

Contents

Keynote lecture by Gilles David (Enertime SAS)	1
ORC AND ENTREPRENEURSHIP IN 2015	
<i>Gilles David</i>	1
Session 1: Working fluids	2
THERMAL STABILITY OF HEXAMETHYLDISILOXANE (MM) FOR HIGH TEMPERATURE APPLICATIONS	
<i>Markus Preißinger, Dieter Brüggemann</i>	2
MULTI-OBJECTIVE OPTIMIZATION OF ORGANIC RANKINE CYCLE POWER PLANTS USING PURE AND MIXED WORKING FLUIDS	
<i>Jesper Graa Andreassen, Martin Ryhl Kærn, Leonardo Pierobon, Ulrik Larsen, Fredrik Haglind</i>	11
EFFECT OF WORKING-FLUID MIXTURES ON ORGANIC RANKINE CYCLE SYSTEM: HEAT TRANSFER AND COST ANALYSIS	
<i>Oyenyi Oyewunmi, Christos Markides</i>	22
INTEGRATED DESIGN OF WORKING FLUID MIXTURES AND ORGANIC RANKINE CYCLES (ORC) IN THE CONTINUOUS-MOLECULAR TARGETING (COMT) FRAMEWORK	
<i>Matthias Lampe, Peter Edel, Johannes Schilling, Joachim Gross, André Bardow</i>	32
A REVIEW OF POTENTIAL WORKING FLUIDS FOR LOW TEMPERATURE ORGANIC RANKINE CYCLES IN WASTE HEAT RECOVERY	
<i>Konstantinos Kontomaris, Jason Juhasz, Luke D. Simoni, Claus-Peter Keller</i>	41
Session 2 – Waste heat recovery from engines I	51
APPLICATION OF REFRIGERANT WORKING FLUIDS FOR MOBILE ORGANIC RANKINE CYCLE SYSTEMS	
<i>Chris Nelson</i>	51
IMPROVING TRAIN ENERGY EFFICIENCY BY ORGANIC RANKINE CYCLE (ORC) FOR RECOVERING WASTE HEAT FROM EXHAUST GAS	
<i>David Serrano, Pascal Smague, Paolino Tona, Pierre Leduc, Arthur Leroux, Andre-Charles Mintsu, Philippe Chevalier</i>	60
PERFORMANCE ANALYSIS OF WASTE HEAT RECOVERY WITH A DUAL LOOP ORGANIC RANKINE CYCLE SYSTEM FOR DIESEL ENGINE	
<i>Hongjin Wang, Hongguang Zhang</i>	70
POTENTIAL OF SMALL-SCALE TURBOMACHINERY FOR WASTE HEAT RECOVERY ON AUTOMOTIVE INTERNAL COMBUSTION ENGINES	
<i>Kévin Rosset, Violette Mounier, Elliott Guenat, Olivier Pajot, Jürg Schiffmann</i>	80
PARAMETRIC OPTIMIZATION AND PERFORMANCE ANALYSIS OF ORGANIC RANKINE CYCLE (ORC) FOR ENGINE WASTE HEAT RECOVERY	
<i>Fubin Yang, Hongguang Zhang</i>	90
Session 3: Large-scale ORC units I	101
INNOVATIVE ORC SCHEMES FOR RETROFITTING ORC WITH HIGH PRESSURE RATIO GAS TURBINES	
<i>Vinayak Hemadri, P.M.V Subbarao</i>	101
UTILIZATION OF WASTE HEAT FROM INTERCOOLED, REHEAT AND RECUPERATED GAS TURBINES FOR POWER GENERATION IN ORGANIC RANKINE CYCLES	
<i>Xurong Wang, Yi Yang, Mingkun Wang, Ya Zheng, Jiangfeng Wang, Yiping Dai</i>	111
TECHNICAL AND ECONOMICAL STUDY OF AN ORC DEDICATED TO THE PRODUCTION OF ELECTRICITY FROM A GEOTHERMAL SOURCE	
<i>Stéphane Schuller, Morgan DaSilva, Christophe Josset, Bruno Awuity, Jérôme Bellettre</i>	121
ORC BOTTOMING FOR COMBINED CYCLE SYSTEMS FED BY BIOMASS	
<i>Mario Gaia, Fredrik Mowill, Claudio Pietra</i>	131
DEVELOPMENT AND TEST OF A 100KW CLASS ORC POWER-GENERATOR FOR LOW TEMPERATURE GEOTHERMAL APPLICATIONS	
<i>Dong Hyun Lee, Young Min Yang, Chun Dong Park, Si Woo Lee, Byung Sik Park</i>	142

Keynote Lecture by Piero Colonna (TU Delft)	151
MINI-ORC TURBOGENERATOR: THE UPCOMING LEAP FORWARD?	
<i>Piero Colonna</i>	151
Session 4: Thermoeconomics I	152
THERMO-ECONOMIC ANALYSIS OF ZEOTROPIC MIXTURES AND PURE WORKING FLUIDS IN ORGANIC RANINKE CYCLES FOR WASTE HEAT RECOVERY	
<i>Florian Heberle, Dieter Brüggemann</i>	152
TECHNO-ECONOMIC ANALYSIS OF THE SUB-CRITICAL ORC WITH OPTIMIZED HEAT TRANSFER PROCESS	
<i>Wei Liu, Dominik Meinel, Christoph Wieland, Hartmut Spliethoff</i>	162
INFLUENCE OF THE HEAT-SOURCE COST ON GEOTHERMAL ORC'S	
<i>Daniël Walraven, Ben Laenen, William D'haeseleer</i>	172
A PERSPECTIVE ON COSTS AND COST ESTIMATION TECHNIQUES FOR ORGANIC RANKINE CYCLE SYSTEMS	
<i>Sanne Lemmens</i>	181
Session 5: Supercritical ORC	191
DESIGN OF WASTE HEAT RECOVERY SYSTEMS BASED ON SUPERCRITICAL ORC FOR POWERFUL GAS AND DIESEL ENGINES	
<i>Oleksii Rudenko, Leonid Moroz, Maksym Burlaka, Clement Joly</i>	191
PERFORMANCE ANALYSIS OF SUPERCRITICAL ORGANIC RANKINE CYCLES (ORCS) BASED ON THE VARIATIONS IN THERMAOPHYSICAL PROPERTIES IN THE PSEUDO-CRITICAL REGION	
<i>Ran Tian, Qingsong An, Lin Shi, Huixing Zhai, Xiaoye Dai</i>	201
INVESTIGATION AND OPTIMIZATION OF THE OPERATION AND DESIGN OF A SMALL SCALE EXPERIMENTAL TRIGENERATION SYSTEM POWERED BY A SUPER-CRITICAL ORC	
<i>Tryfonas Roumpedakis, Konstantinos Braimakis, Sotirios Karellas</i>	211
EXPERIMENTAL TESTING OF A SMALL-SCALE SUPERCRITICAL ORC AT LOW-TEMPERATURE AND VARIABLE CONDITIONS	
<i>George Kosmadakis, Dimitris Manolakos, George Papadakis</i>	222
Session 6: Turbine design I	232
EXPERIMENTAL OBSERVATION OF NON-IDEAL NOZZLE FLOWS OF SILOXANE VAPOR MDM	
<i>Andrea Spinelli, Alberto Guardone, Fabio Cozzi, Margherita Carmine, Renata Cheli, Marta Zocca, Paolo Gaetani, Vincenzo Dossena</i>	232
WAVE SPEED MEASUREMENTS IN NON-IDEAL COMPRESSIBLE FLOWS USING THE FLEXIBLE ASYMMETRIC SHOCK TUBE (FAST)	
<i>Tiemo Mathijssen, Mauro Gallo, Emiliano Casati, Alberto Guardone, Piero Colonna</i> . . .	244
SCALING OF GAS TURBINE FROM AIR TO REFRIGERANTS FOR ORGANIC RANKINE CYCLE (ORC) USING SIMILARITY CONCEPT	
<i>Choon Seng Wong, Susan Krumdieck</i>	255
FAST DESIGN METHODOLOGY FOR SUPERSONIC ROTOR BLADES WITH DENSE GAS EFFECTS	
<i>Elio Bufi, Paola Cinnella, Benoît Obert</i>	270
DEVELOPMENT OF A TURBO-GENERATOR FOR ORC SYSTEM WITH TWIN RADIAL TURBINES AND GAS FOIL BEARINGS	
<i>Young Min Yang, Byung-Sik Park, Si Woo Lee, Dong Hyun Lee</i>	280
EFFICIENCY CORRELATIONS FOR AXIAL TURBINES IN ORC FIELD	
<i>Marco Astolfi, Ennio Macchi</i>	289
Session 7: Small-scale ORC's	301
VOLUMETRIC EXPANDER VERSUS TURBINE – WHICH IS THE BETTER CHOICE FOR SMALL ORC PLANTS?	
<i>Andreas Weiß</i>	301
STUDY OF A VOLUMETRIC EXPANDER SUITABLE FOR WASTE HEAT RECOVERY FROM AN AUTOMOTIVE IC ENGINE USING AN ORC WITH ETHANOL	
<i>José Galindo, Vicente Dolz, Lucía Royo, Régine Haller, Julien Melis</i>	311

COMBINED THERMODYNAMIC AND TURBINE DESIGN ANALYSIS OF SMALL CAPACITY WASTE HEAT RECOVERY ORC <i>Antti Usitalo, Teemu Turunen-Saaresti, Grönman Aki, Honkatukia Juha, Backman Jari</i>	328
EXPERIMENTAL INVESTIGATION OF A RADIAL MICROTURBINE IN ORGANIC RANKINE CYCLE SYSTEM WITH HFE7100 AS WORKING FLUID <i>Tomasz Kaczmarczyk, Grzegorz Zywica, Eugeniusz Ihmatowicz</i>	338
OPERATIONAL EXPERIENCE ON ORC USE FOR WASTE HEAT VALORISATION IN BIOGAS POWER PLANT <i>Arthur Leroux, Coline Gazet, Benoit Paillette, Antonin Pauchet</i>	348
OPTIMIZED EFFICIENCY MAPS AND NEW CORRELATION FOR PERFORMANCE PREDICTION OF ORC BASED ON RADIAL TURBINE FOR SMALL-SCALE APPLICATIONS <i>Kiyarash Rahbar, Saad Mahmoud, Raya Al-Dadah</i>	355
TUTORIAL	365
EFFICIENT EVALUATION OF THERMOPHYSICAL PROPERTIES OF WORKING FLUIDS FOR ORGANIC RANKINE CYCLES <i>Ian Bell</i>	365
Session 8: Scroll expanders	366
EXPERIMENTAL INVESTIGATION OF A SMALL-SCALE TWO STAGE ORGANIC RANKINE CYCLE ENGINE OPERATING AT LOW TEMPERATURE <i>Erika Ntavou, George Kosmadakis, Dimitris Manolakos, George Papadakis, Dimitris Pantonis</i>	366
EXPERIMENTAL STUDY ON ORGANIC RANKINE CYCLE ADOPTING DUAL-EXPANDERS WITH DIFFERENT CAPACITIES IN PARALLEL <i>Eunkoo Yun, Dokyun Kim, Sang Youl Yoon, Kyung Chun Kim</i>	376
THERMO-FLUIDIC AND MECHANICAL LOSSES IN A SCROLL EXPANDER FOR AN R134a ORGANIC RANKINE CYCLE <i>Karthik G.M., Pardeep Garg, Vinod Srinivasan, Pramod Kumar</i>	382
A COMPARISON BETWEEN TWO DIFFERENT CFD APPROACHES OF A REAL SCROLL EXPANDER FOR MICRO-ORC APPLICATIONS <i>Alessio Suman, Carlo Buratto, Nicola Aldi, Michele Pinelli, Pier Ruggero Spina, Mirko Morini</i>	392
Session 9: Heat exchangers	402
DESIGN AND RATING OF AN EVAPORATOR FOR WASTE HEAT RECOVERY ORGANIC RANKINE CYCLE USING SES36 <i>Alihan Kaya, Marija Lazova, Michel De Paepe</i>	402
DESIGN OF A SUPERCRITICAL HEAT EXCHANGER FOR AN INTEGRATED CPV/T-RANKINE CYCLE <i>Marija Lazova, Dieter Daenens, Alihan Kaya, Marnix Van Belleghem, Henk Huisseune, George Kosmadakis, Dimitris Manolakos, Michel De Paepe</i>	412
HEAT STORAGE ORC SYSTEM FOR VEHICLE ICE EXHAUST HEAT RECOVERY <i>Tao Chen, Lei Zhang, Weilin Zhuge, Yangjun Zhang</i>	422
ADVANCED CONTROLS OF ORGANIC RANKINE CYCLE FOR HIGHLY TRANSIENT FLUCTUATIONS DURING INITIAL STARTUP <i>Parsa Mirmobin, Chris Sellers</i>	432
Session 10: Turbine design II	441
UNSTEADY RANS SIMULATION OF THE OFF-DESIGN OPERATION OF A HIGH EXPANSION RATIO ORC RADIAL TURBINE <i>Enrico Rinaldi, Rene Pecnik, Piero Colonna</i>	441
NUMERICAL STUDY OF ORGANIC RANKINE CYCLE RADIAL-INFLOW TURBINES FOR HEAVY-DUTY DIESEL ENGINE COOLANT HEAT RECOVERY <i>Lei Zhang, Weilin Zhuge, Yangjun Zhang, Jie Peng</i>	450
FLUID-DYNAMICS OF THE ORC RADIAL OUTFLOW TURBINE <i>Claudio Spadacini, Lorenzo Centemeri, Dario Rizzi, Massimiliano Sanvito, Aldo Serafino</i>	462

NON-IDEAL COMPRESSIBLE-FLUID DYNAMICS SIMULATIONS WITH SU2: NUMERICAL ASSESSMENT OF NOZZLE AND BLADE FLOWS FOR ORGANIC RANKINE CYCLE APPLICATIONS	
<i>Giulio Gori, Alberto Guardone, Salvatore Vitale, Adam Head, Matteo Pini, Piero Colonna</i>	472
3D FLUID DYNAMIC ANALYSIS OF A HIGH LOADED CENTRIFUGAL ROTOR FOR MINI ORC POWER SYSTEMS	
<i>Salvatore Vitale, Matteo Pini, Antonio Ghidoni, Piero Colonna</i>	482
AUTOMATIC DESIGN OF ORC TURBINE PROFILES BY USING EVOLUTIONARY ALGORITHMS	
<i>Pablo Rodriguez-Fernandez, Giacomo Persico</i>	493
Session 11: Screw expanders	503
SCREW EXPANDERS IN ORC APPLICATIONS, REVIEW AND A NEW PERSPECTIVE	
<i>Henrik Ohman, Per Lundqvist</i>	503
DYNAMIC MODEL FOR THE PERFORMANCE PREDICTION OF A TWIN SCREW EXPANDER IN AN ORC	
<i>Iva Papes, Joris Degroote, Jan Vierendeels</i>	513
COMPARISON OF ORGANIC RANKINE CYCLE SYSTEMS UNDER VARYING CONDITIONS USING TURBINE AND TWIN-SCREW EXPANDERS	
<i>Matthew Read, Ahmed Kovacevic, Ian Smith, Nikola Stosic</i>	522
EXPERIMENTAL INVESTIGATION OF EFFECT OF OPERATING CONDITIONS ON PERFORMANCE OF ORC SYSTEM BASED ON OIL FLOODED TWIN SCREW EXPANDER	
<i>Abhijeet Chougule, Charles Philominraj, Ramakrishna Sonde</i>	532
EXPERIMENTAL STUDY ON ORGANIC RANKINE CYCLE SYSTEM WITH SINGLE-SCREW EXPANDER FOR WASTE HEAT RECOVERY FROM DIESEL ENGINE EXHAUST	
<i>Yuting Wu, Biao Lei, Wei Wang, Yeqiang Zhang, Chongfang Ma</i>	540
EXPERIMENTAL CHARACTERIZATION OF SINGLE SCREW EXPANDER PERFORMANCE UNDER DIFFERENT TESTING CONDITIONS AND WORKING FLUIDS	
<i>Sergei Gusev, Davide Ziviani, Martijn van den Broek</i>	550
Poster session	559
PERFORMANCE ANALYSIS OF ORC SYSTEM WITH IHE USING THE ZEOTROPIC MIXTURE AND THE PURE WORKING FLUID FOR VEHICLE CNG ENGINE	
<i>Songsong Song, Hongguang Zhang</i>	559
A NEW ULTRA-LOW GWP ORC WORKING FLUID	
<i>Gregory Smith, Abdennacer Achaichia, Raymond Thomas</i>	569
REVERSE ENGINEERING OF FLUID SELECTION FOR ORCs USING CUBIC EQUATIONS OF STATE	
<i>Dennis Roskosch, Burak Atakan</i>	570
STUDY OF RECIPROCATING PUMP FOR SUPERCRITICAL ORC AT FULL AND PART LOAD OPERATION	
<i>Arnaud Landelle, Nicolas Tauveron, Philippe Haberschill, Remi Rivelin, Stéphane Colasson</i>	580
INVESTIGATION OF A MASSIVE ELECTRICITY STORAGE SYSTEM BY MEANS OF A GEOTHERMAL HEAT TRANSFER PROCESS INVOLVING CO ₂ TRANSCRITICAL CYCLES	
<i>Fadhel Ayachi, Thomas Tartière, Nicolas Tauveron, Stéphane Colasson, Denis Nguyen</i>	589
AN AUTOMATIC ADJUSTING DEVICE OF THE SPIRAL GROOVE FACE SEAL USED ON ORC TURBINE SHAFT END AND THE ESTABLISHMENT OF CONTROL MODEL	
<i>Ya Zheng, Yue Cao, Dongshuai Hu, Xurong Wang, Yiping Dai</i>	600
FACTOR ANALYSIS OF INTERNAL EXPANSION RATIO FOR SINGLE SCREW EXPANDERS	
<i>Wei Wang, Li-li Shen, Liang Chen, Yuting Wu, Chongfang Ma</i>	610
IMPLEMENTATION OF A SMALL SCALE ORGANIC RANKINE CYCLE TEST BED SYSTEM USING STEAM AS HEAT SOURCE	
<i>Muhammad Usman, Muhammad Imran, Dong Hyun Lee, Byung-Sik Park</i>	620
THERMODYNAMIC STUDY OF INFLECTION POINT OF SATURATED VAPOR CURVE FOR DRY AND ISENTROPIC WORKING FLUIDS	
<i>Xinxin Zhang, Congtian Zhang, Jingfu Wang, Maogang He</i>	630

DESIGN AND NUMERICAL ANALYSIS OF PROCESSES IN SILOXANE VAPOR DRIVEN TURBINE <i>Aleksandr Sebelev, Roland Scharf, Nikolay Zabelin, Maksim Smirnov</i>	640
HIGH-TEMPERATURE SOLAR ORGANIC RANKINE CYCLE – ANNUAL SIMULATION OF VARIOUS SYSTEM DESIGNS <i>Björn Hunstock, Sabine Strauch, Wilhelm Althaus, Björn Bülten, Johannes Grob, Ralf Paucker</i>	650
EXPERIMENTAL STUDY ON A LOW TEMPERETATURE ORC UNIT FOR ONBOARD WASTE HEAT RECOVERY FROM MARINE DIESEL ENGINES <i>Aris - Dimitrios Leontaritis, Platon Pallis, Sotirios Karellas, Aikaterini Papastergiou, Nikolaos Antoniou, Panagiotis Vourliotis, Nikolaos Matthaios Kakalis, George Dimopoulos</i>	660
REDUCING FUEL CONSUMPTION BY UP TO 10% FOR DIESEL-BASED POWER GENERATION BY APPLYING ORC <i>Quirijn Eppinga, Jos van Buijtenen</i>	670
TORQUE RESEARCH OF SINGLE SCREW EXPANDERS <i>Ruiping Zhi, Yuting Wu, Yeqiang Zhang, Biao Lei, Wei Wang, Guoqiang Li, Chongfang Ma</i>	671
EXPERIMENTAL STUDIES ON AN ORGANIC RANKINE CYCLE (ORC) SYSTEM UNDER VARIABLE CONDENSATION TEMPERATURE <i>Feibo Xie, Tong Zhu, Jihua Liu, Naiping Gao, Wei An</i>	681
ADVANCED THERMODYNAMIC MODEL OF ORGANIC RANKINE CYCLE <i>Parsa Mirmobin, Chris Sellers</i>	691
THERMAL EXPANSION AND STRUCTURAL BEHAVIOR OF A CLOSED LOOP THERMAL WIND TUNNEL FOR ORC FLUIDS <i>Maximilian Passmann, Karsten Hasselmann, Felix Reinker, Stefan aus der Wiesche</i>	702
ANALYSIS OF PURE FLUID AND ZEOTROPIC MIXTURES USED IN LOW-TEMPERATURE REHEATING ORGANIC RANKINE CYCLES FOR POWER GENERATION <i>Changwei Liu, Tieyu Gao, Jiamin Xu, Jiangnan Zhu, Xun Xu</i>	712
STRUCTURE RELIABILITY ANALYSIS OF A NEW FREE PISTON EXPANDER <i>Gaosheng Li, Hongguang Zhang</i>	722
WORKING FLUID SELECTION FOR ORGANIC RANKINE CYCLES BASED ON CONTINUOUS-MOLECULAR TARGETS <i>Johannes Schilling, Matthias Lampe, Joachim Gross, André Bardow</i>	732
NUMERICAL AND EXPERIMENTAL INVESTIGATION ON THE ROTARY VANE EXPANDER OPERATION IN MICRO ORC SYSTEM <i>Piotr Kolasinski, Przemyslaw Blasiak</i>	742
THE METHOD OF THE WORKING FLUID SELECTION FOR ORGANIC RANKINE CYCLE (ORC) SYSTEM WITH VOLUMETRIC EXPANDER <i>Piotr Kolasinski</i>	751
THERMODYNAMIC AND DESIGN CONSIDERATION OF A MULTISTAGE AXIAL ORC TURBINE FOR COMBINED APPLICATION WITH A 2 MW CLASS GAS TURBINE FOR DEZENTRALIZED AND INDUSTRIAL USAGE <i>René Braun, Karsten Kusterer, Kristof Weidtmann, Dieter Bohn</i>	761
CONTROL STRATEGIES FOR AUTOMOTIVE RANKINE SYSTEM EVALUATION USING A COSIMULATION PLATFORM <i>Abdelmajid Taklanti, Jin-Ming Liu, Régine Haller</i>	771
PVT PROPERTIES AND VAPOR PRESSURES OF HFO-1336MZZ(E) <i>Katsuyuki Tanaka, Ryo Akasaka, Eiichi Sakaue</i>	782
ORC-DEMONSTRATION-PLANT WITH 1 KW SCROLL EXPANDER - DESIGN AND OPERATIONAL EXPERIENCES <i>Albrecht Eicke, Slawomir Smolen</i>	789
DIESEL ENGINE WASTE HEAT HARNESSING ORC DEVICE <i>Jovana Radulovic</i>	797
SMALL SCALE ORC DESIGN FOR A COGENERATION SOLAR BIOMASS SUPPORTED APPLICATION <i>Joaquín Navarro-Esbrí, Francisco Molés, Bernardo Peris, Adrián Mota-Babiloni</i>	807
CONSTRUCTION AND PRELIMINARY TEST OF AN ORGANIC RANKINE CYCLE (ORC) USING R245FA AND SINGLE SCREW EXPANDER <i>Biao Lei, Yuting Wu, Wei Wang, Chongfang Ma</i>	817
DESIGN AND ANALYSIS OF AN ORGANIC RANKINE CYCLE SYSTEM FOR COGENERATION <i>Peter Collings, Zhibin Yu</i>	818

ON THE OPTIMUM AXIAL FLOW TURBINE DESIGN IN ORGANIC RANKINE CYCLES <i>Luca Da Lio, Giovanni Manente, Andrea Lazzaretto</i>	828
ORC APPLICATIONS FROM LOW GRADE HEAT SOURCES <i>Bernardo Peris, Joaquín Navarro-Esbrí, Francisco Molés, Adrián Mota-Babiloni</i>	844
TESTING AND MODELING A VANE EXPANDER USED IN AN ORC WORKING WITH HEXAMETHYLDISILOXANE (MM) <i>Vaclav Vodicka, Ludovic Guillaume, Jakub Mascuch, Vincent Lemort</i>	853
EFFECT OF WORKING FLUID MIXTURE COMPOSITION ON THE PERFORMANCE OF AN ORGANIC RANKINE CYCLE <i>Peter Collings, Zhibin Yu</i>	863
EVALUATION OF ORC USING LOW GWP WORKING FLUIDS FOR WASTE HEATS <i>Osamu Furuya, Eiichi Sakae</i>	864
COMPARATIVE STUDY OF ORGANIC RANKINE CYCLE(ORC) FOR LOW GRADE EN- ERGY IN TURBINE AND PAT METHOD WITH FLUID <i>Farzam Alimardani, Mohammadreza Rostamzadeh</i>	876
EFFECT OF RADIAL HEAT TRANSFER IN THE PEBBLE BED THERMAL ENERGY STORAGE TANK COUPLED TO A SOLAR ORGANIC RANKINE CYCLE <i>Pardeep Garg, Abhishek Kshirsagar, Pramod Kumar, Matthew Orosz</i>	886
THERMO-ECONOMIC ANALYSIS OF A MIXTURE OF RC-318 AND PENTANE AS WORK- ING FLUID IN A HIGH TEMPERATURE SOLAR ORC <i>Ankit Saini, Karthik G.M., Pardeep Garg, N.C. Thirumalai, Pramod Kumar, Vinod Sriniva- san</i>	896
STUDY ON LABYRINTH SEAL AT THE HIGH-PRESSURE SIDE OF THE SCREW IN SINGLE SCREW EXPANDER <i>Guoqiang Li, Yuting Wu, Ruiping Zhi, Yeqiang Zhang, Chongfang Ma</i>	907
EFFICIENCY OF THE ARCHISOL CONCEPT <i>Harold Lever, Edo Wissink</i>	908
EXPERIMENTAL SETUP OF A SMALL SUPERSONIC TURBINE FOR AN AUTOMOBILE ORC APPLICATION RUNNING WITH ETHANOL <i>Harald Kunte, Jörg Seume</i>	919
PERFORMANCE STUDY OF A SCROLL EXPANDER WITH AMMONIA-WATER <i>James Muye, Juan Carlos Bruno, Rajagopal Saravanan, Alberto Coronas</i>	929
PERFORMANCE ASSESSMENT OF ORGANIC RANKINE CYCLE DRIVEN VAPOR COM- PRESSION HEAT PUMP <i>Violette Mounier, Jürg Schiffmann</i>	937
SYSTEMATIC FLUID-SELECTION IN EARLY STAGES OF ORC DESIGN – A PRACTI- CAL ENGINEERING APPROACH <i>Maximilian Roedder, Christoph Laux, Matthias Neef</i>	938
EXPERIMENTAL STUDY OF AN ORC (ORGANIC RANKINE CYCLE) WITH THERMAL OIL FOR WASTE HEAT RECOVERY OF A DIESEL ENGINE <i>Gegun Shu, Mingru Zhao, Hua Tian</i>	948
AERODYNAMIC DESIGN OF RADIAL INFLOW TURBINE FOR MEDIUM SCALE OR- GANIC RANKINE CYCLE SYSTEM <i>Lei Chen, Boaz Habib, Nick Inskip</i>	958
ADAPTING WASTE HEAT RECOVERY TECHNOLOGIES FOR LOW CARBON OFF- HIGHWAY VEHICLES <i>Apostolos Pesiridis, Fuhaid Alshammari, Benjamin Franchetti Benjamin Franchetti</i>	959
ABOVE GROUND GEOTHERMAL AND ALLIED TECHNOLOGIES – PAVING THE RE- SEARCH ROADMAP <i>Boaz Habib, Nick Inskip, Lei Chen Chen, Mohammed Farid, Brent Young</i>	960
CONNECTION OF A DISTRICT HEATING SYSTEM AND AN ORC GEOTHERMAL PLANT <i>Valdimarsson Pall</i>	961
A NEW DESIGN OF AN ORC PLANT FOR HIGH ENTHALPY GEOTHERMAL RESOURCES <i>Valdimarsson Pall, Markus Sauerborn</i>	962
NOWASTE: WASTE HEAT RE-USE FOR GREENER TRUCK <i>Ludovic Guillaume, Vincent Lemort, Andrea Perosino, Federica Bettoja, Thomas Reiche, Thomas Wagner</i>	963
MODELLING, EXPERIMENTATION AND SIMULATION OF A REVERSIBLE HP/ORC UNIT TO GET A POSITIVE ENERGY BUILDING <i>Olivier Dumond, Carolina Carmo, Sylvain Quoilin, Vincent Lemort</i>	964

EXPERIMENTAL VALIDATION OF A DOMESTIC STRATIFIED HOT WATER TANK MODEL IN MODELICA FOR ANNUAL PERFORMANCE ASSESSMENT <i>Carolina Carmo, Olivier Dumot, Mads Nielsen</i>	965
Session 12: Thermoeconomics II	966
THERMO-ECONOMIC EVALUATION OF ORC'S FOR VARIOUS WORKING FLUIDS <i>Pardeep Garg, Matthew Orosz, Pramod Kumar, Pradip Dutta</i>	966
THERMOECONOMIC ANALYSIS OF ORGANIC RANKINE CYCLE USING ZEOTROPIC MIXTURES <i>Muhammad Imran, Muhammad Usman, Dong Hyun Lee, Byung Sik Park</i>	979
INFLUENCE OF HEAT DEMAND ON TECHNO-ECONOMIC PERFORMANCE OF A BIOMASS/NATURAL GAS MICRO GAS TURBINE AND BOTTOMING ORC FOR COGENERATION <i>Sergio Camporeale, Antonio Pantaleo</i>	990
SIZING AND PARAMETRIC OPTIMIZATION OF A WASTE HEAT TO POWER PLANT BASED ON TRANSCRITICAL ORGANIC RANKINE CYCLE <i>Van Long Le, Michel Feidt, Abdelhamid Kheiri, Vincent Lemort</i>	1002
PRELIMINARY INVESTIGATION INTO THE CURRENT AND FUTURE AFFORDABILITY AND GROWTH OF ORC ELECTRICITY GENERATION SYSTEMS <i>Michael Southon, Susan Krumdieck</i>	1012
Session 13: Waste heat recovery from engines II	1022
STUDY ON THE INFLUENCE OF EVAPORATOR OF ORC SYSTEM ON ENGINE PERFORMANCE <i>Chen Bei, Hongguang Zhang</i>	1022
WASTE HEAT UTILIZATION OF MAIN PROPULSION ENGINE JACKET WATER IN MARINE APPLICATION <i>Errol Yuksek, Parsa Mirmobin</i>	1032
TRANSIENT DUTY CYCLE ANALYSIS FOR MOBILE ORGANIC RANKINE CYCLE APPLICATIONS <i>Miles Robertson, Aaron Costall, Peter Newton, Ricardo Martinez-Botas</i>	1042
THERMODYNAMIC ANALYSIS ON COLD ENERGY UTILIZING ORGANIC RANKINE CYCLE <i>Taehong Sung, Sang Youl Yoon, Kyung Chun Kim</i>	1052
WATER-BASED RANKINE-CYCLE WASTE HEAT RECOVERY SYSTEMS FOR ENGINES: CHALLENGES AND OPPORTUNITIES <i>Gunnar Latz, Olof Erlandsson, Thomas Skåre, Arnaud Contet, Sven Andersson, Karin Munch</i>	1060
TUTORIAL	1070
KEY CONCEPTS IN ORC TURBINE FLUID-DYNAMIC DESIGN <i>Matteo Pini, Salvatore Vitale, Antonio Rubino, Antonio Ghidoni</i>	1070
Session 14: CHP units	1071
PROTOTYPE OF THE DOMESTIC CHP ORC SYSTEM: CONSTRUCTION AND EXPERIMENTAL RESEARCH <i>Grzegorz Zywica, Jan Kicinski, Tomasz Kaczmarczyk, Eugeniusz Ichnatowicz, Tomasz Turzynski, Sebastian Bykuć</i>	1071
SMALL SCALE BIOMASS FUELLED PLANTS FOR COMBINED HEAT AND POWER <i>Stefano Ganassin, Jos van Buijtenen</i>	1080
START-UP RESEARCH ON THE LABORATORY MICRO CHP ORC TEST STAND <i>Sebastian Bykuć, Łukasz Breńkacz, Grzegorz Zywica</i>	1089
FROM TECHNOLOGY DEVELOPMENT TO (PRE-SERIES) PRODUCT – THE EPACK HYBRID <i>Daniela Gewald, Katharina Rostek, Andreas Schuster, Richard Aumann</i>	1099
INTEGRATED CHP CONCEPTS FOR ORC AND THEIR BENEFITS COMPARED TO CONVENTIONAL CONCEPTS <i>Christoph Wieland, Dominik Meinel, Hartmut Spliethoff</i>	1109
Session 15: Modelling and simulation	1120

A PERFORMANCE PREDICTION TOOL FOR ORC APPLICATIONS BASED ON MODELICA <i>Adrian Rettig, Ulf Christian Müller</i>	1120
COMPARISON OF MOVING BOUNDARY AND FINITE-VOLUME HEAT EXCHANGERS MODELS IN THE MODELICA LANGUAGE <i>Adriano Desideri, Jorrit Wronski, Bertrand Dechesne, Martijn van den Broek, Gusev Sergei, Sylvain Quoilin, Vincent Lemort</i>	1130
ORCSIM: A GENERALIZED ORGANIC RANKINE CYCLE SIMULATION TOOL <i>Davide Ziviani, Brandon Woodland, Emeline Georges, Eckhard Groll, James Braun, Travis Horton, Michel De Paepe, Martijn van den Broek</i>	1140
ANALYSIS AND COMPARISON OF DIFFERENT MODELING APPROACHES FOR THE SIMULATION OF A MICRO-SCALE ORGANIC RANKINE CYCLE POWER PLANT <i>Rémi Dickes, Olivier Dumont, Arnaud Legros, Sylvain Quoilin, Vincent Lemort</i>	1150
DESIGN OF ORGANIC RANKINE CYCLE SYSTEMS ACCOUNTING FOR EXPANDER PERFORMANCE <i>Angelo La Seta, Jesper Graa Andreasen, Leonardo Pierobon, Giacomo Persico, Fredrik Haglind</i>	1160
Keynote Lecture by Sylvain Quoilin (University of Liege)	1172
PAST AND CURRENT RESEARCH TRENDS IN ORC POWER SYSTEMS <i>Sylvain Quoilin</i>	1172
Session 16: Advance control strategies	1173
TOWARDS THE OPTIMAL OPERATION OF AN ORGANIC RANKINE CYCLE UNIT BY MEANS OF MODEL PREDICTIVE CONTROL <i>Andres Hernandez, Adriano Desideri, Clara Ionescu, Sylvain Quoilin, Vincent Lemort, Robin De Keyser</i>	1173
OPTIMAL CONTROL OF WASTE HEAT RECOVERY SYSTEMS APPLYING NONLINEAR MODEL PREDICTIVE CONTROL (NMPC) <i>Philipp Petr, Christian Schröder, Jürgen Köhler, Manuel Gräber</i>	1183
WASTE HEAT RECOVERY RANKINE BASED SYSTEM MODELING FOR HEAVY DUTY TRUCKS FUEL ECONOMY ASSESSMENT <i>Vincent Grelet, Vincent Lemort, Madiha Nadri, Pascal Dufour, Thomas Reiche</i>	1193
MODEL BASED CONTROL FOR WASTE HEAT RECOVERY HEAT EXCHANGERS RANKINE CYCLE BASE SYSTEM IN HEAVY DUTY TRUCKS <i>Vincent Grelet, Pascal Dufour, Madiha Nadri, Vincent Lemort, Thomas Reiche</i>	1203
Session 17: Use of solar energy	1213
A NOVEL HYBRID SOLAR POWER GENERATION SYSTEM USING A-SI PHOTOVOLTAIC/THERMAL COLLECTORS AND ORGANIC RANKINE CYCLE <i>Jing Li, Pengcheng Li, Gang Pei, Jie Ji, Jahan Zeb Alvi</i>	1213
OPTIMISATION OF A DOMESTIC-SCALE SOLAR-ORC HEATING AND POWER SYSTEM FOR MAXIMUM POWER OUTPUT IN THE UK <i>James Freeman, Klaus Hellgardt, Christos Markides</i>	1223
IDENTIFICATION OF ORC PARAMETERS FOR OPTIMIZATION OF THERMAL STORAGE MEDIUM COST IN SOLAR ORC <i>Abhishek Kshirsagar, Pardeep Garg, Pramod Kumar, Matthew Orosz</i>	1233
ANALYSIS OF THERMAL ENERGY STORAGE SOLUTIONS FOR A 1 MWe CSP-ORC POWER UNIT <i>David Sánchez, Hicham Frej, Gonzalo S. Martínez, José María Rodríguez, El Ghali Benouna</i>	1243
Session 18: Advanced architectures	1253
THERMODYNAMIC ANALYSIS AND COMPARISON OF AN ORC-OFCCOMBINED POWER GENERATION SYSTEM <i>Jianyong Wang, Jiangfeng Wang, Yiping Dai</i>	1253
PERFORMANCE POTENTIAL OF ORC ARCHITECTURES FOR WASTE HEAT RECOVERY TAKING INTO ACCOUNT DESIGN AND ENVIRONMENTAL CONSTRAINTS <i>Steven Lecompte, Martijn van den Broek, Michel De Paepe</i>	1263

PERFORMANCE COMPARISON OF A NOVEL THERMOFLUIDIC ORGANIC-FLUID HEAT CONVERTER AND AN ORGANIC RANKINE-CYCLE ENGINE <i>Christoph Kirmse, Aly Taleb, Oyeniyi Oyewunmi, Andrew Haslam, Christos Markides . . .</i>	1273
THERMODYNAMIC SIMULATION AND EXPERIMENTAL VALIDATION OF A CASCADED TWO-STAGE ORGANIC RANKINE CYCLE <i>Frithjof H. Dubberke, Klaus-Peter Priebe, Jadran Vrabec, Maximilian Rödder, Matthias Neef</i>	1283
EXPERIMENTAL STUDY ON ADIABATIC TWO-PHASE EXPANSION IN A CYLINDER FOR TRILATERAL CYCLE <i>Hiroshi Kanno, Yusuke Hasegawa, Isao Hayase, Naoki Shikazono</i>	1293
Session 19: Large-scale ORC units II	1303
PERFORMANCE EVALUATION OF NGCC AND COAL-FIRED STEAM POWER PLANTS WITH INTEGRATED CCS AND ORC SYSTEMS <i>Vittorio Tola</i>	1303
FLUID STABILITY IN LARGE SCALE ORCS USING SILOXANES – LONG-TERM EXPERIENCES AND FLUID RECYCLING <i>Tobias Erhart, Jürgen Gölz, Ursula Eicker, Martijn van den Broek</i>	1313
ORC DEPLOYMENT OPPORTUNITIES IN GAS PLANTS <i>John Harinck, Ludovico Calderazzi, Piero Colonna, Hugo Polderman</i>	1323
ON HIGH LEVEL EVALUATION AND COMPARISON OF ORC POWER GENERATORS <i>Henrik Ohman, Per Lundqvist</i>	1333
A MULTI SCALE METHODOLOGY FOR ORC INTEGRATION OPTIMIZATION IN AN INDUSTRIAL PROCESS <i>Cong-Toan Tran, Assaad Zoughaib</i>	1342
TUTORIAL	1350
LOW-ORDER MODELS OF POSITIVE DISPLACEMENT EXPANDERS <i>Vincent Lemort</i>	1350

ORC AND ENTREPRENEURSHIP IN 2015

Gilles David

Enertime SAS

ABSTRACT

The creation from scratch and development of an industrial company in the 21st century is a challenging but rewarding experience. The ORC technology is a perfect choice for would-be industrial entrepreneurs. Gilles David will speak about the genesis of Enertime, an ORC manufacturer he created in 2008. He will explain the technical choices made, the experience gained in creating and establishing a company that design and build large ORC for the international market and his view of the ORC market drivers.

THERMAL STABILITY OF HEXAMETHYLDISILOXANE (MM) FOR HIGH TEMPERATURE APPLICATIONS

Markus Preißinger*, Dieter Brüggemann

University of Bayreuth, Center of Energy Technology (ZET),
Institute of Engineering Thermodynamics and Transport Processes (LTTT),
Universitätsstraße 30, 95447 Bayreuth, Germany
e-mail: zet@uni-bayreuth.de
Web page: <http://www.zet.uni-bayreuth.de>

* Corresponding Author

ABSTRACT

The design of efficient ORC units for the usage of industrial waste heat at high temperatures requires direct evaporating systems without an intermediate thermal oil circuit. Therefore, the thermal stability of high temperature working fluids gains importance. In this study, the thermal degradation of hexamethyldisiloxane (MM) is investigated in an electrically heated tube. The results include qualitative remarks on degradation products as well as the annual degradation rate as quantitative parameter. It is shown that MM is stable up to a temperature of 300 °C with annual degradation rates of less than 3.5 %. Furthermore, the break of a silicon-carbon bond can be a main chemical reaction that influences the thermal degradation. Finally, the impact of the results on the future design of ORC units is discussed.

1. INTRODUCTION

Linear siloxanes like hexamethyldisiloxane (MM) are promising working fluids for high temperature applications like biomass fired power plants (Oberberger, 1998; Oberberger et al., 2002). In such systems, a thermal oil circuit based on synthetic oils with degradation temperatures of more than 300 °C (Mang and Dresel, 2007) is used to avoid thermal stress of the ORC working fluid. However, for industrial waste heat recovery a trend is noticed to direct evaporating systems without thermal oil circuit. The advantages are higher efficiencies, lower investment costs and a much simpler system design. Although evaporation temperatures of MM are limited to a value below 240 °C for typical working pressures of about 17 bar, the film temperature at the heat exchanger surface, hot-spots within the heat exchanger and the failure mode (e.g. standstill of the ORC pump but no shutdown of the heat source) have to be kept in mind.

Therefore, if we want to use MM in a wide range of heat source temperatures, reliable data for its thermal stability are essential. Colonna et al. (2006) report a limit of 400 °C, however, the duration of the experiments, the heating rate and the pressure remain unclear. For cyclic siloxanes, Angelino (1993) gives a similar value of 400 °C. Dvornic (2000, 2008) investigates extensively thermal properties of polysiloxanes, however, without giving quantitative results for the degradation temperature of MM.

To attain such results, different methodologies concerning design of the test rig and evaluation method are found in literature. Ginosar et al. (2011) report a method to separate catalytic from thermal effects within a glass tube. The standard test procedure for the thermal stability of refrigerants is carried out almost similar (ANSI/ASHRAE, 2007). For the same chemical class, the method of adiabatic compression is used to avoid the thermal degradation at hot surfaces (Buravtsev et al., 1994). Thermogravimetric analyses within vacuum (Grassie and Macfarlane, 1978; Grassie et al., 1979; Deshpande and Rezac, 2002) as well as the analysis of different catalysts (Kuramochi et al.,

1993) are also widespread. A test rig designed especially for measurements of ORC working fluids, and in particular of methylbenzenes, is reported by Angelino et al. (1991). Calderazzi and Colonna (1997) use a similar test rig for different refrigerants. In both cases, the sample is located in a metallic cylinder and heated in an oven. Based on isothermal long-time experiments, the degradation rate is calculated.

In the present study, we redesign the test rig by using an electrical heated tube which allows for high heating rates which can be accurately controlled. The main objective is to gain more knowledge on the influence of the working fluid temperature as well as the duration of the experiment. Furthermore, knowledge about the chemical composition of the degradation products is of main interest for a secure operation of direct evaporating ORC systems.

2. METHODOLOGY

2.1 Test rig and procedure

A stainless steel tube with a length of 220 mm and an outer diameter of 18 mm is electrically heated according to Figure 1. The volume of the reactor accounts for 70.2 ml. The power of the heating wire is 850 W on a length of 5 m allowing a continuous and uniform heating of up to 450 °C. Compared to the heating in an oven, faster heating rates are achieved and the heating rate can be chosen constant for all tests. Within a second tube with an outer diameter of 3 mm the temperature within the reactor is measured with a thermocouple and used as pre-set temperature for the isothermal test procedure. To ensure constant test conditions, the reactor volume is flushed with nitrogen and evacuated two times before each test. The vacuum pump has a pressure limit of 1.0E-6 bar. Therefore, the remaining mass of nitrogen in the reactor is negligible. A sample mass of about 7 g is fed into the reactor through the filling valve at the bottom of the tube. Afterwards the reactor is sealed through blind plugs, heated until the preset temperature with a constant heating rate of 0.3 K/s and the time measurement starts. After the test period, the electrical heating is switched off and the reactor is cooled down to ambient temperature through natural convection. Subsequently, the analysis of the time-dependent temperature and pressure curve as well as the analysis of vapour and liquid phase by means of gas chromatography, mass spectroscopy and Karl-Fischer-titration is carried out. The raw material is MM with a purity of 97 % from the company Wacker Chemie in Burghausen, Germany (Wacker® AK 0.65).

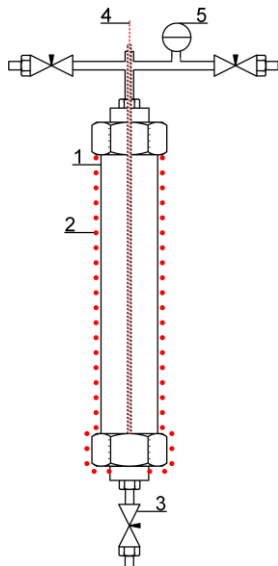


Figure 1: Stainless steel tube (1), electrical heating wire (2), needle valve (3), thermocouple (4) and pressure sensor (5)



Figure 2: Reactor in the lab

2.2 Evaluation method

To describe the evaluation method, an experiment with a temperature of 420 °C and duration of 72 h is selected exemplarily.

First of all, the heating period is analysed. Figure 3 shows the pressure within the tube depending on temperature. The characteristic progression of the bubble line is obtained until a pressure of about 10 bar. However, due to the fact that the heating is much faster than the mixing of the fluid within the reactor, the vapour pressure at a specific temperature is lower than it is expected. Afterwards the slope of the curve drops as the specific volume of MM within the reactor is higher than the critical specific volume (Stephan et al., 2009). Due to the subsequent full mixing within the reactor, the pressure increases marginally at a constant temperature of 420 °C. The slightly right bended part between 120 °C and 160 °C is caused by contaminants within the raw material.

Secondly, the pressure profile during the isothermal test period in Figure 4 shows a value of 15.2 bar with a fluctuation range of 0.05 bar. The pressure changes indicate the formation of molecules with lower or higher molecular mass. The noise signal of the pressure sensor (± 5 mbar) does not affect the result. As the pressure changes are not clearly pronounced, further evaluation methods are needed.

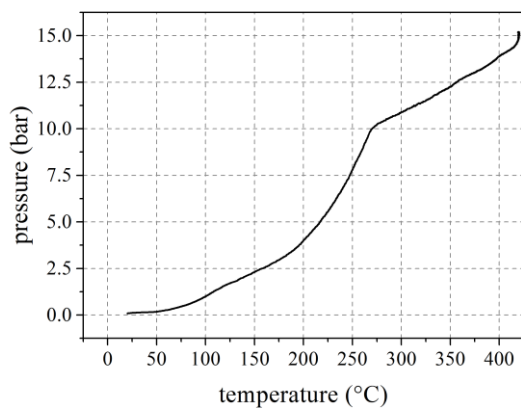


Figure 3: Pressure depending on temperature during heating period ($T = 420$ °C, $t = 72$ h)

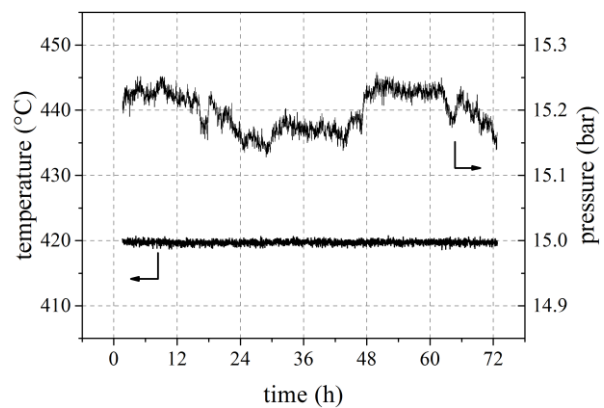


Figure 4: Temperature and pressure depending on time ($T = 420$ °C, $t = 72$ h)

The comparison of the pressure in the reactor before and after the experiment (Figure 5 and Figure 6) confirms the formation of molecules with lower molecular mass than MM. At a constant temperature and a fixed volume of the reactor, the pressure after the experiment is much higher as before which is caused by high vapour pressure of the degradation products.

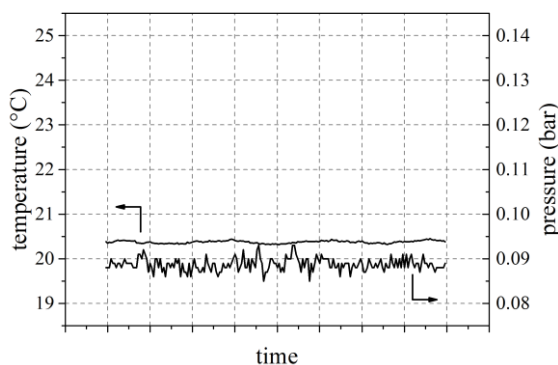


Figure 5: Temperature and pressure before experiment ($T = 420$ °C, $t = 72$ h)

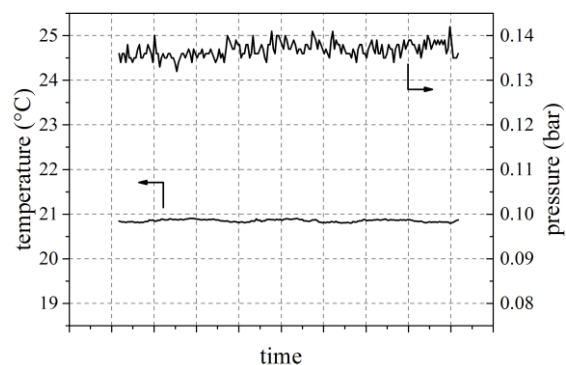


Figure 6: Temperature and pressure after experiment ($T = 420$ °C, $t = 72$ h)

The chemical analysis of the products and the raw material by means of gas chromatography proves the assumption of low molecular substances. The mean relative error caused by the gas chromatograph is lower than 2 %. All components with a mass fraction higher than 0.4 % in the vapour phase are displayed in Figure 7. The mass fraction of MM drops to 58 %. The main

degradation products are low molecular hydrocarbons. This confirms the results from laser impulse experiments of Manders and Bellama (Manders and Bellama, 1985). Within the liquid phase traces of high molecular siloxanes are measured which fits the theory of Dvornic (Dvornic, 2000, 2008). However, the mass fraction of MM within the liquid phase still exceeds 99 % and indicates that the degradation products are mainly found in the vapour phase. As water catalyses the thermal degradation of many organic compounds, the water content of the raw material is measured by means of Karl-Fischer titration which gives a marginal value of 140 ppm. Furthermore, the nitrogen-flushing of the reactor and the subsequent evacuation ensures that no free water or contaminants remain within the tube which would influence the experiments.

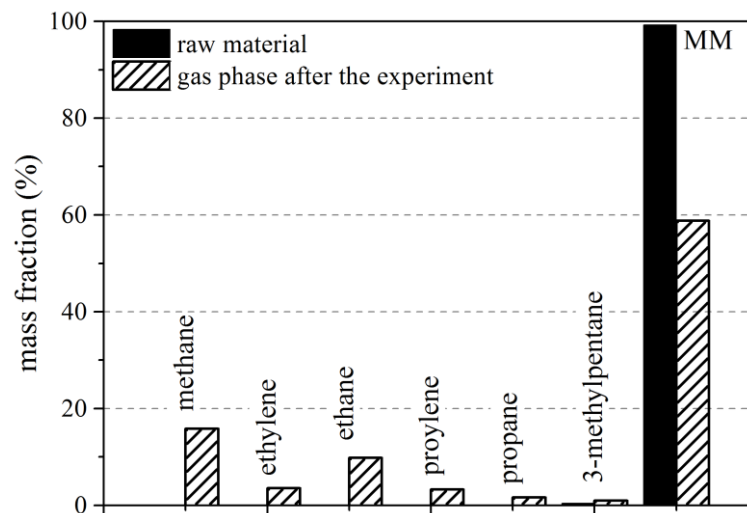


Figure 7: Mass fraction of vapour phase after the experiment and of raw material ($T = 420\text{ }^{\circ}\text{C}$, $t = 72\text{ h}$, relative error caused by gas chromatograph $< 2\%$)

3. RESULTS

3.1 Influence of temperature on thermal degradation

The influence of temperature on the thermal degradation is evaluated in Figure 8. The mass fraction of MM drops with increasing temperature. Below a temperature of $300\text{ }^{\circ}\text{C}$, methane is the dominant degradation product and higher molecular hydrocarbons are hardly detected. At $360\text{ }^{\circ}\text{C}$, higher amounts of ethane and ethylene are detected for the first time. The mass fraction of propane and propylene remains below 1.5% . This value increases up to 7.3% at $420\text{ }^{\circ}\text{C}$. In general, the variation margin of the mass fraction increases with increasing temperature.

3.2 Influence of time on thermal degradation

In general, the retention time within an ORC evaporator is far less than 72 h . However, due to inappropriate mixing and dead volume, high residence times may occur in reality as well. Furthermore, short retention times could give knowledge about the chemical reactions involved in the degradation process. Therefore, the influence of time on the degradation is evaluated. A temperature of $420\text{ }^{\circ}\text{C}$ is chosen to attain high degradation rates which are essential for meaningful results on the influence of time. The mass fraction of MM in Figure 9 drops and the ones of the degradation products increase with increasing time. The slope is almost linear within the first 24 h , for longer times the curves flatten.

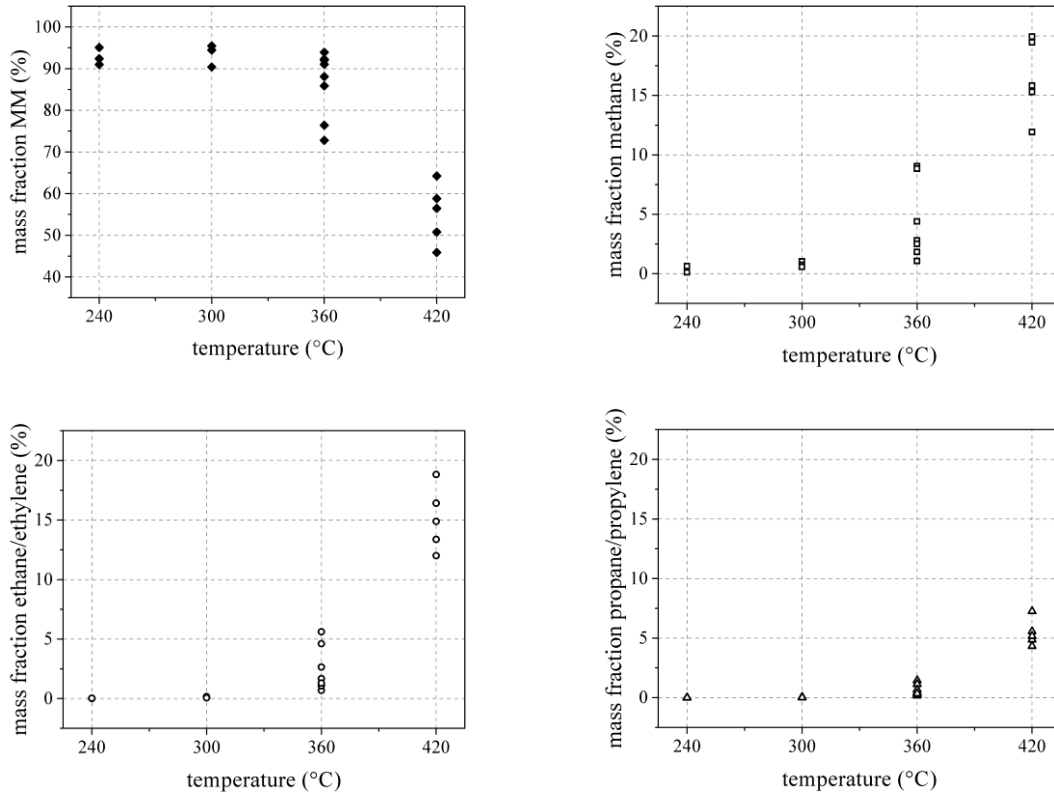


Figure 8: Mass fraction of MM, methane, ethane/ethylene and propane/propylene in the vapour phase after the experiment depending on temperature ($t = 72$ h)

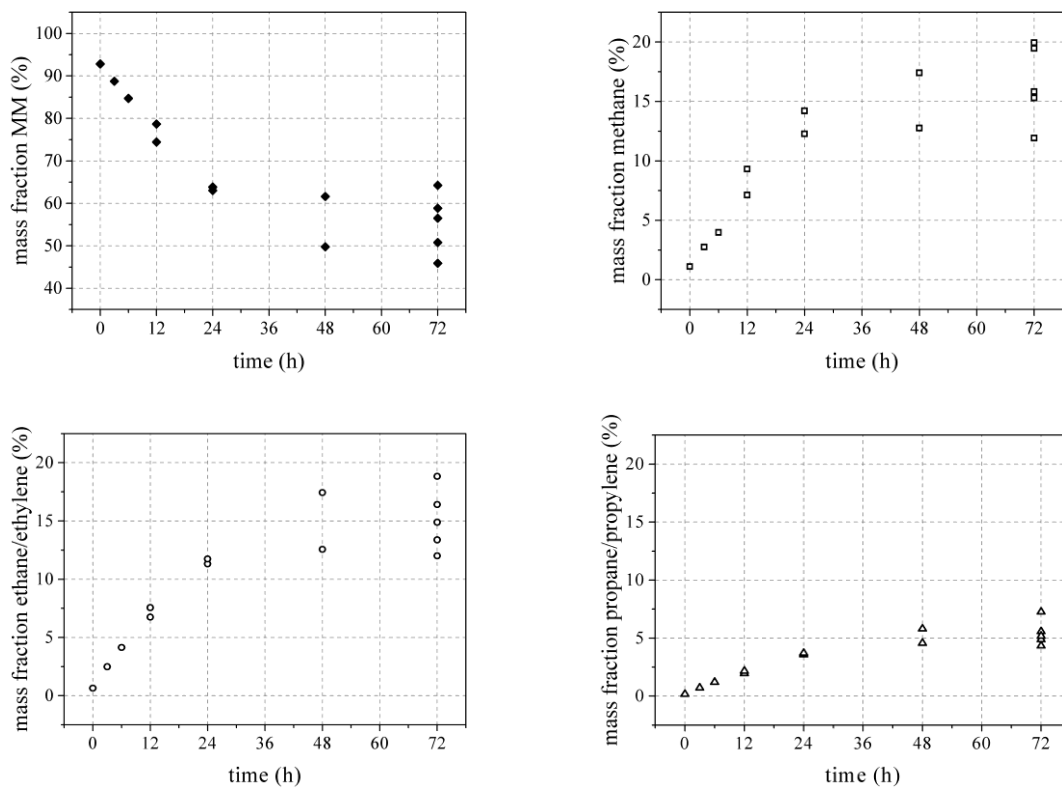


Figure 9: Mass fraction of MM, methane, ethane/ethylene and propane/propylene in the vapour phase after the experiment depending on time ($T = 420$ °C)

4. DISCUSSION

4.1 Qualitative evaluation of degradation products

The formation of C1-/C2- and C3-hydrocarbons suggests that the break of a Si-C-bond and the subsequent formation of methyl radicals can be seen as the start reaction of thermal degradation. The increased variation margin above a temperature of 360 °C in Figure 8 suggests complex recombination effects which differ especially for longer times of the experiment and are strongly influenced by number and kind of available radicals. The theory of free radicals is also supported by the results in Figure 9. The lower the duration of the experiment, the fewer radicals are available and the straighter forward is their influence on the mass fraction especially of MM, methane and ethane/ethylene. This leads to the characteristic linear slope for times lower than 24 h. The number and types of radicals and, therefore, the variation margin increases for longer times of the experiments.

4.2 Quantitative evaluation of degradation

The mass of gaseous MM before and after the experiment is calculated from the composition of the vapour phase. In combination with the overall mass of MM in the reactor, the annual degradation rate is deduced (Figure 10).

The typical exponential progression according to Arrhenius' law is observed. The absolute value for temperatures below 300 °C is mainly lower than the typical leakage rates of 3 %/a (Heberle et al., 2012) that are assumed for geothermal applications. The degradation rate increases considerably for temperatures higher than 300 °C.

Figure 10 also gives the error-containing values for the degradation rate if we assume the following typical errors for the input data of the calculation:

volume of the reactor and mass of MM in the reactor	± 2.0 %
mass fraction of MM in liquid and vapour phase	± 2.0 %
density of MM in liquid and vapour phase	± 1.0 %

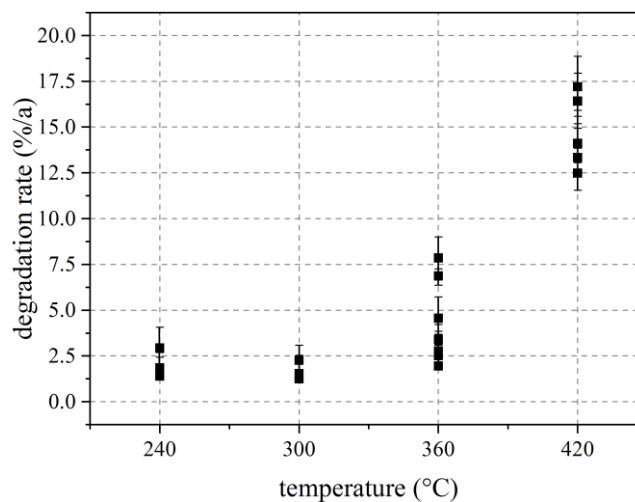


Figure 10: Degradation rate depending on temperature ($t = 72$ h)

The dependency of the annual degradation rate on the duration of the experiments in Figure 11 shows a steep decrease for times lower than 12 h, subsequently the curve flattens. Note that error-containing minimum and maximum values are given again. It is obvious that the relative failure increases for lower durations of the experiment as the values are extrapolated to gain the annual degradation rate. Furthermore, according to Figure 11 the annual degradation rates which were calculated from the experiments for duration of 72 h (Figure 10) are probably higher in real ORC units, in which the retention time of the working fluid in the evaporator is far less. To account for this, a test series is carried out in which MM is just heated up to the pre-set temperature and instantly cooled down

afterwards. Therefore, it is possible to “simulate” the heating in the evaporator and instant cooling in the turbine and condenser in an ORC unit. It is shown that the amount of low molecular hydrocarbons is low until a temperature of 300 °C (Figure 12). At 360 °C, the mass fraction of methane increases. Subsequently, the mass fraction of ethane/ethylene and propane/propylene increases at 420 °C. This again proves the assumption that the break of a Si-C-bondage and the set free methyl radicals influence the thermal degradation of MM.

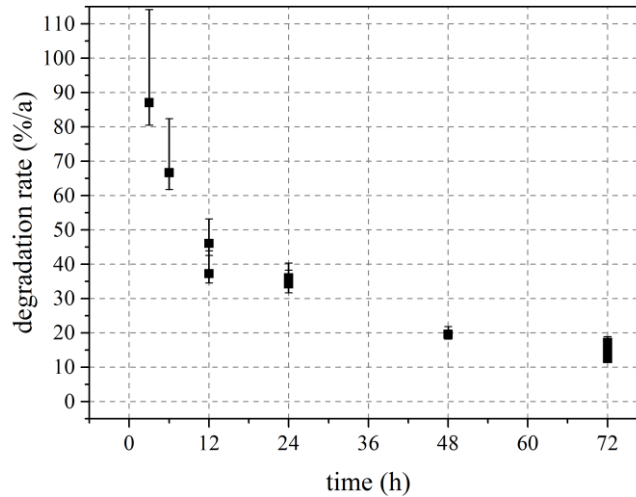


Figure 11: Degradation rate depending on time ($T = 420\text{ °C}$)

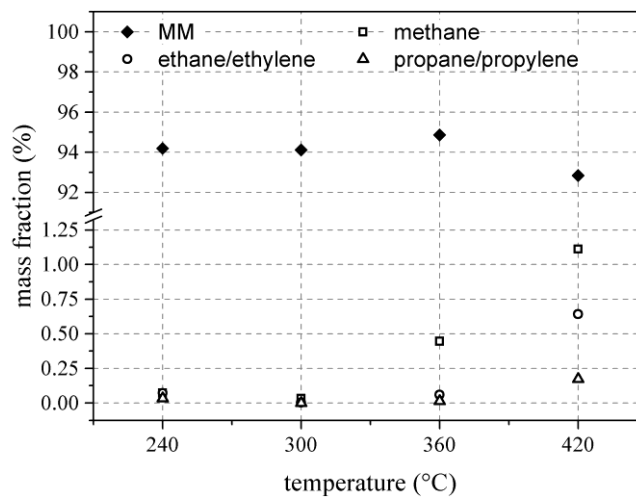


Figure 12: Mass fraction of MM, methane, ethane/ethylene and propane/propylene in the vapour phase after the experiment depending on temperature (test series: heating and instant cooling)

4.3 Impact on the set-up of ORC power units

From the gained results, it can be concluded that the use of MM in ORC units without intermediate thermal oil circuit is possible as long as the fluid temperature does not exceed 300 °C. As the thermodynamic suitable evaporation temperatures are around 240 °C, these conditions can be achieved if special care on evaporator design, particularly concerning film temperature and hotspots, is taken. Furthermore, Figure 12 shows that the formation of methane is an indicator for the thermal degradation. Therefore, in future ORC units a methane sensor could be placed at the top of the evaporator to give evidence on the degradation of MM (for example in case of unforeseen hotspots or in failure mode). In combination with a bleeder valve, the degradation products could be released before influencing the whole ORC system.

5. CONCLUSIONS

The thermal degradation of MM depending on temperature and time was analysed qualitatively and quantitatively and the impact on the set-up of ORC power units was pointed out. The main results can be summarized as follows:

- The main degradation products of MM are low molecular hydrocarbons like methane, ethane/ethylene and propane/propylene.
- The degradation rate is strongly influenced not only by the temperature but also by the retention time.
- MM is stable up to a temperature of 300 °C with annual degradation rates of less than 3.5 %.
- Methane can be used as indicator for ongoing thermal degradation of MM.
- The design of direct evaporating systems based on MM requires special care concerning film temperature and avoiding hot spots in the evaporator.

Ongoing and future work will include the evaluation of free water on the thermal degradation of MM and the comparison with other linear siloxanes (MDM, MD₂M). Furthermore, a dynamic test rig including pump, preheater, evaporator, superheater, throttle valve and condenser is planned to account for mechanical stress of the working fluid due to the cycle as well.

NOMENCLATURE

C	carbon	
MDM	octamethyltrisiloxane	
MD ₂ M	decamethyltetrasiloxane	
MM	hexamethyldisiloxane	
ORC	Organic Rankine Cycle	
Si	silicon	
<i>t</i>	time	(h)
<i>T</i>	temperature	(°C)

REFERENCES

- ANSI/ASHRAE Standard 97-2007, 2007, Sealed glass tube method to test the chemical stability of materials for use within refrigerant systems.
- Angelino, G., 1993, Cyclic Methylsiloxanes as Working Fluids for Space Power Cycles, *Transactions of the ASME - N - Journal of Solar Energy Engineering*, vol. 115, no. 3: p. 130–137.
- Angelino, Gianfranco (Ed.), 1991, Modern research topics in aerospace propulsion, New York, Springer.
- Buravtsev, N., Grigor'ev, A., Kolbanovskii, Y., Ovsyannikov, A., 1994, Thermal and thermooxidative stability of ozone-safe freons, *Russian Journal of Organic Chemistry*, vol. 30, no. 12: p. 1880–1890.
- Calderazzi, L., Colonna, P., 1997, Thermal stability of R-134a, R-141b, R-131I, R-7146, R-125 associated with stainless steel as a containing material, *International Journal of Refrigeration*, vol. 20, no. 6: p. 381–389.
- Colonna, P., Nannan, N., Guardone, A., Lemmon, E., 2006, Multiparameter equations of state for selected siloxanes, *Fluid Phase Equilibria*, vol. 244, no. 2: p. 193–211.
- Deshpande, G., Rezac, M. E., 2002, Kinetic aspects of the thermal degradation of poly(dimethyl siloxane) and poly(dimethyl diphenyl siloxane), *Polymer Degradation and Stability*, vol. 76, no. 1: p. 17–24.
- Dvornic, P. R., 2000, Thermal properties of polysiloxanes. In: Richard G. Jones (Ed.): Silicon containing polymers: The science and technology of their synthesis and applications, Dordrecht, Kluwer Acad. Publ, p. 185–212.

- Dvornic, P. R., 2008, High temperature stability of cyclosiloxanes. In: Gelest Inc. (Ed.): Silicon Compounds: Silanes and Silicones. A survey of properties and chemistry, 2nd Edition: p. 441–454.
- Ginosar, D. M., Petkovic, L. M., Guillen, D. P., 2011, Thermal Stability of Cyclopentane as an Organic Rankine Cycle Working Fluid, *Energy Fuels*, vol. 25, no. 9: p. 4138–4144.
- Grassie, N., Macfarlane, I., 1978, The thermal degradation of polysiloxanes-I. Poly(dimethylsiloxane), *European Polymer Journal*, vol. 14, no. 11: p. 875–884.
- Grassie, N., Macfarlane, I., Francey, K., 1979, The thermal degradation of polysiloxanes-II. Poly(methylphenylsiloxane), *European Polymer Journal*, vol. 15, no. 5: p. 415–422.
- Heberle, F., Brüggemann, D., Obermeier, A., 2012, Mögliche Emissionen bei der Strom- und Wärmeerzeugung aus Geothermie durch den Einsatz von F-Gasen im Energiewandlungsprozess mittels ORC, (in German), Umweltbundesamt (Ed.), Dessau-Roßlau (Climate Change, 16/2012), available online: <http://www.uba.de/uba-info-medien/4323.html>
- Kuramochi, H., Imai, F., Kondoh, H., Kunimori, K., Uchijima, T., Nozoye, H., 1993, Decomposition of cyclopentane on Ni(755): peculiar decomposition behavior of cyclopentane, *Surface Science*, vol. 287–288, part 1: p. 217–221.
- Manders, W. F., Bellama, J. M., 1985, Multiphoton infrared laser-induced degradation of polydimethylsiloxane and hexamethyldisiloxane, *J. Polym. Sci. Polym. Chem. Ed.*, vol. 23, no. 2: p. 351–357.
- Mang, T., Dresel, W., 2007, Lubricants and lubrication. 2nd edition, Weinheim, Wiley-VCH.
- Obernberger, I., 1998, Decentralized biomass combustion: state of the art and future development, Paper to the keynote lecture of the session “Processes for decentralized heat and power production based on combustion” at the 9th European Bioenergy Conference, June 1996, Copenhagen, Denmark, *Biomass and Bioenergy*, vol. 14, no. 1: p. 33–56.
- Obernberger, I., Thornhofer, P., Reisenhofer, E., 2002, Description and evaluation of the new 1000 kW_{el} organic Rankine cycle process integrated in the biomass CHP plant in Lienz, Austria, *Euroheat & Power*, vol. 10: p. 18–25.
- Stephan, P., Schaber, K., Stephan, K., Mayinger, F., 2009, Thermodynamik – Grundlagen und Technische Anwendungen, Band 1: Einstoffsysteme, 18th edition, Berlin, Springer, p. 243.

ACKNOWLEDGEMENT

The authors gratefully acknowledge financial support of the Bayerische Staatsministerium für Bildung und Kultus, Wissenschaft und Kunst within the framework TechnologieAllianzOberfranken.

MULTI-OBJECTIVE OPTIMIZATION OF ORGANIC RANKINE CYCLE POWER PLANTS USING PURE AND MIXED WORKING FLUIDS

Jesper G. Andreasen ^{1*}, Martin R. Kærn¹, Leonardo Pierobon ¹, Ulrik Larsen ², Fredrik Haglind ¹

¹ Technical University of Denmark, Building 403, Nils Koppels Allé, DK-2800 Kgs. Lyngby, Denmark. jgan@mek.dtu.dk*, pmak@mek.dtu.dk, lpier@mek.dtu.dk, frh@mek.dtu.dk

² Department of Shipping and Marine Technology, Chalmers University of Technology, SE-412 96 Gothenburg, Sweden. ulrik.larsen@chalmers.se

* Corresponding Author

ABSTRACT

For zeotropic mixtures, the temperature varies during phase change, which is opposed to the isothermal phase change of pure fluids. The use of such mixtures as working fluids in organic Rankine cycle power plants enables a minimization of the mean temperature difference of the heat exchangers when the minimum pinch point temperature difference is kept fixed. A low mean temperature difference means low heat transfer irreversibilities, which is beneficial for cycle performance, but it also results in larger heat transfer surface areas. Moreover, the two-phase heat transfer coefficients for zeotropic mixtures are usually degraded compared to an ideal mixture heat transfer coefficient linearly interpolated between the pure fluid values. This entails a need for larger and more expensive heat exchangers. Previous studies primarily focus on the thermodynamic benefits of zeotropic mixtures by employing first and second law analyses. In order to assess the feasibility of using zeotropic mixtures, it is, however, important to consider the additional costs of the heat exchangers. In this study, we aim at evaluating the economic feasibility of zeotropic mixtures compared to pure fluids. We carry out a multi-objective optimization of the net power output and the component costs for organic Rankine cycle power plants using low-temperature heat at 90 °C to produce electrical power at around 500 kW. The primary outcomes of the study are Pareto fronts, illustrating the power/cost relations for R32, R134a and R32/R134a (0.65/0.35_{mole}). The results indicate that R32/134a is the best of these fluids, with 3.4 % higher net power than R32 at the same total cost of 1200 k\$.

1. INTRODUCTION

The organic Rankine cycle (ORC) power plant is a technology that enables the utilization of low-temperature heat for electricity production. The working fluid selection for the ORC power plant is a critical design decision which affects the thermodynamic performance and the economic feasibility of the plant. The use of zeotropic mixtures as working fluids has been proposed as a way to improve the performance of the cycle (Angelino and Colonna, 1998). Zeotropic mixtures change phase with varying temperature, which is opposed to the isothermal phase change of pure fluids. As the temperature of the heat source and heat sink change during heat exchange, zeotropic working fluids enable a closer match of the temperature profiles in the condenser and the boiler, compared to pure fluids. This results in a decrease in heat transfer irreversibilities and an increase in cycle performance. The condenser has been identified as the component where the irreversibilities decrease the most when using mixed working fluids (Heberle et al., 2012; Lecompte et al., 2014), and the increment in cycle performance when using zeotropic mixtures instead of pure fluids is largest when the heat source temperature is low (Chys et al., 2012).

Heberle et al. (2012) optimized the performance of ORC systems using zeotropic working fluids for utilization of geothermal heat at 120 °C. Compared to pure isobutane, a mixture of isobutane/isopentane (0.9/0.1_{mole}) achieved an increase in the second law efficiency of 8 %. They also compared the UA -values (the product of the overall heat transfer coefficient and the heat transfer area) of the heat exchangers in the cycle, and found that the mixture compositions resulting in the highest cycle performance also required the highest UA -values. This suggests that the cost of heat exchangers is larger when the mixture is used. Le et al. (2014) performed maximizations of the exergy efficiency and minimizations of the levelized cost of electricity for ORC systems using mixtures of R245fa and pentane as working fluids. Pure pentane was identified as the best fluid, in both optimizations. In the minimization of the levelized cost of electricity, the minimum value for pentane was found to be 0.0863 \$/kWh. The mixtures pentane/R245fa (0.05/0.95_{mass}) and pentane/R245fa (0.1/0.9_{mass}) obtained similar values at 0.0872 and 0.0873 \$/kWh, respectively.

In the present study, we carry out a multi-objective optimization of net power output and component cost for an ORC power plant utilizing a low-temperature water stream at 90 °C. The objective of the study is to investigate and compare the relationship between cost and performance for ORC power plants using pure fluids and zeotropic mixtures as working fluids. The fluids considered are R32, R134a and R32/R134a (0.65/0.35_{mole}). These fluids are selected, since they achieved high thermodynamic performance at subcritical turbine inlet pressure in a previous study (Andreasen et al., 2014).

Previous studies (e.g. (Heberle et al., 2012; Trapp and Colonna, 2013; Andreasen et al., 2014)) which compare pure fluids and zeotropic mixtures focus mainly on the evaluation of the thermodynamic performance of the fluids. These studies indicated that the thermodynamic performance can be increased by using zeotropic mixtures as working fluids, while the size and thereby the cost of the heat exchangers increase. In order to evaluate the feasibility of zeotropic mixtures, it is, therefore, necessary also to assess the cost of equipment such that the working fluids are compared based on the same investment costs. Le et al. (2014) included a single-objective optimization of the levelized cost of electricity. However, they did not consider the simultaneous optimization of thermodynamic performance and cost as is done in the present study. It is advantageous to implement the multi-objective optimization since it enables a comparison of fluid performance based on the same equipment costs.

The paper begins with a description of the methodology in Section 2. The results are presented and discussed in Section 3 and conclusions are given in Section 4.

2. METHODS

The multi-objective optimization method is developed in Matlab version 2014b (Mathworks, 2014) based on the framework described by Pierobon et al. (2014). The steady state ORC system model, capable of handling both pure fluids and mixtures through REFPROP[®] version 9.1 (Lemmon et al., 2013), is adapted from a previous study (Andreasen et al., 2014) and integrated within the simulation tool. A sketch of the ORC power plant is depicted in Figure 1.

The heat source is a low-temperature water stream as investigated in Andreasen et al. (2014). Table 1 shows the hot fluid parameters along with the fixed input parameters assumed for the cycle. The hot fluid and cooling water pumps are denoted as auxiliary pumps.

The optimization variables include cycle and heat exchanger design parameters; see Table 2. The lower boundary for the turbine inlet pressure is defined as the bubble point pressure at a temperature 30 °C higher than the cooling water inlet temperature ($T_{cool,i}$), and the upper boundary is 90 % of the critical pressure (P_c). The superheating degree is defined as the temperature difference between the dew point temperature and the turbine inlet temperature, and the bounds for the baffle spacing are set relative to the shell diameter (d_s). The lower bounds for the pinch points in the condenser and the boiler are set to 0.1 °C. Such low pinch points are not feasible in practice, but they are allowed in this study in order to

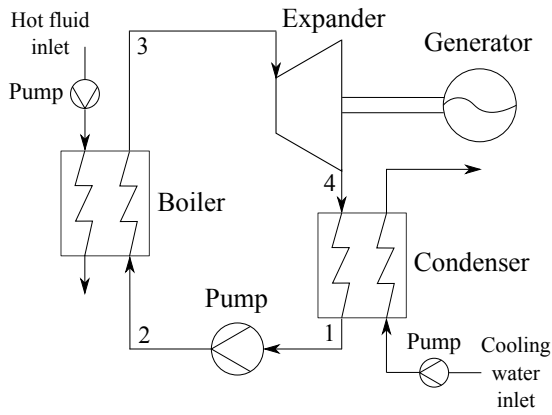


Figure 1: Organic Rankine cycle power system

Table 1: ORC system modelling conditions

Parameter description	Value	Unit
<i>Hot fluid (water)</i>		
Hot fluid inlet temperature	90	°C
Hot fluid mass flow	50	kg/s
Hot fluid pressure	4	bar
<i>Condenser</i>		
Cooling water inlet temperature	15	°C
Outlet vapour quality	0	-
Cooling water pressure	4	bar
<i>Working fluid pump</i>		
Isentropic efficiency	0.8	-
<i>Auxiliary pumps</i>		
Isentropic efficiency	0.7	-
<i>Turbine</i>		
Isentropic efficiency	0.8	-
Minimum outlet vapour quality	1	-

compare the fluids based on a wide range of equipment costs.

The objective functions for the optimization are the net power output and the total cost of the components. The net power is calculated as

$$\dot{W}_{NET} = \dot{m}_{wf}(h_3 - h_4 - (h_2 - h_1)) - \dot{W}_{aux.,pumps} \quad (1)$$

where \dot{m}_{wf} is the working fluid mass flow, h is the mass specific enthalpy and $\dot{W}_{aux.,pumps}$ is the power consumption of the hot fluid and cooling water pumps. The total cost (C_{tot}) of the components is found by adding the cost of the turbine (C_{turb}), working fluid pump ($C_{wf,pump}$), condenser (C_{cond}), boiler (C_{boil}), generator (C_{gen}) and the two auxiliary pumps ($C_{aux.,pumps}$)

$$C_{tot} = C_{turb} + C_{wf,pump} + C_{cond} + C_{boil} + C_{gen} + C_{aux.,pumps} \quad (2)$$

The total cost considered in this paper is the equipment cost, thus further expenses are expected for the construction of the ORC power plants, e.g. installation costs.

Table 2: Optimization variables

Parameter description	Lower bound	Upper bound	Unit
<i>Cycle parameters</i>			
Turbine inlet pressure	$P_{bub}(T_{cool,i} + 30)$	$0.9 \cdot P_c$	bar
Superheating degree	0	40	°C
Condensing temperature	$T_{cool,i} + 5$	$T_{cool,i} + 20$	°C
Boiler pinch point temperature	0.1	20	°C
Condenser pinch point temperature	0.1	20	°C
<i>Condenser design</i>			
Inner tube diameter	16	26	mm
Number of tubes	10	200	-
Baffle spacing	$0.5 \cdot d_s$	$3 \cdot d_s$	mm
<i>Boiler design</i>			
Inner tube diameter	16	26	mm
Number of tubes	10	200	-
Baffle spacing	$0.5 \cdot d_s$	$3 \cdot d_s$	mm

The optimization framework comprises the following steps (Pierobon et al., 2014):

- Calculation of the process states by use of the cycle model (without pressure losses)
- Layout of the geometry of the condenser and the boiler and calculation of the heat transfer area and the pressure losses
- Calculation of the net power output by use of the cycle model (with pressure losses)

- Calculation of the total component cost

2.1 Heat Exchanger Modelling

The heat exchanger models are developed based on the shell-and-tube model used in Kærn et al. (2015). In order to avoid leakage of working fluid, which for zeotropic mixtures can result in undesirable composition shifts, both the boiler and the condenser are designed with the working fluid flowing inside the tubes (Cavallini et al., 2003). The heat exchangers are designed as TEMA E type shell-and-tube heat exchangers with one shell pass and one tube pass. A 60° triangular tube layout is used; see Figure 2.

Table 3 lists the modelling conditions used for the shell-and-tube heat exchangers including the geometric parameters and the ranges for the flow velocities. The velocities must be high enough to avoid excessive fouling, but not so high that the heat exchanger material is eroded. The boundaries for the flow velocities are selected based on recommendations from Nag (2008), Shah and Sekulić (2003) and Coulson et al. (1999). The shell side velocity is only checked at the inlet, since the density variations of the hot fluid and the cooling water are small. The tube side outlet velocity for the condenser is allowed to be lower than the minimum value of 0.9 m/s for liquid in-tube flow found in Shah and Sekulić (2003). Full liquid flow is only present at the end of the condenser tube as all vapour is condensed. It is, therefore, assumed that the liquid velocity can reach 0.5 m/s at the condenser outlet without the risk of excessive fouling formation.

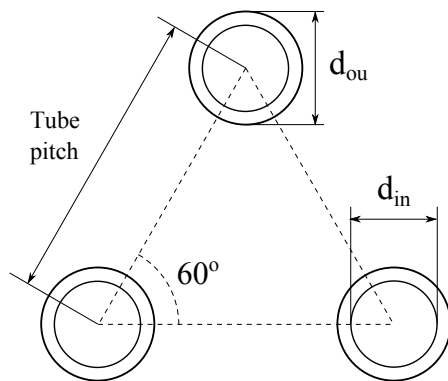


Figure 2: Tube layout

Table 3: Heat exchanger modelling conditions

Parameter description	Value/range	Unit
Tube configuration	Rotated square 45°	-
Tube thickness	3	mm
Tube pitch	1.5 · d _{ou}	mm
Baffle cut	0.25 · d _c	mm
Tube wall conductivity	16	W/mK
Number of control volumes	30	-
<i>Condenser velocities</i>		
Tube side inlet	5 – 22	m/s
Tube side outlet	0.5 – 4	m/s
Shell side inlet	0.3 – 1.5	m/s
<i>Boiler velocities</i>		
Tube side inlet	0.9 – 4	m/s
Tube side outlet	5 – 22	m/s
Shell side inlet	0.3 – 1.5	m/s

The heat transfer and pressure drop characteristics on the shell side are estimated based on the Bell-Delaware method (Shah and Sekulić, 2003). The method is implemented for tubes without fins and for a shell design without tubes in the window section. The effects of larger baffle spacings at the inlet and outlet ducts compared to the central baffle spacing are neglected.

For single-phase flow, the heat transfer coefficient is calculated using the correlation provided by Gnielinski (1976). The two-phase heat transfer coefficient of boiling is estimated based on the correlation provided by Gungor and Winterton (1987) and Thome (1996)

$$\alpha_{2p,boil} = \alpha_L \left[1 + 3000(BoF_c)^{0.86} + 1.12 \left(\frac{x}{1-x} \right)^{0.75} \left(\frac{\rho_L}{\rho_V} \right)^{0.41} \right] \quad (3)$$

where Bo is the boiling number, x is the vapour quality, ρ_L is the density of saturated liquid, ρ_V is the density of saturated vapour and α_L is the liquid only heat transfer coefficient which is calculated using the Dittus-Boelter correlation (Dittus and Boelter, 1930). The ratio of the nucleate boiling heat transfer coefficient to the ideal nucleate boiling heat transfer coefficient, $F_c = \alpha_{nb}/\alpha_{nb,id}$, is calculated by

$$F_c = \left[1 + \left(\frac{\alpha_{nb,id}}{q_{nb}} \right) (T_{dew} - T_{bub}) \left[1 - \exp \left(\frac{-Bq_{nb}}{\rho_L h_{LV} \beta_L} \right) \right] \right]^{-1} \quad (4)$$

where q_{nb} is the nucleate boiling heat flux, T_{dew} is the dew point temperature, T_{bub} is the bubble point temperature, B is a scaling factor, h_{LV} is the enthalpy of vaporization, and β_L is the liquid phase mass transfer coefficient. The values of B and β_L are set to $B = 1$ and $\beta_L = 0.0003$ m/s according to Thome (1996). The ideal nucleate boiling heat transfer coefficient, $\alpha_{nb,id}$ is calculated using the correlation by Stephan and Abdelsalam (1980).

For in-tube condensation, the heat transfer coefficient is estimated using the following correlation (Shah, 2009):

$$\alpha_{2p,cond} = \begin{cases} \alpha_I & J_g \geq 0.98(Z + 0.263)^{-0.62} \\ \alpha_I + \alpha_{Nu} & J_g < 0.98(Z + 0.263)^{-0.62} \end{cases} \quad (5)$$

where Z is Shah's correlating parameter and J_g is the dimensionless vapour velocity.

The heat transfer coefficients α_I and α_{Nu} are calculated as

$$\alpha_I = \alpha_{LT} \left(\frac{\mu_L}{14\mu_V} \right)^{0.0058+0.557P_r} \left[(1-x)^{0.8} + \frac{3.8x^{0.76}(1-x)^{0.04}}{P_r^{0.38}} \right] \quad (6)$$

$$\alpha_{Nu} = 1.32Re_L^{-1/3} \left[\frac{\rho_L(\rho_L - \rho_V)g\lambda_L^3}{\mu_L^2} \right]^{1/3} \quad (7)$$

where α_{LT} is the heat transfer coefficient assuming all mass to be flowing as liquid and Re_L is the Reynolds number for the liquid phase only. The variable α_{LT} is calculated using the Dittus-Boelter equation (Dittus and Boelter, 1930). For mixtures the heat transfer coefficient obtained from equation (5) is corrected using the method proposed by Bell and Ghaly (1973). For in-tube flow, the single-phase pressure drops are calculated based on the Blasius equation (Blasius, 1913) and the two-phase pressure drops are calculated using the correlation by Müller-Steinhagen and Heck (1986).

2.2 Cost Correlations

The cost (in US\$) of the components in the cycle are estimated based on correlations found in the literature. The turbine is assumed to be axial, since axial turbines are commonly used by manufacturers in the range of power (approximately 50-600 kW) considered in the present paper (Quoilin et al., 2013). The cost (in €) of the turbine is estimated based on the correlation provided by Astolfi et al. (2014)

$$C_{turb} = 1.230 \cdot 10^6 \left(\frac{1}{2} \right)^{0.5} \left(\frac{\sqrt{\dot{V}_4}/(\Delta h_{is})^{0.25}}{0.18} \right)^{1.1} \quad (8)$$

where \dot{V}_4 is the volume flow at the turbine outlet and Δh_{is} is the isentropic enthalpy drop across the turbine. An euro-to-dollar conversion factor of 1.2 is used to convert the turbine cost to US\$.

The costs of the pumps, the heat exchangers and the generator are estimated by

$$C_E = C_B \left(\frac{Q}{Q_B} \right)^M f_M f_P f_T \quad (9)$$

where C_E is the equipment cost for equipment with capacity Q , C_B is the base cost for equipment with capacity Q_B , M is a constant exponent, and f_M , f_P are f_T correction factors accounting for materials of construction, design pressure and design temperature.

The economic parameters needed in the cost correlation are listed in Table 4. For the heat exchangers, the pressure correction factor is obtained by linear interpolation between the values reported in Smith (2005). The component costs are corrected for inflation by using the Chemical Engineering Plant Cost Index.

Table 4: Economic parameters

Component	C_B	Q_B	M	f_M	f_P	f_T	Reference
Heat exchangers	32.8 k\$	80 m ²	0.68	1.7	(Smith, 2005)	1	(Smith, 2005)
Pumps	9.48 k\$	4 kW	0.55	1	1	1	(Smith, 2005)
Generator	3.7 k\$	1000 kW	0.95	1	1	1	(Boehm, 1987)

3. RESULTS AND DISCUSSION

Figure 3 shows the Pareto fronts for multi-objective optimizations of net power output and cost for R32, R134a and R32/R134a (0.65/0.35). The results indicate that R32/R134a is the best of the three fluids, since it enables the highest net power output at the lowest component cost. R32 is the second best fluid while R134a is performing worst.

When the fluids are compared based on a single-objective optimization of net power output, R32/R134a (0.65/0.35) reaches 13.8 % higher net power output than R32 and 14.6 % higher than R134a (Andreasen et al., 2014). However, this approach does not account for the equipment cost, and it was therefore not ensured that the fluids were compared based on similar cost. The multi-objective optimization, on the other hand, does enable a fluid comparison based on fixed equipment cost. For a total cost of 1200 k\$, R32/R134a reaches a 3.4 % higher net power than R32 and 10.9 % higher than R134a. At $C_{tot} = 800$ k\$, the mixture obtains 2.1 % higher net power than R32 and 12.6 % higher than R134a. It should be noted that in the single-objective optimization, which was presented in Andreasen et al. (2014), the mixture composition was optimized, but in the multi-objective optimization, carried out in the present paper, it is not. It is, therefore, possible that higher performance can be achieved with the mixture if the composition is optimized in the multi-objective optimization.

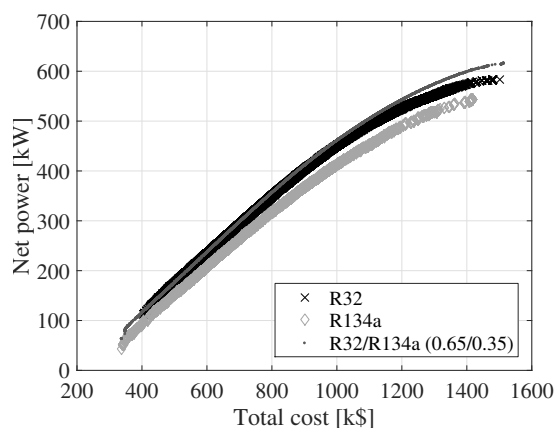


Figure 3: Pareto fronts

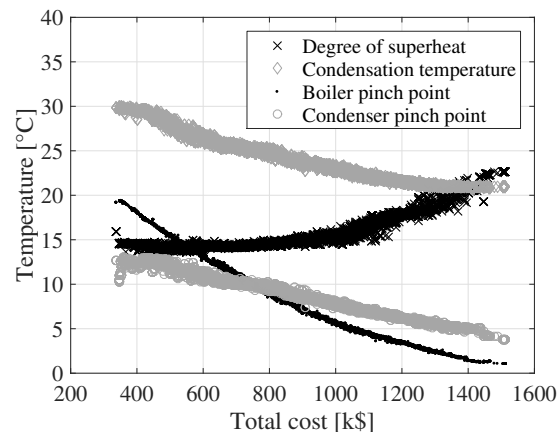


Figure 4: Temperatures, R32/R134a

In Figure 4, the optimal degree of superheating, condensing temperature, boiler pinch point and condenser pinch point are plotted as a function of the total cost for R32/R134a. The degree of superheating increases from about 13 to 23 °C as the total component cost increases. The condensing temperature, boiler pinch point and condenser pinch point all continuously decrease as the total component cost increases. The decrease in boiler pinch point results in an increase in the heat input to the cycle. This trend positively affects the net power output while increasing the investment cost for the boiler. The decrease in the condensing temperature has a positive effect on net power output, but requires larger heat

transfer areas since the temperature difference between the cooling water and the condensing working fluid decreases. The larger heat transfer areas result in higher investment costs for the condenser. For fixed cycle conditions (condensing temperature, mass flow, etc.), the condenser pinch point only affects the net power output of the cycle through the power consumption of the cooling water pump. The pinch point temperature of the condenser thereby primarily affects the cost of the condenser. Therefore, the condenser pinch point tends to be as large as possible, while respecting the following constraints: 1) the cooling water outlet temperature must be larger than the inlet temperature and 2) the flow velocity in the condenser shell should not be higher than 1.5 m/s. A high condenser pinch point results in a low cooling water temperature increase and thereby a high cooling water mass flow and a high shell flow velocity. For R32/R134a, the temperature glide of condensation is 5.3 °C, while the cooling water temperature increase ranges from 5.7 to 14.5 °C. In thermodynamic analyses of zeotropic mixtures, optimum conditions are typically obtained when the temperature glide of the mixture and the temperature increase of the cooling water are matched (Heberle et al., 2012; Chys et al., 2012; Lecompte et al., 2014; Andreasen et al., 2014). The present study does on the other hand indicate that optimum conditions are reached when the temperature increase of the cooling water is larger than the temperature glide of condensation.

For total costs of 1300 k\$, the boiler pinch point drops below 2.5 °C. It is unusual that solutions with pinch points below 2.5 °C represent economically feasible solutions. In Figure 3 at a total cost of 1300 k\$, the curves are levelling off, meaning that an increase in investment cost results in a low increase in net power output compared to when the total cost is lower. It is therefore likely that the more economically feasible solutions are found at total costs below 1300 k\$. It should be noted that the Pareto fronts do not provide information which directly can be used to make an investment decision, since they do not include information about the possible income related to the power delivered by the ORC power plant. Such information is necessary in order to estimate, e.g., net present value or payback periods which are useful figures for making investment decisions. The Pareto fronts should rather be used for assessing the feasibility of working fluids based on equal component costs, thereby ensuring a fair basis for comparison.

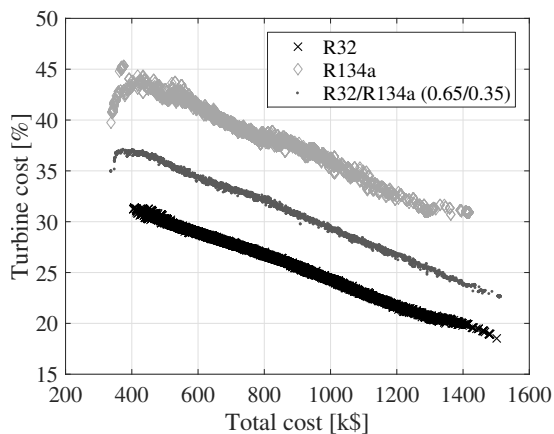


Figure 5: Relative turbine costs

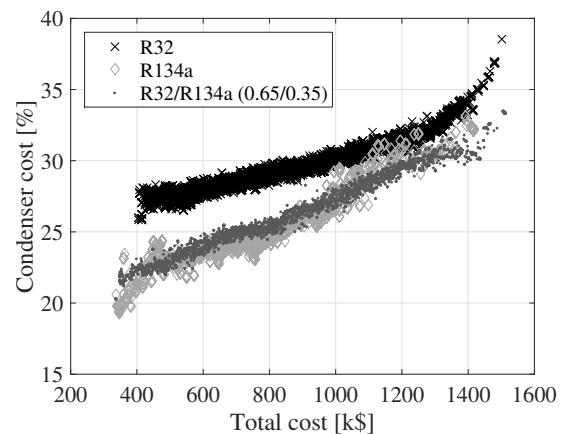


Figure 6: Relative condenser costs

Figures 5, 6 and 7 depict the variation of the cost of the turbine, condenser and boiler as a function of the total cost for the three fluids. The cost values displayed on the y-axes are relative to the total cost. The relative size of the turbine cost decreases, while the relative costs of the condenser and boiler increase. The relative turbine costs decreases since the turbine cost is a function of the turbine outlet volume flow rate and the isentropic enthalpy drop across the turbine. An increase in the outlet volume flow rate or a decrease in the isentropic enthalpy drop results in an increase in the turbine cost. These two parameters can be varied by changing e.g. the boiler pressure or the turbine inlet temperature. By modifying the boiler pressure or the turbine inlet temperature it is, however, not certain that the net power output increases. The cost of the condenser and the boiler can be increased by decreasing the

pinch point temperatures of the heat exchangers or the condensing temperature. This has a positive effect on the net power output. Thus, the cost of the heat exchangers are not as tightly connected to the cycle as the turbine is.

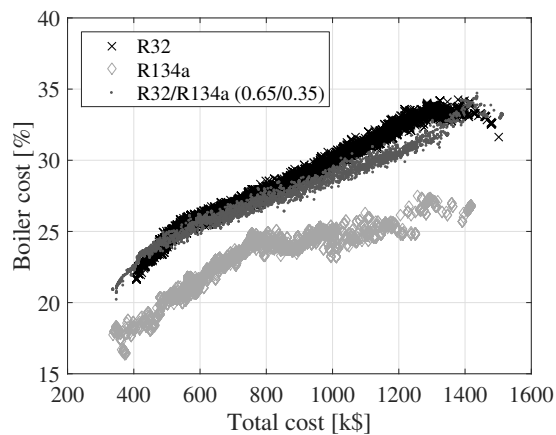


Figure 7: Relative boiler costs

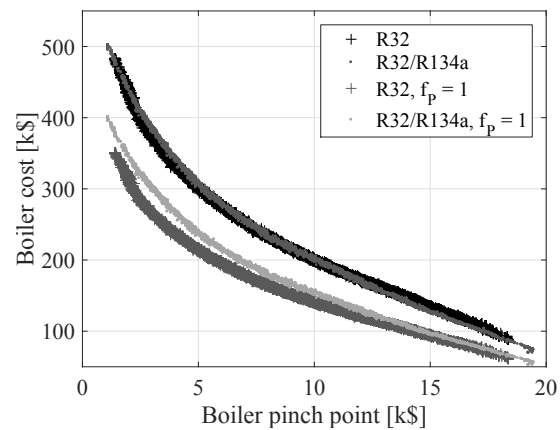


Figure 8: Boiler cost comparison

The boiler pressures range from 39-45 bar for R32, 28-35 bar for R32/R134a and 16-22 bar for R134a. Correspondingly the critical pressures are 57.8 bar, 51.8 bar and 40.6 bar for R32, R32/R134a and R134a, respectively, thus indicating that higher critical pressures are related to higher optimum boiling pressures. Figure 8 displays a comparison of the boiler costs for R32 and R32/R134a with and without the pressure correction factor (f_p). The boiler pinch point is plotted on the x-axis. It is, thereby, possible to compare the boiler costs for a given pinch point temperature difference. When the pressure correction factor is unity, the boiler costs are higher for the mixture compared to R32. When the pressure correction factor is employed as a function of the boiler pressure, the boiler costs are similar for the two fluids. This indicates that the boiler pressure reduction, achieved when using the mixture, can compensate for the increase in boiler cost caused by the degradation of the heat transfer coefficient and the lower temperature difference of heat transfer.

For R32/R134a, the shell length to diameter ratio of the shell-and-tube heat exchanger designs are in a range of 37-110 for the condenser and 76-180 for the boiler. Shah and Sekulić (2003) advise a desirable range of 3-15 for this ratio, meaning that the condensers and the boilers should consist of numerous shorter shell-and-tube heat exchangers in series, in order not to violate this practical limit. The shells designed in this paper are long since the number of tubes must be relatively low in order to ensure reasonable flow velocities in the tubes. Selecting a heat exchanger layout with multiple tube passes is a viable solution for increasing the number of tubes while maintaining high flow velocities in the tubes. Another option is to place the working fluid in the shell rather than in the tubes. This would increase the risk of working fluid leakage, which is problematic in the case of zeotropic mixtures.

4. CONCLUSION

This paper presents the results from a multi-objective optimization of net power output and component cost for ORC power plants using R32, R134a and R32/R134a (0.65/0.35_{mole}). For a low-temperature heat source, the results indicate that R32/R134a (0.65/0.35) is the best fluid and that R134a performs worst. For a total cost of 1200 k\$, the mixture reaches 3.4 % higher net power than R32 and 10.9 % higher than R134a. The relative increase in net power output for the mixture compared to R32 is significantly lower than the 13.8 %, which was estimated in a single-objective optimization of net power, i.e., not considering the cost of the cycle components. This exemplifies the importance of accounting for economic criteria in ORC system optimizations and fluid comparisons. This is especially important when pure fluids and mixtures are compared due to the generally lower temperature difference of heat transfer

and the degradation of heat transfer coefficients for zeotropic mixtures. Moreover, the differences in operating pressures can have a significant effect on the cost of the ORC power plant. It is thus possible to reduce the cost of the boiler by using R32/R134a as the working fluid compared to R32, since the optimum pressure is lower for the mixture.

Future work on this topic will include performance comparisons for a larger group of pure fluids and mixtures and an extension of the economic analysis enabling the estimation of payback periods and net present values, such that the more cost efficient working fluids can be identified. An uncertainty analysis, assessing the influence of the uncertainties related to heat transfer and equipment cost correlations, is also a topic for further investigation, especially in the light of the relatively small performance differences observed for R32 and R32/R134a.

NOMENCLATURE

Symbol			Subscript	
A	heat transfer area	(m ²)	1p	one-phase
B	scaling factor	()	2p	two-phase
Bo	boiling number	()	B	base
C	cost	(US\$)	boil	boiler
d	diameter	(mm)	bub	bubble point
f	correction factor	()	c	critical
F _c	$\alpha_{nb}/\alpha_{nb,id}$	()	cond	condenser
g	gravitational acceleration	(m/s ²)	cool	cooling water
G	mass flux	(kg/(s m ²))	dew	dew point
h	specific enthalpy	(kJ/kg)	E	equipment
J _g	dimensionless vapour velocity	()	gen	generator
M	Exponent in cost correlation	()	HEX	heat exchanger
\dot{m}	mass flow rate	(kg/s)	i	inlet
P	pressure	(bar)	id	ideal
Q	equipment capacity	(m ²), (kW)	in	inner
q	heat flux	(kW/m ²)	is	isentropic
Re	Reynolds number	()	L	saturated liquid
T	temperature	(°C)	LT	all mass as liquid
\dot{V}	volume flow	(m ³ /s)	LV	vaporization
\dot{W}	work	(kW)	nb	nucleate boiling
x	vapour quality	()	NET	net
Z	Shah's correlating parameter	()	ou	outer
α	heat transfer coefficient	(W/(m ² K))	pump	pump
β	mass transfer coefficient	(m/s)	r	reduced
Δ	difference	()	s	shell
λ	thermal conductivity	(W/(m K))	tot	total
μ	viscosity	(kg/(s m))	turb	turbine
ρ	density	(kg/m ³)	V	saturated vapour
			wf	working fluid

REFERENCES

Andreasen, J. G., Larsen, U., Knudsen, T., Pierobon, L., and Haglind, F. (2014). Selection and optimization of pure and mixed working fluids for low grade heat utilization using organic Rankine cycles. *Energy*, 73:204–213.

- Angelino, G. and Colonna, P. (1998). Multicomponent working fluids for organic Rankine cycles (ORCs). *Energy*, 23(6):449–463.
- Astolfi, M., Romano, M. C., Bombarda, P., and Macchi, E. (2014). Binary ORC (Organic Rankine Cycles) power plants for the exploitation of medium-low temperature geothermal sources - Part B: Techno-economic optimization. *Energy*, 66:435–446.
- Bell, K. and Ghaly, M. (1973). An approximate generalized design method for multicomponent/partial condenser. *AIChE Symp. Ser.*, 69:72–79.
- Blasius, H. (1913). Das Ähnlichkeitsgesetz bei Reibungsvorgängen in Flüssigkeiten. In *Mitteilungen über Forschungsarbeiten auf dem Gebiete des Ingenieurwesens 131*, pages 1–41. Springer, Berlin, Germany.
- Boehm, R. F. (1987). *Design analysis of thermal systems*. John Wiley & Sons, Inc., New York, United States of America.
- Cavallini, A., Censi, G., Del Col, D., Doretti, L., Longo, G., Rossetto, L., and Zilio, C. (2003). Condensation inside and outside smooth and enhanced tubes — a review of recent research. *Int. J. Refrig.*, 26(4):373–392.
- Chys, M., van den Broek, M., Vanslambrouck, B., and De Paepe, M. (2012). Potential of zeotropic mixtures as working fluids in organic Rankine cycles. *Energy*, 44(1):623–632.
- Coulson, J., Richardson, J., and Backhurst, J. (1999). *Coulson and Richardson's Chemical Engineering*. Butterworth-Heinemann, Oxford, Great Britain.
- Dittus, W. and Boelter, L. M. K. (1930). Heat transfer in automobile radiators of the tubular type. *Univ. Calif. – Publ. Eng.*, 2(13):443 – 461.
- Gnielinski, V. (1976). New Equation for Heat and Mass Transfer in Turbulent Pipe and Channel Flow. *Int. Chem. Eng.*, 16:359–368.
- Gungor, K. E. and Winterton, R. H. S. (1987). Simplified general correlation for saturated flow boiling and comparisons of correlations with data. *Chem. Eng. Res. Des.*, 65(2):148–156.
- Heberle, F., Preißinger, M., and Brüggemann, D. (2012). Zeotropic mixtures as working fluids in Organic Rankine Cycles for low-enthalpy geothermal resources. *Renew. Energy*, 37(1):364–370.
- Kærn, M. R., Modi, A., Jensen, J. K., and Haglind, F. (2015). An Assessment of Transport Property Estimation Methods for Ammonia–Water Mixtures and Their Influence on Heat Exchanger Size. *Int. J. Thermophys.*
- Le, V. L., Kheiri, A., Feidt, M., and Pelloux-Prayer, S. (2014). Thermodynamic and economic optimizations of a waste heat to power plant driven by a subcritical ORC (Organic Rankine Cycle) using pure or zeotropic working fluid. *Energy*, 78:622–638.
- Lecompte, S., Ameel, B., Ziviani, D., van den Broek, M., and De Paepe, M. (2014). Exergy analysis of zeotropic mixtures as working fluids in Organic Rankine Cycles. *Energy Convers. Manag.*, 85:727–739.
- Lemmon, E. W., Huber, M., and McLinden, M. (2013). NIST Standard Reference Database 23: Reference Fluid Thermodynamic and Transport Properties-REFPROP, Version 9.1, National Institute of Standards and Technology, Standard Reference Data Program, Gaithersburg.
- Mathworks (2014). Matlab 2014b documentation. Technical report, Massachusetts, The United States of America.

- Müller-Steinhagen, H. and Heck, K. (1986). A simple friction pressure drop correlation for two-phase flow in pipes. *Chem. Eng. Process. Process Intensif.*, 20(6):297–308.
- Nag, P. K. (2008). *Power Plant Engineering*. Tata McGraw Hill Education Private Limited, New Delhi, India, 3 edition.
- Pierobon, L., Benato, A., Scolari, E., Haglind, F., and Stoppato, A. (2014). Waste heat recovery technologies for offshore platforms. *Appl. Energy*, 136:228–241.
- Quoilin, S., van den Broek, M., Declaye, S., Dewallef, P., and Lemort, V. (2013). Techno-economic survey of Organic Rankine Cycle (ORC) systems. *Renew. Sustain. Energy Rev.*, 22:168–186.
- Shah, M. M. (2009). An Improved and Extended General Correlation for Heat Transfer During Condensation in Plain Tubes. *HVAC&R Res.*, 15(5):889–913.
- Shah, R. K. and Sekulić, D. P. (2003). *Fundamentals of Heat Exchanger Design*. John Wiley & Sons, Inc., New Jersey, United States of America.
- Smith, R. (2005). *Chemical process: design and integration*. John Wiley & Sons, Inc., West Sussex, England.
- Stephan, K. and Abdelsalam, M. (1980). Heat-transfer correlations for natural convection boiling. *Int. J. Heat Mass Transf.*, 23(1):73–87.
- Thome, J. R. (1996). Boiling of new refrigerants: a state-of-the-art review. *Int. J. Refrig.*, 19(7):435–457.
- Trapp, C. and Colonna, P. (2013). Efficiency Improvement in Precombustion CO₂ Removal Units With a Waste-Heat Recovery ORC Power Plant. *J. Eng. Gas Turbines Power*, 135(4):042311.

ACKNOWLEDGEMENT

The work presented in this paper has been conducted within the frame of the THERMCYC project ("Advanced thermodynamic cycles utilising low-temperature heat sources"; see <http://www.thermcyc.mek.dtu.dk/>) funded by InnovationsFonden, The Danish Council for Strategic Research in Sustainable Energy and Environment. The financial support is gratefully acknowledged.

EFFECT OF WORKING-FLUID MIXTURES ON ORGANIC RANKINE CYCLE SYSTEMS: HEAT TRANSFER AND COST ANALYSIS

Oyeniya A. Oyewunmi and Christos N. Markides*

Clean Energy Processes (CEP) Laboratory, Department of Chemical Engineering,
Imperial College London, London SW7 2AZ, United Kingdom

*E-mail: c.markides@imperial.ac.uk

Web-page: www.imperial.ac.uk/cep

ABSTRACT

The present paper considers the employment of working-fluid mixtures in organic Rankine cycle (ORC) systems with respect to heat transfer performance, component sizing and costs, using two sets of fluid mixtures: *n*-pentane + *n*-hexane and R-245fa + R-227ea. Due to their non-isothermal phase-change behaviour, these zeotropic working-fluid mixtures promise reduced exergy losses, and thus improved cycle efficiencies and power outputs over their respective pure-fluid components. Although the fluid-mixture cycles do indeed show a thermodynamic improvement over the pure-fluid cycles, the heat transfer and cost analyses reveal that they require larger evaporators, condensers and expanders; thus, the resulting ORC systems are also associated with higher costs, leading to possible compromises. In particular, 70 mol% *n*-pentane + 30 mol% *n*-hexane and equimolar R-245fa + R-227ea mixtures lead to the thermodynamically optimal cycles, whereas pure *n*-pentane and pure R-227ea have lower costs amounting to 14% and 5% per unit power output over the thermodynamically optimal mixtures, respectively.

1. INTRODUCTION

Recently, the selection of working fluids for organic Rankine cycle (ORC) systems has received close attention, including a particular interest in multi-component fluid mixtures, due to the opportunities they offer in improving thermodynamic performance. Various authors have carried out investigations to demonstrate and quantify these benefits, which have shown that working-fluid mixtures can exhibit an improved thermal match with the heat source compared to the isothermal profile of (isobaric) evaporation of pure-component fluids, therefore reducing exergy losses due to heat transfer, and increasing thermal and exergy efficiencies (Angelino and di Paliano, 1998; Garg et al., 2013; Wang et al., 2010).

Investigators have carried out both experimental and theoretical studies across a range of heat-source temperatures into the benefits of employing refrigerant (Sami, 2010; Chen et al., 2011; Aghahosseini and Dincer, 2013), hydrocarbon (Heberle et al., 2012; Shu et al., 2014), and siloxane (Dong et al., 2014), working-fluid mixtures. Compared to pure fluids, binary mixtures showed increased power outputs by up to 30% and thermal efficiencies by over 15% in some cases. Excellent second law analyses have also shown significant potential benefits (Lecompte et al., 2014). (Some exceptions to these general trends have also been reported (Li et al., 2014).) Additionally, fluid mixtures can be used to adjust the environmental and safety-related properties of ORC working fluids or to improve design parameters of system components. At the same time, some investigators have begun to develop and apply advanced computer-aided molecular design (CAMD) methodologies (Papadopoulos et al., 2010; Lampe et al., 2014) with a view towards identifying or designing optimal fluids for ORC systems.

While these efforts have demonstrated the potential advantages of working-fluid mixtures, notably in terms of power output and efficiency, many of the associated conclusions have been derived strictly based on thermodynamic cycle analyses that do not fully consider the expected heat transfer performance between the heat source/sink and working-fluid streams in the heat exchangers of ORC engines. In particular, the heat transfer and cost implications of using working-fluid mixtures have not been properly addressed. Refrigerant mixtures are known to exhibit reduced heat-transfer coefficients (HTCs) compared to their pure counterparts (Jung et al., 1989). Specifically, HTCs for refrigerants mixtures are

usually lower than the ‘ideal’ values, linearly interpolated between the mixture components. This, coupled with the reduced temperature difference between the heat source/sink and the working-fluid mixture, will invariably lead to larger and more expensive heat exchangers in an ORC system. Therefore, although working-fluid mixtures may allow a thermodynamic advantage over single-component working fluids, they may also lead to higher system costs owing to a deterioration in their thermal performance.

By presenting a method for evaluating the HTC of working-fluid mixtures, this work aims to explore the effects of using such mixtures on the heat transfer processes in ORC engines, which are important in understanding the role that these fluids play on the overall system performance and cost. A simple ORC engine model is presented that incorporates a suitable heat transfer description of the heat exchangers used for the heat addition and heat rejection processes. The heat exchangers are discretized along their lengths into segments (accounting for phase-change and single-phase regions), with suitable estimates of the HTCs in the different segments. Overall HTCs and heat-transfer areas (HTAs) are then evaluated, and simple cost models are used to estimate the relative costs of the components, and by extension of the entire engine. Using a selection of alkane and refrigerant working-fluid mixtures, the heat transfer characteristics and ORC-system equipment/component costs are thus investigated.

2. THERMODYNAMIC OPTIMIZATION

We begin with a simple thermodynamic optimization of an ORC system in a specified geothermal application with two sets of working-fluid mixtures: the *n*-hexane + *n*-pentane alkane system; and the R-245fa + R-227ea refrigerant system. Earlier studies have shown that these mixtures can provide significant thermodynamic benefits in ORC systems (Lecompte et al., 2014; Chys et al., 2012; Braimakis et al., 2014). Further, pentane and the selected refrigerants are presently being used in actual installations, especially in geothermal ORC setups, such as the one considered here.

2.1 ORC Model

We consider a sub-critical, non-regenerative ORC, consisting of four basic processes (pumping, heat addition, expansion and heat rejection), carried out by an organic working fluid (wf). Briefly, for completeness, the power required to pump the working fluid from State 1 (saturated liquid) to State 2 is:

$$\dot{W}_{\text{pump}} = \dot{m}_{\text{wf}} (h_2 - h_1) = \dot{m}_{\text{wf}} (h_{2s} - h_1) / \eta_{\text{is,pump}} \quad (1)$$

The heat extracted from the heat source is transferred to the working fluid assuming no heat losses and no pressure losses (*i.e.*, an isobaric process). In our engine, the working fluid exits this process as a saturated vapour (State 3), since superheating has been shown to be detrimental to ORC performance (Oyewunmi et al., 2014). Thus, the rate of heat input from the heat source (hs) is given by:

$$\dot{Q}_{\text{in}} = \dot{m}_{\text{hs}} c_{p,\text{hs}} (T_{\text{hs,in}} - T_{\text{hs,out}}) ; \text{ and, } \dot{Q}_{\text{in}} = \dot{m}_{\text{wf}} (h_3 - h_2) \quad (2)$$

The power generated as the working fluid is expanded to State 4 is:

$$\dot{W}_{\text{exp}} = \dot{m}_{\text{wf}} (h_3 - h_4) = \eta_{\text{is,exp}} \dot{m}_{\text{wf}} (h_3 - h_{4s}) \quad (3)$$

During heat rejection, the working fluid transfers heat to a cooling stream (cs) at a rate given by:

$$\dot{Q}_{\text{out}} = \dot{m}_{\text{wf}} (h_4 - h_1) ; \text{ and, } \dot{Q}_{\text{out}} = \dot{m}_{\text{cs}} c_{p,\text{cs}} (T_{\text{cs,out}} - T_{\text{cs,in}}) \quad (4)$$

The pump and expander isentropic efficiencies ($\eta_{\text{is,pump}}$ and $\eta_{\text{is,exp}}$) are taken as 75%, while all necessary fluid properties are calculated with REFPROP 9.1 (Kunz and Wagner, 2012; Lemmon et al., 2013).

2.2 Application

A wide variety of fluid streams can be used as ORC-system heat sources, including thermal oil (*e.g.*, in solar applications), process streams (*e.g.*, in industrial applications), geothermal water/steam, exhaust/flue

gases, etc. For the purpose of this work, it is more appropriate to consider liquid-phase source and sink streams; gaseous streams would dominate the thermal resistances on the source and sink sides of the heat exchangers, thereby overshadowing the thermal resistances on the working-fluid vapour and liquid streams, and limiting the information we hope to derive by employing different working-fluid mixtures. Thus, the heat source selected in the present work is a hot-water stream from the 80 kW_e Birdsville geothermal ORC power-plant in Australia (Beardsmore et al., 2015), with an inlet temperature ($T_{hs,in}$) of 98 °C and a flow rate of 27 kg·s⁻¹ (inlet enthalpy flow of 8.8 MW_{th}). This is typical of what is obtainable from other (low-pressure) geothermal reservoirs and also (low-grade) waste-heat streams in industrial processes. The heat sink is a water stream at ambient conditions (in at 20 °C; out at 30 °C).

An optimization problem is set up to maximize the expansion power-output (\dot{W}_{exp}) and, concurrently, the cycle thermal and exergy efficiencies (η_{th} and η_{ex}) for the specified heat-source enthalpy flow, while specifying that all of the working-fluid cycles are subject to the same (theoretical) total heat input from the source ($\dot{Q}_{in} = 1 \text{ MW}_{th}$; $T_{hs,out} = 89.2 \text{ °C}$). While this latter constraint does not represent the actual working condition in the Birdsville plant, it is imposed in order to ensure the same overall heat-exchange duty across the working-fluid mixtures, thus enabling a uniform basis for comparison. The objective function definition assumes that the pumping-power requirement is at least an order of magnitude smaller than the expansion power-output, $\dot{W}_{pump} \ll \dot{W}_{exp}$. The decision variables are the evaporation and condensation pressures, while an additional constraint concerns the heat exchangers' pinch conditions ($\geq 10 \text{ °C}$).

2.3 Optimal Cycles with Working-Fluid Mixtures

The ORC is optimized for maximum \dot{W}_{exp} , using the Interior Point algorithm (Byrd et al., 1999). The optimal power outputs and associated operating pressures are presented in Figure 1, and the expander performance parameters are presented in Figure 2. All other cycle parameters are given in Table 1.

Table 1: ORC optimization results

$x_{C_6H_{14}}$	η_{th} %	η_{ex} %	w_{exp} kJ/kg	\dot{W}_{pump} kW	\dot{m}_{wf} kg/s	\dot{m}_{cs} kg/s	\dot{Q}_{Ph} kW	\dot{Q}_{Ev} kW	\dot{Q}_{Dsh} kW	\dot{Q}_{Cn} kW	$x_{R-227ea}$	η_{th} %	η_{ex} %	w_{exp} kJ/kg	\dot{W}_{pump} kW	\dot{m}_{wf} kg/s	\dot{m}_{cs} kg/s	\dot{Q}_{Ph} kW	\dot{Q}_{Ev} kW	\dot{Q}_{Dsh} kW	\dot{Q}_{Cn} kW
0.0	7.79	39.5	33.5	1.41	2.37	21.4	251	749	81.0	841	0.0	7.65	39.5	16.7	2.84	4.74	21.4	284	715	62.0	861
0.1	8.24	41.6	36.5	1.33	2.29	21.3	260	740	84.1	833	0.1	8.00	41.5	17.5	3.48	4.78	21.3	318	682	68.5	851
0.2	8.53	43.1	38.5	1.24	2.25	21.2	266	734	86.9	828	0.2	8.12	42.4	17.3	4.05	4.92	21.3	339	661	72.4	846
0.3	8.71	43.9	39.9	1.15	2.21	21.2	270	730	89.3	824	0.3	8.12	42.7	16.7	4.64	5.13	21.3	356	644	75.4	843
0.4	8.70	43.8	40.1	1.04	2.20	21.2	267	732	89.9	823	0.4	8.07	42.8	15.9	5.31	5.40	21.3	373	627	77.8	841
0.5	8.67	43.6	40.0	0.94	2.19	21.2	266	733	90.8	822	0.5	8.03	43.0	15.1	6.12	5.72	21.3	393	607	80.5	839
0.6	8.64	43.4	39.8	0.87	2.19	21.2	265	735	91.9	822	0.6	7.87	42.6	14.0	6.97	6.11	21.4	410	589	82.5	839
0.7	8.56	43.0	39.2	0.79	2.21	21.2	263	737	92.7	822	0.7	7.60	41.7	12.8	7.83	6.57	21.4	426	575	84.3	840
0.8	8.43	42.3	38.1	0.72	2.23	21.2	259	740	92.7	822	0.8	7.32	40.8	11.6	8.77	7.09	21.5	442	559	86.0	842
0.9	8.19	41.1	36.3	0.64	2.27	21.3	252	748	91.4	826	0.9	7.04	39.9	10.5	9.79	7.64	21.6	460	540	86.9	843
1.0	7.85	39.3	33.8	0.55	2.34	21.4	240	760	88.5	833	1.0	6.74	38.9	9.51	10.8	8.23	21.6	478	522	86.4	846

Of the 1 MW_{th} heat inflow to the cycle, roughly ~75% is used to evaporate the alkane working fluids (50% – 70% for the refrigerants), while the rest is used for pre-heating the fluids to their bubble points. On average, about 0.85 MW is rejected during the condensation process. A working-fluid mixture with $x_{C_6H_{14}} = 0.3$ results in the cycle with the highest power output and efficiency. The (pure) *n*-hexane cycle has the lowest power output (Figure 1a), followed closely by the *n*-pentane cycle; their power outputs are 10.5% and 10.1% lower than that of the optimal mixture, respectively. For the R-245fa + R-227ea system, the equimolar mixture ($x_{R-227ea} = 0.5$) is the optimal working fluid (Figure 1b).

The working-fluid mixtures with *n*-hexane fractions between 30 mol% and 60 mol% have the highest power outputs and also the lowest working-fluid flow-rates (from Table 1). This results in cycles with the highest specific work-outputs (defined as $w_{exp} = \dot{W}_{exp}/\dot{m}_{wf}$), with $x_{C_6H_{14}} = 0.4$ having the highest. The pure fluids have the highest mass flow-rates and this, coupled with their lower work-outputs, results in cycles with the lowest work densities, which are about ~16% lower than that of the optimal fluid-mixture. For the R-245fa + R-227ea system, the optimal working-fluid flow-rate increases monotonically from pure R-245fa to pure R-227ea, and R-227ea has the cycle with the lowest specific work.

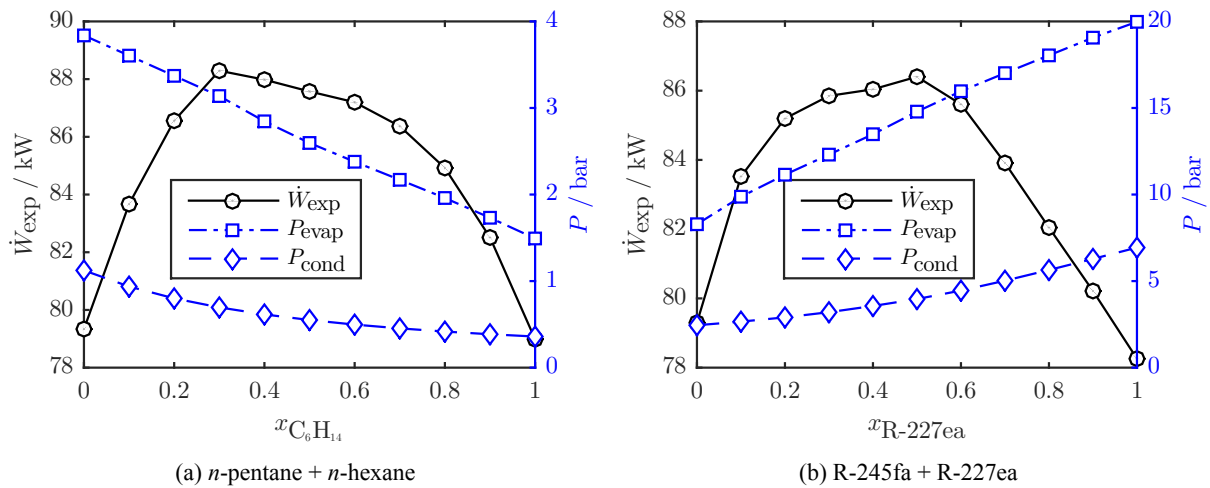


Figure 1: Optimal expander power-output and corresponding operating phase-change pressure

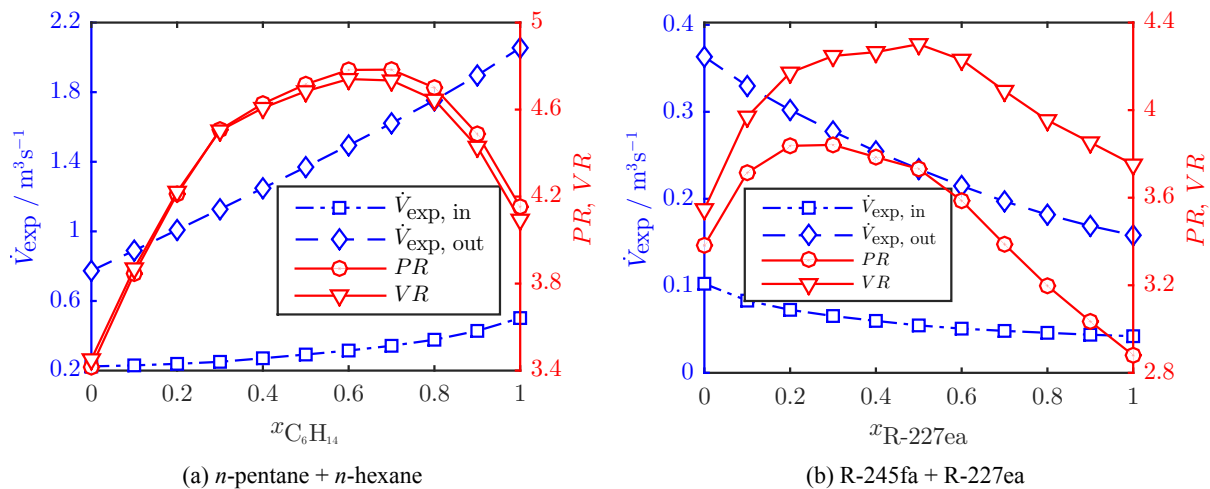


Figure 2: Expander volumetric flow-rate, volume and pressure ratio at optimal power output

The temperature glides (not shown) are smaller in the evaporator than in the condenser. In both heat exchangers these follow a parabolic variation with x , reaching a maximum of 6 – 8 K at the equimolar mixture (n -pentane + n -hexane) and 6 – 9 K at $x_{R-227ea} = 0.3$ (R-245fa + R-227ea). These do not directly correspond to the optimal mixtures, but are close. In fact, the temperature glide is a reasonably good predictor of the maximum power-output in our study, since high power-output mixtures have relatively high temperature glides, which are also closer to the external heat source and sink temperature changes (8 and 10 K). Although this holds true for closely related binary mixtures, it has been suggested that mixtures of highly dissimilar fluids may not follow this trend (Li et al., 2014; Oyewunmi et al., 2014).

The optimal evaporation and condensation pressures (Figure 1a and 1b, RHS axes) reduce linearly from n -pentane (R-227ea) to n -hexane (R-245fa). This is because the saturation pressures of n -pentane (R-227ea) are higher than those of n -hexane (R-245fa) at the same temperature, since the critical temperature of n -pentane (R-227ea) is lower than that of n -hexane (R-245fa). In the R-245fa + R-227ea system, the entire condensation process occurs at above atmospheric pressures, whereas in the n -pentane + n -hexane system, only n -pentane condenses at above atmospheric conditions (the other working fluids condense at sub-atmospheric pressures). The pumping power (while being negligible compared to the expander output) mirrors the behaviour of the optimal evaporation pressure in both working-fluid systems.

The volumetric flow-rates through the expander, \dot{V}_{exp} (Figure 2a and 2b, LHS axes) are linear, increasing steadily from n -pentane (R-227ea) to n -hexane (R-245fa) due to the reduction in the saturation pressures during evaporation and condensation at higher concentrations of n -hexane (R-245fa). The pressure ra-

tio, PR , and expansion ratio, VR , (Figure 2a and 2b, RHS axes) follow similar trends, with a minimum observed for one of the pure-fluid components (n -pentane and R-227ea, respectively), and a maximum observed for a fluid mixture. The low expansion-ratios and volumetric flow-rates for the pure components suggest they would require smaller expanders than the mixtures, potentially leading to cost savings. Also, they would require fewer expansion stages, further increasing the potential cost savings.

3. HEAT TRANSFER ANALYSIS OF OPTIMAL CYCLES

In the previous section we demonstrated the thermodynamic benefits of employing working-fluid mixtures in ORCs, especially for cases when the heat source and sink profiles are constrained. As expected, there are working-fluid mixtures that realize higher power outputs and efficiencies than both pure fluids as a result of the temperature glides during the phase change processes. The associated expansion and pressure ratios of such working-fluid mixtures are comparable to those of the pure working-fluids.

However, these results were derived purely from a thermodynamic perspective; the effects of such mixtures on the heat transfer processes in the heat exchangers, and especially the evaporator and the condenser, have not yet been considered. Experimental investigations have shown that working-fluid mixtures are likely to experience lower HTC's than pure fluids under similar conditions. Thus, it is imperative to examine the consequences of selecting fluid mixtures on the heat transfer processes in an ORC system, with a view towards determining the sizes and costs of the main system components, and therefore their contributions to overall system cost. The pump and expander costs depend on their power ratings and volume/pressure ratios, which were derived from the thermodynamic optimization and thus need no further treatment. The costs of the heat exchangers on the other hand depend on their sizes, which cannot be obtained from thermodynamic calculations alone, and require appropriate heat transfer models.

3.1 Heat Exchanger Sizing

The heat addition process is carried out in two heat exchangers: (1) the Preheater (Ph), used to pre-heat the working fluid to saturated liquid; and (2) the Evaporator (Ev), used to evaporate the working fluid to the saturated vapour state. Similarly, the heat rejection process is carried out in the Desuperheater (Dsh) and the Condenser (Cn). All heat exchangers are modelled as counter-current, shell-and-tube exchangers (shell and tube diameters: 70 mm and 25 mm; tube thickness: $dx = 5$ mm) constructed from carbon-steel (thermal conductivity: $k = 51 \text{ W.m}^{-1}.\text{K}^{-1}$), and are discretized into 100 (variable-sized) segments, i ($= 1 - 100$), each segment having an equal heat transfer/duty, *i.e.*, $\dot{Q}_{in}/100$ or $\dot{Q}_{out}/100$. In all heat exchangers, the working fluid flows through the tube-side (tb), while the heat source and sink streams are the shell-side (sh) fluids. Thus, the total rates at which heat is transferred to/from the working fluid in relation to Equations (2) and (4), respectively, are given by:

$$\dot{Q}_{in} = \dot{Q}_{Ph} + \dot{Q}_{Ev} = \sum_{i=1}^{100} \dot{Q}_i + \sum_{i=1}^{100} \dot{Q}_i ; \text{ and, } \dot{Q}_{out} = \dot{Q}_{Dsh} + \dot{Q}_{Cn} = \sum_{i=1}^{100} \dot{Q}_i + \sum_{i=1}^{100} \dot{Q}_i . \quad (5)$$

Furthermore, for each segment an overall heat-transfer coefficient, U_i , can be defined such that:

$$\dot{Q}_i = U_i A_i \Delta T_{lm,i} ; \text{ where:} \quad (6)$$

$$\Delta T_{lm,i} = \frac{(T_{sh,i+1} - T_{tb,i}) - (T_{sh,i} - T_{tb,i-1})}{\ln[(T_{sh,i+1} - T_{tb,i})/(T_{sh,i} - T_{tb,i-1})]} ; \text{ and, } U_i^{-1} = h_{sh,i}^{-1} + dx/k + h_{tb,i}^{-1} . \quad (7)$$

Single-phase local HTC's (h_{sh} , h_{tb}) can be calculated by using the Dittus-Boelter Nusselt number ($Nu_{i,sp}$) correlation, whereas two-phase HTC's can be calculated by suitably modifying $Nu_{i,sp}$ with empirical functions of the Martinelli parameter, X_{tt} (Jung et al., 1989; Shin et al., 1996). In the present work, this modification was fitted specifically to results from experiments involving horizontal turbulent-flow boiling of refrigerant mixtures, as:

$$Nu_{i,tp} = F(X_{tt}) Nu_{i,sp} ; \text{ where: } F(X_{tt}) = 1 + 1.8X_{tt}^{-0.82} , \text{ and } X_{tt} = \left(\frac{1-q}{q} \right)^{0.9} \left(\frac{\rho_v}{\rho_l} \right)^{0.5} \left(\frac{\mu_l}{\mu_v} \right)^{0.1} . \quad (8)$$

Equation (8) can be applied directly for pure fluids using the overall mixture composition for the liquid and vapour-phase properties. For the fluid mixtures, X_{ft} is calculated using the equilibrium liquid and vapour-phase compositions (not the overall composition) at the saturation temperature and corresponding vapour quality, q on mass basis (Jung et al., 1989). The HTAs of all segments are then calculated from Equation (6) and summed to give the total HTA (A_{HX}) for the heat exchanger of interest.

3.2 Heat Exchanger Sizing for Optimal Cycles

First, we verify the overall HTC's calculated using Equations (7) – (8), especially for the heat exchangers involving phase change (Evaporator and Condenser). The overall HTC's at the 20th, 50th and 80th segments of these heat exchangers, and for the single-phase heat exchangers, are presented in Figure 3 for the R-245fa + R-227ea system. The calculated values are in good general alignment with the experimental data obtainable for flow boiling of refrigerant mixtures found in Jung et al. (1989) and Shin et al. (1996). Also in agreement with experimental observations, the HTC's for the working-fluid mixtures at each of the segments appear lower than the linearly interpolated values between the two pure-fluid components that make up the mixture. While various explanations have been proposed for this phenomenon, most authors contend that it is due to mass-transfer effects caused by the composition differences between the vapour and liquid phases during the phase-change process.

In the single-phase heat exchangers (Preheater and Desuperheater), the overall HTC's for the mixtures are also lower than the linearly interpolated values, although this deviation is less pronounced for the R-245fa + R-227ea mixtures. Overall, the HTC's are highest in the Evaporator, followed by the Condenser, and lowest in the Desuperheater. Higher HTC's are achieved in the Condenser and Evaporator due to change of phase. The working-fluid vapour results in the low HTC values in the Desuperheater.

Based on the knowledge of the HTC's and the associated heat-transfer rates, the HTAs for all segments of the heat exchangers can be calculated from Equation (6). The HTAs of the segments in the Evaporator and the Condenser (for R-245fa + R-227ea) are presented in Figure 4; similar observations can be made by considering *n*-pentane + *n*-hexane. As the mole fraction of R-227ea is increased in the mixture, the HTA is seen to increase and then decrease such that the pure fluids (R-245fa and R-227ea) have heat exchangers with the lowest HTAs. This is the case across all of the segments and in both the Evaporator and the Condenser as a direct result of the lower HTC's of the working-fluid mixtures, with the only exception being that of the Evaporator for R-245fa + R-227ea where some mixtures (*e.g.*, $x_{R-227ea} = 0.8$) have lower HTAs than pure R-245fa; pure R-227ea still has the lowest areas across all of the sections.

The HTA variations are less pronounced in the Evaporator than in the Condenser where large differences exist between the pure fluids and the mixtures. The pure fluids have the smallest areas primarily due to their higher HTC values. For example, even though the Evaporator for the case of pure *n*-hexane has the highest heat-transfer rate (see Table 1), it has the smallest areas because *n*-hexane has the highest overall HTC amongst all the working fluids. In a similar manner, although the condenser for pure R-245fa has the highest duty, its high HTC enables it to have a lower HTA than those of the mixtures.

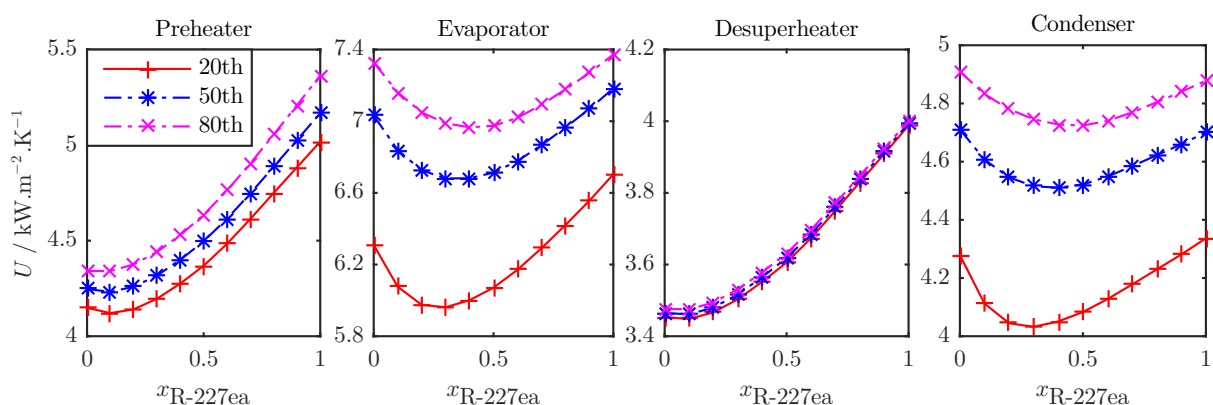


Figure 3: Overall HTC's at segments along the heat exchangers for R-245fa + R-227ea system

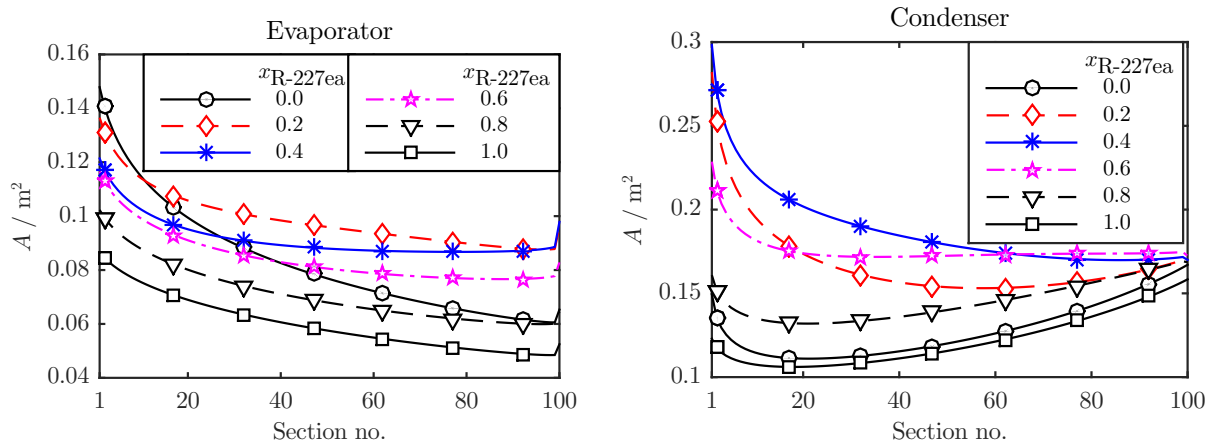


Figure 4: Heat-transfer areas along the Evaporator and Condenser for R-245fa + R-227ea system

The total HTAs for each of the heat exchangers with the different working-fluid mixtures are presented in Figure 5. As expected by consideration of their thermal duties (see Table 1), the Evaporators are generally three times as large as the Preheaters, while the Condensers are 8 – 13 times larger than the Desuperheaters. Although the Condenser thermal-duties are only about 15% higher than those of the Evaporators, the Condensers are twice as large as the Evaporators in most instances. This is due to the lower overall HTC's and the lower temperature differences across the Condensers.

As the concentration of R-227ea in the refrigerant-mixture system is increased, the Ph and Dsh heat duties increase, and so do the total HTAs of both heat exchangers. The Dsh area reaches a maximum at 90 mol% R-227ea and then decreases slightly for pure R-227ea. The Dsh and Ph areas for the *n*-pentane + *n*-hexane systems are also directly governed by their heat duties. It should however be noted that these variations in HTA with working-fluid mixtures (range of 0.13 m² and 0.10 m²; 1.12 m² and 0.31 m²) are much smaller than those associated with the two-phase heat exchangers. This is important, in that it suggests that working-fluid mixtures have a more profound effect on the Evaporator and Condenser sizes than they do on the single-phase heat-exchangers, at least in the present study.

From Figure 5, it is clear that the pure working-fluids have smaller Evaporator HTAs compared to the mixtures. The only exception is found in the R-245fa + R-227ea system, where fluid mixtures with $x_{R-227ea} \geq 0.6$ have lower Ev areas than pure R-245fa. Furthermore, due to the deterioration of HTC's during condensation, the Condensers for the working-fluid mixtures are much larger than those for the pure fluids. In the case of the R-245fa + R-227ea system, the HTAs range from 12.2 m² ($x_{R-227ea} = 1$) to 18.8 m² ($x_{R-227ea} = 0.4$), representing a difference of 54%. Such large differences in HTAs between working-fluid mixtures and pure fluids can lead to considerable differences in plant size and cost.

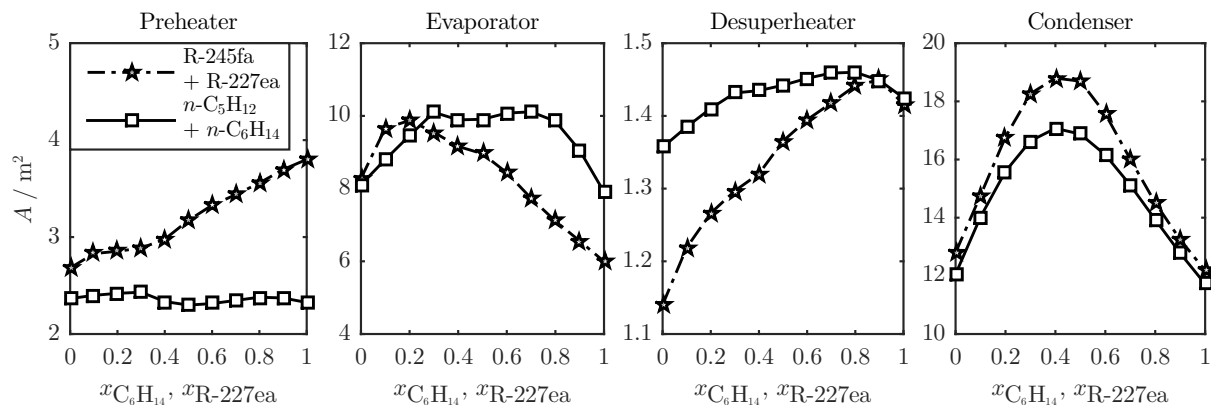


Figure 5: Total heat-transfer areas for heat exchangers with the different working-fluid mixtures

4. COST ANALYSIS OF OPTIMAL CYCLES

We conclude this paper with a brief investigation of the cost implications of employing working-fluid mixtures in ORC systems. The key components affected by the choice of working fluid are those illustrated previously – the working-fluid pump, the expander and the heat exchangers. The costs of these components are added to give an estimate of the plant cost. Although this sum does not give the total installation cost, it is through this amount that the effects of working-fluid choice on plant costs are manifested directly. Other factors that contribute to the plant installation costs would be similar for the various working fluids considered. Component-base costs (C_B , indexed in year 2006; £1 \equiv €1.47, \$1.84) are calculated using logarithmic correlations of component size factors (S) according to Seider et al. (2009) and are presented in Table 2. Also in Table 2 are the cost coefficients (converted to SI units). The calculated component-base costs of the optimal cycles are presented in Figure 6 (LHS axes).

Table 2: Component cost coefficients used in $C_B = (F) \exp\{C_0 + C_1[\ln S] + C_2[\ln S]^2\}$

Component	S	F	C_0	C_1	C_2
Pump	$\dot{V}\sqrt{H}$ ($\text{m}^3 \cdot \text{s}^{-1} \cdot \text{m}^{1/2}$)	2.7	9.0073	0.4636	0.0519
Expander	\dot{W}_{exp} (kW)	1.0	6.5106	0.8100	0.0000
Expander*	\dot{W}_{exp} (kW)	1.0	7.3194	0.8100	0.0000
Heaters/Coolers	A (m^2)	1.0	10.1060	-0.4429	0.0901
Evaporator/Condenser	A (m^2)	1.0	9.5638	0.5320	-0.0002

* Sub-atmospheric pressure discharge expander (applicable to $x_{\text{C}_6\text{H}_{14}} \geq 0.1$)

The pumps cost around £5,200, with the cost reducing monotonically from pure n -pentane (R-227ea) to n -hexane (R-245fa) as a direct result of the lower evaporation pressures as the concentration of n -hexane (R-245fa) in the working fluid is increased (in line with Figure 1). Similarly, the costs of the single-phase heat exchangers (Ph and Dsh) are low (£5,000 – £6,000). However, the evaporator and condenser costs are well in excess of £25,000. The expander costs fall into two classes: (i) sub-atmospheric pressure discharge expanders that cost about £35,000; and (ii) standard expanders with a considerably lower cost of about £15,000. From these results, it is clear that the expander and the phase-change heat exchangers present the dominant costs of the ORC system considered here.

The pure fluids (pure n -pentane and n -hexane; R-245fa and R-227ea) generally have the lowest-cost evaporators and condensers, while the mixtures ($x_{\text{C}_6\text{H}_{14}} = 0.7$ and $x_{\text{C}_6\text{H}_{14}} = 0.4$; $x_{\text{R-227ea}} = 0.2$ and $x_{\text{R-227ea}} = 0.4$ respectively) have the highest costs. The condenser size and cost is smallest for n -pentane despite it having a larger heat duty and working-fluid flow-rate (see Table 1) than those for the mixtures.

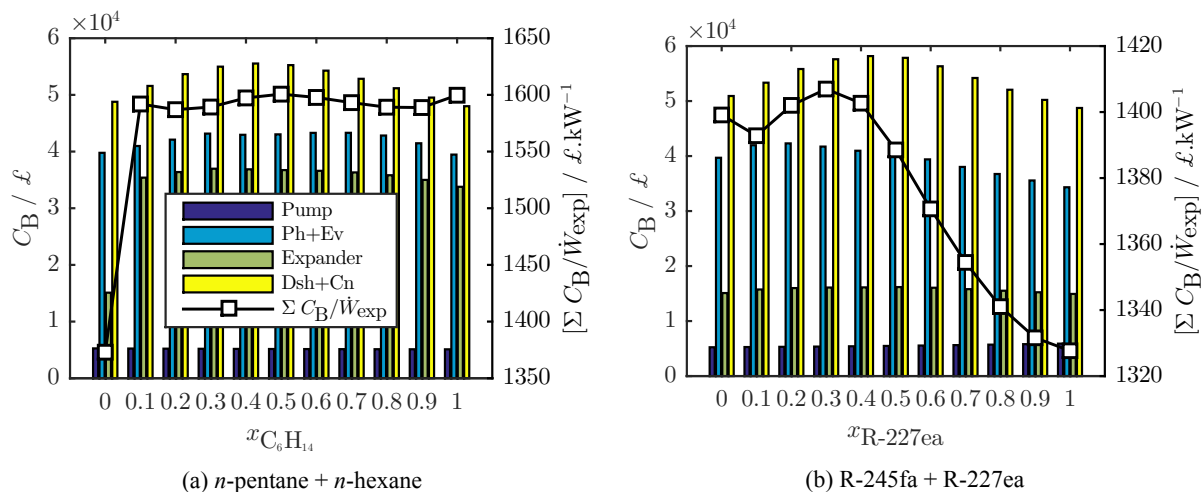


Figure 6: Optimal cycles' component costs (bars; LHS axes) and cost per kW (line; RHS axes)

From Figure 6a and 6b, it is clear that the expander costs mirror the trend exhibited by the optimal power output in Figure 1a and 1b especially as they are correlated with the power output. However, for the *n*-pentane + *n*-hexane system, the expander cost for pure *n*-pentane ($x_{C_6H_{14}} = 0$) is over 50% lower than those of the other working fluids. After expansion, the *n*-pentane vapour exits the expander at above atmospheric pressure while all the other fluids exit at sub-atmospheric pressures and had their expander costs calculated with the low-pressure discharge expander correlation in Table 2. This in turn makes the cost of the *n*-pentane expander much lower than the rest.

We complete the analysis by considering the ‘rated costs’ for the optimal cycles, *i.e.*, cost per kilowatt of power generated ($\Sigma C_B/\dot{W}_{exp}$). This is done such that high power output fluids (especially the fluid mixtures) are not unnecessarily penalized. The rated costs of the optimal cycles are plotted in Figures 6a and 6b (RHS axes). As expected, the ORC system with *n*-pentane as the working fluid has the lowest rated cost (£1,370/kW) due to its very low expander cost compared to the other working fluids while the cycle with $x_{C_6H_{14}} = 0.5$ has the highest rated cost at £1,600/kW. For the R-245fa + R-227ea system, the ORC system with pure R-227ea has the lowest rated cost (£1,330/kW) while that with $x_{R-227ea} = 0.3$ has the highest rated cost. The previously identified, thermodynamically optimal fluid mixtures ($x_{C_6H_{14}} = 0.3$ and $x_{R-227ea} = 0.5$; see Figure 1) have cycle rated costs of £1,600/kW and £1,400/kW respectively. On the other hand, the cost optimal working fluids are *n*-pentane and R-227ea, which give rated cost reductions of 14% and 5% respectively over the thermodynamically optimal working fluids.

5. CONCLUSIONS

The first aim of this study was to investigate the thermodynamic benefits of employing working-fluid mixtures in organic Rankine cycle (ORC) systems, and a second aim was to examine the effects of selecting such mixtures on the sizes and costs of the resulting ORC engines. Two sets of fluid mixtures, namely *n*-pentane + *n*-hexane and R-245fa + R-227ea, were used for this investigation due to their common use in ORC installations. A low-temperature geothermal hot-water heat-source stream was considered. The thermodynamic optimization (maximum expansion power output) resulted in optimal working-fluid mixtures in both cases; the performance indices of these mixtures along with corresponding costs are summarized and compared with those of their constituent pure components in Table 3 below.

Table 3: Performance indices and costs of pure fluids and thermodynamically optimal mixtures

$x_{C_6H_{14}}$	\dot{W}_{exp} kW	PR -	VR -	A_{Ev} m ²	A_{Cn} m ²	$\Sigma C_B/\dot{W}_{exp}$ £/kW	x_{227ea}	\dot{W}_{exp} kW	PR -	VR -	A_{Ev} m ²	A_{Cn} m ²	$\Sigma C_B/\dot{W}_{exp}$ £/kW
0.0	79.3	3.42	3.45	8.11	12.1	1370	0.0	79.3	3.38	3.55	8.28	12.8	1400
0.3	88.3	4.51	4.50	10.1	16.6	1590	0.5	86.4	3.73	4.30	8.96	18.7	1390
1.0	79.0	4.15	4.09	7.91	11.7	1600	1.0	78.3	2.88	3.75	6.00	12.2	1330

The analyses revealed that the temperature glides of the working-fluid mixtures during evaporation and condensation resulted in higher power output and thermal/exergy efficiencies for fluid mixtures. Mixtures containing 30 mol% of *n*-hexane 50 mol% R-227ea had the highest output, more than either set of pure fluids. The pure fluids did however result in smaller expanders due to their low volumetric flow-rates and expansion ratios. Fluid mixtures appeared to have the largest evaporators and condensers, requiring more expensive heat exchangers than the pure fluids. Moreover, due to sub-atmospheric expansion, the expander costs in the case of the *n*-pentane + *n*-hexane working-fluid mixtures (and *n*-hexane) were much higher than those for pure *n*-pentane. Generally, equipment sizes and costs were larger for both set of mixtures than for the constituent pure fluids. Thus, the working-fluid mixtures would require larger plant layout areas, contributing significantly to their overall installation costs.

Although the mixtures were found to have the highest power output, they also had the highest rated cost (equipment cost per kilowatt power generated). On the other hand, ORC systems with pure *n*-pentane working had the lowest rated cost followed by those with *n*-hexane. For the case of R-245fa + R-227ea

working fluids, pure R-227ea had the lowest rated costs. These observations imply that the thermodynamic benefits derived from using the working-fluid mixtures may be outweighed by the increased costs incurred. The fact that these insights were only possible from a direct consideration of thermal and cost factors as exemplified here, underlines the importance of employing a combined thermodynamic, thermal and cost approach in the selection of optimal working-fluid (mixtures) for ORC systems.

REFERENCES

- Aghahosseini, S. and Dincer, I. (2013). Comparative performance analysis of low-temperature organic Rankine cycle (ORC) using pure and zeotropic working fluids. *Applied Thermal Engineering*, 54(1):35–42.
- Angelino, G. and di Paliano, P. C. (1998). Multicomponent working fluids for ORCs. *Energy*, 23(6):449–463.
- Beardsmore, G., Budd, A., Huddleston-Holmes, C., and Davidson, C. (2015). Country update—Australia. In *Proceedings World Geothermal Congress 2015*, pages 19–24.
- Braimakis, K., Leontaritis, A.-D., Preißinger, M., Karellas, S., Brüggeman, D., and Panopoulos, K. (2014). Waste heat recovery with innovative low-temperature ORC based on natural refrigerants. In *27th International Conference on Efficiency, Cost, Optimization, Simulation and Environmental Impact of Energy Systems*.
- Byrd, R., Hribar, M., and Nocedal, J. (1999). An interior point algorithm for large-scale nonlinear programming. *SIAM Journal on Optimization*, 9(4):877–900. doi: 10.1137/S1052623497325107; 26.
- Chen, H., Goswami, D. Y., Rahman, M. M., and Stefanakos, E. K. (2011). A supercritical Rankine cycle using zeotropic mixture working fluids for the conversion of low-grade heat into power. *Energy*, 36(1):549–555.
- Chys, M., van den Broek, M., Vanslambrouck, B., and Paepe, M. D. (2012). Potential of zeotropic mixtures as working fluids in organic Rankine cycles. *Energy*, 44(1):623–632.
- Dong, B., Xu, G., Cai, Y., and Li, H. (2014). Analysis of zeotropic mixtures used in high-temperature organic Rankine cycle. *Energy Conversion and Management*, 84(0):253–260.
- Garg, P., Kumar, P., Srinivasan, K., and Dutta, P. (2013). Evaluation of isopentane, R-245fa and their mixtures as working fluids for organic Rankine cycles. *Applied Thermal Engineering*, 51(1–2):292–300.
- Heberle, F., Preißinger, M., and Brüggemann, D. (2012). Zeotropic mixtures as working fluids in organic Rankine cycles for low-enthalpy geothermal resources. *Renewable Energy*, 37(1):364–370.
- Jung, D. S., McLinden, M., Radermacher, R., and Didion, D. (1989). Horizontal flow boiling heat transfer experiments with a mixture of R22/R114. *International Journal of Heat and Mass Transfer*, 32(1):131–145.
- Kunz, O. and Wagner, W. (2012). The GERG-2008 wide-range equation of state for natural gases and other mixtures: An expansion of GERG-2004. *Journal of Chemical & Engineering Data*, 57(11):3032–3091.
- Lampe, M., Kirmse, C., Sauer, E., Stavrou, M., Gross, J., and Bardow, A. (2014). Computer-aided molecular design of ORC working fluids using PC-SAFT. *Computer Aided Chemical Engineering*, 34(0):357–362.
- Lecompte, S., Ameel, B., Ziviani, D., van den Broek, M., and Paepe, M. D. (2014). Exergy analysis of zeotropic mixtures as working fluids in organic Rankine cycles. *Energy Conversion and Management*, 85:727–739.
- Lemmon, E. W., Huber, M. L., and McLinden, M. O. (2013). NIST standard reference database 23: Reference fluid thermodynamic and transport properties-REFPROP.
- Li, Y.-R., Du, M.-T., Wu, C.-M., Wu, S.-Y., and Liu, C. (2014). Potential of organic Rankine cycle using zeotropic mixtures as working fluids for waste heat recovery. *Energy*, 77(0):509–519.
- Oyewunmi, O. A., Taleb, A. I., Haslam, A. J., and Markides, C. N. (2014). An assessment of working-fluid mixtures using SAFT-VR Mie for use in organic Rankine cycle systems for waste-heat recovery. *Computational Thermal Sciences: An International Journal*, 6(4):301–316.
- Papadopoulos, A. I., Stijepovic, M., and Linke, P. (2010). On the systematic design and selection of optimal working fluids for organic Rankine cycles. *Applied Thermal Engineering*, 30(6–7):760–769.
- Sami, S. M. (2010). Energy and exergy analysis of new refrigerant mixtures in an organic Rankine cycle for low temperature power generation. *International Journal of Ambient Energy*, 31(1):23–32.
- Seider, W. D., Seader, J. D., and Lewin, D. R. (2009). *Product & Process Design Principles: Synthesis, Analysis And Evaluation*. John Wiley & Sons.
- Shin, J. Y., Kim, M. S., and Ro, S. T. (1996). Correlation of evaporative heat transfer coefficients for refrigerant mixtures. In *International Refrigeration and Air Conditioning Conference*, page 316.
- Shu, G., Gao, Y., Tian, H., Wei, H., and Liang, X. (2014). Study of mixtures based on hydrocarbons used in ORC (organic Rankine cycle) for engine waste heat recovery. *Energy*, 74(0):428–438.
- Wang, J. L., Zhao, L., and Wang, X. D. (2010). A comparative study of pure and zeotropic mixtures in low-temperature solar Rankine cycle. *Applied Energy*, 87(11):3366–3373.

INTEGRATED DESIGN OF WORKING FLUID MIXTURES AND ORGANIC RANKINE CYCLES (ORC) IN THE CONTINUOUS-MOLECULAR TARGETING (COMT) FRAMEWORK

Matthias Lampe¹, Peter Edel¹, Johannes Schilling¹, Joachim Gross², André Bardow^{1*}

¹ Chair of Technical Thermodynamics, RWTH Aachen University,
Schinkelstraße 8, 52062 Aachen, Germany
E-mail: andre.bardow@ltt.rwth-aachen.de

² Institute of Thermodynamics and Thermal Process Engineering, Stuttgart University,
Pfaffenwaldring 9, 70569 Stuttgart, Germany

* Corresponding Author

ABSTRACT

Organic Rankine Cycles (ORCs) provide power by exploiting low-temperature heat of renewable sources or waste heat. To enhance the efficiency of ORCs, binary mixtures have been proposed as working fluids. Using a working fluid mixture leads to a temperature glide during evaporation and condensation and thus to a better match between the temperature profile of the heat source and the working fluid. We present a method for the integrated optimization the working fluid mixture, i.e., its components and its composition, and the ORC process parameters. Mixture properties are calculated by the PC-SAFT equation of state. In our design framework, the so-called continuous-molecular targeting (CoMT), the pure component parameters are relaxed in the optimization to allow for a simultaneous optimization of the working fluid mixture and the process. However, the resulting optimal mixture components do in general not coincide with any real fluid. Real fluids are identified in the second step of the CoMT framework, the structure-mapping. In this paper, only the CoMT optimization is employed to quantify the potential benefit of working fluid mixtures. The results show that mixtures are not always thermodynamically beneficial and that their benefit depends on the conditions under which the ORC system is finally installed.

1. INTRODUCTION

Organic Rankine Cycles (ORCs) convert low-temperature heat to power. Typically, the exergy content of such sources is low. Thus, efficiency of the cycle is crucial. To enhance the power output, mixtures have been proposed as working fluids (Angelino and Colonna, 1998). Mixtures have a temperature glide, i.e., the temperature is not constant during the phase-change. Due to the temperature glide, a better match of the temperature profile of working fluid and (sensible) heat source is achieved (see figure 1). Better matching of heat source and working fluids is equivalent to less exergy destruction and thus thermodynamically favorable (Heberle et al., 2012). Therefore, zeotropic mixtures can enhance the efficiency of an ORC system (Angelino and Colonna, 1998; Wang and Zhao, 2009; Heberle et al., 2012). Also economically, mixtures were found to be outperforming pure components. Oyewunmi et al. (2014) state lower investment cost by 20 - 30 % when comparing a mixture to a pure component. However, the comparison of the performance of mixtures and pure working fluids might still be biased by the selection of reference pure working fluids and selection of mixtures for assessment. Only the comparison of optimal working fluid mixture to an optimal pure component enables an unbiased analysis.

The selection of an optimal pure component working fluid is already non-trivial (Quoilin et al., 2013; Bao and Zhao, 2013). The selection of an optimal working fluid *mixture* introduces further complexity. Approaches based on trial and error are prohibitive as the combinatorial nature of the problem cannot

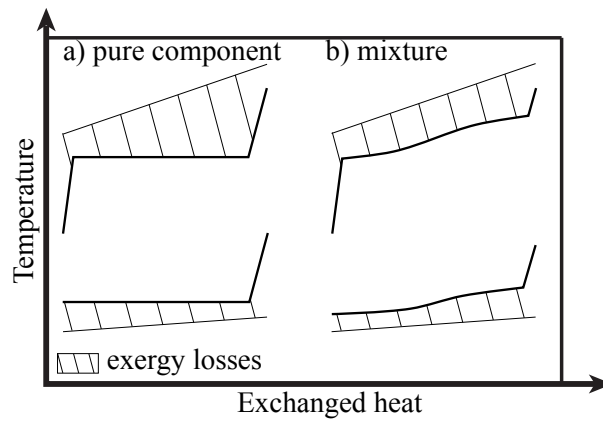


Figure 1: Comparison of the exergy loss during the heat exchange between heat source/sink (thin lines) and the working fluid (thick line), which is a) a pure fluid and b) a mixture. The inlet and outlet temperatures as well as the minimal approach temperature is kept constant. The hatched areas between heat source/sink and working fluid profile reflect the exergy loss due to heat transfer.

be tackled efficiently. Thus, systematic methods for the design of working fluid mixtures are needed (Molina-Thierry and Flores-Tlacuahuac, 2015). Based on their pioneering work for pure fluids (Papadopoulos et al., 2010), Papadopoulos et al. (2013) identify high-performance working fluid mixtures by computer-aided molecular design (CAMD). In their approach, the constituting equations enforcing the feasibility of the component are skipped for one component and an optimal second component is identified. The result is used to limit the search space for the second component and the problem is solved to identify a mixture. Mavrou et al. (2015) compared the resulting mixtures to other proposed mixtures and confirm that the designed mixtures perform better. Furthermore, methods have been developed to select a mixture from a database of components by genetic algorithms (Andreasen et al., 2014).

The continuous-molecular targeting computer-aided molecular design (CoMT-CAMD) framework developed by the authors enables the selection of an optimal working fluid by simultaneously optimizing working fluid and process parameters (Lampe et al., 2014b). Due to the discrete nature of working fluid selection, the simultaneous optimization would lead to a mixed-integer nonlinear program (MINLP) of prohibitive size and complexity. In CoMT-CAMD, the simultaneous optimization is still achieved by exploiting the PC-SAFT equation of state (Gross and Sadowski, 2001, 2002). In PC-SAFT, each working fluid is represented by a set of pure component parameters. These pure component parameters are relaxed to continuous values during the optimization. The relaxation allows for optimization of working fluid and process in a single nonlinear program (NLP). The optimization in the relaxed search-space is the first step of CoMT-CAMD, the continuous-molecular targeting (CoMT). The resulting set of optimal pure component parameters does in general not coincide with the pure component parameters of any real working fluid. Real working fluids are identified in a second step, the so-called structure-mapping. The structure-mapping can be based on a database of existing fluids (Lampe et al., 2014b) or novel working fluids can be generated using CAMD (Lampe et al., 2014a). The CoMT-CAMD framework has also been applied successfully to solvent selection (Bardow et al., 2010; Stavrou et al., 2014).

In this paper, the CoMT-step of the framework is extended for the optimization of binary working fluid mixtures. The extension of the framework allows for the design of an optimal working fluid mixture simultaneously with the optimization of the process itself. The mixture components, the composition and the key process parameters are the degrees of freedom for the optimization. In section 2, the formulation of the integrated mixture and process design is introduced. The continuous-molecular targeting framework is used to identify the optimal working fluid mixture. The resulting optimal hypothetical mixture is compared to the result of the same optimization for a pure component in a case-study (sec. 3). The optimal hypothetical mixture and the hypothetical pure component fluid provide an upper bound on the possible performance for real fluids. Thus, the comparison of an optimal working fluid mixture

to an optimal pure working fluid allows to quantify the potential benefit of employing a working fluid mixture. The results show that mixtures are not always beneficial and that their benefit depends on the conditions under which the ORC system is finally installed.

2. GENERAL PROBLEM FOR WORKING FLUID MIXTURE OPTIMIZATION

In the continuous-molecular targeting, the working fluid mixture and the process are optimized simultaneously. For the formulation of the optimization problem, a generic model of the process is employed.

$$\begin{aligned}
 \min_{x, z_1, z_2, x_{\text{wf}}} \quad & f(x, \theta) && \text{objective function} \\
 \text{s.t.} \quad & g_1(x, \theta) \leq 0 && \text{process model inequalities} \\
 & g_2(x, \theta) = 0 && \text{process model equalities} \\
 & \theta = h(x, z_1, z_2, x_{\text{wf}}) && \text{PC-SAFT} \\
 & A z_1 \leq b && \text{convex hull (fluid 1)} \\
 & A z_2 \leq b && \text{convex hull (fluid 2)} \\
 & x_{\min} \leq x \leq x_{\max} \in \mathbb{R}^n && \text{process variables} \\
 & 0 \leq x_{\text{wf}} \leq 1 \in \mathbb{R} && \text{mixture composition} \\
 & z_{\min} \leq z_1, z_2 \leq z_{\max} \in \mathbb{R}^m && \text{mixture components.}
 \end{aligned} \tag{1}$$

The process model comprises an objective $f(x, \theta)$ (e.g. net power output, efficiency, or second law efficiency) as well as inequality and equality constraints $g_1(x, \theta)$ and $g_2(x, \theta)$, respectively. The process model depends on two vectors of variables: the optimized process parameters x (e.g., mass flow rate, or pressure level) and thermo-physical properties of the working fluid θ (e.g., enthalpies, or entropies of each state point). The thermo-physical properties θ are calculated by PC-SAFT ($\theta = h(x, z_1, z_2, x_{\text{wf}})$). In PC-SAFT, binary mixtures are defined by their composition x_{wf} and two sets of pure component parameters z_1 and z_2 . For the optimized process parameters, bounds can be derived based on the application of the ORC system (e.g., upper and lower pressure level). To limit the search space of the pure component parameters z_i , we construct a convex hull around a database of known pure components. The convex hull yields a set of linear constraints $A z_i \leq b$ for both of the mixture components. Thus, the complete search space of working fluids is feasible for each component.

The simultaneous optimization of mixture and process in eq. (1) identifies the optimal process parameters x^* as well as an optimal working fluid mixture represented by the components z_i^* and the composition x_{wf}^* . The optimization is performed as one single nonlinear program and no discrete degrees of freedom are introduced. However, the resulting optimal mixture components z_i^* do in general not coincide with any real fluid. Real fluids are identified in the second step of the CoMT-CAMD framework, the structure-mapping. In this paper, only the first step of the method is employed. This CoMT step does not identify real components, but yields an upper bound for the performance of any working fluid mixture, as the relaxed problem contains all discrete solutions.

Optimization problem (1) is a nonconvex NLP. In nonconvex problems, multiple local minima can occur. In fact, the search space is symmetric in the compounds of the mixture and thus there at least are two globally optimal solutions, which both represent the same mixture: For any combination of two components z_1 and z_2 , and their composition x_{wf} , an identical symmetric solution can be obtained by exchanging the fluids (i.e., $\bar{z}_1 = z_2$ and $\bar{z}_2 = z_1$) and adapting the composition (i.e., $\bar{x}_{\text{wf}} = 1 - x_{\text{wf}}$). The symmetry of the search space can be prevented by a symmetry breaking constraint, e.g., bounding the mixture composition to $x_{\text{wf}} \leq 0.5$. Symmetry breaking constraints should be employed when global optimization is used to speed up the optimization (Liberti and Ostrowski, 2014). For local search algorithms, symmetry breaking constraints are not always beneficial (Prestwich and Roli, 2005), as additional local minima can be introduced to the problem. In this work, optimization is performed using sequential quadratic programming (SQP) implemented in Matlab (2012) based on (Han, 1977; Powell, 1978, 1979)

Table 1: Specification of the heat source for the generic example.

Parameter	Symbol	Value
heat source mass flow rate	\dot{m}_{HS}	50 $\frac{\text{kg}}{\text{s}}$
heat source specific heat capacity	$c_{p,\text{HS}}$	4.185 $\frac{\text{kJ}}{\text{kg K}}$
heat source inlet temperature	$T_{\text{in,HS}}$	270 °C

on a standard desktop PC (Core i5 CPU, 1.7 GHz with 4 GB RAM) using the default settings. To prevent the solver from converging to a local optimum, different starting values have been used.

3. ILLUSTRATIVE EXAMPLE

The comparison of mixtures of existing working fluids to existing pure components in the literature shows advantages for the mixtures compared to pure components. However, this comparison can be misleading when a good mixture is compared to a bad pure component. Eq. (1) yields an optimal hypothetical mixture and the corresponding process parameters. The same optimization can be performed for a pure working fluid by enforcing a composition of $x_{\text{wf}} = 0$. This allows for the identification of an optimal hypothetical pure working fluid. The results of both optimizations can be used for a unbiased assessment of the potential benefit of mixtures.

To assess the potential of mixtures, a generic example of an ORC system is used. Changing the model for the cooling of the cycle allows to identify how the cold side effects the optimal mixture. A recuperated ORC is considered. The minimal temperature difference to heat source and heat sink are $\Delta T_{\text{min}} = 0$ K. The heat source is defined by a mass flow rate of hot water (see table 1). The degrees of freedom x for the process are the pressure levels for evaporation p_{evap} and condensation p_{cond} as well as the mass flow rate of working fluid \dot{m}_{wf} . The system is optimized for an optimal net power output

$$P_{\text{net}} = \dot{m} [(h_4 - h_5) - (h_2 - h_4)] ,$$

where the enthalpies are calculated assuming boiling liquid after the condenser (state 1) and saturated steam after the evaporator (state 4). To calculate the enthalpy after the turbine (state 5) and after the pump (state 2), constant isentropic efficiencies of turbine and condenser are assumed ($\eta_{\text{T}} = \eta_{\text{P}} = 0.85$). For the recuperator, a minimal approach temperature of $\Delta T_{\text{min}}^{\text{regen}} = 30$ °C is assumed.

For the cooling of the system, different options and model formulations are employed in the following to demonstrate their effect on the optimal working fluid mixture.

3.1 Constant Cooling Temperature

The most simple model of a cooling system assumes a constant lower temperature limit. The lower limit is selected according to a considered cooling system. For this example, a lower temperature limit of 70 °C is considered. Eq. (1) is used to optimize two sets of pure component parameters z_1 and z_2 as well as the optimal mixture composition x_{wf} .

For a constant cooling temperature, the resulting optimal mixture is basically a pure component ($x_{\text{wf}}^* = 0.005$). The illustration of the cycle in a T,h-diagram in figure 2 allows to identify the properties of the working fluid leading to optimality: The working fluid is fitted optimally between the temperature profiles of the heat source and heat sink. As the lower temperature level is constrained by a constant temperature, the temperature glide of a mixture cannot be exploited for the condensation (states 5'-1). For the heating of the system, working fluid and mass flow rate are selected to allow for a minimal temperature difference in the preheating (states 2'-3). This combination of the practically pure working fluid and process is not the most efficient cycle, regarding thermal efficiency. The deficit in efficiency is overcome by matching preheating and heat source such that the heat source is cooled down as far as possible. Thus, the cycle is optimal with respect to the net power output.

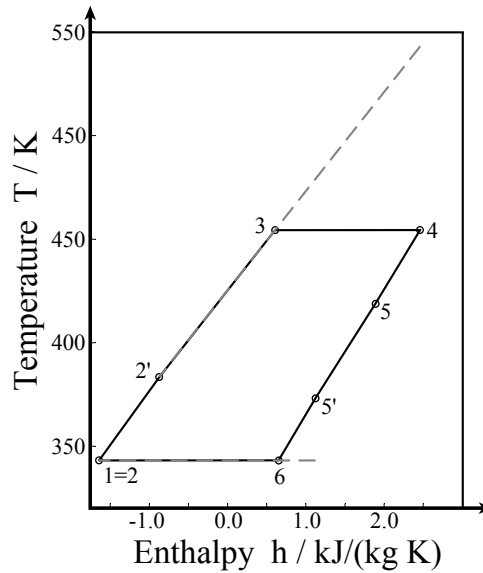


Figure 2: Resulting ORC from the CoMT-optimization for a constant lower temperature limit.

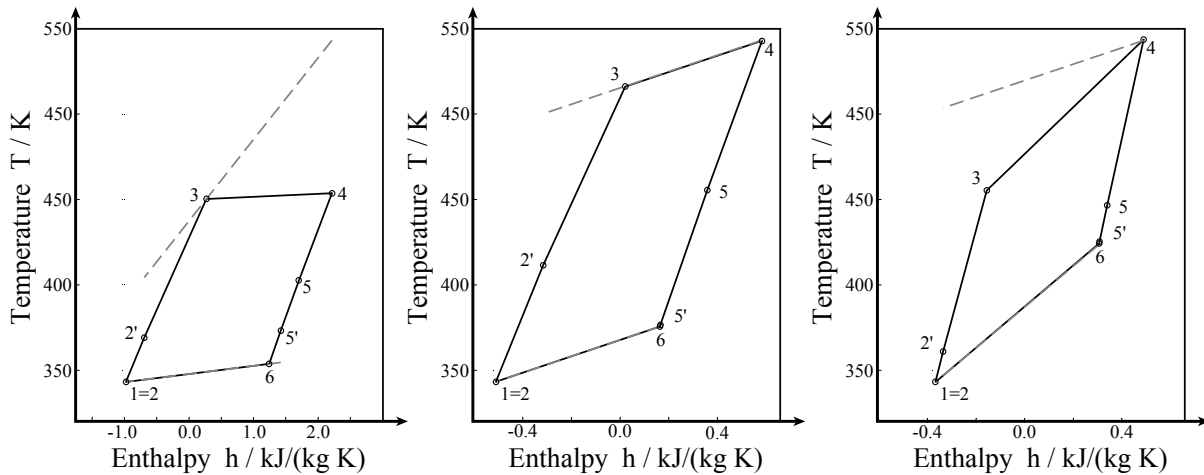


Figure 3: Resulting ORC from the CoMT-optimization for a cooling source with constant mass flow rate of a) $500 \frac{\text{kg}}{\text{s}}$, b) $50 \frac{\text{kg}}{\text{s}}$ and c) $20 \frac{\text{kg}}{\text{s}}$.

The assumption of a constant lower temperature limit leads to the identification of a pure working fluid: due to the constant lower temperature of the cooling system, a pure working fluid already enables an optimal match for a constant lower temperature limit. The effect of a sensible heat carrier in the cooling system is considered in the following.

3.2 Fixed Mass Flow Rate of Cooling Agent

In this section, the cooling system is modeled in the same way as the heat source; i.e., a mass flow rate of cooling agent is supplied with a specified temperature. Three different mass flow rates are assessed to show the effect of a variation of the value of this parameter ($500 \frac{\text{kg}}{\text{s}}$, $50 \frac{\text{kg}}{\text{s}}$, and $20 \frac{\text{kg}}{\text{s}}$). The value of $50 \frac{\text{kg}}{\text{s}}$ corresponds to the same heat capacity flow rate ($\dot{m} c_p$)_{HS} as for the heat source.

In figure 3a, the result of the optimization is shown for a flow rate of $\dot{m}_{CS} = 500 \frac{\text{kg}}{\text{s}}$. The result is a mixture with a composition of $x_{wf} = 0.29$ (see table 2). The temperature glide follows the cooling agent exactly. To enable the perfect match of cooling agent and working fluid the condensation pressure p_{cond} and the mass flow rate \dot{m}_{wf} are selected to the according values. The evaporation pressure p_{evap} is chosen to exploit the minimal allowed temperature difference to the heat source.

Table 2: Resulting mixtures from the CoMT-optimization for different mass flow rates of cooling agent

Parameter	Unit	Values		
\dot{m}_{CS}	$\frac{\text{kg}}{\text{s}}$	500	50	20
x_{wf}	—	0.29	0.1	0.16
m_1	—	1.84	1.91	1.85
σ_1	\AA	3.41	4.32	4.15
$(\frac{\epsilon}{k})_1$	K	503	489	543
m_2	—	2.04	1.84	1.84
σ_2	\AA	4.36	3.91	3.32
$(\frac{\epsilon}{k})_2$	K	392	400	392
p_{evap}	bar	1.26	8.68	5.13
p_{cond}	bar	0.05	0.13	0.25
\dot{m}_{wf}	$\frac{\text{kg}}{\text{s}}$	57.0	15.2	12.5

The results for the varied mass flow of cooling source are similar to this result (figures 3b and 3c). The cooling agent is dominating the value for the temperature glide, regardless of the heat source properties. The optimal match of cooling agent and working fluid leads to a thermodynamically optimal cycle. However, only a comparison based on an economic objective function would give a final answer to the question, if mixtures can outperform pure components: the optimal cycles in this and the previous section exploit a perfect match of working fluid and cooling agent in the condenser. This leads to low temperature differences for the heat transfer and accordingly to large required heat exchange area. The larger heat exchange area might lead to prohibitive investment cost to employ the cycle in a ORC system.

3.3 Modeling of an Air-Cooled System

The comparison based on a constant mass flow rate of cooling agent in section 3.2 might lead to the conclusion that mixtures are performing better for real ORC systems. However, the assumption of a constant mass flow rate of the cooling agent might still be misleading. Besides the negative effect on the heat exchange area, the assumption of a constant mass flow rate of cooling agent is not valid for many applications: When an air-cooled system is employed, the amount of air for cooling the system is not limited by any constraint, in general. The amount of air that is fed to the system results from a tradeoff between cost for the compression of the air and the effectiveness of the cooling-system.

To reflect this tradeoff, a model for the compressor of an air-cooled system is employed. The model is based on a constant isentropic efficiency of the compressor $\eta_{\text{comp}} = 0.75$. The mass flow rate of cooling agent is assumed to be the minimal mass flow rate allowing for the cooling of the cycle. Thus, effort for cooling at lower temperatures is considered in the optimization. The air is entering the compressor at $T_{\text{air, in}} = 15 \text{ }^\circ\text{C}$ and fed to an heat exchanger. The pressure drop to be overcome by the compressor is $\Delta p = 0.01 \text{ bar}$.

Under these conditions, the CoMT optimization results in a mixture (figure 4a and table 3). The optimal process has a lower temperature than the previous cases. The lower temperature is feasible, as the constraint on the lower temperature is less restrictive. A moderate temperature glide is employed (see figure 4a). The net power output optimal mixture with the optimal process is $P_{\text{net}} = 2.76 \text{ MW}$.

For an assessment of the effect of mixtures on the performance of the cycle, the optimization is performed for pure component working fluids. The optimal mixture and an optimal pure component are compared. Thus, the comparison is unbiased by the selection of a specific mixture and a set of pure components.

The result of the CoMT-optimization for the pure component is similar to the result of the mixture optimization (see figure 4b). The optimal pure component has pure component parameters close to com-

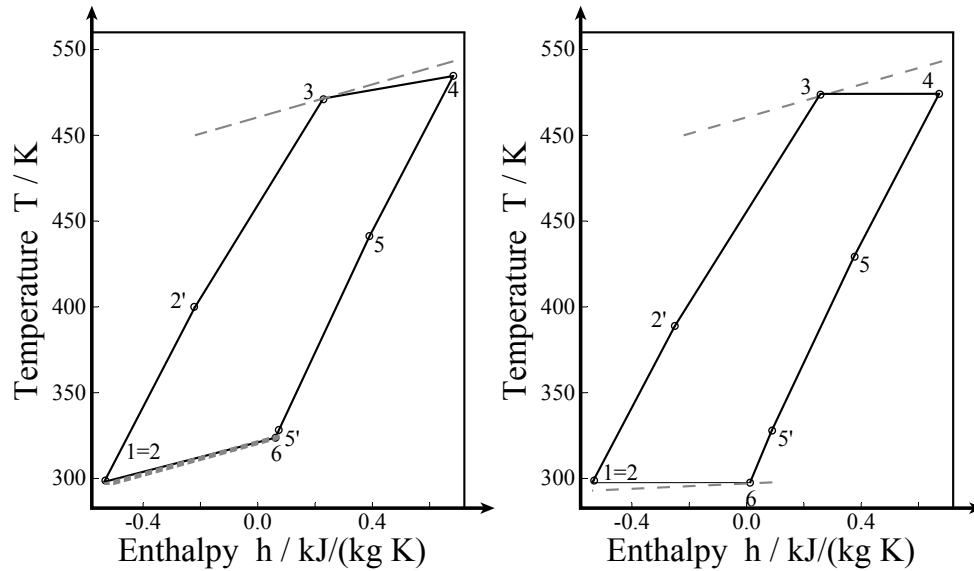


Figure 4: a) Result of the CoMT-optimization employing a model of and air-cooling system. b) Result of the CoMT-optimization for a pure component employing a model of and air-cooling system.

ponent 1 from the optimal mixture (table 3). The net power output of the pure component cycle is $P_{\text{net}} = 2.69$ MW. Thus, the net power output is only 3 % lower than the value for the optimal mixture.

4. SUMMARY

The CoMT method for the integrated optimization of working fluid and process is extended to the design of working fluid mixtures. The optimization was applied successfully to the identification of optimal mixtures under different specifications for the application.

The hypothetical optimal mixture results in a optimal match of the heat transfer profile of the working fluid and the cooling agent in all examples. For a constant temperature of the cooling agent, the optimal working fluid is a pure component. When the mass flow rate of the cooling agent is constant, mixtures are preferable due to their ability to adapt to the temperature profile of the cooling agents.

Overall, the results show that pure component working fluids are competitive with mixtures and indeed optimal in some cases. By employing a model of the cooling system, the trade-off between the efficiency of the cycle and power consumption of the cooling system is reflected. For this case, a mixture is the

Table 3: Results of the CoMT-optimization using an air-cooled system.

Parameter	Unit	Pure component	mixture
x_{wf}	—	-	0.1
m_1	—	1.84	1.84
σ_1	$\dot{\text{A}}$	5.21	5.18
$(\frac{\epsilon}{k})_1$	K	519	543
m_2	—	—	1.89
σ_2	$\dot{\text{A}}$	—	4.35
$(\frac{\epsilon}{k})_2$	K	—	400
p_{evap}	bar	6.79	6.43
p_{cond}	bar	0.01	0.01
\dot{m}_{wf}	$\frac{\text{kg}}{\text{s}}$	14.5	14.6

optimal solution. However, the difference to the optimal pure component working fluid is below 3 %. For the construction of a real ORC system, the small difference might favor the selection of a pure component for simplicity of the system design.

The comparison of mixtures to pure working fluids indicates that there are pure components that can compete with mixtures in terms of thermodynamical performance. Still, economic criteria will decide in practice about the use of working fluid mixtures. Thus, economic criteria should be included in the analysis in future work.

REFERENCES

- Andreasen, J. G., Larsen, U., Knudsen, T., Pierobon, L., and Haglind, F. (2014). “Selection and optimization of pure and mixed working fluids for low grade heat utilization using organic Rankine cycles”. *Energy*, 73:204–213.
- Angelino, G. and Colonna, P. d. P. (1998). “Multicomponent Working Fluids For Organic Rankine Cycles (ORCs)”. *Energy*, 23(6):449–463.
- Bao, J. and Zhao, L. (2013). “A review of working fluid and expander selections for organic Rankine cycle”. *Renewable and Sustainable Energy Reviews*, 24:325–342.
- Bardow, A., Steur, K., and Gross, J. (2010). “Continuous-Molecular Targeting for Integrated Solvent and Process Design”. *Industrial & Engineering Chemistry Research*, 49(6):2834–2840.
- Gross, J. and Sadowski, G. (2001). “Perturbed-Chain SAFT: An Equation of State Based on a Perturbation Theory for Chain Molecules”. *Industrial & Engineering Chemistry Research*, 40(4):1244–1260.
- Gross, J. and Sadowski, G. (2002). “Application of the Perturbed-Chain SAFT Equation of State to Associating Systems”. *Industrial & Engineering Chemistry Research*, 41(22):5510–5515.
- Han, S. P. (1977). “A globally convergent method for nonlinear programming”. *Journal of Optimization Theory and Applications*, 22(3):297–309.
- Heberle, F., Preißinger, M., and Brüggemann, D. (2012). “Zeotropic mixtures as working fluids in Organic Rankine Cycles for low-enthalpy geothermal resources”. *Renewable Energy*, 37(1):364–370.
- Lampe, M., Kirmse, C., Sauer, E., Stavrou, M., Gross, J., and Bardow, A. (2014a). “Computer-aided Molecular Design of ORC Working Fluids using PC-SAFT”. In Eden, M. R., Siirola, J. D., and Towler, G., editors, *Proceedings of the 8th International Conference on Foundations of Computer-Aided Process Design*, volume 34 of *Computer Aided Chemical Engineering*, pages 357–362. Elsevier Science, Burlington.
- Lampe, M., Stavrou, M., Bücker, H. M., Gross, J., and Bardow, A. (2014b). “Simultaneous Optimization of Working Fluid and Process for Organic Rankine Cycles Using PC-SAFT”. *Industrial & Engineering Chemistry Research*, 53(21):8821–8830.
- Liberti, L. and Ostrowski, J. (2014). “Stabilizer-based symmetry breaking constraints for mathematical programs”. *Journal of Global Optimization*, 60(2):183–194.
- Matlab (2012). *The MathWorks Inc., R2012b (8.0.0.783), 32-bit*.
- Mavrou, P., Papadopoulos, A. I., Stijepovic, M. Z., Seferlis, P., Linke, P., and Voutetakis, S. (2015). “Novel and conventional working fluid mixtures for solar Rankine cycles: Performance assessment and multi-criteria selection”. *Applied Thermal Engineering*, 75:384–396.

- Molina-Thierry, D. P. and Flores-Tlacuahuac, A. (2015). “Simultaneous Optimal Design of Organic Mixtures and Rankine Cycles for Low-Temperature Energy Recovery”. *Industrial & Engineering Chemistry Research*, 54(13):3367–3383.
- Oyewunmi, O. A., Taleb, A. I., Haslam, A. J., and Markides, C. N. (2014). “An Assessment of Working-Fluid Mixtures Using SAFT-VR MIE for Use in Organic Rankine Cycle Systems for Waste-Heat Recovery”. *Computational Thermal Sciences: An International Journal*, 6(4):301–316.
- Papadopoulos, A. I., Stijepovic, M. Z., and Linke, P. (2010). “On the systematic design and selection of optimal working fluids for Organic Rankine Cycles”. *Applied Thermal Engineering*, 30(6-7):760–769.
- Papadopoulos, A. I., Stijepovic, M. Z., Linke, P., Seferlis, P., and Voutetakis, S. (2013). “Toward Optimum Working Fluid Mixtures for Organic Rankine Cycles using Molecular Design and Sensitivity Analysis”. *Industrial & Engineering Chemistry Research*, 52(34):12116–12133.
- Powell, M. J. D. (1978). “A fast algorithm for nonlinearly constrained optimization calculations”. In Watson, G., editor, *Numerical Analysis*, volume 630 of *Lecture Notes in Mathematics*, pages 144–157. Springer Berlin Heidelberg.
- Powell, M. J. D. (1979). “Variable metric methods for constrained optimization”. In Glowinski, R., Lions, J., and Laboria, I., editors, *Computing Methods in Applied Sciences and Engineering, 1977, I*, volume 704 of *Lecture Notes in Mathematics*, pages 62–72. Springer Berlin Heidelberg.
- Prestwich, S. and Roli, A. (2005). “Symmetry Breaking and Local Search Spaces”. In Barták, R. and Milano, M., editors, *Integration of AI and OR Techniques in Constraint Programming for Combinatorial Optimization Problems*, volume 3524 of *Lecture Notes in Computer Science*, pages 273–287. Springer Berlin Heidelberg.
- Quoilin, S., Broek, Martijn Van Den, Declaye, S., Dewallef, P., and Lemort, V. (2013). “Techno-economic survey of Organic Rankine Cycle (ORC) systems”. *Renewable and Sustainable Energy Reviews*, 22:168–186.
- Stavrou, M., Lampe, M., Bardow, A., and Gross, J. (2014). “Continuous Molecular Targeting–Computer-Aided Molecular Design (CoMT–CAMD) for Simultaneous Process and Solvent Design for CO₂ Capture”. *Industrial & Engineering Chemistry Research*, 53(46):18029–18041.
- Wang, X. D. and Zhao, L. (2009). “Analysis of zeotropic mixtures used in low-temperature solar Rankine cycles for power generation”. *Solar Energy*, 83(5):605–613.

A REVIEW OF POTENTIAL WORKING FLUIDS FOR LOW TEMPERATURE ORGANIC RANKINE CYCLES IN WASTE HEAT RECOVERY

Jason R. Juhasz, Luke D. Simoni, PhD

The Chemours Company, LLC.
Wilmington, Delaware, USA
jason.r.juhasz@chemours.com
luke.d.simoni@chemours.com

presented by Claus-Peter Keller, Chemours Deutschland GmbH, claus-peter.keller@chemours.com

ABSTRACT

The focus of this paper will be specific to working fluids for use in various technologies for waste heat recovery (WHR) of exhaust heat including internal combustion engines (ICE) and in the use of Organic Rankine Cycles (ORC). Several novel fluids have been developed (DR-2 or HFO-1336mzz(Z) and DR-12) which have a good potential fit for these low temperature heat recovery applications (up to 250°C) and they have been characterized as having desirable working fluid properties such as good safety classification and environmental footprint. Additional properties from an ORC system, where mechanical systems are incorporated, are good thermal stability, chemical compatibility, material compatibility and thermodynamic performance. These systems must be reliable and therefore the interactions with the working fluids are paramount as design basis becomes an important attribute in the development of ORC components. The aforementioned HFO fluids will be assessed on the criteria mentioned to help identify their candidacy in using them in heat recovery technology platform, where interest is specifically ORC based. These novel HFO fluids provide a good alternative to existing working fluids currently under consideration with an added advantage of meeting low GWP regulations.

1. INTRODUCTION

The need to improve energy efficiency and fuel utilization efficiency has been a topic of discussion for the last couple of decades, the direction of integrating heat recovery systems in truck, marine, geothermal, biomass and waste heat from other various heat sources are progressively being adopted to help address this concern. In all of these applications, there are an array of potential different classes of working fluids, CFCs, HCFCs, PFCs, siloxanes, alcohols, hydrocarbons, ethers, amines, fluids mixtures, HCFOs and HFOs, which can be considered for use in ORCs and should be evaluated on a broad basis in order to identify the ideal working fluid for the desired system.

In recent years, an increased scrutiny has been placed on the environmental aspect of these fluids and regulatory pressures are driving global awareness of their impact on the environment. The ozone depletion potential (ODP) and greenhouse gas emissions (GHG) are of particular interest here and emphasis has been placed on choosing a working fluid which demonstrates an ability to meet these climate protection initiatives. When reviewing the various classes of working fluids listed above, certain characteristics will become unviable and as a result, CFCs and PFCs will not be evaluated due to their ODP and high GWP concerns, respectively. The ethers present another concern around

reactivity and stability; the amines have been shown to have major toxicological effects, therefore these components were deemed to be outside the scope of good working fluids.

Within these classes of potential viable working fluids, a select few are provided to show their basic characteristics so a further discussion on relevant use in applications can be made more constructive. Additionally, the novel hydrofluoro-olefin (HFO) based fluids (DR-2 and DR-12) will be discussed as they have been developed specifically to address these concerns as well as having of other favorable characteristics such as being non-flammable and low toxicity concerns.

2. FLUID CHARACTERIZATION FOR LOW TEMPERATURE ORC

2.1 Simple Organic Rankine Cycles

The primary aim in identifying feasibility of working fluids for ORC system rests on conducting a thermodynamic analysis where the cycle configuration is an important variable. Determining the cycle performance is dependent on having precise evaporating and condensing temperatures combined with fluid properties (latent heat of vaporization, temperature, pressure, entropy, enthalpy and liquid and gas densities) and using these variables to determine expander output, required pumping power, net cycle efficiencies, mass flow rates and turbine size parameters for the fluids of interest. Without knowing exact system configurations, it is difficult to assess one fluid's benefits over another so temperature-entropy diagram and vapor pressure versus temperature curve will be provided for selected fluids as a general guideline. The properties shown in *Figures 1 through 3* were calculated by REFPROP and CoolProp software, where each fluid and their respective EOS used are referenced in *Table 1*.

Table 1. EOS reference for Working Fluids using REFPROP and CoolProp

	program/ method	EOS reference:
HCFC-123 (R-123)	REFPROP	Younglove, B.A. and McLinden, M.O., "An International Standard Equation of State for the Thermodynamic Properties of Refrigerant 123 (2,2-Dichloro-1,1,1-trifluoroethane)," J. Phys. Chem. Ref. Data, 23:731-779, 1994.
HFC-134a (R-134a)	REFPROP	Tillner-Roth, R. and Baehr, H.D., "An international standard formulation of the thermodynamic properties of 1,1,1,2-tetrafluoroethane (HFC-134a) for temperatures from 170 K to 455 K at pressures up to 70 MPa," J. Phys. Chem. Ref. Data, 23:657-729, 1994.
HFC-245fa (R-245fa)	REFPROP	"Short Fundamental Equations of State for 20 Industrial Fluids," J. Chem. Eng. Data, 51:785-850, 2006.
DR-12	REFPROP	Peng-Robinson by Pavan Naicker
DR-2	REFPROP	Created at DuPont Based on Experimental Fit of PR-EOS - P. Naicker
SES36	CoolProp	Unpublished report: Monika Thol, Eric W. Lemmon, Roland Span, "Equation of State for a Refrigerant Mixture of R365mfc (1,1,1,3,3-Pentafluorobutane) and Galden [®] HT 55 (Perfluoropolyether)" https://github.com/ibell/coolprop/blob/master/CoolProp/pseudopurefluids/SES36.cpp
HCFO-1233zdE	REFPROP	"Thermodynamic Properties of Trans-1-chloro-3,3,3-trifluoropropene (R1233zd(E)): Vapor Pressure, p-rho-T Data, Speed of Sound Measurements
HMDSO	REFPROP	Multiparameter Equations of State for Selected Siloxanes, Fluid Phase Equilibria, 244:193-211, 2006.
Ethanol	REFPROP	A New Fundamental Equation for Ethanol, Master's Thesis, University of Idaho, 2011.
Toluene	REFPROP	Lemmon, E.W. and Span, R., "Short Fundamental Equations of State for 20 Industrial Fluids," J. Chem. Eng. Data, 51:785-850, 2006.
n-Pentane	REFPROP	Span, R. and Wagner, W. "Equations of State for Technical Applications. II. Results for Nonpolar Fluids," Int. J. Thermophys., 24(1):41-109, 2003.
	REFPROP:	Lemmon, E.W., Huber, M.L., McLinden, M.O. NIST Standard Reference Database 23: Reference Fluid Thermodynamic and Transport Properties-REFPROP, Version 9.1, National Institute of Standards and Technology: Standard Reference Data Program, Gaithersburg, 2013.
	CoolProp:	http://www.coolprop.org/citation.html

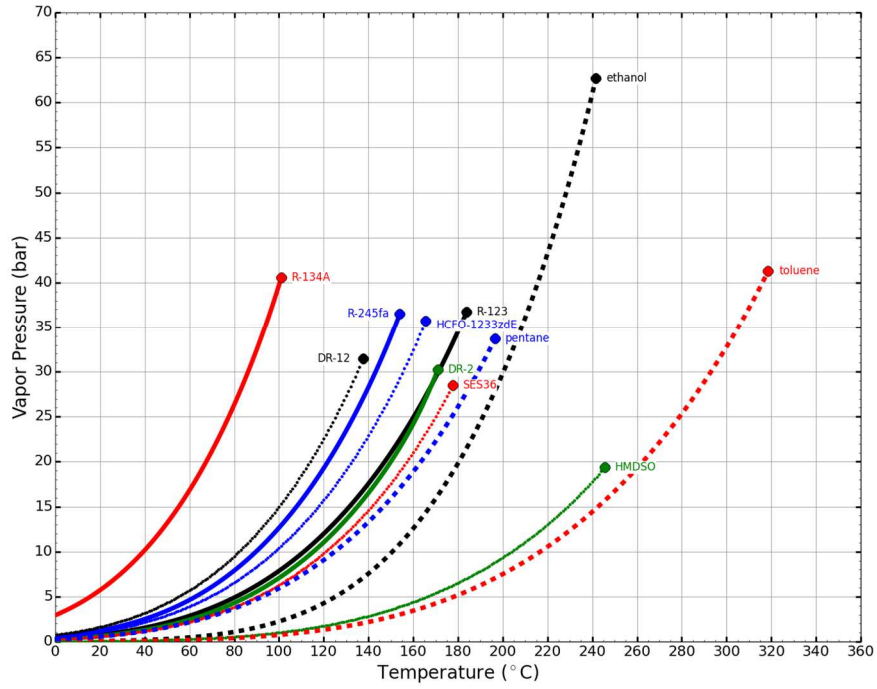


Figure 1. Vapor Pressure of Selected Working Fluids for Comparison

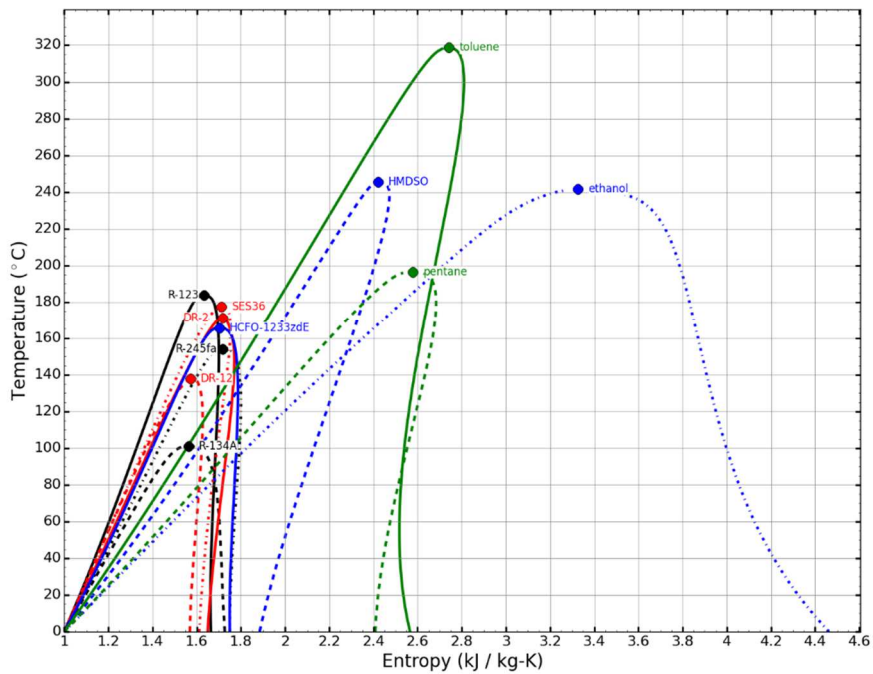


Figure 2. Temperature-Entropy Diagram for Selected Working Fluids for Comparison

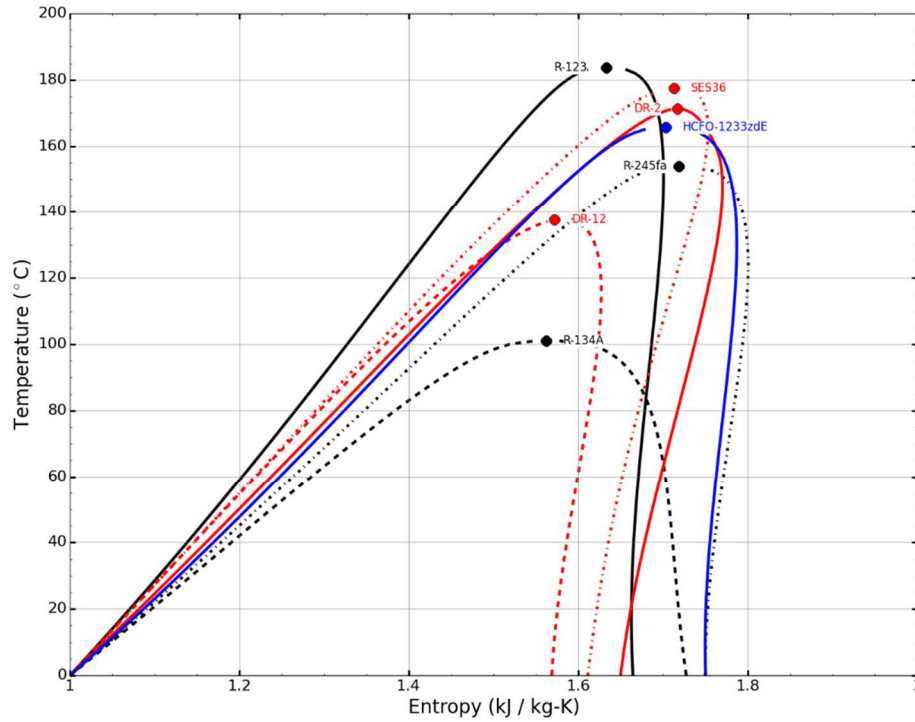


Figure 3. Enlarged Region of Temperature-Entropy diagram for Selected Working Fluids

Examples for Simple Organic Rankine Cycles systems are shown below and *Figure 5* illustrates heat being captured from the exhaust of internal combustion engine (Dupachy *et al.*, 2009).

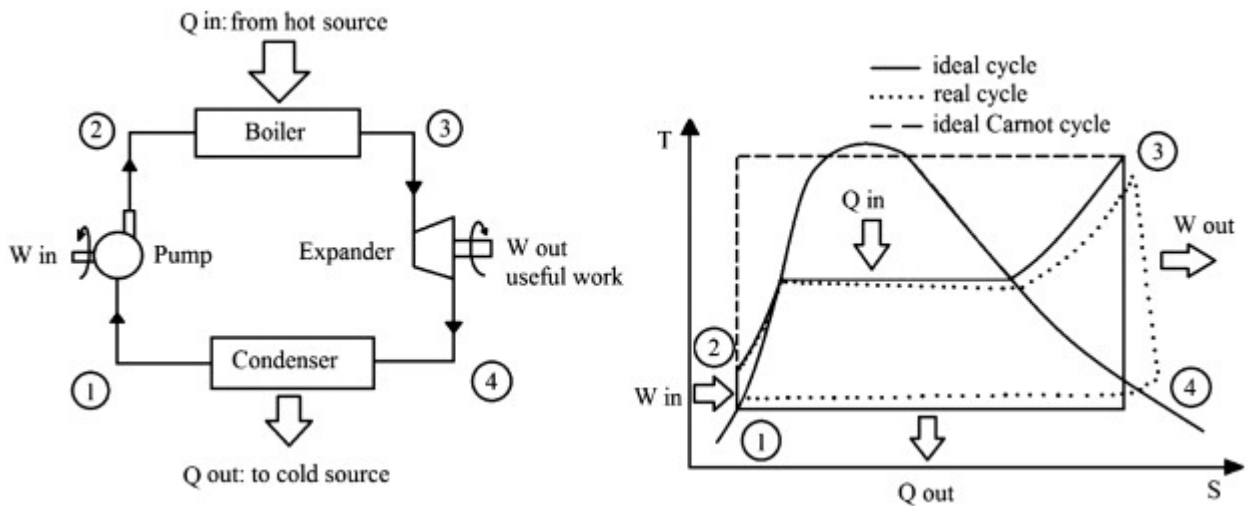


Figure 4. Rankine Cycle System

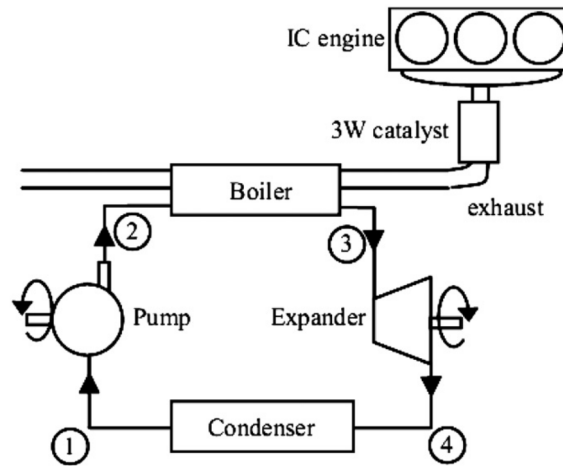


Figure 5. Layout of the waste heat recovery Rankine bottom cycle

Basic component selection for the expanders, pumps and heat exchangers is based on understanding the thermodynamics properties of the working fluids; however, there are other properties which can be overlooked which could be just as critical when selecting a fluid (safety, thermal stability, chemical and material compatibility, viscosity, etc.). These properties could influence reliability, the material construction – plastics, elastomers and metals as well as the robustness of the system where higher operating pressures and/or corrosion potential exists. From the refrigeration industry, many guidelines have been developed to address the safety management piece around the safe handling, storing and personnel exposure. Additional agencies such as NFPA, DOT, CFR, OSHA and TDG have placed many restrictions pertaining to the safe practice of toxic and flammable fluids and thus impose limitation which can affect a distribution and service facilities in terms of cost for electrical classification, breathing apparatuses and/or other infrastructure needs.

2.2 Working Fluids

An effective way to screen out potential working fluid candidates can be an arduous task where emphasis of thermodynamic performance may be deemed as the most important element. Even though this is true, aspects such as flammability and toxicity affect the ability to safely work with the fluids in a given environment. Additionally, ODP and GWP are becoming a growing concerns as environmental restrictions and regulations may be imposed and ultimately negate the use of certain compounds (potential working fluids) as more friendly alternative fluids come into existence. In *Table 2* below, an overview of working fluids are provide to differentiate each based on physical properties, toxicity, flammability, GWP and ODP. Toxicity and flammability characterization for refrigerant fluids is provided in the last row, ratings specifically for HMDSO, ethanol and toluene are conducted by ASHRAE (2000, 2007, 2013) as they use represents a serious safety concern. *Table 3* highlights the general safety classification that is used to characterize working fluids. The category of A and B are used to distinguish the toxicity. The increasing number following the letter distinguishes the increasing flammability aspect of the fluid.

Table 2. Working fluid comparison of key thermodynamic, safety, health and environmental characteristics.

Properties	HCFC-123	HFC-134a	HFC-245fa	DR-12	DR-2	HCFO-1233zd(E)	SES36	n-Pentane	HMDSO ⁽¹⁾	Ethanol ⁽²⁾	Toluene ⁽³⁾
Normal Boiling Point, °C	27.8	-26.1	15.1	7.5	33.4	18.3	36.7	36.1	101	78.4	110.6
Critical Temperatures, °C	185	101.1	154	137.7	171.3	165.6	177.6	196.5	245.5	240.8	318.6
Critical Pressure, Mpa	3.67	4.06	3.65	3	2.9	3.57	2.85	3.36	1.94	6.15	4.13
Latent Heat @ 25 °C (KJ/Kg)	171.37	177.79	190.32	144.96	168.12	191.76	162.75	366.29	229.96	920.66	412.85
Specific Heat @ 0.1 Mpa 25°C (KJ/Kg-K)	1.02	1.43	1.32	1.09	1.19	1.24	1.08	2.32	1.91	2.44	1.7
Toxicity Class	See ASHRAE safety group rating								slightly	NA ⁽⁷⁾	moderate toxic
Flammability Class ⁽⁴⁾									serious flammable	severe flammability	serious flammability
Ozone Depletion Potential	0.02	0	0	0	0	0.0003		0		0	0
Global Warming Potential ⁽⁵⁾	79	1300	858	32 ⁽⁶⁾	2	1	3710	5	ND ⁽⁸⁾	1	3
safety group (ASHRAE)	B1	A1	B1	A1 ⁽⁶⁾	A1	A1	A1	A3	ND ⁽⁸⁾	ND ⁽⁸⁾	ND ⁽⁸⁾

(1) Fisher Scientific, Hexamethyldisiloxane, Material Safety Data Sheet, February 29, 2008.

(2) NCP Alcohols, Ethanol, Material Safety Data Sheet, May 3, 2012.

(3) Honeywell, Toluene, Material Safety Data Sheet, December 21, 2005.

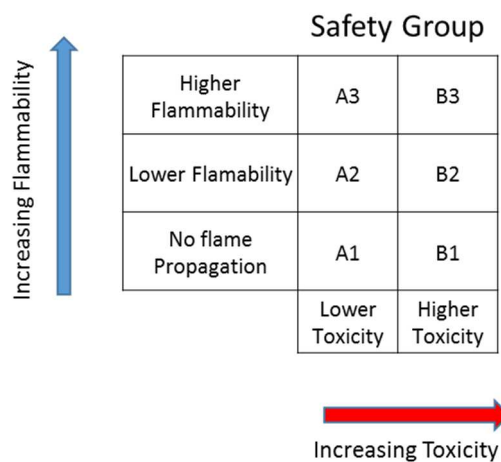
(4) ASTM (2004)

(5) Myhre et al. (2013)

(6) Expected value

(7) Not associated

(8) Not determined

Table 3. General Safety Group Classification

2.3 Thermal Stability

From *Table 2* above, an analysis can be made that the working fluids on the right side present concerns of flammability and of which, two have toxicity issues. A smaller subset of these fluids were screened for thermal stability in sealed tube tests to assess their suitability for higher temperature systems. Four of the fluids investigated, HFCF-123, HFC-245fa, DR-2, DR-12 and HCFO-1233zd(E), and subjected to 250°C for 1 and 7 days with metal coupons. An IC analysis for the anions F⁻ and Cl⁻ were conducted after the exposure conditions on the remaining fluids. Additional stability test of 14 days was carried out on HCFO-1233zd(E) and DR-2; results from HCFO-1233zd(E) were less favorable at 250°C, therefore a lower temperature study was performed at 200°C. As seen in the data in *Table 4*, results for HCFO-1233zd(E) at 200°C reflect significant degradation of the molecule as a function of time. DR-2

and DR-12 showed extremely favorable results. Interesting results were discovered regarding DR-12, where the fluoride ion was below detectable limits. The purity of DR-12 was only 98.1% and has no chlorines in its molecular structure; however, some trace chlorine containing species were present and very evident in the IC analysis as the Cl⁻ ions are seen at these elevated temperatures. These HFO fluids have an unsaturated (double bond) molecule and yet they do not demonstrate poorer thermal stability than saturated compounds. The notion that unsaturated compounds have less stability in a closed system at elevated temperatures is not necessarily correct a correct assumption. In a closed system, with all materials specified, only chemical and material compatibility tests with the exact system (including HFOs) can determine stability. Data presented in *Table 4* below incorporates some results previously presented by Kontomaris *et al.* (2013).

Table 4. Thermal Stability with IC Analysis Results

Fluid	Temperature (°C)	Duration	Coupon	IC Anion Results (PPM)	
				F-	Cl-
HCFO-1233zd-E	200	1 day	steel	8.23	61.5
HCFO-1233zd-E	200	7 days	steel	9.48	143.97
HCFO-1233zd-E	200	14 days	steel	34.28	554.18
HCFC-123	250	1 day	steel	328.43	496.44
HCFO-1233zd-E	250	1 day	steel	11.66	170.45
HFC-245fa	250	1 day	steel	3.6	< MDL
DR-12	250	1 day	steel	< MDL	18.28
DR-2	250	1 day	steel	0.6	11.3
HCFC-123	250	7 days	steel	2460.3	218.96
HCFO-1233zd-E	250	7 days	steel	1400.18	3854.26
HFC-245fa	250	7 days	steel	20	< MDL
DR-12	250	7 days	steel	< MDL	35.23
DR-2	250	7 days	steel	1.55	3.39
HCFO-1233zd-E	250	14 days	steel	2668.5	3194.7
DR-2	250	14 days	steel	1.83	2.02

2.4 Material Compatibility

An investigation was conducted on material compatibility for DR-2 where the study looked at 15 common materials in the presence of POE lubricant oil with DR-2 (Kontomaris, 2014); they were elevated to a temperature of 100°C for 14 days and their weight and hardness changes were measured at the conclusion of the experiment. Results display only a mild interaction between these plastics and elastomers and DR-2; they suggest that DR-2 would be suitable for use. It is recommend that further evaluations be conducted for material and chemical compatibility not only plastics and elastomers, but also covering various metals and lubricating typically found in a heat recovery system. This study is only a subset of current experiments from the lab. Future studies will be available where a selection of lubricant and recommendations will be incorporated as a function of temperature for DR-2 and DR-12.

Table 5. Weight Changes of Various Elastomers and Plastics with DR-2

DR-2 Compatibility with Plastics & Elastomers: (I)		
<u>Weight changes</u> of polymeric specimens after exposure to HFO-1336mzz-Z/POE Lubricant blends for 14 days at 100 °C		
Material	Immediately after Exposure %	Twenty Four Hours after Exposure %
Neoprene	-0.55	-0.98
EPDM	2.39	0.84
Polyester Resin	10.04	4.94
Nylon Resin	-0.74	-0.79
Epoxy	0.66	0.56
Polyester PET	3.73	3.54
Polyester PBT	1.15	1.13
Polycarbonate	0.74	0.75
Polyimide	0.79	0.79
Teflon PTFE	3.05	2.72
Teflon FEP	3.29	3.09
Tefzel ETFE	6.25	5.61
Phenolic	-0.18	-0.31
PVC	0.68	0.70
PEEK	-0.06	0.01

Mild Interactions between HFO-1336mzz-Z and Many Plastics and Elastomers

Table 6. Hardness Changes of Various Elastomers and Plastics with DR-2

DR-2 Compatibility with Plastics & Elastomers: (II)		
<u>Hardness changes</u> of polymeric specimens after exposure to HFO-1336mzz-Z/POE Lubricant blends for 14 days at 100 °C		
Material	Immediately after Exposure %	Twenty Four Hours after Exposure %
Neoprene	7.10	2.58
EPDM	2.56	0.64
Polyester Resin	-1.01	-0.51
Nylon Resin	-1.00	-2.00
Epoxy	-1.01	-3.54
Polyester PET	0.00	0.00
Polyester PBT	-1.00	-1.00
Polycarbonate	-1.00	0.00
Polyimide	0.00	0.00
Teflon PTFE	-0.50	0.00
Teflon FEP	0.00	-0.51
Tefzel ETFE	0.00	0.00
Phenolic	0.00	0.00
PVC	0.00	0.00
PEEK	0.00	0.00

Mild Interactions between HFO-1336mzz-Z and Many Plastics and Elastomers

3. CONCLUSION

The basis of this work was not to provide a deep analysis of ORC systems, but to focus on the viability and the selection process that comes with identifying good working fluid properties. The criteria to develop working fluids which perform under the high temperatures of heat recovery systems is essential as well as the need to have safe and environmental friendly alternatives to choose from. The ultimate goal from this study is to provide insight to existing entities like ASHRAE that review working fluids for the refrigerant industry, where all potential candidates are reviewed by a body of engineers and chemists for safety in use. It is conceivable that different environments may dictate that some safety concerns would represent less of an issue and they should be investigated based on their own merit. In general use, both flammability and toxicity are highlighted to pose significant risks and additional precautions are necessary to address their suitability for use. GWP and ODP represent two additional criteria which will influence working fluid selections in the future as regulations strive to find better alternatives as they affect the environment. Even though these influencers limit the choices of potential candidates, it does not mean that a significant loss of performance must be sacrificed to adhere to these values. The new HFO fluids offer comparable thermodynamic performance similar to fluids in their class and provide thermal stability as well. The DR-2 molecule with its low GWP and no ODP, has shown extremely good thermal stability at temperature up to 250°C. These new class compounds, HFOs, have been shown to exhibit good overall characteristics for use in low and possible medium temperature ORC applications.

NOMENCLATURE

WHR	<i>waste heat recovery</i>
ORC	<i>organic Rankine cycle</i>
GHG	<i>greenhouse gases</i>
ICE	<i>internal combustion engine</i>
ODP	<i>ozone depletion potential</i>
GWP	<i>global warming potential</i>
EOS	<i>equation of state</i>
CFC	<i>chlorofluorocarbon</i>
HCFC	<i>hydrochlorofluorocarbon</i>
HFO	<i>hydrofluoro-olefins</i>
PFC	<i>perfluorocarbons</i>
HMDSO	<i>Hexamethyldisiloxane</i>
NFPA	<i>National Fire Protection Association</i>
DOT	<i>Department of Transportation</i>
CFR	<i>Code of Federal Regulations</i>
TDG	<i>Transportation of Dangerous Goods</i>
OSHA	<i>Occupational Safety and Health Administration</i>
ASHRAE	<i>American Society of Heating, Refrigeration and Air Conditioning Engineers</i>

REFERENCES

- Myhre, G., Shindell D., Breon F., Collins W., Fuglestedt J., Huang J., Koch D., Lamarque J., Lee, D., Mendoza B., Nakajima T., Robock A., Stephens G., Takemura T., Zang H., 2013, Anthropogenic and Natural Radiative Forcing, In: *Climate Change: The Physical Science Basis, Contribution of Working Group I to the Fifth Assessment Report of the Intergovernmental Panel on Climate Change*, Cambridge University Press, Cambridge, United Kingdom and New York, NY, USA.
- Kontomaris, K., Minor B., Hydutsky B., 2013, Low Global Warming Potential Working Fluids for Organic Rankine: DR-2; Chemical Stability at High Temperatures, *2nd International Seminar on Organic Rankine Cycle Power Systems, ASME ORC 2013*, Rotterdam, The Netherlands (October 7-8).
- Kontomaris, K., 2014, Zero-ODP, Low-GWP, Nonflammable Working Fluids for High Temperature Heat Pumps, *ASHRAE 2014 Annual Conference*, Seattle, Washington, USA (June 28- July 2).
- Duparchy A., Leduc P., Bourhis G., Ternel C., 2009, Heat Recovery for the Next Generation of Hybrid Vehicles: Simulations and Design of a Rankine Cycle System, *World Electric Vehicle*, vol. 3, P. 3-6.
- ASTM, 2004, ASTM E681-04, Standard Test Method for concentration Limits of Flammability of Chemicals (Vapors and Gases), American Society for Testing and Materials, Philadelphia, USA.
- ASHRAE, 2000, Addenda to ANSI/ASHRAE Standard-1999, Addenda to Designation and Safety Classifications of Refrigerants, ASHRAE, Atlanta, USA.
- ASHRAE, 2007, ASHRAE Standard 97-2007, Sealed Glass Tube Method to Test the Chemical Stability for Materials for Use within Refrigeration Systems, ASHRAE, Atlanta, USA.
- ASHRAE, 2013, ANSI/ASHRAE Standard 34-2013, Designation and Safety Classification of Refrigerants, ASHRAE, Atlanta, USA.

APPLICATION OF REFRIGERANT WORKING FLUIDS FOR MOBILE ORGANIC RANKINE CYCLES

Christopher R. Nelson*

Cummins Inc, Research & Technology
Columbus, IN, USA
oo647@cummins.com

* Corresponding Author

ABSTRACT

Cummins Inc. has been a leading developer of Organic Rankine Cycle (ORC) systems for application to heavy-duty, on-highway trucks in the United States for several years. Cummins has passed through several generations of ORC system architecture and has fielded several on-highway vehicles equipped with ORC systems as a part of research conducted in partnership with the United States Department of Energy. Throughout this development, Cummins has carefully evaluated potential working fluids for ORC application and has remained committed to using safe and environmentally friendly refrigerants such as R245fa and its recently introduced ultra-low GWP replacements for on-highway use.

Integration of Organic Rankine Cycle (ORC) systems into heavy duty, on-highway vehicles requires consideration of a significant number of factors, not the least of which is the choice of working fluid. The selection of fluid is primarily driven by safety, environmental and health effects of the fluid, potential performance considering the application at hand, availability, serviceability, etc. Given the working fluid, selection/sizing of various system components and optimization of the system architecture may be made.

This paper will briefly review Cummins' ORC history and discuss the background leading to Cummins' selection of refrigerant working fluids for on highway application. Details of technology that allow a refrigerant's safe and effective use in this application will also be discussed. An architecture comparison between systems using a refrigerant such as R245fa and ethanol will be made and a performance comparison between R1233zd(e), an ultra-low GWP replacement for R245fa, and ethanol will be presented.

1. INTRODUCTION

Since approximately 2003, Cummins Inc. has investigated the potential practicality and benefit of applying Organic Rankine Cycles (ORC) to its heavy duty diesel engines applied to on-highway, linehaul vehicles. Cummins settled upon non-flammable refrigerants, such as R245fa, as viable ORC working fluids. Refrigerants were already applied in the ORC industry and had a proven record of effective performance. Cummins evaluated many different working fluids but considerations of safety, environmental responsibility, feasibility, performance, etc., led the researchers to make R245fa their initial prime-path fluid of choice.

Cummins early ORC systems (see Figure 1, below) were designed before the introduction of Selective Catalytic Reduction (SCR) aftertreatment. These ORC systems took advantage of a high flowrate of Recirculated Exhaust Gas (EGR) and were expected to achieve nearly an 8% fuel economy benefit.

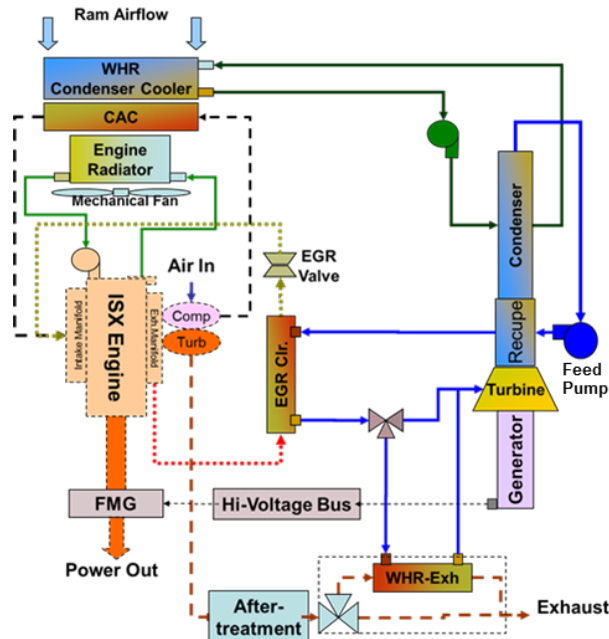


Figure 1: Early Cummins ORC system

At the time, conversion of recovered power to electricity was preferred as integration of the ORC with potential hybrid drive systems was anticipated. Compatibility of electronic systems, cost and complexity of electrical components, and the then expected drive cycle benefit of hybrid systems in linehaul applications drove the ORC architecture away from electrical integration. The concept of mechanically linking recovered power directly to the engine was developed into an architecture as presented in Figure 2, below.

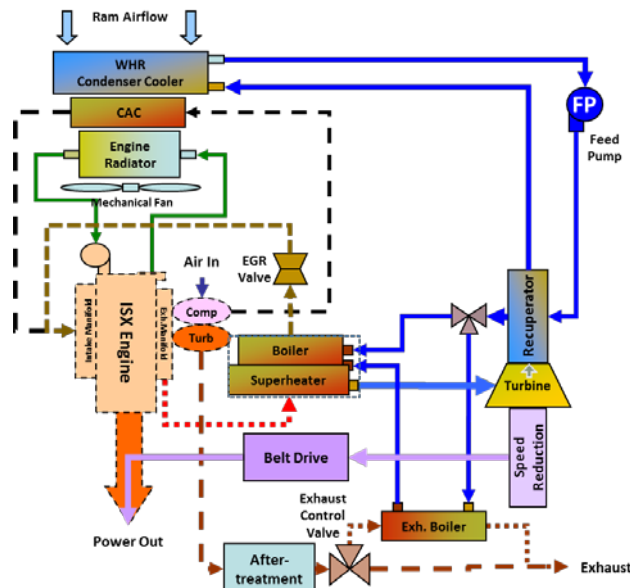


Figure 2: Mechanically-coupled ORC system architecture

Direct-to-air condensing was adopted to avoid an unnecessary pump parasitic. A speed-reducing gearbox and effective, self-contained lubrication system were designed using typical refrigeration-

based technologies. Recovery of charge air heat was not pursued as it did not appear to offer a cost-effective benefit. System performance was reduced to approximately 5% fuel economy benefit at this point due to a significant reduction in EGR flow as a result of adopting SCR aftertreatment. The system architecture settled upon in Figure 2 was successfully demonstrated in-vehicle under the United States Department of Energy's Supertruck Program. Cummins applied R245fa as a working fluid throughout these developments but became aware of refrigeration industry plans to introduce ultra-low Global Warming Potential (GWP) 'drop-in' replacements.

2. Safe and Effective Application

Use of halogenated fluid to cool pre-combustion gases (such as EGR or air) necessarily requires a robust and durable method to prevent leakage of the fluid into the combustion airstream. In response to this challenge, Cummins investigated and embraced a heat exchanger architecture which provides a 'leak to atmosphere' feature. This architecture is described in SAE Paper 2006-01-2163 (David B. Sarraf, Heat Pipe Heat Exchanger with Two Levels of Isolation for Environmental Control of Manned Spacecraft Crew Compartment) and is presented in Figure 4 below. Initially, an isolation method of this nature was considered untenable as it would significantly deteriorate the heat transfer effectiveness of any EGR heat exchanger. However, analysis and hardware evaluation showed that any decrease in effectiveness was negligible. Extensive hardware reliability testing has since shown that a robust EGR heat exchanger design can be successfully executed in this manner. Solutions of this nature are available from several manufacturers.

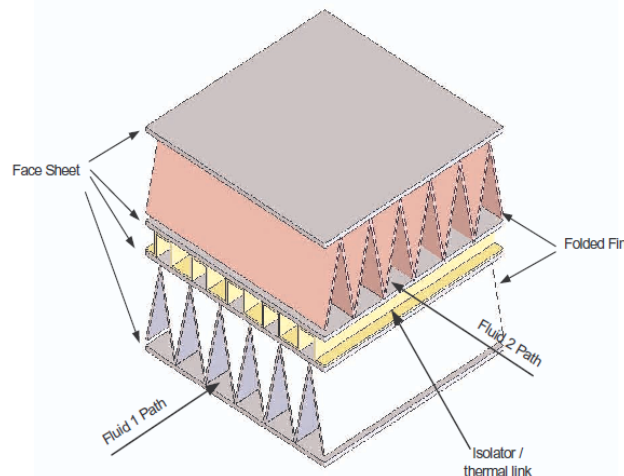


Figure 3: Schematic of a folded fin heat exchanger element with an isolation layer (Ref: SAE 2006-01-2163)

In addition to leakage through heat exchangers into the combustion airstream, leakage of refrigerant working fluid into air within and around the engine compartment was another potential opportunity for generation of harmful emissions. Cummins extensively studied leakage, and the potential for engine ingestion in this regard as well. Recognized standards such as SAE J2773 (Standard for Refrigerant Risk Analysis for Mobile Air Conditioning Systems) and SAE J639 (Safety Standards for Motor Vehicle Refrigerant Vapor Compression Systems) among others were applied to evaluate potential risk. It was concluded that the risk of applying refrigerant as an ORC working fluid posed no significantly greater risk than that which already existed from MAC systems. Impingement of refrigerant leaking upon hot engine surfaces (and tailpipe components) were also studied. It was determined that leaking refrigerant liquid or vapor would not significantly deteriorate but would simply tend to cool those areas of impingement.

3. R245fa Alternatives

Awareness of regulatory restrictions imposed upon Mobile Air Conditioning (MAC) systems in the European Union (EU) led Cummins to investigate alternatives to R245fa. R245fa, with a GWP of

~1000, though with no Ozone Depletion Potential (ODP), applied as a working fluid in a vehicle ORC system would achieve a significant reduction in the emission of carbon dioxide over the life of the vehicle. However, similarity of ORC systems to MAC systems suggested that similar legislated regulations may be applied to ORC systems using refrigerants. Contact with major manufacturers such as Honeywell, DuPont, etc., of R245fa and similar halocarbons revealed intentions to develop and release ultra-low GWP equivalents in the 2015 timeframe. These fluids, such as R1233zd(E), are now available in the market and offer an effective alternative to R245fa. Cummins performed comparative hardware performance testing with several of these alternative fluids (see Figure 4, below) with excellent results. Operating points such as A100, B75, etc. reflect engine operation at Environmental Protection Agency, Federal Test Procedure conditions.

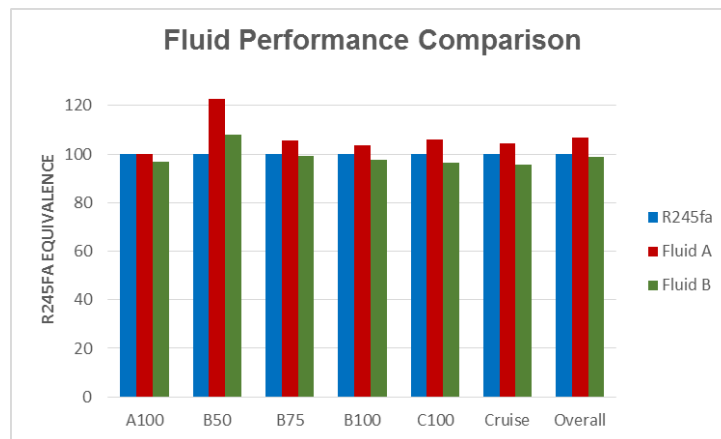


Figure 4: Performance comparison of R245fa against low-GWP equivalents

It was clear from the results that not only were there ‘drop-in’, ultra-low GWP replacements for R245fa readily available, but a slight increase in performance was potentially possible. As a result, Cummins decided upon a low-GWP alternative to R245fa as the concept moves towards a production configuration.

4. Comparisons with Ethanol

4.1 Performance

Ethanol has been taken up as a potential ORC working fluid by many system developers. Ethanol operates very well in this role. At first glance, it is an effective and low-cost choice. Ethanol is generally regarded as non-toxic and environmentally friendly. Typical ethanol ORC system architectures assume rejection of condensation heat into a coolant stream common with the engine (engine and ORC condenser plumbed in parallel, receiving the same radiator return temperature coolant). Many comparisons of performance between R245fa and ethanol simply adopt this cooling system arrangement to evaluate both fluids. However, in doing so, performance potential of R245fa (or R1233zd(e)) is obscured.

A model-based comparison of ethanol and R1233zd(e) at equivalent maximum (225°C) and minimum (80°C) temperatures, maximum operating pressures (2400 kPa) and equally arranged and capable ORC systems (same component efficiencies and effectiveness) shows a stark difference in performance (Figure 5, below).

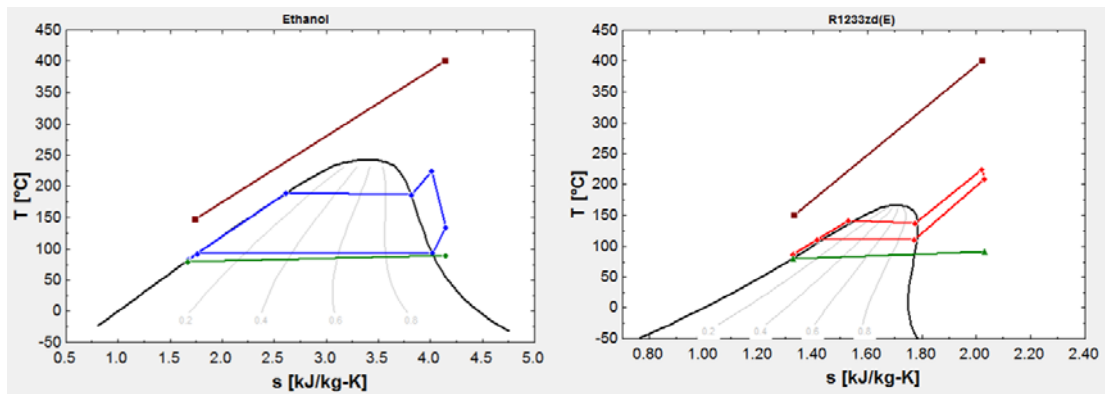


Figure 5: Performance comparison between ethanol and R1233zd(e) in equivalent systems with equal maximum temperatures/pressures and equal condensing temperatures.

For reference, net power from the ethanol system was 18.8 kW, net power from R1233zd(e) was 4.6 kW. Condenser heat rejection was 146 kW for ethanol and 158 for R1233zd(e). Input heat energy to both systems was diesel exhaust at 400°C flowing at 0.6 kg/s. Condensing temperature for ethanol is 93°C, R1233zd(e) is 111°C.

For system application, consideration is necessarily given to the availability of cooling. As presented above, Cummins settled upon a ‘direct to air’ condensing arrangement early in its development. The availability of near ambient air temperature cooling lent further reason to remain with refrigerant working fluids like R1233zd(e).

Ambient air temperature is, on average in the lower contiguous 48 United States approximately 12°C (<http://www.ncdc.noaa.gov/>). Average EU temperature is only slightly higher. In this case, the results are significantly different as presented in Figure 6, below.

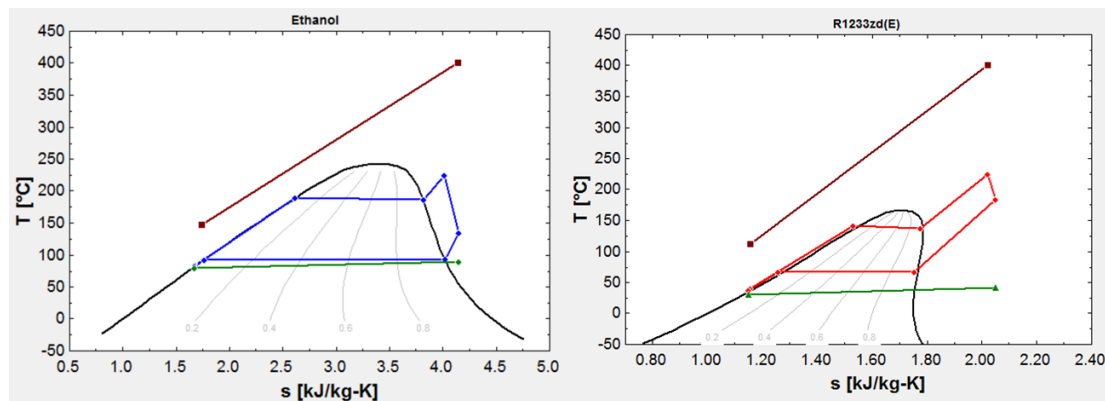


Figure 6: Comparison of ethanol and R1233zd(e) with equivalent systems but with condensing temperature appropriate for an in-vehicle R1233zd(e) system.

For reference in this case, net power from the ethanol system remained at 18.4 kW. Net power from the 1233zd(e) system increased to 14.3 kW. Condenser heat rejection remained 146 kW for ethanol but now increased to 174 kW for R1233zd(e). Input heat energy to both systems as above. Condensing temperature for ethanol remains at 93°C, R1233zd(e) is now 67°C.

An obvious feature of above the R1233zd(e) Temperature-Entropy (T-s) diagram is the opportunity to apply recuperation to the cycle. No such opportunity exists for ethanol due to its ‘wet’ nature. The amount of superheating remaining in the ethanol flow upon leaving the expander is too little to usefully recover. While the addition of a recuperator to an R1233zd(e) system necessarily adds cost to its

arrangement, it provides a significant benefit in power and a reduction in heat rejection. Figure 7 below presents the cycles once again but now the R1233zd(e) cycle has a reasonably effective recuperator (effectiveness of 70%, 50 kPa ‘cold side’ restriction, 10 kPa ‘hot side’ restriction).

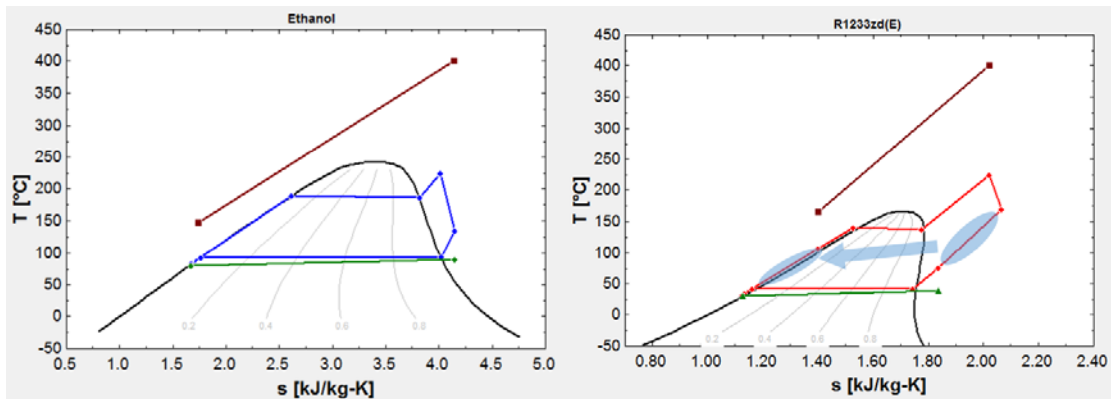


Figure 7: Comparison of ethanol and a recuperated R1233zd(e) cycle.

For reference, net power from the ethanol system remained at 18.4 kW, net power from the R1233zd(e) system increased to 22.7 kW. Condenser heat rejection remained 146 kW for ethanol and but now decreased to 131 kW for R1233zd(e). Input heat energy to both systems as above. Ethanol’s condensing temperature remains at 93°C, R1233zd(e) is now 41°C.

While the results above are only model-based, they represent a fair comparison of the two working fluids considering their potential arrangement in-vehicle. The key take-away is that comparisons between refrigerant and ethanol systems should be made using systems optimized for each fluid. Modeling was performed using Engineering Equation Solver (EES) software with fluid properties currently available through NIST REFPROP. R245fa and R1233zd(e) modeled performance was validated from hardware test experience.

4.2 System Hardware Arrangements

The Cummins R245fa-based ORC system demonstrated during the Supertruck project is illustrated in Figure 8, below.

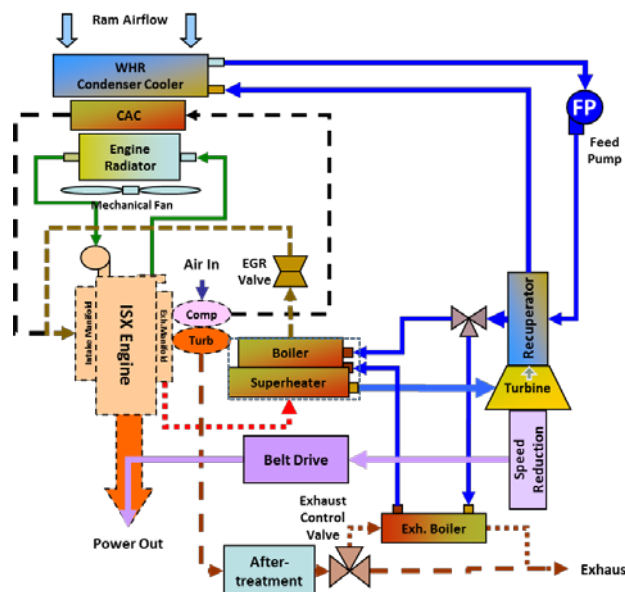
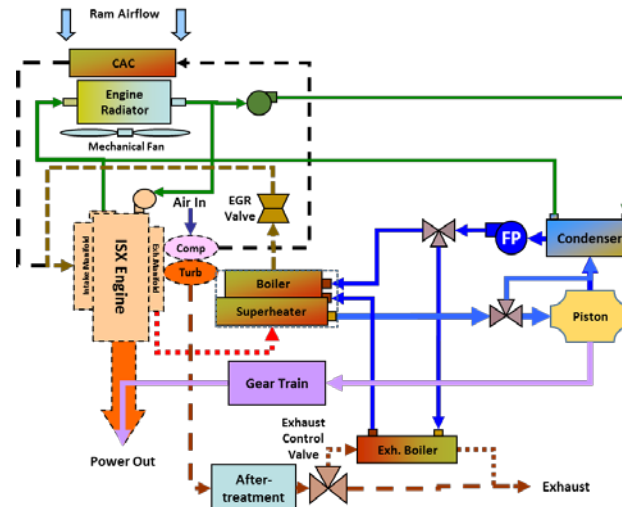


Figure 8: Cummins Supertruck ORC Arrangement

A potential ethanol-based ORC is presented in Figure 9.

**Figure 9:** Potential ethanol ORC system arrangement

In this arrangement, the ethanol system has one fewer heat exchanger than the R245fa system since it doesn't call for a recuperator. In this arrangement, ethanol would be cooled with radiator return temperature coolant. If lower temperature condenser coolant is desired, an additional heat exchanger would be necessary, making the systems equivalent in their number of heat exchangers. It should also be noted that the ethanol condenser, plumbing, etc. must be manufactured from material robust against ethanol corrosion. Typically, stainless steels are applied when dealing with ethanol. In comparison, R1233zd(e) is compatible with aluminum and other lightweight, low-cost materials already commonly deployed in MAC systems.

The ethanol system requires either a shared main engine water pump or a separate water pump, likely electrically driven to provide coolant to that system's condenser. The refrigerant system, being directly cooled to air, does not require this.

An ethanol system, using a low-speed, piston-type expander may directly mechanically couple its power to the engine's geartrain. However, an additional bypass valve around any positive-displacement expander will be necessary to guard against possible liquid ingestion/hydraulic lock and potential damage to the expander and the engine's geartrain. In comparison, refrigerant-based systems using a high-speed turbine expander, will need speed-matching equipment to provide mechanical power coupling to the engine. ORC systems using isentropic or dry working fluids and turbine machines will not need to apply a bypass valve given adequate control of liquid superheating. Turbines are robust to low flowrates of low pressure wet or liquid working fluid. Additionally even a high flow of 'wet' vapor may enter the turbine as, on expansion/acceleration through entry nozzles, the fluid rapidly becomes superheated vapor, leaving little risk of expander blade erosion.

4.3 Other Considerations

Application of either ethanol or refrigerant must consider the arrangement of sealing against the intrusion of outside air. This is not typically an issue during operation as both systems should operate with a 'low-side' (condensing) pressure greater than atmospheric pressure. However, during cold operation or during cold storage, the fluid's saturation pressure can be significantly important. Figure 10, below, presents a comparison of the saturation curves for R1233zd(e) and ethanol.

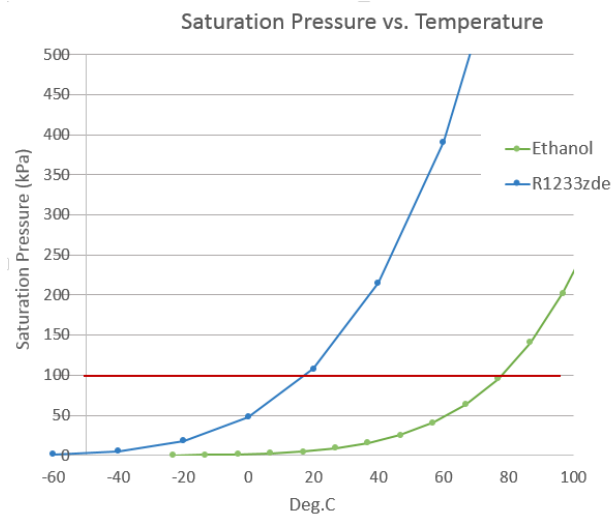


Figure 10: Comparison of saturation pressures

As shown in Figure 10, the saturation pressure of ethanol falls below atmospheric pressure at temperatures less than $\sim 80^{\circ}\text{C}$. At room temperature, it's only about 8 kPa absolute. This means that during shutdown, especially in cold ambient temperatures, there will be a significant risk of air ingress to the ethanol system. Blending ethanol with water further suppresses the saturation pressure. R1233zd(e)'s saturation pressure falls below atmospheric pressure as well at approximately 18°C but it does not reach a significantly hard vacuum until nearly -40°C and degrades at a substantially slower rate. Air ingress will cause unnecessarily high expander back-pressure and decreased system performance. Either system, if executed with mechanical power coupling thus requiring an output shaft seal, would need a seal robust both to pressure during operation as well as vacuum when stored.

Additionally, in regard to low saturation pressures, feedpump cavitation may be expected to occur more frequently in systems using ethanol. Extremely low feedpump Net Pump Suction Head Required (NPSHR) will be a necessary requirement, or an additional 'boost' pump will become necessary. This problem is not only related to cold temperatures. Some ethanol systems have been shown to have vented their condensers to atmosphere in an attempt to increase feedpump inlet available suction head (NPSHA). While this may allow better operation close to sea level, higher altitude operation (and thus lower atmospheric pressure) may lead to feedpump cavitation and a loss of performance if condensing temperatures are below 80°C .

5. Further Development

Application of ORC systems to mobile internal combustion engines is not a new idea but it is certainly not a field whose opportunities have been fully explored. It is hard to imagine the potential performance mobile ORC might provide today had it undergone the same intensity and duration of research and development as the internal combustion engine. Though, as a bottoming cycle, it may never reach the thermal efficiency of the engines to which it is applied, it can certainly grow in its ability and benefit. In doing so it will meet and exceed the economic challenges which have typically kept it from production implementation.

It's quite easy to recovery heat. The real challenge is how to reject it. Thermodynamically, any recovered energy cycled through a heat engine loses some of its energy potential making it more difficult to reject. Given the finite cooling capacity available in current and future heavy duty vehicles, a thorough understanding of cooling system function and its duty-cycle based load will determine how much potential benefit any bottoming cycle can provide. Unused cooling capacity during engine operation below worst case conditions is potential ORC benefit. The optimized sharing of cooling

capacity between the engine and ORC is an area of research ‘outside the cylinder’ which should be developed as vigorously as are combustion, air handling, and aftertreatment.

The engines to which ORC systems are being applied today will certainly change as the emphasis for increased efficiency and reduced emissions continues. Further development of ever more capable NOx reducing aftertreatment may very well result in the removal of EGR. Increased emphasis upon exhaust energy recovery will occur but it will also focus attention to potential recovery of other engine waste heat streams. Charge air and engine coolant may become viable opportunities for cost-effective recovery. An ORC system architecture which can usefully approach these waste heat streams will certainly be the most viable long-term solution. Today’s typical engine coolants offer a bulk temperature considered to be too low for effective use. However, the potential for hotter coolant (and thus more thermally efficient diesel engines) is a real possibility. In this case, an additional ‘necessary’ heat stream (as is EGR today) of recoverable energy will become available for the ORC to convert to useful power.

ORC system components are just beginning to attract the attention of manufacturers. As typical system arrangements coalesce across the industry, availability of more capable and more cost effective components will increase. Development of ORC components is just beginning and will certainly offer performance and efficiency benefits as it grows.

As mobile ORC is a new and relatively undeveloped field which will affect a significant portion of the engine system, there will necessarily be a great deal of work to establish standards, methods, and procedures around its safe and effective application. The handling of its fluids, the ratings of its components, the controls interaction between ORC and other engine systems will all require careful review and consideration by the industry’s governing bodies and professional organizations.

6. Conclusions

This paper covers the use and application of R245f or R1233zd(e) and potentially other halocarbons as working fluids in mobile ORC systems. A brief review of the ORC project at Cummins and system architectures from the project’s early phases through its most recent demonstrations have been shared and discussed. Reasons for Cummins’ choice and adherence to low GWP refrigerant as its on-highway ORC working fluid have been provided. System considerations and features that allow the safe and effective application of these fluids in mobile ORC systems have been shared. Mention and comparison of ultra-low GWP working fluid alternatives to R245fa has been made. A model-based comparison of R1233zd(e) and ethanol has been provided to show that performance between the two working fluids is not quite as different as may be gathered from other work. Application considerations between the two fluids have also been discussed to offer developers some insight as to why R1233zd(e) is an appealing and viable working fluid for application in mobile ORC systems. Considerations for future development have been provided and briefly discussed.

ORC application to on-highway engines was once considered to be a ‘tried and failed’ technology. The emphasis on efficiency and emissions has resurrected it once again. The potential benefit it offers is the most significant efficiency increase available in quite some time and perhaps, for some time to come. New materials, controls, components, and ideas will help it leap the economic hurdle to reach mainstream, production implementation.

ACKNOWLEDGEMENT

The author wishes to acknowledge the United States Department of Energy, Office of Vehicle Technologies without whose partnership and support the opportunity to explore and develop mobile ORC systems would not have been possible.

IMPROVING TRAIN ENERGY EFFICIENCY BY ORGANIC RANKINE CYCLE (ORC) FOR RECOVERING WASTE HEAT FROM EXHAUST GAS

D. Serrano^{1*}, P. Smague¹, P. Tona¹, P. Leduc¹, A.C. Mintsa², A. Leroux² and P. Chevalier³

¹IFP Energies nouvelles (IFPEN), Institut Carnot IFPEN Transports Energie,
1 & 4, avenue de Bois-Préau, 92852 Rueil-Malmaison Cedex, France
E-mail: david.serrano@ifpen.fr

²ENOGIA SAS,
51 rue le Châtelier, 13015 Marseille, France
E-mail: andre-charles.mintsa@enogia.com

³ALSTOM TRANSPORT,
48 Rue Albert Dhalenne - 93482 SAINT OUEN Cedex, France
E-mail: philippe.chevalier@transport.alstom.com

* Corresponding Author

ABSTRACT

In a context of energy cost increase, reducing engine fuel consumption has become a key issue for transportation industry. Many paths exist to achieve substantial fuel savings: downsizing, hybridization, energy recovery... IFPEN has carried out an analysis of heat losses showing that recovering exhaust heat energy is a promising solution for improving fuel economy. Thus, IFPEN and ENOGIA have co-developed an Organic Rankine Cycle (ORC) system for direct recovering energy from exhaust heat. This system has been designed in order to be implemented on a Diesel-electric regional train manufactured by ALSTOM TRANSPORT. The train has several Diesel engines that produce mechanical torque needed for generators used for train electric propulsion. The ORC recovers energy from the exhaust heat of the different Diesel engines.

The project funded by the French national agency for research (ANR) started with OD simulations in order to identify the optimal ORC architecture as well as some promising working fluids. More than 100 fluids were evaluated and finally two fluids were retained for this application thanks to their safety features, eco-friendliness and thermodynamic potential. A pre-design study defined the main components (boiler, condenser, pump...) that answer to the major constraints: cost, compactness, efficiency. ENOGIA developed the "heart" of the ORC, a dedicated turbine coupled with a high-speed generator on the same axle. The objective is that the electricity produced by the turbo-generator is re-injected for the train electrical propulsion. An ORC prototype has been assembled with a special care for avoiding any organic fluid leaks. The prototype has then been tested in an engine bench with the same Diesel engine as in the regional train. At the engine bench, the electricity produced by the ORC is re-injected in the French grid by means of inverters and transformers.

Based on previous experiences, IFPEN has developed an advanced control system for this application, which allows transient control of ORC operation by regulating vapor superheating at evaporator outlet. The machine has been largely instrumented for monitoring Rankine cycle operation. At the time of paper writing, around 10kW of ORC electricity output power has been reached in stable conditions.

1. INTRODUCTION

In Europe, more than 50% of the railway network is not electrified. Thus, Diesel electric trains are widely used for regional passenger transportation. In these trains, the Diesel engines are linked to

high-voltage generators to provide direct current (DC) to the electric train traction. Each regional train has several engines consuming each around 50l/100km of fuel. In a context of energy saving and global warming awareness, train manufacturers have been focusing their research and innovation efforts on the fuel consumption reduction of their engines. But despite all these improvements, engine efficiency is reaching an asymptote around 40-45%. At least 60% of the energy content of the fuel is lost in exhaust gas heat (~30%) and engine coolant (~30%). Many paths exist to achieve substantial fuel savings. Among these, hybrid concepts show significant efficiency improvements but with high cost. That's why some scientists are focusing their interest on how recovering energy from engine losses. Heat conversion to mechanical or electrical work can't only be reduced to energy consideration, then the concept of exergy derived from the second law of thermodynamics has to be introduced. It represents the part of the energy that can be really extracted for a thermodynamic closed system reversibly from its initial state to equilibrium. Exergy (Ex) variation between states 1 and 2 of a system in contact with its environment is defined as:

$$\Delta Ex_{12} = (H_2 - H_1) - T_0 \cdot (S_2 - S_1) \quad (1)$$

El Habchi (2010) shown that recovering energy from the exhaust presents higher potential than coolant energy recovery. As an example, over a specific mission profile (Artemis Motorway, for passenger car) for a 2L gasoline engine, exhaust gas exergy represents 26% of fuel lower heating value whereas coolant exergy is only 3%. Several technologies exist to convert exhaust heat into useful work such as turbo-compound, thermoelectric generator or thermo-acoustic engine and finally thermodynamic systems (Rankine, Stirling, Ericsson cycles). However, the complexity or the cost of some technologies is disproportionally high in comparison to the heat recovery potential: considering this, Rankine cycle seems to be the most promising approach. Heat recovery technology is already widely exploited in stationary equipment or for heavy ships. The implementation on mobile applications is challenging due to the transient behavior of the heat source. No serial production Rankine system exists yet for heavy-duty or train application.

Considering this context, IFPEN and ENOGIA have co-developed an Organic Rankine Cycle (ORC) system for recovering energy from exhaust heat from a Diesel-electric regional train made by ALSTOM TRANSPORT. The train has several Diesel engines developing more than 300kW max. power each. They have a two-stage turbocharging which limits even more exhaust gas temperature compared to a biogas spark-ignited stationary engine for example. The Rankine system produces work by the mean of a working fluid that exchanges heat between a hot source and a cold sink as described in figure 1. The working fluid is circulated and pressurized thanks to a volumetric pump. The fluid is then vaporized inside a boiler by exchanging heat with a hot source, exhaust gas in this case. This vapor at high pressure is then expanded in a turbine generator which produces electricity that is used for electric train propulsion. The working fluid is liquefied in a condenser by exchanging heat with a cold source before it is pumped again. The ORC works in a medium range of temperatures (100 to 200°C) compared to steam Rankine systems that operate at higher temperatures.

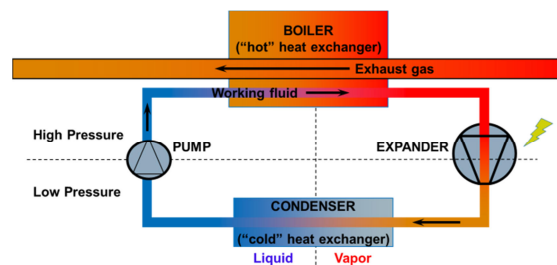


Figure 1: Rankine cycle principle

The project has followed different steps from blank sheet to a prototype: a ORC pre-sizing stage including selection of the ORC architecture and the working fluid, the ORC prototype conception and manufacturing, the testing in realistic conditions at engine bench.

2. SIZING THE ORC

2.1 Heat recovery potential on the train

The first step of this work is to evaluate the heat recovery potential of the train application depending on the hot source and cold sink. To achieve this study, a 0D dynamic low-frequency model of the train system propulsion has been made using the tool LMS Imagine Lab Amesim with IFPEN-Drive engine dedicated library. The IC engine, the generator and electrical load have been simulated using two real mission profiles given by the train manufacturer:

- Profile A: interurban route between two cities at high speed (average speed 120km/h) shown in figure 2.
- Profile B: one suburban route with a lot of stop & go (average speed 77km/h).

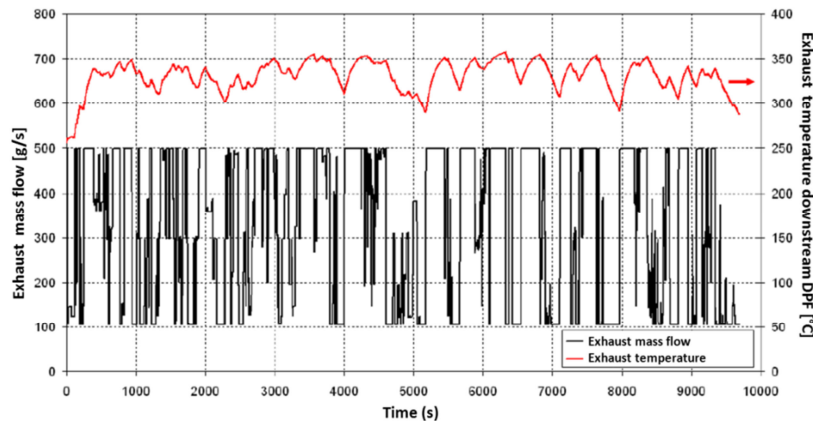


Figure 2: Exhaust mass flow and temperature evolution over mission profile A

The simulator evaluates the recoverable exergy along the chosen mission profiles by using input data of exhaust temperature and exhaust mass flow given by train manufacturer and the heat flow estimation evaluated thanks to REFPROP thermodynamic database of the NIST. Different ORC configurations have been simulated by varying 3 parameters in realistic conditions:

- The cold sink temperature: the ambient temperature impacts the cold sink temperature and thus the exergy recovery potential can be limited.
- The maximum working fluid temperature (for simulating thermo mechanical turbine constraint or limit before chemical degradation of the working fluid).
- The recovery system location: boiler position downstream the Diesel Particulate Filter (DPF).

Table 1: Heat recovery potential simulation results

ORC Configuration	1.	2.	4.	3.	5.
Cold sink T [°C]	50°C	50°C	25°C	50°C	50°C
Max. fluid T [°C]	No limitation	No limitation	200°C	200°C	150°C
Boiler position	Just after DPF	1m downstream DPF	Just after DPF	Just after DPF	Just after DPF
Exergy on profile A [% mech. energy]	48kW (14%)	24kW (7%)	42kW (13%)	39kW (12%)	36kW (12%)
Exergy on profile B [% mech. energy]	49kW (14%)	24kW (7%)	41kW (13%)	38kW (11%)	36kW (10%)

The assumption is that exhaust heat is recovered in both Exhaust Gas Recirculation (EGR) and exhaust line downstream DPF, that's why the levels of exergy are quite high (up to 14%). As EGR heat recovery is deeply intrusive in existent engine architecture and calibration, it has been abandoned at this stage of the project and energy will be recovered only on exhaust line. The main influence factor on recoverable exergy is the recovery system location: the results show that the boiler should be placed as closed as possible downstream DPF to maximize thermal exhaust energy. Then the maximum fluid temperature has a strong influence too: if the max. working fluid temperature is reduced by 50°C, the exergy potential is reduced by ~10%. Finally, the cold sink temperature has a

medium influence on recoverable exergy especially when max. fluid temperature is already limited. Moreover, the 2 different mission profiles have minor impact on exergy potential. These results have to be moderated as the fuel consumption reduction will be different between the 2 mission profiles. Indeed, the ORC turbine has a variable efficiency depending on the operating conditions, especially at part load and during transient conditions, which is hard to be fully taken into account in the simulation.

2.2 Screening the working fluid

The working fluid plays a key role in a Rankine cycle. It is repeatedly vaporized, expanded and re-condensed. The work output for a given temperature gradient differs significantly for different fluids. That's why a screening of different working fluids is carried out to choose the most suitable fluid for this application according to specific criteria:

- Thermodynamic performance: high expansion work output. The pressure in the boiler should be as high as possible to increase the turbine expansion rate. Finally, the pressure downstream the condenser should be as closed as possible to atmospheric pressure also to increase the turbine expansion rate.
- Mollier's diagram shape (temperature versus entropy): the dry working fluids are more suitable as they don't liquefy during their expansion in the turbine. The need for superheating is then reduced and the risk of droplet generation during expansion (leading to turbine blade erosion) is avoided. For a mobile application with high space constraints, the fluid needs to have a high specific heat capacity and latent heat of vaporization to minimize flow rates and by the way the size of components especially the boiler and the required pumping power.
- Safety: inflammability (explosion protection due to critical flashpoint) and toxicity.
- Chemical stability: molecule decomposition under ageing or thermal effects.
- Environment aspects: GWP, ODP.
- Material compatibility: corrosiveness, lubricant properties of the turbine.
- Equilibrium pressure when ORC is stopped: if ORC is under atmospheric pressure when stopped, air can enter inside the circuit if leaks are present and thus degrading Rankine cycle efficiency.
- Low freezing point: compliance with train parking with cold conditions (-30°C).

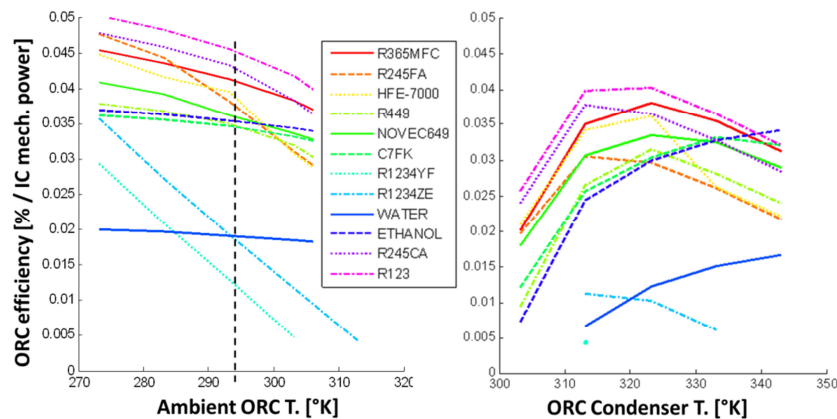


Figure 3: Global ORC efficiency simulated for different fluids for ambient and condenser T. variations

The fluid screening has been carried out with an ORC 0D steady-state model using Matlab platform. Different types of working fluids have been tested including water, ammonia, SO_2 , hydrocarbons, alcohols and hydrofluorocarbons: more than 100 different fluids have been analyzed. The thermodynamic data of the fluids have been estimated thanks to the REFPROP V9.1 software of the NIST. The ORC efficiency is calculated for the engine point producing the maximum power (>300kW) taking into account realistic train conditions. Thus, every ORC component has been described by assumed realistic values of efficiencies for the turbine generator and the pump and using water as cold sink. This water circuit is cooled by an electric cooling fan. The fluid is superheated, its minimal pressure is above 1 bar, its maximum pressure is below 25bar and its maximum temperature

is below 200°C. The Rankine circuit is also optionally composed of a regenerator that exchanges heat between vapor phase from downstream turbine and liquid phase from downstream pump.

Finally, about 500 000 simulations have been carried out in this project. In figure 3, the results show the maximum global ORC efficiency defined as the ratio between the electric output net power of the ORC over the mechanical engine power. This efficiency is between 3 to 5% depending on the conditions (ambient or condenser temperatures...). This global ORC efficiency decreases at low condensing temperatures as more energy is spent to cool the water (cold sink) than the gain in ORC thermal efficiency (Carnot theorem). Because of safety issues, hydrocarbons, alcohols and ammonia are disqualified for train application. Water is also not adapted as efficiencies are really low. Finally, HFC presents good trade-off with a 4% ORC efficiency potential combined with acceptable toxicity and environmental characteristics. Finally, the project has chosen two fluids for experimental testing :

- R245fa: high efficiency and long partner experience with this fluid but high GWP.
- Fluid B: high efficiency, not sensible to condenser water temperature variation, low GWP but high cost.

Table 2: Working fluid specifications

Fluid characteristic	Formula	Max. continuous T	Critical P/T	Inflammability NFPA / HMIS	Toxicity NFPA / HMIS	ODP GWP	Supplier Cost
R245fa	C3H3F5	154°C	154°C 36,5bar	1 / 1 Non flammable	2 / 2	0 950-1030	Honeywell Medium
Fluid B	Confidential	<300°C	<200°C <20bar	0 / 0 Non flammable	Low	0 <50	Confidential High

2.3 Expected performances

Finally, simulations allow to obtain the expected performances for the selected ORC architecture with the two different working fluids. The ORC efficiency expected is around 6 to 7% with both fluids meaning that 6 to 7% of the heat power received by the fluid in the boiler will be re-injected for the electric train traction.

Table 3: Predicted performances at steady-state max. power engine operating point

Fluid	R245fa	Fluid B
Heat power received by the fluid in the boiler	134 kW	122 kW
Heat power lost by the fluid in the condenser	117 kW	107 kW
Electrical power generated by the turbine	16 kW	14 kW
Electrical pump power consumption	1,8 kW	1,6 kW
Cooling power consumption	5,8 kW	3,6 kW
ORC efficiency (compared to heat on fluid)	6,3 %	7,2 %
Fluid mass flow	2150 kg/h	3600 kg/h
P / T in HP branch	25 bar / 167 °C	15 bar / 200 °C
P / T in LP branch	3,6 bar / 41°C	1,5 bar / 50 °C

3. ORC PROTOTYPE AND IMPLEMENTATION AT ENGINE BENCH

3.1 ORC architecture

After the first stage of pre-sizing, IFPEN and ENOGIA co-designed an ORC layout taking into account the previous recommendations in order to be tested at engine bench. The layout is displayed in figure 4. The heat is recovered in the exhaust line downstream the DPF in order to avoid the boiler clogging. The exhaust line has been modified by the implementation of two exhaust throttles allowing the exhaust gas going through the boiler or bypassing it, depending on exhaust thermal energy available. The expansion machine is a turbine that is coupled to a generator for electricity production. Among the conventional components of an ORC cycle, one can notice the presence of a regenerator to improve the cycle efficiency with an intermediate heat exchange in order to pre-heat the pressurized liquid with the vapor after expansion on the turbine. The ORC is instrumented with thermocouples, pressure sensors and flow meters in order to allow real-time monitoring of the ORC energy balance.

3.2 Component description

To pressurize the working fluid, an industrial volumetric pump self-lubricated has been chosen with a variable capacity between 80 to 1000L/min. It is driven by an electrical motor of 3 kW max power with a chain transmission. The boiler has been chosen with specific criteria for maximizing heat exchange with exhaust gas with the minimum pressure drop in exhaust gas (for no impact on engine fuel consumption) and with a reasonable cost. The chosen technology consists in a cross flow stainless steel exchanger mixing tubes (for fluid) and plates (for exhaust gas). Total surface plates (>50m²) is much greater than surfaces of tubes (>3m²) to compensate lower heat transfer coefficient of the gas compared to the liquid. The boiler has been sized to reach the expected performance shown in table 3. ENOGIA has designed and manufactured the expansion machine. It is an axial turbine coupled with a generator on the same axle. The shape of the turbine blades have been adapted to the 2 different fluids based on the experience and know-how of ENOGIA. The robust design of the turbine allows to operate the ORC in flexible operating conditions without any risk of damaging turbine blades and the smart design permits to reduce significantly maintenance intervals of the expander. The condenser and the regenerator are off-the-shelf plate exchangers for cost and planning reasons, taking into account weight and compactness for a further train integration.

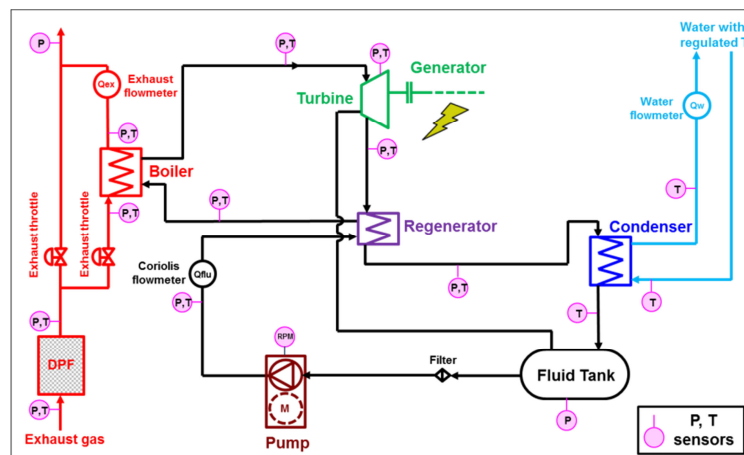


Figure 4: ORC prototype system layout with its measurement equipment for engine bench

3.3 Implementation at engine test bench

The design has taken into account a first level of constraints in terms of train integration. Train integration study has not been fully completed but has highlighted some general guidelines in order that the ORC prototype implemented at engine bench should become compatible with real train integration in the near future. A volume has been defined by the train manufacturer to implement the ORC on the train: it is represented in figure 5 by the tubular frame in blue. This constraint imposed to make a chain transmission between the electrical motor and the fluid pump. Moreover, the condenser and the regenerator had to be inclined to fit in the available room.

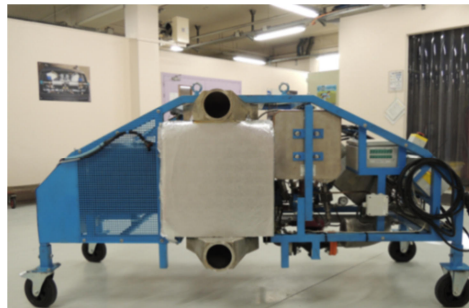


Figure 5: ORC prototype before entering in the test cell

The ORC has been manufactured with the dedicated pressure and temperature sensors. The prototype has been implemented at engine test cell and coupled up with the one Diesel engine identical to the

ones used on the train as presented in figure 6. The exhaust throttles have been mounted: the chosen technology is a flap with an electrohydraulic actuator with position feedback. The electricity generated by the ORC is injected in the test facility grid by means of a smart inverter and a transformer. The smart inverter used in this application, provided by MAVEL, allows a turbine speed regulation and real-time monitoring of the electrical power produced. For each point of the ORC circuit, based on the measurements of pressure and temperature, the fluid and exhaust gas specific enthalpies are tabulated thanks to the thermodynamic data given by the NIST software: REFPROP V9.1. The fluid and exhaust gas heat power are obtained by introducing the measurement fluid mass flow and the enthalpy of a reference state for 20°C. The heat transfer efficiencies of each exchanger are evaluated: boiler, condenser and regenerator ; the turbine efficiency is estimated by making the difference between the isentropic expansion work and the real work measured.

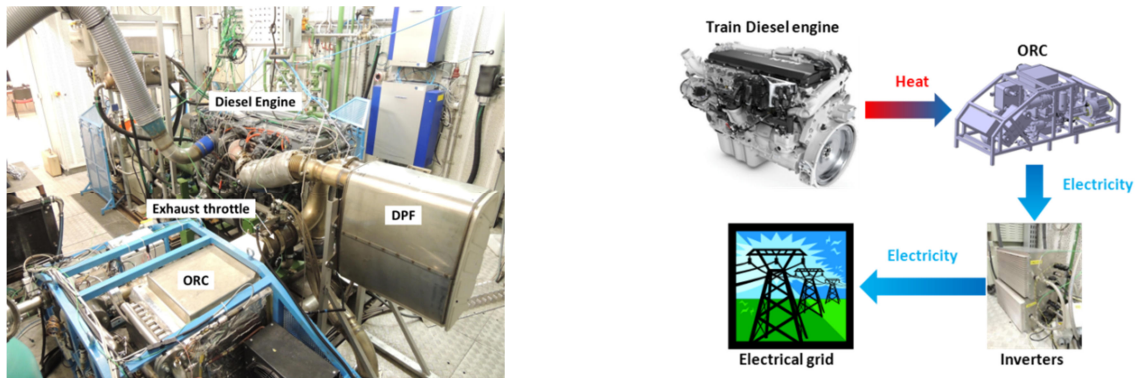


Figure 6: ORC prototype implementation at the engine bench

4. ORC CONTROL SYSTEM

One challenge of this project is to control dynamically the ORC which is a complex system evolving in transient conditions. The principle of the ORC control consists in dynamically adjusting the corner points of the thermodynamic cycle on the Mollier diagram (pressure vs. enthalpy) to ensure safe and efficient operation, with respect to changing external conditions. Ideally, one should be able to adapt both the high pressure (HP) point at evaporator outlet and the low pressure (LP) point at condenser outlet. However, this means being able to control four different thermodynamic variables (two for each point), which is in general unachievable due to the reduced number of available actuators and their lack of control authority. In practice, depending on the ORC configuration, only a few variables can be tightly controlled, and sometimes just one. All the different configurations tested during the project fall into the generic ORC layout shown in figure 7 with the inputs/outputs for control.

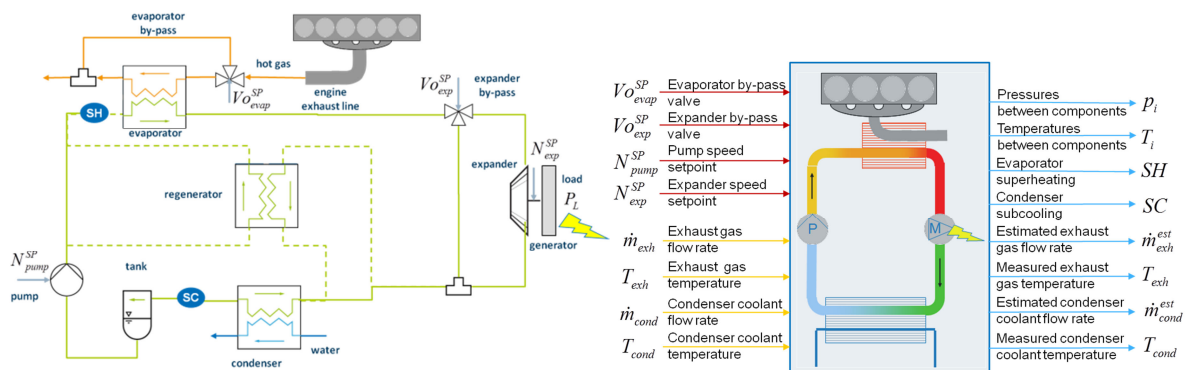


Figure 7: ORC control layout with I/O

(red: manipulated ; yellow: disturbance ; blue: measured/estimated variables)

No actuator is available for control purposes on the condenser side, which means that cooling conditions are entirely seen as an external disturbance. The turbine speed setpoint N_{exp}^{SP} sent to the inverter has little effect in the project conditions and can only be used to optimize turbine efficiency.

The turbine bypass Vo_{exp}^{SP} , which has been integrated in some configurations for safety reasons, cannot be used during nominal (power production) operation. The pump speed setpoint N_{pump}^{SP} is the only actuator with large enough control authority and can be used to control, for instance, the superheating SH at evaporator outlet, a variable which is meaningful both in terms of performance and safety. Thus, a main control loop acting on pump speed to regulate evaporator superheating can be designed, as described in Peralez et al., 2014, for a long-haul truck application. There is one last actuator available, the evaporator bypass Vo_{evap}^{SP} , which has a safety purpose too, but could in principle be used for slow regulation of another variable (HP pressure, for instance), as suggested in Peralez et al., 2014. However, contrary to long-haul truck applications, where ORC systems are most often designed for operation at roughly one third of engine full load (corresponding to flat highway conditions), see for instance Espinosa et al., 2010, the ORC system under investigation is optimized for use at engine full load. Thus, the usefulness of a control loop acting on the proportional evaporator bypass valve to regulate pressure at evaporator (fluid) outlet is very limited in this context.

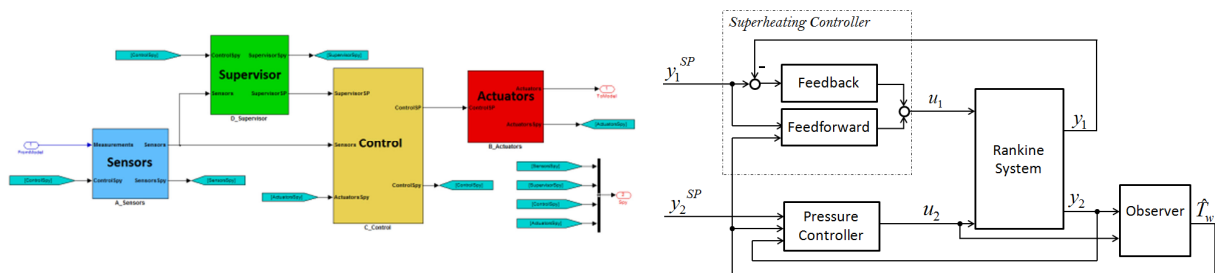


Figure 8: Global supervision and control system in Simulink (left) and decentralized control loops layout (right)

Based on these considerations, in the global supervision and control system in Simulink (figure 8), only the first decentralized control loop (the superheat controller of figure 8, where $u_1 = N_{pump}^{SP}$ and $y_1 = SH$) has been implemented so far. The superheat controller is made of two parts. The feedback part is a gain scheduled PI controller where for the feedforward part two solutions are available: a static feedforward, heuristically calibrated, and the model-based feedforward, presented in Peralez et al., 2013. A first calibration of the gain scheduled PI controller can be directly obtained using a dynamic ORC simulator, based on moving-boundary modeling of heat exchangers coded in Modelica/Dymola, coupled to the control system coded in Simulink. However, a thorough system identification campaign on several operating points is required to obtain an accurate representation of ORC dynamic behavior and finalize controller calibration.

5. EXPERIMENTAL RESULTS

5.1 Relevant results in steady-state conditions

Figure 9 presents the best results on the maximum power engine point ($>300\text{kW}$) for each ORC configuration tested. For confidentiality reasons, the heat power recovered from exhaust gases and the electric power produced at the output of the ORC turbine generator are normalized in reference to the first configuration using R245fa fluid without regenerator. The different bars of the graphs correspond to the different steps of the ORC improvements by the means of the fluid, extra exchanger, mass fluid and boiler optimizations.

The first level of optimization consisted in changing the working fluid from R245fa to fluid B and adding the regenerator. The turbine blades were changed and optimized for the use of fluid B. The chart shows a significant improvement (+22%) on the heat power recovered from the exhaust gases. Thanks to a special shape in its Mollier diagram, fluid B is specially adapted to run with an intermediate exchanger (regenerator) upstream the boiler. Indeed, this exchanger allows pre-heating the pressurized working fluid in liquid state upstream the boiler (the HP branch) with the hot working fluid in vapor state downstream the turbine (the LP branch). The drawbacks of using such exchanger are the extra mass of working fluid (cost issue) and the rising complexity of ORC control. In this project, we estimate the increase of the mass working fluid around 18% leading to an 15% extra cost

of the total ORC fluid cost. This 15% increase cost has to be compared to the 40% ORC electricity production enhancement allowed by this intermediate exchanger and the use of this new fluid B.

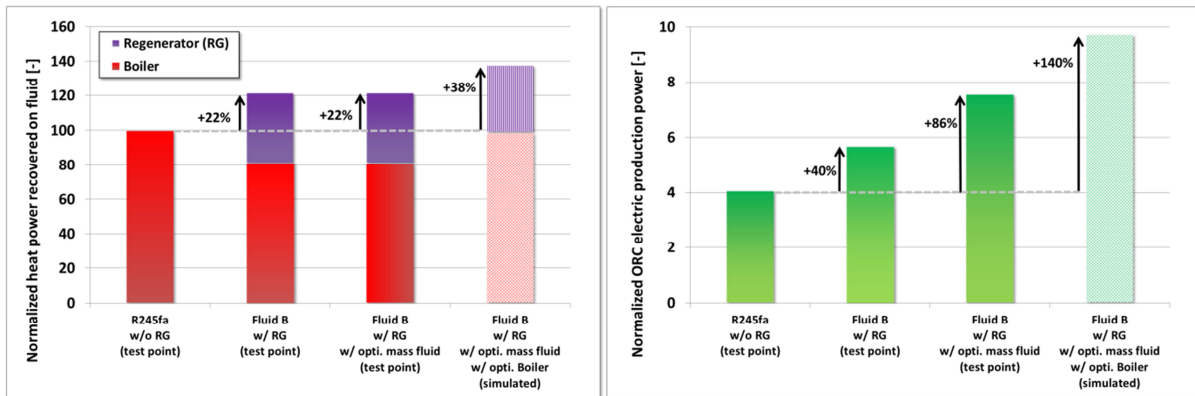


Figure 9: Tests results at max. power engine for different ORC configurations in terms of normalized heat power recovered on the fluid and ORC electric production power

The second step was to optimize the mass of working fluid inside the ORC. This operation is needed to avoid pump cavitation in case of fluid lacking or to avoid non optimized fluid liquefaction in the condenser in case of fluid overload. Furthermore, this optimized working mass fluid allows to maximize the thermodynamic efficiency of the cycle by establishing the optimized pressures in the LP and HP branches. The last step is still ongoing and the tests have not yet been done. Calculations have predicted that with an optimized boiler with higher exchange surface, exhaust gas heat recovering can be improved by 38% compared to the first configuration and ORC electric power output increased by 140%. The tests are still on-going and at the time of paper writing, more than 150hours of ORC operation have been carried out and 600 operating points (steady-state or transient) have been recorded. As a significant achievement, around 10kW of electricity power produced by the ORC turbine generator have been measured continuously in the last tests.

5.2 Boiler hunting

In this project, among all the technical challenges that have been taken up, the boiler has shown sometimes an unstable behavior in steady-state thermal conditions. Indeed, with stabilized constant exhaust gas and working fluid mass flows, temperature periodic oscillations can appear downstream the boiler. This phenomenon is well-known in refrigerating applications like described by Mithraratne et al., 2002, with diphasic exchangers and it has been called “boiler hunting”. More recently, Yuh-Ren et al., 2014, faced the same problem with an ORC using R245fa. In this project, we observed the boiler hunting for both working fluids R245fa and fluid B (see figure 10) with the same boiler but with different signal properties. The signal period were respectively 40s and 17s whereas peak amplitude were respectively 8°C and 6°C for R245fa and fluid B. As a remark, temperature sensors accuracy is around $\pm 0,5^{\circ}\text{C}$. Until now, no consistent scientific explanation exists justifying such behavior. Some scientists assume that the phenomenon depends on the working fluid characteristics and on the boiler internal geometry. This abnormal behavior must be avoided to ensure a robust and consistent ORC control in transient conditions.

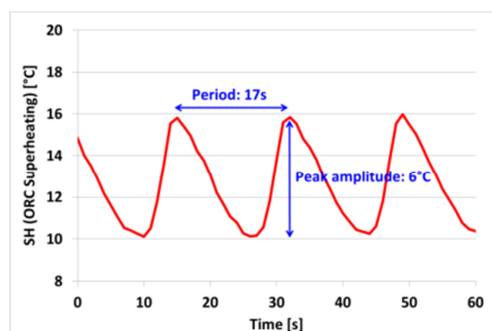


Figure 10: ORC superheating oscillations in steady-state conditions (T, P) after the boiler for fluid B

6. CONCLUSIONS

This pre-industrial project has succeeded in building an operational ORC prototype for a train application by merging the skills of IFPEN and ENOGIA. A pre-sizing study allowed to identify the exergy potential on a realistic train mission profile and the optimal recovery system location provided by ALSTOM TRANSPORT. Then, the screening fluid allowed to choose 2 suitable working fluids for this application considering all the safety, thermodynamic and cost constraints. The expected results were evaluated by simulation. The ORC prototype was built by ENOGIA by selecting the optimal components and respecting a limited volume for further train integration. The prototype has then been implemented at the test bench at IFPEN. An ORC control has been deployed using the know-how of IFPEN previous experiences on Rankine systems. These tools work with the help of exhaustive measures of temperature, pressure and mass flows allowing to evaluate in real-time conditions the energy balance of the whole ORC system. Experimental results showed the high increase of waste heat recovery and electric produced power after each improvement step along the project duration. The change of fluid and the addition of the regenerator increased the electric production by 86% compared to the first configuration. At the time of paper writing, around 10kW of ORC electricity output power has been reached in stable conditions and more than 150h of testing have been carried out. Further improvements should be attainable.

NOMENCLATURE

DPF	Diesel Particulate Filter
GWP / ODP	Greenhouse Warming Potential / Ozone Depleting Potential
IFPEN	IFP Energies nouvelles
NIST	US National Institute of Standards and Technology
ORC	Organic Rankine Cycle
SH/SC	SuperHeating/SubCooling
WHR	Waste Heat Recovery

REFERENCES

- El Habchi, A., Ternel, C., Leduc, P., Hetet, J.F., 2010, Potential of waste heat recovery for automotive engines using detailed simulation, *ASME Conference on Thermal and Environmental Issues in Energy Systems*.
- Espinosa, N., L. Tilman, V. Lemort, S. Quoilin, B. Lombard, 2010, Rankine cycle for waste heat recovery on commercial trucks: approach, constraints and modeling, in Proceedings of the Diesel International Conference and Exhibition, SIA.
- Mithraratne, P., Wijesundera, N.E., 2002, An experimental and numerical study of hunting in thermostatic-expansion-valve-controlled evaporators, *International Journal of Refrigeration*, Volume 25, Issue 7, p. 992-998, ISSN 0140-7007.
- Peralez, J., Nadri, M., Dufour, P., Tona, P. ; Sciarretta, A., 2014, Control design for an automotive turbine Rankine Cycle system based on nonlinear state estimation, *2014 Conference on Decision and Control (CDC)*, IEEE, p. 3316 - 3321.
- Ringler, J., Seifert, M., Guyotot, V., Hübner, W., 2009, Rankine cycle for waste heat recovery of IC engines, *SAE Int. J. engines*, Vol. 2, Issue 1, p. 67-76.
- Yuh-Ren, L., Chi-Ron, K., Chih-His, L., Ben-Ran, F., Jui-Ching, H., Chi-Chuan, W., 2014, Dynamic Response of a 50 kW Organic Rankine Cycle System in Association with Evaporators, *Energies* 7, no. 4: 2436-2448.

ACKNOWLEDGEMENT

The authors would like to thank all the partners of this project: ALSTOM TRANSPORT for providing the engine and the ANR (Agence Nationale de la Recherche) for funding the project. Finally, a special thank you goes to Jocelyn Terver, the technician who performed the tests at the engine bench.

PERFORMANCE ANALYSIS OF WASTE HEAT RECOVERY WITH A DUAL LOOP ORGANIC RANKINE CYCLE SYSTEM FOR DIESEL ENGINE

Hongjin Wang^{1,2*}, Hongguang Zhang^{1,2}

¹College of Environmental and Energy Engineering, Beijing University of Technology, Pingleyuan No.100, 100124 Beijing, China

²Collaborative Innovation Center of Electric Vehicles in Beijing, Pingleyuan No.100, 100124 Beijing, China
e-mail:bjgywanghongjin@163.com

* Corresponding Author

ABSTRACT

To take full advantage of the waste heat from a diesel engine, a set of dual loop organic Rankine cycle system (ORCs) was designed to recover exhaust energy, waste heat from the coolant system, and released heat from turbocharged air in the intercooler of a six-cylinder diesel engine. Aspen plus software was used to model the dual loop ORCs. According to the simulation model, the operating performance of the dual loop ORCs and the fuel economy of the diesel engine were investigated. The results show that the thermodynamic performance and economy performance of the diesel engine can be effectively improved by using the dual loop ORCs. At the engine rated condition, the overall net power output of the dual loop ORCs is up to 43.65 kW. The brake specific fuel consumption (BSFC) and the thermal efficiency of the diesel engine-dual loop ORCs are $191.24 \text{ g}\cdot(\text{kW}\cdot\text{h})^{-1}$ and 37.57%, respectively. Compared with the diesel engine, the thermal efficiency of the combined system can be increased by 13.69% and the BSFC can be reduced by 15.86%.

1. INTRODUCTION

A large amount of petroleum resources has been consumed by automobiles. Meanwhile, given the low utilization rate for internal combustion engine, the thermal efficiency is only 30%-45% for diesel engine and 20%-30% for gasoline engine. And then the remaining heat is released into the atmosphere (Dolz *et al.*, 2012, Roy *et al.*, 2010). Therefore, discovering a more effective way to recover internal combustion engine waste heat so as to increase engine thermal efficiency and decrease fuel consumption has become a hot focus of recent research work.

ORCs has been widely used to recover and utilize the low-grade waste heat and recently numerous scholars have investigated the use of ORCs to recover engine exhaust waste heat energy (Fang *et al.*, 2010, Liu *et al.*, 2012). Shu *et al.* (2014) designed a set of dual loop ORCs to recover exhaust waste heat energy and coolant system waste heat. Results showed that using the dual loop ORCs can effectively improve the thermodynamic performance of the engine. Gao *et al.* (2013) proposed ORCs to recover the exhaust waste heat of a turbocharged diesel engine. The results showed that the net power output of the diesel engine can improve 12%. Meinel *et al.* (2014) compared a two-stage ORC with internal heat recovery with a simple standard ORCs and an ORC with a recuperator based on Aspen Plus software. The thermodynamic efficiencies of the two-stage cycle exceed the corresponding values of reference ORCs by up to 2.25%.

Although many scholars have analyzed the performance of different kinds of ORCs, most research takes only internal combustion engine exhaust energy into account. Few of them have considered recovering the waste heat from the coolant system, and the released heat from turbocharged air in the intercooler of internal combustion engine. In this paper, a set of dual loop ORCs is designed to recover exhaust waste heat energy, waste heat from the coolant system, and released heat from turbocharged air in the intercooler of a diesel engine. Aspen plus software is used to model the dual

loop ORCs, and then the operation performance is analyzed based on the sensitivity analysis under the different high temperature cycle evaporation pressure and the working fluid mass flow rate.

2. MODEL OF DUAL LOOP ORC SYSTEM

2.1 Model of Dual Loop ORCs Based on Aspen Plus

The exhaust temperature of diesel engine is generally high. However, the temperatures of the coolant and the turbocharged air are relatively low. To take full advantage of the waste heat energy from the diesel engine, a set of dual loop ORCs is designed. As shown in Figure 1, the dual loop ORCs contains a high temperature (HT) loop ORCs (the lower part) and a (low temperature) LT loop ORCs (the upper part). The HT loop ORCs is used to recover the high-temperature exhaust energy, while the LT loop ORCs is used to recover the waste heat from the coolant system, the released heat from turbocharged air in the intercooler and the residual heat of low-temperature exhaust energy. Figure 2 and Figure 3 are the T - s diagram of the HT loop and LT loop in the dual loop ORCs, respectively.

The dual loop ORCs system operates according to the following process. In the HT loop ORCs (corresponding to Processes 1-7), the working fluid is pressurized into the saturated liquid state working fluid using Pump 1. Then it is preheated in the Recuperator. Subsequently, the working fluid turns into a saturated vapor state in the Evaporator 1. Then, the saturated vapor enters Expander 1 to produce useful work. Finally, the superheated vapor exported from Expander 1 turns into a saturated liquid state after the heat transfer process in the Recuperator and Condenser 1. With this change, the HT loop ORCs completes one working cycle. Meanwhile, in the LT loop ORCs (corresponding to Processes 10-16), Pump 2 pressurizes the saturated liquid state working fluid and sends it into the Intercooler to exchange heat with the turbocharged intake air. Then, the working fluid flows into the Preheater and is heated up into the two-phase state by the engine coolant. Later, the two-phase working fluid is heated up into a saturated vapor state by the residual heat of the low-temperature exhaust energy in the Evaporator 2. The saturated vapor enters Expander 2 to make it do work. Finally, the superheated vapor exported from Expander 2 condenses into a saturated liquid state in the Condenser 2. The whole process is then completed.

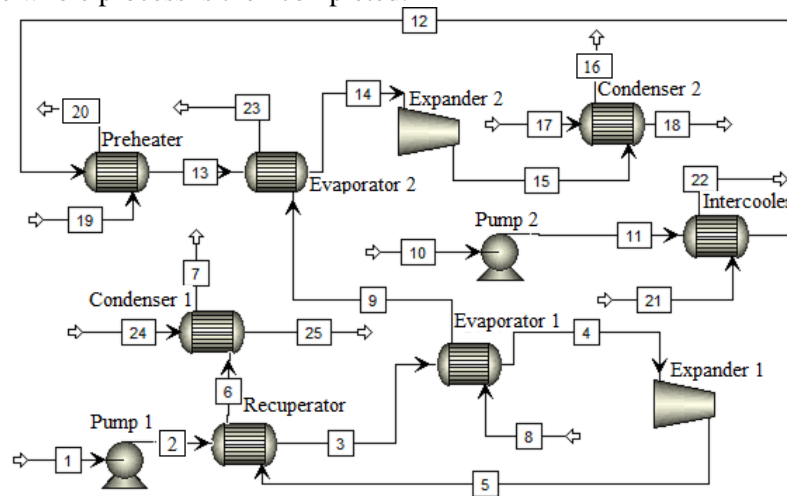


Figure 1: Model of the dual loop ORCs

2.2 Boundary Conditions

- (1) The thermodynamic properties of fluid are calculated based on the Peng-Robinson state equation. R123 is selected as the working fluid, water is selected as the coolant. The diesel engine air fuel ratio is set to 19.7, mass fraction of the exhaust components CO_2 , H_2O , N_2 and O_2 is 15.1%, 5.5%, 71.6% and 7.8%, respectively. (Shu *et al.*, 2014).
- (2) The isentropic efficiencies of expander 1 and expander 2 are both set to 0.7. The isentropic efficiencies of Pump 1 and Pump 2 are both set to 0.65.
- (3) The ambient temperature is set to 291.15 K.
- (4) The working fluid temperature at the evaporator 1 outlet is set to 456K. When the exhaust

temperature drops below the dew point, the exhaust pipes and evaporator surfaces can erode, so the exhaust temperature at the evaporator 2 outlet is set to 380K. (Bahadori, 2011).

(5) The mass flow rate of the HT loop ORCs is set to 0.4-0.8 kg/s; The evaporation pressure of HT loop ORCs is set to 1.0-2.5MPa.

(6) The cooling water inlet temperature and mass flow rate of Condenser1 are set to 285K and 2kg/s (corresponding to Processes 24-25 in Figure 1); The same as the Condenser2 are set to 285K and 3kg/s (corresponding to Processes 17-18 in Figure 1).

(7) The outlet temperature of engine coolant is set to 340K (corresponding to Processes 21-22 in Figure 1)

(8) The outlet temperature of turbocharged intake air is set to 350K (corresponding to Processes 19-20 in Figure 1)

(9) The test parameters of the diesel engine at rated conditions are listed in Table 1.

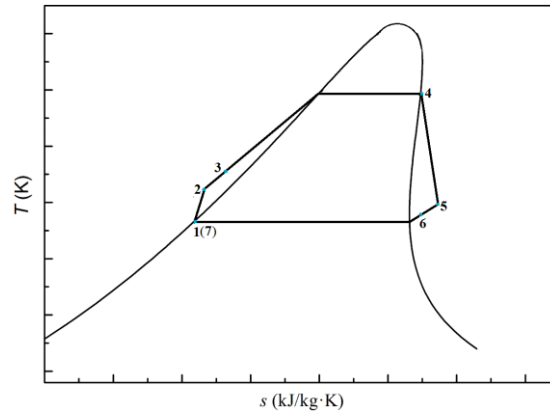


Figure 2: T-s diagram of the HT loop ORCs

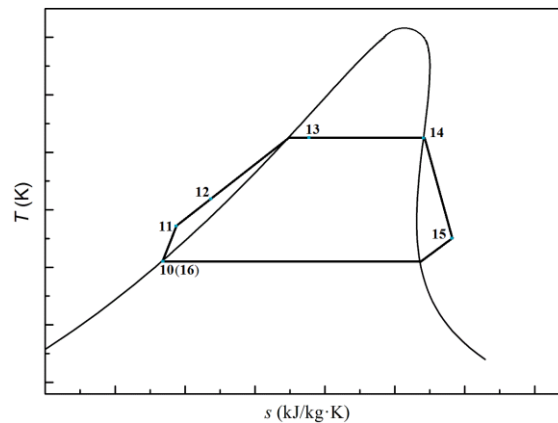


Figure 3: T-s diagram of the LT loop ORCs

Table 1: Test parameters of the diesel engine

Items	value
Rated speed/ r·min ⁻¹	2000
Rated power / kW	275
Exhaust temperature/ K	783
Air intake mass flow rate/ kg·s ⁻¹	0.43
Fuel consumption/ kg·h ⁻¹	60.97
Intake air temperature/ K	407
Engine coolant mass flow rate/ kg·s ⁻¹	1.30
Engine coolant temperature/K	370

2.3 Thermodynamic Model of the Dual Loop ORCs

To evaluate the performance of the dual loop ORCs, the following parameters are selected in the study.

The net power output of HT loop ORCs is given in Equation (1):

$$\dot{W}_H = \dot{W}_{\text{exp1}} - \dot{W}_{\text{p1}} \quad (1)$$

The net power output of LT loop ORCs is given in Equation (2):

$$\dot{W}_L = \dot{W}_{\text{exp2}} - \dot{W}_{\text{p2}} \quad (2)$$

Where \dot{W}_{p1} and \dot{W}_{p2} are the power consumed by pump 1 and pump 2, respectively. \dot{W}_{exp1} and \dot{W}_{exp2} are the power output of the expander 1 and expander 2, respectively.

The overall net power output of the dual loop ORCs is given in Equation (3):

$$\dot{W}_{\text{oa}} = \dot{W}_H + \dot{W}_L \quad (3)$$

The thermal efficiency of the dual loop ORCs is given in Equation (4):

$$\eta_{\text{oa}} = \frac{\dot{W}_{\text{oa}}}{\dot{Q}_{\text{oa}}} \times 100\% \quad (4)$$

Where \dot{Q}_{oa} is the overall heat transfer rate of the dual loop ORCs:

$$\dot{Q}_{\text{oa}} = \dot{Q}_{\text{e1}} + \dot{Q}_{\text{e2}} + \dot{Q}_{\text{int}} + \dot{Q}_{\text{pre}} \quad (5)$$

Where \dot{Q}_{e1} , \dot{Q}_{e2} , \dot{Q}_{int} and \dot{Q}_{pre} are the heat transfer rate of evaporator 1, evaporator 2, intercooler and preheater, respectively.

To assess the economy performance of the diesel engine-dual loop ORC combined system, the brake specific fuel consumption (BSFC) of the combined system is defined as:

$$bsfc_{\text{cs}} = \frac{\dot{F}}{\dot{W}_{\text{eng}} + \dot{W}_{\text{oa}}} \times 1000 \quad (6)$$

Where \dot{F} represents the fuel consumption of the diesel engine; \dot{W}_{eng} represents the power of diesel engine.

The BSFC of the diesel engine is defined as:

$$bsfc_{\text{eng}} = \frac{\dot{F}}{\dot{W}_{\text{eng}}} \times 1000 \quad (7)$$

The improvement ratio of BSFC of the combined system is defined as:

$$\eta_{\text{cs}} = \frac{bsfc_{\text{eng}} - bsfc_{\text{cs}}}{bsfc_{\text{eng}}} \times 100\% \quad (8)$$

The thermal efficiency of the diesel engine is given in Equation (9):

$$\eta_{\text{eng}} = \frac{\dot{W}_{\text{eng}}}{\dot{Q}_{\text{cs}}} \times 100\% \quad (9)$$

Where \dot{Q}_{cs} represents the overall energy generated by fuel combustion of the diesel engine.

The thermal efficiency of the combined system is defined as:

$$\eta_{\text{cst}} = \frac{\dot{W}_{\text{oa}} + \dot{W}_{\text{eng}}}{\dot{Q}_{\text{cs}}} \times 100\% \quad (10)$$

The increasing ratio of thermal efficiency in the combined system is defined as:

$$\eta_{\text{tei}} = \frac{\eta_{\text{cst}} - \eta_{\text{eng}}}{\eta_{\text{eng}}} \times 100\% \quad (11)$$

The exergy destruction rate of the each components are given in Equations (12)-(22):

$$\dot{I}_{\text{p1}} = T_0 \dot{m}_H (s_2 - s_1) \quad (12)$$

$$\dot{I}_{\text{p2}} = T_0 \dot{m}_L (s_{11} - s_{10}) \quad (13)$$

$$\dot{I}_{\text{r}} = \dot{T}_0 \dot{m}_H [(s_6 - s_5) + (s_3 - s_2)] \quad (14)$$

$$\dot{I}_{e1} = T_0 \dot{m}_H [(s_4 - s_3) - \frac{h_4 - h_3}{T_{H,H}}] \quad (15)$$

Where $T_{H,H}$ is the temperature of the high temperature heat source in the HT loop ORCs, and is assumed to be equal to $T_{H,H} = T_4 + 5$.

$$\dot{I}_{e2} = T_0 \dot{m}_L [(s_{14} - s_{13}) - \frac{h_{14} - h_{13}}{T_{L,H}}] \quad (16)$$

Where $T_{L,H}$ is the temperature of the high temperature heat source in the LT loop ORCs, and is assumed to be equal to $T_{L,H} = T_{14} + 5$.

$$\dot{I}_{exp1} = T_0 \dot{m}_H (s_5 - s_4) \quad (17)$$

$$\dot{I}_{exp2} = T_0 \dot{m}_L (s_{15} - s_{14}) \quad (18)$$

$$\dot{I}_{int} = T_0 \dot{m}_L [(s_{12} - s_{11}) - \frac{h_{12} - h_{11}}{T_{int,H}}] \quad (19)$$

Where $T_{int,H}$ is the temperature of the heat source in the intercooler, and is assumed to be equal to $T_{int,H} = T_{12} + 5$.

$$\dot{I}_{pre} = T_0 \dot{m}_L [(s_{13} - s_{12}) - \frac{h_{13} - h_{12}}{T_{pre,H}}] \quad (20)$$

Where $T_{pre,H}$ is the temperature of the heat source in the intercooler, and is assumed to be equal to $T_{pre,H} = T_{13} + 5$.

$$\dot{I}_{con1} = T_0 \dot{m}_L [(s_7 - s_6) - \frac{h_7 - h_6}{T_{H,L}}] \quad (21)$$

Where $T_{H,L}$ is the temperature of the low temperature heat source in the HT loop ORCs, and is assumed to be equal to $T_{H,L} = T_7 - 5$.

$$\dot{I}_{con2} = T_0 \dot{m}_L [(s_{16} - s_{15}) - \frac{h_{16} - h_{15}}{T_{L,L}}] \quad (22)$$

Where $T_{L,L}$ is the temperature of the low temperature heat source in the LT loop ORCs, and is assumed to be equal to $T_{L,L} = T_{16} - 5$.

Note that Eq. (15),(19),(21)and (22) are derived from Ref. (Yang *et al.*, 2014)

3. RESULTS AND DISCUSSION

The variation of the net power output in LT loop ORCs with the evaporation pressure and mass flow rate of the HT loop ORCs is shown in Figure 4. The graph shows that at a certain evaporation pressure of HT loop ORCs, the net power output of the LT loop ORCs decreases gradually with the increase of the mass flow rate of HT loop ORCs. This primarily because that, the heat transfer rate of evaporator 1 increases with the increase of mass flow rate at the HT loop ORCs. Therefore, the heat transfer rate of evaporator 2 decrease. At a certain mass flow rate of HT loop ORCs, the net power output of the LT loop ORCs increases gradually with the increase of the evaporation pressure of HT loop ORCs. When the evaporation pressure and mass flow rate of HT loop ORCs are 2.5 MPa and 0.4 kg·s⁻¹, the net power output of the LT loop ORCs reaches the upper limit and is 24.63 kW.

The variation of the net power output in HT loop ORCs with the evaporation pressure and mass flow rate of the HT loop ORCs is shown in Figure 5. The graph shows that at a certain evaporation pressure of HT loop ORCs, the net power output of the HT loop ORCs increases gradually with the increase of the mass flow rate of HT loop ORCs. At a certain mass flow rate of HT loop ORCs, the net power output of the HT loop ORCs increases gradually with the increase of the evaporation pressure of HT loop ORCs. When the evaporation pressure and mass flow rate of HT loop ORCs are 2.5 MPa and 0.8 kg·s⁻¹, the net power output of the HT loop ORCs reaches the upper limit and is 24.99 kW.

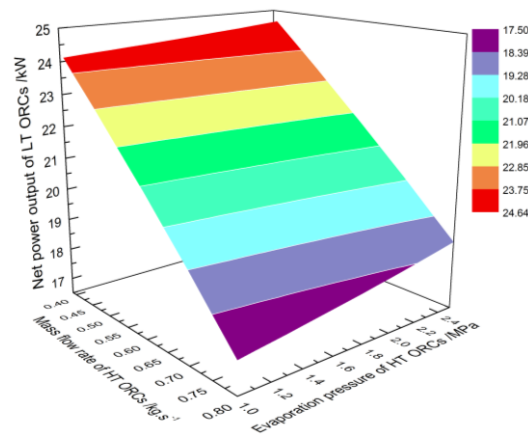


Figure 4: Net power output of the LT loop ORCs

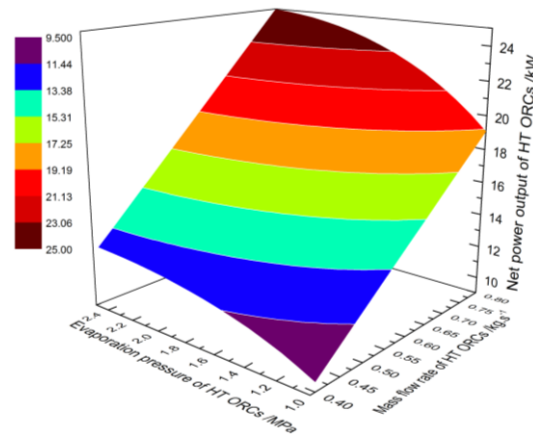


Figure 5: Net power output of the HT loop ORCs

Through the comparison between Figure 4 and Figure 5, it can be concluded that the net power output of the LT loop ORCs and the HT loop ORCs are affected more by mass flow rate of the HT loop ORCs. And the net power output of the LT loop ORC system is greater than that of the HT loop ORC system under the same evaporation pressure of HT ORCs.

The variation of the overall net power output in dual loop ORCs with the evaporation pressure and mass flow rate of the HT loop ORCs is shown in Figure 6. The graph shows that at a certain evaporation pressure of HT loop ORCs, the overall net power output of the dual loop ORCs increases gradually with the increase of the mass flow rate of HT loop ORCs. This primarily because that, with the increase of the mass flow rate of HT loop ORCs, the variation of net power output of HT loop ORCs is relatively higher than that of LT loop ORCs. At a certain mass flow rate of HT loop ORCs, the net power output of the dual loop ORCs increases gradually with the increase of the evaporation pressure of HT loop ORCs. When the evaporation pressure and mass flow rate of HT loop ORCs are 2.5 MPa and $0.8 \text{ kg}\cdot\text{s}^{-1}$, the overall net power output of the dual loop ORCs reaches the upper limit and is 43.65 kW.

The variation of the thermal efficiency in dual loop ORCs with the evaporation pressure and mass flow rate of the HT loop ORCs is shown in Figure 7. Moreover, the thermal efficiency has the same variation tendency with the overall net power output of the dual loop ORCs. The reason can be explained as follows. According to Eq. (4), the thermal efficiency of dual loop ORCs is related to the overall heat transfer rate and the overall net power output of the dual loop ORCs. The overall heat transfer rate is constant due to the constant operating condition of diesel engine, while the overall net power out of dual loop ORCs increases with evaporation pressure and mass flow rate of HT loop ORCs, as shown in Figure 6. When the evaporation pressure and mass flow rate of HT loop ORCs are

2.5 MPa and $0.8 \text{ kg}\cdot\text{s}^{-1}$, the thermal efficiency of the dual loop ORCs reaches the upper limit and is 10.52%.

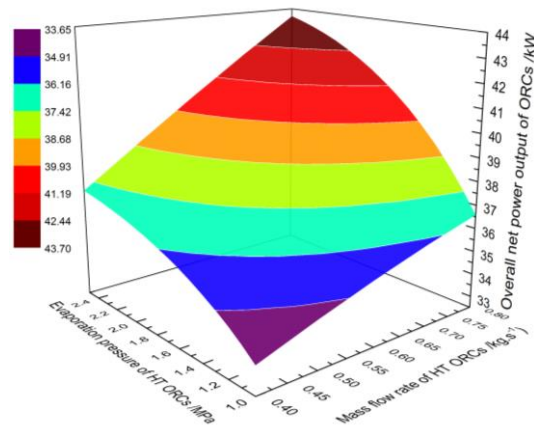


Figure 6: Overall net power output of the dual loop ORCs

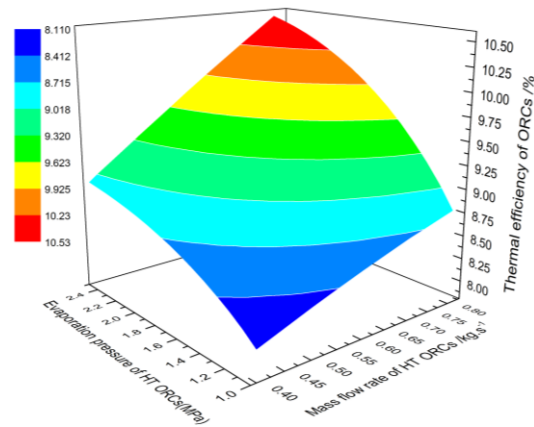


Figure 7: Thermal efficiency of the dual loop ORCs

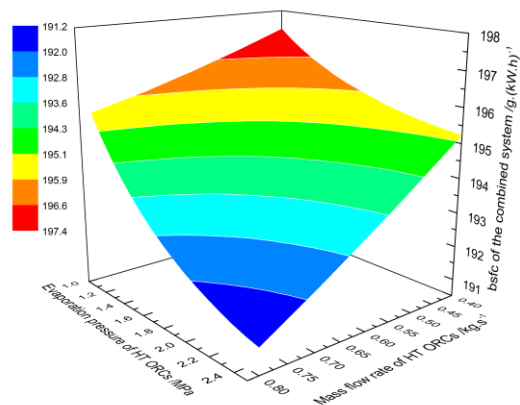


Figure 8: BSFC of the combined system

The variation of the BSFC in diesel engine-dual loop organic Rankine cycle (ORC) combined system with the evaporation pressure and mass flow rate of the HT loop ORCs is shown in Figure 8. The graph shows that at a certain evaporation pressure of HT loop ORCs, the BSFC of the combined system decreases gradually with the increase of the mass flow rate of HT loop ORCs. At a certain mass flow rate of HT loop ORCs, the BSFC of the combined system decreases gradually with the

increase of the evaporation pressure of HT loop ORCs. The reason can be explained as follows. According to Eq. (6), the BSFC of combine system is related to the fuel consumption, the power of diesel engine and the overall net power output of the dual loop ORCs. The fuel consumption and the power of diesel engine is constant due to the constant operating condition of diesel engine, while the overall net power out of dual loop ORCs increases with evaporation pressure and mass flow rate of HT loop ORCs, as shown in Figure 4. When the evaporation pressure and mass flow rate of HT loop ORCs are 2.5 MPa and $0.8 \text{ kg}\cdot\text{s}^{-1}$, the BSFC of the diesel engine-dual loop ORC combined system reaches the minimum and is $191.24 \text{ g}\cdot(\text{kW}\cdot\text{h})^{-1}$.

The variation of the improvement ratio of BSFC in diesel engine-dual loop ORC combined system with the evaporation pressure and mass flow rate of the HT loop ORCs is shown in Figure 9. The graph shows the improvement ratio of BSFC in the combined system gradually increases with evaporation pressure and mass flow rate of HT loop ORCs. Moreover, the minimum improvement ratio of BSFC is 10.9%. When the evaporation pressure and mass flow rate of HT loop ORCs are 2.5 MPa and $0.8 \text{ kg}\cdot\text{s}^{-1}$, the improvement ratio of BSFC in the diesel engine-dual loop ORC combined system reaches the upper limit and is 13.69%.

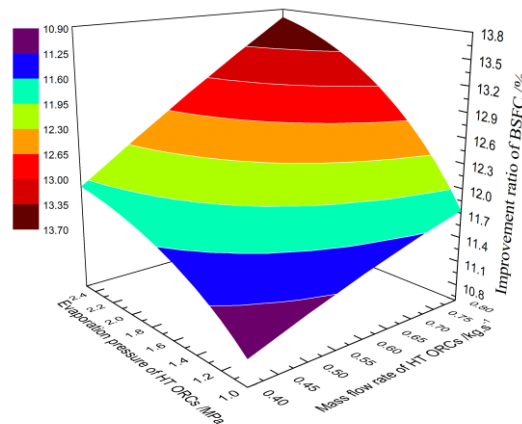


Figure 9: Improvement ratio of BSFC in the combined system

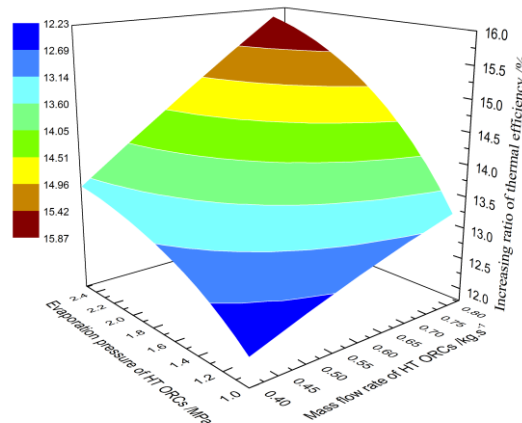


Figure 10: Increasing ratio of thermal efficiency in the combine system

The variation of the thermal efficiency improvement in diesel engine-dual loop ORC combined system with the evaporation pressure and mass flow rate of the HT loop ORCs is shown in Figure 10. Compare with Figure 6, the increasing ratio of thermal efficiency in the combine system has the same variation tendency with the overall net power output of the dual loop ORCs. Moreover, the minimum thermal efficiency improvement is 12.23%. When the evaporation pressure and mass flow rate of HT loop ORCs are 2.5 MPa and $0.8 \text{ kg}\cdot\text{s}^{-1}$, the increasing ratio of thermal efficiency in the diesel engine-dual loop ORC combined system reaches the upper limit and is 15.86%.

Figure 11 shows the variations of the exergy destruction rate in dual loop ORCs under the condition of the overall net power output reaches the upper limit. The graph shows that, the exergy destruction rate of the condenser 2 is bigger than that of other components and is 15.64kW, followed by condenser 1 and evaporator 1. They are 14.70 kW and 13.33 kW, respectively. The exergy destruction of condenser 1 and condenser 2 are all bigger due to the higher temperature difference between the working fluid and cooling water at the condenser. Whereas, the exergy destruction of evaporator 1 is bigger because of the higher temperature difference between the working fluid and exhaust gas at the evaporator 1. The exergy destruction rate of the dual loop ORCs and LT ORCs are 40.78 kW and 29.75 kW, respectively.

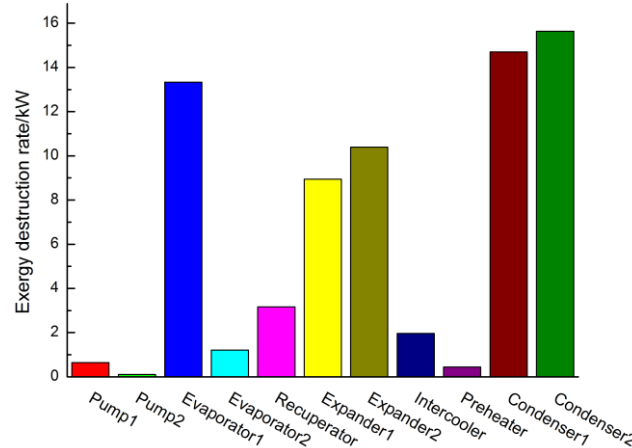


Figure 11: Exergy destruction rate of the dual loop ORCs

4. CONCLUSIONS

- By employing the dual loop ORC system, the waste heat of exhaust energy, coolant system, and released heat from turbocharged air in the intercooler can be effectively recovered and utilized. The overall net power output and thermal efficiency of the dual loop ORCs can reach 43.65kW and 10.52%, respectively.
- The fuel economy of the diesel engine can be notably improved, by employing the dual loop ORCs. When the evaporation pressure and mass flow rate of HT loop ORCs are 2.5 MPa and 0.8 kg·s⁻¹, the BSFC of the diesel engine-dual loop ORC combined system is 191.24 g·(kW·h)⁻¹, which reduced by 13.69% compared with the diesel engine itself.
- The net power output of LT loop ORCs is greater than that of HT loop ORCs. At the maximum overall net power output condition, the exergy destruction rate of the LT loop ORC system is higher than that of the HT loop ORC system and the difference can reach 11.03kW.

NOMENCLATURE

m	mass flow rate	(kg·s ⁻¹)
h	enthalpy	(kJ·kg ⁻¹)
Q	heat transfer rate	(kJ)
S	entropy	(kJ/kg·K)
T	temperature	(K)
W	work	(kJ)
η	efficiency	(%)
F	fuel consumption	(kg·h ⁻¹)
I	exergy destruction	(kW)

Subscript

1,2, 3...	state point in cycle
H	HT loop ORCs/high temperature heat source
L	LT loop ORCs/low temperature heat source
p	pump
e	evaporator
r	recuperator
exp	expander
int	intercooler
pre	preheater
con	condenser
eng	diesel engine
cs	combined system
oa	overall of dual loop ORCs
cst	thermal efficiency of the combined system
tei	thermal efficiency improvement

REFERENCES

- Dolz, V., Novella R., García, A., et al. 2012, HD Diesel engine equipped with a bottoming Rankine cycle as a waste heat recovery system. Part 1: study and analysis of the waste heat energy. *Appl Therm Eng*, vol. 36: p. 269-278.
- Roy, J.P., Mishra, M.K., Misra, A., 2010, Parametric optimization and performance analysis of a waste heat recovery system using Organic Rankine Cycle. *Energy*, vol. 35: p. 5049-5062.
- Fang, J.L., Wei, M.S., Wang, J.R., et al, 2010, Simulation of Waste Heat Recovery from a Heavy-Duty Diesel Engine with a Medium Temperature ORCs. *Transactions of CSICE*, vol. 4, no. 28: p. 362-367.
- Liu, B., Rivière, P., Coquelet, C., et al, 2012, Investigation of a two stage Rankine cycle for electric power plants. *Appl Energ*, vol. 100: p. 285-294.
- Tian, H., Liu, L.N., Shu, G.Q., et al, 2014, Theoretical research on working fluid selection for a high-temperature regenerative transcritical dual-loop engine organic Rankine cycle. *Energ Convers Manage*, vol. 86: p. 764-773.
- Shu, G.Q., Liu, L.N., Tian.H., et al, 2014, Parametric and working fluid analysis of a dual-loop organic Rankine (DORC) used in engine waste heat recovery. *Appl Energ*, vol. 113: p. 1188-1198.
- Gao, W.Z., Zhai, J.M., Li, G.H., et al, 2013, Performance evaluation and experiment system for waste heat recovery of diesel engine. *Energy*, vol.15, no. 55: p. 226-235.
- Meinel, D., Wieland, C., Spliethoff, H, 2014, Effect and comparison of different working fluids on a two-stage organic rankine cycle (ORC) concept. *Appl Therm Eng*, vol. 63: p. 246-253.
- Yu, G.P., Shu, G.Q., Tian, H. et al. 2013, Simulation and thermodynamic analysis of a bottoming Organic Rankine Cycle. *Energy*, vol. 51: p. 281-290.
- Bahadori, A., 2011, Estimation of combustion flue gas acid dew point during heat recovery and efficiency gain. *Appl Therm Eng*, vol. 31: p. 1457-1462.
- Yang, F.B., Dong, X.R., Zhang, H.G. et al, 2014, Performance analysis of waste heat recovery with a dual loop organic Rankine cycle (ORC) system for diesel engine under various operating conditions. *Energ Convers Manage*, vol. 80: p. 243-255.

ACKNOWLEDGEMENT

This work was sponsored by the National Natural Science Foundation of China (Grant No. 51376011), the Beijing Natural Science Foundation Program (Grant No. 3152005), and the Scientific Research Key Program of Beijing Municipal Commission of Education (Grant No. KZ201410005003).

POTENTIAL OF SMALL-SCALE TURBOMACHINERY FOR WASTE HEAT RECOVERY ON AUTOMOTIVE INTERNAL COMBUSTION ENGINES

Kévin ROSSET^{1*}, Violette MOUNIER¹, Elliott GUENAT¹, Olivier PAJOT², Jürg SCHIFFMANN¹

¹Ecole Polytechnique Fédérale de Lausanne, Laboratory for Applied Mechanical Design,
Neuchâtel, Switzerland

kevin.rosset@epfl.ch, violette.mounier@epfl.ch, eliott.guenat@epfl.ch, jurg.schiffmann@epfl.ch

²PSA Peugeot Citroën, Research, Innovation & Advanced Technologies Division,
Lausanne, Switzerland

olivier.pajot@mps.com

* Corresponding Author

ABSTRACT

This paper investigates the waste heat recovery potential of internal combustion engines, using organic Rankine cycles running on small-scale radial turbomachinery. ORC are promising candidates for low-grade thermal sources and the use of dynamic expanders yields very compact systems, which is advantageous for automotive applications. As engine coolant and exhaust gases are the major available heat sources, different cycle configurations and working fluids have been investigated to capture them, in both urban and highway car operation. Pareto fronts showing the compromise between net power output and total heat exchange area have been identified for a set of cycle's variables including turbine inlet conditions and heat exchanger pinches. A preliminary optimization, including only R-1234yf working fluid, shows that a single-source regenerative cycle harvesting the high temperature exhaust gas stream performs averagely better than coolant-driven and dual-source cycles. A more in-depth optimization including eight working fluids as well as aerodynamic and conceptual limitations related to radial turbomachinery and automotive design constraints, finally shows that an ICE exhaust heat recovery ORC could improve the first law efficiency of the driving system by up to 10% when implemented with fluid R-1233zd.

1. INTRODUCTION

Nowadays, concerns about fossil fuel shortage and global warming advocate for a more rational use of primary energy. Transportation, which represents about 28% of the world energy consumption (IEA, 2014), is a sector where efficiency improvements are particularly awaited. Indeed, according to Legros (2014) passenger cars are barely using one third of the available fuel power to drive the wheels. The remaining two thirds are rejected to the environment as waste heat, mainly through coolant and exhaust gas streams. Recovering part of this energy would not only save fuel but also decrease pollutants emissions. The conversion of heat into useful electrical or mechanical energy may be performed by technologies like thermoelectric, thermoacoustic and thermophotovoltaic generators or by various thermodynamic cycles such as Stirling, Brayton and Rankine cycles, according to Legros (2014). Although they are compact, thermoelectric devices require expensive materials and have rather low efficiency, as shown by LeBlanc (2014). As it can be seen in Wu *et al.* (2014) ongoing research on thermoacoustic generators shows good efficiency but prototypes are still bulky. Thermophotovoltaic systems are getting mature but prototypes show limited efficiency and mostly, they require a high temperature source, involving combustion, to efficiently convert heat into thermal radiations (Ferrari *et al.* 2014). Although free-piston Stirling engines are an efficient and mature

technology, they are best suited to slow changing of power output and require long warm-up period (Kongtragool and Wongwises 2003). While open Brayton cycles are adequately exploited in gas turbines and turbojet engines, their efficiency seriously drops when trying to operate them in closed loop with a low temperature heat source. To compensate for this, Wright *et al.* (2006) proposed a design with multiple inter-stage heating/cooling between the expansion/compression stages. The resulting complexity and associated cost make this cycle unsuitable for vehicle integration. Rankine cycles are an attractive candidate, especially when running with organic working fluids, where low- to medium-grade heat sources can be harvested, as shown in the review by Sprouse and Depcik (2013). In such systems, the expansion technology is the most important element since it is responsible for the extraction of the fluid power. For small-scale power generation, volumetric expanders are usually selected since they can handle low fluid flowrates. However, friction between the moving parts causes wear and eventually failure if no lubricant is mixed with the working fluid. In addition to reducing expander and evaporator performance, auxiliary oil circuits add complexity and cost to the system. For these reasons, dynamic expanders would be the preferred solution. In the turbomachinery domain, radial inflow turbines are promising since they can achieve much higher stage pressure ratios than axial machines. Yet, in order to process low flowrates, radial rotors need to be downsized, which is advantageous for vehicle packaging, but however implies high rotor speeds. Improvements in dynamic gas bearing technology make this possible, as shown by Schiffmann and Favrat (2009) and Demierre *et al.* (2015), who successfully operated small-scale radial turbo-compressors and turbo-expanders at speeds up to 210 krpm. The objective of this article is to evaluate the potential of Rankine cycles combined with small-scale turbomachines for waste heat recovery on automotive internal combustion engines. Several cycle topologies and working fluids are included in the investigation to identify the most promising configuration for maximizing waste heat recovery while reducing the required heat exchange area.

2. SYSTEM DESCRIPTION

2.1 Engine characterization

The considered commercial vehicle is equipped with a 96 kW gasoline engine. Test data have been analyzed to extract waste heat flows and temperatures associated with urban (50 km/h) and highway (120 km/h) operations. As shown in Table 1, exhaust gas and coolant streams were identified as valuable heat sources with respect to the engine power. From an exergetic point of view though, coolant yields significantly less recoverable power than exhaust gases, due to its lower temperature.

Table 1: Vehicle power streams characterized in terms of temperature, power and exergy

Vehicle operating point	Engine	Exhaust gases			Coolant			
	\dot{W}_{mec}	T	\dot{Q}	\dot{E}	T_{in}	T_{out}	\dot{Q}	\dot{E}
	kW	°C	kW	kW	°C	°C	kW	kW
Urban	3.80	425	2.64	0.97	105	104	2.17	0.46
Highway	22.9	706	19.2	9.21	105	101	12.6	2.61

2.2 Cycle configurations

In order to extract useful power from engine waste heat, a basic Rankine cycle (Figure 1a) is first considered. In this cycle, a selected working fluid is successively compressed through a pump where little power is consumed (1-2), evaporated through a heat exchanger in contact with a heat source (2-3), expanded through a turbine where useful power is extracted (3-4), and finally condensed through a heat exchanger in contact with a heat sink (4-1) considered to be ambient air in the studied system. To further increase the cycle efficiency, an internal heat exchanger (IHX) can be added as shown in Figure 1b, so that the working fluid is preheated (resp. precooled) before being evaporated (resp. condensed). Yet, in these two configurations, only one single source can be harvested. Since the goal is to maximize heat recovery, two additional configurations are proposed, where both the exhaust gas

and the coolant heat sources are exploited. The first one uses two heat exchangers in series (Figure 1c), with the coolant stream preheating the working fluid and the exhaust gas stream evaporating it. The second one integrates two pumping and expansion stages with heat exchangers in parallel (Figure 1d). In this configuration, the coolant and exhaust gas streams are respectively associated with the intermediate and high pressure evaporators. Although other configurations could have been studied, it was decided, in view of the targeted automotive application where compact packaging is a key aspect, to limit the number of heat exchangers in the evaluated systems to a maximum of three. In order to reduce exergetic losses, all evaporators are considered counter-flow and all condensers cross-flow. The first type is well suited to transfer heat from the engine waste heat streams to the working fluid while the second one is better adapted to reject heat from the working fluid to the ambient air.

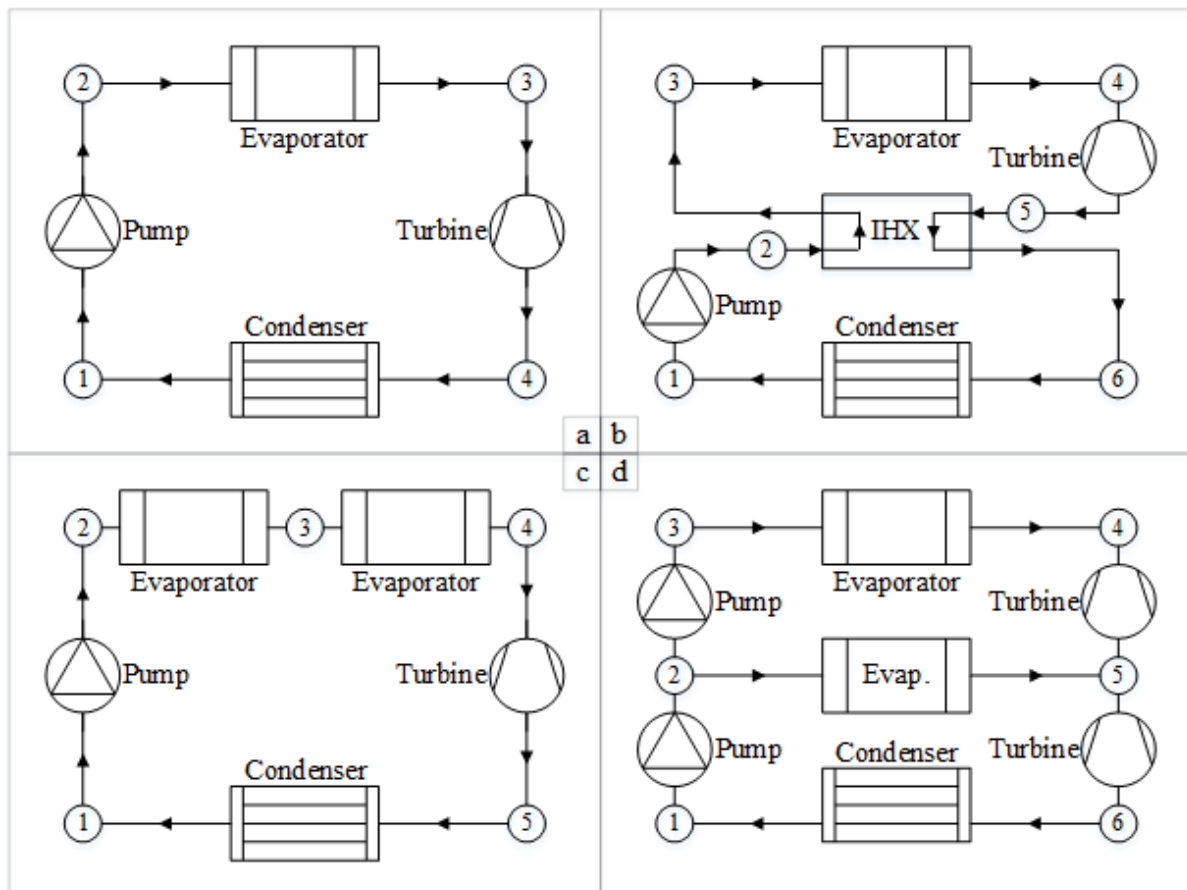


Figure 1: Evaluated Rankine cycle configurations: Basic single-source (a), Regenerative single-source (b), Series dual-source (c), Parallel dual-source (d)

2.3 Fluid candidates

Several working fluids may be appropriate candidates for Rankine cycles. Beyond the critical point, indicating the maximum pressure and temperature levels at which a fluid can experience a two-phase state, environmental indicators are also essential selection criteria. As such, working fluids should show null Ozone Depletion Potential (ODP), low Global Warming Potential (GWP) and low toxicity and flammability (ASHRAE standard 34). Refrigerants R-134a, R-152a and R-245fa were consequently identified as good candidates. Because of their high GWP however, R-134a and R-245fa are likely to be phased out and replaced by their respective counterparts R-1234yf/R-1234ze and R-1233zd, which are therefore included in the evaluation. Other considered fluids are ethanol and water. Table 2 summarizes the selected fluids, also highlighting their expansion behavior from a saturated vapor state at the turbine inlet.

Rankine cycles generally operate close to the saturation lines. Therefore ideal or perfect gas assumptions to retrieve the fluid's thermodynamic properties are not valid. This article uses REFPROP[®] based thermodynamic data to perform cycle calculations.

Table 2: Working fluid candidates

Working fluid	P_{cr} [bar]	T_{cr} [°C]	ODP	GWP	ASHRAE 34	Expansion
R-134a	40.6	101	0	1430	A1	Wet
R-1234yf	33.8	95	0	4	A2L	Dry
R-1234ze	36.3	109	0	6	A2L	Dry
R-152a	45.2	113	0	124	A2	Wet
R-245fa	36.5	154	0	1030	B1	Dry
R-1233zd	35.7	166	0	7	A1	Dry
Ethanol	62.7	242	0	0	-	Wet
Water	220.6	374	0	0	A1	Wet

2.4 Heat sink

In addition to the available heat sources, proposed cycle configurations, and working fluids, a heat sink also has to be characterized. As ambient temperatures ranging from 20 to 25°C were observed in the vehicle test data, the reference cold source temperature is set to 25°C. Assuming a 10°C temperature increase in the cross-flow condensers, an average air exchange temperature of 30°C is then considered.

3. SIMULATION MODELS

In order to assess the performance of a Rankine cycle on the two vehicle operating points, steady-state models have been implemented for each cycle configuration. Typical model inputs are the heat source and sink mass flowrates and temperatures, working fluid subcooling/superheating at the pump/turbine inlets, turbomachines efficiency and heat exchangers temperature pinch. Calculated outputs are the system efficiency, net power output, turbomachinery pre-design (rotor speed and diameter) and heat exchangers area. Model resolution is based on mass and energy conservation laws with the following general assumptions:

- Fluid flow is one-dimensional.
- Fluid kinetic and potential energy variations are neglected.
- Heating and cooling transformations are isobaric.
- Heat exchangers are perfectly insulated.

3.1 Turbomachinery modeling

The net power output of a cycle is calculated from the difference of the generated turbine powers \dot{W}_t and consumed pump powers \dot{W}_p . Each of them is predicted from the product of the working fluid mass flowrate (\dot{m}_t , \dot{m}_p) with the isentropic specific enthalpy difference through the device ($\Delta h_{t,s}$, $\Delta h_{p,s}$), corrected to account for entropy and electromechanical losses:

$$\dot{W}_{net} = \sum_t \dot{W}_t - \sum_p \dot{W}_p = \sum_t (\dot{m}_t \Delta h_{t,s} \cdot \eta_{t,s} \eta_{t,em}) - \sum_p (\dot{m}_p \Delta h_{p,s} / \eta_{p,s} \eta_{p,em}) \quad (1)$$

While electromechanical efficiencies $\eta_{t/p,em}$ are considered fixed for simplicity, isentropic efficiencies $\eta_{t/p,s}$ are extracted from Balje's diagrams (Balje, 1981), that plot iso-efficiency lines as a function of specific speed n_s and specific diameter d_s , defined as:

$$n_s = \frac{\omega \dot{V}^{0.5}}{|\Delta h_s|^{0.75}} \quad (2)$$

$$d_s = \frac{d |\Delta h_s|^{0.25}}{\dot{V}^{0.5}} \quad (3)$$

Determining these two dimensionless parameters from the optimal efficiency on the radial pump / turbine diagram and knowing the fluid flowrate \dot{V} at the pump inlet / turbine outlet as well as the absolute fluid isentropic enthalpy difference $|\Delta h_s|$, both the rotor angular velocity ω and tip diameter d can be estimated. Also, to avoid restricting the feasible design, radial pumps and turbines are not considered coupled on the same shaft.

3.2 Heat exchangers modeling

Predicting the volume of a heat exchanger is a difficult task. It depends not only on the flow conditions, but also on the detailed heat exchanger geometry and materials. Since heat exchangers design is beyond the scope of this work, it was decided to evaluate their size in terms of heat exchange surface. For this purpose, the Logarithmic Mean Temperature Difference (LMTD) method (Incropera *et al.*, 2006) was used. It states that the power \dot{Q} exchanged between two streams is equal to:

$$\dot{Q} = UA\Delta T_{lm} \quad (4)$$

where U is the overall heat transfer coefficient, A the heat exchange area and ΔT_{lm} the logarithmic mean temperature difference. By assuming that fluids are separated by an infinitely thin wall, the heat exchange area becomes identical on each side and the overall heat transfer coefficient derives from an inverted sum of the hot and cold fluid convective heat transfer coefficients U_h and U_c ; which used values are presented in Table 3, depending on the fluid type:

$$\frac{1}{U} = \frac{1}{U_h} + \frac{1}{U_c} \quad (5)$$

Table 3: Typical convective heat transfer coefficients (Marechal, 2012)

	Gas	Liquid	Condensing fluid	Evaporating fluid
$U_{conv} [W/m^2K]$	60	560	1600	3600

The LMTD is given by:

$$\Delta T_{lm} = \frac{\Delta T_2 - \Delta T_1}{\log(\Delta T_2/\Delta T_1)} \quad (6)$$

where ΔT_1 and ΔT_2 are the fluid temperature differences between the two streams on each side of the heat exchanger.

4. OPTIMIZATION RESULTS AND DISCUSSION

The implemented models being highly non-linear, non-differentiable and with numerous inputs, a genetic algorithm has been used to perform the optimizations. The goal is to identify the most promising cycle configuration and working fluid and to determine the possible trade-offs between system performance and size, in accordance with vehicle expectations. Two objective functions were defined: net power output maximization and total heat exchange area minimization. As observed by

Molyneaux (2002) and Leyland (2002), genetic algorithms are well indicated to come up with Pareto frontiers when dealing with complex energy systems.

The optimization was performed in two stages: a first run comparing the four cycles presented in Figure 1 and a second run confronting the eight fluids listed in Table 2.

4.1 Optimization stage I

The first optimization stage aimed at comparing the cycle configurations exposed in Figure 1. It has been performed using refrigerant R-1234yf, which is the standard working fluid replacing R-134a in vehicle cabin air conditioning, with a pump inlet subcooling of 2°C, a pinch of 10°C in all heat exchangers, and no electromechanical losses. Three decision variables were accounted for, as shown in Table 4.

Table 4: Decision variables for optimization stage I

#	Decision variable	Range
1	Working fluid evaporating pressure	2 – 40 bar
2	Working fluid temperature at turbine inlet	60 – 250 °C
3	Exhaust gas temperature at evaporator outlet	80 – 200 °C

Figure 2 presents the Pareto fronts resulting from the first-stage optimization. At first glance, it can be seen that cycles recovering the coolant waste heat only are the least profitable ones and that an internal heat exchanger (IHX) does not increase the extracted power. On the contrary, single-source waste heat recovery using the exhaust gases is much more valuable and, in this case, regeneration through an IHX significantly increases the conversion to useful power. With equal powers for lower areas, the dual-source series configuration always shows better performance than the parallel configuration. This is due to the engine coolant temperature (about 100°C), which imposes the cycle intermediate pressure level (about 30 bar for R-1234yf at 90°C) and therefore limits the topping cycle pressure ratio (1.33 for a maximum pressure of 40 bar) in the parallel configuration.

In urban vehicle operation, the overall Pareto front is shared by the exhaust-gas-driven basic cycle up to 0.13 kW (36% of available power range), the exhaust-gas-driven regenerative cycle from 0.13 to 0.28 kW (42%) and finally the dual-source series cycle from 0.28 to 0.36 kW (22%). In highway vehicle operation however, only exhaust-gas-driven cycles take part in the overall Pareto front, with the basic configuration being optimal up to 1.4 kW (50% of available power range) and the regenerative configuration being optimal from 1.4 to 2.8 kW (50%). Consequently, recovering the engine exhaust gases waste heat using a Rankine cycle that includes an internal heat exchanger, gives the best vehicle efficiency improvement perspectives.

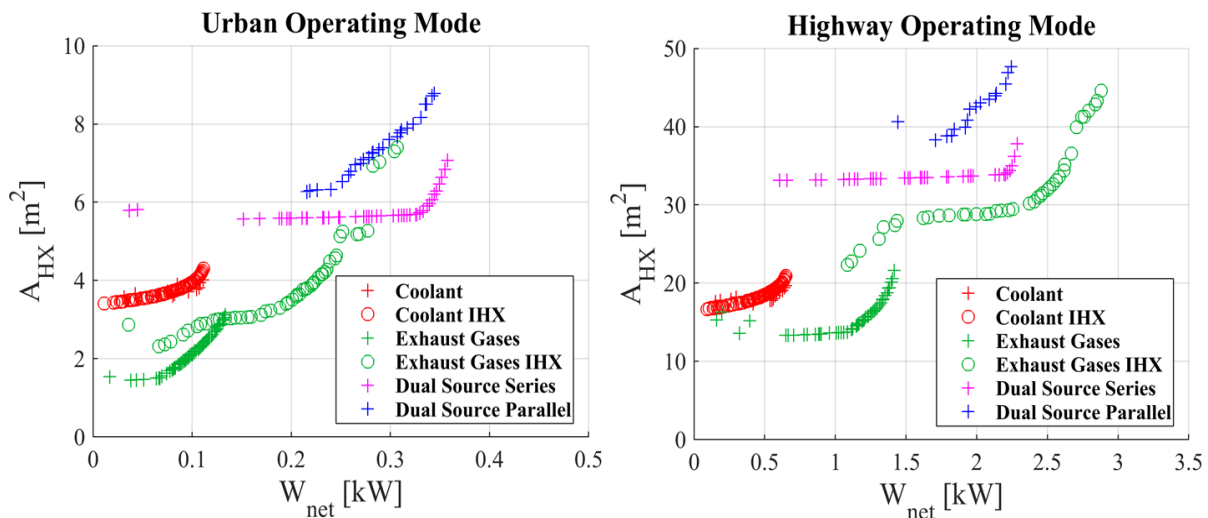


Figure 2 : Heat recovery system Pareto fronts from different cycle configurations

4.2 Optimization stage II

The second optimization stage aimed at comparing the fluid candidates exposed in Table 2. It has been performed using a regenerative exhaust-gas-driven cycle, which is the optimal configuration from the first-stage optimization, with a pump inlet subcooling of 5°C to prevent cavitation, turbomachine electromechanical efficiencies of 85% to account for bearing and generator losses, a minimum working fluid pressure of 1 bar to avoid subatmospheric processes and possible contamination by air, a maximum working fluid pressure of 30 bar to make piping and evaporator costs accessible to automotive industry, a minimum exhaust gas outlet temperature of 150°C to avoid acid condensation in the last section of the exhaust pipe, and a minimum turbine tip diameter of 10 mm for manufacturability. Furthermore, Balje's (1981) predictions for radial pump isentropic efficiencies being overestimated (up to 92%), the pump isentropic efficiency has been fixed to a more realistic value of 60%. Four decision variables were accounted for, as shown in Table 5.

Table 5: Decision variables for optimization stage II

#	Decision variable	Range
1	Working fluid superheating at turbine inlet	0 – 200 °C
2	Condenser pinch	5 – 25 °C
3	Evaporator pinch	5 – 25 °C
4	IHX pinch	5 – 25 °C

In addition to the above constraints, cycle pressure ratio limitations have been considered, so that the expansion is feasible across a single-stage turbine. The advantage is that it significantly decreases the complexity and consequently the manufacturing cost of the turbo-generator unit. Yet, as dynamic machine stage pressure ratio is strongly dependent on rotor design and fluid density differentials, a one-dimensional aerodynamic analysis has been performed on an existing small-scale radial turbine design presented by Demierre *et al.* (2015), which goal was to determine for each working fluid, the maximum stage pressure ratio as a function of the turbine inlet superheating. In this analysis, sonic limitations at the nozzle and rotor throats were accounted for, as well as a maximum rotor peripheral speed of 400 m/s, for mechanical strength reasons.

Results from the second-stage optimization (Figure 3) suggest that whether the vehicle is operated in urban or highway mode, ethanol as well as refrigerants R-245fa and its substitute clearly show the best objectives combinations, with R-1233zd being optimal in terms of net power output. Nonetheless, if the main criterion is to minimize the heat exchange area, ethanol then takes the first place in the ranking. For further comparison, Table 6 presents for each working fluid, some of the main system characteristics at maximum net power output; that is turbine diameter d_t and rotational speed N_t , cycle pressure ratio π , evaporating pressure P_{ev} and efficiency η_c , and system overall efficiency η_s . The first-law efficiencies are defined below, as a function of evaporator load \dot{Q}_{ev} and heat source available power \dot{Q}_{source} .

$$\eta_c = \frac{\dot{W}_{net}}{\dot{Q}_{ev}} \quad (7)$$

$$\eta_s = \frac{\dot{W}_{net}}{\dot{Q}_{source}} \quad (8)$$

It should here be mentioned that the cycle condensing pressures were determined from the average heat sink temperature and accounting for the condenser pinch, subcooling at the pump inlet and minimum pressure constraint. Then, the evaporating pressure was calculated from the optimal pressure ratio at corresponding turbine inlet superheating and accounting for the maximum pressure constraint. As shown in Table 6, this last constraint mainly explains why refrigerants R-152a, R-134a and substitutes exhibit lower performance. On the contrary, with a condensing pressure of 1 bar,

natural working fluids do not suffer from the maximum pressure constraint. While water-based systems performance is limited by the zero-droplet tolerance and by the limitation of the rotor peripheral speed, ethanol-based systems show promising results with the best Pareto frontier from 0.15 to 0.2 kW in urban operating mode and from 1.5 to 1.8 kW in highway operating mode. Nonetheless, these two fluids present relatively high and therefore challenging rotational speeds (300 to 600 krpm), which associated with 20 to 10 mm rotors, lead to much higher peripheral speeds compared to refrigerant-based systems.

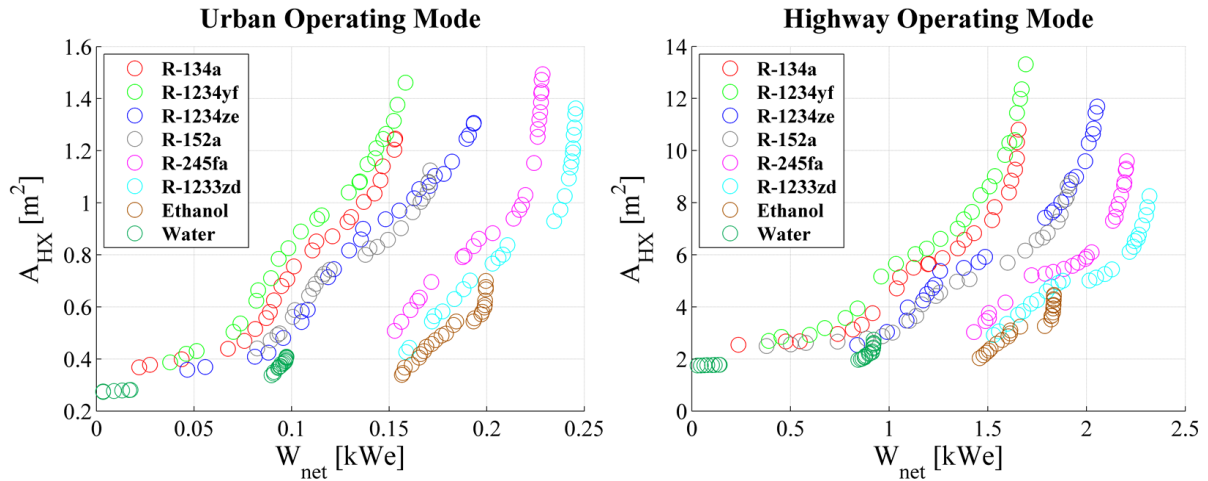


Figure 3: Heat recovery system Pareto fronts from different working fluid candidates

No matter the working fluid, turbine design is always characterized by the smallest accepted design diameter and a high rotational speed when optimizing the heat recovery system for an urban vehicle operation. This is disadvantageous for production and performance since manufacturing tolerances (linked with efficiency) and rotor balancing (linked with stability) become stricter, as observed by Schiffmann and Favrat (2010) and Schiffmann (2013). In addition, efficiencies are lower compared to the highway operation systems. Hence, from this refined optimization and considering both cycle net power outputs and turbine design characteristics, it can be concluded that the waste heat recovery system should be designed for the highway vehicle operation, using refrigerant R-1233zd as cycle working fluid. The expected gain ranges from 1.5 to 2.3 kW of electrical power that is a 6.5 to 10% increase in the first-law efficiency of the vehicle drivetrain.

Table 6: System characteristics at maximum net power outputs

Working fluid	Urban						Highway					
	η_S %	η_C %	P_{ev} bar	π -	N_t krpm	d_t mm	η_S %	η_C %	P_{ev} bar	π -	N_t krpm	d_t mm
R-134a	5.8	8.4	30.0	2.93	261	10.0	8.6	10.5	30.0	2.90	244	12.0
R-1234yf	6.0	8.7	30.0	2.94	250	10.0	8.8	10.8	30.0	2.93	214	12.9
R-1234ze	7.3	10.6	30.0	3.89	293	10.0	10.7	13.1	30.0	3.89	250	13.0
R-152a	6.5	9.4	30.0	3.20	340	10.0	10.0	12.2	30.0	3.27	368	10.9
R-245fa	8.7	12.6	18.2	5.15	309	10.0	11.4	14.0	23.6	5.18	227	15.2
R-1233zd	9.3	13.5	17.4	5.28	329	10.0	12.0	14.7	20.3	5.31	218	16.4
Ethanol	7.6	11.0	5.95	5.95	606	10.0	9.5	11.7	5.94	5.94	335	19.3
Water	3.7	5.4	2.49	2.49	600	10.4	4.8	5.9	2.49	2.49	395	17.9

5. CONCLUSIONS

In view of reducing vehicle fuel consumption and carbon dioxide emissions, Rankine cycle systems have been studied to recover the waste heat from engine coolant and exhaust gas streams. Two representative vehicle operating points were analyzed with four possible cycle configurations and a set of eight working fluids. Targeting both maximum performance and minimum size criteria, multi-objective optimizations were performed, accounting for automotive and turbomachinery design constraints. From the resulting Pareto fronts, it has been found that the optimal recovery system should be designed for the highway vehicle operation, using a regenerative exhaust-gas-driven cycle and refrigerant R-1233zd. The expected benefit is an additional 2.3 kW of electrical power that is a 10% increase in the vehicle efficiency. For achieving this performance, the optimal expander is a 16.5 mm tip diameter radial inflow turbine rotating at about 220 krpm. In order to validate the complete system design, its behavior should now be evaluated for other vehicle operating points, including off-design performance evaluation and engine dynamics.

NOMENCLATURE

Symbols

A	Area	m^2
d	Tip diameter	mm
d_s	Specific diameter	–
\dot{E}	Exergy	W
h	Specific enthalpy	J/kg
\dot{m}	Mass flowrate	kg/s
N	Rotational speed	rpm
n_s	Specific speed	–
P	Pressure	bar
\dot{Q}	Heat	W
T	Temperature	$^{\circ}C$
U	Heat transfer coefficient	W/m^2K
\dot{V}	Volumetric flowrate	m^3/s
\dot{W}	Electrical power	We
\dot{W}	Mechanical power	W
Δh	Specific enthalpy diff.	J/kg
ΔT	Temperature difference	$^{\circ}C$
η	Efficiency	–
π	Pressure ratio	–
ω	Angular velocity	rad/s

Subscripts

C	Cycle
-----	-------

c	Cold
$conv$	Convective
cr	Critical state
em	Electromechanical
ev	Evaporation
HX	Heat exchange
h	Hot
in	Inlet
lm	Logarithmic mean
mec	Mechanical
net	Net
out	Outlet
p	Pump
ref	Reference (Ambient)
S	System
s	Isentropic
t	Turbine

Acronyms

GWP	Global Warming Potential
ICE	Internal Combustion Engine
IHX	Internal Heat Exchanger
ODP	Ozone Depletion Potential
ORC	Organic Rankine Cycle

REFERENCES

- Balje, O. E., 1981, *Turbomachines: A Guide to Design, Selection, and Theory*, John Wiley & Sons Inc., New York, 513 p.
- Demierre, J., Rubino, A., Schiffmann, J., 2015, Modeling and Experimental Investigation of an Oil-Free Microcompressor-Turbine Unit for an Organic Rankine Cycle Driven Heat Pump, *Journal of Engineering for Gas Turbines and Power (ASME)*, vol. 137, no. 3: p. 032602.
- Ferrari, C., Melino, F., Pinelli, M., Spina, P. R., 2014, Thermophotovoltaic energy conversion: Analytical aspects, prototypes and experiences, *Appl. Energy*, vol. 113: p. 1717-1730.
- IEA, 2014, 2014 Key World Energy STATISTICS, *International Energy Agency*.
- Incropera, F. P., DeWitt, D. P., Bergman, T. L., Lavine, A. S., 2007, *Fundamentals of Heat and Mass Transfer*, John Wiley & Sons Inc., New York, 997 p.
- Kongtragool, B., Wongwises, S., 2003, A review of solar-powered Stirling engines and low temperature differential Stirling engines, *Renew. Sustain. Energy Rev.*, vol. 7: p. 131-154.
- LeBlanc, S., 2014, Thermoelectric generators: Linking material properties and systems engineering for waste heat recovery applications, *Sustainable Materials and Technologies*, vol. 1-2: p. 26-35.
- Legros, A., Guillaume, L., Diny, M., Zaïdi, H., Lemort, V., 2014, Comparison and Impact of Waste Heat Recovery Technologies on Passenger Car Fuel Consumption in a Normalized Driving Cycle, *Energies*, vol. 7: p. 5273-5290.
- Leyland, G. B., 2002, Multi-Objective Optimization Applied to Industrial Energy Problems, *Ecole Polytechnique Fédérale de Lausanne*, PhD Thesis no. 2572.
- Marechal, F., 2012, *Process integration techniques for improving the energy efficiency of industrial processes*, EPFL Advanced Energetics coursebook.
- Molyneaux, A., 2002, A Practical Evolutionary Method for The Multi-Objective Optimisation of Complex Integrated Energy Systems Including Vehicle Drivetrains, *Ecole Polytechnique Fédérale de Lausanne*, PhD Thesis no. 2636.
- Schiffmann, J., Favrat, D., 2009, Experimental investigation of a direct driven radial compressor for domestic heat pumps, *Int. J. Refrig.*, vol. 32, no. 8: p. 1918-1928.
- Schiffmann, J., Favrat, D., 2010 Integrated Design and Optimization of Gas Bearing Supported Rotors, *Journal of Mechanical Design*, vol. 132
- Schiffmann, J., 2013 Enhanced Groove Geometry for Herringbone Grooved Journal Bearings, *Journal Of Engineering For Gas Turbines And Power (ASME)*, vol. 135, no. 10, p. 102501.
- Sprouse III, C., Depcik, C., 2013, Review of organic Rankine cycles for internal combustion engine exhaust waste heat recovery, *Appl. Therm. Eng.*, vol. 51, no. 1-2: p. 711-722.
- Wright, S. A., Vernon, M. E., Pickard, P. S., 2006, Concept Design for a High Temperature Helium Brayton Cycle with Interstage Heating and Cooling, *Sandia National Laboratories*.
- Wu, Z., Zhang, L., Dai, W., Luo, E., 2014, Investigation on a 1kW traveling-wave thermoacoustic electrical generator, *Appl. Energy*, vol. 124: p. 140-147.

PARAMETRIC OPTIMIZATION AND PERFORMANCE ANALYSIS OF ORGANIC RANKINE CYCLE (ORC) FOR ENGINE WASTE HEAT RECOVERY

Fubin Yang^{1,2*}, Hongguang Zhang^{1,2}

¹Beijing University of Technology, College of Environmental and Energy Engineering,
Beijing, China
E-mail: yangfubinnuc@163.com

²Collaborative Innovation Center of Electric Vehicles in Beijing,
Beijing, China
E-mail: yangfubinnuc@163.com

* Corresponding Author

ABSTRACT

This study examines the parametric optimization and performance analysis of ORC system using genetic algorithm (GA) for engine waste heat recovery. The effects of three key parameters, including evaporation pressure, superheat degree, and condensation temperature on the net power output per unit heat transfer area and exergy destruction rate under engine various operating conditions are analyzed. Subsequently, the performances of a finned-tube evaporator used in this ORC system are evaluated. The results indicate that the optimal evaporation pressures are mainly influenced by the engine operating conditions. Moreover, superheat degree and condensation temperature presents slight variation over the whole operating range. At rated condition, the ORC system achieves maximum net power output per unit heat transfer area of 0.74kW/m². Furthermore, the ratio of maximum effective heat transfer area to the actual area of the evaporator is 69%, which has great influence on the performance of the ORC system.

1. INTRODUCTION

Over the past few years, the energy consumption has kept increasing with the development of industrialization process in China. Thereinto, internal combustion engines (ICEs) have consumed about 60% of overall oil consumption. Due to the low thermal efficiency of the ICEs, only about one-third of total fuel combustion energy becomes power output. The exhaust waste heat recovery of ICEs presents a potential for converting waste heat into electrical energy to improve the engine thermal efficiency and reduce emissions.

As a solution to the low grade waste heat recovery, Organic Rankine cycle (ORC) has been applied widely because of its high efficiency, low cost and simple structure. Zhai *et al.* (2014) showed that the ORC system is one of the most effective methods for recovering energy from low grade heat sources. Walraven *et al.* (2015) observed that the discount rate, electricity price, brine inlet temperature and annual electricity price evolution have a strong influence on the configuration and efficiency of the ORC and on the economics of the project. Heberle *et al.* (2012) showed that the use of mixtures as working fluids leads to an efficiency increase compared to pure fluids. Li *et al.* (2014) showed that there exists a possible relationship between the critical temperature of working fluids and the economical performance of the system.

Currently, much attention has also been paid to waste heat recovery for the ICEs based on ORC system. Wang *et al.* (2014) indicated that the exhaust energy recovery system serve more applicable on the heavy-duty diesel engine. Teng *et al.* (2006) demonstrated that with the hybrid power system of the

diesel engine and the Rankine engine operated with waste heat, substantial enhancement in engine power and improvement in fuel economy can be achieved. Vaja *et al.* (2010) showed that a 12% increase in the overall efficiency can be achieved compared with the engine with no bottoming.

Based on the aforementioned analysis, the ORC system has already been extensively applied and investigated in low grade heat sources, especially in ICEs waste heat recovery. In this paper, the thermodynamic model of the ORC system is established based on the first and second laws of thermodynamics. The optimal operating parameters of the ORC system are investigated under diesel engine various operating conditions with evaporation pressure, superheat degree, and condensation temperature of the working fluid as optimization parameters for the maximum net power output per unit heat transfer area (POPA) and the minimum exergy destruction rate (EDR) using genetic algorithm (GA).

2. SYSTEM DESCRIPTION

The schematic and T - s diagram of the ORC system for recovering engine exhaust waste heat are shown in Figures 1 and 2. The liquid working fluid is pressurized to the evaporator by the pump. Then the subcooled liquid working fluid absorbs heat from the exhaust gas in the evaporator and turns into saturated or superheated vapor. After that, the vapor flows into the expander to do work and drives the generator to produce electricity. Finally, the superheated vapor exported from the expander condenses into saturated liquid state in the condenser. Subsequently, the liquid working fluid is pressurized by the pump to begin the new cycle again.

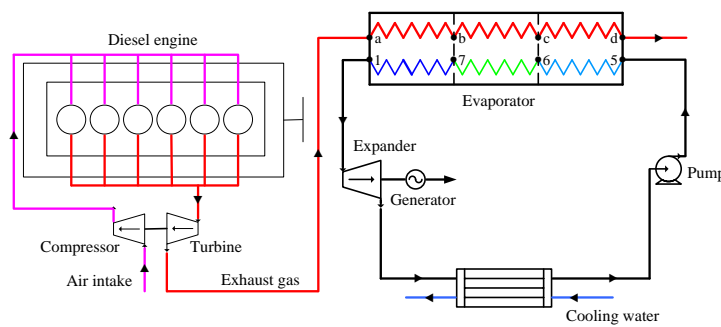


Figure 1: Schematic diagram of the ORC system

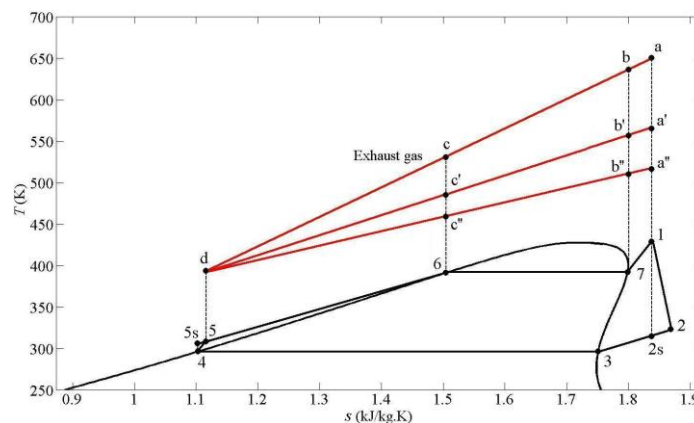


Figure 2: T - s diagram of the ORC system

The optimal working fluid should not only ensure higher waste heat recovery efficiency for the ORC system, but also meet the requirement of environmental protection, safety, and economy. Wang *et al.* (2011) compared nine different pure organic working fluids based on their thermodynamic performances. R245fa is the most suitable working fluid for engine waste heat recovery application.

Therefore, R245fa is selected as the working fluid in this study.

3. MATHEMATICAL MODEL

3.1 Thermodynamic model

Process 1-2 (Expander):

The power output and the exergy destruction rate of the expander are given by:

$$\dot{W}_{\text{exp}} = \dot{m}_{\text{wf}}(h_1 - h_2) \quad (1)$$

$$\dot{I}_{\text{exp}} = T_0 \dot{m}_{\text{wf}}(s_2 - s_1) \quad (2)$$

The isentropic efficiency of expander is given by:

$$\eta_{\text{exp}} = \frac{h_1 - h_2}{h_1 - h_{2s}} \quad (3)$$

Process 2-4 (Condenser):

The heat transfer rate and the exergy destruction rate of the condenser can be expressed as:

$$\dot{Q}_{\text{con}} = \dot{m}_{\text{wf}}(h_2 - h_4) \quad (4)$$

$$\dot{I}_{\text{con}} = \dot{m}_{\text{wf}}[(h_2 - h_4) + T_0(s_2 - s_4)] \quad (5)$$

Process 4-5 (Pump):

The power consumed and the exergy destruction rate of the pump can be determined as:

$$\dot{W}_{\text{p}} = \dot{m}_{\text{wf}}(h_5 - h_4) \quad (6)$$

$$\dot{I}_{\text{p}} = T_0 \dot{m}_{\text{wf}}(s_5 - s_4) \quad (7)$$

The isentropic efficiency of the pump is given by:

$$\eta_{\text{p}} = \frac{h_{5s} - h_4}{h_5 - h_4} \quad (8)$$

Process 5-1 (Evaporator):

The heat transfer rate and the exergy destruction rate of the evaporator can be expressed as:

$$\dot{Q}_{\text{eva}} = \dot{m}_{\text{exh}}(h_a - h_d) = \dot{m}_{\text{wf}}(h_1 - h_5) \quad (9)$$

$$\dot{I}_{\text{eva}} = \dot{m}_{\text{exh}}[(h_a - h_d) + T_0(s_a - s_d)] - \dot{m}_{\text{wf}}[(h_1 - h_5) + T_0(s_1 - s_5)] \quad (10)$$

For each heat transfer area in the evaporator, the heat transfer rate between the exhaust and the working fluid can be calculated using the following equations:

$$\dot{Q}_{71} = \dot{m}_{\text{exh}}(h_a - h_b) = \dot{m}_{\text{wf}}(h_1 - h_7) \quad (11)$$

$$\dot{Q}_{67} = \dot{m}_{\text{exh}}(h_b - h_c) = \dot{m}_{\text{wf}}(h_7 - h_6) \quad (12)$$

$$\dot{Q}_{56} = \dot{m}_{\text{exh}}(h_c - h_d) = \dot{m}_{\text{wf}}(h_6 - h_5) \quad (13)$$

To investigate the heat transfer performance of the evaporator, the ratio of effective heat transfer area to actual area is defined as:

$$\eta_{\text{ht}} = \frac{A_{\text{eff}}}{A_{\text{act}}} \quad (14)$$

The aim of this paper is to conduct the parametric optimization and evaluate the performance of a finned-tube evaporator used in the ORC system. Therefore, the isentropic efficiencies of the pump and the expander are set to constant values. Therein, several assumptions for the thermodynamic model

are listed as follows:

- (1) The ORC system operates under steady state conditions.
- (2) There are no pressure drops in the pipes and the components.
- (3) The heat losses in each component are also neglected.
- (4) The isentropic efficiencies of the pump and the expander are set to 0.65 and 0.7 respectively.
- (5) The ambient temperature is set to 291.15 K.

3.2 Evaporator model

In this study, we select a fin-and-tube evaporator used in our lab for thermodynamic analysis. The schematic and the geometric dimensions of the fin-and-tube evaporator are shown in Figure 3 and Table 1, respectively. The engine exhaust gas flows outside the tube, and the working fluid flows inside the tube. The evaporator model refers to Zhang *et al.* (2013).

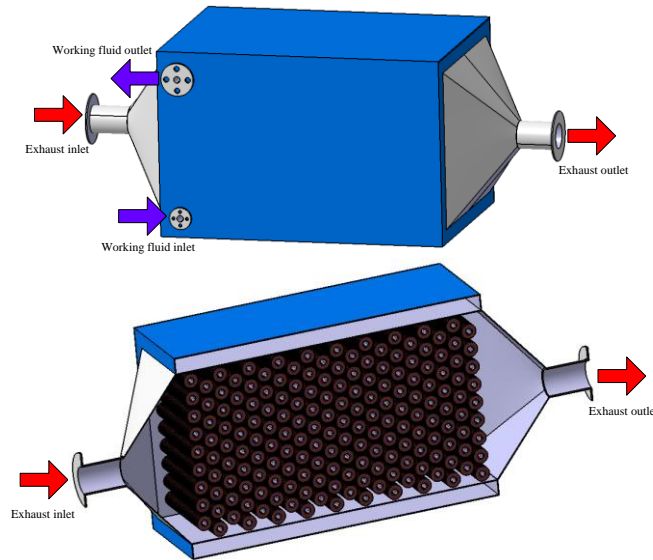


Figure 3: Schematic of the fin-and-tube evaporator

Table 1: Geometric dimensions of the fin-and-tube evaporator

Items	Parameters	Units
Number of tubes in each row	9	-
Number of tube rows	20	-
Tube outer diameter	25	mm
Tube inner diameter	20	mm
Tube pitch	60	mm
Row pitch	100	mm
Fin height	12	mm
Fin width	1	mm
Rib effect coefficient	3	-
Tube row alignment	Staggered type	-
Tube material	Stainless steel316L	-
Fin material	Stainless steel316L	-
Inner heat transfer area	9	m ²
Tube length	8.8	m

4. OPTIMIZATION METHODOLOGY

4.1 Description of genetic algorithm

The diesel engine operates under various operating conditions for the practical applications. Therefore,

the coordinated variation of each operating parameters in the ORC system is indispensable to achieve the optimal performance. Genetic algorithm which was invented by professor Holland (1975) is adaptive heuristic search algorithm based on the evolutionary ideas of natural selection and genetics.

In the present study, the POPA and the EDR are evaluated as objective functions with evaporation pressure, superheat degree and condensation temperature of the working fluid as optimization variables. Therefore the optimization of the ORC system is performed by using GA in MATLAB. The multi-objective optimization function can be described as:

$$\max(\text{POPA})= f(P_7, T_1, T_4) \quad (15)$$

$$\min(\text{EDR})= f(P_7, T_1, T_4) \quad (16)$$

The lower and upper bounds of decision variables and parameter setting of GA are listed in Tables 2 and 3.

Table 2: Lower and upper bounds of decision variables

Decision variables	Lower bound	Upper bound
Evaporation pressure (MPa)	0.8	3
Superheat degree (K)	0	20
Condensation temperature (K)	298.15	353.15

Table 3: Parameter setting of genetic algorithm

Parameters	Value
Population size	150
Selection process	Tournament
Crossover fraction	0.8
Mutation function	Adaptive feasible
Stop generations	600

5. ENGINE WASTE HEAT EVALUATION

The engine used as the topping cycle in this study is a six-cylinder in-line diesel engine. The main technical performance parameters of the diesel engine are listed in Table 4.

Table 4: The main technical parameters of the diesel engine

Items	Parameters	Units
Rated power	247	kW
Maximum torque	1600	N.m
Displacement	11.596	L
Cylinder number	6	
Air intake type	Turbocharged and Intercooled	
Fuel injection system	High pressure common rail	
Speed at maximum torque	1400	r/min
Stroke and cylinder bore	155×126	mm
Compression ratio	17.1	

Figure 4 shows the performance maps of the diesel engine over the whole operating range. The variation of BSFC (brake specific fuel consumption) is illustrated in Figure 4(a), which indicates that the BSFC is mainly influenced by engine torque. When the diesel engine is operating under the high load conditions, it has the lower BSFC within the range of 196 g/(kW.h) to 205 g/(kW.h). Moreover, at the engine rated condition, the power output of the engine reaches a maximum value of 247 kW. Figure 4(b) shows the variation of the exhaust temperature with the engine speed and load. It can be seen that the exhaust temperature varies slightly with engine speed, but increases rapidly with engine

load. When diesel engine is operating under the medium-low speed and medium-high load conditions, the exhaust temperature is relative high and can reach its maximum value of 667 K. The exhaust mass flow rate of the diesel engine, which is the sum of fuel consumption and intake air mass flow rate per unit time, is shown in Figure 4(c). It is obvious that the exhaust mass flow rate increases with engine speed and engine load. At rated condition, the exhaust mass flow rate reaches a maximum of 0.36 kg/s. Figure 4(d) shows the available exhaust energy of the diesel engine over the whole operating range. Note that the available exhaust energy is mainly affected by exhaust mass flow rate and exhaust temperature. Therefore, the available exhaust energy shows the same variation tendency compared with Figures 4(b) and 4(c). Under the medium-high speed and medium-high load conditions, the available exhaust energy ranges from 47 kW to 103 kW. At rated condition, the maximum available exhaust energy of the diesel engine is 103 kW.

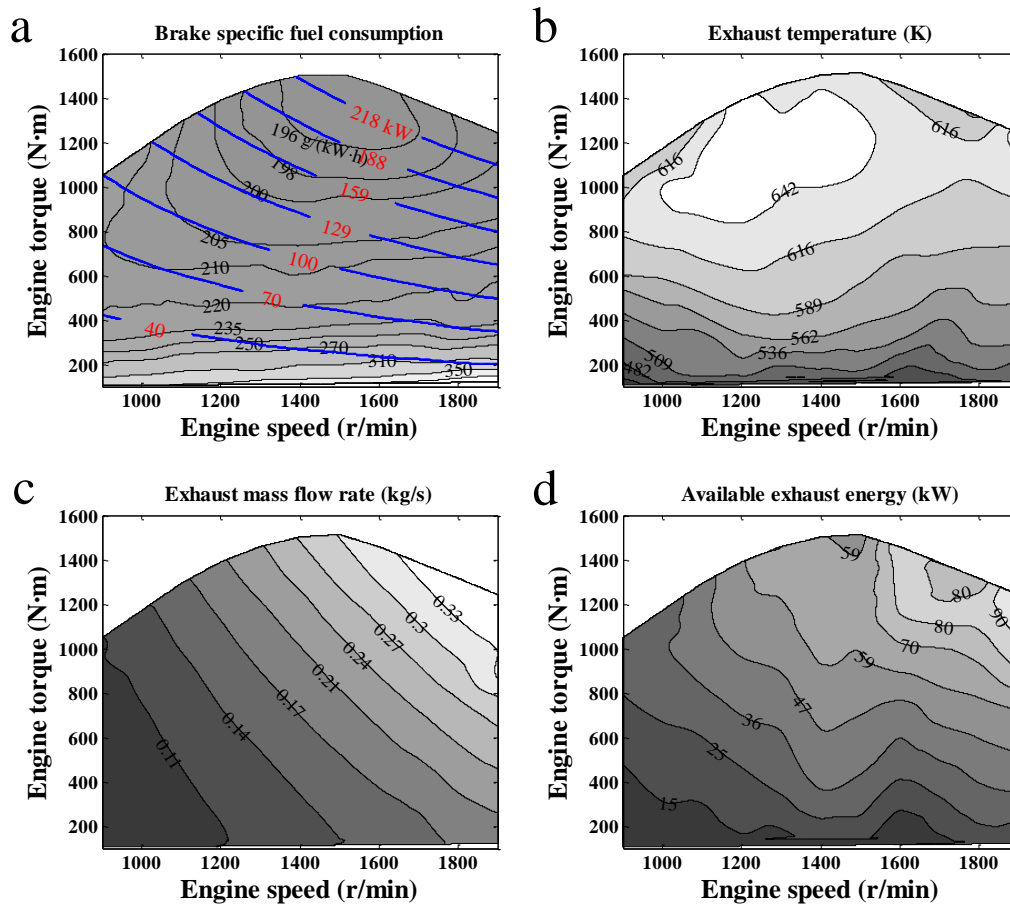


Figure 4: Performance maps of the diesel engine

6. RESULTS AND DISCUSSION

Based on the thermodynamic model established of the ORC system, the optimization using GA for the exhaust waste heat recovery is performed over the whole operating range of the diesel engine. The aim of the optimization process is to achieve the maximum POPA and the minimum EDR.

Figure 5 shows the optimization results of the two objective functions over the whole operating range of the diesel engine. The maximum POPA of the ORC system is presented in Figure 5(a). It can be observed that the maximum POPA is influenced by engine operating conditions significantly, namely available exhaust energy. From Figures 4(d) and 5(a), the maximum POPA increase with the available exhaust energy. This can be explained since the more exhaust energy will lead to an increase in the quantity of evaporated working fluid, which resulted in the increase of the net power output. Over the

whole operating range, the maximum POPA of the ORC system ranges from 0.06 kW/m^2 to 0.74 kW/m^2 . At rated condition, the maximum POPA of the ORC system is 0.74 kW/m^2 . Figure 5(b) shows the variation of the minimum EDR with the engine speed and load. Similarly to the POPA, engine's operating conditions have a great impact on the EDR. When the diesel engine operates under the medium-low speed and medium-low load conditions, the ORC system can provide lower EDR, whose values range from 0.61 kW to 10.75 kW . It also can be seen that when the diesel engine operates under high speed and high load conditions, the ORC system has the higher EDR. This is due to the exhaust temperature increases with the engine speed and load, which resulted in higher temperature difference between the exhaust gas and the working fluid.

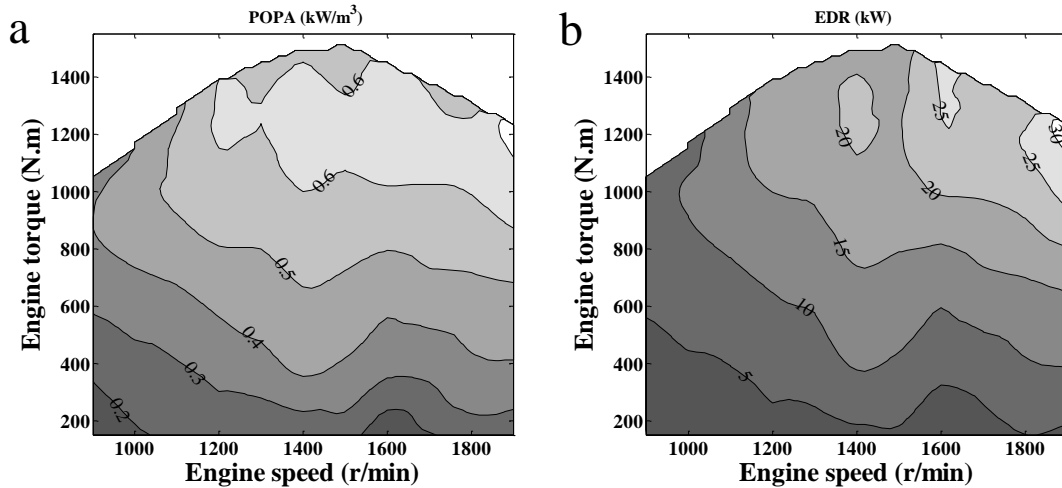


Figure 5: Optimization results of the two objective functions

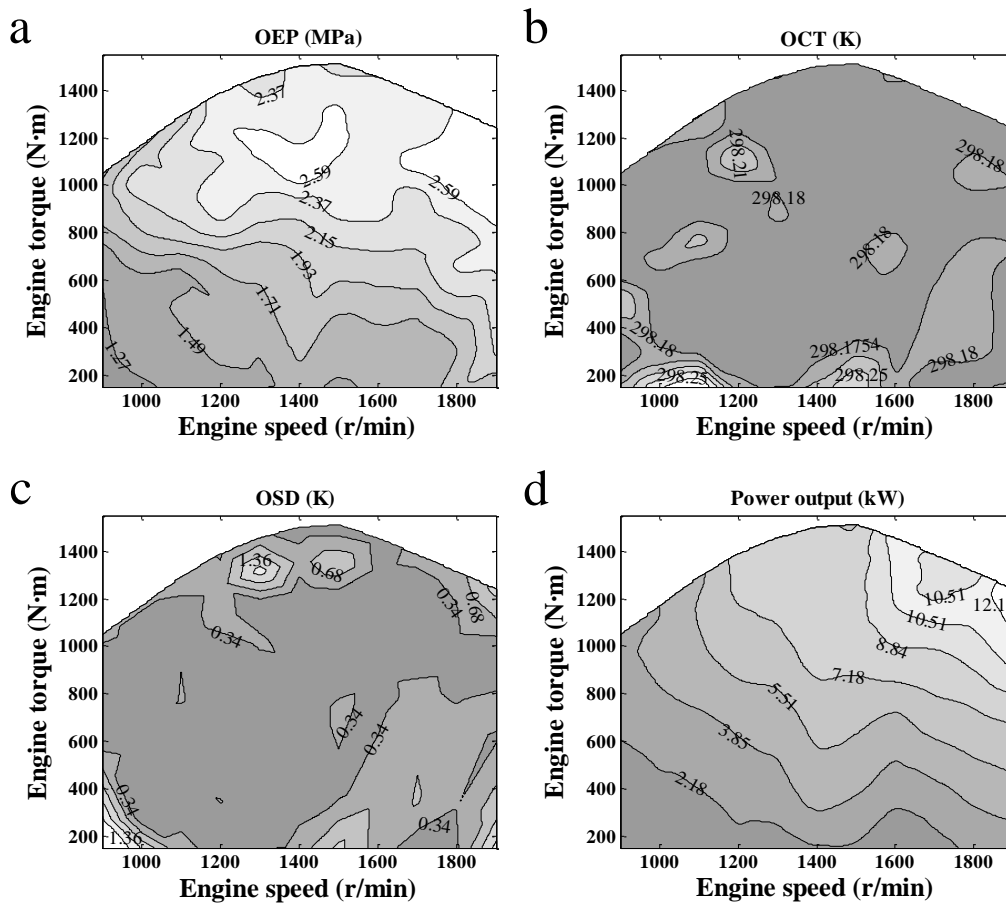


Figure 6: Optimization results of operating parameters and power output for the ORC system

Figure 6 shows the optimization results of operating parameters for the ORC system, including OEP (optimal evaporation pressure), OCT (optimal condensation temperature), and OSD (optimal superheat degree). In addition, the variation of the ORC system power output with the engine's operating conditions is presented in Figure 6(d). Figure 6(a) demonstrates that the overall trend about the OEP increases with the increment of engine speed and engine torque. Over the whole operating range, the OEP for the working fluid is in the range of 1.09 MPa to 2.81 MPa. Therefore, it is necessary to select the OEP for each operating condition of the diesel engine. As can be seen in Figure 6(b), the OCT has a small variation in its range, which is nearly kept constant at 298.15 K. As we all known, higher evaporation pressure and lower condensation temperature will lead to an increase in the thermal efficiency of the ORC system. Therefore, the optimization results of the OEP and the OCT are consistent with the analysis based on the first and second laws of thermodynamics. Figure 6(c) shows the variation of OSD over the engine whole operating range. It can be seen that the OSD is in the range of 0 K to 2.13 K. Under the most operating conditions of the diesel engine, the OSD values are in the range between 0 K to 1 K. That is to say, the working fluid does not need to be superheated, which has the similar results for dry organic fluids with Mago *et al.* (2008). In the practical applications of the ORC system, such small OSD cannot be met perfectly due to the limitation of technology problems. From Figure 6(d), it can be concluded that the net power output exhibits the same variation tendency with available exhaust energy presented in Figure 4(d). The net power output increases with increasing available exhaust energy. Over the whole operating range of the diesel engine, the net power output of the ORC system is in the range of 0.32 kW to 13.84 kW. At the engine rated condition, the net power output is 13.84 kW.

Figure 7(a) shows the thermal efficiency of the ORC system over the whole operating range of the diesel engine. It can be observed that the thermal efficiency of the ORC system is mainly affected by the engine torque. When the diesel engine operates at the high load regions, the ORC system presents higher thermal efficiency. This is due to the increase in the net power output obviously at these regions. At engine rated condition, the thermal efficiency of the ORC system reaches the maximum of 13.33%. The POIR (power output increasing rate) is the ratio of the net power output of the ORC system to the engine power output, which is used to evaluate the performance improvement of the diesel engine. The variation of the POIR over the engine whole operating range is shown in Figure 7 (b). It can be observed that the ORC system generates higher POIR at the low torque regions of the diesel engine. That is to say, when the diesel engine operates at the low torque regions, the ORC system can improve the power performance of the diesel engine notably. At the low torque regions of the diesel engine, the POIR is in the range of 3.23% to 9.41%. When the diesel engine operates at the medium-high torque regions, the POIR changes gently.

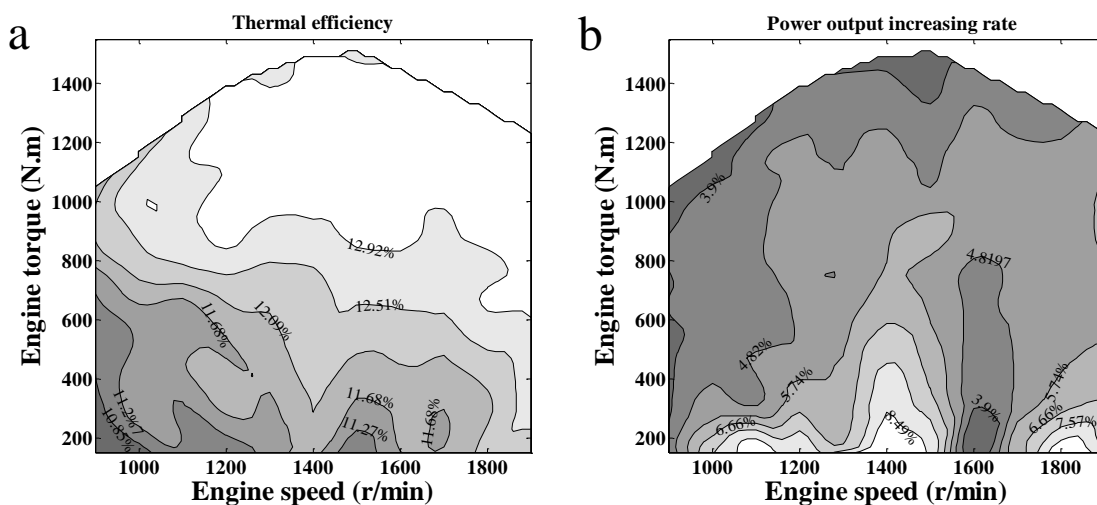
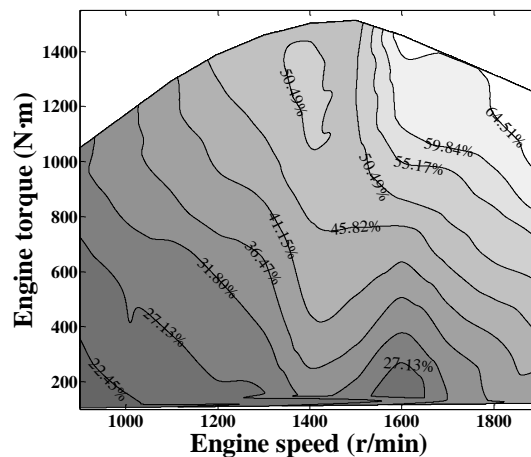


Figure 7: Thermal efficiency of the ORC system and the POIR compared with the diesel engine

Figure 8 shows the ratio of effective heat transfer area to actual area of the evaporator over the whole operating range of the diesel engine. It can be observed that when the diesel engine operates under the medium-low speed or medium-high torque conditions, the ratio of effective heat transfer area to actual area of the evaporator increases with the engine speed and torque. In addition, when the diesel engine operates under the medium-high speed and medium-low torque conditions, the ratio of effective heat transfer area to actual area of the evaporator is mainly affected by the engine torque. That is to say, the operating conditions of the diesel engine have a great effect on the performance of the evaporator. The performances of the evaporator, including heat transfer rate, heat transfer temperature difference, heat transfer coefficient, and heat transfer surface area will vary with the operating conditions of the diesel engine. Over the whole operating range of the diesel engine, the ratio of effective heat transfer area to actual area of the evaporator is in the range of 17.78% to 69.19%.

**Figure 8:** The ratio of effective heat transfer area to actual area of the evaporator

7. CONCLUSIONS

In this study, the parametric optimization and performance analysis of the ORC system using genetic algorithm for recovering exhaust waste heat of a diesel engine are conducted. Based on the first and second laws of thermodynamics, the effects of three key parameters, including evaporation pressure, superheat degree and condensation temperature on the system performances are conducted with net power output per unit heat transfer area and exergy destruction rate as objective functions. The main conclusions can be drawn as follows:

- Over the whole operating range of the diesel engine, the maximum POPA and the net power output are influenced by the engine operating conditions significantly. At rated condition, the maximum POPA and the net power output of the ORC system are 0.74 kW/m^2 and 13.84 kW , respectively.
- The overall trend about the OEP increases with the increment of engine speed and engine torque. Over the whole operating range, the OEP for the working fluid is in the range of 1.09 MPa to 2.81 MPa . The OCT has a small variation in its range, which is nearly kept constant at 298.15 K . The OSD is in the range of 0 K to 2.13 K . Under the most operating conditions of the diesel engine, the OSD values are in the range between 0 K to 1 K .
- For a selected fin-and-tube evaporator, the preheated zone has the maximum heat transfer rate and surface area. Over the whole operating range of the diesel engine, the ratio of effective heat transfer area to actual area of the evaporator is in the range of 17.78% to 69.19% . Considering the OSD almost equals 0, therefore the heat transfer rate and surface area in the superheated zone can almost be neglected.

NOMENCLATURE

\dot{W}	power	(kW)
\dot{Q}	heat transfer rate	(kW)
\dot{m}	mass flow rate	(kg/s)
h	specific enthalpy	(kJ/kg)
s	specific entropy	(kJ/kg.K)
\dot{i}	exergy destruction rate	(kW)
T	temperature	(K)
P	pressure	(MPa)
A	area	(m ²)

Greek letters

η	efficiency
--------	------------

Subscript

0	reference state
1-7,2s,5s	state points in the cycle
exp	expander
wf	working fluid
con	condenser
p	pump
eva	evaporator
exh	exhaust
eff	effective
act	actual

REFERENCES

- Heberle, F., Preißinger, M., Brüggemann, D., 2012, Zeotropic mixtures as working fluids in Organic Rankine Cycles for low-enthalpy geothermal resources, *Renew. Energy*, vol. 37, no. 1: p. 364-370.
- Holland, J. H., 1992, *Adaptation in nature and artificial systems: an introductory analysis with applications to biology, control and artificial intelligence*, MIT Press, Massachusetts.
- Li, Y.R., Du, M.T., Wu, C.M., Wu, S.Y. Liu, C., 2014, Economical evaluation and optimization of subcritical organic Rankine cycle based on temperature matching analysis, *Energy*, vol. 68, p. 238-247.
- Mago, P.J., Chamra, L.M., Srinivasan, K., Somayaji, C., 2008, An examination of regenerative organic Rankine cycles using dry fluids, *Appl. Therm. Eng.*, vol. 28, no. 8-9: p. 998-1007.
- Tong, H., Regner, G., Cowland, C., 2006, Achieving high engine efficiency for heavy-duty diesel engines by waste heat recovery using supercritical organic-fluid Rankine cycle, *SAE paper*, no. 2006-01-3522.
- Vaja, I., Gambarotta, A., 2010, Internal Combustion Engine (ICE) bottoming with Organic Rankine Cycles (ORCs), *Energy*, vol. 35, p. 1084-1093.
- Walraven, D., Laenen, B., D'haeseleer, W., 2015, Economic system optimization of air-cooled organic Rankine cycles powered by low-temperature geothermal heat sources, *Energy*, vol. 80, p. 104-113.
- Wang, E.H., Zhang, H.G., Fan, B.Y., Ouyang, M.G., Zhao, Y., Mu, Q.H., 2011, Study of working fluid selection of organic Rankine cycle (ORC) for engine waste heat recovery, *Energy*, vol. 36, p. 3406-3418.
- Wang, T.Y., Zhang, Y.J., Zhang, J., Peng, Z.J., Shu, G.Q., 2014, Comparisons of system benefits and thermo-economics for exhaust energy recovery applied on a heavy-duty diesel engine and a light-duty vehicle gasoline engine, *Energy Convers. Manag.*, vol. 84, p. 97-107.
- Zhai, H.X., Shi, L., An, Q.S., 2014, Influence of working fluid properties on system performance and screen evaluation indicators for geothermal ORC (organic Rankine cycle) system, *Energy*, vol. 74, p. 2-11.

Zhang, H.G., Wang, E.H., Fan, B.Y., 2013, Heat transfer analysis of a finned-tube evaporator for engine exhaust heat recovery, *Energy Convers. Manag.*, vol. 65, p. 438-447.

ACKNOWLEDGEMENT

This work was sponsored by the Scientific Research Key Program of Beijing Municipal Commission of Education (Grant No. KZ201410005003), the Beijing Natural Science Foundation Program (Grant No. 3152005), the National Natural Science Foundation of China (Grant No. 51376011), and the Key Project of Thirteenth Scientific Research Foundation for Graduate Students in Beijing University of Technology (Grant No. ykj-2014-10708).

INNOVATIVE ORC SCHEMES FOR RETROFITTING ORC WITH HIGH PRESSURE RATIO GAS TURBINES

Vinayak .Hemadri ^{1*}, P.M.V Subbarao ²

¹ Indian Institute of Technology Delhi,
Department of Mechanical Engineering,
New-Delhi, Delhi, India.
vinayakhemadri@gmail.com

² Indian Institute of Technology Delhi,
Department of Mechanical Engineering,
New-Delhi, Delhi, India.
pmvs@mech.iitd.ac.in

* Corresponding Author

ABSTRACT

Combined cycle mode of power generation is one of the efficient ways of generation of power. Combined cycles generally use gas turbine in the topping cycle. However, steam is a standard working fluid in bottoming cycle in present units. Recent studies show that Organic working fluids are most suitable for bottoming cycles under certain range of exhaust gas temperatures. Gas turbines with retrofits like intercooling between the compressor stages and regenerator are not suitable for conventional combined cycle operations. Tapping higher amounts of gas turbine exhaust thermal energy for power generation for high pressure ratio, recuperative gas turbine are feasible with organic working fluids.

Present research work aims at introduction of organic Rankine cycle (ORC) as a bottoming cycle in a conventional combined cycle unit. Commercially available gas turbine models like SGT200 (small capacity) and GE LM -6000 (medium capacity) have been considered for the topping cycle. Saturated Toluene, cyclopentane, butane, MM, MDM, MD₂M, D₄, D₅ are studied parametrically to understand energy recovery potential from the gas turbine exhaust. The working fluid with higher potential for power generation is best suited for ORC.

Use of dry working fluids can achieve the same efficiency as that of other organic working fluids, as they create a scope for use of Internal Heat Exchange (IHE). The advantage of IHE can be understood with reduced condenser loads and enhanced potential for waste heat recovery from the source fluid. It can be either used for thermal applications or power applications depending upon its availability. As siloxanes are deep dry working fluids, their internal regeneration capability is good and hence another bottoming cycle can be thought of with lower boiling point organic working fluid in conjunction with primary bottoming cycle. A very innovative scheme with R-245fa and butane bottoming cycles are studied in conjunction with MM saturated cycle. The power recovery potential by using both the bottoming cycle schemes is studied. This scheme increases complexity of the combined cycle. Hence a dual pressure bottoming cycle scheme is developed using MM as the working fluid. Saturated MM is injected with expanding vapor in the turbine (which is in superheated state). Studying the potential of energy recovery in this arrangement is very creative.

1. INTRODUCTION

Efficiency of power generating cycle improves, if the heat rejection occurs at lowest feasible temperature. This is better achieved by generating power in a combined cycle mode. The commercial combined cycles generally use gas turbine in the topping cycle. The exhaust gas from the topping cycle is used to generate steam for the generation of power in the bottoming cycle. Heavy duty gas turbines with higher exit temperatures from the turbine are techno-economically viable for combined cycle applications.

Combined cycle efficiency depends upon the optimal selection of the gas turbine efficiency. Improving gas turbine efficiency does not necessarily improve the combined cycle efficiency. It is useful only if it does not cause high reduction in steam cycle efficiency. For the same gas turbine inlet conditions, the topping cycle attains higher efficiency at higher pressure ratio. But the efficiency of combined cycle with moderate pressure ratio topping cycle is better than the high pressure ratio topping cycle. This is because steam turbine operates with higher inlet pressure and temperature and contributes greater output. Chacartegui *et al.* (2009a) observed that, gas turbines with retrofits like intercoolers and regenerators are not found suitable in conventional gas and steam combined cycles. Jaheeruddin (2004) observed that steam and gas combined cycles with triple pressure bottoming cycle achieve highest efficiency. Nazzar *et al.* (2003) carried out review of cogeneration opportunity using gas turbine exhaust. Tapping gas turbine exhaust heat to power for a high pressure ratio, recuperative gas turbines needs organic working fluid. It can perform better in the given exhaust temperature range. The integration of ORC with high efficiency, recuperative turbines is carried out by Chacartegui *et al.* (2009b). Bianchi *et al.* (2011) carried out study of different alternative waste heat recovery arrangements like ORC, Stirling engine, inverted Bryton cycle for low to moderate temperature heat sources. Srinivasan *et al.* (2010) and Vaja and Gambarotta (2010) studied integration of ORC with I C engine exhaust. Colonna *et al.* (2006a) (2008a) developed multi parameter Span and Wagner equations for determination of thermodynamic properties of selected siloxanes. The same authors recommend siloxanes for high temperature ORC applications. Drescher and Bruggemann (2007a) and Fernández *et al.* (2011a) suggested use of intermediate thermo oil (recooperer) circuit to exchange energy with source fluid and organic fluid.

This paper presents introduction of ORC as a bottoming cycle in a combined cycle mode. Commercially available gas turbine models of medium to small power capacity are selected for the topping cycle. Saturated toluene, cyclopentane, butane, MM(Hexamethyldisiloxane), MDM(Octamethyl trisiloxane), MD₂M(Decamethyltetrasiloxane), D₄(Octamethylcyclotetrasiloxane), D₅(Decamethylcyclopentasiloxane) are studied parametrically to understand energy recovery potential from the gas turbine exhaust. Thermodynamic analysis of the cycle is carried out with the help of software program developed in C++. Thermodynamic properties of the working fluids calculated using Peng Robnson cubic equations, the constants required to calculate vapor pressure and ideal gas isobaric heat capacity taken from Colonna *et al.* (2006b) (2008b) and Nanan and Colonna (2009) for siloxanes. For toluene, cyclopentane and butane the constants have been referred using Lai Ngoc Anh (2009). To avail the advantage of internal regeneration using IHE, another bottoming cycle in conjunction with MM bottoming cycle has been discussed in sections to follow. A creative multi pressure evaporative scheme is developed to understand the complete power recovery potential from MM

2. DESCRIPTION OF COMBINED CYCLE

Retrofitting high pressure ratio gas turbine topping cycle with ORC bottoming cycle is certainly a challenging task. An intermediate thermo oil circuit (recooperer) circuit is preferred over direct exchange of energy from gas turbine exhaust to the organic working fluid, keeping the safety aspect in focus. Siemens, SGT 200 and high efficiency aero derivative GE LM -6000 are considered for topping cycle. The energy recovery potential for the bottoming ORC cycle using different working fluids is studied for saturated turbine inlet conditions of the bottoming cycle.

2.1 Description of Topping Cycle

The modern heavy duty gas turbine models are not preferred for integration with ORC. The specifications of the gas turbine topping cycles used in this work are provided in Table 1 High efficiency, intercooled and recuperated topping gas turbine cycles produce exhaust gas temperature in the range 355 to 450°C. When there is no process steam requirement, tapping this potential could be possible effectively through organic working fluids.

Figure 1. represents block and *T-s* diagram for combined cycle power plant with gas turbine topping cycle and ORC bottoming cycle with intermediate thermal (thermo) oil circuit. The atmospheric air enters the compressor at point 1_{GT} and it is pressurized to 2_{GT} and then enters the combustor, where it helps to combust the fuel. The hot gases from the combustor 3_{GT} enter the gas turbine, after passing

through the turbine it leaves at 4_{GT} and enter the recoverer (known as heat recovery steam generator HRSB in steam based combined cycle). Dow therm A, thermo oil is used to exchange energy with turbine exhaust. After exchanging energy to the thermo fluid the exhaust gases move to stack and is let out to the atmosphere at prescribed conditions. Thermo fluid after receiving energy from the hot exhaust gases enter the vapor generator of ORC circuit.

Table 1: Specifications of different gas turbine models [Siemens web page, Chacartegui *et al.* (2009c)]

Parameter	SGT200	GE LM-6000
\dot{m}_{ex} (kg/s)	29.3	127
PR	12.2	29.1
TIT(K)		1533
TET(K)	739.15	711
\dot{W} (MW)	6.75	43.4
η (%)	31.5 (ele)	41.8

2.2 Description of ORC Bottoming Cycle

For high pressure ratio recuperative gas turbine topping cycles, steam based bottoming cycle is least efficient. In this scenario, using an organic working fluid in bottoming cycle is a novel idea. The organic working fluid enters the pump at point 1 and it is pressurized to turbine pressure at point 2. Then it flows through the internal heat exchanger (if provided in the circuit) and receives energy from the turbine exhaust of bottoming cycle and leaves at point 2a. It enters the vapor generator and leaves at point 3. After expansion in the turbine point 4, it is in superheated state and made to pass through internal heat exchanger (IHE). It leaves IHE at 4a and passes through condenser; after condensing it enters pump at point 1.

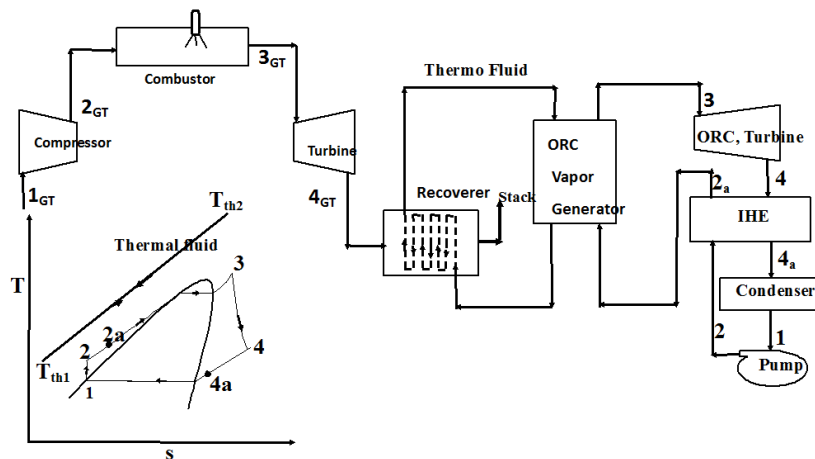


Figure 1: T-s and block diagram for combined cycle power plant

Figure 2. shows temperature $T-\Delta H$ diagram for the generalized combined cycle for bottoming cycles without IHE. It represents heat exchange between exhaust gas to intermediate thermo oil as well as thermo oil to the organic working fluid. The exhaust gas and intermediate thermo oil temperatures for different working fluids is given in Table 2 for SGT 200 integration with organic working fluids. It also explains the operating conditions of the condenser of the ORC circuit. The exhaust gas inlet temperature to the recoverer circuit is denoted by $T_{4_{GT}}$, it is the exit temperature of the flue gas from the topping cycle. The exhaust gas outlet temperature from the recoverer circuit (T_{stack}) is taken as 423.15 K (150°C) based on the suggestions by Meherwan (2002). The inlet and outlet temperature of the thermo oil at the recoverer circuit is denoted by T_{th1} and T_{th2} . T_{th2} is the inlet temperature of the thermo oil to the vaporizer section of ORC and it leaves the vaporizer at a temperature T_{th1} . The maximum temperature of the working fluid is governed by stability and safety criterion of the working fluid. It is given by T_3 in the Figure 2. Since we have carried out a parametric study it is not presented in Table 2. The minimum

temperature of the working fluid is given by condenser conditions. Minimum condenser pressure of 5kPa is recommended by Drescher and Bruggemann (2007b) and Fernández *et al.* (2011b). The condenser temperature ($T_{con}=T_1$) of 323.15K (50°C) is selected for toluene, cyclopentane, butane and MM as their saturation pressure i.e. condenser operating pressure ($P_{con}=P_1$) is above 5kPa. For the working fluids MDM, MD₂M, D₄, D₅ the condenser temperatures (T_1) is elevated to maintain the minimum acceptable condenser pressure.

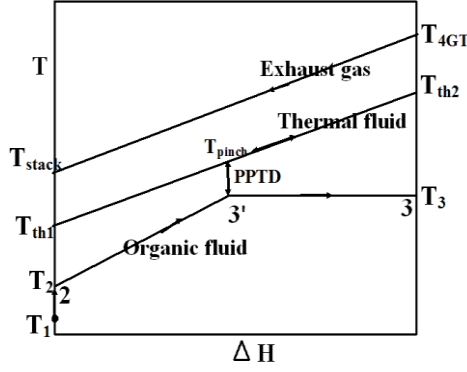


Figure 2: T-ΔH diagram for recuperator and vaporizer

Table 2: Operating temperatures of exhaust gas, thermo oil & working fluid [Refer Figure 2]

Working fluid	T_{4GT} (K)	T_{stack} (K)	T_{th1} (K)	T_{th2} (K)	T_1 (K)	P_1 (kPa)
Toluene	739.15	423.15	343.15	648.15	323.15	9.19
Cyclopentane	739.15	423.15	343.15	648.15	323.15	103.92
Butane	739.15	423.15	343.15	648.15	323.15	494.27
MM	739.15	423.15	343.15	648.15	323.15	17.72
MDM	739.15	423.15	363.15	648.15	343.15	5.83
MD ₂ M	739.15	423.15	393.15	648.15	375.15	5.00
D ₄	739.15	423.15	383.15	648.15	363.15	5.68
D ₅	739.15	423.15	410.15	648.15	390.15	5.29

3. INTEGRATION OF SATURATED ORC BOTTOMING CYCLE WITH TOPING GAS TURBINE CYCLE

Saturated ORC schemes are widely accepted schemes in ORC technology in various applications. These are simple and show good efficiency and preferred over superheated and supercritical schemes for dry working fluids. Different dry type of working fluids like toluene, cyclopentane, butane, MM, MDM, MD₂M, D₄, and D₅ are studied parametrically to understand the energy recovery potential from gas turbine exhaust. The condition of the vapor leaving the turbine is superheated for dry type working fluids. Hence cycles with internal heat recovery using IHE is also studied. An innovative R-245fa bottoming cycle in conjunction with MM bottoming cycle is also studied to understand total recovery potential from gas turbine exhaust. The following assumptions are made in the analysis of the cycle.

- Isentropic efficiency of turbine and pump are assumed as 0.88 and 0.80
- The effectiveness of IHE is 0.8
- PPTD $\geq 10^\circ\text{C}$

3.1 Thermodynamic analysis of the cycle

Selection of pinch point is one of the important parameters in the combined cycle analysis. It can be defined as the temperature difference between the exhaust gas (thermo oil in this case) leaving the evaporator section and saturation temperature of the working fluid at the turbine inlet pressure. It is the lowest temperature difference existing in the evaporator. The calculation of the pinch point and mass flow rates of working fluid is carried out by conducting energy balance. Refer Figure 2. For the notations.

A) Energy exchange in recuperator to calculate mass flow rate of thermal fluid:

Energy lost by the exhaust gas= Energy gained by the thermal fluid

$$\dot{m}_{ex} \times C_{p,ex} \times (T_{4GT} - T_{stack}) = \dot{m}_{th} \times C_{p,th} \times (T_{th2} - T_{th1}) \quad (1)$$

B) Energy exchange in vaporizer section of ORC bottoming cycle to calculate mass flow rate of working fluid:

Energy lost by thermal fluid=Energy gained by the working fluid

$$\dot{m}_{th} \times C_{p,th} \times (T_{th2} - T_{th1}) = \dot{m}_{wf} \times (h_3 - h_2) \quad (2)$$

C) Energy exchange in the evaporator section of the vaporizer to calculate PPTD

$$\dot{m}_{th} \times C_{p,th} \times (T_{th2} - T_{pinch}) = \dot{m}_{wf} \times (h_3 - h_3')$$

$$PPTD = T_{pinch} - T_3' \quad (4)$$

D) The first law efficiency for heat engine can be expressed as:

$$\eta_{th} = \frac{\text{Net work output}}{\text{Heat input}} = \frac{\dot{m}_{wf} \times (w_t - w_p)}{\dot{Q}_{in}} \quad (5)$$

3.1 Integration of Topping Cycle SGT200 with Bottoming ORC Saturated Cycles

In this section integration of different ORC schemes with small capacity gas turbine SGT200 is discussed. Toluene, cyclopentane, butane, MM, MDM, MD₂M, D₄, D₅ working fluids have been studied parametrically to understand the potential for power generation, when connected with gas turbine exhaust. The working fluid with higher potential for power generation is best suited for ORC integration.

The integration with gas turbine cycle for all working fluids considered are studied parametrically at various reduced pressures (P_{-r}) (0.6-0.9). Initially cycles without internal regeneration have been studied followed by cycles with internal regeneration.

Table 3 shows the results obtained for saturated cycles at the maximum permissible temperature limit for individual fluid, expressed in the form of reduced temperature T_{-r} (T_{max}/T_c). The corresponding saturation pressure is also expressed in the form of reduced pressure P_{-r} (P_{max}/P_c). $T_{max} = T_3$, is permissible maximum inlet temperature for the working fluids for integration with SGT200. Toluene is considered at $0.85 P_{max}/P_c$, understanding its safe limit of evaporation for saturated cycles as provided by Chacartegui *et al.* (2009d).

Power produced by any power generating cycle is a function of the mass flow rate of the working fluid and the specific net work output ($w_{net} = w_t - w_p$) of the working fluid. It can be observed that mass flow rate of toluene cycle is less compared to other working fluids, but specific net work output is considerably high over other working fluids. This can be shown with higher level of power recovery from integration with a particular heat source. After toluene, cyclopentane and MM show better exhaust heat to power conversion capabilities. The efficiency of the cycle without IHE is studied initially. Except for butane the potential for internal heat exchange using turbine exhaust is good for all the working fluids considered and hence cycles with IHE have been studied for other working fluids. It can be observed that toluene shows highest efficiency of 25.75% and D₅ exhibits lowest efficiency with a value of 11.38%. The combined cycle efficiency is calculated for gas turbine and ORC integration. The efficiency of the topping gas turbine cycle is referred from Siemens web page and its value is taken as $\eta_{GT} = 0.334$. Highest combined cycle efficiency of 54.11% is observed for toluene with integration with SGT 200.

$$\eta_{cc} = \eta_{GT} + \eta_{ORC} - (\eta_{GT} \cdot \eta_{ORC}) \quad [\text{Murugan and Subbarao (2010)}] \quad (6)$$

Table 3: Results for saturated ORC cycles for all working fluids at $0.9P_{-r}$

Working fluid	T_{-r}	P_{-r}	\dot{m}_{wf} (kg/s)	w_{net} (kJ/kg)	\dot{W} (MW)	$\eta_{(-IHE)}$ %	$\eta_{(+IHE)}$ %	η_{cc} %
Toluene	0.978	0.850	14.847	183.401	2.723	25.75	31.09	54.11
Cyclopentane	0.984	0.900	18.622	117.574	2.189	20.71	22.49	48.38
Butane	0.985	0.900	25.601	57.082	1.461	13.82	----	42.60
MM	0.988	0.900	20.656	78.364	1.619	15.31	24.59	49.78
MDM	0.990	0.900	20.196	76.060	1.536	14.53	27.44	51.68
MD ₂ M	0.989	0.900	21.035	63.105	1.327	12.55	25.53	50.41
D ₄	0.988	0.900	23.191	63.058	1.462	13.83	26.53	51.07
D ₅	0.989	0.900	22.908	52.552	1.204	11.38	24.11	49.46

Parametric study of all the working fluids is done for the P_{-r} range 0.6-0.9. Figure 3(a). shows power recovery potential of all the working fluids. Toluene shows highest power recovery at all the reduced pressures and power recovered by the D₅ is least. This makes toluene most competent working fluid for the integration at all inlet conditions of the turbine. The contribution of bottoming cycle to the total power produced by the combined cycle is expressed by ratio of $\% \dot{W}_{bot} / \dot{W}_{tot}$. Figure 3(b) shows $\% \dot{W}_{bot} / \dot{W}_{tot}$ for toluene, cyclopentane and MM the top three power recovery working fluids. As topping cycles for all the working fluids is same it is obvious that toluene shows higher ratio compared to other

two. Similarly combined cycle efficiency at various reduced pressures is shown in Figure 3(c). The combined cycle efficiency with toluene as the bottoming cycle is highest at all the reduced pressure ranges and it is followed by MM and cyclopentane.

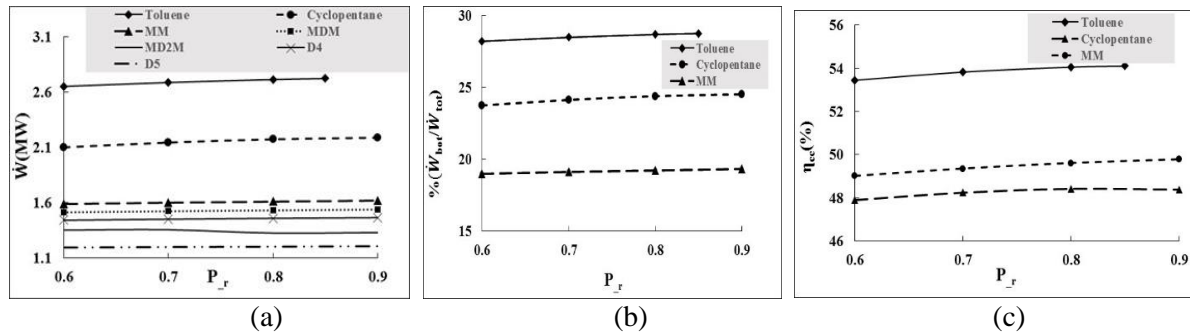


Figure 3 (a, b, c): Total power recovered, $\% \dot{W}_{bot}/\dot{W}_{tot}$, η_{cc}

3.2 Integration of Topping Cycle GELM-6000 with Bottoming ORC Saturated Cycles

The integration of the saturated ORC with different working fluids with medium capacity gas turbine GE LM- 6000 is done in a similar way to SGT 200. The exhaust gas enters the recuperator at 711K at a mass flow rate of 127kg/s and enters the stack at a temperature of 150°C. Thermo fluid is maintained at a temperature of 343.15K and 648.15K at the inlet and out let of the recuperator. Table 4 shows the results obtained for the parametric integration of GE LM- 6000 with different working fluids at $0.9P_{r}$. Power recovery potential of toluene is highest as compared to other working fluids, similar to SGT 200 integration.

Table 4: Results for the parametric integration of GELM-6000 with different working fluids

Working fluid	T_{r}	P_{r}	\dot{m}_{wf} (Kg/s)	\dot{W} (MW)	$\eta_{(-IHE)}$ %	$\eta_{(+IHE)}$ %	η_{cc} %	$\%(\dot{W}_{bot}/\dot{W}_{tot})$
Toluene	0.978	0.85	58.43	10.72	25.07	30.10	59.32	19.80
Cyclopentane	0.984	0.9	73.28	8.62	20.70	22.49	54.89	16.56
MM	0.988	0.9	81.28	6.37	15.31	24.59	56.11	12.80
MDM	0.990	0.9	79.47	6.04	14.53	27.44	57.77	12.22
MD ₂ M	0.989	0.9	82.77	5.22	12.55	25.53	56.66	10.74
D ₄	0.988	0.9	91.26	5.75	13.83	26.53	57.24	11.70
D ₅	0.989	0.9	90.15	4.74	11.38	24.11	55.83	9.84

3.3 Impact of Internal Heat Exchange on Power Recovery:

The advantage of IHE can be understood with reduced condenser loads and enhanced potential for waste heat recovery from the source fluid. It can be either used for thermal applications or power applications depending upon its availability.

Figure 4. shows the advantage of using IHE to the circuit. The temperature of the working fluid increases from T_2 to T_{2a} . And due to this heat addition in a constant pressure process is h_3-h_{2a} instead of h_3-h_2 as represented in the diagram. The effect of this can be observed in thermo oil circuit also, the thermo oil leaves the vaporizer at $T_{th1'}$ instead of T_{th1} . This potential generated due to IHE effect, can be availed either by utilizing it for thermal application or else for power generation. This potential is very small for toluene and cyclopentane and it can be used for small process heat requirement of the industry. As siloxanes are deep dry working fluids, their internal regeneration capability is good and hence another bottoming cycle can be thought with lower boiling point organic working fluid. For the sake of analysis, MM cycle at $0.9P_{r}$ is considered to integrate with another bottoming cycle. R-245fa and butane bottoming cycles are studied in conjunction with MM saturated cycle at $0.9P_{r}$ by using the potential $T_{th1'}-T_{th1}$. As R-245fa produces higher power with the integration and it is presented in the next section.

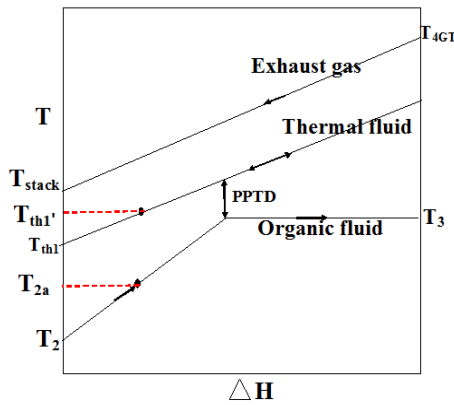


Figure 4: IHE effect on thermal oil circuit

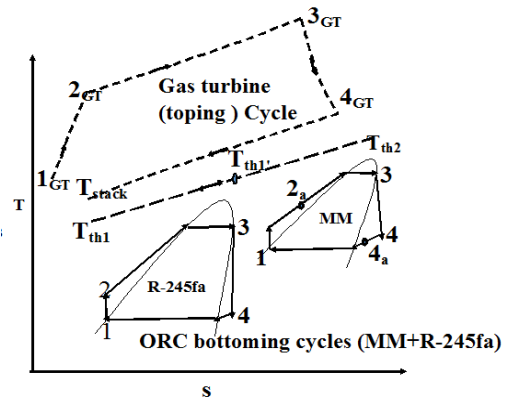


Figure 5: Integration of MM+R-245fa bottoming cycles

3.4 Saturated R-245fa Bottoming Cycle in Conjunction with MM at 0.9P_r for Integration of GE-LM 6000

A very innovative cycle has been developed by understanding the extra potential created due to IHE effect. Figure 5. Shows T-s diagram for saturated R-245fa bottoming cycle which is used in conjunction with MM cycle. The thermo oil leaving the vaporizer of the MM circuit ($T_{th1'}$) is made pass through another vaporizer in which it interacts with low boiling point working fluid R-245fa. After exchanging energy it leaves the vaporizer of R-245fa at T_{th1} , which is the inlet temperature to the heat recoverer. The saturated R-245fa vapor enters the turbine at point 3 after expansion in the turbine the state of the working fluid is slightly superheated. Hence the use of internal heat exchanger is eliminated. The turbine exhaust vapor enters the condenser at point 4. After condensing at point 1 it is pumped to turbine pressure. As this bottoming cycle uses two ORC circuits, it increases complexity of the design, it also adds extra capital investment on all ORC components. The cost associated with this arrangement is not being discussed in this work.

Table 5 shows the parametric study carried for R-245fa cycle for the reduced pressure range of 0.6 to 0.9 P_r. It can be observed that saturated R-245fa at a reduced pressure of 0.9 P_r contributes power of 1.76MW, it is the maximum power obtained from the arrangement. Total power obtained by the two bottoming cycles (MM+R-245fa) is 8.13MW. The efficiency of the combined cycle improves considerably by converting this potential into power. A combined cycle efficiency of 69.57 % is reached by the combination of MM at 0.9 P_r and R-245fa also at 0.9 P_r. The contribution of the bottoming cycle to the combined cycle power is also improved by incorporating this scheme.

Table 5: Results for parametric optimization of R-245fa bottoming cycle used in conjunction with MM at 0.9P_r for integration with GE LM-6000

P _r	\dot{m}_{wf} (kg/s)	$\eta_{(IHE)}$ (%)	\dot{W} (MW)	\dot{W}_{bot} (MM+R245fa)	η_{cc} (%)	% ($\dot{W}_{bot}/\dot{W}_{tot}$)
0.90	58.22	12.63	1.76	8.13	69.57	15.77
0.80	57.24	13.27	1.72	8.09	70.16	15.72
0.70	57.10	13.73	1.67	8.04	70.58	15.63
0.60	57.36	13.99	1.58	7.95	70.82	15.49

4. MULTI PRESSURE EVAPORATION FOR ORC BOTTOMING CYCLES

In this section multi pressure evaporative scheme for bottoming cycle ORC plant is being studied for MM as the working fluid. A very innovative case has been developed and analyzed by using MM as the working fluid.

Due to internal heat exchange between turbine exhaust vapor and exit liquid from pump, the temperature of the thermo oil leaving the vaporizer section of the ORC is increased. This potential has

been utilized by running another bottoming cycle (R-245fa in conjunction with MM cycle). The total power produced by the bottoming cycle by both MM and R245fa is 8.13MW at 0.9P_r as discussed in previous section. It is the maximum power recovery from the combination. Of course it increases the power recovery potential of the bottoming cycle, but it also increases complexity and cost of the cycle by adding one more ORC cycle (components) to the circuit.

4.1. Discussion of Dual Pressure Evaporative MM Cycle

The idea of generating MM vapor and injecting it in the turbine, instead of R-245fa was futile because the condition of MM at lower pressures is superheated and it is not supported by thermodynamics. Therefore a new idea is developed in which instead of generating superheated vapor at the lower pressure (pressure of injection), saturated vapor is being generated and injected in MM turbine. It does lead to slight reduction in exergy of expanding vapor, but it is important that it should produce power comparable to MM and R-245fa combination. After studying feasibility of evaporation at different pressures, it is decided to evaporate MM at 0.3269P_r (0.639MPa) for injection into the turbine.

The block and T-s diagram for the scheme is shown in Figure 6. The condensate from the condenser with flow rate \dot{m}_{wf} at point 1 is divided into two streams: mass \dot{m}_{wf1} and \dot{m}_{wf2} . The mass \dot{m}_{wf1} is pressurized to high pressure in high pressure pump, (2). It is internally regenerated by using the vapor from the exit of the turbine to point, (2a). The regenerated high pressure fluid then enters the high pressure vapor generator at point 2a. It leaves the vapor generator in a saturated state with respect to the turbine inlet pressure, (3). At the same state it enters the turbine and expands till point 4. The condensate \dot{m}_{wf2} is pumped through low pressure pump at 2', the fluid leaving the low pressure pump is internally regenerated using turbine exhaust in the low pressure regenerator to point 2a'. It then enters the low pressure vapor generator and heated till point 4. It is injected into the turbine at the same state. The state of low pressure vapor at point 4 is saturated and the state of the expanding vapor is superheated at point 4. It leads to small amount of exergy destruction of expanding vapor. The temperature of the mixed stream is calculated by this approximation.

Mass flow rate of vapor expanding in turbine at high pressure: $\dot{m}_{wf1} = 81.284 \text{ kg/s}$

Mass flow rate of low pressure vapor: $\dot{m}_{wf2} = 10.8 \text{ kg/s}$

Total mass: $\dot{m}_{wf} = \dot{m}_{wf1} + \dot{m}_{wf2} = 92.084 \text{ kg/s}$ (7)

Temperature of the expanding vapor at point 4: $T_{4,sup} = 480 \text{ K}$

Temperature of the low pressure saturated vapor: $T_{4,sat} = 451.98 \text{ K}$

Mass fraction high pressure expanding vapor: $x_h = \frac{\dot{m}_{wf1}}{\dot{m}_{wf}}$ (8)

Mass fraction of low pressure vapor: $x_l = \frac{\dot{m}_{wf2}}{\dot{m}_{wf}}$ (9)

Hence temperature of the mixed stream is approximated as:

$$T_4 = x_h \times T_{4,sup} + x_l \times T_{4,sat} \approx 477 \text{ K} \quad (10)$$

As both the streams mixing at the same pressure, $P_4 = 0.639 \text{ MPa}$

The further expansion of the mixed stream is considered from P_4 , T_4 to condenser condition till point 5. At point 5 the total mass flow rate of working fluid is divided into two streams. \dot{m}_{wf1} goes to high pressure regenerator and \dot{m}_{wf2} enters low pressure regenerator. After exchanging energy with feed fluid in IHE, both the streams mix together and enter the condenser at point 1' and the cycle continues.

4.2. Thermodynamic analysis of the cycle

Rate of work obtained from high pressure vapor before mixing (3-4) in the turbine:

$$\dot{W}_{t1} = \dot{m}_{wf1} \times (h_3 - h_4) \quad (11)$$

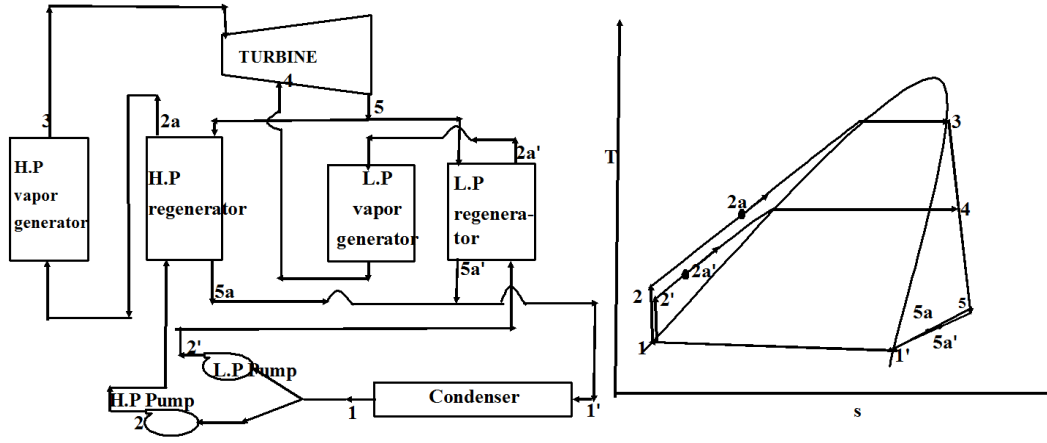


Figure 6: Block and T-s diagram for multi pressure evaporation

Rate of work obtained from the mixed stream (4-5) the turbine:

$$\dot{W}_{t2} = \dot{m}_{wf} \times (h_4 - h_5) \quad (12)$$

$$\text{Total rate of work obtained: } \dot{W}_t = \dot{W}_{t1} + \dot{W}_{t2} \quad (13)$$

$$\text{Rate of work in put to high pressure pump: } \dot{W}_{p1} = \dot{m}_{wf1} \times (h_2 - h_1) \quad (14)$$

$$\text{Rate of Work in put to low pressure pump: } \dot{W}_{p2} = \dot{m}_{wf2} \times (h_2' - h_1) \quad (15)$$

$$\text{Total rate of pump work: } \dot{W}_p = \dot{W}_{p1} + \dot{W}_{p2} \quad (16)$$

$$\text{Net rate of work obtained : } \dot{W}_{net} = (\dot{W}_t - \dot{W}_p) \quad (17)$$

$$\text{Rate of energy input to the cycle: } \dot{Q}_{in} = \dot{m}_{wf1} \times (h_3 - h_{2a}) + \dot{m}_{wf2} \times (h_4 - h_{2a}') \quad (18)$$

$$\text{Efficiency of the cycle: } \eta_{th} = \frac{\text{Net rate of work obtained}}{\text{Total rate of Energy input}} = \frac{\dot{W}_{net}}{\dot{Q}_{in}} \quad (19)$$

Table 6: Results for multi pressure evaporation for MM

T _{r3}	P _{r3}	T _{r4}	P _{r4}	\dot{m}_{wf1} (kg/s)	\dot{m}_{wf2} (kg/s)	\dot{W}_t (kW)	\dot{W}_p (kW)	\dot{W}_{net} (kW)	\dot{Q}_{in} (kW)	η (%)
0.98	0.90	0.87	0.33	81.28	10.80	7540.50	251.48	7289.00	28526.44	25.55

Table 6 shows the results obtained for multi pressure evaporation. It can be observed that net power produced from the multi pressure evaporation is 7.289 MW and the total power produced by bottoming cycle of saturated MM and saturated R245fa at 0.9P_r is 8.13 MW. There is a reduction of power by 841kW by injecting MM saturated vapor in to the turbine, but this cycle is less complicated and simple as it consists only single ORC in the bottoming cycle.

5. CONCLUSIONS

The potential for power recovery using different organic working fluids for saturated ORC schemes is studied for high pressure ratio recuperative gas turbine topping cycles. The cycles are studied for both without IHE and with IHE schemes. Toluene shows highest recovery potential over all the working fluids considered. It generates a power of 2.723MW for integration with SGT200. The advantage of using IHE not only improves efficiency but also creates opportunity for extra power generation using low boiling point working fluid. MM bottoming cycle in conjunction with another low boiling point working fluid (R245fa) recovers a power of 8.13MW(MM+R245fa) for integration with GE-LM 6000. This is lower than toluene bottoming cycle which produces 10.72 MW of power from integration .A multi pressure cycle using MM as the working fluid is discussed at the end for the integration of GE-LM 6000. The advantage of IHE is utilized to generate saturated vapors of MM and injected into the expanding vapor of MM bottoming cycle. The power recovery capability of this innovative idea is compared with (MM+R245fa) combined bottoming cycle. Even though multi pressure evaporation of MM produces less power but it reduces complexity of the cycle.

NOMENCLATURE

List of Symbols		Subscripts	
\dot{m}	Mass flow rate	kg/s	cc Combined cycle
PR	Pressure ratio	(-)	GT Gas turbine
h	Enthalpy	kJ/kg	th Thermo
P	Pressure	MPa	wf Working fluid
T	Temperature	K	sup Superheated
s	Entropy	kJ/(kg-K)	sat Saturated
TIT	Turbine inlet temperature	K	bot Bottoming
TET	Turbine exit temperature	K	tot Total
IHE	Internal heat exchanger	(-)	t Turbine
\dot{W}	Power	MW	p Pump
w	Specific work output	kJ/kg	c Critical
C_p	Specific heat	kJ/(kg-K)	sup Superheated
T_{-r}	Reduced temperature	(-)	sat Saturated
P_{-r}	Reduced pressure	(-)	
Greek Symbols			
η	Efficiency	(%)	

REFERENCES

- Bianchi M., De Pascale A., 2011, Bottoming cycles for electric energy generation: Parametric investigation of available and innovative solutions for the exploitation of low and medium temperature heat sources, *Applied Energy*, 88, 1500–1509.
- Chacartegui R., Sánchez D., Muñoz J.M., Sánchez T., 2009, Alternative ORC bottoming cycles FOR combined cycle power plants, *Applied Energy*, 86, 2162–2170.
- Colonna P., Nannan N.N., Guardone A., Lemmon E.W., 2006, Multiparameter equations of state for selected siloxanes, *Fluid Phase Equilibria*, 244, 193–211.
- Colonna P., Nannan N.N., Guardone A., 2008, Multiparameter equations of state for selected siloxanes, *Fluid Phase Equilibria*, 263, 115–130.
- Drescher U., Bruggemann D., 2007, Fluid selection for the Organic Rankine Cycle (ORC) in biomass power and heat plants, *Applied Thermal Engineering*, 27, 223–228.
- Fernández F.J., Prieto M.M., Suárez I., 2011, Thermodynamic analysis of high-temperature regenerative organic Rankine cycles using siloxanes as working fluids, *Energy*, 36, 5239–5249.
- Jaheeruddin S.K., 2004, Optimization of Erection of Steam Side of a Combined Cycle Power Plant, M-Tech Thesis, Indian Institute of Technology, Delhi.
- Lai Ngoc Anh., 2009, Thermodynamic data of working fluids for energy engineering, Ph.D. Thesis, University of Natural Resources and Applied Life Sciences, Vienna.
- Meherwan P.B., 2002, Hand book for cogeneration and combined cycle power plants, ASME Press, New York.
- Murugan R.S., Subbarao P.M.V., 2008, Efficiency enhancement in a Rankine cycle power plant: combined cycle approach. *Proc. Inst. Mech. Eng. Part A J. Power Energy*. 222:753–760.
- Nannan N.R., Colonna P., 2009, Improvement on multiparameter equations of state for dimethylsiloxanes, *Fluid Phase Equilibria*, 280, 151–152.
- Najjar Y.S.H., Akyurt M., Alrabghi O.M., Alp T., 1993, Cogeneration with gas turbine engines, *Heat Recovery Systems and CHP*, vol.13, no.5:p.471–480.
- Siemens Gas Turbine, Website: <http://www.energy.siemens.com/hq/en/fossil-power-generation/gas-turbines/sgt-200.htm>, [accessed on 01.12.2014].
- Srinivasan K.K., Mago P.J., Krishnan S.R., 2010, Analysis of exhaust waste heat recovery from a dual fuel low temperature combustion engine using an Organic Rankine Cycle, *Energy*, 35, 2387–2399.
- Vaja I., Gambarotta A., 2010, Internal Combustion Engine (ICE) bottoming with Organic Rankine Cycles (ORCs), *Energy*, 35, 1084–1093.

UTILIZATION OF WASTE HEAT FROM INTERCOOLED, REHEAT AND RECUPERATED GAS TURBINES FOR POWER GENERATION IN ORGANIC RANKINE CYCLES

Xurong Wang, Yi Yang, Mingkun Wang, Ya Zheng, Jiangfeng Wang, Yiping Dai*

Xi'an Jiaotong University, School of Energy and Power Engineering,
Xi'an, Shaanxi, P.R. China
*ypdai@mail.xjtu.edu.cn

ABSTRACT

Organic Rankine cycle (ORC) is a very attractive technology for the conversion of low-grade thermal energy into electrical and/or mechanical energy. As the ORC has a wide range of power, it can recover the waste heat from power cycles such as turbines and/or microturbines of gas. The ORC bottoming cycle is currently incorporated into the exhaust of recuperative gas turbines to further lower the temperature of the exhaust gas, yielding similar overall efficiency to that of conventional gas turbine and steam combined cycles. However, a certain amount of thermal energy in the intercooler is not effectively utilized in the intercooled gas turbine cogeneration cycles. The temperature of the compressed air at the intercooler inlet could be found about 120 °C-250 °C. This is an ideal energy source to be used in an ORC for power generation.

In this investigation, a thermodynamic analysis was carried out on combined cycles comprising recuperated, intercooled and reheat gas turbines and two ORCs (recuperated ICRHGT-ORCs) to recover waste heat from the intercooler and the exhaust of recuperated gas turbine. Three existing gas turbines were performed as the topping cycles with appropriate modifications. The following organic fluids were considered as the working fluids in ORCs: R123, R245fa, toluene and cyclohexane. A computer program was then designed for computations of system performance. Thermodynamic analyses were performed to study the effects of parameters including evaporator temperatures and degrees of superheat at the ORC turbine inlet on the combined cycle performance. These parameters were then optimized with thermal efficiency as the objective function by means of a genetic algorithm. It was found that all the three modified gas turbines with bottoming ORCs had higher performance, with thermal efficiency increase of 7.8% to 15.2%, in comparison to their original values.

1. INTRODUCTION

In the low-grade waste heat recovery field, the organic Rankine cycle (ORC) gives a good performance to convert low and medium temperature heats such as renewable energies like solar, wind and geothermal power, low enthalpy heat rejected by industry and exhaust gas of gas turbines into electrical or/and mechanical energy. Much work has been carried out on the application and performance of ORCs (Angelino *et al.*, 1998, Hung, 2001, Wei *et al.*, 2007, Tchanche *et al.*, 2011, Vélez *et al.*, 2012). Typically, the ORC as a bottoming cycle in combined power plants is a promising process to enhance the system efficiency and reduce the fossil fuel consumption. For gas turbine applications, the combination of an ORC bottoming cycle can reduce design and development cost.

The modularity and wide range of power of the ORC system allow repowering of the existing gas turbines to use the thermal power of the exhaust gases typically available in the temperature range of 250 – 300 °C and produce electricity by acting a bottoming cycle. Najjar and Radhwan (1988) proposed a cogeneration system by combining a gas turbine cycle with an ORC bottoming cycle. The results showed that a global combined cycle efficiency slightly below 45.2% with an efficiency improvement of about 54% by using R22 as the organic fluid. Invernizzi *et al.* (2007) investigated the

performance of a 100 kW size micro-gas turbine and ORC combined cycle. They reported that the micro-gas turbine could obtain an additional 45 kW of electricity and an efficiency improvement of 30% to 40%. Yari (2008) conducted parametric analysis and comparison of the micro turbine ORC with or without internal heat exchanger combined cycles. The effects of several parameters on the combined cycle performance were also discussed. Clemente *et al.* (2013) studied a number of different expanders for ORCs with the aim to design a bottoming cycle for a 100 kW recuperated gas turbine. A careful review of these numerous works shows that the bottoming ORC cycle is designed to recover waste heat from the flue gases of a small recuperative gas turbine. However, combined cycles comprising high efficiency heavy duty gas turbines and ORCs in the medium and large scale power generation have not been carefully analyzed. Chacartegui *et al.* (2009) found this shortage and then studied the use of ORC bottoming cycles incorporated into the exhaust of recuperated gas turbines or very high pressure ratio gas turbines, which are characterized by their very high efficiency but low exhaust temperature. Moreover, they modified the topping gas turbines by adding intercooled compression and reheat, showing that the efficiency of the modified combined cycle was up to 3% points higher than conventional single pressure steam combined cycles, depending on the working fluid.

By adding an intercooled compression to the modern high efficiency gas turbines, the low pressure compressor (LPC) outlet temperature varies from 120 °C to 250 °C, depending on the LPC pressure ratio (Bhargava *et al.*, 2002). This amount thermal energy currently is rejected to the coolant like atmospheric air, cooling water or sea water. It is noticed that there may be a continuous increase of efficiency improvement of the current gas turbine and ORC combined cycle by designing an additional ORC bottoming cycle to recover the heat from the intercooled compression. In addition, a limited amount of work has been done on the evaluation of a combined cycle comprising a recuperated, intercooled and reheat (ICRH) gas turbine and two ORC bottoming cycles in cogeneration applications.

This paper investigated the possibility of increasing the performance of recuperated ICRH gas turbines by combining two ORCs which recover the waste heat from the intercooler and the exhaust of recuperated gas turbine. Three existing gas turbines with appropriate modifications were performed as the topping cycles. For the ORC bottoming cycles, the following organic fluids were considered as the working fluids: R123, R245fa, toluene and cyclohexane. A computer program was designed for computations of system performance. Four key parameters in the bottoming cycles including evaporator temperatures and degrees of superheat at the ORC turbine inlet were evaluated to analysis their effects on the combined cycle thermal efficiency. These parameters were then optimized with thermal efficiency as the objective function by means of a genetic algorithm (GA).

2. RECUPERATED ICRHGT-ORCS COMBINED CYCLE DESCRIPTION

In this section, two ORC bottoming cycles are incorporated into the exhaust and two successive compression stages, respectively, of a recuperated ICRH gas turbine cycle, as shown in Figure 1. The purpose of such analysis is to evaluate the interest of the proposed bottoming cycles when integrated with the recuperated ICRH gas turbines. In order to use the exhaust waste heat, an ORC is employed through an evaporator to further decrease the exhaust temperature. Additionally, a second ORC is designed through a suitable evaporator 2 to recover waste heat from the compressed air leaving the LPC.

For the topping cycle, three existing gas turbines are selected and modified to be converted into the recuperated ICRH gas turbine cycles. The selected gas turbines include a modern heavy duty gas turbine Alstom GT 24, a high efficiency aeroderivative gas turbine GE LM-6000 (dry) and a recuperated and intercooled gas turbine Rolls-Royce WR 21. The examples give a large power range from 25 MW to 179 MW. This study converted each of the selected gas turbines into a recuperated ICRH cycle system using the design methodology presented in Bhargava *et al.* (2002). Note that for the Rolls-Royce WR 21 gas turbine, a low pressure turbine (LPT), which is not presented in Figure 1,

is included between the high pressure turbine (HPT) and the combustion chamber 2 (CC2). The calculated main performance of each modified gas turbine is presented in Table 1.

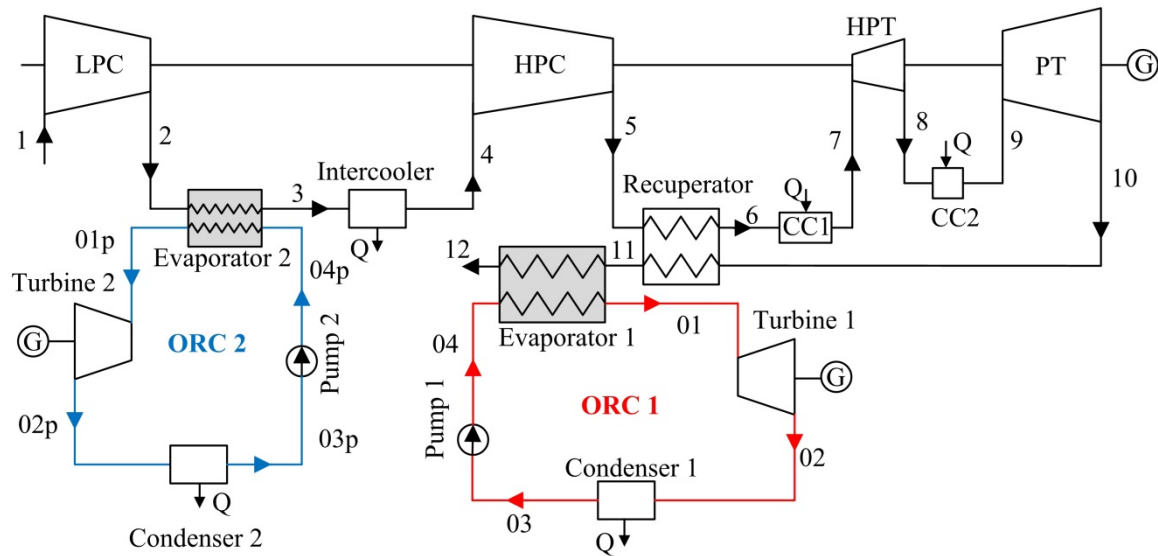


Figure 1: Schematic diagram of reference combined recuperated ICRH gas turbine with two ORC cycles

Table 1: Recuperated ICRH Gas turbines main characteristics

Parameter	GE LM-6000	Alstom GT 24	RR WR 21
Power Output (MW)	96.84	249.75	35.76
Overall Efficiency (%)	47.59	47.32	47.5
Turbine Inlet Temperature (°C)	1260	1260	982
Exhaust Temperature (°C)	462	384	307
LPC outlet temperature (°C)	117	211	152
Exhaust Gas Flow (kg/s)	148.7	391	73.1
Overall Pressure Ratio	34.1	31	16.2
LPC Pressure Ratio	2.65	4.48	3.3
HPT Pressure Ratio	3.44	2.03	1.97
LPT Pressure Ratio	-	-	1.64
PT Pressure Ratio	9.88	15.27	4.94

Data in Table 1 show that each of the recuperated ICRH cycle had impressive efficiency and power output. The modified LM-6000 machine achieved efficiency and power of 47.59% and 96.84 MW, respectively. For the modified GT 24 gas turbine, the efficiency and power were 47.32% and 249.75 MW, respectively. Additionally, the recuperated ICRH cycle derived from WR 21 machine attained efficiency and power of 47.5% and 35.76 MW, respectively. Although the value of exhaust temperature for modified gas turbines is not particularly high due to the presence of the recuperator, it can further drop by addition of an evaporator to transfer its heat to the bottoming cycle. For the modified LM-6000, GT 24 and WR 21 the LPC outlet temperatures were 117, 211 and 152 °C, respectively. The difference in values of LPC outlet temperature for modified gas turbines is due to the fact that the optimum LPC pressure ratio varies.

For the bottoming cycle, two simple configuration of ORC are considered. The ORC uses organic working fluids with low boiling points to recover heat from low- and medium temperature heat sources. The selection of the working fluid substantially affects the performance of the ORC. Table 2 presents a list of some common working fluids considered in this paper along with their critical properties and maximum operating temperatures. The limitation of maximum operating temperature for each working fluid guarantees that fluid degradation is avoided. The working fluid at the ORC

turbine inlet can be either saturated or superheated. The effect of degree of superheat on the combined cycle thermal efficiency will be later discussed.

Table 2: Properties of working fluids used in this study

Working fluid	T_c (°C)	P_c (MPa)	T_{max} (°C)
R123	183.68	3.66	175
R245fa	154.05	3.64	140
Toluene	318.6	4.13	300
Cyclohexane	280.45	4.075	270

3. THERMODYNAMIC ANALYSIS

In this section, the thermodynamic model of combined cycles that use commercially modified gas turbines and ORC bottoming cycles was developed on the basis of available resource in literature (Bhargava *et al.*, 2002, Chacartegui *et al.*, 2009, Yari and Mahmoudi, 2010). It must be noted that the same working fluid is used in both bottoming ORCs for certain recuperated ICRHGT-ORCs combined cycle.

3.1 Assumptions

The following assumptions for the combined cycle are considered in this study:

- (1) The system operates in a steady-state condition; kinetic and potential energy changes are neglected.
- (2) The pressure drops throughout the pipes and heat exchangers are negligible.
- (3) The general assumptions of ORC are listed in Table 3. Saturated liquid is supposed at the condenser outlet with a conservative temperature of 40 °C.
- (4) In thermodynamic calculations special attention is paid to the values of pinch point in evaporator which is not below 2 °C.
- (5) The effectiveness of 0.9 was considered for the intercooler and the recuperator.

Table 3: ORC data assumption

Pump Efficiency (%)	Turbine Efficiency (%)	Evaporator Efficiency (%)	Condensation Temperature (°C)
80	85	90	40

3.2 Performance evaluation

The net power output of the recuperated ICRHGT-ORCs can be expressed as:

$$\begin{aligned} \dot{W}_{net} &= \dot{W}_{net, REC ICRHGT} + \dot{W}_{net, ORCs} \\ &= (\dot{W}_{HPT} + \dot{W}_{PT} - \dot{W}_{LPC} - \dot{W}_{HPC})_{REC ICRHGT} + (\dot{W}_T - \dot{W}_P)_{ORC, 1} + (\dot{W}_T - \dot{W}_P)_{ORC, 2} \end{aligned} \quad (1)$$

The overall efficiency of the combined cycle is given by

$$\eta_I = \frac{\dot{W}_{net}}{\dot{Q}} = \frac{\dot{W}_{net}}{\dot{m}_{air}(h_7 - h_6) + \dot{m}_{mix,1}(h_9 - h_8)} \quad (2)$$

The power ratio is defined as the ratio of bottoming cycles to combined cycle power, which is given as follows

$$\text{Power Ratio} = \frac{\dot{W}_{net, ORCs}}{\dot{W}_{net}} \quad (3)$$

3.3 Optimization method

In order to recover as much waste heat as possible, it is necessary to optimize the combined cycles. The parameters chosen for optimizing recuperated ICRHGT-ORCs combined cycle are evaporator temperatures, pitch point temperature difference and degrees of superheat at the ORC turbine inlet.

The equation of the mathematical model reveal that the optimum value for overall efficiency (η_i) can be expressed as a function of these five operating parameters, as shown in the equation:

$$\text{Maximize } \eta_i(T_{e,1}, T_{e,2}, \Delta T_E, \Delta T_{\text{sup},1}, \Delta T_{\text{sup},2}) \quad (4)$$

Subject to:

$$\begin{aligned} 90 &\leq T_{e,1} \leq T_{\text{max}} \\ 60 &\leq T_{e,2} \leq T_2 - 10 \text{ or } T_{\text{max}} \\ 2 &\leq \Delta T_E \leq 15 \\ 0 &\leq \Delta T_{\text{sup},1} \leq 10 \\ 0 &\leq \Delta T_{\text{sup},2} \leq 10 \end{aligned} \quad (5)$$

where $T_{e,1}$ is the evaporator temperature of the organic fluid in ORC 1, $T_{e,2}$ is the evaporator temperature of the organic fluid in ORC 2, T_2 is the LPC outlet temperature, ΔT_E is the pitch point temperature difference in the evaporator, $\Delta T_{\text{sup},1}$ is the superheat degree at the ORC 1 turbine inlet, $\Delta T_{\text{sup},2}$ is the degree of superheat at the ORC 2 turbine inlet, T_{max} is the maximum operating temperature of the organic fluid.

The constraints as listed in Equation (5) were applied by setting the bounds on each variable. Note that the upper bound of $T_{e,2}$ was limited to either LPC outlet temperature subtracted 10 °C or maximum operating temperature of the organic fluid. This is because the critical temperature of the organic working fluid like R245fa may below the LPC outlet temperature. In the present study, the genetic algorithm (Holland, 1992) is applied to the optimization process to obtain the maximum overall efficiencies for each combined cycle.

4. RESULTS AND DISCUSSION

The results of parametric analysis of the recuperated ICRHGT-ORCs combined cycles are presented in this section. Reference data from the NIST REFPROP database (Lemmon *et al.*, 2007) are used to calculate the working fluid thermodynamic properties. In addition, a code of the recuperated ICRHGT-ORCs combined cycles was developed to perform the simulation of these combined cycles. As toluene has higher critical properties and turbine specific enthalpy than R123, R245fa and cyclohexane, it is used as the working fluid of the bottoming cycles to evaluate effects of key parameters of ORCs on the performance of three modified gas turbine and ORCs combined cycles. Optimizations of recuperated ICRHGT-ORCs combined cycles for different organic working fluids were then conducted.

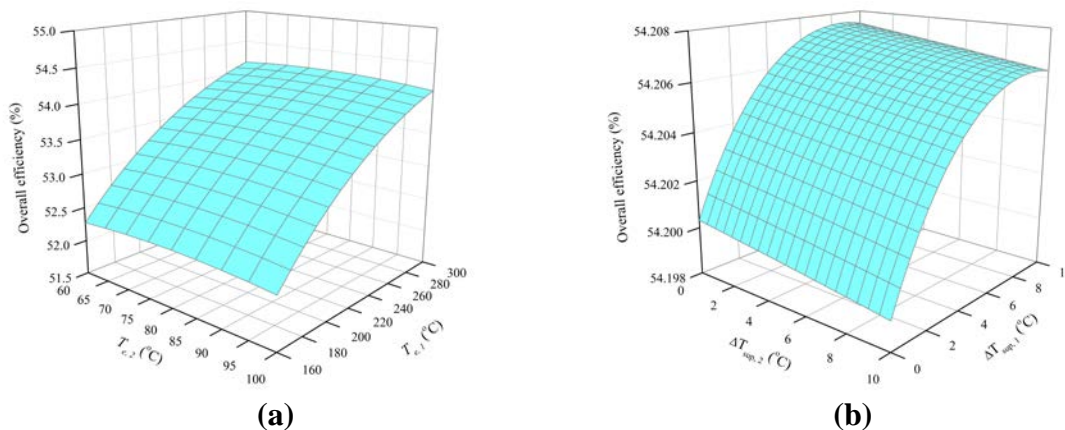


Figure 2: Overall efficiency versus evaporator temperatures (a) and degrees of superheat (b) with toluene as the organic working fluid and the recuperated ICRH LM-6000 gas turbine as the topping cycle

The effect of the evaporator temperatures and degrees of superheat on the overall efficiency of toluene LM-6000-ORCs combined cycle is shown in Figure 2. It can be seen that the overall efficiency strongly increased with an increase in the evaporator temperature $T_{e,1}$. It seems that a greater overall efficiency can be obtained by a higher evaporator temperature in the evaporator 1. This result is understandable because the exhaust temperature of LM-6000 was as high as 465 °C. However, the evaporator temperature $T_{e,2}$ had slight effect on the overall efficiency. It can be seen from Figure 2(b) that there is an optimum value of superheat degree at the ORC 1 turbine inlet with which the efficiency is found to be maximum.

Figure 3 shows the variation of modified GT 24-ORCs combined cycle with evaporator temperatures and degrees of superheat in bottoming cycles with toluene as the working fluid. It can be observed that an increase in evaporator temperature 1 ($T_{e,1}$) led to an increase in overall efficiency. However, an increase in evaporator temperature 2 ($T_{e,2}$) led to an increase and then a decrease in the combined cycle efficiency. These results indicate that the ORC 2 plays an important role in the enhancement of the overall efficiency. This is expected because the LPC outlet temperature of GT 24 was up to 211 °C, and, as a result, the heat recovery from LPC exhaust in evaporator 2 section increased significantly. From Figure 3(b) it can be seen that the overall efficiency decreased with an increase in degree of superheat at ORC 2 turbine inlet. An increase in degree of superheat at ORC 1 turbine inlet, however, led to an increase in the overall efficiency.

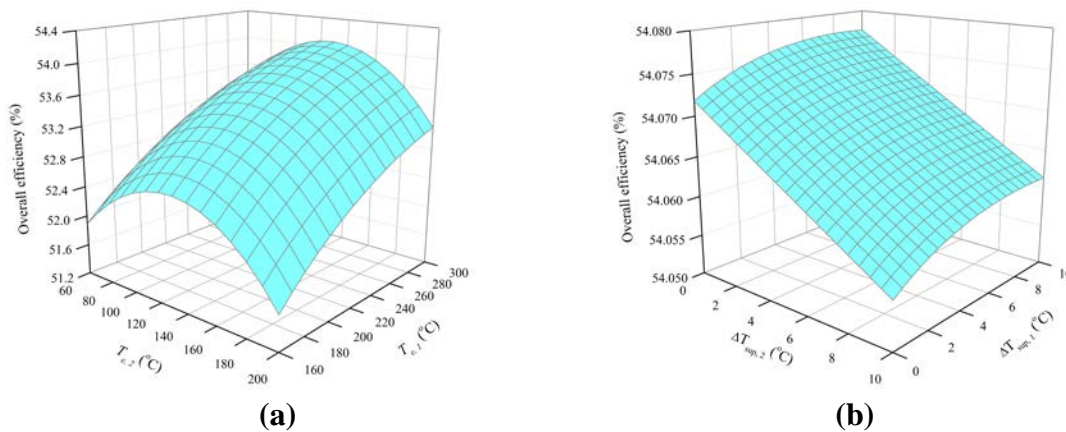


Figure 3: Overall efficiency versus evaporator temperatures (a) and degrees of superheat (b) with toluene as the organic working fluid and the recuperated ICRH GT 24 gas turbine as the topping cycle

Figure 4 presents the effects of evaporator temperatures and ORC turbine inlet vapour superheating on the toluene WR 21-ORCs combined cycle efficiency. It can be seen from Figure 4(a) that an optimum evaporator temperature 2 ($T_{e,2}$) existed and could be found by parameter optimization of the combined cycle. For a higher evaporator temperature 1 ($T_{e,1}$), greater waste heat is transferred to the ORC 1 resulting in an increase of power generation in ORC turbine and therefore the combined cycle efficiency. Figure 4(b) shows that by increasing the degrees of superheat at the turbine inlet both in the ORCs the overall efficiency decreased. It appears that saturated vapour of the organic working fluid is expected at the turbine inlet in both ORCs for the WR 21 and ORCs combined case.

In order to investigate the interest of combining low temperature bottoming cycle with low exhaust temperature intercooled gas turbines, a parametric optimization of the bottoming cycles is now presented depending on the modified gas turbines as described in Table 1 and working fluid in the bottoming cycles. Results are shown in Tables 4, 5 and 6 for different topping gas turbines.

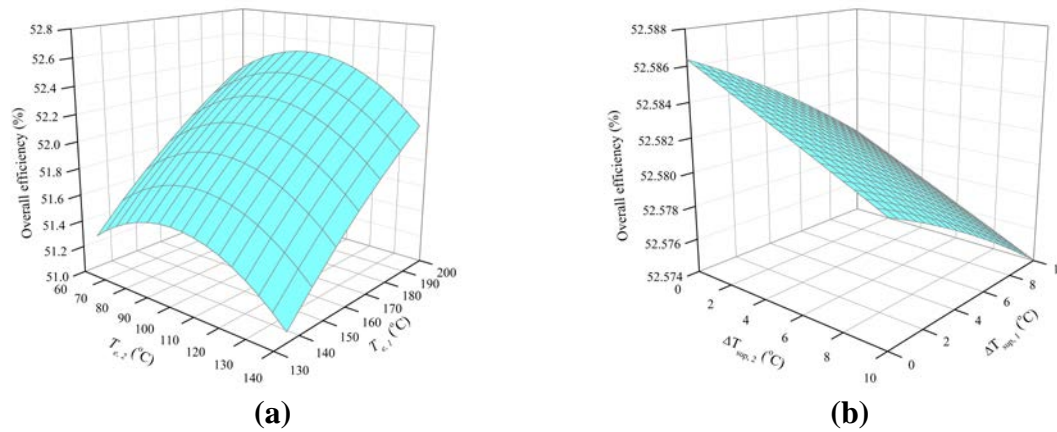


Figure 4: Overall efficiency versus evaporator temperatures (a) and degrees of superheat (b) with toluene as the organic working fluid and the recuperated ICRH WR 21 gas turbine as the topping cycle

Table 4 shows the optimization results of the recuperated ICRH LM-6000-ORCs combined cycle for different organic fluids. It is found that the modified LM-6000-ORCs combined cycle had higher performance, with thermal efficiency increase of 8.75% - 15.18% depending on the organic fluid, in comparison to the original value of stand-alone recuperated ICRH LM-6000. Note that the efficiency enhancement is the overall efficiency of the combined cycle relative to the efficiency of single modified gas turbine. The maximum overall efficiency was obtained by using toluene as the ORC fluid, i.e., 54.81%. Moreover, the toluene REC ICRHGT-ORCs had an overall power output of 111.54 MW with a power ratio of 13.18%. These findings are understandable because the turbine specific work or enthalpy drop of toluene in ORCs is higher when compared with R123, R245fa and cyclohexane. The net additional power produced by the ORCs was about 8.5 - 14.7 MW. The R123 and R245fa ORCs combined cycles demanded mass flow rates of about 231 and 216 kg/s in ORC 1, respectively, which were almost 3 times greater than that the toluene or cyclohexane ORCs combined cycle demanded. The ORC 2 recovering waste heat from the intercooler produced electricity of about 0.5 MW on average for each organic fluid. This amount of power is relatively smaller than the power generated by the ORC 1 due to the limitation of LPC outlet temperature. The optimum operating parameters using the GA are also presented in Table 4. It can be seen that the pinch point temperature difference approached a value of 2 °C for all the organic working fluids, which means that the evaporator size would be large or the evaporator should be well designed to meet the demand of heat transfer. On the other hand, the degree of superheat at the ORC 1 turbine inlet was as high as 10 °C using R123 as the organic fluid, while the degree of superheat at the ORC 2 turbine inlet was relatively small for each organic fluid.

Table 4: Summary of optimization results for maximum overall efficiency of the modified GE LM-6000-ORCs cycle

Parameter	R123	R245fa	Toluene	Cyclohexane
Overall Efficiency (%)	52.62	51.75	54.81	53.89
Efficiency Enhancement (%)	10.57	8.75	15.18	13.24
ORC 1 Power Output (MW)	9.72	7.95	14.21	12.33
ORC 2 Power Output (MW)	0.52	0.53	0.49	0.49
Overall Power Output (MW)	107.08	105.32	111.54	109.66
Power Ratio (%)	9.56	8.05	13.18	11.69
$T_{e,1}$ (°C)	169.9	140	299.7	263.8
$T_{e,2}$ (°C)	80.3	78.1	80.3	75.6
ΔT_E (°C)	2.3	2.1	2.2	2.9
$\Delta T_{sup,1}$ (°C)	10	8	5.7	1.4
$\Delta T_{sup,2}$ (°C)	0.7	2.1	1.2	3.4
ORC 1 Mass Flow Rate (kg/s)	231.4	215.7	72.8	76.7
ORC 2 Mass Flow Rate (kg/s)	31.6	31.4	12.1	14.1

Table 5 shows the optimization performance of the recuperated ICRH GT 24-ORCs combined cycle. It is found that the modified GT 24-ORCs combined cycles had efficiencies of 52.13% - 54.07%, with thermal efficiency increase of 10.17% - 14.26%, in comparison to the original value of stand-alone recuperated ICRH GT 24. The maximum overall efficiency was obtained by using toluene as the ORC fluid, i.e., 54.07%, which is close to the overall efficiency of toluene REC ICRH LM-6000-ORCs combined cycle. Moreover, the toluene REC ICRH GT 24-ORCs had a maximum overall power output of 284.47 MW. The net additional power produced by the ORCs was about 25.4 - 35.6 MW. Furthermore, the power ratios were 9.96%, 9.23%, 12.48% and 10.6% for R123, R245fa, toluene and cyclohexane combined cycles, respectively. The ORC 2 could produce electricity of about 9 MW by using R245fa as the ORC fluid. This amount of power is more than a half of the power generated by the ORC 1 due to the high inlet temperature of ORC turbine 2. Correspondingly, large amount of R245fa is desirable to run the R245fa REC ICRH GT 24-ORCs combined cycle, which, however, may increase the system capital cost. Conversely, organic fluids with high turbine specific enthalpy like toluene and cyclohexane had few mass flow rates in ORCs. The optimum operating parameters using the GA are also presented in Table 5. It can be seen that, similar to the case of modified LM 6000-ORCs combined cycle, the pitch point temperature difference approached a value of 2 °C for all the organic working fluids. On the other hand, the degree of superheat at the ORC 1 turbine inlet ranged from 0.2 °C to 8.2 °C, while the degree of superheat at the ORC 2 turbine inlet was close to zero for all the organic fluids.

Table 5: Summary of optimization results for maximum overall efficiency of the modified Alstom GT 24-ORCs cycle

Parameter	R123	R245fa	Toluene	Cyclohexane
Overall Efficiency (%)	52.55	52.13	54.07	52.93
Efficiency Enhancement (%)	11.06	10.17	14.26	11.85
ORC 1 Power Output (MW)	19.83	16.34	28.99	23.13
ORC 2 Power Output (MW)	7.78	9.06	6.63	6.48
Overall Power Output (MW)	277.36	275.15	284.47	279.36
Power Ratio (%)	9.96	9.23	12.48	10.60
$T_{e,1}$ (°C)	175	140	297	225.7
$T_{e,2}$ (°C)	139	129.4	126.1	150.6
ΔT_E (°C)	2.2	2.2	2	2
$\Delta T_{sup,1}$ (°C)	6.6	8.2	4	0.2
$\Delta T_{sup,2}$ (°C)	0.4	0	0.7	0
ORC 1 Mass Flow Rate (kg/s)	477.6	442.7	150.3	161.9
ORC 2 Mass Flow Rate (kg/s)	230.9	280.9	82.1	68.2

Table 6 shows a summary of optimization performance of the recuperated ICRH WR 21-ORCs combined cycle for different organic working fluids. It is found that the modified WR 21-ORCs combined cycles had efficiencies of 51.19% - 52.62%, with thermal efficiency increase of 7.77% - 10.76%, in comparison to the original value of single recuperated ICRH WR 21. The maximum overall efficiency was obtained by using cyclohexane as the ORC fluid, i.e., 52.62%, which is slightly higher than that by using toluene as the ORC working fluid. Moreover, the cyclohexane REC ICRHGT-ORCs had an overall power output of 39.61 MW with a power ratio of 9.72%. The minimum power ratio was obtained by using R245fa, i.e., 7.21%, where the overall power output was equal to 38.55 MW. The ORC 2 produced electricity of about 0.5 MW on average for each organic fluid. This amount of power is relatively smaller than the power generated by the ORC 1 due to the limitation of LPC outlet temperature and minimum pitch point temperature difference. The optimum operating parameters using a GA are also presented in Table 6. It can be seen that the pitch point temperature difference approached a value of 2 °C for all the organic working fluids. On the other hand, the degree of superheat at the ORC 1 turbine inlet could be as high as 7.8 °C using R123 as the organic fluid, while the degree of superheat at the ORC 2 turbine inlet was relatively small for all the organic fluids in absence of cyclohexane. It can be noticed that the mass flow rate of the working fluid

in ORC 1 in this case was much lower than that of corresponding working fluid in ORC 1 in LM-6000 and GT 24 combined cases as given in Tables 4 and 5. This is because both of the exhaust temperature and the exhaust flow rate of the WR 21 gas turbine were relatively lower, i.e., 307 °C and 73.1 kg/s, respectively, which leads to a decrease in heat transfer to the ORC 1. Compared to the other two high efficiency gas turbines, the modified WR 21 is more suitable to couple ORC bottoming cycles with reasonable operating conditions.

Table 6: Summary of optimization results for maximum overall efficiency of the modified RR WR 21-ORCs cycle

Parameter	R123	R245fa	Toluene	Cyclohexane
Overall Efficiency (%)	51.77	51.19	52.55	52.62
Efficiency Enhancement (%)	8.99	7.77	10.61	10.76
ORC 1 Power Output (MW)	2.68	2.2	3.3	3.34
ORC 2 Power Output (MW)	0.53	0.56	0.5	0.51
Overall Power Output (MW)	38.97	38.55	39.56	39.61
Power Ratio (%)	8.25	7.21	9.59	9.72
$T_{e,1}$ (°C)	170.6	140	205.8	235.7
$T_{e,2}$ (°C)	98	104	95.3	92.7
ΔT_E (°C)	2.2	2	2	2
$\Delta T_{sup,1}$ (°C)	7.8	5.6	0.9	0.8
$\Delta T_{sup,2}$ (°C)	0	0.4	0.4	2.9
ORC 1 Mass Flow Rate (kg/s)	64.8	61.4	23.4	22.5
ORC 2 Mass Flow Rate (kg/s)	23.9	22	9.2	10.1

5. CONCLUSIONS

The main conclusions drawn from this study are the following:

- The analysis of combined cycles based on commercial gas turbines and two ORCs shows that ORCs are an interesting and impressive option when combined with high efficiency gas turbines with low exhaust temperatures. Among the organic fluids in the bottoming cycles, toluene ORC combined cycles for each modified gas turbines present a very attractive overall efficiency.
- The efficiencies of recuperated ICRH gas turbines when coupled with two ORC bottoming cycles were improved by about 7.8% to 15.2% depending on the exhaust temperature and LPC outlet temperature of the topping gas turbine cycle and organic working fluid in ORCs. The use of different organic fluid in the two bottoming cycles may further improve the combined cycle efficiency.
- The heavy duty gas turbines like modified LM-6000 and GT 24 are not preferable to be used in combined cycles with R123 or R245fa ORC as the bottoming cycles resulting from the demand for large amount of mass flow rate in bottoming cycles and further high system capital cost. Gas turbine with relatively small power like WR 21 is more suitable to combine bottoming ORCs with reasonable mass flow rate of the organic fluid.
- The ORC 2 yielded about 0.5 and 0.53 MW on average of the power output for LM-6000 and WR 21 gas turbine combined cycles, respectively. The power could be further increased by using a high pressure ratio LPC and a newly designed HPC of the topping recuperated ICRH gas turbine.

NOMENCLATURE

CC	combustion chamber
G	generator
GT	gas turbine

HPC	high pressure compressor	
HPT	high pressure turbine	
LPC	low pressure compressor	
ORC	organic Rankine cycle	
PT	power turbine	
Q	heat transfer rate	(kW)
REC	recuperator	
T	temperature	(°C)
\dot{W}	power generation	(kW)
\dot{m}	mass flow rate	(kg/s)

Greek letters

η_i	first-law efficiency	(%)
----------	----------------------	-----

Subscript

1,2,3...	cycle locations
c	critical
E	evaporator
I	first law
max	maximum
mix	mixture
sup	superheating

REFERENCES

- Angelino G., Colonna P., 1998, Multicomponent working fluids for Organic Rankine Cycles (ORC), *Energy*, vol. 23, no. 6: p. 449-463.
- Bhargava R., Bianchi M., Peretto A., Spina P.R., 2002, A feasibility study of existing gas turbines for recuperated, intercooled and reheat cycle, *Proc. ASME Turbo Expo Amsterdam: GT-2002-30558*.
- Chacartegui R., Sánchez D., Muñoz J.M., Sánchez T., 2009, Alternative ORC bottoming cycles FOR combined cycle power plants, *Appl. Energy*, vol. 86: p. 2162-2170.
- Clemente S., Micheli D., Reini M., Taccani R., 2013, Bottoming organic Rankine cycle for a small scale gas turbine: A comparison of different solutions, *Appl. Energy*, vol. 106: p. 355-364.
- Holland J.H., 1992, *Adaptation in nature and artificial systems: an introductory analysis with applications to biology, control and artificial intelligence*, MIT Press, Massachusetts.
- Hung T., 2001, Waste heat recovery of Organic Rankine Cycle using dry fluids, *Energy Convers. Manage.*, vol. 42: p. 539–553.
- Invernizzi C., Iora P., Silva P., 2007, Bottoming micro-Rankine cycles for micro-gas turbines, *Appl. Therm. Eng.*, vol. 27: p. 100-110.
- Lemmon E.W., Huber M.L., McLinden M.O., 2007. “NIST standard reference database 23: reference fluid thermodynamic and transport properties-REFPROP”, version 9.0.
- Najjar Y.S.H., Radhwan A.M., 1988, Cogeneration by combine gas turbine engine with organic Rankine cycle, *Heat Recovery Syst. CHP*, vol. 8, no. 3: p. 211-219.
- Tchanche B.F., Lambrinos G., Frangoudakis A., Papadakis G., 2011, Low-grade heat conversion into power using organic Rankine cycles – A review of various applications, *Renew. Sust. Energ. Rev.*, vol. 15: p. 3963-3979.
- Vélez F., Segovia J.J., Martín M.C., Antolín G., Chejne F., Quijano A., 2012, A technical, economical and market review of organic Rankine cycles for the conversion of low-grade heat for power generation, *Renew. Sust. Energ. Rev.*, vol. 16: p. 4175-4189.
- Wei D., Lu X., Lu Z., Gu J., 2007, Performance analysis and optimization of Organic Rankine Cycle (ORC) for waste heat recovery, *Energy Convers. Manage.*, vol. 48: p. 1113–1119.
- Yari M., 2008, Thermodynamic analysis of a combined micro turbine with a micro ORC, *Proc. ASME Turbo Expo Berlin: GT2008-51163*.
- Yari M., Mahmoudi S.M.S., 2010, Utilization of waste heat from GT-MHR for power generation in organic Rankine cycles, *Appl. Therm. Eng.*, vol. 30: p. 366-375.

TECHNICAL AND ECONOMICAL STUDY OF AN ORC DEDICATED TO THE PRODUCTION OF ELECTRICITY FROM A GEOTHERMAL SOURCE

Stéphane Schuller^{1*}, Morgan Da Silva¹, Christophe Josset², Bruno Auvity², Jérôme Bellettre²

¹ Cryostar, Clean Energy,
Hésingue, France
stephane.schuller@cryostar.com, morgan.dasilva@cryostar.com

² Laboratoire de Thermocinétique de Nantes, UMR-CNRS 6607 Université de Nantes,
Nantes, France
christophe.josset@univ-nantes.fr, bruno.auvity@univ-nantes.fr, jerome.bellettre@univ-nantes.fr

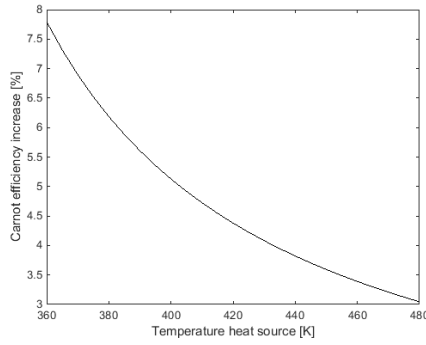
* Corresponding Author

ABSTRACT

This paper presents an original method to design equipment of an organic Rankine cycle power plant. It is based on the entropy production equipartition theorem in the geothermal heat exchanger. The criterion of best pressure in favor of exergy at turbine inlet at given temperature is also used to initialize the problem at an ambient design temperature. According to these design criteria, the price of each main pieces of equipment is estimated. Then the equipment are simulated throughout a typical year, the net electrical production is deduced. The same method is repeated with different ambient temperatures chosen as design temperature. Then the product price per kWh is calculated and compared to the one obtained at the average design temperature. The methods is revealed not monotonous and so a filter is applied to results in order to keep the best cases regarding economical criteria. Three sites are studied. Regarding the ambient temperature climate distribution, a temperature where design appear to be the best, is found. Finally the developed simulation tool of ORC power plant allows to test the relevance of different design criteria.

1. INTRODUCTION

ORCs are proving to be an effective solution to produce mechanical or electrical power from low temperature heat source. These low temperature sources also make them sensitive to the sizing of their equipment (Schuller et al., 2014). Indeed, due to the evolution of the Carnot efficiency for ORCs influenced by ambient temperature (see figure 1 where equation (1) is plotted), the pinches involved in the evaporators or condensers have high consequences. This particular point must be carefully addressed. In these specific conditions, technical and economical trade-offs must be determined in order to make ORC competitive. This paper focuses on the technical-economic study of a supercritical ORC with propane, without regenerator, dedicated to the production of electricity from a geothermal source. The supercritical cycles are chosen for their ability to extract the heat from the hot source and the absence of the phase change plateau that avoids a large pinch inside the steam generator (Schuster et al., 2010). We firstly describe how the four main pieces of equipment (pump, geothermal heat exchanger, turbine and condenser) are designed by applying the entropy production equipartition theorem in the geothermal heat exchanger (Schuller et al., 2014). In the same time a specific criterion (Schuller et al., 2014) regarding working fluid in the turbine is used to constrain the problem and avoid liquid formation in the turbine. The costs of the four main items of equipment are estimated in relation to their sizing parameters (surface of exchanger, turbine power,...) designed at an arbitrarily chosen ambient temperature. The effect of this temperature selection on the design and the overall efficiency (energetic and economic) will be dis-



$$f(T_{hot}) = \frac{(1 - \frac{277}{T_{hot}}) - (1 - \frac{283}{T_{hot}})}{1 - \frac{283}{T_{hot}}} * 100 \quad (1)$$

Figure 1: Carnot efficiency rise for a temperature drop from 283 to 277 K

cussed. Secondly, this paper describes how equipment performances change according to the weather variation throughout the year. A typical ambient temperature distribution along the year is estimated with Meteonorm (Remund and Kunz, 1997)(see figure 2) and is used to calculate the yearly production. Thirdly, the same geothermal source is virtually placed in three sites in the world with different climates. By the previously described method three different ORC plants are designed. The comparison of the three plants is presented. This opens a discussion about the consequence of heat sink temperature variations. The consequence on the characteristics of equipment, designed at a fixed ambient temperature, but used at a variable ambient temperature is observed.

The three places chosen to illustrate the influence of the ambient air as heat sink are:

- Site 1, East of France
- Site 2, Turkey
- Site 3, Caribbean Island

The typical distribution of temperature given by Meteonorm (Remund and Kunz, 1997) for each site is presented in the figure 2 and the mean values are given in table 1

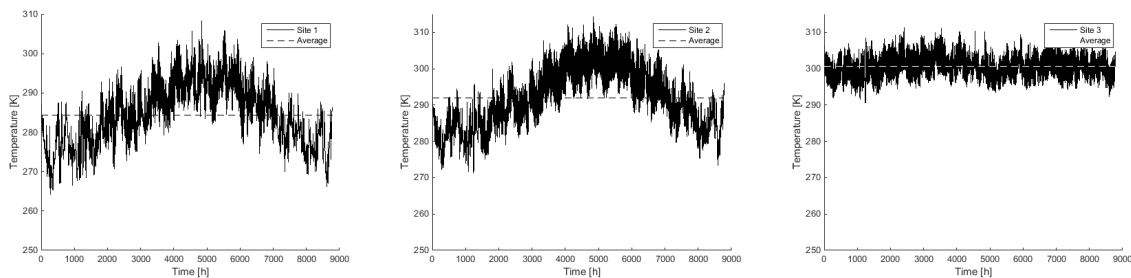


Figure 2: Hourly ambient temperature on typical year

Site	Average temperature (K)	Standard deviation (K)
1	284.5	8.0
2	292.0	8.6
3	300.6	3.5

Table 1: Average and standard deviation of ambient temperature distribution along a typical year

In the present work, the results are obtained by numerical simulations performed with a dedicated simulator developed with Matlab (Schuller et al., 2014).

2. THERMODYNAMICS MODEL

The thermo-physical fluids characteristics are calculated by Refprop (Lemon, 2013), directly linked to Matlab. The main physical properties taken account are summarized in the table 2.

Physical properties	value	unit
Geothermal inlet temperature	435.15	K
Geothermal outlet temperature	273.15	K
Geothermal inlet pressure	2000	kPa
Geothermal mass flow	45	kg/s
Geothermal fluid	pure water	
Working fluid	propane	
Superheating margin (regarding cricon)	≥ 200	kPa
Hex Working fluid outlet entropy	\geq Cricondentrepe entropy	
Pinch Hex	≥ 5	K
Expander inlet temperature	$> T_{crit} + 10$	K
Expander inlet pressure	$> P_{crit} + 50$	kPa
$\Delta T_{Condensation-Ambient\ air}$ (approach design)	18	K
Condenser working fluid pressure drop	20	kPa
Evaporator working fluid pressure drop	100	kPa
Evaporator geothermal fluid pressure drop	200	kPa

Table 2: Hypothesis summary

2.1 Details of equipment model

This supercritical ORC has four main items of equipment ¹:

- a pump transferring and pressurizing the working fluid in liquid phase.
- a geothermal heat exchanger transferring heat from the geothermal source, toward the working fluid.
- a turbine expanding the working fluid to remove the mechanical energy, which coupled to a generator via a gear box will produce electricity then injected on the electrical network.
- a condenser, which desuperheats and then condensates the expanded working fluid, in contact with the cold source, i.e. the ambient air.

Propane is chosen as a working fluid because adapted to the temperature of the hot source (Marcuccilli, 2010) (Sauret, 2011).

2.2 Condenser, cold source

The air cooled condenser is a classic model similar to API661 models that are found in ORC facilities for geothermal applications. The working fluid flows in finned tubes. Air is driven by fans. The power of the fans is calculated according to Robinson and Briggs correlation (Nir, 1991). Fan speed is assumed constant. Fan power depends only on ambient air temperature and its density (calculated directly by Meteonorm). Geometry is fixed, i.e tube length, diameter, fin width, height, fin density, as well as the number of tube rows. Only the number of tubes required by the condensation power is considered for the design calculation, whereas the condensation pressure and temperature will be considered for the off-design calculation.

2.3 Pump

The pump is of centrifugal type. Because of high fluid pressure (beyond its critical pressure), the variation in density between the input and output of the pump is significant. The model considers therefore, for the

¹No regenerator is considered in this study

pump power consumption calculation, a polytropic compression with efficiency depending on its variable speed, head and flow (Troskolanski, 1977). The power and the speed are assumed to be sufficient to reach all the requirements for all off-design points.

2.4 Geothermal heat exchanger, hot source

The geothermal heat exchanger is of the shell and tube type. For cleaning considerations, geothermal water flows in the tubes. The exchanger is discretized in intervals of equally exchanged heat power. The diameter of tubes is considered constant, as well as pitch and baffles spacing and number. The number of parallel tubes depends only on water flow. The length of these tubes is calculated from the required exchange surface at design point.

2.5 Turbine

The turbine is of radial inflow type (Marcuccilli, 2007). The wheel diameter and the speed of rotation are determined to maximize isentropic efficiency (Balje, 1981). Pressure and temperature at turbine inlet are determined according to an optimization procedure (Schuller et al., 2014). The turbine is equipped with variable inlet guide vanes. The turbine inlet pressure is controlled by the position of these inlet guide vanes whereas the inlet temperature is governed by the working fluid mass flow rate (i.e. controlled by the pump).

3. ALGORITHM OF DESIGN AND OFF-DESIGN CALCULATION

The program contains a multitude of parameters. A lot of them are geometric, such as diameter of heat exchanger tube, fin height etc. In this study we focus on the following parameters:

- Ratio of mass flows, water over propane
- Pressure at turbine inlet
- Temperature at turbine inlet
- Design ambient temperature

Simulations are performed in two steps: design step and off-design step. In the design step, a specific ambient design temperature and condenser approach are chosen. Then the four main items of equipment previously presented are designed with respect to some optimization processes (Schuller et al., 2014) (Schuller, 2011). Optimal values of pressure and temperature at turbine inlet (see figure 3) and mass flows ratio are obtained at this stage. In figure 3, the thermal path of water is scaled to propane enthalpy as described in Augustine et al. (2009). In the second step, with off-design calculation, the performances of the designed plant are predicted keeping all the geometrical parameters constant. In this stage, the influence of the varying ambient temperature can be estimated. The flow of propane is calculated to reach the same turbine inlet temperature than at design. In real control scenario, it would be done by varying the speed of the pump. Finally, two different indicators are predicted, one with respect to the annual energy production, the other with respect to the economic efficiency of the plant, depending on the chosen business plan (see paragraph 5). The algorithm is detailed as follows (see figure 4): first, the temperature, at three quarter from supercritical to geothermal source temperature is chosen as the turbine inlet temperature. Thus the corresponding pressure on the curve EMTD² (see figure 3) is deduced for turbine inlet. The turbine outlet pressure is the condensation pressure corresponding to the ambient temperature plus the chosen approach shift from an arbitrary pressure drop. We consider no subcooling³. Then optimization is launched on the turbine inlet pressure and temperature and mass flow of propane, in order to minimize the variance of the reduced temperature difference to the average reduced temperature difference along the geothermal heat exchanger. In other words, the optimization makes the two thermal

²Maximal exergy at given temperature: for a given temperature, there exists a corresponding enthalpy or pressure where the exergy reaches a maximum (Tondeur, 2006)

³The NPSH, net pressure suction head, required by the pump is supplied by the height of the condenser

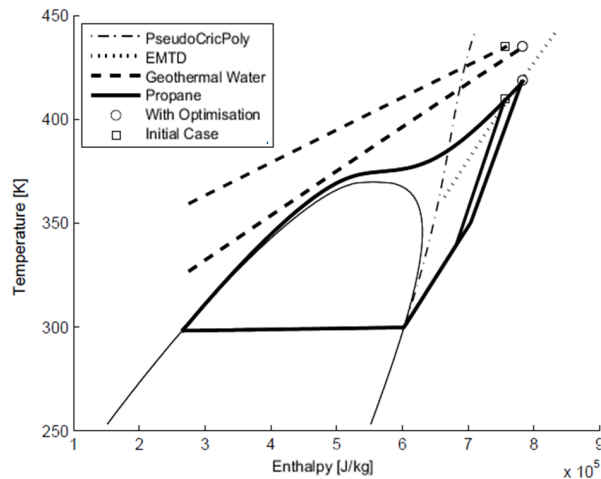


Figure 3: Thermal path of cycles before and after optimization to minimize the criterion of entropy production equipartition

paths (water and propane) as parallel as possible in a diagram of reduced temperature⁴ versus enthalpy. The pinch point is not fixed as recommended by Walraven et al. (2014) for optimum issue, but it is a consequence of using the equipartition criterion. Furthermore, the turbine inlet point should be on the right hand side (in the H,T diagram) of the pseudocricentropic curve (PseudoCricPoly in figure 3) in order to avoid liquid ingress during the expansion through the turbine, with respect of constraints and condition summarized in table 2. At this step, the design is fixed and equipment characteristics are defined. Off-design turbine inlet temperature and pressure are set to the design value. Temperature data from Meteororm are implemented at condenser inlet, and at fixed characteristics, equipment performances are calculated:

- condenser approach
- condensation pressure
- fans power consumption
- pump speed
- pump efficiency and losses
- pump power consumption
- turbine nozzle opening
- turbine efficiency
- turbine, gearbox, generator losses
- generator power
- propane mass flow
- Hex pinch

This off-design is calculated hourly and production is assumed constant during one complete hour. Annual production is the sum of the power at each hour. In the figure 5, the example of site 1, design at average temperature is given. Power and production are reduced by the power and respectively production, produced at the average temperature. The coldest temperature gives the greatest power, but a poor occurrence. Average temperatures give average power values but have the highest occurrences. Hottest temperatures give the lowest power values but have poor occurrences. The consequence is illustrated in figure 6. The power and contribution to annual production are not correlated. Then at which temperature should equipment be designed: at a frequent temperature or at a temperature that gives the best power? To find out, different design temperatures are tested in the paragraph 4.

4. OFF-DESIGN REGARDING THE CHOSEN DESIGN TEMPERATURE

The method described in the paragraph 3 is applied for different design temperatures. These temperatures are chosen among temperature site occurrences, every 0.5 K. All results are reduced by a reference production. This reference is the production of a complete year in site 1, in the case of design at the average temperature of this site. These results are shown in figure 7. The shape of curves are non monotonous. This is due to the chosen criterion of entropy production equipartition. This is different to minimizing the entropy production. The algorithm of optimization is based on a simplex method, with

⁴temperature reduced by the Carnot factor

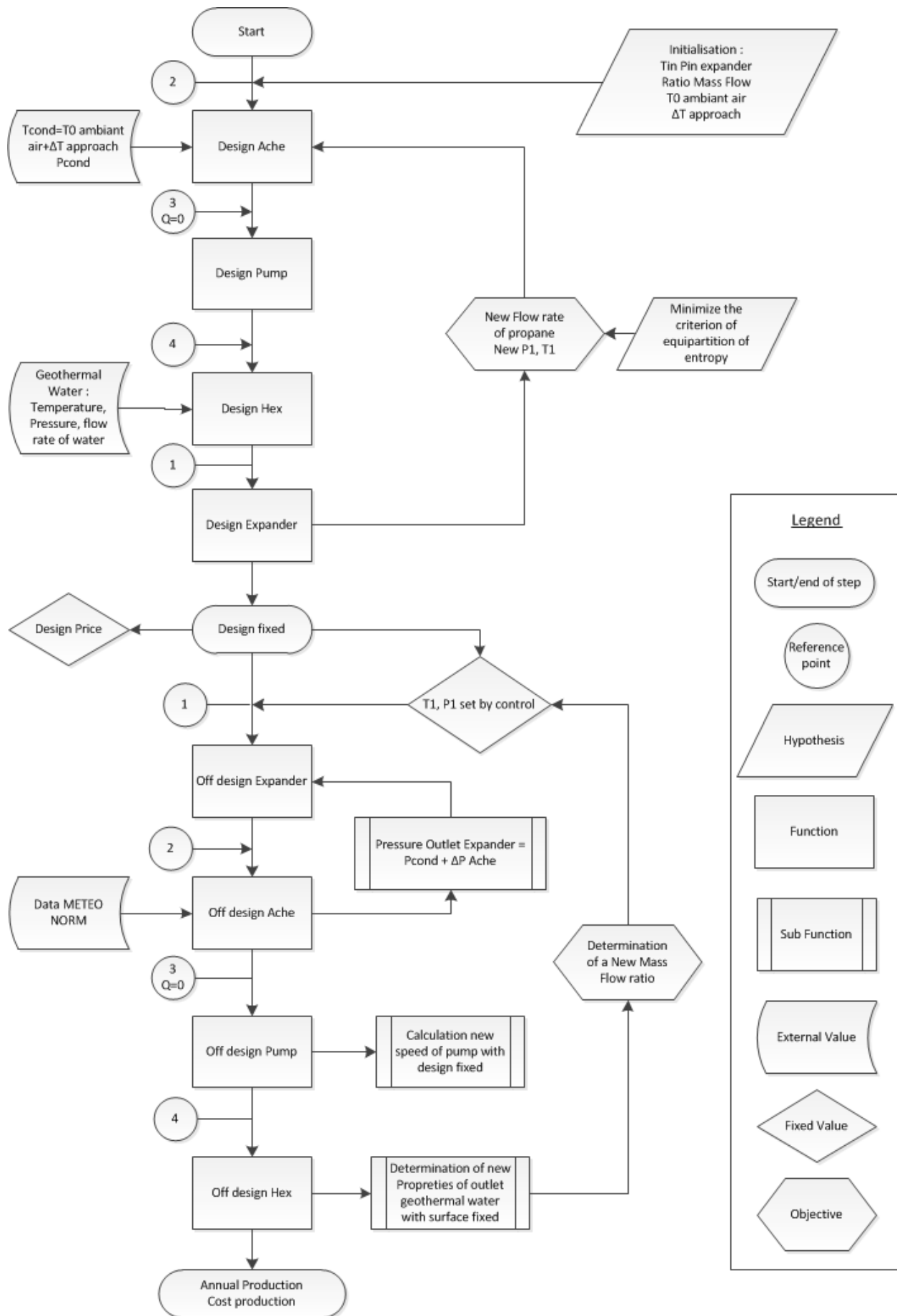


Figure 4: Algorithm logic diagram

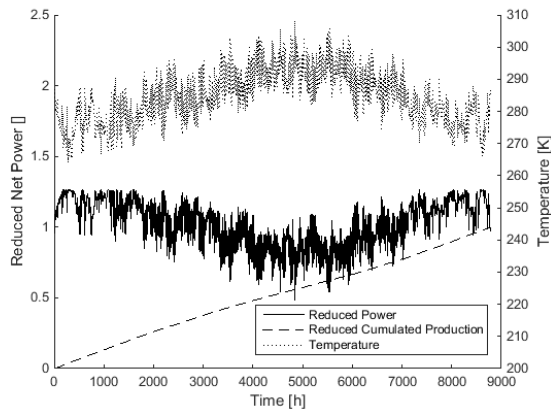


Figure 5: reduced power and production and temperature throughout the year

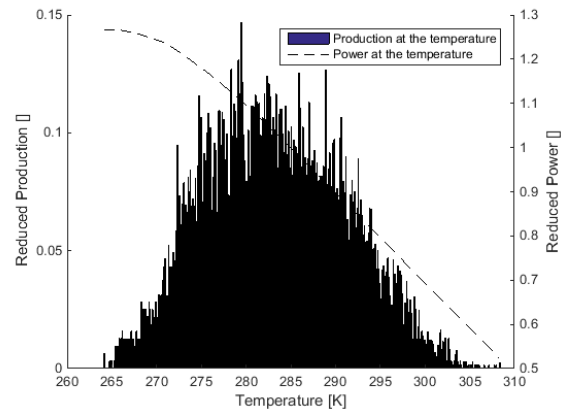


Figure 6: Reduced power and contribution to production vs ambient temperature

three parameters: turbine inlet pressure and temperature and water over propane mass flow ratio. Entropy production is illustrated by the gap between both thermal paths. On the other hand, entropy production equipartition is illustrated by the parallelism between both thermal paths. Sometimes, regarding the equipartition, it is preferable to move the thermal paths away from each other rather than bringing them together while keeping them parallel. This is clearly shown in the example of figure 8:

- The point 1 of figure 7 corresponds to the annual production of a power plant designed at 269.6 K and running at site 1. Its design case is shown with a dotted line in figure 8.
- The point 2 of figure 7 corresponds to the annual production of a power plant designed at 273.6 K and running at site 1. Its designed case is shown with a continuous line in figure 8.

The characteristics of both cases are summarized in the table 3. For only 4 K of design temperature difference, the gap between the two thermal paths of the continuous line case shows that the heat exchanger is smaller than the one of the dotted line case. In consequence the heat exchanger surface of case 1 is three times bigger than that of case 2. Both annual productions are coherent regarding heat exchanger sizes. More generally, pressure rise flattens isobaric curves, while flow ratio changes the slope of the water thermal path. A temperature rise increases the length of the thermal path, thus the range of temperatures taken into account to calculate the average gap between the two fluid temperatures. Finally, by using the equipartition criterion to design equipment and if we assess the production of the designed cycle, we realize that it is not the best method to design equipment that will finally mainly work at off-design conditions. The method is missing a criterion to distinguish between plants that are designed at different ambient temperatures. Thus in paragraph 5, we add some economical criteria.

Case	Design ambient temperature	Propane reduced mass flow	Heat exchanger reduced surface	Turbine inlet temperature	Turbine inlet pressure	Reduced annual production
(Units)	(K)	()	()	(K)	(kPa)	()
1	270	0.91	2.43	421	6900	1.19
2	274	1.28	0.81	408	4500	0.94

Table 3: Comparison between two different design ambient temperature

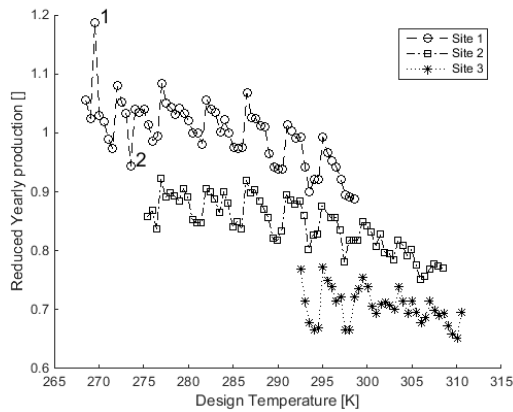


Figure 7: Reduced annual production ("Sum of net kWh produced in one year")

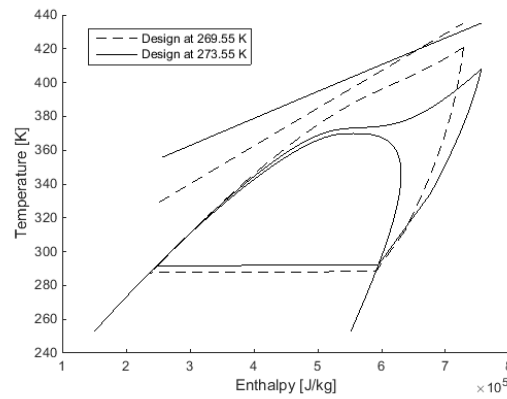


Figure 8: Thermal path of cycles after optimization for two different design ambient temperatures

5. BUSINESS PLAN

One kind of business plan is now implemented. The prices of the four main items of equipment are evaluated by means of Marshall and Swift Index (Turton et al., 2008), then shifted to match some MW ORC scale. From the sum of these items of equipment, by a Lang method (Lang, 1947), updated by Peters et al. (2003), the rest of the cost is estimated by adding rate of this sum. Of course, the business plan depends very sensitively to the place where the plant is built, the local fee, and the price for the kWh sold. The average ambient temperature of site 1 is taken as reference. The results for the other case are then reduced by this reference. The reduced production cost of the reference is then equal to 1, the same goes for its production at the end of one year. As previously done for the calculation of yearly production in paragraph 4, the cost of production is also estimated at different design temperatures. The results are shown in figure 9. This business plan is done for a period of twenty years. The life time of the power plant is assumed to be equal to this duration. The cost of production (see equation 2) is the sum of all cost of charges, salaries and fees to be paid during one year in the power plant. One twentieth of the plant cost is added as depreciation. This amount is divided by the number of kWh produced in one year.

$$Cost_{Production} = \frac{\sum_{year}(fees, charges, salaries) + \frac{1}{20}(capital\ investment)}{\sum_{year}(sold\ electricity)} \quad (2)$$

6. FILTER APPLIED TO DESIGN TEMPERATURE REGARDING BUSINESS PLAN

As shown in figure 7, the yearly production is non monotonous with regards to the design temperature when entropy production equipartition is the optimization criterion chosen. However, once the design is done, off-design is regular and follows the ambient temperature. The business plan brings a new criterion for the evaluation of the results obtained at different design temperatures. Especially the cost of production reveals some more interesting design temperature. We decide to focus on the low production cost plants and the ambient temperature at which they have been designed, as shown in figure 9. The filter keeps all local minima⁵. We plot them with a continuous line for each site. These continuous line reveal more monotonous shapes, with global minima. These minima appear at average minus 1.5 times the standard deviation for site 1 and 2, and the average minus 2 times the standard deviation for site 3. A best design temperature found below the average temperature is coherent with figure 6 data⁶.

⁵the filtered points correspond to the lower bound of the points cloud

⁶The ambient air distribution is symmetric around average, but power is higher at below average temperature

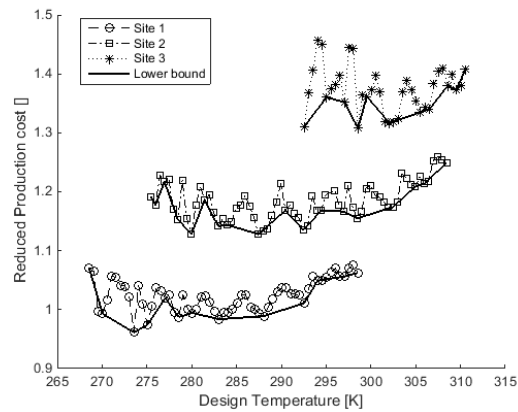


Figure 9: Reduced cost of production ("production cost of kWh")

7. CONCLUSION

Focusing production and comparing between sites, as expected, the coldest site reaches the best result. The entropy production equipartition, used only for design does not have regular trend. Despite this non monotonous characters, it is possible to extract a global regular behavior by filtering data. Due to the sensitivity of the equipartition criterion, it remains necessary to perform the calculations on the entire range of ambient temperature. Each climate has its own optimum. However, based on these three tests, no generic law (rule of thumb) seems to be able to predict a priori the optimal design temperature. Thus, the use of such numerical simulator, coupled with an optimization method seems to be essential in the context of the design of plant like ORC system. The results presented here are closely linked to the choice of the steam generator design criterion, but taking into account other constraints or criteria is easily implementable in the simulator. Thus, in forthcoming publication, we intend as well to test the following points:

- Use a particle swing optimization method to determine the best power plant design.
- Do a systematic calculation on the neighborhood of the assumed optimum found in paragraph 6.
- Use the criterion of entropy production equipartition in off-design control setting⁷.
- Add a constrain to the equipartition criterion to force the mean to reach a target value, figuring indirectly the size of the heat exchanger.
- Calculate the best approach⁸ on the condenser regarding the cost of production.

The combination of multiple criteria is interesting to study. Especially when thermodynamics criterion have benefit to economical optima, which finally is one of the most efficient means to deploy ORC with the support of policymaker.

NOMENCLATURE

T	temperature	(K)	Ache	condenser
T_0	temperature of cold sink	(K)	Hex	geothermal heat exchanger
Q	mass quality		Subscript	
P	pressure of working fluid,	(kPa)	<i>cond</i>	condensation
Δ	difference		<i>in</i>	inlet
EMTD	maximal exergy at given temperature		<i>hot</i>	hot source

⁷Actual control is at fixed turbine inlet temperature and pressure.

⁸Differential temperature between ambient air and condensation temperature.

REFERENCES

- Augustine, C., Field, R., Dipippo, R., Gigliucci, G., Fastelli, I., and Tester, J. (2009). Modeling and analysis of sub- and supercritical binary rankine cycles for low- to mid-temperature. In *Geothermal resource council*, volume 33, pages 689--693.
- Balje, O. (1981). *Turbomachines: A guide to design selection and theory*. Wiley-Interscience.
- Lang, H. (1947). Cost relationships in preliminary cost estimation. *Chemical Engineering*.
- Lemon, E. (2013). *NIST Standard Reference Database 23: Reference Fluid Thermodynamic and Transport Properties (REFPROP), Version 9.1*.
- Marcuccilli, F. (2007). Benefits of using radial inflow turbines for organic rankine cycles. In *Proceeding of World Geothermal congress*. World Geothermal Congress, Geothermal Resource Council.
- Marcuccilli, F. (2010). Optimizing binary cycles thanks to radial inflow turbines. In *Proceeding of World Geothermal congress*. Proceedings European Geothermal Congress.
- Nir, A. (1991). Heat transfer and friction factor correlations for crossflow over staggered finned tube banks. *Heat Transfer Engineering*, 12(1):43--58.
- Peters, M., Timmerhaus, K., and West, R. (2003). *Plant Design and Economics for Chemical Engineers*. Companies, The McGraw-hill, 5th edition.
- Remund, J. and Kunz, S. (1997). *METEONORM: Global meteorological database for solar energy and applied climatology*. Meteotest.
- Sauret, E. (2011). Candidate radial-inflow turbines and high-density working fluids for geothermal power systems. *Energy*, 36-7:4460--4467.
- Schuller, S. (2011). Best exergy point for orc. In *Proceeding of European Geothermal congress*, volume 35, pages 1343--1349. European Geothermal Congress.
- Schuller, S., Josset, C., Auvity, B., and Bellettre, J. (2014). Optimisation par le critère d'équipartition de production d'entropie d'un cycle orc supercritique équipant une source d'eau chaude géothermale et influence sur les performances.
- Schuster, A., Karellas, S., and Aumann, R. (2010). Efficiency optimization potential in supercritical Organic Rankine Cycles. *Energy*, 35(2):1033--1039.
- Tondeur, D. (2006). Optimisation thermodynamique Équipartition de production d'entropie. In *Thermodynamique et Énergétique*, number 8017 in BE, pages 1--15. Techniques de l'ingénieur.
- Troskolanski, A. (1977). *Les turbopompes*. Eyrolles.
- Turton, R., Bailie, R., Whiting, W., and Shaeiwitz, J. (2008). *Analysis, synthesis and design of chemical processes*. Pearson Education.
- Walraven, D., Laenen, B., and D'haeseleer, W. (2014). Optimum configuration of shell-and-tube heat exchangers for the use in low-temperature organic rankine cycles. *Energy Conversion and Management*, 83:177--187.

ORC BOTTOMING FOR COMBINED CYCLE SYSTEMS FED BY BIOMASS

M. Gaia¹, F. Mowill² and C. Pietra^{1*},

¹Turboden s.r.l.,
Via Cernaia, 10
I-20124 Brescia

²OPRA Turbines BV,
Opaalstraat 60
NL-7554 TS Hengelo

e-mail: claudio.pietra@turboden.it

Web page: <http://www.turboden.it>, <http://www.opraturbines.com/en/>

ABSTRACT

In the last two decades ORCs have been largely used to convert the heat from biomass combustion into electric energy. The success of the ORC technology for this application is mainly due to its low maintenance requirements, ease of operation and good partial load performance.

In the quest for higher efficiency systems, biomass gasification, followed by conversion to electric power in a small scale combined cycle, is very promising.

Indeed several gasification systems, integrated with gas cleaning and gas engines for power production, have been put into operation in the past, with different results depending on the adopted solution.

The paper suggests a different approach featuring an innovative gasification device, a gas turbine prime mover, and an Organic Rankine Cycle as bottoming system, typically for a power output of the combined system up around 5 MW. A preliminary study of the system performance is presented.

1. INTRODUCTION

Biomass is a very interesting source for power generation, thanks to a number of reasons, which we try and summarize here:

- it allows storage over extended periods of time, without substantial loss of energy. Hence it allows to cope with a varying power demand, in particular with a seasonally varying power demand.
- it can be transferred to other sites, though at a higher cost than fossil fuels.
- it is, or it can be made, substantially neutral concerning the introduction of carbon dioxide in the atmosphere.
- its cost is strongly related to its origin (residual biomass from agriculture and forestry, energy crop, waste from wood industry etc.), however in many cases the cost per unit of energy content is much lower than the equivalent in a fossil fuel.
- biomass can be transformed into power by quite small power units, down to about one MW of electric power and even less. Hence the related investment can be sustained by small enterprises and limited local resources can be exploited.
- due to the low power level, it is often possible to find, at least for a fraction of the year,

a suitable consumer for the thermal power associated with the generation of electric power.

- On the other hand, if the conversion to power is referred to a Rankine Cycle power plant (steam or ORC), a number of critical aspects have often hindered a more widespread utilisation of biomass for power:
- the cost per kW electric installed is rather high, typically in the range 4000 to 8000 €/kW except for large systems, which are less attractive, for the reasons considered above. An important fraction of the cost is often related to the need to reduce the emission of particulate and of gaseous/VOC pollutants into the atmosphere.
- the efficiency of conversion is up to now rather low in most installations, typically around 15 to 20%, taking into account the whole process, that is the ratio between electric energy produced and the energy content of biomass. Even lower figures can be met for co-generative plants. This low efficiency obviously has the adverse effect of reducing the amount of electric energy which can be produced by a given low cost biomass source, so that in practice, only relatively large sources can be exploited for power generation.
- moreover the ability of today's plants to follow a fast varying load is limited. Hence in the case of an isolated grid, either a mix of power sources is introduced into the grid, or the biomass power unit has to be kept running at high power condition, and the excess power is wasted.

2. DISCUSSION OF GASSIFICATION

Gasification has been proposed as an alternative solution to straight combustion, in order to overcome the problems listed above. In fact, notwithstanding a number of tentative tests, starting back to Rudolf Diesel experiments with pulverized coal, direct utilisation in internal combustion engines of solid biomass, even very finely divided, does not seem to be promising, due to the uneven properties, the energetic cost of pulverisation, the alkali content in ashes, and in general the difficulties of feeding a solid product.

Gas feeding of reciprocating engines on the contrary has been the subject of many analyses and it has been put in to effect in a large number of real applications. A large number of different solutions have been proposed and experimented for the gasifier itself, for the cleaning of the produced gas and the overall implementation of the power plant. Gas turbine systems have been considered too, mostly at larger power level than reciprocating engines.

Specific solutions for gasification are discussed in detail, e.g. in [1] and [2].

The large number of proposed solutions indicate that none is in fact totally satisfactory.

The scope of the present paper is to describe a solution involving an innovative concept gasifier, feeding a combined cycle, composed by a gas turbine and an ORC bottoming unit.

Traditionally the solutions are classified according to the following schemes:

- fixed bed Updraft in which the descending biomass moves counter-current to the ascending gaseous phase, so that the subsequent steps of the process, from the point of view of biomass, are ordered as Drying, Pyrolysis, Reduction, Oxidation (as reported in fig.1-a)
- fixed bed Downdraft in which the descending biomass moves co-current to the descending gaseous phase, so that the subsequent steps of the process, from the point of view of biomass, are ordered as Drying, Pyrolysis, Oxidation, Reduction (fig 1-b)
- fluidized bed of various kinds. In many cases the process cannot be divided in zones and it takes place instead on the surface and within each particle of solid biomass, hence all four transitions take place substantially at the same time in parallel.

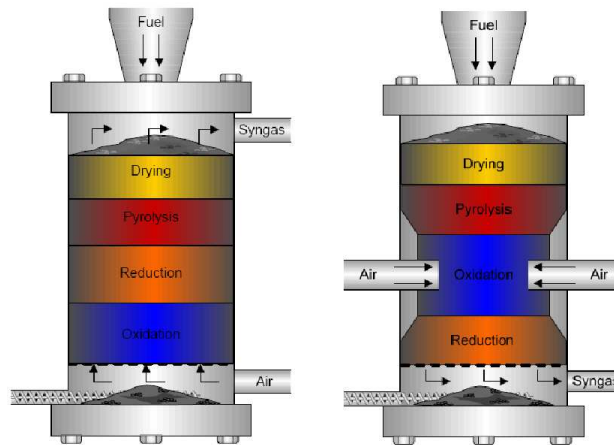


Figure 1 - Traditional fixed bed gasifier schemes [3]

In fixed bed gasifiers, Reduction is the most characterising step, which takes place in the bed of char resulting from the Pyrolysis. In Downdraft gasifiers reduction involves a given dwell time and interaction between the gases and tars resulting from the pyrolysis. As a consequence, besides the main scope of obtaining a gas composition including high H_2 and high CO , the reduction step is very effective at achieving thermal decomposition of tars. In Updraft gasifiers, the produced gas is substantially clean at the top of the reduction zone, but then it flows through the pyrolysis zone and it becomes heavily loaded with tar and moisture. Apparently, a Downdraft solution is preferable in any case. However in practice the transfer of heat to the upper layers undergoing pyrolysis is rather ineffective and it is difficult to keep a uniform flow through the bed, in particular if the bed has a large cross section. Hence the Updraft solution, though not attractive from the tar content point of view, is preferable for relatively large systems. Moreover so as in fact the counter-current flow of hot gas allows an efficient pre-drying of the biomass before it enters the pyrolysis zone and the separated water is added to the produced gas instead of being put to the high temperature reaction zone, allowing to feed the Updraft gasifier with high moisture biomass (up to 50% vs 20% for the Downdraft). [3]

The fluidized bed gasifiers are intermediate, for what concerns both the tar content in the gas point of view and the acceptance of high humidity feed. [4-5]

Fixed bed gasifiers are attractive due to the low parasitic power required and their tolerance of uneven quality biomass. However, the required volume of the reactor is large and the quality of the produced gas is less predictable than with fluidized bed gasifiers.

3. PRESENT PROPOSAL FOR THE GASIFIER

A different approach to the flow within fixed bed gasifiers is here proposed in conjunction with ORC bottoming solution. The new approach should allow to solve the problems reported, that is it should lead to an efficient transfer of heat to the pyrolysis zone and an efficient cleaning of gas thanks to flow within the char bed at high temperature.

The present proposal concerns an innovative co-current fixed bed gasifier, characterized by the fact of utilizing two vessels in parallel, and having an alternate flow of gasifying agent. In this way the produced gas flows back and forth through the bed, ensuring a larger volume of high temperature reactive zones, compared to a conventional downdraft gasifier. Moreover the increase of velocity through the bed activates both the heat exchange between gas and solids and the gasification reactions.

The proposed solution has been given the acronym “Twingas” by the authors of the relevant patent [6], hence here the same name is adopted, too.

A sketch of the Twingas is reported in fig. 2, concerning a system with top to bottom flow of biomass as well as an alternating co-current and counter-current flow of gas.

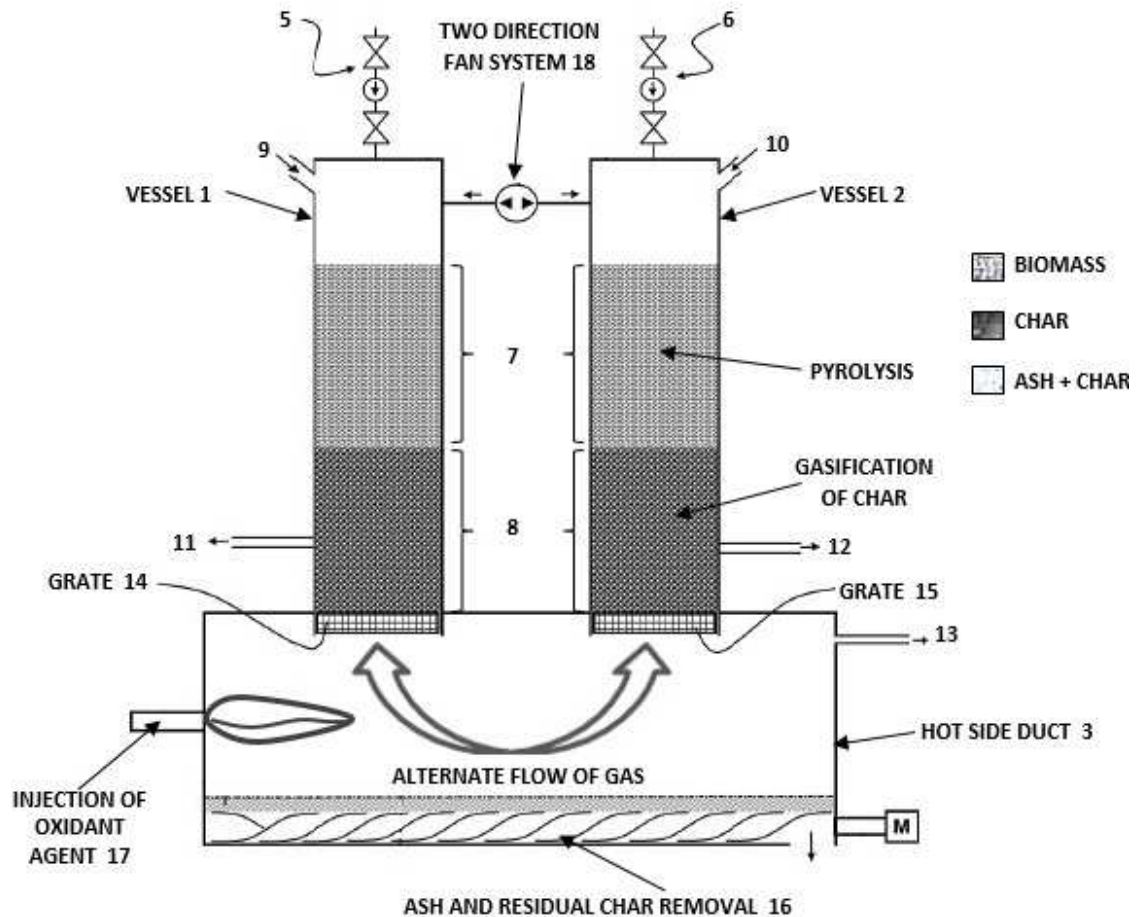


Figure 2 - TWINGAS gasifier solution, with two vessels and alternated flow of gas

The expected results are a higher production per unit of volume of gasifier, a better quality gas and a good tolerance towards non-uniform charge. Twingas is reported more in detail in Appendix I.

4. UTILIZATION OF PRODUCED GAS

The syngas produced by the gasifier can be utilized to generate power according to one of the following schemes:

- 1) Gas is burned in a boiler to generate organic vapour (or steam) for a Rankine cycle, preferably after some treating of the gas, e.g. to reduce the particulate content (fig. 3). Though organic vapour or steam could be also generated by burning the initial solid biomass in a suitable boiler, burning syngas gives some definite advantages, compared to a solid fuel powered furnace and boiler: the combustion can be better controlled, drastically reducing the pollutants in the exhaust, the boiler heat exchange surfaces remain clean, it is possible to change fast the flow of generated vapour/steam, in particular it is possible to reduce/shut-off quickly the combustion, in order to adapt to a the fast load change of a stand-alone unit. Moreover, the inventory of fluid in the boiler is lower, compared to a solid fuel boiler, this feature can be important if a direct exchange between combustion gas and organic working fluid is envisaged.

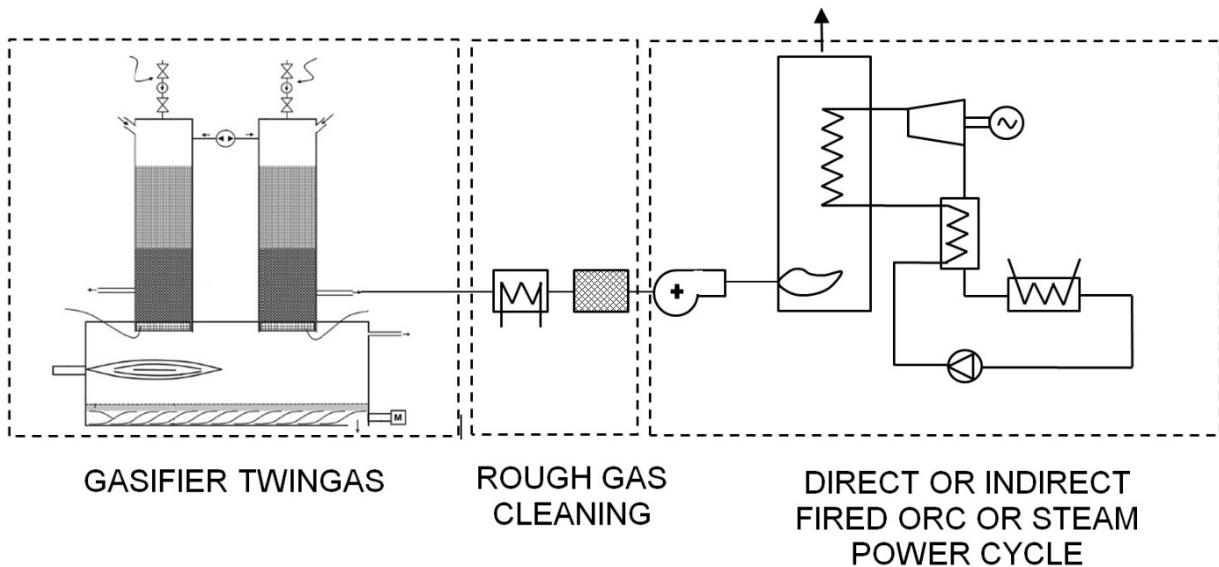


Figure 3 - Utilization of syngas for evaporation of working fluid (ORC or Steam plant)

- 2) Gas is thoroughly cleaned and fed to a reciprocating internal combustion engine (ICE). From the point of view of efficiency this solution is very effective, however past experience has shown that it is difficult to clean the gas consistently to a high purity level, such as to avoid a heavy maintenance burden. The thermal power available in the exhaust downstream from the engine is not large, hence a combined cycle ICE + ORC (fig.4) would get a minor increase of power and efficiency from the ORC itself (the power of the bottoming cycle amounts to some 10% of engine power).

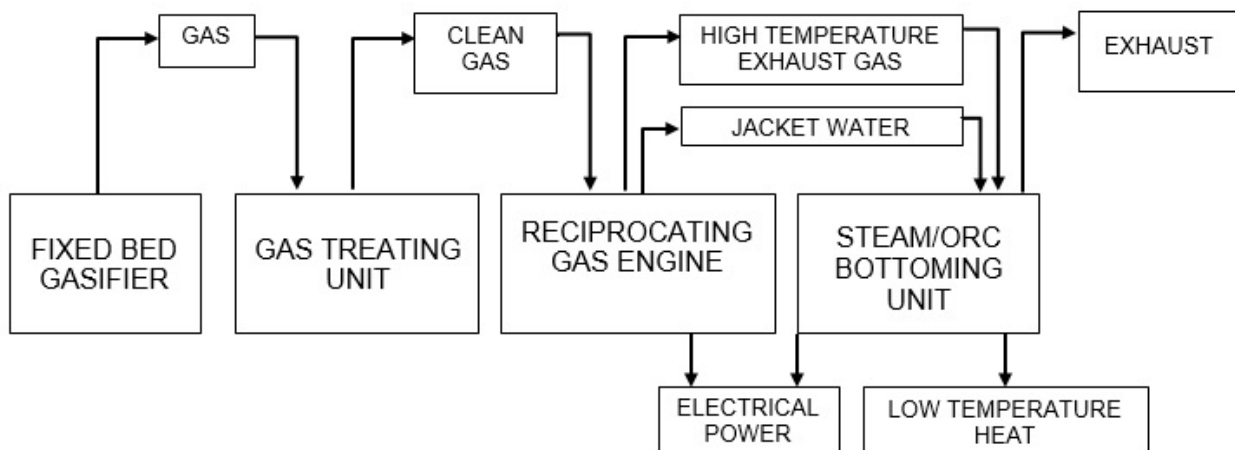


Figure 4 - Schematic of power production from fixed bed gasifier by ICE.

- 3) Gas is thoroughly cleaned, and fed to a compressor which in turn feeds the combustor of a gas turbine (GT). The required purity level for the gas is substantially lower for a gas turbine than for an ICE. The footprint of the gas turbine is small compared to the ICE, its exhaust gas is cleaner, the maintenance load is lower while availability and reliability are higher. The amount of thermal power at high temperature in the exhaust is much larger than in a reciprocating engine, and the addition of a bottoming cycle is instrumental to obtain a high overall efficiency. The bottoming cycle can produce some 30% of the overall power. The rationale for adopting an ORC solution, rather than steam are the following:
- an ORC, if properly designed and constructed is a very reliable, long lasting, and easy to operate unit, featuring a moderate pressure and low rpm turbine,
 - the maintenance cost for ORC is low compared to steam system,

- the ORC concept allows to exploit efficiently low power sources, by adopting suitable working fluid and optimized cycle for the specific heat source,
- fast and repeated start/ stop operation and load variation can be easily fulfilled.

A schematic of the solution is reported in fig.5, with reference to an ORC bottoming unit.

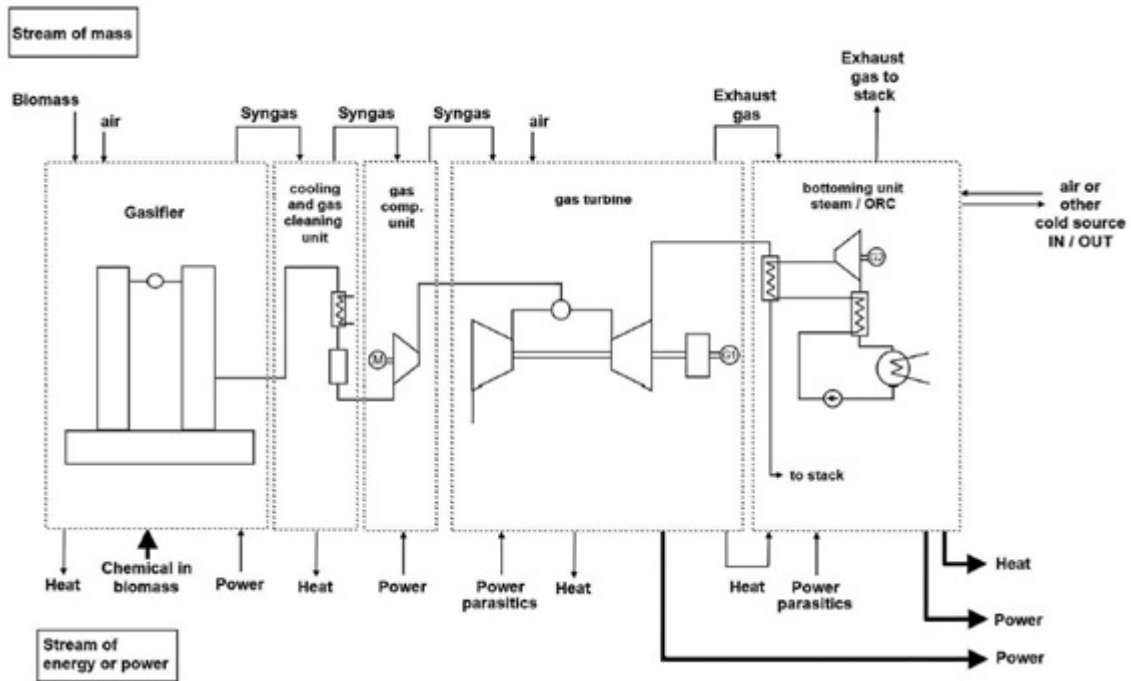


Figure 5 - Schematic of combined cycle fed by gasifier: mass and power streams

The proposed solution for the gasifier should allow to obtain a reliable, low tar, low particulate gas source.

In fact, the best option from the energy efficiency point of view involves the production in the gasifier itself of a pressurized high temperature syngas, hence the whole gas production and supply line to the gas turbine combustor must be under sufficient pressure for power modulation of the gas turbine. To avoid the deposition of its (albeit small) tar content, the temperature of the gas should be kept above some 400 °C.

A preliminary calculation has been performed for a power plant utilizing an OPRA OP16 Gas Turbine [7], organized in a combined cycle, fed by a pressurized Twingas fixed bed gasifier. The bottoming cycle for the combined cycle has been identified as a standard unit (TD 7 by Turboden, with direct recovery from gas turbine exhaust). The working fluid adopted in this case hexamethyldisiloxane.

A simplified scheme is reported in fig.6, featuring direct heat exchange between turbine exhaust gas and ORC working fluid.

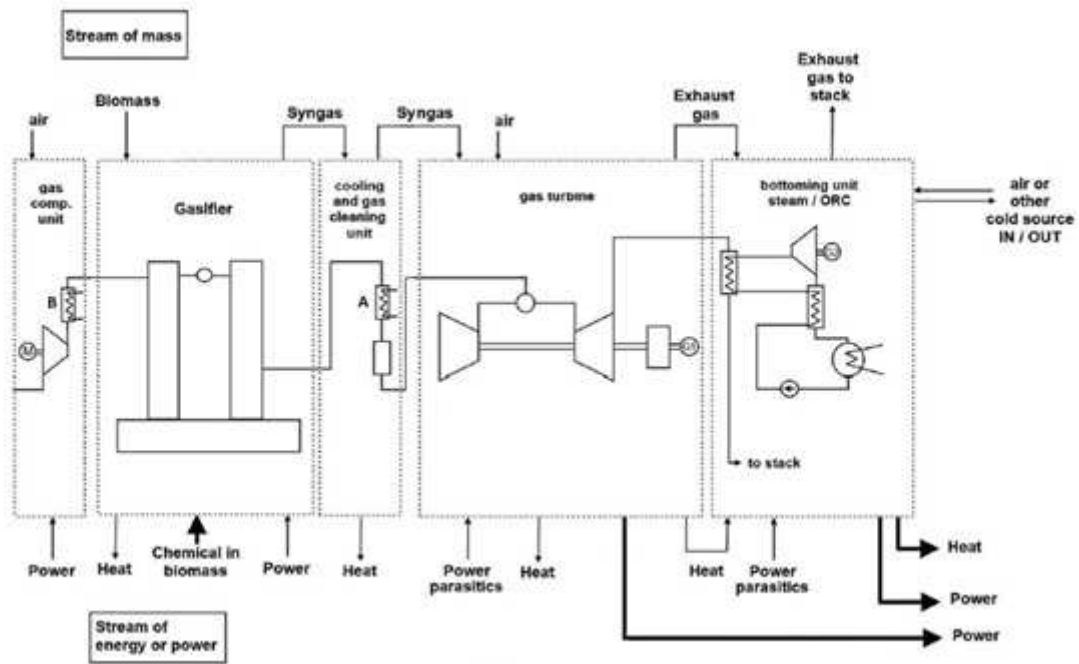


Figure 6 - Schematic of ORC combined cycle fed by pressurized Twingas gasifier: list of mass and power streams

The data adopted for a preliminary evaluation of performance for a case of power only production are reported in Table I (“Standard ORC”), while the preliminary performance is reported in Table II. The design point characteristics for the TD 7 ORC are reported in Tab III [8].

5. ENHANCED ORC BOTTOMING SOLUTIONS

The example reported in the previous chapter concerns the adoption of a standard unit of Turboden as bottoming. In order to explore the power which could be recovered by an ORC system put to the limits, an optimized recovery system has been considered, with two units in series on the exhaust. Moreover, a very high temperature supercritical cycle has been envisaged. The purpose is both to increase the temperature level of the heat input the “high side” of the exhaust flow and to lower the temperature of the exhaust gas leaving the unit, on the “low side”. The same working fluid, hexamethyldisiloxane, is adopted in the two cycles, which can be linked in order to take advantage of a number of shared auxiliaries.

The exchanged power vs temperature diagram is reported in fig.7, and the expected performance is summarized in Table I to III and fig. 8 (“Enhanced ORC”). The power increase is obvious, besides the uncertainties linked to the thermal endurance of the working fluid, in any case the power increase would be obtained at the expense of increased capital cost, and complexity of system.

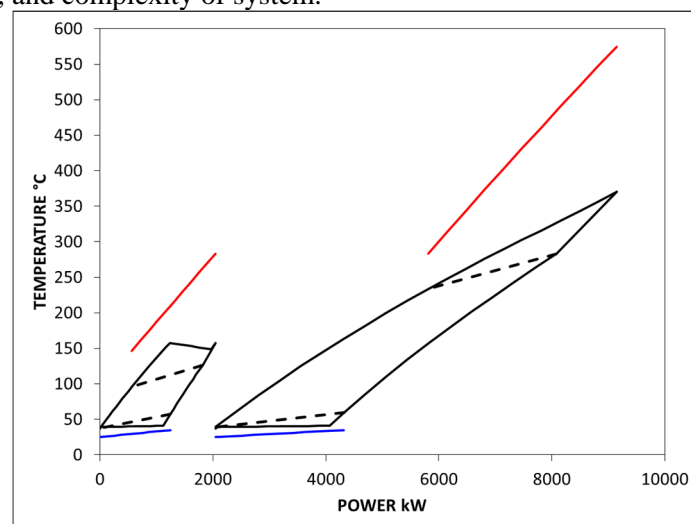


Figure 7 - Q-T diagram for enhanced ORC bottoming solution

Table I : Preliminary data for power-only operation		Standard ORC	Enhanced ORC	
Gasifier	Fuel power input (rel. To NCV)	kW	8362	8362
	<i>NCV fuel (moisture content wood chips 27.5 wt.% w.b.</i>	<i>kJ/kg w.b.</i>	12701	12701
	<i>Fuel input</i>	<i>kg/h</i>	2370	2370
	<i>Ash</i>	<i>kg/h</i>	9,5	9,5
	<i>NCV producer gas (gasifier outlet)</i>	<i>kJ/kg w.b.</i>	5100	5100
	<i>Temperature producer gas out of gasifier</i>	°C	400	400
	Total power output gasifier	kW	8224	8224
	Heat losses producer gas	kW	8	8
	<i>Temperature producer gas after heat loss</i>	°C	396	396
Gas Turbine	Total power input turbine	kW	8216	8216
	<i>Pressure producer gas into turbine</i>	<i>barg</i>	14	14
	<i>Mass flow producer gas into turbine</i>	<i>kg/s</i>	1,47	1,47
	<i>Mass flow air into turbine</i>	<i>kg/s</i>	8,73	8,73
	Electric power output turbine - gross	kW	2054	2054
	Thermal power exhaust gas out of turbine	kW	5916	5916
	<i>Mass flow exhaust gas</i>	<i>kg/s</i>	10,2	10,2
	<i>Temperature exhaust gas out of turbine</i>	°C	575	575
	Heat losses exhaust gas	kW	36	36
	<i>Temperature exhaust gas into ORC</i>	°C	572	572
ORC	Thermal power input ORC - from exhaust gas	kW	4284	4906
	Thermal power input ORC - from cooling PG	kW	-	-
	Conversion losses ORC	kW	27	27
	Electric power output ORC - gross	kW	966	1328
	Thermal power output ORC (not used)	kW	3291	3705
Heat recovery	<i>Temperature exhaust gas out of ORC</i>	°C	197	129
	Low-temperature heat recovery exhaust gas (used)	kW	-	-
	<i>Temperature exhaust gas leaving heat recovery</i>	°C	197	129
	Heat content exhaust gas rest (not used)	kW	1632	1010
	<i>Ambient temperature</i>	°C	15	15

Table II : Preliminary performance data for power-only operation		Standard ORC	Enhanced ORC	
Overall plant	Total electric power output - gross	kW	3020	3382
	Auxiliary power consumption gasifier plant	kW	82	82
	Auxiliary power consumption air cooler	kW	11	11
	Auxiliary power consumption gas turbine	kW	16	16
	Auxiliary power consumption ORC	kW	43	93
	Auxiliary power consumption pumps	kW	10	15
	Auxiliary power consumption compression (air, producer gas)	kW	281	281
	Total electrical power output - net	kW	2577	2884
	Total utilized thermal power output	kW	-	-
	Total electric efficiency - gross	%	36,1	40,4
	Total electric efficiency - net	%	30,8	34,5

Table III: Load case data for power only module

		Standard ORC	Enhanced ORC
Net thermal power processed by ORC	kW	4270	4906
Exhaust gas temperature into ORC	°C	575	575
Exhaust gas temperature out of ORC	°C	197	138
Total exhaust gas flow rate	kg/s	10,2	10,2
Exhaust gas average heat capacity	kJ/kgK	1,1	1,1
Heat losses (on gas-fluid exchanger)	%	-	-
ORC overall net output	kW	920	1237
Thermal power to cooling source	kW	3280	3607
Average air temperature (Dry bulb)	°C	15	15
Cooling water inlet temperature	°C	23	23
Cooling water outlet temperature	°C	35	31

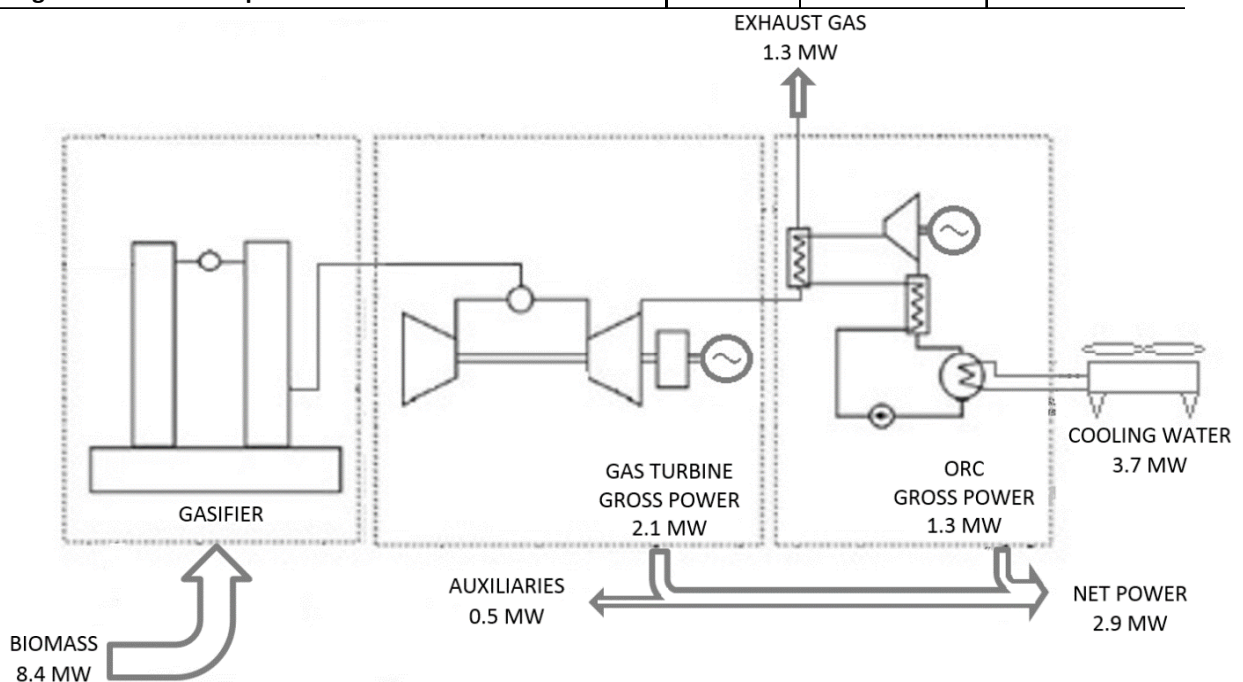


Figure 8 – Simplified block diagram and performance

6. CONCLUSIONS AND FINAL REMARKS

The solution outlined here would allow to obtain a plant, well adapted to converting wood biomass to electric power in the few MW power range, featuring some very attractive points:

- A high overall efficiency of conversion, around 30% for a power-only system with standard ORC.
- Low pollutant content of the exhaust gases.
- Fast modulation of power produced, which could become an important feature for a stand-alone unit.
- Good tolerance concerning the characteristics of the biomass fed to the gasifier, similar to the one of an updraft gasifier.
- Performance with an ORC bottoming system featuring very high temperature supercritical cycle could exceed 34%.

Up to now the solution has been the subject of a number of studies and preliminary evaluations, the technical feasibility, expected performance and cost effectiveness shall be ascertained in the frame of the future activity. If the expected results are confirmed, the proposed solution could give an important contribution to spreading the practical use of small scale biomass sources for power, (typically around 5 MW of electric power produced, by adopting two OPRA Gas Turbine units in parallel), all around the world.

REFERENCES

- [1] Obernberger I., Thek G., Combustion and gasification of solid biomass for heat and power production in Europe – state of the art and relevant future developments, *Proceeding of the 8th European Conference on Industrial Furnaces and Boilers (keynote lecture)*, April 2008, Vilamoura, Portugal, ISBN 978-972-99309-3-5, CENERTEC (Ed.), Portugal.
- [2] Obernberger I., Thek G., Cost assessment of selected decentralized CHP applications based on biomass combustion and biomass gasification, *Proceeding of the 16th European Biomass conference & Exhibition*, June 2008, Valencia, ETA-Renewable Energies (Ed.), Italy.
- [3] Chopra S., Jain A., A review of fixed bed gasification systems for biomass, *Agricultural Engineering International: the CIGR Ejournal*. Invited Overview n° 5. Vol. IX. April, 2007.
- [4] P. Basu, *Combustion and gasification in fluidized beds*, Taylor & Francis, ISDN 0849333962, pp. 335-357, 2006.
- [5] S. Kern, C. Pfeifer, H. Hofbauer, Gasification of wood in a dual fluidized bed gasifier: influence of fuel feeding on process performance, *Chemical Engineering Science*, vol. 90, pp. 284-298, 2013
- [6] R. Bini, M. Gaia, inventors; Turboden srl, assignee. Method for gasifying a biomass and respective gasifier. Patent application N° PCT/IB2015/0502238
- [7] OPRA turbines – Nederland – Technical specification sheets, available online: <http://www.opra.nl/upload/Products/Spec%20sheet%20-%20general%20description.pdf> [Last accessed March 2015]
- [8] Obernberger I., Thonhofer P., Kerchbaumer C., Thechnical and economic pre-assessment of a biomass gasification coupled with a gas turbine and a ORC, Turboden internal study

APPENDIX I- Description of the TWINGAS concept.

With reference to figg.2 and 9, the proposed gasifier is composed of at least two reactors (vessels 1, and vessel 2) and two connecting vessels or ducts, the hot side duct 3, and the cold side duct.

Biomass feed (wood chips, or any other biomass of interest) are fed through the gated feed mechanisms 5 and 6, and flow down in the twin vessels to the high temperature zone at the bottom. The biomass is pyrolyzed to char in zone 7. In the subsequent zone 8 the char reacts with the volatiles generated in the pyrolysis and air from the top air feeds 9,10 (if present) to produce syngas.

The syngas is extracted through ports 11, 12 in the vessels, or through port 13 in the bottom duct. The charcoal column is retained by grates 14, 15 while the ash falling to the bottom of the bottom duct 3 is extracted by a suitable mechanism 16 (screw or other mechanism).

The temperature of the gas in the bottom duct 3 is held at the value required for proper reaction within the vessels by a burner 17, introducing in the gas the correct amount of oxidizing agent (air, oxygen or any oxygen containing gas). The temperature set is one of the main variables in gasifier operation, in principle it should be as high as possible without exceeding the ash melting threshold.

The whole system is characterized by the pumping device 18, a fan which pushes alternatively the gas in the vessel 1 towards the vessel 2 and viceversa. As the head loss through the biomass columns is low compared to the average pressure of the gas, the pumped gas will behave as a nearly incompressible fluid, and a substantially alternate flow of gas will be established throughout the whole system.

This alternate flow involves that the high temperature at the bottom is easily transferred by the flowing gas to the reacting char bed in the twin vessels, thus supplying the required energy for the gasification reactions.

The following advantages are expected from the alternated flow in the two vessels: each vessel is operated, for about half time, as an updraft gasifier. In this phase a gas flow is established from the high temperature zone to the pyrolysis zone and, further up, to the drying zone. This phase allows an effective transfer of heat to the colder zones following a substantially counter-flow scheme. The gas exiting the top layer of biomass of this “updraft” gasifier, is not sent to utilizer, on the contrary it flows through the other vessel, acting in this phase as a “downdraft” gasifier. Flowing down, the gas becomes loaded with steam from the drying section and then with tar, from the pyrolysis zone. It gets progressively at higher temperature, taking heat from the layers it

goes through. It transfers steam and tar to the char bed, where they participate to the gasifying reactions. Tars are decomposed in the bed, CO and H₂ levels are enriched: the typical effects of a downdraft scheme. In order to have this scheme running sustainably, an energy input is required as well as an extraction of the useful product, syngas. Like in most gasifiers, fresh energy is supplied by introducing a sub-stoichiometric amount of oxidizer, typically air, or oxygen-enriched air. A number of different options are possible concerning the site of introduction, the most obvious position being the connecting drum at the bottom of the two vessels. In this area the temperature is high, typically around 800 °C, in order to achieve fast going reactions in the char bed, while avoiding ash softening. Introduction of the oxidizer in this area involves the development of immediate reaction with the gas and allows a good control on the temperature in this area, too. Extraction of produced gas is more tricky, as it should be extracted in a low tar content zone. Also, the temperature should not be too high, to reduce the duty of the heat exchanger preheating of the oxidizer. A position along the two vessels, corresponding to the lower half of the char bed is most probably the best solution. However, due to the pressure drop within the bed, the gas will preferably flow out from the “downdraft” vessel. Hence a gas with a good combination of tar removal and temperature should be obtained. An alternated extraction, controlled by a valve or a fan, can give a number of interesting control strategies.

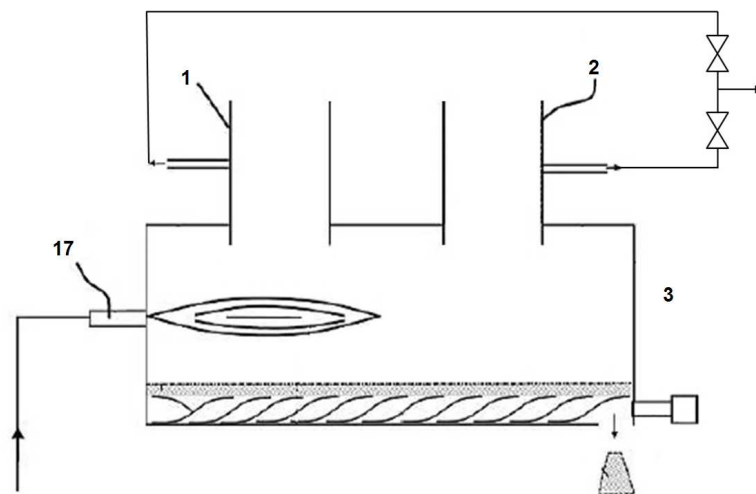


Figure 9 - Extraction points and control values for syngas in Twingas gasifier

In summary, the Twingas solution is expected to allow an effective combination of the advantages of both updraft and downdraft fixed bed gasifiers: moreover so, as it gives new tools for controlling the process, that is the frequency and the intensity of the alternate flow, which are independent from the flow of oxidizer. Moreover it can be expected that, by keeping a larger thickness of char bed at high temperature, the Twingas solution should allow a much faster modulation of load, and in particular a much faster load increase after an extended low load period. This aspect can be very important for systems supplying an isolated grid. The Twingas solution has been here summarized, its analysis is in fact complex and involves a time dependent simulation, much more demanding than the already complex simulation of conventional gasifiers.

DEVELOPMENT AND TEST OF A 100KW CLASS ORC POWER-GENERATOR FOR LOW TEMPERATURE GEOTHERMAL APPLICATIONS

Dong Hyun Lee¹, Young Min Yang^{1,2,3}, Chun Dong Park¹, Si Woo Lee², Byung-Sik Park^{1,3*}

²Energy Efficiency Research Division, Korea Institute of Energy Research,
152 Gajeong-ro, Yuseong-gu, Daejeon 305-343, Republic of Korea
<http://www.kier.re.kr> (e-mail: dhlee@kier.re.kr)

²Jinsol Turbomachinery Co., Ltd.,
94-17 Techno2-ro, Yuseong-gu, Daejeon, 305-509, Republic of Korea
<http://www.jinsolturbo.co.kr> (e-mail: impentacle@jinsolturbo.co.kr)

³Advanced Energy and Technology, Korea University of Science and Technology,
217 Gajeong-ro, Yuseong-gu, Daejeon 305-333, Republic of Korea
e-mail: ymyang@kier.re.kr

ABSTRACT

The major portion of the heat sources is in the lower end of the temperature spectrum. Therefore, the successful utilization of low-grade heat is very essential to energy. The organic Rankine cycles (ORCs) are one of the appropriate technologies to convert low grade heat to power. Korea Institute of Energy Research (KIER) and Jinsol Turbomachinery have jointly developed an ORC power-generator applicable to very low-temperature heat sources. This paper deals with the design, fabrication and test results of the ORC power generator. The ORC system was designed the maximum electric power output of 100kW utilizing geothermal hot water. The ORC has a simple configuration with an evaporator, an expander, a condenser and a pump. The completely hermetic turbo-generator was developed by Jinsol Turbomachinery and applied to the system. The turbo-generator has twin radial inflow turbines connected with high-speed synchronized generator. Two plate heat exchangers are used for evaporator and condenser. The performance test was conducted and the resulted gross electric power output was 91.22kW with cycle efficiency of 7.14%.

1. INTRODUCTION

An organic Rankine cycle (ORC) is a type of a Rankine cycle, which uses organic compounds as a working fluid instead of water. Thanks to the low evaporation temperature of the organic compounds, ORCs could be applied to lower temperature heat sources compared to the steam Rankine cycle. Low grade waste heat, geothermal hot water, solar thermal heat, and biomass combustion can be the heat source for ORCs (Lecompte et al., 2015). There are a couple of alternative technologies for converting low-temperature heat to power, such as Kalina cycle (Kalina, 1984), Uehara cycle (Uehara et al., 1994), Goswami Cycle (Goswami, 1995), trilateral Flash cycle (TFC) and thermoelectric generator. Despite of the high potential of TFC, a lack of efficient two-phase expander is the main obstacle of the TFC. Many researchers have been compared the ORCs and Kalina cycles (Yari et al., 2015, Bombarada et al., 2009, Zare and Mahmoudi, 2015, Yue et al., 2015 and Victor et al., 2013) from a thermodynamic and/or economical perspective. There is still controversy about the best heat recovery power generation technique. However, simple configuration, low pressure level and high freedom of design (selection of working fluids including mixtures, transcritical/supercritical cycle) make the ORS to the most practical technology.

Designing ORC power-generator is quite complex problem due to excessively high freedom of design. Selection of working fluids, configuring a cycle, choosing an expander and heat exchanger types, and etc. Colonna, P. (2013) pointed out that there are 1.6 million alternatives in designing ORCs. Various ORC power-generators are already developed and commercialized in the market. The power ranges of ORCs are from a few kW to tens of MW. Most of the ORCs adopt turbines as expanders, except very small systems due to relatively high isentropic efficiency of turbine. In spite of the long history and successful commercialization of ORCs (Mario Gaja, 2011), many researchers have been making efforts to develop a new and advanced ORC system. Many researchers introduced novel cycles and/or new optimization design method to enhance the cycle efficiency of ORCs (Xiao et al., 2015, Feng et al., 2015 and Imran et al., 2015) and adopting new working fluids (Lecompte et al., 2014 and Mavrou et al., 2015). Several researchers built their own ORCs with various configurations. Yun et al. (2015) designed parallel-expanders ORC for the application with large heat source variations. Yamada et al (2015) developed a prototype of 10W ORC with a scroll expander. They showed the possibility of micro-scaled ORC in spite of low cycle efficiency. Fu et al. (2015) designed and constructed a simple cycle 250kW class ORC with turbine expander and achieved 9.5% thermal efficiency using 120°C hot water.

In the present work, KIER and Jinsol Turbomachinery jointly developed a 100 class ORC power generator for the commercialization purpose. A simple cycle was selected to avoid complexities in construction/maintenance. Instead of that, we focused on improving and optimizing the performances of the ORC system. An originally designed turbo-generator and hybrid type plate heat exchangers are developed and integrated to the present system. This paper will describe the design, fabrication procedures and test results of the system.

2. CYCLE DESIGN

2.1 Design conditions

To design an ORC system, the conditions of heat source and heat sink should be defined. In the present work, one of the hot spring wells in Seokmo Island is selected as a heat source. The heat source temperature is 75°C and the well is expected to produce about 1,400ton of geothermal hot water per day. For a heat sink, dry cooling tower was chosen. The power output of ORCs changes with external temperature and the maximum power is achieved during the winter season. When designing an ORC power generator, not only the rated power but also maximum power output should be considered due to the safety reasons. Therefore, the cooling water temperature of 5°C was assumed for the winter season.

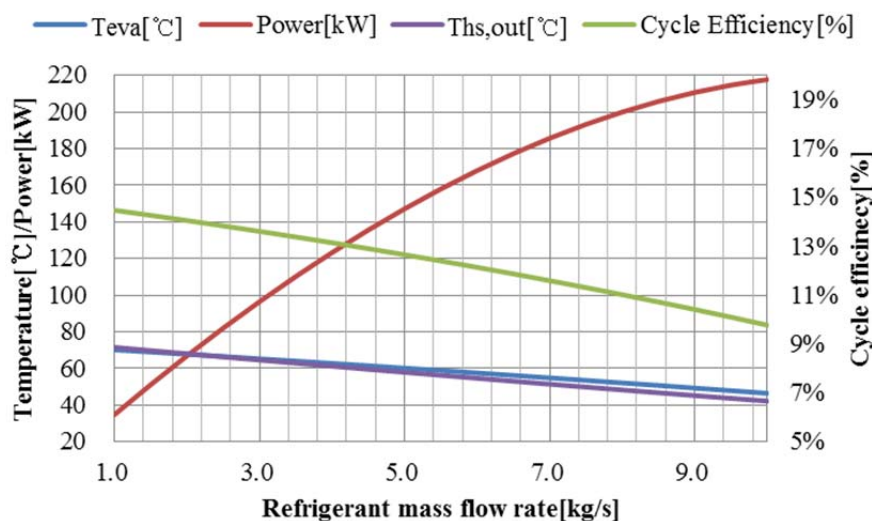


Figure 1: Effects of working fluid flow rate

For the given heat source conditions, the output power of the ORCs increases with the mass flow rate of working fluid, while the cycle efficiency reduces. Therefore, there is no correct answer in deciding a mass flow rate. Hot water in Suokmo Island is planned to be used in hot springs, so the water temperature after the power generation should be high enough for hot springs. Figure 1 shows the effect of mass flow rate of working fluid on evaporation temperature, power output, cycle efficiency and heat source outlet temperature. The working fluid is refrigerant R245fa and the pinch point temperature difference (PPTD) is 2.5°C. For quick estimation, no loss was assumed. Form the calculation, the mass flow rate was determined to 5kg/s with the heat source outlet temperature of 57.9°C.

2.2 System configuration and cycle design

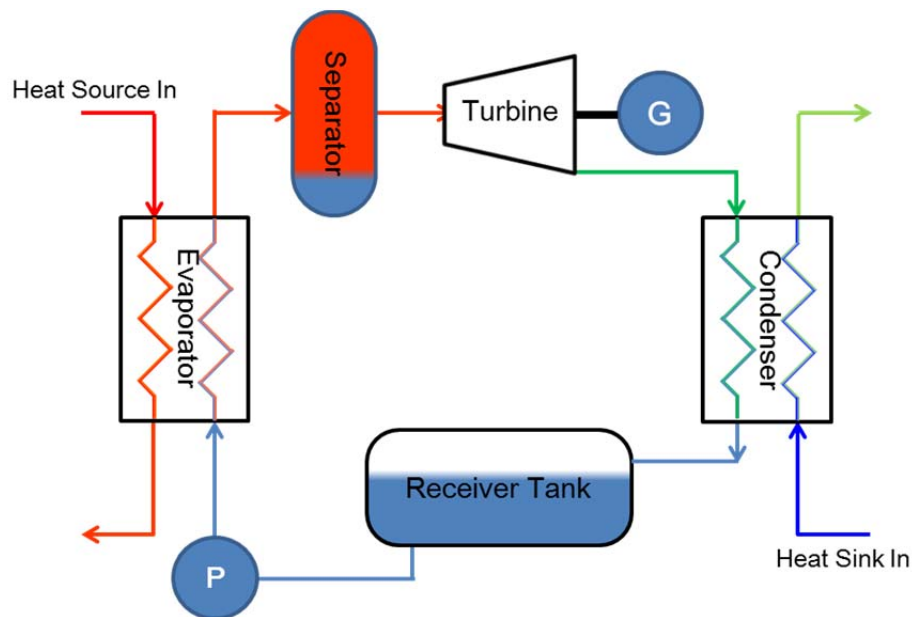


Figure 2: Schematic diagram of ORC power generator

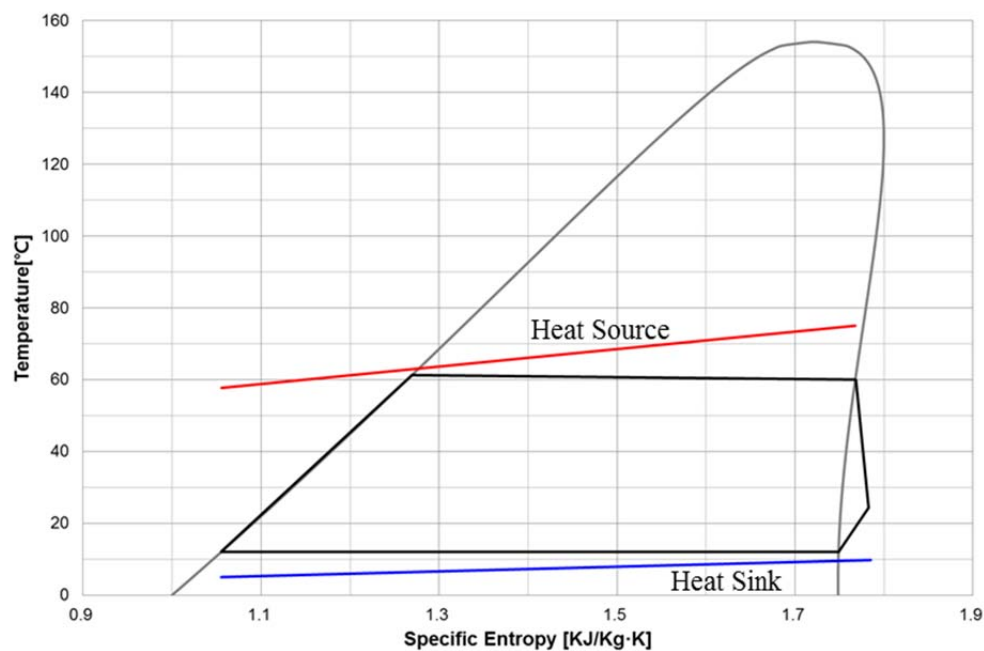


Figure 3: T-s diagram of the present ORC cycle

Figure 2 shows the schematic diagram of the present ORC power generator. The system is consisted of a pump, an evaporator, a separator, turbines, a generator, a condenser and a receiver tank. The R245fa in the receiver tank is assumed an equilibrium state and the temperature and pressure are the same with the condensing condition. For cycle design, efficiencies of the pump, motor, turbine and the generator are assumed to be 0.700, 0.895, 0.850 and 0.950, respectively. And the pressure losses through each component and pipes are considered. The pinch point temperature differences of 2.5°C were applied for both the evaporator and condenser. Required mass flow rate of heat source and heat sink were calculated from the PPTD and were 16.0kg/s and 52.3kg/s, respectively. The T - s diagram of the calculated ORC cycle is shown in Fig. 3. The red and blue lines refer the heat source and heat sink, respectively. The generator power output is 113.1kW with 2.268kW of pumping power consumption. The expected gross cycle efficiency is 9.74% (Net: 9.55%).

3. SYSTEM FABRICATION AND TEST

3.1 Component selection and system fabrication

Design requirements for each component are fixed from the cycle design and summarized in Tables 1 and 2.

Table 1: Design requirements of evaporator and condenser

		Evaporator		Condenser	
		Cold side	Hot side	Cold side	Hot side
Working Fluid		R245fa	Water	Water	R245fa
\dot{m}[kg/s]		5.0	16.0	52.3	5.0
Inlet	T[°C]	12.2	75.0	5.0	24.2
	P[kPa]	479.4	-	-	91.5
Outlet	T[°C]	60.0	-	-	12.0
	P[kPa]	462.3	-	-	89.2
Heat duty	Q[kW]	1161.0		1044.0	

Table 2: Design requirements of turbine and pump

		Turbine	Pump
Working Fluid		R245fa	
\dot{m}[kg/s]		5.0	
Inlet	T[°C]	59.8	12.0
	P[kPa]	456.6	102.6
Outlet	T[°C]	24.3	-
	P[kPa]	95.2	492.8
PR/ΔP[kPa]		4.8/361.4	4.8/390.2

Hybrid type heat exchangers, developed by Innowill, are adopted for both the evaporator and condenser. A Grundfos pump (CRN15-4) was chosen for the present system. A twin radial type turbo-generator was designed and fabricated by Jinsol Turbomachinery. The turbo-generator has twin radial turbines directly coupled with a high speed synchronous generator (Fig. 4). The yellow arrows in Fig. 4 indicate the flow direction of the vapor refrigerant. Details of the turbo-expander are discussed by Yang (2015).

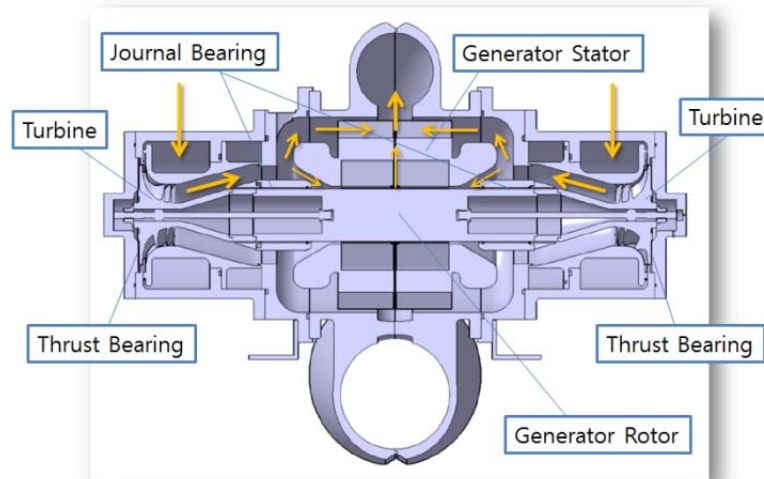


Figure 4: Mechanical Layout of the 100kW turbo-generator for ORC plant (Yang et al., 2015)

A 3ton/hr steam boiler and a plate heat exchanger and hot water tank are used to simulate heat source in Seokmo Island (Fig. 4). The hot water temperature to evaporator was adjusted by controlling steam valve, and the hot water flow rate is fixed. A 500RT cross-flow cooling tower supplies cooling water.

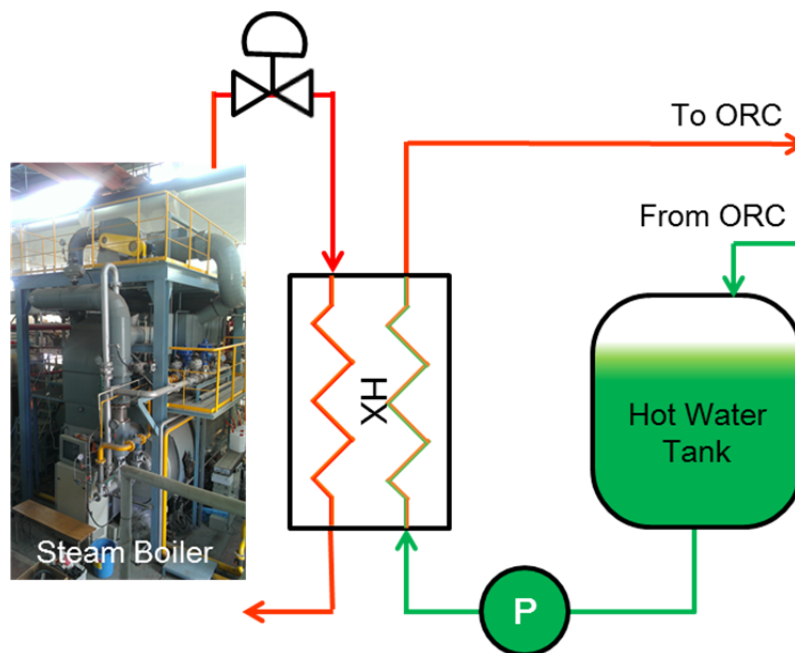


Figure 5: Schematics of hot water supply system

Figure 6 presents the photo of a 100kW ORC turbo-generator installed at KIER. A separator is located just downstream of the evaporator to remove liquid droplet and prevent the possibility of flooding. A small tank is positioned beneath the separator. If the tank is filled with liquid R245fa, an automated control valve opens, so liquid refrigerant can be discharged to receiver tank. Then, hot refrigerant vapor enters the turbines and expands. Since the expanded vapor has very low temperature, it designed to cool the generator instead of external air. Therefore, the vapor refrigerant flows through the generator as shown in Fig. 4. After that it reaches to the condenser and returns to the receiver tank. The receiver tank secures acceptable pump operation pressure for avoiding cavitation and keeps the system stable during unexpected transient behavior, such as over heat input and/or failures in cooling system. A bypass pipe is installed parallel to the turbine.



Figure 6: Photo of a 100kW Geothermal ORC Turbo-generator

3.2 Performance test

For the test and control, pressure transducers with the full scale range of 10bar (GE Druck, PT5072), and RTDs (PT100, 3-wire) are installed as shown in Table 3. The full scale range of the selected pressure transducers is more than double of the operating range. The reason is that the system is pressurized up to 10bar with N_2 gas during the leakage test. The refrigerant flow rate was measured by using Coriolis mass flow meter (OVAL, CA010L) located between the pump and the evaporator. The flow rates of the heat source and cooling water are measured by using magnetic flow meters. The generated electric power was measured at the generator outlet. Precision power analyzer (Yokogawa, WT3000) is used to measure the high frequency electric power.

Figure 7 shows the generator power output (P), refrigerant mass flow rate (\dot{m}) and cycle efficiency (η) during the startup test. When the turbine starts, the bypass valve was partially opened, and part of the refrigerant flows through the bypass line. Therefore, the measured flowrate is higher than that enters the turbines. With increasing of the refrigerant mass flow rate, both the power output and the cycle efficiency increase. When the power output increases up to 70kW, the cycle efficiency reaches maximum value and then stays constant. The effects of mass flow rate are shown in Fig. 8. The condensing temperature rose slightly during the test run. The maximum power output (gross) was recorded 91.22kW and the cycle efficiency was 7.14% at 4.17kg/s of mass flow rate. Both the power output and the cycle efficiency are lower than expected. One of the possible reasons is the absence of insulation. The disagreement between heat release of the source and heat gain of the working fluid is about 10~15% during the test. Based on heat gain of the working fluid, the cycle efficiency was rises up to 9.17%.

Figure 9 compares the designed cycle and test results. Dashed lines indicated designed cycle and solid lines refers the test results. During the test, heat sink temperature was higher than that of design condition. To keep the temperature difference between the heat source and heat sink, the heat source temperature. As a result, the tested condition shifted upward compared to the designed cycle, due to higher heat sink temperature. As shown in Fig. 9, unexpected superheating and subcooling are observed. The degrees of superheat and subcooling were 10.2°C and 5.6°C, respectively. The estimated uncertainty of the measured electric power and calculated cycle efficiency were less than $\pm 1.0\%$ and $\pm 1.46\%$, respectively (Kline and McClintock, 1995).

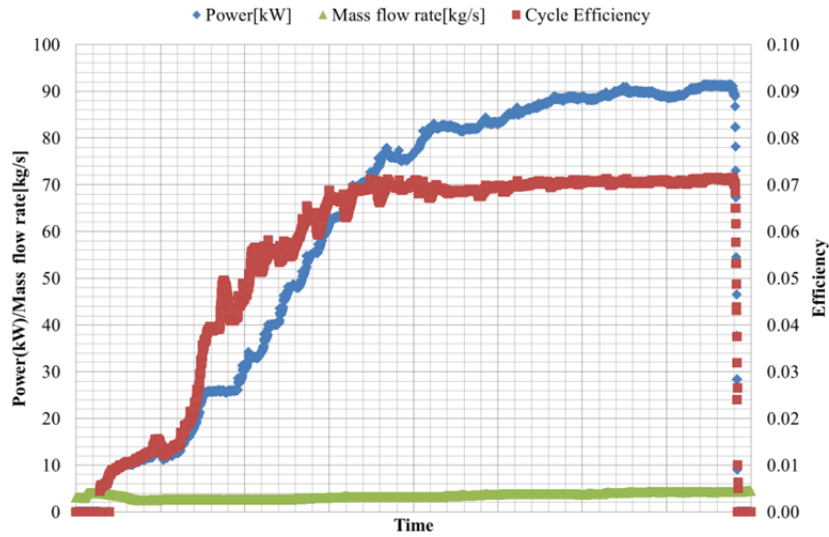


Figure 7: Power and efficiency change during startup

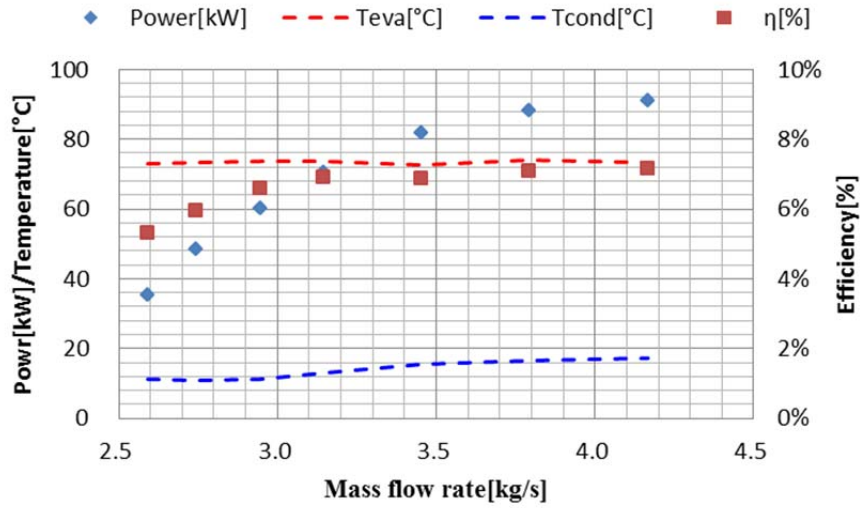


Figure 8: Performance results of 100kW ORC generator

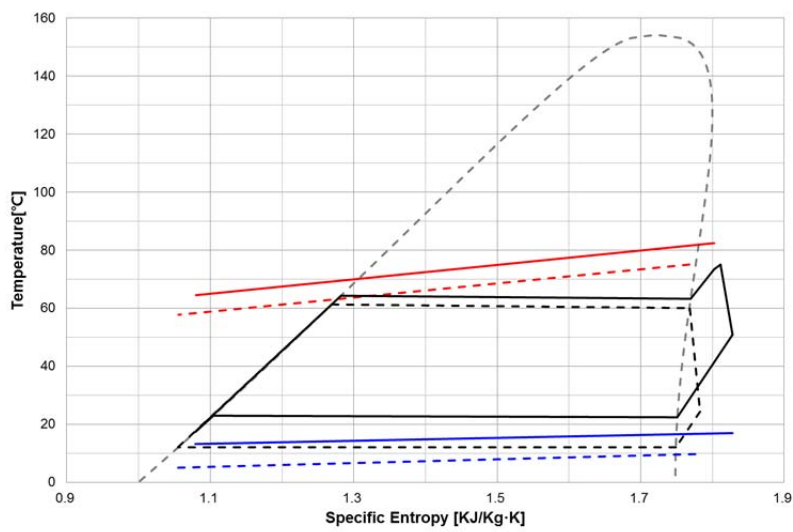


Figure 9: Comparison of designed and tested cycles

6. CONCLUSIONS

A 100kW ORC system adopting a high speed turbo expander was developed for low temperature geothermal heat applications. Performance test has been made and the results are follows:

- The ORC turbo-generator is designed for 113.1kW of gross electric power and 9.74% of cycle efficiency with the refrigerant mass flow rate of 5kg/s.
- The performance test show maximum electric power output was 91.22kW with the cycle efficiency of 7.14%, and the measured refrigerant flow rate was 4.17kg/s.
- High heat sink temperature and heat losses of the evaporator are the possible reason of low cycle efficiency. Based on heat gain of R245fa, the cycle efficiency was 9.17%, which is almost the same with expected value.

NOMENCLATURE

T	temperature	(°C)
P	pressure	(kPa)
\dot{m}	mass flow rate	(kg/sec)
η	cycle efficiency	(%)

Subscript

eva	evaporation
cond	condensation
h	heat source
c	heat sink

ACKNOWLEDGEMENTS

This work was conducted under the framework of Research and Development Program of the Korea Institute of Energy Research (KIER) (B4-2461)

REFERENCES

- Bombarada, P., Invernizzi, C.M., Pietra, C., 2010, Heat recovery from Diesel engines: A thermodynamic comparison between Kalina and ORC cycles, *Applied Thermal Engineering*, vol. 30, no 2-3: p. 212-219.
- Colonna, P., 2013, ORC power systems: the path from the concept to current applications and an outlook to the future, *Proc. of 2nd Int. Seminar on ORC Power Systems*, Rotterdam, The Netherlands.
- Goswami, D.Y., 1995, Solar thermal power-status of technologies and opportunities for research, *Int. Proc. of the 2nd ASME-ISHMT Heat and Mass Transfer Conference*, Tata-McGraw Hill Publishers, New Delhi, India.: p. 57-60.
- Feng, Y. Zhang, Y., Li, B., Yang, J., Shi, Y., 2015, Comparison between regenerative organic Rankine cycle (RORC) and basic organic Rankine cycle (BORC) based on thermoeconomic multi-objective optimization considering exergy efficiency and levelized energy cost (LEC), *Energy Conversion and Management*, vol. 96: p. 58-71.
- Fu, B.-R., Lee, Y.-R., Hsieh, H.-C., 2015, Design, construction, and preliminary results of a 250-kW organic Rankine cycle system, *Applied Thermal Engineering*, vol. 80:, p. 339-346.
- Gaja, M., 2011, 30 years of organic Rankine cycle development, *Proc. of ORC 2011*, Delft, the Netherlands.
- Imran, M., Park B.S., Kim, H.J., Lee, D.H., Usman, M., Heo, M., 2015, Thermo-economic optimization of regenerative organic Rankine cycle for waste heat recovery applications, *Energy Conversion and Management*, vol. 87: p. 107-118.

- Kalina, A.I., 1984, Combined-Cycle System with Novel Bottoming Cycle, *J. Eng. Gas Turbines Power*, vol. 106, no. 4: p. 737-742.
- Kline, S.J., McClintock F.A., 1953, Describing uncertainty in single-sample experiments, *Mech. Eng.* vol. 75: p. 3-8.
- Lecompte, S., Ameel, B., Ziviani, D., van den Broek, M., De Paepe, M., 2014, Exergy analysis of zeotropic mixtures as working fluids in organic Rankine cycles, *Energy Conversion and Management*, vol. 85: p. 727-739.
- Lecompte, S., Huisseune, H., van den Broek, M., Vanslambrouck, B., DE Paepe, M., 2015, Review of organic Rankine cycle (ORC) architectures for waste heat recovery, *Renewable and Sustainable Energy Reviews*, vol. 47: p. 448-461.
- Mavrou, P., Papadopoulos, A. I., Stijepovic, M. Z., Seferlis, P., Linke, P., Voutetakis, S., 2015, Novel and conventional working fluid mixtures for solar Rankine cycles : Performance assessment and multi-criteria selection, *Applied Thermal Engineering*, vol. 75:, p. 384-396.
- Uehara, H., Lkegami, Y., Nishida, T., 1994, OTEC system using a new cycle with absorption and extraction process, *Proc. of 12th Int. Conf. on the Properties of Water and Steam*, pp. 862-869.
- Victor, R.A., Kim, J.K., Smith, R., 2015, Composition optimization of working fluids for organic Rankine cycles and Kalina cycles, *Energy*, vol. 55: p. 114-126.
- Yamada, N., Tominaga, Y., Yoshida, T., 2014, Demonstration of 10- W_p micro organic Rankine cycle generator for low-grade heat recovery, *Energy*, vol. 78: p. 806-813.
- Yari, M., Mehr, A.S., Zare, V., Mahmoudi, S.M.S., Rosen, M.A., 2015, Exergoeconomic comparison of TLC (trilateral Rankine cycle), ORC (organic Rankine cycle) and Kalina cycle using a low grade heat source, *Energy*, vol. 83: p. 712-722.
- Yang, Y.M., Park, B.S., Lee, S.W., Lee, D.H., 2015, Development of a turbo-generator for ORC system with twin radial turbines and gas foil bearings, *Proc. of ASME ORC 2015*, Brussels, Belgium.
- Yue, C., Han, D., Pu, W., He, W., 2015, Comparative analysis of a bottoming transcritical ORC and a Kalina cycle for engine exhaust heat recovery, *Energy Conversion and Management*, vol. 89: p. 764-774.
- Yun, E., Kim, D., Yoon, S.Y., Kim, K.C., 2015, Experimental investigation of an organic Rankine cycle with multiple expanders used in parallel, *Applied Energy*, vol. 145: p. 246-254.
- Zare, V., Mahmoudi, S.M.S., 2015, A thermodynamic comparison between organic Rankine and Kalina cycles for waste heat recovery from the gas turbine-modular helium reactor, *Energy*, vol. 79: p.398-406.
- Xiao, L., Wu, S.-Y., Yi, T.-T., Liu, C., Li, Y.-R., 2015, Multi-objective optimization of evaporation and condensation temperatures for subcritical organic Rankine cycle, *Energy*, vol. 83: p. 723-733.

MINI-ORC TURBOGENERATOR: THE UPCOMING LEAP FORWARD?

Piero Colonna

TU Delft

P.Colonna@tudelft.nl

ABSTRACT

Much R&D is currently devoted to obtain commercial ORC power systems generating few kilowatts up to few tens. The driver application is currently waste heat recovery from long-haul truck engines, but many other applications can be envisaged, once these units successfully reach the market. This is not a new idea, and a brief history will illustrate past developments, useful for the context. The design paradigm of such systems is bound to be quite different from mainstream stationary ORC power plants, as mini systems will be designed for standardized large series production. The small capacity offers at the same time challenges and opportunities. The small and fast turbine is one such challenge, and options and concerned research are briefly addressed. Several new applications based on these miniature power plants are described, and ideas for the path forward proposed.

THERMO-ECONOMIC ANALYSIS OF ZEOTROPIC MIXTURES AND PURE WORKING FLUIDS IN ORGANIC RANINKE CYCLES FOR WASTE HEAT RECOVERY

Florian Heberle* and Dieter Brüggemann

University of Bayreuth, Center of Energy Technology (ZET),
Lehrstuhl für Technische Thermodynamik und Transportprozesse (LTTT),
Universitätsstraße 30, 95447 Bayreuth, Germany
e-mail: zet@uni-bayreuth.de
Web page: <http://www.zet.uni-bayreuth.de>

* Corresponding Author

ABSTRACT

We present a thermo-economic analysis of an Organic Rankine Cycle (ORC) for waste heat recovery. A case study for a heat source temperature of 150 °C and a subcritical, saturated cycle is performed. As working fluids R245fa, isobutane, isopentane and the mixture of isobutane and isopentane are considered. The minimal temperature difference in the evaporator and condenser as well as the mixture composition are chosen as variables in order to identify the most suitable working fluid in combination with optimal process parameters under thermo-economic criteria.

In general, cost-effective systems show a high minimal temperature difference $\Delta T_{PP,C}$ at the pinch-point of the condenser and a low minimal temperature difference $\Delta T_{PP,E}$ at the pinch-point of the evaporator. In case of R245fa, the design parameters $\Delta T_{PP,E} = 1$ K and $\Delta T_{PP,C} = 13$ K lead to minimal costs of 56.8 €/GJ. Choosing isobutane as working fluid leads to the lowest costs per unit exergy with 52.0 €/GJ ($\Delta T_{PP,E} = 1.2$ K; $\Delta T_{PP,C} = 14$ K). Considering the major components of the ORC, specific costs range between 1150 €/kW_{el} and 2250 €/kW_{el}. For the mixture isobutane/isopentane, a mole fraction of 90 % isobutane leads to lowest specific costs per unit exergy. Despite an increased efficiency an overcompensation of the additional expenses for the heat exchange equipment is not achieved compared to isobutane. The pure working fluid is 3.3 % more cost-effective. A sensitivity analysis for the ORC system using isobutane as working fluid shows high sensitivity of the costs per unit exergy to the costs of process integration and the isentropic efficiency of the turbine.

1. INTRODUCTION

Organic Rankine Cycle (ORC) systems for waste heat recovery have a high growth potential (Tchanche *et al.*, 2011). Numerous investigations are performed in order to maximize the efficiency of such power plants by working fluid selection with respect to the heat source temperature. Particularly, the use of zeotropic fluid mixtures is a promising optimisation approach due to a good glide match of the temperature profiles at phase change. In this context, Angelino and Colonna di Paliano (1998) show for a low-temperature application that mixtures of natural hydrocarbons (n-butane/n-hexane) lead to an efficiency increase of 6.8 % compared to the pure working fluid n-pentane. Other case studies for geothermal heat sources prove the potential of zeotropic mixtures as working fluids in ORC systems (Demuth, 1981; Iqbal *et al.*, 1976). For subcritical cycles an increase in efficiency by up to 16 % is obtained compared to pure working fluids, like isobutane or isopentane. More recent investigations include sensitivity analyses for crucial parameters (Borsukiewicz-Gozdur and Nowak, 2007; Wang and Zhao, 2009; Chen *et al.*, 2011; Garg *et al.*, 2013; Dong *et al.*, 2014; Lecompte *et al.*, 2014; Shu *et al.*, 2014). In addition, Heberle *et al.* (2012b) show high second law efficiencies for mixture compositions which lead to an good match of the temperature profiles at

condensation. However, these concentrations show a significant increase in heat exchange capacity. Similar results are obtained by Andreasen *et al.* (2014) considering pure components and their zeotropic mixtures as working fluids for subcritical and transcritical cycles in case of a low-temperature heat source. For a heat source temperature of 120 °C, mixtures of propane and higher boiling natural hydrocarbons as well as isobutane/isopentane show high first law efficiency for the subcritical cycle. At the same time, an increase of the heat exchange capacity for the condenser is presented, which is an indicator for the requirement of high heat transfer areas. Angelino and Colonna di Paliano (2000) compare an equimolar mixture of n-butane/n-hexane and pure n-pentane as ORC working fluids in a case study for waste heat recovery. Fan power savings of the air-cooling system of 49 % by using the zeotropic mixture are determined. However, an additional heat transfer area of 73 % is required. Weith *et al.* (2014) have recently shown for a waste heat recovery unit that the use of a siloxane mixture leads to an efficiency increase of 3 % compared to the most efficient pure component. In consequence, a 14 % higher heat transfer area of the evaporator is determined for the zeotropic mixture.

The described dependence suggests a thermo- or exergo-economic analysis of ORC systems in order to evaluate the increased power output and the additionally required heat exchange area for fluid mixtures. Existing thermo-economic analyses of ORC systems are focused on pure working fluids (Tempesti and Fiaschi, 2013; Astolfi *et al.*, 2014; Heberle and Brüggemann, 2014). Regarding small-scale waste heat recovery ORC units, Quoilin *et al.* (2011) determine specific investment costs for 8 working fluids in the range of 2136 €/kW and 4260 €/kW. For an electric capacity between 30 kW and 120 kW, Imran *et al.* (2014) considered different plant schemes and working fluids. In this context, specific investment costs in the range of 3556 €/kW and 4960 €/kW are obtained. Quoilin *et al.* (2013) indicate specific investment costs between 8000 €/kW and 1000 €/kW for an ORC waste heat recovery module in the range of 10 kW and 7500 kW electrical power output. In case of an geothermal resource, Heberle *et al.* (2012a) identify isobutane as a cost-efficient working-fluid compared to isopentane. The lowest specific costs are obtained for a minimal temperature difference of 3 K in the evaporator and 7 K in the condenser.

Under the consideration of zeotropic mixtures as potential ORC working fluids, we provide a thermo-economic analysis of waste heat recovery ORCs. In order to clarify if an efficiency increase overcompensates the additional heat transfer requirements. A case study is performed for a heat source temperature of 150 °C. In this context, a second law analysis for the ORC working fluids R245fa, isobutane and isopentane as well as for the zeotropic mixture isobutane/isopentane is conducted. Based on processes parameters the required heat exchange equipment is designed. Finally, the specific costs for the generated electricity are calculated. Depending on the working fluid composition and the minimal temperature difference in the condenser and evaporator, the most cost-efficient system is identified.

2. METHODS

2.1 Exergy analysis

For the exergy analysis, steady-state simulations are performed using the software Cycle Tempo (Woudstra, N. and van der Stelt, T.P., 2002). Fluid properties are calculated by RefProp Version 9.1 (Lemmon, E.W. *et al.*, 2013). Process simulations are conducted for a subcritical and saturated cycle. The scheme of the module and the corresponding T,s -diagram in case of a pure working fluid is illustrated in Figure 1.

The present case study is conducted for a low-temperature waste heat source of 150 °C. As a heat transfer medium pressurized water is assumed ($p_{HS} = 6$ bar). The mass flow and the outlet temperature of the heat source are chosen according to a thermal heat input of 3 MW. For the analysis, an air-cooled system is considered. R245fa, isobutane and isopentane as well as the zeotropic mixture isobutane/isopentane are examined as ORC working fluids. For the considered mixture, the composition is varied in discrete steps of 10 mole-%. The temperature difference in the evaporator and condenser is chosen as independent design variables in order to identify the most cost-efficient

process parameters. The analysis is conducted neglecting pressure and heat losses in the pipes and components. In Table 1 the boundary conditions for the cycle simulations are shown.

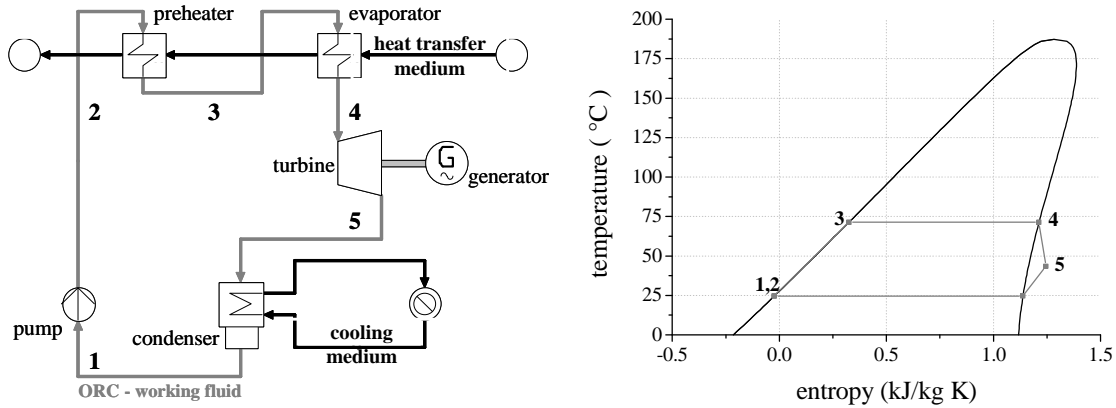


Figure 1: Scheme of ORC system and corresponding T,s -diagram for the working fluid isopentane

Table 1. Boundary conditions assumed for the second law analysis

parameter	
mass flow rate of heat source \dot{m}_{HS}	10 kg/s
outlet temperature of heat source $T_{HS,in}$	80 °C
inlet temperature of cooling medium $T_{CM,in}$	15 °C
temperature difference of cooling medium ΔT_{CM}	15 °C
maximal ORC process pressure p_2	$0.8 \cdot p_{crit}$
isentropic efficiency of feed pump $\eta_{i,P}$	75 %
isentropic efficiency of turbine $\eta_{is,T}$	80 %
efficiency of generator η_G	98 %

To evaluate the cycle efficiency, the net second law efficiency η_{II} of the ORC is calculated by

$$\eta_{II} = \frac{|P_G + P_{Pump} + P_{Fans}|}{\dot{E}_{HS}} = \frac{P_{net}}{\dot{m}_{HS} \cdot e_{HS}} \quad (1)$$

where P_G and P_{Pump} correspond to the power of the generator and the pump. P_{Fans} is related to the power of the air cooler fans. The exergy flow of the heat source \dot{E}_{HS} is obtained by multiplying the specific exergy e_{HS} with the mass flow rate \dot{m}_{HS} . The specific exergy could be calculated by

$$e_{HS} = h - h_0 - T_0(s - s_0) \quad (2)$$

where the subscript 0 corresponds to the reference state ($T_0 = 15$ °C and $p_0 = 1$ bar). Corresponding to (Bejan et al., 1996), the exergy analysis is extended by an exergy balance for each component k of the system

$$\dot{E}_{F,k} = \dot{E}_{P,k} + \dot{E}_{L,k} + \dot{E}_{D,k} \quad (3)$$

where \dot{E}_F and \dot{E}_P describe the exergy flow rate of the fuel and the product. The exergy flow rate \dot{E}_L includes heat losses to the surrounding or exergy that leaves the system in a physical way, like exhaust gases. Here $\dot{E}_L = 0$, due to neglected heat losses. The exergy flow rate \dot{E}_D represents the exergy destruction rate associated to irreversibilities. Exemplarily, the exergy destruction rate of the preheater can be calculated as

$$\dot{E}_{D,PH} = \dot{m}_{ORC} T_0 \left[(s_3 - s_2) - \frac{h_3 - h_2}{T_{m,PH}} \right] \quad (4)$$

where $T_{m,PH}$ corresponds to the thermodynamic mean temperature of the heat source in the preheater.

2.2 Component design and economic analysis

For the major components of the ORC module, the purchased equipment costs (PEC) are estimated based on cost data of Turton *et al.* (2003). Purchased equipment costs C_0 based on ambient operating conditions and a carbon steel construction are calculated in US \$ depending on parameter Y :

$$\log_{10} C_0 = K_1 + K_2 \log_{10}(Y) + K_3 (\log_{10}(Y))^2 \quad (5)$$

where Y represents the capacity or size of a component. The parameters K_1 , K_2 and K_3 are listed in Table 2. To convert the PEC in Euro a conversion ratio of 0.815 is considered. Due to maximal ORC pressures below 35 bar, additional cost factors depending on system pressure are not considered.

Table 2. Equipment cost data used for Equation (5) according to Turton *et al.* (2003)

component	Y ; unit	K_1	K_2	K_3
Pump (centrifugal)	kW	3.3892	0.0536	0.1538
Heat exchanger (floating head)	m ²	4.8306	-0.8509	0.3187
Heat exchanger (air cooler)	m ²	4.0336	0.2341	0.0497
Turbine (axial)	kW	2.7051	1.4398	-0.1776

By setting the corresponding Chemical Engineering Plant Cost Index (CEPCI₂₀₀₁) of 397 into relation to the value of 2014 with 575, the inflation and the development of raw material prices are taken into account Turton *et al.* (2003). For the costs $C_{tot,ORC}$ of the major components of the ORC power plant the PEC are summarized. The total investment costs of the power plant are calculated by multiplying $C_{tot,ORC}$ by the factor $F_{costs} = 6.32$. According to Bejan *et al.* (1996) this parameter represents additional costs like installation, piping, controls, basic engineering and others. The heat exchange area A is determined for the shell and tube heat exchanger in counter flow. Therefore, the overall heat transfer coefficient U_{tot} of each heat exchanger is calculated by

$$\frac{1}{U_{tot}} = \frac{1}{\alpha_o} + \frac{1}{\alpha_i} \frac{r_o}{r_i} + \frac{r_o \ln(r_o / r_i)}{\lambda_t} \quad (6)$$

where α_o represents the heat transfer coefficient at the outside of the tube, respectively, the shell side and α_i corresponds to the heat transfer coefficient at the inside of the tube. The inner and outer radius of the tube are represented by r_i and r_o . The thermal conductivity of the tube corresponds to λ_t . The outer diameter of the tubes is 20 mm and the wall thickness of the tube is 2 mm. In order to calculate the required diameter of the shell and the number of tubes, the maximal flow velocities of 1.5 m/s for liquid flows and 20 m/s for gaseous flows are assumed according to chapter O1 of the VDI Heat Atlas (VDI-GVC, 2010). In general, the ORC working fluid is led inside the tubes. Regarding the tube layout, a squared pitch and a pitch to diameter ratio of 1.22 are assumed. The considered heat transfer correlations for the calculation of α_i , depending on phase state and flow configuration are listed in Table 3. In case of the preheater and the evaporator, the method of Kern (1950) is applied for the shell side (α_o). For the air-cooled condenser a tube bank staggered arrangement is applied. In this context, a cross-flow heat exchanger with finned tubes is considered and the following design parameters are assumed: fin height of 3 mm, a fin thickness of 0.3 mm, a fin spacing of 2 mm and a transversal tube pitch of 60 mm. The air-side heat transfer coefficient is determined by the method of Shah *et al.* (2003). For all considered heat exchangers, the heat transfer surface is finally calculated by

$$\dot{Q} = U_{tot} A F_{LMTD} \Delta T_{log} \quad (7)$$

where ΔT_{log} is the logarithmic mean temperature difference. In general, the logarithmic mean temperature difference correction factor F_{LMTD} is equal 1 for condensation and boiling heat transfer. In this study, the simplifying assumption of $F_{LMTD} = 1$ is also met for single phase heat transfer.

Table 3. References for the considered heat transfer correlations

heat exchanger	tube side
preheater	(Sieder and Tate, 1936)
evaporator (pure working fluid)	(Steiner, 2006)
evaporator (zeotropic mixture)	(Schlünder, 1983)
condenser (pure working fluid)	(Shah, 1979)
condenser (zeotropic mixture)	(Bell and Ghaly, 1973; Silver, 1964)

2.3 Exergy costing

The thermo-economic analysis combines thermodynamic and economic aspects. In this context, the product of the energy conversion as well as each component can be evaluated according to the cost formation process. For the presented analysis, the method by Tsatsaronis and Winhold (1985), also known as exergo-economic method, is used. The exergy costing converts an exergy stream \dot{E} to a cost stream \dot{C} , by multiplying the exergy with corresponding average costs per unit of exergy, respectively, specific costs c . In this context, a system of equations is set up consisting of the cost balance for each component k of system (Bejan *et al.*, 1996), (Heberle *et al.*, 2012a):

$$\dot{C}_{P,k} = \dot{C}_{F,k} - \dot{C}_{D,k} + \dot{Z}_k \quad (8)$$

The cost streams \dot{Z}_k describe the costs of the k -th component depending on operation and maintenance $\dot{Z}_{O\&M}$ and capital investment \dot{Z}_{CI} . In order to calculate the described cost streams the economic boundary conditions listed in Table 4 are assumed.

Table 4. Economic parameters for the calculation of the cost streams \dot{Z}_k

parameter	
lifetime	20 years
interest rate ir	4.0 %
annual operation hours	7500 h/year
Cost rate for operation and maintenance	$0.02 \cdot \dot{Z}_{CI}$
Costs for process integration C_{PI}	$0.2 \cdot C_{tot,ORC}$
Power requirements of the air-cooling system	5 kW _e /MW _{th}
Electricity price €/kWh	0.08 €/kWh

The selected optimization criteria for the system is the minimization of the costs per unit exergy of the total system $c_{P,tot}$. In this study, the generated electricity is considered as the product of the system and the $\dot{E}_{P,tot}$ correspond to the power output of the generator. In this context, the auxiliary power requirements are covered by electricity from the grid. Alternatively, the net power output of the system can be considered in the denominator of Equation (9). The exergy rate of the fuel $\dot{E}_{F,tot}$ represents the exergy rate of the waste heat source transferred to the ORC system.

$$c_{P,tot} = \frac{\dot{C}_{P,tot}}{\dot{E}_{P,tot}} = \frac{(c_{F,tot} \dot{E}_{F,tot} + \sum_k \dot{Z}_k)}{\dot{E}_{P,tot}} \quad (9)$$

In addition, the specific investment costs SIC are calculated:

$$SIC = \frac{C_{tot,ORC}}{P_{net}} \quad (10)$$

3. RESULTS AND DISCUSSION

3.1 Identification of cost-efficient design parameters

For each working fluid the minimal costs per unit exergy $c_{p,tot}$ are identified depending on the minimal temperature difference ΔT_{PP} in the evaporator and condenser. In order to vary the minimal temperature difference, the corresponding upper and lower ORC pressure is adapted. In Figure 2, the resulting specific costs of the product are shown exemplarily for R245fa. The most cost-efficient design parameters for this ORC working fluid are $\Delta T_{PP,E} = 1$ K and $\Delta T_{PP,C} = 13$ K. For these parameters, costs per unit exergy of 56.8 €/GJ are obtained. Considering a minimal temperature difference between 0.5 K and 6 K for the evaporator and 8 K and 14 K for the condenser, the maximum costs per unit exergy of 60.0 €/GJ are calculated ($\Delta T_{PP,E} = 6$ K; $\Delta T_{PP,C} = 8$ K). In general, the cost minimum is a compromise between rising power output and increasing costs with decreasing minimal temperature difference in the heat exchangers. The results show that the condenser is crucial for the total PEC. Due to the highest amount of transferred thermal energy combined with the lowest logarithmic mean temperature difference, the highest heat transfer areas and component costs are obtained for the condenser. Therefore, the most cost-effective parameters show a low ΔT_{PP} for the evaporator and a high value in case of the condenser.

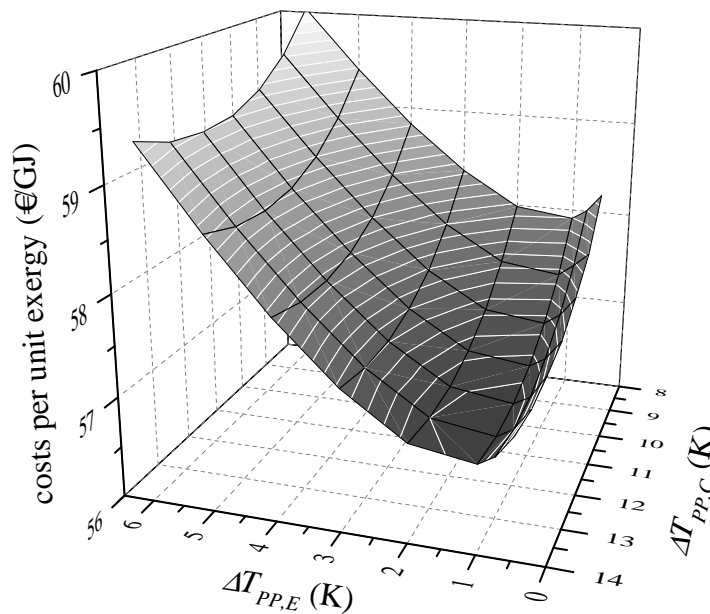


Figure 2: Costs per unit exergy for R245fa as ORC working fluid depending on minimum temperature difference in the evaporator and condenser

3.2 Comparison of ORC working fluids

Power output, heat transfer area and, therefore, capital investment costs for the ORC modules may considerably vary due to the working fluid selection and the corresponding fluid properties. In this context, Figure 3a illustrates the costs per unit exergy for the pure ORC working fluids isopentane, isobutane and R245fa as function of the minimum temperature difference in the condenser. For

$\Delta T_{PP,E}$, always the most cost-effective parameter is shown. In Figure 3b specific costs of the product are shown for selected mole fractions of the zeotropic mixture isobutane/isopentane.

Isobutane is identified as the most cost-effective working fluid for the considered case study with costs per unit exergy of 52.0 €/GJ. The corresponding design parameters are $\Delta T_{PP,E} = 1.2$ K and $\Delta T_{PP,C} = 14$ K. R245fa and isopentane lead to 9.2 % and 15.0 % higher costs per unit exergy (see Table 4). Although, these alternative pure working fluids show optimal design parameters with a lower minimum temperature difference, the power output is 10.8 % and 14.6 % lower. Net second law efficiency is between 1.0 % and 3.0 % lower compared to isobutane. The total heat exchange area differs only slightly and is 0.3 % lower for R245fa and 2.1 % higher for isopentane.

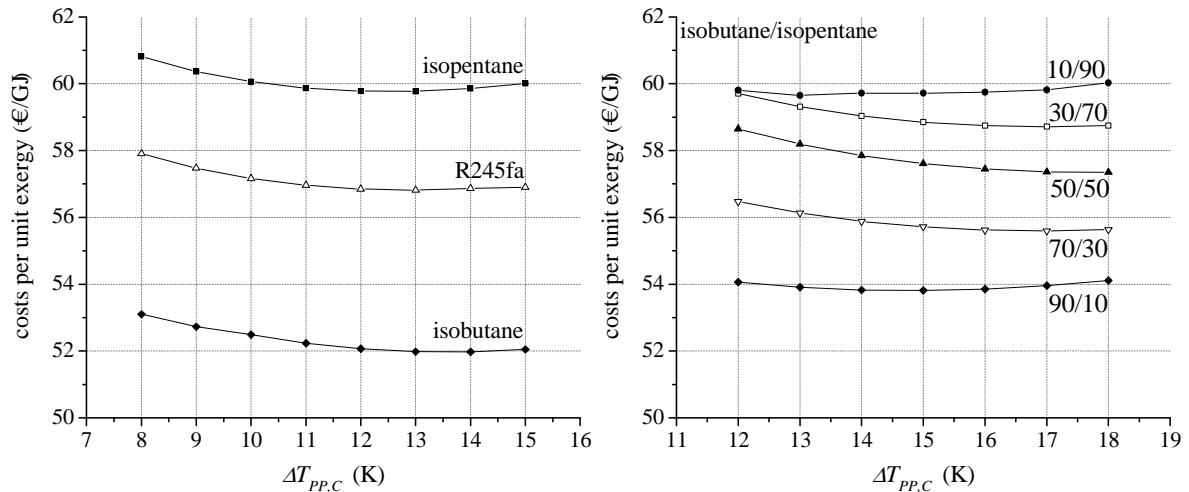


Figure 3: Costs per unit exergy for the pure ORC working fluids (3a) and for the zeotropic mixture isobutane/isopentane (3b) depending on the minimum temperature difference in the condenser

Regarding the mixture isobutane/isopentane, a mole fraction of 90 % isobutane leads to the lowest costs. In case of $\Delta T_{PP,E} = 2$ K and $\Delta T_{PP,C} = 15$ K specific costs of 53.8 €/GJ are obtained. However, the costs per unit exergy are 3.5 % higher compared to the most efficient component isobutane. This is due to a 5.5 % lower power output. At same time the total heat exchange area is only 3.6 % lower for 90/10 compared to isobutane.

Table 4. Selected ORC parameters for the most-effective cycles depending on fluid selection

parameter	isobutane	R245fa	isopentane	isobutane/isopentane
A_{PH} (m ²)	173.2	100.0	90.8	108.1
A_E (m ²)	123.1	118.1	118.6	112.8
A_C (m ²)	747.1	821.7	856.0	785.0
P_G (kW)	387.8	345.9	331.0	366.4
P_{Pump} (kW)	60.1	21.6	12.1	41.4
$\Delta T_{PP,E}$ (K)	1.2	1.0	1.0	2.0
$\Delta T_{PP,C}$ (K)	14.0	13.0	13.0	15.0
η_{II} (%)	30.3	30.0	29.4	30.0
SIC (€/kW)	1161.9	1270.1	1336.23	1203.0
$c_{p,tot}$ (€/GJ)	52.0	56.8	59.8	53.8

3.3 Sensitivity analysis for selected boundary conditions

In order to identify the most cost-important parameters of the estimated boundary conditions, Figure 4 illustrates the costs per unit exergy as function of interest rate, turbine efficiency, costs for process

integration, costs for operation and maintenance and F -factor. The specific costs per unit exergy show the highest sensitivity for the isentropic efficiency of the turbine and the costs for process integration.

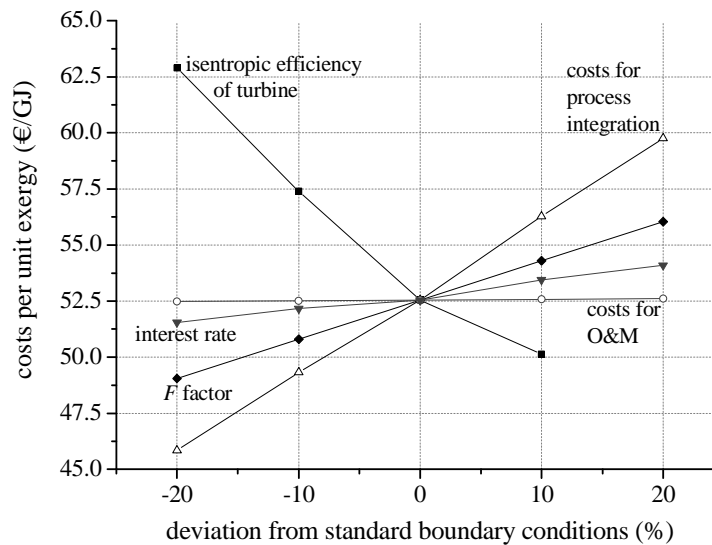


Figure 4: Cost per unit exergy as function of selected parameters for the working fluid isobutane

4. CONCLUSIONS

A thermo-economic case study for waste heat recovery by ORC is conducted. Cost-efficient design parameters concerning the temperature difference at the pinch point are identified in the case of pure working fluids and mixtures. In general, low minimum temperature differences in the evaporator and high values in the condenser are suitable for a cost-efficient ORC system. Isobutane as a working fluid leads to the most cost-effective ORC ($\Delta T_{PP,E} = 1.2$ K; $\Delta T_{PP,C} = 14$ K). Regarding the considered mixture isobutane/isopentane, a mole fraction of 90 % isobutane leads to the lowest costs per unit exergy. The economic parameters show a high sensitivity with respect to the estimated isentropic efficiency of the turbine and the costs for process integration. For further work, a variation of the heat source temperature and the heat exchanger design will be considered. In the context of a reliable estimation of the turbine efficiency, a detailed turbine model will be implemented in the analysis.

NOMENCLATURE

A	heat transfer area	(m^2)
c	costs per unit exergy	(€/GJ)
C	costs	(€)
\dot{C}	cost rate	(€/h)
e	specific exergy	(kJ/kg)
\dot{E}	exergy flow	(kW)
F	cost factor	(-)
h	specific enthalpy	(kJ/kg)
K	constant	(-)
\dot{m}	mass flow	(kg/s)
p	pressure	(bar)
P	power	(kW)
r	radius	(m)
s	specific entropy	(kJ/(kgK))
SIC	specific investment costs	(€/kW)
T	temperature	(°C)
U	overall heat transfer coeff.	(W/(m^2K))

Y	capacity/size parameter	(kW) or (m ²)
\dot{Z}	cost rate	(€/h)
a	heat transfer coefficient	(W/(m ² K))
ΔT	temperature difference	(K)
η	efficiency	(%)

Subscript

C	condenser	log	logarithmic
CI	capital investment	m	mean
CM	cooling medium	net	net
D	destruction	o	outer
E	evaporator	out	outlet
F	fuel	$O\&M$	operation and maintenance
G	generator		
HS	heat source	P	product
i	inner	PH	preheater
is	isentropic	PP	pinch point
II	second law	$Pump$	pump
K	k-th component	t	tube
L	loss	tot	total
$LMTD$	logarithmic mean temperature difference	0	reference state

REFERENCES

- Andreasen, J.G., Larsen, U., Knudsen, T., Pierobon, L., Haglind, F., 2014. Selection and optimization of pure and mixed working fluids for low grade heat utilization using organic rankine cycles. *Energy* 73, 204–213.
- Angelino, G., Colonna di Paliano, P., 1998. Multicomponent Working Fluids For Organic Rankine Cycles (ORCs). *Energy* 23, 449–463.
- Angelino, G., Colonna di Paliano, P., 2000. Air cooled siloxane bottoming cycle for molten carbonate fuel cells, *Proceedings of 2000 Fuel Cell Seminar*. Portland (USA).
- Astolfi, M., Romano, M.C., Bombarda, P., Macchi, E., 2014. Binary ORC (Organic Rankine Cycles) power plants for the exploitation of medium–low temperature geothermal sources – Part B: Techno-economic optimization. *Energy* 66, 435–446.
- Bejan, A., Tsatsaronis, G., Moran, M., 1996. *Thermal Design & Optimization*. John Wiley & Sons, New York.
- Bell, J., Ghaly, A., 1973. An approximate generalized design method for multicomponent/partial condensers. *AIChE Symp Ser. Heat Transf.* 69, 72–79.
- Borsukiewicz-Gozdur, A., Nowak, W., 2007. Comparative analysis of natural and synthetic refrigerants in application to low temperature Clausius-Rankine cycle. *Energy* 32, 344–352.
- Chen, H., Goswami, D.Y., Rahman, M.M., Stefanakos, E.K., 2011. A supercritical Rankine cycle using zeotropic mixture working fluids for the conversion of low-grade heat into power. *Energy* 36, 549–555.
- Demuth, O.J., 1981. Analyses of mixed hydrocarbon binary thermodynamic cycles for moderate temperature geothermal resources, *Proceedings of IECEC Conference*. Atlanta (USA).
- Dong, B., Xu, G., Cai, Y., Li, H., 2014. Analysis of zeotropic mixtures used in high-temperature Organic Rankine cycle. *Energy Convers. Manag.* 84, 253–260.
- Garg, P., Kumar, P., Srinivasan, K., Dutta, P., 2013. Evaluation of isopentane, R-245fa and their mixtures as working fluids for organic Rankine cycles. *Appl. Therm. Eng.* 51, 292–300.
- Heberle, F., Bassermann, P., Preissinger, M., Brüggemann, D., 2012a. Exergoeconomic optimization of an Organic Rankine Cycle for low-temperature geothermal heat sources. *Int. J. Thermodyn.* 15, 119–126.
- Heberle, F., Brüggemann, D., 2014. Thermo-economic Analysis of Hybrid Power Plant Concepts for Geothermal Combined Heat and Power Generation. *Energies* 7, 4482–4497.

- Heberle, F., Preißinger, M., Brüggemann, D., 2012b. Zeotropic mixtures as working fluids in Organic Rankine Cycles for low-enthalpy geothermal resources. *Renew. Energy* 37, 364–370.
- Imran, M., Park, B.S., Kim, H.J., Lee, D.H., Usman, M., Heo, M., 2014. Thermo-economic optimization of Regenerative Organic Rankine Cycle for waste heat recovery applications. *Energy Convers. Manag.* 87, 107–118.
- Iqbal, K.Z., Fish, L.W., Starling, K.E., 1976. Advantages of using mixtures as working fluids in geothermal binary cycles. *Proc. Okla. Acad. Sci.* 56, 110–113.
- Kern, D.Q., 1950. *Process Heat Transfer*. McGraw-Hill, New York.
- Lecompte, S., Ameel, B., Ziviani, D., Van Den Broek, M., De Paepe, M., 2014. Exergy analysis of zeotropic mixtures as working fluids in Organic Rankine Cycles. *Energy Convers. Manag.* 85, 727–739.
- Lemmon, E.W., Huber, M.L., McLinden, M.O., 2013. *NIST Standard Reference Database 23 – Version 9.1*. Physical and Chemical Properties Division. National Institute of Standards and Technology, Boulder, Colorado, US Department of Commerce, USA.
- Quoilin, S., Broek, M.V.D., Declaye, S., Dewallef, P., Lemort, V., 2013. Techno-economic survey of Organic Rankine Cycle (ORC) systems. *Renew. Sustain. Energy Rev.* 22, 168–186.
- Quoilin, S., Declaye, S., Tchanche, B.F., Lemort, V., 2011. Thermo-economic optimization of waste heat recovery Organic Rankine Cycles. *Appl. Therm. Eng.* 31, 2885–2893.
- Schlünder, E.U., 1983. Heat transfer in nucleate boiling of mixtures. *Int. Chem. Eng.* 23, 589–599.
- Shah, M.M., 1979. A general correlation for heat transfer during film condensation inside pipes. *Int. J. Heat Mass Transf.* 22, 547–556.
- Shah, R.K., Sekulic, D.P., 2003. *Heat Exchanger Design Procedures, in Fundamentals of Heat Exchanger Design*, John Wiley & Sons, Inc., Hoboken, NJ, USA
- Shu, G., Gao, Y., Tian, H., Wei, H., Liang, X., 2014. Study of mixtures based on hydrocarbons used in ORC (Organic Rankine Cycle) for engine waste heat recovery, *Energy* 74, 428–438.
- Sieder, E.N., Tate, G.E., 1936. Heat transfer and pressure drop of liquids in tubes. *Ind. Eng. Chem.* 28, 1429–1435.
- Silver, R.S., 1964. An approach to a general theory of surface condensers. *Proc. Inst. Mech. Eng. Part 1*, 179, 339–376.
- Steiner, D., 2006. *Wärmeübertragung beim Sieden gesättigter Flüssigkeiten. (Part H3.1), in: VDI Heat Atlas*. Springer Verlag, Berlin.
- Tchanche, B.F., Lambrinos, G., Frangoudakis, A., Papadakis, G., 2011. Low-grade heat conversion into power using organic Rankine cycles – A review of various applications. *Renew. Sustain. Energy Rev.* 15, 3963–3979.
- Tempesti, D., Fiaschi, D., 2013. Thermo-economic assessment of a micro CHP system fuelled by geothermal and solar energy. *Energy* 58, 45–51.
- Tsatsaronis, G., Winhold, M., 1985. Exergoeconomic analysis and evaluation of energy-conversion plants—I. A new general methodology. *Energy* 10, 69–80.
- Turton, R., Bailie, R.C., Whiting, W.B., 2003. *Analysis, synthesis and design of chemical processes*, 2nd edition. Prentice Hall, Old Tappan, NJ.
- VDI-Gesellschaft Verfahrenstechnik und Chemieingenieurwesen (GVC) (Ed.), 2010. *VDI Heat Atlas*. Springer Verlag, Berlin.
- Wang, X.D., Zhao, L., 2009. Analysis of zeotropic mixtures used in low-temperature solar Rankine cycles for power generation. *Sol. Energy* 83, 605–613.
- Weith, T., Heberle, F., Brüggemann, D., 2014. Performance of Siloxane Mixtures in a High-Temperature Organic Rankine Cycle Considering the Heat Transfer Characteristics during Evaporation. *Energies* 7, 5548–5565.
- Woudstra, N., van der Stelt, T.P., 2002. *Cycle-Tempo: a program for the thermodynamic analysis and optimization of systems for the production of electricity, heat and refrigeration*. Energy Technology Section, Delft University of Technology, The Netherlands.

ACKNOWLEDGEMENT

The work was funded by the Deutsche Forschungsgemeinschaft (DFG) with project No. BR 1713/12. The authors gratefully acknowledge this support.

TECHNO-ECONOMIC ANALYSIS OF THE SUB-CRITICAL ORC WITH OPTIMIZED HEAT TRANSFER PROCESS

Wei Liu^{1,*}, Dominik Meinel¹, Christoph Wieland¹ and Hartmut Spliethoff^{1,2}

¹Institute for Energy Systems, Faculty of Mechanical Engineering, Technische Universität München
Boltzmannstrasse 15, 85748
Garching, Germany

²The Bavarian Center for Applied Energy Research (ZAE Bayern), Division 1: Technology for
Energy Systems and Renewable Energy, Walther-Meissner-Str. 6, 85748
Garching, Germany
wei.liu@tum.de

* Corresponding Author

ABSTRACT

A techno-economic analysis of a sub-critical ORC designed for the utilization of geothermal heat is performed. The thermodynamic optimization of the investigated ORC system is based on a new approach, in which thermal match between the heat source and the working fluid is improved by operating an optimal working fluid at near-critical pressures. The Optimal Heat Source Temperature (OHST) method is used to identify suitable fluids for which the pinch point is located at the inlet (or an intermediate point) of the preheater. As a result, R227ea is selected, which performs best under certain defined conditions, while R245fa is also considered as a reference fluid for further thermo-economic comparison. A heat transfer model is proposed for the plate heat exchanger system in order to determine the pinch point position in the case of near-critical fluid parameters, as well as to obtain the heat transfer area which is required for the calculation of Purchased Equipment Cost (PEC). The economic optimization is based on the minimization of the Levelized Cost of Electricity (LCOE) for the considered fluids. Results from the techno-economic optimizations show that for R245fa the optimum is obtained with a system efficiency of 7.306% and a LCOE of 205.7 €/MWh. In comparison, the proposed approach for R227ea leads to an optimum with a system efficiency of 8.607% and a LCOE of 185.9 €/MWh. The comparison suggests that although the proposed approach aims to improve the thermodynamic performance of the sub-critical ORC, it is also promising in terms of the economic profitability.

1. INTRODUCTION

Interests on power generation from low temperature geothermal heat have grown rapidly in the past decades due to the increase in the electricity consumption worldwide. The Organic Rankine Cycle (ORC) system has been considered as one of the most suitable technologies for the exploitation of such heat source because of several advantages, such as simplicity and relatively high efficiency compared to the conventional water/steam Rankine cycle. However, a great limitation of improving the system efficiency of ORC is the isothermal evaporation which leads to a high exergy destruction in the heat transfer process. Several methods are available, aiming at a better thermal match between the heat source and the working fluid, such as using triangular ORC (Khennich and Galanis, 2012) or super-critical ORC to bypass the isothermal evaporation (Schuster *et al.*, 2010), or using fluid mixtures in order to obtain a non-isothermal evaporation (Heberle *et al.*, 2012). Although these techniques are effective under certain working conditions, the complexity of the ORC system or of the component is increased, causing higher manufacturing costs.

To reduce the exergy destruction caused by isothermal evaporation, an interesting approach is proposed in this paper, where a very high evaporation temperature is applied in order to reduce the absolute heat amount transferred during the evaporation process. The drawback of this approach is, however, obvious: the pinch point which is in most cases located at the evaporator inlet can greatly

limit the mass flow rate of the working fluid, leading to a reduced power output. To overcome this drawback, it is prerequisite for the proposed approach to find a suitable working fluid, for which the pinch point is located not at the evaporator inlet but the preheater inlet. As a result, the whole heat transfer process is optimized, leading to a better thermal match and hence a higher system efficiency (Liu *et al.*, 2014, 2015).

Although the proposed approach has been proven to be an effective method for improving the thermodynamic performance, its impact on the economic performance is still uncertain: the better thermal match in the preheating process does lead to a higher system performance; however, it requires a larger heat transfer area, which increases the purchase cost of the heat exchanger system. Therefore, the main task of the present paper is the thermo-economic investigation of the ORC which is optimized using the proposed approach for the geothermal power generation.

2. Modeling and Thermodynamic Description of Subcritical ORC

Figure 1(a) shows the considered subcritical ORC, which includes the most fundamental components: pump, preheater, evaporator, turbine and condenser. The working fluid at the saturated liquid state (state 1) is pressurized in the pump to a high pressure (state 2). Then it is led to the preheater where the sub-cooled fluid is heated until being liquidly saturated (state 3). Afterwards, the saturated liquid is evaporated under isothermal condition to the saturated vapor (state 4). The vapor then expands in the turbine, which rotates the shaft and generates electricity. At last, the loop is closed by condensing the super-heated vapor (state 5) to the saturated liquid (state 1).

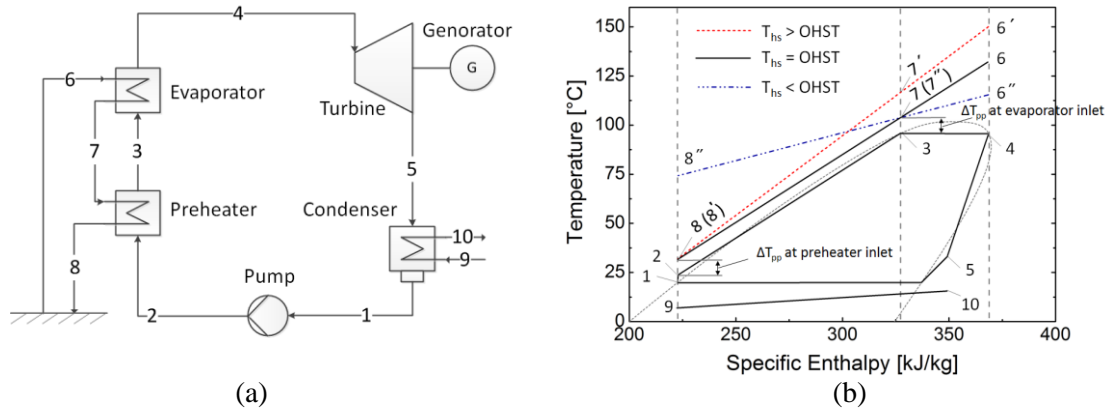


Figure 1: (a) Schematic diagram of a standard ORC, (b) Demonstration of OHST in T-h diagram

The static cycle simulation is performed in Matlab, using fluid properties from REFPROP 9.0 (Lemmon *et al.*, 2012). Simplifications are made that (1) there is no heat loss and no pressure drop through the cycle; (2) auxiliary power consumption, e.g. power required for circulating pump is neglected. The balance strategy is to vary the mass flow rate for the working fluid and the cooling water until the pinch point meets the design criteria in the heat exchanger and condenser, respectively. Unlike the common cycle simulations, the pinch point in the heat exchanger is considered as variable. Table 1 summarizes all boundary conditions for the cycle simulation.

Table 1: Boundary conditions for the investigated subcritical ORC.

Heat source temperature	T_{hs}	140 °C	Cooling water temperature	T_{cw}	8 °C
Heat source pressure	p_{hs}	10 bar	Cooling water pressure	p_{cw}	1 bar
Heat source thermal amount	\dot{Q}_{hs}	50 MW	Isentropic efficiency Turbine	$\eta_{is,turbine}$	0.85
Evaporating pressure	p_{evp}	< 30 bar	Isentropic efficiency Pump	$\eta_{is,pump}$	0.75
Pinch point in heat exchanger	$\Delta T_{pp,HE}$	Variable	Mechanical efficiency	η_{mech}	0.98
Condensation temperature	T_{cond}	20 °C	Generator/Motor efficiency	η_G/η_M	0.95
Pinch point in the condenser	ΔT_{cond}	5 K	Reference state	p_0, T_0	1 bar, 8 °C

Global system efficiency which combines both thermal efficiency η_{th} and heat transfer efficiency η_{HT} of the ORC system is used in this study for the evaluation of the thermodynamic performance. It is given by (Schuster *et al.*, 2010):

$$\eta_{sys} = \eta_{th} \cdot \eta_{HT} \quad (1)$$

Where η_{th} and η_{HT} are equal to:

$$\eta_{th} = \frac{P_{el,net}}{\dot{Q}_{HT}} = \frac{\eta_{mech} \cdot \eta_G \cdot (h_4 - h_5) - (h_2 - h_1)/\eta_{mech}/\eta_M}{h_4 - h_2} \quad (2)$$

$$\eta_{HT} = \frac{\dot{Q}_{HT}}{\dot{Q}_{hs}} = \frac{h_6 - h_8}{h_6 - h_0} \quad (3)$$

Where $P_{el,net}$ is the net power output [kW]; \dot{Q}_{HT} is the heat flow transferred from the heat source to the ORC unit [kW]; \dot{Q}_{hs} represents the available heat of the considered heat source [kW].

Therefore, to increase the thermal efficiency η_{th} of the investigated ORC system with a constant condensation temperature it is practical to increase the evaporating pressure p_4 . To increase the heat transfer efficiency η_{HT} , the heat source outlet temperature T_8 should be lowered as much as possible. More specifically, the maximum of η_{HT} can be observed when the pinch point is located at the preheater inlet.

3. Optimal Heat Source Temperature

The Optimal Heat Source Temperature (OHST) is defined as a heat source temperature, for which the pinch point is evenly located in the preheater (Liu *et al.* 2015). By comparing the OHST with the available heat source temperature, the pinch point position for the investigated ORC can be identified, which is demonstrated by figure 1(b). In the case where $T_{hs} < OHST$, the pinch point is located at the evaporator inlet (states 3-7(7'')). In the case where $T_{hs} > OHST$, however, the pinch point is shifted to the preheater inlet (states 2-8(8')). As the proposed approach requires a pinch point position at the preheater inlet, the working fluid selection should be based on a condition that the OHST is lower than the available heat source temperature.

Assuming a constant specific heat capacity for the homogeneous liquid, the OHST can be estimated as a state quantity depending only on the evaporating pressure (Liu *et al.*, 2015), provided that the pinch point and the condensation temperature are constant:

$$OHST = \frac{h_{evp}}{\bar{c}_{p,wf}} + T_{evp} + \Delta T_{pp,evp} \quad (4)$$

Where the mean specific heat capacity for the working fluid is calculated by:

$$\bar{c}_p = \frac{h_3 - h_2}{T_3 - T_2} \quad (5)$$

Where T_2 is assumed equal to the condensation temperature of the working fluid, since temperature changes only slightly for a homogenous liquid after compression.

The fluid screening is performed based on the OHST theory mentioned above. Firstly, 35 pure fluids with the critical temperatures between 90 and 160 °C are selected out of 121 fluids from the REFPROP database. Afterwards, the OHSTs are calculated for all the considered fluids using equation (4) and (5) given a constant pinch point of 10 K and the evaporating pressure of $0.9 \cdot p_c$, which are summarized in figure 2. It is noted that the constant pinch point is considered in this section only for the purpose of the screening of fluids. Next, taking into account the boundary conditions that $p_{evp} < 30$ bar and $OHST < T_{hs}$ (140 °C), the only fluid, i.e. R227ea which is located near the bottom left corner of figure 2 can be selected for the further cycle simulations. In addition, R245fa which has been widely used in the ORC industry is also selected as a reference fluid for comparison.

It should be noted that in the case of near-critical fluid parameters the pinch point can be located neither in the preheater inlet nor the evaporator inlet, since the heat capacity is strongly dependent on

the temperature. Figure 3(a) presents a possible scenario where the pinch point is located at an intermediate point of the preheater. In order to predict such pinch point position, it is necessary to partition the preheating process into finite number of elements assuming an equal amount of transferred heat, which is detailed in section 4.

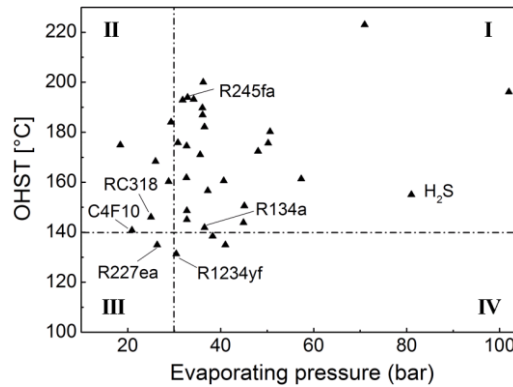


Figure 2: OHST versus evaporating pressure for the considered fluids.

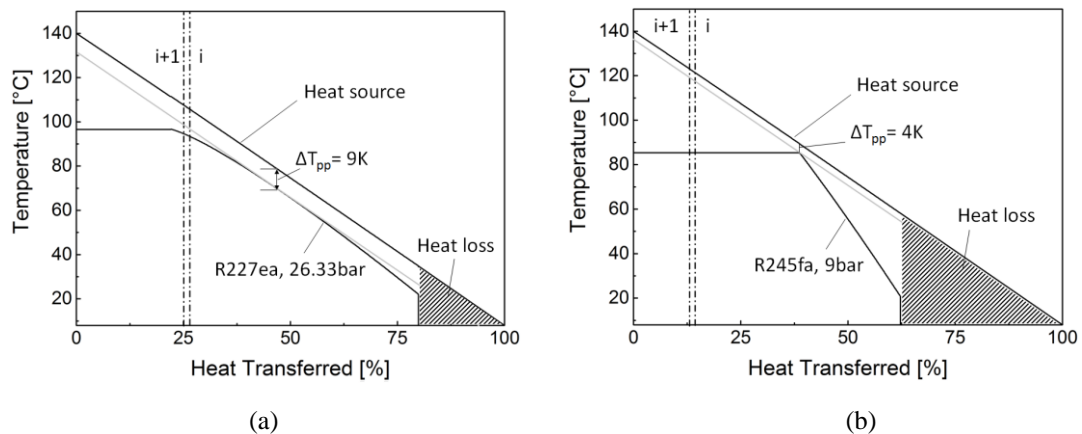


Figure 3: Demonstration of TQ-diagram and pinch point position for (a) R227ea and (b) R245fa, respectively.

4. Heat Transfer calculation

The main aims of the heat transfer calculations are 1) the determination of the pinch point location demonstrated similar to figure 3, and 2) the calculation of the heat transfer coefficient and the required surface area for a counter-flow plate heat exchanger system. The preheater and evaporator are considered as a whole in order to simplify the system components. Assumptions are made that the heat transfer process is stationary and both of the pressure drop and the fouling factor are negligible.

Based on the given geometric parameters of the plate (see table 2), the sizing of a Plate Heat Exchanger (PHE) system requires only few characteristics, i.e. plate arrangement, plates (channel) number and the channel spacing. Figure 4 demonstrates the plate arrangement of the considered PHE system, where plates are arranged into three blocks to form equal number of parallel channels. The channel spacing is set to 3.6 mm. The channel number for each fluid is related to the total required surface area.

Taking into account the temperature dependency of heat capacity, the assumption of an overall temperature difference between the hot and cold fluids cannot be acceptable for the investigated preheating process. For this reason, both of the preheating and evaporating processes are discretized respectively into a number of elements with equal amount of heat flow, as demonstrated in figure 3 and 4. For reduction of the calculation error, the number of elements N_{ele} is set to 500 (Karellas *et al.* 2012).

Table 2: Input parameters for plate.

Plate width	W	0.7 m
Plate height	H	2.31 m
Channel space	b	3.6 mm
Corrugation angle	β	60°
Plate thickness	d_{plate}	0.7 mm
Thermal conductivity	λ_{plate}	15 W/m·K

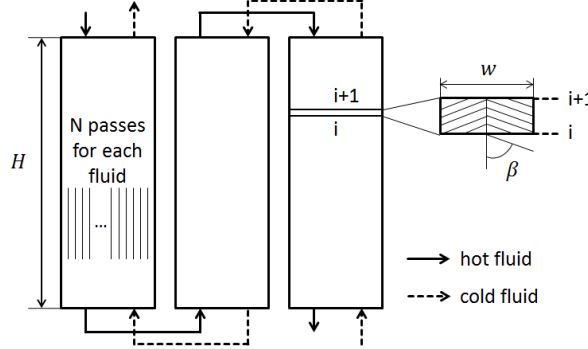


Figure 4: Schematic overview of the plate heat exchanger system.

Within each element, the transferred amount of heat flow is thus given by:

$$\dot{Q}_i = \frac{\dot{Q}_{HT}}{N_{ele}} = U_i \cdot A_i \cdot \Delta T_i \quad (6)$$

$$= \dot{m}_{hs,i} \cdot c_{p,hs,i} \cdot (T_{hs,i+1} - T_{hs,i}) = \dot{m}_{wf,i} \cdot c_{p,wf,i} \cdot (T_{wf,i+1} - T_{wf,i})$$

Where \dot{m}_i is equal to \dot{m}/N_{ch} [kg/s]; and ΔT_i is simplified for each element by assuming:

$$\Delta T_i = T_{hs,i} - T_{wf,i} \quad (7)$$

On this account, the pinch point can be obtained by:

$$\Delta T_{pp} = \min_{1 \leq i \leq N_{ele}} \Delta T_i \quad (8)$$

Assuming the convective heat transfer is dominant, the overall heat transfer coefficient is given by:

$$\frac{1}{U_i} = \frac{1}{h_{wf,i}} + \frac{d_{plate}}{\lambda_{plate}} + \frac{1}{h_{hs,i}} \quad (9)$$

To calculate the convective heat transfer coefficient at an arbitrary point i , it is necessary to obtain the Nusselt number which is defined as the ratio of convective to conductive heat transfer across the elementary boundary:

$$Nu_i = \frac{h_i \cdot D_h}{\lambda_i} \rightarrow h_i = \frac{Nu_i \cdot \lambda_i}{D_h} \quad (10)$$

Where λ_i is the thermal conductivity at point i [W/m²K]; D_h [m] is the hydraulic diameter which is equal to $2Wb/(W + b)$ referring to the investigated plate channel.

Depending on the type of the heat transfer process, the Nusselt numbers are calculated using various empiric correlations. For the single-phase heat transfer process, the Chisholm and Wanniarachchi (Chisholm and Wanniarachchi, 1990) correlation is employed where Nusselt number is given by:

$$Nu = 0.724 \cdot \left(\frac{6\beta}{\pi}\right)^{0.646} \cdot Re^{0.583} \cdot Pr^{0.33} \quad (11)$$

Where Pr is the dimensionless Prandtl number, given by $Pr = c_p \cdot \mu/\lambda$.

For the multi-phase heat transfer, the working fluid undergoes the liquid-gaseous phase transition. Specifically for the evaporating process, Nusselt number is calculated using Yan and Lin's correlation (Yan and Lin, 1999):

$$Nu = 1.926 \cdot Pr_l^{0.33} \cdot Bo_{eq}^{0.3} \cdot Re_{eq}^{0.5} \left[(1-x) + x \cdot \left(\frac{\rho_l}{\rho_v} \right)^{0.5} \right] \quad (12)$$

Where Bo_{eq} is the equivalent boiling number; Re_{eq} is the equivalent Reynold number; ρ_l is the density for saturated liquid [kg/m^3]; ρ_v is the density for saturated vapor [kg/m^3]; x is vapor fraction. It should be noted that for obtaining the continuous heat transfer coefficient the Nusselt number for the evaporative heat transfer is modified by multiplying equation (12) by a factor X_{Nu} given by:

$$X_{Nu} = \frac{Nu_{pre,i=N_{ele}}}{Nu_{evp,i=1}} \quad (13)$$

For the condensation process, Nusselt number is calculated using Yan's correlation (Yan *et al.*, 1999):

$$Nu = 4.118 \cdot Re_{eq}^{0.4} \cdot Pr_l^{0.33} \quad (14)$$

With the rated U_i and ΔT_i , the total heat transfer area A_{tot} can be given by:

$$A_{tot} = \sum_{i=1}^{N_{ele}} A_i \quad (15)$$

However, this calculated surface area must satisfy the input condition, i.e. the plate height of 2.31 m, which is achieved by varying the number of channels for each fluid until the objective error function (equation (16)) is minimized.

$$\Delta H(N_{ch}) = \frac{A_{tot}}{3 \cdot W} - H_{plate} \quad (16)$$

The total number of plates is thus given by:

$$N_{plate} = 3 \cdot (2 \cdot N_{ch} - 1) \quad (17)$$

5. Levelized Cost of Electricity

The economic performance of the considered geothermal ORC system is evaluated by means of the Levelized Cost of Electricity (LCOE) method. Based on the Net Present Value (NPV) method, LCOE is given by (Konstantin, 2013):

$$LCOE = \frac{I_0 + \sum_{t=1}^{t=n} \frac{A_t + I_t}{(1+r)^t}}{\sum_{t=1}^{t=n} \frac{W_{el}}{(1+r)^t}} \quad (18)$$

Where I_0 is the initial investment cost [€]; A_t is the expenditures for Operation & Maintenance (O&M) in the year t [€]; I_t is the investment costs for replacement of equipment in the year t [€]; W_{el} is the Electricity generation in the year t [MWh]; r is the annual discount rate [%]; n is the lifetime of the project in years [a].

Factors accounting for the initial investment cost I_0 are manifold, such as the costs for drilling, purchasing equipment, and other expenses such as site preparation, instrumentation, control, insurance, etc. For a drilling depth of 3.5 km, the drilling cost is estimated to about 21 Mio. € using the correlations from (Schlagermann, 2014). The Purchased Equipment Cost (PEC) related to the component parameters is described in detail see section 5.1. The other expenses for the initial investment are mainly dependent on the drilling process, which approximately accounts for 40% of the total drilling cost (Schlagermann, 2014).

Apart from the initial investment costs in equation (18), the annual expenditures for O&M are estimated to be about $0.03 \cdot I_0$ based on the proposed correlations (Schlagermann, 2014). The investment costs caused by the replacement of system components depend on the lifetime of each component (see table 3). The annual electricity generation is calculated with the consideration of 8000

full-load hours. The annual discount rate is set to 8%. Finally, the lifetime of the project is considered to be 25 years.

It is noted that the correlations used for the economic evaluation are based on an existing geothermal ORC plant in Germany. For more details, the reader is referred to Schlagermann (2014).

Table 3: Constants in equation (19), bare module factors and lifetimes for different system components (Turton *et al.*, 2013) (Schlagermann, 2014)

Equipment	K_1	K_2	K_3	F_B	Lifetime
Pump	3.3892	0.0536	0.1538	4.05	10
Preheater + Evaporator	4.6656	-0.1557	0.1547	3.86	10
Turbine	2.6259	1.4398	-0.1776	6.10	25
Condenser	4.6656	-0.1557	0.1547	3.86	10

5.1 Purchased Equipment Cost (PEC)

The PEC for each component of the ORC system is calculated using the empirical correlations based on a number of industrial data (Turton *et al.*, 2013), which is given by:

$$\log_{10} PEC_0 = K_1 + K_2 \cdot \log_{10} X + K_3 \cdot (\log_{10} X)^2 \quad (19)$$

Where K_1 , K_2 , K_3 are constants depending on the system component (see table 3) and X is the size or capacity for the corresponding component. The calculated PEC_0 is converted into Euro with the average exchange rate of 1.2 for the recent years.

The multiplication factor F_B is used to account for the indirect costs and the use of specific materials (Turton *et al.*, 2013). Therefore, the modified PEC is given by:

$$PEC = PEC_0 \cdot F_B \quad (20)$$

Where F_B is listed in table 3 for each of the system equipment.

The Chemical Engineering Plant Cost Index (CEPCI) is used to evaluate the cost deviation due to inflation. The PEC calculated using equation (20) is based on the CEPCI value of 382 for the year of 1996 (Turton *et al.*, 2013). In the present economic analysis, the updated value of 578.1 for the year of 2014 is employed.

6. Results

The main aim of the thermo-economic optimization is to obtain the minimum of LCOE for the considered two fluids, i.e. the selected R227ea and the reference fluid R245fa.

For R227ea with a constant evaporating pressure in the investigated ORC system, the influence of the pinch point (depicted in figure 3(a)) on the ORC system performance is threefold. Firstly, according to equation (4), increasing the pinch point temperature results in a higher OHST value, which can change the pinch point position to the evaporator inlet in the case of $OHST > T_{hs}$. In order to avoid such changes, the pinch point value is limited up to 15 K for which the OHST is equal to 139.93 °C. Secondly, increasing the pinch point temperature corresponds to a worse thermal match between the thermal water and the working fluid, which reduces the system efficiency. Such influence is illustrated in figure 5 where the global system efficiency for R227ea decreases monotonically with the increase of the pinch point value. Thirdly, the benefit of increasing the pinch point is that it requires a smaller heat transfer area, leading to a lower PEC value particularly for the preheater and the evaporator. Particularly for R227ea, it can be seen from figure 5 that the total PEC for the preheater and the evaporator decreases significantly with the increase of the pinch point value. A small decrease in the other costs mainly referring to the instrumentation & controlling is also observed for a higher pinch point value. The PEC for condenser, turbine and pump are relatively less affected by varying the pinch point. Conclusively, it is reasonable to consider the pinch point in the heat exchanger as the optimization parameter for R227ea.

It is necessary to note that due to the consideration of the constant condensation temperature the variation of the pinch point for the condenser affects only the condenser size but not the power output. Therefore, its influence on the LCOE is relatively limited so that it is not considered in the present techno-economic optimization.

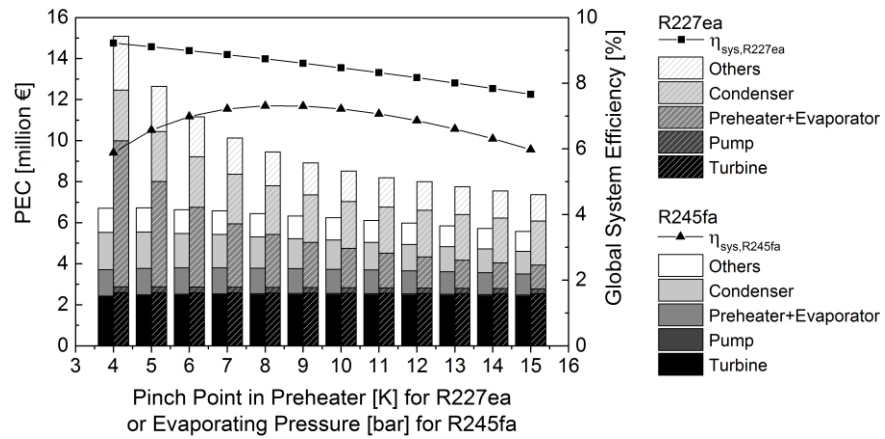


Figure 5: PEC and system efficiency as functions of $\Delta T_{pp, evp}$ and p_{evp} for R227ea and R245fa, respectively.

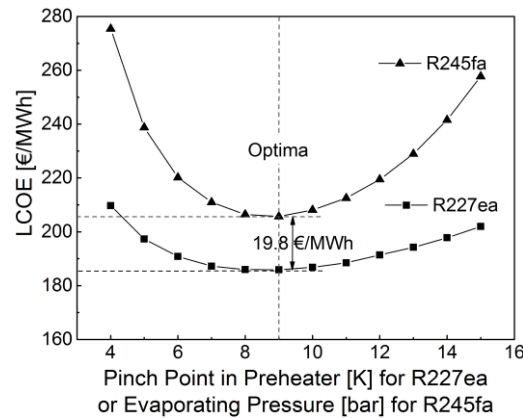


Figure 6: LCOE as functions of $\Delta T_{pp, evp}$ and p_{evp} for R227ea and R245fa, respectively.

Figure 6 shows the resulting LCOE with the variation of pinch point. For R227ea, the minimum of LCOE is observed around 185.9 €/MWh for the pinch point of 9 K. In order for such minimum to make sense, it is required to compare it to the optimum LCOE for some other fluid, e.g. the reference fluid R245fa. The optimization parameter for R245fa, however, is different from that for R227ea. According to equation (4), the OHST for R245fa is significantly higher than the available heat source temperature, indicating that the pinch point is located at the evaporator inlet (see figure 3(b)). In such case to obtain the minimum LCOE, the evaporating pressure is chosen as the optimization parameter (Quoilin *et al.*, 2011). In contrast to R227ea, the pinch point in the preheater is fixed at 4 K for R245fa. In figure 5, the PEC and global system efficiency for R245fa are shown as a function of evaporating pressure, where a maximum global system efficiency can be observed. The LCOE for R245fa is given in figure 6 as a function of evaporating pressure, where a minimum is observed for the evaporating pressure of 9 bar.

For further comparisons, the T-Q diagrams for the optimized R227ea and R245fa are given, illustrating their heat transfer processes, respectively. In addition, table 4 summarizes the parameters resulting from the thermo-economic optimizations for both working fluids. Although the use of R227ea requires higher PEC, more electricity can be produced annually, which leads to reduce the LCOE by 9.63%.

Table 4: Results from the thermo-economic optimizations for R227ea and R245fa

Fluid	Thermodynamic						Economic	
	T_{evp} [°C]	p_{evp} [bar]	$T_{pp, evp}$ [K]	η_{sys} [%]	η_{HT} [%]	W_{el} [MWh]	PEC [m. €]	LCOE [€/MWh]
R227ea	96.60	26.33	9.000	8.607	79.47	29006	8.739	185.9
R245fa	85.33	9	4.000	7.306	63.51	23762	7.306	205.7

7. Conclusions

In the present paper, a new approach for the heat transfer optimization has been developed and thermo-economically investigated for a sub-critical ORC designed for geothermal power generation. The working fluid considered is R227ea, for which the pinch point is not located at the evaporator inlet for the available heat source temperature. A detailed heat transfer model is proposed, aiming at the precise determination of the pinch point position and the calculation of the required heat transfer area. Compared to common works, the optimization parameter considered for R227ea is not the evaporating pressure but the pinch point for the heat transfer process. The results show that the pinch point in the preheater has a great influence on both of the system efficiency and the PEC. An optimum pinch point value is obtained for R227ea, corresponding to a global system efficiency of 8.607% and a minimum LCOE of 185.9 €/MWh. Compared to the optimization results for R245fa, an increase of system efficiency of 17.81% and a reduction of LCOE of 9.63% are observed.

In general, the proposed approach leading to both higher system efficiency and economic profitability seems promising. However, further challenges remain. The numerical results should be compared with the experimental results in the near future. In addition, it is necessary to further include pressure drops through the ORC loops and to investigate their influences on the heat transfer mechanism particularly for the working fluid at the near-critical states.

NOMENCLATURE

A	Surface area or annual cost	(m ² or €)
b	Channel space	(mm)
c_p	Specific heat capacity	(kJ/kg·K)
d	Plate thickness	(mm)
D_h	Hydraulic diameter	(m)
e	Specific exergy flow	(kJ/kg)
F_B	Multiplication factor for PEC	(-)
h	Specific enthalpy	(kJ/kg)
h	Convective heat transfer	(W/kg·m ²)
H	Plate height	(m)
I	Investment cost	(€)
K	Constants for PEC	(-)
m.	million	(€)
\dot{m}	Mass flow rate	(kg/s)
n	Lifetime of project	(a)
Nu	Nusselt number	(-)
p	Pressure	(bar)
P	Power	(kW or MW)
Pr	Prandtl number	(-)
\dot{Q}	Heat flow	(kW)
r	Annual discount rate	(%)
Re	Reynold number	(-)
t	Operation year	(-)
T	Temperature	(°C)
U	Overall heat transfer coeff.	(W/kg·m ²)
W	Plate width	(m)
W	Electricity generation	(MW)
x	Vapor fraction	(-)
X	Size or capacity	(m ² or kW)
β	Corrugation angle	(°)
η	Efficiency	(%)
λ	Thermal conductivity	(W/m·K)

μ	Viscosity	(kg/s·m)
ρ	Density	(kg/m ³)

Subscript

0,1,2, ... 10	Reference or working states	<i>pre</i>	Preheater
<i>el</i>	Electricity	<i>sys</i>	System
<i>ele</i>	Element	<i>th</i>	Thermal
<i>eq</i>	Equivalent	<i>tot</i>	Total
<i>evp</i>	Evaporation	<i>v</i>	Saturated vapor
<i>G</i>	Generator	<i>wf</i>	Working fluid
<i>hs</i>	Heat source	Acronyms	
<i>HT</i>	Heat transferred	<i>LCOE</i>	Levelized Cost of Electricity
<i>l</i>	Saturated liquid	<i>ORC</i>	Organic Rankine Cycle
<i>mech</i>	Mechanical	<i>OHST</i>	Optimal Heat source temperature
<i>M</i>	Motor	<i>PEC</i>	Purchased Equipment Cost
<i>pp</i>	Pinch point	<i>PHE</i>	Plate Heat Exchanger

REFERENCES

- Chisholm, D., Wanniarachchi, A.S., Plate heat exchangers: plate selection and arrangement, *AICHE Meeting*, 18-22.
- Heberle, F., Preißinger, M., Brüggemann, D., 2012, Zeotropic mixtures as working fluids in Organic Rankine Cycles for low-enthalpy geothermal resources, *Renewable Energy*, vol. 37, no. 1, p. 364–370.
- Karellas, S., Schuster, A., Leontaritis, A., 2012, Influence of supercritical ORC parameters on plate heat exchanger design, *Applied Thermal Engineering*, vol. 33-34, p. 70–76.
- Khennich, M., Galanis, N., 2012, Optimal Design of ORC Systems with a Low-Temperature Heat Source, *Entropy*, vol. 14, no. 12, p. 370–389.
- Konstantin, P., 2013, *Praxisbuch Energiewirtschaft. Energieumwandlung, -transport und -beschaffung im liberalisierten Markt*, Springer Vieweg, Berlin, 474.
- Lemmon E.W., Huber, M.L., Nist reference fluid thermodynamic and transport properties-refprop, NIST standard reference database 23-Version 9.0.
- Liu, W., Meinel, D., Wieland, C., Spliethoff, H., 2014: Investigation of hydrofluoroolefins as potential working fluids in organic Rankine cycle for geothermal power generation, *Energy*, vol. 67, p. 106-116.
- Liu, W., Meinel, D., Wieland, C., Spliethoff, H., 2015: Optimal Heat Source Temperature for Optimization of the Organic Rankine Cycle (ORC) process. Submitted In *Energy* 2015.
- Quoilin, S., Declaye, S., Tchanche, B.F., Lemort, V., 2011, Thermo-economic optimization of waste heat recovery Organic Rankine Cycles, *Applied Thermal Engineering*, vol. 31, p. 2885–2893.
- Schlagermann, P., 2014, *Exergoökonomische Analyse geothermischer Strombereitstellung am Beispiel des Oberrheingrabens*, Dr. Hut, Munich, 168.
- Schuster, A., Karellas, S., Aumann, R., 2010, Efficiency optimization potential in supercritical Organic Rankine Cycles, *Energy*, vol. 35, no. 2, p. 1033–1039.
- Turton, R., Bailie, R.C., Whiting, W.B., Shaeiwitz, J.A., Bhattacharyya, D., 2013, *Analysis, Synthesis, and Design of Chemical Processes*, Pearson, NY, 965.
- Yan, Y.Y., Lin, T. F., 1999, Evaporation Heat Transfer and Pressure Drop of Refrigerant R-134a in a Plate Heat Exchanger, *Journal of Heat Transfer*, vol. 121, p. 118–127.
- Yan, Y.Y., Lio, H.C., Lin, T.F., 1999, Condensation heat transfer and pressure drop of refrigerant R-134a in a plate heat exchanger, *International Journal of Heat and Mass Transfer*, vol. 42, no. 6, p. 993–1006.

INFLUENCE OF THE HEAT-SOURCE COST ON GEOTHERMAL ORCS

Daniël Walraven^{1,3}, Ben Laenen^{2,3}, William D'haeseleer^{1,3*}

¹ University of Leuven (KU Leuven) Energy Institute,
TME Branch (Applied Mechanics and Energy Conversion)
Celestijnenlaan 300 Box 2421, B-3001 Leuven, Belgium
daniel.walraven@kuleuven.be, william.dhaeseleer@kuleuven.be

² Flemish Institute for Technological Research (VITO),
Boeretang 200, B-2400 Mol, Belgium
ben.laenen@vito.be

³ EnergyVille (Joint Venture of VITO and KU Leuven),
Dennenstraat 7, B-3600 Genk, Belgium

* Corresponding Author

ABSTRACT

The influence of the cost of the heat source on the performance and configuration of the economically optimal ORC is investigated in this work. This optimal ORC is obtained by performing a system optimization, in which the most important components (heat exchangers, cooling system and turbine) are optimized together with the configuration of the cycle. Minimization of the LCOE (Levelized Cost of Electricity) is chosen as the objective function.

As a result, the LCOE for both water and air-cooled ORCs is given as a function of the heat-source cost and heat-source-wellhead temperature. With these data, an estimation of the LCOE of a geothermal project can be made, based on the depth of the wells and the expected wellhead temperature. By comparing the obtained LCOE with expected electricity prices, the profitability of the project can be estimated.

1. INTRODUCTION

Low-temperature geothermal heat sources are widely available (Tester et al., 2006; IEA, 2011), but the heat-to-electricity conversion efficiency is very low due to the low temperature of the heat source. In many regions in the world, the geothermal heat sources do not manifest at the surface, but drilling of wells is necessary. These wells are often very expensive due to the relative high drilling depth.

In this paper, the combined influence of the drilling costs of the heat source and the temperature of the heat source is investigated. Contour maps of the LCOE (Levelized Cost of Electricity) of economically optimal ORCs are calculated as a function of these two parameters. This LCOE is the fixed electricity price needed to obtain break even at the end of the project. Also the influence of these parameters on the design and performance of the power plants is investigated.

A system optimization is performed, so that the configuration of the main components (heat exchangers, turbine and cooling system) are optimized together with the configuration of the cycle itself. The results in this paper are calculated with a previously developed code and the details of the modeling can be found in Walraven et al. (2015b).

2. MODEL

2.1 ORC

Organic Rankine cycles (ORCs) with different configurations (recuperated, subcritical or transcritical) are modeled in this paper, of which the scheme is given in figure 1. All the possible heat exchangers (economizer, evaporator, superheater and recuperator) are shown, but they are not always necessary. Air-cooled condensers (ACC) or wet cooling towers (WCT) connected to a condenser, and if necessary a desuperheater, can be used for cooling.

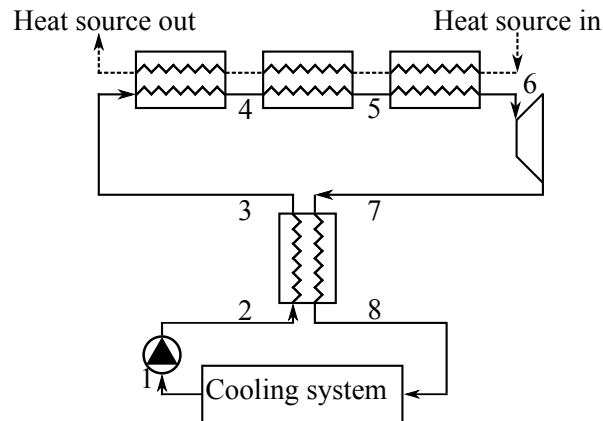


Figure 1: Scheme of a single-pressure, recuperated ORC.

It is assumed that state 1 is saturated liquid and that the isentropic efficiency of the pump is 80%. More information about the modeling of the cycle can be found in Walraven et al. (2013). An axial-inflow, axial-outflow turbine is modeled, based on the results of Macchi and Perdichizzi (1981).

2.2 Shell-and-tube heat exchangers

Figure 2 shows a TEMA E shell-and-tube heat exchanger with its basic geometrical characteristics, which is the only type of heat exchanger used in this paper. The geometrical characteristics are the shell outside diameter D_s , the outside diameter of a tube d_o , the pitch between the tubes p_t , the baffle cut length l_c and the baffle spacing at the inlet $L_{b,i}$, outlet $L_{b,o}$ and the center $L_{b,c}$. More information about the modeling of the heat exchangers can be found in Walraven et al. (2014).

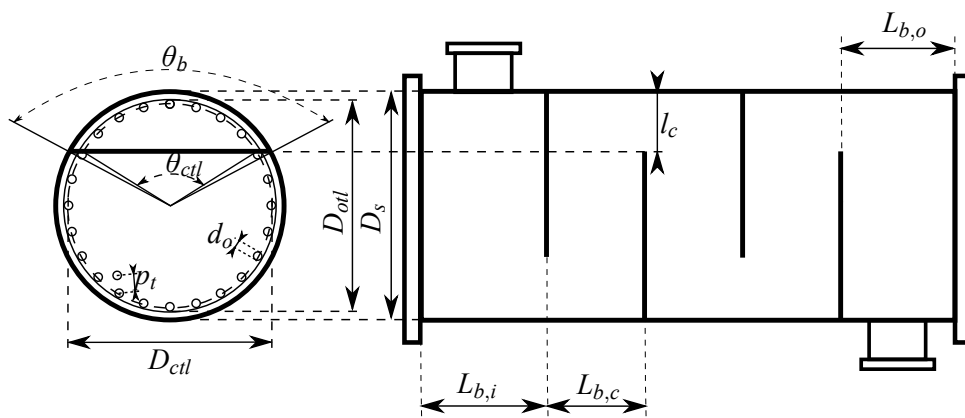


Figure 2: Shell-and-tube geometrical characteristics. Figure adapted from Shah and Sekulić (2003). See also Walraven et al. (2014).

2.3 Cooling system

Figure 3 shows the geometry of the air-cooled condenser (ACC) modeled in this paper. The tube-bundle geometry is determined by the tubes' small width W_s , the fin height H , the fin pitch S , the tubes' large width W_l and the length of the tubes L_t . In an A-frame ACC the tube bundles are placed at an angle θ with the horizontal. More information about the modeling can be found in Walraven et al. (2015a).

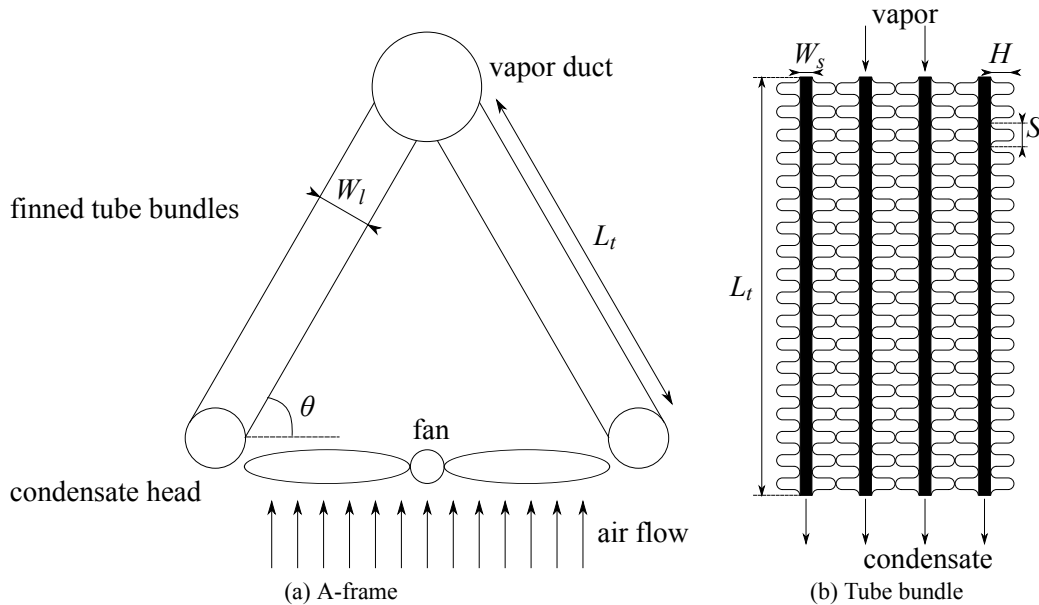


Figure 3: Geometry of an A-frame air-cooled condenser (a) and the bundle geometry of flat tubes with corrugated fins (b).

Another cooling option is the use of a wet cooling tower (WCT) connected to a condenser and, if necessary, a desuperheater. A mechanical-draft wet cooling tower is shown in figure 4. The height of the inlet H_i , the height of the fill H_{fi} , the height of the spray zone H_{sp} and the width of the tower W_t are shown in the figure. The reader is referred to Walraven et al. (2015b) for more information.

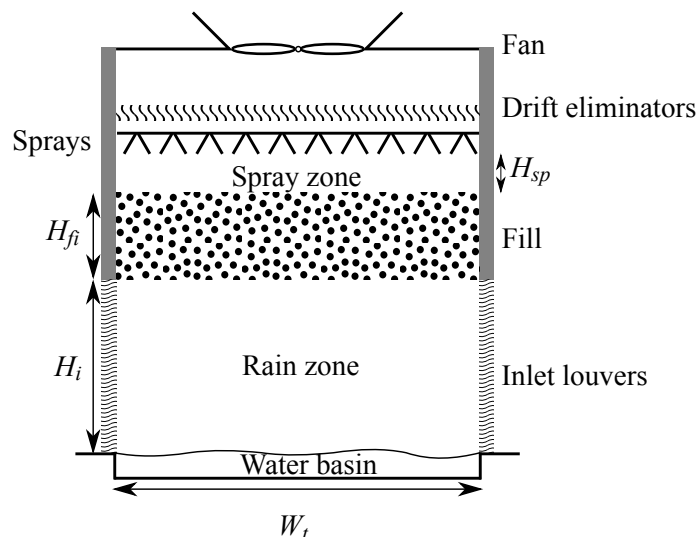


Figure 4: Geometry of an induced mechanical-draft wet cooling tower. Figure adapted from Kloppers (2003).

3. OPTIMIZATION

A *system* optimization is performed by optimizing the cycle parameters and the configuration of all the components together. The software packages CasADi (Andersson et al., 2012) and WORHP (Büskens and Wassel, 2013) are used for the optimization. The models themselves are developed in Python and the fluid properties are obtained from REFPROP (Lemmon et al., 2007).

3.1 Objective function

The objective of the optimization is to minimize the levelized cost of electricity (LCOE). This LCOE is the constant electricity price needed during the lifetime of the power plant to reach break even over the lifetime of the project. The LCOE is calculated in €/MWh_e as (D'haeseleer, 2013)

$$\text{LCOE} = \frac{C_{EPC} + \sum_{t=1}^{t_{LT}} [(C_{O\&M,t} + C_{water,t}) (1+i)^{-t}]}{\sum_{t=1}^{t_{LT}} \dot{W}_{net} N (1+i)^{-t}}, \quad (1)$$

with C_{EPC} the engineering, procurement & construction overnight cost (EPC) of the installation, t_{LT} the lifetime of the installation, $C_{O\&M,t}$ the operations and maintenance cost in year t which is assumed to be 2.5% of the investment cost of the ORC per year (IEA, 2011), $C_{water,t}$ the water cost in year t , \dot{W}_{net} the net electric power output, which takes an electric generator efficiency of 98% into account, expressed in MW_e, N the number of full-load hours per year (an availability of 95% is assumed) and i the discount rate. The EPC cost consists of two parts: the cost of the drilling $C_{drilling}$ and the cost of the ORC C_{ORC} . More information about the cost of the ORC can be found in Walraven et al. (2015b).

3.2 Optimization variables

The optimization variables of a single-pressure, recuperated cycle are the temperature before the turbine, the saturation temperature at the pressure before the turbine, the pressure at the inlet of the pump, the mass flow of the working fluid and the effectiveness of the recuperator (Walraven et al., 2013).

The optimization variables of each shell-and-tube heat exchanger are the shell diameter D_s , tube-outside diameter d_o , tube pitch p_t , baffle cut l_c and the distance between the baffles $L_{b,c}$ (Walraven et al., 2014).

The fin height H , the fin pitch S , the air velocity at the minimum cross section V_{Amin} and the number of tubes n_{tubes} are the optimization variables of the ACC and a non-linear constraint is used to limit the length of the tubes, as done in Walraven et al. (2015a).

The tower width W_t , the inlet height H_i , the relative mass flow of air $\dot{m}_{air}/\dot{m}_{brine}$, the relative cooling-fluid mass flow $\dot{m}_{cf}/\dot{m}_{brine}$ and the minimum cooling-fluid temperature T_{cf}^{min} are the optimization variables of the WCT, as explained in Walraven et al. (2015b).

4. RESULTS AND DISCUSSION

4.1 Reference parameters

The parameters of our "reference" case are given in Table 1, which are based on a proposed geothermal demonstration project in Belgium. In the next subsections, the influence of the well costs and the brine-wellhead temperature on the performance of the ORC is investigated. For each of the parameter variations, a new design optimization is performed with the optimization variables described in Section 3.2 to obtain the minimum LCOE.

4.2 LCOE

In this subsection, the optimal LCOE is given as a function of the brine-inlet temperature and the cost of the wells. They are varied between 100° - 150°C and between 0 - 50 M€, respectively.

Figure 5a shows the LCOE for air-cooled ORCs. As expected, does the LCOE increase for an increasing cost of the wells and a decreasing heat-source-inlet temperature. For the current electricity price of about

Table 1: Parameters of the reference case

Well parameters		Economic parameters	
Brine-wellhead temperature	125°C	Lifetime plant	30 years
Brine production	194 kg/s	Discount rate	4 %/year
Well-pumps consumption	600 kW _e	Water price	0.5 €/m ³
Wells cost	27.5 M€		

Environmental conditions	
Dry-bulb temperature	10.3°C
Wet-bulb temperature	8.6°C
Air pressure	1016 hPa

50 €/MWh_e, only a small part of the investigated temperature-cost range is economically interesting for the investigated reference parameters (Table 1). This "profitable" area is hatched in figure 5. For low heat-source-inlet temperatures, the distance between the LCOE contour lines as a function of the cost of the wells is very low. This is due to the low efficiency of the optimal ORCs for low temperatures.

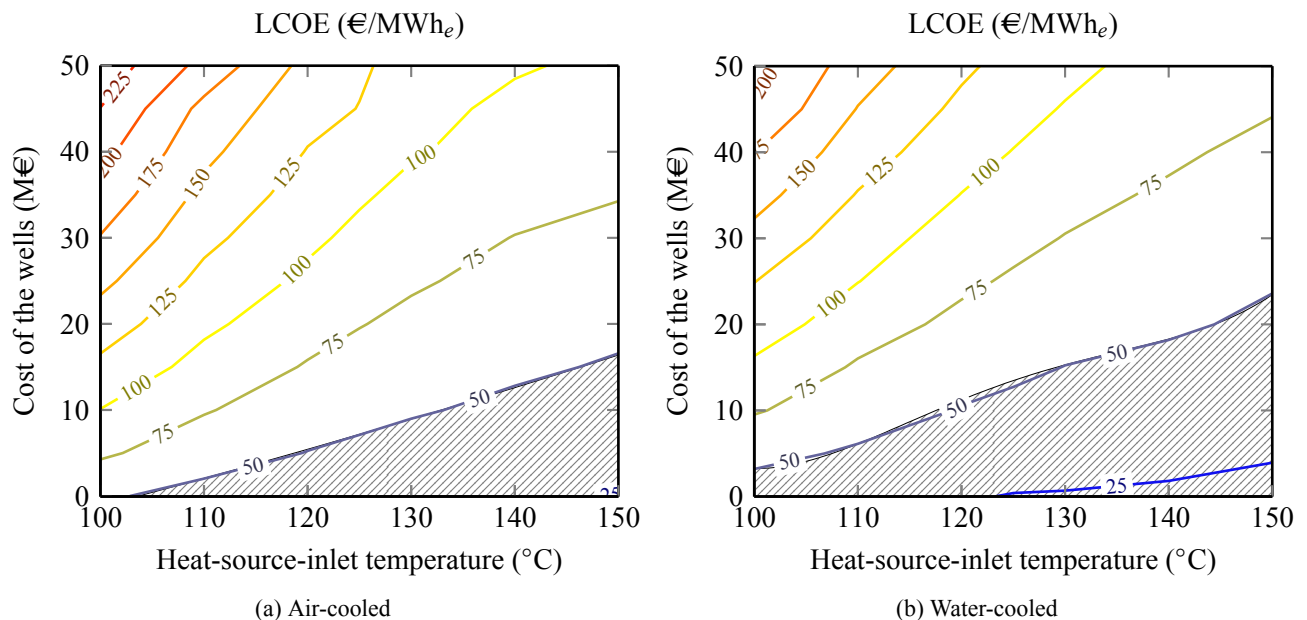


Figure 5: LCOE for air-cooled ORCs (a) and water-cooled ORCs (b) as a function of the heat-source-inlet temperature and the cost of the wells. The hatched area shows the region where the LCOE is lower than the assumed current electricity price of 50 €/MWh_e.

Figure 5b shows the LCOE for water-cooled ORCs. Comparison with Figure 5a shows that the LCOE for water-cooled ORCs is lower than the one for air-cooled ORCs, for the same heat-source-inlet temperature and cost of the wells. So, for the chosen reference parameters, it is better to select water cooling than air cooling.

4.3 Net power output and cost ORC

Figures 6a and 6b give contour lines of the net power output of air and water-cooled ORCs, respectively, as a function of the heat-source-inlet temperature and the cost of the wells. The net power output increases with increasing temperature and with increasing cost of the wells. The former evolution is the consequence of the increasing cycle efficiency with increasing temperature (Carnot). The latter evolution

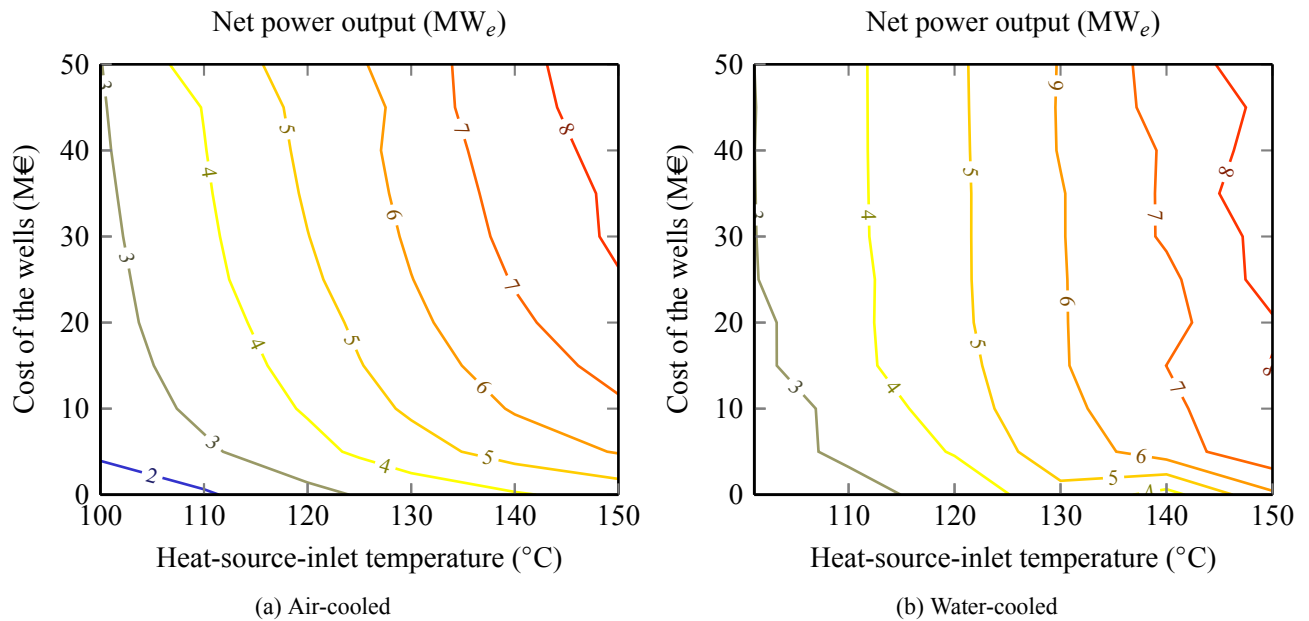


Figure 6: Net power output for air-cooled ORCs (a) and water-cooled ORCs (b) as a function of the heat-source-inlet temperature and the cost of the wells.

is harder to explain. When the cost of the wells $C_{drilling}$ increases, the numerator in equation (1) increases. For an unchanged plant configuration, the LCOE would increase too. The only way to counteract this increase, is by trying to improve the net electric power of the cycle (denominator in equation (1)). This increase of the cycle efficiency can typically be done by decreasing the pinch-point-temperature differences and decreasing the condenser temperature. The consequence of these adaptations is of course that the cost of the ORC C_{ORC} will increase too. For higher well costs, a new optimum is found: the ORC generates more electric power, but also costs more.

Table 2 gives some results of the optimal configurations obtained for air-cooled ORCs at a wellhead temperature of 125°C and for different well costs. From this data, it is clearly seen that the cycle efficiency increases from 7 to almost 10% when the well costs increase from 0 to 50 M€. This is a consequence of the decreasing pinch-point-temperature difference (8 to 4°C) and the decreasing condenser temperature (42 to 28°C).

Well cost (M€)	0	10	30	50
Energetic cycle efficiency (%)	7.3	8.4	9.4	9.6
Pinch-point-temperature-difference in evaporator ($^{\circ}$)	7.6	4.7	3.8	3.7
Condenser temperature ($^{\circ}$)	41.7	34.4	28.7	27.7
Net electric power output (MW_e)	3.1	4.6	5.7	5.9
Brine-outlet temperature ($^{\circ}\text{C}$)	73.3	57.3	49.8	48.9
Exergetic plant efficiency (%)	20.6	31.1	38.4	39.5
Cost ORC (M€)	10.2	17.0	26.0	28.2
Specific cost ORC ($\text{€}/\text{kW}_e$)	3326	3668	4539	4773
Total project cost (M€)	10.2	27.0	66.0	78.2
Specific cost total project ($\text{€}/\text{kW}_e$)	3326	5820	11 521	13 243
Cost ORC/total project cost (%)	100.0	63.0	39.4	36.0
LCOE ($\text{€}/\text{MWh}_e$)	32.2	56.4	94.4	128.3

Table 2: Data of the optimal configurations obtained at different well costs at a temperature of 125°C for ORCs with an ACC.

The relative increase of the net electric power output is larger than the relative increase of the cycle efficiency, because the brine-outlet temperature decreases too with increasing well costs. This is again a consequence of decreasing pinch-point-temperature differences and decreasing condenser temperature, but also because of a decrease in the turbine-inlet temperature.

The consequence of the decreasing pinches and condenser temperature and the increased heat input to the cycle is that the heat exchangers become larger and more expensive. The cost of the ORC increases from 10 to 28 M€ for well costs ranging from 0 to 50 M€, or an increasing cost of the ORC with almost 200%. At the other hand does the specific cost of the ORC "only" increase with 44%.

At the other hand, does the fraction of the cost of the ORC to the total cost of the plant decrease strongly (100-36%) for the investigated increase in the well costs, which is in fact the main reason why the a more efficient and expensive ORC is optimal for higher well costs. As shown by the values of the LCOE in table 2, is the increase in the LCOE also very high due too this increase of the well costs. The increased net electric power output does not manage to compensate for this increased cost to keep the LCOE constant (equation (1)).

Going back to figure 6, it is seen that water-cooled ORCs generate more net electricity than air-cooled ORCs, but the difference is not high enough to explain the large difference in LCOE (Figure 5). This is explained by the difference in cost between the two. Figures 7a and 7b show the contour plot of the costs of the ORC. The difference in cost is a factor of two or more, in favor of the water-cooled ORCs. This is due to the very large cost of an ACC in comparison with a WCT.

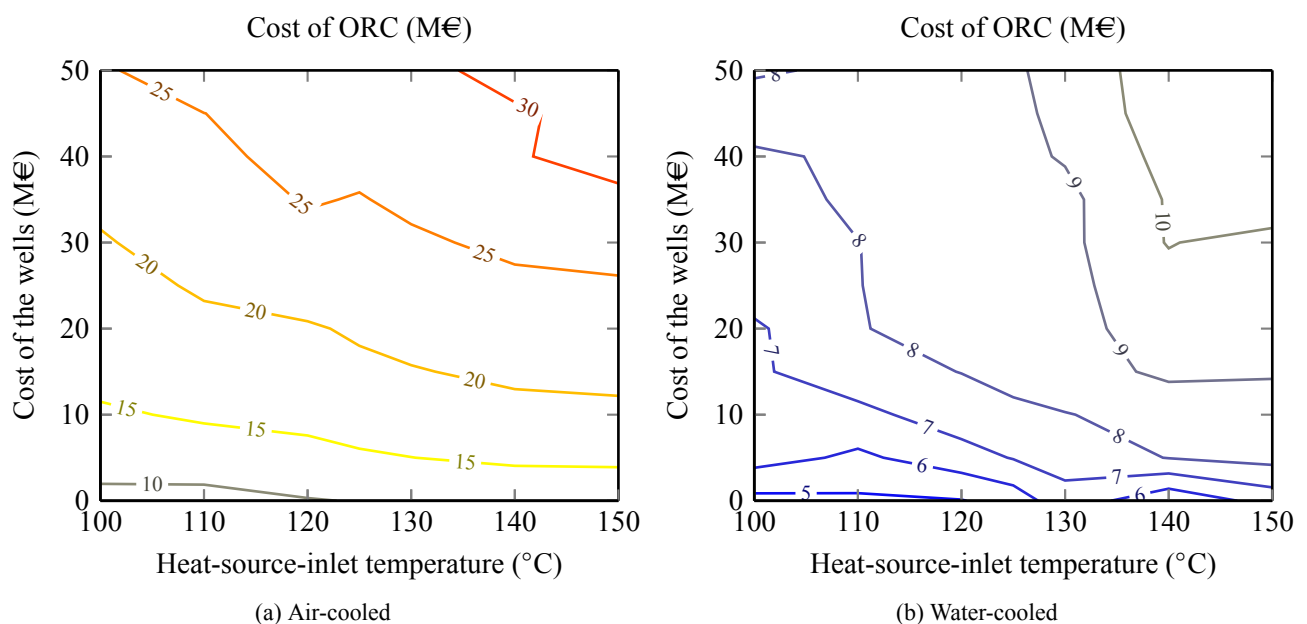


Figure 7: Cost of air-cooled ORCs (a) and water-cooled ORCs (b) as a function of the heat-source-inlet temperature and the cost of the wells.

The optimal ORC becomes more expensive with increasing cost of the wells, as explained above, and with increasing heat-source-inlet temperature. The latter evolution is due to the increased net power output (bigger turbine) and more heat flow (larger heat exchangers, etc.).

5. CONCLUSIONS

The influence of the cost of the wells and the heat-source-inlet temperature on the LCOE, the net power output and the cost of geothermal ORCs is investigated in this paper by performing an economic system optimization. The configuration of the components and the configuration of the cycle are optimized together to obtain the minimum LCOE.

Contour plots of the LCOE are given as a function of the heat-source-inlet temperature and the cost of the wells. With these plots, a first estimate can be made of the electricity price needed for a specific project to become economically profitable.

It is shown that the LCOE of water-cooled ORCs is lower than the one of air-cooled ORCs for the investigated parameters. This is mainly caused by the much higher cost of an ACC in comparison with a WCT, and to a lesser extent by the higher net power output of the water-cooled ORC.

NOMENCLATURE

ACC	Air-cooled condenser	
C	Cost	(€)
d_o	Diameter of a tube	(m)
D_S	Diameter of the shell	(m)
H	Fin height	(m)
H_i	Inlet height	(m)
H_{fi}	Height fill	(m)
H_{sp}	Height spray zone	(m)
L_b	Baffle spacing	(m)
L_t	Length of the tubes	(m)
LCOE	Levelized Cost of Electricity	(€/MWh _e)
N	Full-load hours per year	(-)
p_t	Pitch between tubes	(m)
S	Fin pitch	(m)
WCT	Wet cooling tower	
W_l	Tubes' large width	(m)
\dot{W}_{net}	Net electric power output	(MW _e)
W_S	Tubes' small width	(m)
W_t	Tower width	(m)

Subscript

EPC	Engineering, procurement & construction
O&M	Operations and maintenance
ORC	Organic Rankine cycle

REFERENCES

- Andersson, J., Åkesson, J., and Diehl, M. (2012). CasADi -- A symbolic package for automatic differentiation and optimal control. In Forth, S., Hovland, P., Phipps, E., Utke, J., and Walther, A., editors, *Recent Advances in Algorithmic Differentiation*, volume 87 of *Lecture Notes in Computational Science and Engineering*, pages 297--307. Springer Berlin Heidelberg.
- Büsken, C. and Wassel, D. (2013). The esa nlp solver worhp. In *Modeling and Optimization in Space Engineering*, pages 85--110. Springer.
- D'haeseleer, W. (2013). Synthesis on the economics of nuclear energy. Study for the European Commission, DG Energy. available at: http://ec.europa.eu/energy/nuclear/forum/doc/final_report_dhaeseleer/synthesis_economics_nuclear_20131127-0.pdf.
- IEA (2011). Technology Roadmap: Geothermal Heat and Power. Technical report, International Energy Agency.
- Kloppers, J. C. (2003). *A critical evaluation and refinement of the performance prediction of wet-cooling towers*. PhD thesis, Department of Mechanical Engineering, University of Stellenbosch.
- Lemmon, E., Huber, M., and McLinden, M. (2007). *NIST Reference Fluid Thermodynamic and Transport Properties REFPROP*. The National Institute of Standards and Technology (NIST). Version 8.0.
- Macchi, E. and Perdichizzi, A. (1981). Efficiency prediction for axial-flow turbines operating with nonconventional fluids. *Journal for Engineering for Power*, 103(4):718--724.
- Shah, R. K. and Sekulić, D. P. (2003). *Fundamentals of heat exchanger design*. John Wiley and Sons, Inc.
- Tester, J., Anderson, B., Batchelor, A., Blackwell, D., DiPippo, R., Drake, E., Garnish, J., Livesay, B., Moore, M., and Nichols, K. (2006). The Future of Geothermal Energy: Impact of Enhanced Geothermal Systems (EGS) on the United States in the 21st Century. Technical report, Massachusetts Institute of Technology, Massachusetts, USA.
- Walraven, D., Laenen, B., and D'haeseleer, W. (2013). Comparison of thermodynamic cycles for power production from low-temperature geothermal heat sources. *Energy Conversion and Management*, 66(C):220--233.
- Walraven, D., Laenen, B., and D'haeseleer, W. (2014). Optimum configuration of shell-and-tube heat exchangers for the use in low-temperature organic rankine cycles. *Energy Conversion and Management*, 83(C):177--187.
- Walraven, D., Laenen, B., and D'haeseleer, W. (2015a). Economic system optimization of air-cooled organic rankine cycles powered by low-temperature geothermal heat sources. *Energy*, 80(C):104--113.
- Walraven, D., Laenen, B., and D'haeseleer, W. (2015b). Minimizing the levelized cost of electricity production from low-temperature geothermal heat sources with orcs: water or air cooled? *Applied Energy*, 142(C):144--153.

A PERSPECTIVE ON COSTS AND COST ESTIMATION TECHNIQUES FOR ORGANIC RANKINE CYCLE SYSTEMS

Sanne Lemmens^{1*}

¹University of Antwerp, Department Engineering Management,
Antwerp, Belgium
sanne.lemmens@uantwerpen.be

* Corresponding Author

ABSTRACT

The potential of organic Rankine cycle (ORC) systems is acknowledged by both the considerable amount of ongoing research efforts and the increased occurrence of its applications in practice. A large share of research in this field strives to improve ORC systems by analyzing the performance of various cycle architectures and numerous working fluids. These technical feasibility and optimization studies are at the core of ORC development. Yet, when it comes down to considering practical instalments the economic feasibility of the project is often decisive. Complementary to research efforts on these technical issues this paper approaches the matter from an economic point of view. The costs-dimension of ORC systems is discussed from various perspectives. First of all, this paper provides a brief review of literature knowledge on ORC investment costs. Technical publications on ORC development increasingly include estimates of the costs associated with the system design, but knowledge on actual ORC module and project costs remains scarce. Secondly, this paper takes a closer investigation into the methods used to estimate ORC project costs from the bottom up and the expected accuracies associated with these estimates. Finally, these insights are used to estimate the costs of a known ORC system applied for waste heat recovery. The comparison of the estimated and the actual specific investment costs confirms the existence of a wide accuracy range. The purchased equipment costs obtained with the bottom-up estimate diverge from the actual costs by almost 44% and the deviation leads to differing interpretations on the share of equipment items in the total purchased equipment costs. The results of this analysis are not generalizable since only one real-life study is used for comparison. The main conclusion of the paper is to be cautious when interpreting estimated ORC plant costs.

1. INTRODUCTION

The interest for organic Rankine cycle (ORC) systems is growing increasingly. The concept of using an organic fluid instead of water dates back from right after the invention of the Rankine cycle in 1859, yet it was not until the 1960s and 1970s that ORC technology got more prominent research attention. By today, ORC systems constitute a flourishing research field and its practical possibilities have been proven. The reasons for this success are manifold. Rankine cycles operate with organic fluids, which allows conversion of energy sources in much lower temperature ranges than suitable for conventional steam cycles. ORCs can generate electricity from energy sources such as geothermal wells, biomass, solar and oceanic sources and industrial waste heat. Hence, ORC systems have potential to generate electricity from renewable energy sources as well as to enhance industrial energy efficiency. Both are essential in the transition of energy sectors to more streamlined, efficient, secure and climate-friendly systems. Research on ORC systems is very technical in nature and includes i.a. architecture design and optimization (e.g. Chen, Goswami, and Stefanakos (2010); Lecompte, Huisseune, van den Broek, Vanslambrouck, and De Paepe (2015)), the quest for suitable working fluids (e.g. Hung (2001); Lakew and Bolland (2010)) and the design of new expander types (e.g.

Declaye, Quoilin, Guillaume, and Lemort (2013)). Technical invention and optimization are a necessary first step in the technological innovation process. The subsequent steps are innovation (where the product goes from lab tests to real applications) and diffusion (gradual adoption by firms). The final degree of utilization may impact energy demand. Innovation processes typically follow an s-shaped figure: adoption occurs gradually in the beginning, then with increasing rapidity until the point of saturation. However, there is no guarantee for an invention to go through the entire innovation process and yield market success, even while interesting. For instance, the rate of technological invention and innovation of energy-efficient technologies is found to correlate with energy price increases. The gradual character of the diffusion process stems from the heterogeneity of (potential) adopters, which have a differing expected return. Those firms expecting the investment to be profitable will adopt first. Over time, more firms will adopt due to technology cost reduction, quality improvements and improved information availability. The adoption of energy-efficient technologies is likewise encouraged by higher energy prices, but decreased by adoption costs. Finally, energy-efficient technology adoption is found to be sensitive to the cost of equipment more than to the expected energy costs. (Jaffe, Newell, & Stavins, 2004) Seeing the importance of the economic perspective in technology development and diffusion, the aim of this paper is to complement the large body of literature on technical aspects with an economic viewpoint on ORC installations. A literature review gives insight in current knowledge on the investment costs of ORC systems (section 2). Section 3 elaborates on bottom-up cost estimation techniques and accuracies. In section 4 the investment costs of an actual ORC project are compared to those obtained from a bottom-up estimate. A final chapter discusses the results and conclusions.

2. ORC COSTS: A LITERATURE REVIEW

The body of literature on ORC systems and applications is extensive. The importance of the economic perspective is recognized and increasingly taken along in the engineering studies. At the basis of the economic analysis are the capital costs, particularly important for ORC projects since the annual costs are fairly low. Figure 1 displays the specific investment costs (SIC) estimated for various types of ORC input sources: solar, waste heat recovery (WHR), biomass and geothermal. The references are not included in the figure for clarity, but are included in the reference list. The values in the graph stem from literature and have been adjusted to 2013 Euros to allow for comparison. Geothermal ORC systems are most reported in the larger power output ranges. Figure 2 displays the same values but without the geothermal systems to provide a better view on the other costs. Similarly, Figure 3 limits the graph to smaller size (< 1.2 MW) ORC units. Solar ORC systems appear to be more costly, but most of the other costs are within the 2000 to 4000 €/kW range. Figure 1 suggests lower SIC values for higher power output systems, but additional references would be needed for a more detailed analysis.

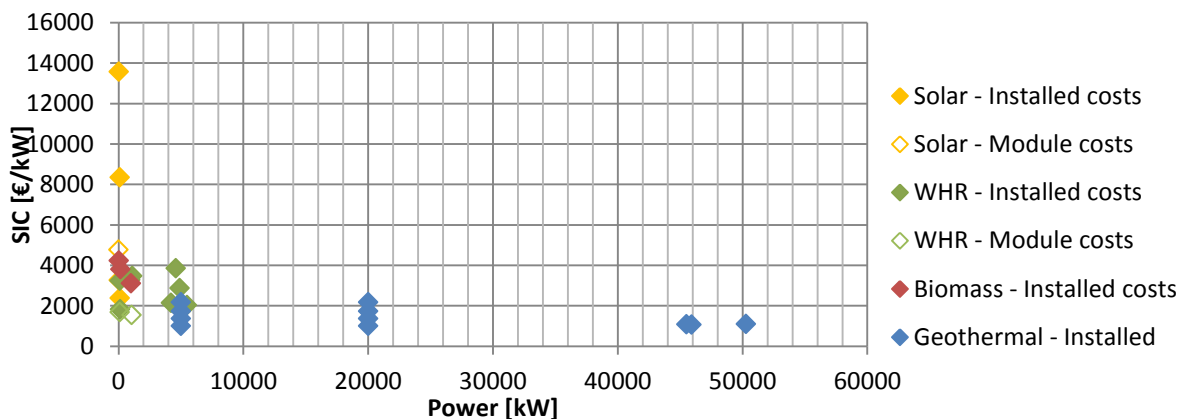


Figure 1: ORC costs in literature

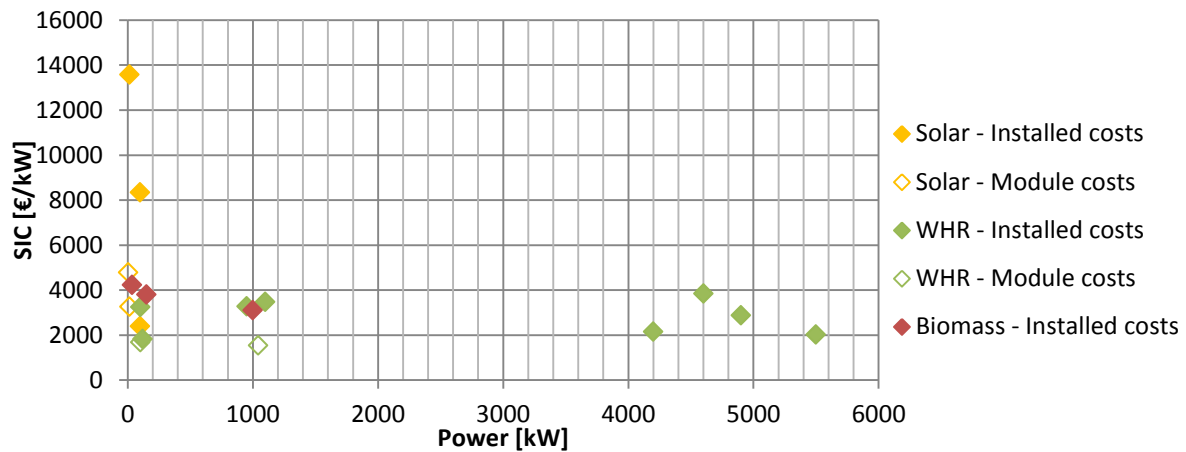


Figure 2: ORC costs in literature - without geothermal references

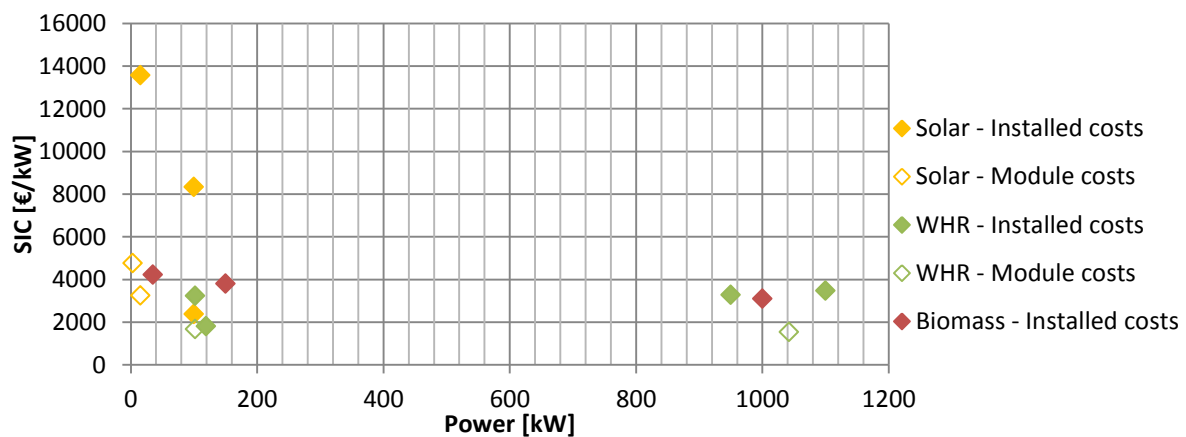


Figure 3: ORC costs in literature – small to medium sized

Not all references reporting ORC costs can be included in such summary graphs, e.g. because only SIC values are given and not the power output. For instance, Quoilin et al. (2011) perform a thermo-economic optimization of ORCs for waste heat recovery. They obtain SIC values between 2136 €/kW and 4260 €/kW, depending on the fluid operated, for small scale ($< 5 W_{\text{net}}$) systems. An important conclusion from their work is that the operating point yielding maximum power does not coincide with that of minimal SIC. Similarly, Imran et al. (2014) utilize thermo-economic optimization to compare cycle setups. The SIC values are in the range of 3274 to 4155 €/kW for the basic ORC, 3453 to 4571 €/kW for the single stage regenerative ORC and 3739-4960 €/kW for the double stage regenerative ORC, depending on the working fluid operated. Unfortunately no indication was given on the power range. Walraven, Laenen, and D'Haeseleer (2015) investigate air-cooled geothermal ORC systems. No exact specific investment costs numbers are presented, but the impact of various factors, such as brine inlet and outlet temperatures, pressure levels, electricity prices, discount rates and electricity price evolutions, on the economics of the ORC project are demonstrated. Other studies are not included here because the economic values are expressed in €/kWh rather than €/kW, such as in Meinel, Wieland, and Spliethoff (2014) who perform a considerate comparison of architecture designs at various sizes. The results were calculated for heat sources of 0.5 MW_{th}, 1 MW_{th} and 5 MW_{th}.

The references in Figure 1 all concern estimates of ORC costs rather than reporting of real ORC costs. Real ORC costs are provided by e.g. Leslie et al. (2009) who report the findings of a 5.5 MW ORC system applied for heat recovery from a gas turbine driving a natural gas pipeline compressor. The system was monitored extensively for one year, the capital costs of the system constitute approximately 2500 €/kW. Prices for biomass fuelled ORC systems are published in the range of 4500 €/kW for a 1803 kW system to 10,200 €/kW for a 345 kW system in 2009 (Duvia, Guercio, & Rossi di Schio, 2009).

3. COST ESTIMATION FOR ORC PLANTS

The up-front estimation of the costs of a new plant is a challenging task. Capital costs, or capital investment, refer to the one-time costs occurring at the beginning of the project. These total investment costs include the costs directly associated with the system (equipment, materials, labor etc. required for the equipment and the installation thereof), indirect costs (engineering, construction costs and contingencies) and other outlays (such as startup costs, working capital, etc.) (Bejan, Tsatsaronis, & Moran, 1996). The estimate of plant capital costs is a practice iterating as the design evolves to increased detail. Plant estimates are classified according to their level of detail and thus their accuracy (Table 1). The accuracy ranges indicate variations regarding technological complexity of the project, suitable reference information, and an appropriate determination of project contingencies (AACE International, 2005). The ranges represented in Table 1 are applicable for process industry projects (AACE International, 2005). Underestimation of capital costs occurs mainly due to incomplete listing of all the equipment needed in the process (Turton, Bailie, Whiting, Shaeiwitz, & Bhattacharyya, 2013, p. 160). An increasing level of detail implies a smaller accuracy range, but similarly an increasing amount of effort and labor hours to make the estimate. Estimates performed in research are generally order-of-magnitude, study and preliminary design estimates.

Table 1: Classification of capital cost estimates (AACE International, 2005; Turton et al., 2013).

Class	Type of estimate	Description	Accuracy ranges
5	Order-of-magnitude estimate (also Ratio / Feasibility)	Based on limited information. Concept screening.	Low: -20% to -50% High: +30% to +100%
4	Study estimate (also Major Equipment / Factored)	List of major equipment. Project screening, feasibility assessment, concept evaluation, and preliminary budget approval.	Low: -15% to -30% High: +20% to +50%
3	Preliminary Design estimate (also Scope)	More detailed sizing of equipment. Budget authorization, appropriation, and/or funding.	Low: -10% to -20% High: +10% to +30%
2	Definitive estimate (also Project Control)	Preliminary specification of all the equipment, utilities, instrumentation, electrical and off-sites. Control or Bid/Tender.	Low: -5% to -15% High: +5% to +20%
1	Detailed estimate (also Firm / Contractor's)	Complete engineering of process and related off-sites and utilities required. Check Estimate or Bid/Tender.	Low: -3% to -10% High: +3% to +15%

The equipment needed for construction of the plant is at the core of most cost estimates. The best approach for the purchase cost of a piece of equipment is a current vendor's price quote. Data from previously bought but similar equipment is next best. (Turton et al., 2013) When the costs of a component are known but its capacity differs from that of the to-be-estimated component, the costs can be roughly estimated using the correlation

$$\frac{c_a}{c_b} = \left(\frac{A_a}{A_b}\right)^n \quad (1)$$

where c and A respectively represent the purchase costs and the equipment cost attribute of the required component (c_a and A_a) and the known component (c_b and A_b) and n is the exponent used to correlate the costs. This exponent n differs per type of equipment, but it is often close to 0.6 for the chemical industry and therefore sometimes referred to as the six-tenths rule. This extrapolation method provides only rough approximations of the actual costs. In case no purchased equipment costs are known, but technical details are available, the costs can be estimated using equipment cost correlations. Guidance, exponents and correlations for various types of process equipment are

provided by i.a. Bejan et al. (1996), Couper, Penney, Fair, and Walas (2012), Smith (2005), Towler and Sinnott (2008), Turton et al. (2013).

The total capital investment of a project can be estimated using various techniques. A simple method is to use a capacity exponent ratio, similarly as previously described for equipment costs estimates. The costs of a planned plant are estimated using the known costs of a similar previously constructed plant. The accuracy of this method is rather low. It should be used for order-of-magnitude or study estimates only. (Peters, Timmerhaus, & West, 2004) Step Count methods take a different approach and utilize the number of functional units or plant sections as a basis to estimate total investment costs. This method is designed for use in the chemical process industry and not so suitable for usage in other manufacturing fields. The accuracy would be in the range of order-of-magnitude estimates. (Towler & Sinnott, 2008) Thirdly, factorial estimation techniques are based on the costs of the major purchased equipment items and apply multiplication factors to obtain the total capital investment. The Lang Factor method is probably the first factorial method. Lang suggested to multiply the total delivered costs of the major equipment parts with a factor that differs according to the type of process. The factors are available for solid, fluid and mixed fluid-solid processing chemical plants. (Towler & Sinnott, 2008) The Lang Factor technique utilizes only one multiplication factor and is therefore expected to yield lower accuracies, it is suggested to use for order-of-magnitude estimates (Peters et al., 2004, p. 252). The Lang Factor method has been adapted numerous times since then. For instance, Hand suggested to utilize multiplication factors for the equipment types instead of the plant type. (Towler & Sinnott, 2008) The utilization of multiple factors implies more detail, but this method would probably still not provide very good accuracies. The detail of the estimate can be improved further using cost factors for different items related to direct costs (erection of equipment, piping, electrical, instrumentation and control, buildings and structures, ancillary buildings, storage, utilities, site preparation). Dividing the process into subunits and applying factors per subunit function improves the estimate's accuracy and reliability. (Towler & Sinnott, 2008) An even more detailed estimate is suggested by Guthrie and accounts the installation, piping and instrumentation costs of each equipment item individually. Inclusion of a factor for the equipment materials used would improve accuracy even more. (Towler & Sinnott, 2008) Still, these estimates would remain within the accuracy of preliminary estimates. Another, somewhat different, factorial method calculates the direct fixed costs and total investment costs as percentages of the delivered-equipment costs. The factors used depend i.a. on the process type, design complexity, location, experience. This percentage of delivered-equipment method is suitable for study and preliminary estimates. (Peters et al., 2004) When the goal is to achieve more detailed estimates than the ones formerly described, this requires more detailed information and engineering effort. For instance, the unit cost method is used for preliminary and definitive estimates. The method requires accurate information on costs from previous projects, detailed estimates of equipment prices, installation labor, instrumentation, electrical and other miscellaneous items. Also engineering hours, drawing efforts, construction, contractor's fee and contingencies are included. This can yield relatively accurate results but requires sufficiently detailed information and engineering time. (Peters et al., 2004) Detailed item estimates, with high accuracies, generally concern advanced project plans. At this stage most details of the project are known, the drawings are finished and the estimates are based preferably on delivered quotations. For most research and development projects, both definitive and detailed cost estimates would range beyond the scope of the project and the information available. Preliminary estimates are feasible, but the accuracy of the results relies strongly on the quality of the information (i.a. factors) used.

Finally, the costs of materials and labor are subject to inflation which implies cost figures from different years are not directly comparable. The most straightforward manner to update historical data is by means of composite cost indices, using equation

$$c_j = c_i * \left(\frac{I_j}{I_i}\right) \quad (2)$$

where c_j and c_i refer to the costs in year j and i respectively, and I_j and I_i are the cost indices for the respective years. These composite indices are a weighted average index of various components costs

commonly used in a particular industry. Updating cost data using cost indices is acceptable for only shorter periods of time, some say four to five years (Jelen & Black, 1983, p. 339). The accuracy of the results decreases when longer time periods are used.

4. A NUMERICAL EXAMPLE

To demonstrate the precarious exercise of bottom-up cost estimation for ORC-plants, this paper compares the costs of an actual case study with the costs obtained from a rough bottom-up estimate. The case study concerns a waste heat recovery ORC installation. The heat source is a low-medium temperature (range 150 – 250°C) flue gas stream from an industrial plant. The ORC system was integrated into the plant using an intermediate thermal oil circuit including a flue gas heat exchanger. The ORC itself has a gross power output of 375 kW and is composed of a centrifugal pump, a one-step radial expander and a generator. The evaporator is a plate heat exchanger and condensation occurs air-cooled. The project has a SIC of 4216 €/kW_{gross}, including installation (in 2013). The partitioning of the costs for this project (Figure 4) demonstrates a major share stems from the ORC unit itself, including pump, expander and generator. The intermediate thermal oil circuit represents about 11% of total investment costs.

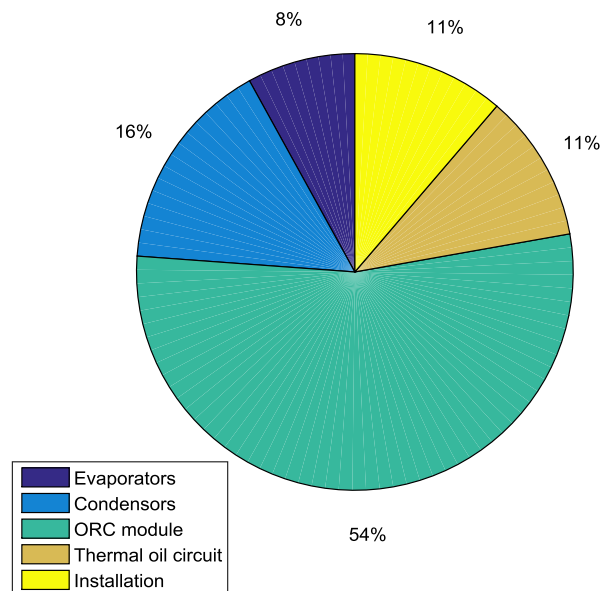


Figure 4: Diagram of the real ORC project costs

Knowing most technical details of the real plant, a rough bottom-up cost estimation was performed using the module costing technique. The module costing technique is a commonly used factorial cost estimation method based on the approach of Guthrie. (Turton et al., 2013). This technique is suitable for preliminary estimates in the range of -20% to +30% accuracy. The costs of the major purchased equipment parts are estimated using available correlations. These base costs are multiplied with the bare module cost factor, that accounts for operating pressures and specific materials of construction, as well as direct and indirect project expenses. This yields the bare module costs. To obtain the total module costs, estimated for integration of the plant into an existing facility, the bare module costs are adapted with another multiplication factor. (Turton et al., 2013) All estimates are converted to 2013 Euros to allow for comparison with the real system. The cost correlations published in Turton et al. (2013) are utilized to estimate most purchased equipment costs, the correlation by Smith (2005) for estimation of the fan costs and the generator costs stem from the correlation given by Toffolo, Lazzaretto, Manente, and Paci (2014). The results obtained from Turton et al. (2013) are in USD₂₀₀₁, they are converted to EUR using a 1.1162 exchange rate (average 2001) and updated to 2013 using the Chemical Engineering Plant Cost Index (CEPCI), with CEPCI₂₀₀₁ and CEPCI₂₀₁₃ values of 397 and 587.3 respectively. Results obtained from Smith (2005) are converted from USD_{Jan,2000} to EUR₂₀₁₃

using an exchange rate of 0.9857 (average Jan 2000) and $CEPCI_{2000}$ equal to 394.1. The correlation from Toffolo et al. (2014) was first published in 1993, so a $CEPCI_{1993}$ of 359.2 was used.

In case only the essential ORC components are considered, and the thermal oil circuit is not accounted for, the estimate yields a result of 1843 €/kW for the purchased equipment costs. In the module costing technique, the purchased equipment costs are used to estimate the total plant costs. An intermediate step is the calculation of the bare module costs. These costs include the direct (equipment, installation materials and labor) and indirect (freight, insurance, taxes, overhead and engineering expenses) costs associated with the project. Accounting for these expenses additional to the purchased equipment costs yields a bare module cost of 4390 €/kW. Finally, the total module costs include also contingencies and contractor fees and auxiliary facilities and are estimated at 5180 €/kW. Note that these estimated costs do not yet include the costs of the thermal oil circuit. Simply adding the costs of the thermal oil system (real costs, not estimated) gives a total module cost of 5642 €/kW. The costs of the thermal oil system are taken as such and not manipulated with bare module or total module factors. Manipulation of the costs for the thermal oil system with a bare module factor of 1.5 and a 1.18 multiplication factor to obtain the total module costs would give a SIC of 5997 €/kW. The bare module factor given for this latter estimate was not given by any reference but expected in line with other bare module factors, a 1.5 factor seems not unreasonable knowing the amount of piping involved with the installation of the system.

Figure 5 displays the real (a) and the estimated (b) purchased equipment costs of the components of the ORC system, excluding installation and thermal oil circuit. The partitioning of purchased equipment costs differs strongly from that of the actual costs. Whereas the evaporators constitute only 10% of purchased equipment costs in reality, the cost estimation leads to a 45% share. The ORC module (expander, generator and pump) represents 69% of actual purchased equipment costs but is estimated at 47%.

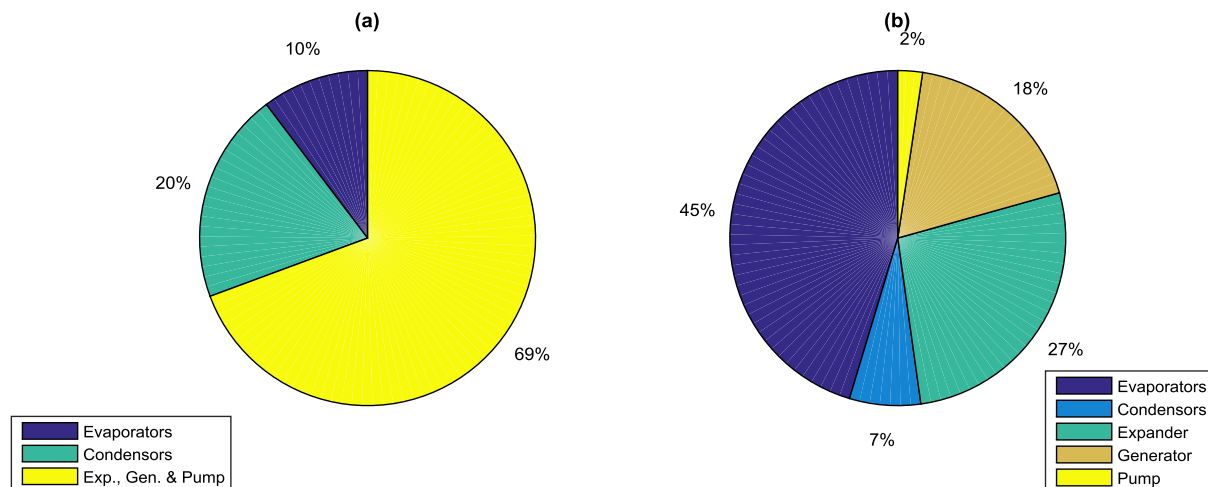


Figure 5: Real (a) and estimated (b) purchased equipment costs

The estimated PEC of 1843 €/kW is significantly lower than the actual PEC of 3280 €/kW (-44 %). If the total module costs are estimated, including the thermal oil circuit but with no adaption of the real costs of the thermal oil system, the obtained costs (5642 €/kW) are 34% higher than the actual total project costs (4216 €/kW). If the thermal oil circuit is included and adapted with bare and total module factors, the estimated cost (5997 €/kW) is even higher and deviates more from the actual costs.

5. DISCUSSION AND CONCLUSIONS

The aim of this paper is to give insight into ORC systems from an economic point of view. Technical invention and innovation are key for evolution to more streamlined and renewables-based energy sectors, but the adoption and diffusion processes of innovative technologies are strongly influenced by

economic factors. There is still not much published information about the actual costs of ORC systems. A brief review of literature knowledge on the investment costs of ORC modules and ORC projects reveals most are in the 2000 – 4000 €/kW range. Geothermal projects tend to be larger with lower SIC values, solar projects are mostly small and can have very high specific investment costs. An increasing number of references utilize thermo-economic and techno-economic optimization techniques and apply bottom-up estimation techniques to estimate the costs of ORC modules or projects. Component cost estimates can simply be made using scale exponent methods, more detailed estimates use factorial estimation techniques. In any bottom-up estimate it is important to consider the expected accuracy range. Simpler methods require less effort but yield lower accuracy. High accuracies are possible making definitive and detailed estimates, but these require a level of plant detail which is commonly not achieved in research estimates. The precariousness of using factorial techniques to approach real plant costs is demonstrated and confirmed for an existing ORC applied for waste heat recovery. The estimated specific purchased equipment costs deviate from the actual project costs by almost 44%. The purchased equipment costs distribution differs largely between the actual and the estimated costs of the components. There are many potential reasons for this deviation. First of all, factorial estimation methods are suitable for preliminary estimates. A deviation of -20% to +30% is therefore not uncommon. The accuracy of factorial estimation methods depends strongly on the quality of the information that was used to establish the multiplication factors. Additional inaccuracies and uncertainties may stem from treatment of costs over time periods. Extrapolation of costs over large periods of time decreases the accuracy of the results. Most of the open-source correlations available in text books are at least nine years old and thus provide less accurate results. Additionally, some of these references refer back to original factors and correlations published in by Guthrie in 1969 or 1974 and updated with few recent data points or using cost indices. This makes these correlations less reliable. Finally, also the choice of indicator for cost escalation and local conditions may have an influence and create additional deviations. This implies that results in such settings should not be interpreted as final, but rather as giving an idea on the expected range of investment costs. This type of estimate can be useful to mutually compare various system designs, where the proportional comparison is more important than the exact outcomes. Finally, it is important to take the difference between costs and prices into consideration in this type of studies. Costs reflect the amount that is required to produce a certain item, the price is the amount you pay to purchase it. The costs associated with producing an ORC system will thus differ from the price paid to acquire that system. Many correlations used to estimate costs are obtained using vendor prices. In case the ORC developer would purchase most equipment instead of developing it this is not a problem. For innovative system designs (e.g. expanders) this method would be less suitable. The main conclusion from this study is to be careful when interpreting results obtained from preliminary bottom-up cost estimates. This is also the case for the results obtained from the estimates in this study. The results confirm a wide accuracy range. Rather than being used as exact results, these estimates could give guidance when comparing several alternatives, estimated with the same method.

NOMENCLATURE

<i>A</i>	equipment cost attribute
<i>c</i>	cost of component (€)
CEPCI	Chemical Engineering Plant Cost Index
ORC	organic Rankine cycle
<i>n</i>	exponent for cost correlation
SIC	specific investment costs (€/kW)
WHR	waste heat recovery

Subscript

<i>a</i>	required component
<i>b</i>	known component
<i>i</i>	year i
<i>j</i>	year j

REFERENCES

- AACE International. (2005). Recommended Practice No. 18R-97. Cost estimate classification system - As applied in engineering, procurement, and construction for the process industries. TCM Framework: 7.3 – Cost Estimating and Budgeting (pp. 10): AACE International.
- Angelino, G., Gaia, M., & Macchi, E. (1984, 13-15 February). *Medium temperature 100kW ORC engine for total energy systems - Experimental results*. Paper presented at the International Seminar of the Commission of the European Communities on Energy Conservation in Industry, Düsseldorf.
- Arslan, O., Ozgur, M. A., & Kose, R. (2012). Electricity Generation Ability of the Simav Geothermal Field: A Technoeconomic Approach. *Energy Sources, Part A: Recovery, Utilization, and Environmental Effects*, 34(12), 1130-1144. doi: 10.1080/15567031003773254
- Barber, R. E. (1978). Current costs of solar powered organic Rankine cycle engines. *Solar Energy*, 20(1), 1-6.
- Bejan, A., Tsatsaronis, G., & Moran, M. (1996). *Thermal design and optimization* New York: Wiley & Sons.
- Chen, H., Goswami, D. Y., & Stefanakos, E. K. (2010). A review of thermodynamic cycles and working fluids for the conversion of low-grade heat. *Renewable and Sustainable Energy Reviews*, 14(9), 3059-3067. doi: 10.1016/j.rser.2010.07.006
- Couper, J. R., Penney, R. W., Fair, J. R., & Walas, S. M. (2012). *Chemical Process Equipment: Selection and Design* (Third ed.): Butterworth-Heinemann.
- Declaye, S., Quoilin, S., Guillaume, L., & Lemort, V. (2013). Experimental study on an open-drive scroll expander integrated into an ORC (Organic Rankine Cycle) system with R245fa as working fluid. *Energy*, 55, 173-183. doi: 10.1016/j.energy.2013.04.003
- Duvia, A., Guercio, A., & Rossi di Schio, C. (2009). *Technical and economic aspects of Biomass fuelled CHP plants based on ORC turbogenerators feeding existing district heating networks*.
- Forni, D., Vaccari, V., Di Santo, D., Rossetti, N., & Baresi, M. (2012, 11–14 September 2012). *Heat recovery for electricity generation in industry*. Paper presented at the ECEEE 2012 Summer Study on energy efficiency in industry, the Netherlands.
- Forsha, M. D., & Nichols, K. E. (1991). Factors affecting the capital cost of binary power plants. *Geothermal Resources Council Transactions*, 15, 99-105.
- Georges, E., Declaye, S., Dumont, O., Quoilin, S., & Lemort, V. (2013). Design of a small-scale organic Rankine cycle engine used in a solar power plant. *International Journal of Low-Carbon Technologies*, 8(suppl 1), i34-i41. doi: 10.1093/ijlct/ctt030
- Huang, Y., McIlveen-Wright, D. R., Rezvani, S., Huang, M. J., Wang, Y. D., Roskilly, A. P., & Hewitt, N. J. (2013). Comparative techno-economic analysis of biomass fuelled combined heat and power for commercial buildings. *Applied Energy*, 112, 518-525. doi: 10.1016/j.apenergy.2013.03.078
- Hung, T.-C. (2001). Waste heat recovery of organic Rankine cycle using dry fluids. *Energy Conversion and Management*, 42, 539-553.
- Imran, M., Park, B. S., Kim, H. J., Lee, D. H., Usman, M., & Heo, M. (2014). Thermo-economic optimization of Regenerative Organic Rankine Cycle for waste heat recovery applications. *Energy Conversion and Management*, 87, 107-118. doi: 10.1016/j.enconman.2014.06.091
- Jaffe, A. B., Newell, R. G., & Stavins, R. N. (2004). Economics of Energy Efficiency. *Encyclopedia of Energy*, 2, 79-90.
- Jelen, F. C., & Black, J. H. (1983). *Cost and optimization engineering* (Second ed.): McGraw-Hill, Inc.
- Kosmadakis, G., Manolakos, D., Kyritsis, S., & Papadakis, G. (2009). Economic assessment of a two-stage solar organic Rankine cycle for reverse osmosis desalination. *Renewable Energy*, 34(6), 1579-1586. doi: 10.1016/j.renene.2008.11.007
- Lakew, A. A., & Bolland, O. (2010). Working fluids for low-temperature heat source. *Applied Thermal Engineering*, 30(10), 1262-1268. doi: 10.1016/j.applthermaleng.2010.02.009
- Law, R., Harvey, A., & Reay, D. (2013). Techno-economic comparison of a high-temperature heat pump and an organic Rankine cycle machine for low-grade waste heat recovery in UK industry. *International Journal of Low-Carbon Technologies*, 8(suppl 1), i47-i54. doi: 10.1093/ijlct/ctt029
- Lecompte, S., Huisseune, H., van den Broek, M., Vanslambrouck, B., & De Paepe, M. (2015). Review of organic Rankine cycle (ORC) architectures for waste heat recovery. *Renewable and Sustainable Energy Reviews*, 47, 448-461. doi: 10.1016/j.rser.2015.03.089
- Lee, K. M., Kuo, S. F., Chien, M. L., & Shih, Y. S. (1988). Parameters analysis on organic rankine energy recovery system. *Energy Conversion and Management*, 28(2), 129-136.
- Leslie, N. P., Sweetser, R. S., Zimron, O., & Stovall, T. K. (2009). Recovered Energy Generation Using an Organic Rankine Cycle System. *ASHRAE Transactions*, 115(Part 1).
- Meinel, D., Wieland, C., & Spliethoff, H. (2014). Economic comparison of ORC (Organic Rankine cycle) processes at different scales. *Energy*, 74, 694-706. doi: 10.1016/j.energy.2014.07.036

- Peters, M. S., Timmerhaus, K. D., & West, R. E. (2004). *Plant Design and Economics for Chemical Engineers* (Fifth ed.): McGraw-Hill
- Quoilin, S., Declaye, S., Tchanche, B. F., & Lemort, V. (2011). Thermo-economic optimization of waste heat recovery Organic Rankine Cycles. *Applied Thermal Engineering*, 31(14), 2885-2893.
- Rentizelas, A., Karellas, S., Kakaras, E., & Tatsiopoulou, I. (2009). Comparative techno-economic analysis of ORC and gasification for bioenergy applications. *Energy Conversion and Management*, 50(3), 674-681. doi: 10.1016/j.enconman.2008.10.008
- Schuster, A., Karellas, S., Kakaras, E., & Spliethoff, H. (2009). Energetic and economic investigation of Organic Rankine Cycle applications. *Applied Thermal Engineering*, 29(8), 1809-1817.
- Smith, R. (2005). *Chemical Process Design and Integration*. West Sussex, England: John Wiley & Sons, Ltd.
- Toffolo, A., Lazzaretto, A., Manente, G., & Paci, M. (2014). A multi-criteria approach for the optimal selection of working fluid and design parameters in Organic Rankine Cycle systems. *Applied Energy*, 121, 219-232. doi: 10.1016/j.apenergy.2014.01.089
- Towler, G., & Sinnott, R. (2008). *Chemical Engineering Design: Principles, Practice and Economics of Plant and Process Design*: Butterworth-Heinemann.
- Turton, R., Bailie, R. C., Whiting, W. B., Shaeiwitz, J. A., & Bhattacharyya, D. (2013). *Analysis, Synthesis, and Design of Chemical Processes* (Fourth ed.). Upper Saddle River, New Jersey: Pearson Education International.
- Walraven, D., Laenen, B., & D'Haeseleer, W. (2015). Economic system optimization of air-cooled organic Rankine cycles powered by low-temperature geothermal heat sources. *Energy*, 80, 104-113. doi: 10.1016/j.energy.2014.11.048

ACKNOWLEDGEMENT

The author is grateful for the financial support granted for this research by the Agency for Innovation by Science and Technology in Flanders. This support was granted in the frame of the IWT SBO-110006 project The Next Generation Organic Rankine Cycles (ORCNext.be).

DESIGN OF WASTE HEAT RECOVERY SYSTEMS BASED ON SUPERCRITICAL ORC FOR POWERFUL GAS AND DIESEL ENGINES

Oleksii Rudenko¹, Leonid Moroz², Maksym Burlaka³, Clement Joly*⁴

¹SoftInWay, Engineering,
Burlington, MA, USA
o.rudenko@softinway.com

²SoftInWay, Engineering
Burlington, MA, USA
l.moroz@softinway.com

³SoftInWay, Engineering
Burlington, MA, USA
m.burlaka@softinway.com

⁴SoftInWay, Engineering
Burlington, MA, USA
clement.joly@softinway.com

* Corresponding Author

ABSTRACT

Nowadays the scientific world community is strongly concerned about problems of efficiency increase and emissions reduction of Internal Combustion Piston Engines (ICPE). The equipment of ICPE with Waste Heat Recovery Systems (WHRS) is an effective solution for the aforementioned problems. This paper focuses on finding the maximum possible heat recovery from the available high and low temperature waste heat flows of a powerful ICPE to produce the maximum amount of additional power while decreasing the load on the engine's cooling system.

Having considered and analyzed existing works devoted to the development of WHRS the most effective ideas were combined to design several thermodynamic cycles for new WHRS of a powerful piston engine (here a G3612 CAT gas petroleum engine is considered). The proposed WHRS is based on a Supercritical Organic Rankine Cycle (SORC) using R245fa as the working fluid where heat is extracted from the waste heat sources by a refrigerant at different pressure levels. Internal recuperation is used to further improve the cycle performances and increase the waste heat recovery. The thermodynamic analysis of the new WHRS showed that up to 19.73% of power boost for the internal combustion engine can be achieved without burning additional fuel which represents significant gains in terms of specific power.

In order to quantify the estimation of the performances for proposed cycles the design of a traditional, high efficiency, a WHRS based on double pressure water steam cycle for the same engine's conditions was performed. This comparison of performances between the steam cycle and the SORC R245fa cycles confirmed a high potential for the designed cycles.

1. INTRODUCTION

Internal combustion piston engines are among the largest consumers of liquid and gaseous fossil fuels all over the world. Despite the introduction of new technologies and constant improving of engines

performances they still are relatively wasteful. Indeed, the efficiency of modern engines rarely exceeds 40-45% (Seher et al. (2012), Guopeng et al. (2013)) and the remainder of the fuel energy usually dissipates into the environment in the form of waste heat. The heat balance diagram of typical engine is given in Figure 1. As is evident from Figure 1, besides the mechanical work energy the heat balance includes a heat of exhaust gas, a heat of charge air, a Jacket Water (JW) heat, a heat of lubricating oil and a radiation heat. The energy from all the heat sources except the last one (radiation), due to its ultra-low waste heat recovery potential, can be used as heat sources for WHRS (Paanu et al. (2012)) and are considered here.

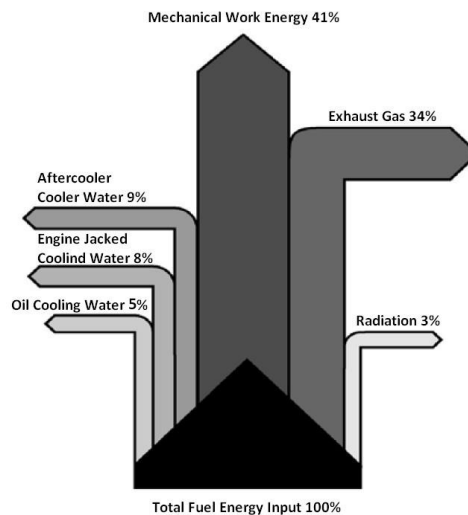


Figure 1: Typical heat balance diagram for CAT engine (Caterpillar (2011))

Waste heat utilization is a very current task because it allows to reduce the harmful influence of ICPE operation on the environment as well as to obtain additional energy and to reduce the load on the engine's cooling system. Different WHRS can produce heat energy, mechanical energy or electricity and combinations of the converted energy forms exist as well. In general, the type of WHRS to be used is determined by the engine type, fuel cost, available energy customers and other factors. In the present paper only WHRS for mechanical power and electricity production were considered because these kinds of energy are preferable for this type of applications and they can be easily converted into other forms of energy.

For vehicle engines the WHRS based on Organic Rankine Cycle (ORC) are the most commercially developed (Paanu et al. (2012)). Because of strict restrictions on weight and dimensions, the mentioned systems typically operate on the base of a simple or recuperated ORC and utilize only high temperature waste heat from the exhaust gases and the exhaust gas recirculation. They usually produce mechanical power or electricity. More complex cycles and a larger number of heat sources are used for waste heat recovery from powerful internal combustion engines where additional weight and dimensions are not crucial factors. Waste heat from stationary, marine and another more powerful ICPE can be recovered using a typical steam bottoming cycle. Steam WHRS allow utilizing almost all a high temperature waste heat and partially utilizing a low temperature heat. The high efficiency steam WHRS are presented in (MAN Diesel & Turbo (2012), Petrov (2006)), they provide up to 14.5% of power boost for the engine.

From the existing works devoted to waste heat recovery range of problems the following methods of efficiency increase can be highlighted:

- Addition of the internal heat recuperation to a WHR cycle;
- Appropriate working fluid selection;
- Increment of initial parameters of bottoming cycle up to supercritical values;
- Maximize waste heat utilization due to the usage of low temperature heat sources;
- Bottoming cycle complexification or usage of several bottoming cycles with different fluids (Maogang (2011)).

This paper focuses on the development of new WHRS as an alternative to high efficiency steam bottoming cycles by accounting for the latest progress in the field of waste heat recovery. The application range of the proposed system extends to powerful and super powerful ICPEs.

2. DEVELOPMENT OF NEW WHRS

The goal of the present work is the development of a new, high efficiency WHRS for powerful and super powerful ICPEs based on ORC principles. To solve the assigned task, a thorough study of the currently existing works was performed and the best ideas were combined. The principles of the maximum waste heat utilization, maximum possible initial cycle parameters, recuperation usage and single working fluid were assumed as a basis for the new WHRS design.

It is well known that the fluid saturation temperature depends on the pressure and the higher the pressure level the higher the saturation temperature. This why the extraction of the waste heat from available sources by a refrigerant at different pressure levels is more effective to achieve a maximum waste heat utilization. The thermodynamic efficiency of a Rankine cycle mainly depends on its maximum cycle parameters (pressure and temperature) and minimum pressure. In the works (Jadhao and Thombare (2013), Braimakis et al. (2014)) is shown that ORC operation with a supercritical top pressure has a positive effect on cycle performances. The internal recuperation, in turn, increases WHRS efficiency due to returning part of the heat after the expander to the cycle.

The process of design of recovery system for waste heat flows from the G3612 CAT gas petroleum piston engine is described hereafter. The process is divided into 4 steps and includes: working fluid selection, definition of main cycle parameters, cycle design and thermodynamic simulation, preliminary design of High Pressure and Low Pressure Turbines (HPT, LPT, respectively). The used engine's data is given in Table 1 and the engine's heat balance is shown in Figure 1.

Table 1: Waste heat flows from G3612 CAT gas petroleum engine (Caterpillar (2011))

Energy Flow	Value, kW	Temperature Potential	Recoverability by WHRS
Total Input Heat From the Fuel	7192	High	-
Mechanical Work	2948.72	-	-
Heat Rejection to Exhaust (Recoverable Exhaust Heat at 120°C)	2445.28 (1644.62)	High	Yes
Heat Rejection to the Aftercooler	647.28	Middle	Yes
Heat Rejection to the Jacket Water	575.36	Low	Yes
Heat Rejection to the Oil Cooler	359.6	Low	Yes
Heat Rejection to the Atmosphere	215.46	Lowest	No

2.1 Working Fluid Selection

Unfortunately, a universal organic working fluid that can be used for a wide range of ORC does not seem to exist and the working fluid selection is one of the most important design steps. There are a lot of works devoted to the mentioned problem (Jadhao & Thombare (2013), Braimakis et al. (2014), DiCarlo & Wallace (2011), Jadhao & Thombare (2013), Nouman (2012)). As a rule, the working fluids are considered according to such criteria as thermodynamic properties, environmental impact, thermal stability and safety. Water, ethanol, R245fa and R134a are among the most popular organic working fluids at the moment. Besides, for a recuperated ORC it is recommended to use either an isentropic or a dry fluid. Here, the working fluid was selected according to its potential to remove heat from the selected sources, at different temperatures, in a pressure range from 1 to 45 bars.

Maogang (2011) used in his work for this purpose the combined thermodynamic cycle. It consists of two cycles: an ORC is used to recover the waste heat of the lubricant and exhaust gas and a Kalina cycle for the recovery of the waste heat of the low-temperature cooling water. Of course, the combined WHRS is effective enough but the use of 2 working fluids essentially complicates the system. For these reasons the Kalina cycle is eliminated here in order to simplify the system.

Based on aforementioned thoughts the R245fa (pentafluoropropane) was selected as the working fluid. Due to its low condensation temperature and relatively high decomposition temperature (higher than 250 °C (Honeywell (2014))) R245fa fits the basic criteria of this study. R245fa fluid properties

were calculated based on the NIST RefProp library (version 9.1). The fluid reference state corresponds to the International Institute of Refrigeration (IIR) convention.

2.2 Main ORC Parameters

The design parameters of the cycle components used in this study are presented in Table 2. The maximum cycle temperature was limited to 240 °C to avoid fluid decomposition. The maximal cycle pressure was set to 45 bars. The subsequent pressure increase does not lead to essential cycle performance increase but it leads to an increase of the WHRS production cost and complication of the HPT design. At the HPT inlet the R245fa is at a supercritical pressure which allows for an increase in the cycle efficiency. The comparison of performances between the SORC and subcritical ORC is given in (Jadhao and Thombare (2013), Braimakis et al. (2014)). For this case the condenser pressure was fixed to 1.3 bars to prevent air ingress into the closed cycle.

Table 2: Design parameters of cycle components

Parameter	Units	Value
Efficiency of HPT and LPT	-	0.8
Efficiency of High and Low Pressure Pumps	-	0.8
Minimal Pinch Point for Heat Exchangers	°C	10
Hydraulic Losses in the Pipelines and Heat Exchangers	-	Ignored

2.3 WHRS Cycle Design and Thermodynamic Simulation

At the initial stage of the ORC design waste heat flows from the G3612 CAT engine (see Figure 1 and Table 1) were considered to provide optimal heat utilization with moderate system complexity. In Figure 2 the distribution of the waste heat flows according to their temperatures and the option of their utilization to generate superheated working fluid for ORC are shown.

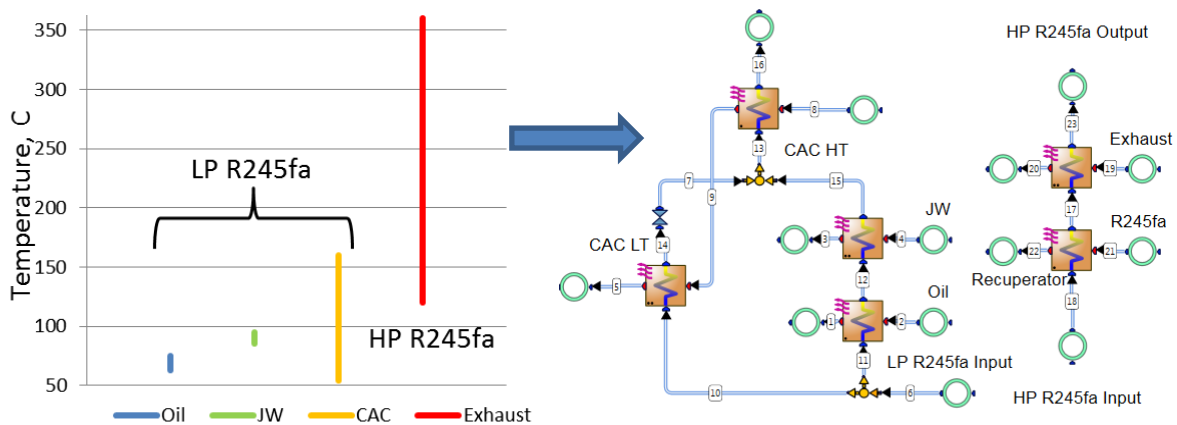


Figure 2: The distribution of heat flows according to their temperatures and the option of their utilization (where LP and HP – low pressure and high pressure; LT and HT – low temperature and high temperature; CAC – charge air cooler)

As is clear from Figure 2, the waste heat from the lubrication oil, the JW and the charge air has a lower temperature potential than the exhaust. It is then rational to use the heat from these sources to preheat the LP flow of R245fa to the necessary conditions. The heat exchangers which transfer heat from the oil and the JW to the low pressure flow of R245fa are connected in series according to their temperature ranges. The Charge Air Cooler (CAC) is divided into two temperature zones; The low temperature CAC (CAC LT heat exchanger in Figure 2) which operates in parallel with the JW and the oil coolers and the high temperature CAC (CAC HT) which is intended for the whole LP flow of R245fa superheat. The pressure of the LP R245fa loop was determined so that the temperature of the working fluid at high temperature CAC outlet is slightly higher than the saturation temperature at the given pressure. Due to the use of a dry working fluid the expansion process in the LPT will take place in the superheated region. In the designed ORC the low pressure loop operates under 7 bars of pressure.

The high pressure loop of the WHRS operates at a maximum pressure of 45 bars. The ORC working fluid is heated through two heat exchangers connected in series (internal recuperator and exhaust gas exchanger). The internal recuperator is used to return to the cycle the part of the heat rejected into condenser. The developed distribution of heat flows for this CAT engine allows utilizing the extra heat in the ORC cycle; almost all of the waste heat can be transferred to the WHRS, the CAC has minimum heat utilization (584.4 kW from the 647 kW available heat). Two alternative cycle concepts for this CAT engine were designed: with separate turbines and with a shared LPT. Both concepts were simulated with the use of the heat balance calculation tool AxCYCLE™ (SoftInWay Inc. (2014)).

2.3.1 Dual loop SORC concept with separate turbines

The flow diagram of the dual loop SORC with the separate turbines is presented in Figure 3. The cycle consists of 6 heat exchangers, 2 turbines (HPT and LPT), 2 pumps (HPP and LPP) and the condenser. Both turbines operate with the same backpressure – 1.3 bars. The flows of R245fa are mixed at the condenser inlet and split at its outlet. The temperature – entropy diagram for the presented cycle is shown on Figure 4. The process 1-2-3-4-5-1 corresponds to the high pressure loop operation and the process 10-20-30-40-10 is for the low pressure loop operation.

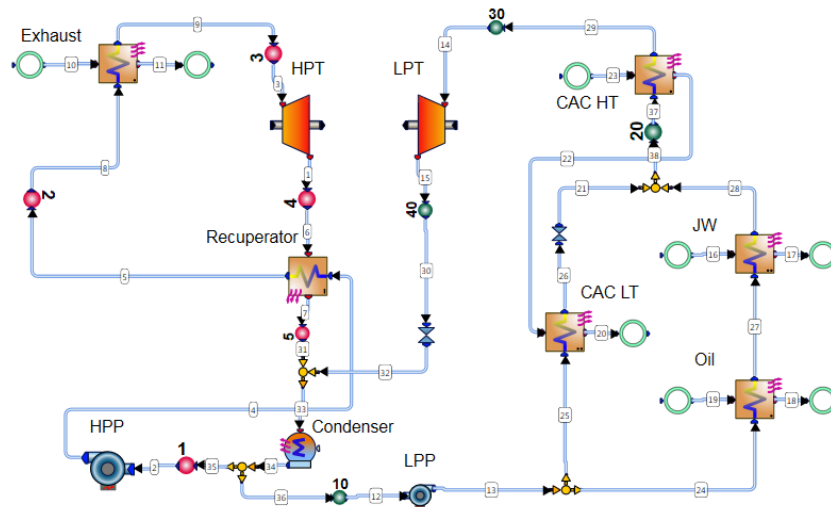


Figure 3: The flow diagram of the SORC with separate turbines

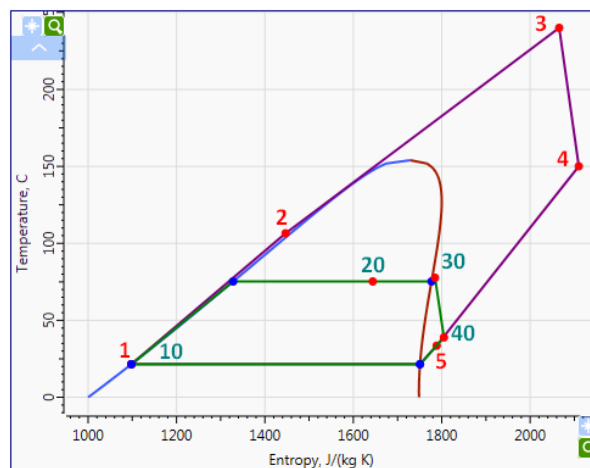


Figure 4: The t-s diagram for the SORC with separate turbines

2.3.2 Dual loop SORC concept with shared LPT

The flow diagram of the dual loop SORC with shared LPT is presented on Figure 5. The considered cycle has the same set of components as the previous one. Unlike in the previous cycle, here the working fluid expands in the HPT up to the pressure of the LP loop (7 bars). After that the flows from the different loops mix and expand in the shared LPT. This means that the mass flow through the LPT is equal to the sum of the HP and LP flows. Flows are again split at the condenser outlet.

The temperature – entropy diagram for the cycle with the shared LPT is shown on Figure 6. In the process 1-2-3 the heat is transferred to the high pressure R245fa flow (45 bars), the process 3-4 is the expansion in the HPT, the process 10-20-30 corresponds to the heat addition to the low pressure flow (7 bars), at point 5 the flows from the different loops mix, between 5 and 6 – the expansion in the LPT occurs and for 6-7 happens a heat transfer in the internal recuperator.

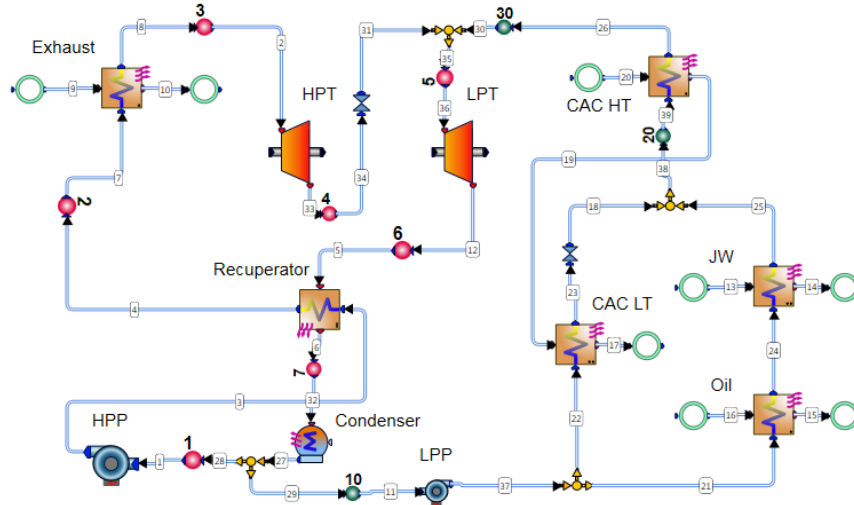


Figure 5: The flow diagram of the SORC with shared LPT

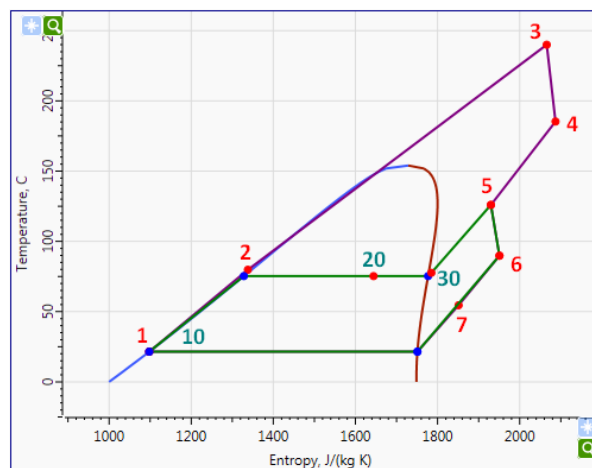


Figure 6: The t-s diagram for the SORC with shared LPT

2.3.3 Performance comparison

In order to quantify the estimation of the performances for the proposed embodiments of the SORC the comparison of their performances with the integral parameters of WHRS based on the double pressure water steam cycle was performed.

The bottoming steam cycle was designed according to materials from (MAN Diesel & Turbo (2012)) for the same CAT engine's conditions given in Table 1. The design parameters used for the steam cycle components are presented in Table 2. The maximum cycle temperature and pressure were limited to 258 °C and to 9 bars, respectively. The pressure at the HPT outlet was set to 3 bars and the condenser pressure was taken as 5.7 kPa. The steam cycle flow diagram and its process in the t – s coordinates are shown on Figure 7. As is evident from Figure 1Figure 7, the use of a steam WHRS allows covering only two sources of the engine's waste heat. This is connected to the thermodynamic properties of water. In this cycle a huge part of the heat is absorbed by the working fluid in the two-phase region under pretty high temperatures (175.35 °C at pressure of 9 bars and 133.52 °C at 3 bars respectively) and the heat of most of the low-temperature sources remains unclaimed. The use of heat from the low temperature sources as well as the steam mass flow is limited by the high temperature source (by the exhaust gas temperature and mass flow).

On the t-s diagram (see Figure 7) between 1 and 2 the total water flow is preheated. After this the flows splits, in the process 2-3-4 the heat is transferred to the high pressure loop and the process 2-8 corresponds to the heat addition to the low pressure flow. The processes 4-5 and 6-7 are for the expansion in the HPT and LPT, respectively.

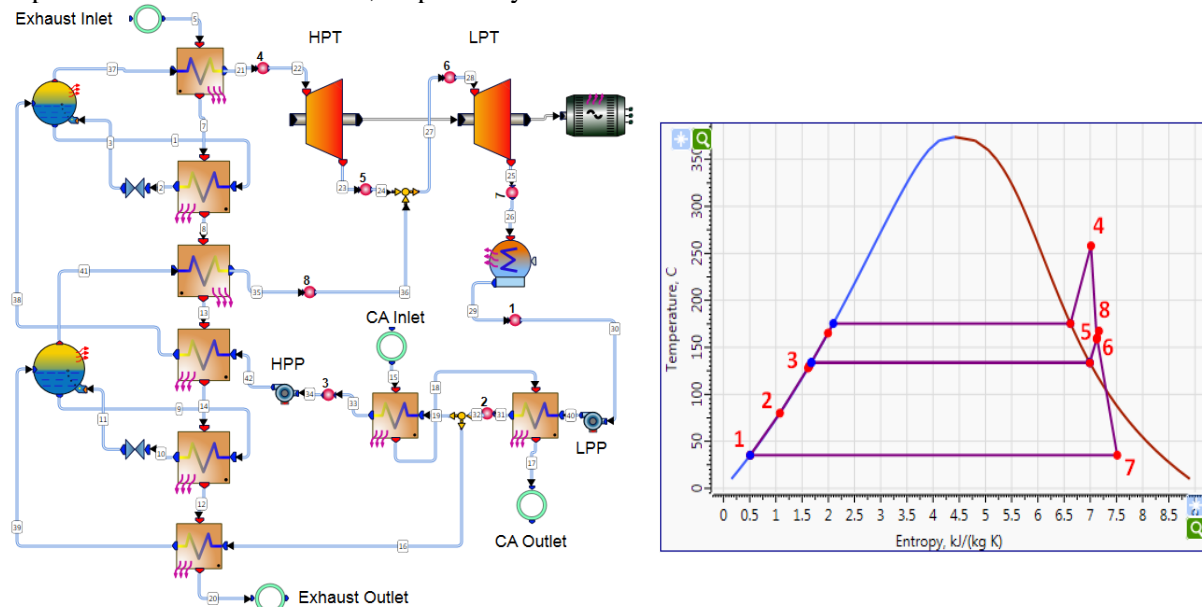


Figure 7: Flow diagram and process in t-s coordinates of the steam cycle

Table 3: The main thermodynamic parameters and the calculated performances of considered cycles

Parameter	Unit	Cycle Embodiments		
		R245fa with Separate Turbines	R245fa with Shared LPT	Steam Cycle
Total Mass Flow	kg/s	12.53	11.77	0.63
Pressure at HPT inlet	bar	45.0	45.0	9.0
Temperature at HPT inlet	°C	240.0	240.0	258.0
Pressure at HPT outlet	bar	1.3	7.0	3.0
Temperature at HPT outlet	°C	150.0	185.3	158.8
Pressure at LPT inlet	bar	7.0	7.0	3.0
Temperature at LPT inlet	°C	77.7	126.0	160.0
Pressure at LPT outlet (Condenser Pressure)	bar	1.3	1.3	0.057
Temperature at LPT outlet	°C	39.0	89.8	35.2
Saturation Temperature at Condenser Pressure	°C	21.5	21.5	35.2
Total Heat Transferred to Cycle	kW	3162.46	3162.46	1750.96
Net Power Production	kW	575.824	531.102	395.728
Power Boost for the CAT Engine	%	19.53	18.01	13.42
Total System Efficiency (ICE+WHRS)	%	49.01	48.38	46.50

The main thermodynamic parameters and the calculated performances of the aforementioned cycles are summarized in Table 3. It can be seen that the steam cycle has the lowest net power production of the three embodiments studied. This fact can be explained by the lowest total amount of waste heat transferred to the WHR cycle. At the same time this cycle has the largest thermal efficiency; it produces 395.728 kW from 1750.96 kW of transferred heat. However, for a WHRS cycle the Net Power Production (NPP) is more attractive since the waste heat is free.

The SORC with separate turbines has a higher NPP due to its higher internal heat recuperation. In that cycle the working fluid temperature at the recuperator inlet (HPT outlet) is 150 °C versus 90 °C in the cycle with the shared LPT. It allows increasing the working fluid mass flow at the HPT inlet (6.02 vs. 5.25 kg/s) which therefore leads to a rise in the mechanical power production. However, the operation of the turbine of the HP loop in the pressure range of the low pressure turbine (cycle concept with

separate turbines) is not a very rational solution. Despite the NPP, the cycle embodiment with the shared LPT is more preferable in the terms of HPT design, production costs and off-design operation. The results of the preliminary design of the HPT and LPT for the SORC with shared LPT are given below.

2.4 Preliminary Design of High Pressure and Low Pressure Turbines

In order to estimate performance and dimensions of these turbines, it was decided to perform a preliminary design for them using SoftInWay turbomachinery design/analysis tool AxSTREAM (Moroz et al. (2005) and (2006)). The boundary conditions for the turbines design are presented in Table 4.

Table 4: Boundary conditions

Parameter	Unit	HPT	LPT
Inlet total pressure	bar	45.00	7.000
Inlet total enthalpy	kJ/kg	621.87	515.63
Static pressure at outlet	bar	7.000	1.300
Mass flow rate	kg/s	5.249	11.77

Rough preliminary estimations showed that both turbines will be rather small in size. For example, the LPT turbine of axial type has 10 stages with a 1st stage nozzle height of about 2 cm and a constant hub diameter of 26 cm. The HPT turbine has up to 20 stages and even smaller blade heights and diameter. It is obvious that it is not reasonable to use axial turbines in these conditions. Taking into account the aforementioned preliminary results it was decided to select a radial turbine type for the further steps. Turbines evaluation was performed in two steps:

1. Turbine design utilizing simplified 1D axisymmetric calculation models by automatic generation of thousands of designs and selection of the best design.
2. Turbine analysis utilizing precise 2D axisymmetric models to get realistic turbine performance.

The Mitrohin-Stepanov loss model was utilized for impeller losses calculation.

Thousands of turbine designs were automatically generated using AxSTREAM’s preliminary design tool. At this step an optimum rotational speed and diameter were selected. After this, 2D calculations were performed for both turbines to obtain their performance. A meridional view of the turbines with some performance data and density field are shown on Figure 8. It should be noted that the turbines picture on Figure 8 are presented using a different scale. Real dimensions can be seen on the vertical and horizontal rulers on the left and the bottom sides of the pictures, respectively. Three-dimensional views of the turbines are presented on Figure 9. Both turbines are of a non-nozzles design type (only impellers and volute). The required inlet angle on impeller blades is achieved by using a special volute design. All performance data and crucial dimensions are collected in Table 5.

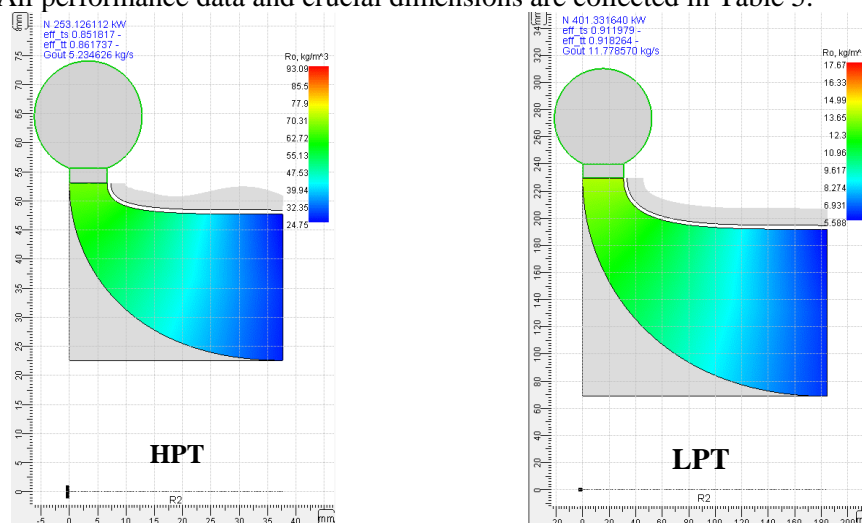


Figure 8: Turbines meridional view with density field

(where, eff_{ts} – turbine internal total-to-static efficiency, eff_{tt} – turbine internal total-to-total efficiency, N – turbine power, G_{out} – turbine mass flow rate, Roh – density)

The HPT is about 4 times smaller than the LPT but its shaft rotational speed is about 5 times higher than for the LPT. The HPT gives 211 kW of mechanical power while the LPT turbine provides about 395 kW. It should be noted that the obtained geometry and performance should not be considered as final. Final configurations might have slightly different performance and dimensions but the difference will not be significant.

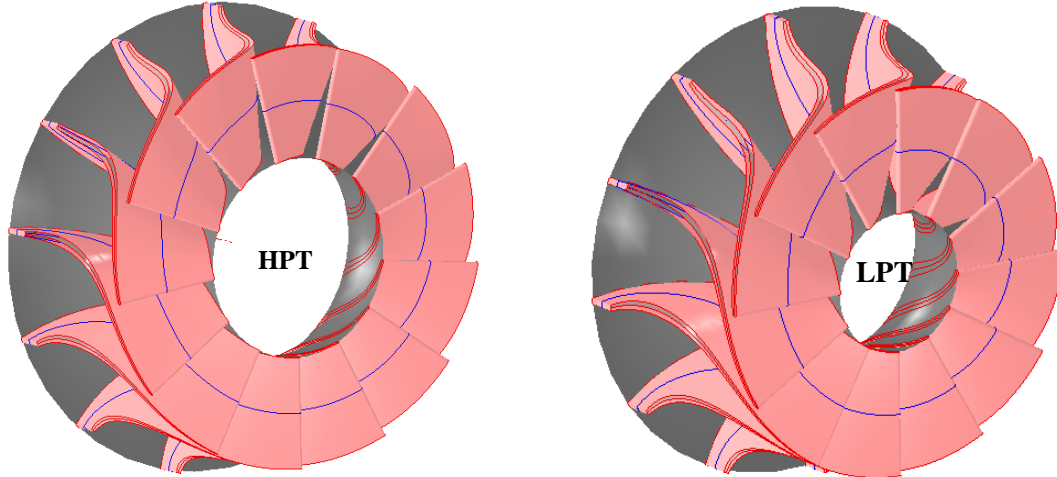


Figure 9: 3D view of the turbines

Table 5: Performance data and crucial dimensions of the turbines

Parameter	Unit	HPT	LPT
Internal total-to-static efficiency	%	85.18	91.33
Power	kW	211.4	394.6
Shaft rotational speed	rpm	40000	7914
Impeller diameter at inlet	mm	106.1	459.2
Mean impeller diameter at outlet	mm	70.3	260.6
Blade height at inlet	mm	6.7	30.9
Blade height at outlet	mm	25.1	122.8
Blade number		13	12

As is evident from Table 5, the obtained turbines efficiency values exceed the previously assumed values (see Table 2). The thermodynamic simulation of the SORC with shared LPT while accounting for the new turbines efficiencies gave 581.86 kW of net power production and 19.73% of power boost for the CAT Engine.

3. FUTURE WORK

The current paper represents a feasibility study and all the received results are not final. In the future, our works on the theme of WHR will be continued in the following directions: off-design WHRS simulation, control system design, estimation of cost and dimensions and more.

4. CONCLUSIONS

- The proposed concepts of dual loop Supercritical Organic Rankine Cycles are a promising technology for maximum waste heat utilization with moderate system complexity. The WHRS designed on the basis of the proposed concepts for powerful and super powerful ICPEs can be either adopted for electricity or mechanical power production.
- The simulation of the new WHRS in AxCYCLE showed that up to 19.73% of power boost for the G3612 CAT gas petroleum engine can be achieved without burning additional fuel which represents significant gains in terms of specific power.
- The comparison of performances between the traditional, high efficiency steam cycle and the SORC R245fa cycles confirmed a high potential for the designed cycles. Both proposed cycles embodiments have a higher net power production compared to the one for the steam cycle in net

power production due to the deep utilization of the low temperature waste heat sources that is not possible using steam.

- For one of the proposed ORC embodiments (the SORC with shared LPT) the evaluation of the turbines size and performance prediction was performed. The designed turbines have high efficiency levels with reasonable dimensions. The internal total-to-static efficiency of the HPT is equal to 85.18 % while it is 91.33% for the LPT. The maximum impeller diameters are equal to 106.1 and 459.2 mm, respectively. The strength characteristics and manufacturability of the designed turbines were not considered in the scope of the present study.

REFERENCES

- Braimakis, K., Leontaritis, A.-D., Preißinger, M., Karellas, S., Brüggeman, D., Panopoulos, K., 2014, Thermodynamic investigation of waste heat recovery with subcritical and supercritical low-temperature organic Rankine cycle based on natural refrigerants and their binary mixtures, *The 27th Int. Conf. of efficiency, cost, optimization, simulation and environmental impact of energy systems*.
- Caterpillar, 2011, *Cooling system*.
- DiCarlo J., Wallace J., 2011, Feasibility study of an organic Rankine cycle system coupled to a diesel engine, *ASME 2011 5th International Conference on Energy Sustainability*, ES2011-54579.
- Guopeng Yu, Gequn Shu, Hua Tian, Haiqiao Wei, Lina Liu, 2013, Simulation and thermodynamic analysis of a bottoming Organic Rankine Cycle (ORC) of diesel engine (DE), *Int. J. Energy*, vol. 51, p. 281-290.
- Honeywell, Revision Date 04/03/2014, *Genetron 245fa Safety Data Sheet*.
- Jumel S., Feidt M., Kheir K., Long Le V., 2012, Working fluid selection and performance comparison of subcritical and supercritical Organic Rankine Cycle (ORC) for low-temperature waste heat recovery, *ECEEE Summer Study on Energy Efficiency in Industry*.
- MAN Diesel & Turbo, 2012, Waste heat recovery system (WHRS) for reduction of fuel consumption, *Emission and EEDI*, no.5510-0136-01ppr.
- Moroz L., Govoruschenko Y., Pagur P., 2006, A uniform approach to conceptual design of axial turbine / compressor flow path, *The Future of Gas Turbine Technology. 3rd International Conference*, Brussels, Belgium.
- Moroz L., Govoruschenko Y., Pagur P., Axial turbine stages design: 1d/2d/3d simulation, experiment, optimization, *Proceedings of ASME Turbo Expo 2005*, Reno-Tahoe, Nevada, USA, GT2005-68614.
- Maogang He, Xinxin Zhang, Ke Zeng, Ke Gao, 2011, A combined thermodynamic cycle used for waste heat recovery of internal combustion engine, *Int. J. Energy*, vol. 36, p. 6821-6829.
- Nouman, J., 2012, Comparative studies and analyses of working fluids for Organic Rankine Cycles – ORC, *Master of Science Thesis EGI-2012-086MSC*.
- Paanu, T., Niemi, S., Rantanen P., 2012, Waste heat recovery – bottoming cycle alternatives, ISSN 1238–7118, *Proc. of the University of VAASA*.
- Petrov, M., 2006, Steam bottoming cycles for the W20V34SG gas engine, *KTH Energy Technology*.
- Seher, D., Lengenfelder, T., Gerhardt, J., Eisenmenger, N., Hackner, M, Krinn, I., 2012, Waste heat recovery for commercial vehicles with a Rankine process, *21st Aachen Colloquium Automobile and engine technology*.
- SoftInWay Inc, 2014, *AxCYCLE user documentation*.

ACKNOWLEDGEMENT

We wish to thank the many people from the SoftInWay Inc. team who generously contributed their time and effort in the preparation of this work. The strength and relevance of the material presented are the result of the inputs and their insightful contributions are greatly appreciated.

PERFORMANCE ANALYSES OF SUPERCRITICAL ORGANIC RANKINE CYCLES (ORCS) WITH LARGE VARIATIONS OF THE THERMOPHYSICAL PROPERTIES IN THE PSEUDOCRITICAL REGION

TIAN Ran¹, AN Qingsong², SHI Lin^{1,*}, ZHAI Huixing¹ and DAI Xiaoye¹

¹Key Laboratory for Thermal Science and Power Engineering of Ministry of Education, Department of Thermal Engineering, Tsinghua University, Beijing, 100084, China

²Key Laboratory of Efficient Utilization of Low and Medium Grade Energy, MOE, School of Mechanical Engineering, Tianjin University, Tianjin 300072, China
e-mail: rnxsl@mail.tsinghua.edu.cn and tianr13@mails.tsinghua.edu.cn

ABSTRACT

Transcritical Organic Rankine cycles (ORCs) are more attractive than subcritical ORCs in terms of their lower exergy losses, higher thermal efficiencies and higher work outputs. This study analyzed the influence of the thermophysical properties variations in the pseudocritical region on the transcritical ORCs performance. For various turbine inlet temperatures and vapor generation pressures, the operating parameters were optimized simultaneously considering the net work output, the thermal efficiency and the total vapor generator area. The results show that the total vapor generator area varied with the turbine inlet temperature along an N-shaped curve. For any heat source temperature, the suitable working fluid should have a pronounced N-shaped curve of the total vapor generator area to guarantee the existence of the optimal parameter region in which all three indicators are optimized. This provides a working fluid selection criterion for heat sources of different temperatures. The analysis simplifies the selections of the operating parameters and the working fluids.

1. INTRODUCTION

Organic Rankine Cycles and their many applications for heat recovery from medium and low temperature heat sources have been widely investigated. Much research interest has been focused on transcritical ORCs because of their high thermal efficiencies, exergy efficiencies and work outputs (Schuster *et al.*, 2010, Karellas and Schuster, 2008, Saleh *et al.*, 2007).

Many studies have considered the working fluid selection and parameter optimization of transcritical ORCs. Maraver *et al.* (2014) provided a general overview of the working fluid selection and optimal design of ORC for different heat sources. They concluded that supercritical cycles are justified for lower critical temperature working fluids if there is no high pressure limitation. However the author did not take into account the working fluid's heat transfer rates. Some researchers have used heat transfer models in heat exchanger area calculations to make economic analyses. Baik *et al.* (2011) compared the transcritical ORC performance of CO₂ and R125 systems using a discretized heat exchanger model to show that R125 has the higher net power output. Li *et al.* (2014) performed thermo-economic analyses with CO₂, R123, R600a, R245fa and R601. Zhang *et al.* (2011) compared the performance of subcritical and transcritical power cycles using optimized cycle parameters. R125 in a transcritical power cycle gave excellent economics and maximized the heat source utilization. Guo *et al.* (2014) investigated the

performance of subcritical and transcritical ORCs based on the pinch point locations in the evaporators. Their results showed that transcritical ORCs have better performance when heat source outlet temperatures are lower.

Although much work has been done on optimizing the thermodynamics and economics of ORC cycles, there are few studies of the heat transfer characteristics or the influence of the thermophysical properties. The thermophysical properties in the supercritical pressure region undergo significant changes in the pseudocritical region (Piro *et al.*, 2011) as shown in Figure 1. These changes affect the working fluid temperature profile and the pinch point location which greatly influence the operating parameter selection and add new requirements to the heat exchanger designs (Karellas *et al.*, 2012). Therefore, the thermophysical properties changes are the key issue for optimization and heat exchanger designs but there are few studies on this topic.

The aims of this study are to investigate the influence of the significant thermophysical property changes in the pseudocritical region on the ORC performance to provide guidance for system designs. First, the turbine inlet temperature, T_3 , and the vapor generation pressure, P_{vap} , were optimized using the net work output W_{net} and the thermal efficiency as the indicators. Then, the variations of the vapor generator surface area, A_{total} , that are related to the changes in T_3 and P_{vap} were analyzed based on the thermophysical property changes. An optimal region was discovered by considering all three indicators, W_{net} , the thermal efficiency and A_{total} . A working fluid selection criterion was then developed based on an analysis of the N-shaped curve for A_{total} at various heat source temperatures.

2. SYSTEM MODELING

2.1 System Description

The basic ORC cycle includes a turbine, condenser, pump and vapor generator. As shown in Figure 2, the working fluid is pressurized to supercritical pressures in the pump and heated by the heat source from point 2 to point 3. In the turbine, the working fluid expands to low pressure to produce work. Finally, the lower pressure vapor is condensed to liquid in the condenser. The working fluid R134a was used as an example.

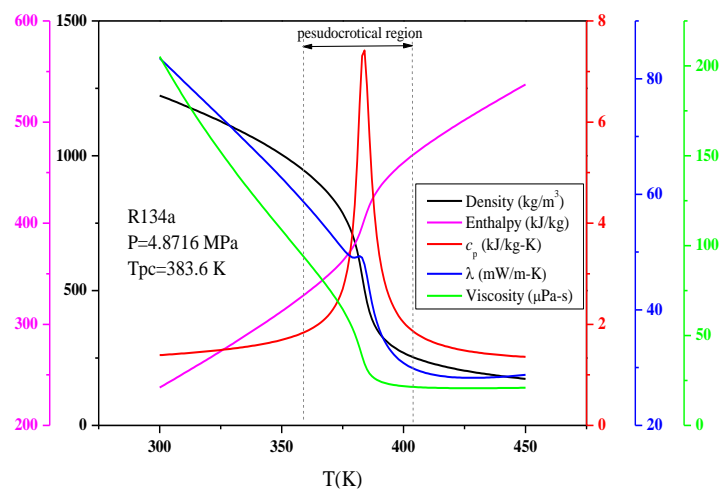


Figure 1: Thermophysical property variations in the pseudocritical region.

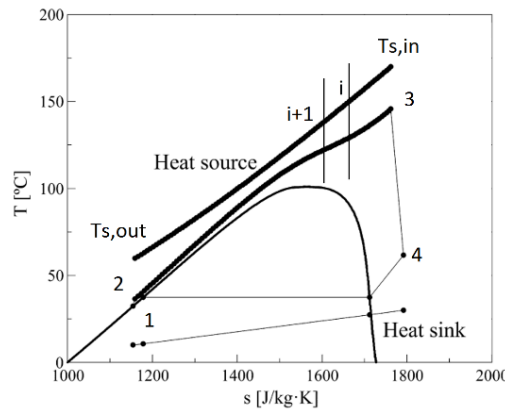


Figure 2: T - s diagram for a transcritical ORC system

2.2 Vapor Generator Model

The working fluid is heated in the vapor generator from liquid to vapor without phase change at supercritical pressures. Due to the significant changes in the thermophysical properties, the vapor generator was divided into n sections in a discretized model assuming equal enthalpy differences as shown in Figure 2. The vapor generator was divided into 100 sections, which has been shown to be reasonable in the literature (Karellas *et al.*, 2012). Section 1 was at the heat source inlet and the working fluid outlet with section 100 as the heat source outlet and the working fluid inlet.

The Nusselt number was calculated using the Jackson correlations (Jackson, 2002) for supercritical pressure fluids:

$$Nu = 0.0183 Re_b^{0.82} Pr_b^{0.5} \left(\frac{\rho_w}{\rho_b} \right)^{0.3} \left(\frac{c_p}{c_{pb}} \right)^n \quad (1)$$

Exponent n is:

$$n = 0.4, \quad \text{for } T_b < T_w < T_{pc} \text{ and for } 1.2T_{pc} < T_b < T_w;$$

$$n = 0.4 + 0.2 \left(\frac{T_w}{T_{pc}} - 1 \right), \quad \text{for } T_b < T_{pc} < T_w;$$

$$n = 0.4 + 0.2 \left(\frac{T_w}{T_{pc}} - 1 \right) \left[1 - 5 \left(\frac{T_b}{T_{pc}} - 1 \right) \right], \quad \text{for } T_{pc} < T_b < 1.2T_{pc} \text{ and } T_b < T_w$$

Where b refers to the bulk fluid temperature and w refers to the wall temperature and T_{pc} is the pseudocritical point temperature. The average specific heat of the working fluid was defined as:

$$\bar{c}_p = \frac{h_w - h_b}{T_w - T_b} \quad (2)$$

The convective heat transfer coefficient in the working fluid was:

$$\alpha_{ORC} = \frac{Nu \lambda}{d} \quad (3)$$

The mean overall heat transfer coefficient was:

$$\frac{1}{U} = \frac{1}{\alpha_{\text{ORC}}} + \frac{1}{\alpha_{\text{HS}}} + \frac{\delta}{\lambda} \quad (4)$$

α_{HS} was calculated using the Dittus Boelter correlation (Sharabi *et al.*, 2008):

$$Nu = 0.023 Pr^n Re^{0.8} \quad (5)$$

Where $n=0.4$ is for heating processes.

The model assumed no heat losses with the logarithmic mean temperature difference (LMTD) used in each element instead of a global temperature difference:

$$Q_{l-i} = \dot{m}_{\text{ORC}} \cdot (h_1 - h_i) = \dot{m}_{\text{HS}} \cdot c_{p,\text{HS}} \cdot (T_{\text{HS},1} - T_{\text{HS},i}) \quad (6)$$

The total vapor generator area, A_{total} , was:

$$A_{\text{total}} = \sum_{i=1}^{i=n} A_i \quad (7)$$

2.3 Global Model

There is no isothermal boiling in the transcritical ORC, so the pinch point location cannot be determined as easily as for the subcritical ORC. The temperature profiles in both the heat source fluid and the working fluid in the vapor generator were calculated using the vapor generator model for the model parameters listed in Table 1. The pinch point location was then determined by modifying the working fluid mass flow rate to get the designed pinch point temperature difference.

Table 1: Simulation parameters for ORC model

Part	Items	Values
Heat source	Inlet temperatures (°C)	160, 170, 180, 190
	Mass flow rate (kg/s)	1
	Pipe pressure (MPa)	1.3
	Pinch point temperature difference (°C)	10
ORC cycle	Condensing temperature (°C)	30
	Isentropic pump efficiency	0.65
	Isentropic turbine efficiency	0.85

3. RESULTS AND DISCUSSION

The calculation used R134a as the working fluid and a 170°C heat source for the parameter optimization (section 3.1) and vapor generator area analysis (section 3.2). R152a and R245fa were used for higher heat source temperatures in section 3.3.

3.1 Parameter optimization based on W_{net} and the thermal efficiency

W_{net} and the thermal efficiency were optimized by changing the turbine inlet temperature, T_3 , and the vapor generation pressure P_{vap} . As shown in Figure 3(a), an optimal W_{net} exists at each P_{vap} . Further, the peak W_{net} move towards higher T_3 as P_{vap} increases. The maximum W_{net} was reached at $1.6P_c$ with only small differences in the maximum W_{net} for various P_{vap} . For example, the maximum W_{net} at $1.3 P_c$ is only 1.14% smaller than that at $1.6 P_c$. Therefore, lower vapor generation pressures should be used to reduce the component requirements and the initial cost with little difference in the work output.

As shown in Figure 3(b), the thermal efficiency increases with T_3 as has been seen in many studies. The thermal efficiency variations with P_{vap} depend on the turbine outlet conditions. For lower T_3 ($T_3 < 393.15\text{K}$), the thermal efficiency decreases with P_{vap} while higher T_3 ($T_3 > 393.15\text{K}$) have maximum thermal efficiency as P_{vap} varies.

Figure 4 shows the variations of W_{net} and the thermal efficiency in response to T_3 and P_{vap} . The shaded area in Figure 4(c) is the optimal region for both W_{net} and the thermal efficiency.

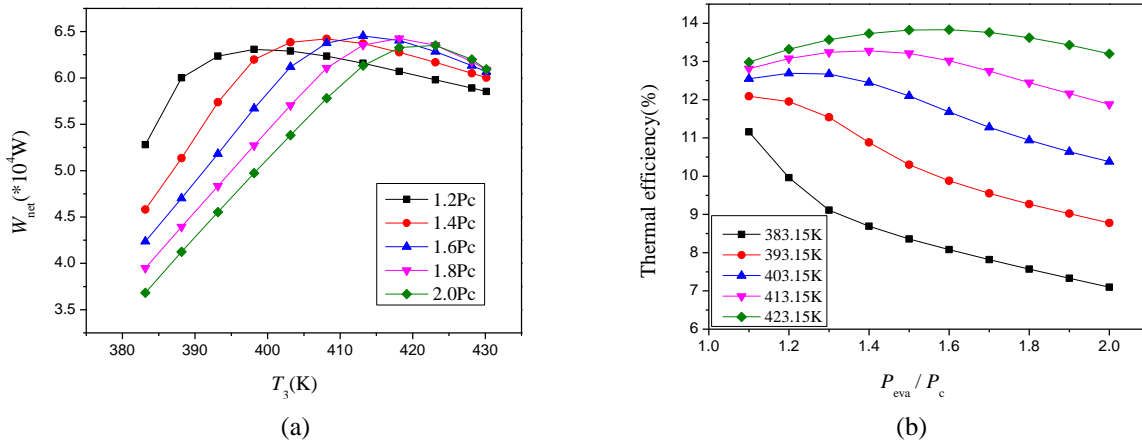


Figure 3: (a) Net work outputs for various turbine inlet temperatures and vapor generator pressures and (b) thermal efficiencies for various vapor generator pressures and turbine inlet temperatures (R134a, $T_s=170^\circ\text{C}$)

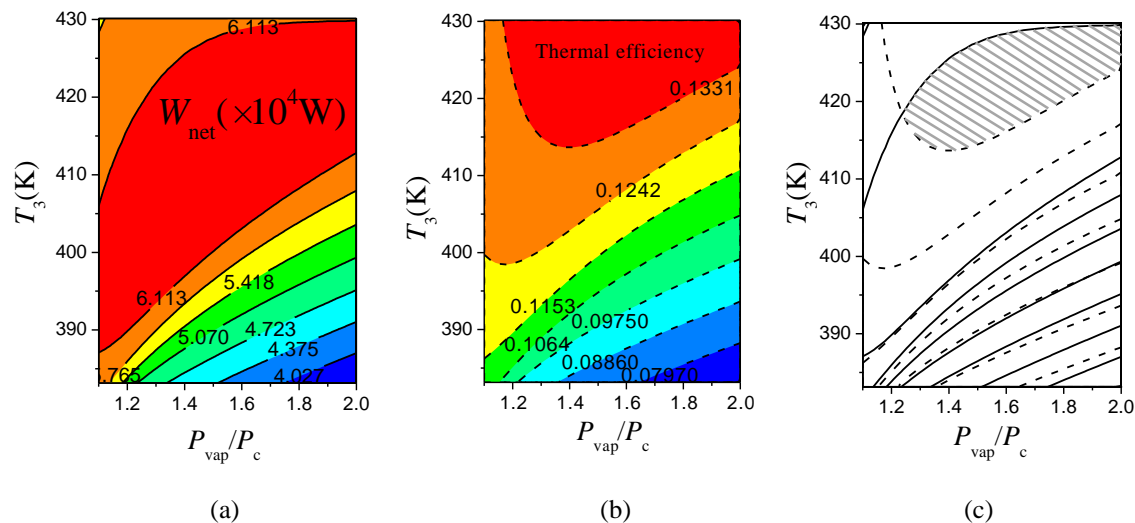


Figure 4: (a) W_{net} for various T_3 and P_{vap} , (b) thermal efficiency for various T_3 and P_{vap} and (c) the optimal operating conditions.

3.2 Vapor Generator Area Analysis

The vapor generator heat exchanger area is the third optimization indicator. The special characteristics of heat transfer at supercritical pressures need to be illustrated by showing the influence of the ORC parameters on the heat exchanger area. Figure 5 shows that the total vapor generator area varies with the turbine inlet temperature along an N-shaped curve.

The N-shaped curve is caused by the variations of the heat transfer coefficient and the LMTD in the pseudocritical region and the movement of the pinch point location. The heat transfer is strongly

affected by the significant changes in the thermophysical properties. As shown in Figure 6(a), the convection heat transfer coefficient of R134a has a peak at temperatures slightly lower than the pseudocritical point and then decreases sharply. The enthalpy sharply increases in the pseudocritical region as shown in Figure 1, so the working fluid temperature gradient, dT/dn , is almost equal to zero, resulting in the temperature profile shown in Figure 6(b). This temperature profile means that the pinch point cannot move across the pseudocritical region. With increasing T_3 , the pinch point moves from the heat source outlet towards the middle, staying at the lower temperature side of the pseudocritical region in the end as shown in Figure 7. The variation of LMTD shown in Figure 8(a) coincides with the temperature profile shown in Figure 6(b), which is the result of the enthalpy variation in the pseudocritical region. In each section of the vapor generator, the elementary area A_i is inversely proportional to the heat transfer coefficient and LMTD, so A_i varies as shown in Figure 8(b). A_{total} is the sum of A_i . Thus, the variations of the heat transfer coefficient and the LMTD in the pseudocritical region and the movement of the pinch point location result in the N-shaped curve for A_{total} .

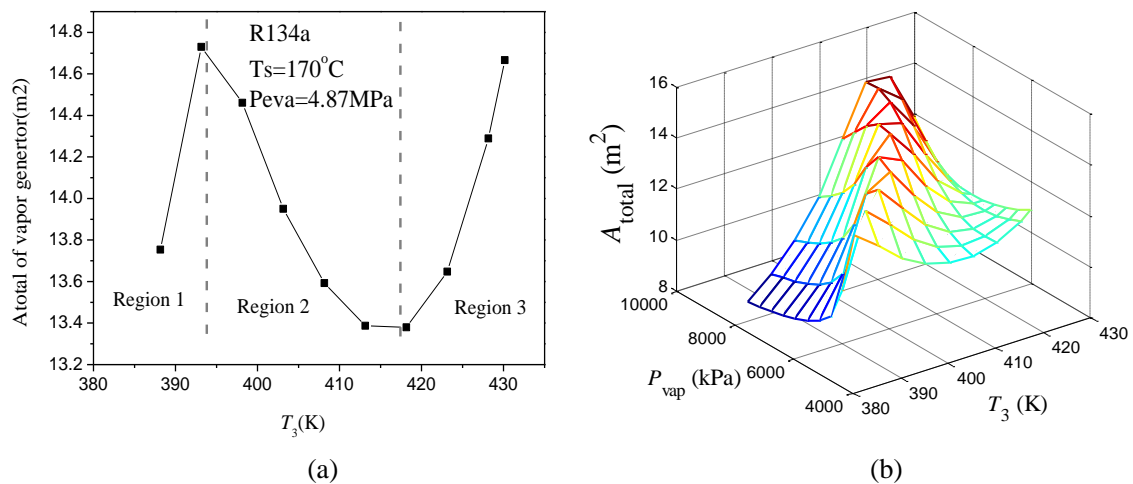


Figure 5: (a) Variation of the vapor generator area A_{total} with the turbine inlet temperature and (b) the variation of A_{total} with the vapor generation pressure and turbine inlet temperature.

A_{total} can be used as the third optimization indicator along with W_{net} and the thermal efficiency. The N-shaped curve in Figure 5(a) can be divided into three regions:

Region 1: $T_3 = 388.15 - 393.15$ K. The pinch point moves from the heat source outlet to the inlet with increasing T_3 as shown in Fig. 8. A_{total} increases with T_3 with the minimum at 388.15 K. However, the transcritical ORC has low W_{net} and thermal efficiency in this region. Therefore, the system should not operate in this region.

Region 2: $T_3 = 393.15 - 418.15$ K. The pinch point moves to the heat source inlet and A_{total} begins to decrease with T_3 . In this region, both W_{net} and thermal efficiency are relatively high, so the system should operate in this region.

Region 3: $T_3 > 418.15$ K, A_{total} increases rapidly in this region due to the higher T_3 and the heat transfer coefficient in this region being much lower than in the other two regions so the heat exchanger area is wasted. For economic reasons, the system should not operate in this region.

The influence of pressure on A_{total} is shown in Figure 5(b). A higher vapor generation pressure results in a larger heat exchanger. Therefore, higher pressures are not economical. The final optimization results considering all three indicators, W_{net} , η_{th} and A_{total} , are shown in Figure 9(b) as the shaded area.

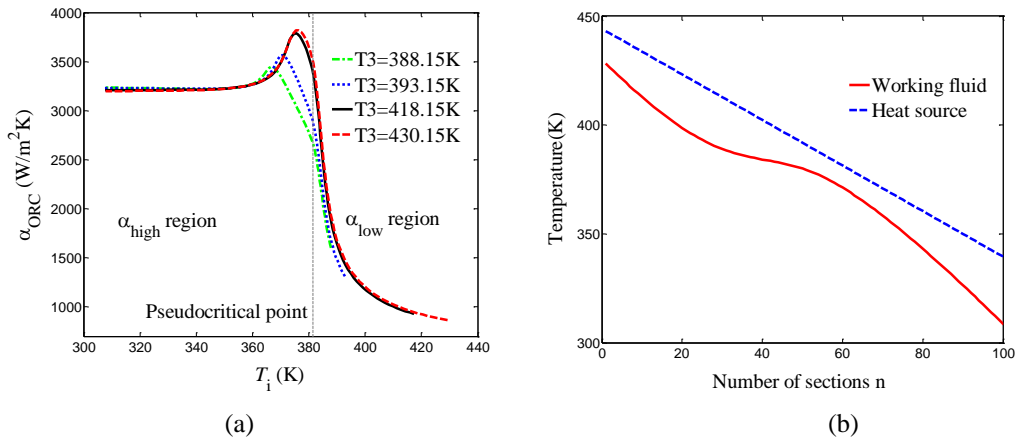


Figure 6: (a) Convection heat transfer coefficient of working fluid in the vapor generator for various turbine inlet temperatures and (b) working fluid and heat source temperature profiles in the vapor generator.

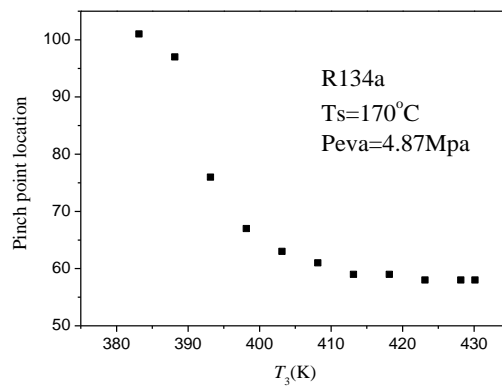


Figure 7: Pinch point locations for various turbine inlet temperatures

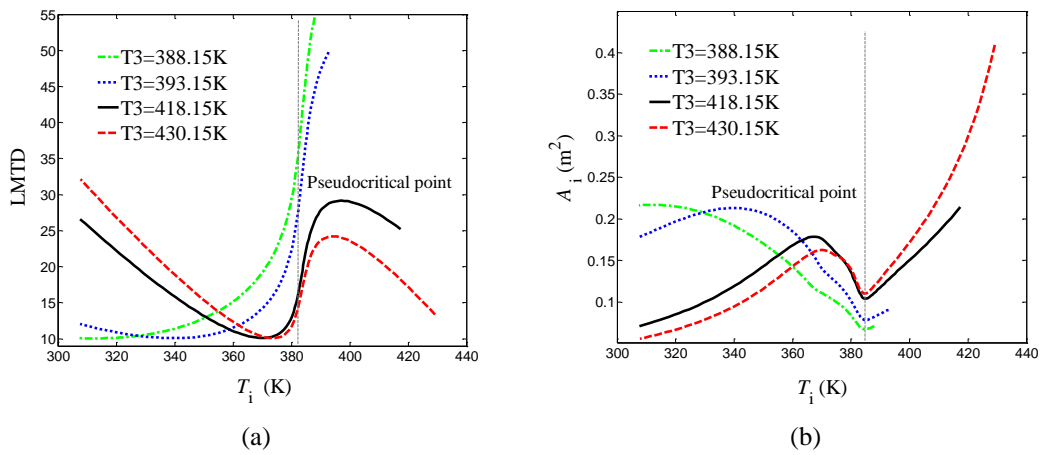


Figure 8: (a) LMTD variations in the vapor generator for various turbine inlet temperatures and (b) the elementary surface area A_i variations in the vapor generator for various turbine inlet temperatures.

3.3 Working Fluid Selection Criterion at Various Heat Source Temperatures

The system performance was also investigated for various heat source temperatures. R134a was used in sections 3.1 and 3.2 with a 170°C heat source. Other heat source temperatures will require other working fluids so that the system has an optimal region as in Figure 9(b). As shown in Table 2, when

the heat source temperature increases from 160°C to 190°C, the higher temperature heat source gives a larger maximum W_{net} , but the corresponding optimal pressure increases from 6.09 MPa to 7.71 MPa. The higher pressure make the system more dangerous and difficult to maintain. As shown in Figure 10, the N-shaped curve of A_{total} for R134a is less pronounced with A_{total} in region 2 increasing significantly with the increasing heat source temperature. Moreover, the higher heat source temperature keeps the pinch point at the heat source outlet as shown in Figure 11. Since the system performance is worse when the pinch point is adjacent to the heat source outlet, the higher heat source temperature will lead to poor performance and there is no optimal shaded area as in Figure 9(b).

In conclusion, when the heat source temperature is much higher than T_c of the working fluid, the optimal area does not exist. While R134a performs well with a 170°C heat source, R134a is not suitable for higher temperature heat sources of 180-190°C. The results in Table 2 show that $W_{net,max}$ and the thermal efficiency of R152a, R245fa, whose T_c are higher than that of R134a, are both higher than that of R134a. The optimal pressures are also much lower than that of R134a for the same heat source temperature. Figures 10 and 11 show that the A_{total} in region 2 using R152a and R245fa are much lower than that of R134a and the pinch point quickly moves to the lower temperature side of the pseudocritical region. The performance is greatly improved by using R152a and R245fa with the 190°C heat source. Thus, if the N-shaped curve for A_{total} is less pronounced or disappears and the pinch point is always stay near heat source outlet, then the current working fluid cannot match the heat source and working fluids with higher critical temperatures are suggested.

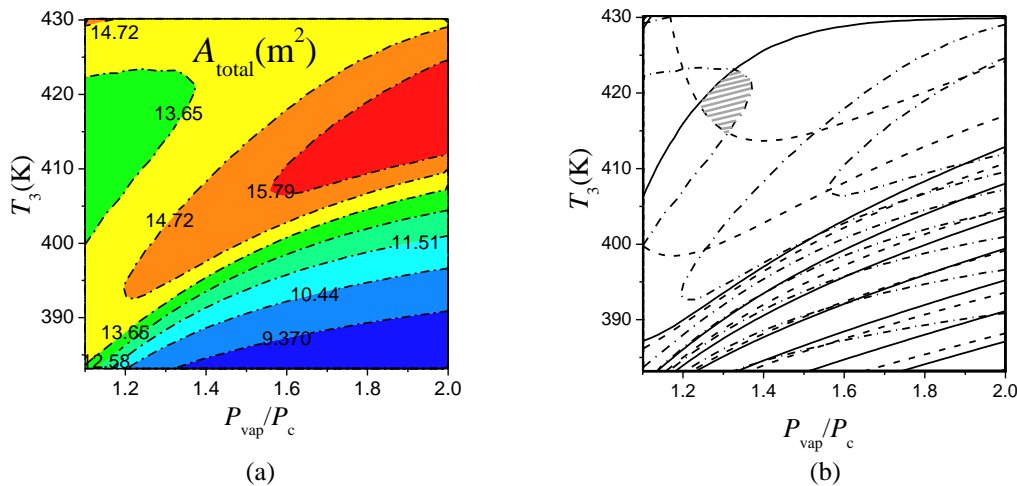


Figure 9: (a) A_{total} variations with T_3 and P_{vap} and (b) the optimal operating region

Table 2: Optimal operating parameters with W_{net} as the optimization objective

	T_c (°C)	P_c (MPa)	T_s (°C)	$W_{net,max}$ (kW)	P_{vap} (MPa)	η_{th} (%)
R134a	101.06	4.0593	160	55.4	6.089	12.10
			170	64.5	6.495	13.02
			180	73.9	6.901	13.76
			190	83.4	7.713	14.29
R152a	113.26	4.5168	180	73.5	6.324	13.85
			190	83.6	6.775	14.70
R245fa	154.01	3.651	190	90.4	4.746	15.22

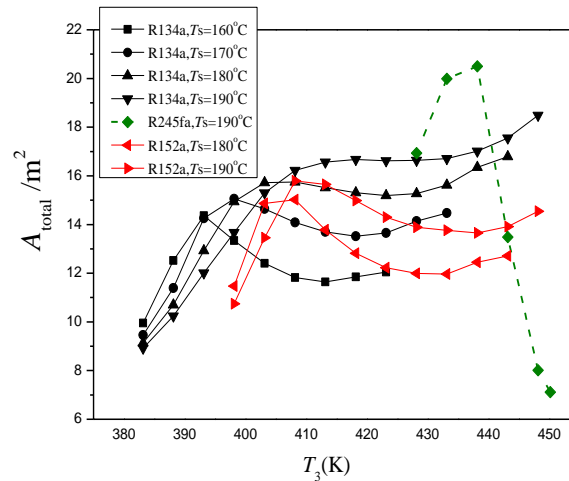


Figure 10: A_{total} variations with the turbine inlet temperature for various heat source temperatures

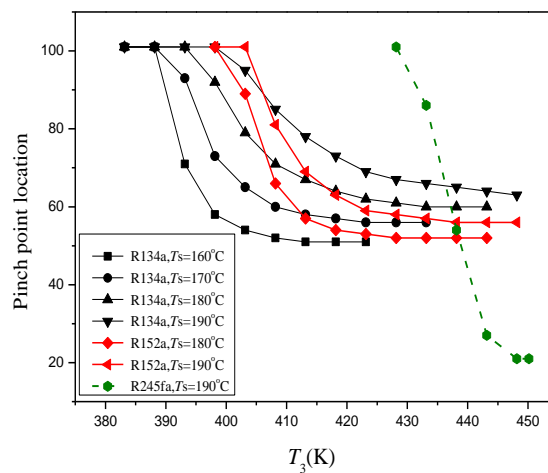


Figure 11: Pinch point location variations with the turbine inlet temperature

4. CONCLUSION

The influence of the large changes in the thermophysical properties in the pseudocritical region was investigated. An optimization method was developed using the net work output, the thermal efficiency and the total vapor generator area. The optimal turbine inlet temperature and vapor generation pressure were found for various operating conditions. The results obtained in this study will simplify working fluid selection for various heat source temperatures. The main conclusions can be summarized as:

1. The thermophysical properties of the working fluid in transcritical ORCs operating at supercritical pressure undergo significant changes, resulting in considerable variations in the heat transfer coefficient and LMTD. Therefore, studies of transcritical ORCs should pay much more attention to the thermophysical property changes in the pseudocritical region. The heat transfer mechanisms at supercritical pressure must be further understood for system optimization and proper heat exchanger design.
2. The total vapor generator area, A_{total} , varies with the turbine inlet temperature T_3 along an N-shaped curve due to the variations of heat transfer coefficient and LMTD in the pseudocritical region and the changes of the pinch point location. The optimal operating conditions should be in region 2 of

the N-shaped curve to give the best area with the best W_{net} and thermal efficiency.

3. A working fluid selection criterion was developed for various heat source temperatures. A suitable working fluid should have a pronounced N-shaped curve for A_{total} to guarantee the existence of the optimal parameter region. When the N-shaped curve for A_{total} is less pronounced or non-existent and the pinch point is always near the heat source outlet, the working fluid cannot match the heat sources, and working fluids with higher critical temperatures are suggested.

REFERENCES

- Baik, Y. J., Kim, M., Chang, K. C., & Kim, S. J. (2011). Power-based performance comparison between carbon dioxide and R125 transcritical cycles for a low-grade heat source. *Applied Energy*, 88(3), 892-898.
- Guo, C., Du, X., Yang, L., & Yang, Y. (2014). Performance analysis of organic Rankine cycle based on location of heat transfer pinch point in evaporator. *Applied Thermal Engineering*, 62(1), 176-186.
- Jackson JD. Consideration of the heat transfer properties of supercritical pressure water in connection with the cooling of advanced nuclear reactors, Proc. 13th Pacific Basin Nuclear Conference, Shenzhen City, China, October 21 – 25, 2002
- Karellas, S., & Schuster, A. (2008). Supercritical fluid parameters in organic Rankine cycle applications. *International Journal of Thermodynamics*, 11(3), 101-108.
- Karellas, S., Schuster, A., & Leontaritis, A. D. (2012). Influence of supercritical ORC parameters on plate heat exchanger design. *Applied Thermal Engineering*, 33, 70-76.
- Li, M., Wang, J., Li, S., Wang, X., He, W., & Dai, Y. (2014). Thermo-economic analysis and comparison of a CO₂ transcritical power cycle and an organic Rankine cycle. *Geothermics*, 50, 101-111.
- Maraver, D., Royo, J., Lemort, V., & Quoilin, S. (2014). Systematic optimization of subcritical and transcritical organic Rankine cycles (ORCs) constrained by technical parameters in multiple applications. *Applied energy*, 117, 11-29.
- Pirola, I., Mokry, S., & Draper, S. (2011). Specifics of thermophysical properties and forced-convective heat transfer at critical and supercritical pressures. *Reviews in Chemical Engineering*, 27(3-4), 191-214.
- Saleh, B., Koglbauer, G., Wendland, M., & Fischer, J. (2007). Working fluids for low-temperature organic Rankine cycles. *Energy*, 32(7), 1210-1221.
- Schuster A, Karellas S, Aumann R. (2010) Efficiency optimization potential in supercritical Organic Rankine Cycles[J]. *Energy*, 35(2): 1033-1039.
- Sharabi M., W. Ambrosini, S. He, J.D. Jackson, (2008) Prediction of turbulent convective heat transfer to a fluid at supercritical pressure in square and triangular channels, *Annals of Nuclear Energy* 35 993e1005
- Zhang, SJ, Wang, HX, & Tao, G. (2011). Performance comparison and parametric optimization of subcritical Organic Rankine Cycle (ORC) and transcritical power cycle system for low-temperature geothermal power generation. *Applied Energy*, 88(8), 2740-2754.

ACKNOWLEDGEMENTS

This work was supported by the State Key Program of the National Natural Science Foundation of China (Grant No.51236004) and the Science Fund for Creative Research Groups (No. 51321002)

INVESTIGATION AND EFFICIENCY MAXIMIZATION OF THE OPERATION AND DESIGN OF A SMALL SCALE EXPERIMENTAL TRIGENERATION SYSTEM POWERED BY A SUPERCRITICAL ORC

Tryfon Roumpedakis*, Konstantinos Braimakis†, Sotirios Karellas†

*National Technical University of Athens,
Heroon Polytechniou 9, 15780 Zografou
Greece
e-mail: roumpedakis_t@hotmail.com

ABSTRACT

In this work, the detailed investigation and the optimization of the operational parameters of an experimental, small scale trigeneration system encompassing a supercritical Organic Rankine Cycle (ORC) and a heat pump are presented. Both the ORC and the heat pump jointly operate with the same working fluid (R227ea). The heat input to the ORC is provided by a 85 kW_{th} biomass boiler. The electricity produced by the ORC, which has a nominal power output of 5 kW_e, is used to power the heat pump, capable of covering a cooling load of 4 kW_{th}, while any surplus electricity is exported to the grid. Meanwhile, the heat generated during the condensation of the working fluid (around 70 kW_{th}) is utilized to produce hot water. The system has therefore the potential to produce combined cooling, heating and electricity, depending on the load requirements, by utilizing a renewable energy source with zero net CO₂ emissions.

The investigation carried out includes the selection process of the working fluid of the system through the comparison of its performance with that of other typical working fluids and by taking into account environmental and safety factors. Furthermore the study presents the optimization procedure for selecting the working temperatures and pressures in order to maximize the cycle's efficiency, given the technological limits of the elements of this system (heat exchangers, scroll expanders etc.). In addition, a supercritical plate heat exchanger model, used for the design of the heat exchanger of the unit, is presented.

1. INTRODUCTION

In the recent years, a significant amount of interest has been focused on multigeneration systems aiming to convert a primary energy source (fossil, solar, waste heat) into combined electricity, cooling and heating. This is in part driven by the fact that traditional electricity generation systems have a restricted efficiency (around 30-40 % [1], [2]), so a great deal of the original heat is rejected to the environment unexploited in the form of waste heat. Due to the policies followed worldwide in order to increase overall system efficiencies and restrain the emissions of greenhouse gas (GHGs), a lot of research focuses on the design of cost competitive co-generation and combined cooling, heating and power systems is carried out. Furthermore, small scale cogeneration and trigeneration systems that use renewable energy sources have gathered significant attention, since they can potentially contribute to a further reduction of emissions, while also ensuring sustainability and fuel independence.

The Organic Rankine Cycle (ORC) has lately gathered substantial interest as a promising technology in the field of power generation from low temperature heat sources, such as solar and geothermal energy and industrial waste heat. The traditional water-steam Rankine cycle, implemented in the conventional high-temperature thermal power plants, is in many cases not economic or technically feasible. This is because its implementation is not favorable for low grade applications and small-scale power outputs [3], such as those encountered in solar thermal plants. The Organic Rankine

Cycle (ORC), on the other hand, poses certain advantages compared to the conventional cycle. Some of these include the potential of low temperature heat recovery due to the lower boiling point of the working fluids used, the overall smaller component size as well as the capability of expander operation under smaller temperatures [4]. Moreover, due to the “dry” organic fluids having a positive dT/dS saturation vapor line, it is not in principle necessary to superheat them [5]. Meanwhile, the supercritical ORC (SORC), in which the working fluid is pressurized to supercritical pressures before its entrance to the heater has been shown to exhibit several advantages, such as improved thermal and also exergetic efficiency [6-8]. The most important characteristic of supercritical ORCs is the fact that, because of the supercritical heating pressures, the working fluid does not gradually evaporate into the gaseous phase. Instead, it changes from the liquid to the supercritical state when its temperature increases above its critical value. Despite, the fact that, compared to a subcritical, the supercritical ORC results in higher operating pressures in the cycle, it is worthy evaluating its competitiveness for small scale systems in a practical way.

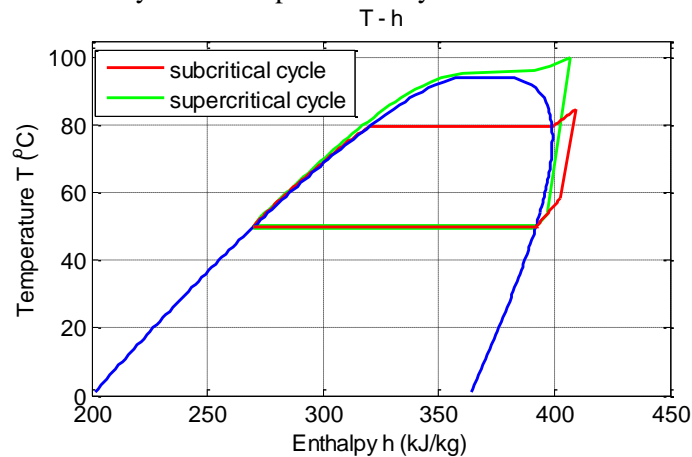


Figure 1: Sub- and supercritical ORC. Example of R1234yf

In this study an experimental trigeneration unit currently under construction in the Laboratory of Steam Boilers and Thermal Plants (LSBTP) in the National Technical University of Athens (NTUA), Greece, is introduced. The system consists of a supercritical Organic Rankine Cycle (SORC) interconnected with a Vapor Compression Cycle (VCC). Heat is provided to the system by a biomass boiler. The two systems are capable of combined electricity, cooling and heating generation, as can be seen in the simplified process diagram of Figure 2. In the present work, the preliminary design and decision process regarding the working fluid selection, the adjustment of some key thermodynamic operational parameters and the selection of equipment is presented and justified.

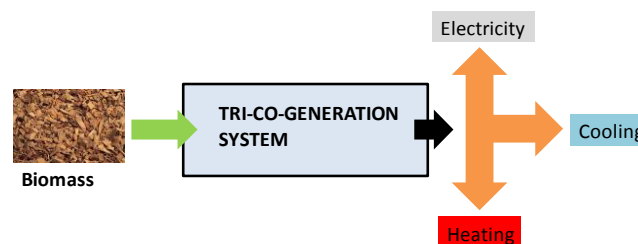


Figure 2: Simple process diagram of the ORC-VCC system under construction

2. SYSTEM DESCRIPTION

2.1 SORC and VCC modules

The system under design and construction consists of three main subsystems, the SORC module, the VCC module and the biomass boiler-heating oil module. The SORC is interconnected to the VCC and both cycles use the same working fluid. The SORC includes a pump and a series of heat exchangers, where energy is transferred from the heat sources to the working fluid. After reaching its maximum temperature the working fluid flows through the expander, producing useful work, which is used to cover the power needs of the system, while any surplus is exported to the grid

The supercritical fluid exiting the expander of the SORC is mixed with the stream exiting the compressor of the VCC and the mixture both enter the condenser of the system. In this way, the condensation step of both cycles takes place in a single condenser under a common pressure, providing the heat output of the system which is used for producing hot water. Apart from the compressor, the VCC is comprised of an expansion valve and an evaporator, where it absorbs heat, thus generating the cooling output of the system.

The power required for the compression of the cooling cycle is provided by the generator of the SORC, while any surplus power can be exported to the electricity grid.

During the winter, when there is no demand for cooling, the VCC can be disconnected from the rest of the system, giving an increased potential for electricity generation. In this manner, the operation mode can alternate between trigeneration and cogeneration. On trigeneration mode, it is necessary that the power produced by the ORC is adequate for the operation of the compressor in order for the system to be independent from external power sources. It must be mentioned, that this system is to operate at steady state conditions, besides the inevitable fluctuations of the biomass boiler.

2.2 Biomass boiler-heating oil circuit

The heat input to the SORC originates from the combustion of biomass in a boiler. The combustion heat is provided to a heating oil which then flows through an intermediate heat transfer loop (HTL) in order to deliver its energy content to the working fluid in the heater of the SORC. The heating oil then returns to the biomass boiler to increase its temperature.

3. MATHEMATICAL MODELING AND SIMULATION

3.1 Mathematical formulation

The first step of the design of the experimental unit is its thermodynamic modeling, which will subsequently allow to select the optimal values of some of its key operational parameters. The simulation of the system is carried out by numerically solving a set of mathematical equations that describe the operation of its components. For the simulation of the system, a steady state operation is assumed, while heat and pressure losses along the equipment are neglected. The equilibrium thermodynamic properties of the working fluid in each state are calculated with the CoolProp database [9] incorporated in the Matlab Software [10]. The most important system performance evaluation indexes used for the design of the facility are the thermal efficiency of the SCORC $\eta_{th,ORC}$, the electrical efficiency of the ORC $\eta_{el,ORC}$, the Coefficient of Performance (COP) of the VCC, the heat production efficiency of the system $\eta_{heat,sys}$ as well as its overall cogeneration efficiency $\eta_{CHP,sys}$. These are described by the following equations:

$$\eta_{th,ORC} = \frac{P_{turb} - P_{pump}}{Q_{ORC,in}} \quad (1)$$

$$\eta_{el,ORC} = \frac{P_{el,net}}{Q_{ORC,in}} \quad (2)$$

$$COP = \frac{Q_{cool}}{P_{el,comp}} \quad (3)$$

$$\eta_{heat,sys} = \frac{Q_{cond}}{Q_{ORC,in}} \quad (4)$$

$$\eta_{CHP,sys} = \frac{Q_{cond} + P_{el,net}}{Q_{ORC,in}} \quad (5)$$

In the above equations, P_{turb} is the work derived in the turbines, P_{pump} is the work consumed in the pump, $P_{el,net}$ is the net electric output of the SORC expander, Q_{cool} is the cooling duty of the VCC, $P_{el,comp}$ is the electricity consumed by the VCC compressor, Q_{heat} is the heat generated in the condenser of the system and $Q_{ORC,in}$ is the heat provided to the working fluid in the heater of the SORC.

3.2 Assumptions

Further assumptions made regarding the operation and the technical specifications of the basic components of the system are summarized in Table 1. The upper pressure level of the SORC was determined by considering the capability to use an open-drive scroll expander, which is commonly proposed for small scale applications such as the one investigated in the current study. The preference towards this type of expander instead of an expander of the hermetic type is justified by its lower cost. Moreover, high pressures (beyond 40 bar) inhibit the use of plate heat exchangers, which are relatively cheap and provide a very attractive heat transfer area-to-volume ratio. The maximum temperature limit of the working fluid of the SORC is imposed by the maximum temperature of the heating oil and the pinch point value of the heater that are assumed to be equal to 120 °C and 10 K respectively. Moreover, it is known that the thermal efficiency of ORCs increases as the condensation temperature decreases. The impact of the condensation temperature on the COP of the VCC is similar. However, it is not possible to decrease this temperature below a certain limit. On one hand, the condensation temperature cannot be lower than the temperature of the cooling water. On the other hand, since the system is intended to produce useful heat, the temperature of the water at the condenser outlet must be at least equal to 50 °C.

Table 1: Heating system and SORC assumptions

<u>Biomass boiler-Heat Transfer Loop</u>	
Boiler efficiency	82.9 %
Biomass Low Heating Value	16920 kJ/kg
Heat duty	85 kW _{th}
Heating oil	BP Transcal N
Heating oil maximum temperature	120 °C
Heating oil temperature difference in boiler	15 K
<u>SORC module</u>	
Pinch point heater	10 K
Pinch point condenser	5 K
Maximum pressure of working fluid	40 bar
Maximum temperature of working fluid	110 °C
Isentropic efficiency of pump	50 %
Isentropic efficiency of expander	65 %
Electromechanical efficiency	85 %
Cooling water temperature at the condenser inlet	
Summer	30 °C
Winter	20 °C
Minimum cooling water temperature at the condenser outlet	40 °C
<u>VCC module</u>	
Pinch point evaporator	5 K
Nominal cooling load	4 kW _{th}
Evaporation temperature	10 °C
Condensation temperature	50 °C
Isentropic efficiency of compressor	75 %

4. WORKING FLUID SELECTION AND THERMAL EFFICIENCY MAXIMIZATION

The selection of the most appropriate working fluid is the first goal of the thermodynamic optimization. In the design process of the experimental unit, the screening method, which is commonly used in the literature, was followed. The two primary criteria used for selecting working fluid candidates are the critical temperature and pressure. Given the operational range of the temperatures and pressures of the system, as given in Table 1, a short list of 11 working fluids was created. These fluids are given in Table 2.

A second group of fluids were chosen from the working fluids of Table 2, by taking into account their Ozone Depletion Potential (ODP), their Global Warming Potential (GWP) as well as their ASHRAE safety group categorization. More specifically, R123 has a high ODP and is to be substituted by HFE7000 by 2030, R1234yf, R143a, R41, Propylene and n-Propane were rejected because of their high inflammability, R134a because of its high critical pressure and R161 because of its very limited market availability. Thus a final list of three working fluids, R125, R227ea and R404a, is assembled (in bold format in Table 2). The optimal working fluid is ultimately chosen by performing a thermodynamic investigation of their performance. The purpose of the optimization process is to determine which fluid exhibits the highest thermal SORC efficiency, when varying certain independent operation variables within the acceptable ranges specified in Table 1. The independent variables are the maximum pressure and temperature of the SORC and the condensation temperature. The evaporation temperature of the VCC is set at 7.5 °C, while a cooling load of 0 (cogeneration mode) and 3 kW (trigeneration mode) is assumed. The results of the optimization process for the three final working fluids are summarized in Table 3.

Table 2 : Preliminary selection of working fluid candidates ($P_{crit} < 40\text{bar}$, $T_{crit} < 110^\circ\text{C}$)

Working fluid	Critical temperature °C [11]	Critical pressure (bar) [11]	ODP [12]	GWP [12]	ASHRAE safety group [13]
R125	66.02	36.18	0	3500	A1
R134a	101.06	40.59	0	1430	A1
R143a	72.71	37.61	0	4470	A2L
R1234yf	94.70	33.82	0	4	A2L
R227ea	101.75	29.25	0	3220	A1
Propylene	92.42	46.65	0	1.8	A3
R41	44.13	58.97	0	92	---
N-Propane	96.70	42.48	0	3.3	A3
R161	102.22	47.02	0	12	--
R410a	72.80	48.60	0	2088	A1
R404a	72.07	37.32	0	3300	A1

As can be seen from Table 3, R227a exhibits both the highest SORC efficiency and the highest COP among the fluids examined. For this reason, it is selected for the experimental unit. It deserves to be noted that, despite it being commonly investigated as a working fluid for ORC applications in the literature [3, 14, 15], R227ea has not been very often used in actual ORC plants or experimental rigs. Moreover, it is rarely used in commercial refrigeration applications. Its market availability is relatively scarce and its cost significantly high, since its price is about eight times the price of R134a.

Table 3 Optimization results of the SORC thermal efficiency for the three final working fluids

	R125	R404a	R227ea
P_{max} (bar)	40	40	30.4
T_{max} (°C)	110	110	110
T_{cond} (°C)	50	50	50
T_{cool} (°C)	10	10	10
$\eta_{th,orc}$	2.16	2.81	4.92
$\eta_{el,net}$ ($Q_c=0$)	0.71	1.17	2.72
$\eta_{el,net}$ ($Q_c=1$)	0.23	0.73	2.30
COP	3.24	3.57	3.78

It can be thus considered as a "novel" working fluid. Based on the optimization results, the operational data of the system are summarized in Table 4.

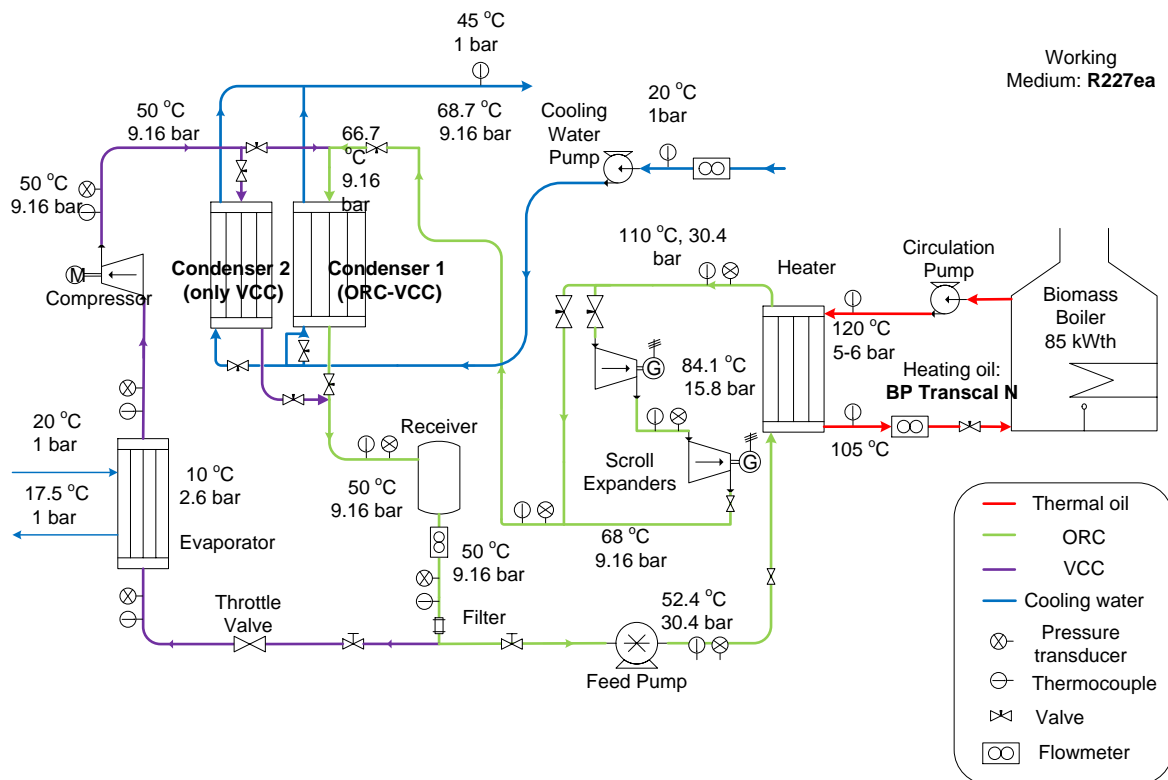


Figure 3: Process flow diagram of the experimental trigeneration facility

5. EQUIPMENT SELECTION

5.1 Overview

A process flow diagram of the experimental unit to be constructed along with operational data and design pressures and temperatures is presented in **Error! Reference source not found.**. The right part of the figure depicts the heating oil circuit along with the biomass boiler (red color) and the left part depicts the VCC (purple color). The SORC is in between these two circuits (green color). Two streams of water (blue color) are used for the cooling and the heating of the working fluid in the Condensers 1 and 2 as well as in the evaporator of the VCC respectively.

As can be seen, it was decided that two identical scroll expanders serially positioned will be used for the expansion process of the working fluid. Each one of these expanders is directly coupled to a generator. This is because of the limited volume flow ratio that is technically possible for these volumetric expanders. According to the literature [16], its value must not be higher than 5. Following a more conservative approach, the volume flow ratio for the expanders of the experimental rig is set between 2 and 3. During the start-up of the operation of the system, the working fluid does not flow through the expanders but goes through a by-pass loop until the vapor reaches the desired pressure and temperature.

Table 4: Design point operational data of the system at trigeneration mode

SORC module	
Mass flow rate	0.699 kg/s
Maximum pressure/temperature	30.4 bar/110 °C
Condensation pressure/temperature	9.16 bar/50 °C
Pressure/temperature after expanders	9.16 bar/68 °C
SORC net electric power output	2.40 kW _e
Overall net electric power output	0.99 kW _e
VCC module	
Mass flow rate	0.056 kg/s
Evaporation pressure/temperature	2.79 bar/10 °C
Condensation pressure/temperature	9.16 bar/50 °C

Pressure/temperature after compressor	9.16 bar/50 °C
Nominal cooling load	4 kW _{th}
<u>Cooling system</u>	
Water inlet temperature (summer/winter)	30 °C/20 °C
Water outlet temperature	45 °C
Mass flow rate	0.730 kg/s
Nominal heating load	85.8 kW _{th}
<u>Heating system</u>	
Heating oil inlet temperature	120 °C
Heating oil outlet temperature	105 °C
Mass flow rate	3.12 kg/s

Furthermore, the system includes two condensers, a large and a small one. The large one is intended for the trigeneration and cogeneration modes, during which the SORC is operational. Due to the significantly lower mass flow rate of the VCC, it is necessary to install a second small condenser, in the case that only the VCC is operational.

A description of the selection process of the equipment of the unit follows.

5.2 Boiler-heating oil circuit

The boiler has the capability to use both biomass pellets and natural gas as combustion fuel. The addition of gas burners is made in order to ensure the versatility of the system and its flexible response to rapidly varying loads. The gas burner consists of two stages. Its heat duty can be varied between 65 to 85 kW_{th} and its maximum fuel flow rate is 6.5 to 18.9 Nm³/h. The flue gas temperature is between 220-230 °C. The pellet burner heat duty ranges between 40 to 80 kW_{th} and its fuel consumption rate between 8 to 20 kg/h. The wood pellets to be used as fuels must have a size around 6-8 mm.

The heating oil circuit includes a centrifugal pump of fixed rotational speed and volume flow rate and is able to handle fluids of temperatures of up to 350 °C. Moreover, the heating oil is stored in a round expansion vessel with a capacity of 250 liters.

The heating system will be automatically controlled through an electronic control panel. The user adjusts the desired heating oil maximum temperature. Since the volume flow rate of the heating oil has a fixed value, the control of this temperature is achieved by automatically shutting down starting up the burners of the boiler based on the readings of a thermostat. In order to investigate the performance of the system at off-design conditions, it is possible to change the heat duty of the burners.

5.3 Heat exchangers

The system includes four heat exchangers: a heater for the heating of the working fluid of the SORC by the heating oil, two cooling water condensers for condensing the working fluid (the requirement for two condensers was explained previously), as well as an evaporator for the VCC module, where the cooling output of the system is produced. All the heat exchangers to be installed are of the plate type. This is because these types of heat exchangers have a number of advantages compared to other types (i.e. shell and tube) for the operational range (pressures, temperatures, heat duty) of the unit under construction. Their advantages include the efficient heat transfer because of the development of high heat transfer coefficients between the fluid streams low volume to heat transfer area ratio and low cost. All heat exchanger models, except for the supercritical refrigerant-heating oil heater were readily proposed on-demand from manufacturers based on their technical specifications. However, most manufacturers were not able to dimension the supercritical heater of the working fluid. This is in part because of the lack of experience with the specific fluid (R227ea) and because of the supercritical conditions of the heat transfer. For this reason, a MATLAB code was used in order to estimate the required heat transfer surface of the heater. Geometrical data of commercially available heat exchanger models were input to the program and the heat transfer area was estimated using the heat exchanger partitioning method [17] and implementing method presented in [18] for calculating the overall heat transfer coefficient. Through a loop computational procedure, a specific plate heat exchanger model with defined number of plates was tested in order to estimate if its available heat

transfer surface would be sufficient for the process. If the available heat transfer surface was estimated to be lower than the required surface, more plates were added and a new loop started. The loop ended when the number of plates ensured that the heat transfer area of the heat exchanger would be higher than the required one. A safety factor was also considered, in order to ensure that the heat exchanger surface would suffice for completing the heat transfer under the desired conditions. The technical characteristics of all heat exchangers are summarized in Table 5.

Table 5: Technical specifications of heat exchangers

Heat exchanger	SORC heater		VCC evaporator		Condenser 1 (large)		Condenser 2 (small)	
	Hot	Cold	Hot	Cold	Hot	Cold	Hot	Cold
Fluid	BP Transcal N	R227ea	Water	R227ea	R227ea	Water	R227ea	Water
Mass flow rate (kg/s)	3.12	0.699	0.382	0.0522	0.643	0.737	0.067	0.062
Inlet pressure (bar)	5.5	30.4	1.013	2.58	9.115	1.013	9.126	1.013
Pressure drop (bar)	-	-	0.0073	0.007	0.062	0.026	0.0051	0.007
Inlet temperature (°C)	120	53	20	8.48 (x=0.4)	66.7	20	50	20
Outlet temperature (°C)	105	110	17.5	7.5	47.336	45	47.407	45
Heat duty (kW _{th})	85		4		77		6.5	
Heat transfer area (m ²)	4.71		0.39		4.32		0.31	

5.4 SORC expanders and VCC compressor

As stated previously, the expanders and the compressor are of the scroll type. Scroll expanders and other positive displacement type machines have been consistently proposed in the literature as ideal for ORCs with outputs in the scale between a few hundred Watts to 10 kW [19-22]. The expanders to be used in the SORC of the experimental unit are commercially available scroll compressors used in trucks, which are modified to enable their reverse operation as expansion machines. The most important considerations to be taken into account when selecting scroll expanders are their maximum operating pressure, their volume flow rate which greatly impacts their rotational speed, the latter being also directly influenced by their swept volume and their expansion ratio. The decision to use open drive scroll expanders instead of hermetic ones was made because of the lower cost and customization capability of the former versus the latter. Two same expanders were chosen to operate at different speeds. The reason for this choice was the fact that this commercial model of scroll compressor has a well-documented performance in expansion mode. The selection of the VCC compressor was simpler, since the operation data of the working fluid at its design point are typical for scroll compressors available in the market.

Table 6: Technical specifications of SORC expanders and VCC compressor

		Built-in swept volume (cc/rev)	Maximum rotational speed (rpm)	Rotational speed at design point (rpm)	Volume flow ratio at design point	Power at design point (kW)
SORC expander	HP	121.1	10000	1384	2.47	2.86
SORC expander	LP	121.1	10000	2632	1.90	2.89
VCC compressor		53.9	10000	1755	3.52	1.06

5.5 SORC pump

The feed pump increases the pressure level of the working fluid before its entrance to the heater. It is also used to control its mass flow rate. This control is achieved by varying the rotational speed of the motor coupled with the pump. The pumps that are commonly used and proposed in ORC units are of the positive displacement type [4]. For this type of pumps, the flow rate is almost proportional to their rotational speed. For the experimental unit, a diaphragm pump will be used. The SORC pump will have a design power output of 2.2 kW at 1450 rpm, which corresponds to a working fluid volume flow rate of around 29 lt/min. As can be seen in **Error! Reference source not found.**, the inlet and outlet pressures of the pump are 9.2 bar and 30.4 bar respectively. The pump is coupled with an electric motor of a nominal power of 3 kW.

5.6 Receiver

The receiver is a feed tank that is positioned after the condensers of the system. It provides a buffer storage of the working fluid during the operation of the unit, since only a certain percentage of its total quantity is circulating through the equipment components and the tubes at any given time (depending on the operating conditions). The feed tank also serves another purpose: it ensures that the working fluid at its outlet is at liquid state and has zero vapor fraction. For the sizing of the working fluid the total mass of the working fluid flowing through the equipment and piping was estimated. The tube diameters at each location of the unit were estimated by considering the proper fluid velocities (1-2 m/s for liquid and 8-10 m/s for gases). An additional volume for the sizing of heat exchangers, as well as an overall safety factor were taken into account. The total required volume of the receiver was thus estimated at around 50 lt.

5.7 System control equipment

The automated control of the system will be realized with the implementation of Programmable Logic Controllers (PLC). The PLC will be programmed to open and close the valves of the system. The PLC will also govern the coupling and the de-coupling between the generators and the scroll expanders. Moreover, they will be responsible for adjusting the rotational speed of the feed pump motor and the generators of the expanders, by the use of power inverters.

6. CONCLUSIONS

The thermodynamic optimization procedure (selection of working fluid, expander inlet pressure and temperature) of a trigeneration experimental unit combining an ORC with a VCC based on the heat input of a 85 kW_{th} biomass/natural gas boiler was developed. The working fluid found to be optimal for the unit is R227ea, while the optimal pressure and temperature are 30.4 bar and 110 °C. At its design point (trigeneration mode), the system will produce 0.99 kW_e, a heating load of 85.8 kW_{th} and a cooling load of 4 kW_{th}.

The selection process of the basic equipment (biomass/natural gas boiler/heating oil circuit, heat exchangers, expanders/compressor, feed pump, receiver and system control equipment) of the experimental unit was also presented. The construction of the experimental system will be completed by the end of 2015 year and measurements on its operation will be carried out in order to evaluate its performance.

ACKNOWLEDGEMENT

The optimization, design and the construction of the unit presented in this work is funded by the national funding program "ARISTEIA II" of the General Secretariat of Research and Technology, Greece.

NOMENCLATURE

η	efficiency	
P	power	kW
Q	heat duty	kW
P	pressure	bar
S	entropy	kJ/K
T	temperature	°C

Subscript

CHP	combined heat and power
comp	compressor
cond	condenser
cool	cooling
crit	critical
el	electric
heat	heat
in	input
max	maximum
net	net value
ORC	ORC working fluid
sys	system
th	thermal

REFERENCES

- [1] Cho H, Mago PJ, Luck R, Chamra LM. Evaluation of CCHP systems performance based on operational cost, primary energy consumption, and carbon dioxide emission by utilizing an optimal operation scheme. *Applied Energy*. 2009;86(12):2540-9.
- [2] Martins LN, Fábrega FM, d'Angelo JVH. Thermodynamic Performance Investigation of a Trigeneration Cycle Considering the Influence of Operational Variables. *Procedia Engineering*. 2012;42(0):1879-88.
- [3] Rayegan R, Tao YX. A procedure to select working fluids for Solar Organic Rankine Cycles (ORCs). *Renewable Energy*. 2011;36(2):659-70.
- [4] Quoilin S, Broek MVD, Declaye S, Dewallef P, Lemort V. Techno-economic survey of Organic Rankine Cycle (ORC) systems. *Renewable and Sustainable Energy Reviews*. 2013;22(0):168-86.
- [5] Pei G, Li J, Ji J. Analysis of low temperature solar thermal electric generation using regenerative Organic Rankine Cycle. *Applied Thermal Engineering*. 2010;30(8-9):998-1004.
- [6] Schuster A, Karellas S, Aumann R. Efficiency optimization potential in supercritical Organic Rankine Cycles. *Energy*. 2010;35(2):1033-9.
- [7] Vetter C, Wiemer H-J, Kuhn D. Comparison of sub- and supercritical Organic Rankine Cycles for power generation from low-temperature/low-enthalpy geothermal wells, considering specific net power output and efficiency. *Applied Thermal Engineering*. 2013;51(1-2):871-9.
- [8] Mikielwicz D, Mikielwicz J. A thermodynamic criterion for selection of working fluid for subcritical and supercritical domestic micro CHP. *Applied Thermal Engineering*. 2010;30(16):2357-62.
- [9] Bell IH, Wronski J, Quoilin S, Lemort V. CoolProp Database.
- [10] TheMathWorks I. MATLAB and Statistics Toolbox Release 2012b,. Natick, Massachusetts, United States.
- [11] Technology NIOsa. REFPROP
- [12] United States Environmental Protection Agency. Official Website of the United States Environmental Protection Agency, <http://www.epa.gov>, Accessed on August 19th, 2014.
- [13] American Society of Heating Refrigerating and Air-Conditioning Engineers. Addenda to Designation and Safety Classifications of Refrigerants. Atlanta, GA 303292000.

- [14] Quoilin S, Declaye S, Tchanche BF, Lemort V. Thermo-economic optimization of waste heat recovery Organic Rankine Cycles. *Applied Thermal Engineering*. 2011;31(14–15):2885-93.
- [15] Delgado-Torres AM, García-Rodríguez L. Analysis and optimization of the low-temperature solar organic Rankine cycle (ORC). *Energy Conversion and Management*. 2010;51(12):2846-56.
- [16] Ibarra M, Rovira A, Alarcón-Padilla DC, Zaragoza G, Blanco J. Performance of a 5 kWe Solar-only Organic Rankine Unit Coupled to a Reverse Osmosis Plant. *Energy Procedia*. 2014;49(0):2251-60.
- [17] Karellas S, Schuster A, Leontaritis A-D. Influence of supercritical ORC parameters on plate heat exchanger design. *Applied Thermal Engineering*. 2012;33–34(0):70-6.
- [18] Walraven D, Laenen B, D'haeseler W. Optimum Configuration of Plate-Type Heat Exchangers for the Use in ORCs for Low-Temperature Geothermal Heat Sources. *Katholieke Universiteit Leuven*; 2013.
- [19] Bao J, Zhao L. A review of working fluid and expander selections for organic Rankine cycle. *Renewable and Sustainable Energy Reviews*. 2013;24(0):325-42.
- [20] Qiu G, Liu H, Riffat S. Expanders for micro-CHP systems with organic Rankine cycle. *Applied Thermal Engineering*. 2011;31(16):3301-7.
- [21] Clemente S, Micheli D, Reini M, Taccani R. Energy efficiency analysis of Organic Rankine Cycles with scroll expanders for cogenerative applications. *Applied Energy*. 2012;97(0):792-801.
- [22] Lemort V, Quoilin S, Cuevas C, Lebrun J. Testing and modeling a scroll expander integrated into an Organic Rankine Cycle. *Applied Thermal Engineering*. 2009;29(14–15):3094-102.

EXPERIMENTAL TESTING OF A SMALL-SCALE SUPERCRITICAL ORC AT LOW-TEMPERATURE AND VARIABLE CONDITIONS

George Kosmadakis*, Dimitris Manolakos and George Papadakis

Department of Natural Resources and Agricultural Engineering,
Agricultural University of Athens, Iera Odos Street 75, Athens 11855, Greece

E-mail: gkosmad@aua.gr, dman@aua.gr, gpap@aua.gr

Web page: <http://www.renewables.aua.gr/>

ABSTRACT

The detailed experimental investigation of an organic Rankine cycle (ORC) is presented, which is designed to operate at supercritical conditions. The net capacity of this engine is almost 3 kW and the temperature of the hot water is always lower than 100 °C. The laboratory testing of the engine includes the variation of the heat input and of the hot water temperature. The maximum heat input is 48 kW, while the hot water temperature ranges from 65 up to 100 °C.

The tests are conducted at the laboratory and the heat source is a controllable electric heater, which can keep the hot water temperature constant, by switching on/off its electrical resistances. The expansion machine is a modified scroll compressor with major conversions, in order to be able to operate with safety at high pressure (max. pressure around 40 bar). The ORC engine is equipped with a dedicated heat exchanger of helical coil design, suitable for such applications. The speeds of the expander and ORC pump are regulated with frequency inverters, in order to control the cycle top pressure and heat input. The performance of all components is evaluated, while special attention is given on the supercritical heat exchanger and the scroll expander.

The performance tests examined here are the ones for hot water temperature of 95 °C, with the aim to examine the engine performance at the design conditions, as well as at off-design ones. Especially the latter are very important, since this engine will be coupled with solar collectors at the final configuration, where the available heat is varied to a great extent.

The engine has been measured at the laboratory, where a thermal efficiency of almost 6% has been achieved, while supercritical operation did not show superior performance as expected, due to the oversized expander. A smaller expander would allow operation at even higher pressures for higher speed with increased electric efficiency, which would probably reveal the full potential of the supercritical operation.

1. INTRODUCTION

The organic Rankine cycle (ORC) technology is suitable for heat recovery applications for low-temperature of even lower than 100 °C (Manolakos *et al.*, 2009a). At such conditions its efficiency is rather low, usually in the range of 3-5%, but still there are cases where its cost-effectiveness can be secured, especially when the heat input comes from waste energy sources. The main advantage at this temperature range is the simple and low-cost heat source circuit, since even pure water can be used with low-pressure piping, while the use of glycol or thermal oil is avoided, as well as a simple ORC configuration with a single expansion machine and no internal heat exchangers (Kosmadakis *et al.*, 2013a).

Supercritical cycles have some interesting features, since a better thermal match exists between the hot source and the organic fluid (Schuster *et al.*, 2010). This aspect is beneficiary for thermal and exergy efficiency, while at the same time some restrictions are introduced to the components selection due to the high pressure operation. This is the common case for steam cycles, which tend towards such configuration, since in large-scale utility steam power plants the use of supercritical cycles has

been already accomplished. But the largest challenges are for the small-scale systems using an ORC, since it is difficult to find and select the appropriate components for such heat-to-power engines. Moreover, low-temperature operation (below 100 °C) brings some additional restrictions, since a limited number of fluids can be used for such purposes and the cycle configuration does not allow any flexibility.

The most important component in ORC engines is the expansion machine and there is intensive research effort for producing expanders (of positive displacement type or even turbines for larger systems). For small-scale systems with power production lower than around 20 kW, scroll expanders have been widely used and showed adequate performance and expansion efficiency (Lemort *et al.*, 2012). The present authors have also used the same expansion technology (both open-drive and hermetic ones) and revealed the good performance at a wide range of pressure ratios (Manolakos *et al.*, 2009a). This brings confident that such expander can be also used at a supercritical cycle, where the biggest challenge is the increased pressure. One positive aspect is that for low-temperature applications, the pressure ratio for both cycle types (supercritical and subcritical) is low and usually in the range of 2-3 (Kosmadakis *et al.*, 2013a). In such pressure ratio range the scroll expander operates with good efficiency.

There are various studies focusing on supercritical ORC at theoretical level (Karellas *et al.*, 2012). Most of the studies provide a thermodynamic overview, focusing on the performance potential of such cycles, while others focus on the fluid selection under such conditions (Chen *et al.*, 2011). These theoretical studies treat some key components as black boxes, providing few details about their performance and operation at off-design conditions (Li *et al.*, 2013), such as the pump and expander, while more focus is given on the heat transfer at supercritical conditions (Lazova *et al.*, 2014).

Such aspects, especially in small-scale systems, are very important, in order to evaluate and compare the performance of a supercritical ORC. Here, an experimental study is implemented, testing a small-scale supercritical ORC with a net capacity of 3 kW under various conditions (Kosmadakis *et al.*, 2014). The heat input is varied, while the hot source temperature is held constant. The first series of measured data are presented, focusing on the whole engine operation, as well as its capability to reach supercritical operation at some conditions.

Such study is very important, since real test data are presented, and the advantages and potential of such technology can be identified. Also, this study provides some first proof, whether a supercritical ORC can be indeed more efficient than a subcritical cycle, and if the theoretical results can be verified. Focus is also given on the expansion machine, evaluating the converted scroll expander at such conditions.

2. THE INSTALLED ENGINE

A small-scale ORC engine has been designed and constructed. One of its biggest challenges during its construction was the modification of a scroll compressor (manufactured by Copeland, type ZP137KCE-TFD with swept volume 127.15 cm³/rev, maximum isentropic efficiency 75.2%, and built-in volume ratio of around 2.6 at compressor mode) to operate as scroll expander (reverse operation). A new casing had to be made, while many internal parts have been re-designed for better matching its operation as expander (such as the inlet volume before the fluid enters the steady scroll). The internal design has been optimized and all issues have been resolved, such as to find an efficient way to get the three wirings of the asynchronous motor out of the casing, ensuring at the same time electrical insulation and pressure sealing. An electric brake is connected with a frequency inverter of the expander, in order to control the test conditions and evaluate this expansion machine. This dynamic brake has a 100% duty cycle and is connected to the frequency inverter of the expander. Its main operation is to convert the variable frequency AC power through transistors into DC electricity, which is then dissipated to heat through a bank of appropriate electrical resistances. This method is followed, in order to have the full control of the expander speed, and find its performance maps.

Also, a dedicated evaporator has been developed for this application, following a helical-coil design. The organic fluid is R-404a. The cooling of the ORC engine is accomplished with a cooling water circuit, using a conventional shell and tube heat exchanger. Cold water with temperature around 16 °C is circulated and drawn from a large water reservoir with capacity of 320 m³, rejecting the heat of the

ORC engine. The condensation temperature of the organic fluid with this method is around 25 °C (fluctuating according to the engine load).

The ORC engine has been then installed at the laboratory for performance tests under controlled conditions. The heat input is provided by an electric heater and its heat production can be altered covering a large range of its capacity (from 25% of the total heat capacity: 12-48 kW_{th}) by operating different number of electric resistances and switching on/off the heater. For the investigation of the ORC engine, the maximum heat produced by the electric heater is around 48 kW_{th}, while the hot source temperature is held constant and equal to 95 °C. The heat transfer fluid (HTF) is pressurized water at around 2.5 bar at such temperature, and circulated with an inline centrifugal pump, operating at constant speed (2900 rpm). A simplified design of the system installed at the laboratory is depicted in Figure 1, together with the heating and cooling circuits (Kosmadakis *et al.*, 2013b).

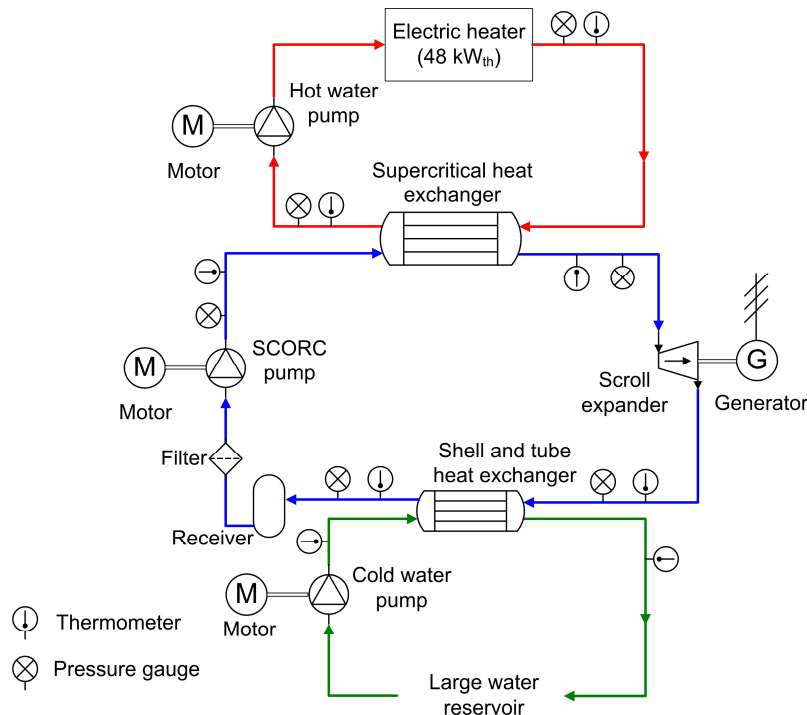


Figure 1: Supercritical ORC design

In Figure 1, the location of the measurement instruments is also depicted at the three circuits (hot water circuit, ORC engine, cold water circuit), in order to measure the key properties and evaluate the performance of this engine at controlled conditions. These instruments are mainly temperature (Pt100 thermocouples, accuracy up to ±0.2 °C) and pressure sensors (pressure transducers, Keller 21Y type, accuracy 1% of the pressure scale), in order to calculate the thermodynamic state of the organic fluid and hot/cold water at each location. With the above uncertainties, the thermodynamic properties are calculated with an accuracy of around 1.2% (Manolakos *et al.*, 2009b). Flow meters are not used, since steady-state conditions are examined, after the engine has reached a balanced operation at each case. The heat input is calculated from the ORC side, since the organic fluid pump is of diaphragm type and has a linear correlation of flow rate/speed, which is provided by the manufacturer (accuracy estimated at 2%). The accuracy of the calculated parameters is given in Table 1 (Manolakos *et al.*, 2009b), with the maximum error concerning the thermal efficiency, since it includes many calculated parameters. Nevertheless, this error is still low and does not influence the relative differences of the results. The installed engine at the laboratory is depicted in Figure 2.

Table 1: Accuracy of calculated parameters

Parameter	Maximum error (%)
Heat input to ORC	2.62

Expander power production	2.62
Pressure ratio	1.40
Expansion efficiency	2.66
Thermal efficiency	3.71

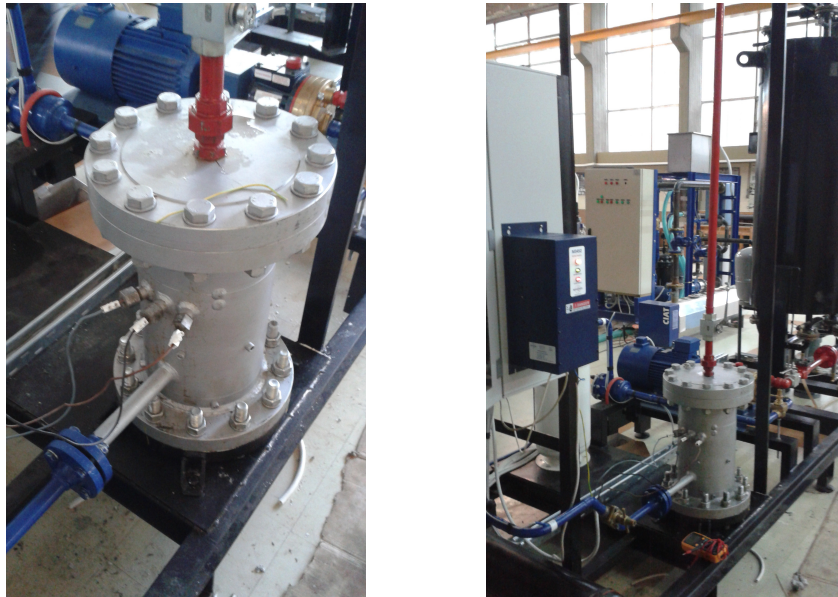


Figure 2: Installed ORC engine. Left: converted hermetic scroll expander. Right: Side view of the ORC engine

3. PERFORMANCE TESTS

The HTF temperature is set constant to 95 °C, while the heat input is varied. The goal is to examine and evaluate the ORC engine performance at these conditions, while supercritical operation is also attempted, in order to identify if and how much the efficiency can be increased at such conditions. The pump frequency is altered from 15 Hz up to 50 Hz (from 288 up to 960 rpm) and the expander frequency is regulated from 10 Hz up to 45 Hz (from 580 up to 2610 rpm). By regulating the pump speed, the heat input is varied up to almost 50 kW_{th}, which is depicted in Figure 3. The variation of the expander speed has just a minor effect on the absorbed heat (see right hand side of Figure 3).

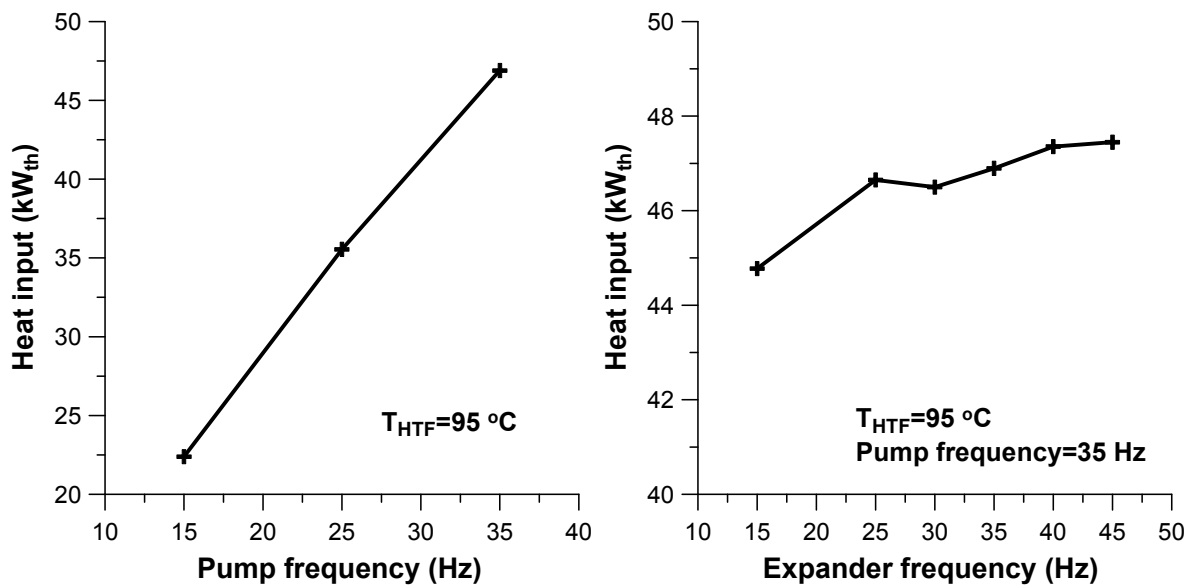


Figure 3: Heat input as a function of the pump and expander frequency

The regulation of the organic fluid pump speed is an effective way to control the heat absorbed by the ORC, while at the same time the flow rate of the organic fluid is adjusted. Therefore, there is the option to keep the speed of the hot water pump constant, simplifying the overall control. In that case, the temperature difference of the HTF would change according to the operating condition (large difference for high heat input). The regulation of the organic fluid pump speed has an important effect on high pressure as well, especially when the expander speed is kept constant, as it will be shown later in this section.

In Figure 4 is shown the expander power production as a function of expander and pump speed, covering a very wide range of operation.

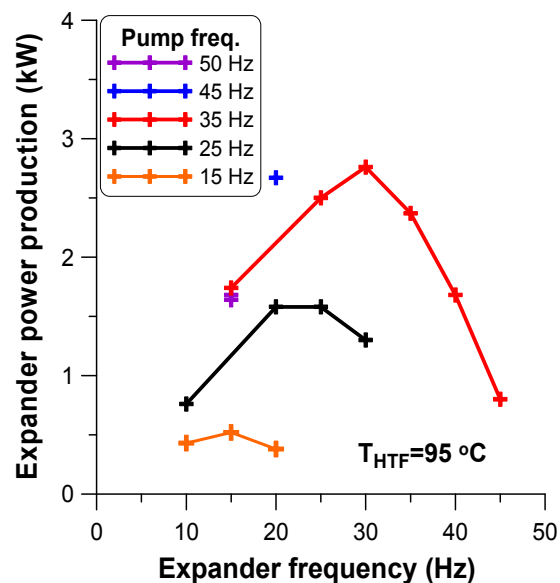


Figure 4: Expander power production as a function of the expander and pump speeds

This power production is actually electricity, since the scroll expander is directly coupled with a three-phase asynchronous motor/generator (capacity of around 10 kW) inside the hermetic casing. This motor operates up to around half of its nominal power, avoiding overheating, due to the absence of cooling (in compressor mode it is cooled by the refrigerant itself).

The power production here reaches 3 kW for the moderate pump frequency of 35 Hz (see Figure 4). For higher pump speed the power production decreases, while additionally more pump power is required. For the pump frequency of 35 Hz and for high expander speed, the power decreases due to lower pressure ratio, while the temperature at the expander outlet is increased. This temperature is shown in Figure 5, together with the expander inlet temperature, which slightly decreases as the expander speed increases.

For high expander speed, the temperature difference across the expander is just 15 °C, which is very low, leading to a poor power production, as already shown in Figure 4. Also, such high outlet temperature provides a first view of the low process efficiency, since large quantities of heat are rejected in this case at the condenser, having to de-superheat the organic fluid. One interesting solution would be to recover this heat, either by using an internal heat exchanger, although it is not recommended for low-temperature applications, or even use this heat for heating purposes (e.g. operation at CHP mode). But the most efficient way is to further adjust and optimize the engine operation, by avoiding operation at such conditions.

The decrease of pressure and pressure ratio for higher expander speed is presented in Figure 6, where the expander inlet pressure and pressure ratio are shown as a function of the expander frequency for pump frequency of 35 Hz. The low cycle pressure is almost constant and equal to 11-12 bar (higher condensation pressure for high load operation). Therefore, the main effect on the pressure ratio is introduced with the variation of the high cycle pressure.

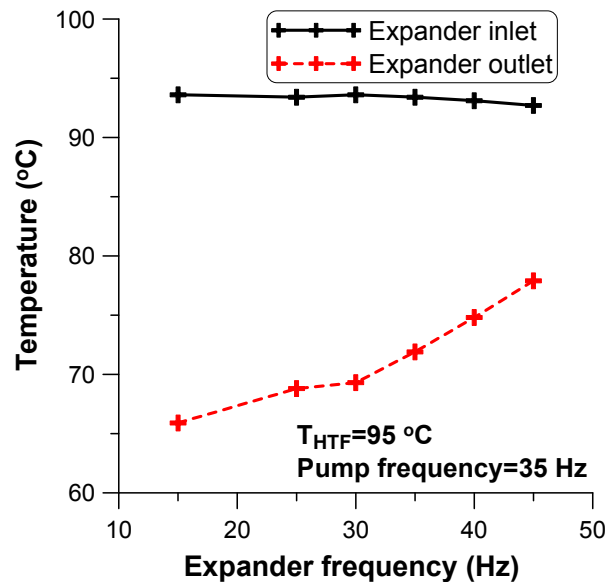


Figure 5: Expander inlet and outlet temperature as a function of the expander speed for pump frequency of 35 Hz

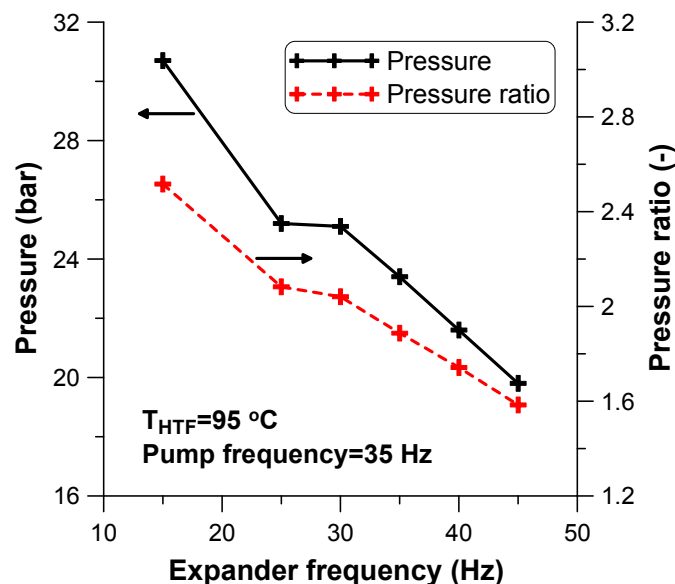


Figure 6: Expander inlet pressure and pressure ratio as a function of the expander speed for pump frequency of 35 Hz

There is a large variation of pressure ratios as the expander speed changes. The maximum pressure ratio is almost 2.6, while the maximum expansion efficiency is observed at a lower expander speed/pressure ratio (equal to around 85%), due to the low electrical efficiency of the asynchronous generator at low speeds, as shown in Figure 7 for three different pump frequencies. It should be mentioned that expansion efficiency is used here as the actual electric power produced divided by the theoretical power produced if the expansion was isentropic. This parameter includes all possible losses (electrical, friction, heat transfer, etc.) and provides a reliable evaluation parameter of all types of expansion machines.

The maximum expansion efficiency is observed for a pressure ratio of 2 (for pump frequency of 35 Hz), which is highly relevant to the built-in volume ratio of the original compressor (Declaye *et al.*, 2013). This pressure ratio value is lower than usual (common values for maximum expansion efficiency are around 3-4), since this compressor is intended for air-conditioning applications, where the pressure/temperature differences are not high. For lower pump speeds and pressure ratios, the

expansion efficiency is decreased. For pump frequency of 25 Hz the pressure ratio with the maximum expansion efficiency of around 80% is 1.87, while for pump frequency of 15 Hz is even lower and equal to 1.62. But again for lower pump speeds, the maximum expansion efficiency is high enough and shows good production potential within a narrow range of operating conditions.

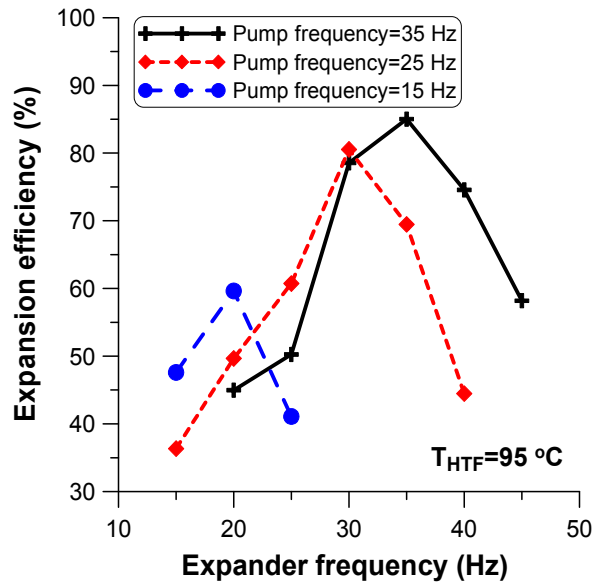


Figure 7: Expansion efficiency as a function of the expander speed for three pump frequencies

The thermal efficiency as a function of pump and expander speeds is depicted in Figure 8. The thermal efficiency is expressed as the net power output (power produced minus the pumping work) divided by the heat input. The maximum values of thermal efficiency are in the range of 5.5%, and are observed for pump frequency of 35 Hz and expander frequency of 30 Hz, which correspond to the conditions, where the maximum expansion efficiency was noticed as well.

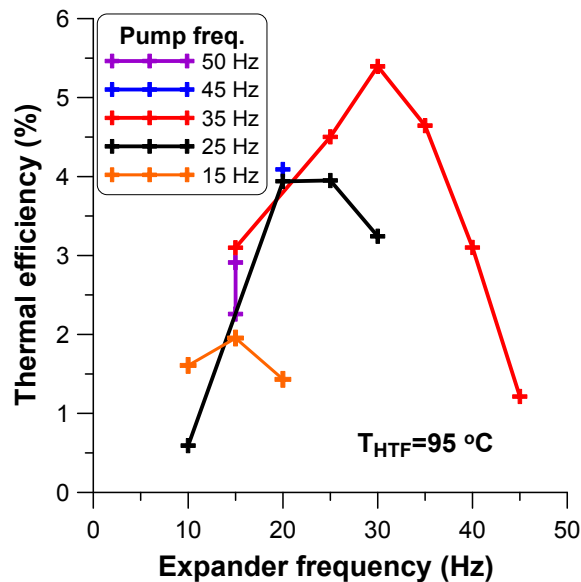


Figure 8: Thermal efficiency as a function of the expander and pump speeds

In all previous tests, supercritical operation was very difficult to be achieved. Although the temperature was over the critical fluid's temperature, the pressure was lower and around 80% of the critical pressure. Such high pressure could be reached only for very large pump speed and low expander speed. One such condition (pump frequency: 50 Hz, expander frequency: 15 Hz) that has

been also recorded showed that the high pressure is 40 bar, which is actually the design pressure, and the expander operated with a pressure ratio of 2.64. The thermal efficiency is equal to 2.9%, due to the low expansion efficiency, being equal to 25% (the low expander speed leads to a low electric efficiency of the generator). Nevertheless, this efficiency value is much higher than all the other recorded for such low expander speed (usually in the range of 1.5-2%), and provides a first positive aspect of the supercritical cycle, although such conditions were difficult to be reached.

The next tests included a lower cooling water flow rate, decreasing the cooling capacity and increasing the condensation pressure/temperature. Such conditions are realistic, since the cooling water had low temperature (around 16 °C), and much higher temperatures are expected to be reached with either air-cooled condenser or evaporative condenser. The pump frequency was high (45 Hz) and the condenser pressure was around 16-17 bar (close to the pump inlet pressure limit). The pressure ratio was not high (equal to 2.2) and the expander frequency varied from 16 up to 30 Hz. The expansion efficiency is observed in Figure 9, where it is shown that the maximum value is almost 80%, which is achieved for moderate expander speed. Moreover, for the supercritical condition (for expander frequency of 16 Hz) the expansion efficiency is low and around 45%, mainly due to the low electrical efficiency of the generator at such conditions.

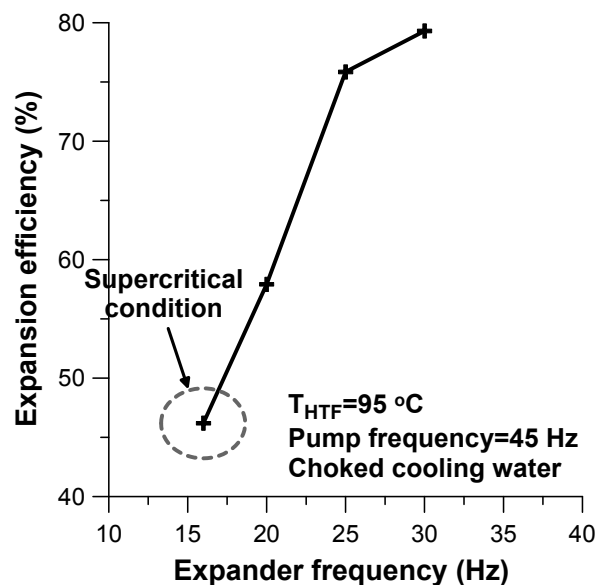


Figure 9: Expansion efficiency as a function of the expander frequency

The thermal efficiency is depicted in Figure 10, where it is shown that the maximum efficiency reached is almost 6% for subcritical operation.

It should be reminded that this high value is reached, when the condensation pressure and temperature are increased, decreasing the power production capability. Therefore, the potential can be even higher than that, which can be achieved with an improved design, especially of the expander, and further testing and development.

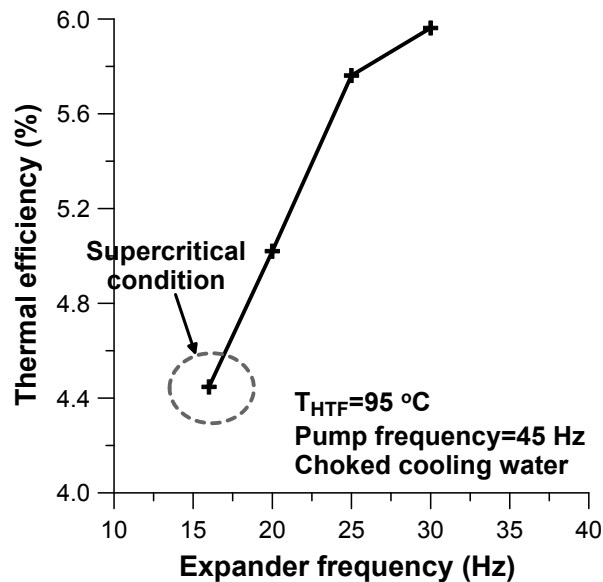


Figure 10: Thermal efficiency as a function of the expander frequency

The efficiency at supercritical condition is lower, mainly due to the low expansion efficiency (see Figure 9). If this condition had a higher expansion efficiency (by including a smaller expander with lower swept volume) and extrapolating the performance curves, then the efficiency would even reach the value of 7%, which is very promising for such small-scale engine at low-temperature and much higher than any other value observed during the current performance tests.

4. CONCLUSIONS

The detailed experimental results of the ORC engine testing at the laboratory have been presented, revealing its performance capability. The tests here concern a constant HTF temperature and equal to 95 °C with variable heat input. This heat is provided by an electric heater and is controlled with the speed variation of the organic fluid pump. A converted hermetic scroll expander is used for power production, showing increased expansion efficiency at some favorable conditions. Various parameters have been examined, mainly when regulating the expander and pump speed, showing the heat-to-power conversion efficiency of such engine.

Moreover, supercritical operation was difficult to be achieved and only when the cooling water flow rate was decreased, could the engine operate at supercritical conditions and maintain such operation. At these conditions, the expander frequency/speed was low (around 15 Hz), keeping a pressure ratio close to the designed one, but leading to a low expansion efficiency, due to the low electric efficiency of the asynchronous generator at these conditions. If the expansion efficiency could be increased (mainly having to do with the frequency operation and the increase of the electrical efficiency), by using a smaller expander, then the thermal efficiency at supercritical conditions seems to be superior to the one at subcritical ones, and fully exploit the theoretical performance.

REFERENCES

- Chen, H., Goswami, D. Y., Rahman, M. M., Stefanakos, E. K., 2011, A supercritical Rankine cycle using zeotropic mixture working fluids for the conversion of low-grade heat into power, *Energy*, vol. 36, no. 1: p. 549-555.
- Declaye, S., Quoilin, S., Guillaume, L., Lemort, V., 2013, Experimental study on an open-drive scroll expander integrated into an ORC (Organic Rankine Cycle) system with R245fa as working fluid, *Energy*, vol. 55: p. 173-183.
- Karellas, S., Schuster, A., Leontaritis, A. D., 2012, Influence of supercritical ORC parameters on plate heat exchanger design, *Applied Thermal Engineering*, vol. 33: p. 70-76.

- Kosmadakis, G., Manolakos, D., Papadakis, G., 2013a, An investigation of design concepts and control strategies of a double-stage expansion solar organic Rankine cycle, *Int J of Sustainable Energy*, DOI: 10.1080/14786451.2013.827682, in press.
- Kosmadakis, G., Manolakos, D., Bouzianas, K., Papadakis, G., 2013b, Heat recovery in low-concentration PV/thermal units using a low-temperature supercritical organic Rankine cycle for improved system performance, Presented at the *2nd Int. Seminar on ORC Power Systems (ASME-ORC2013)*, Rotterdam, The Netherlands, 7-8 October 2013.
- Kosmadakis, G., Manolakos, D., Olsson, O., Ntavou, E., Bystrom, J., Papadakis, G., 2014, Design and implementation of a hybrid low-concentration PV/thermal system, including a bottoming supercritical ORC engine, Presented at the *29th European PV Solar Energy Conference and Exhibition (29th EU PVSEC, 2014)*, Amsterdam, The Netherlands, 22-26 September 2014.
- Lazova, M., Daelman, S., Kaya, A., Huisseune, H., De Paepe, M., 2014, Heat transfer in horizontal tubes at supercritical pressures for organic rankine cycle applications, *10th International Conference on Heat Transfer, Fluid Mechanics and Thermodynamics (HEFAT 2014)*, Proceedings (pp. 1044–1051). Presented at the *10th International Conference on Heat Transfer, Fluid Mechanics and Thermodynamics*, Orlando, Florida, USA.
- Lemort, V., Declaye, S., Quoilin, S., 2012, Experimental characterization of a hermetic scroll expander for use in a micro-scale Rankine cycle, *Proceedings of the Institution of Mechanical Engineers, Part A: Journal of Power and Energy*, vol. 226, no. 1: p. 126-136.
- Li, C., Kosmadakis, G., Manolakos, D., Stefanakos, E., Papadakis, G., Goswami, Y., 2013, Performance investigation of concentrating solar collectors coupled with a transcritical organic Rankine cycle for power and seawater desalination co-generation, *Desalination*, vol. 318, no. 3: p. 107–117.
- Manolakos, D., Kosmadakis, G., Kyritsis, S., Papadakis, G., 2009a, Identification of behaviour and evaluation of performance of small scale, low-temperature Organic Rankine Cycle system coupled with a RO desalination unit, *Energy*, vol. 34, no. 6: p. 767-774.
- Manolakos, D., Kosmadakis, G., Kyritsis, S., Papadakis, G., 2009b, On site experimental evaluation of a low-temperature solar organic Rankine cycle system for RO desalination, *Solar Energy*, vol. 83: p. 646-656.
- Schuster, A., Karellas, S., Aumann, R., 2010, Efficiency optimization potential in supercritical Organic Rankine Cycles. *Energy*, vol. 35, no. 2: p. 1033-1039.

ACKNOWLEDGEMENT

The research leading to these results has received funding from the European Union's Seventh Framework Programme managed by REA-Research Executive Agency, <http://ec.europa.eu/research/rea> ([FP7/2007-2013] [FP7/2007-2011]) under grant agreement n° 315049 [CPV/RANKINE], FP7-SME-2012. The AUA research team would also like to thank its partners for their work within this project.

EXPERIMENTAL OBSERVATION OF NON-IDEAL NOZZLE FLOW OF SILOXANE VAPOR MDM

Andrea Spinelli^{1*}, Alberto Guardone², Fabio Cozzi¹, Margherita Carmine¹, Renata Cheli¹,
Marta Zocca², Paolo Gaetani¹, Vincenzo Dossena¹

¹ Politecnico di Milano, Department of Energy
Via Lambruschini 4, 20156 Milano, Italy
e-mail: andrea.spinelli@polimi.it

² Politecnico di Milano, Department of Aerospace Science and Technology
Via La Masa 34, 20156 Milano, Italy
e-mail: alberto.guardone@polimi.it

* Corresponding Author

ABSTRACT

The first experimental results from the Test-Rig for Organic Vapors (TROVA) at Politecnico di Milano are reported. The facility implements an Organic Rankine Cycle (ORC) where the expansion process takes place within a straight axis convergent-divergent nozzle, which is the simplest geometry representative of an ORC turbine blade passage. In order to reduce the required input thermal power, a batch operating mode was selected for the plant. Experimental runs with air allowed to verify the throttling valve operation and the measurement techniques, which include total pressure and temperature measurements in the settling chamber, static pressure measurements along the nozzle axis. A double-passage Schlieren technique is used to visualize the flow field in the nozzle throat and divergent section and to determine the position of shock waves within the flow field. The first experimental observation of non-ideal nozzle flows are presented for the expansion of siloxane fluid MDM ($C_8H_{24}O_2Si_3$, octamethyltrisiloxane) for vapor expansion in the close proximity of the liquid-vapor saturation curve, at relatively low pressure of operation. A supersonic flow is attained within the divergent section of the nozzle, as demonstrated by the observation of an oblique shock wave at the throat section, where a 0.1 mm recessed step is located. Schlieren visualizations are limited by the occurrence of condensation along the mirror side of the nozzle. Pressure measurements are compatible with the observed flow field.

1. INTRODUCTION

Organic Rankine Cycle (ORC) is a well established and viable technology for the exploitation of energy from low/medium temperature sources, such as renewable or heat-recovery, with applications to low/medium electrical power generation and Combined Heat and Power (CHP) plants. For these applications, the ORC technology is usually preferred over steam cycle due to the simplicity of plant components, high reliability and low operational costs Gaia and Duvia (2002); Bini and Manciana (1996) and relatively high efficiency of the thermodynamic cycle Angelino et al. (1984).

Turbine efficiency in current ORC plants is around 75-85%, see Schuster et al. (2009); Duvia and Tavolo (2008) and recent researches in ORC technology are focused on blade geometry optimization to improve the turbine efficiency. This task is complicated by the fact that the use of organic compounds operating close to the vapor saturation curve in ORC results in highly

non-ideal compressible-fluid flows within the turbine passages, which are usually designed to operate in supersonic flow conditions due to the relatively low speed of sound which characterizes high molecular mass fluids, especially in close-to-saturation flow conditions Harinck et al. (2009). Moreover, the accurate prediction of the flow behavior requires the use of complex non-ideal thermodynamic models. Computational Fluid Dynamics (CFD) codes for non-ideal compressible-fluid dynamics (NICFD) are already available which implement the complex thermodynamics of fluids in ORC turbine passages Colonna and Rebay (2004); Guardone (2007); Cinnella and Congedo (2007); Colonna et al. (2008); Hoffren et al. (2002).

Currently, no experimental data of non-ideal compressible-fluid flows are available to support our understanding of the fluid dynamics of ORC plants and to assess the reliability and accuracy of available thermodynamics models and CFD tools.

To investigate experimentally the non-ideal compressible-fluid flows of organic compounds in typical operating conditions for ORC applications, the *Test Rig for Organic Vapors* (TROVA) was designed and constructed at the Politecnico di Milano, see Spinelli et al. (2013). In the facility, expansion flows of different organic compounds in non-ideal conditions in the close proximity of the liquid-vapor saturation curve can be investigated by independent measurements of pressure, temperature and velocity. The facility implements an ORC (either sub-critical or super-critical), where the expansion process take place within a nozzle replacing the turbine. A straight axis converging-diverging nozzle was chosen, being it the simplest geometry providing an expansion from subsonic to supersonic flow in the operating conditions of interest. The size of the nozzle is large enough to guarantee that within the expanding flow a large isentropic core is preserved, thus making it possible to measure temperature and pressure fields without the use of calibrated probes, see Spinelli et al. (2010). Total pressure and temperature are measured in the settling chamber ahead of the nozzle inlet; static pressure taps at different sections along the nozzle axis are used to follow the flow evolution as it expands from rest to supersonic conditions. In order to reduce the required input thermal power, a batch operating facility has been selected.

The structure of the paper is as follows. In section 2, the general set-up of the test-rig is presented and an overview of the measurement techniques is given. In section 3, experimental results with air are reported. In particular, the operation of the throttling valve is verified and the complete measurement system is tested. The possibility of using the Schlieren visualization to support the interpretation of the pressure measurement is assessed. In section 4, preliminary experimental results for siloxane fluid MDM ($C_8H_{24}O_2Si_3$, octamethyltrisiloxane) are reported. In particular, the heating and degassing procedure is tested and assessed against saturated data for MDM fluid. A very preliminary test run at low pressure (in the range 70-350 mbar) is described and the suitability of the set-up to investigate nozzle flows of non-ideal compressible flows of organic fluids is discussed. Final remarks and observations are gathered in section 5.

2. TROVA: SET-UP AND MEASUREMENT TECHNIQUES

The TROVA operates as a blow-down wind tunnel, namely, in a discontinuous way, to reduce the power requirements. The working fluid to be tested is stored in a high pressure vessel (HPV) (see figure 1) and isochorically heated up to saturated, superheated, or supercritical conditions (point 4 in figure 1) at a pressure P_4 and temperature T_4 above the nozzle stagnation conditions (point 6). The heating elements consist of electrical bands and wires externally clung to the vessel. The control valve (MCV) regulates the feeding total pressure P_{T6} at the inlet of the nozzle during the entire test. Small fluctuations in pressure around the set-point are acceptable since they are characterized by a time scale extremely large if compared to the nozzle characteristic

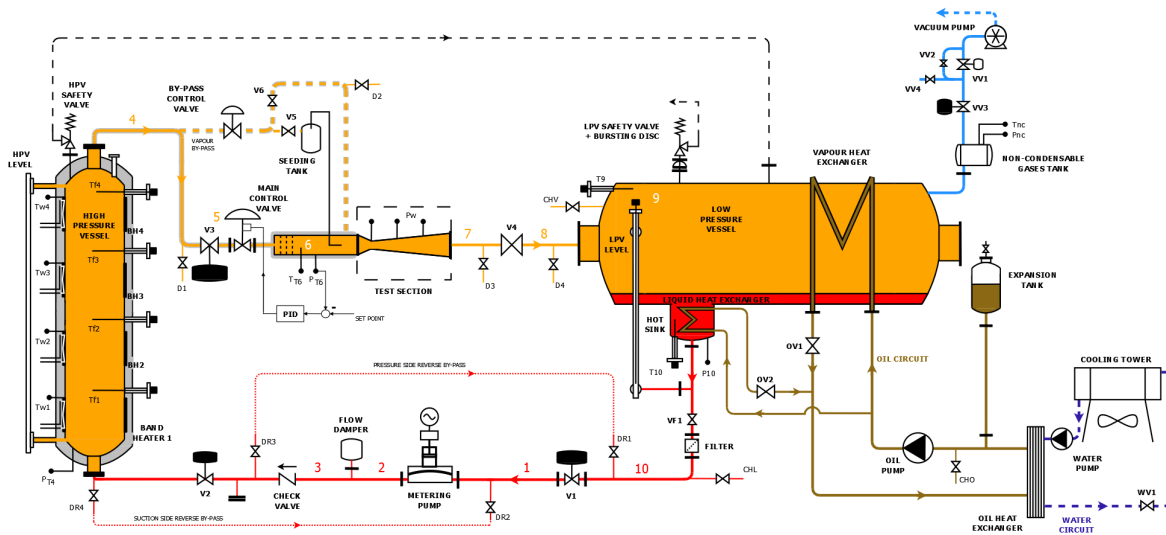


Figure 1: Scheme of the TROVA test-rig. The total pressure and temperature in the settling chamber are measured by sensors P_{T6} and T_{T6} , respectively. Static pressure taps in the test section are indicated by P_w .

Fluid	P_{T6} (bar)	T_{T6} (°C)	Z_{T6}	β	P_7 (bar)	M_7	t (s)
MDM	4.0	253.2	0.85	10.0	0.4	2.05	~ 40

Table 1: Operating conditions for the first MDM test and expected duration. The expansion ratio β , exit pressure P_7 and exit Mach number M_7 refer to adapted conditions.

time. Similarly, the reduction of the nozzle inlet total temperature T_{T6} due to the HPV emptying process is small, thanks to the high molecular complexity of the working fluid, i.e., large heat capacity, and occurs at a very small time rate. However, in the settling chamber ahead of the nozzle, the stagnation conditions data P_{T6} and T_{T6} are acquired at frequency of orders of magnitude higher with respect to the frequency content of each signal. The organic vapor is then expanded (to state 7) through the nozzle, where wall pressure measurements are performed. The vapor is discharged into a large area pipe (point 8), where it is slowed and brought in a low pressure vessel (LPV, state 9) where the fluid is collected and condensed (state 1). The loop is closed by the liquid compression to the HPV (point 2), performed by a membrane metering pump. Further details concerning all components can be found in Spinelli et al. (2013).

The design test scheduled for the TROVA concerns the expansion flow of siloxane MDM. Due to its relatively high critical temperature ($T_C = 290.94$ °C), its thermal stability, non-toxicity and low cost, this fluid is of particular interest for industrial ORC plant exploiting relatively high temperature sources (e.g. biomass, solar radiation). The operating conditions for this test have been selected as a compromise between the requirement of moderate temperatures, in order to avoid fluid decomposition during the early tests, and the need of expanding the vapor through thermodynamic regions where non-ideal compressible-fluid effects are appreciable. The resulting conditions are reported in table 1.

2.1 Test section and instrumentation

The test section is made of a planar converging-diverging nozzle (see figure 2); the diverging portion of the nozzle profile was designed by applying the method of characteristics coupled with state-of-the-art thermodynamic models for the siloxane MDM (Guardone et al. (2013), Colonna

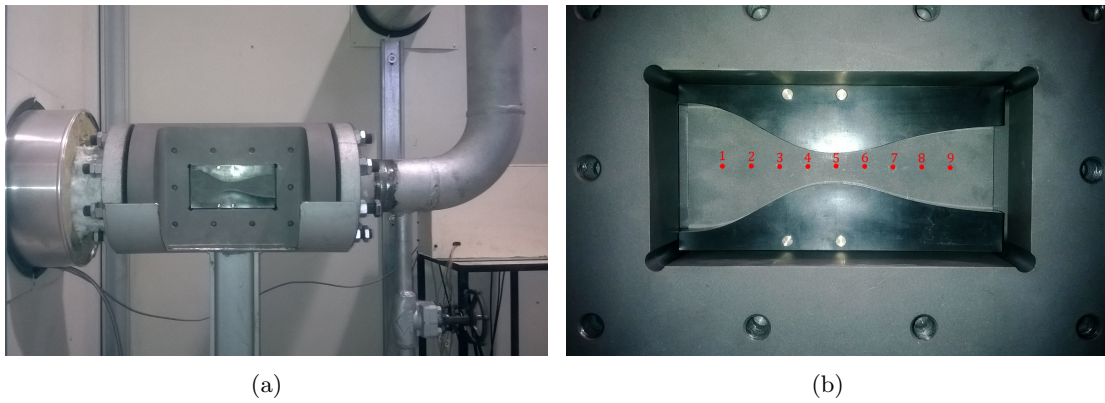


Figure 2: Overview of the test section (a) and details of the nozzle within the test section (b). The flow is from left to right. The settling chamber is on the left and it is enclosed in the white box which contains the TROVA and it is separated from the laboratory for safety. The front window is made of quartz to allow for optical access, the back closure is a mirror (not installed to take the picture). Static pressure taps are located along the symmetry axis and are marked with red dots.

Property	Sensor	Type	CR P (bar)	CR T (°C)	$U_2 P$ (%FS)	$U_2 T$ (°C)
T_T	Thermocouple	J (Fe - Cu/Ni)	-	25-250	-	0.4
P_T, P_w	Piezo-resistive	Kulite XTEH	1-FS (3.5-40)	25-250	0.07	-

Table 2: Type, calibration range (CR) and expanded uncertainty (U_2) of the instruments employed for pressure and temperature measurements. FS is the transducer full scale.

et al. (2006)), while the converging portion was represented by a 5th order polynomial profile which realizes a smooth transition from the inlet to the throat section. At the geometrical throat a recessed step of 0.1 mm depth (1.2% of the nozzle semi-height at the throat) was machined on both the top and bottom contoured profiles, in order to fix the location of the minimum nozzle area, independently from boundary layer unsteadiness.

The front planar wall is a quartz window which guarantees optical access, while the rear wall is made by a steel plate and it houses 9 pressure taps along the nozzle axis. Behind each tap a 25 mm long pneumatic line-cavity system is machined in the plate body, connecting the tap with the sensing element of a piezo-resistive pressure transducer. For the present experimentation, the plate surface has been mirror polished, in order to allow the implementation of the double-passage Schlieren visualization technique detailed in section 2.2. The stagnation conditions are measured in the settling chamber ahead of the test section. A wall pressure tap/line/transducer system (similar to the nozzle ones) is used for the total pressure, due to the very low flow velocity in the chamber; the total temperature is measured by a J type thermocouple whose hot junction is located at the chamber axis.

The pneumatic lines connecting each pressure measurement point with the corresponding transducer are characterized by very short length (~ 25 mm) and small diameter ducts (0.3 to 1.5 mm); similarly the volume of the capacities ahead of the transducer sensing element is extremely small (~ 45 mm³). A natural frequency of about 900 Hz has been estimated for the transmission lines. All pressure sensors are piezo-resistive transducers (Kulite XTEH-7L series) operating at high temperature (up to 343 °C) and chemically compatible with almost all working fluids of interest for the ORC industry. The data acquisition (DAQ) system consist

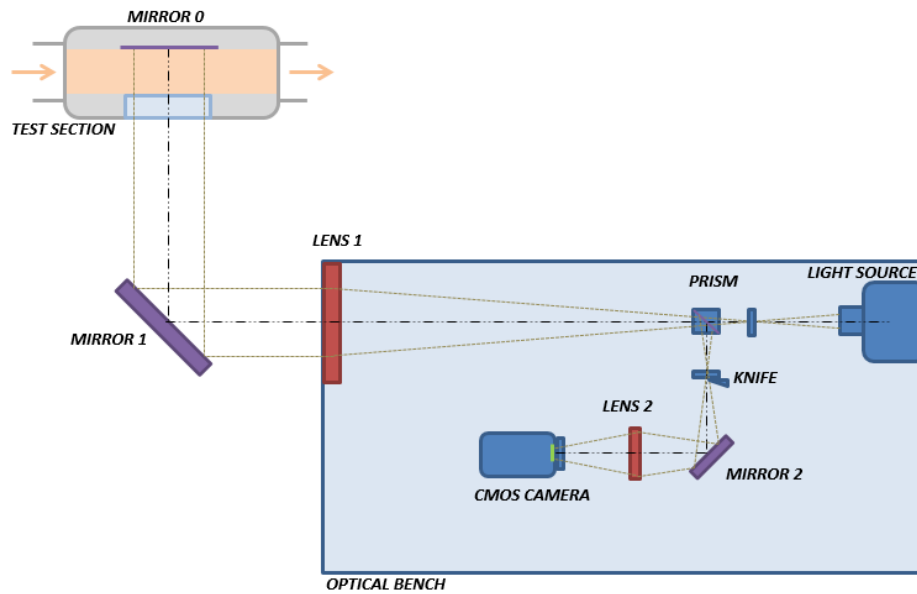


Figure 3: Functioning scheme of the double-passage Schlieren set-up.

of analog modules employed to provide the voltage supply to the transducers and to amplify the measurement signals (including the thermocouple output voltage) and of a high speed data acquisition board.

The J thermocouple has been calibrated in the temperature range 25-250 °C. Due to the large sensitivity of the pressure transducers to temperature variation and the consequent uncertainty increase, the pressure sensors were calibrated both in pressure and in temperature in the range 1-FS bar for the pressure and 25-250 °C for the temperature. The final accuracy, expressed in terms of expanded uncertainty, obtained for each sensor is summarized in table 2. Notice that the acquisition channels and the supply/amplification modules are kept unchanged during both the calibration and the measurement processes.

2.2 Schlieren set-up

A double pass-type parallel light Schlieren system with the emitting and receiving optical components mounted on an optical table was used. This configuration is shorter and easier to align with respect to the classical Z-type system. A schematic sketch of the system is shown in figure 3. A 100 W Hg arc-lamp is used as the light source. The light from the lamp is focused by a F/1.5 silica lens into a circular spot of about 3 mm in diameter and then collimated to form parallel light rays by a Schlieren lens head (Lens 1 in figure 3). The latter has a diameter of 150 mm and a focal length of 1000 mm. The collimated light beam is deflected by a circular mirror (Mirror 1 in figure 3) before traversing the test section. It is then reflected back to the Schlieren head by the metallic mirror 0 (namely, by the polished nozzle back wall) and focused on the vertically aligned knife edge (knife in figure 3)). The knife orientation allows to visualize the density gradient along the nozzle axis. A cubic beamsplitter (prism in figure 3) separate the light beam originated by the light source and the reflected one. A lens of 160 mm focal length and 50 mm diameter is located behind the knife (Lens 2 in figure 3) and forms a real image of the test section on the sensor of a high speed CMOS camera. To allow a suitable long recording time the CMOS camera resolution and frame rate were respectively set to 1024 x 512 pixels and to 100 fps (frames per second), while the exposure time was set to 20 μ s.

Fluid	P_{T6} (bar)	T_{T6} (°C)	Z_{T6}	β	P_7 (bar)	M_7	t (s)
Air	4.0	20-60	1.0	20.0	0.2	2.59	~ 40

Table 3: Operating conditions for the air test and expected duration. The expansion ratio β , exit pressure P_7 and exit Mach number M_7 refer to adapted conditions.

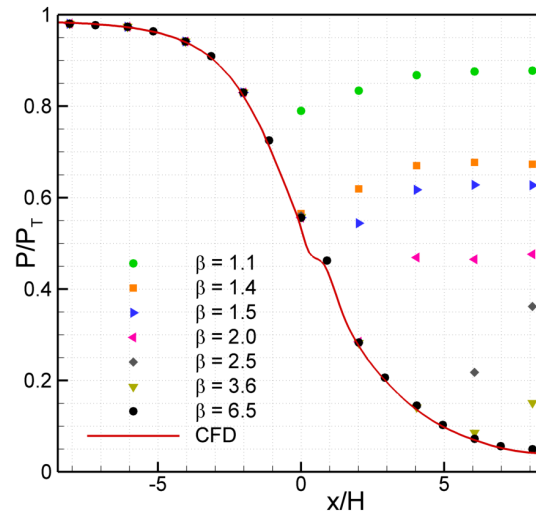


Figure 4: Pressure measurement along the nozzle axis for different values of the expansion ratio β . Pressure is made non-dimensional by the upstream total pressure P_T . The throat is located at $x/H = 0$. H is the nozzle semi-height at the throat.

3. EXPERIMENTAL RESULTS WITH AIR

3.1 Equivalent test with air

In order to verify the suitability of the test procedure and of the measuring strategy in giving reliable measurements and an accurate description the nozzle flow field, an equivalent test is designed and performed using dry air as working fluid. This allows for a comparison with theory based on the ideal gas model, with similar experiments in nozzle (available from the literature), and with standard CFD simulations. The equivalent test was designed in order to have a comparable duration with respect to the MDM 1st test (see table 1), thus a similar dynamic operation of the plant. Therefore, the capability of the control valve MCV in keeping a reasonably constant pressure at the nozzle inlet during the test can be verified. The converging-diverging nozzle profile designed for the MDM 1st test was used. However, when operated with air, the nozzle adapted expansion ratio and exit Mach number considerably differ from the corresponding design values for MDM expansion. The operating conditions of the equivalent test are summarized in table 3.

The air tests were performed by storing in the HPV air at a pressure of about $P_{T4} = 12$ bar and at a temperature in the range $T_{T4} = 20-160$ °C. The LPV pressure is brought to $P_{T9} = 0.08$ bar by evacuating the reservoir. Therefore, at the initial time ($P_7 = P_{T9}$) the nozzle is under-expanded, since the expansion ratio is $\beta = P_{T6}/P_7 = 50$. The test start is dictated by the opening of the ball valve V3 (see figure 1) which also triggers the CMOS camera recording, in such a way that the pressure and temperature data are synchronized with the Schlieren images. The control valve operates with low frequency oscillations (of the order of 1 Hz) keeping the nozzle inlet total pressure at a value of about $P_{T6} = 4 \pm 0.1$ bar for approximately 25 s, than the MCV is fully opened and the pressure across the valve is balanced ($P_{T4} = P_{T6}$). The test

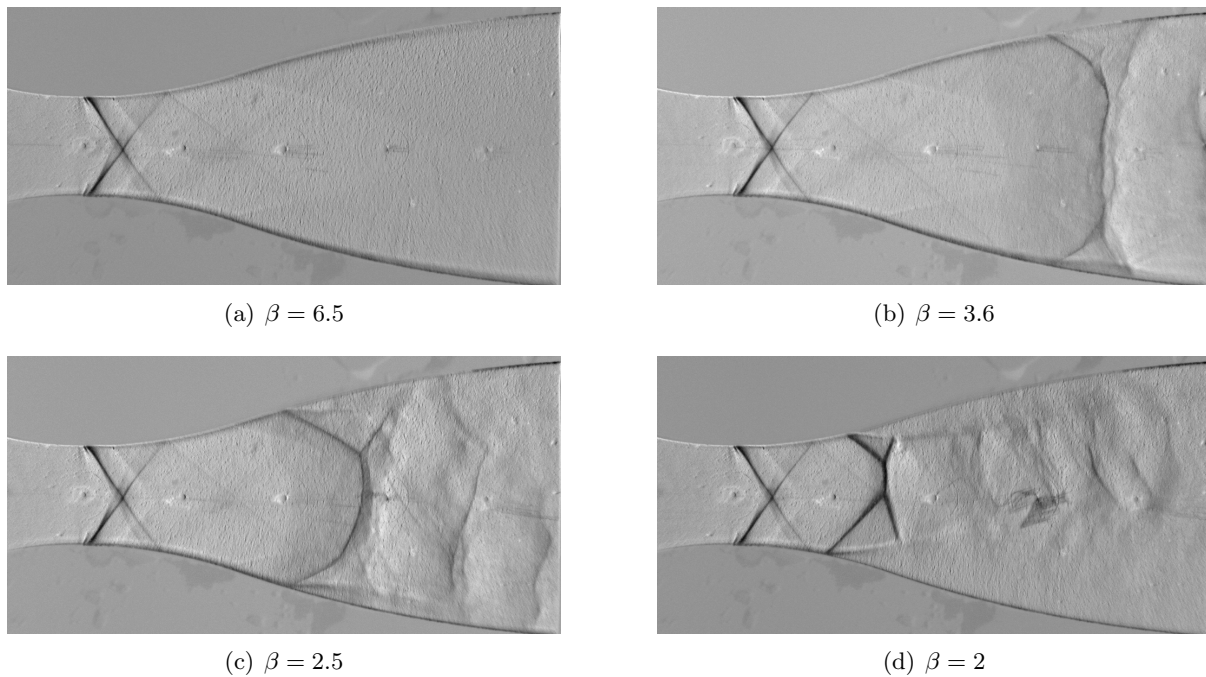


Figure 5: Schlieren visualization of nozzle operation in air in choked conditions for four values of the expansion ratio β , corresponding to adapted conditions (a) and subsonic outflow with a shock wave in the divergent section (b,c,d). A recessed step 0.1 mm deep is machined at the throat section of geometry shown on top: a fan-shock-fan system originates at the step location. Pressure measurements are reported in figure 4.

proceeds for additional 15 s (with a reducing and uncontrolled P_{T6}) until the pressure of the two reservoirs are balanced ($P_{T4}=P_{T9}$) (due to the HPV emptying and the LPV filling). According to this test scheme, the entire range of possible flow regimes in the nozzle are observed during the test: from under-expanded/adapted/over-expanded to fully subsonic flow.

3.2 Test results

The values of the static to total pressure ratio are reported in figure 4 for all static pressure taps along the nozzle axis and for different values of the expansion ratio β . Note that pressure taps along the back plate are not symmetric and up to 17 different measurement station can be obtained if different tests are carried out by changing the plate orientation. Numerical simulations of the expansion process, including the geometry of the recessed step, agree fairly well with the adapted flow conditions within the nozzle ($\beta = 6.5$) in figure 4. Note that the isentropic expansion profile is perturbed by the presence of the recessed step at the nozzle throat, as confirmed by the numerical simulations as well as by the experimental results. At lower values of β , the measured pressure profiles depart from the adapted one, as expected from the gasdynamic theory of nozzle flows.

Indeed, as confirmed also by the Schlieren measurements in figure 5, shock waves occurs in the divergent portion of the nozzle for low enough expansion ratios. For $\beta = 1.1$ and $\beta = 1.4$ (see figure 4) a fully subsonic flow is observed in both the convergent and the divergent section of the flow; notice that in case of $\beta = 1.4$ sonic conditions are reached at throat. Remarkably, the recessed step at the nozzle throat produces significant perturbation in the flow field, which are clearly visible in all Schlieren visualizations in figure 5 and in the pressure profiles in figure 4. Supersonic flow expansion at the step location results in the formation of a Prandtl-Meyer fan

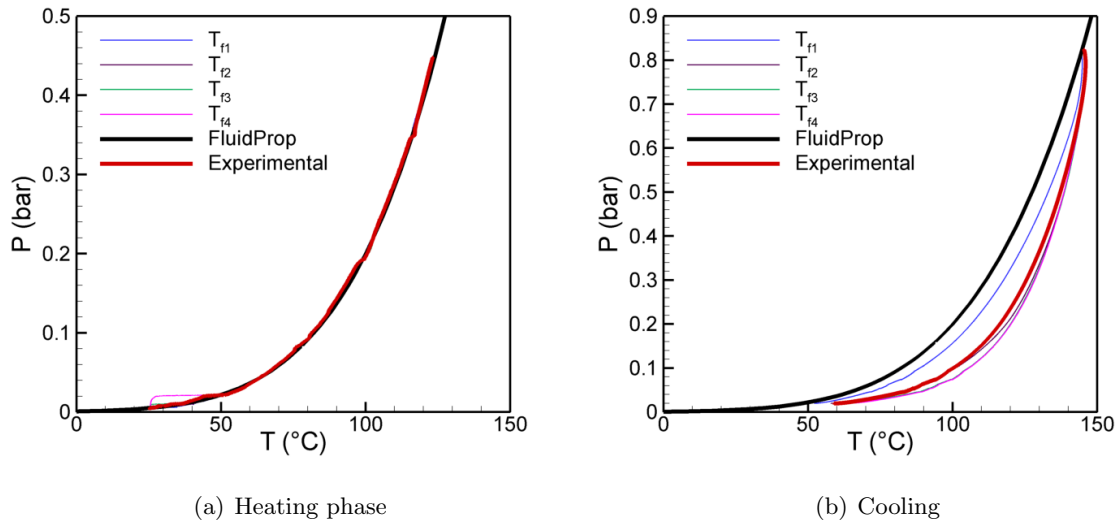


Figure 6: Pressure-temperature profile during the heating (a) and cooling (b) phase and saturation curve of fluid MDM.

(light gray in the Schlieren images) and causes flow separation around the step corner. Flow re-attachment at the nozzle surface results in the formation of a shock wave (dark gray). A further expansion is visible at the geometric discontinuity at the end of the machined portion of the nozzle. The resulting fan-shock-fan combination is clearly seen to propagate and to interact with the nozzle walls in the adapted flow conditions shown in 5a).

4. PRELIMINARY RESULTS FOR MDM VAPOR

4.1 Fluid preparation and heating/cooling procedure

The preliminary steps required to prepare the MDM test include the fluid charge and the execution of cycles of isochoric heating and cooling within the HPV for removing incondensable gases, most notably air, from the fluid. The fluid was charged at the condenser (LPV) after a complete plant evacuation, which was carried out using the plant vacuum pump. The final pressure before the charge (at each section) was of the order of 1 mbar. Depending on the test conditions a proper fraction of the liquid is pumped to the HPV by the metering pump, whose operation was also verified. The mass of fluid charged at each section is such that, at room temperature, the fluid is always in saturated conditions, therefore at a pressure well below the atmospheric pressure.

The heating/cooling cycles were performed from room temperature ($\sim 20^\circ\text{C}$) to about 180°C , therefore below the critical point and always maintaining saturated conditions, namely by keeping the fluid within the two-phase region. It's worth reminding that the HPV is electrically heated from the vessel external walls and it is not equipped with a cooling system, therefore cooling can be obtained only by heat exchange with the external environment.

Figure 6 shows that the experimental P - T saturation curve obtained during the heating process is finely captured by the thermodynamic model Colonna et al. (2006), whereas the agreement is lost during the cooling process. Indeed, during the heating process the convective heat transfer between the fluid and the thermocouple (industrial K type) hot junctions (located at the reservoir axis) is promoted by the expected convective motion within the reservoir (activated by the liquid boiling in the lower portion of the reservoir, where most of the thermal energy enters the system). This heat transfer mechanism is expected to prevail over the conduction

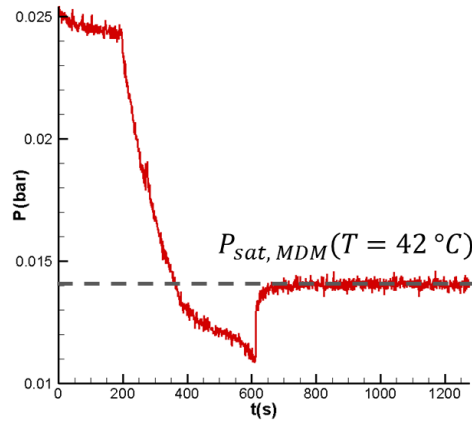


Figure 7: Pressure in the HPV during the degassing cycle at a temperature of 42 °C.

Fluid	P_{T6} (bar)	T_{T6} (°C)	Z_{T6}	β
MDM	0.35-0.07	120-80	0.97	50-10

Table 4: Operating conditions for the early MDM tests.

along the thermocouple stem and the radiation from the vessel wall. During the cooling process, convective motions are strongly inhibited, since the the entire HPV (and especially its top portion) is not provided with a cooling system and it is strongly insulated. Therefore, the thermocouple are presumably heated by conduction and radiation from the vessel wall at a temperature constantly higher than the condensing fluid temperature.

After each heating/cooling cycle, the HPV pressure is significantly higher than the saturation pressure at the fluid temperature (see figure 7, at $t < 200$ s). This could be related to the presence of air sucked by HPV from the surrounding environment, to liquid degassing or to fluid decomposition, since MDM is expected to form more volatile fractions after decomposition. For this reason, after each cycle the HPV has been degassed, by means of the vacuum pump. The process is depicted in figure 7. It can be seen that as the vacuum pumps is operating (staring at $t \simeq 200$ s) the HPV pressure reduces at a large rate (until $t \simeq 400$ s) this behaviour is probably related to volatile gas extraction (air, non-condensable gas, possible decomposition products). As the pressure diminishes the rate of decrease also reduces, indicating the approaching of the saturation pressure and the consequent probable extraction of MDM vapor. As the vacuum pump is stopped (at $t \simeq 600$ s), the pressure rapidly rise, reaching and keeping constant the saturation value, thus indicating that no fluid decomposition occurred. This matching is also a confirmation of the consistency between the experimental and the calculated P-T value at this saturation point ($P = 0.014$ bar, $T = 42$ °C).

4.2 Experimental results

Due to the difficulties related to the accurate setting of the MCV PID parameters, the early test with MDM are performed with a constant valve opening set at 25%. The resulting test conditions are reported in table 4.

A picture of the test section during the experimental runs with MDM is shown in figure 10. Condensation of MDM vapor occurred along the back plate, which is not heated, in all performed tests. Condensation prevented the use of the double-passage Schlieren techniques, since liquid

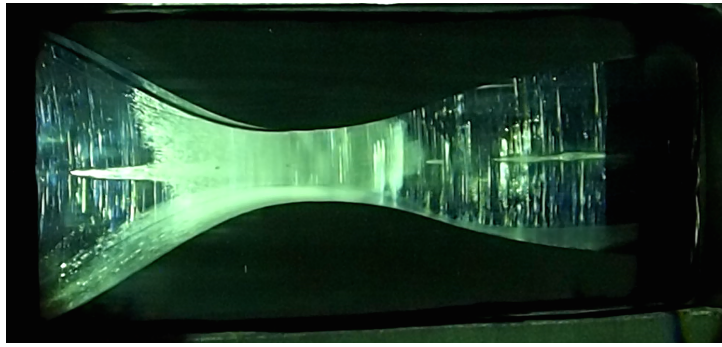


Figure 8: Picture of the test section during the experimental runs with MDM. The flow is from left to right. Condensation along the back plate is clearly visible. A liquid film is also visible in the convergent section of the nozzle.

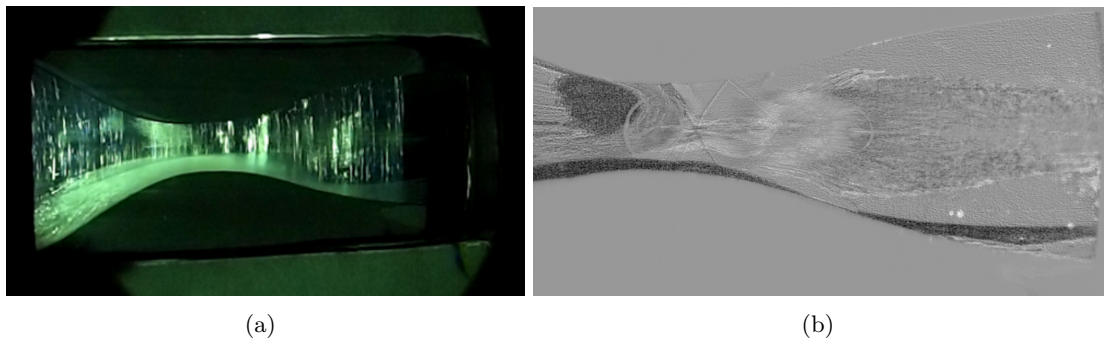


Figure 9: Last part of the experimental run with MDM. The flow is from left to right. Total inlet conditions at this time are $P_{T6} = 100$ mbar, $T_{T6} = 84$ °C; the downstream pressure is $P_9 = 6$ mbar. (a) Picture of the test section; the liquid film is largely evaporated at the back plate. (b) Schlieren visualization; oblique shock waves immediately downstream of the recessed step are clearly visible.

drops and film over the back plate produced reflected rays featuring highly distortion in different directions, thus preventing the detection of the density gradients in the vapor phase. Direct observation of the test section revealed that indeed condensation occurs only along the metal plate. Moreover, two shock waves originating from step position were observed thus confirming the possibility of observing a supersonic nozzle flow in the vapor phase. This is also proved by partial Schlieren visualization of figure 9 obtained during the last part of the test, when the test section heating provided by the vapor flow is such that the liquid film is largely evaporated. The oblique shock waves originated immediately after the recessed step are clearly visible (together with their reflection at the contoured wall), thus confirming the occurrence of a supersonic flow of MDM vapor within the nozzle.

Figure 10 reports the instantaneous Mach number at the pressure tap located along the nozzle axis and at the throat section. The Mach number is computed from isentropic relations using the instantaneous values of the total and static pressure ratio and according to the pertinent thermodynamic model. From small-perturbation theory of transonic flows, the value of the Mach number in this peculiar location is independent from the fluid thermodynamics. Therefore the ideal-gas value measured for air (about 0.96) should be equal to that obtained for MDM in non-ideal conditions. Indeed a good agreement is observed during the first 15 s of the experiment, thus confirming the consistency of the pressure measurements. Departure from the expected value is believed to be related also to the presence of a thick liquid film along the bottom surface of the nozzle, probably caused by liquid entrainment within the main vapor flow from

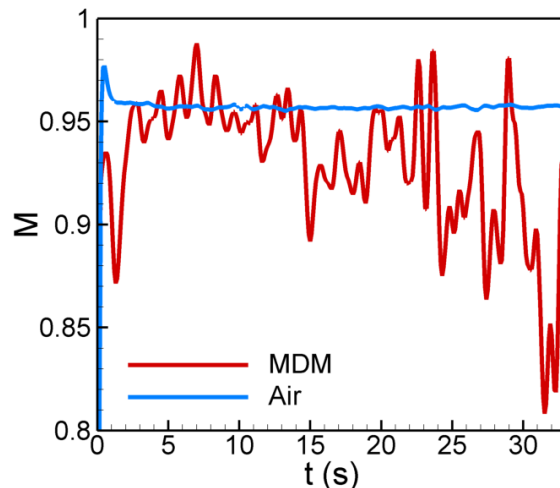


Figure 10: Mach number from the pressure tap located along the nozzle axis and at the throat section for the air and MDM test runs.

the settling chamber.

5. CONCLUSIONS

Preliminary results from the Test-Rig for Organic Vapors (TROVA) at Politecnico di Milano were reported. Pressure measurements are in good agreement with theoretical predictions for air, thus confirming the accuracy of the measurement chain and the efficiency of the throttling valve. The Schlieren bench is functional and provides an overview of the flow field, including the location of shock waves which is required to understand the pressure signal in the diverse operating conditions. Regarding the test run with the organic fluid MDM, the loading procedure and the liquid pump operation was verified. Degassing of the fluid is satisfactory: after vacuumising the HPV, the pressure immediately sets back to the vapor pressure at the considered temperature. The fluid follows the saturation curve while heating, thus indicating that no contaminants are present. Preliminary results for nozzle flow of MDM were found to be consistent with those obtained for air, though condensation along the back plate prevented its use as a mirror for the optical measurements. The appearance of shock waves induced by the recessed step confirms the occurrence of a supersonic nozzle flow of MDM in the vapor phase, during the last part of the test. The test-rig is currently being retrofitted with a new heating system to avoid condensation during the fluid heating phase, most notably in the piping connecting the HPV and the test section, and during the test runs.

REFERENCES

- Angelino, G., Gaia, M., and Macchi, E. (1984). A review of italian activity in the field of organic rankine cycles. In *VDI Berichte - Proceedings of the International VDI Seminar, Zurich*, volume 539, Dsseldorf. VDI Verlag.
- Bini, R. and Manciana, E. (1996). Organic rankine cycle turbogenerators for combined heat and power production from biomass. In *Energy Conversion from Biomass Fuels, Current Trends and Future System, Munich*.
- Cinnella, P. and Congedo, P. M. (2007). Inviscid and viscous aerodynamics of dense gases. *J. Fluid Mech.*, 580:179–217.

- Colonna, P., Harinck, J., Rebay, S., and Guardone, A. (2008). Real-gas effects in organic rankine cycle turbine nozzles. *J. Prop. Power*, 24:282–294.
- Colonna, P., Nannan, R., Guardone, A., and Lemmon, E. W. (2006). Multi-parameter equations of state for selected siloxanes. *Fluid Phase Equilib.*, 244:193–211.
- Colonna, P. and Rebay, S. (2004). Numerical simulation of dense gas flows on unstructured grids with an implicit high resolution upwind Euler solver. *Int. J. Numer. Meth. Fluids*, 46(7):735–765.
- Duvia, A. and Tavolo, S. (2008). Application of orc units in the pellet production field: technical-economic considerations and overview of the operational results of an orc plant in the industry installed in madau (germany). Technical report, Turboden s.r.l., Italy.
- Gaia, M. and Duvia, A. (2002). Orc plants for power production from biomass, 0.4-1.5 MWe: technology, efficiency, practical experiences and economy. In *7th Holzenergie Symposium*. ETH Zurich.
- Guardone, A. (2007). Three-dimensional shock tube flows of dense gases. *J. Fluid Mech.*, 583:423–442.
- Guardone, A., Spinelli, A., and Dossena, V. (2013). Influence of molecular complexity on nozzle design for an organic vapor wind tunnel. *ASME Journal of Engineering for Gas Turbines and Power*, 135:042307.
- Harinck, J., Guardone, A., and Colonna, P. (2009). The influence of molecular complexity on expanding flows of ideal and dense gases. *Phys. of Fluids*, 21:086101, 1–14.
- Hoffren, J., Talonpoika, T., Larjola, J., and Siikonen, T. (2002). Numerical simulation of real-gas flow in a supersonic turbine nozzle ring. *J. Eng. Gas Turbine Power*, 124:395–403.
- Schuster, A., Karellas, S., Kakaras, E., and Spliethoff, H. (June 2009). Energetic and economic investigation of organic rankine cycle applications. *Applied Thermal Engineering*, 29(8-9):1809–1817.
- Spinelli, A., Dossena, V., Gaetani, P., Osnaghi, C., and Colombo, D. (2010). Design of a test rig for organic vapours. In *Proceedings of ASME Turbo Expo, Glasgow, UK*.
- Spinelli, A., Pini, M., Dossena, V., Gaetani, P., and Casella, F. (2013). Design, simulation, and construction of a test rig for organic vapours. *ASME Journal of Engineering for Gas Turbines and Power*, 135:042303.

ACKNOWLEDGEMENT

The research is funded by the European Research Council under Grant ERC Consolidator 2013, project NSHOCK 617603. The initial layout of the plant was funded by Turboden S.r.l..

WAVE SPEED MEASUREMENTS IN NON-IDEAL COMPRESSIBLE FLOWS USING THE FLEXIBLE ASYMMETRIC SHOCK TUBE (FAST)

T. Mathijssen¹, M. Gallo¹, E. Casati¹, A. Guardone², P. Colonna^{1*}

¹ Propulsion & Power, Delft University of Technology
2629 HS, Delft, The Netherlands
P.Colonna@tudelft.nl

² Department of Aerospace Science & Technology, Politecnico di Milano
Via La Masa 34, Milano 20156, Italy

* Corresponding Author

ABSTRACT

Non-ideal compressible fluid dynamics (NICFD) are defined as compressible fluid flows occurring in the dense vapour, dense vapour-liquid equilibrium or supercritical thermodynamic region. This type of flow can occur in expanders of organic Rankine cycle power plants. In order to study NICFD, a Ludwig tube-type facility has been designed and constructed at Delft University of Technology. A large variety of fluids can be employed in the facility, but for this study D₆ siloxane is chosen as working fluid due to its high thermal stability and the possibility of encountering non-classical gasdynamic phenomena. This compound belongs to the siloxane class, which are also used as working fluids in ORC power systems. Gasdynamic experiments within the NICFD region are presented from which the wave speed and speed of sound can be inferred using the time-of-flight technique. These data can be used to improve and validate thermodynamic models.

1. INTRODUCTION

The field of fluid mechanics studying the motion of fluids in the dense-vapour, dense-vapour-liquid and supercritical thermodynamic region is called Non-ideal compressible fluid dynamics (NICFD). Such flows are characterized by, among other interesting phenomena, a quite different variation of the sound speed compared to that of ideal gases. This feature can be investigated by considering the fundamental derivative of gasdynamics Γ , defined by Thompson (1971) as

$$\Gamma \equiv 1 + \frac{\rho}{c} \left(\frac{\partial c}{\partial \rho} \right)_s, \quad (1)$$

in which ρ , c and s denote the fluid density, speed of sound, and entropy respectively. For an ideal gas, Γ is constant and equal to $(\gamma + 1)/2$ in ideal gases, in which γ is the ratio of specific heats. Whenever Γ is variable among the thermodynamic states of the fluid flow, NICFD occurs (Thompson, 1988).

The working-fluid flows within turbomachinery of Organic Rankine Cycle (ORC) power systems is one example where NICFD is encountered (Cramer, 1989; Brown and Argrow, 2000; Colonna et al., 2015). Other examples encompass supercritical carbon dioxide (scCO₂) power systems (Conboy et al., 2012; Rinaldi et al., 2015) and high temperature heat pumps (Zamfirescu and Dincer, 2009).

Flow measurements in the dense vapour region of complex organic fluids can contribute to the improvement of thermodynamic models and to the understanding of NICFD. ORC turbine designs benefit from better thermodynamic models through a more accurate prediction of flow patterns, such as shock waves. However, measurements in dense vapours of high molecular weight fluids are scarce (Nannan et al.,



Figure 1: Picture of the FAST setup. In the foreground the LPP is visible, with the charge tube extending to the other side of the room. The vapour generator and condenser are not visible in this image.

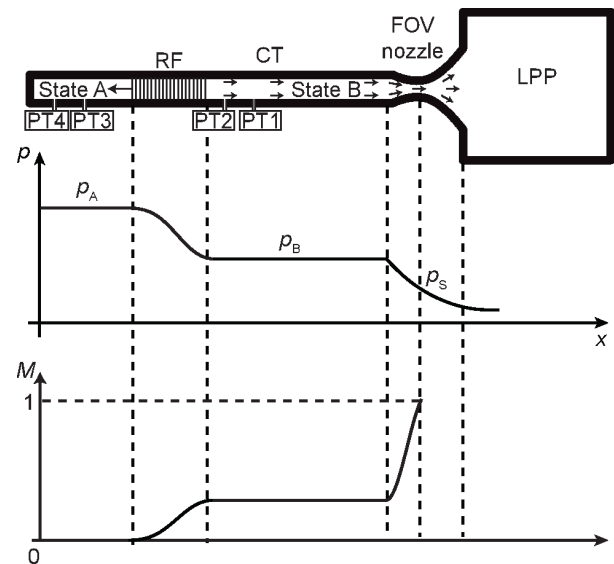


Figure 2: Schematic overview of a rarefaction wave experiment after opening the FOV. A rarefaction fan (RF) propagates into the charge tube (CT) at sonic speed W . The rarefaction starts a flow from stagnant condition A in the CT to condition B. It flows through a choked nozzle to the low pressure plenum (LPP). The pressure p and Mach number M along the tube are displayed qualitatively.

2007; Weith et al., 2014). In order to fill this gap, the flexible asymmetric shock tube (FAST), an unconventional Ludwieg tube, is designed and installed at Delft University of Technology (Colonna et al., 2008a), in the Netherlands, with the aim of studying wave propagation in the dense vapour of organic compounds.

This work documents the FAST set-up and the first experimental results of wave propagation measurements in the dense vapour of dodecamethylcyclohexasiloxane (D_6). Fig. 2 shows a schematic overview of a classical rarefaction wave experiment. The charge tube (CT) is filled with the dense organic vapour and kept at the desired pressure and temperature. The fast-opening valve (FOV), initially closed, is opened, thus allowing the fluid to flow towards the low pressure plenum (LPP), which is maintained at a lower pressure. Consequently a rarefaction travels into the CT.

A description of the set-up is provided in Sec. 2: it provides details about the components equipping the complete system as-built, the experimental procedure, and an overview of the control and data acquisition system. The results of the rarefaction wave experiments in a variety of incondensable gases are reported and discussed in Sec. 3. In Sec. 4 results from preliminary rarefaction wave measurements in D_6 are reported. Sec. 5 summarizes concluding remarks and outlines future work.

2. THE FAST AND THE EXPERIMENTAL PROCEDURE

The mechanical and heating equipment is described in Sec. 2.1 by outlining the procedure of a typical experiment. The measurement and monitoring instruments as well as the control system are briefly reported in Sec. 2.2.

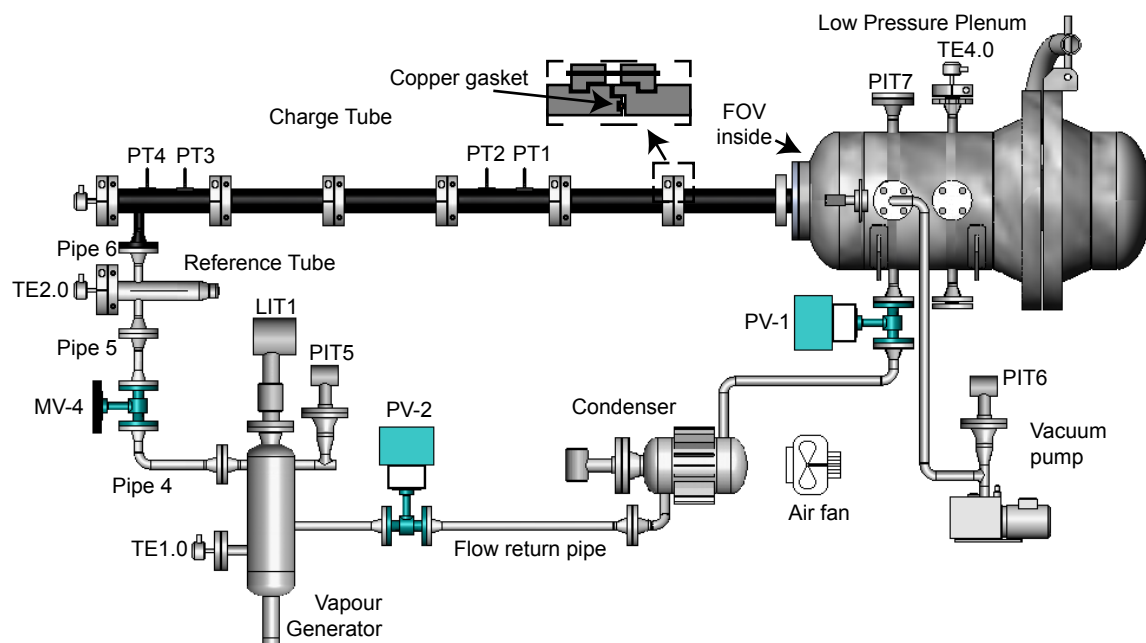


Figure 3: Overview of the FAST setup. Relevant labels are placed to the equipment and instruments. The fast-opening valve is placed inside the low pressure plenum.

2.1 Equipment & procedure

A schematic representation of the FAST is reported in Fig. 3. All pipes, vessels, and parts in contact with the working fluid are made of stainless steel (316Ti).

Before starting an experiment the working fluid needs to be purified in order to remove air and moisture deemed as the main causes of thermal decomposition of the adopted organic compounds at high temperature (Dvornic, 2004). The fluid, after being filtered with a 3Å molecular sieve and a paper filter, is inserted into a stainless steel Swagelok cylinder (type 304L-HDF-81CAL) and a Pfeiffer vacuum pump (type Duo 5 M) is used to extract any incondensable gases. By immersing the cylinder in a pool of liquid nitrogen, the fluid freezes and, as a consequence, releases the dissolved gases that are extracted by using a vacuum pump once the fluid has melted. This freezing-thawing procedure is repeated at least 2 times before filling the vapour generator through pipe 1, see Fig. 4.

The vapour generator is a custom made 5.9 liter vessel, designed to heat and evaporate the working fluid isochorically (valves MV-4 and PV-2 closed, see Fig. 3) up to the desired pressure and temperature by utilizing electric heaters. Most of the thermal energy is supplied to the vapour generator by a 1.5 kW Kurval ceramic band heater (custom built ETB HRHK-type) covering the bottom section, see Fig. 4, because the lower part of the vapour generator is always in contact with liquid. This ensures a high heat transfer coefficient between the heater and the liquid fluid inside the vessel and helps avoiding hot spots that could trigger thermal decomposition of the fluid. Preliminary tests revealed periodic instabilities of the thermal control induced by condensation phenomena occurring in the unheated section of the vessel (pipe 2 and 3, Fig. 4). By heating all the walls of the vapour generator, these instabilities were eliminated. Therefore, the main section of the vessel is heated by a 2.8 kW ceramic band heater (custom built ETB HRHK-type). The complex geometry of the top section made the implementation of a band heater impossible, so the upper section of the vapour generator is heated with a 6 m long 1 kW Welvy Joule dissipation heating wire (type HSQ/060). Another heating wire of the same type is wrapped around pipe 2 and 3, and a third wire around pipe 4, see Fig. 3. Where possible to apply, the heating element presses into a KWX 2 mm conducting graphite layer (type KU-CBGA2000-0H) to improve the thermal contact, which also ensures an even surface temperature distribution, thanks to its high in-plane thermal

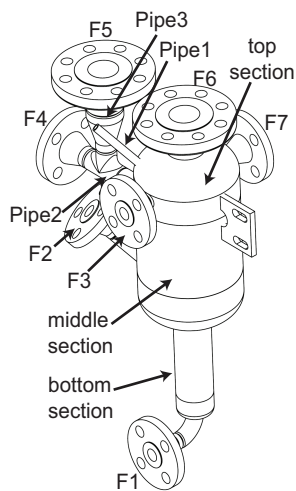


Figure 4: Drawing of the vapour generator. The numbers correspond to the flanges connecting with the following equipment: **F1:** outlet to extract liquid, **F2:** PT-100 sensor, **F3:** return pipe from the LPP, **F4:** burst disc, **F5:** static pressure transducer, **F6:** liquid level meter, **F7:** reference tube

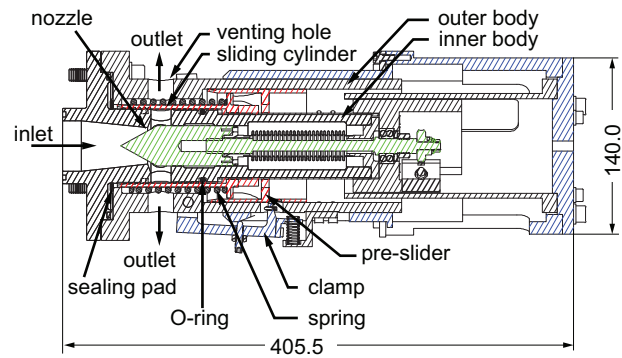


Figure 5: Drawing of the cross-section of the Fast Opening Valve. The actuation system (in blue) slides slowly to the right side, which pushes the clamps outward. Once the clamps release the pre-slider, the fast moving components (in red) come into motion because the compressed spring pushes the sliding cylinder and the pre-slider away. After the sliding cylinder is pushed across the venting holes, the fluid is free to flow from the inlet to the outlet. The nozzle insert (in green) can be moved in the longitudinal direction in order to control the throat area.

conductivity. This is required to obtain a uniform temperature and to prevent hot spots that could promote thermal decomposition. The entire vapour generator is covered with a layer of minimum 50 mm rockwool insulation to limit heat losses to the environment.

Once the desired pressure is attained in the vapour generator, a manually operated Tyco 19.05 mm globe valve MV-4 (type Megastar) is opened and vapour flows through pipe 4 to the reference tube (RT) and charge tube (CT), see Fig. 3. The purpose of the RT is to finely control the vapour superheating and to provide a reference for the thermal control of the CT, as further explained in Sec. 2.2. The RT is a 500 mm long tube with an internal diameter of 40 mm and 15 mm thick walls. The thickness of the walls enhances an even distribution of the thermal power. The thermal energy is supplied by two Tyco custom-made heating jackets around the tube, which includes a 25 mm glass silk insulation layer. A 335 W version is placed around the RT and a 180 W version around the flange of the RT. To prevent condensation in pipe 6, see Fig. 3, a 2.1 m long 370 W Welvy Joule dissipation heating wire (type HSQ/021) is applied with a 2 mm thick graphite layer placed underneath.

The geometry of the CT and of the RT are identical, except for their length. The CT is composed of six pipe segments, each 1520 mm long. The pipe segments feature a male-to-female connection and a red copper seal (see the zoomed section in Fig. 3) which allow for satisfactory sealing both in case the inner volume is at superatmospheric pressure, or under vacuum conditions. The CT assembly measures 9 m in total and is placed on a sliding support to allow for its thermal expansion when at high temperature. Each segment is fitted with a custom made Tyco 950 W Glass Silk heating jacket and the couplings between the elements are fitted with two 0.5m Welvy 180 W Joule heating electric wire (type: HBQ/005), all covered by a 25 mm glass silk insulation layer. Immersion of temperature sensors in the CT would inherently disturb the flow field of interest. Instead, the outside wall temperature is measured both in the RT and CT. Due to the geometric equivalence of the RT and the CT, imposing the same temperature on the walls results in the same fluid temperature inside the tube.

The end of the CT is closed off by a FOV, arguably the most complex mechanical part of the setup, see Fig. 5. This custom designed valve is able to operate at high temperatures without lubrication to

avoid contamination of the working fluid. It might however be expected that the siloxane working fluids act as a lubricant. The valve is contained in the LPP and can be operated remotely, keeping the entire facility hermetically sealed for multiple experiments. In the opened position, the working fluid can flow through venting holes present in the inner and outer body in the radial direction. In the closed position, a sliding cylinder is pushed between these bodies, obstructing the flow through the venting holes. The sliding cylinder presses into a Kalrez compound sealing pad on the flange to ensure sealing. On the other side, the sealing is performed by a Kalrez O-ring with a diameter of 47.22 mm and a thickness of 3.53 mm between the sliding cylinder and the inner body. Since the thermal swelling of the O-ring has a strong effect on the friction of the sliding cylinder during the fast opening, a 3 mm thermocouple (K-type) inserted in a hole in the mounting flange of the FOV monitors the temperature of the steel. An Inconel steel spring is compressed and three radial clamps engage the pre-slider to prevent the spring from being released. To open the valve, the clamps are moved in the outward direction, allowing the spring to push the sliding cylinder and the pre-slider away, thus leaving the venting holes open. A nozzle insert creates a throat area in order to choke the flow, thus preventing flow disturbances from travelling upstream. For this reason the throat is located upstream of the sealing, as opposite to solutions that are typical in Ludwig tubes (Schrijer and Bannink, 2010; Knauss et al., 1999). The nozzle insert can be moved remotely in the longitudinal direction to change the throat area section, between approximately 420 mm² and 600 mm², and this allows to modulate the strength of the rarefaction waves.

The FOV is contained in the LPP, a 113 liter cylindrically shaped vessel, see Fig. 3, with an outer diameter of 406.4 mm and 9.53 mm thick walls. The electric motor triggering the FOV and the manual nozzle positioning gear are mounted on the LPP with feedthrough shaft connections sealed with copper gaskets. A lid gives access to the vessel interior for installation of the FOV, and is sealed by a graphite gasket. The LPP can be heated by 4 custom built Tyco heating jackets with a nominal power of 1450, 425, 960 and 490 W respectively.

The vapour flows from the LPP through globe valve PV-1 into a condenser. The condensed liquid accumulates in a flow return pipe and returns via globe valve PV-2 into the vapour generator, see Fig. 3.

2.2 Instruments & Control

The thermal energy supply to the various sections of the facility is regulated by digital PID controllers, which modulates the electrical voltage to the heating elements via RKC 1-phase thyristors (model: THV-1PZ-020-5*NN-6).

In the vapour generator, the static pressure had initially been used as process variable for the main heater at the bottom section, measured by a Klay pressure transmitter (type 2000-SAN-4-F(w)-I-HT-G43) with a specified accuracy of 0.1% of the full range of 30 bar. Because the operating pressure range of the vapour generator spans from very far from the critical point to close-to-critical conditions, the response in pressure to the supplied thermal power changes dramatically, due to the difference in the pressure derivative with respect to temperature at constant specific volume $(\frac{\partial P}{\partial T})_v$. Consequently, the PID parameters should also be adapted depending on the operated pressure. This is avoided by converting the pressure into a saturation temperature with the help of in-house software (Colonna et al., 2012) implementing suitable fluid thermodynamic property models, (see, e.g. Nannan and Colonna 2009). Now the same PID parameters can be used throughout the entire operating range, because the change in specific heat capacity is sufficiently moderate. At the same time, the fast response of the pressure transmitter is still exploited for the control. The fluid saturation temperature is compared by a direct measurement of the liquid temperature as sensed by a Klay 4-wire Pt-100 sensor with insertion length of 180 mm and 6 mm diameter (type TT-E-D-F-L180xD6-S-P2-P13), which is calibrated using a Presys calibration oven (type T-350P) to within a tolerance of 0.12 °C. The other heaters on the vapour generator are each regulated based on the temperature difference as measured by the Pt-100 and a 1 mm thick thermocouple (K-type) applied underneath each heater.

The heat supply to the RT is regulated by a PID controller with as process variable the superheating of

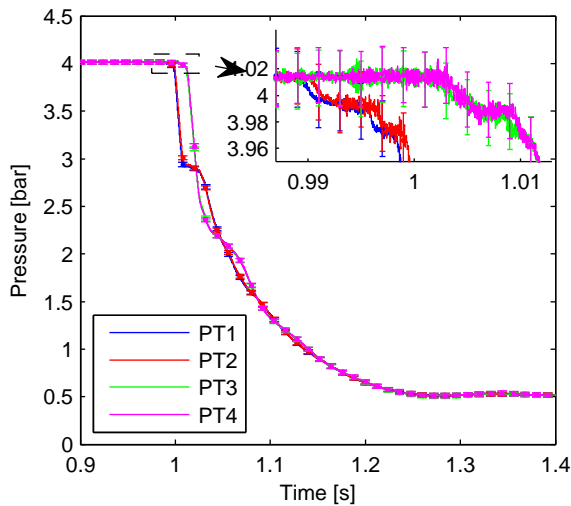


Figure 6: Pressure signals of experiment 25 measured by transducers PT1 to PT4. The valve opening results in a pressure drop from 3.97 bar to 2.88 bar, which is preceded by two other small pressure drops. These are attributed to an initial leakage flow that starts as soon as the FOV sliding cylinder detaches from the seal.

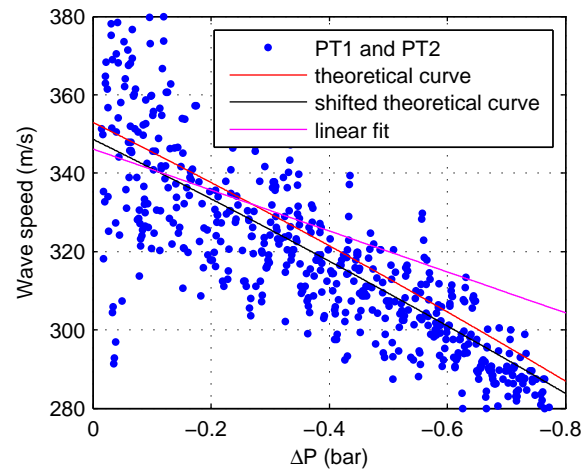


Figure 7: Wave Speed in N_2 as a function of the pressure drop. The blue dots are the experimental results obtained with the time-of-flight method. The red line is the theoretical curve. The black line is a shift of the theoretical curve with the average deviation from the theoretical curve. The magenta line is a linear fit of the data. The shifted theoretical curve and the linear fit are made based on 25 % of $\Delta p_{rel} = -0.2$ bar

the vapour, measured by the difference in temperature of the vapour in the RT and of the liquid in the vapour generator. The temperature in the RT is measured with a Klay 3-wire Pt-100 sensor (type TT-E-D-F-L250xD6-S-P2-P13) with 250 mm insertion length and 6 mm diameter, and is calibrated in the same manner as the one in the vapour generator. An identical resistance temperature detector (RTD) as the one in the RT is used to monitor the temperature in the CT.

The fluid temperature inside the CT is controlled by imposing the same wall temperature on the CT as on the RT, which are geometrically equivalent, except for the length. The process variable of each control loop is the difference in wall temperature between the RT and the respective CT pipe segment and coupling. Instead of measuring the temperature of the two thermocouples and calculating the difference in temperature, here the two thermocouples are connected to each other and the voltage difference is directly measured to reduce the measurement error. The 1 m long and 0.5 mm thick thermocouple (type K) is placed in a groove in the RT and in each CT element, bonded to the tube with Aremco silver-filled conductive ceramic adhesive (type 597A) to ensure the measurement of the wall temperature.

To measure the passing rarefaction, four dynamic pressure measurement stations PT1-PT4 are created by flush mounting a high-temperature Kulite fully active four arm wheatstone bridge pressure transducer (type XTEH-10LAC-190M-21bar-A) that measures the pressure with an accuracy of 0.5 % of the full scale of 21 bar along the CT at a distance of 4, 4.3, 8.4 and 8.7 m from the FOV respectively, see Fig. 3. The signals acquire at a frequency of 250 kHz and are scaled after each experiment with the more accurate value of the pressure before and after the experiment, measured by the static pressure transducers. The sensors are placed in pairs to give the possibility to have a time of flight measurement at two different locations in the tube.

nr	fluid	P_{CT} [bar]	T_{CT} [°C]	Γ [-]	ΔP_{wave} [bar]	A_{nozzle} [mm ²]	c_{model} [m/s]	c_{fit} [m/s]	c_{shift} [m/s]
1	He	6.01	17.3	1.34	1.74	459	1006	998	964
2	He	4.90	22.7	1.34	0.28	79	1014	1014	1028
3	He	6.09	48.9	1.34	1.69	438	1059	1005	1072
4	He	6.50	50.0	1.34	0.32	67	1060	1121	955
5	He	6.66	99.2	1.34	2.01	483	1138	1274	1169
6	He	6.02	149.4	1.34	1.84	489	1212	1225	1182
7	He	7.29	269.4	1.34	0.33	62	1373	1547	1348
8	He	8.47	269.9	1.34	0.44	72	1374	1424	1483
9	air	6.31	17.6	1.21	1.62	456	343	341	341
10	air	4.08	18.0	1.20	0.97	418	343	338	339
11	air	7.01	19.1	1.21	1.81	459	344	338	339
12	air	4.86	20.0	1.21	0.21	67	344	359	350
13	air	5.39	20.0	1.21	0.23	68	344	344	353
14	air	7.13	22.0	1.21	0.30	67	345	338	347
15	air	6.15	49.1	1.21	1.62	468	361	353	356
16	air	6.98	95.0	1.20	0.27	61	386	375	388
17	air	6.80	99.5	1.20	1.76	461	388	390	384
18	CO ₂	5.99	18.0	1.13	1.50	471	262	257	259
19	CO ₂	6.42	50.0	1.12	1.59	465	275	274	273
20	CO ₂	6.64	100.3	1.12	1.64	464	296	294	293
21	CO ₂	6.13	149.7	1.11	1.50	459	314	321	315
22	N ₂	1.09	25.3	1.20	0.35	576	352	337	338
23	N ₂	1.12	25.4	1.20	0.33	531	352	379	349
24	N ₂	4.00	25.7	1.20	1.00	443	353	360	353
25	N ₂	4.01	25.8	1.20	1.08	481	353	346	349
26	D ₆	1.26	264.2	0.86	0.09	169	89.8	89.5	88.4
27	D ₆	1.26	293.7	0.91	0.15	278	94.3	94.0	94.1
28	D ₆	1.27	298.0	0.91	0.18	328	94.8	96.9	93.9
29	D ₆	1.27	300.1	0.92	0.14	254	95.1	98.3	94.0
30	D ₆	2.52	301.1	0.79	0.26	254	84.6	84.9	83.5
31	D ₆	2.38	302.3	0.81	0.21	220	86.2	83.5	82.7
32	D ₆	2.53	305.1	0.79	0.29	286	85.4	84.3	83.5

Table 1: Results from rarefaction measurements. p_{CT} and T_{CT} are the measured initial pressure and temperature in the charge tube. Γ and c_{model} are the fundamental derivative of gasdynamics and speed of sound respectively calculated using the most accurate thermodynamic model for the measured conditions (uncertainty unknown). Δp_{wave} is the pressure difference across the rarefaction. A_{nozzle} is the nozzle area calculated using the pressure drop across the expansion. c_{fit} and c_{shift} are the speed of sound as measured by fitting the experimental time-of-flight results using a linear function and by shifting the theoretical curve with the average deviation respectively.

3. RAREFACTION WAVES IN INCONDENSABLE GASES.

In order to verify the correct functioning of the facility, a series of experiments are performed using incondensable gases in the ideal gas regime. The CT is filled with the gas under pressure, while the LPP is kept at vacuum conditions. The FOV is opened after which a rarefaction wave propagates into the CT, see Fig. 2. A flow starts from the CT into the LPP, which is attaining a sonic speed in the throat.

The pressure recordings of rarefaction experiment 25 (see Table 1) are displayed in Fig. 6. The working fluid in that experiment is nitrogen and the pressure is 4.01 bar in the CT and < 10 mbar in the LPP, both at an ambient temperature of 25.8 °C. The FOV opening sequence can be inferred from these pressure data: as soon as the FOV opening is initiated, the sliding cylinder is pushed by the compressed spring, see Fig. 5. A small opening is created when the sliding cylinder does not touch the seal anymore, and the flow gets choked close to this position. This causes a small pressure drop of approximately 20 mbar. As the slider moves further, the position of minimum cross-section of the flow changes to a section between the slider and the inner body, which is slightly larger than the initial choked section. This is revealed by

a second small drop in the pressure of approximately 20 mbar. Finally the sliding cylinder passes over the venting hole of the inner body, and the flow chokes at the designated nozzle. This is seen as the large pressure drop down to 2.88 bar.

The nozzle throat cross-sectional area is not easily recovered from the FOV geometry and therefore it is inferred from the measurements by assuming a steady flow from state B through the nozzle, see Fig. 2. The mass flow in state B is evaluated using the density calculated by using the isentropic relations from state A, the known cross-sectional area of the CT and the evaluated flow velocity using the Riemann invariant from state A. The isentropic relations are used to calculate the density and velocity in the throat. The calculated throat area ranges from 418 to 576 mm². Several experiments were performed using a special nozzle insert, for which the calculated throat area ranges from 61 to 79 mm², see Table 1.

The local wave propagation speed in the CT equals the local speed of sound minus the local flow velocity. A theoretical curve can be constructed by calculating the wave propagation speed as a function of the pressure drop of the rarefaction. At zero pressure drop, the wave propagation speed equals the speed of sound, since stagnant conditions are assumed in the CT before opening the valve, and is evaluated using the reference equation of state. For a given pressure drop, the wave propagation speed is evaluated by calculating the local speed of sound using the isentropic relations, while the local flow velocity is calculated by evaluating the Riemann invariant in the undisturbed state (Thompson, 1988).

By applying the time-of-flight method to the signals of two pressure transducers, an experimental value of the local wave propagation speed is obtained. This is done by first selecting the relevant part of the pressure signal as follows: the beginning of the wave at $t = t_{start}$ is formally identified as the time when the pressure departs more than 15 mbar from the initial value P_{CT} . The threshold is chosen such that it exceeds the noise level. The end of the unperturbed portion of the signal is chosen when the head of the wave is expected to reach the end of the CT at $t = t_{end}$. The estimate is performed by using the speed of sound from the accurate reference thermodynamic model, therefore $t_{end} = t_{start} + \Delta x / c_{model}$, where Δx is the distance between the sensor location and the end of the CT. The relevant portion of the signal ΔP_{rel} spans from P_{start} to P_{end} . This span is divided into intervals of two times the resolution of 0.32 mbar of the pressure signal of the current measurement system. The time-of-flight method is applied to corresponding subintervals from different sensors to compute the local wave propagation speed. The measurements of sensors PT3 / PT4 are quickly influenced by the reflection of the rarefaction from the CT end wall, so only the measurements of sensors PT1 / PT2 are considered.

Fig. 7 shows for the example of experiment 25 the charts that can be obtained, from which the speed of sound can be retrieved at $\Delta p \rightarrow 0$. Wave speed values as a function of the measured pressure drop are shown together with fitting curves used to estimate the speed of sound. To reduce inaccuracies introduced by the FOV in the determination of the speed of sound to a negligible level, only the first 25 % of the relevant pressure span is taken, while keeping a minimum of 40 mbar, such that $\Delta p_{max} = \max(0.25p_{rel}, 0.04 \text{ bar})$. Two methods are used to fit the experimental data: a simple linear fit and a fit obtained by shifting the theoretical curve with the average deviation of the measurement points with respect to this curve. The resulting speed of sound c_{fit} and c_{shift} are reported in table 1. For air, CO₂ and N₂, both methods deliver an accurate estimate of the speed of sound, compared to the value obtained from the reference thermodynamic model (Lemmon et al., 2013), which corresponds to the ideal gas model in this regime. The only exception is the linear fit for experiment 23. The average error and standard deviation with respect to the model are $2.1 \pm 1.6 \%$ and $1.1 \pm 1.1 \%$ for the linear fit and the shifted theoretical curve respectively. For helium, the average error and standard deviation with respect to the model are $5.1 \pm 4.6 \%$ and $4.0 \pm 3.1 \%$ for the linear fit and the shifted theoretical curve respectively. The reason for the larger error is due to the higher speed of sound of helium in combination with the finite process start-up time of the FOV resulting in a very small usable relevant portion of the signal.

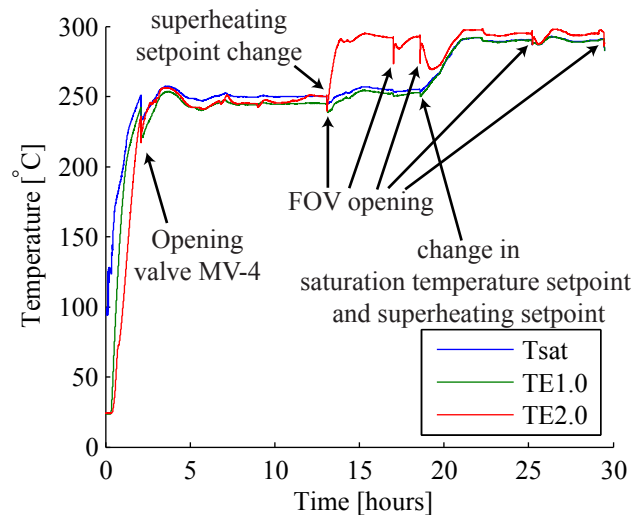


Figure 8: Temperature recordings during the experimental campaign on siloxane D_6 . T_{sat} is obtained from the measured pressure in the vapour generator by means of the suitable thermodynamic model from Nannan and Colonna (2009). TE1.0 is the temperature measured by the PT-100 sensor in the vapour generator. TE2.0 is the temperature measured by the PT-100 sensor in the reference tube.

4. RAREFACTION WAVES IN SILOXANE D_6

Experiments to measure the expansion wave speed in D_6 (dodecamethylcyclohexasiloxane, $C_{12}H_{36}O_6Si_6$) are performed from which the speed of sound is estimated. Gaschromatographic analysis confirmed the specification of the supplier that the fluid has a 96 % purity. Experiments were conducted at several thermodynamic states, see experiments 26 to 32 in Table 1. Fig. 8 shows the temperature of the fluid in the vapour generator and in the reference tube during the entire test campaign. Part of the liquid in the vapour generator is flashed each time valve MV-4 is opened after an experiment. The measured temperature fluctuations in the reference tube and charge tube had a period of approximately 2 hours with an amplitude of up to 3 °C for both temperature levels.

Pressure recordings of experiment 28 are displayed in Fig. 9. Calculations using the resulting pressure drop from the experiments result in a significantly lower nozzle area than the 460 to 600 mm² that was expected based on the geometry, see Table 1, which may indicate that there is accumulation of condensed fluid in the unheated FOV.

The wave propagation speed has been computed from the experimental data and compared with the theoretical curve, which is constructed in the same manner as for the incondensable gases. The ideal gas model can not be used in this case, and consequently the Riemann invariant can not be integrated analytically. The local flow velocity is instead evaluated by integrating the Riemann invariant numerically. Estimation of the speed of sound is obtained with the best available thermodynamic model for pure D_6 , which shows a 30 % deviation on the speed of sound with the sole reliable measurement, which is performed in the liquid state (Colonna et al., 2008b). Results from experiment 28 are displayed in Fig. 10. The wave speed calculated from experimental data for this experiment is within 8 % of the value predicted by the thermodynamic model. Only for a pressure drop lower than 12 mbar the deviation is higher, because the pressure gradient is very low, thus the influence of noise more significant. By fitting the experimental data in the same manner as illustrated for the case of incondensable gases, i.e. using a linear fit, and by shifting the theoretical curve, the speed of sound c_{fit} and c_{shift} is obtained. The average error and standard deviation with respect to the value predicted by the thermodynamic model are 1.6 ± 1.2 % for the linear fit and 1.6 ± 1.1 % for the shifted theoretical curve. The experimental results are unexpectedly close to model predictions, considering that, differently from the case of incondensable

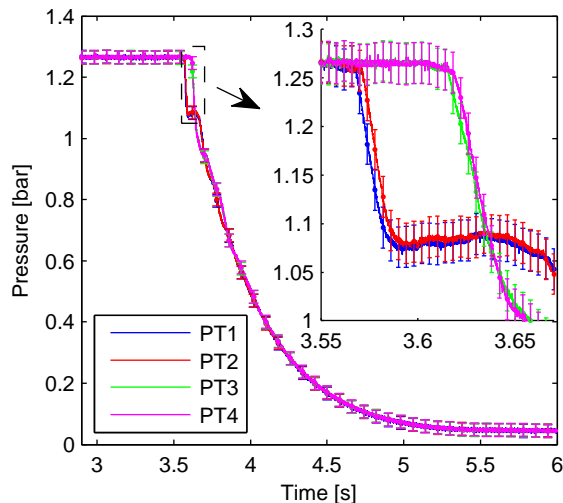


Figure 9: Pressure recordings during a D_6 experiment. The conditions in the CT are 1.27 bar and 298 °C. PT1 to PT4 are the pressure recordings of the sensor closest to the FOV to furthest away from the FOV, respectively.

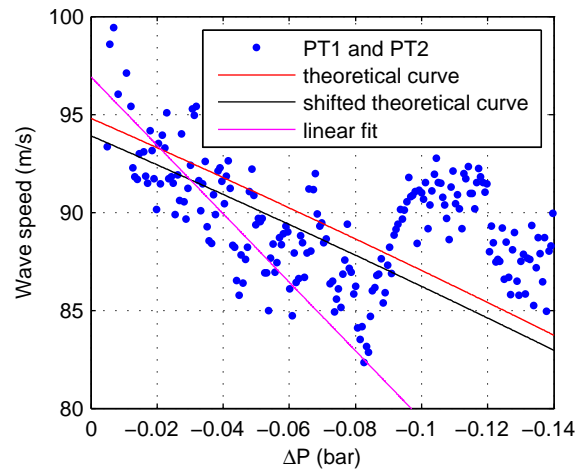


Figure 10: Wave speed in D_6 siloxane as a function of the pressure drop. The blue dots are the experimental results obtained with the time-of-flight measurements. The red line is the theoretical curve. The black line is a fit of the experimental data using a shift of the theoretical curve. The magenta line is a linear fit of the data.

gas, the D_6 thermodynamic model is expected to be rather inaccurate for states in the close proximity of the saturation curve.

5. CONCLUSION & FUTURE WORK

A novel Ludwig-tube-type facility has been commissioned at Delft University of Technology, with the purpose of performing measurements on rarefaction waves in dense organic vapours. The pressure and temperature of the working fluid can be regulated independently from each other, such that any thermodynamic state can be achieved within the limits of the measurement system of 21 bar and 400 °C. Experiments on rarefaction waves in a number of incondensable gases have been conducted to validate the correct functioning of the facility. A novel algorithm is devised to estimate the speed of sound from rarefaction experiments. Experiments using siloxane D_6 show the feasibility of the original design concept up to 300 °C: rarefaction wave speed measurements were successfully performed, providing values of the speed of sound that are within 1.6% of the predictions of the best available thermodynamic model (the model itself is known to be affected by uncertainties of 30 % for the speed of sound).

REFERENCES

- Brown, B. and Argrow, B. (2000). Application of Bethe-Zel'dovich-Thompson fluids in organic Rankine cycle engines. *J. Propul. Power*, 16(6):1118--1124.
- Colonna, P., Casati, E., Trapp, C., Mathijssen, T., Larjola, J., Turunen-Saaresti, T., and Uusitalo, A. (2015). Organic Rankine cycle power systems: From the concept to current technology, applications and an outlook to the future. *J. Eng. Gas Turb. Power*, 137(10):100801.
- Colonna, P., Guardone, A., Nannan, N., and Zamfirescu, C. (2008a). Design of the dense gas flexible asymmetric shock tube. *J. Fluids Eng.*, 130(3). 034501.
- Colonna, P., Nannan, N. R., and Guardone, A. (2008b). Multiparameter equations of state for siloxanes:

$[(\text{CH}_3)_3\text{-Si-O}_{1/2}]_2\text{-[O-Si-(CH}_3)_2]_{i=1,\dots,3}$ and $[\text{O-Si-(CH}_3)_2]_6$. *Fluid Phase Equilib.*, 263(2):115--130.

- Colonna, P., van der Stelt, T. P., and Guardone, A. (2012). FluidProp (Version 3.0): A program for the estimation of thermophysical properties of fluids.
- Conboy, T., Wright, S., Pasch, J., Fleming, D., Rochau, G., and Fuller, R. (2012). Performance characteristics of an operating supercritical CO₂ Brayton cycle. *J. Eng. Gas Turb. Power*, 134(11).
- Cramer, M. S. (1989). Shock splitting in single-phase gases. *J. Fluid Mech.*, 199:281--296.
- Dvornic, P. R. (2004). High temperature stability of polysiloxanes. *Silicon Compounds: Silanes and Silicones, Gelest Catalog*, pages 419--432.
- Knauss, H., Riedel, R., and Wagner, S. (1999). The shock wind tunnel of Stuttgart university - a facility for testing hypersonic vehicles. In *9th International Space Planes and Hypersonic Systems and Technologies Conference*, number AIAA 99-4959.
- Lemmon, E., Huber, M., and McLinden, M. (2013.). NIST standard reference database 23: Reference fluid thermodynamic and transport properties-REFPROP, version 9.1.
- Nannan, N. and Colonna, P. (2009). Improvement on multiparameter equations of state for dimethylsiloxanes by adopting more accurate ideal-gas isobaric heat capacities: Supplementary to P. Colonna, N. R. Nannan, A. Guardone, E. W. Lemmon, *Fluid Phase Equilib.* 244, 193 (2006). *Fluid Phase Equilib.*, 280(1--2):151--152.
- Nannan, N., Colonna, P., Tracy, C., Rowley, R., and Hurly, J. (2007). Ideal-gas heat capacities of dimethylsiloxanes from speed-of-sound measurements and ab initio calculations. *Fluid Phase Equilib.*, 257(1):102--113.
- Rinaldi, E., Pecnik, R., and Colonna, P. (2015). Computational fluid dynamic simulation of a supercritical CO₂ compressor performance map. *J. Eng. Gas Turb. Power*, 137(7):072602.
- Schrijer, F. and Bannink, W. (2010). Description and flow assessment of the delft hypersonic ludwig tube. *J. Spacecraft Rockets*, 47(1):125--133.
- Thompson, P. A. (1971). A fundamental derivative in gasdynamics. *Phys. Fluids*, 14(9):1843--1849.
- Thompson, P. A. (1988). *Compressible Fluid Dynamics*. McGraw-Hill.
- Weith, T., Heberle, F., Preißinger, M., and Brüggeman, D. (2014). Performance of siloxanes mixtures in a high-temperature organic Rankine cycle considering the heat transfer characteristics during evaporation. *Energies*, 7:5548--5565.
- Zamfirescu, C. and Dincer, I. (2009). Performance investigation of high-temperature heat pumps with various BZT working fluids. *Thermochim. Acta*, 488(1--2):66 -- 77.

ACKNOWLEDGEMENT

This research is partly funded by Dutch Technology Foundation STW, the Technology Program of the Ministry of Economic Affairs (DSF 11143) and by the European Research Council under grant ERC Consolidator 2013 (NShock 617603)

SCALING OF GAS TURBINE FROM AIR TO REFRIGERANTS FOR ORGANIC RANKINE CYCLE (ORC) USING SIMILARITY CONCEPT

Choon Seng Wong^{1*}, Prof. Susan Krumdieck²

^{1,2}Department of Mechanical Engineering, University of Canterbury,
Private Bag 4800, Christchurch 8041, New Zealand.
choon.wong@pg.canterbury.ac.nz¹, susan.krumdieck@canterbury.ac.nz²

* Corresponding Author

ABSTRACT

Organic Rankine Cycle (ORC) could be used to generate power from low temperature heat sources or improve overall cycle efficiency in waste heat applications with minimal environmental pollution. The design and development of an ORC turbine, however, is a complex and costly engineering problem. The common refrigerants for an ORC application exhibit non-ideal gas behaviour and some unfavourable characteristics, such as flammability and toxicity. These characteristics further increase the complexity of the design and laboratory testing process of a turbine. Similitude, or similarity concept, is an essential concept in turbomachinery to allow the designer to scale a turbine design to different sizes or different working fluids without repeating the whole design and development process. Similarity concept allows the testing of a turbo-machine in a simple air test bench instead of a full scale ORC test bench. The concept can be further applied to adapt an existing gas turbine as an ORC turbine using different working fluids.

This paper aims to scale an industrial gas turbine to different working fluids, other than the fluid the turbine was originally designed for. Three different approaches using the similarity concept were applied on the turbine performance data using compressed air to generate the performance curve for two refrigerants, namely R134a and R245fa. The scaled performance curves derived from the air performance data were compared to the performance map generated using 3D computational fluid dynamics (CFD) analysis tools for R134a and R245fa. The three approaches were compared in term of the accuracy of the performance estimation, and the most feasible approach was selected. The result shows that complete similarity cannot be achieved using two turbo-machines with different working fluids, even at the best efficiency point for particular expansion ratio. Constant $\Delta h_{0s}/a_0^2$ is imposed to achieve similarity, but the volumetric ratio is varying using different working fluids due to the variation of sound speed. The differences in the fluid properties and the expansion ratio lead to the deviation in turbine performance parameters, velocity diagram, turbine's exit swirl angle, and entropy generation. The use of $\Delta h_{0s}/a_0^2$ further limits the application of the gas turbine for refrigerants with heavier molecular weight to a pressure ratio less than the designed pressure ratio using air. The specific speed at the best efficiency point with different expansion ratio was shifted to a higher value if higher expansion ratio was imposed. A correction chart for R245fa was attempted to estimate the turbine's performance at higher expansion ratio as a function of volumetric ratio.

1. INTRODUCTION

The adaptation of an existing turbines for ORC application using different working medium can reduce the developmental effort involved in turbomachinery design aspects, such as re-designing the turbine wheel, prototyping and re-conducting the laboratory testing. The lack of documentation in literature about the adaptation of off-the-shelf turbines in applications other than the application for which they were originally designed has impeded the further development for ORC new-entrants. Turbines are usually designed for a particular set of specific speed and operating conditions, for a

specific working fluid and a specific application. The adaptation of an existing turbine for the ORC application using a different working medium is fundamentally subjected to the similitude of the design analysis of turbomachinery, which is also known as similarity concept.

. Non-dimensional parameters of turbomachines for similarity concept have been derived using the Buckingham Pi theorem. In turbomachinery there are numerous dimensionless groups possible from the seven fundamental variables, such as flow coefficient, head coefficient, power coefficient, and Reynolds number. These non-dimensional groups serve as fundamental parameters for turbomachines handling compressible or incompressible fluids. A number of other important turbine parameters include specific speed, specific diameter, and loading coefficients. The introduction of specific speed allowed the rapid development in the experimental testing of hydraulic turbines in the 1900s (Meher-Homji, 2000) and facilitated the selection of turbomachines' types for different applications (Balje, 1981). The performance mapping using flow coefficient and loading coefficient has facilitated the preliminary design process for both axial flow turbines (Dixon & Hall, 2010) and radial inflow turbines (Chen & Baines, 1994). These parameters also allow turbomachinery designers to scale a turbine from one application to another application, with different wheel size, different inlet operating conditions, and different working mediums (Aungier, 2006; Japikse & Baines, 1995).

Scaling of turbomachines using the previously discussed non-dimensional parameters is feasible if the machine is geometrically similar, which implies that the number of blades, blades thickness, blade angle, machine size, radii and operating clearance are scaled proportionally (Japikse & Baines, 1995). Scaling from large sizes to small sizes imposes some difficulties, attributed to the surface finish, the manufacturing limit and the increased cost for increased geometrical tightness at small size. The Reynolds number imposes the next major constraint, in which a correction factor has to be applied. A number of correction charts are recommended to take into account of the Reynolds number effect in the laboratory testing of centrifugal compressors at different operating conditions (Casey, 1985; Strub et al., 1987). The geometrical scaling of turbomachinery from one size to another requires the tip speed to be constant to maintain similar effects from windage loss, tip clearance loss, external losses and mechanical effects (Japikse & Baines, 1995).

Scaling of turbomachines for different operating conditions within the same working fluid is a common practice in turbomachinery testing. The inlet operating condition is scaled to reduce the pressure and temperature into the compressor or the turbine during the performance test. This practice can reduce the operational cost and the capital cost of the testing equipment. The Reynolds number cannot be scaled and a correction factor is required either from the published literature or based on in-house knowledge.

The increasing interest in Organic Rankine Cycles has prompted the need for ORC turbines that can operate with various working mediums. The most common working fluid in existing commercial installations is n-Pentane (working fluid patented by ORMAT) (S. Quoilin & Lemort, 2009). Other working fluids are actively proposed and recommended under different conditions for a better thermodynamic cycle efficiency (Bao & Zhao, 2013) and a more cost-efficient design of heat exchanger (Sylvain Quoilin, Declaye, Tchanche, & Lemort, 2011). The testing of the turbine, however, is not a simple task. A full scale ORC set-up is favorable for turbine performance test but it imposes high design, development, and installation cost and efforts in the concerns of system layout, pump, heat exchanger and piping. Refrigerants typically introduce some side effects to either the environment, atmosphere, and health and safety issues. The refrigerants have to be sealed properly with minimal leakage, which further increases the operational cost of the test facility. A simple compressed air test bench is favorable as the compressed air is safe to be released to the atmosphere without any environmental issues. The testing via compressed air, however, might introduce some important deviations, as the real gas effects cannot be accounted accurately. The variation of density of real gas across blade passage during the expansion process and the machine Reynolds number cannot be scaled precisely from one fluid to another, which further limits the similitude using real gas. The lack of published correction chart for Mach number and Reynolds number for different working mediums has further limited the application of the similarity concept. These issues make it difficult for the turbomachinery designers or the

engineers to apply the turbine performance curve generated using compressed air to an application using real gas, such as n-Pentane.

This study explores the feasibility of utilizing the similarity concept to estimate the turbine performance using real gas. Three different approaches using the similarity concept were proposed to scale air performance data to generate performance curves for two refrigerants, namely R134a and R245fa. A full computational fluid dynamic (CFD) analysis was then performed to generate the performances curves for the selected refrigerants. The approaches using the similarity concept were then compared to the result from the CFD analysis. The most feasible approach in scaling a turbine from air to refrigerants was selected. The accuracy of the performance prediction through the similarity analysis of the ORC turbomachine was estimated. The deviation in turbine's performance for different working fluids was presented and discussed.

2. METHODOLOGY

An industrial gas turbine with published turbine geometry (Sauret, 2012) was selected for this study. The selected gas turbine was initially designed for Sundstrand Power Systems (SPS) T-100 Multipurpose Small Power Unit (MPSPU) with a single-shaft configuration to accommodate the ground-based auxiliary power application (Jones, 1996). The nominal power of the selected turbine is 37 kW with a growth capability up to 75 kW (Jones, 1996). A CFD model was previously conducted on the gas turbine using air as the working medium and the result from the numerical modelling was compared to the experimental data (Jones, 1996; Wong & Krumdieck, 2014). The result from the CFD model agreed with the experimental data with less than 1% error in term of total-to-static efficiency. The CFD method was employed to generate the performance curve using two selected refrigerants, namely R134a and R245fa to validate the precision and accuracy of three different approaches of similarity concept in scaling the gas turbine from one working medium with ideal gas behavior to another working medium with real gas behavior.

The first part of this study re-generated the performance map of the selected gas turbine using air as the working medium and the performance curve served as a benchmark to determine the turbine performance using R134a and R245fa via similarity concept. The fluid properties of air were estimated using polytropic ideal gas equations. Three different approaches for similarity analysis were applied in this study. The performance curve scaled from the air data was plotted as a function of velocity ratio and specific speed for comparison.

The second part utilized the CFD methodology as outlined in previous study (Wong & Krumdieck, 2014) to generate the performance map of the selected gas turbine using R134a and R245fa. The performance map generated from the CFD tools was compared to the scaled performance map. The fluid properties of the refrigerants were extracted from REFPROP developed by National Institute of Standards and Technology (E. W. Lemmon, Huber, M.L., McLinden, M.O, 2013), and the details of the mathematical expressions to represent the real gas behavior of the selected refrigerants should be referred to the work by Lemmon (E. W. Lemmon & Span, 2006). The three different approaches were compared to the performance map by CFD tools, and the accuracy of each method was discussed.

The third part discusses the deviation in the turbine's performance using different working fluids at the best efficiency point. The fluid flow field and the blade loading across the blade passage, the velocity diagram at the turbine inlet and the outlet, and the Reynolds number effect on the turbine's performance were investigated. The limitation of the selected approach was presented, and a correction factor was generated to predict the best efficiency point of the turbine at higher expansion ratio (including super-sonic expansion).

2.1 Similarity Analysis

Similarity analysis, or similitude, provides a quick solution to scale a fluid machine for different operating conditions and different incompressible fluids without resorting to the full scale three-dimensional CFD methods. The performance of a turbomachine is dependent on the machine size, machine speed, and the fluid properties. Turbomachines are designed to handle either compressible or incompressible flow. Two extra terms are employed for turbomachines handling compressible flow, compared to the fluid machines handling incompressible flow, to take account of the compressible flow properties and the change of density during the expansion/compression process (Dixon & Hall, 2010). The performance parameters of a compressible flow turbomachine is expressed as a function of some variables, as listed in equation (1).

$$\Delta h_{0s}, P, \eta = f(N, D, \dot{m}, \rho_{01}, a_{01}, \gamma, \mu) \quad (1)$$

Where Δh_{0s} is the total-to-static enthalpy drop of the fluid across the turbine at the designed pressure ratio, P is the shaft power, η is the isentropic efficiency, and the efficiency is evaluated using the inlet stagnation and outlet static condition in this study, N is the rotational speed of the shaft, D is the diameter of the turbine wheel, \dot{m} is the inlet mass flow rate, ρ_{01} is the density evaluated using the inlet stagnation condition, a_{01} is the sonic velocity at the inlet, γ is the specific heat, and μ is the dynamic viscosity. Buckingham π theorem was applied in equation (1) and three variables, density, ρ_{01} , shaft speed, N , and wheel diameter, D were selected to reduce the original expression into five dimensionless groups, as presented in equation (2). The full mathematical derivation should be referred to the work by Dixon (Dixon & Hall, 2010).

$$\frac{\Delta h_{0s}}{a_{01}^2}, \eta, \frac{P}{\rho_{01} a_{01}^3 D^5} = f \left\{ \frac{\dot{m}}{\rho_{01} N D^3}, \frac{\rho_{01} N D^2}{\mu}, \frac{N D}{a_{01}}, \gamma \right\} \quad (2)$$

The current dimensionless group is not an explicit formulation where the parameters, such as density and sonic velocity, cannot be measured directly. The dimensionless groups can be reduced to a number of variables which allows direct measurement from the experiments if the compressible flow is modelled as a perfect gas. The dimensionless parameters were then reduced to a function of temperature and pressure at both inlet and outlet stations of the turbine, as listed in equation (3).

$$\frac{p_{02}}{p_{01}}, \eta, \frac{\Delta T_0}{T_{01}} = f \left\{ \frac{\dot{m} \sqrt{\gamma R T_{01}}}{p_{01} D^2}, Re, \frac{N D}{\sqrt{\gamma R T_{01}}}, \gamma \right\} \quad (3)$$

Where p is pressure, T is temperature, Re is machine Reynolds number, and R is the gas constant. The mathematical simplification of the dimensionless groups using perfect gas model are available from the works by Baines, Aungier, and Dixon (Aungier, 2006; Dixon & Hall, 2010; Japikse & Baines, 1995). Complete similarity can be achieved when

- 1) complete geometrical similarity is achieved (Aungier, 2006; Japikse & Baines, 1995), in which the turbine is scaled up or scaled down proportionally, *and*
- 2) dynamic similarity is achieved, in which the velocity components and forces are equal (Aungier, 2006).

Three different approaches are trialed to scale the performance data using air into the performance map using refrigerants. The scaled performance curve from each approach was compared to the performance curve from CFD analysis and the accuracy for each method was evaluated.

The *perfect gas approach* assumes that the selected refrigerants, R245fa and R134a are perfect gas. Three non-dimensional groups are hold constant, which are pressure ratio, blade speed coefficient in equation (4), and mass flow coefficients in equation (5). The outlet static pressure of the refrigerants

is determined given the pressure ratio of the turbine using air. Equation (4) is employed to calculate the shaft's rotational speed whereas equation (5) is applied to determine the mass flow rate at the turbine inlet.

$$\frac{ND}{a_{01}} = \text{constant} \quad (4)$$

$$\frac{\dot{m}}{\rho_{01}ND^3} = \text{constant} \quad (5)$$

The *variable pressure ratio approach* is similar to the perfect gas approach, but the pressure ratio does not remain constant. The pressure ratio using the selected refrigerants is determined using the correlation in equation (6). Equation (4) and equation (5) are then employed to determine the shaft speed and the mass flow rate, respectively.

$$\frac{\Delta h_{0s}}{a_{01}^2} = \text{constant} \quad (6)$$

The *constant specific speed approach* assumes constant pressure ratio, velocity ratio, v and the specific speed, N_s for the selected working medium. The optimal velocity ratio and specific speed of a turbomachine typically fall in a narrow range of operation for maximum efficiency. Both are hold constant to determine the shaft speed and the mass flow rate by using equations (7) and (8), respectively.

$$v = \frac{U}{C_{is}} = \frac{U}{\sqrt{2\Delta h_{0s}}} \quad (7)$$

Where U is turbine inlet tip speed, and C_{is} is the fictitious velocity when the fluid is expanded in an isentropic process across a nozzle, with the pressure ratio equals to the pressure ratio of the turbine stage.

$$N_s = \frac{\omega \sqrt{\dot{m}/\rho_{exit}}}{\Delta h_{0s}^{0.75}} \quad (8)$$

Where ρ_{exit} is the density at the turbine outlet.

2.2 Evaluation of Aerodynamic Performance using CFD Analysis

CFD analysis was conducted on the gas turbine to determine the overall performance of the turbine stage and evaluate the fluid dynamics across the blade passage. The CFD analysis was performed using ANSYS CFX version 15.0 and the overall procedure is illustrated in Figure 1. The solid models of both nozzle and rotor blades were constructed in ANSYS BladeGen by providing the principal geometry and the distribution of the wrap angle along the meridional position. Hexahedral meshes were then applied on the fluid zone across both the nozzle and turbine blades. A two-dimensional topography was generated on the hub surface, mid span and close-to-shroud surface as a framework to smoothen the formation of meshes. The mesh quality was controlled by refining the mesh size and manipulating the number of elements across the boundary layer of the blade surface. The skew meshes were eliminated to avoid ill-meshes. The operating condition and the boundary condition were then set up at each stations (nozzle inlet, interface between nozzle and turbine rotor, and rotor outlet). A suitable working fluid was selected from the in-built fluid database or the fluid properties can also be imported from the external fluid database. $k-\varepsilon$ model was selected to model the turbulence across the blade passage. The

Navier-Stokes equations were solved numerically and the result was evaluated as velocity vector field and distribution of thermodynamics properties across the blade passage.

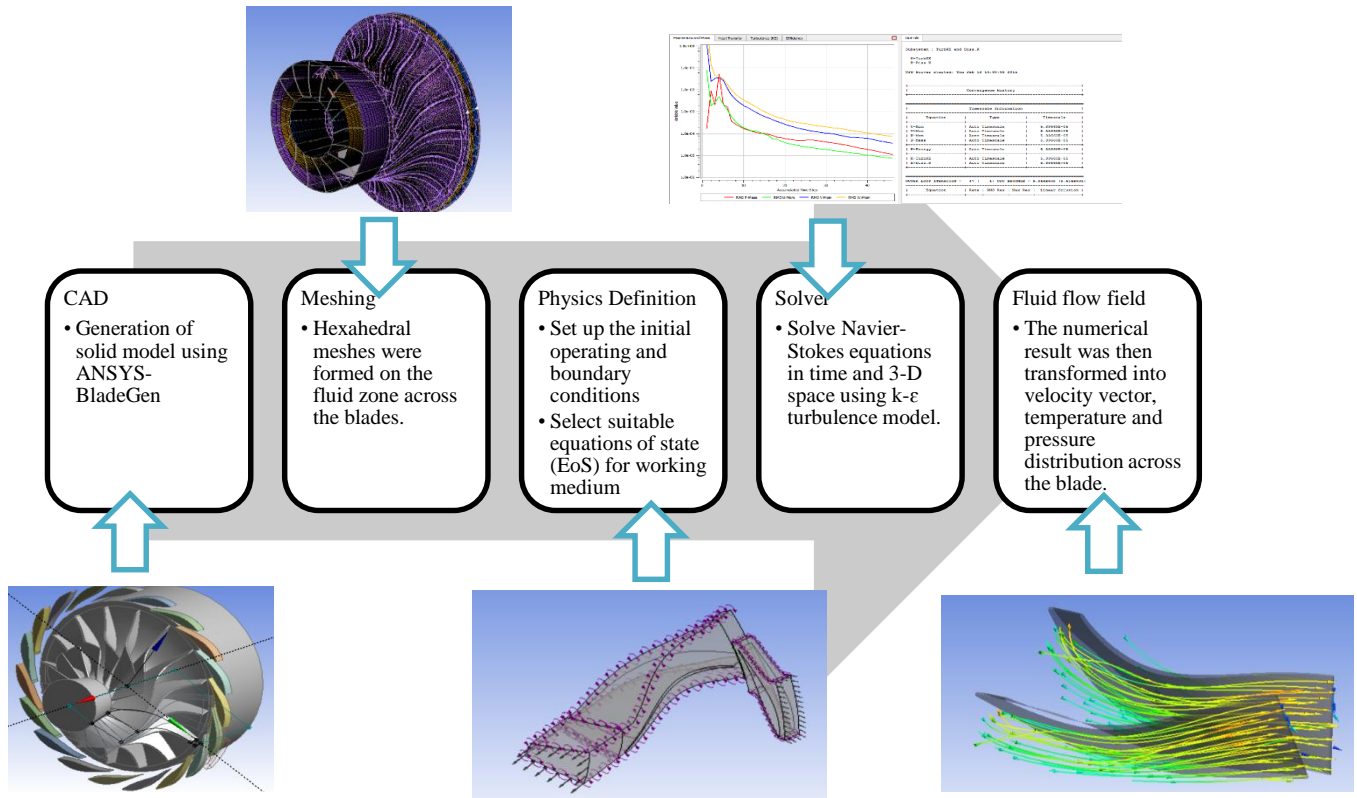


Figure 1: Overall procedures of CFD simulation using ANSYS Turbomachinery Package

3. RESULT

The three different approaches were applied to scale the performance curve from air to R134a and R245fa with the operating conditions in Table 1.

Table 1: Operating condition of air and selected refrigerants

	Unit	Air	R134a	R245fa
Molecular weight, M	g/mol	28.97	102.03	134.05
Inlet total temperature	K	1056.5	386	406.1
Inlet total pressure	kPa	580.4	2380	2334
Compressibility factor at inlet	-	1	0.786	0.630
Speed of sound at inlet	m/s	635	153.4	108.6
Outlet static pressure	kPa	101.3	420	420
Compressibility factor at outlet	-	1	0.931	0.904

R134a was superheated up to 35 degree before entering the turbine to avoid the formation of moisture at the end of the expansion process since it is a wet fluid. The scaled performance curves of R134a using the three approaches were compared to the result from the CFD analyses, in terms of velocity ratio in Figure 2, and specific speed in Figure 3. The three similarity approaches and the CFD analyses were compared in term of specific speed for R134a in Figure 3, and R245fa in Figure 4.

The *perfect gas approach* shows that the optimal velocity ratio is under-estimated. The optimal value from the *perfect gas approach* is 0.48, whereas the estimated value from the CFD analysis is 0.60.

The optimal velocity ratio from the *variable pressure ratio approach* and the *constant specific speed approach* agrees closely to the estimated values from the CFD analysis, with an error less than 10%, as illustrated in Table 1. The optimal operating shaft speed would be predicted incorrectly if the *perfect gas approach* was applied.

The overall trend of the turbine performance is similar between the CFD analysis and the *constant specific speed approach*, but the trend is different for the *variable pressure ratio approach*. The *variable pressure ratio approach* shows fairly flat efficiency for the range of velocity ratio between 0.55 and 0.70, and the range of specific speed between 0.33 and 0.42. However, the CFD analysis shows that the turbine is very sensitive to the operating point, as shown in Figure 2 and Figure 3. The turbine performance drops significantly at the operating points away from the best efficiency point. The best efficiency point is defined as the point with the maximum total-to-static isentropic efficiency at certain pressure ratio. The result shows that the *variable pressure ratio approach* provides a good prediction of optimal velocity ratio, optimal specific speed, and maximum efficiency. However, the approach does not provide a good estimation of performance for the operating points away from the best efficiency point, as presented in Table 2.

The *constant specific speed approach* assumes constant pressure ratio, specific speed and velocity ratio. The trend of the performance is similar between the *constant specific speed approach* and the CFD analysis for R134a and R245fa, based on Figure 3 and Figure 4. However, the turbine efficiency was over-estimated with errors between 10 and 20%, for the investigated range of velocity ratio and specific speed. This approach provides a better estimation in the turbine performance away from the best efficiency point, compared to another two approaches. However, the *constant specific speed approach* yields over 10% error in estimating the optimal velocity ratio, optimal specific speed, and maximum turbine efficiency, whereas the *variable pressure ratio approach* yields an error between 7% and 8%, as listed in Table 2.

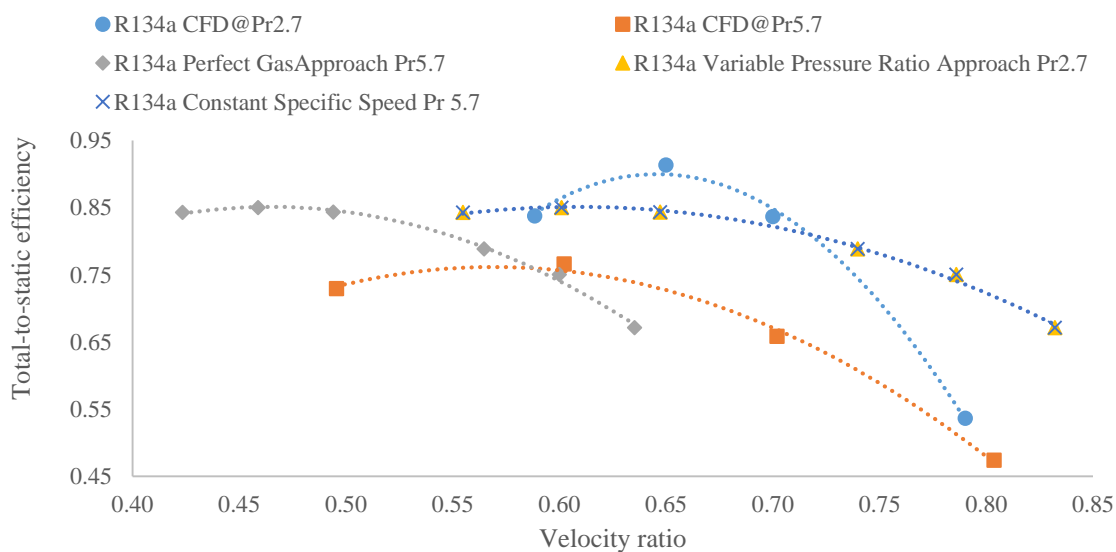


Figure 2: Comparisons of scaled performance from air data and CFD result for R134a as a function of velocity ratio

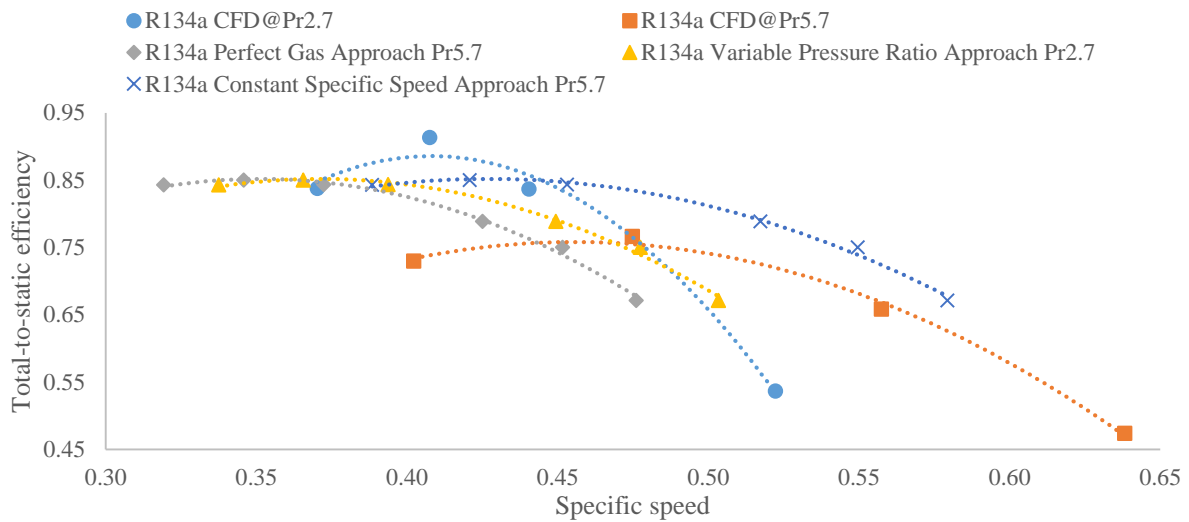


Figure 3: Comparisons of scaled performance from air data and CFD result for R134a as a function of specific speed

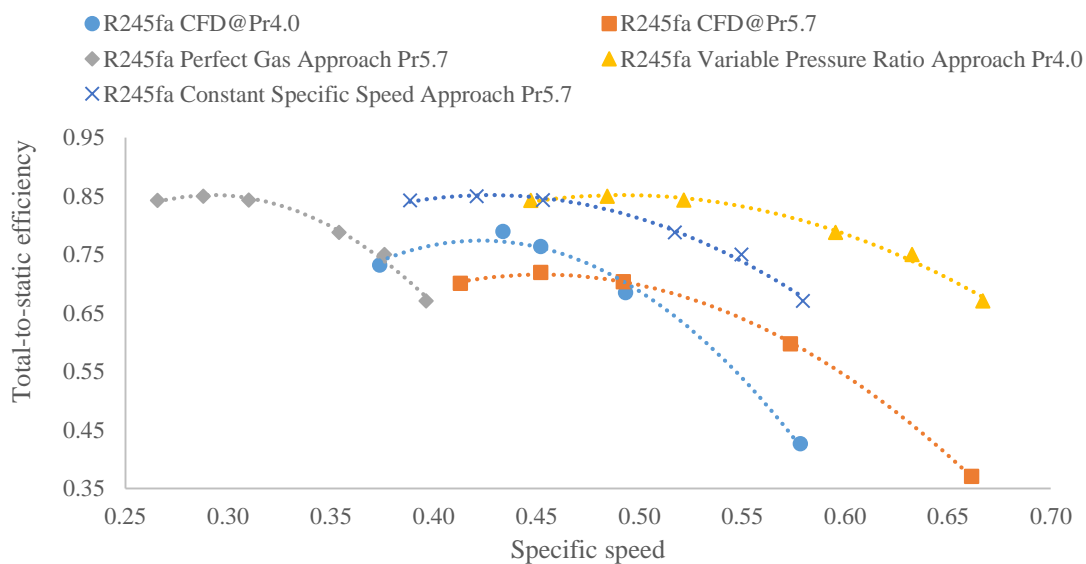


Figure 4: Comparisons of scaled performance from air data and CFD result for R245fa as a function of specific speed

The estimation of the inlet mass flow rate by the three similarity approaches and the CFD analysis was compared. The *perfect gas* approach and the *variable pressure ratio* approach utilize the mass flow coefficient in equation (5) whereas the *constant specific speed* approach uses the specific speed correlation in equation (8) to estimate the inlet mass flow rate. The result in Table 2 shows that the mass flow rate was under-estimated using all three approaches. The mass flow coefficient predicts the inlet mass flow rate with a better accuracy, with an error less than 10%, as opposed to the specific speed correlation, with error in the range of 15 and 25%. Hence, the *perfect gas* approach and the *variable pressure ratio* approach provide better estimations in the inlet mass flow, compared to the *constant specific speed* approach.

Table 2: Numerical error for different scaling approaches

	Working medium	Pressure ratio	Optimal velocity ratio	Optimal specific speed	Maximum total-to-static efficiency	Mass flow rate (kg/s)	Average Error (%)
Benchmark	Air	5.7	0.6	0.42	0.85	0.29	
Approach 1 (Perfect Gas)	R134a	5.7	0.46	0.35	0.85	3.46	
	Error (%)		23.3	25.5	11.8	4.6	16.3
	R245fa	5.7	0.38	0.29	0.85	3.75	
	Error (%)		31.9	35.9	18.4	9.0	23.8
Approach 2 (Variable Pressure Ratio)	R134a	2.7	0.6	0.37	0.85	3.46	
	Error (%)		7.7	9.8	6.6	4.7	7.2
	R245fa	4.0	0.6	0.48	0.85	3.75	
	Error (%)		2.9	13.5	9.4	9.0	8.7
Approach 3 (Constant Specific Speed)	R134a	5.7	0.6	0.42	0.85	2.99	
	Error (%)		0.0	10.6	11.8	17.6	10.0
	R245fa	5.7	0.6	0.42	0.85	3.15	
	Error (%)		7.5	7.2	18.4	23.5	14.1
CFD	R134a	2.7	0.65	0.41	0.91	3.63	
		5.7	0.60	0.47	0.76	3.63	
	R245fa	4.00	0.58	0.42	0.78	4.12	
		5.7	0.56	0.45	0.72	4.12	

4. DISCUSSION

The discrepancy in the turbine efficiency if a turbine stage is scaled from one operating condition into another is attributed to the variation in machine Reynolds number and Mach number. Various Reynolds number corrections were proposed for centrifugal compressors, such as ASME PTC-10 (PTC, 1997) and the efficiency-deficiency chart by Pampreen (Pampreen, 1973). The machine Reynolds number, however, does not have significant effect on the change in efficiency in this study as the effects of viscosity and thermal conductivity can be neglected at high Reynolds number (Harinck, Guardone, & Colonna, 2009). Reynolds number, $Re = \rho U D / \mu$ is a function of density, ρ , tip speed, U , wheel diameter, D , and dynamic viscosity, μ . The dynamic viscosity of the refrigerants is much smaller, rendering a higher value in the Reynolds number, in the magnitude of 100×10^6 , as opposed to the Reynolds number of steam, air, and water in the magnitude of 1×10^6 . The turbine inlet condition was varied using the CFD analysis to investigate the correlation between the machine Reynolds number and the turbine performance, as illustrated in Figure 5. The turbine's performance is fairly consistent in a wide range of Reynolds number, between 10 and 90. Hence, the Reynolds number effect can be neglected in this study.

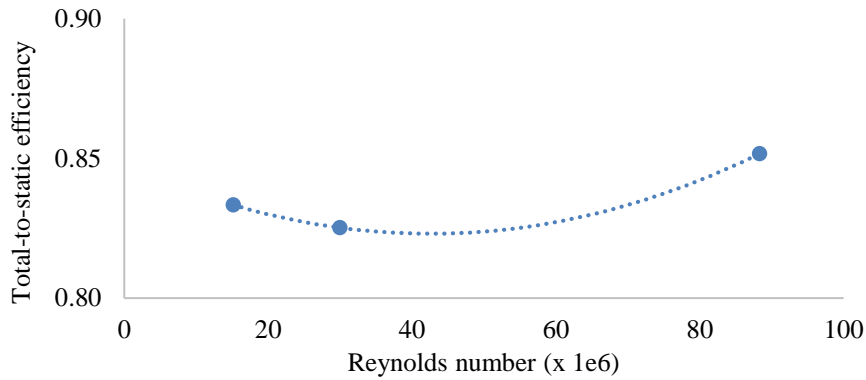


Figure 5: Effect of machine Reynolds number on turbine’s performance using R134a

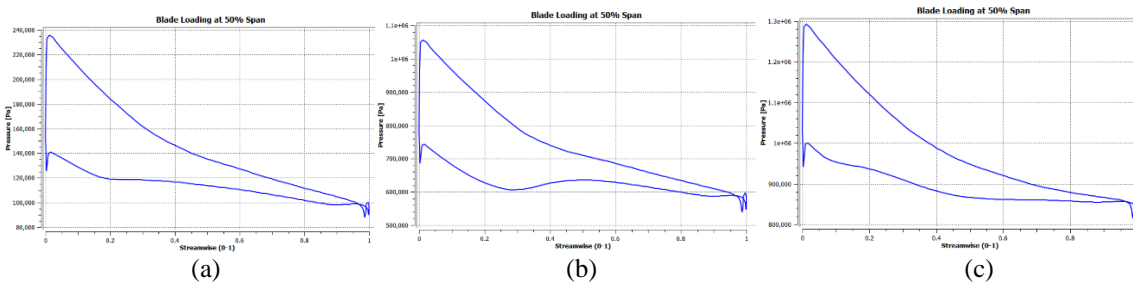


Figure 6: Blade loading and density at blade surface using air at pressure ratio of 5.7 (a), R245fa at pressure ratio of 4.0 (b) and R134a at pressure ratio of 2.7 (c)

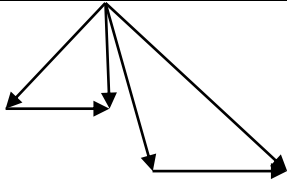
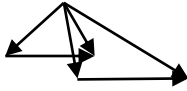
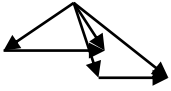
The blade loading along the pressure and suction surfaces at optimal specific speed using the *variable pressure ratio* approach are similar for all three working fluids; air, R134a and R245fa. Constant pressure drop was observed for air (modelled as ideal gas), R134a and R245fa (modelled as real gas) along pressure surface, but pressure fluctuation was observed for R245fa along the suction surface. The fluctuation is related to the adverse pressure gradient near the leading edge of the suction surface, which forms a vortex and local backpressure downstream of the vortex, as illustrated by the velocity vector in Figure 7. The flow re-attaches downstream of the vortex with gradual pressure drop along the blade passage.

The maximum isentropic efficiency for air, R134a and R245fa is different although the pressure loading along the blade passage at the optimal specific speed is similar. The highest turbine efficiency is achieved by R134a, followed by air, and R245fa. The deviation can be explained as a function of compressibility effect. The compressibility factor is a ratio of actual specific volume to the ideal volume of selected fluids. The compressibility effect of the expansion process across the turbine was measured qualitatively by volumetric flow ratio (Macchi & Perdichizzi, 1981). Macchi and Perdichizzi found that the increase in the volumetric flow ratio gives rise to a reduction in the turbine efficiency at optimal specific speed (Macchi & Perdichizzi, 1981), and the volumetric flow ratio has to be less than 50 to achieve a high turbine stage efficiency greater than 0.80 (Angelino, Invernizzi, & Macchi, 1991). The volumetric flow ratio is different for different working fluid using the *variable pressure ratio* approach. The volumetric flow ratio was determined as 5.7 for air, 4.9 for R245fa, and 2.7 for R134a. The use of equation (9) justifies the highest efficiency using R134a at low pressure ratio. Equation (9) is the change of entropy of a perfect gas in a closed system.

$$\Delta s = c_v \ln\left(\frac{T_3}{T_1}\right) + R \ln\left(\frac{v_3}{v_1}\right) \quad (9)$$

Where Δs denotes the entropy generation, c_v isochoric heat capacity, R specific gas constant, T temperature, and v specific volume. The increase in volumetric flow ratio generates a larger entropy difference. The larger the entropy differences, the larger the irreversibility of the system and the lower the turbine's efficiency. Hence, the highest efficiency is achieved by R134a with the lowest pressure ratio among all three working fluids. However, the turbine's efficiency using R245fa (expansion ratio of 4.9) is 78%, which is lower than air at 85% (expansion ratio of 5.7). This shows that the volumetric flow ratio is not the sole contributor to the drop in turbine performance using different fluids.

Table 3: Performance parameters for different working fluids, using Variable Pressure Ratio Approach

Fluids	Air	R134a	R245fa	
Velocity triangle				
Pressure ratio		5.7	2.7	4.0
Volumetric flow ratio		5.7	2.7	4.9
Degree of Reaction		0.42	0.47	0.44
Flow coefficient		0.245	0.172	0.249
Stage loading coefficient		1.040	0.974	0.995

The differences in the volumetric flow ratio also gives rise to the change in a number of turbine parameters. Optimum degree of reaction decreases whereas optimal flow coefficient increases with increasing expansion ratio. These yield some changes in the velocity diagram at the turbine exit, as shown in Table 3. The complete similarity is not achieved as the velocity vector at the turbine exit is not conserved. Hence, the *variable pressure ratio* approach does not achieve complete similarity, and this gives rise to the error in estimating the velocity ratio, specific speed, and turbine performance.

The flow field diagrams of R245fa, R134a, and air using the *variable pressure ratio* approach were compared in Figure 7. The flow undergoes turning from axial direction to tangential direction, and gives rise to Coriolis effect in the radial direction (Moustapha, Zelesky, Baines, & Japiske, 2003). The flow undergoes a non-uniform velocity distribution in the spanwise direction, with lowest velocity near the end wall surface of the hub. The radial gradient of the flow velocity in the spanwise direction gives rise to the imbalance in the pressure gradient in the spanwise direction. The end result of the Coriolis effect and the non-uniform velocity give rise to a complex flow field, which is illustrated in Figure 7 in term of flow angle. The bulk flow moves from suction surface near the shroud to pressure surface near the hub. The flow is compensated by a number of passage vortices, and the flow vector diagram can be found in Kitton's work (also presented by Baines in his work (Moustapha et al., 2003)). This phenomena exists in the best efficiency point, attributed to the turning of the flow from axial to tangential direction. The distribution of the swirl angle at the trailing edge was averaged and the flow angle was determined as 1° for air, 33° for R134a and 37° for R245fa. The result implies that the turbine exit swirl angle might increase monotonically with the molecular weight of the working fluids, with the highest by R245fa and the lowest by air. Positive swirl angle is non-favorable as the fluid internal energy would be lost as kinetic energy. The specific work output would decrease with a positive swirl angle, based on Euler turbomachinery equation.

$$W_x = U_2 C_{\theta 2} - U_3 C_{\theta 3} = U_2 C_{m2} \tan \alpha_2 - U_3 C_{m3} \tan \alpha_3 \quad (10)$$

Where W_x is specific work output, U_2 is rotor inlet tip speed, U_3 is rotor outlet tip speed, C_θ is tangential velocity component, C_m is meridional velocity component, and α is swirl angle.

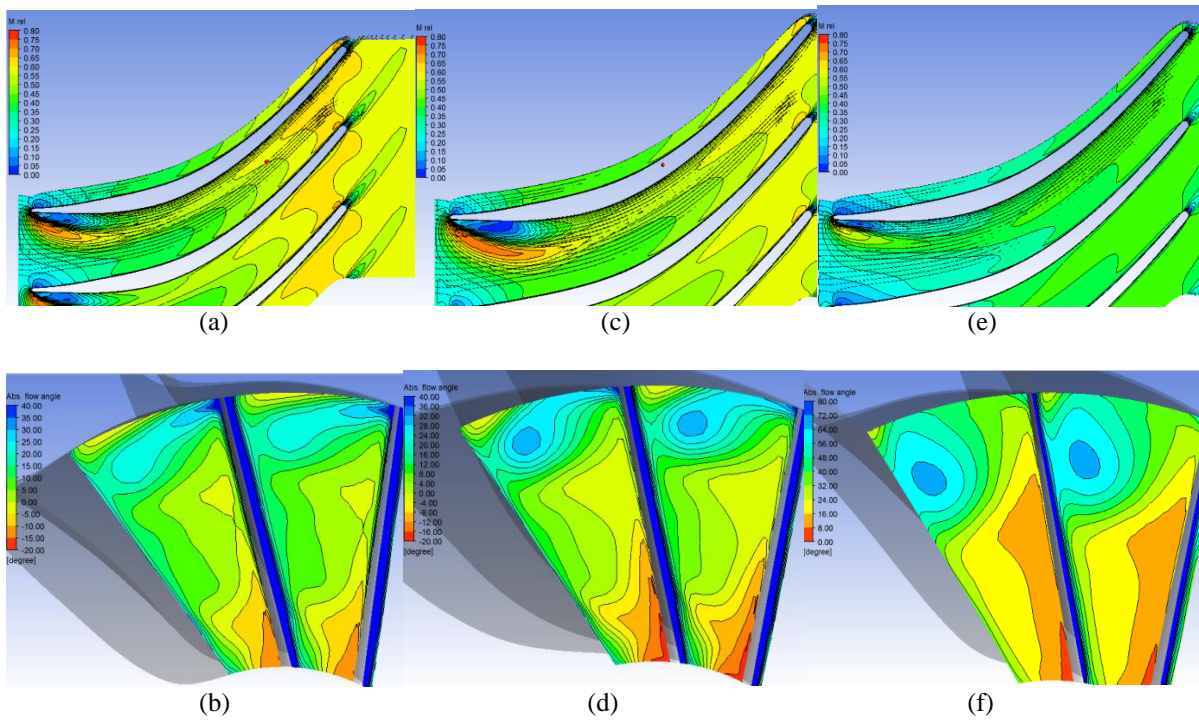


Figure 7: Distribution of relative Mach number in the meridional plane and distribution of absolute flow angle at the trailing edge using air at pressure ratio of 5.7 (a-b), R245fa at pressure ratio of 4.0 (c-d) and R134a at pressure ratio of 2.7 (e-f)

The conventional radial inflow turbine is typically designed for low pressure ratio application, which is between 1.2 and 3.0 for automotive turbochargers, and less than 10 for single stage gas turbines to avoid choking and shock waves in supersonic expansion. The selected gas turbine has a design pressure ratio of 5.7. Different pressure ratio was determined for R134a and R245fa assuming constant value of $\Delta h_{0s}/a_{01}^2$ (using the *variable pressure ratio* approach) and plotted in Figure 8. The limiting line on the left represents the saturation lines of the refrigerants. The calculated pressure ratio for the selected refrigerants is less than 5.7, which is the pressure ratio imposed on the turbine using air. The local sound speed of refrigerants with heavier molecular weight is less than the local speed of sound using air. The local speed of sound is between 90 and 190 m/s for R134a and between 75 and 160 m/s for R245fa for the temperature range of 300 and 450 K, and pressure range of 0.5 and 4.0 MPa, which is less than the local speed of sound of air at 635 m/s with the given operating condition in Table 1. The smaller the local speed of sound, the smaller the isentropic enthalpy drop and the smaller the pressure ratio across the turbine. Hence, the *variable pressure ratio* approach is limited to a pressure ratio less than the design pressure ratio using air. This limits the applicability of the approach in ORC application, which is characterized for high pressure ratio expansion.

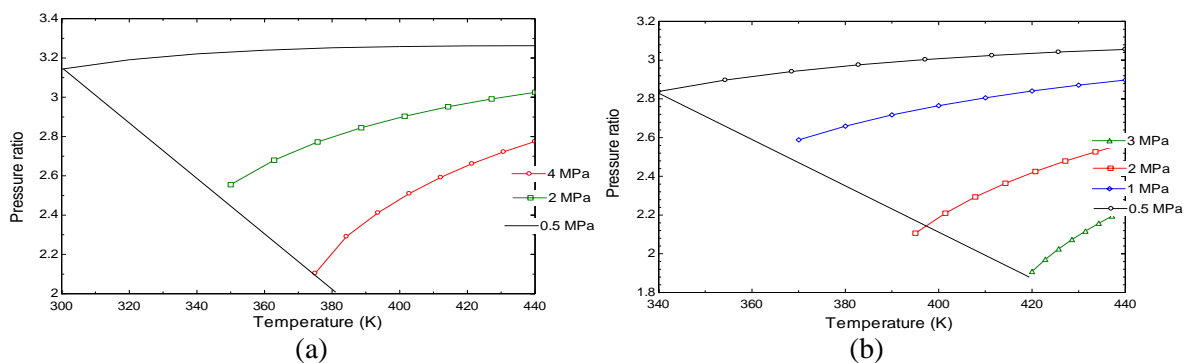


Figure 8: Range of applicability using equation (6) for R134a (a) and R245fa (b)

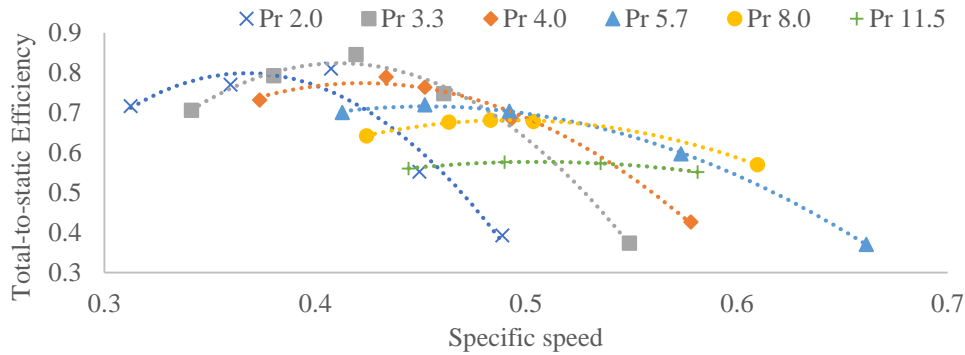


Figure 9: Performance map of R245fa at different specific speed and pressure ratio

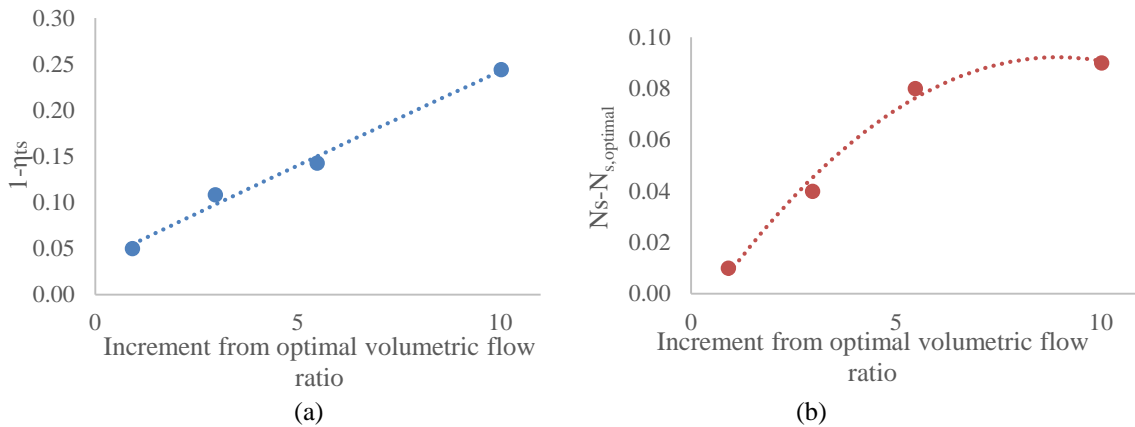


Figure 10: Deviation of best efficiency point and the corresponding specific speed at increasing volumetric flow ratio

The prediction of the turbine performance at higher pressure ratio or expansion ratio is required for ORC application. A correction chart for R245fa at different expansion ratio was developed using Figure 9. The turbine’s performance map for R245fa was generated for different pressure ratio (2 – 11.5) and specific speed (0.3 – 0.7), and plotted in Figure 9. The result shows that the maximum turbine performance was achieved at a pressure ratio of 3.3 (equivalent to volumetric flow ratio at 4.0). The maximum efficiency point at the pressure ratio of 3.3 is used as a benchmark to calculate the deficiency in efficiency and deviation of optimal specific speed at higher volumetric flow ratio. The turbine losses increase linearly with increasing volumetric flow ratio as shown in Figure 10(a). The location of the specific speed for the best efficiency point at increasing volumetric ratio is increasing, as shown in Figure 9. The deviation in the optimal specific speed is plotted as a function of volumetric flow ratio in Figure 10. The result shows that the deviation in optimal specific speed increases with increasing volumetric flow ratio until the blade passage is choked (with the relative Mach number around 1). The further increment in volumetric flow ratio does not have any effect on the value of $N_s - N_{s,optimal}$, as illustrated in Figure 10.

5. CONCLUSION

Three different approaches using the similarity concept were proposed and investigated to scale the selected gas turbine from air to R134a and R245fa in this study. The *perfect gas* approach assuming the real gas as perfect gas provides the largest error in terms of optimal velocity ratio, optimal specific speed, and maximum efficiency. The *variable pressure ratio* approach shows the highest averaged accuracy in predicting the optimal velocity ratio, optimal specific speed, maximum efficiency and mass flow rate. The *constant specific speed* approach is recommended to estimate the turbine’s performance away from the best efficiency point.

Constant value of $\Delta h_0/a_0^2$ was imposed in the *variable pressure ratio* approach to achieve the similarity but a number of deviations was observed, including swirl angle at the turbine outlet, volumetric flow ratio, best efficiency point and the corresponding specific speed. The Reynolds number effect does not influence the scaling using refrigerants as the effect of viscosity is negligible at high Reynolds number using refrigerants with low viscosity. The swirl angle at the turbine outlet was observed as a function of molecular weight, in which the increment in molecular weight increases the swirl angle and reduces the specific work output. The *variable pressure ratio* approach does not ensure a constant volumetric flow ratio, hence the complete similarity cannot be achieved. The *variable pressure ratio* approach is limited to pressure ratio less than the design pressure ratio using air, which is not suitable to scale an ORC turbine. Therefore, a correction chart was developed to scale the performance of the gas turbine for higher volumetric ratio using R245fa. The deficiency in turbine efficiency is linearly correlated to the increased volumetric flow ratio. The correction chart provides a good estimation in selecting a suitable turbine for a particular ORC application. However, the correction chart has to be validated against the experimental data for better accuracy.

NOMENCLATURE

a	local speed of sound	(m/s)
C	absolute flow velocity	(m/s)
C _{is}	isentropic flow velocity	(m/s)
c _v	isochoric heat capacity	(J/kg.K)
D	turbine wheel diameter	(m)
Δh_0	enthalpy drop	(kJ/kg)
\dot{m}	mass flow rate	(kg/s)
N	shaft speed	(rev/min)
N _s	specific speed	(-)
p	pressure	(kPa)
P	shaft power	(kW)
R	gas constant	(J/kg.K)
Re	Reynolds number	(-)
T	temperature	(K)
U	tip speed	(m/s)

Greek letter

α	swirl angle	(degree)
θ	tangential direction	(-)
γ	ratio of specific heats	(-)
η	efficiency	(-)
ρ	density	(kg/m ³)
v	velocity ratio	(-)
ω	shaft speed	(rad/s)

Subscript

01	nozzle inlet stagnation condition
02	rotor inlet stagnation condition
03	rotor outlet stagnation condition
1	nozzle inlet static condition
2	rotor inlet static condition
3	rotor outlet static condition
m	meridional plane
s	isentropic process

REFERENCES

- Angelino, G., Invernizzi, C., & Macchi, E. (1991). Organic Working Fluid Optimization for Space Power Cycles. In G. Angelino, L. De Luca & W. A. Sirignano (Eds.), *Modern Research Topics in Aerospace Propulsion* (pp. 297-326): Springer New York.
- Aungier, R. H. (2006). *Turbine aerodynamics: axial-flow and radial-inflow turbine design and analysis*: ASME Press.
- Balje, O. E. (1981). *Turbomachines: A Guide to Design Selection and Theory*: Wiley.
- Bao, J., & Zhao, L. (2013). A review of working fluid and expander selections for organic Rankine cycle. *Renewable and Sustainable Energy Reviews*, 24, 325-342.
- Casey, M. V. (1985). The Effects of Reynolds Number on the Efficiency of Centrifugal Compressor Stages. *Journal of Engineering for Gas Turbines and Power*, 107(2), 541-548. doi: 10.1115/1.3239767
- Chen, H., & Baines, N. C. (1994). The aerodynamic loading of radial and mixed-flow turbines. *International Journal of Mechanical Sciences*, 36(1), 63-79. doi: 10.1016/0020-7403(94)90007-8
- Dixon, S. L., & Hall, C. (2010). Fluid Mechanics and Thermodynamics of Turbomachinery Retrieved from <http://canterbury.ebib.com.au/patron/FullRecord.aspx?p=534952>
- Harinck, J., Guardone, A., & Colonna, P. (2009). The influence of molecular complexity on expanding flows of ideal and dense gases. *Physics of Fluids (1994-present)*, 21(8), 086101. doi: <http://dx.doi.org/10.1063/1.3194308>
- Japikse, D., & Baines, N. C. (1995). *Introduction to turbomachinery*: Concepts ETI.
- Jones, A. C. (1996). Design and Test of a Small, High Pressure Ratio Radial Turbine. *Journal of Turbomachinery*, 118(2), 362-370. doi: 10.1115/1.2836651
- Lemmon, E. W., Huber, M.L., McLinden, M.O. (2013). NIST Standard Reference Database 23: Reference Fluid Thermodynamic and Transport Properties-REFPROP, Version 9.1. Gaithersburg: Standard Reference Data Program.
- Lemmon, E. W., & Span, R. (2006). Short fundamental equations of state for 20 industrial fluids. *Journal of Chemical & Engineering Data*, 51(3), 785-850.
- Macchi, E., & Perdichizzi, A. (1981). Efficiency prediction for axial-flow turbines operating with nonconventional fluids. *ASME Journal of Engineering for Power*, 103, 718e724.
- Meher-Homji, C. B. (2000). *The Historical Evolution of Turbomachinery*. Paper presented at the Proceedings of the 29th Turbomachinery Symposium, Texas A&M University, Houston, TX.
- Moustapha, H., Zelesky, M., Baines, N. C., & Japikse, D. (2003). *Axial and Radial Turbines*: Concepts Eti.
- Pampreen, R. (1973). Small turbomachinery compressor and fan aerodynamics. *Journal of Engineering for Gas Turbines and Power*, 95(3), 251-256.
- PTC, A. (1997). PTC 10-1997, Performance test code on compressors and exhausters. *American Society of Mechanical Engineers, New York*, 3.
- Quoilin, S., Declaye, S., Tchanche, B. F., & Lemort, V. (2011). Thermo-economic optimization of waste heat recovery Organic Rankine Cycles. *Applied Thermal Engineering*, 31(14-15), 2885-2893. doi: 10.1016/j.applthermaleng.2011.05.014
- Quoilin, S., & Lemort, V. (2009, 14-17 April). *Technological and economical survey of Organic Rankine Cycle systems*. Paper presented at the 5th European Conference Economis and Management of Energy in Industry, Algarve, Portugal.
- Sauret, E. (2012). *Open design of high pressure ratio radial-inflow turbine for academic validation*. Paper presented at the Proceedings of the ASME 2012 International Mechanical Engineering Congress and Exposition, Houston, Texas.
- Strub, R. A., Bonciani, L., Borer, C. J., Casey, M. V., Cole, S. L., Cook, B. B., . . . Strite, M. A. (1987). Influence of the Reynolds Number on the Performance of Centrifugal Compressors. *Journal of Turbomachinery*, 109(4), 541-544. doi: 10.1115/1.3262145
- Wong, C. S., & Krumdieck, S. (2014). *Energy and Exergy Analysis of an Air-Cooled Geothermal Power Plant with Fixed Nozzle Turbine in Subsonic Expansion and Supersonic Expansion via CFD Analysis*. Paper presented at the 36th New Zealand Geothermal Workshop Auckland University.

ACKNOWLEDGEMENT

The project is supported by Heavy Engineering Research Association (HERA) as part of the Above Ground Geothermal and Allied Technology (AGGAT) program with funding from NZ Ministry for Business, Innovation and Employment contract: HERX1201.

FAST DESIGN METHODOLOGY FOR SUPERSONIC ROTOR BLADES WITH DENSE GAS EFFECTS

Elio Antonio Bufi¹, Benoit Obert², Paola Cinnella^{3*}

¹ Laboratoire DynFluid
Arts et Metiers ParisTech, Paris (France)
Polytechnic of Bari, Bari (Italy)
Email: elio-antonio.bufi@ensam.eu

² ENERTIME, Courbevoie (France)
Email: benoit.obert@enertime.com

³ Arts et Metiers ParisTech, Paris (France)
Email: paola.cinnella@ensam.eu

* Corresponding Author

ABSTRACT

This work describes a fast 2-D design methodology based on the method of characteristics (MOC) for rotor blade vanes of supersonic axial Organic Rankine Cycle (ORC) impulse expanders. The MOC is generalized to gases governed by complex equations of state to fully account for dense gas behavior characteristic of ORC turbines. The fluid thermodynamic properties are described by highly accurate multiparameter equations of state based on Helmholtz free energy. Several working fluids are considered, including R245fa, R134a, R227ea, R236fa. The designs generated by the generalized MOC are compared with those obtained under the classical perfect gas model. Finally, CFD simulations of both isolated rotor blades and a full turbine stage are carried out to assess the performance of the designs using the ANSYS CFX solver.

1. INTRODUCTION

In recent years, the Organic Rankine Cycle (ORC) technology has received great interest from the scientific and technical community because of its capability of generating electric power using low temperature sources with good performances. For compactness, mechanical design simplicity and cost reasons, ORC plants often use single stage expander characterized by high pressure ratios, which leads to supersonic flow conditions. Furthermore, ORC working fluids are often characterized by the so-called dense-gas effects (see, e.g. (Congedo et al., 2011) and references cited therein).

The gas dynamics of dense gases can be described through a key thermodynamic property, known as the fundamental derivative of gas dynamics (Thompson, 1971):

$$\Gamma = 1 + \frac{\rho}{a} \left(\frac{\partial a}{\partial \rho} \right)_s \quad (1)$$

Equation (1) represents a measure of the rate of change for the local speed of sound with respect to density in isentropic transformation (Colonna et al., 2009). For light fluids, $\Gamma > 1$. This is the case of perfect gases, which have a constant $\Gamma = (\gamma + 1)/2$.

For fluid with sufficient molecular complexity and under specific thermodynamic conditions, $\Gamma < 1$, which leads to a reverse behaviour of the speed of sound in isentropic perturbations with respect to classical case: a decreases in isentropic compressions and grows in isentropic expansions.

The aerodynamic modelling of such a system is made difficult by dense gas effects characterizing the thermodynamic behaviour of the working fluid in the vicinity of the critical point and the saturation curve.

The need for a compact turbine working with high pressure ratios implies the choice of an impulse turbine architecture. This can be justified by considering a typical impulse blade and its velocity triangle (figure 4).

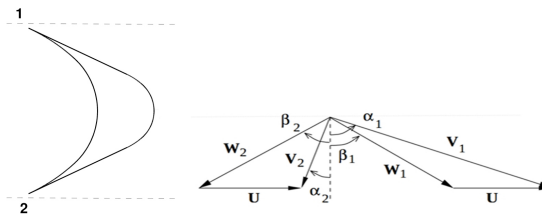


Figure 1: Example of impulse blade geometry and velocity triangles

By imposing an axial outlet flow for the impeller ($\alpha_2 = 0$), with the axial absolute velocity component kept constant, the work coefficient can be expressed as:

$$\psi = \frac{\Delta H_0}{U^2} = 2(1 - \Lambda) \quad (2)$$

In equation (2), U represents the peripheral velocity at a specified radius, ΔH_0 the total enthalpy drop per unit mass across the impeller and Λ the degree of reaction. For an impulse turbine ($\Lambda = 0$), the total enthalpy drop is two times greater than for a 0.5 reaction degree turbine. This property allows extracting a large amount of work from a single stage, with a maximum for a vane outlet swirl equal to 67° and rotor turning to 116° ($\beta_1 = \beta_2 = 58^\circ$) (Paniagua et al., 2014). However, particular care must be addressed to the rotor and stator blades aerodynamic design because both behave as supersonic nozzles. Moreover, the typical operating conditions for an ORC turbine are in the proximity of the working fluid saturation curve or sometimes supercritical. Due to the presence of strong dense gas effects, models used to design the blade shapes have to be modified accordingly. Several authors in the past have addressed the design of dense gas nozzles and stator blades (Cramer and Tarkenton, 1992; Guardone et al., 2013; Wheeler and Ong, 2013; Bufi et al., 2015). All of them generally rely on extended versions of the Method of Characteristics (MOC) for 2D supersonic flows. The aim of this work is to develop, for the first time to the Authors knowledge, a methodology for the design of rotor blades of axial supersonic ORC impulse turbines, which takes properly into account dense gas effects. This is based on the MOC along with the vortex flow field approach, previously introduced for perfect gas flows (Goldman, 1968; Paniagua et al., 2014), extended to the dense gas case.

The performances of blade shapes obtained with MOC using different organic working fluids are then evaluated by means of numerical simulations carried out using the ANSYS CFX code, both for the isolated rows and for a supersonic turbine stage.

2. SUPERSONIC IMPULSE TURBINE BLADES DESIGN

In this Section we first recall the Method of Characteristics (MOC) for the design of perfect gas supersonic nozzles and its extension to dense gas flows. Then, we present its application to the design of supersonic rotor blades, in conjunction with a free-vortex methodology.

2.1 MOC for supersonic nozzle design

The MOC is a classical method for the design of the divergent part of supersonic nozzles under the hypotheses of 2D, steady and homentropic flow. Such a flow is governed by the 2D isentropic Euler equations, which represent an hyperbolic system of conservation laws characterized by two families of characteristic lines. These are defined by equations of the form (Délery, 2010; Zucrow and Hoffman, 1976):

$$\frac{dy}{dx} = \tan(\varphi \mp \mu) \quad (3)$$

where φ is the local flow angle and $\mu = \arcsin(M^{-1})$ is the Mach angle. Rewriting the governing equations in the characteristic reference frame, one gets the so-called compatibility equations, which are just ordinary differential equations, of the form:

$$d\varphi \pm \sqrt{M^2 - 1} \frac{dV}{V} = 0 \quad (4)$$

where V is the velocity magnitude and the sign + or – denotes a left-running or – a right-running characteristic line, respectively. For a perfect gas, equations (4) can be integrated analytically after rewriting dV/V in terms of the Mach number and by making use of the equation of state, leading to the well-known Prandtl-Meyer relations:

$$\varphi \pm v(M) = \text{constant (along a characteristic)} \quad (5)$$

The preceding equations, along with the equations of the characteristic lines (3) are then used as described in (D elery, 2010) to design the nozzle wall contour. In the case of a dense gas, equation (4) can no longer be integrated analytically. Instead, we use a numerical method for ordinary differential equations, namely, Heun's second-order predictor-corrector method to carry out the integration along characteristic lines. The discretized compatibility equation is supplemented by dense gas equations of state to compute all of the required thermodynamic properties. Precisely, we make use of the thermodynamic library REFPROP (Lemmon et al., 2013), which contains reference multiparameter equations of state for many dense gases of potential interest as ORC working fluids. Extensions of the MOC to dense gases were proposed in the past by (Guardone et al., 2013; Wheeler and Ong, 2013) with focus on the design of De-Laval nozzles or radial turbine injectors, respectively. In (Bufi et al., 2015) the methodology is extended to dense gas models by using reference EOS and applied to axial turbomachinery design. Once the nozzle divergent has been designed via the MOC, a geometrical postprocessing procedure is applied to generate a supersonic turbine nozzle. Some geometrical parameters are imposed in order to control the final blade geometry (see figure 2): the stagger angle θ , the angular extension Φ and the radius of the leading edge arc cb , the radius R of the leading edge arc cd and the trailing edge thickness ef .

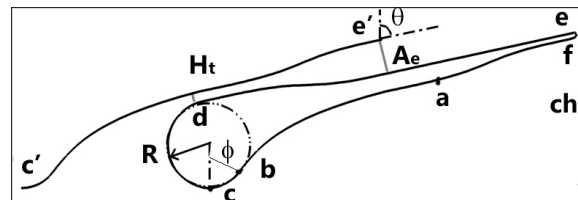


Figure 2: Example of supersonic stator blade geometry designed with MOC.

2.2 Design of dense gas supersonic rotor blades

For the design of supersonic rotor blades we follow the procedure described in (Paniagua et al., 2014; Goldman, 1968) for perfect gas flows and we extend it to dense gases.

The flow at the rotor inlet is assumed as a uniform one that is simply deflected by the rotor blades. To achieve this deflection, the flow passes through a transition region delimited by upper and lower transition arcs and by characteristic lines. For clarity, the transition region is sketched in figure 3, where AB and CD are transition arcs and the dashed lines are used to represent the characteristics. Through this region, the uniform inlet flow is converted into a free vortex flow, for which $V \cdot R = \text{constant}$, with R the radius of curvature of a streamline and V the constant velocity along it, following an isentropic transformation.

Figure 4 shows a schematic description of the rotor blade geometry designed with MOC. We use the same notation of the MOC for perfect gases reported in (Paniagua et al., 2014; Goldman, 1968) and we refer to them for details. In order to start with the design procedure for dense gases, the following input parameters are defined: inlet total pressure and temperature; inlet/outlet relative flow angle β_i/β_o ;

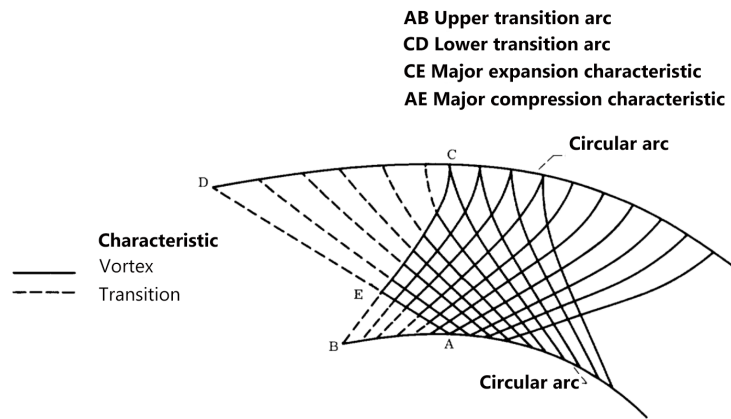


Figure 3: Scheme of the system of characteristic lines in the rotor vane. (Goldman, 1968)

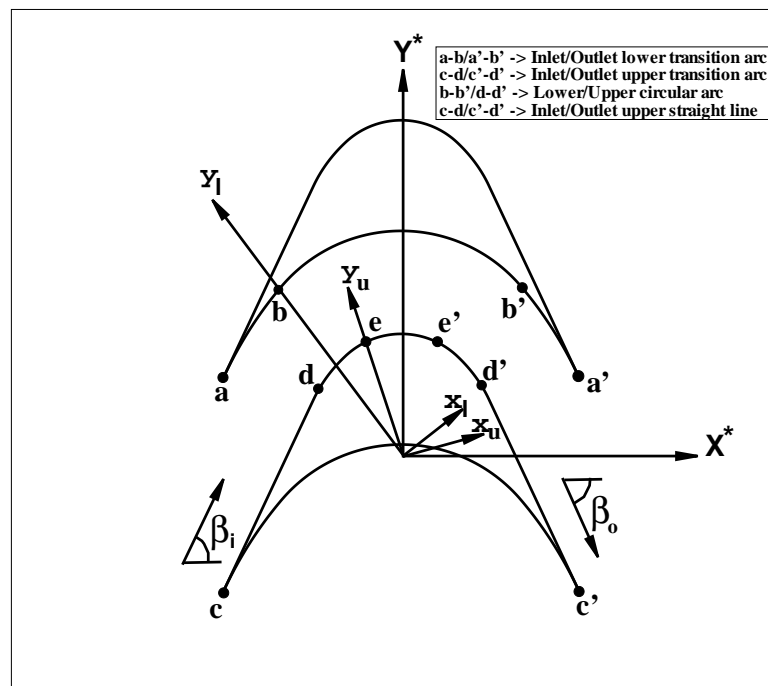


Figure 4: Schematic description of the rotor blade design.

inlet/outlet Mach number M_i/M_o ; the lower arc Mach number M_l , assigned on the lower circular arc b-b'; the upper arc Mach number M_u , assigned on the upper circular arc d-d'. As for the perfect gas model, the lower and upper transition arcs (a-b/a'-b' and d-e/d'-e' for inlet and outlet, respectively) are determined in the unrotated lower/upper reference systems (denoted with subscripts l and u). The geometry is then rotated in the $X^* - Y^*$ reference system and completed with the straight line parts c-d/c'-d' and the circular arcs b-b'/d-d'.

The MOC for perfect gas algorithm makes use of the analytical expressions of the Prandtl-Meyer function $\nu = \nu(M)$ and of the critical Mach number $M^* = M^*(M)$ (with $M^* = V/a^*$ and a^* the critical speed of sound) for perfect gases. For a dense gas, no such analytical expressions are available.

The calculation of the critical Mach number is replaced by the following iterative procedure:

1. The critical speed of sound is first computed from the known values of the total pressure p_0 and temperature T_0 by using a thermodynamic library available in REFPROP
2. An initial tentative value $M^{*(0)}$ for the critical Mach number is prescribed.
3. At each iteration of the method, an updated value of the velocity magnitude is computed as $V^{(m)} =$

$$M^{*(m-1)} a^*$$

4. The latter is used to compute an updated value of the specific static enthalpy $h^{(m)}$, given the total enthalpy $h_0 = h_0(p_0, T_0)$.
5. The speed of sound is then updated by using the thermodynamic relation $a^{(m)} = f(h^{(m)}, s)$, where the entropy s is constant everywhere and is known from the prescribed inlet conditions.
6. Finally, an updated value of the Mach number $M^{(m)} = V^{(m)}/a^{(m)}$ is obtained.
7. If $M^{(m)} - M^{(m-1)}$ is below a given tolerance, the procedure is stopped. Otherwise, a new value is assigned for $M^{*(m+1)}$ (by using a bisection procedure) and the iteration is started again.

The design procedure above is completed by adding a finite leading-edge/trailing-edge thickness. Besides, non-symmetrical blades with various degrees of reaction can be designed if different inlet/outlet input parameters are imposed. In this work, unique incidence problems related to the supersonic relative flow on the rotor inlet are neglected on design stage, due to the interest on viscous effects which could make useless any incidence angle calculation based on inviscid theory.

2.3 Example of rotor blade designs

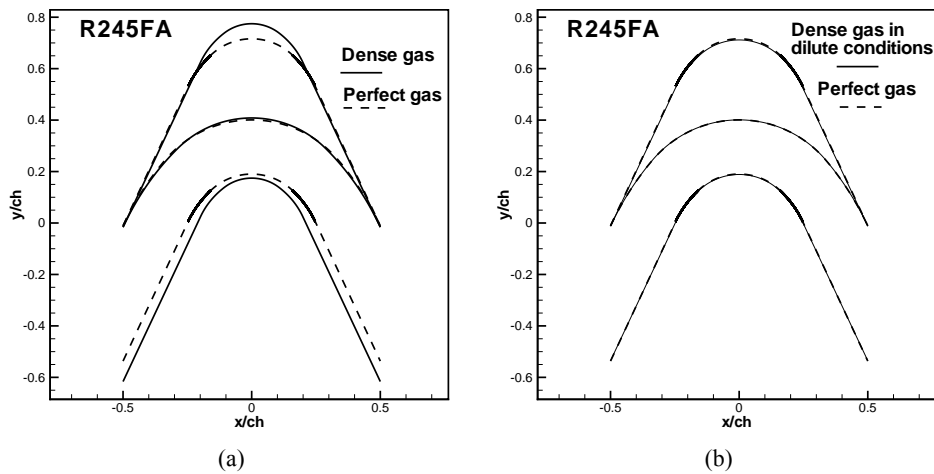


Figure 5: Blade designs for R245FA at operating conditions ($p_r^0 = 1.05, T_r^0 = 1.05$) (a) and at conditions ($p_r^0 = 0.055, T_r^0 = 1.15$) (b). Dashed lines represent designs obtained under the perfect gas model.

Four organic working fluids are used to test the MOC. Their critical properties are shown in table 1, where γ is the specific heat ratio in the dilute gas limit along the critical isotherm curve (Guardone et al., 2013). The design algorithm for rotor blades has been run for a typical ORC working fluid, namely

Table 1: Thermophysical properties for different organic substances, based on reference EOS (from REFPROP ver. 9.1).

	R245fa	R227ea	R134a	R236fa
p_c [MPa]	3.651	2.93	4.06	3.2
T_c [K]	427.16	374.9	374.2	398.07
ρ_c [kg/m ³]	516.08	594.2	511.9	551.3
M_w [g/mol]	134.05	170.03	102.03	152.04
γ	1.061	1.056	1.092	1.059

R245FA, whose thermophysical properties are given in table 1 and used to investigate the impact of real gas effects on the resulting geometry. The degree of reaction is set to zero, so that the resulting geometry is symmetric. Figure 5 shows a comparison of geometries calculated with different operating

conditions and gas models. The first operation point (characterised by the reduced pressure $p_r^0 = 1.05$ and the reduced temperature $T_r^0 = 1.05$) is very close to the R245FA upper saturation curve and this affects the rotor geometry, leading to larger cross section variations with respect to perfect gas. Indeed, a greater generic area to throat area ratio is addressed to the REF geometry. This is a typical behavior already seen in supersonic stators (Guardone et al., 2013). It is due to the effect of Γ that, being lower than one in dense gas regions, provides higher exit-to-throat area ratios.

Figure 5b shows the design obtained for a lower total pressure ($p_r^0 = 0.055$) and higher total temperature ($T_r^0 = 1.15$), so that the thermodynamic conditions at rotor inlet lie far from the dense gas region. Here, the blade designed with a dense gas EOS is very similar to that obtained with the perfect gas model. Then,

Table 2: Geometrical output parameters for four different organic fluids under the same operating condition ($p_r^0 = 1.28$, $T_r^0 = 1.28$, $M_{in} = M_{out} = 1.5$, $M_l = 1$, $M_u = 2$, $\beta_{in} = \beta_{out} = 65^\circ$).

	R245fa	R227ea	R134a	R236fa
σ	1.82	1.81	1.85	1.82
ch^*	2.31	2.32	2.30	2.31
ph^*	1.27	1.28	1.24	1.27

a parametric study for several working fluids suitable for ORC applications at the same reduced input conditions has been carried out. Fluid properties are also given in table 1. For all of the fluids, the input thermodynamic conditions and design parameters are set to ($p_r^0 = 1.28$, $T_r^0 = 1.28$, $M_{in} = M_{out} = 1.5$, $M_l = 1$, $M_u = 2$, $\beta_i = \beta_o = 65^\circ$). Table 2 provides the following geometrical parameters for the resulting designs: blade solidity σ , defined as the axial chord to pitch ratio; the axial chord ch^* and pitch ph^* normalized respect to the critic radius r^* , the latter defined as the radius of the sonic streamline in the vortex flow field. It can be noticed that the lower is the fluid molecular complexity (as for the R134A fluid) the higher is the solidity.

3. NUMERICAL SIMULATIONS

Viscous 2-D numerical simulations have been carried out for both an isolated rotor blade row and a full turbine stage designed using the MOC methods presented in this paper. The CFD software used is the commercial code Ansys CFX 16.0. The turbulence model used is k-omega SST (Shear Stress Transport). The thermodynamic properties of the fluids are modelled using the real gas properties (rgp) library (ANSYS, 2015). The rgp files contain property tables mapped as a function of temperature and pressure along the turbine expansion and allow accurately taking into account dense gas effects.

In table 3 the parameters used to design the blade shapes and to perform the simulations with the R245FA working fluid are shown. In order to assess the presence of dense gas effects it is important to evalu-

Table 3: Rotor blade design parameters.

Parameters	Values
Inlet total relative pressure [bar]	6
Inlet total relative temperature [K]	393.15
Inlet relative Mach number	1.5
Inlet relative flow angle [$^\circ$]	60
Suction side circular arc Mach number	1.9
Pressure side circular arc Mach number	1.1

ate the position of the operating point on the working fluid state diagram. In figure 6a the isentropic evolution of the expansion on the T-S diagram is shown. The presence of strong dense gas effects is expected, since fundamental derivative Γ is below 1 throughout the expansion (see figure 6b). It can be noticed that, for this application, the strongest dense gas effects occur mainly inside the nozzle, where

the enthalpy drop is elaborated. This is due to the "dry" nature of R245FA fluid which allows to have the last part of expansion farther from the saturation curve. Simulations for an isolated supersonic rotor

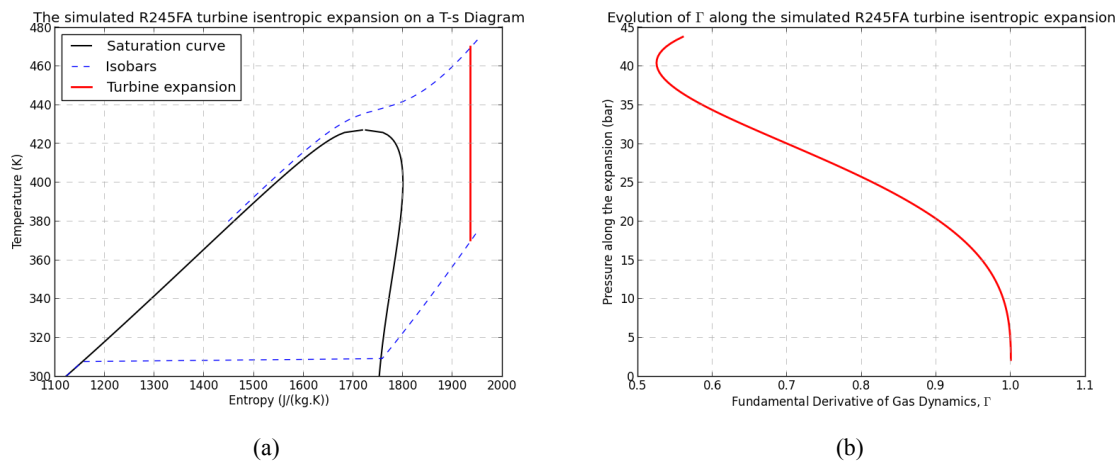


Figure 6: Isentropic turbine expansion on the R245FA T-S diagram (a); Fundamental Derivative of gas dynamics Γ evaluated along the turbine expansion (b).

blade row using fluid R245FA have been carried out in the relative reference system. The blade row considered is symmetric, so the outlet conditions are identical to the inlet conditions. The inlet rotor angle is prescribed according to the stator exit conditions.

By using the Zweifel empirical coefficient (Zweifel, 1945), the number of rotor to stator blades ratio is set to 2. The 2-D computational grid for the full stage simulation is composed of C-shaped blocks around the blades and of H-shaped blocks at stage inlet and outlet shown in figure 7a. It is generated using Ansys TurboGrid and refined to obtain y^+ values less than 1 at the blade walls with 330066 total number of elements (121704 overall elements for the rotor row and 208362 elements for the stator row). Simulations for a full turbine stage involving a supersonic rotor blade row and a supersonic stator blade row both designed by the means of the MOC procedures presented in this paper are carried out. The total temperature, the total pressure and the velocity components are imposed at the inlet. Average static pressure is set at the outlet and a mixing-plane boundary condition is set at the stator-rotor interface. Table 4 presents the main turbine working parameters, taken from a real-world application (they are different from those used in the previous section 2.4). In order to maximize the impact of dense gas effects, we choose supercritical turbine inlet conditions (see figure 6a). Only the results for R245FA fluid are shown because of the absence of substantial differences among the other fluids considered in this paper (see table 1). Figure 7b presents the relative Mach number distribution for the full turbine stage simulation. The flow is accelerated in the stator vanes up to the design absolute Mach number of 2.4 and, thanks to the accurate design with the MOC algorithm, no normal shocks are formed in the divergent part of the nozzle. Thanks to the accurate design with the MOC algorithm, no normal shocks are formed in the divergent part of the nozzle. However, weak oblique shocks are generated at the trailing edge of the stator due to the rounded trailing edge. These shocks interact with the viscous wake, visible on the stator outlet. Due to the mixing plane interface, interactions of the latter with the rotor row can not be observed. The flow in the rotor vanes is characterised by weak oblique shocks departing both from the leading and trailing edge of the blades due to the finite thickness of the actual rotor geometry. The turbine is found to be in a "started" configuration, since a normal shock at the inlet is avoided and the flow inside the rotor vanes is supersonic (Kantrowitz et al., 1945). The flow in the relative reference frame is then deflected by the blade vanes up to a relative Mach number slightly lower than the design one due to the set of oblique shocks departing both from leading and trailing edge. To better analyse the flow behaviour in the rotor vanes an isolated rotor simulation has been performed (see figure 8b). At the inlet of the rotor vanes, the presence of an oblique shock wave is noticed. Two oblique shocks depart also from trailing

edge: one impinges the suction side while the other one interacts with the viscous wake. The careful design of the rotor blade prevents the formation of a normal shock at the inlet that would slow down the flow to subsonic conditions within the blade passage. The calculated total to total isentropic efficiency for this turbine is 92.9%. In order to assess the main source of losses in the turbine stage, it is useful to analyse the entropy deviation $(S - S_{in})/S_{in}$, with S_{in} the specific entropy at inlet. The entropy deviation is shown in figure 8a for the isolated rotor. Entropy is mainly generated with the viscous boundary layers and wakes, whereas entropy generation across shocks is extremely weak. This demonstrates that the proposed methodology provides blade designs with negligible shock losses. The presence of viscous effects also modify the design degree of reaction, set to zero for the design here proposed. The actual degree of reaction evaluated after simulations is found to be 0.042. This effect can be addressed to the modification of the effective blade vane geometry due to the boundary layer thickness, which lead to lower passage sections going from inlet to outlet.

Table 4: Main turbine full stage working parameters.

Parameters	Values
Inlet total reduced pressure	1.2
Pressure ratio	20.6
Inlet total reduced temperature	1.1
Stator nozzle outlet design Mach number	2.4
Stator stager angle [°]	70
Rotor blade speed [m/s]	141.37

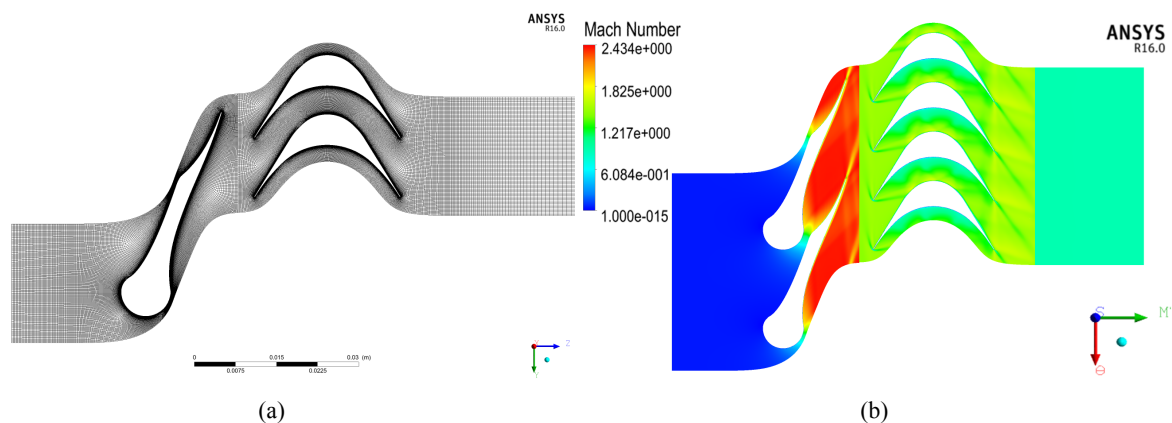


Figure 7: Computational block structured grid for full turbine stage (330066 elements) (a); relative Mach number distribution for R245FA fluid (b).

4. CONCLUSIONS

An efficient design procedure for supersonic ORC turbine rotor blades taking carefully into account dense gas effects has been developed. It is based on the method of characteristics and allows designing blade vanes by imposing the momentum conservation through a free vortex flow condition. Significant differences are found between geometries obtained with the ideal and dense gas models. The numerical simulations show that the accurate blade design in dense gas flow regime allows accounting for the dense gas phenomena during expansion and avoiding the focusing of characteristic lines into strong right shocks inside the blade vanes. The main source of loss of performances can be then addressed to the viscous phenomena, as confirmed by the entropy deviation analysis.

Future developments of the supersonic ORC turbine stage design process will lead to the unsteady nu-

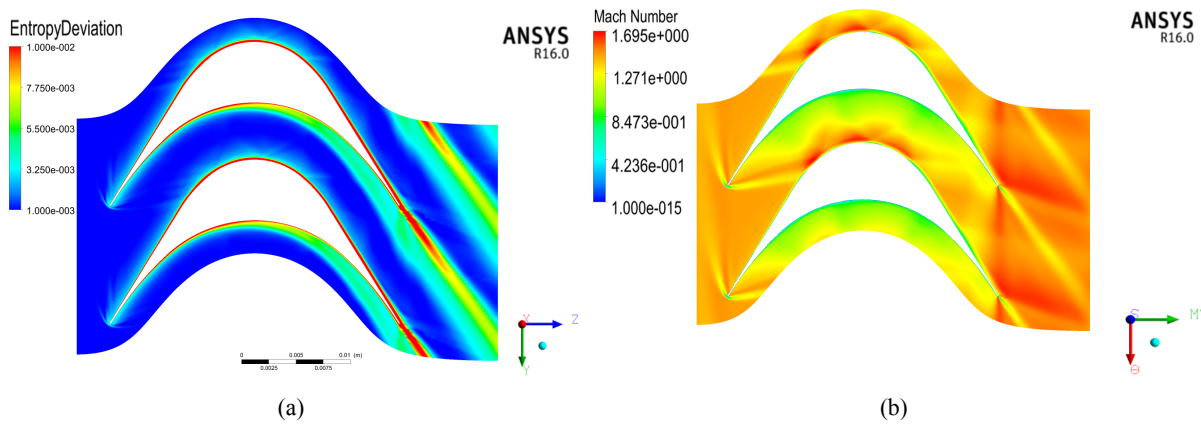


Figure 8: Entropy deviation contour plot for the isolated rotor (R245FA fluid) (a); Mach number distribution for the isolated rotor (R245FA fluid) (b).

merical analysis of the entire turbine stage in order to take into account the interactions between stator and rotor due to viscous phenomena along with the 3-D turbine full stage design.

ACKNOWLEDGEMENTS

The authors would like to thank ADEME (Agence de l'Environnement et de la Maîtrise de l'Energie), PS2E (Paris-Saclay Efficacité Énergétique) and Total who partially funded the works presented in this paper.

REFERENCES

- ANSYS, I. (2015). Ansys cfx-solver modeling guide.
- Bufi, E. A., Cinnella, P., and Merle, X. (2015). Sensitivity of supersonic orc turbine injector designs to fluctuating operating conditions. *Proceedings of the ASME 2015 Turbo Expo Turbine Technical Conference, ASME TURBO EXPO 2015 June 15-19, 2015, Montreal, Canada (Submitted and accepted)*.
- Colonna, P., Nannan, N., Guardone, A., and Van der Stelt, T. (2009). On the computation of the fundamental derivative of gas dynamics using equations of state. *Fluid Phase Equilibria*, 286(1):43--54.
- Congedo, P., Corre, C., and Martinez, J.-M. (2011). Shape optimization of an airfoil in a BZT flow with multiple-source uncertainties. 200(1-4):216 -- 232.
- Cramer, M. and Tarkenton, G. (1992). Transonic flows of bethe-zel'dovich-thompson fluids. *Journal of Fluid Mechanics*, 240:197--228.
- Délery, J. (2010). *Handbook of compressible aerodynamics*. ISTE.
- Goldman, L. J. (1968). Analytical investigation of supersonic turbomachinery blading. 1/2-analysis of impulse turbine-blade sections.
- Guardone, A., Spinelli, A., and Dossena, V. (2013). Influence of molecular complexity on nozzle design for an organic vapor wind tunnel. *Journal of Engineering for Gas Turbines and Power*, 135(4):042307.
- Kantrowitz, A., Donaldson, C., Laboratory, L. A., and for Aeronautics, U. S. N. A. C. (1945). *Preliminary Investigation of Supersonic Diffusers*. National Advisory Committee for Aeronautics.
- Lemmon, E. W., Huber, M. L., and McLinden, M. O. (2013). *NIST Reference Fluid Thermodynamic and Transport Properties - REFPROP Version 9.1*. NIST.

- Paniagua, G., Iorio, M., Vinha, N., and Sousa, J. (2014). Design and analysis of pioneering high super-sonic axial turbines. *International Journal of Mechanical Sciences*, 89:65--77.
- Thompson, P. A. (1971). A fundamental derivative in gasdynamics. *Physics of Fluids (1958-1988)*, 14(9):1843--1849.
- Wheeler, A. P. and Ong, J. (2013). The role of dense gas dynamics on orc turbine performance. In *ASME Turbo Expo 2013: Turbine Technical Conference and Exposition*, pages V002T07A030--V002T07A030. American Society of Mechanical Engineers.
- Zucrow, M. J. and Hoffman, J. D. (1976). Gas dynamics. *New York: Wiley, 1976*, 1--2.
- Zweifel, O. (1945). The spacing of turbomachine blading, especially with large angular deflection. *Brown Boveri Review* 32.

NOMENCLATURE

a	Speed of sound	(m/s)
ch	Axial chord	(m)
p	Pressure	(Pa)
ph	Blade pitch	(m)
G	Mass-flow rate	(kg/s)
H	Specific enthalpy	(J/kg)
M	Mach number	
R	Radius for the design of the convergent	(m)
R_g	Specific gas constant	(J/kg * K)
S	Specific entropy	(J/kg * K)
T	Temperature	(K)
V	Velocity	(m/s)
β_a	Leading edge attach angle	(rad)
γ	Specific heat ratio	
η_{is}	Isentropic efficiency	
θ	Stagger angle	(rad)
μ	Mach angle	(rad)
ν	Prandtl-Meyer function	
v_s	Specific volume	(m ³ /kg)
ρ	Density	(kg/m ³)
σ	Blade solidity (chord to pitch ratio)	
φ	Flow angle	(rad)
Φ	Leading edge angular extension.	(rad)

Subscript

r	Reduced: normalised respect to critical conditions.
c	Critical thermodynamic property.
0	Total/reservoir thermodynamic property.

Superscript

*	Critic (sonic) parameter.
---	---------------------------

Acronyms/abbreviations

<i>MOC</i>	Method Of Characteristics.
<i>REF</i>	REFPROP model.
<i>EOS</i>	Equation Of State.
<i>CFD</i>	Computational Fluid Dynamics.
<i>ORC</i>	Organic Rankine Cycle.

DEVELOPMENT OF A TURBO-GENERATOR FOR ORC SYSTEM WITH TWIN RADIAL TURBINES AND GAS FOIL BEARINGS

Young Min Yang^{1,2,3}, Byung Sik Park^{1,2*}, Si Woo Lee³, Dong Hyun Lee²,

¹Advanced Energy and Technology, Korea University of Science and Technology,
217 Gajeong-ro, Yuseong-gu, Daejeon 305-333, Republic of Korea
e-mail: ymyang@kier.re.kr

²Energy Efficiency Research Division, Korea Institute of Energy Research,
152 Gajeong-ro, Yuseong-gu, Daejeon 305-343, Republic of Korea
<http://www.kier.re.kr> (e-mail: bspark@kier.re.kr)

³Jinsol Turbomachinery Co., Ltd.,
94-17 Techno2-ro, Yuseong-gu, Daejeon, 305-509, Republic of Korea
<http://www.jinsolturbo.co.kr> (e-mail: impentacle@jinsolturbo.co.kr)

ABSTRACT

The interest in ORC plant is increasing over recent years in terms of the energy and the environment costs. But the capital cost and maintenance cost of an ORC plant are the main obstacles of the wide spread in the global market. To overcome them, it is necessary to decrease the manufacturing and maintenance cost, and to increase the turbine efficiency and the system availability.

Korea Institute of Energy Research (KIER) and Jinsol Turbomachinery have jointly developed a novel turbo-generator applicable to the low temperature heat sources to meet those needs.

The turbo-generator developed is almost maintenance-free, highly efficient and completely hermetic. A high speed permanent magnet synchronous generator (PMSG) was applied to get the high efficiency. Radial turbines were directly coupled with the PMSG without a gear box to reduce the power transfer loss and cost. The rotor shaft was supported by gas foil bearings to increase the system availability through the non-contacting bearings. Twin radial turbines were assembled with the rotor shaft in the way of face-to-face to cancel out the axial load caused by the pressure difference. This configuration made it possible to apply a gas foil bearing as a thrust bearing despite of its low load capacity. A gas foil bearings is the simple and cheap solution for the rotor support system and the completely hermetic turbo-generator. The high efficiency of the radial turbine was acquired by the real gas modelled turbine design with optimum specific speed.

The developed turbo-generator was integrated with the 100kWe ORC plant installed at KIER and it showed that the turbo-generator efficiency was about 80% as the result of the performance test with the temperature difference of 70°C between the heat source inlet and the heat sink inlet.

1. INTRODUCTION

In terms of energy issues and environmental aspects, the interest in ORC (Organic Rankine Cycle) plant is increasing over recent years because of its applicability and availability for low temperature heat sources. An ORC has nearly the same components with a conventional steam Rankine cycle except using organic compounds instead of water. The organic compounds applicable to the low temperature heat source (<100~150°C) usually have lower boiling point than the water because ORC plants are applied to generate power from low-temperature heat sources (Quoilin *et al.*, 2013).

³rd International Seminar on ORC Power Systems, October 12-14, 2015, Brussels, Belgium

Although ORC power plant is considered as one of the promising technologies for generating power from low-temperature heat sources, its high capital cost and maintenance cost are the main obstacles in the wide spread on the global market (Quoilin *et al.*, 2013 and Wang *et al.*, 2011). Mainly the high capital cost and low cycle efficiency cause the low IRR for the ORC power plant. It is necessary to improve the capital cost, maintenance cost, cycle efficiency and system availability to obtain high IRR. In terms of cost, the capital cost of heat exchanges should be reduced at first because it is more than half of the total power plant capital cost and the costs of other components should be reduced secondly. The maintenance cost also should be reduced more. For revenue from the power generation, it is more important to obtain high cycle efficiency (by the components with high efficiency and system optimization) and high system availability (low maintenance shut-down by the robust components) to get more power from the given conditions.

In spite of its drawbacks, ORMAT, Turboden, BNI, UTC, Electrathem, Access Energy and so on have supplied their ORC power plant in the global market. And new manufacturers appear in the market continuously. Most of them select the turbines as their expanders while some others such as Electrathem and Kobelco use the screw type expanders especially in small power capacity plant (Kang, 2012, Takahashi *et al.*, 2013, Yuksek and Mrimobin, 2013). Many research studies were conducted with various types of expanders. According to the summary of Fu *et al.* (2015), a scroll expander is dominant in the ORC system with less than 50kW power output. But the reason is that the power capacities of the investigated studies are less than 10kW except some cases.

The expander and the generator are the most important components in the ORC power plant because they convert the electric power from the temperature difference between the heat source and heat sink. To overcome ORC's disadvantages, the expander and the generator must be highly efficient and robust at design point and off-design points. In addition, the expander-generator set must have the advantages such as high system availability, low manufacturing cost, light weight, small volume, easy maintenance, hermetic configuration, and excellent endurance performance.

This study presents the design and development of a novel turbo-generator applicable for low temperature heat sources in 100kW class ORC power plant to meet the needs suggested above. In addition, this paper presents the test results of the 100kW-class turbo-generator under some operation points.

2. DESIGN OF TURBO-GENERATOR

This 100kW power class turbo-generator was integrated to the 100kW class ORC power plant in the Korea Institute of Energy Research (KIER), Korea. R245fa was selected as the working fluid in the ORC system on the basis of the available heat source and heat sink temperature. Although various refrigerants were adopted in the numerous studies (Fu *et al.*, 2015, Bao and Zhao, 2013), there exists the proper refrigerant which might be used in the ORC system considering the various aspects such as cycle efficiency, fluid density, safety, and environmental effects.

2.1 Mechanical Layout

The turbo-generator was designed to meet the requirements listed above: high efficiency, high system availability, low manufacturing cost, light weight, small volume, easy maintenance, hermetic configuration, and excellent endurance performance. The turbo-generator was suggested to adopt the radial in-flow turbine, permanent magnet synchronous generator, gas foil bearing, and direct coupling between turbine and generator. The mechanical arrangement was that the twin radial in-flow turbines are located in the front-to front way and the generator is located between them as shown in Figure 1.

By selecting the radial in-flow turbine, the manufacturing cost can be reduced with the high efficiency. And compact size and light weight can be obtainable. The high rotational speed of turbine is inevitable to meet the optimum specific speed but this high speed makes the turbo-generator compact and small.

Due to the high speed, the high speed permanent magnet synchronous generator (PMSG) and the low

speed generator with a gear box can be the candidates. For this turbo-generator, the PMSG was selected as a generator. It has higher efficiency than other type generators, light weight, and small volume due to the high rotational speed. It can rotate at various speeds regardless the grid power frequency. That makes the radial turbine rotate at its optimum speed with the maximum efficiency. But its small volume has small surface area for its cooling. It makes hard to design the cooling system in spite of its low heat generation due to its high efficiency. Also it needs power converting system (PCS) to convert the generator side power-generating-frequency that depends on the rotational speed of generator to grid side one. But the power converting efficiency is higher than that of a gear box. PCS does not need the lubrication oil, an oil cooling system, and its maintenance such as oil change. It is more attractive to adopt the PMSG and PCS in the turbo-generator for ORC power plant.

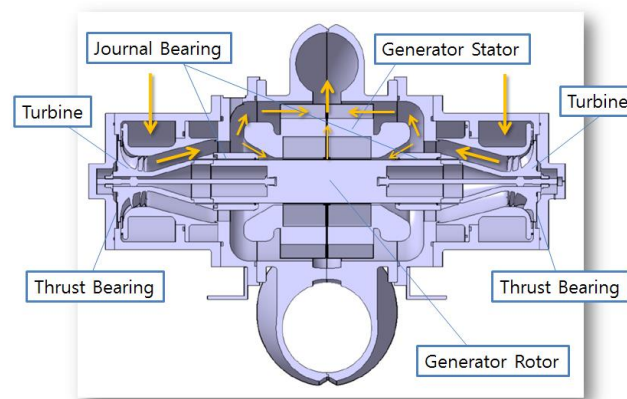


Figure 1: Mechanical Layout of the 100kW turbo-generator for ORC plant

A gas foil bearing was applied in the rotor support for the journal bearing and the thrust bearing. It is the gas foil bearing that is one of the non-contact bearing and oil free bearing. It makes the maintenance-free turbo-generator possible due to its special characteristics mentioned above. A magnetic bearing also has these characteristics but it has many complicate components (its own exclusive controller, position sensors and so on) and more power consumption. It may increase the cost of the ORC plant.

But the gas foil bearing has small load capacity. While it is not the problem in journal bearing, it can be a severe problem in thrust bearing because it should have the load capacity for the axial load caused by the pressure difference between the front side and back side of the radial turbine.

Table 1: Design requirements of radial turbine

Parameters	Unit	Values
Inlet Temperature	°C	59.8
Inlet Pressure	bar	4.56
Expansion Ratio	-	4.67
Mass Flow Rate	kg/s	2.5 (for each turbine) (total: 5 for twin turbines)
Output Power	kW	58.5 (for each turbine) (total: 117 for twin turbines)
Efficiency	%	85
Working Fluid	-	R245fa

As shown Figure 1, the turbine and the generator's rotor were coupled directly to skip the gear box and its oil handling system. And the twin turbines were arranged in the front-to front formation. It makes possible to cancel out the axial load caused by the pressure difference in each single turbine.

Theoretically the axial load caused by the turbine is zero, which allowed us to use the gas foil bearing as the thrust bearing. The thrust bearing was located at the back face of each twin turbines as shown in Figure 1. In addition, the generator was located between the twin turbines' exits. The relatively cool working fluid can flow into the generator from the turbine exit after expansion. It can cool down the generator by the cooling passage shown in Figure 1. It makes possible to omit the other cooling passage and to save the loss of working fluid for the cooling passage. Table 1 shows the design requirements of radial turbine on the basis of ORC plant cycle design.

2.2 Radial Turbine and PMSG

The radial turbine was designed on the basis of the thermodynamic properties of working fluid, R245fa to meet the specification shown in Table 1. The stage efficiency of the radial turbine was expected as high as 90% with Reynolds Number effect corrected. The rotational speed of the turbine was selected as an optimal value which corresponds to the optimal specific speed. The main flow sections of the turbine stage, i.e. rotor exit, rotor inlet were designed on the basis of optimum velocity triangles which makes the rotor exit relative flow velocity at the tip radius and the rotor inlet absolute flow velocity as minimum respectively and no swirl at the rotor exit. The minimum velocity design minimizes the aerodynamic losses and no swirl at the outlet of turbine rotor makes the radial component of the exit velocity negligible (Aungier, 2006). The dimension of the main flow path is shown in Table 2 for the designed radial turbine.

Table 2: Dimension of the main flow path from the design results of radial turbine

Items	Unit	Values
Stator Inlet Radius	mm	105
Stator Outlet Radius	mm	82
Stator Blade Height	mm	10.6
No. of Stator Blade	-	20
Rotor Inlet Radius	mm	76
Rotor Inlet Blade Height	mm	10.6
Rotor Outlet Tip Radius	mm	54.6
Rotor Outlet Tip Radius	mm	20
No. of Rotor Blade	-	14

The wall contour of the turbine rotor and the blade profiles were generated with the proprietary in-house design code on the basis of the main flow path shown in Table 2 and the real gas model of R245fa using REFPROP developed by NIST. The final radial turbine is shown in Figure 2. Figure 2 (a) shows one of the twin turbine rotors and Figure 2 (b) shows one of the twin turbine stators.

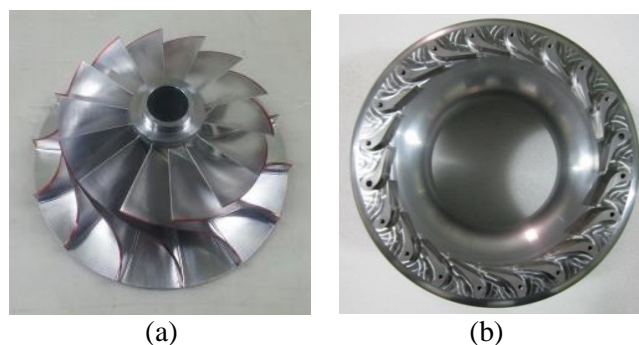


Figure 2: Radial Turbine Rotor (a) and Stator (b)

The generator was designed in the type of PMSG to obtain higher efficiency. A type of the rare earth magnet was used to get the strong permanent magnet. A samarium-cobalt magnet ($\text{Sm}_2\text{Co}_{17}$) is

preferred as the rotor magnet for PMSG because of its higher demagnetized temperature than others. Due to this, it can operate at higher temperature. The design specification and design results are shown in Table 3. The stator core was designed and constructed to have several cooling fins along the outside of it extended in the radial direction as shown in Figure 3 (a) to dissipate the heat generated by the iron loss and copper loss of the stator. It has also cooling passage in the middle of the stator core along the axial direction shown in the Figure 1 and Figure 3 (b). The cooling passage in the middle of the stator core is mainly the one for rotor shaft cooling, which can dissipate the heat from the can loss and the permanent magnet loss of the rotor shaft.

Table 3: Design specification and its result of PMSG

Items	Unit	Values
No. of Phase	-	3
No. of Poles	-	2
Rated Voltage(line-to-line)	V	480
Rated Current	A	137
Rated Power	kW	110
Efficiency	%	95
No. of Slots in Stator	-	24
Stator Outer Radius	mm	220
Stator Inlet Radius	mm	89
Rotor Radius	mm	85
Length of the Rotor Magnet	mm	150

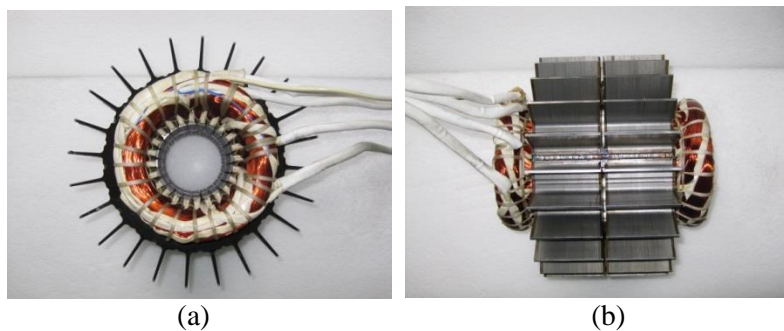


Figure 3: Stator for the PMSG Type Generator

2.3 Gas Foil Bearings

Twin turbine rotors were assembled at each end of the generator rotor shaft which was the part of the turbo-generator rotor to obtain the face-to-face configuration. The whole rotor was supported by the journal bearings and the thrust bearings as shown in Figure 1. The journal bearings support the radial load caused by the rotor weight and the thrust bearings support the axial load caused by the pressure difference between turbines, respectively. According to the literatures, the load capacity of a journal foil bearing is given by Equation (1) (Kus and Neksa, 2013).

$$C_{JB} = f_{JB} L_{JB} D_{JB}^2 N \quad (1)$$

For the thrust bearing, the axial load on the rotor shaft could be ideally cancelled out to be zero because the rotor shaft is bilaterally symmetric. Therefore the axial load on the rotor is not significant. The thrust load capacity that can be supported by a thrust foil bearing, also is given by Equation (2) (Kus and Neksa, 2013).

$$C_{TB} = f_{TB} \pi W D_{TB}^2 N \quad (2)$$

According to the in-house design practice, the journal and thrust bearings were designed and made as shown in Figure 4. Figure 4 (a) is the top foil of the journal bearing and Figure 4 (b) shows the bump foil of the journal bearing placed between the top foil and the bearing housing. Figure 4 (c) is the thrust bearing located at the backside of each twin turbine.

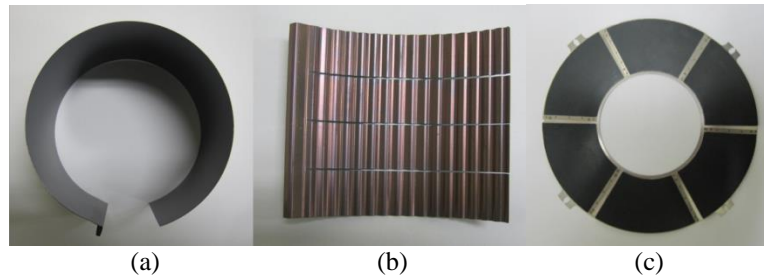


Figure 4: Gas Foil Bearing: Journal Bearing (Top Foil: a, Bump Foil: b) and Thrust Bearing (c)

3. TEST RESULTS AND DISCUSSION

Figure 5(a) shows the experimental apparatus for the turbine performance test. Actually the whole ORC power plant system was required to run the turbo-generator and to test its performance by the electrical power output from the generator. Then, the performance of the turbo-generator could be evaluated.

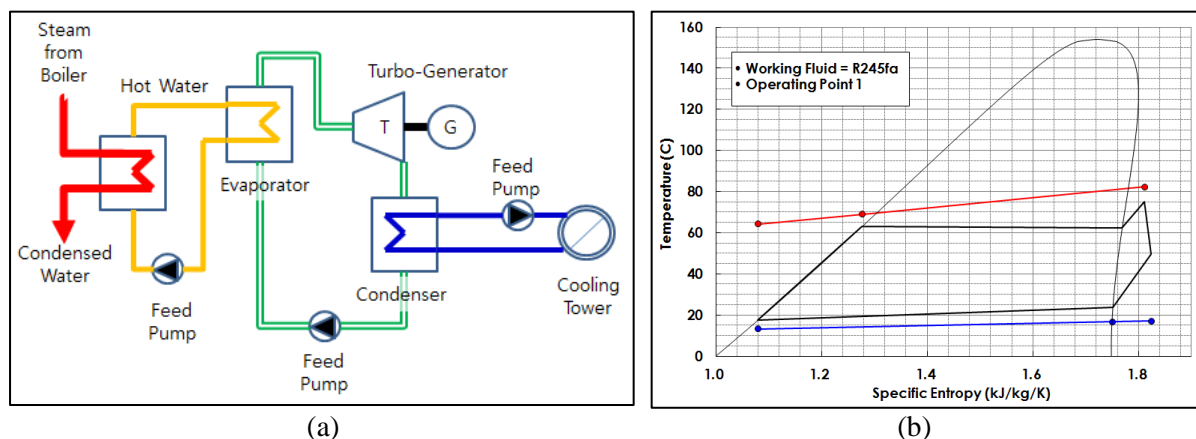


Figure 5: ORC power plant as a turbo-generator performance test rig

The orange line loop in Figure 5(a) is the hot water loop heated by the steam from the boiler as a heat source. The green line loop is the working fluid (R245fa) loop. The blue line loop is the cooling water line to absorb the heat rejection from the condensation of the working fluid. Steam line (red) and hot water loop (orange) were installed to simulate the hot-water type heat source. Figure 5(b) shows a plot of thermodynamic cycle in the temperature entropy diagram (T-S diagram) for an operating point. Table 4 together with Figure 6 (a) show the operating conditions of the ORC power plant and the electrical power output at each operating point. The performance of the turbo-generator was evaluated on the basis of this power output. The mass flowrate of the heat source (hot water) was set to a constant value, 17kg/s. And the temperature difference between the heat source inlet and the heat sink inlet was also controlled to a constant value, about 70°C. Since the temperature difference was nearly

constant, the rotational speed of turbine was also kept nearly constant within 6% deviation. Figure 6 (a) also shows that the electrical power output was proportional to the mass flow rate of the working fluid.

The electrical power output was measured at the power output terminal of the generator. The (gross) cycle efficiency which is defined in Equation (3) increased from 5.2% to 7.3% while the mass flowrate increased. That means 40.4% increase along the flowrate increase. The efficiency of the turbo-generator means that of the total equipment composed of the turbine and generator. It is shown in Equation (4) that the efficiency is the ratio of the electrical power output to the ideal power output from the turbine.

Table 4: Electrical power output and control inputs at each measured operation point

Operating Point	Electric Power Output (kW)	Control Inputs			
		Working Fluid Flowrate (kg/s)	Heat Source Inlet Temperature (°C)	Heat Sink Inlet Temperature (°C)	ΔT (°C)
1	91.20	5.17	82.32	13.17	69.14
2	81.50	4.71	82.78	12.48	70.30
3	70.43	4.16	82.85	11.62	71.23
4	60.34	3.69	81.77	10.94	70.84
5	48.93	3.15	82.52	10.27	72.26
6	35.17	2.60	81.93	10.15	71.78

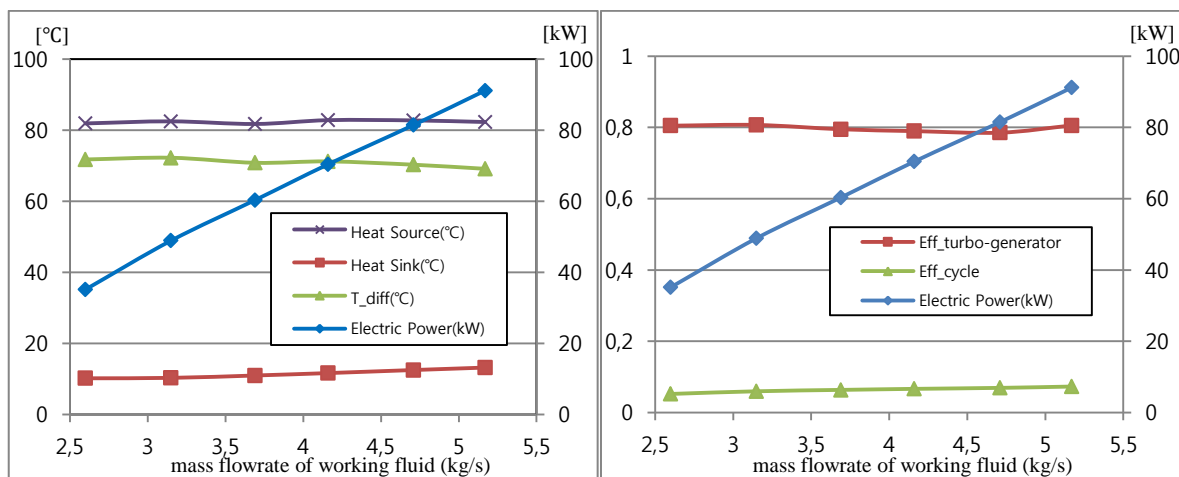


Figure 6: Operation conditions and performance results

It was difficult to measure the temperature and pressure right after turbine exit because of the unique configuration of this turbo-generator. The temperature and the pressure were measure merely near the end-turn of the generator. Assuming that the pressure drop between them is negligible, ideal enthalpy drop can be calculated from the turbine inlet and outlet conditions. But the temperature difference was not negligible because of the temperature rise due to the generator loss and windage loss. Therefore only the turbo-generator efficiency was evaluated instead of the turbine efficiency. The calculated efficiencies of the turbo-generator ranged from 78.5% to 80.7% as shown in Figure 6. It matched well with the product of the design efficiency of the turbine and generator (0.85*0.95) without considering the windage loss.

$$\eta_{cycle} = \frac{P_e}{\dot{Q}_{in}} \quad (3)$$

$$\eta_{t-g} = \frac{P_e}{\Delta h_i \cdot \dot{m}_{ref}} \quad (4)$$

$$\eta_{t-g} = \eta_t \cdot \eta_g \cdot (1 - \xi_{wl}) \quad (5)$$

As shown in Equation (5), the efficiency of the turbo-generator is the product of the turbine efficiency, the generator efficiency, and the efficiency decrease due to the windage loss of the rest part of the rotor except the generator shaft. If the generator is designed with the specified efficiency (95%) and the windage loss is ignored, the turbine efficiency was 85% in the case of the maximum turbo-generator efficiency (80.7%).

4. CONCLUSION

The present study was the design and construction of a novel turbo-generator applicable for the low temperature heat sources to meet the market needs. It is almost maintenance free, highly efficient and completely hermetic. A unique configuration was developed including high speed permanent magnet synchronous generator (PMSG), twin radial turbines, and gas foil bearings. Twin radial turbines were assembled to the rotor shaft in the face-to-face configuration.

The performance test results of the turbo-generator showed that the maximum power output was 91.2kW. The maximal efficiency of the turbo-generator and cycle efficiency were 80.7% and 7.3%, respectively under the condition of 70°C temperature difference between heat source and heat sink.

And the future study will focus on the clarification of the turbine and generator efficiencies, cost estimation compared with the other types, turbine efficiency change with respect to the operation points, and dynamic response of turbo-generator.

NOMENCLATURE

C	load capacity	(N)
D	diameter	(m)
f	bearing performance coefficient	(N/m ³ /krpm)
L	axial length	(m)
\dot{m}	mass flow rate	(kg/sec)
N	rotor speed	(krpm)
P	power	(kW)
\dot{Q}	heat flow rate	(kW)
w	radial extent of the top foil	(m)
ξ	energy loss coefficient	(-)
η	efficiency	(-)
Δh	enthalpy difference	(kJ/kg)

Subscript

JB	journal bearing
TB	thrust bearing
t-g	turbo-generator

t	turbine
g	generator
e	electric
i	ideal
ref	refrigerant
wl	windage loss

REFERENCES

- Aungier, R. H., 2006, *Turbine Aerodynamics; axial-flow and radial-inflow turbine design and analysis*, ASME Press, New York: p. 197-290
- Bao, J., Zhao, L., 2013, A review of working fluid and expander selections for organic Rankine cycle, *Renewable and Sustainable Energy Reviews*, vol. 24: p. 325-342.
- Fu, B., Lee, Y., Hsieh, J., 2015, Design, construction, and preliminary results of a 250-kW organic Rankine cycle system, *Applied Thermal Engineering*, vol. 80: p. 339-346
- Kang, S., 2012, Design and experimental study of ORC and radial turbine using R245fa working fluid, *Energy*, vol. 41, no. 1: p. 514-524
- Kus, B., Neksa, P., 2013, Development of one-dimensional model for initial design and evaluation of oil-free CO₂, *International Journal of Refrigeration*, vol. 36: p. 2079-2090.
- Quoilin, S., Broek, M., Declaye, S., Dewallef, P., Lemort, V., 2013, Techno-economic survey of Organic Rankine Cycle(ORC) systems, *Renewable and Sustainable Energy Reviews*, vol. 22: p. 168-186.
- Takahashi, K., et al., 2013, Binary Cycle Power Generation System for Hot Water, "*R&D*" *Kobe Steel Engineering Reports*, vol. 63, no. 2: p. 2-5
- Wang, H., Peterson, R., Harada, K., Miller, E., Ingram, R., Fisher, L., 2011, Performance of a combined organic Rankine cycle and vapor compression cycle for heat activated cooling, *Energy*, vol. 36, no. 1: p. 447-458.
- Yukse, E., Mirmobin, P., 2013, High efficiency low temperature ORC system, *2nd International Seminar on ORC Power Systems*, Rotterdam

ACKNOWLEDGEMENT

This work was conducted under the framework of Research and Development Program of the Korea Institute of Energy Research (KIER) (B4-2461) and Contract Based Department Program of Korea University of Science and Technology.

EFFICIENCY CORRELATIONS FOR AXIAL FLOW TURBINES WORKING WITH NON-CONVENTIONAL FLUIDS

Marco Astolfi^{1*}, Ennio Macchi¹

¹Politecnico di Milano, Energy Department,
Milano, Italy

*marco.astolfi@polimi.it

ABSTRACT

This work aims at defining a set of general correlations for the estimation of axial-flow turbine efficiency in Organic Rankine Cycle (ORC) field. A dedicated numerical tool is used for the optimization of several hundreds of turbines and the results are presented in specific parameters (SP , V_r and Ns) according to similarity rules. The analysis is carried out for single, two and three stages turbines. For each case a correlation of efficiency at optimal rotational speed is calibrated in function of the equivalent single stage SP and the total isentropic V_r . Three sensitivity analyses are proposed in order to highlight the effects of each single parameter on stage efficiency. Finally, the effect of fluid choice on turbine performance and dimension is discussed with a numerical example.

1. INTRODUCTION

The energy market is today more and more oriented to technical solutions able to exploit renewable energy sources and waste heat from industrial processes with the aim at reducing air and water pollution and increasing systems efficiency. In this context Organic Rankine Cycle (ORC) is one of the most reliable and mature solution for the exploitation of various energy sources characterized by a small available thermal power and/or a low maximum temperature. Typical fields of application of ORC technology are the geothermal energy, the solar energy, the biomass combustion and the heat recovery from industrial processes. ORCs have a simple layout characterized by a limited number of components; in addition they are extremely flexible showing good off-design performances in a large range of working conditions. The main advantage of ORCs is the possibility to select the most appropriate working fluid among a wide list of candidates guaranteeing high efficiency cycles in a large range of applications (Astolfi *et al*, 2014a). Despite their simplicity, the study of ORCs requires cross-functional expertise because the design and the optimization of these plants is largely influenced by the availability of (i) accurate equations of state (EoS), (ii) reliable cost correlations and (iii) efficiency correlations able to describe components performance. In particular, the expander is the key component of an ORC and the estimation of its efficiency and dimension is crucial to obtain a reliable evaluation of system performance and cost. The assumption of a fixed expander efficiency, independent of (i) the operative conditions (inlet and outlet thermodynamic states), (ii) the working fluid and (iii) the expected power output, may lead to unrealistic results (Astolfi *et al*, 2014b). In ORC field different types of expanders are used depending on the plant power output and the expansion ratio. Axial flow turbine is the most common choice and it is used by main market leaders like Ormat and Turboden, while Exergy has recently introduced high efficiency radial outflow turbines, especially suitable for high volume ratio expansions (Xodo *et al*, 2013). Radial inflow turbines are designed by Atlas Copco and by Calnetix GE in a large range of dimensions: from few tens of kW to tens of MW in geothermal applications. Finally, positive displacement expanders (scroll, pistons or screw devices) are proposed for small size applications like solar power plants and automotive ORC. This work is focused on axial-flow turbines because of their large market share and their capability to cover a large range of applications with high isentropic efficiency.

Various correlations, charts and diagrams for the estimation of axial turbine efficiency are proposed in literature but usually they lack in to account some variables of crucial interest in ORC field. The use of

complex and heavy fluids entails a design of ORC turbines which is different from either gas or steam turbines. Organic fluids generally operate at moderate temperatures and show a small isentropic enthalpy drop in expansion leading to the design of compact turbines with a reduced number of stages and low load coefficients (k_{is}). Peripheral speed is generally not a critical issue while in gas and steam turbines this is the key limiting factor in the selection of stage number due to both mechanical stresses and high temperatures. On the other hand, organic fluids usually have large volume ratios per stage and a low speed of sound. Both these aspects make the design of an ORC turbine a quite challenging task which cannot be faced without the support of a specific optimization software. Simple correlations such as Smith (1965) diagrams and Baljé and Binsley (1968) plots cannot catch these ORC turbines peculiarities. As already demonstrated by Macchi (1977), Macchi and Perdichizzi (1981) and Lozza *et al.* (1981), a rigorous design of an axial flow turbine should take into account real blade dimensions and the effects of Mach numbers especially if supersonic flows are present. These aspects are crucial for organic fluids, where blades are characterized by a large height variation, large flaring angles and supersonic velocities. In particular in Macchi (1977), the effect of both the volume ratio and the specific speed is analyzed for different single stage turbines operating with heavy and complex fluids while in Lozza *et al.* (1981) a sensitivity analysis is carried out varying the number of stages for turbines with two different size parameters. A further step ahead is provided in the work of Macchi and Perdichizzi (1981) with the definition of a map of efficiency for single stage turbines at optimized rotational speed as function of size parameter and volume ratio. The purpose of this paper is to propose an efficiency correlation for single, two and three stage axial flow turbines at optimized rotational speed in a wide range of volume ratios and dimensions.

2. SCOPE OF WORK AND METHODOLOGY

Except for some biomass applications, in ORC field each turbine is designed *ex novo* because each plant differs in the available thermal power and in the temperature of both the heat source and the cooling medium. Turbines in ORC can operate with different fluids in a large range of pressure and volume ratios, size and power output. For these reasons, it is interesting to adopt a non-dimensional approach which allows comparing optimal turbine designs on the basis of specific parameters. According to similarity rules (Dixon, 1998), the results achieved for a certain turbine stage can be extended to any other case if the stages respect the following conditions (Macchi and Perdichizzi, 1981):

1. They have the same specific speed;
2. The geometric similarity is fully verified (all the geometrical ratios are equal);
3. The flow is fully turbulent so that the Reynold number effects are negligible
4. the Mach numbers are similar;
5. The volumetric behaviour of the two fluids is the same, namely the volume flow rate variation across the stage is equal for the two fluids. This condition is verified if the two fluids are incompressible or if they are ideal gas with the same pressure ratio and the same heat capacity ratio;

ORC turbines ranges from micro scale to very big machines and so the geometrical similarity cannot be always verified because of the presence of technological constraints like the minimum trailing edge thickness and the minimum tip clearance gap. Very small turbines are intrinsically less efficient because of the increase of profile and leakage losses. On the other hand, high value of volume ratios affect the turbine stage design which requires converging diverging blades and relevant variation of blade height in a single row with detrimental effects on stage efficiency.

The parameters suggested as independent variables for a parametric analysis are: the size parameter $\left(SP = \frac{V_{out,is}^{0.5}}{\Delta h_{is}^{0.25}} \right)$ and the volume ratio $\left(V_r = \frac{V_{out,is}}{V_{in}} \right)$ while the specific speed $\left(Ns = \frac{RPM}{60} \frac{V_{out,is}^{0.5}}{\Delta h_{is}^{0.75}} \right)$ will be optimized for each case. The physical significance of SP , V_r and Ns and their influence on the turbine efficiency will be discussed later.

In order to obtain efficiency maps with a sufficient detail and covering a large range of ORC applications, hundreds of turbines have been optimized. Independent variables range between a minimum and a maximum value which is 0.02 m -1 m for SP and 1.2-200 for Vr .

The optimizations presented in next sections are realized assuming a complex ideal gas with a γ value equal to 1.05 as representative of a generic organic fluid. We found this simplifying hypothesis appropriate for the scope of the present analysis, i.e. to obtain quite accurate preliminary prediction of turbine efficiency for a large variety of ORC cycles and working fluids. The results in section 6 confirm the validity of this assumption. Of course, in the final turbine design a proper EoS should be considered. In this study, Reynolds numbers are not considered as independent variables since for Re greater than 10^6 the effect on stage performance is negligible, while the influence of Mach numbers on blade geometry, flow angles and losses are accounted for. Even if the Mach numbers resulting from the adopted ideal gas assumption differ from the real ones, these deviations cause minor effects on the predicted stage efficiency (Macchi and Perdichizzi, 1981).

All the results presented in the next sections are obtained with Axtur tool, an *in house* optimization code for axial flow and radial outflow turbines developed by Macchi and Lozza at the Energy Department of the Politecnico di Milano. The code is based on a pseudo 1D approach and both blade channels geometry and velocity triangles are defined at mean diameter for each blade row (see Fig 1 for nomenclature details). Blade heights are hence obtained from continuity equation and the actual blade geometry is considered in efficiency losses calculation. Efficiency loss for each row is computed using correlations from literature to take into account the presence of the boundary layer, supersonic flows, flow angle variations and other losses.

Axtur, starting from a feasible initial point, performs multivariable constrained optimizations of turbines with a maximum stage number equal to three. Every stage is fully defined by nine parameters. Three of them define stage quantities: the stage isentropic load (k_{is}), the isentropic degree of reaction (r^*) and the isentropic volume ratio (V_r). The other six (three for each row) parameters are representative of stage geometrical ratios (o/s , o/b and b/r_m). These parameters are the optimization variables of the problem and they can be varied by the optimization algorithm between a lower and an upper bound whose values are defined according to the limits of the correlations used to compute the efficiency losses.

In addition, nonlinear constraints are considered for other variables of interest, like maximum Mach numbers, maximum number of blades and flaring angles and for technological limitations. Penalty factors are introduced if the upper or the lower bounds are not respected.

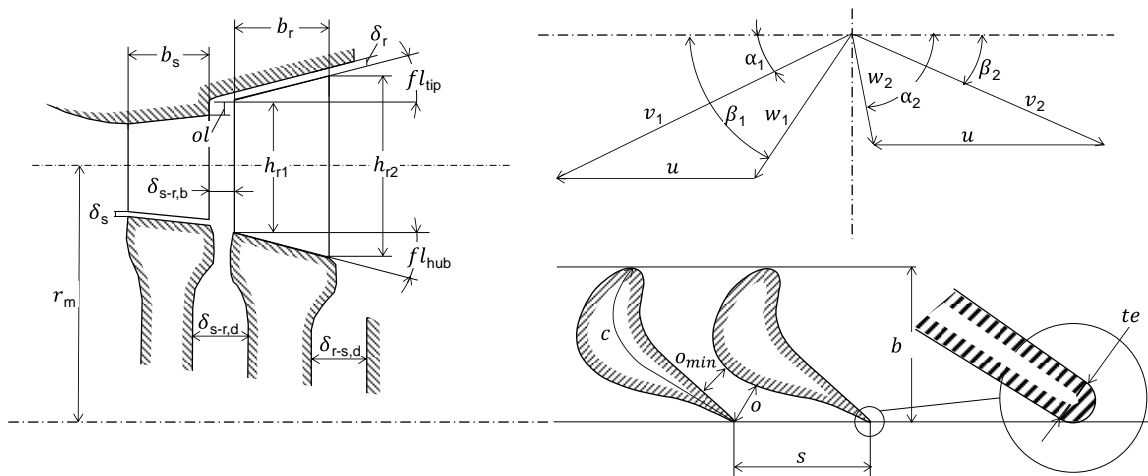


Figure 1 - Notation used in Axtur for the blade geometry and the velocity triangles. Converging-diverging blades are used by the code when $Ma > 1.4$ otherwise $o = o_{min}$. In the velocity triangle the v vector represents the absolute velocity while w one the velocity relative to the rotor blade; u vector is the peripheral speed. Subscripts 1 and 2 refer to the inlet and the outlet of the rotor blade respectively.

For a single stage Axtur optimizes the total to static efficiency corrected by the fraction of kinetic energy recovered by the diffuser according to eq. 4.

$$\eta = \frac{W}{\Delta h_{T-S} - \varphi_E \frac{v_{2,a}^2}{2}} \quad (1)$$

Where φ_E is the efficiency of the diffuser; it is assumed that 50% of the kinetic energy of the discharge absolute velocity axial component can be recovered.

The approach is not completely rigorous because the recovery of kinetic energy entails a reduction of the pressure at turbine discharge and so a higher pressure drop and a higher power production while here the effect is accounted subtracting the same term from the denominator. As proved by Macchi [6], the approximation is generally valid and does not affect the quality of the solution in terms of turbine efficiency. For multistage turbine the code maximizes the power output imposing $\varphi_E = 1$ for all the stages except the last one, but introducing annulus losses between blade rows.

The results provided by Axtur consist in a complete characterization of blade geometry in both blade to blade and meridional planes and velocity triangles. Furthermore, the breakup of the efficiency losses is reported considering the following effects:

- *Profile loss* (Craig&Cox [10]): due to the blade shape and effects related to friction, fluid vane deflection and boundary layer dissipation. This loss mainly depends on blade pitch, blade axial chord length, trailing edge thickness and roughness of blade surface, angular deflection and relative velocity ratio.
- *Secondary losses* (Craig and Cox, 1970): caused by secondary flow structures mainly described by passage vortex, horseshoe vortex, trailing edge vortex and corner vortex. These losses are affected by the same parameters which have influence on profile losses plus blade height.
- *Annulus losses* (Craig and Cox, 1970 or Kacker and Okapuu, 1981): due to the passage of fluid in the gap between two blade rows. This loss is calculated for all the stages except for the last one.
- *Leakage losses* (Craig and Cox, 1970): caused by the unwanted passage of fluid above blade tip whose expansion does not contribute to power production. This kind of loss is mainly related to radial clearance, blade length and blade overlap. They can be null for the first stator blades only.
- *Disk windage losses*: due to velocity gradient in the clearance between stator and rotor disk walls. They are strongly affected by rotational speed and by both absolute disk clearance and disk diameter.
- *Kinetic energy loss*: it is the fraction of kinetic energy of discharge velocity which cannot be recovered with the diffuser. Usually it is defined with a coefficient φ_e smaller than unit respect to the kinetic energy of the axial component.

Exit flow angles are computed according with the flow condition: (i) Subsonic flow (Ainley and Mathieson, 1951), (ii) Supersonic flow with after expansion (Vavra, 1969), (iii) Supersonic flow with converging diverging nozzle (Deich, 1965). Experimental data from Deich (1965) are used for accounting of additional losses related to supersonic flows at blade exit, while an empirical correlation introduced by Macchi (1977) accounts for losses related to relative transonic velocities at rotor inlet.

3. SINGLE STAGE TURBINES

More than five hundreds of turbines are optimized varying SP and V_r and optimizing Ns . It is important to remember that, according to similarity rules, the results here obtained are representative of any other turbine stage with the same set of independent parameters. Different volumetric fluid behavior and molar mass affect variables like speed of revolution, pressure ratio, temperature and enthalpy drop and mass flow rate but they have small influence on the final optimal design which has the same geometrical aspect and the same isentropic efficiency. The validity of this assumption is verified in the test case presented in chapter 6.

In Fig 2.a each point represents the maximum efficiency attainable for any combination of SP , V_r and N_s . It is possible to notice that for each couple of SP and V_r parameters an optimal specific speed is found, while detrimental effects on the efficiency can be highlighted increasing the V_r and decreasing the SP . As a general consideration, there is a large range in SP and V_r where the optimal specific speed is between 0.1 and 0.15, as already pointed out in Macchi [6]. For small SP and for high V_r the optimal N_s decreases down to 0.05. This is justified by the presence of lower and upper bounds on some geometrical dimensions like minimum blade height and maximum h/D ratio at the discharge section. In these cases, a N_s value above 0.1 entails an almost unfeasible design of the blade with a strong increase of secondary losses due to fluid leakages and high flaring angles.

The maximum point for every curve is representative of the maximum attainable efficiency at optimized rotational speed and optimal results are collected in a contour map reported in Fig 2.b. For a better understanding of the effects occurring in the definition of optimized stage geometry, three parametric analyses are proposed in the following. The first focuses on the effect of N_s at fixed SP and V_r , while the other two are carried out varying one by one V_r and SP at optimized rotational speed.

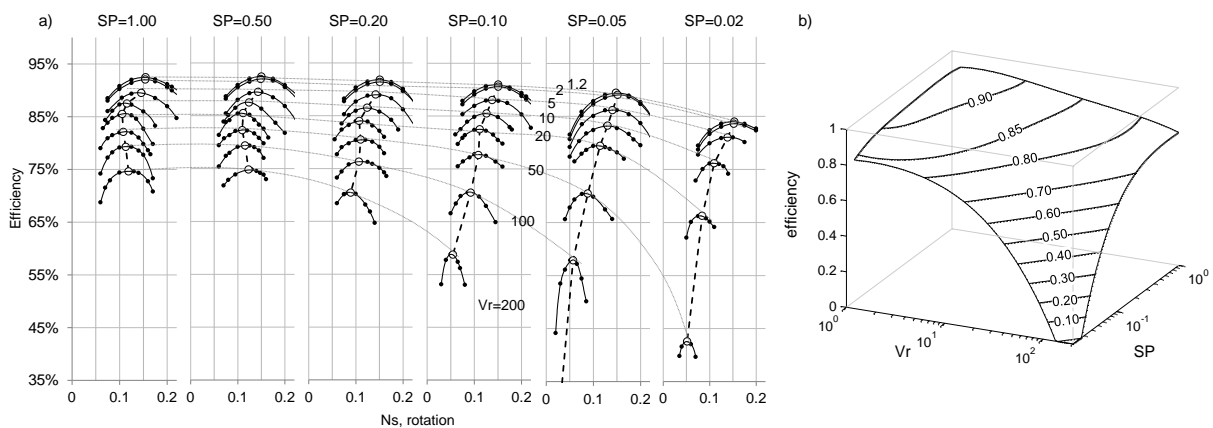


Figure 2 – a) Results for the single stage turbines. Black markers (●) are representative of the optimal turbine configuration for each combination of SP , V_r and N_s . White markers (○) identify the turbine designs at optimized rotational speed. b) map of efficiency for a single stage turbine at optimal N_s .

2.1. Effect of N_s

The first analysis regards the optimization of N_s for a single stage turbine at fixed SP and V_r equal to 0.4 m and 4 respectively (similar results are obtained for any other SP and V_r combination). Results are reported in Fig 3. In this case, both the volume flow rate at turbine exit and the isentropic enthalpy drop are constant and so N_s parameter has a direct effect on the speed of revolution and turbine mean diameter. At low specific speed the turbine stages have large mean diameter because of the necessity to maintain optimal u velocity above a certain value, to reduce the stage load.

Stages in this region have small h/D parameters and they are affected by high leakage and secondary losses. Velocity triangles are representative of impulse stages with an almost axial absolute velocity v_2 , thus the kinetic losses are minimized. Disk windage loss is noticeable because of the large diameter interested by this dissipation effect.

Increasing the rotational speed allows reducing both the secondary and leakage losses thanks to higher blades and a larger h/D ratio while the profile and the kinetic losses become more and more relevant. Optimal N_s value is equal to about 0.15 corresponding to well-proportioned turbine stages and an almost 50% reaction velocity triangle with an axial absolute velocity at turbine outlet.

On the other hand, for higher N_s values, the rotational speed is higher and the stage mean diameter is strongly reduced leading to high values of h/D parameter. Both the secondary and the leakage losses are

minimized but the distorted shape of the velocity triangles entails high values of discharge velocity which cannot be maintained in axial direction. As a consequence, kinetic energy losses increase because of the high value of v_2 and the presence of a tangential component which cannot be recovered by the diffuser. The trade-off between these opposite effects leads to the presence of an optimum value of Ns which yields the maximum efficiency.

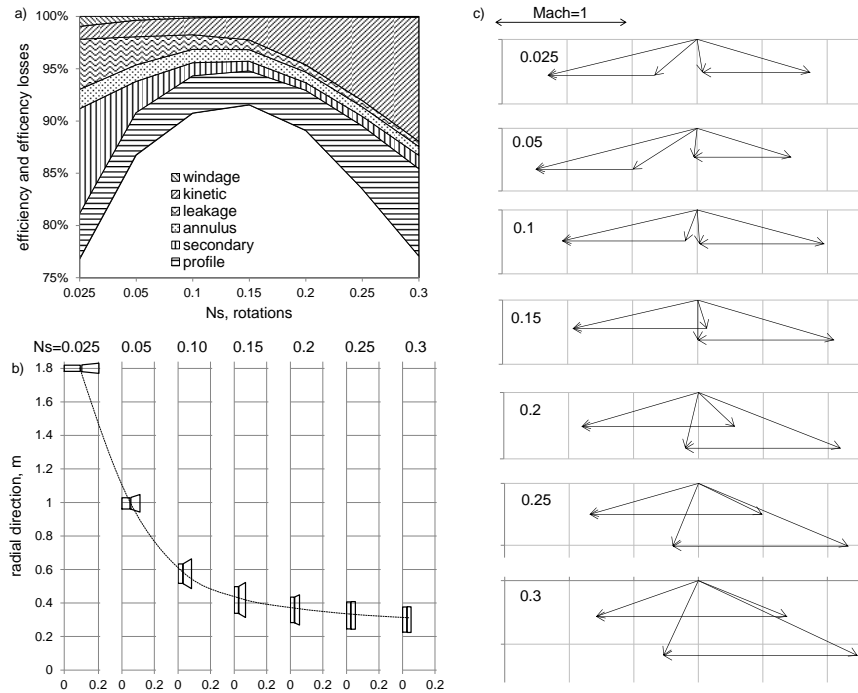


Figure 3 – Results of the parametric analysis varying Ns for a single stage turbine with $SP=0.04$ and $Vr=4$: a) Efficiency losses breakup, b) blade profiles and c) velocity diagrams. Mach numbers for inlet and outlet triangles are evaluated using the fluid SoS at stator and rotor outlet section respectively.

2.2. Effect of Vr at optimized Ns

Optimized results for single stage turbines, with different Vr and a fixed SP equal to 0.05, are presented in Fig 4. The breakdown of efficiency losses shows that the maximum attainable efficiency is a decreasing function of Vr . For really low volume ratios, namely values below twice than the $V_{r,crit} = 1.64$, velocity triangles are always subsonic, the load is limited and 50% reaction stages with high efficiency can be designed, h/D ratio is favourable, no flaring is required and both secondary and profile losses are small. Increasing Vr , Mach numbers greater than unit are obtained, in particular for v_1 and w_2 velocities, with an increase of profile losses. Converging-diverging stator nozzles are required for Vr above 5, while they are needed also for rotor blades for values beyond 10. For Vr greater than 20, a velocity close to the sonic one is obtained at w_1 vector with problems of shock waves at rotor inlet. The loss coefficient which takes into account this effect contributes to penalize the overall efficiency.

Velocity triangles become more and more distorted due to the necessity to handle higher volume flow variations and contextually maintaining a velocity vector v_2 close to the axial direction and limiting Mw_1 . Increasing the volume ratio involves a higher isentropic enthalpy drop and optimized stages with a higher peripheral speed u and a larger mean diameter in order to limit the stage load. Solutions move toward impulse stages with very small blade heights and high secondary losses due to unfavorable h/D ratio and disk windage loss increases due to larger surface interested by the phenomena. In conclusion, adopting Vr higher than 5 for a small SP single stage turbine entails a strong limitation in the attainable efficiency and multistage turbines should be considered in order to contain the load on each stage.

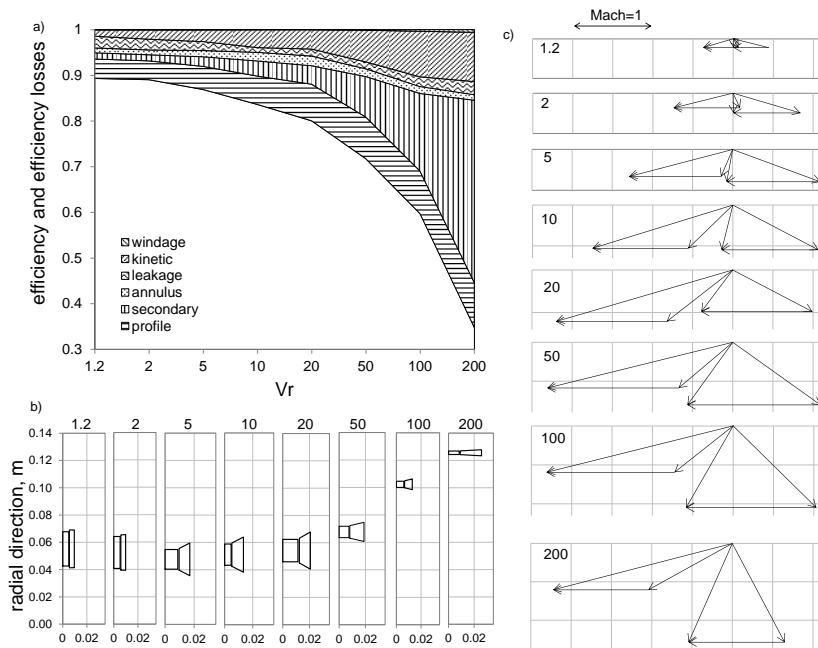


Figure 4 – Results of the parametric analysis for different single stage turbines having the same $SP=0.05$ m at the optimal specific speed: a) Efficiency losses breakup, b) blade profiles and c) velocity diagrams.

2.3. Effect of SP at optimized Ns

The last sensitivity analysis is realized for different single stage turbines with the same $V_r = 20$ but different SP and results are reported in Fig 5. Size parameter is varied from 0.02 m to 1 m which is a value representative of turbines close to the maximum size of normal ORC expanders. All the stages work with the same isentropic enthalpy drop but they notably differ in volumetric flow rate because of the quadratic dependence on the SP . Small size parameters lead to very small volume flow rates at turbine inlet section with a reduced passage area. Due to geometrical limits on minimum blade height and minimum δ_r/h ratio, the mean diameter gets smaller with an increase of rotational speed in order to maintain the optimal value of specific speed. These two effects result in a strong efficiency drop for small turbines with a considerable increase of secondary and leakage losses. Similar results are obtained for smaller V_r , even if the efficiency drop related to small SP decreases.

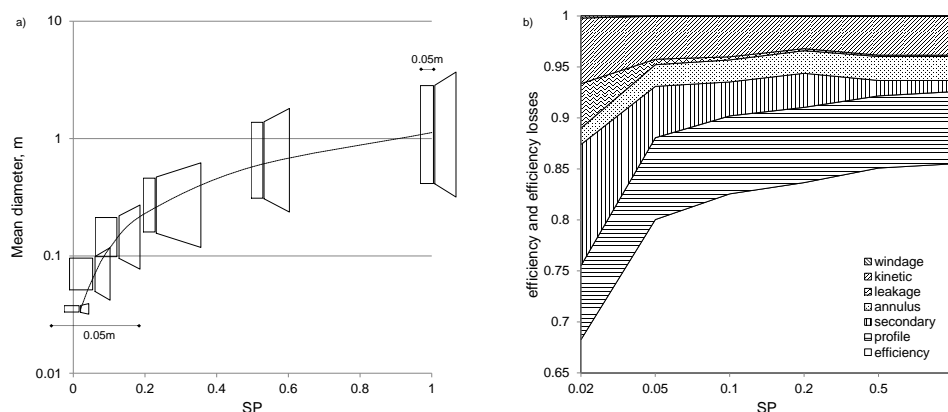


Figure 5 – Results of the parametric analysis for different single stage turbines having the same $Vr=20$ at the optimal specific speed: a) blade profiles and b) efficiency losses breakup.

4. MULTI STAGE TURBINE

In previous section, single stage turbines have been considered highlighting that their efficiency is strongly penalized by high volume ratios with even more marked reduction at small size parameters. In ORC field, multistage turbines are commonly adopted because they can achieve a higher efficiency exploiting the repartition of the whole volume flow variation on two or more stages. In this work only two and three stage turbines are considered because in most of the applications the benefit in adopting a higher number of stages is limited with an increase of component cost and a higher cost of electricity. For common applications, axial turbines are usually overhung with rolling bearing on the generator side of the shaft. This design allows an easy inspection of the turbine during maintenance operation and it is generally preferred even if it limits the number of stages to three because of rotodynamic issues. For turbines directly coupled to generator, a rotodynamic analysis performed by Exergy (Spadacini *et al*, 2013) shows that for a number of stages greater than three the natural frequencies of the turbine shaft get closer to 50 (or 60 Hz) with the risk of resonance during normal operation. A technical solution to increase the number of stages and the overall volume ratio without incurring in these problems is represented by radial outflow turbines.

The same analysis presented in the previous section is repeated for both two and three stage machines. The results, obtained optimizing the rotational speed for each turbine, are presented in terms of V_r and SP calculated for the overall expansion as though it is exploited by a single stage.

In Fig 6.a the comparison between the maximum efficiencies achievable for a single stage and a two stage turbine is reported while in Fig 6.b the increment of efficiency is displayed.

Increases of efficiency are not constant over the considered range of SP and V_r . The most relevant increments are obtained for high overall volume ratios and small SP . For V_r equal to 5 the efficiency increment is greater than 2 percentage points independently of SP value: an increment that usually justifies a more expensive device with the adoption of a two stage turbine.

Benefits are obviously larger for higher V_r and the efficiency increase reaches values above 10% for medium-small machines and volume ratios greater than 50. Last observation regards the possibility to extend the domain of solution: in particular for a SP lower than 0.02 m and V_r of 100 and 200 it is not possible to design a full-admission single stage turbine with a reasonable efficiency. The high load on such a small stage and the presence of geometric constrains entail a non-feasible execution of the optimization algorithm with variables values always outside of the efficiency losses correlation limits.

This problem does not arise for two stage turbines and the whole range of SP and V_r is explored.

Similar considerations can be done comparing two stages and three stage turbines. Results are reported in Fig 7.a and Fig. 7.b. The attainable efficiency increase is lower than in the previous case but, once again, notable advantages are highlighted for high volume ratios and small turbines. Finally, a graphical comparison of the performance maps for the single stage, the two stage and the three stage turbine are reported in Fig 6.c and 7.c.

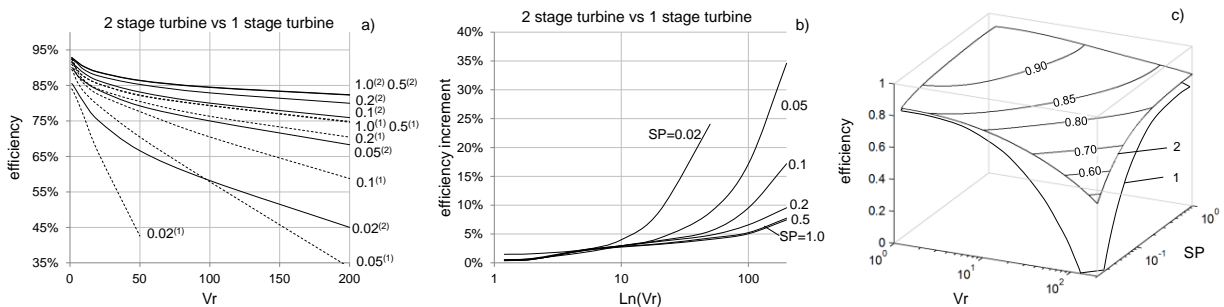


Figure 6 - Comparison between attainable efficiency adopting a two stage turbine instead of a single stage turbine (a) and corresponding efficiency increases (b). Graphical representation of maps of efficiency (c).

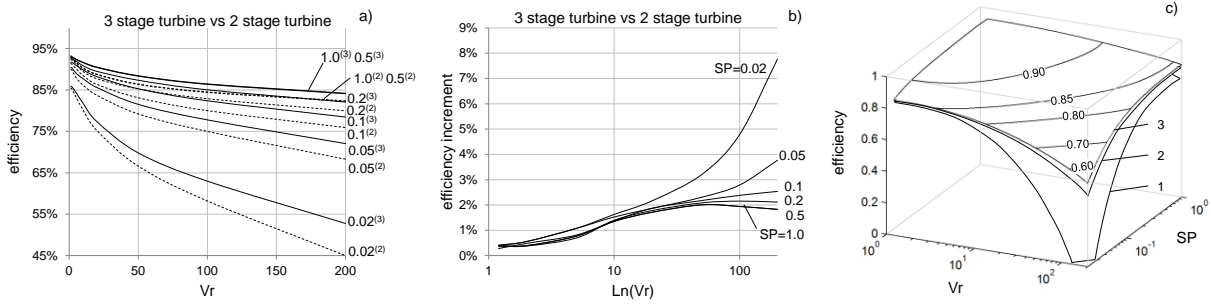


Figure 7 - Comparison between attainable efficiency adopting a three stage turbine instead of a two stage turbine (a) and corresponding efficiency increases (b). Graphical representation of maps of efficiency (c).

5. NUMERICAL CORRELATIONS OF EFFICIENCY

The set of data of maximum attainable turbine efficiency are regressed with a OLS regression performed in Gretl. The most suitable terms function of SP and V_r are selected and a process of exclusion of the less influencing ones is carried out in order to obtain the maximum value of the adjusted R^2 coefficient. All the proposed correlations have a functional form reported in eq 2 while the numerical values of the retrieved coefficients can be found in Table 1.

$$\eta = \sum_{i=0}^{15} A_i F_i \quad (2)$$

Table 1 - Regressed coefficients to be used in the correlation of turbine efficiency for single, two and three stage turbines

Stages number		1	2	3
n	F_i	A_i		
0	1	0.90831500	0.923406	0.932274
1	$\ln(SP)$	-0.05248690	-0.0221021	-0.01243
2	$\ln(SP)^2$	-0.04799080	-0.0233814	-0.018
3	$\ln(SP)^3$	-0.01710380	-0.00844961	-0.00716
4	$\ln(SP)^4$	-0.00244002	-0.0012978	-0.00118
5	V_r	-	-0.00069293	-0.00044
6	$\ln(V_r)$	0.04961780	0.0146911	-
7	$\ln(V_r)^2$	-0.04894860	-0.0102795	-
8	$\ln(V_r)^3$	0.01171650	-	-0.0016
9	$\ln(V_r)^4$	-0.00100473	0.000317241	0.000298
10	$\ln(V_r) \ln(SP)$	0.05645970	0.0163959	0.005959
12	$\ln(V_r)^2 \ln(SP)$	-0.01859440	-0.00515265	-0.00163
12	$\ln(V_r) \ln(SP)^2$	0.01288860	0.00358361	0.001946
13	$\ln(V_r)^3 \ln(SP)$	0.00178187	0.000554726	0.000163
14	$\ln(V_r)^3 \ln(SP)^2$	-0.00021196	-	-
15	$\ln(V_r)^2 \ln(SP)^3$	0.00078667	0.000293607	0.000211
Adjusted R^2		0.99790	0.99935	0.99954

6. MODEL VALIDATION

In this section an example about the capabilities of the proposed correlations is provided. In particular, the aim is underling how the volume ratio and the dimension of a real turbine stage can affect the turbine performance. To validate the proposed methodology two fluids (R125 and hexane) are considered and two turbine sizes (isentropic power of 5 MW and 250 kW) are analysed. Both fluids expand from a temperature of 155°C down to a pressure equal to the saturation at 30°C as representative of a low temperature heat source application with a cooling water condenser. A supercritical cycle is considered for R125 with a turbine inlet pressure of 36,2 bar while a saturated cycle is imposed for hexane according to its high critical temperature and the overhanging saturated vapour line which allows for a dry expansion. In Table 2 the main thermodynamic properties of the fluids are reported with other quantity of direct interest for the evaluation of turbine efficiency. Both R125 and hexane show real gas effects at turbine inlet with a compressibility factor equal to 0.85 and 0.79 respectively while a behaviour closer to ideal gas is founded at turbine discharge with values of 0.91 and 0.99. The overall expansion coefficients (γ) are different from the value assumed for the ideal gas in the previous sections and are equal to 1.10 and 1.06. The two turbine stage differ in both the Vr and the SP . The expansion of R125 shows a very limited variation of density because of the high condensation pressure and the high degree of superheating. On the contrary hexane according to the corresponding state principle (Poling and Prausnitz, 2000) has a lower condensing pressure (a vacuum pump is required at the condenser to remove air leakage) and a larger volume flow rate variation across the turbine. Hexane mass flow rate is lower than the R125 one but the SP is larger because of the very low density at turbine outlet section. Using the correlation of efficiency previously described the turbine efficiency is calculated: R125 turbine shows a very high (90%) efficiency while for hexane the presence of supersonic flows and limitation of flaring angles play a detrimental role in the final efficiency which is close to 83%. In this case the positive effect of a larger SP is not sufficient to compensate the difficulties in realizing a high Vr stage. Reducing the size of the turbines the presence of geometrical constraints (minimum o/s and maximum o/b) bound the final solution and leads to a decrement of about 3 point of efficiency confirming the overall trend presented in previous analyses.

Table 2 – Characteristics of the considered fluids and main results of the analysis

	R125		hexane	
critical properties				
MM	120.02		86.18	
T_{crit} , °C	66.02		234.67	
p_{crit} , bar	36.18		30.34	
expansion data				
W_{is} , kW	5000	250	5000	250
p_{in} , bar	36.200		8.290	
p_{out} , bar	15.685		0.250	
ΔT_{sh} , °C	88.980		0	
m , kg/s	237.71	11.89	40.78	2.04
$V_{out,is}$, m ³ /s	3.79	0.19	55.24	2.76
specific parameters				
V_r	2.293	2.293	34.389	34.389
SP , m	0.162	0.036	0.397	0.089
$\eta_{is}^{correlation}$	0.903	0.877	0.833	0.799
Axtur results				
η_{is}^{Axtur}	0.907	0.872	0.828	0.795
RPM	6000	31000	5500	2800
Ns	0.111	0.129	0.104	0.118
D , m	0.420	0.086	0.900	0.180

The four turbines are hence designed in Axtur considering real fluid properties (i.e. compressibility effects, Mach numbers, etc.) and optimizing the rotational speed. It is possible to highlight a good accordance among the efficiencies calculated with the two methods confirming the validity of the proposed approach. The optimal rotational speed, the optimal N_s and the resulting optimal diameter are reported in table as well.

7. CONCLUSIONS

In this work three correlations of performance are provided for axial turbines with a maximum number of stages equal to three. This study aims to complete the work done in previous publications about the estimation of maximum efficiency attainable with 1D optimization techniques. The correlations can be used for a preliminary estimation of turbine performance in the numerical optimization of ORC even if the results are affected by inaccuracy mainly related to the quality of efficiency losses correlations and the simplified volumetric behavior assumed in the generation of the performance maps.

On the basis of the present analyses the following conclusions can be addressed:

- Rotational speed must be always optimized since relevant efficiency decrements are highlighted for values lower and higher than the optimal one. The use of slow generators with more than two couple of poles is recommended for large turbines while a gearbox or a power electronic system is required for small size machines having an optimal rotational speed higher than 3000 RPM;
- Geometrical similarity cannot be always verified because of the presence of geometrical constraints related to blade machining and limits of loss correlations. Decreasing the size of the turbine the maximum efficiency is reduced mainly because of the increasing of profile and leakage losses;
- Isentropic volume ratio strongly affects stage design and efficiency. A single stage turbine with high V_r is penalized because of the presence of big flaring angles, supersonic flows and high kinetic losses and it is advantageous to split the expansion in two or more stages
- The contemporary presence of small SP and high VR strongly penalizes the attainable efficiency of single stage machines and suggests the adoption of multi-stage solutions.

NOMENCLATURE

Variables

A	coefficients for the efficiency correlations	(-)
b	axial chord	(m)
β	pressure ratio	(-)
η	efficiency	(-)
F	terms of the efficiency correlations	(-)
φ_E	kinetic energy recovery factor	(-)
γ	ratio of specific heats	(-)
k_{is}	Isentropic load coefficient	(-)
h	enthalpy or blade height	(m)
h/D	blade height-blade mean diameter ratio	(-)
m	mass flow rate	(kg/s)
N_s	specific speed	(-)
o	blade channels throat	(m)
p	pressure	(bar)
r	radius	(m)
ρ	density	(kg/m ³)
s	blade step	(m)

SP	Size Parameter	(m)
T	temperature	(°C)
V	volume flow rate	(m ³ /s)
v	absolute velocity	(m/s)
u	mean peripheral speed	(m/s)
V _r	volume ratio	(-)
W	power	(kW)
w	relative velocity	(m/s)

Subscripts

crit	critical property
eva	evaporation
cond	condensation
is	isentropic
re	real
T-S	Total to Static

REFERENCES

- Ainley, D.C., Mathieson, G.C.R., 1951, A method of performance estimation for axial-flow turbines, *British Aeronautical Research Council*, Vol. R&M 2974.
- Astolfi, M., Romano, M., Bombarda, P., Macchi, E., 2014a, Binary Orc Power Plants For The Exploitation Of Medium-Low Temperature Geothermal Sources. Part A Thermodynamic Optimization, *Energy*.
- Astolfi, M., Romano, M., Bombarda, P., Macchi, E., 2014b, Binary Orc Power Plants For The Exploitation Of Medium-Low Temperature Geothermal Sources. Part B Techno-Economic Optimization, *Energy*.
- Baljè, O.E., Binsley, R.L., 1968, Axial turbine performance evaluation: part B - optimization with and without constraints, *ASME Journal of Engineering for Power*. pp. 349-360.
- Craig, H.R.M., Cox, H.J.A., 1970, Performance estimation of axial flow turbines, *Proceedings of the institution of mechanical engineers*. pp. 407-423. Vol. 185 32/71.
- Deich, M.E., Filippov, G.A., Lazarev, L.Y., 1965, Atlas of axial turbine blade characteristics. Moscow, *Maschinostromie Publishing House*.
- Dixon, S. L., 1998, Fluid Mechanics, *Thermodynamics of turbomachinery*, Fifth Edition, Eselvier.
- Kacker, S.C., Okapuu, U., 1981, A mean line prediction method for axial flow turbine performance prediction, *ASME paper 81-GT-58*.
- Lozza, G., Macchi, E., Perdichizzi, A., 1981, On the influence of the number of stages on the efficiency of axial flow turbines, *Journal for Engineering for Power*.
- Macchi, E., 1977, Design criteria for turbines operating with fluids having a low speed of sound. Closed cycle gas turbines, Von Karman Institute for Fluid-dynamics, lecture series 100.
- Macchi, E., Perdichizzi, A., 1981, Efficiency prediction for axial flow turbines operating with non-conventional fluids, *J. Eng. Gas Turbines Power*.
- Poling, E. B., Prausnitz, J. M., O'Connell. J. P., 2000, Properties of Gases and Liquids, Fifth Edition., *McGraw-Hill Education*.
- Smith, M. H., 1965, A simple correlation of turbine efficiency, *Journal of Royal Aeronautical Society*.
- Spadacini, C., Rizzi, D., Saccilotto, C., Salgarollo, S., Centemeri, L., 2013, The Radial Outflow Turbine Technology: Impact On The Cycle Thermodynamics And Machinery Fluid- And Rotordynamic Features. *2st International Seminar on ORC Power Systems*, Rotterdam.
- Vavra, M.H., 1969, Axial flow turbines, *Von Karman Institute for Fluid-dynamics*, lecture series 15.
- Xodo, G. L., Spadacini, C., Astolfi, M., Macchi, E., 2013, Comparison Of Axial And Radial Outflow Turbines In A Medium-High Enthalpy Waste Heat Recovery Orc Application. *2st International Seminar on ORC Power Systems*, Rotterdam.

VOLUMETRIC EXPANDER VERSUS TURBINE – WHICH IS THE BETTER CHOICE FOR SMALL ORC PLANTS?

Andreas P. Weiß

Competence Center for CHP Systems,
University of Applied Sciences Amberg-Weiden,
Kaiser-Wilhelm-Ring 23, 92224 Amberg, Germany
e-mail: a.weiss@oth-aw.de
Web page: <http://www.oth-aw.de>

ABSTRACT

Since the steam turbine replaced the steam reciprocating engine by the end of 19th century it has been the only expander type in Clausius Rankine Cycle (CRC) and Organic Rankine Cycle (ORC) power plants at least above 1 MW_{el}. Positive displacement expanders like scroll or screw machines have often been applied for smaller units – in particular below 100 kW_{el}. One reason for this is that in cooling or compressed air technology these machines are cheaply available as compressors which can be “easily” converted to expanders. In contrast, up to now small turbines are rather seldom in this market segment. One goal of this paper is to discuss whether there are other reasons than those already mentioned to justify the choice of volumetric expanders for small ORC plants and to clarify whether small turbines provide benefits which could not have been used in the past just due to the lack of appropriate machines.

The paper briefly introduces the working principles of positive displacement and turbine expanders and evaluates them concerning their application in small ORC-plants. In the author’s opinion, the advantages of turbines outweigh their disadvantages. Nevertheless, in the following the decision between e.g. impulse or reaction type, axial or radial, single or multistage turbine has to be made. The paper discusses and explains the “pro and cons” of these turbine types. This paper aims to identify the best expander for a given application and in addition evaluates the different expanders with regard to their suitability for a so-called “micro-expander-construction-kit” which should help to design and build an appropriate expander for any given application out of a wide range of boundary conditions and working fluids. Here, the single stage impulse turbine was identified as the best compromise

1. INTRODUCTION

By the end of 19th century the steam turbine had superseded the steam reciprocating engine in power generation as well as vessel propulsion because of its superiority with regard to power density and higher allowable steam temperatures and thus higher cycle efficiencies. Since that time, the turbine has been dominating the power generation at least above 1 MW power output. It is generally accepted that turbines outclass volumetric expanders regarding large power output and processing huge mass flows. However, on the lower end of the power generation range, i.e. 1 MW or even below 100 kW power output the situation seems to be different. For small ORC or CRC units very often volumetric expanders are applied (Figure 1, see Branchini et. al., (2013)). Many publications e.g. Glavatskaya *et.al* (2012), Lemort *et. al.* (2013) postulate that for small power output or rather small mass flow a piston, screw, scroll or rotating vane expander would be the better choice regarding efficiency, rotational speed, size, costs etc.. This statement will be discussed in the following.

The author is convinced that besides the above-mentioned reasons there is another very simple reason for the frequent use of small volumetric expanders for small plants: These machines were cheaply available in the past from refrigeration or compressed air technology where they acted as compressors. Compared to small compressors, small turbines appear rather seldom. There is one exception: Small radial inflow, (axial outflow) turbines which are typical for automotive

turbochargers. However, these turbines are designed for rather low expansion ratios (ER). Furthermore, they are only available as turbocharger units equipped with oil bearings which rely on the internal combustion engine's oil system. Thus, the application of a turbocharger turbine as ORC expander is a bit elaborate.

The goal of the paper is to determine whether turbines can be a reasonable choice for small ORC units in the range of 3 to 100 kW_{el}. This question is in particular interesting for the development of a „micro-expander-construction kit“ for small ORC expanders which has to cover different temperature levels, mass flow rates, as well as fluids.

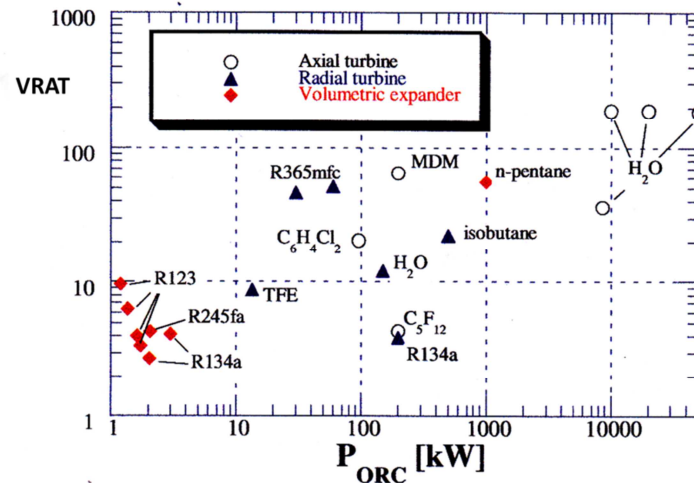


Figure 1: Actual VRAT values of existing ORC expanders with specified fluids (Branchini *et. al.*, 2014)

Figure 1 suggests that the volumetric expanders seem to dominate the power range below 10 kW. Furthermore, a first limitation of the volumetric expander can be identified: It is obviously restricted to small volumetric expansion ratios VRAT < 10. This is due to their built-in volume ratio. This geometrical volume ratio is for screw or scroll expanders about 5 and in the range of 10 for piston expanders (Lemort *et. al.*, 2013). However, higher expansions ratios may be advantageous e.g. for automotive waste heat recovery where small heat fluxes are combined with rather high temperatures or temperature differences, respectively. High temperature differences in an ORC usually result in high volume flow ratios for the expander.

2. VOLUMETRIC VERSUS DYNAMIC EXPANDER

2.1 Selection Criteria for Small Expanders

There are many criteria which may influence the choice of an expander for an ORC plant (Table 1). The design engineer tends to focus on efficiency, whereas for the „end-user“ the return of investment is the most important issue. Thus, beside efficiency, costs are a major criterion, which are strongly influenced by the design of the expander, its complexity, number of parts, the expected wear maintenance etc..

Table 1: Selection criteria for small ORC expanders

Economic Criteria	Technical Criteria
<ul style="list-style-type: none"> costs 	<ul style="list-style-type: none"> efficiency
<ul style="list-style-type: none"> availability on market 	<ul style="list-style-type: none"> rotational speed (bearing, generator)
<ul style="list-style-type: none"> reliability 	<ul style="list-style-type: none"> lubrication (pollution of working fluid)
<ul style="list-style-type: none"> maintainability 	<ul style="list-style-type: none"> sealing
	<ul style="list-style-type: none"> power level (volume flow rate)

	<ul style="list-style-type: none"> • working fluid
	<ul style="list-style-type: none"> • wear
	<ul style="list-style-type: none"> • complexity
	<ul style="list-style-type: none"> • adaptability (fluid, VRAT etc.)

Furthermore, if the focus is not only on one ORC unit for one set of boundary conditions but a „micro-expander-construction-kit“-system with the intention to cover different levels of heat source/heat sink temperature, power output and different fluids, the adaptability of the expander design has also to be taken into consideration.

2.2 Comparison of Working Principles

The working principles of a volumetric and a dynamic expander are quite different (Figure 2). Volumetric expanders use the expansion work directly by changing the volume of a working chamber. Therefore, they deal with high pressures, big forces and small velocities of flow and machine parts. The built-in volume ratio and the swept volume are the main design parameters of volumetric expanders which limit their reasonable application range. The built-in volume ratio determines the specific work and the volume flow ratio (VRAT) which can be implemented per stage. A multi-stage arrangement for high VRAT is conceivable, but also elaborate due to additional piping, clutches etc.. The swept volume in combination with the rotational speed results in the volume flow rate which can be processed. Furthermore, both parameters determine the required size of the expander. Usually, due to their relative low rotational speed volumetric expanders can drive a standard generator directly without a gear. Part load (p. l.) e.g. reduced mass flow in an ORC can easily be handled by adjusting the rotational speed. The working chamber of the volumetric expander must be closed. Hence, it needs a contact sealing, which generates friction losses and wear and requires lubrication.

In a first step, dynamic expanders i.e. turbines convert the vapor’s internal energy into kinetic energy by means of nozzles. Therefore, pressure and forces are rather small but flow velocities are high. In a second step the kinetic energy is converted into mechanical work by turning the flow within the rotor blading. The circumferential speed u of the wheel has to be in the magnitude of the flow velocity i. e. high. The high circumferential velocity u in combination with a small diameter D leads to a necessary rotational speed usually in the range of 10,000 to 100,000 rpm or even more ($u \sim n \cdot D$). Thus, turbines cannot be coupled directly to a standard generator. In addition, a gear or a high-speed generator must be used. In a turbine the fluid volume change during expansion is not just implemented by changing a chamber volume but by simultaneously increasing flow velocity and area. High expansion ratios can be implemented even in a single stage if supersonic flow is accepted, which leads to lower achievable efficiency. This is the reason why a turbine design with fixed main dimensions (e. g. diameter, length) can cover a wide range of boundary conditions (mass flow rate, expansion ratio etc.) just by adapting nozzle length and area, blade height and/or degree of admission. Partial admission (p. a.) is a means to handle part load (see chapter 3). In a turbine there are no contact seals. Hence, no lubrication is necessary. However, there is a certain leakage which cannot be avoided. Due to the high flow velocities, the absence of valves and the continuously working principle, turbines can process high volume flows in a small construction volume.


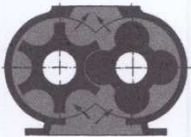

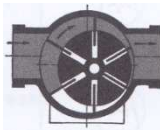
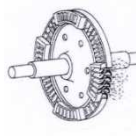


volumetric expanders $work = \int v dp$				dynamic expanders $work \sim u^2$		
						
piston	screw	scroll	vane	axial	cantilever	radial

Figure 2: Expander types

2.3 Construction Types of Volumetric Expanders (Figure 2)

Piston: The classical volume expander is the reciprocating piston expander. It can show high expansion efficiencies (e.g. 70% in Eilts *et.al.* (2012)). The achievable volume ratios of volumetric expanders are in the range of 10 (Lemort *et. al.*, 2013) or slightly higher. However, it needs a lot of bearings and in addition inlet and outlet valves which makes the design complex and costly. Liquid in the cylinder can cause damage. Thus, the piston expander should not be applied for wet expansion. The machine and the flow are oscillating. Hence, the machine needs balancing and is prone to vibrations.

Screw: The screw expander expands the fluid continuously. It does not need any valves but at least four bearings for the two rotors. The rotors are not in contact with each other. Lubrication is required for sealing purposes. Even lubricated the necessary rotational speed is the highest for volumetric expanders. Without lubrication the rotational speed must be high (> 10,000 rpm). Therefore, standard generators are not suitable. Possible volume ratios (VRAT) are in the range of 5, efficiencies of around 50% (Eilts *et.al.*, 2012) might be acceptable. A certain amount of wetness can be handled by a screw expander.

Scroll: A scroll expander is a comparatively simple device: it consists of two spirals, one of which is rotating. It can be mounted directly on the shaft of the generator avoiding any additional bearing. Volume ratio is below 5 (Lemort *et. al.*, 2013). Wang *et. al.* (2009) reported measured efficiencies in the range of 70% even for a quite small machine (< 1 kW). Droplets are no problem for a scroll expander.

Vane: The rotating vane expander is working continuously with a rather small rotational speed. Built in volume ratios are rather small (VRAT < 5). The vanes are in contact with the casing. Lubrication is required, which can spoil the working fluid. Furthermore, high friction losses and wear have to be expected. Rotating vane air motors are well known and widely used in industry. Their efficiencies are usually in the range of 30-40%. However, Badr *et.al.* (1984) report measured efficiencies of 80%.

Dry Runners: All the discussed volumetric expanders are available as dry runners, i. e. without lubrication, to avoid the spoiling of the working fluid. Usually, dry runners suffer from higher friction losses and leakages. Therefore, their efficiency is lower than that of their lubricated counterparts.

2.4 Construction of Small Dynamic Expanders - Turbines

Turbines are simple devices (Figure 2), comparable to volumetric expanders in terms of design. The turbine shaft needs two bearings. For small single stage turbines the rotor wheel can be mounted directly on the shaft of the high-speed generator. Because of the absence of contact seals, no lubrication is needed which could spoil the working fluid. Droplets at the end of expansion cause erosion in turbines. However, most of the applied organic working fluids show an isentropic or even dry saturation vapor curve. So, generally droplets are no problem in ORC applications. Small turbines suffer from a high relative surface roughness, big relative clearances and a big relative trailing edge thickness, etc.. Thus, they do not achieve efficiencies in the range of their bigger counterparts. All these statements hold true for axial and radial turbines of reaction or impulse type as well. The advantages and disadvantages of the different types of turbines will be discussed in more detail in chapter 3.

2.5 Which Expander Type for the “Micro-Expander-Construction Kit?”

Table 2 summaries the results of this first evaluation. As long as efficiency is not the main focus or the only issue of consideration and as long as high speed generators are available, the turbine can compete with any volumetric expander. From the author’s point of view its main advantages are its simplicity, the possibility to adjust one basic turbine design quickly to different boundary conditions (e. g. VRAT) without changing the overall size and finally, that lubrication in contact with the working fluid can be avoided. Already Quoilin *et. al.* (2012) concluded that a turbine does have the broadest application map of all expander types. Hence, the author’s research group (Weith *et. al.*, 2013) decided to build up the ORC “micro-expander-construction kit” based on turbines.

Table 2: Evaluation of small expander types

expander type	η	VRAT	n	p. l.	size	adapt-ability	lubri-cation	wear	wet-ness	vib-ration	com-plexity	Σ
volumetric												
piston	2	1	2	2	0	0	0	1	1	0	0	9
screw	1	0	1	2	0	0	0	2	2	2	0	10
scroll	1	0	2	2	1	2	0	1	2	2	2	15
vane	0	0	2	2	1	1	0	0	2	2	1	11
dynamic												
	1	2	0	1	2	2	2	2	1	2	2	17

3. COMPARISON AND ASSESSMENT OF DIFFERENT TURBINES

Although the decision was made in favor of a turbine expander there are still many different types of turbines e. g. impulse or reaction turbines, axial or radial turbines and radially inflow or outflow turbines which can be considered. In the following, these turbines will be compared and evaluated regarding their applicability as a basis for the “micro-expander-construction kit”.

3.1 Impulse versus Reaction Turbine

Figure 3 compares the blading and the velocity triangles of an impulse stage and a 50% reaction stage. In an impulse stage the nozzles convert the entire required stage enthalpy drop Δh_{is} into kinetic energy. Thus, the nozzle exit velocity c_1 is very high. The rotor blades turn the flow without changing the magnitude of velocities ($|w_1| = |w_2|$). The pressure p in the rotor blading remains constant. In a 50% reaction stage the conversion of the stage enthalpy drop is equally distributed between nozzle and rotor blades. Thus, the nozzle exit velocity c_1 is not as high as in the impulse stage. The following acceleration ($|w_2| > |w_1|$) and pressure drop in the rotor blades has the same magnitude as in the nozzle blades. These differences in velocity triangles result in certain differences in stage characteristics:

- Higher velocities mean higher losses: the efficiency potential of an impulse stage is lower than that of a reaction stage.
- Thanks to the constant pressure via the rotor blading, impulse stages can be designed to work with partial admission (p.a.). This means that a portion of the total arc of the annulus is blocked off. Hence, the flow impinges only on-parts of the rotor blading. Partial admission is an option to implement part load with reasonable efficiency or to build turbines for very small power output without requiring blading heights that are too small to be manufactured with sufficient accuracy. Additionally, in this respect the impulse rotor blading benefits from the circumstance that it is subjected to the minimum pressure in the ORC plant and thus works with the maximal volume flow rate occurring in the cycle.
- The pressure drop via the reaction rotor blading generates non-negligible axial thrust. It either has to be balanced or the bearing must be able to withstand it.
- Furthermore, due to the pressure drop, the reaction stage efficiency is more sensitive to radial clearances.
- Applying the simplified Euler equation (1) for turbo machines ($u_1 = u_2$)

$$\Delta h_{blading} = u * (c_{u1} - c_{u2}) \quad (1)$$

it becomes obvious (Figure 3), that

$$\Delta h_{blading,impulse} = 2 * u^2 \text{ and } \Delta h_{blading,reaction} = 1 * u^2 \quad (2), (3)$$

Since $\Delta h_{blading} \approx \Delta h_{is}$ it follows that

$$u_{opt,impulse} = \frac{1}{\sqrt{2}} * \sqrt{\Delta h_{is}} \text{ and } u_{opt,reaction} = 1 * \sqrt{\Delta h_{is}} \quad (4), (5)$$

i.e. for an identical stage enthalpy drop Δh_{is} the impulse stage requires only a significantly lower optimal circumferential speed ($u_{opt,impulse} = u_{opt,reaction} / \sqrt{2}$) than the reaction stage. This is a big advantage of the impulse stage applied as a small expander.

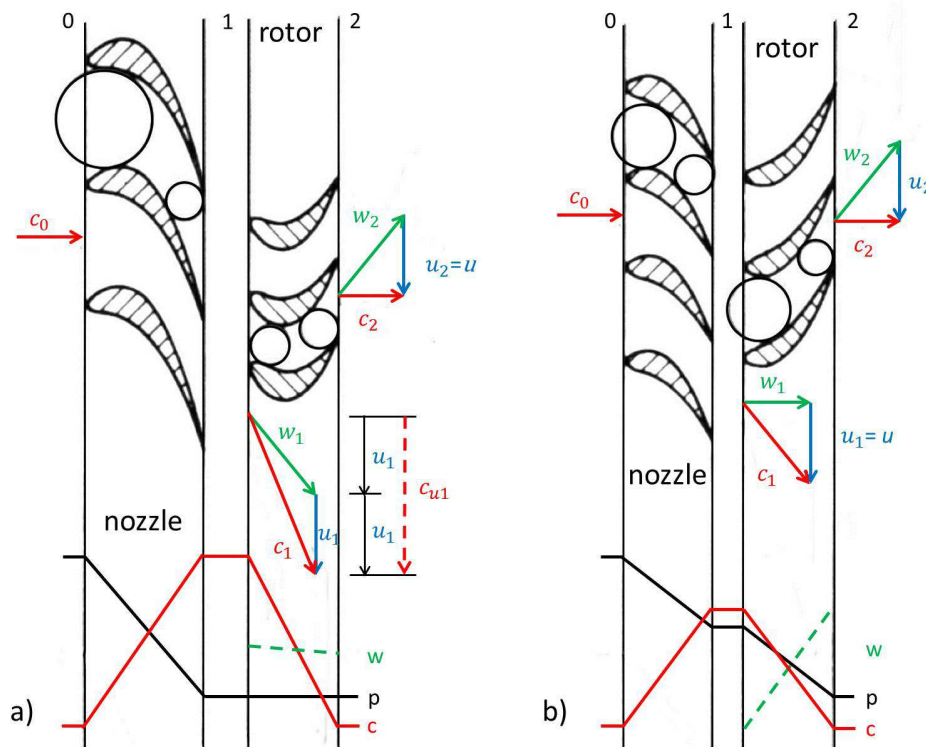


Figure 3: Comparison impulse (a) and reaction stage (b)

It has often been stated in literature - e. g. Bao and Zhao (2013) - that radial inflow turbines are better suited for low mass flow rates and high pressure ratios than axial ones. This is correct in principle. Nevertheless, for radial inflow turbines which are usually designed as reaction stages a maximal expansion ratio in the range 8 to 10 is reasonable (Moustapha *et al.*, 2003). For higher values not only the nozzles but also the impeller would choke. That is why Bao and Zhao (2013) or Quoilin *et al.* (2013) limit the rotor relative exit Mach number to 0.85 in their considerations. However, impulse stages can even cope with supersonic relative Mach number ($Ma_2 \approx Ma_1$) with acceptable efficiencies of 70%-80% (Vernau, 1987). As a consequence, very high stage expansion ratios $ER > 100$ (Rinaldi *et al.*, 2013) or volume flow ratios (VRAT) can be put in practice.

Table 3: Impulse versus reaction turbines

turbine axial – cantilever - radial	impulse	reaction
efficiency potential (ts) \approx	80%	90%

turbine	η	VRAT	n	axial thrust	p. a.	leakages	minimal power/size	Σ
impulse	0	2	2	2	2	2	2	12
reaction	2	0	0	0	0	0	0	2

To summarize (Table 3), for small power output the impulse turbine (axial or radial) is obviously the more flexible and also a simpler approach for a micro ORC expander. The classical radial (reaction) inflow turbine might be more efficient for certain tasks but is probably less suitable for an ORC “micro- expander-construction-kit”. The impulse turbine can be easily adapted to a wide range of

mass flow rate, fluids, inlet and exit pressures just by changing the nozzle area (-ratio), the blade height and/or the degree of admission.

3.2 Axial versus Radial Turbine (Figure 4)

Equation (6) below is valid for all types of turbines and shows the Euler work $\Delta h_{blading}$ processed in the rotor as difference between the squared rotor inlet (1) and exit (2) velocities (compare Figure 3). For an axial turbine, in particular for a small one with short blades the Δu^2 -term is almost or exactly zero.

$$\Delta h_{blading} = \frac{1}{2} * [(c_1^2 - c_2^2) - (w_1^2 - w_2^2) + (u_1^2 - u_2^2)] \tag{6}$$

If the flow through a turbine wheel is subjected to a significant change in radius e.g. a change in circumferential velocity, the Δu^2 -term contributes a substantial part to the overall enthalpy conversion like in a radial inflow reaction turbine. As a result, the radial inflow turbine can process higher expansion ratios than an axial stage without getting transonic or supersonic.

The radial inflow cantilever turbine benefits from this Δu^2 -effect as well – however to a lesser extent. The author’s research group has recently developed small cantilever „quasi-impulse“ turbines which do not work with acceleration in the rotor ($|w_1| = |w_2|$). Nevertheless, caused by the Δu^2 -term there is a small amount of reaction. Thus, the nozzles are slightly relieved. The Mach numbers at nozzle exit and rotor inlet remain smaller than for the axial counterpart. Although a small amount of reaction is used, this type of cantilever turbine can be applied using partial admission. Of course, this benefit does have a disadvantage: the cantilever „quasi-impulse“ turbine requires a slightly higher circumferential speed.

The significant advantages of radial outflow turbines are mainly twofold:

1. a flow direction from a smaller to a bigger radius corresponds to an area increase of the flow path which is helpful for expanding organic fluids with high volume flow ratios (VRAT)
2. centrifugal flow direction easily enables a multi stage arrangement if the expansion ratio of one stage is not sufficient.


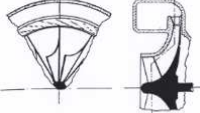
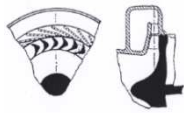

turbine type								
axial	radial inflow		cantilever inflow		cantilever outflow			
								
turbine type	η	VRAT	n	axial thrust	p.a.	multi stage	complexity	Σ
axial ($r \approx 0$)	1	2	2	2	2	2	2	13
radial inflow ($r \approx 0,5$)	2	0	0	0	0	0	1	3
cantilever inflow ($r > 0$)	2	1	1	1	2	0	2	9
cantilever outflow ($r \approx 0,5$)	2	2	0	0	0	2	1	7

Figure 4: Axial versus radial turbine

One main disadvantage of the radial outflow turbine stage is the fact that the Δu^2 -term is working against the others terms (equation 6). I.e. in a radial outflow turbine the velocities (absolute, circumferential) and Mach numbers must be higher than in its inflow competitor for the same enthalpy drop.

The construction of a single stage axial turbine or a radial inflow cantilever turbine can be very simple. The manufacturing of the nozzle rings and the integral wheels does not need a 5-axis milling machine like for a radial inflow turbine. At least for small expanders the design and arrangement of a radial out-flow stage seems to be more challenging. Therefore, it was decided to rely on the single-stage impulse turbine for the “micro-expander-constructing-kit”.

3.3 The Micro Turbo Generator Concept

Figure 5 displays the developed micro turbo generator concept which relies on the “micro expander construction kit”. Its main features are:

- hermetically sealed turbine-generator (3 -100 kW_{el}, implemented with 5 manufactured sizes)
- single stage axial impulse turbine (10.000 – 70.000 rpm)
- integrally manufactured turbine wheel (Ø 50 – 250 mm)
- permanent magnet high-speed generator
- turbine wheel directly mounted on generator shaft: just one set of bearings required, no gear, no coupling
- roller bearings, slide bearings or aerodynamic bearings - depending on task
- compact design, low material usage
- design can be easily adapted to different boundary conditions, fluids etc.

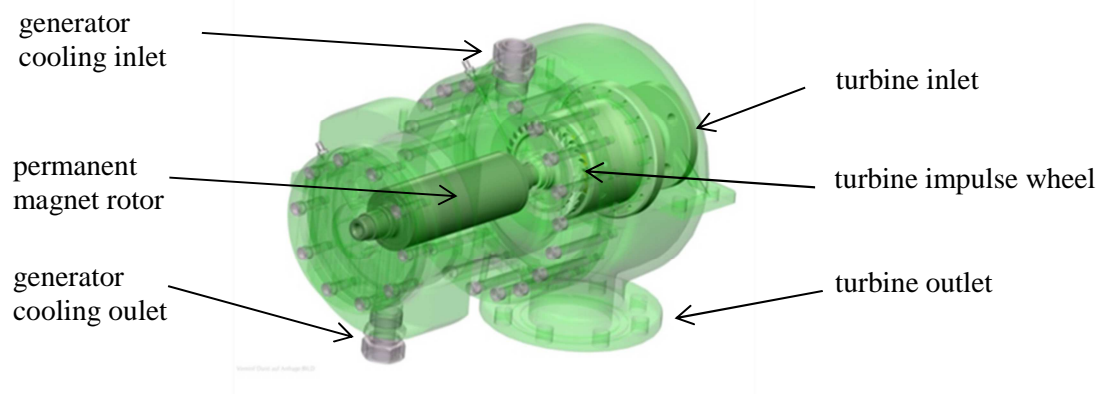


Figure 5: The micro turbo generator concept

3.4 Test Results of Developed Small Turbines

Based on the introduced concept several small axial and cantilevered turbines for steam, air and different organic fluids (Table 4) have already been built and successfully tested.

Table 4: Test results of built small turbines

#	turbine type		fluid	ØD m	n rpm	VRAT -	p.a. %	P kW	η _{ts} %
①	impulse	axial	steam	0,05	70000	3,9	30	1,0	40 ¹
②	impulse	axial	r245fa	0,08	21000	3,4	90	11,0	70 ²
③	impulse	axial	cyclopentane	0,12	30000	16,0	55	11,0	65 ³
④	impulse	axial	air	0,08	49000	6,4	60	5,4	60 ¹
⑤	low reaction	cantilever	air	0,08	49000	6,4	50	5,7	63 ¹

¹: brake efficiency ²: including generator losses ³: based on measured inlet/outlet temperatures and pressures

The small axial steam turbine ① was developed for automotive waste heat recovery. The r245fa- and the Cyclopentan-turbine (②, ③) were designed and built for small waste heat recovery ORC plants as bottoming cycles for biogas engines. The air turbines (④, ⑤) are just demonstrators to investigate the pro and cons of the cantilever design compared to the axial design. The cantilever designed showed the expected higher efficiency. Nevertheless, the axial impulse design provides many other

advantages (see Figure 4) as discussed. Due to different constraints (e.g. maximum rotational speed of the bearing technology) none of the turbines could be designed to operate with its optimal circumferential speed (u_{opt}). Therefore, the efficiencies are rather too low but still acceptable for the given application.

4. CONCLUSIONS

For small and micro ORC plants costs per kW are usually high and it is questionable if those small units will work economically. Therefore, all components, especially the expander must be simple and cheap in series production. From the author's point of view, this requirement rules out the reciprocating piston and screw expanders. The rotating vane expander has already been produced in big numbers for compressed air application. Due to the scrubbing (sealing) vanes it shows usually poor expansion efficiency and high wear. Using a scroll expander mounted on the standard generator shaft a very simple expander unit can be implemented. However, the scroll expansion ratios are limited to the lower end. Thus, only smaller temperature differences can be processed efficiently in an ORC if a scroll expander is to be applied.

The single stage axial impulse turbine can cope with small volume rates and high expansion ratios. Thus, a wide range of boundary conditions and working fluids can be covered with the introduced „micro-expander-construction-kit“. Combined with a high-speed generator a compact, simple and cost-efficient turbo expander unit can be put into practice.

NOMENCLATURE

c	absolute velocity	(m/s)
D	diameter	(m)
ER	expansion ratio	(-)
h	enthalpy	(J/kg)
Ma	Mach number	(-)
n	rotational speed	(rpm)
P	power	(W, kW)
p	pressure	(N/m ²)
u	circumferential velocity	(m/s)
v	specific volume	(m ³ /kg)
VRAT	volume flow ratio	(-)
w	relative velocity	(m/s)
Δ	difference	
η	efficiency	(-)

CRC	Clausius Rankine Cycle
ORC	Organic Rankine Cycle
p. a.	partial admission
p. l.	part load

Subscript

0	nozzle blading/stage inlet
1	nozzle blading outlet, rotor blading inlet
2	rotor blading/stage outlet
el	electric
is	isentropic
opt	optimal
ts	total to static
u	in circumferential direction

REFERENCES

- Badr, O., O'Callaghan, P. W., Hussein M., Probert, S. D., 1984,
Multi-Vane Expanders as Prime Movers for Low-Grade Energy Organic Rankine Cycle Engines
Applied Energy 16, p129-146
- Bao, J., Zhao, L., 2013,
A review of working fluid and expander selections of organic Rankine cycle
Renewable and Sustainable Energy Reviews 24, p 325-342
- Branchini, L., De Pascale, A., Peretto, A., 2013,
Systematic comparison of ORC configurations by means of comprehensive performance indexes
Applied Thermal Engineering 61, p 129-140
- Eilts, P., Seume, J., Brümmner A., 2012,
Zwischenbericht über das Vorhaben 1060 – CO₂-Sonderforschungsprogramm
Expansionsmaschine, *FVV Informationstagung 2012, Heft R558*, Bad Neuenahr
- Glavatskaya, Y., Podevin, P., Lemort, V., Shonda O., Descombes G., 2012,
Reciprocating Expander for an Exhaust Heat Recovery Rankine Cycle for Passenger Car
Application,
Energies, 5, p 1751-1765
- Lemort, V., Ludovic, G., Arnaud, L., Declaye, S., Quoilin, S., 2013,
A comparison of piston, screw and scroll expander for small Rankine cycle systems
Proceedings of the 3rd International Conference on Microgeneration and Related Technologies,
Naples, Italy
- Moustapha, H., Zelesky, M. F., Baines, N. C., Japikse, D., 2003,
Axial and Radial Turbines
Concepts NREC, ISBN 0-933283-12-0
- Quoilin, S., Declaye, S., Legros, A., Guillaume, L., Lemort, V., 2012
Working fluid selection and operation maps for Organic Rankine Cycle expansion machines
International Compressor Engineering Conference at Purdue, July 16-19
- Rinaldi, E., Buonocore, A., Pecnik, R., Colonna, P., 2013,
Inviscid stator/rotor interaction of a single stage high expansion ratio ORC turbine
ASME Organic Rankine Cycle 2013, *2nd International Seminar on ORC Power Systems*, October
7-8, Rotterdam 2013
- Verneau, A., 1987,
Supersonic Turbines for Organic Fluid Rankine Cycles from 3 to 1300 kW
von Karman Institute for Fluid Dynamics, Lecture Series 1987-07, Brussels
- Wang, H., Peterson, R. B., Herron, T., 2009,
Experimental performance of a compliant scroll expander for an organic Rankine cycle
Proc. IMechE Vol. 223 Part A: J. Power and Energy, pp 863-872
- Weith T., Heberle F., Weiß A. P., Zinn G., 2013,
Development of a Small Scale ORC for Waste Heat Recovery
ASME Organic Rankine Cycle 2013, *2nd International Seminar on ORC Power Systems*, October
7-8, Rotterdam 2013

ACKNOWLEDGEMENT

This project was funded by the Bavarian State Ministry of Education, Science and the Arts.

STUDY OF A VOLUMETRIC EXPANDER SUITABLE FOR WASTE HEAT RECOVERY FROM AN AUTOMOTIVE IC ENGINE USING AN ORC WITH ETHANOL

José Galindo¹, Vicente Dolz^{1*}, Lucía Royo¹, Regine Haller², Julien Melis³

¹CMT – Motores Térmicos, Universitat Politècnica de València, Valencia, Spain

² Valeo Systèmes Thermiques, La Verriere, France

³Exoès, Gradignan, France

* Corresponding Author (vidolrui@mot.upv.es)

ABSTRACT

Waste Heat Recovery in exhaust gas flow of automotive engines has proved to be a path to increase the overall efficiency of automotive vehicles. Recovery potential of up to 7% are shown in several works in the literature. However, most of them are theoretical estimations. Some of them presents results from prototypes fed by steady flow generated in an auxiliary gas tank and not with actual engine exhaust gases.

This paper deals with the simulation model of a volumetric expander, integrated in an ORC mock-up, coupled to a 2 l turbocharged gasoline engine and using ethanol as working fluid. An experimental facility of an ethanol ORC using a swash-plate expander coupled to an Ecoboost 2.0 engine has then been used to correlate it.

The target is to understand the physical phenomena which are not predictable by simulation and can only be observed by experimentation and secondly, to carry out some parametric studies showing the potential for optimizing different elements of the expander machine.

1. INTRODUCTION

In the last years, the interest in improving energy efficiency in reciprocating internal combustion (ICE) engines of vehicles has increased, together with the entry into force of ever more stringent anti-pollution regulations. Many of these works are focused on the development of new technologies to recover waste heat from IC engines. Saidur et al. (2012) propose four different groups to classify these technologies: the thermoelectric generators (TEG) (Yang, 2005), organic Rankine cycles (ORC) (Apostol et al., 2015), six-stroke cycle IC engine (Conklin & Szybist, 2010) and new developments on turbocharger technology (Dolz et al., 2012) and (Serrano et al., 2012). The turbocharging technology has been deeply developed for vehicle IC engines in recent decades. In fact, turbochargers are used in practically all Diesel engines used in automotive vehicles. Regarding other present technologies and considering this classification, ORC technology is one of the most promising because of its implementation in the near future engines. ORC technology to recover low-grade heat sources has been widely developed in biomass, geothermal or solar power plants and also in combined heat and power (CHP) in industrial processes. There are many studies about these facilities, both theoretical and experimental. Some of these theoretical studies describe mathematical models in different ORC facilities for the recovery of these low temperature heat sources. Table 1 presents a summary of several studies with the main characteristics of the described models.

Table 1: Summary of papers about ORC modeling

Reference	Model features	Software	Max. Power	Working fluid
(Bracco et al., 2013)	ORC with a scroll expander	AMESim	1.5kW (mechanical)	R245fa
(Lecompte et al., 2013)	ORC for CHP with a volumetric expander	Matlab with RefProp	207kW (output)	R152a, R1234yf, R245fa
(Manente et al., 2013)	Dynamic ORC model with a turbine	Matlab (Simulink)	8MW (net power)	Isobutene and R134a
(Quoilin et al., 2010)	ORC with a scroll expander	EES	1.8kW (mechanical)	HCFC-123
(Wei et al., 2008)	Dynamic ORC model with a turbine	Modelica and Dymola	100kW	R245fa
(Ziviani et al., 2014)	ORC with a scroll expander	AMESim	2.16kW (mechanical)	R245fa
(Carlos et al., 2014)	scroll expander	-	260W (mechanical)	air and ammonia
(Cipollone et al., 2014)	sliding vane rotary expander	-	2kW (mechanical)	R236fa
(Ferrara et al., 2013)	reciprocating expander	WAVE and EES	2.26kW (output)	water
(Giuffrida, 2014)	scroll expander	Matlab with Refprop	2kW (mechanical)	several fluids
(Lemort et al., 2009)	scroll expander	-	1.8kW (mechanical)	HCFC-123
(Wenzhi et al., 2013)	reciprocating expander	Matlab (Simulink)	11.5kW (output)	water

At present, some studies try to adapt this technology to waste heat recovery (WHR) on vehicle IC engines. In these engines, space and weight restrictions are higher than in industrial installations, which greatly hinders their adaptation. On the other hand, the thermal power available in these engines for WHR is lower than in industrial processes. So the optimized expander, mass flows and working fluids for heat recovery in IC engines can be different than the options considered in other applications. Typically, the expanders used in industrial ORC facilities are turbines, screws, scrolls or rotary vane expanders (Qiu et al., 2011). However, ORC design for automotive engines generally presents a reciprocating machine as the optimal solution to recover waste heat energy into mechanical energy, due to low working fluid flow, high values in expansion ratios and space restrictions.

Regarding the working fluids, ethanol is considered by several authors as a promising fluid due to its good features in the temperature range of a vehicle application (450°C-100°C). Although ethanol is positively evaluated taking into account environmental, thermo-physical properties and cost features, it has been classified as serious hazard by NFPA due to its high flammability. (Seher et al., 2012) concluded that ethanol is one of the most favorable solution when a reciprocating machine is used as expander. (Howell & Gibble, 2011) selected ethanol as the best working fluid for a successful ORC for a HD truck.

Despite of these theoretical studies, where the ethanol has proven to be the most suitable working fluid for this type of installations, experimental ORC works with this fluid have not been published due to the flammability properties. Therefore, it is necessary to take safety measures to prevent accidents arising from the use of this fluid.

In previous studies, some methodologies to design these cycles for vehicle IC engines have been proposed (Macián et al., 2013) and applied to define the main characteristics of an ORC facility for WHR in automotive IC engines. This experimental facility has been assembled and tested in order to estimate the viability of this technology. This installation uses a swash-plate reciprocating expander to recover heat losses into mechanical energy and ethanol as working fluid. The main objective of this

paper will consist in describing and validating a model in AMESim of this facility in order to evaluate the main thermo-physical magnitudes of these cycles.

2. SYSTEM LAYOUT

As the expander is the most innovative element of these cycles the description of this system layout has been divided in two parts: first part, where a general ORC layout is described and a second part, where the expander is characterized.

2.1 Organic Rankine Cycle layout

In order to perform an experimental evaluation of this system, an ORC test bench was designed and built at CMT-Motores Térmicos in Universitat Politècnica de València (Figure 1) in a research project with the companies Valeo Systèmes Thermiques and Exoès. This facility can be coupled to different types of automotive combustion engines (an automotive diesel engine, a Heavy Duty diesel engine and an automotive petrol engine). The test bench recovers energy from exhaust gases of a turbocharged 2 l gasoline engine and exchanges thermal energy to the ethanol side.



Figure 1: ORC mock-up

Figure 2 shows the most relevant components of the ORC mock-up. The running principle is as follows: engine exhaust gases pass through the boiler to the working fluid, in this case, ethanol. Then, it is pumped into the high pressure loop and then is evaporated in the boiler and slightly superheated. Thus, working fluid under high temperature and high pressure is generated. After that, the vapor flows into the expander where enthalpy is converted into effective work measured by a torque measuring unit. Low pressure vapor is extracted from the expander and flows to the condenser, reducing its temperature by cooling water and producing condensed ethanol. Therefore, the cycle starts again. The ORC cycle contains as main elements: a boiler, a swash-plate expander, a condenser, a fluid receiver, a subcooler, an expansion vessel and a pump. The main elements have been carefully insulated to avoid heat losses to the ambient. The thermodynamic properties of the ethanol (pressure and temperature) have been measured upstream and downstream of all components, verifying energy balances and power estimations. Table 2 synthesizes the absolute uncertainties of all the sensors installed in the ORC mock-up.

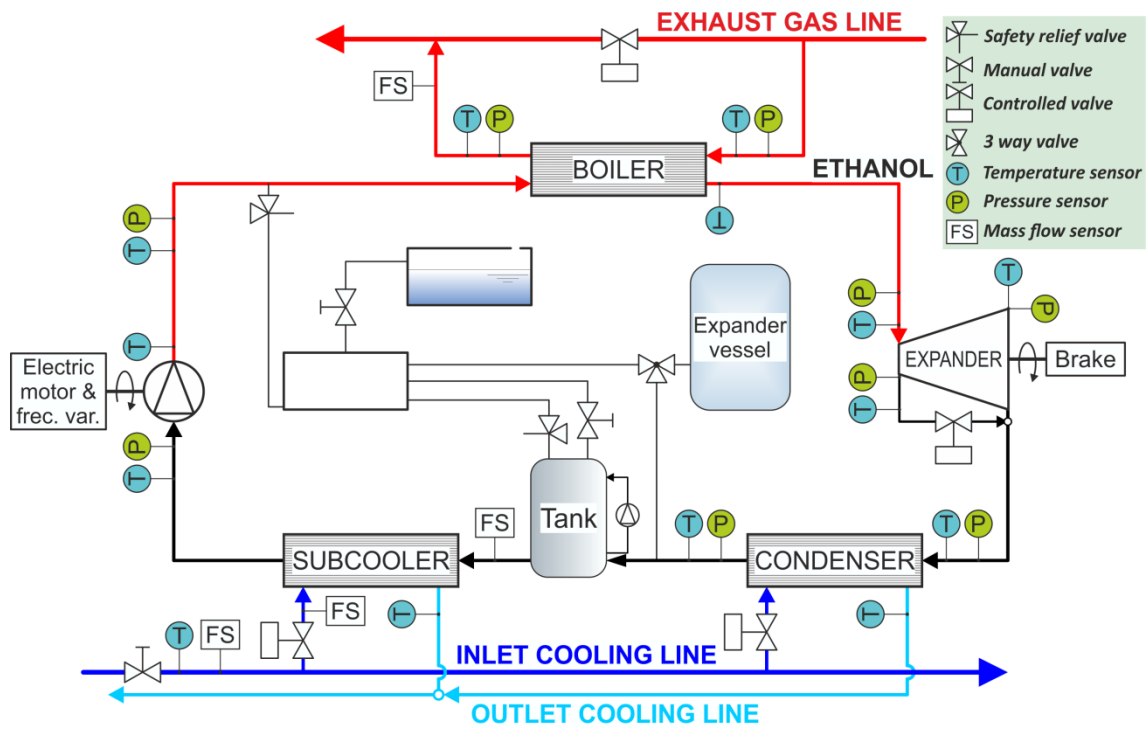


Figure 2: ORC scheme

Table 2: Range and accuracy of sensors

	Measurement principle	Range	Accuracy
Exhaust gas pressure	Piezoresistive	0-2 bar	0.05% FS
Ethanol high pressure loop	Piezoresistive	0-50 bar	0.05% FS
Ethanol low pressure loop	Piezoresistive	0-5 bar	0.05% FS
Temperatures	K-type thermocouples (Class 2)	(-270)-(1,372)K	±2.5°C
Ethanol flow meter	Coriolis flow meter	0-2,720 kg/h	±0.1%
Water flow meter	Electromagnetic flow sensor	0.3-1 m/s	±0.5% of rate
Expander rotational speed	Optical tachymeter	0-20,000 rpm	±1 rpm
Expander torque meter	Strain gauges	0-200 Nm	0.05%FS

2.2 Swash-plate expander layout

The expander machine used in this installation is a Swash-plate expander. Lower flow rates and higher expansion ratios could be reached in this machine, thus displacement expanders are considered the main technology for recovering waste heat from low temperature sources and low expander power in vehicle applications. The geometrical features of the expander are listed in Table 3 and Figure 3 shows a picture of the Swash-plate expander delivered by Exoès.

Table 3: Swash-plate characteristics

Swash-plate characteristics	
Pistons number	3
Bore	40 mm
Stroke	31 mm
Maximum expander speed	4500 rpm

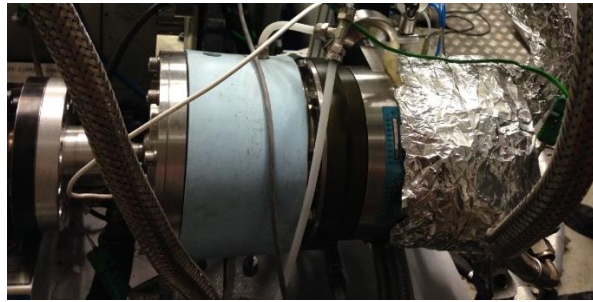


Figure 3: Swash-plate expander delivered by Exoès

The expander performance has been characterized through the calculation of the indicated diagram (P-V). One AVL GU13P piezoelectric pressure sensor was placed on the chamber of one of the pistons to evaluate the pressure variations. It allows tracking pressure variations during filling and emptying processes. The piezoelectric transducer was connected to a Kistler 5015 charge amplifier. The pressure-volume diagram is used to describe changes of volume and pressure of a system. A swash-plate expander is a positive displacement machine. It works as a two stroke machine, which means that during one revolution, with a piston movement from the Top Dead Centre to the Bottom Dead Centre and back again, one working cycle is completed. The superheated steam flows through the intake valve into the cylinder whose piston is near top dead center. Moving the piston downwards, the steam expands and lead out by exhaust ports in the cylinder (slits) situated near the bottom dead center. Finally, the upmoving piston closes the exhaust ports and compresses the steam remained in the cylinder and the cycle starts again. Furthermore, a TDC sensor is used to know the position of the BDC. TDC is an eddy current-Sensor which delivers a signal correlating to the distance between sensor and the swashplate. The piezoelectric pressure signal has been referenced using low frequency measurement (piezoresistive sensor). The analysis of P-V diagrams in different expanders could be very convenient to evaluate possible irreversibilities and improvements in the expansion machine. All the signals were recorded with a sampling frequency of 50 kHz and processed with Labview program. Each cycle was obtained as an average of at least 30 cycles to avoid dispersion in measurements.

3. MODELLING

A comprehensive theoretical model of both the Organic Rankine Cycle and the Swash-plate expander has been developed by the authors using AMESim®. The software package provides a 1D simulation suite to model and analyze multi-domain intelligent systems, and to predict their multi-disciplinary performances. This software consists of available object-oriented libraries, where the user should connect them properly and fix the parameters. The purpose of these models will be: Firstly, it should be used to help the understanding of those physical phenomena which are difficult to observe by means experimentation and secondly, in order to estimate the behavior of the cycle without the need for experimental tests under operating conditions that may cause danger to the installation and / or people. Both models have been validated using tests measured in the mock-up.

3.1 Organic Rankine Cycle model

A simple layout of the ORC consisting of a boiler, a positive displacement pump, a volumetric expander, a fluid receiver, a condenser and an expansion vessel is considered in this model.

Figure 4 shows the AMESim® model of the cycle based on the ORC installation. A detailed description for modelling each component will be presented in the following subsections.

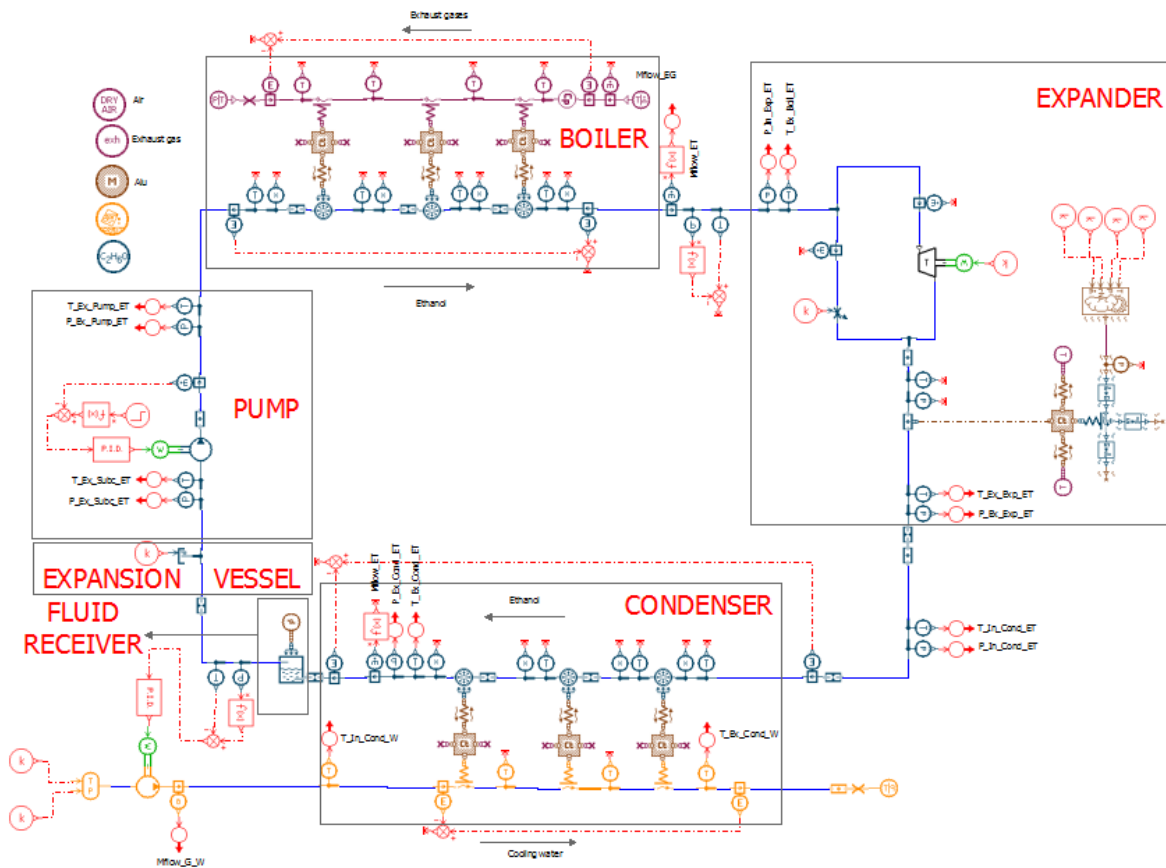


Figure 4: Organic Rankine Cycle model

3.1.1 Working fluid: In the modelling of a particular working fluid it is crucial to be able to reproduce both the thermodynamic and transport properties of the working fluid. AMESim® provides built-in physical-thermo property data of different fluids. In this case the working fluid is ethanol, which is considered by several authors as a promising fluid due to its great features in energy recovery aspect in the temperature range of a vehicle application. Table 4 summarizes the main characteristics of the working fluid.

Table 4: Properties of Ethanol

Chemical structure	C ₂ H ₆ O		
Critical Temperature	T _c	240.9	°C
Critical pressure	P _c	61.4	bar
Atmospheric boiling point	T _b	78.3	°C
Ozone depletion potential	ODP	0	-
Global Warming Potential	GWP	n/a	-
NFPA health hazard	H	2	-
NFPA flammability hazard	F	3	-
Auto ignition temperature	T _{ign}	363	°C

3.1.2 Heat Exchangers: The boiler ensures the heat transfer from exhaust gases to working fluid, based on plate and fin technology. A prototype was specifically designed for this application supplied by Valeo Systèmes Thermiques. The condenser and the subcooler are plate and fin heat exchangers chosen among industrial residential products. Plate and fin technology is preferred by the vast majority of the applications due to its compactness and high level of efficiency.

A 2D discretization model of both elements (boiler and condenser) is represented by a two-counter flow streams. In the case of the boiler, the exhaust gases and the ethanol represents the hot and cold source respectively. In the case of the condenser, the ethanol and the refrigerant (water) represent the hot and cold source respectively. In each element the volume has been divided in 3 small volumes, which in global terms exchanges the net thermal power of the global element. The heat exchange process takes into account both convective and conducting (just in longitudinal direction) process. Depending on the process (boiling or condensation) different correlations implemented in AMESim® have been taken into account.

3.1.3 Volumetric expander: The Swash-plate expander is the main element of the ORC system because it has a great impact in the overall system efficiency. Several tests have been done using turbines and expanders, most of them corresponds to scroll expanders and rotary vane ones. Between reciprocating machines, swash-plate expanders are increasingly taking into account due to its versatility and compactness. Swash-plate expanders could work with high pressure ratios, low flow regimes, lower rotational speeds and could tolerate fluid drops during its expansion. The expander model uses three parameters to characterize the performance of the expander, i.e. isentropic efficiency in Equation (1), mechanical efficiency in Equation (2) and volumetric efficiency in Equation (3).

$$\eta_{iso} = \frac{P_{ind}}{P_{iso}} \quad (1)$$

$$\eta_{mec} = \frac{P_s}{P_{ind}} \quad (2)$$

$$\eta_{vol} = \frac{\dot{m}_{ET}}{\rho_{ET} * N_{Exp} * Disp} \quad (3)$$

$$P_{iso} = \dot{m}_{ET} * (h_{in_Exp_ET} - h_{out_Exp_ET_iso}) \quad (4)$$

$$P_{ind} = W_{cyl} * n_{cyl} * N_{Exp} * \frac{1}{60} \quad (5)$$

$$P_s = T_{Exp} * N_{Exp} \quad (6)$$

Where P_{iso} , P_{ind} and P_s are isentropic, indicated and shaft power respectively. They have been calculated using Equation (4), (5) and (6) respectively, where \dot{m}_{ET} is the mass flow through the expander, $h_{in_Exp_ET}$ is the enthalpy at the inlet of the expander (calculated by using temperature and pressure at the inlet), $h_{out_Exp_ET_iso}$ is the isentropic enthalpy at the outlet of the expander (calculated by using pressure at the outlet and entropy at the inlet), W_{cyl} is the energy extracted from the system (calculated by integrating P-V diagram), N_{Exp} is the expander speed and n_{cyl} the number of cylinders of the expander. Regarding the volumetric efficiency, ρ_{ET} is the density of the ethanol at the inlet of the expander and $Disp$ is the volume displaced by the expander.

No leakages and internal pressure drops have been taken into account in this expander model. Thermal conduction with internal walls of the swash-plate expander is considered to consider heat losses to the ambient.

3.1.4 Pump: A fixed displacement pump is used in this model. The mass flow rate is obtained from volumetric efficiency. The enthalpy increase is defined by the mechanical and isentropic efficiency and the swept volume. No correlations have been considered for efficiencies. Instead, some fixed values were specified for the points simulated.

3.1.5 Pipes and pressure drops: Internal piping losses in the system have been taken into account using hydraulic resistances. The transformation process is pretended to be isenthalpic. Using these elements both enthalpy and mass flow are computed.

Pressure drops in the system have been calculated using correlations available in AMESim®. The hydraulic diameter and the cross-sectional area were used to model different cross-sectional geometries. The pressure drops are regular and the friction factor depends on the flow regime and the relative roughness of the duct. Depending on the state of the fluid different correlations were applied: In a single phase flow (liquid or vapour) the Churchill (Churchill, 1977) correlation is used, while in a two phase flow correlation the user can choose between Mac Adams (McAdams, W.H., Woods, W.K., and Bryan, 1942), Cichitti (Cicchitti, Lombardi, Silvestri, Soldaini, & Zavattarelli, 1959), Dukler (Dukler, A.E., Wicks, M., and Cleveland, 1964), Friedel (Friedel, 1979) and Muller-Steinhagen-Heck (Müller-Steinhagen & Heck, 1986). In this case the Mac Adams correlation was implemented.

3.1.6 Expansion vessel: The expansion vessel is modelled using a tank with modulated pressure and constant specific enthalpy. The user must specify the low pressure value with a constant.

3.2 Swash-plate expander model

As shown in section 3, the volumetric expander tested in this installation is a Swash-plate expander. Although in the global ORC model an AMESim® submodel of the TPF library was used for modelling the expander using volumetric, isentropic and mechanical efficiencies, the need for a physical model of the expander has led to the development of a specific model for just the Swash-plate expander. Figure 5 shows the particular model of the Swash-plate expander in AMESim®. This model could be used as a design and optimization tool in future developments.

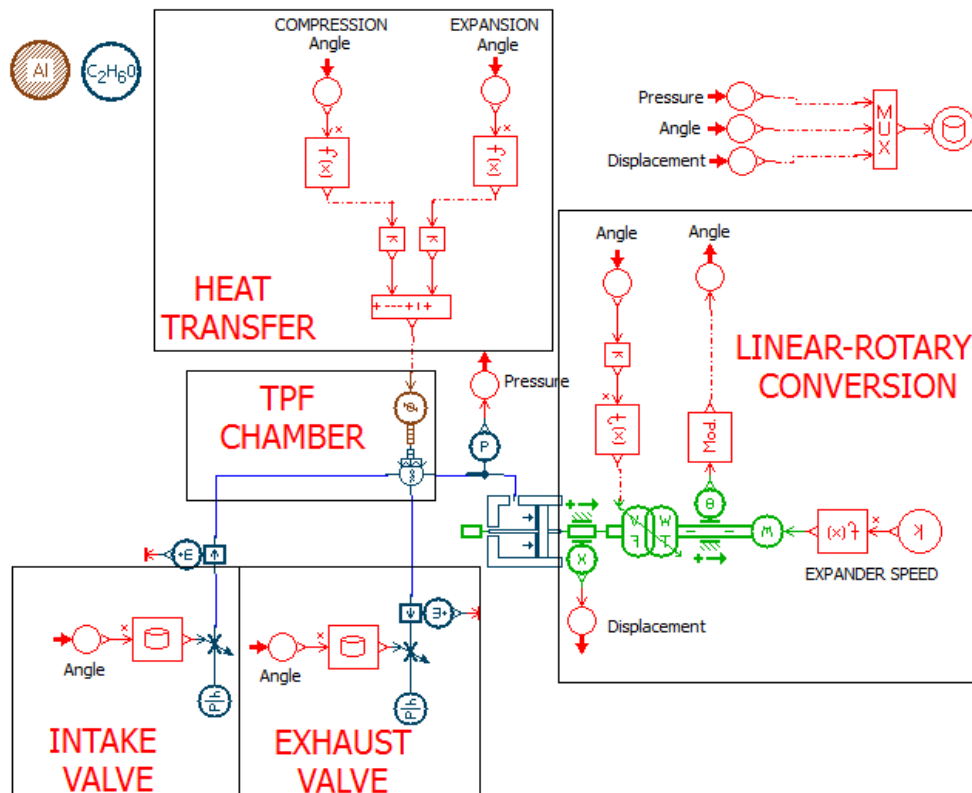


Figure 5: Swash-plate expander model

The fluid dynamic behavior of the Swash-plate was modelled using AMESim® and validated with the experimental tests developed in the expander. The comparison between P-V diagrams (simulated and tested) was used to quantify the error and accuracy of the model.

The main part of the model consists of a two phase flow chamber with variable volume and pressure and temperature dynamics. This submodel was modified respect the original model of the AMESim® library to take into account heat transfer during compression and expansion. The filling (Intake) and emptying (Exhaust) valves provide the mass and pressure exchanges during the process. The angle signal (obtained from the expander speed) is used in three parts of the model:

- In the heat transfer element: Although the expander was insulated, the expansion and compression process never follows an adiabatic law. The transformation is rather polytropic with a heat exchange between the working fluid and the expander walls due to friction, temperature differences and possible condensation effects in the piston chamber. Therefore, the angle signal was used to consider the angles of compression and expansion and to apply for each process a heat transfer coefficient.
- In the valves: The angle was considered to take into account the discharge coefficient for the intake and the exhaust valve at each particular angle. Thus, the valves were modeled as orifices with constant area and variable discharge coefficient.
- In the rotary-linear transformer: It was considered to calculate the absolute displacement in Equation (7) and therefore the volume variation in Equation (8) of the piston as a function of the Swash-plate angle.

$$X(\Phi) = R_{sw} * (1 - \cos(\Phi)) * \tan(\alpha_{sw}) \quad (7)$$

$$V(\Phi) = V_d + \pi * \frac{A^2}{4} * X(\Phi) \quad (8)$$

Where R_{sw} is the radius of Swash Plate (m), α_{sw} is the swash plate angle (°), Φ is the angle covered by the piston, V_d is the dead volume (m³), A is the bore (m), $X(\Phi)$ is the displacement of the piston (m) and $V(\Phi)$ is the volume of the piston (m³). No leakages effects have been modelled.

4. RESULTS

4.1 Organic Rankine Cycle results

In order to characterize the ORC system three points have been tested at different steady working conditions of the ORC system. The points presented in this study aims to show the recovery features at different expander operating points. In these tests, the system has been controlled commanding three parameters: the speed of the pump, in order to control the mass flow of ethanol flowing through the installation, the balloon pressure of the expansion vessel, in order to control the outlet pressure of the expander, and the expander speed, in order to control the high pressure at the inlet of the expander. These points correspond to a heat exchange in the boiler of 25 kW and three conditions of expander (expander speed of 2000, 2500 and 3000 rpm). Table 5 shows the inputs of the ORC model. For each point (P1, P2 and P3), the mass flow of the expander, the pressure at the inlet of the pump, the expander speed, the temperature at the inlet of the boiler at the EG side, the pressure at the boiler at the EG side, the mass flow of the EG and the temperature at the inlet of the condenser at the water side were fixed.

Table 5: Inputs of the ORC model

	P1	P2	P3	Units
Mf_ET	73.85	75.99	74.79	kg/h
P_in_P_ET	1.571	1.899	1.589	bar
N_Exp	2001	2502	3003	rpm
T_in_B_EG	749.48	740.28	748.92	°C
P_out_B_EG	1.018	1.024	1.018	bar
Mf_EG	154.98	159.47	155.25	kg/h
T_in_C_W	48.42	49.01	47.58	°C

Table 6 shows the volumetric, the isentropic, the mechanical efficiency (calculated using Equation (1),(2) and (3)) and the global efficiency of the expander (defined by the isentropic efficiency times the mechanical efficiency). They have been fixed in the model.

Table 6: Experimental efficiencies of the Swash-plate expander

	P1	P2	P3	Units
P_ind	1739	2007	1874	W
P_mec	1649	1543	1531	W
P_iso	3431	3413	3338	W
η_{vol}	19.37%	17.21%	14.54%	-
η_{iso}	50.68%	58.81%	56.14%	-
η_{mec}	94.81%	76.90%	81.72%	-
η_{glob}	48.05%	45.22%	45.88%	-

Table 7 presents the outputs of the model for the three points tested. For each point three columns are presented, the first one, called “P_i Exper.,” corresponds to the experimental values, the second one, called P_i Sim., corresponds to the simulation values and the last one, called Error, corresponds the absolute error between both values. Temperatures are given in °C, pressures in bar, torque in Nm and pump speed in rpm. As regards temperatures, the maximum deviation corresponds to the temperature at the inlet of the expander at medium expander speed (2500 rpm), with a value of 3.28%. The remainder temperatures of the cycle are obtained with an error lower than 3%. Regarding pressures, the maximum deviation corresponds to the pressure at the inlet of the condenser, with a value of 4.48%. The remainder pressures in the system are calculated with an error of 3%. The last two simulation parameters are the torque and the pump speed, in which the maximum deviation is 5%.

Table 7: Outputs of the ORC model

	P1 Exper.	P1 Sim.	Error	P2 Exper.	P2 Sim.	Error	P3 Exper.	P3 Sim.	Error
T_out_P_ET	47.39	46.39	0.31%	47.13	46.33	0.25%	48.60	46.33	0.70%
T_out_B_ET	210.23	208.65	0.33%	215.14	199.12	3.28%	208.29	201.34	1.44%
T_out_Exp_ET	104.74	116.21	3.04%	109.14	107.23	0.50%	111.05	109.89	0.30%
T_in_C_ET	103.79	102.55	0.33%	103.41	99.06	1.16%	102.26	97.12	1.37%
T_out_C_ET	48.27	48.58	0.10%	47.95	48.51	0.17%	47.88	48.60	0.22%
T_in_P_ET	46.67	45.76	0.28%	46.51	45.76	0.23%	47.47	45.76	0.53%
T_out_C_W	73.85	71.39	0.71%	67.25	69.03	0.52%	72.88	71.55	0.38%
P_out_P_ET	34.26	34.26	0.01%	31.01	31.48	1.51%	31.77	31.16	1.92%
P_in_Exp_ET	28.65	29.57	3.20%	27.00	26.53	1.74%	26.01	26.36	1.33%
P_in_C_ET	1.89	1.89	0.20%	2.01	2.10	4.48%	1.90	1.88	0.95%
T	7.81	7.98	2.18%	5.86	5.59	4.47%	4.87	4.96	1.85%
N_P	300	312	3.81%	305	321	5.14%	301	316	4.94%

4.2 Swash-plate expander results

The simulated and experimental curves of the pressure variation inside the expander chamber as a function of the volume were compared for the three points tested in previous sections.

Figure 6,

Figure 7 and

Figure 8 show the comparison carried out with the three expander speeds of 3000 rpm, 2500 rpm and 2000 rpm. Red and green crosses indicate the intake and exhaust valve closing angle (or volume) respectively. Red and green circles indicate the intake and exhaust valve opening angle (or volume) respectively. It was found a quite good agreement between experimental and simulation results in terms of indicated power delivered by the expander. In the right corner of these diagrams both the indicated power and the expander speed were added. Slight differences could be found in these simulations due to pressure drop in the valves and effects of pulsating flow, which cannot be modelled in AMESim® with the Two-Phase flow library.

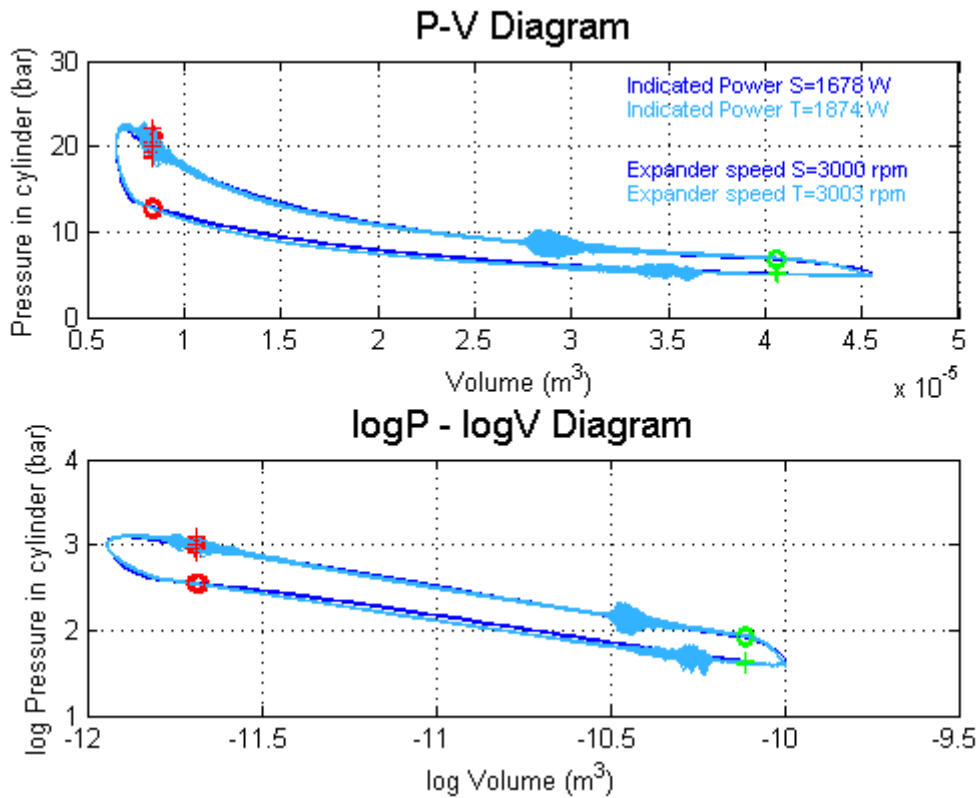


Figure 6: P-V and logP-logV Diagram 3000 rpm

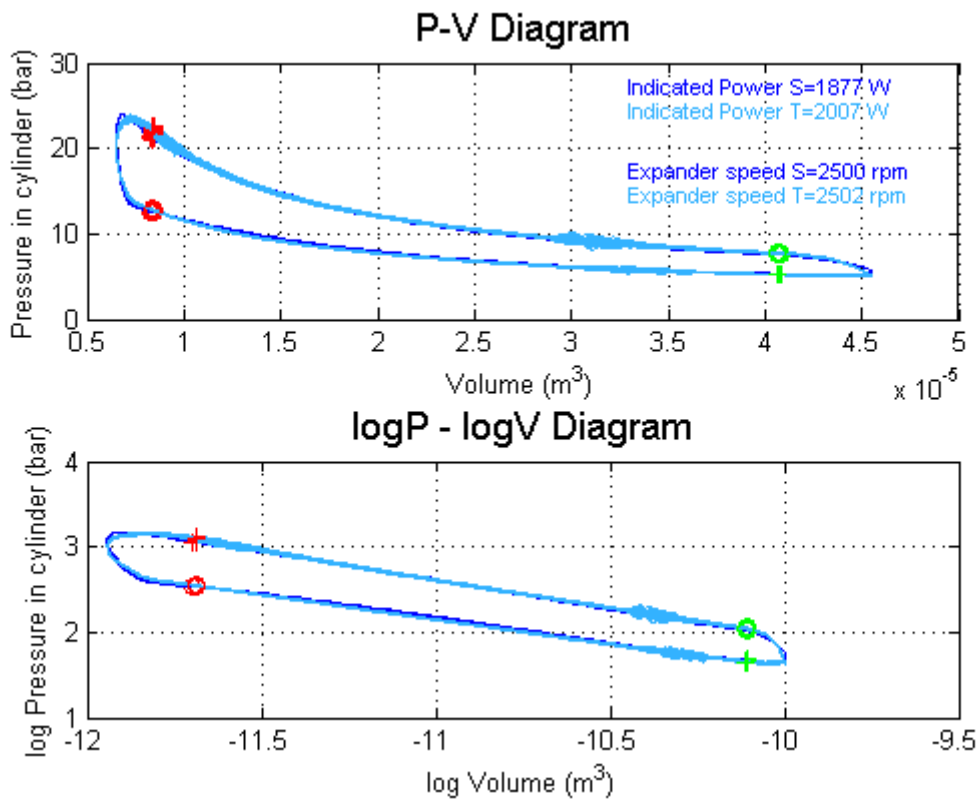


Figure 7: P-V and logP-logV Diagram 2500 rpm

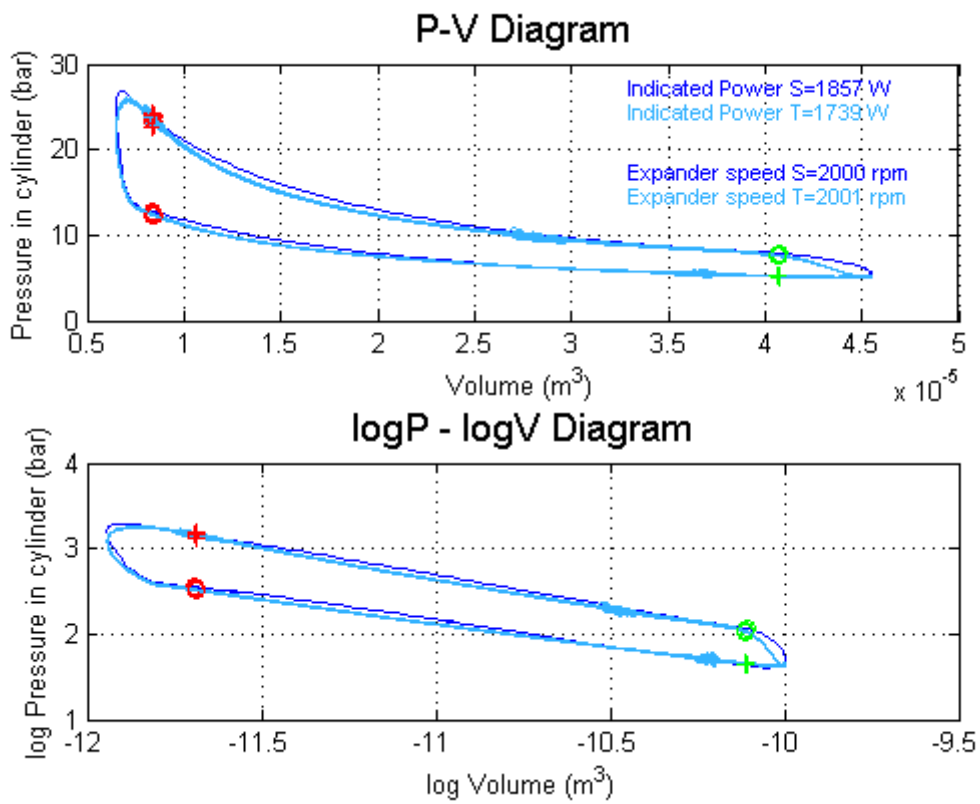


Figure 8: P-V and logP-logV Diagram 2000 rpm

Table 8 summarizes the results of the simulation. The inputs of the model were obtained from pressure measurements at the inlet of the expander and expander speed. In order to take into account differences between heat transferred in the three points, the coefficients of compression and expansion were modified. In this model the higher the expander speed is, the higher heat transfer rate should be imposed in the model. The maximum deviation of the model from measurements corresponds to 10% in the point of 3000 rpm, which is considered acceptable to predict flow behavior. Besides, the model predicts properly the filling and emptying processes as it can be seen in Figure 6, Figure 7 and Figure 8.

Table 8: Results of the Swash-plate model

	P1	P2	P3	Units	I/O
P_B	25	25	25	kW	-
P_in_Exp_ET	28.65	27.00	26.01	bar	Input
N_Exp	2001	2502	3003	rpm	Input
P_ind_T	1739	2007	1874	W	-
P_ind_S	1857	1877	1678	W	Output
Error (%)	6.79%	6.48%	10.46%	-	-

5. CONCLUSIONS

The presented work describes and analyzes two models based on an experimental ORC installation installed in a turbocharged 2.0 l gasoline engine to recover waste heat in exhaust gases. These models correspond on one side to the global ORC cycle and on the other side the dynamic of the Swash-plate expander. The comparison of performance parameters have been made in three points by means of changing the inputs and obtaining the outputs of the model. The results are summarized in the following points:

- An ORC model is developed using the software AMESim®. This model allows to simulate the main parameters measured in the cycle. Comparing the three steady operating points, a maximum deviation of 4% regarding pressures and temperatures and a value of 5% regarding torque was attained.
- A Swash-plate expander model is presented using the software AMESim®. This model represents the fluid dynamic behavior of the Swash-plate using discharge coefficients, displacement laws and heat transfer coefficients. The P-V diagram was measured by a piezoelectric pressure sensor and compared to the simulation. Maximum deviation of 10% was achieved at point of 3000 rpm.

Waste heat recovery technologies seem to assume an essential role in the new regulations of the forthcoming decade. Therefore, ORC will be considered in increasingly growing markets to solve some of the actually environmental challenges, among which it can be pointed out ICEs. In these systems a large number of features should be contemplated, i.e. working fluid, heat exchangers, volumetric machine, pressure and temperature levels, etc.... Thus, in order to optimize and improve these systems it is crucial the development of reliable models to avoid huge number of tests. The proposed models develop in this article using AMESim® are consistent due to its slight deviation between tests and simulation results. Thus, it could be considered a valuable tool in future ORC installed in ICEs.

NOMENCLATURE

ORC	Organic Rankine Cycle
P-V	Pressure Volume
TDC	Top Dead Center
BDC	Bottom Dead Center
T	Tested
S	Simulated
TPF	Two Phase Flow
Mf	Mass flow
N	Speed
T	Torque
P	Power

Subscript

ET	Ethanol
W	Water
EG	Exhaust Gases
P	Pump
Exp	Expander
C	Condenser
B	Boiler
in	inlet
out	outlet
iso	isentropic
ind	indicated
s	shaft
vol	volumetric
mec	mechanical
cyl	cylinder
sw	swash-plate
glob	global

REFERENCES

- Apostol, V., Pop, H., Dobrovicescu, A., Prisecaru, T., Alexandru, A., & Prisecaru, M. (2015). Thermodynamic Analysis of ORC Configurations Used for WHR from a Turbocharged Diesel Engine. *Procedia Engineering*, *100*, 549–558. doi:10.1016/j.proeng.2015.01.402
- Bracco, R., Clemente, S., Micheli, D., & Reini, M. (2013). Experimental tests and modelization of a domestic-scale ORC (Organic Rankine Cycle). *Energy*, *58*, 107–116. doi:10.1016/j.energy.2012.12.016
- Carlos, L., Carles, J., Lemort, V., & Coronas, A. (2014). Characterization and modeling of a scroll expander with air and ammonia as working fluid. *Applied Thermal Engineering*, *70*, 630–640. doi:10.1016/j.applthermaleng.2014.05.069
- Churchill, S. W. (1977). Friction-factor equation spans all fluid flow regimes. *Chem. Eng.*, 91–92.

- Cicchitti, A., Lombardi, C., Silvestri, M., Soldaini, G., & Zavattarelli, R. (1959). TWO-PHASE COOLING EXPERIMENTS: PRESSURE DROP, HEAT TRANSFER AND BURNOUT MEASUREMENTS. Retrieved from <http://www.osti.gov/scitech/biblio/4181977>
- Cipollone, R., Bianchi, G., Di Battista, D., Contaldi, G., & Murgia, S. (2014). Mechanical energy recovery from low grade thermal energy sources. *Energy Procedia*, 45, 121–130. doi:10.1016/j.egypro.2014.01.014
- Conklin, J. C., & Szybist, J. P. (2010). A highly efficient six-stroke internal combustion engine cycle with water injection for in-cylinder exhaust heat recovery. *Energy*, 35(4), 1658–1664. doi:10.1016/j.energy.2009.12.012
- Dolz, V., Novella, R., García, A., & Sánchez, J. (2012). HD Diesel engine equipped with a bottoming Rankine cycle as a waste heat recovery system. Part 1: Study and analysis of the waste heat energy. *Applied Thermal Engineering*, 36(1), 269–278.
- Dukler, A.E., Wicks, M., and Cleveland, R. G. (1964). Pressure drop and hold-up in two-phase flow Part A: A comparison of existing correlations Part B: An approach through similarity analysis. *AIChE Journal*, 10, 38–51.
- Ferrara, G., Manfrida, G., & Pescioni, a. (2013). Model of a small steam engine for renewable domestic CHP (combined heat and power) system. *Energy*, 58, 78–85. doi:10.1016/j.energy.2013.03.035
- Friedel, L. (1979). Improved friction pressure drop correlations for horizontal and vertical two-phase pipe flow. In *European Two-Phase Group Meeting, Isra, Italy*.
- Giuffrida, A. (2014). Modelling the performance of a scroll expander for small organic Rankine cycles when changing the working fluid. *Applied Thermal Engineering*, 70(1), 1040–1049. doi:10.1016/j.applthermaleng.2014.06.004
- Howell, T., & Gibble, J. (2011). Development of an ORC system to improve HD truck fuel efficiency. *Deer 2011 Conference*, 1–21.
- Lecompte, S., Huisseune, H., van den Broek, M., De Schamphelre, S., & De Paepe, M. (2013). Part load based thermo-economic optimization of the Organic Rankine Cycle (ORC) applied to a combined heat and power (CHP) system. *Applied Energy*, 111, 871–881. doi:10.1016/j.apenergy.2013.06.043
- Lemort, V., Quoilin, S., Cuevas, C., & Lebrun, J. (2009). Testing and modeling a scroll expander integrated into an Organic Rankine Cycle. *Applied Thermal Engineering*, 29(14-15), 3094–3102. doi:10.1016/j.applthermaleng.2009.04.013
- Macián, V., Serrano, J. R., Dolz, V., & Sánchez, J. (2013). Methodology to design a bottoming Rankine cycle, as a waste energy recovering system in vehicles. Study in a HDD engine. *Applied Energy*, 104, 758–771.

- Manente, G., Toffolo, A., Lazzaretto, A., & Paci, M. (2013). An Organic Rankine Cycle off-design model for the search of the optimal control strategy. *Energy*, 58, 97–106. doi:10.1016/j.energy.2012.12.035
- McAdams, W.H., Woods, W.K., and Bryan, R. L. (1942). Vaporization inside horizontal tubes -II- Benzene-oil mixtures. In *Trans. ASME* (p. 193).
- Müller-Steinhagen, H., & Heck, K. (1986). A simple friction pressure drop correlation for two-phase flow in pipes. *Chemical Engineering and Processing: Process Intensification*, 20(6), 297–308. Retrieved from <http://www.sciencedirect.com/science/article/pii/0255270186800083>
- Qiu, G., Liu, H., & Riffat, S. (2011). Expanders for micro-CHP systems with organic Rankine cycle. *Applied Thermal Engineering*, 31(16), 3301–3307. doi:10.1016/j.applthermaleng.2011.06.008
- Quoilin, S., Lemort, V., & Lebrun, J. (2010). Experimental study and modeling of an Organic Rankine Cycle using scroll expander. *Applied Energy*, 87(4), 1260–1268. doi:10.1016/j.apenergy.2009.06.026
- Saidur, R., Rezaei, M., Muzammil, W. K., Hassan, M. H., Paria, S., & Hasanuzzaman, M. (2012). Technologies to recover exhaust heat from internal combustion engines. *Renewable and Sustainable Energy Reviews*, 16(8), 5649–5659. doi:10.1016/j.rser.2012.05.018
- Seher, D., Lengenfelder, T., Gerhardt, J., Eisenmenger, N., Hackner, M., & Krinn, I. (2012). Waste Heat Recovery for Commercial Vehicles with a Rankine Process. *21 St Aachen Colloquium Automobile and Engine Technology 2012*.
- Serrano, J. R., Dolz, V., Novella, R., & García, A. (2012). HD Diesel engine equipped with a bottoming Rankine cycle as a waste heat recovery system. Part 2: Evaluation of alternative solutions. *Applied Thermal Engineering*, 36(1), 279–287.
- Wei, D., Lu, X., Lu, Z., & Gu, J. (2008). Dynamic modeling and simulation of an Organic Rankine Cycle (ORC) system for waste heat recovery. *Applied Thermal Engineering*, 28, 1216–1224. doi:10.1016/j.applthermaleng.2007.07.019
- Wenzhi, G., Junmeng, Z., Guanghua, L., Qiang, B., & Liming, F. (2013). Performance evaluation and experiment system for waste heat recovery of diesel engine. *Energy*, 55, 226–235. doi:10.1016/j.energy.2013.03.073
- Yang, J. (2005). Potential applications of thermoelectric waste heat recovery in the automotive industry. *ICT 2005. 24th International Conference on Thermoelectrics, 2005.*, 1–5. doi:10.1109/ICT.2005.1519911
- Ziviani, D., Beyene, A., & Venturini, M. (2014). Advances and challenges in ORC systems modeling for low grade thermal energy recovery. *Applied Energy*, 121, 79–95. doi:10.1016/j.apenergy.2014.01.074

ACKNOWLEDGEMENT

This work is part of a research project called “Evaluation of bottoming cycles in IC engines to recover waste heat energies” funded by a National Project of the Spanish Government with reference TRA2013-46408-R.

COMBINED THERMODYNAMIC AND TURBINE DESIGN ANALYSIS OF SMALL CAPACITY WASTE HEAT RECOVERY ORC

Antti Uusitalo*, Teemu Turunen-Saaresti, Aki Grönman, Juha Honkatukia, Jari Backman

¹ Larjola Laboratory of Turbomachinery, School of Energy Systems

Lappeenranta, Finland

Contact Information (antti.uusitalo@lut.fi)

* Corresponding Author

ABSTRACT

In this paper, the design of small-capacity ORC turbines for a waste heat recovery application is studied and discussed. A turbine design tool was coupled with a thermodynamic analysis tool in order to evaluate the effect of different working fluids and process parameters, not only by taking into account the thermodynamic aspects of the process design, but also evaluating the availability to design turbines with a relatively high efficiency and feasible geometry. The studied turbine type is a radial inflow turbine since radial turbines represent relatively simple geometries when compared to multistage configurations, can have a high expansion ratio over a single stage, and have a better efficiency at a low power capacity than the axial counterparts. The results indicate that the main difficulties in the design of small capacity ORC turbines are related to high rotational speeds, small dimensions, and large blade height ratios. In addition, the use of single stage turbines leads to highly supersonic flow in the stator even when adopting low or moderate flow velocities. The results of this study highlight the importance of combining both the thermodynamic process design and the turbine design when evaluating suitable working fluids and operational parameters.

1. INTRODUCTION

Organic Rankine Cycles (ORC) are a widely implemented technology in geothermal, biomass, and in different waste heat recovery applications. The use of organic working fluids allows to design small-scale power systems that are capable of utilizing efficiently low temperature heat sources. The current ORC applications and the most important design aspects of ORCs are presented and discussed e.g. in (Colonna et al., 2015). In small power output ORCs (about 10-50 kW) a volumetric expander, namely screw or scroll expanders, are typically preferred instead of a turbine whereas a turbine is typically used as an expansion machine in larger scale ORC applications (Colonna et al., 2015). The limitations of using volumetric expanders are related to the lower achievable expansion ratios over an expander when compared to the use of turbines and thus, the use of volumetric expanders disables the use of high molecular weight and high critical temperature fluids characterized by high expansion ratios and high thermodynamic efficiencies. Therefore, the use of turbines could enable the design of high efficiency small-scale ORCs, especially for high temperature applications.

The turbine types used in the ORCs are typically axial or radial turbines (Colonna et al., 2015). Studies on using multistage radial outflow turbines have been carried out in the recent years (Pini et al., 2013). The expansion ratio over the turbine can be very high, especially in high-temperature ORCs, which can result in high Mach numbers and significantly large rotor blade height ratio between the rotor outlet and inlet (Macchi, 1977; van Buijtenen et al., 2003; Uusitalo et al., 2013). In addition, the real gas effects in the expansion become significant, especially when fluids having a high molecular complexity are used and when the expansion occurs near the critical point of the fluid (Harinck et al., 2009; Guardone et al., 2013). In many ORC turbines, the flow is supersonic since the organic fluids have a low speed of sound. This causes losses related to the occurrence of shock waves in the flow passages. The design and flow

analysis of supersonic ORC turbine stators have been presented for radial turbines e.g. in (Harinck et al., 2010, Uusitalo et al., 2014) and for axial turbine stator e.g. in (Colonna et al., 2006). Geometry optimization methods by using automated CFD-design have been developed in the recent years in order to further improve the performance of supersonic ORC turbines (Harinck et al. 2013). The results by Harinck et al. (2013) indicated that the losses caused by the occurrence of shock waves can be reduced significantly by bending and turning the stator flow channels instead of using straight nozzles.

Few experimental works on small-scale ORC turbines are available in the literature. Verneau (1987) presented the experimental results for two high pressure ratio ORC turbines, having a power output of 50 kW and using FC 75 as the working fluid. The first turbine design was a supersonic two-stage axial turbine and the second design was a single-stage axial turbine. The pressure ratios of the designed turbines were about 150. The experiments showed that a relatively high turbine efficiency in a range of 70 to 80 % was achieved for both the two-stage and single-stage turbine designs. An experimental study on a small-scale ORC having a high speed radial turbine was presented by Kang (2012). The turbine and generator were assembled to a single shaft having a rotational speed of 63 000 rpm. The system used R245fa as the working fluid and the evaporation temperature was in a range from 70 °C to 90 °C. The measured power output was 32.7 kW and the turbine efficiency of 78.7 % was achieved. Additionally, Klonowicz et al. (2014) presented experimental results of a low-temperature ORC using R227ea. The system had a 10 kW hermetic turbogenerator and the designed turbine was a partial admission axial turbine. The electric efficiency of the turbogenerator of less than 60 % was measured including the losses in the turbine and in the generator.

Despite several studies on high-expansion ratio ORC turbines, guidelines to design such expanders, especially for small-scale systems are lacking and only few studies have presented experimental results on the performance of small ORC turbines. In addition, a large number of publications have discussed the working fluid selection from the thermodynamic point of view, but totally neglecting the effect of the working fluid on the turbine design. Maraver et al. (2014) included a preliminary turbine size evaluation for different working fluids in a thermodynamic study by using a size parameter (SP), but no further assessment on the turbine rotational speeds, geometry, or Mach numbers were included. This paper presents a method of combining the thermodynamic process analysis and preliminary turbine design tool to evaluate suitable working fluids and cycle design parameters for a small-scale ORC from the point of view of the turbine design. In addition, the most critical aspects of designing radial turbines for small-scale ORCs are highlighted and discussed. The studied application is exhaust heat recovery of small-scale gas turbines.

2. DESIGN METHODS

The design of an ORC process utilizing exhaust gas heat is studied by using exhaust gas values typical for small-scale gas turbines (Invernizzi et al., 2007). The exhaust gas temperature at the ORC evaporator inlet is 300 °C, and the mass flow rate of the exhaust gas was set to 1 kg/s. The exhaust gas temperature at the evaporator outlet was varied in the analysis in order to study the effect of the exhaust gas outlet temperature on the cycle power output and turbine design. A commercial thermodynamic library Refprop was used for calculating the fluid properties. The studied fluids are hydrocarbons toluene, cyclohexane, and pentane; siloxanes MDM and MM; and fluorocarbons R245fa and R365mfc. The main thermodynamic properties of the studied fluids are presented in Table 1.

In the thermodynamic analysis of the process, the evaporation pressure of the working fluid was optimized to reach a minimum pinch-point temperature difference of 15 °C in the evaporator with the given heat source values. If the temperature difference in the evaporator remained sufficient, a limit of $p_{ev}/p_{crit} = 0.95$ was used for the evaporation pressure. A condensing temperature of 60 °C was used, the cycle included a recuperator and all the studied fluids were superheated by 10 °C, since a flow through type of evaporator was considered. Turbine efficiency of 80 %, generator efficiency of 95 %, efficiency

Table 1: Studied working fluids and main thermodynamic properties.

fluid	T_{crit} , [$^{\circ}C$]	p_{crit} , [bar]	MW, [kg/kmol]	p_{cond} (@ 60 $^{\circ}C$), [bar]
toluene	318.6	41.3	92.1	0.2
cyclohexane	280.5	40.75	84.2	0.5
pentane	196.6	33.7	72.1	2.1
MDM	290.9	14.2	236.5	0.04
MM	245.6	19.4	162.4	0.3
R245fa	154.0	36.5	134.0	4.6
R365mfc	186.9	32.7	148.1	2.0

of the frequency converter of 97 %, and the efficiency of feed pump of 60 % were used in the analysis.

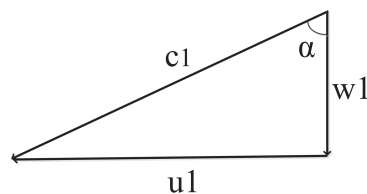
The design tool of radial turbines calculates the main dimensions and velocity triangles of the turbine. The turbine inlet and the outlet conditions were obtained as a result from the process thermodynamic design. The evaluation of the turbine rotational speed, n , was carried out by using the non-dimensional parameter, turbine specific speed N_s defined as,

$$N_s = \frac{\omega q_v^{0.5}}{\Delta h_s^{0.75}}. \quad (1)$$

According to the performance diagram for radial turbines operating with compressible fluids, the highest efficiencies are obtained with specific speeds in a range from 0.4 to 0.8 (Balje, 1981). The intermediate static pressure between the stator and rotor was selected by using the degree of reaction which is defined by dividing the enthalpy change in the turbine rotor by the total enthalpy change in the turbine stator and rotor

$$r = \frac{\Delta h_{rot}}{\Delta h_{tot}}. \quad (2)$$

The rotor outlet blade tip to rotor inlet diameter ratio D_{2t}/D_1 , the blade hub-to-tip diameter ratio D_{2h}/D_{2t} at the outlet as well as the stator exit flow angle α_1 were evaluated by following the guidelines of (Rohlik, 1972). The velocity calculations were based on the continuity equation and on the Euler turbomachine equation. The velocity vectors were solved at the rotor inlet and at the rotor outlet. An example of the turbine velocity triangle at the rotor inlet is presented in Fig. 1. The tangential component of the absolute velocity, c_u , was used in monitoring the shape of the velocity triangle at the rotor inlet by using a velocity ratio c_u/u while the radial component of the absolute velocity, c_r , was used in the continuity equation to calculate the blade height at the rotor inlet. The stator efficiency of 82 % was used in the calculations to estimate the static enthalpy at the stator outlet. The turbines were designed to have the rotor discharge in axial direction, and thus, the tangential component of the absolute velocity at the rotor outlet $c_{u2} = 0$. The calculations of the turbine geometry were based on the assumption that the flow velocity at the rotor discharge is relatively low and thus, an assumption of $h_{2,st} \approx h_{2,tot}$ was used and no analysis for the turbine diffuser was included.

**Figure 1:** An example of a velocity triangle at the rotor inlet, having a radial relative velocity ($w_{u1} = 0$).

It should be noted that the results of the process calculations were based on the 80 % turbine efficiency

with all the studied fluids and process design parameters. This kind of approach can be well justified in the preliminary evaluation of turbine dimensions and rotational speeds, but it should be noted that the turbine efficiency has an effect on the size of the rotor wheel and on the optimal turbine rotational speed. Thus, a more accurate turbine design would be achieved in a case if the turbine efficiency used in the process design were iteratively changed based on the obtained turbine dimensions and Mach number at the stator outlet. However, this would require detailed numerical simulations of the turbine since there is very limited data available about the losses and applicable loss correlations for radial ORC turbines.

3. RESULTS

3.1 Comparison to radial turbine designs available in the literature

A comparison was made between the turbine geometries designed with the code used in this study and ORC radial turbine designs available in the literature to verify the design method. The working fluid mass flow rate, the turbine inlet state, the turbine efficiency and the turbine outlet pressure, as well as the degree of reaction and the specific speed if available, were set to the same values as presented in (Kang, 2012; van Buijtenen et al, 2003). The turbine isentropic efficiency of 75 % was used in the comparison of (Kang, 2012) and 80 % in the comparison of (van Buijtenen et al., 2003). The absolute flow angle at the stator outlet of 75 ° was used for the both turbines designs. The results of the comparison are presented in Table 2. In general, based on the results of the comparison the developed turbine design code has a good agreement in the turbine diameter and rotational speed with the radial ORC turbine designs selected for the comparison. The found agreement shows the reliability of the design method and gives a good foundation for the analysis in the following sections.

Table 2: Comparison of the turbine rotor diameter and rotational speed between Turbine 1 (Kang, 2012), Turbine 2 (van Buijtenen et al., 2003), and the used turbine design code.

	fluid	P_t , kW	q_m , kg/s	N_s , -	r , -	$p_{t,in}$, bar	$T_{t,in}$, °C	$p_{t,out}$, bar	D_{rot} , mm	n_{rot} , rpm
Turbine 1	R245fa	≈ 30.0	1.58	na	na	7.3	80	1.78	125	20 000
comparison	R245fa	31.0	1.58	0.45	0.47	7.3	80	1.78	124.1	21 597
Turbine 2	toluene	≈ 200	1.24	0.44	0.26	32.3	325	0.27	224	28 300
comparison	toluene	191.6	1.24	0.44	0.26	32.3	325	0.27	227.5	28 081

3.2 Results with different working fluids

The process and turbine design results with different working fluids are presented in this section. The results presented in this section were calculated for turbines having the specific speed of 0.5 and the degree of reaction of about 0.5. The results of the cycle power output, the cycle efficiency and the evaporation pressure as a function of the exhaust gas temperature at the evaporator outlet are presented in Fig. 2a, Fig. 2b and Fig. 2c. The results for the power output show that the studied hydrocarbons represent the highest simulated cycle power output, above 30 kW, and the fluorocarbon R245fa represents the lowest power outputs, especially with the high exhaust gas temperatures at the evaporator outlet. The fluids with the highest critical temperatures represent the highest values for the power output with the higher exhaust gas temperatures at the evaporator outlet when compared to the fluids with the lowest critical temperatures. The highest cycle efficiencies are reached with hydrocarbons toluene and cyclohexane, and the lowest efficiencies with R245fa and R365mfc. It should be noted that these power output and efficiency results are based on the use of constant turbine isentropic efficiency with all the studied fluids and cycle parameters. A more detailed analysis would require the turbine efficiency to be iteratively changed according to the obtained turbine geometries. The evaporation pressure limit of $p_{ev}/p_{crit} = 0.95$ is reached with fluids having the lowest critical temperatures, namely R245fa, R365mfc, pentane, and MM, since the temperature difference between the working fluid and the exhaust gas remains sufficient. Evaporation pressures well below the critical pressures are adopted with each fluid when the lowest ex-

haust gas outlet temperatures are considered in order to maintain a sufficient temperature difference of 15 °C in the evaporator.

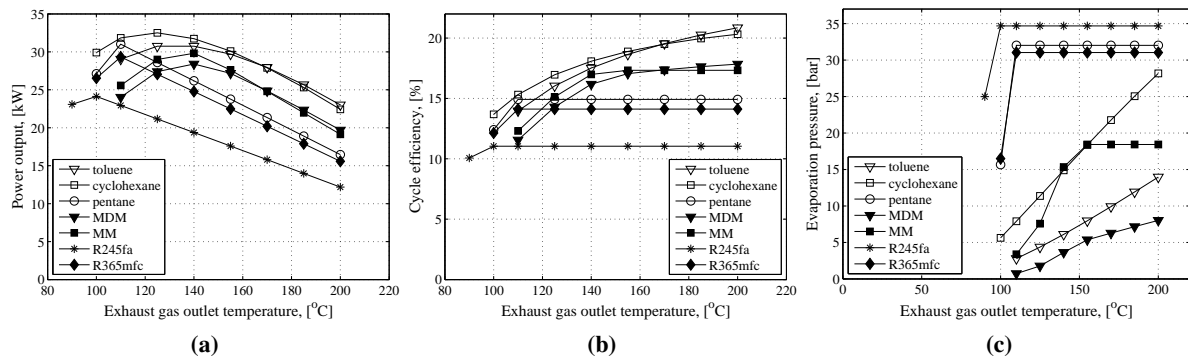


Figure 2: Results of a) power output, b) cycle efficiency, and c) evaporation pressure as a function of exhaust gas temperature at the evaporator outlet.

The working fluid mass flow rate is presented in Fig. 3a, the enthalpy change in the turbine in Fig. 3b, and the expansion ratio over the turbine in Fig. 3c as a function of the exhaust gas outlet temperature. The studied fluorocarbons, R245fa and R365mfc, represent the highest mass flow rates in the process, while the studied hydrocarbons, toluene, cyclohexane, and pentane represent the lowest mass flow rates. The studied hydrocarbons represent the highest enthalpy drop in the turbine and the studied fluorocarbons represent the lowest enthalpy drop. The studied siloxanes and high critical temperature hydrocarbons represent significantly higher expansion ratio over the turbine than the other fluids, especially when the exhaust gas temperature at the evaporator outlet is high. This can be explained by the low condensing pressure of these fluids and if the exhaust gas temperature is high at the evaporator outlet a high evaporation pressure was obtained, resulting in a large expansion ratio over the turbine. The studied fluorocarbons and pentane, which are the fluids having the lowest critical temperatures, represent the lowest expansion ratios over the turbine.

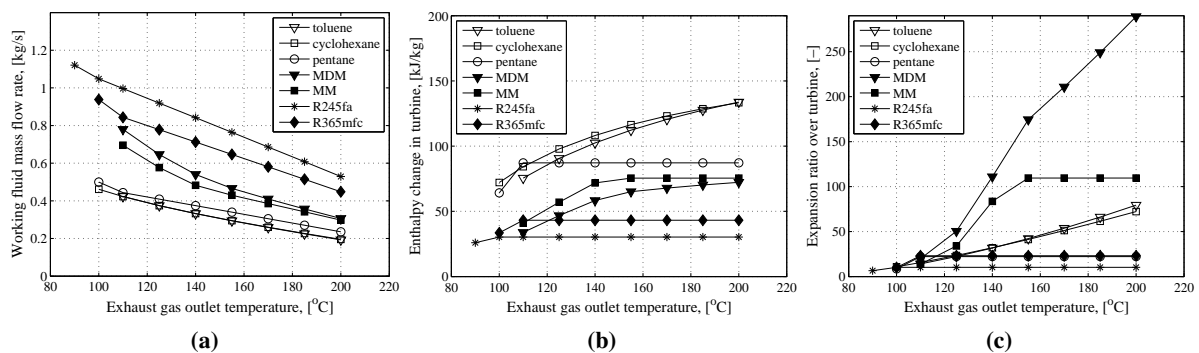


Figure 3: Results of a) working fluid mass flow rate, b) enthalpy change over the turbine, and c) expansion ratio over the turbine as a function of exhaust gas temperature at the evaporator outlet.

The calculated turbine diameters are presented in Fig. 4a, the blade height at the rotor inlet in Fig. 4b, and the rotor outlet-to-inlet blade height ratio in Fig. 4c. Based on the results, the fluids having the lowest critical temperatures presents the smallest turbine wheels and small blade heights at the turbine rotor inlet. The studied siloxanes and the hydrocarbons with the highest critical temperatures, toluene and cyclohexane, represent the largest rotor wheels and highest blade heights at the rotor inlet, especially when a low exhaust gas outlet temperature is used. These fluids also represent significantly large rotor blade

height ratios, especially with the high exhaust gas outlet temperatures. This can be mainly explained by the high expansion ratio over the turbine with these fluids, which requires a large change in the flow area over the turbine wheel. The blade heights at the rotor inlet are significantly small ranging from 1 mm to 2 mm when a high exhaust gas outlet temperature is adopted. The small blade height is estimated to cause turbine efficiency reductions due to the high tip clearance losses and relatively thick boundary layers when compared to the height of the flow channel, as well as difficulties in manufacturing the turbine wheel. On the other hand, the effect of the tip clearance at the rotor inlet on the radial turbine efficiency has been reported to be less significant when compared to significance of tip clearance loss in axial turbines (Dambach et al., 1999). The large rotor blade height ratio might cause flow separation in the rotor and thus, reducing the turbine efficiency.

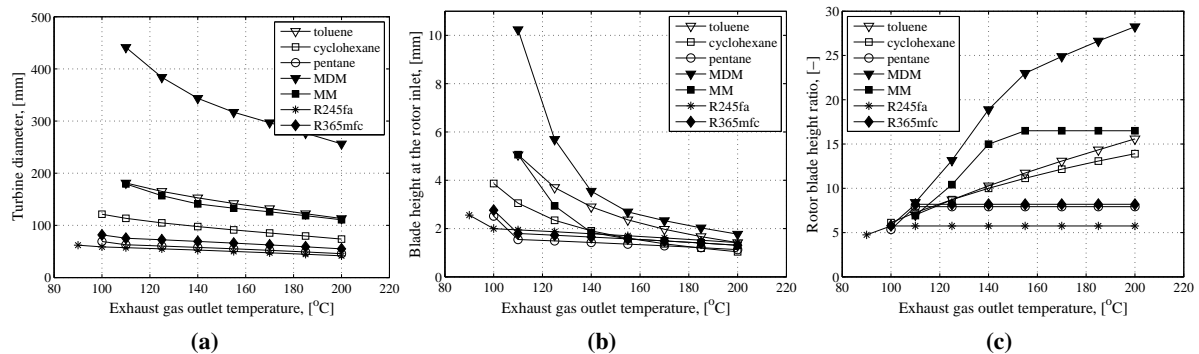


Figure 4: Results of turbine design values as a function of exhaust gas temperature at the evaporator outlet: a) rotor diameter, b) blade height at the rotor inlet, and c) rotor blade height ratio.

The Mach number at the stator outlet is presented in Fig. 5a, the peripheral speed at the turbine rotor inlet in Fig. 5b, and the turbine rotational speed in Fig. 5c. Fig 5a shows that all the studied fluids have a supersonic flow at the turbine stator outlet. The studied siloxanes and the hydrocarbons, toluene and cyclohexane, represent the highest Mach numbers at the stator outlet while the fluids with the lowest critical temperatures, namely R245fa, R365mfc, and pentane represent the lowest Mach numbers. The highly supersonic flow requires the use of accurate design methods for the stator flow channel in order to reduce the losses. In addition, the losses related to the stator-rotor interaction and to the reflection of shock waves from the rotor blades have been identified as a significant source of losses in this type of turbines (Rinaldi et al., 2013). The studied hydrocarbons represent the highest peripheral speed at the rotor inlet and the studied fluorocarbons represent the lowest values of peripheral speed. The high peripheral speed causes higher stresses for the turbine wheel, which should be taken into account in the mechanical design of the turbine wheel. The highest turbine rotational speed is achieved with pentane and the lowest rotational speed is achieved with the siloxane MDM. The high rotational speed increases the turbine shaft mechanical and windage losses and sets demands for the bearing design.

In general, the results indicate that by designing the cycle for low exhaust gas outlet temperatures and thus, resulting in a low evaporation pressure, several benefits can be achieved from the point of view of the turbine design. The working fluid mass flow rate and the blade height at the rotor inlet are higher and the turbine wheel is larger. In addition, the rotor blade height ratio, expansion ratio over the turbine, rotational speed and the Mach number at the stator outlet are lower when compared to a cycle designed with a higher evaporation pressure.

3.3 Effect of specific speed on turbine design

The effect of the turbine specific speed on the turbine design is presented and discussed in the following. The working fluid is toluene and the degree of reaction is about 0.5 in the calculated cases. The effect of the turbine specific speed on the rotor diameter is presented in Fig. 6a and on the turbine rotational

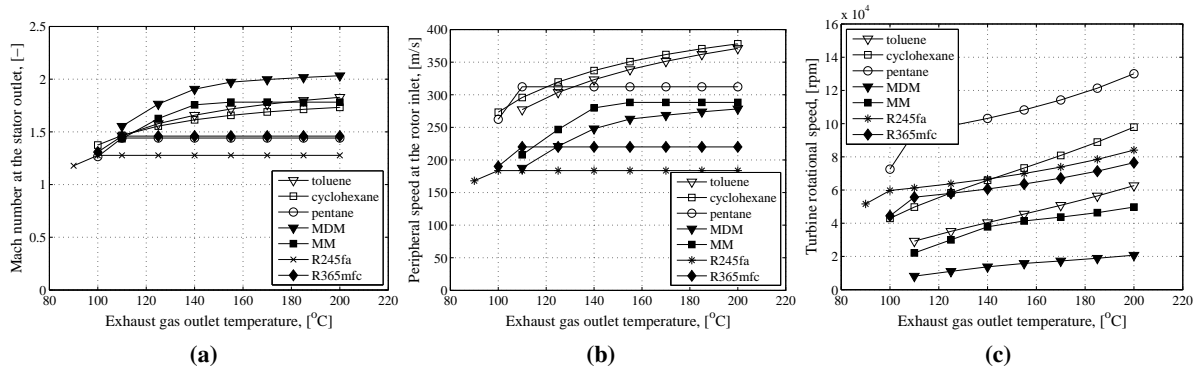


Figure 5: Results of a) Mach number at the stator outlet, b) peripheral speed at the turbine rotor inlet, and c) turbine rotational speed.

speed in Fig. 6b. The effect of the turbine specific speed on the blade height at the rotor inlet is presented Fig. 6c, and on the turbine rotor blade height ratio in Fig. 6d. The results presented in Figs. 6a-d, show

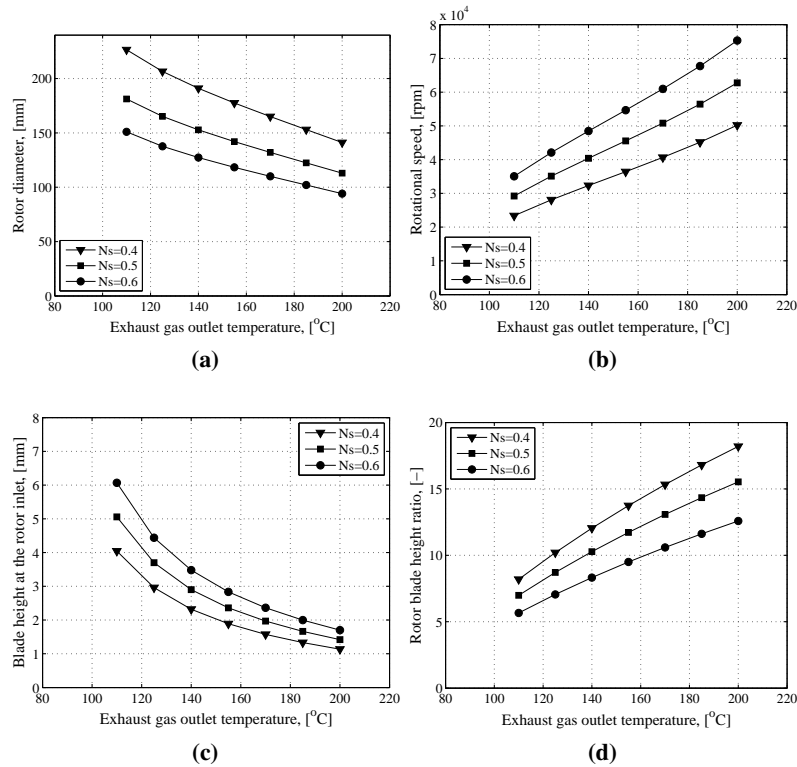


Figure 6: The effect of turbine specific speed on a) rotor diameter, b) rotational speed, c) blade height at the rotor inlet, and d) rotor blade height ratio. The working fluid is toluene.

that by selecting a low specific speed the turbine wheel is larger and the rotational speed is lower, when compared to a turbine design with a high specific speed. Thus, a turbine with a low specific speed can be considered if the turbine tends to be fast rotating and having a small diameter with a high specific speed. On the other hand, the results indicate that the blade height at the rotor inlet is smaller and the rotor blade height ratio is higher, possibly resulting to lower turbine efficiency when a low specific speed is selected, when compared to a turbine designed for higher specific speed.

3.4 Effect of degree of reaction on turbine design

The effect of the turbine's degree of reaction on the turbine design is presented and discussed in this section. The working fluid is toluene and the specific speed is 0.5 in the calculated cases. The effect of the degree of reaction on the rotor diameter, on the blade height at the rotor inlet, on the turbine rotor blade height ratio and on the Mach number at the stator outlet is presented in Fig. 7a, 7b, in Fig. 7c and 7d, respectively. The results presented in Figs. 7a-d, show that by selecting a low degree of reaction

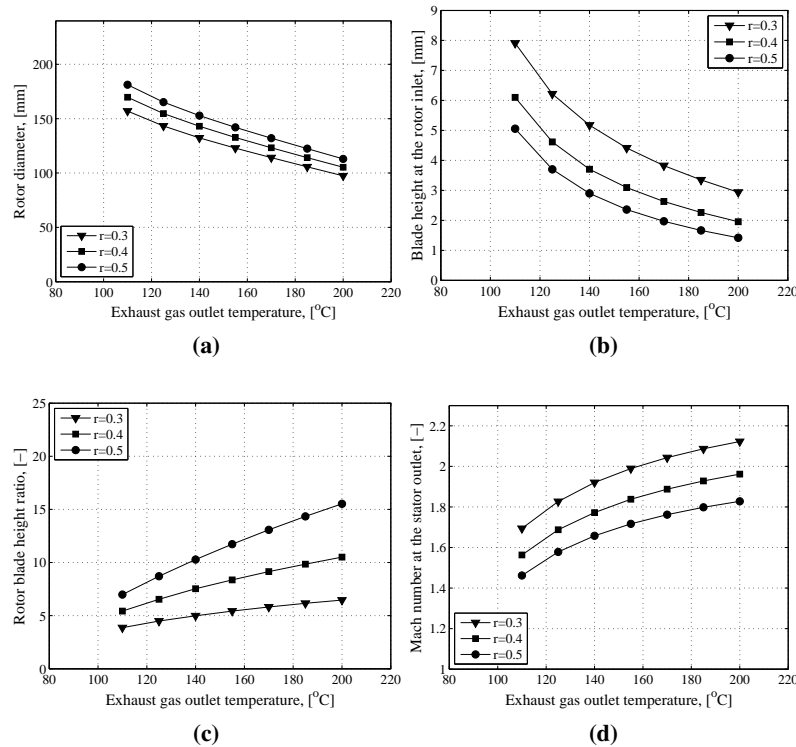


Figure 7: The effect of the degree of reaction on a) rotor diameter, b) blade height at the rotor inlet, c) rotor blade height ratio, and d) Mach number at the stator outlet. The working fluid is toluene.

the rotor wheel is smaller and the blade height at rotor inlet is higher when compared to a higher value of degree of reaction. In addition, the rotor blade height ratio is significantly reduced by selecting a low degree of reaction. However, the Mach number at the stator outlet is higher when a low degree of reaction is adopted. This can be explained by the fact that the pressure ratio over the turbine stator is high when a low degree of reaction is selected resulting in a high stator outlet velocity. In addition, the selection of low degree of reaction increases the velocity ratio c_{u1}/u_1 and there is a risk of a flow separation at the rotor inlet caused by a large incidence angle of the relative velocity if radial blades at the rotor inlet are considered. Thus, the use of bent blades at the rotor inlet, as were used e.g. in the turbine presented in (van Buijtenen et al. 2003), could be considered if a low degree of reaction is selected.

4. CONCLUSIONS

In this study, a simplified design tool of a radial turbine was coupled with a thermodynamic analysis tool to evaluate and compare different working fluids, not only from the thermodynamic point of view, but taking into account the turbine design considerations as well. Based on the results the selection of working fluid highly influences not only the thermodynamic performance of the cycle, but has a significant impact on the turbine dimensions and rotational speed as well. In general, the design of small-scale ORC turbines is difficult because the turbine wheels tend to be small and fast rotating, and represent small blade heights at the rotor inlet. The largest turbine wheels and the lowest rotational speeds were

obtained with fluids having the highest critical temperatures. However, the results indicate that the use of a fluid with a high critical temperature leads to a high expansion ratio over the turbine and thus, represents highly supersonic flow at the stator outlet and large rotor blade height ratio, which is estimated to reduce the achievable turbine efficiency. The results indicate that by designing the cycle for a low evaporation pressure several benefits can be achieved from the turbine design point of view. The working fluid mass flow rate and the blade height at the rotor inlet is higher and the turbine wheel is larger. In addition, the rotor blade height ratio, expansion ratio over the turbine, the rotational speed and the Mach number at the stator outlet are lower when compared to a cycle designed for a higher evaporation pressure. Thus, if a small-scale ORC adopting a single-stage turbine is considered, it might be beneficial to design the cycle for a low evaporation pressure despite the reduction in the cycle efficiency. It was also observed that the turbine dimensions are very sensitive on the choice of turbine specific speed and degree of reaction. Loss correlations for high expansion ratio radial turbines for ORC applications should be created and implemented in the future. The authors suggest that more experimental work on ORC turbines should be carried out to provide knowledge on the performance and feasibility of small-scale ORC systems based on turbine technology.

NOMENCLATURE

c	absolute velocity	(m/s)
h	specific enthalpy	(kJ/kg)
P	power	(kW)
p	pressure	(bar)
q_m	mass flow rate	(kg/s)
q_v	volumetric flow rate	(m ³ /s)
T	temperature	(°C)
c	absolute flow velocity	(m/s)
N_s	specific speed	(-)
n	rotational speed	(rpm, 1/s)
w	relative velocity	(m/s)
u	tangential/peripheral velocity	(m/s)
D	diameter	(m)
r	degree of reaction	(-)
α	absolute flow angle	(deg)
ω	angular speed	(rad/s)

Subscript

ev	evaporation
s	isentropic
st	static
rot	rotor
t	turbine/blade tip
h	blade hub
0	turbine inlet
1	rotor inlet/stator outlet
2	rotor outlet
u	tangential component
r	radial component

REFERENCES

- Balje, O.E., 1981, Turbomachines: A Guide to Design, Selection and Theory. John Wiley and Sons, New York.
- Colonna P., Rebay S., Harinck J., and Guardone A., 2006, Real-Gas Effects in ORC Turbine Flow

- Simulations: Influence of Thermodynamic Models on Flow Fields and Performance Parameters. Proceedings of ECCOMAS CFD, September 5-8.
- Colonna P., Casati E., Trapp C., Mathijssen T., Larjola J., Turunen-Saaresti T., and Uusitalo A., 2015, Organic Rankine Cycle Power Systems: from the Concept to Current Technology, Applications and an Outlook to the Future. *J. Eng. Gas Turbines and Power*, vol. 137:10.1115/1.4029884.
- Dambach R., Hodson H.P., and Huntsman I., 1999, An Experimental Study of Tip Clearance Flow in a Radial Inflow Turbine. *Journal of Turbomachinery*, vol. 121(4): 644-650.
- Guardone A., Spinelli A., and Dossena V., 2013, Influence of Molecular Complexity on Nozzle Design for an Organic Vapor Wind Tunnel. *J. Eng. Gas Turbines and Power*, vol. 135:042307.
- Harinck J., Guardone A., and Colonna P., 2009, The Influence of Molecular Complexity on Expanding Flows of Ideal and Dense Gases. *Physics of Fluids*, vol. 21:086101.
- Harinck J., Turunen-Saaresti T., Colonna P., Rebay S., and van Buijtenen J., 2010, Computational Study of a High-Expansion Ratio Radial Organic Rankine Cycle Turbine Stator. *J. Eng. Gas Turbines and Power*, vol. 132:054501.
- Harinck, J., Pasquale, D., Pecnik, R., van Buijtenen, J., and Colonna, P., 2013, Performance improvement of a radial organic Rankine cycle turbine by means of automated computational fluid dynamic design. *Journal of Power and Energy*, vol. 227(6), p.637-645.
- Kang S.H., 2012, Design and experimental study of ORC (organic Rankine cycle) and radial turbine using R245fa working fluid. *Energy*, vol.41(1), p.514-524.
- Klonowicz P., Borsukiewicz-Gozdur A., Hanausek P., Krylłowicz W., and Brüggemann., 2014, Design and performance measurements of an organic vapour turbine. *Applied Thermal Engineering*, vol.63(1), p.297-303.
- Macchi E., 1977, Design criteria for turbines operating with fluids having a low speed of sound. Von Karman Institute for Fluid Dynamics. Closed Cycle Gas Turbines, Lecture series 100, May 9-13.
- Maraver D., Royo J., Lemort V., and Quoilin S., 2014. Systematic optimization of subcritical and transcritical organic Rankine cycles (ORCs) constrained by technical parameters in multiple applications. *Applied energy*, 117, p.11-29.
- Pini M., Persico G., Casati E., and Dossena V., 2013, Preliminary Design of a Centrifugal Turbine for Organic Rankine Cycle Applications. *J. Eng. Gas Turbines and Power*, vol. 135(4):10.1115/1.4023122.
- Rinaldi E., Buonocore A., Pecnik R., and Colonna P., 2013, Inviscid stator/rotor interaction of a single stage high expansion ratio ORC turbine. 2nd International Seminar on ORC Power Systems. Rotterdam, The Netherlands, 7-8 October.
- Rohlik H., 1972, Radial Inflow Turbines, Chapter 10 in Glassman A. J., Turbine Design and Application: Volume 1-3, NASA, 388 pages.
- Uusitalo A, Honkatukia J, Turunen-Saaresti T, Colonna P, Larjola J., 2013, Siloxanes as working fluids for mini ORC turbogenerators based on "high speed technology". *J. Eng. Gas Turbines and Power*, vol.135;042305.
- Uusitalo A., Turunen-Saaresti T., Guardone A., and Grönman A., 2014, Design and Modeling of Highly Supersonic Small Scale Radial ORC Turbine Stator with High Molecular Complexity Working Fluids. ASME Turbo Expo 2014, 16-20 June 2014, Germany.
- van Buijtenen J.P., Larjola J., Turunen-Saaresti T., Honkatukia J., Esa H. and Backman J., 2003, Design and validation of a new high expansion ratio radial turbine for ORC application. 5th European conference on Turbomachinery, Prague, March 17-22.
- Verneau A., 1987, Supersonic Turbines for Organic Fluid Rankine Cycles from 3 to 1300 kW: Small High Pressure Ratio Turbines. Von Karman Institute for Fluid Dynamics, Lecture series 7, June 15-18.

EXPERIMENTAL INVESTIGATION OF A RADIAL MICROTURBINE IN ORGANIC RANKINE CYCLE SYSTEM WITH HFE7100 AS WORKING FLUID

Tomasz Z. Kaczmarczyk*, Grzegorz Żywica, Eugeniusz Ihnatowicz

The Szewalski Institute of Fluid-Flow Machinery, Polish Academy of Sciences
Centre of Mechanics of Machines, Department of Turbine Dynamics and Diagnostics
Gen. J. Fiszera 14 st., 80-231 Gdańsk, Poland
tkaczmarczyk@imp.gda.pl, gzywica@imp.gda.pl, gieihn@imp.gda.pl

* Tomasz Z. Kaczmarczyk, e-mail: tkaczmarczyk@imp.gda.pl

ABSTRACT

The paper presents the results of experimental investigation of the ORC system with prototype microturbine. The prototype of biomass boiler has been used as a heat source. The boiler with a power rating of 25 kW_{th} is powered by biomass (wood pellets) using an auger. The biomass boiler heats thermal oil which is directed to the evaporator where the low boiling refrigerant evaporates. The maximum temperature of the thermal oil in the evaporator is about 210 °C – 215 °C. The solvent HFE7100 was used as the working fluid in the ORC system. The prototype of four-stage radial microturbine and biomass boiler has been designed and built at the Institute of Fluid-Flow Machinery of the PAS in Gdańsk. The designed electric capacity of microturbine is 2.7 kW_e at maximum speed of 24000 rpm. The isentropic efficiency for this fluid-flow machine is about 70%. The generated electricity is dissipated by an electric heater with a power of 5 kW_e and eleven light bulbs 100 W_e each. Electrical load can be adjusted according to your needs. At the inlet of the microturbine a condensate separator was applied to protect the blades from erosion and to ensure the proper operation of gas bearings. In the initial phase the steam microturbine is supplied with a high degree of superheat in the range from 30 K to 40 K (the warm phase of the microturbine). During normal operation of the microturbine, superheating degree of the low boiling fluid is in the range of 5 K to 10 K. The working fluid after expansion in microturbine is directed to the regenerator and then to the condenser. The heat supplied to the condenser is dissipated by a fan cooler with maximum power of 50 kW_{th}. Depending on the flow rate of the glycol in the condenser the absolute pressure is in the range of 1.2 bar - 3 bar and a temperature of the working fluid in the range from 20 °C to 65 °C can be obtained. The paper presents the characteristics of the ORC system and radial microturbine for different variants of flow rates for different working mediums (thermal oil, HFE7100, glycol). During testing of the ORC system with the prototype of radial microturbine and the biomass boiler (fired with wood pellets) the maximum electrical output power was around 1551 W_e.

1. INTRODUCTION

The Directive 2009/28/WE, approved by the European Union, has committed the majority of its Member States to increase the share of renewable energy sources in total energy consumption to 20% by 2020 (15% in Poland). This is not only an active fight against global climate change, but also a key contribution to boosting the development of modern technologies. That is why the scientists continue to search for new energy-saving technologies. One idea is to use new RES systems or modify existing systems by making use of CHP installations. Combined heat and power (CHP) production, e.g. in ORC systems, can be an alternative for traditional power engineering systems. The cogeneration systems are characterized by energy savings and environmental-friendly technologies. The use of micro-CHP system can easily satisfy single-family home demand for heat and electricity, reducing CO₂ emissions to atmosphere. It is estimated that in order to satisfy these demands for one single-family house, one needs to use a CHP system whose electrical power does not exceed 10 kW_e. For multi-family buildings, power capacity of CHP systems should be in the range of 10 – 30 kW_e (Liu et

al., 2011, Onovwiona et al., 2006, Quoilin et al., 2010). In order to meet the EU directives and trends, for systems using RES, a domestic micro power plant (based on the ORC cycle) has been built at the Institute of Fluid-Flow Machinery, in Gdańsk. An expansion device is seen as a key element in any ORC installation which principally decides of the whole system efficiency. That is why many scientists carry out research on ORC cycles with various types of expanders i.e. vane, scroll, piston, screw expanders as well as Stirling engines or turbines. Mayer et al. (2013) investigated into the ORC system with a scroll expander and HFC-M1 as the working fluid. The scroll Air Squared expander had the following rated parameters: expansion coefficient 3.5, nominal rotational speed 3600 rpm, pressure 13.8 bar, displacement 12 cm³/rev. Purified exhaust gases from the Capstone gas turbine were used as a heat source. The temperature of gas was about 220 °C and its mass flow was about 0.3 kg/s. The Carnot efficiency was about 10.1% and the thermal efficiency reached 5.7%. Lemort et al. (2009) investigated the ORC system with a prototype of scroll expander and working medium HCFC-123. As an expansion device a modified oil-free scroll compressor was applied. Two hot air flows were used as a heat source. The isentropic expander effectiveness was in the range from 42% to 68% for the pressure ratio of the expander in the range from 2.7 to 5.4. The maximum cycle efficiency was about 7.4%. Quoilin et al. (2010) have proposed different analytical models of components and parameters of the ORC system. Difference between the measured electric power generated by the expander and power value calculated by a numerical model was less than 10%. Declaye et al. (2013) investigated the oil-free scroll expander in an ORC system with R245fa. The scroll expander was obtained by modifying an open-drive scroll compressor to run in reverse. The maximum isentropic efficiency depends on the rotational speed. For an inlet pressure 12 bar, it ranges from 71.3% at 3500 rpm to 75.7% at 2500 rpm. The maximum shaft power is 2.00 kW at 3500 rpm for a pressure ratio of 7.18 and an inlet pressure of 12 bar. The minimum shaft power is 0.21kW at 3000 rpm for a pressure ratio of 2.36 and an inlet pressure of 9 bar. The maximum cycle efficiency is 8.54% at 3000 rpm for a pressure ratio of 7.1 and an inlet pressure of 12 bar. The minimum cycle efficiency is 0.1% at 3000 rpm for a pressure ratio of 2.36 and an inlet pressure of 9 bar. The exergetic efficiency is 48% at 3000 rpm for pressure ratio 4.32 and an inlet pressure of 12 bar. Qiu et al. (2012) tested the ORC system with 50 kW_{th} biomass-pellet boiler and vane-type air motor as an expander. The experimental results show that the CHP system generated about 860 W_e of electricity, efficiency of electricity generation was 1.41% and CHP efficiency was 78.69%. Bahrami et al. (2013) performed thermodynamic analysis of an ORC cycle, in conjunction with a Stirling engine. The following working mediums were tested: FC72, FC87, HFE7000, HFE7100, Novec649, n-pentane, R245fa and toluene. Operating temperatures of ORC was between 80 °C and 140 °C. The steam turbine was used as an expansion device. Total power efficiency in the range 34% to 42% was observed for different cases. The ORC cycle efficiency was in the range of 15-19%, depending on the used working medium. They found that the best mediums in this cycle were: toluene, HFE7100 and n-pentane. Smith et al. (2006) carried out research on the ORC cycle with R124 as a working medium. Twin screw compressor was used as an expander. The machine was coupled to a generator, rotating at 1800 rpm, using a vee belt drive. Initial tests showed that the expander generated 22 kW of shaft power with an adiabatic efficiency of 74%. The unit cost is in the range of \$1500-2000/kW_e (water cooled) and \$2500/kW_e (air cooled). Seher et al. (2012) performed experimental studies and computational simulations of the ORC system equipped with two expanders, turbine and piston machine. The heat source was a 12 l heavy duty engine. The thermal power input to the WHR (waste heat recovery) system was from 100 kW_{th} to 300 kW_{th}. They analyzed several working mediums, including water, toluene, ethanol, R246fa and MM (Hexamethydisiloxane). The piston expander operated as a single-cylinder double acting type and power take-off was at engine speed. Dimensions of the piston machine are: displacement 0.9 l, stroke 81 mm, piston diameter 87 mm. The calculated effective power of the piston machine amounts to 12 kW_e (that is about 5% of the Diesel engine power). The measured mechanical power was around 14 kW (that is about 4.3% of the engine power). The experiment was carried out using water as a working medium. The maximum water pressure reached around 32 bar and the maximum temperature was about 380 °C. The double-stage constant-pressure turbine was the second expander. The maximum speed of the turbine was 150000 rpm. The numerical simulation of the ORC cycle with water as a working medium gave the following results: maximum turbine output power 10 kW with an efficiency of 66%. The results of the measurements were as follows: maximum power reached around 9 kW at turbine's rotational speed of about 120000 rpm. The most favourable solutions are

either a piston machine using water or ethanol as working fluid and a turbine using ethanol. Kaczmarczyk et al. (2013a), Kaczmarczyk et al. (2013b) investigated the ORC system with an expansion valve (simulating work of a microturbine) and a radial microturbine. The experimental investigation conducted in the regenerative ORC test bench with a gear pump and a radial microturbine gave the following physicochemical parameters of HFE7100 (working medium): temperature 180 °C, pressure 11.76 bar, working medium flow rate 0.16 kg/s. Reaching the shaft rate of 254 Hz, the microturbine generates electric power of 360 W_e. The Carnot efficiency of the regenerative ORC system with a microturbine was about 32% and the thermal efficiency of the regenerative ORC system with a microturbine was about 5.2%. Liu et al. (2010) used a modified air turbine motor as a turbine in the ORC system. The turbine was connected to a car alternator, which was loaded with resistors and light bulbs. The researchers used two heat sources: electric heater 9 kW_e and a biomass-fired boiler with power 25 kW_{th}. As the working fluid the HFE700 and HFE7100 were used. In the ORC system with electric heater maximum electrical power was 96 W_e, electrical efficiency was 1.06% and the efficiency of the CHP system was over 83%. In the ORC system with biomass boiler electrical efficiency was 1.34%, the efficiency of the CHP system was 88%, and the maximum electric power was about 284 W_e. Li et al. (2011) presented a theoretical and experimental study of heat loss in the radial-axial turbine (with power 3.3 kW_e) in the ORC system. It was a quantitative study on the convection and radiation heat transfer. The results show that the external radiative and convective heat loss coefficient was about 3.2 W/m²K and 7.0 W/m²K respectively, when the ORC operated around 100 °C. The total heat loss coefficient in the ORC experimental test was about 16.4 W/m²K, where its value was estimated at 94.5 W_e. The expander efficiency will be overestimated by about 2.9% if the external heat loss is not taken into consideration. Pei et al. (2011) presented the results of a prototype of radial-axial turbine operating in ORC cycle with R123 as a working fluid. The turbine isentropic efficiency is about 62.5% and ORC efficiency is around 6.8%. The turbine shaft power was about 1 kW.

2. EXPERIMENTAL STAND – ORC INSTALLATION

The ORC installation in the Laboratory of Cogenerative Micro Power Plants is composed of three basic cycles: a heating cycle, cooling cycle and a working fluid cycle. The ORC test bench with a HFE7100 droplet separator is presented in Figure 1.

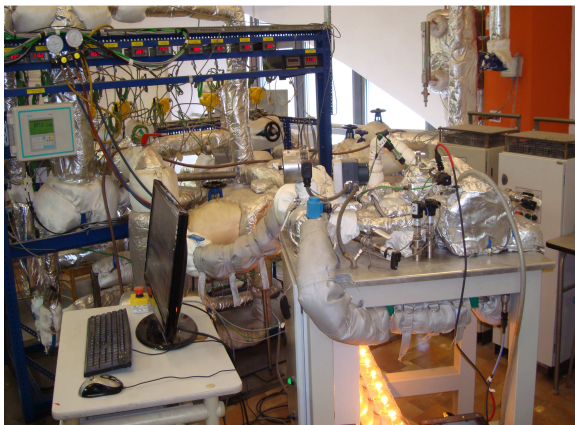


Figure 1: The ORC system with a microturbine and a set of heaters in the test bench

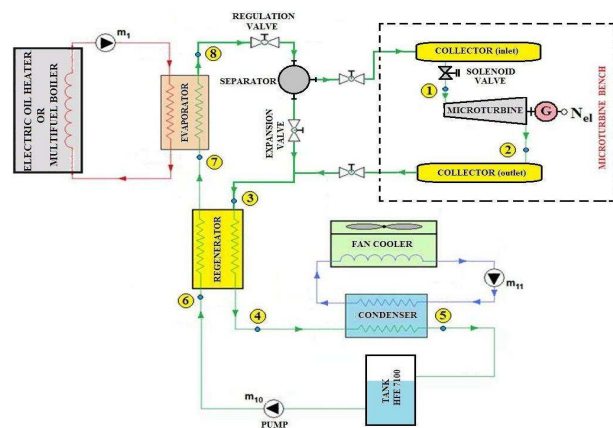


Figure 2: Measurement scheme of the regenerative ORC with a microturbine

The heating cycle consists of oil gear pumps made by Tapflo (model TG L018) and two independent heat sources: a prototypical multifuel boiler and a set of two prototypical electric thermal oil heaters that can operate independently or in series/in parallel. The regulation of rotational speed of the oil gear pumps was carried out through the frequency converter made by Bonfiglioli Synplus (model SPL200 03 F). The ORC installation can operate using an expansion valve (simulating operation of a microturbine), microturbine or a group of expanders. The gear pump used in the experimental system to feed liquid HFE7100 is supplied by Scherzinger (model 4030). The pump can provide a maximum operating pressure of 14 bar, flow rate of 15.75 l/min and rotation speed of 4000 rpm. The maximum

power output of the pump is 0.75 kW. The output capacity pump can be adjusted from 0-100%, using a frequency inverter made by LS (model iG5A). The measurement scheme of the regenerative ORC system with a microturbine is presented in Figure 2. The characteristic points 1 – 8 for the regenerative cycle have been marked. These points were used to determine the changes in thermodynamic state of the working medium in the ORC installation.

2.1 Microturbine

The ORC system cooperates with a high-speed four-stage radial microturbine whose parameters are as follows: nominal power 2.7 kW_e, nominal rotational speed 24000 rpm and isentropic efficiency of about 70%. Figure 3 presents a photograph of the microturbine.

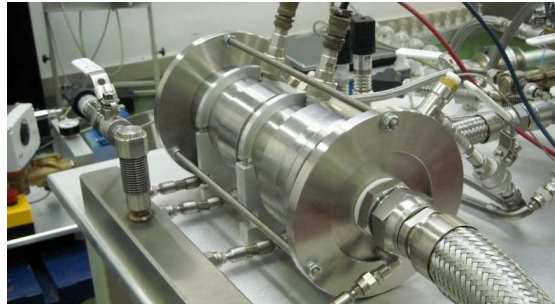


Figure 3: Experimental stand of the microturbine

The turbine shaft is integrated with an electric energy generator and encased in a sealed housing. Given the hermetic construction and the high rotational speed, aerostatic gas bearings powered by a low-boiling medium vapor were used. The microturbine is equipped with a control and measurement system which assures good functioning of the device as well as reception and conditioning of electric energy.

2.2 Heat sources

As it has previously been mentioned, the heating cycle has two heat sources. The first one is a multifuel boiler, alternatively fuelled with biomass, town gas, or gas obtained by gasification of biomass. The other heat source is a prototypical electric flow heater for thermal oil. Both the multifuel boiler (Figure 4) and the electric heater (Figure 5) can operate independently or in series. The prototypical electric flow heater for thermal oil consists of two modules: LKM-25/75-300 and LKM-25/75-301.



Figure 4: Prototype multi-fuel boiler with a solid fuel reservoir (biomass-pellets)



Figure 5: Prototype electric flow heater for thermal oil

Both modules can operate independently or in series and are designed to heat non-conductive fluids (thermal oil) to the temperature of about 250 °C with low power flow density (below 3 W/cm²) and the power of 2x24 kW_e. The heater is powered from the network with alternative (50 Hz), three-phase voltage of 3x400 VAC. The boiler is equipped with a coil heat exchanger for double exhaust gas circulation which increases its effectiveness. The maximal boiler power during biomass combustion (pellets of about 5 mm diameter) is about 30 kW_{th}.

2.3 Cooling system

The third cycle in the ORC installation is the cooling system consisting of fan coolers made by GEA (model TDR 01 06 53-C) with a water spraying system, glycol pump made by LFP (model 25 POeC100 Mega) with inverters, JAD-type and plate heat exchangers and piping. The cooling system of the ORC installation performs two tasks. First, it enables cooling of the thermal oil coming to the evaporator, and thus increases the range of adjustment of oil temperature. Moreover, additional cooling of oil protects the system against the excessive temperature rise or enables quick cooling of thermal oil in case of loss of electricity or a breakdown, which assures higher safety while operating the ORC installation. Oil cooling is performed with the use of a JAD-type heat exchanger, cooling glycol pump and a fan cooler. The other important task of the cooling system is quick cooling of the HFE7100 vapor in the condenser (plate exchanger), in a way to obtain liquid of the temperature of 65 °C at the inlet of the circulation pump.

2.4 The measuring and data acquisition system

The measuring system is based on the National Instruments (NI) devices. The NI PXIe-8130 controller, with appropriate software, controls the operation of the system. Signals from temperature, pressure, power and flow rate sensors, after adjustment in the SCXI-1102b module, are converted into digital form using the data acquisition (DAQ) boards: PXI-6280 and PXI-6251. The NI SCXI-1102B amplifier module with the SCXI-1303 terminal block, the SCXI-1125 and the SCXI-1313 were applied to generate both analogue and digital control signals. The software for the measurement system was made using the NI LabVIEW graphical programming platform. All temperatures were measured with a type K (model TP-211K-b) thermocouple having a diameter of 0.5 mm and a length of 100 mm, with an accuracy of $\pm 0.1^\circ\text{C}$ (made by Czaki). All pressures were measured with pressure transducers made by Trafag (model NAH 8253), with accuracy of 0.15% over the full scale range (16 bar). Differential pressure were measured with a smart differential pressure transmitters by Aplisens (model APR-2000ALW and APR-2200ALW) with permissible measuring error $\pm 0.1\%$, accuracy of 0.075% over the full scale range (0.5 bar). The Flow rate of the thermal oil was measured with an ultrasonic flowmeter made by Simens (model Sitrans FUS1010,) with 1% at $v \geq 0.3$ m/s. The flow rate of the HFE7100 was measured using Coriolis mass flowmeter made by Simens (model Sitrans FC Massflo Mass 2100) with an accuracy of $\pm 0.1\%$. The flow rate of the glycol was measured using turbine flowmeter made by Hoffer (model HO3/4X3/4-30-B-1) with an accuracy of $\pm 0.25\%$. The electric power output of the generator was measured using a meter of network parameters made by Lumel (model ND20) with phase current and voltage $\pm 0.2\%$; power (active, reactive and apparent) $\pm 0.5\%$; tangent $\varphi \pm 1\%$; frequency $\pm 0.2\%$ of the measured value, active/reactive energy $\pm 0.5\%$.

2.5 Measurement process

As a result of heating the working medium (thermal oil, HFE7100 and glycol), the changes in the flow rate take place, being caused by the change of physicochemical parameters (i.e. density, viscosity). The definition of steady state was introduced. Steady state denotes the state in which the flow rate change of the working medium does not exceed 1% of the maximum flow rate for 15 minutes. The acceptable maximal (1%) flow rates are: for the thermal oil 0.004 kg/s, for the HFE7100 0.002 kg/s and for the glycol 0.005 kg/s. Additionally, the change of average pressure in the steady state should not exceed 0.12 bar (i.e. 1% of the maximum pressure value) for 15 minutes, and the changes in temperature values should not exceed $\pm 1^\circ\text{C}$.

3. EXPERIMENTAL RESULTS OF MICROTURBINE IN THE ORC CYCLE

3.1 Thermal-flow characteristics of the ORC installation

Figure 6 presents the graph of the working medium (HFE7100 and thermal oil) temperature changes in the evaporator (system with an electric flow heater for thermal oil).

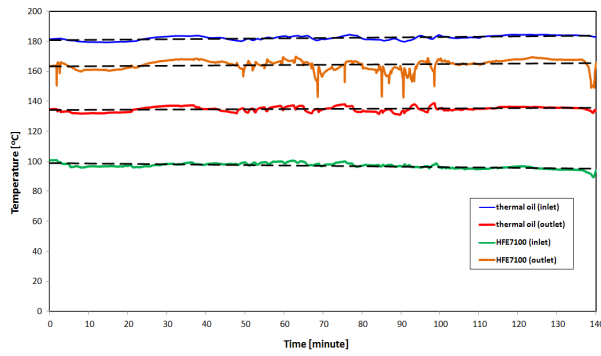


Figure 6: The temperature of HFE7100 and thermal oil in the evaporator vs time

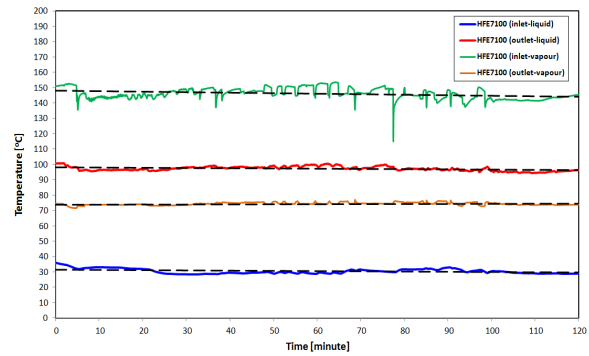


Figure 7: The temperature of HFE7100 in the regenerator vs time

Figure 6 shows that the temperature of thermal oil at the inlet to the evaporator was stable reaching about 182 °C and was about 138 °C at the outlet. The temperature of HFE7100 at the inlet to the evaporator was about 100 °C and reached about 163 °C at the outlet. The temperature changes of HFE7100 in the regenerator on the liquid and vapor sides in the steady state are presented in Figure 7. Figure 7 shows that the temperature of HFE7100 at the inlet to the vapour side of the regenerator was about 145 °C, and about 75 °C at the outlet, which gives the temperature difference of about 70 °C. The temperature of HFE7100 at the inlet to the liquid side of the regenerator was about 30 °C and about 98 °C at the outlet. Figure 8 presents the temperature changes in the HFE7100 and glycol in the condenser in the steady state.

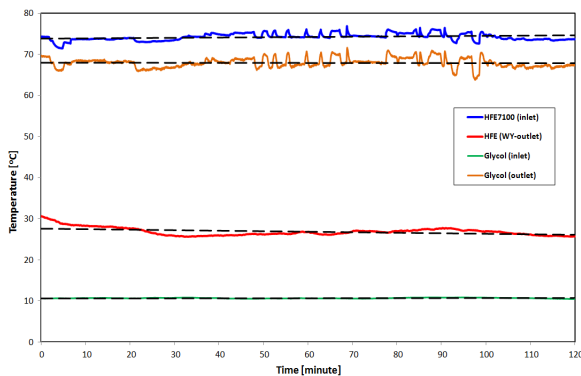


Figure 8: The temperature of HFE7100 and glycol in the condenser vs time

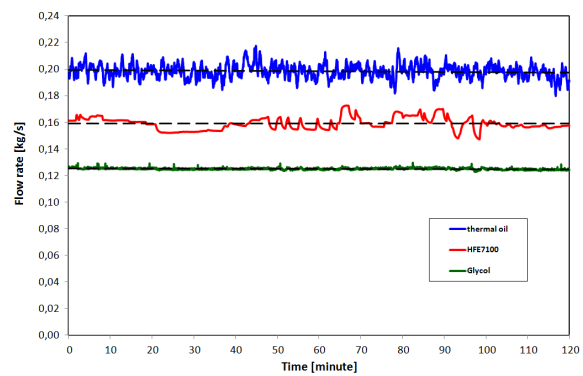


Figure 9: The flow rate of working medium vs time (during microturbine operation)

The temperature of glycol (Figure 8) at the inlet to the condenser was about 10 °C and 68 °C at the outlet. The temperature of HFE7100 at the inlet to the condenser reached about 75 °C and was 28 °C at the outlet. Figure 9 presents the flow rate waveforms for thermal oil, HFE7100 and glycol measured during microturbine operation. The analysis of the measurement data shows that the average flow rate of the thermal oil was about 0.21 kg/s. Moreover, the average flow rate values for the HFE7100 and glycol were around 0.162 kg/s and 0.125 kg/s, respectively.

3.2 The radial microturbine characteristics

Figure 10 presents the output voltage curve of the radial microturbine recorded during the measurement. Load current diagram of the microturbine generator was shown on Figure 11.

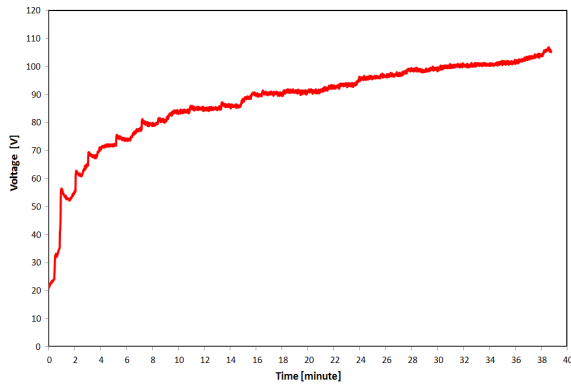


Figure 10: Voltage generated of the radial microturbine vs time

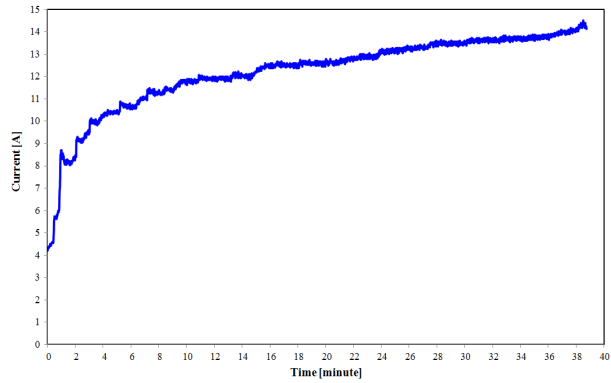


Figure 11: Load current of the radial microturbine vs time

Maximum voltage generated by the microturbine was around 107 V, while the maximum load current was about 14.5 A. Electrical power curve for the radial microturbine operating in the ORC system was shown in Figure 12. The Figure 13 presents the graph containing the course of microturbine rotational speed in relation to the measurement time.

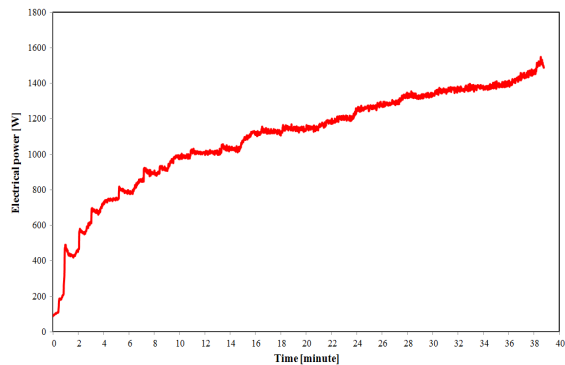


Figure 12: Electric power curve registered during microturbine operation

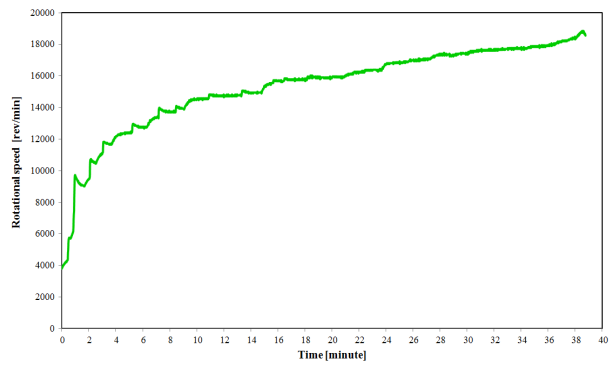


Figure 13: Microturbine rotational speed registered during the measurement

The maximum electric power generated by the microturbine reached the level of 1551 W_e, at the rotational speed of about 18700 rpm. The electric power generated by the microturbine versus rotational speed and pressure drop in the microturbine are shown in Figures 14 and 15 respectively.

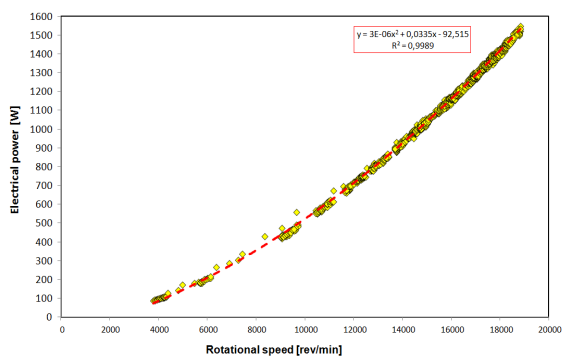


Figure 14: Electric power generated by the microturbine vs rotational speed

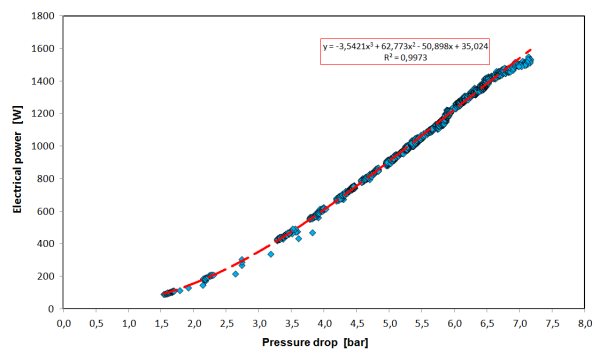


Figure 15: Electric power generated by the microturbine vs pressure drop

On the basis of Figures 14 and 15, knowing the value of rotational speed or pressure drop in the microturbine, electric power of the microturbine can be assessed quickly and easily across the entire power range. These two figures contain red dashed lines representing linear regression, the coefficients of which were calculated by the least squares method. The regression lines are presented

with their corresponding equations and coefficients (R^2). The electric power generated by the microturbine versus pressure ratio and inlet pressure is shown in Figures 16 and 17, respectively.

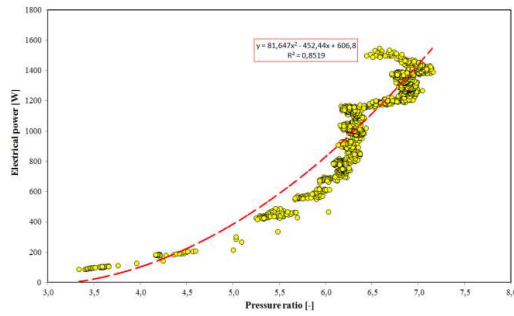


Figure 16: Electric power generated by the microturbine vs pressure ratio

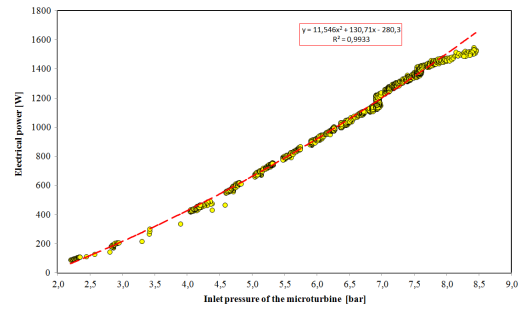


Figure 17: Electric power generated by the microturbine vs inlet pressure

Figure 16 shows that when the pressure ratio is equal to 7, the power generated by the microturbine amounts 1480 W_e. The maximum electric power was generated by the microturbine when the supply pressure was 8.5 bar (Figure 17) and reached about 1550 W_e. The Figures 16 and 17 contain linear regression lines with their corresponding equations and coefficients (R^2). Figures 18 and 19 present the diagram T-s and P-v for the HFE7100 in the ORC system with regeneration, respectively.

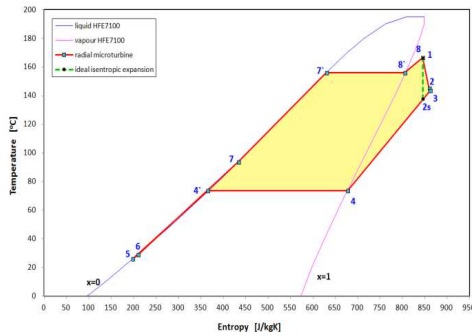


Figure 18: T-s diagram ORC system

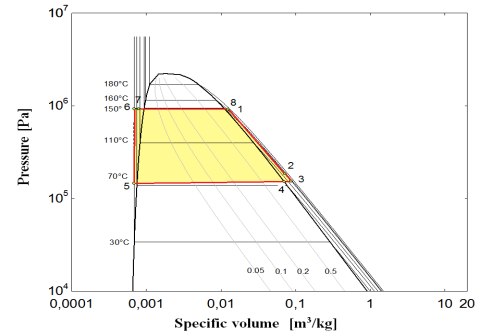


Figure 19: P-v diagram ORC system

Figures 18 and 19 shows the temperatures of HE7100 in inlet and outlet of the microturbine were 166.5 °C and 145 °C respectively. The pressure value at the microturbine inlet was 9.21 bar and outlet 1.86 bar. In this case, efficiency of the radial microturbine amounted to 70.61% and the ORC system efficiency was 5.95%. The calculated Carnot efficiency equalled 31.98% and the exergetic efficiency equalled 18.55%. The equations (1 - 4) on the basis of which the above-mentioned efficiencies were calculated are presented below. The Carnot efficiency was calculated by the relation:

$$\eta_c = 1 - \frac{T_{\min}}{T_{\max}} \quad (1)$$

where T_{\min} and T_{\max} – temperature for the upper and lower heat source, respectively. The isentropic radial microturbine efficiency was calculated from the relation

$$\eta_{s,turb} = \frac{h_1 - h_2}{h_1 - h_{2s}} \quad (2)$$

where h is the refrigerant enthalpy, the subscript numbers indicate the state, and the subscript s refers to the isentropic process. The thermal efficiency of the ORC system was calculated by

$$\eta_{ORC} = \frac{(h_1 - h_2) - (h_6 - h_5)}{h_8 - h_6} \quad (3)$$

where h_1, h_2, h_5, h_6 and h_8 are the specific enthalpy of the HFE7100. The exergetic efficiency was calculated from the relation

$$\eta_{exerg} = \frac{\eta_{ORC}}{\eta_C} \tag{4}$$

where η_{ORC} – thermal efficiency of the ORC system, η_C – Carnot efficiency.

Figure 20 presents comparison of the power generated by a rolling-piston expander – Zheng et al. (2013), a scroll expander – Yun et al. (2015) and a radial microturbine – present data, versus pressure ratio. Yun et al. (2015) and Zheng et al. (2013) as the working fluid used a R245fa.

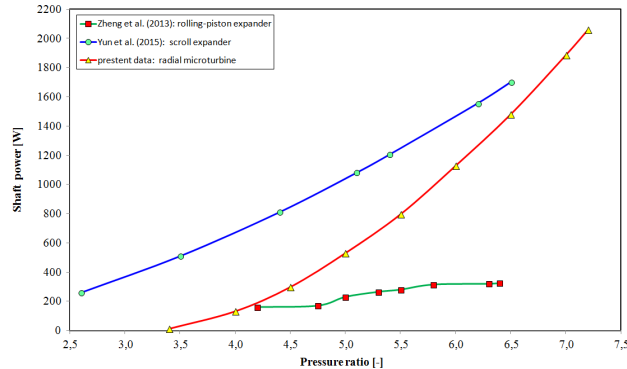


Figure 20: Comparison of the power generated by different expanders and radial microturbine vs pressure ratio

As can be seen in Figure 20, the power curves possess a similar trend. For example, for the pressure ratio 6 the output power of the scroll expander was 1450 W_e, the radial microturbine amounted to 1100 W_e, whereas in the case of the rolling-piston expander it was 300 W_e. The difference between their values manifests itself through the following fact. The values of measured power were obtained using different expansion devices and different working mediums were used.

4. CONCLUSIONS

On the basis of the conducted research on the ORC system with regeneration it was found that the maximum electrical power generated by the radial microturbine reached 1551 W_e. This value was obtained at the rotational speed of 18700 rpm and the HFE7100 supply pressure of 9.21 bar (at the microturbine inlet). The efficiency of the radial microturbine amounted to 70.61%, and the ORC system efficiency was 5.95%. The Carnot efficiency and exergetic efficiency amounted to 31.98% and 18.55%, respectively. The power characteristics contain regression lines along with their corresponding equations in order to facilitate the analyses and comparisons for other researchers.

NOMENCLATURE

h	specific enthalpy	(J/kg)
η	efficiency	(-)
T	temperature	(°C)

Subscript

C	Carnot
e	electrical
exerg	exergy
min	minimum
max	maximum
ORC	organic Rankine cycle

s	isentropic
th	thermal
turb	turbine

REFERENCES

- Bahrami, M., Hamidi, A. A., Porkhial, S., 2013, Investigation of the effect of organic working fluids on thermodynamic performance of combined cycle Stirling-ORC. *International Journal of Energy and Environmental Engineering*, 4: p. 1 -9.
- Declaye, S., Quoilin, S., Guillaume, L., Lemort, V., 2013, Experimental study on an open-drive scroll expander into an ORC (Organic Rankine Cycle) system with R245fa as working fluid, *Energy*, 55: p. 173-183.
- Kaczmarczyk, T. Z., Ihnatowicz, E., Żywica, G., Bykuć, S., Kozanecki, Z., 2013a, Z., Initial experimental investigation of the ORC system in a cogenerative domestic power plant with a microturbine, *8th World Conference on Experimental Heat Transfer, Fluid Mechanics, and Thermodynamics*, Lisbon, Portugal.
- Kaczmarczyk, T. Z., Ihnatowicz, E., Bykuć, S., Żywica, G., Kozanecki, Z., 2013b, Experimental investigation of the ORC system in a cogenerative domestic power plant with a microturbine and an expansion valve, *ASME ORC 2nd International Seminar on ORC Power System*, Rotterdam, The Netherlands.
- Lemort, V., Quoilin, S., Cuevas, C., Lebrun J., 2009, Testing and modeling a scroll expander integrated into an Organic Rankine Cycle, *Applied Thermal Engineering*, 29: p. 3094-3102.
- Li, J., Pei, G., Li, Y., Ji, J., 2011, Evaluation of external of heat loss from a small-scale expander used in organic Rankine cycle, *Applied Thermal Engineering*, 31: p. 2694-2701.
- Liu, H., Qiu, G., Shao, Y., Daminabo, F., Riffat, S. B., 2010, Preliminary experimental investigations of a biomass-fired micro-scale CHP with organic Rankine cycle, *International Journal of Low-Carbon Technologies*, 5: p. 81-87.
- Liu, H., Shao, Y., Li, J., 2011, A biomass-fired micro-scale CHP system with organic Rankine cycle (ORC) – Thermodynamic modelling studies, *Biomass and Bioenergy*, 35: p. 3985-3994.
- Meyer, D., Wong, Ch., Engel, F., Krumdieck, S., 2013, Design and build of 1 kilowatt Organic Rankine Cycle power generator, *35th New Zealand Geothermal Workshop*, Rotorua, New Zealand.
- Onovwiona, H. I., Ugursal, V. I., 2006, Residential cogeneration systems: review of the current technology, *Renewable and Sustainable Energy Reviews*, 10: p. 389-431.
- Pei, G., Li, J., Li, Y., Wang, D., Ji J., 2011, Construction and dynamic test of a small-scale organic rankine cycle, *Energy*, 36: p 3215-3223.
- Qiu, G., Shao, Y., Li, J., Liu, H., Riffat, S. B., 2012, Experimental investigation of a biomass-fired ORC –based micro-CHP for domestic applications, *Fuel*, 96: p. 374 – 382.
- Quoilin, S., Lemort, V., Lebrun, J., 2010, Experimental study and modeling of an Organic Rankine Cycle using scroll expander, *Applied Energy*, 87: p. 1260-1268.
- Seher, D., Lengenfelder, T., Gerhardt, J., Eisenmenger, N., Hackner, M., Krinn, I., 2012, Waste Heat Recovery for Commercial Vehicles with a Rankine Process, *21st Aachen Colloquium Automobile and Engine Technology*, Aachen, Germany.
- Smith, I. K., Stosic, N., Kovacevic, A., Langson, R., 2006, Cost effective small scale ORC for power recovery from low enthalpy geothermal resources. *Proceedings of ASME International Mechanical Engineering Congress and Exposition*, Chicago, Illinois, USA.
- Yun, E., Kim, D., Yoon, S. Y., Kim, K. Ch., 2015, Experimental investigation of an organic Rankine cycle with multiple expanders used in parallel, *Applied Energy*, 145: p. 246-254.
- Zheng N., Zhao L., Wang X.D., Tan Y.T.: Experimental verification of a rolling-piston expander that applied for low-temperature Organic Rankine Cycle, 2013, *Applied Energy*, 112, p. 1265-1274

ACKNOWLEDGEMENT

The research work presented in this article was supported by the scientific project POIG.01.01.02-00-016/08 “Model agroenergy complexes as an example of distributed cogeneration based on local renewable energy sources”.

OPERATIONAL EXPERIENCE ON ORC USE FOR WASTE HEAT VALORIZATION IN BIOGAS POWER PLANT

Coline Gazet¹, Arthur Leroux¹, Benoit Paillette¹, Antonin Pauchet¹

¹ENOGIA SAS,
www.enogia.com
19 Avenue Paul Hérault
13015 Marseilles, France

ABSTRACT

In the overall market of ORC, even though there is a lack of offer in the smaller power ranges (less than 100kW electrical), the potential markets and applications remain very significant. That is why the company ENOGIA was founded in 2009 by four French engineers, which purpose was to develop its own micro-turbine/alternator technology instead of the more classic “modified refrigeration screw or scroll compressor”.

The development of the ENOGIA turbo-expander took several years in order to bring an efficient, reliable and affordable expander, as well as the complete ORC system. The development path of these will be presented, as well as the many prototypes built and tested.

The current target market of ENOGIA is biogas power plant efficiency enhancement, and in order to bring efficient and cost efficient solutions for this market, we aim to improve our products with experience from real on-site demonstrators. Different ORC layouts for biogas plants enhancement were identified and will be presented. The two main approaches used are: The hot loop can use water from the biogas engine jacket, which provides low input temperatures, and can be coupled to an exhaust gas exchanger. In order to obtain higher input temperatures, it is possible to design the ORC in “direct evaporation” configuration using directly the exhaust gases. With this layout, higher condensing temperatures can be achieved and heat can therefore be used for customer applications.

In order to show return of experience on the proposed ORC for biogas plant layouts, operational perspectives from significant references of ENOGIA will be presented. Eventually those were positive experiences and ENOGIA is currently developing the product range for future projects.

1. INTRODUCTION

In the overall market of ORC, although there is a lack of commercial offer in the smaller power ranges (less than 100kW electrical), there are very significant potential markets and numerous applications, from waste heat valorization to biomass or geothermal renewable electricity production. This is the reason the company ENOGIA was founded in 2009 by four French engineers. The purpose of ENOGIA was to develop its own micro turbine expander / generator module instead of the more classic approach of “modified refrigeration screw or scroll compressor”, because it allows much more design flexibility of the ORC system.

The development of the ENOGIA turbo-expander started in 2009 and took several years in order to bring an efficient, reliable and affordable expander, as well as the complete ORC system. Hereunder is presented the development path of these, as well as the many prototypes built and tested.

2. TURBINE EXPANDER DEVELOPMENT

The first turbine was a small 3kW demonstrator with a very short lifetime of the bearing system. It was meant to be a proof of concept of the high speed close coupled turbine generator, in a hermetic housing. Thanks to this prototype, size of stators and rotors, shape of bladings, were adjusted and tested in both design and off design conditions. Even if this prototype showed significant weaknesses in the bearing system and the sealing system, the main purpose remained showing that the ENOGIA turbine is technically feasible before focusing on its lifetime in order to minimize maintenance costs.



Figure 1: First turbine prototype and bladings

The second version represented the first prototype for a 10kW unit. The expander bearing system was significantly improved with an active oil lubrication system in order to have a better long-term holding. Thanks to adapted components, we succeeded in having a very satisfying fluid-tightness. However this second version met the limitations of the electric generator, which had unsatisfying thermal transfer from the windings to the water cooling system.



Figure 2: Second turbine prototype

A third version used a different permanent magnet generator type, with direct contact between the steel laminations of the stator and the cooling system, and proved to be very reliable and thermally efficient, with reasonable temperature levels in the windings, even at full power or even higher than maximum specified power.

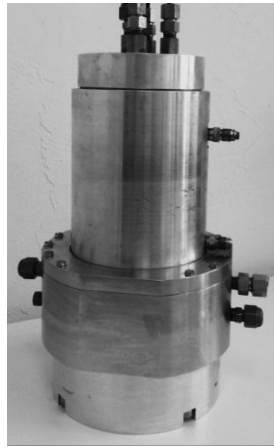


Figure 3: Third turbine prototype

An important difference between the first turbine prototypes and the operational ORC modules for biogas units are the temperatures reached at the evaporator of the ORC unit. Indeed the first tests were made in regenerative cycle with relatively high temperatures, when the biogas genset gives to the ORC warm water at 90°C, sometimes even less. Because of this, ENOGIA had to adapt its technology for biogas applications, especially the working fluid and associated rotors and stators. The company is now able to produce the two products in standardize version: low temperatures without regeneration and medium temperatures with HFE fluid and regenerative cycle.

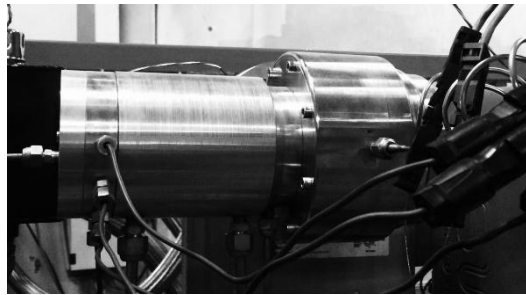


Figure 4: Commercial ENOGIA 10LT-V6 turbine in operation

One of the next steps was the improvement of the fluidic part including some modifications in the overall architecture to minimize pressure losses. The machining was also optimized to obtain the smoothest lines as possible. Moreover, the made-to-measure electric generator and shaft were another required stage to guarantee the turbine performance and reliability. The last changes were related to maintenance, making disassembly easier. ENOGIA is now following an optimization policy concerning mechanical parts in order to reduce production costs.

2. ORC FOR FARM BIOGAS

The current target market of ENOGIA is biogas power plant efficiency enhancement, and in order to bring efficient and cost efficient solutions for this market, the company aims to improve the products with experience from real on-site demonstrators.

3.1 System architecture

Different ORC layouts for biogas were identified and the two main approaches used are:

- The hot loop can use water from the biogas engine jacket, which provides low input temperatures, generally at 90°C. It can be coupled to an exhaust gas exchanger in order to recover a maximum of waste heat. In this configuration, the cold loop temperatures are around 30°C which is often too low and more complicated to reuse than higher temperatures. Sometimes, farmers can use this output heat to dry cereals, to dry straw, to heat greenhouses or to have pre-heat water for cattle. Nevertheless, given the low temperatures, the ORC is usually used only to generate more electricity.

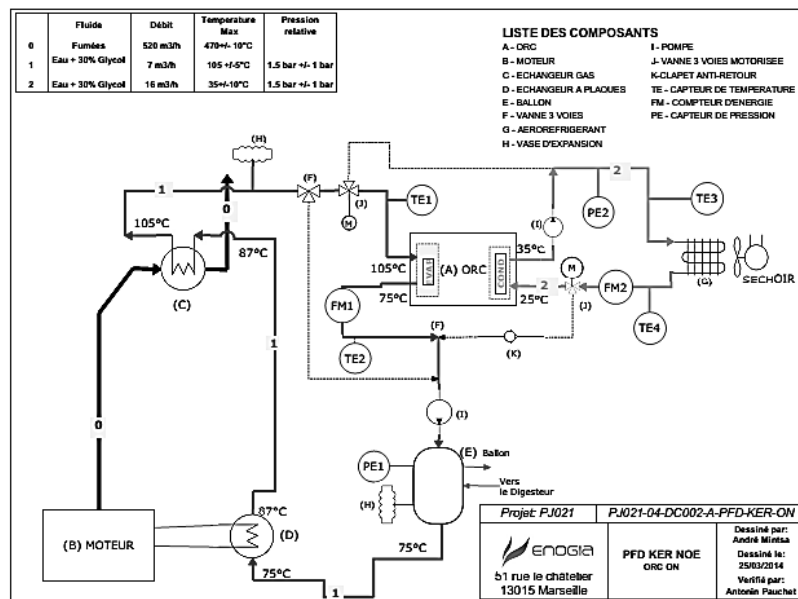


Figure 5: hot water ORC layout (Ker Noé, France)

- In order to obtain higher input temperatures, it is possible to design the ORC in “direct evaporation” configuration using directly the exhaust gases. With this layout, higher condensing temperatures can be achieved and heat can therefore be used for further customer applications especially domestic hot water. The first testing session on this technology with an ENOGIA prototype ORC unit was successfully achieved and the results are really promising.

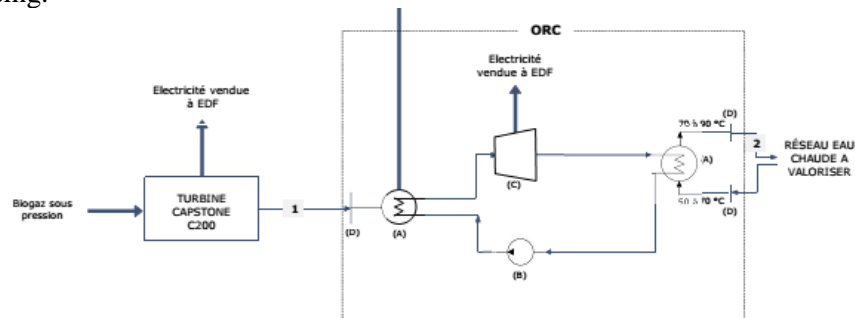


Figure 6: Exhaust gas ORC layout

3.2 Operational experience

In order to show return of experience on the proposed ORC for biogas plant layouts, operational perspectives from significant references of ENOGIA will be presented.

The first reference is the Treviso project in Italy. The ORC is a standard 10 kW unit using low temperatures: 90-70°C for hot loop with a thermal power of about 65kW and cooling ground water around 10-15°C. The main issue was the configuration of the existing plant. The exchanger of the biogas engine was too far from the ORC and piping not enough isolated, resulting in a huge loss of thermal power before the exchanger. The cooling ground water lead to working parameters quite specific (very low condensing pressures) when almost all projects use dry coolers. Thanks to this project, ENOGIA could learn and improve its technology especially concerning pump cavitation, efficiency, lubrication and vibrations besides the biogas engine.



Figure 7: Treviso ORC container with exhaust heat recovery

The second significant reference is the Ker-Noé project in France. It is the same configuration than the unit in Italy, except the cooling loop working with dry coolers. The owner uses the extra heat to dry cereals so that there is a minimum of waste heat in his biogas plant. The main feedback of this project was that theoretical pressure ratios were different from the operational ones so that ENOGIA could redesign the turbo-generator injectors. After almost a year of working, performances of the ORC were analyzed with data from tele-monitoring. The theoretical power production was about 7 kW_e with a thermal power input of 121kW_{th}.

Although the engine thermal power was lower than predicted (about 20kW_{th} less), the ORC produces more than 6kW_e with the best adapted cooling. Finally, the power delivered corresponds to 90% of what ENOGIA expected.

At full load, the isentropic efficiency of the ORC expander reaches 70% no matter the cooling temperatures are, with a generator estimated efficiency of 80%. Except little changes in the regulation law to improve it, the other theoretical parameters were adapted to the existing installation. After these improvements, efficiencies attained 5 to 7 percent range with the very low grade heat available (90/70°C CHP water loop).



Figure 8: Ker Noé ORC unit

As it was said hereinabove, ENOGIA was working on another configuration since 2013, using directly exhaust gases. The issue of “direct evaporation“ was to design an adapted gas-fluid exchanger.

This technology was tested for a special non-stationary demand with the help of IFP Energies Nouvelles (also called IFPEN), a major research and innovation center, trusted partner of ENOGIA. The tests made during 2014 and 2015 were very successful and prove the high performance of this technology, which attained approximately 10% gross efficiency.

What makes the ORC unit more efficient is also the regenerative cycle used in conjunction with a novel working fluid, a HFE fluid from 3M; indeed it improves about 30% the overall performance. Another strong point of this technology is the capability to operate with higher condensing temperatures, in the 70°C range, allowing using the ORC unit as a real CHP.

On another side, ENOGIA had been forecast the necessity of security components in the conception phase, knowing what high temperatures imply. During testing, the by-pass on the exhaust gases had been engaged several times. A unit has been recently delivered for an installer of biogas solutions and the hope will be to include an ORC on each of its installation as the technology seems really efficient.

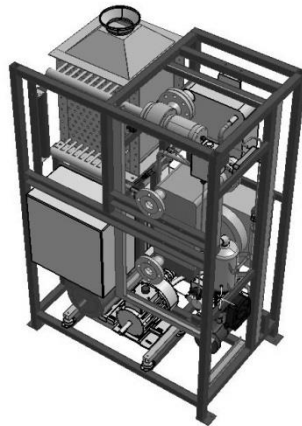


Figure 9: 10kW “Direct Evaporation” ORC unit

3. CONCLUSION

Since 2009, several ORC turbines were engineered and tested for small ORC applications, resulting in a commercial product that is available from ENOGIA, the ENO-10LT 10 kW low temperature ORC module.

This product has been tested at several customer premises in France and in Italy. Eventually those were positive experiences and ENOGIA is currently developing the product range for future projects. The company has developed a wider range of power and has already built 20kW, 40kW and 100kW units, although the last one uses a technology of turbine completely different given the higher power. Current prices go from 1800 to 3000 € per kW, depending on size and features, for ENOGIA's small ORC product range.

ENOGIA R&D team currently develops products with a direct gases evaporator, which will be available for farm biogas, and which first unit will be installed on the exhaust of a Capstone C65 turbine in a farm biogas plant in France. A key advantage of this technology will be that it will also produce hot water, improving the electrical efficiency of the biogas plant, but with very few loss of heating power as well.

ACKNOWLEDGEMENT

This R&D effort was funded by ENOGIA S.A.S., which is a French innovative company aiming to develop ORC units for small scale waste heat valorization. It is located 19 Avenue Paul Hérault 13015 Marseilles, France.

Further information is available on www.enogia.com or by email: info@enogia.com.

OPTIMIZED EFFICIENCY MAPS AND NEW CORRELATION FOR PERFORMANCE PREDICTION OF ORC BASED ON RADIAL TURBINE FOR SMALL-SCALE APPLICATIONS

Kiyarash Rahbar^{1*}, Saad Mahmoud¹, Raya K. Al-Dadah¹

¹ School of Mechanical Engineering,
University of Birmingham, Edgbaston,
Birmingham, UK, B15-2TT
e-mail: kxr965@bham.ac.uk

* Corresponding Author

ABSTRACT

The expander is considered as the most critical component of the ORC. Radial inflow turbine exhibits unique advantages of high efficiency, compact structure and light weight compared to the axial turbine when employed in the small-scale applications such as distributed CHP systems. In most of the ORC studies the turbine efficiency is assumed as a constant input for the optimization of cycle without assuring that the specified turbine efficiency can be achieved by the imposed thermodynamic conditions. In addition, atypical properties of the high-density working fluid and the near-critical operating condition of the ORC requires the turbine design procedure and parameters to be customized for the ORC. This study presents the optimization of a radial ORC turbine for maximum efficiency using mean-line modelling and genetic algorithm (GA). In contrast to the previous studies, real gas equation of state and the most advanced and recent loss models are employed in the code to capture the non-ideal behaviour of the working fluid. The optimized turbine efficiency is achieved by the GA for a wide range of operating conditions and for four organic fluids (R123, R245fa, R1233zd and isobutane). Such results are presented through new generalized maps based on the non-dimensional parameters as the flow and loading coefficients, specific speed and specific diameter. Using regression analysis a new correlation for the turbine efficiency is also presented. These new maps and the correlation are preliminary steps toward improving the previous constant turbine efficacy assumption and have great potential to be integrated with the general optimization methods of the ORC.

1. INTRODUCTION

Recently, ORC technology has received a growing attention due to its competitive performance and flexibility for small to medium scale power generation applications. Majority of studies about the organic Rankine cycle (ORC) are mainly devoted to the methods of selecting appropriate fluid for different applications (Aleksandra and Władysław, 2007, Al-Sulaiman *et al.*, 2011, Dolz *et al.* 2012, Rayegan and Tao, 2011) or to the thermodynamic optimization of the cycle based on a range of performance indexes such as the thermal and exergy efficiencies, net power output or heat exchangers area (Rashidi *et al.* 2011, Hettiarachchi, 2007, Wang *et al.*, 2013). On the other hand, little attention has been paid to the design and performance characteristics of the expander. In all above studies that seek the optimum cycle parameters, fixed values are assigned to the turbine efficiency for a wide range of operating conditions and for various working fluids while ignoring the feasibility that the turbine is capable of achieving these efficiencies in practice. In addition, due to the specific thermodynamic properties of the organic fluids (i.e. large molecular weight and low speed of sound), the turbine can behave differently from those that operate with steam or other gases and needs a special design. Moreover, operating near critical point of organic fluids makes the ideal gas models unsatisfactory and requires the real gas formulation of the turbine expansion. Considering these facets, the use of conventional generalized performance correlation charts such as (Rodgers and Geiser 1987, Balje 1981, Chen and Baines 1994) can become inaccurate when used for performance prediction of turbines operating with organic fluids. In this study a new approach for performance prediction of ORC based

on radial turbine is presented that is suitable for small scale applications such as distributed combined heat and power (CHP) systems with power capacity of up to 50kW. In this novel approach the conventional radial turbine performance maps are updated and optimized based on the real gas properties of organic fluids, genetic algorithm (GA) optimization technique and the most advanced and recent loss models by Aungier (2006). A mean-line model for design, analysis and performance prediction of radial turbines is developed in the engineering equation solver (EES) platform and directly embedded with the ORC system code. Such model allows for replacement of the fixed turbine efficiency by an interactive value that is calculated based on the ORC thermodynamic conditions and working fluids properties and assures that the optimized turbine efficiencies are achievable in practice. Such turbine efficiencies are correlated through new maps against loading and flow coefficients, specific speed and specific diameter for four different organic fluids as R123, R245fa, R1233zd and isobutane. Furthermore, a new correlation for turbine efficiency is presented by employing the regression analysis, though, it is considered to be a preliminary one as it requires to be validated against ORC experimental data which are very limited in the literature and also be extended to other working fluid families such as ethers and siloxanes.

2. NON-DIMENSIONAL PARAMETERS

Turbomachines require a set of non-dimensional parameters that can readily describe the machine's overall performance for assessment, selection and comparison. Following Whitfield and Baines (1990), the basic parameters that influence the behaviour of a turbomachine are collected in the form of a functional relation shown by equation (1).

$$\eta_{ts} = f\left(\text{ER}_{ts}, \frac{\dot{m} \sqrt{RT_t}}{P_t \pi \frac{d^2}{4}}, \frac{\omega d \pi}{60 \sqrt{RT_t} \gamma}, \text{Re}, \gamma\right) \quad (1)$$

With the assumption of single working fluid passes through the turbine and fully developed turbulent flow regime, equation (1) is simplified into a more common form as shown by equations (2) and (3).

$$\eta_{ts} = f(\phi, \psi, \text{Ma}) \quad (2)$$

$$\eta_{ts} = f(N_s, d_s, \text{Ma}) \quad (3)$$

Where ϕ , ψ , N_s , d_s and are the flow and loading coefficients, specific speed and specific diameter and are defined by equations (4) to (7) respectively.

$$\phi = \frac{C_{m5}}{U_4} \quad (4)$$

$$\psi = \frac{\Delta h_{actual}}{U_4^2} \quad (5)$$

$$N_s = \frac{\omega \sqrt{Q_5}}{\Delta h_s^{0.75}} \quad (6)$$

$$d_s = \frac{d_4 \Delta h_s^{0.25}}{\sqrt{Q_5}} \quad (7)$$

Since the ORC turbines are often operating at high expansion ratios, the effect of compressibility (Mach number) is quite significant on the expander efficiency and should be included in the final correlation. However, the Mach number is always an outcome of the turbine design procedure and there is no prior knowledge of this parameter unless the detailed turbine design procedure is conducted. Since the aim of this study is to provide a correlation that can estimate the turbine efficiency without performing the turbine design process, which is clearly impractical, and using only non-dimensional parameters, volumetric expansion ratio (VR) introduced by Macchi and Perdichizzi (1981) is also included in the analysis to address the effect Mach number. VR is the ratio of the turbine stage outlet volumetric flow rate to the turbine stage inlet volumetric flow rate and is defined by equation (8).

$$VR = \frac{Q_5}{Q_1} \quad (8)$$

VR is a more meaningful parameter (in place of expansion ratio or Mach number) that explicitly correlates the degradation of turbine efficiency due to the high Mach numbers (Macchi and Perdichizzi, 1981). In other words, VR accounts for the compressibility effect in a more generalized way than other equivalent parameters (expansion ratio and Mach number) and one can estimate its value from the cycle analysis (based on the desired cycle requirements) and without the need for completing the turbine design procedure. Hence, the efficiency of organic turbines (characterized by high Mach numbers) can be more accurately explained in the following functional form:

$$\eta_{ts} = f(\varphi, \psi, VR) \quad (9)$$

In the classical work of Balje (1981) the turbine efficiency is correlated against N_s and d_s in which the best turbine designs lay on the Cordier line. The optimum radial turbine efficiencies are obtained at N_s values in the range of 0.5 to 0.7, however, the selection of an appropriate N_s does not necessarily yield the optimum turbine design. The selection of the optimum N_s can immediately achieve the optimum d_s and eventually the turbine rotor tip diameter, though, no other information is provided regarding to other turbine geometry. Chen and Baines (1994) employed data from a wide range of designs and various applications to correlate the radial turbine efficiencies against the other set of non-dimensional parameters as φ and ψ . They showed that the maximum radial turbine efficiency is obtained at the loading and flow coefficients in the range of 0.9 to 1 and 0.2 to 0.3 respectively. The use of φ - ψ couple is advantageous compared to N_s - d_s as more information about the turbine principal dimensions such as passage areas, inlet and exit blade height and velocity triangles is achieved. The N_s - d_s or φ - ψ performance correlation charts (such as Balje, 1981 and Chen and Baines, 1994) are often dated and may not accurately represent the performance of the modern radial turbines. In addition, atypical characteristics of ORC systems such as high expansion ratios (high Mach number), real gas behavior of working fluids and small turbine dimensions makes the use of these conventional charts questionable. Therefore, it is necessary to update these charts based on real gas properties and advanced loss models while employing an optimization scheme to maximize the radial turbine efficiency.

3. INTEGRATED MODELING AND OPTIMIZATION OF RADIAL TURBINE AND ORC SYSTEM

The methodology for the integrated modeling of the ORC system with the mean-line modeling of radial turbine is followed by the previous works of authors (Rahbar *et al.* 2015a, Rahbar *et al.* 2015b). The ORC system consists of four main components as the evaporator, turbine, condenser and pump. The turbine itself consists of the volute, nozzle and rotor. Figure 1 shows the schematic of the ORC and radial turbine together with their corresponding temperature-entropy and enthalpy-entropy diagrams respectively. The turbine-ORC model is developed in the EES software to utilize its reliable thermodynamic property functions for real gas modeling of the turbine-ORC system. EES uses the fundamental (Helmholtz free energy) equation of state for determining the thermodynamic properties of the selected organic fluids and details of which can be found in (Lemmon *et al.* 2006). Modelling of the radial turbine is based on a one-dimensional assumption in which there is a mean streamline through the stage that represents the average of passage condition and the thermodynamic properties and flow features (i.e. velocity triangles) are obtained at key stations (shown in Figure 1) across the mean line. With the choice of turbine input variables listed in Table 1 and the initial estimate of the turbine efficiency, the model determines the key geometry parameters for the rotor, nozzle and volute. Using the calculated geometry and the well-established loss correlations the model determines a more accurate estimation of turbine performance. This process is repeated until convergence is achieved for the turbine efficiency. Then with the calculated turbine exit thermodynamic properties (T_5 , P_5 , h_5 , S_5) and the ORC model input variables listed in Table 1, the main cycle parameters such as thermal efficiency, net power output and pump power consumption are determined. However, selection of arbitrary values from the range of input parameters shown in Table 1 does not necessarily yields the maximum efficiency for the turbine. Therefore an optimization scheme called genetic algorithm is coupled with the turbine-ORC model to maximize the radial turbine efficiency based on the input variables of Table 1. Moreover, the

optimization algorithm is constrained by some of the critical turbine geometry parameters, flow features and ORC characteristics to assure the feasibility of the optimized turbine dimensions and to achieve high cycle and turbine performances. Figure 2 shows the flow chart of the turbine-ORC model with integrated optimization scheme that details the overall procedure. More information regarding to the detailed modeling, optimization procedure and the imposed constraints can be found in (Rahbar *et al.* 2015a, Rahbar *et al.* 2015b). The turbine loss models employed in this study are expressed as total pressure loss coefficients and include the profile, incidence, blade loading, hub to shroud, tip clearance and distortion losses which are shown by equations (10) to (15) (Aungier, 2006). It should be mentioned that the majority of loss models are developed for the gas turbines with air or flue gases as the working fluids and due to the lack of experimental data in the open literature about the performance of ORC with small-scale organic radial turbines, such loss models should be taken with some care. However, the relative comparison of the performance with different fluids is believed to be primarily correct.

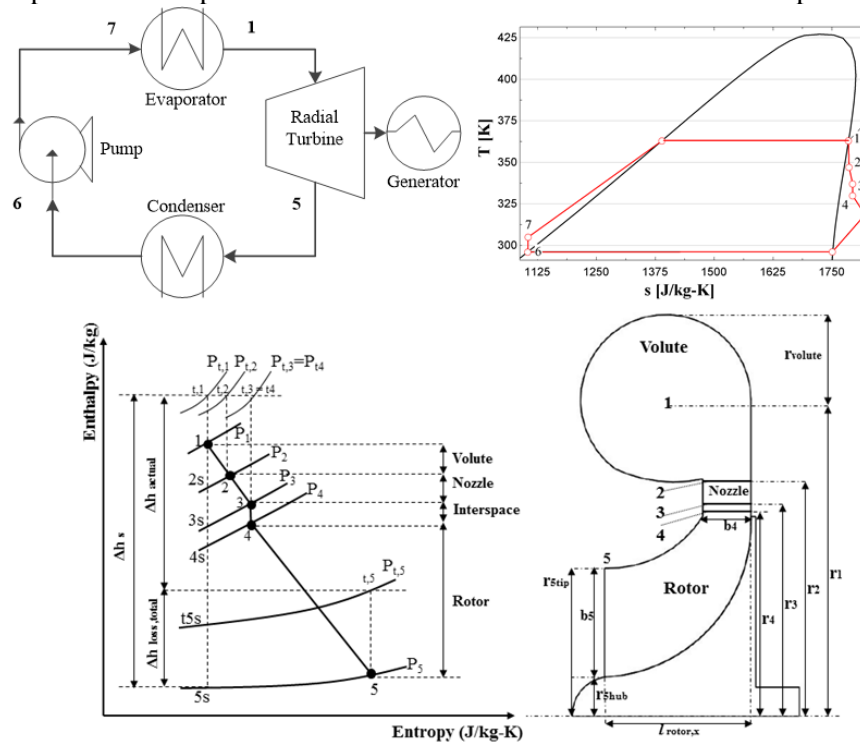


Figure 1: Schematic of the ORC system (top left), ORC temperature-entropy diagram (top right), radial turbine section view (bottom right), radial turbine enthalpy-entropy diagram (bottom left),

Table 1: Input parameters of the turbine-ORC model

Parameter	Unit	Value/Range
Turbine inlet total temperature ($T_{t,i}$)	K	343 - 393
Turbine inlet total pressure ($P_{t,i}$)	kPa	Saturation pressure
Turbine inlet degree of super heating ($T_{superheating}$)	K	1 - 5
Turbine total-to-static expansion ratio (ER_{ts})	-	2 - 8
Turbine rotational speed (ω)	rpm	30000 - 70000
Turbine loading coefficient (ψ)	-	0.7 - 1.4
Turbine flow coefficient (ϕ)	-	0.15 - 0.5
Turbine rotor exit absolute flow angle (α_5)	deg	-15 - 15
Turbine rotor exit hub to inlet radii ratio (r_{shub}/r_4)	-	0.2 - 0.3
Turbine nozzle inlet to exit radii ratio (r_2/r_3)	-	1.2 - 1.3
Turbine volute swirl coefficient (SC)	-	0.95
Turbine volute pressure loss coefficient (k_{volute})	-	0.1
ORC mass flow rate of working fluid (m)	kg/s	0.2 - 1
ORC pump efficiency (η_{pump})	-	0.7
ORC generator efficiency ($\eta_{generator}$)	-	0.96
ORC mechanical efficiency ($\eta_{mechanical}$)	-	0.96

$$Y_{profile} = \frac{2\Theta + \Delta^2}{(1 - \Delta)^2} \quad (10)$$

$$Y_{incidence} = \cos^2(\alpha_4 - \arctan(\frac{C_{m4}}{\sigma[U_4 - C_{m4} \tan(\beta_4)]})) (\frac{P_{rel,t,4} - P_4}{P_{rel,t,5} - P_5}) \quad (11)$$

$$Y_{blade,loading} = \frac{1}{24} \left[\frac{2\pi |r_5 C_{\theta 5} - r_4 C_{\theta 4}|}{l_{rotor,x} Z_{rotor} W_5} \right]^2 \quad (12)$$

$$Y_{hub,to,shroud} = \frac{1}{6} \left[\frac{\kappa b_5 \frac{W_4 + W_5}{2}}{W_5 \cos(\alpha_5)} \right]^2 \quad (13)$$

$$Y_{tip,clearance} = \frac{0.816 \sqrt{2\rho_{average} (P_{rel,t,4} - P_4)} l_{rotor,x} Z_{rotor} \epsilon}{\dot{m}} \left(\frac{P_{rel,t,4} - P_4}{P_{rel,t,5} - P_5} \right) \quad (14)$$

$$Y_{distortion} = \left(\frac{\frac{r_1 C_1}{C_2} - C_{\theta 2}}{C_2} \right)^2 \quad (15)$$

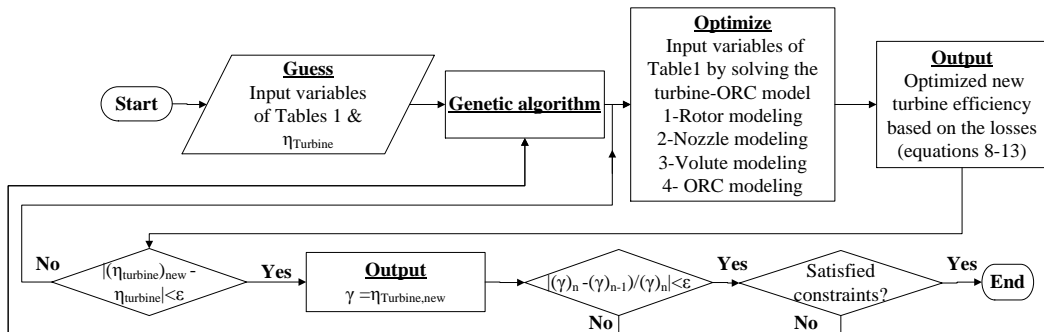


Figure 2: Flow chart for integrated modelling of turbine and ORC system with embedded optimization algorithm

4. RESULTS AND DISCUSSION

In order to conduct the optimization of turbine efficiency it is necessary to determine which parameters have the most significant effects on $\eta_{turbine}$. Following (Rahbar *et al.* 2015a, Rahbar *et al.* 2015b), among the listed parameters in Table 1, $T_{t,1}$, $P_{t,1}$, $T_{superheating}$, ER_{ts} , ω , ψ , φ , α_5 and m have the most significant effects on the $\eta_{turbine}$ and are included in the optimization using genetic algorithm. In order to correlate the variation of the optimized turbine efficiency with non-dimensional parameters and update the conventional φ - ψ and N_s - d_s charts the following specification for the design parameters are set to cover a wide range of designs.

$$\begin{aligned} T_{t,1} &\in (343:393:10) \\ \psi &\in (0.7:1.4:0.1) \\ \varphi &\in (0.15:0.5:0.05) \end{aligned} \quad (16)$$

Where the first and second terms are the upper and lower boundaries and third term is the step of variation for each parameter. The optimization is conducted for all possible combination of the above design parameters, however, only the optimized updated ϕ - ψ and N_s - d_s charts for the turbine inlet temperature of 373K are shown for brevity. As presented in Figure 3, the maximum turbine efficiencies are achieved at low flow coefficients with the maximum value of 86% obtained by R1233zd. In the ϕ - ψ performance charts, the maximum turbine efficiencies vary in the range of 82% to 86% compared to the maximum value of 88% shown by Chen and Baines (1994). This is due to the higher expansion ratios of ORC turbines (about 8) and corresponding supersonic losses compared to the conventional radial gas turbines with the maximum expansion ratios of about 4. In addition, implementation of back swept blading at rotor inlet is advantageous since the turbine efficiency increases at loading coefficients in excess of unity (Rahbar *et al.* 2015b). Comparing the ϕ - ψ charts shown in Figure 3 with Chen and Baines (1994) reveals that the turbine efficiency increases by a maximum of 3% at loading coefficients greater than unity. In other words the contours of maximum efficiency are slightly shifted to higher loading coefficients. Figure 4 presents the optimized updated N_s - d_s performance charts for the four investigated fluids. Similar to Balje (1981) diagram, the optimum region of N_s - d_s still exists in all charts in which the line of maximum efficiency is equivalent to the theoretical curve that almost gives $N_s d_s = 2$. But in contrast to the conventional radial turbines that the maximum efficiency occurs at the specific speed values of between 0.5 to 0.7, for ORC turbines this optimum value has been shifted to lower specific speed values of between 0.35 to 0.55 as shown in Figure 4.

Although the optimized performance charts shown in Figures 3 and 4 are essential for performance prediction of the ORC turbines, it is more beneficial to present the variation of the optimized turbine efficiency in the form of a mathematical equation. Therefore, linear regression analysis is employed in order to correlate the optimized turbine efficiencies with volumetric expansion ratio, flow and loading coefficients using all the generated design points. Figure 5 shows the linear regression plot for both the turbine inlet temperature of 373K (5a) and also for the complete range of inlet temperature from 343K to 393K (5b). As can be seen in Figure 5 the values of R^2 are quite high and assures that the regression analysis can fairly accurately predict the performance of the ORC radial turbines. Equation 17 shows the first order polynomial obtained based on this regression analysis using all the 417 created design points shown in Figure 5(b) and correlates the turbine efficiency with the volumetric expansion ratio, loading and flow coefficients.

$$\eta_{turbine} = 0.925 - 0.416\phi + 0.0279\psi - 0.00675VR \quad (17)$$

It should be underlined that the obtained correlation shown by equation 17 is assumed to be a preliminary correlation for performance prediction of ORC radial turbines and is considered as the initial step towards improvement in performance prediction of ORC based on the radial turbines. This is primary due to the fact that the employed loss models are originally developed for gas turbines using air as the working fluid and they should be used with some care. In addition, due to the lack of experimental data for performance of the ORC turbines it is required to validate the developed correlation with real test data upon their availability in open literature. However, it is believed that the proposed methodology is quite novel and has great potential to be further improved and extended for a wider range of organic fluids and broader range of operating conditions.

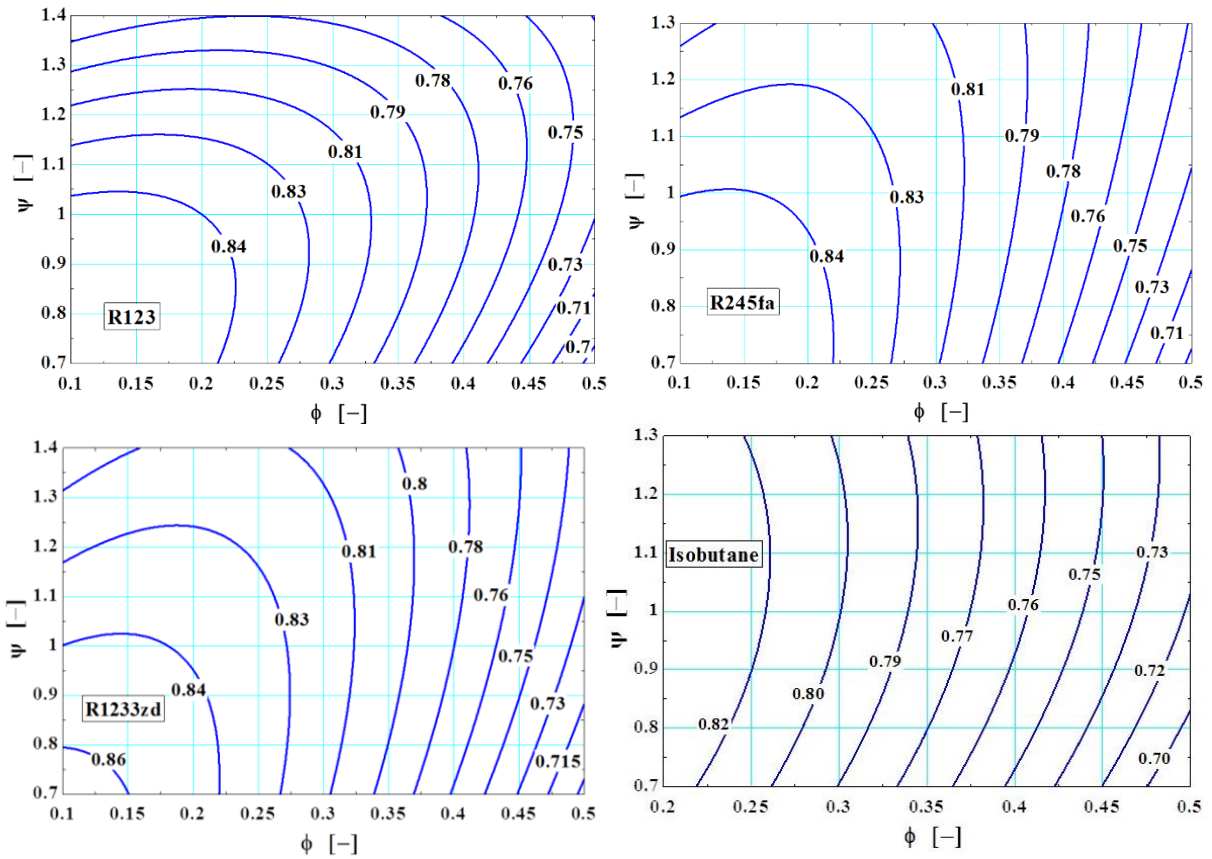


Figure 3: Contours of optimized turbine efficiency based on flow and loading coefficients for four organic fluids as R123, R245fa, R1233zd and isobutane at turbine inlet temperature of 373K

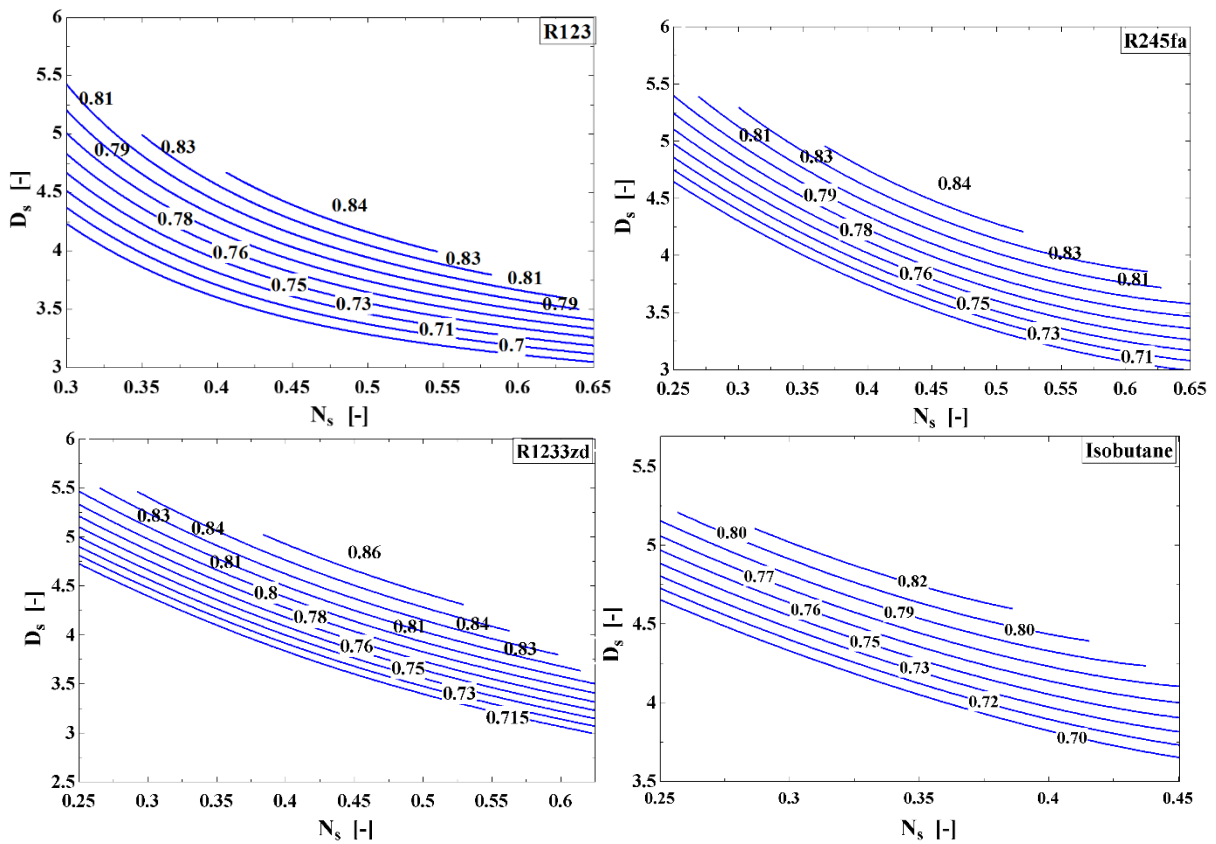


Figure 4: Contours of optimized turbine efficiency based on specific speed and specific diameter for four organic fluids as R123, R245fa, R1233zd and isobutane at turbine inlet temperature of 373K

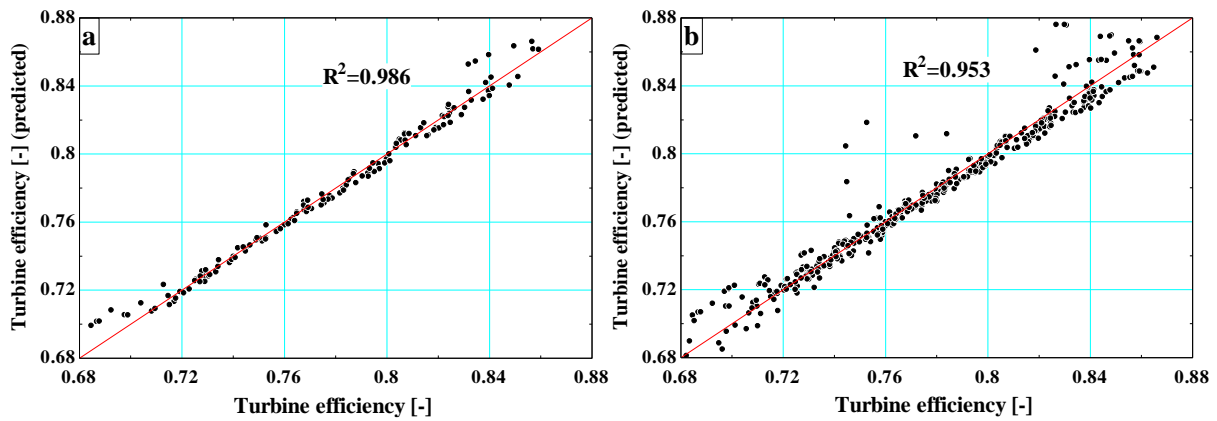


Figure 5: Predicted optimized turbine efficiency as a function of turbine efficiency at turbine inlet temperature of 373K (a) at the full range of turbine inlet temperature from 343K to 393K (b)

5. CONCLUSIONS

This study presents a novel approach that combines the modeling of the ORC system with modeling of radial turbine and allows for optimization of turbine efficiency based on a wide range of input variables. The paper shows that the conventional performance charts are no more sufficient for reliable performance predication of ORC radial turbines. These charts are updated and optimized based on the most advanced loss models and characteristics of organic fluids and ORC system (i.e. real gas behavior and high expansion ratios). The updated performance charts showed that there are considerable variations between them and the conventional ones as the contours of maximum efficiency are shifted to larger loading coefficients and smaller specific speeds respectively. In addition, the optimized charts showed that the maximum efficiency of ORC radial turbines are about 2% lower than the maximum efficiency of radial gas turbines. The R^2 values from the regression analysis showed that the established first order polynomial correlation can fairly accurately predict the performance of ORC turbines, though, it is required to be further modified and validated with the ORC experimental data (which are very scarce in the open literature). These new charts and the correlation could be a useful tool in general optimization procedures of the ORC systems that avoid any arbitrary assumption of turbine efficiency and yield a more accurate estimation of the turbine performance.

NOMENCLATURE

b	blade height	(m)
C	absolute velocity	(m/s)
d	diameter	(m)
d_s	specific diameter	(-)
ER	expansion ratio	(-)
h	enthalpy	(J/kg)
Δh_{actual}	actual specific enthalpy drop	(J/kg)
Δh_s	isentropic specific enthalpy drop	(J/kg)
l	flow path length	(m)
m	mass flow rate	(kg/s)
Ma	Mach number	(-)
N_s	specific speed	(-)
P	pressure	(Pa)
Q	volumetric flow rate	(m ³ /s)
R	gas constant	(J/kg-K)
r	radius	(m)
Re	Reynolds number	(-)
T	temperature	(K)
U	rotor blade velocity	(m/s)
VR	volumetric expansion ratio	(-)

W	relative velocity	(m/s)
Y	total pressure loss coefficient	(-)
Z_{rotor}	number of rotor blades	(-)
α	absolute flow angle to meridional	(degree)
β	relative flow angle to meridional	(degree)
κ	mean surface curvature	(m ⁻¹)
σ	slip factor	(-)
γ	specific heat ratio	(-)
ε	rotor casing clearance	(m)
η	efficiency	(-)
φ	flow coefficient	(-)
ψ	loading coefficient	(-)
ω	rotational velocity	(rad/s)
Θ	normalized momentum thickness	(-)
Δ	normalized mass thickness	(-)

Subscript

1-5	stations across the turbine
m	meridional direction
rel	relative value in rotating coordinate system
t	total conditions
ts	total to static
x	axial direction
θ	tangential direction

REFERENCES

- Aleksandra, B.G., and Władysław, N., 2007, Maximizing the working fluid flow as a way of increasing power output of geothermal power plant. *Appl Therm Eng*, 27, p. 2074–8.
- Al-Sulaiman, F.A., Hamdullahpur, F., and Dincer, I., 2011, Greenhouse gas emission and exergy assessments of an integrated organic Rankine cycle with a biomass combustor for combined cooling, heating and power production. *Appl Therm Eng*, 31, p. 439–46.
- Aungier, R.H., 2006, *Turbine aerodynamics, axial-flow and radial-inflow turbine design and analysis*. ASME Press, New York.
- Balje, O.E., 1981, *Turbomachines: a guide to design, selection and theory*. Wiley: New York.
- Chen, H., and Baines, N.C., 1994, The aerodynamic loading of radial and mixed flow turbines. *Int. J. Mech Sci*, 36, p. 63-79.
- Dolz, V., Novella, R., García, A., and Sánchez, J.H.D., 2012, Diesel engine equipped with a bottoming Rankine cycle as a waste heat recovery system. Part 1: Study and analysis of the waste heat energy. *Appl Therm Eng*, 36, p.269–78.
- Hettiarachchi, H.D.M., Golubovic, M., Worek, W.M., and Ikegami, Y., 2007, Optimum design criteria for an Organic Rankine cycle using low- temperature geothermal heat sources. *Energy*, 32, p.1698–1706.
- Lemmon, E.W., Span, R., 2006, Short Fundamental Equations of State for 20 Industrial Fluid. *Chemical & Engineering Data*, 51, p. 785-850
- Macchi, E., Perdichizzi, A., 1981, Efficiency prediction for axial flow turbines operating with nonconventional fluids. *J Eng gas turbines power*, 103, p. 718-24.
- Rahbar, K., Mahmoud, S., Al-Dadah, R.K., and Moazami, N., 2015, Modeling and optimization of organic Rankine cycle based on a small-scale radial inflow turbine. *Energy Convers and Manag*, 91, p. 186-98.
- Rahbar, K., Mahmoud, S., Al-Dadah, R.K., and Moazami, N., 2015, Parametric analysis and optimization of a small-scale radial turbine for organic Rankine cycle. *Energy*, 83, p.696-711.
- Rashidi, M.M., Galanis, N., Nazari, F., Basiri Parsa, A., and Shamekhi, L., 2011, Parametric analysis and optimization of regenerative Clausius and organic Rankine cycles with two feed water heaters using artificial bees colony and artificial neural network. *Energy*, 36, p. 5728-40.
- Rayegan, R., and Tao, Y.X., 2011, A procedure to select working fluids for solar organic Rankine Cycles (ORCs). *Renewable Energy*, 36(2), p. 659–70.
- Wang, J., Yan, Z., Wang, M., Li, M., and Dai, Y., 2013, Multi-objective optimization of an organic

Rankine cycle (ORC) for low grade waste heat recovery using evolutionary algorithm. *Energy Convers and Manag*, 71, p. 146-58.

Rodgers, C., and Geiser, R., 1987, Performance of a high efficiency radial/axial turbine. *Trans ASME J of Turbomachinery*, 109, p. 151-4.

Whitfield, A., and Baines, N.C., 1990, *Design of radial turbomachines*. Longman, New York.

EFFICIENT EVALUATION OF THERMOPHYSICAL PROPERTIES OF WORKING FLUIDS FOR ORGANIC RANKINE CYCLES

Ian Bell

National Institute of Standards and Technology
Boulder, CO
USA

ABSTRACT

The overall topic of this tutorial session is a description of the models that underpin the state-of-the-art thermophysical property libraries, and how these properties can be retrieved in a computationally efficient manner. The emphasis will be placed on the use of the REFPROP property library developed at the National Institute of Standards and Technology (NIST), though other libraries will also be described in some detail.

The first topic of the tutorial session will be a theoretical description of how the models (equations of state, mixture models, transport property formulations, etc.) are constructed. The emphasis of this section will be to describe the theory in a way that is relevant to end-users, such that they can understand the implications of these model formulations on their own code that they write.

Secondly, we will describe the use of the NIST REFPROP library to calculate the parameters of interest, including thermodynamic properties, derivatives of thermophysical properties, mixture phase envelopes, etc. An emphasis will be placed on the different means that can be used to maximize computational efficiency. Furthermore, the various options available for interfacing with REFPROP will be described, including the use of the CoolProp thermophysical property library.

Finally, we will present work that has been recently carried out to use the bicubic tabular interpolation methods of CoolProp to achieve computational speeds for fixed-composition mixtures from REFPROP that are on the order of the computational speed of mixtures that are treated as pseudo-pure fluids. This should be of particular interest to researchers that are carrying out dynamic simulation studies with zeotropic mixtures, as has been proposed in the literature for Organic Rankine Cycles.

EXPERIMENTAL INVESTIGATION OF A SMALL-SCALE TWO STAGE ORGANIC RANKINE CYCLE ENGINE OPERATING AT LOW TEMPERATURE

Erika Ntavou^{1,*}, George Kosmadakis², Dimitris Manolakos³, George Papadakis⁴ and Dimitris Papantonis⁵

^{1,*} Agricultural University of Athens, Department of Natural Resources and Agricultural Engineering, Athens, Attica, Greece
edavou@aua.gr

² Agricultural University of Athens, Department of Natural Resources and Agricultural Engineering, Athens, Attica, Greece
gkosmad@aua.gr

³ Agricultural University of Athens, Department of Natural Resources and Agricultural Engineering, Athens, Attica, Greece
dman@aua.gr

⁴ Agricultural University of Athens, Department of Natural Resources and Agricultural Engineering, Athens, Attica, Greece
gpap@aua.gr

⁵ National Technical University of Athens, Department of Mechanical Engineering Fluid Section, Athens, Attica, Greece
papan@fluid.mech.ntua.gr

* Corresponding Author

ABSTRACT

A prototype two-stage heat-to-power engine based on the Organic Rankine Cycle (ORC) has been developed for operation at a wide thermal load input range, coming from variable thermal sources, such as evacuated tube solar collectors. The system is used to produce electrical energy through the expansion of a refrigerant (R245fa) in two scroll expanders which are connected in series. The intense fluctuation of the temperature and heat input dictates the use of a two-stage engine, for flexible and efficient operation even at low thermal load, thus these expansion machines can operate within a narrow pressure ratio range, showing high expansion efficiency up to 70%. When operating at high heat input both expanders operate, while for low heat input, the first expander is completely bypassed. The net capacity of the ORC engine is 10 kWe, when supplied with 100 kW of heat at a temperature of 130 °C.

This engine has been tested in an appropriate test-rig at the laboratory, using a controllable electrical heater as the heat source. The power produced by the two hermetic scroll expanders is driven to an electric panel through frequency inverters. This study presents the ORC engine testing results, when the heat transfer fluid is water with temperature of 95 °C (part-load operation). The engine is tested under both single and two-stage configuration and the heat input is varied with the regulation of the ORC feed pump speed. The measurements have shown that even at such low-temperature the thermal efficiency is adequate (up to 7% for single- and two- stage operation), and that the second expander can operate with increased isentropic efficiency up to 66%, while for the first one this value is much lower, due to its under-expansion (pressure ratio 1.7-2.7 for the first and 3-7 for the second expander).

The maximum thermal efficiency is observed for low pump speed, while the highest power production of 3.5 kW was noticed at single-stage operation, slightly higher than the 3.3 kW produced at the two-stage operation.

1. INTRODUCTION

In recent years, organic Rankine cycle (ORC) technology has become a field of intense research and it appears as a promising technology for conversion of low grade heat into useful work or electricity (Desai and Bandyopadhyay, 2009, Mago *et al.*, 2008). The research so far has been focused on both single and two-stage systems. The single-stage Organic Rankine Cycle using solar collectors as a heat source has been experimentally evaluated (Manolakos *et al.* 2005, 2007, 2009a, 2009b, Manolakos, 2006), along with the detailed simulation of its performance (Manolakos 2006, Manolakos *et al.* 2005, 2009a, 2009b). Concerning the two-stage ORC systems, the research is increasing in the aspect of design and simulation, in order to identify the improvement in efficiency in comparison to the single stage system (Kosmadakis *et al.*, 2010). In the present work a prototype two-stage engine, which has been constructed as a result of intense research, design and simulation work, is being experimentally evaluated for operation at 95°C for variable heat input. The engine is being tested for both single and two-stage operation and the heat in the laboratory is provided by an electrical heater of a capacity of 100 kW_{th}. A two-stage system is being selected for the current experiment in order to evaluate the expected offered flexibility to the system, since this design promises an efficient operation in a wide range of thermal power input. Even at partial or low thermal load, the first expander can be completely by passed if needed, and a *sufficient* operation is realized with only the second expander. The expander is a key element of the ORC. The choice of the expander strongly depends on the operating conditions and on the size of the facility and two main types of machines can be distinguished: the dynamic (turbo) and displacement (volumetric) type (Lemort *et al.*, 2009). Displacement type machines are more appropriate to the small-scale ORC unit because they are characterized by lower flow rates, higher pressure ratios and much lower rotational speeds than turbo-machines. Moreover, these machines can tolerate two-phase conditions, which may appear at the end of the expansion at some operating conditions. Among positive displacement machines, the scroll machine is a good candidate for the ORC application, because of its reduced number of moving parts, reliability, wide output power range, and broad availability. Moreover, it is a proven technology in compressor mode due to its extensive use in refrigeration and air-conditioning industry. However, up to now, the use of scroll machines in expander mode has mainly been limited to experimental work and so far numerous scroll expander prototypes have been tested for different fluids. In the current test, two hermetic sealed scroll compressors have been used as expanders (i.e. operated in reverse mode) after modification and their operation is carefully and separately tested. The hermetic expanders show the great advantage that they include in one compact unit all the necessary sub-systems (generator, lubrication system) that work efficiently and the chance of leakage is small while their cost is relatively low. The working fluid used is the refrigerant R-245fa.

2. DESCRIPTION OF THE SYSTEM

The two-stage ORC configuration that has been developed after intense research and which is being tested in the present work, is based on the use of an integrated system with the use of a single organic fluid and two scroll expanders (scroll compressors in reverse operation), connected in series. The organic fluid that has been selected according to previous analysis is R-245fa (Kosmadakis *et al.*, 2009). This configuration has been proven to be the best solution concerning the efficiency in a wide load range, as well as the cost and simplicity of the control system (Hung *et al.* 1997, Kosmadakis *et al.* 2010, Mago *et al.* 2008). In operation at a load lower than around 50-60% of the nominal, the first expander is being by-passed with the use of an electro valve, thus the evaporated organic fluid is being expanded only in the second expander. In this way, the pressure ratio fluctuation on which the expander efficiency is depended, is kept low in the whole load range (Manolakos *et al.* 2009a, 2009b). The main components of the developed engine are the heat transfer fluid pump, the organic fluid pump, the evaporator, the scroll expanders and the condenser. The organic fluid pump is a Wanner

axial- piston pump and it can operate at sufficiently high pressures with low mass flow, a combination needed in the present tested system. The maximum volume flow is 29 L/min and the maximum motor capacity is 2.2 kW at 960 rpm (50 Hz). The scroll expanders are Copeland scroll compressors that have been modified to operate reversely. The models that have been chosen are ZR125KCE-TFD for the first expander, with maximum inlet pressure 32 bar and power at the nominal pressure ratio 6.15 kW (isentropic efficiency 70.9% at compressor mode) and ZR190KCE-TFD for the second expander, with maximum pressure 32 bar and power at nominal pressure ratio 9.2 kW (isentropic efficiency 69.2% at compressor mode). Both compressors have an inner volume ratio around 3. The first expander is smaller than the second one in terms of swept volume (167.15 cm³/rev for the first and 249.16 cm³/rev for the second compressor). The heat exchangers are of plate type that secure a good heat convection and negligible pressure drop from the inlet to the outlet. Their active surface is 9 m² and their capacity is 100 kW (both evaporators and the condenser). They are manufactured by Ciat and they are Exl 14 70 type. Such a configuration is shown in Figure 1.

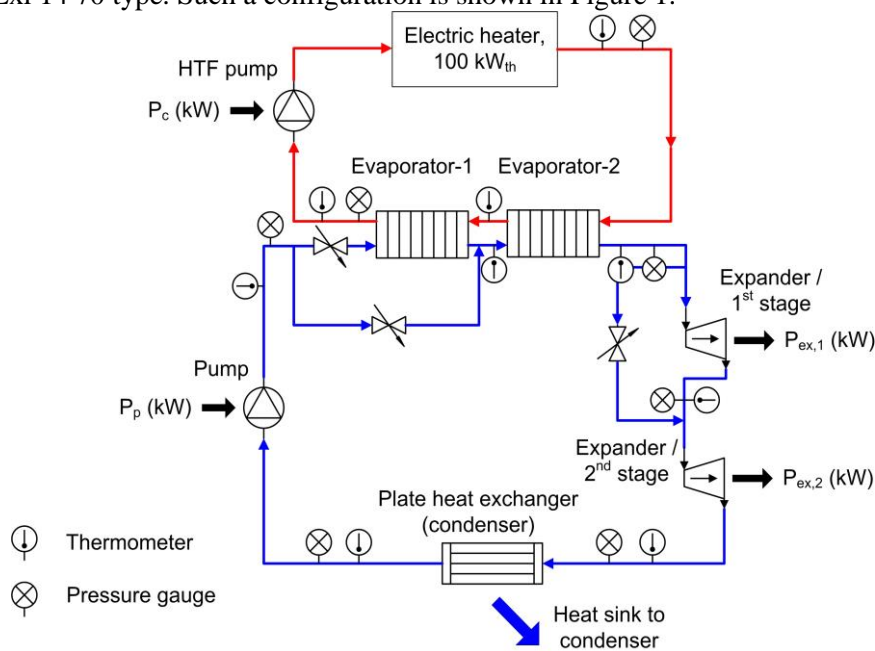


Figure 1: A two- stage ORC configuration with two expanders connected in series

For the heat source simulation, an electrical heater of a capacity of 100 kW_{th} is used and the heat transfer working fluid is water. At every inlet and outlet of each component, appropriate measurement instrumentation is used (thermocouples and pressure transducers). The digital output is shown on the electric panel of the engine. The fluid pump is driven by a frequency inverter, while the speed of the two expanders is regulated as well with the use of inverters connected with the dynamic electric brake. The single or two stage operation is set with the help of an electro valve, which allows a full by- pass of the first expander in medium/low load operation. Two ball-valves, which completely isolate the first branch of the first expander for maintenance service, are manually controlled for additional safety while changing the operation from one to two-stage.

The tests that were implemented at the laboratory aid in the evaluation of the engine's operation at several temperatures and conditions. The temperature and pressure of each location that are shown on the electrical panel are used to determine the organic fluid's condition. Consequently, the engine's efficiency can be calculated, as well as the characteristic properties for every operational point. In the present work the engine is being examined for the operation at 95°C and for variable heat input to the ORC evaporator (plate heat exchanger with capacity of 100 kW_{th}). In Figure 2, the integrated system that is installed in the laboratory as well as a close view of the scroll expanders are shown;



Figure 2: The integrated system installed in the laboratory and the scroll expanders

3. EXPERIMENTAL RESULTS AND EVALUATION

For water temperature of 95°C, the ORC engine has been tested for single and two-stage operation. In Figure 3 below, the optimum (i.e. highest efficiency value for each pump and expander(s) frequency combination) power production as a function of the heat input for each pump rotation speed is observed, in one and two-stage operation. The x- axis represents the total thermal input (in kW_{th}) which is given by Equation (1) below;

$$Q_{th} = (h_{orc\,ev\,out} - h_{orc\,ev\,in}) * m_{orc\,p} \quad (1)$$

where $h_{orc\,ev\,out}$ and $h_{orc\,ev\,in}$ are the enthalpy [kJ/kg] in the evaporator's output and input accordingly and $m_{orc\,p}$ is the organic fluid's mass flow rate [kg/s],

The y- axis represents the sum of the power production of each expander ($P_{orc\,ex}$) and is the sum of the measured produced power in [kW]

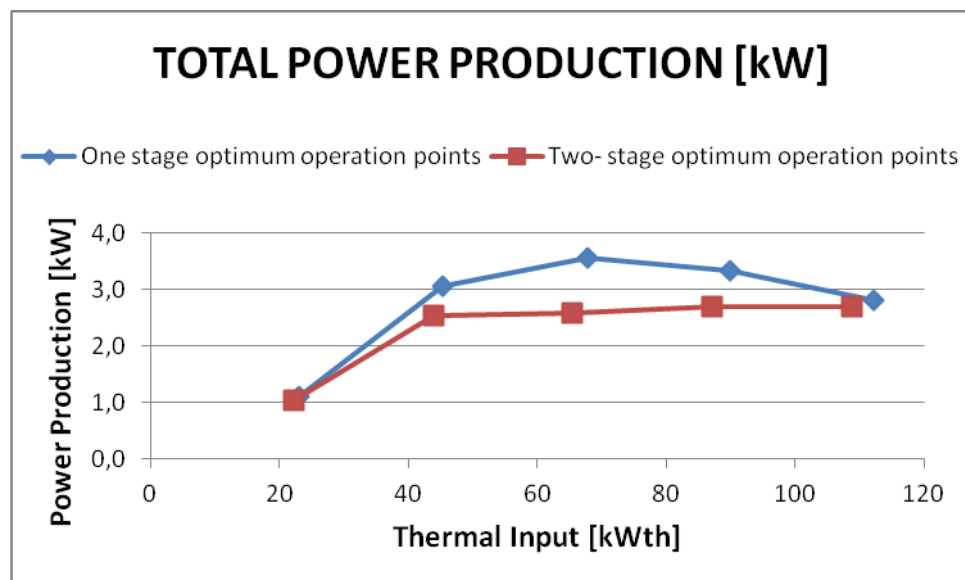


Figure 3: Power production as a function of the thermal input, one and two- stage operation

In Figure 3, it is observed that the maximum power production for one stage operation is noticed at around 3.5 kW for thermal input around 70 kW_{th} and pump rotation at 30 Hz frequency and expander

frequency at 40 Hz. As the pump rotation speed increases, the organic fluid mass that can absorb the transferred heat increases and as a result the power production increases accordingly up to the maximum value of 3.5 kW. However, from that point, in high pump rotation speed, the expander is not capable of expanding the fluid so efficiently, and the power production starts to decrease. In Figure 3, it is also observed that in two- stage operation, the maximum power production is around 2.7 kW for 40 and 50 Hz pump's frequency and 20 Hz at the first and 50 Hz at the second expander. The thermal load for these operating points is above 90 kW_{th}. Beyond that point, the curve tends to get a constant value, as noticed in Figure 3, and the system power production remains under 3 kW. It should be high lightened though, that the operation temperature (95 °C) is still moderate in comparison to the design temperature of the engine (120°~ 140°C), and this is one of the reasons that the produced power remains below the expected one (~10kW_e).

In Figure 4 the total thermal efficiency of the ORC engine is presented as a function of the thermal input, for the optimum operation points for several pump rotation speeds, in one and two stage operation. The x- axis represents once again the thermal input Q_{th} given from Equation (1), while the y- axis represents the thermal efficiency given by Equation (2);

$$n_{th} = \frac{[(P_{orc}]_{ex} - P_{orc p})}{Q_{th}} * 100 \quad (2)$$

where $P_{orc ex}$ is the sum of the measured expanders' power production (see above) and $P_{orc p}$ represents the pump's power consumption (in kW) and is equal to ;

$$P_{orc p} = [(h)_{orc p out} - h_{orc p in}] * m_{orc p} \quad (3)$$

where $h_{orc p out}$ and $h_{orc p in}$ are the enthalpy [kJ/kg] at the output and the input of the ORC pump accordingly.

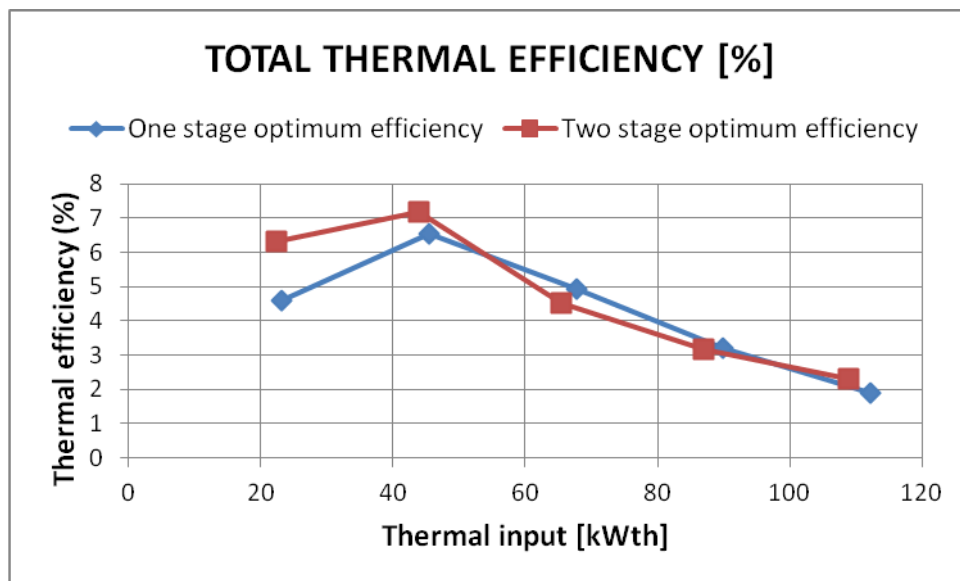


Figure 4: Thermal efficiency as a function of the thermal input, one and two- stage operation

In Figure 4 is observed that in one stage operation the thermal efficiency is noticed at around 6.8 % for thermal input at around 50 kW_{th} while in two- stage operation it is slightly increased reaching 7.2 % for thermal input at around 50 kW_{th}. In both cases, the thermal efficiency is decreased with the increase of pump's speed due to the increase of the own- consumption of the system (organic fluid pump consumption), since the efficiency is the ratio of the net power production to the thermal input.

In Figure 5, the relation between the heat input and the organic fluid pump’s rotational speed in one and two- stage operation is presented;

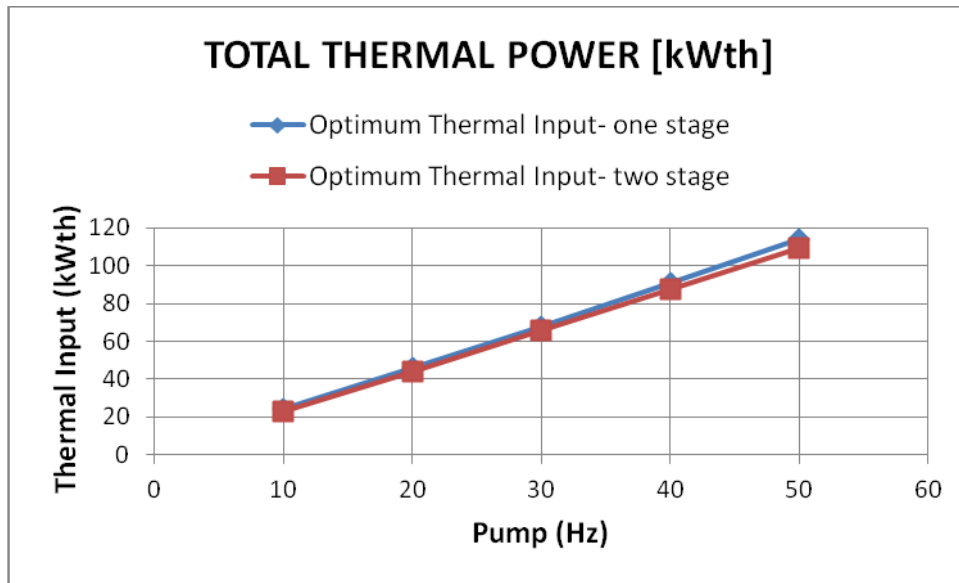


Figure 5: Thermal input as a function of the pump’s frequency, one and two- stage operation

As presented in Figure 5, the thermal input in one stage operation reaches slightly higher levels than in two- stage operation, since the maximum is noticed at around 119 kW_{th}. However, for the most of the organic fluid pump’s operation, the thermal input curves almost coincide for both operations.

Finally, since the two scroll expanders have been modified from commercial scroll compressors and their operation is crucial for the evaluation of the whole system’s operation, it is important to examine their operation separately. In Figure 6, the relation between the pressure ratio and the expander’s frequency for several pump’s rotation speeds is presented, while in Figures 7 and 8 the same curves are being drawn for the two expanders in the two- stage operation. The x- axis represents the second expander’s set frequency at each operation point, while the pressure ratio is given by the ratio;

$$Pressure\ ratio = \frac{P_{orc\ ex\ in}}{P_{orc\ ex\ out}} \tag{4}$$

where $P_{orc\ ex\ in}$ and $P_{orc\ ex\ out}$ are the measured pressure [bar] at the inlet and outlet of the expander under investigation, accordingly.

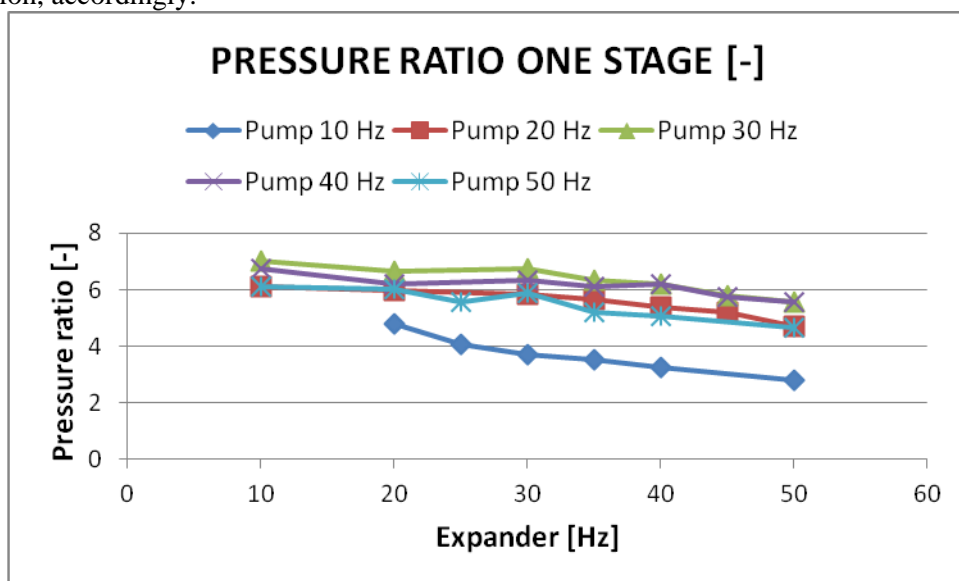


Figure 6: Pressure ratio as a function of the expander’s frequency, one stage operation

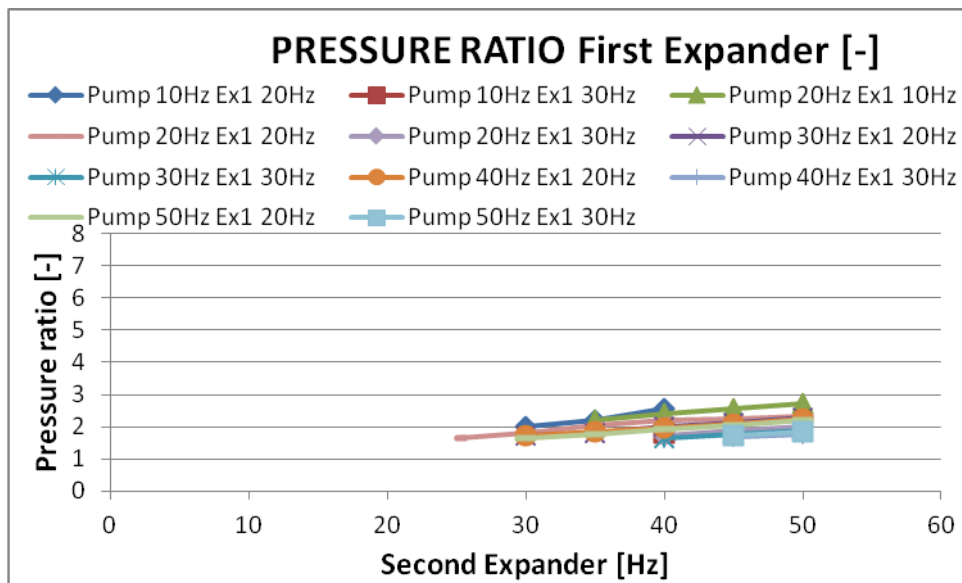


Figure 7: Pressure ratio as a function of the first expander's frequency, two- stage operation

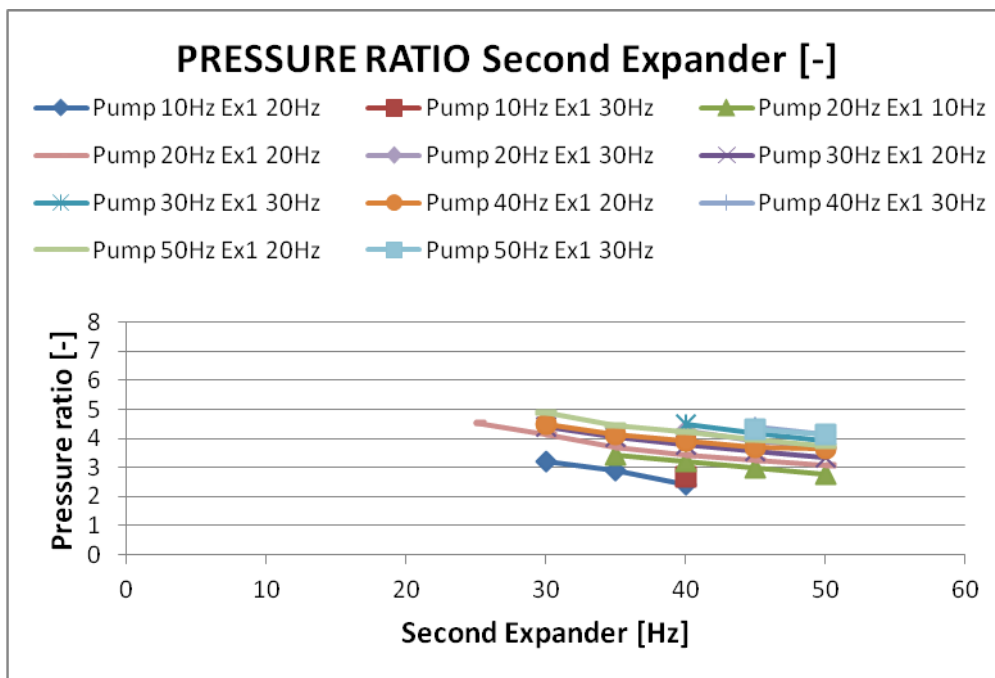


Figure 8: Pressure ratio as a function of the second expander's frequency, two- stage operation

In one stage operation the pressure ratio is around 6 and 7 for medium and high pump frequency, while for low pump frequency it is lower. As the expander's frequency increases for constant pump rotational speed, the organic fluid's inlet pressure decreases thus the pressure ratio decreases as well. The maximum pressure ratio which shows the most efficient operation point is noticed for pump frequency at 30 Hz and expander's frequency at 10 Hz.

In Figures 7 and 8, it is observed that the pressure ratio of the first expander is significantly lower, since for constant operation it gets values from 1 to 3 lower than the second one. With the increase of the pump's frequency the pressure ratio of the first expander decreases (inlet pressure lower than the pressure at the exit) while the ratio of the second increases. With the increase of the second

expander's frequency the first expander's pressure ratio increases while the second expander's decreases, due to a decrease of the inlet pressure. Consequently the pressure ratio decreases.

A good evaluation of the expanders' operation derives from their isentropic efficiency (the ratio of the actual work output of the expander to the work output of the expander if the expander undergoes an isentropic process between the same inlet and outlet pressure). In Figures 9 and 10 the isentropic efficiency of the second expander (with higher swept volume) is presented for single and two- stage operation. The x- axis represents the expander's frequency set for each operation point, while the y- axis represents the isentropic efficiency of each expander given by the Equation (5);

$$n_{orc\ is} = \frac{P_{orc\ ex}}{m_{orc\ p} * (h_{orc\ ex\ in} - h_{orc\ ex\ out\ is})} * 100 \tag{5}$$

where $h_{orc\ ex\ in}$ is the enthalpy at the expander's inlet and $h_{orc\ ex\ out\ is}$ is the isentropic enthalpy of the expander [kJ/kg].

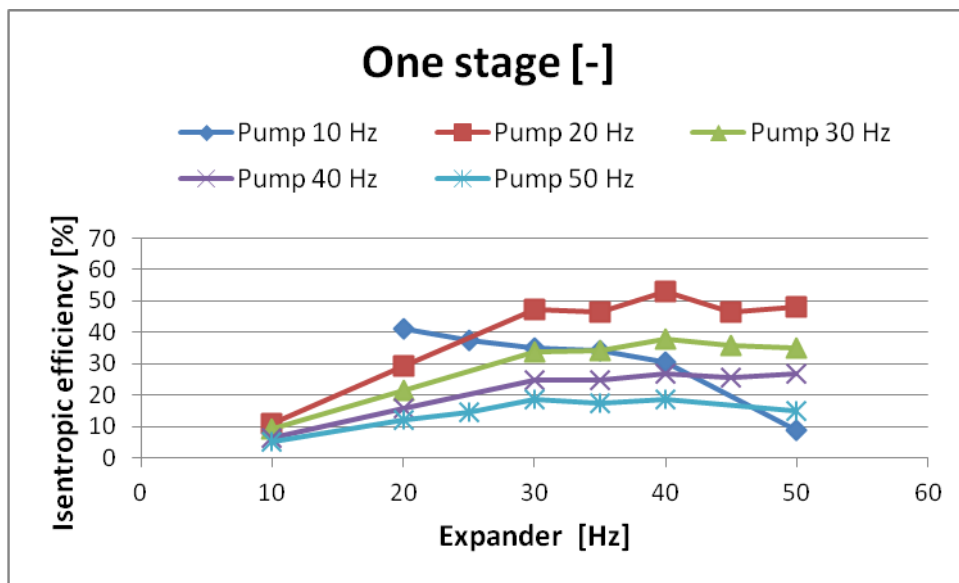


Figure 9: Isentropic efficiency of the second expander, one stage operation

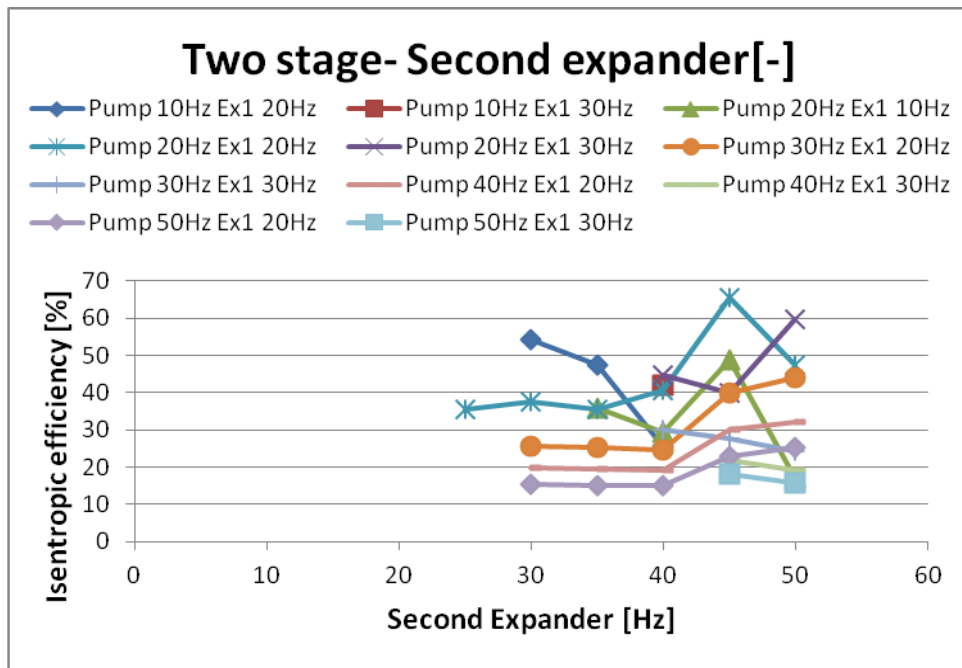


Figure 10: Isentropic efficiency of the second expander, two- stage operation

In both Figures 9 and 10, it is noticed that the second expander can operate with increased isentropic efficiency up to 66%, which implies a very good operation. According to Lemort *et al.* (2009), a tested open-driven scroll expander achieved a maximum isentropic efficiency of 68%, while Zanelli and Favrat (1994) carried out an experimental investigation on a hermetic scroll expander generator fed with refrigerant R134a and showed that the machine produced a power ranging from 1.0 to 3.5 kW with a maximal isentropic efficiency of 65%. The isentropic efficiency of the current expander is similar to those studies and signifies an effective operation. In Figure 10, it is also noticed that as the pump's frequency increases (thus the fluid mass flow increases) and the power production decreases, the expander's isentropic efficiency decreases as well, since the pressure ratio decreases, even if the electric efficiency of the asynchronous generator increases.

4. CONCLUSIONS

According to the tests in the laboratory the designed and manufactured engine worked efficiently even at a moderate temperature in comparison to the nominal design temperature. Even at one stage operation, a significant power production has been noticed for the whole heat load range, with a good efficiency throughout the whole operation. The selected and modified expanders have shown an efficient operation throughout the whole operation range of the pump and even if theoretically a pressure ratio of around 3 was expected for each expander in order to get the most of the two stage expansion, the first (and smaller) expander reached a pressure ratio of around 2 while the second one around 5 (total pressure ratio equals 10). In the current temperature (95°C), the single stage operation shows a slightly higher power output, since the power production is higher than the two- stage system, while the thermal efficiency is slightly lower. However, it should be stressed that the water temperature of the current test is still considerably lower than the design temperature of the modified two-stage ORC engine which is 130 °C and this is the main reason that the two- stage system has not proven any special improvement in comparison to the single stage system. What is of great importance is that the system tested shows that the two- stages expansion offers flexibility and these results deploy the potential of this technology, which appears to be promising possibly in combination with renewable energy heat sources.

REFERENCES

- Desai N.B., Bandyopadhyay S., 2009, Process integration of organic Rankine cycle, *Energy*, vol. 34, no.10: p.1674-1686
- Hung TC, Shai TY, Wang SK., 1997, A review of organic Rankine cycle (ORCs) for the recovery of low grade waste heat, *Energy*, vol. 22, no.7: p.661–67.
- Kosmadakis G., Manolakos D., Davou E. and Papadakis G., 2013, Implementation of a two-stage Organic Rankine Cycle using scroll expanders, operating under variable heat input, *2nd Int. Seminar on ORC Power Systems (ASME-ORC2013)*, Rotterdam, The Netherlands.
- Kosmadakis G., Manolakos D., Papadakis G., 2010, Parametric theoretical study of a two-stage solar organic Rankine cycle for RO desalination, *Renewable Energy*, vol. 35, no.5: p.989-996
- Kosmadakis G, Manolakos D, Kyritsis S, Papadakis G., 2009, Comparative thermodynamic study of refrigerants to select the best for use in the high-temperature stage of a two-stage organic Rankine cycle for RO desalination. *Desalination*, vol. 243, no. 1–3: p.74–94.
- Lemort V., Quoilin S., Cuevas C. and Lebrun J., 2009, Testing and modeling a scroll expander integrated into an Organic Rankine Cycle, *Applied Thermal Engineering*, vol. 29, no.14-15: p.3094-3102.
- Manolakos D, Papadakis G, Kyritsis S, Bouzianas K., 2007, Experimental evaluation of an autonomous low-temperature solar Rankine cycle system for reverse osmosis desalination. *Desalination*, vol.203, no.1-3: p.203-366.
- Manolakos D., 2006, Development of an Autonomous Low Temperature Solar Rankine Cycle System for Reverse Osmosis Desalination. *Ph.D thesis*, Agricultural University of Athens (in Greek, http://www.aua.gr/~kyritsis/abstract_workshop_Manolakos.pdf).
- Manolakos D, Kosmadakis G, Kyritsis S, Papadakis G., 2009, On site experimental evaluation of a low-temperature solar organic Rankine cycle system for RO desalination. *Solar Energy*, vol.83, no.5: p.646-656.
- Manolakos D, Kosmadakis G, Kyritsis S, Papadakis G., 2009, Identification of behavior and evaluation of performance of small scale, low temperature organic Rankine cycle system coupled with an RO desalination unit. *Energy*, vol.34, no.6: p.767-774.
- Manolakos D, Papadakis G, Mohamed Essam Sh, Kyritsis S, Bouzianas K., 2005, Design of an autonomous low-temperature solar Rankine cycle system for reverse osmosis desalination. *Desalination*, vol.183, no.1-3: p.73-80.
- Mago P.J., Chamra L.M., Srinivasan K., Somayaji C., 2008, An examination of regenerative organic Rankine cycles using dry fluids, *Appl Therm Eng*, vol. 28, no.8-9: p. 998–1007.
- Nguyen V.M., Doherty P.S. and Riffat S.B., 2001, Development of a prototype low-temperature Rankine cycle electricity generation system, *Appl. Therm. Eng.*, Vol. 21, no. 2, p.169–181.
- Quoilin S, Orosz M, Hemond H, Lemort V., 2011, Performance and design optimization of a low-cost solar organic Rankine cycle for remote power generation. *Solar Energy*, vol.85, no.5: p.955–966.
- Zanelli R., Favrat D., 1994, Experimental investigation of a hermetic scroll expander- generator, *Proceedings of the International Compressor Engineering Conference at Purdue*, paper 1021.

ACKNOWLEDGEMENT

The present work is conducted within the framework of the project with contract No. 09SYN-32-982, partly funded by the Greek General Secretary of Research and Technology (GSRT).

EXPERIMENTAL STUDY ON PARALLEL EXPANDER ORGANIC RANKINE CYCLE WITH TWO DIFFERENT CAPACITY EXPANDERS

Eunkoo Yun¹, Dokyun Kim¹, Sang Youl Yoon^{2*} and Kyung Chun Kim^{1*}

¹School of Mechanical Engineering, Pusan National University
Busan, 609-735, Korea

kooo8282@pusan.ac.kr, dogyunkim@pusan.ac.kr, kckim@pusan.ac.kr

²Rolls-Royce University Technology Centre, Pusan National University
Busan, 609-735, Korea
yoonsy@pusan.ac.kr

* Corresponding Author

ABSTRACT

Recently, an organic Rankine cycle (ORC) with dual expanders in parallel called as parallel-Expanders ORC (PE-ORC) has been proposed for more efficient waste heat recovery in applications in which there are large heat variations such as distributed energy system with multiple internal combustion engines. This study describes a PE-ORC adopting two expanders with different capacities. The system could have three operating modes according to the operated expanders. An ORC loop with 1 kW and 3kW class expanders in parallel are prepared for the test. The ORC test bench has a 100kW heater as the heat source, and an air-cooled chiller as the heat sink. R245fa was used as working fluid. In order to evaluate the performance characteristics of the system for each operating mode, efficiencies and shaft powers were obtained under various evaporative heat transfer conditions. The appropriateness of utilizing proposed ORC system and optimal operation mode which can produce higher power output will be discussed with experimental results.

1. INTRODUCTION

Some applications including internal combustion engine (ICE) have large heat variation of sources. Single-expander ORC system in those fields could be operated at off-design points, and thus the efficiency could be severely reduced, or the ORC system might not be operated (Choi and Kim, 2013). Recently, an organic Rankine cycle (ORC) with multiple expanders in parallel called as parallel-Expanders ORC (PE-ORC) has been proposed for more efficient waste heat recovery in applications in which there are large heat variations such as distributed energy system with multiple internal combustion engines (Yun *et al.*, 2015). They showed the feasibility of the PE-ORC by experimental evaluation of simple PE-ORC which had two identical scroll expanders. The study showed the PE-ORC with two identical expanders could have two design points which can achieve the maximum performance. The number of the design points and the number of operating mode depend on the number of expander and each expander capacity.

In this study, a PE-ORC adopting two expanders with different capacities is tested, and thus the tested system has three design points and three operating modes. The performance for each operating mode has been evaluated.

2. EXPERIMENTAL SETUP

A schematic diagram of ORC test bench adopting two expanders with different capacities is given in Figure 1. The ORC loop consists of two expander modules, an evaporator, a condenser, a working fluid pump, and a liquid receiver. Two scroll expanders, Expander 1 and Expander 2, with different

capacities were assembled in parallel between distribution and mixing chambers. The separated working fluid through the distribution chamber flows into both expanders, and merges in mixing chamber after expansion, and then is fed into the condenser. Manual open-close valves for switching between operating modes are installed at the entrances of both expanders. Brazed plate heat exchangers were used for the evaporator and condenser, respectively. The feed pump for working fluid was a volumetric Diaphragm type pump whose rotational speed was controlled using a frequency drive. Pressurized hot water heated by an electric heater was used as heat source, and an air-cooled chiller was connected with condenser in order to supply cooling water at a constant temperature. A 3-D schematic model of ORC system and Expander 1, and a photograph of Expander 2 are shown in Figure 2.

Technical overview of each expander unit is summarized in Table 1. Expander 1 was an oil-free open-drive scroll air compressor has been adapted to run in an expander mode by reversing the flow direction. A container for preventing leakage was designed as shown in Figure 2 (Wang *et al.*, 2011). Expander 2 is a commercially available oil-free scroll expander unit manufactured by Air Squared, Inc. The shaft of each expander is directly coupled with torque sensor to measure the shaft power and permanent magnetic motor to control the rotational speed in series. The specifications of sensors are listed in Table 2. R245fa was used as the working fluid because of its thermodynamic suitability for low-temperature heat recovery, non-flammability, and lack of toxicity (Declaye *et al.*, 2013).

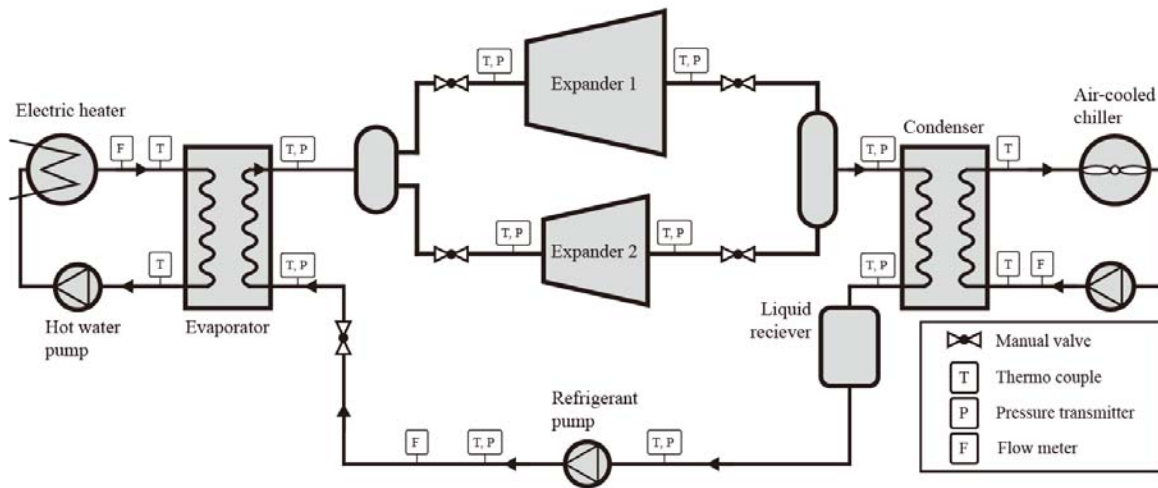


Figure 1: Schematic diagram of Dual-expander ORC test rig

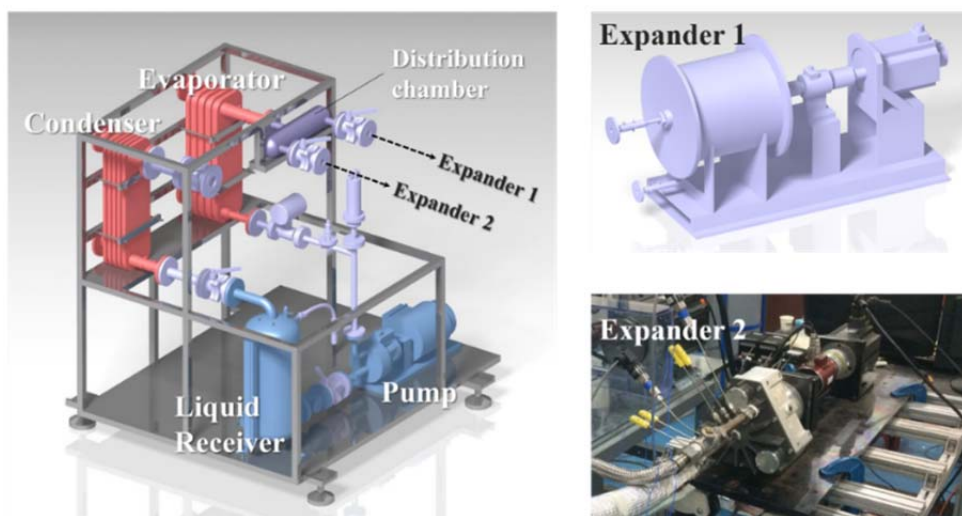


Figure 2: Schematics of ORC system and Expander 1, and a photograph of Expander 2

Table 1: Technical overviews of Expander 1 and 2

Component	Expander 1 (Modified from oil-free scroll air compressor)	Expander 2 (Commercial oil-free scroll expander)
Model numbers	BC-KL52H	E15H22N4.25
Manufacturer	Kyungwon Machinery Co, LTD.	Air Squared, Inc.
Max. pressure	10 bar (Compressed air)	13.8 bar
Expansion ratio	4	3.5
Rated speed	2900 rpm	3600 rpm
Output (nominal)	3.7 kW (Motor spec.)	1 kW
Swept volume/rev	30.34 cm ³ /rev	12 cm ³ /rev

Table 2: Specifications of sensors used in test rig

Measurement	Type	Range	Accuracy
Pressure	Piezo resistive	0-20 bar	± 0.5 % F.S.
Flow rate	Oval gear type	0.5-30 l/min	± 0.5 % F.S.
Rotational speed	Magneto type	0-10000 rpm	± 1 rpm
Torque	Strain gauge	0-50 N-m	± 1 % F.S.

3. RESULTS AND DISCUSSION

In this study, only Expander 2 has been tested because the Expander 1 is in modification for improving its tightness. The preliminary tests were conducted according to various expander inlet pressure conditions under the fixed shaft rotational speed. The preliminary test conditions for Expander 2 summarized in Table 3. For assessment of expander performances, several factors such as filling factor, power output, and isentropic efficiency should be considered with expander model used in previous studies (Lemort *et al.*, 2009).

The filling factor represented the volumetric performance of the expander, and is defined as given in Equation (1).

$$FF = \frac{\dot{m}_{wf,meas} \cdot v_{ex,in}}{\dot{V}_s} \quad (1)$$

Measured shaft power and internal expansion power can be calculated by using Equation (2) and (3).

$$\dot{W}_{ex,meas} = \tau \cdot \omega \quad (2)$$

$$\dot{W}_{int} = \dot{m}_{int} [(h_{ex,in} - h_{ad}) + v_{ad} (P_{ad} - P_{ex,out})] \quad (3)$$

The total mass flow rate entering the expander can be defined as sum of internal and leakage mass flow rate, and is expressed in Equation (4)

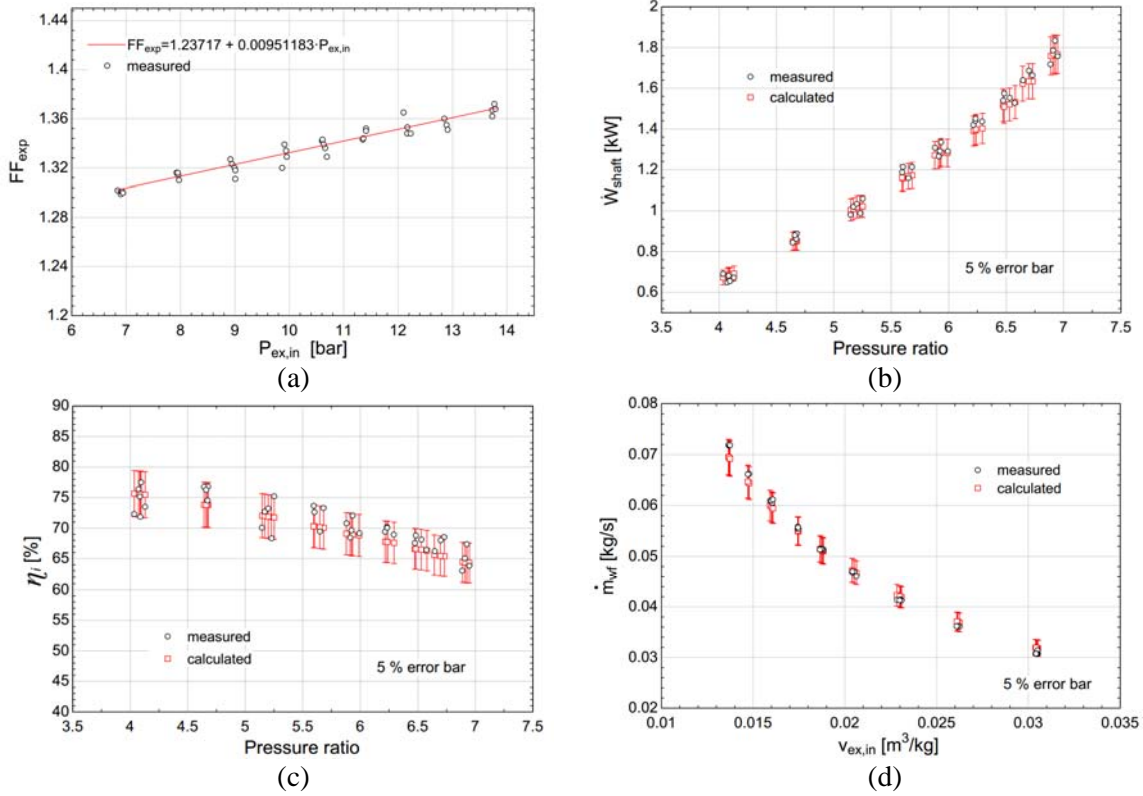
$$\dot{m} = \dot{m}_{int} + \dot{m}_{leak} = \frac{\dot{V}_s}{v_{ex,in}} + \dot{m}_{leak} = \frac{N \cdot \dot{V}_s}{v_{ex,in}} + \dot{m}_{leak} \quad (4)$$

The leakage mass flow rate can be calculated by mass and energy conservation equations through isentropic converging nozzle, which has a lumped leakage area (A_{leak}) at the nozzle throat, as given in Equation (5).

$$\dot{m}_{leak} = \frac{A_{leak}}{v_{leak,thr}} \sqrt{2(h_{ex,in} - h_{leak,thr})} \quad (5)$$

Table 3: Preliminary testing condition for Expander 2

Unit	N_{ex} [rpm]	$P_{ex,in}$ [bar]	$P_{ex,out}$ [bar]	$T_{H,in}$ [°C]	$T_{C,in}$ [°C]
Expander 2	3600	6.84-13.8	1.7-1.98	120	18

**Figure 3:** Measured and calculated results of performance characteristics for Expander 2

The lumped leakage area (A_{leak}) of Expander 2 is empirically identified to 2.85 mm². The nozzle outlet pressure should reach to the critical pressure due to the narrow throat area. The critical pressure at the throat can be calculated by Equation (6).

$$P_{leak,thr} = P_{ex,in} \left[\left(\frac{2}{\gamma+1} \right)^{\frac{\gamma}{\gamma-1}} \right] \quad (6)$$

In this study, the thermal losses by heat transfer could be neglectable because the temperatures and pressures was measured direct after inlet and outlet of expander. The expander isentropic efficiency is defined as given in Equation (7).

$$\eta_i = \frac{\dot{W}}{\dot{m}_{wf,meas} \cdot \Delta h_i} \quad (7)$$

Figure 3 shows the measured and calculated results of performance characteristics for Expander 2. The filling factor linearly increases as the expander inlet pressure increases. As shown in Figure 3 (b)-(d), the results calculated through the expander model closely match the experimental results. The maximum shaft power measured was 1.8 kW at the maximum pressure ratio. The maximum isentropic efficiency measured was about 77 % at a pressure ratio of 4.1. The calculated mass flow rates of working fluid by expander model are in good agreement with the experimental results. With the confidence of the analytical expander model, the performances of Expander 1 and Expander 2 have been determined by using the expander model, respectively. The leakage area of Expander 1 is assumed to 5.86 mm². In order to predict the performance characteristics of PE-ORC system cycle

analysis was conducted and, main parameters used for the cycle analysis are summarized in Table 4. Figure 4 shows the calculated isentropic efficiencies against evaporative heat transfer using the expander model and simple cycle model.

In simple cycle model, the cycle efficiency was calculated by Equation (8).

$$\eta_c = \frac{(\dot{W}_{in} - \dot{W}_{pp})_{total}}{\dot{Q}_{ev,total}} \quad (8)$$

The simulated results of power outputs and cycle efficiencies against the evaporative heat transfer are graphically represented in Figure 5. The selected mode changing points were for maximization of the total power output and cycle efficiency.

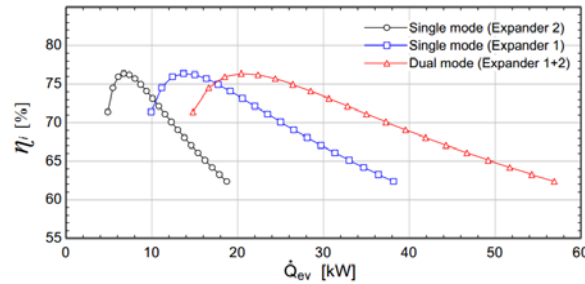


Figure 4: Predicted isentropic efficiencies for three operating modes (Single modes and Dual mode)

Table 3: Parameters for cycle model

$P_{ex,in}$ [bar]	$P_{ex,out}$ [bar]	$T_{superheat}$ [°C]	$T_{subcool}$ [°C]	η_{pp} [%]
4.5-13.8	1.8	5	3	80

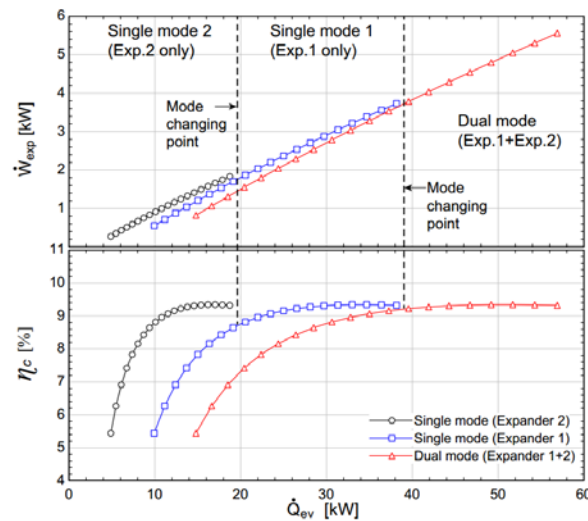


Figure 5: Predicted power outputs and cycle efficiencies for three operating modes (Single modes and Dual mode) and mode changing points for maximizing cycle efficiency

5. CONCLUSIONS

In this study, the preliminary test of a PE-ORC adopting two expanders with different capacities is carried out, and the performance for each operating mode has been predicted by the expander model and the simple cycle model.

- Expander 2 has been tested according to various inlet pressure conditions for validation of expander model.
- The calculations by the expander model closely match the experimental results.

- The performance characteristics of PE-ORC were predicted by simple cycle model, and mode changing points selected for maximizing cycle efficiency.

NOMENCLATURE

h	enthalpy	(kJ/kg)
η	efficiency	(–)
\dot{m}	mass flow rate	(kg/s)
P	pressure	(bar)
\dot{Q}	heat	(kW)
T	temperature	(°C)
v	specific volume	(m ³ /kg)
\dot{V}	volumetric flow rate	(m ³ /s)
\dot{W}	work	(kW)

Subscript

ad	adapted
c	cycle
ev	evaporator
ex	expander
i	isentropic
in	inlet
int	internal
meas	measured
out	outlet
pp	pump
wf	working fluid

REFERENCES

- Choi, B. C., Kim, Y. M., 2013, Thermodynamic analysis of a dual loop heat recovery system with trilateral cycle applied to exhaust gases of internal combustion engine for propulsion of the 6800 TEU container ship, *Energy*, vol. 58: p. 404-416.
- Yun, E., Kim, D., Yoon, S. Y., Kim, K. C., 2015, Experimental investigation of an organic Rankine cycle with multiple expanders used in parallel, *Applied Energy*, vol. 145: p. 246-254.
- Wang, E. H., Zhang, H. G., Fan, B. Y., Ouyang, M. G., Zhao, Y., Mu, Q. H., 2011, Study of working fluid selection of organic rankine cycle (ORC) for engine waste heat recovery, *Energy*, vol. 36: p. 3406-18.
- Declaye, S., Quoilin, S., Guillaume, L., Lemort, V., 2013, Experimental study on an open-drive scroll expander integrated into an ORC (Organic Rankine Cycle) system with R245fa as working fluid, *Energy*, vol. 55: p. 173-183.
- Lemort, V., Quoilin, S., Cuevas, C., Lebrun, J., 2009, Testing and modeling a scroll expander integrated into an Organic Rankine Cycle, *Applied Thermal Engineering*, vol. 29, no. 14: p. 3094-3102.

ACKNOWLEDGEMENT

This research was supported partially by Basic Science Research Program through the National Research Foundation of Korea (NRF) funded by the Ministry of Education (NRF-2013R1A1A2012173), partially by the Energy Efficiency and Resources of the Korea Institute of Energy Technology Evaluation and Planning (KETEP) granted financial resource from the Ministry of Trade, Industry & Energy, Republic of Korea (No. 20112010100030).

THERMO-FLUIDIC AND MECHANICAL LOSSES IN A SCROLL EXPANDER FOR AN R134A ORGANIC RANKINE CYCLE

Karthik G. M.¹, Pardeep Garg^{2*}, Vinod Srinivasan³ and Pramod Kumar⁴

Indian Institute of Science Bangalore
C V Raman Ave, Bengaluru, Karnataka 560012

¹karthik.gm1@gmail.com

²pardeep_1127@yahoo.com

³vinods@mecheng.iisc.ernet.in

⁴pramod_k24@yahoo.com

*Corresponding author

ABSTRACT

In a scroll device, the loss mechanisms can be categorized into two major types; a) thermal fluidic and b) mechanical losses. Further, these losses are found to be strong functions of aspect ratio of a scroll (ratio of scroll diameter and height) and need to be optimized for the best isentropic efficiency. In this paper, a general methodology is developed to optimize the scroll expander geometry for the given operating conditions in any ORC. Detailed results from this methodology are presented for the case study of an ORC with R-134a as a working fluid for different operating conditions. Dependence of individual losses on aspect ratio is understood and presented.

1. INTRODUCTION

Unmatched demand and supply of energy continues to motivate the engineering community to efficiently realize even the marginal potential of low temperature heat sources (~ 150 °C) which are abundantly available in the form of renewable sources of energy such as geothermal and low concentration solar energy. The scale of these energy sources ranging from a few kW_{th} to MW_{th}, makes scalability a key feature of any chosen energy conversion technology. ORC is a promising technology which is both scalable in the above range and can efficiently generate electricity at low temperatures (Tchanche *et al.*, 2011). In a typical ORC, while pump and heat exchangers are scalable and standardized for a wide range of capacities, choice of expander becomes crucial at power scales below 100 kW_e. At these scales, the conventional turbine type expanders tend to have high rotational speeds ($>10^4$ rpm) (Fiaschi *et al.*, 2012) and suffer from low isentropic efficiency. Positive displacement devices such as scroll expanders are a possibility in the range of 1 to 100 kW_e (Qui *et al.*, 2011).

Traditionally, scroll has been used as a compressor in refrigeration and air conditioning industry and more recently has started garnering interest as an expander for power generation in micro-scale ORCs. Scientific literature on scroll as an expander can be broadly classified into three major categories, a) experimental testing of scroll in an ORC facility (Saitoh *et al.*, 2007 and Wang *et al.*, 2009), b) numerical simulation using computational fluid dynamic (CFD) (Ooi *et al.*, 2004 and Rogers *et al.*, 1990) and c) analytical modeling including semi-empirical or deterministic models (Quoilin *et al.*, 2010). To predict the overall ORC performance with scroll as an expander, semi-empirical or deterministic models have been developed using the knowledge base generated by above mentioned experimental and computational studies (Lemort *et al.*, 2009 and Guangbin *et al.*, 2010).

A typical feature of these models is to analyze thermal-fluidic losses in detail and assume either a lumped value for calculating the mechanical losses (friction between solid components due to relative motion) (Lemort *et al.*, 2009) or neglecting them (Guangbin *et al.*, 2010). However, mechanical losses being an inherent feature of any scroll machine need to be properly examined to design the most efficient geometry, as was done in the case of compressors by Ishii *et al.* (1992) who found that an

optimum combination of scroll height and involute base circle radius results in the maximum efficiency. Such studies are rarely found in the case of scroll expanders. In this paper, a comprehensive study of mechanical and thermal-fluidic losses is carried out for a scroll expander which uses R134a as a working fluid. Furthermore, an optimum combination of geometric parameters is generated for the chosen operating conditions and power capacity of 100 kW_e. Despite being proposed only for applications below 10 kW_e, a 100 kW_e scroll can be physically realized due to low volumetric flow rates observed for the chosen operating conditions.

2. THERMODYNAMIC CYCLE

2.1 ORC details

Figure 1 shows the schematic of the thermodynamic cycle considered in this paper. Low pressure and low temperature liquid at state 1 is pumped to a higher pressure state 2. High pressure fluid at this state is preheated in a regenerator from state 2 to 5 by recovering heat from the expander exhaust wherein the low pressure gas is cooled from state 4 to 6. Remaining heat addition from state 5 to 3 occurs in a heater via a heat transfer fluid (HTF) where it losses heat from state i,HTF to o,HTF. The working fluid is then expanded in a scroll device till state 4. Regenerator outlet on the low pressure side (state 6) is then cooled in an air cooled condenser till state 1 to complete the cycle. Ideal cycle requires the pumping and expansion processes be isentropic and heat transfer processes be isobaric. But real processes are plagued by heat transfer and pressure drop losses, the details of which can found in (Garg *et al.*, 2013 and 2015) .The major assumptions are briefed here.

2.1.1 Cycle assumptions

- i. Minimum cycle temperature (T_l) is 45 °C.
- ii. To obtain the operating conditions across the scroll, its isentropic efficiency is assumed to be unity which later on is calculated using the scroll model.
- iii. Power generation is 100 kW_e.

2.2 Scroll Details

A scroll device consists of a fixed scroll and a moving scroll which translates in a circular orbit. The two scrolls conjugate forming compartments known as chambers. Gas at high temperature and pressure enters at the eye of the scroll and expands as it passes through the various expansion chambers during which it performs work on the moving scroll. Figure 2 shows a typical schematic of the scroll expander. Profile of these scrolls is given by the equation of involute of a circle (equation 1), where r_b is the radius of the base circle.

$$\begin{aligned} x &= r_b (\cos \theta + \theta \sin \theta) \\ y &= r_b (\sin \theta - \theta \cos \theta) \end{aligned} \tag{1}$$

2.2.1. Scroll related assumptions

- i. The number of scroll turns (wraps) is fixed such that scroll exhaust pressure equals condenser pressure.
- ii. The scroll thickness is 5mm which ensures sufficient strength of the scroll walls at the operating pressures analyzed in this paper.
- iii. The radial and flank clearance are fixed at 60µm and 80µm respectively

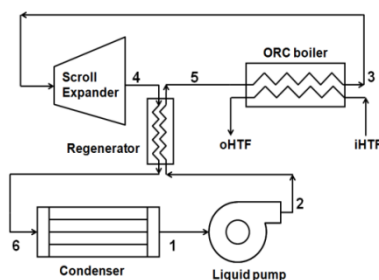


Figure 1: Schematic of an ORC

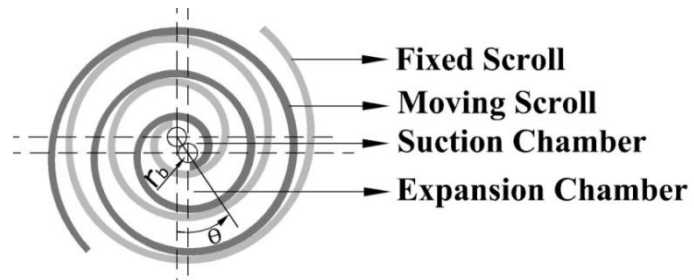


Figure 2: Typical schematic of a scroll expander

3. SCROLL MODELLING

A detailed algorithm for optimizing the scroll geometry is illustrated in Figure 3. For a given scroll inlet temperature, scroll operating conditions are decided by the thermodynamic modeling of the ORC such that they are optimized for the best cycle efficiency. These operating conditions are then fed to the geometric model which generates a number of geometries with different aspect ratios for the given power capacity. These geometries are subsequently evaluated against the best isentropic efficiency by minimizing thermal-fluidic and mechanical losses. These models are herein briefly discussed.

3.1 Geometric Modeling

Based on the required mass flow rate, geometries with different aspect ratios are generated with the various combinations of scroll height (b) and involute base circle radius (r_b). Characteristic parameters of these geometries are also calculated in this model, for example, variation of the chamber area, chamber volume and leakage area, corresponding to flank and radial leakage, with orbiting angle.

3.2 Thermodynamic model

This model calculates the variation of chamber pressure with the orbiting angle which is used to evaluate the loss in isentropic efficiency. Following sub-models are used to calculate the major thermal-fluidic losses.

3.2.1 Supply pressure drop

Ideally, the suction process in a scroll expander is isobaric. However, this is not so due to irreversibilities caused by a pressure drop when the working fluid moves from the suction port to the suction chamber in a finite time. Using the mass flow rate, the corresponding pressure drop can be calculated using equation 2.

$$\dot{m} = A_{su} \rho \sqrt{2(h_{su} - h)} \quad (2)$$

3.2.2 Radial Leakage

Fluid leaking out of the clearances between the moving scroll and the fixed scroll at their top and bottom plane along the spiral length is termed as radial leakage. Modeling of radial leakage is based on Poiseuille's law characterized by laminar flow.

3.2.3 Flank Leakage

Fluid leakage from high to low pressure chamber along the flank walls of the scroll is termed as flank leakage. Leakage amount is calculated using a similar nozzle equation (equation 2) but substituting suction area with flank leakage area.

3.2.4 Heat Transfer

A lumped model is used to calculate the heat transfer losses from the scroll as derived by Lemort *et al.*, 2009 which accounts for the supply and exhaust heat transfer.

3.3 Gas Forces

Chamber pressure variation with orbiting angle already obtained from the thermodynamic model is used to calculate the corresponding gas forces on scroll, namely, F_t (tangential force), F_r (radial force) and M_o (gas moment). Detailed formulations of these forces are given in Ishii *et al.*, 1986.

3.4 Mechanical Modelling

Ishii *et al.* (1986) built a comprehensive scroll compressor mechanical model. In this paper, their model is adapted to a scroll expander and integrated into the ORC model. The various geometrical elements of the scroll are parameterized according to the power capacity of the scroll expander. The following moment equation is derived for the case of an expander at a particular orbiting angle θ of the moving scroll:

$$(I_o + m_s r_o^2 + m_o r_o^2 \sin^2 \theta) \ddot{\theta} - m_o r_o^2 \sin \theta \cdot \cos \theta \cdot \dot{\theta}^2 = -N + F_t r_o - \{L_Q + L_S + (f_{x1} + f_{x2}) r_o \cos \theta + (f_{y1} + f_{y2}) r_o \sin \theta + (f_{t1} + f_{t2}) r_o\} \quad (3)$$

On integrating equation 3 over an entire rotation, while considering steady state with constant angular velocity, and expressing the average of each term over the rotation in terms of work, the following equation is obtained.

$$N\omega = \underbrace{F_t r_o \omega}_A - \left\{ \underbrace{L_S + L_Q}_C + \underbrace{(f_{t1} + f_{t2}) r_o}_D + \underbrace{\frac{1}{2\pi} \int_0^{2\pi} (f_{x1} + f_{x2}) r_o \cos \theta d\theta + \frac{1}{2\pi} \int_0^{2\pi} (f_{y1} + f_{y2}) r_o \sin \theta d\theta}_E \right\} \omega \quad (4)$$

In equation 4, A is the power output/generator load, B is the work available due to the gas force, C is the loss due to friction in the crank pin and journal bearing, D is the frictional loss in the thrust bearing and E is the frictional loss due to the Oldham coupling. The losses C, D and E have been described below. These frictional losses have been calculated using Coulomb’s law of friction and using coefficient of friction $\mu=0.027$ (Ishii *et al.* 1986).

3.4.1 Frictional loss at crank pin and Journal bearing (C)

The crank pin is fixed on the offset crank and is allowed to rotate within the orbiting scroll sleeve bearing, providing the necessary degree of freedom to convert orbiting motion of the scroll to shaft rotation. L_S represents the frictional torque loss at the crank pin. The crankshaft which transfers power from the scroll to the generator passes through a journal bearing. The frictional loss at this bearing is represented by L_Q .

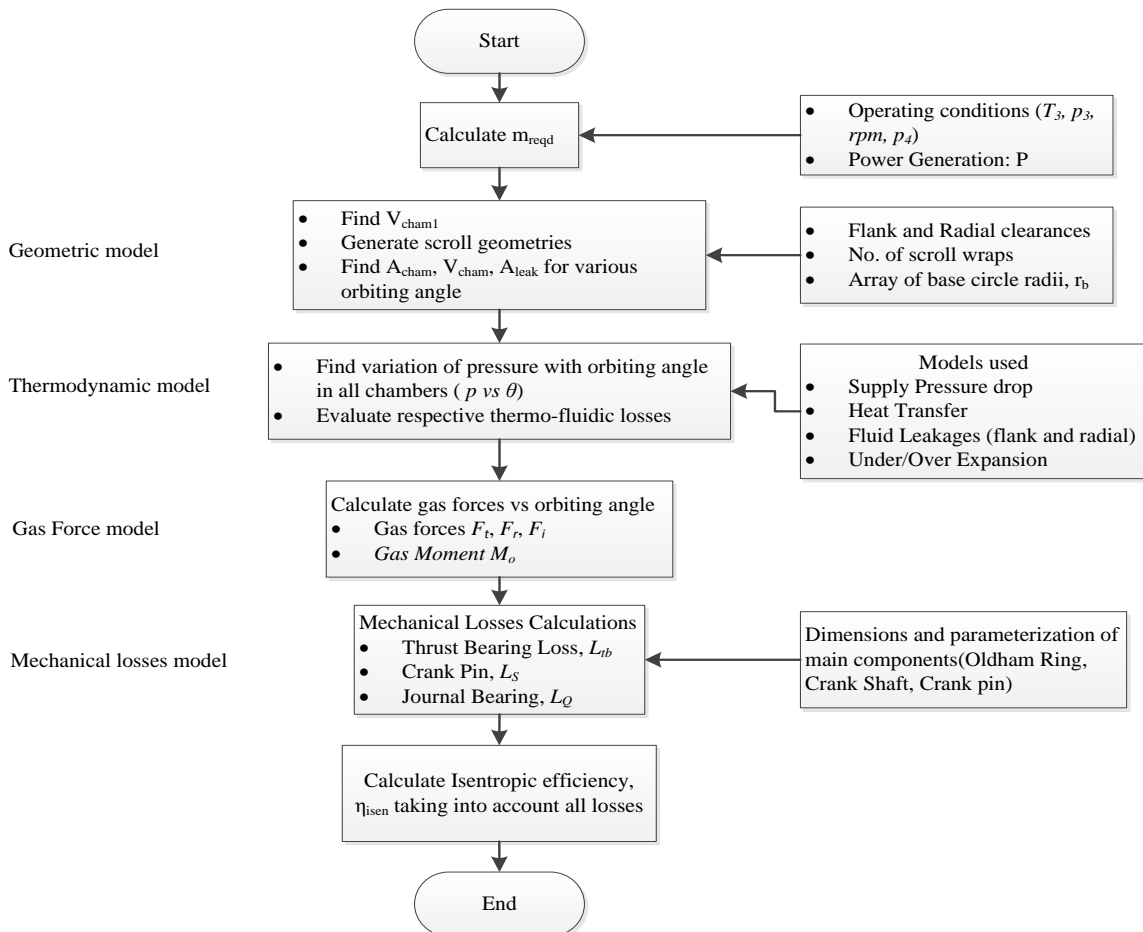


Figure 3: Algorithm followed to optimize the scroll geometry for the given operating conditions of ORC

3.4.2 Thrust Bearing Losses (D)

The resultant thrust force due to gas pressure inside the chamber along with the constraint forces preventing the overturning of the orbiting scroll are supported by the thrust bearing surface. The reaction thrust forces have corresponding frictional forces which represent the thrust bearing losses.

3.4.3 Frictional loss at Oldham coupling (E)

The Oldham coupling slides between the moving scroll and the guide slot on the casing of the scroll machine. The frictional loss due to sliding is very small compared to the other losses.

All calculations were carried out on MATLAB (R-2011b) platform, which was programmed to invoke REFPROP 9.0 database for all thermodynamic property calculations.

4. RESULTS AND DISCUSSIONS

We validated our model against experimental results from Declaye et al. (2013) for an ORC having expander inlet temperature of 105 °C and expander inlet pressure of 12 bar using R245fa as the working fluid. The rotational speed of the scroll was 3000 rpm. Figure 4 shows the isentropic efficiency predicted by our model, which lies within the error limits of Declaye’s experimental data. And Figure 5 compares the non-dimensional power generated from the scroll and that predicted by our model.

Scroll geometries studied in this paper are generated for rotational speed of 3000 rpm and various expander inlet temperatures ranging from 100 to 150 °C in the steps of 10 °C. Corresponding expander inlet pressures are chosen at which the cycle efficiencies are maximum and are reported in Table 1. Scroll exhaust pressure is fixed to 12.01 bar corresponding to the saturation pressure of R134a at 45 °C. Various other data like volumetric and pressure expansion ratio across the scroll are also tabulated in Table 1. For a chosen set of operating conditions, a number of scroll geometries are possible with different scroll heights as shown in Figure 6. These geometries need to be optimized for maximum isentropic efficiency. These geometries are then subjected to the evaluation of thermal-fluidic and mechanical losses as described in sections 4.1 and 4.2 respectively. A range of 1 cm to 10 cm was chosen for the height (*b*) of the scroll since optimal geometry with respect to minimum losses was seen within this range for the chosen operating conditions. All the losses are presented in a fractional form as shown below, where X represents the loss model referred to.

$$\eta_{loss,X} = 1 - \frac{\text{scroll work in case loss 'X' is switched on}}{\text{scroll work with all loss switched off}} \quad (5)$$

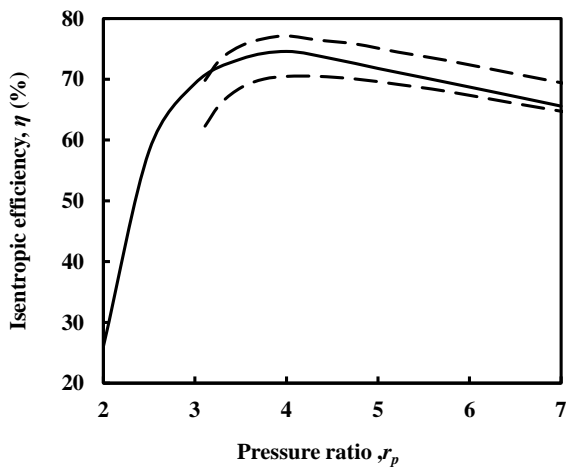


Figure 4: Isentropic efficiency vs pressure ratio
 Legend: — Predicted, - - - Experimental Limits (Declaye *et al.*, 2013)

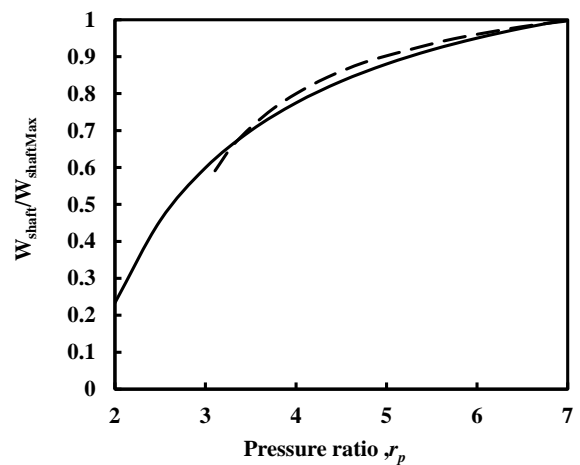
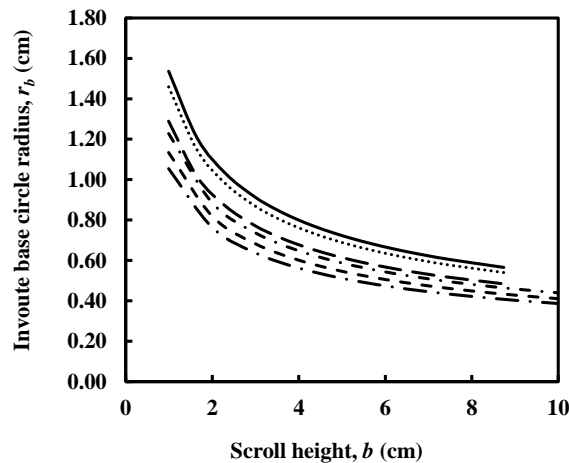


Figure 5: Non dimensional shaft power vs pressure ratio. Legend: — Predicted, - - - Experiment (Declaye *et al.*, 2013)

Table 1: Pressure and volumetric expansion ratio at the various scroll inlet temperatures for an exhaust pressure of 12.1 bar in case of R134a

T_3 (°C)	Optimum R_p	Optimum $\eta_{cycle}(\%)$	Optimum R_v	p_3 (bar)
100	2.80	10.17	3.17	33.61
110	2.97	11.11	3.30	35.76
120	3.31	12.31	3.66	39.74
130	3.63	13.50	3.99	43.61
140	4.01	14.68	4.38	48.15
150	4.40	15.85	4.78	52.90

**Figure 6:** Scroll base circle radius vs scroll height. Legend: — $T_3=100$ °C, $T_3=110$ °C, — — — $T_3=120$ °C, - - - $T_3=130$ °C, - . - $T_3=140$ °C, — · — $T_3=150$ °C

4.1. Thermal-fluidic losses

Fractional loss due to supply pressure drop against the scroll height is plotted in Figure 7. As scroll height increases, gas inlet area to the scroll decreases which results in higher supply pressure drop and hence the losses associated with it. At constant scroll inlet temperature, these losses are found to be roughly linear with scroll height. However, increase in scroll inlet temperature (T_3) decreases the supply pressure drop losses due to lower mass flow rates required to generate the same power output.

For the given scroll operating conditions, there exists a unique scroll geometry for which heat transfer losses are minimized as observed in Figure 7. Further, scroll geometry resulting in minimum heat transfer losses corresponds to minimum scroll surface area. As expected, heat transfer losses increase with scroll inlet temperature.

The loss due to flank leakage, Figure 8, is noted to increase with height of the scroll expander which can be directly attributed to the increase in leakage area along the flank of scroll wall. Also the leakage losses increase with supply temperature due to a corresponding increase in supply pressure. There is no distinct optimum scroll height observed for minimization of flank leakage losses contrary to the heat transfer losses.

Losses due to radial leakage are directly proportional to the spiral length of the scroll as can be seen in Figure 8, which in turn decreases with increase in scroll height. For higher scroll inlet temperatures, higher radial leakage losses are noted which is again attributed to higher scroll inlet pressure

4.2 Mechanical losses

As seen in Figure 9, fractional loss due to friction in the thrust bearing decreases with increase in height of scroll due to a corresponding decrease in the thrust bearing area of the scroll. Also a minima

is seen after which the losses rise marginally, indicating existence of an optimal choice of height (b) of the scroll. Its behavior is independent of the supply temperature.

The losses in the crank pin and journal bearing show minima at a particular height. Furthermore, this optimal height is seen to decrease with increase in supply temperature, which could be attributed to a corresponding increase in supply pressure.

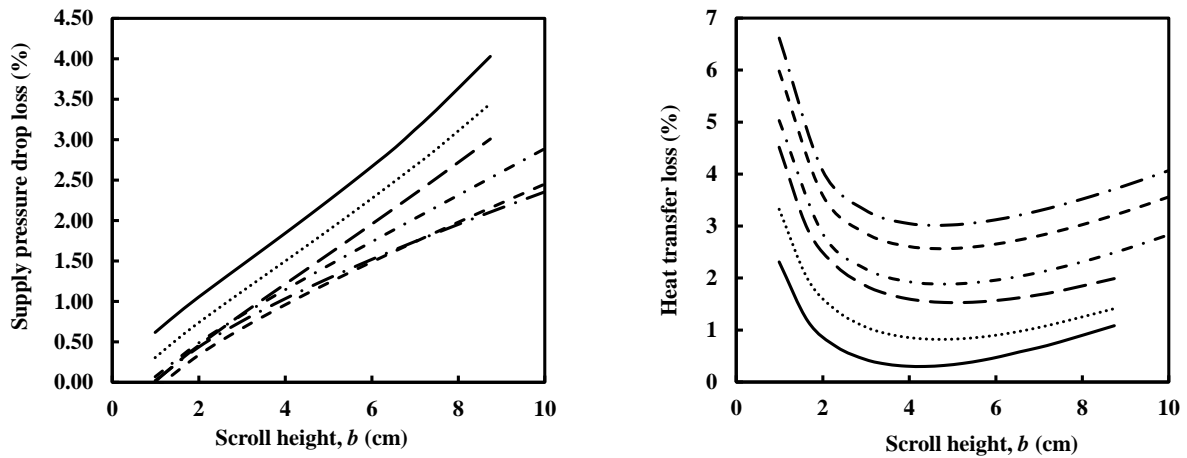


Figure 7: Variation of Supply Pressure drop losses and Heat transfer losses with scroll height. Legend: — $T_3=100^\circ\text{C}$, $T_3=110^\circ\text{C}$, — — — $T_3=120^\circ\text{C}$, - · - · - $T_3=130^\circ\text{C}$, - - - $T_3=140^\circ\text{C}$, — · — · — $T_3=150^\circ\text{C}$

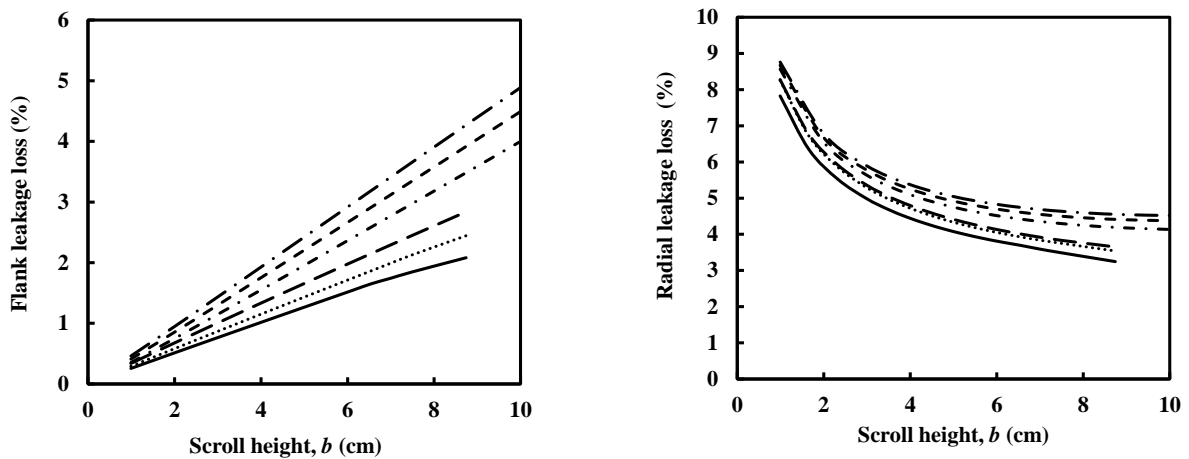


Figure 8: Variation of Flank leakage loss and Radial leakage loss with scroll height. Legend: — $T_3=100^\circ\text{C}$, $T_3=110^\circ\text{C}$, — — — $T_3=120^\circ\text{C}$, - · - · - $T_3=130^\circ\text{C}$, - - - $T_3=140^\circ\text{C}$, — · — · — $T_3=150^\circ\text{C}$

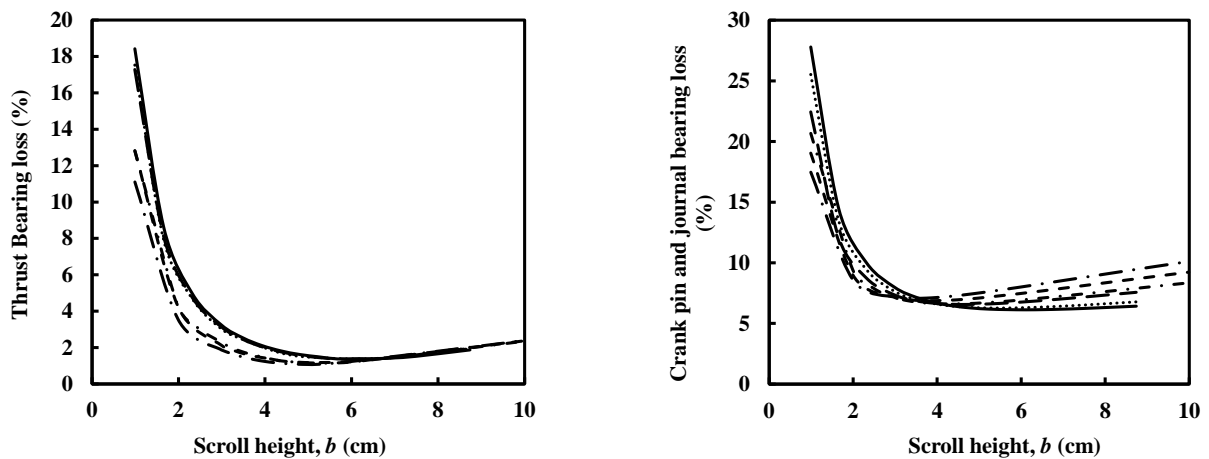


Figure 9: Variation of Thrust bearing losses and Crank pin and Journal bearing loss with scroll height. Legend: — $T_3=100^\circ\text{C}$, $T_3=110^\circ\text{C}$, — — — $T_3=120^\circ\text{C}$, - · - · - $T_3=130^\circ\text{C}$, - - - $T_3=140^\circ\text{C}$, — · — · — $T_3=150^\circ\text{C}$

4.3 Overall Losses

The distribution of the various losses can be seen in Figure 10 for the case of $T_3 = 120\text{ }^\circ\text{C}$.

Figure 11 shows the overall isentropic efficiency of the scroll expander as a function of scroll height. This graph includes the effect of all the losses discussed above. As can be seen there exists an optimal height at which maximum isentropic efficiency of the scroll expander exists. Also this optimal height is a function of the expander inlet temperature and monotonically decreases with increase in the expander inlet temperature as can be seen in Figure 12. The following equation can be used to obtain the optimal height as a function of temperature.

$$b_{opt} = -0.000387T_3 + 0.2061 \quad (4)$$

Also for the case of constant expander inlet pressure p_3 of 33.16 bar and varying expander inlet temperature T_3 , the optimal height is seen to be almost constant indicating the influence of expander inlet pressure on the optimal geometry of the scroll expander.

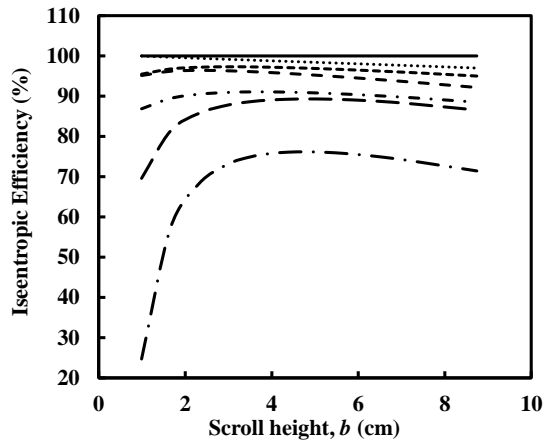


Figure 10: Variation of overall Isentropic efficiency with scroll height for scroll inlet temperature of $120\text{ }^\circ\text{C}$. Legend: — Ideal, +Supply Pressure Drop, -----+ Heat Transfer Loss, - - -+ Flank Leakage, - · - · - +Radial Leakage, ——— Thrust Bearing Losses, — · — · — Journal Bearing Losses

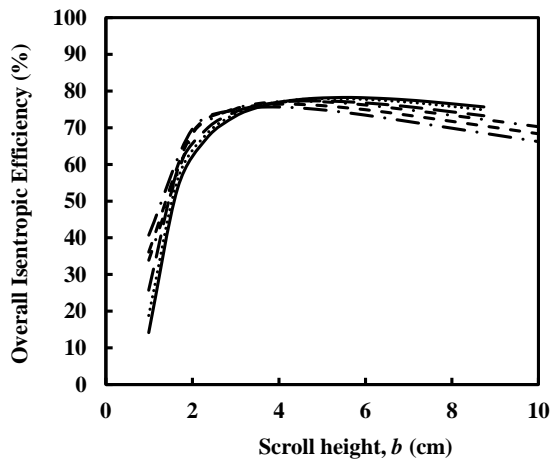


Figure 11: Variation of overall Isentropic efficiency with scroll height. Legend: — $T_3=100\text{ }^\circ\text{C}$, $T_3=110\text{ }^\circ\text{C}$, ----- $T_3=120\text{ }^\circ\text{C}$, - · - · - $T_3=130\text{ }^\circ\text{C}$, - - - $T_3=140\text{ }^\circ\text{C}$, — · — · — $T_3=150\text{ }^\circ\text{C}$

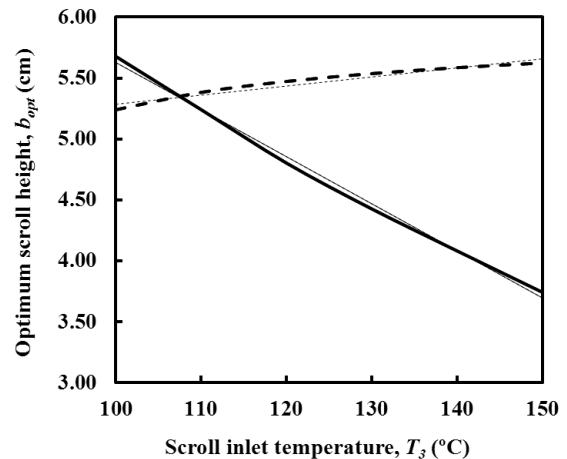


Figure 12: Optimum Scroll Height vs Supply Temperature. Legend: — Optimum P_3 corresponding to T_3 , - - - $p_3=33.16\text{ bar}$

5. CONCLUSIONS

In this paper, a procedure to optimize the scroll geometry for maximum isentropic efficiency for the given operating conditions and choice of working fluid in an ORC is presented. Selection of optimum geometry is based on minimizing the major losses in a scroll device namely, thermal-fluidic and mechanical losses which strongly depend upon the aspect ratio. Key findings from the case study of R134a ORC are as follows:

- i. Break up of these losses predicts mechanical losses to be of significant importance and hence, mechanical losses need to be properly accounted for.
- ii. Lumped models for mechanical losses may miss the optimum scroll geometry as the mechanical losses are found to be strong functions of scroll aspect ratios.
- iii. Keeping the pressures across the scroll identical, the optimum scroll height remains fairly constant with increase in scroll inlet temperature. On the other hand, if pressures in the scroll increase, optimum height decreases indicating higher aspect ratios.

Further, the tool developed herein can be implemented for the various working fluids and for different power scales to draw a comparison among them on the basis of optimum isentropic efficiency, scroll dimensions and cost.

NOMENCLATURE

A_{su}	suction area	m^2
b	scroll height	m
b_{opt}	optimum scroll height	m
F_i	axial force	N
F_r	radial force	N
F_t	tangential force	N
$f_{x1}, f_{x2}, f_{y1}, f_{y2}$	frictional force at Oldham ring	N
h	enthalpy	kJ/kg
I_o	crank shaft moment of inertia	kgm^2
L_Q	frictional torque at crank journal	Nm
L_S	frictional torque at crank pin	Nm
m	mass flow rate	kg/s
M_o	gas moment	Nm
m_s	mass of orbiting scroll	kg
N	generator load	W
p	pressure	N/m^2
r_b	base circle radius	m
r_o	orbiting radius	m
R_p	Pressure ratio	(-)
R_v	Expansion ratio	(-)
T	temperature	K
V	volume	m^3
θ	scroll orbiting angle	rad
ω	angular speed	rad/s
ρ	density	kg/m^3

REFERENCES

- Declaye, S., Quoilin, S., Guillaume, L., Lemort, V., 2013, Experimental study on an open-drive scroll expander integrated into an ORC (Organic Rankine Cycle) system with R245fa as working fluid. *Energy*, vol. 55, p: 173-183.
- Fiaschi, D., Manfrida, G., Maraschiello, F., 2012, Thermo-fluid dynamics preliminary design of turbo-expanders for ORC cycles, *Applied Energy*, vol. 97: p. 601–608.

- Garg, P., Kumar, P., Srinivasan, K., Dutta, P., 2013, Evaluation of carbon dioxide blends with isopentane and propane as working fluids for organic Rankine cycles, *Applied Thermal Engineering*, vol. 52, p: 439-448
- Garg, P., Kumar, P., Srinivasan, K., 2015, A trade-off between maxima in efficiency and specific work output of super- and trans-critical CO₂ Brayton cycles, *The Journal of Supercritical Fluids*, vol. 98, p: 119–126
- Guangbin, L., Yuanyang, Z., Liansheng, L., Pengcheng, S., 2010, Simulation and experiment research on wide ranging working process of scroll expander driven by compressed air, *Applied Thermal Engineering*, vol. 30, no. 14: p. 2073-2079.
- Lemort, V., Quoilin, S., Cuevas, C., Lebrun, J., 2009, Testing and modeling a scroll expander integrated into an Organic Rankine Cycle, *Applied Thermal Engineering*, vol. 29, no. 14: p. 3094-3102.
- Ooi, K. T., Zhu, J., 2004, Convective heat transfer in a scroll compressor chamber: a 2-D simulation, *International Journal of Thermal Sciences*, vol. 43, no. 7: p. 677-688.
- Tchanche, B. F., et al, 2011, Low-grade heat conversion into power using organic Rankine cycles – A review of various applications, *Renewable and Sustainable Energy Reviews*, vol. 15, no. 8: p. 3963–3979.
- Quoilin, S., Lemort, V., Lebrun, J., 2010, Experimental study and modeling of an Organic Rankine Cycle using scroll expander, *Applied energy*, vol. 87, no. 4: p. 1260-1268.
- Saitoh, T., Yamada, N., Wakashima, S. I., 2007, Solar Rankine cycle system using scroll expander, *Journal of Environment and Engineering*, vol. 2, no. 4: p. 708-719.
- Wang, H., Peterson, R. B., Herron, T., 2009, Experimental performance of a compliant scroll expander for an organic Rankine cycle, *Proceedings of the Institution of Mechanical Engineers, Part A: Journal of Power and Energy*, vol. 223, no. 7: p. 863-872.
- Ishii, N., Fuhushima, M., Sano, K., Sawai, K., 1986, A study on dynamic behavior of a scroll compressor, *International Compressor Engineering Conference*, Paper 578.
- Ishii, N., Yamamoto, S., Muramatsu, S., Yamamura, M., Takahashi, M., 1992, Optimum combination of parameters for high mechanical efficiency of a scroll compressor, *International Compressor Engineering Conference*, Paper 798.
- Morishita, E., Sugihara, M., Inaba, T., Nakamura, T., 1984, Scroll Compressor Analytical Model, *International Compressor Engineering Conference*, Paper 495.
- Rogers, R. J., Wagner, R. C., 1990, Scroll compressor flow modeling: experimental and computational investigation, *International Compressor Engineering Conference*, Paper 707.

ACKNOWLEDGEMENT

This research is based upon work supported by the Solar Energy Research Institute for India and the U.S. (SERIUS) funded jointly by the U.S. Department of Energy subcontract DE AC36-08G028308 (Office of Science, Office of Basic Energy Sciences, and Energy Efficiency and Renewable Energy, Solar Energy Technology Program, with support from the Office of International Affairs) and the Government of India subcontract IUSSTF/JCERDC-SERIIUS/2012 dated 22nd Nov. 2012.

A COMPARISON BETWEEN TWO DIFFERENT CFD APPROACHES OF A REAL SCROLL EXPANDER FOR MICRO-ORC APPLICATIONS

Alessio Suman^{1,a}, Carlo Buratto^{1,2,b},
Nicola Aldi^{1,c}, Michele Pinelli^{1,d}, Pier Ruggero Spina^{1,e},
Mirko Morini^{3,*}

¹Engineering Department in Ferrara (EnDiF), University of Ferrara, Ferrara, Italy

²Fluid-A s.r.l., Pieve di Cento, Bologna, Italy

²Industrial Engineering Department, University of Parma, Parma, Italy

^a alessio.suman@unife.it, ^b carlo.buratto@unife.it, ^c nicola.aldi@unife.it, ,

^d michele.pinelli@unife.it, ^e pier.ruggero.spina@unife.it

* mirko.morini@unipr.it

ABSTRACT

In this paper, CFD analyses of real scroll compressor are developed for a two-dimensional real geometry of a scroll compressor obtained by means of a Reverse Engineering (RE) of a commercial scroll compressor to be used as an expander in a microORC system. The analyses are carried out by means of CFD numerical simulations involving two type of approaches: (i) Dynamic Mesh (DM) and (ii) Chimera Strategy (CS). The particularity of these types of transient analyses consists in being able to reproduce the real operation of the machine through a sequence of relative positions between fixed and moving spirals. The results discuss the difference between the two numerical approaches in terms of ability to represent the actual flow features in a positive displacement machine. Analysis of the performance in terms of pressure and mass flow rate profiles, volumetric efficiency and shaft torque are reported.

1. INTRODUCTION

Scroll expander has recently become a good solution for micro and small scale ORC applications because of its reliability, compact structure, fewer moving parts, lower level of noise and vibration. Many experimental applications (up to 10 kW) can be found in literature (Bao and Zhao, 2013). In order to meet the increasing demands of efficiency and cost, the need for an experiment dedicated to each individual component of the energy system arose where the individual components are derived from applications other than those for which they are originally used. Laboratory micro- and sub-systems have been developed in order to study and optimize the entire energy system starting from *ad hoc* designed prototypes. In particular, a number of applications concerns small- and micro- size systems, for which the achievement of engineered solutions is particularly difficult. Bao and Zhao (2013) pointed out that for micro-energy system, the volumetric expander technology is the most preferable in terms of efficiency and cost. In particular, for applications in the range of (1 — 10) kWe, scroll, screw and rotary vane expanders are the most suitable for the ORC power-plants. The “*off-the-shelves*” availability of these components is very scarce and insufficient to meet the increasing demand of micro-scale component. In many cases, the designers have to be reinvented the volumetric expander taken from other applications (such as air condition, refrigeration, etc.). In these cases, the mathematical definition of the volumetric machine, that allows the preliminary analysis by studying the relationship between pockets evolution and the volumetric machine overall performance, is not possible. In this case, a new methodology, called Reverse Engineering (RE), represents a very useful method for generating a computational geometry of the real machine. The RE procedure and

instruments have improved their accuracy in recent years and, at the same time, the progress in software development allows three-dimensional representation of the real object to be obtained in a very short time. The RE method has recently gained importance in product development, maintenance/recovery and remanufacturing fields (Bagci, 2009 and Gameros *et al.*, 2015). The application of RE approach is an ever increasing methodology in fluid machinery studies, but its application in conjunction with the CFD approach is the early stage when dealing with small size positive displacement machines.

In this paper, the real geometry of the commercial SANDEN TRSA09-3658 scroll compressor has been acquired. The scroll performance in the expansion mode was studied by means of a CFD numerical analysis. CFD applications to positive displacement machine have been increasingly proposed in literature (Song *et al.*, 2015), thanks to the evolution of capability both in terms of algorithms and computational resources and, in some cases, the CFD results could be used for setting up lumped parameter model (Ziviani *et al.*, 2014).

A very recent interesting review is presented in Song *et al.* (2015). In their work, the Authors states that CFD simulation for the scroll machine is still in early stage because of the complex geometry and unique motion of orbiting scroll wrap, which is also one of the main issues faced in the present paper. The CFD simulations, refer to a transient numerical simulation in which the computational mesh is modified (regenerated and/or moved) at each time step to accommodate the shape and size change of the gas pockets. The numerical simulations regard a two-dimensional or three-dimensional computational domain. The validity of 2D versus 3D simulation is still an open question. In fact, in Song *et al.* (2015) claim that 2D numerical models cannot reflect the accurate spatial distribution and variation of the flow field. At the same time, Chang *et al.* (2014), demonstrated that the pressure variation on the expansion process by 2D geometry is slightly higher than that of 3D model, but the overall tendency is similar and the deviation is acceptable.

The analyses presented in this paper consist of: (i) the acquisition of the scroll compressor Sanden TRSA09-3658 geometry through a RE procedure and its CAD reconstruction as an expander, (ii) the generation of the numerical domain in order to allows the CFD analysis by means of a two type of approaches, (iii) the transient simulation with the DM approach by using ANSYS Fluent, (iv) the transient simulation with the CS approach by using CD-ADAPCO STAR-CCM+ and (v) the analysis of the performance in terms of pressure and mass flow rate profiles volumetric efficiency and shaft torque. Both of the numerical strategies are able to reproduce the real operation of the machine through a succession of a relative positions between the fixed and moving profiles and the following variation of the scroll gas pocket size.

The CFD model allows the evaluation of the influence of leakage flows, e.g. due to radial (flank) gaps, which play a key role in the determination of the performances of the machine. Moreover, it allows the tuning of analytical and thermodynamic models with fewer resources in the design phase. For this reason, the computational effort and time represent a key parameter on this type of approach. This paper deals with this issues and compare two different numerical strategies for which the Authors will highlight differences and similarities of different CFD methods.

2. REAL SCROLL RECONSTRUCTION AND GEOMETRIC ANALYSIS

The real geometry of the Sanden TRSA09-3658 scroll was obtained through an RE procedure. The RE of the real component has been performed by means of a Romer laser scanner and the subsequent parametric CAD representations. At first, a 3D polygonal geometry of the real geometry is obtained by interpolating the point cloud derived from the laser scanner by means of the Polyworks V12 software.

In Tab. 1 the scroll geometrical characteristics are reported while in Fig. 1, a real scroll device is shown. As can be seen from Tab. 2, the scroll flank gaps are non-uniform flank gaps during the orbit. Some considerations can be drawn after the RE procedure:

- before RE, no evidence of variable-with-orbit flank gap was expected. Their variability observed on the actual machine, after RE, can be due to: (i) the functional discrepancy between ideal CAD geometry and actual geometry after manufacturing; (ii) the actual geometry of the stator and

Table 1: Scroll compressor characteristics

Volume ratio	3.1055	
Maximum inlet volume [mm³]	85,900	
Spiral height [mm]	33.5	
End-plate diameter [mm]	120.0	
Axial duct diameter [mm]	12.0	
Radial duct diameter [mm]	12.5	
Flank gap [μm]	0° (inlet chambers close)	20
	90°	36
	180°	94
	270°	36

rotor assembly during standard working operation; (iii) the error inherent to the laser scanner device and to the subsequent interpolating process of the cloud points;

- the maximum inlet volume of the Sanden scroll compressor delivered by the manufacturer is different from the measured one. In particular, the manufacturer value is equal to 85,700 mm³. The discrepancy between the two values are equal to 200 mm³. After an order of magnitude calculation, this value was estimated to be equivalent to an uncertainty on the mass flow rate of about 1.5 %, which is acceptable if compared to typical experimental uncertainty on mass flow rate as reported by Matos and Rodrigues (2013).

The reproduction of the scroll as obtained by RE is shown in Fig 1 where the scroll profile is made regular and continuous by means of Spline curves. The CAD geometry of the real scroll is then exported in the CAD software SolidWorks through an interchange file format, e.g .stp or .iges format.

The computational domain consists of a bi-dimensional representation of the scroll machine. A 2D section has been obtained by intersecting the 3D polygonal model with a plane perpendicular to the rotation axis. In Fig. 2a, the 2D surface used for CFD simulation is outlined. To perform the subsequent 2D CFD simulation, the outlet boundary condition has been imposed in correspondence to the outlet duct (right-top duct in Fig. 2a), while the inlet boundary condition has been imposed in correspondence to the central volume of the machine by means of an opening on the fixed profile. In Fig. 2b, the detail of the central volume of the scroll in which the inlet section has been placed is presented. This numerical domain will use for both numerical analysis (DM and CS).

The 2D numerical domain uses the actual flank gaps derived from the RE. The consequent numerical simulation has to allow the resolution of the numerical model when very small (always lower than 100 μm with a minimum as equal to 20 μm) and variable-with-orbit flank gaps afflicted the scroll operation. For this reason the computational mesh e the transient simulation have to be accurately defined.

**Figure 1:** Scroll Sanden TRSA09-3658

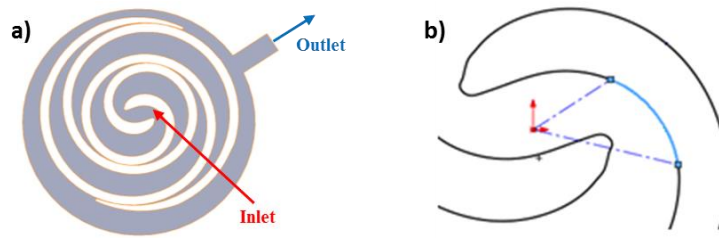


Figure 2: 2D Numerical domain

3. DYNAMIC MESH APPROACH

Since the scroll machine operation is based on the variation of the gas pocket volume according to the crack shaft position, the numerical domain and the resolution strategy are developed in order to accommodate this process. Two different numerical approaches are adopted and compared.

3.1 Dynamic mesh approach

The CFD simulations were carried out as a 2D transient numerical model by using a Dynamic Mesh (DM) strategy implemented in ANSYS Fluent 13.0. This transient analysis is able to reproduce the real operation of the machine through a sequence of relative positions between the fixed and moving profile by imposing an angular increment.

The use of 2D CFD analysis by using a DM for studying some particular fluid dynamic phenomena in the gear pumps. In particular, Castilla *et al.* (2010) put the attention to the turbulence structure in the suction chamber, while Del Campo *et al.* (2012) analyzed the pressure variation and cavitation phenomena. In these cases, the 2D strategy allows the comprehension of the major fluid dynamic phenomena involved in volumetric devices.

In this paper, with the DM strategy, the mesh inside the fixed and moving (orbiting) profiles is regenerated at each time step to accommodate the shape and size change of the gas pockets. The mesh regeneration could follow element size criteria and/or element quality criteria (such as skewness).

The numerical domain of the real scroll is discretized through the use of a triangular mesh. The mesh was composed of about 900,000 triangular elements. The maximum element skewness of the initial mesh is smaller than 0.33 (0.60 before smoothing) and a minimum orthogonal quality at least equal to 0.655 was achieved. To increase the resolution of the mesh close to the walls, a local mesh refining approach was adopted. The local refining around the walls is shown in Fig. 3. In the flank gap there are at least two triangular mesh elements in agreement with the data reported in literature (Castilla *et al.*, 2010 and Del Campo *et al.*, 2012) for volumetric displacement.

3.1 Chimera approach

Overlapping grid, subsequently named the Chimera approach, was first introduced in the early

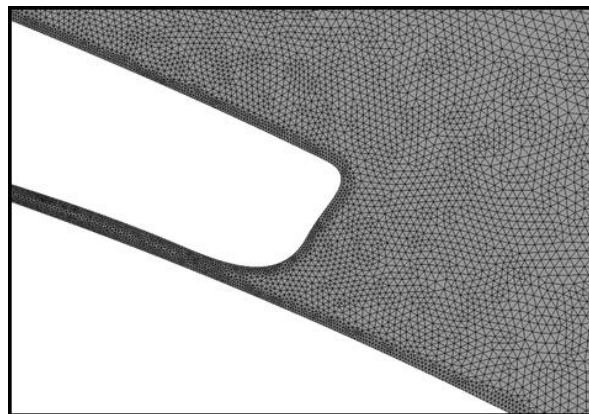


Figure 3: Local mesh refinement around the scroll edge in the case of DM strategy

1980's (Steger and Benek, 1987) when several grid assembly packages have become available (Roget and Sitaraman, 2014). In the present paper, the simulation of the scroll expander with the Chimera Strategy (CS) was carried out by means of CD-ADAPCO STAR-CCM+ 9.04. The overset method consist in the contemporary use of active cells and passive cells. In active cells, regular discretized equations are solved, while in passive cells, no equation is solved, they are temporarily or permanently de-activated. Active cells along interface to passive cells refer to donor cells at another grid instead of the passive neighbors on the same grid. The first layer of passive cells next to active cells are called acceptor cells. The solution is computed on all grids simultaneously. Grids are implicitly coupled through the linear equation system matrix. Different interpolation functions can be used to express values at acceptor cells via values at donor cells. The donor cells must be active cells, and the change of cell status is automatically controlled by the solver. Overset grids usually involve one background mesh, which is adapted to environment, and one or more overset grids attached to bodies, overlapping the background mesh and/or each other as reported in Fig. 4. Each grid (background and overset) can move according to the motion models implemented in the CFD software. In literature, the comparison between the CS and other CFD strategies are limited. Togasci *et al.*, 2001 and Hoke *et al.*, 2009 report the applications of the overset grid for a rocket booster and a 2D airfoil, respectively. Comparison with experimental data (Togasci *et al.*, 2001) and other CFD solutions (Hoke *et al.*, 2009) demonstrated that the CS is reliable for different fluid dynamics applications. The major difference with respect to the DM approach consists that CS does not deform the mesh during the calculation.

In the present paper the background mesh and the overlapping mesh are reported in Fig. 5. The overlapping mesh bounded the moving scroll spiral and are obtained by an offset of 1.5 mm from the actual moving scroll spiral. Overlapping mesh is made up with 171,073 elements while the background mesh (that refers to the scroll stator and fixed spiral) is made up by 529,547 elements. Overlapping and background mesh are constitute by polyhedral elements and prism layer close to the wall. In the particular reported in Fig. 5 clearly visible are the polyhedral elements in the core regions while the prism layer close to the wall allow the grid refinement and the good representation of the flank leakage.

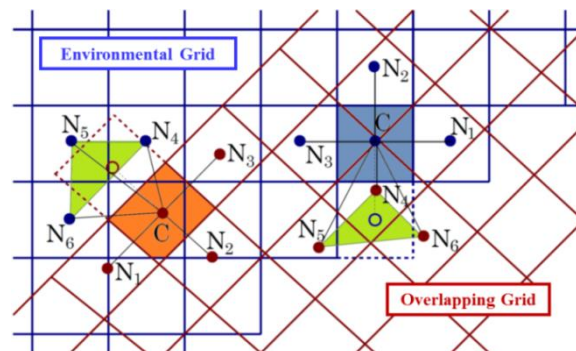


Figure 4: N_1, N_2, N_3 neighbors from same grid; N_4, N_5, N_6 neighbors from overlapping grid (Schreck and Perić, 2012)

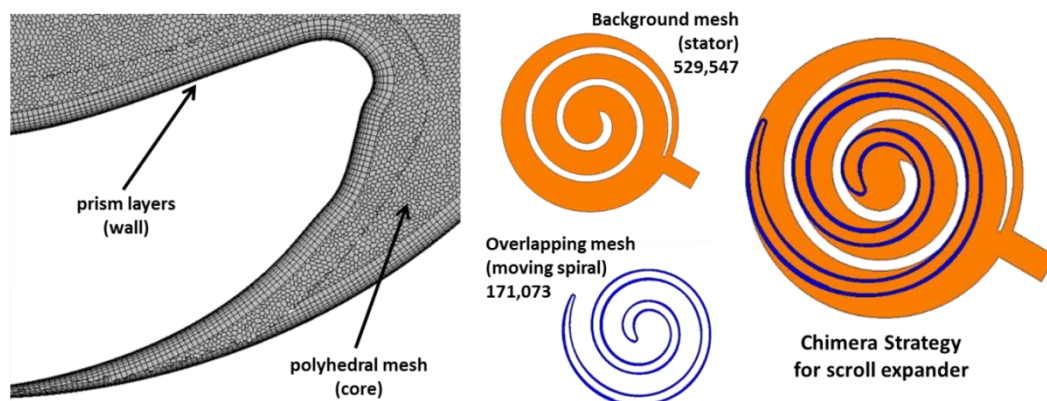


Figure 5: Background and overlapping mesh

5. COMPARISON

5.1 Boundary conditions

To perform a comparative analysis, the same boundary conditions were applied in the two numerical simulations. To perform the two-dimensional CFD simulations, the inlet boundary condition has been imposed in correspondence to the central volume of the machine by means of an opening on the fixed profile as reported in Fig. 2b. Both simulations (DM and CS) were conducted by imposing a pressure ratio of 3.5. The reference pressure is 101,325 Pa. The rotational velocity was imposed equal to 2,000 rpm. The turbulence model chosen, in accordance with Cui (2006), is the $k-\epsilon$ model combined with standard wall functions. The fluid considered for the comparisons between the DM and CS simulation is air at standard conditions. Simulation of scroll machines by using real gas equations is numerically very challenging and could drain most of the computational resources during the simulation. Moreover, the specific geometry under consideration is characterized by time-varying sliding narrow gaps which result in tough convergence issues when using air as the working fluid. These issues are even more relevant when refrigerant is used. For these reasons, for the purposes of this paper (i.e. sensitivity analyses and the comparison between two different simulation strategies) only air is considered as the working fluid. The time step of the transient analyses is equal to $5.21 \cdot 10^{-6}$ s that corresponds to an angular increment of 0.0625° of the scroll crank. The advection scheme adopted for both analyses is the second order Upwind.

5.2 Pressure field and fluctuations at the ports

In Fig. 6, the trends of the inlet chamber pressure of the scroll expander are presented as a function of the normalized angular position of the orbit covered by the moving spiral profile. The solution provided by the CS shows a smooth trend in discharge pressure even if, the pressure fluctuation showed by the DM solution (at $3/4$ of the orbit) is contained in few Pa (less than 0.75 %).

Comparing the contour plots referring to the latter expander orbits angles ($3/4$ and 1) DM and CS solutions show a different pressure for the twin discharge pockets. This phenomenon is related to the asymmetric position of the inlet and outlet ports and strongly linked to the design of the scroll machine even if in the Chimera Strategy this phenomenon is less appreciated. Pressure fields are comparable and clearly visible, in both solutions, are the pressure evolutions inside the isolated pockets: (i) the inlet pocket (which the pressure graph referred), (ii) the intermediate pocket and finally (iii) the discharge pocket and the outlet duct.

The pressure trends and the pressure field representation allow the definition of which pressure fluctuations affect the machine during standard operation. These results are very important to understand the vibration and noise generated by the machine.

5.3 Flow rate and velocity field

In Fig. 7, the trends of the mass flow of the scroll expander are reported as a function of the normalized angular position of the orbit covered by the moving spiral profile. The trends of the mass flow rate are very similar in both of the scroll expander ports. In the inlet section, the same mass flow rate fluctuation can be observed for the two numerical strategies. The higher mass flow rate operated

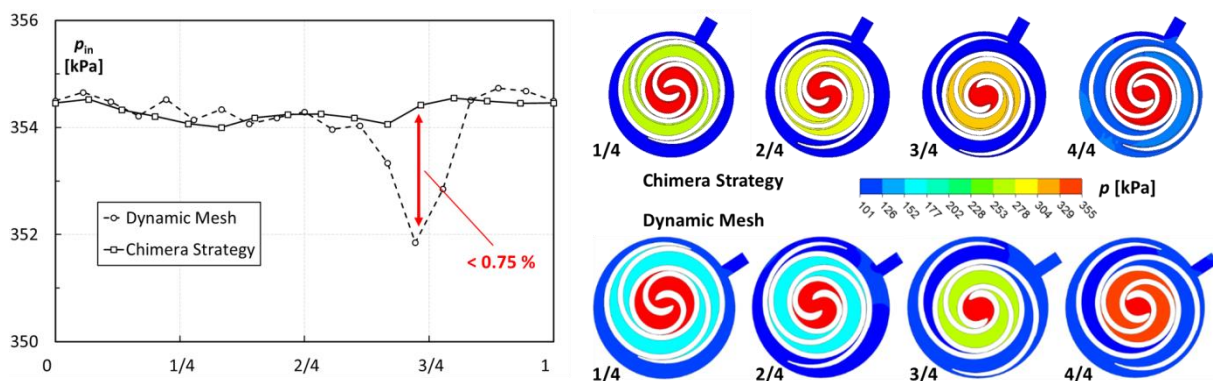


Figure 6: Inlet pressure and pressure fields during the orbits

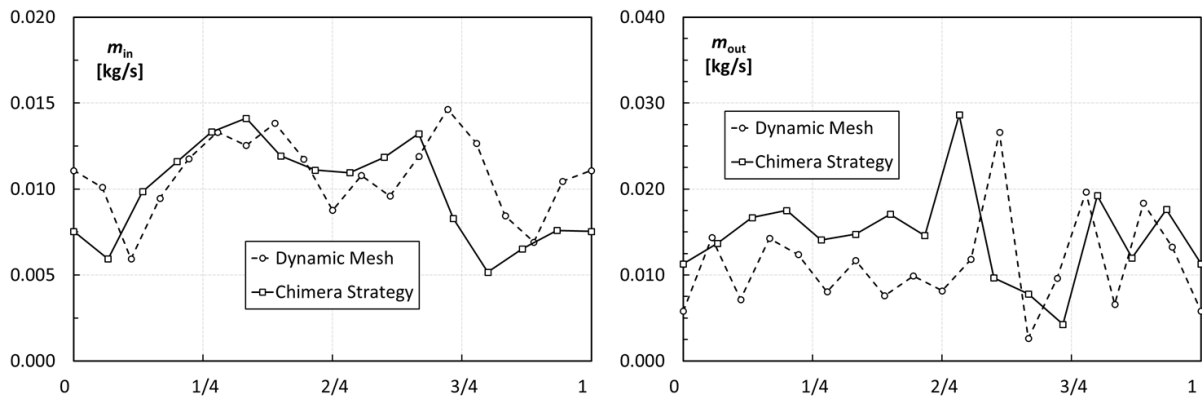


Figure 7: Mass flow rate

by the scroll expander in the orbit angle range from 1/4 to 3/4 is due to the position of the moving spiral that is in the opposite position with respect to the inlet port. This phenomenon is well described by the two numerical strategies. The average values of the inlet mass flow rate are: (i) 0.0108 kg/s in the DM solution and (ii) 0.0098 kg/s in the CS solution. The deviation is equal to 0.001 kg/m s that corresponds to the 9 % with respect to the higher value. Considering the (i) different numerical approaches that reflect in different mesh topology, (ii) different solution strategies and (iii) the scroll machine peculiarities, these values are considered acceptable.

Regarding the discharge mass flow rate, same consideration can be done. The fluctuations is well reproduced by the two strategies even if the CS solution shows a higher values in the first half of the scroll orbit. Pressure fluctuations reported above and mass flow rate discontinuities are due to interaction between the moving spiral and the outlet port positioned closer to the upper gas pocket (as can be seen in Fig. 2). Comparing the phase of the two mass flow rate trends it is possible to note the phase shift. Chimera Strategy solution appears in advance with respect to the DM solution for the inlet mass flow rate trend and for the outlet mass flow rate trend up to 2/4 orbit. However, in the last part of the orbit, in the case of outlet mass flow rate the DM solution appears in advance with respect to the CS solution. The difference highlighted for the mass flow rate values are due to resolution of the flank gaps that allow the fluid in the scroll expander to by-pass the moving scroll towards the discharge outlet. The mesh refinement close to the walls (realized in both cases) are able to describe this phenomenon as can be seen in Fig. 8, but, due to the different numerical approach, the global solution of this local fluid dynamic phenomenon is different. In Fig. 8 there are two representations of the flank leakage that affect the scroll expander. In this operation mode, the fluid overpasses the spiral through the flank gaps without energy exchanges (and thus work) with the mobile spiral. Figure 8 shows the flank leakages (i) from the discharge chamber to the outlet volume (casing), (ii) from the expansion chamber to the discharge chamber and finally (iii) from the suction chamber to the expansion chamber. In Fig. 9, the evolution of the velocity fields inside the expander scroll are presented. From these plots, the back flow at the inlet port during compression mode can be clearly observed. This aspect seems to be due to the dimension of the external case of the scroll machine. This result may not be very representative of the actual scroll machine. In fact, in these bi-dimensional simulations the operation fluid does not have the possibility to move along the rotating axis of the machine, and thus, possible three dimensional flows are neglected from the results reported in this paper.

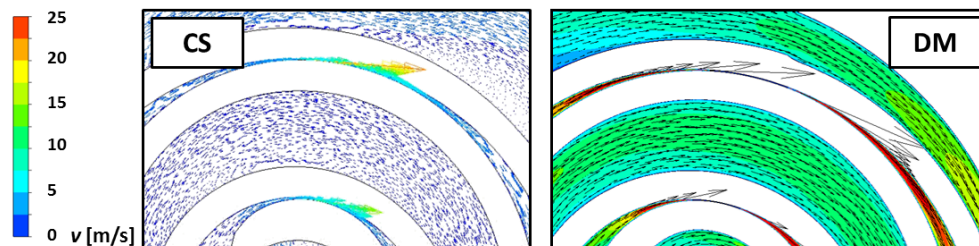


Figure 8: Flank leakage in the scroll expander

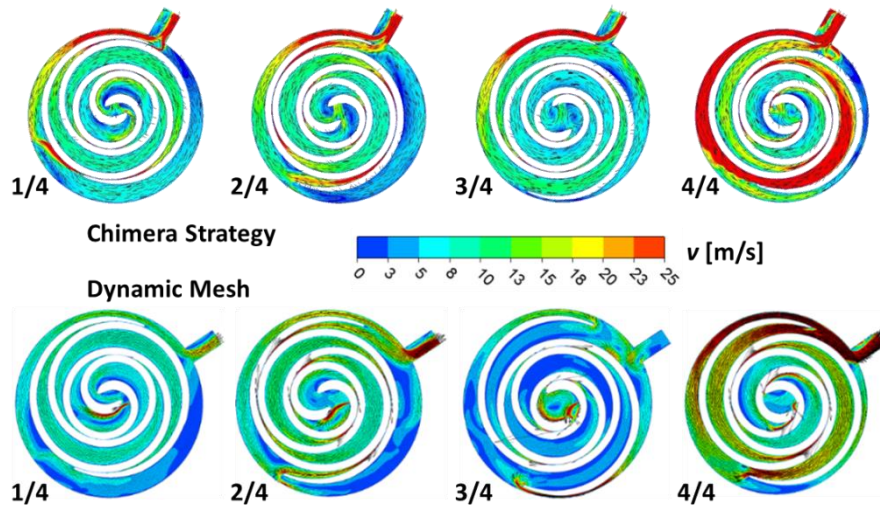


Figure 9: Velocity fields

5.4 Shaft torque and volumetric efficiency

The comparison between the two numerical approaches was carried out also by the scroll performance. Starting from the CFD results, in this paragraph the authors have reported the scroll performance related to (i) shaft torque and (ii) volumetric efficiency.

Figure 10 reports the shaft torque trends for CS and DM simulations. Also in this case, the two shaft torque trend as a function of the normalized angular position of the orbit covered by the moving spiral profile are very consistent to each other. The shaft torque generated by the moving spiral varying in the range from 2.20 Nm to 0.35 Nm. The CS solution shows a more smooth trend. The pressure and mass flow rate fluctuations highlighted in correspondence of the position equal to 3/4 of the orbit angle determine a shaft torque variation, especially in the DM solution.

The volumetric efficiency of the scroll machine was also estimated by means of CFD results for both of the solutions. The volumetric efficiency of the scroll expander, VFM (Volumetric Flow Matching ratio), was obtained as the ratio of the ideal volume flow rate determined through the theoretical volume isolated by the scroll and the CFD calculated volume flow operated by the scroll. The VFM value should be as close as possible to one for optimal performance. Greater values indicate higher volumetric losses.

The VFM resulted equal to (i) 3.06 in the case of DM solution and (ii) 2.80 in the case of CS solution. The deviation is due to the deviation highlighted for the values of the mass flow rate at the expander inlet port. These high values, consistent with the data presented by Mathias *et al.* (2009), are closely related to the value of the flank gap imposed between the fixed scroll and the moving scroll. As previously mentioned, the magnitude of the flank gap influences the performance of the scroll machine (in particular the volumetric efficiency). By using the CFD simulations, leakage flows in the flank gap, that affect the operation of both machines, can be clearly observed as reported in Fig. 8.

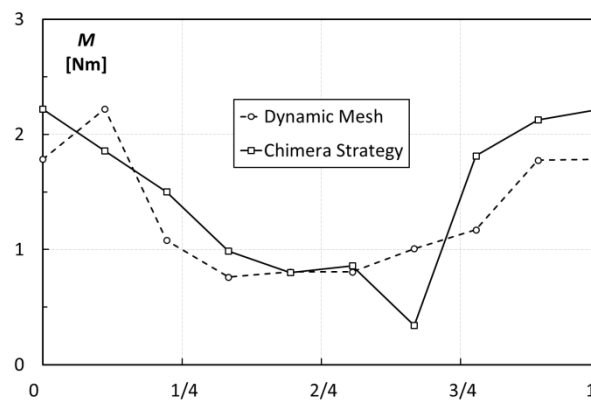


Figure 10: Shaft torque

The flank leakages are, in general, driven by (i) the magnitude of the flank gaps, (ii) the density of the operating fluid, (iii) the presence of the lubricating oil and (iv) the pressure difference between two consecutive isolated pockets. In general long spirals allow the reduction of the pressure difference between two consecutive isolated pockets (and thus there is less flank leakage) but the scroll machine becomes bigger and more expensive. In the same way, the use of lubricating oil allows the reduction of leakages thanks to its phase (liquid) and viscosity but the scroll machine and, in this case, the entire circuit become more complicated and expensive.

6. CONCLUSIONS

In this paper a comprehensive performance and fluid dynamic assessment of a real scroll machine was presented by means of CFD analyses. The numerical analysis based on the comparison between two different numerical approaches for the analysis of a real scroll machine used as an expander.

Thanks to the use of a reverse engineering procedure, an unknown scroll compressor geometry was reconstructed and digitalized. The use of CFD simulation allows the study of the detailed working features of the machine that are not completely visible with other types of analyses (such as thermodynamic or lumped approach). Two CFD methods were developed by means of a transient numerical simulations. Dynamic mesh approach and Chimera Strategy are used in order to reproduce the real operation of the machine through a sequence of relative positions between fixed and moving spirals. The CFD transient simulations allowed the evaluation of time profile of the mass flow rate and pressure fluctuations at the inlet and outlet sections of the machine.

The comparison between the two numerical strategies on a real scroll machine was carried out through the analysis of (i) pressure field inside the scroll pocket, (ii) the mass flow rate at the inlet and outlet ports, (iii) velocity field and the influence of the flank gap and finally (iv) shaft torque and volumetric efficiency.

Results show that both of numerical strategies are able to reproduce the pressure fluctuation (deviation less than 0.75 % at the inlet port) and the mass flow rate variation at the ports. Differences were highlighted for the phase of fluctuations of the mass flow rate trend. Scroll expander performance such as shaft torque and volumetric efficiency are very consistent between the two numerical strategies.

The capability of the two approaches to calculate the pressure and mass flow rate fluctuations represent a key results and both of this method could represent an very useful tool during the design phase. All of fluid dynamic phenomena impact on the scroll performance, and only through their comprehension it is possible to optimize the scroll design by the modification of the spiral profile or the position and dimension of the inlet and outlet port. Pressure fluctuations are closely related to vibrations and noise generated by the machine in operation.

NOMENCLATURE

M	torque	[Nm]
m	mass flow rate	[kg/s]
N	grid node	
p	pressure	[Pa]
v	velocity	[m/s]

Subscript

in	inlet
out	outlet

Acronyms

CFD	Computational Fluid Dynamics
CS	Chimera Strategy
DM	Dynamic Mesh

RE Reverse Engineering
VFM Volumetric Flow Matching ratio

REFERENCES

- Bagci, E., 2009, Reverse engineering applications for recovery of broken or worn parts and re-manufacturing: Three case studies, *Adv. Eng. Software*, **40**, pp. 407-418.
- Bao, J., Zhao, L., 2013, A review of working fluid and expander selections for organic Rankine cycle”, *Renewable and Sustainable Energy Rev.*, **24**, pp. 325-342.
- Castilla, R., Gamez-Montero, P. J., Ertürk, N., Vernet, A., Coussirat, M., Codina, E., 2010, Numerical simulation of turbulent flow in the suction chamber of a gear pump using deforming mesh and mesh replacement, *Int. J. Mech. Sci.*, **52**, pp. 1334-1342.
- Chang, J. C., Chang, C. W., Hung, T. C., Lin, J. R., Huang, K. C., 2014, Experimental study and CFD approach for scroll type expander used in low-temperature organic Rankine cycle, *Appl. Therm. Eng.*, **73**, pp. 1444-1452.
- Cui, M. M., 2006, Numerical Study of Unsteady Flows in a Scroll Compressor, *J. Fluids Eng.*, **128**, pp. 947-55.
- Del Campo, D., Castilla, R., Raush, G. A., Gamez-Montero, P. J., Codina, E., 2012, Numerical Analysis of External Gear Pumps Including Cavitation, *J. Fluids Eng.*, **134**, p. 081105.
- Gameros, A., De Chiffre, L., Siller, H. R., Hiller, J., Genta, G., 2015, A reverse engineering methodology for nickel alloy turbine blades with internal features, *CIRP J. Manuf. Sci. Technol.*, art. in press (9 pages).
- Hoke, C., Decker, R., Cummings, R., McDaniel, D., Morton, S., 2009, Comparison of Overset Grid Deformation Techniques Applied to 2-Dimensional NACA Airfoils, 19th AIAA Computational Fluid Dynamics Conference, 22 - 25 June 2009, San Antonio, Texas, US.
- Mathias, J. A., Johnston, J. R. J., Cao, J., Priedeman, D. K., Christensen, R. N., 2009, Experimental Testing of Gerotor and Scroll Expanders Used in, and Energetic and Exergetic Modeling of, an Organic Rankine Cycle, *J. Energy Res. Technol.*, **131**, p. 012201.
- Matos, M. A., Rodrigues, N., 2013, Gas mass-flow meters: Measurement and uncertainties, *Flow Meas. Instrum.*, **33**, pp. 45-54.
- Roget, B., Sitaraman, J., 2014, Robust and efficient overset grid assembly for partitioned unstructured meshes, *J. Comput. Phys.*, **260**, pp. 1-24.
- Schreck, E., Perić, M., 2012, Overset Grids in STAR-CCM+: Methodology, Applications and Future Developments, STAR Japanese Conference 2012.
- Song, P., Wei, M., Shi, L., Danish, S. N., Ma, C., 2015, A review of scroll expanders for organic Rankine cycle systems, *Appl. Therm. Eng.*, **75**, pp. 54-64.
- Steger, J. L., Benek, J. A., 1987, On the use of composite grid schemes in computational aerodynamics, *Comput. Methods Appl. Mech. Eng.*, **64**, pp. 301-320.
- Togashi, F., Nakahashi, K., Ito, Y., Iwamiya, T., Shimbo Y., 2001, Flow Simulation of NAL Experimental Supersonic Airplane/Booster Separation Using Overset Unstructured Grids, *Comput. Fluids*, **30**(6), pp. 673-688.
- Ziviani, D., Suman, A., Lecompt, S., De Paepe, M., van den Broek, M., Spina, P. R., Pinelli, M., Venturini, M., Beyene, A., 2014, Comparison of a Single-Screw and a Scroll Expander under Part-Load Conditions for Low-Grade Heat Recovery ORC Systems, Proc. of 6th International Conference on Applied Energy (ICAE2014), Taipei, 30 May - 2 June, 2014, Paper n. 78, pp. 1-4.

ACKNOWLEDGEMENT

The research was partially supported by the Italian Ministry of Economic Development within the framework of the Program Agreement MSE-CNR “Ricerca del Sistema elettrico nazionale (RdS)”.

DESIGN AND RATING OF AN EVAPORATOR FOR WASTE HEAT RECOVERY ORGANIC RANKINE CYCLE USING SES36

Alihan Kaya^{1*}, Marija Lazova¹ and Michel De Paepe¹

¹Ghent University,
Department of Flow, Heat and Combustion Mechanics,
Ghent, Belgium
e-mail: alihan.kaya@ugent.be

* Corresponding Author

ABSTRACT

The paper presents a design and rating study of a 4MW evaporator having plain horizontal carbon steel tubes having diameters of 25,4 mm, 31,8 mm and 38 mm, to be used in waste heat recovery via Organic Rankine cycle (ORC). SES36 is chosen as working fluid due to its low boiling point, which makes it suitable for low-grade waste heat recovery with subcritical ORCs. Waste heat carrier industrial air arrives at the evaporator bundle at 280°C. Inlet temperature of the working fluid is 40°C and the evaporation occurs at 125°C and 1,09 MPa. Furthermore, a design sensitivity analysis is made by means of using 13 different in-tube flow boiling correlations. The resulting design and rating parameters yielded by each correlation are compared to each other. By those means, a design error margin of various thermo-hydraulic heat exchanger parameters is revealed, when different in-tube flow boiling heat transfer calculation methods are used. The change in the error margins are investigated with respect to changing tube outer diameter, tube wall thickness, fin density and tube layout (staggered and inline).

1. INTRODUCTION

Waste heat recovery as an alternative energy source is receiving more and more attention from the industry and scientific world, as the energy shortage and environmental concerns in the world are rising. Organic Rankine cycles (ORCs) are promising applications for waste heat recovery, due to their heat recovery efficiencies and environmental-friendly features (Quoilin *et al.*, 2013). ORCs are applicable with a wide range of waste heat sources rooting from industrial operations such as metallurgical industry, incinerators, combustion engines, annealing furnaces, drying, baking, cement production etc. ORCs are typically being applied on waste heat sources with the temperature range from 100°C up to 400°C, by being usually referred as low-temperature waste heat (100°C-250°C) and high-temperature waste heat (250°C-400°C). ORCs have a similar working principal with the conventional Rankine cycle which utilizes water or steam, however they utilize organic fluids as working fluid. Two among the most commonly used zero ozone depletion potential (ODP) working fluids for low-grade waste heat recovery are R245fa and Solkatherm® SES36. Their thermodynamic and environmental properties can be seen in the Table 1.

Table 1: Properties of proposed fluids

Working Fluid	GWP	ASHRAE Criteria	M. Mass (g.mol ⁻¹)	Boiling Point (K)	T _{crit} (K)	P _{crit} (MPa)
R245fa	950	B1	134,05	288,05	427,2	3,64
Solkatherm® SES36	3710	Non-Flammable	184,53	308,79	450,7	2,85

The case-specific working conditions are the main determining parameters for an ORC system design. The efficiency of the cycle strongly depends on the considered working fluid. A reasonable selection process can be done by taking the fluids' thermodynamic, stability, safety, legislative and environmental aspects into consideration for a particular case. Moreover, the critical temperature and

critical pressure values of the working fluid are the main criterion for distinguishing the cycle conditions (subcritical, transcritical and supercritical) of an ORC. R245fa is reported to be a suitable refrigerant for ORC applications by various researchers (Maalouf *et al.*, 2012; Saleh *et al.*, 2007; Shengjun *et al.*, 2011; Liu *et al.*, 2012). Although, there are empirical examples of promising ORC efficiency of SES36 (Mikielewicz *et al.*, 2012; Mikielewicz, 2010; Riva *et al.*, 2006; Siddiqi and Atakan, 2011; Galvez, 2009), the ORC research with SES36 is still at its infancy. With the light of its reported promising features in accordance to the aforementioned aspects, Solkatherm® SES36 is chosen as the working fluid for the present study related to the subcritical ORC evaporators.

Waste heat recovery can be performed efficiently through a direct evaporator (e.g. finned tube bundles) where the hot flue gas coming from a heat source (Ribatski and Thome, 2007) is in direct contact with the heat exchanger outer surface. However, the thermodynamic efficiency of an evaporator relies on heat transfer and pressure drops, the sizing of an evaporator needs to be performed accordingly (Quoilin *et al.*, 2013). In a design problem, the accuracy of the design method might have a significant impact on the aspects related to heat transfer and thermo-economic efficiency. A too small sized evaporator not capable to perform a complete evaporation might cause turbine or expander damage in some cases. On the other hand, a too large evaporator will cause excessive working fluid superheating, which may lead to a negative impact on system performance and a higher heat exchanger cost (Fischer, 2011). Design of evaporators is often being done by means of commercial software, where various generally applicable calculation methods are implemented, yet the methods are usually undisclosed. Moreover, the validity range of those methods usually do not overlap with present conditions. Thus, the accuracy of using different heat transfer correlations from the aspect of specific ORC evaporator design and rating parameters is not known yet. In that manner, the accuracy of in-tube flow boiling calculations might have an observable influence on the end design, even though the design of evaporator for waste heat recovery ORC applications is significantly dependent on flue gas heat carrier side. For having a concrete idea of the largest possible error margin of using various flow boiling heat transfer methods, a design sensitivity analysis is performed by means of using 13 different a priori flow boiling heat transfer correlations. The investigated correlations are listed in Table 2.

Table 2: Used flow boiling correlations

Author(s)	Year	Source
Kandlikar	1990	(Kandlikar, 1990)
Gungor & Winterton	1987	(Thome, 2004)
Gungor & Winterton	1986	(Gungor and Winterton, 1986)
Wattelet <i>et al.</i>	1994	(Dobson <i>et al.</i> , 1993)
Butterworth	1970	(Schlunder, 1986)
Chen	1966	(Chen, 1966)
Bennett <i>et al.</i>	1959	(Bennett and Chen, 1980)
Palen	1983	(Schlunder; 1986)
Shah	2009	(Shah, 1976)
Klimenko	1990	(Klimenko, 1988)
Liu & Winterton	1991	(Liu and Winterton, 1991)
Steiner & Taborek	1992	(Steiner and Taborek, 1992)
Chun & Seban	1971	(Chun and Seban, 1971)

The error margin sensitivity analysis is made for a typical low-temperature ORC waste recovery case where the working fluid enters to the evaporator at 40°C and the evaporation occurs at 125°C and 1,09 MPa. The waste heat carrier fluid is industrial air and has a temperature of 280°C at the evaporator inlet. The required capacity is 4 MW. The fixed and variable geometrical parameters of the evaporator is given at the Table 3. It is important to mention that number of tubes and fin diameter changes directly with the outer tube diameter. Moreover, an illustration of the evaporator is shown in the Figure 1. Moreover, Figure 2 shows the geometric parameters of the inline and staggered layout, as well as the geometrical definitions related to the fins around tubes.

Table 3: Evaporator properties and parameters

D_{out} (mm)	25,4 – 31,8 – 38
# of Tubes	66 – 59 – 54
t_w (mm)	2,11 – 2,77
L_{tube} (m)	3
W (m)	4
Tube Material	Carbon Steel
D_f (mm)	57 – 60,35 – 70
t_f (mm)	0,4
P_f (fins/m)	236 – 275 – 314 – 354 – 393 – 432
Fin Material	Aluminum
D_{bend} (mm)	$3 \times D_{out}$
Tube Layout	Staggered (60°) - Inline

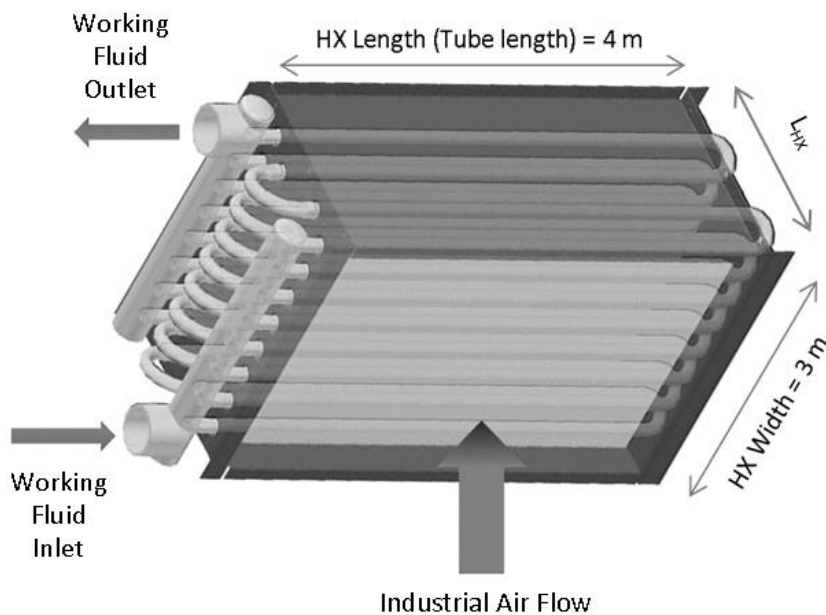


Figure 1: Evaporator drawing

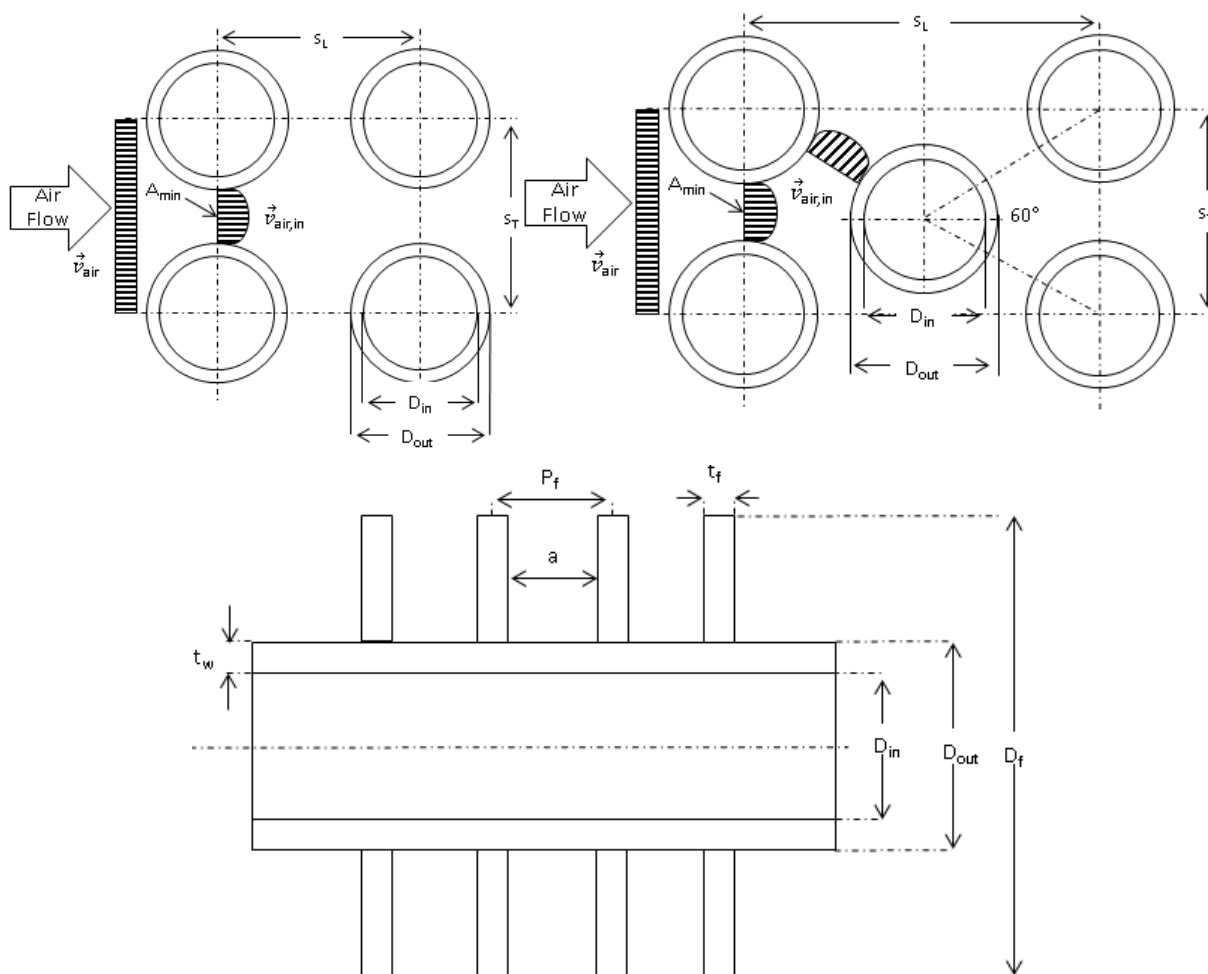


Figure 2: Inline (upper left) and staggered (upper right) tube layouts; fin geometry (lower center)

2. DESIGN METHODOLOGY

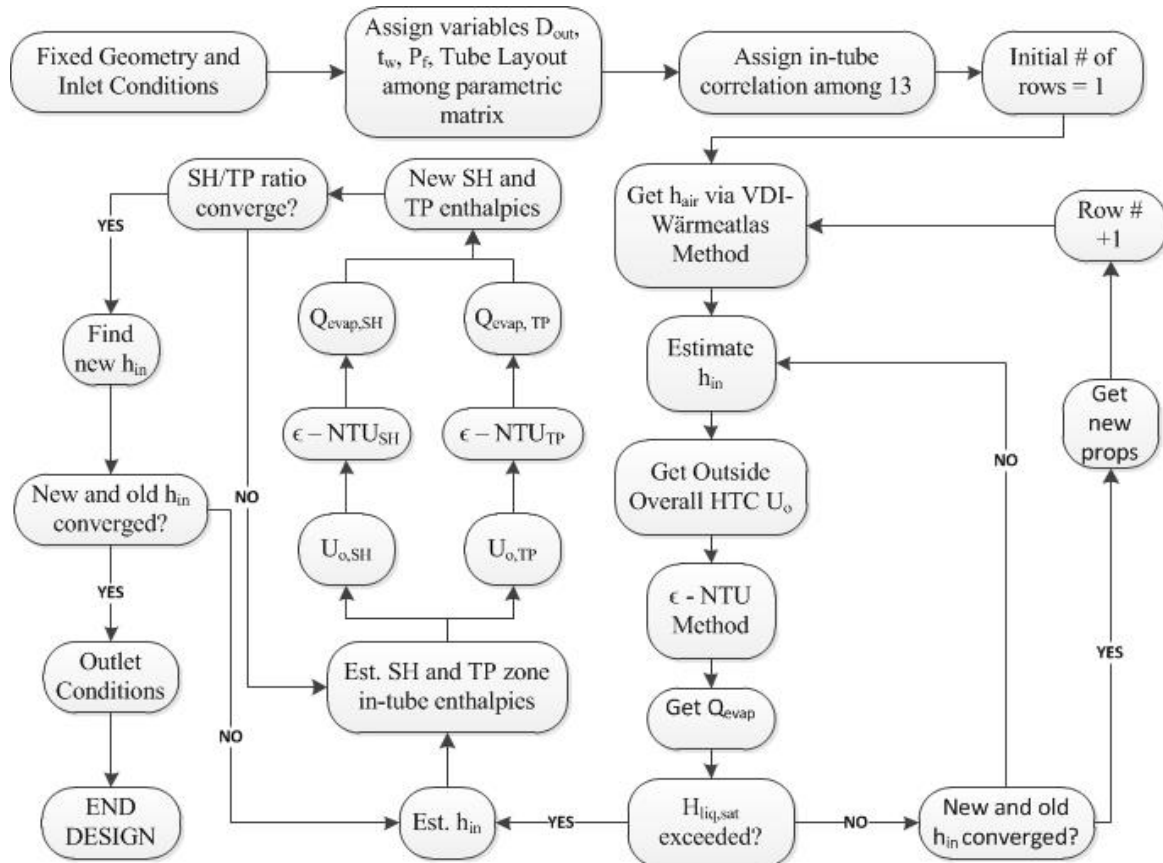


Figure 3: Flow chart of iterative evaporator design methodology

A generic design methodology is implemented for finding the number of required rows in an iterative manner, and the flow of the method is illustrated in Figure 3. The method starts with single row of tubes in accordance with the diameter and heat exchanger width. The transferred heat (via ϵ -NTU method, separate relations for superheated single-phase zone denoted as “SH” and two-phase zones denoted as “TP”) and subsequently the working fluid exit enthalpy are calculated for that particular row. The rows are increased by one incrementally until saturated (and also superheated) vapour is attained at the last tube. The vapour quality (if saturation conditions are reached) is calculated through linear ratio of latent heat and exit enthalpy at that particular tube. The air properties are calculated at each new row encountered, whereas the working fluid property change (i.e. temperature glide) is neglected due to very low pressure drops. At the end, a design solution for each combination of in-tube convective coefficient correlation, tube diameter, tube wall thickness, fin density and tube layout ($13 \times 3 \times 2 \times 6 \times 2 = 936$ design combinations in total) is attained.

Air-side convective coefficient is found through VDI-Wärmeatlas method given for forced convection on finned tubes in cross flow (VDI-Wärmeatlas, 2010). The heat transfer equations for inline (Eqn. 1) and the staggered (Eqn. 2) layout are given as:

$$Nu_D = 0,22Re_D^{0,6} \left(\frac{A}{A_{to}}\right)^{-0,15} Pr^{1/3} \quad (1)$$

$$Nu_D = 0,38Re_D^{0,6} \left(\frac{A}{A_{to}}\right)^{-0,15} Pr^{1/3} \quad (2)$$

The in-tube convective coefficients at the subcooled zone and the superheated zone are calculated through Dittus-Boelter equation given as (for liquid and vapour phase):

$$h = 0,023Re^{0,8}Pr^{0,4} \left(\frac{k}{D_{in}}\right) \quad (3)$$

For evaluating the in-tube and outer pressure drops, Friedel correlation (Friedel, 1979) and Robinson & Briggs correlation (Thome, 2004) were used, respectively. Two-phase pressure drop at U-bends were calculated with Muller-Steinhagen and Heck correlation (Muller-Steinhagen and Heck, 1986). The fouling outside (industrial air) and inside the tubes (working fluid) are determined as 0,0004 m²K/W and 0,0002 m²K/W, respectively. The fan power is estimated as:

$$Fan\ Power = G_{air} A_{min} \frac{\Delta P_{air}}{\rho_{air}^{0.85}} \quad (4)$$

where the fan efficiency is assumed as 85%. The cost is estimated for comparative reasons and is calculated by taking European market values of carbon steel tubing and welding labor cost per U-bend into consideration, whereas the fin cost is excluded.

3. DESIGN SENSITIVITY ANALYSIS

The design solutions mentioned in the previous chapter are compared with each other by means of fixing all geometric parameters except tube diameter, tube wall thickness, fin density and tube layout, respectively. For each of those four variables, influence of the deviation of two-phase heat transfer coefficients h_{tp} on estimated heat exchanger cost, fan power, total transferred heat Q_{tot} , number of bends N_{bends} , total longitudinal heat exchanger length L_{hx} , total tube length L , overall heat transfer coefficient U , air-side pressure drop ΔP_{air} and refrigerant-side pressure drop ΔP_{ref} is assessed for each changing geometric variable. At a particular case, the error margin among the values yielded by 13 correlations were calculated for each parameter with the formula below:

$$Error\ Margin = \frac{Standard\ deviation\ of\ the\ 13\ values}{Average\ of\ 13\ values} \times 100 \quad (5)$$

The changes in the error margins are illustrated with 3D graphs and the exact values are provided at the corresponding tables underneath. At each table, maximum and minimum deviations are shown with yellow and green highlighting, respectively. The unchanging error margins and in-between values are not indicated with any color. It is important to note that the deviations of cost, total tube length, count of U-bends and longitudinal heat exchanger length are quite similar as they are directly related to each other. Table 4 and Figure 4 show the deviations of a design case having **staggered layout, SES36 as working fluid, 3 m of tube length, 4m of heat exchanger width, D_{out}=1/2” and t_w=2,11 mm** with respect to 6 values of P_f **changing between 236 - 432 fins/m**. Apparently the maximum deviation usually occurs (except Q_{tot} and L_{hx}) when the fin density is 314 fins/m, which corresponds to a heat transfer coefficient deviation of 29,1%. The minimum deviation of convective coefficient occurs at the highest fin density (432 fins/m) as 24,6%. There is no linear but a Gaussian-like tendency in error margin change with changing fin density. Thus, it can be said that the error margins are relatively smaller at the lowest and then the highest fin density. Largest deviations occur at ΔP_{ref} and cost (10,7% and 11,6%), where Q_{tot} is the least deviating parameter observed in all cases.

Table 4: Influence of h_{tp} deviation on all parameters for 6 fin density values

P_f	h_{tp}	Q_{tot}	Cost	U	Fan Power	L	L_{hx}	N_{bends}	ΔP_{air}	ΔP_{ref}
236	27,2%	3,1%	5,5%	4,0%	5,0%	4,6%	4,2%	4,3%	4,3%	10,2%
275	28,2%	2,9%	7,7%	5,6%	7,1%	6,4%	4,4%	5,9%	5,9%	9,8%
314	29,1%	3,8%	11,6%	8,3%	10,5%	9,5%	4,9%	8,7%	8,7%	10,7%
354	27,8%	4,3%	10,4%	7,3%	9,3%	8,4%	5,3%	7,7%	7,7%	10,7%
393	25,7%	4,3%	9,0%	6,3%	8,1%	7,3%	5,6%	6,7%	6,7%	9,3%
432	24,6%	3,6%	6,8%	4,7%	6,1%	5,5%	5,6%	5,0%	5,0%	7,1%

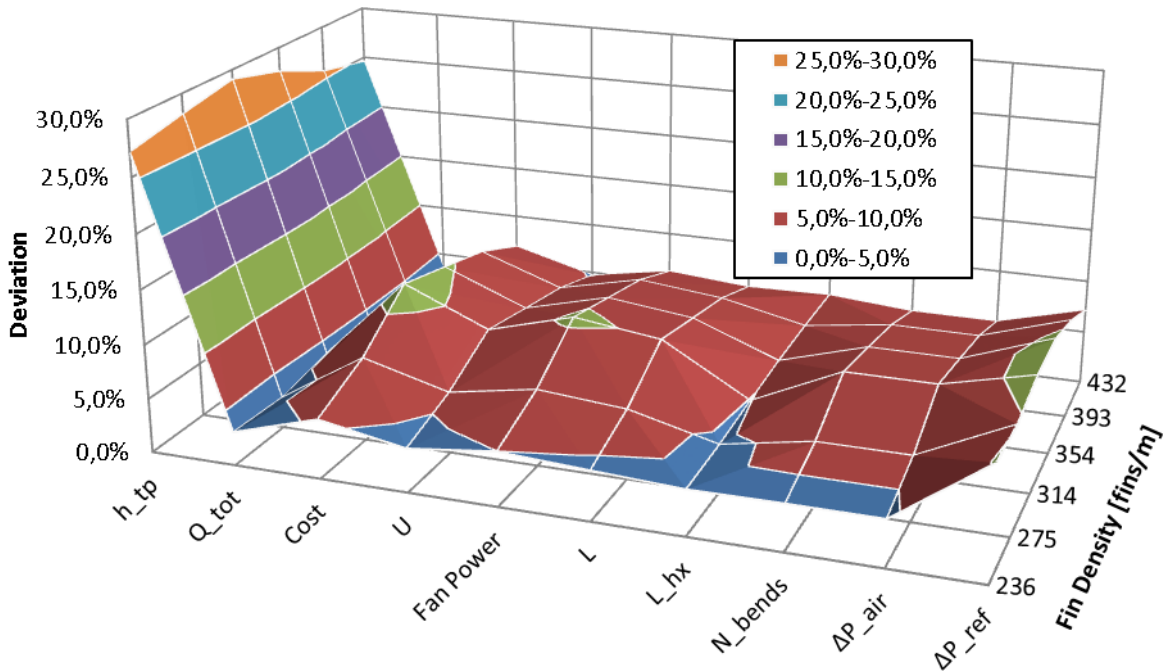


Figure 4: Influence of h_{tp} deviation on all parameters for 6 fin density values

Table 5 and Figure 5 show the deviations of a design case having **staggered layout, SES36 as working fluid, 3 m of tube length, 4m of heat exchanger width, $D_{out}=1/2''$ and $P_f=236$ fins/m** with respect to 2 values of t_w **changing between 2,11 – 2,77 mm**. As can be observed from the table, the change in error margin is considerably low as the tube wall thickness changes. The convective coefficients derive between 27% to 27,2%. As the wall thickness shrinks, the error margin gets somewhat larger, but at a negligible value (0,6%) at ΔP_{ref} , where largest change in deviations occur.

Table 5: Influence of h_{tp} deviation on all parameters for 2 tube wall thickness values

t_w	h_{tp}	Q_{tot}	Cost	U	Fan Power	L	L_{hx}	N_{bends}	ΔP_{air}	ΔP_{ref}
2,11	27,2%	3,1%	5,5%	4,0%	5,0%	4,6%	4,2%	4,3%	4,3%	10,2%
2,77	27,0%	3,0%	5,5%	4,0%	5,0%	4,6%	4,0%	4,2%	4,2%	10,8%

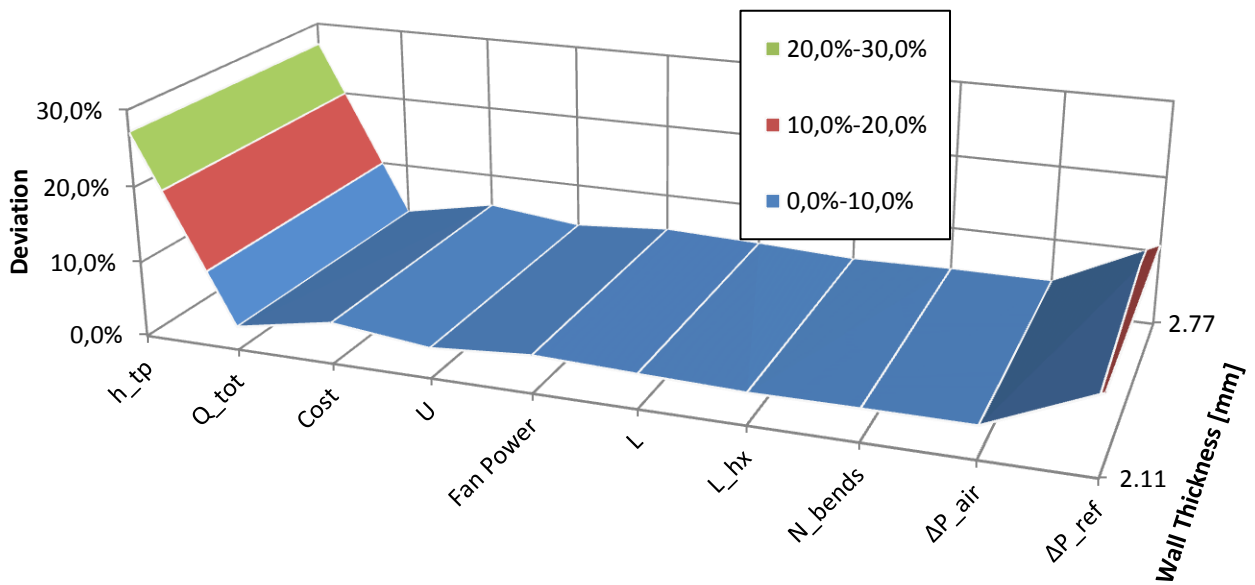


Figure 5: Influence of h_{tp} deviation on all parameters for 2 tube wall thickness values

Table 6 and Figure 6 show the deviations of a design case having **staggered layout, SES36 as working fluid, 3 m of tube length, 4m of heat exchanger width, $D_{out}=1/2''$ and $P_f=236$ fins/m** with respect to 2 values of t_w **changing between 2,11 – 2,77 mm**. Deviation of convective coefficients change between 27,2% and 28,1%. In most of the investigated parameters, the error margin increase as the tube layout is changed from staggered to inline. The largest deviation occur with ΔP_{ref} as 10,2%. Smallest deviations are observed at Q_{tot} which changes between 2,7% and 3,1%.

Table 6: Influence of h_{tp} deviation on all parameters for 2 tube layouts

Layout	h_{tp}	Q_{tot}	Cost	U	Fan Power	L	L_{hx}	N_{bends}	ΔP_{air}	ΔP_{ref}
Staggered	27,2%	3,1%	5,5%	4,0%	5,0%	4,6%	4,2%	4,3%	4,3%	10,2%
Inline	28,1%	2,7%	6,6%	5,3%	6,2%	5,8%	3,0%	5,3%	5,3%	10,2%

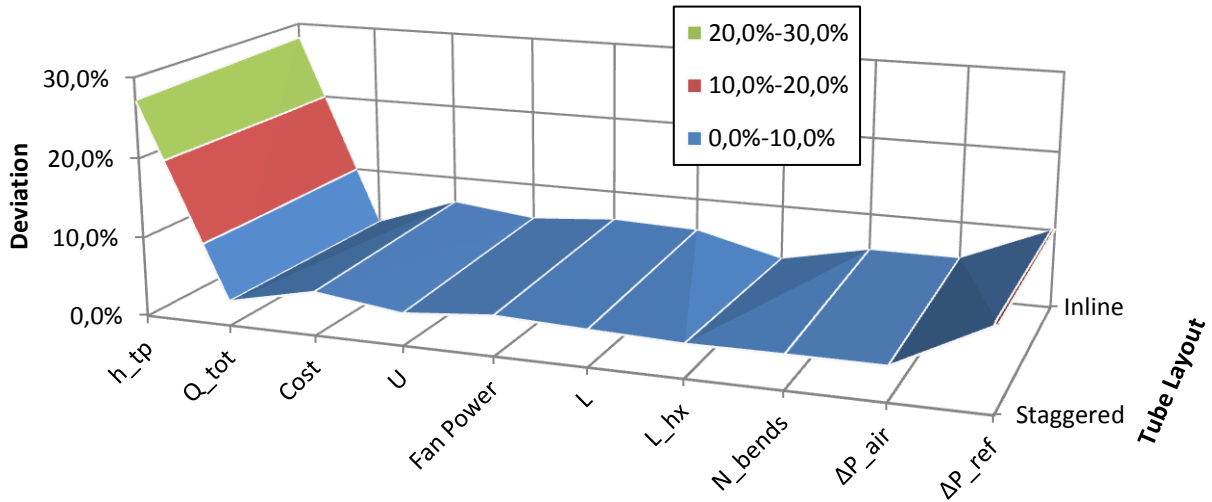


Figure 6: Influence of h_{tp} deviation on all parameters for 2 tube layouts

Table 7 and Figure 7 show the deviations of a design case having **staggered layout, SES36 as working fluid, 3 m of tube length, 4m of heat exchanger width, $t_w=2,11$ mm and $P_f=236$ fins/m** with respect to 3 values of D_{out} **changing between 25,4 – 38 mm**. The convective coefficients change between 27,2% and 30,2%. Among the three investigated outer diameter values, smallest diameter (25,4 mm) yields the smallest error margins at all parameters. In general, the least deviating parameter is observed to be L_{hx} , where the largest occurs at ΔP_{ref} . There is again a non-linear but a Gaussian-like change in the error margins as the diameter increases. In other words, the largest deviations are observed at the middle-size diameter (31,8 mm).

Table 7: Influence of h_{tp} deviation on all parameters for 3 tube outer diameters

D_{out}	h_{tp}	Q_{tot}	Cost	U	Fan Power	L	L_{hx}	N_{bends}	ΔP_{air}	ΔP_{ref}
25,4	27,2%	3,1%	5,5%	4,0%	5,0%	4,6%	4,2%	4,3%	4,3%	10,2%
31,8	27,4%	6,4%	13,4%	10,0%	12,1%	11,2%	4,6%	9,9%	9,9%	17,0%
38	30,2%	7,3%	12,6%	9,8%	11,5%	10,7%	5,6%	9,8%	9,8%	11,2%

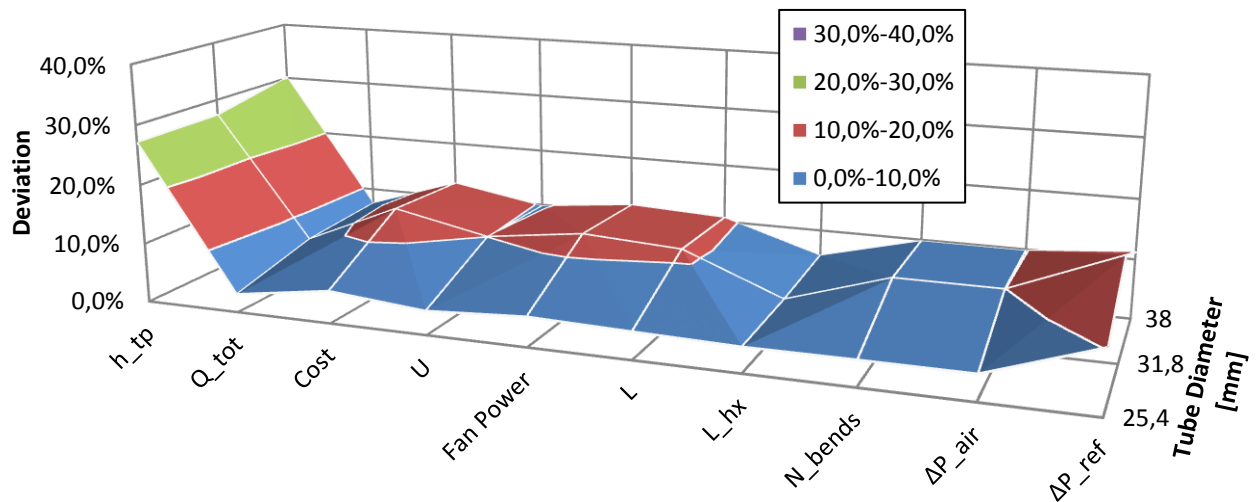


Figure 7: Influence of h_{tp} deviation on all parameters for 3 tube outer diameters

It is important to note that Chun & Seban and Chen correlations usually underpredict the heat transfer coefficients in comparison to the other methods. Thus, they calculate larger tube lengths required for heat transfer. It can be said that those two correlations play a significant role in increasing the possible general error margin. Moreover, the deviation between all of the correlations occur due to their varying reported application ranges, conditions and own prediction errors. None of the investigated correlations were validated experimentally for Solkatherm® SES36 as well. As a result of all the mentioned reasons of error, the obtained percentage values represent the maximum error that the end design can have when a conventional flow boiling correlation is used for in-tube heat transfer calculations.

4. CONCLUSIONS

For four changing geometric variables (fin density, tube wall thickness, tube layout and tube outer diameters) a design sensitivity analysis is done for investigating the influence of in-tube convective heat transfer coefficient calculated via 13 correlations on 10 thermo-hydraulic heat exchanger parameters. By including many flow boiling correlations, a general error margin in those parameters is deduced. The error margins can be regarded as the maximum error that exists in the end design of a low-temperature direct evaporator for waste heat recovery ORCs. The found conclusions include:

- Keeping the fin density as low or high as possible can help decreasing the error margin,
- Higher tube wall thickness can decrease the error margin,
- Using staggered tube layout instead of inline can decrease the error margin,
- Using smaller tube outer diameters can help decreasing the error margin,
- A high deviation of in-tube convective heat transfer coefficient usually causes a higher deviation in investigated parameters, although the changing geometric variables should be considered at the same time as well for having an idea of expected error margin,
- Using newer calculation methods can decrease the error margins in design
- In most of the cases and investigated parameters, the error margins remain under 10%, with a maximum observed error margin of approximately 30% at convective coefficients.
- More correlations can be included to the study for expanding the general applicability scope of sensitivity analysis.
- An experimental investigation is necessary for having a more accurate idea.

NOMENCLATURE

A	area	(m ²)
D	diameter	(mm)
G	mass flux	(kg/m ² s)
h	convective coefficient	(W/m ² K)
H	Enthalpy	(J/kg)
k	thermal conductivity	(W/mK)
L	Length	(m)
N	number of	(-)
P	pressure, pitch	(Pa, fins/m)
Pr	Prandtl number	(-)
Re	Reynold's number	(-)
Q	transferred heat	(W)
t	thickness	(mm)
T	temperature	(°C)
U	overall heat transfer coeff.	(W/m ² K)
W	width	(m)

Subscript

air	air-side
bends	U-bends
crit	critical
evap	evaporation
hx	heat exchanger
in	in-tube side
liq	liquid phase
min	minimum
out	outer-tube side
ref	refrigerant side
sat	saturation
tp	two-phase
tot	total

Greek

ρ	density	(kg/m ³)
Δ	difference	(-)

REFERENCES

- Bennett, D.L., Chen, J.C., 1980, Forced convective boiling in vertical tubes for saturated pure components and binary mixtures, *AIChE Journal.*, vol. 26, no. 3: p. 454-461.
- Chen, J.C., 1966, Correlation for boiling heat transfer to saturated fluids in convective flow, *Industrial & Engineering Chemistry Process Design and Development*, vol. 5, no. 3: p. 322-329.
- Chun, K.R., Seban, R.A., 1971, Heat transfer to evaporating liquid films, *Journal of Heat Transfer*, vol. 93, no. 4: p. 391-396.
- Dobson, M.K., Wattelet, J.P., Chato, J.C., 1993, *Optimal sizing of two-phase heat exchangers*, Project Deliverable ACRC TR-42, 21 pages, Air Conditioning and Refrigeration Center. College of Engineering. University of Illinois at Urbana-Champaign.
- Fischer, J., 2011, Comparison of trilateral cycles and organic Rankine cycles, *Energy*, vol. 36: p. 6208-6219.
- Friedel, L., 1979, Improved friction pressure drop correlations for horizontal and vertical two-phase pipe flow, In *European two-phase flow group meeting, Paper E*, vol. 2: p. 1979.

- Galvez, J.B., 2009, Publishable Executive Summary – Final Report, mechanical power generation based on solar thermodynamic engines (POWERSOL), Project No: 032344, 42 pages
- Gungor, K.E., Winterton, R.H.S., 1986, A general correlation for flow boiling in tubes and annuli, *International Journal of Heat and Mass Transfer*, vol. 29, no. 3: p. 351-358.
- Kandlikar, S.G., 1990, A general correlation for saturated two-phase flow boiling heat transfer inside horizontal and vertical tubes, *Journal of heat transfer*, vol. 112, no. 1: p. 219-228.
- Klimenko, V.V., 1988, A generalized correlation for two-phase forced flow heat transfer, *International Journal of heat and mass transfer*, vol. 31, no. 3: p. 541-552.
- Liu, C., He, C., Gao, H., Xu, X., Xu, J., 2012, The optimal evaporation temperature of subcritical ORC based on second law efficiency for waste heat recovery, *Entropy*, vol. 14, no. 3: p. 491-504.
- Liu, Z., Winterton, R.H.S., 1991, A general correlation for saturated and subcooled flow boiling in tubes and annuli, based on a nucleate pool boiling equation. *International journal of heat and mass transfer*, vol. 34, no. 11: p. 2759-2766.
- Maalouf, S., Boulawz-Ksayer, E., Clodic, D., 2012, ORC finned-tube evaporator design and system performance optimization, *International Refrigeration and Air Conditioning Conference*, Purdue, Paper 2370, 10 pages.
- Mikielewicz, D., Wajs, J., Gliński, M., Zrooga, A.B.R., 2012, Experimental investigation of dryout of SES 36, R134a, R123 and ethanol in vertical small diameter tubes, *Experimental thermal and fluid science*, vol. 44: p. 556-564.
- Mikielewicz, J., 2010, Micro Heat and Power Plants Working in Organic Rankine Cycle, *Polish J. of Environ. Stud*, vol. 19, no. 3: p. 499-505.
- Müller-Steinhagen, H., Heck, K., 1986, A simple friction pressure drop correlation for two-phase flow in pipes, *Chemical Engineering and Processing: Process Intensification*, vol. 20, no. 6: p. 297-308.
- Quoilin, S., van den Broek, M., Declaye, S., Dewallef, P., Lemort, V., 2013, Techno-economic survey of Organic Rankine Cycle (ORC) systems, *Renewable and Sustainable Energy Reviews*, vol. 22: p. 168-186.
- Ribatski, G, Thome, J.R., 2007, Two-Phase Flow and Heat Transfer across Horizontal Tube Bundles- A Review, *Heat transfer engineering*, vol. 28, no. 6: p. 508-524.
- Riva, M., Flohr, F., Fröba, A., 2006, New fluid for high temperature applications, *International Refrigeration and Air Conditioning Conference*, Purdue, Paper R106, 9 pages.
- Saleh, B., Koglbauer, G., Wendland, M., Fischer, J., 2007, Working fluids for low-temperature organic Rankine cycles, *Energy*, vol. 32, no. 7: p. 1210-1221.
- Schlunder, E.U., 1986, *Heat exchanger design handbook. Supplement 3*, Taylor & Francis Inc, USA.
- Shah, M.M., 1976, A new correlation for heat transfer during boiling flow through pipes, *Ashrae Trans*, vol. 82, no. 2: p. 66-86.
- Shengjun, Z., Huaixin, W., Tao, G., 2011, Performance comparison and parametric optimization of subcritical Organic Rankine Cycle (ORC) and transcritical power cycle system for low-temperature geothermal power generation, *Applied Energy*, vol. 88, no. 8: p. 2740-2754.
- Siddiqi, M.A., Atakan, B., 2011, Investigation of the criteria for fluid selection in Rankine cycles for waste heat recovery. *International Journal of Thermodynamics*, vol. 14, no. 3: p. 117-123.
- Steiner, D., Taborek, J., 1992, Flow boiling heat transfer in vertical tubes correlated by an asymptotic model. *Heat transfer engineering*, vol. 13, no. 2: p. 43-69.
- Thome, J.R., 2004, *Engineering data book III*, Wolverine Tube Inc., Switzerland
- VDI-Gesellschaft Verfahrenstechnik und Chemieingenieurwesen, & VDI Gesellschaft (Eds.), 2010, *VDI Heat Atlas*, Springer, Germany, 1606 pages.

DESIGN OF A SUPERCRITICAL HEAT EXCHANGER FOR AN INTEGRATED CPV/T-RANKINE CYCLE

Marija Lazova^{1*}, Dieter Daenens¹, Alihan Kaya¹, Marnix Van Belleghem¹, Henk Huisseune¹, George Kosmadakis², Dimitris Manolakos², Michel De Paepe¹

¹Ghent University - UGent, Department of Flow, Heat and Combustion Mechanics,
Ghent, Belgium
Marija.Lazova@UGent.be

²Agricultural University of Athens, Department of Natural Resources & Agricultural Engineering,
Athens, Greece
gkosmad@aua.gr

* Corresponding Author

ABSTRACT

The worldwide interest for low grade heat utilization by using Organic Rankine Cycle (ORC) technologies has increased significantly. An Organic Rankine Cycle can be combined with several renewable sources, such as solar energy. Concentrating solar power is a well proven technology and it can be efficiently combined with ORC technology for electricity generation. The goal was achieved by utilizing the excess heat source from PV collectors through a low temperature supercritical heat exchanger in the Organic Rankine Cycle. The motivation for working at supercritical state in the heat exchanger is the better thermal match between the heat source and the working fluid, leading to better overall cycle efficiency.

A designed prototype is a helical coil heat exchanger with R404a used as working fluid flowing in the coil and the heat source fluid in the shell. The design of this heat exchanger was done using heat transfer and pressure drop correlations available from literature. There is a large uncertainty on these correlations for the considered application because they were derived for working fluids water, CO₂, R410a and R404a more than ten years ago. In order to have adequate performance and heat transfer rate the heat exchanger was oversized by 20%. Next, the prototype was built and installed in a test set-up. In this paper measurements on the supercritical heat exchanger prototype are reported. The measurements on the prototype show that the heat exchanger is indeed oversized. Based on the measurements, a new heat transfer correlation is suggested. In future design this correlation can be used as less oversized (and thus cheaper) heat exchanger.

1. INTRODUCTION

An increased demand for energy and environmental issues on a worldwide level have stimulated a number of researchers to work on improving the efficiency of thermodynamic cycles and look for ways of utilizing renewable energy sources. Concentrated solar power is one of the renewable energy sources that have great potential for electric power generation. A new system integrating two technologies the Concentrated Photovoltaics/Thermal (CPV/T) and Supercritical Organic Rankine Cycle (SCORC) was developed and implemented in Athens, Greece. One solar collector presents a combination of photovoltaic panel and a solar thermal collector that simultaneously generates heat and electricity. The SCORC engine includes the supercritical heat exchanger that is used for recovery of the low grade excess heat from the CPV/T loop. In the SCORC, R404a is used as working medium where the critical pressure and temperature is 37.29 bar and 75.02 °C respectively.

The reason of introducing this innovative concept CPV/T in combination with the SCORC was because the Organic Rankine Cycle is considered a suitable technology for converting low-grade heat

sources (e.g. from process industry, solar energy, geothermal, etc.) to electric power generation. This is because the organic (working) fluid has relatively lower critical pressure and temperature compared to water/steam used in classical Rankine cycle. In order to have a good performance of the cycle, not only a good selection of the working fluid is important but also a proper design and selection of the cycle components is essential. A way of enhancing the overall cycle efficiency of an ORC is introduced with supercritical heat transfer in the heat exchanger.

A main challenge to work with supercritical ORCs is a better thermal match of the temperature profiles of the heat source and the working (organic) fluid in the heat exchanger. Moreover, at supercritical state there are strong variations of the thermophysical properties of the fluid. As the value of the heat transfer coefficient depends on these variations, it is important to study and understand the behaviour of the fluid properties when going from subcritical to supercritical state. In order to have a proper design of heat exchanger suitable to work at supercritical conditions it is important to determine the local heat transfer coefficients and correlations.

Other important parameters that influence on the heat transfer are the working fluid flow direction, tube diameter, heat and mass flux, buoyancy and selection of proper organic fluid.

A lot of research activities regarding supercritical heat transfer started in the second half of the 20th century. Many studies were related to heat transfer at critical and near-critical region for a variety of working fluids such as water, carbon dioxide and helium. Back in 1957, Bringer and Smith (1957a) [1] were the pioneers on experimental research for heat transfer to supercritical fluids. Because of the rapid variations of thermal conductivity, viscosity and density they have found out that the existing empirical and semi-theoretical correlations did not give accurate results. The rapid variations of thermal conductivity, viscosity and density were identified as the main reasons for the deviation between experimental results and expectations from the correlation. Dickinson and Weich (1958) [2] are one of the first researchers who did investigation about heat transfer to supercritical water. The work was followed by Shitsman (1959) [3] who did heat transfer research at the near critical region, not only on water but on oxygen and CO₂ as well. Krasnoschekov and Protopopov (1959) [4] published a work related to the heat transfer at the supercritical region in tubes for the fluids such as water and CO₂. In 1963 Shitsman (1963) [5] published a work related to impairments on heat transmission at supercritical pressure. Bishop *et al.* (1964) [6] investigated the forced convection heat transfer to water at near critical temperatures and supercritical pressure. In 1970, Ackerman (1970) [7] investigated the parameters that influence on the pseudo-boiling heat transfer to supercritical water in smooth and ribbed tubes. Yamagata *et al.* (1972) [8] conducted research related to forced convection heat transfer to supercritical water flowing in vertical tubes. Jackson and Fewster (1975) [9] did work on forced convection to supercritical fluids. Most of the experimental investigations had been mainly done in vertical positioning of the tube. In 1964, Vikrev and Lokshin [10] performed one of the earliest studies about supercritical heat transfer to water at horizontal flow. This study is of great importance because it was first attempt to quantitatively formulate deterioration of heat transfer coefficients in supercritical conditions. The buoyancy effect in a turbulent and vertical flow was first studied by Jackson and Hall (1979) [11].

In order to provide accurate correlations for design of a heat exchanger the heat transfer process to the working fluids at supercritical conditions has to be studied. Even though the research activities regarding supercritical heat transfer started long time ago the first published paper found in the literature regarding supercritical ORC dates from 1981. Haskins (1981) [12] performed research activities of solar receiver coupled to a supercritical ORC engine in order to maximize the thermal efficiency by using toluene as working fluid. Furthermore, ten years later a first paper regarding numerical investigations of the flow pattern and forced convective heat transfer in supercritical flows, such as those encountered in compact heat exchangers had been published [13]. While the first work related to ORC and the influence of the parameters on plate heat exchanger design was presented by Schuster *et al.* (2012) [14].

Many heat transfer and pressure drop correlations have been proposed from the authors mentioned above. It is important to notice that the correlations are derived mainly for fluids such as water, CO₂ and helium. However, it is important to be pointed out that this does not marginalize the importance and the scientific value of previously performed research.

From the literature review by Lazova *et al.* (2014) [15] can be concluded that there is very limited experimental and heat transfer data at supercritical state for organic fluids used in transcritical ORCs. The main reason is the difference of the working conditions of an ORC plant such as relatively higher

temperature and pressure. This lack of knowledge necessitates the development of new heat transfer correlations suitable for working fluids used under the supercritical conditions in ORC. Inaccurate correlations lead to an over-sizing of heat exchangers, thus resulting in a lower economic feasibility of such cycles. The heat exchanger is a key component in every ORC engine. This component dictates the efficiency of the cycle and the total cost of an ORC plant. It is estimated that the cost of the heat exchangers is usually up to 30% of the total cost of an ORC where evaporator, (regenerator) and condenser are taken into account Zhang *et al.* (2010) [16]. The cost of the heat exchanger in the CPV/T-Rankine prototype system is only 12% because the major part belongs to the solar collectors. Because the ratio of the total heat exchanger area to net power output in an ORC is considerably high it presents an important issue of consideration.

Hence, from the arguments mentioned above it can be concluded that more accurate design of the heat exchanger with appropriate correlations leads to improved cycle efficiency and lowering the cost of such installation. In this work a supercritical heat exchanger is designed and constructed using literature correlations. Next, the heat exchanger is tested and the measurements are compared to the design specs.

2. DESCRIPTION OF THE CPV/T – RANKINE TEST SET-UP

A new test set-up that integrates two technologies such the Concentrated Photovoltaics/Thermal (CPV/T) and Supercritical Organic Rankine Cycle (SCORC) was developed and built in Athens, Greece. The supercritical heat exchanger is the component that couples the CPV/T field from one side with the SCORC engine. For the first measurements the supercritical heat exchanger was tested in the laboratory where an electrical heater was used instead of solar collectors. The final engine is coupled with solar collectors. Heat sources that are of interest in this research work are with temperature range between 70°C to 100°C. Figure 3 illustrates simplified layout of the experimental test set-up. During the experimental campaigns temperature and pressure measurements were conducted, while the mass flow rate of the organic fluid was determined from correlations of the positive displacement pump (SCORC feed pump). The positioning of the pressure and temperature sensors is indicated in Figure 3. In order to evaluate the performance of the heat exchanger, one temperature sensor is placed at the inlet and one at the outlet of the heat exchanger and the heat source respectively. It is important to be mentioned that the system is well insulated, which means that the heat loss to the environment is reduced

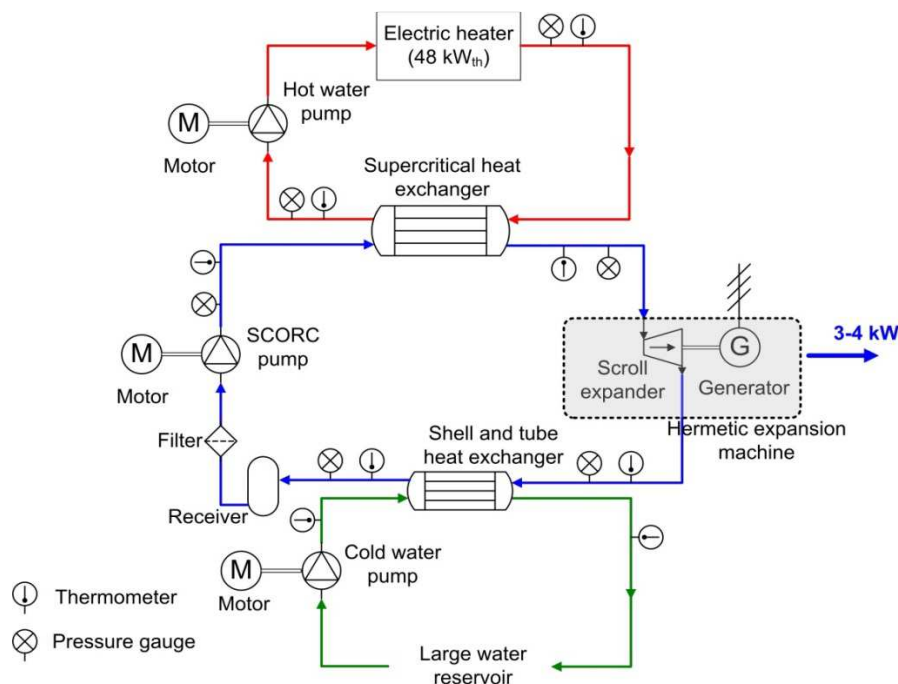


Figure 3: Simplified layout of the experimental test set-up

Several measurements campaigns were done, where the supercritical state was achieved under the following conditions presented and compared with the designing condition in Table 1; While running the measurements these values were held constant. As presented in Table 1, there is variation between the design and measurements conditions which gives lower heat transfer capacity.

Table 1: Summary of the design and measurement conditions

	MEASUREMENTS		DESIGN	
m_{wf}	2,7	[kg/s]	2,5	[kg/s]
T_{hf_in}	101	[°C]	95	[°C]
m_{wf}	0,226	[kg/s]	0,2539	[kg/s]
T_{wf}	36,3	[°C]	27,37	[°C]
p_{crit}	1,026		1,034	
Q	36	kW	41	kW

The difference between the initially designed model and the built component in the terms of heat transferred is 41 kW and 36 kW respectively.

The aim of these measurements was to evaluate the performance of the heat exchanger working at supercritical state. This component is first of its kind specially designed and build for an ORC installation, suitable to operate at relatively higher pressure and temperature.

3. DESIGN OF A SUPERCRITICAL HEAT EXCHANGER

The heat exchanger is part of the SCORC engine that is coupled to the CPV/T circuit in one system. This component was designed by using correlations (Pethukov, Garimella, Mokry) available from literature. The heat capacity of this supercritical heat exchanger is 41 kW_{th}. According to the results of the simulations helical coil type heat exchanger was selected based on its ability to withstand high pressure, compact size, performance, easy integration to the system, relatively simple manufacturing and cost. This component is first of this kind specially designed and built for ORC application suitable to operate at supercritical conditions.

3.1 Design characteristics

A counter flow heat exchanger of helical coil type Patil *et al.* (1982) [17] is fabricated out of metal coil - tube that is fitted in annular portion of two concentric cylinders. The dimensions of both cylinders are determined by the velocity needed to meet heat transfer requirements. At the annulus side in downward direction the heat source (water-glycol) flows while the working fluid R404a runs in upward direction in the helical coil. The heat transfer takes place across the coil wall. Figure 4 presents the configuration of the helical-coil heat exchanger.

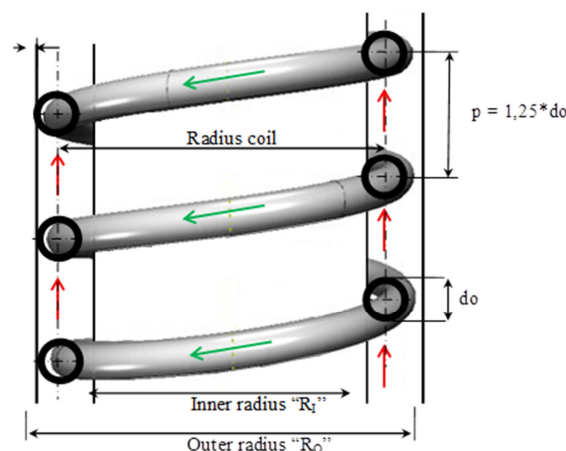


Figure 4: Schematic representation of the helical coil heat exchanger

A representative supercritical heating process is presented in Figure 5, showing the temperatures of the heat transfer fluid and an organic fluid R404a, with a pinch point temperature difference of 10 K, which exists at the organic fluid's outlet.

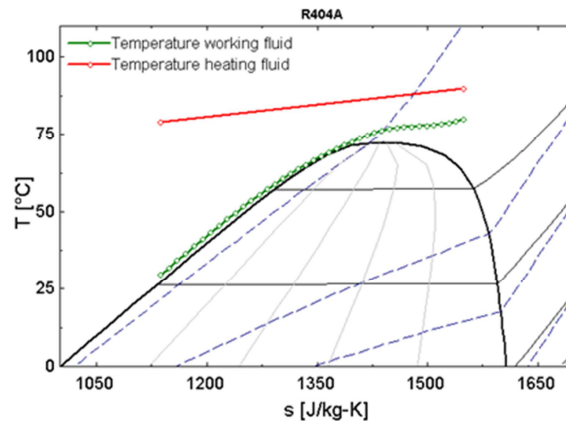


Figure 5: T,s-diagram of the heating process in the supercritical heat exchanger

The design of the heat exchanger is accomplished taking into account that the velocity and pressure drop in the coil-tube and annulus are within the allowable ranges. In the calculation procedure, the velocity ranges of the working fluid R404a were fixed at minimum 0.5 m/s and maximum 2.17 m/s, while the overall pressure drop was neglected. It was calculated afterwards and should be lower than 40 kPa. The heating fluid is flowing relatively slow ($Re = 4200 - 5900$).

3.2 Methodology for designing the heat exchanger

A widely used method of calculating the heat transfer capacity (UA) and eventually sizing the heat exchanger is the logarithmic mean temperature difference (LMTD) method, applied between the inlet and outlet of the heat exchanger Cayer *et. al* (2010) [18], Roy *et. al* (2010) [19], Claesson (2005) [20] and given by Eq. (1).

$$\dot{Q} = U \cdot A \cdot \Delta T_{log} = U \cdot A \cdot \frac{\Delta T_1 - \Delta T_2}{\ln\left(\frac{\Delta T_1}{\Delta T_2}\right)} \quad (1)$$

where Q is the heat transferred, U the overall heat transfer coefficient, A the total heat exchanging surface and ΔT_{log} is the logarithmic temperature difference or LMTD, and '1' and '2' is the ends of the heat exchanger at which the hot and cold streams enter or exit on either side.

However, the LMTD-method is based on constant fluid properties. When working with fluids at supercritical state this assumption leads to incorrect results. An alternative solution is to discretise the heat exchangers to a large number of control volumes so that the properties variation in each step is small and an average constant value can be assigned within each volume. The discretization is performed in EES (Engineering Equation Solver) by dividing the overall enthalpy change for one of the streams in N (here $N = 20$) equal differences dh . Discretization is advisable to be in the range between 20 and 40 equal distances. Lower than 20 leads to inaccurate results, while above 40 is not suggested, due to the large increase of required computational time (the accuracy is more or less the same).

3.2.1 Heat transfer coefficient at the shell side (annulus): In a helical-coil heat exchanger, the heating fluid is circulated in the annulus. As the flow rate of the heating fluid is rather low, the following Nusselt-correlation, valid for Reynolds number (Re) between 50 and 10000 can be used Eq. (2) Coates (1959) [21]

$$Nu = 0,6Re^{0,5}Pr^{0,31} \quad (2)$$

where Pr is the Prandtl number.

For higher Reynolds number ($Re > 10000$), Eq. (3) is used Kern (1950) [22]

$$Nu = 0,36Re^{0,55}Pr^{\frac{1}{3}}(\mu/\mu_w)^{0,14} \quad (3)$$

where μ is the fluid's bulk viscosity and μ_w is the fluid's viscosity at the wall temperature.

3.2.2 Heat transfer coefficient at the helical coil side: At the helical coil side supercritical fluid is circulated in upward flow. Several correlations can be found in the literature for the calculation of the heat transfer coefficient at supercritical conditions. In this work three correlations for sizing of the heat exchanger are identified and compared. The conventional heat transfer correlations for single phase flow (calculation of the Nusselt number) cannot be used in the current case, due to the variations of the fluid properties around the critical point. For the calculations of the helical coil heat exchanger, three heat transfer correlations are compared.

Petukhov *et al.* (1961) [23] developed correlations for supercritical fluid parameters. The correlations have a correction factor, which neutralizes the effect of the variations of the thermo-physical properties around the pseudo-critical point and provides more stable and accurate results. The proposed Nusselt-correlation originally developed for carbon dioxide in the supercritical range at high temperature drops takes into account the difference in properties between the wall and the bulk, and is given below.

$$Nu_b = Nu_{0,b} \left(\frac{\bar{c}_p}{c_{p,b}} \right)^{0,35} \left(\frac{\lambda_b}{\lambda_w} \right)^{-0,33} \left(\frac{\mu_b}{\mu_w} \right)^{-0,11} \quad (4)$$

where b refers to the bulk fluid temperature and w to the wall temperature.

The heat-transfer coefficient of the organic fluid flowing inside the coil is calculated using the correlations for supercritical heat transfer in a straight pipe. This coefficient is then corrected for a coiled tube by multiplying it by a factor: $F_{helical}$ given by Schmidt's correlation, which has a large application range

$$F_{helical} = 1 + 3,6 \left[1 - \frac{d_i}{D_H} \right] \left(\frac{d_i}{D_H} \right)^{0,8} \quad (5)$$

This expression is applicable for $2 \times 10^4 < Re < 1,5 \times 10^5$ and for $5 < R/a < 84$, with R the radius of the coil [m] and a the radius of the tube [m].

The term $Nu_{0,b}$ is calculated using the following Petukhov-Kirillov (1958) correlation [24] and the bulk temperature of the fluid.

$$Nu_{0,b} = \left(\frac{\frac{f_b}{8} Re_b \bar{Pr}}{12,7 \left(\frac{f_b}{8} \right)^{0,5} \left(\frac{Pr^2}{3} - 1 \right) + 1,07} \right) \quad (6)$$

where the Darcy friction factor (f) is expressed as:

$$f = (1,82 \log_{10}(Re_b) - 1,64)^{-2} \quad (7)$$

The average specific heat \bar{c}_p is defined as:

$$\bar{c}_p = \frac{h_b - h_w}{T_b - T_w} \quad (8)$$

Garimella (2005) [25] developed correlations for supercritical heat transfer based on measurement data from refrigerants bends R410a and R404a. Three regions of heat transfer were identified based on the state of the heat transferring fluid: Liquid-like region, Pseudo-critical transition and Gas-like region. For each region a separate correlation for Nusselt number and friction factor was identified. However, these correlations were developed for smaller diameter (9,4 and 6,2 mm) and for supercritical heat transfer cooling applications. As already mentioned, the tube diameter influences the heat transfer rate. The designed supercritical heat exchanger has relatively higher inner diameter of 26 mm and the working conditions are different from one for ORC application. Therefore, these correlations were taken into account and compared to other without completely relying during the design process. The average uncertainties in these heat transfer coefficients were $\pm 10\%$. These correlations are listed in continuation;

Liquid-like region:

$$Nu = 1,421 Nu_{churchil-modified} (C_{p,w}/C_{p,b})^{0,444} (d_{actual}/d_{baseline})^{-0,183} \quad (9)$$

Pseudo-critical transition:

$$Nu = 1,350Nu_{churchil-modified} (C_{p,w}/C_{p,b})^{0,249} (d_{actual}/d_{baseline})^{-0,066} \quad (10)$$

Gas-like region:

$$Nu = 1,556Nu_{churchil-modified} (C_{p,w}/C_{p,b})^{-0,212} (d_{actual}/d_{baseline})^{-0,308} \quad (11)$$

These correlations are valid for the following working range: $200 \text{ kg/m}^2\text{s} < G < 800 \text{ kg/m}^2\text{s}$ and $1.0 < P/P_{cr} < 1.2$. Also there are correction factors developed for all flow regimes boundaries.

The majority of empirical correlations were proposed in the 1960s – 1970s, when experimental techniques were not at the same advanced level as they are today. Also, thermo-physical properties of water have been updated since that time (for example, a peak in thermal conductivity in critical and pseudo-critical points within a range of pressures from 22,1 to 25 MPa was not officially recognized until the 1990s). Therefore, a new or an updated correlation, based on a new set of heat-transfer data and the latest thermo-physical properties was recently developed and evaluated by Mokry et al. (2011) [26]

$$Nu = 0,0061Re^{0,904}Pr^{0,684}(\rho_w/\rho_b)^{0,564} \quad (12)$$

This correlation is valid for the following working range: $200 \text{ kg/m}^2\text{s} < G < 1500 \text{ kg/m}^2\text{s}$.

3.3 Dimensions of the heat exchanger

As summary, the final design of the heat exchanger leads to coil length of 66 m and inner diameter of the coil of 26 mm. To account for heat transfer correlation uncertainty the heat exchanger is oversized by about 20%. Table 1 presents summary of the heat exchanger design.

Table 2: Summary of the heat exchanger design

Helical coil heat exchanger										
d_o [mm]	t [mm]	L [m]	D_i [m]	D_o [m]	D_c [m]	H [m]	A [m ²]	Q [kW]	h_{hf_avg} [W/m ² K]	h_{wf_avg} [W/m ² K]
33.7	4	66	0.526	0.674	0.6	1.508	6.988	41	403	2200

where d_o is the tube outer diameter, t the tube thickness, D_i the inner shell diameter, D_o the outer shell diameter, D_c the coil diameter, H the height of the HX and A the total heat exchanger surface. Q is the heat transfer capacity of the heat exchanger coefficient. h_{avg} is the average heat transfer coefficient.

4. COMPARISON OF THE CALCULATED WITH THE MEASURED DATA OF THE SUPERCRITICAL HEAT EXCHANGER

4.1 Analysis of the constraints of the designed and built model

To check the performance of the helical coil heat exchanger, the influence of changing mass flow rate to the heat transferred and the outlet temperatures at cold and hot side is investigated. The constraints are presented in Table 2. The outlet temperatures at the cold and hot side and the pinch point temperature difference are determined by the flow rates and inlet temperatures. In figures 6 and 7 the pinch point temperature difference (design and measurements) is presented.

Changing the flow rate of the heating fluid without changing the flow rate of the working fluid will result in a decrease of the outlet temperature of the heating fluid, a decrease of the outlet temperature of the working fluid and an increase of the pinch point temperature difference.

The designed pinch point temperature difference is 10 K. From the sets of measurements covering supercritical operation it is shown that the main advantage is the very low temperature differences between the heating fluid and the organic fluid R404a (in the range of 1.5-2.5 °C). Moreover, the pressure drop of the heating fluid is very small and equal to 0.1-0.2 bar, while that of the organic fluid R404a is higher and in the range of 0.6-1 bar. This value is low, which should be however considered during the design stage, in order to select the correct size of this component.

In figure 6 and 7 the pinch point temperature difference (design and measurements) between the heating fluid and the working fluid R404a is presented.

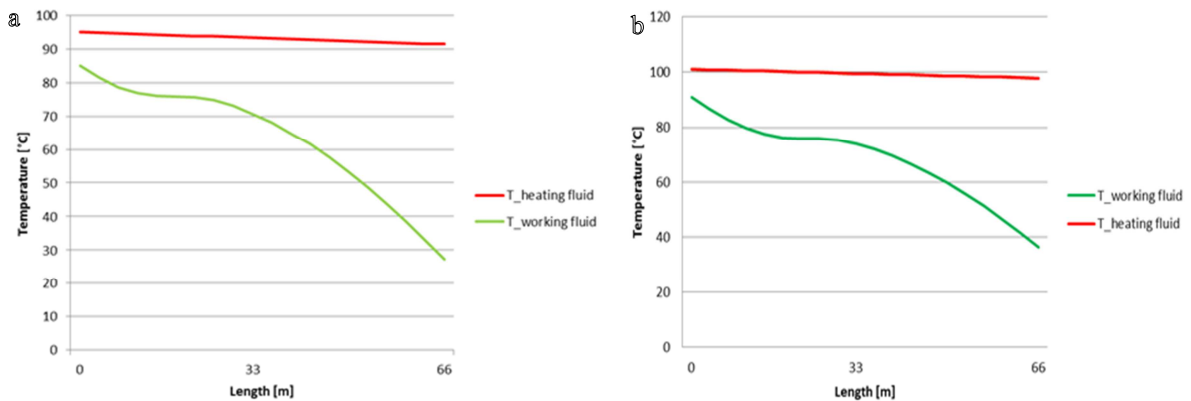


Figure 6: Pinch point temperature differences: a. designed model; b. built model

4.2 Development of new correlation suitable for helical coil heat exchanger

Using a modified Wilson method introduced by Shah (1990) [27], Jose *et. al* (2005) [28] the mean value of the convection coefficient outside the tubes and the convection coefficient inside the tubes as a function of the working fluid mass flow (or velocity) are obtained. Figure 8 is logarithmic graph that describes the Nu number as a function of the Re and Pr numbers. This graph presents a comparison of the experimental data and the correlations used from the literature. Moreover, the coefficient C and the exponent of the Reynolds number m of the general dimensionless correlation $Nu = CRe^mPr^n$ are also obtained, thus the general correlation is determined assuming only the value of the exponent of the Prantdl number, n.

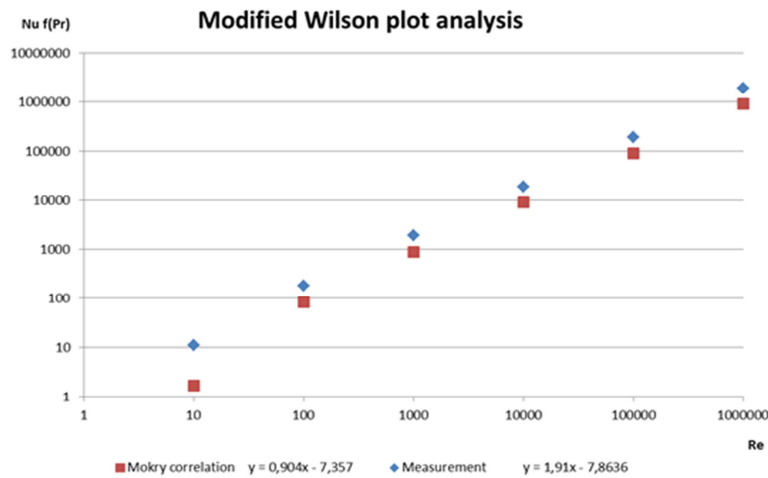


Figure 8: Logarithmic graph describing the Nu number as a function of the Re and Pr numbers (comparison of calculated with measured data)

$$Nu = 0,0044Re^{1,91}Pr^{0,4} \quad (13)$$

In the design process of this supercritical heat exchanger, three calculation methods for supercritical heat transfer were implemented and compared (Petukhov, Garimella, and Mokry). These heat transfer correlations were developed independently. A safety factor was implemented to account for heat transfer correlation uncertainty. The measurements and the new correlation derived from this experiment indicate (Figure 8) that the measured heat transfer is about 10% higher than the used correlations. Hence, the size of the heat exchanger can be reduced by 10% and still keeping the good

performance (heat transfer rate). On the other hand, by reducing the size of this component, the cost will be decreased and an economic benefit on the whole plant will be achieved. The benefit would be more accurate design and use of less material, which leads to lower costs and lower pressure drop for both fluid circuits.

6. CONCLUSIONS

In this work a supercritical heat exchanger suitable for ORC applications is investigated. Even though ORC is not new technology, there is still room for improvement by working at supercritical state of the organic fluid. However, there is still lack of experimental (accurate) data, especially suitable for ORC installations. A helical coil heat exchanger was designed and built. Correlations available from literature were used. These correlations were developed for water, CO₂ and refrigerants like R404a and R410a. The correlations were derived for smaller diameter and different working conditions than ORCs. In order to check the performance of the designed and built heat exchanger at supercritical working conditions, measurements have been conducted. The inlet temperatures of the working and heating fluid were held constant 36,3°C and 101°C respectively. For this measurement the mass flow rate was 0,226 kg/s and the heat exchanger showed good performance. The pinch point temperature difference at these working conditions is lower than 10K. From the mentioned arguments in this work, it can be concluded that more accurate design of the heat exchanger with appropriate correlations leads to improved cycle efficiency and lowering the cost of such installation.

REFERENCES

1. Bringer, R.P., Smith, J. M., , *Heat transfer in the critical region*. AIChE Journal, 1957. **3**(1): p. 49 - 55.
2. Dickinson, N.L. and C.P. Weich, *Heat transfer to supercritical water*. ASME 80, 1958: p. pp.745-751.
3. Shitsman, M.E., *Heat transfer to water, oxygen and carbon dioxide in the approximately critical range*. Teploenergetiky, No.1, 1959: p. pp.68-72.
4. Krasnoshchekov, E.A. and V.S. Protopopov, *Heat transfer at supercritical region in flow of carbon dioxide and water in tubes, (In Russian)*. Thermal Eng., 1959. **12**: p. 26–30.
5. Shitsman, M.E., *Impairment of the heat transmission at super-critical pressures*. . Teplofiz. Vys. Temp. 1, 1963. **No. 2** (1963).
6. Bishop, A.A., R.O. Sandberg, and L.S. Tong, *Forced convection heat transfer to water at near critical temperatures and supercritical pressures*., WCAP-2056-P, Part-III-B, 1964(February, 1964.).
7. Ackermann, J.W., *Pseudo-boiling heat transfer to supercritical pressure water in smooth and ribbed tubes*. Journal of Heat transfer, 1970. **Vol. (1970)**: p. pp.490-498.
8. Yamagata, K., et al., *Forced convection heat transfer to supercritical water flowing in tubes* International Journal of Heat and Mass Transfer,., 1972. **15**: p. pp.2575-2593.
9. Jackson, J.D. and J. Fewster, *Forced Convection Data for Supercritical Pressure Fluids*. HTFS 21540, 1975.
10. Vikrev, Y.V., Lokshin, V.,, *An experimental study of temperature conditions in horizontal steam generating tubes at supercritical pressures*. Teploenergetika 1, 1964. **11**(3): p. 12 -16
11. Jackson, J.D., Hall, W. B. , *Influences of buoyancy on heat transfer to fluids flowing in vertical tubes under turbulent conditions*. Turbulent Forced Convection in Channels and Rod Bundles, 1979. **2**(published by Hemisphere Publishing Corporat): p. 613-640.
12. Haskins, H.J., R.M. Taylor, and D.B. Osborn, *Development of solar receiver for an organic Rankine cycle engine*, in *Proceedings of the 16th Intersociety Energy Conversion Engineering Conference. 'Technologies for the Transition'*, 1981. p. 1764-9, vol.2.
13. Amon, C.H.M., B B; , *Spectral Element Simulations of Unsteady Forced Convective Heat Transfer: Application to Compact Heat Exchanger Geometries* Numerical Heat Transfer, Part A 1991. **19**: p. 1-19.
14. Schuster A, K.S., Leontaritis AD. , *Influence of supercritical ORC parameters on plate heat exchanger design*, , in *Applied Thermal Engineering* 2012; . p. 70-76.
15. Lazova M., K.A., Huisseune H., and De Paepe M., *Heat transfer in horizontal tubes at supercritical pressures for ORC application*, in *HEFAT 2014*, 2014.
16. Zhang C-L, Y.L., Shao L-L. , *Comparison of heat pump performance using fin-and-tube and microchannel heat exchangers under frost conditions*. , in *Appl Energy*, 2010. p. 1187–97.
17. Patil R. K., S.B.W., Ghosh P.K. , *Designing a helical-coil heat exchanger*. Chemical Engineering 1982. **13**.

18. Cayer E, G.N., Nesreddine H. , *Parametric study and optimization of a transcritical power cycle using a low temperature source*, . Applied Energy 2010; . **87**: : p. 1349-1357. .
19. Roy P, D.M., Galanis N, Nesreddine H, Cayer E. , *Thermodynamic analysis of a power cycle using a low-temperature source and a binary NH₃-H₂O mixture as working fluid*. . Int J Thermal Sci 2010. **49**(1): p. 48–58.
20. Claesson, J., *Correction of logarithmic mean temperature difference in a compact brazed plate evaporator assuming heat flux governed flow boiling heat transfer coefficient*. . Int J Refrig, 2005. **28**(4): p. 573–78.
21. Coates J, P.B., *Heat Transfer to Moving Fluids*, in *Chem Eng* 1959. p. 67–72.
22. Kern, D.Q., *Process Heat Transfer*. , 1950.: McGraw-Hill, New York.
23. Petukhov BS, K.E., Protopopov VS. , *An investigation of heat transfer to fluids flowing in pipes under supercritical conditions.*, in *ASME* 1961: University of Colorado, Boulder, CO, USA. p. 569-78.
24. Petukhov BS, K.V., *On heat exchange at turbulent flow of liquid in pipes*. Teploenergetika 1, 1958. **4**: p. 63–81.
25. Garimella, S., *High condensing temperature heat transfer performance of low critical temperature refrigerants*, 2006, Air-conditioning and refrigeration technology institute, ARTI 21CR program contract number 610-20060, : Arlington, Virginia, USA.
26. Mokry S, P.I., *Development of supercritical water heat-transfer correlation for vertical bare tubes*. , in *Nuclear Engineering and Design*, 2011. p. 1126–1136.
27. Shah, R.K., *Assesment of modified Wilson plot techniques used for obtaining heat exchanger design data in Heat Transfer*, in *9th International heat transfer Conference* 1990. p. 51-56.
28. Jose Fernandez-Seara, J.S.a.A.C., *Experimental apparatus for meauring heat transfer coefficients by the Wilson plot method*. European Journal of Physics 2005.

ACKNOWLEDGEMENT

The research leading to these results has received funding from the European Union's Seventh Framework Programme managed by REA-Research Executive Agency, <http://ec.europa.eu/research/rea> ([FP7/2007-2013] [FP7/2007-2011]) under grant agreement n° 315049 [CPV/RANKINE], FP7-SME-2012

The results presented in this paper have been obtained within the frame of the IWT SBO-110006 project The Next Generation Organic Rankine Cycles (www.orcnex.be), funded by the Institute for the Promotion and Innovation by Science and Technology in Flanders. This financial support is gratefully acknowledged.

HEAT STORAGE ORC SYSTEM FOR VEHICLE ICE EXHAUST HEAT RECOVERY

Tao CHEN¹, Lei ZHANG¹, Weilin ZHUGE¹, Yangjun ZHANG^{1,*}

¹ State Key Laboratory of Automotive Safety and Energy, Tsinghua University, Beijing, 100084, China

t-chen14@mails.tsinghua.edu.cn

zlei11@mails.tsinghua.edu.cn

zhugewl@tsinghua.edu.cn

yjzhang@tsinghua.edu.cn

* Corresponding Author

ABSTRACT

A new Organic Rankine Cycle (ORC) system for vehicle internal combustion engine (ICE) waste heat recovery (WHR) is presented in this paper, which can effectively reduce the influence of exhaust gas fluctuation caused by vehicle driving cycle. An evaporator with heat storage material inside is used in this system to make it possible that the ORC expander working under more stable condition, and the conceptual scheme of the heat-storage ORC system is presented. The dynamic model is established, and a heavy diesel engine exhaust experimental data is used as heat source in the performance simulation. The heat resistance effect and the heat capacity effect are the main effects of heat storage ORC system, and the influence of these two effects are analyzed and discussed, meanwhile, the system designing criteria is presented. Compared with conventional system, the fluctuation of ORC evaporator outlet temperature can be decreased by 50 % and the system overall efficiency can be increased from 6 % to 7 %.

1. INTRODUCTION

Interest in WHR of vehicle ICE has grown dramatically recently, as CO₂ emission regulations are becoming stricter. Around 60-70 % of the fuel energy is lost in the exhaust and coolant (Endo *et al.*, 2007), and many researchers recognize WHR is one of the most potential methods to improve ICE efficiency. Furthermore, the technologies for WHR of vehicle ICE can also be used to save energy in the industry.

The four main sources of waste heat in a vehicle are the exhaust, coolant, exhaust gas recirculation (EGR) cooler and charge air cooler (Teng *et al.*, 2007). Exhaust has the highest temperature with the largest mass flow rate heat sources among them, so exhaust heat recovery (EHR) is the most attractive part of WHR. Researchers have proposed many methods for EHR, such as, Rankine Cycle, Organic Rankine Cycle (ORC), Brayton Cycle. By comparison, ORC system has the best performance (Bailey, 1985). Then a series of model and experimental researches of ORC system for vehicle WHR show that brake specific fuel consumption BSFC can be improved by up to 15-30% under the ideal working condition (Morgan *et al.*, 1973; Poulin *et al.*, 1984; Chammas & Clodic, 2005). On the other side, it means that thermal efficiency and net output power of the engine can be improved by 18-40%.

Selection of the working fluid and calculation of steady system performance used to be the primary focus of this research field (Hung *et al.*, 1997; Sprouse & Depcik, 2013; Roy *et al.*, 2010). Recently, researchers paid more attention to the heat fluctuation caused by the vehicle varying working condition, because fluctuation could significantly influence the performance of ORC system in the application. The fluctuation not only can reduce the efficiency, but also can break the components of ORC system, especially when the expander is a turbine. If the turbine inlet working condition fluctuation is too large, it will work in low-efficient range at most of the time. What's worse, if the working fluid is unsaturated at the turbine inlet, the droplet will break the blade.

Using the active control is a method to deal with the influence of the heat fluctuation, and keep the system in a safe working condition range. In the last decade, some active control strategies have been researched (Quoilin *et al.*, 2011; Horst *et al.*, 2013; Pralez *et al.*, 2013). Horst *et al.* (2013) controls the ORC system by four actuators, which are the pump rotation speed, the expander speed and two valves. Although the active control method can make the system under a safety working condition, the fluctuation of the turbine inlet temperature and pressure can't be reduced. As a result, the turbine will work in the low-efficient range at most of the time.

This paper proposes a heat-storage ORC system to deal with the heat fluctuation instead of using complex active control system. In the HS evaporator, the heat of exhaust is absorbed by heat storage material firstly, and then the heat will be conducted from heat storage material to the working fluid. The heat fluctuation will be reduced by the heat storage material, therefore the ORC system can work in a relative steady condition. This heat-storage ORC system makes it feasible that using a fixed-speed motor to drive pump, at the same time the turbine will work around the design point with a high efficiency.

The description of this system is proposed in Section 2, where introduces the conceptual scheme of the new system as well as the key components. Then this work establishes the system dynamic model in Section 3. Later, the simulated performance of the new ORC system and discussions are shown in Section 4. Section 5 presents the conclusion and the summary of the whole work.

2. SYSTEM DESCRIPTION & METHODOLOGY

Figure 1 presents the conceptual scheme of the heat-storage ORC system. The heat-storage evaporator is the key component, which adds a layer of heat-storage material between the heat source and working fluid. Figure 2 shows the principle diagram of heat-storage evaporator. There are two homocentric pipes separating the heat storage material from exhaust and working fluid instead of the only one pipe in the conventional evaporator. The expander is a turbine expander connected with a high speed generator. The safety valve avoids the unsaturated vapor go into the turbine. The working process of this system is shown as follows.

Working fluid is pressed in the pump, and then it evaporates in the evaporator. After that, the working fluid will be expanded in the expander and generate electricity. At last, working fluid will be condensed back to the fluid reservoir. When the temperature of heat storage material becomes higher than the Start-Temperature, the working fluid pump start to work and the safety valve will be closed. When the engine stops working, the safety valve will be opened, as well as the pump is stopped. If the evaporator outlet temperature is lower than the Safety-Temperature, the safety valve will be opened, but the pump won't be stopped. Adding the heat storage material greatly reduces the times of opening and closing the safety valve which makes this system more feasible.

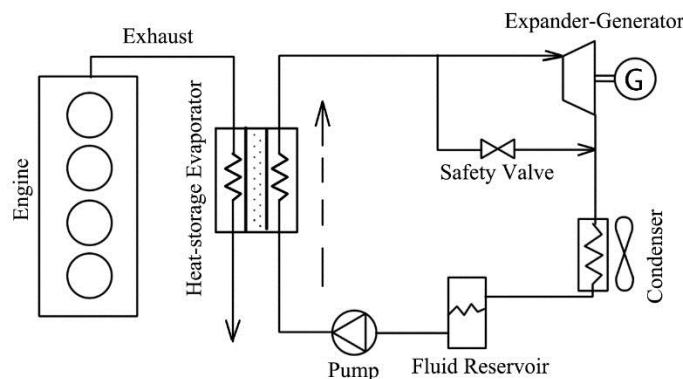


Figure 1: Conceptual scheme of heat-storage ORC system

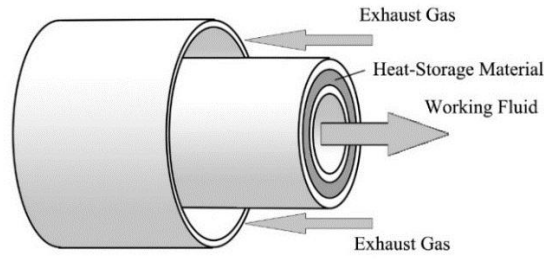


Figure 2: Principle diagram of heat-storage evaporator

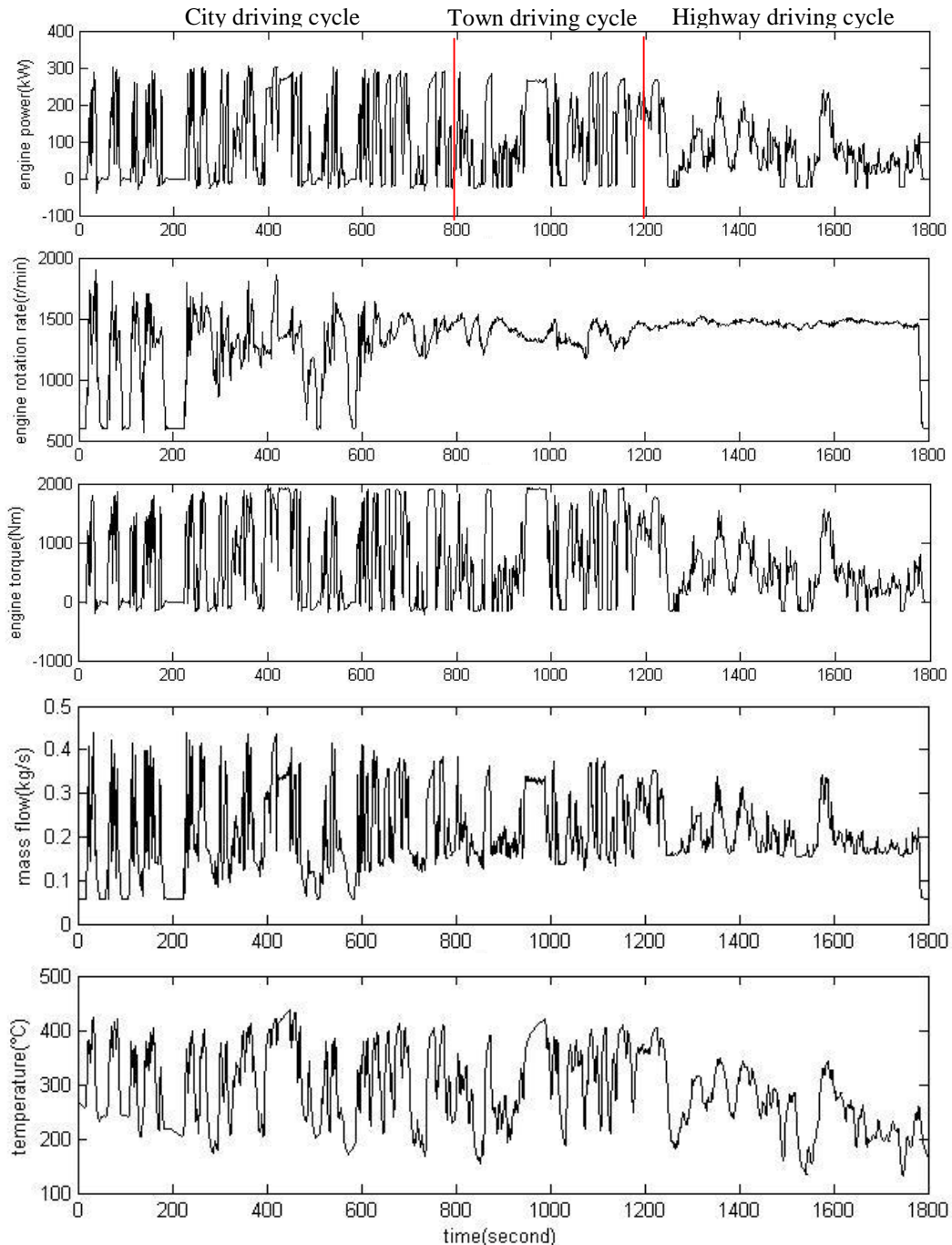


Figure 3: Vehicle diesel engine exhaust experimental data in ETC cycle

R245fa is selected as the working fluid of ORC system, as Malavolta *et al* (2010) researches that R245fa is a suitable working fluid to recover the heat in exhaust. This paper focuses on the influence of heat storage material, so the special research of working fluid selection is simplified.

Table 1: Reference properties of the heat storage material

Parameters	Value	Parameters	Value
Density	1667 kg/m ³	Thermal conductivity	0.8 W/(m*K)
Heat capacity	1.6 kJ/kg		

Table 2: Main parameters of the diesel engine

Parameters	Value	Parameters	Value
Numbers of cylinders	6	Rated power	300 kW
Displacement	12 L	Rated rotation speed	1900 r/min
Compression ratio	17	Maximum torque	1900 Nm

The selection of heat storage material is the key problem for this new ORC system. At the same time, there are hundreds of inorganic salts can be chosen, which include nitrite salts, nitrate salts, carbonate salts and so on. Herrmann U *et al* (2002), Reilly HE& Kolb WJ (2001) and Zalba B *et al* (2003) have summarized the properties of the inorganic salts in their researches, it shows that the density is in the range of 1400-2200 kg/m³, the thermal conductivity is in the range of 0.5-2 W/(m*K) and the heat capacity is in the range of 1.5-1.8 kJ/kg. This work doesn't select a special material, while the reference properties is selected in the reliable range, in Table 1, because the purpose of this work is researching the performance of the HS ORC system and presenting the criterion for the heat storage material selection. A special heat storage material will be selected in the future.

The waste heat recovery performance of the heat-storage ORC system for a heavy duty diesel engine operating under ETC driving cycle was investigated. The main parameters of the diesel engine is shown in Table 2. ETC cycle is the standard test for vehicle engine transient performance evaluation. It consists of three parts, city driving cycle, town driving cycle, and highway driving cycle, which include the typical working conditions of the engine in China. The engine rotation rate and torque must follow the text requirement, which is shown in Figure 3. It also shows the experimental data of the exhaust temperature and mass flow rate of the engine operating under ETC cycle. The heat source of the evaporator is determined by the exhaust experimental data.

3. DYNAMIC MODELING

3.1 Heat-storage Evaporator

Figure 4 shows the simplified model of the evaporator. Finite difference method is used in this model, and the evaporator is simplified as a 1D pipe with the constant shape of transverse section. The loss of pressure is ignored and the pump is working in a steady condition, so the pressure of exhaust and working fluid is assumed as a constant in the whole flow field. Both of the exhaust and working fluid are considered as inviscid fluid. According to these assumptions, the energy conservation equation (Eq. 1) is considered.

$$\frac{DU}{Dt} = \dot{Q} + \dot{W} \quad (1)$$

The simplified form based on the above assumptions is given as follows:

$$\int_v \left(\rho \frac{\partial H}{\partial t} - \rho \cdot u \frac{\partial H}{\partial x} \right) dv = \int_A \dot{q} \cdot dA \quad (2)$$

One order upwind scheme is used for discretization of exhaust and working fluid flow field:

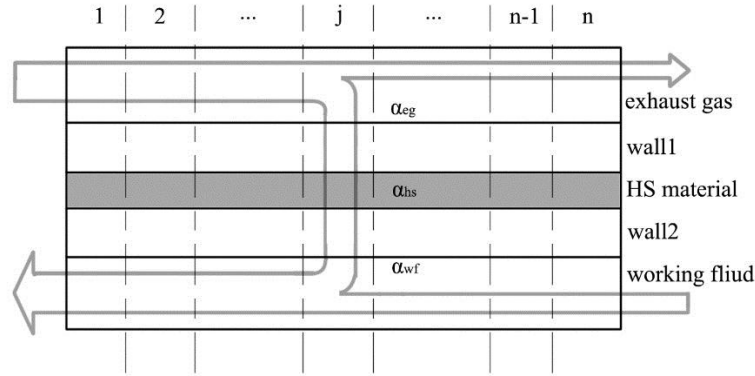


Figure 4: Discrete model of evaporator

Table 3: Main parameters of the HS-evaporator

Parameters	Value	Parameters	Value
Area	3 m ²	α_{exh}	1000 W/m ² K
V _{exh}	0.04 m ³	$\alpha_{wf,liquid}$	260 W/m ² K
V _{wf}	0.009 m ³	$\alpha_{wf,evapor}$	360 W/m ² K
M _{wall1}	10 kg	n	40
M _{wall2}	10 kg	M _{sto}	5 kg
C _v wall	4600 J/kg	α_{sto}	800 W/m ² K

$$\frac{\rho_{exh,j} V_{exh,i}}{\rho_{exh,j} V_{exh,i}} \frac{\partial H_{exh,j}}{\partial t} = \dot{M}_{exh} \frac{H_{exh,j+1} - H_{exh,j}}{2} - A_i \dot{q}_{exh,j} \quad (3)$$

$$\frac{\rho_{wf,j} V_{wf,i}}{\rho_{wf,j} V_{wf,i}} \frac{\partial H_{wf,j}}{\partial t} = -\dot{M}_{wf,j} \frac{H_{wf,j} - H_{wf,j-1}}{2} + A_i \dot{q}_{wf,j} \quad (4)$$

The energy conservation equation of pipe wall and heat-storage material is shown as follows. The heat transfer between different respective elements is ignored.

$$M_{sto,i} \cdot \frac{dE_{sto,j}}{dt} = A_i (\dot{q}_{sto1,j} - \dot{q}_{sto2,j}) \quad (5)$$

$$C_{v_{wall1}} M_{wall1,i} \cdot \frac{dT_{wall1,j}}{dt} = A_i (\dot{q}_{exh,j} - \dot{q}_{sto1,j}) \quad (6)$$

$$C_{v_{wall2}} M_{wall2,i} \cdot \frac{dT_{wall2,j}}{dt} = A_i (\dot{q}_{sto2,j} - \dot{q}_{wf,j}) \quad (7)$$

The heat transfer coefficient is calculated by:

$$\dot{q}_{exh,j} = \alpha_{exh} (T_{exh,j} - T_{wall1,j}) \quad (8)$$

$$\dot{q}_{sto1,j} = \alpha_{sto} (T_{wall1,j} - T_{sto,j}) \quad (9)$$

$$\dot{q}_{sto2,j} = \alpha_{sto} (T_{sto,j} - T_{wall2,j}) \quad (10)$$

$$\dot{q}_{wf,j} = \alpha_{wf,j} (T_{wall2,j} - T_{wf,j}) \quad (11)$$

The heat transfer coefficient of exhaust side and heat storage material side is considered as a constant, while that of working fluid side depends on the state. Liquid and gas coefficients are constant respective (Quoilin *et al*, 2011), and the two-phase coefficient is calculated by Eq.12 (Horst *et al*, 2013).

$$\frac{\alpha_{wf, ev}}{\alpha_{wf, bub}} = \left((1-x)^{0.01} \left((1-x)^{1.5} + 1.9x^{0.6} \left(\frac{\rho_{wf, bub}}{\rho_{wf, dew}} \right)^{0.35} \right)^{-2.2} + x^{0.01} \left(\frac{\alpha_{wf, dew}}{\alpha_{wf, bub}} \left(1 + 8(1-x)^{0.7} \left(\frac{\rho_{wf, bub}}{\rho_{wf, dew}} \right)^{0.67} \right) \right)^{-2} \right)^{-0.5} \quad (12)$$

Other main parameters are shown in Table 3, the heat transfer coefficients of R245fa and exhaust are referenced to Quoilin *et al*,(2011).

Software REFPROP® is used to provide the properties of R245fa, and software Matlab® is used for ORC modeling.

3.2 Other components

The turbine working condition is relatively steady, as the mass flow rate and pressure are constants. The inlet temperature is the only unsteady parameter which makes a limited difference in the turbine performance. The isentropic efficiency just changes less than 2% in the range of the temperature (350-450 K) calculated by the turbine design results of Fiaschi *et al* (2015). As a result, the turbine isentropic efficiency is considered as a constant: $\eta_{turbine} = 0.75$.

The pump of the heat-storage system is under a steady working condition, which means the pressure ratio and volume flow rate are constants. Therefore, the isentropic efficiency is considered as a constant: $\eta_{pump} = 0.7$.

The condenser is an air-cooled condenser installed in the front of the vehicle, so the cooling capacity is good enough to make sure the outlet temperature close to the ambient temperature. The ambient temperature in this work is 25 °C, and the outlet temperature is set to 40 °C.

4. PERFORMANCE SIMULATION & DISCUSSION

Several cases have been simulated for comparing the heat-storage ORC system with the conventional system. Two main effects are found, which are caused by adding the heat storage material, and they are the heat resistance effect and heat capacity effect. Heat resistance effect is bad for the system performance, while the heat capacity effect is favorable. The details are shown in this section.

4.1 Heat resistance effect

It is easy to comprehend that adding heat storage material in the evaporator pipe (Figure 2) will resist the heat transfer. In conventional system, thermal energy is conducted by the route: exhaust-pipe-working fluid, while in this system it is conducted by the route: exhaust-pipe1-heat storage material-pipe2-working fluid. Obviously there are two more heat transfer steps, which increase the overall heat resistance of the system. The heat transfer coefficient between pipe and heat-storage material is the key parameter of the heat resistance effect, which depends on its thickness and heat conductivity.

The heat resistance effect will reduce the heat transfer capability of the evaporator. A steady simulation is conducted and the influence of the heat transfer coefficient is shown in Figure 5, where the exhaust temperature is 330 °C and the exhaust mass flow rate is 0.15 kg/s. It can be found that the superheating temperature at evaporator outlet decreases as the heat transfer coefficient decreases. It also means that if we keep the identical superheating temperature, the mass flow rate will be smaller as the heat transfer coefficient decreases.

The heat resistance effect will reduce the heat fluctuation of the exhaust, which is shown in Figure 6. It is the result of the unsteady simulation, when the heat source of this system is 200 seconds among the ETC cycle which can represent the characters of the ICE exhaust. The result is calculated in two steps. A steady simulation is finished at first, and then it will be used as the initial condition of the unsteady simulation. In the steady simulation, the heat source is the mean value of the exhaust temperature and mass flow rate along the 200 seconds, and an iterative computation is done to make sure that the evaporator outlet superheating temperature is about 50 K, so the mass flow rates of the curves are different. In the unsteady simulation, the working fluid mass flow rate is a constant respectively, and the exhaust temperature and mass flow rate are unsteady. The evaporator outlet superheating temperature is shown in the Figure 6, as a result, heat fluctuation is reduced as the heat transfer coefficient going down.

The system performance depends on the heat transfer capability and the fluctuation of the evaporator outlet superheating temperature. A smaller the fluctuation means that the working fluid at the evaporator outlet has smaller possibilities to be unsaturated, as a result that the working fluid mass flow rate can be set large. If the fluctuation is large, the working fluid at the evaporator outlet will be unsaturated vapor some time, at that time, the safety valve will be opened to protect the turbine from droplet harming and the output power will be null. The heat transfer capability influences the working fluid mass flow rate straightly as is shown in Figure 5, which is discussed above.

Figure 7 shows the system performance changes as the working fluid mass flow rate increases. The vertical coordinate represents the overall efficiency, which is a calculation of net power output divided by the total thermal energy in the exhaust during that time, and an identical trend is found in the average net output power and the engine power improvement. When the mass flow rate is small, the working fluid at the evaporator outlet is saturated vapor during almost all the time, so the performance is better as the mass flow rate increases. While the mass flow rate is large, the unsaturated time is longer which makes the performance worse as the mass flow rate increases. As a result, there is a performance maximum in the middle mass flow rate. The curves represent the ORC system with different heat transfer coefficients, and it is shown that the maximum performance decreases as the heat transfer coefficient decreases. So the heat resistance effect is a bad effect for the system performance.

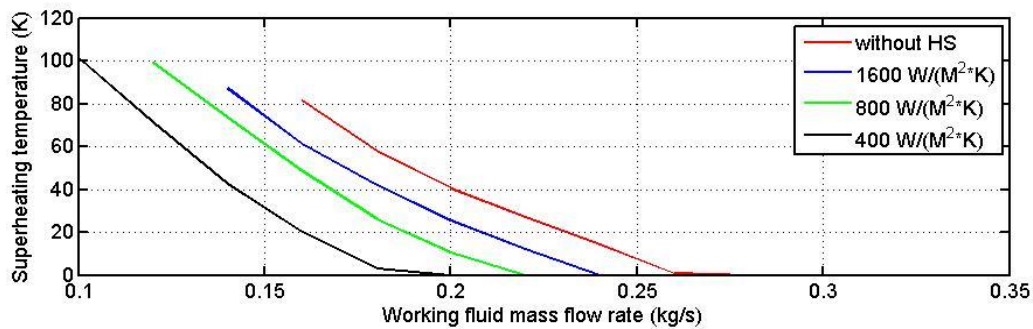


Figure 5: Superheating temperature at the evaporator outlet vs. working fluid mass flow rate

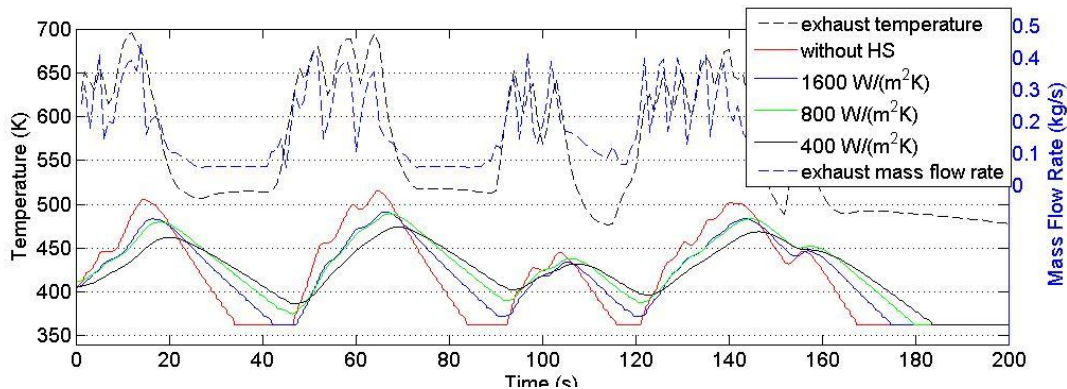


Figure 6: Fluctuation of the evaporator outlet temperature

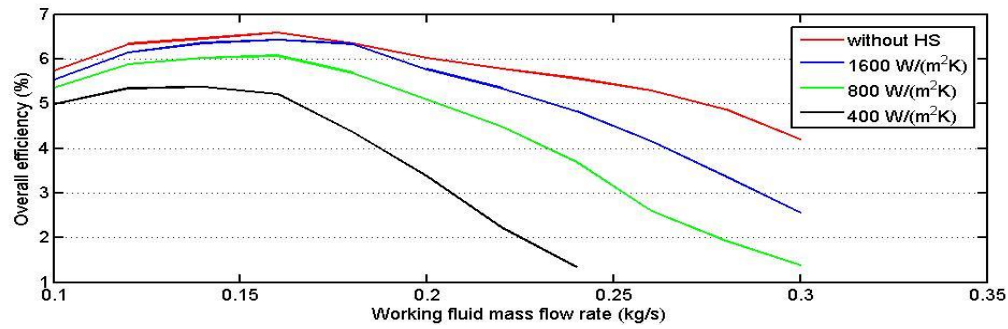


Figure 7: System overall efficiency vs. working fluid mass flow rate

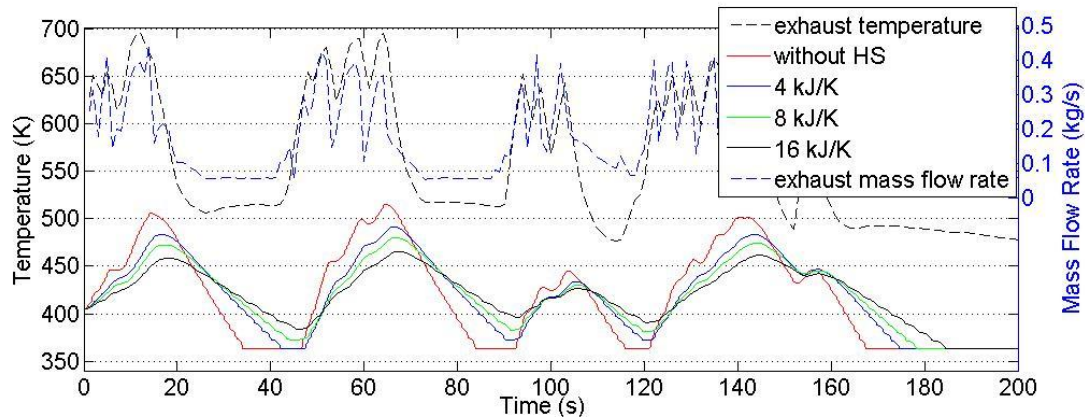


Figure 8: Fluctuation of the evaporator outlet temperature

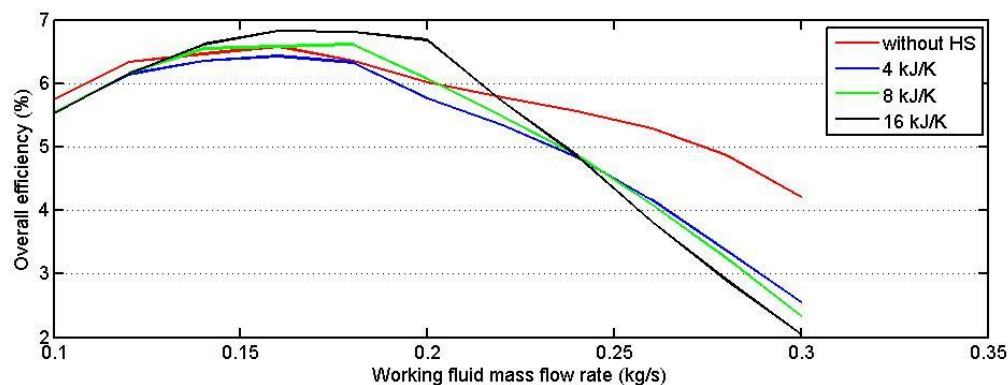


Figure 9: System overall efficiency vs. working fluid mass flow rate

4.2 Heat capacity effect

The heat capacity effect is produced by the heat capacity of the heat-storage material, while it is unrelated to the heat transfer coefficient, however, it also can reduce the fluctuation which is shown in Figure 8. In these cases, the heat transfer coefficient is set to $1600 \text{ W}/(\text{m}^2\text{K})$, and different curves represent the systems with different total heat capacities of the heat storage material. It shows that the fluctuation is reduced as the heat capacity decreases. It is worth noting that the heat capacity effect is in helpful to improve the system overall efficiency, which is shown in Figure 9. The overall efficiency can be improved from 6 % to 7 % in these calculation cases, and the larger total heat capacity is, the better the system performance is.

4.3 System performance discussion

The two effect's influence has been conducted in above sections, and the conclusion is valuable for selecting the heat storage material and designing the evaporator construction.

The heat transfer coefficient depends on the thickness and the heat conductivity of the heat storage material:

$$\alpha_{sto} = 2 \frac{\lambda_{sto}}{h_{sto}} \quad (13)$$

The total heat capacity depends on the total volume and the volumetric heat capacity of the material:

$$C_{sto} = c_{v,sto} \cdot V_{sto} \quad (14)$$

The thickness and volume is the parameter of the evaporator construction, and the relationship between them is fixed if the heat transfer area is fixed:

$$A = \frac{V_{sto}}{h_{sto}} \quad (15)$$

It shows that there is a trade-off between the heat resistance effect and the heat capacity effect, which is related to the thickness of the heat storage material. It means that a good heat storage evaporator can be designed by optimizing the heat storage material thickness. At the same time, it should be noted that the thickness of the heat storage material shouldn't be too large, because it leads to the increasing of weight and volume of the evaporator, which are limited in the vehicle.

On the other hand, a conclusion can be drawn that the system performance will be improved when selecting a heat storage material with both of the larger heat conductivity and the larger volumetric heat capacity. Except the conventional heat storage material which store the heat by temperature rising, the phase change heat storage material and the chemical heat storage material have great potential in the heat-storage ORC system. M. Medrano *et al* (2010), A. Gil *et al* (2010) and M.M. Kenisarin (2010) summarized the phase change heat storage materials, their works showed that nearly any melting temperature can be realized in the range of 100-400 °C by adjusting the component of inorganic salt mixtures. If the phase change reacts along the temperature range instead of at a special temperature, it will be more valuable for this system.

5. CONCLUSIONS

The heat storage ORC system for the vehicle ICE EHR reduces the heat fluctuation by 50%, at the same time, it improves the overall efficiency of the ORC system. In the cases of this paper the overall efficiency can be increased from 6 % to 7 %. Furthermore, this system has the potential to reduce the heat fluctuation more and improve the system performance more by selecting a better heat storage material.

Two effects of the system are proposed and analyzed in this paper. Both of them have the ability to reduce the heat fluctuation, but the heat resistance effect is unfavorable for the system performance while the heat capacity effect is advantageous for it. If the latter is greater than the former, the system efficiency will be improved. As a result, it is better to increase the heat transfer coefficient as well as the total heat capacity during designing the heat storage ORC system evaporator. At the same time, it should be noted that the thickness of the heat storage material shouldn't be too large because of the limitation of weight and space in the vehicle.

The selection of the heat storage material is important for the system performance, the material with larger heat conductivity and larger volumetric heat capacity are the better one. The latent heat storage material has the potential, among which the phase change heat storage material is much more feasible.

REFERENCES

Endo T., Kawajiri S., Kojima Y., Takahashi K., Baba T., Ibaraki S., Takahashi T., et al., 2007, Study on Maximizing Exergy in Automotive Engines, *SAE Int*, Publication 2007-01-0257

- Teng H., Regner G., Cowland C., 2007, Waste Heat Recovery of Heavy-Duty Diesel Engines by Organic Rankine Cycle Part I: Hybrid Energy System of Diesel and Rankine Engines, *SAE Int*, Publication 2007-01-0537.
- Bailey M., 1985, Comparative Evaluation of Three Alternative Power Cycles for Waste Heat Recovery from the Exhaust of Adiabatic Diesel Engines, *Lewis Research Center, Cleveland (OH)* Report No. NASA TM-86953.
- Morgan D., Patel P., Doyle E., Raymond R., Sakhuja R., Barber K., 1973, Laboratory Test Results Low Emission Rankine-Cycle Engine with Organic-Based Working Fluid and Reciprocating Expander for Automobiles, *SAE*, Publication 739062 (1973).
- Poulin E., Demler R., Krepchin I., Walker D., 1984, Steam Bottoming Cycle for an Adiabatic Diesel Engine, *Foster-Miller Inc., Waltham (MA)*, 1984 Mar, Report No. NASA CR-168255.
- Chammas R., Clodic D., 2005, Combined Cycle for Hybrid Vehicles, *SAE Int*, Publication 2005-01-1171.
- Hung T., Shai T., Wang S., 1997, A review of organic Rankine cycles (ORCs) for the recovery of low-grade waste heat, *Energy*, Vol. 22, no. 7: p. 661-667.
- Sprouse C., Depcik C., 2013, Review of organic Rankine cycles for internal combustion engine exhaust waste heat recovery, *Applied Thermal Engineering*, Vol. 51, no. 1-2: p. 711-722.
- Roy J., Mishra M., Misra A., 2010, Parametric optimization and performance analysis of a waste heat recovery system using Organic Rankine Cycle, *Energy*, Vol. 35, no. 12: p. 5049-5062.
- Quoilin S., Aumann R., Grill A., Schuster A., Lemort V., Spliethoff H., 2011, Dynamic modeling and optimal control strategy of waste heat recovery Organic Rankine Cycles, *Applied Energy*, Vol. 88, no.6: p. 2183-2190.
- Horst T., Rottengruber H., Seifert M., Ringler J., 2013, Dynamic heat exchanger model for performance prediction and control system design of automotive waste heat recovery system, *Applied Energy*, Vol. 105, p. 293-303.
- Peralez J., Tona P., Lepreux O., Sciarretta A., Voise L., Dufour P., Nadri M., 2013, Improving the Control Performance of an Organic Rankine Cycle System for Waste Heat Recovery from a Heavy-Duty Diesel Engine using a Model-Based Approach. *2013 IEEE Conference on Decision and Control (CDC), Florence : Italy (2013)*.
- Fiaschi D., Manfrida G., Maraschiello F., 2015, Design and performance prediction of radial ORC turboexpanders, *Applied Energy*, Vol.138, p. 517-532.
- Malavolta M., Beyene A., Venturini M., 2010, Experimental implementation of a micro-scale ORC based CHP Energy system for domestic applications, *ASME Paper*, IMECE2010-37208.
- Herrmann U, Geyer M, Kearney D, 2002, Overview on thermal storage systems. In *Workshop on thermal storage for trough power systems*. p. 20-21.
- Reilly HE, Kolb WJ., 2001, Evaluation of molten salt power tower technology based on the experience of solar two. *Sandia National Laboratories Report No. SAND2001-3674*.
- Zalba B, Mari'n JM, Cabeza LF, Mehling H., 2003, Review on thermal energy storage with phase change: materials, heat transfer analysis and applications. *Applied Thermal Engineering*, Vol. 23, no. 3: p. 251-283.
- Medrano M., Gil A., Martorell I., et al, 2010, State of the art on high-temperature thermal energy storage for power generation. Part 2—Case studies, *Renewable and Sustainable Energy Reviews*, Vol. 14, no. 1: p. 56-72.
- Gil A., Medrano M., Martorell I., et al, 2010, State of the art on high temperature thermal energy storage for power generation. Part 1—Concepts, materials and modellization, *Renewable and Sustainable Energy Reviews*, Vol. 14, no. 1: p. 31-55.
- Kenisarin M., 2010, High-temperature phase change materials for thermal energy storage. *Renewable and Sustainable Energy Reviews*, Vol. 14, no. 3: p. 955-970.

ACKNOWLEDGEMENT

The authors would like to thank the National Basic Research Program of China (2011CB707204) for the support.

ADVANCED CONTROLS OF ORGANIC RANKINE CYCLE FOR HIGHLY TRANSIENT FLUCTUATIONS DURING INITIAL STARTUP

Parsa Mirmobin*, Chris Sellers

Calnetix Technologies, LLC
16323 Shoemaker Ave, Cerritos, CA 90703
USA

e-mail: pmirmobin@calnetix.com, csellers@calnetix.com

Web page: <http://www.calnetix.com>

* Corresponding Author

ABSTRACT

Organic Rankine Cycles are typically utilized in systems with a steady heat source and condensing condition. In highly transient cases, the working fluid undergoes violent phase transition within the evaporator. The resulting forces are experienced by the heat exchanger, expander, and associated piping. This ultimately results in premature and catastrophic component failure.

This paper discusses pressure and flow instability which occurs during initial startup of an ORC. The instability is a result of the interaction between the nonlinear pressure field within the evaporator and the pressure source (centrifugal pump.) The phenomenon is characterized by a rapid oscillation in pressure and flow and resembles similar effects observed in low pressure boilers and axial compressors. Experimental data is examined and a method for reducing or eliminating this effect is presented.

1. INTRODUCTION

Organic Rankine Cycles (ORC) may experience large oscillations in evaporator outlet pressure, mass flow, and temperature during initial startup. These oscillations cause unstable operation, premature shutdown, and increased component wear. When designing an overall control scheme, it is important to account for this phenomenon to ensure a safe and stable startup.

Two-phase flow instabilities were first studied by Ledinegg (1938). He observed the internal characteristic curve (system curve) for an evaporator has a region of negative slope region caused by the phase change from liquid to vapor. Figure 1 below is a graphical representation of the negative sloped curve.

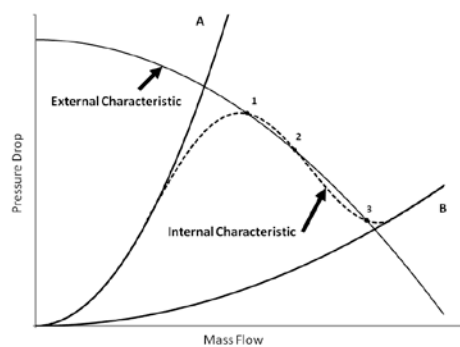


Figure 1: Negative Slope of Internal Characteristic Curve

Curve A represents the internal characteristic of an evaporator filled primarily with vapor. Curve B represents the internal characteristic of an evaporator filled primarily with liquid. As the pressure and mass flow increase, the evaporator's internal characteristic transitions between curves A and B along the dotted line. In Figure 1 the external characteristic (pump curve) intersects the evaporator's internal characteristic at points 1, 2, and 3. Points 1, 2, and 3 each represent stable operating conditions for the pump. A small perturbation in the mass flow or pressure drop will cause the pump to jump from one point to the other. Thus this operating condition is unstable.



Figure 2: Model to Describe Density Wave Oscillations

Subsequent studies focused on dynamic instabilities with a repeating oscillatory pattern. The most common type of dynamic instability is the density wave oscillation, DWO, first discussed by Stenning (1964). Figure 2 shows the classical model used to describe DWO. It consists of a pipe with throttling valves upstream and downstream of a heated section. The pressure at the pipe inlet and exit are constant at P_i and P_e . At some time "t" the pressure at P_2 undergoes a small drop of the order ΔP . This pressure drop may be caused by unsteady flow conditions, fluctuations in the two-phase region, etc. The pressure at P_1 drops nearly instantly by an equal value of ΔP . The pressure difference between P_i and P_1 increases and thus the fluid velocity into the heated section increases by:

$$u \propto \sqrt{P_i - P_1} \quad (1)$$

This sends a surge of higher density fluid through the heated section from P_1 to P_2 . The high density fluid causes an increase of the pressure of P_2 by a value ΔP . The pressure at P_1 sees an equal increase and corresponding drop in the inlet velocity by Equation (1). Now a low density surge of fluid is sent from P_1 to P_2 , and the cycle repeats itself.

Flow stall and reversal plays a major role in the flow instabilities present during an ORC system's startup. A parallel may be drawn with compressor surge oscillations. Axial compressors exhibit a sharp drop in the head output at very low flows. Surge oscillations occur when an axial compressor operates with high throttling and a large compressible volume in the downstream plenum. The oscillation cycle is described as:

1. Pressure builds downstream in the plenum.
2. Compressor flow decreases and pressure output increases following the compressors external characteristic curve.
3. The pressure output reaches a peak value after which flow separation occurs on the compressor blade surface. This causes the compressor head output to drop dramatically.
4. Pressure in the plenum decreases and flow reversal may occur due to the breakdown of the flow field within the compressor.
5. Once the plenum pressure is sufficiently low, the flow within the compressor stabilizes. Flow begins to move forward into the plenum and the pressure begins to rise again.

The interested reader is referred to Moore and Greitzer (1986) for a more detailed description.

In the next section experimental results will be presented, and attempt will be made to provide a qualitative description of the oscillation process which occurs during the startup of an ORC system.

2. EXPERIMENTAL RESULTS

2.1 Methodology

Data was collected using the Calnetix ORC test cell partially depicted in Figure 3. The working fluid was R245fa refrigerant. A Calnetix ORC system was operated with the turbine in bypass. A

throttling valve was used to represent the pressure drop action of the turbine. Heat was added to the system via a PID controlled hot water loop. The hot water loop was operated at two heating condition: 21 kg/s at 71°C and 28 kg/s at 82°C. The working fluid pump was stepped from 6Hz to 35Hz in 1Hz increments over a period of 75 minutes. The stepping procedure was stopped at various frequencies in order to allow transient phenomena to decay and capture the sustained oscillatory phenomena. Table 1 provides a description of each sensor in the test apparatus. Data was acquired with a sampling frequency of 5Hz for TT106, FM101, TT111, PT112, and PT113 and with a sampling frequency of 0.333 Hz for TT20 and PT20. The initial condition for these sensors prior to pump operation are listed in Table 1.

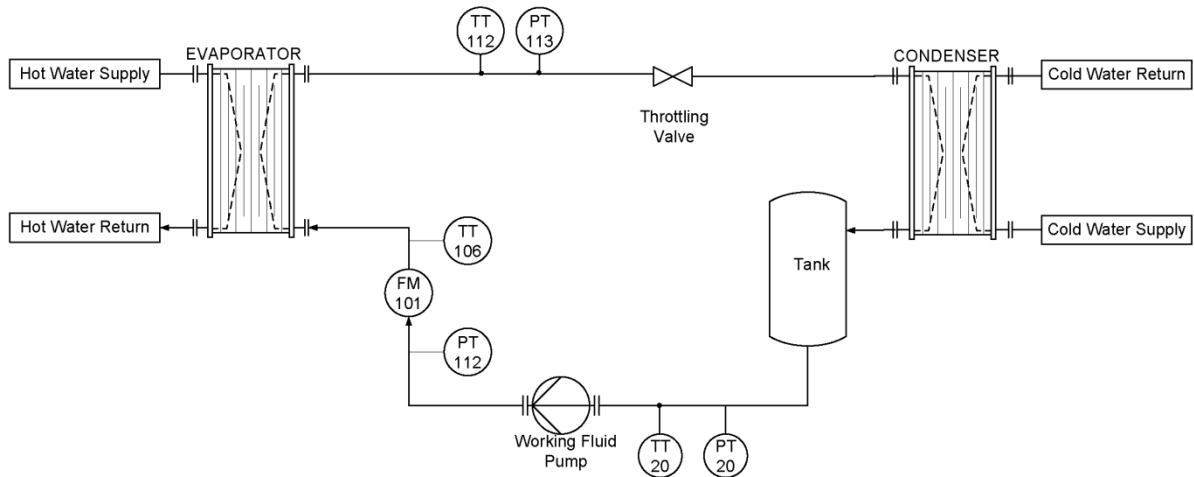


Figure 3: Test Apparatus

Table 1: Test Apparatus Sensor Descriptions

Sensor Tag	Description
TT20	Working fluid Tank Temperature
PT20	Working fluid Tank Pressure
TT106	Evaporator Inlet Temperature
PT112	Evaporator Inlet Pressure
TT112	Evaporator Outlet Temperature
PT113	Evaporator Outlet Pressure
FM101	Working fluid Mass Flow Meter

Table 2: Sensor Initial Conditions

Sensor Tag	Initial Values
TT20	19.7 °C
PT20	1.4 Bar
TT106	25.6 °C
PT112	1.3 Bar
TT112	61.6 °C
PT113	2.3 Bar
FM101	0.2 kg/s

2.2 Results and Discussion

Figure 4 shows a representative diagram of the oscillatory process.

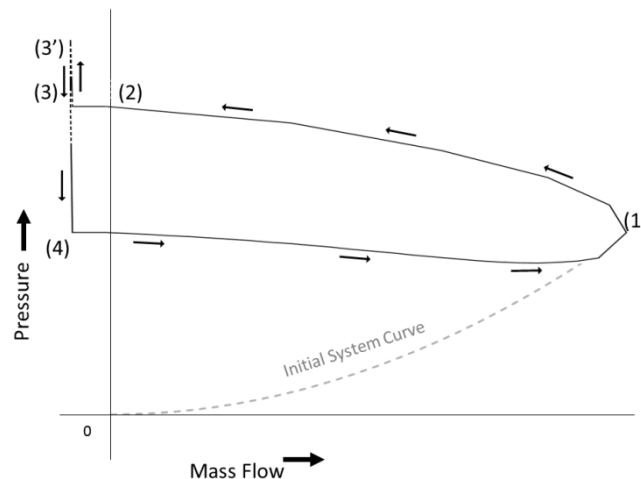


Figure 4: Diagram of Pressure/Mass Flow Oscillations

Initially the evaporator is completely filled with vapor. The pump is operated to some driving frequency and high density liquid flows into the evaporator. The pressure in the evaporator rises to point 1 following a path similar to Curve A in Figure 1. The liquid quickly vaporizes and an imbalance forms between vapor production and mass flow out of the evaporator. The accumulation of mass within the evaporator and increasing system enthalpy causes a local rise in pressure. The mass flow begins to slow down as the evaporator pressure rises, and the system transitions from operating point 1 to 2 along the pumps external characteristic curve. Flow stall and partial reversal occurs from points 2 to 3. At low pump frequencies, the evaporator pressure continues to build up to point 3' as the remaining liquid is vaporized. From point 3 (or 3') to point 4 the evaporator pressure drops as the gas expands forward through the throttling valve and backwards into the piping section between the pump and evaporator. Once the evaporator pressure reaches the original conditions at point 1, the pump is able to reestablish forward flow and the diagram transitions from point 4 to 1. The pump is again operating at point 1 and the cycle repeats.

It is believed flow reversal occurs due to flow separation along the impeller blade surfaces. The measured value for flow reversal was 0.18kg/s. At low frequencies, test data indicated gas was present in the pipe section between the pump and evaporator inlet. This would only occur if gas flows backwards from the evaporator. Additionally the temperature at the bottom of the working fluid tank shows a rapid spike during the flow reversal period. This is believed to be caused by higher temperature fluid from within the pump pushed backwards to the sensor.

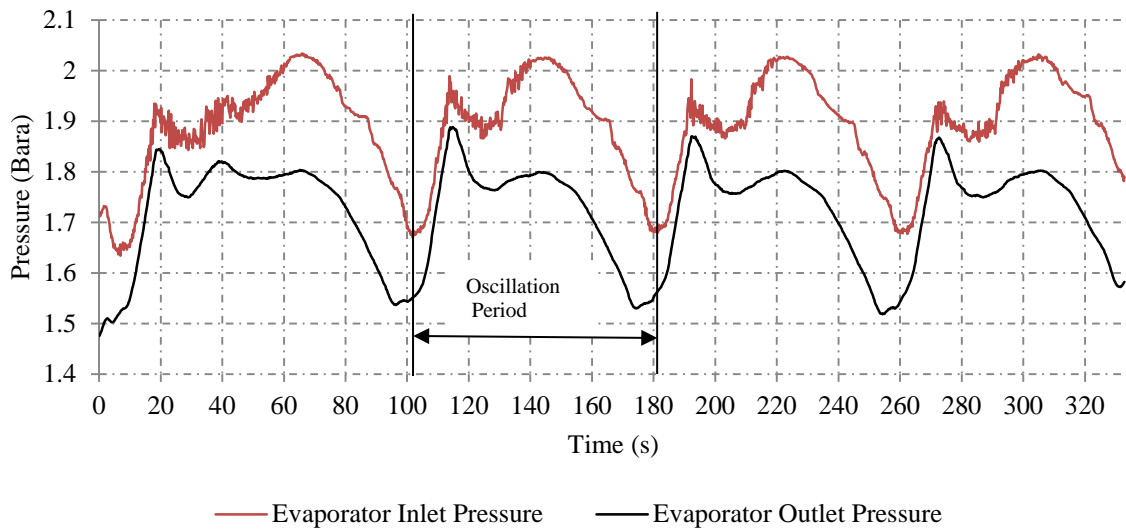


Figure 5: Low Frequency Pressure Oscillations at Pump Driving Frequency of 14 Hz

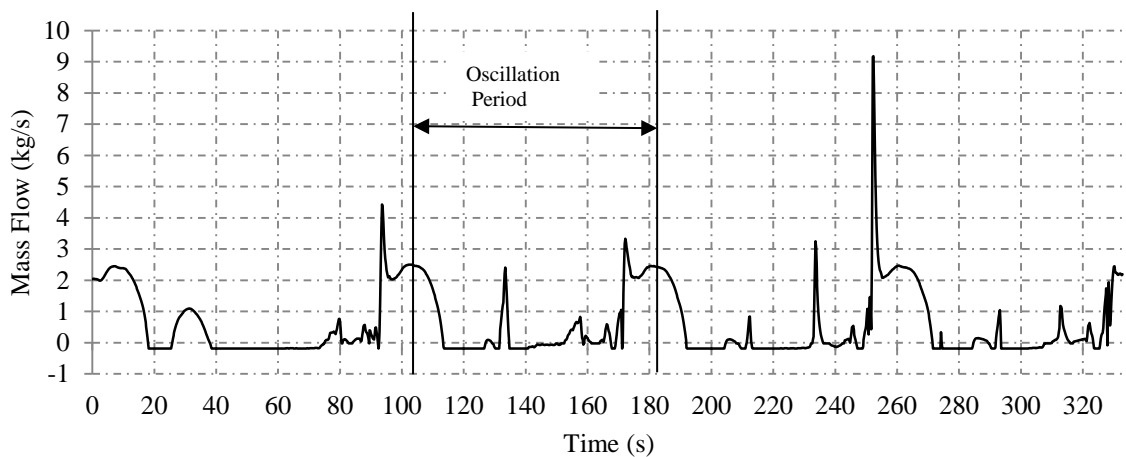


Figure 6: Low Frequency Mass Flow Oscillations at Pump Driving Frequency of 14 Hz

At low pump frequencies the pressure and mass flow oscillations resemble those depicted in Figure 5 and Figure 6. The oscillatory period ranges from 102 to 81 seconds. The period decreases with increasing pump frequency. The oscillations are characterized by a long flow stall and reversal period followed by a sudden surge in liquid flow. It is believed the lengthy flow stall/reversal period is caused by the residual liquid vaporizing within the evaporator. High frequency oscillations with periods shorter than the sampling frequency appear in the evaporator inlet pressure after the onset of flow reversal. These may be a product of pump cavitation induced by recirculating flow at the pump outlet.

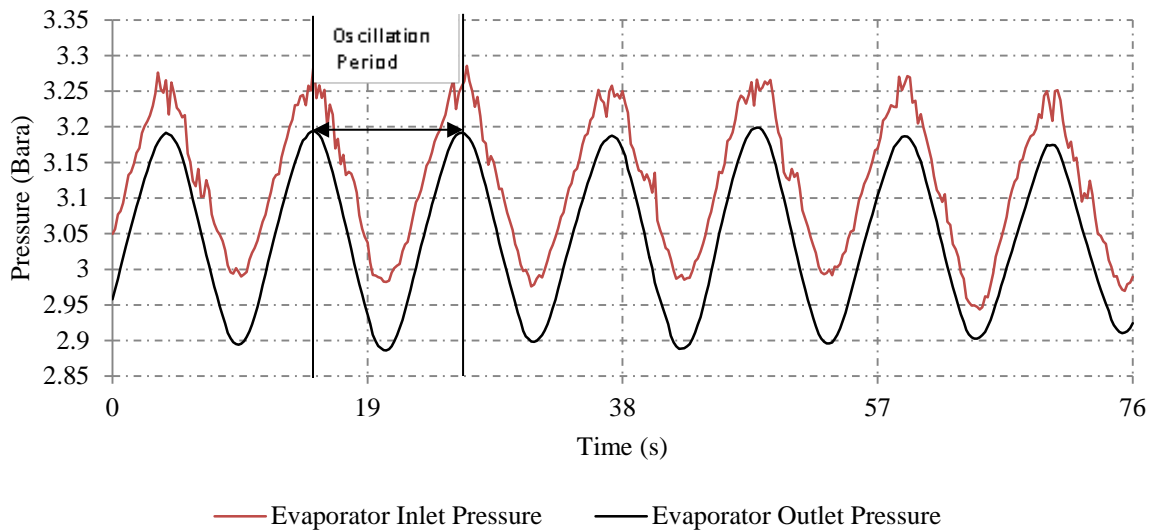


Figure 7: High Frequency Pressure Oscillations at Pump Driving Frequency of 25 Hz

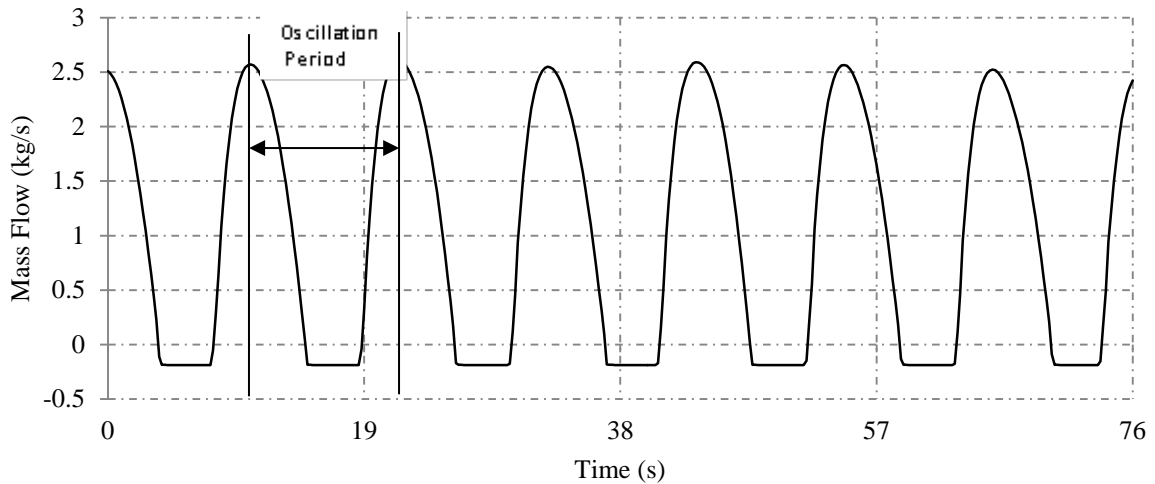


Figure 8: High Frequency Mass Flow Oscillations at Pump Driving Frequency of 25 Hz

As the pump driving frequency is increased further, a transition occurs from the low frequency pattern (Figure 5 and Figure 6) to a high frequency pattern shown in Figure 7 and Figure 8. The period of this high frequency oscillation ranged from 17 to 9 seconds. As before the oscillation period decreased with increasing pump driving frequency. These oscillations are characterized by a shorter mass flow stall/reversal period (~5 seconds vs ~70 seconds.) The shape of the pressure and mass flow oscillation is significantly more regular with a sinusoidal quality. Additionally the amplitude of the pressure and mass flow oscillations increased with increasing pump drive frequency.

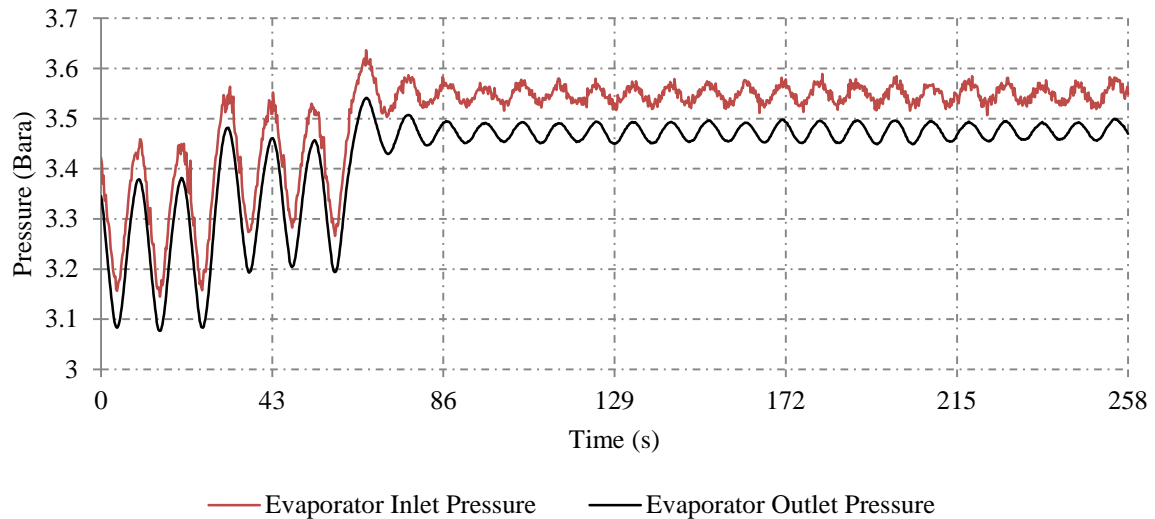


Figure 9: Pressure Oscillation Stabilization at Pump Driving Frequency of 27 Hz

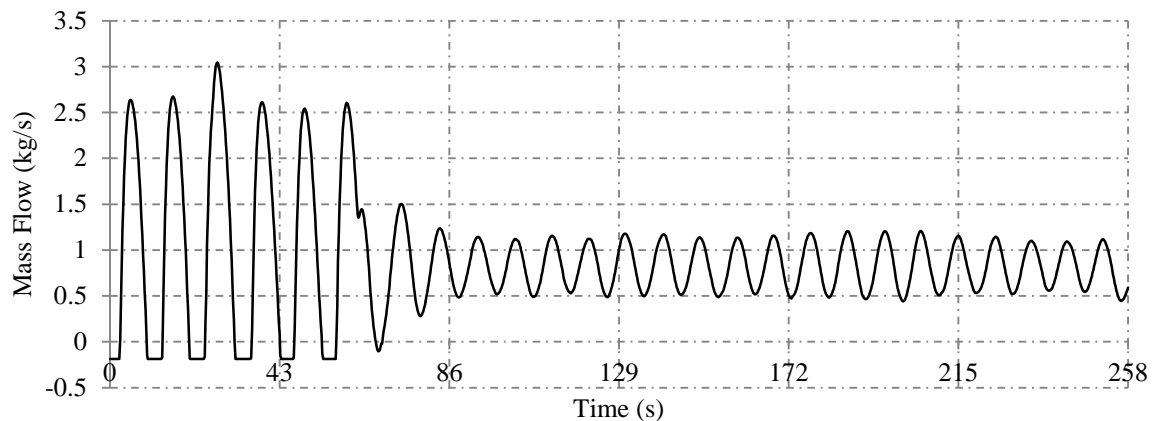


Figure 10: Flow Oscillation Stabilization at Pump Driving Frequency of 27 Hz

Figure 9 and Figure 10 show the pressure/mass flow oscillations stabilizing at high pump frequency. The flow stall/reversal pattern is no longer present. The large swings in flow and pressure stabilize to relatively smaller fluctuations. This stabilization may occur as the internal characteristic of the evaporator completes the transition from curve A to B in Figure 1, or it may be a result of the pump's external characteristic curve being sufficiently large to prevent flow stall/reversal.

The oscillatory patterns were very similar at the two source temperature and mass flow conditions. Increasing the source temperature and mass flow had the effect of increasing the stabilization frequency. Additionally the oscillation amplitude was greater for the higher temperature operation. It is believed this is due to increased pumping power at higher frequencies. This is in agreement with field observations which show the phenomena was more severe for higher temperature applications (e.g. those involving high temperature steam and exhaust gas.)

All the preceding data was collected for evaporator exit superheats on the order of 30°C. It was observed for superheat values less than ~10°C oscillations were not present. This may indicate a compressible volume is necessary for large amplitude oscillations to occur.

Based on the observations described above, it is believed evaporators with lower pressure loss (i.e. shell and tube) may be less prone to this type of instability. These types of evaporator are less commonly used in the field due to added cost of refrigerant charge and space limitations.

Additionally the use of a volumetric pump vs. a centrifugal pump may reduce or eliminate the oscillatory phenomena due to the steep external characteristic. In fact this type of pump is recommended in literature to avoid a Ledinegg type instability.

3. CONTROL AND DETECTION STRATEGIES

As seen in the previous section, the system stabilizes once the working fluid pump has reached a sufficiently large speed. Thus the simplest means to reduce pressure and flow oscillations is to ramp the pump speed quickly through the unstable operating conditions. Figure 11 shows the operation of a constant ramp pump signal and its primary control value, superheat.

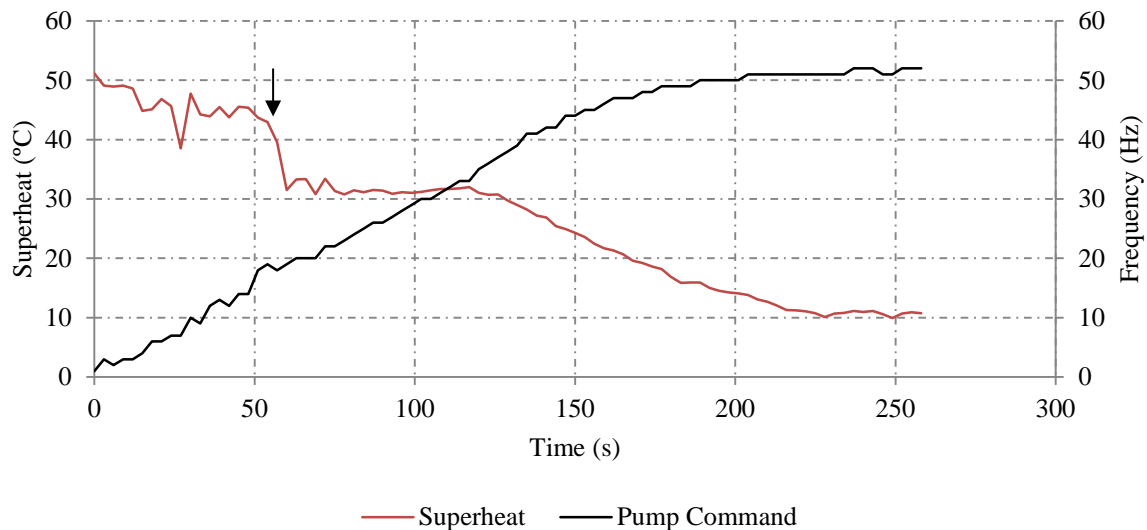


Figure 11: Fast Ramp through Unstable Region

There is a large drop in the superheat from approximately 45°C to 30°C at the 60 second mark (see arrow.) This is the result of a Ledinegg type flow excursion which occurs as the evaporator transitions from a primarily vapor to primarily liquid internal characteristic. During testing this excursion is accompanied by a "honking" noise and rush of fluid. The cause of this noise is not well understood. After the flow excursion, the superheat value is very stable and follows closely with the pump signal.

Detection of the onset of flow/pressure oscillations is accomplished by calculating the rate of change of the effected process value(s) as in Equation (2) below:

$$\frac{|X_n - X_{n-1}|}{\Delta t} \geq \alpha \quad (2)$$

where X is the process value of interest (e.g. superheat, pressure, or flow), the subscript "n" and "n-1" indicate the most recent sample and previous sample respectively, Δt is the sampling time, and α is a threshold value. When the rate of change of the process value exceeds the threshold value, flow/pressure oscillations are present. From field testing a threshold value may be derived which allows accurate detection of the oscillatory phenomena.

It should be noted, Equation (2) is prone to false detection due to signal noise. Noise filtering would require higher sampling frequency than the existing platform (PLC) allows. Inclusion of more historical terms in the equation will cause additional unacceptable delays due to slow sampling frequency. Therefore a more pragmatic approach has been devised to deal with the phenomena. After detection, the controller takes action to reduce the effects of the oscillatory phenomena. These actions

may result in an operating state which is not optimal for the desired system power output. Thereafter the system gradually migrates to the normal operating state. In this way even a false positive may be accommodated without causing the system to respond erratically or shutdown.

The control strategy present above has been successfully implemented in multiple field installations. Advanced control strategies require a more complete understanding of the underlying mechanism for the oscillatory phenomena and design factors which influence it (e.g. choice of evaporator, piping system design, etc.) This is the subject of future research projects.

4. CONCLUSION

In this paper an important source of instability in Organic Rankine Cycles is described, namely oscillatory pressure and mass flow within the evaporator. The underlying physical phenomena that lead to the oscillatory behavior have been discussed in detail. Experimental results show clear evident of the phenomena together with characteristics of such behavior. The paper goes on to outline the principles for detecting the oscillatory phenomena in operation. This sets the cornerstone for developing controls to mitigate or reduce this phenomena resulting in more stable and longer life operation.

REFERENCES

Ledinegg, M., 1938, "Instability of flow during natural and forced circulation", *Die Wärme*, Vol.61, No.8: P.891-898

Moore, F.K., Greitzer, E.M., 1986 "A Theory of Post-Stall Transients in Axial Compression Systems: Part I-Development of Equations, *J. Eng Gas Turbines Power*, 108: P.68-76

Hawkins, L., Zhu, L., Blumber, E., Mirmobin, P., and Erdlac Jr., R., 2012, Heat-To-Electricity with High-Speed Magnetic Bearing/Generator System, *GRC 2012 Annual Meeting*, Reno, NV.

Stenning, A.H., 1964, "Instabilities in the flow of a boiling liquid" *J. Basic Eng. Trans. ASME*, Ser. D.86: P.213-228

UNSTEADY RANS SIMULATION OF THE OFF-DESIGN OPERATION OF A HIGH EXPANSION RATIO ORC TURBINE

Enrico Rinaldi¹, Rene Pecnik^{1*}, Piero Colonna²

¹ Delft University of Technology, Process & Energy Department,
Delft, The Netherlands
e.rinaldi@tudelft.nl, r.pecnik@tudelft.nl

² Delft University of Technology, Propulsion and Power,
Delft, The Netherlands
p.colonna@tudelft.nl

* Corresponding Author

ABSTRACT

The design of Organic Rankine cycle (ORC) turbines is a challenging task due to the complex thermodynamic behaviour of the working fluid, the typical high expansion ratio which leads to a highly supersonic flow, and the continuous shift of operation between on- and off-design conditions. Computational fluid dynamic (CFD) simulations provide useful insights on the turbine flow field which help the analysis, design, and optimization process. Steady state CFD computations are becoming nowadays common practice in the design of ORC turbines. However, the inherent unsteadiness of the problem requires time resolved simulations to capture a number of phenomena otherwise ignored, e.g., shock/shock and shock/boundary layer interactions, which are expected to dominate the flow evolution. This paper presents a numerical investigation of the off-design operation of a single stage high expansion ratio (>100) ORC radial turbine. Two-dimensional unsteady Reynolds-averaged Navier-Stokes simulations are presented to highlight the main flow characteristics and to study the stator/rotor interaction in terms of time dependent turbine performance parameters and blade loads. An in-house flow solver was used, which accounts for the non-ideal behaviour of the fluid via look-up tables generated using a multiparameter equation of state model. The documented analysis shows unique insights on the unsteady flow field in a supersonic ORC turbine and represents the first step toward a new component design approach based on non-stationary flow characteristics.

1. INTRODUCTION

Organic Rankine cycle (ORC) turbogenerators are a widely pursued technology for the conversion of external heat sources in the low power range (from few kW_e to few MW_e), such as waste heat from industrial processes or solar radiation. The working principles of an ORC are the same as for a steam Rankine cycle, the only difference being the use of an organic fluid which permits to have moderate cycle maximum pressures, allows for a dry turbine expansion and can be used as a lubricant. It also represents an additional degree of freedom to the designer which can be used to best match the external heat source, therefore making the ORC power system extremely flexible. More details on ORC turbogenerators are given by Colonna et al. (2015).

In terms of turbine design, the use of an organic compound leads to small enthalpy drops and to few stages and low rotational speed machines as a consequence. In the low power range, ORC turbines can reach much higher efficiencies if compared to steam turbines. However, the design

of efficient ORC expanders is a challenging task due to the strongly non-ideal thermophysical behaviour of the fluid, especially in the first stages. In fact, the turbine expansion usually occurs in the fluid dense gas region, whereby the ideal gas law does not hold and real gas effects dominate. Moreover, the typically low speed of sound for an organic fluid often results in supersonic flow conditions for high turbine expansion ratios.

Recently, the use of computational fluid dynamics (CFD) in the design of this non-conventional turbomachinery has gained momentum, as the work of Harinck et al. (2013) and Pasquale et al. (2013) demonstrates showing significant performance improvement of an existing ORC turbine by automated shape optimization of the stator vanes based on steady state CFD computations. Simplified models, as quasi-1D or throughflow calculations, are also common practice and can provide an optimal choice of the main design parameters in the first stages of a machine development, see for example the work of Pini et al. (2013) and Casati et al. (2014).

However, rotating machines present an inherent unsteadiness which becomes more prominent in case of transonic/supersonic flow regimes, as it is the case for ORC turbines. This makes time resolved CFD simulations crucial to represent and study unsteady phenomena otherwise ignored, e.g., shock/shock, shock wave/boundary layer and wake/boundary layer interactions, which affect the turbine operation and performance. Extensive studies were conducted in the past on standard steam and gas turbines. The blades boundary layer evolution and transition under external disturbances was studied by Schulte and Hodson (1998), and the effect on the blade heat load distribution and cooling was analyzed by Michelassi et al. (1999); Teng et al. (2000); Didier et al. (2002). Unsteady blade forces were investigated by Mailach et al. (2004); Rodriguez et al. (2007); Hushmandi et al. (2011). Finally, efficiency increase by vanes clocking in multistage machines was considered by Huber et al. (1996); Griffin et al. (1996); Hummel (2002); Mailach and Vogeler (2004); Schennach et al. (2008).

This paper presents a numerical investigation of the stator/rotor interaction in an ORC high expansion ratio (>100), single stage radial turbine by means of quasi-3D unsteady RANS simulations. Shock/shock and shock/boundary layer interactions are described, and their effect on the blade loads highlighted. An in-house CFD solver is coupled to state-of-the-art thermo-physical models to have the highest possible accuracy in the fluid property evaluation. The present work demonstrates the importance of using unsteady simulations to study and design supersonic ORC turbines and provides unique insights on their fluid dynamic operation.

The paper is structured as follows. Sec. 2 presents the turbine geometry and computational grid. The CFD code is briefly described in Sec. 3. Time-averaged pressure distributions on the stator and rotor blades are analyzed in Sec. 4. Sec. 5 presents the time evolution of the turbine flow field and describes unsteady shock/shock and shock/boundary layer interactions. Time dependent rotor blade loads are discussed in Sec. 6. Sec. 7 summarizes the conclusions.

2. TURBINE GEOMETRY

The preliminary design of a single stage, radial inlet turbine operating in a commercial ORC unit is considered in this study. The turbine is made of 18 stator blades and 47 rotor blades. In order to exploit the machine periodicity and to perform CFD simulations on a reduced computational domain, the number of rotor blades was reduced to 45 in the numerical model, so that $\Delta\theta = 40$ deg only could be modeled. The numerical domain therefore contains 2 stator blades and 5 rotor blades. Figure 1 depicts the real machine and the modeled geometry. The latter was obtained extracting a 2D plane at half the channel height and placing one cell only along the direction perpendicular to the plane. However, the real cross-sectional area variation was maintained as a function of the distance from the axis of rotation, therefore defining a so-called quasi-3D mesh which allows the fluid to expand in a similar manner as it would do in the real 3D geometry. The mesh counts approximately 200,000 hexahedra, which were

Table 1: Turbine boundary conditions. The subscript 0 indicates total conditions and the subscript r denotes reduced quantities, i.e., normalized by the vapour-liquid critical point value.

$T_{0,in}$	$T_{0r,in}$	$P_{0,in}$	$P_{0r,in}$	P_{out}	ω	Walls
314.5 °C	0.99	31.9 bar	0.77	$\nabla P = 0$	24 krpm	Adiabatic

clustered at the walls to ensure that $y^+ \approx 1$. In order to perform CFD simulations, constant total temperature and pressure conditions were set at the inlet of the domain to their design values; a Neumann boundary condition was applied at the supersonic outlet. The stator/rotor sliding interface was treated using a flux-conserving scheme. The solid walls were considered adiabatic. The rotational speed only was set to an off-design value, $\omega = 24,000$ rpm, which is about 8% lower than the design rotational speed, $\omega = 26,000$ rpm. Table 1 summarizes the boundary conditions used for the CFD analysis.

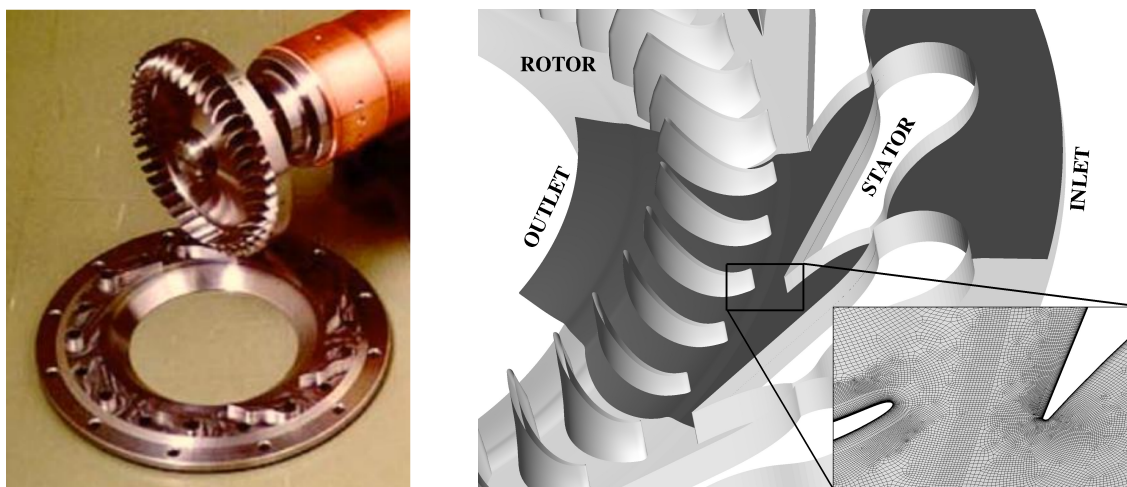


Figure 1: Turbine real geometry (left) and computational domain (right).

3. DENSE GAS CFD SOLVER

A Reynolds-averaged Navier–Stokes solver based on a finite volume formulation on unstructured grids was used. A thorough description of the numerical methods implemented is given by Pecnik et al. (2012b). The one equation turbulence model of Spalart and Allmaras (1994) models the Reynolds stresses. The numerical fluxes and Jacobians are formulated for a general equation of state as described by Rinaldi et al. (2014a). The code was previously validated for applications relevant for this study, see Pecnik et al. (2012a, 2013); Rinaldi et al. (2014b, 2015). Implicit time integration (BDF2) was used to perform the unsteady simulations with a fixed time step chosen such that a period was discretized in 100,000 steps, which lead to a maximum Courant number $CFL \approx 1.5$.

Due to the proximity of the working fluid (Toluene) inlet conditions to its vapour-liquid critical point, the ideal gas model is not applicable. A state-of-the-art multiparameter equation of state model is used instead to model the thermophysical fluid behaviour. Detailed descriptions of the models adopted for thermodynamic and transport properties are given by Olchoway and Sengers (1989); Polt et al. (1992); Lemmon and Span (2006); Santos et al. (2006); Assael et al. (2012). In order to reduce the computational cost of the fluid property evaluation during the CFD simulation, a look-up table built on the above mentioned models is used. A comprehensive analysis of the method is presented by Rinaldi et al. (2014a). The accuracy of the interpolation

on the tabulated thermodynamic area used in this study was verified in a pre-run step. Average and maximum relative errors of the order of 10^{-6} and 10^{-4} , respectively, were calculated for the properties used by the CFD code on a 400×400 nodes table which covers the range $\rho_r = [0.005, 145]$ kg/m^3 and $T = [310, 690]$ K, otherwise expressed in reduced values as $\rho = [1.8 \times 10^{-5}, 0.52]$ and $T_r = [0.52, 1.17]$.

4. TIME-AVERAGED RESULTS

The time-averaged pressure profile along the rotor and stator blades is reported in Fig. 2, together with the maximum and minimum values envelope. The rotor blade profile shows large deviations along the whole blade length as a consequence of the highly unsteady flow evolution in the rotor vanes. On the other hand, the pressure profile in the supersonic part of the stator vane shows no time deviations on Side 1, where the fluid is continuously expanded until the trailing edge of the blade. Small pressure bumps indicate local weak oblique shocks which are a consequence of the thickening of the boundary layer, which changes the wall curvature seen by the flow, and of a possibly low level of smoothness of the surface. Indeed, local differences of the curvature of the surface with respect to the design shape, which was obtained by the method of characteristics, result in compression waves which coalesce into shocks, which can be more clearly observed in Fig. 3. On the opposite side, a similar profile is observed until a shock wave recompresses the fluid at a radial distance from the axis of rotation of about $r \approx 0.123$. At this location, the envelop indicates that the shock impingement position is not fixed but fluctuates. The reason for this oscillations will be highlighted in Sec. 5, where the time evolution of the flow field is described.

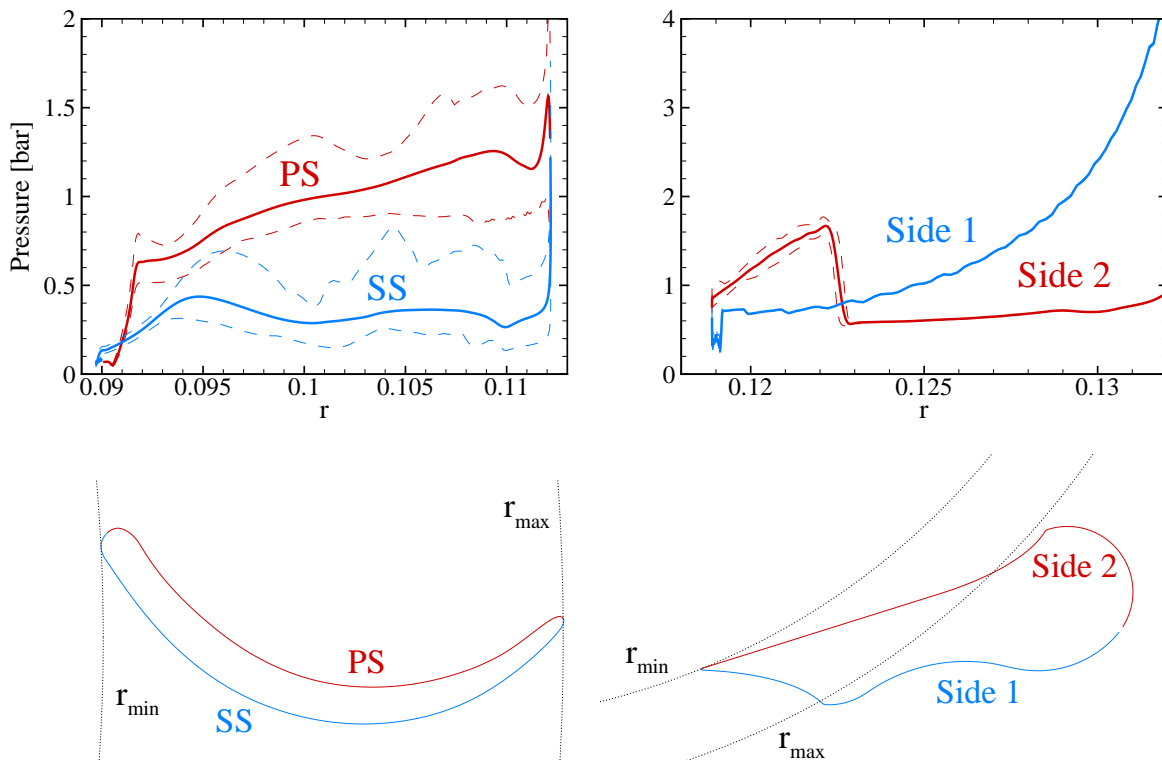


Figure 2: Time-averaged (solid lines), maximum and minimum values (dashed lines) of pressure on the rotor (left) and stator (right) blades. Quantities are functions of the radial distance r from the axis of rotation. LE and TE denote the blade leading edge and trailing edge, respectively.

5. UNSTEADY FLOW EVOLUTION

The evolution of the flow field over a rotor blade passage is studied in this section. Due to the periodicity of the turbine geometry, hereafter we will focus on the passage of one rotor blade, namely blade 0, over one stator vane only. In terms of normalized time $\tau = t/T$, where t denotes the physical time and $T = \Delta\theta/\omega$, this means that the analysis is limited to $\tau = [0, 0.5]$.

Figure 3 displays the pressure gradient magnitude field, by which the strong recompressions induced by the shock waves are easily identifiable. The main flow features are highlighted at $\tau = 0$. The flow is accelerated to sonic conditions in the stator vane throat (TH) and subsequently expands to supersonic conditions in the diverging part of the vane, up to $M \approx 2.8$. Two strong oblique shock waves (ST1 and ST2) are originated from the stator blade trailing edge and recompress the fluid. ST1 directly propagates in the rotor, while ST2 first hits the stator blade wall and then is reflected (R) downstream in the rotor. The rotor flow field shows steady bow shocks (BS) in front of the blunt rotor blades leading edge due to supersonic conditions in the relative frame of reference. BS shocks can be avoided operating the machine at higher rotational speeds. Oblique shock waves (OS) are located on the suction side of the blades and are responsible for large flow separations, largely contributing to the turbine losses, see Fig. 4. Similarly to the stator blade trailing edge, two oblique shocks stem from the rotor blades trailing edge (RT1 and RT2).

At $\tau = 0$, the shock R penetrates the bow shock in front of blade 0 and the oblique shock on the suction side, eventually impinging on the suction side itself in the subsequent time steps. Between $\tau = 2/12$ and $\tau = 4/12$ a similar interaction occurs with ST1. As the blade rotates, BS hits the stator wall near the trailing edge. The shock/boundary layer interaction location moves downstream until the pressure perturbation induced by the shock interacts with the shocks ST1 and ST2, determining their oscillation. This mechanism is responsible for the fluctuation of the reflection point of ST2 into R observed in terms of time-averaged pressure profile in Fig. 2.

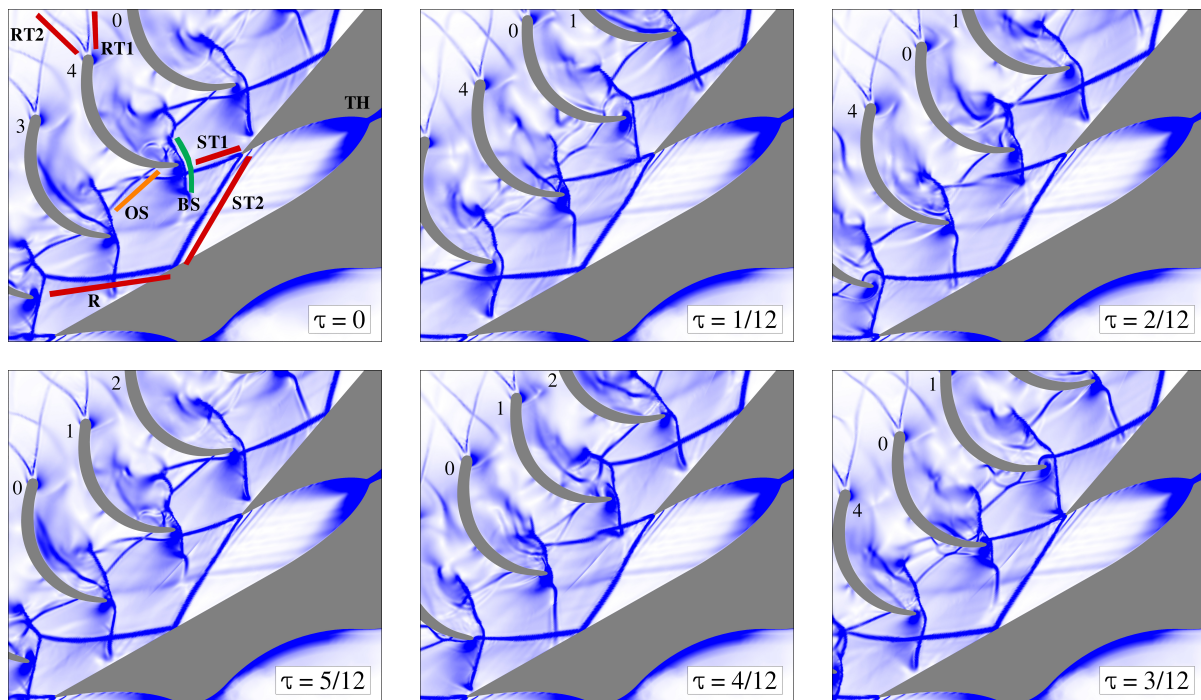


Figure 3: Absolute value of the pressure gradient. The range of values goes from 5 bar/m (white) to 300 bar/m (blue).

The time evolution of the vorticity field is depicted in Fig. 4. A thickening of the boundary layer (black circles, T1 and T2) is observed on the wall of the stator blade and is due to the interaction between the ST2 and BS shocks respectively. As the rotor blades move, T2 follows BS and moves downstream toward the stator blade trailing edge. The wake of the stator blade does not show any vortex shedding, however peaks of vorticity are visible along the wake downstream of the bow shock fronts (dashed lines, SF). The rotor field is dominated by large separation areas (S) on the suction side of the blades, which are induced by the oblique shocks OS depicted in shown in Fig. 3, and which are responsible for most of the losses in the rotor.

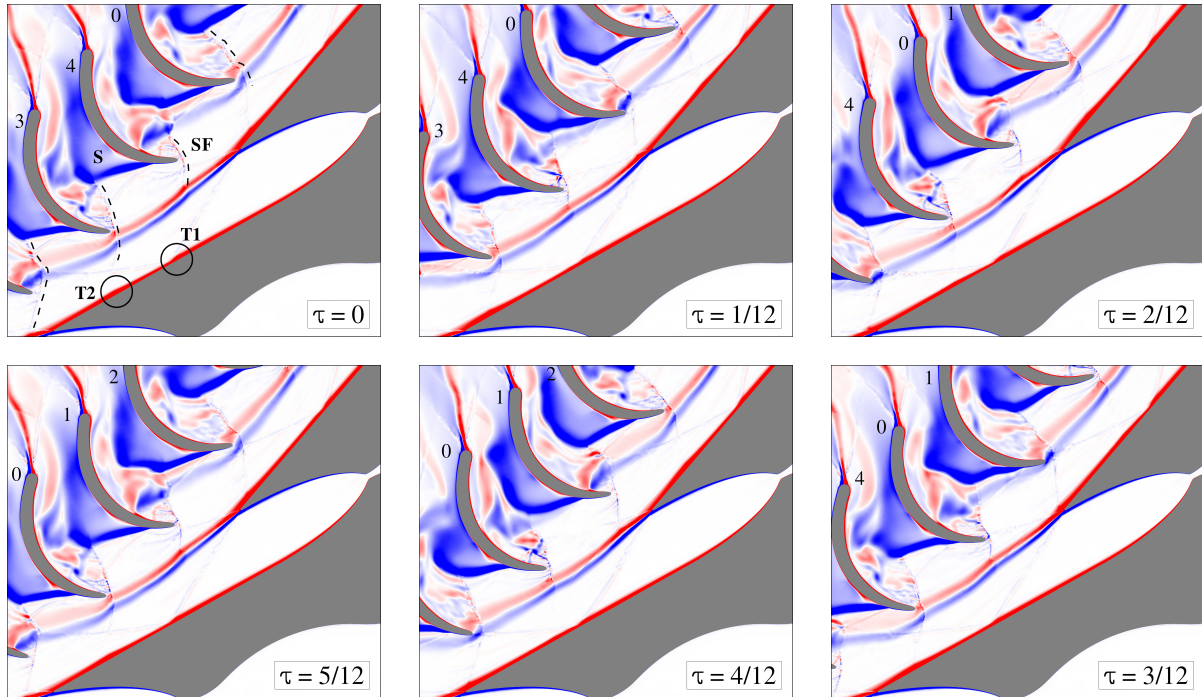


Figure 4: Vorticity field. The range of values goes from -1.5×10^5 1/s (blue) to 1.5×10^5 1/s (red).

6. BLADE LOADS

The rotor blade forces and torque profiles are shown in Fig. 6 for the rotor blade 4 as a function of time over one period. Forces are decomposed on a local frame of reference centered in the center of gravity and aligned with the radial and tangential directions, F_r and F_t respectively, with respect to the center of rotation, see Fig. 5. F_r , F_t and M_z were calculated integrating the pressure over the blade surface. The viscous contribution was neglected since it amounts to $\approx 1\%$ of the pressure's.

Forces and torque profiles show large fluctuations induced by the unsteady shock interactions described in the previous section. The deviation from the time averaged value can be as high as 50% for F_r , 40% for F_t and 90% for M_z .

At $\tau = 0.15$ the tangential component of the force suddenly increases in magnitude due to the detachment of a shock wave from the pressure side of the blade. Therefore, pressure increases along the front part of the pressure side, and as a consequence F_t . This mechanism can be observed in Fig. 3 at $\tau = 2/12$ and $\tau = 2/12$ on the rotor blade 4, and at $\tau = 0$ on blade 3 (the load profiles on the 5 rotor blades only differ by a shift in time by $\tau = 0.2$). A stronger tangential component of the force in the front part of the blade determines a larger (in magnitude) torque, as confirmed by the steep change of M_z at $\tau = 0.15$. The opposite occurs when the tail of the

R shock impinges on the rotor blade suction side at $\tau = 4/12$. Pressure increases locally leading to a drop in the magnitude of F_r and a smaller torque.

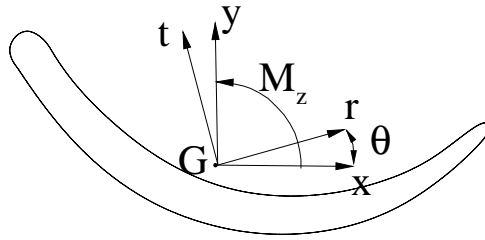


Figure 5: Local frame of reference used to calculate forces and torque on the rotor blades.

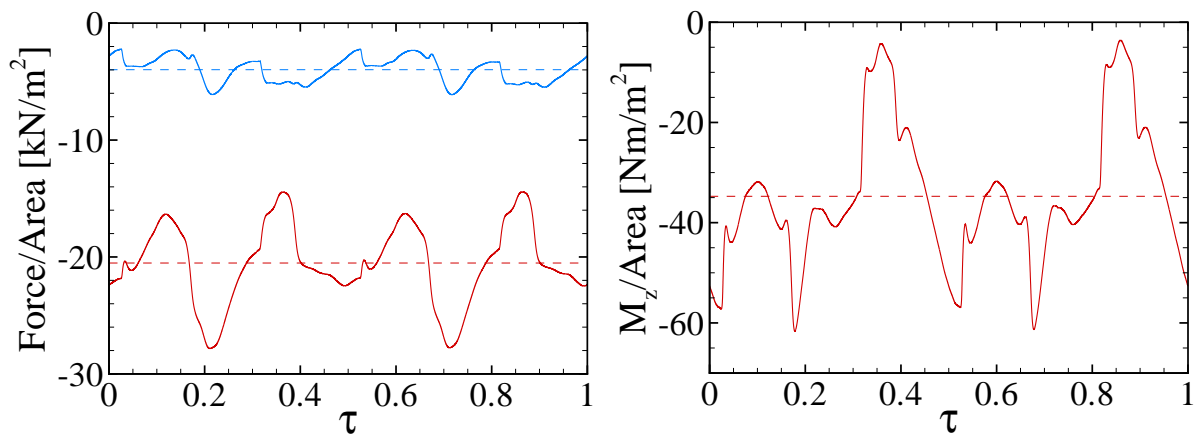


Figure 6: Time evolution of the blade forces and torque. Radial (blue) and tangential (red) components are displayed in the left plot, torque (red) in the right plot. Time-averaged values are also included (dashed lines).

7. CONCLUSIONS

The fluid dynamics of an ORC single stage, high-expansion ratio, radial turbine in off-design conditions was investigated for the first time by means of quasi-3D RANS simulations. An in-house CFD code suited for dense gas flows simulations was used for the study. State-of-the-art thermophysical models were coupled to the CFD code by means of look-up tables, which strongly reduced the computational cost of the fluid property evaluations.

The main interactions between shocks and boundary layers were studied over a time period and identified as the main loss sources the strong trailing edge shocks in the stator, which dynamically interact with the stator blade boundary layer, and the suction side oblique shocks in the rotor, which induce large separation areas. Time-averaged and unsteady rotor blades load profiles were analyzed and showed large forces and torque fluctuations which can be as high as 50% for F_r , 40% for F_t and 90% for M_z . The physical reasons for these sharp load variations were discussed in terms of shock waves interaction with the rotor blades.

The presented study demonstrates the importance of time resolved unsteady CFD simulations

to understand the fluid dynamic operation of supersonic ORC turbines, which are dominated by unsteady flow structures interactions. This investigation highlighted the main loss sources and the fluid dynamic mechanisms responsible for large blade loads fluctuations. This paper represents the first step toward a new ORC turbine design optimization approach based on knowledge and data provided by unsteady CFD simulations.

REFERENCES

- Assael, M. J., Mylona, S. K., Huber, M. L., and Perkins, R. A. (2012). Reference correlation of the thermal conductivity of toluene from the triple point to 1000 K and up to 1000 MPa. *J. Phys. Chem. Ref. Data*, 41(2):023101.
- Casati, E., Vitale, S., Pini, M., Persico, G., and Colonna, P. (2014). Centrifugal turbines for mini-organic Rankine cycle power systems. *J. Eng. Gas Turb. Power*, 136(12):122607.
- Colonna, P., Casati, E., Trapp, C., Mathijssen, T., Larjola, J., Turunen-Saaresti, T., and Uusitalo, A. (2015). Organic Rankine cycle power systems: From the concept to current technology, applications, and an outlook to the future. *Journal of Engineering for Gas Turbines and Power*, 137(10):100801.
- Didier, F., Dénos, R., and Arts, T. (2002). Unsteady rotor heat transfer in a transonic turbine stage. *J. Turbomach.*, 124(4):614–622.
- Griffin, L., Huber, F., and Sharma, O. (1996). Performance improvement through indexing of turbine airfoils: Part 2 - Numerical simulation. *J. Turbomach.*, 118(4):636–642.
- Harinck, J., Pasquale, D., Pecnik, R., van Buijtenen, J., and Colonna, P. (2013). Performance improvement of a radial organic Rankine cycle turbine by means of automated computational fluid dynamic design. *Proc. IMechE, Part A: J. Power and Energy*, 227(6):637–645.
- Huber, F., Johnson, P., Sharma, O., Staubach, J., and Gaddis, S. (1996). Performance improvement through indexing of turbine airfoils: Part 1 - Experimental investigation. *J. Turbomach.*, 118(4):630–635.
- Hummel, F. (2002). Wake-wake interaction and its potential for clocking in a transonic high-pressure turbine. *J. Turbomach.*, 124(1):69–76.
- Hushmandi, N., Fridh, J., and Fransson, T. (2011). Unsteady forces of rotor blades in full and partial admission turbines. *J. Turbomach.*, 133(4).
- Lemmon, E. W. and Span, R. (2006). Short fundamental equations of state for 20 industrial fluids. *J. Chem. Eng. Data*, 51(3):785–850.
- Mailach, R., Müller, L., and Vogeler, K. (2004). Rotor-stator interactions in a four-stage low-speed axial compressor - Part II: Unsteady aerodynamic forces of rotor and stator blades. *J. Turbomach.*, 126(4):519–526.
- Mailach, R. and Vogeler, K. (2004). Rotor-stator interactions in a four-stage low-speed axial compressor - Part I: Unsteady profile pressures and the effect of clocking. *J. Turbomach.*, 126(4):507–518.
- Michelassi, V., Martelli, F., Dénos, R., Arts, T., and Sieverding, C. (1999). Unsteady heat transfer in stator-rotor interaction by two-equation turbulence model. *J. Turbomach.*, 121(3):436–447.

- Olchoway, G. A. and Sengers, J. V. (1989). A simplified representation for the thermal conductivity of fluids in the critical region. *Int. J. Thermophys.*, 10(2):417–426.
- Pasquale, D., Ghidoni, A., and Rebay, S. (2013). Shape optimization of an organic Rankine cycle radial turbine nozzle. *J. Eng. Gas Turb. Power*, 135(4):042308.
- Pecnik, R., Rinaldi, E., and Colonna, P. (2012a). Computational fluid dynamics of a radial compressor operating with supercritical CO₂. *J. Eng. Gas Turb. Power*, 134(12):122301.
- Pecnik, R., Terrapon, V. E., Ham, F., Iaccarino, G., and Pitsch, H. (2012b). Reynolds-averaged Navier-Stokes simulations of the HyShot II scramjet. *AIAA J.*, 50(8):1717–1732.
- Pecnik, R., Witteveen, J. A. S., and Iaccarino, G. (2013). Assessment of uncertainties in modeling of laminar to turbulent transition for transonic flows. *Flow Turbulence Combust.*, 91:41–61.
- Pini, M., Persico, G., Casati, E., and Dossena, V. (2013). Preliminary design of a centrifugal turbine for organic Rankine cycle applications. *J. Eng. Gas Turb. Power*, 135(4):042312.
- Polt, A., Platzer, B., and Maurer, G. (1992). Parameter der thermischen Zustandsgleichung von Bänder fuer 14 mehratomige reine Stoffe. *Chem. Tech.(Leipzig)*, 44(6):216–224.
- Rinaldi, E., Pecnik, R., and Colonna, P. (2014a). Exact Jacobians for implicit Navier–Stokes simulations of equilibrium real gas flows. *J. Comput. Phys.*, 270:459–477.
- Rinaldi, E., Pecnik, R., and Colonna, P. (2015). Computational fluid dynamic simulation of a supercritical CO₂ compressor performance map. *J. Eng. Gas Turb. Power*, 137(7):072602.
- Rinaldi, E., Suarez Raspopov, R., Colonna, P., and Pecnik, R. (2014b). Modeling curvature effects on turbulence transition for turbomachinery flows. In *Proceedings of the ASME Turbo Expo*, pages 1–11.
- Rodriguez, C., Egusquiza, E., and Santos, I. (2007). Frequencies in the vibration induced by the rotor stator interaction in a centrifugal pump turbine. *J. Fluid. Eng.-T. ASME*, 129(11):1428–1435.
- Santos, F. J. V., Nieto De Castro, C. A., Dymond, J. H., Dalaouti, N. K., Assael, M. J., and Nagashima, A. (2006). Standard reference data for the viscosity of toluene. *J. Phys. Chem. Ref. Data*, 35(1):1–8.
- Schennach, O., Pecnik, R., Paradiso, B., Göttlich, E., Marn, A., and Woisetschlager, J. (2008). The effect of vane clocking on the unsteady flow field in a one-and-a-half stage transonic turbine. *J. Turbomach.*, 130(3):031022.
- Schulte, V. and Hodson, H. (1998). Unsteady wake-induced boundary layer transition in high lift LP turbines. *J. Turbomach.*, 120(1):28–35.
- Spalart, P. R. and Allmaras, S. R. (1994). One-equation turbulence model for aerodynamic flows. *Rech. Aerospatiale*, (1):5–21.
- Teng, S., Sohn, D., and Han, J.-C. (2000). Unsteady wake effect on film temperature and effectiveness distributions for a gas turbine blade. *J. Turbomach.*, 122(2):340–347.

NUMERICAL STUDY OF ORGANIC RANKINE CYCLE RADIAL-INFLOW TURBINES FOR HEAVY-DUTY DIESEL ENGINE COOLANT HEAT RECOVERY

Lei Zhang¹, Weilin Zhuge¹, Yangjun Zhang^{1*}, Jie Peng²

¹State Key Laboratory of Automotive Safety and Energy, Tsinghua University, Beijing, 10084, China

zlei11@mails.tsinghua.edu.cn

zhugewl@tsinghua.edu.cn

yjzhang@tsinghua.edu.cn

²Department of Engineering Mechanics, Tsinghua University, Beijing, 10084, China

peng-jie@tsinghua.edu.cn

* Corresponding Author

ABSTRACT

Low rotating speed radial-inflow turbines are promising for the organic Rankine cycle systems in the small power size applications such as heavy-duty trucks and passenger cars waste heat recovery. Small mass flow rate and low rotating speed will lead to the turbine design specific speed lower than the optimal range of 0.34 to 0.72. Until now, few literatures reported the performance characteristics and loss mechanisms of low specific speed ORC radial-inflow turbines. The present study makes a RANS simulation of the low specific speed of 0.28 radial-inflow turbine using R245fa as working fluid to evaluate its performance characteristics and investigate the loss mechanisms. An optimal specific speed of 0.47 radial-inflow turbine in the same nominal operating condition and working fluid is also simulated for comparative analysis. The CFD results indicate that the low specific speed turbine nominal efficiency decreases 1.7% compared with the optimal one. And furthermore the off-design efficiency decreases are in the range of 2.6% to 0.6% from low to high pressure ratio conditions. The effect of specific speed on the efficiency characteristics mainly lies on rotor tip clearance and passage losses. The low specific speed turbine shows larger tip clearance losses but smaller passage losses compared with the optimal specific speed turbine. Flow field analysis of rotor entropy generation indicates that for the low specific speed turbine, the entropy generation caused by the tip clearance flow is much larger, and the tip clearance loss is mainly located on the suction surface in the inducer to midchord region, but on the pressure surface in the exducer region.

1. INTRODUCTION

More and more attention is being paid by the automobile research institutes and manufacturers to the organic Rankine cycle (ORC) power system, which can significantly improve the internal combustion engine efficiency by recovering the waste heat like exhaust gas and coolant. The use of organic fluids instead of water makes the power system suitable for low (below 230 °C) to middle (230-650 °C) temperature waste heat recovery. Furthermore, single stage expanders can satisfy the pressure ratio demand for most applications, and there exists no need of superheating and no risk of blades erosion when dry or isentropic type organic fluids are used (Tchanche *et al.*, 2011).

Radial-inflow turbines have been widely researched in the power size from 50 to 5000kW in the ORC system. However, when the power size is below 50kW or even 10kW with applications in the range of heavy-duty trucks to passenger cars it is not considered as a potential expander type compared with scroll expanders (Quoilin *et al.*, 2013). The high design rotating speed to satisfy the optimal specific speed of radial-inflow turbines is the main reason. Low specific speed radial-inflow turbines can be competitive in the small power size applications.

Specific speed, which is used extensively in studies of radial-inflow turbines, is a correlation between design features and efficiencies. **Figure 1** is the classic chart of the relationship between radial-inflow turbine specific speeds and losses documented by Rohlik (1968) based on various loss models. The results showed peak total-to-static efficiency of 87% close to dimensionless specific speed around 0.6, with efficiencies diminishing at lower and higher specific speed. The chart showed that the efficiency would drop to 80% when the specific speed was 0.3, and the efficiency would further drop to 70% when the specific speed was 0.15. The experimental research by Kofskey and Nusbaum (1972) also showed that a maximum peak total-to-static efficiency of 89% could be obtained at the specific speed of about 0.51. The efficiencies would be above 80% within the specific speed range of 0.34 to 0.72. There was a rapid decrease in efficiencies at both ends of the specific speed curve.

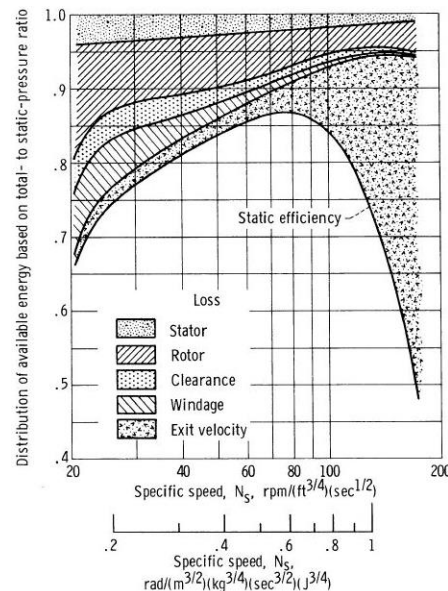


Figure 1: Prediction of radial-inflow turbine loss breakdown (Rohlik, 1968)

Numerical analysis of ORC turbine performance characteristics and loss mechanisms just starts in the recent five years. The mainly researched turbines still follow the basic principle, which is to select the design rotating speed to make the specific speed within the optimum range of 0.34 to 0.72. Li *et al.* (2011) studied a 3.8kW partial admission radial turbine with R11 as working fluid. The design specific speed was about 0.41, and the efficiency can only reach 62.5%. The authors depict the effects of partial admission on the flow field in the rotor passage. Some losses arise because of the mixing of high and low momentum fluid, interaction of some vortexes and vortexes dissipation. Cho *et al.* (2014) designed a partial admission impulse radial turbo-expander for 30kW application with specific speed of 0.39, and simulated the performance characteristics in two power size, 30kW and 3kW. The authors showed the results of optimal rotating speed and nozzles numbers under different inlet total temperatures. As for the turbine efficiency, it was shown that the partial admission rate had great influence, the value of which dropped from 77% to 62% in 30kW, and from 52% to 39% in 3kW as the partial admission rate decreased. Sauret and Gu (2014) studied a 400kW radial-inflow turbine with R143a as working fluid. The specific speed was 0.60, and the nominal total-to-static efficiency was 83.5%. And also large amount of off-design conditions were simulated to analyze its performance characteristics. The results showed that efficiencies would drop 10-20% when the rotating speed increased or decreased by 20%. Zhang *et al.* (2014) simulated a 10kW radial-inflow turbine with R123 as working fluid to discuss the real gas effects in the nozzle and rotor. The design specific speed was 0.58, and the nominal total-to-static efficiency was 83.5%. The authors mainly focused on the property differences between real and perfect gas model simulation results, thus the discussion about performance characteristics did not mentioned. Wheeler and Ong (2014) analyzed a 155kW shrouded radial-inflow turbine with pentane as working fluid. The design specific speed was 0.34, and the reported total-to-static efficiency was 85.8% without taking tip clearance loss into account. The authors demonstrated that as the Mach number in the nozzle outlet reached near 1.4, using the

constant height inducer would lead to relative flow acceleration and then high peak Mach number in the inducer. Through the inducer shape redesign, 1.3% efficiency improvement was obtained. Since the mainly reported ORC radial-inflow turbines are designed within the optimum specific speed range, there exist few literatures relating to the performance characteristics analysis of low specific speed turbines. In the present work, three-dimensional steady RANS simulations were carried out to study the performance characteristics of 0.28 specific speed ORC radial-inflow turbine for heavy-duty diesel engine coolant heat recovery. Furthermore an optimal specific speed of 0.47 radial turbine is also simulated for comparative analysis. The paper was organized as following, the two specific speed turbines in the same nominal condition were preliminarily designed in section 2. And then, the numerical method and grid independence analysis were described Section 3. Section 4 proceeded with the comparative study of the performance characteristics of the low and optimal specific speed turbines and furthermore the discussion of loss mechanics, followed by the conclusions.

2. PRELIMINARY DESIGN

First of all, dimensionless parameters of specific speed n_s and blade-to-jet speed ratio v are used to determine the rotating speed ω and rotor inlet radius r_4 , which is also the radial-inflow turbine feature size. The definitions of these two parameters are,

$$n_s = \omega \sqrt{Q_6} / (h_{0,sg} - h_6)_{is}^{3/4} \quad (1)$$

$$v = \omega r_4 / \sqrt{2(h_{0,sg} - h_6)_{is}} \quad (2)$$

Besides the specific speed n_s and blade-to-jet speed ratio v , the preliminary design process cannot be completed until some other essential empirical parameters are determined. During the last several decades, the recommended values of these empirical parameters for perfect gas axial and radial turbine design developed a lot on the benefit of aero engine rapid development. Now it is an opportunity for the ORC turbine to rapidly develop on the benefit of organic Rankine cycle technologies promising future. However, as the lack of abundant design cases of the ORC turbine, it is preferred to utilize the recommended empirical values for perfect gas turbines in the ORC radial-inflow turbine preliminary design process. The essential eight empirical parameters and their recommended values are listed in **Table 1**. And the principal geometry parameters and locations of different subscript numbers are illustrated in **Figure 2**.

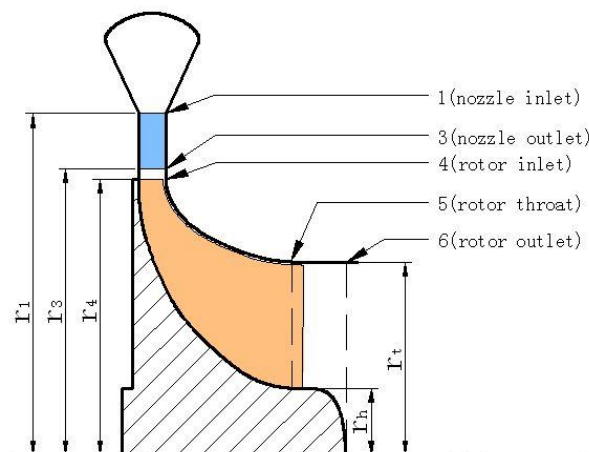


Figure 2: A diagram of radial-inflow turbine principal geometry parameters and locations

As few discussions about nozzle vane number determination, it is set to the number equal to the rotor blade number. Furthermore, the rotor blade numbers are the values calculated based on Glassman method minus three to avoid excessive blockage and high friction losses. The geometry design results of low and optimal specific speed ORC radial-inflow turbines are shown in **Table 2**.

Table 1: Empirical parameters and their recommended values in the preliminary design process

Empirical Parameter	Symbol	Recommended Values
Nozzle vane exit angle	α_{b3}	characterized by specific speed (Rohlik,1968)
Nozzle vane number	Z_n	few recommendations
Nozzle vane radius distance	r_1-r_3	$0.4r_4$ (Concepts NREC, 2014)
Interspace radius distance	r_3-r_4	$2b_3\cos\alpha_3$ (Watanabe <i>et al.</i> , 1971)
Rotor blade exit angle	β_{b6}	-55 (Whitfield, 1990)
Rotor blade number	Z_r	$(\pi/30)(110-\alpha_3)\tan\alpha_3$ (Glassman, 1976)
Rotor exit tip to inlet radius ratio	$r_{6,t}/r_4$	characterized by specific speed (Rohlik,1968)
Rotor exit hub to tip radius ratio	$r_{6,h}/r_{6,t}$	0.35 (Zhang, 2013)

Table 2 : Preliminary design results of low and optimal specific speed ORC turbines

Component	Geometry Parameters	Low Specific Speed Turbine	Optimal Specific Speed Turbine
Dimensionless parameters	Specific speed	0.28	0.47
	Blade-to-jet speed ratio	0.70	0.70
Volute	Throat radius [mm]	129	85
	Throat area [mm ²]	1017	908
Nozzle	Inlet radius [mm]	100	62
	Inlet vane angle [°]	70	67
	Exit radius [mm]	84	52
	Exit vane angle [°]	80	77
	Number of vanes	15	12
Interspace	Exit radius [mm]	82.5	50
Rotor	Rotating speed [rpm]	15,000	25,000
	Inlet blade height [mm]	5	5
	Exit tip radius [mm]	50	35
	Exit hub radius [mm]	18	12
	Exit blade angle[°]	-55	-55
	Number of blades	15	12
	Tip clearance [mm]	0.3	0.3
Predicted performance	Mass flow rate [kg/s]	0.761	0.756
	Power [kW]	10.1	10.3
	Total-to-static efficiency	80.6%	83.0%

3. NUMERICAL METHOD

The steady state simulation of the ORC radial-inflow turbines designed in section 2 were carried out using the commercial CFD code FINE™/Turbo. FINE™/Turbo is a Reynolds-average Navier-Stokes equation solver that is based on the finite volume method, and uses 5 stage explicit Runge-Kutta scheme and multi-block structured meshing strategy (NUMECA, 2014). The turbulence model used in this calculation is the SST $k-\omega$ model.

The treatment of the real gas model for R245fa in this CFD code has been discussed in the former study (Zhang, 2014). Some setting parameters are modified. The Helmholtz energy equation of state (Lemmon and Span, 2006) fitted for organic fluid R245fa is utilized to calculate the gas properties. The available temperature is limited to the range of 273K to 433K, and available pressure is from 0.05MPa to 4.00MPa. The grid number of data tables are increased by 60%, and bicubic interpolation method replaced the bilinear interpolation method. The purpose of all these modifications is to improve accuracy of the datum used for evaluating R245fa properties in the CFD code.

The CFD domain consists of three components: the nozzle ring, the rotor wheel, and the exhaust pipe, shown in **Figure 3**. The domain was meshed using the multi-block structured tool AutoGrid5™. A fine mesh with 1,234,428 number of grid points was generated, which kept y^+ lower than 4 in the nozzle vane surfaces and 2 in the rotor blade surfaces. The distribution of the mesh was 175,263 grid points within the nozzle ring passage, 833,072 grid points within the rotor wheel passage and 226,093 grid points within the exhaust pipe passage. The grid independency study showed that the increase of grid

point number by 100% in each orthogonal grid direction only made a 0.2% difference in the predicted mass flow rate and 0.4% difference in the predicted torque. It indicated that the discretization error was reduced to an acceptable error in the current grid point number.

Total pressure and total temperature with velocity direction after the volute were used as the inlet boundary condition because the CFD domain did not include the volute. The values of inlet boundary conditions were obtained from the one-dimensional calculation results. The averaged static pressure was used as the exit boundary condition. All of the wall boundaries were treated as smooth and adiabatic. Another important consideration is the interface between the rotating and stationary domain. The “Mixing Plane” method using Conservative Coupling by Pitchwise Row scheme was adopted.

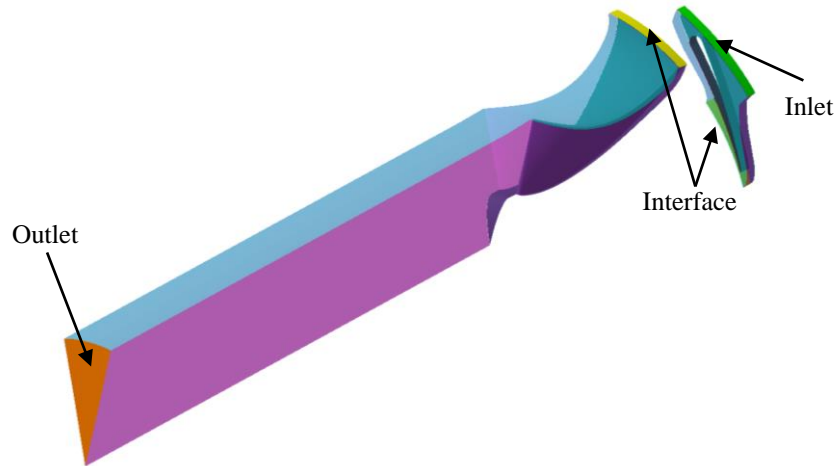


Figure 3: CFD domain of the radial turbine

4. RESULTS AND DISCUSSIONS

In this section, the CFD simulation results are analyzed. Firstly, the performance characteristics of low and optimal specific speed turbines are compared. And then six loss models are used to break down the losses based on the CFD datum to explain the influence of specific speed on efficiency differences. Finally, the flow field comparisons of rotor entropy generation between low and optimal specific speed turbines are carried out to discuss the loss mechanisms.

4.1 Turbine Performance Characteristics

Mass flow rate and efficiency are the two main performance parameters for turbines. In general, the reduced mass flow rate \dot{m}_{rd} and total-to-static isentropic efficiency η_{ts} are used for the radial-inflow turbine performance description. The definitions of these two performance parameters are,

$$\dot{m}_{rd} = \frac{\dot{m} \sqrt{T_{0,sg}}}{p_{0,sg}} \quad (3)$$

$$\eta_{ts} = \frac{P}{\dot{m}(h_{0,sg} - h_{6})_{is}} \quad (4)$$

Figure 4 and **Figure 5** show the performance characteristics of the low and optimal specific speed turbines. Three rotating speed lines besides the design rotating speed line were simulated, the values of which were set to 0.7, 0.85 and 1.15 times of the design rotating speed. The calculated pressure ratios were in the range of 2.0 to 4.5. As is shown in **Figure 4(a)** and **Figure 5(a)**, when the pressure ratio is above 3.0, the turbine is choked. In this pressure ratio range (above 3.0), the reduced mass flow rate only has relationship with the pressure ratio, and it changes a little as the pressure ratio increases. However, in the low pressure ratio range (below 3.0), the mass flow rate has relationship with the pressure ratio and rotating speed, and it changes a lot based on the pressure ratio. The reduced mass flow rate is determined by nozzle throat area. As the throat area is the same for the two

turbines, the difference of choked reduced mass flow rate is within 1% for the low and optimal specific speed turbines.

As for the total-to-static isentropic efficiency shown in **Figure 4(b)** and **Figure 5(b)**, the nominal efficiency of low specific speed turbine is 1.7% lower than that of the optimal specific speed turbine. The off-design operating conditions mainly locate in the envelope line of the efficiency curves. For the low specific speed turbine, the total-to-static efficiencies change in the range of 79.5% to 83.3% when the pressure ratios increase from 2.0 to 4.5. For the optimal specific speed turbine, it is obvious that higher efficiencies can be achieved in the envelope line. The maximum improvement of 2.6% occurred in the condition of pressure ratio equal to 2.0, and the minimum improvement of 0.6% occurred in the condition of pressure ratio equal to 4.0. In addition, for the off-design operating conditions, which are below the efficiency envelope line, the specific speed also has great influence. For the operating conditions, where the rotating speed is high and the pressure ratio is low, the efficiencies of low specific speed turbine is 7-9% lower; for the operating conditions, where the rotating speed is low and the pressure ratio is high, but in contrary the efficiencies of low specific speed turbine is slightly higher. It indicates that the specific speed has great influence on the turbine nominal and off-design efficiencies, especially on the operating conditions that pressure ratio is lower than the design value.

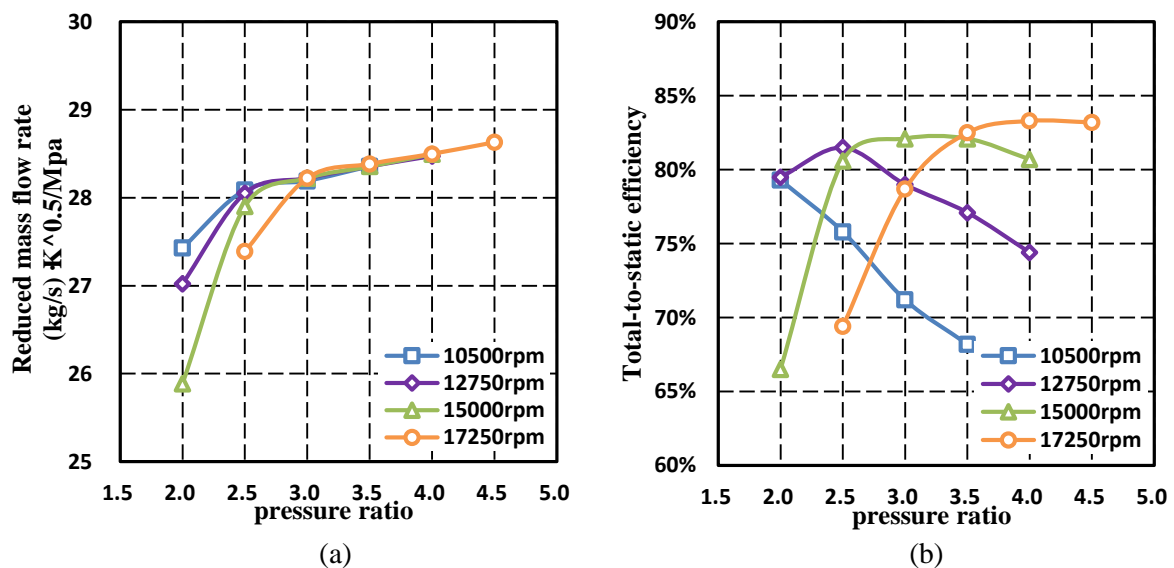


Figure 4: Performance characteristics of the low specific speed turbine

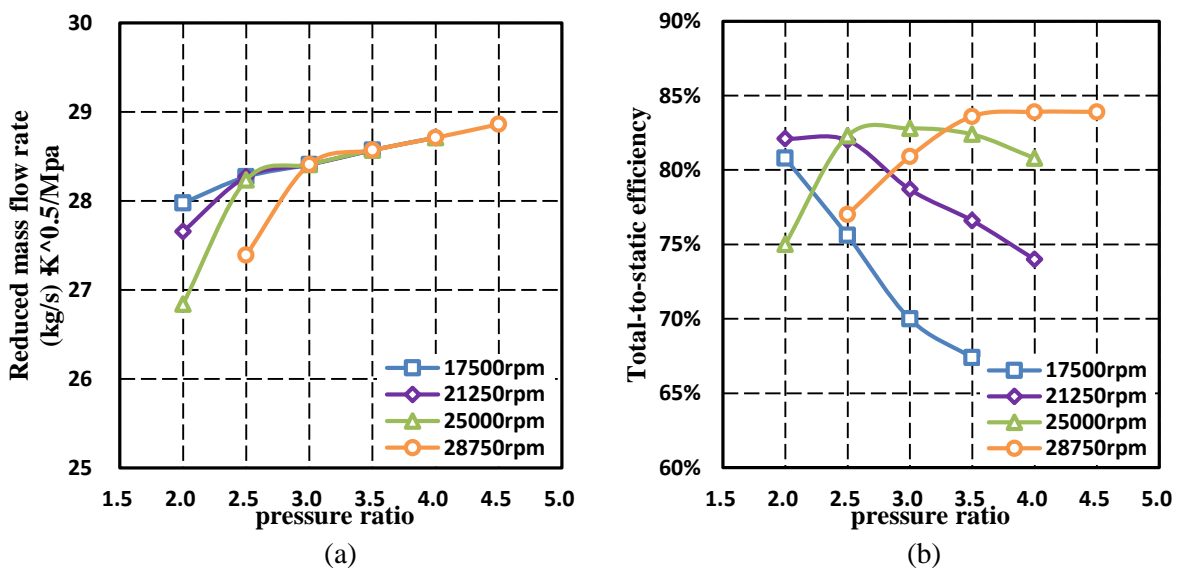


Figure 5: Performance characteristics of the optimal specific speed turbine

4.2 Breakdown of Losses

The breakdown of losses can illustrate that which component has the greatest influence on the efficiency dropping. A way to divide losses in a radial-inflow turbine stage was documented by Rohlik (1968), he divided them into stator loss, rotor loss, clearance loss, windage loss and exit velocity loss. In the present study, based on the authors' experience, the radial-inflow turbine stage loss is divided into stator loss, inlet incidence loss, rotor passage loss, trailing edge loss, tip clearance loss, and exit velocity loss (seen in **Figure 6**). Each loss is represented by a mathematic model which has some basis in the turbine physical processes. The windage loss is not taken into consideration.

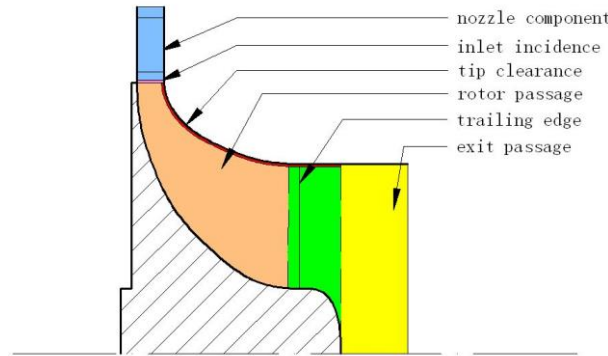


Figure 6: Division of the radial-inflow turbine stage for analysis of loss distribution

The nozzle loss model was developed by Rodgers (1987). It was based on Rodgers' own test data and the Ricardo data. A static enthalpy loss coefficient ξ_n was proposed based on the nozzle exit Reynolds number Re_3 , nozzle blade solidity, and throat aspect ratio,

$$\xi_n = \frac{h_3 - h_{3, is}}{h_{3, sg} - h_3} = \frac{0.05}{Re_3^{0.2}} \left(\frac{3 \tan \alpha_{b3}}{s/c} + \frac{o}{b_3} \right) \quad (5)$$

where $Re_3 = \rho_3 C_3 b_3 / \mu_3$.

The inlet incidence loss L_i refers to any work of the organic fluid turning from its direction of approach to the rotor to the direction required by the blade passage. The incidence loss is the contribution to the entropy generated, when the turbine is operating away from its design point and the rotor inlet flow angle is not equal to its optimum $\beta_{4, opt}$ (Wasserbauer and Glassman, 1975).

$$L_i = \frac{1}{2} W_4^2 \sin^2(\beta_4 - \beta_{4, opt}) \quad (6)$$

where $\beta_{4, opt} = 10^\circ$.

The rotor passage loss L_p includes the losses due to cross-stream or secondary flows, the mixing which these bring about, and the blockage and loss of kinetic energy due to the growth of boundary layers. The rotor passage loss formulation based on the mean kinetic energy of the fluid in the blade passage are widely used, and its developed form by Wasserbauer and Glassman (1975) is based on the meridional component of kinetic energy at inlet but the whole kinetic energy at the rotor throat.

$$L_p = \frac{1}{2} K_p (W_4^2 \cos^2(\beta_4 - \beta_{4, opt}) + W_5^2) \quad (7)$$

where K_p is an empirical coefficient, for which a value of 0.3 is recommended.

The rotor passage loss formulation applies between the inlet and throat of the rotor, and the trailing edge loss L_{trl} is modeled between the throat and rotor outlet. The tangential component of absolute velocity is assumed to be constant, and a trailing edge loss is based on a sudden expansion from the rotor throat to an area just downstream of the rotor outlet (Moustapha *et al.*, 2003).

$$L_{trl} = \frac{1}{2} (C_{5, m} - C_{6, m})^2 \quad (8)$$

The tip clearance loss L_{ctr} refers to the leakage flow through the gap between the tip and shroud. The leakage flow can be written in terms of separate leakage gaps in the axial, radial and cross-coupling portions (Dambach *et al.*, 1998).

$$L_{ctr} = \frac{U_4^3 Z_r}{8\pi} (K_a \varepsilon_a C_a + K_r \varepsilon_r C_r + K_c \sqrt{\varepsilon_a \varepsilon_r C_a C_r}) \quad (9)$$

where $C_a = \frac{1-(r_{6,t}/r_4)}{C_{4,m} b_4}$ and $C_r = \left(\frac{r_{6,t}}{r_4}\right) \frac{z-b_4}{C_{6,m} r_6 b_6}$. And K_a , K_r and K_c are the discharge coefficients for the axial, radial and cross-coupling portions of the tip gap respectively. Good agreement with test data was achieved with $K_a = 0.4$, $K_r = 0.75$ and $K_c = 0.3$.

The exit velocity loss L_e relates to the exit absolute velocity of the organic fluid which cannot be used.

$$L_e = \frac{1}{2} C_6^2 \quad (10)$$

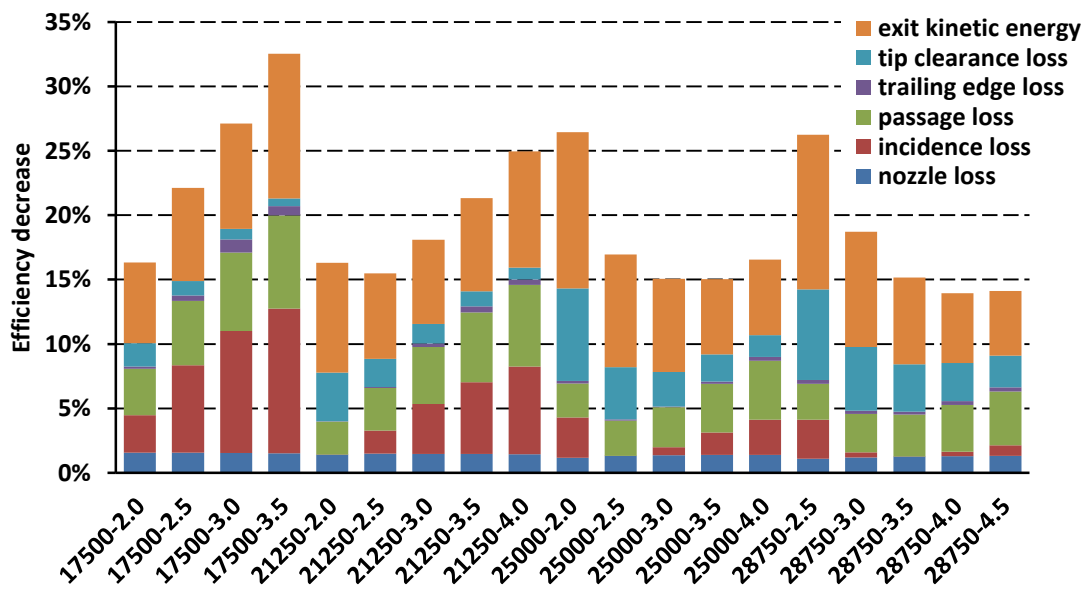
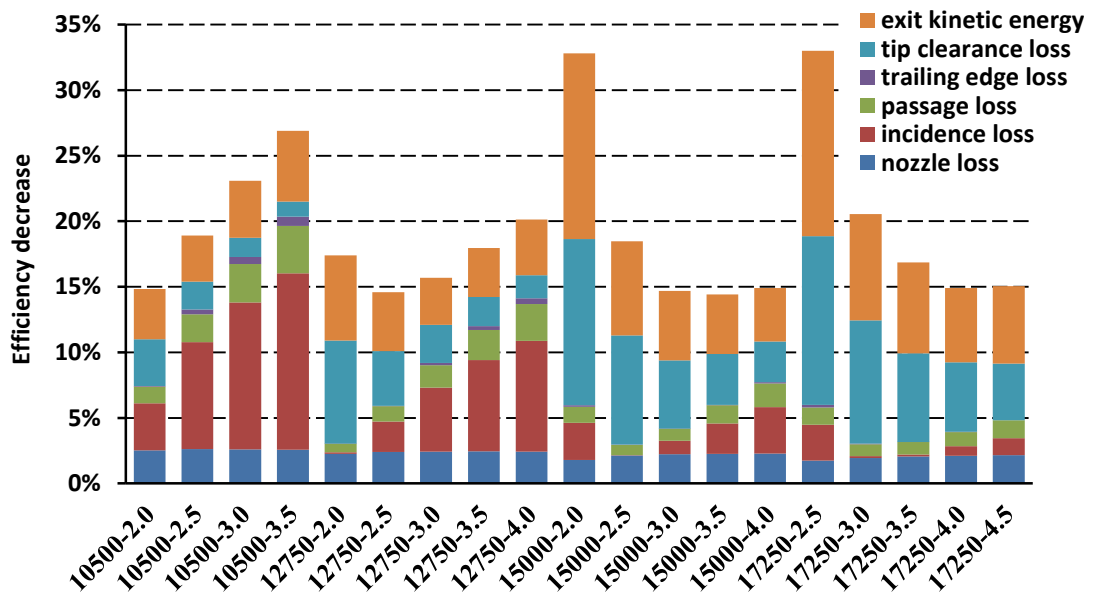


Figure 7: Breakdown of losses for the low and optimal specific speed turbines

Figure 7 shows the breakdown of losses for the low and optimal specific speed turbines. Each column is a specific operating condition, where the first number represents the rotating speed and the second one is the pressure ratio. In general, compared with rotor losses, the stator losses are much smaller in all the operating conditions of the two turbines. The losses related to the rotor dominate the turbine efficiency dropping, except the high rotating speed with low pressure ratio operating conditions, where the exit velocity losses are dramatically large. For the high rotating speed with low pressure ratio conditions, the exit kinetic energy losses are much larger than the average values of all the operating conditions, and also the tip clearance losses are larger than the average values. Both of these two losses make the efficiency drop a lot. What's more, as the tip clearance losses of low specific speed turbine increase much larger, the efficiencies of low specific speed turbine in these conditions are much lower than those of optimum specific speed turbine.

When comparing the loss distributions related to rotor between low and optimal specific speed turbines, it leads to the following results. The low specific speed turbine shows larger tip clearance losses but smaller passage losses compared with the optimal specific speed turbine; the trailing edge losses are much smaller compared with other losses; incidence losses are determined by the operating conditions. For low rotating speed with high pressure ratio operating conditions, incidence losses are very large, even can dominate the rotor loss in some extreme operating conditions. It is mainly caused by the very large positive incidence angles. What's more, low specific speed turbine show smaller exit kinetic velocity losses in these conditions, which lead to a slight improve of the efficiencies. For the operating conditions located in the efficiency envelope line, the incidence losses are much smaller, and the losses are dominated by the tip clearance loss and rotor passage loss.

A typical operating condition in the efficiency envelope line is the nominal operating condition. For the nominal operating condition, the tip clearance loss of low specific speed turbine can be as much as above 8% accounting for more than 40% of the total loss, but the tip clearance loss of optimal one is only 4%. However, the passage loss of low specific speed turbine is only 0.8% compared with 2.7% of the optimal specific speed turbine. The similar situation occurred for the off-design point located in the efficiency envelope line. On the one hand, these differences can be explained by the differences of geometry parameters in **Table 2**. The low specific speed design will lead to larger geometry size for the same design power output. Furthermore, it will lead to smaller magnitude of velocity parameters but larger values of parameters related to tip clearance. Hence, it would decrease the passage losses but increase the tip clearance losses. On the other hand, the efficiency differences can be better explained when the flow field of rotor entropy generation is well understood.

4.3 Rotor Entropy Generation

The rotor flow field comparison in the nominal condition is carried out to discuss the influence of specific speed on the entropy generation in the rotor tip clearance and passage. As described in the tip clearance loss model, the tip clearance loss is mainly caused by the fluid moving from pressure surface (PS) to the suction surface (SS) of the blades. The kinetic energy carried by the fluid is dissipated into the main flow, and at the same time it may enhance the vorticity in the rotor passage, which will further increase the loss. From the research by Dambach et al. (1998), the tip clearance flow in a radial-inflow turbine can be divided into three regions, inducer, midchord, and exducer. The flow field of vorticity and entropy in these three regions are shown in **Figure 8** and **Figure 9**.

Compared with the optimum specific speed turbine, **Figure 8(a)** illustrates that in the inducer region larger contribution of entropy generation is caused by the tip clearance on the suction surface, and the scrapping effect caused by relative casing motion is also stronger to increase the passage loss. In the midchord region shown in **Figure 8(b)**, tip clearance also makes larger contribution of entropy generation on the suction surface, and further the vortex is generated by the tip clearance flow. Although complicated rotor passage vortexes are shown in **Figure 8(b)**, it seems that the vortex caused by the stronger scrapping effect in **Figure 9(b)** causes larger rotor passage loss compared with the low specific speed turbine. **Figure 8(c)** and **Figure 9(c)** illustrate that in the exducer region, the entropy generation caused by the tip clearance moves from suction surface to pressure surface. And a large vortex dominates the contribution of passage entropy generation for both of low and optimum specific speed turbines. To summarize, for the low specific speed turbine, much larger entropy generation is caused by the tip clearance flow, which is consistent with the results of loss model analysis, and flow field analysis of entropy generation indicates that the tip clearance loss is located on the suction

surface in the inducer to midchord region, but on the pressure surface in the exducer region. Further analysis of tip clearance flow may be an important aspect to improve the low specific speed turbine efficiency.

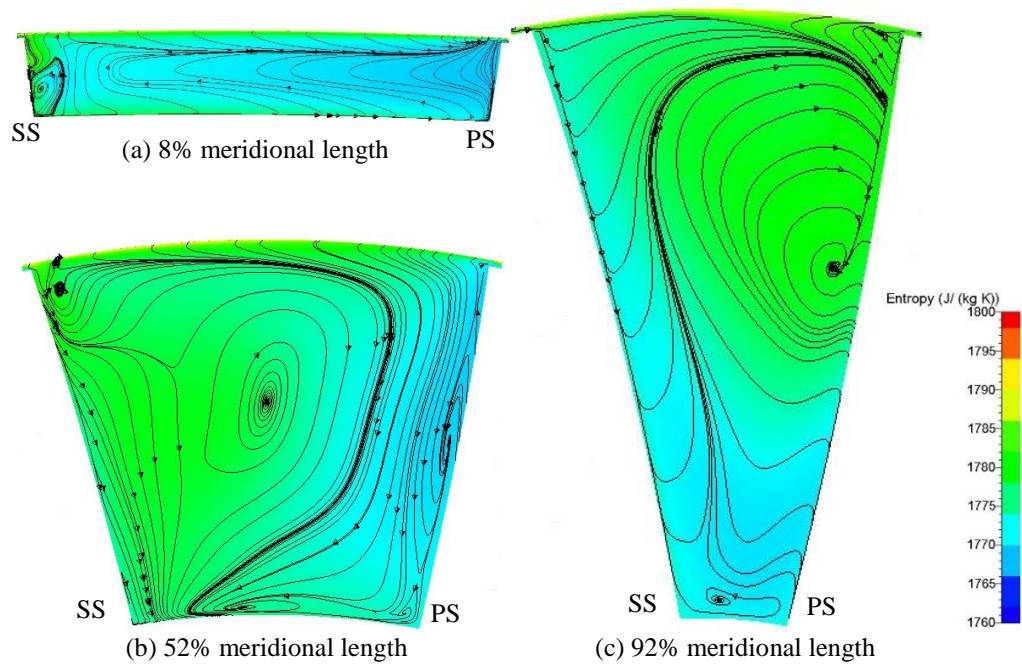


Figure 8: Vorticity and entropy on cross sections of the low specific speed turbine in the nominal condition

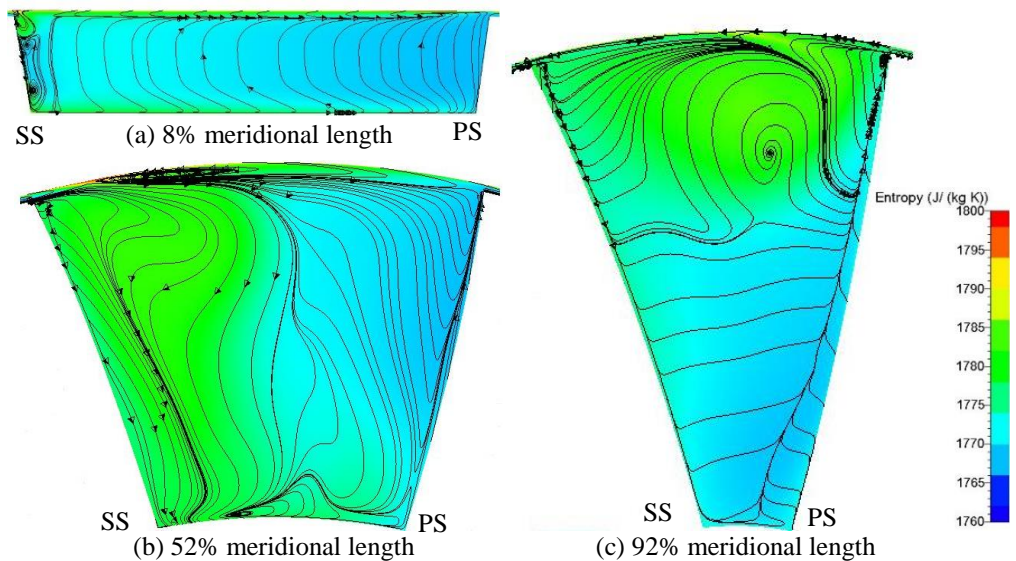


Figure 9: Vorticity and entropy on cross sections of the optimal specific speed turbine in the nominal condition

5. CONCLUSIONS

In the present study, three-dimensional steady RANS simulations have been carried out to investigate the performance characteristics and loss mechanisms of the ORC radial-inflow turbine using R245fa as working fluid applied for heavy-duty diesel engine coolant heat recovery. The comparison of performance characteristics and flow fields between low and optimal specific speed turbines has been analyzed. The results from this work suggest the following conclusions.

- When comparing the turbine performance characteristics between design specific speed of 0.28 and 0.47, the low specific speed turbine nominal efficiency decreases 1.7%. And furthermore in the efficiency envelope curve, the efficiency decreases are in the range of 2.6%

to 0.6% from low to high pressure ratio conditions. It indicates that the specific speed has great influence on the turbine nominal and off-design efficiencies, especially in the low pressure ratio conditions.

- The breakdown of losses indicates that the effect of specific speed on the performance characteristics mainly lies on rotor tip clearance and passage losses. The low specific speed turbine shows larger tip clearance losses but smaller passage losses.
- Flow field analysis of rotor entropy generation indicates that for the low specific speed turbine, much larger entropy generation is caused by the tip clearance flow, which is consistent with the results of loss model analysis, and furthermore the tip clearance loss is mainly located on the suction surface in the inducer to midchord region, but on the pressure surface in the exducer region.

In the future, a further study on the tip clearance flow in the low specific speed turbine rotor will be carried out to find out a flow control method to improve efficiencies of this kind of turbines.

NOMENCLATURE

C	absolute velocity	(m/s)
P	output power	(kW)
Q	volute flow rate	(m ³ /s)
T	temperature	(K)
U	rotating velocity	(m/s)
W	relative velocity	(m/s)
Z_n	nozzle vane number	
Z_r	rotor blade number	
b	blade height	(m)
c	stator vane chord	(m)
h	enthalpy	(J/kg)
\dot{m}	mass flow rate	(kg/s)
o	stator throat opening	(m)
p	pressure	(Mpa)
r	radius	(m)
s	stator spacing	(m)
z	turbine axial length	(m)
α	absolute flow angle	($^\circ$)
α_b	nozzle vane angle	($^\circ$)
β	relative flow angle	($^\circ$)
β_b	rotor blade angle	($^\circ$)
ε	tip clearance	(m)
μ	viscosity	(Pa s)
ρ	density	(kg/m ³)
ω	rotating speed	(rad/s)

Subscript

0	volute inlet position
1	nozzle inlet position
3	nozzle outlet position
4	rotor inlet position
5	rotor throat position
6	rotor outlet position
a	axial direction
h	rotor hub position
is	isentropic process
m	meridian component
r	radial direction

sg stagnation condition
t rotor tip position

REFERENCES

- Cho S.Y., Cho C.H., Ahn K.Y., Lee Y.D., 2014, A study of the optimal operating conditions in the organic Rankine cycle using a turbo-expander for fluctuations of the available thermal energy, *Energy*, 64:900-911.
- Concepts NREC, 2014, Rital 8.3 Help.
- Dambach R., Hodson H.P., Huntsman I., 1998, An experimental study of tip clearance flow in radial inflow turbines, ASME Paper No. 98-GT-467.
- Glassman A.J., 1976, Computer program for design and analysis of radial inflow turbines, NASA Technical Note TN D-8164.
- Kofskey M.G., Nusbaum W.J., 1972, Effects of specific speed on experimental performance of a radial-inflow turbine, Tech. rep., NASA Technical Note TN D-6605.
- Lemmon E.W., Span R., 2006, Short Fundamental Equations of State for 20 Industrial Fluids, *J. Chem. Eng. Data*, 51, 785-850.
- Li P., Chen J.H., Zhang D., Xie Y.H., 2011, Study on the steady and unsteady aerodynamic performance of a radial inflow turbine with small partial admission in a miniature ORC system, *Proceedings of the ASME 2011 Power Conference*.
- Mousapha H., Zelesky M.F., Baines N.C., Japikse D., 2003, Axial and Radial Turbines, Concepts NREC, USA.
- NUMECA, 2014, FINETTM/Turbo v9.1 Theoretical Manual.
- Quoilin S., Broek M., Declaye S., Dewallef P., Lemort V., 2013, Techno-economic survey of Organic Rankine Cycle (ORC) systems, *Renewable and Sustainable Energy Reviews*, 22:168-186.
- Rodgers C., 1987, Mainline performance prediction for radial inflow turbines, Tech. rep., VKI Lecture Series.
- Rohlik H. E., 1968, Analytical determination of radial inflow turbine design geometry for maximum efficiency, Tech. rep., NASA Technical Note TN D-4384.
- Sauret E., Gu Y.T., 2014, Three-dimensional off-design numerical analysis of an organic Rankine cycle radial-inflow turbine, *Applied Energy*, 135:202-211.
- Tchanche B.F., Lambrinos G., Frangoudakis A., Papadakis G., 2011, Low-grade heat conversion into power using organic Rankine cycles – A review of various applications, *Renewable and Sustainable Energy Reviews*, 15:3963-79.
- Wasserbauer C.A., Glassman A.J., 1975, FORTRAN program for predicting the off-design performance of radial inflow turbines, NASA Technical Note TN D-8063.
- Watanabe I., Ariga I., Mashimo T., 1971, Effects of dimensional parameters of impellers on performance characteristics of a radial inflow turbines, *Trans ASME Journal of Engineering for Power*, 93:81-102.
- Wheeler A., Ong J., 2014, A study of the three-dimensional unsteady real-gas flows within a transonic ORC turbine, *Proceedings of ASME Turbo Expo 2014*.
- Whitfield A., 1990, The preliminary design of radial inflow turbines, *Trans ASME Journal of Turbomachinery*, 112:50-57.
- Zhang L., Zhuge W.L., Peng J., Liu S.J., Zhang Y.J., 2013, Optimization of the blade trailing edge geometric parameters for a small scale ORC turbine, *IOP Conf. Series: Materials Science and Engineering* 52(2013) 042016.
- Zhang L., Zhuge W.L., Zhang Y.J., Peng J., 2014, The influence of real gas effects on ICE-ORC turbine flow field, *Proceedings of ASME Turbo Expo 2014*.

ACKNOWLEDGEMENT

The authors would like to thank the National Basic Research Program of China (2011CB707204) for the support.

FLUID-DYNAMICS OF THE ORC RADIAL OUTFLOW TURBINE

Claudio Spadacini*, Lorenzo Centemeri, Dario Rizzi, Massimiliano Sanvito and Aldo Serafino

Exergy SpA,
Via Santa Rita 14, 21057, Olgiate Olona (VA)
Italy
e-mail: info@exergy.it
Web page: <http://www.exergy-orc.com>

ABSTRACT

It is well documented that axial turbines and radial inflow turbines have traditionally been the selected solutions for ORC, both with an overhung configuration. In the last years a different turbine technology for ORC has been developed, engineered, manufactured and tested by Exergy: the radial outflow turbine.

In order to better understand its potential and limits, the present study has the purpose of conducting a fluid-dynamic study of the ORC radial outflow turbine. To pursue this aim, here firstly a summary description of the radial outflow turbine and of its features is given, by means of mechanical and thermodynamic fundamentals.

Secondly, moving from the hypothesis of direct coupling with generator, boundary conditions for a 2 MW case are chosen and a radial outflow turbine is studied, focusing on fluid-dynamic design: after a preliminary mean line study a CFD simulation of the machine is performed.

The described analysis includes also a comparison with an axial ORC turbine with the overhung configuration directed coupled with a generator: this approach could allow to valuate fluid-dynamic losses in both technologies and can explain the reason why the radial outflow turbine shows a higher efficiency than the axial overhung one in many ORC applications.

1. INTRODUCTION

In these days the ORC market is in expansion and as a matter of fact a rising interest about it can be observed in the scientific community. In terms of system performance, turbine is the most important and critical component of ORC systems (Macchi, 2013) and for this reason it is subject to many researches and studies.

An interesting innovation in this panorama is the ORC radial outflow turbine developed by Exergy, which has several unique characteristics qualifying this unconventional configuration as advantageous for many ORC applications, as it ideally matches the process conditions typical for these kinds of uses. In fact it has been demonstrated (Macchi, 2013 – Frassinetti et al., 2013) that this machine is competitive with both axial and radial inflow turbines, solutions usually adopted in ORC applications with the overhung configuration as it allows to have compact machines and to reduce sealing problems (Salucci et. al, 1983).

2. THE ORC RADIAL OUTFLOW TURBINE AT A GLANCE

To better understand the particular features of the radial outflow turbine (see Figure 1) some considerations about turbomachinery fluid-dynamics and about thermodynamics are necessary.

The well-known general Euler equation for turbomachinery, ignoring minor negligible losses, provides a formulation of the specific work for a single stage as (for instance Stodola, 1927):

$$l = u_1 c_{t1} - u_2 c_{t2} \quad (1)$$

where:

- u is the Peripheral velocity,
- c_t is the Tangential component of the absolute velocity,
- 1 is the Inlet section of the turbine,
- 2 is the Outlet section of the turbine.

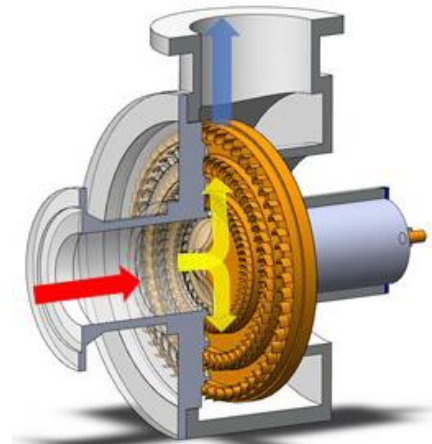


Figure 1: Radial outflow turbine

As a result of Equation (1) in order to maximize the specific work of a single stage, the first term should be significantly higher than the second: assuming that in a turbine C_{t1} must be much bigger than C_{t2} , the highest specific work of a single stage is thus achieved by the radial inflow configuration, which has intrinsically a higher peripheral velocity at the inlet and a lower one at the outlet.

The radial outflow configuration has instead a low specific work per stage due to the increase of the peripheral velocity while expanding the vapor ($U_1 < U_2$). Furthermore, from thermodynamics it is known that the expansion of fluids with low molecular weight, like water, at operative conditions which are typical for power production, is characterized by high enthalpy drops, high volumetric flows and high volumetric ratios (Poling et al., 2000).

Thus, the choice of the radial outflow turbine with water steam faces a serious limit: a significant number of stages is mandatory to convert the enthalpy drop of the fluid into mechanical energy. Owing to this reason, Ljungstrom developed his counter rotating radial outflow turbine configuration, in order to reduce the number of the turbine stages by increasing their specific work.

Moreover, due to the remarkable volumetric flow and its ratio between the inlet and outlet section (considerable for steam), the turbine blades would necessarily have a large height even for small power output turbines. Thus, for the very large diameter disk necessary to accommodate all the required stages and for the too long blades, the radial outflow turbine configuration demonstrated severe limitations while processing steam and was therefore deemed not suitable.

These issues led to no significant development of such type of turbine, which was phased out for steam applications by axial turbines.

At the operative conditions typical for ORC, fluids with high molecular weight lead to significantly lower enthalpy drops, volumetric flows and volumetric ratios than steam (Poling et al., 2000): this made possible for Exergy to reconsider the radial outflow turbine configuration for this application in binary power plants, as the intrinsic limits of this type of technology are no longer relevant.

If compared to traditional organic fluid turbines, meaning overhung axial turbines, Exergy overhung radial outflow turbine demonstrates several mechanical and fluid-dynamic differences hereby summarized.

2.1. Mechanical analysis

Axial turbines are characterized by having only one stage mounted on each single disk (in this paper called single-disk / single stage configuration). This arrangement in overhung axial turbines limits the number of stages, for rotordynamics reasons, to up to 3 stages. The radial outflow turbine allows instead to have several stages arranged on the same disk (see Figure 1).

The single-disk / multi stage configuration has thus the advantage of minimizing vibrations and static and dynamic loads on the bearings, due to the reduced distance between bearings and the turbine center of gravity. This makes possible to decrease the maintenance and to extend the useful life of the rotating components (see Figure 2).

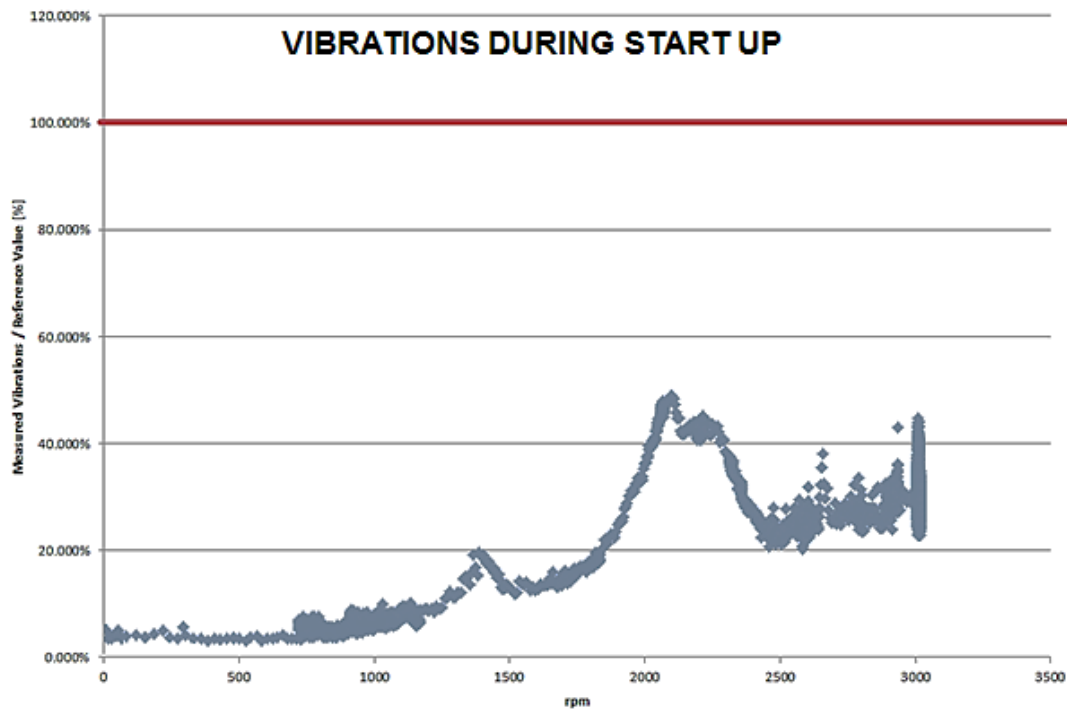


Figure 2: Vibrations during start up. Reference Value from ISO 10816-3 (From Frassinetti et al., 2013)

Finally, being the peripheral velocity constant along the blade span, velocity triangles at hub and tip do not change and the blades are prismatic instead of twisted.

2.2. Fluid-dynamic analysis

Having a cross section increasing proportionally to the radius, during the expansion the radial outflow turbine matches the volumetric flow behavior better than the axial turbines, which usually require high flaring angles. This means that it is possible to have lower blades at the last stage, leading to evident mechanical advantages, and higher blades at the first stages, thus reducing the endwall and leakage losses (for instance Sieverding, 1985 - Sharma and Butler, 1987 or Duden et al, 1999).

For these reasons, as initial stages have a better aspect ratio, they do not need partial admission, avoiding additional losses related to this aspect (Suter and Traupel, 1959 – Horlock, 1966). As a consequence, the possibility to manage higher volumetric flow ratio allows to have a higher pressure at turbine inlet while keeping the same condensing pressure, therefore giving the opportunity to increase the thermodynamic cycle efficiency.

Finally, as the enthalpy drop of the fluid is divided on several stages for the single-disk / multi stage configuration, the radial outflow turbine is characterized by a better recovery factor (Horlock, 1966 - Dixon, 1998 - Lakshminarayana, 1986 or Moustapha et al., 2003) and by lower stage work coefficients. This results in a subsonic or at most transonic expansion (in spite of the low speed of sound of organic fluids), instead of supersonic one typical of the other configuration and in a higher fluid-dynamic efficiency both in nominal and off-design conditions.

3. THE FLUID-DYNAMIC STUDY

In the last years a rising interest in the radial outflow turbine has been noticed and some studies about its fluid-dynamics have been proposed (Spadacini et al., 2011 - Pini et al., 2013 - Persico et al., 2013 - Spadacini et al., 2013).

Until today this configuration has been studied alone. In this work we would like to focus our attention on a comparison between the radial outflow and the axial configurations, considered as the reference technology.

3.1. Case study description

To perform the above mentioned comparison a common case study has been used for both configurations. The boundary conditions are listed in Table 1.

Table 1: Boundary conditions for common case study

Fluid	[-]	Pentane
Turbine Inlet Pressure	[bar]	10.3
Turbine Inlet Temperature	[°C]	130
Turbine Outlet Pressure	[bar]	1
Turbine Mass Flow Rate	[kg s ⁻¹]	25

In order to simplify the mechanical configuration of the system and to reduce costs of investment, operation and maintenance due to the presence of gear, a direct coupling with the generator is chosen: so both turbines must rotate at 3000 rpm.

An in-house made 1D code has been used to design the two machines: the code simulates the expansion of the working fluid in the turbine and it uses the losses model by AMDCKO (Ainley and Mathieson, 1951 – Dunham and Came, 1970 – Kacker and Okapuu, 1981); thermodynamic properties are calculated with Refprop 9.1 (NIST, 2013).

As output the radial outflow turbine results in having 5 stages and producing an estimated power of 1924 kW, with an isentropic efficiency of 85.50%; the axial turbine, with 3 stages, has instead the power of 1852 kW and an efficiency of 82.30%.

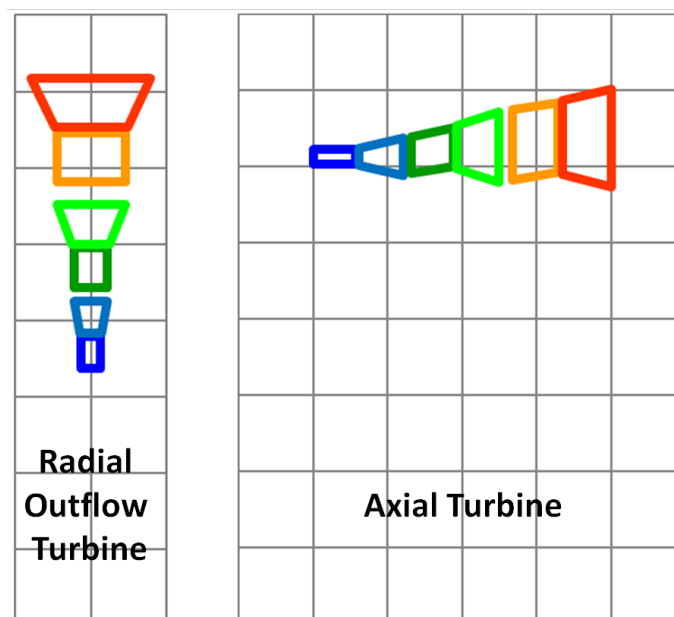


Figure 3: Example of modeled geometry for the radial outflow turbine (left) and axial turbine (right) – From Spadacini et al., 2011

In Table 2 the main results of the 1D analysis are provided respectively for the radial outflow and axial turbine.

Table 2: Main results of 1D mean line analysis

		Radial Outflow Turbine	Axial Turbine
Profile and T.E. losses	[%]	3.572%	5.353%
Endwall losses	[%]	6.635%	6.925%
Leakage losses	[%]	2.974%	4.110%
Disk friction	[%]	1.332%	1.332%

In Table 2 four categories of fluid-dynamic losses are listed: the profile and trailing edge losses and the endwall ones are defined as in AMDCKO model (Ainley and Mathieson, 1951 – Dunham and Came, 1970 – Kacker and Okapuu, 1981).

Leakage losses are calculated as indicated by Egli (Egli, 1935) and disk friction as Daily and Nece (Daily and Nece, 1960): to compute these losses, clearances are supposed to be the same for both configurations.

Important conclusions can be deduced by analyzing results in Table 2.

In fact profile losses in the axial configuration are higher than in the radial outflow, as the first results to have its stages more loaded than the other one with a highly supersonic flow; on the other side the expansion in the radial outflow turbine is at most transonic.

The axial turbine has also higher endwall losses, as a consequence of the lower h/c and h/d ratios (Traupel, 1966 – Horlock, 1966 - Dixon, 1998 - Lakshminarayana, 1986 or Moustapha et al., 2003). Finally, as axial blades are smaller than the radial ones and because of the lower h/d ratio, leakage losses are minor in the radial outflow turbine.

As a consequence of this considerations, for the present case study the radial outflow turbine results to have a higher efficiency than the axial one.

3.2. CFD simulation

After the conclusions reported above, the comparison must be continued; for this reason a viscous 3D CFD analysis of both turbines is performed. The code employed in this step is ANSYS CFX.

In both of the domains periodic boundary conditions are used and for interface between the two cascades the stage method is utilized for modeling frame change (ANSYS, 2013).

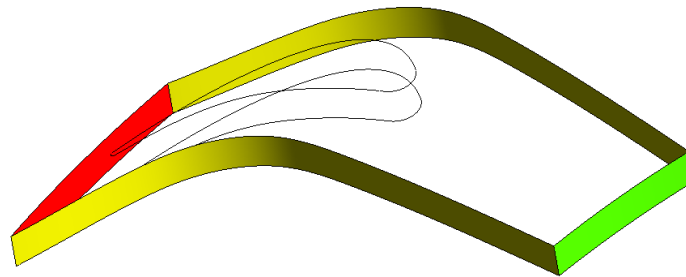


Figure 4: Interfaces for each cascade studied (periodic boundary conditions on yellow surfaces)

To generate blades of both the turbines an in-house database has been used. For thermodynamic properties look-up tables (Pini et al., 2015) are compiled with data from Refprop 9.1 (NIST, 2013).

The used turbulence model is the k-omega SST with the high resolution advection scheme (ANSYS, 2013).

In a first step for both the turbines a computational grid of about 2 million nodes and 7.5 million of tetra and hexa elements has been used; mesh has been then refined to about 8.5 million nodes and 30 million elements with differences in calculated results below 1%. Skewness has been always below 0.9 and maximum Aspect Ratio results to be 62.

3.3. CFD results

The hypotheses just described lead to the following results: the radial outflow turbine with a mass flow rate of 25 kg s^{-1} produces 1938 kW, while the axial produces 1857 kW; the calculated isentropic efficiencies are respectively 86.10 % for the first and 82.5 % for the second one.

A piece of information about the expansion in both of the turbines can be extracted from Figure 5 and Figure 6, which confirm that stages in the radial outflow turbine are at most transonic, while in axial turbine they are highly supersonic.

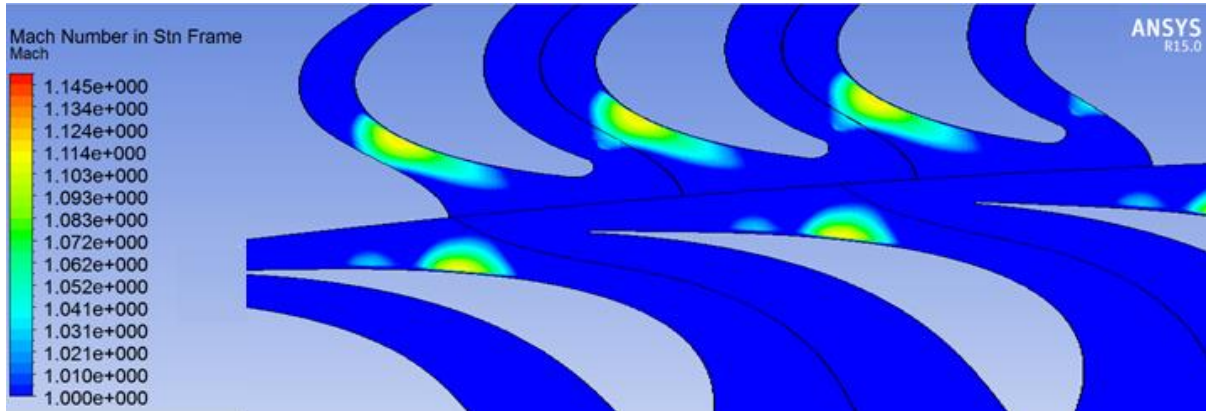


Figure 5: Maximum absolute Mach number at the outlet of stator vanes in the radial turbine

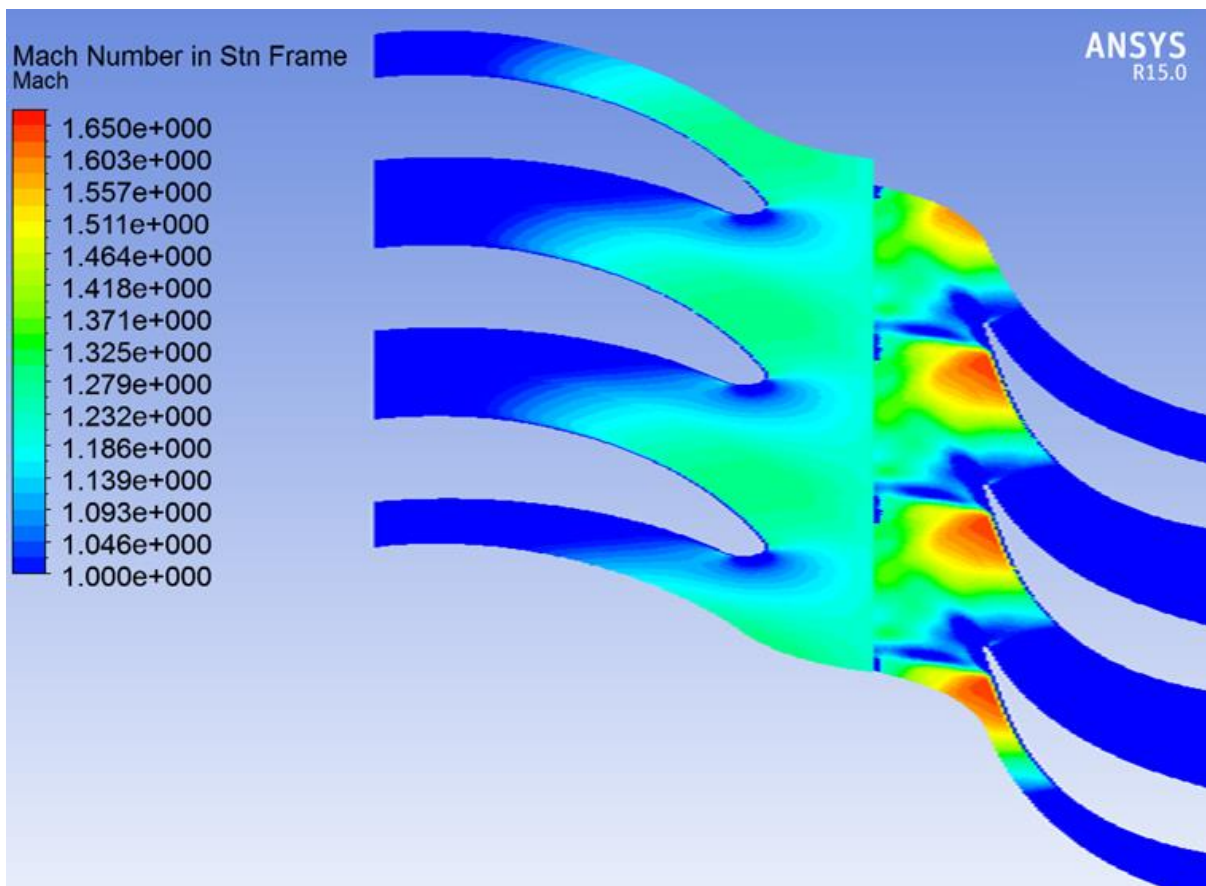


Figure 6: Maximum absolute Mach number at the outlet of stator vanes in the axial turbine

To complete information given by Figure 5 and Figure 6, in the radial turbine the maximum expansion ratio is about 1.6 while in the axial turbine the average value is about 2.8.

To analyze dissipations and losses during the expansion process in both turbines two parameters are chosen: entropy (Figure 7 and Figure 8) and turbulent kinetic energy (Figure 9 and Figure 10).

In fact from thermodynamics it is known that the entropy generated in a process is a measure of the internal irreversibilities (Moran and Shapiro 2004 or Gyftopoulos and Beretta, 1991, for instance). In turbomachinery the sources of entropy are in general viscous effects due to boundary layer and mixing processes and shock waves (Denton, 1993): all these phenomena lead to the losses discussed before in Paragraph 3.1.

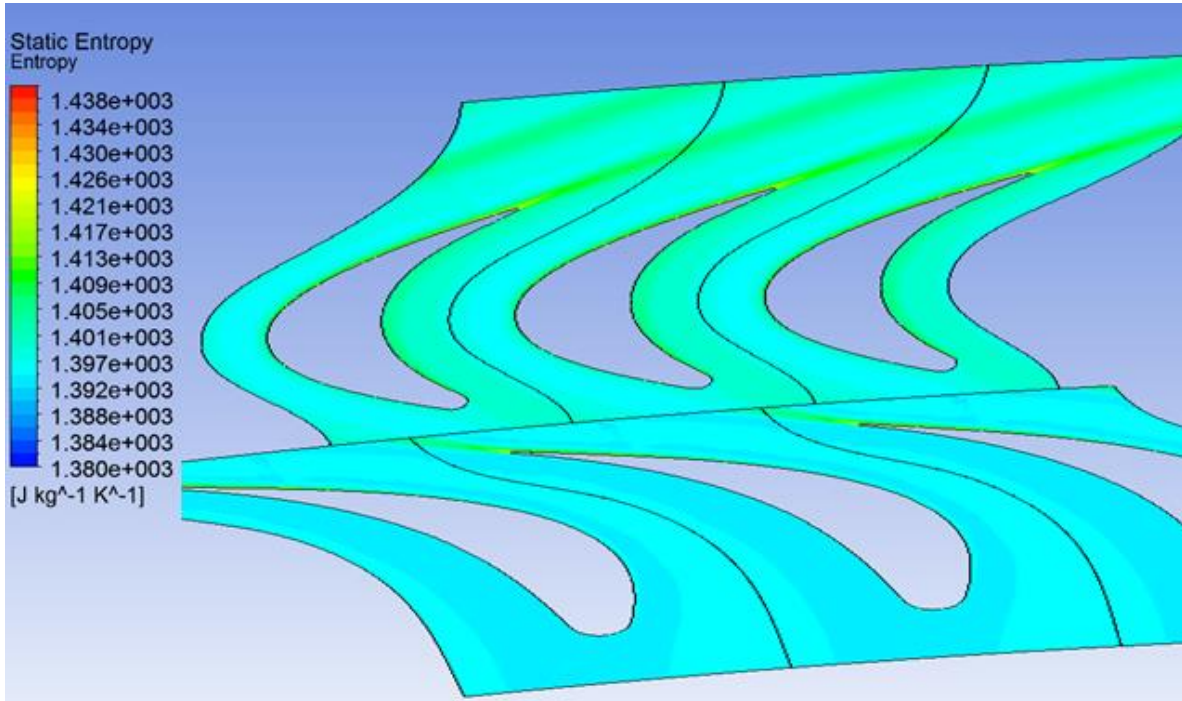


Figure 7: Generated entropy at the last stage of the radial turbine

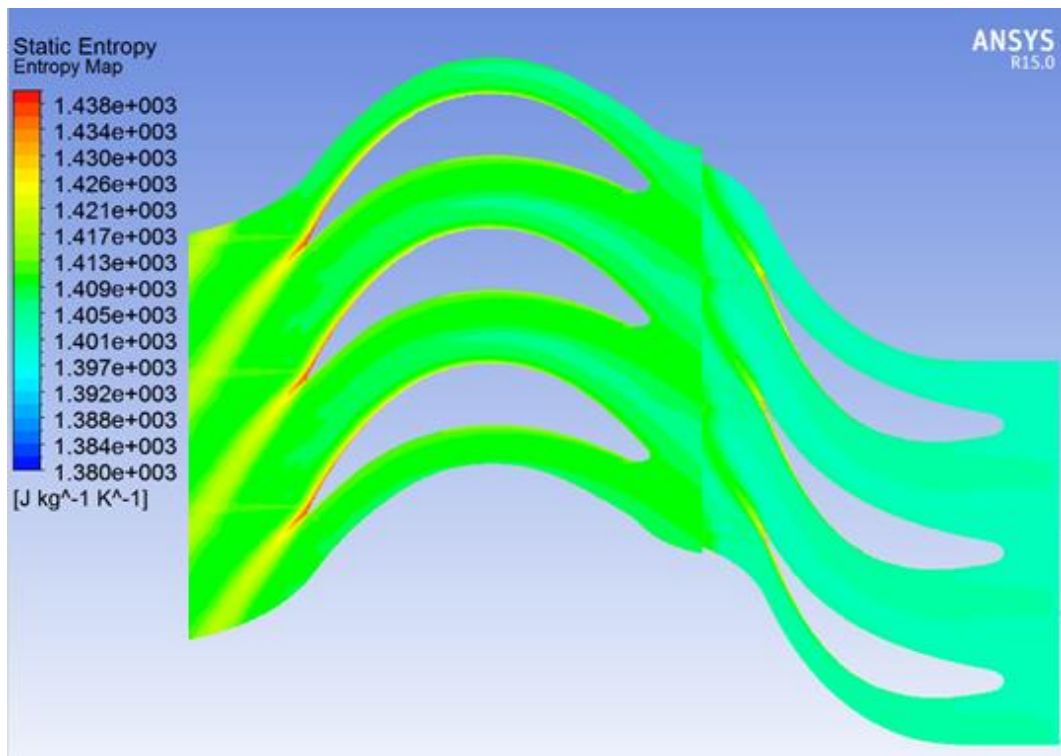


Figure 8: Generated entropy at the last stage of the axial turbine

In addition another important piece of information about losses and dissipation can be deduced from the turbulent kinetic energy distribution. In fact, turbulent kinetic energy (Hinze, 1975) is considered to be an indicator of viscous actions on total pressure losses (Gregory-Smith, 1988 - Moore, 1987).

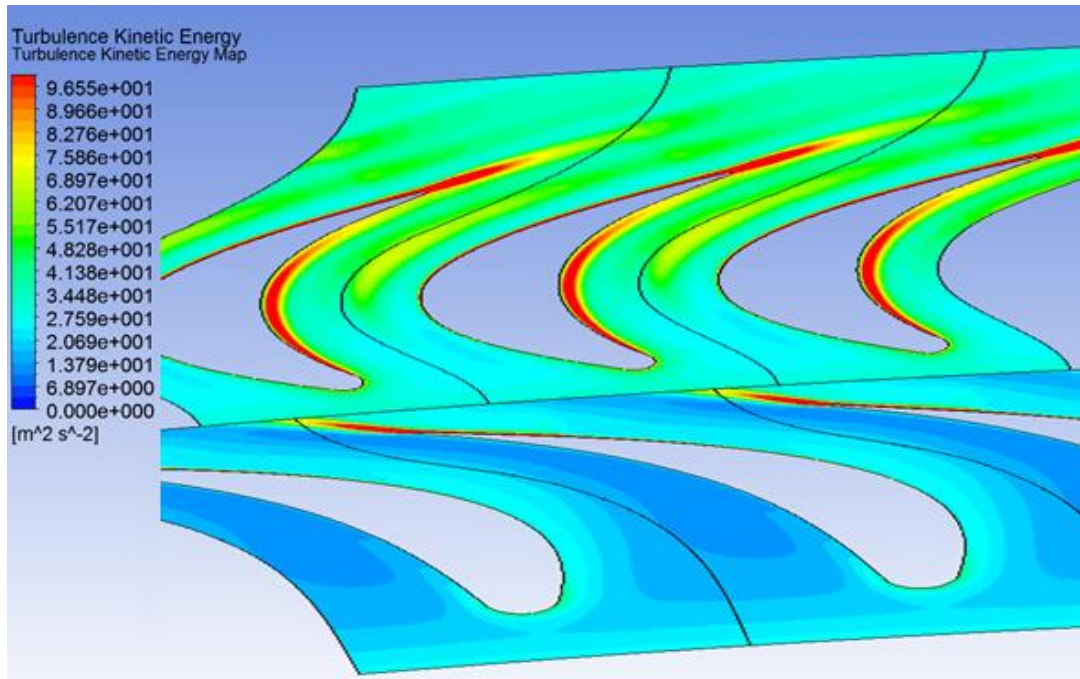


Figure 9: Turbulent kinetic energy at the last stage of the radial turbine

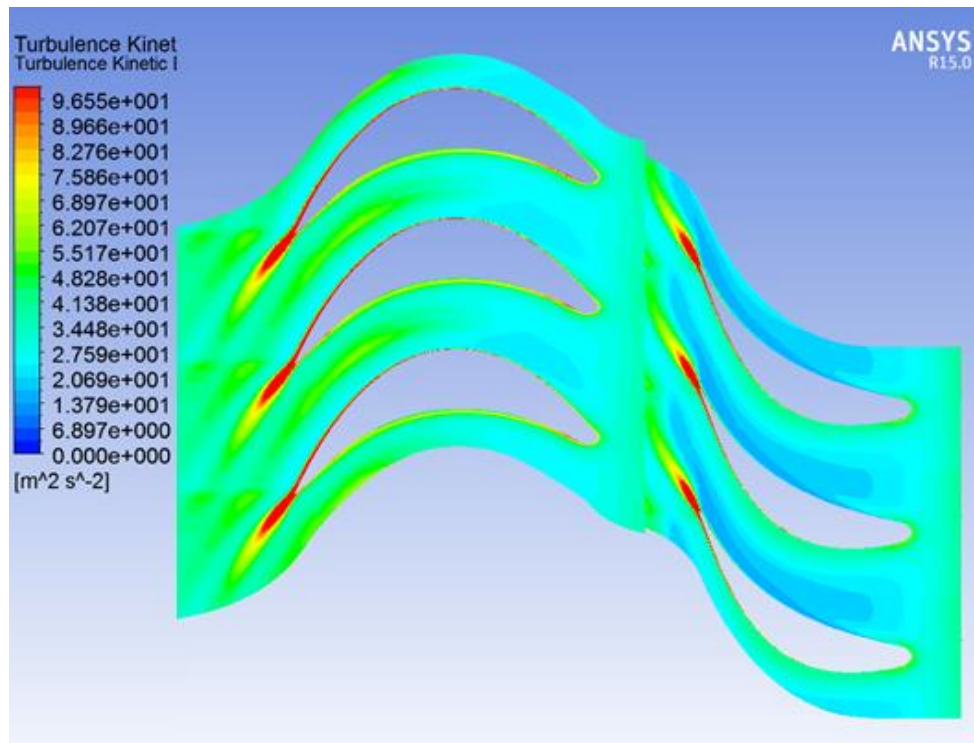


Figure 10: Turbulent kinetic energy at the last stage of the axial turbine

4. CONCLUSIONS

It has been highlighted that the radial outflow turbine is a solution well matching with the typical ORC process characteristics, i.e. high molecular weight, low speed of sound and limited volumetric expansion ratio. Furthermore, for a 2 MW case with the rotational speed of 3000 rpm, a study of the fluid-dynamics of this configuration has been carried out, firstly with mean line 1D methods and then with a CFD 3D simulation. As a result of this analysis, because of the feature of having more stages on a single disk, fluid expansion is characterized by lower losses and dissipations compared to the axial turbine. Consequently, the radial outflow turbine in some ORC applications can be more efficient than the axial one.

Future development of this work should focus on investigating the behavior of the ORC radial outflow turbine in off-design conditions, better if by a comparison with the axial overhung one.

REFERENCES

- ANSYS, 2013, "ANSYS CFX-Solver Modeling Guide".
- Ainley D.G. and Mathieson G.C.R., 1951, "A method of Performance Estimation for Axial-Flow Turbines", R&M 2974, Aeronautical Research Council, London.
- Daily J.W. and Nece R.E., 1960, "Chamber Dimension Effects on Induced Flow and Frictional Resistance of Enclosed Rotating Disk", Trans. ASME, J. of Basic Engineering, Mar, pp. 217-232.
- Dixon S.L., 1998, "Fluid Mechanics and Thermodynamics of Machinery", Elsevier.
- Duden A., Raab I. and Fottner L., 1999, "Controlling the Secondary Flow in a Turbine Cascade by a Three-Dimensional Airfoil Design and Endwall Contouring", ASME, J. of Turbomachinery, April, pp. 191-199.
- Dunham J. and Came P.M., 1970, "Improvements to the Ainley-Mathieson Method of Turbine Performance Prediction", Trans. ASME, J. of Engineering for Power, July, pp. 252-256.
- Egli A., 1935, "The Leakage of Steam Through Labyrinth Glands", Trans. ASME, 57, pp. 115-122.
- Frassinetti M., Rizzi D., Serafino A., Centemeri L. and Spadacini, C., 2013, "Operational Results of the World's First Orc Radial Outflow Turbine, and its Future Development", in Proc. of 2nd Int. Sem. on ORC Power Systems, Oct., Rotterdam.
- Gyftopoulos E.P. and Beretta G.P., 1991, "Thermodynamics: Foundations and Applications", MacMillan Publishing Company, New York.
- Gregory-Smith, D. G., Walsh, J. A., Graves, C. P., and Fulton, K. P., 1988, "Turbulence Measurements and Endwall Flows in a Turbine Rotor Cascade," ASME J. Turbomach., Vol.110.
- Hinze, J. O., 1975, Turbulence, 2nd ed., McGraw-Hill, New York.
- Horlock J.H., 1966, "Axial-Flow Turbines", Butterwoths, London.
- Kacker S.C. and Okapuu U., 1981, "A Mean Line Prediction Method for Axial Flow Turbine Efficiency", Paper No. 81-GT-58, ASME, New York.
- Lakshminarayana B., 1986, "Fluid Dynamic and Heat Transfer of Turbomachinery", J. Wiley & Sons.
- Macchi E., 2013, "The Choice Of Working Fluid: The Most Important Step For A Successful Organic Rankine Cycle (And An Efficient Turbine)", in Proc. of 2nd Int. Sem. on ORC Power Systems, Oct., Rotterdam.
- Moore, J., Shaffer, D. M., and Moore, J. G., 1987, "Reynolds Stresses and Dissipation Mechanisms Downstream of a Turbine Cascade," ASME J. Turbomach., 109, pp. 258-267.
- Moran M.J. and Shapiro H.N., 2004, "Fundamentals of Engineering Thermodynamics", 5th Ed., Wiley.
- Moustapha H., Zelesky M. F., Baines N. C. and Japiske D., 2003, "Axial and Radial Turbines", Concepts ETI.
- NIST, 2013, "Reference Fluid Thermodynamic and Transport Properties—REFPROP Version 9.1".
- Persico G., Pini M., Dossena V. and Gaetani P., 2013, "Aerodynamic Design and Analysis of Centrifugal Turbine Cascade", in ASME Turbo Expo 2013, Paper No. GT2013-95770.
- Pini M., Persico G., Casati E. and Dossena V., 2013, "Preliminary Design of a Centrifugal Turbine for ORC Applications", ASME J. Eng. Gas Turb. Power, Apr., Vol. 115.
- Pini M., Spinelli A., Persico G., and Rebay S., 2015, "Consistent look-up table interpolation method for real-gas flow simulations", Computers & Fluids, Jan., Vol. 107, pp. 178-188.

- Poling B.E., Prausnitz J.M., O'Connell J.P., 2000, "The Properties of Gas and Liquids", McGraw-Hill.
- Salucci B., Centemeri L., Caniato G., 1983, "Bench Testing of a 500 kW Organic Rankine Cycle Plant", Proc. Of the Third International Seminar on the Results of EC Geothermal Energy Research, Nov., Munich.
- Sieverding C.H., 1985, "Recent Progress in the Understanding of Basic Aspects of Secondary Flows in Turbine Blades Passages", ASME, J. Eng. Gas Turbines Power, April, pp. 248-257.
- Sharma O.P. and Butler T.L., 1987, "Predictions of Endwall Losses and Secondary Flows in Axial Flow Turbine Cascades", ASME, J. of Turbomachinery, April, pp. 229-236.
- Spadacini C., Centemeri L., Xodo L.G., Astolfi M., Romano M.C. and Macchi E., 2011, "A New Configuration for Organic Rankine Cycle Power Systems", in Proc. of 1st Int. Sem. on ORC Power Systems, Sept., Delft.
- Spadacini C., Rizzi D., Saccilotto C., Salgarollo S., Centemeri L., 2013, "The Radial Outflow Turbine Technology: Impact On The Cycle Thermodynamics And Machinery Fluid- And Rotordynamic Features", in Proc. of 2nd Int. Sem. on ORC Power Systems, Oct., Rotterdam.
- Stodola A. and Lowenstein L.C., 1927, "Steam and Gas Turbines", McGraw-Hill, New York.
- Suter P. and Traupel W., 1959, "Untersuchungen Über den Ventilationsverlust von Turbinenradern", Mitteilungen aus dem Inst. für Thermische Turbomaschinen, ETH, Zürich.
- Traupel W., 1966, "Thermische Turbomaschinen", Springer-Verlag, Berlin.

NON-IDEAL COMPRESSIBLE-FLUID DYNAMICS SIMULATION WITH SU2: NUMERICAL ASSESSMENT OF NOZZLE AND BLADE FLOWS FOR ORGANIC RANKINE CYCLE APPLICATIONS

G. Gori^{1*}, A. Guardone¹, S. Vitale², A. J. Head², M. Pini², P. Colonna²

¹ Politecnico di Milano, Department of Aerospace Science and Technologies,
Via La Masa 34, 20156 Milano, Italy
giulio.gori@polimi.it

² Delft University of Technology,
Kluyverweg 1, 2629 HS Delft
s.vitale@tudelft.nl

ABSTRACT

The growing interests towards Organic Rankine Cycle (ORC) turbo-machinery calls for reliable and well-established simulation and design tools, including Computational Fluid Dynamics (CFD) software, accounting for non-ideal thermodynamic behaviour in close proximity to the liquid-vapour saturation curve and critical point, as well as two-phase properties. SU2, an open-source CFD solver originally developed at Stanford University, Palacios et al. (2013, 2014), was recently extended to deal with non-ideal thermodynamics, including state-of-the-art multi-parameter equations of state implemented in the FluidProp library, Colonna and van der Stelt (2004), and it is now in the process of becoming a reliable simulation tool for academic and industrial research on ORC machinery. The investigation of SU2 performances in connection with the numerical simulation of steady nozzle and turbine flows of interest for ORC applications are provided. Numerical simulations refer to both inviscid and viscous flow, with diverse thermodynamic (ideal gas, Van der Waal gas, Peng- Robinson Stryjek-Vera, Span-Wagner multi-parameter equation of state) and turbulence (Spalart-Allmaras, SST-k) models. Considered geometries include straight axis planar nozzle, and a typical ORC turbine blade passage.

1. INTRODUCTION

Nowadays applications involving non-ideal compressible flows can be found in numerous industrial problems and are spread over heterogeneous fields. During the last decade Organic Rankine Cycle turbo-machinery became of utmost importance for the future design of highly efficient energy production systems. In practical applications the ORC machinery make use of particular fluids that, under certain conditions of pressure and density, may show non-ideal thermodynamic behaviour. For these fluids the ideal gas law is proved to fail in describing accurately the thermodynamic behaviour when pressure and temperatures are close to the liquid-vapour saturation curve, in the region near the critical point. The rising of non-ideal compressible fluid phenomena thus calls for more complex equations of state, like for instance the Van der Waals or the Peng-Robinson Stryjek-Vera equation of state or the multi-parameter equation of state. These complex gas models are of utmost importance and can possibly provide a more accurate description of the thermodynamic behaviour that characterizes these fluids. Nowadays the community can only rely on a few computational tools capable of dealing with real fluid flows. One of these tools is *zFlow*, developed by S. Rebay and P. Colonna, a solver suitable for compressible inviscid dense gas flows where an hybrid Finite-volume/Finite-element discretization scheme is adopted, Colonna et al. (2002). Such code has been already proved to provide accurate predictions of the flow field inside ORC three-dimensional radial turbine. Today the academic community and the industry desire for a more reliable and well-maintained investiga-

tion tool, to prove the accuracy of the state-of-the-art equation of state and to foster the design of new, more efficient, power production systems. This tool should serve as a framework from which users can start developing their own real-gas models, including new numerical algorithms and customized features, without worrying about the maintenance of the overall structure. The Stanford University Unstructured (SU2) software suite recently became a promising candidate for this role. SU2 is a popular open-source platform for solving multi-physics PDE problems and PDE-constrained optimization problems on general, unstructured meshes. The core of SU2 is a Reynolds-averaged Navier-Stokes (RANS) solver dedicated to the simulation of compressible, turbulent flows. The capabilities of this solver are various and their number is growing quickly as developers from the international team contribute to improve the code, providing new features and extending its capabilities. A joint research team composed by researchers from Delft University of Technology, from the Politecnico di Milano, and from the Stanford University recently undertook a collaborative effort to bring the SU2 at the cutting-edge for non-ideal compressible fluid-dynamics (NICFD) simulation, Vitale et al. (2015), extending SU2 capabilities to a wider range of pertinence with the inclusion of the Van der Waals and the Peng-Robinson Stryjek-Vera equation of state. The early work has been lately extended with the inclusion of the FluidProp, Colonna and van der Stelt (2004), thermodynamic library which opens the path to the exploitation of the state-of-the-art multi-parameter equation of state. The SU2 suite already included a library for thermo-physical properties of reacting non-equilibrium flows, such as those involving combustion, though a computational framework for NICFD simulation was completely missing. In compliance with the open-source philosophy of the project all the modifications are made available to the community, thus contributing to promote a worldwide access to state-of-the-art analysis tool for NICFD. The actual characteristics of dense vapours, supercritical flows and compressible two-phase flows, in close proximity to the saturation curve near the critical point, entail that the thermodynamic behaviour of the fluid differs considerably from that described by the perfect gas law and, under particular conditions, they may even exhibit non-classical gas-dynamic phenomena. The nature of this particular phenomena is related to the value of the fundamental derivative of gas-dynamics Γ . A non-monotonic Mach number trend along expansion is typical for values of Γ enclosed between 0 and 1, while negative values may bring to the occurrence of inverse gas-dynamics phenomena such as rarefaction shock waves, splitting waves or even composite waves. Heavy complex molecule in the vapour region are expected to show inverse gas-dynamics behaviour, Colonna et al. (2007), and recently two-phase rarefaction shock waves have been recognized as physically realizable close to the critical point of simple compounds, Nannan et al. (2014).

The paper is organized as follows: the first part recalls a brief description of the governing equations for an arbitrarily complex fluid at equilibrium condition and a short review of the numerical method implemented in the SU2 suite. In the second part we present some exemplary results involving simple geometries such as straight axis planar nozzles and a typical ORC turbine blade passage.

2. NUMERICAL MODEL

This section outlines the most distinguishing features of the SU2 solver for non-ideal compressible fluid flows. We first remember that, differently from past attempts and commercial alternatives, the modular and open-source infrastructure of the SU2 suite is largely suitable to build upon the existing flow model new knowledge and methods for fundamental and applied studies for non-ideal fluid flows. Currently, SU2 solves the equilibrium compressible RANS equations, Landau and Lifshitz (1993), by leveraging on a general formulation enabling the use of arbitrary thermo-physical models. The system of PDE equations including the inviscid and

viscous terms is written as

$$\partial_t U + \nabla \cdot \vec{F}^c - \nabla \cdot \vec{F}^v = Q \quad \text{in } \Omega, t > 0 \quad (1)$$

Equation (1) describes how mass, momentum and energy evolve in a control domain. \vec{U} symbolizes the vector of conservative variables, i.e. $\vec{U} = (\rho, \rho v_1, \rho v_2, \rho v_3, \rho E)^T$, where ρ is the fluid density, E is the total energy per unit mass, and $\vec{v} = (v_1, v_2, v_3) \in \mathbb{R}^3$ is the flow velocity in a Cartesian coordinate system. The imposition of the boundary conditions follows the approach proposed in Guardone et al. (2011) to automatically detect inflow/outflow boundaries for hyperbolic systems. Notably the convective and viscous fluxes are given by

$$\vec{F}_i^c = \begin{pmatrix} \rho v_i \\ \rho v_i v_1 + P \delta_{i1} \\ \rho v_i v_2 + P \delta_{i2} \\ \rho v_i v_3 + P \delta_{i3} \\ \rho v_i H \end{pmatrix}, \quad \vec{F}_i^v = \begin{pmatrix} \cdot \\ \tau_{i1} \\ \tau_{i2} \\ \tau_{i3} \\ v_j \tau_{ij} + k_{\text{tot}} \partial_i T \end{pmatrix}, \quad i = 1, \dots, 3 \quad (2)$$

P is the static pressure, T is the temperature, H is the total enthalpy, δ_{ij} is the Kronecker delta function, and the viscous stresses can be compactly written as $\tau_{ij} = \mu_{\text{tot}} (\partial_j v_i + \partial_i v_j - \frac{2}{3} \delta_{ij} \nabla \cdot \vec{v})$. The total viscosity and the total thermal conductivity result from a molecular, $\mu_{\text{mol}}, k_{\text{mol}}$ and a turbulent, $\mu_{\text{tur}}, k_{\text{tur}}$ contribution. Convective fluxes are properly reconstructed by means of the generalized Roe's approximate Riemann solver (ARS) proposed in Montagne and Vinokur (1990). Second-order accuracy is resolved using a Monotone Upstream-centered Schemes for Conservation Laws (MUSCL) approach, van Leer (1979), with gradient limitation. On the other hand, viscous fluxes are evaluated by averaging the flow variables, flow derivatives, and transport properties at two neighbouring cells whereas the *Thin Shear-Layer* approximation, Blazek (2005), is employed for gradient calculation.

For pure fluids and mixture of given composition in a stable equilibrium state the thermodynamic state can be retrieved by using ρ and internal energy e as follows

$$\rho = U_1, \quad e = \frac{U_5}{U_1} - \frac{(U_2 + U_3 + U_4)^2}{2U_1^2} = E - \frac{\|v\|^2}{2}. \quad (3)$$

The required thermo-physical quantities are conveniently expressed as a function of the ρ, e , i.e. $P = P(\rho, e) = P(U), T = T(\rho, e) = T(U), \mu_{\text{mol}} = \mu_{\text{mol}}(\rho, T(\rho, e)) = \mu_{\text{mol}}(U), k_{\text{mol}} = k_{\text{mol}}(\rho, T(\rho, e)) = k_{\text{mol}}(U)$. The SU2 embeds polytropic models (Van der Waals and Peng-Robinson) for rough and quick estimate of non-ideal flows properties. The other properties characterizing the fluid such as the specific heat capacity C_p and all the transport quantities can be conveniently expressed as

$$\begin{aligned} \mu_{\text{mol}} &= \mu_{\text{mol}}(\rho, T) = \mu_{\text{mol}}(\rho, T(\rho, e)) = \mu_{\text{mol}}(U), \\ k_{\text{mol}} &= k_{\text{mol}}(\rho, T) = k_{\text{mol}}(\rho, T(\rho, e)) = k_{\text{mol}}(U), \\ C_p &= C_p(P, T) = C_p(P(\rho, e), T(\rho, e)) = C_p(U). \end{aligned} \quad (4)$$

For more accurate predictions the SU2 embedded thermo-physical library was recently extended with the inclusion of the FluidProp software, Colonna and van der Stelt (2004), a general purpose thermo-physical database originally accomplished at Delft University of Technology. FluidProp contains several thermo-physical models and provides easy access to the quantities necessary for SU2 simulation, with possibility of handling look-up table interpolations Pini et al. (2014) to fasten the calculation. This opens the path to a wide variety of new capabilities: the properties of fluids –such as viscosity and thermal conductivity– whose thermodynamic state is characterized by a value of pressure and temperature close to the liquid-vapour saturation curve in the region near the critical point, can now be computed with a higher level of accuracy.

The aforementioned non-ideal fluid models now available for SU2 make it possible to represent non-ideal and non-classical phenomena such as rarefaction shock waves or compression fans. Beyond the embedded thermodynamic models, the high flexibility of SU2 and the re-usable thermodynamic infrastructure allows for the future implementation of novel fluid models.

This more general approach calls then for a reformulation of the equations involved by the numerical method. Indeed the ideal gas assumption does not apply anymore and a general formulation can be obtained from the spectral decomposition of the Roe's averaged state Jacobian. By means of the Roe averaging procedure (5), it follows that a supplemental condition arises (6), namely:

$$\left(\vec{F}_i^c - \vec{F}_j^c\right) = \bar{A}(U_i - U_j), \quad \bar{A} = A(\bar{U}) \quad (5)$$

$$\bar{\chi}(\rho_i - \rho_j) + \bar{\kappa}(\rho_i e_i - \rho_j e_j) = (P_i - P_j), \quad (6)$$

where $\bar{\chi}$ and $\bar{\kappa}$ are the average of these two thermodynamic quantities defined in eq. (7) and (8).

$$\chi = \left(\frac{\partial P}{\partial \rho}\right)_{\rho e} = \left(\frac{\partial P}{\partial \rho}\right)_e - \frac{e}{\rho} \left(\frac{\partial P}{\partial e}\right)_\rho \quad (7)$$

$$\kappa = \left(\frac{\partial P}{\partial \rho e}\right)_\rho = \frac{1}{\rho} \left(\frac{\partial P}{\partial e}\right)_\rho \quad (8)$$

For a PIG fluid this last condition is automatically satisfied as χ equals to zero and κ is constantly equal to $\gamma - 1$. On the other hand, using a NICF model only one relation (6) is provided for the two unknowns $\bar{\chi}$ and $\bar{\kappa}$. Therefore, the Roe-average state remains uniquely defined if and only if a proper closure condition is given.

3. RESULTS

In this section we present some exemplary test cases in order to show the reliability of the SU2 suite and to highlight some typical applications which may take advantages from the SU2 extended thermo-dynamic library. The considered test cases include simple geometries such as straight axis two-dimensional planar nozzles and a typical ORC turbine blade passage.

3.1 2-D TROVA nozzle

The TROVA (Test Rig for Organic Vapors) experimental facility was built at Laboratorio di Fluidodinamica delle Macchine (LFM) of Politecnico di Milano, Spinelli et al. (2012), and Guardone and Dossena (2012), in collaboration with Turboden s.r.l. and within the frame of the project Solar. In this section we show the flow field predicted by SU2 for a MDM fluid at operating conditions listed in table 1: MDM properties, such as thermal conductivity or viscosity, are assumed to be constant through the nozzle. Values are given for the fluid at the inlet conditions and were computed using FluidProp. Results for three different fluid models, namely the polytropic ideal gas law, the polytropic Van der Waals and the polytropic Peng-Robinson Stryjek-Vera from the embedded SU2 thermo-dynamic library, are compared to show how a different level of accuracy in the description of the fluid behaviour may bring to different results. The domain represents a planar two-dimensional straight axis nozzle discharging into a reservoir: the computational grid is a hybrid mesh, hexahedrons were used to describe the boundary-layer region while tetrahedrons to discretize the core region and the reservoir. With reference to Fig 1: a no-slip condition is applied along nozzle wall and on the vertical wall in $x \approx 0.18$, symmetry condition is imposed at the centreline and at the upper boundary of the reservoir. Inlet and outlet conditions are resumed in table 1. The grid in the boundary layer region is extremely refined: this is due to the fact that properties needed for the computation of the first cell height—such as kinematic viscosity—are difficult to determine accurately for the

Fluid	MDM
Gas Constant	35.152 ($J/K/kg$)
Specific heat ratio	1.0125
Critical temperature	564.1 $^{\circ}K$
Critical pressure	1415000 Pa
Acentric factor	0.529
Total inlet temperature	526.35 $^{\circ}K$
Total inlet pressure	400000 Pa
Static outlet pressure	1000 Pa
Molecular viscosity	1.376E-5 $Pa \times s$
Thermal conductivity	0.04728 $W/m/K$
Turbulence model	SST- $k\omega$ and SA
Spatial scheme	Upwind generalized Roe 1 nd order

Table 1: Test conditions for the 2D TROVA nozzle simulation.

involved fluid. Indeed the first cell height for this test case is $\approx 1e^{-7}[m]$ –flow involving air in standard condition requires $\approx 1e^{-5}[m]$ –. The nozzle is studied when the discharge occurs in off-design conditions, namely when the coefficient of expansion is 5.58 (design conditions correspond indeed to 10), in this test case the nozzle is then operating in an under-expanded regime. The predicted flow-field is shown in figure 1: the upper half of the picture refers to a grid composed by $\approx 75k$ elements while Mach contours in the lower half is related to a $\approx 180k$ cells mesh. This result was obtained using the ideal gas law to describe the fluid thermodynamic behaviour and the SST- $k\omega$ for modelling turbulence. At the discharge section a Prandtl-meyer expansion occurs: the flow is turned outwards and redirected towards the reservoir wall, where a symmetry boundary condition holds. The supersonic flow hence hits the boundary fostering the rise of a compression shock-wave: a system of reflected shock-wave then propagates through the reservoir. Figure 1 shows how a more refined discretization of the reservoir is needed in order to represent the wave reflecting system with a higher level of resolution. This was expected since a numerical scheme of the first order is highly dissipative and hence strongly dependent on the grid spacing: shock-wave in the coarser mesh is indeed smeared out moving along the nozzle axis. Mach and pressure trends along the centreline for the three different equation of state, computed using the SST- $k\omega$ turbulence model, are reported in figure 2 and 3.

3.2 2-D ORCHID nozzle

The ORCHID (Organic Rankine Cycle Hybrid Integrated Device) is an experimental facility being constructed at the Aerospace Propulsion and Power (APP) Lab. of the Delft University of Technology. It will be used to perform gas dynamic studies of non-ideal expansions and performance comparisons of high-speed ORC turbomachinery. The facility has been set up in collaboration with Robert Bosch GmbH (Solar ORC turbogenerator for zero-energy buildings) and by Dana-Spicer Corp (Mini-ORC turbogenerator for combined cycle powertrains). In this section we show a flow field simulated by SU2 for the linear siloxane hexamethyldisiloxane (MM); namely one of the working fluids considered in the design of the ORCHID with simulation parameters and set values specified in Table 2. RANS equations are solved with the slip condition at the walls and symmetry along the mid-plane. The FEQ Helmholtz equation of state implemented in the FluidProp thermo-dynamic library is used to model the fluid behaviour, the result is compared to the output from the integral balance equations for an adiabatic flow and a steady oblique shock wave. The test case is presented in Figure 4; a two-dimensional converging-diverging nozzle generated with a MoC code, Guardone and Dossena (2012), with a model placed 18 mm from the throat with a flow turning angle $\theta = 20^{\circ}$ along the centreline. Figure 5 depicts the terminology used, with β corresponding to the oblique shock wave angle and V to the velocity before and after the shock. The shock wave resulting from the CFD computation is 45.0° and is reflected off the nozzle profile wall, subsequently

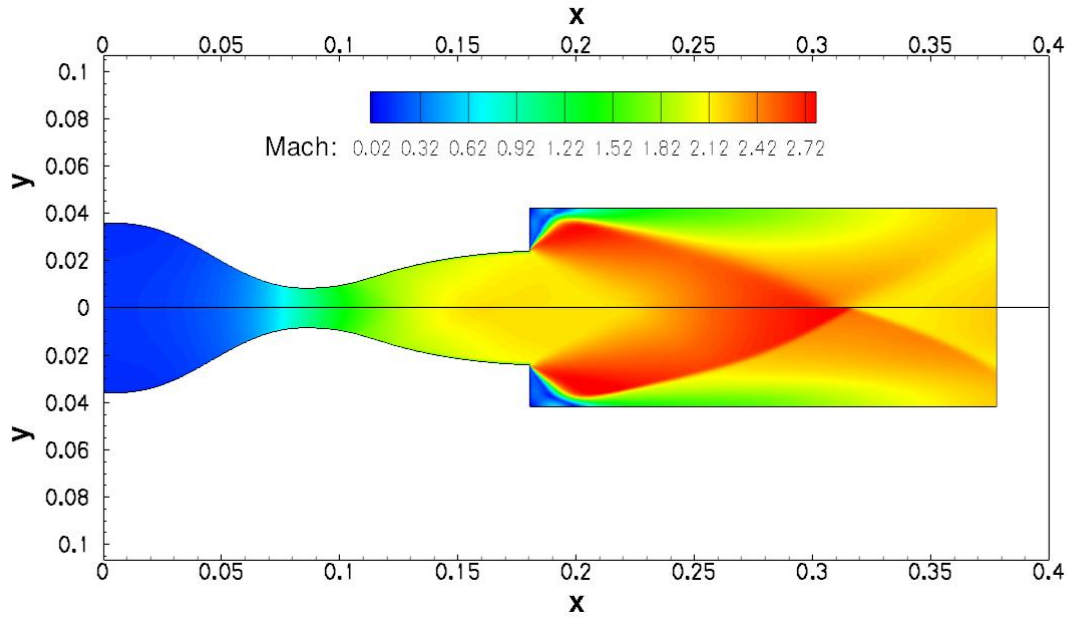


Figure 1: Mach contour in TROVA nozzle using polytropic ideal gas equation of state and SST- $k\omega$ turbulence model for two different level of mesh refinement: respectively $\approx 74k$ elements (upper side) and $\approx 180k$ elements (lower side). Axis refers to dimensional length [m].

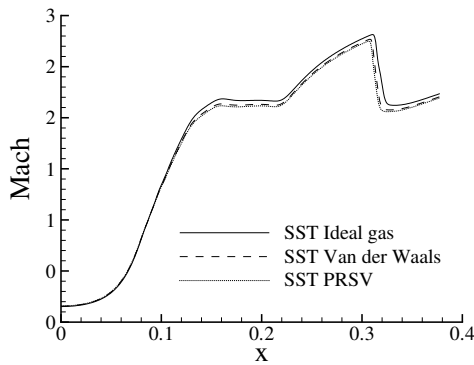


Figure 2: Comparison of Mach number trends along the centreline.

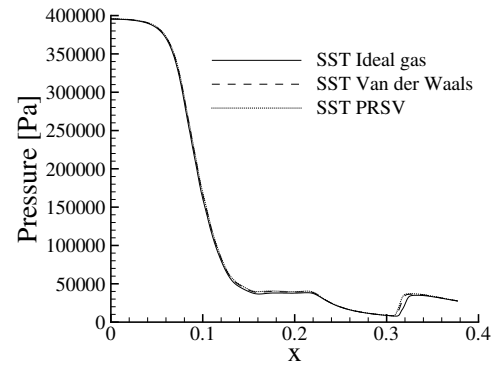


Figure 3: Comparison of pressure trends along the centreline.

Fluid	MM
Thermodynamic model	FEQ Helmholtz
Critical temperature	518.75 K
Critical pressure	19.39 bar
Total inlet temperature	525.15 K
Total inlet pressure	18.4 bar
Spatial scheme	Upwind generalized Roe 2 nd order
Turbulence model	SST- $k\omega$
Inlet turbulence intensity	0.001
Reynolds Number Throat	1.642E6
Spatial scheme	Upwind generalized Roe 2 nd order

Table 2: Main parameters of the 2D ORCHID supersonic nozzle simulation.

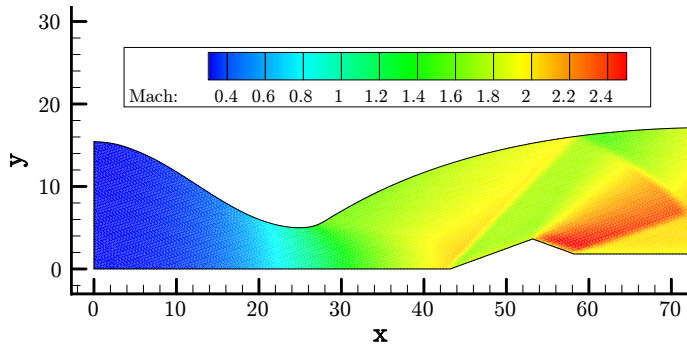


Figure 4: Mach contours of the 2D nozzle.

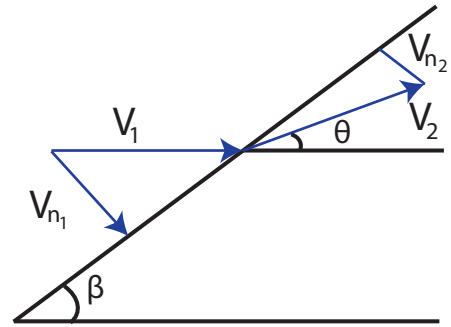


Figure 5: Oblique Shock Wave Angles and Vectors.

cutting the expansion fan that is generated from the back of the model. It is well known that the conditions across the surfaces of discontinuities are governed by the integral conservation equations. The jump conditions across a steady shock-wave for the continuity, momentum and energy equations cannot be solved with a simple closed-form expression as is the case for an ideal gas. The Rankine-Hugoniot relations are rendered obsolete and thus, for a non-ideal gas which uses more complicated equations of state, an iterative calculation procedure is employed to obtain the thermodynamic change across a shock wave and is given by Grossman (2000). It is now possible to determine the relationship between the M_1 - β - θ variables and when providing inputs such as θ , V_1 , P_1 and ρ_1 , properties after the shock may be calculated. This allows calculation of relevant data such as shock strength, angle and the location along the mid-plane where detachment occurs, while maintaining relatively fast computational times. The resulting β is 44.3° and represents a 1.5 % deviation in the solution compared to the results in Figure 4 above.

3.3 Supersonic ORC turbine stator

In this test-case the capabilities of the new NICFD solver are tested in predicting the flow feature of a supersonic ORC turbine cascade. The calculations are performed using the inviscid solver, the SA and the SST- $k\omega$ turbulence models. Table 3 summarizes the main inputs for the solver.

Figure 6 plots the Mach contour of the simulation using the SST- $k\omega$, and, as can be noticed, the flow field is characterized by intense shocks and expansion fan interactions at the outlet. It is important to predict these phenomena with high accuracy because they generally represent the main source of fluid-dynamic losses for these particular applications. As can be seen indeed from Fig. 7 no distinctions can be appreciated in the pressure distribution trends plotted for the three different simulations. Figure 8 confirms the predominance of supersonic effect on the flow solutions, and a very low discrepancy can be appreciated on the flow Mach number trend at the outlet section.

4. CONCLUSIONS

In this paper SU2 CFD suite was considered as a possible candidate for representing a reliable investigation tool for the study and for the design of Organic-Rankine Cycle turbo-machinery. SU2 simulating capabilities were recently extended to real gas flows by the inclusion of an embedded collection of fluid models, which comprehend three different equation of state—polytropic ideal gas, polytropic Van der Waals and polytropic Peng-Robinson Stryjek-Vera—for the description of fluid behaviour and also by the inclusion of the FluidProp thermo-physical library.

Fluid	MDM
Specific heat ratio	1.0214
Total inlet temperature	545.17 °K
Total inlet pressure	800000 Pa
Static outlet pressure	10000 Pa
Molecular viscosity	1.0461E-5 Pa × s
Thermal conductivity	0.028085 W/m/K
Turbulence model	SST- $k\omega$ and SA
Inlet turbulence intensity	0.05
Spatial scheme	Upwind generalized Roe 2 nd order

Table 3: Test conditions for the 2D supersonic stator.

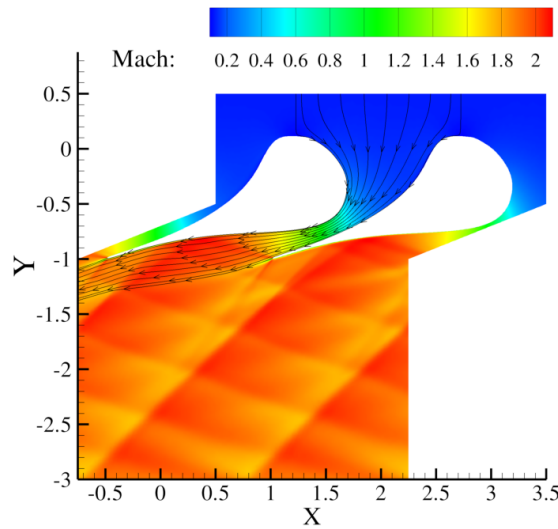


Figure 6: Mach flow field of the 2D supersonic stator fusing the SST- $k\omega$ turbulence model. Units on the axis are scaled due to industrial secrecy.

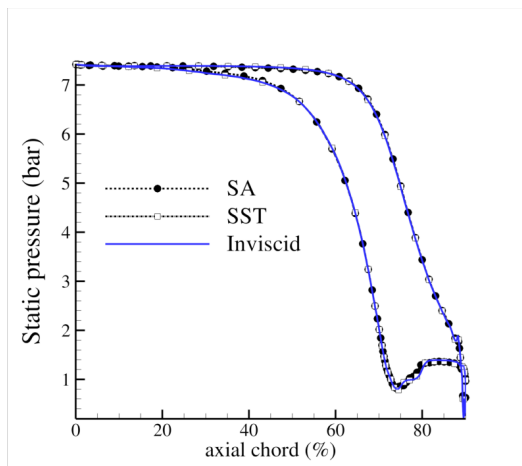


Figure 7: Pressure distribution around the blade profile for the inviscid case and with SA and SST turbulence models.

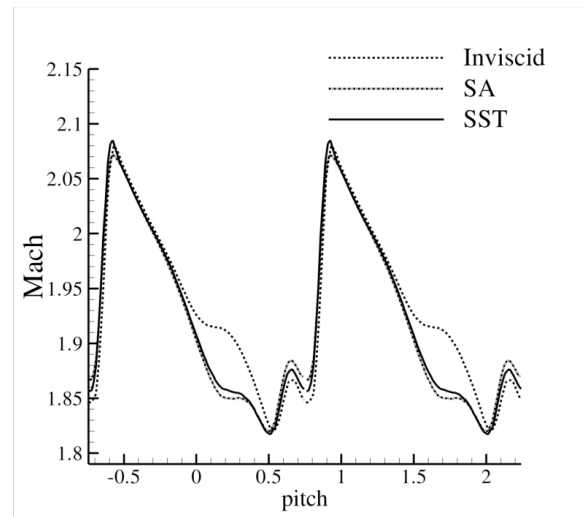


Figure 8: Mach trend at the outlet for the inviscid case and with SA and SST turbulence models.

Within the aim of SU2 it is possible to manage non-ideal compressible flows that may exhibit

non-classical gas-dynamic phenomena. This include fluid flows that slightly depart from an ideal behaviour but also fluid flows that give birth to rarefaction shock-waves and compression fans. The open-source trait opens the path to a wide range of possibilities: the integration of new software packages devoted to real gas applications is easily achievable within the SU2 framework. In this paper we showed that SU2 is already capable of tackling problems that engineers or researchers may face in typical ORC applications: simulation involving geometries of utmost importance such as nozzles and a typical ORC turbine blade passage were carried out. Different equation of state were used to describe the thermodynamic behaviour of fluids characterized by a highly complex molecular structure and using both first and second order numerical schemes.

REFERENCES

- Blazek, J. (2005). *Computational Fluid Dynamics: Principles and Applications*. Elsevier, Oxford.
- Colonna, P., Guardone, A., and Nannan, N. R. (2007). Siloxanes: a new class of candidate Bethe-Zeldovich-Thompson fluids. *Physics of Fluids*, 19.
- Colonna, P., Rebay, S., and Silva, P. (2002). Computer simulations of dense gas flows using complex equations of state for pure fluids and mixtures and state of the art numerical schemes. Technical report.
- Colonna, P. and van der Stelt, T. P. (2004). FluidProp: a program for the estimation of thermo physical properties of fluids. software.
- Grossman, B. (2000). Fundamental concepts of real gasdynamics. Technical report, Virginia Polytechnic Institute and State University.
- Guardone, A., Isola, D., and Quaranta, G. (2011). Arbitrary Lagrangian Eulerian formulation for two-dimensional flows using dynamic meshes with edge swapping. *Journal of Computational Physics*, 230(20):7706–7722.
- Guardone, A. Spinelli, A. and Dossena, V. (2012). Influence of molecular complexity on nozzle design for an organic vapor wind tunnel. *J. of Eng. For Gas Turb. And Power*.
- Landau, L. and Lifshitz, E. (1993). *Fluid Mechanics (2nd Edition)*. Pergamon Press.
- Montagne, J. and Vinokur, M. (1990). Generalized flux-vector splitting and Roe average for an equilibrium real gas. *Journal of Computational Physics*, 89(2):276–300.
- Nannan, N., Guardone, A., and Colonna, P. (2014). Critical point anomalies include expansion shock waves. *Physics of Fluids*, 26:021701–7.
- Palacios, F. et al. (2013). Stanford university unstructured (su2): An open-source integrated computational environment for multi-physics simulation and design. *AIAA Paper 2013-0287*.
- Palacios, F. et al. (2014). Stanford university unstructured (su2): Open-source analysis and design technology for turbulent flows. *AIAA Paper 2014-0243*.
- Pini, M., Spinelli, A., Persico, G., and Rebay, S. (2014). Consistent Look-up Table Interpolation Method for Real-Gas Flow Simulations. *submitted to Computers & Fluids*.
- Spinelli, A. et al. (2012). Design, simulation, and construction of a test rig for organic vapors. *J. of Eng. For Gas Turb. And Power*.

- van Leer, B. (1979). Towards the ultimate conservative difference scheme V. a second-order sequel to Godunov's method. *Journal of Computational Physics*, 32(1):101–136.
- Vitale, S. et al. (2015). Extension of the SU2 Open Source CFD code to the simulation of turbulent flows of fluids modelled with complex thermophysical laws. *AIAA (accepted for publication)*.

ACKNOWLEDGEMENT

The research is partially funded by the European Research Council under Grant ERC Consolidator 2013, project NSHOCK 617603.

FLUID DYNAMIC DESIGN AND ANALYSIS OF A HIGHLY LOADED CENTRIFUGAL ROTOR FOR MINI ORC POWER SYSTEMS

Salvatore Vitale^{1*}, Matteo Pini¹, Antonio Ghidoni² and Piero Colonna¹

¹ Delft University of Technology, Propulsion and Power,
Delft, The Netherlands
s.vitale@tudelft.nl

² Università degli studi di Brescia, Department of Mechanical and Industrial Engineering,
Brescia, Italy

* Corresponding Author

ABSTRACT

This article presents the fluid-dynamic design and analysis of a high-loaded centrifugal rotor for mini ORC applications. Recently a vast interest about mini ORC turbogenerators is growing up. These systems must be equipped with high-efficient turbines to maximize their overall efficiency. Recent works demonstrated that, among the various alternatives, the multi-stage centrifugal turbine may be extremely attractive for such applications. However, this turbine is characterized by a very high loaded first stage whose design has a key role for the success of the technology. In order to cope with these severe conditions we propose a design methodology specifically tailored for radial-outflow cascades. The method combines NURBS curves and flow passage area control to "physically" drive the construction of the profiles. As exemplary test case, we apply the new procedure to the design of the first rotor of a $10kW_e$ micro centrifugal turbine for heat recovery application. Finally, we assess the performance of the designed rotor by means of 2D and 3D turbulent simulations, providing an extensive comparison against preliminary estimates based on Traupel and Craig&Cox loss correlations. The results show that the design method is flexible and quick enough to minimize losses by few manual iterations. Furthermore, it turned out that both loss models fairly well estimate profile losses, even if Traupel seems to be more accurate than Craig&Cox model to predict secondary and tip clearance loss effects.

1. INTRODUCTION

Organic Rankine Cycles (ORC) power systems are, nowadays, a well-established technology for the conversion of thermal energy sources in the small-to-medium power range (from 100 kW_e to few MWe), D'Amelio (1935); Tabor and Bronicki (1964); Angelino et al. (1984); Verneau (1987). Miniaturized (5-30 kW_e) systems are particularly attractive for waste heat recovery onboard mobile applications, e.g. trucks or aircrafts, and for decentralized energy production in combination with solar heat sinks.

The realization of successful mini ORC (*mORC*) power systems demands to design highly efficient (>75%) mini-turboexpanders, to be competitive with respect to existing alternatives like fuel-cells. As well documented, the use of organic media generally leads to unusual turbine configurations, Macchi (1985, 1977): few axial stages or a single centripetal stage, often characterized by supersonic flows and strong shocks. These phenomena are even worse in small blade passages, due to the interaction with tip and secondary vortex structures. The achievement of high-efficient mini-turbines implies a full redefinition of the design strategy of the expander, starting from the turbine concept, passing through dedicated preliminary design optimization, Pini et al. (2013); Casati et al. (2014), and eventually arriving at a complete new definition of the optimal blade profiles through advanced methodologies, Persico et al. (2013); Pini et al. (2014).

Recently, the multi-stage radial-outflow turbine (ROT) has been thoroughly studied for ORC power sys-

tems. This configuration naturally accommodates the high volumetric flow ratios typical of ORC fluids and allows for compact multi-stage arrangements, thus preventing high supersonic flows. Although in a previous work the authors already demonstrated with a preliminary investigation that ROT may allow for compact and efficient turbo-expanders for *m*ORC systems, Casati et al. (2014), many challenges are still to be addressed for the success of this architecture. One of the open issue regards the design and performance evaluation of the first stage, which operates under very unfavorable flow conditions. Notably, this stage usually features a rotor characterized by high flow deflection, low aspect ratio and significant tip-to-blade height clearance, resulting in low fluid dynamic performance that may compromise the efficiency of the whole machine. Moreover, the rotor is subject to non-inertial effects, i.e. centrifugal and Coriolis fictitious forces, and to a high increase of the flow passage in the radial direction that pose additional concerns during the blade design process.

Consequently, demonstrating that the first rotor can be designed with acceptable efficiency is crucial to quantify the actual gain offered by the ROT concept for *m*ORC with respect to axial and radial-inflow competitors. For this reason the objective of this work is to perform a trustworthy fluid dynamic design of the first rotor of a 5-stages small centrifugal turbine preliminary which was designed following the methodology provided in Casati et al. (2014). The study is supported by detailed 2D and 3D CFD analysis and complemented by a comparison between the computed and predicted (by means of the widely used empirical correlations Craig and Cox (1971); Traupel (1977)) loss coefficients.

The blade profile definition is carried out by a novel methodology for the aerodynamic design of centrifugal blades based on NURBS curves and flow passage area detection. The algorithm is implemented in a new CAD Turbine Blade Modeler (TBM) exploiting the Python API of the open-source (LGPL License) Software FreeCAD Falck and Collette (2012). The TBM is in turn automatically linked with two in house mesh generators (named UMG2 and UMG3, respectively) to create high quality 2D and 3D grids. The flow calculations are carried out by resorting to the SU2 solver, recently extended by the authors to deal with arbitrary thermo-physical models Vitale et al. (2015).

The paper is organized as follows: Section 2 illustrates the procedure devised for the design of centrifugal cascades, Section 3 extensively describes the design of the first rotor of a *m*ORC for heat recovery applications, while section 4 analyses the performance of the considered cascade with blade-to-blade and 3D simulations.

2. METHODOLOGY

This section briefly recalls the tools adopted in this work and reports extensively the methodology devised for the design of centrifugal blades.

2.1 Numerical Methods

The CFD solution is obtained by coupling the in-house mesh generation software UMG2 and UMG3, Ghidoni et al. (2006), to the SU2 suite. SU2 discretizes and solves the fluid governing equations using the finite volume approach on unstructured grids. The code has been recently extended by the authors to treat non-ideal compressible fluid flows that commonly occur in ORC turbines. An exhaustive description of the solver characteristics alongside the numerical validation process can be found in Vitale et al. (2015).

2.2 Centrifugal Blade Construction

In the centrifugal architecture the peripheral speed does not change along the blade span allowing to resort to untwisted blades. For this reason, the construction of a centrifugal blade reduces to the definition of a 2D blade profile simply lofted to construct the 3D geometry.

Figure 1 illustrates the construction of the centrifugal camber-line using NURBS curve. The camber-line is completely defined by the inlet blade angle β_{in} , the outlet blade angle β_{out} , the stagger angle γ , the radial chord c_{rad} and the *LE* position. As a matter of fact the *TE* position is uniquely defined by the *LE*,

γ and c_{rad} , and an additional third point P_{int} resulting from the intersection of the inlet and outlet lines. These two lines follow the direction of β_{in} and β_{out} , respectively, which are defined in the radial reference of framework.

Using three *CPs* the camber-line assumes a quadratic shape, and changing the weight value of the intersecting control points the ensemble of the quadratic curves can be represented as an arc of parabola ($w_{int} = 1.0$), hyperbole ($w_{int} > 1.0$), ellipse or circle ($w_{int} < 1.0$) Piegl and Tiller (1997).

The approach used for the construction of the pressure and suction side is based partially on the work of Vestraete (2010) for the construction of 2D axial turbine blade. The *SS* and *PS* are NURBS curves themselves whose shape is specified by distributing the *CPs* according to a thickness law as a function of the camber-line length. Figure 2 shows an example of *TD* for the suction side, and, on top, the corresponding distribution of the *CPs* on the *SS* along the blade camber-line. It is worth to note that by properly tuning the *TD* law any desired blade loading trend can be met.

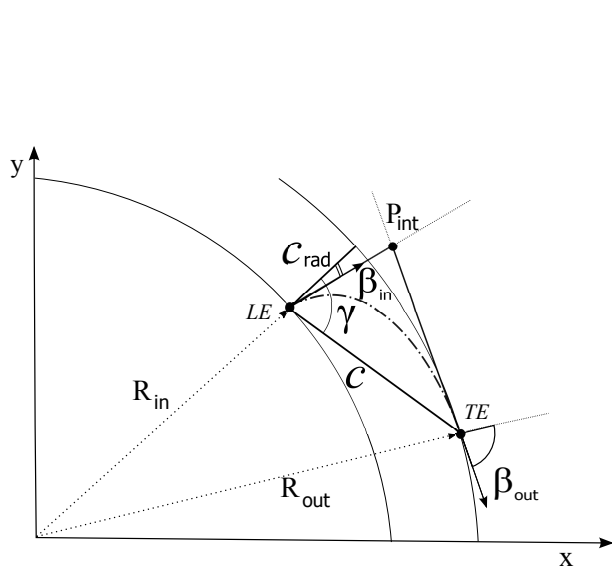


Figure 1: Camber-line construction for a centrifugal turbine using NURBS curve.

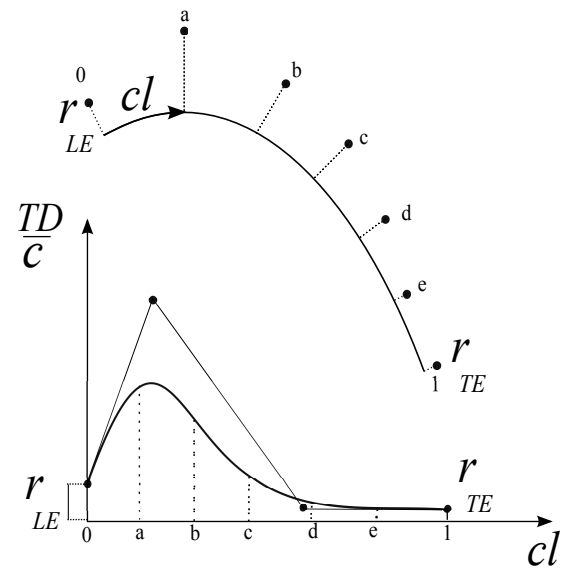


Figure 2: 2D centrifugal profile construction using NURBS curve.

3. 2D DESIGN OF A CENTRIFUGAL ROTOR FOR MINI-ORC APPLICATIONS

This section presents the design of a high loaded centrifugal rotor by using the TBM and the NICFD solver in an iterative manner to attain a convenient blade shape.

3.1 Design of the Rotor Blade

We here consider the first rotor of the 5-stage small-scale transonic ROT as exemplary test case. The total efficiency of the machine was predicted by the Traupel's loss model to be approximately 80%. The main data for the blade geometry construction and the boundary conditions for the CFD simulation are provided in Table 1 and 2, respectively. Figure 3 shows the trends of the main parameters influencing the performance of the turbine cascades: blade deflection, aspect ratio and the tip clearance. The first rotor (blade row n°2 in Fig.3) is characterized by the most severe conditions: extremely high flow deflection, low aspect ratio and high tip clearance to blade height ratio. Additionally, Fig. 4 reports the relative increase of the passage area and peripheral speed of each blade row for the same turbine. Due to the high increase of the peripheral speed along the stream-wise direction, the first rotor is furthermore subject to a significant rise of the (relative) fluid mechanical energy from the inlet to the outlet. As a consequence, higher Mach numbers are expected to occur at the rotor outlet compared to stationary cascades of similar geometry, working under the equivalent expansion ratio. On the other hand, if not properly handled, the radial evolution of the machine may lead to unexpected converging-diverging passage areas even

adopting purely converging blades with sudden flow supersonic excursions and generation of strong shocks.

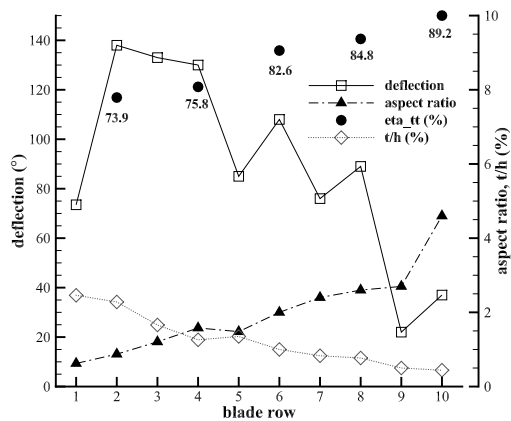


Figure 3: Flow deflection, aspect ratio, tip clearance for each blade row and total total efficiency for each stage of the 5-stage mini centrifugal turbine.

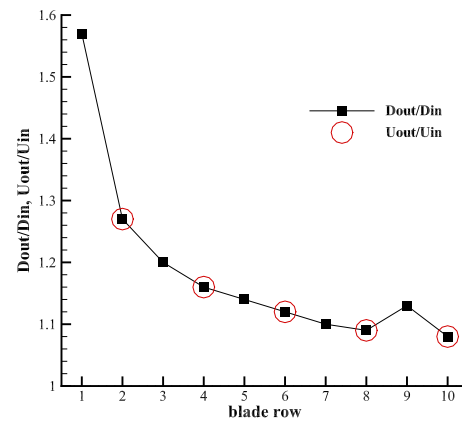


Figure 4: Rate of increase of the diameter for each blade row and of the peripheral speed for each rotor blade of the 5-stage mini centrifugal turbine.

The design of centrifugal profiles cannot follow any standard design rule established for axial cascades, as already pointed out in Persico et al. (2015), where the analysis was restricted to slender profiles for low deflection radial cascades and suggested rather simple design criteria, i.e. elliptic mean-arc and thickness distribution taken from existing profiles, that are almost useless in presence of high-loaded blades with relevant radial area evolution. Hence, we adopt the more general approach explained in the previous section to achieve a suitable blade profile for such unconventional configuration.

As anticipated the degrees of freedom for the 2D profile are the stagger angle γ and the thickness distribution for the pressure (TD_{PS}) and suction side (TD_{SS}). R_{in} , c_{rad} , β_{out} , N_{blades}^o , TE_{th} are the inputs for the TBM, while the prescribed blade throat width o_{out} is achieved by selecting the appropriate TD_{PS} , TD_{SS} , and γ .

R_{in}	1.88 cm
c_{rad}	0.5 cm
β_{in}	66.0 °
β_{out}	-74.1 °
N_{blades}^o	38 [-]
o_{out}	0.1 cm
te_{th}	100 μ m

Fluid	D4
$T_{t,in}$	305.79 °C
$P_{t,in}$	3.66 bar
$P_{s,out}$	1.655 bar
$\beta_{flow,in}$	66.0 °
N	19000.0 rpm

Table 1: Geometrical parameters for the desing of the rotor blade. **Table 2: Main input data for the CFD simulation.**

Figure 5 shows the designed rotor cascade. As highlighted in the top picture of Fig. 6, the radial evolution of the cascade dictates an unusual non-monotonic trend of the flow passage area (PA). The inlet semi-bladed region is characterized by a throat located where the flow encounters the SS at the LE . Then the PA increases until the flow reaches the PS . If not conveniently controlled this trend may generate undesired supersonic flow bubbles with high risk of flow separation on the SS . Consequently strong adverse pressure gradients may establish on both pressure and suction sides with the increasing of the boundary layer. Also in the semi-bladed outlet region the PA increases, triggering the onset of strong shock waves on the suction side.

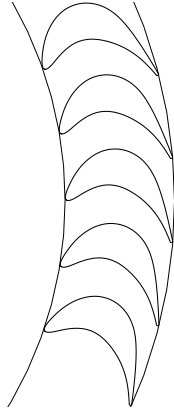


Figure 5: Centrifugal rotor 2D profile.

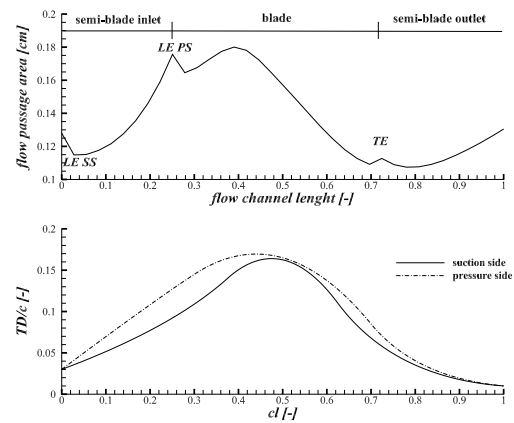


Figure 6: Flow passage area distribution and TD_{SS} and TD_{PS} of the 2D centrifugal rotor.

The optimal rotor configuration should mitigate all these loss mechanisms. The final blade shape was derived by iteratively changing the TD_{SS} , the TD_{PS} and the γ . Each blade profile was tested by means of 2D viscous simulations using the SST turbulence model and few design adaptations were necessary to minimize the fluid-dynamic losses. The bottom picture of Fig. 6 displays the final TD_{SS} and TD_{PS} laws used to construct the final profile. A value of 22.5 was set for the stagger angle. It can be observed that the LE thickness is thin, especially on the SS , in order to avoid the creation of a throat in the semi-bladed inlet region; in the middle part the profile is rather thick so as to better guide the flow and prevent separations; the TE is conversely set to the smallest value, compatible with manufacturing limits, in order to reduce wake and mixing losses. Figure 7 shows the relative Mach contour of the designed centrifugal rotor; it can be appreciated that no shocks appear upstream of the blade and no flow separations occur on both suction and pressure sides. As expected, shock waves are clearly visible downstream of the blade as a result of the flow over-expansion on the rear suction side.

A further improvement of the rotor performance can be certainly achieved by means of shape optimization algorithms. However, as demonstrated, a thorough understanding of the physical problem can already aid the initial design of the cascade without the need of expensive optimization procedures. Furthermore, the present algorithm can greatly help to drive the automated design algorithms in the early steps.

4. NUMERICAL VERIFICATION OF THE CENTRIFUGAL ROTOR

In this section we illustrate the fluid-dynamic performance of the designed high loaded centrifugal rotor by means of blade-to-blade and fully 3D simulations.

4.1 2D CFD analysis

The blade-to-blade performance of the final rotor configuration are now discussed in detail. The siloxane D4 is modeled as a polytropic Peng-Robinson gas. Table 3 summarizes the main results of the 2D simulation. The profile losses are estimated by resorting to the mixed-out average at inlet section and at a section placed 5% of the radial chord downstream of the trailing-edge. At nominal conditions the corresponding kinetic energy loss coefficient is nearly 3.9%, while values predicted by the Traupel's and Cox's model are about 3.2% and 5%, respectively. Considering that these correlations were developed for axial cascades, we can conclude that, at least at a preliminary level, they provide a reasonable measure of the 2D performance of the cascade and can be used in the design phase of $mORC$.

\dot{m}_l	1.64 kg/s/m
M_{out}	1.05 [-]
$\beta_{out,flow}$	74.49 °
ζ_{is}	3.9 [-]

Table 3: Main results of the blade to blade simulations

When assembling the full row we considered the number of blades as a fixed input from the preliminary design phase. However, as well known in turbomachinery theory, the solidity largely affects the overall fluid-dynamic performance of the cascade. In case of radial *m*ORC the direct application of the solidity correlations for axial turbines is somewhat questionable and therefore accurate numerical predictions may be necessary to determine the optimal value. Figure 8 presents a study of the optimal number of blades to minimize the profile losses. All the profiles have the same TD_{SS} and TD_{PS} , yet a different stagger angle in order to keep constant the gauging angle ($\frac{\rho}{s}$). The minimum profile losses arises for 38 blades, surprisingly in accordance with the number of blades estimated by the Zweifel criterion, Zweifel (1945), and used in the preliminary design phase. Figure 9 shows that in all cases two successive shock waves occur on the suction side though of different intensity. The first shock, that is weaker for the row with 32 blades, is generated by the interaction of the suction flow with the expansion fan impinging on the suction side. It is interesting to note that increasing the number of blades the flow experiences larger acceleration on the suction side, leading to a stronger fishtail shock wave. All these phenomena are amplified by the diverging shape of the streamtube along the radial direction, which emphasizes the flow accelerations and arrests. An opposite trend manifests just upstream of the trailing-edge. The reduction of blade loading induces lower velocities and adverse pressure gradients, resulting in a much weaker second shock for the case with 45 blades. The profile losses are greatly influenced by the combination of these two shocks and the final optimum solidity is reached with 38 blades, which may represent the trade-off between the two opposite situations.

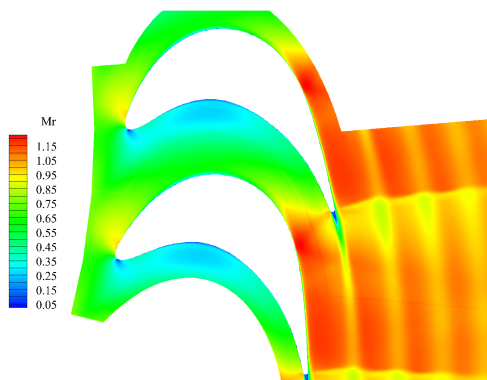


Figure 7: Mach contour of the designed centrifugal rotor.

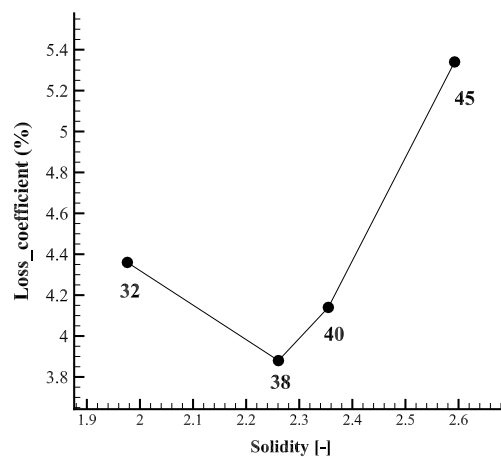


Figure 8: CFD blade to blade results of the solidity optimization for the centrifugal rotor.

Besides the major role on the fluid dynamic losses, the solidity parameter influences the flow slip and, eventually, the work extraction from the radial cascade. Figure 10 shows the angular difference between the rotor simulated as a rotating cascade and as a stationary cascade (provided consistent relative boundary conditions) for different number of blades. In order to avoid any post expansion and post compression effect, that can modify the outlet flow angle, the boundary conditions for the static case are chosen to obtain the same averaged flow Mach number at the outlet. The results are qualitatively in

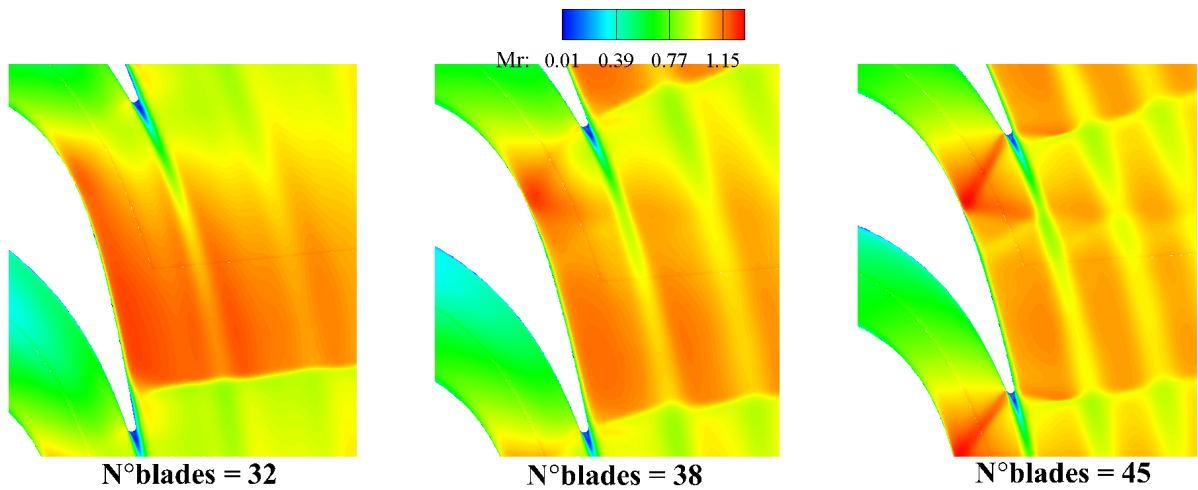


Figure 9: Rotor profile and its blade channel curve.

agreement with the general theory of circulation, which admits, for purely radial cascades, the presence of a counter-rotating vortex acting on the blade to blade plane ($\nabla W = -2\omega$). The net effect is the appearance of a fictitious force deflecting the flow (slip effect) in the tangential direction, namely in the opposite direction to the verse of rotation of the turbine. As expected, the slip vanishes for a high number of blades, as occurs in the first rotor of *mORC*turbines.

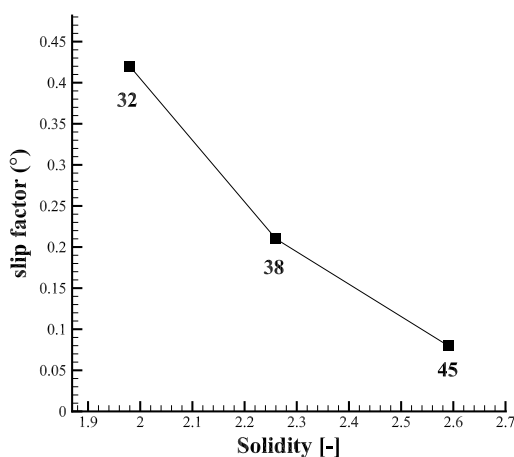


Figure 10: Slip factor for 3 centrifugal cascade with 32, 38 and 45 blades.

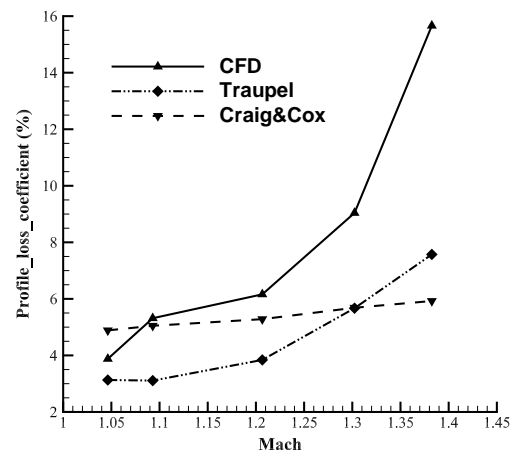


Figure 11: Comparison of the profile losses estimation.

Another key aspect of the radial cascades is their behaviour at off-design conditions. This is particularly relevant for small-scale turbines, as their functioning is intimately connected to the energy demand of the load. The blade to blade analysis of the 38 blade cascade is herein extended at moderate partial loads, until reaching an outlet Mach number of 1.4. To aid the reader we remember that Mach 1.4 is the traditional design limit in axial configurations to retain purely converging blades. The objective of the study is twofold: to assess the reliability of the correlations, and to gain knowledge about the characteristic of converging centrifugal blades for weakly supersonic flows. The outcomes are illustrated in Fig.11. As well visible, the results show that up to Mach 1.2 the predictions of the loss models are fairly in accordance with CFD results. While the C & C correlation displays a smaller deviation and fails to capture the correct slope of the loss curve, the Traupel's correlation provides a more reliable trend, even if it underestimates the losses for the whole range of operating conditions. This suggests that using such

correlations for weakly and fully supersonic flows in *m*ORC turbines may result in the over-prediction of the expander total-to-total efficiency. Likewise some general recommendations can be drawn on the basis of the CFD predictions. The exponential-like growth of the rotor losses above Mach 1.2 indicates that radial-outward converging blades optimized for transonic regimes may suffer of severe drawbacks already at moderate off-design conditions, strengthening the idea that robust fluid-dynamic design of mini-ROT can be truly achieved by fully multi-stage robust optimization procedures.

4.2 3D CFD analysis

This section briefly describes the 3D CFD analysis of the rotor cascade. As previously mentioned the 3D profile is generated simply lofting the 2D profile. The blade height ($blh = 0.43$ cm) is calculated by using the linear mass flow computed with the blade to blade analysis and the expected mass flow ($\dot{m} = 0.266$ kg/s) of the turbine ($blh = \frac{\dot{m}}{\dot{m}_1}$).

Three 3D configurations have been considered to investigate the different loss mechanisms occurring in the 3D blade passage: a geometry i) with slip end-walls to determine the profile losses, ii) with no slip end-walls to estimate secondary flows, and iii) with a tip clearance $tcl = 100\mu\text{m}$ and $tcl = 200\mu\text{m}$ to examine the tip loss mechanism.

The calculations were performed using the same boundary conditions specified for the 2D case and unstructured meshes of about 3 million elements. Convergence was approximately reached after 10000 iterations (10 hours on 20 cores, Intel® Xeon(R) CPU E5-2687W 3.10GHz).

Table 4 shows the breakdown of the loss sources. As expected the tip clearance losses highly penalize the performance of small-scale ORC cascades. As a matter of fact, as depicted in Fig. 13, even with tcl over blh around $\frac{1}{40}$, the tip clearance vortex covers about 25 % of the flow passage area. Such vortex structure causes a considerable distortion of the flow angle at tip, see Fig. 12, which eventually leads to a lower averaged outlet flow angle and, hence, a significant reduction of work extraction. Indeed a even worse situation would occur by doubling the tcl to $200\mu\text{m}$. Finally, Table 5 compares the fluid dynamics losses estimated by the CFD and empirical correlations. The C & C model fails in predicting the secondary and tip losses whereas the Traupel, though with some overestimation, better captures the trends.

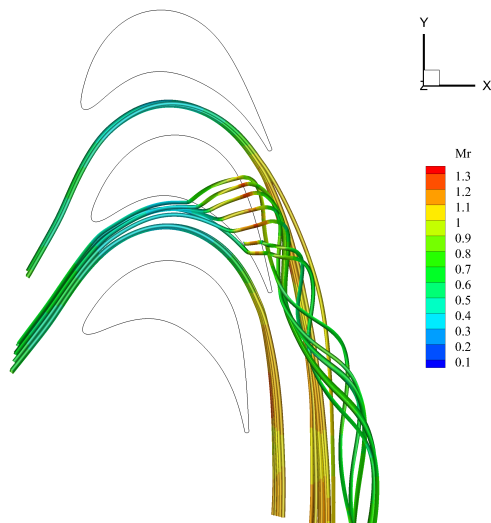


Figure 12: 3D stream lines of the flow solution with tip clearance $100\mu\text{m}$ top view.

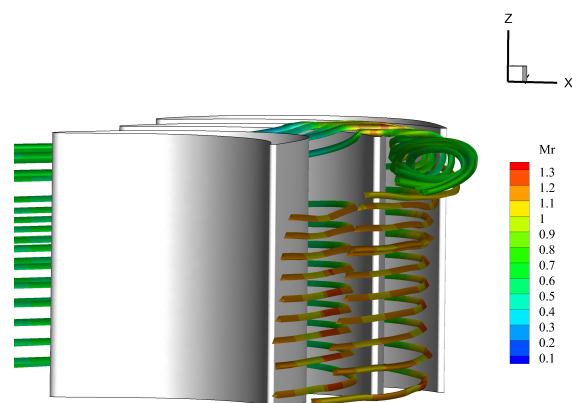


Figure 13: 3D stream lines of the flow solution with tip clearance $100\mu\text{m}$ downstream view.

5. CONCLUSIONS

This work illustrated the application of a novel blade design methodology to the development of a high loaded centrifugal blade for mini-ORC turbines. The use of a physical-based approach allows to obtain a

case	$\zeta_{is,tot}$	$\beta_{flow,out}$	ew
Blade to blade	3.9	74.5	6.84
3D no tip	7.3	74.4	6.66
3D 100 μm tip	17.0	72.24	6.20
3D 200 μm tip	24.8	70.5	6.05

Table 4: Main results of the simulations.

tool	$\zeta_{is,p}$	$\zeta_{is,s}$	$\zeta_{is,tcl,100}$	$\zeta_{is,tcl,200}$
CFD	3.9	3.4	9.7	17.5
C & C	4.9	11.7	3.8	8.3
Traupel	3.2	5.9	14.1	22.7

Table 5: Comparison between the CFD results and the loss models.

blade design, comparable with the performance predicted at a preliminary design level. However, CFD results show that, due to the complexity of the fluid-dynamic phenomena involved (shock wakes and vortex interactions), there is indeed room to further improve the actual efficiency of the blade by resorting to advanced shape optimization methods. Finally the loss models used for the preliminary design of the turbine were assessed against CFD predictions. For the specific application here considered the Traupel's model outperforms the Craig & Cox model, which fails in reproducing secondary and tip phenomena. Hence, the use of the Traupel's model at a preliminary design level may lead to a more reliable design for such unconventional turbines.

NOMENCLATURE

NICFD	Not Ideal Compressible Fluid-Dynamics	
ROT	Radial-Outflow Turbine	
TBM	Turbine Blade Modeler	
β	blade and flow angles	($^{\circ}$)
γ	stagger angle	($^{\circ}$)
LE	leading-edge	
TE	leading-edge	
P	pressure	(bar)
T	temperature	(C°)
N	rotational speed	(rpm)
blh	blade height	(rpm)
c	blade chord	(m)
cl	camber-line length	(m)
o	throat width	(m)
tcl	tip-clearance	(m)
\dot{m}	mass flow	(kg/s)
M	flow Mach number	($-$)
ζ_{is}	kinetic energy loss coefficient	($\%$)
ew	eulerian work	(kJ/kg)
TD	thickness distribution	
SS	suction side	
PS	pressure side	
CPs	control points	
w	weight of the NURBS	

Subscript

is	isentropic
int	intersected
l	linear
th	thickness

REFERENCES

- Angelino, G., Gaia, M., and Macchi, E. (1984). A review of Italian activity in the field of Organic Rankine Cycles. In *VDI Berichte - Proceedings of the International VDI Seminar*, volume 539, pages 465--482, Düsseldorf. VDI Verlag.
- Casati, E., Vitale, S., Pini, M., Persico, G., and Colonna, P. (2014). Centrifugal Turbines for Mini-Organic Rankine Cycle Power Systems. *ASME Journal of Engineering for Gas Turbines and Power*, 136(122607):1--11.
- Craig, H. and Cox, H. (1971). Performance estimation of axial flow turbines. *Proceedings Institution of Mechanical Engineers*, 185-32/71:407--424.
- D'Amelio, L. (1935). *Impiego di vapori ad alto peso molecolare in piccole turbine e utilizzazione del calore solare per energia motrice*. Industria Napoletana Arti Grafiche.
- Falck, D. and Collette, B. (2012). *FreeCAD [How-to]*. Packt Publishing.
- Ghidoni, A., Pelizzari, E., Rebay, S., and Selmin, V. (2006). 3d anisotropic unstructured grid generation. *International journal for numerical methods in fluids*, 51(9-10):1097--1115.
- Macchi, E. (1977). *Lecture series 100 on Closed-Cycle gas turbines*, chapter Design criteria for turbines operating with fluids having a low speed of sound. Von Karman Institute for Fluid Dynamics.
- Macchi, E. (1985). Design limits: basic parameter selection and optimization methods in turbomachinery design. volume 97 Av 2, pages 805--828, Izmir, Turk. Martinus Nijhoff Publ., Dordrecht, The Netherlands.
- Persico, G., Pini, M., Dossena, V., and Gaetani, P. (2013). Aerodynamic Design and Analysis of Centrifugal Turbine Cascades. In *ASME Turbo Expo 2013*, number GT2013-95770.
- Persico, G., Pini, M., Dossena, V., and Gaetani, P. (2015). Aerodynamics of Centrifugal Turbine Cascades. *Journal of Engineering for*, 19.
- Piegl, L. and Tiller, W. (1997). *The NURBS Book (2Nd Ed.)*. Springer-Verlag New York, Inc., New York, NY, USA.
- Pini, M., Persico, G., Casati, E., and Dossena, V. (2013). Preliminary design of a centrifugal turbine for organic Rankine cycle applications. *Journal of Engineering for Gas Turbines and Power-Transactions of the ASME*, 135:042312--1--9.
- Pini, M., Persico, G., Pasquale, D., and Rebay, S. (2014). Adjoint method for shape optimization in real-gas flow applications. *Journal of Engineering for Gas Turbines and Power*, 137(3):032604--032604.
- Tabor, H. and Bronicki, L. (1964). Establishing criteria for fluids for small vapor turbines. In *SAE National Transportation, Powerplant, and Fuels and Lubricants Meeting*, number 640823.
- Traupel, W. (1977). *Thermische Turbomaschinen*. Springer-Verlag, Berlin.
- Verneau, A. (1987). *Lecture series 1987-07*, chapter Small high pressure ratio turbines. Supersonic turbines for organic Rankine cycles from 3 to 1300 kW. Von Karman Institute for Fluid Dynamics.
- Vestraete, T. (2010). CADO: a Computer Aided Design and Optimization Tool for Turbomachinery Applications. 2nd International Conference on Engineering Optimization.

Vitale, S., Gori, G., Pini, M., Guardone, A., Palacios, F., Economon, T., Alonso, J., and Colonna, P. (2015). Extension of the SU2 Open Source CFD code to the simulation of turbulent flows of fluids modelled with complex thermophysical laws. In *AIAA 22th Computational Fluid-Dynamics Conference*, number CFD-16, 2148971, Dallas.

Zweifel, O. (1945). The spacing of turbo-machine blading especially with large angular deflection. *Brown Boveri Review*.

ACKNOWLEDGEMENT

Salvatore Vitale would like to acknowledge the FPP master student Roel de Koning, for his collaboration on the development of the TBM, and the support of the STW and Dana Spicer on the CC-PowerTrain project.

AUTOMATIC DESIGN OF ORC TURBINE PROFILES USING EVOLUTIONARY ALGORITHMS

Pablo Rodriguez-Fernandez, Giacomo Persico

Laboratorio di Fluidodinamica delle Macchine,
Politecnico di Milano,
Via Lambruschini 4, I-20156 Milano, Italy
e-mail: giacomo.persico@polimi.it
Web page: <http://www.lfm.polimi.it>

ABSTRACT

In this paper, an automated design tool for Organic Rankine Cycle (ORC) turbines is presented. Supersonic flows and real-gas effects featuring ORC turbines complicate significantly their aerodynamic design, which may benefit significantly from the application of systematic optimization methods. This study proposes a complete method to perform shape optimization of ORC turbine blades, constructed as a combination of a generalized geometrical parametrization technique, a high-fidelity Computational Fluid Dynamic (CFD) solver (including real gas and turbulence models) and an evolutionary algorithm. As a result, a non-intrusive tool, with no need for gradients definition, is developed. The high computational burden typical of evolutionary methods is here tackled by the use of a surrogate-based optimization strategy, for which a Gaussian model is applied. Application to ORC turbines has been proved to be successful, resulting in a comprehensive method for a very wide range of applications. In particular, the present optimization scheme has been applied to the re-design of the supersonic nozzle of an axial-flow turbine. In this design exercise very strong shocks are generated in the rear blade suction side and shock-boundary layer interaction mechanisms occur. Optimization aiming at a more uniform flow at the blade outlet section is shown to minimize the shock losses, resulting in a significant improvement in the nozzle efficiency. The optimal configuration determined with the present design tool is also successfully validated against the outcome of a previous optimization performed with a gradient-based method, demonstrating the reliability and the potential of the design methodology here proposed.

1. INTRODUCTION

Thanks to the progressive increase of computational capability, optimization techniques based on high-fidelity flow models play a key role in the present-day design process of turbomachinery. The turbomachinery design process offers optimization challenges at different fidelity levels, from the zero-dimensional stage-by-stage definition (Pini et al. (2013)), to the axisymmetric design (Larocca (2008); Pasquale et al. (2014)), up to the detailed blade shape definition (Verstraete et al. (2010); Pini et al. (2014)).

In the last decades several CFD-based shape optimization procedures were specifically developed in Aerodynamics, such as inverse design methods (Demeulenaere et al. (1997)), adjoint-based gradient methods (Peter and Dwight (2010)), or evolutionary algorithms (Coello (2000)). These latter techniques allow to explore a wider range of feasible solutions, identifying the best individual, and also allow to handle multi-objective optimization problems (Pierret et al. (2006)).

In this paper, a novel optimization package is presented, based on evolutionary algorithms, specifically oriented to the design of turbomachinery blades. Thanks to the high-fidelity flow model, which includes turbulence models and a generalized thermodynamic treatment of the working fluid, the method is particularly attractive for ORC turbines, that feature severe supersonic flows and strong real-gas effects. Several optimization algorithms are tested and the application of the design tool to a highly complex

ORC turbine indicates that dramatic performance improvement is achievable by systematic application of the proposed optimization method.

The paper is structured as follows: in Section 2, the methodology behind the shape optimization tool is described in detail; in Section 3, the different optimization strategies applied and the environment in which they are implemented are discussed. Section 4 finally reports the results of the application to a supersonic ORC turbine nozzle, considering the effectiveness of optimization as well as its implications on the cascade aerodynamics.

2. METHODOLOGY

The optimization strategy here presented is constructed by combining four main blocks, namely a geometry parameterization code, a high-fidelity CFD solver, a library of evolutionary algorithms, and a meta-model interpolation tool. All these items are discussed in detail in the present Section. In particular, Subsection 2.1 describes how B-Spline curves are used to generate the blade geometry; in Subsection 2.2, the CFD model employed for the present high-fidelity calculations is summarized; in Subsection 2.3, genetic algorithms and evolutionary strategies are presented; finally, in Subsection 2.4 the surrogate model used in this study is defined.

2.1 Geometry Parameterization

A key feature of shape-optimization problems in aerodynamics is the technique used to reconstruct the shape of profiles by employing a minimum number of variables. In this work, B-Spline curves are used to parameterize the blade geometry, as the shape can be easily described by a certain number of so-called control points. Thanks to this and other features, B-Spline curves are presently recognized as a powerful tool in both application and theory for aerodynamic designs (Farin (2002)).

A B-Spline can be defined as a piecewise curve with components of degree n that provide local support and whose smoothness and continuity can be adjusted. Thus, a B-Spline curve can be described as a weighted sum of basis functions as follows:

$$x(u) = \sum_{j=0}^L d_j N_j^n(u) \quad (1)$$

where $\{d_j\}$, with $j = 0, \dots, L$, are the control points, and $N_j^n(u)$ are the corresponding n -degree B-Spline bases. These can be defined recursively in the form:

$$N_j^k(u) = \frac{u - u_{j-1}}{u_{j+k-1} - u_{j-1}} N_j^{k-1}(u) + \frac{u_{j+k} - u}{u_{j+k} - u_j} N_{j+1}^{k-1}(u) \quad (2)$$

$$N_j^0(u) = \begin{cases} 0 & \text{if } u_{j-1} \leq u < u_j, \\ 1 & \text{otherwise} \end{cases}$$

where $\{u_j\}$, with $j = 0, \dots, K$, is the knot sequence and u is a parameter. Notice that $K = L + n - 1$.

At this point, a first algorithm can be developed to generate a B-Spline curve from a given set of control points, as it is depicted in Figure 1.

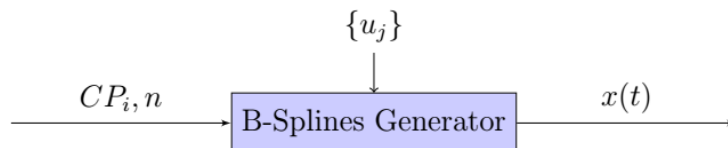


Figure 1: Geometry generation algorithm. CP_i and n are the control points and the degree of the curve, respectively; $\{u_j\}$ is the knot sequence. As output, the B-Spline curve $x(t)$ is generated.

The optimization tool described in this study is able to build an approximate representation of the shape of the blade using a B-Spline curve, defined and manipulated by the position of the control points. In order to generate this curve, the baseline geometry needs to be interpolated. In this work, a least squares interpolation method is used.

It is assumed that $P + 1$ data points p_i are given, with $i = 0, \dots, P$, and we seek to find the approximated B-Spline curve $x(u)$ of degree n and $K + 1$ knots u_k , with $k = 0, \dots, K$. This B-Spline curve will be defined by $L + 1$ control points d_j , with $j = 0, \dots, L$, such that $L = K - n + 1$. The error of the approximation for a given point can be expressed as $\|p_i - p(w_i)\|$, where w_i , with $i = 0, \dots, P$, are the data parameters of the problem. Therefore, the objective is to minimize the total approximation error:

$$f(x) = \sum_{i=0}^P \|p_i - x(w_i)\| \quad (3)$$

If we rewrite Equation (3) using Equation (1) and perform a least squares minimization process, a final expression for the $L + 1$ normal equations is derived:

$$\sum_{j=0}^L d_j \sum_{i=0}^P N_j^n(w_i) N_k^n(w_i) = \sum_{i=0}^P p_i N_k^n(w_i); \quad (4)$$

This equation leads to a linear system $A \cdot x = B$ that is solved, in this work, by using Cholesky Decomposition. At this point, a new algorithm can be defined, to find the control points that best represent a given geometry, as it is depicted in Figure 2.

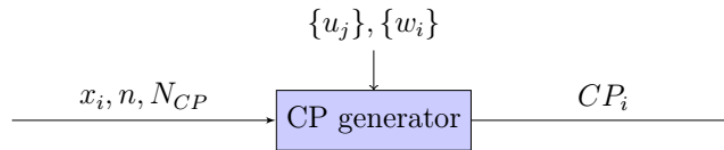


Figure 2: Interpolation algorithm. x_i , n and N_{CP} are the data points, the degree of the B-Spline curve and the desired number of control points, respectively. $\{u_j\}$ and $\{w_j\}$ are the knot sequence and the data parameters. As output, the control points CP_i of the B-Spline are generated.

The sequence of data parameters $\{w_i\}$ is built using a centripetal parameterization. With regard to the knot sequence, it can control the shape of the final interpolated B-Spline. It divides the curve into segments, defined on a knot span. In this work, the knot sequence is used to regulate the position of the control points that serve as design variables of the optimization problem. In this way, one can identify areas prone to optimization and thus assign a different number of control points for each region during the interpolation process.

In this study, both pressure and suction sides of the blade are generated with a unique B-Spline curve. However, the trailing edge will be considered separately, as it is best represented by a circular arc. As a result, the B-Spline curve is constrained to pass through the first and last data points to create a closed curve along with the circular-shaped trailing edge. Continuity and regularity are ensured by imposing same derivative. Additionally, no weights for the control points are used during the interpolation.

2.2 CFD Codes

The present optimization strategy makes use of high-fidelity numerical simulations of the selected blade configurations, performed applying a fully-turbulent and real-gas CFD model based on the ANSYS-CFX solver. As only blade-to-blade effects are of interest, quasi-3D simulations are carried out, using 2D profiles generated with the geometry parameterization algorithm and considering a straight streamtube around midspan. The effects of turbulence are introduced by resorting to the $\kappa - \omega$ SST model,

providing a proper clustering of the cells in the near-wall region so to ensure y^+ below unity along the blade. The real-gas thermodynamic behavior of the working fluid is treated by means of a Look-up-Table (LuT) interpolation method; the LuT was constructed in primitive variables (P, T) by resorting to the Span-Wagner equations of state implemented in the FluidProp database (Colonna et al. (2008)). Total conditions, flow angles, and turbulence quantities are assigned at the inlet, and static pressure is given at the outlet. The onset of spurious pressure wave reflections from the downstream boundary is avoided by placing the outflow boundary three axial chords away from the trailing edge. High resolution numerical schemes are used for advective and diffusive fluxes.

2.3 Genetic Algorithms

The interest in single and multi-objective optimization has grown dramatically in the last decades, thanks to the progressive increase of computational power. In engineering, this has led to the development of several methods which apply the concepts of optimization to support the design of components. Thus, design-oriented optimization can be pursued by applying inverse design methods, gradient-based methods, or heuristic methods. For aerodynamic design purposes, the application of heuristic methods is particularly attractive, as it can be performed by using direct calculation models (such as CFD).

Within the class of heuristic methods, Evolutionary Algorithms (EAs) have become very interesting in a wide range of applications, due to many advantages that make them outperform other optimization methods. Among them, Genetic Algorithms (GAs) have the possibility of dealing with oscillating or smooth-less objective functions; they also allow to introduce constraints in a relatively easy way, and to treat multi-objective optimization as well. Furthermore, genetic algorithms are global optimization methods and, hence, are best suited for optimization problems with multiple local optima, for which gradient methods are too computationally expensive or not readily available. In many optimization problems, GAs quickly identify promising regions of the design space where the global optimum might be located. The interested reader is invited to consult Reeves and Rowe (2002) for a complete description of different GA approaches.

However, the flexibility and simplification provided by GAs are achieved through a massive application of the direct computational model of interest, and thousands of evaluations are usually needed to identify the optimum. Shape-optimization problems in aerodynamics require the application of CFD models, which are expensive tools requiring at least some minutes of calculation to achieve convergence (a reliable optimization requires, in general, fully turbulent flow models and an appropriate grid resolution). As a consequence the direct application of CFD-based genetic optimization is usually not feasible for aerodynamic design purposes. To tackle this unacceptable computational cost, surrogate models can be used. Surrogate models, also known as meta-models or response surfaces, are analytical functions that relate the design variables with performance (i.e., the objective function) in an approximate way. A mathematical representation is selected for the objective function with no relation with the physical phenomena of the real problem (namely, with the CFD model). As it will be discussed later, the mathematical model is trained along the process, resulting in a dramatic reduction of computational burden, as the genetic algorithm is applied directly to the meta-model.

2.4 Surrogate Models

An extensive theory about surrogate models has been developed and many schemes are currently available (the interested reader is referred to Simpson et al. (2001) for a review of available techniques). In this study, the Kriging model is used as the mathematical approximate objective function or non-linear constraint. The Kriging technique is based on a set of interpolation methods, sometimes called Gaussian Processes, originally developed for geostatistic problems and nowadays widely used in many engineering fields. The mathematical model of Kriging can be understood as the linear combination of a trend function and the implementation of a stochastic process. The most common form of a Kriging model is as follows:

$$\tilde{f}(x) = g(x)^T \beta + r(x)^T R^{-1} (f - G\beta) \quad (5)$$

where x is the point to be evaluated; $g(x)^T \beta$ is the trend function evaluated at x , whose coefficients are estimated using a least squares approach; $r(x)$ is the correlation vector with the data points; R is the correlation matrix for all of the data points; f is the response values vector; and $G\beta$ is a vector that contains the trend function evaluated at all data points. The terms in the correlation vector ($r(x)$) and correlation matrix (R) are computed using a Maximum Likelihood Estimation (MLE) procedure.

The implementation of this meta-model in the evolutionary optimization strategy is described in Section 3.

3. IMPLEMENTATION

In this study the optimization problem has been assembled in the object-oriented framework Dakota (Adams et al. (2013)). Dakota provides optimization algorithms, i.e. single-objective and multi-objective genetic algorithms, as well as surrogate models and optimization strategies.

To perform the optimization using genetic algorithms, the JEGA library is used. JEGA (Java Engine for Genetic Algorithms) is a framework that provides a flexible and extensible optimization environment for computational models. Different optimization approaches have been considered and tested to investigate the performance and eventually improve the automatic design tool developed in this research. The initial database is built using Latin Hypercube sampling technique. Usually the size of the population is taken as 2 to 4 times the number of design variables. For example in the present case, a population of 50 individuals is chosen, in line with the 16 design variables used. The probability of crossover and mutation are 80% and 20%, respectively. Elitism is used as selection technique.

To determine the Kriging parameters, the Surfpack library is employed. In this case, it uses a global search method called *DiRect* algorithm (dividing rectangles), a derivative-free global optimization method that balances search in promising and unexplored regions. The trend function is built using a reduced quadratic expression. When working with non-linear constraints, a Kriging model is also built as a mathematical expression for each of them.

Regarding optimization strategies, local and global schemes are tested. In **surrogate-based local optimization** (SBLO), also called Trust Region technique, the optimization algorithm operates directly on a surrogate model that is built using an initial database composed by a certain number of individuals. However, the surrogate model has a limited reliability (especially at the beginning of the process), and hence the fidelity of the approximation is assessed by comparing with the high-fidelity expensive tool (by running the CFD solver). The main feature of the local optimization is the use of a trust region approach, which defines the extent of the approximation. SBLO method needs to generate and update the data fit in each trust region, performing high-fidelity evaluations over a design of experiments. Although a local approach, each sampling in the trust region can be performed globally, which allows to extract relevant global design trends. The comparison between the surrogate and the high-fidelity evaluations, formulated as a trust region ratio, is used to define the step acceptance and trust region size and position of the next iteration.

On the other hand, in a **surrogate-based global optimization** (SBGO), the algorithm is not supported by a trust-region approach. It starts from an initial sample of points and the optimizer operates on that surrogate, by updating its parameters after a new optimum is found and added to the sample. This approach should be used carefully, as there is no guarantee of convergence. It should be used either when there exists the need of using an initial database or when the surrogate needs, somehow, to be updated globally. The surrogate becomes more accurate as the iterations progress. In the present study, both global and local schemes are compared and tested.

4. RESULTS

An exercise of shape-optimization is discussed in the following to demonstrate the capabilities of the design tool presented in this paper. To show the flexibility and the wide range of application of the technique, a particularly severe test-case is considered, namely a converging-diverging supersonic nozzle for an axial-flow ORC turbine operating with MDM. The original blade geometry, shown in Figure 3 and called Baseline in the following, was designed by means of the method of characteristics (MOC) for the diverging part and features a highly smooth leading edge to reduce the sensitivity to incidence variations. The optimization process aims at maximizing the performance of the cascade operating with an expansion ratio of 8 starting from a superheated condition ($P_{T,in} = 8\text{bar}$, $T_{T,in} = 272\text{C}$) close to the saturation line. As a result, supersonic flows are induced (in fact, the cascade-exit Mach number exceeds 2) and strong real-gas effects occur in the expansion, justifying the use of a LuT approach for the thermodynamic modeling of the fluid.

The blade geometry has been first interpolated and parametrized using the method described in Subsection 2.1. Once the right number of control points is established, their relative position can be adjusted by modifying the knot sequence. In this work, 30 control points have been found to be sufficient to provide an accurate interpolation. From the complete set, the vertical positions (y-coordinate) of 16 control points define the set of design variables for the optimization problem (see Figure 3). The leading edge and the front part (roughly up to the throat) are kept fixed during the optimization process and a larger number of control points is chosen in these regions. The trailing edge width is kept constant so to guarantee the structural resistance of the blade, and therefore only one control point is needed to determine the location of the trailing edge.

High-fidelity calculations were performed on structured grids composed by 400,000 hexahedral elements. The reliability of the numerical model used in this context was previously assessed against experiments performed by the authors themselves on a research turbine stage installed at Politecnico di Milano (Persico et al. (2012)). The CFD model was shown to accurately predict the fully three-dimensional and unsteady flow physics of the whole turbine stage, and provided estimates of stage efficiency within 1% of the experimental datum, i.e. comparable to the uncertainty of the measurement technique.

In the following, several optimization tests are discussed, with the aim of investigating the impact of different approaches on both the computational cost and the fitness of the design outcome. Different surrogate strategies are considered, also in comparison to gradient-based optimization techniques; it is shown how the proposed automatic design tool provides, in addition to the specific optimized geometry, some intuitive design guidelines for supersonic ORC turbines.

4.1 Impact of the optimization strategy

At first, the comparison between the Global (training) and Local (trust regions) optimization strategies is performed. For both cases the same objective function is used, defined as the standard deviation of the azimuthal pressure distribution evaluated half axial chord downstream the blade trailing edge. The minimization of this quantity in a supersonic cascade is expected to reduce the shock strength, thus increasing the cascade performance.

For the construction of the Kriging surrogate model, a minimum sample size of 5 times the number of design variables is commonly considered. In this study, 16 design variables are set to optimize the geometry, and hence a database of 80 individuals is, in all cases, considered. In the global approach,

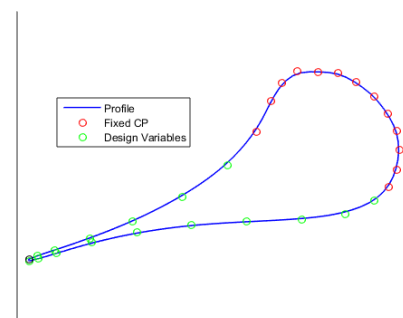


Figure 3: Baseline profile shape and control points distribution. Green circles indicate design variables, while red ones are kept fixed during optimization. The black circle indicates the control point that moves accordingly to keep the trailing edge width constant.

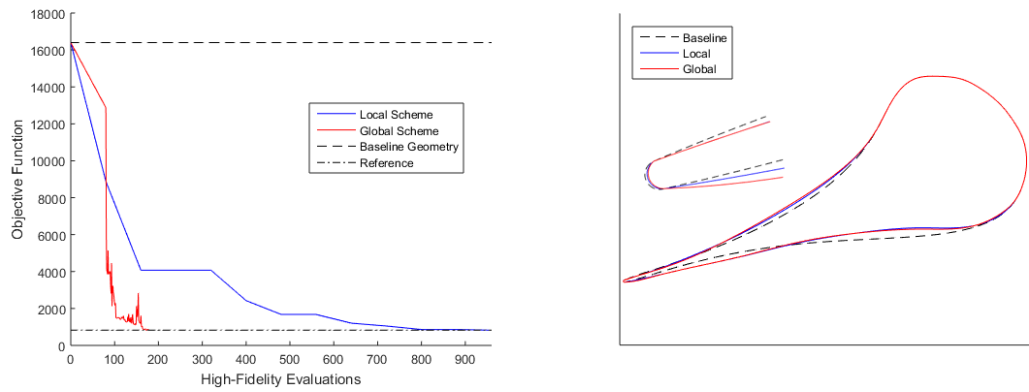


Figure 4: Left: convergence history of global and local strategies for surrogate-based optimization. Right: optimized geometry using global and local strategies for surrogate-based optimization.

this means that the code builds the initial Kriging model over this initial sample. After a complete GA-optimization applied only to the mathematical model, the result is assessed via the high-fidelity tool and added to the population (updating the Kriging parameters in each iteration). On the other hand, the local approach builds a new Kriging model after each GA-optimization. These different features are clearly visible in the left frame of Figure 4, where the paths towards optimization are compared for the two methods; in particular, it is observed how the local scheme advances only each 80 high-fidelity evaluations, while the global method advances continuously after the initial 80 iterations. As a result the local approach shows a much slower trend, even though the local and global schemes obtain a very similar minimization of the objective function, significantly reduced with respect to the baseline configuration. For this reason, in the following only the global scheme will be used.

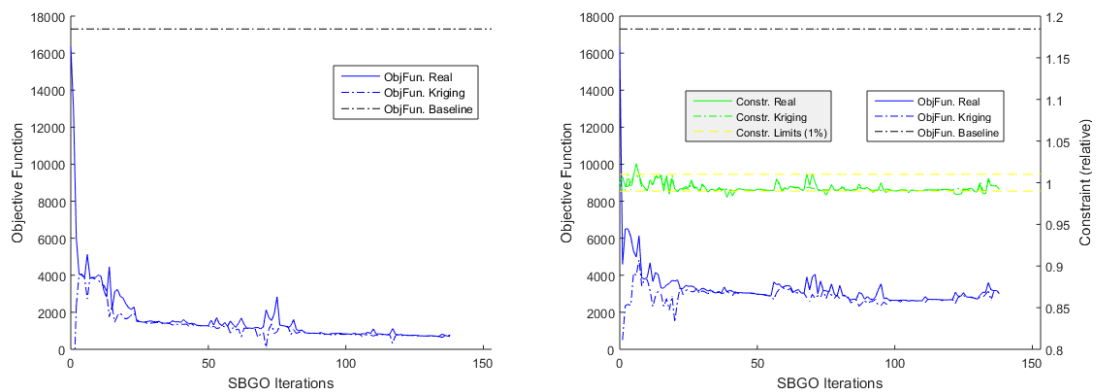


Figure 5: Convergence history of Kriging model for (left) non-constrained, and (right) constrained optimization, using a global strategy for surrogate-based optimization.

When performing evolutionary optimization using surrogate strategies, the convergence of the approximate model to the actual response surface of the problem needs to be verified. The left frame of Figure 5 shows that the surrogate model quickly matches the high-fidelity tendency, except for some spikes of progressively reduced amplitude as the algorithm converges to the optimum. This allows to conclude that the training procedure chosen for the Kriging model is appropriate for the present design problem. The smooth convergence trends observed so far have been achieved without the application of explicit constraints to the optimization. However from the engineering perspective it is interesting to investigate how the optimization proceeds when a relevant quantity is constrained; for example, when looking to

the turbine cascade performance, the flow rate is usually a fixed parameter whose variation needs to be limited in a narrow range. The right-hand side of Figure 5 shows the results a non-linear constrained optimization, by forcing the flow rate to stay within $\pm 1\%$ with respect to the baseline value. A specific Kriging model is built for the constraint. It is observed how, after a significant reduction of the objective function in the initial phase, the constraint prevents the optimization from progressing further, resulting in a lower fitness of the outcome. It is also very interesting to note that the flow rate of the optimized cascade achieved via non-constrained global optimization is, in fact, within the limits. This is probably because the front part of the blade up to the throat is kept fixed and hence the flow rate is somehow imposed indirectly in the present choked flow configuration. This seems to be a more effective procedure when dealing with supersonic cascades.

4.2 Aerodynamic analysis

The flow configuration established in the cascade optimized via the non-constrained global strategy is now discussed, in comparison to the baseline configuration and to another optimized case. This latter configuration was obtained by applying an adjoint-based gradient method developed by Pini et al. (2014); it was performed using the same objective function used here and was based on an inviscid flow solver; the result here reported is, however, the high-fidelity calculation of that optimized configuration.

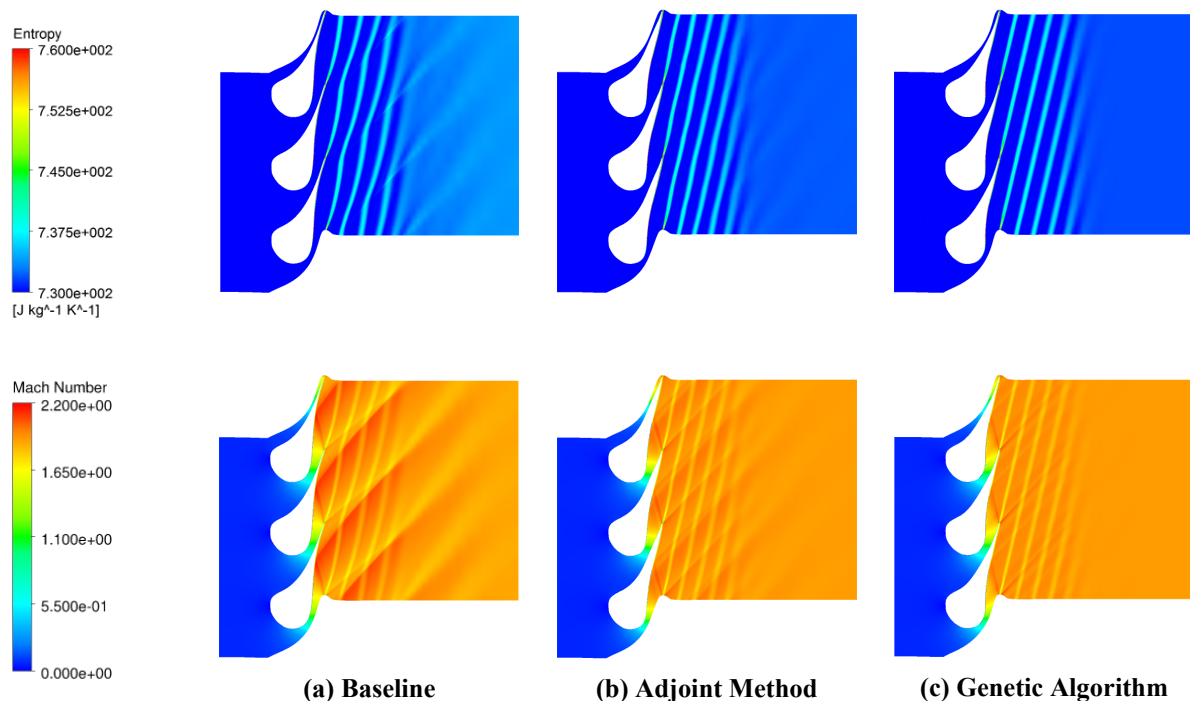


Figure 6: Comparison of the Mach number (bottom) and Entropy (top) distributions for (a) Baseline, (b) Adjoint method (Pini et al. (2014)), and (c) present study using the global strategy.

The entropy and Mach number field on the blade-to-blade surface are reported for the three cases in Figure 6. The effect of the optimization is clearly visible by comparing the optimized and baseline configurations; in particular the minimization of the pressure oscillations downstream of the cascade leads to a dramatic reduction of the main shock strength. Hence, the severe pressure gradient observed in the baseline case is highly weakened and the weaving path of the blade wakes is almost eliminated. As a result, the overall entropy generation is significantly reduced in the optimized cases. The two optimized blades exhibit very similar flow configurations, even though the two approaches make use of very different methods based on different flow models; this suggests that both the methods are converging towards the same optimum, which is probably the global optimum for the present problem. The evolutionary optimization leads, in fact, to a slightly more uniform flow, due to the slightly weaker fishtail shock system

at the blade trailing edge; such a shock system is not accurately captured by the inviscid flow model used in the adjoint-based optimization (due to the missing displacement thickness of the boundary layers), and this may explain the slight differences observed. However the outcome of the adjoint optimization still remains an excellent result considering its extremely limited computational cost (less than an hour on a standard PC) with respect to that of the present GA strategy (20 hours on a 15-processor cluster).

Figure 7 reports the pressure distribution on the three blades, in the form of isentropic Mach number, and explains the reason for the improved performance of the optimized configurations. Both optimal blades move ahead the acceleration of the flow on the suction side, just downstream of the sonic throat and still within the bladed channel; as a result the over-speed on the rear suction side is limited and hence the subsequent diffusion is eliminated. In this way the onset of the strong shock observed in the baseline configuration is prevented. Once again the two optimized configurations show very similar trends, with local differences especially close to the trailing edge.

To quantify the impact of the optimization on the cascade performance the Total Pressure Loss Coefficient is used, defined as the total pressure loss referred to the exit dynamic pressure ($Y = \frac{P_{T,in} - P_T}{P_{T,in} - P}$). The results, considering an outlet placed at 2 chords downstream the blade (where the flow can be considered mixed-out) are summarized in Table 1. It can be concluded that the more uniform flow achieved in the downstream region leads to a relevant decrease of the total pressure loss coefficient, which reduces from 15.0 to 9.3%.

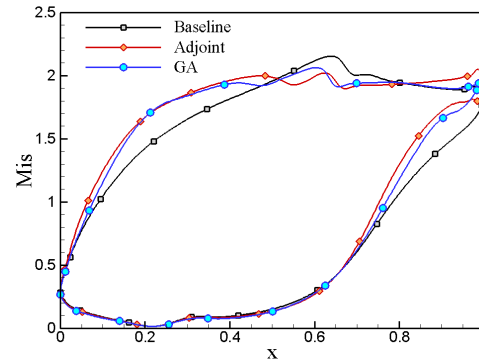


Figure 7: Isentropic Mach Number distribution over the blade for the Baseline configuration, the optimized blade using the Adjoint Method (Pini et al. (2014)) and using genetic algorithms.

	Baseline	Adjoint Method	GA
Y	0.15	0.11	0.093

Table 1: Total Pressure Loss Coefficient at two axial chords downstream the blade.

5. CONCLUSIONS

This paper has presented a novel package for the automatic design of ORC turbines based on an evolutionary strategy. Detailed descriptions of all the steps of the optimization scheme have been provided, namely the geometry parametrization, the high-fidelity flow solver and the genetic algorithm.

The blade shape is parametrized via B-Splines, whose local control capability allowed a detailed shape reconstruction while preserving surface smoothness. The implementation of advanced high-fidelity flow models, of paramount importance for ORC turbines, is easily attained thanks to the non-intrusive character of the evolutionary optimization strategy here used. To tackle the computational burden typical of CFD-driven evolutionary strategies, the genetic algorithm is coupled to a surrogate model that reflects the influence of the design variables on the objective function. Several optimization strategies have been discussed to evaluate the convergence process and the associated computational cost.

Application to a supersonic ORC turbine nozzle has demonstrated that relevant performance improvements can be achieved by maximizing flow uniformity downstream the blade. A further comparison, for the same test case, against an alternative optimization approach has assessed the validity of the present design methodology. Results have also allowed to quantify the impact of the application of high-fidelity flow models within the optimization process. Future research will be addressed towards the applica-

tion of the present shape-optimization tool to the design of novel turbine blade configurations for ORC applications.

REFERENCES

- Adams, B., Bauman, L., Bohnhoff, W., Dalbey, K., Ebeida, M., Eddy, J., Eldred, M., Hough, P., Hu, K., Jakeman, J., Swiler, L., and Vigil, D. (2013). Dakota, a multilevel parallel object-oriented framework for design optimization, parameter estimation, uncertainty quantification, and sensitivity analysis: Version 5.4 user's manual. *Sandia Technical Report SAND2010-2183*.
- Coello, C. (2000). An updated survey of GA-based multiobjective optimization techniques. *ACM Computing Surveys*, 32(2):109–143.
- Colonna, P., Nannan, N., and Guardone, A. (2008). Multiparameter equations of state for siloxanes: $[(\text{ch}_3)_3\text{-si-o}1/2]_2\text{-[o-si-(ch}_3)_2]_i, i=1, \dots, 3$, and $[\text{o-si-(ch}_3)_2]_6$. *Fluid Phase Equilibria*, 263(2):115 – 130.
- Demeulenaere, A., Leonard, O., and Van Den Braembussche, R. (1997). A two-dimensional Navier-Stokes inverse solver for compressor and turbine blade design. *Journal of Power and Energy*, 211(4):299–307.
- Farin, G. (2002). *Curves and Surfaces for CAD: A Practical Guide*. Morgan Kaufmann Publishers Inc., San Francisco, CA, USA, 5th edition.
- Larocca, F. (2008). Multiple objective optimization and inverse design of axial turbomachinery blade. *Journal of Propulsion and Power*, 24(5):1093–1099.
- Pasquale, D., Persico, G., and Rebay, S. (2014). Optimization of Turbomachinery Flow Surfaces Applying a CFD-Based Troughflow Method. *Journal of Turbomachinery*, 136(3):031013 1–11.
- Persico, G., Mora, A., Gaetani, P., and Savini, M. (2012). Unsteady aerodynamics of a low aspect ratio turbine stage: Modeling issues and flow physics. *Journal of Turbomachinery*, 134(6).
- Peter, J. and Dwight, R. (2010). Numerical sensitivity analysis for aerodynamic optimization: A survey of approaches. *Computers & Fluids*, (39):373–391.
- Pierret, S., Coelho, R., and Kato, H. (2006). Multidisciplinary and multiple operating points shape optimization of three-dimensional compressor blades. *Structural and Multidisciplinary Optimization*, 33(1):61–70.
- Pini, M., Pasquale, D., Persico, G., and Rebay, S. (2014). Adjoint method for shape optimization in real-gas flow applications. *Journal of Engineering for Gas Turbines and Power*, 137:032604.
- Pini, M., Persico, G., Casati, E., and Dossena, V. (2013). Preliminary design of a centrifugal turbine for ORC applications. *ASME Journal of Engineering for Gas Turbines and Power*, 135(042312).
- Reeves, C. R. and Rowe, J. E. (2002). *Genetic Algorithms: Principles and Perspectives: A Guide to GA Theory*. Kluwer Academic Publishers, Norwell, MA, USA.
- Simpson, T., Poplinski, J., Koch, P. N., and Allen, J. (2001). Metamodels for computer-based engineering design: Survey and recommendations. *Engineering with Computers*, 17(2):129–150.
- Verstraete, T., Alsalihi, Z., and Van Den Braembussche, R. (2010). Multidisciplinary Optimization of a Radial Compressor for Microgas Turbine Applications. *Journal of Turbomachinery*, 132:031004.

SCREW EXPANDERS IN ORC APPLICATIONS, REVIEW AND A NEW PERSPECTIVE

Henrik Ohman^{1*}, Per Lundqvist²

¹KTH, Royal institute of Technology,
Department of Energy Technology,
Stockholm, Sweden
henrik@hohman.se

²KTH, Royal Institute of Technology,
Department of Energy Technology,
Stockholm, Sweden
per.lundqvist@energy.kth.se

* Corresponding Author

ABSTRACT

Performance of Organic Rankine Cycles is sensitive not only to the entry temperature ratio between heat source and heat sink but also to the temperature degradation of the heat source flow, caused by the heat transfer to the process in pre-heater, evaporator and super heater. In order to adopt the cycle to the great variety of heat sources a multitude of fluids are required. Alternatively fluid mixtures, trans-critical or supercritical fluid conditions can be used to match the process temperatures with the heat source. Screw expanders offer an alternative, new approach to the matching problem of ORC's as they allow for flexible multi-phase expansion. Hereby the vapour fraction at the expander entry can be used to partially match the temperatures of the process to a particular heat source. To provide a perspective on the use of such screw expanders in ORC-systems previous experimental and commercial experience have been reviewed and discussed.

Screw expanders are versatile machines used for the production of mechanical work in power ranges from 3kW to 1.5MW. As the functional characteristics differ significantly from dynamic expanders the explanatory models used to generalise results are different. Plenty of research has resulted in well generalized explanatory models for dynamic expander analysis. For screw expanders similar explanatory models exist mainly in commercially confidential environments. A few public sources disclose test data. In the few cases data has been investigated the analyses tend to rely on thermodynamic models suitable for dry gas expansion. Typically that leads to reasonable replication of test results but seldom to models suitable for detailed understanding of the process. In applications with 2-phase expansion the theories used to simulate functional characteristics is entirely insufficient. The main reason for the scarcity of work in this field is probably the empirical difficulties in obtaining good measuring data in multi-phase conditions.

This paper describes a review of multi-phase screw expander experiences and explains why a unique theory is required to model its characteristics. In the absence of such a unique theory a correlation based in empirical data is presented. This allow for estimations of screw expander efficiency in multi-phase conditions. Measured efficiency with dry expansion, or such efficiency simulated, can be used to estimate adiabatic efficiency with expansion entry vapor fractions ranging from 0 to 1 by using this correlation. Hence estimating expansion efficiency during multi-phase expansion is simplified, allowing for better optimisation of the ORC-systems. This way a new perspective of screw expander potential in ORC system integration can be presented.

1. INTRODUCTION

Historical background, experiences with screw expanders in ORC's, 2-phase expansion and the implications of using 2-phase expansion in ORC's are explained to create a perspective of the future potentials in combining the two.

Helical, rotating piston-type, fluid expansion machines have been around as long as their equivalent fluid compression machines. The ideas for developing such devices constitute natural progressions of the Archimedes Screw, known by the ancients. Heinrich Krigar patented a twin rotor helical liquid pump in 1878, with an alternative use as *presse*. The latter term would be similar to the modern term *blower*, i.e. a positive displacement fan with no internal compression. In the 1920's jet engine designer Alf Lysholm started the development of a series of twin screw compressors for the application of combustion chamber air compression in airborne jet engines and turbo-props, see Figure 1. Lysholm and Boestad (1935) describe a fully industrialized twin screw compressor, sold on five continents only two years later. After that an impressive evolution of designs and applications for twin screw compressor technology emerged. They have revolutionized technical systems architecture in combustion engines, refrigeration and air conditioning plants, industrial gas cleaning and pressurized air systems.

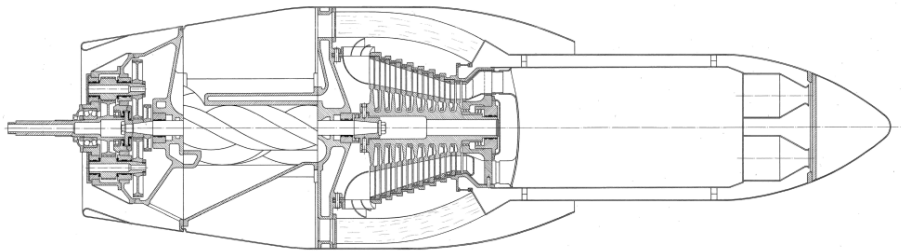


Figure 1. Early integration of twin screw machine in Gas Turbine aircraft engine.

The opportunity of reverse use, i.e. twin screw expanders, was obvious to anyone involved. However markets for supply of shaft power always tended to be smaller than for supply of compressed gases. Therefore commercial volumes, and consequently the variations of designs, are significantly less for screw expanders than its reversely operating sibling. From the same reasons scientific investigation of twin screw expanders is limited and many industrial records have been cleaned out.

One branch of screw expander applications is steam expansion with dry entry. Such applications were common before the advent of affordable, variable speed, electric drives and have seen a revival in modern small scale distributed power generation. Significant knowledge exists in industry and science and that branch will not be specifically addressed in this paper.

With modern developments towards local small scale power generation, as well as widespread availability of thermodynamic computational tools, development of various ORC systems has increased. The use of screw expanders in such applications is still in its infancy and requires more scientific study. Furthermore the screw expanders currently used tend to be limited to designs based on screw compressor design optimizations, leaving room for significant improvements of the machine design itself.

One of the perhaps most interesting possibilities to improve the technology of ORC's is implementing the unique characteristic of allowing efficient expansion of mixtures of gas and liquid from the beginning of the expansion process. Sample effects on ORC system efficiency and specific cost were demonstrated in Öhman and Lundqvist (2014). Using standard practice thermodynamic analysis tools economic optimization of cycle design, and cost allocation, becomes trivial provided that the efficiency of the mixed phase expansion process can be estimated.

Little information on 2-phase expansion efficiency of screw expanders is available. Part of the historic experience of using screw expanders is therefore presented below as well as state-of-the-art on performance prediction and its implications on ORC system optimization.

2. PRIOR FIELD EXPERIENCES WITH ORC'S

Very little of industrial knowledge prior to the digital revolution is traceable without having access to proprietary archives. Also such information is hard to come by as most companies involved has ceased to exist over time and their records scattered. Traces however can be found, often tracked in interviews with elderly engineers and scientists, or in technical periodicals.

One cannot write about twin screw machines without briefly mentioning the late engineering company ALÅ/SRM, 1908-2011. *Aktiebolaget Ljungströms Ångturbin, later renamed Svenska Rotor Maskiner AB*. As described in Timuska (2008) and Svenningsson et al (2010) SRM dominated the systematic development of twin screw machines and by licensing the technology to most suppliers on the market the impact of their development cannot be overestimated. SRM's archives originally contained design calculations and performance data from worldwide screw expander power generation systems from 1932 to 2011. Unfortunately that archive is only partly available and could be expected to be partly shattered. The information in this paper is based on interviews with experienced engineers and available publications.

ORC's using screw expanders was well known in the 1960's. Minto (1967) describe an automotive version of an ORC and Behrendt (1970) cites Minto implementing it in 2 different full scale cars, one of them using a 112mm, A-profile screw expander and R114 as seen in Figure 2.

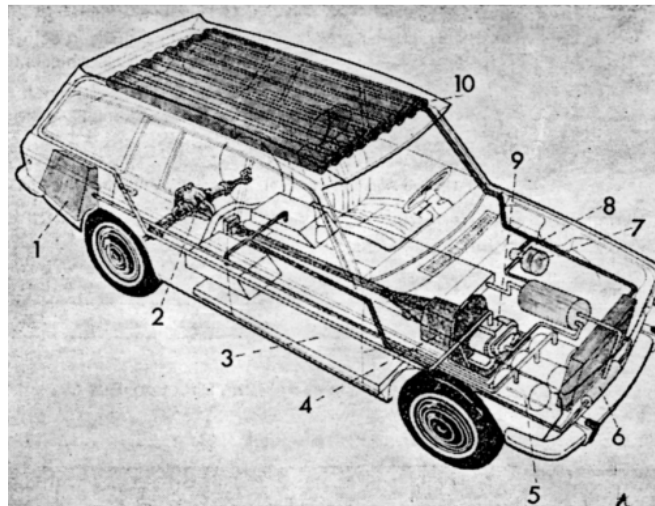


Figure 2. Schematic image of a Datsun station wagon equipped with a Minto ORC drive train.

Before Mintos automotive ORC, Linde created so called MK-systems integrating an ORC-system with an air conditioning system, also using R114. 5 sizes of such machines were developed in the 1960's, using integrated screw expander-screw compressor-liquid pump units as described by Öhman (1997). CIT-ALCATEL sold ORC-units for solar energy pumping stations in the 1970's, developed in the 1960's. They used a 112mm, A-profile, screw expander and R114, see Figure 3, similar to at least one of Mintos ORC-driven prototype vehicles. Thermofrost developed a 10kW waste heat driven ORC with a screw expander, followed by a similar 350kW ORC, with screw expanders reengineered from standard screw compressors of Japanese making. One of the latter was using waste heat from Korsnäs Pulp factory in mid-Sweden. A German supplier built a handful of ORC screw expanders for waste heat recovery purposes in the 1980's and 1990's as well as one 60kW, iso-butane ORC-expander in Biburg, Germany as of 2004.

Rumors of several sizes of field applications with ORC's using screw expanders from Japanese suppliers echoes from 1970's to 1990's though that information has not been verified. In 2003 ITRI installed a field pilot of a 50kW ORC in a waste heat recovery plant in Taiwan. They used a 113mm, semi-hermetic, screw expander using R141b.

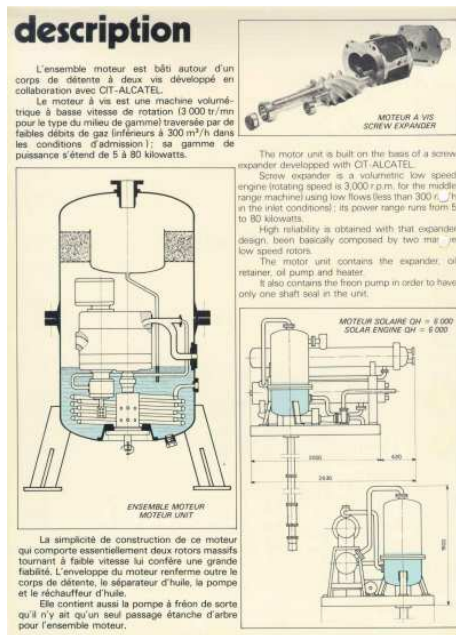


Figure 3. Detail of commercial leaflet on Solar driven ORC. *Mid 1970's, not dated.*

Between 2005 and 2012 a Swedish supplier commissioned 4 waste heat recovery ORC units with 254mm screw expanders; 350kW/R410a, 750kW/NH₃ described in Öhman and Lundqvist (2012), 650kW/R410a and 600kW/R236fa. The latter was installed for jacket cooling water waste heat recovery on a 14MW marine diesel in a commercial freight ship. Allegedly they are still in operation. During the same time period a UK supplier commissioned a significant number of 65kW ORC units using R245fa. *Data for those screw expanders are yet unavailable to the authors.* An Australian supplier commissioned a 450kW screw expander ORC for waste heat recovery on a gas turbine in 2014. Biederman and Brasz (2014) describe four parallel 1MW/R245fa geothermal ORC expanders in Lightning Dock, New Mexico. Reports are coming in on some recent Chinese pilot installations of screw expander ORC's. This list of experiences is not conclusive but indicates that significant amount of industrial experience is available though scarcely seen in scientific literature.

3. TWO PHASE EXPANDERS

A screw expander consists of two rotating, helical bodies creating "chambers" with certain characteristics between them. Each chamber starts from a volume of zero, is expanded to a maximal volume and thereafter compressed to a volume of zero. The typical cycle time for one chamber process is about 700 degrees rotation of the Male rotor. Figure 4 indicates that during the first part of volume expansion the chamber is in contact with a suction line, feeding fluid into the chamber at almost constant pressure. During the second part of chamber expansion the chamber is isolated, forcing the pressure to decline. After passing the apex of volume the chamber comes into contact with a discharge line, emptying the expanded fluid at almost constant pressure. Work is produced during the expansion by a combination of rotational speed and distribution of fluid forces onto the two rotors. The rotors can be separated by lubrication liquid or external synchronization gear wheels depending on type of design. Rotor combinations can be designed in multiple ways with two, three or more rotors interacting. Twin screw expanders are the most common and will be discussed further under the name *screw expanders*. Triple screw machines, with one Male rotor and two Gate rotors also called

single screw machines, and multiple screw design are mechanically complex and therefore less suitable in 2-phase expansion applications.

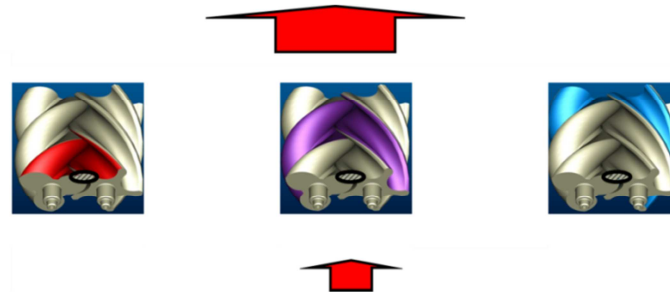


Figure 4. Schematic image of screw expander rotors indicated entry port and chamber volume development.

Screw expander rotors can be designed in multiple manners. The most common is two parallel rotors with constant diameter and constant helix. Olofsson (1989) showed a variant with non-constant helix rotors and non-parallel shaft centers. *Herring bone* arrangements, with minimal axial bearing forces as in Figure 5, were popular in the 1960's but disappeared from the market, most likely due to difficulties of manufacture.

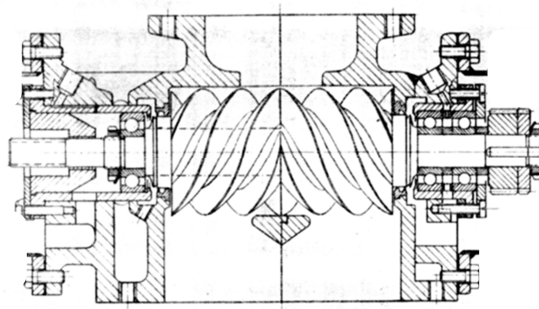


Figure 5. Example of a Herring bone type screw expander from the Japanese market.

Regardless of macro-design parameters, such as diameters, lengths, helix and shaft angles all screw expander rotors need a suitable profile. It is defined by micro-design parameters controlling the seals between chambers, port flow velocities, bending, vibrational stability and substrate erosion. Rotor profiles are typically defined as hypo-cycloids or epi-cycloids alternatively generating mating geometries with a predefined distribution of clearances to allow machining tolerances and material deflections.

During the 1950's and 1960's a series of design rules for screw compressors were issued by some of the manufactures. Also design rules for screw expanders were produced. They all have in common being based on three design handbooks from SRM, popularly called the *Compressor Bibles* and the *Expander Bible*. Such documents are of course currently replaced by computer models. Interestingly enough designs according to the *Expander Bible* are still competitive to most available designs on the market. The *Bibles* were distributed among screw compressor manufacturers but due to their age few can be expected to be still available. As determining the geometrical entities of screw expanders is known this paper focus on the significantly more difficult issue of predicting, and consequently optimizing, functional efficiency.

3.1 Experience from testing of 2-phase expansion in screw expanders

Wagenius (1958) show test data from a 40mm screw expander with a mixture of air and oil. Weiss et al (1975), Steidel et al (1977), Steidel et al (1981), McKay (1982) and Kauder and Kliem (2003) reported on 2-phase expansion with steam. Kliem (2005) tested improved filling solutions with 2-phase steam expansion. Schibbye (1959) reports test data from 3-phase expansion, gas/liquid/solid, of air and humidity. Sprankle (1973), Brasz (2003) and Öhman (2004) discuss the expansion of flashing liquid in screw expanders, also displaying some test data. Merigaux and Pocard (1978), Smith et al (1994) and Öhman and Lundqvist (2013) present data on 2-phase expansion of refrigerants.

The nature of 2-phase screw expander applications is such that pressure level, nominal power, temperatures, fluid and machine tip speed often differs, making comparison difficult. Furthermore the design of each screw expander is unique. Oil injected machines are to be compared to synchronized, sleeve bearing designs to anti friction bearing designs and stiff rotors to weak rotors. Also the built in volume ratio is not always optimal for the test conditions and seldom explicitly stated. Öhman and Lundqvist (2013) explain the logical complexity of simulating 2-phase expansion in a screw machine and yet, to date, there are no physics based models claiming to predict adiabatic efficiency of such expansion with any accuracy. In the same article a method according to Equation (1) is established using information on peak efficiency and efficiency at saturated gas conditions in order to determine adiabatic efficiency as a function of expansion entry vapor fraction.

$$\eta_{ad}(X_{entry}) = \eta_{ad,sat} + \psi_{2phase} \cdot (1 - X_{entry}) \cdot 10 \quad (1)$$

The correlation is defined by Equation (2), as of Öhman and Lundqvist (2013)

$$\psi_{2phase} = \frac{d\eta_{ad}}{dX_{entry}} = -0.15 \cdot \eta_{ad,peak} + 0.09 \quad (2)$$

Note that the sign of the first term is derived from table data and graph in the reference. There is an obvious typographic error regarding the sign in the equation in the reference.

In reality adiabatic efficiency of screw expanders is relatively insensitive to the degree of superheat at expansion entry why Equation (3) is more practical to use. *Note that the correlation only allows us to estimate the effect of variations in adiabatic efficiency. The magnitude needs to be determined by physical tests or simulations using dry expansion entry conditions.*

$$\eta_{ad}(X_{entry}) = \eta_{ad,peak} + \psi_{2phase} \cdot (1 - X_{entry}) \cdot 10 \quad (3)$$

As can be seen in Figure 6 the correlation predicts a linear relation between vapor fraction and adiabatic efficiency. *Seemingly too simple the sources support the conclusion of a linear relation, see for example Figure 2-6, p. 2-27 in McKay (1982) or Figure 8, p. 1217 in Öhman and Lundqvist (2013).* Hereby cycle simulations can be performed as discussed in Chapter 4.

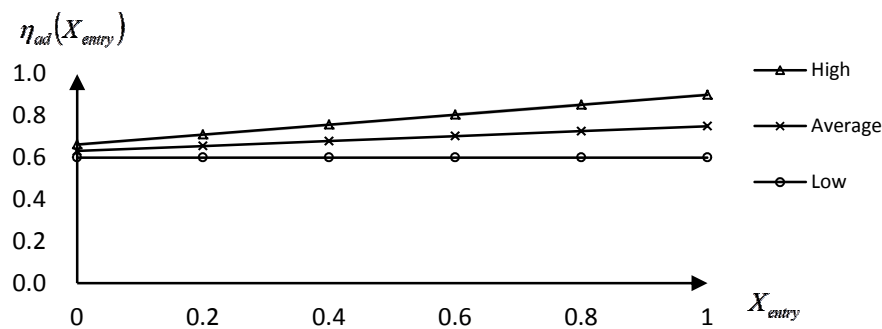


Figure 6. Adiabatic efficiency with 2-phase expansion entry vs. vapor fraction. Peak efficiencies High (90%), Average (75%), Low (60%) as of Öhman and Lundqvist (2014)

3.2 On the difficulty of modeling performance of a 2-phase screw expander

A 2-phase mixture of working fluid needs to be in equilibrium to be stable. Equations of state, used to determine the energy of a fluid, assume that such equilibrium exists, *quasi-static conditions*. The problem with a 2-phase screw expander is that no quasi-static conditions will exist. Therefore any modeling using conventional thermodynamic entities of the fluid will be susceptible to errors by definition.

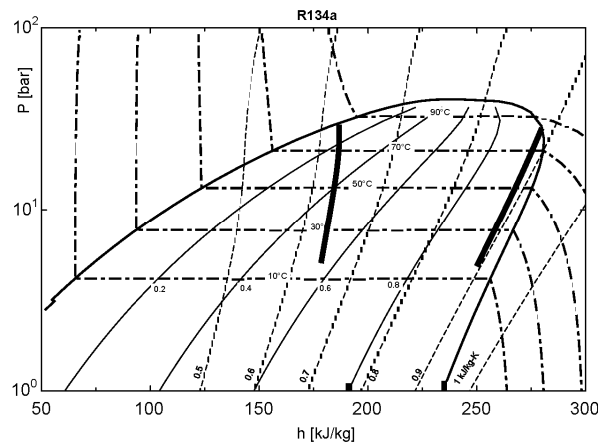


Figure 7. Schematic indication of non-reversible expansion of left side: saturated liquid, right side: saturated gas, R134a

One way to explain the process is to use the simplified Figure 7. The mixture can be schematically separated into; expansion of liquid, left side of the diagram and of gas, right side of the diagram.

Expansion of the pure liquid leads to immediate flashing of liquid, a process well handled in refrigeration condensate valve technology and conventional Trilateral Flash Cycles. The evaporated gas tends to counteract the pressure reduction in the chamber meaning that we need very detailed information on the flashing in order to predict chamber pressure. Flashing also absorbs heat from the liquid, a process also requiring detailed simulation in order to predict the consequential chamber pressure. Expansion of the saturated gas, as in a conventional ORC without superheat, would quasi-statically lead to an immediate condensation of some fluid. The condensation is however not immediate, something well known to engineers designing screw expanders for ice production. Instead the gas can exist in sub-cooled conditions for a remarkably long time. Theories for sub cooled gas behavior are established in steam turbine expansion thermodynamics. However, in screw expanders the two expansion processes co-exist in the same chamber with undefined thermal contact, interacting with each other. This disqualifies any existing theory for dynamic expansion.

Commonly used models, using this logic of Figure 7, assume local equilibrium to simulate fluid states. To the knowledge of the authors no evidence of accuracy suitable to explain details of the expansion process, nor to predict performance for practical use, has been published. Research on flashing of liquid is ongoing, see Polanco et al (2010), but the methodologies are not yet well adapted to flash expansion in volumetric machines.

Physically modeling the expansion seems complicated but not impossible. However, on top of the basic thermodynamics we need to add strong centrifugal effects within the chamber, leakage of hot/cold gas/liquid of non-quasi-static conditions as well as the existence of lubrication oil. Solubility of fluid in oil is a function of pressure and temperature. Further increasing complexity by using fluid mixtures limits the probability designing a theoretical model to predict performance.

With the perspective of the above the approach of Equations (1) and (3) seems as a better short term alternative to predict performance and thereby implementing the unique characteristics of 2-phase expansion in screw expanders.

4. A NEW PERSPECTIVE ON ORC CYCLE DESIGN

In optimizing ORC performance adaption of cycle temperature to that of the heat source has critical impact on the results. Of course a balanced approach is required due to the trade-off between high cycle efficiencies and high cost of heat exchanger area. Saleh et al (2007), Pierobon et al (2014) and many others have developed methodologies to choose an appropriate working fluid for any particular application. Woodland et al (2013) showed that the combination of mixed flow expansion and fluid blends can provide opportunities to improve ORC design. *The downside of choosing the appropriate working fluid/fluid blend for every application is obviously the lack of standardization and the difficulty of moving one ORC unit from one application to another, or shifting its operating conditions.*

Öhman and Lundqvist (2014) showed that when ORC's can be optimized on expansion entry vapor fraction then the sensitivity to choice of working fluid is significantly reduced. Thus an ORC unit, designed for variable vapor fraction, can more easily be adapted to various heat sources and achieve better industrial cost efficiency. In the comparison a marine diesel engine cooling water waste heat recovery application was investigated assuming 3 radically different working fluids, R717/R134a/R245fa. To estimate the effects of component efficiencies three grouped efficiency classes were used, see reference for details.

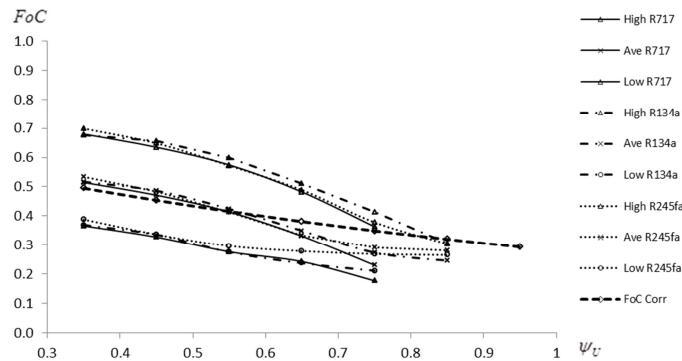


Figure 8. Fraction of Carnot vs. Utilization, both non-dimensional, in a marine diesel waste heat recovery ORC optimized on vapor fraction using R717, R134a and R245fa. *High, Ave and Low indicate grouped component efficiency class levels as of Öhman and Lundqvist (2014). FoC Corr is an estimation of current market product performance for the same conditions, same reference.*

As seen in Figure 8 the optimized thermal efficiency of the three different fluids was found very similar, with concern taken to different component efficiency classes. *If the ORC cycles would have been limited to saturated, or superheated, expansion entry conditions the outcome of the three different working fluids would have been significantly more different.* Another observation from the comparison was that there are specific cost minima with significant effects on plant architecture. Those specific cost minima are strongly dependent on the vapor fraction.

5. DISCUSSION

As far as is known by the Authors very few publications addressing variable vapor fraction ORC system optimization exists. The work in Öhman and Lundqvist (2014) only demonstrates the effects and the subject matter needs further investigations in order to establish limitations of opportunities. However, the work supports the assumption that by using screw expanders to allow variable vapor fraction expansion entry conditions opportunities exist to significantly increase cost efficiency of ORC systems compared to current practice.

An obvious weak point in the theoretical simulations is the correlation of adiabatic expansion efficiency explained in Chapter 3.1. The proposed correlation in Equation (2) is based on a limited

amount of test data with many unknown parameters. Further refinement of that correlation is however time consuming and costly. One could argue that a wiser use of such resources might be to focus more on simulation of the physical processes inside the chamber.

A reflection on the work is that there is an apparent need to rethink our assumptions on what an ORC is and reconsider our approaches to choice of working fluid. The Authors look forward to further improvements in the methodologies for design choice of working fluid in the perspective of the above. Equation (2) means that fundamentally new modeling tools are not immediately required.

6. CONCLUSIONS

This review shows that a multitude of experience of using twin screw expanders in ORC applications exists. However such experience seems to be mostly industrial and not well explained scientifically. The review also shows that multi-phase expansion in screw machines is a well proven technology. Also, in determining expansion efficiency, while having mixed flow at expansion entry, a correlation can be used. A final conclusion is that the above findings allows for a new perspective on optimization of ORC's to its heat sources and significantly affects opportunities to standardize choices of working fluid.

NOMENCLATURE

X_{entry}	Vapor fraction at expansion entry	(-)
η_{ad}	Adiabatic efficiency (isentropic and adiabatic)	(-)
$\eta_{ad,sat}$	Adiabatic efficiency, with saturated gas entry	(-)
$\eta_{ad,peak}$	Adiabatic efficiency, at peak efficiency entry condition	(-)
Ψ_{2phase}	Correlation factor due to vapor fraction	(-)
FoC	Fraction of Carnot, ratio of real-to-reversible thermal efficiency	(-)
Ψ_U	Utilization of available heat transport from source to sink	(-)

REFERENCES

- Behrendt, E., 1970, Freon-Motor als Fahrzeugantrieb, *Automobil Revue.*, vol. 6, no. 3, p. 32-33, (In German)
- Biederman, T., Brasz, J., 2014, Geothermal ORC systems using large screw expanders, 22nd *International Compressor engineering Conference at Purdue. July 14-17. 2014*, Nr. 1470, Purdue University, Purdue,
- Brasz, J., 2000, Screw expessor testing on R134a chiller-efficiency, liquid carry over and chiller benefit, *Compressors and their systems*, ISSN:1356-1448, ISBN:1860584179, ImechE Conference Transactions., vol. 2,
- Kauder, K., Kliem, B., 2003, *The operating conditions of 2-phase screw motors with internal evaporation*, ISSN:0945-1870, Dortmund University, Dortmund, vol. 11, p. 69-84, (In German),
- Kliem, B., 2005, *Fundamentals of the two-phase screw-type engine*, Dortmund University, Dortmund , 140 p., (In German)
- Lysholm, A., Boestad, G., 1935, Compressor apparatus, US Patent nr 2111560,
- McKay, R., 1982, *Helical screw expander evaluation project final report*, DOE/ET/28329-1, Jet Propulsion Laboratory, US Department of Energy, (JPL-Pub-82-5),
- Merigoux, J. M., Pocard, P., 1980, Solar power units with screw expanders, *Solar 3 (1980).*, 80/25169, p. 1293-1317,
- Minto, W. L., 1967, Low entropy engine, US Patent nr 3479817,
- Öhman, H., 1997, Refrigerant expanders for use in Organic Rankine Cycles (ORC), *SRM Technical Screw Compressor Conference 1997.*, SRM, p. 2-6,

- Öhman, H., 2004, Test results of a screw type expander/compressor and the implication of phase separators on the refrigeration process, *International Refrigeration and Air Conditioning Conference at Purdue. July 12-15. 2004*, R025, Purdue University, Purdue,
- Öhman, H., 2012, Implementation and evaluation of a low temperature waste heat recovery power cycle using NH₃ in an Organic Rankine Cycle, *Energy.*, vol. 48, p. 227-232
- Öhman, H., Lundqvist, P., 2013, Experimental investigation of a Lysholm turbine operating with superheated, saturated and 2-phase inlet conditions, *Applied Thermal Engineering.*, vol. 50, p. 1211-1218, (<http://dx.doi.org/10.1016/j.applthermaleng.2012.08.035>)
- Öhman, H., Lundqvist, P., 2014, *Organic Rankine Cycles with variable vapor fraction expansion entry*, TRITA-REFR REPORT 14:2, KTH, Stockholm. Sweden, ISBN 978-91-7595-224-6,
- Olofsson, H., 1989, Rotary positive displacement machine for compressible working fluid, US Patent nr 4863357,
- Pierobon, L., Casati, E., Casella, F., Haglind, F., Colonna, P., 2014, Design methodology for flexible energy conversion systems accounting for dynamic performance, *Energy.*, vol. 68, p. 667-679
- Polanco, G., Holdo, A., E., Munday, G., 2010, General review of flashing jet studies, *Journal of Hazardous Materials.*, vol. 173, p. 2-18,
- Saleh, B., Koglbauer, G., Wendland, M., Fischer, J., 2007, Working fluids for low-temperature Rankine cycles, *Energy.*, vol. 32, no. 7, p. 1210-1221, (doi:10.1016/j.energy.2006.07.001)
- Schibbye, H., 1959, *Performance of gearless screw expander*, SRM Technical report 1045/M-25, SRM, Stockholm, (opcon.se/web/Reports_2.aspx, 06.12.2011),
- Smith, I. K., Stocik, N., Aldis, C. A., 1994, Lysholm machines as two-phase expanders, *International Compressor Engineering Conference*, Paper 957, Purdue University, Purdue, (<http://docs.lib.purdue.edu/icec/957>),
- Steidel, R., Weiss, H., Hower, J. E., 1977, *Performance characteristics of the Lysholm engine as tested for geothermal power applications in the Imperial valley*, Rept. UCRL-80151, Lawrence Livermore Laboratory, Livermore, California, USA,
- Steidel, R., Pankow, D., Berger, R. E., 1981, Performance characteristics of the Lysholm engine as tested for geothermal applications, *16th Intersociety Energy Conversion Engineering Conference, IECEC.*, vol. 2,
- Svenningsson, K., Sjölin, U., Öhman, H., 2010, *The screw compressor development at SRM*, SRM, Stockholm, www.opcon.se/web/History_4.aspx, 02.12.2015,
- Timuska, K., 2008, *100 years of energy efficiency*, SRM, Stockholm, www.opcon.se/web/History_1.aspx, 02.20.2015,
- Wagenius, B., 1958, SRM machines of helical body type, for compression and expansion; their operational characteristics, design and application in refrigeration technology, *Kylteknisk Tidskrift.*, vol. 1, p. 1-7, (In Swedish),
- Wiess, H., Steidel, R., Lundberg, A., 1975, *Performance characteristics of a Lysholm engine*, Rept. UCRL-51861, Lawrence Livermore Laboratory, Livermore, California, USA,
- Woodland, B., J., Krishna, A., Groll, E., A., Brown, J., E., Horton, W., T., Garimella, S., V., 2013, Thermodynamic comparison of organic rankine cycles employing liquid-flooded expansion or a solution circuit, *Applied Thermal Engineering.*, vol. 61, p. 859-865

DYNAMIC MODEL FOR THE PERFORMANCE PREDICTION OF A TWIN SCREW EXPANDER IN AN ORC

I. Papes*, J. Degroote, J. Vierendeels¹

¹Ghent University, Department of Flow, Heat and Combustion Mechanics,
Ghent, Belgium

*iva.papes@ugent.be

ABSTRACT

The Organic Rankine Cycle (ORC) is well known and proven technology for waste heat recovery. The current generation of twin screw expanders used for low-grade heat recovery are in fact compressors working in the opposite sense. In this paper a mathematical model for calculating the performance of a twin screw expander is presented. The model is based on geometrical parameters which describe volume and leakage areas for every angular position. With these functions the entire design of a screw expander is determined. The differential equations used in the model are derived from the mass and energy conservation laws and are solved together with the appropriate Equation of State in the instantaneous control volumes. Since R245fa is selected as a working fluid, the Aungier Redlich-Kwong Equation of State has been used. The results of the mathematical model are compared to the 3D Computational Fluid Dynamics (CFD) calculations of the same twin screw expander using the same working fluid. To calculate the mass flow rates through the leakage paths formed inside the screw expander, flow coefficients are considered as constant and they are derived from 3D CFD calculations. The outcome of the mathematical model is the P-V indicator diagram which is compared to CFD results of the same twin screw expander. It is shown that the developed model accurately predicts the performance of the expander.

1. INTRODUCTION

With increasing concerns over energy pollution and consumption constraints the interest in waste heat recovery has grown in the past years. A large portion of waste heat is available at low temperatures (350K-400K) from industrial processes which can be converted into mechanical power. The most widely used technology for waste heat recovery is the Organic Rankine Cycle (ORC). Although ORC systems are now well developed, efforts have been increasingly directed towards higher efficiencies and power outputs. The key element for the power generation in ORC systems is the expander. The choice of the expander is crucial and it depends on the amount of available heat and operating conditions. For small scale ORC system studied in this paper, displacement machines are highly suitable (Lemort, 2013).

The first analytical procedure for the expander's performance prediction has been reported by (Margolis, 1978). More recently, the numerical and experimental study of an oil injected twin screw expander for both air and R113 has been presented in (Wang, 2010). A mathematical model was verified with an experimental study and flow coefficients used in the leakage models were derived from it.

The capability to analyse the performance of such complex screw machines by thermodynamic models which describe the behaviour of the fluid are often limited because of inability to get

proper experimental data. With Computational Fluid Dynamic (CFD) it is possible to analyse the flow within screw expanders and to get a better view on different phenomena that occur within such machines. In previous studies the authors presented a 3D CFD simulation of a twin screw expander using R245fa (also known as 1,1,1,3,3-Pentafluoropropane) as the working fluid (Papes, 2014). R245fa is characterized by a positive slope of the saturated vapor line in a T-s diagram which will prevent the formation of liquid droplets at the exit of the expander. The mesh motion is handled by an in-house code which generates a block-structured grid with the help of solutions of Laplace problems on an unstructured triangular grid (Vande Voorde, 2004).

The aim of this paper is to present a mathematical model of a twin screw expander and to validate it with CFD results. Moreover, the goal is to extract the coefficients used in the isentropic converging nozzle leakage model from the 3D CFD analysis. Several objective performance indicators such as mass flow rates, pressure-volume diagrams and power output are used to compare these two models.

2. GEOMETRY

The geometry of a twin screw expander used in this study is shown in Figure 1a. There are four male lobes and six female lobes with asymmetrical rotor profiles. The outer diameter of the male and female rotors is approximately 70mm with L/D ratio of 1.9.

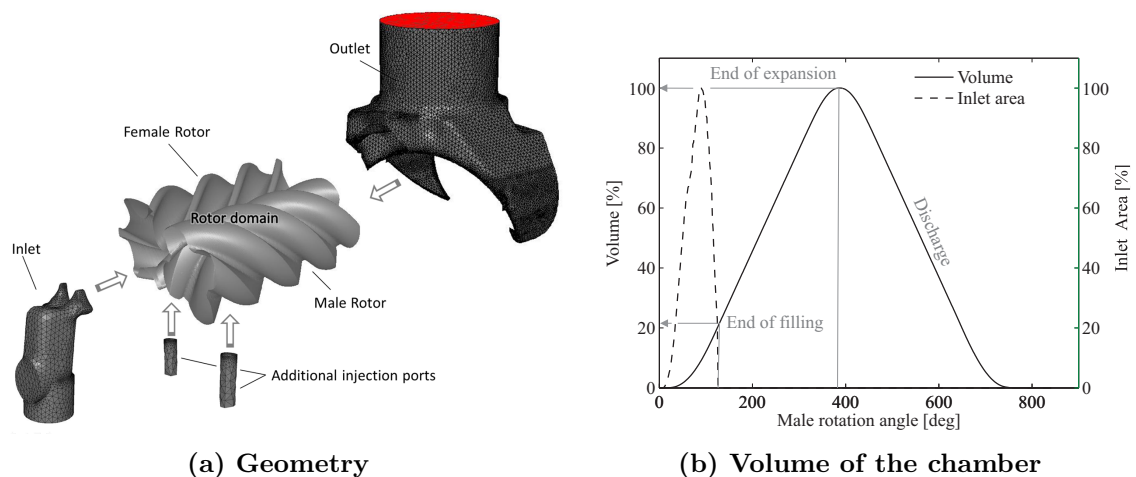


Figure 1: Geometry of a twin screw expander with the analytical description of the geometrical parameters used in the mathematical model

The volume curve of the screw expander is shown in Figure 1b. The formation of a chamber starts at $\theta = 0^\circ$ in Figure 1b. When $\theta = 7^\circ$, the chamber is in connection with the inlet port. As the rotor rotate, the volume of the chamber increases with increasing inlet surface area, and the chamber is filled with the working fluid. When the inlet area starts to decrease, the volume of the chamber is still increasing. This can already cause the **pre-expansion** of the working fluid. The filling ends at $\theta = 126^\circ$ after which the working fluid expands with increasing volume of the chamber. At $\theta = 387^\circ$, the working chamber is connected to the outlet and the working fluid is discharged through the outlet port.

Within twin screw expanders, it is possible to identify four types of leakage paths. All four types of leakages in screw expanders are depicted in Figure 2 and are characterized by the length of the leakage path and the area of the clearance.

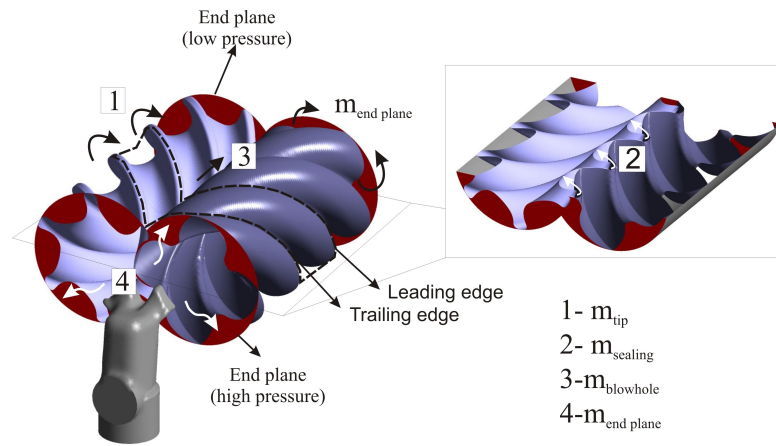


Figure 2: Different leakage types inside the twin screw expander

3. CFD ANALYSIS

The flow calculations inside a screw expander are performed by Ansys Fluent with the use of User Defined Functions (UDFs) to handle the grid movement and real gas model as presented in (Papes, 2014). The mathematical model consists of a set of momentum, energy and mass conservation equations, which are accompanied by the Aungier Redlich-Kwong (ARK) EoS and $k - \varepsilon$ turbulence model. The spatial discretization is second order upwind. Both CFD and mathematical model presented in this paper used the same geometry from Figure 1b. A result of the CFD analysis for pressure ratio of 6 is presented in Figure 3.

In order to calculate flow coefficients for different leakage paths, the mass flow rate through the corresponding leakage path was correlated with the pressure ratio between chambers that are forming that leakage path and its area according to equation of isentropic converging nozzle.

By analysing the results of CFD calculations, it was seen that pulsations in the inlet pipe play an important role in the pressure difference which influences the mass flow during the filling. These pulsations can be captured with 3D CFD calculations or with a one-dimensional model. In this study pulsations in the pipe before the inlet port are obtained from the CFD results and are used in the developed mathematical model. The results of pressure pulsations for different

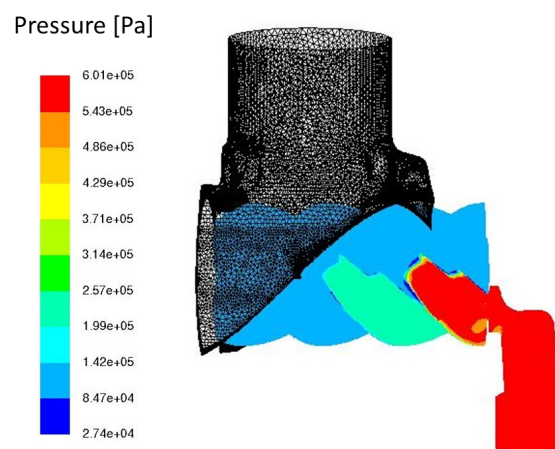


Figure 3: Pressure within twin screw expander (results of CFD analysis)

pressure ratios and rotational speeds were calculated through the reference plane as shown in Figure 4.

4. EQUATIONS GOVERNING SCREW EXPANDER PROCESS

The zero-dimensional mathematical model described in this paper employs the mass and energy conservation equations, accompanied by the geometrical model which describes the change in volume with the time or angular position, as well as change in the inlet and leakage path areas. Also in this model, the ARK EoS is used to describe real gas effects of R245fa.

When analysing the flow within the screw expander, the following assumptions have been made:

- The heat transfer between the working fluid and the rotor or between the casing and the ambient are not included in the model (they are also neglected in CFD simulations).
- Mechanical losses of the screw expander are not included in the model.
- Potential and kinetic energy of the working fluid are negligible.
- The flow through the leakage paths and inlet port is assumed to pass through an isentropic nozzle.
- Leakage flows through the end planes are not included in the model since they are not modelled. in the CFD calculations.
- The discharge process occurs at constant pressure.

The following equations were applied for each working chamber:

$$\frac{dm_{ch}}{dt} = \sum_i \dot{m}_i \quad (1)$$

$$\frac{dT}{dt} = \frac{-T \left(\frac{\partial \rho}{\partial T} \right)_v \left[\frac{dV}{dt} - v \frac{dm_{ch}}{dt} \right] - h \frac{dm_{ch}}{dt} + \sum_i \dot{m}_i h}{m_{ch} c_v} \quad (2)$$

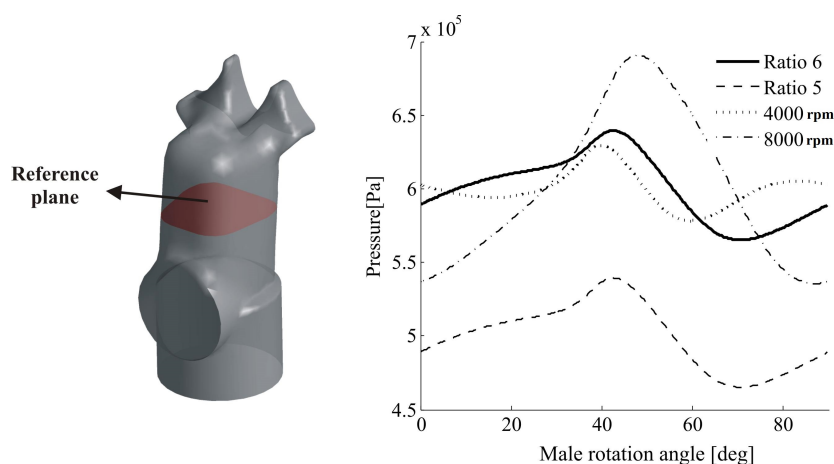


Figure 4: Pressure pulsations in the reference plane of the inlet port (results from CFD analysis)

This system of differential equations is solved by using the forward Euler method applied simultaneously on all chambers. Once the geometrical inputs (volume change and leakage areas) have been provided to the model, the pressure and the temperature are initialized with guess values. After that, for each iteration step, the mass flows going in or out of the chamber are calculated and the temperature in the next step is obtained. Since the mass, the volume and the temperature are then known, the pressure and the density can be updated.

The mass flow through the leakage paths and the inlet port is calculated using the isentropic nozzle model (Bell, 2011):

$$\dot{m}_{nozzle} = CA\sqrt{p_{up}\rho_{up}}\sqrt{\frac{2k}{k-1}\left(p_{ratio}^{2/k} - p_{ratio}^{(k+1)/k}\right)} \quad (3)$$

Where the function of pressure ratio is defined as:

$$p_{ratio} = \begin{cases} \left(1 + \frac{k-1}{2}\right)^{k/(1-k)} & p_{down}/p_{up} \leq \left(1 + \frac{k-1}{2}\right)^{k/(1-k)} \\ p_{down}/p_{up} & p_{down}/p_{up} > \left(1 + \frac{k-1}{2}\right)^{k/(1-k)} \end{cases}$$

Flow coefficients C are constant in time and are obtained from CFD calculations. The indicated work of a twin screw expander can be expressed as the area of the P-V indicator:

$$W_{ind,cycle} = \int_{cycle} V dp \quad (4)$$

The power of the twin screw expander can be then calculated as:

$$P_{ind} = \frac{W_{ind,cycle}zn}{60} \quad (5)$$

with z the number of lobes and n the rotational speed.

5. RESULTS AND DISCUSSION

There are different parameters to be compared between the developed mathematical model and the CFD analysis. One is the P-V indicator diagram of the screw expander, which will show how the pressure in every moment is changing with the instantaneous volume. If the calculated P-V indicator diagram agrees with the results of CFD analysis, the overall performance will be well predicted. However, additional parameters like mass in the chamber or leakage flow through the clearance paths should be checked and compared.

In Table 1, comparison for power and mass flow rate between the developed model and the CFD analysis are presented. The comparison has been made for pressure ratios $\pi = 6, 5$ and 4 and for rotational speeds of 6000rpm (nominal speed), 4000rpm and 8000rpm.

5.1 Evaluation with different pressure ratio

In Figure 5 the P-V indicator diagrams for pressure ratio of $\pi = 6, 5$ and 4 are shown. From Table 1 it can be seen that the difference in power outputs between CFD analysis and developed model is from 2 – 6%.

Pressure ratio	Speed	CFD		MODEL	
		Flow rate [kg/s]	Power [kW]	Flow rate [kg/s]	Power [kW]
6	6000	0.1469	4.72	0.1415	4.61
5	6000	0.1210	3.46	0.1160	3.30
4	6000	0.0955	2.18	0.0922	2.05
6	4000	0.1055	3.18	0.1028	3.23
6	8000	0.1618	5.11	0.1619	5.30

Table 1: Results for mass flow rates and power outputs for the developed model and the CFD analysis

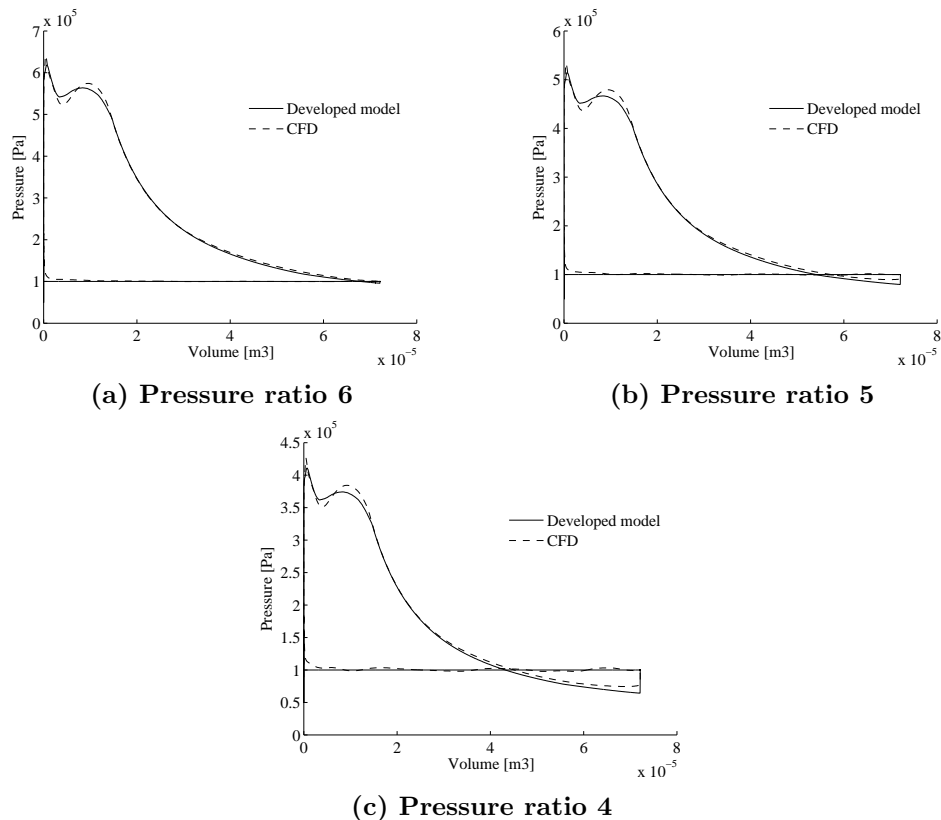


Figure 5: Model predicted and CFD calculated results

5.2 Evaluation with speed change

The performance of the expander was also examined with variations in speed (Figure 6). With change in speed, the P-V indicator shows a difference during the filling phase. Due to the shorter duration of the filling period with the rise in rotational speed, it can be seen that the throttling loss increases. The difference between the developed model and the CFD analysis is around 4% for a rotational speed of 8000rpm and around 2% for a rotational speed of 4000rpm.

5.3 Mass in the chamber

The comparison of the total mass in the chamber between the developed model and the CFD results is shown in Figure 7. This parameter is very important because it shows if the mass in the chamber after the filling is close to CFD results. This shows if the filling process in the developed model is described correctly. But also, it shows if the leakage flows are reducing the mass in the chamber in the same way as in CFD results.

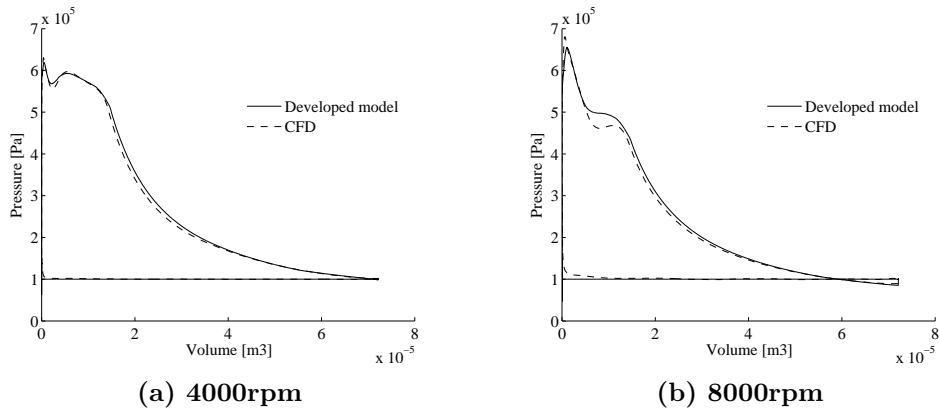


Figure 6: Model predicted and CFD calculated results for changes in rotational speed

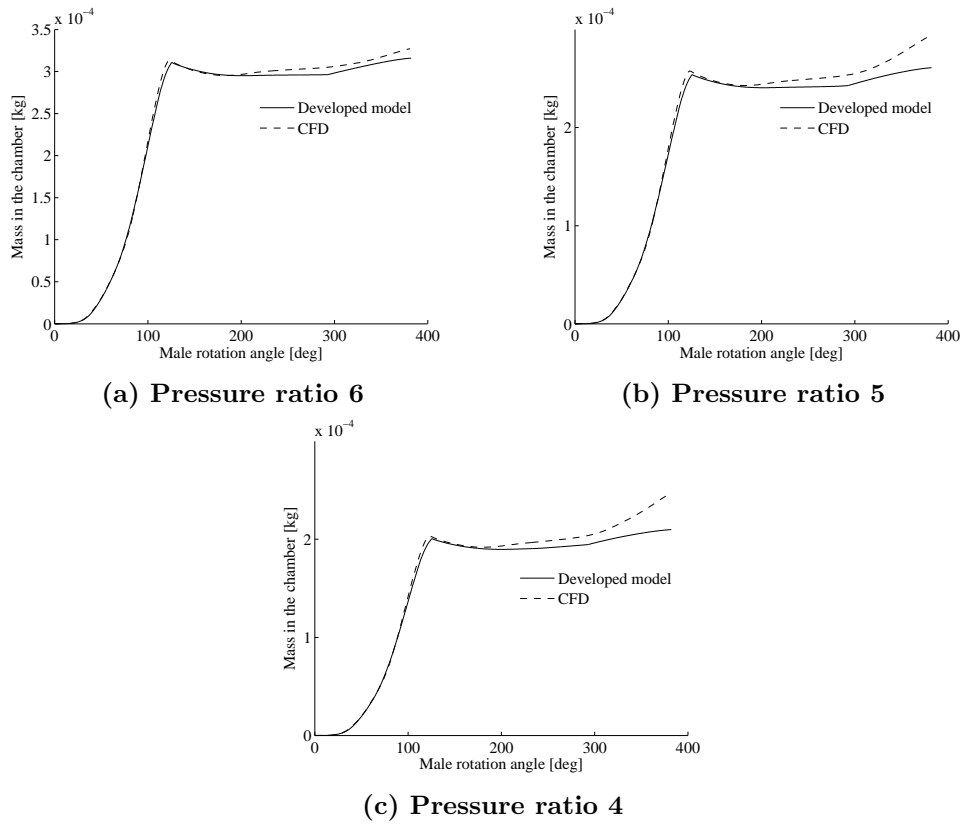


Figure 7: Model predicted and CFD calculated results of the mass in a chamber for changes in pressure ratio

5.4 Leakage flows

The last two parameters are the mass flow rates through the tip and sealing leakage path (Figure 8). Here it is very important to see if using the constant flow coefficient derived from the CFD calculations can estimate these flows correctly. It can be clearly seen that the trend of these curves is matching well with CFD results. Although slight deviations are present, it should be noted that mass flow rates through the leakage gaps are already very low comparing to the total mass flow rate.

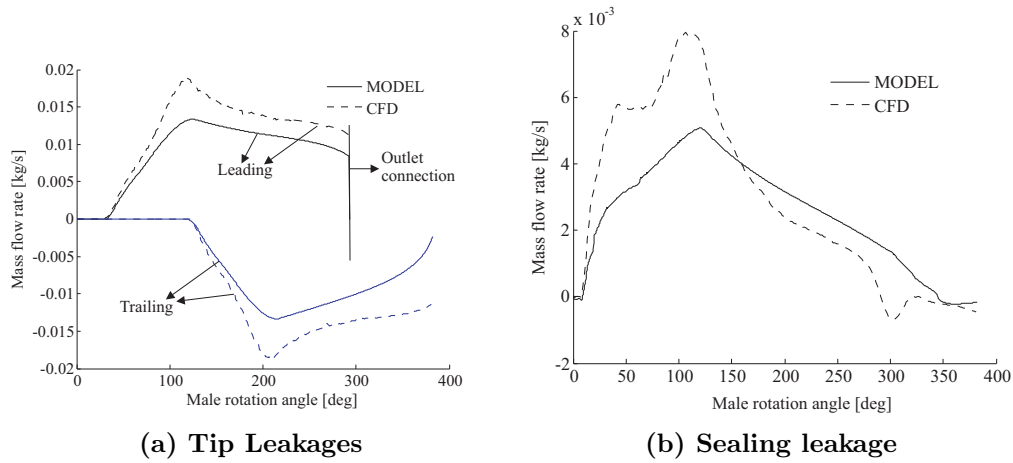


Figure 8: Model predicted and CFD calculated results in the screw expander with pressure ratio 6 and rotational speed of 6000rpm

6. CONCLUSION

A mathematical model for the performance prediction of a twin screw expander has been developed. From the mass and energy conservation laws, differential equations are derived which are then solved together with the Aungier Redlich-Kwong Equation of State for R245fa in the instantaneous control volumes. The mathematical model employs all geometrical parameters such as chamber volume, suction and leakage areas. To calculate the mass flow rates through the leakage paths formed inside the screw expander, flow coefficients are derived from CFD analysis. All geometrical inputs in terms of rotational angle of male rotor are employed in the model. It is shown that the developed model accurately predicts the performance of the expander.

7. NOMENCLATURE

NOMENCLATURE		T	Temperature (K)
Symbols		V	Volume (m^3)
\dot{m}	Mass flow rate (kg/s)	W	Work (J)
ρ	Density (kg/m^3)	z	Number of lobes ($-$)
A	Area of the leakage path/inlet area (m^2)	Subscripts	
C	Flow coefficient ($-$)	ch	Chamber
h	Specific enthalpy (kJ/kg)	$down$	Downstream
k	Specific heat ratio ($-$)	i	Number of boundaries of the working chamber
m	Mass (kg)	in	Indicated
n	Rotational speed (rpm)	up	Upstream
P	Power (W)		

REFERENCES

- Lemort V., Guillaume L., Legros A., Declaye S. and Quoilin S., 2013, A comparison of piston, screw and scroll expanders for small scale Rankine cycle systems In Proc. 3rd Int. Conf. on Microgeneration and Related Technologies
- Papes I., Degroote J. and Vierendeels J., 2014, Analysis of a Twin Screw Expander for ORC Systems using Computational Fluid Dynamics with a Real Gas Model Int. Compressor Engineering Conf. at Purdue University
- Papes I., Degroote J. and Vierendeels J., 2013, 3D CFD Analysis of an Oil Injected Twin Screw Expander ASME International Mechanical Engineering Congress and Exposition
- Margolis D. L., 1978, Analytical Modelling of Helical Screw Turbines for Performance Prediction ASME J. Engr. for Power, **100**, 482
- Wang Z., Zhang Y., Sun T. and Wei L., 2010, Numerical simulation and experimental study on the performance of screw expander ASHRAE Transactions part 2, **116**, 218-225
- Aungier R. H., 1995, A fast, accurate real gas equation of state for fluid dynamic analysis applications J. of Fluids Engineering, **117**, 277-281
- Vande Voorde J., Vierendeels J., Dick E., 2004, Development of a Laplacian-based mesh generator for ALE calculations in rotary volumetric pumps and compressors Computer Methods in Applied Mechanics and Engineering, **193**, 39-41, 4401-4415
- Bell I. 2011, Theoretical and Experimental Analysis of Liquid Flooded Compression in Scroll Compressors *PhD Thesis*

ACKNOWLEDGEMENT

The results presented in this paper have been obtained within the frame of the IWT SBO-110006 project The Next Generation Organic Rankine Cycles (www.orcnext.be), funded by the Institute for the Promotion and Innovation by Science and Technology in Flanders. This financial support is gratefully acknowledged.

COMPARISON OF ORGANIC RANKINE CYCLE SYSTEMS UNDER VARYING CONDITIONS USING TURBINE AND TWIN-SCREW EXPANDERS

M. Read*, A. Kovacevic, I.K. Smith and N. Stosic

City University London,
Northampton Square, London EC1V 0HB, United Kingdom
e-mail:m.read@city.ac.uk

* Corresponding Author

ABSTRACT

A multi-variable optimization program has been developed to investigate the performance of Organic Rankine Cycles (ORCs) for low temperature heat recovery applications. This cycle model contains detailed thermodynamic models of the system components, and the methods used to match the operation of the expander to the requirements of the cycle are described. Two types of ORC system are considered; one containing a turbine to expand dry saturated or superheated vapour, and one with a twin-screw machine allowing expansion of partially evaporated fluid.

Modelling of the ORC system with a twin-screw expander has been described previously (Read et al. 2014a, 2014b). The performance of the turbine in the superheated ORC has been modelled using available operational data for single stage, reaction turbines, where correlations have been used to estimate the efficiency of the turbine at 'off-design' conditions using either fixed or variable nozzle geometries.

The capability of the cycle model has been demonstrated for the case of heat recovery from a source fluid at 120°C. The system parameters are optimised for a typical operating condition, which determines the required size of heat exchangers and the expander characteristics. Performance at off-design conditions can then be optimized within these constraints. This allows a rigorous investigation of the effect of air temperature variation on the system performance, and the seasonal variation in net power output for the turbine and twin-screw ORC systems is estimated.

1. INTRODUCTION

The Organic Rankine Cycle (ORC) provides a means of recovering useful energy from low temperature heat sources. In comparison with conventional high temperature steam Rankine cycles, the low temperature of these heat sources means that the attainable cycle efficiency is much lower, while the required surface area of the heat exchangers per unit power output is much higher. The lower latent heat of evaporation of organic fluids relative to steam also means that the feed pump work required in ORCs is a significantly higher proportion of the gross power output.

Maximising the net power output from an ORC is a compromise between increasing the mean temperature of heat addition (which, in accordance with Carnot's principle, can increase cycle efficiency) and increasing the amount of heat extracted from the source, which requires a lower evaporation temperature.

Especially at lower source temperatures, up to approximately 120°C inlet, the only cycle normally considered is that where the working fluid enters the expander as dry saturated vapour, as shown in Figure 1a. However, in most cases, this leads to the working fluid leaving the expander with some superheat, which must be removed before condensation begins. By the use of a screw expander, instead of the more conventional turbine, it is possible to admit the working fluid to the expander as

wet vapour and thereby eliminate both the need to de-superheat the vapour after expansion and, simultaneously to raise the evaporation temperature, as shown in Figure 1b, thus improving the cycle efficiency. The potential cost and performance benefits of using screw expanders in ORC systems have been extensively studied for geothermal applications by Smith et al. (2001, 2004, 2005).

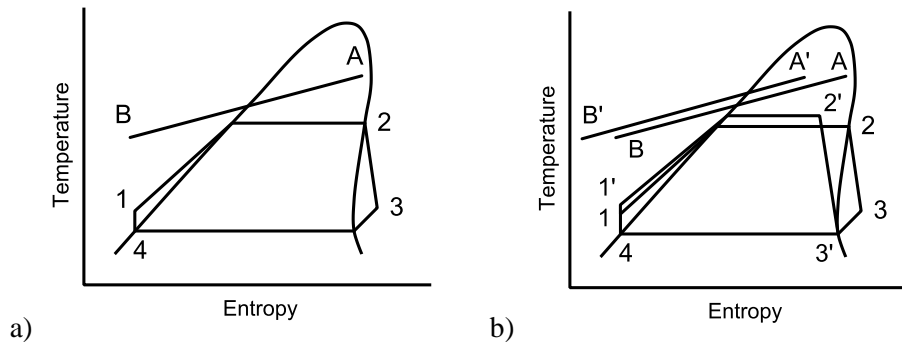


Figure 1: Illustrative T-s diagrams showing a) conventional ORC with dry saturated vapour at the expander inlet, and b) how the expansion of wet vapour can avoid superheated vapour

However, screw expander efficiencies are more sensitive to expansion pressure ratio than turbines and the expansion ratio increases as the expander inlet vapour dryness fraction decreases. To determine the value of inlet dryness fraction that leads to the maximum system power output, it is therefore necessary to include estimates of how both the screw expander and the feed pump performance vary as the inlet dryness fraction of the working fluid is changed in such a wet ORC (WORC) system. The performance of these systems has previously been studied for operation at both design and off-design conditions (Read et al., 2014a, 2014b). In order to gain more insight into the performance of these systems, they must however be assessed in comparison with equivalent optimised ORC systems using convention turbine expanders. This requires an understanding of how turbine efficiency varies with inlet conditions and required mass flow rate of the working fluid. The aim of this study is to present a comparative analysis of the design and off-design performance of twin-screw WORC and turbine ORC systems.

2. ORC MODEL FOR OPTIMISATION ANALYSIS

The performance of ORC systems has been assessed using a computational model of the cycle. This has been written as an object-oriented program in the C# language, which provides a convenient structure as it allows a generic description of heat sources, heat sinks and cycle components. Each of these cycle elements contains definitions for all the necessary input and output parameters along with the required calculations. Both simple cycles such as those shown in Figure 1, and more complex cases (including multiple heat source streams, multiple paths for the working fluid or varying working fluid composition) can be analysed by creating models of the required components and providing the necessary input parameter values. The key cycle components are discussed in more detail below.

2.1 Turbine model

Single stage radial inflow reaction turbines are commonly used in ORC applications. These turbines must be sized for specified design point conditions. The flow of working fluid is choked at the throat of the turbine inlet nozzle, and the cross-sectional area at this point must be chosen in order to achieve the required mass flow rate. The operation of the turbine can be characterised by considering the conditions at the throat (denoted by the superscript *) assuming isentropic expansion from turbine inlet conditions (subscript *turb, i*) as described by Wendt and Mines (2013). The pressure, density, enthalpy and velocity of the working fluid at the throat can be calculated using the relationships in equations (1)-(3), where the critical conditions of the working fluid are denoted by the subscript *c*.

$$p^* = 0.67 p_{turb,i} \left(\frac{p_{turb,i}}{p_c} \right)^{0.2} \left(\frac{T_c}{T_{turb,i}} \right) \quad (1)$$

$$\rho^*, h^* = f(p^*, s_{turb,i}) \text{ , where values can be found using an appropriate equation of state} \quad (2)$$

$$u^* = \sqrt{2(h_{turb,i} - h^*)} \quad (3)$$

For the mass flow rate required at design conditions (denoted by subscript d), the cross-sectional area at the throat of the nozzle can then be calculated using equation (4).

$$\dot{m}_d = (\rho^* A^* u^*)_d \quad (4)$$

The mass flow rate of the working fluid in the cycle will vary at off-design conditions, and two possibilities have therefore been considered for the turbine design:

- i. Fixed nozzle geometry, with constant throat area of $(A^*)_d$,
- ii. Variable nozzle geometry, allowing the value of A^* to be adjusted.

For the fixed geometry case, an upstream throttle valve is required to reduce the turbine inlet pressure to a value which achieves the required mass flow rate through the fixed design throat area. Using variable geometry, the value of A^* may be varied between zero and a specified maximum value to achieve the required mass flow rate.

To characterise the effect of varying inlet and exhaust conditions on turbine performance, the turbine isentropic efficiency can be related to a velocity ratio, r_u , for the turbine. The velocity ratio is the ratio of the turbine tip speed, u_{tip} , to the spouting velocity, defined as the velocity achieved if the enthalpy change for an isentropic expansion were entirely converted to kinetic energy, as shown in Equation 5 (where $h_{turb,os}$ is the isentropic turbine outlet enthalpy).

$$r_u = u_{tip} / \sqrt{2(h_{turb,i} - h_{turb,os})} \quad (5)$$

The correlations proposed by Wendt and Mines (2013) have been used to characterise the change in turbine efficiency as a function of both the change in the nozzle throat area resulting from manipulating the nozzle geometry, and the change in the velocity ratio for the expansion process. In the current study, a constant turbine rotational speed has been used in all cases. As the power output of the turbine is in the region of 100 kW, a representative maximum isentropic efficiency of 75% has been assumed, rather than the 82% proposed for much higher power systems (Wendt and Mines, 2013). The REFPROP database developed by NIST has been used to calculate all thermodynamic properties of the working fluid. The working fluid used in this study is the refrigerant R245fa, which has a critical temperature of 154°C. This is sufficiently high to ensure sub-critical pressure in the evaporator. While using fluids with higher critical temperature may increase the achievable net power output by reducing the pressure difference across the feed pump and expander, the reduced vapour density at condenser pressure would significantly increase the size and cost of cycle components. The cost of the R245fa fluid itself is relatively low, and it is widely used for low temperature ORC applications.

The aim of this study is to understand how changes in operating conditions affect the performance of the conventional ORC system and compare this with the results of previous analysis of a WORC system. Using the method described above, the actual size and operating speed of the turbine are not required to estimate cycle performance, and the detailed design of the turbine has therefore not been considered.

2.2 Heat exchanger models

A discretized approach has been taken to the calculation of the required surface area in the heat exchangers. Once the temperatures of the source, sink and working fluids have been defined, the heat exchangers are split into a number of short sections and the heat transfer and the log-mean temperature difference (LMTD) are calculated. Representative values for the overall heat transfer coefficient in conventional shell and tube heat exchangers with different fluid phases (Roetzel and Spang, 2010) are shown in Table 1, and have been used to calculate the heat transfer surface areas. These are then lumped into two overall heat exchanger areas for ‘heat addition’ (combined feed-heater, evaporator and, if required, super-heater) and ‘heat rejection’ (combined de-superheater, condenser and sub-cooler) which can be sized for design-point conditions. The calculation of heat exchanger areas is essential for the analysis of off-design system operation, and while this simple approach is not expected to be highly accurate for design purposes, it can be used to gain some insight into the requirements of the different cycles.

Table 1: Representative values of overall heat transfer coefficient for ORC shell and tube heat exchangers with different states for the heat transfer fluids

State of the heat transfer fluids:		Approximate overall heat transfer coefficient (W/m ² K):
Liquid or 2-phase	Liquid	1200
Liquid or 2-phase	Gas	70
Gas	Gas	35

2.3 Integrated cycle model and optimisation analysis

There are two important aspects to applying the component models in an integrated cycle model. Firstly, the mass flow rate identified by consideration of the heat transfer between the source fluid and the working fluid must be matched to the mass flow rate in the expander itself. However, the expander mass flow rate is calculated as a function of the inlet conditions (which may be throttled) and the turbine geometry; an iterative approach is therefore required in order to bring the error between these two calculated mass flow rates below an acceptable value, and identify the required operating conditions for the expander. For turbines with either fixed or variable nozzle geometry, if the required mass flow rate cannot be achieved by the turbine through throttling and/or nozzle area control then the isentropic efficiency is set to zero.

Secondly, although the heat transfer surface area of the heat exchangers can be calculated for the design point optimisation, during off-design operation these values must remain fixed. The varying cycle conditions cause changes in the integrated LMTD and the heat transferred in each heat exchanger. Two separate iterative loops are therefore required to identify the pinch point temperature differences required to achieve the required area of the boiler/evaporator and the de-superheater/condenser/sub-cooler units to within an allowable error. If, for any reason, the required heat exchanger areas cannot be achieved with particular cycle conditions, the expander efficiency is again set to zero.

Applying these iterative subroutines allows the cycle to be completely defined, and the net power output can be calculated. An evolutionary algorithm has been used to identify the optimum operating conditions for the cycle model. This is a flexible and stable numerical approach which allows for optimisation with any number of variables and is particularly good for distinguishing global from local maxima and coping with discontinuities in the target function. A population of solutions is defined in which each individual solution has a unique ‘gene’ consisting of a ‘chromosome’ for each of the cycle optimisation variables under consideration (e.g. boiler pressure, condenser pressure, degree of superheat). The values of the chromosomes are initially randomly generated, and a function (in this study, the net power output of the cycle) is defined in order to calculate the ‘fitness’ of a

particular solution. Over successive generations of the calculation procedure, 'fitter' genes are used to create new solutions through both combination and random mutation of the chromosomes. In this study, the optimisation method was implemented as follows:

- i. An initial estimate was made of the optimal system operating conditions.
- ii. An initial population of 5000 randomly generated solutions were created, centred on the estimated values.
- iii. The combination and mutation algorithm was implemented for 5000 generations, and the best solution identified.
- iv. A check was performed by creating a random population of 5000 centred on the best solution, and if a new best solution was identified the procedure was repeated.

3. LOW TEMPERATURE HEAT RECOVERY CASE STUDY

In order to demonstrate the cycle analysis described in Section 2, a simple case study has been performed for the recovery of heat from a geothermal brine source fluid. This liquid stream has an inlet temperature of 120°C and contains a recoverable heat content of 2.7 MW if cooled to an ambient temperature of 10°C; however, a minimum allowable brine temperature of 70°C has been imposed as this represents a typical limit for controlling the formation of precipitates.

The study presented below has investigated the generation of power from this heat source using an ORC with the following characteristics:

- The working fluid is refrigerant R245fa.
- An air cooled condenser is used with 2°C sub-cooling of the working fluid at the exit.
- Minimum pinch point temperature differences of 5°C and 10°C respectively have been applied for the boiler and condenser for the design-point optimisation.
- The efficiency of the feed pump has been characterised as a function of volumetric flow and pressure difference rate using data from manufacturers.
- An efficiency of 95% has been assumed for the electrical generator and 90% for pump/fan motors.

For this type of application, where the minimum allowable source temperature is well above the feed pump exit temperature when operating at design conditions, cycle efficiency and hence power output can be improved via recuperation, although the close temperature matching between the superheated vapour and sub-cooled liquid often necessitates a relatively large heat exchanger. In order to simplify the system analysis and the matching of the heat exchanger areas at off-design conditions, this study assumes that no recuperation is used to recover heat from the superheated turbine exit vapour.

Operation of the ORC system has been considered for average climate conditions in Nevada, USA where there are significant geothermal resources of this type. The annual mean temperature is 10.5°C, with monthly variations in the average maximum and minimum temperatures shown in Figure 2. A design-point optimisation has been performed for the annual mean temperature; the fixed parameters for this optimisation are shown in Table 2, and the results are shown in Table 3.

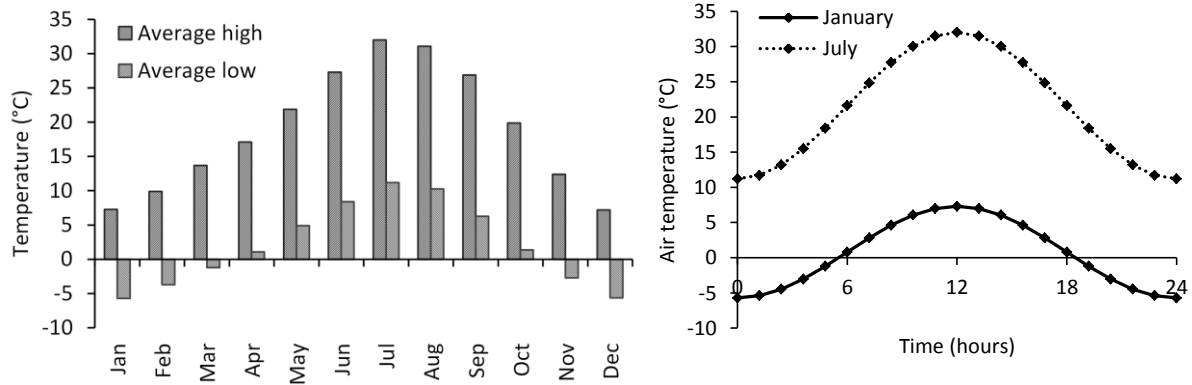


Figure 2: Monthly average maximum and minimum air temperatures in Nevada USA, and examples of assumed daily sinusoidal variation of air temperature

Table 2: Fixed parameters for design point optimisation of ORC system

Working fluid	-	R245fa
Boiler design pinch point	°C	5
Condenser design pinch point	°C	10
$T_{air,design}$	°C	10.5
$T_{source,in}$	°C	120
$T_{source,min}$	°C	70

Table 3: Optimised parameters for ORC with turbine expander operating at the design point conditions stated in Table 2

$p_{evaporator,in}$	bar	8.3
$p_{condenser,in}$	bar	1.7
$\Delta T_{superheat}$ at turbine inlet	°C	0
$\Delta T_{superheat}$ at turbine exit	°C	16
\dot{m}_{wf}	kg/s	5.4
$T_{brine,out}$	°C	70
$P_{expander}$ (electrical)	kWe	103
$P_{condenser fan}$ (electrical)	kWe	18.1
$P_{feed pump}$ (electrical)	kWe	4.6
P_{net} (electrical)	kWe	81.0

3.1 Off-design analysis of ORC with turbine

The off-design performance of the optimised ORC has been investigated by identifying the conditions required to achieve maximum net power output from the system defined in Table 2 for a range of air temperatures from -10 to 40°C. In all cases, the off-design analysis has achieved an error of less than 0.1% between the design-point and off-design values of the heat transfer surface area for the boiler and condenser heat exchangers. Reducing this allowable error was found to have negligible effect on the net power output from the system; with an air temperature of 30°C for example, a maximum error

of 1×10^{-6} in the heat exchanger areas was found to change the calculated net power output by less than 0.05%. The resulting system performance for off-design operation is shown in Figures 3 and 4, where the heat recovery efficiency refers to the fraction of available heat that is transferred into the cycle, and the cycle efficiency is the net power output divided by the heat input, as defined in equations (6) and (7).

$$\eta_{\text{heat recovery}} = \frac{T_{\text{source},i} - T_{\text{source},o}}{T_{\text{source},i} - T_{\text{air}}} \quad (6)$$

$$\eta_{\text{cycle}} = \frac{P_{\text{net}}}{\dot{m}_{\text{source}}(h_{\text{source},i} - h_{\text{source},o})} \quad (7)$$

3.2 Comparison of results for turbine ORC and twin-screw WORC

In order to assess the effect that the off-design performance has on the operation of the ORC system throughout the year, it has been assumed that for a typical day, the temperature has a sinusoidal variation between the average monthly maximum and minimum temperatures as shown in Figure 2. The variation in power with temperature through the course of a typical day in each month can then be calculated, and the mean power output for each month can be found. Figure 5 shows the time-averaged power output from the ORC for each month. The values of net power output calculated for both design-point and time-averaged annual conditions are compared in Figure 6. In Figures 3-6, results are also shown for the WORC using a twin-screw expander, as described by Read et al. (2014b). Finally, Figure 7 shows a comparison between the calculated heat transfer areas for heat addition and reject in both the WORC and ORC systems.

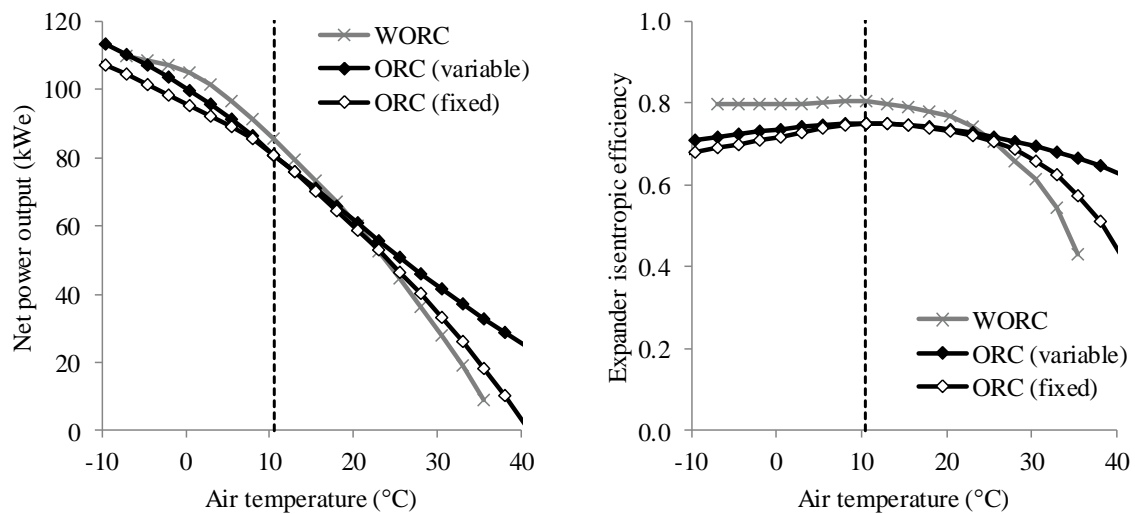


Figure 3: Maximum net power output as a function of air temperature and corresponding expander isentropic efficiency for WORC using twin-screw and ORC using fixed and variable nozzle turbines

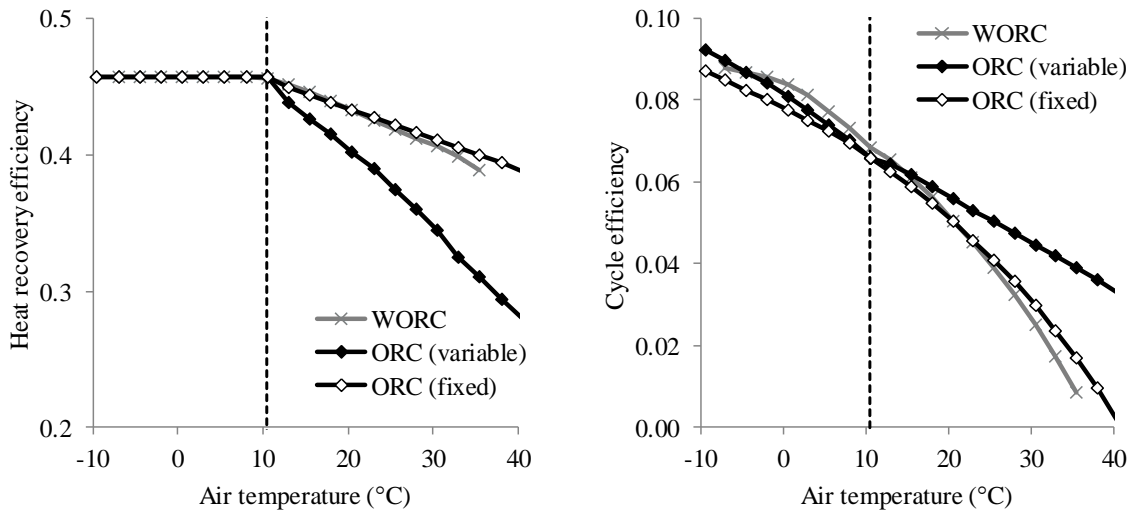


Figure 4: Heat recovery efficiency and cycle efficiency as functions of air temperature for WORC using twin-screw and ORC using turbine with fixed and variable nozzle geometry

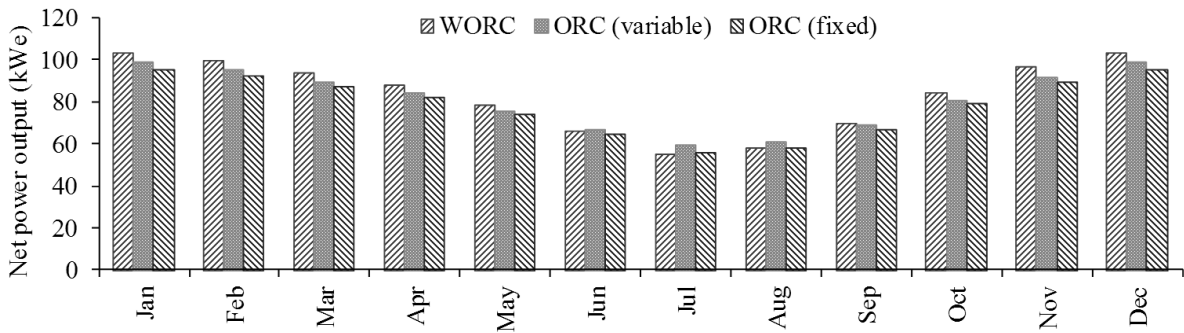


Figure 5: Comparison of monthly time-averaged net power output for the WORC, and ORC using turbine with fixed and variable nozzle geometry

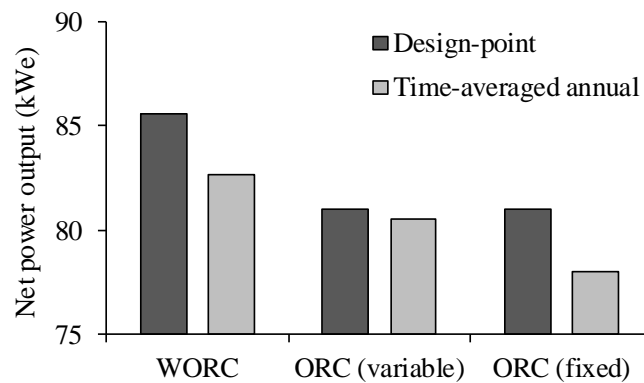


Figure 6: Comparison of net power output from WORC and ORC systems (with fixed and variable turbine nozzle geometries) for design-point and time-averaged annual conditions

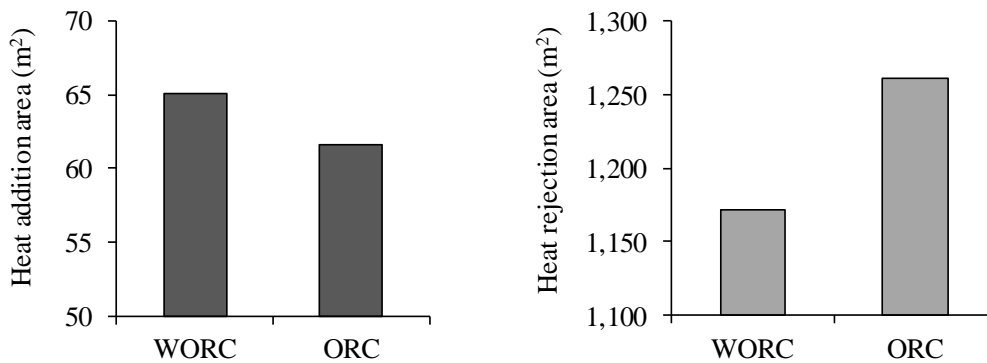


Figure 7: Comparison of predicted heat exchanger areas for WORC and ORC systems sized for design-point conditions

4. DISCUSSION

The results in Figures 3-7 show that similar overall performance is achieved by different ORC systems. The design-point net power output is largest for the WORC, largely due to the slightly higher expander isentropic efficiency predicted for the twin-screw machine, which was also able to maintain higher efficiency at off-design conditions with lower air temperature. The fixed geometry turbine was seen to achieve a lower efficiency than the variable geometry machine at all off-design conditions, but this decrease in efficiency was largely offset by a higher relative recovery of heat from the source fluid at higher air temperatures. The efficiency of the twin-screw machine in the WORC is seen to drop rapidly at higher air temperatures, due to the fixed built-in volume ratio of the machine leading to over-expansion of the working fluid. It may therefore be possible to improve the high temperature performance of the WORC system by allowing optimisation of the expander speed and/or built-in volume ratio in order to better match the volume ratio of the expansion process; the increase in net power output is however expected to be small due to the limited periods of time spent operating at these higher air temperatures. The time-averaged net power output from all cycles is seen to be very similar for all systems, at around 80 kWe, and the use of the average annual temperature to perform the design point calculations is seen to provide a good initial estimate of the real-world system performance.

The results presented above also give some insight into cost implications for the ORC systems. Compared to the optimised WORC, the area required for heat addition in the ORC is reduced by 5%, but the heat rejection area is increased by 8% due to the requirement to cool the superheated vapour at the turbine exit. As the air-cooled condenser is likely to represent a significant proportion of the total system cost due to its large size, this difference could be economically significant. However, more detailed consideration of the design and performance of heat exchangers and the associated heat transfer coefficients would be required to confirm this. The possible economic benefits of using twin-screw machines in WORC systems has already been discussed in detail (Leibowitz et al., 2006), and the results here suggest that performance can match or exceed conventional ORCs for relatively low power applications. It is however worth noting that the isentropic efficiency of turbines increases with power up to a maximum of around 83% for large-scale geothermal applications (Wendt and Mines, 2013). While the efficiency of twin-screw machines also generally improves with size and power output (due to the relative reduction in leakage flows), there is a practical limit of around 0.5 metres for the maximum rotor diameter. Applied to a WORC, isentropic efficiencies of around 84% and a net power output of around 590 kWe are predicted (Read et al., 2014b) and represent an upper limit to WORC operation using twin-screw expanders.

5. CONCLUSIONS

In this paper, the optimisation and part-load simulation of low temperature heat recovery systems has been demonstrated. The case study considered above suggests that similar overall performance can be achieved by ORC systems using both twin-screw and turbine expanders. The results indicate that for the application considered (where the heat source conditions remain constant) there is little benefit, in terms of average power output, in using a variable geometry turbine over the fixed type. While the efficiency of the screw expander is seen to decrease more rapidly than the turbine at higher air temperatures, the WORC is predicted to achieve comparable design-point and time-averaged performance and offers the potential for a low cost and low complexity system. The model described can be used for a wide range of applications, and allows comparative studies of the technical and economic performance of low temperature heat recovery systems and their components.

REFERENCES

- Leibowitz, H., Smith, I.K., Stosic, N., 2006, Cost Effective Small Scale ORC Systems for Power Recovery from Low Grade Heat Sources, *Proceedings of IMECE2006*, ASME, p. 521-527
- Read, M.G., Smith, I.K., Stosic, N., 2014a, Multi-Variable Optimisation of Wet Vapour Organic Rankine Cycles with Twin-Screw Expanders, 22nd International Compressor Engineering Conference at Purdue, Paper 2359.
- Read, M.G., Smith, I.K., Stosic, N., 2014b, Effect of Air Temperature Variation on the Performance of Wet Vapour Organic Rankine Cycle Systems, Transactions of the 38th GRC Annual Meeting, Portland OR .
- Roetzel, W., Spang, B., 2010, VDI Heat Atlas: C3 Typical Values of Overall Heat Transfer Coefficients, pp 75-78, Springer Berlin Heidelberg
- Smith, I.K., Stosic, N., Aldis, C.A., 1996, Development of the Trilateral Flash Cycle System: Part 3: The Design of High-Efficiency Two-Phase Screw Expanders, *Proceedings of the Institution of Mechanical Engineers, Part A: Journal of Power and Energy*, 210(1): 75-93.
- Smith, I.K., Stosic, N., Kovacevic, A., 2001, Power recovery from low cost two-phase expanders, *Transactions of Geothermal Resource Council*, p. 601-606.
- Smith, I.K., Stosic, N., Kovacevic, A., 2004, An improved System for Power Recovery from Higher Enthalpy Liquid Dominated Fields, *GRC Annual Meeting, Indian Wells*.
- Smith, I.K., N Stosic, N., Kovacevic, A., 2005, Screw expanders increase output and decrease the cost of geothermal binary power plant systems, *Transactions of Geothermal Resource Council*, p. 25-28.
- Stosic, N., Hanjalic, K., 1997b, Development and Optimization of Screw Machines with a Simulation Model - Part I: Profile Generation, *Journal of Fluids Engineering*, 119(3): 659-663.
- Wendt, D.S., Mines, G.L., 2013, Simulation of Air-Cooled Organic Rankine Cycle Geothermal Power Plant Performance, Report number: INL/EXT-13-30173, prepared for U.S. Department of Energy.

EXPERIMENTAL INVESTIGATION OF EFFECT OF OPERATING CONDITIONS ON PERFORMANCE OF ORC SYSTEM BASED ON OIL FLOODED TWIN SCREW EXPANDER

Abhijeet Chougule^{1,2*}, Charles Philominraj¹, Dr. Ramakrishna R. Sonde¹

¹Thermax Limited,
D-13, MIDC Industrial Area, R D Aga Road, Chinchwad, Pune - 411019, India
E-mail: abhijeet.chougule@thermaxindia.com

²Savitribai Phule Pune University,
Ganesh Khind, Pune - 411007, India

* Corresponding Author

ABSTRACT

The paper discusses the following aspects on the experimental investigation of effect of operating conditions on volumetric expander (oil flooded twin screw expander) based ORC system.

- Experimental investigation of oil flooded twin screw expander performance in an ORC system
- Experimental investigation and analysis of oil separator pressure drop and its effect on volumetric/isentropic efficiency of the expander
- Variable speed versus constant speed operation - Effect on isentropic efficiency of expander and cycle efficiency. The variable speed operation gives optimum isentropic efficiency (80 to 85%) at all loads of low potency heat recovery for power generation.
- Field experience of 30 and 100 kW screw expander based ORC system

1. INTRODUCTION

Organic Rankine Cycle (ORC) is emerging as one of the most suitable technology for harnessing low potency (low temperature) heat for electrical power generation.

Currently it is needless to emphasize the importance of harnessing low potency heat since it has become “the need” for any industry. However there are several challenges in harnessing low potency heat (Goel *et al.*, 2014):

- Higher cost of heat recovery due to low logarithmic mean temperature difference (LMTD)
- The conversion efficiency is low as the heat source becomes lower and lower. Although very high isentropic efficiencies of the organic fluid expander/turbines is achieved, the cycle efficiency has always remained low since the limiting Carnot efficiency is itself low at these temperatures.
- Availability of equipment in terms of reliability and uninterrupted operating hours

This paper discusses/reports the investigations carried out in overcoming some of these challenges to make ORC more and more viable. The experimentally investigated ORC system consists of a volumetric expander (oil flooded twin screw expander).

The investigation is based on understanding the mechanical and thermal performance of the ORC system, with respect to thermodynamic parameters of operating fluid and variable conditions of heat source and heat sink. The key experiments investigated are the effect of operating shaft speed on the expander performance at part load conditions and the effect of oil separator pressure drop on performance of the system (Mujic *et al.*, 2010).

The later part of the paper covers the challenges involved to make the ORC technology viable and reliable for various applications (Goel *et al.*, 2014). It also focuses on identifying the key areas of development to make the ORC system cost competitive and reliable in operation.

2. EXPERIMENTAL INVESTIGATION

The ORC experimental facility is designed for testing ORC system and its different components. The system uses low temperature saturated steam (at around 130°C) as the heat source and wet cooling tower (with water cooled condenser) for heat rejection. It is designed to test various capacities of ORC expanders/ turbines from shaft power capacity of 10 to 100 kW. The shaft power is measured by using an eddy current dynamometer (capacity 110 kW). The system is also designed for different operating fluids ranging from HCFC, HFC families to pure Alkanes. The photograph of the test facility is as shown in Figure 1.

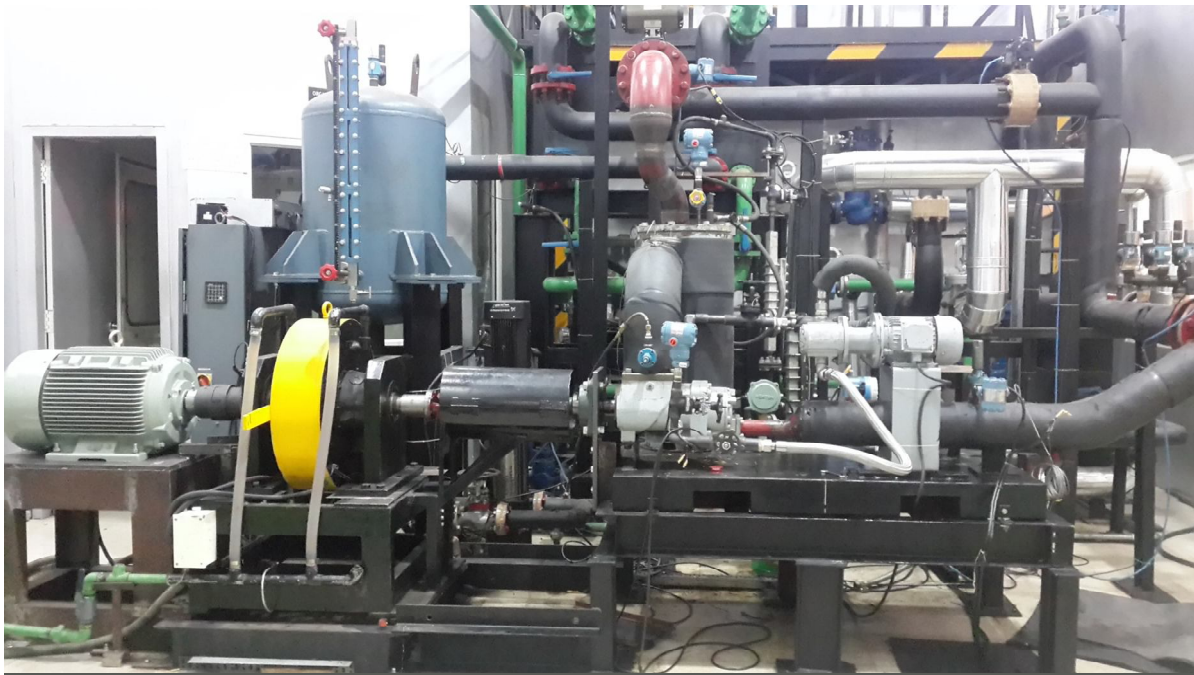


Figure 1: ORC test facility (with screw expander)

The current research work is oriented towards investigation of oil flooded twin screw expander for addressing the parametric performance of twin screw expander. The selected expander is a 4/5 lobe type design with designed displacement volume of 0.00292 m³ per revolution with volumetric compression ratio of 4.5. The rotor length is 245 mm. The maximum withstanding pressure of the expander casing is 18 bar abs. Hence during operational trials, the expander inlet pressure is limited up to 16 bar abs. The operating fluid used is R245fa (1,1,1,3,3 pentafluoropropane). The expander was tested for variable speed as well as constant speed operation. The variable speed operation was tested in the operating speed range of 1000 to 4500 rpm. The Constant speed operation was tested at 1500, 2000 and 3000 rpm. The experimental investigation was conducted with maintaining a superheat vapor condition (degree of superheat at 20°C) at expander inlet. The lube oil for bearing was pumped inside the expander using a positive displacement pump with constant flow rate.

Experimental results obtained from the performance testing of the expander operating at a constant shaft speed condition of 1500 rpm and 2000 rpm with steady state heat source and heat sink parameters of full load capacity, are presented in Figure 2 and 3 respectively. The experiments were conducted at steady state conditions of heat sink and heat source. The performance of the expander was monitored at steady conditions of constant flow of cooling water (heat sink fluid) and steam (heat

source fluid). The expander performance is observed through the isentropic efficiency of the expander. The isentropic efficiency of the expander is calculated from Equation (1).

$$\eta_{isentropic} = \frac{h_1 - h_2}{h_1 - h_2'} \quad (1)$$

The performance of the expander was monitored on the calculated isentropic efficiency based on measured operating parameters of pressure and temperature at expander inlet and outlet.

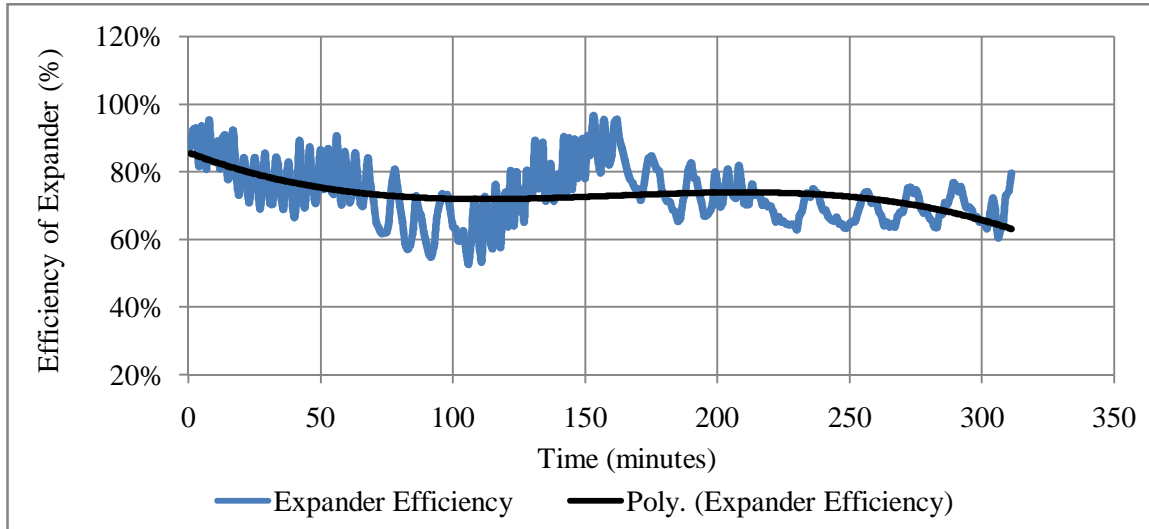


Figure 2: ORC experimental analysis (1500 rpm) - Expander isentropic efficiency

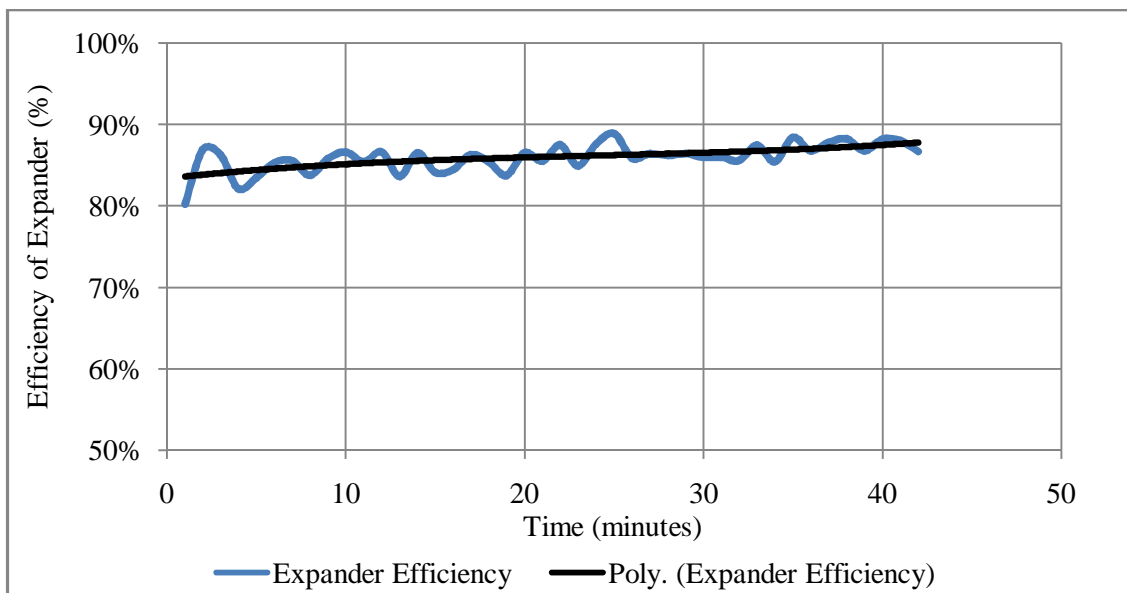


Figure 3: ORC experimental analysis (2000 rpm) - Expander efficiency

From Figure 2, it can be observed that the isentropic efficiency of expander operating at constant speed of 1500 rpm was in the range of 60 to 95%. The stable zone of operation indicated the expander isentropic efficiency in the range of 60% to 80%. Similarly from Figure 3 it can be observed that the isentropic efficiency of the expander operating at constant speed of 2000 rpm is in the range of 80% to 88%. This investigation indicates that the isentropic efficiency of the expander increases with increase in shaft speed. The cyclic variations in the isentropic efficiency graph of expander are due to

the dynamometer loading and unloading to maintain the expander shaft speed constant and with the feed pump operating to maintain constant degree of superheat at expander inlet.

2.1 Comparison of variable speed versus constant speed operation

In scenarios where heat source is varying (ORC system operating at part load conditions), the ORC system can be operated in two modes: constant speed and variable speed. The impact of operating mode on the isentropic efficiency of expander is experimentally investigated. The tests were conducted for the constant condensing temperature of 40°C (saturation pressure of 2.5 bar abs.) and variable heat input. The system was operated in constant speed mode at 1500 rpm and in variable speed mode. The shaft speed was varying between 1000 to 3000 rpm in variable speed mode operation. The experimental results obtained during this investigation are shown in figure 4.

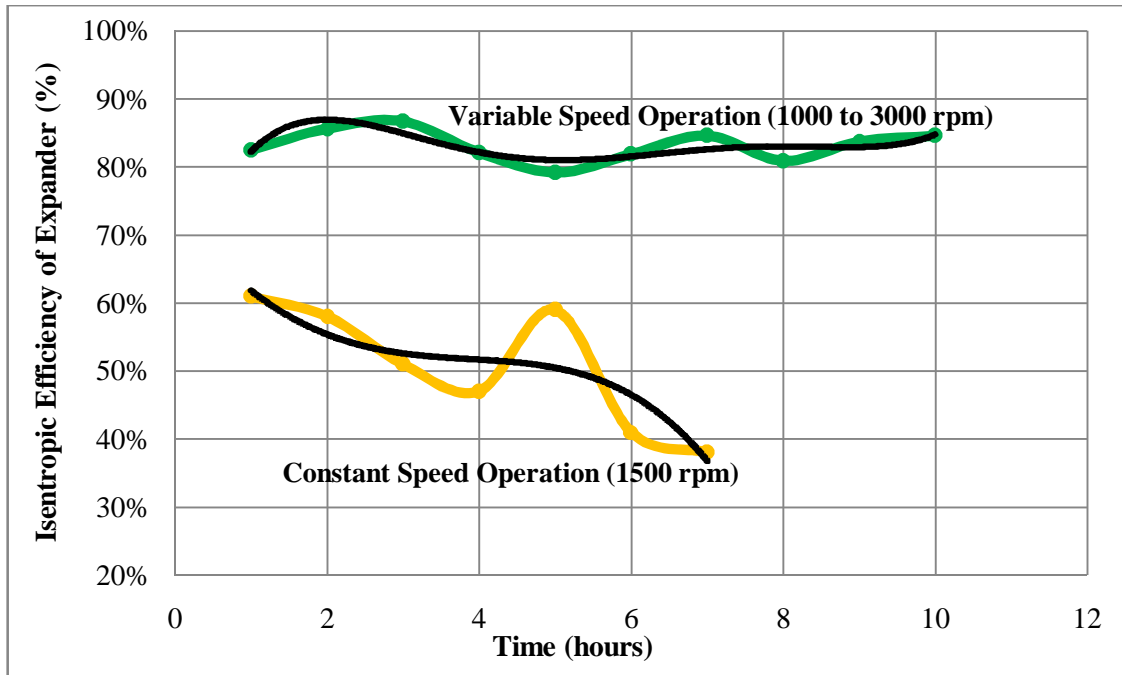


Figure 4: ORC Test result - Constant speed versus variable speed

From Figure 4, it is observed that the isentropic efficiency of the expander started reducing from 60% to less than 40%, at constant shaft speed mode with respect to reduction in heat input. The expander shaft speed was forced to be maintained at 1500 rpm using a dynamometer. The speed was maintained constant by varying the breaking torque on the expander shaft. That resulted in reduction of expander inlet pressure from 14.3 bar abs. to 5.7 bar abs. (expander pressure ratio decreased from 3.58 to 1.43) with respect to heat input reduction from 100% to 30%. The reduction in pressure ratio has resulted in poor expander efficiency.

In variable speed mode, the Shaft was allowed to vary by maintaining constant breaking torque on the dynamometer. The shaft speed variation was resulted by reduction in heat input from 100% to 30% load. The reduction in heat input actually resulted in reduced mass flow of operating fluid (as the pump flow modulated to maintain required degree of superheat at expander inlet). The effect of this change in mass flow resulted in fairly constant expander inlet pressure in the range of 13.6 to 14.3 bar abs. The obtained expander isentropic efficiency in this mode of experiment is in the range of 80 to 85%.

The conclusion drawn from this investigation is that, the operating pressure ratio of the expander impacts the expander isentropic efficiency. Higher pressure ratio is possible in variable speed operation and not in constant speed operation. Hence for part load operations and varying heat input

conditions, the performance of the system is efficient at variable speed mode operation and not with constant speed mode operation.

2.2 Effect of oil separator pressure drop

The lube oil is injected inside the oil flooded twin screw expander which is required for lubrication of bearings and for providing the sealing between two helical screws. Majority quantity of lube oil is pumped to the bearings mounted at both the ends of expander shafts (main rotor and gate rotor). A small quantity of lube oil gets mixed with operating fluid inside expander and then provides the required sealing between two screws. After lubrication the oil from bearings also gets mixed with the operating fluid and it comes out from low pressure port along with operating fluid. This oil has to be separated and circulated back to the expander for continuous lubrication and sealing. The oil separator performs the function of oil separation and also provides the required head for lube oil pump. The location of oil separator in the ORC system is between the expander outlet and condenser inlet. It is as shown in figure 5.

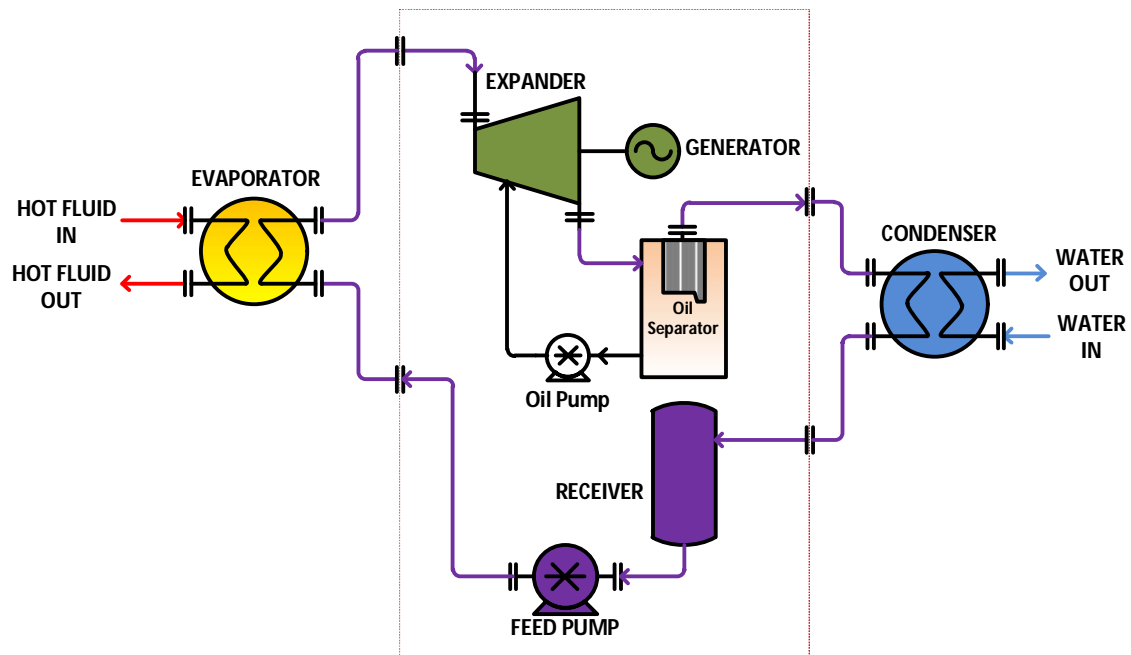


Figure 5: ORC system block diagram (with oil separator)

The oil separator tank is provided with two stage oil separation. In first stage, the bigger droplets of oil are separated by centrifugal action which is supported by the tangential entry of fluid oil mixture coming out from expander. After the first stage separation, the direction of flow is reversed and then the fluid is filtered using a clothed filter element for small oil droplet removal. This filter element is installed in the inner cavity of the oil flow reversal chamber. The smaller oil droplets are captured in the walls of filter element. These captured oil droplets trickle down, and get collected at the inner cavity of the element. Due to these changes in flow direction and filter element, the oil separator has an inherent pressure drop of the process fluid.

The conventional design of oil separator which is used along with screw compressors was incorporated in the experimental investigation. In experimental study the pressure drop observed across the oil separator was in the range of 2.4 to 2.6 bar. This resulted in increased expander outlet pressure (i.e. reduced pressure ratio) which caused reduction in power output from the expander. To decrease this pressure drop and to increase the pressure ratio across the expander, the oil separator inlet and outlet ports along with interconnecting piping was redesigned for low pressure parameters of operating fluid. After redesign, the pressure drop across the oil separator was observed to be reduced by 40%.

The effect of oil separator redesign is experimentally investigated (for improvement in expander efficiency) and compared with the results obtained with original oil separator design. The obtained results are shown in Figure 6. The reduced pressure drop across oil separator resulted in improved expander efficiency by 5%.

The experimental investigation of pressure drop across the oil separator was carried in term of its effect on the isentropic efficiency of the expander while operating at constant condensing conditions which are maintained by constant flow of heat sink and heat source fluid. The experiment was carried out at steady operating conditions of operating parameters across the expander. It was compared with earlier performance of the expander which had higher pressure drop across the oil separator.

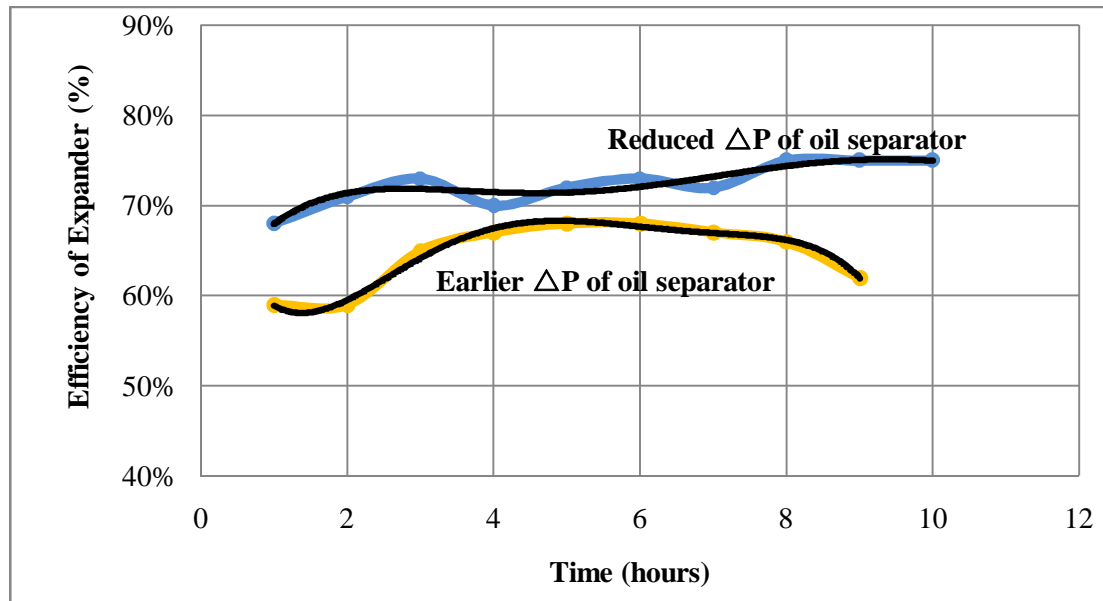


Figure 6: ORC Test result - Effect of oil separator pressure drop

Based on this experimental investigation, it can be inferred that, reduction in pressure drop across the oil separator has reduced the irreversibility from the expander and improved the expander isentropic efficiency. It can also be inferred that removal of oil separator will further enhance the expander efficiency and thus the overall efficiency of the system. This improved isentropic efficiency of expander is effect of improved pressure ratio across the expander as the expander outlet pressure has approached towards the condenser pressure. The higher pressure ratio resulted in increased power output and better efficiency.

However, in the absence of oil separator, the lube oil will be carried over to condenser. The oil carry over to condenser will foul the heat transfer surface. This is not an issue while the ORC system is operating at full load condition, as the oil percentage in operating fluid will be less than 3%. (<http://handbooks.swep.net/>) But at part load, the oil percentage in operating fluid will be more than 35% which affects heat transfer in side condenser. Therefore it is required to have sufficient over surface area in condenser design. The oil collection and recirculation to the expander also need to be addressed in this case.

2.3 Mechanical performance

Experimental set-up was initially designed with a velocity range of 20 m/s at expander inlet port. However during experimentation, the vibrations were noted at expander inlet piping. The cause of these vibrations was the increased velocity at expander inlet due to convergent nozzle to reduce pipe diameter of 114.3 mm to 60.3 mm neat the inlet port of expander. The nozzle was initially located close to the expander inlet port which did not provide enough straight length of pipe to stabilize the

operating flow. The redesign for flow stabilization resulted in reduction of these vibrations and improved the expander reliability.

3. 100 kW PROTOTYPE

The learning from all these experimental investigations of ORC system, are implemented in first prototype of capacity 100 kW, which is under commissioning and testing at a solar thermal based power plant. The photograph of this prototype ORC system is as shown in Figure 7.



Figure 7: First prototype of ORC system: Capacity 100 kW

The key features included are the variable speed operation for part load conditions to keep higher pressure ratio across the expander and improved design of oil separator to get lower expander outlet pressure. The expander inlet flow stabilization is also implemented to reduce the vibration at the expander. The mechanical vibration from the rotary systems i.e. expander and electrical generator are decoupled from each other by implementation of timing belt drive arrangement.

The experimental investigation of 100 kW prototype system are yet to be carried out as the system is under commissioning stage and will be produced in further work to improve the next version of the ORC systems.

4. CONCLUSION

- The ORC system is more efficient at operations with variable speed for varying source heat input and at part load conditions. The isentropic efficiency of the expander at variable speed mode of operation is 80-85%, which is at least 30% higher than that in constant speed mode. The variable speed operation improves the viability of ORC system.
- The redesigned oil separator improved the expander efficiency by 5% due to reduction in pressure drop across it by 40%. Inclusion of any additional component between expander outlet and condenser reduces the expander efficiency as well as cycle efficiency due to the pressure drop across the component.

- The removal of oil separator will certainly improve the efficiency of the system as pressure ratio across the expander. However this will increase the heat transfer area required in condenser. This has to be further investigated to arrive at an optimum system design.
- The performance of the expander was improved by reducing the flow induced vibrations at expander inlet. The availability and reliability of the screw expander for enhanced mechanical performance has to be further investigated by implementing vibration mitigation techniques, shaft seal development and arriving at optimized mechanical design parameters.

NOMENCLATURE

η	efficiency	(%)
h	enthalpy of fluid	(kJ/kg)
N	number	(-)

Subscript

1	expander inlet
2	expander outlet
'	isentropic condition

REFERENCES

- Velez F., Segovia J., Martin M., Antolin G., Chejne F., Quijano A., Nov 2012, "Comparative study of working fluids for a Rankine cycle operating at low temperature", *Fuel Processing Technology*, vol. 103, p 71-77.
- Stosic N., Smith I., Kovacevic A., 2005, "Screw Compressors - Mathematical modelling and performance calculation", ISBN-10,3-540-24275-9 Springer, New York, 138 p.
- Quoilin S., Lemort V., 2009 "Technological and economic survey of organic Rankine cycle systems", *5th European conference Economic and Management of Energy in Industry*, p 1-12
- Quoilin S., Aumann R., Grill A., Schuster A., Lemort V., Spliethoff H., 2011, "Dynamic Modelling and optimal control strategy of waste heat recovery Organic Rankine Cycles", *Applied Energy*, vol. 88, p 2183-2190
- National Institute of Standards & Technology, REFPROP 9.0, Fluid property database
- Mujic E., Kovacevic A., Stosic N. and Smith I., 2010 "Advanced design environment for screw machines". *International compressor engineering conference*, 1243, p 1-8.
- Karl, J. 2004, "Decentralized energy systems, new technologies in liberalized energy market", "Dezentrale Energiesysteme, (Neue Technologien im liberalisierten Energiemarkt) Oldenbourg Wissenschaftsverlag, Munchen", (in German)
- Goel S., Herzog O., Datta A., Sonde R., Deshpande K., Fink J., Schumacher T., June 2014, "Market potential study for organic Rankine cycle technology in India - A Publication on Industrial Energy Efficiency" Indo-German Energy Forum Support Office (IGEF-SO), New Delhi, 68 p.
- Charles P., Dec 2013, "Compacting heat transfer systems in new and advanced power cycle systems: Addressing major challenge in waste and renewable energy technologies" Proceedings of Indo-US workshop on "Recent advances in micro/ nano-scale heat transfer and applications in clean energy technologies"
- Bianchi M., De Pascale A., 2011, "Bottoming cycle for electric energy generation: Parametric investigation of available and innovative solutions for the exploitation of low and medium temperature heat sources", *Applied Energy*, vol. 88, p 1500-1509

EXPERIMENTAL STUDY ON ORGANIC RANKINE CYCLE SYSTEM WITH SINGLE-SCREW EXPANDER FOR WASTE HEAT RECOVERY FROM DIESEL ENGINE EXHAUST

Yuting Wu*, Biao Lei, Wei Wang, Yeqiang Zhang, Chongfang Ma

Key Laboratory of Enhanced Heat Transfer and Energy Conservation of Ministry of Education and Key Laboratory of Heat Transfer and Energy Conversion of Beijing Municipality, College of Environmental and Energy Engineering, Beijing University of Technology, Beijing 100124, PR China

Contact Information: wuyuting@bjut.edu.cn

ABSTRACT

A single-screw expander prototype with 155 mm diameter screw was developed. An ORC (organic Rankine cycle) experimental system for waste heat recovery from diesel engine exhaust was built. Experiments were conducted for different expander torque and diesel engine loads. The experimental results indicated: (1) Single-screw expander is suitable for small/medium scale ORC system, and it can obtain good performance at low-medium rotational speed. The maximums of power output 10.38 kW and shaft efficiency 57.88% are achieved at 1538 rpm. (2) The maximums of volumetric efficiency, adiabatic efficiency and expansion ratio of single-screw expander are 90.73%, 73.25% and 4.6, respectively. (3) The performance of ORC system is affected not only by the working case of diesel, but also by the torque of single-screw expander. The biggest ORC efficiency is 6.48%, which is gotten at 250 kW diesel power output and 64.43 Nm of single-screw expander. (4) With ORC system, the specific fuel consumption of diesel is effectively decreased. When the power output of diesel is 250 kW, the specific fuel consumption is decreased by 3.5%, and the overall system efficiency is 43.8%, which is increased by 1.53%. (5) With the reducing of mass flow rate pumped into evaporator, the dryness of vapor is accelerated, and heat exchange quantity almost linearly decreases. Volumetric flow rate of vapor into single-screw expander increases with increase of inlet vapor dryness but volumetric efficiency decreases with that. The rising of expansion rate is due to increase of inlet pressure and decrease of outlet pressure with the increase of inlet vapor dryness and the biggest expansion ratio is 4.7. With the increase of inlet vapor dryness, torques and power outputs of single-screw expander are rising.

1. INTRODUCTION

Over the past century, the diesel engine has been a primary power source for automobiles, long-haul trucks, locomotives, and ships. The efficiency of a modern diesel engine is about 30%~40% in an ideal case. The other energy dissipated is lost by transmission to the environment through exhaust gas, cooling water, lubrication oil and radiation. In driving conditions, energy loss is even close to 80%. Improving the utilization of low temperature energy can significantly increase the integrated energy efficiency and remarkably reduce the fuel consumption, so it is a promising path for energy saving and consumption reducing for diesel engine. Of interest, many researchers recognize that waste heat recovery (WHR) from engine exhaust has the potential to decrease fuel consumption without increasing emissions, and recent technological advancements have made these systems viable and cost effective (Chammas et al., 2005).

The ORC is a Rankine cycle in which an organic substance is used instead of water-vapor. ORC system is an environmentally friendly system with no emissions of exhaust gases such as CO, CO₂, NO_x, SO_x and other atmospheric pollutants. The most important feature for an ORC is its capability of utilizing various kinds of low-grade heat sources for power generation. Most studies choose ORC for WHR due to its simplicity and ability to operate with low to moderate temperature differences. Another primary advantage of ORC is the use of widely available and affordable components.

In an ORC system, there are two main types of expanders: the velocity-type expanders, such as axial turbine expander, and the volume-type expanders, such as screw expander, scroll expander and reciprocal piston expander (Qiu et al., 2011). Turbine expander has many advantages, but it is generally applied in power cycles with power output greater than 50kW, because its efficiency would

be unacceptable in small scale power cycles (Peterson et al., 2008). Turbine expander is suitable for superheated vapor. With saturated steam, the problems of using turbine expander are water erosion to blades and low shaft efficiency of the unit. In addition, turbine has faster rotational speed, and an excess gear box is indispensable if it is utilized in a small scale ORC. Compared with the velocity-type expanders, volume-type expanders are suitable for the ORC-based waste heat recovery because they are characterized by lower flow rates, higher expansion ratios and much lower rotational speeds.

Recently, scroll expander has been gaining some interests as the expanders in small scale ORC (Peterson et al., 2008, Lemort et al., 2009). This device does not require inlet or exhaust valves which reduces noise and improves the durability of the unit. Another advantage is that the rolling contacts provide a seal such that large volumes of oil used as a sealant are not required and the leakage is reduced. Compared with other volume-type expanders, scroll expander may be applied in a very small scale power system, such as 0.1~10kW.

There are two types of screw expanders: twin-screw expander and single-screw expander. Twin-screw expander has been widely used in Rankine cycle system, especially for geothermal and waste heat applications. Twin-screw expander depends on precise numerically-controlled machining to achieve a leak-resistant fit. Compared with twin-screw expander, the single-screw expander has a lot of advantages, such as long service life, balanced loading of the main screw, high volumetric efficiency, low noise, low leakage, low vibration and simple configuration, and so on. Single-screw expander can realize 1-200 kW range of power output, and it is more suitable for low temperature and small scale of ORC system for waste heat recovery. Recent studies have reported the performance of in-house built single screw expander for low power capacity. Wang et al. (2011) presented a 5 kWe machine with an isentropic efficiency of up to 59%. He et al. (2013) built and tested a 22 kWe single screw expander reaching a maximum isentropic efficiency of 55% at 2800 rpm. Wang et al. (2013) analyzed the influence of the gaterotor/shell and the screw/shell gap by building and testing three different single screw expanders. Desideri et al (2013) described experimental results of a small scale ORC system which utilizes a single-screw expander modified from a single-screw compressor. In total, 120 steady-state experimental data points have been measured and the adiabatic efficiency of expander is from 27.3% to 56.35%.

According to the power output of different type of expanders, turbine is suitable for waste heat recovery from exhaust of diesel engine which power output is more than 1MW, and scroll expander is suitable for that with diesel engine power output less than 100kW. For the power output of ORC for waste heat recovery from exhaust of 100kW~1MW diesel engine is generally from 1kW to 10's of kW, single-screw expander is the most appropriate candidate.

In this paper, an ORC experimental system with single-screw expander was developed for waste heat recovery from exhaust of a 336hp diesel engine. Experiments were carried out to investigate the influence of engine condition and expander torque on the performance of ORC system and overall engine system with ORC.

2. DEVELOPMENT OF ORC SYSTEM

2.1 The single-screw expander

A single-screw expander has been developed by our team, as shown by fig.1. The reference of this prototype's design is a single-screw compressor. Then the arrangement of screw and gaterotors, the installment of bearings, and the apparent structure are similar to a single-screw compressor. In order to simplify the construction and reduce the friction resistance, packing seal with PTFE is used as the shaft seal. The balance hole which connects high pressure leakage room with low pressure discharge volume of this expander is drilled on the shell which is different to that drilled on the screw or main shaft. The parameters of this single-screw expander used in the test are shown in table 1.

2.2 Evaporator

A spiral-tube type evaporator has been developed for the waste heat recovery system. In the evaporator, a spiral titanium tube is placed in a cylinder and baffles are also inserted in the cylinder to enhance heat transfer in the evaporator. In order to reduce the weight of this evaporator, titanium tube

is used instead of stainless steel tube. Heat is transferred from exhaust to spiral titanium tube, and working fluid is heated by spiral titanium tube and is evaporated in the tube. The design temperature is 550°C, and the design capacity is 150kW. The design pressures of organic substance side and the gas side are 2.5MPa and 0.1MPa, respectively. Because the organic substance volume continuously increases for being heated, the cross section area needs to increase correspondingly. The evaporating process is divided into 5 tube sides. The first and second tube sides both have 8 tubes, the third tube side has 16 tubes, the fourth tube side has 24 tubes and the fifth tube side has 32 tubes. The length of each tube is 6.8m and the wall thickness is 1.2mm. The parameters of the evaporator are shown in Table. 2.

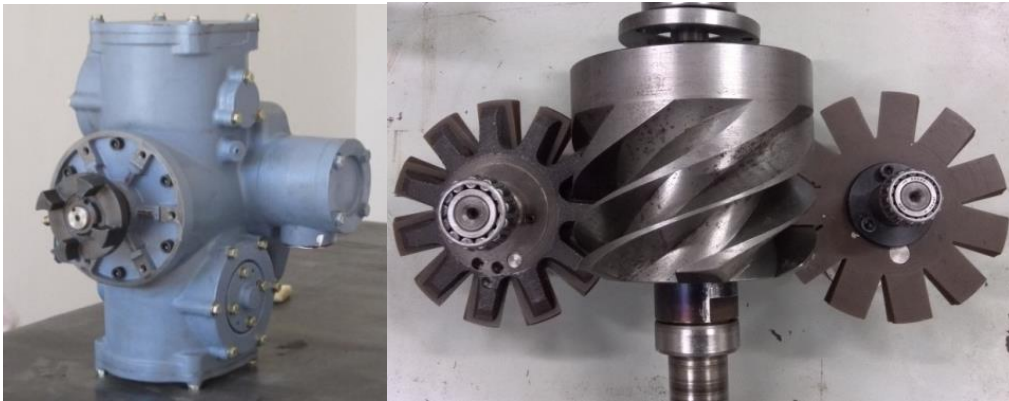


Fig.1: Photograph of the single-screw expander

Table.1: The parameter of single-screw expander

Parameters	Value	Parameters	Value
Diameter of screw(mm)	155	Diameter of gaterotor(mm)	155
Groove number of screw	6	Tooth number of gaterotor	11
Center distance(mm)	124		

Table.2: The parameter of the spiral-tube evaporator

parameters	value	parameters	value
Diameter of spiral tube(mm)	16	Wall thickness of shell (mm)	4
Wall thickness of spiral tube(mm)	1.2	Evaporator weight (kg)	147
Shell diameter (mm)	500	Heat exchange area (m ²)	12
Shell length (mm)	1500	Heat input capacity (kW)	142

2.3 Condenser

An aluminum multi-channel parallel type condenser has been developed for the waste heat recovery system. In order to enhance the heat transfer on air side, high performance louvered fins are used. While, the application of aluminum multi-channel tubes strengthens the ability of heat transfer from working fluid to air. Fig.3 shows the photograph and configuration of the aluminum multi-channel parallel type condenser. The working fluid enters the header and flows through tubes. It is important to reduce the flow resistance because of the significant effect on the power output of single-screw expander. In the design, parallel structure of dual-condenser is used and the total flow process is divided into two tube sides. The working fluid is averaged to 70 tubes in each first tube side, and then averaged to 48 tubes in each second tube side after working fluid condensation from the first tube sides. The calculation results that the total flow resistance is less than 0.1MPa. A fan is used to

enhance the air flow and the bending type construction of the condenser would improve its utilization. The parameters of the evaporator are listed in Table. 3.

Table.3: The parameter of the parallel type condenser

parameters	value	parameters	value
Tube width (mm)	25.47	Heat transfer area in air side (m ²)	1.02
Tube thickness (mm)	2	Size of condenser (mm)	980×980×1255
Fins spacing (mm)	1.4	Condenser weight (kg)	78
Fins height (mm)	6.85	Heat rejection capacity (kW)	150
Louvered angle(°C)	27	Fan size (m)	φ860×64

2.4 Pump

The pump is a multistage centrifugal pump called CR5-32 and is provided by GRUNDFOS. The pump was running at rated speed. In order to adjust the flow rate of working fluid, a throttling bypass valvewas installed between the pump and the storage tank of working fluid. The parameters of the pump are shown in Table. 4.

Table.4: The parameter of the pump

parameters	value	parameters	value
Rotational speed (rpm)	2919	Stages	32
Designed volume flow (m ³ /h)	2.98	Net weight (kg)	81.9
Designed head (m)	205		

2.5 Configuration of the ORC system

The prototype of ORC system for WHR is shown in fig.2. The ORC system included a single-screw expander, an evaporator, a condenser, a storage tank of working fluid, a multistage centrifugal pump, etc. R123 was used as the working fluid because of its outstanding ability to improve the ORC performance. R123 was first heated to vapor by exhaust waste heat of engine in the evaporator, and then the vapor expanded and generated power output in the single-screw expander. The vapor from expander was condensed into liquid by ambient air in the condenser. The R123 liquid in condenser was pumped to the evaporator. There was a storage tank in the ORC system for supplying working fluid.



Fig.2: ORC system prototype

3. EXPERIMENTAL APPARATUS AND DATA DERIVATION

3.1 Experimental system

Fig.3 illustrates the concept of experiment. Heat source is the exhaust of a diesel engine whose power output can reach 336 horsepower. Operations start at the firing of the diesel engine. Pump begins to work when the power output of engine rises to 40 kW, then working fluid is circling in the system. It does not directly flow into the expander because a bypass is opened. When the power output of engine is over 80 kW, valves at inlet and outlet of the expander are opened, while a valve at the bypass is closed and the fan of condenser is switched on to start the working cycle. Working fluid passes through the expander, and the expander rotates. The power output of diesel engine increases gradually to the preset point. After the temperature of exhaust at inlet of the evaporator becomes steady, different torque of expander is adjusted, and experimental data are collected until the end of experiment. Pump in ORC system rotates at rated speed. In order to adjust the flow rate of working fluid into evaporator, a throttling bypass valve is installed. In the test, by adjusting the excitation of an eddy current dynamometer linked with the shaft of single-screw expander, the torque of single-screw expander can be changed.

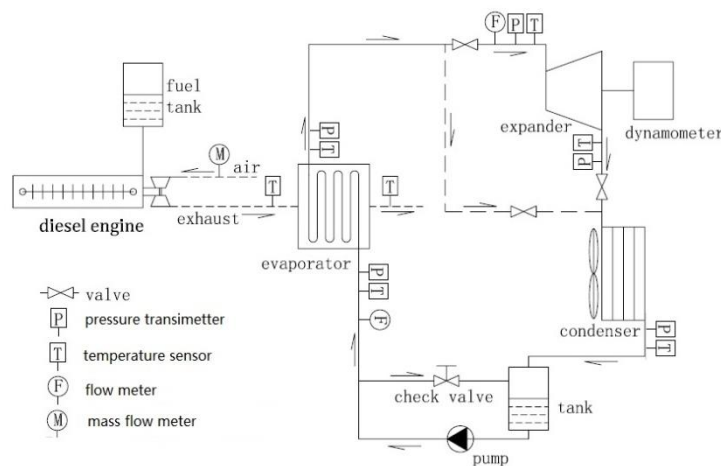


Fig.3: ORC system diagram

The power output and rotational speed of the single-screw expander are recorded by the dynamometer. Temperature probes and pressure transducers were installed on the organic substance side at inlet and outlet of the evaporator, expander, and outlet of condenser to determine the state of the working fluid. Temperature probes were installed on the exhaust side of the inlet and outlet of evaporator to determine the temperature of the exhaust. Temperature probes use PT100 with an accuracy of $\pm 0.5^\circ\text{C}$ besides the temperature probes on the exhaust side which are N-type thermocouple with an accuracy of $\pm 1.5^\circ\text{C}$. The pressure sensors of SMP131 with an accuracy of $\pm 0.5\%$ FS and measurement range of 0~2MPa were used to measure the working fluid pressure, and a pressure sensor of SMP121 is used to measure the exhaust pressure with an accuracy of $\pm 0.2\%$ FS and measurement range of 0~0.1MPa. These temperature probes and pressure sensors are provided by Shanghai Leeg Instruments CO., LTD. The mass flow rates of working fluid were measured using a rotameter(model H250) with an accuracy of $\pm 1.0\%$ FS which was installed on the organic substance side at inlet of evaporator and a vortex flow meter (model VFM4070G) with the accuracy of $\pm 0.5\%$ FS installed at inlet of expander. These two instruments are manufactured by KROHNE. The exhaust mass flow is calculated by the fuel consumption meter of FC2210 with the accuracy of $\pm 0.4\%$ FS supplied by Hunan xiangyi dynamic test instrument CO., LTD and the air mass flow measured by thermal gas mass flow meter of 20N150 with the accuracy of $\pm 1\%$ FS provided by Shanghai ToCeil Engine Testing Equipment CO., LTD installed at inlet of engine. In order to measure the rotational speed and power output of expander, an eddy current dynamometer of GW40 supplied by Hunan xiangyi dynamic test instrument CO., LTD. was installed. The maximum measurement of torque and rotational speed are 160N·m with an accuracy of $\pm 0.2\%$ FS and 10000rpm with an accuracy of

±1rpm, respectively. All the output signals of experimental data were transported to a computer and stored as a function of time there.

3.2 Data derivation

(1) Power output: this indicates the ability of single-screw expander to output power, and is defined as

$$Pe = \frac{N \cdot \omega}{1000} \quad (1)$$

(2) Dryness is defined as the fraction of the total mixture which is vapor, based on mass. That is

$$x = \frac{\dot{m}''}{\dot{m}' + \dot{m}''} \quad (2)$$

(3) Shaft efficiency of single-screw expander: this is the ratio of power output to enthalpy drop of working fluid in an ideal adiabatic process, which is defined as

$$\eta_{exp} = \frac{Pe_{exp} \times 3.6}{\dot{m}_{R123} \Delta h_{s,exp}} \times 100\% \quad (3)$$

(4) The effect of leakage in expansion process can be evaluated by volumetric efficiency, which is defined by

$$\eta_V = \frac{V_i}{V_m} \quad (4)$$

(5) ORC efficiency: this is the ratio of available energy to overall energy obtained from thermal source, and is expressed as

$$\eta_{ORC} = \frac{(Pe_{exp} - Pe_{pump}) \times 3.6}{\dot{m}_e (h_{e,in} - h_{e,out})} \times 100\% \quad (5)$$

(6) Specific fuel consumption: this indicates the economic performance of engine, which is defined by

$$d = \frac{\dot{m}_{fuel}}{(Pe_{exp} + Pe_{engine})} \times 10^3 \quad (6)$$

(7) Overall system efficiency

$$\eta_{t,system} = \frac{3.6 \times (Pe_{exp} + Pe_{engine} - Pe_{pump})}{\dot{m}_{oil} \times H_{oil}} \times 100\% \quad (7)$$

4. EXPERIMENTAL PERFORMANCE ANALYSES

In the test, temperature and mass flow of exhaust were varied by changing in the power output and the rotational speed of diesel engine. Table 5 lists detailed specification and temperature and mass flow for different conditions of diesel engine (denoted as different cases), and table 6 gives the influences of the ORC system to diesel engine.

Table.5: Parameters of different conditions of diesel engine

item	Unit	Case1	Case2	Case3	Case4	Case5	Case6
Power output	kW	140	160	180	200	220	250
Rotational speed	rpm	1800	1800	1800	1900	1900	1900
Temperature of exhaust	°C	417	430	448	425	451	485
Mass flow of exhaust	kg/h	958	1024	1092	1205	1272	1315

Table.6:Influences of the ORC system to diesel engine

Case	Power output	Rotational speed	Specificoil consumption without ORC	Specificoil consumption with ORC	Increment of specific oil consumption	Exhaust overpressure without ORC	Exhaust overpressure with ORC	Increment of exhaust overpressure
	kW	rpm	kg/h	kg/h	%	kPa	kPa	%
1	140	1800	28.7	29	1.05	6.4	7.3	14.06
2	160	1800	32.2	32.8	1.86	7.3	8.6	17.81
3	180	1800	36.6	37.1	1.37	8.3	9.8	18.07
4	200	1900	39.4	40	1.52	9	10.7	18.89
5	220	1900	43.3	44	1.62	10.2	12.7	24.51
6	248	1900	49.5	50.1	1.21	11.6	13.3	14.65

Note: in case 6 the power output of diesel engine is 250kW with ORC system.

Fig.4 shows the changes of temperature drop of exhaust with torque of single-screw expander. In the first three cases, the temperature drop decrease linearly and the changes are very small; however, the changes of temperature drop in the other cases are much larger. It is obvious that the temperature drop does not increase with the increase of diesel power output. In case 4 and case 5, some points are lower than ones in the first three cases. The influence of expander's torque on the heat quantity absorbed from exhaust is shown in fig.5. The decreases of the quantity of exchanged heat are too little to consider in the first three cases, while it decreases obviously in cases 4 through 6 with the increase of torque of single-screw expander. Because the mass flow of exhaust keeps steady at a case, the quantity of exchanged heat is mainly affected by temperature drop. From this figure, it is shown that the quantity of exchanged heat increases with the increase of the power output of diesel engine also. Although the temperature drop does not increase with the increase of diesel power output, the quantity of exchanged heat keeps increasing due to the increase of the mass flow of exhaust.

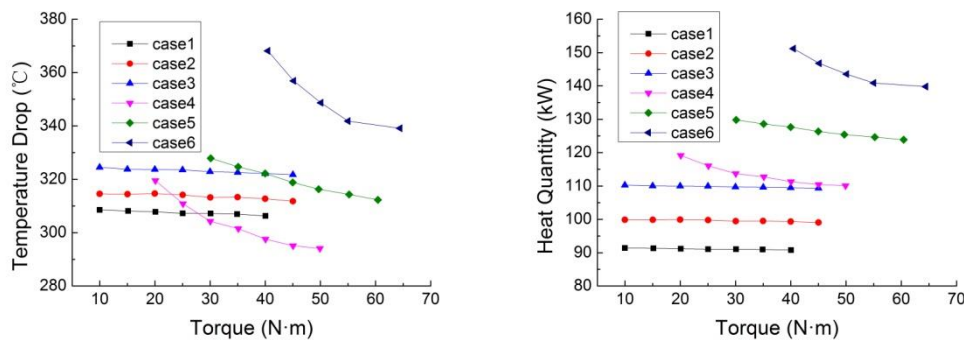


Fig.4:Temperature of exhaust gas vs. torque **Fig.5:**Quantity of exchanged heat vs. torque

Power output of single-screw expander can be calculated and its changes with the torque are shown in fig.6. It is shown that the power output of single-screw expander increased in the form of a parabola with rising expander torque. In the first four cases of experiments, when the torques of the expander are 30N·m, 40N·m, 40N·m and 50N·m, the maximums of power output of the expander are 3.63kW, 4.69kW, 5.55kW and 6.64kW, respectively. In case 5 and case 6 the maximums of power output of the expander are not achieved due to the restriction of the experimental conditions. But the increase of the power output becomes slow with the increase of the torque, and the maximums obtained are 7.81kW and 10.38kW, respectively.

Fig.7 shows the change of the shaft efficiency of the single-screw expander. From the figure, there are maximums of the shaft efficiency in every group of data in the first five cases, they are 41.45%, 46.73%, 47.59%, 49.90 and 49.93%, respectively. The shaft efficiency increases with the torque of expander in case 6, and the maximum is 57.88% at 64.43N·m of torque. The inflection point of the shaft efficiency in case 6 doesn't occur, because the increase of lubricating oil's temperature is too fast and it soon exceeds 105°C, then the engine could not go on working.

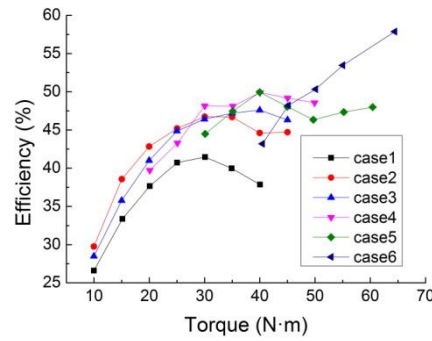
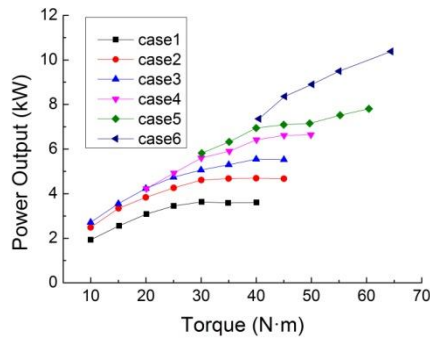


Fig.6:Power output vs. torque**Fig.7:**Total efficiency vs. torque

Fig.8 shows the variation of ORC efficiency. From this figure, the maximums of ORC efficiency are obtained in the first four cases; they are 3.04%, 3.74%, 4.04% and 5.13%, respectively, corresponding to the expander's torque of 35Nm, 40Nm, 40Nm and 50Nm. In case 5 and case 6, the power output of the single-screw expander increases with the torque while the quantity of exchanged heat decreases with the torque, so, the ORC efficiency increases with the torque, and the maximums obtained in the test are 5.34% and 6.48%, respectively.

The overall system efficiency of diesel engine with ORC is an improvement over that of diesel engine without ORC, as shown in fig.9. From the figure, the smallest improvement is 0.81% at 140kW, and the biggest improvement is 1.53% at 250kW. It is obvious that 43.80% is the highest overall system efficiency with ORC system when the power output of diesel engine is 250kW.

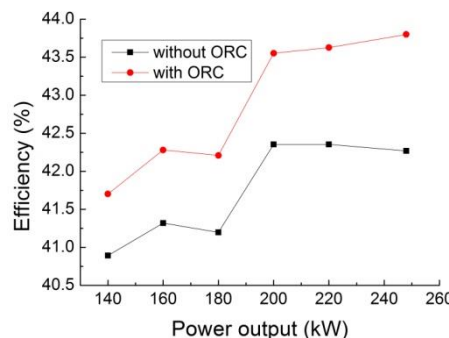
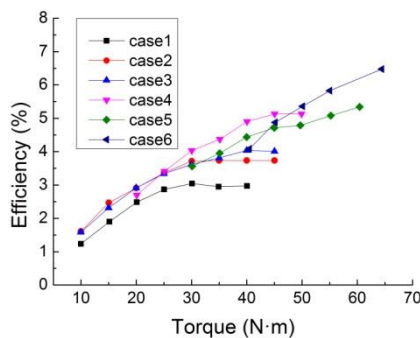


Fig.8: ORC efficiency vs. torque**Fig.9:** Overall system efficiency vs. power output of diesel engine

Power output indicates the performance of work output for single-screw expanders. Fig.10 shows that power output increases with dryness. The increase is faster at low dryness than it is at high dryness. But there is little difference between the values of power output for different rotational speed at the same dryness, and the biggest power output is 5.12kW, which is shown in fig.10.

Although the power output increases with the increase of inlet vapor dryness, the shaft efficiency of single-screw expander decreases with the increase of dryness, and the maximum is 7%~8% bigger than the minimum, as shown in fig.11. From this figure, it can also be observed that the shaft efficiency at 1200rpm is bigger than that at 900rpm, and the biggest efficiency is nearly 50%.

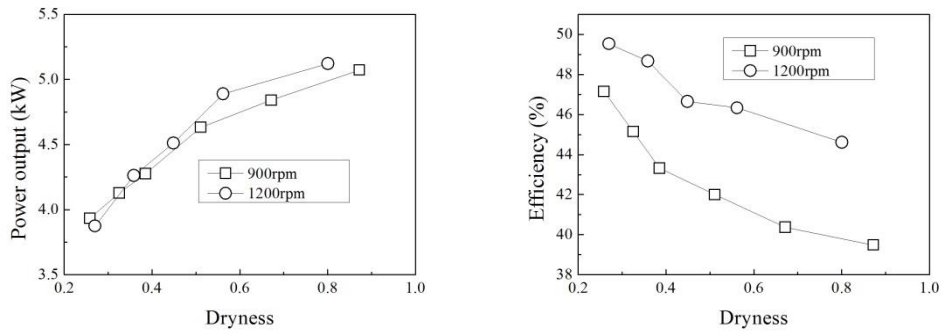


Fig.10: Power output versus inlet vapor dryness**Fig.11:**Shaft efficiency versus inlet vapor dryness

5. CONCLUSION

In this study, the influence of torque of single-screw expander on the performance of ORC used in waste heat recovery is obtained for different conditions of diesel engine. The effects on performance indices of single-screw expander and heat-work conversion efficiency are investigated. Based on the present analysis, the following results are concluded:

- (1) Single-screw expander is suitable for small/medium scale ORC system, and it can obtain good performance at low-medium rotational speed. The maximums of power output 10.38kW and shaft efficiency 57.88% are gotten at 1538rpm.
- (2)The maximums of volumetric efficiency, adiabatic efficiency and expansion ratio of single-screw expander are 90.73%, 63.46% and 4.6, respectively.
- (3) The performance of ORC system is affected not only by the working case of diesel, but also by the torque of single-screw expander. The biggest ORC efficiency is 6.48%, which is gotten at 250kW diesel power output and 64.43N.m of single-screw expander.
- (4) With ORC system, the specific fuel consumption of diesel is effectively decreased. When the power output of diesel is 250kW, the specific fuel consumption is decreased by 3.5%, and the overall system efficiency is 43.8%, which is increased by 1.53%.
- (5)With the increase of inlet vapor dryness, torque and power output of single-screw expander are rising and the biggest power output is 5.5kW, but the shaft efficiency of single-screw expander is decreased by 7%~8%.

In summary, the results of test basically reach the expectation. Meanwhile, it also has great room for improvement. On the one hand, increasing the rotational speed to 2800~3000rpm and decreasing the outlet pressure of the single-screw expander can obtain more power output. On the other hand, optimizing the layout of system and decreasing the weight of main equipment can realize the compact and lightweight design for utilization in a truck. With the continuous improvement of equipment and testing, the system for waste heat recovery from exhaust of fixed and moving internal combustion engine would have great prospects in saving fuel and improving overall system efficiency.

Nomenclature

Variables

d :	specific oil consumption [kg/(kW·h)]
h :	specific enthalpy [kJ/kg]
H :	heating value [kJ/kg]
\dot{m} :	mass flow rate [kg/h]
N :	torque [N·m]
P :	pressure [bar]

Subscripts

e :	exhaust gases
$engine$:	diesel engine
exp :	expander
i	ideal
in :	inlet
is :	isentropic

Pe :	power [kW]	m	measurement
t :	time [s]	oil :	diesel oil
V :	volume flow rate [m ³ /h]	ORC :	ORC system
x	vapor dryness	out :	outlet
ε :	expansion ratio [-]	$pump$:	pump in ORC system
η :	efficiency [-]	$R123$:	R123
Δ :	difference [-]	sys :	system
ω :	angular velocity [rad/s]	$total$:	total

REFERENCES

- Chammas. R. El, Clodic.D, Combined Cycle for Hybrid Vehicles. SAE Int. Publication 2005-01-1171 (2005).
- Qiu, G. Q., Liu, H., Riffat, S., 2011. Expanders for micro-CHP systems with organic Rankine cycle. *Appl. Therm Eng.*, Vol. 31: p. 3301-3307.
- Peterson, R.B., Wang,H.,Herron, T.,2008. Performance of small-scale regenerative Rankine power cycle employing a scroll expander, *Proceedings of the Institution of Mechanical Engineers Part A-Journal of Power and Energy*, Vol. 222:p.271-282.
- Lemort,V., Quoilin,S.,Cuevas, C., Lebrun,J., 2009. Testing and modeling a scroll expander integrated into an Organic Rankine Cycle, *Appl. Therm Eng.*, Vol. 29: p. 3094-3102.
- Wang,W.,Wu, Y. T.,Ma, C. F.et al., 2011.Preliminary experimental study of single-screw expander prototype. *Appl. Therm Eng.*, Vol. 31: p.3684-3688.
- He, W., Wu, Y., Peng, Y., Zhang, Y., Ma, C., and Ma, G. (2013). Influence of intake pressure on the performance of single screw expander working with compressed air. *Applied Thermal Engineering*, Vol. 51:p. 662 -- 669.
- Wang, W.,Wu, Y.,Ma, C.,Xia, G. andWang, J.,2013. Experimental study on the performance of single screw expanders by gap adjustment, *Energy* Vol. 62: p. 379-384.
- Desideri,A.,Broek M. van den, GusevS. et al.,2014.Experimental campaign and modeling of a low-capacity waste heat recovery system based on a single screw expander. *22nd International Compressor Engineering Conference at Purdue*, Paper ID: 1451, P.1-10.

ACKNOWLEDGEMENTS

The authors are also grateful to the financial support by the National Basic Research Program (also called 973 Program) of China under grant number 2011CB707202 and National Key Technology Support Program of China under grant number 2014BAJ01B05.

EXPERIMENTAL COMPARISON OF A SINGLE SCREW EXPANDER UNDER DIFFERENT OPERATING CONDITIONS AND WORKING FLUIDS

Sergei Gusev*, Davide Ziviani, Martijn van den Broek

Department of Flow, Heat and Combustion Mechanics, Ghent University,
Ghent, Belgium
servei.gusev@ugent.be, davide.ziviani@ugent.be, martijn.vandenbroek@ugent.be

* Corresponding Author

ABSTRACT

During the last years, one of the most popular ways to recover low-grade waste heat is the organic Rankine cycle (ORC). This technology is widely studied and continuously optimized and, as a result, there are many efficient installations available on the market utilizing heat with stable parameters such as from geothermal sources or from the biomass combustion process. However, if a variable hot source in terms of either temperature or flow rate is introduced, the expansion devices have to work at non-optimal conditions, which decrease the global efficiency of ORC installations, e.g. in the case of waste heat recovery. In order to characterize the performance of a positive displacement expander close enough to the optimum, the influence of pressure ratios, filling factor, and working fluid properties on power output is studied. In this paper, experimental results obtained on a small-scale ORC test setup based on an 11 kWe single-screw expander are presented. Two working fluids are used during the tests, i.e. R245fa and SES36 (Solkatherm). These working fluids are common for ORC installations exploiting low-temperature waste heat. The waste heat source is simulated by an electrically heated thermal oil loop with adjustable temperature and flow rate. Various waste heat inlet flow rates are considered in order to find an optimal evaporation pressure and to maximize the power output with different heat source profiles. Based on the experimental data, the expander model is developed. For each working fluid, optimal working conditions are determined. In most cases, there is under-expansion due to a relatively small built-in volume ratio, causing certain losses. By means of the model, the ideal expansion process is simulated and compared with the real one obtained experimentally to quantify these losses and conclusions can be drawn whether significant benefits can be offered by using an optimized expander instead of an "off-the-shelf" reversed compressor.

1. INTRODUCTION

The organic Rankine cycle (ORC) is mainly used to produce electricity or useful work from heat at lower temperature, which are renewable energy sources, such as solar or geothermal, and low-grade heat produced in an industrial process which cannot be recovered (van den Broek et al., 2012). Solar, with exception of concentrated solar technologies, and geothermal applications are often also characterized by relatively low temperature levels. The ORC technology utilizes this heat, reducing the use of primary energy and CO₂ emission.

A test rig (Fig. 1) was built to demonstrate the ORC technology in the frame of a project granted by IWT Flanders and it is currently used in the ORCNext project (www.orcnext.be) aiming to improve the ORC technology by introducing new types of expanders, advanced cycles, model based predictive control algorithms in combination with an economical analysis. The results obtained during extensive experiments are introduced in this paper in order to contribute to the study on the working fluids behavior in actual installations, e.g. Bracco et al. (2013) and Farrokhi et al. (2013), and to evaluate the impact of different working fluids on the same installation (Huck et al., 2013). While theoretical investigations on

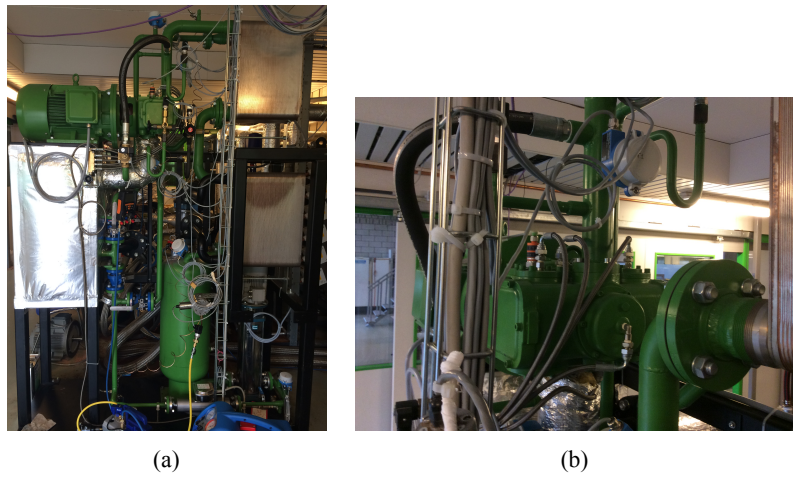


Figure 1: (a) ORC at UGent, Campus Kortrijk; (b) close view of the single screw expander installed.

the comparison of fluid properties can be found in literature e.g. Badr et al. (1985); Saleh et al. (2007); Quoilin et al. (2011), publications about practical use of different fluids and the relative performance are still rare. In this work, the performance of a unit built from "off the shelf" components and filled subsequently with two working fluids SES36 (Solkatherm) and R245fa is mapped and analyzed, the maximum power output regimes are indicated.

2. ORC TEST SETUP

The ORC test setup is shown in Fig. 1(a). A standard single-screw air compressor has been adjusted by BEP Europe (Ziviani et al., 2014) to operate as an expansion device and connected to an asynchronous generator with 11 kW nominal electric power. A closer view of the expander is shown in Fig. 1(b). The electrical power produced by the generator is injected into the electric grid by means of a four-quadrant inverter, which also allows to vary the generator rotational speed from 0 to 3600 rpm. The speed of a circulating 14-stage centrifugal pump can also be varied from 0 to 3000 rpm introducing a variable evaporation pressure up to 14 bar. The evaporator, internal heat exchanger and the condenser are three identical brazed plate heat exchangers. A more detailed description of the setup and the sensors installed can be found in a previous publication (Gusev et al., 2014). Thermodynamic parameters which can not be measured directly are calculated in real time using the CoolProp library (Bell et al., 2014). In this analysis, the power consumed by auxiliary equipment is neglected. The thermal power input, $\dot{Q}_{T66, ev, in}$, is guaranteed by a controllable 250 kW electric heater with Therminol 66 (T66) as working medium. The electric power injected to the grid is measured by the inverter. The net power produced by the ORC is obtained by subtracting the pump power from the electric power measured at the grid:

$$\dot{W}_{el, net} = \dot{W}_{el, grid, exp} - \dot{W}_{pp} \quad (1)$$

Due to the absence of a torque meter to measure the expander shaft power, an overall isentropic efficiency that includes the expander and the generator/inverter is defined as follows:

$$\eta_{is, oa, meas} = \frac{\dot{W}_{el, grid, exp}}{\dot{W}_{is, exp}} = \frac{\dot{W}_{el, grid, exp}}{\dot{m}_{r, exp} (h_{su, exp} - h_{ex, is, exp})} \quad (2)$$

In order to obtain the isentropic efficiency at the shaft, the generator efficiency and the inverter effectiveness should be accounted for as follows,

$$\eta_{is, sh, exp} = \frac{\dot{W}_{sh, exp}}{\dot{W}_{is, exp}} = \frac{\dot{W}_{el, grid, exp}}{\eta_{mech, gen} \epsilon_{el, inv} [\dot{m}_{r, exp} (h_{su, exp} - h_{ex, is, exp})]} \quad (3)$$

The correlations for the generator and the inverter efficiency have been obtained from Melotte (2012). The filling factor is given by:

$$\Phi_{FF} = \frac{\dot{m}v_{su,exp}}{\dot{V}_{swept,th}} = \frac{\dot{m}v_{su,exp}}{2z_{sr}V_{g,su}(N_{rot,exp}/60)} \quad (4)$$

where the volume of the groove at suction closure, $V_{g,su}$, is determined by the geometric model described in details in Ziviani et al. (2015). Finally, the net cycle efficiency can be expressed as:

$$\eta_{ORC,net} = \frac{\dot{W}_{el,grid,exp} - \dot{W}_{pp}}{\dot{Q}_{T66,ev,in}} \quad (5)$$

The main measured and calculated parameters for both working fluids are summarized in Table 1.

3. EXPERIMENTAL RESULTS

The choice of the experiment operating conditions is based on some typical solar and geothermal applications described in literature (Barbier, 2002; Tchanche et al., 2009; Liu et al., 2013; Zhou, 2014). The temperature of the heat source in many cases is stable over time and therefore has been kept constant during the experiments. Typical temperature range of the heat source considered is between 90 °C and 125 °C. However, the maximum temperature of the heat carrier (Therminol66) is limited to 125 °C because of the expander design that does not allow higher operating temperatures. Another limitation is represented by the maximum pressure that the expander can handle safely. Throughout the tests, the maximum pressure never exceeded 14 bar. The operating conditions of the working fluids are shown in Fig. 2. It can be noted that the condensing pressure of SES36 is typically below atmospheric pressure. Challenges arise to avoid air infiltration in the system, in particular during the idle state. In fact, the design of the installation does not allow to completely prevent leakages because the components are designed for general purposes.

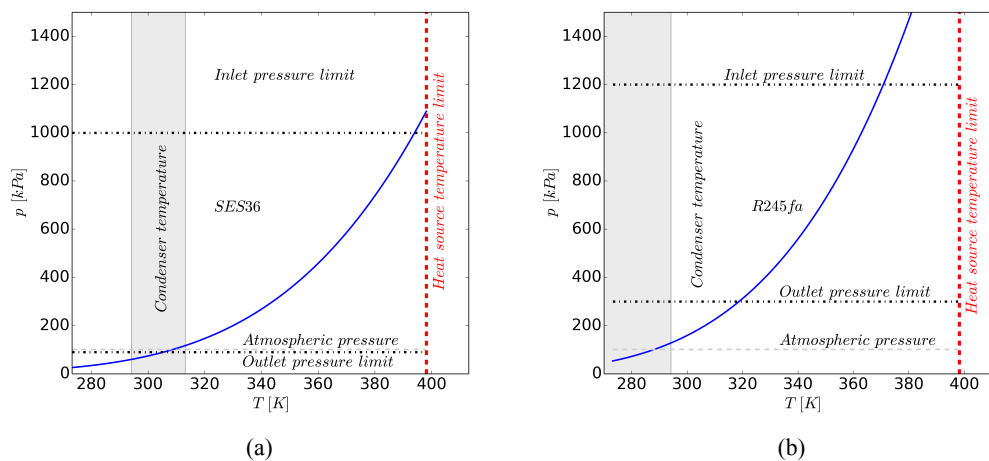
The first experiments were performed with SES36 and successively the installation has been charged with R245fa. Due to the fact that the installation relies on an air-cooler installed on the roof top, the cooling capacity strongly depends on the weather conditions. The fluids have been tested in different months of the year and therefore it is not possible to draw general conclusions on the maximum performance achievable by the system. However, a comparison of the operating conditions of the ORC with the different working fluid has been carried out. Two typical thermodynamic plots (T-s diagram) of the cycle with SES36 and R245fa are shown in Fig. 3.

In order to maintain a stable operation of the setup, a certain superheating level of 10-15 K before the expander was kept, in the case of SES36. The maximum achievable evaporating pressure in this case was about 8 bar, therefore the same pressure was used during the R245fa experiments in order to have a fair comparison. The superheating level of R245fa at the same conditions is much higher, up to 40 K. This cycle configuration leads to a significant exergy loss. Potentially, the heat source can be cooled down much deeper if a lower flow rate is chosen. As a result, a lower power output is detected. Moreover, during the experiments with SES36, a significant subcooling was detected.

One of the aims of the experimental campaign was the characterization of the expander with two different fluids and under different operating conditions. To this end, the mass flow rate is imposed by adjusting the frequency of the pump. However, it was noted that also the rotational speed of the expander influences the mass flow rate of the system. One of the reasons is that the pump is a centrifugal-type and as a consequence the mass flow rate is dependent on the evaporation pressure. Instead the expander is a volumetric machine and the volumetric flow rate is only dependent on the rotational speed. The tests were conducted by varying the frequency of the pump from minimum to maximum at a fixed expander rotational speed. The same procedure has been applied for all the considered expander rotational speeds. In particular, for SES36 only 2000 rpm and 3000 rpm have been tested. Four different speeds have been

Table 1: Summary of the minimum and maximum measured values of the variables considered for both working fluids.

	$p_{su,exp}$ (kPa)	$p_{ex,exp}$ (kPa)	$T_{su,exp}$ (°C)	\dot{m}_r (kg/s)	$\dot{W}_{el,grid}$ (W)	$T_{ex,exp}$ (°C)	T_{cd} (°C)	ΔT_{sh} (K)	ΔT_{sc} (K)	$\eta_{is,oa,exp}$ (-)	η_{ORC} (-)	Φ_{FF} (-)
SES36												
Min	450	90.6	91.65	0.150	1283	73.99	30.91	0.13	9	0.135	0.010	0.897
Max	1028	177.9	125	0.406	7865	102.0	50.87	28	14	0.647	0.092	1.117
R245fa												
Min	566	120	106.7	0.12	1283	75.5	18.82	26	1.9	0.205	0.014	1.038
Max	1230	232	124.9	0.37	7364	104.6	37.12	56	3.7	0.519	0.077	1.331

**Figure 2: Working fluid operating conditions during the tests: (a) SES36; (b) R245FA.**

tested in the case of R245fa, i.e. 2000 rpm, 2500 rpm, 3000 rpm and 3300 rpm. A total of 43 and 59 steady-state points have been determined for SES36 and R245fa, respectively. The comparison of the fluids is proposed in terms of operating maps as function of power output, isentropic efficiency, mass flow rate, pump and expander rotational speeds as well as ORC efficiency.

4. COMPARISON OF THE WORKING FLUIDS PERFORMANCE

As it can be seen in Fig. 2, an ORC unit filled with R245fa operates at higher working pressures compared with SES36, resulting in lower pressure ratios within the same temperature region. As a consequence, the thermodynamic efficiency of the ORC running with R245fa is slightly lower. The condenser pressure is very close to the expander limit of 3 bar, especially during summer. This pressure corresponds to a temperature of about 45 °C. Taking into account a certain temperature difference between the condenser and the ambient temperatures caused by the air-type cooling loop, the current combination of working fluid and expander is not appropriate for regions with a hot climate. An expander suitable to withstand higher working pressures is needed in order to avoid emergency shut-downs if R245fa is used. An advantage of R245fa over SES36 is that the condensing pressure is higher than the ambient which prevents non-condensable gases in the system. On the other hand, higher working pressures mean in general higher leakage flows and the loss of working fluid through flanges and shaft seals. The cost of the low-GWP working fluids is non-negligible especially for larger installations. The absence of subcooling caused by non-condensable gasses in the condenser is an advantage from a thermodynamic point of view but increases the duty of the circulating pump. A saturated working fluid can start boiling in the suction line due to a certain local pressure drop preventing pump to work properly. In some cases under a variable

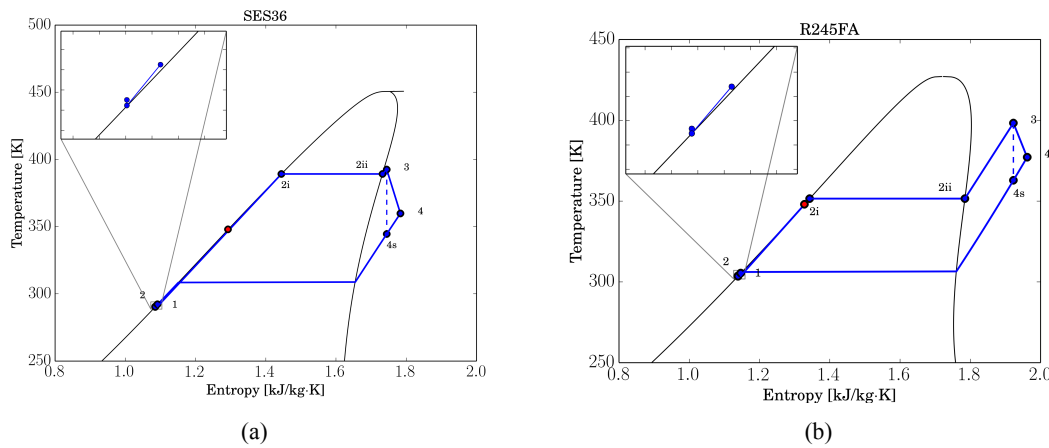


Figure 3: Examples of thermodynamic plots obtained from the experiments: (a) SES36 ; (b) R245fa. The outlet state of the regenerator prior entering the evaporator is marked with a red dot.

cooling temperature this phenomenon can completely block the flow.

The steady-state points obtained for both fluids are plotted in Fig. 4, where the power output of the expander, $\dot{W}_{el,grid}$, is given as function of the pressure ratio, $r_{p,exp}$, for different rotational speeds. The isentropic efficiency is indicated by a color scale. It is possible to notice that there is a quasi-linear trend between power output and pressure ratio.

For most of the points, the power output increases with the increase of both pressure ratio and rotational speed. This can be easily observed by considering the rotational speeds of 2000 rpm and 3000 rpm. Regarding the rotational speeds of 2500 rpm and 3300 rpm for R245fa, shown in Fig. 4(b), a similar consideration can be made, i.e. the higher the rotational speed and the pressure ratio, the higher the power output, by keeping in mind that these steady-state points were obtained during a very warm day which affected the condensing pressure. The pressure ratio range achievable was limited both at high pressure side (limit set by maximum pressure of expander) and low pressure side because of high external temperature.

The ORC installation operates most of the time at pressure ratios higher than the pressure ratio corresponding to the built-in volume ratio of the expander, $r_{v,built-in} = 4.7$ (Ziviani et al., 2015), causing an over-expansion. While the power output at the same pressure ratio is similar for both fluids, the expander isentropic efficiency is slightly higher in the case of SES36. At low pressure ratios and power, the influence of the expander rotational speed is limited. Maximum and minimum values of the performance of each fluid are listed in Table 1.

The operating conditions of both working fluids are presented with three performance maps shown in Fig. 5, 6, 8. In Fig. 5, 6, the mass flow rates of SES36 and R245fa and the isentropic efficiency versus the expander and the pump rotational speeds are shown, respectively. A higher mass flow of R245fa at the same conditions is caused by its lower density in comparison with SES36. The influence of the expander rotational speed is less significant than the pump rotational speed for both fluids. The trend for the pump rotational speed is almost linear, as shown in Fig. 7, so higher rotational speeds can be recommended in order to achieve a higher performance. The maximum isentropic efficiency of the expander is achieved at the nominal speed of 3000 rpm for both fluids. The third set of performance maps, in Fig. 8, assesses the optimum operating conditions, in terms of cycle efficiency, η_{ORC} , of the ORC system for different thermal input, \dot{Q}_{T66} , and degree of superheating, ΔT_{sh} . The cycle efficiency is related to the degree of superheating and the working fluid. In particular, in the case of SES36, the maximum cycle efficiency is observed with a range of the degree of superheating of 5-10 K, as shown in Fig. 8(a). Instead, in the

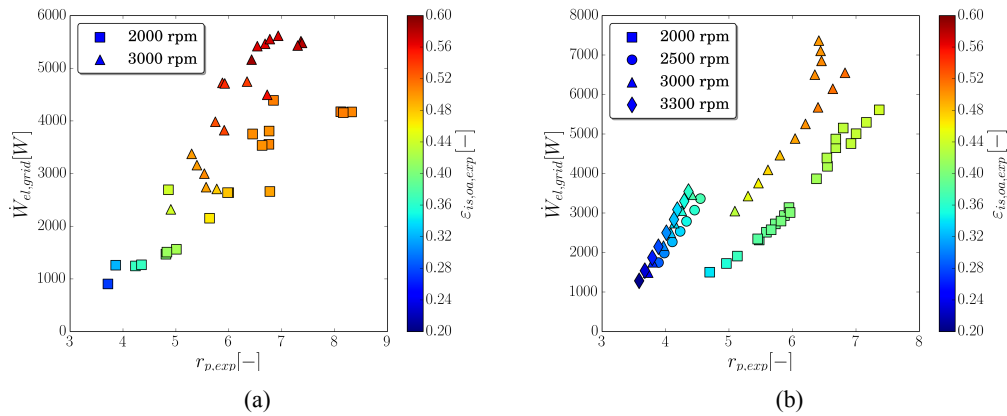


Figure 4: Power output as a function of different pressure ratios: (a) SES36 ;(b) R245fa. The color scale indicates the overall isentropic efficiency.

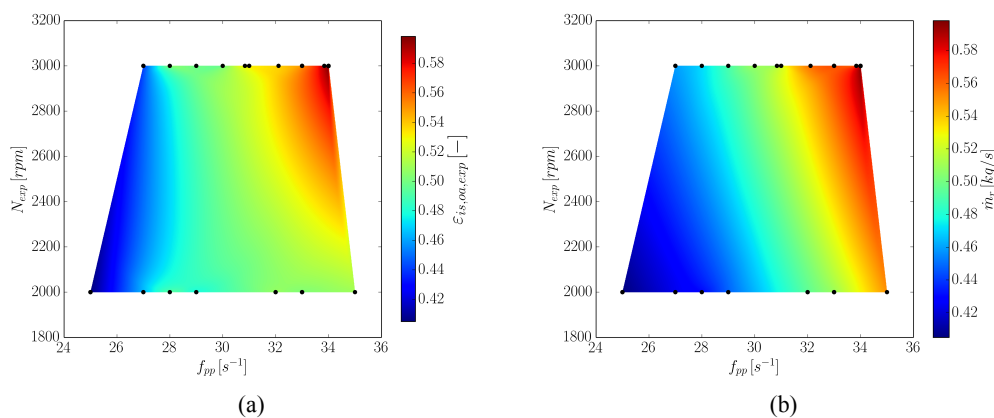


Figure 5: Operating maps of SES36: (a) overall isentropic efficiency as function of pump and expander rotational speeds; (b) mass flow rate as function of pump and expander rotational speeds.

case of R245fa, the cycle efficiency is maximized at higher values of the superheating, 30-35 K, Fig. 8(b).

The operating stability of the system and different conditions have also been investigated. During the experiments, an unstable operation characterized by a fluctuating mass flow rate of the working fluid was detected when the working fluid was entering the expander close to the vapor saturation point. A decrease of the evaporation pressure resulted in an increase of the mass flow rate, which is a sign of a wet expansion. A drop in both power output and isentropic efficiency occurred.

5. CONCLUSIONS

In this paper, the performance of a non-optimized ORC unit operating subsequently with two different working fluids under the same conditions is mapped. The efficiency of the ORC system components is not constant during operation and it is influenced by the dynamic behavior of each component. Based on the experimental results, an optimal rotational speed of the circulating pump and the expander can be found for each typical working condition such as the flow rate, the temperature of the heat source and the ambient temperature. These settings could be implemented in a feed-forward control of an installation that operates with a variable heat input.

For the given temperature level and the current installation, SES36 is more optimal than R245fa. For

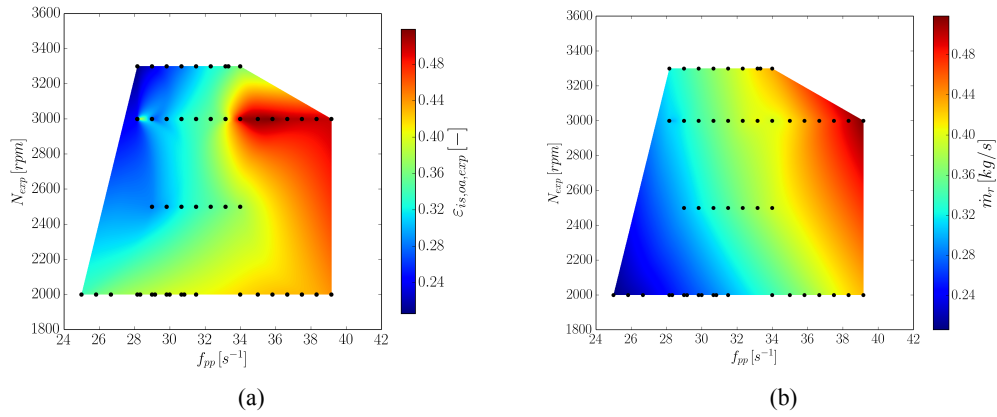


Figure 6: Operating maps of R245fa: (a) overall isentropic efficiency as function of pump and expander rotational speeds; (b) mass flow rate as function of pump and expander rotational speeds.

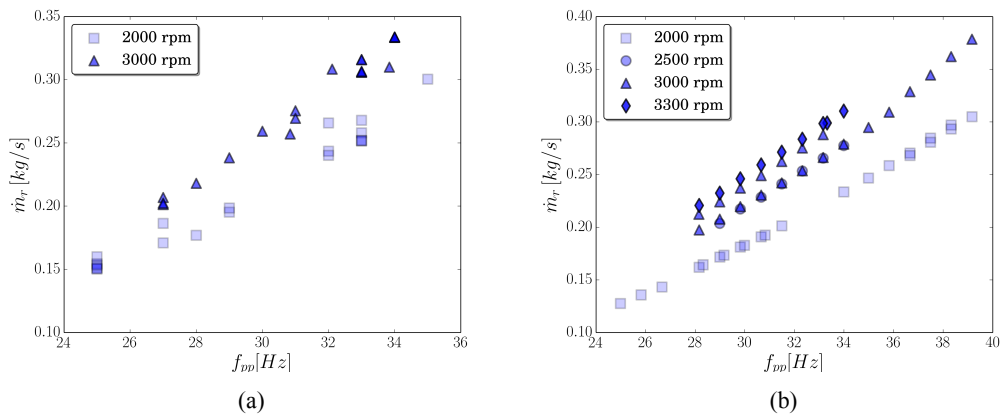


Figure 7: Influence of the pump frequency on the mass flow rate at different expander rotational speeds: (a) SES36; (b) R245fa.

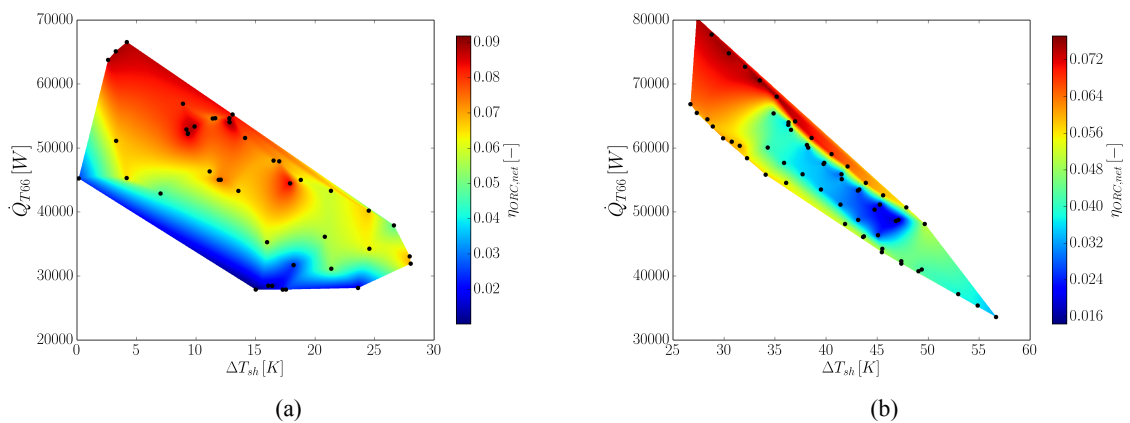


Figure 8: Net cycle efficiency as function of thermal power and degree of superheating: (a) SES36; (b) R245FA.

both fluids, operation at superheating levels lower than 5 K should be avoided due to difficulties in maintaining a stable mass flow rate.

REFERENCES

- Badr, O., Probert, S. D., and O'Callaghan, P. (1985). Selecting a working fluid for a Rankine cycle engine. *Applied Energy*, 21:1–42.
- Barbier, E. (2002). Geothermal energy technology and current status: an overview. *Renewable and Sustainable Energy Reviews*, 6:3–65.
- Bell, I. H., Wronski, J., Quoilin, S., and Lemort, V. (2014). Pure and pseudo-pure fluid thermophysical property evaluation and the open-source thermophysical property library CoolProp. *Industrial & Engineering Chemistry Research*, 53(6):2498–2508.
- Bracco, R., Clemente, S., Micheli, D., and Reini, M. (2013). Experimental tests and modelization of a domestic-scale ORC (organic Rankine cycle). *Energy*, 58(1):107–116. ISSN 0360-5442.
- Farrokhi, M., Noie, S. H., and Akbarzadeh, A. A. (2013). Preliminary experimental investigation of a natural gas-fired ORC-based micro-CHP system for residential buildings. *Applied Thermal Engineering*, 7. ISSN 1359-4311.
- Gusev, S., Ziviani, D., Bell, I., De Paepe, M., and van den Broek, M. (2014). Experimental comparison of working fluids for organic Rankine cycle with single-screw expander. In *Proceedings of the International Refrigeration and Air Conditioning Conference*. Paper 1548.
- Huck, P., Laursen, A. L., Zia, J., and Woolley, L. (2013). Identification and test of low global warming potential alternatives to HFC-245fa in organic Rankine cycles. In *Proceedings of the 2nd International Seminar on ORC Power Systems*, Rotterdam, Netherlands.
- Liu, Q., Duan, Y., and Yang, Z. (2013). Performance analyses of geothermal organic Rankine cycles with selected hydrocarbon working fluids. *Energy*, 63:123–132. ISSN 0360-5442.
- Melotte, N. (2012). Experimental study and dynamic modeling of a waste heat recovery organic Rankine cycle. Master's thesis, University of Liege.
- Quoilin, S., Declaye, S., Tchanche, B. F., and Lemort, V. (2011). Thermo-economic optimization of waste heat recovery organic Rankine cycles. *Applied Thermal Engineering*, 31(14):2885–2893.
- Saleh, B., Koglbauer, G., Wendland, M., and Fischer, J. (2007). Working fluids for low temperature organic Rankine cycles. *Energy*, 32:1210–1221.
- Tchanche, B. F., Papadakis, G., Lambrinos, G., and Frangoudakis, A. (2009). Fluid selection for a low-temperature solar organic Rankine cycle. *Applied Thermal Engineering*, 29:2468–2476.
- van den Broek, M., Vanslambrouck, B., and De Paepe, M. (2012). Electricity generation from biomass: Organic Rankine cycle versus steam cycle. In *Proceedings of the Conference and Exhibition on Biomass for Energy*, Jönköping, Sweden.
- Zhou, C. (2014). Hybridisation of solar and geothermal energy in both subcritical and supercritical organic Rankine cycles. *Energy Conversion and Management*, 81:72–82. ISSN 0196-8904.
- Ziviani, D., Bell, I., van den Broek, M., and De Paepe, M. (2014). Comprehensive model of a single-screw expander for ORC-systems. In *Proceedings of the International Compressor Engineering Conference*. Paper 2357.

Ziviani, D., Bell, I. H., De Paepe, M., and van den Broek, M. (2015). Update on single-screw expander geometry model integrated into an open-source simulation tool. In *9th Int. Conf. on Compressors and their Systems, City University of London, London*, number 39.

NOMENCLATURE

c_p	specific heat at constant pressure	(J/kg-K)	Subscript	
\dot{m}	mass flow rate	(kg/s)	exp	expander
f_{pp}	pump frequency	(Hz)	el	electric
N	rotational speed	(rpm)	ev	evaporator
p	pressure	(Pa)	gen	generator
\dot{Q}	heat rate	(W)	is	isentropic
r_p	pressure ratio	(-)	in	inlet
T	temperature	(K, °C)	inv	inverter
v	specific volume	(m^3/kg)	meas	measured
V	volume	(m^3)	oa	overall
\dot{W}	power	(W)	pp	pump
z_{sr}	number of starwheel tooth	(-)	r	refrigerant
Φ_{FF}	filling factor	(-)	sc	subcooling
ϵ	effectiveness	(-)	su	supply
η	efficiency	(-)	sh	superheating
Subscript				shaft
cd	condenser		th	theoretical
ex	exhaust		T66	Therminol66

ACKNOWLEDGEMENT

The financial support is provided by the Institute for the Promotion and Innovation by Science and Technology in Flanders. All data and results presented in this survey have been obtained in the frame of the IWT SBO-110006 project “The Next Generation Organic Rankine Cycles”: www.orcnnext.be

PERFORMANCE ANALYSIS OF ORC SYSTEM WITH IHE USING THE ZEOTROPIC MIXTURE AND THE PURE WORKING FLUID FOR VEHICLE CNG ENGINE

Songsong Song^{1,2*}, Hongguang Zhang^{1,2}

¹College of Environmental and Energy Engineering, Beijing University of Technology, Pingleyuan No.100, 100124 Beijing, China
e-mail: qihsong@126.com

²Collaborative Innovation Center of Electric Vehicles in Beijing, Pingleyuan No.100, 100124 Beijing, China

* Corresponding Author

ABSTRACT

In order to improve the thermal efficiency of compressed natural gas (CNG) engine, a set of organic Rankine cycle (ORC) system with internal heat exchanger (IHE) is designed to recover exhaust waste heat from the CNG engine. The working fluids under investigation are the pure working fluid R245fa and the zeotropic mixture R416A. Subsequently, the influence of the two different working fluids on performance parameters such as net power output, thermal efficiency, exergy efficiency and output energy density of working fluid are analyzed. The results show that the zeotropic mixture R416A performs better. Finally, a combined CNG engine and ORC system with IHE is defined to evaluate the performance improvement. Results show that compared with the CNG engine, the thermal efficiency of the combined system can be increased by a maximum 7%.

1. INTRODUCTION

The thermal efficiency of most compressed natural gas (CNG) engines are 30% or so and they are lower than that of diesel engines, large amount fuel energy are rejected from CNG engines to the surroundings as waste heat, with a significant fraction through the exhaust. Therefore, recovering the exhaust waste heat from CNG engine so as to improve thermal efficiency and save fuel has become a hot focus of recent research work (Wang *et al.*, 2014).

The organic Rankine cycle (ORC) is a promising method to recover waste heat from internal combustion engines (ICE) exhaust gas (Chiew *et al.*, 2011, Wang *et al.*, 2011, Zhang *et al.*, 2014). Vaja *et al.* (2010) designed a power cycle equipment to match a stationary internal combustion engine, and accordingly chose three pure working fluids to examine three different ORC schemes separately. The analysis demonstrated that a 12% increase in the total efficiency could be achieved with respect to the engine with no ORC cycle. Yang *et al.* (2014) designed a set of dual loop ORC system to recover exhaust energy, waste heat from the coolant system, and released heat from turbocharged air in the intercooler of a six-cylinder diesel engine. R245fa was selected as the working fluid for both loops. The results showed that the dual loop ORC system achieves the largest net power output at 27.85 kW at the engine rated condition. Compared with the diesel engine, the thermal efficiency of the combined system can be increased by 13%. Yu *et al.* (2013) built an ORC system to recover waste heat both from engine exhaust gas and jacket water using R245fa as working fluid. Results indicated that the ORC system performances well under the rated engine condition with expansion power up to 14.5 kW, recovery efficiency up to 9.2% and exergy efficiency up to 21.7%. Combined with bottoming ORC system, thermal efficiency of diesel engine can be improved up to 6.1%.

For the working fluids of ORC system, the match of working fluids with heat source and systems significantly affects system performance. Zeotropic mixtures have a property called “temperature glide” in evaporation and condensation process and this can reduce exergy destruction rate due to heat transfer temperature difference (Wu *et al.*, 2012). Radulovic and Castaneda (2014) proposed six zeotropic mixtures for conducting a parametric optimisation of supercritical Rankine cycle powered by low temperature geothermal heat source. And then a comparative analysis between the zeotropic mixtures and pure R-143a was studied. The results showed that the cycle efficiency can be improved by 15% at the same operational conditions. Lecompte *et al.* (2014) examined the thermodynamic performance of non-superheated subcritical organic Rankine cycles (ORCs) with zeotropic mixtures as working fluids based on a second law analysis. The results showed that an increase in second law efficiency in the range of 7.1% and 14.2% is obtained compared to pure working fluids. Furthermore, between optimized ORCs with zeotropic mixtures as working fluid the difference in second law efficiency varies less than 3 percentage points.

According to abovementioned analysis, zeotropic mixtures have bigger potential in optimizing the ORC system performances than pure working fluids, whereas few scholars use zeotropic mixtures for an ORC system in recovering the exhaust energy from a CNG engine.

2. EVALUATION OF EXHAUST WASTE HEAT FROM CNG ENGINE

To design an optimal ORC system that can efficiently recover the exhaust waste heat from CNG engine, it is necessary to analyze the energy distribution in the running process of the engine. In this paper, a six-cylinder four-stroke CNG engine was employed, and the main performance parameters were listed in Table 1. Based on the performance test data of engine experimental system, the running performances and exhaust energy of the CNG engine under various operating conditions were analyzed. During the experiment, the CNG engine speed ranged from 1800 r/min to 2200 r/min at an interval of 200 r/min. The eleven operating condition points were selected and tested under each engine speed.

Table 1:Main technical performance parameters of the CNG engine

Items	Parameters	Units
Cylinder number	6	
Rated power	206	kW
Displacement	8.3	L
Stroke and cylinder bore	135×114	mm
Compression ratio	10.5	
Maximum torque	1050	N.m

The universal characteristic of CNG engine is shown in Figure 1. As seen in this figure, the blue contour lines indicate the variations in the effective power output of the engine under engine various operating conditions. The black contour lines indicate the variations in the brake specific fuel consumption (BSFC) of the engine under engine various operating conditions. At the engine rated condition, the effective power output of the CNG engine is 206.9 kW. In addition, the brake specific fuel consumption (BSFC) is relatively low in the engine’s medium speed with medium-high load regions. On the contrary, the brake specific fuel consumption (BSFC) is relatively higher in the engine’s low load region, particularly in the high speed region. When the engine speed is 1400 r/min and engine torque is 1050 N.m, the CNG engine achieves the optimal fuel economy, and the BSFC is 199 g/(kW.h).

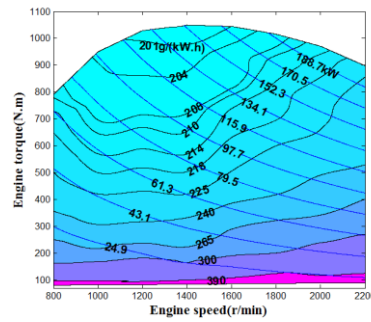


Figure 1: Universal characteristic of CNG engine

Figure 2 shows the thermal efficiency under engine various operating conditions. The thermal efficiency η_{en} can be calculated using the following equation:

$$\eta_{en} = \frac{\dot{W}_{en}}{\dot{Q}_f} \quad (1)$$

Where, \dot{W}_{en} is the effective power output of CNG engine, \dot{Q}_f is the fuel combustion energy which can be calculated using the fuel consumption rate and fuel lower heating value. In this paper, the fuel lower heating value is 50050 kJ/kg.

As seen in the Figure 2, the thermal efficiency increases with the engine torque. On the other hand, the thermal efficiency firstly increases and then decreases with engine torque, whereas the variation trend is not especially obvious in the engine's low load region. When the engine speed is 1400 r/min and engine torque is 1050 N.m, the thermal efficiency of CNG engine can reach up to a maximum of 36.14%.

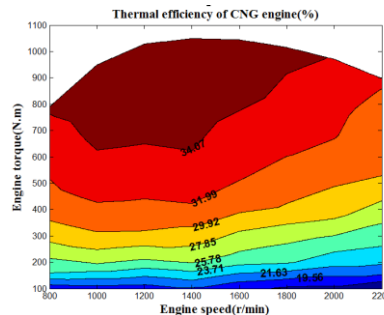


Figure 2: Thermal efficiency of CNG engine

Figure 3 illustrates the variation of exhaust temperature in different engine speed with the engine torque. As shown in Figure 3, exhaust temperature is relatively low under low speed with low torque conditions, and relatively high under both medium-high speed and medium-high torque conditions. But the overall variation trend is complex. From Figure 3 it can be seen that exhaust temperature is in the range of 730 K to 900 K.

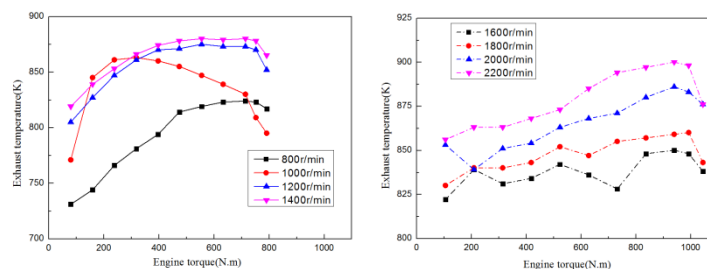


Figure 3: Exhaust temperature of CNG engine

When calculating exhaust energy, methane is assumed to be the natural gas fuel and other substances contained in the natural gas are ignored for this study. Air-fuel ratio of the CNG engine is set to 17.2 (by mass). According to chemical reaction equation for the combustion process, mass fraction of the exhaust components CO_2 , H_2O and N_2 is 15.1%, 12.4% and 72.5%, respectively. Subsequently, the specific enthalpy of the exhaust under a specific temperature is calculated using the thermodynamic calculation method of ideal gas and REFPROP 9.0 software. In addition, exhaust mass flow rate \dot{m}_{exh} can be calculated using air-fuel ratio and fuel consumption which measured by experiment. Finally, the exhaust energy \dot{Q}_{exh} of CNG engine can be calculated using equation (2).

$$\dot{Q}_{\text{exh}} = \dot{m}_{\text{exh}} h_{\text{exh}} \quad (2)$$

Where, h_{exh} is the specific enthalpy of the exhaust.

In practical ORC system, exhaust energy can not be totally absorbed by working fluids (Yu *et al.* 2013). Therefore, in this paper, the exhaust temperature and pressure at the outlet of evaporator are set to 378 K and 97.8 kPa, respectively. Subsequently, specific enthalpy of the exhaust under the set exhaust temperature and pressure is calculated using REFPROP 9.0 software. Finally the available exhaust energy rate can be calculated using equation (3).

$$\dot{Q}_{\text{ava}} = \dot{m}_{\text{exh}} (h_{\text{in}} - h_{\text{out}}) \quad (3)$$

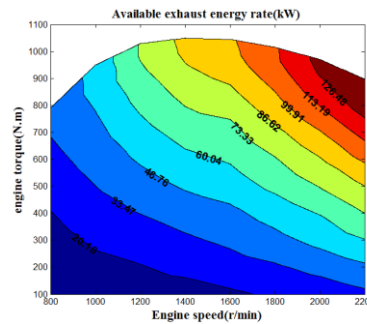


Figure 4: Available exhaust energy rate of CNG engine

According to the performance test data of CNG engine, the variation tendency of available exhaust energy rate under engine various operating conditions is shown in Figure 4. It is evident that available exhaust energy rate increases over the engine whole operating range, achieving 139.58 kW at the engine rated condition.

3. EXHAUST WASTE HEAT RECOVERY SYSTEM BASED ON ORC WITH IHE

3.1 System Description

In order to recover the exhaust waste heat from CNG engine efficiently, the ORC system with IHE is designed as shown in Figure 5. The system consists of an evaporator, a condenser, an expander, a recuperator (namely IHE), a pump, a reservoir and a generator. At first, the exhaust gas exchanges heat with the organic working fluid in the evaporator, then the exhaust gas is released through evaporator into the atmosphere. Meanwhile the organic working fluid turns into high-temperature and high-pressure gas and soon enters expander to generate electricity. Later, the organic working fluid exhausted from the expander goes into the recuperator to exchange heat with the liquid organic working fluid which exported from the pump. Subsequently, the cooled working fluid that is exhausted from recuperator condenses into a saturated liquid state and flows into the reservoir. The organic working fluid is pressurized by using pump and then absorbs heat in the recuperator. Finally, the organic working fluid flows into the evaporator to absorb the heat from engine exhaust.

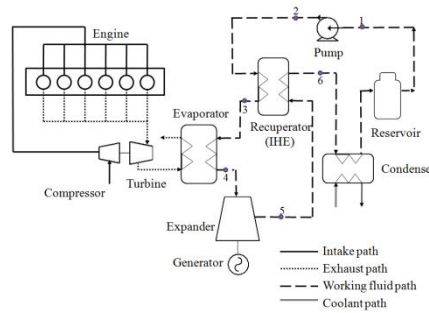


Figure 5: Schematic diagram of ORC system with IHE

3.2 Working Fluid Selection

The selection of working fluids has an important impact on thermodynamic performances of the ORC system. In this paper, there are two kinds of working fluids have been selected to study the performances of ORC system. Therein R245fa has performed well as the working fluid in ORC systems in many studies (Wang *et al.* 2011, Wang *et al.* 2012). In addition, because of the good environment friendliness and safety, zeotropic mixture R416A with property of temperature glide has been selected from the existing serial-numbered refrigerant for this study. The properties of R416A and R245fa are listed in Table 2.

Table 2: Properties of R416A

Parameters	R416A	R245fa
Components	R134a/R124/R600	~
Composition (mass fraction)	0.59/0.395/0.015	~
Critical temperature (K)	380.23	427.16
Critical pressure (MPa)	3.98	3.651
Glide temperature (K)	1.86	~
Safety	A1	B1
Environment friendliness (Yes/No)	Yes	Yes
Fluid type	Wet	Dry

Glide temperature: standard atmospheric pressure.

3.3 Thermodynamic Model

Figure 6 is the $T-s$ diagram of the working fluid. Therein Process 1-2 is the actual pressurization process of pump, process 1-2s is the isentropic pressurization process. Process 2-3 is the isobaric endothermic process of the working fluids in the recuperator. Process 3-4 is the isobaric endothermic process, Process 4-5s is the isentropic expansion process, while the process 4-5 is the actual expansion process. Process 5-6 is the isobaric exothermic process of the organic working fluid in the recuperator. Process 6-1 is the isobaric condensation process. Process $T_{exh_in} - T_{exh_out}$ is the heat transfer process of the engine exhaust in the evaporator, T_{exh_in} is the exhaust gas temperature at the inlet of the evaporator, T_{exh_out} is the exhaust gas temperature at the outlet of the evaporator.

Based on the first and second laws of thermodynamics, the performance parameters of ORC system with IHE are calculated using the following equations:

In the process 1-2, the power consumption \dot{W}_p is calculated with the equation below.

$$\dot{W}_p = \dot{m}(h_2 - h_1) = \frac{\dot{m}(h_{2s} - h_1)}{\eta_p} \quad (4)$$

Where, \dot{m} is mass flow rate of organic working fluid, η_p is isentropic efficiency of pump.

In the processes 2-3 and 5-6, the heat transfer rate \dot{Q}_r of the recuperator is calculated using the following equation:

$$\dot{Q}_r = \dot{m}(h_3 - h_2) = \dot{m}(h_5 - h_6) \quad (5)$$

ε is the effectiveness of recuperator, which can be calculated using equation (6):

$$\varepsilon = (T_5 - T_6)/(T_5 - T_2) \quad (6)$$

In the process 3-4, the heat transfer rate \dot{Q}_e of the evaporator is calculated using the following equation:

$$\dot{Q}_e = \dot{m}(h_4 - h_3) \quad (7)$$

In the processes 4-5 and 4-5s, the power output \dot{W}_s of the expander is calculated using the following equation:

$$\dot{W}_s = \dot{m}(h_4 - h_5) = \dot{m}(h_4 - h_{5s})\eta_s \quad (8)$$

Where, η_s is isentropic efficiency of expander.

In the process 6-1, the heat transfer rate \dot{Q}_c of the condenser is calculated using the following equation:

$$\dot{Q}_c = \dot{m}(h_6 - h_1) \quad (9)$$

In the all equations, h and its subscripts represent the specific enthalpy value of each state point in the T - s diagram.

According to the above analysis, the net power output, thermal efficiency and exergy efficiency of ORC system with IHE are respectively calculated using the following equations:

$$\dot{W}_n = \dot{W}_s - \dot{W}_p \quad (10)$$

$$\eta_{th} = \frac{\dot{W}_n}{\dot{Q}_e} \quad (11)$$

$$\eta_{ex} = \frac{\dot{W}_n}{\dot{Q}_e(1 - \frac{T_L}{T_H})} \quad (12)$$

Where, T_H is the temperature of the high temperature heat source that can be calculated using equation (13). T_{exh_in} can be measured through engine test. T_{exh_out} is the exhaust temperature at the outlet of evaporator. T_L is the temperature of the low temperature heat source.

$$T_H = (T_{exh_in} - T_{exh_out}) / \ln(T_{exh_in} / T_{exh_out}) \quad (13)$$

In addition, output energy density of working fluid ρ is defined to evaluate the capability to produce useful work for per unit of mass of working fluids. Its calculation equation as follows:

$$\rho = \frac{\dot{W}_n}{\dot{m}} \quad (14)$$

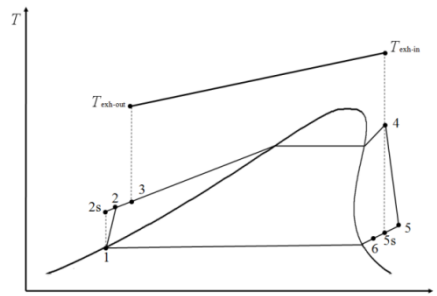


Figure 6: T - s diagram of ORC system with IHE

4. RESULTS AND DISCUSSION

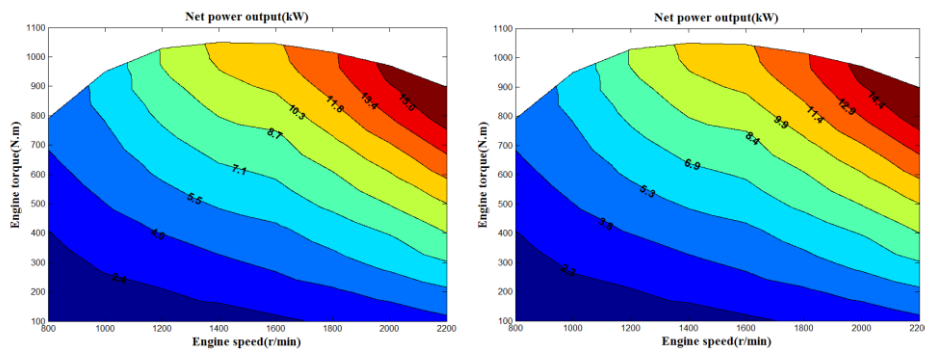
4.1 Boundary Conditions

In order to analyze the effects of R416A and R245fa on the performance of ORC system with IHE, in this paper, the boundary conditions are set as follows:

- (1) Pressure drop and heat loss in each component as well as pipelines are neglected.
- (2) Evaporation pressure is set to 2.5 MPa.
- (3) The degree of superheat and T_L are set to 30 K and 293 K, respectively.
- (4) The isentropic efficiencies of the expander and the pump are both set to 0.8.
- (5) The working fluid releases heat in the condenser and then turns into a saturated liquid state.
- (6) The expansion ratio of expander is set to 4.
- (7) The effectiveness of recuperator is set to 0.85.

4.2 Results Analysis

Figure 7 illustrates how the net power output of the ORC system with IHE using the two different working fluids changes over the engine whole operating range. As shown in Figure 7(a) and (b), the variation tendency of the net power output using the two different working fluids are consistent, while the values are different. The net power output of the ORC system with IHE using the two working fluids increases with the increase of the engine's speed and load. At the engine's rated condition, the net power output for R416A reaches a maximum of 16.6 kW and a maximum of 16.0 kW for R245fa. Additionally, comparing Figure 7(a) and (b) shows that the net power output for R416A is larger than that of R245fa for each engine operating conditions. Therefore, by employing zeotropic mixture R416A, the performance of ORC system with IHE has better characteristics of power output.



(a) Net power output of R416A

(b) Net power output of R245fa

Figure 7: Net power output of ORC system with IHE

The results of the ORC system with IHE using the two different working fluids are summarized in Table 3. As shown in Table 3, the thermal efficiency and output energy density of working fluid for R416A are all larger than that of R245fa. For the same net power output of ORC system with IHE, the higher output energy density of working fluid, the less mass flow rate of working fluid is required for ORC system that can obviously reduce the working fluid mass filled in the ORC system. The total weight of the ORC system not only can be reduced but also the risk of environmental pollution can be significantly decreased.

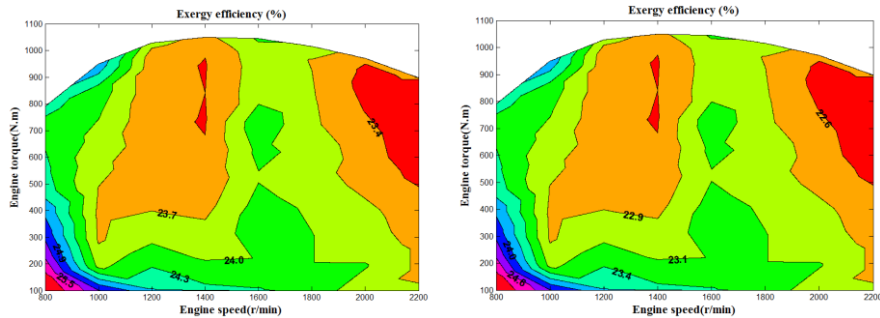
Table 3: The results of two different working fluids

Performance parameters	Working fluids	
	R416A	R245fa
Thermal efficiency (%)	11.9%	11.4%
Condensing temperature (K)	299.7	344.1
Output energy density of working fluid (kJ/kg)	22.8	21.8

On the other hand, as listed in Table 3, we can see that the condensing temperature for R416A is lower than that of R245fa. As we all know, condensing temperature is one of the key factors which

can influence the running performance of ORC system. Although the lower condensing temperature is beneficial for the running of ORC system, in practical application, the lower condensing temperature needs the higher-performance cooling system which can increase the cost of ORC system.

Figure 8 illustrates the variation of exergy efficiency with CNG engine speed and load. As shown in the Figure 8 (a) and (b), the variation tendencies of exergy efficiency using the two different working fluids are consistent. Namely, the exergy efficiency of ORC system with IHE is higher in the engine's low speed with low load regions. Whereas the exergy efficiency is lower in the engine's medium-high speed with medium-high load regions. The reason can be analyzed as follows: according to the equation (12), for the selected working fluid, exergy efficiency only depends on the exhaust temperature on the condition that the temperature of low temperature heat source is constant. Moreover, the variation trend of exhaust temperature is shown in Figure 3.



(a) Exergy efficiency of R416A

(b) Exergy efficiency of R245fa

Figure 8:Exergy efficiency of ORC system with IHE

According to all of the results described above, we can conclude that the ORC system with IHE using R416A as the working fluid displays superior thermodynamic properties. Therefore, in order to optimize the power system as a whole and evaluate the improvement in overall power output, a “combined CNG engine and ORC system with IHE” is defined. The thermal efficiency of combined system η_{com} is calculated using the following equation:

$$\eta_{com} = \frac{\dot{W}_n + \dot{W}_{en}}{\dot{Q}_f} \quad (15)$$

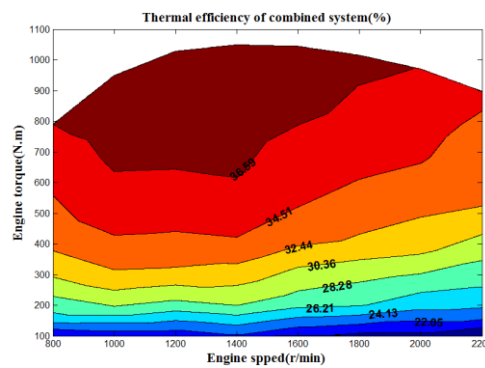


Figure 9:Thermal efficiency of combined system

The thermal efficiency of combined system is shown in Figure 9. When the engine speed is constant, the thermal efficiency of combined system increases with engine torque. On the other hand, when the engine torque is constant, the thermal efficiency of combined system firstly increases and then decreases with engine speed. When the engine speed is 1400 r/min and engine torque is 1050 N.m, the maximum thermal efficiency of combined system is 38.67%, which is higher than that of CNG engine by 7.0%.

5. CONCLUSIONS

- When evaporation pressure is 2.5 MPa and expansion ratio of expander is 4, the output energy density of working fluid, net power output, thermal efficiency, and exergy efficiency of ORC system with IHE using zeotropic mixture R416A are all superior to the same system using R245fa. Therefore, zeotropic mixtures have bigger potential in optimizing the ORC system performances than pure working fluids
- For the ORC system with IHE, condensing temperature for R416A is lower than that of R245fa. Although the lower condensing temperature is beneficial for the running of system, in engineering application, extremely low condensing temperatures cause difficulties in economically providing a low temperature heat source.
- The thermal efficiency of combined system increases with engine load, which is higher than that of CNG engine by 7.0%. From the viewpoint of power performance, the ORC system with IHE is a promising scheme to recover the exhaust waste heat from a CNG engine.

NOMENCLATURE

h	enthalpy	(kJ/kg)
s	entropy	(kJ/kg K)
\dot{m}	mass flow rate	(kg/s)
\dot{W}	power	(kW)
T	temperature	(K)
\dot{Q}	heat transfer rate	(kW)
η	efficiency	(-)
ε	effectiveness of recuperator	(-)

Subscript

1,2,2s,3,4,5,5s,6	state point in cycle
p	pump
e	evaporator
s	expander
r	recuperator
n	net
c	condenser
exh	exhaust gas
in	inlet
out	outlet
L	low temperature heat source
H	high temperature heat source
th	thermal
com	combined system
en	engine
ex	exergy
f	fuel
ava	available

REFERENCES

Zhang, J., Zhang, H.G., Yang, K., et al, 2014, Performance analysis of regenerative organic Rankine cycle (RORC) using the pure working fluid and the zeotropic mixture over the whole operating range of a diesel engine, Energy Convers Manage, vol. 84, p. 282-294.

- Yang, F.B., Dong, X.R., Zhang, H.G., et al, 2014, Performance analysis of waste heat recovery with a dual loop organic Rankine cycle (ORC) system for diesel engine under various operating conditions, *Energy Convers Manage*, vol. 80, p. 243-255.
- Yu, G.P., Shu, G.Q., Tian, H., et al, 2013, Simulation and thermodynamic analysis of a bottoming Organic Rankine Cycle(ORC) of diesel engine(DE), *Energy*,vol. 51, p. 281-290.
- Wang, E.H., Zhang, H.G., Fan, B.Y., et al, 2011, Study of working fluid selection of organic Rankine cycle (ORC) for engine waste heat recovery, *Energy*, vol. 36, p. 3406-3418.
- Wang, J.L., Zhao, L., Wang, X.D., 2012, An experimental study on the recuperative low temperature solar Rankine cycle using R245fa, *Appl Energ*, vol.94, p. 34-40.
- Wang, T.H., Zhang, Y.J., Zhang, J., et al, 2014, Comparisons of system benefits and thermo-economics for exhaust energy recovery applied on a heavy-duty diesel engine and a light-duty vehicle gasoline engine, *Energy Convers Manage*, vol. 84, p. 97-107.
- Wang, T.H., Zhang, Y.J., Peng, Z.J., et al, 2011, A review of researches on thermal exhaust heat recovery with Rankine cycle, *Renew Sustain Energy Rev*, vol. 15, p. 2862-2871.
- Wu, W., Zhao, L., Ho, T., 2012, Experimental investigation on pinch points and maximum temperature differences in a horizontal tube-in-tube evaporator using zeotropic refrigerants, *Energy Convers Manage*, vol. 56, p. 22-31.
- Vaja, I., Gambarotta, A., 2010, Internal Combustion Engine (ICE) bottoming with Organic Rankine Cycles (ORCs), *Energy*,vol. 35, p. 1084-1093.
- Radulovic, J., Castaneda, B.I.N., 2014, On the potential of zeotropic mixtures in supercritical ORC powered by geothermal energy source, *Energy Convers Manage*, vol. 88, p. 365-371.
- Lecompte, S., Ameel, B., Ziviani, D., et al, 2014, Exergy analysis of zeotropic mixtures as working fluids in Organic Rankine Cycles, *Energy Convers Manage*, vol. 85, p. 727-739.
- Chiew, L., Clegg, M.W., Willats, R.H., et al, 2011, Waste heat energy harvesting for improving vehicle efficiency, SAE paper:2011-01-1167.

ACKNOWLEDGEMENT

This work was sponsored by the Scientific Research Key Program of Beijing Municipal Commission of Education (Grant No. KZ201410005003), National Natural Science Foundation of China (Grant No. 51376011), Beijing Natural Science Foundation Program (Grant No. 3152005).

A NEW ULTRA-LOW GWP ORC WORKING FLUID

Gregory L. Smith*, Abdennacer Achaichia[†] and Raymond H. Thomas*

*Honeywell International
20 Peabody Street, Buffalo, NY
USA
Gregory.Smith2@Honeywell.com
Raymond.Thomas@Honeywell.com

[†]Honeywell Belgium N.V.
Interleuvenlaan 15, 3001 VB, Heverlee
Belgium
Nacer.Achaichia@Honeywell.com

ABSTRACT

Organic Rankine Cycle system designs that operate with hydrofluorocarbon working fluids such as HFC-134a (1,1,1,2-tetrafluoroethane) and HFC-245fa (1,1,1,3,3-pentafluoropropane) have been operating in the field for a number of years, and HFC-245fa has emerged as a leading working fluid choice.

These systems have demonstrated environmental benefits that validate their current and future use. Even so, there is great interest among system OEMs, equipment end-users, regulatory agencies, and the public to embrace new low global warming technologies. Honeywell has developed a fluid that can serve as a replacement for HFC-245fa in foam expansion, aerosols, and organic Rankine cycle applications, which has an ultra-low global warming potential of 1. This working fluid is fluorinated olefin R-1233zd(E) (1-chloro-3,3,3-trifluoroprop-1-ene). The environmental and thermo-physical properties of this fluid are reviewed, and theoretical thermodynamic efficiency and ORC system calculations are presented for R-1233zd(E) and are compared to HFC-245fa. Thermal stability data for R-1233zd(E) is also presented, along with the results of a high-temperature material compatibility study.

REVERSE ENGINEERING OF FLUID SELECTION FOR ORCS USING CUBIC EQUATIONS OF STATE

D. Roskosch^{1*}, B. Atakan²

¹University of Duisburg-Essen, IVG, Thermodynamics,
Duisburg, Germany
dennis.roskosch@uni-due.de

² University of Duisburg-Essen, IVG, Thermodynamics
Duisburg, Germany
burak.atakan@uni-due.de

* Corresponding Author

ABSTRACT

Fluid selection for thermodynamic cycles like organic Rankine cycles remains an actual topic. Generally the search for a working fluid is based on experimental approaches or on a not very systematic trial and error approach. An alternative theory based reverse engineering approach is proposed and investigated here: The process should start with a model process, designed with respect to the boundary conditions and with (abstract) properties of the fluid needed to fit into this process, best described by some general equation of state and the corresponding fluid-describing parameters. These should be analyzed and optimized with respect to the defined model process, which also has to be optimized simultaneously. The degrees of freedom of the process are restricted to some crucial state variables with variation regimes defined with respect to the boundary conditions like the heat source, heat sink, technical restrictions etc.

Knowing the optimal fluid parameters, real fluids can be selected or even synthesized which have fluid defining properties in the optimum regime like critical temperature T_c or ideal gas capacities of heat c_p , also allowing to find new working fluids, not considered so far. The number and kind of the fluid-defining parameters is mainly based on the choice of the used equation of state (EOS). In the present work the cubic Peng-Robinson equation was chosen due to its moderate numerical expense, sufficient accuracy and a general availability of the fluid-defining parameters for many compounds.

The considered model-process is designed for a typical geothermal heat source with a temperature level of 423.15 K. The objective function is the thermal efficiency as a function of critical pressure p_c , T_c , acentric factor and c_p . Also, some crucial process variables have to be regarded as a problem variable. The results give clear hints regarding optimal fluid parameters of the analyzed process and deepen the thermodynamic understanding of the process. Finally, a strategy for screening large databases is explained. Several fluids from different substance groups were found to have high thermal efficiencies. These fluids will also have to fulfill further criteria, prior to their usage, but the method appears to be a good base for fluid selection.

1. INTRODUCTION

In the context of the expanded use of renewable energies and the increased use of low-temperature heat sources (geothermal, solar thermal, waste heat etc.) for electric power generation, ORCs find wider application. A crucial step in the development process of an ORC is the fluid selection according to different, criteria. Quoilin et al. have listed in their review [1] the most important criteria of fluid selection. Here the focus will be on thermodynamic criteria only, like a high thermal efficiency η and net power output P_{net} as well as acceptable pressures (evaporator and condenser).

Today, the basic thermodynamic approach of fluid selection starts with a model process, designed to defined boundary conditions like heat source and heat sink temperatures. Several preselected fluids, for which thermodynamic data are available, are tested with respect to a specific process parameter like thermal efficiency, exergy loss etc. and finally, the fluid which performs best is selected. For this approach, ample literature is available e.g.: [2,3]. An advanced approach is to combine the fluid selection step with the process optimization (e.g.: [4–6]); fitting the process to the respective working fluid improves the results considerably. Most of these studies are theoretical and use thermodynamic databases or EOS (equation of state) to calculate properties like enthalpy, entropy etc. Due to the ample scientific literature regarding fluid selection, a broader range of compounds were discussed as potential candidates, however, only a few are actually used in commercial ORC power plants [1]. The number of chemical compounds, which are in principle suitable as working fluids, will surely be larger. One problem of the basic approach is the high experimental or computational cost for every fluid to be tested, limiting the number of tested fluids and thus, there is the risk of neglecting potentially good fluids in the preselection step. Furthermore, the fluid rating is not objective; it is only based on the investigated fluid group or on results of other studies. An objective reference point, like the performance of an optimal fluid is missed.

An alternative for fluid selection is a reverse engineering approach with simultaneous process optimization, proposed and investigated here for ORCs. Very recently, we have applied this approach to heat pump cycles [7]; the main procedure has already been described in detail there, thus, here only a brief overview of the method is given. The main idea is to find the optimal properties a fluid should have for the considered process with the defined boundary conditions. Therefore, fluid-descriptive parameters are regarded as continuous variables which are simultaneously optimized with chosen process parameters and with respect to an objective function like thermal efficiency or net power output. Every variable is restricted to physically reasonable values; furthermore, the optimization of process and fluid parameters is constrained by boundary conditions like temperature levels of heat source and heat sink, temperature differences at the pinch point, pressure limits, steam quality at the turbine outlet etc. The type of fluid-descriptive parameters depends on the chosen EOS (equation of state). It can either be defined on the macroscopic scale like critical point values combined with capacities of heat, as used e.g. in cubic EOS or based on a molecular description, as used by the PC-SAFT EOS [8]. After optimizing both, these abstract parameters and the process, the found optimal parameter combination, generally will not fit to real fluids. Thus, the approach continues with the search of real fluids with parameters near to the optimal values. One of the advantages is that also fluids would be considered which would not be investigated in the standard approach.

Comparable approaches for pure fluid selection for ORCs with various heat source temperatures, using some kind of reverse-engineering approach, are found in: [9–11]. Furthermore, a reverse-engineering approach was also used to find optimal fluid mixtures for ORCs [12,13]. All of these investigations are based on a Computer-Aided Molecular Design (CAMD) method; thus, the molecular structure is the optimized parameter. The calculation of the fluid properties is usually done via a group contribution method. A common intermediate step in all is the calculation of critical properties and of heat capacities. In the present work, those fluid parameters are directly optimized. The fluid property model is based on the less complex cubic Peng-Robinson EOS [14], also because the needed fluid parameters (see section 2.1) are known for many fluids. Often it was assumed that the cubic EOS are not accurate enough to describe the performance of fluids as working fluids. Analysis of our own and of others [15,16] for several refrigerants using a typical refrigeration cycle have shown that a fluid property model based on the Peng-Robinson EOS combined with the heat capacity of the ideal gas is accurate enough for the first step of fluid selection (see section 2.1). The reverse engineering approach for ORC-processes shall be investigated in the present paper for a simple ORC with a geothermal heat source at 423.15 K. The fluid and process optimizations are carried out regarding the thermal efficiency.

2. METHODS

The optimization is based on a simple Rankine cycle (see Figure 1) as found in any standard thermodynamic textbook (e.g.: [17]). It consists of a pump, an evaporator, a turbine and a condenser.

The process works between two fluid and temperature dependent pressure levels, with the high pressure in the evaporator and the low in the condenser. The condensation temperature is chosen to be 303.15 K and a mass flow of $\dot{m}_{gw} = 100 \text{ kg/s}$ of geothermal water with a constant heat capacity of $75 \text{ J}/(\text{mol}\cdot\text{K})$ enters the evaporator at 423.15 K. According to a scenario that can be used for combined heat and power generation, the outlet temperature is 403.15 K, constantly. Condenser and evaporator are isobaric and the isentropic efficiencies of pump and turbine are chosen to be $\eta_p^s = 0.6$ and $\eta_t^s = 0.8$.

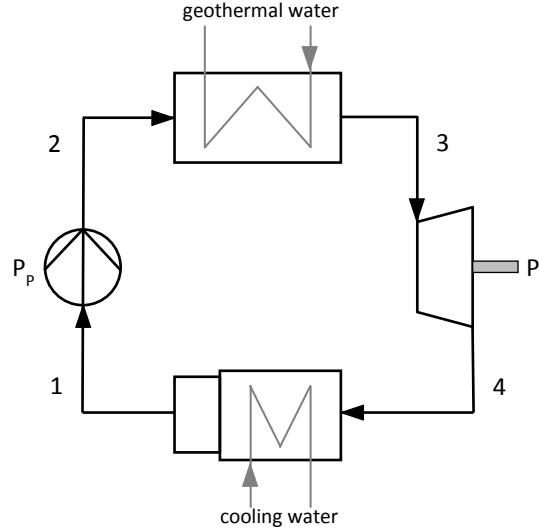


Figure 1: Working principle of the model process

The working fluid leaves the condenser at the condensation temperature and the fluid-dependent pressure as saturated liquid ($x_1 = 0$). From state 1 to 2 the fluid is pumped to the evaporator pressure which depends on the evaporation temperature, which is also a problem variable, constrained by the temperature profile of the geothermal water and a minimum pinch-temperature of 10 K. After heat is supplied (st2 – st3), the fluid is expanded in the turbine and finally, condensed from st4 to st1. Based on the inlet states of pump and turbine (st1, st3), the isentropic efficiencies and by means of the isentropic outlet states (st2^s, st4^s) the real outlet states can be calculated. The procedure as well as the respective equations can be found in any thermodynamic textbook (e.g.: [17]). Finally, the enthalpies at the outlet states apply to:

$$h_2 = \frac{h_2^s - h_1}{\eta_p^s} + h_1 \quad (1)$$

$$h_4 = h_3 + \eta_t^s(h_4^s - h_3) \quad (2)$$

State 3 can be saturated or superheated steam; it is defined by the temperature in state 3 which is also a degree of freedom for process optimization. It is constrained by the evaporation temperature and the geothermal water inlet temperature, taking into account the minimum pinch-temperature. The lower limit of the steam quality at state 4 is restricted to 0.9. From the energy balances for the various components the net power output and the input heat flow are calculated by:

$$|P_{net}| = |P_t| - P_p = \dot{n}_f[(h_3 - h_4) - (h_2 - h_1)] \quad (3)$$

$$\dot{Q}_{in} = \dot{n}_f(h_3 - h_2) \quad (4)$$

The molar flow rate of the working fluid is calculated from the energy balance of the geothermal water and equation (4):

$$\dot{n}_f = \frac{\dot{n}_{gw} \cdot c_{p,gw}(T_{gw,in} - T_{gw,out})}{h_3 - h_2} \quad (5)$$

Equations (3) and (4) lead to the well known expression of the thermal efficiency η :

$$\eta = \frac{|P_{net}|}{\dot{Q}_{in}} \quad (6)$$

By means of the energy balance $|P_{net}| = \dot{Q}_{in} - \dot{Q}_{out}$, the Gibbs equation $Tds = dh - vdp$ and the thermodynamic mean temperatures it can also be written as:

$$\eta = 1 - \frac{T_{m,low}(s_4 - s_1)}{T_{m,high}(s_3 - s_2)} \quad (7)$$

2.1. The fluid property model

The calculations of the objective function η requires the determination of the different thermodynamic properties temperature T , pressure p , specific volume v , enthalpy h , entropy s and the steam quality x for the different states.

The property model used here is based on the Peng-Robinson EOS and the T dependent ideal gas heat capacity. Within the simulations only a linear temperature dependence of the heat capacity was used, since it turned out that this is accurate enough for the small considered temperature ranges (T_3 - T_4). In order to find real fluids based on the optimal values the heat capacity were taken at 350 K together with the linear gradient at this temperature. Overall, the fluid descriptive parameters within the optimizations are T_c , p_c , ω , together with A and B for the temperature dependent ideal gas heat capacity $c_p(T) = A + B \cdot T$. All equations used in our property model can be found in Sandler's book [17]. The vapor liquid equilibrium calculation is done by means of the Ambrose-Walton method [18]; it is an empirical method and also based on T_c , p_c and ω . The Peng-Robinson EOS based property model is a good basis for fluid optimizing and screening, since it is easily and quickly solved, numerically and is sufficiently accurate, as shown earlier [7] the accuracy of our model appears to be reasonably good to be used in fluid screening purposes.

Table 1: Variable range for optimization, process parameters and constraints

parameter	value / range
critical temperature	$430 \leq T_c \leq 700$ K
acentric factor	$0.05 \leq \omega \leq 0.8$
heat capacity (ideal gas) at 350 K	$35 \leq c_p \leq 150$ J/(mol·K)
slope of heat capacity at 350 K	$0.01 \leq B \leq 0.6$ J/(mol·K ²)
evaporation temperature	T_{evap}^a
temperature in state 3	T_3^a
critical pressure	$3.0 \leq p_c \leq 12.0$ MPa
system pressure limits	$0.01 \leq p_{sys} \leq 2$ MPa
minimum steam quality in St 4	$x_{4,min} = 0.9$

^a Depending on the actual fluid parameter and a minimum pinch of 10 K

2.2. The optimization routine

The computer programs for optimizing and calculating the fluid properties are written in the programming language Python [19]. The optimization routine was the NLP-algorithm (Non-Linear-Problem) combined with the solver "ralg" taken from the OpenOpt package [20] which can handle both non-linear and non-smooth functions; furthermore, every optimizing parameter can be box-bounded and the optimization might be generally constrained.

2.3. Boundary conditions

It turned out, that the critical pressure has only an indirect impact on the thermal efficiency; the critical pressure influences the suitability range of the critical temperature with respect to the system pressure limits, and thus, it has a mediate impact on the thermal efficiency. As a result, p_c cannot be optimized with the chosen solver, and the optimizations are repeated for 10 values of p_c between 3.0

and 12.0 MPa with 1.0 MPa steps. Thus, the optimization parameters are T_c , ω , the evaporation temperature, the temperature at state 3 and the coefficients A and B of the linear temperature dependent function of the ideal gas heat capacity. Only subcritical processes are considered, therefore, the difference between T_c and the evaporation temperature must always be larger than 20 K. Besides this restriction, the evaporation temperature and the temperature in state 3 are limited by the temperature profile of the geothermal water and a minimum pinch of 10 K. Furthermore, T_3 has to be larger than T_{evap} . The parameter ranges of the ideal gas heat capacity at 350 K as well as the gradient were chosen so that values of most real fluids are within the limits. Here, the variable A is calculated from the slope of the linear equation and the value of c_p at 350 K. Table 1 gives an overview of the defined parameter limits and also over the remaining process variables, now.

As in the literature [9], the system pressures (p_{evap} , p_{cond}) are constrained between 0.01 and 2.0 MPa; they depend on the corresponding temperature levels, on the critical point and the acentric factor. Furthermore, for protection of the turbine the minimum steam quality ($x = m_v/m_{\text{total}}$) at the turbine outlet has to be larger than 0.9.

3. RESULTS AND DISCUSSION

Fluid and simultaneous process optimizations with the discussed parameters and constraints were carried out with the thermal efficiency η as objective function.

Table 2 shows the results of the η optimizations with respect to each critical pressure. It gets clear, that the optimal values of the thermal efficiency are always larger than 0.17 and increase with the critical pressure, marginally. The same is true for the associated critical temperatures, which increase from 602.75 K to 646.07 K. The optimal values of T_c correspond in combination with the optimal acentric factors to the respective maximum of T_c , which fulfills the pressure limits. However, investigations showed that p_c has no direct impact on η ; in fact, it influences only the suitability limit of the critical temperature with respect to the lower pressure limit. Higher critical pressures allow higher values of T_c , which lead to higher thermal efficiencies. The optimal acentric factor also increases with the critical pressure from 0.07 to 0.13; the values are near the lower boundary of ω ($\omega_{\text{min}} = 0.05$). This investigation showed that the direct impact of ω on the thermal efficiency is marginal; however, ω influences the suitability range of T_c with respect to the pressure limits. Lower values of the acentric factor lead to a shift of the T_c suitability limit to higher critical temperatures, which results in increased thermal efficiencies. Regarding the optimizations, a further reduction of ω is in conflict with the pinch condition at the starting point of evaporation; thus, smaller values of ω

Table 2: Results from η optimization

p_c [MPa]	T_c [K]	ω []	A [J/(mol·K)]	B [J/(mol·K ²)]	$c_p(350\text{K})$ [J/(mol·K)]	T_{evap} [K]	T_3 [K]	x_4 []	η []
3.0	602.75	0.07	0.01	0.10	35.01	396.62	413.15	0.92	0.175
4.0	607.75	0.09	0.00	0.10	35.00	396.57	413.15	0.92	0.175
5.0	619.91	0.09	0.00	0.10	35.00	396.47	413.15	0.92	0.176
6.0	625.36	0.10	0.03	0.10	35.03	396.43	413.15	0.92	0.176
7.0	626.54	0.12	0.01	0.10	35.01	396.42	413.15	0.91	0.176
8.0	638.33	0.10	0.00	0.10	35.00	396.33	413.15	0.91	0.176
9.0	647.55	0.09	0.04	0.10	35.04	396.27	413.15	0.91	0.176
10.0	645.16	0.11	0.00	0.10	35.00	396.28	413.15	0.91	0.177
11.0	647.56	0.12	0.02	0.10	35.02	396.26	413.15	0.91	0.177
12.0	646.07	0.13	0.00	0.10	35.00	396.27	413.15	0.91	0.177

lead to the need of decreasing the evaporation temperature, which results in a significant decrease of η , again. Therefore, the optimal acentric factors are slightly shifted to higher values. Regarding the molar heat capacity at the reference temperature ($T = 350$ K), the optimal value of $c_p(350\text{K}) = 35$ J/(mol·K) is independent of p_c , which correspond to the lower boundary of the $c_p(350\text{K})$ -domain. This

is also true for the parameter A which is always at the lower boundary. The optimal value of the parameter B (c_p gradient) is constantly 0.1, corresponding to the lowest value fulfilling the $c_p(350\text{K})$ restriction with respect to $A = 0$. The optimizations lead to evaporation temperatures slightly higher than 396 K; which is the respective maximum with regards to the minimum pinch point-temperature difference at the inception of evaporation. The temperature in state 3 is 413.15 K which is the maximum temperature which fulfills the pinch point requirement. All steam qualities at the turbine outlet (state 4) are larger than 0.91 and thus, above the boundary ($x_{4,\min} = 0.9$). The results of former fluid optimizations by Lampe et al. [9], Palma Flores et al. [11] and Papadopoulos et al. [10] show a different picture with respect to the optimal fluid properties. Although similar temperature domains were regarded here, fluids with lower critical temperatures and higher heat capacities reach the highest thermal efficiencies. As main difference to our scenario the authors did not specify the outlet temperature of the heat carrier; their objective was generating the highest possible net power output with respect to a defined heat carrier mass flow with fixed inlet temperature. Regarding such a scenario, our approach also leads to fluids with lower values of T_c and higher heat capacities. Thus, the exact design of the process influences the optimal fluid, essentially and a fluid recommendation based only on the heat source temperature seems to be not reasonable.

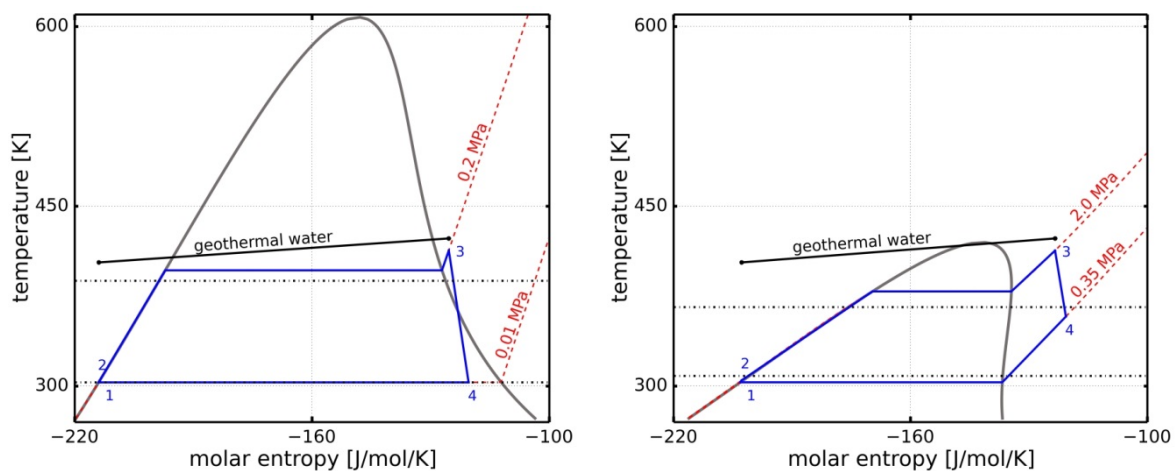


Figure 2: T-s plots of the η optimized fluid for $p_c = 4.0$ MPa (left) and of butene (right)

Butene is one of the recommended fluids for a heat source temperature between 420 and 445 K [21] and has a critical pressure of 4.04 MPa and thus, it is interesting to compare it with the optimal fluid at 4 MPa. Further fluid properties of butene can be found in Table 3. Figure 2 shows the Ts-diagram of the η optimized fluid for $p_c = 4.0$ MPa (left) and for the optimized process using butene as working fluid (right). Isobars (dashed lines), lines for the resultant thermodynamic mean temperatures (dash-dotted lines) and the temperature regime of the geothermal water are included. With respect to the discussed boundary conditions and based on the optimized process with butene a thermal efficiency of $\eta = 0.1245$ is reached, while the optimal fluid has a thermal efficiency of $\eta = 0.175$. First of all, a direct comparison of the two fluids shows a significantly elongated saturation regime for the optimal fluid, which results mainly from the higher critical temperature. The lower value of T_c (for butene) leads also to increased vapor pressures (η -opt: $p_{\text{cond}} = 0.01$ MPa, butene: $p_{\text{cond}} = 0.35$ MPa) and a significantly increased pressure difference (η -opt: $\Delta p_{12} = 0.19$ MPa, butene: $\Delta p = 1.65$ MPa), although the temperature difference ($T_{\text{evap}} - T_{\text{cond}}$) is smaller. Furthermore, smaller evaporation entropies at constant temperature levels are constituted by lower values of T_c . The flatter slope of the saturated liquid line and the partially negative gradient of the saturated steam line for butene result mainly from the higher value of the heat capacity (η -opt: $c_p(350\text{K}) = 35$ J/(mol·K), butene: $c_p(350\text{K}) = 103.86$ J/(mol·K)). The small slope of the isobaric line at evaporation pressure in the domain of the subcooled liquid, the smaller evaporation entropy and the decreased evaporation temperature lead to a significantly reduced thermodynamic mean temperature at the higher pressure level. Based on the superheating in st3 and the regime of the saturated steam line, butene leaves the turbine as superheated steam resulting in a higher value of the thermodynamic mean temperature at

condensation pressure. The spreading of either thermodynamic mean temperature is directly related to the thermal efficiency of the process (eq. (7)); therefore, a higher spreading results in larger values of η , in general. Due to it, the smaller spreading for butene, compared to the optimal fluid, leads to a strongly reduced thermal efficiency.

Finally, the optimizations of the thermal efficiency lead to fluids with small values of $c_p(350\text{K})$, highest possible critical temperatures and small acentric factors. Such fluids are wet fluids with an elongated saturation regime, typically.

3.1. (Real) fluid selection

After having found optimal fluid parameters, real fluids with similar parameters must be found or could even be synthesized. A detailed description of the fluid selection process was discussed for heat pumps and is found in [7]. Here, we give only a brief description of the selection process. A small fluid database with 284 records taken from different sources [22–24] was used here. It contains values of T_c , p_c , ω and 4 or 5 coefficients for an equation for the isobaric ideal gas heat capacity for every record. In order to compare with optimization results, the value of $c_p(350)$ as well as the gradient at this temperature were calculated. The fluid selection process is ordered in three steps and can also be efficiently applied to large databases:

Step I – Preselection with respect to the pressure limits

Using the Ambrose-Walton equation [18], vapor pressures at given temperatures can be calculated, analytically. The aim of step I is the exclusion of fluids, which do not fulfill the pressure restrictions at the given temperature levels. While, the condensation temperature is clearly defined as 303.15 K and the vapor pressure can directly be calculated; the evaporation temperature is a problem variable and is not defined, explicitly. However, it is assumed that fluids not fulfilling the higher pressure limit at the poor condensation temperature of 340 K will not reach good thermal efficiencies and are omitted. Additionally, it was found that fluids with good thermal efficiencies have vapor pressures significantly below the limit. In the present work with the used database, the above-mentioned temperature levels and the boundary conditions ($0.01 \leq p_{\text{sys}} \leq 2 \text{ MPa}$), from this step the number of potential fluids was reduced from 284 to 106.

Step II – Fit of a function for η estimation

From the presented optimizations it was found that small values of $c_p(350\text{K})$ and ω as well as critical temperatures between 600 and 650 K (depending on p_c) lead to high values of η . Further investigations pointed out that T_c and $c_p(350\text{K})$ are the critical and most sensitive variables for the thermal efficiency. The critical pressure has no direct impact and the effect of ω is marginal and can be neglected. Basically, with respect to this knowledge, fluids with properties near the optimum can be chosen for further investigation. However, finding a fluid with properties very close to the optimum is not probable, thus, fluid selection represents usually a compromise. Because of the unknown sensitivity of η with respect to the individual parameters, the fluid selection along this path is always in danger of missing attractive combinations of the parameters. Thus, by means of the optimization algorithm a function for η estimation as a function of T_c , $c_p(350\text{K})$ and the optimized process parameters (T_{evap} , T_3) was fitted to 100 combinations of T_c and $c_p(350\text{K})$. Ten critical temperatures between 360 and 600 K as well as 10 values of $c_p(350\text{K})$ between 35 and 150 J/(mol·K) were selected. The critical pressure was fixed at 4.0 MPa and the acentric factor was set to 0.10, which is the mean value resulting from the optimizations. Here, pressure restrictions were not considered, since in step I all fluids not fulfilling the restrictions were excluded. Four polynomials, each of degree 3, with overall 12 coefficients were fitted to the optimization results. A comparison between the values of η estimated by the polynomials and calculated by our fluid property model results in an absolute mean percentage error of 7.6 %, from the 106 fluids remaining from step I. However, the largest errors are found for fluids with poor η ; comparing only fluids with $\eta > 0.16$ (35 records) the absolute mean percentage error is decreased to 1.96 %. Finally, by means of the fit also large databases can be screened efficiently for good fluids.

The 2nd step requires the greatest computational effort of the 3 matching steps. The 100 optimizations for the fit can be done by a common computer (CPU: i5-3750, RAM: 8 GB) in about 30 minutes.

Step III - Final fluid selection for further investigation

With the results of step II, fluids with probably high thermal efficiencies can be chosen for further investigations, regarding other fluid criteria. Besides the estimation by the polynomials, the process optimization should be repeated once again for this limited number of fluids, to obtain the correct values. In step II 35 fluids with $\eta > 0.16$ were found; Table 3 shows 10 of them, exemplarily. Furthermore, the 5 fluids recommended by Wang et al. [21] for heat source temperatures between 420 and 445 K are also listed (No. 11 – 15). Those fluids all have thermal efficiencies smaller than 0.1245 and are with respect to the process regarded in this work much less efficient than the fluids resulting from our selection. Using our approach for a similar process as regarded in this work, but without fixing the heat source outlet temperature (regarding only power generation) leads also to the fluids 11-15 as top ranked. It follows, that besides the heat source temperature, further process parameters influence the choice of optimal fluids. Among the top-ranked fluids are conventional refrigerants like R150, R20 or R30 as well as fluids like bromine or acetonitrile, which are extremely toxic and/or corrosive compounds. However, this investigation is only meant as an example and perhaps some of the fluids like methanol, ethanol or acetone appear to be worth further investigations regarding other suitability criteria.

Table 3: Top-ranked fluids resulting from the fluid selection (No. 1-10), as well as fluids recommended by [21]

No.	Fluid	η []	T_c [K]	p_c [MPa]	ω []	$c_p(350K)$ [J/(mol·K)]
1	Bromine	0.1737	584.1	10.30	0.129	36.47
2	Acetonitrile	0.1711	545.5	4.83	0.334	59.46
3	Methanol	0.1700	512.5	8.08	0.565	50.35
4	1,2-Dichloroethane (R150)	0.1693	566.0	5.36	0.250	88.77
5	Chloroform (R20)	0.1685	536.5	5.55	0.229	71.49
6	Ethanol	0.1685	514.0	6.15	0.645	77.86
7	Dichloromethane (R30)	0.1676	510.1	6.08	0.198	57.49
8	Benzene	0.1673	562.0	4.90	0.210	106.00
9	Fluorobenzene	0.1655	560.0	4.55	0.248	118.38
10	Acetone	0.1654	508.3	4.70	0.306	88.62
11	Butene	0.1245	419.9	4.04	0.189	103.86
12	Isobutene	0.1237	417.9	4.00	0.199	100.44
13	1,1,1,2,3,3-Hexafluoropropane (R236ea)	0.1218	412.4	3.50	0.379	140.81
14	1-Chloro-1,1-difluoroethane (R142b)	0.1145	409.6	4.33	0.251	94.73
15	Isobutane (R600a)	0.1122	407.8	3.64	0.184	118.52

4. CONCLUSIONS

In this work the reverse engineering approach for fluid selection, recently introduced for heat pump cycles, is now applied to ORCs. It appears to be a more promising approach to first start thinking about an optimal process with optimal fluid parameters, instead of screening well investigated fluids. Furthermore, based on the reverse engineering approach, fluids that were not well investigated so far, can be found, and also more is learned about the fluid properties which are important for the cycle. This also leads to an objective value which represents the performance of a hypothetical best fluid. The presented approach consists of the simultaneous numerical optimization of fluid-descriptive parameters and some process parameters, the latter could easily be extended. Here, the fluid property model is the cubic Peng-Robinson equation of state and a linear equation for the temperature dependent isobaric ideal gas heat capacity. Thus, the needed fluid-descriptive parameters are the

critical temperature, the critical pressure, the acentric factor and two coefficients for the heat capacity. These values are not too numerous and available for many compounds and could in future also be extended to apply group additivity methods to search for further fluids or for calculations of other fluid properties like thermal conductivity and viscosity, without increasing the number of parameters to be optimized.

First of all, it was shown, that the reverse engineering approach also can be applied to ORCs, efficiently. It was pointed out, that the results of the optimization are thermodynamically reasonable and lead to a deeper understanding of the interrelation of fluid and process parameters. Based on the optimized fluid parameters a procedure was presented to find real fluids near the optimum. Therefore, an equation for the prediction of η based on the most important variables was fitted.

Several fluids with higher values of η than the usually recommended ones for the here defined heat source temperature were found. Some of them, like bromine or acetonitrile will probably never be used as working fluids, but other like acetone or methanol may be worth further investigation. Comparing the optimal fluid parameters found in this work to the results of fluid optimizations by other authors allow the conclusion, that, besides the heat source temperature, also other criteria and parameters influence the optimal fluid choice, clearly. Further investigations regarding the influence of the process design or boundaries on the optimal fluid parameters are needed for a deeper insight.

NOMENCLATURE

A	coefficient of the molar isobaric heat capacity (intercept)	(J/mol/K)
B	coefficient of the molar isobaric heat capacity (gradient)	(J/mol/K ²)
c_p	molar isobaric heat capacity	(J/mol/K)
h	molar enthalpy	(J/mol)
\dot{m}	mass flow rate	(kg/s)
\dot{n}	molar flow rate	(mol/s)
P	power	(MW)
P	pressure	(MPa)
\dot{Q}	heat flow	(MW)
s	molar entropy	(J/mol/K)
st	state	(-)
T	temperature	(K)
\dot{V}	volume flow rate	(m ³ /s)
v	molar volume	(m ³ /mol)
w	molar work	(MJ/mol)
x	steam quality	(-)
η	thermal efficiency	(-)
ω	acentric factor	(-)

Subscripts

c	critical
cond	condensation
evap	evaporation
gw	geothermal water
f	working fluid
p	pump
s	isentropic
sys	system
t	turbine

REFERENCES

- [1] Quoilin S, Broek, Martijn Van Den, Declaye S, Dewallef P, Lemort V; 2013; Techno-economic survey of Organic Rankine Cycle (ORC) systems; *Renewable and Sustainable Energy Reviews*:168–86.
- [2] SALEH B, KOGLBAUER G, WENDLAND M, FISCHER J; 2007; Working fluids for low-temperature organic Rankine cycles; *Energy*(7):1210–21.
- [3] Siddiqi MA, Atakan B; 2012; Alkanes as fluids in Rankine cycles in comparison to water, benzene and toluene; *Energy*(1):256–63.
- [4] Tchanche BF, Papadakis G, Lambrinos G, Frangoudakis A; 2009; Fluid selection for a low-temperature solar organic Rankine cycle; *Applied Thermal Engineering*(11-12):2468–76.
- [5] Long R, Bao YJ, Huang XM, Liu W; 2014; Exergy analysis and working fluid selection of organic Rankine cycle for low grade waste heat recovery; *Energy*:475–83.
- [6] Heberle F, Brüggemann D; 2010; Exergy based fluid selection for a geothermal Organic Rankine Cycle for combined heat and power generation; *Applied Thermal Engineering*(11-12):1326–32.
- [7] Roskosch D, Atakan B; 2015; Reverse engineering of fluid selection for thermodynamic cycles with cubic equations of state, using a compression heat pump as example; *Energy*(81):202–12.
- [8] Gross J, Sadowski G; 2001; Perturbed-Chain SAFT: An Equation of State Based on a Perturbation Theory for Chain Molecules; *Ind. Eng. Chem. Res.*(4):1244–60.
- [9] Lampe M, Stavrou M, Bücker HM, Gross J, Bardow A; 2014; Simultaneous Optimization of Working Fluid and Process for Organic Rankine Cycles (ORCs) using PC-SAFT; *Ind. Eng. Chem. Res.*(53(21)):8821–30.
- [10] Papadopoulos AI, Stijepovic M, Linke P; 2010; On the systematic design and selection of optimal working fluids for Organic Rankine Cycles; *Applied Thermal Engineering*(6-7):760–9.
- [11] Palma-Flores O, Flores-Tlacuahuac A, Canseco-Melchor G; 2015; Optimal molecular design of working fluids for sustainable low-temperature energy recovery; *Computers & Chemical Engineering*:334–49.
- [12] Papadopoulos AI, Stijepovic M, Linke P, Seferlis P, Voutetakis S; 2013; Toward Optimum Working Fluid Mixtures for Organic Rankine Cycles using Molecular Design and Sensitivity Analysis; *Ind. Eng. Chem. Res.*(34):12116–33.
- [13] Molina-Thierry DP, Flores-Tlacuahuac A; 2015; Simultaneous Optimal Design of Organic Mixtures and Rankine Cycles for Low-Temperature Energy Recovery; *Ind. Eng. Chem. Res.*(13):3367–83.
- [14] Peng DY, Robinson DP; 1976; A New Two-Constant Equation of State; *Ind. Eng. Chem. Fundam.*(15(1)).
- [15] Brown JS; 2007; Predicting performance of refrigerants using the Peng-Robinson Equation of State; *International Journal of Refrigeration-Revue Internationale du Froid*(8):1319–28.
- [16] Brown JS, Brignoli R, Daubman S; 2014; Methodology for estimating thermodynamic parameters and performance of working fluids for organic Rankine cycles; *Energy*:818–28.
- [17] Sandler SI; 2006; *Chemical, biochemical, and engineering thermodynamics*. Hoboken, N.J (USA): John Wiley; xiv, 945.
- [18] Ambrose D, Walton J; 1989; Vapour pressures up to their critical temperatures of normal alkanes and 1-alkanols; *Pure and Applied Chemistry*(8).
- [19] Python.org; Available from: www.python.org/. [19/05/2015].
- [20] OpenOpt; Available from: www.openopt.org/. [19/05/2015].
- [21] Wang D, Ling X, Peng H, Liu L, Tao L; 2013; Efficiency and optimal performance evaluation of organic Rankine cycle for low grade waste heat power generation; *Energy*:343–52.
- [22] Poling BE, Prausnitz JM, O'Connell JP; 2001; *The properties of gases and liquids*. New York (USA): McGraw-Hill; 1 v. (various).
- [23] 2006; *VDI-Wärmeatlas*. Berlin (GER), Heidelberg (GER), New York (USA): Springer; 1432 S. in getr. Zählung.
- [24] Lemmon, E.W., Huber, M.L., McLinden, M.O; 2023; *NIST Standard Reference Database 23: Reference Fluid Thermodynamic and Transport Properties-REFPROP*. Gaithersburg: National Institute of Standards and Technology.

STUDY OF RECIPROCATING PUMP FOR SUPERCRITICAL ORC AT FULL AND PART LOAD OPERATION

Arnaud Landelle^{1,2,3,4*}, Nicolas Tauveron^{1,2}, Philippe Haberschill³, Rémi Revellin³, Stephane Colasson^{1,2}

¹ Université Grenoble Alpes, F-38000 Grenoble, France

² CEA, LITEN, LS2T, F-38000 Grenoble, France

³ Université de Lyon, CNRS, INSA-Lyon, CETHIL, UMR5008, Villeurbanne F-69621, France

⁴ ADEME, 20 Av. du Grésillé, BP90406, 49004 Angers Cedex 01, France

* arnaud.landelle@cea.fr

ABSTRACT

Recovery of waste heat in industrial processes is an important component of energy savings worldwide. At low temperature levels, thermodynamics prevents any high efficiency in the heat-to-electricity conversion; such dedicated systems have to be optimized and should achieve a maximum heat recovery, at partial and full load. These technical and technological problematic are also common with renewable natural resources use (solar, geothermal, biomass). Supercritical organic Rankine cycle is quite well investigated in the scientific community, but rarely experimentally studied, especially off-design and dynamic behaviors of such systems. The CEA/LITEN is developing a 10kWe prototypes of supercritical ORC to investigate experimental potential of such technology for low grade power generation. The first task is to characterize various components behavior in supercritical regimes. In such cycles, the pump plays a strategic role, as for supercritical operations the back work ratio is a key parameter to consider. Performance data of a reciprocating pump drive by an induction motor with variable speed drive are measured. Maximum pump efficiency achieve is 82% and maximum global efficiency (pump & drive) achieve is 41%. Losses are evaluated and a power model is proposed and compared with experimental data. Results of this work aim to give a better knowledge for ORC pump design and optimization.

1. INTRODUCTION

Organic Rankine Cycles (ORC) are known since the 19th century, but in recent decades research and commercial development increased exponentially (Quoilin *et al.*, 2013). Most research focused on nominal steady-state optimization, screening working fluid and operating conditions. Optimization criteria vary from study to study (energetic efficiency, exergetic analysis, power, or cost). Several study shows supercritical ORC have a high potential (Schuter *et al.*, 2010; Shu *et al.* 2013) especially in the low temperature range (~150°C) (Astolfi *et al.*, 2014; Toffolo *et al.*, 2014) but supercritical conditions mean high pressure and more constrains on components. For components optimization, most research focuses on the expander that is the critical components (Bao and Zhao, 2013), heat exchangers and evaporators especially are also investigated, but few researchers discuss of the pump. However, Quoilin *et al.* (2013) describes the pump as a key component that should be carefully chosen according to its controllability, tightness, Net Positive Suction Head (NPSH) and efficiency. Pump efficiency becomes a crucial parameter for low temperature and supercritical cycles. Back Work Ratio defines as the ratio between pump electrical consumption and expander outlet power is introduced to evaluate pump impact. In supercritical ORC, Maraver *et al.* (2014) shows that pump efficiency have a major impact on cycle exergetic efficiency. Using R-134a, cycle exergetic efficiency decrease from 46

to 40% if the pump efficiency decrease from 75 to 50 %. From authors' point of view, it is therefore essential to investigate the pumping system for on and off design ORC operation. The author listed only two pump efficiency correlation used for ORC models. A correlation is proposed by Lippke (1995) for centrifugal pump, losses related to the driver are also discussed. Quoilin *et al.* (2011) uses an empirical correlation proposed by Vetter (2006) for rotary positive displacement pump and add a constant electromechanical efficiency for driver losses. While most of feed pumps used in experimental ORC are reciprocating positive displacement pumps. Furthermore, as Miao *et al.* (2015) emphasized, confusions and simplifications are made about pump power consumption and efficiency. Results of this study aim to propose an experimental approach for pump characterization, a behavioural off-design reciprocating pump model for losses and efficiency that can be used for ORC system model, and provide knowledge assets for pump selection and optimal use.

2. EXPERIMENTAL SETUP

An experimental investigation is carried out on a diaphragm pump integrated into an experimental bench using R-134a as fluid. The test bench described in Figure 1 is use for subcritical and supercritical heat transfer investigation. This paper only focuses on the pumping system.

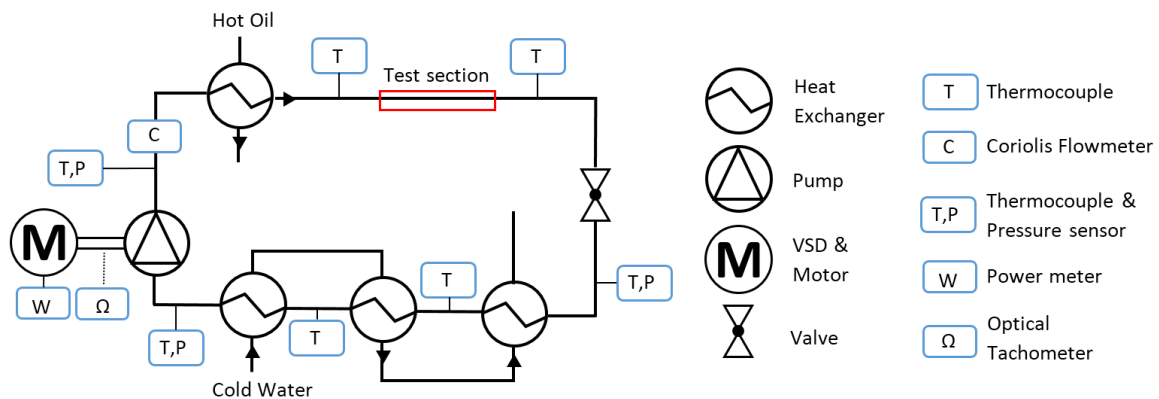


Figure 1: Scheme of the test bench

2.1 Test Bench

The pumping system is composed by a diaphragm pump (Wanner Hydra-Cell, model G03X), using a triplex single-acting reciprocating positive displacement technology. This technology is often used in small supercritical ORC because of its tightness and high efficiency at high pressure, low flow rate. And, a three-phase induction motor (Leroy-Sommer, model LS90L 1,8kW) integrating a Variable Speed Drive (VSD) (Leroy-Sommer, model Varmeca 32). The frequency can vary from 10 to 50 Hz, corresponding to a shaft rotational speed from 300 to 1500 revolutions per minute (rpm). At nominal speed (1500 rpm), the volume flow is around 0,58 m³/h and the maximum outlet pressure is 70 bar. The pump is located at the bottom of the bench after all condensers to increase the NPSH. The fluid is evaporate and expanded through a valve that control the pressure differential at the pump ends. The electrical consumption is measured by a power quality clamp meter. The mass flow rate is measured by a Coriolis flowmeter. The shaft rotational speed is measured by an optical tachometer. Measurement accuracy are shown in Table 1.

2.2 Test Description

In order to characterize the pump, different kinds of tests are done. Since there is no torque meter between the motor and the pump, uncoupled motor tests are done to characterize the motor and VSD. Experimental data cover the full speed range, with 52 points. Unloaded pump test are done to estimate the unloaded volume flow (\dot{V}_0), valves are open to reduce the pressure differential at the pump ends (ΔP), 48 points cover the full speed range. For pump on load, total of 87 experimental points are achieved, covering a ΔP range from 0 to 35 bar at five different speed shaft (350 to 650 rpm). For each point, measurement are averaged during 1-2 minutes, to smooth variations. NPSH is kept as high as possible to reduce its impact on the volumetric efficiency (Miller, 1988).

Table 1 : Measuring range and accuracy

Variable	Range	Uncertainty
Supply pressure	0-17 bar	± 0,3 bar
Exhaust pressure	0-50 bar	± 0,1 bar
Temperature	0-120 °C	± 0,5 °C
Shaft rotational speed	0-1500 rpm	± 1 rpm
Electrical power	0-700W	± 20 W
Mass flow rate	0-0,1 kg/s	± 5.10 ⁻⁴ kg/s

3. DATA REDUCTION

3.1 System Energetic Model

An energetic model of the pumping system is proposed in Figure 2 to identify losses. \dot{W}_{el} is the measured electrical consumption, \dot{W}_{mech} is the mechanical shaft power, \dot{Q}_{los} are powers dissipated by different components in the ambient environment. Fluid pumping is assumed to be fast enough to consider no heat transfer between the pump and the fluid. $\dot{W}_{flu,pp}$ the power transferred by the pump to the fluid is made of $\dot{W}_{hyd} = \int v \cdot dP$ the hydraulic power (ie. useful) and internal frictions which are represented by a fictive heat power $\dot{Q}_{los,flu}$. Different efficiencies are defined from these power: the global efficiency of the pumping system $\eta_{global} = \dot{W}_{hyd} / \dot{W}_{el}$, the pump efficiency $\eta_{pump} = \dot{W}_{hyd} / \dot{W}_{mech}$ and the isentropic efficiency of the pump $\eta_{is} = \dot{W}_{hyd} / \dot{W}_{flu,pp}$.

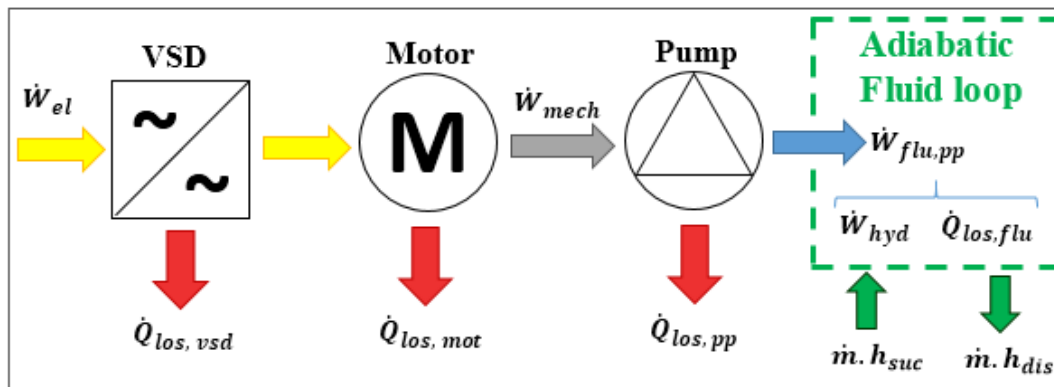


Figure 2: Energetic conceptual scheme of the pumping system

3.2 Motor and VSD Losses

Motor and VSD dissipated power should be estimated to get the mechanical power. Assumptions are made based on the literature review. De Almeida *et al.* (2014) and IEC 60034-31 explained that losses in VSD is a sum of constant loss and loss proportional to the output power. Kari (2009) performed tests and showed that in modern VSDs, losses increase with speed and torque. At low torque, losses are nearly constant and independent of the rotational speed. In tests performed for this study, motor and VSD operate under 50 % of the nominal torque. It is assumed that VSD losses ($\dot{Q}_{los,vsd}$) are constant, as did Deprez *et al.* (2010) for its VSD and motor losses approximation.

Induction motors have been more widely studied and normalized, even under variable speed and load. The IEC 60034-31 provide a part load efficiency formula based on manufacturer motor data. In this formula, motor losses are a linear function of \dot{W}_{mech}^2 . Li *et al.* (2015) improved it with a new correlation for motor efficiency drive by a VSD, assuming the voltage is proportional to the frequency at the VSD output. From this correlation and assuming a constant power factor over the test, motor losses are expressed as: $\dot{Q}_{los,mot} = C_2 \cdot \dot{W}_{mech}^2 + C_3 \cdot \Omega^2$ with C_2 and C_3 constant parameters function of motor design. Figure 3 shows estimated losses for the motor used in this study, with both correlations. Correlations show small differences at nominal speed, correlation developed by Li is used for motor losses estimation. Therefore, the shaft power is estimated with one empirical constant (C_1) for VSD losses. $\dot{W}_{mot,n} \cdot \eta_{mot,n} \cdot \Omega_n$ are respectively the nominal motor power, the efficiency and the rotational

speed, provided by the manufacturer. \dot{W}_{el} and $\dot{\Omega}$ are measured parameters. The quadratic equation (1) is solved to find \dot{W}_{mech} .

$$\dot{W}_{mech} = \dot{W}_{el} - \dot{Q}_{los,pwd} - \dot{Q}_{los,mot} = \dot{W}_{el} - C_1 - \left[\left(\frac{1}{\eta_{mot,n}} - 1 \right) \dot{W}_{mot,n} \left(0,7 \frac{\dot{W}_{mech}^2}{\dot{W}_{mot,n}^2} + 0,3 \frac{\dot{\Omega}^2}{\dot{\Omega}_n^2} \right) \right] \quad (1)$$

From uncoupled motor tests, assuming $\dot{W}_{mech} = 0$, experimental value of C_1 is find to be 240W.

3.3 Pump Data

Volume flow rate is estimated from the mass flow rate and the fluid density using pressure and temperature at the pump outlet. Density, as other fluid properties, are computed with R-134a property equations provided by Tillner-Roth and Baehr (1994) used on EES. $\dot{W}_{flu,pp} = \dot{m}_{flu} \cdot \Delta h_{pp}$ and enthalpy is computed from pressure and temperature. Hydraulic power is define as: $\dot{W}_{hyd} [W] = \dot{V} [m^3/s] \cdot \Delta P [Pa]$. Therefore, $\dot{Q}_{los,pp}$ and $\dot{Q}_{los,flu}$ are estimated. Volumetric efficiency is the ratio between the real volume flow (\dot{V}) and the theoretical flow, product of displaced volume by rotational speed ($\dot{V}_{th} = V_{disp} \cdot \dot{\Omega}$). When the pump runs unloaded ($\Delta P = 0$), η_{vol} is near 100%. Therefore, manufacturer theoretical flow is compared with experimental no load flow (\dot{V}_0). Manufacturer displaced volume (V_{disp}) is estimated at 6,84 cm³, experimental at 7,15 cm³. Since the same method is used to estimate the volume flow on load and unloaded, experimental no load flow is taken to compute the volumetric efficiency: $\eta_{vol} = \dot{V} / \dot{V}_0$.

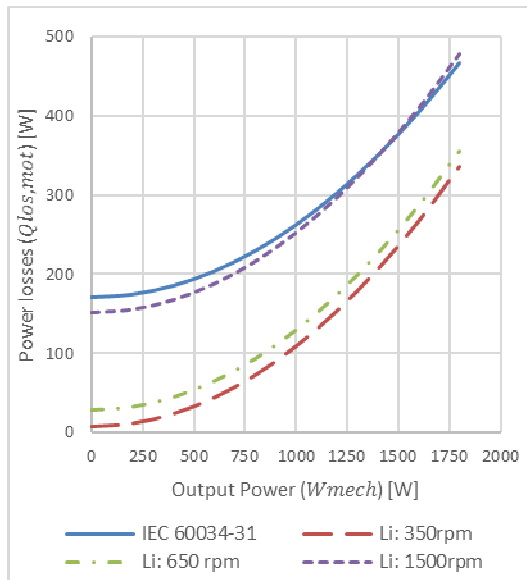


Figure 3: Motor losses function of load

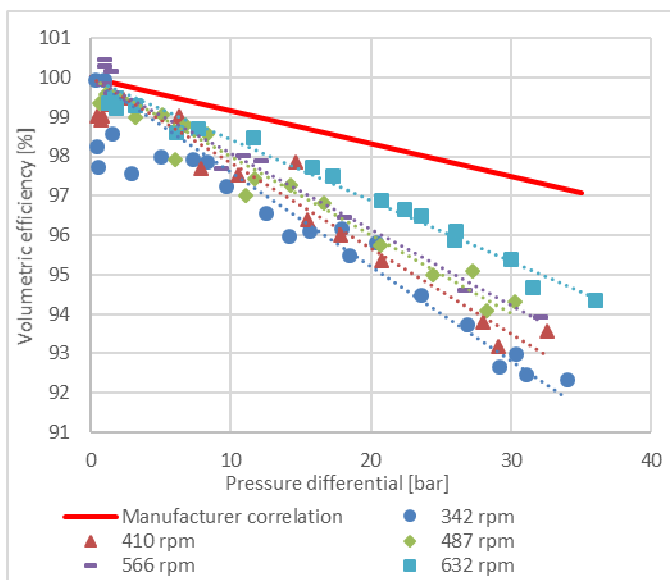


Figure 4: Effect of ΔP on volumetric efficiency for different mean rotational speed

4. RESULTS & ANALYSIS

4.1 Volumetric Efficiency

On load tests are performed at constant speed reference. Since an induction motor is used, slip increases between the speed reference and the real shaft speed when load increase. Therefore, the rotational speed should be measured at every step to compute corresponding no load flow and volumetric efficiency. As shown in Figure 4 volumetric efficiency is found to be dependent of the pressure differential and rotational speed while in theory, manufacturer data shown it is only proportional to the ΔP . Manufacturer and experimental result should be compared with caution since manufacturer data are mainly computed for cold water.

Literature shows different factors affecting the volumetric efficiency. As previously noted, NPSH affects the volumetric efficiency (Miller, 1988). For reciprocating pump, the NPSHr is defined by ANSI/HI 6.1-6.5 and 6.6 as a reduction of 3 % in the volumetric efficiency compared to the max

efficiency, at the same speed and pressure differential. Therefore, sub-cooling is essential to keep a good volumetric efficiency. Here, NPSH impact is neglected. Reciprocating pumps use valves, Miller (1995), Singh and Madavan (1987) and Johnston (1991) mentioned continuous valve leakage under high pressure and backflow when piston changes direction due to delays in the valves closing. If the closing delays is assumed to be inversely proportional to the rotational speed and since the number of cycle is proportional to the rotational speed, the average backflow time is considered constant. Therefore, backflow and continuous leakage are approximated by a continuous leakage flow rate using the equation proposed by De Chageres and Rey (2009): $\dot{V}_{leak} = A \cdot \Delta P / \mu$ with A an empirical geometric coefficient.

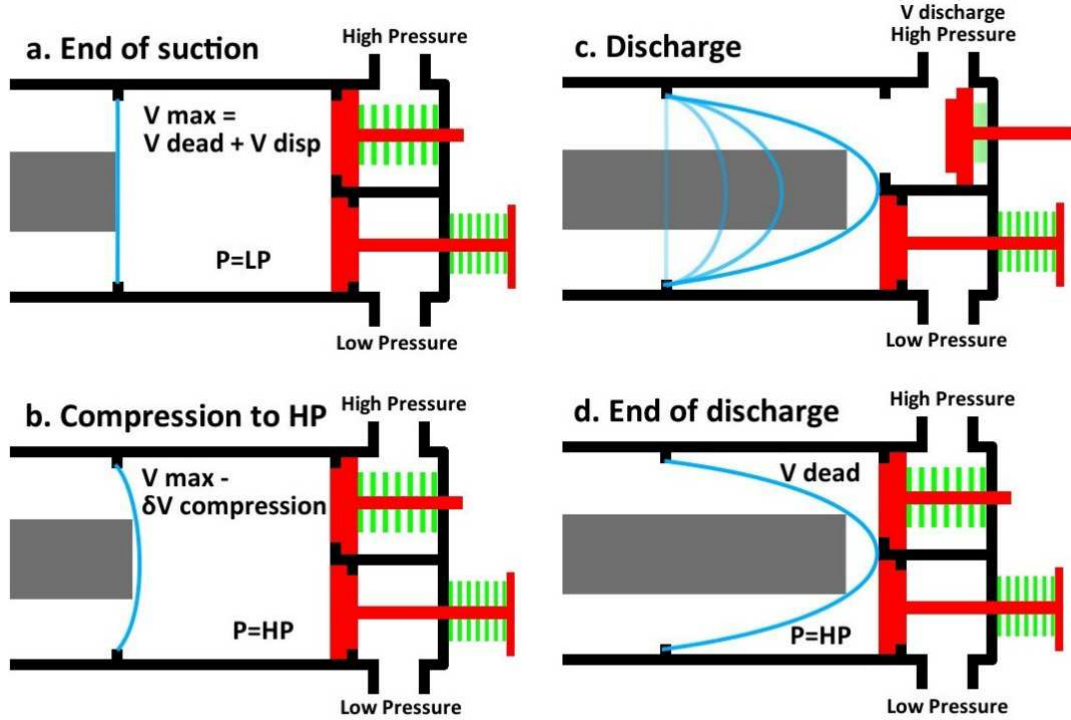


Figure 3: Reciprocating pump discharge process

Fluid compressibility is the third and most important factor. This factor creates a likelihood of confusion: the volumetric efficiency could be defined using the suction (Tackett *et al.*, 2008) or the discharge volume flow rate (Miller, 1995). Since outlet conditions are used to compute the volume flow, the second formulation is used. Figure 5 presents steps of the discharge process. Isothermal compressibility factor $\beta_T = -\frac{1}{V} \cdot \left(\frac{\partial V}{\partial P}\right)_T$ is introduced to write the volume discharge per stroke:

$$V_{dis} = (V_{max} - \Delta V_{compression}) - V_{dead} = V_{disp} - \Delta P \cdot \beta_T \cdot (V_{disp} + V_{dead}) \quad (2)$$

Adding valve leakage, discharge flow and volumetric efficiency equations are:

$$\dot{V}_{dis} = \dot{\Omega} \cdot V_{disp} \cdot \left(1 - \Delta P \cdot \beta_T \cdot \left(1 + \frac{V_{dead}}{V_{disp}}\right)\right) - A \cdot \frac{\Delta P}{\mu} \quad (3)$$

$$\eta_{vol} = \frac{\dot{V}_{dis}}{\dot{\Omega} V_{disp}} = 1 - \Delta P \cdot \beta_T \cdot \left(1 + \frac{V_{dead}}{V_{disp}}\right) - \frac{A \cdot \Delta P}{\mu \cdot V_{disp} \cdot \dot{\Omega}} \quad (4)$$

$$= 1 - \left(\frac{C_4}{\dot{\Omega}} + C_E\right) \cdot \Delta P \quad \text{with } C_4 = \frac{A}{\mu \cdot V_{disp}} \quad \text{and } C_E = \beta_T \cdot \left(1 + \frac{V_{dead}}{V_{disp}}\right) \quad (5)$$

Slope coefficients of Figure 4 are reported in Figure 6 corresponding to $(a/\dot{\Omega} + b)$ coefficient. V_{disp} is known from 3.3, μ and β_T are fluid properties computed from outlet conditions. Therefore, geometrical leakage coefficient is estimated $A \cong 1,3 \cdot 10^{-10} \text{ cm}^3$ and the dead volume $V_{dead} \cong 5,5 \text{ cm}^3$. Uncertainties on those values are high since there are only five data points used. Data at nominal speed will give more confidence in those results. However, manufacturer slope is constant, which could be explained if valve leakages were neglected ($C_4=0$), and leads to a single coefficient $C_5=0,000835 \text{ bar}^{-1}$, close to the experimental one ($C_5=0,000837$).

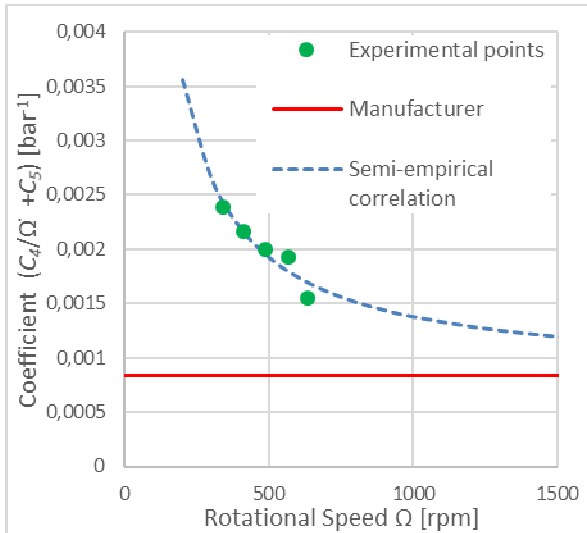


Figure 6: Volumetric efficiency slope coefficient

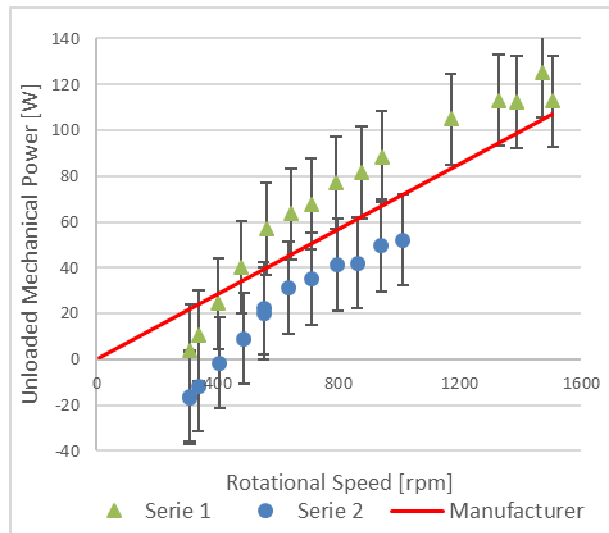


Figure 7: Unloaded mechanical power

4.2 Power & Pump Efficiency

Manufacturer proposes an equation to estimate the required power:

$$W_{mech} = C_6 \cdot \dot{\Omega} + C_7 \cdot W_{hyd} \quad (6)$$

The first term corresponds to friction losses, the second to pumping work efficiency. Manufacturer coefficient values are compared with experimental data. Coefficient C_6 is estimated from unloaded tests, the hydraulic power is neglected. For more accuracy, VSD and motor losses are not computed from Equation (1) to estimate W_{mech} . Instead, experimental losses from uncoupled tests is used. In addition, the hydraulic power, even low, is subtracted (assuming $C_7=1$). Figure 7 shows two series of test and the linear interpolation, C_6 is estimated at $0,0723 \text{ W/rpm}$ with the same order of magnitude as the manufacturer value: $0,0711 \text{ W/rpm}$. From on load tests, coefficient C_7 is estimated at $1,212$ (manufacturer: $1,174$). Mechanical power computed from motor & VSD model (Equation 1 with experimental W_{elec}) and pump model (Equation 6 with experimental W_{hyd}) are compared in Figure 8.

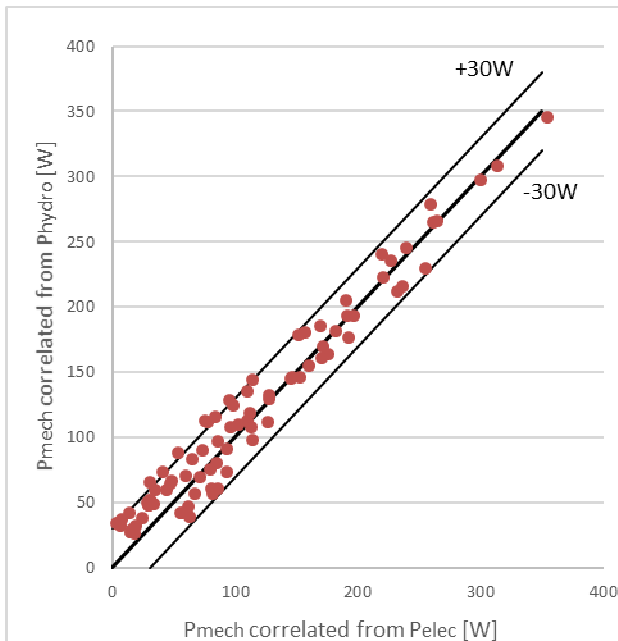


Figure 8: Correlated Mechanical Power: Pump model (equation 6) vs Motor model (equation 1)

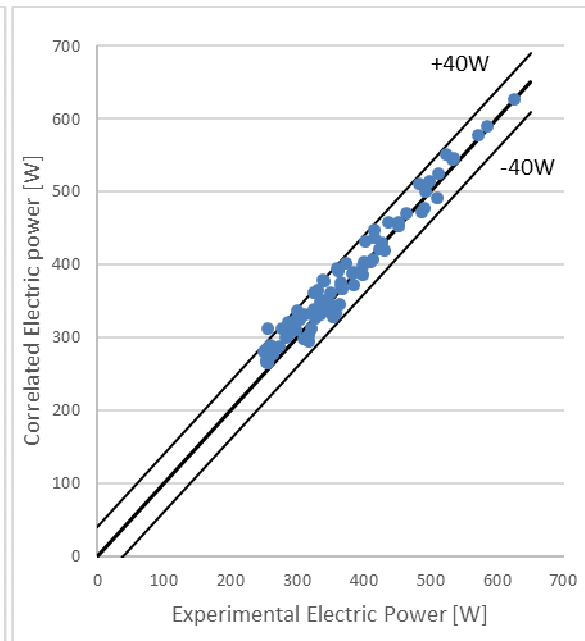


Figure 9: Experimental vs Correlated Electric Power

From Equation (6), pump efficiency becomes $\eta_{pump} = \dot{W}_{hyd} / (C_6 \cdot \dot{\Omega} + C_7 \cdot \dot{W}_{hyd})$ Miller (1995) and Tackett (2008) have the same kind of pump efficiency dependence with the load. The maximum pump efficiency is directly revealed: $\eta_{pump,max} = 1 / C_7 = 82,5\%$. Power consumption \dot{W}_{el} is estimated from \dot{W}_{hyd} and $\dot{\Omega}$ using Equation (1) and (6), experimental and correlated values are compared in Figure 9.

Enthalpies are not known with enough accuracies to provide accurate $\dot{W}_{fluid,pmp}$ and therefore isentropic efficiencies values. A solution should be to use more accurate temperature sensors or use a calorimeter to estimate $\dot{Q}_{loss,pmp}$. However, the isentropic efficiencies mean trend seems similar to the pump efficiency trend. If $\dot{Q}_{loss,pmp}$ is assumed negligible, then, as a first approximation $\eta_{is} \cong \eta_{pump}$.

4.2 Model Overview

Table 2 summarize the main equation useful for the pumping system modelling. The first equation provide a relation between the volume flow (or the volumetric efficiency), the shaft rotational speed and the pressure drop. It could be used for flow control purpose or volume flow rate estimation. The second equation provide a relation between the pump mechanical shaft power, the rotational speed, the pressure drop and the flow rate. The flow rate could be compute from the first equation. This equation is use for pump losses and efficiency. The third equation provide a relation between the electric consumption, the rotational speed and the motor shaft power. When each equation are combined, it provide the net electric power request for a given pressure drop and rotational speed (or flow rate). This is useful for modelling or design purpose.

Table 2 : Models equations and parameters overview

Volume Flow Rate	$\dot{V}_{dis} = \dot{\Omega} \cdot V_{disp} \left[1 - \left(\frac{A}{\dot{\Omega} \cdot \mu \cdot V_{disp}} + \beta_T \cdot \left(1 + \frac{V_{dead}}{V_{disp}} \right) \right) \cdot \Delta P \right]$			
Input parameters	$\dot{\Omega}$	rpm	Rotational speed	
	ΔP	bar	Pressure differential	
Model coefficients	V_{disp}	m ³	Displaced volume	<i>Experimental:</i> Unloaded pump test
	A	m ³	Leakage coefficient	<i>Experimental:</i> On-load pump test
	V_{dead}	m ³	Dead volume	
Fluid properties	μ	Pa.s	Dynamic viscosity	Computed from outlet pressure & temperature
	β_T	Pa ⁻¹	Isothermal compressibility	
Pump power	$\dot{W}_{mech} = C_6 \cdot \dot{\Omega} + C_7 \cdot \dot{W}_{hyd} = C_6 \cdot \dot{\Omega} + C_7 \cdot \dot{V}_{dis} \cdot \Delta P$			
Input parameters	$\dot{\Omega}$	rpm	Rotational speed	
	ΔP	Pa	Pressure differential	
	\dot{V}_{dis}	m ³ /s	Volumetric flow	
Model coefficients	C_6	W/rpm	Friction coefficient	<i>Experimental:</i> On-load pump test
	C_7	-	Efficiency coefficient	
VSD & Motor power	$\dot{W}_{el} = C_1 + \dot{W}_{mech} + C_2 \cdot \dot{W}_{mech}^2 + C_3 \cdot \dot{\Omega}^2$			
Input parameters	$\dot{\Omega}$	rpm	Rotational speed	
	\dot{W}_{mech}	W	Mechanical power	
Model coefficients	C_1	W/rpm	VSD losses coefficient	<i>Experimental:</i> Uncoupled motor test
	C_2	W ⁻¹	Part-load coefficient	<i>Motor data :</i> $C_2 = 0.7 \cdot \frac{(1/\eta_{motor} - 1)}{\dot{W}_{motor}}$
	C_3	W/rpm ²	Motor friction coefficient	<i>Motor data :</i> $C_3 = 0.3 \cdot \dot{W}_{motor} \cdot \frac{(1/\eta_{motor} - 1)}{\dot{\Omega}_n^2}$

6. CONCLUSIONS

An energetic analysis of a pumping system for ORC is proposed. For each component, a semi-empirical power model based on literature and experimental analysis is presented. This model could be used for the design or simulation of a reciprocating pump integrated into an Organic Rankine cycle, at part and full load. The volumetric efficiency equation could be used for simulation, process control or flow rate estimation if no flowmeter is available. Clarification of the different efficiencies useful for ORC design or simulation is proposed. The method and model deserve a deeper investigation for validation, as torque measurement between motor and pump or VSD electric power output. Measurement are in progress on a bigger pump for comparison and scale-up. Experimental analysis shows that reciprocating pump can achieve good efficiency at high pressure (more than 80%), but falls when the pressure decrease. Pump driver should be carefully chosen and designed as well as the pump. Oversize leads to lower efficiency, especially when the process runs often at part-load operation. The electric motor should be chosen according to the process nominal power and not the pump maximum power, avoiding a motor oversizing due to pump oversize. It should also be noted that new legislation on motor minimal efficiency are implemented in most countries.

NOMENCLATURE

h	specific enthalpy	(J/kg)	\dot{W}	power	(W)
\dot{m}	mass flow rate	(kg/s)	β_T	isothermal compressibility	(Pa ⁻¹)
P	pressure	(bar)	Δ	difference	(-)
\dot{Q}	heat power	(W)	η	efficiency	(-)
V	volume	(m ³)	μ	dynamic viscosity	(Pa.s)
\dot{V}	volume flow rate	(m ³ /h)	Ω	rotational speed	(rpm)

Subscript

0	unloaded	mech	mechanical
dis	discharge	mot	motor
disp	displaced	n	nominal
el	electrical	pp	pump
flu	fluid	suc	suction
hyd	hydraulic	th	theory
is	isentropic	vol	volumetric
los	losses	vsd	variable speed drive

REFERENCES

- Astolfi, M., Romano, M.C., Bombarda, P., Macchi, E., 2014. Binary ORC (Organic Rankine Cycles) power plants for the exploitation of medium–low temperature geothermal sources – Part B: Techno-economic optimization. *Energy*, vol. 66: p. 435–446
- Bao, J., Zhao, L., 2013. A review of working fluid and expander selections for organic Rankine cycle. *Renewable and Sustainable Energy Reviews*, vol. 24: p. 325–342
- De Almeida, A., Falkner, H., Fong, J., Jugdoyal, K., 2014. EuP lot 30 - Electric motors and drives (Final Report). for European Commission: 209p.
- De Charger, B., Rey, R., 2009. Pompes volumétriques pour liquides, *Techniques de l'Ingénieur*.
- Deprez, W., Lemmens, J., Vanhooydonck, D., Symens, W., Stockman, K., Dereyne, S., Driesen, J., 2010. Iso efficiency contours as a concept to characterize variable speed drive efficiency. *10th International Conference on Electrical Machines*, Rome.
- Maraver, D., Royo, J., Lemort, V., Quoilin, S., 2014. Systematic optimization of subcritical and transcritical organic Rankine cycles (ORCs) constrained by technical parameters in multiple applications. *Applied Energy*, vol. 117: p. 11–29.

- Miao, Z., Xu, J., Yang, X., Zou, J., 2015. Operation and performance of a low temperature organic Rankine cycle. *Applied Thermal Engineering*, vol. 75: p. 1065–1075
- Miller, J.E., 1988. Characteristic of the reciprocating pump. *Proc. of the 5th International Pump Users Symposium*, Houston.
- Miller, J.E., 1995. *The Reciprocating Pump Theory, Design, And Use*, Krieger Publishing Co: 484 p.
- Johnston, D.N., 1991. Numerical modelling of reciprocating pumps with self-acting valves. *Proceedings of the Institution of Mechanical Engineers, Part I: Journal of Systems and Control Engineering*, vol. 205: p. 87–96.
- Kari, R., 2009. AC Drive comes with losses - Technical Description. ABB.
- Li, Y., Liu, M., Lau, J., Zhang, B., 2015. A novel method to determine the motor efficiency under variable speed operations and partial load conditions. *Applied Energy*, vol. 144: p. 234–240
- Lippke, F., 1995. Simulation of the part load behavior of a 30 MWe SEGS plant. Sandia National Laboratories
- Quoilin, S., Aumann, R., Grill, A., Schuster, A., Lemort, V., Spliethoff, H., 2011. Dynamic modeling and optimal control strategy of waste heat recovery Organic Rankine Cycles. *Applied Energy*, vol. 88: p. 2183–2190
- Quoilin, S., Broek, M.V.D., Declaye, S., Dewallef, P., Lemort, V., 2013. Techno-economic survey of organic rankine cycle (ORC) systems. *Renewable and Sustainable Energy Reviews*, vol. 22: p. 168–186
- Schuster, A., Karellas, S., Aumann, R., 2010. Efficiency optimization potential in supercritical Organic Rankine Cycles. *Energy*, vol. 35: p. 1033–1039
- Shu, G., Liu, L., Tian, H., Wei, H., Xu, X., 2013. Performance comparison and working fluid analysis of subcritical and transcritical dual-loop organic Rankine cycle (DORC) used in engine waste heat recovery. *Energy Conversion and Management*, vol. 74: p. 35–43.
- Astolfi, M., Romano, M.C., Singh, P.J., Madavan, N.K., 1987. Complete Analysis and Simulation of Reciprocating Pumps Including System Piping. *Proc. of the 4th International Pump Users Symposium*, Houston, p. 53–73.
- Tackett, H.H., Cripe, J.A., Dyson, G., 2008. Positive Displacement Reciprocating Pump Fundamentals - Power and Direct Acting Types. *Proc. of the 24th International Pump Users Symposium*.
- Tillner-Roth, R., Baehr, H.D., 1994. An International Standard Formulation for the Thermodynamic Properties of 1,1,1,2-Tetrafluoroethane (HFC-134a) for Temperatures from 170 K to 455 K and Pressures up to 70 MPa. *Journal of Physical and Chemical Reference Data*, vol. 23: p. 657.
- Toffolo, A., Lazzaretto, A., Manente, G., Paci, M., 2014. A multi-criteria approach for the optimal selection of working fluid and design parameters in Organic Rankine Cycle systems. *Applied Energy*, vol. 121: p. 219–232.
- Vetter, G., 2006. *Rotierende Verdrängerpumpen für die Prozesstechnik*, Vulkan-Verlag GmbH. 337 p.
- ANSI/HI 6.1-6.5, 2000. Reciprocating Power Pumps for Nomenclature, Definitions, Application and Operation. American National Standards Institute.
- ANSI/HI 6.6, 2000. Reciprocating Pump Tests. American National Standards Institute.
- IEC 60034-31, 2010. Guide for the selection and application of energy efficient motors including variable-speed applications. International Electrotechnical Commission.

ACKNOWLEDGEMENT

This work was supported by the French Environment and Energy Management Agency (ADEME) and the Atomic Energy Commission (CEA)

INVESTIGATION OF A MASSIVE ELECTRICITY STORAGE SYSTEM BY MEANS OF A GEOTHERMAL HEAT TRANSFER PROCESS INVOLVING CO₂ TRANSCRITICAL CYCLES

Fadhel Ayachi¹, Thomas Tartière², Nicolas Tauveron^{1*}, Stéphane Colasson¹, Denis Nguyen³

¹CEA, LITEN – DTBH/SBRT/LS2T, 17 rue des Martyrs, 38054 Grenoble, France
fadhel.ayachi@cea.fr, nicolas.tauveron@cea.fr; stephane.colasson@cea.fr

²Enertime, 1 rue du Moulin des Bruyères, 92400 Courbevoie, France
thomas.tartiere@enertime.com

³BRGM Languedoc-Roussillon, 1039 rue de Pinville, 34000 Montpellier, France
d.nguyen@brgm.fr

* Corresponding Author

ABSTRACT

This work presents a specific application of the Rankine cycle and heat pump technologies: electricity storage. A multi-megawatt thermo-electric energy storage based on thermodynamic cycles is studied as a promising alternative to PSH (Pumped-Storage Hydroelectricity) and CAES (Compressed Air Energy Storage) systems. As a preliminary work, the main objective is to assess the performances of the massive storage technology based on transcritical CO₂ heat pump for charging and transcritical CO₂ Organic Rankine Cycle for discharging, with power output in the 1-10 MWe range.

The general concept of the system is presented, along with its thermodynamic modeling. A parametric analysis is carried out showing that it is possible to reach roundtrip efficiencies up to 53% that are competitive with other technologies. This work also shows the strong dependency between the different parameters of the system, and how an economic optimization will have to take all the subcomponents into account.

1. INTRODUCTION

Organic Rankine Cycles (ORC) have been used in a wide range of applications, including geothermal, biomass or solar power plants, waste heat recovery from industrial processes or combustion engines, ocean thermal energy conversion... and a wide range of power outputs from a few kW to tens of MW. The possibility to use ORC to produce electricity from heat that has been previously stored as a large-scale electricity storage technology remains more confidential but has been the subjects of recent studies [1].

As it is well-known, the massive integration of intermittent renewable energy production generates new challenges for the supervision and regulation of electric grids. The use of flexible but carbon-intensive technologies such as gas turbines has been the main solution in order to ensure the balance between demand and supply, maintaining grid frequency and power quality. However, large-scale electricity storage is a promising alternative with a much lower environmental impact. In addition, it would enable a decentralized access to electricity and lower the dependency on fossil fuels. If storage is still expensive today, it could become increasingly viable as the price of carbon rises.

Several technologies exist or are under development for large-scale energy storage. Pumped Hydro Storage (PHS) is the most common one, accounting for more than 99% of the worldwide bulk storage capacity, representing around 140 GW over 380 locations [2]. When there is an excess of power supply, water is pumped to an upper reservoir, from where it can be discharged to drive a turbine

when power demand is high. Reported roundtrip efficiencies are typically between 70% and 85%. Despite having a long lifetime and being the most cost-effective energy storage technology, these systems have a low energy density and require the construction of large reservoirs, leading to a high environmental impact. In addition, the most suitable locations have already been used in developed countries. Other possibilities would be to include pre-existing dams or the ocean, as in the 30 MW Yanbaru project in Japan [3].

In a Compressed-Air Energy Storage (CAES) system, ambient air is compressed and stored underground. Reported roundtrip efficiencies are around 50%. The capital cost of CAES power plants is competitive with PHS and their power output can reach hundreds of MW. In contrast to PHS, only 2 CAES power plants exist in the world: a 290 MW plant in Huntorf, Germany (1978) [4], and a 110 MW plant in McIntosh, USA (1991) [5]. A much higher efficiency of up to 70% could be achieved by storing the heat of compression before the pressurized air is sent to the cavity [6][7]. This Advanced Adiabatic CAES (AA-CAES) technology is still under development. As for PHS, CAES systems require very specific sites and cannot be installed everywhere.

Thermo-electric energy storage (TEES) is a promising alternative to existing technologies that would allow widespread and large-scale electricity storage. It has a high energy density and is independent from geological or geographical constraints. During periods of excess electricity generation, a vapor compression heat pump consumes electricity and transfers heat between a low-temperature heat source and a higher temperature heat sink. The temperature difference between the heat sink and the heat source can be maintained for several hours, until a power cycle is used to discharge the system and generate electricity during peak consumption hours.

Mercangöz [1] gave references of thermo-electric energy storage studies as old as 1924 and described the general concept of this technology, based on two-way conversion of electricity to and from heat. He stated that the main challenges of TEES are to closely match the heat source and heat sink with the working fluid, and to find an optimum between roundtrip efficiency and capital cost. He analyzed a TEES system with transcritical CO₂, hot water and ice as storage materials. The ABB Corporate Research Center [8][9] described a way to store electricity using two hot water tanks, ice storage and transcritical CO₂ cycles. For similar systems, Morandin [10][11][12] defined a design methodology based on pinch analysis and calculated a 60% maximum roundtrip efficiency for a base case scenario with turbomachinery efficiencies given by manufacturers.

Sensible heat storage with hot water tanks is often considered, since water has high thermal capacity, is very cheap and environmental-friendly. Latent heat storages based on phase change materials (PCMs) have also been widely investigated. The heat sink of the system can be either the ambient or ice. This second option ensures a constant low-pressure for the process that is favorable to turbomachines. A mixture of salt and water can be used to adjust the heat sink temperature between 0°C and -21.2°C (corresponding to the eutectic point with 23.3% of NaCl in the mixture) [10].

Different working fluids can be considered for the thermodynamic cycles. Desrués [13] presented a TEES process based on Argon in forward and backward closed Brayton cycles. Henchoz [14] analyzed the combination of solar thermal energy with TEES based on Ammonia cycles. Kim [15] reviewed current TEES systems and showed that using transcritical CO₂ cycles instead of Argon Brayton cycles leads to a higher roundtrip efficiency even if the required temperature difference between the heat storages is much smaller. He also proposed an isothermal energy storage system based on transcritical CO₂ cycles and liquid piston compressors/expanders.

Carbon dioxide is a natural refrigerant with many advantages. It is a low-cost fluid that is non-toxic, non-flammable, chemically stable, and readily available. In addition, the high fluid density of supercritical CO₂ leads to very compact systems. Many studies have been published to evaluate the potential of supercritical CO₂ as working fluid in power cycles and heat pumps [16][17]. Cayer carried out an analysis [18] and optimization [19] of transcritical CO₂ cycle with a low-temperature

heat source. More recently, the use of CO₂ for multi-megawatt power cycles has reached a commercial step with the American company Echogen [20].

The purpose of this article is to introduce a new type of electro-thermal energy storage process for large scale electric applications, based on transcritical CO₂ cycles and ground heat storage. The conceptual design of the TEES system is addressed here only from a thermodynamic point of view and economic analysis are left for future works.

2. THERMODYNAMIC MODELING

The electro-thermal energy storage system is a high-capacity storage concept that includes:

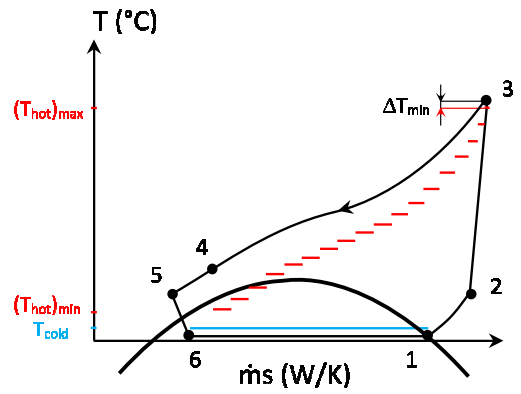
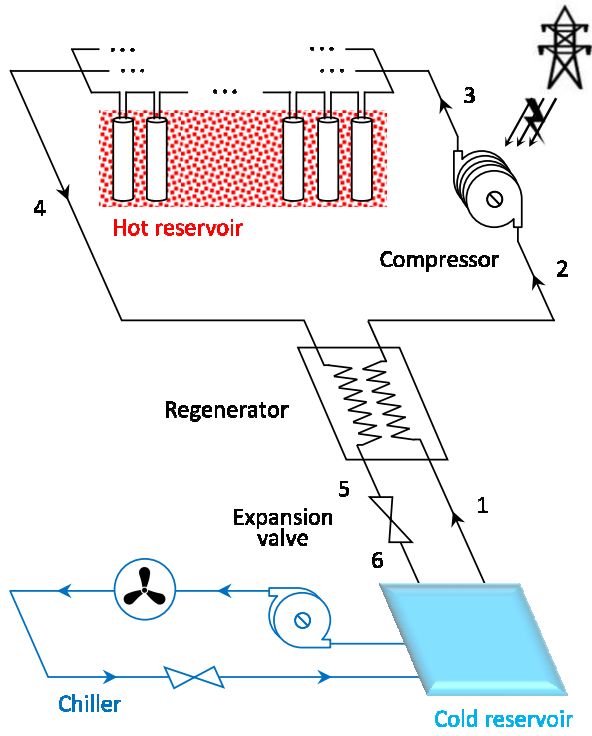
- i- a hot reservoir made of a set of ground heat exchangers in a low diffusivity rock ;
- ii- a cold reservoir using either ice ($T_{\text{cold}} \leq 0^{\circ}\text{C}$) or a phase-change material ($T_{\text{cold}} > 0^{\circ}\text{C}$);
- iii- two thermodynamic cycles as charging and discharging processes, both using carbon dioxide as working fluid;

The layouts of the thermodynamic cycles are given by Fig. 1 and Fig. 2. Due to the high storage capacity (typically 100 MWh of heat) and the rock low diffusivity, this technology is suitable for long discharge durations (typically >10 hours) and will not offer the same kind of services to the grid than batteries. Therefore, the parameters of the system will vary very slowly with time, and provided that the system is not discharged further than a certain point, can be considered as constant, as a preliminary step. Therefore, the processes are assumed to be at steady state and the system parameters are reported in Table 1. The thermodynamic model is implemented with Engineering Equation Solver (EES) [21].

During off-hours, a transcritical heat pump is used for charging the system: the working fluid leaves the cold reservoir heat exchanger as a saturated vapor at $T_1 = T_{\text{cold}} - \Delta T_{\text{min}}$ and is preheated (1 → 2) through a regenerator, before being adiabatically compressed (2 → 3) with isentropic efficiency $\eta_{s,c}$. At the compressor outlet, the fluid at $T_3 = (T_{\text{hot}})_{\text{max}} + \Delta T_{\text{min}}$ and supercritical high pressure $P_3 = P_H$ is cooled through the hot reservoir exchangers (3 → 4) and releases heat to the ground, before being subcooled in the regenerator (4 → 5). The liquid is then expanded (5 → 6) to subcritical low pressure P_L and is finally evaporated in the cold reservoir exchanger (6 → 1).

Table 1. Input parameters

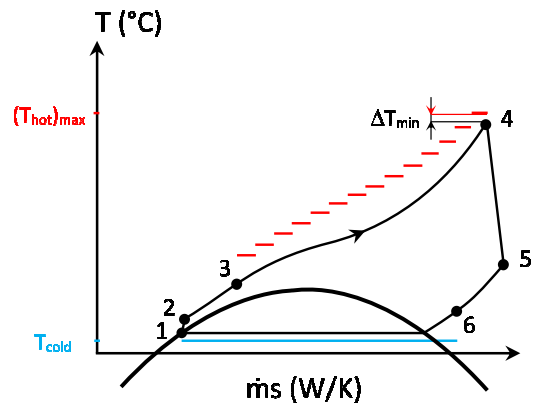
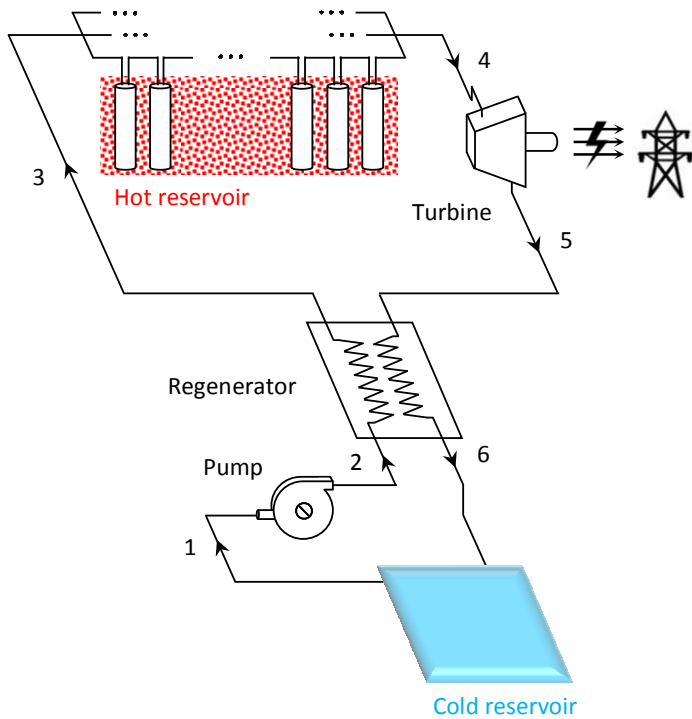
Storage	
Hot storage max temperature	Variable
Cold storage temperature	Variable
Min temperature difference between heat reservoir and CO ₂ ΔT_{min}	1 K
Charging cycle	
Compressor isentropic efficiency $\eta_{s,c}$	0.85
Motor efficiency η_m	0.98
$(T_4)_{\text{min}}$	30°C
Regenerator pinch	5 K
Discharging cycle	
Net power output \dot{W}_{el}'	1 – 10 MW _{el}
Pump isentropic efficiency $\eta_{s,p}$	0.80
Turbine isentropic efficiency $\eta_{s,t}$	0.90
Generator efficiency η_g	0.98
Regenerator pinch	5 K
Chiller	
Compressor isentropic efficiency	0.85
Motor efficiency	0.98
Condensing temperature	20°C
Evaporating temperature	Same than for discharge cycle



(a)

(b)

Fig. 1. Charging process: a) process layout, b) (T, ṁs) diagram.



(a)

(b)

Fig. 2. Discharging process: a) process layout, b) (T, ṁs) diagram.

High pressures in the range 100-150 bars will require the use of Printed-Circuit Heat Exchangers (PCHE) [22] or more unlikely costly tubular heat exchangers for the regenerator heat exchanger.

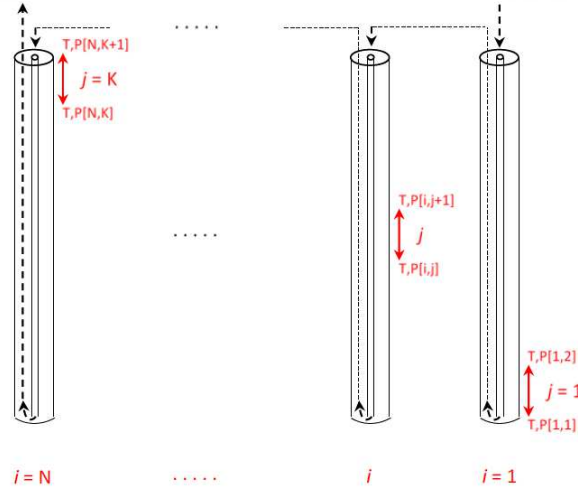


Fig. 3. Principle of the ground heat exchangers

Fig. 3 shows the general principle of the ground heat storage. The fluid at supercritical pressure is injected at the bottom of each column through a central tube and then flows up to an annular exit, transferring heat with the surrounding rock. Several series of ground heat exchangers are installed in parallel in order to reach the required thermal input/output. Detailed simulations of the overall ground heat storage system are being investigated and will enable to estimate the head losses in that component and adjust the cycle parameters. As a preliminary work, pressure losses in the thermodynamic cycles are neglected.

Given the cold storage temperature T_{cold} and ΔT_{min} as input parameters, it is possible to calculate the saturation temperature T_1 and thus the saturation pressure P_L . Similarly, knowing the hot storage temperature, ΔT_{min} and the compressor isentropic efficiency, it is possible to calculate the high pressure P_H . The thermodynamic states of the charging cycle can be obtained from the energy balances of each components:

$$(h_1 - h_2) + (h_4 - h_5) = 0 \quad (1)$$

$$\dot{W}_c + \dot{m}(h_2 - h_3) = 0 \quad (2)$$

$$\dot{Q}_{hot} + \dot{m}(h_3 - h_4) = 0 \quad (3)$$

$$h_5 - h_6 = 0 \quad (4)$$

$$\dot{Q}_{cold} + \dot{m}(h_6 - h_1) = 0 \quad (5)$$

h_i (J/kgK) and \dot{m} (kg/s) being respectively the specific enthalpy at state i and the mass flow rate in the charging cycle. $\dot{W}_c = \dot{m}(h_{3s} - h_2) / \eta_{s,c} > 0$, $\dot{Q}_{hot} < 0$ and $\dot{Q}_{cold} > 0$ are respectively the compressor power, the heat flux transferred to the hot reservoir and the heat flux transferred from the cold reservoir.

Adding equations 1 to 5 leads to the energy balance of the charging cycle:

$$\dot{W}_c + \dot{Q}_{hot} + \dot{Q}_{cold} = 0 \quad (6)$$

During peak-hours, a transcritical Organic Rankine Cycle is used for discharging the system: the working fluid leaves the cold reservoir heat exchanger at saturation $T_1' = T_{cold} + \Delta T_{min}$ and is pumped (1 → 2) with isentropic efficiency $\eta_{s,p}$. At the pump outlet, the fluid at supercritical high pressure $P_2' = P_H'$ is preheated in the regenerator (2 → 3), then heated in the hot reservoir exchanger (3 → 4) where it recovers heat from the ground and reaches $T_4' = (T_{hot})_{max} - \Delta T_{min}$. The fluid is then adiabatically expanded (4 → 5) with isentropic efficiency $\eta_{s,t}$ to the subcritical pressure P_L' , producing mechanical power. Finally, the fluid is cooled in the regenerator (5 → 6) before being condensed through the cold reservoir exchanger (6 → 1).

The reservoir temperatures T_{cold} and $(T_{hot})_{max}$ and the hot pressure $P_H' \approx P_H$ being known, the thermodynamic states can be obtained from the energy balances of each component:

$$\dot{W}_p' + \dot{m}'(h_1' - h_2') = 0 \quad (7)$$

$$(h_2' - h_3') + (h_5' - h_6') = 0 \quad (8)$$

$$\dot{Q}_{hot}' + \dot{m}'(h_3' - h_4') = 0 \quad (9)$$

$$\dot{W}_t' + \dot{m}'(h_4' - h_5') = 0 \quad (10)$$

$$\dot{Q}_{cold}' + \dot{m}'(h_6' - h_1') = 0 \quad (11)$$

h_i' (J/kgK) and \dot{m}' (kg/s) being respectively the specific enthalpy at state i and the mass flow rate of the discharging cycle. $\dot{W}_p'(W) = \dot{m}'(h_2' - h_1') / \eta_{s,p} > 0$, $\dot{W}_t'(W) = \dot{m}'(h_4' - h_5') \eta_{s,t} < 0$, $\dot{Q}_{hot}'(W) > 0$ and $\dot{Q}_{cold}'(W) < 0$ are respectively the pump power, the turbine power, the heat flux transferred from the hot reservoir and the heat flux transferred to the cold reservoir.

Adding equations 7 to 11 gives the energy balance of the discharge cycle:

$$\dot{W}_p' + \dot{Q}_{hot}' + \dot{W}_t' + \dot{Q}_{cold}' = 0 \quad (12)$$

As an example, the Temperature-Entropy diagram of the charging and discharging cycles, for hot storage at 130°C and cold storage at 0°C, are given in Fig. 4.

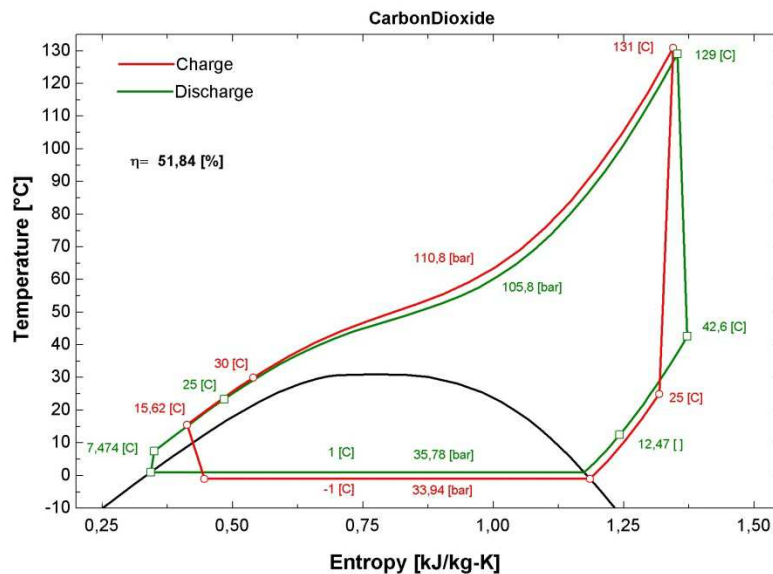


Fig. 4. T-S diagram for hot storage at 130°C and cold storage at 0°C ($\Delta T_{min} = 1K$).

The net power output of the discharge cycle $\dot{W}'_{el} = \eta_g \cdot \dot{W}'_c - \dot{W}'_p$ is defined as an input parameter, in the range 1-10 MWel. The thermal energy stored in the ground heat exchangers is $\dot{Q}'_{hot} \cdot t_{discharge} = -\dot{Q}'_{hot} \cdot t_{charge}$. As a first step, we assume similar charging and discharging time so $\dot{Q}'_{hot} \cong -\dot{Q}'_{hot}$. This gives the mass flow rates \dot{m} and \dot{m}' and then the net power input of the charging cycle $\dot{W}_{el} = \dot{W}_c / \eta_m$. Having a different charge duration would only change the mass flow rate of the charging heat pump cycle, and therefore its power input, but does not affect the thermodynamic analysis.

Furthermore, by adding equations 6 and 12 and using $\dot{Q}'_{hot} = -\dot{Q}'_{hot}$, it follows that:

$$\dot{W}_c + \dot{Q}'_{cold} + \dot{W}'_p + \dot{W}'_t + \dot{Q}'_{cold} = 0 \quad (13)$$

Based on Equation 13, we can define the thermal asymmetry of the system such as:

$$\delta\dot{Q}'_{cold} = \dot{Q}'_{cold} + \dot{Q}'_{cold} = -(\dot{W}_c + \dot{W}'_p + \dot{W}'_t) < 0 \quad (14)$$

The charging and discharging cycles are not perfectly reversible. Even if the discharging cycle can consume the same amount of heat than provided by the charging cycle ($\dot{Q}'_{hot} = -\dot{Q}'_{hot}$), the amount of cold produced by the heat pump cycle is smaller than the amount needed during the discharge. Therefore, the thermal asymmetry of the system represents the amount of additional cooling that is needed to discharge the system and that should be provided by an auxiliary CO₂ chiller working in parallel with the charging cycle (Fig. 1a).

A thermodynamic model of a single-stage chiller, with parameters given in Table 1, is developed using EES in order to calculate this additional electrical consumption $\dot{W}'_{el}(W)$, expressed by equation 15.

$$\dot{W}'_{el} = \frac{-\delta\dot{Q}'_{cold}}{COP} \quad (15)$$

Finally, assuming similar charging and discharging durations, the overall roundtrip efficiency of the system can be defined as:

$$\eta_{sys} = \frac{\dot{W}'_{el}}{\dot{W}_{el} + \dot{W}'_{el}} \quad (16)$$

This steady-state analysis provided a limited but useful first analysis of the system, in order to assess the main characteristics of each component and the dependency between the charging and discharging cycles. A time-dependent model of the system is under development but requires a detailed simulation of the diffusion through the ground heat exchangers, and a thorough understanding of the convection heat transfer coefficient between the supercritical CO₂ and the rock. These two topics are being investigated and will be detailed in future works.

3. PARAMETRIC ANALYSIS

Based on this preliminary thermodynamic modeling, it is possible to carry out a parameter analysis of the system. Figure 5 shows the efficiency of the system with respect to the temperature of the heat storages. As we can see, it is possible to reach roundtrip efficiencies up to 53% with high storage temperatures and 1 K-temperature difference between the charging and discharging cycle (ΔT_{min}).

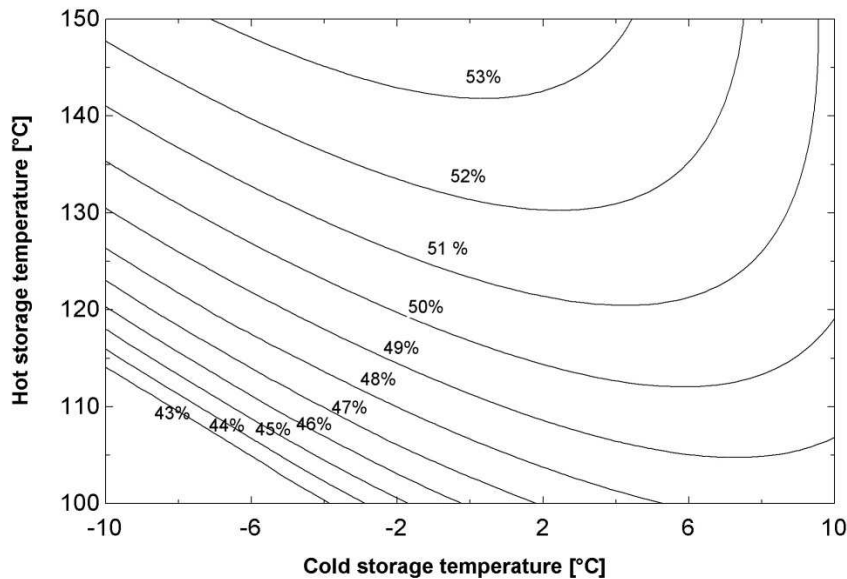


Fig. 5. Overall efficiency of the storage system with respect to the design storage temperatures ($\Delta T_{\min} = 1\text{K}$).

The choice of temperatures for the hot and cold storages will not only impact the overall electrical efficiency but also the size of the storages and the initial investment cost. For example, Fig. 6 gives the roundtrip efficiency as a function of the cold storage temperature for a hot storage at 130°C. In that case, it is possible to reach a maximum overall efficiency of 51.8% for a cold storage at 2°C. This is mainly due to the fact that the heat pump COP increases significantly when the cold storage temperature is increased, thus decreasing the electricity consumption of the system. In addition, this also reduces the pressure ratio in the two thermodynamic cycles and therefore simplifies the design of the turbomachines.

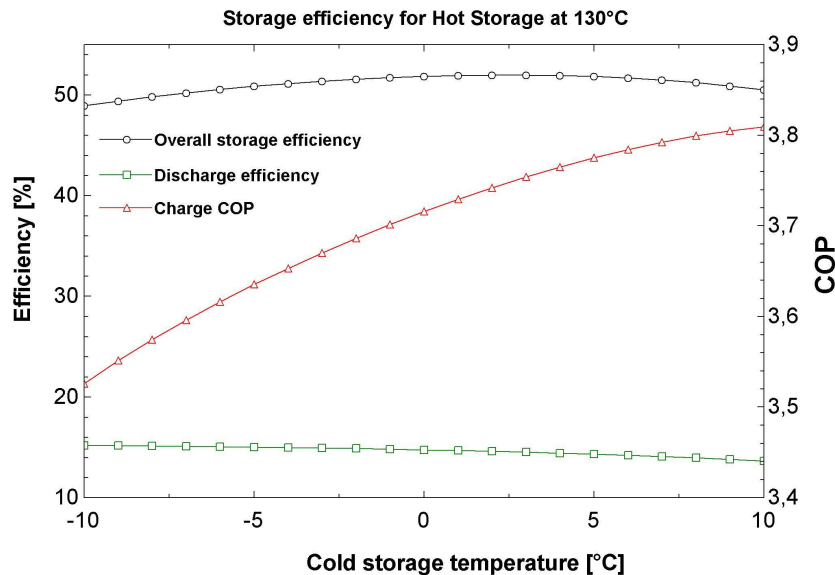


Fig. 6. Storage efficiency as a function of cold storage temperature ($(T_{\text{hot}})_{\max} = 130^{\circ}\text{C}$, $\Delta T_{\min} = 1\text{K}$).

Figure 7 shows the thermal asymmetry of the system, as defined by Equation 13, as a function of the cold storage temperature, for a hot storage at 130°C. We can see that the increase in storage efficiency shown in Figure 6 when changing the cold storage temperature from -10°C to 0°C is also due to a smaller asymmetry between the charging and discharging cycles. In addition, the performance of the chiller that provides this additional cooling is improved with higher cold storage temperatures.

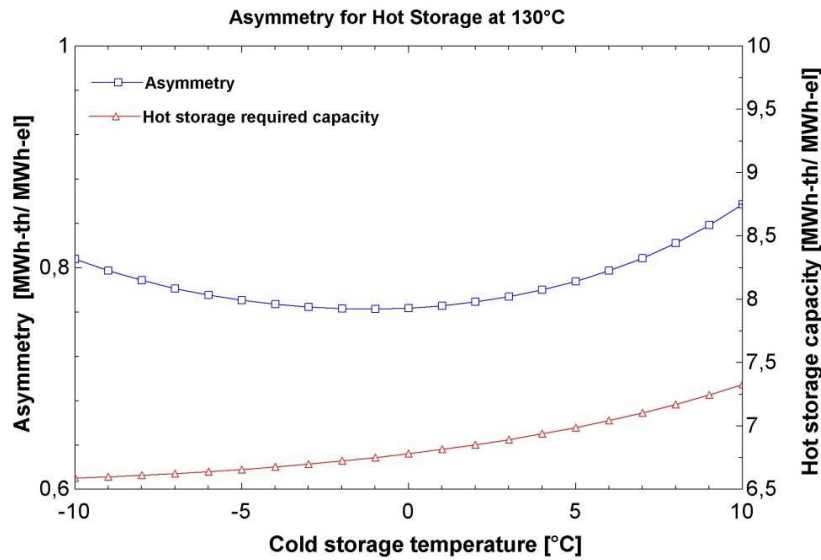


Fig. 7. Asymmetry as a function of cold storage temperature ($(T_{hot})_{max} = 130^{\circ}C$, $\Delta T_{min} = 1K$).

However, decreasing the temperature difference between the two storages reduces the power cycle efficiency. This means that the discharging cycle has to consume more heat in order to produce the same electrical power output. Therefore, the hot storage has to be bigger, leading to an increase of about 11% between the cases of cold storage at $-10^{\circ}C$ and $10^{\circ}C$. In addition, for a given hot storage temperature, the high pressure of the system increases with warmer cold storage temperatures, as shown in figure 8.

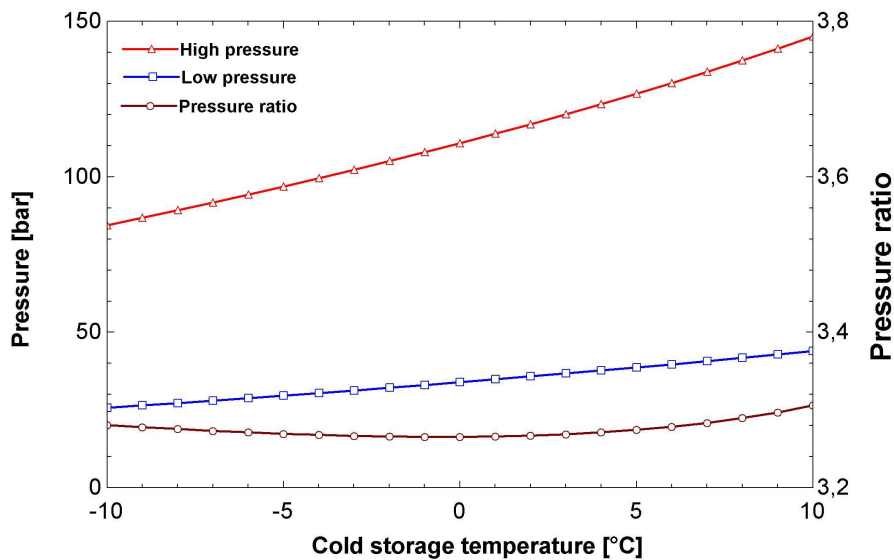


Fig. 8. Pressures of the system as a function of cold storage temperature ($(T_{hot})_{max} = 130^{\circ}C$, $\Delta T_{min} = 1K$).

As we can see, the system optimization has to take all these elements into account in order to find a trade-off between efficiency and investment cost. Further works will take turbomachinery and heat storage designs into account in the process design, enabling a cost optimization of the storage system.

4. CONCLUSION

This work carries out the analysis of a novel system storing electricity in the form of ground heat and ice, using transcritical Heat Pump and transcritical ORC cycles for the charging and discharging processes. A thermodynamic modeling is presented and a parametric analysis shows roundtrip efficiencies of up to 53% that are competitive with other technologies. Further work through the SELECO₂ project will include turbomachinery and heat storage designs in order to have a more detailed overview of the system and of the dependency between the charging and the discharging processes which can represent large off-design conditions. Furthermore transient simulations of the complete charging/discharging cycle will be performed and confirm (or not) the efficiency value and the general interest of the device.

REFERENCES

- [1] Mercangöz M, Hemrle J, Kaufmann L, Z'Graggen A, Ohler C. Electrothermal energy storage with transcritical CO₂ cycles. *Energy* 2012; 45: 407–415.
- [2] ENEA Consulting, Facts & Figures : Le Stockage d'Énergie. 2012; Available at: <<http://www.enea-consulting.com/wp-content/uploads/ENEA-Consulting-Le-Stockage-d'Énergie.pdf>> [accessed 22.01.2015].
- [3] Fujihara T, Imano H, Oshima K. Development of Pump Turbine for Seawater Pumped-Storage Power plant. *Hitachi Review* 1998 : 47 (5): 199-202.
- [4] Crotofino F, Mohmeyer K-U, and Scharf R. Huntorf CAES: More than 20 Years of Successful Operation. Proc of SMRI Spring Meeting, Orlando, Florida, USA, 15-18 April 2001.
- [5] PowerSouth Energy Cooperative, CAES McIntosh Alabama. Available at: <http://www.powersouth.com/mcintosh_power_plant/compressed_air_energy> [accessed 23.01.2015]
- [6] Chris Bullough, Christoph Gatzen, Christoph Jakiel, Martin Koller, Andreas Nowi, Stefan Zunft, Advanced adiabatic compressed air energy storage for the integration of wind energy, in: Proceedings of the European Wind Energy Conference, London UK, 2004.
- [7] Grazzini G, Milazzo A. Thermodynamic analysis of CAES/TES systems for renewable energy plants. *Renewable Energy* 2008;32:1998-2006.
- [8] Mercangoez M, Hemrle J, Kaufmann L. Thermoelectric energy storage system having two thermal baths and method for storing thermoelectric energy. Patent EP2241737 (A1) [Internet]. 20.10.2010. Available at: www.google.com/patents/EP2241737A1 [accessed 22.05.15].
- [9] Ohler C, Mercangoez M. Thermoelectric energy storage system and method for storing thermoelectric energy. Patent EP2182179 (A1) [Internet]. 05.05.2010. Available at: www.ipo.gov.uk/p-ipsum/case/PublicationNumber/EP2182179 [accessed 22.01.15].
- [10] Morandin M, Maréchal F, Mercangöz M, Buchter F. Conceptual design of a thermo-electrical energy storage system based on heat integration of thermodynamic cycles - Part A: Methodology and base case. *Energy* 2012;45:375e85.
- [11] Morandin M, Maréchal F, Mercangöz M, Buchter F. Conceptual design of a thermo-electrical energy storage system based on heat integration of thermodynamic cycles - Part B: Alternative system configurations. *Energy* 2012;45:386-96.
- [12] Morandin M, Mercangöz M, Hemrle J, Maréchal F, Favrat D. Thermoeconomic design optimization of a thermo-electric energy storage system based on transcritical CO₂ cycles. *Energy* 2013; 58: 571–587.
- [13] Desrués T, Ruer J, Marty P, Fourmigué JF. A thermal energy storage process for large scale electric applications. *Applied Thermal Engineering* 2010;30(5):425-32
- [14] Henchoz S, Buchter F, Favrat D, Morandin M, Mercangoez M. Thermoeconomic analysis of a solar enhanced energy storage concept based on thermodynamic cycles. *Energy* 2012;45(1):358e65.
- [15] Kim YM, Shin DG, Lee SY, Favrat D. Isothermal transcritical CO₂ cycles with TES (thermal energy storage) for electricity storage. *Energy* 2013; 49: 484–501.

- [16] Kim YM, Kim CG, Favrat D. Transcritical or supercritical CO₂ cycles using both low- and high-temperature heat sources. *Energy* 2012; 43: 402–415.
- [17] Li M, Wang J, Li S, Xurong Wang, He W, Dai Y. Thermo-economic analysis and comparison of a CO₂ transcritical power cycle and an organic Rankine cycle. *Geothermics* 2014; 50: 101–111.
- [18] Cayer E, Galanis N, Désilets M, Nesreddine H, Roy P. Analysis of a carbon dioxide transcritical power cycle using a low temperature source. *Applied Energy* 2009;86:1055–63.
- [19] Cayer E, Galanis N, Nesreddine H. Parametric study and optimization of a transcritical power cycle using a low temperature source. *Applied Energy* 2010;87:1349-1357
- [20] Held T., Initial Test Results of a Megawatt-class Supercritical CO₂ heat engine. The 4th International Symposium – Supercritical CO₂ Power Cycles; 2014 Sept 9-10; Pittsburgh, USA.
- [21] S.A. Klein, Engineering Equation Solver. F-Chart Software, Middleton, WI, 2010.
- [22] Le Pierres R., Southall D., Osborne S. Impact of Mechanical Design Issues on Printed Circuit Heat Exchangers, in: Proceedings of SCO₂ Power Cycle Symposium, Boulder, 2011

ACKNOWLEDGEMENT

The authors acknowledge the support of the French Agence Nationale de la Recherche (ANR), under grant ANR-13-SEED-0004 (project SELECO₂).

AN AUTOMATIC ADJUSTING DEVICE OF THE SPIRAL GROOVE FACE SEAL USED ON ORC TURBINE SHAFT END AND THE ESTABLISHMENT OF CONTROL MODEL

Ya Zheng¹, Yue Cao², Dongshuai Hu³, Xurong Wang⁴, Yiping Dai^{5*}

^{1,2,3,4,5}Xi'an Jiaotong University, Institute of Turbomachinery,
Xi'an, Shaanxi, China
ypdai@mail.xjtu.edu.cn

* Corresponding Author

ABSTRACT

ORC system has to solve the seal problem for the inflammable, explosive, corrosive and toxic working fluids. The real-time monitoring of seal systems is particularly important to ensure 'zero-leakage'. In recent decades, the development of automation technology, testing and measurement technology, advanced process technology and some related regulations for the rotating machinery promote the research and application of monitoring technology of the spiral groove face seals. This paper mainly focuses on the real-time response of the seal system to the change of working parameters. A new method is proposed to achieve the automatic control of seal pressure. The experiment and numerical simulation is conducted at first to obtain the maximum differential pressure between inlet and outlet, which can ensure zero leakage of the seal system in different working parameters. Then, the control system of pump is established to adjust the pressure of feed pump in real time when the pressure of sealed medium (the pressure of end face outlet) changes. Consequently, the pressure of end face inlet is adjusted to make the differential pressure between inlet and outlet less than or equal to the maximum differential pressure.

1. INTRODUCTION

Organic Rankine Cycle system has been confirmed to be an efficient approach to utilize low grade waste heat and this system is considerable mature for immense amounts of concrete research during these years. However, the leakage of organic fluid is still the persistent problem of the ORC system which can cause toxic substances diffusion and efficiency decrease. The spiral groove seal using liquid as sealed medium was proposed by Josef (1980) firstly. Then researchers mainly use the advanced virtual instrument technology on testing system of spiral groove face seals. It is creative to combine the machinery and electricity on the basis of virtual instrument technology, which contribute to build a complete set of testing and monitoring system of spiral groove face seals. The appropriate sensors can ensure the stable operation of turbine units. Since the concept of controlled end face seal was proposed, it has been researched by many scholars. Wolff and Salant (1995) used electronic technique to control mechanical seal for aerospace applications. Heilala (1987), Etsion *et al.* (1991) tried to prevent mechanical seal from dry running and severe wear through adjusting and controlling the end face temperature. Zou *et al.* (2000) monitored the non-contacting mechanical face seal in real time, Zhou and Gu (2009) focused on the controllability of spiral groove face seals, and concluded the relationship between sealing performance and the fluid film. Zheng *et al.* (2012) built detailed models of spiral groove face seal in commercial computational software ANSYS/FLUENT to analyze the effect of structural and operational parameters of spiral groove face seals.

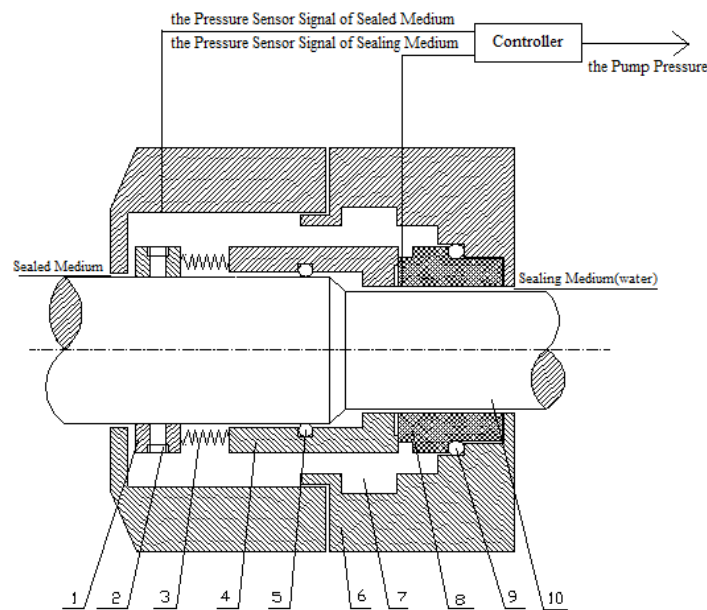
According to the various characteristic parameters tests of seals, the measurement and control of liquid film pressure is vitally important to monitor the status of seals and ensure it operates stably

and safely. In general, engineers use pressure tap to measure the pressure of liquid film on the surface, however it may cause the change of flow distribution around the pressure tap which draws into error to the measurement results finally. In order to solve this situation, this paper proposes to install sensors at different positions of the end face to measure pressure of each point. Firstly, these sensors will be fitted like a parabolic curve. Secondly, they will be integrated in the whole face which can calculate the opening force of liquid film. Therefore, the seal system can be stable and safe by controlling the opening force and closing face of the spring.

2. THE STRUCTURE AND PRINCIPLE OF AUTOMATION SPIRAL GROOVE FACE SEAL

The structure of spiral groove face seal is similar to the mechanical seal, as shown in Figure 1. And the affiliated automatic control system is also illustrated in this figure. When the rotating ring begins to turn, it will pump sealed media of low voltage side to the side of the high pressure seal chamber. The razor-thin liquid film (micron-scaled) is produced between the moving and static rings what plays a significant role in preventing leakage.

In order to make the fastest response timelier according to the changes of sealed medium pressure and avoid leakage to the most extent on the seal system, it is necessary to install a sensor on the static ring for shaft position. By real-time measurement of sealing medium (water) pressure in the spiral groove end face inlet and the cover, two pressure values can be obtained. To compare the two pressure values and feed back to the controller. At last, the results will be used to adjust the speed of the motor through the controller, thereby, it can adjust the pressure of feed pump to make sealing medium pressure of end face inlet rise or fall.



1-coil spring, 2-fastening screw, 3-spring, 4-rotating ring, 5-seals of rotating ring, 6-gland, 7-seal chamber, 8-stationary ring, 9-seals of stationary ring, 10-shaft

Figure 1: Structure and automatic control system of the spiral groove face seal

ORC system uses organism as working medium, such as R245fa, R134, and R123 (Dai *et al.*, 2009). The various working medium is considered as sealed medium in the automation spiral groove face seal system. Therefore, their physical properties should be considered including toxicity, water solubility and so on. It can be easily ingored that the sensor and other materials face the risk of corrosion. In this paper, water is used as the sealing medium due to it can decrease

complexity of computation and it should be realized that lubricating oil will be used in the practical industry.

3. SIMULATION OF SPIRAL GROOVE FACE SEAL

The CFD analysis provides a visual insight to the sealed and sealing medium behavior inside the spiral groove face seal. However, the flow complexity caused by high rotation speed and micro-scale need to be solved by accurate equation approach and flow model.

3.1 Governing Equations

The simple criterion of distinguishing laminar flow and turbulent flow is the Reynolds Number. The method of calculating Re is given as:

$$Re = \frac{\rho Lu}{\eta} \quad (1)$$

By the calculation, Re number is 102 and it is greater than the Re number used to determinate the laminar and turbulent flow on engineering which is 2600 (Moxey et al., 2010) It could be considered that the flow is in laminar motion. ANSYS/FLUENT provides four segregated types of algorithms: SIMPLE, SIMPLEC, PISO, and (for time-dependant flows using the Non-Iterative Time Advancement option (NITA)) Fractional Step (FSM). In ANSYS/FLUENT, both the standard SIMPLE algorithm and the SIMPLEC (SIMPLE-Consistent) algorithm are available. SIMPLE is the default, but many problems will benefit from using SIMPLEC, particularly because of the increased under-relaxation that can be applied. The governing equations are following:

(a) The equation for conservation of mass, or continuity equation, can be written as follows:

$$\frac{\partial \rho}{\partial t} + \nabla \cdot (\rho \bar{v}) = 0 \quad (2)$$

(b) Transport of momentum in an inertial (non-accelerating) reference frame is described by

$$\frac{\partial}{\partial t} (\rho \bar{v}) + \nabla \cdot (\rho \bar{v} \bar{v}) = -\nabla p + \nabla \cdot (\bar{\tau}) + \rho \bar{g} + \bar{F} \quad (3)$$

where p is the static pressure, $\bar{\tau}$ is the stress tensor (described below), and $\rho \bar{g}$ is the gravitational body force, \bar{F} contains other source terms that may arise from resistances, sources, etc.

(c) The energy equation for a fluid region can be written in terms of sensible enthalpy h as

$$\frac{\partial}{\partial t} (\rho h) + \nabla \cdot (\rho h \bar{v}) = \nabla \cdot [(k + k_t) \nabla T] + S_h \quad (4)$$

where k is the molecular conductivity, k_t is the conductivity due to turbulent transport, and the source term S_h includes any volumetric heat sources you have defined.

3.2 Simulation Model

The two dimensional structure of sealing ring is presented in Figure 2. Software of Gambit and ANSYS/Fluent were used to accomplish geometric modeling and numerical simulation of internal flow field of spiral groove respectively.

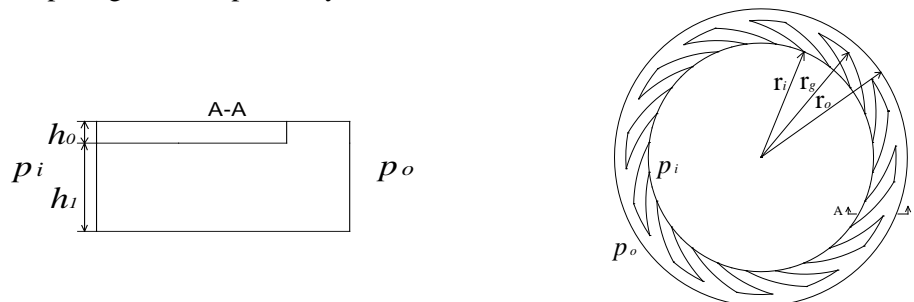


Figure 2: Structure of slotted end face of spiral groove face seal

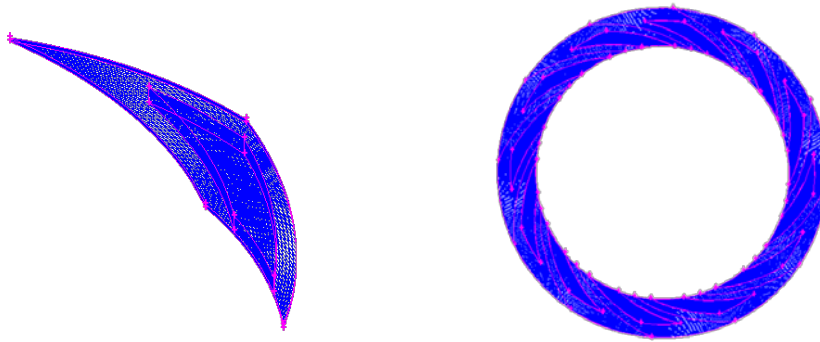


Figure 3: Computational mesh of spiral groove face seal

The spiral groove seal was modeled by the professional 3D modeling software-Gambit, and used CFD codes together with structured hexahedral mesh as shown in Figure 3. The grid number of single spiral groove is 129536 and the grid number of whole circle is 1554432.

3.3 Simulation Results

To combine the design of sealing device and the given medium (water) parameters, the spiral groove face seal was simulated under different working parameters in this paper to ensure the differential pressure without leakage. When the seal structure and the shaft rotate, the sealing medium is constant. To calculate the pressure of end face inlet based varying sealing medium pressure (the pressure of end face outlet) within 2 to 3 MPa. In all working conditions, using the minimum value among the maximum differential pressure regarded as safety limits to be control value which can ensure no leak. The specific working parameters are presented in Table 1.

The inlet pressure is assumed to be 0.1MPa and increasing the outlet pressure gradually, it can be found that the end face has backflow when the outlet pressure p_0 is 0.6413MPa. The backflow becomes more serious as p_0 increases, what illustrates the happen of leakage. The simulation results are shown in Figure 4.

Table1: The value and range of all parameters

Items	Value	Items	Value
Inner diameter r_i / mm	25	Spiral angle/°	21
External diameter r_o /mm	32.5	Length ration of Slot and dam L_g	0.67
Thickness of film h_0 / mm	0.003	Rotate speed n/r·min ⁻¹	3000
Groove width ratio γ_g	0.5	Medium	water
Number of grooves N	12	Working temperature T /°C	20
Groove depth h_1 / mm	0.0125	Inlet pressure/MPa	0.1~2
Radius of the junction of slot and dam r_g / mm	30	Outlet pressure/MPa	0.1~3

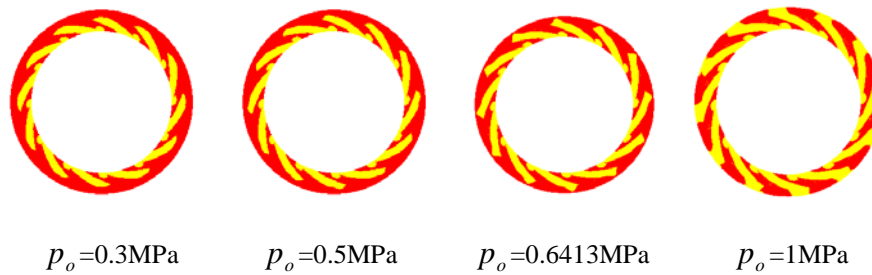


Figure 4: Radial velocity contours with different outlet pressures

Figure 4 shows the radial velocity contours when the inlet pressure is 0.1MPa and the outlet pressure is 0.3MPa, 0.5MPa, 0.6413MPa, 1MPa respectively. The yellow section represents the radial velocity direction of flow that points the center of a circle, and the red section represents the radial velocity direction of flow that points the back to center of a circle. When the outlet pressure p_o is 0.6413MPa, the yellow section penetrates the whole circle what demonstrates the medium flows from the external to the inner, the sealing medium begins leaking. And the backflow is intensified with the increasing outlet pressure. To calculate the corresponding outlet pressure without leakage respectively when the inlet pressure is 0.1MPa, 1MPa and 2MPa. Finally we can get the differential pressure with leakage happening under these three working conditions, using the minimum value of these three differential pressures (0.54MPa) to be the control condition in this paper.

4. THE AUTOMATIC CONTROL SYSTEM OF SPIRAL GROOVE FACE SEAL

The automatic control system used for the spiral groove face seal cannot be establishment without high precision and micro sensor, extremely refine processing technic, and the sensitive controller. Moreover, the control condition which is the major part in the system has been calculated through CFD simulation in the above section. The control system mentioned in the paper need to prevent leak from happening with the differential pressure becomes 0.54MPa suddenly under all working conditions, therefore, it is vitally important for the control system to make timely and accurately responses.

4.1 Control Model

The control model of the automatic control system is shown in Figure 5. Comparing the feed pump output pressure P_v (the pressure of sealing medium) with seal medium pressure P_s , the controller transfer signal to change the valve opening of pump outlet to regulate the flow, thereby the differential pressure can be stay at 0.54MPa.

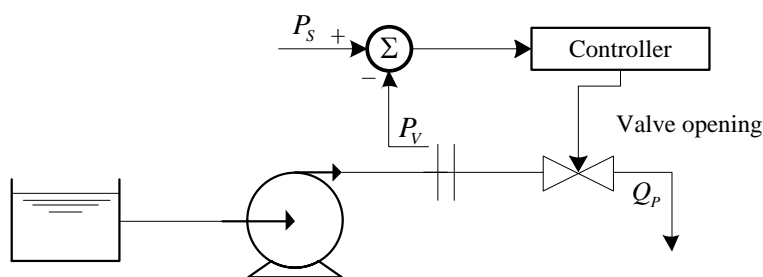


Figure 5: Pressure control model of automation spiral groove face seal

The mathematical model of centrifugal pump was established based on the characteristic curve of the pump as shown in Figure 6. Figure 6 shows the relationship between the capacity and head of the pump (Hu *et al.*, 2015).

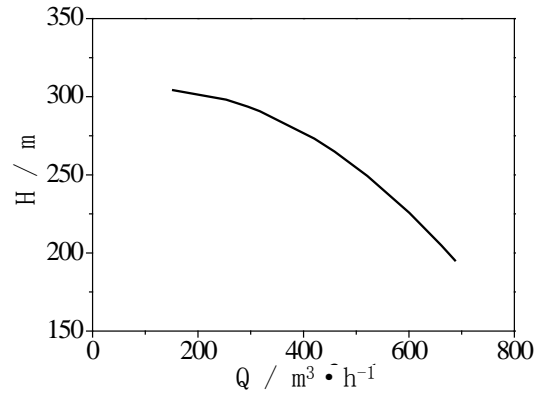


Figure 6: Characteristics curve of the feed water pump

The pump flow is determined by the valve opening and pressure difference between the front and behind of the valve and the relationship is given in Equation (5)

$$Q = k\sqrt{P_V - P_a} \quad (5)$$

Where, k represents the valve opening, P_V and P_a represent the pressure of front and behind of valve respectively. In this system, the P_a is just atmosphere pressure. When P_V is gage pressure, the Equation can be expressed as:

$$Q = k\sqrt{P_V} \quad (6)$$

The Bernoulli equation (Shames, 1982) used for the pump without considering frictional resistance and flow losses is given as:

$$\frac{P_{in}}{\rho g} + \frac{v_{in}^2}{2g} + z_1 + H = \frac{P_{out}}{\rho g} + \frac{v_{out}^2}{2g} + z_2 \quad (7)$$

To the system in this paper, $z_1 = z_2$, $v_{in} = v_{out}$, the lift of pump is:

$$H = \frac{P_{out} - P_{in}}{\rho g} \quad (8)$$

When P_V is gage pressure, the pressure of the inlet of seal end face is :

$$P_V = \alpha \rho g H \quad (9)$$

Where α represents partial loss coefficient of the pump outlet and the valve inlet what is equivalent to the flow loss of working medium in the process of the whole flow.

4.2 Control Strategy

According to the theories above, the detailed automation spiral groove end face seal model was established in MATLAB/SIMULINK as shown in Figure 7. And, the PI controller was used to control the pressure of sealing medium. To increase the proportionality coefficient can reduce static error, but oversize proportionality coefficient can take unstableness to the closed-loop system. The principle of PI controller is presented in Equation (10),

$$G_C = K_P e(t) + K_I \int_0^t e(\tau) d\tau \quad (10)$$

where $e(t)$ represents the deviation between set value and actual value, K_P and K_I represent proportionality coefficient and integral coefficient, respectively.

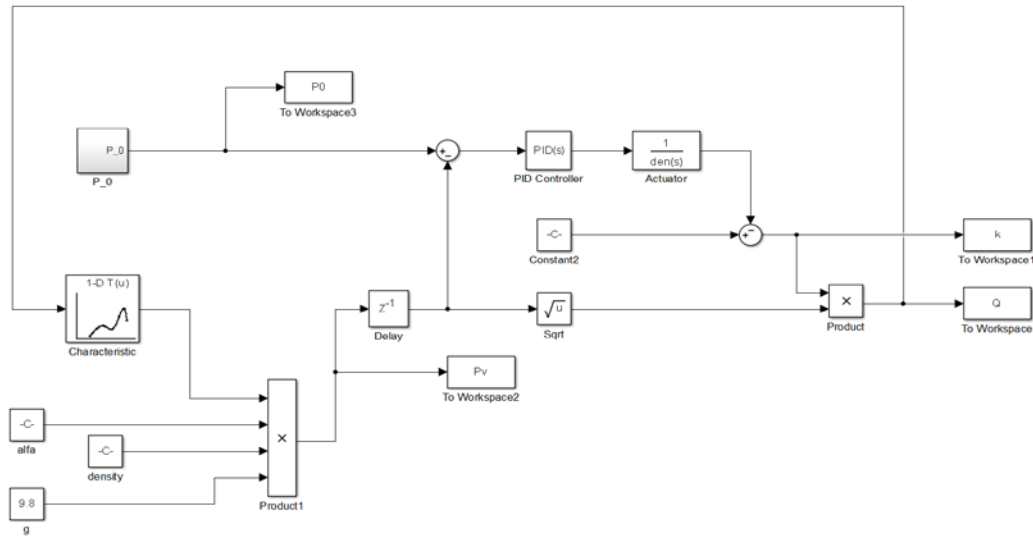


Figure 7: Control model and program of automation spiral groove face seal

4.3 Results

The paper designs proportional-integral (PI) control (Byung-Su and Edgar, 1998) for the system. For the dynamic response characteristic simulation of the system, to compare the pressure (p_i) of sealing medium provided by the feed pump with the value (p_0) of the sealed pressure subtracts 0.54MPa. Assuming the initial pressure of the feed pump is 2.5 MPa, and p_0 changes from 2.5MPa to 3MPa through stepping. After setting controller parameters, the variation of pressure provided by pump under PI control is shown in Figures 8 and 9. Figure 8 shows the pressure step disturbances (0.1MPa, 0.3MPa and 0.5MPa) of sealed medium and Figure 9 shows the pressure responses of sealing medium under the controller.

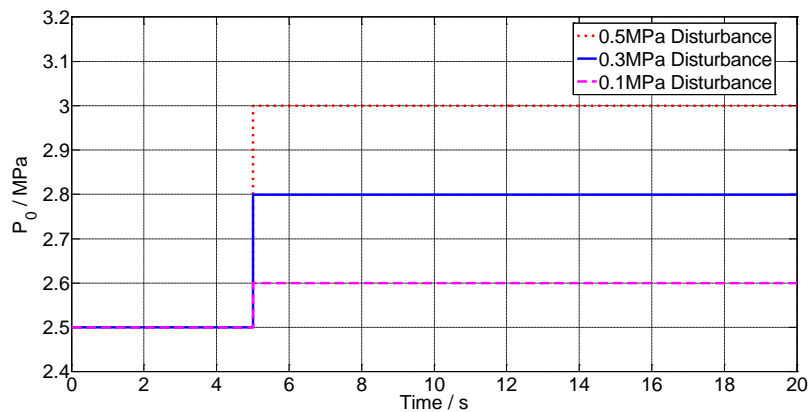


Figure 8: Pressure step disturbance of sealed medium

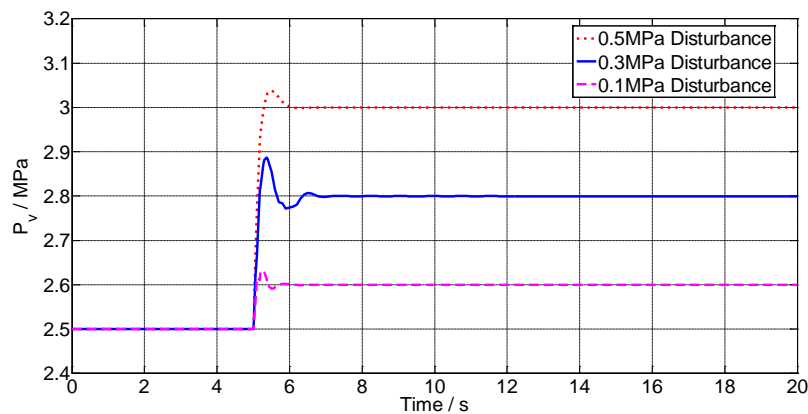


Figure 9: Pressure responses of sealing medium under varying disturbances

It can be seen that when p_0 changes from 2.5MPa to 3MPa through stepping, the sensor accepts the variation of p_0 and comparing with the pressure of the front of outlet valve. The controller adjusts the outlet valve opening by accepting the signal of differential pressure. However, more flow makes the pressure provided by pump smaller when the rotating speed of pump is constant. Figure 9 proves PI control has no static error and system overshoot. From the dynamic process of adjusting, the PI control is immediately reacting for deviation. As long as there is deviation, the integral accumulation will affect control until the deviation is zero.

The dynamic response curves of flow and valve opening are shown in Figures 10 and 11, respectively.

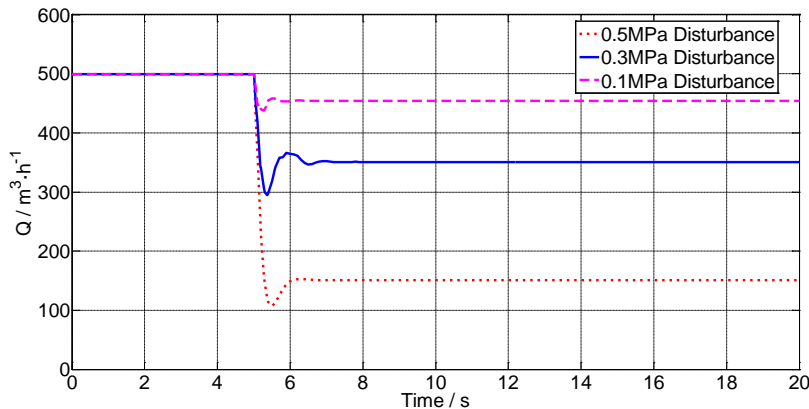


Figure 10: Dynamic response curves of flow under varying disturbances

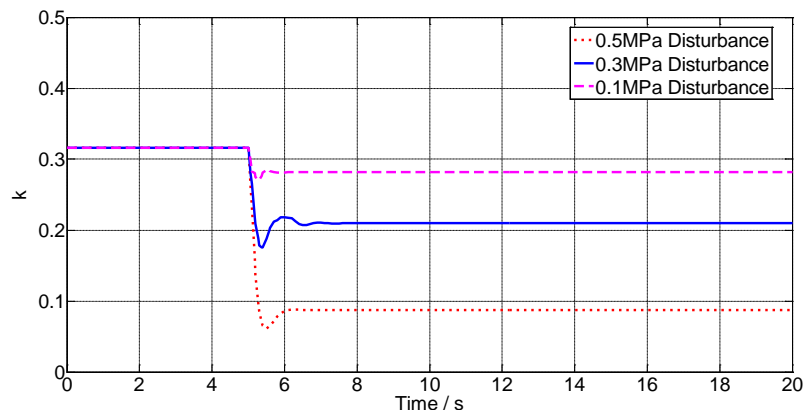


Figure 11: Dynamic response curves of valve opening under varying disturbances

The original state of system: the pressure provided by pump is 2.5MPa, the valve opening is 0.316 by calculating. To reduce the deviation from p_0 in order to increase the pressure provided by pump. Thereby the valve opening should decrease gradually by the controller. Figure 11 shows the PI control can achieve the zero static error with p_0 through adjusting valve opening. The flow variation is determined by valve opening and pressure difference on both ends of valve. According to Equation (5), it can be calculated that the flow with the pressure provided by pump and valve opening at some point. The flow decreases with valve opening decreasing. However, the relationship between the flow and pressure provided by pump is nonlinear according to the pump characteristic curve.

The working points curve of the pump under the control above as shown in Figure 12. It can be seen that A point is the original value of working point, B, C and D are the working points after PI control making system steady under different disturbances respectively. The PI control makes the working point move from A to the terminal points (B, C and D) in a curve of the second degree, the growth rate of pressure become slower with the decrease of flow.

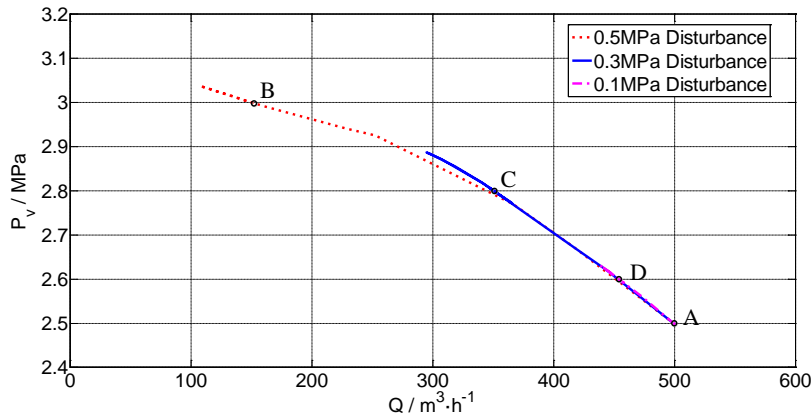


Figure 12: Dynamic response curve of the pump working points under varying disturbances

5. CONCLUSIONS

The paper proposes an automatic adjusting device of the spiral groove face seal used on ORC turbine shaft end. It can achieve zero leakage through a complete automatic control system. This paper mainly includes two parts: using CFD to simulate the spiral groove face seal in order to ensure the differential pressure, using SIMULINK to establish the automatic control model. Based on the analytical and simulative investigations presented in this paper, the following conclusions can be drawn:

- 1 The spiral groove face seal with automatic control system can achieve zero leakage which can be used for the ORC turbine.
- 2 The CFD method provides an insight way to investigate the internal flow of the spiral groove seal and calculates the differential pressure (0.54MPa).without leakage. Additionally, the outlet pressure contributes to the backflow.
- 3 This control system with PI controller has good robustness and strong resistance for disturbance under the off-design conditions.

NOMENCLATURE

g	gravitational acceleration	(m/s ²)
h	mean specific enthalpy	(J/kg)
k	valve opening	(m)
L	length	(m)
P_{in}	inlet pressure of pump	(Pa)
P_{out}	outlet pressure of pump	(Pa)
p	pressure	(Pa)
u	velocity	(m/s)
v_{in}	inlet velocity of pump	(m/s)
v_{out}	outlet velocity of pump	(m/s)
z_1	inlet height of pump	(m)
z_2	outlet height of pump	(m)

Greek symbol

ρ	density	(kg/m ³)
η	absolute viscosity	(kg/m·s)
τ	time	(s)

REFERENCES

- Sedy J., 1980, *U.S. Patent No. 4,212,475*, Washington, DC: U.S. Patent and Trademark Office.
- Wolff P.J., Salant R.F., 1995, Electronically controlled mechanical seal for aerospace applications- Part II: Transient tests, *Tribol. trans.*, vol. 38, no. 1: p. 51-56.
- Heilala A. J., Kangasneimi A., 1987, Adjustment and control of a mechanical seal against dry running and severe wear, *Proc. 11th Int. Conf. Fluid Sealing*, p. 548-575.
- Etsion I. Z. J. N., Palmor Z. J., HARABRI N., 1991, Feasibility study of a controlled mechanical seal, *Lubr. Eng.*, vol. 47, no. 8: p. 621-625.
- Zou M., Dayan J., Green I., 2000, Dynamic simulation and monitoring of a non-contacting flexibly mounted rotor mechanical face seal, *Proc. Inst. Mech. Eng., Part C: J. Mech. Eng. Sci.*, vol. 214, no. 9: p. 1195-1206.
- Boqin Z. J. G., 2009, Controllability of Spiral Groove Mechanical Seal, *Chin. J. Mech. Eng.*, 1, p. 20.
- Ya Z., Ying W., Yiping D., 2012, Numerical simulation and characteristics analysis of the turbine shaft end spiral groove mechanical seal, *Digital Manuf. Autom. (ICDMA), 2012 Third Int. Conf. IEEE*: p. 558-561
- Dai Y., Wang J., Gao L., 2009, Parametric optimization and comparative study of organic Rankine cycle (ORC) for low grade waste heat recovery, *Energy Convers. Manage.*, vol. 50, no. 3: p. 576-582.
- Moxey D., Barkley D., 2010, Distinct large-scale turbulent-laminar states in transitional pipe flow, *Proc. Nat. Acad. Sci.*, vol. 107, no. 18: p. 8091-8096.
- Hu D., Li S., Zheng Y., Wang J., Dai Y., 2015, Preliminary design and off-design performance analysis of an Organic Rankine Cycle for geothermal sources, *Energy Convers. Manage.*, vol. 96: p. 175-187.
- Shames I.H., Shames I.H., 1982, *Mechanics of fluids*, p. 359, New York, NY: McGraw-Hill.
- Ko B.S., Edgar T.F., 1998, Assessment of achievable PI control performance for linear processes with dead time, *Am. Control Conf., 1998. Proc. 1998* vol. 3: p. 1548-1552.

ACKNOWLEDGEMENT

The authors gratefully acknowledge the financial support by the National High-tech Research and Development Program (Grant No.2012AA053002) and the National Key Technology R&D Program (Grant No.2011BAA05B03).

FACTOR ANALYSIS OF EXPANSION RATIO FOR SINGLE SCREW EXPANDERS

Wei WANG*, Li-li SHEN, Liang CHEN, Yu-ting WU, Chong-fang MA

* Beijing University of Technology,
College of Environmental and Energy Engineering,
Key Laboratory of Enhanced Heat Transfer and Energy Conservation, Ministry of Education and Key
Laboratory of Heat Transfer and Energy Conversion, Beijing municipality,
100 PIN LE YUAN, Chaoyang District, Beijing, P R China
E-mail: wang_wei@bjut.edu.cn

*Wei WANG

ABSTRACT

For low temperature waste heat recovery, Organic Rankine Cycle (ORC) is generally considered the most promising choice in varieties of potential technologies, and become a hotspot of research and development in international academic and industrial fields. However, reviewing the research results related ORC system in recent years, the actual situation was not optimistic. There were many technical bottlenecks hindered the application of ORC, especially for small scale system. Among those problems, the performance of expander was the key issue, and how to improve it was two aspects. First one was improving the shaft efficiency of expander, and it was the common sense of the researchers in this field. Second one was controlling appropriate expansion ratio (ε), and it was special requirement of small scale ORC system. Due to relative small expansion ratio, the thermal efficiency of ORC was low even if high efficiency of expanders. In actual conditions, the high efficiency and expansion ratio of expanders were hardly obtained simultaneously. So, it is necessary to carry out the special discussion about expansion ratio. Single screw expander was a type of volumetric prime mover. Due to special configuration, it had the potential of realized relative high expansion ratio. So, it makes possible getting high thermal efficiency of ORC. In this paper, we tried to analyze the influence factors of internal expansion ratio for single screw expanders. Firstly, the thermodynamic model of ORC was described, and the analysis of expansion ratio influenced cycle thermal efficiency was carried out. From the calculation results, it was found that thermal efficiency was increased with expansion ratio, but the accelerated velocity was decreased gradually. Considering the actual efficiencies of expander and pumps, appropriate expansion ratio should be existed. Secondly, the analysis of the influence factors of internal expansion ratio for single screw expanders was carried out, from the aspects of configuration, process and condition. From the results, high expansion theoretically could be obtained by changing the configuration of screw and gaterotor, inlet and outlet structure. The maximum volumetric ratio could above 20, and it could completely cover the temperature range of low temperature waste heat recovery. However, in actual condition, different meshing and fit clearances would influence leakage and cause expansion ratio reduced. So, configuration design and clearance control were key issues to improve the expansion ratio of single screw expanders.

1. INTRODUCTION

Nowadays, research and development of low temperature heat efficient thermal power conversion system becomes a hot research field in the world. Among the research of different type thermodynamic cycles, ORC was considered the most potential technology and obtained the most attention in the world.

For ORC research, thermodynamic cycle analysis was the most popular field all over the world, and the most academic articles focused on it. Reviewing most articles in this topic, the result was still existed the problems of ideal and bad suitable for actual situation. Especially for small scale low temperature heat source, the restriction of expander was the key problem, and it was indicated overestimating expander efficiency and ignoring the influence of expansion ratio. Referring the efficiency of large scale steam turbine, expander efficiency was usually assumed above 0.8. Moreover,

the actual performance of working fluid pump was another key problem, and the pump efficiency was significantly overestimated in many articles, the value was about 0.65-0.85. Hence, the performance indexes of ORC were overestimated obviously, and thermal efficiency of ORC was higher than 10%, even above 15%.

For experimental study of ORC system, we can get quite different situation. There are many articles carried out the research of this topic, we just took some examples. The result data of some experimental study articles was showed in Table 1. From the results of those articles, we can find that the types of working fluid pump were included diaphragm and multistage centrifugal, although most of the articles did not gave actual pump efficiency, but the data of Quoilin et al. (2010) could reflect the real situation, it was only 15%. In other words, the actual pump efficiency was very lower than assumption, but we had to choose diaphragm and multistage centrifugal pumps because of high pressure requirement. It was very difficult to obtain high pressure, small flow rate and high efficiency at the same time, so how to improve the efficiency of working fluid pump was a key issue for ORC, especially for small scale system. We also can find that the types of expander were included scroll, rolling piston, radial turbine and single screw. Actually, every type expanders have been studied. From the results, it was obvious that radial turbine had the biggest capacity, second was single screw, and scroll and rolling piston was smaller. The working conditions of each article were quite different, but the temperature difference of evaporation and condensation were all about 30-50°C. Because several articles did not mentioned the degree of supercooled, so the actual temperature difference between expander's inlet and outlet should below above value. It indicated that the real energy utilization percentage of ORC was significantly lower than analyzed results, it was also indicated that the limitation of expander was a key bottleneck for sufficiently utilization low temperature thermal energy. From the data of table 1, we can find that the expansion ratio was about 2.5 to 6.6. Considering the thermophysical property of working fluid, the temperature difference between inlet and outlet for expander was estimated about 40-60°C, and it was obviously lower than the temperature difference between low temperature heat source and surrounding. Meanwhile, if expander efficiency was not good enough, the performance of ORC would be worse than desired. Unfortunately, the real efficiency of expanders was not satisfied, it was just about 40%-60%. Kang et al. (2012) presented the tested efficiency of radial turbine beyond 80%, but its expansion ratio was below 2.72, so the maximum value of thermal efficiency was about 5.65%, lower than the case of higher expansion ratio. The results of unsatisfied expansion ratio and expander efficiency were unacceptable thermal efficiency of ORC.

Reviewing the research results related small scale ORC system, we can get three bottlenecks for ORC performance: expander efficiency, expansion ratio and the efficiency of pump and fan. For small scale expanders, improving efficiency was a tuff job, and working fluid pump had similar situation. So, improving expansion ratio was an easier measure for obtaining higher thermal efficiency at present. There are many factors influencing expansion ratio, such as working fluid types, expander configurations and working conditions, etc.

Single screw configuration is composed of a screw and several gaterotors, and generally divides into four types of PC, PP, CC and CP. C and P were the abbreviations of cylinder and plate, respectively. The first abbr. means the shape of screw and the second one means the shape of gaterotor. CP type is the most common configuration of single screw because of easily processing. A single screw expander mainly consists of screw, gaterotors and shell. The screw groove, the internal wall of shell and the profile surfaces of the gaterotor teeth constitutes a closed space, which was to change the volume with the rotation of screw and gaterotor. In this paper, we tried to analyze the influence factors of expansion ratio for single screw expanders, and try to provide the technical measures to improve it.

Table 1: List of the performance indexes of some experimental study articles

Author	Work fluid pump	Expander	Working fluid	W_G/kW	$T_{eva}/^{\circ}C$	$T_{con}/^{\circ}C$	$\eta_E/\%$	ε	$\eta_H/\%$	$\eta_P/\%$
Li et al. (2013)	Diaphragm	Radial turbine	R123	6.07	90.7	39.4	58.53	4.19	7.98	No
Bracco et al. (2013)	Diaphragm	Scroll	R245fa	1.1-1.8	85.4-101.4	27-30	60-74	4.6-6.6	8.8-9.8	No
Quoilin et al. (2010)	Diaphragm	Scroll	R123	0.5-1.8	-	-	42-68	2.7-5.4	Max. 7.4	15%
Zheng et al. (2013)	Diaphragm	Rolling piston	R245fa	0.16-0.32	72.4-82.6	14.6-33.2	Max. 44	4	2-6	No
Zhou et al. (2013)	Multistage centrifugal	Scroll	R123	Max. 0.645	85.5-114.9	34.9-49.6	Max. 57	5	Max. 8.5	No
Kang et al. (2012)	Multistage centrifugal	Radial turbine	R245fa	24.5-31.2	77-83	44.5-47.3	76-82.2	2.62-2.72	5.05-5.65	No
Gu et al. (2009)	Multistage centrifugal	Scroll	R600a	Max. 1.1	-	-	Max. 50.1	-	Max. 2.9	Assumed 85%
Zhang et al. (2014)	Multistage centrifugal	Single screw	R123	Max. 10.38	123.6-140.2	79-101	Max. 57.9	2.5-4.6	Max. 6.5	No

2. INFLUENCE FACTORS FOR ORC SYSTEM

Due to the limitation of expanders, low temperature heat energy could not make full use for small scale ORC system. A remarkable phenomenon was outlet temperature of working fluid higher than condensation temperature, and it was caused by relative lower expansion ratio of expanders. In this section, we tried to analysis expansion ratio how to influence the performance of ORC system.

2.1 Thermodynamic model

Firstly, a thermodynamic model was described, and specific information was showed in Figure 1.

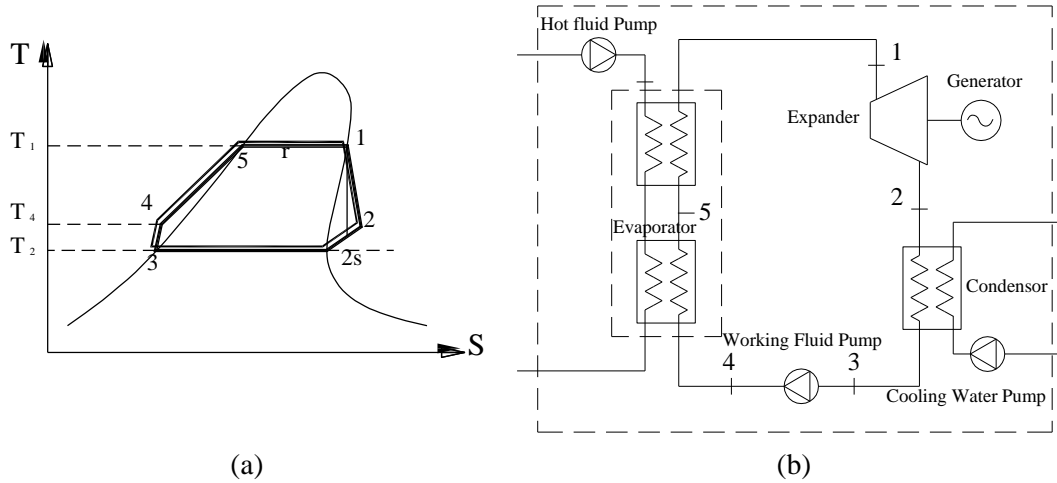


Figure 1: Organic Rankine cycle
(a) T-S chart; (b) Schematic diagram of thermal system

The thermodynamic model of power generation system was described as follow. Point 1, 3 and 5 were assumed to saturation state.

The absorption heat of working fluid in evaporator is calculated by

$$Q_1 = m(h_1 - h_4) \quad (1)$$

The generating capacity of expander is calculated by

$$w_G = (h_1 - h_{2s})\eta_a\eta_M\eta_G \quad (2)$$

The consumption of working fluid pump is calculated by

$$w_P = \frac{v_3(p_4 - p_3)}{\eta_P\eta_{EM}} = \frac{(h_4 - h_3)}{\eta_P\eta_{EM}} \quad (3)$$

The net generation of ORC is calculated by

$$W_{net,ORC} = W_G - W_P = m(w_G - w_P) \quad (4)$$

The thermal efficiency (thermodynamic first law efficiency) of ORC is defined as

$$\eta_{H,ORC} = \eta_{I,ORC} = \frac{W_{net,ORC}}{Q_1} = \frac{(h_1 - h_2) - (h_4 - h_3)}{h_1 - h_4} \quad (5)$$

The thermodynamic second law efficiency of ORC is defined as

$$\eta_{II,ORC} = \frac{\eta_{H,ORC}}{1 - \frac{T_3}{T_1}} \quad (6)$$

Because of the limitation of expansion ratio (ε), when working fluid type and evaporation temperature was assumed, outlet pressure was calculated by expansion ratio. So, the relationship between inlet pressure and outlet pressure is defined as

$$\varepsilon = \frac{p_1}{p_2} \quad (7)$$

2.2 Result and discussion

Before calculated, we must assume some conditions. Here, R123 was selected by working fluid, because it had higher critical point. Generator efficiency and electric motor efficiency of working fluid pump was assumed 0.95, respectively.

2.2.1 Expansion ratio

Here, adiabatic and mechanical efficiency were assumed about 0.7 and 0.95, respectively. So the total efficiency of expander was about 0.65, and it was very near experimental results. Working fluid pump efficiency was assumed 0.8. **Condensation temperature was assumed 30°C**

Figure 2 was the variation of thermal efficiency with expansion ratio of R123. At the same evaporation temperature, thermal efficiency increased with expansion ratio, until the condensation temperature was near environmental temperature. At the same expansion ratio, thermal efficiency decreased very slightly with the increase of evaporation temperature. However, with the absolute pressure rising, pump efficiency would be reduced in actual condition. So, it was indicated that lower evaporation temperature should be adopted at the condition of determined expansion ratio.

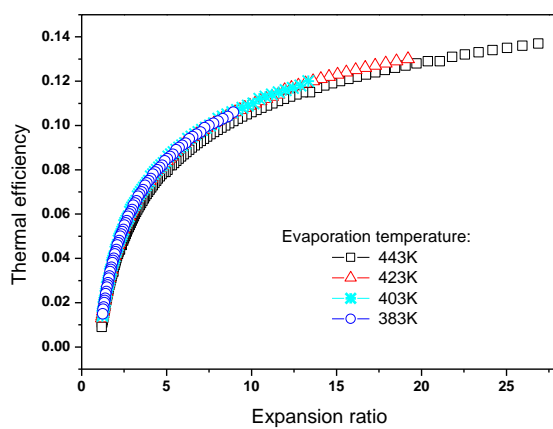


Figure 2: Variation of thermal efficiency with expansion ratio of R123

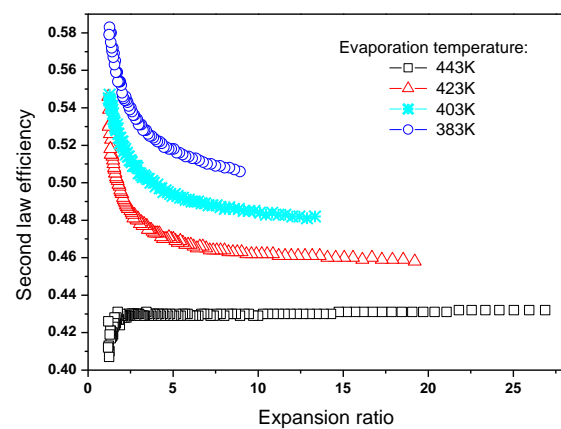


Figure 3: Variation of Second law efficiency with expansion ratio of R123

Figure 3 was the variation of second law efficiency with expansion ratio of R123. At the same evaporation temperature, second law efficiency decreased quickly with expansion ratio, until the condensation temperature was near environmental temperature. With the increase of evaporation temperature, the decrease velocity become gently. The reverse trend occurred with evaporation temperature closing critical point. At the same expansion ratio, second law efficiency accelerated declined with the increase of evaporation temperature. Summary above calculating result, it was indicated that improving expansion ratio was an effective method to increase the thermodynamic performance of ORC, however, if considering expander and pump efficiency would decrease with the increase of expansion ratio, so expansion ratio should existed suitable range.

2.2.2 Adiabatic efficiency

Here, mechanical efficiency was assumed 0.95. Expansion ratio was assumed 6. Working fluid pump efficiency was assumed 0.8.

Figure 4 was the variation of thermal efficiency with adiabatic efficiency of R123. At the same evaporation temperature, thermal efficiency lineal increased with adiabatic efficiency. At the same adiabatic efficiency, thermal efficiency decreased slightly with the increase of evaporation temperature, the trend was more obvious in the situation of lower adiabatic efficiency. So, it was indicated that improving evaporation temperature should not a reasonable method if expansion ratio fixed. Figure 5 was the variation of second law efficiency with adiabatic efficiency of R123. It has similar trend compared with thermal efficiency, just a little different. With the increase of adiabatic efficiency, the difference of second law efficiency was gradually added among different evaporation temperature. The phenomenon could explain that thermodynamic perfection will be improved with the increase of adiabatic efficiency and far away from critical point.

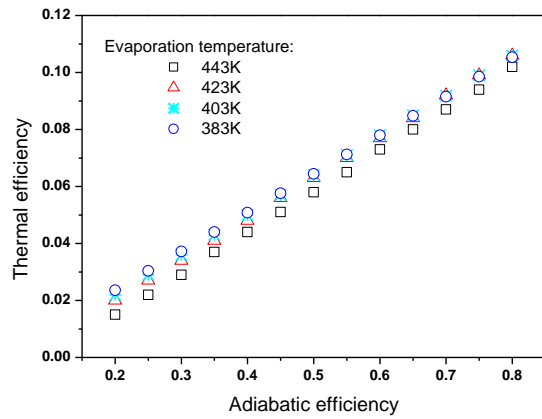


Figure 4: Variation of thermal efficiency with adiabatic efficiency of R123

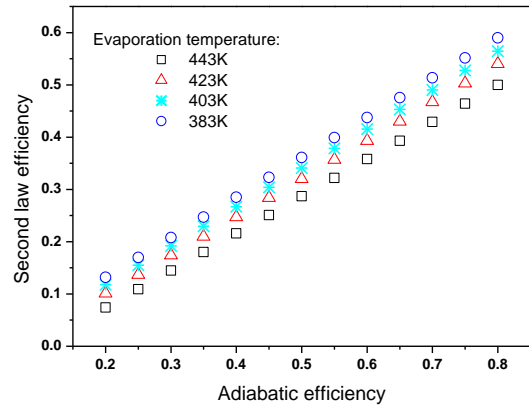


Figure 5: Variation of second law efficiency with adiabatic efficiency of R123

2.2.3 Pump efficiency

Here, adiabatic and mechanical efficiency were assumed about 0.7 and 0.95, respectively. Expansion ratio was assumed 6.

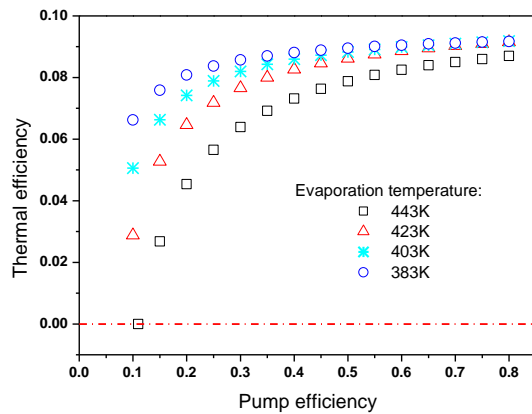


Figure 6: Variation of thermal efficiency with pump efficiency of R123

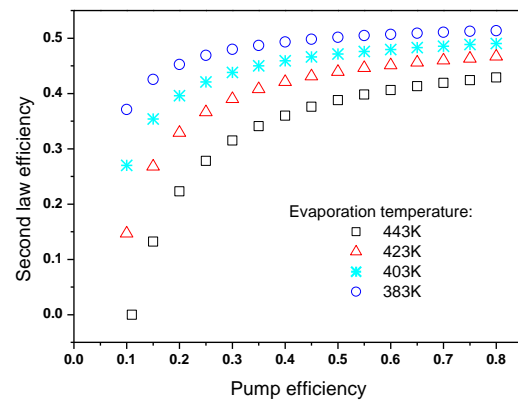


Figure 7: Variation of second law efficiency with pump efficiency of R123

Figure 6 was the variation of thermal efficiency with pump efficiency of R123. At the same evaporation temperature, thermal efficiency accelerated declined with pump efficiency decrease. At the same pump efficiency, thermal efficiency decreased accelerated with the increase of evaporation temperature, the trend was more obvious in the situation of lower pump efficiency. From the result, it was also found that the influence of pump efficiency was weakened at relative lower evaporation temperature, even lower than 0.3. So, it was indicated that improving evaporation temperature should not a reasonable method if low pump efficiency. Figure 7 was the variation of second law efficiency with pump efficiency of R123. It has similar trend compared with thermal efficiency.

Summary above calculating result, it could be found that improving expansion ratio could increase thermodynamic performance of ORC system. If expansion ratio could not be improved, increase evaporation temperature was no use to improve performance.

3. EXPANSION RATIO OF SINGLE SCREW EXPANDERS

According to the different working principles, expanders can be classified two types: velocity and positive displacement. Velocity expanders mainly include single stage and multi-stage axial turbine, single stage and multi-stage radial turbine, etc. Positive displacement expanders mainly include piston, scroll, twin screw and single screw, etc. According to the different movement forms, positive displacement expanders can be classified two types: reciprocating and rotary. Piston expander is the former, and scroll, twin screw and single screw are the latter.

For velocity expanders, increasing rotational speed could improve expansion ratio. But, if the rotational speed was increased too high, mechanical loss would be significantly raised. So, multi-stage configuration was adopted usually in order to improve expansion ratio. Generally speaking, expansion ratio of single stage for axial turbine was lower than radial turbine. So, the stage numbers of axial turbine should be more than radial turbine if obtained the same expansion ratio.

For positive displacement expanders, expansion ratio (ε) was influenced by internal volumetric ratio (τ) and adiabatic index of working fluid. The function existed in ideal condition:

$$\varepsilon = \left(\frac{V_{out}}{V_{in}} \right)^\kappa = \tau^\kappa \quad (8)$$

For reciprocating expanders, expansion ratio could be changed through controlling inlet and exhaust phases. However, if the expansion ratio was improved too high, adiabatic efficiency would greatly decrease due to the clearance volume. For rotary expanders, if the configuration and working fluid has been determined, expansion ratio was fixed. There are two methods to improve it: the one is modify the configuration of expanders, and the other is added capacity adjustment mechanism, for example, slide valve.

Single screw expander is positive displacement type, and belongs to rotary type too. Considering actual situation, mainly influence factors of expansion ratio included three aspects: internal volumetric ratio, working fluid type and working condition.

3.1 Internal volumetric ratio

Because CP type single screw configuration was the simple and widely use among different single screw types, so it was selected for the case to analysis. Geometric structure of single screw meshing pair was showed on Figure 8. Mainly parameters include screw radius R_1 , gaterotor radius R_2 , the center distance between screw and gaterotor A , meshing angle α_1 , discharge angle α' , half angle of teeth width δ , teeth width of gaterotor b_0 , minimum thickness of screw rib Δb . When R_1 , R_2 , A , b_0 were assumed, other parameters could be calculated.

In order to obtain internal volumetric ratio, intake and exhaust volume should be calculated. Exhaust volume was the maximum volumetric element. Making reference to the handbook (Yu et al, 2012), the maximum volumetric element can be calculated by

$$V_1 = \int_{\alpha_1 - \delta}^{\alpha_1 + \delta} \int_{-\frac{b_0}{2}}^{\frac{b_0}{2} \sin(\alpha_1 - \alpha)} \frac{R_1^2 - (A - \sqrt{R_2^2 - b^2 \cos \alpha + b \sin \alpha})^2}{2 \cos \alpha} \omega db d\alpha \quad (9-1)$$

$$V_2 = \int_{\alpha'}^{\alpha_1 - \delta} \int_{-\frac{b_0}{2}}^{\frac{b_0}{2}} \frac{R_1^2 - (A - \sqrt{R_2^2 - b^2 \cos \alpha + b \sin \alpha})^2}{2 \cos \alpha} \omega db d\alpha \quad (9-2)$$

$$V_t = V_1 + V_2 \quad (9-3)$$

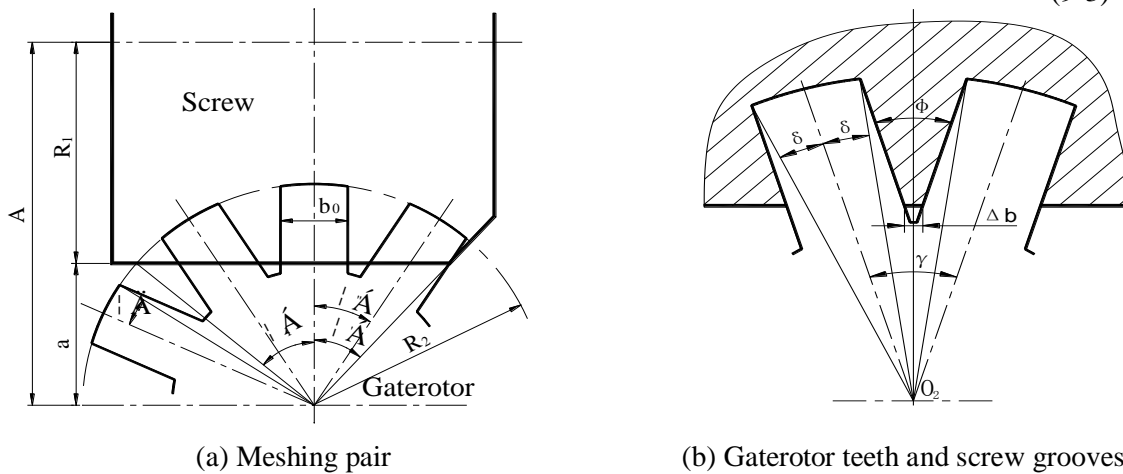


Figure 8: Geometric structure of meshing pairs

Intake volume was determined by intake triangle port and screw groove width (equal to gaterotor teeth width). When the arc length of the circumferential direction of intake triangle port was assumed, the rotary angle of screw could be calculated. Then, it was converted into the rotary angle of gaterotor. So, the rotary angle of gaterotor of intake process was the angle above sentence mentioned plusing teeth width angle (2δ). Thus, intake volume could be calculated by equation (9). Of course, the limits of integration should be changed.

Obviously, if we want to improve expansion ratio, intake volume should be reduced. According to above describe, there were two measures to realize it: the one was reduced the dimension of intake triangle port, and another was reduced screw groove width. The minimum dimension was zero, so the maximum internal volumetric ratio should be existed when screw groove width as certain value. Reducing screw groove width also can improve internal volumetric ratio, but it was limited by the requirement of gaterotor mechanical strength.

Here, we give an example to analysis. R_1 , R_2 , A , b_0 were assumed as 58.5mm, 58.5mm, 96mm and 17.1mm, respectively. Variation of maximum volumetric element and maximum internal volumetric ratio with minimum thickness of screw rib was showed on Figure 9. With the increase of minimum thickness of screw rib, maximum volumetric element was declined linearly, and maximum internal volumetric ratio was increased accelerated. From calculation result, appropriate reducing screw groove width could make maximum internal volumetric ratio to reach above 30. Considering the dimension of intake triangle port, internal volumetric ratio could be easy to realize above 20. Summery above analysis, for single screw expanders, internal volumetric ratio could be improved theoretically by configuration adjustment to satisfy the requirement of ORC system.

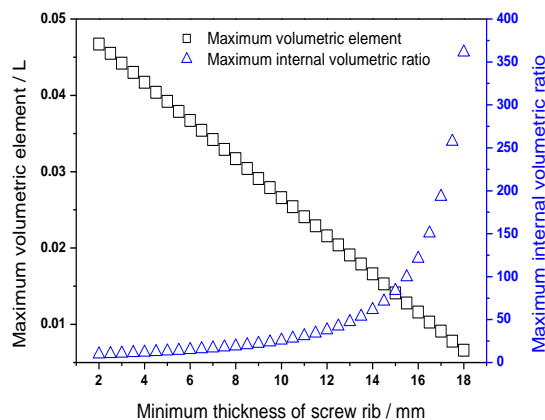


Figure 9: Variation of maximum volumetric element and maximum internal volumetric ratio with minimum thickness of screw rib (Screw diameter = 117mm)

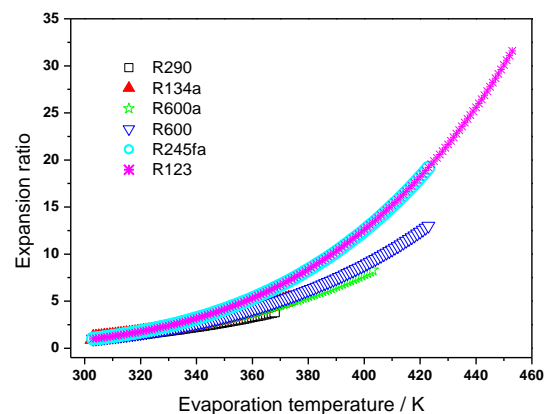


Figure 10: Variation of expansion ratio with evaporation temperature for six working fluids

3.2 Working fluids

Thermophysical properties of working fluid influencing expansion ratio was reflected in two aspects. The one was pressure ratio between evaporation and condensation temperature. Assuming condensation temperature was 303K, R290, R134a, R600a, R600, R245fa and R123 were selected to analyze. Figure 10 was the variation of expansion ratio with evaporation temperature for six working fluids. From the results, at the same temperature difference between evaporation and condensation, working fluid of higher critical point has higher expansion ratio, however, for working fluid of lower critical point, the absolute pressure was significantly higher than the former. In addition, expansion ratio of higher critical point working fluids can beyond 20, even 30 in subcritical region. So, if we want to sufficiently use low temperature heat source, expansion ratio of expanders should be improved.

On the other hand, adiabatic index of working fluids was another important factor. In common sense, working fluid has more complex of molecular structure, the adiabatic index has smaller. Furthermore, from some research result of, adiabatic index of many Freon was significant declined with pressure increase, and it was slightly changed with temperature increase in the situation of lower pressure

(about 200kPa), but it was decreased with temperature increase in higher pressure. For example, the adiabatic index of air was 1.4, R22 was about 1.12-1.19 and R600a was about 1.02-1.05. It was showed that adiabatic index of Freon was obviously lower than air. For refrigeration, it was a good characteristic because of reducing compression power consumption. But for expansion, the situation was opposite. Lower adiabatic index caused lower expansion ratio at the same configuration of expanders.

3.3 Working conditions

The above analysis was based on ideal conditions. But in actual working condition, the situation was more complex. For single screw expanders, many leakage passes were existed due to clearance fit requirement, and leakage will cause the increase of discharge temperature and pressure, so the possess index was lower than adiabatic index, at last, expansion ratio reduced. However, experimental study of this field was much lacked.

4. CONCLUSIONS

In this paper, expansion ratio influencing single screw expanders was discussed. Firstly, a simple thermodynamic model was described, and then expansion ratio influencing ORC system was analyzed. Secondly, the influence factor of expansion ratio for single screw expanders was analyzed. Through those works, five conclusions are obtained:

- (1) With the increase of expansion ratio, thermal efficiency of ORC was improved, and improving speed was fast firstly, and then slowed down. Considering the actual efficiencies of working fluid pump and expander, appropriate improving expansion ratio was the effective technical measure to improve ORC performance.
- (2) At the same expansion ratio, increase intake temperature was no use improving thermal efficiency, and could reduce second low efficiency. So, increase intake parameters were not a good measure to improving ORC performance when the configuration of expander was fixed or regulation system was not existed.
- (3) For a certain configuration of single screw expander, maximum internal volumetric ratio was existed. Through adjusting the demission of intake triangle port and screw groove width, internal volumetric ratio could be changed.
- (4) Thermophysical properties of working fluid would influence expansion ratio, especially adiabatic index. In next research, process index should be obtained by experimental study.

REFERENCES

- Li M, Wang J, He W, et al, 2013. Construction and preliminary test of a low-temperature regenerative Organic Rankine Cycle (ORC) using R123. *Renew. Eng.*, vol.57: p. 216-222.
- Bracco R, Clemente S, Micheli D, et al, 2013. Experimental tests and modelization of a domestic-scale ORC (Organic Rankine Cycle). *Eng.*, vol.58: p. 107-116.
- Quoilin S, Lemort V, Lebrun J, 2010. Experimental study and modeling of an Organic Rankine Cycle using scroll expander. *Appl. Eng.*, vol.87, no.4: p.1260-1268.
- Zheng N, Zhao L, Wang X D, et al, 2013. Experimental verification of a rolling-piston expander that applied for low-temperature Organic Rankine Cycle. *Appl. Eng.*, vol.112: p.1265-1274.
- Zhou N, Wang X, Chen Z, et al, 2013. Experimental study on Organic Rankine Cycle for waste heat recovery from low-temperature flue gas. *Eng.*, vol.55: p. 216-225.
- Kang S H, 2012. Design and experimental study of ORC (organic Rankine cycle) and radial turbine using R245fa working fluid. *Eng.*, vol.41: p. 514-524.
- Gu Wei, 2009. Theoretical and Experimental Study of Organic Rankine Cycle for Low and Medium Grade Heat Source Utilization [D]. School of Mechanical Engineering, Shanghai: Shanghai Jiao Tong University
- Zhang Ye-Qiang, Wu Yu-Ting, Xia Guo-Dong, et al, 2014. Development and experimental study on organic Rankine cycle system with single-screw expander for waste heat recovery from exhaust of diesel engine. *Eng.*, vol.77: p. 499-508.

Yu Yong-zhang, Jiang Pei-zheng, Sun Si-ying, 2012. *Compressor Engineering Handbook*. China Petrochemical Press, Beijing, 1070p.

ACKNOWLEDGEMENT

The work was supported by China National Natural Science Foundation (51006002) and the 973 Program' Project (2011CB707202 and 2011CB710704).

IMPLEMENTAION OF A SMALL SCALE ORGANIC RANKINCE CYCLE TEST BED SYSTEM USING STEAM AS HEAT SOURCE

Muhammad Usman^{‡†}, Muhammad Imran^{‡†}, Dong Hyun Lee[†] and Byung-Sik Park^{*‡†}

[‡]Korea University of Science and Technology, 217 Gajeong-ro, Yuseong-gu, Daejeon 305-350, South Korea
usman@ust.ac.kr / usman7@live.com
Web page: <http://www.ust.ac.kr/>

[†]Korea Institute of Energy Research,
152 Gajeong-ro, Yuseong-gu, 305-343, Daejeon, South Korea
^{*}Corresponding Authur e-mail: bspark@kier.re.kr
Web page: <http://www.kier.re.kr>

ABSTRACT

Organic Rankine cycle based power systems are well known for waste heat recovery application due to their adaptability to follow heat source variations. Industrial exhaust steam has an appreciable potential for the installation of waste heat recovery units. Korea Institute of Energy Research has developed waste heat recovery units which can generate power in the range of hundreds of kilowatts. In order to, rigorously test new cycle configurations and control strategies with least cost for heat source, a small-scale organic Rankine cycle test bed was implemented which a has steam condensing heat exchanger for using steam as a heat source in similar configurations as of larger units. The test bed was equipped with data logging and standalone control system and was configured for the electrical output around 1kW using R245fa as a working fluid. The system is composed of plate type heat exchangers, scroll type expansion machine, screw type working fluid pump and control valves with actuators. This work will present the difficulties, solutions and operational results in terms of design, equipment selection, fabrication and operational experience of system for small-scale power generation with efficiency over 5.2 % for a temperature difference of 120°C. Complexities involved in superheat control of working fluid for the system powered by steam will also be discussed.

INTRODUCTION

Organic Rankine cycle system (ORC) is the accepted viable technology for low-temperature heat conversion to electricity (Lecompte et al. 2015). Statistical analysis suggests that low-grade waste heat accounts for more than 50% of the total heat generated in the industry (Hung et al. 1997). Utilization of this waste heat energy to harness electrical power output will be a necessity of future to stay within energy budget allocations, to compete with the growing economies of the world. Low-grade waste heat power generation has been experimentally tested in many studies, where (Zhang et al. 2014), (Wenzhi et al. 2013), (Peris et al. 2015) & (Minea 2014) are the few works to mention in low-grade waste heat recovery works. Most of the published works presented their heat source as hot water or exhaust gas.

Korea Institute of Energy Research has implemented 100kW class ORC systems for low-grade industrial waste heat. The implementation of a very small-scale ORC system was to be tested for performance, controllability, and net power output using low-temperature exhaust steam (<135°C), as a heat source. As this system will be operated for 1kW power output with condensing steam as a heat source, already published literature rarely contain information for such configuration of a small power system with such heat source. The implemented test bed system will be used to test thermodynamic parameters and control strategies by using negligible operational costs as compared to the already installed 100kW scale system. It is suggested that for a small-scale power generation system (under 5kW) scroll machine is the best choice (Quoilin et al. 2012). Following the previous findings, a scroll machine is used in this work. The working fluid is an important factor of choice for ORC power system design, R245fa is known for its safety levels and environmental impacts for waste heat application (Wang et al. 2011). R245fa is also the best choice based on the criteria of net power and suitable working pressure (He et al. 2012). Thus, R245fa is selected as the suitable working fluid for the proposed system.

This work describes the design, fabrication and technical difficulties involved in the implementation of ORC system of such small power out using available components from the market. The test results are presented with performance evaluation for different degrees of superheating of the working fluid at expander inlet.

Materials & Method

The system's operational success is dependent upon its design and implementation. For small scale systems, it is customary to design the thermodynamic cycle for optimum performance at given source and sink conditions to obtain required power output and then finding the equipment (expansion machine, pump, heat exchangers, etc.) from the market, which can operate at required conditions of the power cycle. Contrarily, for bigger systems, it is common to design the components to strictly fulfil the performance requirements. For smaller systems, it is not viable to design and manufacture every single component as per requirements. In that case, components which match closely are selected and can be operated at slightly off design, compromising on performance. Component sizing & selection is difficult when the unusually small power requirement and cycle configurations are imposed. The mismatched components cause a lower overall performance of the system.

The system was designed to be operated by steam in the pressure range of 0~2 bar gauge pressure and the sink temperature at 12°C was available. Numerous working fluids have been under investigation for the usage in organic Rankine cycle based system for low-grade waste heat recovery. R245fa was selected for its closest match of required thermodynamic properties for available heat source and sink conditions and favorable environmental impact. The design procedure was initiated by fixing the pinch point temperature difference in heat exchangers (evaporator and condenser). Having fixed the pinching temperatures allowed to fix evaporation and condensing temperature of the organic Rankine cycle. The pressure ratio was calculated from evaporation and condensing pressures. Although when optimizing the performance of the waste heat ORC system, an optimum evaporating temperature exists that maximizes the output power (or overall efficiency) (Quoilin et al. 2011) but for prototypes and small systems it is more feasible to follow the equipment specifications. In current case, the expander inlet pressure for required output was selected as evaporation pressure. Isentropic enthalpy change was calculated at the calculated pressure ratio. Isentropic efficiency of the scroll type expansion machine was estimated from published literature (Song et al. 2014). The mass flow rate for the proposed system can be calculated from Equation (1).

$$\dot{W}_{shaft} = \dot{m} \cdot (h_1 - h_{2s}) \eta_{isen} \quad (1)$$

Power output for net electric power includes the mechanical losses in expander, coupling and generator. Also the generator efficiency reduces the generator output. In order to obtain 1kW electric output, \dot{W}_{shaft} is estimated to be higher than 1kW. After performing the design calculations for the system, the scheme was modelled in cycle tempo software (Cycle Tempo) for verification and ease of study for

various operational parameters. Major thermodynamic parameters at design point are presented in Table 1.

Table 1: Thermodynamic parameters at design point from design calculation and verified by cycle-tempo software simulation

Parameters	Value
Evaporator pressure	12.5bar
Condenser pressure	1.1bar
Expander Isentropic efficiency	50%
Working fluid mass flow rate	0.051kg/s
Heat source temperature (saturated steam)	120°C
Sink Temperature	16°C
Sink mass flow rate	0.73kg/s
Expander inlet temperature	101.5°C
Condenser subcooling	3°C

Table 2: Details of Equipment selected for implementation of test bed

Sr. no	Equipment	Details
1	Expander	Scroll Type expander (Airsquared Inc.), 12cc/rev, 1kW Nominal output, Magnetic coupling linked to 60Hz Generator 110V AC generator
2	Evaporator & Condenser	Braze plate heat exchangers (Janghan Engineers, Inc.) 60 & 50 plates, area of 6.5 & 5.38 square meter for evaporator & condenser, respectively
4	Feed Pump	Screw type pump (Tuthill Pump Company). Displacement of 2.6ml/rev Magnetic coupling linked to 0.75kW 3 phase 380V generator
5	Load Bank	Electric Bulbs of various power ratings were connected to the generator using single push single throw (SPST) type relays. Bulbs for 110V, were used in different power rating combination. 200W, 100W, 60W, 30W watt bulbs are used to obtain various step of resistive load connected to the generator
6	Heat Sink	Cooling tower already installed in facility
7	Heat Source	LNG based boiler with steam generation capacity of 500 kg/hr maximum
8	Flow rate meters	Working fluid with Coriolis type flow meter, sink flow rate measurement with electromagnetic flow rate meter, sink flow rate measurement with vortex type flow meter
9	Valves	Butterfly valves and globe valve for steam flow control (actuator controlled)
10	Temperature Measurement	T -type thermocouples for temperature measurement & RTD (PT100) for evaporator and expander inlet/exit
11	Pressure Transducers	Pressure Transducers with range of 0~16bar
12	Data Acquisition & Control	NI - cRIO 9074 with 8 slot integrated controller, NI I/O C-series model and Labview software

Table 2 presents the detail of selected equipment for test bed construction. Very few off the shelf expansion machines are available in the market, which can be used directly without alteration, but in this work a scroll machine designed for ORC application was available. Pump selection is another tough choice because of low flow rate, and large pressure head, no suitable centrifugal machine was found. A screw pump was able to cater our requirement with confidence as far pressure and flow rate requirements were required, but resulted in poor efficiency (<30%). Load bank was made by connecting electric bulbs of various power ratings to generator circuit and connections were controlled by relay operation.

Figure 1 presents the piping and instrumentation diagram for the test rig which was constructed according to the CAD diagram of system presented in Figure 2. Figure 3 presents the test rig in final fabricated form and under organic Rankine cycle system operation for power output.

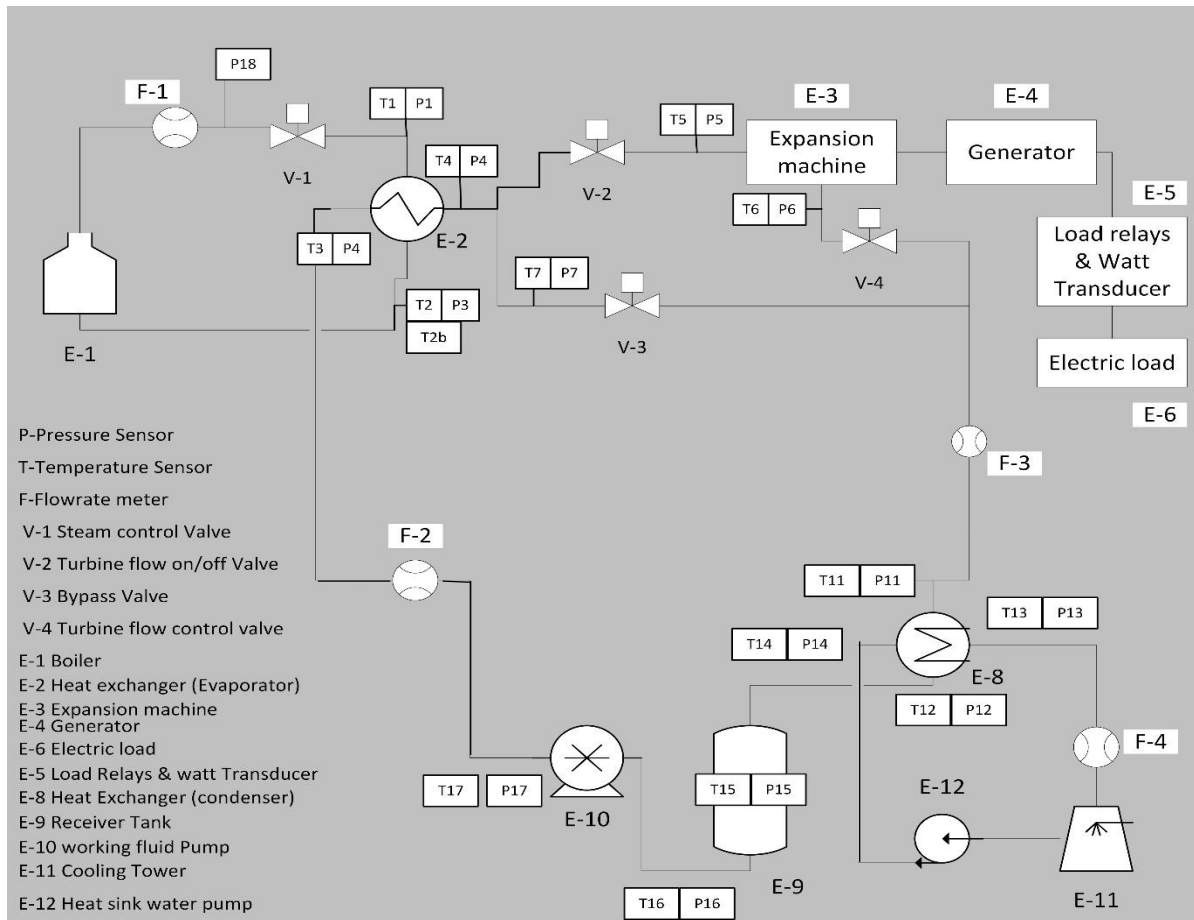


Figure 1: P&ID Scheme for proposed system

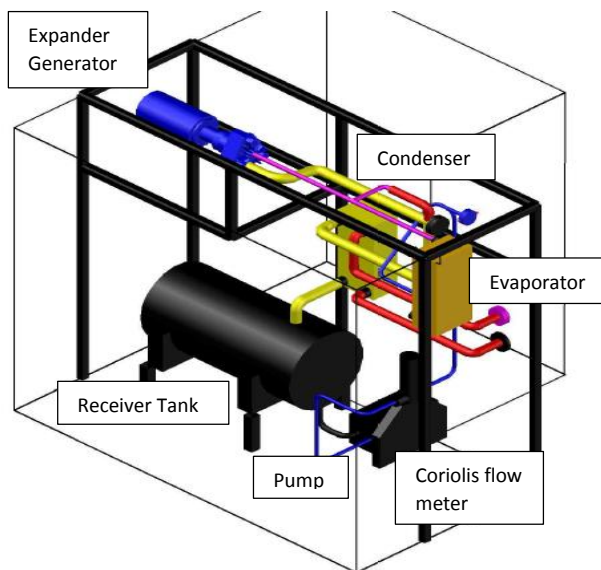


Figure 2: Isometric view of implemented system



Figure 3: System under operation

Results & Discussion

Figure 4 presents organic Rankine cycle test bed operational parameters for 20 minutes of its operating time. The system was operated in a way that the expander speed was kept below 3600RPM to follow safety recommendations from the manufacturer. Electric bulbs were connected to the load circuit one after another until a total of load of 1060W was imposed to the electric generator. After increasing the electric load, the pump speed controlled by variable frequency drive was increased to increase the mass flow rate and increase the evaporator pressure which increase the expander speed. After attaining the expander speed around 3600RPM, next electric bulb was connected which would reduce the expander speed as the torque on generator increased and for the same power output the rotational speed was decreased. Increasing the mass flow rate further, increased the evaporator pressure which allowed higher power output from the expander. The Figure shows that the evaporator pressure follows the pump speed (Mass flow rate). Generator power output increased to a maximum value of 1020W, when evaporator pressure is around the maximum operating design point of 11.5 barg. Expander speed was 3400 RPM while the generator was connected to a circuit of 8 bulbs (200W x 4, 100W x 2, 30W x 2) rated at 110V which summed up to yield 1060W resistive load.

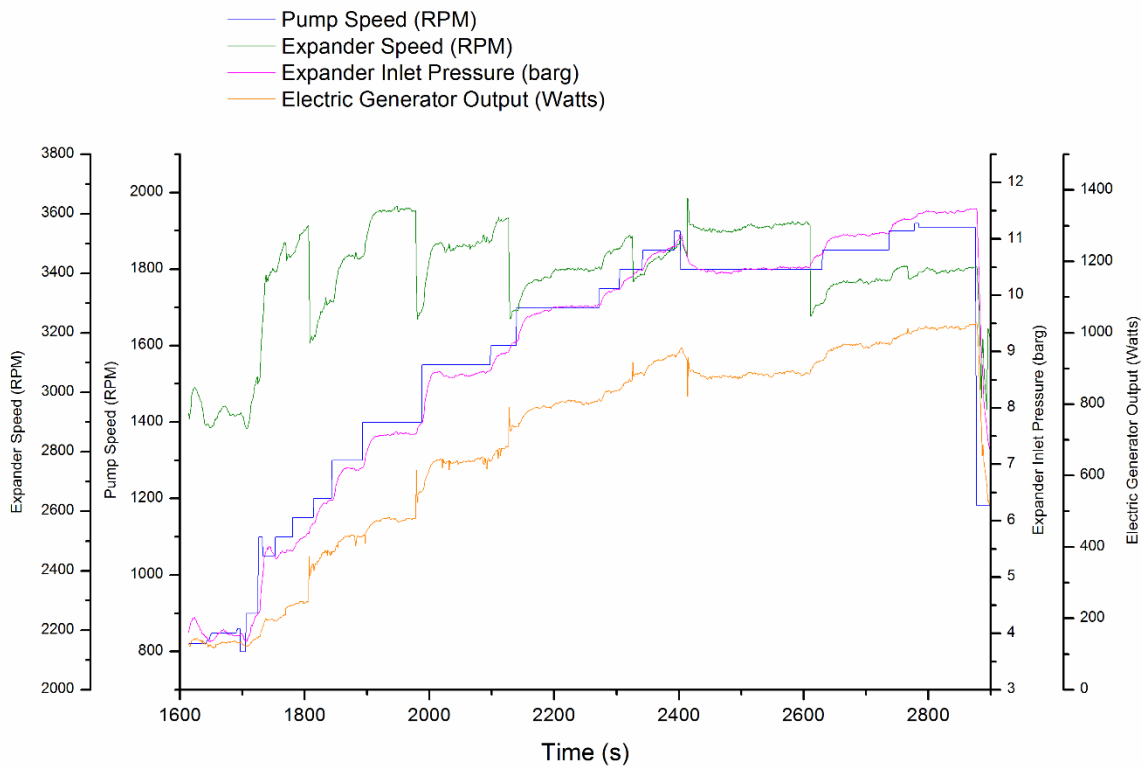


Figure 4: Organic Rankine cycle system operational parameters for different power output range

The sharp spikes in generator power output data occurred at the same time when expander speed was reduced at constant pump speed, increasing the imposed torque reduced the expander speed for the same power output. This was due to the connection of the relay with bulb. When the applied load increased as a step change the expander speed was reduced, to get back to recommended expander speed, pump speed was carefully adjusted to carry higher loads.

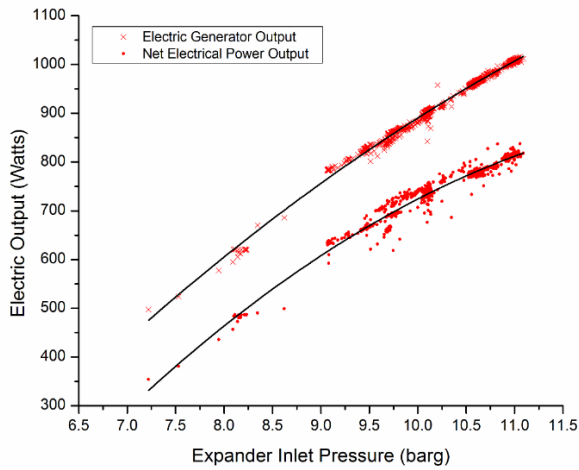


Figure 5: Electric Generator Output and Net Output vs Expander Inlet Pressure

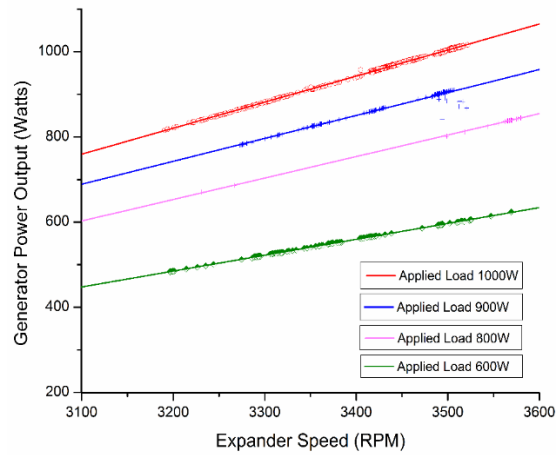


Figure 6: Electric Generator Power Output power vs Expander Speed

Figure 5 presents the electric output of generator with respect to the evaporator pressure while condenser conditions were held constant at 0.3barg. The figure also presents the net electric power output from the system. The pump electric power consumption was measured and used for evaluation. Both data plots are fitted with a 2nd order polynomial for analysis. Figure 6 presents generator output at various electric loading conditions. An applied load of 1000W refers to the connected electric bulbs with a combined power rating of 1000W to the electric generator circuit.

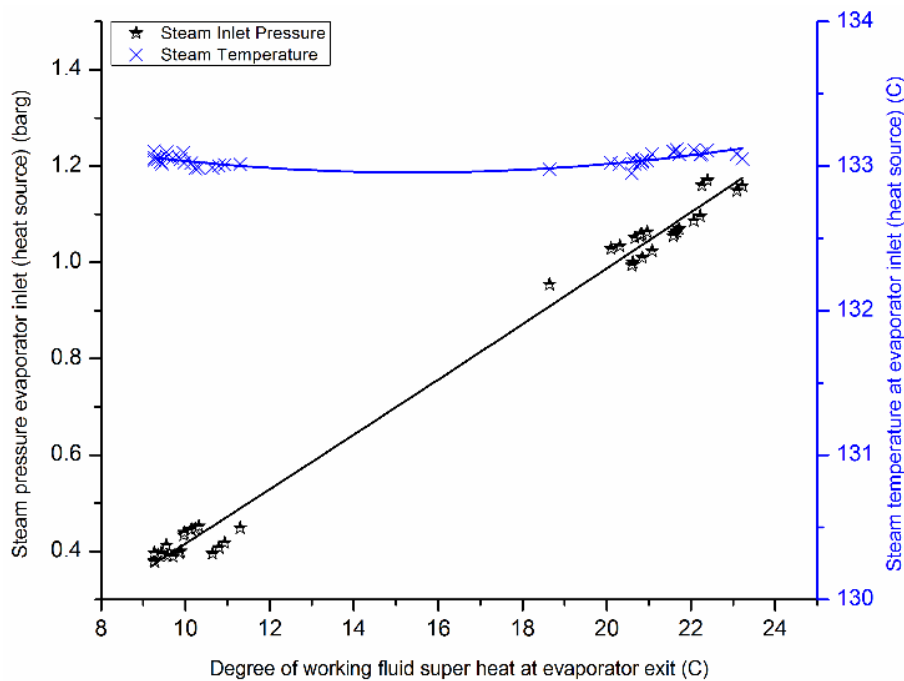


Figure 7: Variation of degree of super heat of working fluid at evaporator exit with respect to steam (heat source) pressure at heat source inlet side.

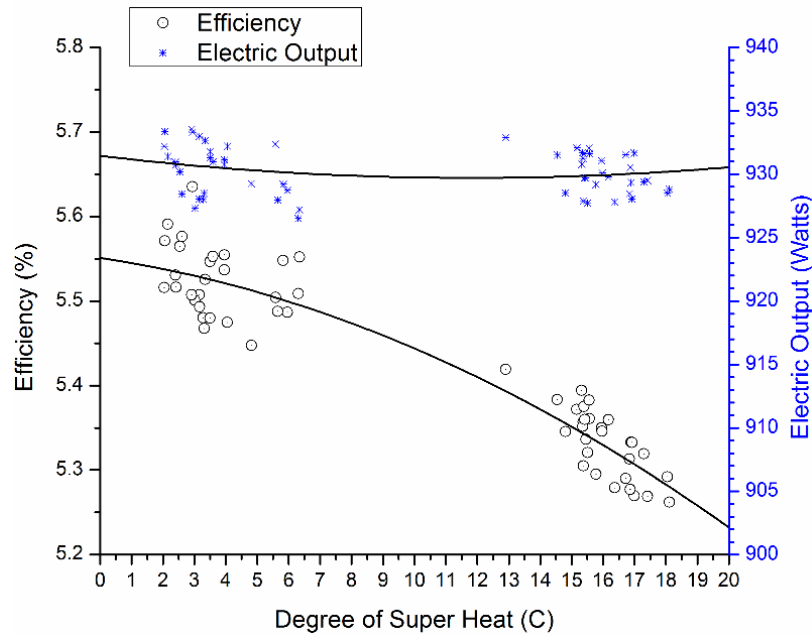


Figure 8: Effect of degree of super heat of working fluid at expander inlet vs electrical efficiency for same power output

An experiment to investigate the effects of superheat of the working fluid at expander inlet was performed. Extensive research and theoretical background suggested the lesser the degree of superheating, the better would be the performance for a system without recuperator using R245fa working fluid. In reality to maintain, superheat value of 0 would be ideal but is very challenging task to maintain a stable working fluid output with all vapor exit quality without any superheating. The ability to maintain the minimum superheating degree depends on various equipment and control characteristics. Evaporator type, size & geometry, plays an important role in this regard. In case of plate heat exchanger, the number of channels, aspect ratio, port design & thermal inertia influence the performance in such a way that to obtain a superheat of 0 is very difficult. The heat source type is also an important factor when considering the controllability of superheating of the working fluid at evaporator exit. In case of current system the heat source is steam, which is condensed in evaporator and subcooled to certain level.

Control of heat source was performed by using a globe valve which has been carefully sized and custom manufactured for the current conditions of steam pressure & flow rates. The actuator controlled valve allowed control of heat source for a steam requirement of less than 40 kg/hr. Figure 7 presents the controllability of working fluid superheat at evaporator exit. The globe valve which has an upstream steam pressure of 1.95 ~ 2 barg was opened in such a way that the downstream pressure of globe valve was increased. As a result, condensing pressure in evaporator (heat source side/steam) was increased. Superheat at evaporator exit (Working fluid side) was observed as 10°C when source pressure was 0.4 barg, when steam pressure was increased to 1.1 barg the super heat value was observed around 21°C. While the source temperature was observed around 133°C in both cases. Figure 8 presents superheating degree at expander inlet and cycle efficiency for same electrical power output. Figure 7 and Figure 8 present data from same experiment, but the Figure 8 presents superheat value at expander inlet while Figure 7 presents the superheat value for evaporator exit. The difference in super heat values is due to heat loss in piping network when the working fluid flows from evaporator to expander. The data in Figure 9 and 8 is used to plot 2nd order polynomial fits for analysis. Electrical efficiency of system was obtained by equation (2).

$$\eta_{elec} = \frac{\text{Electric Generator Power Output (kW)}}{\dot{Q}_{\text{evaporator, working fluid (kW)}}} \quad (2)$$

Where

$$\dot{Q}_{e,wf} (kW) = \dot{m}_{wf} (h_{eo} - h_{ei}) \quad (3)$$

Figure 8 data results used to obtain 2nd order polynomial relation which suggest the drop in efficiency of system with increasing super heat value. The relation is presented as Equation (4)

$$\zeta = 5.55084 - 0.00542(\theta) - 0.0005245(\theta)^2 \quad (4)$$

Where

ζ – electric efficiency (percentage) as a function of superheat

θ – is degree of superheat (Celcius) at expander inlet

Equation 4 can be used to estimate the reduction in efficiency with respect to superheating degree for the same electrical power generated. In this case power output was held constant by maintaining a constant expander speed to hold power output around 930W and heat source carefully adjusted to obtain different superheat values. It was noted that for current system an increase in 1°C of super heat will reduce 0.011% in electric efficiency if evaporator superheat is around 10°C. As the relation is nonlinear curve it suggests reduction in electric efficiency of 0.025% with increase of 1°C after super heat at heat exchanger exit is above 20°C. The relation is only valid for current system and is a basis for the future research work to be carried out to establish relationship for efficiency and superheating degree for various systems of various power range.

Conclusion

In this work, design, equipment selection and fabrication of a small scale organic Rankine cycle test bed system, using steam as heat source was performed. The fabricated test rig was operated and following conclusion were made:

- 1kW scale organic Rankine cycle system can be designed and fabricated with major components available from market.
- Design requirement of components and availability causes mismatching in component selection, whereas losses (isentropic, frictional, electrical etc.) involved in components should be carefully analyzed to achieve required performance.
- A 1kW scale ORC system is capable of producing net electrical output if components are precisely selected
- The system was able to produce 1kW electric output with efficiency value of 5.2%.
- The best efficiency points are not at the highest output power.
- Using a steam condensing evaporator for small flow rates of steam and working fluid superheat control at constant pressure is difficult procedure.
- Efficiency depreciation with increasing superheat level can go as high as 0.02% per degree Celsius for this system.
- An attempt to establish a practical approach for relating efficiency depreciation with higher superheat is initiated. The future work will incorporate various types of systems at various power range will be studied for efficiency drop due to superheat to highlight how much research attention and work will be required for improvement of control systems and heat exchangers to obtain minimum super heat levels.

3rd International Seminar on ORC Power Systems, October 12-14, 2015, Brussels, Belgium

NOMENCLATURE

ORC	Organic Rankine Cycle
\dot{W}_{shaft}	Expander shaft power output
\dot{m}_{wf}	Working fluid mass flow rate (R245fa)
h_{eo}	Working fluid enthalpy at evaporator outlet
h_{ei}	Working fluid enthalpy at evaporator inlet
η_{isen}	Expander Isentropic efficiency
η_{elec}	Thermal to electric conversion efficiency
$\dot{Q}_{e,wf}$	Heat transfer to the working fluid

REFERENCES

- Cycle Tempo. TU Delft (Delft University of Technology), <http://www.asimptote.nl/>
- He, C. et al., 2012. The optimal evaporation temperature and working fluids for subcritical organic Rankine cycle. *Energy*, 38(1), pp.136–143.
- Hung, T.C., Shai, T.Y. & Wang, S.K., 1997. A review of organic rankine cycles (ORCs) for the recovery of low-grade waste heat. *Energy*, 22(7), pp.661–667.
- Lecompte, S. et al., 2015. Review of organic Rankine cycle (ORC) architectures for waste heat recovery. *Renewable and Sustainable Energy Reviews*, 47, pp.448–461.
- Minea, V., 2014. Power generation with ORC machines using low-grade waste heat or renewable energy. *Applied Thermal Engineering*, 69(1-2), pp.143–154.
- Peris, B. et al., 2015. Experimental characterization of an ORC (organic Rankine cycle) for power and CHP (combined heat and power) applications from low grade heat sources. *Energy*, 82, pp.269–276.
- Quoilin, S. et al., 2011. Thermo-economic optimization of waste heat recovery Organic Rankine Cycles. *Applied Thermal Engineering*, 31(14-15), pp.2885–2893.
- Song, P. et al., 2014. A review of scroll expanders for organic Rankine cycle systems. *Applied Thermal Engineering*, 75, pp.54–64.

3rd International Seminar on ORC Power Systems, October 12-14, 2015, Brussels, Belgium

Wang, E.H. et al., 2011. Study of working fluid selection of organic Rankine cycle (ORC) for engine waste heat recovery. *Energy*, 36(5), pp.3406–3418.

Wenzhi, G. et al., 2013. Performance evaluation and experiment system for waste heat recovery of diesel engine. *Energy*, 55, pp.226–235.

Zhang, Y.-Q. et al., 2014. Development and experimental study on organic Rankine cycle system with single-screw expander for waste heat recovery from exhaust of diesel engine. *Energy*, 77, pp.499–508.

ACKNOWLEDGEMENT

This work was conducted under the framework of Research and Development program of the Korea Institute of Energy Research and University of Science & Technology (b4-5524).

THERMODYNAMIC STUDY OF INFLECTION POINT OF SATURATED VAPOR CURVE FOR DRY AND ISENTROPIC WORKING FLUIDS

Xinxin ZHANG^{1*}, Congtian Zhang¹, Jingfu WANG¹, Maogang HE²

¹Key Laboratory of Enhanced Heat Transfer and Energy Conservation, Ministry of Education
Key Laboratory of Heat Transfer and Energy Conversion, Beijing Municipality
College of Environmental and Energy Engineering, Beijing University of Technology
Beijing 100124, P R China
xinxinzhang@bjut.edu.cn

²Key Laboratory of Thermo-Fluid Science and Engineering, Ministry of Education
School of Energy and Power Engineering, Xi'an Jiaotong University
Xi'an, Shaanxi 710049, P R China
mghe@mail.xjtu.edu.cn

* Corresponding Author Xinxin ZHANG

ABSTRACT

In this paper, the definition of inflection point on saturated vapor curve of dry fluid and isentropic fluid was given according to the shape of the saturated curve of working fluids in a T-s diagram. On this basis, the model of near-critical region triangle was established. Using this model, the effect of inflection point on saturated vapor curve on performance of organic Rankine cycle(ORC) was studied when 38 kinds of dry and isentropic organic working fluids was adopted in ORC. The performance includes relationship between the inflection point temperature and the area of near-critical region triangle, the relationship between the exergy at the inflection point and the area of near-critical region triangle, and the relationship between the area of near-critical region triangle and reciprocal value of slope of saturated vapor curve. On this basis, if the type of heat source is taken into account, the theoretical analysis results show that heptane, cyclohexane, octane, nonane, decane, and dodecane are the suitable working fluids for open-type heat source utilization.

1. INTRODUCTION

The organic Rankine cycle(ORC) which applies the principle of the steam Rankine cycle, but uses organic working fluids with low boiling points was first invented and introduced by Ray and Moss (1966) who used fluorochemicals as working fluid in small Rankine cycle power units. Since then, the ORC technology has become more and more popular in both the waste heat recovery and renewable and sustainable energy utilization field.

As known to all, working fluid plays a very important role in thermodynamic cycle. The efficiency, the operation condition, the impact on the environment, and the economic feasibility of thermodynamic cycle are greatly affected by working fluid selection and the nature of the working fluid. In ORC, organic working fluid plays a decisive role. It is the lower boiling point of organic working fluid compared with water that makes a higher saturation pressure at lower temperatures. Accordingly, work can be produced at a lower temperature because of good thermodynamic performance of organic working fluid.

Organic working fluid can be classified into three categories according to the slope of the saturated vapor curve in a T-s diagram. They are dry fluid with a positive slope(e.g. isopentane), wet fluid with a negative slope(e.g. R22), and isentropic fluid with a vertical slope(e.g. R11)(Hung, 2001; Liu *et al.*,

2004; Chen *et al.*, 2010). The working fluids of dry or isentropic type are more appropriate for ORC systems(Liu *et al.*, 2004). The literature shows extensive researches on organic working fluid selection under certain predefined temperature conditions and certain operation conditions. If we observe the shape of saturated vapor curve of dry and isentropic fluid in a T - s diagram, we will find an inflection point on saturated vapor curve. In this paper, we defined this inflection point and established a model of near-critical region triangle. Using this model, the effect of inflection point on saturated vapor curve on performance of organic Rankine cycle(ORC) was studied when 38 kinds of dry and isentropic organic working fluids was adopted in ORC. On this basis, taking the type of heat sources into account, the suitable working fluid was analyzed and selected through theoretical calculation.

2. DEFINITION OF INFLECTION POINT ON SATURATED VAPOR CURVE

2.1 Type of Working fluid

As mentioned in Section 1, a working fluid can be classified as a wet, dry, or isentropic fluid according to the slope of the saturated vapor curve (dT/ds) in its T - s diagram as depicted in Figure 1. Considering the value of dT/ds is infinity for an isentropic fluid, the reciprocal value of the slope(e.g ds/dT) is used to judge the type of a working fluid. Here we define $\zeta = ds/dT$, if $\zeta > 0$, then it is a dry fluid, and $\zeta \approx 0$ for an isentropic fluid and $\zeta < 0$ for a wet fluid. Near critical point, there is an inflection point on saturated vapor curve of dry and isentropic working fluid. In order to study the effect of this inflection point on the performance of organic Rankine cycle for waste heat recovery, first we have to judge the type of a working fluid according to its value of ζ and the shape of its T - s diagram.

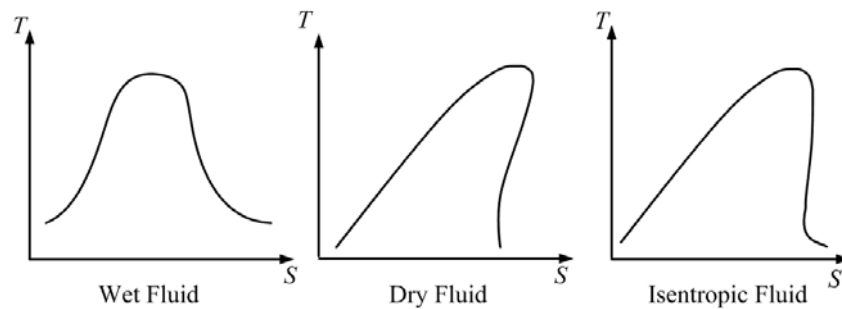


Figure 1: Temperature-entropy (T - s) diagrams of different fluids

Liu *et al.*(2004) introduced an equation for calculating the value of ζ , which is:

$$\zeta = \frac{c_p}{T_H} - \frac{[(n \cdot T_{rH}) / (1 - T_{rH})] + 1}{T_H^2} \Delta H_H \quad (1)$$

where, ζ (ds/dT) denotes the reciprocal value of the slope of saturated vapor curve in a T - s diagram, n is suggested to be 0.375 or 0.38(Poling *et al.*, 2001), $T_{rH}(=T_H/T_c)$ denotes the reduced evaporation temperature, and ΔH_H is the enthalpy of vaporization.

The calculation value of ζ according to Equation (1) and corresponding type of a working fluid is listed in Table 1. The calculation values have a good agreement with the shape of saturated vapor curves in a T - s diagram.

2.2 Definition and Determination of Inflection Point on Saturated Vapor Curve

From the classification of working fluid introduced in the last subsection, it can be seen that in a T - s diagram, a significant difference between dry(or isentropic) fluid and wet fluid is the existence of a point on its saturated vapor curve on which the entropy value reaches the maximum. This point is located near the critical point. After passing this point, the entropy value on saturated vapor curve of

dry fluid decreases. For isentropic fluid, the entropy value basically keeps unchanged. However, we cannot find out such a point on saturated vapor curve of wet fluid.

Table 1: The calculation value of ζ and corresponding type of a working fluid

Working Fluid	Calculation Value of ζ	Fluid Type
Water	-13.1818	Wet
Ethanol	-5.4299	Wet
R11	-0.3903	Isentropic
R123	0.1202	Isentropic
HFE7100	1.8252	Dry
n-Pentane	1.2835	Dry
Iso-pentane	1.1801	Dry
Benzene	0.3316	Isentropic
Toluene	1.0600	Dry
p-Xylene	1.5390	Dry
butane	0.0083	Dry
butene	0.0065	Dry
cis-butene	0.0059	Dry
cyclohexane	0.0112	Dry
decane	0.0146	Dry
dodecane	0.0149	Dry
heptane	0.0121	Dry
hexane	0.0106	Dry
isobutane	0.0083	Dry
isobutene	0.0071	Dry
isohexane	0.0113	Dry
nonane	0.0124	Dry
octane	0.0121	Dry
pentane	0.0098	Dry
perfluorobutane	0.0051	Dry
perfluoropentane	0.0056	Dry
R113	0.0030	Isentropic
R114	0.0033	Isentropic
R115	0.0032	Isentropic
R124	0.0030	Isentropic
R141b	0.0030	Isentropic
R142b	0.0029	Isentropic
R218	0.0045	Isentropic
R227ea	0.0042	Isentropic
R236ea	0.0043	Isentropic
R236fa	0.0038	Isentropic
R245ca	0.0046	Isentropic
R245fa	0.0044	Isentropic
R365mfc	0.0056	Dry
RC318	0.0043	Isentropic
trans-butene	0.0067	Dry

Considering this unique characteristic of dry and isentropic fluid, here we define an inflection point on saturated vapor curve of dry or isentropic fluid as a point whose entropic reaches the maximum value ranging from freezing point to critical point. [Figure 2](#) illustrates the inflection point on saturated vapor curve of dry and isentropic fluid.

According to the definition of inflection point on saturated vapor curve, its location is determined by the entropic value of dry or isentropic fluid given by REFPROP 8.0 software developed by the National Institute of Standards and Technology Laboratories (NIST)(Lemmon et al., 2007). Dry and isentropic working fluids are selected from all the working fluids in REFPROP 8.0 according to the

calculation value of ζ . The T - s diagrams of these two types of working fluids are made by software. Observe the shape of saturated vapor curve in T - s diagram, and obtain the entropy value under each temperature from the critical point to freezing point using 0.5K as a step. For dry fluid, it can be seen that on saturated vapor curve the entropy value increases with the temperature decrease from critical point until inflection point. As for isentropic fluid, the entropy value basically keeps constant when temperature is around the inflection point. Therefore, we define the inflection point of isentropic fluid as the closest point to critical point with the maximum entropy value on saturated vapor curve. Table 2 lists the temperature on inflection point of 38 working fluids(dry and isentropic) studied in this paper.

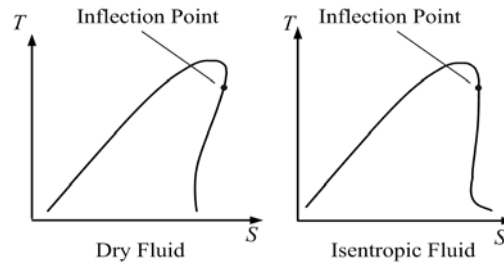


Figure 2: Inflection point on saturated vapor curve of dry and isentropic fluid

3. DEFINITION AND AREA OF NEAR-CRITICAL REGION TRIANGLE

Figure 3 describes the typical process(1-2s-2'-3-4-5) of an organic Rankine cycle with dry working fluids. The thermal efficiency of an ideal ORC can be calculated from the following equation.

$$\eta_i = \frac{w}{q_1} = \frac{w - w_p}{h_1 - h_4} = \frac{h_1 - h_{2s} - (h_4 - h_3)}{h_1 - h_4} \quad (2)$$

where, h denotes enthalpy value, w denotes work, and q denotes heat. The number on subscript stands for the state point of the ORC.

The thermal efficiency of a practical ORC can be calculated from the following equation.

$$\eta_r = \frac{w}{q_1} = \frac{w_r - w_p}{h_1 - h_4} = \frac{h_1 - h_2 - (h_4 - h_3)}{h_1 - h_4} \quad (3)$$

From the above two equations, it can be seen that the enthalpy value of point 1 significantly effects the thermal efficiency of an ORC. Therefore, the inflection point introduced in this paper focuses on the characteristics of point 1 in an ORC. The inflection point usually has a relatively high temperature. Moreover, latent heat of vaporization reaches the maximum value at the inflection point for dry and isentropic fluid(In the range between critical point and inflection point). However, the temperature between critical point and inflection point doesn't offer any help for improving the thermal efficiency of an ORC. In order to study the effect of inflection point on saturated vapor curve on the thermal efficiency of an ORC, we have to define a parameter to measure the meaningless part surrounded by saturated curve of dry or isentropic fluid for improving the cycle thermal efficiency. This meaningless part will be described by the area of near-critical region triangle.

In T - s diagram, draw a line through the inflection point and make it parallel to the s axis. This straight line will make two intersections with the saturated liquid curve and saturated vapor curve. These two intersections, with the critical point, make a triangle. This triangle is defined as the near-critical region triangle. The base of the near-critical region triangle stands for the entropy difference between the

saturated liquid state and the saturated vapor state at the inflection point temperature. The height of the near-critical region triangle stands for the temperature difference between the critical point and the inflection point. **Figure. 4** illustrates the near-critical region triangle of dry and isentropic fluid. The unit of entropy difference is $\text{kJ/kg}\cdot\text{K}$ (triangle base), and that of temperature difference is K (triangle height), therefore, the area of near-critical region triangle has a unit of kJ/kg which is the same as the unit of enthalpy.

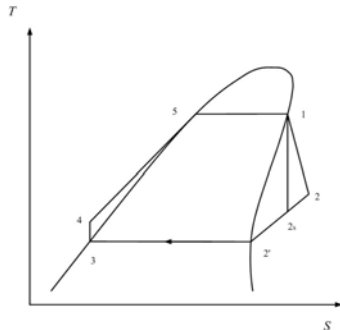


Figure 3: Typical process of an organic Rankine cycle with dry working fluids

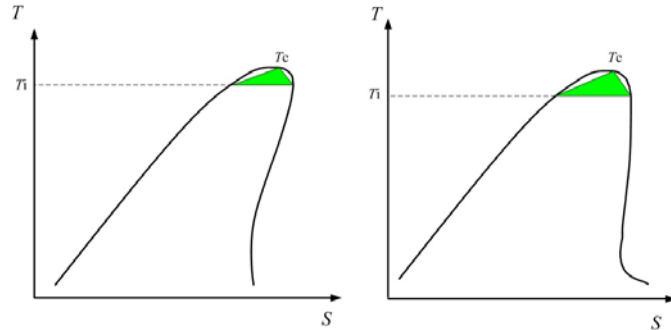


Figure 4: Near-critical region triangle of dry and isentropic fluid

From the database of REFPROP 8.0 software, 38 kinds of dry and isentropic fluids are selected for calculation and analysis. **Table 2** lists the basic thermophysical characteristics of these 38 kinds of fluids. According to these parameters and the definition of near-critical region triangle, the areas of near-critical region triangle of these 38 kinds of working fluids were calculated. **Figure 5** depicts the relation between the inflection point temperature and the area of near-critical region triangle. From the figure, it can be seen that dodecane and perfluoropentane has the smallest area of near-critical region triangle. However, dodecane has the highest inflection point temperature among these 38 kinds of working fluids. Most of working fluids have inflection point temperatures ranging from 350K to 500K. Here it has to be mentioned that the critical temperature of R116(hexafluoroethane) is 293.03K which is much lower than the operation temperature of an ORC which is from 353K to 673K. Therefore, R116 will not be included in the following analysis.

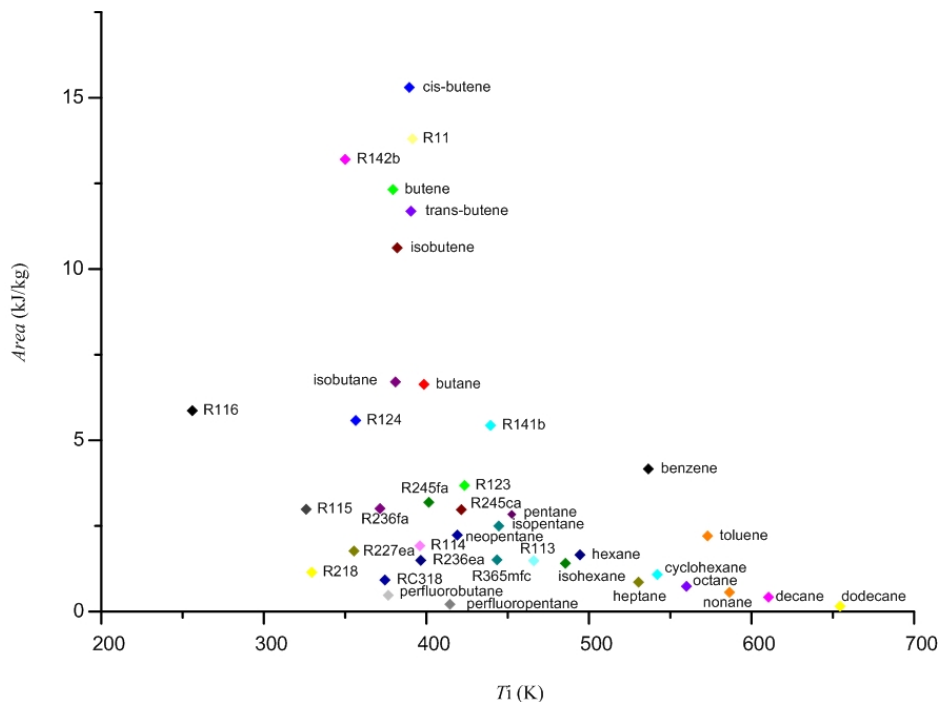


Figure 5: Relation between the inflection point temperature and the area of near-critical region triangle

Table 2: Basic thermophysical characteristics of 38 working fluids

Working Fluid	Critical Temperature/ K	Temperature on inflection point/ K	Vapor entropy on inflection point/ $\text{kJ}\cdot(\text{kg}\cdot\text{K})^{-1}$	Liquid entropy on inflection point/ $\text{kJ}\cdot(\text{kg}\cdot\text{K})^{-1}$
benzene	562.05	536.5	1.3865	1.0710
Butane	425.13	398.5	1.357	1.0539
Butene	419.29	379.5	1.1707	1.0303
cis-butene	435.75	389.5	1.2149	1.0565
Cyclohexane	553.64	542	1.4009	1.0711
Decane	617.7	610.5	0.47934	0.3824
Dodecane	658.1	654.5	0.4546	0.3836
Heptane	540.13	530.5	1.6772	1.3305
Hexane	507.82	494.5	1.6776	1.5374
Isobutane	407.81	381	1.5635	1.3951
Isobutene	418.09	382	1.4151	1.1946
Isohexane	497.7	485.5	1.2371	0.9202
Isopentane	460.35	444.5	1.7003	1.4793
Neopentane	433.74	419	1.5991	1.3125
Nonane	594.55	586.5	1.8847	1.5986
Octane	569.32	560	1.7887	1.3505
Pentane	469.7	452.5	1.369	1.2213
perfluorobutane	386.33	376.5	1.5087	1.3263
perfluoropentane	420.56	414.5	1.6921	1.5041
R11	471.11	391.5	1.6371	1.4109
R113	487.21	466	1.8634	1.6349
R114	418.83	396	1.7999	1.5510
R115	353.1	326	1.9259	1.7425
R116	293.03	256	1.5085	1.3759
R123	456.83	423.5	1.2	0.9647
R124	395.43	356.5	1.5067	0.8932
R141b	477.5	439.5	1.3865	1.0710
R142b	410.26	350	1.357	1.0539
R218	345.02	329.5	1.1707	1.0303
R227ea	374.9	355.5	1.2149	1.0565
R236ea	412.44	396.5	1.4009	1.0711
R236fa	398.07	371.5	0.47934	0.3824
R245ca	447.57	421.5	0.4546	0.3836
R245fa	427.16	401.5	1.6772	1.3305
R365mfc	460	443.5	1.6776	1.5374
RC318	388.38	374.5	1.5635	1.3951
Toluene	591.75	573	1.4151	1.1946
trans-butene	428.61	390.5	1.2371	0.9202

4. EFFECT OF INFLECTION POINT ON PERFORMANCE OF AN ORC

Exergy is used to evaluate the quality of energy. Under ambient condition, the energy that can be converted into useful work is called exergy. Through exergy analysis of an ORC, we can find out the part that needs to be improved. As for an ORC, the exergy loss caused by expansion process cannot be ignored. Based on this consideration, the exergy at inflection point temperature of working fluid and its area of near-critical region triangle is compared. [Figure. 6](#) depicts this comparison result. From the figure, it can be seen that heptane, cyclohexane, octane, nonane, decane, and dodecane has a relatively small area of near-critical region triangle but a high exergy.

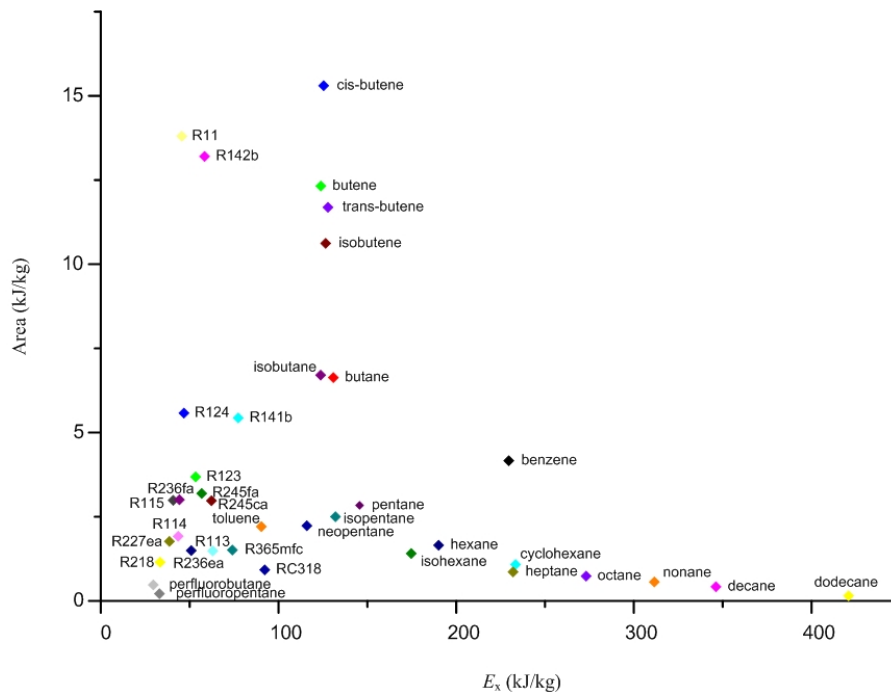


Figure 6: Relation between the area of near-critical region triangle and the exergy at inflection point temperature

From the previous discussion, it is known to all that the drier working fluid is, the more benefit an ORC gets from an expander's perspective. What is the relation between the area of near-critical region triangle of a working fluid and its type. Figure 7 depicts this relation. The value of ζ can be used to judge the type of a working fluid. The dry fluid has a positive value of ζ . From the figure, it can be seen that compared with other working fluids, decane and dodecane has a relatively big value of ζ and a relatively small area of near-critical region triangle. These two working fluids are good candidates for selection.

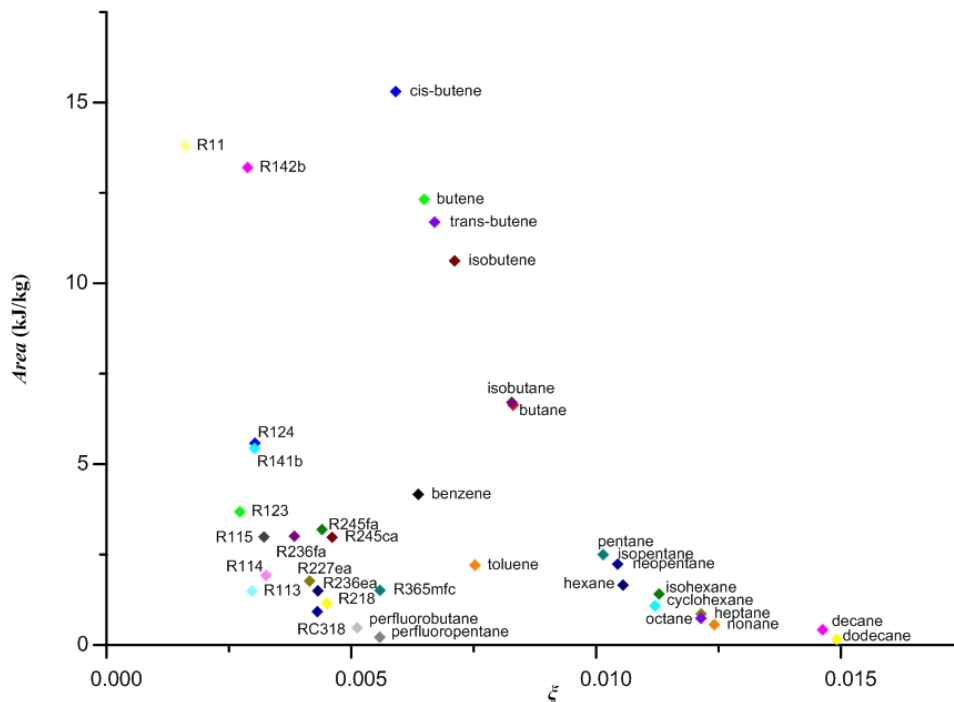


Figure 7: Relation between the area of near-critical region triangle and the type of working fluid

There are two types of waste heat (Yan, 1982; Zhao and Qian, 1984; He *et al.* 2014). One is called open type. The other is called closed type. For the open type, the inlet temperature and the mass flow rate are known, and the working mass of the heat source is directly discharged after being used. For the closed type, the heat release is specific and the working mass of the heat source is usually recycled after releasing heat. Therefore, the standards used to measure the waste heat recovery of these two types of heat source are different (Yan, 1982; Zhao and Qian, 1984). For the open type, the maximum net power output is used as the criterion. However, for the closed type, the maximum thermal efficiency is the criterion. Accordingly, the selection principle of working fluid for waste heat recovery with different heat source is different (Yan, 1982; He *et al.* 2014). For the open type, the working fluids with high liquid specific heat and low latent heat of evaporation should be selected as the working fluids. In contrast, the working fluids with low liquid specific heat and the high latent heat of evaporation are better for the closed heat source.

According to the above conclusion, the liquid specific heat at the inflection point temperature and the latent heat of evaporation at the inflection point temperature for 38 kinds of organic working fluids are listed in Table 3. Moreover, Figure 8 depicts the relation between these two parameters.

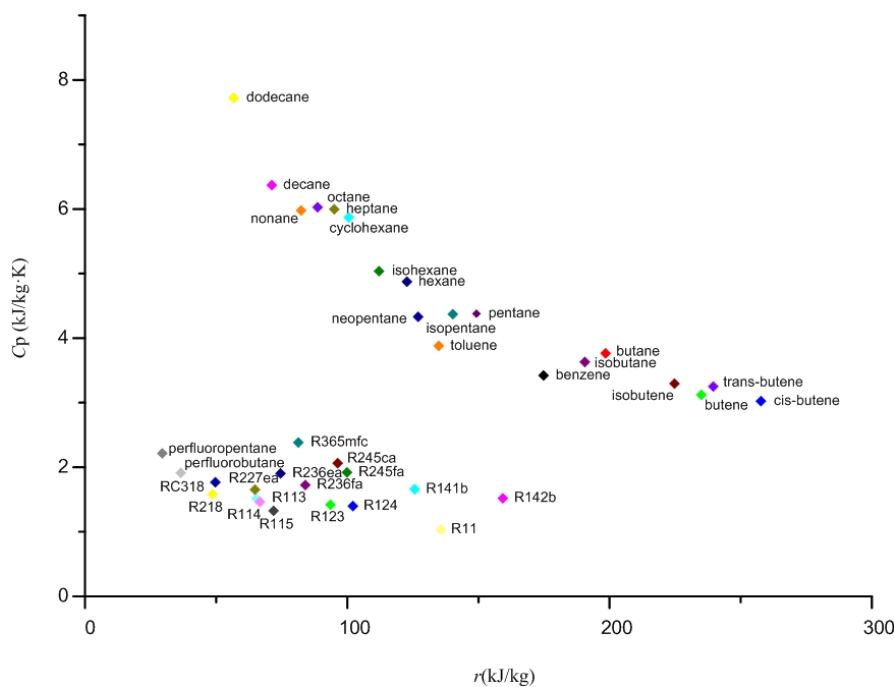


Figure 8: Relation between the liquid specific heat at the inflection point temperature and the latent heat of evaporation at the inflection point temperature

Scanning the figure carefully, it can be seen that the working fluids at the upper left corner should be selected for waste heat recovery of open type heat source. In contrast, the working fluids at the bottom right corner are better for the closed type heat source. The working fluids at the upper left corner (heptane, cyclohexane, octane, nonane, decane, and dodecane) are just the ones we have selected through the previous discussion. However, butene and its isomers which are at the bottom right corner are not selected due to their big areas of near-critical region triangle.

5. CONCLUSIONS

Through scanning the shape of saturated curve of dry and isentropic fluid, it can be seen that there is an inflection point on its saturated vapor curve. We define an inflection point on saturated vapor curve of dry or isentropic fluid as a point whose entropic reaches the maximum value ranging from freezing point to critical point. On this basis, we define the near-critical region triangle which is used to measure the meaningless part surrounded by saturated curve of dry or isentropic fluid.

Table 3: Liquid specific heat and latent heat of evaporation at the inflection point temperature of 38 working fluids

Working Fluid	Liquid specific heat at the inflection point temperature, $C_p / \text{kJ} \cdot (\text{kg} \cdot \text{K})^{-1}$	Latent heat of evaporation at the inflection point temperature, $/ \text{kJ} \cdot \text{kg}^{-1}$
Benzene	3.4216	174.84
Butane	3.7638	198.48
Butene	3.1208	235.01
cis-butene	3.0254	257.72
Cyclohexane	5.8695	100.62
Decane	6.3693	71.25
Dodecane	7.7228	56.71
Heptane	5.9967	95.04
Hexane	4.8754	122.74
Isobutane	3.6316	190.56
Isobutene	3.2953	224.77
Isohexane	5.0375	112.11
Isopentane	4.3709	140.24
Neopentane	4.3319	126.99
Nonane	5.9777	82.37
Octane	6.0278	88.7
Pentane	4.378	149.26
perfluorobutane	1.9117	36.51
perfluoropentane	2.2151	29.42
R11	1.036	135.75
R113	1.5117	65.34
R114	1.4625	66.67
R115	1.3247	71.88
R123	1.419	93.57
R124	1.3982	102.14
R141b	1.6606	125.71
R142b	1.5201	159.3
R218	1.5841	48.68
R227ea	1.6539	64.82
R236ea	1.9049	74.52
R236fa	1.7247	84.03
R245ca	2.0641	96.31
R245fa	1.9207	99.91
R365mfc	2.3851	81.37
RC318	1.7678	49.66
Toluene	3.8798	134.84
trans-butene	3.2499	239.57

Using these two model, the effect of inflection point on saturated vapor curve on performance of organic Rankine cycle(ORC) was studied when 38 kinds of dry and isentropic organic working fluids was adopted in ORC. The analysis results show that heptane, cyclohexane, octane, nonane, decane, and dodecane are the suitable working fluids. On this basis, if the type of heat source is taken into account, a same theoretical analysis results is gotten for open-type heat source utilization. However, for the closed-type heat source, there is no suitable working fluid if using these two models for analysis due to the big areas of near-critical region triangle of butene and its isomers.

REFERENCES

- Ray, S.K., Moss, G., 1966, Fluorochemicals as working fluids for small rankine cycle power units, *Adv. Energy. Convers.*, vol. 6, no.2: p. 89-102.
- Hung, T. C., 2001, Waste heat recovery of organic Rankine cycle using dry fluids, *Energy. Convers. Manage.*, vol. 42: p. 539-553.
- Chen, H., Goswami, D.Y., Stefanakos, E.K., 2010, A review of thermodynamic cycles and working fluids for the conversion of low-grade heat, *Renew. Sust. Energ. Rev.*, vol. 14: p.3059-3067.
- Liu, B.T., Chien, K.H., Wang, C.C., 2004, Effect of working fluids on organic Rankine cycle for waste heat recovery, *Energy*, vol.29: p.1207-1217.
- Poling, B.E., Prausnitz, J.M., O'Connell, J.P., 2001, The properties of gases and liquids, 5th ed., McGraw-Hill, New York.
- Lemmon, E.W., McLinden, M.O., Huber, M.L., 2007, NIST reference fluid thermodynamic and transport properties-REFPROP version 8.0, National Institute of Standard Technology, Boulder.
- Yan, J.L., 1982, Thermodynamic principles and formulas for choosing working fluids and parameters in designing power plant of low temperature heat. *J. Eng. Thermophys.*, vol. 3, no.1: p.1-7.[In Chinese]
- Zhao, G., Qian, L., 1984, Exergy analysis and its application, Higher Education Press, Beijing.[In Chinese]
- He, C., Liu C., Zhou, M. et al., 2014, A new selection principle of working fluids for subcritical organic Rankine cycle coupling with different heat sources, *Energy*, vol.68: p. 283-291.

ACKNOWLEDGEMENT

This work was supported by the National Key Basic Research Program of China (973 Program, No.2013CB228306). The authors gratefully acknowledge them for financial support of this work.

DESIGN AND NUMERICAL ANALYSIS OF PROCESSES IN SILOXANE VAPOR DRIVEN TURBINE

A. Sebelev*¹, R. Scharf², N. Zabelin¹, M. Smirnov¹

¹Peter the Great St. Petersburg Polytechnic University (SPbPU),
Department “Turbines, Hydro machines and aero-engines”
St. Petersburg, Russia;

²Leibniz Universität Hannover,
Institut für Kraftwerkstechnik und Wärmeübertragung
Hannover, Germany
e-mail: a.sebelev.turbo@mail.ru

ABSTRACT

The problem of decreasing of fossil fuel consumption and energy efficiency is one of today's major conceptions in the field of energy economics. Waste heat recovery is one of the promising solutions for this problem. One of the ways to increase efficiency of the waste heat recovery process is using siloxanes as working fluids for organic Rankine cycles (ORC).

SPbPU scientists have analyzed peculiarities of the steady-state expansion process in the siloxane vapor driven turbine. The design of the nozzle and the blade wheel of the turbine is supersonic due to the low speed of sound of siloxanes. Initial parameters of siloxane were subcritical; a pressure ratio of the turbine was 25. Progressive steps of the initial temperature, pressure ratio and rotational velocity were used to obtain convergence of the solution process. The changings of positions of the nozzle and blade wheel critical sections were established. The details of the supersonic vortices interaction in the blade wheel flow range were analyzed.

The efficiency and power output of the investigated turbine stage were estimated as 0.699 and 309.1 kW, respectively.

1. INTRODUCTION

Waste heat recovery is one of the promising solutions to increase efficiency of different plants and industrial processes (Larjola (1995), Vescovo (2009)). The highest volume of waste heat resources takes place at different thermal power plants, cement, metallurgical and chemical productions. In Russia it is also the gas transport industry. The estimation of waste heat thermal power at the all gas compressor stations of “Gazprom” is 87.9 GW (Lykov *et al.* (2013)). Rough estimations of waste heat thermal power at different productions in Russia, made on the base of Key World Energy Statistics (2014), are: 3.9 GW at the all cement production plants, 2.8 GW at the all metallurgical production plants and 1.9 GW at the all chemical production plants. In the other words, all this waste heat may be turned to 14.5 GW of electrical power by the most conservative estimate.

In most cases using of organic Rankine cycles (ORC) for recovery plants provides higher efficiency of the recovery plants in comparison with water steam Rankine cycle due to low temperature levels of the waste heat streams (Larjola (1995), Hung *et al.* (1997), Vescovo (2009)). The average temperature level of the waste heat streams in the whole Russian gas transport system is 390°C by the estimation of Lykov *et al.* (2013). The average temperature level of the waste heat streams at other productions in Russia varies from 150°C to 350°C. One of the most important questions in the recovery plant designing is the choosing of a working fluid. Nowadays the aspects of using of various hydrocarbons, freons and alcohols in ORC are widely researched by different authors (Iqbal *et al.* (1977), Hung *et al.* (1997), Shuster *et al.* (2010), Gao *et al.* (2012)). Modern requirements for environment safety determine ozone depletion potential (ODP) and global warming potential (GWP) as main criteria for

choosing of a working fluid. It was shown that in this case the most promising alternatives to different hydrocarbons, freons and alcohols are zeotropic mixtures and siloxanes (Heberle *et al.* (2012), Chys *et al.* (2012), Weith *et al.* (2014)). The aspects of using of siloxanes in ORC were investigated by Lai *et al.* (2011), Fernandez *et al.* (2011), Uusitalo *et al.* (2013). It was shown that in this case the efficiency of ORC may be increased up to 23 – 25%.

The turbines for organic working fluids have essential differences in details of the expansion process in comparison with typical gas and steam turbines. The special supersonic design is required for such turbines due to low speed of sound of different organic working fluids. The aspects of designing of the ORC driven turbines were outlined by different authors. Yamamoto *et al.* (2001) designed and tested R-123 centripetal turbine; Kang (2012) designed and tested R-245fa radial-inflow turbine; Casati *et al.* (2014) described designing method of the ORC centrifugal microturbines. Guardone *et al.* (2013) described the influence of molecular complexity on nozzle design.

Despite the high volume of investigations in the area of organic working fluids expansions the peculiarities of siloxanes behavior during the expansion process still haven't been outlined. Thus, the scope of the present paper is to investigate the siloxane expansion process and to outline its peculiarities.

2. INVESTIGATION OBJECT

2.1. Initial parameters of the expansion process

Hexametyldisiloxane (MM) was chosen as working fluid for the expansion process. The initial pressure p_0 was set as 1 MPa. The initial temperature T_0 was set as a vapor saturation temperature at chosen initial pressure. The turbine pressure ratio has been chosen as 25 to provide the required turbine enthalpy drop upon the condition of 300 kW power output of the turbine stage. Trans- and supercritical initial parameters were not considered.

Positive slope of MM vapor saturation curve provides inability of intersection between expansion process curve and two-phase region as shown in figure 1. It means that there is no possibility of droplet formation in the turbine stage.

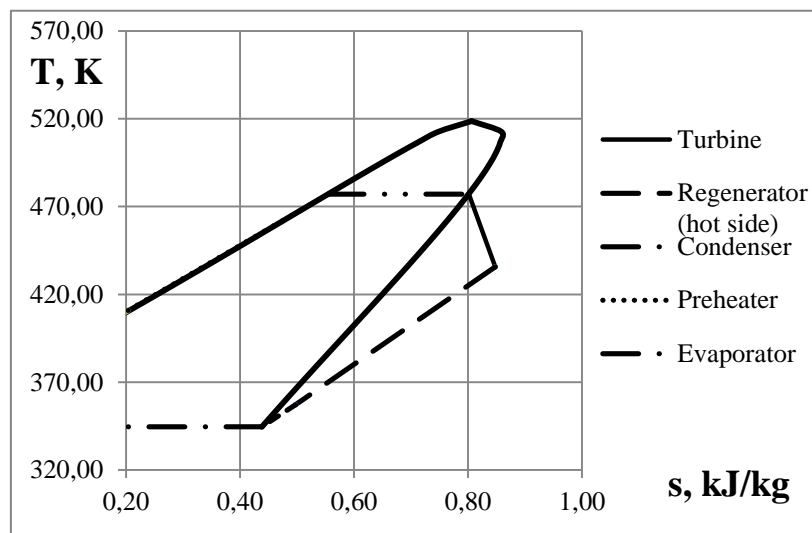


Figure 1: T-s diagram of the expansion process

2.2. The turbine

A single-stage double-flow axial turbine was chosen as the expander machine. The choice of the double-flow design was made due to high axial forces acting on the turbine rotor. The subsonic part of the nozzle was designed according to Vitoshinski profile. The supersonic part of the nozzle was designed using the SPbPU high pitch-chord ratio design. The main features of the high pitch-chord ratio design, described in details by Rassokhin (2004), are:

- small angles α_1 (3..5°) and β_1 (8..14°);

- high blade wheel flow turning angle ($\Omega = 151..164^\circ$);
- high pitch-chord ratio for the nozzle and blade wheel blades ($t_N/b_N > 4$, $t_{BW}/b_{BW} > 1.1$);
- high enthalpy drops at one turbine stage (up to 800 kJ/kg).

The supersonic blade profile C9022B was chosen for the blade wheel. This blade profile was described in details by Dejch *et al.* (1965). The reason to use blade profile with thick leading edge is strong changing of MM properties with relation to thermodynamic parameters. The design of the nozzle and blade wheel is supersonic due to low MM speed of sound. Involutions of the nozzle and blade wheel at the mean diameter are shown in figure 2. The blade wheel of the turbine has a tip shroud. The main geometric parameters of the single-flow turbine stage are given in table 1.

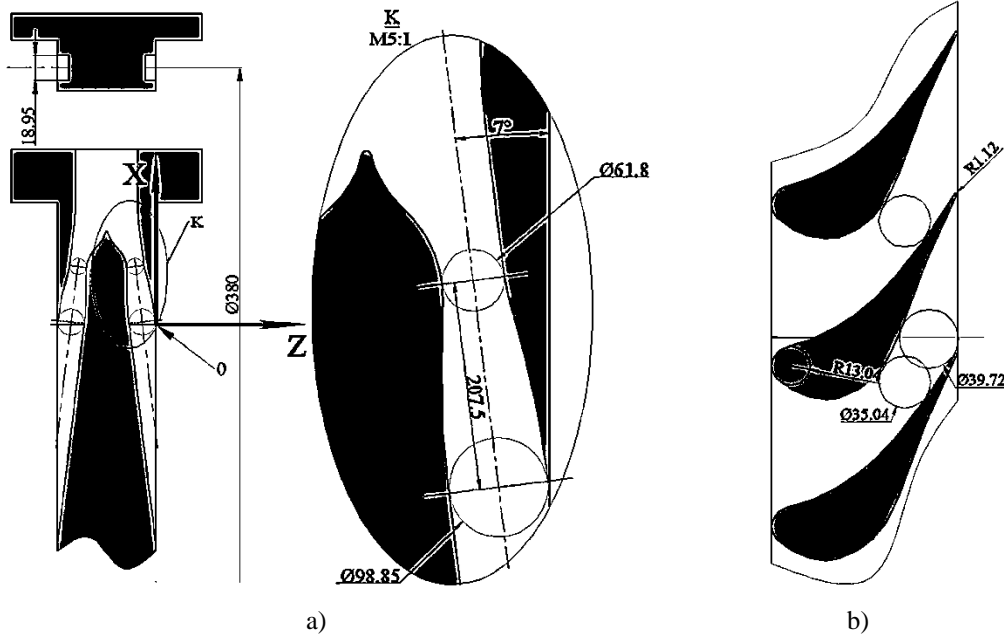


Figure 2: Involutions of the nozzle (a) and blade wheel (b) at the mean diameter

Table 1: The main geometric parameters of the one-flow turbine stage

Parameter	Dimensions	Value	Parameter	Dimensions	Value
D_m	mm	380	α_1	deg.	7.00
n	rev/min	12000	ΔL_{ax}	mm	7.00
H_0	kJ/kg	66.26	ΔL_{tc}	mm	0.30
G	kg/s	6.86	β_1	deg.	90.00
C_{ax}/u	-	1.52	Z_2	-	55
ε	-	0.97	l_2	mm	24.75
Z_1	-	7	β_2^*	deg.	30.00
l_1	mm	18.95	Ω	deg.	60.00

3. NUMERICAL SIMULATION METHOD

The SPbPU method for numerical simulation of processes in supersonic turbines, described by Zabelin *et al.* (2013), was used. ANSYS CFX was used to provide the numerical simulation.

The original relation between the number of nozzles and number of working blades is 7/55. The relation 1/8 and periodic boundary conditions were used in the computational model. This assumption is correct to be used with Frozen Rotor interface between the nozzle and blade wheel areas because the relation between connecting areas in this case is 1:1.018. The modeling of blade wheel tip shroud was also considered in numerical model in assumption of rotating motion of tip shroud domain. The computational model of the single-flow turbine stage is presented in figure 3.

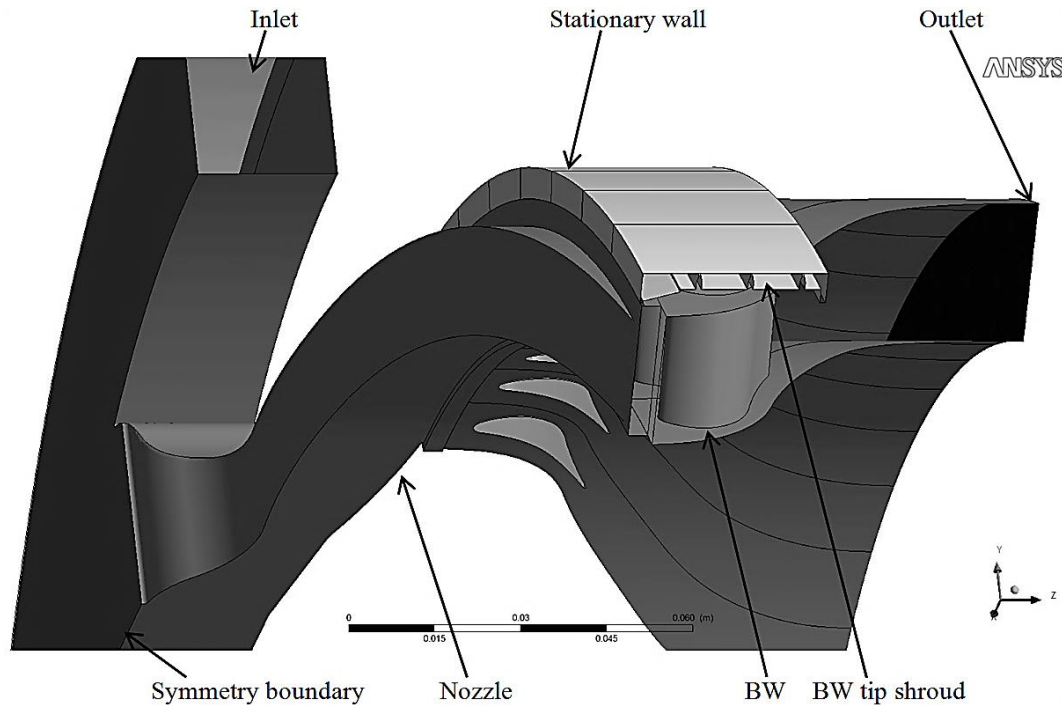


Figure 3: Computational model of the single-flow turbine stage

High-Reynolds version of the $k-\omega$ SST turbulence model was used. Steady-state Frozen rotor interface between the nozzle and blade wheel areas was used to model rotor-stator interaction. Flow parameters of the turbine stage were obtained by averaging of their values for 4 positions of blade wheel relatively to the nozzle in the range of blade wheel pitch angle.

Aungier Redlich Kwong real gas equation of state was used to model thermodynamic properties of MM during the expansion process. The main parameters need to be specified are: molar mass, critical temperature and pressure, acentric factor and boiling temperature. Zero pressure polynomial coefficients were obtained with using REFPROP databases to evaluate specific heat capacity of MM. Kinetic Theory models were used to model transport properties of MM. Rigid Non Interacting Sphere model was used to model MM dynamic viscosity behavior.

Total parameters at inlet ($p_0 = 1$ MPa, $T_0 = 477.1$ K) and static pressure at outlet ($p_0 = 0.04$ MPa) were specified as boundary conditions in computational model. Progressive steps of the boundary conditions were used to obtain convergence of the solution process. The iteration steps between the changings of boundary conditions were different to decrease their negative influence on the solution process. Monitoring of the RMS residuals, imbalances and turbine efficiency and power output were used to control convergence of the solution process. The criteria of the convergent solution in present research were:

- drop of the RMS residuals more than 10^2 ;
- imbalances less than 0.5%;
- fluctuation of the turbine efficiency and power output less than 5%.

Three different types of computational domains discretization were compared to obtain grid independent solution. The results of the grid independency study are presented in table 2.

Table 2: The results of the grid independency study

Grid type	1 nozzle sector, millions of nodes	8 blade wheel sectors, millions of nodes	8 tip shroud sectors, millions of nodes	Difference in the turbine efficiency with the previous grid, %	Difference in the turbine power output with the previous grid, %
Coarse	0.68	3.21	3.15	-	-
Medium	1.15	6.85	4.26	10.2	15.4
Fine	1.98	10.64	5.32	4.2	4.8

The medium grid was used in further calculations. The grid structure is presented in figure 4.

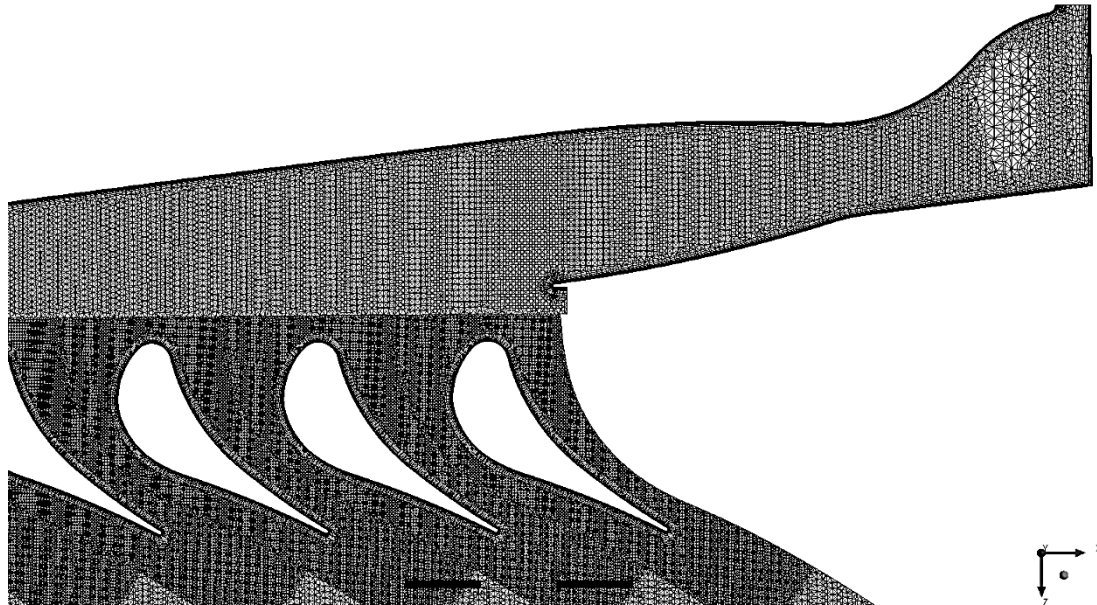


Figure 4: The grid structure

4. DISCUSSION OF THE RESULTS

The values of the calculated thermodynamic and transport properties were compared with the values obtained with using REFPROP databases to estimate tolerance of the obtained results. Maximum deviation between CFX and REFPROP results was less than 5% for specific heat capacity and dynamic viscosity. It is noteworthy that isentropic exponent of MM has a strong nonlinear dependence on temperature and pressure in superheated vapor area as shown in figure 5a. In this case it is incorrect to use constant isentropic exponent in preliminary turbine calculations. Rough boundary in figure 5a is a consequence of discrete steps of temperature and pressure.

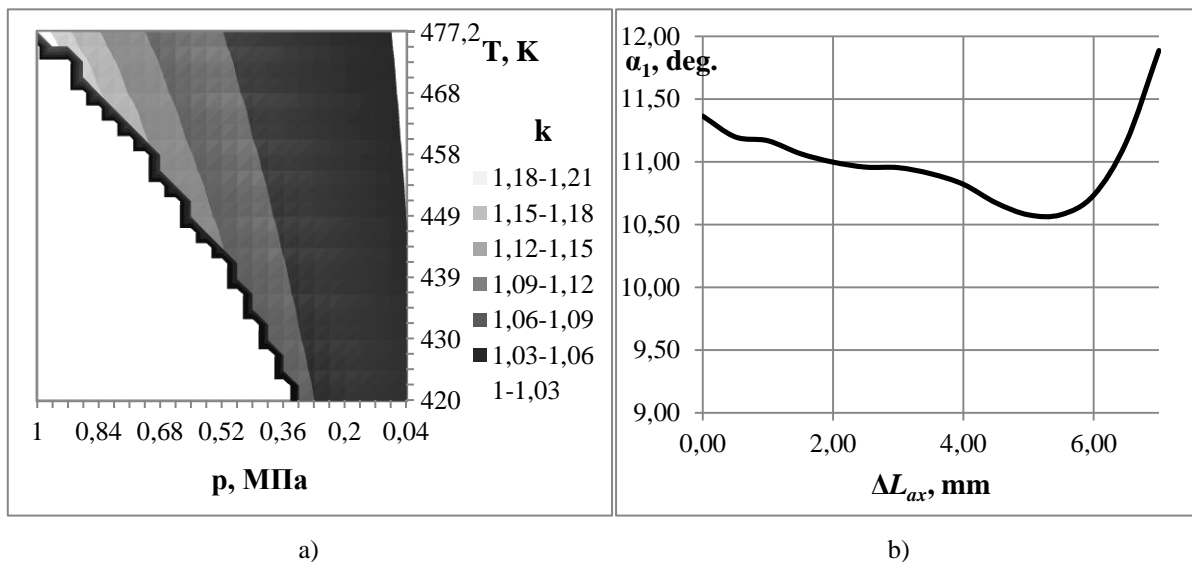


Figure 5: MM isentropic exponent dependence on temperature and pressure in superheated vapor area (a) and varying of the nozzle outlet angle outbound of the nozzle (b)

The analysis of Mach number field in the nozzle (figure 6) shows that the flow in the critical section is not fully supersonic. It can be seen in details in figure 7. Physically, it means that the position of real critical section changed to the downstream direction in comparison with its design position. This

phenomenon was established by Reichert and Simon (1997). This fact means that the theoretical mass flow rate through the supersonic nozzle, defined as:

$$G_t = \frac{p_0 \cdot S_{cs}}{\sqrt{T_0}} \sqrt{\frac{k}{R} \left(\frac{2}{k+1} \right)^{\frac{k+1}{k-1}}}, \quad (1)$$

should be based on the cross-sectional area of the real critical section. Additionally, the velocity profile near the critical section is highly distorted towards to the straight nozzle wall. This is a consequence of the non-symmetric shape of the nozzle and was also outlined by Reichert and Simon (1997). The same situation takes place near the blade wheel critical section.

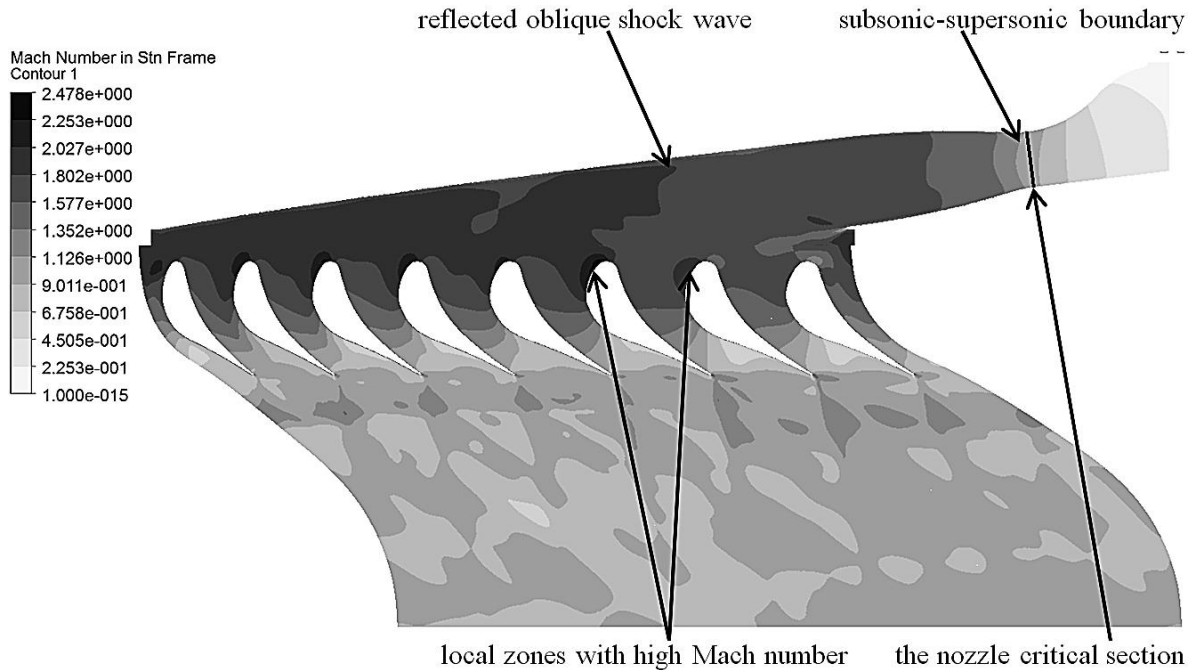


Figure 6: Mach number field in the turbine stage at the mean diameter

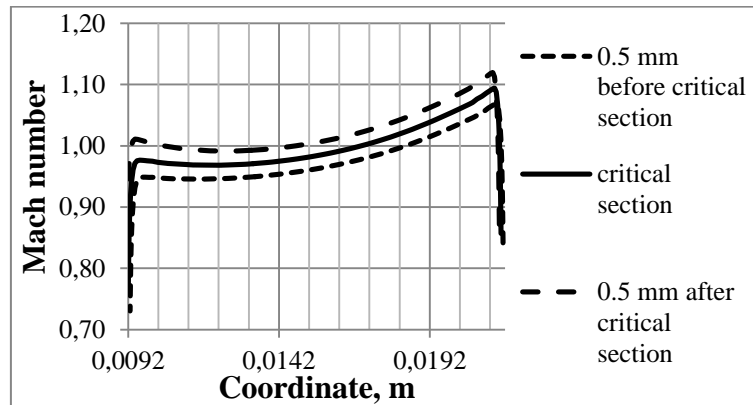


Figure 7: Velocity profiles near the nozzle critical section at the mean diameter

The oblique shock wave from the nozzle reflects from the nozzle wall and then impinges on the leading edge of the blades. This leads to the appearing of the local zones with high Mach number (up to 2.5 in stationary frame) at the blades leading edges. Such flow behavior is typical for axial supersonic turbines and was described in details by Kirillov (1972) and Traupel (1977). It should be outlined that the nozzle outlet angle, defined as:

$$\alpha_1 = \arctg\left(\frac{G \cdot D_m \cdot c_{1z}}{2M_N}\right), \quad (2)$$

has a decreasing value outbound of the nozzle as shown in figure 5b. Zabelin *et al.* (2013) showed that this phenomenon is a consequence of the blade wheel influence on the nozzle in trans- and supersonic turbines. The nozzle torque in equation (2) was calculated directly in CFD-Post.

The analysis of the flow structure in the blade wheel shows that double vortex structure appears at the blade wheel inlet as shown in figure 8. It is a consequence of complex phenomena which take place at the edges of the nozzles active flow sectors. These phenomena related to the flow separation and were described by Natalevich (1979). The hub vortex rotates clockwise and rests against the blade wheel hub. The shroud vortex has a counterclockwise rotation and rests against the blade wheel shroud because of the inertial forces. This flow separation leads to additional energy losses at the boundary of vortices interaction as shown in figure 9.

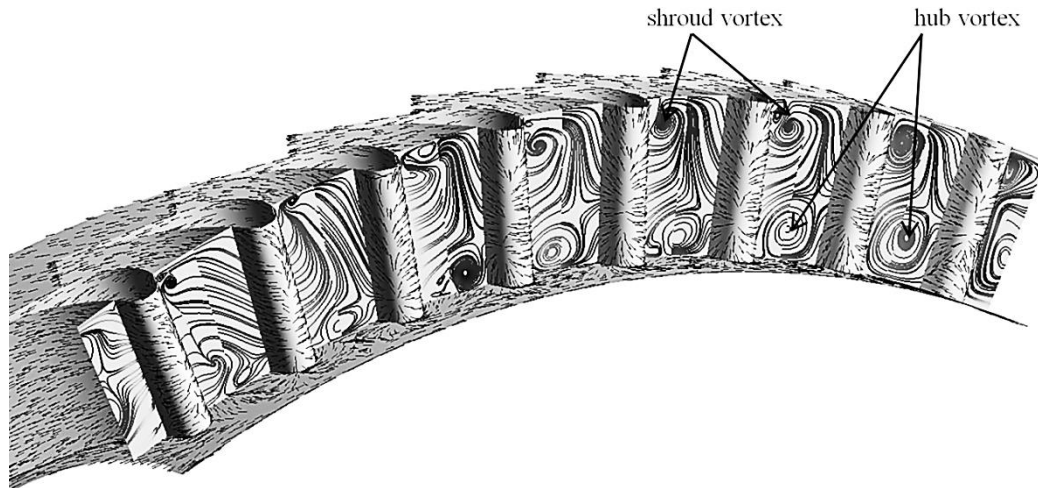


Figure 8: Flow structure at the blade wheel inlet

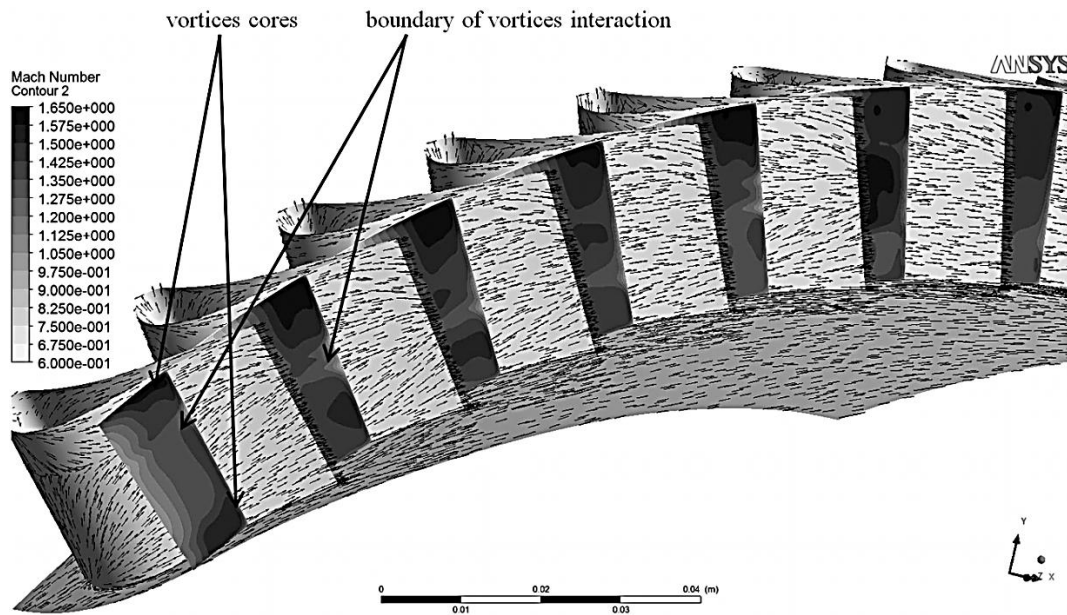


Figure 9: Flow structure at the blade wheel outlet

Another peculiarity that should be highlighted is a specific shape of the shock wave after the blade wheel. As it can be seen in figures 8 and 9 the hub vortex increases as it drew in the blade wheel flow range. This leads to the decreasing of the shroud vortex and increasing of the Mach number at the blade wheel shroud. This process is illustrated in figures 9 and 10. The zones with low velocities at the blade wheel shroud in figure 10 are the zones of the tip shroud leakage interaction with the main flow. High volume of the hub vortex together with strong dependence of the MM density on thermodynamic parameters leads to appearing of the normal shock wave at the blade wheel outlet as

shown in figure 10. The intensity of the normal shock wave decreases from hub to shroud due to low volume of the shroud vortex in comparison with the hub vortex. This is also the reason for the high Mach number zones appearing at the blade wheel shroud. The volume of the high Mach number zones increases with distance from the blade wheel. It means that shroud vortex is underexpanded and continues its expansion after the blade wheel.

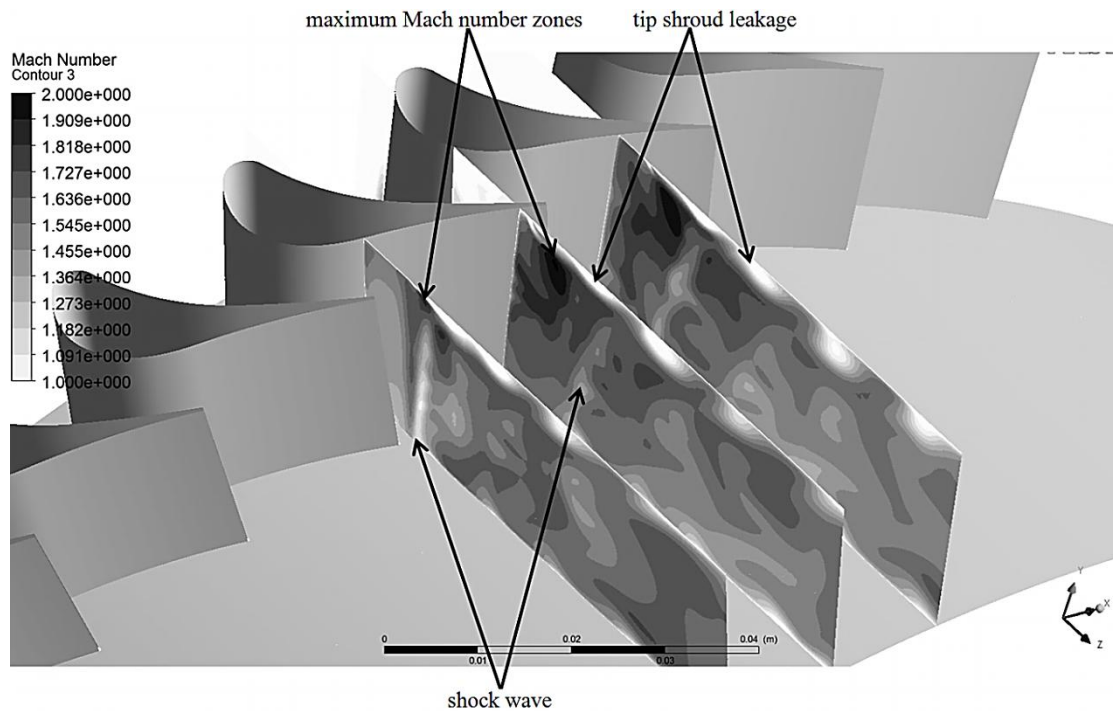


Figure 10: Shock wave at the blade wheel outlet

The efficiency and power output of the investigated turbine stage were calculated with using following equations:

$$\eta_i = \frac{M_{BW} \cdot \pi \cdot n}{30 \cdot G \cdot H_0}, \quad (3)$$

$$N = \frac{M_{BW} \cdot \pi \cdot n}{30}. \quad (4)$$

The calculated values of the efficiency and power output for investigated single-flow turbine stage are 0.699 and 309.1 kW respectively.

5. CONCLUSIONS

The expansion process in the siloxane vapor driven turbine was modeled. The peculiarities of the siloxane expansion process were outlined. The important conclusions about the calculations of theoretical mass flow rate through the supersonic nozzles were made. It was shown that in case of the supersonic nozzles the equation for theoretical mass flow rate should be based on the cross-sectional area of the real critical section. It was also shown that it is unacceptable to use constant isentropic exponent in case of the preliminary ORC turbines calculations.

Most of the outlined peculiarities are typical for the supersonic axial microturbines because of subcritical initial parameters of the siloxane vapor. However, the strong relation of the siloxane properties to the thermodynamic parameters determines its nonconventional behavior during the expansion in the blade wheel. Complex interaction between two supersonic vortices in the blade wheel leads to additional energy losses and appearing of the normal shock wave after the blade wheel. As a result, calculated efficiency of the investigated turbine stage is 0.699. This value is close to the efficiency of the water steam microturbines with mean diameter up to 500 mm.

NOMENCLATURE

GW	Gigawatt	
GWP	Global Warming Potential	
kW	Kilowatt	
MM	Hexametyldisiloxane	
ODP	Ozone Depletion Potential	
ORC	Organic Rankine Cycle	
SPbPU	Peter the Great St. Petersburg Polytechnic University	
C_{ax}/u	stage load coefficient	
c_{1z}	axial component of velocity at the nozzle outlet	m/s
D_m	mean diameter	m
G	mass flow rate	kg/s
H_0	isentropic enthalpy drop	kJ/kg
k	isentropic exponent	
l_1	nozzle height	mm
l_2	blade height	mm
M	torque	N·m
n	rotational speed	rev/min
p_0	nozzle inlet pressure	MPa
p_2	blade wheel outlet pressure	MPa
R	individual gas constant	J/(kg·K)
S	cross-sectional area	m ²
T_0	nozzle inlet temperature	K
Z_1	number of nozzles	
Z_2	number of blades	
α_1	nozzle outlet angle	deg.
β_1	blade wheel inlet angle in relative frame	deg.
β_2^*	blade wheel outlet angle in relative frame	deg.
ΔL	clearance value	mm
ε	partial admission ratio	

Subscript

BW	blade wheel
N	nozzle
ax	axial
cs	critical section
i	internal
t	theoretical
tc	tip clearance

REFERENCES

- [1] Casati, E., Vitale, S., Pini, M., Persico, G., Colonna, P., 2014, Centrifugal turbines for mini-organic Rankine cycle power systems, *Journal of Engineering for Gas Turbines and Power*, vol. 136, 122607.
- [2] Chys, M., van den Broek, M., Vanslambrouck, B., De Paepe, M., 2012, Potential of zeotropic mixtures as working fluids in organic Rankine cycles, *Energy*, vol. 44, pp. 623 – 632.
- [3] Dejch, E.M., Filipov, A.G., Lazarev, J.L., 1965, *Atlas profilej reshetok osevyh turbin*, Mashinostroyenie, Moscow, 96p.
- [4] Fernandez, F.J., Prieto, M.M., Suarez, I., 2011, Thermodynamic analysis of high-temperature regenerative organic Rankine cycles using siloxanes as working fluids, *Energy*, vol. 36, pp. 5239 – 5249.

- [5] Gao, H., Liu, Ch., He, Ch., Xu, Xi., Wu, Sh., Li, Y., 2012, Performance Analysis and Working Fluid Selection of a supercritical Organic Rankine Cycle for low grade waste heat recovery, *Energies*, vol. 5, pp. 3233 – 3247.
- [6] Guardone, A., Spinelli, A., Dossena, V., 2013, Influence of molecular complexity on nozzle design for an organic vapor wind tunnel, *Journal of Engineering for Gas Turbines and Power*, vol. 135, 042307.
- [7] Heberle, F., Preißinger, M., Brüggemann, D., 2012, Zeotropic mixtures as working fluids in Organic Rankine Cycles for low-enthalpy geothermal resources, *Renewable Energy*, vol. 37, pp. 364 – 370.
- [8] Hung, T.C., Shai, T.Y., Wang, S.K., 1997, A review of Organic Rankine Cycles (ORCs) for the recovery of low-grade waste heat, *Energy*, vol. 22, pp. 661 – 667.
- [9] Iqbal, K.Z., Fish, L.W., Starling, K.E., 1977, Isobutane geothermal binary cycle sensitivity analysis, *Proceedings Oklahoma Academic Science*, The University of Oklahoma, pp. 131 – 137.
- [10] Kang, S.H., Design and experimental study of ORC (organic Rankine cycle) and radial turbine using R245fa working fluid, 2012, *Energy*, vol. 41, pp. 514 – 524.
- [11] Key World Energy Statistics, *International Energy Agency*, 2014.
- [12] Kirillov, I.I., 1972, *Teorija turbomashin*, Mashinostroyenie, Leningrad, 533p.
- [13] Lai, N.A., Wendland, M., Fischer, J., 2011, Working fluids for high-temperature organic Rankine cycles, *Energy*, vol. 36, pp. 199 – 211.
- [14] Larjola, J., 1995, Electricity from industrial waste heat using high-speed organic Rankine cycle (ORC), *International journal of production economics*, vol. 41, pp. 227 – 235.
- [15] Lykov, A.V., Zabelin, N.A., Rassokhin, V.A., 2013, Estimation of waste heat resources in Russian unified system of gas supply, *St. Petersburg State Polytechnical University Journal*, vol. 183 (4), pp. 136–145.
- [16] Natalevich, A.S., 1979, *Vozdushnye mikroturbiny*, Mashinostroyenie, Moscow, 192p.
- [17] Rassokhin, V.A., 2004, Turbiny konstrukcii LPI: preimushhestva, harakteristiki, opyt razrabotki i primenenie, *St. Petersburg State Polytechnical University Journal*, vol. 491, pp. 152 – 161.
- [18] Reichert, A.W., Simon, H., 1997, Design and flow field calculations for transonic and supersonic radial inflow turbine guide vanes, *Journal of turbomachinery*, vol. 119 (1), pp. 103 – 113.
- [19] Shuster, A., Karellas, S., Aumann, R., 2010, Efficiency optimization potential in supercritical Organic Rankine Cycles, *Energy*, vol. 35, pp. 1033 – 1039.
- [20] Traupel, W., 1977, *Thermische Turbomaschinen*, 3. Aufl., Springer, Berlin, 579p.
- [21] Uusitalo, A., Turunen-Saaresti, T., Honkatukia, J., Colonna, P., Larjola, J., 2013, Siloxanes as working fluids for mni-ORC systems based on high-speed turbogenerator technology, *Journal of Engineering for Gas Turbines and Power*, vol. 135, 042305.
- [22] Vescovo, R., 2009, ORC recovering industrial heat, *Cogeneration and On-Site Power Production*, vol. 2, pp. 53 – 57.
- [23] Weith, T., Heberle, F., Preißinger, M., Brüggemann, D., 2014, Performance of siloxane mixtures in a high-temperature Organic Rankine Cycle considering the heat transfer characteristics during evaporation, *Energies*, vol. 7, pp. 5548 – 5565.
- [24] Yamamoto, T., Furuhashi, T., Arai, N., Mori, K., 2001, Design and testing of the organic Rankine cycle, *Energy*, vol. 26, pp. 239 – 251.
- [25] Zabelin, N.A., Rakov, G.L., Rassokhin, V.A., Sebelev, A.A., Smirnov, M.V., 2013, Investigation of fluid flow highlights in low flow-rated LPI turbine stages, *St. Petersburg State Polytechnical University Journal*, vol. 166 (1), pp. 45–53.

HIGH-TEMPERATURE SOLAR ORGANIC RANKINE CYCLE – ANNUAL SIMULATION OF VARIOUS SYSTEM DESIGNS

Björn Hunstock^{1*}, Sabine Strauch², Wilhelm Althaus, Björn Bülten, Johannes Grob, Ralf Paucker

Fraunhofer UMSICHT
Department Energy Systems Engineering
46047 Oberhausen, Germany
¹bjoern.hunstock@umsicht.fraunhofer.de
²sabine.strauch@umsicht.fraunhofer.de

* Corresponding Author

ABSTRACT

This paper deals with the simulation of high-temperature solar organic Rankine cycles. In contrast to previous simulations the diurnal variations and the effect of charging and discharging the thermal energy storage are taken into account. Furthermore, the presented simulations cover one full year. The simulations use discrete time steps with a constant operation over a period of one hour. Considering a full year, 8 760 connected simulations have been carried out to describe the full and part load operation of one plant. Annual simulations allow a detailed evaluation of a solar organic Rankine cycle. The work describes the effect of varying solar field area and thermal energy storage capacity with different design points. High values of irradiance result in small solar fields. These fields often cannot provide enough thermal energy to produce the nominal electrical power at time steps with low irradiance. Design points using a low value for irradiance allow full load operations during the winter season. On the other hand, they generate a large percentage of waste heat during summer, which cannot be used due to limited storage and power capacity. The presented annual simulations show that different design points for a solar organic Rankine cycle cause various results for the plant performance over a full year. A design point in December leads to a large solar field and a thermal energy storage with a high capacity. The annual simulations show the continuous operation over a full year and are used to evaluate the plant designs.

1. INTRODUCTION

A comprehensive use of solar energy for power production is one approach for global sustainable electricity generation. Many rural areas with high potential of solar radiation (e. g. Northern Africa) are still supplied with power from stand-alone diesel generators (Szabó *et al.*, 2011). Hence, small decentralized power plants using renewable energies can reduce the consumption of fossil fuels in such areas. Concentrated solar power (CSP) is a promising technology to generate power in areas with high direct solar radiation that is non-scattered radiation. Small CSP plants are able to replace or support existing diesel generators.

The organic Rankine cycle (ORC) efficiently converts heat into power and can be used as a decentralized power plant. High-temperature ORC (evaporation temperatures of more than 200 °C) utilizing solar thermal power suits to be combined with the state-of-the-art mid- or high-temperature parabolic trough collectors. These solar driven ORC is called solar organic Rankine cycle (SORC) Providing high evaporation temperatures, parabolic trough collectors enable ORC to operate at high

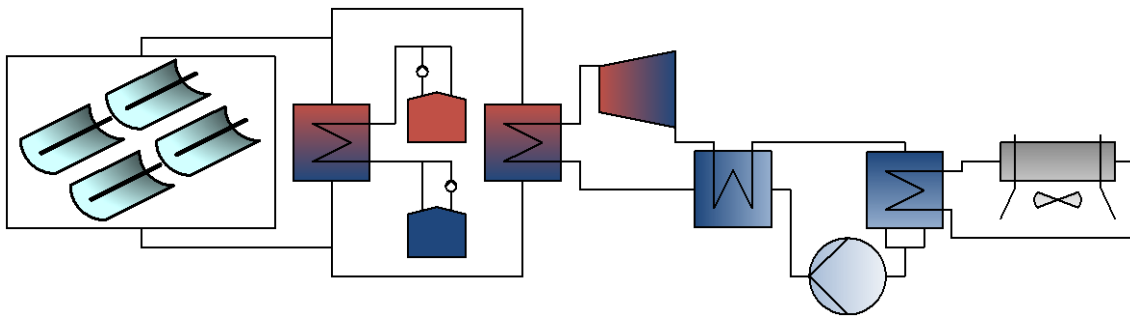


Figure 1: Scheme of a SORC plant

cycle efficiencies. Furthermore, an additional thermal energy storage (TES) increases the full load hours of the power plant. In consequence a SORC can theoretically cover a continuous load if a well-sized TES is integrated and the solar field is sufficiently large. Figure 1 shows the scheme of a SORC plant. The plant consists of two different cycles. The first one is the solar field which converts solar irradiation into thermal energy. The second one utilizes this thermal energy to generate electricity. The first cycle includes the TES which consists of two tanks (one hot and one cold tank). The indirect storage system is charged and discharged by a heat exchanger. During times with sufficient irradiance the solar field charges the TES and at the same time supplies the ORC with thermal energy. At night the stored thermal energy is used to evaporate the ORC working fluid.

Only a few high-temperature SORC plants have been built yet. Most of these SORC originate from research projects. Stine and Geyer (2001) mentioned three different SORC plants with the electrical power of 19 kW, 37 kW and 150 kW which were used to supply the pumps for wells. In 2006 a SORC with an electrical gross power of 1.35 MW started operation at Arizona Public Service in the USA (Sinai and Fisher, 2007; Canada *et al.*, 2004). A thermocline storage was planned for a future expansion of this SORC to store the thermal energy for a full load operation of six hours. Orosz *et al.* (2010a) developed a small scaled SORC with 1 kW_{el} for decentralized power generation tested in Lesotho, Africa. Kane (2003) presented operation data of a 15 kW_{el} ORC connected to linear Fresnel collectors, whereas Moustafa *et al.* (1984) showed a SORC plant that uses parabolic dishes to produce thermal energy for a 100 kW_{el} ORC.

The academic research focuses on the simulation of SORC. For different applications the cycle has been simulated and optimized to achieve a high cycle efficiency. Delgado-Torres and García-Rodríguez (2007a) and (2007b) simulated different SORC and compared different ORC working fluids. The simulations used a constant direct normal irradiance (DNI). The steady-state simulations did not consider a TES and determined the collector area taking into account different condensation temperatures for recuperative and non-recuperative ORC. Several other works dealt with the simulation of SORC systems, for example Bruno *et al.* (2008), Nafey and Sharaf (2010), Orosz *et al.* (2010b) and Quoilin (2011). A thermal energy storage is considered by Price and Hassani (2002), McMahan (2006), He *et al.* (2012) and Al-Sulaiman *et al.* (2011), but the operation for different values of irradiance was not included. Orosz *et al.* (2010b) developed a design tool for small scaled SORC on the basis of the plant design described in Orosz *et al.* (2010a). The continuing impact of the hourly varying direct irradiance during a full year on a SORC has not been focused by research yet.

Hence, this paper deals with the annual simulation of SORC plants considering the charge and discharge of an integrated TES. Different SORC configurations are analyzed. Plant parameters are varied to show the effects in operation. Technical or economic interests are not taken into account. An ORC power capacity of 500 kW_{el} serves as an example for decentralized power supply applications. SORC of this plant size are considered to be technically mature and available (Dürr Cyplan, 2015).

First of all, it is shown how the design of a SORC can differ depending on varying values of DNI. For different solar field sizes and TES capacities the daily variation of produced energy is computed to preselect design points. The parameters are varied to show the influence on the annual solar capacity

factor. Considering these results annual simulations with hourly time steps for three different designs are carried out and main results of the annual simulations are analyzed.

2. EVALUATING DESIGN POINTS FOR SORC PLANTS

2.1 Basics for simulations

The simulation of the SORC including solar field, TES and power block are carried out with the commercial software THERMOFLEX. The program allows modeling several thermal systems, e. g. steam power plants, gas turbines etc. Thermodynamic properties for various fluids are included in the model. Therefore different working fluids for an ORC can be taken into account. The software allows predicting the part load behavior of an energy system with an off-design simulation mode.

At first, a design is specified and simulated. The chosen design is used to simulate the off-design behavior, for example the part load operation caused by low irradiance. Discrete time steps are used to calculate time dependent results. Each time step represents one hour. A higher time step resolution would increase the duration of calculation. The direct normal irradiance as input parameter does not cause fast load changes. Only for sunrise and sunset a higher time step resolution would increase the precision. Therefore, one steady state simulation runs for each hour of the day. The state of charge (SOC) of the TES depends on the previous SOC and on the actual charging or discharging rate. Therefore, the SOC of the TES at the end of a time step is used as input value for the following time step. Heat capacity of plant material and flow simulation are not taken into account.

To simplify, the ambient temperature for every simulation is fixed at 15 °C. This satisfies the requirements of the approach chosen in this paper, which does not consider exact efficiency losses caused by high ambient temperatures. For an economic analyze it must be kept in mind.

The size of a solar field is often specified as dimensionless factor, the solar multiple. According to the definition in Montes *et al.* (2009) the solar multiple SM equals the ratio between the thermal power of solar field at design point and the thermal power required for full load operation of the power block.

$$SM = \frac{\dot{Q}_{th, SF}}{\dot{Q}_{th, ORC}} \quad (1)$$

According to this approach for this ORC application the SM is calculated by dividing the thermal power required for full load operation of the ORC $\dot{Q}_{th, ORC}$ by the thermal power of the solar field $\dot{Q}_{th, SF}$ (compare Equation (1)). Following this definition, a solar field with a solar multiple $SM = 2$ causes a collector area twice as much as a solar field with $SM = 1$. The solar multiple mainly depends on the used irradiance and the power capacity of the power block.

A calculation shows the impact of the amount of DNI on the required solar field area. For this calculation all losses are assumed to be negligible during energy conversion to prove the direct interrelationship between solar field area and direct normal irradiance. Table 1 demonstrates the dependency of the solar field area and the normal component of the beam irradiance. Equation (2) outlines this correlation.

$$\dot{Q}_{th, SF} = \eta_{SF} \cdot G_{bn} \cdot A_{ap} \quad (2)$$

The thermal power of the solar field is calculated by multiplying the solar field efficiency η_{SF} , the

Table 1: Required solar field area to produce 2 MW_{th} for different values of irradiation

DNI	Solar field area
400 W/m ²	5 000 m ²
600 W/m ²	3 333 m ²
800 W/m ²	2 500 m ²

collected direct normal irradiance G_{bn} , and the aperture area of the solar field A_{ap} . Hence, assuming a high irradiance, e. g. in the summer season, the calculation results in a small solar field. A solar field at that size might not be able to provide sufficient thermal energy to operate the ORC during winter times. In Table 1 each solar field area delivers a thermal power of 2 MW. Assuming that an ORC requires the same thermal power, each solar field would have a SM of 1, although the area differs.

The annual performance of a CSP plant can be described with the annual solar capacity factor CF_{sol} . Equation (3) shows this ratio between the electrical energy yield and the product of the DNI on aperture and the aperture collector area.

$$CF_{sol} = \frac{\sum_{i=1}^{8760} P_i \cdot \Delta t_i}{\sum_{i=1}^{8760} G_{bn,i} \cdot A_{ap} \cdot \Delta t_i} \quad (3)$$

2.2 SORC without a TES

To show the influence on the plant design and operation three different dates of the year are used to design a SORC with the same process parameters.

The site location is assumed to be at a longitude of 30° north of the equator. Table 2 summarizes the main design parameters of the SORC. The design points are on March 21th (spring equinox) as well as June 21st and December 21st (summer and winter solstice). The irradiance on the spring and autumn equinox is identical, therefore only March 21st is taken into account. For every design point a solar time of 12:00 o'clock is assumed to estimate the irradiance.

The ORC uses toluene as working fluid and an internal heat exchanger to recuperate the thermal energy of the superheated steam after expansion. Previous research studies favored toluene as working fluid, which allows a high cycle efficiency compared to other fluids (Delgado-Torres and

Table 2: Relevant simulation parameters for comparison of different design points without a TES

	March 21 st	June 21 st	December 21 st	
<i>Site</i>				
Longitude	30			° north
Solar time (decimal)	12.00			h
Direct normal irradiance on aperture area	719.1	869.8	429.2	W/m ²
Day of the year	80	172	355	-
<i>ORC</i>				
ORC Gross power	500			kW _{el}
Working fluid	Toluene (C7H8)			-
Evaporation pressure	25.00			bar
Condensing pressure	0.14			bar
ORC gross efficiency	24			%
<i>Solar field</i>				
Heat transfer fluid	Therminol 66			-
Aperture area	4 624	3 542	9 756	m ²
Solar multiple	1			-
Thermal power	2 039			kW
Outlet temperature	320			°C
Inlet temperature	250			°C
Solar field efficiency	61.3	66.2	48.7	%

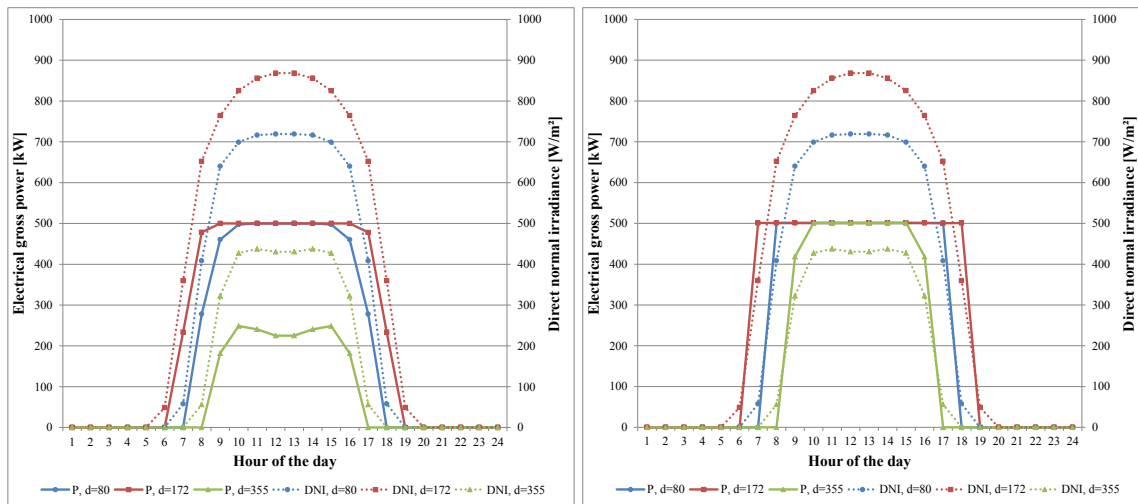


Figure 2: Electrical gross power of the SORC for the design point March 21st (left) and December 21st (right)

García-Rodríguez, 2007a). The inlet pressure of the turbine is 25 bar at about 280 °C. This prevents thermal decomposition that may occur above 300 °C. The condensing pressure of the cycle is 0.14 bar at about 53 °C. For the design point a turbine isentropic efficiency of 75 % is used and a feed pump isentropic efficiency of 75 %. With a gross power of 500 kW_{el} the ORC achieves a gross efficiency of 24 %.

Each design uses a solar field with $SM = 1$. Due to the different direct normal irradiance, the required area of the solar field varies. The used heat transfer fluid is Therminol 66 and the thermal power of each configuration is about 2 039 kW. A TES is not considered in the first run, but will be added in following simulations. The solar field efficiency depends among other parameters on the ambient temperature and solar irradiance, which is the reason for varying efficiencies presented in Table 2. Hourly off-design simulations are carried out for each design on all design dates. The irradiance for one time step is constant. The value is determined at the middle of one hour. This means, that for the twelfth hour of a day (11:00 to 12:00) the solar time 11:30 is used to estimate the irradiance for the entire time step.

Figure 2 shows the results of the off-design simulations using March 21st ($d = 80$) and December 21st ($d = 355$) as design points (right chart). On the left ordinate the electrical gross power of the SORC in kW is plotted, while the right ordinate gives the DNI on the aperture area in W/m². The March design allows six hours of full load operation on the design day and eight hours on June 21st ($d = 172$). The higher irradiance in June and the long sunshine duration allow two more hours with full load operation for the ORC. In contrast, the available solar field area does not allow a full load operation on December 21st. In this case, a solar field of a larger area with $SM > 1$ is necessary to satisfy the required thermal power of a 500 kW_{el} ORC. As shown in Table 2 the solar field size nearly doubles, but it allows full load operation with a low irradiance at the design point in December. On the other side, this large solar field causes a great amount of excess thermal energy in March and June. This waste heat can only be utilized when using a TES.

Choosing the optimal design point for the SORC is essential to satisfy a local power demand. Increasing the solar field size causes more full load hours during sunshine duration especially in times of low DNI. A TES or an auxiliary boiler allow operation after sunset. In conclusion, a TES is considered in the following simulations.

2.3 SORC with a TES

For these simulations the design point is March 21st. A TES of 17.7 MWh capacity is included to enable a 500 kW_{el} ORC for six hours of full load operation. The solar multiple takes the values 1, 2 and 4 to size the solar field. The off-design simulations are carried out for March 21st, June 21st and December 21st. Each of these days is analyzed on the SOC and electrical power. The SOC of the TES at the end of the last time step is equal to the SOC at the beginning of the first time step. This condition ensures realistic behavior of the plant for sequent days with nearly the same irradiance profile.

Figure 3 shows the trend for three different days for a SORC plant with a solar multiple of 1 and 2. The system design with $SM = 1$ leads to a small solar field and, therefore, not sufficient thermal energy is supplied to the storage on December 21st and March 21st. On June 21st there are higher irradiance and more sunshine hours available to increase the SOC. The peak of the storage level is at the 17th hour with a value of approximately 30 %. A solar field with $SM = 1$ does not allow charging the TES. The solar field is too small to use a TES appropriately. A solar field twice as big ($SM = 2$) enables a more effective use of the TES in March and June, and it allows full load operation in December. The TES is charged between morning and afternoon while the ORC is supplied directly. When the irradiance decreases, the TES is discharged and the ORC operates nearly at 90 % load. The reason for this is the lower temperature of the heat transfer fluid after discharging due to the temperature difference at the pinch point. The TES is integrated as an indirect system and uses a heat exchanger to store the thermal power of the solar field. In storage mode the heat exchanger reduces the temperature twice for the reason of charging and discharging. The bigger solar field allows a full load operation during sunshine in December, whereas operation during that time is not possible at $SM = 1$.

In Figure 4 the performance of two storage capacities, namely six and twelve hours, are compared with each other. The design point is March 21st and the SM is 4. The off-design simulations are carried out for the same days as in Figure 2 and under the same cycle conditions for each day. Compared to the results of the simulations for $SM = 2$ the full load operation on December 21st is increased by using a large solar field. This even allows operation of 90 % load in the evening.

In March and June the TES is already fully charged in the morning, but at the beginning of the day the storage is totally discharged. This shows that the storage capacity is too small for 24 hours of operation and an increased solar field does not result in more full load hours. The TES with a capacity of 12 hours in chart of Figure 4 allows this operation in March and June. The solar field size does not

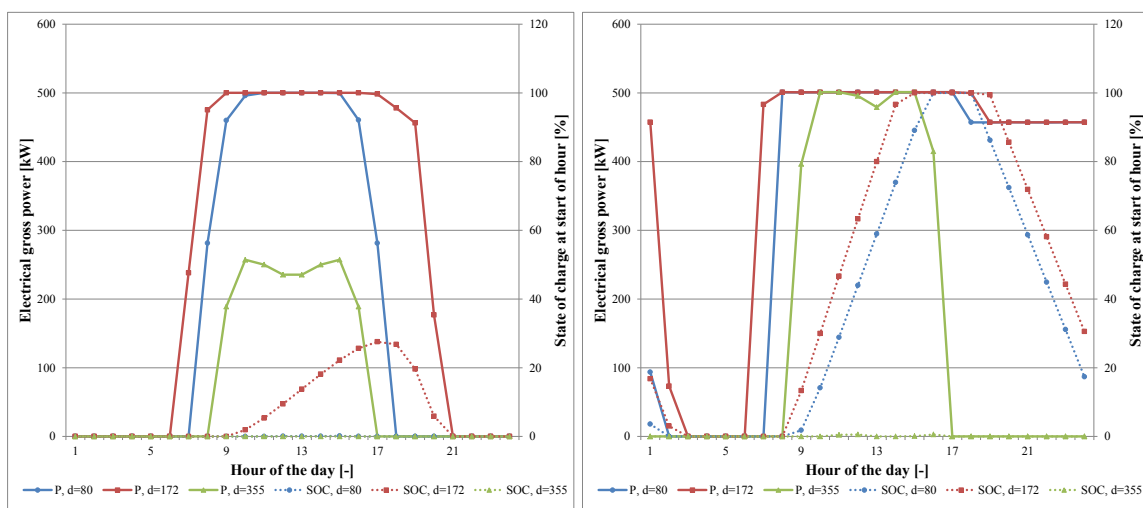


Figure 3: Electrical gross power (left ordinate) and state of charge at start of hour (right ordinate) for off-design simulations with $SM = 1$ (left chart) and $SM = 2$ (right chart).

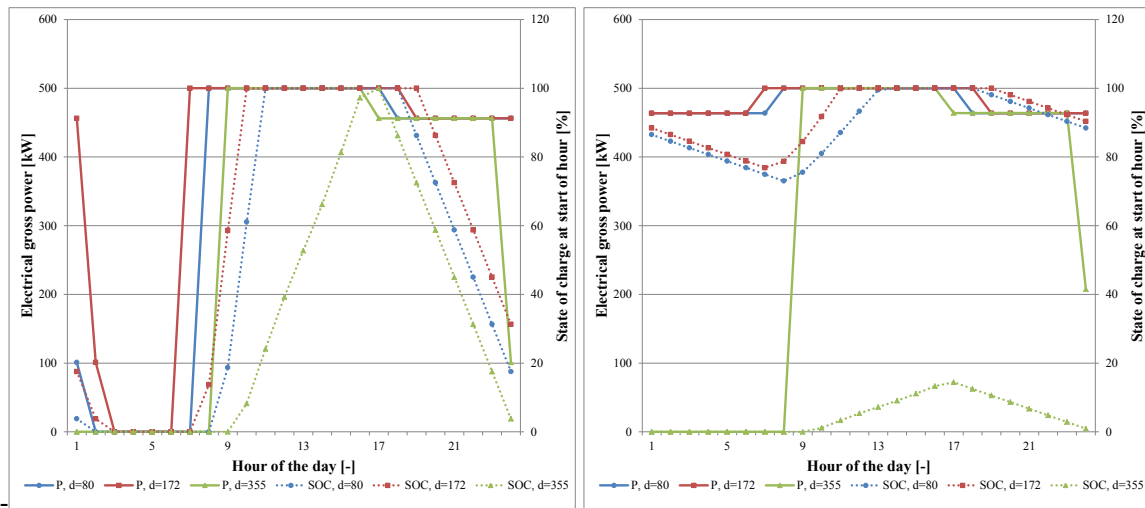


Figure 4: Electrical gross power (left ordinate) and state of charge at start of hour (right ordinate) for off-design simulations with a storage capacity of 6 hours (left chart) and 12 hours (right chart).

change and the excessive thermal energy is stored in the TES. On December 21st the collected thermal energy does not suffice to operate the ORC from the beginning of the day. For this amount of irradiance the solar field is too small and the storage cannot be charged sufficiently. At the charge peak only 15 % of the capacity is used. On March 21st and June 21st the TES is not discharged totally. The minimum SOC reaches only 72 % (March 21st) and 75 % (June 21st). Hence, in these cases the designed storage is oversized and does not suit the solar field size. Furthermore, this design does not suffice for continuous operation on December 21st.

The previous simulations made it possible to evaluate different designs on independent days. However, these daily simulations are not suitable to predict the real behavior of a SORC on successional days, but they are essential to specify characteristic design points. This approach is beneficial regarding aspects of time required for computing and simulating. The preselection using the characteristic design points helps to avoid surplus annual simulations.

Hence, annual simulations for three different design points are carried out in a case study to evaluate the annual performance of a SORC plant.

3. CASE STUDY – ANNUAL SIMULATION OF A SORC

Considering the results of the simulations prior to this, three different annual simulations are carried out. Case 1 refers to the 21st of March (80th day of the year), case 2 to June 21st (172nd day of the year) and case 3 to December 21st (355th day of the year). As in the previous simulations, the ORC has an electrical nominal gross power of 500 kW. The TES is sized with a capacity of 12 full load hours for the ORC and the solar field has a *SM* of 4. The DNI at 12:00 o' clock solar time is used as design point. Table 3 shows the main results of the annual simulation for each design point.

The different DNI on aperture of collector influences the solar field area. In December the low irradiance results in the need of a big solar field, nearly twice as big as the solar field with design point in June. The sunshine duration of an entire year is 4 382 hours. Hence, a TES has to cover the remaining hours for continuous operation. As shown in Figure 4, the design points in March and June lead to the fact that the solar field is too small to charge the TES in winter times when the irradiance is low. The bigger solar field in case 1 allows more operation hours compared to case 2. Whereas, the solar field in case 3 allows 8 760 operation hours for the SORC. The amount of hours out of operation is a theoretical value since e. g. no maintenance stops are taken into account for these simulations. For case 3 the annual electrical energy yield is 4 202 MWh. The solar field and thermal energy storage

Table 3: Case study: results of annual simulation

	Case 1	Case 2	Case 3	Unit
Design point	March 21 st	June 21 st	December 21 st	-
Aperture direct normal irradiance	719.1	869.8	429.2	W/m ²
Solar field aperture area	18 596	14 418	39 286	m ²
Sunshine duration	4 382			h
Hours out of operation	485	1 022	0	h
Annual aperture direct normal irradiation	2.306			MWh/m ²
Annual collected normal irradiation	42 885	33 248	90 597	MWh
Annual collected thermal energy	18 596	14 882	16 580	MWh
Annual electrical energy yield	3 955	3 690	4 202	MWh
Annual solar capacity factor	9.2	11.1	4.6	%

allow SORC operation in every simulated time step. However, the huge solar field causes a low annual solar capacity factor of 4.6 %. The annual solar capacity factor of case 1 is about 9.2 % and for case 2 11.1 %.

To evaluate one SORC design in detail an in-depth view has to be carried out. An annual simulation can be reviewed by looking closely at single days. Hence, in Figure 5 the course of various parameters for March 21st and June 21st of the annual simulation of case 3 is presented. For both entire days the electrical gross power, the direct normal irradiance and the SOC of the TES at the beginning of every time step are plotted. The solar field and the TES ensure the continuous power production of the SORC plant. The TES is charged within a few hours. This is caused by the fact that the simulation allows a higher heat flux than the nominal thermal heat flux for the ORC. If this heat flux is limited, charging times will become longer. The trend of the SOC shows that only about 30 % of the TES load are used on December 21st. Therefore, the storage capacity and the solar field size are not regarded to be well designed for this plant since in this case a huge percentage of the storage fluid is not needed during most of the year. Finding a more suitable design will need several more simulations of further designs which on their part again have to be evaluated by annual simulations.

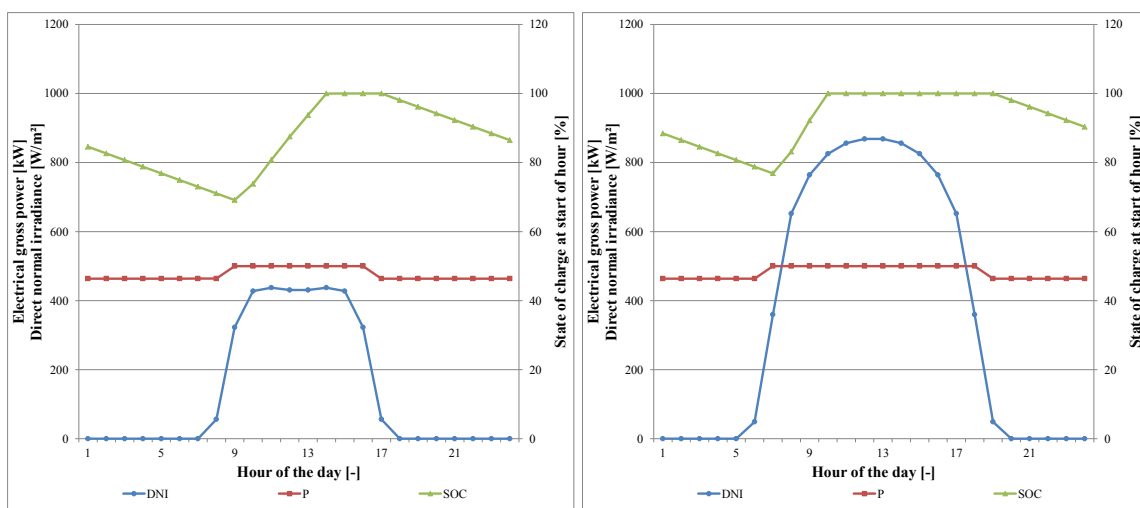


Figure 5: Gross power P, DNI (both left ordinate) and SOC (right ordinate) for December 21st (left chart) and June 21st (right chart), all charts are created with the results of case 3 plant design

4. CONCLUSIONS

Many options exist to design and engineer a SORC. The size of TES and of solar field are directly linked to plant availability and the number of annual operation hours at full and part load. The solar field size and the TES size influence the capacity factor of the SORC. For sizing the solar field and the TES an appropriate design point has to be chosen. Annual simulations describe accurately the full and part load behavior of a SORC plant. With these simulations the chosen design can be evaluated.

In detail, the simulations carried out in this paper conclude in the following:

- A time step approach is used to describe the full and part load behavior of a SORC. A steady-state simulation is not considered to be a suitable approach.
- Choosing an appropriate design point is essential when designing and evaluating a SORC plant with annual simulations.
- The available irradiance and the required thermal power for the ORC influence the solar field size significantly.
- When sizing the TES, the following parameters have to be taken into account at least: the solar field size, full load hours, demand profile and direct normal irradiance over a period of one year.
- Specifying the most suitable design for solar field and TES with simulations results in an optimization problem characterized by a large number of degrees of freedom.
- To determine the best SORC plant design (including economic parameters) an optimization is required.

The simulations described in this paper do not consider economic constraint, auxiliary equipment such as boilers or load profile for power demand. In these cases the simulation needs to be extended by the relevant parameters to optimize a design and to compare it to a diesel generator.

Further works focus on the design of an optimization model. This model will aim at finding the most suitable basic engineering parameters, e. g. capacity of ORC and TES and size of solar field, for a SORC design as a decentralized power plant. The optimization model will contain an economic objective function and uses, among others things, a power demand and an irradiance profile as constraints. The model will include part load behavior for the SORC to satisfy a load dynamic.

NOMENCLATURE

A_{ap}	aperture area	(m ²)
d	day of year	(-)
G_{bn}	beam (direct) normal irradiance	(W/m ²)
P	electrical power	(kW)
\dot{Q}	thermal power	(kW)
SM	solar multiple	(-)
Δt	duration of time step	(h)
η	efficiency	(-)
CF	capacity factor	(-)

Subscripts

el	electrical
i	time step 'i'
sol	solar
th	thermal

Abbreviations

DNI	direct normal irradiance
ORC	organic Rankine cycle
SF	solar field
SORC	solar organic Rankine cycle
SOC	state of charge
TES	thermal energy storage

REFERENCES

- Al-Sulaiman, F. A., Dincer, I., Hamdullahpur, F., 2011, Exergy modeling of a new solar driven trigeneration system, *Solar Energy*, vol. 85, no. 9: p. 2228-2243.
- Bruno, J. C., López-Villada, J., Letelier, E., Romera, S., Coronas, A., 2008, Modelling and optimisation of solar organic rankine cycle engines for reverse osmosis desalination, *Applied Thermal Engineering*, vol. 28, 17-18: p. 2212-2226.
- Canada, S., Cohen, G., Cable, R., Brosseau, D., Price, H., 2004, Parabolic Trough Organic Rankine Cycle Solar Power Plant, *Proceedings of the 2004 DOE Solar Energy Technologies Program Review Meeting*, National Renewable Energy Laboratory:
- Delgado-Torres, A. M., García-Rodríguez, L., 2007a, Comparison of solar technologies for driving a desalination system by means of an organic Rankine cycle, *Desalination*, vol. 216, 1-3: p. 276-291.
- Delgado-Torres, A. M., García-Rodríguez, L., 2007b, Preliminary assessment of solar organic Rankine cycles for driving a desalination system, *Desalination*, vol. 216, 1-3: p. 252-275.
- Dürr Cyplan, 2015, Hochtemperaturanlagen ohne Wärmenutzung, <http://www.durr-cyplan.com/de/energietechnik-produkte/ht-anlagen-ohne-waermenutzung/>, last access: 18 May 2015.
- He, Y.-L., Mei, D.-H., Tao, W.-Q., Yang, W.-W., Liu, H.-L., 2012, Simulation of the parabolic trough solar energy generation system with Organic Rankine Cycle, *Applied Energy*, vol. 97: p. 630-641.
- Kane, M., 2003, Small hybrid solar power system, *Energy*, vol. 28, no. 14: p. 1427-1443.
- McMahan, A. C., 2006, *Design & Optimization of Organic Rankine Cycle Solar-Thermal Powerplants*, Masterthesis, Madison (Wisconsin).
- Montes, M. J., Abánades, A., Martínez-Val, J. M., Valdés, M., 2009, Solar multiple optimization for a solar-only thermal power plant, using oil as heat transfer fluid in the parabolic trough collectors, *Solar Energy*, vol. 83, no. 12: p. 2165-2176.
- Moustafa, S., Hoefler, W., El-Mansy, H., Kamal, A., Jarrar, D., Hoppman, H., Zewen, H., 1984, Design specifications and application of a 100 kW_{el}(700 kW_{th}) cogeneration solar power plant, *Solar Energy*, vol. 32, no. 2: p. 263-269.
- Nafey, A. S., Sharaf, M. A., 2010, Combined solar organic Rankine cycle with reverse osmosis desalination process: Energy, exergy, and cost evaluations, *Renewable Energy*, vol. 35, no. 11: p. 2571-2580.
- Orosz, M. S., Mueller, A., Quoilin, S., Hemond, H., 2010a, Small Scale Solar ORC System for Distributed Power, *Eurosun 2010: 2nd International Congress on Heating, Cooling and Buildings*.
- Orosz, M. S., Quoilin, S., Hemond, H., 2010b, SORCE: A design tool for solar organic Rankine cycle systems in distributed generation applications, *Eurosun 2010: 2nd International Congress on Heating, Cooling and Buildings*.
- Price, H., Hassani, V., 2002, *Modular Trough Power Plant Cycle and Systems Analysis*, National Renewable Energy Laboratory, 118 p.
- Quoilin, S., 2011, *Sustainable Energy Conversion Through the Use of Organic Rankine Cycles for Waste Heat Recovery and Solar Applications*, Dissertation, Liège, 138 p.
- Sinai, J., Fisher, U., 2007, 1 MW Solar Power Plant using Ormat® Energy Converter, *Proceedings of the 14th Sede Boqer Symposium on Solar Electricity Production*, Ben-Gurion University of the Negev: p. 53-56.
- Stine, W. B. and Geyer, M., 2001, Power From The Sun, Online book, <http://powerfromthesun.net/book.html>, last access: 27 January 2014.
- Szabó, S., Bódis, K., Huld, T., Moner-Girona, M., 2011, Energy solutions in rural Africa: mapping electrification costs of distributed solar and diesel generation versus grid extension, *Environ. Res. Lett.*, vol. 6, no. 3: p. 1-9.

EXPERIMENTAL STUDY ON A LOW TEMPERATURE ORC UNIT FOR ONBOARD WASTE HEAT RECOVERY FROM MARINE DIESEL ENGINES

Aris-Dimitrios Leontaritis¹, Platon Pallis¹, Sotirios Karellas^{1*}, Aikaterini Papastergiou¹, Nikolaos Antoniou¹, Panagiotis Vourliotis¹, Nikolaos Matthaios Kakalis², and George Dimopoulos²

¹Laboratory of Steam Boilers and Thermal Plants, School of Mechanical Engineering, National Technical University of Athens, 9 Iroon Polytechniou, 15780, Athens, Greece.

Web page: <http://www.lsbtp.mech.ntua.gr/>

²DNV GL Strategic Research & Innovation East Med., Black & Caspian Seas/ Piraeus Hub

* Corresponding Author
e-mail: sotokar@mail.ntua.gr

ABSTRACT

The aim of this work is the experimental study of an ORC prototype unit which has been designed as a waste heat recovery system for the jacket water of marine diesel auxiliary internal combustion engines (ICEs). In order to simulate the operating characteristics of such engines, the heat input is in the order of 90kWth at low-temperature (90 °C) and is supplied by a natural gas boiler. The ORC unit produces 5 kWel of net electrical power, using as working medium the refrigerant R134a at a design cycle pressure of 25 bar and a temperature of 82 °C.

The experimental evaluation of the unit focuses more on operational issues than overall performance which has already been experimentally studied by a number of researchers. Accordingly, this study includes the investigation of the behaviour of the whole ORC system as well as of its key components under varying operational parameters, such as the occurrence of cavitation in the system feed pump and optimal scroll expanders operation. These outcomes contribute to an optimized configuration of the ORC system components and of the necessary measuring equipment as well as to the development of an efficient automatic control strategy of a dedicated ORC test bench which could then be directly coupled to an adequately sized marine auxiliary ICE for real time operation assessment.

1. INTRODUCTION

The energetic consumption of a commercial ship consists of propulsion and internal consumption electricity needs, which are entirely covered by specially designed marine diesel engines (main and auxiliary respectively). For large ships, the fuel expenses constitute about 30-55% of the total operational costs, depending on the type of vessel (Kalli et al., 2009). Strong motivation exists within the marine sector to reduce fuel expenses and to comply with ever stricter efficiency regulations, e.g. the EEDI -Energy Efficiency Design Index (Larsen et al., 2014a). Moreover, regarding emissions of CO₂ and oxides of sulfur and nitrogen (SO_x and NO_x) the international regulations are changing towards stricter limits (IMO, 2011). Currently, emphasis is being put on the improvement of the thermal efficiency of engines by optimizing their configuration in order to achieve lower fuel consumption (Jaichandar and Annamalai, 2012; Park, 2012). Also, research has been focused on advanced combustion technologies, such as the HCCI (Gan et al., 2011; Yao et al., 2009), the lean combustion (Zheng and Reader, 2004), and the stratified combustion (Park et al., 2012; Lu et al., 2011), in order to achieve a higher overall efficiency and reduce overall emissions. However, as these technologies have achieved quite a matured stage, it becomes harder to achieve further improvements by using these methods and thus a valuable alternative approach to improve overall energy efficiency is to capture and reclaim the “waste heat” (Shu et al., 2013). Hence, in times of high fuel prices,

there are significant economic advantages associated with investing in marine diesel engine waste heat recovery (WHR) systems (MAN, 2012; Shu et al., 2013). WHR systems for electrical or mechanical power production can significantly contribute to dealing with these issues, with the ORC (Organic Rankine Cycle), the Kalina cycle and the steam Rankine cycle receiving the majority of attention in the literature. The steam Rankine cycle is focused on higher temperature WHR mainly from the exhaust gases of the main engines of a ship, while the ORC/Kalina cycles are more suitable for smaller engines (MAN, 2012), like the marine auxiliary ones, while at the same time they can also be used for WHR from lower temperature heat sources (e.g. the jacket water of diesel engines). However, optimisation results suggest that the Kalina cycle possess no significant advantages compared to the ORC or the steam cycle (Larsen et al., 2014a).

Although the Diesel process is highly efficient, large marine diesel engines are particularly well suited to be coupled with a WHR system (Larsen et al., 2014b), as the engine loses a large part of the fuel energy to the environment, mainly with the exhaust gases (up to 25% of the input energy) and the jacket water (up to 5.1% of the input energy; MAN, 2012). However, both of these heat sources, originating from the main engine, are used for covering the internal heating needs of a ship (e.g. heavy fuel oil pre-heating, fresh water generation, exhaust gas boiler), while the respective ones from the auxiliary engines remain unused. Several researchers have proposed WHR systems for main marine diesel engines (Larsen et al., 2014a-2014b; Bounefour and Ouadha, 2014; MAN, 2012; Yang and Yeh, 2014), but no experimental study or even a theoretical analysis has ever been conducted regarding the jacket water of auxiliary engines. In this perspective, the present work focuses on the recovery of heat from the auxiliary engines and more specifically from their jacket water. For the scale and heat source temperature level considered, both the ORC and the Kalina could be used as bottoming cycles. Bombarda et al. (2010) compared the two processes applied for WHR on large marine engines and found that both cycles, when optimized, produced equal power outputs. In the present paper, an ORC WHR system, specially designed for the jacket water of a marine auxiliary diesel engine is experimentally studied.

2. THE MARINE ORC PROTOTYPE TEST BENCH

The marine ORC prototype unit is based on a conventional low-temperature subcritical Organic Rankine Cycle using R134a as working medium. This experimental unit has been designed as a waste heat recovery system for the jacket water of marine diesel auxiliary internal combustion engines (ICEs). In order to simulate the operating characteristics of such engines, the heat input is in the order of 90kW_{th} at a low-temperature (90°C), and is supplied by a natural gas boiler via an intermediate plate heat exchanger (evaporator). The boiler thermal output is adjustable and thus part load operation can be simulated as well. A schematic diagram of the unit is presented in **Figure 1**.

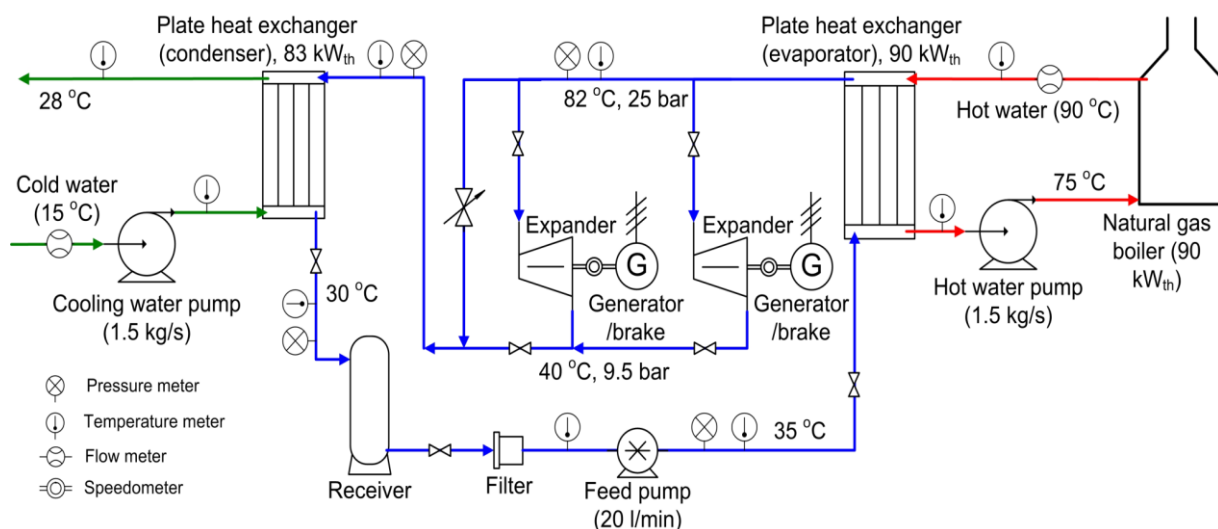


Figure 1: Schematic diagram of the ORC prototype unit.

2.1 Operation and control parameters of the experimental unit

The cycle is fed by a receiver (feed tank) at an average pressure of 9.5 bar and an average temperature of 30 °C. These parameters are controlled by the cold water flow in the condenser, which is adjusted by a regulatory valve.

The feed pump is a positive displacement multi-diaphragm pump that subsequently raises the pressure of the fluid at about 22-25 bar, depending on the operational conditions, and leads it to the evaporator. At a nominal speed of 960rpm a flow rate of 20lt/min is achieved. The rotational speed of the pump is controlled by a frequency drive. As a result, the refrigerant mass flow rate can be adjusted according to the unit load and the desired superheating temperature of the vapor, given the fact that the delivered volume flow rate of diaphragm pumps is in most cases a linear function of their rotational speed.

The high pressure vapor is expanded in two parallel scroll expanders, while a by-pass section controlled by an electromagnetic valve can alternatively lead the flow directly to the condenser. Actually, these expanders are two open-drive scroll compressors in reverse operation as it is thoroughly explained in the next paragraph. Each scroll expander drives an asynchronous motor/generator through a 1:1 belt drive, which can be coupled and uncoupled by an electromagnetic clutch. Both generators are connected to the 50Hz/400V electrical grid via a regenerative inverter module, which provides both grid stability and rotational speed control of the generators and hence of the expanders. For a given pump rotational speed (and thus mass flow rate), the inlet pressure of the scroll expanders is directly adjusted by their rotational speed, since the processed mass flow rate for volumetric machines is given by the product of the inlet density (ρ_{in}) multiplied by the swept volume (V_H) and the rotational speed (N_{rot}) of the machine (1).

$$\dot{M} = \rho_{in} \cdot V_H \cdot N_{rot} \quad (1)$$

An increase (decrease) of the rotational speed allows for a decrease (increase) of the density of the refrigerant at the expander inlet and thus causes a decrease (increase) of the respective inlet pressure. Finally, the expanded vapor is led to the condenser (plate heat exchanger), the condensate returns to the feed tank, and the cycle starts over. The ORC unit (**Figure 2**) produces 5 kW_{el} of net electrical power, at a design cycle pressure of 25bar and a temperature of 82°C.

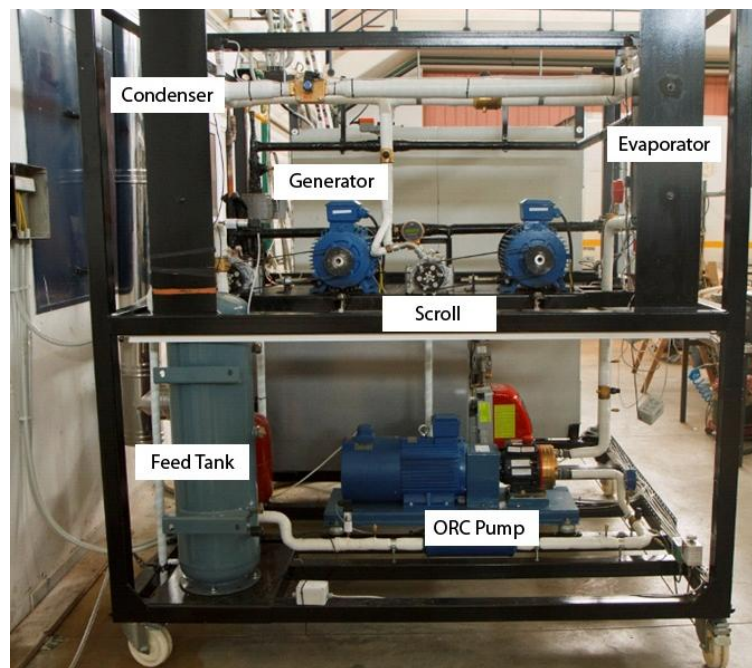


Figure 2: The Marine-ORC experimental unit

Various instruments have been mounted at all key-points of the cycle (**Figure 1**), in order to evaluate the performance of the different components of the ORC unit. Thermocouples and pressure transducers record the thermodynamic procedure; an electromagnetic flow-meter supervises the hot

water volume flow rate and two tachometers the scrolls' actual rotational speed. All important parameters regarding the electrical motors of both the pump and the generators, such as the consumed/produced active power are retrieved by the respective frequency drives.

It is noted that the automatic control of the system (including the frequency drives), the measurements and the data logging is materialised with the use of an industrial PLC (Programmable Logic Controller) and a SCADA (Supervisory Control and Data Acquisition) environment, which constitutes an important step towards the standardization and commercialization of such micro-scale units.

2.2 The scroll expanders

The expansion machine of an ORC system is a key component with critical influence on the overall system performance. Volumetric expanders are mostly suitable for micro-scale ORC systems (Declaye et al., 2013) as they are characterized by low mass flows, relatively high pressure ratios and much lower rotational speeds compared to turbo-machines (Quoilin, 2011). Scroll machines, in particular, are more favorable for such applications due to high performance and reliability, reduced number of moving parts, low price and broad availability at a wide power output range (Zanelli and Favrat, 1994).

In the power range of micro scale ORCs (up to a few kW) there are currently no dedicated commercial scroll expanders available at an affordable price. Therefore, a viable solution is the use of a modified commercial scroll compressor (hermetic or open drive), designed either for air compression or for refrigeration applications, at reverse operation (Declaye et al., 2013).

In this study, two identical commercial open drive scroll compressors, originally designed for trucks' A/C systems were used as expanders. Their modification mainly focused on the inlet/outlet connectors and on the removal of the outlet (at compressor mode) check-valves so that they don't block the flow at reverse operation (expander mode).

Table 1: Scroll expanders characteristics

Swept volume (compressor mode)	121 cm ³ /rev
Maximum Pressure	35bar
Built-involume ratio	≈2.3
Nominal Power output (expander mode)	3.5 kW

3. RESULTS and DISCUSSION

3.1 Cavitation effect on the ORC pump operation

A typical problem in micro scale ORC systems is the cavitation effect on the feed pump. Indeed, this problem was faced during the first steps of operation of the presented experimental unit, causing serious oscillations in its operation (mass flow rate, cycle pressure and temperature). In order to thoroughly understand this problem and finally solve it, an analysis of the pump operational conditions was conducted and is presented next.

First of all, in order to ensure stable operation of a pump, the **available** Net Positive Suction Head (**NPSHa**) at the pump inlet should exceed the respective **required** Net Positive Suction Head (**NPSHr**), given by the operation curves provided by the manufacturer, by at least 100mbar or an equivalent of 1 mH₂O. The NPSHa (mH₂O) is calculated by the following equation:

$$NPSHa = P_t + H_z - H_f - H_a - P_{vp} \quad (2)$$

Where:

P_t = Pressure at the pump inlet

H_z = Vertical distance from liquid surface to pump center line

H_f = Friction losses in suction piping

H_a = Acceleration head at pump suction

P_{vp} = Absolute pressure of liquid at pumping temperature

The acceleration head factor (Ha) is calculated by equation (3).

$$Ha = \frac{C \cdot L \cdot V \cdot N}{K \cdot G} \quad (3)$$

Where:

C = Constant determined by type of pump (in our case Wanner Engineering, Hydra Cell D/G10)

L = actual length of suction line

V = Velocity of liquid in suction line

N = RPM of crankshaft

G = Gravitational constant

K = Constant to compensate for compressibility of the fluid

For the operation conditions at the design point of the experimental unit the NPSHr is 500mbar, $H_z=0.3m$, $Ha \approx 200mbar$, and $H_f=200mbar$.

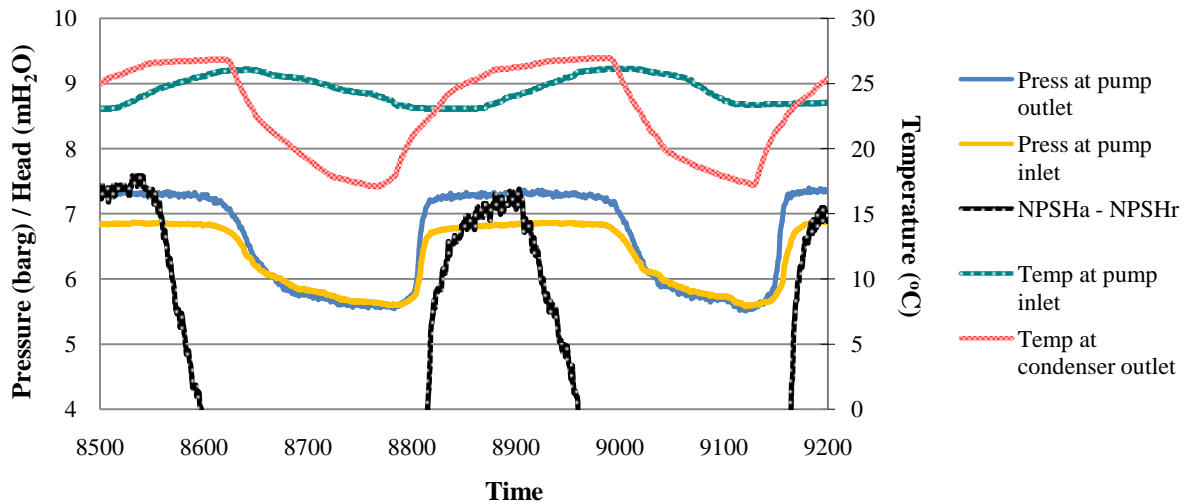


Figure 3: Cavitation effect on ORC pump operation.

The main parameters of the ORC feed pump under operation with cavitation effect are depicted in **Figure 3**. In fact, the ORC pump was tested while just circulating the refrigerant around the ORC circuit via the scroll by-pass section and thus practically no pressure raise is implemented by the pump. Analyzing the pump operation at the first oscillation cycle (cold start), it is observed that initially the pressure at the pump inlet/outlet remains constant with time, indicating a constant mass flow rate, and that the NPSHa - NPSHr difference is maintained well above the threshold of 100mbar (1 mH₂O). As the whole system is ramping up, the temperature at the condenser outlet raises due to the increase of the evaporator outlet temperature. Consequently, the temperature at the pump inlet raises but with a significant time lag caused by the thermal inertia of the feed tank, which stands between the condenser outlet and the pump inlet. With raising temperature at the pump inlet, the absolute pressure of the refrigerant (factor P_{vp} of equation (2)) raises and as a result the NPSHa drops. When the difference NPSHa - NPSHr reaches a critical value of around 100mbar (1 mH₂O), the cavitation effect is initiated and the circulating mass flow rate drops significantly. Simultaneously, the pressure of the circuit (controlled by the condensation temperature which drops due to the reducing refrigerant mass flow rate) also drops (factor P_t of equation (2)) and the unit's operation practically collapses. To make things worse, even though at this point the refrigerant temperature at the condenser outlet drops dramatically, since there is practically a zero mass flow rate, the feed tank needs time to cool down and keeps feeding the pump at relatively high temperature (and thus high P_{vp}); at this point the NPSH difference is strongly negative. Eventually the feed tank cools down, lowering the pumping temperature and thus raising the NPSH difference. Gradually the cavitation effect fades, the mass flow rate raises, and a new cycle starts over.

In order to solve this problem a water cooled heat exchanger was installed in the suction line of the ORC pump, downstream of the liquid receiver, so that the pumping temperature and thus the absolute

pressure of the refrigerant (factor P_{vp} of equation (2)) are maintained at lower values, ensuring stable pump operation. The main parameters of the ORC pump under operation with the additional sub-cooling heat exchanger are depicted in **Figure 4**. The measurements have been obtained at similar operation conditions with **Figure 3**, allowing their direct comparison. The sub-cooling heat exchanger causes an average 2K temperature drop at the suctioned refrigerant which has proved to be sufficient for the stable operation of the unit. As it can be seen in the diagram, the NPSHa is constantly kept above 17 mH₂O with a required NPSH of 5 mH₂O. Its main fluctuations are caused by the suction pressure, which in turn depends on the cooling water mass flow at the condenser (or equivalently on the condenser outlet temperature) and naturally by the temperature at the pump inlet which affects the factor P_{vp} as already discussed. Accordingly, between $t=300$ and $t=690$ the NPSHa is slightly dropping even though the suction pressure is slightly raising, due to the greater influence of the raising temperature at the pump inlet (factor P_{vp}). The evident drops of NPSHa at $t=700$, $t=840$ and 1040 are caused by marginal steps of increasing cooling water mass flow rate at the condenser which directly influence the pressure at the pump inlet and thus the NPSHa. At the respective intervals the observed NPSHa raise is caused by the slightly decreasing temperature at the pump inlet. It is finally noted that the stable operation of the feed pump can be confirmed by the observation of the almost constant delivered Head of the pump over time (P_{out} -Pin).

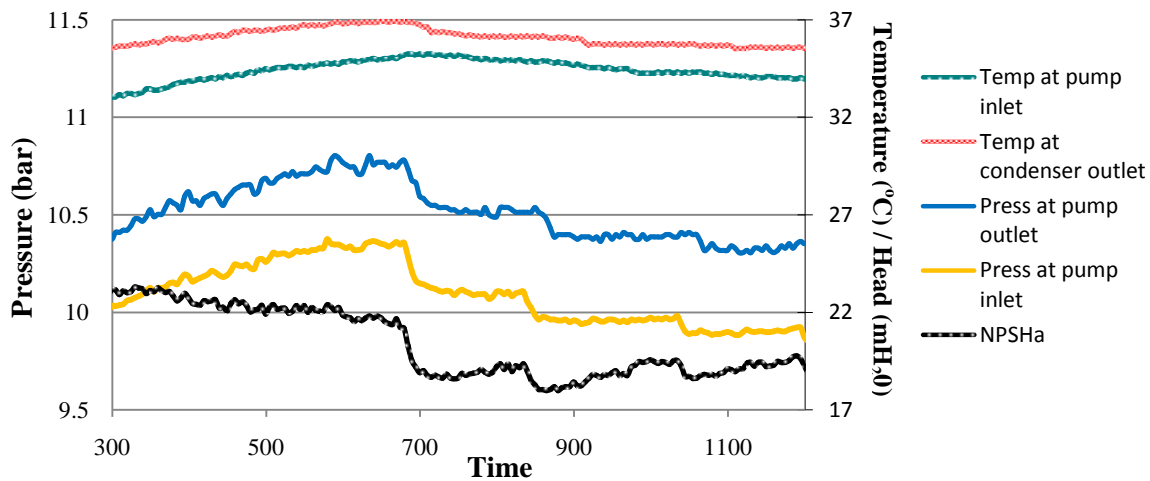


Figure 4: Cavitation free ORC pump operation with the addition of a sub-cooling heat exchanger

Extensive testing under different load and other operational conditions proved this solution as sufficiently effective to ensure the stable operation of the ORC pump and thus of the whole system. All the results presented from this point on in this paper refer to the experimental unit with the fitted additional heat exchanger. However, there are indications of partial cavitation occurrence at high pump rotational speeds which need to be further studied. As cavitation can be detected by the reduced delivered mass flow under constant pump rotational speed, a coriolis type mass flow meter has to be installed to the test rig in order to further investigate this issue, while the influence of the sub-cooling degree also requires to be studied.

3.2 Scroll expanders' operation

In this section the scroll expander's operation is presented through diagrams of its main operational parameters. It is noted that at this point of studying, the presented data can be used for a qualitative analysis of the behavior of the used scroll expanders under various conditions and its comparison with the findings of other researchers. **Figure 5** depicts the influence of the **scroll rotational speed** ($N_{rot,exp}$) and the **supply (inlet) temperature** (T_{su}) of the refrigerant on the **overall isentropic efficiency** (ϵ_{is}). The presented surface has been produced by the statistical fitting of the experimental data. ϵ_{is} is defined as:

$$\epsilon_{is} = \frac{Pel_{gross}}{\dot{M}_{in} \cdot (h_{su} - h_{ex,is})} \quad (4)$$

Where:

- $P_{el, gross}$ the gross electrical power output of the ORC unit (equal to the net electrical power output of the two scroll expanders)
- \dot{M}_{in} the total circulating mass flow rate
- h_{su} the supply enthalpy of the refrigerant at the expander inlet
- $h_{ex, is}$ the enthalpy at the ideal isentropic expansion point at the measured exhaust pressure

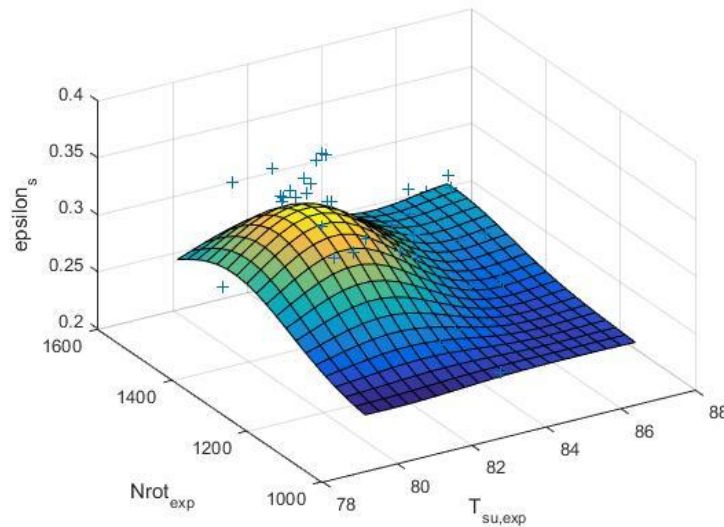


Figure 5: Scroll expander overall isentropic efficiency as a function of supply temperature ($T_{su,exp}$) and rotational speed ($N_{rot,exp}$)

Using this definition for the isentropic efficiency, all electromechanical losses, which can account for up to 40% of the gross generated electrical power, are included and that is the reason why the efficiency appears to be quite low.. The use of inverter frequency drives and induction motors/generators gives much room for improvements which is part of the work planned ahead. This was confirmed by low measured values of the power factor which indicates the low electrical efficiency of the generators. In order to study the behaviour of the expander itself separately a dynamometer or torque meter should be installed directly on its shaft. At any case, the results are useful for the qualitative analysis of the system. Analysing this diagram, the first obvious observation is that the isentropic efficiency is maximised near the nominal design conditions ($N_{rot,exp}=1500$ rpm / $T_{su}=82^{\circ}C$). From a thermodynamic point of view, this was expected since the optimisation objective during the design of this system (as in most heat recovery systems) was the power output and not the cycle thermal efficiency (Bramakis et al., 2015; Quoilin et al., 2011). Moreover, the expander itself is expected to have a better efficiency near its design point (i.e. when the imposed volume/pressure ratio is near the built in volume ratio of the expander) where over-expansion and under-expansion losses are minimized.

Focusing on the influence of the supply temperature, it is concluded that a 4 to 5K degree of superheating of the live vapor gives the optimum results (at 25 bar the saturated vapor has a temperature of $77.5^{\circ}C$). As other researchers have pointed out (Quoilin et al., 2011; Mago et al., 2008; Yamamoto et al. 2001), the superheating at the evaporator exhaust should be at low levels when using high molecular weight organic fluids, such as R134a .

The impact of the rotational speed can be better understood by the explanation of Figure 6, which presents the overall isentropic efficiency of the expander as a function of the filling factor (Φ) under various rotational speeds. The filling factor expresses a relative measure for the internal mass flow leakages and the respective power losses. The filling factor is defined as:

$$\Phi = \frac{\dot{M}_{in}}{V_{swept} \cdot N_{rot} \cdot \rho_{su}} > 1 \quad (5)$$

Where:

- \dot{M}_{in} the total circulating mass flow rate
- V_{swept} the built in swept volume of the scroll machine at expander mode
- N_{rot} the expander rotational speed
- ρ_{su} the supply density of the refrigerant at the expander inlet

As expected, the rotational speed highly affects Φ , and as it can be observed in the diagram, the lower the rotational speed is the higher the filling factor gets due to the larger relative impact of the internal leakages. This effect has also been noted by Lemort et al. (2009) in an experimental analysis of an open drive scroll expander. Other operational parameters such as the inlet pressure and the imposed pressure ratio also affect the filling factor and that is the reason why its value varies for constant rotational speeds. Naturally, Φ in turn affects the overall isentropic efficiency which gets reduced by increasing internal leakages.

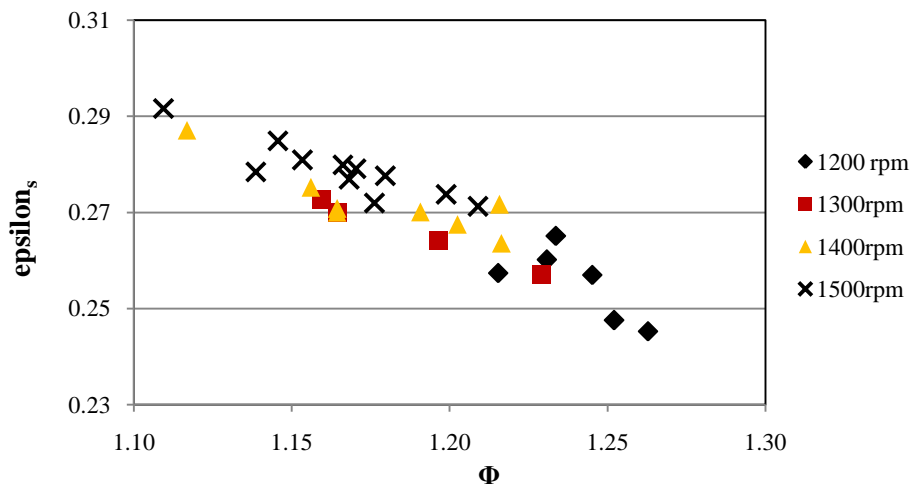


Figure 6: Scroll expander overall isentropic efficiency as a function of the filling factor (Φ)

Another interesting issue is the actual mass flow rate that circulates through the ORC circuit. Currently this value is calculated through the heat balance in the evaporator. The temperature and pressure of the heat source (water) as well as the volume flow rate are measured so the heat input rate (\dot{Q}_{in}) is known. At the same time the inlet and outlet conditions (pressure and temperature) of the refrigerant are also measured and thus considering zero heat exchange losses the circulating mass flow rate (\dot{M}_{in}) can be calculated by the following equation:

$$\dot{M}_{in} = \frac{\dot{Q}_{in}}{(h_{out} - h_{in})_{refrigerant}} \quad (6)$$

A cross-check of this value can be done through the heat balance at the system condenser. For this purpose an ultrasonic mass flow meter and two thermocouples (condenser inlet-outlet) were installed at the cooling water circuit and the dissipated heat rate was this way indirectly measured. In the following diagram (Figure 7), the values of the measured condenser dissipated heat rate (Q_{meas}) vs the respective calculated values (Q_{calc}) using the above-mentioned value (equation 6) of the mass flow rate (\dot{M}_{in}) are presented. The relative declination ($\Delta Q\%$) between these values is within 2-8% which is satisfactory for the needs of the present study. Moreover, the total system heat balance ($Q_{tot} = Q_{evap} + W_{pump} - W_{scrolls} - Q_{cond} - Q_{subcooler} - Q_{amb}$) gives a calculated Q_{amb} of about 600W which is a realistic value for the non calculated ambient heat losses through the pipes of the system. However, in order to investigate certain operational issues such as the occurrence of partial cavitation in the ORC pump and the filling factor of the expander, accurate measurements of the mass flow meter with a coriolis mass flow meter are absolutely necessary.

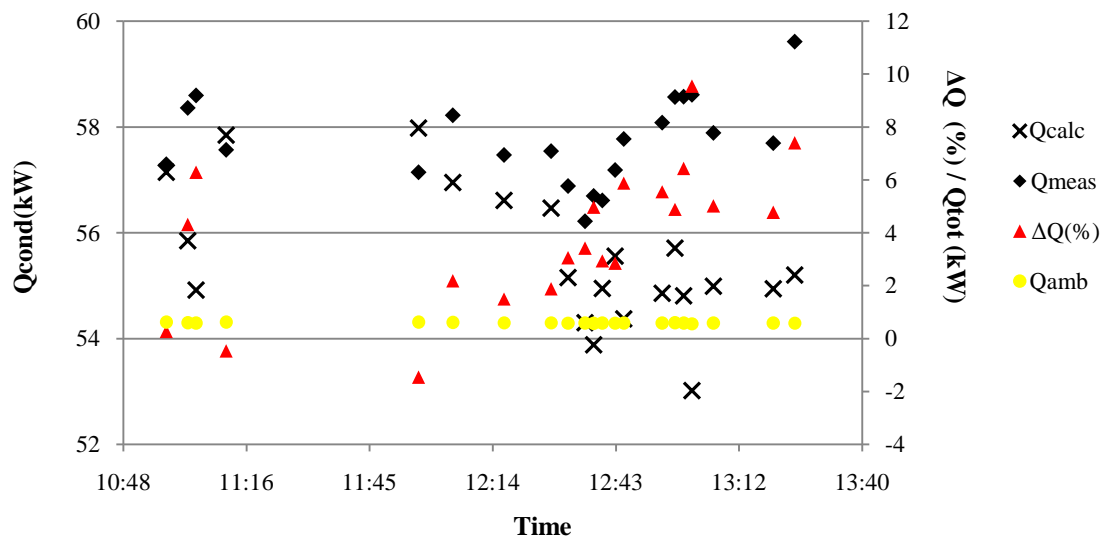


Figure 7: Condenser and overall heat balance

4. CONCLUSIONS

- A coriolis mass flow meter is an indispensable part of the measuring equipment of such experimental benches.
- Cavitation effect in ORC feed pumps can be dealt with the addition of a sub-cooling heat exchanger at the suction line of the pump. The effect of the sub-cooling degree on the cavitation effect as well as on the system performance needs further investigation.
- Partial cavitation at high pump loads and/or rotational speeds and its effect on the feed pump as well as on the overall system efficiency is another issue that requires further studying.
- The relatively low overall scroll expanders isentropic efficiency implies a low conversion of mechanical power into electrical. This was confirmed by low measured values of the power factor. Much room for performance enhancement through the optimization of the main operational parameters of the the induction motors/generators, such as the motor control method and its relative slip speed.
- A torque meter has to be installed directly on the expander's shaft in order to evaluate its performance separately. This is also necessary for the performance optimization of the electrical power generation sub-system.

REFERENCES

- Bombarda, P., Invernizzi, C.M., Pietra, C., 2010, Heat recovery from diesel engines: a thermodynamic comparison between Kalina and ORC cycles. *Applied Thermal Engineering*, vol.30, no 2-3: p. 212-219.
- Bounefour, Ouadha, a., 2014, Thermodynamic analysis and thermodynamic analysis and working fluid optimization of a combined ORC-VCC system using waste heat from a marine diesel engine, *Proceedings of the ASME 2014 International Mechanical Engineering Congress and Exposition IMECE2014 November 14-20, 2014, Montreal, Quebec, Canada*.
- Braimakis, K., Preißinger, M., Brüggemann, D., Karellas, S., Panopoulos, K., 2015, Low grade waste heat recovery with subcritical and supercritical Organic Rankine Cycle based on natural refrigerants and their binary mixtures, *Energy*, In Press, Corrected Proof, doi: 10.1016/j.energy.2015.03.092
- Declaye, S., Quoilin, S., Guillaume, L., Lemort, V., 2013, Experimental study on an open-drive scroll expander integrated into an ORC (Organic Rankine Cycle) system with R245fa as working fluid, *Energy*, vol.55, no.1: p. 173-183.

- Gan, S., Ng, H.K., Pang, K.M., 2011, Homogeneous Charge Compression Ignition (HCCI) combustion: implementation and effects on pollutants in direct injection diesel engines. *Applied Energy*, vol.88, no.1: p.559–67.
- IMO, The International Maritime Organisation, 2011, IMO and the environment, URL: imo.org
- Jaichandar, S., Annamalai, K., 2012, Effects of open combustion chamber geometries on the performance of pongamia biodiesel in a DI diesel engine. *Fuel*, vol. 98, no. 1: p.272–279.
- Kalli, J., Karvonen, T., Makkonen, T., 2009, Sulphur content in ships bunker fuel in 2015, Technical Report, Helsinki, Finland: Ministry of Transport and communications.
- Larsen, U., Nguyen, T., Knudsen, T., Haglind, F., 2014b, System analysis and optimisation of a Kalina split-cycle for waste heat recovery on large marine diesel engines, *Energy*, vol. 64, no. 1: p. 484-494.
- Larsen, U., Sigthorsson, O., Haglind, F., 2014a, A comparison of advanced heat recovery power cycles in a combined cycle for large ships, *Energy*, vol. 74, no.1 : p. 260-268.
- Lemort, V., Quoilin, S., Cuevas, C., Lebrun, J., 2009, Testing and modeling a scroll expander integrated into an Organic Rankine Cycle, *Applied Thermal Engineering*, vol. 29, no.1: p. 3094–3102.
- Lu, X., Shen, Y., Zhang, Y., Zhou, X., Ji, L., Yang, Z., 2011, Controlled three-stage heat release of stratified charge compression ignition (SCCI) combustion with a two-stage primary reference fuel supply. *Fuel*, vol. 90, no. 1: p. 2026–38.
- Mago, P.J., Chamra, L.M., Srinivasan, K., Somayaji, C., 2008, An examination of regenerative Organic Rankine Cycles using dry fluids, *Applied Thermal Engineering*, vol. 28, no. 1: p. 998-1007.
- MAN, Diesel & Turbo, Denmark, 2012, Waste heat recovery systems (WHRS). URL: www.mandieselturbo.com [accessed 30.08.13].
- Park, C., Kim, S., Kim, H., Moriyoshi, Y., 2012, Stratified lean combustion characteristics of a spray-guided combustion system in a gasoline direct injection engine. *Energy*, vol. 41, no. 1 : p. 401–407.
- Park, S., 2012, Optimization of combustion chamber geometry and engine operating conditions for compression ignition engines fueled with dimethyl ether. *Fuel*, vol. 97, no.1: p. 61–71.
- Quoilin S., 2011, Sustainable Energy Conversion through the use of Organic Rankine Cycles for waste heat recovery and solar applications, Liege, PhD Dissertation: p.12-15.
- Quoilin S., Lemort, V., 2011, Thermo-economic optimization of waste heat recovery Organic Rankine Cycles, *Applied Thermal Engineering*, vol. 31, no.1: p. 2885-2893.
- Shu, G., Liang, Y., Wei, H., Tian, H., Zhao, J., Liu, L., 2013, A review of waste heat recovery on Two-stroke IC engine aboard ships, *Renewable Sustainable Energy Review 2013*, vol. 19, no.0: p. 385-401.
- T. Yamamoto, T., Furuhashi, T., Arai, T., Mori, T., 2001, Design and testing of the Organic Rankine Cycle, *Energy*, vol. 26, no. 1: 239-251.
- Yang, M.H., Yeh, R.H., 2014, Analyzing the optimization of an organic Rankine cycle system for recovering waste heat from a large marine engine containing a cooling water system, *Energy Conversion and Management*, vol. 88, no. 1: p. 999-1010.
- Yao, M., Zheng, Z., Liu, H., 2009, Progress and recent trends in homogeneous charge compression ignition (HCCI) engines. *Progress in Energy and Combustion Science 2009*, vol. 35, no.1: p. 398–437.
- Zanelli R., Favrat D., 1994, Experimental investigation of a hermetic scroll expander generator. In: *Proceedings 12th international compressor engineering conference at Purdue*: p. 459-64.
- Zheng, M., Reader, G.T., 2004, Energy efficiency analyses of active flow aftertreatment systems for lean burn internal combustion engines, *Energy Conversion and Management*, vol. 45, no.1 : p. 2473–93.
- (Quoilin et al., 2011; Mago et al., 2008; Yamamoto et al. 2001)

ACKNOWLEDGEMENT

This study has been conducted within the Marine-ORC project funded by “DNV GL, Strategic Research & Innovation East Med., Black & Caspian Seas/ Piraeus Hub”.

**REDUCING FUEL CONSUMPTION BY UP TO 10 % FOR
DIESEL-BASED POWER GENERATION BY
APPLYING ORC**

Quirijn Eppinga & Jos P. van Buijtenen

Tri-O-Gen B.V.,
PO Box 25, 7470 AA Goor, The
Netherlands E-mail:
Jos.vanbuijtenen@triogen.nl

ABSTRACT

A high efficiency Organic Rankine Cycle (ORC) power unit has been developed by Tri-O-Gen B.V. of The Netherlands. The ORC system is based on a thermally stable hydro-carbon as a working fluid, hence suitable for direct use of intermediate temperature heat sources. The unit is capable of transforming heat flows at temperatures between 350 and 600 °C into electricity. Typical applications involve the exhaust gasses of gas- or diesel engines and small gas turbines. These can be either fuelled by bio-gas, landfill gas, mine gas, or by natural gas as CHP units, where the power-to-heat ratio can be improved considerably. Unit power ranges from 65 to 165 kWe. Generally, the power produced by the ORC is considered as extra (renewable) power.

This paper describes the effect of applying this technology to Diesel engine based power generation, by recovering the heat in the exhaust gas and converting it into electricity. Here, the effect is a direct saving on fuel, as the power output is generally a number dictated by the grid. For a given amount of power, the Diesel engine can run in part-load, reducing its fuel consumption by up to 10 % and increasing its life, and also reducing its emissions of CO₂ and other harmful constituents. Applications are in decentralized and remote power, where fuel costs are generally high.

An economic evaluation will be given, together with some application examples and recent operating experience.

TORQUE RESEARCH OF SINGLE SCREW EXPANDERS

Ruiping Zhi^{1*}, Yuting Wu¹, Yeqiang Zhang¹, Biao Lei, Wei Wang¹, Guoqiang Li¹
and Chongfang Ma

¹Key Laboratory of Enhanced Heat Transfer and Energy Conservation of Ministry of Education and

¹Key Laboratory of Heat Transfer and Energy Conversion of Beijing Municipality, College of Environmental and Energy Engineering, Beijing University of Technology, Beijing 100124, PR China

*E-mail: Zhiruiping@gmail.com

ABSTRACT

In recent years, people have paid much attention to single screw expanders. Many experiments have been carried out on the performance of single screw expanders in fundamental applications such as industry waste heat recovery, compressed air power system, and pressure energy recovery. This paper presents a theoretical torque model of single screw expander under the conditions of ideal adiabatic expansion and air as working fluid. It was found that the torque ratio is independent of inlet pressure of single screw expander and is close to 1. It indicates that the single screw expander runs smooth. Besides, the calculated output power based on the theoretical torque model was close to the measured output power by experiments, if the shaft efficiency from experiments results and output work loss under over-expansion process were considered. And it demonstrates that this model can be used to estimate the output power of single screw expander before designing it according to the diameter of main rotor, volume ratio, inlet and back pressure of single screw expander.

1. INTRODUCTION

In recent years, with heavy fog and haze dominating our life, people realized the bad effects of PM2.5, such as coughs, asthma, sore throats and other respiratory illnesses. Many researchers and industries have realized the importance of using low-grade energy so that we can contribute to a permanent "Beijing Blue". Without doubt, ORC system is a great technology to save energy and keep the energy clean. A whole ORC system is basically composed of evaporator, expander, condenser and working fluid pump. Among these components, the selection of expander type is crucial to this efficiency of the system because the expander decides how much pressure energy is converted to power.

Among piston expanders, turbo expanders, scroll expanders and screw expanders, single screw expanders (SSEs) have received much attention in recent years due to its unique advantages, such as balanced loads, long working life, simple structure, low vibration and so on. In 2008, Ma Chongfang and his team [1] first reported the SSEs with 10kW and 40kW in Science Times. He et al. [2] carried out the study on the power system of compressed air based on three-stage SSEs. By programming and mathematical modeling results, it is shown that the single screw expander (SSE) has a good potential to be used in power systems. Liu et al. [10] verified the feasibility of SSE on ORC system with heat source of flue gas. Wang et al. [3] used compressed air as working fluid to verify the performance of SSE prototype. The designed flow rate of SSE is 1.1Nm³/min. The performance tests were conducted under different conditions including different intake flow, different humidity, constant torque and constant rotational speed. According to the experimental results, it is shown that the output power is 5kW at rotary speed of 2850r/min, discharge temperature is -45°C, the maximum temperature drop was about 62°C, and the maximum of adiabatic efficiency and total efficiency were 59% and 32.5% respectively. And it also shows that this SSE prototype has good part-load performance. And lubrication may be a factor to cause low adiabatic efficiency. He et al. [4] carried out experiments on the performance of the SSEs with compressed air as working fluid under different intake pressures and showed that the measured torque has a large increase as the intake pressure increases and has a slight decrease as the rotational speed increases. Desideri et al. [5] evaluated the SSE modified from a standard compressor and developed a steady-state model of the whole ORC unit. In this experiment,

the working fluid is Solkatherm (the azetropic mixture of HFC365mfc and YR-1800), the volume ratio of the expander is 5 and the diameter of main rotor is 155mm. The results show that the maximum expander isentropic efficiency and generated power are 64.78% and 7.8 kWe respectively. The whole cycle efficiency peaked at 9.8% with the evaporating temperature of 108°C. Ziviani et al. [6] established a detailed model of SSE based on the geometric parameters, heat transfer model and governing equations. And then verified the calculated data using experiment data between mass flow rates and output power.

Although the performance of SSE have been carried out in the ORC system and power system, little attention has been paid to the theoretical torque model of SSE which can be used to predict if the SSE works in a good state and also can be used to estimate how much output power are produced. The paper presents a detailed torque model of single screw expander and gives out comparison of calculated torque and experimental data.

2. Theoretical torque calculation of single screw expander

2.1 Main Parameters of Single Screw Expanders

The main rotor and a pair of gate rotors are the key components in SSE (shown in Figure 1). In this paper, the SSE is designed by our laboratory team. The single screw expander belongs to CP type. It means that the main rotor is machined by a cutting tool with straight line like a single tooth of gate rotor. The gate rotor is generated by envelope of main rotor. The main rotor and gate rotor are machined by special purpose machine developed by our team (shown in Figure 2). Their meshing relations are just like worm gears. The main structure parameters of meshing pair are the foundation to calculate the basic volume, the volume ratio and the whole design of SSE. The main parameters are illustrated in Figure 3.



Figure 1: Single screw expander



Figure 2: Main rotor and gate rotor

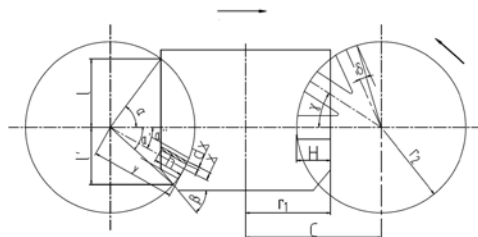


Figure 3: Structure of single screw meshing pair

$$i = \frac{\theta_1}{\theta_2} = \frac{z_2}{z_1} \quad (1)$$

$$\gamma = \frac{2\pi}{z_2} \quad (2)$$

$$k_0 = \frac{r_2}{r_1} \quad (3)$$

$$k = \frac{H}{r_1} \quad (4)$$

$$C = r_1(1 + k_0 - k) \tag{5}$$

$$l = r_1 \sqrt{2k_0k - k^2} \tag{6}$$

$$\alpha = \arcsin\left(\frac{\sqrt{2k_0k - k^2}}{k_0}\right) \tag{7}$$

$$\alpha' = \arcsin\left(\frac{l'}{r_1k_0}\right) \tag{8}$$

$$l' = 0.7l \tag{9}$$

$$\xi = \frac{e}{2r_1} \tag{10}$$

$$b = 2r_1[(k_0 - k) \sin\left(\frac{\gamma}{2}\right) - \xi \cos\left(\frac{\gamma}{2}\right)] \tag{11}$$

$$b_s = \frac{b}{2r_2} = \frac{(k_0 - k) \sin\left(\frac{\gamma}{2}\right) - \xi \cos\left(\frac{\gamma}{2}\right)}{k_0} \tag{12}$$

$$\delta = \arcsin(b_s) \tag{13}$$

2.2 Swept Volume Equation

In this paper, based on the method used by Sun Guangsan (1988), we calculate the whole single groove basic volume of the main rotor. The method mainly refers to the area of the gate rotor and the centroid of the gate rotor when meshing with the main rotor. The whole single groove basic volume is divided into two parts. One part is the volume of the gate rotor sweeping the groove of the main rotor from the front edge of the gate rotor just coming into the groove to the back edge of the gate rotor just coming to the groove (in Figure 4). The other part is the volume of the gate rotor sweeping the groove from the back edge of the gate rotor just coming into the groove to just beginning discharge. However, there is some difference between the volume equation inferred by Sun Guangsan and this volume equation in this paper. This volume equation of this paper is mainly expressed by non-dimensional coefficients of k and k_0 and the radius (r_1) of main rotor. The formulae are as follows:

$$V = V_1 + V_2 = \int_{\alpha-\delta}^{\alpha+\delta} A \cdot i\bar{R}_1 d\theta_2 + \int_{\alpha_{ds}}^{\alpha-\delta} A \cdot i\bar{R}_2 d\theta_2 \tag{14}$$

$$A_{\alpha-\delta} = k_0^2 r_1^2 \arcsin(b_s) + b_s \sqrt{1 - b_s^2} - 2b_s k_0 r_1^2 (k_0 - k) \sec(\alpha - \delta) \tag{15}$$

$$\left\{ \begin{aligned} A &= A_{\alpha-\delta} \cdot \left(\frac{\alpha + \delta - \theta_2}{2\delta}\right)^2; \alpha - \delta \leq \theta_2 \leq \alpha + \delta \end{aligned} \right. \tag{16}$$

$$A = \int_{\frac{b}{2}}^{\frac{b}{2}} (\sqrt{k_0^2 r_1^2 - x^2} - (k_0 r_1 - H) \sec \theta_2 + x \tan \theta_2) dx; \theta_{db} \leq \theta_2 \leq \alpha - \delta$$

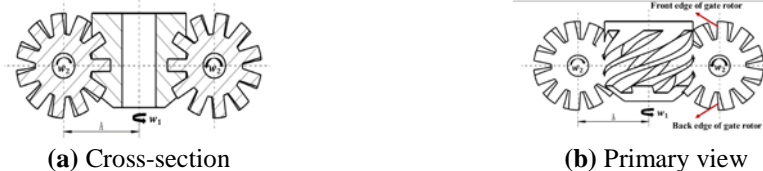


Figure 4: Movement relations of single screw meshing pair

For the single screw expander, the whole expansion process is divided into three phases. It is suction, closed expansion and discharge respectively. The first part volume (V_1) is an inherent suction volume for every main rotor when the angle of gate rotor is between $\alpha - \delta$ and $\alpha + \delta$. So when we calculate the expander suction volume at any time during the suction phase, the formula is as follows:

$$V = \begin{cases} V_1 = \int_{\alpha-\delta}^{\alpha+\delta} A \cdot i\bar{R}_1 d\theta_2, \alpha - \delta \leq \theta_2 \leq \alpha + \delta \\ V_1 + V_2 = \int_{\alpha-\delta}^{\alpha+\delta} A \cdot i\bar{R}_1 d\theta_2 + \int_{\theta_2}^{\alpha-\delta} A \cdot i\bar{R}_2 d\theta_2, \theta_{se} \leq \theta_2 < \alpha - \delta \end{cases} \quad (17)$$

When we calculate the closing expansion volume at any time during the closing expansion phase, the formula is as follows:

$$V = \int_{\alpha-\delta}^{\alpha+\delta} A \cdot i\bar{R}_1 d\theta_2 + \int_{\alpha-\delta}^{\theta_2} A \cdot i\bar{R}_2 d\theta_2, \theta_{db} \leq \theta_2 < \theta_{se} \quad (18)$$

When we calculate the discharge volume at any time during the discharge phase, the formula is as follows:

$$V = \begin{cases} \int_{\alpha-\delta}^{\alpha+\delta} A \cdot i\bar{R}_1 d\theta_2 + \int_{\alpha-\delta}^{2\theta_{db}-\theta_2} A \cdot i\bar{R}_2 d\theta_2, 2\theta_{db} - \alpha + \delta \leq \theta_2 < \theta_{db} \\ \int_{\alpha-\delta}^{\alpha+\delta} A \cdot i\bar{R}_1 d\theta_2, 2\theta_{db} - \alpha - \delta \leq \theta_2 < 2\theta_{db} - \alpha + \delta \end{cases} \quad (19)$$

2.3 Calculation of Instantaneous and Average Torque

For the single screw expander, the instantaneous torque of main rotor is equal to product of the force on the gate rotor tooth area and the distance from the centroid of the gate rotor tooth area to the center of main rotor. Assuming that the pressure on the lower teeth surface of gate rotor is equal to the discharge pressure and the instantaneous torque is divided into three phases according to the operation process of single screw expander. Assuming that the expansion is a perfect adiabatic process and that the working fluid is compressed air, the formulae of the instantaneous torque are as follows:

$$\begin{cases} F = (p_{in} - p_{out})A, \alpha - \delta < \theta_2 \leq \alpha + \delta \\ F = (p_{in} - p_{out})A, \theta_{se} < \theta_2 \leq \alpha - \delta \\ F = p_{in} \left(\frac{V_2}{V_1} \right)^k A, \theta_{db} < \theta_2 \leq \theta_{se} \\ F = (p_{out} - p_{out})A = 0, 2\theta - \alpha - \delta \leq \theta_2 \leq \theta_{db} \\ T = (p_{in} - p_{out})A\bar{R}_1, \alpha - \delta < \theta_2 \leq \alpha + \delta \\ T = (p_{in} - p_{out})A\bar{R}_2, \theta_{se} < \theta_2 \leq \alpha - \delta \\ T = p_{in} \left(\frac{V_2}{V_1} \right)^k A\bar{R}_2, \theta_{db} < \theta_2 \leq \theta_{se} \\ T = (p_{out} - p_{out})A\bar{R}_2 = 0, 2\theta_{db} - \alpha - \delta \leq \theta_2 \leq \theta_{db} \end{cases} \quad (20)$$

$$\begin{cases} T = (p_{in} - p_{out})A\bar{R}_1, \alpha - \delta < \theta_2 \leq \alpha + \delta \\ T = (p_{in} - p_{out})A\bar{R}_2, \theta_{se} < \theta_2 \leq \alpha - \delta \\ T = p_{in} \left(\frac{V_2}{V_1} \right)^k A\bar{R}_2, \theta_{db} < \theta_2 \leq \theta_{se} \\ T = (p_{out} - p_{out})A\bar{R}_2 = 0, 2\theta_{db} - \alpha - \delta \leq \theta_2 \leq \theta_{db} \end{cases} \quad (21)$$

Therefore, the average torque is given by the following equation (22):

$$T_{a1} = \frac{\int_{t_1}^{t_2} T dt}{t_2 - t_1} \quad (22)$$

The theoretical output power can be written as

$$P_{el} = \frac{T_{a1}n}{9550} \quad (23)$$

2.4 Output Power Loss Percentage of Over or Under Expansion Process

It is known that the single screw expander is a positive displacement expander without discharge valve. As a result, there is a built-in volume ratio (η_{iv}) for the single screw expander. If the inlet pressure of expander (P_{in}) is certain, the internal outlet pressure (P_{iout}) is a certain value when the expansion ends and the expander begins discharging. But the internal outlet pressure finally needs to be equal to the back pressure (P_d) of the discharge pipe, so that the working fluid can be discharged. The internal and external expansion ratio (ε_i and ε_d) can be obtained in the following equation (24-25). If the internal outlet pressure P_{iout} is equal to the external outlet pressure P_d , the expansion process is called as ‘full expansion’ (shown in Figure 5a). If the internal outlet pressure P_{iout} is less than the external outlet pressure P_d , the expansion process is called as ‘over expansion’ (shown in figure 5b). If the internal outlet pressure P_{iout} is greater than the external outlet pressure P_d , the expansion process is called as ‘under expansion’ (shown in Figure 5c). For the over and under expansion, there is additional power consumption and it will decrease the output power. The output work loss Δw is shown in the triangle with shadow part. The output power loss percentage η_w can be calculated in equation 26.

$$\varepsilon_i = \frac{P_{in}}{P_{iout}} \tag{24}$$

$$\varepsilon_d = \frac{P_{in}}{P_d} \tag{25}$$

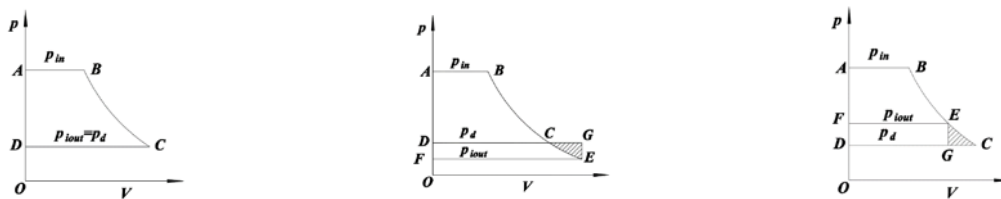
$$\eta_w = \frac{\Delta w/t}{w_d/t} = \frac{\Delta w}{w_d} = \frac{\left(\frac{\kappa-1}{\kappa} \varepsilon_d^{-1} \varepsilon_i^{\frac{1}{\kappa}} - \varepsilon_d^{\frac{1-\kappa}{\kappa}} + \frac{1}{\kappa} \varepsilon_i^{\frac{1-\kappa}{\kappa}}\right)}{1 - \varepsilon_d^{\frac{1-\kappa}{\kappa}}} \tag{26}$$

Hence, the output power P_{e2} after considering the output power loss under different expansion type can be written as

$$P_{e2} = P_{e1}(1 - \eta_w) \tag{27}$$

Furtherly considering the shaft efficiency η_s , the output power P_{e3} is given by

$$P_{e3} = P_{e1}(1 - \eta_w)\eta_s \tag{28}$$



(a) Full expansion

(b) Over expansion

(c) Under expansion

Figure 5: Expansion type

3. Results and Discussions

3.1 Experimental Results

The single screw expander designed by our laboratory is installed in a compressed air power system. This whole system includes five parts: air intake and exhaust circuit, oil lubrication circuit, power testing system, water cooling system and data acquisition system. The air source comes from a compressed air storage tank. The rotary speed of single screw expander is 3000r/min. And the inlet air measured pressure was varied from 4.97bar to 9.975bar. The main parameters of SSE are listed in

Table 1. The measured variables and their uncertainties are shown in Table 2. And the experimental results are shown in Table 3.

The built-in volume ratio of single screw expander is 5. This experiment uses the air as working fluid. And the adiabatic exponent of air is assigned as an ideal value of 1.4. Assuming that the expansion process is an adiabatic process, according to the adiabatic equation of air, the ideal adiabatic expansion ratio is 9.518. As can be seen from Table 3, the expansion ratios calculated by experiments data are less than that of ideal adiabatic expansion ratio. So this single screw expander was in an over-expanded working state. This inlet pressure in this experiment just sets less than 10 bar, because there is an upper end of measured output power for the eddy current dynamometer (0~10 kW). That's the reason that experiments with higher inlet pressure cannot be carried out.

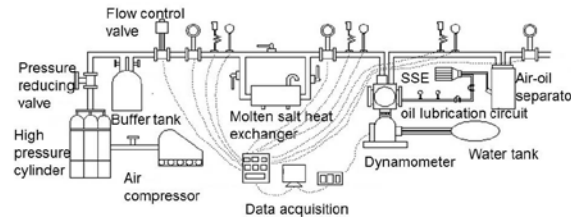


Figure 6: General layout of experimental setup with air compressor

Table 1: Main parameters of single screw expander

Parameters	
Diameter of main rotor	155mm
Diameter of gate rotor	155mm
Transmission ratio	11/6
Center distance	124mm
Volume ratio	5
Tooth width of gate rotor	23.4mm

Table 2: Measured variables and their uncertainties

Variable	Units	Uncertainties
Temperature	°C	0.5%
Pressure	bar	0.5%
flow	m ³ /h	1.5%
Torque	N.m	±0.2~0.4% FS
Rotate speed	r/min	±1%

Table 3: Experimental results of single screw expander

Inlet pressure P_{in} (bar)	Rotate speed n (r/min)	Torque T_{ex} (N.m)	Output Power P_{ex} (kW)	Outlet Pressure P_d (bar)	External expansion ratio ε_d	Shaft efficiency η_s (%)
4.971	2999	11.464	3.600	0.500	3.981	48.189
5.976	3000	15.785	4.958	0.600	4.340	51.387
7.033	2999	20.166	6.333	0.700	4.725	54.046
8.010	2999	24.028	7.457	0.800	5.005	56.393
8.975	3000	27.776	8.72	0.967	5.073	57.679
9.975	3000	31.583	9.92	1.100	5.226	58.274

3.2 Calculated Torque and Torque Ratio of Single Screw Expander

Based on the equation presented in this paper, the Matlab codes are programmed and developed to calculate the instantaneous torque of single screw expander with the rotary angle changes of main rotor. Assuming that the inlet pressure is equal to the measured values by experiments, the expansion process is a perfect adiabatic expansion, and that there is no mechanical and frictional loss. From the Figure 7, the output torque value appears again with period 60 degrees. In a period, no matter how much the inlet pressure is equal to, all the relative highest point and lowest point appears at the same degrees (46degrees and 30degrees respectively). In Figure 7, it is shown that the output torque of single screw expander increases with the increase of inlet pressure. This trend is in accordance with that of experimental results.

Torque ratio is defined as theoretical torque at different angle of main rotor in to average torque of single screw expander and can be calculated in equation (shown in equation 29). Torque ratio can reflect the operation performance of single screw expander. The torque ratio is closer to 1, the single screw expander runs smoother. It can be observed in Figure 8 that the torque ratio is independent of inlet pressure, and that there is a small fluctuation for torque ration around at the horizontal line (Torque ratio of the horizontal line is equal to 1). It could be concluded that the single screw expander runs steadily.

$$\lambda = \frac{T}{T_{a1}} \tag{29}$$

3.2 Calculated and Measured Output Power of Single Screw Expander

According to the trapezoid rule of numerical integral formulas, the average torque in one period is obtained by equation (22), and then by equation (23-28), the calculated output power can be calculated (shown in Table 5). The relative error can be obtained by the following equation (30). As listed in table 5, it reveals that the over-expansion would cause great output power loss and that the output power loss percentage will decrease sharply with a slow increase of external expansion ratio.

$$Er = \frac{P_{e3} - P_{ex}}{P_{ex}} \tag{30}$$

It can be observed in Figure 9 that the output power of single screw expander increases linearly with growth of inlet pressure. The relative error of output power is given in Table 4. The difference value of output power is around at 1 and there is almost no change for ΔP , but the relative error is bigger compared to the change of difference value ΔP of it. Because the output power value itself is not a big value. Although the relative error is not much small, the output power by this mathematical model still can be accepted. That's because in this model, the leakage and friction loss are not considered.

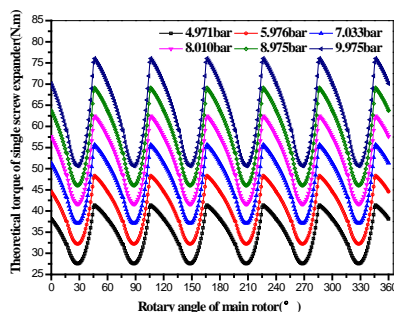


Figure 7: Theoretical torque of main rotor at different rotary angle of main rotor

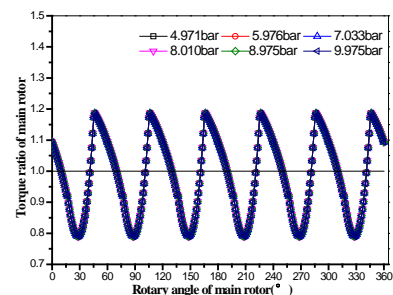


Figure 8: Torque ratio at different angle of main rotor

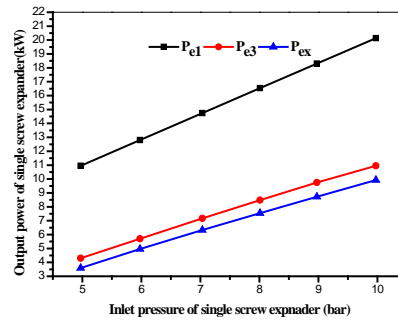


Figure 9: Output power of single screw expander with changes of inlet pressure

Table 4: The relative error, the theoretical output power, the output power after considering shaft efficiency and output power loss percentage and the measured output power

Inlet Pressure(bar)	P_{el} (kW)	η_w (%)	P_{e3} (kW)	P_{ex} (kW)	ΔP (kW)	Er (%)
4.971	10.949	18.46	4.301	3.600	0.701	19.5
5.976	12.800	13.48	5.704	4.958	0.746	15.0
7.033	14.739	10.01	7.168	6.333	0.834	13.2
8.010	16.537	7.98	8.479	7.547	0.932	12.4
8.975	18.301	7.57	9.748	8.725	1.023	11.7
9.975	20.135	6.67	10.951	9.920	1.031	10.4

4. Conclusions

In this paper, based on the modified mathematical model of basic volume for main rotor, the theoretical model torque model of single screw expander is established under ideal adiabatic expansion process and air as working fluid. And this paper presents the output power loss percentage equation during under or over expansion process. According to the present analysis, the following results are concluded:

- (1) From the torque equation, it can be found that the theoretical torque mathematical model is independent of rotation speed of single screw expander. The instantaneous torque and the torque ratio reflect that the single screw expander runs steadily.
- (2) The output power loss percentage equation can also be applied to polytropic process in twin screw expanders and single screw expanders. The κ value in equation (26) is replaced by the polytropic exponent n .
- (3) By comparison between calculated output power by mathematical model and measured torque by experiments, this relative error is 10%~19% while the differential value ΔP between calculated and measured output power is just around at 1. Hence, this model can be used to estimate the output power of SSE under given diameter of main rotor, inlet pressure, built-in volume ratio and back pressure when design the SSE. And there is a rapid increase for η_w with a slight decrease of external expansion ratio. So the SSE should avoid over-expansion process when design it in order to lower great output power loss.

This theoretical mathematical model can just be used to estimate the operation state and output power of SSE under ideal adiabatic expansion process and air as working fluid, if the diameter of main rotor, inlet pressure, volume ratio and back pressure are given. But there is still some room to improve. On the one hand, the inlet pressure loss should be included in the future study in order to make the

calculated torque be closer to the measured torque. On the other hand, in order to calculate the torque of SSE in ORC system, the state equation of organic fluid need to be studied. With the continuous improvement of this model, this model will be more accurate.

NOMENCLATURE

Variable	definition	units
i	transmission ratio	(-)
z	number of grooves or teeth	(-)
γ	indexing angle of gate rotor	(rad)
r	radius	(mm)
k_0	ratio of the main rotor radius in to the gate rotor radius	(-)
k	meshing depth coefficient	(-)
H	the maximum meshing depth	(mm)
C	Center distance of single screw meshing pair	(mm)
l	axial length of the discharge side	(mm)
α	meshing angle of the discharge side	(-)
α'	meshing angle of the suction side	(-)
l'	axial length of the suction side	(-)
b_s	tooth width coefficient	(-)
b	tooth width of the gate rotor	(mm)
δ	half angle of the tooth width	(rad)
e	the minimum width of the groove wall	(mm)
ξ	coefficient of the groove wall	(-)
A	area of gate rotor tooth meshing with main rotor	(mm ²)
V	volume of main rotor groove	(mm ³)
θ	rotary angle	(rad)
p	inlet or outlet pressure of single screw expander	(Mpa)
p_d	back pressure	(Mpa)
p_{iout}	internal expansion pressure of single screw expander	(Mpa)
T	instantaneous output torque of single screw expander	(N.m)
T_{a1}	theoretical average output torque	(N.m)
P	output power of single screw expander	(kW)
η_s	shaft efficiency of single screw expander	(-)
η_w	output power loss percentage of single screw expander	(-)
λ	torque ratio	
Er	relative error	(-)
ε_i	internal expansion ratio	(-)
ε_d	external expansion ratio	(-)
ΔP	differential value of output power	(kW)
Subscript		
1	main rotor	
2	gate rotor	
e1	theoretical	
e2	after considering output power loss percentage	
e3	after considering shaft efficiency	

ex	experimental results
in	inlet
out	outlet
se	suction ending
db	discharge beginning

REFERENCES

- [1] <http://news.sciencenet.cn/sbhtmlnews/2008/12/214421.html> (2008) (in Chinese)
- [2] HE, W., Wu, Y.T., Ma, C.F., Ma, G.Y., (2010). Performance study on three-stage power system of compressed air vehicle based on single-screw expander [J]. *Science China Technological Sciences*, 2010, 53(8): 2299-2303.
- [3] Wang, W., Wu, Y.T., Ma, C.F., Liu, L.D., and Yu, J., (2011). Preliminary experimental study of single screw expander prototype. *Applied Thermal Engineering*, 31:3684 - 3688.
- [4] He, W., Wu, Y.T., Peng, Y.H., Zhang, Y.Q., Ma, C.F., and Ma, G.Y., (2013). Influence of intake pressure on the performance of single screw expander working with compressed air. *Applied Thermal Engineering*, 51:662-669.
- [5] Desideri, A., van den Broek, M., Gusev, S., and Quoilin, S., (2014). Experimental campaign and modeling of a low-capacity waste heat recovery system based on a single screw expander. In *International Compressor Engineering Conference*. Paper 1506.
- [6] Ziviani, D., Bell, I., Paepe, D., and M., van den Broek, M., (2014). Comprehensive model of a single screw expander for orc-systems applications. In *2014 Purdue Conferences: Compressor Engineering Refrigeration and air conditioning high performance building*. Paper 1451.
- [7] Lu, Y.W., He, W., Wu, Y.T., Ji, W.N., Ma, C.F., and Guo, H., (2013). Performance study on the compressed air refrigeration system based on single screw expander. *Energy*, 55:762--768.
- [8] Sun, G., (1988). The investigation of some basic geometric problems of the single screw co. In *International Compressor Engineering Conference*. Paper 630.
- [9] ZHANG, Y.Q., WU, Y.T., XIA, G.D., Ma, C.F., Ji, W.N., Liu, S.W., Yang, K., and Yang, F.B., (2014). Development and experimental study on organic Rankine cycle system with single-screw expander for waste heat recovery from exhaust of diesel engine [J]. *Energy*, 77: 499-508.
- [10] Liu, L.D., (2010). Research of the single screw expander and organic Rankine cycle system [D]. (in Chinese)
- [11] Peng, Y.H., (2013) Performance study of the compressed-air power system based on single-screw expanders[D].(in Chinese)
- [12] Peng, Y.H., Wu, Y.T., He, W., Ji, W.N. And Ma, C.F., (2014) Experimental study of single screw engine at different intake pressure.(in Chinese)

ACKNOWLEDGEMENTS

The authors are grateful to acknowledge the financial support provided by the National Basic Research Program of China with Grant Numbers 2011CB710704 and 2013CB228306, International S&T Cooperation Program of China with Grant Numbers 2014DF60600.

Thanks for experimental data supported by Yeqiang Zhang, Weining Ji and Yanhai Peng. If there is no their hard work, there will be no model validation of this paper. I am quite grateful for the guide from Biao Lei. Thanks for good suggestions from Wei Wang. Thanks them very much for their help.

EXPRIMENTAL STUDIES ON AN ORGANIC RANKINE CYCLE (ORC) SYSTEM UNDER VARIABLE CONDENSATION TEMPERATURE

Feibo Xie, Tong Zhu *, Jihua Liu, Naiping Gao, Wei An

College of Mechanical Engineering, Tongji University,
Siping Road 1239, Shanghai, China
E-mail: zhu_tong@tongji.edu.cn
Tel: 86-21-65983867

* Corresponding Author

ABSTRACT

For a thermal power system the operating condensation temperature fluctuates significantly throughout the year in many areas due to the change of ambient temperature. Therefore, off-design operation of an Organic Rankine Cycle (ORC) system is unavoidable. The present paper focuses on the test and analysis of an ORC system using R123 as the working fluid under various condensation temperature conditions. A scroll expander was integrated into the ORC system and connected with a synchronous generator. The exhaust gas from a furnace and the water from the cooling tower were adopted to simulate the low-grade heat source and the cold source, respectively. The temperature of the exhaust gas was about 180 °C. With the increasing of the cold water temperature from 22 °C to 42 °C, the condensation temperature of the working fluid varied from 50 °C to 65 °C and the pressure from 0.21MPa to 0.32MPa, respectively. It affected the expansion ratio and the temperature difference between the inlet and outlet of the expander. The performances of the expander, evaporator, condenser and the whole system were influenced subsequently. The measured electric power output declined from 2.36kW to 1.54kW, and the thermal efficiency fell from 7.25% to 5.52% as well. Under the operation conditions, the electric power and thermal efficiency decreased, by 34.75% and 23.86%, respectively. These results indicate that the operating condensation temperature plays a key role on the performance of the ORC system, and suggest that a proper condensation temperature is important to the design and operation of the ORC system.

1. INTRODUCTION

Energy crisis and global warming have greatly accelerated the development of low grade heat recovery technologies. An Organic Rankine Cycle (ORC) is regarded as a reasonable and promising way for power generation from low grade heat sources due to its high efficiency and flexibility (Tchanche B. et al., 2011; Velez F. et al., 2012; Ziviani D. et al., 2014). Compared to steam Rankine Cycles (RC), ORCs prefer organic fluids to low boiling points to improve the efficiency in low temperature applications. Several large scale ORCs have been available on the market (Quoilin S. et al., 2013; Tchanche B. et al., 2014). However, most of small-scale ORCs are still at the initial stage and receive increasingly striking attention due to its great market potential in low grade heat sources. ORCs show dramatic potential in utilization of geothermal (Gu Z. et al., 2002; Franco A. et al. 2009), solar energy (Joan B. et al., 2008; Pei G. et al., 2010), industrial waste heat (Liu B. et al., 2004; Dai Y. et al., 2009; Srinivasan K. et al., 2010; Zhou N. et al., 2013), engine exhaust gas (Invernizzi C. et al., 2007) and biomass (Martina P. et al., 2010). Over the past several decades, this wide range of applications has encouraged researchers' efforts to provide suitable ORC solutions. Thus various investigations have been carried out for working fluid selections (Hung T. et al., 2001; Saleh B. et al., 2007; Tung T. et al., 2010) and parameter optimizations (Wei D. et al., 2008; Quoilin S. et al., 2010; Quoilin S. et al., 2011; Lee Y. et al., 2012; Bracco R. et al., 2013; Minea V. et al., 2014).

Unlike RCs, ORCs, especially small scale, easily suffer the influence of off-design operation conditions. Heat sources for ORCs are usually unsteady. An industrial waste heat source usually fluctuates in a certain range because of the variation of the upstream production process. The solar radiation intensity fluctuates with the time of day and the season. The variable operation has been becoming a hotspots of ORCs studies recently. Many studies indicate that the performance and operating parameters of an ORC are sensitive to the changes in the heat source temperature (Bamgbopa M. et al.,2013; Ibarra M. et al., 2014), the working fluid flow rate (Bracco R. et al.,2013;Miao Z. et al.,2015) and the load (Miao Z. et al.,2015). And variations of the entering cooling fluid temperature also have an important influence on the output power and cycle efficiency of the ORC (Lee Y. et al.,2012; Li J. et al., 2014).

Additionally the expander is a critical component of an ORC. Among positive displacement expansion machines, a scroll expander is widely regarded as a potential and promising candidate for a kW-scale ORC due to compactness, high efficiency, few movement part, broad availability and so on (Bao J. et al., 2013; Song P. et al., 2015). Generally, the scroll expander is mainly modified from a scroll compressor (Lermort V. et al.,2009; Declaye S. et al., 2013; Liu G. et al.,2015), and elaborately designed for an ORC are hardly reported.

In the present work, an ORC using an oil-free scroll expander is tested and analyzed. R123 was adopted as the working fluid. The authors focus on the steady-state expander operation characteristic and performance of the ORC system under various cooling water temperature conditions, which simulates seasonal and daily variations of the ambient temperature. Under these conditions, the key operating parameters, which mainly includes pressures and temperatures at the expander inlet and outlet, electric output power and cycle efficiency, are analyzed,.

2. TEST BENCH DESCRIPTION

2.1 Experimental testing rig

In this section, the brief schematic diagram of the ORC is shown in Figure 1 (a). The thermodynamics of the ORC is similar to that of the RC. The T-s diagram of the thermodynamic processes is shown in Figure 1 (b). The liquid working fluid pressurized by the working fluid pump in the evaporator absorbs the heat from the low temperature heat source and becomes the high pressure superheating vapor. The high pressure and temperature vapor expands in the scroll expander to drive the synchronous generator. The low pressure superheating vapor exhausted from the scroll expander evolves through precooling to condensing to overcooling process in the condenser and is changed into liquid, and then feeds back to the evaporator via the pump. Then this process completes a power circulation.

The major components of the ORC include an evaporator, a scroll expander, a condenser, a working fluid pump, a cooling water tower, a synchronous generator, and other auxiliary equipments. R123 was selected as the working fluid. The exhaust gas from a furnace burning flue gas was utilized to simulate a low grade heat source. A cooling water tower installed in the outdoor cooled down the cooling water from the condenser.

A tube-shell heat exchanger with the heat transfer area of 4.9 m² was used as the condenser. And here the superheated working fluid is pre-cooled, condensed and slightly sub-cooled by the cooling water.

The working fluid pump is a diaphragm metering pump and its displacement can be adjusted by its stroke, which allowed controlling the R123 flow rate through the cycle. It could provide the maximum volumetric flow rate and pressure, 800L/h and 2MPa, respectively.

A finned-tube exchanger was selected as the evaporator according to the type of the low temperature heat source, and its total heat transfer area is 14m².

An oil-free scroll expander was used for the expansion process, which was elaborately designed for the ORC by Air Squared. Some basic parameters about the scroll expander are listed in Table 1.

An synchronous generator was driven by the scroll expander through belt- pulley coupling. The rated outpower and rated rotate speed was 5kW and 1500rpm, respectively. Several bulbs was used to consume electricity from the generator.

In the test rig, the measured parameters included the pressure and temperature at inlet and outlet of four primary devices, flow rates of the working fluid and the cooling water. In addition, the detailed information of these main measurement instruments is listed in Table 2.

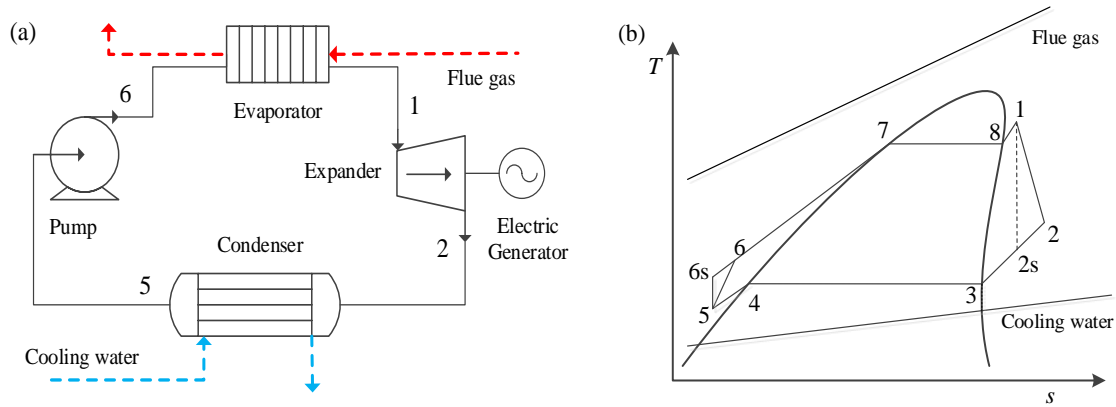


Figure 1: Schematic diagram of (a) the ORC and (b) T-s of the ORC

Table 1: Basic parameters of the scroll expander

Parameters	Unit	Value
Type	--	E22H38N4.25(oil-free)
Suction volume	cm ³ /r	73.6
Max. rotational speed	rpm	3600
Max. inlet pressure	MPa	1.38
Max. inlet temperature	°C	175
Built-in volume ratio	--	3.5

2.2 Thermodynamic analysis equations

Severale different parameters were used for the analysis of the experimental data obtained under the variation of the entering cooling water temperature condition.

Table 2: Main instruments used in the test rig

Parameters	Sensors	Range	Accuracy
Temperature	K-type thermocouple	0-1580K	±0.1K
Pressure	diffused silicon pressure transmitter	0-2.5MPa	±0.2%
Liquid turbine flowmeter	LWGY-2Y	1-10m ³ /h	±0.1%
vortex-shedding flowmeter	BF-LUGB32246	15-150m ³ /h	±1.5%

The heat absorbed by the working fluid from the low temperature heat source in the evaporator is caculated by Equation (1):

$$Q_{\text{evap}} = m_{\text{wf}} (h_{\text{wf, evap, out}} - h_{\text{wf, evap, in}}) \tag{1}$$

The heat released by the working fluid towards the cooling water in the condenser is caculated by Equation (2):

$$Q_{\text{cond}} = m_{\text{wf}} (h_{\text{wf, cond, in}} - h_{\text{wf, cond, out}}) \tag{2}$$

The working fluid pump consumption is calculated by Equation (3):

$$W_p = m_{wf} (h_{wf,pump,out} - h_{wf,pump,in}) \quad (3)$$

The net electric output power in the test is calculated by Equation (4):

$$W_{net} = W_{ele} - W_p \quad (4)$$

where W_{ele} is the electric power from synchronous generator which is measured by the electro-dynamometer as the power consumed on the bulbs.

The cycle electric efficiency is defined by Equation (5):

$$\eta_{ORC} = \frac{W_{net}}{Q_{evap}} \quad (5)$$

The expander isentropic efficiency and electric isentropic efficiency, is defined by Equation (6) and (7), respectively:

$$\varepsilon_s = \frac{h_{wf,exp,in} - h_{wf,exp,out}}{h_{wf,exp,in} - h_{wf,exp,out,s}} \quad (6)$$

$$\varepsilon_{s,ele} = \frac{W_{ele}}{m_{wf} (h_{wf,exp,in} - h_{wf,exp,out,s})} \quad (7)$$

The pressure ratio of the expander, is defined by Equation (8):

$$r_p = \frac{P_{exp,in}}{P_{exp,out}} \quad (8)$$

2.3 Operating procedure

The ORC rig was tested under varying the cooling water inlet temperature. For this, as the ambient temperature cannot be controlled, different operating conditions had been achieved during the tests by replacing the higher temperature water in the outdoor cooling tower. On the other hand, the flue gas inlet temperature and flow rate kept steady by the flue gas flow rate and air-input amount, and the flow rate of the cooling water was imposed with a fixed frequency set point in the centrifugal water pump. In Table 3, it can be seen that the operating range obtained during the tests for each variable.

Table 3: The operating parameters during the tests

Parameter	Unit	Value
t_{hf}	°C	180
$V_{cf,cond}$	m ³ /h	20
$t_{cf,cond,in}$	°C	20-45
$P_{exp,in}$	MPa	0.9-1.1
$P_{exp,out}$	MPa	0.2-0.35

3. RESULTS AND DISCUSSION

From the experimental data obtained during the tests, an analysis has been conducted, and these results are exposed and discussed in this section.

Figure 2 shows the variation of the pressure and saturation temperature at the condenser inlet under the different cooling water temperature. The pressure was found to be approximately proportional to the entering cooling water temperature. The saturation temperature also increased linearly. This phenomenon was in accordance with the mechanism of heat transfer at the condenser. This was because when the entering cooling water temperature increase and other parameters (for example flow rates of the working fluid and cooling water), the coefficient and area of heat transfer had little effect on. The increase of the pressure at the condenser inlet inevitably results into the increase of the pressure at the expander outlet, and this could have a great effect on the expander performance.

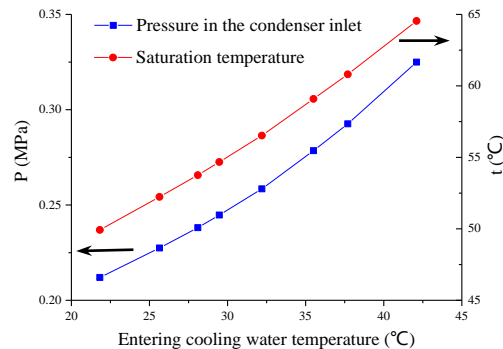


Figure 2: The pressure and saturation temperature at the condenser inlet vs. the entering cooling water temperature

The variation of vapor pressure, temperature and superheating degree at the expander inlet are shown in the Figure 3. The vapor pressure slightly increased, and the temperature and the degree of superheating decreased with the increase of the entering cooling water temperature. This phenomenon agreed with the scroll expander characterization and the heat transfer mechanism in the evaporator. The higher scroll expander back pressure increased the discharge resistance and resulted in the higher pressure at the expander inlet. The higher vapor pressure meant the higher evaporation temperature in the evaporator. When the temperature and flow rate of the heat source at the evaporator inlet was relatively steady, it meant that the heat-transfer temperature difference decreased. The preheating and evaporating area enlarged, and the superheating area shrank. The decrease in the superheating area led to the slight decrease of the vapor temperature at the expander inlet. And this process made the superheating degree decrease.

Figure 4 shows the variation of vapor pressure, temperature and superheating degree at the expander outlet. Generally speaking, the vapor temperature at the expander outlet decreased with the entering cooling water temperature, and the vapor pressure increased. So these reduced the superheating degree. These are because the lower heat flux in the evaporator at higher entering cooling water temperature reduced the heat transfer load of the evaporator and the temperature at the expander inlet decreased. Moreover, it is obvious that the superheating degree at the expander outlet, about 50 °C is relatively high, especially under the lower entering cooling water temperature, and it could be a good choice to recover this part of heat by an internal heat exchanger (IHE). This could benefit to promote the thermal efficiency of the ORC.

The pressure ratio and temperature drop through the scroll expander were calculated and analyzed by using data from tests and is shown in Figure 5. The pressure ratio in Figure 5 is known as external pressure ratio because of the pressure sensors at the tubes connecting with the expander inlet and outlet. A higher pressure ratio through the expander leads a higher driving force for the expander. When the entering cooling water temperature increased, the relative increase of the vapor pressure at the expander outlet is larger than that at the inlet. This process results in the decrease of the pressure ratio and the pressure, and the output power could decrease.

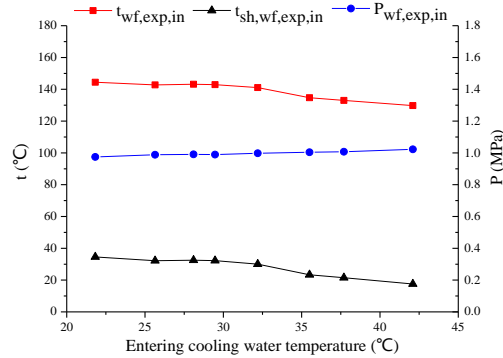


Figure 3: The key operating parameters characterization at the expander inlet during the tests

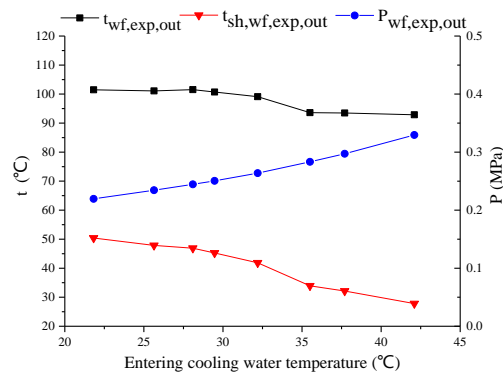


Figure 4: The key operating parameters characterization at the expander outlet during the tests

Based on the collected operating parameters of the expander, the isentropic efficiencies is calculated and shown in Figure 6. It can be shown clearly that firstly the scroll expander isentropic efficiencies slightly descended with the increase in the entering cooling water temperature, increased dramatically, and slight decreased with the further increase in the entering cooling water temperature. The maximum isentropic efficiency was obtained when the entering cooling water temperature was 35.5 °C, and at this time the volume ratio was 3.6, which was very closed to the design value 3.5. In addition, the isentropic efficiencies calculated by Equation (6) was relative too high because the heat losses the scroll expander was not negligible during the test (Declaye S. et al., 2013). So it is hardly expected to elucidate the trends only by means of the experimental results because many factors, such as pressure losses, mechanical friction and leakage, affected the isentropic efficiency. Beside the scroll expander electric isentropic efficiency slightly decreased with the increase of the cooling water temperature, seen in Figure 6.

Figure 7 shows the variation of the measured electric power output and the cycle thermal efficiency with the increase of the entering cooling water temperature. Definitely, the electric power output and the cycle thermal efficiency decrease with the increase of the entering cooling water temperature. When the entering cooling water temperature increase from 21 °C to 42 °C, the measured electric power output declines from 2.36kW to 1.54kW, and the cycle thermal efficiency falls from 7.25% to 5.52% as well. These mean that when the entering cooling water temperature increases by 1 °C, the electric power output decreases by 1.65%. Under the operating conditions, the electric power output and thermal efficiency decreases, by 34.75% and 23.86%, respectively. It is noted that the relative decrease in the electric power output was more important than that in the thermal efficiency. The reason is likely that the heat absorbed by the working fluid from the heat source at the evaporator also decreases with the entering cooling water temperature, but the variation slowered by lower than that of the electric power output. The heat absorbed by the working fluid at the evaporator decreases because the saturation temperature in the evaporator and the enthalpy at the evaporator inlet increase.

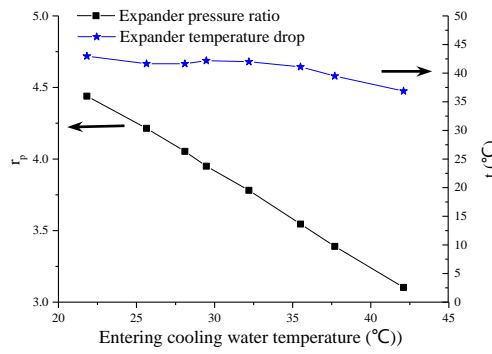


Figure 5: The pressure ratio and temperature drop through the expander during the tests

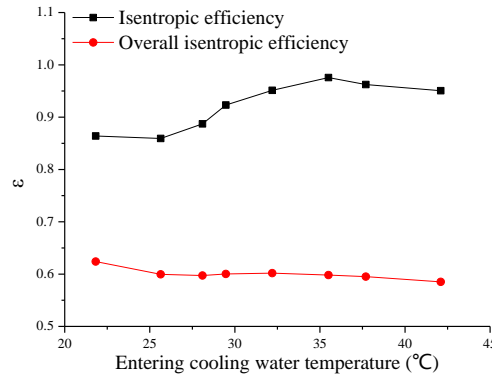


Figure 6: The isentropic efficiency characterization during the tests

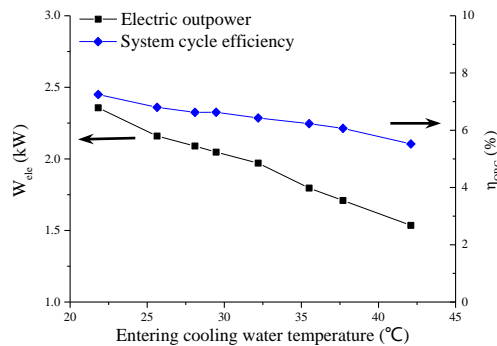


Figure 7: The ORC performance characterization during the tests

6. CONCLUSIONS

Focused on the exploration of kW-scale ORC system, this investigation presents the test and analysis of the operation characteristic and performance of an ORC rig with R123 as the working fluid. A oil-free scroll expander was adopted and then converted heat energy into mechanical power. Operation characteristics were compared under various cooling water temperatures from 22 °C to 42 °C, which the condensation temperature of the working fluid varied from 50 °C to 65 °C and the pressure from 0.21MPa to 0.32MPa, respectively. The measured electric power output declined from 2.36kW to 1.54kW, and the cycle thermal efficiency fell from 7.25% to 5.52% as well. Under the operation conditions, the electric output power and thermal efficiency decreased, by 34.75% and 23.86%, respectively.

For the tests, the entering cooling water temperature has a great effect on the electric output power and thermal efficiency by the variation of the pressure at the scroll expander outlet. And this means that the performance of the ORC could be sensitive to the seasonal and daily variation of the ambient temperature and suggest that a proper condensation temperature is important to the design and operation of the ORC system.

NOMENCLATURE

h	enthalpy	kJ/kg
m	mass flow rate	kg/s
P	pressure	MPa
Q	thermal power	kW
r_p	pressure ratio	-
r_v	volume ratio	-
s	entropy	kJ/kg/K
t	temperature	°C
V	volume	m ³
W	power	kW

Greek symbols

ε	efficiency	%
η	efficiency	%
ρ	density	kg/m ³

Subscript

cf	cooling fluid
cond	condenser
ele	electric
evap	evaporator
exp	expander
hf	heat fluid
in	inlet
oc	overcooling
out	outlet
p	pump
s	isentropic
sat	saturation
sh	superheat
wf	working fluid

REFERENCES

- Bambgopa, M., Uzgoren, E., 2013, Numerical analysis of an organic Rankine cycle under steady and variable heat input, *Applied Energy*, vol. 107 : p. 219-228.
- Bao, J., Zhao, L., A review of working fluid and expander selections for organic Rankine cycle, *Renewable and Sustainable Energy Reviews*, vol. 24 : p. 325-342.
- Bracco, R., Clemente, S., Micheli, D., Reini, M., 2013, Experimental tests and modelization of a domestic-scale ORC (Organic Rankine Cycle), *Energy*, vol. 58 : p. 107-116.
- Dai, Y., Wang, J., Gao, L., 2009, Parametric optimization and comparative study of organic Rankine cycle (ORC) for low grade waste heat recovery, *Energy Conversion and Management*, vol. 50 : p. 576-582.
- Declaye, S., Quoilin, S., Guillaume, L., Lemort, V., 2013, Experimental study on an opendrive scroll expander integrated into an ORC (Organic Rankine Cycle) system with R245fa as working fluid, *Energy*, vol. 55 : p. 173-183.
- Franco, A., Villani, M., 2009, Optimal design of binary cycle power plants for water-dominated, medium-temperature geothermal fields, *Geothermics*, vol. 38 : p. 379-391.
- Gu, Z., Sato, H., 2002, Performance of supercritical cycles for geothermal binary design, *Energy Conversion and Management*, vol. 43 : p. 961-971.

- Hung, T., 2001, Waste heat recovery of organic Rankine cycle using dry fluids, *Energy Conversion and Management*, vol. 42 : p. 539-553.
- Ibarra, M., Rovira, A., Alarcon-Padilla, D., Blanco, J., 2014, Performance of a 5kWe Organic Rankine Cycle at part-load operation, *Applied Energy*, vol. 120 : p. 147-158.
- Invernizzi, C., Iora, P., Silva, P., 2007, Bottoming micro-Rankine cycles for micro-gas turbines, *Applied Thermal Engineering*, vol. 27 : p. 100–110.
- Joan, B., Jesús, L., Eduardo, L., Silvia, R., Alberto, C., 2008, Modelling and optimisation of solar organic Rankine cycle engines for reverse osmosis desalination, *Applied Thermal Engineering*, vol. 28 : p. 2212–2226.
- Lee, Y., Kuo, C., Wang, C., 2012, Transient response of a 50 kW organic Rankine cycle system, *Energy*, vol. 48 : p. 532-538.
- Lemort, V., Quoilin, S., Cuevas, C., Lebrun, J., 2009, Testing and modeling a scroll expander integrated into an organic Rankine cycle, *Applied Thermal Engineering*, vol. 29 : p. 309-3102.
- Li, J., Pei, G., Ji, J., Bai, X., Li, P., Xia, L., 2014, Design of the ORC (organic Rankine cycle) condensation temperature with respect to the expander characteristics for domestic CHP (combined heat and power) applications, *Energy*, vol. 77 : p. 579-590.
- Liu, B., Chien, K., Wang, C., Effect of working fluids on organic Rankine cycle for waste heat recovery, *Energy*, vol. 29 : p. 1207–1217.
- Liu, G B., Zhao, Y., Yang, Q., Wang, L., Tang, B., Li, L., 2015, Theoretical and experimental research on scroll expander used in small-scale organic Rankine cycle system, *Journal of Process Mechanical Engineering*, vol. 229 : p. 25-35.
- Martina, P., Shane, W., Philip, O., 2010, Evaluation of energy efficiency of various biogas production and utilization pathways, *Applied Energy*, vol. 87 : p. 3305–3321.
- Miao, Z., Xu, J., Yang, X., Zou, J., 2015, Operation and performance of a low temperature organic Rankine cycle, *Applied Thermal Engineering*, vol. 75 : p. 1065-1075.
- Pei, G., Li, J., Ji, J., 2010, nalysis of low temperature solar thermal electric generation using regenerative organic Rankine cycle, *Applied Thermal Engineering*, vol. 30 : p. 998–1004.
- Quoilin, S., Aumann, R., Grill, A., Schuster, A., Lemort, V., Spliethoff, H., 2011, Dynamic modeling and optimal control strategy of waste heat recovery Organic Rankine Cycles, *Applied Energy*, vol. 88 : p. 2183-2190.
- Quoilin, S., Broek, M., Declaye, S., Dewallef, P., Lemort, V., 2013, Techno-economic survey of Organic Rankine Cycle (ORC) systems, *Renewable and Sustainable Energy Reviews*, 2013, vol. 22 : p. 168-186.
- Quoilin, S., Lemort, V., Lebrun, J., 2010, Experimental study and modeling of an organic Rankine cycle using scroll expander, *Applied Energy*, vol. 87 : p. 1260-1268.
- Saleh, B., Koglbauer, G., Wendland, M., Fischer, J., 2007, Working fluids for lowtemperature organic Rankine cycles, *Energy*, vol. 32 : p. 1210-1221.
- Song, P., Wei, M., Shi, L., Danish, S., Ma, C., 2015, A review of scroll expanders for organic Rankine cycle systems, *Applied Thermal Engineering*, vol. 75 : p. 54-64.
- Srinivasan, K., Mago, P., Krishnan, S., 2010, Analysis of exhaust waste heat recovery from a dual fuel low temperature combustion engine using an organic Rankine cycle, *Energy*, vol. 35 : p. 2387-2399.
- Tchanche, B., Lambrinos, Gr., Frangoudakis, A., Papadakis, G., 2011, Low-grade heat conversion into power using organic Rankine cycles – A review of various applications, *Renewable and Sustainable Energy Reviews*, vol. 15 : p. 3963-3979.
- Tchanche, B., Petrissans, M., Papadakis, G., 2014, Heat resource and organic Rankine cycle machine, *Renewable and Sustainable Energy Reviews*, vol. 39 : p. 1185-1199.
- Tung, T., Wang, S., Kuo, C., Pei, B., Tsai, K., 2010, A study of organic working fluids on system efficiency of an ORC using low-grade energy sources, *Energy*, vol. 35 : p. 1403-1411.
- Vasile, M., 2014, Power generation with ORC machines using low-grade waste heat or renewable energy, *Applied Thermal Engineering*, vol. 69 : p. 143-154.

- Velez, F., Segovia, J., Martin, C., Antolin G., Chejne F., Quijano, A., 2012, A technical, economical and market review of organic Rankine cycles for the conversion of low-grade heat for power generation, *Renewable and Sustainable Energy Reviews*, vol. 16 : p. 4175-4189.
- Wei, D., Lu, X., Lu, Z., Gu, J., 2008, Dynamic modeling and simulation of an Organic Rankine Cycle (ORC) system for waste heat recovery, *Applied Thermal Engineering*, vol. 28 : p. 1216-1224.
- Zhou, N., Wang, X., Chen, Z., Wang, Z., 2013, Experimental study on Organic Rankine Cycle for waste heat recovery from low-temperature flue gas, *Energy*, vol. 55 : p. 216-225.
- Ziviani, D., Beyene, A., Venturini, M., 2014, Advances and challenges in ORC systems modeling for low grade thermal energy recovery, *Applied Energy*, vol. 121: p. 79-95.

ACKNOWLEDGEMENT

The authors want to acknowledge the financial support by National Fundamental Research Program 973 project (2014CB249201) "Research on the stability of complex energy system integrated natural gas and renewable energy" and ENN-Tongji Institute for Advanced Clean Energy under the project "Research on the key technologies in power generation from low-grade waste heat".

ADVANCED THERMODYNAMIC MODEL OF ORGANIC RANKINE CYCLE

Parsa Mirmobin*, Chris Sellers

Calnetix Technologies, LLC
16323 Shoemaker Ave, Cerritos, CA 90703
USA

e-mail: pmirmobin@calnetix.com, csellers@calnetix.com

Web page: <http://www.calnetix.com>

* Corresponding Author

ABSTRACT

Low-grade heat from geothermal or industrial processes is an eco-friendly resource for electric power production. The Organic Rankine Cycle (ORC) has become a popular means to exploit these energy sources. This growing popularity has resulted in the need for rapid, accurate simulation tools for plant design and specification.

In this paper, an advanced, steady state, thermodynamic model of an ORC is developed. The model is composed of several sub components including: an evaporator and condenser, centrifugal pump, turbine expander, and pipe elements. Each of these components is modeled independently and their inputs/outputs are combined together to form the overall system.

The model is developed using simple programming language (VBA) in excel and utilizes NIST Refprop for calculation of state properties. This medium was chosen because of its simplicity and low cost; however, the general model structure can easily be implemented in any programming language. The model predictions are validated against field data collected from ORC systems operating at several evaporating and condensing conditions.

1. INTRODUCTION

Rising energy costs, the demand for improved system efficiency, and government programs to reduce plant emissions have led to a surge in the popularity of the Organic Rankine Cycle (ORC.) Advanced modeling techniques are required to estimate the electrical power produced by an ORC system and to choose appropriate system components. The demand for simulation tools which can quickly and cheaply accomplish these tasks has grown in lockstep with ORC demand.

Commercially available process simulators (e.g. ASPEN HYSYS, CHEMCAD) are powerful but often expensive and cumbersome to work with. These “all encompassing” simulators are excellent for plant designs yet lack modeling for key components necessary to develop a high fidelity ORC system simulator. The following paper will describe the development of a low cost, flexible model written in Excel VBA. The model has been used to design over 100 plants and shows excellent agreement with field installations.

The model is divided into three main sections:

- 1) The working fluid loop
- 2) The evaporator
- 3) The condenser

The working fluid loop model is composed of several component models arranged in series to represent the ORC system. The following sections will describe each component model in detail.

2. MODELING METHODOLOGY

2.1 Pipe Section Model

The pipe model estimates the pressure and temperature losses experienced by the fluid as it flows through a pipe section. It links the major components (e.g. pump, evaporator, etc.) together in the working fluid loop model. The inputs are temperature, pressure, and mass flow and the outputs are temperature and pressure losses. Additionally there are several descriptive inputs: roughness, height, length, diameter, overall heat transfer coefficient, and ambient temperature. The pressure drop is found using the Darcy-Weisbach equation.

$$\Delta P = 8\pi f L \frac{\dot{m}^2}{\rho_{in,pipe} D^3} \quad (1)$$

The inlet density in Equation (1) is calculated from the inlet temperature and pressure. The Darcy friction factor in Equation (1) is found from an iterative solution to the equation below, Colebrook (1939).

$$\frac{1}{\sqrt{f}} = -2 \log_{10} \left(\frac{\epsilon}{3.7D} + \frac{2.51}{Re\sqrt{f}} \right) \quad (2)$$

The Reynolds number in Equation (2) is calculated using the inlet density and viscosity. These properties are calculated at the inlet temperature and pressure. Treating the pipe section as a cylinder with 1-D convective heat transfer and a constant ambient temperature, the temperature drop across the pipe section is calculated by (Incropera and DeWitt 2002):

$$\Delta T = (T_{amb} - T_{in}) e^{-\frac{\pi U D L}{\dot{m} c_p}} \quad (3)$$

The overall heat transfer coefficient in Equation (3) is adjusted based on test data of a production ORC. The specific heat is calculated at the pipe inlet temperature and pressure.

The pressure loss of system fittings within the working fluid loop (i.e. filters, valves, etc.) may be modeled as an equivalent length of pipe for a given diameter.

2.2 Pump Model

The pump model simulates the operation of a centrifugal pump as utilized in the Calnetix ORC product. The inputs are inlet temperature, inlet pressure, mass flow and outlet pressure. The outputs are the exit temperature and motor power. The calculation begins with determining the inlet density, enthalpy, and entropy at the inlet temperature and pressure. Next the volumetric flow and hydraulic head are calculated by:

$$G = \frac{\dot{m}}{\rho_{in}} \quad (4)$$

$$\Delta H = \frac{(P_{out} - P_{in})}{\rho_{in} g} \quad (5)$$

The values for volumetric flow rate and hydraulic head are input into a table map which outputs the pump efficiency, η_{pump} .

$$\eta_{pump} = MAP(\Delta H, G) \quad (6)$$

Next the ideal outlet enthalpy is calculated at the inlet entropy and outlet pressure. The true pump outlet enthalpy is calculated using:

$$h_{out} = \eta_{pump}(h_{out,s} - h_{in}) + h_{in} \quad (7)$$

Combining the output from Equation (7), the mass flow, and inlet enthalpy, the pump power is found using:

$$W_{pump} = \dot{m}(h_{out} - h_{in}) \quad (8)$$

Finally the outlet temperature may be calculated at the outlet pressure and outlet. The MAP used by Equation (6) was developed experimentally from the centrifugal pump model used in Calnetix ORC products. Maps for other types of pumps may be developed in the same manner.

2.3 Integrated Power Module (IPM)

The integrated power module, IPM, plays a pivotal role in the working fluid loop model by setting the system mass flow and determining the grid power output. The Calnetix IPM consists of a nozzle, turbine wheel, rotor, and generator stator. The rotor/wheel assembly is levitated by magnetic bearings within the generator stator, see Figure 1 below.

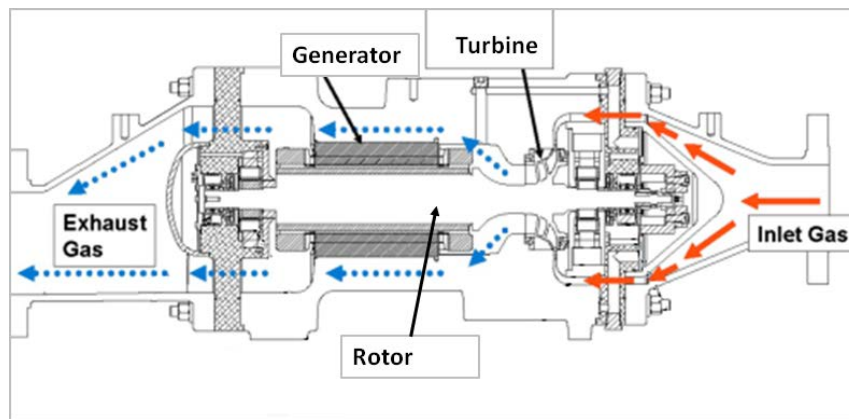


Figure 1: Calnetix IPM

The working fluid flows into the nozzle, through the turbine, over the rotor, and around the generator. Heat from turbine efficiency losses, rotor windage, and generator efficiency losses are added into the fluid stream increasing the exit enthalpy. These losses are estimated using table maps and correlations developed using CFD and empirical test data.

The inputs to the IPM model are inlet temperature, inlet pressure, outlet pressure, and turbine speed. Additionally there are several internal variables used from the previous calculation. These values are the static speed of sound at the nozzle inlet a^* , the static density at the nozzle inlet ρ^* , the dimensionless enthalpy drop across the wheel, the dimensionless wheel rotation speed, and the flow parameter at the wheel exit. The outputs are grid power, temperature at the IPM outlet, and working fluid loop mass flow.

The model calculation is carried out in several steps. Initially the internal input variables are input into map files which represent the turbine operation. The outputs are the isentropic efficiency (η_T) of the nozzle turbine system, the dimensionless inlet flow parameter (ϕ_{in}), and the turbine exit swirl angle (θ).

$$\eta_T = MAP \left(\frac{\Delta h_s}{(a^*)^2}, \frac{N}{a^*} \right) \quad (9)$$

$$\phi_{in} = MAP \left(\frac{\Delta h_s}{(a^*)^2}, \frac{N}{a^*} \right) \quad (10)$$

$$\theta = MAP \left(\frac{\Delta h_s}{(a^*)^2}, \frac{N}{a^*} \right) \quad (11)$$

Next the turbine exit swirl angle and wheel exit flow parameter are used to find the percentage pressure drop across the generator, $\Delta P_{Gen} \%$.

$$\Delta P_{Gen} \% = MAP(\theta, \phi_{out}) \quad (12)$$

The pressure at the wheel outlet is determined from:

$$P_{out} = (1 + \Delta P_{Gen} \%) P_{out,IPM} \quad (13)$$

Next the entropy and enthalpy at the nozzle inlet are calculated at the IPM inlet temperature and pressure. The ideal enthalpy at the wheel exit is calculated at the wheel outlet pressure and entropy at the nozzle inlet. The true enthalpy at the wheel exit is calculated by combining values from:

$$h_{out} = h_{in} - \eta_T (h_{in} - h_{out,s}) \quad (14)$$

Next the system mass flow is calculated from the inlet flow parameter (ϕ_{in}), static speed of sound at the nozzle inlet (a^*), and static density at the nozzle inlet (ρ^*). The model accounts for turbine leakage as follows:

$$\dot{m}_T = (1 - \alpha) \dot{m} \quad (15)$$

Combining the values from Equations (14), (15), and the nozzle inlet enthalpy, the turbine work may be calculated as:

$$W_T = \dot{m}_T (h_{in} - h_{out}) \quad (16)$$

The generator converts the turbine work calculated in Equation (16) to electrical power. A portion of the mechanical work is lost due to viscous effects acting on the rotor and wheel outer surfaces. These losses are called "windage" losses and are calculated through the aid of correlations from Norris (1970) and Vrancik (1968.) Additionally there are electrical losses due to resistance in the copper windings of the stator and iron losses due to changes in the magnetic field. An energy balance across the wheel/rotor control surface results in:

$$W_{Gen} = W_T - Q_{Loss} - W_{windage} \quad (17)$$

Where Q_{loss} is the heat lost from generator due to inefficiencies. Equation (17) may be simplified by introducing the generator efficiency, η_{Gen} , which relates the portion of turbine work lost due to generator efficiencies as:

$$\eta_{Gen} = \frac{W_T - Q_{Loss}}{W_T} \quad (18)$$

Thus combining Equations (17) and (18) then generator work may be expressed as (19):

$$W_{Gen} = \eta_{Gen} W_T - W_{windage} \quad (19)$$

The generator efficiency is found from a map lookup with inputs turbine work and generator frequency. The final step in the grid power calculation is to account for losses due to inefficiencies in the electrical power rectification and conversion process. These losses are accounted for with the power electronics efficiency number, η_{PE} , and related to the generator power and grid power by:

$$W_{PE} = \eta_{PE} W_{Gen} \quad (20)$$

To determine the temperature at the exit of the IPM, the enthalpy at the exit of the generator must be determined. This is found by forming an energy balance for the control surface surrounding the fluid flowing into and out of the generator:

$$\dot{m}(h_{out,Gen} - h_{in,Gen}) = Q_{Loss} + W_{windage} \quad (21)$$

The enthalpy at the generator inlet is found from a mass weighted average of the enthalpy exiting the turbine and leakage enthalpy. Using Equation (15) and values for the wheel outlet enthalpy and nozzle inlet enthalpy:

$$h_{in,Gen} = (1 - \alpha)h_{out} + \alpha h_{in} \quad (22)$$

Thus using Equations (18), (21), and (22) and solving for the generator outlet enthalpy, we arrive at:

$$h_{out,Gen} = (1 - \alpha)h_{out} + \alpha h_{in} + \frac{[(1 - \eta_{Gen})W_T + W_{windage}]}{\dot{m}} \quad (23)$$

Finally the exit temperature of the wheel is a function of the IPM outlet pressure and the enthalpy. The Calnetix ORC utilizes a reaction type turbine, thus the model is readily compatible with different types of reaction turbines. With appropriate map files, the model may be modified to accommodate other types of turbines.

2.4 Updating IPM Model Internal Variables

Once the calculations from section 2.3 are completed, the internal variables are updated for the next calculation loop. These values converge after several iterations. The first step in the update process is to calculate the static speed of sound and static density at the nozzle inlet.

The initial speed of sound is calculated at the nozzle inlet temperature and pressure. Using the value for enthalpy at the nozzle inlet found earlier, an intermediary enthalpy is found. by subtracting the square of the initial speed of sound:

$$h_i = h_{in} - \frac{a_i^2}{C} \quad (24)$$

Next the speed of sound is recalculated using the intermediary enthalpy, h_i , and the nozzle inlet entropy:

$$a_i = a(h_i, s_{in}) \quad (25)$$

The new speed of sound value is placed back into Equation (24) and the process is repeated until the value for a_i converges. This converged value is the static speed of sound at the nozzle inlet, $a_{in,nozzle}^*$. The final value of h_i is the static enthalpy at the nozzle inlet, h^* . The static density is now calculated from the value h^* and the entropy at the nozzle inlet.

Next the values for the static speed of sound at the nozzle inlet, nozzle inlet enthalpy, ideal nozzle exit enthalpy, and rotor speed are used to calculate the quantities $\Delta h_s / (a^*)^2$ and N/a^* . A new inlet flow parameter is calculated using the mass flow calculated by the IPM model. Finally the flow parameter at the wheel exit may be calculated using the procedure described above with the temperature, pressure, enthalpy, and entropy at the wheel exit.

2.5 Combining the Working fluid loop Components

Integrating the working fluid loop components is depicted graphically in Figure 2 below:

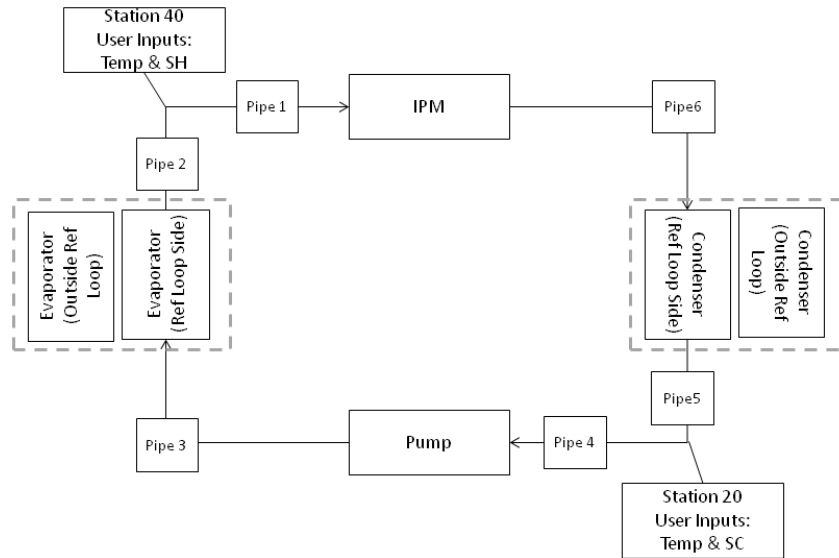


Figure 2: Working fluid loop Diagram

The overall user inputs to the working fluid loop model are temperature at station 40, superheat at station 40, temperature at station 20, and sub-cooling at station 20. From these values the pressure is calculated at stations 40 and 20 respectively. The pressure drop across each pipe element is added or subtracted from the P_{40} and P_{20} . Thus the pressure inputs to each component are calculated by:

$$P_{in,IPM} = P_{40} - \Delta P_1 \quad (26)$$

$$P_{out,IPM} = P_{20} + \Delta P_5 + \Delta P_{Cond} + \Delta P_6 \quad (27)$$

$$P_{in,Pump} = P_{20} - \Delta P_4 \quad (28)$$

$$P_{out,Pump} = P_{40} + \Delta P_2 + \Delta P_{Evap} + \Delta P_3 \quad (29)$$

The inlet temperature to each component is found using the temperature loss for each pipe section with Equation (3). In some cases the temperature loss is calculated in reverse and added to the user input temperature. The input/output temperature values are updated with each successive calculation of the working fluid loop. Convergence is achieved after several iterations.

2.6 Evaporator and Condenser Models

The evaporator and condenser models estimate the source mass flow and heat exchanger surface area needed. The user inputs are inlet temperature and pressure of the source, source side pressure loss coefficient, working fluid side pressure loss coefficient, exit temperature of the source, and overall heat transfer coefficient. Additionally these models take inputs of working fluid inlet temperature/pressure, outlet temperature/pressure, and heat exchanger duty which are all calculated by the working fluid loop model. The pressure drop on the source and working fluid sides are calculated by the minor loss equation:

$$P_{out} = P_{in} - \xi \frac{\dot{m}^2}{\rho_{in}} \quad (30)$$

The inlet density in Equation (30) is calculated at the inlet temperature and pressure. The pressure loss coefficient, ξ , is typically given by the heat exchanger manufacturer. The heat exchanger duty is calculated from the inlet enthalpy, outlet enthalpy, and mass flow on the working fluid side by:

$$Q = \dot{m}(h_{in} - h_{out}) \quad (31)$$

The source mass flow is calculated by dividing the heat exchanger duty calculated by Equation (31) by the enthalpy change between the inlet and outlet of the source:

$$\dot{m}_{source} = \frac{Q_{HEX}}{(h_{out,source} - h_{in,source})} \quad (32)$$

The inlet enthalpy for the source is calculated at the source inlet temperature and pressure. The outlet enthalpy is calculated from the source outlet temperature and pressure. The source outlet pressure is updated iteratively using Equation (30), (31), and (32).

The heat exchanger surface area is found using a discrete integration process. The process begins by determining the enthalpy and pressure step sizes for both the source side and working fluid sides of the evaporator and condensing with:

$$\Delta h = \frac{h_{out} - h_{in}}{k} \quad (33)$$

$$\Delta P = \frac{P_{out} - P_{in}}{k} \quad (34)$$

From Equations (33) and (34), a discretized pressure and enthalpy field for the source and working fluid sides is defined by:

$$h_i \in \{h_{in} + i\Delta h\} \text{ for } i = 0, 1, 2, \dots, k \quad (35)$$

$$P_i \in \{P_{in} + i\Delta P\} \text{ for } i = 0, 1, 2, \dots, k \quad (36)$$

By Equation (36)(37), the pressure field is evenly spaced with the enthalpy change for both the source and working fluid sides. The discrete temperature field may be calculated from each enthalpy and pressure pair as:

$$T_i \in \{T(h_i, P_i)\} \text{ for } i = 0, 1, 2, \dots, k \quad (37)$$

The heat flux through each heat exchanger section is defined for both the source and working fluid sides as:

$$Q_i \in \{(1/\dot{m})(h_i - h_{i-1})\} \text{ for } i = 1, 2, \dots, k \quad (38)$$

Next the log mean temperature difference for each section is found from:

$$T_{i,LMD} \in \left\{ \frac{(T_{i,Source} - T_{k-i,Ref}) - (T_{i-1,Source} - T_{k-i-1,Ref})}{\ln \frac{(T_{i,Source} - T_{k-i,Ref})}{(T_{i-1,Source} - T_{k-i-1,Ref})}} \right\} \quad (39)$$

The index "i" in Equation (39) takes integer values from 0 to k. Using Equations (38) and (39) and the relationship between heat flux, the overall heat transfer coefficient, heat exchanger surface area, and log mean temperature difference:

$$(UA)_i \in \{Q_i/T_{i,LMD}\} \text{ for } i = 1, 2, \dots, k \quad (40)$$

Finally the heat exchanger surface area is found by summing the values in Equation (40) and dividing by the user input overall heat transfer coefficient, U .

$$A = \frac{1}{U} \sum_{i=1}^k (UA)_i \quad (41)$$

The model described above is intentionally simple for the following reasons:

- 1) The model is iterated many times to arrive at the desired set point. A simpler component model reduces the overall computation time.
- 2) Complex models require parameters such as local friction factor which need to be determined experimentally or analytically across a broad range of fluid conditions. This data is often unavailable from heat exchanger manufacturers.

3. CASE STUDIES

The model described above is used extensively by Calnetix to assess new applications as well as validate unit performance at specific operating conditions. The data tabulated below is from 4 distinct applications in the field. The applications are all commercial, utilizing generated power within the facility or exporting power to local utilities. The working fluid in these cases was R245fa refrigerant. The model output in general shows good agreement with field data. The Gross Efficiency is defined as the gross electrical power exported to the grid divided by the rate of heat is transferred to the working fluid.

Table 1: Saturated Steam Plant- Japan

	Model	Field data
Heat Source Temp (°C)	145	145
Heat Source Pressure (Bar)	1.95	1.8
Heat Source Flow Rate (kg/s)	0.35	0.35
Coolant Temperature (°C)	26	26
Coolant Pressure (Bar)	1.38	No Value
Turbine Inlet Temperature (°C)	122	119
Turbine Inlet Pressure (Bar)	16.4	15.5
Condenser Exit Temperature (°C)	29	29.5
Condenser Exit Pressure (Bar)	1.9	1.95
Gross Power Output (kW)	100.7	101
Gross Efficiency (%)	11.1	11.0

Table 2: Hot Water from an Incineration Plant- Japan

	Model	Field data
Heat Source Temp (°C)	98.7	98.7
Heat Source Pressure (Bar)	2.9	2.9
Heat Source Flow Rate (kg/s)	7.25	12.28
Coolant Temperature (°C)	20.2	20.2
Coolant Pressure (Bar)	1.4	1.4
Turbine Inlet Temperature (°C)	67.8	67.8
Turbine Inlet Pressure (Bar)	4.9	4.9
Condenser Exit Temperature (°C)	21	21
Condenser Exit Pressure (Bar)	1.47	1.47
Gross Power Output (kW)	100.8	124.7

Gross Efficiency (%)	7.0	6.7
----------------------	-----	-----

Table 3: Geothermal Low Pressure Steam- Japan

	Model	Field data
Heat Source Temp (°C)	125	128
Heat Source Pressure (Bar)	2.1	2.9
Heat Source Flow Rate (kg/s)	0.47	0.45
Coolant Temperature (°C)	25	24
Coolant Pressure (Bar)	1.3	1.5
Turbine Inlet Temperature (°C)	120	126
Turbine Inlet Pressure (Bar)	17.3	18.2
Condenser Exit Temperature (°C)	31.4	29.9
Condenser Exit Pressure (Bar)	2.06	1.99
Gross Power Output (kW)	125	125
Gross Efficiency (%)	12	12

Table 4: Flue Gas from Clay Factory Using Intermediate Oil Loop- Europe

	Model	Field data
Heat Source Temp (°C)	148	160
Heat Source Pressure (Bar)	7	No Value
Heat Source Flow Rate (kg/s)	20.8	20
Coolant Temperature (°C)	19	28
Coolant Pressure (Bar)	1	1
Turbine Inlet Temperature (°C)	128	130
Turbine Inlet Pressure (Bar)	18.7	18.6
Condenser Exit Temperature (°C)	25.7	30
Condenser Exit Pressure (Bar)	1.8	2.8
Gross Power Output (kW)	125	125
Gross Efficiency (%)	12.6	12.4

4. CONCLUSION

The development of an advanced thermodynamic model of an Organic Rankine Cycle was discussed. The model is implemented in Excel VBA script and uses Refprop as an equation of state. Each major component of the ORC is modeled in detail and combined together to form the completed system. The model obviates the need for complex and expensive process simulation tools, and delivers a highly accurate output. This affords a high degree of confidence to Calnetix and its customers when selecting balance of plant components and arriving at sensitive capital investment decisions.

NOMENCLATURE

α	turbine seal leakage	(%)
ϵ	roughness height	(m)
θ	swirl angle	(°)
η	efficiency	(%)
ξ	minor loss coefficient	(MPa-m ³ -s ² /kg ³)
ρ	density	(kg/m ³)
Φ	flow parameter	(m ²)
A	surface area	(m ²)
a	speed of sound	(m/s)
C	unit conversion constant	(J-s ² /kg-m ²)
c_p	specific heat	(J/kg-°C)

D	diameter	(m)
f	Darcy friction factor	(-)
G	volumetric flow rate	(m ³ /s)
g	gravitational constant	(m/s ²)
H	hydraulic head	(m)
h	specific enthalpy	(J/kg)
k	number of heat exchanger sections	(-)
L	length	(m)
MAP	value lookup table	(-)
\dot{m}	mass flow rate	(kg/s)
N	rotational speed	(RPM)
P	pressure	(MPa)
Q	heat	(Watts)
Re	Reynolds number	(-)
T	temperature	(°C)
U	overall heat transfer coefficient	(W/m ² -°C)
W	work	(Watts)

Subscript

*	static condition
amb	ambient
Cond	condenser
Evap	evaporator
Gen	generator
i	index integer
in	inlet condition
IPM	integrated power module
LMD	log mean difference
Loss	heat loss
out	outlet condition
PE	condition or item related to the power electronics
pipe	condition or item related to the pipe model
Ref	working fluid side of the condenser or evaporator
s	isentropic
Source	source side of the condenser or evaporator
T	condition or item related to the turbine
Windage	energy loss associated with windage

REFERENCES

Colebrook, C.F., 1939, "Turbulent flow in pipes, with particular reference to the transition region between smooth and rough pipe laws", *Journal of the ICE*, vol. 11, no. 4: P.133-156

Incropera, F.P., De-Witt, D.P., 2002, *Fundamentals of Heat and Mass Transfer* 5th ed., John Wiley & Sons, New York, 981p

Hawkins, L., Zhu, L., Blumber, E., Mirmobin, P., and Erdlac Jr., R., 2012, "Heat-To-Electricity with High-Speed Magnetic Bearing/Generator System", *2012 GRC Annual Meeting*

Norris R., Buckland F., Fitzroy N., General Electric Company Corporate Research and Development, 1970, *Heat Transfer and Fluid Flow Data Book*, G408.3, G408.5

Vrancik, J., 1968, "Prediction of Windage Power Loss in Alternators", National Aeronautics and Space Administration, TN D-4849

Yukse, E., Mirmobin P., 2015, "Electricity Generation from Large Marine Vessel Engine Jacket Water Heat", *ASME Power Energy 2015*

THERMAL EXPANSION AND STRUCTURAL BEHAVIOR OF A CLOSED LOOP THERMAL WIND TUNNEL FOR ORC FLUIDS

Maximilian Passmann, Karsten Hasselmann,
Felix Reinker, Stefan aus der Wiesche

Department of Mechanical Engineering
Muenster University of Applied Sciences,
48565 Steinfurt, Germany
e-mail: f.reinker@fh-muenster.de

ABSTRACT

The Organic Rankine Cycle (ORC) offers great potential for recovering waste heat and using low-temperature sources for power generation. However, the ORC thermal efficiency is limited by the relatively low temperature level, and therefore, designing ORC components with high efficiencies and minimized losses is of major importance. The use of organic fluids creates new challenges for turbine and component design, due to dense gas behavior and the low speed of sound leading to high Mach numbers.

Computational fluid dynamics (CFD) offers great potential for design and optimization of ORC components. But the employment of CFD methods requires careful validation by means of experimental data. For ORC components, such an experimental approach requires the use of specially designed wind tunnels for organic vapors.

The closed wind tunnel, presented in this contribution, is designed as a pressure vessel system to allow for pressure levels up to $p = 10$ bars and temperatures up to $\theta = 180^\circ\text{C}$. The investigation of heavy weight organic fluid flows at superheated state also needs for higher temperature levels. Heating and cooling units are therefore used to achieve steady state conditions inside of the test section.

In this contribution the design process of a closed loop wind tunnel is presented, focusing on the thermal expansion of the system. Thermal finite element method (FEM) analysis is applied to calculate temperature distributions, considering thermal loads and heat losses of the facility. Based on these data, linear FEM analysis is used to investigate thermal stress in the closed loop vessel system. Supporting points and critical zones are assessed in a more detailed analysis. A method to analyse the transient behavior of the structure and to determine allowable heating rates during heat-up phase is presented.

The testing facility is part of a large research project aiming at obtaining loss correlations for performance predictions of ORC turbines and processes, which is supported by the German Ministry for Education and Research (BMBF).

1. INTRODUCTION

The Organic Rankine Cycle represents a viable technical approach for conversion of low temperature sources, like waste heat or geothermal reservoirs, to electricity or to combined electricity and heat. An ORC process consists of a Rankine cycle employing an organic compound as working fluid. This technology is usually preferred over steam cycles, due to the higher thermodynamic cycle efficiency, in case of low-grade heat sources [1, 4, 9]. The design and performance prediction of steam and gas turbines have been initially based on measurements and numerical simulations of flow through two-dimensional cascades of blades [5]. In case of ORC turbines and related fluids, such an approach requires the use of specially designed wind tunnels and dedicated instrumentation. The Laboratory for Thermal and Power Engineering of Muenster University of Applied Sciences, Germany is building up

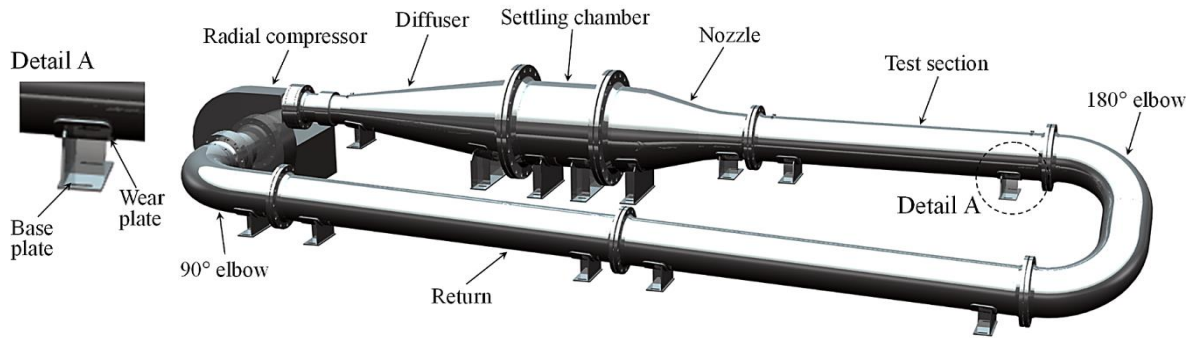


Figure 1: 3D model of the closed circuit wind tunnel for ORC fluids.

a closed loop wind tunnel for investigating real gas effects in dense gas flows of organic vapors in nozzles and axial turbine blades.

The basic test section, as shown in Fig. 1, acts as a barrel-type casing allowing for different inserted test sections like simple nozzle geometries or axial turbine blade test sections. The maximum Mach number upstream the blade section will lie in the transonic region ($M = 1$). Shadow schlieren visualization utilizing a high speed camera will be used for qualitative flow characterization in the test section. For local flow field investigation Laser Doppler Anemometry will be used. Besides optical measurements, classical pneumatic measurement techniques will also be performed, as for instance to measure the pressure field alongside the nozzle axis.

Subject of the present contribution is the examination of thermal expansion and structural behavior of the facility by means of structural and thermal linear finite element analysis. Fig. 1 shows a 3D model of the closed circuit wind tunnel in its current development status. To allow for operating conditions of up to $p = 10$ bars internal pressure at $\theta = 180^\circ\text{C}$, all pressurized components are laid out according to pressure rating PN16 [13]. The support saddles (cf. Fig. 1, detail A) are designed on the basis of DIN 28080 [6] with a wall thickness of 10 mm for the wear plate and 8 mm for all other components. The entire unit rests on a rigid steel subframe (not shown in Fig. 1). The saddle base plates act as bearing areas. Sliding plates will be installed between subframe and base plates, to reduce friction forces and to avoid thermal bridging to the ground.

The dimensions of the wind tunnel are approximately 7200 mm in length and 1600 mm in width. The 180° elbow is angled at 30° , resulting in a maximum level difference of 610 mm between test section and return. An overview of the dimensions is given in Tab. 1.

The first part of this paper focuses on the overall bearing concept of the unit, taking into account thermal and structural influences. A simplified shell model is used to investigate three different bearing concepts under steady-state conditions. In the second part, temperature distribution and thermal stress, occurring during heat-up phase, will be addressed based on the example of the settling chamber.

Table 1: Dimensions of the closed circuit wind tunnel for ORC fluids.

Component	Length	Midsurface diameter		Wall thickness
	l [mm]	d_{min} [mm]	d_{mout} [mm]	s [mm]
Diffuser	1745	216.1	601.2	8.8
Settling chamber	690		601.2	8.8
Nozzle	1073	601.2	318.5	8.8
Test section	2067		318.5	7.1
Return	5454.3		318.5	7.1
	Radius	Midsurface diameter	Length in x-direction	Length in y-direction
	r [mm]	d_m [mm]	l_x [mm]	l_y [mm]
90° elbow	486	318.5	648	486
180° elbow	486	318.5	1221	564

2. FINITE ELEMENT ANALYSIS OF THE STATIC SHELL MODEL

2.1 Finite Element Model

Linear finite element analysis utilizing NX Nastran version 8.5 (SOL101) [10] is used to investigate expansion and stress distribution resulting from both, thermal and structural loads under steady-state conditions. Based on the 3D solid model of the wind tunnel, as depicted in Fig. 1, a midsurface model was generated. Mapped meshing was utilized to mesh the midsurface with 8-noded shell elements (CQUAD8). For singly curved shells like cylinders this element type performs better than the 4-noded CQUAD4 element [10]. The coordinate system and calculated stresses for this type of element are shown in Fig. 2. CQUAD8 elements are isoparametric with four corner and four mid-side grid points. Stresses, as shown in Fig. 2, are evaluated at the centroid and at the vertices. For plane strain analysis the von Mises equivalent stress σ_{VFEM} is defined by:

$$\sigma_{VFEM} = \sqrt{\frac{1}{2} \cdot [(\sigma_x - \sigma_y)^2 + (\sigma_y - \sigma_z)^2 + (\sigma_z - \sigma_x)^2] + 3 \cdot \tau_{xy}^2} \quad (1)$$

with the stress component in z-direction being $\sigma_z = 0$. A thorough description of the finite element method and theoretical backgrounds concerning shell elements can be found in [3].

Multiple mesh collectors were generated, to account for different wall thicknesses and materials in pipe sections and support saddles. The meshed model is shown in Fig. 3. The pressure vessel is made from high-alloy austenitic steel (X5CrNi18-10), whereas the support saddles are made from construction steel. For both materials all physical and mechanical properties were implemented into NX as temperature dependent values [12]. Typical values are given in Section 2.2.

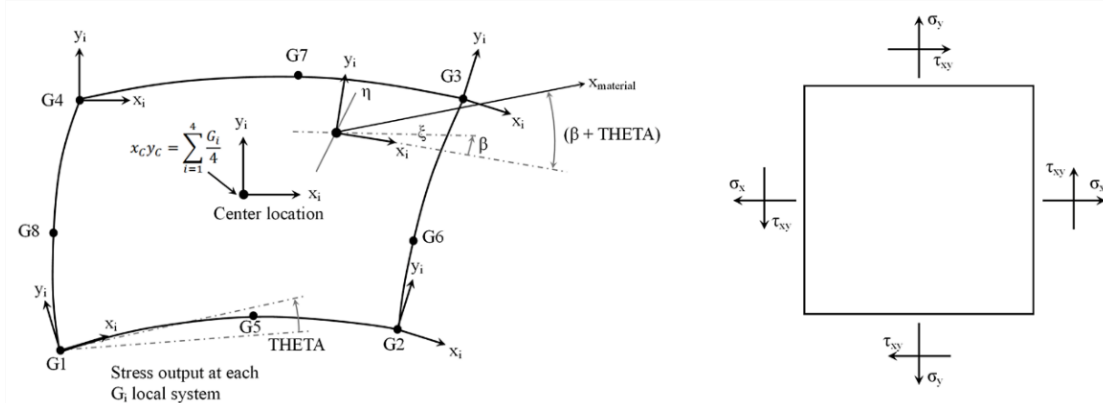


Figure 2: CQUAD8 coordinate system and stresses in shell elements.

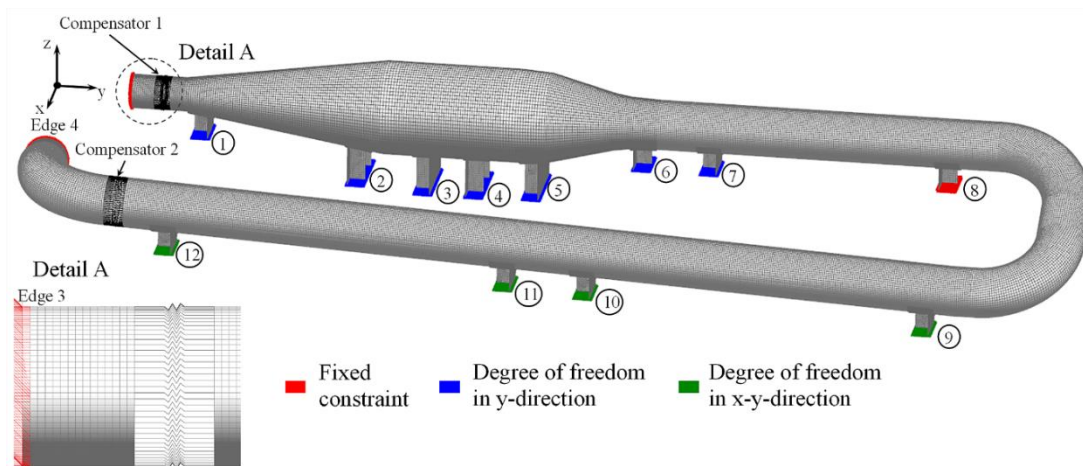


Figure 3: Meshed finite element shell model with boundary conditions.

The two axial compensators were modeled with elastic 1D elements (CELAS) which behave like simple extension or compression springs (cf. Fig. 3, detail A). The axial spring stiffness for compensator 1 and 2 were assumed as $k = 257 \text{ N/mm}$ and $k = 705 \text{ N/mm}$ respectively.

A surface-to-surface glue constraint was applied to connect each wear plate of the saddle to the pressure vessel. Glue constraints allow to join dissimilar meshes by creating weld-like connections, preventing relative motion in all directions between the glued surfaces. At the same time, displacements and loads are transferred correctly, resulting in an accurate strain and stress condition between glued surfaces [10].

The boundary conditions were modeled according to Fig. 3. All nodes on edge 3 and 4 representing the connection between pressure vessel and radial compressor were fixed, as was the lower face of the base plate of saddle 8. Support saddles 1 to 7 act as movable bearing points with a single degree of freedom (DOF) in x-direction at the lower face of the saddle base plates. For the remaining saddles 9 to 12 the base plates were fixed in all degrees of freedom but in x- and y-direction. This concept was modified later on as described in Section 2.3. The entire vessel was loaded with $p = 10 \text{ bars}$ internal pressure and a temperature of $\theta = 180 \text{ }^\circ\text{C}$.

2.2 Material Properties

Two materials were used in the simulation. The pressure vessel whose inner surface is in contact with the organic fluid is made from X5CrNi18-10. The support saddles are made from construction steel. The temperature dependency of mechanical and physical properties are taken into account in the finite element model. Typical values for both materials at $\theta = 20^\circ\text{C}$ and $\theta = 180^\circ\text{C}$ are given in Tab. 2.

The decisive strength parameter for both X5CrNi18-10 and construction steel is the yield strength $R_{p0.2}$ which is depicted in Fig. 4 as function of temperature θ . Especially in the case of X5CrNi18-10, the operating temperature of $\theta = 180^\circ\text{C}$ leads to a significant decrease in strength, resulting in a value of $R_{p0.2} = 131 \text{ N/mm}^2$ compared to a nominal value of $R_{p0.2} = 190 \text{ N/mm}^2$ at $\theta = 20^\circ\text{C}$.

Table 2: Mechanical and physical properties of construction steel and X5CrNi18-10 at $\theta = 20^\circ\text{C}$ and $\theta = 180^\circ\text{C}$.

Material	Temperature	Density	Young's module	Yield strength	Coefficient of linear expansion
	θ				
	[$^\circ\text{C}$]				
Construction steel	20	7830	207000	140	11
	180	7830	207000	134	12.3
X5Cr-Ni18-10	20	7900	200000	190	16
	180	7900	186000	131	17

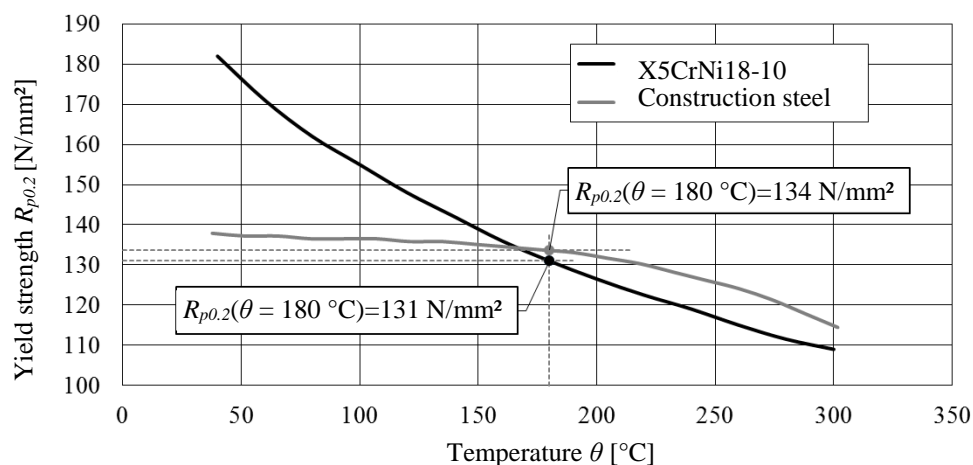


Figure 4: Temperature dependency of yield strength $R_{p0.2}$ for construction steel and X5CrNi18-10.

2.3 Results of the Static Shell Model

The decisive strength parameter for evaluating the results is the allowable stress at design temperature σ_{aDT} , with the yield strength $R_{p0.2}$ at design temperature and the safety factor $S = 1.5$ according to [13]:

$$\sigma_{aDT} = \frac{R_{p0.2}}{S}. \quad (2)$$

For the given temperature of $\theta = 180^\circ\text{C}$ the allowable stress for X5CrNi18-10 results in a value of approximately $\sigma_{aDT} = 90 \text{ N/mm}^2$. One-dimensional thermal expansion can be estimated for a given temperature difference $\Delta\theta$, thermal expansion coefficient α , and geometric dimension l from [8]:

$$\Delta l = \alpha \cdot l \cdot \Delta\theta \quad (3)$$

with values for α according to Tab. 2 and dimension l according to Tab. 1.

Three different bearing-concepts were investigated (cf. Tab. 3). Starting point for the calculations was concept a) as shown in Fig. 3. The position of saddles 8, 9 and 13 are shown in Fig. 6. For concepts a) and b) only saddles 8 and 9 were considered. In concept c) an additional saddle 13 was added in front of the 90° elbow.

Fig. 5 shows the effects of temperature, pressure and the combination of both on nodal displacements. The basis for this calculation is concept a). In the first step, only a temperature load of $\theta = 180^\circ\text{C}$ was applied to the structure (cf. Fig. 5, left side). The resulting displacements in x- and y-direction are consistent with analytical values calculated from Eq. 3. In the second step, only an internal pressure load of $p = 10 \text{ bars}$ was applied to all pressurized parts (cf. Fig. 5, in the middle). The resulting radial stresses in the test section, diffuser, settling chamber, and nozzle compare well to the analytical values derived from standard equations as found for instance in [8, 13]. However, the major effect of the pressure load is the tendency to bend up the 180° elbow. This movement is allowed due to the fact that saddles 9 to 12 of the return section have DOFs in x- and y- direction, while saddle 8 of the test section is fixed. Therefore, the axial compensator of the return section with its low spring stiffness of $k = 705 \text{ N/mm}$ offers little resistance and acts as an extension spring. The resulting maximum displacements in the 180° elbow lie in the order of 20 mm.

In a final step the combination of temperature and pressure loads were considered (cf. Fig. 5, right side). Both individual influences can be superimposed [11]. While the tendency to straighten up the 180° elbow remains, the expansion of the axial compensator is substantially reduced. This can be attributed to the fact that the displacement of the return section, resulting from the thermal load, is in reverse direction to the displacement caused by internal pressure. The main portion of the resulting strain can be attributed to the effect of pressure. High values of strain can result in critical stress values especially in the area of the 180° elbow. Fig. 6 shows displacement and resulting stress values for different bearing concepts. For each of the three evaluated concepts the bearing concept was gradually modified to optimize strain and stress distribution. Each time the structure was loaded with a temperature of $\theta = 180^\circ\text{C}$ and internal pressure of $p = 10 \text{ bars}$. Average and maximum stress values for 180° elbow, return, 90° elbow, and test section are shown in Fig. 7.

Table 3: Bearing concepts for the static shell model.

Saddle	8	9	13
	Degree of freedom (DOF)		
Concept a)	fixed	x-y	-
Concept b)	fixed	x	-
Concept c)	fixed	x	x

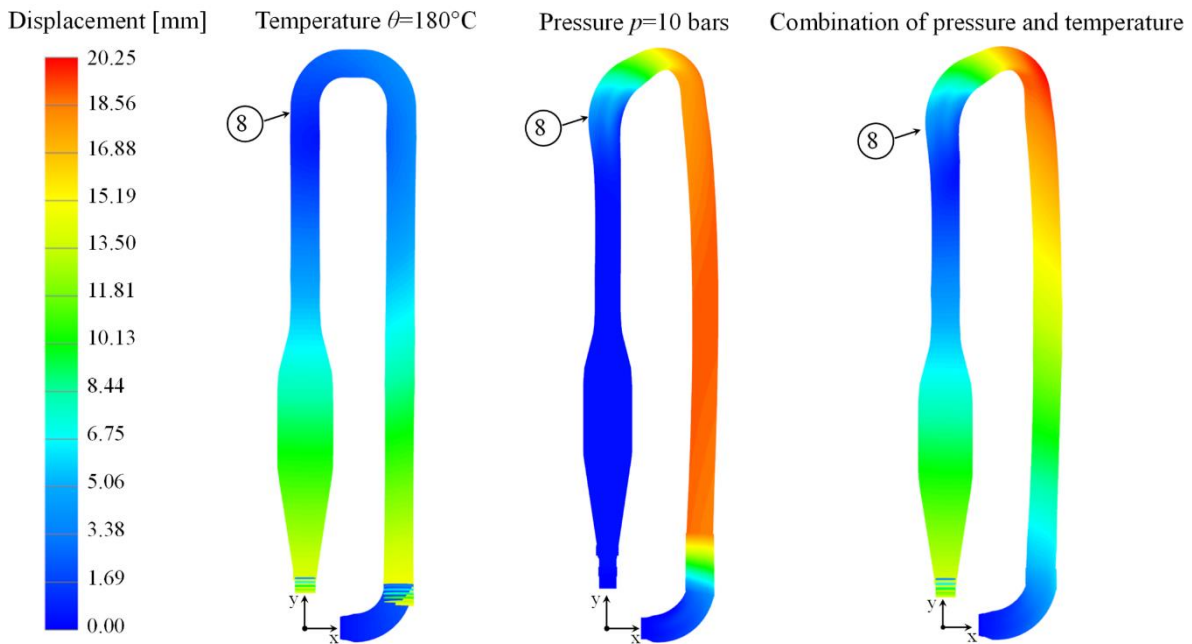


Figure 5: Effect of temperature and pressure on displacement for the basic model as shown in Figure 3.

For concept a) saddle 8 at the end of the test section was fixed. All saddles at the return section have DOFs in x- and y- direction. The results are high values of stress in the 180° elbow, test section and return. The maximum stress values in all four sections exceed the allowable stress of $\sigma_V = 90 \text{ N/mm}^2$ by a factor of 1.3 up to 2.4. For concept b) saddle 9 in addition to saddle 8 was fixed in y-direction to prevent the tendency to straighten up the 180° elbow, allowing only for movement in x-direction. As a result, average and maximum stress values found in the 180° elbow, test section and return are greatly reduced and lie below the allowable stress level. With a maximum of $\sigma_V = 144 \text{ N/mm}^2$ in the 90° elbow, concept b) still leads to an overloading of this section. Therefore, saddle 13 was added for concept c). By locking the DOF in y-direction, the reaction force of the axial compensator is no longer affecting the 90° elbow but is absorbed by the saddle. The resulting maximum stress of $\sigma_V = 79.7 \text{ N/mm}^2$ was almost halved compared to the $\sigma_V = 144.4 \text{ N/mm}^2$ from concept b).

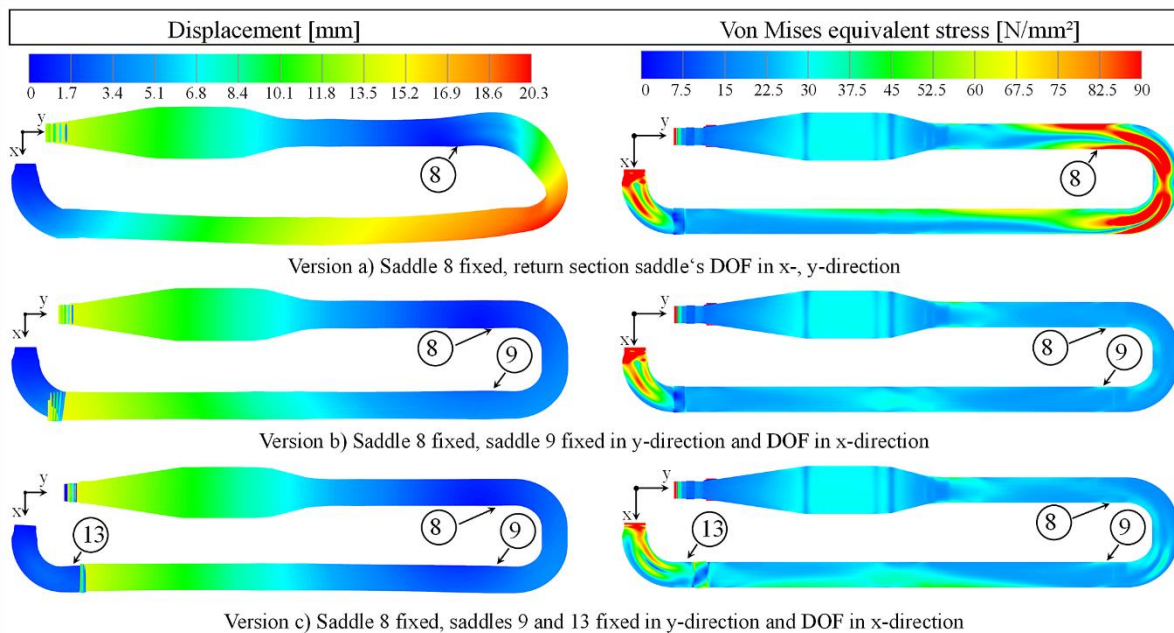


Figure 6: Effect of different bearing-concepts on displacement and von Mises stress.

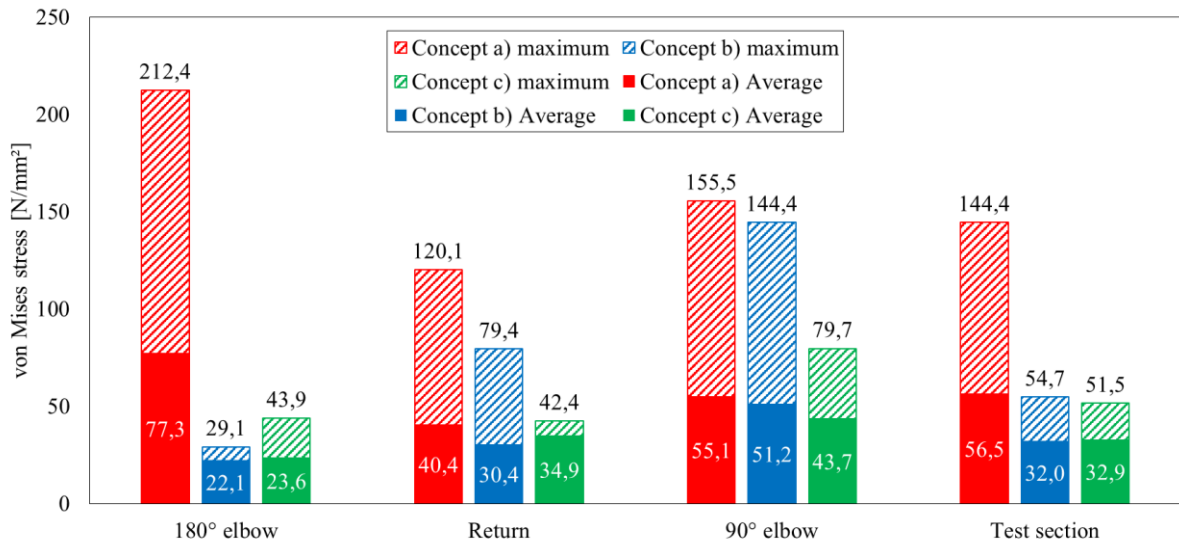


Figure 7: Maximum and average von Mises equivalent stress for concepts a), b) and c).

3. TRANSIENT ANALYSIS

During the start-up process, thick-walled parts and areas of high material accumulation lead to significant temperature differences within the material. The resulting thermal strain evokes high residual stress states [11]. In general, thermal stresses are directly proportional to the temperature difference ($\theta_i - \theta_m$) of a local temperature θ_i to the average wall temperature θ_m . Thermal stresses are also known to be proportional to the square of the wall thickness. Therefore, thick-walled components usually determine allowable heating and load change rates [11]. Thermal expansion and resulting thermal stresses during heat-up phase were investigated using the example of the settling chamber, which was assumed to be critical due to its massive flanges.

Analytical methods for estimating the maximum temperature differences and resulting thermal stresses exist for simple geometries like spheres, cylinders or plates [2, 11]. Applying the procedure given by [2], the progression of the wall temperature difference ($\theta_i - \theta_m$) in a plate, resulting from a sudden temperature change, was plotted over a period of two hours (cf. Fig. 8). According to Fig. 8, the maximum temperature difference hence the maximum thermal stress in a plate will occur within the first 30 minutes. Assuming a similar transient behavior for the settling chamber, the following investigations were confined to a time frame of 60 minutes.

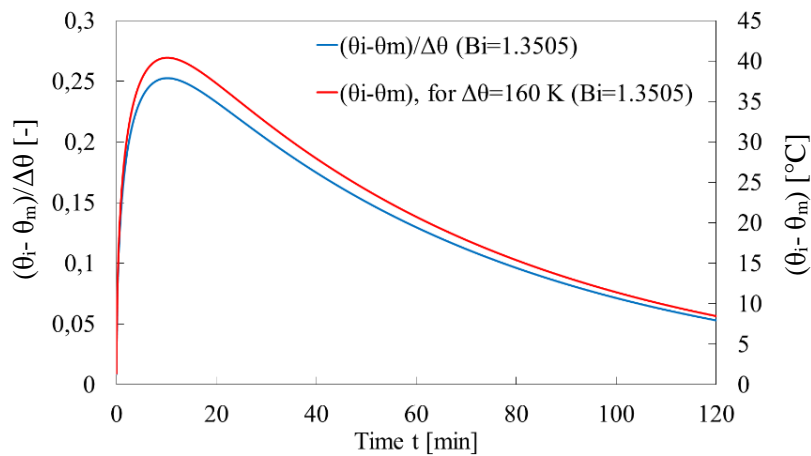


Figure 8: Wall temperature difference over time for a sudden temperature change in a plate.

3.1 Finite Element Model for Transient Analysis

In the First step, a thermal finite element model was built, which provided the temperature distribution throughout the structure. This was achieved using the NX Thermal solver in advanced transient settings [7]. In an interim step, a mapping solution mapped the nodal temperatures to the structural model, which in turn provided strain and stress distribution. For the structural computations linear finite element analysis utilizing NX Nastran (SOL 101) was used. Symmetry to the y-z-plane was exploited for all models to reduce computing time.

The thermal model, as shown in Fig. 9 on the left hand side, was meshed with 4-noded tetrahedral elements. As the whole structure will be insulated with a layer of mineral wool, a solid body of 100 mm thickness was added. The introduction of heat into the structure will be achieved by electric heating sleeves applied to the pressure vessel. A thermal load was applied to the outer surface of the pressure vessel to model the heating sleeves (cf. Fig. 9, Detail A), assuming the thermal resistance between heating sleeves and pressure vessel to be negligibly small. The thermal load is regulated by a PID controller with a specified target temperature of $\theta = 180^\circ\text{C}$. A number of elements from the mesh of the pressure vessel were chosen as sensors for the controller. Natural convection at the outer surface of insulation and saddle was added utilizing built in correlations provided by NX for cylinder, horizontal and vertical plate. The assumed ambient temperature is $\theta = 22^\circ\text{C}$. As the pressure vessel will be under vacuum during the start-up process, the inner surface of the vessel is adiabatic in this model.

The structural model was meshed utilizing mapped meshing with 20-noded hexahedral elements. Mesh refinement was carried out in the area of the pressure vessel, to ensure 4 element layers across the wall thickness. The bended wear plate of the saddle was meshed with 10-noded tetrahedral elements. In the symmetry y-z-plane a symmetrical constraint was applied (DOF in y- and z-direction). At the right end of the model the raised surface of the flange (flange gasket contact area) was fixed. The cross section of the pressure vessel at the left end was elastically supported by grounded springs. The springs represent the axial compensator with a spring stiffness of $k = 257 \text{ N/mm}$.

For the pressure vessel and saddle the same materials as described in Section 2.1 were used. The thermal model additionally contains the insulation layer. A material file was generated using physical properties of mineral wool assuming isotropic material behavior. Mineral wool possesses an average thermal conductivity of $\lambda = 0.05 \text{ W/(m}\cdot\text{K)}$, a density of $\rho = 100 \text{ kg/m}^3$ and a specific heat capacity of $c_p = 0.84 \text{ kJ/(kg}\cdot\text{K)}$ [12].

3.2 Results of the Transient Analysis

Temperature distribution and thermal stress were evaluated for two different configurations over a period of 60 minutes. For configuration a) a thermal load of $\dot{q} = 2500 \text{ W/m}^2$ was applied to the outer surface of the pressure vessel as described in Section 3.1. For configuration b) the thermal load was split up into two

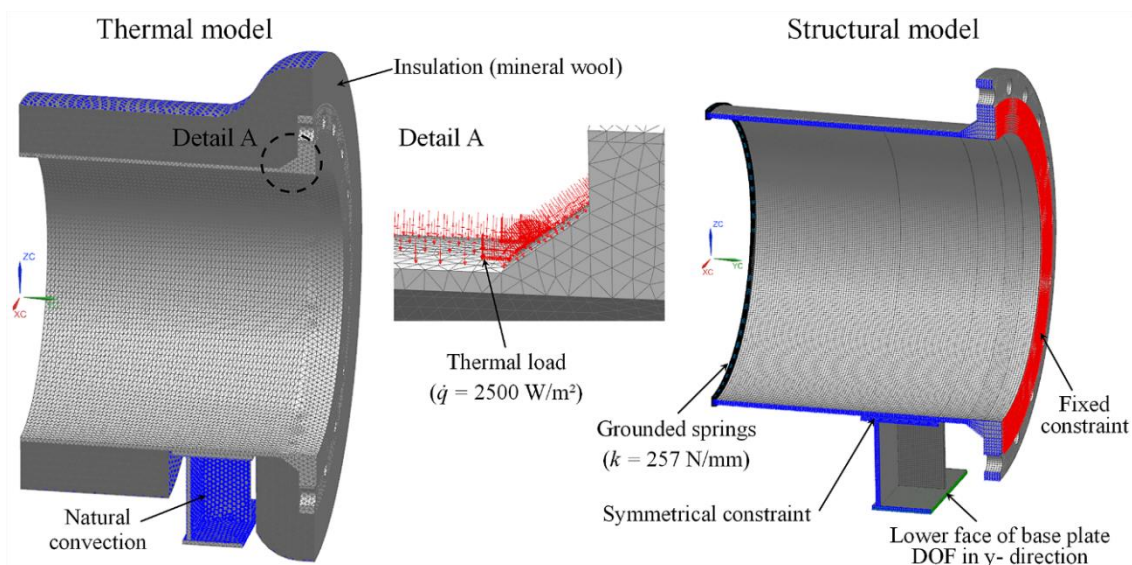


Figure 9: Meshed thermal and structural finite element model of settling chamber.

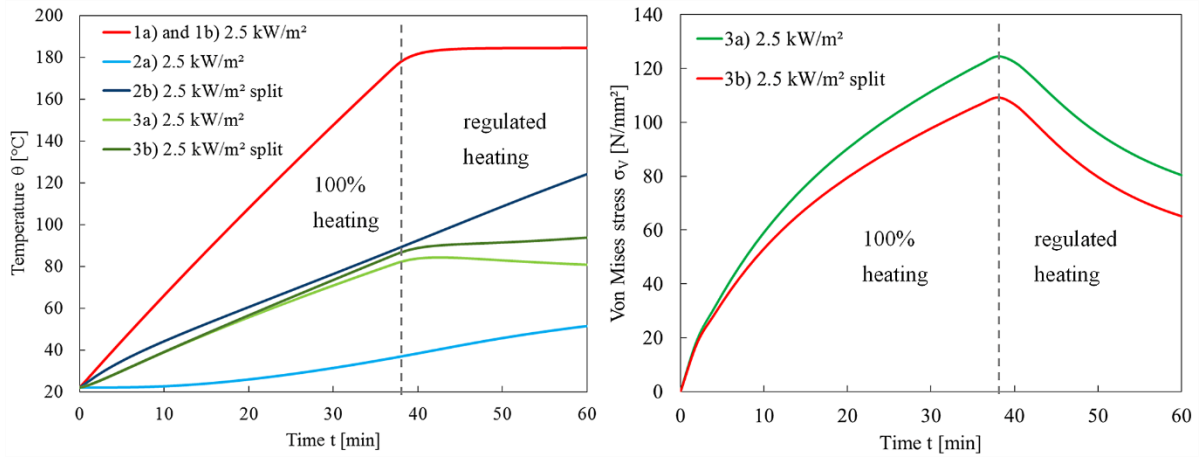


Figure 10: Development of temperature θ and von Mises stress σ_v over the first hour during heat-up phase for a thermal load of $\dot{q} = 2500 \text{ W/m}^2$ at different structural points.

areas. The first load was defined for the pressure vessel itself, whereas the second one only covered the surface area of the flange. The weld, joining pressure vessel and flange, was chosen as the parting line between the two areas. In this configuration each thermal load had its own PID controller assigned to it.

The development of temperature θ and von Mises stress σ_v within the first hour for a thermal load of $\dot{q} = 2500 \text{ W/m}^2$ is shown in Fig. 10. The positions of the points 1) to 3) are illustrated in Fig. 11. In the thin walled pressure vessel, represented by points 1a) and 1b), the temperature curve is identical for both configurations. After approximately 40 minutes this area has reached its target temperature of $\theta = 180^\circ\text{C}$. After that the PID controller reduces the thermal load to maintain the target temperature. A similar behavior can be observed for points 3a) and 3b).

The maximum stress values occur in the areas of the weld seam, joining pressure vessel and flange, and the weld seam, joining pressure vessel and saddle. As becomes evident from Fig. 10 (right hand side), configurations a) and b) both yield failure critical stress values of up to $\sigma_v = 123 \text{ N/mm}^2$. However, by splitting up the thermal load and defining two separate areas a more uniform temperature distribution in vessel and flange can be achieved resulting in lower thermal stress values.

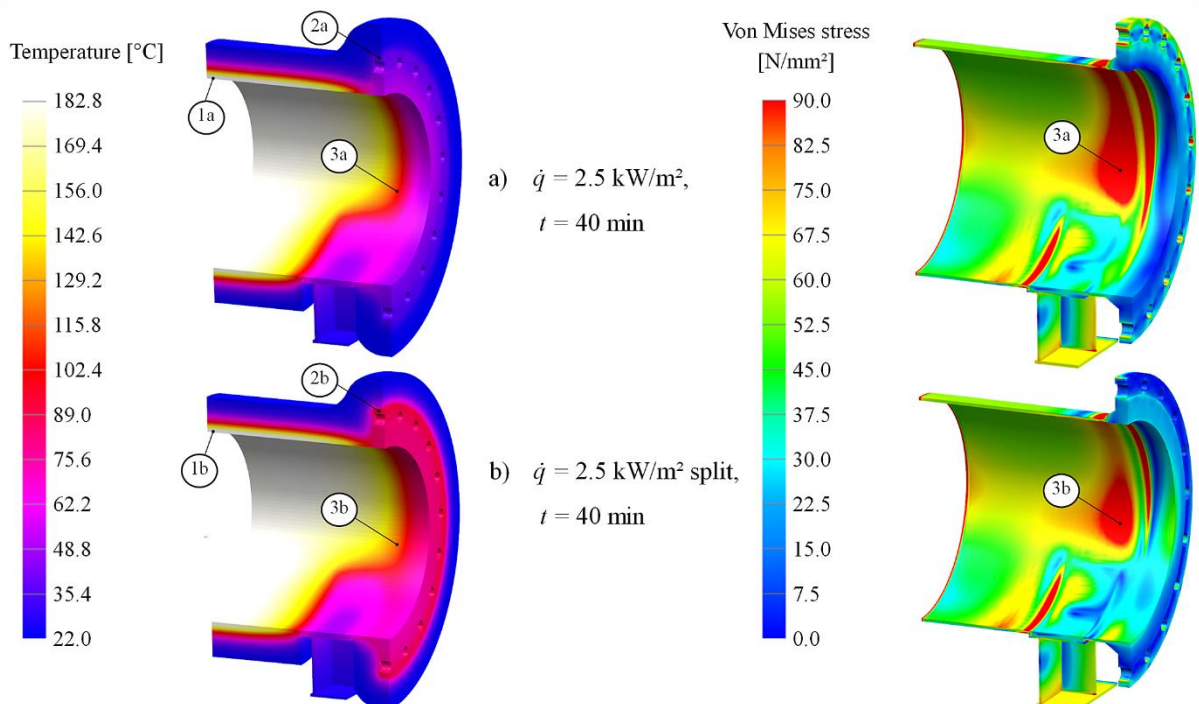


Figure 11: Temperature θ and von Mises stress σ_v distribution at $t = 40 \text{ min}$ for a thermal load of $\dot{q} = 2500 \text{ W/m}^2$.

4. CONCLUDING COMMENTS

This paper describes a method to design and analyse the bearing concept of a closed wind tunnel for organic fluids by means of linear finite element analysis. A simplified shell model was built up and three different concepts were considered. The basic impacts of temperature and pressure loads were identified. Based on these findings an optimized bearing concept, leading to an equal strain and stress distribution, was developed.

Temperature distribution and thermal stress during heat-up phase were investigated using combined thermal and structural finite element analysis. The thermal model provided transient temperature distributions, which were used to calculate thermal stresses. A method was presented to reduce these thermal stresses by way of achieving a uniform temperature distribution throughout the structure. As the resulting stress values presented in this paper are still above the critical yield strength, further investigations are needed. This includes the determination of permitted heating rates, the ideal configuration of the heating sleeves and their individual regulation.

5. NOMENCLATURE

c_p	Specific heat capacity	$\text{kJ}/(\text{kg}\cdot\text{K})$
d_m	Midsurface diameter	mm
E	Young's modulus	N/mm^2
k	Spring stiffness	N/mm
l	Length	mm
\dot{q}	Heat flux	W/m^2
r	Radius	mm
$R_{p0.2}$	0.2%-yield strength	N/mm^2
s	Wall thickness	mm
t	Time	s
α	Coefficient of linear expansion	$1/\text{K}$
θ	Temperature	K
ρ	Density	kg/m^3
σ_v	Von Mises equivalent stress	N/mm^2
τ	Shear stress	N/mm^2

6. REFERENCES

- [1] Adam, A. W., ed., 1995. *Organic Rankine Cycles. Encyclopedia of Energy Technology and the Environment*, John Wiley & Sons, New York, 3024 p.
- [2] Baehr, H.D., Stephan, K., 2013. *Wärme- und Stoffübertragung*, Springer, Berlin, Heidelberg, 804 p.
- [3] Bathe, K.J., 2002. *Finite Elemente Methode*, Springer, Berlin, Heidelberg, 1253 p.
- [4] Chen, H., Goswami, D. Y., and Stefanakos, E. K., 2010. *A review of thermodynamic cycles and working fluids for the conversion of low-grade heat*, Renewable and Sustainable Energy Reviews, 14(9), pp. 3059-3067.
- [5] Dixon, S. L., 1998. *Fluid mechanics and thermodynamics of turbomachinery*, Butterworth-Heinemann, Boston, 556 p.
- [6] German Institute for Standardization, 2003. *DIN 28080:2003-08, Saddle supports for horizontal apparatus - Dimensions*, Berlin, 12 p.
- [7] Maya Heat Transfer Technologies Ltd., 2012. *NX Thermal Reference manual*, 544 p.
- [8] Scholz, G., 2012. *Rohrleitungs- und Apparatebau*, Springer, Berlin, Heidelberg, 411 p.
- [9] Schuster, A., Karellas, S., Kakaras, E., and Spliethoff, H., 2009. *Energetic and economic investigation of organic rankine cycle applications*, Applied Thermal Engineering, 29(8-9), pp. 1809-1817.
- [10] Siemens Product Lifecycle Management Software Inc., 2012. *NX Reference manual*.
- [11] Strauß, K., 2009. *Kraftwerkstechnik*, Springer, Berlin, Heidelberg, 522 p.
- [12] VDI e.V., ed., 2013. *VDI-Wärmeatlas*, Springer, Berlin, Heidelberg, 1760 p.
- [13] Verband der TÜV e.V., ed., 2006. *AD 2000 - Regelwerk*, Carl Heymanns Verlag, Berlin, 796 p.

ANALYSIS OF PURE FLUID AND ZEOTROPIC MIXTURES USED IN LOW-TEMPERATURE REHEATING ORGANIC RANKINE CYCLES FOR POWER GENERATION

Changwei Liu¹, Tieyu Gao^{2*}, Jiamin Xu³, Jiangnan Zhu⁴, Xun Xu⁵

¹School of Energy and Power Engineering, Xi'an Jiaotong University
Xi'an, Shaanxi, P.R.China
876180495@qq.com

²School of Energy and Power Engineering, Xi'an Jiaotong University
Xi'an, Shaanxi, P.R.China
sunmoon@mail.xjtu.edu.cn

³School of Energy and Power Engineering, Xi'an Jiaotong University
Xi'an, Shaanxi, P.R.China
88342276@qq.com

⁴School of Energy and Power Engineering, Xi'an Jiaotong University
Xi'an, Shaanxi, P.R.China
zhujiangnan1234@126.com

⁵School of Energy and Power Engineering, Xi'an Jiaotong University
Xi'an, Shaanxi, P.R.China
402270702@qq.com

ABSTRACT

The shortage of fossil energy sources boosts the development and utilization of renewable energy. Among various novel techniques, recovering energy from low-grade heat sources including industrial waste heat, geothermal energy and solar energy through power generation via organic Rankine cycle (ORC) has been one of the focuses. ORC is one of the effective methods to recover low-grade heat, which makes use of environment-friendly organics as working fluids, and low temperature thermal energy as the driving energy. Investigations have indicated that reheating ORC can improve the thermal performance of the system. In this paper, the cycle performance is measured by the system net power output. By using pure fluid R245fa, R123 and zeotropic mixtures R245fa/R21, R123/R21, R245fa/R123 as the cycle working fluids, the influences of working fluid, mixtures component ratio and reheat pressure ratio on low-temperature reheating ORC system are investigated. The optimal reheat pressure ratios of reheating ORC system using different working fluids are obtained. In addition, zeotropic mixtures R245fa/R21(0.65/0.35) is superior in the improvement of the system net power output. In practical application, the optimal reheat pressure ratio and component ratio should be determined based on the mixture and evaporation temperature to ensure the net power output of reheating ORC system maximum.

1. INTRODUCTION

As the world's energy situation becomes aggravate, the recovery of low-temperature heat sources has become one of the research focuses. Due to the fact that conventional steam Rankine cycle does not allow efficient energy conversion at low temperatures, organic Rankine cycle (ORC) has been extensively studied for the conversion of low-grade heat into power for its simplicity and relatively high efficiency (Chen *et al.*, 2011).

Recently, some researchers have studied the reheating ORC system. Li *et al.* (2102) investigated the net power output and thermal efficiency of pure R245fa in reheating ORC system aiming at low-temperature heat source below 120°C. Xu *et al.* (2009) proposed a determination method for optimal reheating pressure of ORC system using R123 as working fluid, which could ensure a highest system efficiency. Li *et al.* (2013) studied the low-temperature heat source utilization of reheating ORC systems using different working fluids, then gained the variation regularity of the net power output and thermal efficiency with evaporation temperature and reheat pressure ratio. Wang *et al.* (2013) chose R601 and R245ca as the working fluids and investigated the influence of the reheat pressure ratio on the net power output, thermal efficiency and exergy efficiency of the system, then obtained the optimal reheat pressure ratios.

In order to improve the efficiency of ORC system, using mixtures has become an important method (Zheng *et al.*, 2008). The temperature glide of zeotropic mixture in phase transformation zone can provide a good temperature matching of cold and heat fluids for heat-exchanges, which could reduce the irreversible entropy production caused by the heat transfer temperature difference (Maizza *et al.*, 2001). Wang *et al.* (2010) compared low-temperature solar ORC systems using pure fluid and zeotropic mixture as the working fluid by experiments, and the results showed that using zeotropic mixture as working fluid could improve both output work and exergy efficiency of the system. Angelino *et al.* (1998) calculated performance of waste heat recovery ORC system and geothermal power generation ORC system using mixtures as working fluids which were composed of silicone oil and different hydrocarbon by the PRSV state equation and WS mixing rule. The results indicated that cycle performance was closely relative to the component ratio of mixtures, so the component ratio must be optimized when mixture was used.

Above studies indicate that reheating process and zeotropic mixtures can both effectively improve the thermodynamic performance of ORC system. At present, very few studies on low temperature reheating ORC system for power generation using zeotropic mixtures are reported, and the optimal component ratio of zeotropic mixtures has not been fully studied. In this paper, influences of zeotropic mixtures' kind and component ratio, as well as the reheating pressure ratio on the net power output of reheating ORC system are investigated. The results show that zeotropic mixtures can effectively improve the net power output of reheating ORC system when the mixture's kind and component ratio are suitable.

2. ANALYSIS OF REHEATING ORC SYSTEM AND SELECTION OF WORKING FLUIDS

2.1 Reheating ORC System

Compared with the simple ORC system, Reheating ORC system includes a high pressure expander and a low pressure expander instead of a single expander. A reheating ORC system includes evaporator, high pressure turbine 1, reheater, low pressure turbine 2, condenser and pump, as shown in Figure 1. The circulation specifically include the following processes:

5-6: Adiabatic compression process. The saturated liquid working fluid is compressed adiabatically into high pressure unsaturated liquid in pump, then enters evaporator.

6-1: Isobaric heating process. High pressure unsaturated liquid is heated into high temperature and high pressure saturated vapor by absorbing heat of the low-temperature heat source in evaporator, then enters high pressure turbine 1.

1-2: Adiabatic expansion process. Saturated vapor expands in high pressure turbine 1 to do work and generate electricity, and the pressure and temperature of working fluid drop, then enters the reheat.

2-3: Isobaric heating process. Vapor is heated in reheater, and its temperature increases to the same value of that of state 1, then enters low pressure turbine 2.

3-4: Adiabatic expansion process. Vapor expands in low pressure turbine 2 to do work, then becomes low temperature and low pressure superheated vapor.

4-1: Isobaric condensation process. Vapor is condensed into saturated liquid by heat exchange with cooling water in condenser.

In this paper the system is in a stable flow state, and no heat exchange occurs between each thermal device and the environment. The pressure losses of evaporator, reheater, condenser and the connecting pipes are negligible. The working fluid at outlet of the condenser is saturated liquid while the working fluid at outlet of the evaporator is saturated vapor. The tephigram of reheating ORC system is shown in Figure 2.

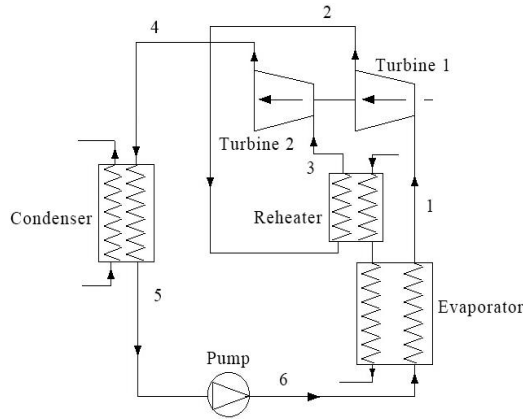


Figure 1: Reheating ORC system

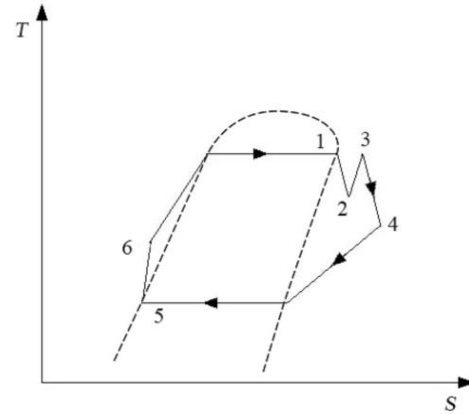


Figure 2: Tephigram of reheating ORC system

2.2 The Choice of Working Fluids

Studies of simple ORC system show that choice of the working fluid has an important influence on the system thermal performance (Ni *et al.*, 2013). The working fluid should have superior stability, good environmental protection and excellent thermal physical properties which match well with heat source (Maizza *et al.*, 1996). Drying and wetting of working fluid is an important feature in low grade heat source ORC system, which is determined by the slope of saturated vapor line in the tephigram. The slope of dry working fluid is greater than zero while the slope of wet working fluid is lower than zero, and the slope of isentropic fluid is close to zero. High temperature and high pressure vapor of dry working fluid and isentropic working fluid becomes superheated vapor after expanding in turbine, thus there is no droplet appearing in the process (Gu *et al.*, 2008).

Table 1: Thermophysics property parameters of working fluids.

Working Fluid	Molecular Weight /kg mol ⁻¹	Standard Boiling Point /K	Critical Temperature /K	Critical Pressure /Mpa	ODP	GWP (100 Years)
R21	102.92	282.01	451.48	5.1812	0.04	151
R245fa	134.05	288.29	427.16	3.6510	0	1050
R123	152.93	300.97	550.0	3.6618	0.01	77

R21, R123 and R245fa are common working fluids used in ORC system, and the values of ODP (Ozone Depression Potential) and GWP (Global Warming Potential) of the three fluids are relatively small, which means they are eco-friendly (Gu *et al.*, 2007). Thermophysics property parameters of three pure working fluids are shown in Table 1 (Calm *et al.*, 2011). Using R245fa/R21 as working fluid could effectively improve the net power output of the ORC system (Li *et al.*, 2012). Therefore, we select R21, R123, R245fa as pure fluids and R245fa/R21, R123/R21, R245fa/R123 as zeotropic mixtures in this paper. In this study, the working fluid is set as saturated vapor at the outlet of the evaporator, and dry working fluid or isentropic working fluid should be used to avoid the water hammer at the tail of turbine (Xu *et al.*, 2011). R21 is a typical wet working fluid while R245fa and

R123 are dry working fluids. To guarantee the zeotropic mixtures are dry working fluids or isentropic working fluids, the mass fraction of R21 must be no more than 0.35 in mixture R245fa/R21 and no more than 0.2 in mixture R123/R21 from REFPROP's calculations. Figure 3 is the tephigram of saturated R245fa/R21 (0.65/0.35), and Figure 4 is the tephigram of saturated R123/R21 (0.8/0.2). As shown in two figures, these two mixtures are isentropic working fluids under the corresponding proportion.

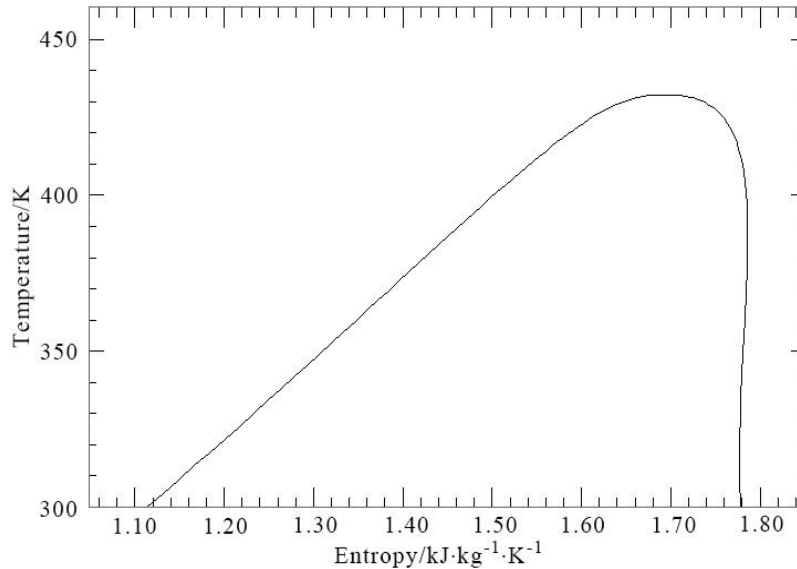


Figure 3: Tephigram of saturated R245fa/R21 (0.65/0.35)

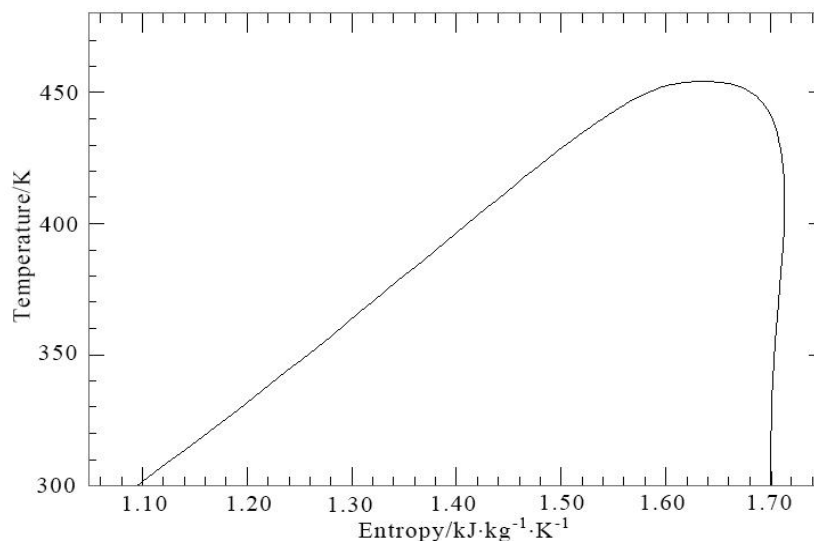


Figure 4: Tephigram of saturated R123/R21 (0.8/0.2)

3. THE PERFORMANCE ANALYSIS OF REHEATING ORC SYSTEM

3.1 System Parameters Setting and The Research Method

In this research, the condensing temperature is 300K which is constrained by environmental temperature. In the case of zeotropic mixtures, the temperature of working fluid at outlet of the condenser is regarded as the condensing temperature. The heat source temperature is 400K, and the maximal evaporation temperature is 380K which is constrained by heat source temperature. In the

case of zeotropic mixtures, the temperature of working fluid at outlet of the evaporator is regarded as the evaporation temperature. The adiabatic efficiency of the turbines is 85%, and the mechanical efficiency is 90%. The adiabatic efficiency of the pump is 80%, and the mass flow of working fluid is 1 kg s^{-1} . In addition, the working fluid is set as saturated liquid at the outlet of the condenser and saturated vapor at the outlet of the evaporator. The Reheat pressure ratio is defined as the ratio of inlet pressure of Turbine 2 and that of Turbine 1. To ensure the inlet pressure of Turbine 2 is greater than its outlet pressure, which is condensation pressure, we set the minimal reheat pressure ratio as 0.3. The parameter values of each state point are calculated by REFPROP.

For low-temperature heat energy generating system, the important thing is to improve the total output work, not the thermal efficiency. Therefore the system performance is evaluated by net power output of the reheating ORC system in this article. Fundamental equations are as follows:

Work of high pressure turbine 1:

$$W_1 = \dot{m} \cdot (h_1 - h_2) \cdot \eta_m \quad (1)$$

Work of low pressure turbine 2:

$$W_2 = \dot{m} \cdot (h_3 - h_4) \cdot \eta_m \quad (2)$$

Consumed work of pump:

$$W_p = \dot{m} \cdot (h_6 - h_5) \quad (3)$$

Net power output of the system:

$$W = W_1 + W_2 - W_p \quad (4)$$

Where: \dot{m} is mass flow of the working fluid, which is 1 kg s^{-1} in this research; h_1 is specific enthalpy of the working fluid at inlet of high pressure turbine 1, kJ kg^{-1} ; h_2 is specific enthalpy of the working fluid at outlet of high pressure turbine 1, kJ kg^{-1} ; h_3 is specific enthalpy of the working fluid at inlet of low pressure turbine 2, kJ kg^{-1} ; h_4 is specific enthalpy of the working fluid at outlet of low pressure turbine 2, kJ kg^{-1} ; η_m is the mechanical efficiency of the turbines, which is 90% in this research; h_5 is specific enthalpy of the working fluid at inlet of pump, kJ kg^{-1} ; h_6 is specific enthalpy of the working fluid at outlet of pump, kJ kg^{-1} .

3.2 The Performance Analysis of Reheating ORC System Using Pure Working Fluid

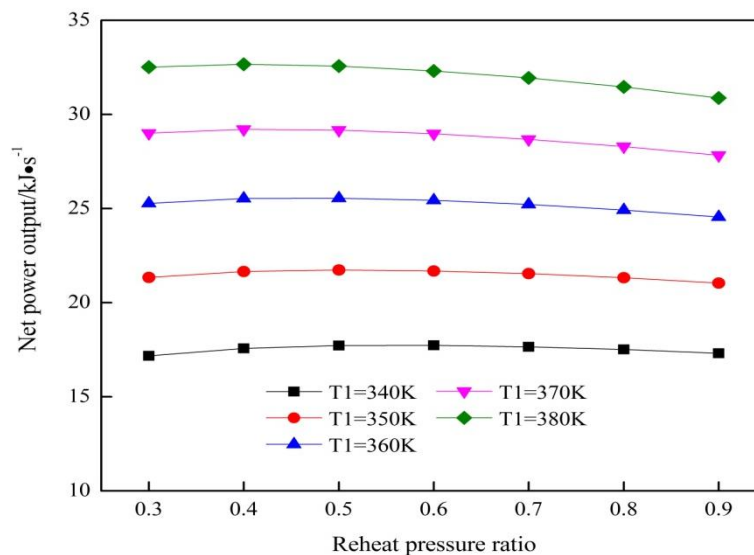


Figure 5: The influences of reheat pressure ratio and evaporator temperature on net power output (working fluid is R245fa)

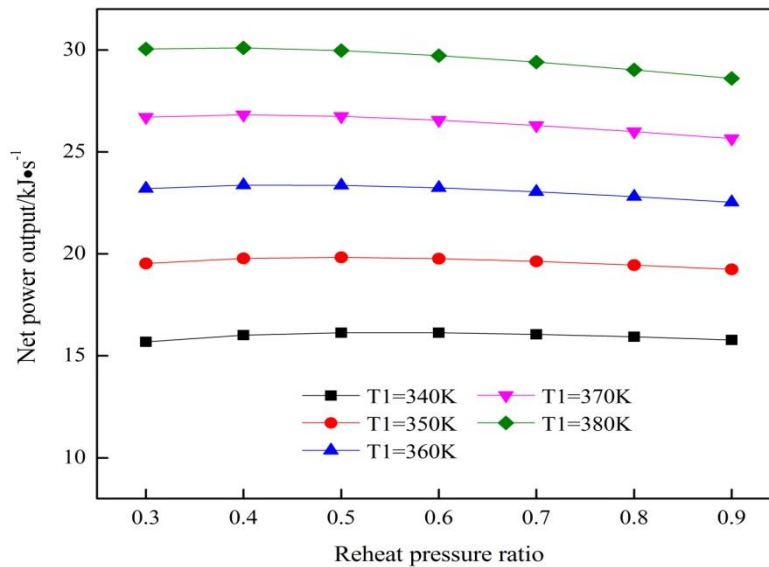


Figure 6: The influences of reheat pressure ratio and evaporator temperature on net power output (working fluid is R123)

Net power outputs of the reheating ORC system using R245fa and R123 as working fluids are calculated at different temperatures (340K-380K) and different reheat pressure ratios (0.3-0.9), and the results are shown in Figure 5 and Figure 6. T_1 denotes evaporation temperature in the figures.

As shown in the two figures, the net power output increases gradually with the increasing evaporating temperature. net power output of the reheating ORC system using R245fa as working fluid is about 9% greater than that of the reheating ORC system using R123 at the same evaporating temperature and reheat pressure ratio, indicating that the performance of R245fa is better than that of R123.

Table 2: The optimal reheat pressure ratios

Evaporating Temperature/K	Working Fluid	Optimal Reheat Pressure Ratios	Maximum Net Power Output /kJ·s ⁻¹
340	R245fa	0.56	17.743
	R123	0.55	16.141
350	R245fa	0.50	21.741
	R123	0.49	19.829
360	R245fa	0.46	25.566
	R123	0.44	23.387
370	R245fa	0.43	29.211
	R123	0.40	26.895
380	R245fa	0.40	32.665
	R123	0.37	30.112

In addition, with reheat pressure ratio increases, net power outputs of reheating ORC system using different working fluids all first increase then decrease. The reheat pressure ratio which makes the net power output maximum is regarded as the optimal one and the optimal reheat pressure ratio is related to working fluid type and evaporating temperature. The optimal reheat pressure ratios under different evaporating temperatures are gained through further calculations, and the results are shown in Table 2. From Table 2 we can see that, the optimum reheat pressure ratios of reheating ORC systems using this two kinds of working fluids gradually reduce with the evaporating temperature increasing; and the optimum reheat pressure ratio is smaller when R245fa is used as working fluid at the same evaporating temperature .

3.3 The Performance Analysis of Reheating ORC System Using Zeotropic Mixtures

We select 360K as characteristic evaporation temperature and respectively calculate the net power outputs of ORC system using R245fa/R21, R123/R21 and R245fa/R123 as working fluids under different reheat pressure ratios and component ratios. The results are shown in Figure 7-9.

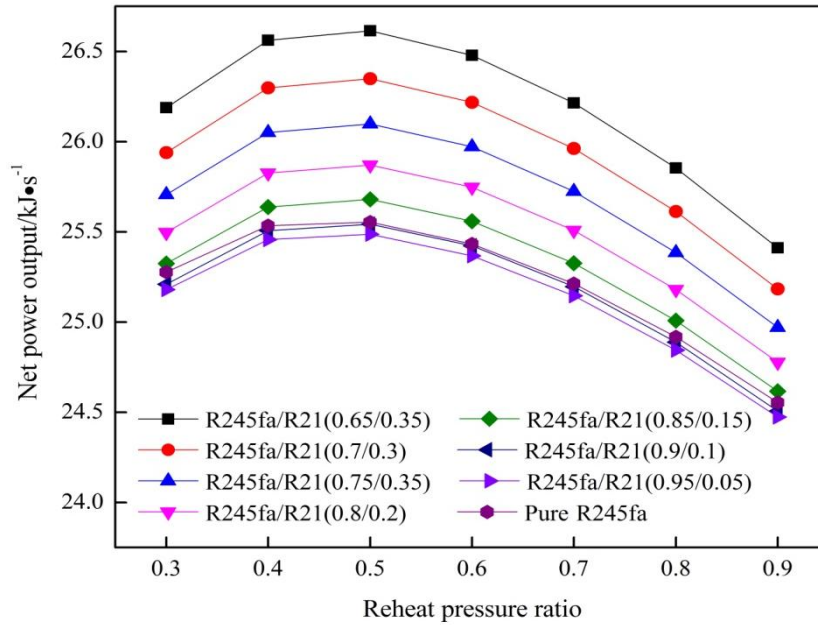


Figure 7: The influences of reheat pressure ratio and component ratio on net power output (working fluid is R245fa/R21)

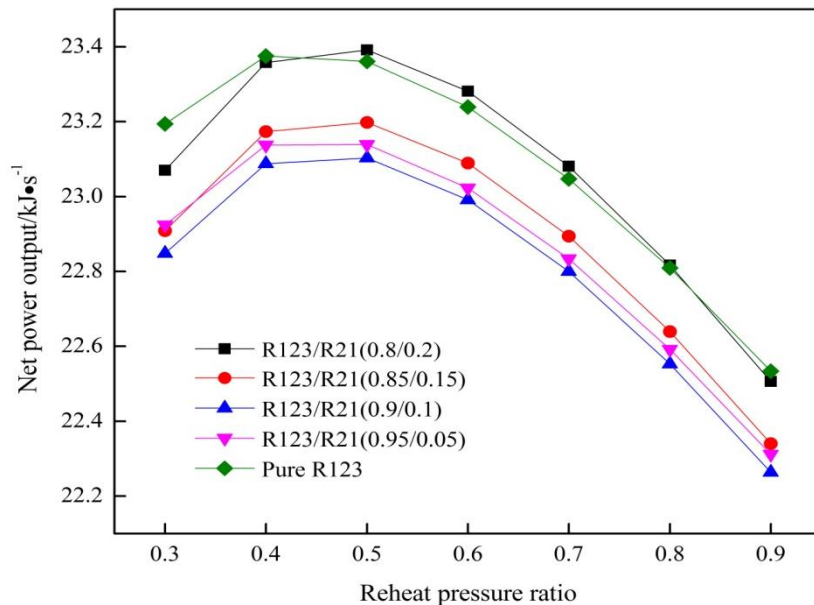


Figure 8: The influences of reheat pressure ratio and component ratio on net power output (working fluid is R123/R21)

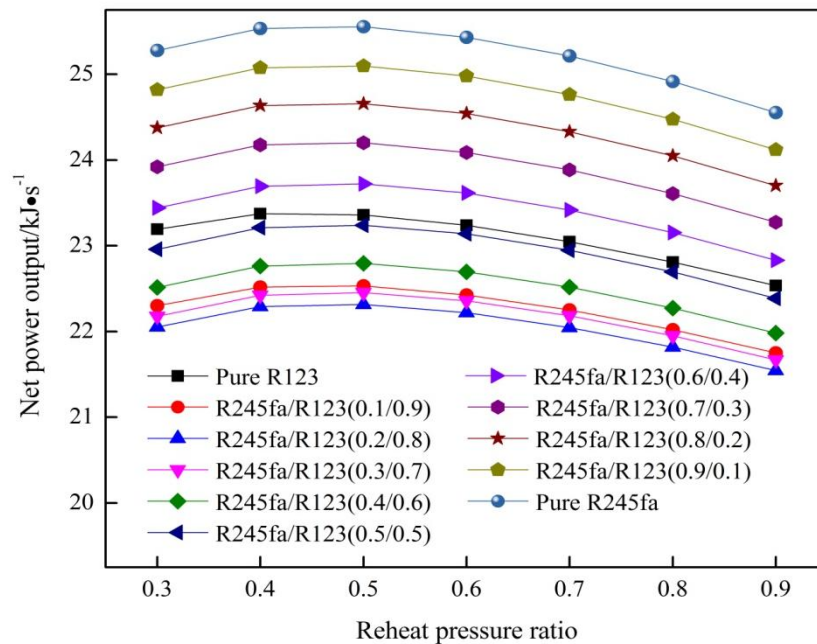


Figure 9: The influences of reheat pressure ratio and component ratio on net power output (working fluid is R245fa/R123)

Figure 7 shows that with an increase in the component ratio of R245fa, the net power output of reheating ORC system gradually decreases. As we can see from Figure 7, net power output of the reheating ORC system using R245fa/R21 as working fluid is greater than that of the reheating ORC system using pure R245fa when the component ratio of R245fa is less than 0.9. This is because that zeotropic mixtures present variable temperature profile during the phase change process, which could considerably reduce the mismatch between heating or cooling sources and the evaporating or condensing working fluid mixtures respectively, so the system irreversibilities could be minimized. Consequently, an appropriate choice of zeotropic mixtures could improve the enthalpy drop between the turbine import and export, thus raising the net power output of ORC system. Net power output of the reheating ORC system using R245fa/R21 (0.65/0.35) as working fluid is about 4% greater than that of the reheating ORC system using pure R245fa at the same reheat pressure ratio. With a further calculation, we acquire that when the evaporation temperature is 360K, the optimal reheat pressure ratio of the reheating ORC system using R245fa/R21 (0.65/0.35) as working fluid is 0.47, and the maximum net power output is 26.622 kJ s^{-1} , which is 4.13% greater than that of the reheating ORC system using pure R245fa.

Figure 8 shows that the net power output of reheating ORC system using R123/R21 (0.8/0.2) or pure R123 as working fluid is relatively large while the net power output of reheating ORC system using R123/R21 (0.9/0.1) is smallest. With a further calculation, we acquire that when the evaporation temperature is 360K, the optimal reheat pressure ratio of the reheating ORC system using R123/R21 (0.8/0.2) as working fluid is 0.47, and the maximum net power output is 23.399 kJ s^{-1} , which is 0.05% greater than that of the reheating ORC system using pure R123. We could obtain that using mixtures R123/R21 as working fluid could hardly improve the net power output of reheating ORC system.

Figure 9 shows that net power output of the reheating ORC system using R245fa/R123 as working fluid is smaller than that of the reheating ORC system using pure R245fa. It is interesting to find that when the component ratio of R123 is larger than 0.5, net power output of the reheating ORC system using R245fa/R123 as working fluid is even smaller than that of the reheating ORC system using pure R123. We could obtain that using mixtures R123/R21 as working fluid could not improve the net power output of reheating ORC system.

4. CONCLUSIONS

In this paper, the research object is reheating ORC system utilizing low temperature waste heat, and the evaluation standard is net power output of the ORC system. The reheating ORC systems using R245fa, R123, R245fa/R21, R123/R21 and R245fa/R123 as working fluids were investigated. The main conclusions can be extracted as follow:

- For reheating ORC systems using pure R245fa and R123 as working fluids, with an increase in evaporation temperature, the net power output gradually increases. Net power output of the reheating ORC system using pure R245fa as working fluid is about 9% greater than that of the reheating ORC system using pure R123 at the same temperature and reheat pressure ratio. There is an optimal reheat pressure ratio making the net power output of ORC system maximum. The optimal reheat pressure ratios of reheating ORC systems using pure R245fa and R123 as working fluids decrease with the evaporation temperature increasing. The optimal reheat pressure ratio of reheating ORC system using pure R245fa as working fluid is slightly smaller than that of reheating ORC system using pure R123 at the same evaporation temperature.
- When the evaporation temperature is 360K, the maximum net power output of reheating ORC system using mixtures R245fa/R21 as working fluid is 4.13% greater than that of reheating ORC system using pure R245fa while the maximum net power output of reheating ORC system using mixtures R123/R21 as working fluid is only 0.05% greater than that of reheating ORC system using pure R123. The optimal mixtures component ratios are R245fa/R21 (0.65/0.35) and R123/R21 (0.8/0.2). Using mixture R245fa/R123 as working fluid cannot increase the net power output of reheating ORC system.
- Zeotropic mixture can effectively improve the net power output of reheating ORC system when the mixture's category and component ratio are suitable. In practical application, the optimal reheat pressure ratio and component ratio should be determined based on the mixture and evaporation temperature to ensure the net power output of reheating ORC system maximum.

REFERENCES

- Angelino, G., Paliano, P., 1998, Multicomponent Working Fluids for Organic Rankine Cycles, *Energy*, vol. 23, no. 6: p. 449-463.
- Calm, J M., Hourahan, G C., 2011, Physical, Safety and Environmental Data for Current and Alternative Refrigerants, *Proceedings of 23rd International Congress of Refrigeration.*, ICR.
- Chen, H., Goswami, D Y., Rahman, M M., *et al.*, 2011, A Supercritical Rankine Cycle Using Zeotropic Mixture Working Fluids for the Conversion of Low-grade Heat Into Power, *Energy*, vol. 36, no. 1: p. 549-555.
- Gu, W., Weng, Y., Cao, G. *et al.*, 2007, The Research Status and Development Trend for Low Temperature Heat Energy Power Generation, *Journal of Engineering for Thermal Energy and Power*, vol. 22, no. 2: p. 115-119.
- Gu, W., Weng, Y. *et al.*, 2008, Thermodynamic Analysis of Power Generation System Based on Closed Organic Rankine Cycle, *Acta Energetica Sinica*, vol. 29, no. 5 p:608- 612.
- Li, M., Bai, H. *et al.*, 2013, The Study on Thermodynamic Performance of Reheating Organic Rankine Circulation System, *Journal of Inner Mongolia University of Science and Technology*, vol. 32, no. 1: p. 50-53.
- Li, N., Zhang, X., Bai, H. *et al.*, 2012, The Study on Thermal Performance of Power Generation System Using Organic Rankine Cycle and Reheating Cycle System, *Industrial Heating*, vol. 41, no. 2: p. 44-47.
- Maizza, V., Maizza, A., 1996, Working Fluids in Non-steady Flows for Waste Energy Recovery Systems, *Applied Thermal Engineering*, vol. 16, no. 7: p. 579-590.
- Maizza, V., Maizza, A., 2001, Unconventional Working Fluids in Organic Rankine Cycles for Waste Energy Recovery Systems, *Applied Thermal Engineering*, vol. 21, no. 3: p. 381-390.

- Ni, Y., Zhao, L., Liu, C. *et al.*, 2013, Recovery of Waste Heat of Low Temperature Flue Gas by Parametric Optimization on Organic Rankine Cycle with Non-Azeotropic Mixtures, *CIESC Journal*, vol. 64, no. 11: p. 3985-3992.
- Wang, J., Zhao, L., Wang, X., 2010, A Comparative Study of Pure and Zeotropic Mixtures in Low-Temperature Solar Rankine Cycle, *Applied Energy*, vol. 87, no. 11:p.3366-3373.
- Wang, Z., Yu, Y. *et al.*, 2013, Parameter Optimization on Low Temperature Reheating Organic Rankine Cycle, *Thermal Power Generation*, vol. 42, no. 5: p. 22-29.
- Xu, J., Dong, A. *et al.*, 2011, Working Fluid Selecting of Organic Rankine Cycle for Low and Medium Grade Heat Source Utilization, *Energy Conservation Technology*, vol. 29, no. 167: p. 204-210.
- Xu, J., Li, X., Gu, C. *et al.*, 2009, Determination of Optimal Reheating Pressure in Organic Rankine Cycle System, *Journal of Tianjing Polytechnic University*, vol. 28, no. 2: p. 83-85.
- Zheng, H., Tang, K., Jin, T. *et al.*, 2008, Advances in Working Fluids for Organic Rankine Cycle, *Energy Engineering*, no.4: p.5-11.

STRUCTURE RELIABILITY ANALYSIS AND EXPERIMENTAL VERIFICATION OF A NEW FREE PISTON EXPANDER

Gaosheng Li^{1,2*}, Hongguang Zhang^{1,2}

¹College of Environmental and Energy Engineering, Beijing University of Technology,
Pingleyuan No.100, 100124 Beijing, China

²Collaborative Innovation Center of Electric Vehicles in Beijing,
Pingleyuan No.100, 100124 Beijing, China
E-mail: gao.sheng2005@163.com

* Corresponding Author

ABSTRACT

A new free piston expander coupled with liner generator (FPE-LG) has been proposed in this paper, which can be used as a thermo-electric conversion device for organic Rankine cycle (ORC). Compared to other expanders, the free piston expander (FPE) seems to be the most suitable working component for small scale ORC system owing to good sealing, variable compress ratio and compact structure if the inlet/outlet control is worked out accurately. Thus, a physical prototype with a novel valve train has been manufactured, which is experimentally validated in an air test rig before it is integrated into whole ORC system.

In this paper, a general engineering methodology is adopted to analyze the structure reliability of the FPE valve train at different input frequencies. The dynamics simulation of the valve train is carried out via ADMAS software firstly, the obtained contact force results are set as boundary conditions of stress analysis. Based on elastic mechanics theory and finite element method, more precise calculation results about stress distribution on the valve train are obtained through transient structural module in ANSYS® Workbench V14.5. The results show that the maximal von Mises stress is 231.71MPa which mainly concentrate on the root of the valve slider. Although the maximal von Mises stress on the valve slider does not exceed its material allowable stress when the servomotor input frequency is 8Hz, the fluctuation of the stress is obvious, which leads to mechanical failure. FPE prototype with the valve train can realize the suction, expansion and discharge processes properly in the air test rig and can work stably in a relatively wide range of servomotor input frequency from 1Hz to 8Hz. The stress analysis and dynamics simulation results can provide a significant reference value for the mechanical performance optimization of the next generation FPE and further validation of the FPE-LG in the ORC system will be conducted in the near future.

1. INTRODUCTION

About one third of the energy which is produced by the automotive fuel combustion has been utilized, however, the majority has been wasted in the form of exhaust gases, cooling water and mechanical friction loss. Utilizing exhaust energy has recently become a more efficient and effective method by which to save energy and reduce emissions (Ou *et al.*, 2013, Boretti, 2012). The organic Rankine cycle (ORC) system is not only a reliable and promising method for converting waste heat of vehicle exhaust into useful work but also a most likely industrialization technology (He *et al.*, 2012).

As the core working part, the performance of expander has a direct influence on output power of automotive ORC system. Owing to small flow rate constraint and compact structure requirement, the

traditional expanders such as the turbine, screw, scroll expanders have certain difficulties in application for the small scale automotive ORC system respectively. For instance, although the screw expander is widely used in ORC system, of which helix rotor surface with high accuracy must be manufactured by special equipment and tools (Wang *et al.*, 2011). Furthermore, the screw expander can't reach the end pressure as high as reciprocating piston expander when the expansion process is completed (Gao *et al.*, 2013). Due to large leakage under high pressure difference, the scroll expander has a low efficiency. Hence, very tight clearance design is required in order to achieve a satisfactory efficiency, which will make the manufacturing costs increased. As for the turbine expander, the rotating speed will exceed 200,000 to meet to this small flow rate, which is a great challenge associated with the reliability and mechanical strength. However, the free piston expander (FPE) is suitable to the condition of small flow and low output power (Han *et al.*, 2014, Zhang *et al.*, 2007). At present, studies of free piston expander mainly focus on the refrigeration field. No public reports about using free piston expander as working part for vehicle internal combustion engine (ICE) waste heat recovery has been seen in published literatures yet. Thus, free piston expander coupled with a liner generator has been proposed in this paper, which can be used as a thermo-electric conversion device in vehicle ICE waste heat recovery. Moreover, the FPE-LG prototype is preliminary validated in the air test rig under low intake pressure and steam flow rate condition before it is integrated into the whole ORC system.

2. DESCRIPTION OF THE FPE-LG PROTOTYPE

2.1 The system description of free piston expander coupled with liner generator (FPE-LG)

The thermo-electric conversion components in conventional automotive ORC system consists of independent expander and generator, which need more space for installation and make the ORC system very difficult to application in the vehicle. The FPE-LG unit can be used as a substitute for thermo-electric conversion components in the small scale automotive ORC system owing to compact structure. The basic concept presents in this work is illustrates in Fig.1.

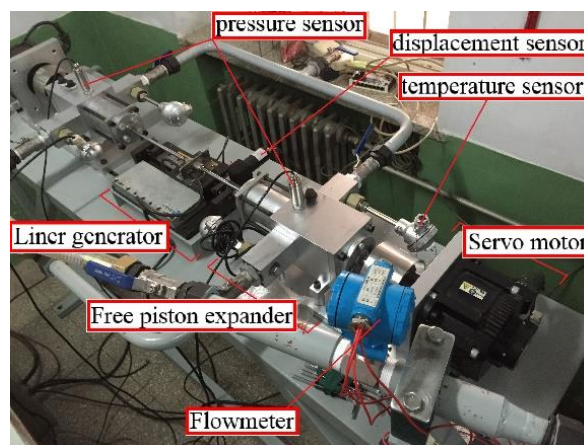


Figure 1: System diagram of FPE-LG

As shown in Fig.1, FPE-LG unit is mainly composed of four components: expander, liner generator, servomotor, measurement and control system. Compared to the opposed arrangement form with two free piston expanders, the piston returning of an independent free piston expander needs an additional return spring what will decrease the reliability in working process. Furthermore, electric energy production by the liner generator need reciprocating movement of the mover. Thus, the former scheme is adopted. Both the output ends of the two opposed FPEs are jointed together with the mover of the liner generator through two flexible joints, and enable the mover to free reciprocate without additional return springs under the support of stator which is fixed on the test-bed. Working principle of the FPE-LG is discussed in detail in the following section.

2.2 Structure layout of free piston expander

During the concept design phase of the prototype, what we mainly focus on is the total electric energy production of liner generator which is decided by piston velocity of FPE according to Faraday's electromagnetic induction law. While the pressure and flow rate of the working fluid in the small scale ORC system have a significant influence on the piston velocity of FPE. Thus, it is very important to select appropriate structure parameters in order to satisfy these design requirements. Subsequently, the diameters of the expander cylinder and the stroke are calculated according to the assumed compression ratio. Moreover, the important factors which are mentioned above have been taken into consideration overall. The final geometric parameters of the FPE are determined as shown in Table.1.

Table 1: Structure parameters of free piston expander

Items	Value	Units
Cylinder bore	80	mm
Working frequency	1-8	Hz
Stroke	102	mm
Piston rod diameter	10	mm
Compression ratio	8	
Intake/exhaust port diameter	20	mm

Fig.2 shows the structure of the free piston expander. The FPE mainly includes following components: cylinder head, piston group, cylinder, valve seat, cylinder block, valve train, valve sleeve, fixed plate, cover, guide sleeve, input shaft. Simultaneously, the output end of a 200V servomotor is connected to input shaft of the expander with a flexible coupling joint which can ensure alignment of center line. Thus, working fluid inflow and outflow of the FPE can be adjusted via the valve train which movement is controlled by the servomotor. In order to reduce the loss of friction, the closed space between the cover and fixed plate is filled with lubricating oil which can be added through a small hole on the cover. We select aluminum alloy for constituting the moving parts including valve and piston while the other main parts are constituted with 304 stainless steel, since aluminum alloy has high-strength which is used generally in ICE piston design, it can bear the high pressure and temperature in ORC system and maintain its mechanical property in these conditions while 304 stainless steel has good resistance to corrosion. Owing to the mechanical wear between the piston group and cylinder head, a guide sleeve constituted with aluminum bronze is placed in the cylinder head which can improve the service life of piston rod and meet the high precision demand of the piston group installed.

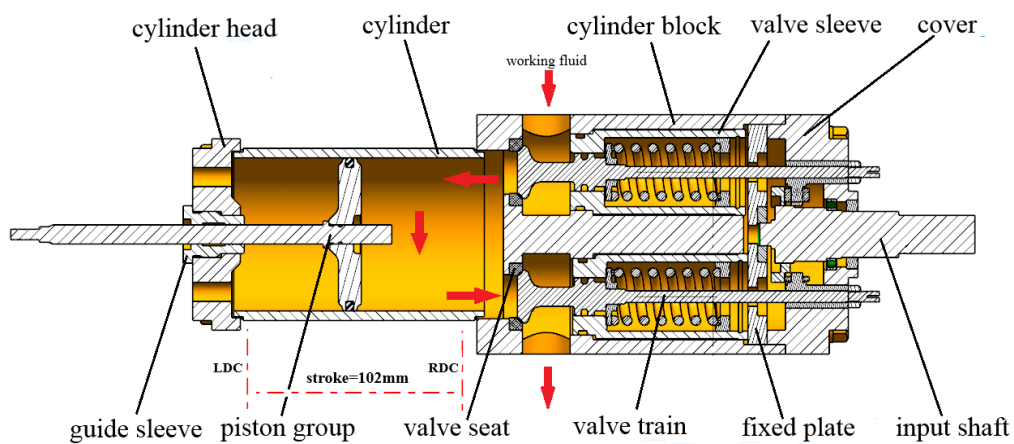


Figure 2: Structure diagram of free piston expander

Based on the description about main structure of the free piston expander and selection of key parts above, the working process of the FPE-LG prototype can be simply described as following: firstly,

two servomotors are set to certain phase difference before the FPE-LG operates, which can ensure the inlet valve of expander on one side opens while the outlet valve on other side closes. Taking the expander on the right side (as shown in Fig.2) as an example, the exhaust gas exchanges heat with the organic working fluid in the evaporator when ORC system works. Meanwhile the organic working fluid turns into high-temperature and high-pressure gas, which is injected into the expander intake port and then enters into the expander cylinder when the inlet valve opens, driving the piston to the LDC. Simultaneously, the outlet valve of the left expander opens which is controlled by another servomotor and the in-cylinder pressure is lower than the right side. So the piston is pushed to the RDC under the action of force produced by the right expander. In this process, the liner generator mover can move together with expander piston groups, cutting the magnetic induction lines to produce electric energy.

2.3 The expander inlet/outlet control method

The free piston expander seems to be the most suitable thermal-power conversion component for small scale ORC system if the inlet/outlet control is carried out successfully, since it has the greatest potential for practical application owing to the good sealing, less mechanical loss and simple structure. In fact, the development of the free piston concept at the TU Dresden seems to be the most promising one up till now, because the efficiency was reported to approach 50% and the prototype expander was verified to be feasible. The electronically controlled valve is abandoned owing to the high cost and complex control system. Thus, a novel mechanical valve train has been created for the FPE in this paper and a full scaled CAD model of the valve train which is built via CATIA V5R21[®] is prepared for the subsequent analyses, as shown in Fig.3.

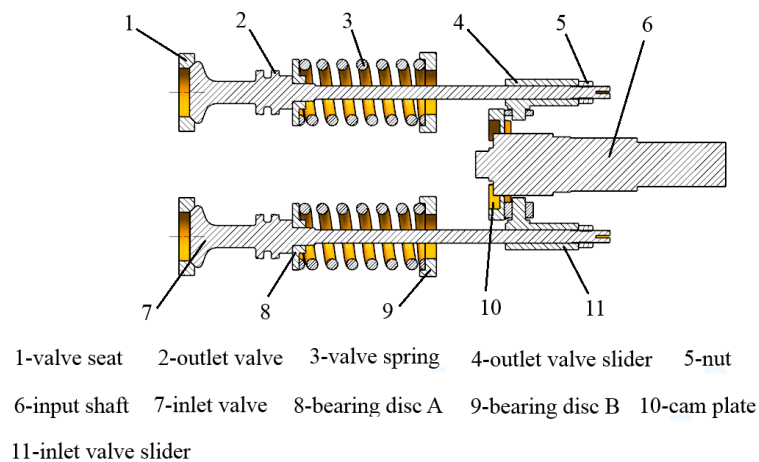


Figure 3: Structure diagram of FPE valve train

The structure of the FPE valve train is illustrated in Fig.3. It is mainly composed of several parts: valve seat, valve spring, cam plate, inlet/outlet valve slider, input shaft, inlet/outlet valve, bearing disc A and B. The cam plate is processed into stepped shape with a height difference of 3 millimeter. The surface of upward and downward position is processed into arc surface in order to reduce the resistance of the valve opening and closing. The valve spring with a pre-compressing quantity of 5.5 millimeter is fixed between bearing disc A and B when the expander is assembled. An axial hole through the center of valve slider is manufactured which can be used to fix the valve with a nut. And the gap between bearing disc B and cam plate can be adjusted by changing the mounting position of bearing disc B after the valve train is assembled into the FPE cylinder block. Through this kind of design approach, the valve slider can be compressed on the cam plate. Thus, the valve opening and closing which is driven through the rotating movement of the cam plate can be achieved.

Considering that the reliability and durability of the valve train is mainly determined by spring load, natural frequency, fatigue resistance and relaxation properties, 55CrSi has been selected for

constituting the mechanical spring of the valve train owing to wide applications in the field of high stress spring and excellent mechanical character which can insure the air tightness at the same time. According to the design parameters of the mechanical spring, as shown in Table 2, spring stiffness (f) can be calculated with following equation:

$$f = \frac{G \cdot d^4}{8 \cdot D^3 \cdot n} \quad (1)$$

Table 2: Mechanical spring parameters

Parameters	Mean	Value	Units
G	Shearing modulus of elasticity	8×10^4	N/mm ²
d	Spring diameter	25	mm
D	Wire diameter	5	mm
n	Effective number of turns	5.5	-
f	Stiffness	72.7	N/mm
L	Spring relaxation length	67	mm
c	damping	0.66E-003	N·s/mm

3. DYNAMICS SIMULATION OF THE FPE VALVE TRAIN

3.1 Dynamics simulation model description

The irregular contact surface between cam plate and valve slider will cause a serious problem of calculation convergence in the process of stress analysis. Owing to the difficulty of the nonlinear problem in transient structural solution, we adopt a general engineering methodology. Firstly the dynamics simulation is carried out via ADMAS software, which is a professional mechanical dynamics simulation software. Then the contact force simulation results between the valve silders and cam plate are exported and be set as stress analysis boundary conditions in transient structural module of ANSYS® Workbench V14.5. Furthermore, it is also convenient to analyze the valve train movement rule and the design parameters of cam plate profile through ADMAS.

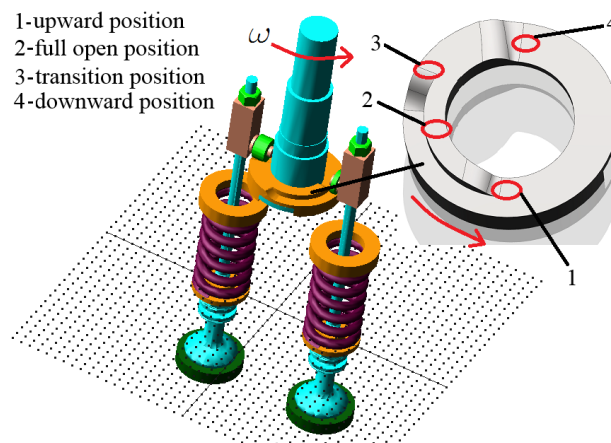


Figure 4: Dynamics simulation model of the valve train

As shown in Fig.4, aim to get the force conditions in the contact location between valve sliders and cam plate, the CAD model we prepared has been imported into the ADMAS. And then, constraints and loads are added according to the true motion. In order to obtain precise results, the spring, valve sliders and valves are set as flexible parts which are divided into suitable mesh, while the rest are set as rigid parts. Simultaneously, the time of the cam plate rotates a cycle is defined as the end time of simulation in order to observe the change of force more clearly, while the simulation steps are defined to one thousand which can ensure the accuracy of dynamics simulation results.

3.2 Analysis of the simulation results and boundary conditions extraction

Force conditions between the inlet/outlet valve sliders and cam plate at different servomotor input frequencies is analyzed. We select 2Hz, 5Hz, 8Hz, 10Hz as input simulation variables to prove the reliability of the valve train at design frequency.

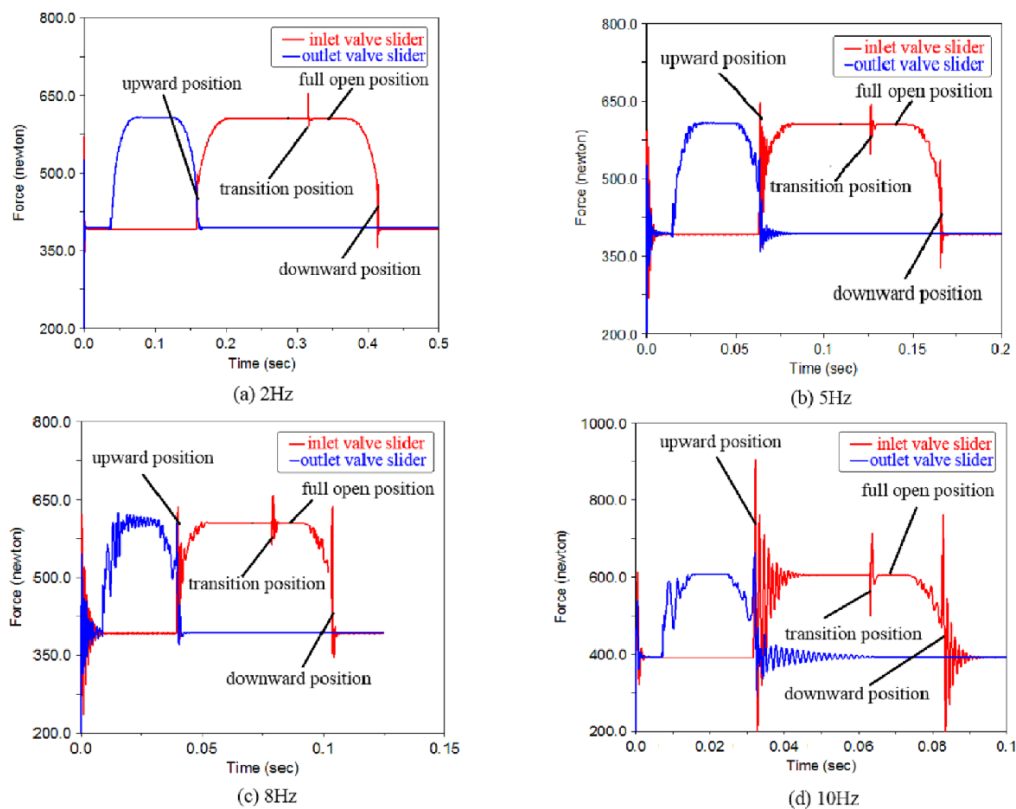


Figure 5: Total contact force of valve sliders at different servomotor input frequencies

Fig.5 shows the total contact force comparisons between the inlet and outlet valve slider at different input frequencies. The sudden change of contact force on inlet valve slider increased significantly with improvement of the servomotor input frequencies when it reaches the upward and downward position, while the change rule of outlet valve slider is not obvious at low input frequency. There is hardly any sudden change of the force in the inlet valve opening and closing process in Fig.5(a), however, as we can see in Fig.5(b) (c) (d) the fluctuating intensities and the magnitudes of the force changes obviously. Simultaneously, a sudden change of contact force occurred at the transition position owing to the sudden decreasing of the contact surface between inlet valve slider and cam plate. However, the contact surface between outlet valve slider and cam plate is constant, so the variation of contact force between the outlet valve slider and cam plate at the transition position is very different from it. Meanwhile, both contact force of the inlet and outlet valve slider has no significant change at the full open position. Then, the force data of inlet/outlet valve sliders in three coordinate directions is exported, which can be set as the force load in following stress analysis.

4. FINITE ELEMENT MODLE OF THE FPE VALVE TRAIN

Based on analysis of the simulation results above, the left side where inlet valve is settled as shown in Fig.4 is taken as main research object owing to the complexity of the contact force change. The finite element (FE) model of the valve train used in the numerical analysis is constructed, the assembled finite element model includes inlet valve, valve spring, inlet valve slider, nut, circular bearing disc A and B, as shown in Fig.6.

In order to precisely simulate the real contact and load conditions in stress analysis, the simplified model is meshed using SOLID187, a higher order three-dimensional solid element, which has a quadratic displacement behavior and well suited to model irregular meshes. The element is defined by 10 nodes having three transitional DOF at each node. The valve train FE model has 319795 elements and 484079 nodes.

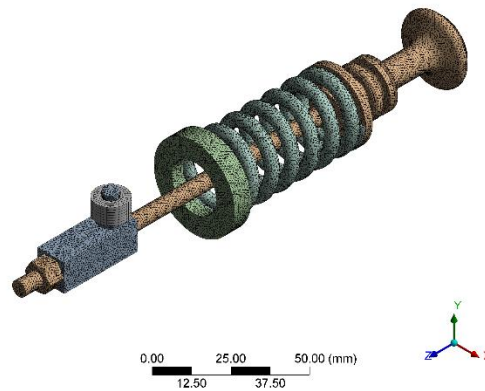


Figure 6: Finite element model of the valve train

4.1 simplification of boundary conditions and imposing load

In order to ensure convergence of calculation, the boundary conditions such as force and displacement of each part or part contacts must be simplified according to actual conditions before the solution program of FE model has been carried out.

Based on the actual working conditions, an equivalent intake pressure which is imposed on the inlet valve head has been ignored. The total friction of contact portions has much less influence on the calculation results in the design conditions owing to splash lubrication. Then, the contact force of inlet valve slider in three coordinate directions which is obtained via ADMAS is imported into transient structural module as calculation boundary. Considering that it is approximately liner contact between the inlet valve slider and cam plate, main load is defined to nodal force which magnitude depends on the dynamic simulation results. Completely bonded contact is assigned to the interface between components. A displacement constraint which is limited the X, Y directions and free the Z direction is applied to four profiles of the valve slider and a fix constraint is assigned to the cylindrical surface of the bearing disc B. Finally, an equivalent spring contact is assigned to the contact surface between two bearing discs which stiffness, damping, preload is defined to 72N/mm, 0.66E-003Ns/mm and 400N according to the calculation results in section 2.3, respectively.

4.2 Experimental validated of FPE-LG in air test rig

In order to validate the correctness of working principle of the expander and the valve train, an air test rig has been set up. As shown in Fig.7, it includes high pressure air compressor, air receiver, connecting pipe, FPE-LG, acquisition system. Furthermore, test of the valve train in actual working conditions is conducted to validate the results of stress simulation, which is discussed in detail in the following section.

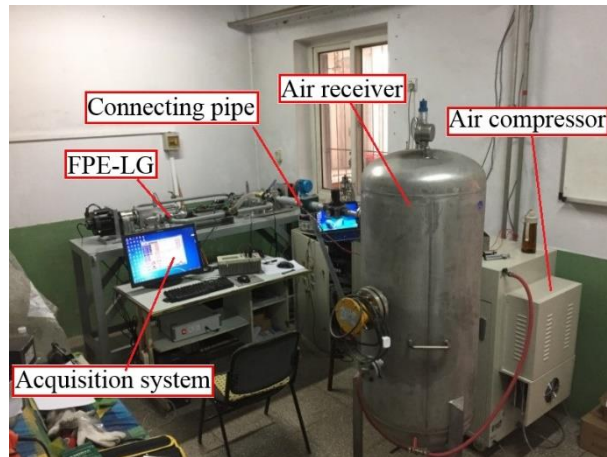


Figure. 7: FPE-LG test bench

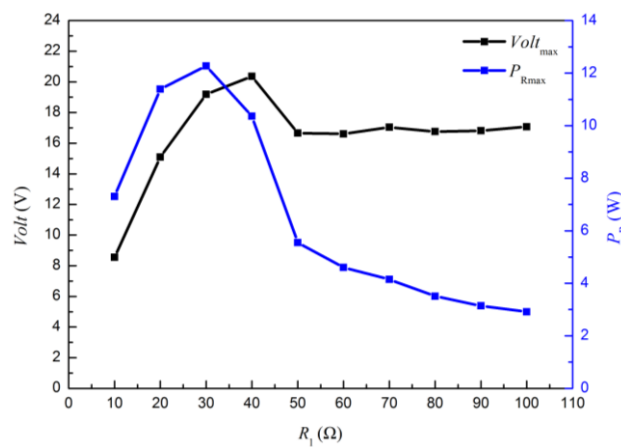


Figure. 8: Load peak voltage and peak power for different load resistance

In order to assess the thermoelectric conversion capacity of the FPE-LG, preliminary experiment is carried out at a certain condition, which intake pressure, input frequency, external load resistance is 0.2MPa, 1.5Hz and 10Ω - 100Ω respectively. As illustrated in Fig.8, the maximum transient voltage is 20.4V when the external load resistance value is 40Ω . The maximum output power is 12.3W when the external load resistance value is 30Ω according to the Ohm's law. Since the compressed air is selected as working fluid in this pneumatic test, the working pressure and temperature are lower than conventional ORC system. However, the transient maximum output power of FPE-LG is considerable. More experiments about other variable factors includes intake pressure, input frequency, evaporating temperature will be conducted when the FPE-LG is integrated into a small scale ORC system.

The FPE-LG prototype can operated stably at different servomotor input frequencies from 1Hz to 8Hz. The maximal pressure in cylinder can reach 5 bar. Although the FPE-LG prototype can operate at a higher input frequency and pressure, we don't further improve it since the collision between piston and cylinder head increases obviously with input frequency improving.

5. ANALYSIS OF SIMULATION RESULTS

The prototype can operate steadily at different input frequencies in the air test rig. However, crack of the inlet valve slider mainly originates from the same region after long time running, which is marked with A in Fig.9.



Figure 9: Actual failure region of the inlet valve slider

FE analyses results illustrates that the root of inlet valve slider is subjected to stress concentration which make it easily failure region and can cause a premature failure problem. This is consistent with the actual damage conditions. Owing to high speed and frequent collision with the cam plate, a large quantities of heat is generated through friction, which can also reduce the serve life of the inlet valve slider.

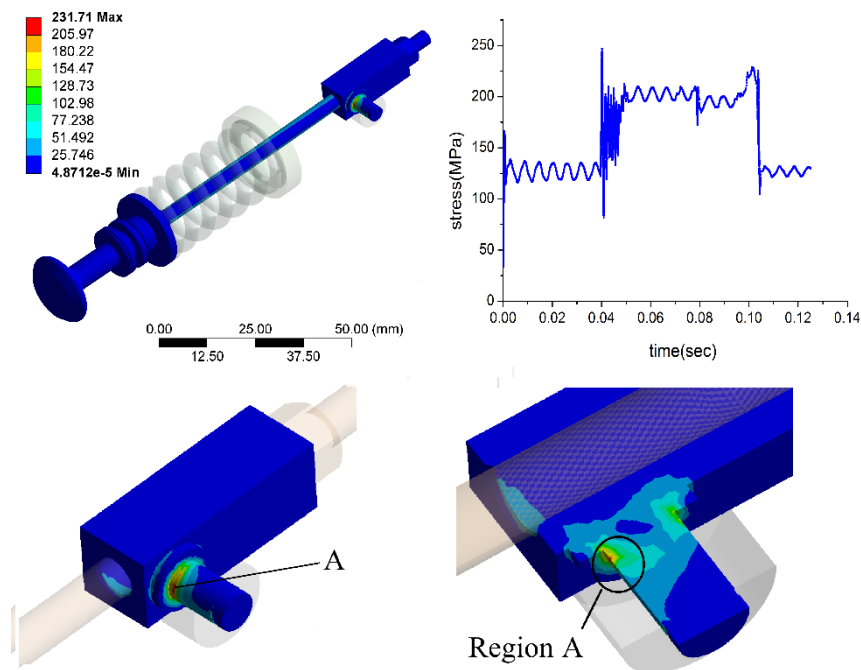


Figure 10: Equivalent von Mises stress (MPa) distribution on the inlet valve slider

Fig.10 shows equivalent von Mises stress distribution obtained from the FE analysis when the servomotor input frequency is 8Hz which is the maximum value in actual test conditions. It can be seen that the maximum von Mises stress is 231.71Mpa which mainly concentrates on the root of inlet valve slider when it moves from upward position to full open position. Simultaneously, the fluctuation of the von Mises stress is obvious in one working cycle. The results are agreement with actual situations. The maximum stress is meet limit yield of material which is selected to constitute the valve slider. However, the stress in this area (marked with A) is close to the mechanical strength of the material, which indicates that the region is a critical area and prone to be failed. Enhancement of the fatigue life of the inlet valve slider is dependent on the decreases of the stress concentration. Hence, adding a fillet to the root of inlet valve slider and taking heat treatment are both the effective methods to eliminate the stress concentration. Because of the exact value of stress distribution on the root of

valve slider is difficult to measure in practice, the proposed method of analyzing the failure of valve slider, which takes into account of several key position, is predictive and applicable.

6. CONCLUSIONS

In this paper, an engineering methodology is adopted to analyze the structure reliability of the FPE valve train. And experimentally validated of FPE-LG in an air test rig is conducted before it is integrated into whole ORC system. The main conclusions can be drawn as follows:

- The results of the stress analysis indicated that the region of stress concentration on the inlet valve slider is in coincidence with the real failure areas. The maximum value of the von stress is 231.71MPa in a working cycle. The stress concentration and fluctuation are two main factors which strongly affects the structural reliability of the valve train. The methodology is feasible and low-cost in the prototype design. And the mechanical damage of the operated prototype indicates that FPE can't work normally when it deviated from the analysis results in this paper.
- The FPE-LG with the novel valve train was validated in the air test system. The results shows that the FPE-LG can operate in a wide range of input frequencies from 1Hz to 8Hz which reveals that the inlet/outlet control scheme is feasible. Furthermore, the pressure in cylinder can reach 5 bar. The FPE-LG prototype described in this work is shown to be successful in meeting its design goals.
- Further experimental validation about the FPE-LG will be conducted in a miniature ORC system in near future.

REFERENCES

- Ou, X.M., Yan, X.Y., Zhang, X., Zhang, X.L., 2013, Life-cycle energy use and greenhouse gas emissions analysis for bio-liquid jet fuel from open pond-based micro-algae under China conditions, *Energies*, vol. 6, p. 4897-4923.
- Boretti, A., 2012, Recovery of exhaust and coolant heat with R245fa organic Rankine cycles in a hybrid passenger car with a naturally aspirated gasoline engine, *Appl Therm Eng*, vol. 36, p. 73-77.
- He, Y.L., Mei, D.H., Tao, W.Q., Yang, W.W., Liu, H.L., 2012, Simulation of the parabolic trough solar energy generation system with Organic Rankine Cycle, *Appl Energ*, vol. 97, p. 630-641.
- Wang, W., Wu, Y.T., Ma, C.F., Liu, L.D., Yu, J., 2011, Preliminary Experimental Study of Single Screw Expander Prototype, *Appl Therm Eng*, vol. 31, p. 3684-3688.
- Gao, W.Z., Zhai, J.M., Li, G.H., Bian, Q., Feng, L.M., 2013, Performance evaluation and experiment system for waste heat recovery of diesel engine, *Energy*, vol. 55, p. 226-235.
- Han, Y.Q., Kang, J.J., Zhang, G.P., et al, 2014, Performance evaluation of free piston compressor coupling organic Rankine cycle under different operating conditions, *Energ Convers Manage*, vol. 86, p. 340-348.
- Zhang, B., Peng, X., He, Z., Xing, Z., Shu, P., 2007, Development of a double acting free piston expander for power recovery in transcritical CO₂ cycle, *Appl Therm Eng*, vol. 27, p. 1629-1636.

ACKNOWLEDGEMENT

This work was sponsored by the Beijing Natural Science Foundation Program (Grant No. 3152005), the National Natural Science Foundation of China (Grant No. 51376011), and the Scientific Research Key Program of Beijing Municipal Commission of Education (Grant No. KZ201410005003).

WORKING FLUID SELECTION FOR ORGANIC RANKINE CYCLES BASED ON CONTINUOUS-MOLECULAR TARGETS

Johannes Schilling¹, Matthias Lampe¹, Joachim Gross², André Bardow^{1*}

¹ Chair of Technical Thermodynamics, RWTH Aachen University,
Schinkelstraße 8, 52062 Aachen, Germany
E-mail: andre.bardow@ltt.rwth-aachen.de

² Institute of Thermodynamics and Thermal Process Engineering, Stuttgart University,
Pfaffenwaldring 9, 70569 Stuttgart, Germany

* Corresponding Author

ABSTRACT

Organic Rankine Cycles (ORCs) transform heat from low-temperature sources to electrical power. To ensure optimal use of a heat source, the cycle needs to be tailored to the specific application. Tailoring the cycle means optimizing both process and working fluid. Simultaneous optimization of process and working fluid is enabled by the Continuous-molecular targeting (CoMT) framework. Herein, working fluid properties are calculated by the perturbed-chain statistical associating fluid theory (PC-SAFT). The pure component parameters representing the working fluid are relaxed during the optimization leading to an efficient nonlinear program (NLP). The solution is an optimal combination of working fluid and process. Due to the relaxation, the pure component parameters of the optimal working fluid, in general, do not coincide with any real working fluid. Thus, real working fluids with similar properties are searched for in the following step, the so-called structure-mapping. Currently, a Taylor approximation of the objective function around the hypothetical optimal working fluid is used to estimate the objective function value of real working fluids. The Taylor approximation does not account for changes in the active set of constraints leading to occasional poor classification of the working fluids. To overcome this shortcoming, we present an adaptive structure-mapping: An additional Taylor approximation is added around a sampling point, if its approximation is poor. All Taylor approximations are combined using inverse distance weighting. The resulting adaptive structure-mapping improves the quality of the result and efficiently identifies the best working fluids. The approach is demonstrated in a case study for working fluid selection of a solar ORC.

1. INTRODUCTION

Organic Rankine Cycles enable the utilization of low-temperature heat to generate electrical power. Low-temperature heat is available from different sources, e.g., solar (Tchanche et al., 2009), geothermal (Heberle and Brüggemann, 2010), biomass (Drescher and Brüggemann, 2007) or waste heat (Wang et al., 2012). To ensure optimal use of a heat source, the cycle needs to be tailored to the specific application. For tailoring the cycle, both have to be optimized: process and working fluid.

Today, working fluid selection and process optimization are commonly carried out separately following a two-step approach (Tchanche et al., 2009; Drescher and Brüggemann, 2007; Quoilin et al., 2013): In a first step, working fluid candidates are preselected by experience and based on heuristic guidelines defining favorable working fluid properties. In the second step, the process is optimized for each preselected working fluid. For the preselection, a variety of different, partly conflicting heuristic criteria have been proposed. Papadopoulos et al. (2010) combine therefore computer-aided molecular design (CAMD) methods and multi-objective optimization for working fluid selection. Importantly, the proposed criteria can not reflect the actual operating conditions. However, if the heuristic knowledge underlying

the preselection fail, meaningful and promising working fluids are excluded leading to suboptimal solutions. Working fluid selection is inherently coupled to process optimization. Thus, recent reviews (Quoilin et al., 2013; Bao, J. and Zhao, L., 2013) recommend including working fluid selection in process optimization to obtain an overall optimal solution. However, the direct integration of these two design tasks leads to a mixed integer nonlinear program (MINLP) of prohibitive size and complexity for practical applications (Lampe et al., 2014). Recently, Papadopoulos et al. (2013) use a process-related objective function. The working fluid properties are modeled by a cubic equation of state and combined with a process model.

Simultaneous optimization of process and working fluid is achieved in the Continuous-molecular targeting framework by relaxation of the pure component parameters describing the working fluid (Bardow et al., 2010; Lampe et al., 2014; Stavrou et al., 2014). Here, in a first step, a hypothetical working fluid is identified maximizing a process-based objective function. Then, real working fluids with similar properties are identified in the second step, the so-called structure-mapping. For this purpose, a Taylor approximation around the hypothetical optimal working fluid is used to estimate the objective function value of real working fluids. However, this local approximation suffers from occasional poor classification of real working fluids. In this work, we present a method for adaptive structure-mapping to allow for efficient identification of the best working fluids.

The paper is structured as follows: in section 2, the current CoMT framework is briefly reviewed. Our method for adaptive structure-mapping is introduced in section 3. In section 4, the adaptive structure-mapping is applied to a case study and the results are analyzed. Conclusions are drawn in section 5.

2. CONTINUOUS-MOLECULAR TARGETING FRAMEWORK

Selecting a suitable working fluid is a generic problem with applications beyond ORC processes. Bardow et al. (2010) propose a generic approach, the so-called continuous-molecular targeting (CoMT). The approach was first applied to achieve simultaneous optimization of solvents and processes. Lampe et al. (2014) successfully applied the CoMT framework for the simultaneous process and working fluid optimization of ORC processes (Figure 1).

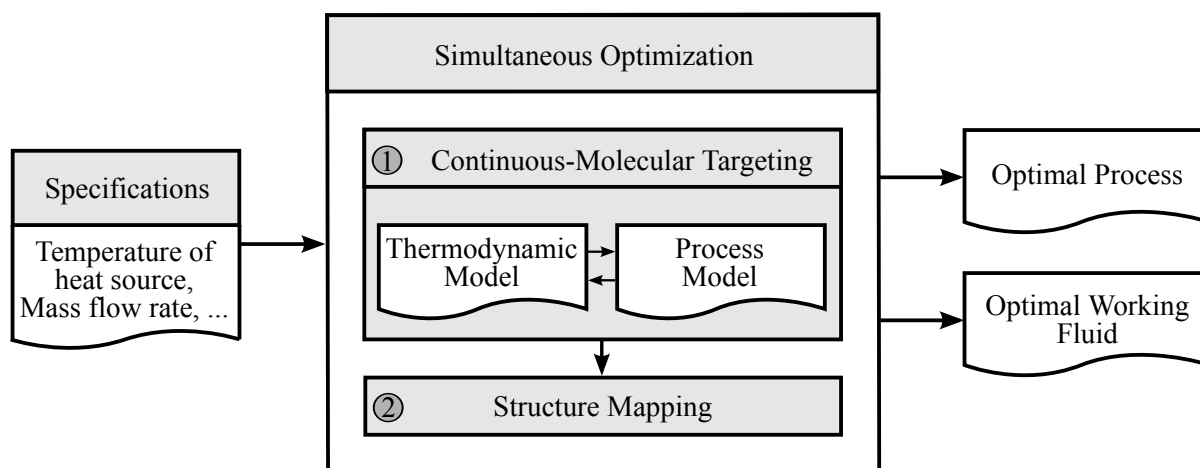


Figure 1: Simultaneous optimization of working fluid and process using the CoMT framework

To allow for the integrated process and working fluid optimization, we exploit the rich molecular picture underlying the perturbed-chain statistical associating fluid theory (PC-SAFT) equation of state (Gross and Sadowski, 2001). PC-SAFT is a model of the Helmholtz energy, which ensures a consistent picture of all equilibrium properties of the working fluid. A set of typically up to seven pure component parameters describes each working fluid (Stavrou et al., 2014). For simplicity, non-polar and non-associative

working fluids are considered in this work. Each working fluid is then described by three parameters: the segment number m , the segment diameter σ , and the segment dispersion energy ϵ/k .

A direct formulation of the integrated optimization using the pure component parameters as variables leads to a MINLP of prohibitive size and complexity, because a discrete degree of freedom is added to the problem for each real working fluid. Here, the MINLP is avoided by relaxing the pure component parameters during the simultaneous optimization of process and working fluid. Relaxation transforms the MINLP into a NLP of the form

$$\begin{aligned}
 & \max_{x,y} f(x,y) \\
 & s.t. \quad g(x,y) \leq 0 \\
 & \quad \quad h(x,y) = 0 \\
 & \quad \quad Ay \leq b \\
 & \quad \quad x_{\min} \leq x \leq x_{\max} \in \mathbb{R}^n \\
 & \quad \quad y_{\min} \leq y \leq y_{\max} \in \mathbb{R}^m
 \end{aligned} \tag{1}$$

where x denotes the process variables, y denotes the pure component parameters and $f(x,y)$ denotes the objective function to be optimized. Here, any objective function can be employed, which is based on equilibrium thermodynamics. First approaches are available to even calculate transport properties based on PC-SAFT (Novak, 2011; Lötgering-Lin and Gross, 2015). The integration of such approaches would allow for a thermoeconomic objective function still requiring only PC-SAFT parameters to describe the working fluid. Without loss of generality, maximization is considered. The inequality and equality constraints of the process as well as PC-SAFT are formed by $g(x,y)$ and $h(x,y)$. The solution of Problem (1) is a hypothetical optimal working fluid y^* and the corresponding optimal process parameters x^* . In general, the hypothetical optimal working fluid does not coincide with a real fluid. To identify real fluids, a database of pure component parameters is used in this work. The values of the database can, in turn, be used to constrain the search space for optimization. For this purpose, a convex hull around the pure component parameters of real working fluids y_k of a database is used. The convex hull is represented by the set of linear constraints $Ay \leq b$ in Problem (1).

In the second step, real working fluids with similar properties as the hypothetical optimal working fluid are identified (Figure 1). Currently, a second degree Taylor approximation around the hypothetical optimal working fluid is used to estimate the objective function value of real working fluids (Bardow et al., 2010; Lampe et al., 2014; Stavrou et al., 2014). For this purpose, it is necessary to rewrite the objective function $f(x,y)$ as

$$\begin{aligned}
 \tilde{f}(y) &= \max_x f(x,y) \\
 s.t. \quad & g(x,y) \leq 0 \\
 & h(x,y) = 0 \\
 & x_{\min} \leq x \leq x_{\max} \in \mathbb{R}^n.
 \end{aligned} \tag{2}$$

From Problem (2), the Taylor approximation around optimum values y^* is calculated:

$$T(y) = \tilde{f}(y^*) + J(y^*)(y - y^*) + \frac{1}{2}(y - y^*)^T H(y^*)(y - y^*). \tag{3}$$

Here, $J(y^*)$ denotes the Jacobian and $H(y^*)$ the Hessian of $\tilde{f}(y)$ at the sampling point y^* . Thus, the approximation of the performance for a working fluid is solely characterized by pure component parameters y_k . Based on the approximation $T(y_k)$, a ranking of potential working fluids is obtained. Each working fluid is classified by the rank r of the ranking. However, the Taylor approximation does not account for changes in the active set of constraints (Lampe et al., 2014), whereby a substantial deviation between the Taylor approximation and the real objective function value occurs (Figure 2a). Thus, working fluids are classified wrongly. To overcome these shortcomings, an adaptive structure-mapping is presented.

3. ADAPTIVE STRUCTURE-MAPPING

The adaptive structure-mapping iteratively identifies sampling points to adapt the approximation. In section 3.1, the method for selection of additional sampling points is presented. The adaption of the current approximation is detailed in section 3.2.

3.1 Algorithm

The key idea for the adaption of approximation is to apply a Taylor approximation not only once at the hypothetical optimal working fluid, but also at additional sampling points. The individual Taylor approximations $T_i(y)$ are combined to an adapted approximation $A(y)$ (Figure 2). The sampling points are selected in regions with a substantial deviation between the current approximation and the objective function. Through an iterative selection of suitable sampling points, the approximation, and therefore the structure-mapping, is adapted until a sufficient accuracy is achieved.

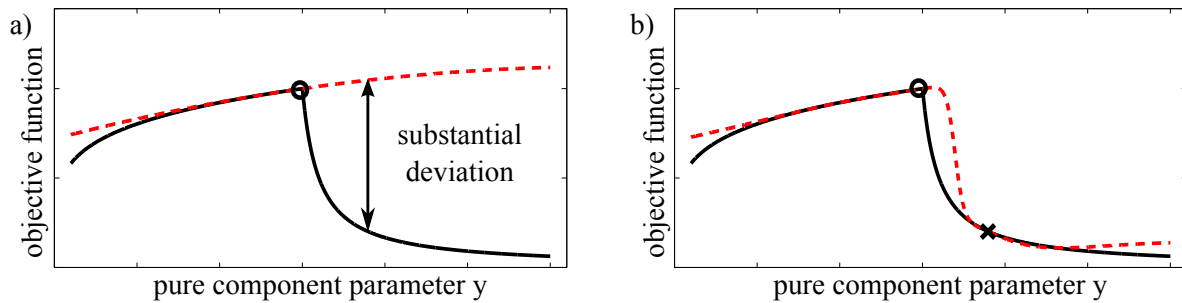


Figure 2: Qualitative illustration of the adapted approximation of the objective function $\tilde{f}(y)$ (black, solid) in the mapping step: a) Taylor approximation $T(y)$ (red, dashed) around the optimum y^* (marker \circ), b) adapted approximation $A(y)$ (red, dashed) with an additional sampling point (marker \times) in a region with previous substantial deviation between the objective function and the approximation.

The starting point is the ranking based on the Taylor approximation around the hypothetical optimal working fluid (step 1 in Figure 3). The selection of the next sampling point is performed by a systematic analysis of the current ranking (step 2). Beginning with the highest ranked working fluid $r = 1$ and following the order of the ranking, the real objective function value $\tilde{f}(y_r)$ of the r -th ranked working fluid y_r is calculated from Problem (2) (step 2a). This procedure continues, until the absolute difference ΔA_r between approximation $A(y_r)$ and real objective function value $\tilde{f}(y_r)$ exceeds a threshold ΔA_{\max} (step 2b)

$$\Delta A_r = |A(y_r) - \tilde{f}(y_r)| > \Delta A_{\max}. \quad (4)$$

Here, r denotes the rank of the working fluid in the current ranking. In this work, the threshold ΔA_{\max} is set to 5% of the objective function value of the hypothetical optimal working fluid. If the absolute difference ΔA_r exceeds the threshold, the pure component parameters of this r -th ranked working fluid are selected as additional sampling point. The approximation $A(y)$ is adapted by taking a Taylor approximation of the additional sampling point into account (step 3, see section 3.2 for details). A revised ranking of potential working fluids is obtained based on the adapted approximation (step 4). Subsequently, a termination criterion is checked (step 5). The algorithm stops, if for the first 15 ranks of the revised ranking a process optimization is performed in a previous iteration. If the termination criterion is not fulfilled, the algorithm continues at step 2. Beginning with the highest ranked working fluid $r = 1$, the algorithm analyzes the revised ranking systematically to select one more additional sampling point. Thus, the approximation is iteratively adapted to the objective function, since a region with previous poor approximation is improved by an additional Taylor approximation in each iteration. As a result, the method yields a ranking based on the real objective function values of the already calculated working fluids and the approximations of all further working fluids. The adaptive structure-mapping improves the quality of the ranking and allows for efficient identification of the best working fluids.

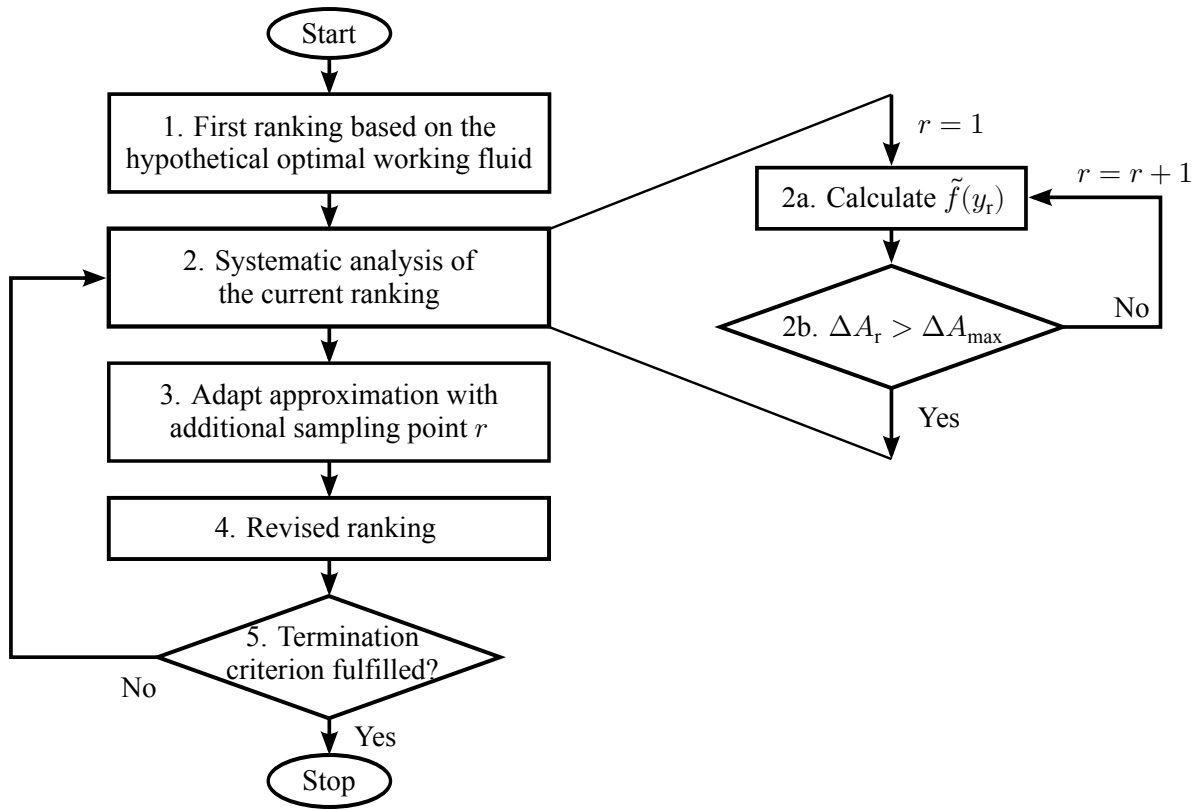


Figure 3: Flow chart for adaptive structure-mapping.

3.2 Adaptive approximation

The adaptive approximation $A(y)$ is a weighted sum of individual Taylor approximations $T_i(y)$. The Taylor approximations $T_i(y)$ are calculated by Equation (3), whereby the pure component parameters of the hypothetical optimal working fluid y^* are replaced by the sampling points y_i . The individual Taylor approximations $T_i(y)$ around the sampling points y_i are multiplied by a weighting factor $w_i^*(y)$ and combined to an adapted overall approximation $A(y)$ of the objective function

$$A(y) = \sum_{i=1}^S w_i^*(y) \cdot T_i(y), \quad (5)$$

whereby S denotes the number of sampling points. The weighting factor $w_i^*(y)$ increases the influence of Taylor approximation $T_i(y)$ the closer the pure component parameters y are to the corresponding sampling point y_i . A suitable method for this purpose is the so-called inverse distance weighting. In this work, the distance between two points in the three-dimensional space spanned by the pure component parameters $y = (m, \sigma, \epsilon/k)^T$ is considered. The pure component parameters have different magnitudes and units. To prevent effects of different scaling, the pure component parameters are normalized to one by

$$m_n = \frac{m - m_{\min}}{m_{\max} - m_{\min}}, \quad \sigma_n = \frac{\sigma - \sigma_{\min}}{\sigma_{\max} - \sigma_{\min}}, \quad (\epsilon/k)_n = \frac{(\epsilon/k) - (\epsilon/k)_{\min}}{(\epsilon/k)_{\max} - (\epsilon/k)_{\min}}, \quad (6)$$

yielding normalized pure component parameters $y_n = (m_n, \sigma_n, (\epsilon/k)_n)^T$. Here, parameters $y_{j,\min}$ and $y_{j,\max}$ are the smallest and largest value of the pure component parameters of the database respectively. The inverse distance $d_i^p(y)$ of the Taylor approximation $T_i(y)$ around a sampling point y_i is calculated by (Dumitru et al., 2013):

$$d_i^p(y) = \frac{1}{\|y_n - y_{n,i}\|^p}. \quad (7)$$

The weighting factor depends on the so-called power parameter p . The best results are typically obtained for $p = 2$ (Dumitru et al., 2013). To ensure that the approximation at the sampling point matches the

objective function value, the sum of all inverse distances is normalized to one leading to a weighting factor $w_i^*(y)$:

$$w_i^*(y) = \frac{d_i^{-P}(y)}{\sum_{u=1}^S d_u^{-P}(y)}. \quad (8)$$

The approximation $A(y)$ does not explicitly account for changes in the active set of constraints. However, the adaption captures the behavior of the objective due to the changes in the active set.

The adaptive approximation improves the solution but it can also produce suspicious solution as shown in the following. Figure 4 illustrates a qualitative one-dimensional example for the objective function and its approximation. A second degree Taylor approximation around a sampling point in a region with strong convex curvature leads to unphysical approximation and slow convergence of the adaptive structure-mapping (Figure 4a). This difficulty is circumvented by using a first degree Taylor approximation instead of a second degree Taylor approximation in regions with convex curvature (Figure 4b).

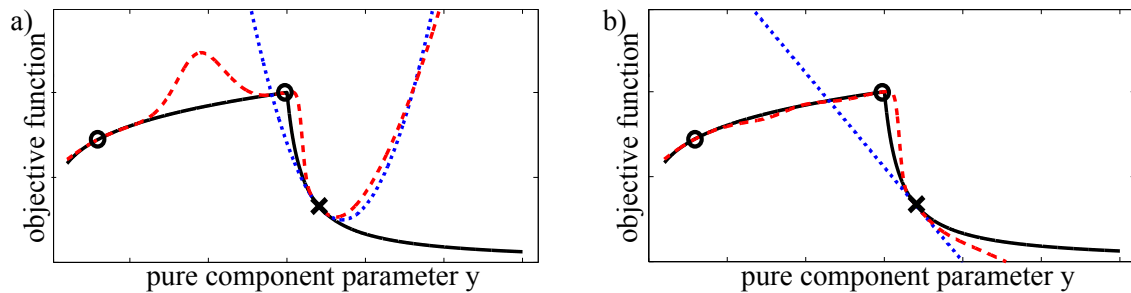


Figure 4: Approximation $A(y)$ (red, dashed) of the objective function $\tilde{f}(y)$ (black, solid) with a) second degree and b) first degree Taylor approximation $T_i(y)$ (blue, dotted) around a sampling point in a region with strong convex curvature (marker \times)

In the multidimensional case, a function is considered to be concave, if a concave curvature exists in all spatial directions. In the major part of the considered parameter space, the objective function shows both concave and convex curvatures in the various spatial directions. If first degree Taylor approximations are used whenever one spatial direction has convex curvature, a first degree Taylor approximation is chosen for almost all sampling points. This leads to slow convergence of the adaptive structure-mapping and, thus, longer computing time, since the approximation is much less accurate.

For this reason, we classify the vicinity of a sampling point as concave, if possible convex curvatures in all directions are negligible compared to the concave curvature. Curvature is evaluated from the eigenvalues of the Hessian $\tilde{H}(y_i)$ of the objective function $\tilde{f}(y)$. In order to ensure comparability of the eigenvalues, the Hessian is transformed to the normalized parameter space (Equation (6)). Positive eigenvalues characterize convex and negative concave curvature; the magnitude is a measure for the strength of the curvature. We allow convex curvature, if the highest eigenvalue λ_{\max} of the normalized Hessian is at least an order of magnitude smaller than the amount of the lowest eigenvalue λ_{\min} . With this restriction, the Hessian $H(y_i)$ in Equation (3) is

$$H(y_i) = \begin{cases} \tilde{H}(y_i), & \text{if } 10 \cdot \lambda_{\max} < |\lambda_{\min}| \\ 0_{3,3}, & \text{otherwise.} \end{cases} \quad (9)$$

Using this heuristic, more second degree Taylor approximations are selected, while avoiding unphysical impact of the convex curvature. This curvature approach proves suitable in all case studies.

4. CASE STUDY – SMALL-SCALE SOLAR THERMAL ORC SYSTEM

The adaptive structure-mapping is applied to the optimization of a ORC process with direct solar evaporation based on Casati et al. (2011). A recuperator is used to increase the efficiency. The net power

output P_{net} is considered as objective function. The degrees of freedom in the process model are: pressure of the condenser p_{cond} , pressure of the evaporator p_{evap} , degree of superheating ΔT_{sh} and mass flow rate of the working fluid \dot{m}_{wf} . We assume a fixed heat flow of the solar field \dot{Q}_{solar} at the temperature T_{Q} (Table 1). A minimal temperature difference in the heat exchangers ΔT_{pinch} is imposed to ensure feasible heat transfer. The pressure levels in the cycle are further constrained by minimal and maximal absolute pressures p_{min} and p_{max} , respectively.

Table 1: Solar source specifications and constraints for the case study

Parameter	Symbol	Value
temperature of heat source	T_{Q}	380 °C
heat flow of the solar field	\dot{Q}_{solar}	463 kW
temperature of heat sink	T_{S}	80 °C
maximal absolute pressure	p_{max}	50 bar
minimal absolute pressure	p_{min}	0.05 bar
minimal temperature difference	ΔT_{pinch}	10 K
isentropic turbine efficiency	η_{T}	80 %
generator efficiency	η_{G}	95 %
isentropic pump efficiency	η_{P}	70 %
mechanic pump efficiency	$\eta_{\text{P,mech}}$	90 %

The adaptive structure-mapping is applied to a database of 223 working fluids. In order to evaluate the results of the structure-mapping, an individual process optimization for all working fluids of the database is performed. A real ranking is obtained, which serves as an unambiguous measure for the quality of the ranking from the adaptive structure-mapping. Thus, the database is comparatively small to allow for an efficient validation. The database can easily be extended to consider more fluids. Alternatively, computer-aided molecular design can be employed for the design of working fluids (Lampe et al., 2015). For this case study, the adaptive structure-mapping terminates after two iterations, i.e., three sampling points are used for the overall approximation. All sampling points are approximated by a second degree Taylor approximation. To evaluate the results of the adaptive structure-mapping, the ranking after each iteration is compared to the real ranking. Spearman's rank correlation coefficient ρ_s serves as a measure for the correlation (Puth et al., 2015): The closer the correlation coefficient ρ_s is to one, the better is the correlation. The corresponding real rank is plotted for the 60 highest ranked working fluids of the structure-mapping (Figure 5).

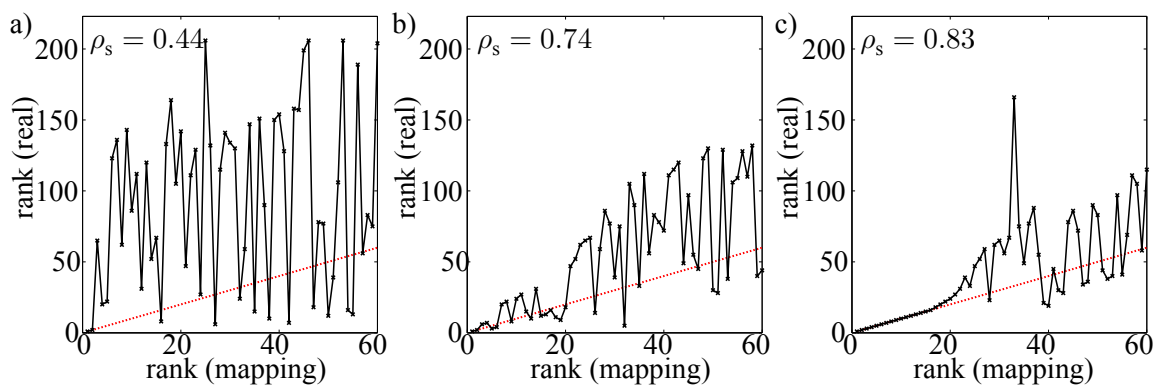


Figure 5: Comparison of result of the CoMT-CAMD approach (black, solid) with one (a), two (b) and three (c) sampling points and the ideal result (red, dotted)

The original structure-mapping with only one Taylor approximation around the hypothetical optimal working fluid identifies the best two working fluids but shows large deficits (Figure 5a): Many working fluids are overestimated and ranked too well. Here, Spearman's rank correlation coefficient is $\rho_s = 0.44$.

The result with two sampling points shows a better correlation ($\rho_s = 0.74$, Figure 5b). In particular, the top 20 are already well captured. The final result with three sampling points identifies the top 20 nearly in the correct order ($\rho_s = 0.83$, Figure 5c).

The original structure-mapping with one Taylor approximation around the hypothetical optimal working fluid identifies only 2 working fluids of the top 10 (4 of the top 20). This result is improved significantly by the adaptive structure-mapping: all working fluids of the top 10 and 18 of the top 20 are identified correctly. The improvement is archived by a more accurate approximation of the objective function in the relevant region. To visualize the functionality of the adaptive structure-mapping, the working fluid ethylcyclohexane is examined ($m = 3.0$, $\sigma = 4.0 \text{ \AA}$, $\epsilon/k = 283.8 \text{ K}$). Ethylcyclohexane is ranked 9th in the real ranking. Figure 6 shows the optimal net power output \tilde{f} as function of the segment number m for constant segment diameter σ and segment dispersion energy ϵ/k corresponding to the pure component parameters of ethylcyclohexane. The pure component parameters of the hypothetical optimal working fluid y^* are $m^* = 1.8$, $\sigma^* = 4.1 \text{ \AA}$, and $(\epsilon/k)^* = 408.6 \text{ K}$ and are not in the plane of Figure 6. Additionally, the approximation function $A(y)$ with one, two, and three sampling points are plotted. The Taylor approximation around the optimum is not sufficient to approximate the objective function in this region. A substantial deviation between the approximation $A(y)$ and the objective function $\tilde{f}(y)$ occurs: ethylcyclohexane is underestimated and ranked 69th. However, the approximation with three sampling points corresponds well to the objective function. Ethylcyclohexane is correctly ranked 9th in the final ranking.

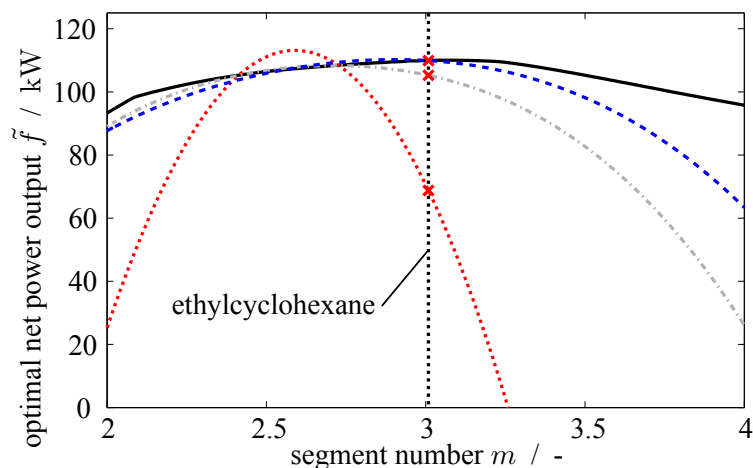


Figure 6: Optimal net power output \tilde{f} (black, solid) and the approximation function $A(y)$ with one (red, dotted), two (gray, dash-dotted) and three (blue, dashed) sampling points as function of the segment number m for constant segment diameter $\sigma = 4.0 \text{ \AA}$ and segment dispersion energy $\epsilon/k = 283.8 \text{ K}$ corresponding to the pure component parameters of ethylcyclohexane. The optimal values are $m^* = 1.8$, $\sigma^* = 4.1 \text{ \AA}$ and $(\epsilon/k)^* = 408.6 \text{ K}$.

Finally, the effectiveness of the method is evaluated based on the required computing effort. The number of function evaluations of the objective function in the optimizations for both the adaptive structure-mapping and the calculation of the real ranking are compared. For the adaptive structure-mapping, the function evaluations of the CoMT-optimization, the calculation of Jacobians and Hessians by finite differences, and the calculation of real objective function values are considered. For the real ranking, the function evaluations to calculate the individual process optimizations of each working fluid of the database are counted.

The calculation of the real ranking requires 31,537 function evaluations. The calculation of the case study by the adaptive structure-mapping takes 3,951 function evaluations, which corresponds to savings of 87.5%. Thus, the adapted CoMT framework is far more efficient than an individual optimization of each working fluid to identify the best working fluids. Considering a larger database, the number

of function evaluations to calculate the real ranking would increase with the number of working fluids. In contrast, in our experience, there is no direct correlation between the number of working fluids and function evaluations in the CoMT framework, so that overall, the efficiency of the CoMT framework is expected to increase.

If the heuristic regarding the negligible convex curvature is not made (see Section 3.2), the adapted CoMT framework requires 12,805 function evaluations and 10 sampling points to identify the ten best working fluids. In this case, five first degree Taylor approximations and five second degree Taylor approximations are employed. If exclusively first degree polynomials are used, the CoMT framework requires 17,838 function evaluations and 24 sampling points. The results demonstrate the advantage of using second degree polynomials and the heuristic regarding negligible convex curvature.

5. CONCLUSIONS

Simultaneous design of ORC process and working fluid is enabled by the Continuous-molecular targeting framework. However, mapping of the targets onto real working fluids occasionally failed. For this purpose, an adaptive structure-mapping is presented to identify the best working fluids for ORC processes based on continuous-molecular targets. The approximation used for the structure-mapping is iteratively adapted by combining several Taylor approximations around different sampling points. A method to select sampling points is presented and a heuristic for the selection of the degree of the Taylor approximations is proposed. The result of the method is a ranked set of working fluids. The adaptive structure-mapping improves the quality of the ranking and allows for efficient identification of the best working fluids.

The adaptive structure-mapping is successfully applied to a case study, where the original mapping only identifies 2 working fluids out of the top 10 correctly. The adaptive method correctly identifies all working fluids of the top 10. Thereby, the adaptive structure-mapping is more efficient than an individual optimization of each working fluid: In this case study, the function evaluations are reduced by 87.5 %.

NOMENCLATURE

A	approximation function	(-)	T	Taylor approximation	(-)
d^{-p}	inverse distance	(-)	w^*	normalized weighting factor	(-)
f, \tilde{f}	objective function	(-)	x	process variables	(-)
g	inequality constraints	(-)	x^*	optimal process parameters of y^*	(-)
H, \tilde{H}	Hessian	(-)	y	pure component parameters	(-)
h	equality constraints	(-)	y^*	hypothetical optimal working fluid	(-)
J	Jacobian	(-)	ϵ/κ	associating energy	(K)
m	segment number	(-)	λ	eigenvalues	(-)
p	power parameter	(-)	ρ_s	rank correlation coefficient	(-)
S	number of sampling points	(-)	σ	segment diameter	(Å)

Subscript

i	sampling point	min	minimal
k	real working fluid of the database	n	normalized
max	maximal	r	rank

REFERENCES

- Bao, J. and Zhao, L. (2013). A review of working fluid and expander selections for organic rankine cycle. *Renewable and Sustainable Energy Reviews*, 24:325–342.
- Bardow, A., Steur, K., and Gross, J. (2010). Continuous-molecular targeting for integrated solvent and process design. *Ind. Eng. Chem. Res.*, 49(6):2834–2840.

- Casati, E., Colonna, P., and Nannan, N. R. (2011). Supercritical ORC turbogenerators coupled with linear solar collectors. In *Proceedings of the ISES solar world congress 2011, Kassel, Germany, 2011*.
- Drescher, U. and Brüggemann, D. (2007). Fluid selection for the organic rankine cycle (ORC) in biomass power and heat plants. *Applied Thermal Engineering*, 27(1):223 – 228.
- Dumitru, P. D., Plopeanu, M., and Badea, D. (2013). Comparative study regarding the methods of interpolation. In *1st European Conference of Geodesy & Geomatics Engineering 2013, Recent Advanced in Geodesy and Geomatics Engineering—Conference Proceedings, 45-52pp, Antalya, Oct. 8*, volume 10.
- Gross, J. and Sadowski, G. (2001). Perturbed-chain SAFT: An equation of state based on a perturbation theory for chain molecules. *Ind. Eng. Chem. Res.*, 40(4):1244–1260.
- Heberle, F. and Brüggemann, D. (2010). Exergy based fluid selection for a geothermal organic rankine cycle for combined heat and power generation. *Applied Thermal Engineering*, 30(11-12):1326 – 1332.
- Lampe, M., Stavrou, M., Bücker, H. M., Gross, J., and Bardow, A. (2014). Simultaneous optimization of working fluid and process for organic rankine cycles using PC-SAFT. *Ind. Eng. Chem. Res.*, 53(21):8821–8830.
- Lampe, M., Stavrou, M., Schilling, J., Sauer, E., Gross, J., and Bardow, A. (2015). Computer-aided molecular design in the continuous-molecular targeting framework using group-contribution PC-SAFT. *Computers & Chemical Engineering*.
- Lötgering-Lin, O. and Gross, J. (2015). A group contribution method for viscosities based on entropy scaling using the perturbed-chain polar statistical associating fluid theory. *Ind. Eng. Chem. Res.*, submitted.
- Novak, L. T. (2011). Fluid viscosity-residual entropy correlation. *Int. J. Chem. React. Eng.*, 9(1).
- Papadopoulos, A. I., Stijepovic, M., and Linke, P. (2010). On the systematic design and selection of optimal working fluids for organic rankine cycles. *Applied Thermal Engineering*, 30(6-7):760 – 769.
- Papadopoulos, A. I., Stijepovic, M., Linke, P., Seferlis, P., and Voutetakis, S. (2013). Toward optimum working fluid mixtures for organic rankine cycles using molecular design and sensitivity analysis. *Ind. Eng. Chem. Res.*, 52(34):12116–12133.
- Puth, M.-T., Neuhäuser, M., and Ruxton, G. D. (2015). Effective use of spearman’s and kendall’s correlation coefficients for association between two measured traits. *Animal Behaviour*, 102:77 – 84.
- Quoilin, S., Broek, M. V. D., Declaye, S., Dewallef, P., and Lemort, V. (2013). Techno-economic survey of organic rankine cycle (ORC) systems. *Renewable and Sustainable Energy Reviews*, 22:168 – 186.
- Stavrou, M., Lampe, M., Bardow, A., and Gross, J. (2014). Continuous molecular targeting-computer-aided molecular design (CoMT-CAMD) for simultaneous process and solvent design for CO₂ capture. *Ind. Eng. Chem. Res.*, 53(46):18029–18041.
- Tchanche, B. F., Papadakis, G., Lambrinos, G., and Frangoudakis, A. (2009). Fluid selection for a low-temperature solar organic rankine cycle. *Applied Thermal Engineering*, 29(11-12):2468 – 2476.
- Wang, Z. Q., Zhou, N. J., Guo, J., and Wang, X. Y. (2012). Fluid selection and parametric optimization of organic rankine cycle using low temperature waste heat. *Energy*, 40(1):107 – 115.

ACKNOWLEDGEMENT

We thank the Deutsche Forschungsgemeinschaft (DFG) for funding this work (BA2884/4-1).

NUMERICAL AND EXPERIMENTAL INVESTIGATION ON THE ROTARY VANE EXPANDER OPERATION IN MICRO ORC SYSTEM

Piotr Kolasinski*¹, Przemysław Błasiak²

^{1,2}Wrocław University of Technology,
Department of Thermodynamics, Theory of Machines and Thermal Systems
Wrocław, Poland
E-mail: ¹piotr.kolasinski@pwr.edu.pl, ²przemyslaw.blasiak@pwr.edu.pl

* Corresponding Author

ABSTRACT

Volumetric expanders are nowadays used in micro, small and medium power ORC systems. As it was indicated by Bao and Zhao (2013) most often spiral and screw machines are applied. However, it can be seen that the application of rotary vane expanders is also growing (Tchanche et al. (2011)). Rotary vane expanders are particularly interesting because of the many advantages they have. The most important features of such expanders are: very simple construction; high power in relation to the dimensions; the ability to operate in low inlet pressure and wet gas conditions; low weight; lack of clearance volume; lack of steering valves; possibility to construct an oil-free machines; ease of sealing; the ability to operate at low rotational speeds and a low price. As it was described by Gnutek and Kolasinski (2013) power range of the rotary vane expanders is 0.1—7 kW, thus these machines are particularly interesting for micro and domestic ORC systems. Vane expanders used in ORC systems are very similar to these commonly used in pneumatic systems, however, it is necessary to carry out the appropriate adaptation of the machine. This includes special hermetic sealing, lubrication and cooling. As a part of the research works on ORC power systems with vane expanders conducted by the authors on Wrocław University of Technology a research test-stand (comprehensively described by Gnutek and Kolasinski (2013)) was designed and realized. This micro power, R123 based, ORC prototype enables experimental analysis of the vane expander operation under different conditions. In this article authors present the results of numerical simulation of vane expander operation in ORC prototype and compared them with the results of experiment. 3D model of the expander was built and analyzed in ANSYS CFX based on the geometrical data obtained by complete disassembly of the machine. The numerical analysis included the same, as in the case of the experiment, expander operating conditions, i.e. pressure, temperature and R123 flow rate at the inlet and outlet of the expander.

1. INTRODUCTION

As it was indicated by Lund and Münster (2006) effective energy recovery from renewable and waste energy sources is one of the most important present-day problems. Advanced energy systems based on local waste heat, renewables and fossil fuel resources can give the opportunity for an increase of consumers energy safety and continuity of energy supply. However, implementation of local energy systems requires the relevant energy conversion technologies.

One of the promising energy conversion technologies is a ORC system. ORC power systems may differ in power, purpose and technical configuration. Available are: micro power (0.5—10 kW), small power (10—100 kW), medium power (100—500 kW) and a large power (500 kW and more) systems. As it was presented by Vanslambrouck (2009) they can operate as power plants, CHP's and multi-generation systems.

The most important problems connected with ORC system design are the suitable working fluid and expander selection. Expander selection is mainly based on the system power and its purpose. In

general, two types of expanders can be applied in ORC systems. One are the turbines, the others are volumetric machines.

Turbines are mainly applied in an large and medium power ORC systems powered by the heat sources with high thermal capacity (1 MW and more) and temperature (150 °C and more), such as large industrial waste sources e.g. steam boilers or gas turbine exhaust gases. Volumetric expanders are applied mainly in micro and small power systems such as domestic and agriculture plants. One of the most important problems in this case is the dynamic thermal characteristic of the heat source also characterized by small capacity, thermal power and temperature (up to 150 °C). Variation in the heat source properties has a negative influence on the continuity of the system operation and difficulty in system adjustment. Therefore the design and construction of small and micro power ORC systems is very difficult and most of the existing systems are still at the level of prototype or under research. In low and micro power ORCs applicability of turbines is very limited due to the machine operational characteristics requiring large flow of the working medium. Moreover microturbines are very small in dimensions what results in very high rotational speeds and difficulty of a rotor balancing and bearing. The necessity of a very precise parts fitting result in high manufacturing costs. This is the contrary to the aim of small ORC systems which should be simple, cheap and easy to use.

Volumetric expanders are a good option for systems where the low pressures and low working medium flows are expected. In general piston, screw, spiral, vane and the rotary lobe expanders can be applied in small and micro ORC plants. The general advantages of volumetric expanders resulting from comparison with the turbines were comprehensively described by Gnutek and Kolasiński (2013). Vane expanders are especially interesting for small and micro ORC systems. Currently they became a subject of different experimental and numerical scientific analyses (Montenegro et al. (2014)). Micro vane expander has a number of advantages resulting from comparison with other volumetric expanders. The most important are: very simple design, high power in relation to the dimensions, suitability for wet gas conditions, low weight, ease of gas-tight sealing and very low price. There are no ORC-dedicated vane expanders available, however, standard pneumatic air motors can be easily adapted.

As a part of the research works on ORC power systems with vane expanders, conducted by the authors on Wrocław University of Technology, a research test-stand (comprehensively described by Gnutek and Kolasiński (2013)) was designed and realized. This micro power, R123 based, ORC prototype enables experimental analysis of the vane expander operation under different conditions.

The authors decided to carry out the experiment on the test-stand and to compare the results with numerical analysis of the applied vane expander. 3D model of the expander was built and analyzed in ANSYS CFX based on the geometrical data obtained by complete disassembly of the machine. The numerical analysis included the same, as in the case of the experiment, expander operating conditions i.e. pressure, temperature and R123 flow rate at the inlet and outlet of the expander.

2. DESCRIPTION OF THE TEST-STAND, THE EXPANDER AND THE EXPERIMENTAL RESULTS

An experimental test-stand was designed and realized in order to study the influence of the different operational conditions on the operation of the rotary vane expander. Figure 1 shows a simplified construction scheme of the test-stand. The main test-stand components are: the gas central heating boiler (featuring maximal thermal power of 24 kW) (1), the shell-and-tube evaporator (2), the working fluid pump (3), the reservoir of working fluid (4), the plate condenser (5) and the micro multivane expander connected with DC generator (6). The working fluid is R123. The test stand is based on manual control of operational parameters with the help of regulation valves. The manual control helps in simulating different operational conditions e.g. it is possible to change the working medium flow direction in the evaporator from a counter-flow to the co-current. The measurements are carried out using the following methods: temperatures are measured with the use of T-type thermocouples, pressures are measured with the use of tube pressure gauges. The flow rate of R123 as well as the flow rate of cooling and heating water are measured with the use of rotameters (See Fig. 1 for the measurement sensors locations: p – manometer, t – thermocouple, V – rotameter).

The heat source for the system is hot water from the gas central heating boiler (1). The temperature of the heat source can be regulated in the range of 40–85 °C. This allows the evaluation of operational conditions of the ORC power system for variable heat sources.

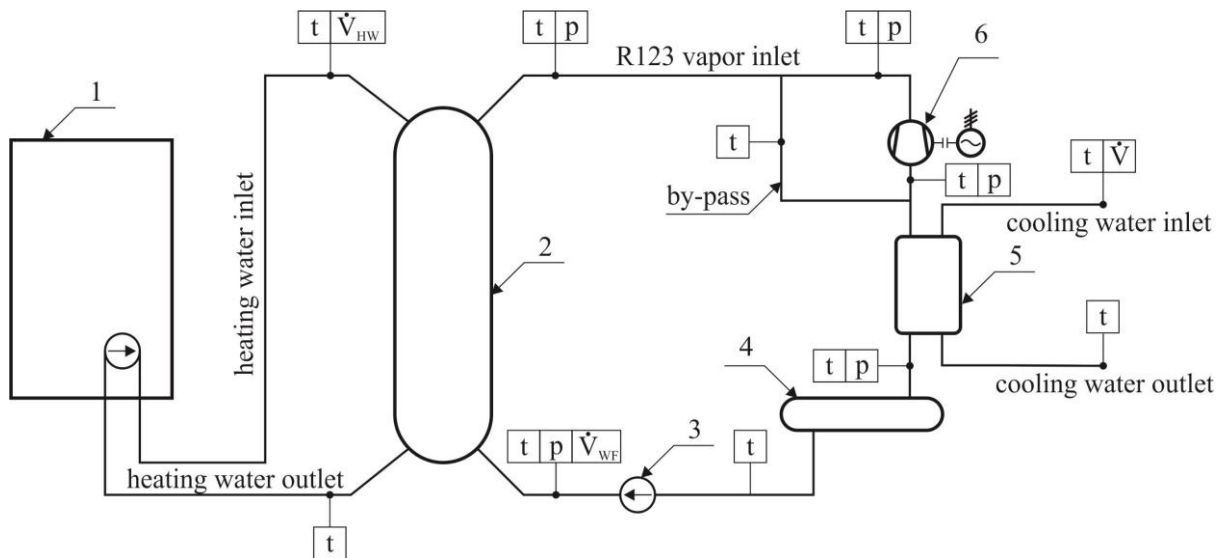


Figure 1: The simplified construction scheme of the test-stand.

- 1 – gas central heating boiler, 2 – shell-and-tube evaporator, 3 – working fluid pump,
4 – reservoir of working fluid, 5 – plate condenser, 6 – multivane expander with DC generator

A more detailed description of the test stand was presented by Gnutek and Kolasiński (2013). The expansion device is a micro four-vane air motor featuring a maximum power of 600 W. The expander was specially adapted for low-boiling working fluid e.g. the special seals and bearings were used. Moreover, a number of changes in the expander design were made in order to maximize the machine power. The expander is connected by gas-tight clutch with a small DC generator. Figure 2 shows a view of the expander-generator unit disassembled from the test-stand.



Figure 2: The view of the expander-generator unit disassembled from the test-stand

The design of the above described rotary vane expander is presented in figure 3. It consists of cylindrical stationary cylinder of inner diameter 37.5 mm and rotating rotor of outer diameter 34.0 mm. The rotor is placed eccentrically relative to the cylinder. Eccentricity is 1.75 mm. Length of the cylinder is 22.0 mm. Rotor is equipped with four flat vanes, which can move in the slots due to centrifugal forces. Vanes are positioned to the cylinder surface in the right angles. Thickness of each vane is 1.5 mm. Rotary vane expander is fed with R123 working fluid via cylindrical pipe of inner

diameter 8.5 mm. Pipe is tangentially located at side surface of the cylinder. On the second side there is identical outlet pipe where gas leaves the expander chamber to the condenser. The operation principle of rotary vane expander is as follows: high pressure at inlet acts on the vanes and results in rotary motion of the rotor. Due to eccentricity and moving blades, working chamber constantly changes its volume from lowest to highest. The working fluid is trapped in chamber which volume increases with increase of angle of rotation. Consequently working fluid expands and exits through the outlet to the condenser. Rotational energy of the rotor is transformed into mechanical work which is the main output of the rotary vane expander.

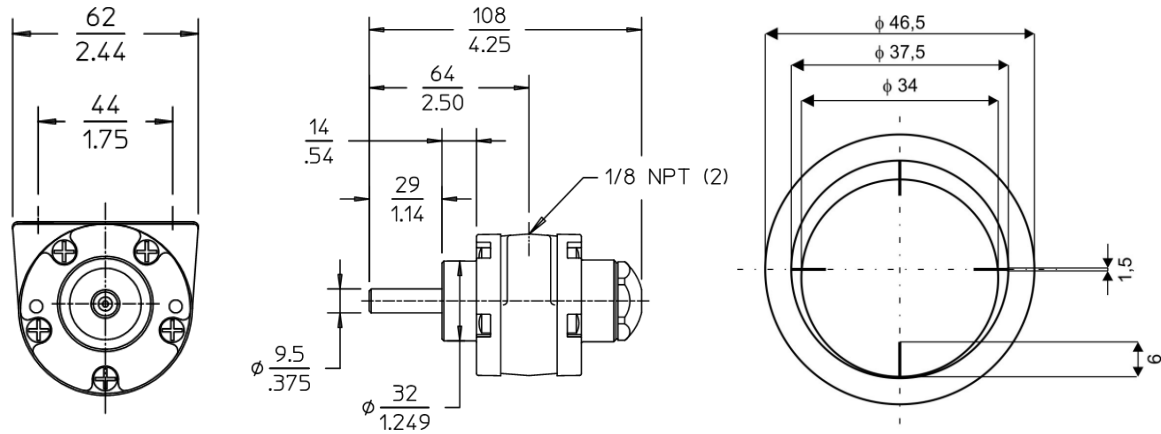


Figure 3: Dimensions of the rotary vane expander being considered.

In order to determine the working fluid thermal properties at the inlet and the outlet of the expander the experiment was carried out on the test-stand. The authors decided to carry out this experiment for the maximum temperature of the heat source ($t = 85\text{ }^{\circ}\text{C}$) and maximum working medium pressure allowed for this expander ($p = 0.5\text{ MPa}$). For this conditions the measured thermal properties of the working fluid at the inlet to the expander were $p_{in} = 0.5\text{ MPa}$ and $t_{in} = 80\text{ }^{\circ}\text{C}$. The measured outlet temperature was $t_{out} = 65\text{ }^{\circ}\text{C}$ and the outlet pressure was $p_{out} = 0.1\text{ MPa}$. The measurement results together with the corresponding values of specific enthalpy and the specific entropy (determined with the SOLKANE software) are presented in table 1.

Table 1: The experimental results

\dot{m}_{R123}	t_{in}	p_{in}	t_{out}	p_{out}	h_{in}	s_{in}	h_{out}	s_{out}
kg/s	$^{\circ}\text{C}$	MPa	$^{\circ}\text{C}$	MPa	kJ/kg	kJ/kgK	kJ/kg	kJ/kgK
0.0615	81	0.5	65	0.1	429.48	1.6788	424.88	1.7472

Presented above experimental results are the input data to the described below numerical analysis.

3. NUMERICAL MODELING

3.1 Numerical domain

In the figure 4 three dimensional numerical domain and mesh are depicted. Additionally the mesh details near the tip of the vanes and inlet/outlet areas are also visible. Numerical domain consists of fluid regions only and housing walls of the rotary vane expander are modelled via boundary conditions. Additionally numerical domain was divided into two areas: stationary inlet and outlet pipes and rotating part including fluid residing in the working chambers of the rotary vane expander. Dimensions of the numerical domain are the same as described in the previous section. The inlet and outlet are in the distance 45 mm from the Y axis of the rotary vane expander. Inner cylinder surface is

represented by the CYLINDER surface and outer surface of the rotor by ROTOR surface. Due to small differences between rotor and cylinder diameter it was hard to provide good quality mesh in the case of vane thickness 1.5 mm. In order to overcome this difficulties vane thickness in the model was set up to 0.5 mm. This simplification does not introduce significant error during the calculation because impact of vane thickness on heat transfer and fluid flow is negligible. Additionally it was impossible to use gap value between vane tip and cylinder wall less than 0.15 mm due to strong curvature of the geometry. Therefore for each time step during the simulation gap was hold to 0.3 mm for each vane to avoid creation of negative volumes in the numerical mesh. It results in eccentricity 1.45 mm whereas in the real rotary vane expander it equals to 1.75 mm. Nevertheless, in the reality small gaps always exists due to sealing rings and small gaps should be taken into account in order to model leakage phenomenon (Montenegro et al., 2014). In the present study hexahedral mesh was used for rotor domain with 9 control volumes in the gap and number of hexahedrons equal to 75492. For the inlet and outlet pipes tetrahedral mesh was used with total number of tetrahedrons equal to 109383.

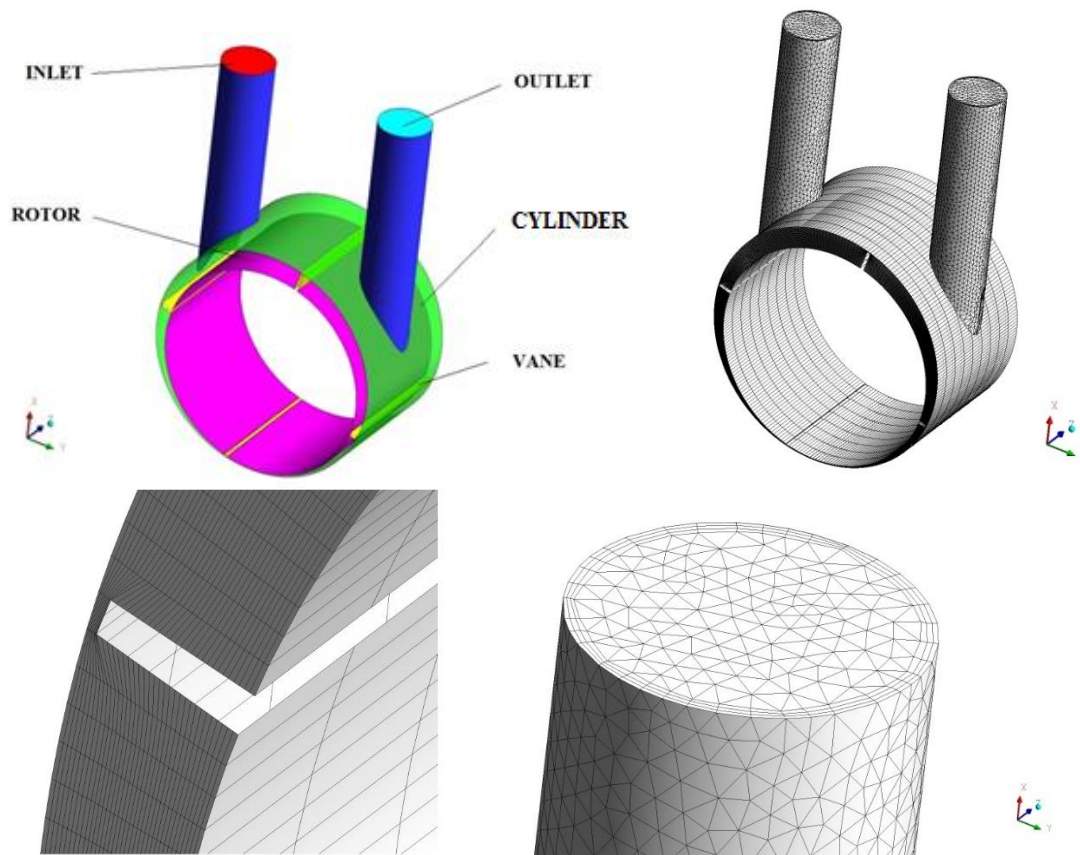


Figure 4: Three dimensional numerical domain of the rotary vane expander and numerical mesh. At the bottom mesh details near the vane tip and inlet/outlet areas

3.2 Numerical model

Non-isothermal, incompressible turbulent flow in the rotary vane expander has been considered. Transport equations of mass, momentum and energy were solved with the use of commercial solver (Ansys, 2014). In the absence of a phase change, radiation and with neglecting dissipation function term these equations can be written in the following vector form

Continuity equation

$$\nabla \cdot \mathbf{U} = 0 \quad (1)$$

Momentum equation

$$\frac{\partial \rho \mathbf{U}}{\partial \tau} + \nabla \cdot (\rho \mathbf{U} \mathbf{U}) = -\nabla p + \nabla \cdot [\mu (\nabla \mathbf{U} + \nabla \mathbf{U}^T)] \quad (2)$$

Energy equation

$$\rho c_p \left[\frac{\partial T}{\partial \tau} + \nabla \cdot (T \mathbf{U}) \right] = \nabla \cdot (k \nabla T) \quad (3)$$

where \mathbf{U} stands for total velocity vector, i.e. difference between velocity vector and moving mesh velocity vector. It is due to the incorporated deforming mesh method (Ansys, 2014) in order to take into account movement of the rotor and vanes. Deforming mesh method consists in calculating in each time step the shape of the moving boundaries. Additionally the nodes distribution in the mesh is calculated according to the following diffusion equation

$$\nabla \cdot (\Gamma_{disp} \nabla \delta) = 0 \quad (4)$$

where δ is the displacement relative to the previous mesh locations and Γ_{disp} is the mesh stiffness, which determines the degree to which regions of nodes move together (Ansys, 2014). It is so-called displacement diffusion model and preserves the relative mesh distribution of the initial mesh. Deforming mesh method requires additional computational resources, but it provides most accurate results for issues with moving parts. Due to simple geometry of the rotary vane expander for each of the boundary surface equations of motion were specified via CEL expressions (CFX Expression Language). They are basically code routines written in Fortran programming language and can be easily incorporated in the solver. The deforming mesh method is inherently transient because shape of the numerical domain changes constantly and has to be determined for each time step. In the present study rotor moves at constant rotational speed $n = 3000$ rev/min. The time step used in the simulations corresponds to the rotation of the rotor about 0.1 degree. Very high rotational speed results in fully turbulent flow. In order to turbulent flow standard k- ϵ model was used. Both convection, temporal and turbulent terms in the transport equations were solved with use of high resolution scheme. For each wall no-slip boundary condition was applied. The vane and the rotor surfaces were treated as adiabatic. On the cylinder and side walls convective boundary condition was imposed with heat transfer coefficient $h = 5$ W/(m²K) and ambient temperature $t_{amb} = 20^\circ$ C. Working fluid enters the inlet pipe under 0.5 MPa pressure and in temperature 81 °C and exits through outlet in temperature 65 °C. The outlet pressure is equal to 0.1 MPa. In order to provide information transfer between stationary and rotating subdomains, interface boundary condition was used. The working fluid used in the simulation was R123. It was treated as Newtonian with having constant thermo-physical properties determined from the Refprop software for the mean temperature 73 °C and presented in table 2. Calculations were conducted up to five full rotor revolutions and then periodic steady state was assumed. It was reasonable due to small differences between successive fourth and fifth rotation. In terms of residuals, within each timestep calculations were conducted to achieve convergence below 10^{-6} .

Table 2: Thermo-physical properties of R123 used in the simulation

ρ	c_p	μ	k	Pr
kg/m ³	J/(kgK)	μ Pa·s	W/(mK)	-
10.00	750.00	12.388	0.01201	0.77

4. NUMERICAL RESULTS AND DISCUSSION

Figure 5 shows the pressure distribution in the working chambers during rotor movement. As it can be seen from this figure the highest pressure of the working fluid is in the inlet port and filled working chamber. During the rotor movement working fluid pressure decreases with the decreasing volume of the working chamber. The lowest pressure is in the outlet port during the evacuation of the working fluid from the machine. Figure 6 shows the working fluid velocity vectors during the rotor movement. The highest velocities can be observed in the 2nd and the 3rd working chamber, where the chamber volume is minimal. Relatively low working fluid velocities can be observed in the inlet and the outlet ports. Also, in these areas, vortices can be observed. These vortices have negative influence on the expander operation, as they result in working fluid pressure changes and mixing, thus the edges of the inlet and the outlet port of the expander should be redesigned and optimized. Figure 7 shows the temperature distribution in the working fluid during the expander operation. As it can be seen in this figure the working fluid temperature decreases during the expansion. In the inlet and the outlet port the local temperature fluctuations are appearing. These fluctuations are resulting from both the leakage between the vane and the cylinder (the hot gas flowing into the 1st expander working chamber mixes with the gas in the 4th expander working chamber and the gas flowing through the outlet port) and vortices appearing in these areas (increased velocity of the fluid and change in the fluid internal energy).

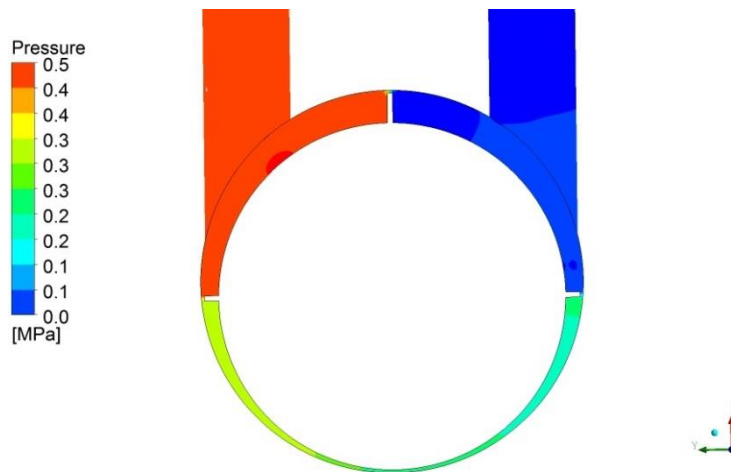


Figure 5: Pressure distribution in the plane for $z = 0.011$ m

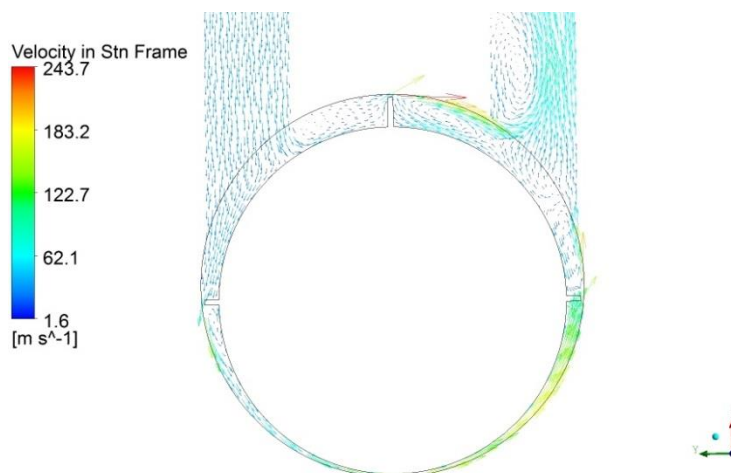


Figure 6: Vectors of velocity in the stationary frame of reference in the plane for $z = 0.011$ m

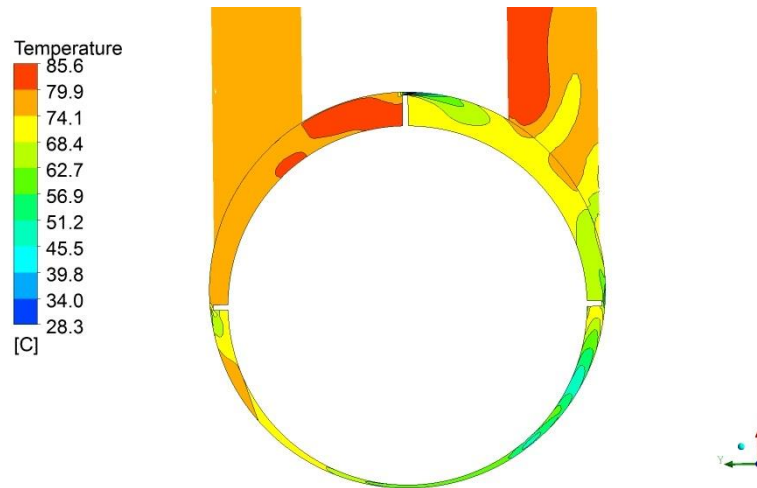


Figure 7: Temperature distribution in the plane for $z = 0.011$ m

5. SUMMARY AND CONCLUSIONS

In this study the numerical and experimental analysis of the micro-power rotary vane expander operation in ORC system were presented. Numerical analysis was based on 3D model of the expander which was built basing on the geometrical data obtained by complete disassembly of the experimentally tested machine. Numerical analysis of the expander operation was performed in ANSYS CFX, basing on the thermodynamic parameters measured on the test-stand.

The results of the analysis showed the distributions of the pressure, velocity vectors and the temperature of R123 in the expander working chambers. The calculated results show that in the case of volumetric machines the working fluid velocities inside the working chambers are low when compared to the turbines. Moreover, the velocity vectors distribution indicated that in the inlet and the outlet port of the expander large vortices are appearing. These vortices have negative influence on the expander operation, and should be optimized by the change in the expander design. Thus, the sharp edges of the inlet and the outlet port should be redesigned. One of the possible solutions is the change of the inlet and the outlet port diameter to the larger and rounding the edges. Also, the optimization of the expander design should include the change of the rotor diameter to the lower and the length of the cylinder to the larger, in order to increase the volume of the working chambers. Increased volume of the working chambers will result in the increase of the expander power. The authors are currently working on further numerical and experimental analyses concerning the optimization of the volumetric expanders design.

NOMENCLATURE

The nomenclature should be located at the end of the text using the following format:

δ	relative displacement	(–)
Γ	mesh stiffness	(–)
μ	dynamic viscosity	($\mu\text{Pa}\cdot\text{s}$)
ρ	density	(kg/m^3)
τ	time	(s)
c	specific heat	(J/kgK)
h	specific enthalpy	(kJ/kg)
h	heat transfer coefficient	($\text{W}/\text{m}^2\text{K}$)
k	thermal conductivity	(W/mK)
\dot{m}	mass flow	(kg/s)
p	pressure	(Pa)

Pr	Prandtl number	(–)
s	specific entropy	(kJ/kgK)
T	temperature	(K)
t	temperature	(°C)
U	total velocity vector	(–)

Subscript

amb	ambient
in	inlet
out	outlet
p	related to the isobaric process
R123	related to the R123 working fluid

REFERENCES

- Anslys CFX v. 14.5, 2014, Ansys CFX Theory Guide,
- Bao, J., Zhao, L., 2013, A review of working fluid and expander selections for organic Rankine cycle, *Renewable and Sustainable Energy Reviews*, Vol. 24: pp. 325-342,
- Gnutek, Z., Kolasiński, P., 2013, The application of rotary vane expanders in ORC systems – 479 thermodynamic description and experimental results. *Journal of Engineering for Gas Turbines and Power*, Vol. 135(6): pp. 1-10,
- Lund, H.; Münster, E., 2006, Integrated energy systems and local energy markets. *Energy Policy*, Vol. 34: pp. 1152-1160,
- Montenegro, G., Della Torre, A. D., Fiocco, M., Onorati, A., Benatzky, Ch., Schlager, G., 2014, Evaluating the Performance of a Rotary Vane Expander for Small Scale Organic Rankine Cycles using CFD tools, *Energy Procedia*, Vol. 45: p. 1136-1145,
- Montenegro, G., Della Torre, A., Onorati, A., Broggi, D., Schlager, G., Benatzky, C., 2014, CFD simulation of a sliding vane expander operating inside a small scale ORC for low temperature waste heat recovery, *SAE Technical Papers*, Vol.1,
- Tchanche, B. F., Lambrinos, Gr., Frangoudakis, A., Papadakis, G., 2011, Low-grade heat conversion into power using organic Rankine cycles – A review of various applications, *Renewable and Sustainable Energy Reviews*, Vol. 15: pp. 3963-3979,
- Vanslambrouck, B., 2009, The Organic Rankine Cycle: Technology and Applications, *International Symposium: Waste Heat Recovery by ORC*, Howest De Hogeschool West-Vlaanderen

ACKNOWLEDGEMENT

Calculations have been carried out using resources provided by Wroclaw Centre for Networking and Supercomputing (<http://wcss.pl>).

This work is co-financed by the European Union as part of the European Social Fund.

THE METHOD OF THE WORKING FLUID SELECTION FOR ORGANIC RANKINE CYCLE (ORC) SYSTEM WITH VOLUMETRIC EXPANDER

Piotr Kolasinski*¹

¹Wrocław University of Technology,
Department of Thermodynamics, Theory of Machines and Thermal Systems
Wrocław, Poland
E-mail: piotr.kolasinski@pwr.edu.pl

* Corresponding Author

ABSTRACT

Volumetric expanders are nowadays used in micro, small and medium power ORC systems. Tchanche (2011) indicated that most often spiral, screw and the rotary vane machines are applied. Volumetric machines have a number of specific features determining their operation. The most important are: the possibility of building expanders for small and very small capacities; small and moderate frequency of operating cycle - allowing for consideration of the processes taking place in the machine as a quasi-static; the ability to operate at high pressure drops in a single stage and ease of the hermetic sealing. The most important feature of the volumetric expander operation is the relationship of the expander power and the expansion ratio (the ratio of the inlet and outlet pressure). Each type of volumetric expander also has the optimum value of the expansion ratio. Unlike the turbines, volumetric expanders can operate at low working fluid flow rates and lower pressures. Thus, it is possible to apply volumetric expanders in ORCs powered by low-temperature heat sources, such as e.g. domestic waste heat. The task of a suitable working fluid selection to the ORC system with volumetric expander should be considered differently than in the case of the turbine-based systems. It is caused by low thermal parameters of the cycle and indicated earlier volumetric expander characteristic features. In this paper a new method of the working fluid selection to the ORC system working with volumetric expander was presented. The method is based on the dimensionless parameters useful for the comparative analysis of different working fluids. Dimensionless parameters were defined for selected thermal properties of the working fluids, namely the ability of heat absorption from the heat source, heat removal, mean temperature of the heat supply and the efficiency of the energy conversion. These comparative parameters were calculated for selected low-boiling ORC working fluids and selected temperature of the heat source and the heat sink. Basing on the values of these parameters the working fluids comparison was presented and applicable working fluids were selected.

1. INTRODUCTION

As it was indicated by Bao and Zhao (2013) the most important problems connected with ORC system design are the suitable working fluid and expander selection. They also showed that currently there is a wide range of applicable working fluids available. Expander selection is mainly based on the system power and its purpose. In general two types of expanders can be applied in ORC systems. One are the turbines, the others are volumetric expanders.

Turbines are mainly applied in an large power (1 MW and more) ORC systems powered by the heat sources with high thermal power and temperature (150 °C and more). Such heat sources are generated as waste heat in large industrial power machines e.g. steam boilers (waste steam) or gas turbines (exhaust gases). Lai et. al. (2011) showed that in the large power systems silicone oils (e.g. MM (hexamethyldisiloxane) or MDM (octamethyltrisiloxane)) are mainly adopted as working fluids.

Gnutek and Kolasiński (2013) indicated that volumetric expanders are applicable mainly in micro and small power systems such as domestic and agriculture plants powered by the heat sources with small capacities, thermal power and temperature (up to 150 °C). Low thermal parameters of heat source influences also the working fluid selection. Only the low-boiling working fluids are possible for application in this case. Such working fluid are the refrigerants and similar substances e.g. classical R123 ($C_2HCl_2F_3$) and R245fa ($C_3H_3F_5$), as well as new specially designed fluids e.g. R1234yf ($C_3F_4H_2$), R1234ze ($C_3F_4H_2$), or SES36 ($CF_3CH_2CF_2CH_3/PFPE$).

Volumetric expanders are a good option for systems where the low pressures and low working medium flows are expected. In general piston, screw, spiral, vane and rotary lobe expanders can be applied in ORC plants. Piston expanders are good option for the ORC systems where high (up to 20 MPa in case of the single stage expanders) inlet pressures of the working fluid are expected, as they have the high expansion ratios (the ratio of the inlet and outlet pressure). Piston expanders can be used in the ORC systems powered by heat sources with stable characteristic of the thermal power output as these expanders must work in dry vapor conditions in order to avoid liquid phase in the cylinder. Screw expanders can be applied in systems powered by heat sources with changeable characteristic (both in terms of the temperature, capacity and power) as in this type of the expanders moist vapor can be expanded without problems. The expansion ratio of the screw expander typically is in the range of $\sigma = 10$ –15. Spiral expanders are applied in many of the ORC systems as they are compact and relatively cheap. Vane expanders are applied mostly in the ORC prototypes and test-stands and most of them is under research and development. The expansion ratio of the rotary vane expanders typically is in the range of $\sigma = 5$ –7. Rotary lobe expanders are also under research and development, but these type of the expanders are promising because of their advantages such as e.g. ability to expand the moist vapor, low operating pressures and simple design. The range of working pressures and expansion ratios of different types of volumetric expanders are presented in table 1.

Table 1: Range of the working pressures and expansion ratios for different types of the volumetric expanders (Więckiewicz and Cantek (1985))

Expander type	$P_{in\ max}$ MPa	P_{out} MPa	σ_{max} -
Piston (single stage)	20	0.1	200
Screw	1.5	0.1	15
Spiral	1.0	0.1	10
Vane	0.7	0.1	7
Rotary lobe	0.6	0.1	6

The most important feature of the volumetric expander is the relationship of the expander power and the expansion ratio. This issue was discussed in details by Gnutek and Kolasiński (2011). Each type of volumetric expander also has the optimum value of the expansion ratio. Unlike the turbines, volumetric expanders can operate at low working fluid flow rates and low pressures. The task of a suitable working fluid selection to the ORC system with volumetric expander should be thus considered differently than in the case of the turbine-based systems.

2. THERMODYNAMIC PROPERTIES OF WORKING FLUIDS SUITABLE FOR ORC SYSTEMS WITH VOLUMETRIC EXPANDERS

As it was indicated in the introduction volumetric expanders are good option for ORC systems powered by low temperature heat sources and each type of the volumetric expander has specific range of the expansion ratio. Taking into account this specific conditions (low temperature of the heat source and expander operational conditions) only the selected working fluids can be applied in ORC system with volumetric expanders. Selected working fluids that can be used in low-power ORC systems with volumetric expanders are presented in table 2.

Working fluids can be described by well-known thermodynamic relationships (equations of the state, the expressions for the specific heat, heat of a phase change or the thermodynamic functions), and the coefficients defined for the description and analysis of specific applications. The above-mentioned thermodynamic relations are presented in the form of algebraic or differential equations, tables, graphs or software. Level of completeness of this description in relation to the substances, presented in table 2, is very different, which does not facilitate the thermodynamic analyzes. Figure 1 shows the general T-s diagram for the low-boiling substance. The characteristic values of thermal properties are indicated on this graph with taking into account the ambient parameters. The areas of the individual phases can therefore be highlighted: superheated vapor, moist vapor, liquid, the area of the critical point (C_r), the dry saturated vapor line ($x = 1$) and the line of boiling liquid ($x = 0$). Working fluid with ambient temperature T_a has the pressure $p(T_a)$, typically different from the ambient pressure p_a . Evaporation temperature T_{ev} at ambient pressure (p_a) is one of the basic quantities describing the substance, just like the corresponding heat of condensation $q_c(p_a)$ (isobar, isotherm e-f). The critical point parameters – p_{cr} , T_{cr} are another key parameters describing the substance. Isobar passing through this point is important in the division of the operating range of the power plant and organization of the cycle. In contrast, the critical isotherm determines the usefulness of a substance to act as a heat transfer fluid in a power plant. If $T_c < T_a$ it would be not possible to condense the vapor and liquid compression, which is the basic principle of a power plant operation. On the background of the described T-s graph the power plant cycle was presented (red lines).

Table 2: The working fluids suitable for low-power ORC systems with volumetric expanders

No.	Margin Position	Chemical formula	Molar mass	Normal boiling point	Critical point			Range of applicability		
					t_{cr}	p_{cr}	ρ_{cr}	t_{min}	t_{max}	p_{max}
			M	t_n	t_{cr}	p_{cr}	ρ_{cr}	t_{min}	t_{max}	p_{max}
			kg/kmol	°C	°C	MPa	kg/m ³	°C	°C	MPa
1	R113	CCl ₂ FCClF ₂	187.38	47.5	214.06	3.39	560.00	-36.22	251.85	200
2	R114	C ₂ Cl ₂ F ₄	170.92	3.6	145.68	3.25	579.97	0	233.85	21
3	R123	CHCl ₂ CF ₃	152.90	27.8	183.68	3.66	550.00	-107.15	326.85	40
4	R124	CF ₃ CHClF	136.50	-11.9	122.28	3.62	560.00	-153.15	196.85	40
5	R1234ze	CHF=CHCF ₃	114.04	-18.9	109.37	3.63	489.24	-104.53	146.85	20
6	R134a	CH ₂ F-CF ₃	102.00	-26.0	101.06	4.06	512.00	-103.3	181.85	70
7	R152a	CHF ₂ CH ₃	66.05	-24.0	113.26	4.51	368.00	-118.59	226.85	60
8	R227	CF ₃ CHFCF ₃	170.03	-16.3	101.75	2.93	594.25	-126.8	201.85	60
9	R236fa	CF ₃ CH ₂ CF ₃	152.00	-1.4	124.92	3.20	551.30	-93.63	226.85	40
10	R245fa	CF ₃ CH ₂ CHF ₂	134.05	15.1	154.01	3.65	516.08	-102.1	166.85	200
11	R365mfc	CF ₃ CH ₂ CF ₂ CH ₃	148.07	40.1	186.85	3.22	473.84	-34.15	226.85	35
12	R409A	-	97.40	-34.2	107.00	4.60	-	-	-	-
13	SES 36	CF ₃ CH ₂ CF ₂ CH ₃ /PFPE	184.85	35.6	177.60	2.85	-	-	-	-

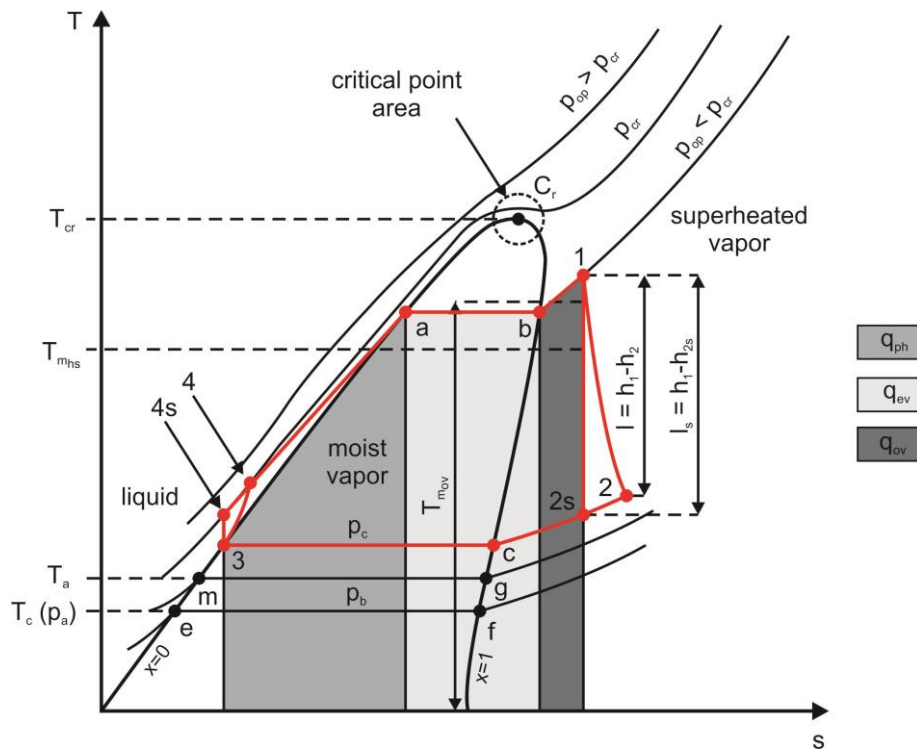


Figure 1: T-s diagram for low-boiling working fluid

Depending on the working fluid type the characteristic curve can have different shapes. Figure 2 shows the characteristic curves for selected working fluids. Also the temperature range for low potential heat sources is presented on this figure with dashed lines (90—150 °C).

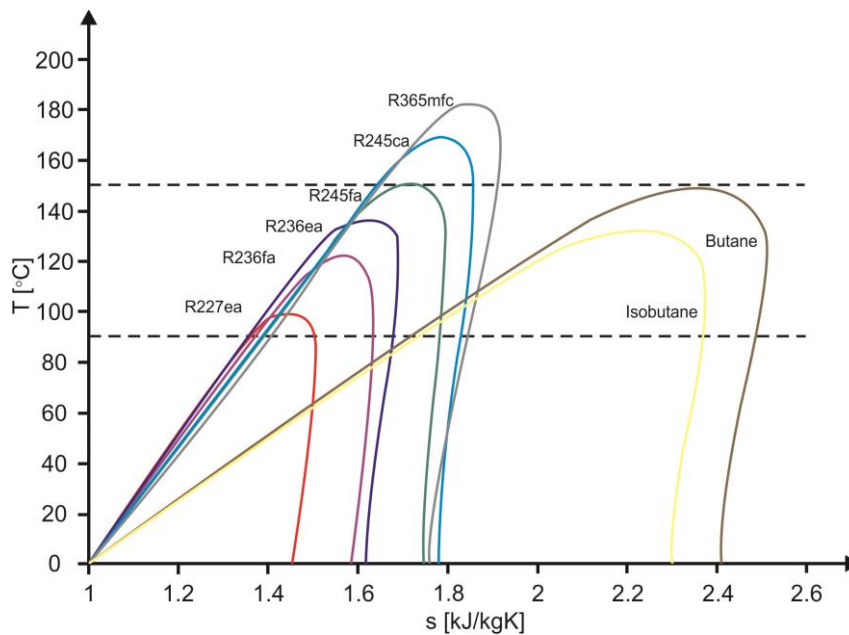


Figure 2: Characteristic curves for different working fluids (Trapp and Colonna (2013))

3. THE METHOD OF WORKING FLUID SELECTION

Figure 3 shows the comparison of two ideal power plant cycles (blue and red lines) for two different low-boiling working fluids on T-s plane, which is the basis for further considerations. This graph is

built with the assumption that both of the cycles are powered by the same heat source with the same heat supply temperature (T_{hs}). Moreover it is assumed that both of the cycles are cooled by the same heat sink with the same condensation temperature (T_c).

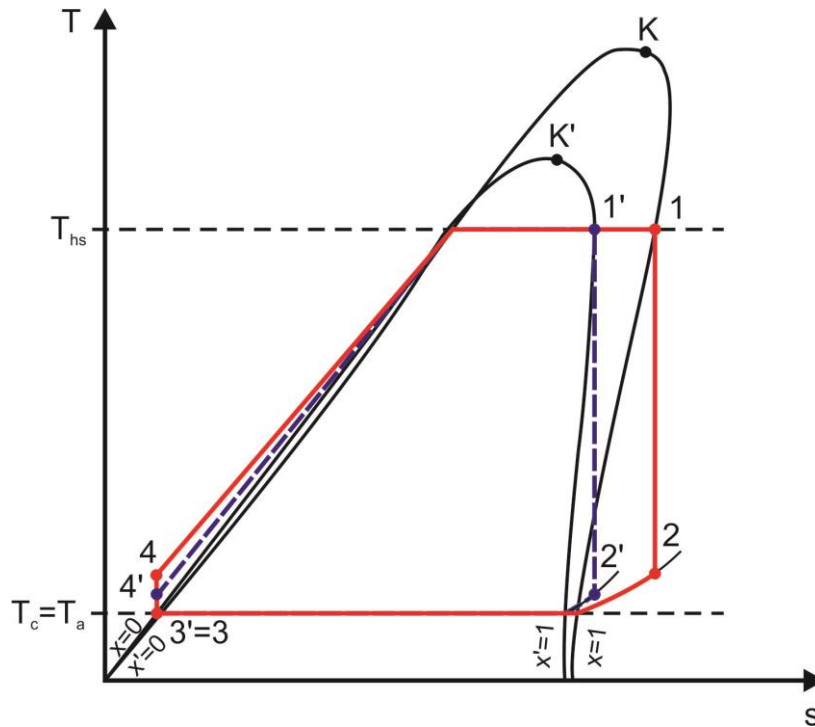


Figure 3: T-s diagram with the power plant cycles for two different working fluids

Comparison of two different substances is possible basing on many parameters (e.g. toxicity, ODP, HGWP, etc.), but the most important are the thermal properties as they have the influence on the ORC system power, efficiency and quality of operation. Thus, in this methodology, it is proposed to analyse the substances basing on the following thermal properties:

- The amount of the heat absorbed from the heat source in the evaporator,
- The mean temperature of the heat supply,
- The amount of the heat removed by the heat sink in the condenser,
- The efficiency of thermal energy conversion.

Moreover the following assumptions are needed to carry out the comparison (see Fig. 3 for details):

- The temperatures of the heat source and the heat sink are the same for both substances,
- Both working substances are thermally stable in the described on Fig. 3 temperature range,
- One of the substances is the reference.

In order to compare two substances with taking into account above mentioned properties and assumptions it is useful to define dimensionless comparative parameters, described in the following.

3.1 α_{hs} - The parameter of the absorbed heat

α_{hs} parameter characterizes the working fluid in terms of ability to absorb heat at the possible highest supply temperature (T_{hs}). This parameter can be useful when comparing the working fluids in terms of maximizing the heat amount absorbed from the heat source. The comparison of α_{hs} parameter calculated for two different working fluids and two different ORC cycles (the reference one and compared one, as presented on Fig.3) allows the selection of a working fluid with larger heat absorption capacity, i.e. one that will maximize the heat absorption from the heat source. This parameter can be defined with the expression

$$\alpha_{hs} = \left(\frac{\dot{Q}_{ORC1}^+}{\dot{Q}_{ORC2}^+} \right)_{(T_{hs}-T_a), p} \quad (1)$$

$$\dot{Q}_{ORC1}^+ = \dot{m}_{ORC1} \cdot (h_1 - h_4) \quad (2)$$

$$\dot{Q}_{ORC2}^+ = \dot{m}_{ORC2} \cdot (h_1' - h_4') \quad (3)$$

Where:

\dot{m}_{ORC1} - the working medium mass flow in the compared cycle,

\dot{m}_{ORC2} - the working medium mass flow in the reference cycle,

\dot{Q}_{ORC1}^+ - the heat transfer rate absorbed by the working fluid during the evaporation in the compared cycle,

\dot{Q}_{ORC2}^+ - the heat transfer rate absorbed by the working fluid during the evaporation in the reference cycle.

3.2 α_{mhs} - The parameter of the mean heat supply temperature

α_{mhs} parameter characterizes the working fluid in terms of ability to absorb heat at the highest possible mean heat delivery temperature T_{mhs} . This parameter can be useful for comparing the working fluids in terms of maximizing the heat delivery temperature and comparative analyses of working fluids in terms of maximizing ORC plant efficiency. This parameter can be defined with the expression

$$\alpha_{mhs} = \left(\frac{T_{ORC1}^{mhs}}{T_{ORC2}^{mhs}} \right)_{(T_{hs}-T_a), p} \quad (4)$$

$$T_{ORC1}^{mhs} = \frac{q_{ph} + q_{ev} + q_{sh}}{\Delta s} \quad (5)$$

$$T_{ORC2}^{mhs} = \frac{q_{ph}' + q_{ev}' + q_{sh}'}{\Delta s'} \quad (6)$$

Where:

T_{ORC1}^{mhs} - mean temperature of the heat supply in the compared cycle,

T_{ORC2}^{mhs} - mean temperature of the heat supply in the reference cycle,

q_{ph} - heat of preheating,

q_{ev} - heat of evaporation,

q_{sh} - heat of superheating,

Δs - change in the medium entropy during the preheating, evaporation and superheating.

3.3 α_o - The parameter of the removed heat

α_o parameter characterizes the working fluid in terms of ability to remove the heat at the lowest possible heat removal temperature $T_c \cong T_a$. This parameter can be useful for comparing the working fluids in terms of minimizing the temperature of the heat sink. This parameter can be defined as:

$$\alpha_{hr} = \left(\frac{\dot{Q}_{ORC1}^-}{\dot{Q}_{ORC2}^-} \right)_{(T_{hs}-T_a), P} \quad (7)$$

$$\dot{Q}_{ORC1}^- = \dot{m}_{ORC1} \cdot (h_{ORC1}'' - h_{ORC1}') \quad (8)$$

$$\dot{Q}_{ORC2}^- = \dot{m}_{ORC2} \cdot (h_{ORC2}'' - h_{ORC2}') \quad (9)$$

Where:

\dot{m}_{ORC1} - the working medium mass flow in the compared cycle,

\dot{m}_{ORC2} - the working medium mass flow in the reference cycle,

\dot{Q}_{ORC1}^- - the heat transfer rate removed during the condensation in the compared cycle,

\dot{Q}_{ORC2}^- - the heat transfer rate removed during the condensation in the reference cycle.

3.4 α_e – The parameter of the efficiency of thermal energy conversion

α_e parameter characterizes the working fluid in terms of ability to maximize the efficiency of the energy conversion. This parameter can be useful when comparing the working fluids in terms of maximizing the efficiency of conversion of the heat supplied from the heat source to the other energy forms. This parameter can be defined as:

$$\alpha_e = \left(\frac{E_{ORC1}}{E_{ORC2}} \right)_{(T_{hs}-T_a), P} \quad (10)$$

$$E_{ORC1} = P_{ORC1} + Q_{TORC1} + Q_{LORC1} \quad (11)$$

$$E_{ORC2} = P_{ORC2} + Q_{TORC2} + Q_{LORC2} \quad (12)$$

Where:

E_{ORC1} - the energy generated and dissipated in the compared cycle,

E_{ORC2} - the energy generated and dissipated in the reference cycle,

P - electric power output (the electric power on the output of the current generator),

Q_T - thermal power output (heat generated for the central heating purposes),

Q_L - heat losses (heat losses via convection and radiation from the surfaces of the pipelines, the evaporator, the condenser and the other system devices).

The above defined parameters can be useful for comparative selection of the ORC system working fluid, when the thermal characteristic of the heat source and the heat sink (namely the heat source and the heat sink temperatures) are known. The selection criteria are the maximal values of the α_{hs} , α_{mhs} , α_{hr} and α_e parameters. Moreover, basing on the comparison of the calculated parameters and the values of the expansion ratio as well as specific expansion work it is possible to select a suitable volumetric expander to the ORC system. The importance of the α_{hs} , α_{mhs} , α_{hr} and α_e parameters is always connected with the application of the ORC system. For the example in the ORC system dedicated for heat recovery from the cooling mediums (e.g. in internal combustion engines) the heat removal from the medium is the priority. Thus, the most important parameter in this case is the α_{hs} and it should be maximized during the expander and working fluid selection. In each ORC system

cycle efficiency is also very important, thus in all of the applications α_e parameter should be maximized.

4. COMPARATIVE ANALYSIS OF THE WORKING FLUIDS

In the following the comparative analysis of the selected low-boiling working fluids suitable for application in ORC powered by low temperature heat sources is presented. The analysis was performed for working fluids listed in table 2. The values of thermal properties (i.e. specific enthalpy and the specific entropy) were calculated with the Refprop and Solkane software.

The following assumptions were taken into account in the calculations:

- The temperature of the heat source is $t_{hs} = 95$ °C,
- The expander internal efficiency is $\eta_i = 0,7$,
- Temperature of the heat sink is $t_c = 20$ °C,
- The reference substance is R123,
- There is no heat generated for central heating and heat losses in the system are negligible.

The defined earlier comparative parameters (α_{hs} , α_{mhs} , α_{hr} and α_e) together with the expansion ratio and expander specific work were calculated for each of the working fluid. Calculations were made for cycles presented in fig. 3. The results of these calculations are presented in table 3 (indexes of the thermal properties according to fig. 3).

Table 3: The results of the calculations

Working fluid	t_1	p_1	t_2	p_2	h_1	s_1	i_2	s_2	h_3'	s_3'	l	σ	α_{hs}	α_{mhs}	α_{hr}	α_e
	°C	bar	°C	bar	kJ/kg	kJ/kgK	kJ/kg	kJ/kgK	kJ/kg	kJ/kgK	kJ/kg	-	-	-	-	-
R113	95	3.87	50.26	0.37	417.07	1.6262	391.75	1.6527	218.09	1.0639	25.32	10.55	0.91	1.00	0.91	0.92
R114	95	12.83	48.42	1.82	390.81	1.5562	369.83	1.5783	219.44	1.0684	20.98	7.05	0.79	0.99	0.79	0.76
R123	95	7.02	42.45	0.76	438.19	1.6890	410.56	1.7188	220.05	1.0763	27.63	9.24	1.00	1.00	1.00	1.00
R124	95	21.54	23.65	3.27	404.41	1.5971	381.89	1.6220	222.09	1.0779	22.52	6.59	0.84	0.99	0.84	0.82
R1234ze	95	27.39	28.02	4.27	252.31	0.7610	229.22	0.7931	51.019	0.1856	23.09	6.41	0.92	0.98	0.94	0.84
R134a	95	35.91	20.00	5.72	421.12	1.6504	397.73	1.6770	227.47	1.0960	23.39	6.28	0.89	0.98	0.89	0.85
R152a	95	31.79	20.00	5.13	540.50	2.3412	501.80	2.3852	234.77	1.4755	38.70	6.20	1.40	0.99	1.40	1.40
R227	95	25.50	37.64	3.90	369.04	1.5025	352.37	1.5206	222.81	1.0806	16.67	6.54	0.67	0.98	0.68	0.60
R236fa	95	17.44	43.36	2.30	416.85	1.6370	393.91	1.6615	224.62	1.0867	22.94	7.60	0.88	0.99	0.89	0.83
R245fa	95	11.30	43.05	1.22	471.29	1.7885	440.70	1.8213	225.86	1.0912	30.59	9.21	1.13	0.99	1.13	1.11
R365mfc	95	5.20	56.16	0.46	492.00	1.8487	459.26	1.8824	226.90	1.0956	32.74	11.30	1.22	0.99	1.22	1.18
R409A	95	35.99	19.33	5.78	412.28	1.6186	387.37	1.6474	215.20	1.0495	24.91	6.23	0.90	0.97	0.90	0.90
SES 36	95	5.61	60.64	0.58	414.77	1.6176	390.30	1.6423	220.28	1.0705	24.47	9.67	0.89	1.00	0.89	0.89

As it can be seen from the calculation results, three of the working fluids (R152a, R245fa and R365mfc) have better thermal properties in comparison to R123 as the comparative parameters are greater than 1.

For the assumed ORC system working conditions, the best working fluid is R152a when compared to R123. In case of R152a the calculated values of the α_{hs} , α_{hr} and α_e are equal (1.4). This means that R152a is 40% better than R123 in the heat absorption, heat removal and thermal energy usage efficiency. The α_{mhs} parameter is lower ($\alpha_{mhs} = 0.99$) in case of R152a when compared to R123, thus the mean heat supply temperature is lower for R152a. Also, the value of the expansion ratio is lowest ($\sigma = 6.2$) in case of R152a in comparison to other analyzed substances, and the specific expansion work is highest ($l = 38.7$ kJ/kg). However, in case of R152a the pressure on the expander inlet is high ($p_1 = 31.79$ bar) and the choice of the suitable volumetric expander is limited only to the piston expander (see Table 1 for maximum expansion ratio of different volumetric expanders).

The second, better than R123 working fluid, is R365mfc. In case of R365mfc the calculated values of the α_{hs} , α_{hr} and α_c are 1.22, 1.22 and 1.18 correspondingly. This means that R365mfc is 22% better than R123 in the heat absorption and heat removal and 18% better in the thermal energy usage efficiency. Similarly to the earlier described comparison α_{mhs} parameter is also lower ($\alpha_{mhs} = 0.99$) in this case. The value of the expansion ratio in case of R365mfc is higher than in the case of R123 ($\sigma = 11.3$), but the operational pressures are lower ($p_1 = 5.20$ bar and $p_2 = 0.46$ bar) and the specific expansion work is higher ($l = 32.74$ kJ/kg) when compared to R123. Low operational pressures and the value of the expansion ratio makes that screw expander will be optimal in this case.

The third, better than R123, working fluid is R245fa. In case of R245fa the calculated values of the α_{hs} , α_{hr} and α_c are 1.13, 1.13 and 1.11 correspondingly. This means that R245fa is 13% better than R123 in the heat absorption and heat removal and 11% better in the thermal energy usage efficiency. Similarly to the earlier described comparisons α_{mhs} parameter is also lower ($\alpha_{mhs} = 0.99$) in this case. The value of the expansion ratio in case of R245fa is lower than in the case of R123 ($\sigma = 9.21$), but the operational pressures are higher ($p_1 = 11.30$ bar and $p_2 = 1.22$ bar). The specific expansion work is higher ($l = 30.59$ kJ/kg) when compared to R123. The moderate pressures and the value of the expansion ratio in this case makes that two types of the volumetric expanders (screw and spiral) can be applied in this case. As it can be seen from the results α_{hs} and α_{hr} are similar for the analyzed substances. This is due to the similar shapes of the saturation curves for these substances and similar ratio of the heat needed for preheating, evaporation and superheating of the substance in relation to the heat of condensation. The other working fluids (R113, R114, R124, R1234ze, R134a, R227, R236fa, R409A and SES 36) have worse thermal properties when compared with R123. The calculated comparative parameters are lower for these substances in comparison to R123.

5. CONCLUSIONS

This study presents the comparative working fluid selection method for ORC system powered by low temperature heat source. This method is based on comparison of selected thermal properties of working fluids with the use of the defined parameters describing the substance in the following properties: the amount of the heat absorbed from the heat source, the mean temperature of the heat supply, the amount of the heat removed by the heat sink and the efficiency of thermal energy conversion. Described method can be useful for the working fluid selection to the ORC system with known thermal parameters (temperatures) of the heat source and the heat sink. Moreover, it is possible to select the suitable volumetric expander basing on the comparison of the calculated parameters, the expansion ratio and the specific expansion work. The comparison example presented in point 3 of this paper and valid for the ORC system powered by the low-temperature (95 °C) heat source, where R123 is the reference working fluid, shows that in considered case three different working fluids (R152a, R245fa and R365mfc) can be more efficient alternatives to R123. Also, the suitable volumetric expanders were selected using the presented method for each of the working fluids alternatives. Presented method can also easily be adopted to other working substances and other assumptions. Thus, using this method, it is possible to analyze many different ORCs powered by different heat sources.

NOMENCLATURE

The nomenclature should be located at the end of the text using the following format:

α	comparative parameter	(–)
η	efficiency	(–)
ρ	density	(kg/m ³)
σ	expansion ratio	(–)
E	energy	(J)
h	specific enthalpy	(kJ/kg)
l	specific work	(kJ/kg)
M	molar mass	(kg/kmol)

m	mass flow	(kg/s)
P	power	(W)
p	pressure	(Pa)
r	heat of evaporation	(kJ/kg)
q	specific heat	(kJ/kg)
Q	heat transfer rate	(W)
s	specific entropy	(kJ/kgK)
T	temperature	(K)
t	temperature	(°C)
x	vapor quality	(–)

Subscript

1, 2, ..., n	1 st , 2 nd , ... n th
a	ambient
c	condensation
cr	critical
e	efficiency
ev	evaporation
hs	heat supply
i	internal
in	inlet
L	losses
m	mean
max	maximal
min	minimal
out	outlet
op	operational
ORC1	related to the compared cycle
ORC2	related to the reference cycle
sh	superheating
ph	preheating
s	isentropic
T	thermal

REFERENCES

- Bao, J., Zhao, L., 2013, A review of working fluid and expander selections for organic Rankine cycle, *Renewable and Sustainable Energy Reviews*, Vol. 24: pp. 325-342,
- Gnutek, Z., Kolasiński, P., 2013, The application of rotary vane expanders in ORC systems – 479 thermodynamic description and experimental results. *Journal of Engineering for Gas Turbines and Power*, Vol. 135(6): pp. 1-10,
- Lai, N.A., Wendland, M., Fischer, J., 2011, Working fluids for high-temperature organic Rankine cycles. *Energy*, Vol. 36: pp. 199-211,
- Tchanche, B. F., Lambrinos, Gr., Frangoudakis, A., Papadakis, G., 2011, Low-grade heat conversion into power using organic Rankine cycles – A review of various applications, *Renewable and Sustainable Energy Reviews*, Vol. 15: pp. 3963-3979,
- Trapp, C., Colonna, P., 2013, Efficiency Improvement in Precombustion CO₂ Removal Units With a Waste-Heat Recovery ORC Power Plant, *Journal of Engineering for Gas Turbines and Power*, Vol. 135(4): pp. 1-12,
- Więckiewicz, H., Cantek, L., 1985, *Volumetric Compressors - Atlas*, 2nd ed.; Gdańsk University of Technology Publishing, Gdańsk, Poland, pp. 380,

THERMODYNAMIC AND DESIGN CONSIDERATION OF A MULTISTAGE AXIAL ORC TURBINE FOR COMBINED APPLICATION WITH A 2 MW CLASS GAS TURBINE FOR DEZENTRALIZED AND INDUSTRIAL USAGE

René Braun^{1*}, Karsten Kusterer¹, Kristof Weidtmann¹, Dieter Bohn²

¹B&B-AGEMA,
Aachen, NRW, Gemany
braun@bub-agema.de

²Aachen University,
Aachen, NRW,Germany
Dieter.bohn@rwth-aachen.de

* Corresponding Author

ABSTRACT

The continuous growth of the part of renewable energy resources within the future mixture of energy supply leads to a trend of concepts for decentralized and flexible power generation. The raising portion of solar and wind energy, as an example, requires intelligent decentralized and flexible solutions to ensure a stable grid and a sustainable power generation.

A significant role within those future decentralized and flexible power generation concepts might be taken over by small to medium sized gas turbines. Gas turbines can be operated within a large range of load and within a small reaction time of the system. Further, the choice of fuel, burned within the gas turbine, is flexible (e.g. hydrogen or hydrogen-natural gas mixtures). Nevertheless, the efficiency of a simple gas turbine cycle, depending on its size, varies from 25% to 30%.

To increase the cycle efficiencies, the gas turbine cycle itself can be upgraded by implementation of a compressor interstage cooling and/or a recuperator, as examples. Those applications are cost intensive and technically not easy to handle in many applications. Another possibility to increase the cycle efficiency is the combined operation with bottoming cycles. Usually a water-steam cycle is applied as bottoming cycle, which uses the waste heat within the exhaust gas of the gas turbine. In small to mid-sized gas turbines the temperature and heat amount within the exhaust gas are often not sufficient to operate a water steam cycle efficiently. Further, in industrial applications, a part of the heat, within the exhaust gas, is often used in secondary processes which lower the total amount of heat, which can be transferred to a bottoming cycle.

An alternative to water-steam bottoming cycles can be given by organic Rankine cycles (ORC) based on organic fluids. An advantage of organic fluids is the characteristic of evaporating at lower temperatures and lower heat amounts and thus, the usability in a Rankine cycle even at low heat source temperatures.

This paper discusses an ORC process design for a combined application with a simple cycle gas turbine in the 2 MW class. The thermodynamic cycle configuration is shown and it will be pointed out that the cycle efficiency (simple GT) of 26.3% can be increased to more than 36% by application of a bottoming ORC cycle (simple GT+ORC). A key component within the ORC cycle is the turbine. This paper shows the results of an extended aerodynamic ORC axial turbine pre-design based on the thermodynamic cycle considerations. Within the design study the real gas properties of the organic fluid are taken into account. Based on the outcome of the pre-design a 3D aerodynamic axial turbine design is investigated. By application of CFD simulations the turbine design has been optimized and the ORC power output could be increased from 636kW (0D-design) to 659 kW (CFD-design), which lead to a combined cycle efficiency of more than 36%.

1. INTRODUCTION

During the last decade the importance of intelligent, flexible and sustainable energy conversion systems is steadily growing. Thereby the application of systems based on organic Rankine cycles (ORC) get more and more in focus in several technical disciplines as Quoilin et al. (2013) have shown in their survey of ORC systems. The technology of Organic Rankine cycles are nowadays applied to many kinds of technology fields, such as solar thermal, geothermal or biomass power plants, in offshore platform applications, waste heat recovery systems and even in heavy trucks.

This paper deals with the application of ORC system as bottoming cycles for usage of waste heat from a primary cycle. Due to the trend of decentralized power generation, as a consequence of the growing part of renewables within the future energy mixture, small to mid-sized flexible power generation systems are required. The application of gas turbines can full fill the requirements in terms of system flexibility and variable sizes. A disadvantage of simple gas turbine cycles are the low efficiencies. A possibility to increase the simple cycle efficiency is the application of a bottoming cycle. In many cases a conventional bottoming cycle based on water/steam is not economical. In such cases a bottoming cycle based on organic fluids can be a successful alternative. Nguyen et al. (2012) and Pierobon et al. (2013) have shown in their investigations the significant benefit which can be achieved by the application of ORC system as bottoming cycle to a gas turbine for offshore solution. Kusterer et al. (2013) have shown the potential of a combined cycle configuration of a 2 MW class gas turbine with an ORC within a conceptual process design study.

As various kinds of organic fluids are available, a usage-oriented working fluid selection process is necessary, in order to find the best candidate for the process of interest. As the fluid properties of organic fluids are different in a huge range and the consideration of the real gas behavior of such fluids is of highest importance within those selection analyzes, many researchers have investigated in this field (e.g. Quoilin et al. (2012); Saleh et al. (2007)) For the best choice of suitable fluids the practicability and feasibility of the thermodynamic results have to be taken into account, but also the design of the cycle, the heat transfer behavior within the heat exchanger and the relating volume flows through the expansion machines are of highest interest for an ORC fluid selection. There is a significant amount of literature dedicated to the evaluation of suitable working fluids, due to the complexity of the topic (e.g. Kusterer et al.(2014); Fernandez et al. (2011); Lai et al. (2011); Sauret et al. (2011); Chen et al. (2011)).

The calculation of ORC processes has to consider the real gas properties of the analyzed fluids, as the approximation with ideal gas equations is not valid for the most of the fluids. Therefore the development of suitable equation of states for analyzing of organic fluids is investigated by a lot of researchers (e.g. Weingerl et al. (2001), Wei et al. (2000), Miyamoto and Watanabe (2003)). Harink et al (2010) have analyzed the influence of different CFD solvers, turbulence models and equation of states to the performance of a radial ORC turbine predicted by the application of different CFD solvers. They have shown that the accuracy of the results is highly addicted to the related models and solvers.

This paper deals with the applicability of conventional steam turbine design procedures and how far those are transferrable to the design of axial turbines using organic mediums. The analyzed design is based on a thermodynamic process study of a combined application of an ORC and a simple gas turbine (2 MW class). As organic working fluid pentane is used in the ORC cycle

2. Thermodynamic Cycle Modeling

2.1 Software tool for process calculations

The thermodynamic cycle modeling of the combined gas turbine and ORC has been performed by a "Thermodynamic Design Tool" (TDT) application, developed by B&B-AGEMA. TDT supports the design and calculation of single and combined energetic processes based on a 0D thermodynamic approach, using different fluids selected by the user. Combined cycles (e.g. gas turbine + ORC) can be investigated directly and with consideration of interactions. It comprises real gas behavior of several fluids and mixtures. The thermodynamic processes can be visualized in parametric

thermodynamic diagrams, e.g. enthalpy/entropy, temperature/pressure, including precisely tabled thermodynamic values. The calculation method for compression and expansion processes under real gas behavior are based on Lütke (2004).

2.2 Combined Cycle Calculation (0D-TDT)

The cycle design of the combined gas turbine and organic Rankine cycle configuration is shown in Figure 1. The combined cycle contains a simple cycle gas turbine and a recuperated organic Rankine cycle. On the right hand side of the Figure the thermodynamic parameter of the single components are illustrated in order to classify the cycles. The simple gas turbine cycle results in an efficiency of 26.3%, this efficiency includes a thermal to electrical factor of 0.893, which approximates the mechanical losses of rotating parts and transmission losses within the generator.

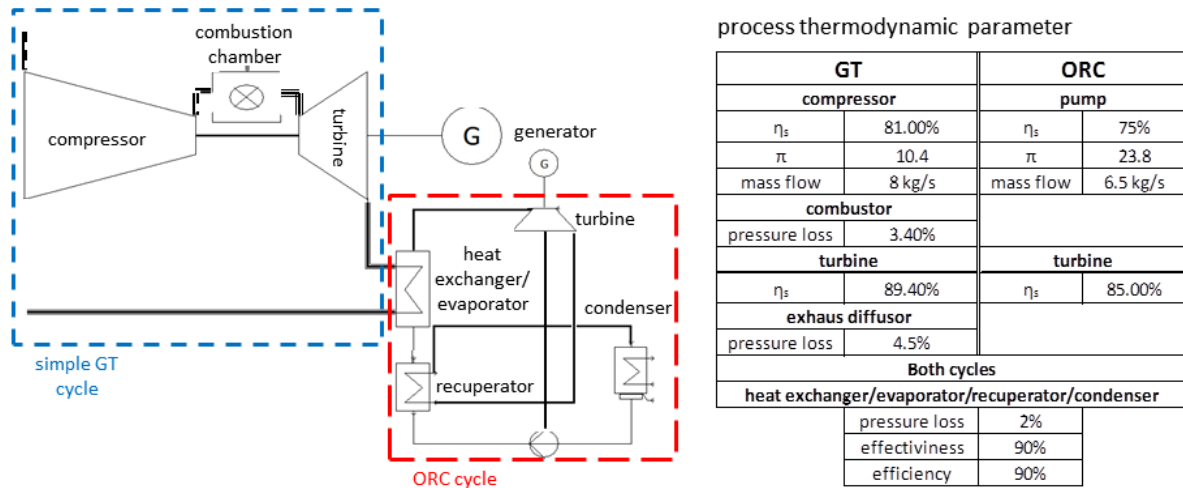


Figure 1: combined cycle configuration of simple gas turbine and organic Rankine cycle

The resulting combined cycle efficiency is 35%, whereas the power output of the ORC is 625.6 kW (without consideration of the condenser energy consumption and an assumed thermal to electrical factor, similar as for the GT cycle, of 0.9). Thus, the efficiency of the simple cycle could be increased by more than 8%pts., by application of a bottoming ORC cycle.

As the focus of this paper is on the design of the axial turbine, the calculated turbine power within the thermodynamic 0-D process calculation (TDT) has to be seen as reference and starting point for the more detailed turbine design. The ORC 0-D net turbine power output is 707 kW which is conform to a specific work of 108.8 kJ/kg. For the further design study the specific work is set as value of comparison.

3. ORC Turbine Design

3.1 Definition of Main Turbine Parameter and Boundary Conditions

As first, a simple 1D design approach has been performed by calculating the characteristic machine parameters ψ_{yM} , δ_M and σ_M . The characteristic machine parameters are defined as:

$$\psi_{yM} = \frac{\left(\frac{n}{n-1}\right)RT\left(\pi^{\frac{n-1}{n}} - 1\right)}{\frac{1}{2}u^2} \quad (1)$$

$$\delta_M = \frac{|\psi_{yM}|^{\frac{1}{4}}}{\left|\frac{4Vu}{\pi D_B^2}\right|^{\frac{1}{2}}} \quad (2)$$

$$\sigma_M = \frac{\left|\frac{4Vu}{\pi D_B^2}\right|^{\frac{1}{2}}}{|\psi_{yM}|^{\frac{3}{4}}} \quad (3)$$

Based on the characteristic machine parameters a first assumption of rotational speed and stage numbers can be defined for the turbine by using the Cordier diagram (see Figure 2) and by variation of the reference diameter and the rotational speed. The Cordier diagram presents ranges of machine characteristic parameters and is based on empirical data of real single stage machines. The diagram has been developed by O. Cordier in 1953. The Cordier diagram and the definitions of the characteristic machine parameters are only defined for single stage compressors and turbines, but they are useful to get a first impression of the needed stage numbers, the reference diameters and the rotational speed of compressors and turbines. Thus, the diagram is used in order to determine the rotational speed and stage number for the ORC turbine.

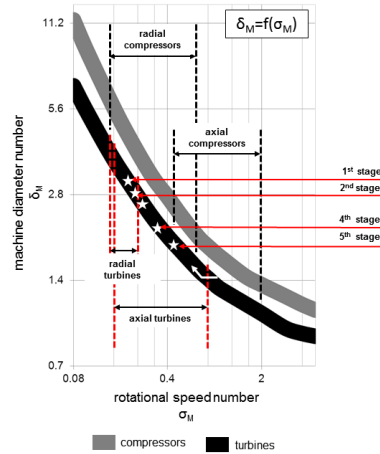


Figure 2: Cordier Diagram

The analysis based on the Cordier diagram and the related formulas (Equ.2 and 3) leads to a rotational speed of the turbine of 300 s^{-1} , which is related to a σ_M of 0.14 for the whole turbine. The number of stages is evaluated with 5, by calculating the characteristic parameters for each stage and manipulating the stage loading and influencing parameters till all stages are within the range of experienced axial machines of the Cordier diagram. By this procedure the required number of stages can be assumed and has to be verified as feasible in the detailed turbine design.

For simplification purposes the 5 stages of the turbine shall be designed as quasi-repetition stages, with constant stage flow coefficients φ

$$\varphi = \frac{c_m}{u} \quad (4)$$

where u is the circumferential velocity of the blade outlet and c_m the velocity of the flow in the meridian section. By the stage load coefficient ψ_h the loading of each stage is characterized:

$$\psi_h = \frac{\Delta h}{u^2 \frac{1}{2}} \quad (5)$$

where Δh describes the difference of the specific total enthalpy between outlet and inlet of the stage. Another important parameter within the design of a turbomachine is the enthalpy reaction number ρ_h :

$$\rho_h = \frac{\Delta h_{vane}}{\Delta h_{vane} + \Delta h_{vblade}} \quad (6)$$

it describes the load distribution between the vane and the blade of a stage.

Within the iterative 1D mean line design approach φ , ψ_h , ρ_h , the rotation rate, the mass flow of the organic medium and the diameter of the hub contour are initial values. Those values are necessary, in order to start the iterative process presented within the following section. The characteristic stage parameters are given in Table 1.

Table 1: turbine stage parameter

	1. stage	2. stage	3. stage	4 stage	5. stage
φ	0,3	0,3	0,3	0,3	0,3
ρ_h	0,5	0,5	0,5	0,5	0,5
ψ_h	-2,1	-2,1	-2	-2	-1,6

3.2 1D Mean Line ORC Turbine Design

In order to evaluate the main design parameters (e.g. geometrical parameters, flow parameters, etc.) of the ORC turbine, a 1D design has to be performed. A common design practice for gas or steam turbines is the application of a 1D Mean Line approach. This paper analyses the applicability of the common design procedure for the design of the axial ORC turbine and if the conventional design laws and methods are also applicable for turbines working with organic mediums. Therefore the changes of state, which have to be calculated within the mean line approach, have been iteratively solved by consideration of real gas equations and by implementation of property tables based on the data base implemented within the thermodynamic design tool (TDT). The iterative solving of the change of state is illustrated. The iteration is done till two criteria (ϵ_p and ϵ_T) are fulfilled. The main equations (7 and 8) to solve the change of state are based on RIST (1996) and shall not be further explained here. Thus, the 1D mean Line approach for application for ORC turbines becomes more complex as for example for gas or steam turbines in cause of missing data correlations or applicable real gas models.

$$\frac{p_2}{p_1} = \left[1 + \frac{\Delta h_s + (K_T \cdot v)_{1,2} \cdot p_1 \left(\frac{p_2}{p_1} - 1 \right)}{c_{p_{1,2s}} \cdot T_1} \right]^{\left(\frac{\kappa \cdot [1 + K_T]}{\kappa \cdot [1 - K_p] - 1} \right)_{1,2}} \quad (7)$$

$$\frac{p_2}{p_1} = \left(\frac{T_2}{T_1} \right)^{\left(\frac{\kappa \cdot [1 + K_T]}{\kappa \cdot [1 - K_p] - 1} \right)_{1,2}} \cdot \exp \left(- \frac{\Delta s}{(K \cdot R_N \cdot [1 + K_T])_{1,2}} \right) \quad (8)$$

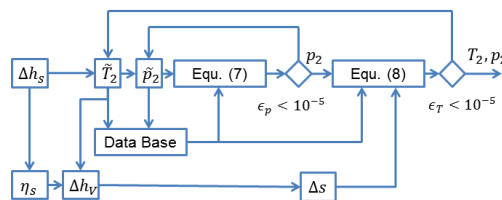


Figure 3: iterative scheme of solving the change of state

The 1D mean line process is illustrated in Figure 4. As it can be seen, due to the consideration of the real gas behavior of the organic fluid, the design process of the 1D mean line approach becomes complex and requires an iterative solutions. However, the results of the mean line approach are the flow angles in the mean line and the geometrical information about the hub and casing contour. Due to feasibility issues, additional boundary (BC) conditions have been considered within the design approach. Therefore the minimal size of a blade height is set to 5mm and additionally, in order to avoid a supersonic flow within the cascade, the inflow Mach number (Ma) should be lower than 0.3 and the outflow Ma lower than 0.9 (for each blade). Aerodynamic losses as well as profile losses have been approximated within the 1D design approach by empirical loss models (LM) with corresponding loss coefficients ξ . Those models are addicted to empirical models used for the design of steam turbines, as specific models are not available for organic mediums. The mean line approach is mainly divided into two sections, the thermodynamic (TD) and aerodynamic (AD) part as illustrated in Figure 4.

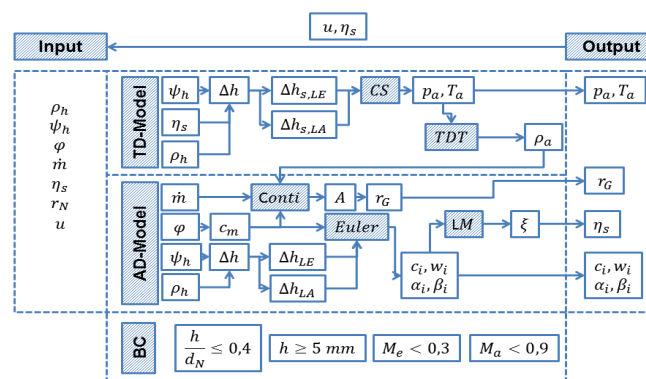
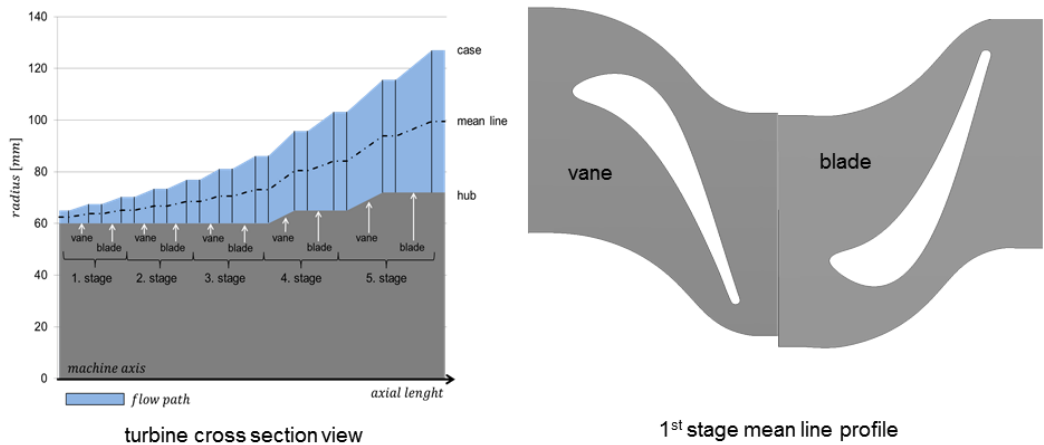


Figure 4: mean-line design process

The mean line approach results in the main geometrical information for the turbine design, as the hub and casing contour as well as the flow angles within the mean line section. Based on this information the main flow path and the profiles of the vanes and blades can be designed, as illustrated in Figure 5.



		vane	blade	vane	blade	vane	blade	vane	blade	vane	blade
aerodynamic mean line results											
velocity (abs. frame of reference)	in	35,350	130,662	37,222	137,367	39,206	143,180	41,525	163,851	47,954	174,503
	out	130,662	37,222	137,367	39,205	143,180	41,525	163,851	47,954	174,503	57,021
velocity (rel. frame of reference)	in	-	36,456	-	378,465	-	399,075	-	45,467	-	57,185
	out	-	133,353	-	140,667	-	147,798	-	171,435	-	187,073
angle (abs. frame of reference)	in	90,00	16,015	98,355	15,939	99,090	16,184	95,804	16,106	97,438	17,699
	out	16,015	98,355	15,939	99,091	16,184	95,804	16,106	97,438	17,699	99,266
angle (rel. frame of reference)	in	-	81,433	-	85,386	-	90,289	-	91,363	-	111,918
	out	-	163,969	-	164,026	-	163,767	-	163,897	-	162,493

Figure 5: mean line results - flow passage and flow angles

Due to the quasi-repetition stage design the mean line is not following on a constant radial position, but increasing in its radial position in axial direction. The resulting flow passage and the mean line location can be seen in on the left hand side in Figure 5. On the right hand side the contour of the vane and blade profiles of the 1st stage is exemplarily shown. Based on the resulting flow angles, the profiles have been designed within an in-house profile generator, which is not be further explained. As the hub and casing contour is known, a 3D turbine design can be evaluated. The first design considers non twisted airfoils, which means constant shapes in radial direction.

The calculated specific work is 104.54 kJ/kg, a difference of 3.9% to the 0-D process calculation. The reasons can be seen in the application of an iterative solving of the changes of state and the application of empirical loss models.

4. ORC Turbine CFD Simulation

The CFD simulations within this study are performed with the commercial code STARCCM+. The simulation set up considers the realizable k-ε turbulence model for the turbulence expression and considers the thermodynamic fluid properties of pentane as pressure and temperature depended tables for the thermal conductivity and dynamic viscosity. The specific heat has been prescribed as polynomial function. To consider the real gas behavior the Peng Robinson real gas model has been selected. The inlet conditions are prescribed as total conditions of temperature and pressure and the outlet is considered as a static pressure outlet.

4.1 CFD Simulation of first mean line design approach

The results of the numerical analysis (CFD 1st) in comparison to the 1D and 0-D design results are listed in Figure 6. It can be seen that small deviations are calculated by each approach by a direct comparison. The main key factors why there are differences are driven by two main factors: i) the consideration of the real gas behavior and ii) the consideration of losses. Within the numerical

analyses those two factors are directly connected to each other, in the 1D design there are indirect connected via loss models and in the 0-D design the losses are indirect considered by the prediction of isentropic component efficiencies. Thus, the different applications of the losses lead to small deviations, which need to be adjusted and fine-tuned.

Nevertheless, in a direct comparison of CFD and 1D design, the turbine principally shows the expected behavior by comparing the calculated pressure expansion line through the turbine, shown on the right hand side of Figure 6. The pressure lines are perfectly overlapping, whereas the static temperature distribution shows a difference. The difference of the static temperature is mainly produced within the first stage, the location where the applied real gas model within the CFD shows its highest failure in the calculation of the change of state, which has then direct influence to the prediction of the static parameters. After the first stage the static temperature lines are nearly parallel, this shows a similar prediction of CFD and 1D.

The accuracy of applicable real gas models in STARCCM+ in regard of the real gas factor determined by the real gas model versus the data base is as well illustrated in Figure 6. The failure rate is decreasing along the expansion line and has its maximum in the first stage for all models, but the Peng Robinson model shows the smallest deviations. Within the first stage the real gas factor of pentane is around 0.5 and as smaller the real gas factor as higher the failure rate of the real gas models. The models are not validated for pentane and thus have increasing failure rates for low real gas factors and this failure rate is then transported throughout the calculation of the static parameters.

Nevertheless, it can be said that the numerical investigation has shown a good performance of the turbine and the results are within an acceptable range of deviation for the first run.

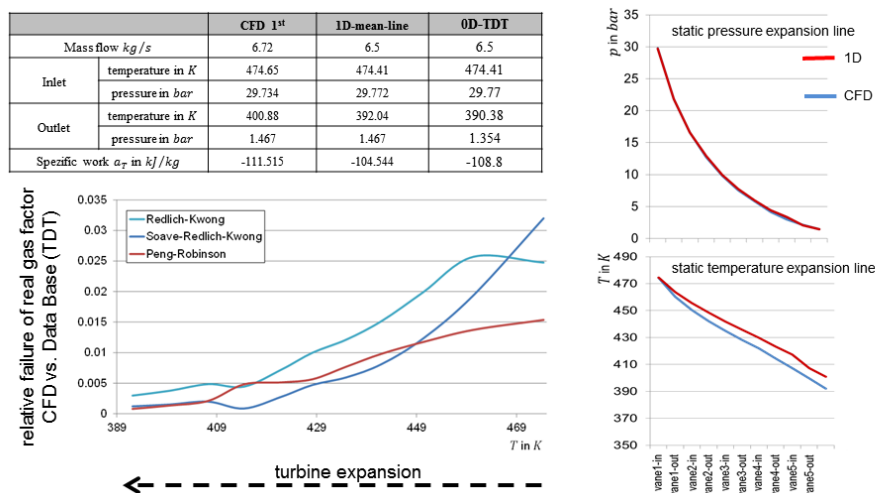


Figure 6: CFD results compared to 1D mean line design parameter

In order to compare the results, the specific work can be taken into account. It can be seen, that the prediction of the CFD is 6.3% higher than the estimated work by the 1D mean line design, whereas the deviation between the 1st CFD and the thermodynamic process calculation is 2.5%. Of course, a certain value of uncertainty is not avoidable but it can be assumed, that the implemented models within the 1D-design are not perfectly transferrable to the analyzed ORC turbine, as most of the correlations (especially for loss prediction, etc.) are specialized for steam turbine designs. Nevertheless, the 1D-design based on common practices of steam turbine design procedures is applicable and the resulted design is already close to a feasible design also for an organic fluid application. Based on the CFD results a turbine optimization process can be started to further increase the power output and to optimize the aerodynamic behavior. This can be done for instance by optimizing the shape of the profiles and/or to twist the blades.

4.2 CFD based optimization: consideration of radial twisting

Despite the deviations between the CFD and the 1D mean line results, an optimization of the turbine can be performed based on the results and experiences observed from the CFD analysis. Thus, a twisting of the blades has been analyzed and compared on the basis of a numerical delta analysis with

the first step CFD calculation of section 4.1. The evaluation of the twist parameters can be evaluated on two approaches: i) directly by evaluation of flow angles within the CFD or ii) by empirical models. For the determination of the twist parameters of the blades the second method has been chosen, as empirical models can be directly applied to a 1D Mean Line approach and thus show more potential to be considered in an early design stage. Two models have been compared: a free vortex model and a stator outflow angle model (Schuh (2012)). The models determine the radial flow angle distribution of the blades based on the result of the mean line calculation. The twist of the blade can then be realized within the profile generator. In order to validate the applicability of the models, the predicted flow angles from the two models have been compared to the flow angles from the CFD analysis. A comparison is shown exemplarily for the outlet of the 3rd vane in Figure 7. Within the analysis the free vortex model has been evaluated as best practice for an application.

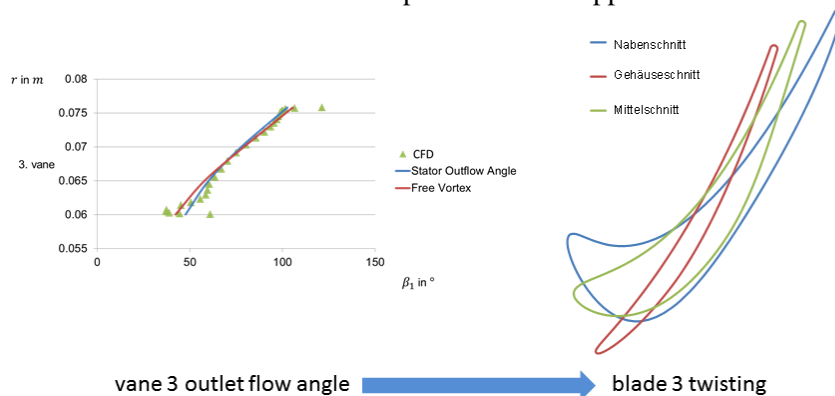


Figure 7: radial outlet flow angle distribution of vane 3 and blade 3 twist

The main results of the CFD considering the twisted profiles are shown and compared in Figure 8. Due to a twist of the profiles the flow losses induced by incidence could be reduced and thus, the specific work has been decreased by 1.4%.

		CFD twist	CFD-1st	1D-mean-line	0D-TDT
Mass flow kg/s		6.48	6.72	6.5	6.5
Inlet	temperature in K	474.76	474.65	474.41	474.41
	pressure in bar	29.81	29.734	29.772	29.77
Outlet	temperature in K	399.8	400.88	392.04	390.38
	pressure in bar	1.467	1.467	1.467	1.354
Specific work a_T in kJ/kg		-113.034	-111.515	-104.544	-108.8

Figure 8: comparison of results

6. CONCLUSIONS

Within this paper the design of an ORC turbine has been presented. Based on the results of a 0D thermodynamic process calculation a 1D turbine design has been performed on the basis of a mean line approach. The turbine has been designed as quasi repetition stages with consideration of empirical loss models and correlations applied from the design of steam turbines. The design has been transferred to a 3D turbine design and calculated by CFD. The main results of the analysis are that the design rules and methods of designing steam turbines are applicable for the design of ORC turbines. Nevertheless, some deviations and uncertainties are carried out, which require an adjustment of correlations and loss models in order to increase the accuracy of the ORC turbine design. The analysis by CFD requires a high accuracy in defining the fluid properties and the chosen physical models within the calculation. In order to minimize the design effort of an ORC turbine, it is intended to achieve a good turbine design already in early design steps, as within the 1D design approach. Therefore the implementation of empirical models and correlations are necessary. Those models are available for steam turbine design but not verified for organic turbines. The analysis of empirical

models for twisted blade designs has shown the applicability of those models as well for a pentane axial turbine.

The thermodynamic process design has shown the potential of the application of ORC systems as bottoming cycles to small and middle size gas turbines as the cycle efficiency could be increased from 26% to 36%. Especially the application of axial turbine designs offer a high potential, as high turbine efficiencies can be achieved.

NOMENCLATURE

A	specific work	[kJ/kg]
A	Flow channel area	[mm ²]
c	velocity magnitude (absolute system)	[m/s]
d	diameter	[mm]
w	velocity magnitude (relative system)	[m/s]
c _m	velocity in meridian section	[m/s]
D _B	reference diameter	[m]
h	specific enthalpy	[kJ/kg]
P	static pressure	[kg/m ²]
r	radius	[m],[mm]
R	specific gas constant	[J/(kg*K)]
T	static temperature	[K]
u	circumferential velocity	[m/s]
\dot{V}	volume flow	[m ³ /s]
α	absolute flow angle	[°]
β	relative flow angle	[°]
δ_M	machine diameter number	
σ_M	rotational speed number	
ϕ	flow coefficient	
ψ_h	stage loading number	
ψ_{yM}	machine loading number	
ρ_h	enthalpy reaction number	
η	efficiency	
π	pressure ratio	

Subscript

a	outlet position
e	inlet position
G	casing
i	inlet position
N	hub
n	counting variable
s	isentropic

Abbreviation

AD	Aerodynamic
CFD	Computational Fluid Dynamics
Conti	Continuity
CS	Change of State
Euler	EULER equations
GT	Gas Turbine
LA	blade
LE	vane
LM	Loss Models
ORC	Organic Rankine Cycle
TD	Thermodynamic
TDT	Thermodynamic design Tool

REFERENCES

- Chen, Y., Lundqvist, P., Johansson, A., "A comparative study of the carbon dioxide transcritical power cycle compared with an organic Rankine cycle with R123 as working fluid in waste heat recovery", *Applied Thermal Engineering*, 2006, 26, 17-18, 2142-2147
- Cordier, O., 1953, "Ähnlichkeitsbedingungen für Strömungs-maschinen, Brennstoff-Wärme-Kraft", *J. Strömungsmaschinen*, **5/10**
- Fernandez, F.J., Prieto, M.M., Suarez, I., "Thermodynamic analysis of high temperature regenerative Organic Rankine Cycles using Silohexanes as working fluids" *Energy*, 2011, 36, 8, 5239-5249
- Harinck, J., saaresti, T.T., Colonna, P., Rebay, S., Buijtenen, v.J., "Computational Study of a high.expansion ratio radial Organic Rankine Cycle Turbine Stator, *Journal of Engineering for Gas Turbines and Power*, May 2010, vol. 132 /054501-1
- Kusterer, K., Braun, R., Bohn, D., 2014, Organic Rankine Cycle Working Fluid Selection and Performance Analysis for Combined Cycle Application with a 2MW class Gas Turbine, *Proc. of ASME Turbo Expo 2014, GT2014-25439*, Düsseldorf, Germany
- Kusterer, K., Braun, R., Köllen, L., Tanimura, K., Sugimoto, T., Bohn, D., "Combined Solar Thermal Gas Turbine and Organic Rankine Cycle Application for Improved Cycle Efficiencies", *Proc. of ASME Turbo Expo 2013, GT2013-94713*, San Antonio, USA
- Lütke, K., "Process Centrifugal Compressors: *Basics, Function, Operation, Design, Application*", Springer Verlag GmbH, 2004
- Lai, N.A., Wendland, M., Fischer, J., Working fluids for high temperature Organic Rankine Cycles", *Energy*, 2011, 36, 1, 199-211
- Miyamoto, H., Watanabe, K., "Helmholtz-Type Equations of State for Hydrocarbon Mixtures of Propane/n-Butane, Propane/Isobutane, n-Butane/Isobutane, and Propane/n-Butane/Isobutane", *International Journal of Thermophysics*, Vol. 254, No. 4, 2003
- Nguyen, T.V., Elmegaard, B., Pierobon, L., Haglind, F.H., Breuhaus, P., „Modeling and analysis of offshore energy systems on north sea oil and gas platforms", *Proc. of the 53rd Scandinavian Simulation and Modeling Society Conference*, October 4-6, 2012, Reykjavik, Iceland
- Quoilin S., v.d. Broek, M., declaye, S., Dewallef, P., Lemort, V., 2013, Techno-economic survey of Organic Rankine Cycle (ORC) system, *Renewable and Sustainable Energy Reviews*, no. 22, p.168-186
- Quoilin, S., Declaye, S., Legros, A., Guillaume, L., Lemort, V., 2012, "Working fluid selection and operating maps for Organic Rankine Cycle expansion machines", *International Compressor Engineering Conference at Prudue*, July 16-19, 2012
- Rist, D., 1996, *Dynamik Realer Gase. Grundlagen, Berechnungen und Daten für Thermogasdynamik, Strömungsmechanik und Gastechnik*. Springer, Berlin, 1996
- Saleh, B., Koglbauer, G., Wendland, M., Fischer, J., 2007, Working fluids for low-temperature organic Rankine cycles", *Journal of Energy*, 32, p. 1210-1221
- Sauret, E., Rowlands, A.S., "Candidate radial-inflow turbines and high density working fluids for geothermal power systems", *Energy*, 2011, 36, 7, 4460-4467
- Schumann, J.; Sahren, D.; Jeschke, P.; Harbecke, U.; Polklas, T.; Schwarz, M., 2012, Impact of Secondary Flow on the Accuracy of Simplified Design Methods for steam turbine stages, *Proceedings of ASME Turbo Expo*, 2012
- Tveitaskog, A.K., Haglind, F., "Optimization of advanced liquid natural gas fuelled machinery systems for a high speed ferry", *Proc. of ASME Turbo Expo 2012, GT2012-69022*, Copenhagen, Denmark
- Weingerl, U., Wendland, M., Fischer, J., Müller, A., Winkelmann, J., „Backbone family of equations of state: 2. Nonpolar and polar fluid mixtures", *Journal of AIChE* , 47, 705-17, 2001
- Wei, S.Y., Sados, R.J., "Equations of State for the calculation of fluid phase equilibria", *Journal of AIChE*, 46, 169-196, 2000

CONTROL STRATEGIES FOR AUTOMOTIVE RANKINE SYSTEM EVALUATION USING A COSIMULATION PLATFORM

Abdelmajid Taklanti*, Jin-Ming LIU, Regine Haller, Samy Hammi, Bertrand Nicolas, Yulia Glavatskaya and Mohamed Yahia

Valeo Thermal Systems
8, rue Louis Lormand 78321 le Mesnil saint Denis
Contact Information (abdelmajid.taklanti@valeo.com)

ABSTRACT

Today, several solutions to recover wasted heat in automotive power train are considered and evaluated in order to reduce vehicle fuel consumption and to meet new emission regulation targets (El Habachi *et al.* (2010), Abbe Horst *et al.* (2014), Domingues *et al.* (2013) and Haller *et al.* (2014)). One of the solutions is to use Organic Rankine Cycle to recover waste heat from engine cooling system and/or engine exhaust gas and transform it to mechanical or electrical power. Automotive environment is very severe and very transient, the key point for operating such system is to set up and validate a suitable control strategy to maximize the recovered output power.

In automotive industry development processes the control strategies are mainly described in a control tool environment. Commonly, the control is then tested and the control parameters are set up using physical mockups and prototypes of the studied system on a test bench. Afterwards the control is coded into a control unit and integrated in a vehicle or a demo-car in order to validate and tune up the control strategies and parameters. This process is very long and time consuming because physical prototype and demo-car are needed.

In this paper, we are going to present a methodology using a virtual model of a R134a low temperature Rankine system integrated in a vehicle platform developed in a system simulation tool environment and coupled to a Rankine control system developed in a control tool environment. This methodology and co-simulation (see Taklanti *et al.*, 2013) allow us to test and evaluate different control strategies, to select the optimal one and to set up control parameters prior to physical mockup or demo car availability.

Finally, some results are presented showing the performance of a low temperature R134a Rankine system in a vehicle environment and the performance of a control strategy for constant velocities and transient driving cycles.

1 INTRODUCTION

The efficiency of an Internal Combustion Engine used in passenger cars is at maximum 45% and about 18% in average during the NEDC driving cycle. This means, 55% to 78% of the chemical energy in the fuel is emitted to the environment as heat through the exhaust line and the engine cooling system. Many investigations have been done to exploit these losses. Direct use of heat to enhance engine warm up, thermoelectricity, turbo-compound, for example, are technical solutions mainly valorizing the exhaust losses. Among those technologies, Rankine Cycle seems very promising and potentially able to use low or high temperature heat losses considering a well adapted working fluid and component technologies.

Haller *et al.* (2014) compared Rankine waste heat recovery system performance versus car velocity at high and low heat source temperature. It appears that the low temperature system is better than the high temperature one at lower engine loads which corresponds to lower vehicle speeds. An additional parameter is the ambient temperature as it affects the performance of the heat sink. The high

temperature system is well adapted for high engine load at high speed driving and less sensitive to ambient condition. Depending on the ambient temperature the crossing point is variable, but approximately at a vehicle speed of 100km/h for an ambient temperature of 22°C.

In this paper the methodology for the control strategy development of the Rankine system and the optimization of the recovered power will be presented. This methodology is applied to a R134a low temperature Rankine system integrated into a vehicle power train.

2 R134A LOW TEMPERATURE RANKINE SYSTEM

Different Rankine system architectures are possible for automotive applications. Figure 1 presents the low temperature system layout chosen for the current study. The engine coolant picks up the waste heat of the engine which is then used to evaporate the working fluid in the water evaporator (or boiler). The expansion of high pressure vapor through the refrigerant expander (RExp) produces mechanical power. Then, the low pressure vapor condenses in the water condenser cooled by a low temperature coolant circuit. Finally a subcooler guarantees sub-cooled liquid at pump inlet to prevent the pump from cavitations.

Exhaust gas heat recovery exchanger (EHR) may be considered in the high temperature coolant loop prior to the evaporator. With higher coolant temperature the potential of recovery power increases and the system efficiency may be improved.

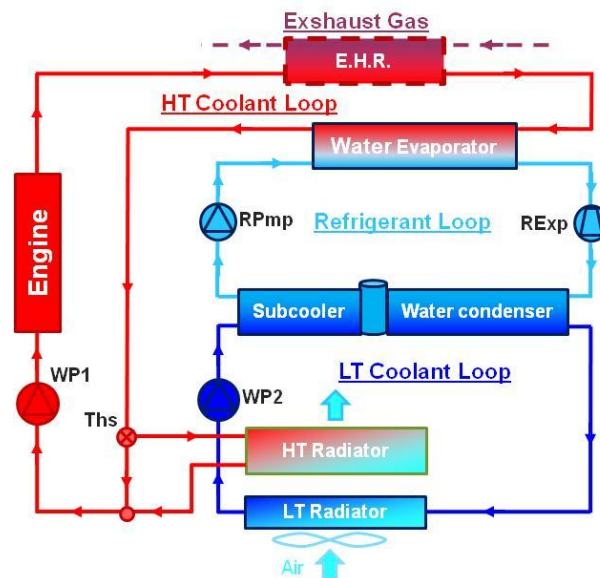


Figure 1 : Low temperature Rankine Architecture

For the integration of the Rankine system in a vehicle different solutions are possible. In the architecture considered in this study, the evaporator is placed at engine coolant outlet. The thermostat (Ths) controls the temperature setting at engine outlet by adjusting the coolant flow distribution between high temperature radiator and the radiator bypass. In the low temperature circuit, the electrical water pump WP2 ensures the coolant circulation in the water condenser and subcooler. The low temperature radiator is placed in the vehicle front end upstream, or in parallel of, the high temperature radiator.

3 SIMULATION MODEL DEVELOPMENT

3.1 R134a Rankine Cycle Model

A simulation model of a R134a Rankine cycle was developed in a multi-physics systems simulation tool. Figure 2 presents a sketch of the Rankine cycle composed of 3 main circuits: High temperature

coolant loop, refrigerant loop and low temperature coolant loop. Those loops integrate the main components of the system: evaporator, expander, condenser, receiver, subcooler, refrigerant pump, low temperature radiator and water pump.

A co-simulation block developed on control tool representing the Rankine control system is linked to the Rankine system model developed on system simulation tool.

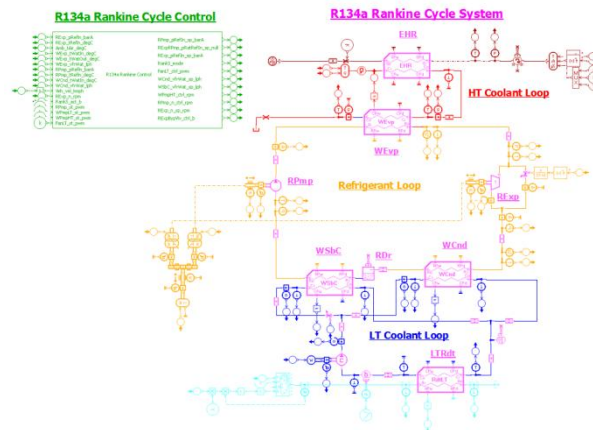


Figure 2 : R134a Rankine cycle simulation model

Large experimental investigations were performed on a low temperature Rankine cycle prototype as shown in figure 3 (see also Haller *et al* (2014)). The characteristics of this low temperature R134a Rankine prototype and part of the experimental results were used to set up the simulation model and to define and calibrate parameters of the physical component models.

4 R134A RANKINE SYSTEM CONTROL DEVELOPMENT

4.1 Rankine System Operation

Figure 3 represents a Rankine cycle operation in R134a Mollier Diagram (temperature/entropy and pressure/enthalpy). The mechanical power recovered by the Expander is:

$$P_{W_{rExp}} = (H_{rExp_i} - H_{rExp_o}) * Q_{m_{rExp}} \quad (1)$$

$$P_{W_{mExp}} = P_{W_{rExp}} * Eff_{mExp} \quad (2)$$

To maximize the recovered power by the expander it is necessary to maximize the product of refrigerant mass flow rate $Q_{m_{rExp}}$ and the difference between inlet and outlet enthalpy of Expander ($H_{rExp_i} - H_{rExp_o}$) weighted by the Expander mechanical efficiency Eff_{mExp} . These variables depend on a set of external and internal parameters of the Rankine cycle.

The principal external parameters are:

- Temperature and volume flow rate of the high temperature coolant at evaporator inlet
- Temperature and mass flow rate of ambient air at low temperature radiator

The principal internal parameters are:

- Refrigerant pump speed
- Refrigerant expander speed

Other internal parameters which affect the Rankine system performance are the sizing of the heat exchangers and other components, the volume of the refrigerant loop and the refrigerant charge, volume and mass flow rate of high temperature and low temperature coolant loops.

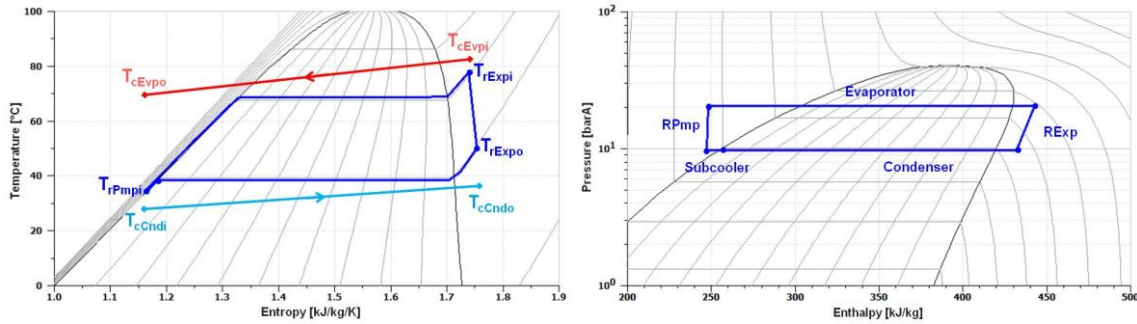


Figure 3 : R134a TS and Mollier diagram of Rankine cycle

In practice, maximizing the power $P_{w_{mExp}}$ of the expander isn't enough, because the refrigerant pump has to be driven electrically or mechanically, in fact we should maximize the net power produced by the Rankine system. This is to say, for a predefined external condition, it is important to control pump and expander speeds in order to maximize the recovered net power $P_{w_{mNet}}$ defined by:

$$P_{w_{mNet}} = P_{w_{mExp}} - P_{w_{mPmp}} \quad (3)$$

In mean time the control system should ensure the Rankine system protection for all operating points:

1. Avoid that high pressure exceeds a maximal limit HP_{work_max} .
2. Ensure a superheat at expander inlet higher than Sh_{work_min} and avoid droplets formation at evaporator outlet, since it can damage the expander.
3. Avoid cooling down the coolant at the evaporator outlet below a minimum temperature limit $T_{w_out_min}$.
4. Ensure a minimum subcooling at pump inlet higher than Sb_{work_min} to avoid pump cavitations.

4.2 Optimal Rankine System operation

In order to find the best compromise of pump and expander speeds a matrix of steady state operating conditions is defined. It corresponds to ambient temperatures variation between $-20^{\circ}C$ and $+45^{\circ}C$ and vehicle speed variation from 30 to 180 km/h (low temperature radiator air velocity variation from 0.75 m/s to 7 m/s without Fan functioning).

For each external operating condition steady states simulations are performed for a set of pump speeds variation and expander speeds variation. Points with high pressure values exceeding the maximum working pressure $HP_{work_max}=32$ bar are removed. The same for points with a superheat at evaporator outlet or condenser inlet lower than $Sh_{work_min} = 5$ K. The target of these simulations is to identify points with the highest Rankine mechanical net power $P_{w_{mNet}}$ defined by equation 3.

Figure 4 presents an example of Rankine mechanical net power versus pump speed and expander speed obtained for an operating condition of $20^{\circ}C$ ambient temperature, 2.5 m/s air velocity at the radiator, $90^{\circ}C$ coolant temperature, 1500 l/h HT coolant flow rate and 1200 l/h LT coolant flow rate.

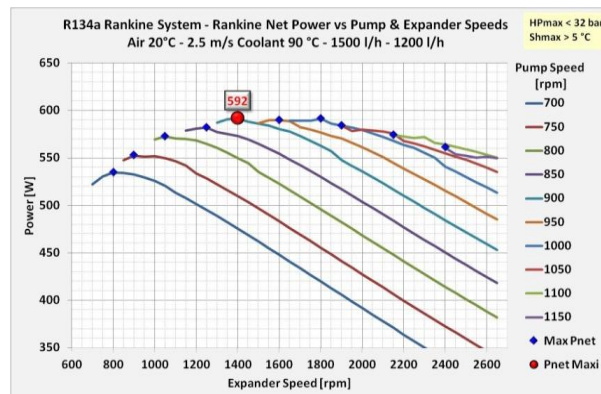


Figure 4 : Rankine net power for condition :

$$T_{aExt} = 20^{\circ}C \quad V_{aExt} = 2.5 \text{ m/s} \quad T_{cEvpi} = 90^{\circ}C \quad Q_{V_{Evpi}} = 1500 \text{ l/h} \quad Q_{V_{Cnd}} = 1200 \text{ l/h}$$

The blue dot points represent for a given pump speed, the expander speed with the maximum Rankine net power. The red dot point represents the optimal pump speed and optimal expander speed with the highest possible Rankine net power.

The next two figures present for the optimal Rankine net power obtained for different operating conditions. Figure 5a presents the effect of high temperature coolant loop temperature varying from 80°C to 115°C and for two ambient air temperatures of 20°C and 0°C. Figure 5b presents the effect of ambient air temperature variation from -20°C to 35°C for two high temperature coolant temperatures of 90°C and 110°C.

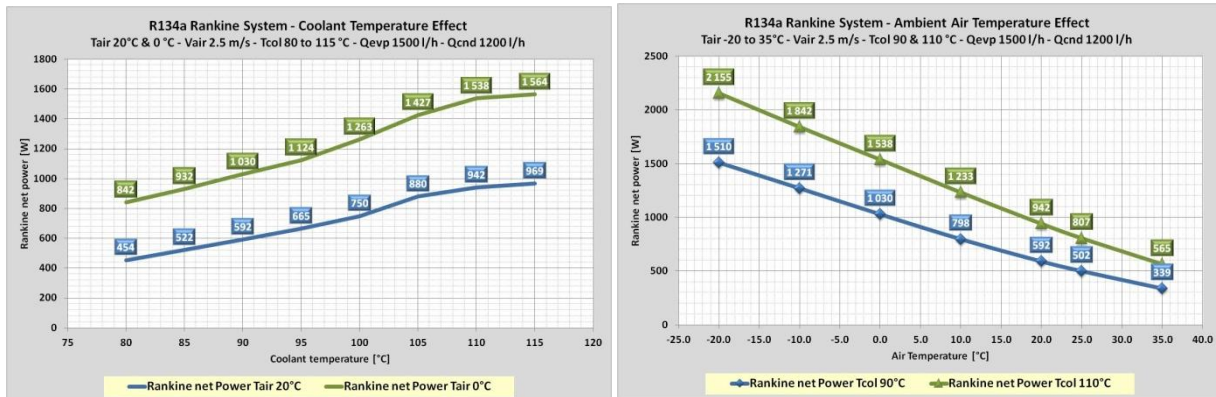


Figure 5 : Effect of operating conditions on optimal Rankine system performance
 a: HT coolant temperature effect b: Ambient air temperature effect

As expected, the Rankine net power increases when the coolant temperature increases and when the ambient air temperature decreases. The Rankine net power vary from 339W at 35°C Ambient temperature and 90°C coolant temperature to 2155 W for -20°C ambient temperature and 110°C coolant temperature.

We can observe also that for a coolant temperature higher than 105°C, the slope of variation of the net power decreases. This is due to the limitations in high pressure $HP_{work,max}$. For example, at ambient air of 20°C, and coolant temperature of 110°C, the maximum Rankine net power without limitation in high pressure is 1005 W with a high pressure of 37 bars to be compared to 942 W with high pressure limited to 32 bars or 815 W with high pressure limited to 28 bars.

5 RANKINE SYSTEM CONTROL ALGORITHM

As stated in §4.1, the objective of the Rankine control system is to control the refrigerant pump speed and the expander speed in order to maximize the recovered net power $P_{w,mNet}$ and protect the system during operating.

Quoilin, S., (2011) propose three control strategy of a small-scale ORC based on the regulation of evaporating temperature and superheating in order to control the expander and the pump speeds. A relationship of optimal evaporating temperature is defined by a linear regression of optimal results obtained from a set of 31 steady state workings points where condensing temperature, working fluid mass flow rate and heat source temperature are varying in certain range. The superheating is imposed to a constant value.

The control strategies developed in this paper are based on an estimation of the optimal evaporating high pressure and the optimal condensing low pressure, and they are also based on the high pressure limit and the minimal superheat limit. To estimate the optimal working points, we write down the equation of the recovered power in the evaporator, the rejected power in condenser, the shaft power produced by the expander and the power consumed by the pump. These equations are then simplified by using a set of assumptions. An analytical treatment allows us to define optimal roots that maximize the Rankine net power.

5.1 Expander speed control.

To control the expander speed, we estimate an evaporating high pressure set point P_{rEvpo_sp} corresponding to the optimal evaporator power recovered from high temperature coolant loop $P_{W_{rEvpo_Opt}}$. To do that, we set a number of assumptions in order to simplify the equation of $P_{W_{mNet}}$. After derivation $\partial P_{W_{mNet}} / \partial P_{W_{rEvpo}} = 0$ and assuming some parameters as constants, we obtain a solution $P_{W_{rEvpo}}$ that maximize $P_{W_{mNet}}$ of the form: (f is a defined function of T_{cEvpi} , T_{aExt} , Q_{VcEvpo} , Q_{VcCnd} , V_{aExt} and the system components characteristics)

$$P_{W_{rEvpo_Opt}} = f(T_{cEvpi}, T_{aExt}, Q_{VcEvpo}, Q_{VcCnd}, V_{aExt}) \quad (4)$$

From $P_{W_{rEvpo_Opt}}$ of equation 4 we define the evaporating high pressure set point P_{rEvpo_sp} that will be used to control the expander speed.

5.2 Refrigerant pump speed control

To control the pump speed, we estimate a condensing low pressure set point P_{rCndi_sp} or a pressure ratio set point P_{rat_sp} corresponding to the maximum expander net power $P_{W_{mNet}}$. To do that, we used the equation of $P_{W_{mNet}}$ and the high pressure set point P_{rEvpo_sp} defined in §5.1. After different mathematical manipulations and some assumptions to simplify the equations, we set the derivative $\partial P_{W_{mNet}} / \partial P_{ratio} = 0$ and we obtain a solution P_{ratio_sp} that maximize $P_{W_{mNet}}$ of the form: (g is a defined function of P_{rEvpo_sp} , T_{aExt} and the system components characteristics)

$$P_{ratio_sp} = g(P_{rEvpo_sp}, T_{aExt}) \quad (5)$$

From P_{ratio_sp} of equation 5 and P_{rEvpo_sp} we define the condensing low pressure set point P_{rCndi_sp} that will be used to control the pump speed.

5.3 Control system architecture

Figure 6 presents the diagram of the Rankine control system. For this control strategy we use the following sensor data:

- From vehicle control unit:
 - T_{aExt} : Air temperature at low temperature radiator inlet
 - V_{aExt} : Air velocity at low temperature radiator inlet
 - Q_{VcEvpo} : High temperature coolant volume flow rate at evaporator inlet
- From Rankine system :
 - T_{cEvpi} : High temperature coolant temperature at evaporator inlet
 - P_{rExp_i} : Refrigerant pressure at evaporator outlet or at expander inlet
 - T_{rExp_i} : Refrigerant temperature at evaporator outlet or at expander inlet
 - P_{rExp_o} : Refrigerant pressure at expander outlet or at pump inlet

An evaporating high pressure set point P_{rEvpo_sp} and a condensing low pressure set point P_{rCndi_sp} are estimated by the control system. The high pressure is then regulated by controlling the expander speed and using the estimated high pressure set point. The low pressure set point and the condition on the minimum superheat are used to control the pump speed.

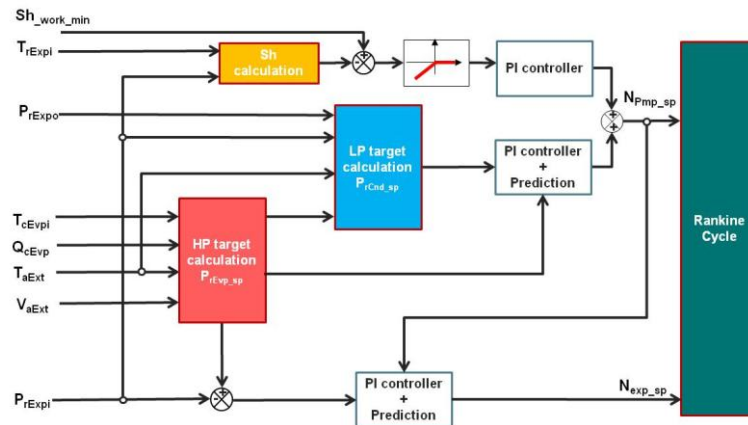


Figure 6 : Control system diagram

5.4 Rankine control system validation.

Different algorithms to estimate the optimal evaporating high pressure and condensing low pressure were tested. In order to evaluate the performance of these algorithms, we tested the Rankine control system with the Rankine system alone without the vehicle model. Steady state simulations are performed on the matrix of operating conditions defined in §4.2.

Because of the assumptions and approximations used to estimate the optimal Rankine system working points, the Rankine net power obtained with the different control algorithms is, in general, lower than the reference net power. The differences are between 0 W to 40 W.

Figure 7 illustrates the performance of the selected control algorithm. The first graph 7a shows the comparison on the effect of evaporator coolant temperature from 80°C to 110°C. Ambient temperature is 20°C. The control allows us to obtain a very good level of Rankine net power with a maximum difference of 17 W corresponding to 3% compared to the optimal power. The second graph 7b shows the comparison on the effect of radiator air velocity from 0.75 m/s to 5 m/s. The maximum difference on Rankine net power is 20 W corresponding to 4% of the optimal power.

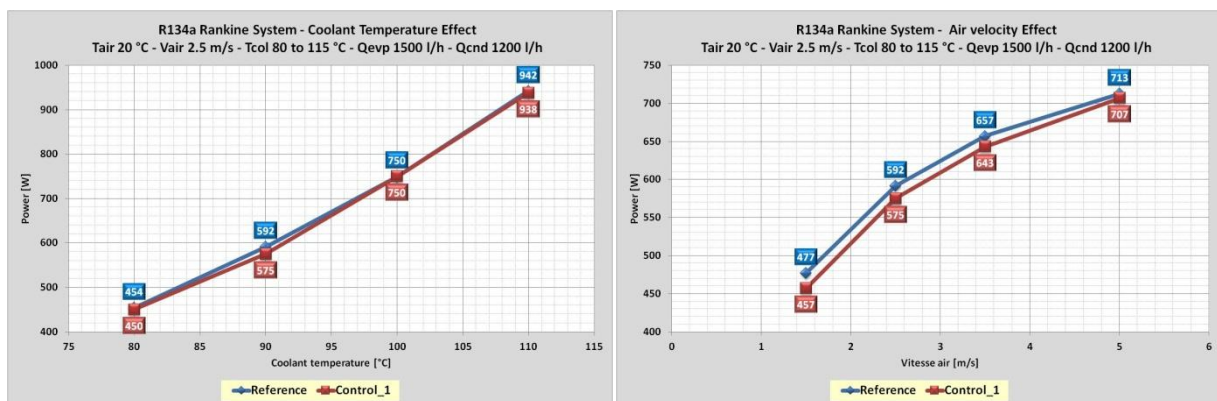


Figure 7 : Comparison of control algorithm performance on steady state conditions

6 VEHICLE INTEGRATION

6.1 Vehicle Energy and Thermal Management Simulation Platform

A simulation platform developed in the multi-physics systems simulation tool allows vehicle energy management and vehicle thermal management simulations of a vehicle equipped with a 2.0 liter turbocharged gasoline engine.

The R134a Rankine cycle model presented in Figure 2 and the control system were integrated into the Vehicle platform in order to simulate Rankine cycle with operating conditions close to real life

vehicle conditions. The interactions between vehicle and Rankine system are taken into account. However, in this study, the use of recovered power by the Rankine system electrically or mechanically by the vehicle power train is not considered. We only evaluate the recovered mechanical net power. The use of this power will be up to the carmaker strategy and will depend on the vehicle and the power train architecture and engine control strategy.

6.2 Application to constant velocities driving cycles

Figure 8 presents the Rankine net power obtained for constant vehicle velocities from 30 km/h to 180 km/h and for ambient temperature from -10°C to 25°C . The thermostat temperature setting is 90°C .

The following remarks can be stated:

- The Rankine net power increases when the vehicle speed increases. This is due to an increase of the available waste heat that can be recovered by the evaporator on one side, and an improvement of condensation performance due to the radiator air velocity increases with vehicle velocity on the other side.
- The Rankine net power is higher for low ambient temperature than for high ambient temperature. This is due to the improvement of condensation performance.
- The Rankine net power is limited by the recovered heat which is limited by the condensation side of the system, the pump and expander size.

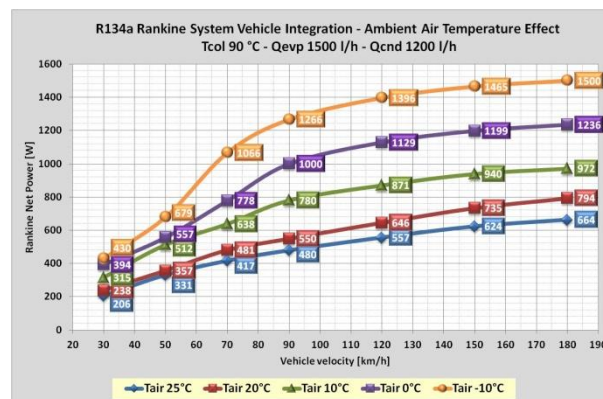


Figure 8 : Rankine net power versus vehicle speed and ambient air temperature

6.3 Application to transient driving cycle

To illustrate the performance of the Rankine control system, results are presented for transient WLTC driving cycles. WLTC is the driving cycle of the upcoming Worldwide harmonized Light vehicle Test Cycle. WLTC is more representative of real life driving in urban and sub urban conditions than driving cycles like NEDC. The duration of the WLTC cycle is 1800s and the average vehicle velocity is 46 km/h with a maximum vehicle velocity of 130 km/h. The simulations are performed for a period of 3600 s corresponding to two times the WLTC cycle duration in order to compare a WLTC with cold start engine and a WLTC cycle with warm engine.

Figure 9 presents the evolution of different Rankine cycle variables during the two WLTC driving cycles at 10°C ambient temperature. We can distinguish different phases:

- Phase I: At the start of the driving cycle, we assume that the vehicle temperature is constant and equal to the ambient temperature of 10°C . During the first 780 s period, the engine and the coolant are not hot enough and the Rankine system is switched off. The expander speed is zero and the pump speed is zero (In fact, for numerical reasons, the pump speed is set to a small value in order to ensure a minimal refrigerant circulation)
- Phase II: The coolant temperature is now higher than a coolant temperature high limit setting of 85°C , the Rankine system is activated and the pump and the expander are controlled in order to

regulate high pressure set point and low pressure set point with the constraint on minimum superheat Sh_{work_min} .

- Phase III (highlighted zones): The vehicle speed is too low or the vehicle is stopping. There is no more sufficient energy to be recovered. The air velocity at the radiator vanishes unless we switch on the Fan. The coolant outlet temperature is decreasing and reaches a low temperature limit setting of 80°C . So, the Rankine system is switched off and the pump and the expander are stopped.

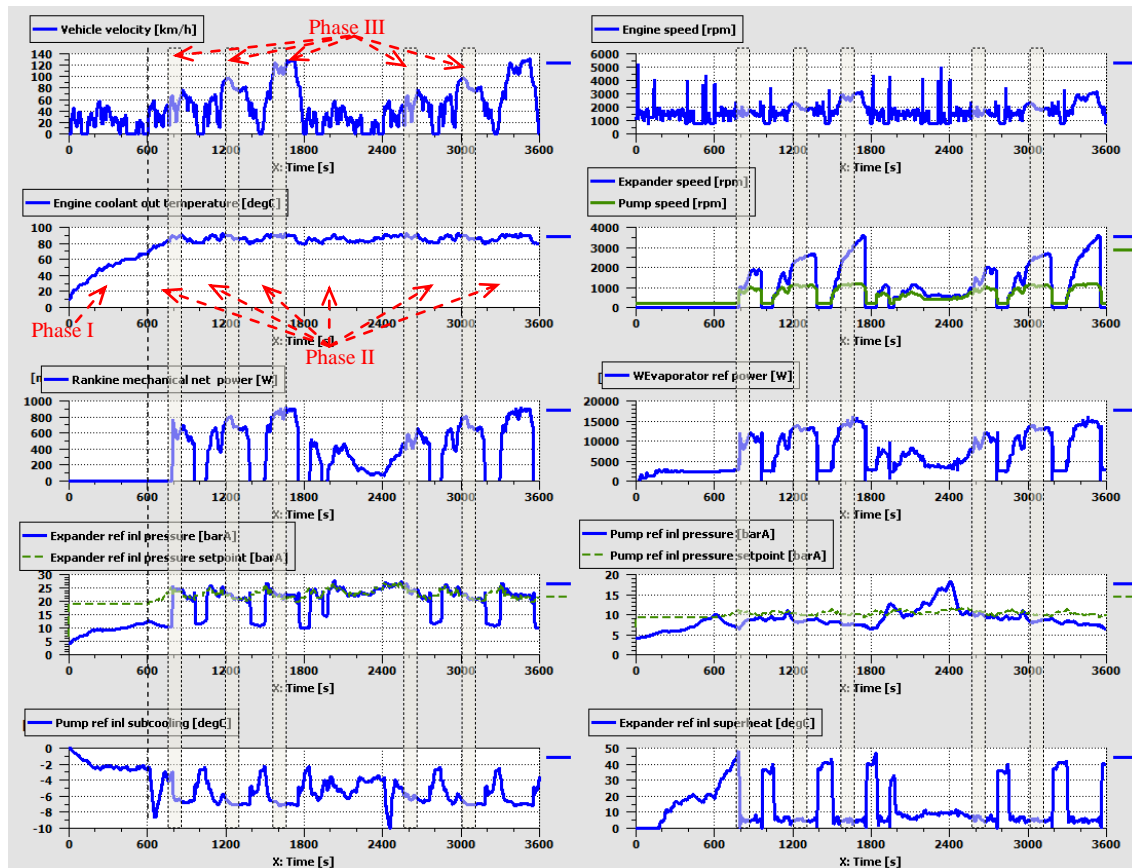


Figure 9 : Rankine system operation during WLTC driving cycle

Figure 10 presents a zoom showing the performance of the regulation of the evaporating high pressure and the condensing low pressure. The first graph shows the regulation of evaporation high pressure. The simulated high pressure follows correctly the estimated high pressure evolution defined by the control system with a delay of about 5s. The high pressure drops down when the Rankine system is switched off and the expander is stopped. The second graph presents the control of condensation low pressure. The condensing low pressure is 3 to 4 bars lower than the optimal low pressure defined by the control. In fact, to increase the level of low pressure we need to increase the pump speed. However, the superheat is very low as shown in the fourth graph. If the pump speed increases, the superheat will decrease below the Sh_{work_min} limitation. So, during these operating conditions the pump speed is controlled here by the superheat limit instead of by the condensation low pressure.

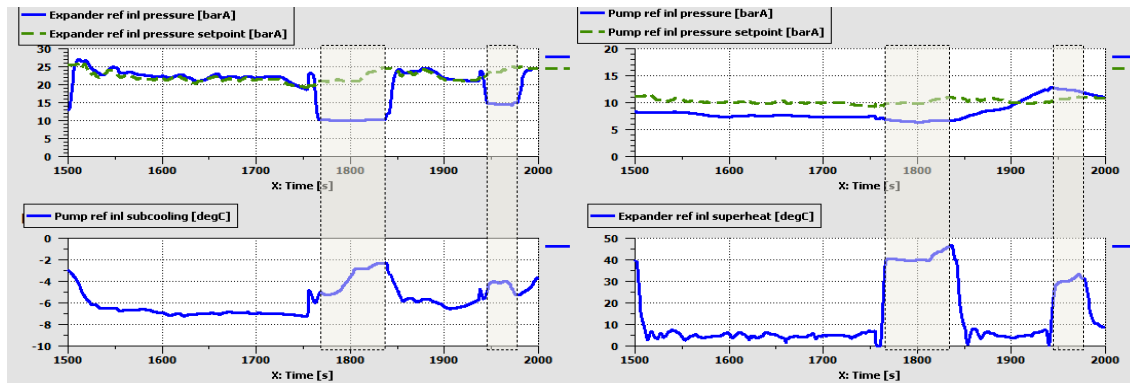


Figure 10 : Evaporating high pressure and condensing low pressure control

7 CONCLUSION

In this paper, we presented a methodology to develop and validate a control system of a low temperature waste heat recovery Organic Rankine Cycle system based on a co-simulation between a control tool and a systems simulation tool.

In the first part, a model of R134a Rankine cycle developed in a multi-physics systems simulation tool is presented. The model is based on a R134a Rankine prototype developed and tested at Valeo on a test bench. Experimental results obtained on the prototype are used to set up, calibrate and validate the models of the components and the Rankine system models.

The Rankine system model is then integrated into a global vehicle energy and thermal management model allowing simulation of Rankine system in various vehicle operating conditions corresponding to constant vehicle velocities.

A control algorithm is derived from an analytical analysis of the Rankine system equations. Different estimation of optimal evaporating high pressure and condensing low pressure are extracted and used to control the expander speed and the pump speed. The control algorithm programmed in a control tool is coupled to the physical model of a vehicle with Rankine system. The selected control algorithm was validated in steady state conditions and showed a good performance. The estimated Rankine net power obtained with the control system is no more than 20 W lower than the maximum possible net power.

Finally, the Rankine control system is applied to a transient WLTC driving cycle at different ambient conditions. It shows the ability of the control system to regulate the Rankine system with highly transient external and internal operating conditions in order to maximize the recovered mechanical net power and ensure a good conditions for a safe Rankine system functioning.

The developed control strategy and the methodology presented here can be adapted to different Rankine cycle architectures and different working fluids. It allows us also to study and evaluate different vehicle integration architectures and different options to use the mechanical power recovered by the expander directly to assist the engine and bring part of the power needed to accessories functioning or indirectly by producing electricity with an electrical generator.

NOMENCLATURE

Eff_{mExp}	Expander mechanical efficiency	[-]
HP_{work_max}	High pressure maximal working limit	[barA]
H_{rExp_i}	Refrigerant enthalpy at expander inlet	[J/kg]
H_{rExp_o}	Refrigerant enthalpy at expander outlet	[J/kg]
P_{ratio_sp}	Ratio of high and low pressure set point	[-]
P_{rCndi_sp}	Refrigerant pressure set point at condenser inlet	[barA]
P_{rEvpo_sp}	Refrigerant pressure set point at evaporator outlet	[barA]

P_{rExp_i}	Refrigerant pressure at expander inlet	[barA]
P_{rExp_o}	Refrigerant pressure at expander outlet	[barA]
PW_{mExp}	Expander mechanical power	[W]
PW_{mNet}	Rankine mechanical net power	[W]
PW_{rEvap}	Evaporator refrigerant power	[W]
PW_{rEvap_Opt}	Optimal evaporator refrigerant power	[W]
Qm_{rExp}	Expander refrigerant mass flow rate	[kg/s]
QV_{cCnd}	Coolant volume flow rate at condenser inlet	[m ³ /s]
QV_{cEvap}	Coolant volume flow rate at evaporator inlet	[m ³ /s]
Sb_{work_min}	Subcooling minimal working limit	[K]
Sh_{work_min}	Superheat minimal working limit	[K]
T_{aExt}	Ambient air temperature	[°C]
T_{cCnd_i}	Coolant temperature at condenser inlet	[°C]
T_{cCnd_o}	Coolant temperature at condenser outlet	[°C]
T_{cEvap_i}	Coolant temperature at evaporator inlet	[°C]
T_{cEvap_o}	Coolant temperature at evaporator outlet	[°C]
T_{rExp_i}	Refrigerant temperature at expander inlet	[°C]
T_{rExp_o}	Refrigerant temperature at expander outlet	[°C]
T_{rPmp_i}	Refrigerant temperature at refrigerant pump inlet	[°C]
$T_{w_out_min}$	Coolant temperature return minimal working limit	[°C]
V_{aExt}	Air velocity at low temperature radiator inlet	[m/s]

REFERENCES

- El Habchi, A., Ternel, C., Leduc, P., Hetet, J.F., 2010, Potential of waste heat recovery for automotive engines using detailed simulation, *ASME-ATI Conference on Thermal and Environment Issues in Energy Systems, Sorrento, Italy, May 16-19*.
- Abbe Horst, T., Tegethoff, W., Eilts, P., Koehler, J., 2014, Prediction of dynamic Rankine Cycle Waste heat recovery performance and fuel saving potential in passenger car applications considering interactions with vehicles energy management, *Energy Conversion and Management, vol. 78, p. 438-451*.
- Domingues, A., Santos, H., Costa, M., 2013, Analysis of vehicle exhaust waste heat recovery potential using a Rankine Cycle, *Energy vol. 49 p. 71-85*.
- Haller, R., Nicolas, B., Hammi, S., Taklanti, A., Labaste-Mauhe, L., Glavatskaya, Y., Yahia, M., 2014, Comparison of high and low temperature working fluids for automotive Rankine waste heat recovery systems, *SIA Powertrain, Rouen, France, May 21-22; 2014*.
- Taklanti, A., Liu, J.M., Yahia, M., 2013, Toward verification and optimization of electrical vehicle thermal management control strategies based on virtual vehicle model, *SAE Thermal Management Systems Symposium, Troy, Michigan October 22-24; 2013*.
- Quoilin, S., Aumann, R., Grill, A., Schuster, A., Lemort, V., Spliethoff, H., 2011, Dynamic modeling and optimal control strategy of waste heat recovery Organic Rankine Cycles, *Applied Energy vol. 88 p 2183-2190*.

PVT PROPERTIES AND VAPOR PRESSURES OF HFO-1336MZZ(E)

Katsuyuki TANAKA^{1*}, Ryo AKASAKA², Eiichi SAKAUE³

¹Nihon University, Department of Precision Machinery Engineering,
Chiba, Japan
ktanaka@eme.cst.nihon-u.ac.jp

²Kyushu Sangyo University, Department of Mechanical Engineering,
Fukuoka, Japan
ryo-a@ip.kyusan-u.ac.jp

³Toshiba Co. Ltd., Power System Company,
Kanagawa, Japan
eiichi.sakaue@toshiba.co.jp

* Corresponding Author

ABSTRACT

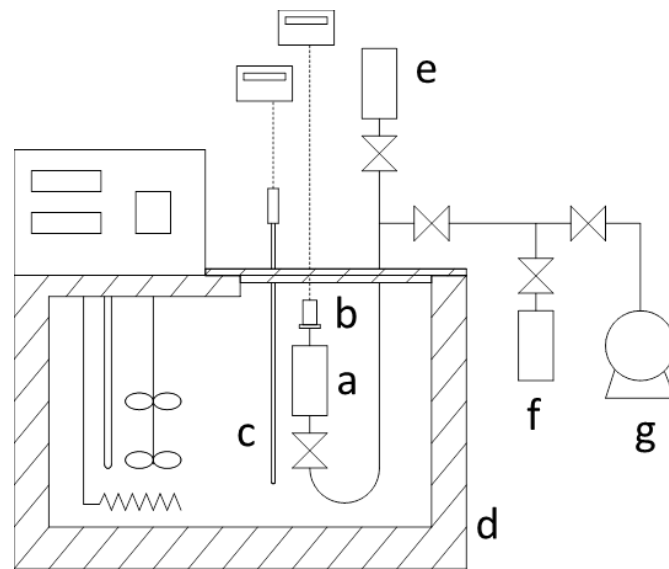
Experimental data of PVT properties and vapor pressures are presented for trans-1,1,1,4,4,4-hexafluoro-2-butene (HFO-1336mzz(E)). HFO-1336mzz(E) can be an alternative for conventional working fluids. However, reliable property information on the refrigerant is scarce at this time. This work performed measurements of the PVT properties at temperatures from 323 K to 443 K and pressures up to 10 MPa, including supercritical region. An isochoric method was employed with a constant volume cell designed for operation at high temperatures and high pressures. The critical temperature, pressure, and density were estimated from the PVT properties in the critical region. The saturation properties were also obtained.

1. INTRODUCTION

Regarding effective energy utilization, organic Rankine cycle systems are expected for power generation systems using waste heat energy which is relatively low-temperature heat sources. And then, several kinds of working fluids should be able to be selected according to temperature of heat sources. HFO-1336mzz(E) (CAS registry no.66711-86-2, molecular weight is 164.05) is definitely one of possible candidates for the working fluid whose boiling point is near and less than room temperature. HFO-1336mzz(E) is geometrical isomer of HFO-1336mzz(Z) whose boiling point is more than room temperature. In this study, PVT properties and vapor pressures for HFO-1336mzz(E) were measured to develop the thermophysical property data base of working fluids for organic Rankine cycle systems.

2. EXPERIMENTAL

A schematic diagram of the experimental apparatus is shown in Figure 1. Sample of HFO-1336mzz(E) produced by SynQuest Laboratories, Inc. was used. Measurements of PVT (Pressure-Volume-Temperature) properties were conducted by the isochoric method. The sample was filled in a sample cell with constant volume. The mass of sample was determined from difference in the mass of a sample bomb before and after filling the sample. The density was obtained from the volume of the cell and the mass of sample. Temperature of the sample was controlled by a thermostat oil bath. Pressure of the sample was measured by a pressure sensor. PVT properties were obtained along several isochoric lines by changing the mass of sample filled in the sample cell.



a: Sample cell, b: Pressure sensor, c: Temperature sensor, d: Thermostat oil bath, e: Filling bottle, f: Sample bottle, g: Vacuum pump

Figure 1 Schematic diagram of the apparatus

3. RESULTS AND DISCUSSIONS

3.1 PVT properties

The data of PVT properties for HFO-1336mzz(E) was obtained at temperatures from 323 K to 443 K at 10 K interval and pressures up to 10 MPa, along 17 isochores as shown in Figure 2. The data arranged along isotherms are shown in Figure 3.

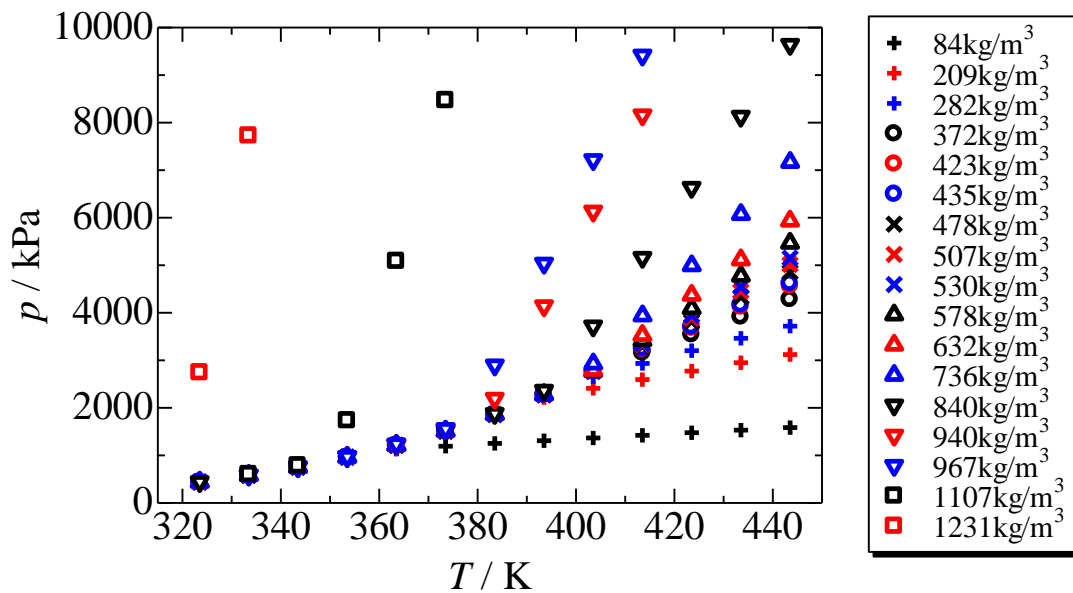


Figure 2 Experimental PVT data on pressure-temperature diagram

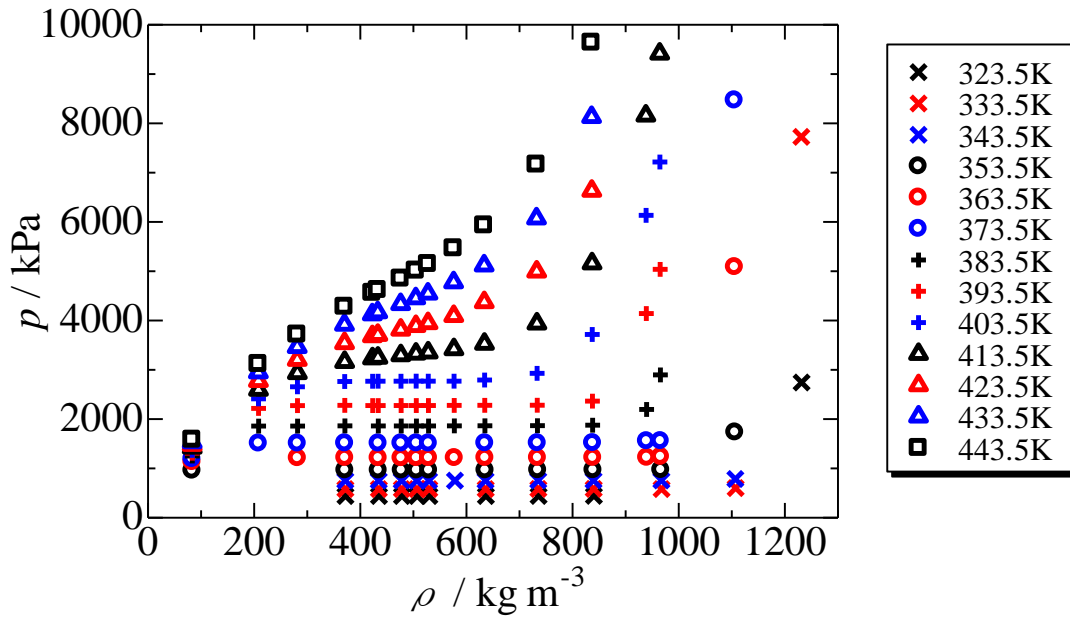


Figure 3 Experimental PVT data on pressure-density diagram

Figure 4 is an enlarged view of the critical region in Figure 3. The isotherm of 403.5 K includes data in two-phase region, because the pressure is constant in the density range from 400 kg/m³ to 600kg/m³. The isotherm of 413.5K consists of only data in the super critical region, because the pressure increases monotonously. These observations suggest that the critical temperature is located between 403 K and 413 K and that the critical density is to be found between 400 kg/m³ and 600 kg/m³.

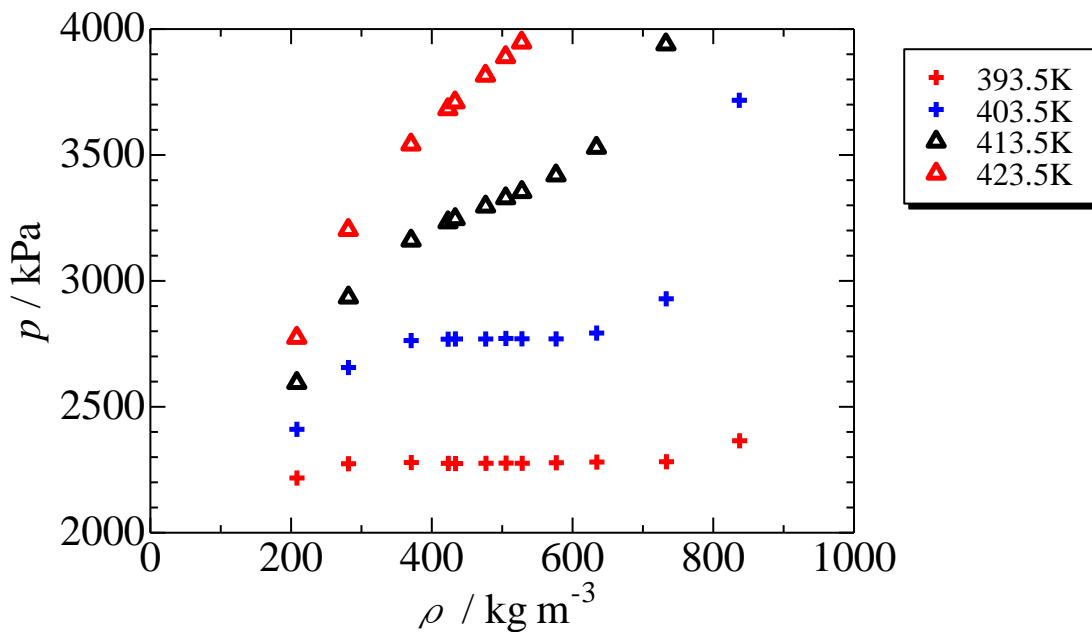


Figure 4 Experimental PVT data on pressure-density diagram in the temperature range from 393.5 K to 423.5 K

3.2 PVT properties near the critical point

In order to find more accurate location of the critical point, additional PVT measurements were performed in the critical region. PVT properties in the temperature range from 403.5 K to 413.5 K at 1K interval and in the density range from 384 kg/m³ to 605 kg/m³ along seven isochores were obtained. The data is shown in Figure 5 on the pressure-temperature diagram. They are also shown in Figure 6 on the pressure-density diagram, and its enlarged figure is shown in Figure 7 in the temperature range from 403.5 K to 405.5 K. These figures indicate that the critical point is located between 403.5 K and 404.5 K for temperature, between 2770 kPa and 2820 kPa for pressure, and between 476 kg/m³ and 528 kg/m³ for density.

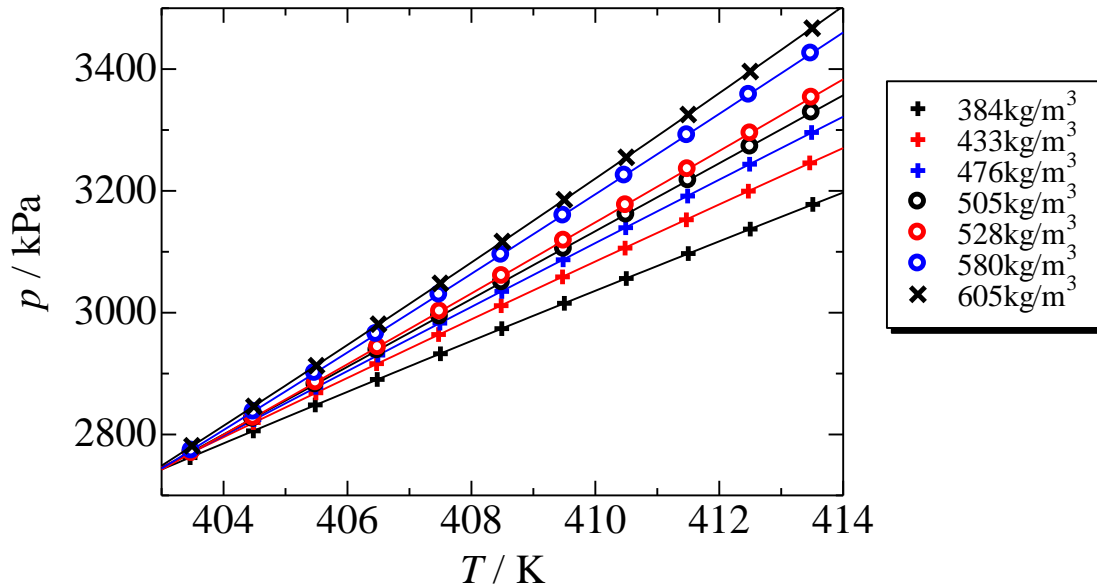


Figure 5 Experimental PVT data on pressure-temperature diagram near critical point

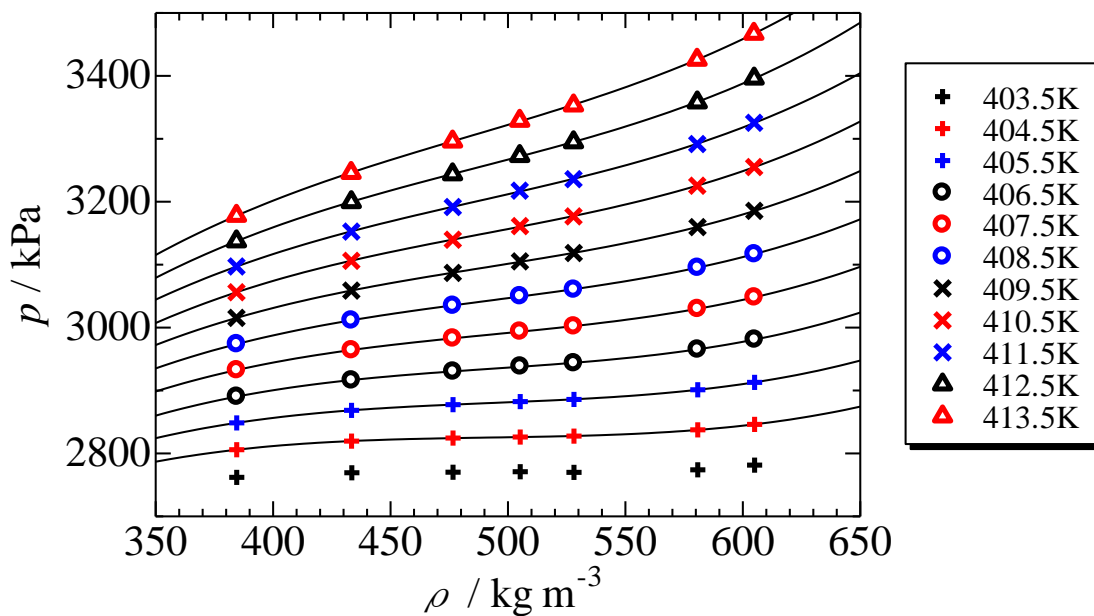


Figure 6 Experimental PVT data on pressure-density diagram near critical point

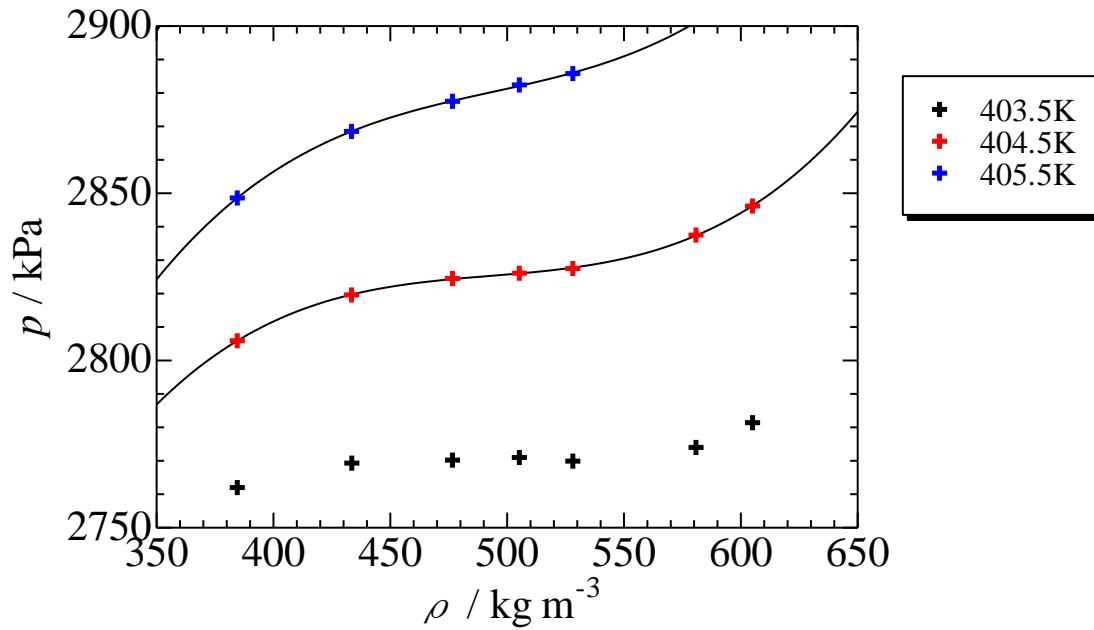


Figure 7 Experimental PVT data on pressure-density diagram near critical point (from 403.5 K to 405.5 K).

3.3 Vapor pressure

Vapor pressures are obtained from two-phase region data in the isotherms. Temperature dependence of the vapor pressures is shown in Figure 8.

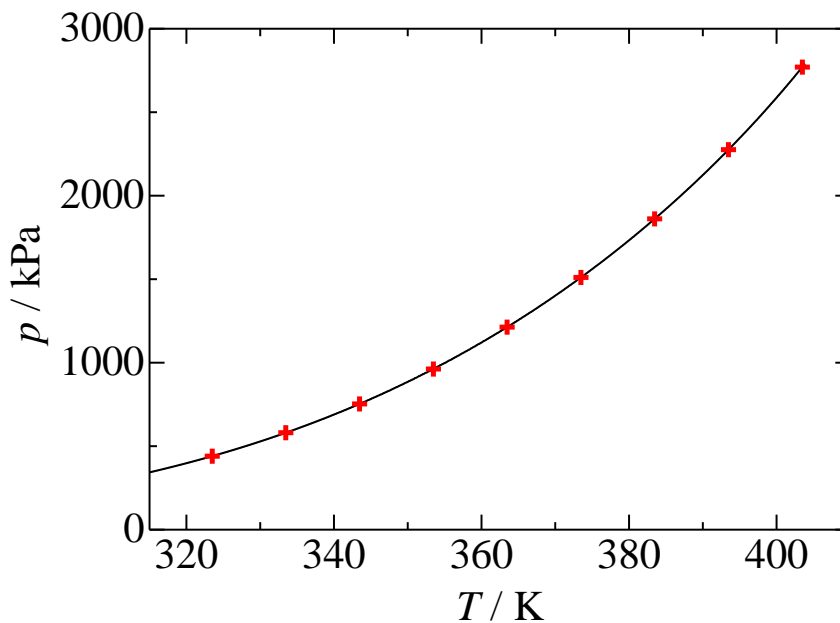


Figure 8 Vapor pressure of HFO-1336mzz(E)

3.4 Saturated densities

The saturated liquid or vapor densities were determined from intersections of the vapor pressure curve and several isochores, as shown in Figure 9. Eleven data points of saturated densities were obtained as shown in Figure 10.

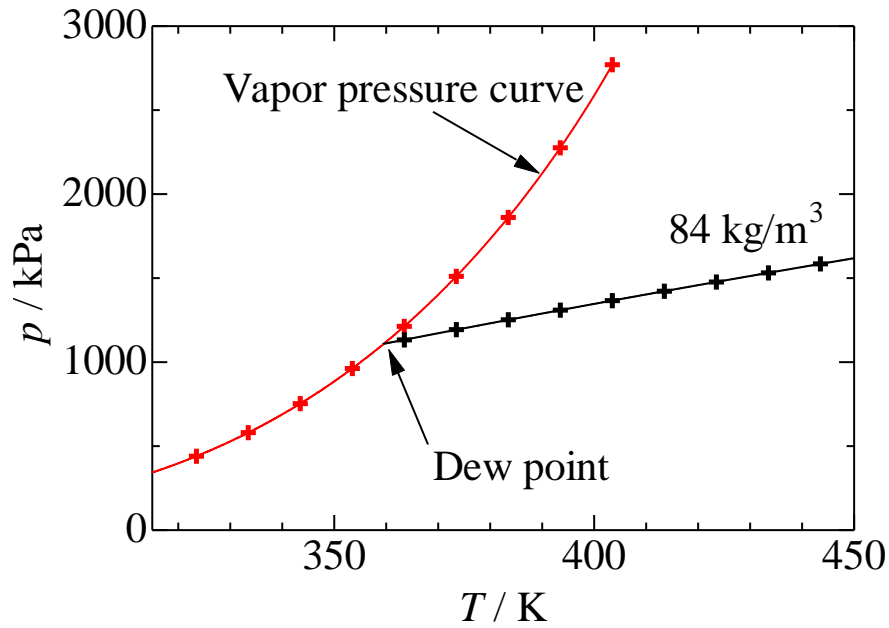


Figure 9 Determination of the saturated densities. Example for isotherm of 84 kg/m^3 .

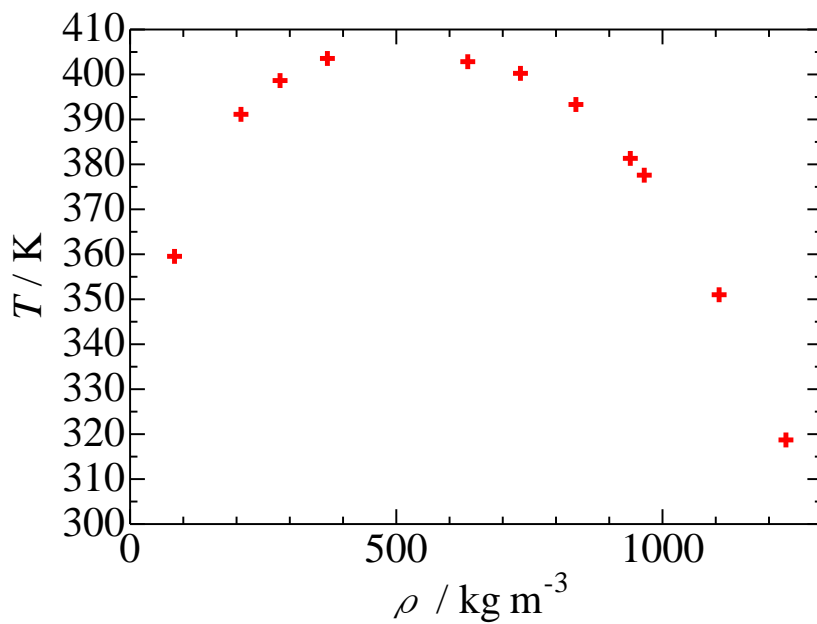


Figure 10 Saturated liquid and vapor densities of HFO-1336mzz(E)

4. CONCLUSIONS

Conclusions of this work are summarized as follows:

- Seventy seven data points of PVT properties for HFO-1336mzz(E) were obtained in a wide ranges of temperature and density, including the critical region.
- Nine data points of the vapor pressures for HFO-1336mzz(E) were obtained from two-phase region data.
- Eleven data points of the saturated densities of HFO-1336mzz(E) were determined from intersections of the vapor pressure curve and isochores.

NOMENCLATURE

p	pressure	(kPa)
T	temperature	(K)
V	volume	(m ³ /kg)
ρ	density	(kg/m ³)

ACKNOWLEDGEMENT

This work was supported by the Japan Science and Technology Agency (JST) under the Strategic International Collaborative Research Program (SICORP).

ORC-DEMONSTRATION-PLANT WITH 1 KW SCROLL EXPANDER – CONCEPT, DESIGN AND OPERATIONAL EXPERIENCES

Albrecht Eicke¹
Slawomir Smolen²

University of Applied Sciences Bremen
Julius Robert Mayer – Institute for Energy Technology
Neustadtswall 30, Bremen, 28199, Germany

¹ Albrecht.Eicke@hs-bremen.de

² Slawomir.Smolen@hs-bremen.de

ABSTRACT

The development and optimization of the ORC technology can be divided into two general groups of tasks and challenges: theoretical investigations and practical system and component improvement. One of the main practical challenges is the adoption of proper and effective expansion devices.

In this paper the current project – an ORC demonstration and test plant with an oil free expander - will be presented. The core of the micro power plant is a scroll-expander with a nominal power of 1 kW. A commercially available scroll expander (Air Squared Inc., E15H22N4.25) with generator was used as expansion machine of the plant, in order to check the capabilities and the theoretical and practical limitations. In the first testing phase, compressed air has been used as working fluid in the expansion machine and the characteristic curves (electric power versus revolution speed with overall efficiency) have been plotted. These results can be extrapolated on other working fluids theoretically and are an indicator for the limitations of the scroll expander coupled with the electric generator. In the main phase of the project, the complete ORC-Installation with R245fa as working fluid is going to be tested and evaluated.

In the future the installation will be coupled to solar collectors, which will provide the heat to keep the ORC process running. Alternatively the heat can be generated by an electric driven thermal heater rated at a nominal power of 17 kW to demonstrate the functionality of the ORC itself without using solar energy. Disregarding the source of the heat, it is transmitted by two plate heat exchangers to the working fluid (R245fa). The extensive measurement instrumentation will be able to evaluate the entire process and the components used for the installation, especially the effectiveness of the expansion device.

1. INTRODUCTION

Organic Rankine Cycle (ORC) installations use an organic fluid instead of water as working fluid and are potentially feasible in heat recovery systems - especially for energy conversion on low and middle temperature levels. Many practical applications have been designed and installed to use low enthalpy heat sources like geothermal energy, industrial waste heat, solar energy, biomass combustion plants, small scale cogeneration systems, domestic boilers and others.

Within the framework of many projects and activities in the JRM-Institute and Laboratory for Energy Engineering at the University of Applied Sciences in Bremen, several practical and theoretical aspects of energy transformation using Organic Rankine Cycle have been investigated.

The prior activities focused on two general optimization and designing tasks. A special procedure and program has been elaborated and developed in the area of universal theoretical analysis, which facilitates working fluid selection in Organic Rankine Cycle for waste energy recovery from potential low and medium temperature level sources. In order to identify the most suitable organic fluids, several criteria have to be taken into consideration. An essential part of the program is a wide range database of organic fluids and the elaborated tool should create a support by choosing an optimal

working fluid for special applications and become a part of a bigger optimization procedure by different boundary conditions.

The theoretical research areas to develop and optimize the ORC technology can be divided into two general groups of tasks and challenges. The first big area is the thermodynamic system optimization which means not only the efficiency improvement within the cycle but also analysis of the complex system: heat source coupled with ORC-process (Smolen, 2014). This analysis should be performed by minimizing energy and exergy losses (Srinophakum, 2001, Invernizzi, 2007, Hung, 2001, and others). The second theoretical field is the working fluid selection as optimization measure of the cycle and the entire process heat transfer from heat source. However, the selection of working fluids and operational conditions are very important to system performance. The thermodynamic properties of working fluids will affect the system efficiency, operation, and environmental impact (Smolen, 2011, Saleh, 2006, Angelino, 1998, Borsukiewicz-Gozdur, 2007, Liu, 2004 and others)

The ORC-Process is not the only alternative to use low enthalpy heat sources. Some technologies are available and efficient, some other technologies are still been developed but seem being promising. Among those technologies the water-ammonia cycle, the supercritical CO₂ cycle, the Stirling and Ericsson cycles, the Kalina cycle and the thermoelectric generator can be mentioned. There are many criteria and boundary conditions to compare the different approaches and methods of energy conversion but generally the Organic Rankine Cycle is preferred to those technologies, because of its simplicity and its limited number of components, all of them being very common and in the typical applications commercially available.

One of the practical limitations and challenges of developing of new ORC-installations are expansion devices, or lack of suitable machines for special applications in small and middle range of performance (especially micro- and mini ORC-installations). There are many approaches and practical solutions and technologies like using micro turbines, scroll expanders, screw machines, special reciprocation engines and others. The internal efficiency of expansion process is one of the biggest sources of energy and exergy losses which restrict system's efficiency. As example of practical possibilities and solutions, the application of a screw compressor as expansion device of ca. 30 kW has been investigated and the unique installation has been put into operation within a prior theoretical and practical work (Eicke, 2014). The project work presented in this paper deals with smaller range of performance and uses existing components in order to extend the practical and theoretical experiences and potential applicability.

2. OBJECTIVES AND REQUIREMENTS TO THE TEST AND DEMONSTRATION 1 KW ORC-PLANT

The general goal of the work was concept development, design, evaluation and optimization of an ORC plant in power range of ca. 1 kW. One of the practical intensions of the project was to investigate a commercially available scroll expander (Air Squared Inc., E15H22N4.25) with generator as core piece of the plant, to adopt the installation to this specific expansion device and to check the capabilities and the theoretical and practical limitations.

In the first stage of development, the heat source should be "simulated" by an electric heater but, as final solution, the test plant will be coupled with a solar installation in order to demonstrate the application as renewable energy conversion and use. Subject of the presented paper is only the first stage of the project and the relevant subsequent subtasks are:

- technical optimization by concept development and permanent improvement after the first operational experiences;
- thermodynamic process evaluation and optimization by using advanced measurement technology;
- theoretical validation and transfer of the measurement results to changeable temperature levels and different working fluids. (This possibility is limited by the existing installation and the reconfiguration require additional measures like component replacement);
- evaluation of the practical application possibilities in different energy supply systems.

Furthermore some additional aspects have been taken into consideration like flexibility by required modifications and improvement measures, safety aspects, analysis and prevention of operational

accidents, demonstration effects and others. Advanced measurement technology should facilitate thermodynamic and technical evaluation and optimization of the plant and additionally support the demonstration effect.

3. DEMONSTRATION PLANT CONCEPT AND MAIN COMPONENTS

As already mentioned, the general goal of the installation concept has been adapted to the requirements and performance of the scroll expander (Air Squared Inc., E15H22N4.25). All components and parts of the installation have been calculated and selected, in order to use the possibilities and potential of the existing expansion device in an optimal way. The temperature, pressure and flow rate sensors have been installed in all relevant points not to be able to evaluate the whole cycle but also to validate the components and the auxiliary equipment. The connection scheme of the plant is shown in figure 1.

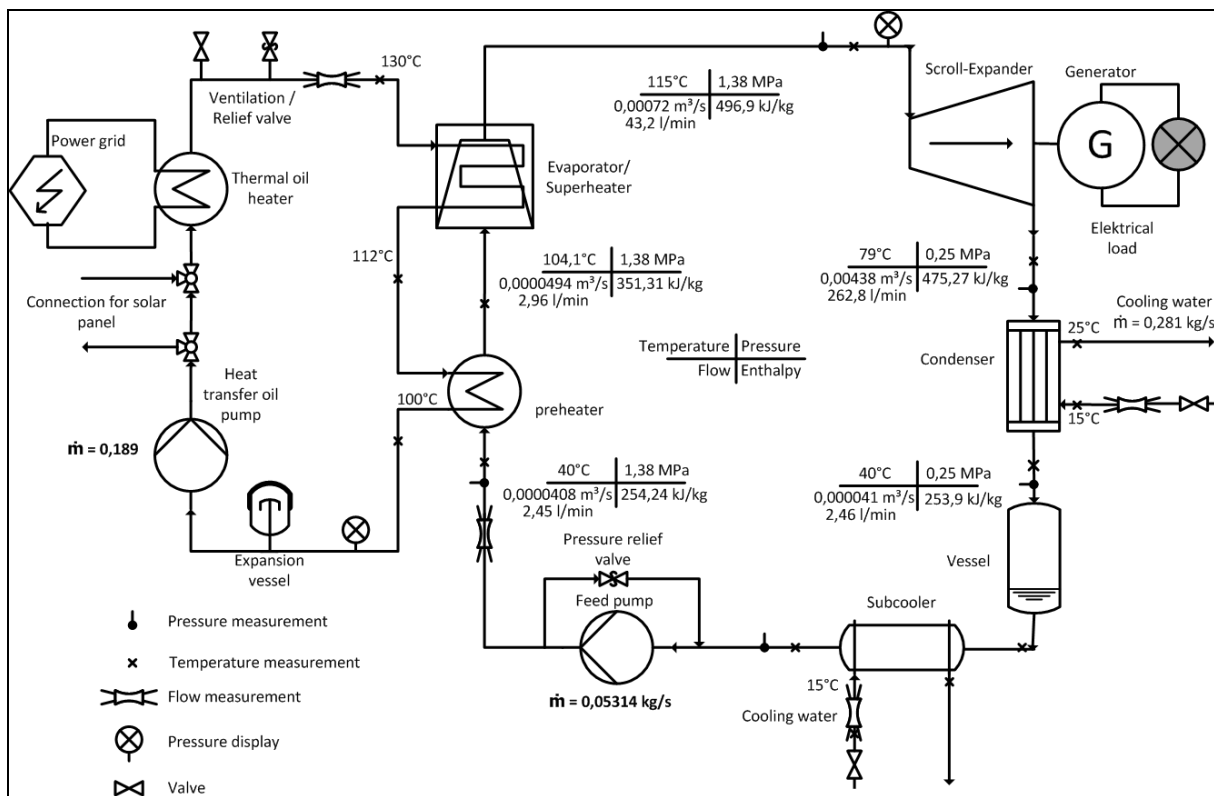


Figure 1: ORC demonstration plant – connection schema

In the first stage of the project the heat power is provided by electric heater and the heat transfer medium is thermal oil. The typical ORC-installation consists of preheater, evaporator, scroll expander, condenser and feed pump. An additional special part is the refrigerant sub cooler after the storage tank. This one facilitates the operational quality, especially by putting into operation or changeable performance (experiences from the bigger installation mentioned in the introduction). The thermodynamic cycle is shown in figure 2 (log p–h–Diagram).

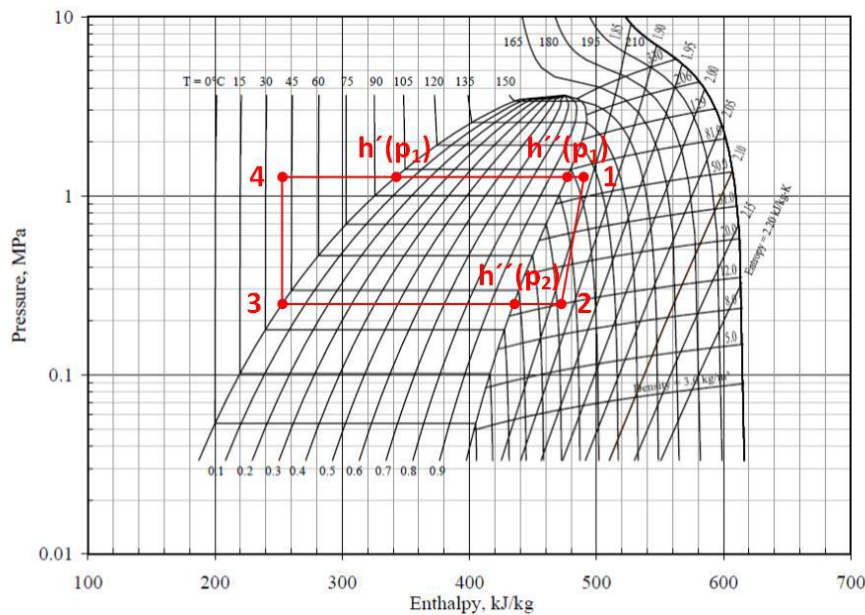


Figure 2: ORC cycle parameter in log-p-h-diagram

For the test bench the working fluid R245fa was selected but some alternatives are possible and can be taken into consideration. The calculated (expected) efficiency amounts to ca. 8.7 %. This efficiency has been calculated as total efficiency, it means electrical energy output to thermal energy input (4-1 in Fig. 2). The expected internal efficiency of expansion (1-2 in Fig. 2) has been considered as well as pumping power (3-4 in Fig. 2). Heat losses in heat exchangers (evaporator, condenser) and in connecting pipes are negligible - when good insulated - and were not calculated.

The following table specifies some important data and characteristics to the main components of the installation.

Table 1: Components of the plant – selected data and characteristics

No.	Component	Parameter
1.	Scroll expander	Air Squared Inc., E15H22N4.25, expansion ratio 3.5
2.	Generator	AB30 Hydro, 50Hz, 2400W at 3000min ⁻¹
3.	Electric thermal oil heater	Typ HF/SE-20, $t_{max} = 130^{\circ}\text{C}$, Power = 20kW
4.	Feed pump (refrigerant)	Slide pump with magnetic coupling
5.	Heat exchanger	Preheater: Plate heat exchanger, GPL 25-8 Evaporator: Plate heat exchanger, GPL 25-14 Condenser: Plate heat exchanger, GPL 1-20 Sub cooler: Pipe in pipe heat exchanger Typ HE1.5
6.	Heat transfer pump	small centrifugal pump for Therminol ADX10
7.	Electric installation (energy use)	15 Halogen bulb each 100W electrical load

4. DESIGN OF THE INSTALLATION

The installation has been designed and built in the Laboratory for Energetics of the Hochschule Bremen within a master project work (Haberkorn *et al.*, 2015). All the requirements and objectives mentioned above has been considered and as demonstration effect the front side of the box shaped stand is designed as thermodynamic part, the expander and generator is mounted on the top and the electric and control devices are placed on the back – as shown in figure 3. On the right the electrical power can be visualized by luminous halogen lamps, which are controlled by a special board. For the second stage of the project, the connections to the solar installation have been designed too.

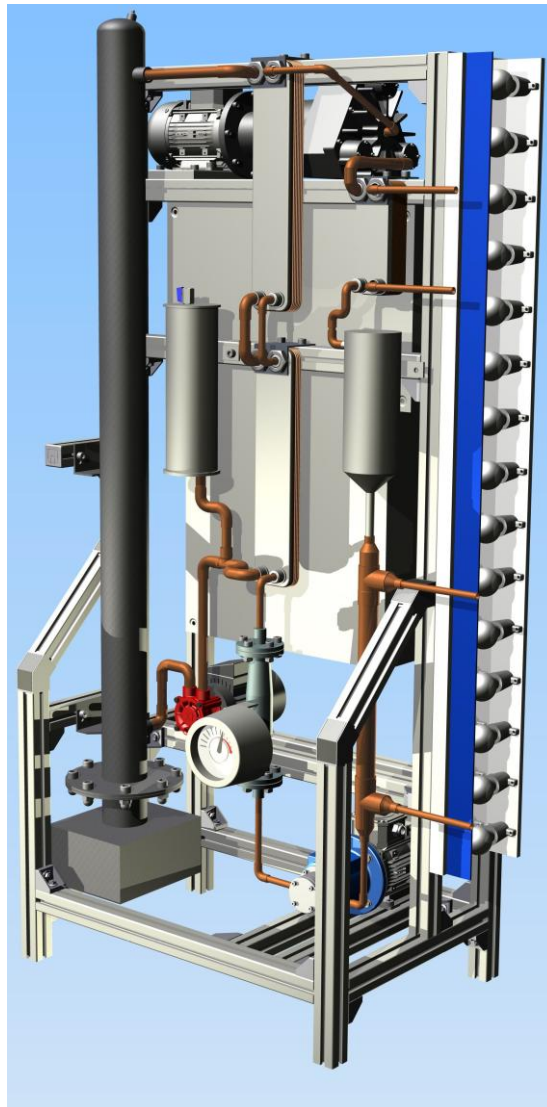


Figure 3: Design of the 1 kW ORC demonstration plant

5. LABVIEW CONTROL SYSTEM

This ORC-plant is developed to demonstrate a steam cycle and to show the function of its components. A Data Acquisition System cDAQ 9178 was used for measuring the temperature and the pressure in each condition, the electric power, the volume flow and the revolution of the scroll expander. This system is built up in a modular way and cause of the integrated signal condition the sensors are clearly arranged and direct connected. The voltage and current flow of the generator are converted by a hall effect transducer into a signal of up to 5 Volt so that the effective electric power could be calculated. The measurement equipment is shown in figure 4 and is located in a separate switchboard to reduce electric noise from inverter and motor.

To hold the required voltage and the frequency, for example 230 Volt at 50 Hz, a LabVIEW program calculates the electric load and turns on additional light bulbs or switches them off (each light bulb has nominal 100 Watt at 230 Volt). A maximum number of 15 light bulbs can show directly the produced power of the specific operating point.

The software searches for the measured temperature and pressure the values for enthalpy and entropy to the main condition points from a table. Additional to the heat power, the electrical power, the revolution and the efficiency these points are also visualized in a h-s-diagram and a T-s-diagram.

The speed of the feed pump is controlled over an inverter, shown in figure 4, to steer the mass flow of the refrigerant in the cycle to hold the evaporating temperature on one hand and to control the revolution of the scroll expander on the other hand.

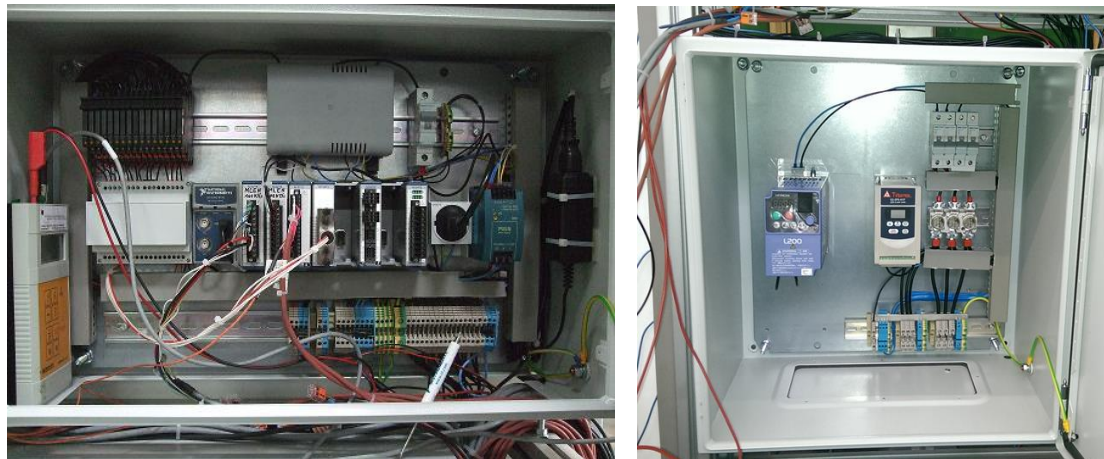


Figure 4: The measurement equipment (left) and frequency inverter to control the feed pump (right)

The electric thermal oil heater was not delivered in time, so that the scroll expander was tested with compressed air to check the control loop, the sensors and the electric load.

6. COMPRESSED AIR TEST BENCH FOR SCROLL EXPANDER TESTS

The test bench was enlarged with air pipes and an air flow meter to test the scroll expander and the generator. The supply grid for compressed air of the Laboratory for Energetics is limited to 0.95 MPa therefore it was not possible to test the expander with the maximum pressure of 1.38 MPa.

In the beginning the characteristic of the generator (voltage versus speed) was measured. The first run showed that the generator is self-excited and built up a magnetic field when the break-through-voltage of the diode is over 100 Volt the first time – like shown in figure 5. The following tests show a useful voltage of 80 Volt when the revolution per minute is higher than 1500 min⁻¹.

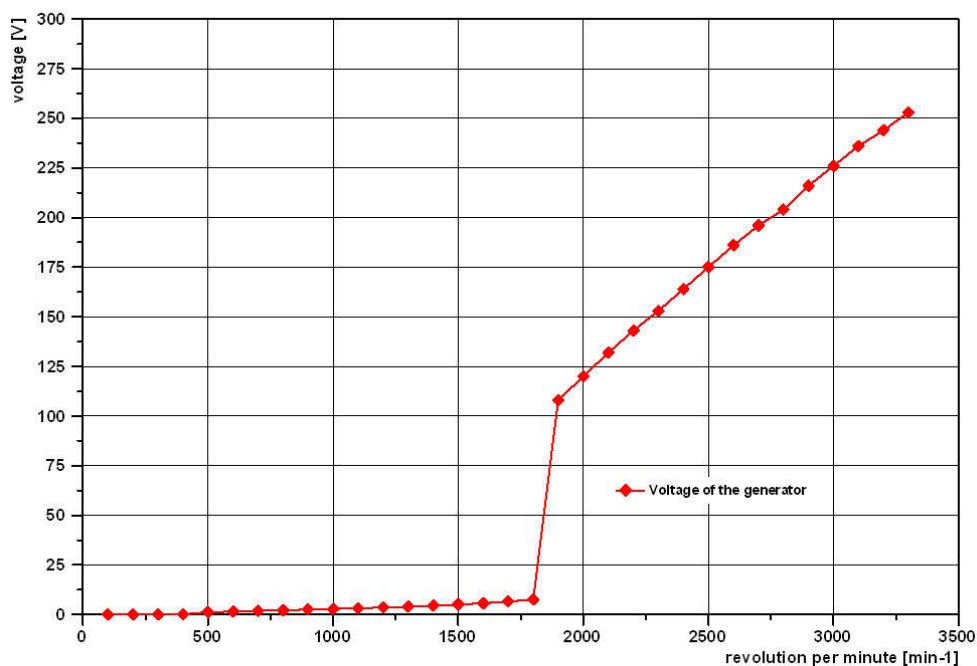


Figure 5: Characteristic of the generator Voltmaster AB30 2400 Watt - voltage vs rpm

The compressed air is expanded in the scroll expander from an inlet temperature of 19°C with a volume ratio of 3.5 to a low temperature of 10 degrees below zero at the end of the expansion that the duration of the test is limited not to risk a damage of the expander. The enthalpy and the thermal properties of the air is not comparable with the 115°C hot refrigerant of the real fluid. It is therefore necessary to increase the load of the test bench at lower revolutions per minute by external excitation of the rotor to measure the full curve of the electric power. The real refrigerant fluid with its higher energy content would cause higher speeds of the scroll engine than for air operation and is therefore in the correct speed range. Figure 6 shows the electric power versus revolution per minute for a pressure from 0.50 MPa to the maximum of 0.94 MPa. The overall efficiency is noted in numbers at every second point. The volume flow through the scroll engine increases with the increase of speed but the torque goes down to zero at maximum speed. The efficiency is higher with higher suction pressure and rise up to a maximum value a little bit higher than the half of the revolution per minute with no load. For example the efficiency for a pressure of 0.94 MPa at 3600 rpm is zero and rise up to $\eta = 0.43$ at 2200 rpm.

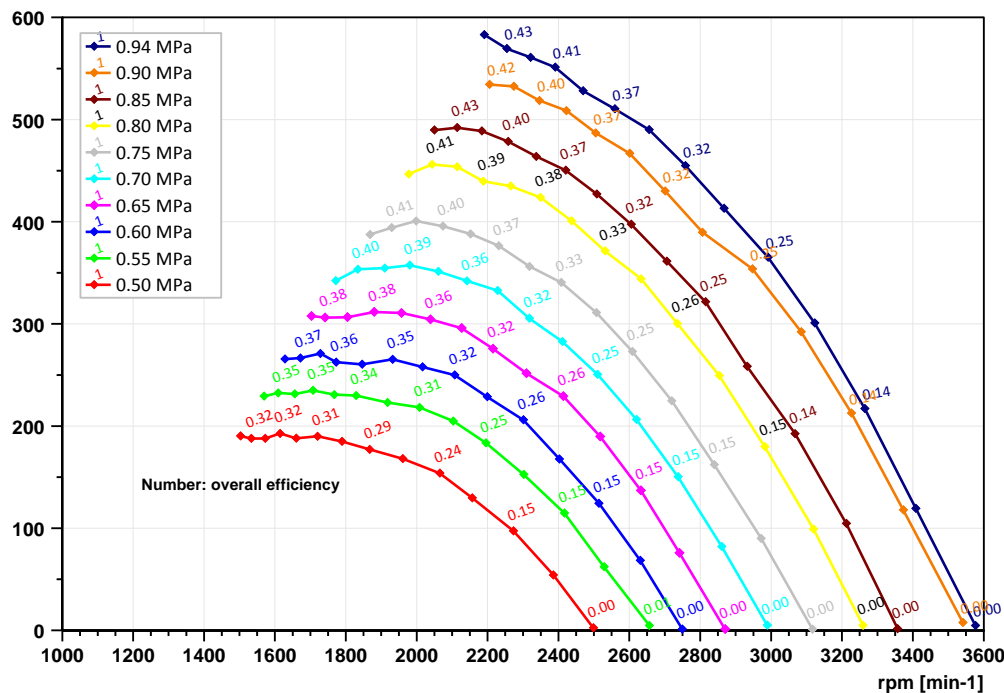


Figure 6: Electric Power versus rpm with overall efficiency

7. CONCLUSIONS AND OUTLOOK

As result of the practical orientated work, a unique 1 kW ORC installation on the base of scroll expander has been developed, designed and built, which facilitates process improvement and demonstration effects. Additionally, a test bench for scroll expander tests with pressurized air has been developed and equipped in order to investigate operational features of the expansion device as the first practical step. These preliminary tests are essential for the subsequent thermodynamic process improvement and optimization. The final presentation is going to include the first operation experiences and test results.

Related to the second stage of the ORC project a solar installation has been calculated and planed, which is going to be installed and coupled with the ORC-plant to extend it to a complex installation using a renewable energy source.

Parallel to this technical project, an additional aspect – namely economical one - has been taken into consideration by investigating the practical applicability. One concrete application possibility of the 1 kW plant for waste heat use from an industrial process was evaluated from economical point of view, in fact with a negative result. (The economic efficiency calculations have been conducted for German

energy prices and economical boundary conditions and the calculation's details would be beyond the scope of this paper). The main reason for the economic ineffectiveness is of course the costs of the unique installation, which cannot justify profitable operation under the terms of conventional economy.

REFERENCES

- Angelino, G., Di Palliano, P.-C., Multicomponent working fluids for organic Rankine cycles (ORCs), *Energy*, vol. 23, No. 6, 1998, pp. 449-463.
- Borsukiewicz-Gozdur, A., Nowak, W., Comparative analysis of natural and synthetic refrigerants in application to low temperature Clausius-Rankine cycle, *Energy*, vol. 32, 2007, pp. 344-352.
- Eicke, A., Smolen, S., Screw Engine as Expansion Machine Applied in an ORC-Test-Installation – the First Operating Experiences – Lubrication System for a Screw Machine in Reverse Rotation, *VDI-Berichte (Energy and Environment)*, International Conference on Screw Machines, TU Dortmund University - 2014, ISSN 0083-5560, ISBN 978-3-18-092228-7.
- Haberkorn, P., Herrmann, L., Sax, M., Speckmann, B., Zoche, D., KAI-ORC, Technical Project Documentation, University of Applied Sciences Bremen (Hochschule Bremen, Advisor: Smolen, S., Eicke, A.), Februar 2015, not published.
- Hung, T.-C., Shai, T.-Y., Wang, S.-K., A review of organic Rankine cycles (ORCs) for the recovery of low-grade waste heat, *Energy*, Vol. 22, No. 7, 1997, pp. 661 – 667.
- Hung, T.-C., Waste heat recovery of organic Rankine cycle using dry fluids, *Energy conversion and management*, vol. 42, 2001, pp. 539-553.
- Invernizzi, C., Iora, P., Silva, P., Bottoming micro-Rankine cycles for micro-gas turbines, *Applied Thermal Engineering*, vol. 27, 2007, pp. 100-110.
- Liu, B.-T., Chien, K.-H., Wang, C.-C., Effect of working fluids on organic Rankine cycle for waste heat recovery, *Energy*, vol. 29, 2004, pp. 1207-1217.
- Saleh, B., Koglbauer, G., Wendland, M., Fischer J., Working fluids for low-temperature Organic Rankine Cycles, *Energy (2006)*, doi:10.1016/j.energy.2006.07.001., Elsevier Ltd.
- Smolen, S., Boertz, H., Calculation and optimization of heat transfer between the low enthalpy heat source and Organic Rankine Cycle applied to heat recovery systems, *Key Engineering Materials*, Vol. 597 (2014), © (2014) Trans Tech Publications, Switzerland doi:10.4028/www.scientific.net/KEM.597.45
- Smolen, S., Bandean, D., Working Fluid Selection for Organic Rankine Cycle Applied to Heat Recovery Systems, *WREC, World Renewable Energy Congress 2011*, Sweden, Linköping, May 2011, www.wrec2011.com
- Smolen, S., Simulation and Thermodynamic Analysis of a Two-Stage Organic Rankine Cycle for Utilization of Waste Heat at Medium and Low Temperature Levels, *Energy Science and Technology (Peer Reviewed Journal)*, Volume 1, Number 1, 28 February 2011, Canadian Research & and Development Center of Science and Cultures, www.ascanada.net, ISSN 1923-8460 [Print], ISSN 1923-8479 [Online]
- Srinophakum, T., Laowithayangkul, S., Ishida, M., Simulation of power cycle with energy utilization diagram, *Energy Conversion and Management*, vol. 42, 2001, p. 1437-1456.

DIESEL ENGINE WASTE HEAT HARNESSING ORC

Jovana Radulovic^{1*}, Simon Taylor¹

¹University of Portsmouth, School of Engineering,
Portsmouth, PO1 3DJ, United Kingdom
jovana.radulovic@port.ac.uk

ABSTRACT

Use of ORCs in waste heat recovery is widely seen as a viable and promising solution for increasing energy efficiency and emission reduction efforts, with “on-board” vehicular concepts becoming increasingly popular. In this study, the potential of an ORC harnessing exhaust energy from a diesel generator is considered. Preliminary fluid selection was based on satisfactory thermodynamic performance, and expander size requirement as the limiting parameter.

Both simple and recuperative ORC systems were considered. The effect of the exhaust temperature and the high operational pressure of the ORC model were evaluated in terms of energetic and exergetic performance. For the toluene ORC, moderate pressure values were dictated by the expander size limitation, yet this can be alleviated by high exhaust temperatures. Simple ORCs required a larger heat input and had lower exergetic efficiency. Recuperative ORCs showed better thermal efficiency and lower overall exergy destruction. The expander efficiency was identified as a vital parameter for cycle design and thermodynamic performance.

1. INTRODUCTION

With ever increasing global energy consumption and climate change concerns, reducing greenhouse gases emissions and improving energy efficiency of power systems are immediate priorities. Organic Rankine Cycle (ORC) has been long recognised as a promising technology to support the shift from conventional fossil fuels towards renewable energy sources. A number of published studies evaluated ORC potential in conjunction with biomass, solar and geothermal energy sources (Tchanche *et al.*, 2011). Additionally, ORC is a powerful tool for harnessing waste heat (Quoilin *et al.*, 2013) (Kolsch and Radulovic, 2015).

Basic ORC is founded on well-known transformations found in the conventional steam Rankine systems. However, the use of a volatile organic liquid as the working fluid allows for low-grade heat sources to be used. ORC is considered to be flexible in terms of the type and temperature of the heat source, and requires low maintenance. The versatility of the heat source and its modular design make ORC an attractive option, especially when waste heat is used for power generation.

Conversion of waste heat into electricity through so-called bottoming ORC improves the overall efficiency of the system whilst reducing heat pollution. The efficiency of the waste heat recovery through an ORC depends on a number of parameters: the state and quantity of the stream matter, its availability and especially its temperature. In fact, waste heat sources are categorized according to their temperature range as: low heat (< 230°C); medium heat (230°C - 650°C); and high heat (> 650°C) (Tchanche *et al.*, 2011). In particular, harnessing of diesel engine exhaust heat has been the focus of recent research. Larsen *et al.* (2013) studied a plethora of potential ORC fluids for waste heat recovery in marine applications. Yu *et al.* (2013) concluded that the thermal efficiency of a diesel engine can be improved up to 6.1% through bottoming ORC implementation. Wang *et al.* (2014) proposed a dual-loop ORC system. Katsanos *et al.* (2012) evaluated the possibility of ORC installation on a diesel truck engine. Feasibility of several on-board vehicular ORC recovery systems has also been performed (Capata and Toro, 2014).

Selection of the working fluid in an ORC is a much debated issue (Tchanche *et al.*, 2011). Fluid properties dictate thermodynamic performance, but also have overarching influence on cycle design. Fluid stability and flammability have to be taken into account in order to ensure the safe operation of the device. Fluid toxicity and environmental impact must also be considered. Thus far, the scientific community agrees an ideal ORC working fluid cannot be selected, and that ‘optimal’ fluid choice depends on the particular application, nature and temperature of the heat source, cycle operational parameters, etc.

In this paper, an ORC implementation harnessing waste heat from a diesel generator is considered. The analysis was based on a Rolls Royce Field Electrical Power Supply (FEPS) 40 kW unit. This features a Deutz 912, air-cooled, 6 cylinder inline, direct injection diesel engine. According to the manufacturer’s specification, the maximum exhaust temperature is 500°C. In this paper a small-size compact ORC, powered by the above described exhaust waste heat, for additional power generation is considered. Comprehensive fluid selection and evaluation of the cycle energetic and exergetic performance was carried out, with size limitation being the primary factor.

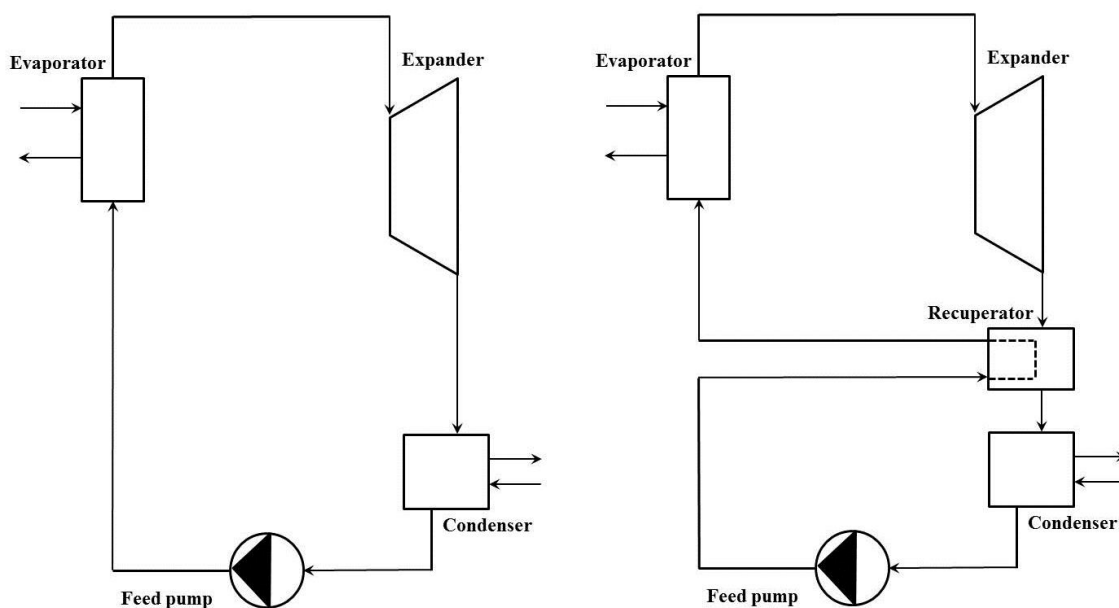


Figure 1: Schematics of simple and recuperative ORC.

2. METHODOLOGY

2.1 ORC model

Two ORC designs were considered: a simple cycle and a recuperative cycle, as shown in Figure 1. The basic processes of the ORC, and the assumptions made in our model, are as follows: pump pressure increase; isobaric heating in the evaporator by the exhaust stream; expansion; isobaric cooling of the working fluid until saturation and condensation. If the working fluid is in the superheated state at the expander outlet, it is possible to use a recuperator (Yang *et al.*, 2014). The recuperator element allows for internal heat transfer between ‘hot’ low pressure stream from the expander outlet and ‘cold’ high pressure stream leaving the pump; thus, working fluid is being preheated before entering the evaporator. The pressure drop through the recuperator heat exchanger was assumed to be negligible and the low pressure stream at the outlet of the heat exchanger was assumed to be in a saturated vapour state. Further assumptions which were made included a steady-state steady-flow system, negligible kinetic and potential energy losses as well as negligible heat losses in all components and pipes.

The condenser outlet was assumed to be a saturated liquid at 298K; this assumption was used to set the operational pressure of the condenser. High cycle pressure and temperature were varied in a selected range in order to evaluate ORC performance and size requirements at different operational parameters. In the initial assessment, isentropic efficiency of the pump and the expander were fixed at 80% and 75%, respectively, although these parameters are analysed afterwards in more detail. All fluid properties were evaluated using REFPROP 9.1. Work and heat exchanges were calculated from the enthalpy gradient at specified points of the cycle. A detailed set of equations can be found in (Radulovic and Castaneda, 2014). Energy and exergy balance was carried out for individual cycle components as well as the whole system:

$$w_P + q_{in} = w_E + q_{out} \quad (1)$$

$$ex_{in} + q \left(1 - \frac{T_0}{T} \right) = ex_{out} + w + i \quad (2)$$

in order to evaluate thermal and exergy efficiency:

$$\eta_{th} = \frac{w_{net}}{q_{in}} \quad (3)$$

$$\eta_{ex} = 1 - \frac{i_{total}}{ex_{in}} \quad (4)$$

where overall exergy destruction was calculated as

$$i_{total} = i_P + i_B + i_E + i_C (+ i_R) \quad (5)$$

Table 1: Preliminary assessment of suitable working fluids

Fluid/ Performance	Benzene	Toluene	Cyclohexane	Propyl cyclohexane	Undecane	MDM
w_{net} (kJ/kg)	186.3	199.7	177.7	200.4	207.7	110.3
q_B (kJ/kg)	936.5	934.5	1029.3	1027.7	1059.2	761.1
η_{th} (%)	19.9	21.4	17.3	19.5	19.6	14.5
VR (-)	69.8	238.8	72.4	1840.9	20552.7	2270.2
i_{total} (kJ/kg)	496.4	481.7	572.8	548.9	564.6	444.6
η_{ex} (%)	27.3	29.3	23.7	26.8	26.9	19.9

2.2 Fluid selection

The maximum exhaust temperature of the diesel generator is stated by the manufacturers to be 773K, indicated the need for a working fluid appropriate for high temperature application. Suitable candidates have been much debated in the literature. A number of fluids shortlisted in Tchanche *et al.* (2011) for high-temperature ORC systems were considered. Assuming a high cycle temperature of 616K and a moderate operational pressure of 1MPa, preliminary assessment of fluid behavior in a simple ORC was performed. Results are summarised in Table 1. The toluene cycle yielded the highest thermal and exergy efficiency. The MDM fluid family had the lowest exergetic and thermal efficiency, and the worst work output. The largest net work was calculated for the undecane cycle. However, undecane, and similarly-performing propyl cyclohexane, had unacceptably high volume

ratios. Heptane and octane, hydrocarbons with a lower molecular weight, were also evaluated, but were subsequently excluded due to the high exhaust temperatures considered here. Aromatics generally require lower heat input than cycloalkanes. Low volume ratios were found for benzene and cyclohexane expanders. Nonetheless, overall exergy destruction was found to be lower in the toluene ORC. Taking everything into consideration, toluene was selected as a fitting and manageable working fluid. Given the critical temperature and pressure of toluene, 591.75K and 4.1263 MPa respectively, only subcritical cycles were considered. Being a dry fluid, as shown on the $T-s$ diagram in Figure 2, there is no risk of toluene condensation occurring at the expander outlet, which allows for the use of the recuperating element in the cycle. Notwithstanding the superior thermodynamic performance of toluene, there are other aspects that have to be considered. According to ASHRAE Standard 34 – Refrigerant safety group classification, toluene is in the A3 group (A – lower toxicity; 3 – higher flammability). Despite this feature, highly flammable fluids are commonly considered in ORC studies (Song *et al.*, 2015). Use of toluene in an ‘on-board’ ORC device would therefore pose a safety risk. Nonetheless, toluene-based ORC systems are already in use.

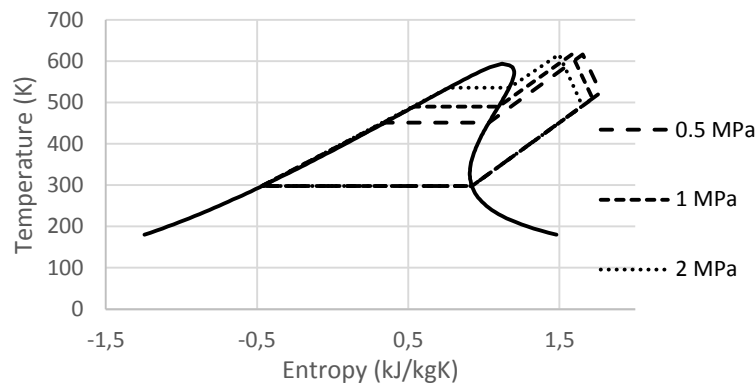


Figure 2: High pressure variation in simple toluene ORC with expander inlet temperature of 616K.

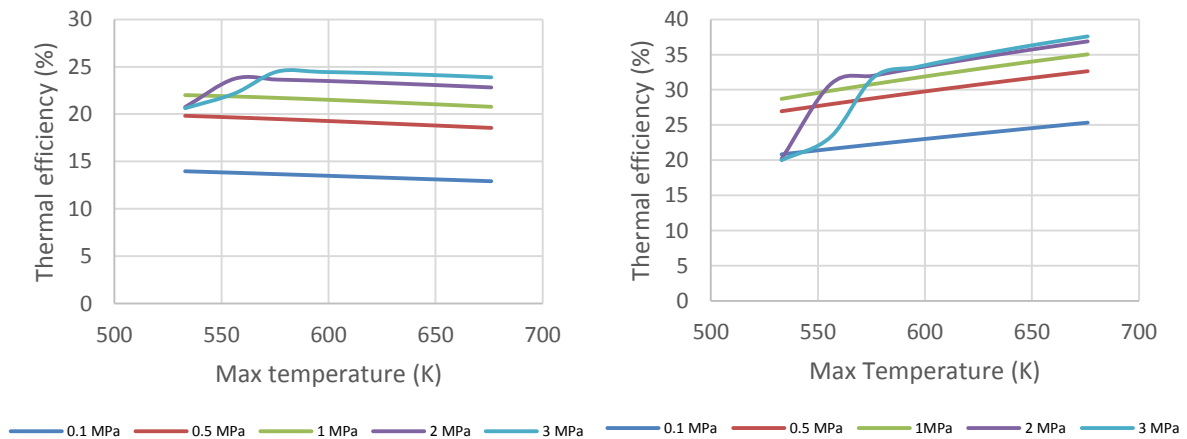


Figure 3: Thermal efficiency of simple ORC (left) and recuperative ORC (right).

2.3 Cycle Operational Parameters

The performance of a bottoming ORC is directly affected by the state of the exhaust from the diesel generator. Based on the maximum exhaust temperature specified above, the expander inlet temperature was varied between 530K and 670K. Our ORC is to operate on a subcritical cycle; therefore a high pressure limit of 3 MPa was applied. The range of high cycle temperatures and pressures is generous, mostly to allow for comprehensive thermodynamic analysis. Medium temperatures of around 616K, as assumed above, are of practical significance. A reasonably high

cycle pressure of 2 MPa is commonly mentioned in literature (Larsen *et al.*, 2013) as the expected high pressure limit. High pressures are often favoured, especially for dry fluids like toluene, as they improve the cycle performance. However, apart from boosting the efficiency, high pressure levels also increase the expander volume ratio, which requires a large-sized turbine. In our case, space limitation and manageable volume ratios were prerogatives. The high pressure of our ORC is dictated by the expansion ratio it necessitates, rather than being a compromise between the desired cycle performance and the element size. Thus, pressures well below 2 MPa are desirable.

3. RESULTS AND DISCUSSION

3.1 Energetic analysis

The performance of the simple and recuperative ORC was evaluated. The effect of high cycle temperature and pressure on thermal efficiency is presented in Figure 3. As expected, the toluene cycles benefit from high evaporator pressures. The simple cycle is energetically somewhat insensitive to high cycle temperatures; in fact, efficiency decreases with high degree of superheat at the expander inlet. The exception being the combination of high pressure and low temperature, when the fluid is roughly at the saturated vapour state and the efficiency is low. In the whole range of expander inlet temperatures considered with the pressure of 1 MPa, a simple cycle efficiency above 20% is reached. Selecting a high pressure of 2 MPa leads to a 2.0% increase on average, while selecting 0.5 MPa as the operational pressure decreased the efficiency by approximately 2.2%. Naturally, recuperative ORC showed an improved energetic performance. Conversely to the simple cycle, the recuperative cycle efficiency increases with the degree of superheat at the expander inlet, making the high operational pressure a secondary parameter. Minor enhancement of the thermal performance was observed at pressures above 1 MPa (1.5%), and above 2 MPa any enhancement is practically undistinguishable. Decreasing the operational pressure of the recuperative ORC to 0.5 MPa reduces the thermal efficiency by 2.1%, like for the simple ORC.

While the recuperator increases energy efficiency, it does not alter the work output. As shown in Figure 4, net work of the cycle increases with both temperature and pressure. Similarly to the thermal efficiency, the effect of pressure is lessened above 1 MPa. While the increase in high cycle pressure improves thermal performance and work output, it also requires a larger expander. Progression of the volume ratio with high cycle pressure is presented in Figure 4, assuming a high temperature of 616K. The volume ratio grows almost linearly with pressure for the set high temperature. Hence, a compromise between acceptable values of the volume ratio and the high cycle pressure which dictates the overall system performance is necessary. Based on the calculated VR values, and having in mind the size limitation, our optimal high pressure is likely to be in 0.5-1 MPa range. Nevertheless, increase in expander inlet temperature can greatly influence the net work output and therefore act as a high pressure 'substitute'. In a simple ORC this leads to a slightly reduced thermal performance, but not in a recuperative one. Due to the internal heat transfer between expander and pump outlet streams, overall heat input in the system is significantly reduced, as shown in Figure 5. Higher operational pressures generally require larger heat inputs, yet the effect of pressure is minor. Increase of expander inlet temperature entails a greater heat supply. Again, this is largely reduced in a recuperative ORC case.

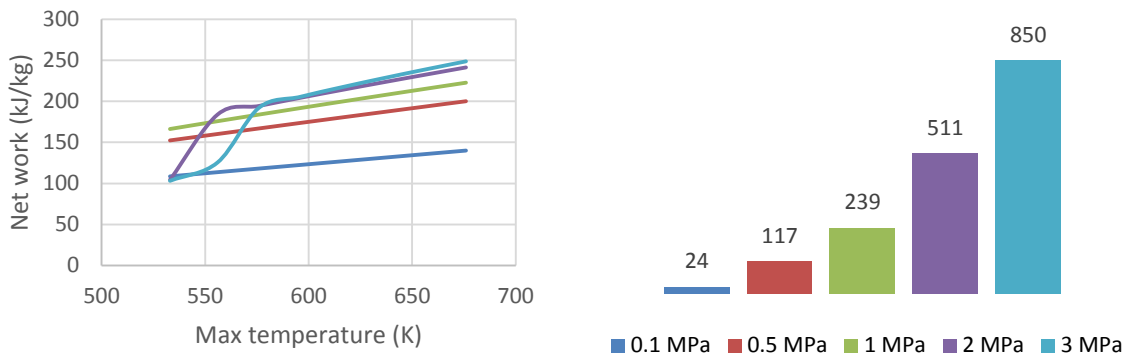


Figure 4: Effect of the high cycle pressure on net work and expander volume ratio.

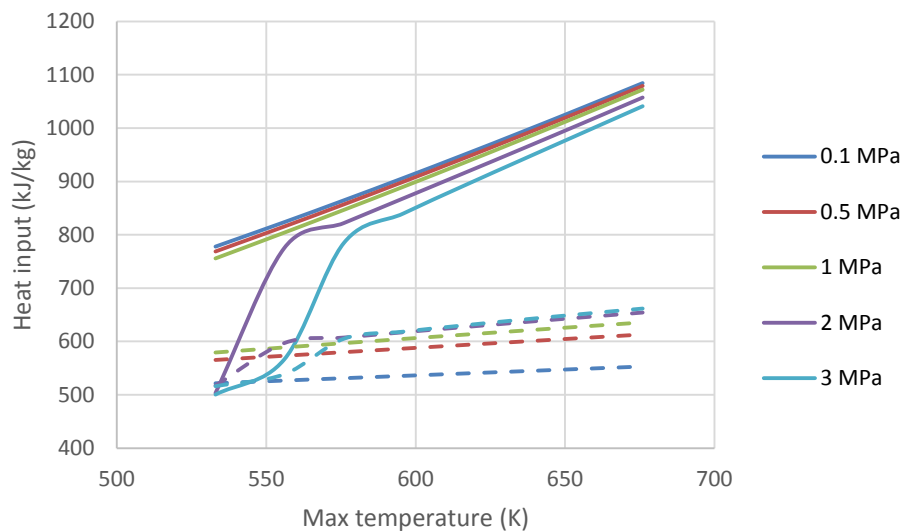


Figure 5: Required heat input in simple ORC (solid line); recuperative ORC (dashed line).

3.2 Exergetic analysis

Second law efficiency and specific exergy destruction in individual cycle components was evaluated for both simple and recuperative toluene cycles. Internal heat transfer improves the thermal performance of the ORC, but does not necessarily lead to higher exergy efficiency. Hence, use of the recuperator appears to be somewhat controversial, and a much debated issue in scientific community (Maraver *et al.*, 2014). Comparison of exergetic performances as a function of high cycle temperature and pressure is given in Figure 6. The recuperative ORC achieved higher exergetic efficiencies than the simple one. Notwithstanding the peculiarity of low temperature - high pressure combination, an increase in evaporator pressure in the recuperative cycle raises the exergy efficiency. For the simple ORC, even at high operational pressures, exergetic efficiency did not reach 35%, whereas higher exergetic efficiencies were achieved at 0.5 MPa pressure in the recuperative case. Exergetic performance also improves with an increase in the expander inlet temperature for a recuperative ORC. The opposite trend is observed for the simple ORC system, in which case exergy efficiency slightly decreases with increasing high temperature.

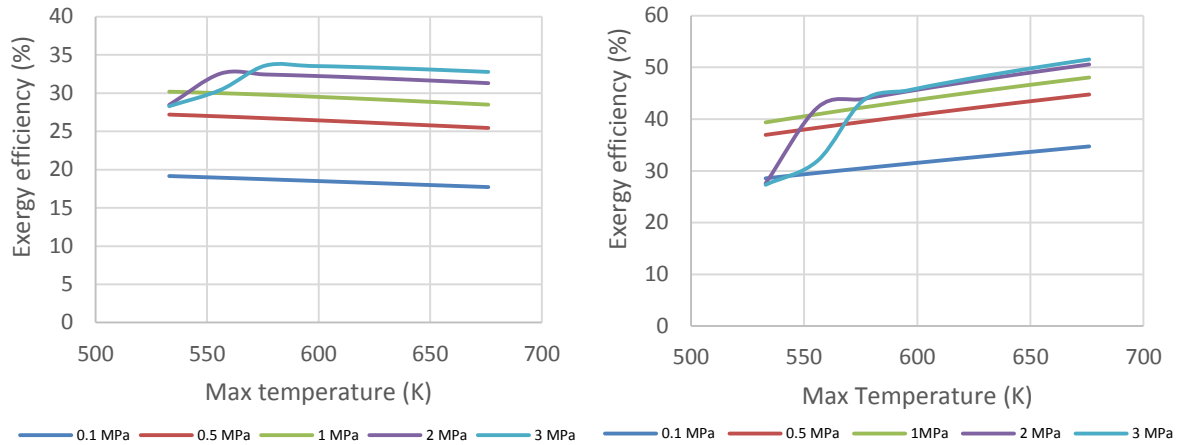


Figure 6: Exergetic efficiency of simple ORC (left) and recuperative ORC (right).

The extent and distribution of the exergy destruction in individual cycle elements is of interest. While exergy efficiency is lower for the recuperative cycle, the overall exergy destruction is greatly reduced, as shown in Figure 7. Irreversibilities decrease with increasing pressure, marginally so for the recuperative ORC. Naturally, the greatest exergy destruction rate is observed for the evaporator, which decreases with increasing pressure, for both the simple and the recuperative ORC. Approximately 10% of total irreversibilities in the simple ORC occurred in the condenser. Given that the condenser inlet state in the recuperative cycle was fixed at the saturated vapour point, the exergy destruction during the heat removal process was the same in all inspected cases, comparable to minor irreversibilities commonly evaluated for the pump. In a recuperative ORC, the heat exchanger is a more significant source of irreversibilities. The turbine destruction rate remains the same regardless of the use of the recuperating element, and it increases with the pressure. However, in the recuperative ORC exergy destruction during the heat addition process is lower, as less of heat is needed to power the cycle. Hence, the expander exergy destruction becomes more significant.

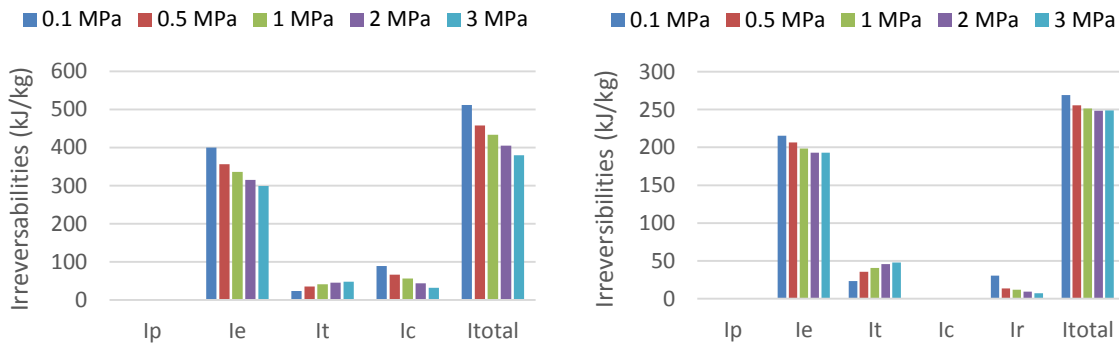


Figure 7: Exergy destruction in simple ORC (left) and recuperative ORC (right).

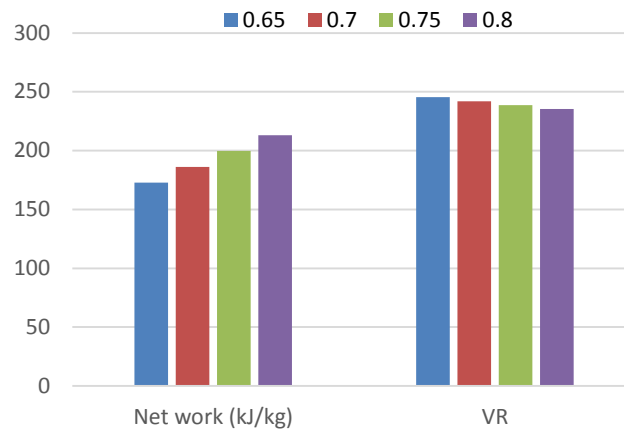


Figure 8: Net work and volume ratio of simple and recuperative ORC for variable expander efficiency at operating parameters of 1MPa and 616K.

3.3 Effect of expander efficiency

The expander, as a core component of the ORC system, has received significant scientific attention (Gao *et al.*, 2015, and references within). In order to better assess the effect of the expander behavior, energetic and exergetic cycle performance was evaluated by modifying the expander isentropic efficiency to 65%, 70% and 80%. For brevity, only the results for 616K and 1MPa, as a representative temperature and pressure, are presented in Figures 8 and 9. Naturally, power output increases with improved expander efficiencies, namely ~7% higher net work is achieved per 5% expander efficiency increase, as shown in Figure 8. An equivalent rise in the cycle efficiency is found for the simple ORC. The volume ratio decreases by 1.4% on average, across all examined pressures. In the recuperative cycle, a higher expander efficiency results in less heat being available for preheating the fluid in the heat exchanger. Hence, the heat input increases by 2%, which reduces the overall improvement in the recuperative cycle efficiency to ~5%. Exergetic efficiency in a simple ORC increases due to a reduction in expander irreversibilities. In the case of the recuperative cycle, the total exergy input is higher, yet exergy destruction in the heat exchanger is lower for higher expander efficiency, and the overall exergetic efficiency improves. Still, exergetic efficiency increase is reduced compared to the simple ORC.

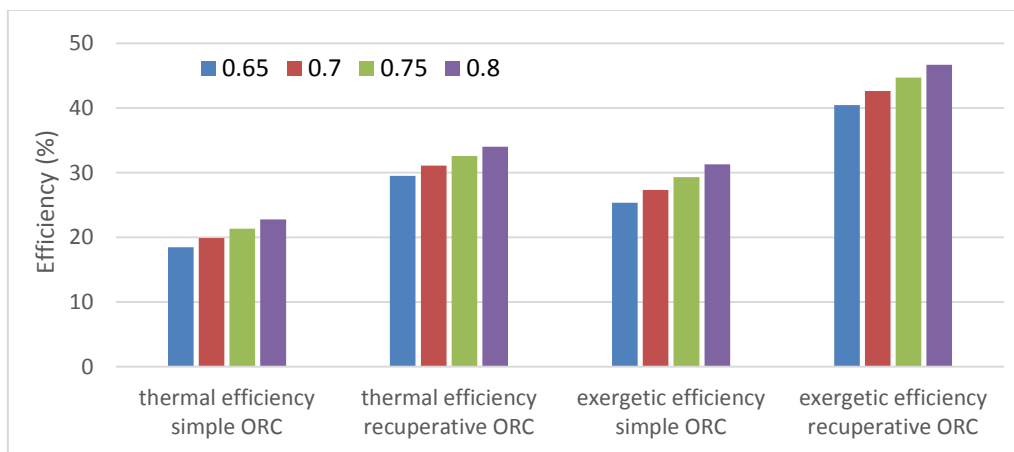


Figure 9: Thermal and exergetic efficiency of simple and recuperative ORC for variable expander efficiency at operating parameters of 1MPa and 616K.

6. CONCLUSIONS

The high temperature toluene ORC is a promising solution for diesel exhaust waste heat recovery. As a dry fluid, toluene achieves better thermodynamic performance at high pressures. However, for 'on-board' applications, size of the device is critical, and high pressures may result in an unacceptably large expander volume ratio. Hence, a compromise has been made between maximization of desired power and required expander size, indicating intermediate pressures, around 1MPa, may be the best solution. Additionally, the high temperature of the available exhaust stream may compensate for lower selected pressures.

Both simple and recuperative ORC systems were considered. The recuperative ORC reached a higher thermal efficiency, which was further augmented by the temperature increase, and required a lower heat input. Total exergy destruction was significantly reduced for the recuperative ORC, which resulted in better exergetic efficiency. Considerable effect of expander efficiency was evaluated: better thermal and exergetic performance, higher power output and a reduction in the volume ratio.

NOMENCLATURE

ex	specific exergy	(kJ/kg)
i	irreversibility	(kJ/kg)
q	specific heat	(kJ/kg)
T	temperature	(K)
VR	volume ratio	(-)
w	specific work	(kJ/kg)
η	efficiency	(-)

Subscript

0	dead state
B	boiler
C	condenser
E	expander
ex	exergetic
in	input
out	output
P	pump
R	recuperator
th	thermal

REFERENCES

- Capata, R., Toro, C., 2014, Feasibility analysis of a small-scale ORC energy recovery system for vehicular application, *Energ Convers Manage*, vol. 86: p. 1078-1090.
- Gao, P., Jiang, L., Wang, L. W., Wang, R. Z., Song, F. P., 2015, Simulation and experiments on an ORC system with different scroll expanders based on energy and exergy analysis, *Appl Therm Eng*, vol. 75: p. 880-888.
- Katsanos, C. O., Hountalas, D. T., Pariotis, E. G., 2012, Thermodynamic analysis of a Rankine cycle applied on a diesel truck engine using steam and organic medium. *Energ Convers Manage*, vol. 60: p. 68-76.
- Kölsch, B., Radulovic, J., 2015, Utilisation of diesel engine waste heat by Organic Rankine Cycle. *Appl Therm Eng*, vol. 78: p. 437-448.

- Larsen, U., Pierobon, L., Haglind, F., Gabriellii, C., 2013, Design and optimisation of organic Rankine cycles for waste heat recovery in marine applications using the principles of natural selection. *Energy*, vol. 55: p. 803-812.
- Maraver, D., Royo, J., Lemort, V., Quoilin, S., 2014, Systematic optimization of subcritical and transcritical organic Rankine cycles (ORCs) constrained by technical parameters in multiple applications. *Appl Energ*, vol. 117: p. 11-29.
- Quoilin, S., Broek, M. V. D., Declaye, S., Dewallef, P., Lemort, V., 2013, Techno-economic survey of Organic Rankine Cycle (ORC) systems. *Renew Sust Energ Rev*, vol. 22: p. 168-186.
- Radulovic, J., Beleno Castaneda, N. I., 2014, On the potential of zeotropic mixtures in supercritical ORC powered by geothermal energy source. *Energ Convers Manage*, vol. 88: p. 365-371.
- Song, J., Song, Y., Gu, C., 2015, Thermodynamic analysis and performance optimization of an Organic Rankine Cycle (ORC) waste heat recovery system for marine diesel engines. *Energy*, vol. 82: p. 976-985.
- Tchanche, B. F., Lambrinos, G., Frangoudakis, A., Papadakis, G., 2011, Low-grade heat conversion into power using organic Rankine cycles – A review of various applications. *Renew Sust Energ Rev*, vol. 15, no. 8: p. 3963-3979.
- Wang, E. H., Zhang, H. G., Fan, B. Y., Ouyang, M. G., Yang, F. Y., Yang, K., Wang, Z., Zhang, J., Yang, F. B., 2014, Parametric analysis of a dual-loop ORC system for waste heat recovery of a diesel engine. *Appl Therm Eng*, vol. 67, no 1-2: p. 168-178.
- Yang, F., Dong, X., Zhang, H., Wang, Z., Yang, K., Zhang, J., Wang, E., Liu, H., Zhao, G., 2014, Performance analysis of waste heat recovery with a dual loop organic Rankine cycle (ORC) system for diesel engine under various operating conditions. *Energ Convers Manage*, vol. 80: p. 243-255.
- Yu, G., Shu, G., Tian, H., Wei, H., Liu, L., 2013, Simulation and thermodynamic analysis of a bottoming Organic Rankine Cycle (ORC) of diesel engine (DE). *Energy*, vol. 51: p. 281-290.

SMALL SCALE ORC DESIGN FOR A COGENERATION SOLAR BIOMASS SUPPORTED APPLICATION

J. Navarro-Esbrí^{1,2,*}, F. Molés¹, B. Peris¹, A. Mota-Babiloni¹

¹ISTENER Research Group, Jaume I University,
Campus de Riu Sec s/n, E12071, Castellón
Spain
e-mail: navarroj@uji.es

²EXPANDER TECH,
Campus de Riu Sec s/n, E12071, Castellón
Spain

* Corresponding Author

ABSTRACT

Combined Heat and Power (CHP) systems and bottoming power cycles for waste heat recovery have received considerable attention over the past decades. Among the several proposed power cycles, the Organic Rankine Cycle (ORC) has been attracting increasing attention. ORCs have been proved as a feasible technology for low temperature (< 250 °C) and small scale (< 1 MW) applications, converting renewable energy into heat and power.

The aim of this work is to present the design process of a micro scale ORC (< 100 kW), suitable for a Combined Cold, Heat and Power (CCHP) application, through an adsorption chiller, that uses solar biomass supported renewable energy as heat source. The ORC module has to be designed in order to work in cogeneration mode and generation mode (power only).

Therefore, this work deals with the preliminary design of the ORC module, including working fluid and configuration selection, from the technical requirements of the equipment imposed by the application. The optimization of the operating conditions is also addressed in order to maximize the efficiency of the system. Finally, an expander has been proposed and characterized. The experimental results from the expander have been used in order to predict the expected behavior of the ORC module in cogeneration mode, producing hot water up to 70°C.

1. INTRODUCTION

Due to environmental constrains, Combined Heat and Power (CHP) systems and bottoming power cycles for waste heat recovery have received considerable attention. Several power cycles have been proposed for low temperature heat recovery. Among them, the Organic Rankine Cycle (ORC) has been attracting considerable attention (Vélez, 2012). Several ORC systems have been installed for recovering waste heat from power plants (Dolz *et al.*, 2012), industrial processes (Peris *et al.*, 2015a) or from internal combustion engines (Peris *et al.*, 2013). ORC systems have also been widely used for converting renewable energy, such as solar (Wang *et al.*, 2013), biomass (Huang *et al.*, 2013) and geothermal (El-Emam and Dincer, 2013) energy into power. ORCs have been studied by various authors, commonly classifying heat sources with temperatures ranging between 100°C and 250°C as “low temperature” heat sources and above 250°C as “high temperature” heat sources. Brasz *et al.* (2005) considered low temperature applications and Zabek *et al.* (2013) studied waste heat recovery at high temperatures, demonstrating ORC feasibility in both cases. Focusing on residential and commercial applications, the ORC has been proposed as a suitable energy conversion technology,

since it can achieve great efficiencies from low grade heat sources and can result cost-effective for small scale and micro-scale applications, often referred to an electrical power lower than 1 MW and 15 kW, respectively (Peris *et al.*, 2015b).

The choice of the ORC working fluid has an important influence on the system efficiency, and numerous works on this subject can be found in the literature. Lai *et al.* (2011) investigated potential single-component working fluids for high temperature ORC processes and found that siloxanes and selected hydrocarbons are promising. Shale *et al.* (2007), Shengjun *et al.* (2011) and Quoilin *et al.* (2011) evaluated various working fluids for low to medium temperature applications, highlighting that hydrofluorocarbons with low critical temperatures, such as HFC-134a and HFC-245fa, are suitable. Molés *et al.* (2014) predicted attractive thermodynamic performance of ORC systems for low temperature heat sources using HCFO-1233zd-E and HFO-1336mzz-Z as low Global Warming Potential (GWP) alternatives to HFC-245fa.

About cycle configuration, different suitable configurations for low grade heat sources recovery using ORCs can be found in the literature. One of the most commonly used is the regenerative ORC, which can be performed in three ways: with an internal heat exchanger (Wang *et al.*, 2013), with open and closed feed fluid heaters using turbine bleeding (Gang *et al.*, 2010) or using a vapor injector as a regenerator (Xu and He, 2011). Another configuration proposed for low grade heat sources is based on superheating the fluid in a single stage (Roy *et al.*, 2011) or through various reheat stages (DiGenova *et al.*, 2013). Two pressure levels and the use of an ejector have been also studied by Li *et al.* (2012), increasing the output capacity compared to the basic ORC. Finally, transcritical configurations have been also proposed to allow a better temperature matching with low irreversibilities (Ho *et al.*, 2012), generally requiring higher operating pressures.

Regarding expander technology, Peris *et al.* (2015c) indicated that the volumetric expander type is most appropriate for low grade heat sources and micro-scale application. The reason is that volumetric expanders results more appropriate than turbomachines, as they are characterized by lower flow rates, higher pressure ratios, much lower rotational speeds, besides to exhibit good effectiveness and tolerate liquid phase during expansion (Quoilin, *et al.*, 2013). In this way, recent works continues improving volumetric expanders, such as rotary volumetric expanders based on the Wankel concept (Antonelli *et al.*, 2014), scroll (Song *et al.*, 2014) or screw expanders (Zhu *et al.*, 2014). Furthermore, an appropriate operating pressure ratio for the expander, a suitable working fluid and an efficient configuration are also recommendations to increase the electrical gain (Peris *et al.*, 2013).

The aim of this work is to present the design process of a small scale ORC, suitable for a Combined Cold, Heat and Power (CCHP) application that uses solar biomass supported renewable energy as heat source. So, the work presents the technical requirements of the equipment imposed by the application, discusses the working fluid selected, reports the thermodynamic cycle, presents the experimental characterization of an expander prototype and, finally, summarizes the main conclusions.

2. TECHNICAL REQUIREMENTS

The technical requirements of the equipment imposed by the application are the boundary conditions that constrain the design process of the ORC system. The overall scheme of the system is presented in Figure 1. The cogeneration unit is planned to work on two different operating modes: generation mode and cogeneration mode.

Attending to the renewable heat source activation, it consists on a solar biomass supported heat source. The heat transfer fluid will be thermal oil. The solar collectors will work at temperatures up to 270°C, but the thermal oil inlet temperature into the ORC is expected to be, due to buffers/collectors and thermal losses, up to 245°C. In order to maintain fixed the inlet temperature on the ORC, a buffer tank is required to avoid the solar field disturbances.

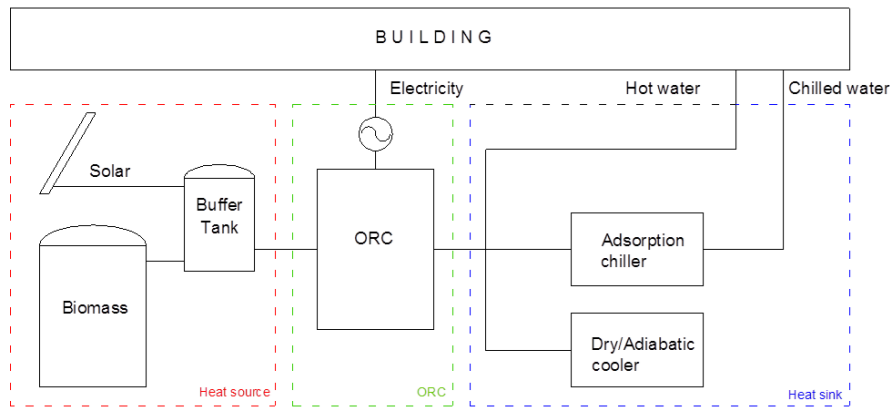


Figure 1: Overall scheme of the system

Regarding the heat sink, the different modes of the cogeneration unit result in two different condensation temperatures, fixed by the heat sink transfer fluid temperatures, in the ORC: 30°C for generation mode and 70°C for cogeneration mode. In generation mode the condensation heat is rejected to the ambient through a dry/adiabatic cooler. In cogeneration mode the heat sink is used to produce hot water for heating or hot water to activate an adsorption chiller. Water has been selected as the heat transfer fluid for the heat sink loop.

3. WORKING FLUID

The working fluid is a key parameter that determines the operating pressures, maximum allowable temperature, system efficiency, optimal configuration and components technology. So, it has a great influence on achieving the target. Furthermore, there are other criteria to be considered in the working fluid selection, such as security characteristics (toxicity and flammability) and environmental issues (ODP and GWP). In ORC systems with high temperature heat sources, working fluids as toluene, hydrocarbons or silicone oils are used. However, looking for security and environmental characteristics with high efficiencies at low temperatures, the following fluid families have been considered: hydrofluorocarbons (HFC), hydrofluoroether (HFE), and hydrofluoroolefins (HFO).

Table 1: working fluid candidates properties

Fluid	Toxicity PEL (ppm) / Flammability	GWP	ODP	T_{crit} (°C)	P_{crit} (bar)	T_{max} (°C)
HFC-134a	1000/Non-flammable	1300	0	101	40.59	<200
HFC-245fa	300/Non-flammable	950	0	154	36.51	<250
SES36	1000/Non-flammable(*)	3710	0	177.55	28.49	190
HFO-1234yf	500/Low-flammability	4	0	94.7	33.82	<200
HFO-1234ze(Z)	500/Non-flammable	1	0	150	35.30	<200
HCFO-1233zd-E	300/Non-flammable	5	0	165.6	35.71	200
HFO-1336mzz-Z	500/Non-flammable	9	0	171.3	29	<250

Different working fluid options have been analyzed and evaluated for their application in the current application based on the suitable fluids found in the literature. Special attention has been taken in security properties, as toxicity and flammability, thermal stability and environmental properties, like Global Warming Potential (GWP) and Ozone Depletion Potential (ODP). Relevant thermo-physical properties of the working fluid candidates are summarized in Table 1.

Maximum allowable temperature supposes another constrain in order to avoid degradation in the working fluid. So, HFC-134a, SES36, HFO-1234yf and HCFO-1233zd-E have been discarded. HFO-1336mzz-Z is not commercially available nowadays, despite its desirable properties, as low GWP, among others. Finally, HFC-245fa has been selected as the best available working fluid candidate, with low toxicity, no flammable, maximum allowable temperature below 250°C (240°C) and good

expected efficiencies. HFC-245fa is commonly selected as working fluid for similar heat sources when safety levels and environmental impacts are considered (Wang *et al.*, 2011).

4. THERMODYNAMIC CYCLE

In the framework of a systematic investigation approach, various possible modifications to the simple ORC plant layout are analyzed and compared, in order to improve the ORC recovery performance; arrangements such as recuperation, superheated cycle, transcritical conditions, regenerative cycle and their combinations are taken into account.

From the analysis of the different options for the configuration of the ORC cycle, the most suitable of them, for the range of operating conditions of the targeted application, have been investigated. The adoption of a recuperative heat exchanger has been considered, due to the high temperature of the heat source compared with the critical temperature of the working fluid selected, having to work with high superheat degree. The possibility of working in transcritical conditions has been studied to allow a better temperature matching with low irreversibilities, although generally requiring higher operating pressures and more pump consumptions. Therefore, various cycles are proposed, showing their schemes in Figure 2.

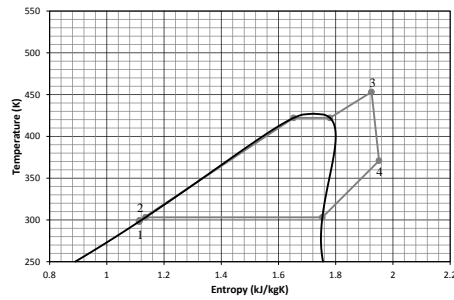
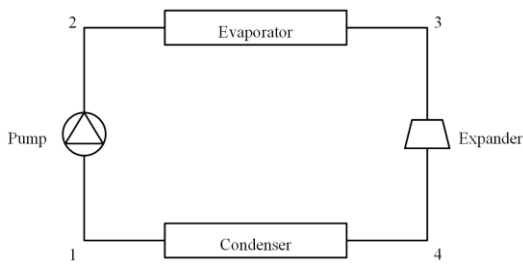
After the analysis of the configurations proposed, the possibility of working in transcritical conditions has been rejected due to the increase on the pump consumption that reduces the net efficiency of the cycle. The increase on the pump consumption due to the transcritical operation can suppose, depending on the operating conditions, a 10% of the gross power produced by the expander, higher in comparison with the 5% of the pump consumption in subcritical operation. The adoption of a recuperative heat exchanger has been selected, due to the improvement on the efficiency by reducing the thermal power required. The adoption of a recuperative heat exchanger improves the efficiency between 12.5% and 31.5%, depending on the operating conditions. Finally, the best configuration is the use of a recuperative heat exchanger in subcritical conditions. This configuration has been previously selected as optimal for HFC-245fa as working fluid with similar heat source conditions for Branchini *et al.* (2013).

5. EXPERIMENTAL APPROACH

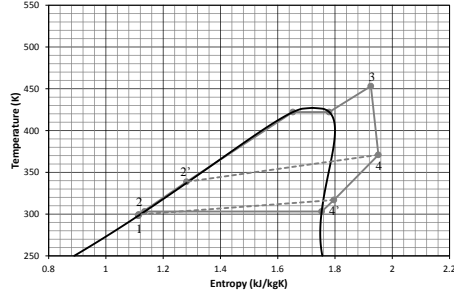
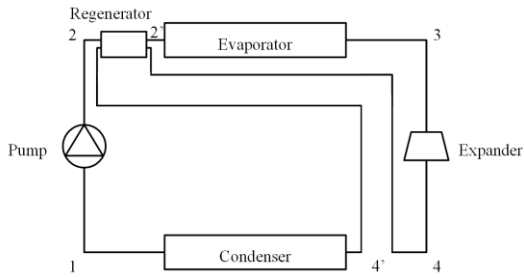
With the working fluid, configuration and operating conditions selected, the next step has been the selection of the components of the ORC module and their design. Knowing that the expander is a key parameter on the ORC efficiency, its design has been addressed constructing and testing various prototypes.

The expander technology selected to meet the prototype requirements has been analyzed and a volumetric expander is proposed. As previously introduced, the volumetric technology shows better results for low grade heat sources and small scale applications. So, the volumetric technology has been adopted for the expander design.

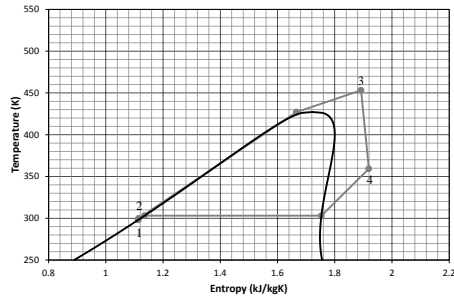
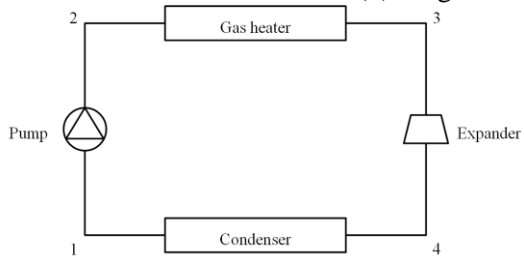
The main challenge in the expander design is the different operating conditions presented in generation and cogeneration mode, taking into account the maximum temperature allowable at the expander inlet of 240°C. In this way, different designs are analysed looking for optimizing the efficiency of the system in all the range of expected operating conditions, not only the electrical efficiency but also cost, size, weight, flexibility... Therefore, two different designs are considered, one specially designed for optimizing generation mode and the other looking for optimal energy profit in cogeneration mode.



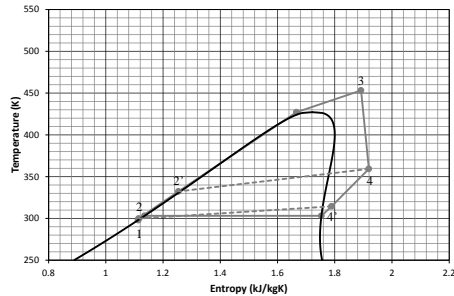
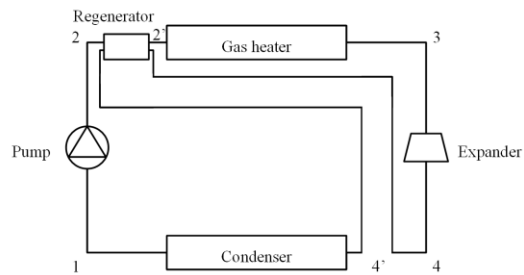
(a) Basic cycle - subcritical



(b) Regenerative cycle - subcritical



(c) Basic cycle - transcritical



(d) Regenerative cycle - transcritical

Figure 2: Configurations proposed

The design optimized for generation mode achieves a good efficiency condensing below 30°C but it is highly penalized above 40°C of condensing temperature and, besides, has serious disadvantages as high cost, control handicaps, high size and weight, making the future product non feasible. On the other hand, the expander design optimized for cogeneration mode presents the best efficiency in cogeneration mode and, although it is slightly penalized in generation mode, it shows a good performance in the operating range (for the expected range of condensing temperatures) and being a cost-effective solution with the advantage of reducing considerably size and weight and simplifying ORC control.



Figure 3: Simulated and constructed prototype and the ORC test bench

Finally, the expander prototype has been designed according to the second proposal, optimizing the cogeneration mode, since the overall efficiency in this mode is much higher than in generation mode and due to the advantages exposed before. The expected performance of this expander prototype has been experimental tested in the test bench constructed ad-hoc for the expander tests. Thermal and electrical power haven been scaled down to meet the disposal thermal power on the test bench, with a 1:3 scale.

In the following, the main parameters measured of the test bench are presented. Firstly, the thermal power input is monitored in the hot side through inlet and outlet thermal oil temperatures, using surface thermocouples, and the thermal oil volumetric flow rate, that is measured using a vortex flow meter. The working mass flow rate is obtained through a Corioliss mass flow meter. The pressure and temperature at the inlet and outlet port of the expander are measured for monitoring its performance. Furthermore, its electrical power output is measured using a wattmeter located at the electric generator, while the pump electrical consumption is measured in the electric motor through another wattmeter.

The measuring devices uncertainties, extracted from manufacturer's data sheets, and the calculated parameters uncertainties, obtained as a function of the uncertainty on each measured variable by using the RSS method (Taylor, 1997), are collected in Table 2.

Table 2: uncertainties of measured and calculated parameters

Parameter	Uncertainty
Temperature (°C)	1
Pressure (%)	0.5
Mass flow rate (%)	0.3
Thermal oil volumetric flow rate (%)	0.75
Electrical power (%)	1.2
Electrical isentropic effectiveness (%)	4.89
Pressure ratio (%)	0.71

For the analysis of the experimental data obtained during tests, the performance of the expander is defined as the electrical expander effectiveness by Eq. 1, often also named expander overall efficiency. This equation expresses the relationship between the electrical power measured in the electric generator and the maximum that could be ideally obtained. The pressure ratio in the expander is calculated through Eq. 2.

$$\varepsilon_{x,is} = \frac{\dot{W}_x}{\dot{m}(h_{x,in} - h_{x,out,is})} \quad (1)$$

$$P_r = \frac{P_{x,in}}{P_{x,out}} \quad (2)$$

The electrical expander effectiveness achieved by the expander prototype in the test bench is represented in Figure 4.

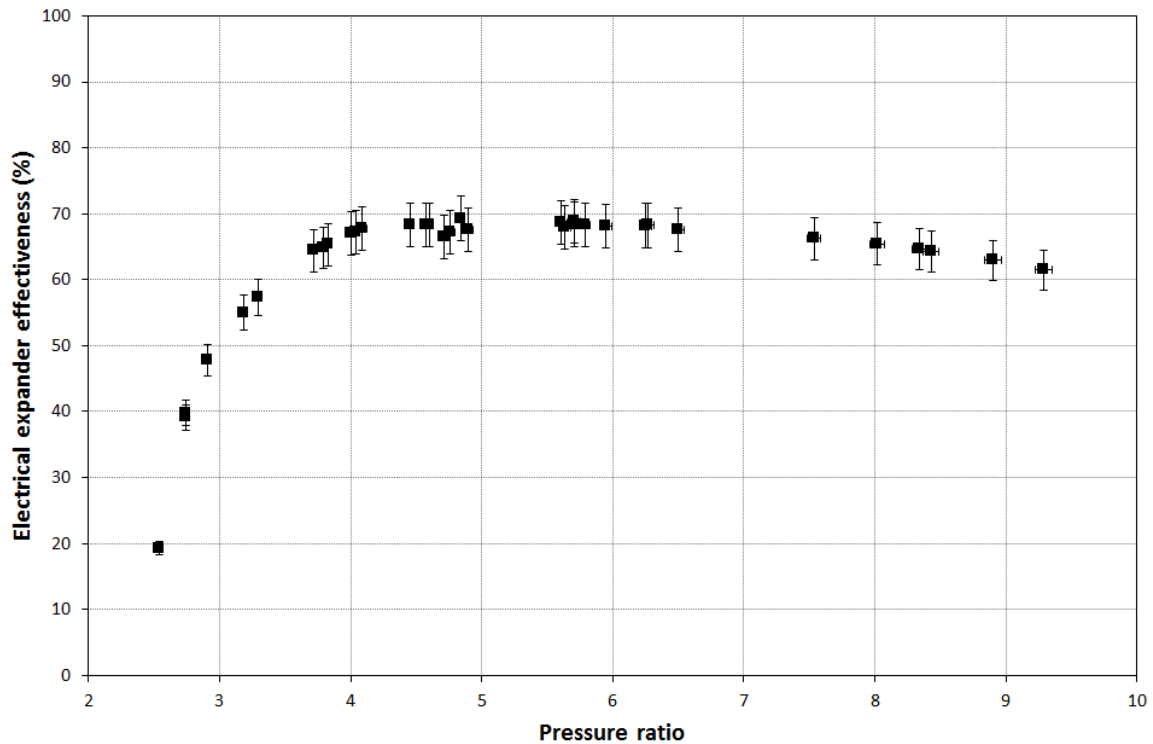


Figure 4: Electrical expander effectiveness achieved

The experimental results from the expander have been used in order to predict the expected behavior of the ORC module. The performance of the cogeneration system, producing hot water at 70°C, is summarized in Table 3, with an uncertainty of ±15%.

Table 3: cogeneration mode performance

Heat source transfer fluid	Thermal oil
Heat source inlet temperature (°C)	245
Heat source outlet temperature (°C)	173.3
Heat source flow rate (m³/h)	11.8
Heat source thermal power (kW)	480
Heat sink transfer fluid	Water
Heat sink inlet temperature (°C)	60
Heat sink outlet temperature (°C)	70
Heat sink flow rate (m³/h)	34.1
Heat sink thermal power (kW)	390
Gross electrical power (kW)	70

6. CONCLUSIONS

This work presents the design process of a micro scale ORC, suitable for a Combined Cold, Heat and Power (CCHP) application that uses solar biomass supported renewable energy as heat source. The technical requirements of the equipment, working fluid selection, thermodynamic cycle configuration, design and expected performance are presented.

The technical requirements of the equipment imposed by the application are the boundary conditions that constrain the design process of the ORC system. Attending to the renewable heat source activation, it consists on a solar biomass supported heat source. The heat sink is used to produce hot water for heating or hot water to activate an adsorption chiller.

Different working fluid options have been analyzed and evaluated for their application in the current application based on the suitable fluids found in the literature. Special attention has been taken in security properties, as toxicity and flammability, thermal stability and environmental properties. HFC-245fa has been selected as the best available working fluid candidate, with low toxicity, no flammable, maximum allowable temperature below 250°C and good expected efficiencies.

Various possible modifications to the simple ORC plant layout are analyzed and compared, in order to improve the ORC recovery performance. The possibility of working in transcritical conditions has been rejected due to the increase on the pump consumption that reduces the net efficiency of the cycle. The adoption of a recuperative heat exchanger has been selected, due to the improvement on the efficiency by reducing the thermal power required.

With the working fluid, configuration and operating conditions selected, the next step has been the selection of the components of the ORC module and their design. The expander design has been addressed and an expander prototype has been obtained. The performance of this expander prototype has been experimental characterized in the test bench constructed ad-hoc for the expander tests. Finally, the experimental results from the expander prototype have been used to obtain the expected performance of the ORC module working in cogeneration mode and producing hot water at 70°C to activate the adsorption chiller.

NOMENCLATURE

ε	efficiency	(%)
h	specific enthalpy	(kJ/kg)
m	mass flow rate	(kg/s)
P	pressure	(bar)
T	temperature	(°C)
W	electrical power	(kW)

Subscripts

crit	critical
in	inlet
is	isentropic
max	maximum
out	outlet
r	ratio
x	expander

REFERENCES

Antonelli, M., Baccioli, A., Francesconi, M., Desideri, U., Martorano, L., 2014, Operating maps of a rotary engine used as an expander for micro-generation with various working fluids, *Appl. Energy*, vol. 113, no. 1: p. 742-750.

Branchini, L., Pascale, A., Peretto, A., Systematic comparison of ORC configurations by means of comprehensive performance indexes, *Appl. Therm. Eng.*, vol. 61, no. 1: p. 129-140.

Brasz, J.J., Biederman, B.P., Holdmann, G., 2005, Power production from a moderate temperature geothermal resource, *GRC Annual Meeting*.

DiGenova, K.J., Botros, B.B., Brisson, J.G., 2013, Method for customizing and organic Rankine cycle to a complex heat source for efficient energy conversion, demonstrated on a Fischer Tropsch plant, *Appl. Energy*, vol. 102, no. 1: p. 746-754.

Dolz, V., Novella, R., García, A., Sanchez, J., 2012, HD diesel engine equipped with a bottoming Rankine cycle as a waste heat recovery system. Part 1: study and analysis of the waste heat energy, *Appl. Therm. Eng.*, vol. 36, no. 1: p. 269-278.

El-Emam, R.S., Dincer, I., 2013, Exergy and exergoeconomic analyses and optimization of geothermal organic Rankine cycle, *Appl. Therm. Eng.*, vol. 59, no. 1: p. 435-444.

Gang, P., Jing, L., Jie, J., 2010, Analysis of low temperature solar thermal electric generation using regenerative organic Rankine cycle, *Appl. Therm. Eng.*, vol. 30, no. 8: p. 998-1004.

Ho, T., Mao, S.S., Greif, R., 2012, Comparison of the organic flash cycle (OFC) to other advanced vapor cycles for intermediate and high temperature waste heat reclamation and solar thermal energy, *Energy*, vol. 42, no. 1: p. 213-223.

Huang, Y., Wang, Y.D., Rezvani, S., McIlveen-Wright, D.R., Anderson, M., Mondol, J., Zacharopolous, A., Hewitt, N.J., 2013, A techno-economic assessment of biomass fuelled trigeneration system integrated with organic Rankine cycle, *Appl. Therm. Eng.*, vol. 53, no. 2: p. 325-331.

Lai, N.A., Wendland, M., Fischer, J., 2011, Working fluids for high-temperature organic Rankine cycles, *Energy*, vol. 36, no. 1: p. 199-211.

Li, X., Zhao, C., Hu, X., 2012, Thermodynamic analysis of organic Rankine cycle with ejector, *Energy*, vol. 42, no. 1: p. 342-349.

Molés, F., Navarro-Esbrí, J., Peris, B., Mota-Babiloni, A., Barragán-Cervera, A., Kontomaris, K., 2014, Low GWP alternatives to HFC-245fa in Organic Rankine Cycles for low temperature heat recovery: HCFO-1233zd-E and HFO-1336mzz-Z, *Appl. Therm. Eng.*, vol. 71, no. 1: p. 204-212.

Peris, P., Navarro-Esbrí, J., Molés, F., 2013, Bottoming organic Rankine cycle configurations to increase Internal Combustion Engines power output from cooling water waste heat recovery, *Appl. Therm. Eng.*, vol. 61, no. 2: p. 364-371.

Peris, P., Navarro-Esbrí, J., Molés, F., Collado, R., Mota-Babiloni, A., 2015a, Performance evaluation of an Organic Rankine Cycle (ORC) for power applications from low grade heat sources, *Appl. Therm. Eng.*, vol. 75, no. 1: p. 763-769.

Peris, P., Navarro-Esbrí, J., Molés, F., Martí, J.P., Mota-Babiloni, A., 2015b, Experimental characterization of an Organic Rankine Cycle (ORC) for micro-scale applications, *Appl. Therm. Eng.*, vol. 79, no. 1: p. 1-8.

Peris, P., Navarro-Esbrí, J., Molés, F., González, M., Mota-Babiloni, A., 2015c, Experimental characterization of an ORC (organic Rankine cycle) for power and CHP (combined heat and power) applications from low grade heat sources, *Energy*, vol. 82, no. 1: p. 269-276.

Quoilin, S., Declaye, S., Tchanche, B.F., Lemort, V., 2011, Thermo-economic optimization of waste heat recovery organic Rankine cycles, *Appl. Therm. Eng.*, vol. 31, no. 14: p. 2885-2893.

Quoilin, S., Van Den Broek, M., Declaye, S., Dewallef, P., Lemort, V., 2013, Techno-economic survey of organic Rankine cycle (ORC) systems, *Renew. Sustain. Energy Rev.*, vol. 22, no. 1: p. 168-186.

Taylor, J.R., 1997, An introduction to error analysis; The study of uncertainties in physical measurements, *University Science Books*, Sausalito, USA.

Roy, J.P., Mihsra, M.K., Misra, A., 2011, Performance analysis of an organic Rankine cycle with superheating under different heat source temperature conditions, *Appl. Energy*, vol. 88, no. 9: p. 2995-3004.

Saleh, R., Koglbauer, G., Wendland, M., Fischer, J., 2007, Working fluids for low-temperature organic Rankine cycles, *Energy*, vol. 32, no. 7: p. 1210-1221.

Shengjun Z., Huaixin W., Tao, G., 2011, Performance comparison and parametric optimization of subcritical Organic Rankine Cycle (ORC) and transcritical power cycle system for low-temperature geothermal power generation, *Appl. Energy*, vol. 88, no. 8: p. 2740-2754.

Song, P., Wei, M., Shi, L., Danish, S.N., Ma, C., 2014, A review of scroll expanders for organic Rankine cycle systems, *Appl. Therm. Eng.*, vol. 75, no. 1: p. 54-64.

Vélez, F., Segovia, J.J., Martín, M.C., Antolín, G., Chejne, F., Quijano, A., 2012, A technical, economical and market review of organic Rankine cycles for the conversion of low-grade heat for power generation, *Renew. Sustain. Energy Rev.*, vol. 16, no. 6: p. 4175-4189.

Wang, E., Zhang, H., Fan, B., Ouyang, M., Zhao, Y., Mu, Q., 2011, Study of working fluid selection of organic Rankine cycle (ORC) for engine waste heat recovery, *Energy*, vol. 36, no. 1: p. 3406-3418.

Wang, M., Wang, J., Zhao, Y., Zhao, P., Dai, Y., 2013, Thermodynamic analysis and optimization of a solar-driven regenerative organic Rankine cycle (ORC) based on flat-plate solar collectors, *Appl. Therm. Eng.*, vol. 50, no. 1: p. 816-825.

Xu, R.J., He, Y.L., 2011, A vapor injector-based novel regenerative organic Rankine cycle, *Appl. Therm. Eng.*, vol. 31, no. 6: p. 1238-1243.

Zabek, D., Penton, J., Reay, D., 2013, Optimization of waste heat utilization in oil field development employing a transcritical Organic Rankine Cycle (ORC) for electricity generation, *Appl. Therm. Eng.*, vol. 59, no. 1: p. 363-369.

Zhu, Y., Jiang, L., Jin, V., Yu, L., 2014, Impact of built-in and actual expansion ratio difference of expander on ORC system performance, *Appl. Therm. Eng.*, vol. 71, no. 1: p. 548-558.

ACKNOWLEDGEMENT

The result presented in this paper is part of the BRICKER project (www.bricker-project.com). This project has received funding from the European Union's Seventh Framework Programme for research, technological development and demonstration under grant agreement No 609071.

CONSTRUCTION AND PRELIMINARY TEST OF AN ORGANIC RANKINE CYCLE (ORC) USING R245FA AND SINGLE SCREW EXPANDER

Biao Lei *, Yuting Wu, Wei Wang and Chongfang Ma

* Beijing University of Technology,
Ping Le Yuan 100, Chaoyang District, Beijing,
China
e-mail: leibiao@emails.bjut.edu.cn

ABSTRACT

Organic Rankine Cycle (ORC) is one of the most promising methods for converting low-grade heat into power. In this paper, an experimental ORC system, which includes a single screw expander, a shell and tube evaporator, an air-cooled fin-and-tube condenser and a metering pump, has been built. R245fa was adopted as the working fluid considering of its good performance and environmentally-friendly characteristics. The heat source of the experimental system is the conduction oil which was heated by electricity. In the evaporator of the system, R245fa was evaporated into vapor by the high-temperature conduction oil. Experiments were conducted to analyze the operational characteristics and performance of the developed ORC. The key parameters of the ORC, such as the efficiency of the cycle and the expander, were obtained. In addition, the factors which influence the performances of the developed ORC were analyzed and discussed.

REFERENCES

- [1] Tchanche BF, Lambrinos G, Frangoudakis A, Papadakis G. Low-grade heat conversion into power using organic Rankine cycles – A review of various applications. *Renewable and Sustainable Energy Reviews*. 2011;15:3963-79.
- [2] Vélez F, Segovia JJ, Martín MC, Antolín G, Chejne F, Quijano A. A technical, economical and market review of organic Rankine cycles for the conversion of low-grade heat for power generation. *Renewable and Sustainable Energy Reviews*. 2012;16:4175-89.
- [3] Quoilin S, Aumann R, Grill A, Schuster A, Lemort V, Spliethoff H. Dynamic modeling and optimal control strategy of waste heat recovery Organic Rankine Cycles. *Applied Energy*. 2011;88:2183-90.
- [4] Quoilin, S.; Broek, M.V.D.; Declaye, S.; Dewallef, P.; Lemort, V. Techno-economic survey of Organic Rankine Cycle (ORC) systems. *Renewable and Sustainable Energy Reviews* 2013, 22, 168-186

ORGANIC RANKINE CYCLE WITH ZEOTROPIC MIXTURES OF ALKANES AS WORKING FLUIDS FOR COGENERATION

Peter Collings¹, Zhibin Yu^{2*}

¹University of Glasgow, University Avenue
Glasgow, United Kingdom
(E-mail: p.collings.1@research.gla.ac.uk)

²University of Glasgow, University Avenue
Glasgow, United Kingdom
(E-mail: Zhibin.Yu@glasgow.ac.uk)

* Corresponding Author

ABSTRACT

Organic Rankine Cycles for the utilisation of low-temperature heat sources suffer from inherently low efficiency due to Carnot limitations, with first law efficiencies of 10-15% for heat source temperatures below 200°C. The large amount of heat rejection in the condenser that this entails means that they are potentially ideal candidates for combined heat and power schemes. This paper analyses the performance of a cycle with a recirculating heat source, using a zeotropic mixture of alkanes as the working fluid. Changing the mixture composition changes the bubble and dew points of the cycle, and introduces a temperature change during phase change, known as “glide”. As the condenser outlet temperature is determined by the pinch point at the condensation temperature, the introduction of glide can increase the condenser and evaporator loading for a given condenser outlet temperature for cogeneration supply. This can work against any added benefit gained by creating a working fluid blend tailored to a specific heat source and sink. When the temperature glide is small, there is a smooth drop in condenser pressure and associated smooth increase in efficiency, When the glide is larger, the change in efficiency happens more abruptly at either end of the transition from one fluid to another, with a period of more gentle change in efficiency in between. The effect these changes have on the performance of the cycle and possible applications in cycle optimisation are an exciting area for future research.

1. INTRODUCTION

Much current research focuses on the development of systems to generate electricity from lower-quality heat sources, with temperatures of less than 250°C. However, the actual proportion of energy demand accounted for by electricity is relatively small. Figure 1, adapted from (UK DECC, 2014a), shows that only 22.8% of non-transport energy usage in the UK is accounted for by electricity.

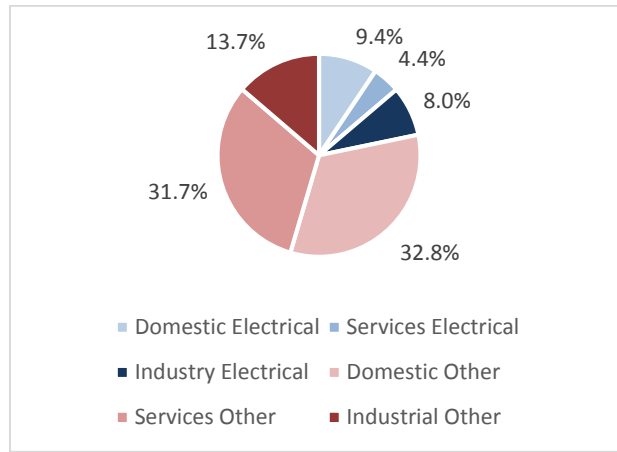


Figure 1: 2013 UK Energy Usage by Fuel and Sector (UK DECC, 2014a)

Table 1: 2013 UK Energy Usage divided into Heating and Other (UK DECC, 2014a)

Space and Water Heating	Domestic	41.9%	
	Service	13.9%	
	Industry	2.8%	58.7%
Other	Domestic	8.8%	
	Service	9.3%	
	Industry	23.2%	41.3%

Table 1, also adapted from (UK DECC, 2014a), shows the breakdown of 2013 UK non-transport energy usage into space and water heating, and other. Although this data does not account for “crossover” usage of energy, such as electric space and water heaters, or heat used for things other than space heating, for example, preheating feedstock in the chemical industry, its implications are clear; there is a large potential market for waste heat, such as that developed by power generation. This is borne out by the UK Department of Energy and Climate Change who, in their report on waste heat utilisation, estimate that there is a demand for 18.7 TWh/yr of low-grade heat (<250°C) for industrial processes (UK DECC, 2014b).

Previous research indicates that small-scale Organic Rankine Cycle systems are capable of efficiencies of the order of 10% (Fu, et al., 2005), (Shu, et al., 2014), (Kang, May 2012). The remaining ~90% of the heat that enters the system is rejected to the environment in the condenser. If this heat can be recovered and used for space and water heating, ORC systems could be ideal for CHP purposes.

This is contingent on the water outflow from the condenser being of sufficient temperature for space or water heating applications. Water heating for washing, for example, requires a temperature of 40°C (UK DECC, n.d.). Underfloor heating requires a temperature of 35-50°C (UK DECC, May 2012) (UK DECC, 2012b) (UK DECC, 2012a). Radiators may require a temperature of 60°C (Institution of Civil Engineers, 2012). To achieve this, district heating schemes usually provide heat at 90-100°C (UK DECC, 2012c) (Poyry Energy Consulting, 2009).

The application of Organic Rankine Cycle for cogeneration has attracted considerable attentions. Twomey et al (Twomey, et al., 2013) considered a solar-powered ORC system providing water heated by the condenser at 65°C, and using a scroll device as their expander. They showed electrical efficiency of 3.47%. Stoppato (Stoppato, 2012) performed an energetic and economic investigation of an existing ORC cogeneration plant in Italy, providing district heating water at 80°C from a 310°C heat source. This cycle aims to increase exergy efficiency by splitting the flow between a regenerative heat exchanger and a fluid preheater using the primary heat source, and achieves an electrical efficiency of 18.6%, modelling the cycle components as black boxes with performance varying based

on empirical data. Uris et al (Uris, et al., 2014) performed an analysis of a biomass cogeneration plant with a 300°C heat source providing heat from 65-90°C, using various sub-and supercritical working fluids. This showed a maximum first law thermal efficiency of 22.62% for a subcritical recuperative cycle.

Typical sources of heat for ORC systems include solar thermal, geothermal, and waste heat from industry. The UK contains several potential geothermal resources with temperatures of up to 180°C (UK DECC, 2013a). Unlike geothermal resources, solar thermal resources vary in temperature depending on the incident radiation and the degree of concentration. Temperatures in excess of 700°C have been generated in practice (Deutsches Zentrum für Luft- und Raumfahrt, n.d.). For industrial waste heat, most high-temperature sources are in the solid phase (steel billets, etc.) which is hard to effectively recover energy from. If these are excluded, 88.9% of easily-utilised waste heat, i.e. that which is available in sources in the liquid or gaseous phase, are at low temperatures, less than 250°C (UK DECC, 2014b).

So far, most research and development of ORC systems has considered single-component organic working fluids. This has several shortcomings: (i) There is always a mismatch of temperature profiles between heat transfer fluid and the working fluid because the single working fluid evaporates and condenses at fixed temperatures while the heat transfer fluid changes temperature during heat transfer. This mismatch leads to irreversibility and reduces the cycle efficiency (Chys, et al., 2012). (ii) An ORC power plant is currently designed by selecting a working fluid to match the heat source and sink temperatures. Considering that these temperatures differ from one customer to another, and the design options are limited by the availability of suitable organic fluids, installation costs are high. A wider choice of working fluids is desirable to reduce installation and operating costs (Chys, et al., 2012).

It is proposed here that these challenges can all be addressed by using zeotropic mixtures, which have the following advantages: (i) A zeotropic mixture has a variable temperature during phase change. **Figure 2** shows the bubble and dew lines of a zeotropic mixture formed by Butane and Heptane. For example, for a mixture with 20% of the high-boiling-point component Heptane, the evaporation starts at the temperature T_{bubble} and ends at T_{dew} . The differential ($T_{\text{bubble}} - T_{\text{dew}}$) is the temperature ‘glide’ of this mixture, which can be used to match the temperature change of heat transfer fluid in counter flow heat exchangers, so that the irreversibility can be reduced (Rajapaksha, n.d.). The use of suitable zeotropic mixtures as working fluids can increase cycle efficiency and power production of ORC systems, especially for lower temperature applications (<250 °C) [22]. (ii) Zeotropic mixtures display bubble- and dew-point temperatures between those of the two member components, and this varies predictably with mixture percentage. This allows the formation of a mixture with a particular composition to match heat sink temperatures so that more options of working fluids are available.

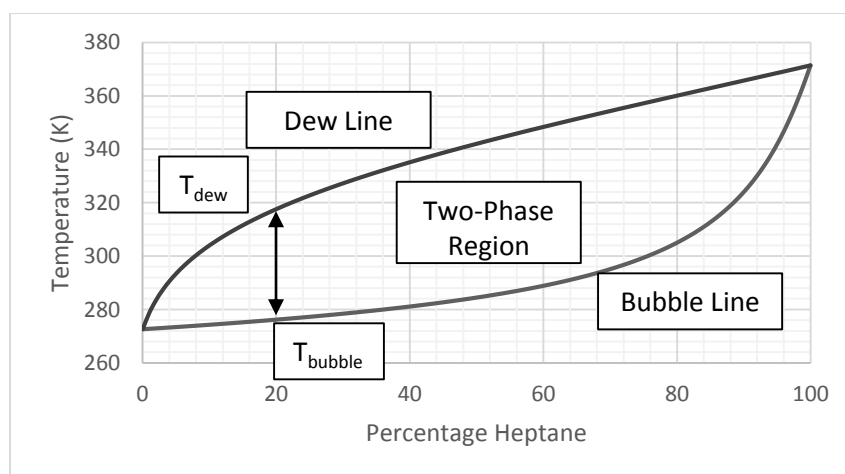


Figure 2: Glide curve of a mixture of Heptane and Butane at 1 bar

In this research, the working fluids selected for the cycle were zeotropic mixtures of alkanes. Specifically pentane, hexane and heptane, and their mixtures with butane. These substances are thermodynamically and chemically quite similar, being non-polar, dry fluids, minimising the number of independent variables to be considered when comparing results.

2. THEORY

The coolant outlet temperature from the condenser is primarily determined by the dew point of the working fluid at condenser pressure. If the dew point is at a lower temperature, or a higher enthalpy, the flow rate of coolant required to maintain the pinch point temperature difference will be greater.

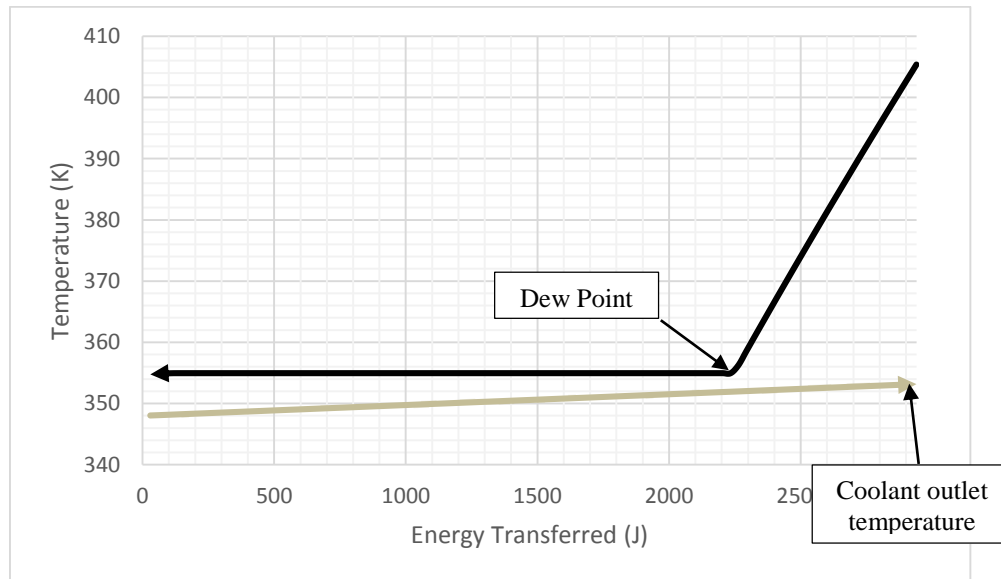


Figure 3: Condenser Temperature Profile for Heptane

Figure 3 demonstrates this principle. The pinch point in the condenser occurs at the dew point. If the dew point moves downwards (lower temperature) or to the right (higher enthalpy), the slope of the lower line must decrease in order for it to maintain the temperature gap at the pinch point. Decreasing the slope results in a lower coolant outlet temperature. In physical terms, this can be achieved by increasing the flow rate of coolant through the condenser.

When a fluid with a lower boiling point is added to one with a higher boiling point, two primary effects occur. One is that the bubble and dew points of the fluid are decreased, the other is that a degree of glide, or temperature change during phase change, is introduced. This means that the dew point increases more quickly than the bubble point. The aim of this paper is to investigate the effects these changes in bubble and dew points have on the required condenser pressures and efficiency of an Organic Rankine Cycle used for cogeneration.

3. NUMERICAL SIMULATION

There was assumed to be no pressure or heat loss from piping or heat exchangers, and no significant effects from velocity, momentum, change in elevation, or compressibility in the flow. A numerical simulation in MATLAB using REFPROP 9.1 (Lemmon, et al., 2013) was developed to analyse a cogeneration system using zeotropic working fluids. The naming convention for points in the cycle was as shown in figure 4:

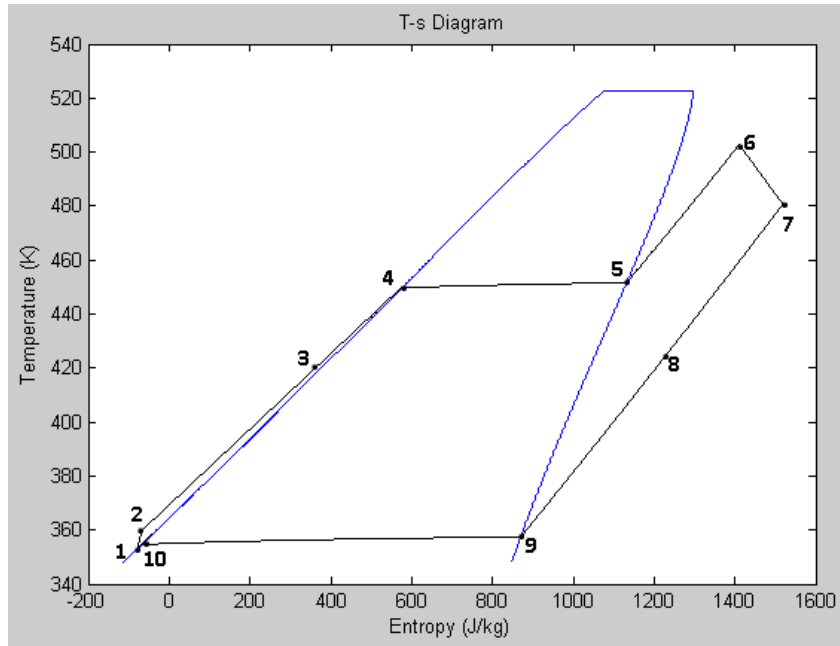


Figure 4: Cycle Diagram, with numbered points.

The pinch point temperature difference in the condenser was taken to be 5°C , which is consistent with previous research (Liu, et al., 2014), (Stefano Clemente, 2012). The coolant inlet temperature was taken to be 80°C , to represent mains water, and the outlet temperature to be 90°C , to represent a district heating scheme. The condenser pressure was then increased from an initial value of 10kPa until the pinch point opened up to the desired 5°C .

REFPROP allows for the calculation of each of the fluid properties on its extensive list given any two other properties, so temperature and pressure information is sufficient to also calculate the enthalpy and entropy of the fluid at this point.

The heat source temperature was taken to be 250°C , and the condenser pressure set to 1600kPa , which was low enough to ensure that the highest boiling point fluid, heptane, would fully vaporise at this temperature.

$$T_6 = 250^{\circ}\text{C} \quad (4)$$

$$P_{\text{evap}} = 1600\text{kPa} \quad (5)$$

The isentropic efficiency of the pump and the expander were taken to be 90% and 70% respectively. Assuming isentropic pumping and expansion, $h_{2,\text{isentropic}}$ and $h_{7,\text{isentropic}}$ can then be obtained from REFPROP, and used to calculate the actual values, using the equations:

$$h_2 = h_1 + \eta_{\text{pump}} * (h_{2,\text{isentropic}} - h_1) \quad (6)$$

$$h_7 = h_6 - \eta_{\text{expander}} * (h_6 - h_{7,\text{isentropic}}) \quad (7)$$

Once this has been done, two properties are known for each of the four key points in the cycle; pump outlet, evaporator outlet, expander outlet and condenser outlet, and so equation 8 can be used to calculate the efficiency of the cycle.

$$\eta_{cycle} = \left(\frac{(h_6 - h_7) - (h_2 - h_1)}{h_6 - h_2} \right) \quad (8)$$

This allowed for the efficiency of the cycle to be calculated.

Keeping the evaporator pressure the same for comparability, the process was then repeated as the second fluid was added to the base fluid of butane in 10% increments of mass fraction. Limiting the evaporator pressure reflects the design considerations in real-world ORC plants, where higher pressures increase the cost and suffer from diminishing returns in efficiency.

This whole process was repeated using pentane, hexane and heptane as the second fluid, and the effects on the performance of the cycle observed.

The model was validated against experimental results obtained by Kang (Kang, May 2012) by using the same initial parameters, and produced results that were within 2% of his values for all points of the cycle as shown previously by the authors (Collings & Yu, 2014). This was considered reasonable in light of the assumptions that had been made in the production of the model, which offered us the confidence to apply this model to cogeneration application as presented in this paper.

4. RESULTS

As described in section 3, the heat source temperature was set to 250°C and the evaporator pressure to 1600kPa. The coolant inlet and outlet temperatures were set to 80 and 90°C respectively.

For all of the fluids under consideration, their addition to butane increased the bubble and dew points of the mixture, and allowed the condenser pressure to be dropped while maintaining the same temperature of water for cogeneration purposes at the condenser outlet, increasing the pressure ratio and therefore the efficiency of the cycle.

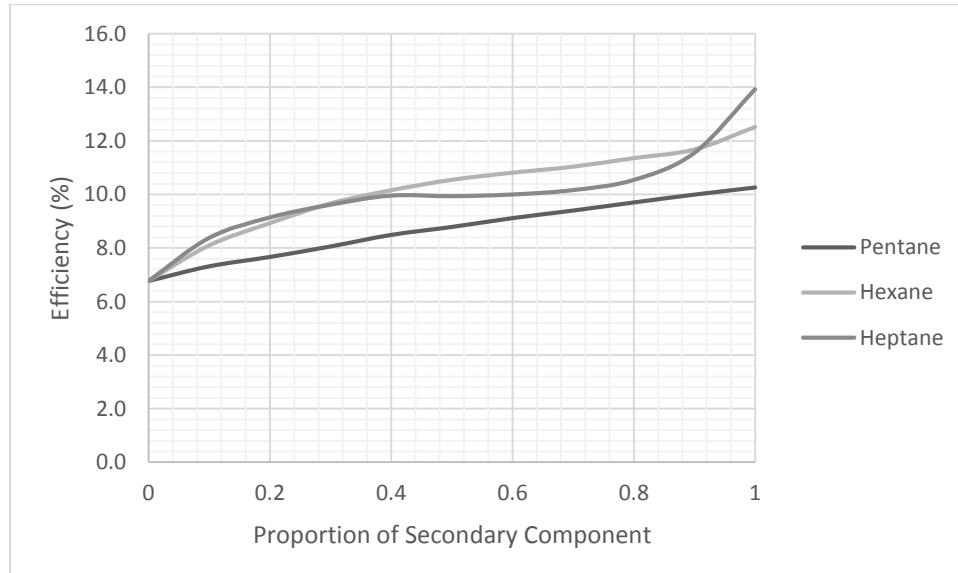


Figure 4: Performance of the system against the proportion of different secondary fluids

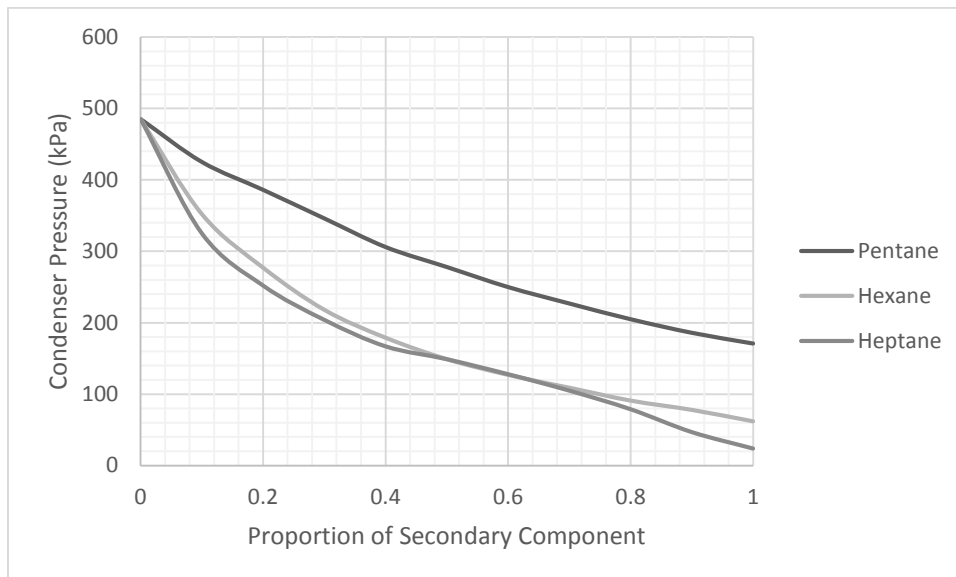


Figure 5: Performance of the system with changing condenser pressure for different secondary fluids

As shown in figures 4 and 5, the addition of pentane to butane smoothly decreases the condenser pressure and increases the efficiency, with a slightly more rapid rate of increase for lower mass fractions of butane.

A similar effect can be seen for the addition of hexane and heptane. The addition of hexane reduces the condenser pressure and increases the efficiency of the cycle. However, this change is less smooth, and the increase in the slope of the efficiency-composition line is more pronounced at very high and very low mass fractions of butane. For heptane, the increased slope at either end of the plot is far more obvious in, although the general trend of decreasing condenser pressure and increased efficiency remains.

A possible explanation for the observed shape of plot is that adding a higher-boiling-point component to the working fluid, such as heptane to butane, will tend to increase the dew point of the cycle, while leaving the bubble point largely unchanged. This allows for the condenser pressure to be dropped without closing the pinch point located at the fluid's dew point to unacceptable levels.

The rate of increase moderates between 20% and 70% heptane, due to the fact that in this region, the glide changes far more slowly, and the condenser pressure is able to decrease smoothly. Above 70% hexane, the bubble point begins to increase rapidly, which results in a sharp decrease in evaporator loading while maintaining roughly the same work output in the expander.

For pentane and hexane, these effects are also present, but the lower overall amount of glide means that the slopes of the bubble and dew lines are more similar at all compositions and results in a smoother profile as the composition changes. This is shown in **Figure 6**. The curve for butane-pentane features less glide, and so the bubble and dew curves have more similar slopes, meaning that the initial changes in bubble and dew points at each end of the scale are less drastic. The overall result of this is that the efficiency of the cycle will vary smoothly as the composition is changed, as shown in the earlier figures.

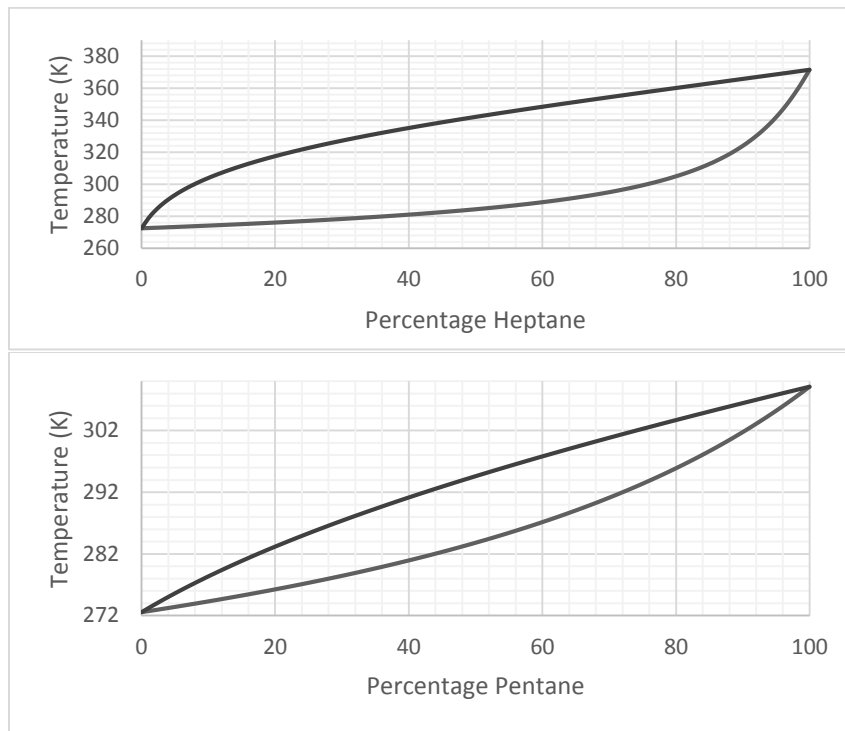


Figure 6: Comparison of glide curves for Butane-Heptane and Butane-Pentane

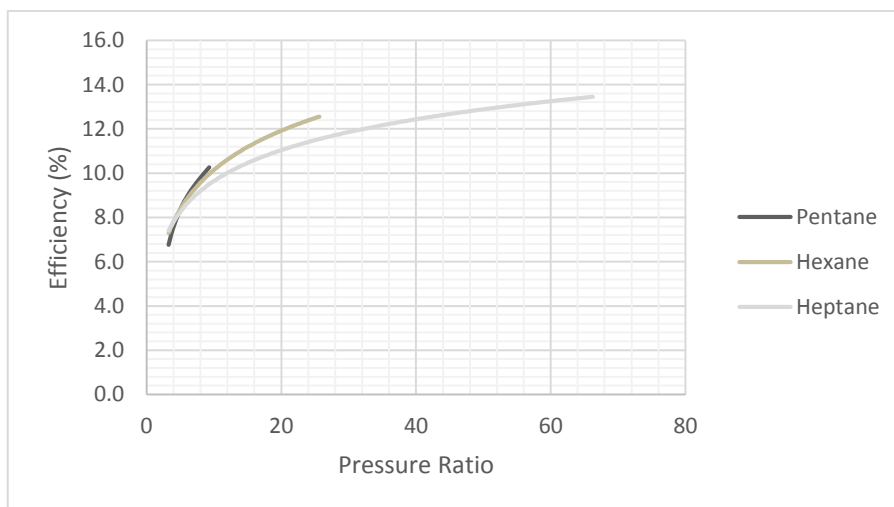


Figure 7: Relationship between pressure ratio and efficiency for different secondary fluids

For all secondary fluids, the efficiency increased as the pressure ratio increased, as shown in

Figure 7, with the increase tapering off, as even an infinitely large pressure ratio will never be able to overcome the Carnot limitation on the cycle.

Figure 7 also shows that the efficiency is higher at lower pressure ratios for lower boiling point secondary components, perhaps because butane-heptane mixtures exhibit higher glide for the same condenser pressure, increasing the condenser and evaporator loading without increasing expander work.

The practical implication of this for the implementation of Organic Rankine Cycles limited by condenser water outlet temperature is that working fluids can be tailored to match heat source and

sink temperatures by mixing them together, but ideally the components of the mixture must be selected to have relatively similar boiling points, otherwise sharp drops in efficiency will be observed as the composition is changed. For situations in which the pressure ratio is limited by any reason, such as the pressure rating of the evaporator and condenser, lower boiling-point secondary components, such as Pentane or Hexane, can be more efficient, however, the use of a higher boiling-point secondary component fluids in a system with a limited evaporator pressure is capable of achieving a higher pressure ratio, as the permitted condenser temperature is lower. In practice, the optimal solution will be determined by the exact configuration and limitations of the system. The higher the achievable pressure ratio, the more likely that Heptane will be the better option.

5. CONCLUSION

It has been shown that zeotropic mixtures can cause changes in the condensing temperature and pressure of a cycle, and that these changes can affect the efficiency of the cycle for a fixed coolant outlet temperature. For zeotropic mixtures consisting of components with relatively similar boiling points, this change in efficiency and condenser pressure is relatively smooth. However, if the temperature glide is too great, the larger changes in bubble and dew point at either end of the scale cause correspondingly abrupt changes in efficiency at these points.

For all mixtures, the benefit in efficiency from tailoring the working fluid to the heat source and sink outweighs the negative effect caused by the increased condenser and expander loading. This benefit is greater for a given pressure ratio when the two components of the working fluid have similar boiling points, as this results in a lower temperature glide, minimizing evaporator and condenser loading.

Potential utilisation of these effects to improve the efficiency of ORCs for cogeneration is a fertile area for future research.

NOMENCLATURE

h	Enthalpy	J/kg
P	Pressure	kPa
s	Entropy	J/kg K
T	Temperature	K
η	Efficiency	%

Subscript

1	Pump Inlet
2	Pump Outlet
3	Regenerator Outlet, cold (unused)
4	Bubble point, evaporator
5	Dew Point, evaporator
6	Expander Inlet
7	Expander Outlet
8	Regenerator Outlet, hot (unused)
9	Dew Point, condenser
10	Bubble Point, condenser
Critical	Property at critical point of the fluid

REFERENCES

- Chys, M., Broek, M. v. d., Vanslambrouck, B. & Paepe, M. d., 2012. Potential of zeotropic mixtures as working fluids in Organic Rankine Cycles. *Energy*, Volume 44, pp. 623-632.
- Collings, P. & Yu, Z., 2014. *Modelling and Analysis of a Small-Scale Organic Rankine Cycle System with a Scroll Expander*. s.l., s.n.
- Deutsches Zentrum für Luft- und Raumfahrt, n.d. *The Jülich Solar Power Tower*, s.l.: s.n.
- Fu, B.-R., Lee, Y.-R. & Hsieh, J.-C., 2005. Design, construction, and preliminary results of a 250-kW organic Rankine cycle system. *Applied Thermal Engineering*, April, Volume 80, pp. 339-346.
- Institution of Civil Engineers, 2012. *Energy Briefing: Heat*, s.l.: s.n.
- Kang, S. H., May 2012. Design and experimental study of ORC (organic Rankine cycle) and radial turbine using R245fa working fluid. *Energy*, 41(1), pp. 514-524.
- Lemmon, E., Huber, M. & McLinden, M., 2013. *NIST Standard Reference Database 23: Reference Fluid Thermodynamic and Transport Properties-REFPROP, Version 9.1*, Gaithersburg: s.n.
- Liu, Q., Duan, Y. & Yang, Z., 2014. Effect of condensation temperature glide on the performance of organic Rankine cycles with zeotropic mixture working fluids. *Applied Energy*, pp. 394-404.
- Oudkerk, J., Quoilin, S. & Lemort, V., 2011. *Evaluation of an ORC-Based micro-CHP system involving a hermetic scroll expander*. s.l., s.n.
- Poyry Energy Consulting, 2009. *The Potential and Costs of District Heating Networks*, s.l.: s.n.
- Rajapaksha, L., n.d. Influence of special attributes of zeotropic refrigerant mixtures on design and operation of vapour compression refrigeration and heat pump systems. *Energy Conversion and Management*, Volume 48, pp. 539-545.
- Shu, G. et al., 2014. Study of mixtures based on hydrocarbons used in ORC (Organic Rankine Cycle) for engine waste heat recovery. *Energy*, September, Volume 74, pp. 428-438.
- Stefano Clemente, D. M. M. R. T., 2012. Energy efficiency analysis of Organic Rankine Cycles with scroll expanders for Cogenerative Applications. *Applied Energy*, Volume 97.
- Stoppato, A., 2012. Energetic and Economic Investigation of the Operation Management of an Organic Rankine Cycle cogeneration Plant. *Energy*, May, 41(1), pp. 3-9.
- Twomey, B., Jacobs, P. & H.Gurgenci, 2013. Dynamic Performance Estimation of Small-Scale Solar Cogeneration with an Organic Rankine Cycle using a Scroll Expander. *Applied Thermal Engineering*, March, 51(1-2), pp. 1307-1316.
- UK DECC, 2012a. *Detailed analysis from the first phase of the energy-saving trust's heat pump field trial*, s.l.: s.n.
- UK DECC, 2012b. *First Year of Monitoring of Exhaust Air Heat Pumps with Underfloor Heating*, s.l.: s.n.
- UK DECC, 2012c. *The Future of Heating: A Strategic Framework for Low-Carbon heat in the UK*, s.l.: s.n.
- UK DECC, 2013a. *Deep Geothermal Review Study - Final Report*, s.l.: s.n.
- UK DECC, 2014a. *Energy Consumption in the UK, 2014 Update*, s.l.: s.n.
- UK DECC, 2014b. *The Potential for Recovering and Using Surplus Heat from Industry*, s.l.: s.n.
- UK DECC, May 2012. *Report on Under-Floor Heating Design*, s.l.: s.n.
- UK DECC, n.d. *A consultation on proposed changes to the Government's Standard Assessment Procedure*, s.l.: s.n.
- Uris, M., Linares, J. I. & Arenas, E., 2014. Techno-economic feasibility assessment of a biomass cogeneration plant based on an Organic Rankine cycle. *Renewable Energy*, June, Volume 66, pp. 707-713.

ACKNOWLEDGEMENT

This research is funded by Royal Society (RG130051)

ON THE OPTIMUM AXIAL FLOW TURBINE DESIGN IN ORGANIC RANKINE CYCLES

Luca Da Lio¹, Giovanni Manente^{2*}, Andrea Lazzaretto³

^{1,2,3}University of Padova, Department of Industrial Engineering,
Via Venezia 1, 35131 Padova, Italy

(¹luca.dalio@studenti.unipd.it, ²giovanni.manente@unipd.it, ³andrea.lazzaretto@unipd.it)

* Corresponding Author

ABSTRACT

Organic Rankine Cycles (ORCs) can effectively recover low grade heat for electricity production from industrial wastes and renewable energy. The general design problem of an ORC system is not trivial due to the choice of several design variables related to the thermodynamic cycle and equipment. Most of the optimization studies in the literature search for the optimum cycle configuration, design parameters and working fluid, disregarding the influence of these choices on expander design and efficiency. Indeed, the latter is often fixed to a constant value implicitly assuming that it will be achieved by a proper expander design in a subsequent design phase. This approach may be weak especially for the working fluids operating in ORCs having a high molecular weight and a low speed of sound. In these applications the high volumetric expansion ratios which may occur even at small temperature differences between turbine inlet and outlet markedly decrease the expander efficiency. Moreover, this efficiency is strongly affected by expander size that may vary from only few kW up to several MWs. The aim of this study consists in searching for the optimum axial flow turbine design parameters (so called duty parameters) in a wide range of ORC operating conditions. Flow coefficient, loading coefficient and degree of reaction are selected as input values in a mean line design procedure that generates the main turbine geometrical characteristics and evaluates the turbine efficiency according to recent loss correlations. The variation of turbine efficiency with duty parameters is then shown in efficiency charts (like the Smith's one) to highlight suboptimal design options. This procedure is repeated for a range of ORC duty specifications (mass flow rate and expansion ratio) to detect their influence on turbine efficiency. So, any penalty associated with the selection of non-optimum duty parameters is clearly separated from the efficiency decay deriving from more severe operating conditions (e.g., high expansion ratios and small sizes).

keywords: Organic Rankine Cycles, axial turbine design, optimization, efficiency prediction.

1. INTRODUCTION

Organic Rankine Cycles are a viable option for the efficient use of low to medium temperature heat sources by simple cycle layouts. ORC systems are applied in the 50 to 500 kW sizes to recover heat from the exhaust gases of gas turbines or internal combustion engines, to exploit the heat content of biomass combustion gases, solar radiation or geothermal sources (Toffolo et al., 2014). Many studies in the literature compare the effects of the working fluid on plant performance for a fixed expander efficiency (Heberle and Brüggemann, 2006), whereas little focus is given to the peculiar design and characteristics of the expander. However, the specific thermodynamic properties of organic fluids necessarily affect the design of the expander, suggesting turbine configurations that differ from those operating with steam or other gases. In particular, the enthalpy drop in the expansion processes of Organic Rankine Cycles is lower than the steam enthalpy drop over the same temperature interval because of the higher molecular weight of organic fluids. The relatively small specific work can be disposed in a low number of stages with benefits in terms of turbine cost and size. On the other hand, the high expansion ratio per stage and the low speed of sound of organic fluids may result in transonic and supersonic flow conditions with

additional loss phenomena such as shock waves, which reduce turbine efficiency and ask for a specific turbine design.

Regardless of the turbine type, the consequence of all mentioned aspects is that the use of traditional tools for preliminary design and efficiency estimate (e.g., Smith chart, Balje diagram) becomes questionable when dealing with organic fluids. Hence new charts are required for organic fluids to have a reliable assessment of the expander efficiency as a function of turbomachinery design parameters. The importance of predicting real efficiency values becomes evident when the designer has to choose the thermodynamic cycle parameters (mass flow rate, evaporation and condensation temperature, kind of fluid, etc., for a given thermal source) which maximize (or minimize) a specified objective function.

In the search for the optimum cycle parameters many studies in the literature (Tchanche et al., 2009), (Khennich and Galanis, 2012) simply assume turbine efficiency values, disregarding the real possibility for the turbine to achieve these efficiencies in practice. Other studies (Sauret and Rowlands, 2011) check the assumed efficiency values only after evaluating optimum cycle parameters. A relevant contribution to the development of new preliminary design tools and efficiency charts for axial turbines operating with fluids having a low speed of sound is given by Macchi (1977), Macchi and Perdichizzi (1981). The authors warn about using efficiency charts (Balje, 1981) that depend on specific speed (n_s) and specific diameter (d_s) only, because i) they are obtained for a given range of Mach numbers and fixed ratio of specific heats and ii) do not account for the effect of reduced turbine dimensions on performance. They develop new charts based on Craig and Cox loss correlations (Craig and Cox, 1971) that link turbine efficiency and optimum specific speed to the volumetric expansion ratio (V/R) and size parameter (SP). Recently, Lazzaretto and Manente (2014) have used these charts at each step of an automatic optimization procedure of the ORC system to calculate the turbine efficiency on the basis of the current thermodynamic variables. This approach eliminates the need of an arbitrary assumption about turbine efficiency at the beginning of the thermodynamic optimization procedure and supplies reliable optimum turbine efficiencies in conjunction with optimum values of other thermodynamic parameters.

In this study the axial flow turbine efficiency charts are updated by taking advantage of the current availability of real gas properties calculation programs Lemmon et al. (2010) and recent loss correlations (Aungier, 2006), which improve the classical models by (Ainley and Mathieson, 1957), (Kacker and Okapuu, 1982) and (Craig and Cox, 1971). A one dimensional meanline model of an axial flow turbine operating with *R245fa* is built in *Matlab*[®] environment to evaluate efficiency and main geometrical parameters. The predicted efficiencies are collected into two groups of maps: in the first one they are correlated to the parameters traditionally selected by the turbine designer (i.e, the so called "duty parameters"); in the second one to the volumetric expansion ratio and size parameter to highlight the influence of working fluid properties, thermodynamic cycle parameters and turbine size on the achievable turbine efficiency (see also (Angelino et al., 1984)).

These maps are similar to those recently obtained by the authors in (DaLio et al., 2014), the main differences being due to a more accurate evaluation of profile losses and a different evaluation of radial clearance. Moreover some preliminary results obtained for isobutane are shown. The main goal of the work is to extract all possible information from these efficiency maps in order to improve the design of turbines operating with a wide set of high molecular weight fluids and having various dimensions, and to increase the power output of the associated ORC systems.

2. THEORETICAL BACKGROUND

According to the dimensional analysis the efficiency of geometrically similar turbomachinery can be predicted in terms of dimensionless variables. In the formulation proposed by Shepherd (1956) the efficiency is a function of five independent variables: specific speed, specific diameter, Reynolds number, Mach number and specific heat ratio (Eq. 1):

$$\eta = f(n_s, d_s, Re, Ma, \gamma) \quad (1)$$

where specific speed and specific diameter are defined as:

$$n_s = \omega \frac{\dot{V}_3^{0.5}}{\Delta h_{0s}^{0.75}} \quad (2)$$

$$d_s = d \frac{\Delta h_{0s}^{0.25}}{\dot{V}_3^{0.5}} \quad (3)$$

When dealing with a turbomachinery operating with a specific fluid in a fully developed turbulent flow regime the effects of γ and Re can be neglected. So, the independent variables of Eq. (1) reduce to three. If the fluid is incompressible and Mach is below 0.5 (Csanady, 1964) the effect of Ma can be ignored, as well. The Balje diagrams (Balje, 1981) show the relationship between n_s , d_s and η under these assumptions for different types of turbomachinery.

The Balje diagram is particularly useful to calculate the turbine diameter, but it does not provide other information on turbine geometry. Other dimensionless parameters such as the loading and flow coefficients (ψ and ϕ), in the form

$$\psi = \frac{h_{01} - h_{03}}{u^2} \quad (4)$$

$$\phi = \frac{V_x}{u} \quad (5)$$

may give additional insights on turbine geometry. These dimensionless parameters are used as design parameters in this work. The well known Smith chart (Smith, 1965) clearly shows that the choice of these parameters affects axial flow turbine efficiency: the highest efficiencies generally occur at low ϕ and ψ values. Both Balje diagrams and Smith charts assign the same efficiency to turbomachinery having the same $n_s - d_s$ or $\psi - \phi$ values. Accordingly, the efficiency penalties associated with i) the high expansion ratios (high Mach number) typical of organic fluids, ii) the small turbine dimensions, iii) the different degrees of reaction, cannot be directly detected through these charts.

These effects can be explicitly taken into account by i) the volumetric expansion ratio VR ii) the size parameter SP (introduced by (Macchi and Perdichizzi, 1981)), and the degree of reaction R :

$$VR = \frac{\dot{V}_3}{\dot{V}_1} \quad (6)$$

$$SP = \frac{\dot{V}_3^{0.5}}{(h_{01} - h_{03})^{0.25}} \quad (7)$$

$$R = \frac{h_2 - h_3}{h_1 - h_3} \quad (8)$$

In this paper turbine efficiency is directly predicted from the classical ψ - ϕ complemented with the information on VR , SP and R , keeping the advantages of the traditional design tools (Smith charts) but enlarging the application to a wider spectrum of working fluids and operating conditions.

VR was preferred to the pressure ratio as an indicator of compressibility, as suggested by Macchi (1977), because it makes the correlation of the efficiency decay with expansion ratio less dependent on the working fluid being considered. On the other hand, SP accounts for the efficiency decay due to the different

ratio between viscous and inertia forces for turbomachinery of different size (Lozza, 2006) and for manufacturing limits which impose that some elements of the machine (e.g., trailing edge thickness, radial clearance, surface finish) cannot be scaled proportionally to the absolute dimension (see Table 2).

According to the suggested approach a turbine design based on given values of ψ , ϕ and R can be transferred to other turbines having the same values of these parameters only if they have the same VR and SP .

3. THE TURBINE DESIGN MODEL AND OPTIMIZATION PROCEDURE

The meanline design model described in this section aims at defining an optimum design and providing a simple procedure to predict the efficiency of a single stage axial flow turbine. The choice of non-dimensional parameters (ψ , ϕ and R) along with a first guess estimate of the turbine efficiency are used in the turbine model to define the main turbine design parameters under a given set of design specifications (T_{evap} , \dot{m}) properly selected to span a wide range of SP and VR (see the flowchart in Fig. 1).

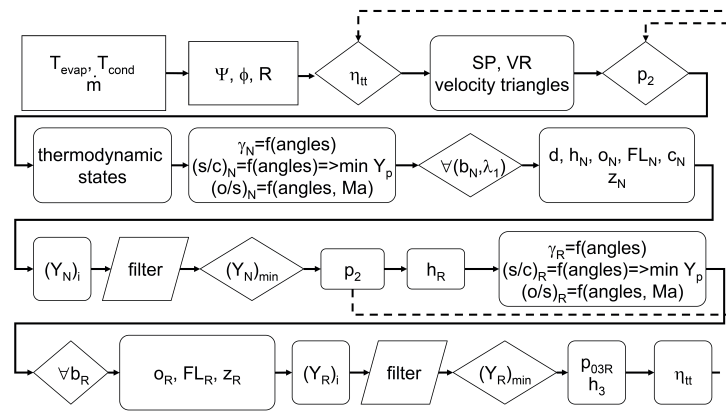


Figure 1: Model's flowchart: dotted arrows indicate updates for guess values.

The resulting geometry is then used to predict turbine design efficiency by means of an iterative procedure which embeds adequate loss models that properly take into account the effects of the high Mach numbers typical of heavy fluids working in ORCs. These models are presented in detail in Appendix A. While traditional loss models either disregard (Ainley and Mathieson, 1957) or overestimate shock and post expansion losses (Dunham and Came, 1970), the more recent Aungier's model that is applied here supplies a better estimate of the magnitude of these losses. This choice has a direct impact on turbine efficiency, and provides the performance gap and associated variation in the design parameters compared to previous literature that generally relies on the Craig and Cox (e.g. Macchi and Perdichizzi (1981)). An accurate analysis of all the loss sources occurring in the blade rows is performed to form a reliable estimate of the overall total pressure losses within the stator and rotor (Y_N and Y_R , respectively, in Fig. 1). Real fluid properties taken from *NIST Refprop* (Lemmon et al., 2010) are considered to accurately evaluate the thermodynamic behavior, particularly at high pressure and close to the vapor saturation curve. Unlike Macchi and Perdichizzi (1981) this model assumes the three requirements of a "normal" stage (named also "repeating" stage):

$$V_x = constant \quad d = constant \quad \alpha_1 = \alpha_3 \quad (9)$$

where V_x is the axial velocity, d is the root mean square diameter, α_1 and α_3 are the absolute flow angles at stations 1 and 3.

A schematic of the circumferential and meridional section of the blade row is drawn in Figures 2(a) and 2(b) to highlight the main geometrical parameters calculated by the design optimization procedure.

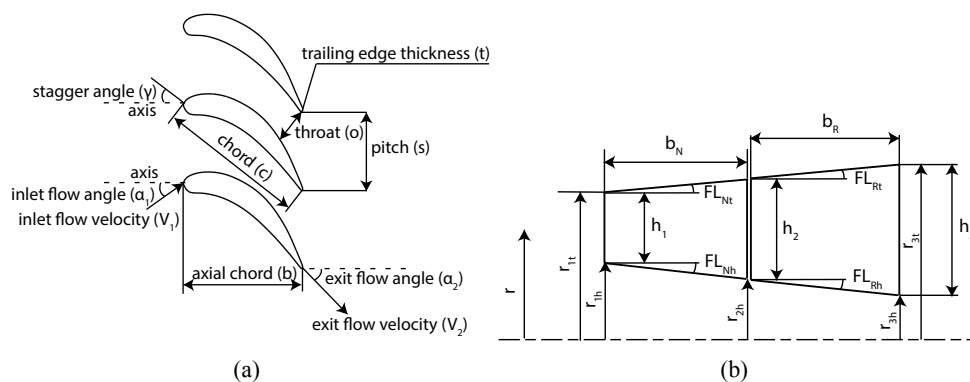


Figure 2: (a) Main geometrical blade parameters, and (b) Schematic representation of turbine stage meridional channel.

Table 1: Upper and lower bounds of the free variables in the optimization procedure.

	min value	max value
λ_1	0.30	0.95
λ_3	0.30	1
FL_N ($^\circ$)	-20	20
FL_R ($^\circ$)	-25	25
$(h/d)_3$	0	0.25
$\arcsin(o/s)_N$ ($^\circ$)	13	60
$\arcsin(o/s)_R$ ($^\circ$)	13	60
$(b/d)_N$	0	0.25
$(b/d)_R$	0	0.25
b_N (mm)	3	100
b_R (mm)	3	100
z_N	10	100
z_R	10	100

A detailed explanation of all steps required to optimize the design of the axial turbine stage, as shown in the flow chart of Fig. 1, is given in Appendix B.

4. RESULTS

The main outcomes of the design procedure presented in Section 3 are the geometry and efficiency of an axial flow turbine fulfilling given design specifications (i.e., mass flow rate and specific work). For each design specifications different turbine designs are generated assuming different values of the design parameters ψ , ϕ and R . Accordingly new Smith charts are generated showing the maximum efficiency achievable by $R245fa$ at different ψ - ϕ - R values. Only Smith charts referring to optimum degree of reaction are shown for brevity (see Fig. 3). Starting from each design specification the optimum design parameters (ψ - ϕ) and efficiency are drawn from the associated Smith charts and used to build a general efficiency map in the SP - VR plane (see Fig. 4(a)).

To cover a wide spectrum of SP and VR conditions, the whole analysis is carried out by considering the following set of design specifications: evaporation temperatures (T_{evap}) in the range 50 to 110 $^\circ\text{C}$ at steps of 10 $^\circ\text{C}$, and mass flow rates (\dot{m}) equal to 10, 30, 50 and 100 100 kg/s. The turbine outlet pressure

Table 2: Geometric parameters in (m) the rigorous similarity of which cannot be maintained at low actual turbine dimensions.

e	2×10^{-6}
δ	$\max(0.0005 \text{ or } 0.015h_3)$
t	$\max(0.001 \text{ or } 0.05 \phi)$

is fixed in all cases at 1.97 bar, being determined by the assumed condensation temperature (33 °C). The range and step of variation of the design parameters are:

$$\Psi \in (0.8 : 0.01 : 2.80)$$

$$\phi \in (0.40 : 0.01 : 0.90)$$

$$R \in (0.00 : 0.01 : 0.60)$$

where the first and third terms are the upper and lower bounds and the step of variation is shown in the middle.

All possible combinations of design specifications and design parameters are simulated to generate the new charts shown in the following.

4.1 New Smith charts

Assuming that half of the axial kinetic energy in the discharge section is recovered (Macchi and Perdichizzi, 1981) the turbine efficiency becomes:

$$\eta = \frac{h_{01} - h_{03}}{h_{01} - h_{3ss} - 0.5 \frac{V_x^2}{2}} \quad (10)$$

Efficiency values calculated at optimum R through Eq. (10) are shown in ψ - ϕ plane in Figs. 3 for two extreme values of VR (Fig. 3(a) and 3(b)) and SP (Fig. 3(c) and 3(d)).

It clearly appears that the highest efficiencies are obtained at low flow coefficients and low loading coefficients, as in the original Smith chart. High ψ values imply larger deflections which require a larger blade surface area in contact with the fluid and in turn higher friction losses. As the flow coefficient ϕ increases, the deflection decreases but the axial velocity increases, resulting in additional losses (Moustapha et al., 2003).

The volumetric expansion ratio has a strong influence on turbine efficiency. The chart in Fig. 3(a) refers to $VR \approx 2.3$ ($T_{evap} = 60$ °C) and shows a maximum efficiency equal to 88.4% obtained at $\phi = 0.4$ and $\psi = 1.01$. The chart in Fig. 3(b) refers to a much higher VR ($T_{evap} = 100$ °C), and shows a maximum efficiency equal to 86.1% which is obtained at $\phi = 0.4$ and $\psi = 1.11$. These results demonstrate that the efficiency markedly decreases (-2.3%-points) and the optimum ψ slightly increases (+0.10) with VR . Similarly the effect of size parameter on turbine efficiency is shown in Figs. 3(c) and 3(d) where the efficiency penalties become 2.2%-points moving from $SP=0.27$ m to 0.09 m, decreasing the turbine diameter from 0.50 m to 0.16 m.

Table 3 compares the geometrical features and losses for two turbines having different volumetric expansion ratios in the optimum points of Figures 3(a) and 3(b). All loss sources are shown in Table 3 to explain the efficiency gap between the two cases. It clearly appears that the efficiency penalties for the higher pressure ratio is due to the high post expansion losses (in the stator they account for more than half of the total losses) which are absent for the lower pressure ratio. Indeed, the flow is supersonic both at stator and rotor outlet. Moreover, the higher secondary losses and the occurrence shock losses further reduce the efficiency.

Table 4 referring to the two optimum designs in Figs. 3(c) and 3(d) shows a significant increase of secondary, profile and clearance losses when reducing the size.

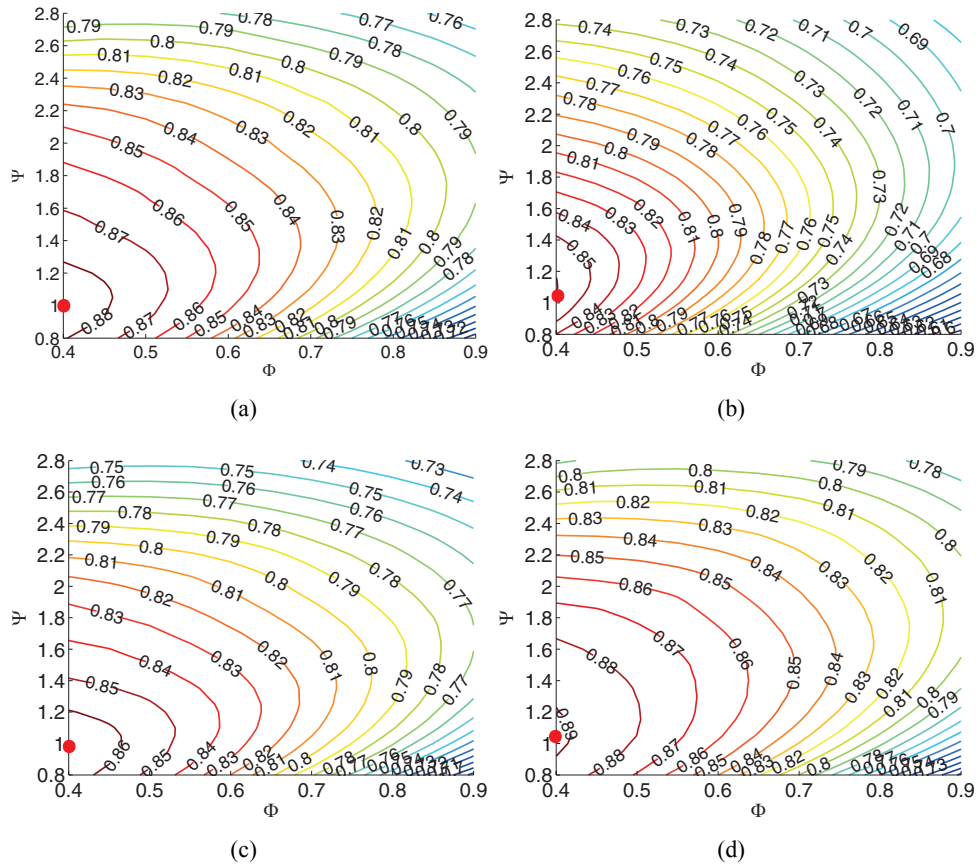


Figure 3: Smith charts showing lines at constant η for: (a) $\dot{m} = 50 \text{ kg/s}$, $T_{evap} = 60 \text{ }^\circ\text{C}$ ($SP \approx 0.16 \text{ m}$, $VR \approx 2.3$); (b) $\dot{m} = 50 \text{ kg/s}$, $T_{evap} = 100 \text{ }^\circ\text{C}$ ($SP \approx 0.16 \text{ m}$, $VR \approx 7$); (c) $\dot{m} = 10 \text{ kg/s}$, $T_{evap} = 60 \text{ }^\circ\text{C}$ ($SP \approx 0.09 \text{ m}$, $VR \approx 2.3$); (d) $\dot{m} = 100 \text{ kg/s}$, $T_{evap} = 60 \text{ }^\circ\text{C}$ ($SP \approx 0.27 \text{ m}$, $VR \approx 2.3$). Red dots indicate the best efficiency points.

Table 3: Main performance parameters and losses in the optimum points of Figs. 3(a) and 3(b).

	VR	2.3		6.9		
	ϕ	0.4		0.4		
	Ψ	1.01		1.11		
	n_s	1.02		0.93		
	R	0.47		0.45		
	η	0.884		0.861		
	V_x (m/s)	47.4		66.6		
	d (m)	0.36		0.31		
	ω (rad/s)	663		1081		
	u (m/s)	118		166		
	stator	rotor		stator	rotor	
<i>Mach inlet</i>	0.36	0.35		0.54	0.50	
<i>Mach exit</i>	0.97	0.91		1.42	1.28	
<i>deflection</i>	65	69		71	83	
<i>h/c</i>	0.93	1.73		0.51	1.10	
<i>t/o (%)</i>	7.74	8.11		7.69	7.91	
<i>δ/h_3 (%)</i>		1.5			1.5	
<i>flaring tip (°)</i>	11	17		12	18	
<i>flaring hub (°)</i>	14	25		14	25	
<i>b (m)</i>	0.046	0.041		0.045	0.057	
	stator	rotor	total	stator	rotor	total
<i>profile</i>	0.022 (32.4%)	0.020 (13.7%)	0.042 (19.6%)	0.019 (10.5%)	0.021 (8.9%)	0.040 (9.6%)
<i>secondary</i>	0.039 (57.3%)	0.029 (19.9%)	0.068 (31.8%)	0.050 (27.6%)	0.039 (16.6%)	0.089 (21.4%)
<i>trailing edge</i>	0.008 (11.8%)	0.008 (5.5%)	0.016 (7.5%)	0.008 (4.4%)	0.008 (3.4%)	0.016 (3.9%)
<i>shock</i>	0 (0%)	0 (0%)	0 (0%)	0.015 (8.29%)	0.008 (3.4%)	0.023 (5.5%)
<i>postexpansion</i>	0 (0%)	0 (0%)	0 (0%)	0.089 (49.2%)	0.049 (20.9%)	0.138 (33.2%)
<i>clearance</i>		0.089 (60.9%)	0.089 (41.6%)		0.110 (46.8%)	0.110 (26.4%)
<i>total</i>	0.068 (100%)	0.146 (100%)	0.214 (100%)	0.181 (100%)	0.235 (100%)	0.416 (100%)

4.2 SP-VR maps

In this section the effects of the design specifications on the optimum turbine design parameters and efficiency are analyzed. To this end the simulation model is run at different mass flow rates and evaporating temperatures to find the optimum designs in the range SP 0.05 ÷ 0.30 m and VR 2 ÷ 9. Each Smith chart contributes in the following SP - VR maps with its maximum efficiency point.

Figure 4(a) clearly shows that the highest turbine efficiencies are located in the region of low VR s and high SP s. At fixed SP , large volume variations cause relevant losses mainly due to high Mach flow regimes (i.e., high velocities). At fixed VR , small turbines are disadvantaged because of larger ratios between viscous and inertia forces and manufacturing limits which lead to higher clearance losses.

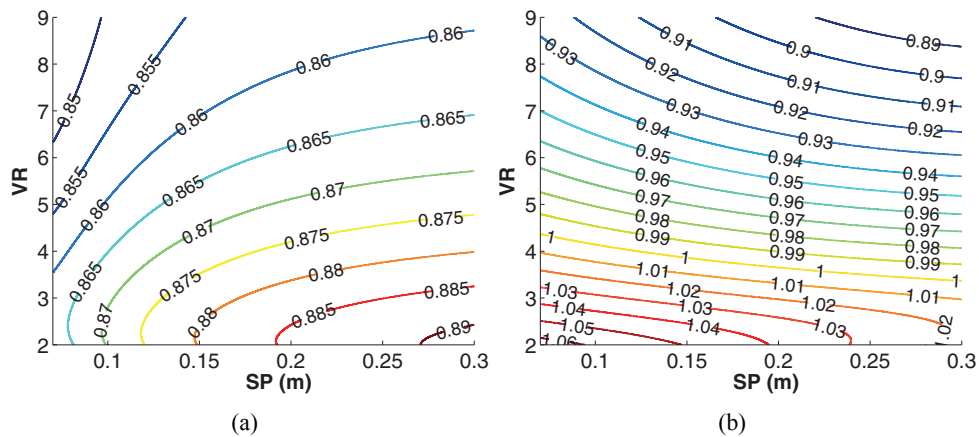


Figure 4: (a) Optimum turbine efficiency, and (b) optimum specific speeds versus SP and VR for $R245fa$

Figure 4(b) shows the specific speed trend in the SP - VR plane. In agreement with the literature the

Table 4: Main performance parameters and losses in the optimum points of Figs. 3(c) and 3(d)

	SP	0.086		0.27			
	ϕ	0.4		0.4			
	Ψ	0.97		1.01			
	n_s	1.04		1.03			
	R	0.48		0.47			
	η	0.866		0.888			
	V_x (m/s)	48		47			
	d (m)	0.16		0.50			
	ω (rad/s)	1506		471			
	u (m/s)	120		119			
		stator	rotor	stator	rotor		
<i>Mach inlet</i>		0.36	0.35	0.36	0.35		
<i>Mach exit</i>		0.95	0.91	0.97	0.91		
<i>deflection</i>		73	68	72	73		
<i>h/c</i>		0.50	0.92	1.22	1.72		
<i>t/o (%)</i>		7.7	8.0	7.8	8.1		
δ/h_3			1.56		1.5		
<i>flaring tip</i> (°)		6	10	15	17		
<i>flaring hub</i> (°)		6	15	19	25		
<i>b</i> (m)		0.038	0.033	0.050	0.057		
		stator	rotor	total	stator	rotor	total
<i>profile</i>		0.024 (27.0%)	0.023 (13.4%)	0.047 (18.1%)	0.021 (35.0%)	0.016 (11.4%)	0.037 (18.5%)
<i>secondary</i>		0.058 (65.2%)	0.043 (25.1%)	0.101 (38.8%)	0.032 (53.3%)	0.028 (20.0%)	0.060 (30.0%)
<i>trailing edge</i>		0.008 (9.0%)	0.008 (4.7%)	0.016 (6.2%)	0.008 (13.3%)	0.008 (5.7%)	0.016 (8.0%)
<i>shock</i>		0 (0%)	0 (0%)	0 (0%)	0 (0%)	0 (0%)	0 (0%)
<i>postexpansion</i>		0 (0%)	0 (0%)	0 (0%)	0 (0%)	0 (0%)	0 (0%)
<i>clearance</i>			0.098 (57.3%)	0.098 (38%)		0.089 (63.6%)	0.089 (44.5%)
<i>total</i>		0.089 (100%)	0.171 (100%)	0.260 (100%)	0.060 (100%)	0.14 (100%)	0.20 (100%)

optimum values of n_s increase as the turbine dimensions and VR decrease. At constant SP (i.e., for constant d) the increase of n_s towards low VR is a consequence of lower enthalpy drops, which oppose to the effect of the progressive decrease of the angular speed ω due to the decrease in turbine peripheral speed (u).

These maps can be compared with those originally obtained by Macchi and Perdichizzi (1981) reported here in Fig. 5, where the SP - VR domain considered in this work is highlighted in red. The range of turbine efficiency is narrower in the present work varying between 0.85 and 0.89. The rising trend of turbine efficiency with SP up to 0.30 m at fixed VR is confirmed in this analysis, as well as the decreasing trend at increasing VR .

The decrease of optimum specific speed with VR is observed in this paper too. Specific speeds are higher than the optimum ones calculated by Macchi and Perdichizzi (1981) especially in the high VR and SP region and show a weaker dependence from SP (note that angular speeds are expressed in rpm instead of rad/s).

Fig.6 shows the SP - VR -efficiency map for *isobutane*. At given values of the couple SP - VR higher efficiencies are achieved by *isobutane* compared to *R245fa*. However the general trend is maintained.

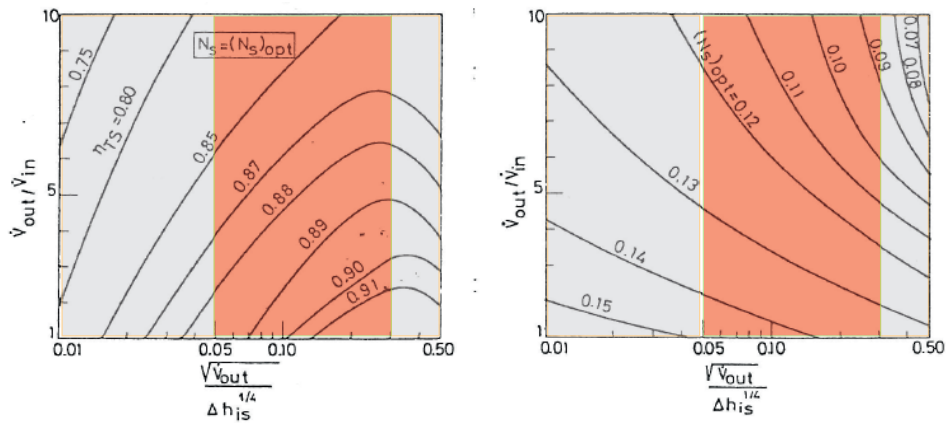


Figure 5: Efficiency prediction and optimum values of specific speed for a turbine stage (reproduced from Macchi and Perdichizzi (1981))

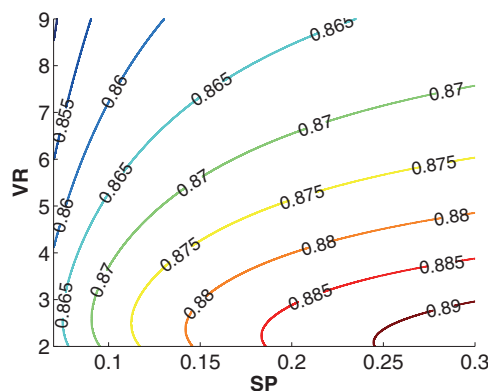


Figure 6: Optimum turbine efficiency versus SP and VR for *isobutane*.

5. CONCLUSIONS

The paper shows that new design procedures are needed for a reliable design of ORC expanders operating with high molecular weight fluids due to the wider range of operating conditions (e.g., size, pressure ratios) compared to traditional applications using conventional fluids (e.g., air or flue gases). The model of the single stage axial flow turbine developed in this work explicitly accounts for the influence of the volumetric expansion ratio (VR) and size (SP) parameters in addition to the flow and loading coefficients and degree of reaction. Expansion ratio and size parameters are found to significantly affect the achievable efficiency and cannot be disregarded even in a preliminary ORC expander design. For *R245fa*, the increase of VR from 2.3 to 7 causes a decrease of the optimum efficiency of 2.3%-points (from 88.4% to 86.1% at $SP \approx 0.16$ m). Similarly, the penalty in the optimum efficiency reaches 2.2%-points when the size is reduced from SP 0.27 m to ≈ 0.16 m (i.e., from 88.8% to 86.6% at $VR \approx 2.3$). The analysis has also highlighted the effects of VR and SP on the optimum design parameters ψ , ϕ and n_s . When VR increases from 2.3 to 7 at fixed SP (≈ 0.16 m), the optimum loading coefficient ψ increases from 1.01 to 1.11, the optimum flow coefficient ϕ remains unchanged (0.4) and the specific speed n_s reduces from 1.02 to 0.93. The comparison *R245fa-isobutane* demonstrate that the efficiency map is not strictly general but is affected by the peculiar properties of the working fluid. The developed maps improve the prediction of ORC expander performance, but they could certainly be improved by a proper tuning with new experimental data specifically retrieved from tests on real ORC systems. Nonetheless a good agreement is found with results of theoretical analyses reported in the literature.

The resulting charts could be a useful tool in a general optimization procedure of the ORC systems

design that takes into account the real turbine behavior in the search for the best thermodynamic cycle parameters.

A. LOSS MODEL

The general structure of the loss model used here is derived from Aungier's work (Aungier, 2006). The total pressure loss coefficient through the blade rows is expressed as the sum of several terms representing specific loss sources: profile, secondary, trailing edge, post expansion, shock and clearance losses.

$$Y = Y_p + Y_s + Y_{te} + Y_{ex} + Y_{sh} + Y_{cl} \quad (\text{A.1})$$

In this section the formulation of all these loss sources is presented. Although these equations are written for a fixed row (i.e., stator) they are still valid for a rotor provided that relative flow angles (β) are substituted for absolute ones (α). When using the following equations flow angles must be expressed consistently with the blade angle convention, so that:

$$\alpha_1 = 90 + \arctan(V_{t1}/V_x) \quad (\text{A.2})$$

$$\alpha_2 = 90 - \arctan(V_{t2}/V_x) \quad (\text{A.3})$$

$$\beta_2 = 90 - \arctan(W_{t2}/V_x) \quad (\text{A.4})$$

$$\beta_3 = 90 + \arctan(W_{t3}/V_x) \quad (\text{A.5})$$

The output of the loss model is the total pressure loss coefficient of the stator (Y_N) and rotor (Y_R), respectively defined by:

$$Y_N = \frac{p_{01} - p_{02}}{p_{02} - p_2} \quad (\text{A.6})$$

$$Y_R = \frac{p_{02R} - p_{03R}}{p_{03R} - p_3} \quad (\text{A.7})$$

A.1 Profile losses

The profile loss is due to skin friction on the blade surface and depends on the blade area that is in contact with the fluid, the surface roughness, and Reynolds and Mach numbers. The profile loss coefficient Y_p is evaluated using a modified form of the Ainley-Mathieson model:

$$Y_p = k_{mod} k_{inc} k_p k_{Re} k_M \left((Y_{p1} + \xi^2(Y_{p2} - Y_{p1})) \left(\frac{5t_{max}}{c} \right)^\xi - \Delta Y_{te} \right) \quad (\text{A.8})$$

where:

- Y_{p1} and Y_{p2} represent the profile losses in nozzle blades and impulse blades, respectively, and ξ is the ratio between the inlet and outlet flow angles and governs the amount of profile losses for blade configurations that are intermediate between nozzle and impulse ones. Both Y_{p1} and Y_{p2} show a minimum at an optimum pitch to chord ratio, which varies depending on the discharge flow angle.
- k_{mod} , k_{inc} , k_p , k_{Re} and k_M are correction factors accounting for:
 - i) Superior performance of modern designs due to improved design technology (k_{mod}). A value equal to 0.67 is used as suggested by Kacker-Okapuu;
 - ii) Off-design incidence flow angles (k_{inc}). k_{inc} is set to 1 because only design conditions are considered;

- iii) Beneficial influence of high Mach numbers (k_p) (thin boundary layers and flow separations avoided) compared to flow conditions in cascade tests;
 - iv) Effects of Reynolds number and surface roughness on the friction coefficient (k_{Re});
 - v) discharge Mach number in subsonic flow regimes (k_M).
- ΔY_{te} is the trailing edge loss term that is evaluated separately from the profile losses in the Aungier's model.

A.2 Secondary losses

Secondary flows are vortices that occur as a result of the boundary layers and curvature of the blade passage causing fluid deviations from the main flow direction. Secondary losses are calculated using an updated version of the AMDC model originally proposed by Dunham and Came (Dunham and Came, 1970) and subsequently refined by Kacker and Okapuu (Kacker and Okapuu, 1982) and Aungier (Aungier, 2006). According to this model the total pressure loss Y_s is calculated starting from the loading factor Z :

$$Z = \left(C_L \frac{c}{s} \right)^2 \frac{\sin^2 \alpha_2}{\sin^3 \alpha_m} \quad (\text{A.9})$$

where C_L is the lift coefficient defined by:

$$C_L = 2(\cot \alpha_1 + \cot \alpha_2) \frac{s}{c} \sin \alpha_m \quad (\text{A.10})$$

A preliminary estimate of the secondary flow loss coefficient can be calculated as:

$$\tilde{Y}_s = 0.0334 F_{AR} Z \frac{\cos \alpha_2}{\cos \alpha_{1b}} \quad (\text{A.11})$$

where F_{AR} is a correction factor based on blade span and chord.

Aungier further refines Eq. (A.11) by imposing an asymptotic upper limit of about 0.365 to the secondary losses. Moreover, correction factors accounting for Reynolds and Mach number (k_{Re} , k_s) are also included to get:

$$Y_s = k_{Re} k_s \sqrt{\frac{\tilde{Y}_s^2}{1 + 7.5 \tilde{Y}_s^2}} \quad (\text{A.12})$$

A.3 Trailing edge losses

Trailing edge losses account for pressure losses due to trailing edge blockage. The trailing edge loss coefficient is expressed as a function of the ratio between trailing edge thickness and blade throat according to the following expression:

$$Y_{te} = \frac{\Delta p_0}{0.5 \rho V_2^2} = \left(\frac{t_2}{o_2 - t_2} \right)^2 \quad (\text{A.13})$$

A.4 Shock losses

Shock losses account for the formation of shock waves also at moderate average inlet Mach numbers due to the local acceleration at blade leading edges. Although these shock waves take place next to the blading hub endwall they can be evaluated as a contribution to the mean line losses through \tilde{Y}_{sh} that enters in the definition of Y_{sh} in Eq. (A.1):

$$\tilde{Y}_{sh} = 0.8 X_1^2 + X_2^2 \quad (\text{A.14})$$

$$Y_{sh} = \sqrt{\frac{\widetilde{Y}_{sh}^2}{1 + \widetilde{Y}_{sh}^2}} \quad (\text{A.15})$$

X_1 and X_2 both depend on inlet and outlet Mach numbers.

A.5 Supersonic expansion losses

Due to the low speed of sound of heavy fluids and high pressure ratios it is quite usual to deal with supersonic velocities which generate additional pressure losses as result of shock waves in the trailing edge wake. The phenomena underlying these losses are difficult to be described in an easy but reliable way using a meanline analysis approach. We observed that the models proposed by (Dunham and Came, 1970), (Li et al., 2004) give non meaningful results (that are either overestimated or underestimated, respectively) when dealing with high Mach numbers. More reliable results are instead provided by the following Aungier's correlation:

$$Y_{ex} = \left(\frac{Ma_2 - 1}{Ma_2} \right)^2 \quad (\text{A.16})$$

A.6 Blade clearance losses

The loss coefficient is computed for the rotor only using the following expression:

$$Y_{cl} = 0.47 Z \frac{c}{h} \left(\frac{\delta}{c} \right)^{0.78} \quad (\text{A.17})$$

B. DETAILED DESIGN PROCEDURE

1. The values of the mass flow rate (\dot{m}) and evaporation and condensation temperatures (T_{evap} , T_{cond}) are known from the thermodynamic cycle analysis, and represent design specifications. A saturated vapor condition is assumed at turbine inlet so that states 1 and 3_{ss} are completely defined;
2. Proper ranges of variation of ψ , ϕ and R are selected (see Section 4) to get all absolute and relative flow angles by means of Eqs. (B.1) and (B.2):

$$\begin{cases} \tan \alpha_3 = \frac{1-R-\Psi/2}{\phi} \\ \tan \alpha_2 = \frac{1-R+\Psi/2}{\phi} \end{cases} \quad (\text{B.1})$$

$$\begin{cases} \tan \beta_3 = -\frac{R+\Psi/2}{\phi} \\ \tan \beta_2 = -\frac{R-\Psi/2}{\phi} \end{cases} \quad (\text{B.2})$$

3. h_3 is calculated by assuming a guess value of the total-to-total efficiency η_{tt} . So, the rotor outlet state is known and VR , SP can be calculated; h_2 , u and V_x are calculated from R , ψ and ϕ , respectively;
4. All the velocity triangles can be obtained by means of trivial trigonometric calculations. So, the total states 01 , 03 , 03_{ss} can be calculated;
5. Assuming a guess value for the pressure p_2 , state 2 is located in the enthalpy-entropy plane;
6. The passage area A_1 at the inlet of the stator is calculated from the mass flow rate definition. A set of couples "stator inlet hub-to-tip radius ratios ($\lambda_1 = r_{1h}/r_{1t}$ - see Fig. 2(b)) - nozzle axial chord (b_N)" is considered to calculate a wide spectrum of the following geometrical parameters: chord (c_N), root mean square diameter ($d = 2A_1/\pi\sqrt{(1-\lambda_1^2)/(1+\lambda_1^2)}$), blade span (h_N) (from continuity equation), blade pitch (s_N), number of blades (z_N) and throat opening (o_N). The set of

generated stator geometries are compared on the basis of the associated losses (Eq. (A.1)) to select the best performing one. Unfeasible solutions in the set $(\lambda_1 - b_N)$ are eliminated according to the constraints summarized in Table 1, among which the most binding are those associated with the flaring angle ($FL_N < 20^\circ$) and the hub-to-tip radius ratio at rotor outlet ($\lambda_3 \geq 0.30$). Among all feasible solutions, the couple $(\lambda_1 - b_N)$ yielding the lowest total nozzle pressure loss coefficient (Y_N) is chosen. The blade spans (h) along the stator and rotor blade channels are then found from the continuity equation (see Fig. 2(b));

7. At this point the stator outlet pressure (previously assumed as a guess value at point 5) can be calculated from the definition of total pressure loss coefficient, being Y_N known:

$$Y_N = \frac{p_{01} - p_{02}}{p_{02} - p_2} = \frac{p_{01} - f(h_{02}, s_2)}{f(h_{02}, s_2) - p_2} \quad (\text{B.3})$$

So, state 2 can be located in the enthalpy-entropy diagram. Note that the total pressure at stator outlet (p_{02}) is calculated from the known values of h_{02} and s_2 to properly take compressibility into account (i.e., the dynamic pressure in the denominator of Eq. (B.3) is not calculated as $0.5\rho_2 V_2^2$, as commonly suggested in the literature);

8. The calculation procedure of the rotor geometry and losses is similar but simpler than the stator one. In fact, the only free variable is b_R , being λ_3 ($\lambda_3 = r_{3h}/r_{3t}$ in Figure 2(b)) evaluated from λ_1 (that is known from the calculations in the stator, see step 6). Indeed, it can be demonstrated from the continuity equation that the hub-to-tip radius ratios of two consecutive sections i and j in a normal axial turbine stage can be linked to each other by means of the volumetric expansion ratio VR :

$$\lambda_j = \sqrt{\frac{1 + \lambda_i^2 - VR(1 - \lambda_i^2)}{1 + \lambda_i^2 + VR(1 - \lambda_i^2)}} \quad (\text{B.4})$$

For each value of b_R the rotor geometrical parameters (s_R, z_R, o_R , etc.) and total rotor pressure loss (Y_R) are calculated (see the flowchart in Fig. 1), from good engineering practice (see (Moustapha et al., 2003)). The rotor design yielding the lowest Y_R and fulfilling all the constraints is selected. Starting from the definition of Y_R , p_{03R} is then calculated and used to find a new value of h_3 , which updates the h_3 calculated from the η_{tt} guess at step 3;

9. A new estimate of the total-to-total efficiency is calculated from:

$$\eta_{tt} = \frac{h_{01} - h_{03}}{h_{01} - h_{03ss}} \quad (\text{B.5})$$

This estimate is used as input for the next iteration until convergence.

NOMENCLATURE

α	absolute flow angle	($^\circ$)
β	relative flow angle	($^\circ$)
δ	rotor radial clearance	(m)
\dot{m}	mass flow rate	(kg/s)
\dot{V}	volumetric flow rate	(m^3/s)
η	efficiency	()
γ	sweep angle	($^\circ$)
λ	hub to tip radius ratio	()
ω	angular velocity	(rad/s)

ϕ	flow coefficient	()
ψ	loading coefficient	()
ρ	density	(kg/m ³)
A	area	(m ²)
b	blade axial chord	(m)
c	blade chord	(m)
d	root mean square diameter	(m)
e	blade surface roughness	(m)
FL	flaring angle	(°)
h	blade span	(m)
h	specific enthalpy	(J/kg)
Ma	Mach number	()
n_s	specific speed	()
o	blade throat	(m)
p	pressure	(Pa)
R	degree of reaction	()
Re	Reynolds number	()
s	blade pitch	(m)
SP	size parameter	(m)
T	temperature	(°C)
t	trailing edge thickness	(m)
u	peripheral velocity	(m/s)
V	absolute velocity	(m/s)
V_x	meridional velocity	(m/s)
VR	volumetric flow ratio	()
w	relative velocity	(m/s)
Y	total pressure loss coefficient	()
Z	loading factor	()
z	blade number	()

Subscript

0	total state
1	stator inlet
2	stator exit and rotor inlet
3	rotor exit
cond	condensing
evap	evaporating
h	hub
m	mean direction
N	stator
R	rotor
s	isentropic
t	tip
tt	total to total

REFERENCES

- Ainley, D. G. and Mathieson, G. C. R. (1957). A method for performance estimation for axial-flow turbines. *ARC Technical Report, R. and M. No.2974, Great Britain.*
- Angelino, G., Gaia, M., and Macchi, E. (1984). A review of italian activity in the field of Organic Rankine Cycles. *Proceedings of International VDI-Seminar, Zurich.*

- Aungier, R. H. (2006). *Turbine Aerodynamics: Axial-Flow and Radial-Flow turbines Design and Analysis*. ASME, New York.
- Balje, O. E. (1981). *Turbomachines: A Guide to Design, Selection and Theory*. Wiley, New York.
- Craig, H. R. M. and Cox, H. J. A. (1971). Performance estimation of axial flow turbines. *Proceedings of the Institution of Mechanical Engineers* 185, No.32: 407-423.
- Csanady, G. T. (1964). *Theory of Turbomachinery*. McGraw-Hill, Waterloo.
- DaLio, L., Manente, G., and Lazzaretto, A. (2014). New efficiency charts for the optimum design of axial flow turbines for organic rankine cycles. *Energy* 77: 447-459.
- Dunham, J. and Came, P. (1970). Improvements to the Ainley-Mathieson method of turbine performance prediction. *Trans. ASME Journal of Engineering for Power* 92: 252-256.
- Heberle, F. and Brüggemann, D. (2006). Exergy based fluid selection for a geothermal organic Rankine cycle for combined heat and power generation. *Applied Thermal Engineering* 30, 1326-1332.
- Kacker, S. C. and Okapuu, U. (1982). A mean line prediction method for axial flow turbine efficiency. *Trans. ASME Journal of Engineering for Power* 104: 111-119.
- Khennich, M. and Galanis, N. (2012). Optimal design of ORC systems with a low-temperature heat source. *Entropy* 14, 370-389.
- Lazzaretto, A. and Manente, G. (2014). A new criterion to optimize ORC design performance using efficiency correlations for axial and radial turbines. *International Journal of Thermodynamics Accepted for publication*.
- Lemmon, E. W., Huber, M. L., and McLinden, M. O. (2010). NIST standard reference database 23: reference fluid thermodynamic and transport properties-RERPROP, version 9.0. *National Institute of Standards and Technology, Standard Reference Data Program, Gaithersburg*.
- Li, S. M., Chu, T. L., Yoo, Y. S., and Ng, W. F. (2004). Transonic and low supersonic flow losses of two steam turbine blades at large incidences. *Trans. ASME Journal of Fluids Engineering* 126: 966-975.
- Lozza, G. (2006). *Turbine a gas e cicli combinati*. (In Italian). Progetto Leonardo, Bologna, Italy.
- Macchi, E. (1977). Design criteria for turbines operating with fluids having a low speed of sound. *Lecture Series n.100, Closed Gas Turbines, Von Karman Institute*.
- Macchi, E. and Perdichizzi, A. (1981). Efficiency prediction for axial flow turbines operating with nonconventional fluids. *Trans. ASME Journal of Engineering for Power* 103: 718-724.
- Moustapha, H., Zalesky, M. F., Baines, N. C., and Japikse, D. (2003). *Axial and Radial Turbines*. Concepts ETI.
- Sauret, E. and Rowlands, A. S. (2011). Candidate radial-inflow turbines and high-density working fluids for geothermal power systems. *Energy* 36, 4460-4467.
- Shepherd, D. (1956). *Principles of Turbomachinery*. The Macmillan Company, New York.
- Smith, S. F. (1965). A simple correlation of turbine efficiency. *Journal of Aeronautical Society* 69: 467-470.
- Tchanche, B. F., Papadakis, G., Lambrinos, G., and Frangoudakis, A. (2009). Fluid selection for a low-temperature solar organic Rankine cycle. *Applied Thermal Engineering* 29, 2468-2476.
- Toffolo, A., Lazzaretto, A., Manente, G., and Paci, M. (2014). A multi-criteria approach for the optimal selection of working fluid and design parameters in Organic Rankine Cycle systems. *Applied Energy* 121: 219-232.

ORC APPLICATIONS FROM LOW GRADE HEAT SOURCES

Bernardo Peris^{1*}, Joaquín Navarro-Esbrí^{1,2}, Francisco Molés¹, Adrián Mota-Babiloni^{1,3}

¹ISTENER Research Group. Jaume I University
Castellón de la Plana, Castellón, Spain
bperis@uji.es

²EXPANDER TECH, Campus de RiuSec s/n, E12071, Castellón, Spain

³Institute for Industrial, Radiophysical and Environmental Safety. Polytechnic University
Valencia, Spain

* Corresponding Author

ABSTRACT

The Organic Rankine Cycle (ORC) has been proven as an efficient way to benefit from low grade heat sources, with a great interest in waste heat recovery and use of renewable heat sources. In this way, this work deals about three different applications implemented in Spain. The first application consists of a power only system for industrial waste heat recovery, taking advantage from the exhaust air of a ceramic furnace to produce a rated electrical power of 20 kW. The second application is a Combined Heat and Power (CHP) system integrated as a bottoming power cycle of an Internal Combustion Engine (ICE), with the purpose to recover waste heat from exhaust gases. This system is installed in a hospital to increase the ICE electrical production and generate hot water up to 90 °C. The third application can operate producing power only or heat and power. In this last case, the ORC module is used to profit thermal energy from a biomass supported solar thermal system and producing a maximum electrical power about 6 kW and hot water above 80 °C.

Moreover, focusing on the ORC modules performance, experimental data obtained from tests developed under different operating conditions in the three application cases are analyzed and discussed.

1. INTRODUCTION

The ORC (organic Rankine cycle) has been proven as an efficient way for power generation from low grade heat sources (Yamada *et al.*, 2014). It is a similar power cycle to the steam Rankine cycle, but uses more volatile fluids instead of water to improve the efficiency in low temperature applications (Li *et al.*, 2012). Its operating principle consists of recovering the thermal energy from the heat source through the evaporation of the working fluid and reducing the enthalpy in an expander to produce mechanical work, which is turned into electricity by an electric generator. This is a closed system, which condenses the vapor from the expander outlet and pressurizes the liquid to restart the cycle again. So, it is considered a simple cycle that requires little maintenance, compared to other power cycles like Kalina (Bombarda *et al.*, 2010), Goswami, transcritical cycle or trilateral-flash cycle (Chen *et al.*, 2010); in addition to its mature and proven technology against direct conversion techniques (thermo-electric, thermionic or piezoelectric) (Tchanche *et al.*, 2011).

The application of ORC systems are mainly focused on renewable and waste heat sources, with several examples like: solar thermal (M. Wang *et al.*, 2013), geothermal (Franco, 2011), oceanic (Tchanche *et al.*, 2011), biomass (Algieri & Morrone, 2012), waste heat from power plants (Dolz *et al.*, 2012), waste heat from industrial processes (D. Wang *et al.*, 2012) or others (H. Wang *et al.*, 2011).

Moreover, the ORC systems can be used for combined heat and power applications. Thus, the ORC can be used as a power only generation system (Yamada *et al.*, 2014), recovering the thermal energy from the heat source to produce electricity with the maximum efficiency achievable and rejecting the thermal energy from the condenser to the cold side. On the other hand, the thermal energy from the condenser also could be produced with a profitable temperature for users, reducing the electrical efficiency of the system, but increasing its global efficiency (Dentice d'Accadia *et al.*, 2003). Thereby, the ORC operates as a combined heat and power (CHP) system, requiring lower primary energy consumptions compared to a separate heat and power production, besides reducing global energy costs and pollutant emissions to the atmosphere.

Regarding to the ORC use for power applications, various studies can be found in the literature. So, Zhou *et al.* (2013) tested an ORC for waste heat recovery from flue gases. The authors used a liquefied petroleum gas stove to simulate the heat source and to control the temperature in the range of 90 to 220 °C. The working fluid selected was R123 and a scroll expander, obtaining a maximum power output of 0.645 kW and a cycle efficiency of 8.5 %. Bracco *et al.* (2013) tested a small-size ORC, that used R245fa as working fluid and a scroll expander, for waste heat recovery. The heat source was simulated using an electric boiler, achieving a cycle efficiency between 8 and 9 %. Casci *et al.* (1981) used an ORC, with a rated electrical power of 40 kW, in a ceramic kiln to profit from flue gas waste heat. Forni *et al.* (2012) summarized various analysis of an ORC manufacturer in cement, glass, steel and oil&gas industries. The net electrical production went from 7.6 to 39.2 GWh/y, allowing payback periods from 7.2 to 9.2 years.

With respect to the ORC use for CHP applications, a great interest has received for residential and commercial applications. In this way, Dong *et al.* (2009) reviewed small and micro-scale biomass-fuelled CHP systems, comparing the ORC to other conversion technologies. The researchers pointed that the ORC encounters technical and economical obstacles, in comparison to medium and large-scale systems, requiring to reduce the specific investment cost and increment the electrical and CHP efficiencies. Experimental results obtained in a preliminary investigation were presented by Farrokhi *et al.* (2014) about a gas-fired ORC-based micro-CHP system for residential buildings. Thereby, using isopentane as working fluid and a vane type of expander, a maximum electrical power output of 0.774 kW and a net cycle electrical efficiency of 1.66% were achieved. Similarly, Qiu *et al.* (2012) experimented with a biomass-pellet boiler and an ORC for micro-CHP applications, by heating to 46 °C the cooling water of the condenser outlet. The main working fluid used was HFE7000 and, again, a vane type of expander. So, 0.861 kW were generated with a gross electrical efficiency of 1.41% and a CHP efficiency of 78.69%. Declaye *et al.* (2013) characterized an oil-free scroll expander using R245fa as working fluid, showing that the cycle could produce up to 50 °C of useful heat, a maximum shaft power of 2.1 kW and mechanical efficiency of 8.5%.

From the reviewed information, different applications and uses for the ORC can be observed. However, few works address the final application of the ORC and its experimental performance when a commercial module is used. In this way, this work deals about three different ORC applications implemented in Spain. The first application consists of using an ORC as a power only system, the second one uses the ORC as a CHP system and the last application was designed to operate with the ORC in both modes, power only and CHP. Thereby, these applications are addressed in this paper. Moreover, experimental data obtained from the tests developed in each ORC module are exposed and discussed.

For this purpose, the rest of the paper is organized as follows. Section 2 presents the three application cases. Section 3 describes the main characteristics of the ORC modules. Section 4 exposes the main results of the experimental characterization. Finally, Section 5 summarizes the main conclusions of the work.

2. APPLICATIONS DESCRIPTION

This section describes the three applications addressed in this work.

2.1 Power only application

This application consists of profiting waste heat from exhaust gases of a ceramic furnace. Specifically, recovering the waste heat available in the indirect cooling air, which are clean gases with high temperature, due to its proximity to the furnace burners the furnace. The recovery facility is mainly composed by a recuperator heat exchanger, located in a bypass of the cooling air duct, and a heat transfer loop with thermal oil that transports the thermal energy from the heat source to the ORC module, as Fig. 1.a to Fig. 1.c show. Moreover, Fig. 1.d shows the scheme of the facility.

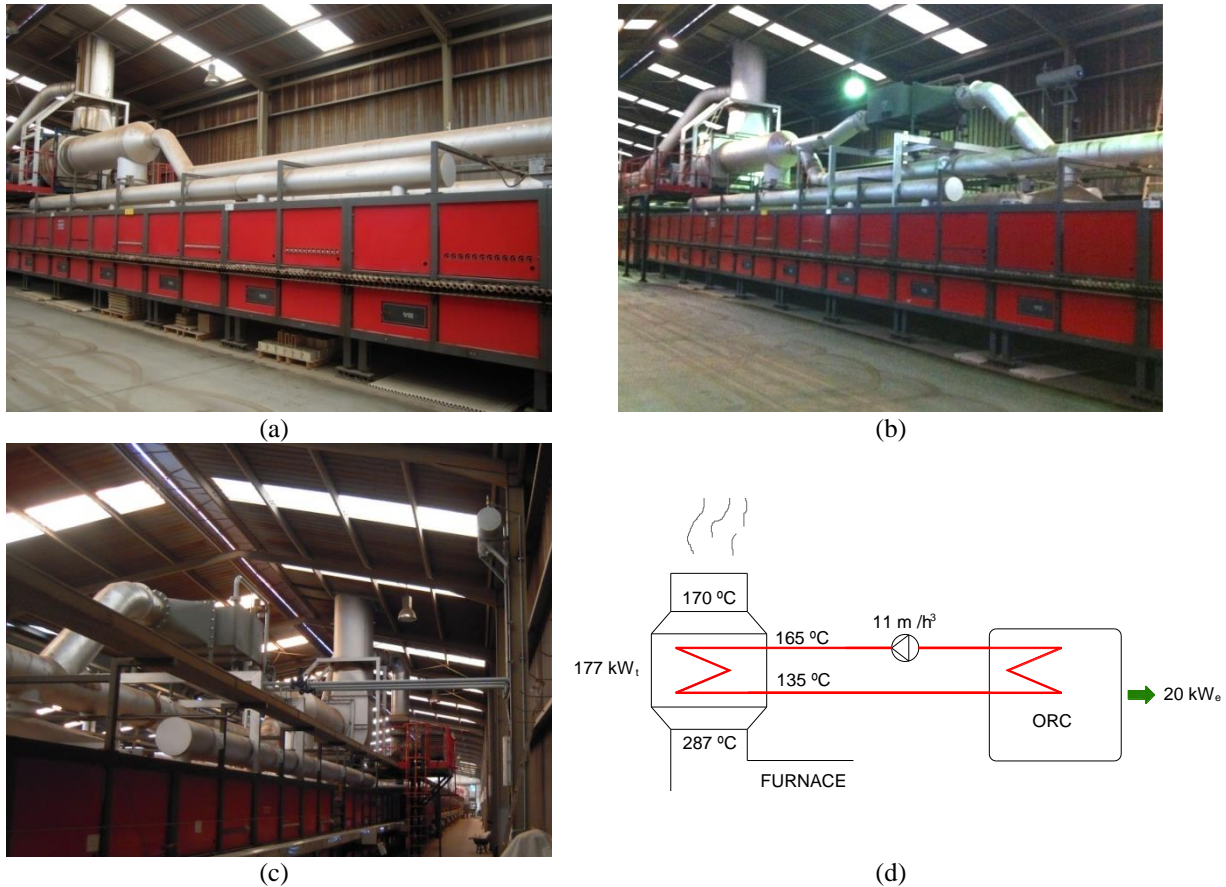


Figure 1: Industrial furnace of Keros Ceramica and heat recovery facility: (a) original facility, (b) modified facility, (c) heat transfer loop, (d) facility scheme.

The main features of the recuperator heat exchanger are listed in Table 1. This heat exchanger was designed to recover a thermal power of 177 kW from the heat source and provide thermal oil at 165 °C to the ORC module.

Table 1: Recuperator heat exchanger features.

Thermal capacity (kW)	177
Air volumetric flow rate (Nm ³ ·s ⁻¹)	1.15
Air temperatures (°C)	287/170
Oil temperatures (°C)	135/165
Air pressure drop (mbar)	1.90
Thermal oil pressure drop (bar)	0.8
Surface (m ²)	65.6

2.2 Combined heat and power application

The original facility consisted of an Internal Combustion Engine (ICE) for a CHP application in a hospital located in Ourense (Spain). This ICE was designed to provide a rated electrical power of 1,200 kW and up to 400 kW of useful heat from the exhaust gases, as Fig. 2.a represents. Then, the aim of the project was to replace the heat exchanger by an ORC system, producing a similar useful heat, at the same temperature of 90 °C, and more electricity, as Fig. 2.b represents.

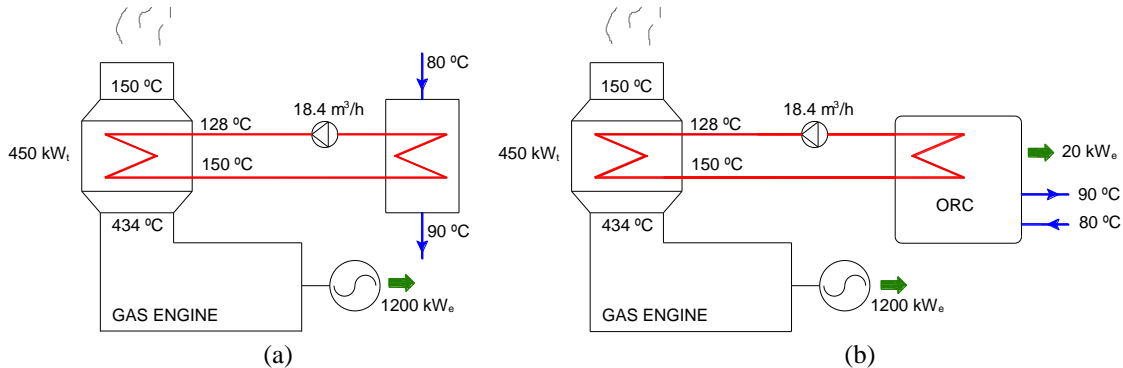


Figure 2: Heat source of the ORC system: (a) scheme of the original facility with heat exchanger, (b) scheme of the improved facility through ORC.

The main features of the recuperator heat exchanger, integrated in the chimney, are listed in Table 2. This heat exchanger was designed to recover a thermal power of 450 kW from the heat source and provide pressurized water at 150 °C to the ORC module.

Table 2: Recuperator heat exchanger features.

Thermal capacity (kW)	450
Exhaust gas flow rate (kg/h)	5,191
Exhaust gas temperatures (°C)	434/150
Pressurized water temperatures (°C)	128/150
Exhaust gas pressure drop (mbar)	17
Pressurized water pressure drop (mbar)	50
Surface (m ²)	76

2.3 Power and CHP application

This system was designed to operate with renewable heat sources, specifically a biomass supported solar thermal system. Thus, the ORC should operate efficiently in both modes, power only generation and CHP production.

A typical architecture of the facility in which the ORC is integrated is illustrated in Fig. 3.a. Fig. 3.b shows the scheme of the facility. Furthermore, the design specifications from customers of this module are listed in Table 3.

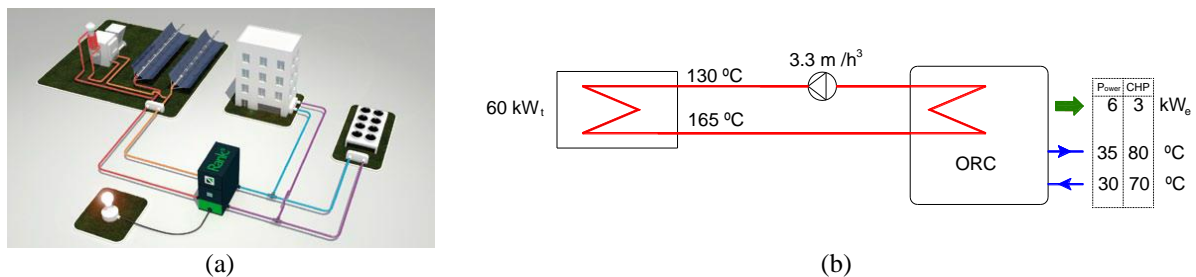


Figure 3: Power and CHP applications: (a) typical architecture, (b) facility scheme.

Table 3: Design specifications.

Thermal power input (kW)	60
Thermal fluid	Oil or Water-glycol (10%)
Inlet temperature of the thermal fluid (°C)	165
Inlet temperature of cooling water in generation mode (°C)	30
Inlet temperature of cooling water in CHP mode (°C)	70

3. ORC MODULES DESCRIPTION

This section describes the main characteristics of the ORC modules, shown in Fig. 4, addressing the cycle configuration, working fluid, expander and dissipation system.

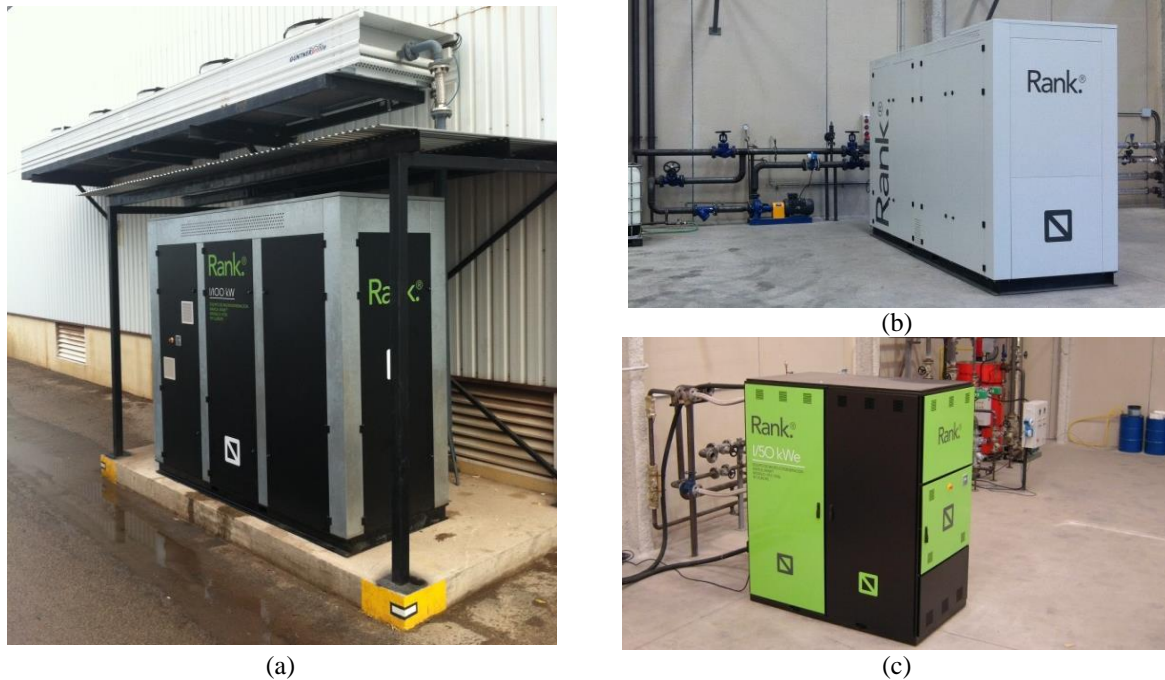


Figure 4: ORC modules: (a) Power generation system integrated in the industrial application, (b) CHP system during tests, (c) Power only and CHP system during tests.

3.1 Cycle configuration and working fluid

All the ORC systems used in these applications are commercial modules from Rank®, whose main characteristics are summarized in Table 4. In these studied cases, the modules employ the same architecture and use the same working fluid. Regarding to the architecture, the regenerative configuration is used. This configuration allows recovering the thermal energy from the heat source, besides the waste heat from the expander outlet to preheat the liquid, improving the cycle electrical efficiency. The working fluid used is R245fa, commonly used among ORC manufacturers (Vélez *et al.*, 2012) and the researches reviewed. This is a non flammable fluid with low toxicity and moderate environmental properties, which also has been proven as an efficient fluid for low grade waste heat recovery (Peris *et al.*, 2013). However, the characteristics of the expander differ in function of each application.

Table 4: Main characteristics of the ORC modules used.

Cycle configuration	subcritical, regenerative with superheating
Working fluid	R245fa
Expander technology	volumetric
Heat exchangers type	brazed plate
Maximum operating temperature (°C)	170
Maximum dissipating temperature (°C)	90

3.2 Expander

The ORC modules use rotary volumetric expanders, whose sizes, speeds and volume ratios (V_i) have been optimized to achieve the maximum efficiency during the operating point, established as design conditions. In this way, Table 5 collects the maximum efficiency ($\varepsilon_{el, ise}$) of the expanders and the pressure ratio (r_p) in which it was achieved. As it can be seen, the ORC designed for the power application operates efficiently at a high pressure ratio (Peris *et al.*, 2015a). In contrast, the ORC designed for the CHP application only operates efficiently at low pressure ratios. On the other hand, the third application can operate with an intermediate efficiency in both modes, being a suitable solution for a flexible system.

Table 5: Experimental expander efficiencies and its associated pressure ratios.

	$\varepsilon_{el, ise}$ (%)	r_p	References
Power application	64.89	7.93	(Peris <i>et al.</i> , 2015b)
CHP application	68.54	2.61	(Peris <i>et al.</i> , 2015c)
Power and CHP	63.77	4.10	(Peris <i>et al.</i> , 2015d)

3.3 Dissipation system

The dissipation system varies in function of the type of application. So, in a power application the thermal energy from the condenser is rejected to the ambient. For this, the dissipation system was directly implemented through an air condenser, previously shown in Fig. 4.a. This system allows reducing exergetic losses compared to a dry cooler with cooling water, besides simplifying the scheme, since there is not required another pump nor its associated safety and control devices.

On the other hand, in a CHP application the thermal energy from the condenser is considered as useful heat for users. So, the hot water from the outlet of the condenser could directly feed consumers. In order to simulate this consumption, a dry cooler with cooling water was used during tests. Thereby, reducing the dry coolers fans velocity, the condensing temperature was controlled. So, both modes, power, with fans at full velocity, and CHP, with fans at reduced velocity, were simulated during tests. The dissipation systems used in the tests are shown in Fig. 5.

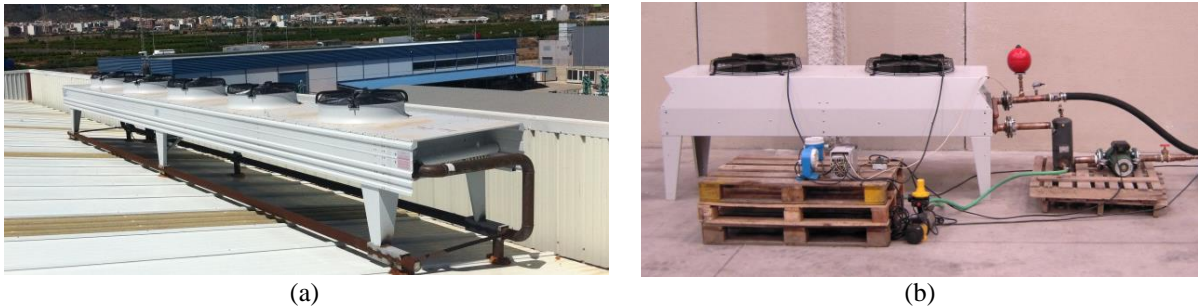


Figure 5: Dissipation systems: (a) CHP system, (b) power and CHP system.

4. RESULTS

In this section, the gross electrical efficiency of the cycle (η_g) and the expander electrical isentropic effectiveness ($\varepsilon_{el, ise}$) obtained during tests are presented and discussed.

Regarding to the ORC for power applications, Fig. 6.a shows that a maximum gross electrical efficiency of 12.47% is obtained. This efficiency is reached with a pressure ratio about 8, being a system optimized for its operating conditions. Moreover, Fig. 6.b shows that the expander operates with a stable effectiveness for high pressure ratios.

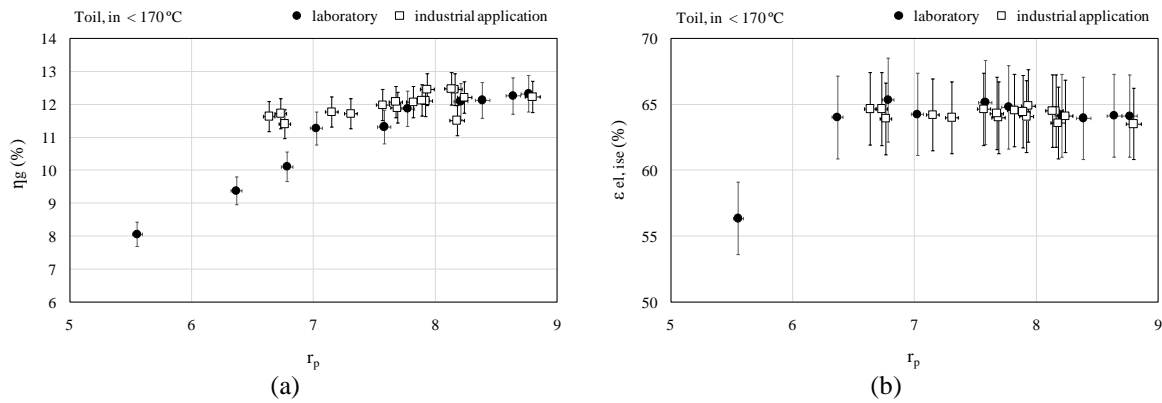


Figure 6: ORC for power applications: (a) gross electrical efficiency, (b) expander electrical isentropic effectiveness.

Regarding to the ORC for CHP applications, Fig. 7.a shows that a maximum gross electrical efficiency of 9.40% is obtained. This low value, compared to the latter, is mainly due to the different expander used. So, Fig. 7.b shows that the expander is optimized for a pressure ratio between 2-3, which is a suitable value to operate in CHP applications, but a poor value for power only generation.

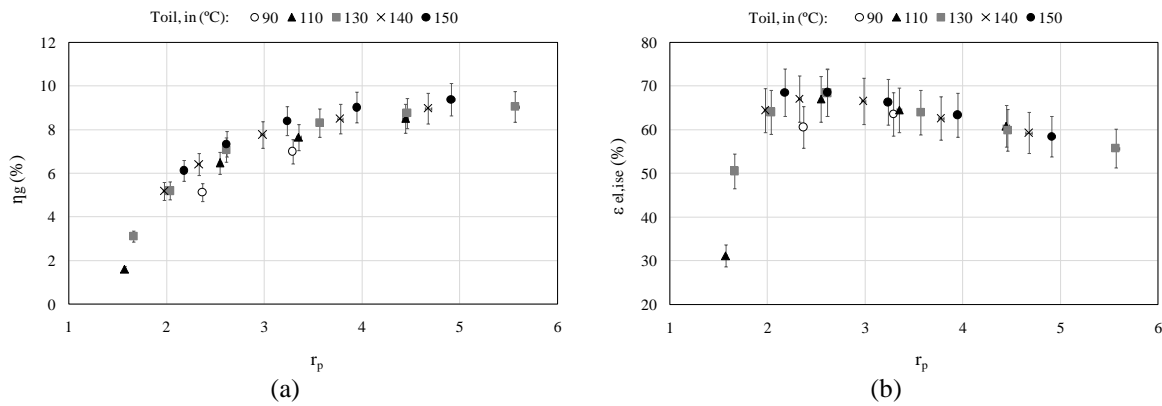


Figure 7: ORC for CHP applications: (a) gross electrical efficiency, (b) expander electrical isentropic effectiveness.

As it has been said above, the third application was designed using an expander with an intermediate V_i , that allows the operation in both modes, power only and CHP. Thereby, Fig. 8.a shows that the maximum value of electrical efficiency remains between the two previous ORC systems, with a maximum of 10.64%. The electrical effectiveness of the expander was maximized for a pressure ratio above 4, as Fig. 8.b shows, being a module suitable to operate with a moderate efficiency in both modes, but not optimized in comparison with the previous two modules.

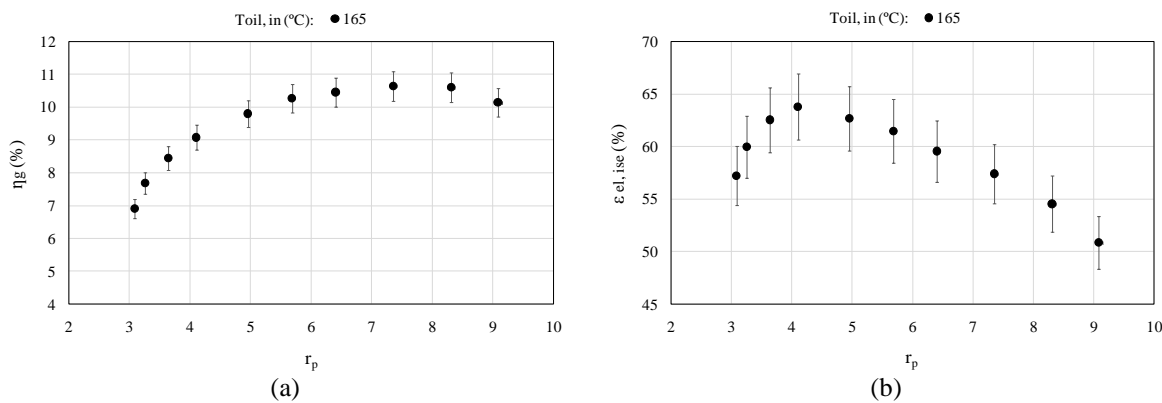


Figure 8: ORC for power and CHP applications: (a) gross electrical efficiency, (b) expander electrical isentropic effectiveness.

5. CONCLUSIONS

This work deals about three different applications developed using ORC systems in Spain. For this, the heat source, dissipation system and the main characteristics of the ORC are addressed. Moreover, the main results of the experimental characterization of each module are presented and analyzed.

In this way, the results show that the expander plays a key role in the optimization of a system for a specific application. So, a large V_i is recommended to operate in power applications, demonstrating a gross electrical efficiency of 12.47% with activation temperatures about 165°C. A small V_i is preferable for CHP applications, being able to provide hot water up to 90 °C with an acceptable gross electrical efficiency of 9.40%, with activation temperatures about 150°C. However, if the system requires operating in both modes, power and CHP, an intermediate V_i results a suitable solution. So, the experimental data show a maximum gross electrical efficiency of 10.64% with activation temperature about 165°C.

NOMENCLATURE

ε	effectiveness (%)
η	efficiency (%)
r_p	pressure ratio
V_i	built-in volume ratio

Subscripts

el	electrical
g	gross
ise	isentropic

REFERENCES

- Algieri, A., & Morrone, P., 2012, Comparative energetic analysis of high-temperature subcritical and transcritical Organic Rankine Cycle (ORC). A biomass application in the Sibari district, *Applied Thermal Engineering*, 36, 236–244.
- Bombarda, P., Invernizzi, C. M., & Pietra, C., 2010, Heat recovery from Diesel engines: A thermodynamic comparison between Kalina and ORC cycles, *Applied Thermal Engineering*, 30(2-3), 212–219.
- Bracco, R., Clemente, S., Micheli, D., & Reini, M., 2013, Experimental tests and modelization of a domestic-scale ORC (Organic Rankine Cycle), *Energy*, 58, 107–116.
- Casci, C., Angelino, G., Ferrari, P., Gaia, M., Giglioli, G., & Macchi, E., 1981, Heat recovery in a ceramic kiln with an organic rankine cycle engine, *Journal of Heat Recovery Systems*, 1, 125–131.
- Chen, H., Goswami, D. Y., & Stefanakos, E. K., 2010, A review of thermodynamic cycles and working fluids for the conversion of low-grade heat, *Renewable and Sustainable Energy Reviews*, 14(9), 3059–3067.
- Declaye, S., Quoilin, S., Guillaume, L., & Lemort, V., 2013, Experimental study on an open-drive scroll expander integrated into an ORC (Organic Rankine Cycle) system with R245fa as working fluid, *Energy*, 55, 173–183.
- Dentice d'Accadia, M., Sasso, M., Sibilio, S., & Vanoli, L., 2003, Micro-combined heat and power in residential and light commercial applications, *Applied Thermal Engineering*, 23, 1247–1259.
- Dolz, V., Novella, R., García, a., & Sánchez, J., 2012, HD Diesel engine equipped with a bottoming Rankine cycle as a waste heat recovery system. Part 1: Study and analysis of the waste heat energy, *Applied Thermal Engineering*, 36, 269–278.
- Dong, L., Liu, H., & Riffat, S., 2009, Development of small-scale and micro-scale biomass-fuelled CHP systems - A literature review, *Applied Thermal Engineering*, 29(11-12), 2119–2126.

- Farrokhi, M., Noie, S. H., & Akbarzadeh, a. a., 2014, Preliminary experimental investigation of a natural gas-fired ORC-based micro-CHP system for residential buildings, *Applied Thermal Engineering*, 69(1-2), 221–229.
- Forni, D., Vaccari, V., Santo, D. Di, & Baresi, M., 2012, Heat recovery for electricity generation in industry, ECEE 2012 Summer Study on Energy Efficiency in Industry, 523–534.
- Franco, A., 2011, Power production from a moderate temperature geothermal resource with regenerative Organic Rankine Cycles, *Energy for Sustainable Development*, 15(4), 411–419.
- Li, J., Pei, G., Li, Y., Wang, D., & Ji, J., 2012, Energetic and exergetic investigation of an organic Rankine cycle at different heat source temperatures, *Energy*, 38(1), 85–95.
- Peris, B., Navarro-Esbrí, J., & Molés, F., 2013, Bottoming organic Rankine cycle configurations to increase Internal Combustion Engines power output from cooling water waste heat recovery, *Applied Thermal Engineering*, 61(2), 364–371.
- Peris, B., Navarro-Esbrí, J., Molés, F., Mota-Babiloni, A., 2015, Experimental study of an ORC (organic Rankine cycle) for low grade waste heat recovery in a ceramic industry, *Energy*, doi:10.1016/j.energy.2015.03.065.
- Peris, B., Navarro-Esbrí, J., Molés, F., Collado, R., & Mota-Babiloni, A., 2015, Performance evaluation of an Organic Rankine Cycle (ORC) for power applications from low grade heat sources, *Applied Thermal Engineering*, 75, 763–769.
- Peris, B., Navarro-Esbrí, J., Molés, F., González, M., & Mota-Babiloni, A., 2015, Experimental characterization of an ORC (organic Rankine cycle) for power and CHP (combined heat and power) applications from low grade heat sources, *Energy*, 82, 269–276.
- Peris, B., Navarro-Esbrí, J., Molés, F., Martí, J. P., & Mota-Babiloni, A., 2015, Experimental characterization of an Organic Rankine Cycle (ORC) for micro-scale CHP applications, *Applied Thermal Engineering*, 79, 1–8.
- Qiu, G., Shao, Y., Li, J., Liu, H., & Riffat, S. B., 2012, Experimental investigation of a biomass-fired ORC-based micro-CHP for domestic applications, *Fuel*, 96, 374–382.
- Tchanche, B. F., Lambrinos, G., Frangoudakis, a., & Papadakis, G. (2011), Low-grade heat conversion into power using organic Rankine cycles - A review of various applications, *Renewable and Sustainable Energy Reviews*, 15, 3963–3979.
- Vélez, F., Segovia, J. J., Martín, M. C., Antolín, G., Chejne, F., & Quijano, A., 2012, A technical, economical and market review of organic Rankine cycles for the conversion of low-grade heat for power generation, *Renewable and Sustainable Energy Reviews*, 16(6), 4175–4189.
- Wang, D., Ling, X., & Peng, H., 2012, Performance analysis of double organic Rankine cycle for discontinuous low temperature waste heat recovery, *Applied Thermal Engineering*, 48, 63–71.
- Wang, H., Peterson, R., & Herron, T., 2011, Design study of configurations on system COP for a combined ORC (organic Rankine cycle) and VCC (vapor compression cycle), *Energy*, 36(8), 4809–4820.
- Wang, M., Wang, J., Zhao, Y., Zhao, P., & Dai, Y., 2013, Thermodynamic analysis and optimization of a solar-driven regenerative organic Rankine cycle (ORC) based on flat-plate solar collectors, *Applied Thermal Engineering*, 50(1), 816–825.
- Yamada, N., Tominaga, Y., & Yoshida, T., 2014, Demonstration of 10- W p micro organic Rankine cycle generator for low-grade heat recovery, *Energy*, 78, 806–813.
- Zhou, N., Wang, X., Chen, Z., & Wang, Z., 2013, Experimental study on Organic Rankine Cycle for waste heat recovery from low-temperature flue gas, *Energy*, 55, 216–225.

ACKNOWLEDGEMENT

The authors are indebted to the Minister of industry of ‘GeneralitatValenciana’ (Spain) for its financial assistance under project INIDIV2010022 and Rank®, the ORC manufacturer, for its support in this project. Also to thank greatly the Jaume I University for its financial support under the PhD grant PREDOC/2013/28 of ‘Convocatòriad’ajudespredoctorals per a la formació de personal investigadordelPla de promoció de la investigació de la UniversitatJaume I de Castelló (Spain)’.

TESTING AND MODELING A VANE EXPANDER USED IN AN ORC WORKING WITH HEXAMETHYLDISILOXANE (MM)

Vaclav Vodicka^{1*}, Ludovic Guillaume², Jakub Mascuch³ and Vincent Lemort⁴

^{1,3} University Centre for Energy Efficient Buildings
Czech Technical University in Prague
Trinecka 1024, 273 43 Bustehrad
Czech Republic

¹ e-mail: vaclav.vodicka@uceeb.cz

³ e-mail: jakub.mascuch@uceeb.cz

^{2,4} Thermodynamics Laboratory
University of Liège
Campus du Sart Tilman, B49, 4000 Liège
Belgium

² e-mail: ludovic.guillaume@ulg.ac.be

⁴ e-mail: vincent.lemort@ulg.ac.be

* Corresponding Author

ABSTRACT

Waste heat from industrial production carries considerable potential for further use. Organic Rankine Cycle (ORC) brings a possibility to produce electrical energy from heat, originally intended to be released to the surroundings. For ORC systems with power output up to 10 kW, small-scale turbines are still expensive to manufacture and their use can be problematic in terms of high shaft speed or quality of inlet vapor. It is therefore preferable to use positive displacement expanders. The first part of this paper presents and analyses the measurements conducted on a prototype of vane expander. This vane expander characterized by a 1 kW power output operates in an ORC heat engine that uses hexamethyldisiloxane as a working fluid. The expander inlet temperature varies approximately from 135 °C to 150 °C, inlet pressure varies approximately from 200 to 300 kPa abs, isentropic efficiency from 0.4 to 0.58. The second part of the paper proposes a grey-box model, which is calibrated on the base of the measured data. This lumped-parameter model takes into consideration major losses of the expander: supply and discharge pressure losses, under and over-expansion, internal leakages and mechanical losses. The model is finally used to assess the impact of each source of losses on the overall performance of the expander.

1. INTRODUCTION

ORC technology seems to be a promising solution for waste heat recovery (WHR) and combined heat and power (CHP) generation especially in a small scale (up to 10 kW_{el}). Waste heat can be recovered from many industrial processes or combustion engines; small scale CHP units for households and small businesses fit into the concept of smart grids. Rising amount of publications focused on devices with low power output shows strong importance of this topic. According to Qiu et al. (2011) the use of positive displacement expanders especially scroll or vane type is a good choice for low power ORC applications because of their low cost and good efficiency over a wide range of operating conditions. One of the most noticeable advantages of positive displacement expanders is insensitivity on a quality of admission vapor compared to turbine technology. This allows a simplification of design of a cycle and its controlling algorithms. Only a few recently published papers (e.g. Cipollone, 2014, Xia, 2013,

Yang, 2008) present experimental measurement and evaluation of sliding vane expanders. This paper presents an experimental characteristics of a sliding vane expander used in an ORC operating with hexamethyldisiloxane (MM) as a working fluid. This ORC was built and is operated at University Centre for Energy Efficient Buildings (UCEEB) at Czech Technical University (CTU) in Prague. Ongoing project at UCEEB are focused on market favorable technology especially in terms of specific cost. Various topics related to decentralized power generation were in focus at Faculty of Mechanical Engineering (FME) at CTU in Prague. Both technical and economic issues were investigated. Current experimental work at UCEEB is based on nearly 6 years experiences from ORC construction and its operation at FME. According to economic analysis presented by Mascuch and Dlouhy (2011) a new approach to low power ORC design was developed at FME. Small CHP unit with a biomass boiler was built and operated. Boiler was separated from ORC by thermal oil circuit. Isopropylbenzene was used as a working fluid. Many engineering challenges had to be solved during this work. In general, this type of design was not successful. It was found out that the ORC has to be redesigned to be as simple as possible for the future commercial success. Total gross electrical efficiency was about 5.7% and a vane expander reached 38% of thermodynamic efficiency. Numbers were more than 50% lower than design estimations.

2. DESCRIPTION OF EXPERIMENTAL ORC TEST RIG

The experimental test rig with organic Rankine cycle at UCEEB is used for testing not only single components but also the whole cycle. Its scheme is shown in figure 1. ORC is designed as single-circuit. In the working fluid (MM) is dissolved about 5% of lubricating oil. Heat input to the cycle is approximately 20-23 kW. Main components are the evaporator, the expander, the condenser, the condensate receiver and the feed pump. Evaporator is a spiral tube exchanger. Flue gas from diesel burner is used as a source of heat. Flue gas inlet temperature ranges between 370 °C and 410 °C, outlet temperature is between 100°C and 130°C.

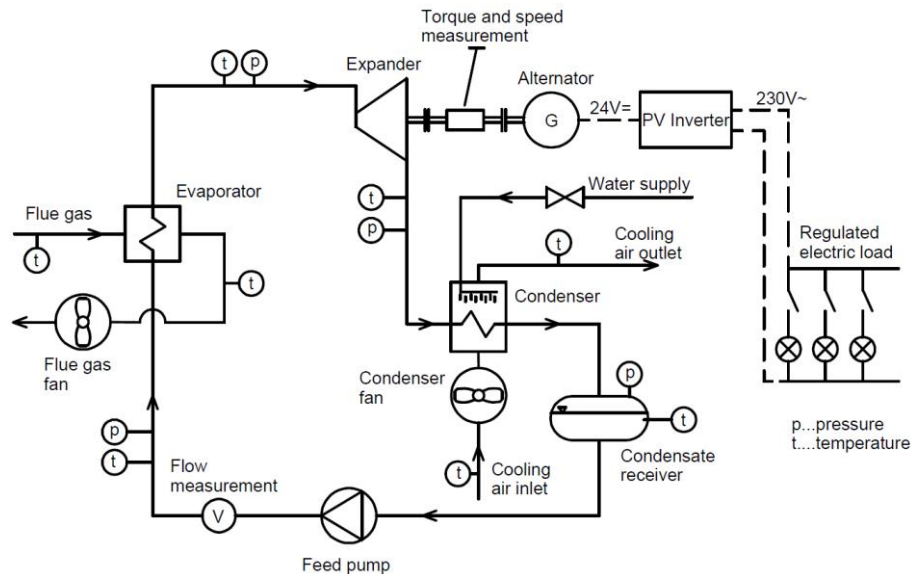


Figure 1: Scheme of the test rig

Generated vapor comes into a vane expander of own design. The expander is connected directly with the evaporator without any control valve. The expander drives a 24 VDC automotive alternator, which is connected with a common photovoltaic inverter. Bulbs with a total power consumption of 635 W are used as an electric load. Regulation step is 5 W. It is possible to connect additional load with constant power consumption as well. Condenser is similar to evaporator. It is a spiral tube exchanger designed with focus on low pressure drop. Condensation occurs inside the tubes. Condenser is air-cooled; fan speed is regulated by frequency inverter. Cooling air temperature at the inlet was about

30 – 35 °C. Water sprinkler that improves the cooling performance of the condenser was mounted above the condenser to decrease the condensing pressure even more. Condenser is followed by condensate receiver under which is placed a gear pump. The pump is connected with an asynchronous motor with nominal speed of 1500 RPM. Speed can be regulated with frequency inverter. Maximum flow is 8.5 l/min at nominal speed.

Position of all sensors can be seen in figure 1. The test rig allows measurement of temperatures at important points of the cycle, pressures, volumetric flow at the pump outlet, shaft speed of the expander and torque. Temperature of the flue gas at evaporator inlet and outlet and cooling air temperature at condenser inlet and outlet is also measured. Unfortunately it is not possible to measure the flow of flue gas and cooling air reliably. All the temperatures are measured with Pt100 sensors. Pressures are measured with common industrial piezoresistive pressure transducers. Turbine flow meter with pulse output is used for measurement of volumetric flow. Torque and speed is measured within one sensor – speed with pulse output, torque with bridge strain gauge with transducer. The data from the sensors are collected with common industrial PLC. Table 1 summarizes accuracy of used sensors.

Sensor	Range	Accuracy
Pressure - low pressure side	(0-400) kPa abs.	±0.5% f.s.
Pressure - high pressure side	(0-1000) kPa abs.	±0.5% f.s.
Temperature	(-196 - +600) °C	±(0.30°C+0.005 t)
Volumetric flow	(1-10) l/min	±3% of reading
Torque	(0-30) Nm	±0.2% f.s.
Speed	(0-15000) RPM	±0.2% f.s.

Table 1: Range and accuracy of used sensors

Different working conditions can be reached in several ways. The shaft speed of expander can be regulated by switching the electric bulbs on and off. Decrease in the electric load results in torque reduction of alternator and shaft speed increase. Superheating of vapor can be influenced by changing the speed of pump. Lower speed leads to lower flow rate through the evaporator and larger superheating. Pressure in condenser and isentropic enthalpy gradient of expander can be influenced by changing the speed of the condenser fan and by use of the additional cooling with the water sprinkler. Performance of diesel burner slightly varied during the experiments due to decreasing of the level of fuel in a tank. Unfortunately this phenomenon cannot be controlled.

3. PROTOTYPE OF VANE EXPANDER

Expander is one of the most important components of the ORC. Its performance has significant impact on the efficiency of the whole cycle. As already written, expansion is ensured by the vane expander. This prototype was designed and built because there is no commercially available and cheap expander with a low power output of several kW. Vane expander was selected because of simple design, low manufacturing costs, reliability and possibility of reaching good thermodynamic efficiency in case of optimal design (Aoun, 2008). Design of tested expander is shown in figure 2. Expander is semi-hermetical; torque transmission is ensured by a magnetic coupling with permanent magnets. Stator is designed as a monoblock, in which a cylindrical working space, space for bearings and inlet and outlet chamber are milled. Supply and exhaust of the working fluid is radial. Rotor faces with bearings are mounted to the rotor with bolts. The bearings are placed in the stator with radial clearance, the axial movement of rotor is allowed. Rotor faces have grooves which serve for guiding the vanes during rotation. Rotor faces also create boundary of the working chambers. All the parts of the expander are made of stainless steel except the vanes, which are made of graphite. Expander has 8 working chambers with displacement of 7.66 cm³ per one chamber. Nominal built-in volumetric expansion ratio is 3. Expander is designed to produce 1 kW of mechanical power with overall efficiency of 0.41 at the nominal conditions of the cycle. Nominal shaft speed is 3020 RPM.

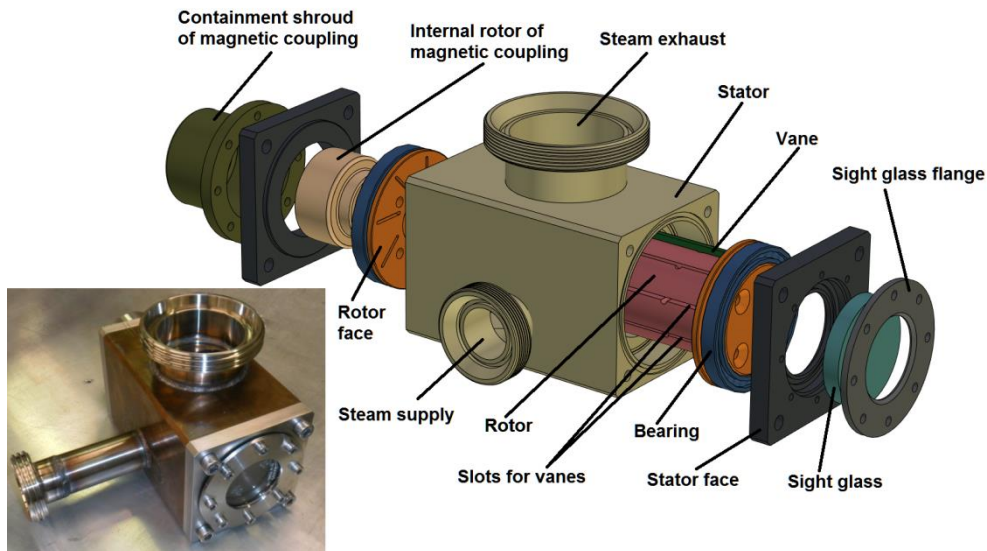


Figure 2: Design of the vane expander

It is necessary to ensure permanent contact of vanes with the inner stator surface for a proper function of the expander so that the working chambers are separated and there is no flow between adjacent chambers. Vanes are drawn out due to centrifugal force but only in case that this force is greater than a force resulting from the pressure difference above and below the vanes. Force resulting from pressure difference can be much higher than the centrifugal force especially during the initial phase of expansion. Therefore each slot for the vane in the stator has two milled grooves which connect working chamber with the space below the vane to balance the pressures. Similar solution is described by Peterson and McGahan (1972) for a vane compressor with the difference that the grooves are milled in the vanes. Another solution is to use the springs below the vanes as described e.g. by Yang *et al.* (2008).

4. EXPERIMENTAL CAMPAIGN

The measured data were recorded every second during the experiments. They were evaluated always in steady states. All the recorded values were averaged at each stable state with a period of 3 to 7 minutes. 60 steady states were captured and evaluated.

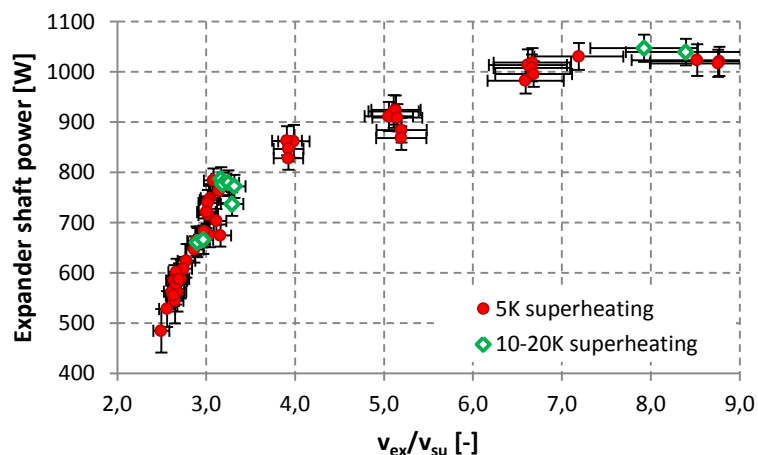


Figure 3: Measured values of expander shaft power

Admission temperature ranged from 135 to 157°C, admission pressure from 221 to 296 kPa abs., discharge pressure from 27 to 117 kPa abs. Superheating of admission vapor was maintained

at 5 K ($\pm 0.5K$) during most of measurements. Several states were measured with the superheating of 10-20 K. Figure 3 shows dependence between expander shaft power and a ratio of specific volume of vapor at expander outlet and inlet (v_{ex}/v_{su}). It can be seen that the performance rises rapidly in the area where $v_{ex}/v_{su} = 2.5-3.2$.

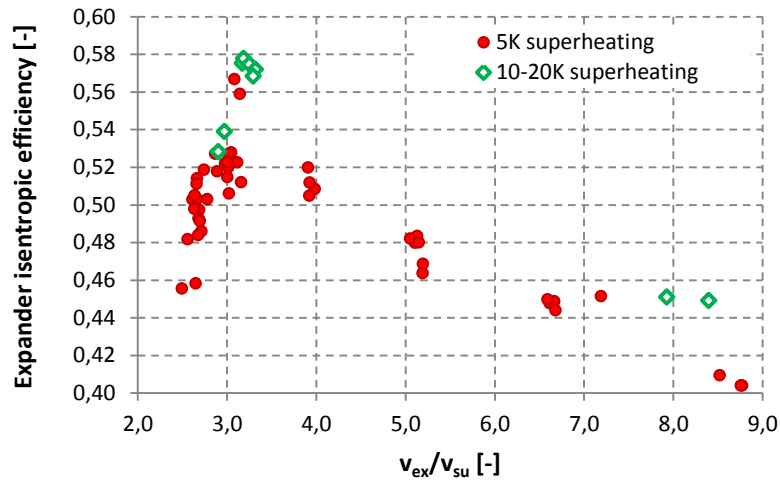


Figure 4: Expander isentropic efficiency vs. v_{ex}/v_{su}

The expander isentropic efficiency defined in equation 1 is shown in figure 4.

$$\eta_s = \frac{\dot{W}_{shaft}}{\dot{M}_{wf} \cdot (h_{su} - h_{ex,s})} \quad (1)$$

Rapid increase of efficiency can be seen in the same range of values v_{ex}/v_{su} . The highest values of expander efficiency are at $v_{ex}/v_{su} = 3.2$. This value approximately corresponds to the built-in volumetric expansion ratio of the expander ($r_{v,in}=3$). The efficiency falls in case that the value v_{ex}/v_{su} is higher than approximately 3.5. Performance of the expander ranged from 480 to 1050 W. Expander efficiency ranged from 0.4 to 0.58. Efficiency curve corresponds to the theoretical model. Fluctuation of values of efficiency is caused mainly because of a fluctuation of speed and, to a lesser extent, probably due to other effects. The points with superheating of 10-20 K are also highlighted in the graph in fig. 4. Only 10 stable states were measured in these conditions. It can be seen that the higher superheating mean higher efficiency in all cases. However, this fact is needed to be confirmed by further measurements. The dependence between expander efficiency and admission vapor superheating should be also measured in the future.

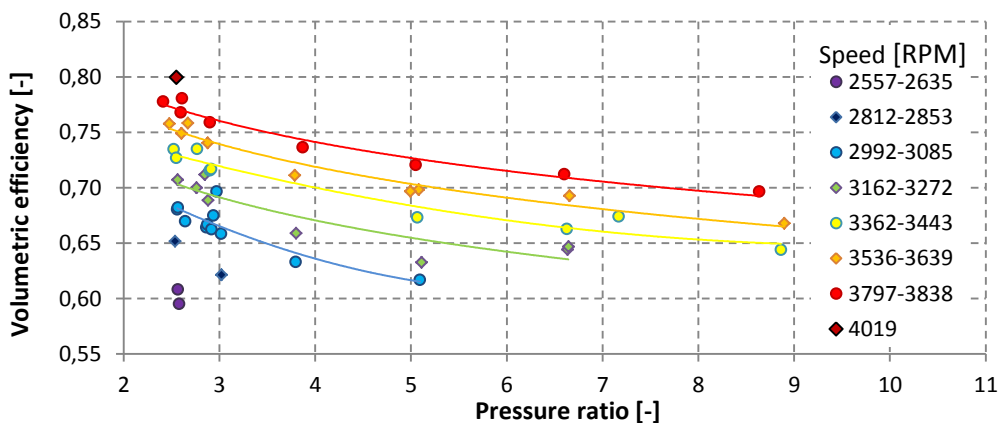


Figure 5: Volumetric efficiency vs. pressure ratio and speed, 5K superheating

Figure 5 shows the dependency of volumetric efficiency (which is defined by the equation 2) on pressure ratio and expander shaft speed. Shaft speed ranged from approximately 2550 to 4000 RPM.

$$\eta_{vol} = \frac{N_{rot,exp} \cdot c \cdot V_c}{60 \cdot \dot{M}_{wf} \cdot v_{su}} \quad (2)$$

It was difficult to maintain precise speed of expander due to characteristics of built-in regulator in alternator. For this reason the speed and the volumetric efficiency fluctuate a bit. Nevertheless it can be seen that the value of volumetric efficiency rises with the increase of speed. This is caused by rising of the overall flow through the expander when the total leakage within the expander remains almost the same. There is also declining trend of volumetric efficiency with increasing of pressure ratio within the expander. Higher pressure ratio leads to greater leakage of working fluid from the working chambers of the expander.

5. MODELING

A semi-empirical model was calibrated on the base of the measured data. This lumped-parameter model takes into consideration major losses of the expander such as supply and discharge pressure losses, under and over-expansion, internal leakages and mechanical losses (figure 6). The model parameters were identified for the expander under investigation, integrated into a Rankine cycle and fed with hexamethyldisiloxane.

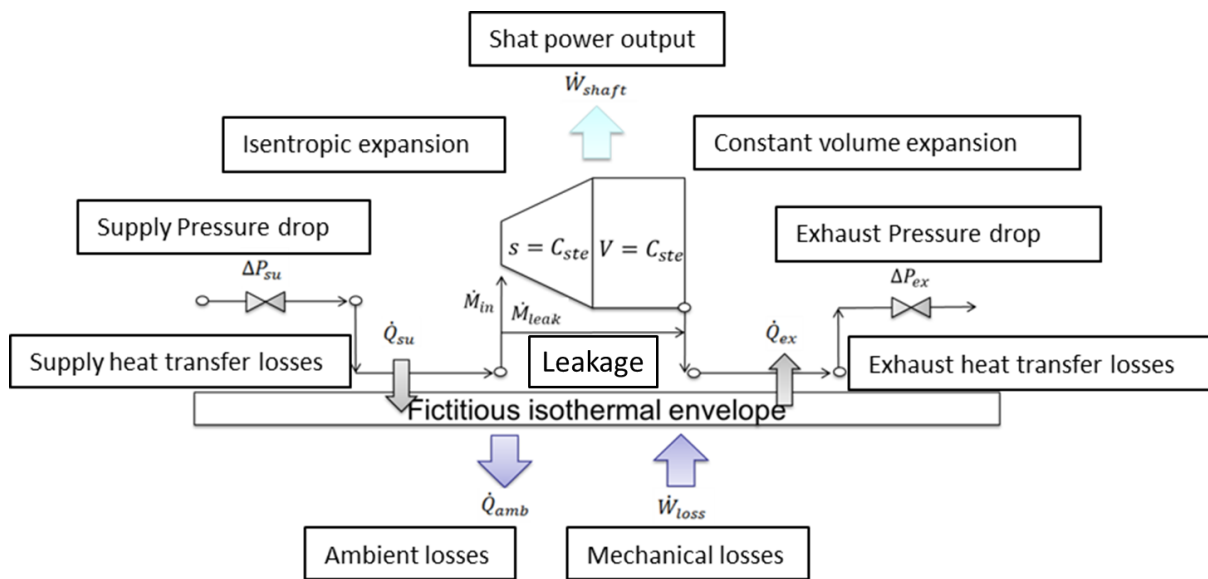


Figure 6: Schematic of the semi-empirical model

The parameter identification process was illustrated by Lemort (2009). The input variables of the model are the supply pressure, the supply temperature, the exhaust pressure and the rotational speed of the expander. The model then calculates the mass flow rate displaced by the expander, the delivered mechanical power and the exhaust temperature. A particular attention was dedicated to the identification of the leakage area parameter. Indeed, as it can be seen, this parameter almost evolves as the inverse of the rotational speed (figure 7). But it could also be shown that it depends on the pressure difference over the expansion machine and of the fluid inlet temperature.

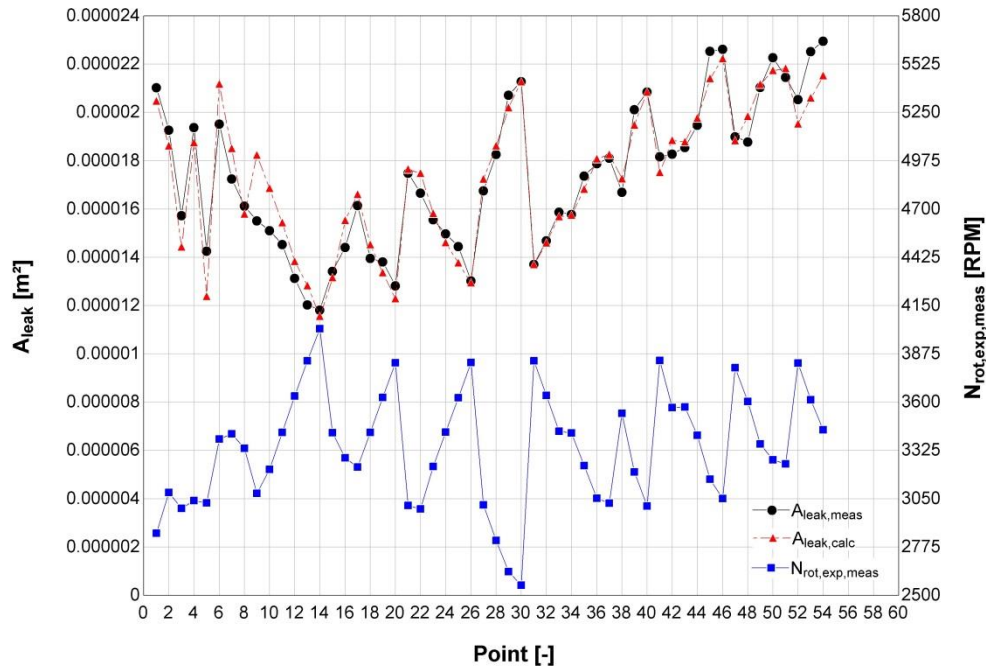


Figure 7: Identification of the fictive flow rate area

The validation of the model was realized comparing the predicted and measured values for the mass flow rate, mechanical power and the exhaust temperature of the expander. Figure 8 compares the evolutions of the mass flow rate measured and predicted by the model. It can be observed that the agreement between the measurement and the prediction by the model is very good. The maximum deviation is 3%.

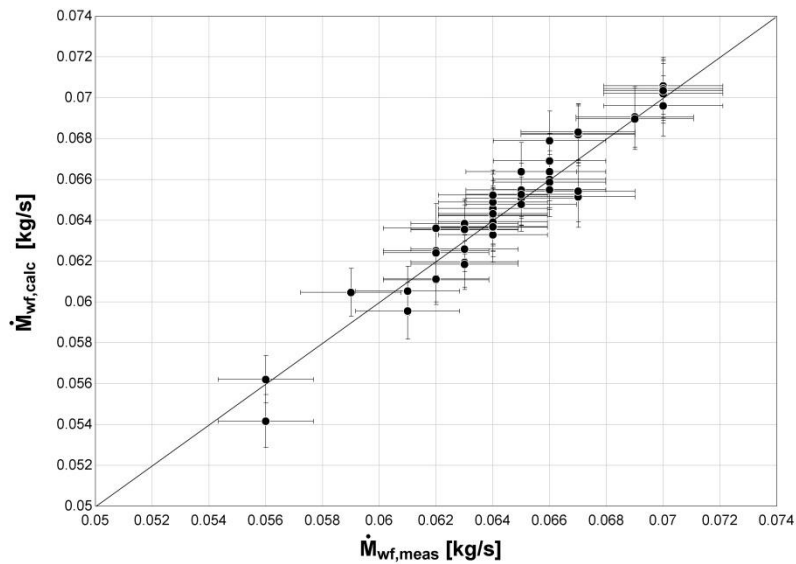


Figure 8: Validation of the expander model - comparison between predicted and measured mass flow rate

The evolutions of the shaft power, measured and predicted by the model are compared in Figure 9. It can be observed that the agreement is good. The maximum deviation between the model predictions and the measurements is 8%.

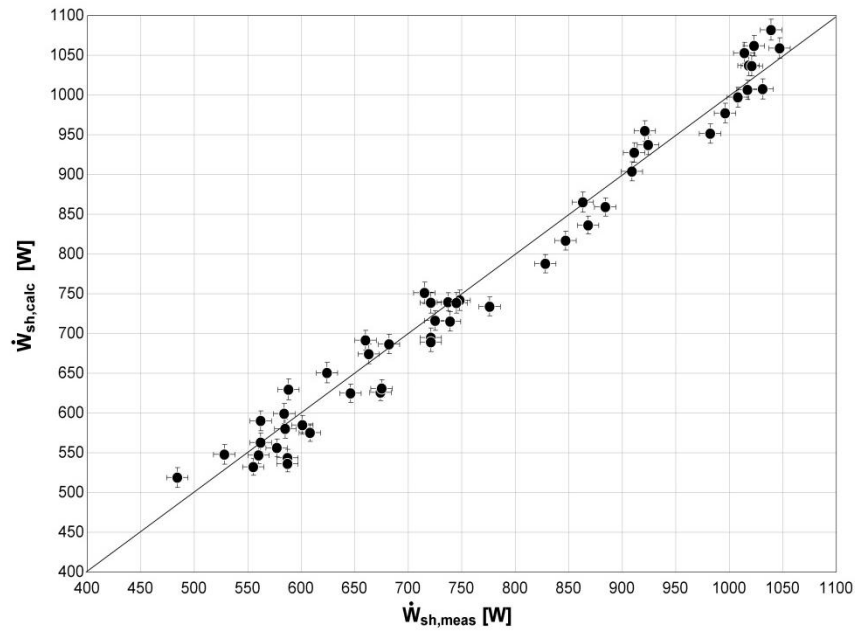


Figure 9: Validation of the expander model - comparison between predicted and measured shaft power

The model predicts the exhaust temperature within 4 K and seems to slightly underestimate it. This could be – among other things – the result of an error in the temperatures measurements during the experimental campaign. Indeed, the energy balance over the expander revealed to be incorrect and led to negative ambient losses (see equation 3). However, the balance is very sensitive to precise temperature measurement and small errors have a great influence on the difference ($h_{su} - h_{ex}$).

$$\dot{Q}_{amb} = \dot{M}_{wf} (h_{su} - h_{ex}) - \dot{W}_{shaft} < 0 \quad (3)$$

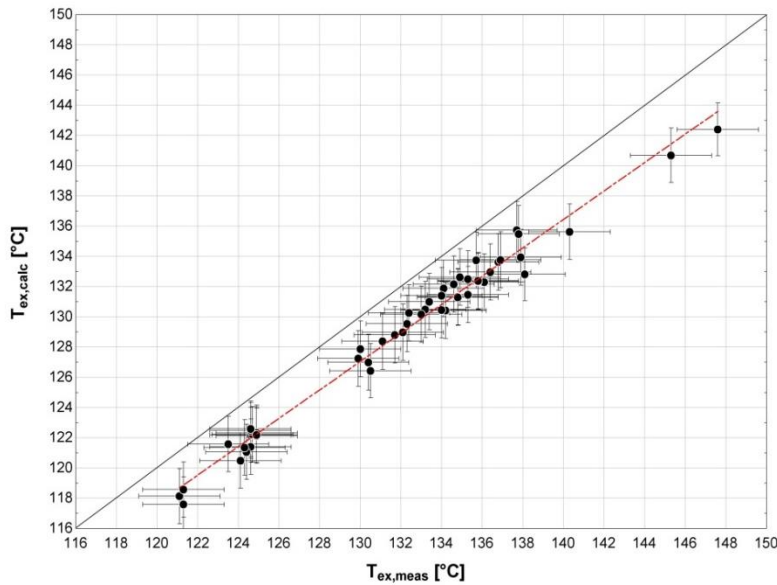


Figure 10: Validation of the expander model - comparison between predicted and measured exhaust temperature

The validated model of the expander can then be used to quantify the different losses. Figure 11 shows the evolution of the overall isentropic efficiency with the pressure ratio imposed to the expander for a particular rotational speed of 3000 RPM. The evolution at the top of the figure is

predicted by a model that only accounts for under- and over-expansion losses. The efficiency equals 1.0 at a pressure ratio adapted to the built-in volume ratio ($r_{v, in} = 3$) of the expander (top curve). For smaller and larger pressure ratios, the fluid is over-expanded and under-expanded respectively. The isentropic efficiency then decreases when accounting for the heat transfers (green curve) mainly because of the supply cooling down of the fluid. It also decreases when taking into account the mechanical losses (purple curve) mainly caused by the friction of the vanes on the stator. Introducing the supply pressure drop in the modeling largely reduces the isentropic effectiveness (blue curve). A more detailed investigation should answer the question of how to reduce this pressure drop by modifying the expander geometry. The internal leakage is responsible for the major part of the performance loss (red curve). Further work should investigate the possibility of reducing this leakage without increasing the mechanical losses of the expander.

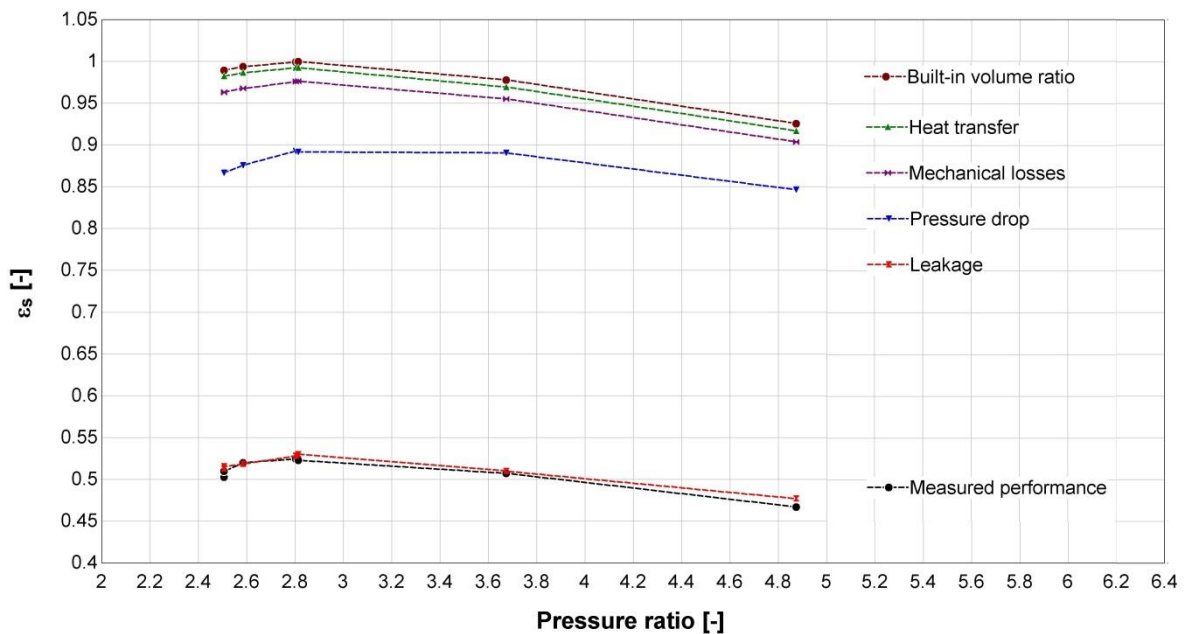


Figure 11: Model analysis - evolution of the calculated overall isentropic effectiveness with the imposed pressure ratio for a rotational speed of 3000 RPM.

6. CONCLUSION

The paper describes experimental measurements and modeling of the vane expander prototype used in an experimental ORC which uses hexamethyldisiloxane as a working fluid. The ORC is cooled by air and uses flue gas as a source of heat. The vane expander reached the maximum shaft power of 1.05 kW with the isentropic efficiency 0.45. The maximum reached isentropic efficiency was 0.58 at 800 W of shaft power. It is obvious that highest efficiencies were obtained when the ratio v_{ex}/v_{su} roughly corresponds to the internal built-in volume ratio of the expander. Further attention should be paid to the optimal superheating which apparently affects the expander efficiency. Presented results of a semi-empirical model show good agreement between calculated and measured mass flow rate and shaft power respectively. The model shows that the internal leakage is responsible for the major part of performance loss. The supply pressure drop has also significant influence on the overall performance. Therefore, further work should be focused on investigation how to reduce these major losses.

NOMENCLATURE

c	number of working chambers	(-)
ΔP	pressure drop	(Pa)

h	specific enthalpy	(J/kg)
\dot{M}	mass flow rate	(kg/s)
N_{rot}	rotational speed	(RPM)
\dot{Q}	heat transfer rate	(W)
$r_{v, in}$	internal built-in volumetric ratio	(–)
s	specific entropy	(J/kg.K)
v	specific volume	(m ³ /kg)
V	volume	(m ³)
V_c	initial volume of working chamber	(m ³)
\dot{W}	mechanical power	(W)
η, ε	efficiency	(–)

Subscript

amb	ambient
calc	calculated
ex	exhaust
exp	expander
in	internal
leak	leakage
loss	losses
meas	measured
s	isentropic
shaft	shaft
su	supply
vol	volumetric
wf	working fluid

REFERENCES

- Aoun, B., 2008, *Micro Combined Heat and Power Operating on Renewable Energy for Residential Building*, PhD thesis, École Nationale Supérieure des Mines de Paris, Paris, 151 p.
- Cipollone, R., Contaldi, G., Bianchi, G., Murgia, S., 2014, Energy recovery using sliding vane rotary expanders, *8th International Conference on Compressors and their Systems*, p.183-194.
- Lemort, V., Quoilin, S., Cuevas, C., Lebrun, J., 2009, Testing and modeling a scroll expander integrated into an Organic Rankine Cycle, *Applied Thermal Engineering*, 29, p. 3094–3102.
- Mascuch, J., Dlouhy, T., 2011, Natural Gas Decentralized Micro CHP: The Czech Republic Case, *5th Annual International Travelling Conference for Young Researchers and PhD Students ERIN 2011*, p. 81-86.
- Peterson, C. R., McGahan, W. A., 1972, Thermodynamic and Aerodynamic Analysis Method for Oil Flooded Sliding Vane Compressor, *International Compressor Engineering Conference*, Purdue University, p. 1-8.
- Xia, C., Zhang, W., Bu, G., Wang, Z., Shu, P., 2013, Experimental study on a sliding vane expander in the HFC410A refrigeration system for energy recovery, *Applied Thermal Engineering*, 59, p. 559–567.
- Yang, B., Peng, X., He, Z., Guo, B., Xing, Z., 2008, Experimental investigation on the internal working process of a CO₂ rotary vane expander, *Applied Thermal Engineering*, 29, p. 2289–2296.

ACKNOWLEDGEMENT

This work has been supported by the European Union, OP RDI project No. CZ.1.05/2.1.00/03.0091 – University Centre for Energy Efficient Buildings and OP RDI project No. CZ.1.05/3.1.00/13.0283 – Intelligent Buildings.

EFFECT OF WORKING FLUID MIXTURE COMPOSITION ON THE PERFORMANCE OF AN ORGANIC RANKINE CYCLE

Peter Collings, Zhibin Yu*

University of Glasgow,
University Avenue
Glasgow
United Kingdom
p.collings.1@research.gla.ac.uk, zhibin.yu@glasgow.ac.uk

ABSTRACT

Whereas single-component working fluids exhibit phase changes at a constant temperature, working fluid mixtures containing two or more components can exhibit a change in temperature across a phase change, known as “glide”. These fluid mixtures are termed “zeotropic”. Zeotropic mixtures can possess several advantages when used as working fluids in ORC systems. Similarly to supercritical cycles, they can match the temperature profiles on the hot and cold sides of the evaporator, resulting in less of a need for superheating, and increasing second law efficiency. The major advantage of a zeotropic fluid over a supercritical one is that this effect can also be felt in the condenser, which can greatly reduce the need for coolant for a given cycle efficiency. This is of particular benefit in desert areas, where cooling water is not readily available. In general, zeotropic cycles can be made to exhibit significant temperature glide at far lower pressures than an equivalent supercritical cycle.

A temperature glide can also result in a greater amount of energy being transferred in a recuperator, should one be included in the system, by increasing the difference in temperature between the cold fluid leaving the pump, and the hot fluid leaving the expander, which results in a greater transfer of energy for a given cycle configuration, especially when this enables a certain amount of phase change to occur in the recuperator.

This paper uses a numerical simulation in MATLAB to analyse the effects of varying the composition of a zeotropic mixture of R245fa and R134a on the overall performance of a cycle, both with and without a recuperator installed.

Evaluation of ORC using Low GWP Working Fluids for Waste Heats

Katsuya Yamashita^{1*}, Osamu Furuya^{1*}, Eiichi Sakaue^{1*}

¹Toshiba Corporation Power Systems Company, Power and Industrial Systems R&D Center,
New Energy and Generator Group
Yokohama, Kanagawa, Japan
Katsuya2.yamashita@toshiba.co.jp

ABSTRACT

In this study, to evaluate Organic Rankine cycle (ORC) system using low GWP working for waste heat of lower temperature (180°C waste gas), R1233zd and R1234ze(E) as low GWP working have been selected comparing with the used R245fa, and evaluated ORC system efficiency. As a result, R1233zd and R1234ze(E) are more useful than R245. R1233zd is particularly found out effective and easily.

INTRODUCTION

Ironworks have various furnaces and have been exhausting waste heats of various temperatures. Though waste heats of more than 250°C have already been utilized for electricity, heating, drying and all that. But, those of lower than 200°C have not been effectively utilized yet. For 40 years, electric power generation system using organic working fluid has been commercialized for the geothermal hot water of lower than 200°C in geothermal power plants. But due to environmental problems of organic working fluids, electric power generation system using organic working fluid has not been applied in the lower waste heats. Organic working fluid's problems for commercial application are toxicity, flammability, ozone depletion (ODP) and global warming potential (GWP). Recently, in respect of climate change, low GWP working fluids have been paid attention and developed. Some are being released into market. The low GWP working fluids are more degradable in high atmosphere and have much shorter lifetime than existing organic working fluid such as R134a and R245fa and less flammability than flammable working fluid such as pentane, butane, propane due to its molecule structure.

In this study, to design ORC system using low GWP working for 180°C waste gas, various kinds of thermal properties of those low GWP have been evaluated using publicized reliable database like NIST, for the first step. Also other properties such as stability, productivity are evaluated to find out effective low GWP working fluids. As the second step, power generation efficiency for waste gas of lower than 200°C using low GWP working fluids such as R1233zd and R1234ze(E) was evaluated compared with conventional one, R245fa. Various power generation system types are evaluated such as subcritical Rankine cycle, supercritical Rankine cycle and recuperated Rankine cycle, based on depending on critical temperature of working fluids and turbine outlet gas superheated temperature. Evaluations also take into accounts following factors, such as turbine efficiency, working fluid pump efficiency, generator efficiency, pinch-point temperature difference and pressure loss of heat recovery heat exchanger, condenser, recuperator, and pipe pressure loss. Since, expected power generation output is more than 1MW, and turbine inlet pressure is more than 1MPa, multi-stage axial turbine is picked up.

As the result, power generation gross efficiency and the modified efficiency are estimated and heat exchangers scales are determined by basic designation.

1. Low-GWP Working Fluids

Table.1 shows Low GWP working fluids and used R245fa. R1233zd and R1234ze(E) are 5-6 GWP, about 1/200 to R245fa. R1234ze(E) is lower than R245fa at the boiling point, the critical point, and then ORC Plant is higher pressure. And also there is flammable range. On the other hand, R1233zd has similar thermal characteristics. But the critical temperature is about 10C higher than R245fa, and is capable to generate the higher temperature vapor to the turbine.

Table.1. Comparisons of Low GWP Working Fluids

		R245fa	R1233zd	R1234ze(E)
Boiling Point	Tb	15.3	16.0	-19.0
Critical Temp	Tc	154.0	165.6	109.0
Critical Pressure	Pc	3.65	3.57	3.97
Molecular Mass		134	130.5	114
GWP		1030	5.0	6.0
Flammability		None	None	7.0-9.5
ODP		0.0	0.0	0.0

2. Organic Rankine Cycle of Waste Heat

2.1 Power Plant System

Fig1 shows the schematic Rankine cycle including recuperator. Rankine cycle is generally used the steam power plant using fossil fuels and the turbine inlet temperature attained to over 600C. For the turbine inlet temperature more than 230C, steam power plants using water as working fluid were generally more effective than organic working fluids like hydrocarbon as Propane, Butane, and Pentane.

Organic Rankine cycles have been applied for example geothermal power plant, solar power plant, biomass power plant, heat recovery power plant. Cycle applications of low temperature source about less than 200C have been used practically and been commercialized. Schematic figure of Rankine cycle (including the recuperation) is shown in Fig1. Rankine cycle without recuperator is less advantageous, because the hot temperature level (potential) of heating fluids is made good use of. And also the outlet temperature of heating fluids is lower; the utilizing rate of heating fluids' inlet temperature is more decreasing. The recuperated Rankine cycle is more effective, because the inlet temperature of feed liquid to heat exchanger being heated by heating source, is close to the outlet temperature of heating fluids. In other word, on condition of same heating rate from the heating source, the circulating working fluid rate of cycle is increased and turbine output is higher than that without recuperator.

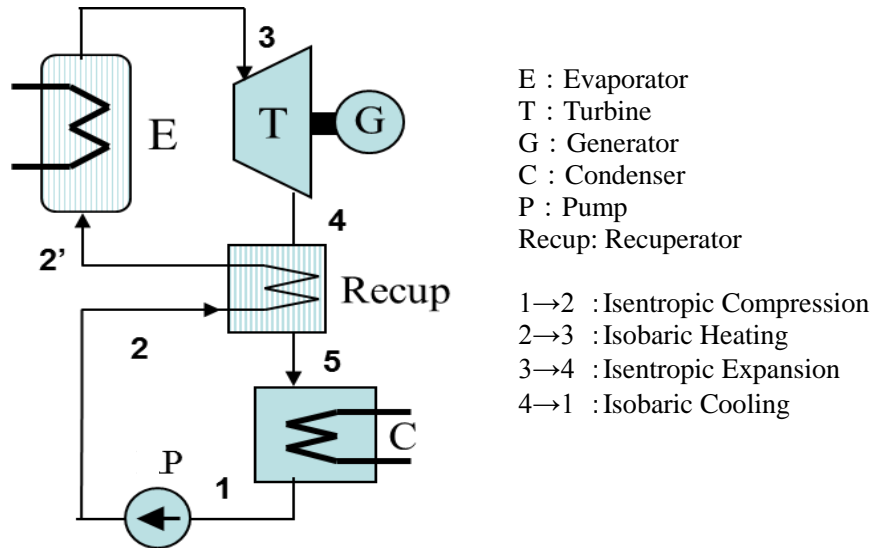


Fig1. Schematic Rankine Cycle System

2.2 ORC Type of Investigating

Alternate low GWP working fluids are R1233zd, R1234ze (E). The critical temperature of R1233zd is 165.6C close to waste heat gas inlet temperature 180C. And then the subcritical Rankine cycle have been investigated like used working fluid R245faas Fig2. And also super heating of evaporator is not necessary because those studied organic working fluids have the tendency of superheating by isentropic expansion in subcritical condition. Above mentioned, in subcritical Rankine cycle condition, the lower the outlet temperature of heating fluids is, the more effective power plant output is. That cycle characteristics, which the power output is unmatched the subcritical Rankine cycle efficiency is weak point of ORC.

One of heat cyclic way of improving the weak point of simple Rankine cycle is super critical Rankine cycle in fig.2. In the super critical Rankine cycle, the isobaric heating' process has not temperature limit, and then the evaporator outlet temperature can be getting close to the inlet temperature of heating fluid. The important point of super critical Rankine cycle is to been selecting the turbine inlet pressure according to working fluid, in view point of the critical condition that critical temperature, pressure, (volume). The other R1234ze(E)' critical temperature is 109C, far from waste heat gas temperature, and then the supercritical Rankine cycle have been investigated for R1234ze(E) as Fig2.

Another of heat cyclic way is the recuperated Rankine cycle in Fig.3, which is different than regenerated Rankine cycle like the steam power plant. The regenerated Rankine cycle which have been used large power plant using high pressure steam Rankine cycle, is the cycle of heating feed water using various pressure extraction steam from Steam turbine. Organic working fluids have less amount of latent heat than water, and the tendency of superheating gas by isentropic expansion. And turbine exhausted gas is higher than the feed liquid temperature of the organic fluid pump. In Fig3 the feed liquid temperature can increased by recuperator and the flow rate of the isobaric heating of evaporator (1-2) can be increased and then turbine output can be augment. The recuperated cycles have been studied for each working fluid.

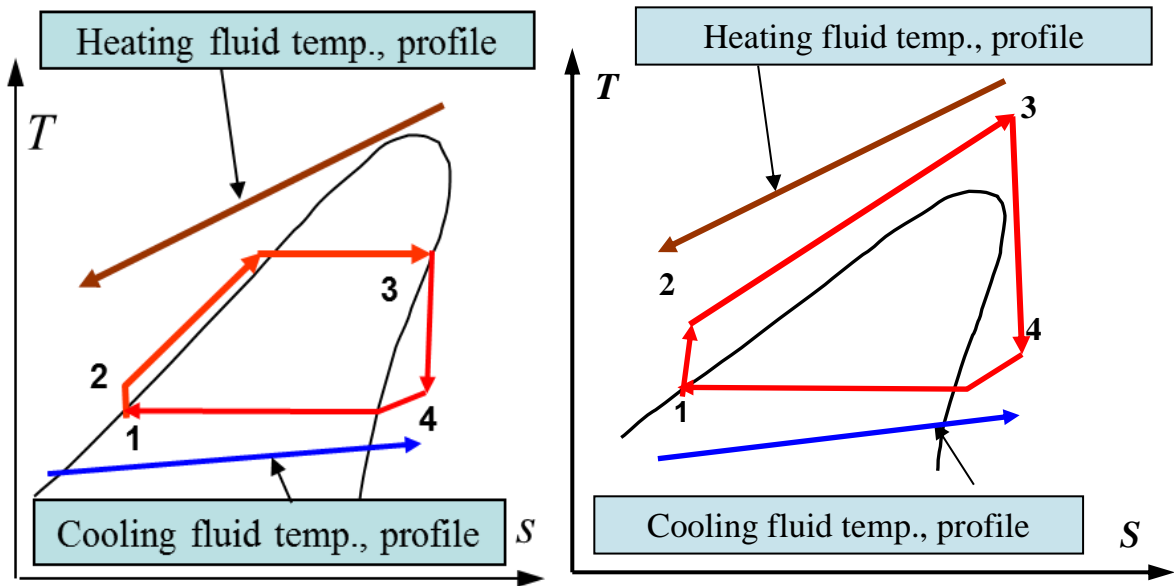


Fig.2. Subcritical & Supercritical Rankine Cycle T-S Diagram

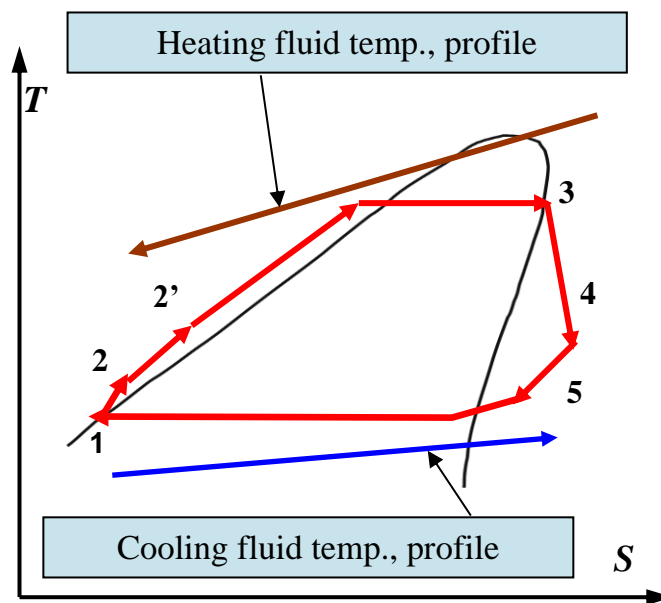


Fig.3. Recuperated Rankine Cycle T-S Diagram

2.2 Components of ORC

The above-mentioned schematic cycles are shown in Fig4-Fig5. The waste heat gas temperature is fixed at 180C. The heat recovery evaporator (HREVA) and the heat recovery preheater (HRPRE) are shown separately on the subcritical condition in Fig4 because of existing header of saturated vapor, on the other hand, the supercritical condition has one heat exchanger, the supercritical evaporator (HR-SUP EVA), because of not-restricting without turbine inlet condition, temperature, pressure. In Fig5, the recuperator (RECUP) is connecting from the organic turbine to the condenser and the recuperator heat load is determined to the pinch-point temperature difference from the condenser inlet to the high pressure feeding liquid. The cooling source is the cooling water by the cooling tower.

The main components are as follows

- Heat Recovery Evaporator

There are two kind of heating fluids, liquid state and gas state in ORC. As mentioned above, the lower waste heats of the ironworks are almost gas state. The waste gases have low density and then became large volume flow rate. Utilizing the existing gas duct, the heat transfer portions are packed inside, the preheater and the evaporator needs to be low pressure loss of waste gas side.

In general, like the natural circulating boiler, there is liquid-vapor separating header and the evaporating tube bundles in the upper waste gas stream, the preheating tube bundle in the downstream. In under-mentioned supercritical evaporator, the header is not necessary because of not existing phase-boundary, the heat-exchanged portion is composed of the one-through tubes. The heat transfer rate of waste gas is lower than that of inner tube heat transfer, and the high fin tube is practical used. The heat transfer rates of the supercritical fluids are practically used for inner tube. And then application of supercritical cycle to waste heats gas is reasonable.

- Turbine

The aim of ORC development using the low temperature waste heat of ironworks is to investigate high efficiency and more than MW class power plant. Because low power plant like 50~200kW is less applicability of heavy electrical duty like ironworks. In general the axial turbine is effective and practically used for more than MW electrical generation. And then the axial turbine is applied to the ORC system.

- Condenser

Organic working fluids are lower than water in thermal conductivity. The condensation heat transfer is lower, and then shell tube type condenser utilizing the enhanced tube like low-fin horizontal tube is used practically.

- Recuperator

Recuperator is heat exchanging between the high pressure working fluids' liquid and low pressure turbine exhaust vapor. The low pressure exhaust vapor is much larger volume than the working fluids' liquid and has low heat transfer rate. And then the tube bundle configuration like the above heat recovery evaporator is installed into the shell because the turbine exhaust vapor is more than atmospheric pressure

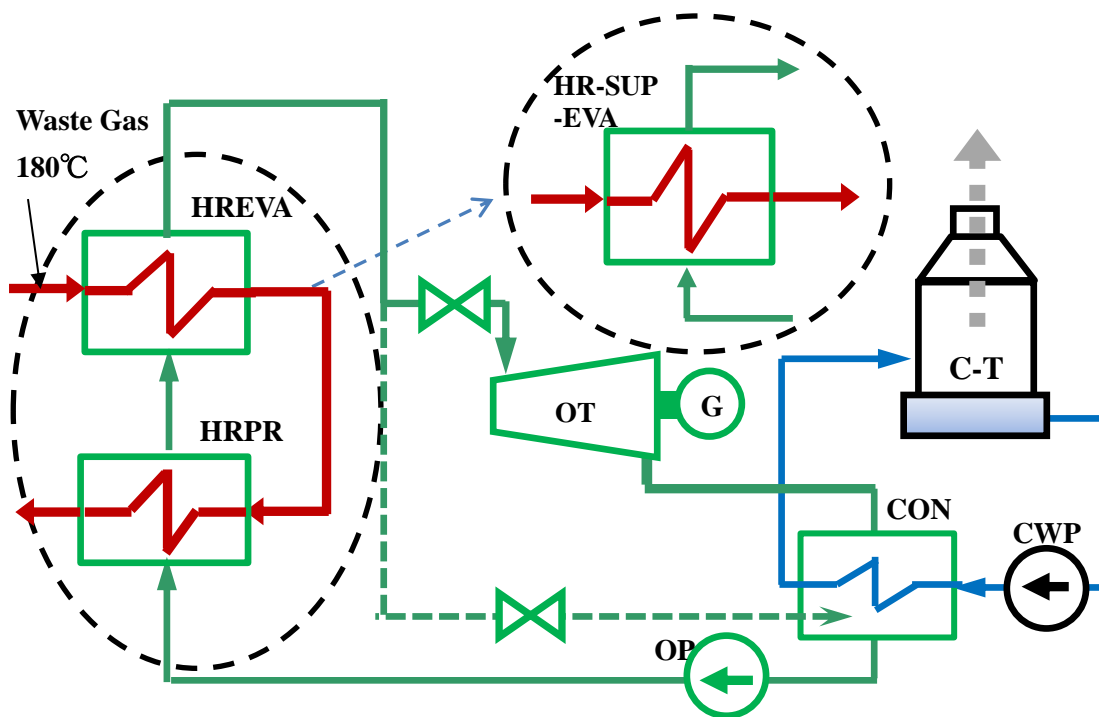


Fig.4. Schematic Subcritical & Supercritical Rankine System

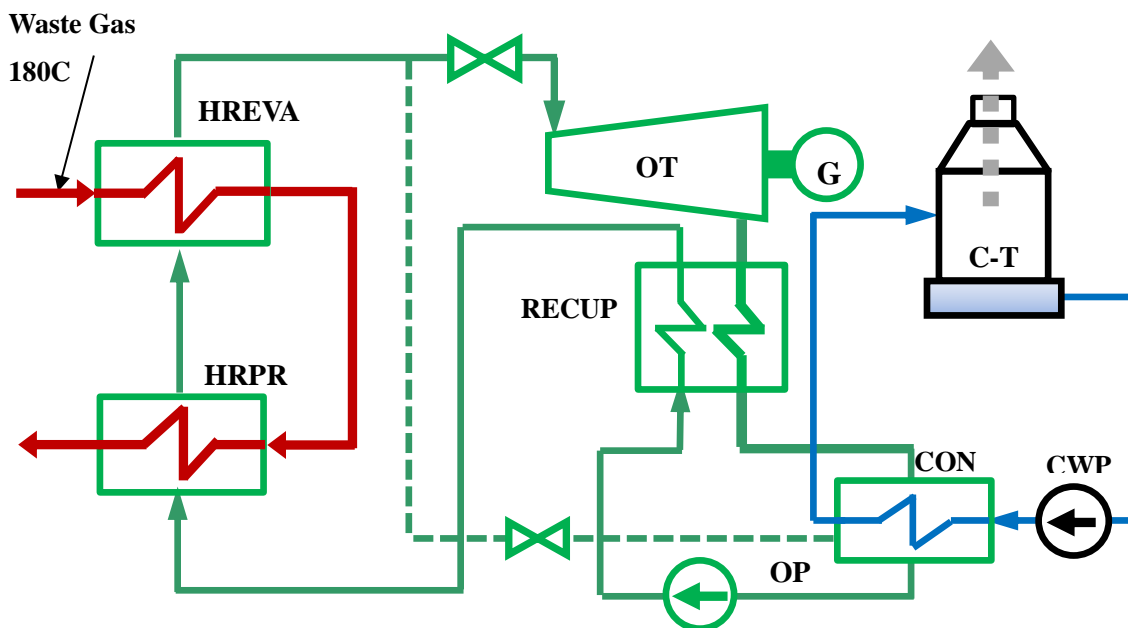


Fig.5. Schematic Recuperated Rankine System

HREVA	Heat Recovery Evaporator	HRPRE:	Heat Recovery Preheater
HR-SUP EVA:	Supercritical Evaporator	OT :	Organic Turbine
G :	Generator	CON :	Condenser
OP :	Organic Fluid Pump	CWP :	Cooling Water Pump
RECUP:	Recuperator	C-T:	Cooling Tower

3. Organic Rankine Cycle Evaluation

3.1. Rankine Cycle (Supercritical Rankine Cycle) Evaluation

The using working fluids, R245fa has the high GWP shown in Table.1. As Low GWP Organic working fluids, R1234ze(E) and R1233zd has been promising in air-conditioning, foaming agents. Inlet temperature of the waste heat gas is lower than 180°C, and the range of outlet temperature are 110–140°C, on grounds of exhausting condition and gas's contamination. Comparing the critical temperatures of working fluids with waste gas inlet temperature, R245fa and R1233zd have been analyzing as subcritical Rankine cycle, and R1234ze(E) has been analyzing as supercritical Rankine cycle as shown in Fig2. The composing difference of subcritical and supercritical cycle is evaporator and preheater which are generating the working fluids steam (gas). In subcritical cycle, there are preheater which is heating the feed liquid to the temperature close to saturation temperature (evaporating steam temperature) and evaporator which is generating steam (gas) at a certain pressure. But in supercritical cycle, there is no phase change at the heating and gas generating process, there is one heat exchanger. There is one more characteristic in supercritical cycle that is selecting temperature profile changeable by setting pressure. The comparing results of Gross Output Efficiencies of working fluids are shown in Fig.3.

The analyzing conditions are followers.

- i. The heating gas is dry air and inlet temperature is 180C.
- ii. The pinch point temperature difference is more than 10C of heating and evaporating heat exchangers
- iii. The line of the isentropic expansion of turbine is outside of the saturated gas line in working fluid.
- iv. Turbine isentropic efficiency is due to the working volume flow
- v. The Generating output takes account of gear, generator, and turbine efficiency.
- vi. The turbine outlet pressure loss is 4%
- vii. The Condensing temperature is 32C, and the cooling water outlet temperature is 25C.
- viii. The pressure loss from evaporator to turbine is 4 % including main-stop valve loss
- ix. The working fluids side pressure loss is calculating at base of the pressure loss of waste heating gas is 20kPa.

As shown in Fig2 the gross output of each (every) working fluids are decreasing in proportion to the output temperature of waste heats. It means that each thermal efficiencies of their output temperature of waste heats is almost equal. It is due to that the turbine inlet temperatures have hardly any changed according to the outlet temperatures of waste heats. Fig3 shows the tendencies clearly. The gross efficiency of supercritical Rankine cycle using Low GWP working fluid R1234ze(E) is lower than that of R245fa. But varying the turbine inlet pressure and setting the pinch point temperature of the evaporator 10C, the gross efficiency is a bit more than that of r245fa. On the other hand, That of R1233zd is more than R245fa about 1.0% because of the turbine temperature of R1233zd is more than that of R245fa.

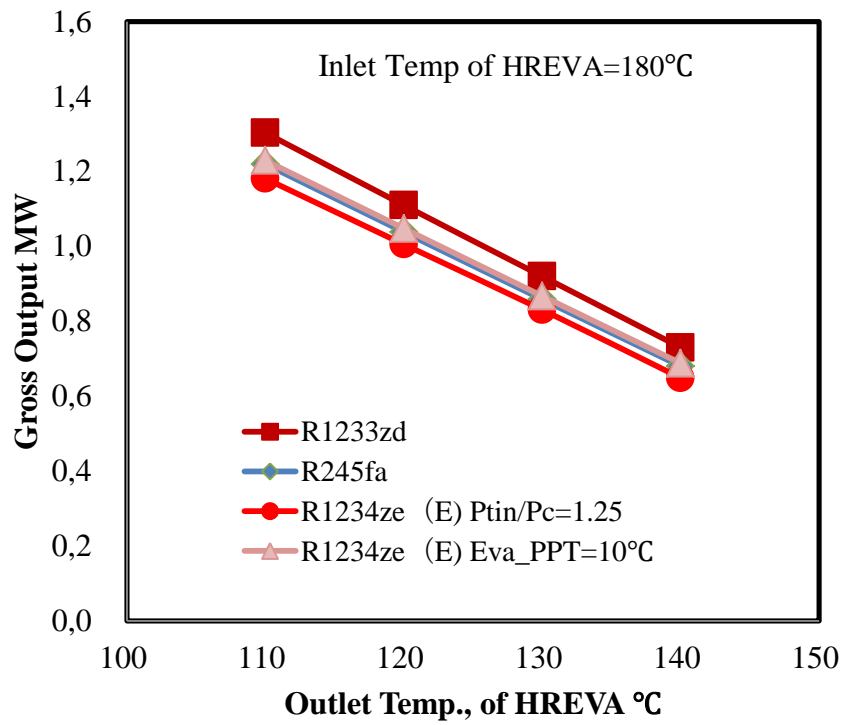


Fig.6. Gross Output of Working Fluids

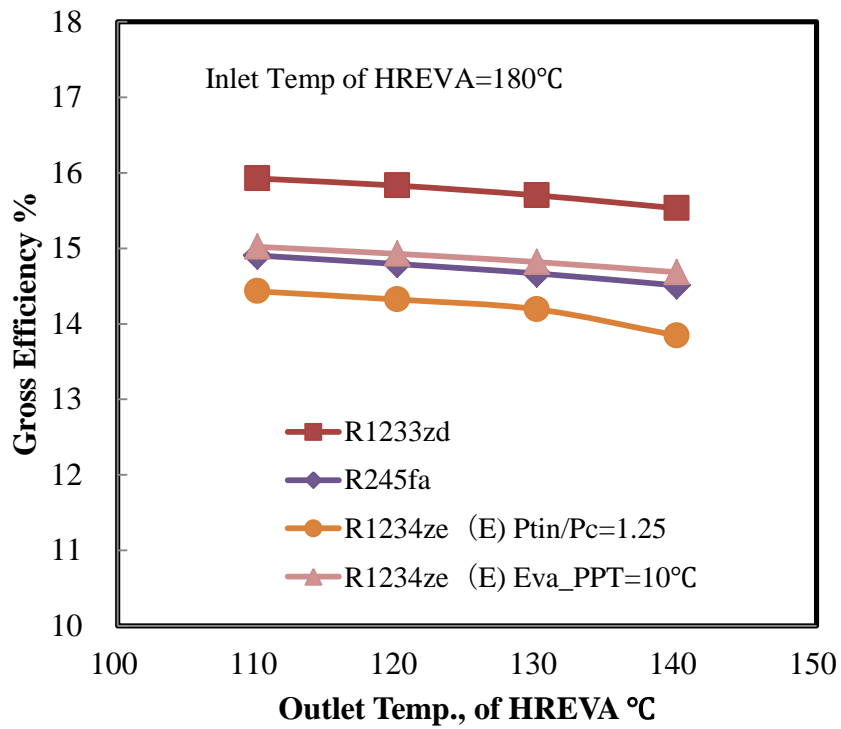


Fig.7. Gross Efficiency of Working Fluids

3.2. Recuperated Rankine Cycle (Supercritical Rankine Cycle) Evaluation

Generally Organic working fluids have the tendency which the line of the isentropic expansion is off from the saturated gas line. Turbine isentropic efficiency is about 80%, the outlet steam (gas) is more off and became superheated steam (gas). And then heating the feed liquid using the superheated temperature is recuperator (Fig5)

Superheated rate of turbine outlet is different among the investigating working fluids, supercritical cycle of R1234ze(E) has most superheated ratio, R245fa, R1233zd in order. The gross efficiency by recuperating has been shown in Fig8-Fig9. The Gross efficiency of Recuperated cycle of R245fa & R1233zd in Fig6-8, have been little increased about 1%. Their two working fluids are about same critical temperature and about same superheated rate. And then the recuperated capability is low and the recuperating ratio (= Recuperator heat load/Condenser heat load) are 6-7%.

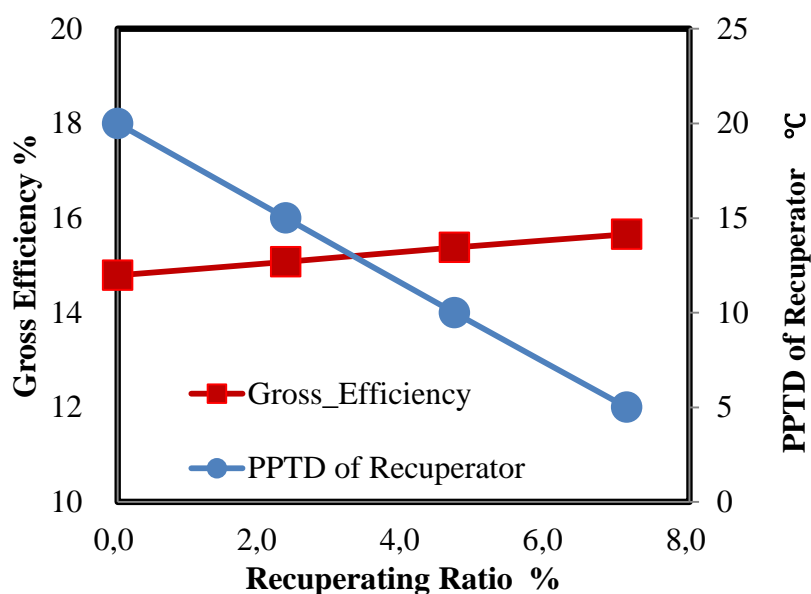


Fig.8. Gross Efficiency of R245fa by Recuperating

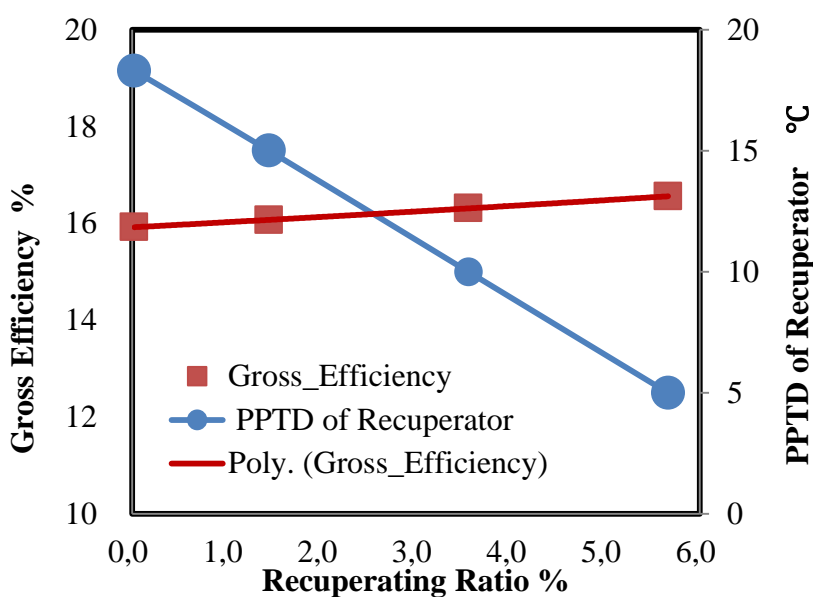


Fig.9. Gross Efficiency of R1233zd by Recuperating

Another working fluid, R1234ze(E) which is supercritical Rankine Cycle, has high recuperating ratio to 30%. And then the gross efficiency has been to 19%, as to about 30% recuperating ratio. The R1234ze(E) supercritical cycle's turbine inlet temperature attains to 168C, that is 55C superheated at the turbine outlet vapor. The superheated temperature became to more than 30°C, the condenser performance is lower than that of saturate vapor. The recuperator is indispensable to the R1234ze(E) supercritical cycle. But it is not necessary for R245fa and R1233zd subcritical cycle.

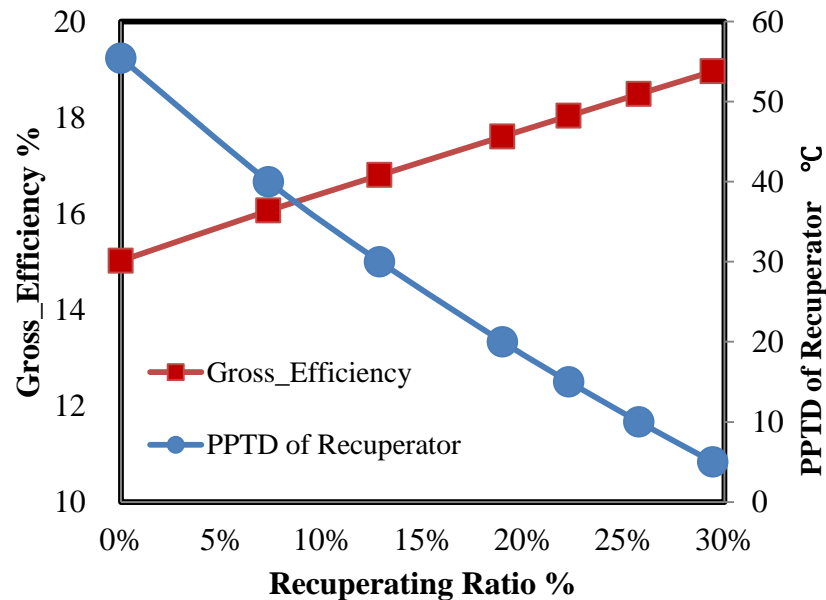


Fig.9. Gross Efficiency of R1234ze (E) Supercritical Cycle by Recuperating

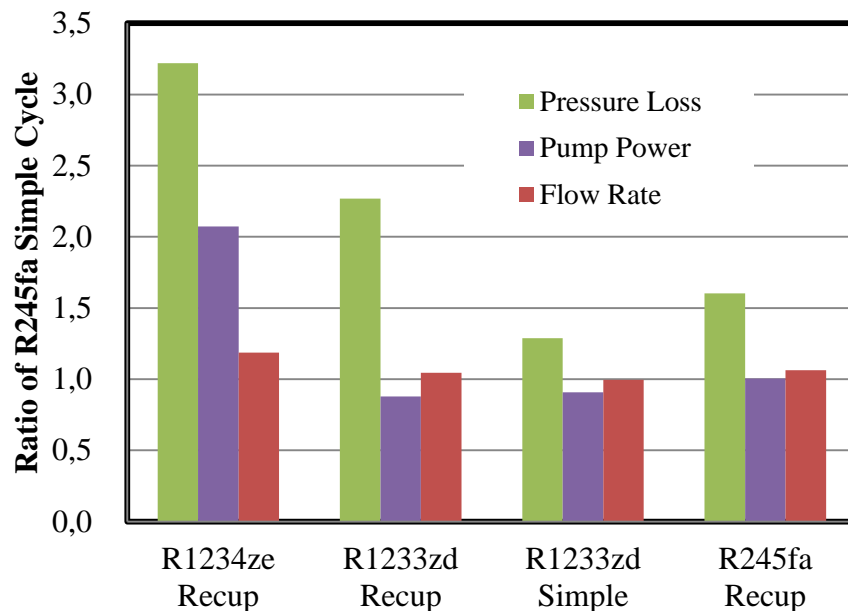


Fig.10. Comparison of Flow Rate Pump-power pressure loss Ratio

4. Comparison of R1233zd and R1234ze(E)

R1234ze (E)' supercritical recuperated Rankine cycle is highest Gross efficiency. On the investigation of Low GWP ORC, Comparison of components has been carried out. Because R1233zd is not suitable for the supercritical recuperated Rankine cycle due to the critical temperature and isentropic expansion line closed to the saturated gas line. But it is possible of R1233zd cycle that components are smaller than the R1234ze(E) cycle. Fig.10 shows the concerned value of components' size. The values of Fig.10 are the ratio of the working fluid flow rate, pump-power and pressure loss ratio heat recovery evaporator and recuperator at R245fa cycle. R1233zd is lower than R245fa both the flow rate and pump power. But all values of R1234(E) supercritical recuperated cycle is more than that of R245fa, In particular the pump power is more than twice because of supercritical cycle.

Table.2 shows the modified output which draws the pump power from the gross power. The table shows the value comparing the R245fa recuperated cycle. The recuperated Rankine cycle of R1233zd is highest output augmentation, the second is R1234ze(E) supercritical recuperated cycle which is highest gross efficiency. but if the organic pump efficiency is improved, R1234ze(E) supercritical recuperated cycle can have best performance.

R1233zd simple Rankine cycle is 8.0% higher than R245fa, replacing R245fa in used ORC power plant with R1233zd can be effective.

Table.2.Modified Output Augmentation Based on R245fa

Working fluid & Cycle	R1234ze(E)	R1233zd	R1233zd	R24fa
Evaporation Pressure	Supercritical	Subcritical	Subcritical	Subcritical
Recuperated Rate	29%	5.6%	None	6.4%
Modified Output Augmentation	11.5%	12.6%	8.0%	5.9%

5. Conclusion

The investigation of organic Rankine cycle has been carried out using Low GWP working fluids, instead of used High GWP working fluid R245fa, this paper has shown the results for 180C waste heat gas as follows

- Alternate low GWP working fluids, R1233zd, R1234ze(E) have higher gross efficiency than the used working fluid, R245fa.
- Without recuperating, R1233zd' cycle is highest gross efficiency.
- In recuperated Rankine of working fluids, R1234ze(E) is most recuperating ratio and then is highest gross efficiency of about 30% recuperating.
- On the modified output augmentation distracting the organic pump consumption, R1233zd is highest output.

6. Acknowledgement

This work was supported by the Japan Science and Technology Agency (JST) under the Strategic International Collaborative Research Program (SICORP).

7. References

1. Bala V.DATLA, Joost J.BRASZ “*Organic Rankine Cycle System, Analysis for Low GWP Working Fluids*” IRACC at Purdue, July 16-19,2012
2. Sotirios Karellas, Andreas Schuster, “*Supercritical Fluid Parameters in Organic Rankine Cycle Applications*” Int.J.of Thermodynamics, Vol.11(No.3) pp.101-108, September,2008
3. Bala V.DATTA, Joost J.BRASZ “Comparing R1233zd and R245fa for Low Temperature ORC Application” IRACC at Purdue, July 14-19,2014
4. Enrico Saverio Barbieri, Mirko Morini, Michele Pinelli “*Development of A Model for The Simulation of Organic Rankine Cycles Based Contribution Techniques* ” ASME Turbo Expo GT2011,June 6-10,2011

COMPARATIVE STUDY OF ORGANIC RANKINE CYCLE(ORC) FOR LOW GRADE ENERGY IN TURBINE AND PAT METHOD WITH FLUID

Mohammadreza Rostamzadeh¹, Farzam Alimardani^{2*}

¹University of Tabriz, Faculty of Mechanical Engineering,
Tabriz, East Azerbaijan, Iran

E-mail: Mr.Rostamzade@Tabrizu.ac.ir

²University of Tehran, Faculty of New sciences and Technologies,
End of the North Karegar St., Tehran, Tehran, Iran

E-mail: F.alimardani@ut.ac.ir

* Farzam Alimardani

ABSTRACT

In this paper, the organic fluid open Rankine cycle is analyzed when the variable expander is common assumption. The cycle arrangement in this plan is semi-open that is the layout is as a semi-cycle and the exhaust gas is directed to a drain tank. The effect of various parameters such as the inlet pressure on the expander, inlet temperature, pressure limit, injection rate on the thermal efficiency, the second law efficiency is measured and energy conversion to work is done with laboratory fixed effects. The highlighted characteristic in this study is the source serviceability capability in low-temperature and introduction of different blades as expander and its using to determine different organic fluids serviceability. This study shows that to what extent is the efficiency of the organic serviceable liquid R11, R22, R134a and how is each relation with the critical temperature and the impact of various changes on the cycle will be displayed and changes in temperature and flow rate, pressure and weights change will be analyzed and in the next stage expander replacement effect on results process will be shown. But what is important for us in this study project is to get work from lower temperature source, today's using water is used as fluid as the main and original factor in powers with high costs to raise the water temperature to 1500°C and using low temperature energy sources as the new energy for the future has importance and should be studied.

Keywords: Pump as turbine; Organic Rankine cycle; low temperature; R11; R22; R134a

1. Introduction

Many power-plants, including simple steam power plants work at a cycle, that is working-fluid passes a process and finally is returned to the first state. Although it is possible that motor passes a mechanics cycle but working-fluid will not pass a thermodynamics cycle, therefor, working-fluid will have a different state at final moment against first moment. Sometimes it is said that such equipment work in open cycle (in this case using cycle word is meaningless), while the steam power-plants work in a closed cycle. Difference between open and closed cycles may also exist in relation to refrigeration equipment. However, open and closed cycles are useful for both types of equipment that is we analyze performance of a hypothesized closed-cycle that is like as actual cycle. Such a method will be useful in determining the effect of parameters on performance [8].

In recent years, the increasing consumption of fossil fuels has led to more and more environmental problems such as global warming, ozone depletion and atmospheric pollution. Furthermore, along with the fast development of industry, energy shortages and blackouts have appeared more and more frequently all over the world. Due to all these reasons, utilizing low-grade waste heat for energy

production has attracted more and more attention for its potential in reduction the fossil fuel consumption.

When utilizing low-grad waste heat, the traditional steam Rankine cycle does not give a satisfying performance due to its low thermal efficiency and large volume flows; and thus, so called organic rankine cycles (ORCs) have been proposed [20-24]. These cycles use organic substances as working fluids and the systems consist of at least five principal components: evaporator, turbine, condenser, pump and working fluid [23].

Conserving energy while exploring renewable, environmentally-friendly energy resources is of crucial importance to keeping up with increasing energy demands. Small hydropower with its characteristics of available worldwide became attractive to energy utilization after the oil crisis of the seventies.

Pumps are relatively simple machines, easy to manufacture and maintain and readily available all over the world. Experiments have shown that in relatively low power outputs, pumps with high technological standards in reverse operation can compete with conventional turbines in respect to maximum efficiency [25]. Thus, PAT is one of the cheap and attractive alternatives in high pressure fluid and small hydropower resources exploration. Research on PAT was started around 1930 [26]. With increasing energy demands, it will be more economical to exploit such energy resources in future.

Nomenclature	
M_s	Rate of mass in measure force
RPM	Radius speed (revolutions per minute)
D_h	Height shade in water pipe
H3	Evaporator outlet enthalpy (kJ/kg)
\mathcal{V}	Specific volume (m ³ /kg)
T, P	Temperature & Pressure of internal fluid (K & pa)
H4	Turbine outlet enthalpy (kJ/kg)
H _{is}	External isentropic enthalpy from Turbine (kJ/kg)
M	Mass flow rate of working fluid (hg/s)
Q	heat addition of working fluid (kW)
W	Production Power in a real process (kW)
W _{is}	Production Power in an isentropic process (kW)
η_{ts}	Turbine Isentropic efficiency
η_{th}	Turbine thermal efficiency
h out	Exhausting Enthalpy from the Turbine (kJ/kg)
Subscript	
2,3,4,4s	state point

1.1. Rankine cycle thermodynamic analysis and modeling with organic fluid

The main advantage of the ORC is its superior ability in recovering waste heat with a low to medium temperature. There is a wide range of heat sources which can be applied to ORCs, such as waste heat from the condenser of a steam power plant, from industrial processer, solar radiation and geothermal energy [27,28]. This is especially important since, such as in Iran, 88% of waste heat belongs to this category. In general, recovery of waste heat with temperature below 370°C is not economically feasible, and this kind of heat is usually exhausted and becomes a source of pollution. Therefore, power generation using an ORC in recovering the waste heat is beneficial in many aspects: economical utilization of the energy, reduced electrical loads and reduced emission of CO₂.

Practically, due to the irreversibility in a real life thermodynamic system, it is impossible to convert all the available thermal energy into useful work.

These assumptions are used in this analysis:

1. The system modeling conditions is steady state.
2. Components heat transfer to the environment is ignored.
3. Pump and turbine process is real.
4. The pressure drop in interface tubes and heat exchangers is ignored.

Rankine cycle arrangement with Organic Fluid is shown in Fig.1.

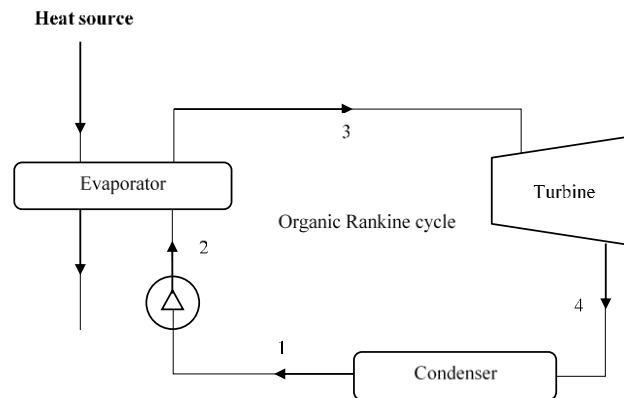


Fig.1. Schematic diagram of basic organic Rankine cycle

1.1.1. Pump: Isentropic efficiency and pump work for cycle is calculated with the below equations:

$$\eta_p = \frac{W_{p1,s}}{W_{p1}} \quad (1)$$

$$W_{p1,s} = V_1 \cdot (P_2 - P_1) \quad (2)$$

$$W_{p1} = h_2 - h_1 \quad (3)$$

η_p : Isentropic efficiency

W_p : Consumption Power in a real process

H_1, P_1 : Enthalpy and pressure of pump inlet

H_2, P_2 : Enthalpy and pressure of pump outlet

1.1.2. Evaporator: Fluids is heated in evaporator and reaches to the turbine inlet conditions. In this point steam can be as saturated or superheated steam. Heat transfer in evaporator and first law of thermodynamics for simple cycle and the recovery cycle are obtained as follows:

$$Q_{evap} = \dot{m}_{ORC} (h_{13} - h_{12}) \quad (4)$$

h_{13} and h_{12} are fluid enthalpy in evaporator input and output.

1.1.3. Turbine: Outlet steam in evaporator is entered into the turbine in order to produce mechanical power in turbine, this highly temperature and highly pressure vapor passing through blades are converted into lowly pressure and temperature flow and turbine isentropic efficiency for simple cycle Rankine with organic fluid is written as follows:

$$\eta_{Is_{turbine}} = \frac{h_{13} - h_{14}}{h_{13} - h_{14,s}} \quad (5)$$

$\eta_{T,ORC}$: Turbine Isentropic Efficiency

h_{13} : flow special enthalpy of turbine Inlet

h_{14} : flow special enthalpy of turbine outlet that is calculated as below during isentropic process

Turbine specific work is calculated using the following equation:

$$h_{4,s} = h_{4,s}(S_3, P_4) \quad (6)$$

$$\dot{W} = \dot{m} \cdot (h_3 - h_4) \quad (7)$$

1.1.4. Condenser: Outlet working-fluid state from the turbine is converted to saturated liquid through constant pressure in condenser. The rate of heat lost to the ambient is as simple cycle, cycle with internal heat exchanger and cycle with recovery [4].

$$Q_{cond} = \dot{m}_{ORC}(h_{14} - h_{11}) \quad (8)$$

1.2. Pressure and temperature effect on Rankine cycle

It can be said that Rankine cycle efficiency can be increased by lowering discharge pressure, that pressure increase during the addition of heat, and superheating steam. The quality of the output steam from turbine will be increased by superheating water steam and will be decreased by lowering the outlet pressure and increased pressure in which heat is added [19]. Some factors should be considered in the case of the deviation of actual cycles from ideal cycles that the most important factors are drops of turbines, pumps, piping and the condensers [18,6].

2. Pump instead of turbine in the power system

Pump system as the expander of the power system is known as one of the power production system and energy. In this system, we focus on pump system instead of turbine system. This system has effect on advances of countries that don't have turbine production technology and type and way of turbine selection is not important, however, the aim of selection is proper efficiency in a system that the pump shows turbine efficiency and selection optimization based on working conditions is among the most important issues in this system [15].

2.1. What is the hydraulic power system?

A hydraulic power system is resulted from fluid movement and its effect on a mechanical equipment, this space is established in natural spaces like mountains and waterfalls and there is need to construction that it can be used with any size and in any phenomenon. Hydraulic power system is a term for explaining small systems that describe hydroelectric power generation under 5KW. Pump systems components instead of turbine is:

- 1) Water flow entrance into the system
- 2) The substance that covers the entrance
- 3) A tool designed to guide the flow into the inlet channel
- 4) In case that steam is far from using point, channel is designed that is not necessary, but its use is recommended
- 5) The Actuator force

- 6) Actuators for pumping
- 7) Turbine or generator or electric utility chamber
- 8) Pump instead of turbine that makes possible energy conversion
- 9) Motor has efficiency for pumping and generator for turbine
- 10) Channel that converts power chamber water into the steam when the turbine outlet is nearly steam, this chamber is not required [10,11,14,15].

3. Experimental set-up

in basic design of the factor equipment and the injection path, as it has been identified in Fig.2, water reservoir is designed as boiler in which the working-fluid capsule is set and its floor is designed so that capsule can't move and adjustable electric heater is set to change water temperature that leads to change working-fluid temperature so that fluid attain into the vapor-phase by temperature increase and enter designing path. In the path, firstly regulator is set to regulate the pressure and the pressure changes are adjustable, then flow rate measuring will be done as follow and then thermometer and manometer are set to determine the pressure and temperature at the expander entrance [2,3].

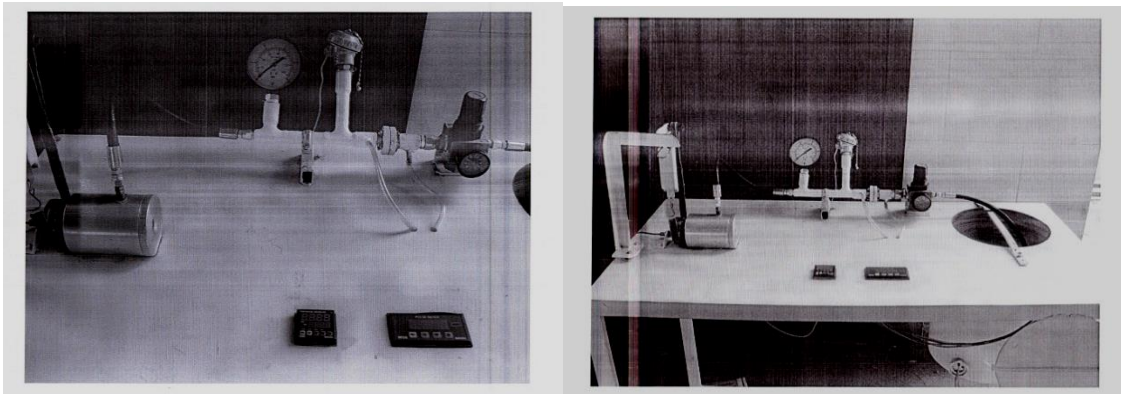


Fig.2. general schematic of made equipment

3-1. Flow rate calculations

For flow rate measurement in the main path, aluminum plate with ratio of hole diameter to path diameter is set after regulator and two holes are set before and after the plate to attach to the U shape path of manometer tube to determine the height difference and the flow rate which flow rate is calculated by following calculations it should be remembered that Boiler's heat changes by \dot{m} (flow rate) change [17].

$$\Delta H_{R11} = \frac{\Delta P_{R11}}{\gamma_{R11}} \quad (9)$$

$$\rho_{R11} = \frac{1}{\gamma_{R11}} \quad (10)$$

$$D_h = \Delta H_w \quad (11)$$

$$\Delta P_{R11} = \rho_{water} \cdot g \cdot \Delta H_{wat} = \gamma_w \cdot D_h \quad (12)$$

$$V_{ideal} = \sqrt{2 \cdot g \cdot \rho_w \cdot \gamma_{R11} \cdot \Delta H_w} \quad (13)$$

$$V_{act} = C_d \cdot V_{ideal} \quad (14)$$

$$\dot{m} = \rho C_d V_{ideal} = \rho \cdot C_d \cdot \sqrt{2 \cdot g \cdot \rho_w \cdot \gamma_{R11} \cdot D_h} = \rho \cdot C_d (2 \cdot g \cdot \rho_w \cdot \gamma_{R11} \cdot D_h)^{1/2} \quad (15)$$

3.2. Force calculation principles

For dynamometer, a base attached to the pulley with the lubricant bearing is used in that a belt with proper width in one hand is attached to the base of dynamometer and is attached to pulley base from below and is attached to pulley in back and is attached to weight plate on the other hand and work and power are calculated as below:

$$W = \frac{\pi}{30} \cdot (RPM) \cdot (F - m \cdot g) \cdot R \quad (17)$$

h_{is} is obtained theoretically in software. Expansion phenomenon is constant Entropy phenomenon and isentropic enthalpy is obtained with pressure discharge form to atmosphere and fixing entropy in entrance and exhaust [5].

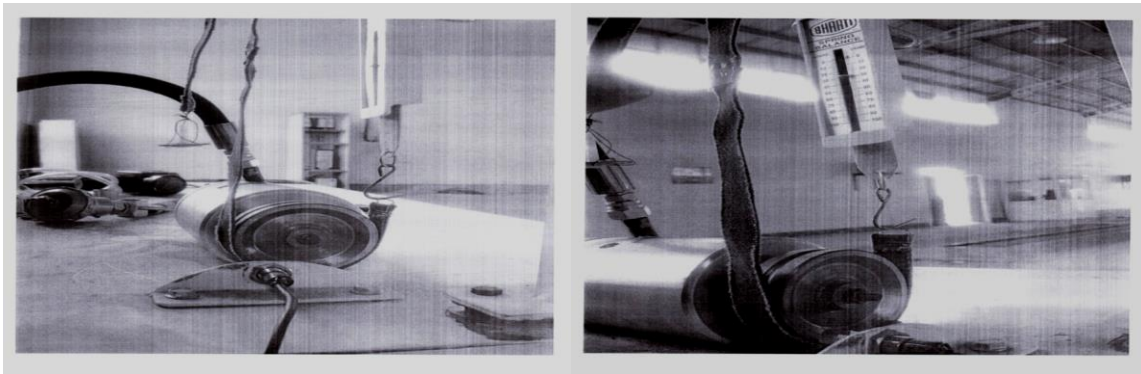


Fig.3. Dynamometer equipment schematic

3.3. Expansion chamber

In this paper, the design of the expander and its chamber is done specifically and solely for this study that is a cylindrical steel chamber with two nozzles that depending on the injection direction has the capability of conversion from expander to pump system instead of turbine and it is inside blades Chamber which is Hyundai car's supercharger blade and is considered as a hydraulic pump with smooth bearings to facilitate the movement of the blades. Fluid outlet is a closed chamber which is linked drain tank by a hole of expander exhaust by tubing and dynamometer is done by principles set out. The important thing to note is that refrigerants are very corrosive and corrosion-resistant metals should be selected for materials. To determine round a of the mechanical-digital sensor is used, so that a pulley is v to the expander blade main shaft and a tiny papillae is attached on the outer radius of the pulley and a round sensor with a minimal round is considered as papillae and round numbers are shown as data in indicator attached to sensor [9].

4. Result

Fig. 4,5,6,7,8,9 show the variation of net power output with the various expander inlet pressure for 3 different working fluids for their respective optimal temperature. In fluid R11, R22, R134a, The first law efficiency of the Rankine cycle increase with the increasing of turbine inlet pressure and efficiency increase acceleration is high in R22 fluid than R11 and when fluid efficiency increases it is high in R22 fluid than R11 and by inlet pressure increase, whole waste of the cycle is nearly ignorable. With excessive inlet temperature to expander, minor changes can be observed at the efficiency increasing, but these changes are sensible. This is an advantage for Rankine cycle with a

low temperature source that is operational in the low temperature. Compared to the actual and isentropic work, fluid performance of R22 is better than R11. By pressure increasing in the fluid, more rotation are observed of blade movements and in R22 fluid, rotation are increased by pressure increasing from 1.2 to 3 bar but in R11 this acceleration is as little slope. Clear relation between flow rate and pressure in flow rate measuring is seen at two sides of main path, flow rate injection is increased by pressure increasing and vice versa. Thermodynamic efficiency increases with pressure increase and the relation of this efficiency with pressure increase is different from temperature and flow rate increase and has ascension relation than temperature, flow rate and other changes. Specific volume and pressure increase followed by inlet superheated steam result in increased performance. Entropy increase with temperature increase has better entrance into superheated steam area and therefore fluid has better improved performance.

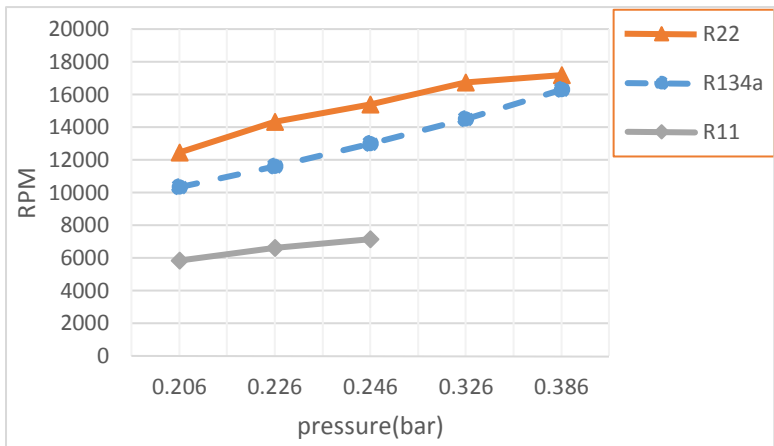


Fig.4. pressure- RPM for expand system.

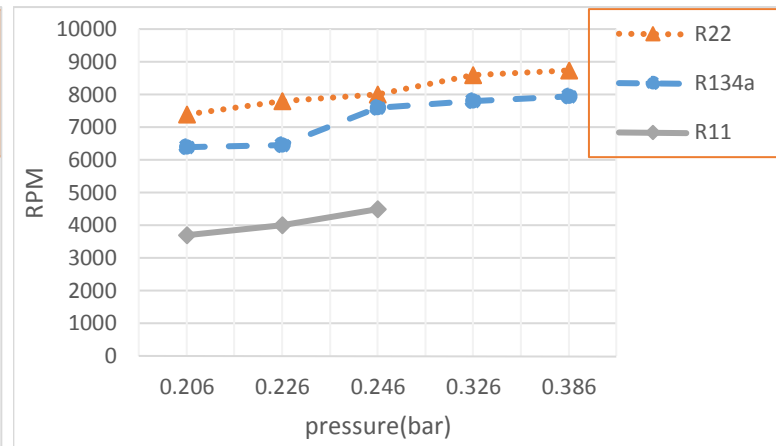


Fig.5. pressure- RPM for pat system.

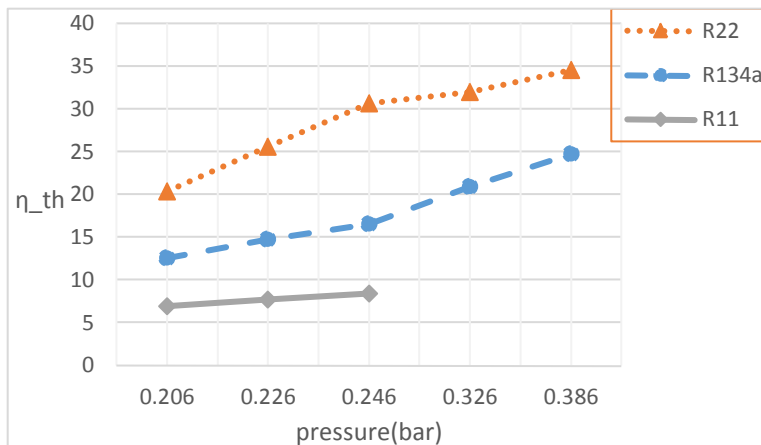


Fig.6. pressure-thermal efficiency for expand system.

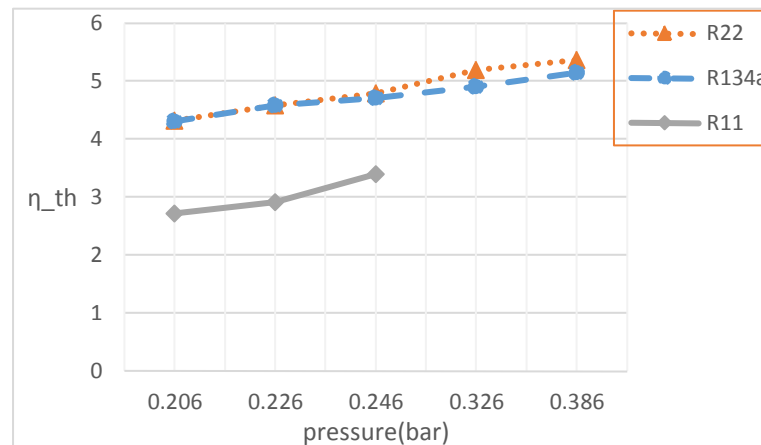


Fig.7. pressure-thermal efficiency for pat system.

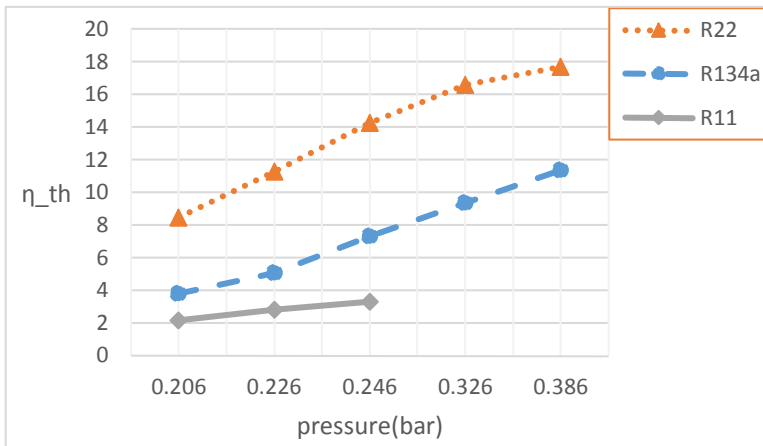


Fig.8. Pressure-real work for expand system.

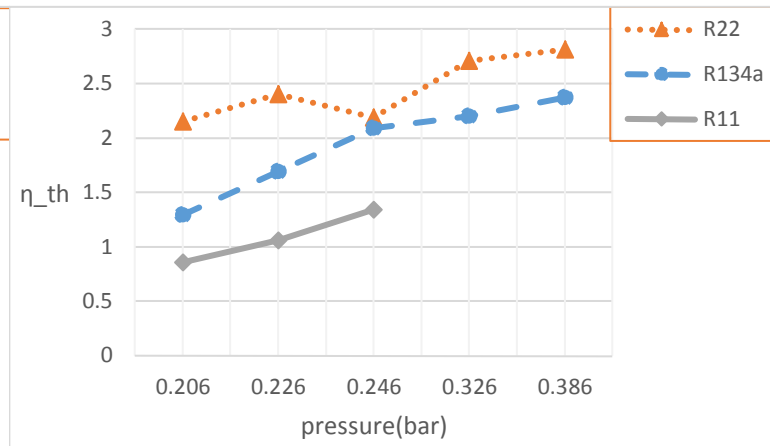


Fig.9. pressure-real work for pat system

5. Discussion

Fluid thermodynamic efficiency of R22 is higher than R11, this is because of R22 fluid ability to quickly convert into steam phase. Selecting fluids such as R12 and R13 and R14 and R114 give better results than fluids we've used because they have less critical temperature and less entropy range and better converting ability to steam vapor phase. But selecting fluids such as R123 and R500 and R502 and RC318 and R23 will give results near to R-22 that have close temperature limit and close entropy and their pressure-specific volume diagram are close to each other. We should attempt select liquids that have operating functionality, in selection of these fluids, the fluid with a high critical temperature should not be selected and their freezing temperature should not be very low. The high critical temperature is not the only sufficient requirement and diagram slope should be steeper than critical point that is diagram's downward region of temperature-entropy and should have sharper end slope and entering the superheated steam area should be soon in this state efficiency is better. The gas or fluid tension in the direction is one of the problems that need to be checked before the test and data giving phase. What is done in experimental observations were as below: Low efficiency of pump as turbine system rather than the turbine mode, which is resulted from the reverse movement of the blade, therefore entering minor data was avoided and it is exploitable only because using pump system instead of turbine for efficiency is a false choice and only has laboratory usage or it is exploitable in countries which do not have turbine technology. Isentropic efficiency is about 12% and have points that should be noted: First, due to the lack of laboratory fluid and organic capsule in our country there was possibility of using fluids with higher efficiency. Second, the increase in temperature due to the capsule explosion including fluid is not possible and experiment is done in biphasic region. Third, due to flow rate measurement in orifice plate mode there was huge losses than the case without orifice. According to testing procedure and with regard to flow rate measurement, plate removal was not possible and path losses and leakages are factors that affect the performance of Isentropic, while the expander's losses were higher than supposed amount. Wholly taking into account above items and if this test is ideal, by supposing efficiency mortality rate of 40% it was expected that efficiency and performance is practical.

6. Conclusion

In the present study, thermodynamic and experimental analysis of Rankine cycle with organic fluid and expander is designed that has the capability of converting pump system instead of the turbine, and is presented based on first law of thermodynamic. The main conclusion can be summarized as follow:

- 1) Rankine cycle has clear exit power and different fluids can flow in it. The effects of selecting various fluids and parameters such as temperature into expander, inlet pressure and injections flow rate have been studied in ORC and results are announced.
- 2) The study was done with Hyundai vehicle supercharger blade and has the ability to pump liquidity system instead of turbine but the important point in the design is lubrication process and moving with low friction that using lubricant bearings is recommended.
- 3) For measuring flow rate in designed path, pressure must not exceed a limit because it mix tube path water with factor fluid of main path and this factor is more effective in data measuring and should be followed.

Acknowledgement

The authors would like to thank Dr.Elnaz Shaseb for experimental setup and data collection of this work.

References

- [1] Nagatomo, S., Ootaka, T., and Morishima, A. Effects of operating conditions on expander performance characteristics. *Trans. JSRAE*, 1999, 16(1), 59-66.
- [2] Bearing catalogue, Hanwha, 2003.
- [3] Shigley, J. and Mischke, C. *Mechanical engineering design*, 6th edition, 2001 (McGraw-Hill, New York).
- [4] Wei, D., Lu, Z., and Gu, J. Performance analysis and optimization of organic Rankine cycle (ORC) for waste heat recovery, *Energy Convers. Manage.*, 2007, 48, 1113-1119.
- [5] Badr, O., Naik, S., and O'Callaghan, P. W. Expansion machine for a low-power-output steam Rankine-cycle engine. *Appl. Energy*, 1991, 39, 93-116.
- [6] Lee, K. M., Kuo, S. R. Chien, M. L., and Shih, Y. S. Parameter analysis on organic Rankine cycle energy recovery system. *Energy Confers. Manage.*, 1988, 28, 129-136.
- [7] Takahisa Yamamoto, Tomohiko Furuhashi, Norio Arai, Koichi Mori, Design and testing of the Organic Rankine Cycle. *Energy* 26 (2001) – 239-251.
- [8] Adrian B. *Advanced engineering thermodynamics*. New York: Wiley, 1997.
- [9] Hyoudou T. Ishida Y. *Design of turbine*. Tokyo: Power Co, 1969.
- [10] Williams A. *Pump as turbines - a user's guide*. 2nd ed. Warwickshire: ITDG Publishing; 2003.
- [11] Williams, *Pumps as Turbines Users Guide*, International Technology Publication, London, 1995.
- [12] Yiping Dai, Jiangfeng Wang, Lin Gao, Parametric optimization and comparative study of organic Rankine cycle (ORC) for low grade waste heat recovery. *Energy* 50(2009)576-582.
- [13] Mariano Arriaga, Pump as turbine- A pico- hydro alternative in Lao People Democratic Republic, *Renewable Energy* 35 (2010) 1109-1115.
- [14] Maher P. Smith N. Williams A. Assessment of pico hydro as an option for offgrid electrification in Kenya" *Micro hydra Centre - Nottingham Trent University*; 2003. pp. 1357-69.

- [15] Rawal S. KshirsagarJT. Numerical simulation on a pump operating in a turbine mode. Texas A&M University System, Turbomachinery Laboratory; 2007.
- [16] James A. Mathias, Job R. Johnston, Jr., Jiming Cao., Douglas K. Predeman., Richard N. Christensen., Experimental Testing of Gerotor and Scroll Expanders Used in, and Energetic and Exergetic Modeling of, an Organic Rankine Cycle, Energy, Vol. 131, 2009, pp:012201-1.
- [17] Shames, fluid of mechanic, 1995.
- [18] Nagatomo, S., Ootaka, T., and Morishima, A. Effects of operating conditions on expander performance characteristics. Trans. JSRAE, 1999, 16(1), 59-66.
- [19] G. J. Van Wylen and R. E. Sonntag. Fundamentals of Classical Thermodynamics. 3rd ed. New York: John Wiley & Sons, 1985.
- [20] G. Angelino, P.C.D. Paliano, Multicomponent working fluid for organic rankine cycle (ORCs), Energy 23 (6) (1998) 449-463.
- [21] B.T. Liu, K.H.chien, C.C.Wang, effect on working fluid on organic rankine cycle for waste heat recovery, energy 29 (2004) 1207-1217.
- [22] T.C. Hung, T.Y. Shai, S.K. Wang, a review of organic rankine cycles (ORCs) for the recovery of low-grade waste heat, Energy 22 (7) (1997) 661-667.
- [23] T.C. Hung, Waste heat recovery of organic rankine cycle using dry fluids, Energy convers. Manage. 42 (2001) 539-553.
- [24] T.Yamamoto, T.Furuhata, N.Arai, K.mori, Design and testing of the organic rankine cycle, Energy 26 (2001) 239-251.
- [25] Chapallaz JM, Eichenberger P, Fischer G. Manual on pumps used as turbines, Vieweg, Braunschweig; 1992.
- [26] Kittredge CP, Thoma D. Centrifugal pumps operated under abnormal conditions. Power 1931:881-4.
- [27] Drake RL. Turbomachin Int 1985;26:31.
- [28] Badr O, Probert D, O'Callaghan PW. Appl Energy 1986;23:1.

EFFECT OF RADIAL HEAT TRANSFER IN THE PEBBLE BED THERMAL ENERGY STORAGE TANK COUPLED TO A SOLAR ORGANIC RANKINE CYCLE

Pardeep Garg^{1*}, Abhishek N. Kshirsagar², Pramod Kumar^{1#}, Matthew S. Orosz⁴

¹ Indian Institute of Science Bangalore
C V Raman Ave, Bengaluru, Karnataka, India

*E-mail: pardeep_1127@yahoo.com

#E-mail: pramod_k24@yahoo.com

² Pune Vidyarthi Griha's College of Engineering and Technology
Vidyanagari, Pune, Maharashtra, India
E-mail: kshirsagar_abhishek@yahoo.com

⁴ Massachusetts Institute of Technology
Cambridge, Boston, USA
E-mail: mso@mit.edu

ABSTRACT

This paper analyzes the heat transfer mechanisms in the pebble-bed storage medium and reports the issues associated with it. A cylindrical geometry is considered for the storage tank in the present analysis for three different geometrical configurations which are solved using CFD commercial solver, Fluent 6.0, ANSYS. These configurations have different positions for inlet and outlet ports, namely, a) central inlet and outlet configuration (C-IOC), b) uniform inlet and outlet configuration (U-IOC) and c) diametrically opposite inlet and outlet ports on the lateral surface or the side inlet and outlet configuration (S-IOC) of the cylindrical TES tank. A comparative analysis of these three configurations is presented and internal heat transfer issues in the radial direction are identified. A new parameter called effectiveness of the TES tank is proposed to quantify the energy stored in the tank at the end charging process. Finally, the side inlet and outlet case is found to be a practically realizable as well as an effective alternate.

1. INTRODUCTION

Thermal energy storage (TES) is one of means of suppressing the adverse effects arising due to solar fluctuations on the power cycles and is also recognized as a cheaper option to store energy to generate electricity during non-solar hours (Taljan *et al.*, 2012). There are a number ways in which energy can be stored for example in form of sensible and latent heat. Herrmann and Kearney (2002) optimized these technologies on the basis of techno-economic analysis and emphasized on the need of reducing the cost of storage media. One possible way to reduce the cost of storage medium is to store partial amount of heat in the inexpensive rocks or pebbles as suggested by Meier *et al.* (1991). Pertaining to this, the economic advantages of pebble-bed TES (PB-TES) have been established by Zavattoni *et al.* (2013). Various studies have been made for understanding the heat storage mechanisms in these systems by modeling the heat transfer processes in it. For example, Ismail and Stuginsky (1999) modeled packed bed as porous media, Shah and Furbo (2003) analyzed the heat transfer fluid (HTF) entrance effects into the tank and Benmasour *et al.* (2006) treated uniformly sized spherical capsules as pebble bed in a two dimensional computational domain. These models are generally simplified and do not capture temperature gradients in the radial direction. However, the present paper finds that these effects can significantly lower the heat storage potential in a PB-TES system and hence the same need to be accounted for in the governing equations. Further, various inlet and outlet configurations of the PB-TES system are considered to show their effect on the energy stored in a given PB-TES system and in a given charging time.

2. SOLAR-ORC DETAILS AND CASE STUDY

Physical layout of the solar-ORC considered in this paper consists of two closed loops, a) heat transfer fluid (HTF) and b) working fluid loop as shown in Fig. 1. In the HTF loop, cold HTF from a PB-TES is pumped to a parabolic trough collector where it gets heated up and is then sent for the storage in a PB-TES tank. Working fluid loop is a regenerative ORC where the expander exhaust heat is recovered to heat up the pump outlet fluid. The two loops interact via a heat exchanger termed as an HEX (boiler for the working fluid) in this paper where the HTF coming from a PB-TES tank is cooled and working fluid in turn is heated up to the expander inlet temperature. TES is modeled in such a way that temperature drop across the HTF in HEX and PB-TES are identical.

2.2 TES details

Heated HTF from solar field enters the PB-TES tank from the inlet port (at or near the top) where it loses heat to the pebbles and the cold HTF around. The same amount of cold HTF leaves the tank from the outlet port (at or near the bottom) and is passed to the solar collectors to heat it up again. The process of storing heat from the solar collectors is termed as charging of the PB-TES whereas utilizing of the heat from the PB-TES in the power block is called discharging of the tank. In a real scenario, both the processes occur simultaneously and the one dominating over the other decides the net energy stored at any instance in the tank. To simplify the actual phenomenon occurring in the tank, only the charging process is simulated in this paper to understand the effect of location of inlet and outlet ports on a PB-TES. Schematics of these configurations are shown in Figure 2.

2.1 Case study

A detailed study of heat transfer mechanisms in a PB-TES system is carried out for a solar-ORC yielding a steady output of 100 kWe for the duration 600 Hrs. to 1800 Hrs. The working fluid used in the ORC is R-134a operating between 175 °C and 45 °C with the expander inlet pressure of 52 bar (transcritical cycle) optimized for maximum efficiency equal to ~10 %. Details of cycle modeling can be found in Garg *et al.*, (2013). HTF operating temperatures across the boiler are found to be 358 and 438 K. Location selected for study of the solar and DNI characteristics is 23.5°, 80° (latitude chosen is Tropic of Cancer which represents roughly the average of extreme Indian latitudes) and the day chosen is Vernal Equinox. The TES system selected is a pebble-bed system with fused silica as the pebble material and ethylene glycol as the HTF with their thermo-physical properties mentioned in section 3. Various assumptions made regarding the tank are listed below.

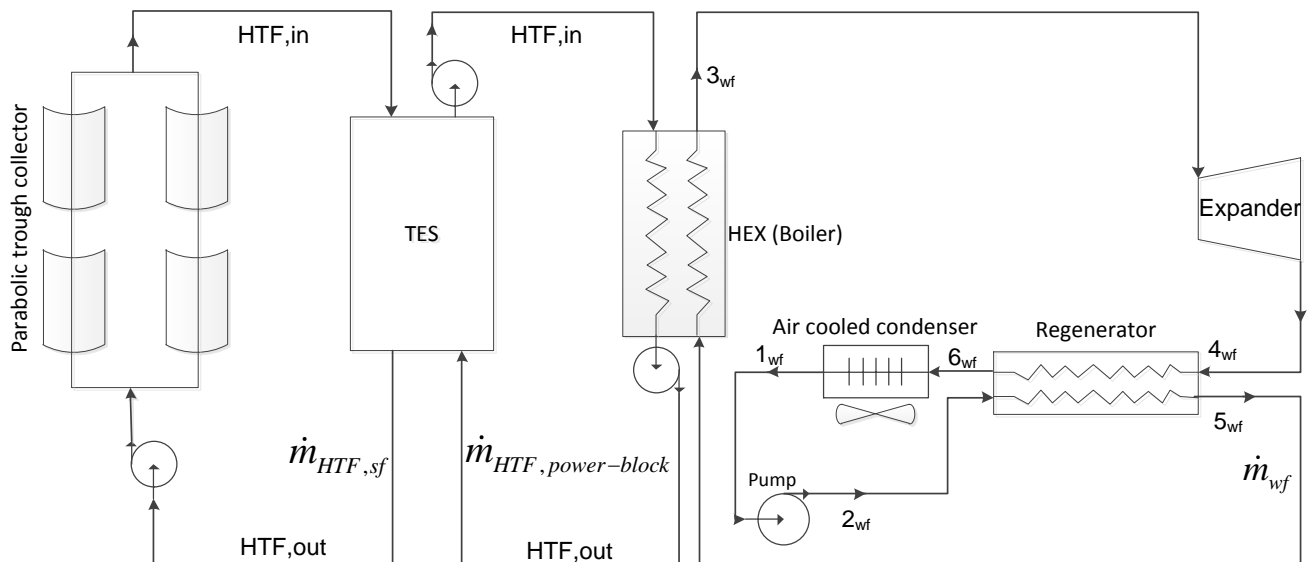


Fig 1: Schematic of an ORC coupled to parabolic trough collector

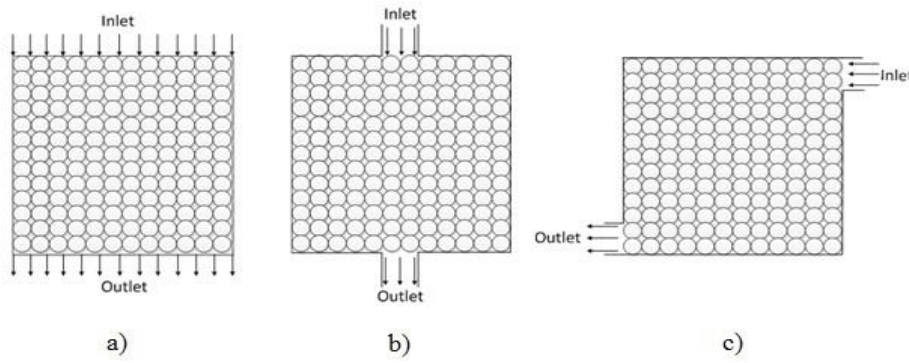


Figure 2: Schematic representation of cross-section at inlets and outlets of all the configurations

Assumptions:

- i. Control strategy followed in the solar field is the regulation of mass flow rate to achieve steady $T_{HTF,in}$. However, for the simulation purposes, mass flow rate across the PB-TES is averaged out and assumed to be constant during the charging process.
- ii. Though, thermo-physical properties of HTF are assumed to be the function of temperature as given in the section 3, for the given operating conditions of HTF, these are taken to be the average of those at $T_{HTF,mean}$ defined as

$$T_{HTF,mean} = \frac{T_{HTF,in} + T_{HTF,out}}{2} \tag{1}$$

- iii. The porosity (ϕ) is 0.45 and the geometry selected has an aspect ratio (L_{PB-TES}/D_{PB-TES}) of unity.
- iv. TES has adiabatic walls.

3. METHODOLOGY

The basic methodology for PB-TES sizing is given in detail in Kshirsagar *et al.*(2015), but the salient features are repeated for the sake of completeness of this paper in Appendix A. PB-TES with uniformly sized spherical balls is modeled as a porous media in Fluent 6.0 and the following governing equations are solved to capture heat transfer issues in radial direction.

$$\phi \frac{\partial \rho_f}{\partial t} + \nabla \cdot (\rho_f \mathbf{v}) = 0 \tag{2}$$

$$\rho_f \left[\frac{1}{\phi} \frac{\partial \mathbf{v}}{\partial t} + \frac{\mathbf{v}}{\phi} \nabla \cdot \left(\frac{\mathbf{v}}{\phi} \right) \right] = -\nabla P + \frac{\mu}{\phi \rho_f} \nabla^2 \mathbf{v} - \frac{\mu}{K} \mathbf{v} \tag{3}$$

$$\left((1-\phi)(\rho c)_s + \phi(\rho c_p)_f \right) \frac{\partial T}{\partial t} + (\rho c_p)_f \nabla T = \nabla \cdot (k_s \nabla T) + \phi \nabla \cdot \nabla T (k_f - k_s) \tag{4}$$

Condition of local thermal equilibrium is assumed to prevail in the tank in the above equation. Also, the flow considered here is laminar as the Reynolds number is well within its range (~400). The HTF inlet is chosen as velocity inlet. The internal surface or volume is selected as porous zone. The walls are chosen as stationary with a no slip condition (Versteeg and Malalasekera, 2007). Viscous resistance in all the directions calculated using Darcy’s law and Ergun’s equation comes out to be $4.878 \times 10^6 \text{m}^{-2}$. The thermo-physical properties of fused silica and ethylene glycol are as follows:

Properties	Ethylene glycol	Fused silica
Density, ρ (kg/m ³)	882	2200
Specific heat, C_p (J/kgK)	3000	740
Thermal conductivity, K (W/mK)	0.1951	1.3
Dynamic viscosity, μ (Pa.s)	6.535×10^{-4}	-

Table 1: Thermo-physical properties of ethylene glycol as HTF and fused silica as pebble material

3.1 Boundary conditions

The mass flow rate during the charging process at the inlet and the outlet is taken as 0.6846 kg/s. The inlet temperature is chosen as 438 K and the tank is initially kept at 358 K. An ‘outflow’ boundary condition is used for the HTF outlet since the details of flow velocities and pressure are not known prior to solving the flow problem (Ansys Inc., 2009). The C-IOC and the U-IOC are axisymmetric in nature and are likewise simulated. The S-IOC is simulated as a three dimensional geometry. The simulation is done for the charging process during excess period of the day. Table 1 shows different characteristics of tank for all the IOCs. The inlet and outlet diameters of ports are so chosen in order to minimize the pressure drop across unit length of the tube to 0.1 kPa/m.

Characteristic	U-IOC	C-IOC	S-IOC
Height (m)	3.4	3.4	3.4
Diameter (m)	3.4	3.4	3.4
Porosity	0.45	0.45	0.45
IO port diameter (m)	3.4	0.4	0.4

Table 2: Characteristics of tank for different IOCs

3.2 Parameter of interest

A new parameter called effectiveness of the TES tank is introduced defined as the ratio of actual to ideal case energy stored at the end of charging process in a PB-TES system designed ignoring radial effects.

$$\varepsilon = \frac{E_{PB-TES,actual}^{t=\text{charging time}}}{E_{PB-TES,ideal}^{t=\text{charging time}}} \quad (5)$$

4. RESULTS AND DISCUSSIONS:

Three different inlet and outlet configurations namely central, uniform and the side are analyzed and compared for the given parameters as mentioned in Table 1. Firstly, U-IOC which is the closest to the ideal configuration is studied. In this case, at any instance, both the fluid and the pebbles in a horizontal plane tend to achieve local equilibrium and no temperature gradients are found. This is mainly due to the fact that all the radial positions in any plane in the tank have an equal access to flow and hence thermal energy. Thus, there are no thermally insulated corners in the tank and hence the storage potential is realized to its maximum as shown in Figure 3.

Though the U-IOC produces the best results, it is not practically realizable as the uniform distribution of fluid is hard to achieve in a real scenario. The second and most popular configuration in literature is reported to be the C-IOC. At the end of charging time (t_{full}), TES system is found to have the isolated corners in the bottom extreme of the tank as shown in Figure 4 depicting the inability of the TES to store energy to its fullest.

In both the scenarios mentioned above, the outlet is placed on the bottom of tank which needs a submersible pump leading to higher exergy losses (Pacheco et al., 2002) and a complicated system. An alternative could be to have the side inlet and outlet configuration (S-IOC) which is easily realizable and has the potential to offer better performance indicators than the central one. Temperature distribution in this case is plotted in Figure 5 at t_{full} wherein thermally isolated corners near the lateral wall are visible.

Effect of these TES configurations is then studied on the ORC performance. Further, envelope heat transfer losses are assumed to minimize the heat recovered potential by 5 %. Thus, in an ideal (U-IOC) scenario designed for a 100 kW system for a vernal equinox day, electricity collected would be around 1140 kWh. The other configurations like C-IOC and S-IOC would deliver only 912 and 997.5 kWh of electricity. These details are shown in Table 3.

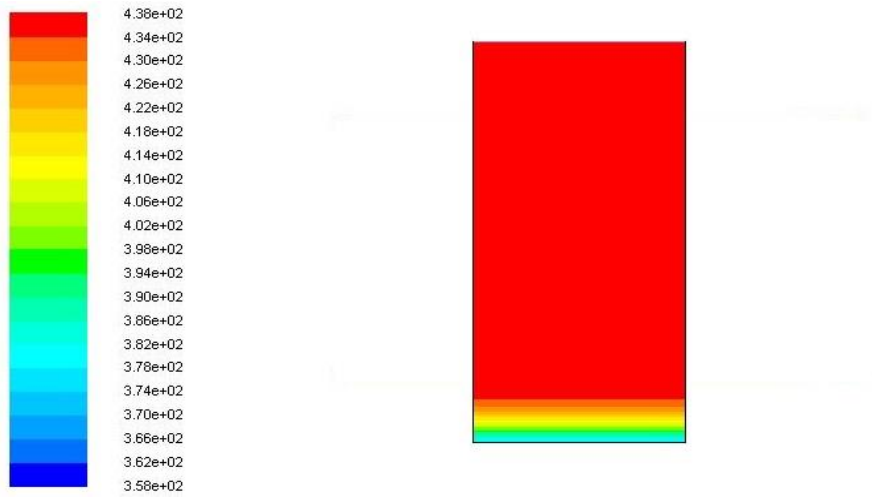


Figure 3: Contours of static temperature for U-IOC after t_{full} (left vertical axis of cylinder denotes the center of tank)

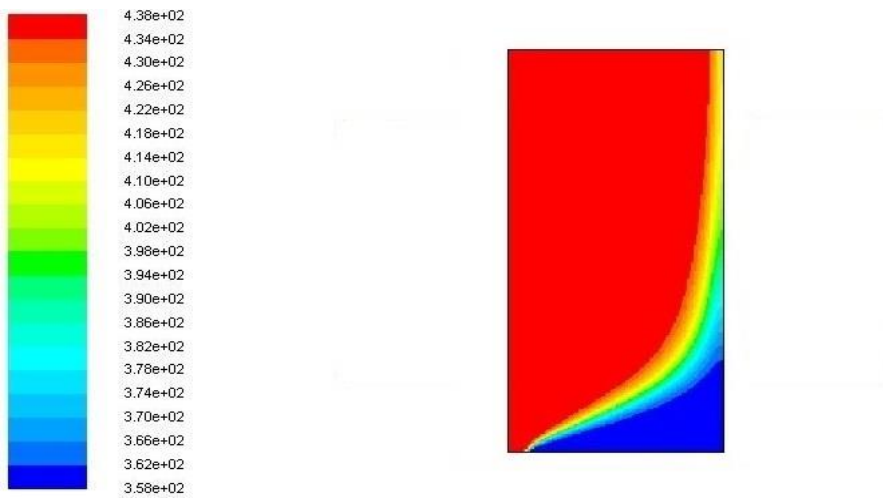


Figure 4: Contours of static temperature for C-IOC after t_{full} (left vertical axis of cylinder denotes the center of tank)

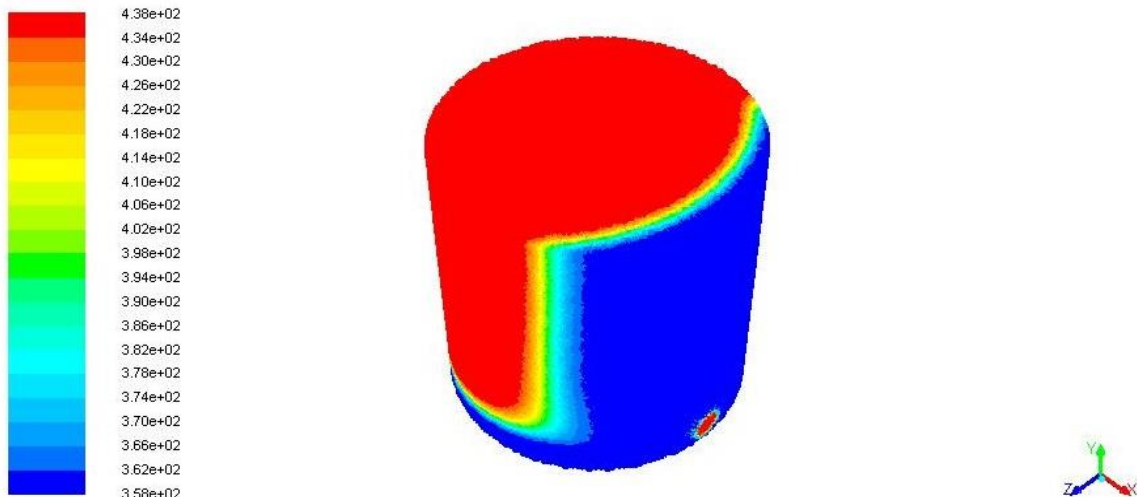


Figure 5: Contours of static temperature for S-IOC after t_{full}

Next, we perform the comparison among the three configurations on the basis of evolution of energy stored and net energy stored at t_{full} . In this regard, Figure 6 shows the variation of HTF outlet temperature with respect to flow time. It can be seen that the HTF outlet temperature in case of uniform configuration stays almost steady throughout t_{full} (358 K) except for the time when thermocline zone reaches the bottom part of the tank (~ 29000 s). In rest of the two cases, HTF outlet temperature starts increasing from its base value of 358 K at the instant (denoted as $t_{short-circuit}$) when the high temperature fluid is near to the bottom part of the tank resulting in isolated corners. In case of C-IOC, $t_{short-circuit}$ is found to be ~ 12000 s whereas for the side inlet and outlet case it is ~ 18000 s. Higher value of $t_{short-circuit}$ for the latter can be explained using the fact that HTF tends to travel more in the tank (along the diagonal) before it reaches the bottom part than in the latter where the HTF travels vertically. These indicate that the heat transfer characteristics of both the configurations are consistent with the above discussion. Finally, the figure shows the side configuration to have intermediate properties between those of the central and uniform.

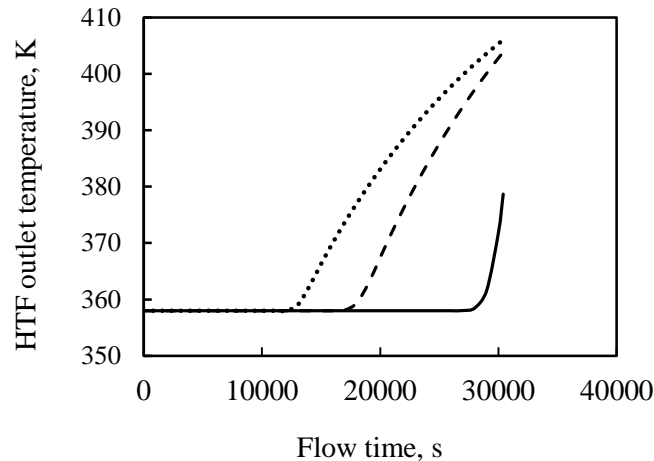


Figure 6: HTF outlet temperature versus flow time for U-IOC, S-IOC and C-IOC.
 Legend: ———U-IOC, ———S-IOC,C-IOC.

Pertaining to the figures above, energy stored in the tank with respect to flow time is plotted in figure 7. Rate at which the energy is stored remains constant with time for the U-IOC throughout the charging process. The same is not true in the other two scenarios. After $t=t_{short-circuit}$, the rate of energy storage decreases which at the end of charging time leads to the lower amount of energies stored. Further, S-IOC fares on the parameter of effectiveness which can store 87.5 % energy as compared to 80 % in the central inlet and outlet case (Table 3).

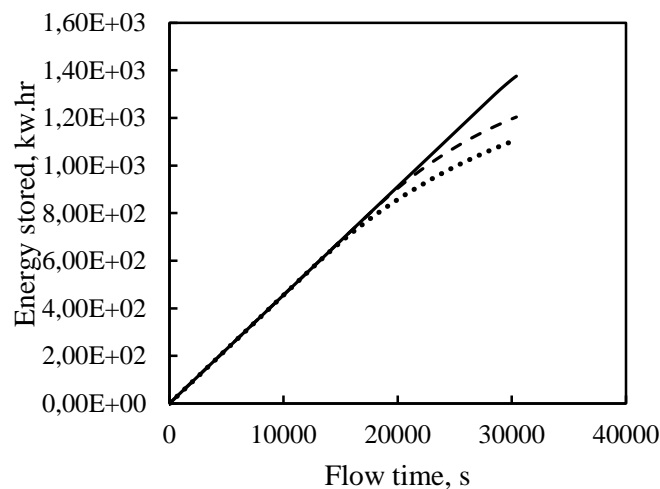


Figure 7: HTF outlet temperature versus flow time for U-IOC, S-IOC and C-IOC.
 Legend: ———U-IOC, ———S-IOC,C-IOC.

Inlet and outlet configuration	Effectiveness (ϵ)	Energy stored per day($1200 \times 0.95 \times \epsilon$)
Uniform	1	1140 kWhr
Central	0.8	912 kWhr
Side	0.875	997.5 kWhr

Table 3: Effectiveness of various IOCs

5. CONCLUSION

CFD simulation of pebble bed based thermal energy storage systems establishes the fact that temperature gradients in the radial direction can significantly affect the heat storage efficiencies which in turn are dependent on the inlet and outlet configuration. A comparative analysis of these systems with different inlet and outlet configurations is presented. The U-IOC is found to be the closest to the ideal case wherein radial temperature gradients are absent. However, practical issues like placement of the discharge pump in this scenario motivates for other alternates. Such an alternate is a configuration with S-IOC which is found to store 7.5 % higher energy than the present state of art with the C-IOC. The future scope of this work may involve rating these different TES tanks for various aspect ratios along with the modeling of simultaneous modeling of charging and discharging process.

REFERENCES

- Garg P., Kumar P., Srinivasan K., Dutta P., 2013, Evaluation of carbon dioxide blends with isopentane and propane as working fluids for organic Rankine cycles, *Applied Thermal Engineering*, Vol. 52, pp 439-448.
- Gregor Taljan, Gregor Verbi, Milos Pantos, Manfred Sakulin, Lothar Fickert, 2012, Optimal sizing of biomass-fired Organic Rankine Cycle CHP system with heat storage, *Renewable Energy*, vol. 41 p. 29-38
- Ulf Herrmann, David W. Kearney, 2002, Survey of Thermal Energy Storage for Parabolic Trough Power Plants, *Journal of Solar Energy Engineering*, Vol. 124/145-152
- G. Zanganeh, A. Pedretti, S. Zavattoni, M. Barbato, A. Steinfeld, 2012, Packed-bed thermal storage for concentrated solar power – Pilot-scale demonstration and industrial-scale design, *Solar Energy*, vol. 86 p. 3084–3098
- Mawire, M. McPherson, 2009, Experimental and simulated temperature distribution of an oil-pebble Bed thermal energy storage system with a variable heat source, *Applied Thermal Engineering*, vol. 29 p. 1086–1095A.
- Hasnain SM. Review on sustainable thermal energy storage technologies. Part1. Heat storage materials and techniques, *Energy Convers Manage*, J1998;39(11):1127–38
- Quoilin, S., Orosz, M., Hemond, H., Lemort, V., 2011, Performance and design optimization of a low-cost solar organic Rankine cycle for remote power generation, *Solar Energy*, vol. 85, no. 5: p. 955-966.
- Orosz, M. S., 2012, ThermoSolar and photovoltaic hybridization for small scale Distributed Generation: Applications for Powering Rural Health, Doctoral dissertation, Massachusetts Institute of Technology.
- Orosz, M. S., Quoilin, S., Hemond, H., Sorce: A Design Tool For Solar Organic Rankine Cycle Systems In Distributed Generation Applications
- Curran, H. M., 1993, Mechanical systems and components, *In: Lof, G. O. G., Active Solar Systems*, MIT Press, Cambridge, MA: p. 693-743

Appendix A

Following steps are used to calculate mass of HTF required operating ORC at its steady operating conditions

a) Energy stored in the TES

The rate at which the energy is available to the TES from the collector is given by eq. 1.

$$\dot{Q}_{collector} = \eta_{collector} DNI_N A_{collector} \quad (A.1)$$

Heat required in power block is given by

$$\dot{Q}_{power-block} = \frac{\dot{P}}{n_{ORC}} \quad (A.2)$$

Also, area (ABCD) = area (AGHD) for the continuous operation of power block for Δt_h time

$$\dot{Q}_{power-block} \Delta t_h = \int_{t_{1h}}^{t_{4h}} \dot{Q}_{collector} dt_h \quad (A.3)$$

It can be noted that heat available from the collector exceeds that of required in the power block in the hours between t_{2h} to t_{3h} and can be stored in the PB-TES. The stored heat can then later be used in the hours between t_{1h} to t_{2h} and t_{3h} to t_{4h} when the heat available from the collector is not enough to run the power block. It can be seen that the heat stored in the surplus hours should be equal to energy used in the deficit hours for the steady operation of power block. Energy that need to be stored in the PB-TES is thus given as

$$\Delta E_{PB-TES} = \text{area}(\text{arc}(BC)) - \text{area}(BCFE) \quad (A.4)$$

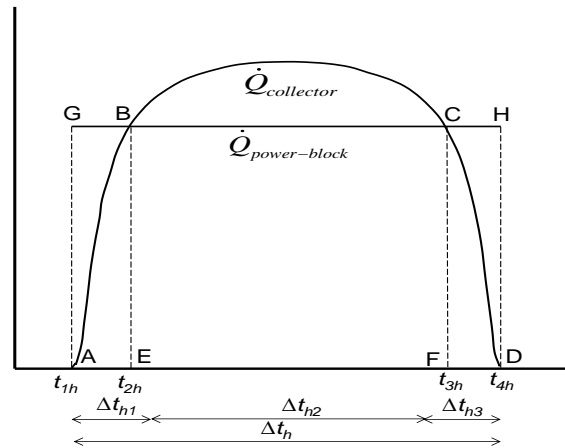


Figure A.1 Plot of a typical DNI profile with a constant power output

Eq.3 can be used to calculate the area of collector required. Eqs. (A.1) and (A.2) are plotted in Fig. 3.

$$\Delta E_{PB-TES} = \text{area}(\text{arc}(BC)) - \text{area}(BCFE) \quad (A.5a)$$

Or

$$\Delta E_{PB-TES} = \int_{t_{2h}}^{t_{3h}} \dot{Q}_{collector} dt_h - \dot{Q}_{power-block} \Delta t_{3h} \quad (A.5b)$$

b) Mass of HTF stored in PB-TES

Total energy stored in the PB-TES is given by

$$\Delta E_{PB-TES} = \Delta E_{HTF} + \Delta E_{Pebble} \quad (A.6)$$

Where,

$$\Delta E_{HTF} = M_{HTF} c_{p_{HTF}} \Delta T_{HTF} \quad (A.7)$$

$$\Delta E_{Pebble} = M_{Pebble} c_{p_{Pebble}} \Delta T_{Pebble} \quad (A.8)$$

Condition of local thermal equilibrium is assumed to be persistent in the PB-TES making the temperature of HTF and pebble equal.

PB-TES can be modeled as a porous media with porosity or void fraction equal to φ where,

$$\varphi = \frac{V_{HTF}}{V_{Total}} \quad (A.9)$$

Where V_{Total} and V_{HTF} is the volume of the PB-TES.

V_{Total} can be calculated from the above equation.

$$\Delta E_{PB-TES} = (\varphi \rho_{HTF} c_{p_{HTF}} + (1 - \varphi) \rho_{Pebble} c_{p_{Pebble}}) V_{Total} \Delta T_{HTF} \quad (A.10)$$

Using Eqs. (B.7), (B.10) and (B.4), M_{HTF} can be simplified to

$$M_{HTF} = \frac{\Delta E_{PB-TES}}{c_{p_{HTF}} \Delta T_{HTF}} - M_{Pebble} \frac{c_{p_{Pebble}}}{c_{p_{HTF}}} \quad (A.11)$$

Above equation establishes an inverse relationship between M_{HTF} and ΔT_{HTF} .

NOMENCLATURE

l	Latitude	(°)
ω	Hour angle	(°)
n	Day number	(-)
δ	Declination	(°)
β	Solar altitude angle	(°)
φ	Solar azimuth angle	(°)
γ	Surface solar azimuth angle	(°)
θ	Angle of incidence	(°)
α	Tilt angle	(°)
A	Apparent solar irradiation at air mass equal to zero	(W/m ²)

B	Atmospheric extinction coefficient	(-)
C_N	Clearness number	(-)
T	Temperature	(K)
M	Mass	(kg)
E	Energy	(J)
V	Volume	(m ³)
$A_{collector}$	Area of collector field	(m ²)
\dot{Q}	Power	(W)
\dot{P}	Output power	(W)
t	Time	(Hours)
c_p	Specific heat	(J/kgK)
η	Efficiency	(-)
ρ	Density	(kg/m ³)
ε	Effectiveness	(-)
\dot{m}	Mass flow rate	(kg/s)
ϕ	Porosity	(-)
v	Seepage velocity	(m/s)
k	Thermal conductivity	(W/mK)
μ	Dynamic viscosity	(Pa.s)

Subscript

h	hour
HTF	heat transfer fluid
$Pebbles$	pebble
$PB-TES$	pebble bed thermal energy storage
$power-block$	power block
$collector$	collector
$Total$	total tank
f	fluid
s	solid
$full$	full
$short-circuit$	condition when HTF at 438 K reaches outlet

Abbreviations

TES	thermal energy storage
HTF	heat transfer fluid
DNI	direct normal insolation
PB-TES	pebble-bed thermal energy storage
ORC	organic Rankine cycle
IOC	inlet and outlet configuration
U-IOC	uniform inlet and outlet configuration
C-IOC	central inlet and outlet configuration
S-IOC	side inlet and outlet configuration

ACKNOWLEDGEMENT

This research is based upon work supported by the Solar Energy Research Institute for India and the U.S. (SERIUS) funded jointly by the U.S. Department of Energy subcontract DE AC36-08G028308 (Office of Science, Office of Basic Energy Sciences, and Energy Efficiency and Renewable Energy, Solar Energy Technology Program, with support from the Office of International Affairs) and the Government of India subcontract IUSSTF/JCERDC-SERIIUS/2012 dated 22nd Nov. 2012.

THERMO-ECONOMIC ANALYSIS OF A MIXTURE OF RC-318 AND PENTANE AS A WORKING FLUID IN A HIGH TEMPERATURE ORC

Ankit Saini¹, Karthik G.M.²⁺, Pardeep Garg^{2*}, Thirumalai N.C.³, Pramod Kumar^{2†}, Vinod Srinivasan^{2‡}

¹PEC University of Technology, Vidya Path,
Sector 12, Chandigarh 160012, India
E-mail: ankitsaini.bemec12@pec.edu.in

²Indian Institute of Science, C V Raman Ave,
Bengaluru, Karnataka 560012, India
⁺E-mail: karthik.gm1@gmail.com
^{*}E-Mail: pardeep_1127@yahoo.com
[†]E-Mail: pramod@mecheng.iisc.ernet.in
[‡]E-Mail: vinods@mecheng.iisc.ernet.in

³Center for Study of Science, Technology & Policy, No. 18,
Mayura Street, 10th Cross, Papanna Layout, Nagashettyhalli,
RMV 2nd stage, Bengaluru, Karnataka 560094, India
E-mail: thirumalai@cstep.in

*Corresponding author

ABSTRACT

In this paper, the potential of realizing a low cost power block in concentrated solar power applications is investigated. A conventional steam Rankine cycle operates under vacuum pressures in the condenser which manifests in considerably high volumetric flow rates at the expander exhaust. This calls for large equipment size and makes the power block expensive. This paper presents the idea of substituting the conventional power block by a high temperature (~ 350 °C) and equally efficient organic Rankine cycle (ORC) which works on a mixture of pentane and RC-318 (70 % and 30 % on a molar basis). A comparison is made on a one-to-one basis with identical operating conditions for a given solar field equipment. It is found that the proposed mixture has an initial investment cost ~ 25 % lower than steam in the Rankine cycle due to its significantly lower volumetric flow rates.

1. INTRODUCTION

As demand for energy increases across the world along with proliferation of awareness about humankind's responsibility towards nature, major advancements have been made in the search for cleaner sources of energy. Amongst the renewable energy resources, a lot of impetus has been put on concentrated solar thermal (CST) and as a consequence, it has witnessed great technological leaps in the past decade.

Conventional steam Rankine cycles used in fossil fuel based power plants have been directly adapted to CST since it has evolved as an efficient power block over the last two centuries. Despite this, steam suffers from low densities at the expander exhaust resulting in prodigious size of the equipment. Furthermore, issues like wet expansion render the turbine systems complicated. These limitations have led to other cycles being suggested for CST technology. Garg et al. (2013a, 2014) investigated and proposed CO₂ cycles for solar thermal applications, suggesting that the compactness of such cycles could be explored as means of lowering the levelized cost of energy (LCOE). Contemporarily, organic fluids have also been suggested to supersede steam as a working fluid and reviewed by Tchanche et al. (2011), albeit for low temperature heat sources such as waste heat recovery or geothermal. Significant amount of work by Quoilin exists on thermo-economic evaluation of organic

Rankine cycles (Quoilin et al. 2009, Quoilin et al. 2011a and Quoilin 2011b). Furthermore, different ORC working fluids have been investigated by Mikielwicz and Mikielwicz (2010), Wang et al. (2011) and Garg et al. (2013c). Low Carnot efficiencies of these cycles when coupled to a comparatively expensive solar field result in higher investment costs and encourage investigation of high temperature ORCs. Buoyed by this motivation, present paper suggests a new working fluid for a high temperature ORC which can compete with the solar steam Rankine cycle on thermo-economic platforms.

2. SOLAR-ORGANIC RANKINE CYCLE DETAILS

Figure 1 shows a schematic of a solar-ORC power block which consists of two closed loops, namely a) heat transfer fluid (HTF) loop and b) working fluid loop. Parabolic troughs concentrate sunlight onto tube-like receivers carrying cold HTF from a (Thermal Energy Storage) TES tank where it gets heated up and makes its way back to the TES tank. The heat from the hot HTF is thus stored in the TES tank and is then transferred to the working fluid in a heat exchanger to produce pressurized vapor, which is further used to drive turbines to generate power.

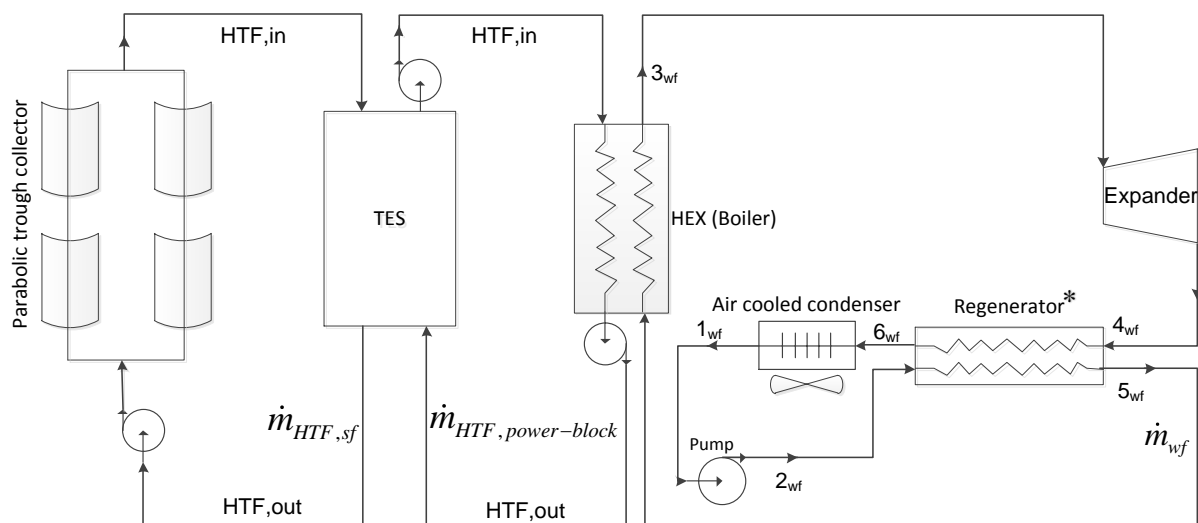


Figure 1: Schematic of an ORC. *Regenerator is not present in case of steam Rankine cycle

In an ORC, low pressure and low temperature liquid at state 1_{wf} is pumped to a higher pressure state, 2_{wf} which is then preheated in a regenerator to state 5_{wf} by recovering heat from cooling the expander exhaust from state 4_{wf} to state 6_{wf} . Remaining heat addition from state 5_{wf} to 3_{wf} occurs in a heater via a heat transfer fluid. Working fluid is then further expanded in a turbine till state 4_{wf} . Regenerator outlet on low pressure side at state 6_{wf} is then cooled in an air cooled condenser till state 1_{wf} to complete the cycle. The power block of a steam Rankine cycle is very similar to the one above except that it does not incorporate a regenerator.

2.1 Choice of working fluid for high temperature ORCs

NIST REFPROP database is exhaustively searched and 18 fluids are shortlisted based on the criteria of having zero ozone depletion potential (ODP) and/or pressure inside the condenser at $45\text{ }^{\circ}\text{C}$ above the atmospheric pressure. These fluids are listed in Table 1. The maximum temperature limit up to which the equation of state (EOS) used in REFPROP is valid is also mentioned. Very few fluids have EOS valid beyond $300\text{ }^{\circ}\text{C}$, out of which propane and R143a have high saturation pressures at $45\text{ }^{\circ}\text{C}$ ($>15\text{ bar}$) demanding very high upper cycle pressure ($p_{2,wf}$) and hence cannot be used economically for ORC applications. On the other hand butane, pentane and RC318 have manageable condenser pressures but suffer from issues like flammability or high global warming potential (GWP). Based on the conclusions drawn from our previous studies (Garg et al., 2013b), mixture of RC318 (high GWP) with butane or pentane (flammable) can be made non-flammable if its molar concentration of flammable component is equal to or less than 70 % (Zabetakis, 1924). It turns out that these mixtures

have acceptable GWPs as well. The mixture of RC-318 and pentane was chosen over the RC-318 and butane mixture since it exhibited a greater temperature glide in the condenser. The rationale was that a greater temperature glide facilitates the use of cheaper and more compact condenser heat exchangers by increasing the LMTD. Also, alkanes with five or more carbon atoms tend to result in high pressure systems.

Table 1: Shortlisted fluids from the NIST REFPROP database

<i>Fluid</i>	<i>Saturation pressure at 45 °C (bar)</i>	<i>Maximum temperature (°C)</i>	<i>Maximum pressure (bar)</i>
<i>R-1234yf</i>	11.5	137	300
<i>R-1234ze</i>	8.8	147	200
<i>R-218</i>	14.4	167	200
<i>R-245fa</i>	2.9	167	2000
<i>R-134a</i>	11.6	182	700
<i>R-142b</i>	6.0	197	600
<i>R-227ea</i>	8.0	202	600
<i>R-365mfc</i>	1.2	227	350
<i>R-245ca</i>	2.1	227	600
<i>R-236ea</i>	3.9	227	600
<i>R-152a</i>	10.4	227	600
<i>R-125</i>	22.6	227	600
<i>R-141b</i>	1.6	227	4000
<i>Butane</i>	4.3	302	2000
<i>Pentane</i>	1.3	327	1000
<i>RC-318</i>	5.7	350	600
<i>R143a</i>	20.6	377	1000
<i>Propane</i>	15.3	377	10000

3. METHODOLOGY

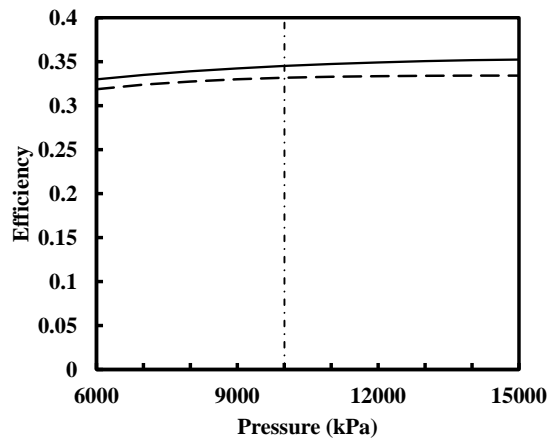


Figure 2. Effect of increasing the evaporator pressure on the efficiency of the steam Rankine cycle
Legend: — steam Rankine cycle, - - - ORC.

To facilitate comparison between a solar steam Rankine cycle and an ORC on a one-to-one basis, both the cycles are modelled with the same solar field aperture area. Hence, the thermal heat input for the both the cycles is the same and the cost associated with the solar equipment is not considered in this paper. Further, the evaporator pressure and lowest temperature of the both the cycles is fixed at 100 bar and 45 °C respectively using the same rationale. 100 bar was chosen as the evaporator pressure for both the cycles because it was observed that with increasing the pressure beyond 100 bar, the

efficiency increased only marginally. Figure 2 illustrates the decreasing benefits, in terms of efficiency, of increasing the evaporator pressure.

3.1 Solar field

The solar field is assumed to provide a supply of HTF with inlet and outlet temperatures of 293 °C and 393 °C, respectively to either cycle which is in accordance with a majority of parabolic trough CST plants across the world. The place chosen for the case study is Ahmedabad, India, situated at 23.07 °N, roughly near the Tropic of Cancer and the day assumed is vernal equinox, i.e. 21st March. Table 2 lists all the solar field details.

Table 2. Solar side details assumed for the case study. DNI stands for direct normal insolation.

	Steam	ORC
<i>DNI (kW-hr_{th}/m²-day)</i>	5.3	5.3
<i>Solar-field aperture area (m²)</i>	40,000	40,000
<i>Collector efficiency (%)</i>	70	70
<i>Storage efficiency (%)</i>	95	95
<i>Thermal energy storage (hours)</i>	12	12
<i>Thermal heat input (MW_{th})</i>	143	143

3.1. Power cycles

T-s and *p-h* charts for the steam Rankine cycle and ORC are shown in Figures 3 and 4, respectively. Note that the pumping processes 1_{wf} → 2_{wf} are not visible on the *T-s* charts of either cycle since the temperature and entropy changes across the pump are relatively negligible. Modeling details for such an ORC could be found in Garg et al. (2013b) and for the sake of completeness are repeated here.

- i. The ambient temperature is assumed to be 30 °C.
- ii. Turbine and pump isentropic efficiencies are assumed to be 0.9 i.e.

$$\eta_{turbine} = \frac{h_{3,wf} - h_{4,wf}}{h_{3,wf} - h_{4,wf}} = 0.9 \quad (1)$$

$$\eta_{pump} = \frac{h_{2,wf} - h_{1,wf}}{h_{2,wf} - h_{1,wf}} = 0.9 \quad (2)$$

- iii. All heat exchangers are modelled as counter flow heat exchangers with approach temperature of 20 °C. Mathematically,

$$T_{3,wf} = T_{HTF,in} - T_{approach} \quad (3)$$

and for the ORC regenerator,

$$T_{6,wf} = T_{2,wf} + T_{approach} \quad (4)$$

- iv. Thermodynamic property data is extrapolated by 25 °C for the sake of comparison.

3.2 Cost functions

To compute the initial investment cost of the power blocks, appropriate cost functions are formulated for the major cycle components, namely heat exchangers, turbines and pumps and condensers. The expressions are summarized in detail in Table 3.

For the pump, the cost function listed by Arsalis (2008) is used. For all heat exchangers other than condensers, Ho et al. (2015) is referred to and appropriate cost function is used. Turbine costs have been adapted from Silveira and Tuna (2003) which agree well with numbers extrapolated from Black & Veatch, NREL (2012). Finally, condenser cost numbers are based on quotations received from one of the leading air cooled condenser manufacturers. Correction factors have been applied wherever applicable.

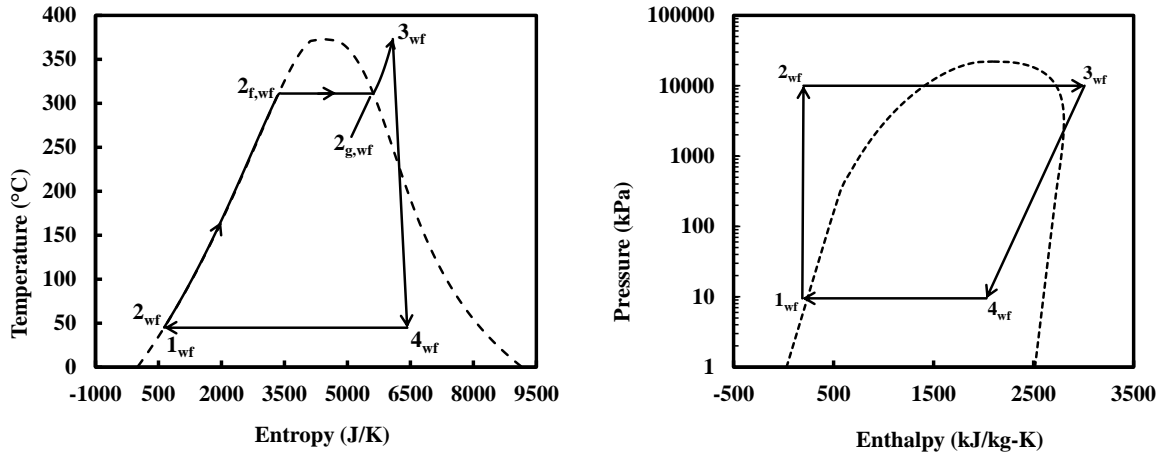


Figure 3: Steam Rankine cycle on $T-s$ and $p-h$ charts (100 bar, 373 °C).

Legend: — — — saturation curve, — cycle processes.

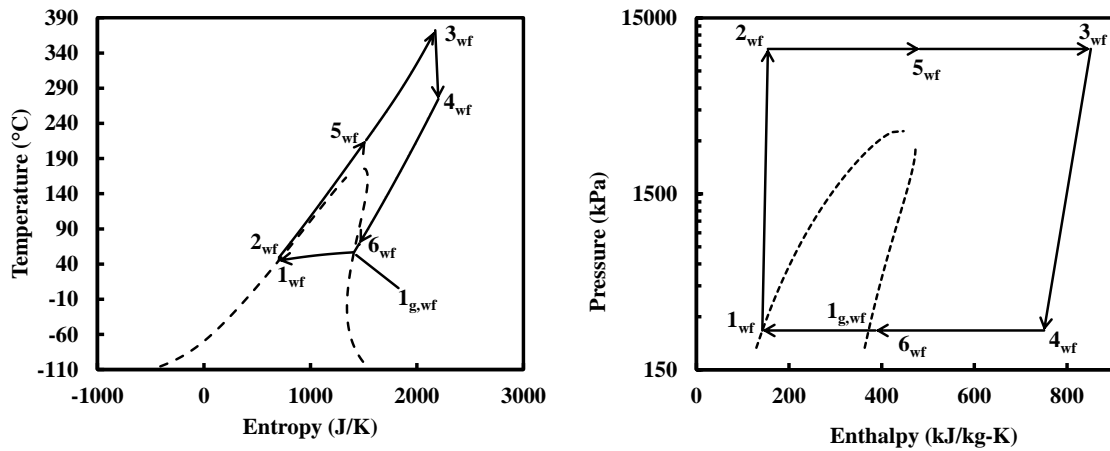


Figure 4: ORC on $T-s$ and $p-h$ charts (100 bar, 373 °C).

Legend: — — — saturation curve, — cycle processes

Table 3. Component cost models.

	Variable description	Model equation	
C_{pump}	Pump component cost	$C_{pump} = 442 \cdot (\dot{W}_{pump})^{0.71} \cdot 1.41 f_{\eta}$	(5)
f_{η}	Efficiency correction factor	$f_{\eta} = 1 + \left(\frac{1-0.8}{1-\eta_{pump}} \right)$	(6)
C_{boiler}	Boiler component cost	$C_{boiler} = f_1 \cdot A^{f_2} \cdot f_M \cdot f_p + f_3$	(7)
		where f_1, f_2, f_3 depend upon the type of heat exchanger, f_M is the material correction factor and f_p is the pressure correction factor	
$C_{turbine}$	Turbine component cost	$C_{turbine} = 3540 \cdot \dot{W}_{turbine}^{0.71}$	(8)
$C_{condenser}$	Condenser component cost	$C_{condenser} = 876.6 \cdot A_{frontal} + 1.311 \times 10^6$	(9)

3.3 Performance indicators

The parameters of interest are the overall thermal efficiency of cycle defined as

$$\eta_{th,steam} = \frac{(h_{3,wf} - h_{4,wf}) - (h_{2,wf} - h_{1,wf})}{h_{3,wf} - h_{2,wf}} \quad (10)$$

$$\eta_{th,orc} = \frac{(h_{3,wf} - h_{4,wf}) - (h_{2,wf} - h_{1,wf})}{h_{3,wf} - h_{5,wf}} \quad (11)$$

volumetric flow rate for a heat addition of \dot{Q} in the boiler heat exchanger, calculated as

$$vfr_{steam} = \frac{\dot{Q}}{(h_{3,wf} - h_{2,wf}) \times \rho_{steam}} \quad (12)$$

$$vfr_{mixture} = \frac{\dot{Q}}{(h_{3,wf} - h_{5,wf}) \times \rho_{mixture}} \quad (13)$$

and temperature glide in the ORC, calculated as

$$\Delta T_{glide} = T_{1_{g,wf}} - T_{1_{wf}} \quad (14)$$

where $1_{g,wf}$ corresponds to the intersection of condenser isobar and saturation vapor line. As pointed out earlier, a greater temperature glide in the condenser increases the LMTD and thereby, reduces the heat transfer area required. This allows for more compact and cheaper heat exchangers.

The final performance parameter is the cost of cycle per unit of electricity generated (\$/W_e)

All calculations are carried out on MATLAB 8.3.0.532 (R-2014a) platform, which is programmed to invoke REFPROP for all thermodynamic property calculations.

4. RESULTS AND DISCUSSIONS

4.1 Efficiency

For identical thermal input from the solar field for the steam Rankine cycle and the ORC, the efficiencies computed are 34.52 % and 33.18 %, respectively which manifest into net-work outputs of 49.43 MW and 47.51 MW, respectively. Hence, on a one-to-one thermodynamic comparison, steam Rankine cycle is slightly more efficient and economic analysis needs to be performed. On further study of the costs involved, evidence in support of ORC begins to accumulate.

4.2 Component Costs

4.2.1 Pump

The pressure ratios in the steam Rankine cycle and mixture based ORC are around 1000 and 40, respectively. However, the pump work in the case of the ORC is roughly 8 times more than the same in steam Rankine cycle. This is expected since the specific volume of water is less as compared to the mixture. Arsalis (2008) performed a thermo-economic analysis of a hybrid solid oxide fuel cell-gas turbine-steam turbine power plants. Correspondingly, cost functions for pumps have been adopted for this paper which are applicable to power scales considered here.

4.2.2 Regenerative heat exchanger

The regenerative heat generator is absent in the case of steam Rankine cycle while in ORC, its heat duty is 127.3 MW. The hot working fluid is at a pressure of 2.5 bar with inlet and outlet temperatures of 272 °C and 68 °C, respectively while the cold fluid is at a pressure of 100 bar with inlet and outlet temperatures of 49 °C and 215 °C, respectively. The log mean temperature difference (LMTD) computed is 37 °C. The temperature profile of the ORC regenerator is shown in Figure 5. An appropriate pressure correction factor is considered while modifying the cost function for ORC application suggested by Taal et al. (2003).

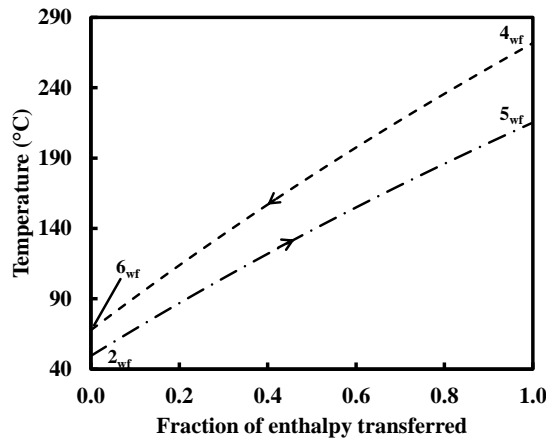


Figure 5. Temperature profile in the ORC regenerator. Legend: --- hot working fluid, - · - · - cold working fluid

4.2.3 Boiler

Since the thermal heat input from solar field is identical for both the cycles, the heat duty of the boilers are identical as well at 143.2 MW. The LMTD for the steam Rankine cycle is found to be 83 °C while for the ORC, it is 49 °C. Figure 6 shows the temperature profiles in the boilers for both the cycles. Note that phase change occurs inside the boiler for the steam Rankine cycle whereas there is no phase change inside the ORC boiler. The ORC is transcritical. Boiler cost estimated is in good agreement with estimations from Taal et al. (2003).

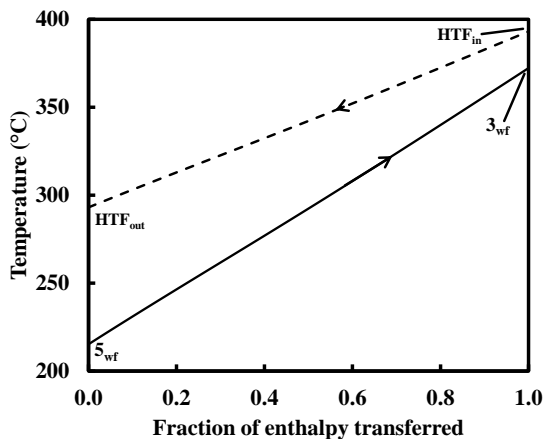


Figure 6a: Temperature profile in the ORC boiler. Legend: --- HTF, — working fluid

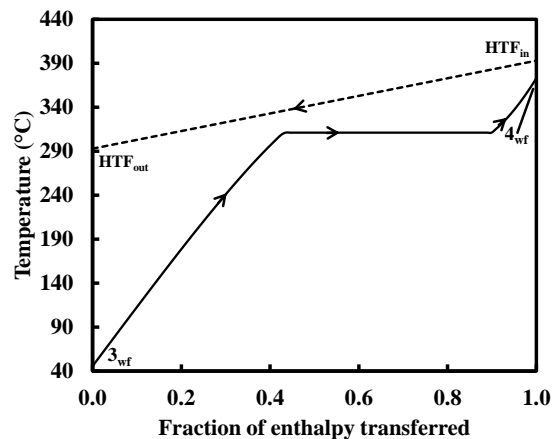


Figure 6b: Temperature profile in the steam Rankine cycle boiler. Legend: --- HTF, — working fluid

4.2.4 Turbine

The volumetric flow rates at the turbine exhaust for the ORC is about one-tenth of the same for the steam Rankine cycle. This flow rate promises decisive savings in equipment size for the ORC. A cost estimate was first made using the function suggested by Silveira and Tuna (2003) and cross validated with numbers suggested by Black & Veatch (contracted by NREL, 2012) for steam turbines employed in a pulverized coal fired Rankine cycle in a 606 MW plant. Furthermore, additional care is taken to scale the cost thus obtained by a factor of 2 since steam turbines are rated according to temperatures achieved in coal fired Rankine cycles, which are generally around 600 °C. For a solar steam Rankine cycle working at a maximum temperature of about 370 °C, the specific work output is 2 times the specific work output for a coal powered Rankine cycle. The corresponding cost for a turbine operating in the ORC cycle is taken to be one-fifth of the cost of a turbine operating in the solar Rankine cycle. The rationale behind this number is the fact that the volumetric flow rates in the ORC is one-tenth the volumetric flow rates in the steam Rankine cycle. Hence, ideally, the turbine cost would be close to

one-tenth but following a conservative approach and allowing for non-linear variation of cost of the turbine with flow rates, one-fifth fraction is set as the maximum limit.

4.2.5 Condenser

Air cooled condenser (ACC) is considered to reject the cycle waste heat to the ambience. Turchi et al. (2010b) proposed that air cooled condenser are more cost-effective for solar Rankine cycles than evaporative cooling. A detailed model for ACC can be found in Vidhi et al. (2014). The algorithm to optimize the ACC area and hence cost is different in both the cycles. In steam, the criterion is to minimize the pressure drop on the steam side as the work output is highly sensitive to steam pressure drop in condenser. For example, a 3 % pressure drop in steam condenser is found to drop the cycle efficiency by 1 %. However, in case of ORC, the parameter to optimize is fan power which is set at 1 % of the plant output. Furthermore, in case of mixture based ORC, temperature glide across the condenser increases the effective LMTD resulting in lower condenser area. Table 4 lists the condenser details for either cycle.

Table 4. Condenser design details for steam Rankine and ORC.

<i>Condenser details</i>	<i>Steam</i>	<i>ORC</i>
<i>Frontal area (m²)</i>	23600	8200
<i>Fan power (kW)</i>	15.52	64.9
<i>Pressure drop on working fluid side (kPa)</i>	0.61	1.8
<i>LMTD (°C)</i>	15	27.2
<i>Temperature glide (°C)</i>	0	11.17

Table 5 compares the operation parameters and the component costs for each cycle and the resulting \$/kW_e. The 916 \$/kW for the steam Rankine cycle is found to be in good agreement with the cost of the power block (940 \$/kW in 2010) suggested by Turchi et al. (2010a).

Although the ORC heat exchangers are more expensive than their steam counterpart due to lower LMTDs, the cost savings achieved in a more compact turbine (due to lower volumetric flow rates) and condenser (due to temperature glide) sufficiently compensate with the result that the mixture based ORC has a significantly lower initial investment cost for a 50 MW_e plant studied in this paper. This suggests a scope of realizing lower energy generation costs.

6. CONCLUSIONS

A thermo-economic evaluation of a steam Rankine cycle and an ORC for similar operation conditions and power outputs suggests the promise of organic working fluids for high temperature ORCs. Key conclusions are listed below:

1. The thermal efficiency of steam Rankine is only marginally better than that of the ORC.
2. The volumetric flow rate at the exhaust of turbine in the ORC is one-tenth of the same in steam Rankine. Hence, significant cost savings can be realized in the ORC turbine.
3. Temperature glide of the working fluid across the ORC condenser manifests into a higher LMTD and thus lesser heat transfer area facilitating a more compact and cheaper condenser. The cost savings in condenser are decisive in realizing its lower initial investment costs.
4. Although regenerator heat exchanger contributes to additional cost for the ORC, the significant difference in the \$/kW_e for the two cycles suggests that high temperature ORCs are viable substitutes for the steam Rankine cycle and worth investigating further in detail.

It must be appreciated that although the imposed operating conditions constrained the cycles from operating at their thermo-economic optima, the cost numbers generated nevertheless encourage further investigation of high temperature ORCs. Future scope of work may include comparison of the two cycles operating at their thermo-economic optima, use of more accurate functions or database for

thermodynamic data points and LCOE computations. Inhibiting feature is the thermal stability of organic fluids at high temperatures.

Table 5. Steam Rankine cycle and ORC design, performance

	<i>Steam</i>	<i>ORC</i>
$T_{max}(\text{°C})$	373	373
$T_{min}(\text{°C})$	45	45
$P_{max}(\text{MPa})$	10	10
$P_{min}(\text{MPa})$	0.009	0.250
<i>Pressure ratio</i>	1111	39.8
$\eta_{turbine}(\%)$	0.9	0.9
$\eta_{pump}(\%)$	0.9	0.9
$T_{amb}(\text{°C})$	30	30
$\Delta T_{htf}(\text{°C})$	100	100
$v_{fr}(\text{m}^3/\text{s})$	604.6	62.95
$\dot{W}_{turbine}(\text{MW}_e)$	50	52.2
$\dot{W}_{pump}(\text{MW}_e)$	0.6	4.7
<i>Net Power</i> (MW_e)	49.4	47.5
<i>Efficiency</i> (%)	34.52	33.18
<i>Boiler</i> ($\$/\text{kW}_e$)	157	261
<i>Regenerator</i> ($\$/\text{kW}_e$)	N/A	110
<i>Cooling</i> ($\$/\text{kW}_e$)	445	175
<i>Compression</i> ($\$/\text{kW}_e$)	4	16
<i>Expansion</i> ($\$/\text{kW}_e$)	311	130
<i>Total</i> ($\$/\text{kW}_e$)	917	692

NOMENCLATURE

Symbols

C	component cost	US \$
c_p	specific heat at constant pressure	kJ/kg K
f	efficiency correction factor	–
\dot{m}	mass flow rate	kg/s
p	pressure	bar
\dot{Q}	heat transfer rate	kW
T	temperature	K
\dot{W}	power output	kW
v_{fr}	volumetric flow rate	m^3/s

Greek letters

η	efficiency	–
ρ	density	kg/m^3

Subscripts

amb	ambient
-----	---------

f	saturated liquid
g	saturated vapor
htf	heat transfer fluid
in	inlet
out	outlet
η	efficiency
th	thermal
wf	working fluid
1 to 6	states on ideal thermodynamic cycle

Superscripts

'	states on real thermodynamic cycle
---	------------------------------------

REFERENCES

- Arsalis, A., 2008, Thermo-economic modeling and parametric study of hybrid SOFC-gas turbine-steam turbine power plants ranging from 1.5 to 10MW_e, *Journal of Power Sources*, vol. 181: p. 313-326
- Black & Veatch, 2012, Cost and performance data for power generation technologies, *Prepared for National Renewable Energy Laboratory*
- Garg, P., Kumar, P., Srinivasan, K., 2013a, Supercritical carbon dioxide Brayton cycle for concentrated solar power, *The Journal of Supercritical Fluids*, vol. 76: p. 54-60
- Garg, P., Kumar, P., Srinivasan, K., Dutta, P., 2013b, Evaluation of isopentane, R-245fa and their mixtures as working fluids for organic Rankine cycles, *Applied Thermal Engineering*, vol. 51: p. 292-300
- Garg, P., Kumar, P., Srinivasan, K., Dutta, P., 2013c, Evaluation of carbon dioxide blends with isopentane and propane as working fluids for organic Rankine cycles, *Applied Thermal Engineering*, vol. 52: p. 439-448
- Garg, P., Srinivasan, K., Dutta, P., Kumar, P., 2014, Comparison of CO₂ and Steam in Trans-critical Rankine Cycles for Concentrated Solar Power, *SolarPACES 2013 International Conference*, Energy Procedia: p. 1138-1146
- Ho, C.K., Carlson, M., Garg, P., Kumar, P., 2015, Cost and performance tradeoffs of alternative solar-driven S-CO₂ Brayton cycle configurations, *ASME 2015 Power and Energy Conversion Conference*
- Mikielewicz, D., Mikielewicz, J., 2010, A thermodynamic criterion for selection of working fluid for subcritical and supercritical domestic micro CHP, *Applied Thermal Engineering*, vol. 30: p. 2357-2362
- Peard, M.G., Stubbs, F.J., Hinshelwood, C., Danby, C.J., 1952, The kinetics of thermal decomposition of branched-chain paraffin hydrocarbons, *Proceedings of the Royal Society of London. Series A, Mathematics and Physical Sciences*, vol. 214: p. 330-338
- Quoilin, S., Declaye, S., Tchanche, B.F., Lemort, V., 2011a, Thermo-economic optimization of waste heat recovery Organic Rankine Cycles, *Applied Thermal Engineering*, vol. 31: p. 2885-2893
- Quoilin, S., Lemort, V., 2009, Technological and Economical Survey of Organic Rankine Cycle Systems, *Economics and management of energy in industry*
- Quoilin, S., Orosz, M., Hemond, H., Lemort, V., 2011b, Performance and design optimization of a low-cost organic Rankine cycle for remote power generation, *Solar Energy*, vol. 85: p. 955-966
- Silveira, J.L., Tuna, C.E., 2003, Thermo-economic analysis method for optimization of combined heat & power systems. Part 1, *Progress in Energy and Combustion Science*, vol. 29: p. 479-485
- Taal, M., Bulatov, I., Klemes, J., Stehlik, P., 2003, Cost estimation and energy price forecasts for economic evaluation of retrofit projects, *Applied Thermal Engineering*, vol. 23: p. 1819-1835
- Tchanche, B.F., Lambrinos, Gr., Frangoudakis, A., Papadakis, G., 2011, Low-grade heat conversion into power using organic Rankine cycles – A review of various applications, *Renewable and Sustainable Energy Reviews*, vol. 15: p. 3963-3979
- Turchi, C., 2010, Parabolic Trough Reference Plant for Cost Modeling with the Solar Advisor Model (SAM), *Technical Report NREL/TP-550-47605*

- Turchi, C., Mehos, M., Ho, C.K., Kolb, G.J., 2010, Current and Future Costs for Parabolic Trough and Power Tower Systems in the US Market, *SolarPACES 2010 International Conference*, NREL/CP-5500-49303
- Vidhi, R., Garg, P., Orosz, M.S., Goswami, D.Y., Kumar, P., 2014, Ground Cooling System for Improving the Efficiency of Low Temperature Power Generation, *ASME 8th International Conference on Energy Sustainability*, doi. 10.1115/ES2014-6618
- Wang, E.H., Zhang, H.G., Fan, B.Y., Ouyang, M.G., Zhao, Y., Mu, Q.H., 2011, Study of working fluid selection of organic Rankine cycle (ORC) for engine waste heat recovery, *Energy*, vol. 36: p. 3406-3418
- Zabetakis, M.G., 1924, Flammability Characteristics of Combustible Gases and Vapors, *U.S. Dept. of Interior, Bureau of Mines*, TN23.U4 NO. 627 622.06173

ACKNOWLEDGEMENT

This research is based upon work supported by the Solar Energy Research Institute for India and the U.S. (SERIUS) funded jointly by the U.S. Department of Energy subcontract DE AC36-08G028308 (Office of Science, Office of Basic Energy Sciences, and Energy Efficiency and Renewable Energy, Solar Energy Technology Program, with support from the Office of International Affairs) and the Government of India subcontract IUSSTF/JCERDC-SERIIUS/2012 dated 22nd Nov. 2012.

STUDY ON LABYRINTH SEAL AT THE HIGH-PRESSURE SIDE OF THE SCREW IN SINGLE SCREW EXPANDER

Guoqiang Li *, Yuting Wu, Ruiping Zhi, Yeqiang Zhang and Chongfang Ma

* Beijing University of Technology,
Ping Le Yuan 100, Chaoyang District, Beijing,
China
e-mail: guoqiang121913@126.com

ABSTRACT

Single-screw expander can be used in small scale ORC power system in which the output power is from 1 to 500 kW. There are many advantages of single screw expander, such as long working life, balanced loading of the screw, high volumetric efficiency, low noise, low leakage, low vibration and simple configuration. However, reliable seal is required at the high-pressure side of the screw for single screw expander.

Labyrinth seal is a widely used seal method in the scope of industry. It is characterized by simple structure, well-adapted, great stabilization, long lifetime and convenient maintenance. It is widely used to seal compressors, steam turbines, gas turbines and blowing plants. Therefore it is very promising that single screw expander adopts labyrinth seal to get well sealing at high-pressure side of the screw.

In this paper, several models were built, and then numerical simulation was conducted. Sequentially, the operating principles of labyrinth seal were analysed according to the simulation results. In addition, the influences of the labyrinth seal parameters, such as types of organic working fluids, pressures at inlet and outlet, size of clearance (length & width), tooth width, tooth height, tooth distance, number of teeth, and angle of inclination, were studied.

REFERENCES

- [1] Bao J, Zhao L. A review of working fluid and expander selections for organic Rankine cycle. *Renewable and Sustainable Energy Reviews*. 2013;24:325-42.
- [2] Wang W, Wu Y-t, Ma C-f, Liu L-d, Yu J. Preliminary experimental study of single screw expander prototype. *Applied Thermal Engineering*. 2011;31:3684-8.
- [3] Wang W, Wu Y-t, Ma C-f, Xia G-d, Wang J-f. Experimental study on the performance of single screw expanders by gap adjustment. *Energy*. 2013;62:379-84.

EFFICIENCY OF THE ARCHISOL CONCEPT

H.M.D. Lever¹, E.B. Wissink²

¹Archimedes Solutions,
Diepenveen, The Netherlands
e-mail: archimedessolutions@solcon.nl Web
page: www.archimedessolutions.nl

²Wageningen UR Food & Biobased Research,
Wageningen, The Netherlands
e-mail: edo.wissink@wur.nl
Web page: www.wageningenur.nl/fbr/postharvest

ABSTRACT

A simplified ORC cycle is proposed for small temperature differences. The most important simplification is the replacement of the pump section by a hydraulic column. The weight difference between the downward moving liquid column and the upward moving gas column provides the driving pressure for the cycle. Because the effect of this weight difference bears resemblance to the law of Archimedes, it is called the Archisol Concept

Especially for Ocean Thermal Energy Conversion applications, it is expected to be an advantage that less mechanical components are necessary for the cycle.

The University of Wageningen has carried out some first order calculations to check the thermodynamic feasibility.

The calculation shows that it is possible to produce electrical power with the Archisol concept for both scenarios; ocean ($T_{\text{water hot/cold}} = 27/6 \text{ } ^\circ\text{C}$) (i) and residual/geothermal heat ($T_{\text{water hot/cold}} = 70/20 \text{ } ^\circ\text{C}$)

Typical for the ocean scenario is:

- The refrigerant cycle itself is has a limited height, about 15 m, and operates with low pressure.
- A large part of the produced power output is consumed by the pumps of the evaporator and the condenser, which makes the outcome of the calculations very dependent on the energy consumption of the pumps. Most critical in the performance is the internal pressure drop of the water in the heat exchangers itself. The calculations are based on 0.3, but fact is that water supply lines are open systems, which can and will be polluted by dirt and biofouling, which can increase the water flow resistance strongly”

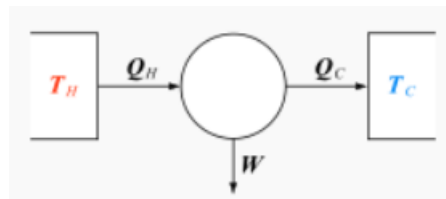
This leads to an efficiency of just over 2 % for the ORC cycle and 0,7 % for the complete process, taking secondary pump use for the water streams into account. The authors expect that the simplicity of the design could be attractive for further OTEC research and projects.

Further research is planned to demonstrate the viability of the proposed simplified ORC cycle.

1. INTRODUCTION

Power production out of waste heat recovery or natural heat sources (geothermal energy or temperature difference in deep ocean waters) can be marked as durable, because they do not make (direct) use of fossil energy sources. Given the limited temperature level of the heat source, the power production will have two important characteristics:

1. According to Carnot, the efficiency of the power production using waste heat recovery or natural heat sources is limited by the temperature levels of the hot and cold source. The Carnot efficiency is defined as the ratio of work W (which can be transferred into electrical power) and the hot source heat input. See figure 1.



$$\eta = \frac{W}{Q_H} = 1 - \frac{T_C}{T_H}$$

Figure 1: Definition of Carnot efficiency

Given the relative small temperature differences of these applications between the hot and cold source, relative large volumes of heat are required. The critical success factor is how efficient the power cycle can handle large heat flows. A good design reduces the hardware requirements and reduces the need for auxiliary power for pumps and fans.

2. The power cycle itself should match low temperature level of the heat- and cooling source in order to operate with acceptable pressure levels. Given the low temperature levels and looking for an continue cycle which can create a large power output, the use of the principle of the Organic Rankine Cycle is a logic choice. The ORC cycle exist of a closed refrigerant loop using the following components pump-evaporator-expander and condenser.

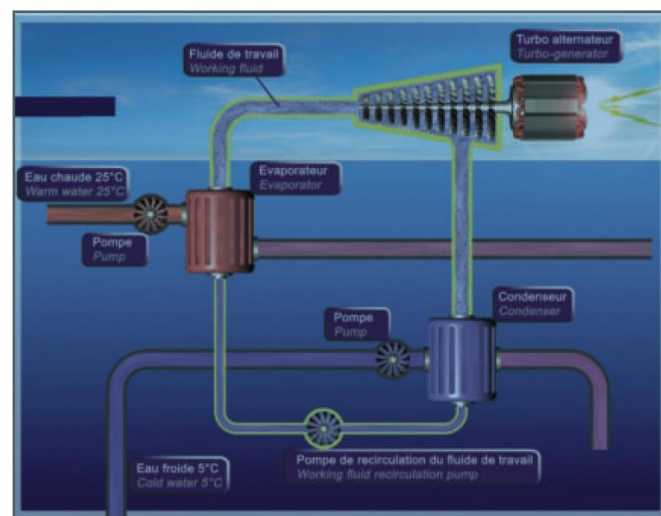


Figure 2: standard ORC cycle applied in Ocean Thermal Energy Conversion (Source: DCNS)

Archimedes Solutions has designed the so called Archisol concept. This Archisol concept is based on a modified ORC-principle. To evaluate the technical feasibility of this concept, Archimedes Solutions has asked Wageningen UR to make some first order feasibility calculations. These first order feasibility calculations include flow- and heat losses. The auxiliary power requirements of pumps and/or fans are calculated based on usual and common used efficiencies of the components in the system.

The feasibility calculations are made for the following applications/scenario's.

1. Ocean Thermal Energy Conversion (OTEC)

OTEC uses the ocean's warm surface water with a temperature up to 27 °C to vaporize fluid and condensation of it takes place with cold seawater coming from deeper sea levels. Depending on the depth, the temperature of ocean water ranges from 6.5 to 8.5 °C. Using colder water from deep sea levels increases the efficiency of the cycle, but also requires more pumping power to transport it to the condensing heat exchanger. Table 1 gives an example of the temperature profile of deep ocean waters used as used in the calculations.

Depth (m)	Temperature (°C)
0	27
100	24
200	11
300	8.5
400	7.8
500	7
600	6.5

Table 1: Temperature distribution of deep ocean waters that is used in the calculations.

2. Geothermal/residual heat energy conversion

The application of power generation makes use of geothermal/residual heat of 70 °C water. In the most ideal situation cooling water of 20 °C is available as well. Additionally a calculation will be made what the energy- and water consumption is when a cooling tower is used to produce 20 °C cooling water when the ambient temperature is 15 °C and a humidity is 70%.

2. DESCRIPTION OF THE ARCHISOL-concept

2.1 General

The Archisol-cycle is based on a standard Organic_Rankine_cycle. Where the ORC makes use of a pump to increase the refrigerant liquid pressure, the Archisol-concept uses the weight of a liquid refrigerant column itself to increase the liquid pressure. The advantage of not having a pump is that it increases the reliability and reduces the auxiliary energy to drive the pump. The disadvantage is that the installation needs sufficient height, which makes the cycle Archisol-concept less compact than the standard ORC. The authors have no knowledge of previous research where gravity is used to pressurize the liquid, so as far as they are aware this can be considered a new concept in an ORC like setup. The height of the liquid column corresponds with the pressure build up and the choice of the working fluid. The pressure build up corresponds with the available temperature difference. The Archisol concept is therefore most suitable for situations with small temperature differences and large streams of warming and cooling power.

2.2 Description of Archisol-cycle

The Archisol concept exists of a closed loop cycle, based on four sequential stages: condensing, increasing liquid pressure, evaporation and gas expansion. See figure 3. A short functional description of each stage is given below:

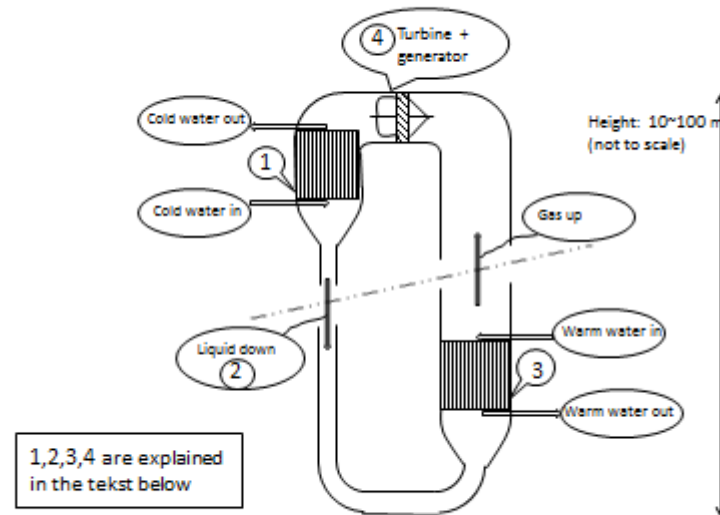


Figure 3: Cycle configuration with gas expansion

1. Condensing:

Working fluid is condensed near to water surface in the condenser (10), using water with a low temperature pumped up from a water level deep below the surface (11).

Condensing temperature:
$$T_c = T_{\text{cold water condenser in}} + \Delta T_{\text{condenser hex}} \quad (1)$$

2. Increasing liquid pressure:

The liquid from the condenser is pressurized by the weight of the liquid column. The height of the liquid column is self-adjusting until there is the following equilibrium:

Maximum liquid pressure:
$$P_o = P_c + \rho_{\text{liquid}} \cdot g \cdot h_{\text{liquid column}} - \Delta P_{\text{flow losses liquid}} \quad (2)$$

3. Evaporation (/super heater)

The working fluid is evaporated in the evaporator (6) in the lower part of the cycle, using warm water from the surface (7) pumped downwards to the evaporator. To prevent liquid formation during gas expansion in the turbine, gas should have an minimum superheating. The superheat may be controlled by controlling the liquid flow to the evaporator. The required superheat reduces the maximum evaporation temperature T_o .

$$\text{Evaporation temperature: } T_0 = T_{\text{warm water evap in}} - \Delta T_{\text{evaporator hex}} - \Delta T_{\text{min required superheat}} \quad (4)$$

4. Gas expansion

The pressurized gas is expanded in the expansion device (14) at the higher part cycle. Expansion of gas reduces both temperature and pressure. The ideal gas expansion process, which produces the most power, is the isentropic expansion. The practical power production can be calculated by making use of the isentropic efficiency of the expansion device. The power production is dependent on the available pressure difference and the gas flow. The pressure difference is basically the difference between the evaporation pressure and the condenser pressure, minus the additional pressure losses in the cycle. To prevent liquid formation during expansion, the gas should be superheated adequately. This limits the evaporator pressure and thus reduces the practical available pressure difference.

The available pressure difference over turbine is:

$$\begin{aligned} \Delta p_{\text{turbine}} &= P_o - P_c - \Delta p_{\text{flow losses gas}} - \Delta p_{\text{gas column}} \\ &= P_o - P_c - \Delta p_{\text{flow losses gas}} - \rho_{\text{gas}} \cdot g \cdot h_{\text{cycle}} \end{aligned} \quad (4)$$

The maximum theoretical power production of the gas driven turbine is calculated by single stage isentropic expansion:

$$W_{\text{turbine isentropic}} = \dot{m} \cdot (h_{\text{gas in}} - h_{\text{gas out,s}}) \quad (5)$$

2.4 Auxiliary systems

To drive the cycle auxiliary systems are required. Their power consumption is very important in calculating the net power production.

The two most important auxiliary systems are the pipe lines with their water pumps. These are required to transport cold water to the condenser and warm water to the evaporator.

In order to determine the electrical power consumption of these pumps, the hydraulic power has been calculated based on the flow and the pressure difference over the pump.

The pressure difference over a pump is based on the static pressure difference caused by the difference in density of the water itself plus the dynamic friction losses caused by the flow.

$$\Delta p_{\text{pump}} = \Delta p_{\text{static}} + \Delta p_{\text{dynamic}}$$

The static pressure difference caused by the difference in density of the water in the pipe compared with the average density out of the pipe. The used density of sea water is given in figure 4.

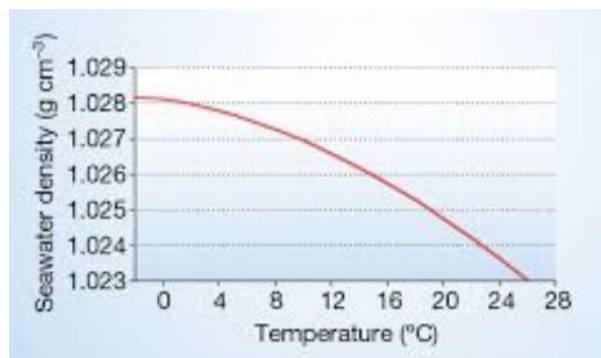


Figure 4: Salt water temperature- density relation

The dynamic pressure difference is caused by the flow losses in the pipe and in the heat exchanger. The flow losses in the pipe have been calculated by using the friction factor of a turbulent flow in a round pipe with a roughness factor (ϵ/d) of 0.001.

The pressure loss in the condenser and evaporator is an important design parameter, because it will strongly influence the outcome of the calculations. The calculation is made assuming a pressure loss of 0.3 bar*.

** Note that the water supply lines are open systems, which means that these can and will be polluted by dirt and organic material. This will increase internal resistance of the pipeline and the condenser and evaporator. The latter will have more impact. This all means an increase of the actual pressure drop over time compared to the design value.*

Once the pressure difference over the pump and water flow are known, the electric power consumption of these pump can be calculated when the efficiency of the pump and the used electromotor are known:

$$P_{\text{elec pump}} = W_{\text{hydraulic}} / (\eta_{\text{pump}} * \eta_{\text{electromotor}}) = Q * (\Delta p_{\text{static}} + \Delta p_{\text{dynamic}}) / (\eta_{\text{pump}} * \eta_{\text{electromotor}}) \quad (6)$$

Thermal losses

Apart from the auxiliary power consumption these water transport systems have also thermal losses. These have been calculated, assuming the use of a 5mm PP coating on the inner diameter of the pipe. Compared to other losses, the thermal losses appeared to be small for high capacity systems. In the calculations the water pipe diameter is 1 m. The largest losses are the thermal losses of the cold water supply line and these are less than 0,1 K. This means that thermal losses are negligible for large capacity systems.

3. CALCULATION RESULTS

3.1 General

In order to calculate the power production and the auxiliary power requirements of pumps and/or fans assumptions have to be made for losses and efficiency of components. The efficiency values used in the calculation of the most important components are given in table 2. The calculation results are given in the next paragraphs of this chapter.

pump evaporator water		unit
efficiency electromotor	0.85	-
efficiency pump	0.8	-
pump condenser water		
efficiency electromotor	0.85	-
efficiency pump	0.8	-
Turbine efficiency		
turbine efficiency	0.9	-
generator efficiency	0.85	-
Heat exchanger		
Pressure drop	0,3	bar

Table 2: Main parameters required to make the efficiency calculations.

3.2 Performance calculations for ocean application

The following table gives the results for the Ocean application:

Refrigerant	R134a	
Power production turbine	647	kW
P elect LT water pump	318	kW
P elect HT water pump	112	kW
Net power production	217	kW
Condenser water transport pipe		
length	600	m
d-pipe	1	m
flow speed	3	m/s
Mass flow	2419	kg/s
Twater condenser in	6.6	°C
Twater condenser out	9.6	°C
Evaporator water transport pipe		
length	11.63	m
d-pipe	1	m
flow speed	3.07	m/s
Mass flow	2475	kg/s
Twater evaporator in	27.0	°C
Twater evaporator out	24.0	°C
Δp condenser water pump	0.92	bar
Δp evaporator water pump	0.31	bar
Condenser capacity Q_c	28516	kW
Evaporator capacity Q_o	29163	kW
Maximum possible Carnot efficiency	6.8	%
Calculated efficiency	0.7	%
Height liquid column	12	m
Max system pressure	5.8	bar(a)
Total refrigerant contents	739	kg

Table 3: Main results of efficiency calculations ocean/refrigerant R134a scenario.

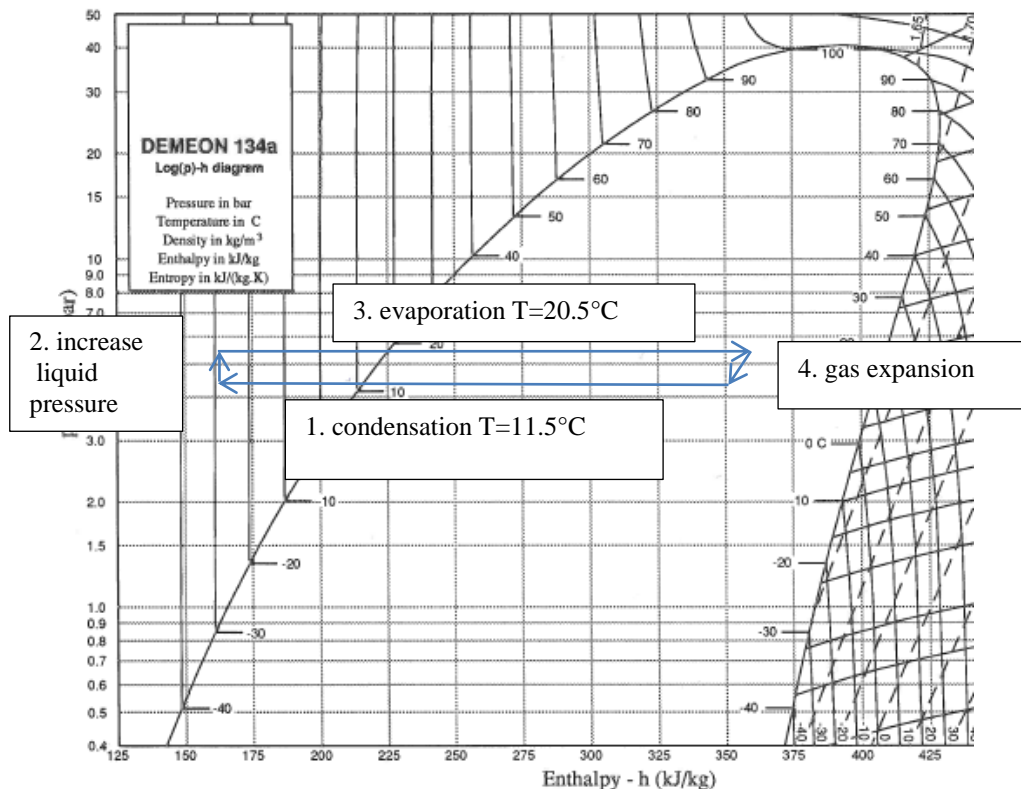


Figure 5: Process cycle of gas expansion ocean scenario indicated in h – log p diagram

The results show that a large part of the produced power is consumed as auxiliary power for the pumps. This is indirect a result of making use of a relative small temperature difference of the ocean water, with a corresponding low Carnot efficiency number. This means that relative large heat flows are required to drive the cycle. These relative high heat flows increase the investment for the heat exchangers and the use of their auxiliary power.

Result is that the outcome of the calculations is very dependent on the energy consumption of the pumps of the evaporator and the condenser. Most critical in the performance is the internal pressure drop of the water in the heat exchangers itself. This is a design parameter and is assumed to be 0,3 bar. This is possible for a clean and well-designed heat exchanger, for example an oversized shell and tube heat exchanger, but fact is that water supply lines are open systems, which can and will be polluted by dirt and other organic substances, which will increase the water flow resistance strongly.

The refrigerant cycle itself is has a limited height, about 15 m, and operates with low pressures.

The largest components of the total system are:

- the long pipeline to get cold water supply (diameter= 1 m and length= 600 m)
- the heat exchangers with their pumps

3.2 Economic considerations for ocean application

The main advantages concerning the Ocean application are considered to be:

- No working fluid pump and therefor lower investment and maintenance cost and no use of auxiliary power to drive the pump
- Compact platform design for applications at sea because of vertical placement of components
- The use of non-dangerous working fluid

The main issues are comparable to other OTEC systems:

- Overall thermodynamic efficiency is low because of the small temperature differences,
- Pump power use is high because of the long water pipelines and the pressure drop in the heat exchangers

Overall it is expected that the Archisol concept can bring economic advantages for OTEC applications, mainly due to the compacter platform design and the lower maintenance costs.

3.3 Performance calculations for residual/geothermal heat application

Refrigerant	R134a	
Power production turbine	2292	kW
P elect LT water pump	212	kW
P elect HT water pump	131	kW
Net power production	1949	kW
Condenser water transport pipe		
length	345	m
d-pipe	1	m
flow speed	3	m/s
Mass flow	2356	kg/s
Twater condenser in	20.00	°C
Twater condenser out	23.00	°C
Evaporator water transport pipe		
length	75	m
d-pipe	1	m
flow speed	3.07	m/s
Mass flow	2411	kg/s
Twater evaporator in	70.00	°C
Twater evaporator out	67.00	°C
Δp condenser water pump	0.61	bar
Δp evaporator water pump	0.37	bar
Condenser capacity Q_c	29547	kW
Evaporator capacity Q_o	31839	kW
Maximum possible Carnot efficiency	14.6	%
Calculated efficiency	6.1	%
Height liquid column		
Height liquid column	98	m
Max system pressure	18.2	bar(a)
Total refrigerant contents	6102	kg

Table 4: Main results of efficiency calculations. Scenario: residual heat/ refrigerant R134a

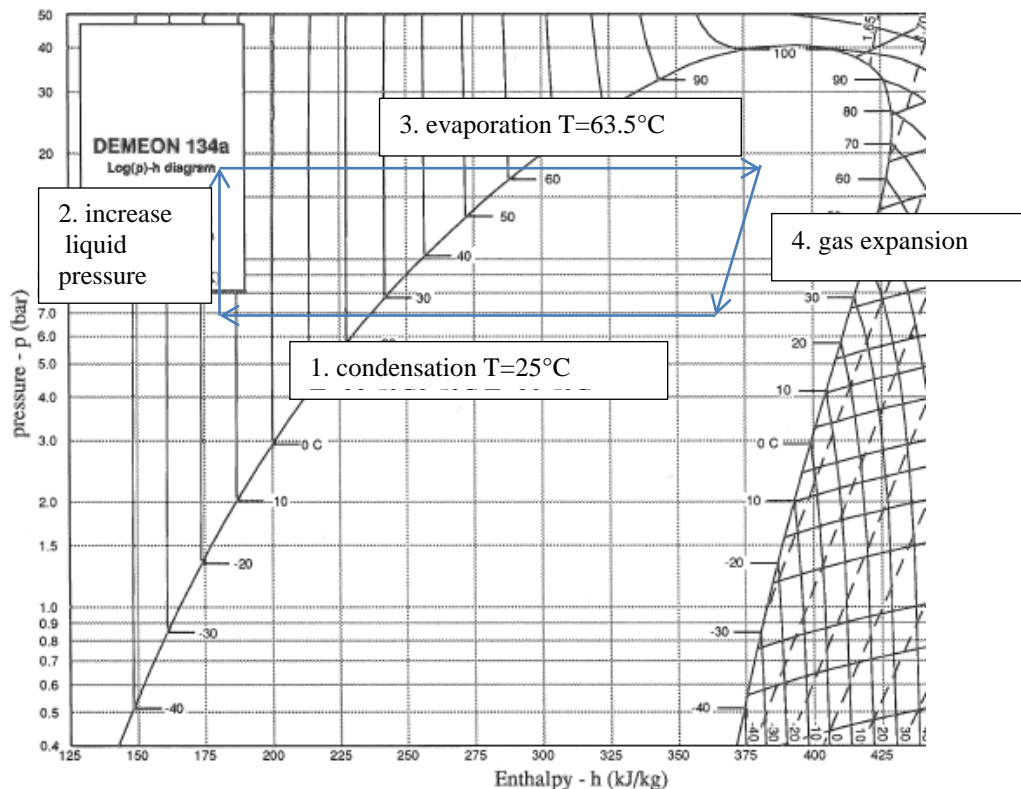


Figure 6: Process cycle of gas expansion residual heat scenario indicated in $h - \log p$ diagram

Compared to the results of the ocean application, here a smaller part of the produced power is consumed as auxiliary power for the pumps. This is a result of making use of a larger temperature difference, with a corresponding high Carnot efficiency number.

The outcome of the calculations is dependent of the energy consumption of the pumps of the evaporator and the condenser, but is here less critical than compared to the ocean application. Critical issue in this application is the presence of cooling water for the condenser. If not, air has to be used and that increases the investment and the auxiliary energy use..

The refrigerant cycle itself has a significant, height, about 100m and operates with moderate pressure. The largest components of the total system are:

- the pipeline of the cold water supply (diameter= 1 m and length= 345m)
- the pipeline of the warm water supply (diameter= 1 m and length= 75 m)
- the heat exchangers with their pumps

The cold water supply line is quite long because of the fact that the water in and outflow should not be close to each other and the fact that the condenser is situated at a height of minimal 98 m. In order to reduce the pump power requirements the potential energy of the water flow has to be recovered by using a down flow pipe.

4. Conclusion

This article describes the feasibility study of the Archisol concept for both the ocean application and the geothermal heat application. The Archisol-concept is an ORC without a liquid pump. The functionality of the pump is replaced by the column weight of the liquid refrigerant.

The feasibility study has been made for a large capacity system, because auxiliary power consumption is a deciding factor. The ocean application has a lower efficiency than the geothermal application, 0.7% against 6.1%. This is mainly caused by the relative small difference between the surface and deep water temperature (27/6.6°C). The main risk is the increase of auxiliary power consumption by pollution of the open seawater heat exchangers. This is however common for OTEC applications. When comparing the Archisol concept to existing OTEC applications the simplified cycle design (no working fluid pump required) and a compact platform design are expected to be advantageous.

The residual/geothermal application has a better thermodynamic feasibility, especially when large scale cooling water is available. The use of ambient air for cooling the condenser reduces the efficiency or consumes large quantities of water.

Reference:

Kempener, Ruud (IRENA), Neumann Frank (IMIEU) OCEAN THERMAL
ENERGY CONVERSION
IRENA 2014 TECHNOLOGY BRIEF

EXPERIMENTAL SETUP OF A SMALL SUPERSONIC TURBINE FOR AN AUTOMOTIVE ORC APPLICATION RUNNING WITH ETHANOL

Harald S. Kunte, Joerg R. Seume

Institute of Turbomachinery and Fluid Dynamics, Leibniz University Hannover,
Lower Saxony, Germany
kunte@tfd.uni-hannover.de; seume@tfd.uni-hannover.de

ABSTRACT

Waste heat recovery by bottoming Organic Rankine Cycles (ORC) is a promising method to increase the efficiency of automotive transportation based on combustion engines. The efficiency of these ORCs is significantly dependent on the efficiency of the expansion machine. For this reason, a supersonic impulse turbine with a variable partial admission was developed for such an ORC. The design of the blade profiles and the design parameters for this turbine are presented. The high rotational speed and the ambitious working fluid were the most challenging aspects in the design process of the expansion machine, hence the mechanical design of the expansion machine, the methods of power conversion, the seals and bearings are shown. The presented prototype has been manufactured and is been experimentally investigated at an ORC test facility at the Institute of Turbomachinery and Fluid Dynamics. This test facility provides two possibilities to measure the efficiency, which will be discussed; firstly, the determination of the turbine power with the enthalpy drop from inlet to outlet; secondly, the direct measurement of the power of the generator with the power electronics and a motor analyzer.

NOMENCLATURE

D	[m]	diameter	<u>subscripts</u>
h	[m]	blade height	in inlet
\dot{m}	[kgs ⁻¹]	mass flow	out outlet
N	[-]	number	R rotor
n	[min ⁻¹]	rotational speed	S stator
p	[bar]	pressure	Shroud diameter of the shroud
		pressure probe	t total thermodynamic conditions
T	[K]	temperature	
		temperature probe	<u>abbreviations</u>
δ	[m]	blade tip clearance	FFKM perfluoro-elastomer
ϵ	[-]	partial admission	ORC Organic Rankine Cycle
			PTFE polytetrafluoroethylene

1 INTRODUCTION

Automobile manufacturers are currently focused on reducing fuel consumption and emissions. This can be achieved by increasing the efficiency of the combustion engine. The investigation of the energy flow in such a combustion engine showed that a significant part of the added chemical energy is lost as thermal energy in the exhaust gas (Bourhis and Leduc (2010)). A possible way to increase the efficiency of these combustion engines is to recover some of that energy. Different systems for such a recovery are conceivable, e.g. thermo electric systems, a Stirling motor, a Joule Cycle or an Organic Rankine Cycle (ORC). Span et al. (2011) performed a thermodynamic investigation of the last three processes and compared the achievable power output. They identified the ORC as the most suitable for the temperature levels encountered in the engine exhaust.

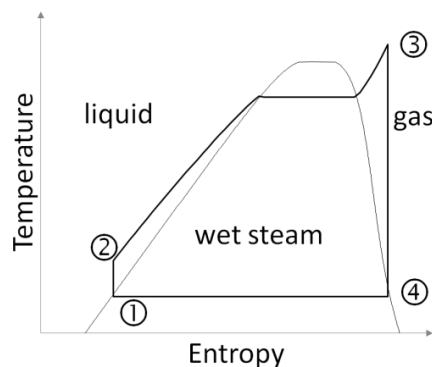


Figure 1: Isentropic ORC, schematically

The ideal isentropic temperature-entropy plot of such an ORC is schematically shown in figure 1. The efficiency and power output of such an ORC is highly dependent on the working fluid used, on its boundary conditions, and the expansion machine. The working fluid has to be selected with consideration of the allowable temperature and pressure levels. For this reason, suitable fluids must be determined for each individual application. Additionally, the overall efficiency of the ORC is highly dependent on the efficiency of the expansion machine. As the ORC application in automobiles is still under development, no standard expansion machine has established yet. Potential expansion machines for this application are: Piston expanders (Glavatskaya (2012)), screw expanders (Oomori and Ongino (1993)) and turbines (Patel and Doyle (1976), Freyman et al. (2008)). Piston expanders and screw expanders use the displacement principle, thus they seem to be more appropriate for the high pressure ratio and the low mass flow. However, supersonic impulse turbines are also able to be operated at these boundary conditions (Kunte and Seume (2013), Verneau (1987), Uusitalo et al. (2014)). In addition, they promise a more compact design. Experimental data of such turbines are rarely accessible in the literature, because the introduction into the commercial market has not yet occurred. A supersonic impulse turbine is being developed for this application at the Institute of Turbomachinery and Fluid Dynamics Hannover, in order to determine the performance potential experimentally and to validate the numerical simulations.

The scope of this work is to present the aerodynamic and the mechanical design of the turbine. The supersonic flow requires the use of special blade profiles. These blade profiles and the resulting turbine parameters are described. The resulting turbine is mounted on one shaft with the generator, which requires a special high-speed generator and demands suitable bearings and seals. For this reason the chosen overall design of the expansion machine is presented. This expansion machine will be investigated by experiments to determine the performance. However, the challenge of an accurate performance determination is also well known from turbochargers, where heat losses at the turbine housing can falsify the measured performance. Based on that experience, two independent methods are provided in the test facility for an accurate determination of performance, in term of power and efficiency.

2 The Boundary conditions of the ORC

Table 1: Operating conditions of the turbine

Parameter	Units	Design	Min	Max
Fluid	ethanol (95% mass), water (5% mass)			
$\dot{m}_{S,in}$	kg s ⁻¹	0.045	0.006	0.091
$T_{S,in}$	K	539	458	539
$P_{t,S,in}$	bar	40	10	40
$P_{R,out}$	bar	0.81	0.81	0.81

The diesel engine of a truck with a cubic capacity of 12.8 liters and a maximum power of 375 kW was chosen as heat source. An operating point of medium load with a power of 228 kW is the selected design operating point. In prior studies, Kunte and Seume (2013) performed a thermodynamic analysis at this operating point to determine the

optimal boundary conditions of the ORC. It was shown that using ethanol as the working fluid promises the highest power output of the ORC for the given exhaust gas conditions of the combustion engine. Deviating from the prior study, a mass fraction of 5% water is now added to the ethanol. This additive has no thermodynamic purpose, but it improves the corrosion resistance of the titanium turbine rotor, which can be damaged by stress corrosion in pure ethanol environments. Additionally, the inlet temperature of the turbine must be raised from 530 K to 539 K to avoid condensation and droplet impact erosion damage to the turbine rotor. The higher process temperature, the higher thermal capacity, and the higher enthalpy of vaporization of water reduce the mass flow from 0.052 kg/s to 0.045 kg/s. The maximum inlet pressure of 40 bar and the outlet pressure of 0.81 bar remain unchanged. Additionally a minimum and a maximum operating point were defined. These operating points have no corresponding operating point in the combustion engine, rather they represent the boundaries of the performance map of the turbine. The resulting thermodynamic boundary conditions are summarized in table 1.

2.1 Aerodynamic design of the supersonic impulse turbine

The chosen boundary conditions for the ORC are quite challenging for a turbine. Firstly, the mass flow is very low. This leads to a small turbine diameter and a low blade height and consequently effects like wall friction and tip gap losses will increase. Secondly, the pressure ratio of 49 is very high for a single stage turbine. As this turbine should be used in an automotive application, the premise was to use a single stage turbine to minimize the manufacturing cost and the size.

However, Verneau (1987) showed that supersonic impulse turbines expand high pressure ratios per stage at a good level of efficiency. In spite of the high pressure ratio, this type of turbine promises an acceptably low rotational speed, which can be used by a gear or a generator. Additionally, this type of turbine can be operated at partial admission. That means that only a part of the circumference of the stator is equipped with passages while the rest of the circumference is blocked. Although partial admission causes additional losses, it allows the blade height to be raised to an acceptable value. In this case, the reduced tip gap loss can exceed the losses due to the partial admission and thus the partial admission can raise turbine efficiency.

A supersonic impulse turbine with partial admission was designed to this end. Impulse turbines are characterized by degree of reaction close to 0. This means, that the whole pressure ratio is expanded in the stator and the subsequent rotor only redirects the flow without a change in speed. The blade profiles chosen for this turbine are shown in figure 2. The stator passages are formed like Laval nozzles, consisting of a convergent and a divergent part. The flow enters the stator in the convergent part of the nozzle at subsonic velocity ① and is accelerated to the speed of sound up to the throat ②. A further acceleration takes place in the divergent part of the nozzle ③. The design specifications from Humble et al. (1995) were used, to determine the radii of the throat and the shape of the

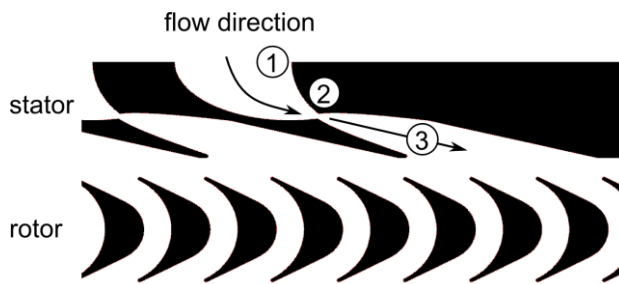


Figure 2: ORC Blade profile of the turbine

divergent part of the nozzle, which is formed like a bell nozzle. The rotor blades are formed like a redirecting blade row. The cross section of the passage is constant from inlet to outlet. The leading and trailing edges of the rotor should be as thin as possible because of the supersonic approach velocity of the rotor. However, very thin leading and trailing edges are not able to withstand the expected aerodynamic forces and to ensure the mechanical integrity of the blade. Already Boxer et al. (1952) have given geometrical specifications for such

leading and trailing edges. However, the small dimensions of the turbine make the implementation of such geometries very challenging due to manufacturing tolerances. Thus a radius of 0.2 mm was chosen for the leading and trailing edges.

A model of the turbine design is shown in figure 3. The flow angles were determined by a flow coefficient of 2 and a 0 degree of reaction. This results in a shroud diameter of 63.1 mm and a rotational speed of 85,000 rpm at the design point. At this point, the turbine operates with a partial admission of 40 %. This leads to a rotor blade height of 3.43 mm. This low blade height can cause very high tip gap losses, if the radial tip gap is chosen too large. Hence, a minimum tip gap of 0.13 mm was determined after consideration of manufacturing tolerances, thermal expansion, and centrifugal forces.

The amount of thermal energy, provided by the combustion engine of the truck, varies over time. As a result, the mass flow of the ethanol-water-mixture varies, too. This would lead to a highly differing inlet pressure of the turbine, if the total area of the nozzle throats would be fixed. However, Kunte and Seume (2013) showed, that a variable partial admission of the turbine allows adjusting the overall area by opening additional nozzle throats, to keep the turbine inlet pressure within an acceptable range. This ensures to operate the Laval nozzles under nearly ideal conditions at a high efficiency. The designed turbine is able to vary its degree of partial admission stepwise between 20 %, 40%, 60% and 80 % with a predicted power of up to 19 kW. The design parameters of the turbine are listed in table 2.

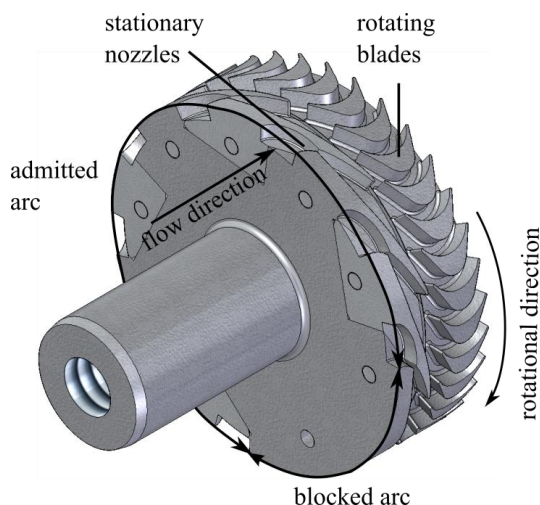


Figure 3: Model of the turbine

Table 2: Parameters of the investigated turbine

Parameter	Units	Values
D_{Shroud}	m	0.0631
h	m	0.00343
δ	m	0.00013
n_{Design}	rpm	85,000
N_s		8
ϵ_{Design}		0.4
ϵ		0.2, 0.4, 0.6, 0.8
N_R		33

2.2 Mechanical design of the expansion machine

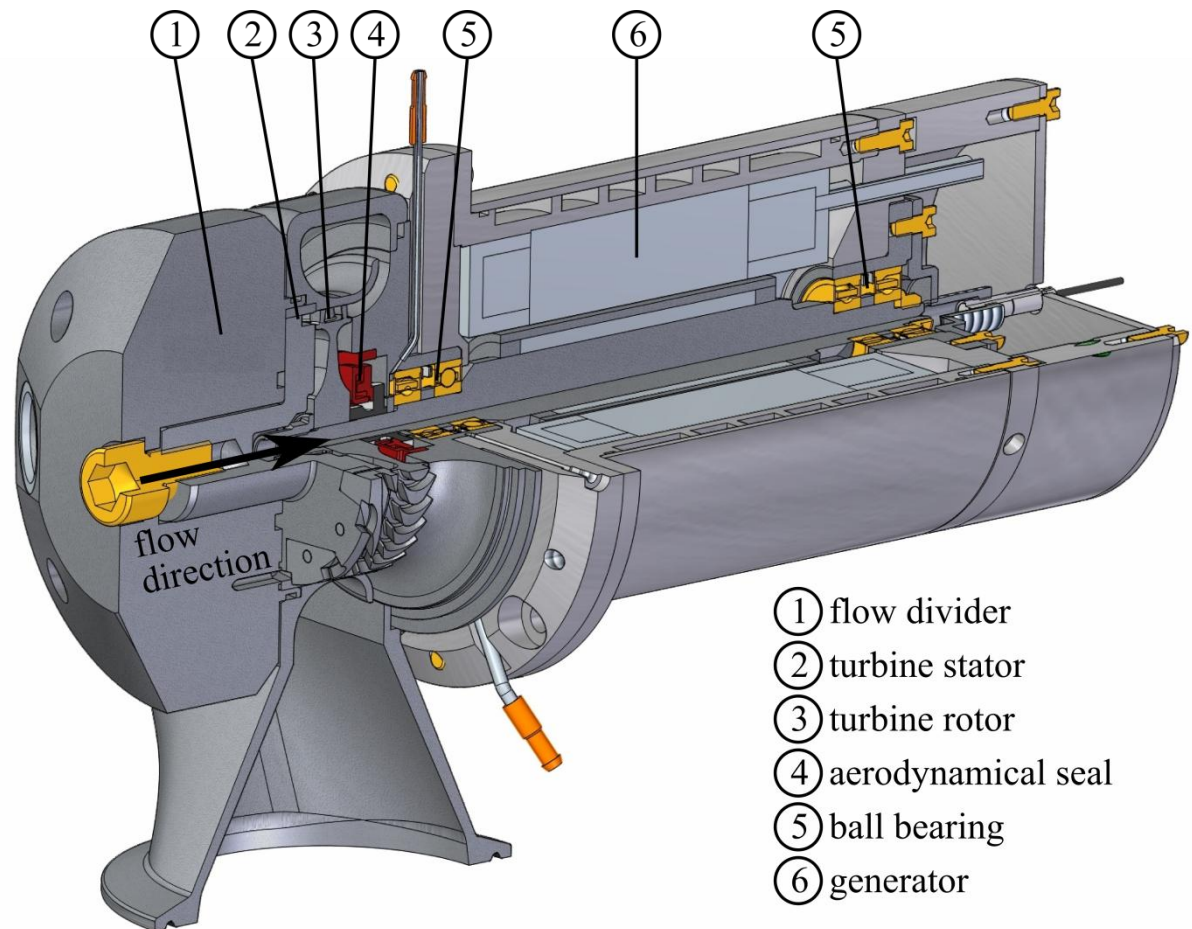


Figure 4: Mechanical design of the expansion machine

Due to the high rotational speed of the turbine, it is not easy to utilize the mechanical power gained. A direct coupling with the combustion engine is not possible because of the differing rotational speeds. Two possibilities were considered to allow the utilization of the power generated: Firstly, reducing the rotational speed with a gear box and secondly, directly coupling the turbine to a high-speed generator. A comparison of these options showed advantages of the high-speed generator over the gearbox. The generator has a more compact expansion machine design and generators suitable for these rotational speed and power levels are technically realizable. Additionally, suitable gears for this application are not available on the market as a standard unit and have no cost advantage over the generator. Hence, a turbine generator unit was designed.

This expansion machine is depicted in figure 4. The flow enters a flow divider (①), which splits the flow and guides it to every individual stator nozzle. The stator nozzles (②) are attached to a stationary disc with an anchor, which connects the stator with the divider. Each of these stator nozzles is individually sealed on the contact surface to avoid bypass flows between the stator nozzles. After the stator, the flow passes the turbine rotor (③) which converts the kinetic energy of the flow into rotational energy. Behind the rotor, the flow direction is turned radially and the flow is collected in a plenum. The turbine rotor is mounted on the shaft, which transfers the rotational power to the generator rotor. The seal used is an aerodynamically lubricated axial face seal (④). The shaft is

mounted on two pairs of high precision ball bearings (5). The turbine rotor is in an overhung position. This is disadvantageous for the rotor dynamics, however it makes sealing the ethanol cycle easier. The generator is placed in the middle of the bearings. These components will be described in detail in the following sections.

2.2.1 Seals

The ORC can be divided into a high pressure section and a low pressure section. In the high pressure section temperatures of up to 539 K and pressures of 40 bar must be sealed. Leaks must be avoided to prevent the formation of explosive gas mixtures outside the machine. On the other hand, the seals must avoid the penetration of air into the low pressure section of the turbine, which would contaminate the working fluid and thus deteriorate the cycle. In the high pressure section, only static seals are necessary. In addition to the static seals, dynamic seals are necessary on the rotor shaft in the low pressure section.

The O-rings in the high-pressure section as well as in the low-pressure section are made of FFKM. FFKM is resistant to ethanol and its use is permitted for operating temperatures up to 598 K, which is much higher than the maximum temperature of 539 K in the cycle. Additionally, FFKM is a flexible elastomer. For this reason, FFKM is suitable for the O-rings, which have to be stretched, for example for positioning in notches of a shaft seal. One disadvantage of FFKM is the high cost of this material. For this reason, a different sealing material was searched for the flat seals, which provides the required thermal and chemical resistance, but does not need the flexibility of FFKM. PTFE and graphite seals satisfy these requirements. Both PTFE and graphite are resistant to ethanol, but graphite has a higher thermal resistance of up to 673 K compared to 533 K for PTFE.

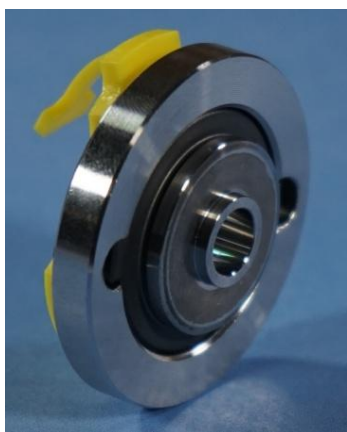


Figure 5: Aerodynamically lubricated seal

A generator housing, which is enclosed together with the ORC, is not an option because the ball bearings and their lubricant are not resistant to ethanol. Thus, the fast rotating shaft has to be sealed to separate the generator cavity from the turbine cavity with the ethanol. However, the sliding speeds are too high for contacting seals while non-contacting seals such as labyrinth seals have to be provided with purge air for a complete separation from the Rankine cycle. Therefore, an aerodynamically lubricated seal is used instead to seal the shaft. This seal was developed for turbocharger applications to minimize oil losses of the bearings (figure 5) (Simon et al. (2010)). This seal consists of three main components, a rotating steel element, a stationary graphite ring and the housing. If the shaft is not rotating, a spring pushes the non-rotating ring in axial direction against the steel element. When the shaft starts to turn, grooves on the front face of the rotating element induce a radially-oriented flow film between the stationary ring and the rotating element, thus separating the two elements. The shape of the grooves transports a small amount of ethanol against the pressure gradient into a cavity. This cavity is purged by a permanent nitrogen flow. This means a small loss of ethanol over the time, but prevents the contamination of the ethanol cycle. The housing material of the seal was modified, due to the fact, that the standard aluminum housing is not resistant to ethanol. For this reason, stainless steel housing was used.

2.2.2 Bearings



Figure 6: Ball bearings and spring

For the shaft, different bearing solutions were investigated. Three requirements were defined, which should be fulfilled by the bearing. Firstly, the bearing should work oil-free, respectively the bearings should have their own seals to avoid a pollution of the generator with oil. Secondly, the rotordynamics should be favorably affected, which prohibits the presence of harmful eigenfrequencies in the operating range. Thirdly, the bearing and their design should be low-priced. These demands can be met with high precision ball bearings. Ball bearings (HCB7000-C-2RSD-T-P4S) from the Schaeffler Group were used in a paired O-arrangement and are pre-loaded by a spring (figure 6). This arrangement was chosen, because it improves the rotordynamic behavior due to its higher bending stiffness. These bearings are also able to absorb the axial forces of the turbine, hence no additional axial thrust bearing is necessary. They are lubricated for life and self-sealed.

2.2.3 Generator

The generator used is a high-speed synchronous generator with a maximum power of 19.5 kWe and a maximum rotational speed of 110,000 rpm (ATE (2012)). The bipolar permanent magnet, mounted on the shaft is made of neodymium. The magnet itself is covered by a steel jacket, which resists the centrifugal forces. Due to the high power density of the generator, water cooling of the generator is required. Thus, the generator stator is mounted in a cooling jacket made of aluminum. This cooling jacket also functions as the generator housing.

3 Measurement methods for the efficiency determination of the turbine

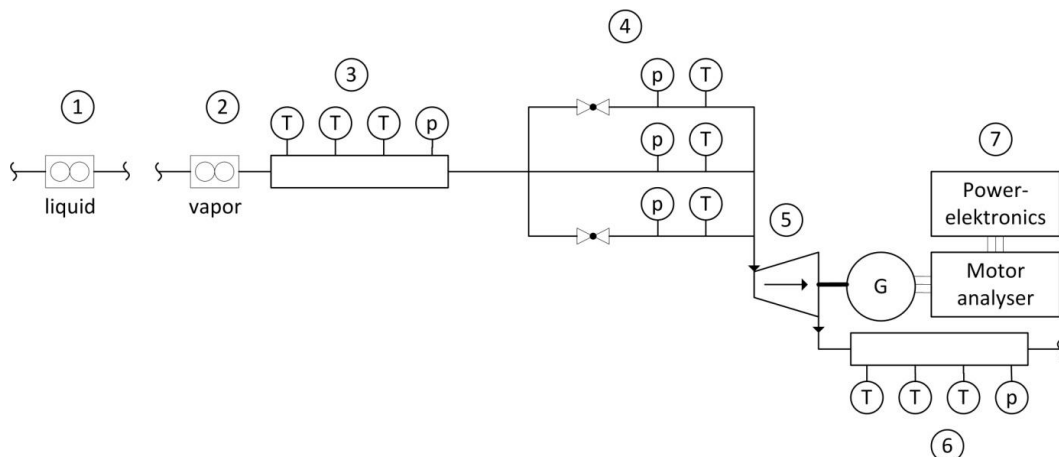


Figure 7: Instrumentation for the determination of the turbine efficiency

Instrumentation for the efficiency determination is shown in figure 7. Two mass-flow meters are positioned in the cycle. The first one is positioned in the liquid section of the test facility (1). At this position, the temperatures are low, which simplifies the measurement and increases the accuracy. However, the test facility has a bypass which can direct the flow past the expander. Therefore, a

second flow meter is integrated, which measures the flow passing through the expansion machine ②. It is possible to operate the cycle without bypassing. In this case, the mass flow meters measure the same flow and can be compared. The inlet and the outlet of the expansion machine are equipped with three temperature probes and a pressure probe ③⑥. This arrangement ensures that the average temperature and pressure profiles are measured and enhances the accuracy of the efficiency determination. Additionally, the expansion machine is equipped with its own temperature and pressure probes. These probes are positioned in each of the tubes of the control unit for the variable partial admission directly in front of the turbine inlet ④. This unit consists of three tubes, which can supply a part of the stator nozzles with ethanol. One of these tubes is continuously opened and represents the minimal partial admission. The degree of partial admission can be controlled with ball valves, which open additional tubes to vary the degree of partial admission. Within this, the temperature and pressure probes have two purposes. Firstly, the pressure probes check the correct function of the ball valves by comparing the pressure level with the target pressure. Secondly, pressure and temperature losses occur in the pipes between measuring tube ③ and the turbine inlet. These losses can be detected by the additional probes in front of the turbine and the accuracy is improved. Using the measurement of these thermodynamic conditions, the energy flow out of the system can be determined. In adiabatic systems, this energy flow represents the turbine power from which the efficiency can be calculated.

However, it is known from experiments with turbochargers, that turbine applications are not adiabatic and heat losses can significantly affect the measured efficiency (Casey and Fesich (2010)). For this reason, a second possibility for the determination of the turbine power is implemented. The power electronics provides the possibility to measure the torque and power of the expansion machine, too (Sieb & Meyer (2013)). The power electronics are not intended for measurement applications, which require a very high accuracy. For this reason, an additional motor analyzer is required, which is able to determine the power with the desired accuracy. However, the measured power is not the turbine power, because friction losses in the bearings and in the seal occur. These losses have to be investigated and determined in order to consider them in the final determination of the turbine efficiency.

4 Description of the test facility



Figure 8: ORC test facility of the Leibniz University Hannover

The experiments will be performed on an ORC test facility (figure 8). This test facility is designed with approved components that comply with all governmental regulations, such as the pressure equipment directive or the ATEX directives. Size-optimized components, which are currently in development for automotive applications do not fulfill these requirements and are not used for the standard configuration. However, the test facility has a modular design, which enables the exchange of individual components. This gives the opportunity to investigate other prototype components of ORCs with this test facility, as well. The currently implemented instrumentation is designed to measure the operating conditions of each component. Additionally, the test facility is designed for several working fluids besides ethanol.

5 Conclusion

Automotive waste heat recovery is a promising opportunity for increasing the efficiency of vehicles powered by internal combustion engines. Prior studies have shown that an ORC is a most suitable candidate for such a recovery. However, the efficiency of these ORCs is significantly dependent on the efficiency of the expansion machine.

A supersonic impulse turbine has been developed at the TFD for this application. This impulse turbine is faced with challenging boundary conditions, firstly a high pressure ratio of 49 and secondly a very low mass flow of 45 g/s. In the aerodynamic design, special blade profiles were used which promise a high efficiency under these conditions. The stator is formed like a Laval nozzle with a divergent bell-shaped nozzle part. Additionally, a partial admission of 40 % was chosen for the design point to maintain acceptably high blade heights in spite of the small mass flow. Furthermore, automotive applications demand high variability in the expansion machine to cover the performance map of the combustion engine. For this reason, the degree of partial admission can be varied stepwise between 0.2, 0.4, 0.6, 0.8. This turbine promises an output power of up to 19 kW.

A prototype of this turbine was manufactured at the TFD to validate it experimentally. The high rotational speed and ethanol as a working fluid, made the design of the prototype challenging. The turbine and the generator are mounted on one shaft. A high speed generator was used because of the high rotational speeds. The shaft was mounted with two pairs of preloaded ball bearings, which are greased for life. An aerodynamically lubricated seal, developed for a turbocharger application, was used to seal the rotating shaft and avoid the leakage of ethanol. FFKM, PTFE, and graphite are used for static seals.

Additionally, instrumentation for the determination of efficiency was implemented which provides two options for the determination of efficiency. Firstly, the enthalpy drop from inlet to outlet can be measured. Secondly, the power output and the torque absorbed by the generator can be measured. This instrumentation is part of the ORC test facility of the Leibniz University at Hannover.

Acknowledgement

This investigation was funded by industry fees in the context of the Sonderforschungsprogramm CO₂ of the Forschungsvereinigung Verbrennungskraftmaschinen e.V. (FVV) and the Forschungsvereinigung Antriebstechnik e.V. (FVA) which is gratefully acknowledged. Also the authors would like to thank the “Regional Computer Centre of Lower Saxony” (RRZN) for supporting this study.

The ORC Test Facility was partly financed by the European Community under an EFRE grand and co-financed by the Institute of Power Plant Technology at the Leibniz University Hannover, headed by Prof. Dr.-Ing. R. Scharf. The ORC Test Facility is located at the EFZN, an energy research center of Lower Saxony at Goslar/Germany.

Reference

- ATE, Antriebstechnik und Entwicklungs GmbH, technical data sheet of the generator, No. 582 0001 100, 2012-07-13
- Bourhis G., Leduc P.; Energy and Exergy Balances for Modern Diesel and Gasoline Engines; Oil and Gas Science and Technology; Vol. 65; 2010
- Boxer E., Sterret J. R., Wlodarski J.; Application of Supersonic Vortex-Flow Theory to the Design of Supersonic Impulse Compressor – or Turbine-Blade Sections; NACA Report: RM 152B06; 1952
- Casey M. V., Fesich T. M., The Efficiency of Turbocharger Compressors With Diabatic Flows; Journal of Engineering for Gas Turbines and Power; Vol.132/072302; 2010
- Freymann R., Strobl W., Obieglo A.; Der Turbosteamer: Ein System zur Kraft-Wärme-Kopplung im Automobil; Motortechnische Zeitschrift; 05/2008; Wiesbaden; 2008
- Glavatskaya Y., Podevin P., Lemort V., Shonda O., Descombes G.; Reciprocating Expander for an Exhaust Recovery Rankine Cycle for a Passenger Car Application; energies; ISSN 11996-107; 2012
- Humble R.W.; Henry G.N.; Larson W.J.; Space Propulsion Analysis and Design; Space Technology Series; The McGraw-Hill Companies Inc.; New York; ISBN: 0-07-031320-2; 1995
- Kunte H. S.; Seume J. R. ; Partial Admission Impulse Turbine for Automotive ORC Application; SAE-Paper 2013-24-0092; 2013
- Oomori H., Ogino S.; Waste Heat Recovery of Passenger Car Using a Combination of Rankine Bottoming Cycle and Evaporative Engine Cooling System; SAE technical paper 930880; 1993, doi: 10.4271/930880
- Patel P., Doyle W.; Compounding the Truck Diesel Engine with an Organic Rankine-Cycle System; SAE technical paper 760343; 1976
- Sieb & Meyer AG; Einspeiseeinheit SD2R (25 kW) Hardwarebeschreibung, P-TD-0000202.3, 2013-10-09
- Simon C., Lang K., Feigl K., Bock E.; Turboladerdichtung für Null Ölverbrauch und minimiertes Blow-By; MTZ; 2010-04
- Span R.; Eifler W.; Struzyna R.; Nutzung der Motorwärme durch Kreisprozesse; presented at the FVV Informationstagung Motoren/Turbomaschinen; Bad Neuenahr; 2011
- Uusitalo A., Turunen-Saaresti T., Guardone A., Grönman A.; Design and Flow Analysis of a supersonic small scale ORC Turbine Stator with high Molecular Complexity Working Fluid; ASME Turbo Expo 2014; GT2014-26204; Germany; 2014
- Verneau A.; Supersonic Turbines for Organic Fluid Rankine Cycles from 3 to 1300 kW; von Karman Institute for Fluid Dynamics; Lecture Series 1987-07, Bertin; France; 1987

PERFORMANCE OF A SCROLL EXPANDER WITH AMMONIA-WATER

James Muye^{1*}, Joan Carles Bruno¹, Rajagopal Saravanan², Alberto Coronas¹

¹Universitat Rovira I Virgili, Department of Mechanical engineering,
Tarragona, Spain

²Anna University, Department of Mechanical engineering,
Chennai, India

* jamesmuye.mwangome@urv.cat

ABSTRACT

This paper examines the performance of an open drive scroll compressor modified to work as an expander operating on ammonia-water working medium. The modelling and simulation of the scroll expander is carried out with EES program. In this study a simulation of the expander performance at various pressure ratios (2-4), expander speeds (2500-7500 rpm) and ammonia concentrations (0.8-0.99) at a constant supply pressure (5 bar) and temperature (105°C) has been presented. The scroll expander produced a work output of 0.29 to 1.5 kW, with isentropic efficiencies of between 0.48-0.64. At the assumed inlet conditions, the optimum expansion ratio for the expander is 3.

1. INTRODUCTION

Rankine cycles can use a variety of working fluids including mixtures. One of these mixtures is the ammonia-water mixture using absorption and desorption processes. In the ammonia-water mixture, the low boiling point of ammonia makes it attractive for low/medium grade heat utilization; and the tendency to boil and condense at a range of temperatures of the ammonia-water mixture provides a good match between the heat source and working fluid. Also the similar molecular weights of ammonia and water make it possible to utilize the standard steam turbine components (Ganesh and Srinivas, 2010). This binary mixture can find applications in the Kalina and Goswami cycles. The efficiency of the Kalina cycle can be as much as 1.9 times higher than that of the Rankine Cycle system, at the same border conditions (Kalina, 1984).

The expander plays a critical role in systems converting heat into power. It has been established that utilizing a scroll expander can be a viable option for small scale applications. Song *et al.* (2014) gave a comprehensive review on the application and research of scroll expanders. Synthetic refrigerants have been the common working fluid in organic systems integrating scroll expanders (Bracco *et al.*, 2013; Twomey *et al.*, 2013; Jradi *et al.*, 2014). The scroll expander can also be useful in absorption power and cooling cycles. Ayou *et al.* (2013) provided an overview of the numerous combined absorption power and cooling cycles proposed in the literature. To investigate the viability of these cycles, Villada *et al.* (2014) modelled and simulated different solar absorption power-cooling systems that use ammonia based working fluid mixture to simultaneously produce cooling and mechanical power with a single system. They concluded that solar collectors could be used to drive combined absorption power and cooling cycles.

Demirkaya (2011) integrated a scroll expander in an absorptive power and cooling cogeneration system utilizing low temperature heat sources and performed a theoretical and experimental analysis. He modified an off the shelf open drive scroll compressor used in truck refrigeration units and warned that when using a scroll device for an absorption based cycle oil can be carried to the absorber and mix with the strong solution ammonia-water mixture by the vapor flow. The performance of the

expander was between 30-40%. The investigation however did not include characterization of the scroll device.

Mendoza *et al.* (2014) experimentally characterized and modeled a scroll expander with air and ammonia as working fluid. They studied how the main operating variables (supply pressure and temperature, pressure ratio, rotational speed and lubrication) influence the performance of the scroll expander and used a semi-empirical model to determine the scroll expander performance. A constant lubrication mass fraction of 2% was determined as the optimum lubrication amount. The semi-empirical model could predict mechanical power, exhaust temperature and supply mass flow rate of the expander at accuracy levels of $\pm 9\%$, ± 4 K and $\pm 5\%$, respectively.

The objective of this study is to investigate the performance of an open drive scroll compressor modified to work as an expander operating on ammonia-water working medium. In this paper a simulation of the expander performance for ammonia-water has been presented. Experiments to validate the model are being performed. The results of the complete study will be relevant in the future development of small capacity ammonia-water energy conversion systems driven at low/medium temperatures.

2. METHODOLOGY

The expander model adopted by Mendoza *et al.* (2014) for ammonia working fluid uses four semi-empirical parameters. The semi-empirical parameters required for this model are: the swept volume of the compressor (obtained from manufacturer's data), built in volume ratio (obtained from geometrical measurements of the device), work loss (from no load tests) and the theoretical leakage area (deduced from experimental data). The input parameters for the model are pressure and temperature at the expander inlet, pressure at the outlet and the expander rotational speed. It then predicts mechanical power, exhaust temperature and supply mass flow rate of the expander. This model is similar to the one proposed by Lemort *et al.* (2009), the only difference is that in the present model heat transfer with the environment has been assumed adiabatic because of the small heat transfer area of the expander. For simplicity the current model also neglects the effects of lubrication.

Figure 1 shows the model outline of the expander. The working fluid stream supplied to the expander (m_{su}) is split into two: a work producing stream (m_{in}) and a non-work producing steam (m_{leak}) which leaks between the scrolls. The work producing stream is expanded in two stages: the first process is adiabatic and reversible (from su to int) then followed by a constant volume process (int to ex_2). After the expansion processes there is adiabatic mixing of the two streams (m_{leak} and m_{in}) at ex_1 . The stream ex_1 then captures heat that was generated from mechanical losses such as friction to produce the exhaust stream ex .

The total work and actual work resulting from the two expansion stages can be calculated as:

$$W_{total} = m_{in} \{ (h_{in} - h_{int}) + v_{int} (P_{int} - P_{ex}) \} \quad (1)$$

$$W_{net} = W_{total} - W_{loss} \quad (2)$$

To calculate the isentropic efficiency of the expander, the actual work output is compared to the isentropic scenario. The isentropic efficiency of the expander can be expressed as:

$$\eta_{iso.exp} = W_{net} / \{ m_{su} (h_{su} - h_{iso.exp}) \} \quad (3)$$

The volumetric efficiency of the expander is the ratio between the theoretical mass flow rate and the actual mass flow rate as expressed in equation (4).

$$\eta_{v.exp} = (V_{swept} N \rho_{su}) / m_{su} \quad (4)$$

The mechanical efficiency of the expander is the ratio between the useful work and total work produced by the expander.

$$\eta_{m,exp} = W_{net} / W_{total} \quad (5)$$

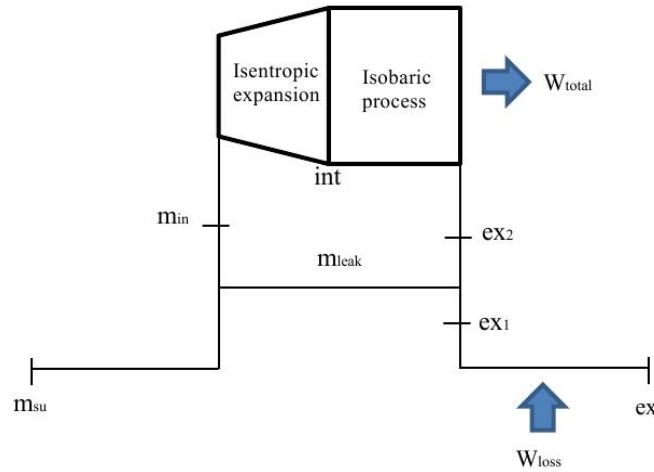


Figure 1: Model outline of the expander

Thermodynamic properties for the ammonia-water mixture are obtained from the (Engineering Equation Solver) EES (2014) external routines database. In a future study, a comparison will be made between the experimental data and simulated data. If the two sets of data do not agree, then the expander will need to be characterized specifically for ammonia-water.

3. RESULTS AND DISCUSSION

Figure 2 shows the expander production and performance at various concentrations and pressure ratios. Pressure at the expander inlet (P_{su}), temperature at the inlet (T_{su}) and rotational speed (N) were kept constant at 5 bar, 105°C and 5000 rpm respectively. The expander output increases with pressure ratio due to the improving expansion ratio across the expander. For all the three pressure ratios considered, the expander output decreases by 32W as the concentration (X) improves from 0.8 to 0.99. There is slightly more work produced at lower concentrations as expected because water has a higher enthalpy than ammonia. The expander registered the best isentropic efficiency ($\eta_{iso,exp}$) when operated at a pressure ratio of 3 ($Pr = 3$). The relationship between isentropic efficiency and pressure ratio depends on the rate of increase of actual work and ideal work (no entropy generation) as pressure ratio increases. Both actual work and ideal work increase with pressure ratio but at different rates. Thus at $Pr = 3$ actual work is closer in value to ideal work, this implies less entropy generation than at $Pr = 2$. Increasing the concentration improves $\eta_{iso,exp}$ at $Pr = 4$, however improving the concentration diminishes $\eta_{iso,exp}$ at $Pr = 2$. Therefore in the $Pr = 2$ case, improving the concentration increases irreversibilities however when $Pr = 4$ the reverse is true.

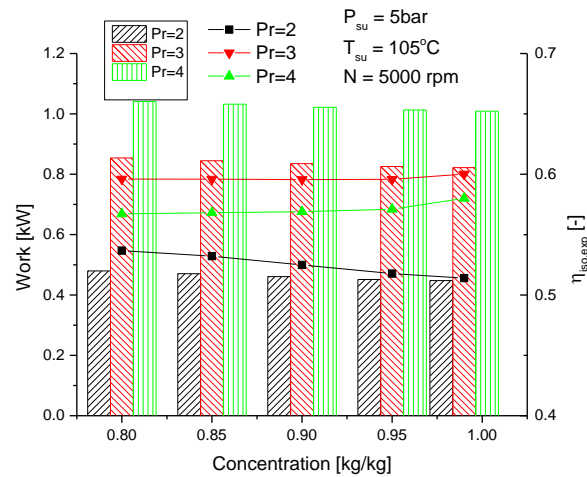


Figure 2: Expander work (bars) and isentropic efficiency (lines) at varying concentrations and pressure ratios

Figure 3 shows the expander work and isentropic efficiency at varying concentrations and expander speeds (P_{su} and T_{su} constant). At a speed of 2500 rpm, work output diminished by 16W as concentration improved from 0.8 to 0.99. It diminishes by 32W and 48W at 5000 rpm and 7500 rpm respectively. The best $\eta_{iso,exp}$ was observed at $Pr = 3$ for all the three rotational speeds considered. By design, the expander becomes more efficient and more productive as the rotational speed is increased since leakages are minimized at high speeds. The improvement in performance is more pronounced at $Pr = 4$ than at $Pr = 2$. Therefore high pressure ratios are not effective in low rotational speeds, the converse applies also. As depicted in Figure 2, increasing the concentration was found to improve $\eta_{iso,exp}$ at $Pr = 4$, however $\eta_{iso,exp}$ diminishes as the concentration is improved for the $Pr = 2$ case.

Figure 4 shows the expander exit temperature and mechanical efficiency at various concentrations and pressure ratios (P_{su} , T_{su} and N constant). A big pressure ratio implies a big expansion ratio across the scroll device which results to low expander exit temperatures because most of the enthalpy of the working fluid is harnessed by the expander. Therefore the expander exit temperature drops with increasing pressure ratio. The mechanical efficiency of the expander ($\eta_{m,exp}$) improves with pressure ratio because the work loss becomes insignificant as more work is produced. Because water has a better enthalpy than ammonia, the exit temperature generally reduces as the ammonia concentration improves. We can predict that the expander exit temperatures will drop further when the rotational speed is increased. Nonetheless the exit temperature, T_{ex} will increase when the supply temperature (T_{su}) is increased. Therefore by taking into account T_{su} , the value of T_{ex} can indicate the productivity of the expander. For example if two similar expanders are subjected to the same conditions, the expander with a lower T_{ex} will be the most productive.

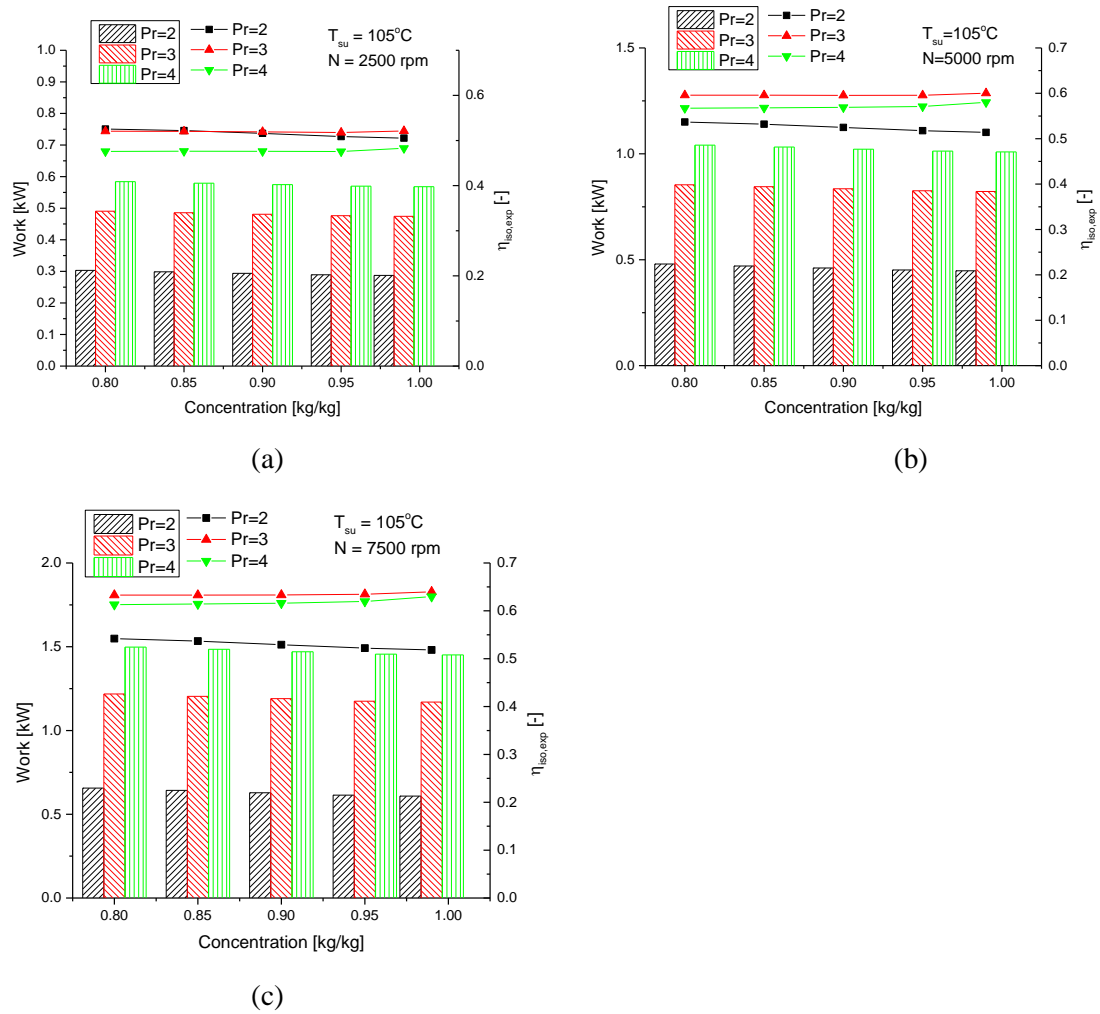


Figure 3: Expander work (bars) and isentropic efficiency (lines) at varying concentrations and expander speeds: (a) 2500 rpm (b) 5000 rpm and (c) 7500 rpm

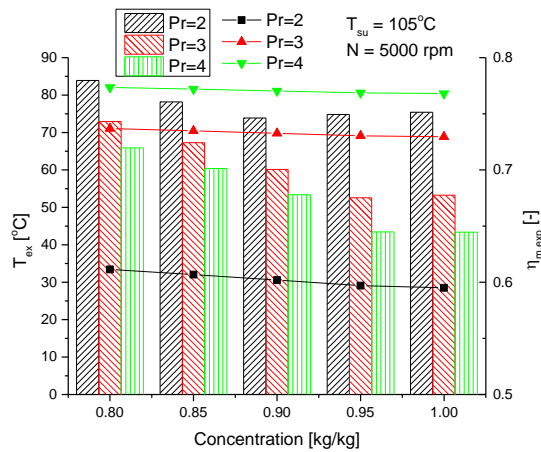


Figure 4: Expander exit temperature (bars) and mechanical efficiency (lines) at various concentrations and pressure ratios

At constant P_{su} , T_{su} and N the variation of volumetric efficiency and mass flow rate at various concentrations and pressure ratios is shown in Figure 5. The mass flow is fairly constant (at a

particular pressure ratio) with regard to changes in ammonia concentration however improving the pressure ratio increased the mass flow. The scroll expander is a fixed volume device therefore a high mass flow rate translates into a low volumetric efficiency as indicated in Figure 5.

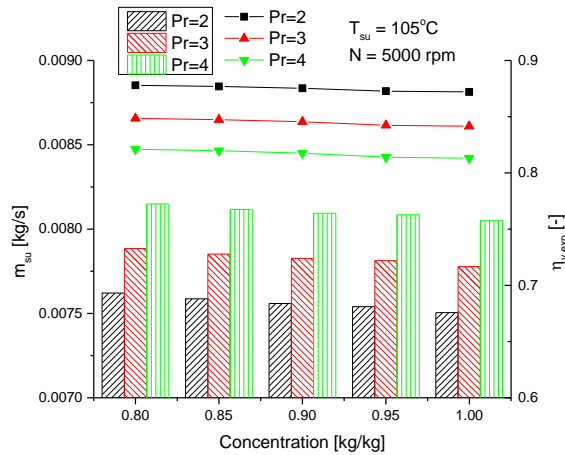


Figure 5: Volumetric efficiency (lines) and the mass flow (bars) through the expander at various concentrations and pressure ratios.

4. CONCLUSIONS

A simulated performance study of a scroll expander working with ammonia-water working fluid has been presented. The effects of pressure ratio, ammonia concentration and expander rotational speed on the performance of the expander was investigated. Generally the work output improved by increasing the pressure ratio and rotational speed or by reducing the ammonia concentration. When considering the expander isentropic efficiency, a pressure ratio of 3 ($Pr = 3$) was found to be ideal for the expander with a supply pressure and temperature of 5 bar and 105°C respectively and at rotational speeds of between 2500-7500 rpm. Also it is important to remark that high pressure ratios are not ideal at low rotational speeds and vice versa. At a supply pressure and temperature of 5 bar and 105°C respectively, the maximum $\eta_{iso,exp}$ is 63.96% achieved at $X = 0.99, Pr = 3, N = 7500$ and the maximum work output is 1.5 kW attained at $X = 0.8, Pr = 4, N = 7500$. The lowest $\eta_{iso,exp}$ is 47.59% at $X = 0.8, Pr = 4, N = 2500$ and the minimal work produced is 0.29 kW when $X = 0.99, Pr = 2, N = 2500$. A low expander exit temperature can imply either: a high expansion ratio (pressure ratio), a high rotational speed or simply a low supply temperature. Because the scroll expander is a fixed volume device, a high mass flow rate transforms into a low volumetric efficiency.

NOMENCLATURE

h	specific enthalpy	(kJ/kg)
m	mass flow rate	(kg/s)
N	rotations per minute	(rpm)
P	pressure	(bar)
Pr	pressure ratio	(-)
T	temperature	(°C, K)
V	volume	(m ³)
v	specific volume	(m ³ /kg)
W	work	(kW)

X concentration (kg/kg)

Subscripts

ex exiting the device
exp expander
in in to the device
int internal
iso isentropic
leak leakage
loss lost
m mechanical
net net
su supply
swept swept volume of device
total total
v volumetric

Greek symbols

η efficiency
 ρ density

REFERENCES

- Ganesh N.S., Srinivas T., 2010, Thermodynamic properties of binary mixture for power generation systems, *ARPJ Journal of Engineering and Applied Sciences*, vol.5, no. 10: p.49–54.
- Kalina A. I., 1984, Combined cycle system with novel bottoming cycle, *J Eng Gas Turbines Power*, Vol.106, no. 4: p.737–742.
- Song P., Wei M., Shi L., Danish S. N., Ma C., 2014, A review of scroll expanders for organic Rankine cycle systems, *Applied Thermal Engineering*, vol.75 : p. 54-64.
- Bracco R., Clemente S., Micheli D., Reini M., 2013, Experimental tests and modelization of a domestic-scale ORC (Organic Rankine Cycle), *Energy*, vol.58: p. 107-116.
- Twomey B., Jacobs P. A., Gurgenci H., 2013, Dynamic performance estimation of small-scale solar cogeneration with an organic Rankine cycle using a scroll expander, *Applied Thermal Engineering*, vol.51, no.1-2: p.1307-1316.
- Jradi M., Li J., Liu H., Riffat S., 2014, Micro-scale ORC-based combined heat and power system using a novel scroll expander, *International Journal of Low-Carbon Technologies*, vol. 9: p. 91–99.
- Ayou D. S., Bruno J. C., Saravanan R., Coronas A., 2013, An overview of combined absorption power and cooling cycles, *Renew. Sust. Energy Rev.*, vol. 21: p. 728–748.

Villada J. L., Ayou D. S., Bruno J. C., Coronas A., 2014, Modelling, simulation and analysis of solar absorption power-cooling systems, *International Journal of Refrigeration*, Vol. 39: p. 125–136.

Demirkaya G., 2011, *Theoretical and Experimental Analysis of Power and Cooling Cogeneration Utilizing Low Temperature Heat Sources*, PhD thesis, University of South Florida

Mendoza L. C., Navarro-Esbrí J., Bruno J. C., Lemort V., Coronas A., Characterization and modeling of a scroll expander with air and ammonia as working fluid, *Applied Thermal Engineering*, vol. 70, no.1: p. 630 – 640.

Lemort V., Quoilin S., Cuevas C., Lebrun J., 2009, Testing and modeling a scroll expander integrated into an Organic Rankine Cycle, *Applied Thermal Engineering*, Vol. 29, no.14–15: p. 3094–3102

EES, Engineering Equation Solver, 1992-2014. F-Chart Software. www.fchart.com.

ACKNOWLEDGEMENT

The authors acknowledge the support of Spanish Ministry of Economy and Competiveness (DPI2012-38841-C02-01) and the Government of India-Department of Science and Technology (DST/TM/SER1/2K12/74(C)). James Muye thanks Universitat Rovira i Virgili for the Martí i Franquès Predoctoral Research Staff Programme grant (2013PMF-PIPF-85).

PERFORMANCE ASSESSMENT OF ORGANIC RANKINE CYCLE DRIVEN VAPOR COMPRESSION HEAT PUMP

Violette Mounier*, Jürg Schiffmann[‡]

Laboratory of Applied Mechanical engineering,
Ecole Polytechnique Fédérale de Lausanne, EPFL
Rue de la Maladière 71b,
Neuchâtel, 2000, Switzerland

* corresponding author : violette.mounier@epfl.ch
<http://lamd.epfl.ch>

ABSTRACT

Vapor compression cycle heat pumps driven by thermal engines such as organic Rankine cycles (HP-ORC) are able to provide both heating and cooling for domestic applications for a large set of heat sources. Recently, an oil-free Compressor-Turbine Unit (CTU) in a HP-ORC has been investigated in which both the radial ORC turbine [1] and the radial heat pump compressor are running on the same gas bearing supported shaft [2]. The radial compressor and the radial inflow turbine have tip diameters of the order of 20 mm. The CTU has been tested at rotor speeds in excess of 200 krpm with shaft powers up to 2.4 kW. The compressor and the turbine were operated at pressure ratios of up to 2.8 and 4.4, while reaching isentropic efficiencies in excess of 70%, thus validating the concept based on small-scale turbomachinery[3]. Based on reduced order models, a study has been conducted to investigate the feasibility of the HP ORC system using an optimized CTU running with different working fluids and with different operating conditions. The effect of a regenerator and of the turbine inlet pressure has been investigated. The results reveal that HP-ORC systems can achieve a theoretical COP up to 2.11 and exergetic efficiencies up to 80% with R134a working fluid for an heating capacity of 40 kW, a sink temperature of 35 °C, an inlet turbine temperature of 180 °C and an evaporation temperature of 7 °C while preliminary experimental results [4] show COP up to 1.55 and exergetic efficiency up to 41%. It turns out that these cycles are of great interest since they are highly flexible, offer a wide operation range and can run on low GWP, hazard less fluids. Since heating power has a direct impact on the CTU-unit the scaling effects on the turbomachinery design and on rotor speed are investigated and presented in this article.

REFERENCES

- [1] J. Demierre, "Theoretical and Experimental Study of Thermally Driven Heat Pump Based on a Double Organic Rankine Cycle. Ph.D. thesis,," Ecole Polytechnique Fédérale de Lausanne, 2012.
- [2] J. Schiffmann, "Integrated Design , Optimization and Experimental Investigation of a Direct Driven Turbocompressor for Domestic Heat Pumps, Ph.D thesis," Ecole Polytechnique Fédérale de Lausanne, 2008.
- [3] J. Demierre, A. Rubino, and J. Schiffmann, "Modeling and experimental investigation of an oil free micro compressor turbine unit for an ORC driven Heat Pump," in *ASME Turbo Expo 2014*, 2014.
- [4] J. Demierre, D. Favrat, J. Schiffmann, and J. Wegele, "Experimental investigation of a Thermally Driven Heat Pump based on a double Organic Rankine Cycle and an oil-free Compressor-Turbine Unit," *Int. J. Refrig.*, vol. 44, pp. 91–100, 2014.

SYSTEMATIC FLUID-SELECTION IN EARLY STAGES OF ORC DESIGN – A PRACTICAL ENGINEERING APPROACH

Maximilian Roedder*, Christoph Laux and Matthias Neef

University of Applied Sciences Duesseldorf,
Josef-Gockeln-Str. 9, 40474 Duesseldorf, Germany
E-mail: maximilian.roedder@fh-duesseldorf.de
Web page: <http://mv.fh-duesseldorf.de/Neef>

ABSTRACT

The selection of a working fluid plays a major role in the design phase of organic Rankine cycles (ORC). Therefore, a suitable working fluid builds the foundation for a high power production in an ORC, which also leads to high cycle efficiencies and is hence one of the most significant selling arguments. But the selection of a working fluid should not only depend on the power output of the ORC. There are technical rules for example given by the legislator, which also have to be respected with highest priority.

For a quick evaluation of potential working fluids a selection procedure was developed. The method uses 23 criteria – in total – out of six main categories (*thermodynamical, procedural/thermodynamical, safety, environmental, economical and chemical*), which should be considered with adequate priority related to the implementation of the ORC. During the first tests, not all of the criteria were evaluated, therefore, the process was improved with an accurate elaboration of the omitted criteria and by the integration of the working fluid mass flow directly into the selection process.

The procedure itself is divided into four main steps, the *pre-selection*, the *elimination process*, the *ranking process* and the *final fluid choice*. Such procedure requires the subdivision of the 23 criteria into elimination criteria (EC) and tolerance criteria (TC). An advantage of this disposition into a structured process in the early design phase of the ORC is the direct elimination of working fluids in the pre-selection- and elimination-phase. The application of the selection procedure into the design process leads also to a saving in development time and helps to make an educated decision.

This contribution deals with a comprehensive compilation of all 23 criteria deemed as relevant for the fluid selection and shows examples of fluid selections.

1. INTRODUCTION

With the perpetual increasing standards in the development of renewable energy technologies the ORC technology has to prove its own worth. To keep the competitive ability of ORCs the plant cost has to remain small while the power production and the electric cycle efficiency should increase.

Designing the cycle components as high-end equipment (e.g. pumps, fans and multistage turbines) surely leads to higher efficiencies but usually by acceptance of immensely rising plant cost.

The power production of an ORC depends also on the cycle design and the optimization of operation parameters as well as the selection of a suitable organic working fluid.

For industrial use, competitive systems must not exceed an upper boundary for the cost per installed kW of about 5000€ while the cycle efficiency should be as high as possible, which can partially be achieved by the selection of the most suitable working fluid.

However, a suitable working fluid has to combine a multitude of specific characteristics depending on the area of application and with respect to the manufacture's and the legislator's requirements. Quoilin et al. [6] observed, that commercial ORC power plants usually operate with common working fluids despite to the broad range of fluids, which have been analyzed and reviewed in numerous scientific fluid selection studies [1,2,3,4,5,7].

Hence, it might be of general interest to initiate a trend in the standardization of a working fluid selection procedure in the early design phase of ORCs without losing any kind of freedom in the individuality of the ORC plant design itself.

The recommendation for the integration of a structured procedure for the selection of organic working fluids into the ORC design phase was already expressed by Roedder et al. [8], where also the definition of the selection criteria with relation to earlier works from several authors and the development of the selection procedure is explained in more detail.

With the first application of the method by selecting a low temperature (LT) and a high temperature (HT) working fluid for a two stage ORC it was recognized that the integration of all criteria into the process workflow requires a more accurate revision.

In this work a revision of the suggested elimination criteria (EC) and tolerance criteria (TC) [8] is presented.

The present paper contains a short briefing about the selection method. The main focus is directed at additional criteria with respect to [8]. The significance of all criteria is then evaluated to compile a final version of the relevant elimination and tolerance criteria.

2. SYSTEMATIC APPROACH

The selection procedure itself is based on an evaluation method for the validation of technical systems [9], which provides a split of selection methods into partitions. A subdivision of the procedure enables a structured process, which increases the quality of the evaluation method that also depends strongly on the defined selection criteria. Hence it is important that the customer requirements are carefully included and explicitly considered while the criteria elaboration.

A split of the procedure into four main steps (the *pre-selection*, the *elimination*, the *ranking* and the *final fluid choice*) is evidentially practical for the evaluation of organic working fluids [8]. The suggested work flow ensures the elimination of working fluids in an early step of the method, which leads to a saving in time due to the rating of only passed fluids. A well-structured working instruction also leads to minimization of failures in the approach and hence carefulness for beginners and also advanced users in ORC design.

3. THE SELECTION PROCEDURE

The application of the procedure is demonstrated by selecting an organic working fluid for a custom designed single-stage HT-ORC for training intention and applied research. Due to the integration of an adjustable electric heating rod into the heat supplying thermo-oil cycle the system allows operation modes at different temperature levels. Using dry or isentropic fluids – where the turbine outlet condition is almost settled in the superheated area – enables the recovery of the excessive condensation heat by integration of a recuperator (R) behind the turbine (T).

After the selection of a suitable working fluid for the given HT-ORC (Figure 1) the design and the thermodynamical cycle calculation is performed with “EBSILON®Professional” [12], a simulation tool for thermodynamic cycle calculations.

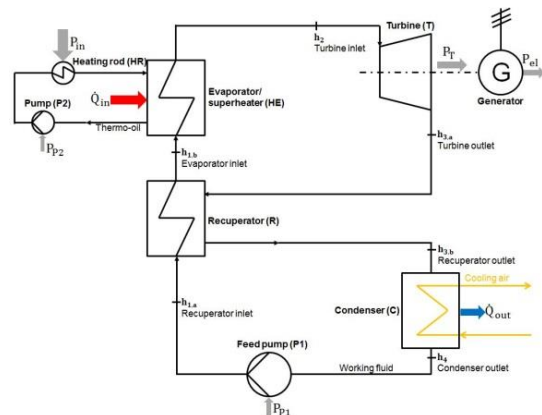


Figure 1: HT-ORC for training intention and applied research

If not indicated otherwise thermodynamic variables are calculated with the in “EBSILON®Professional” [12] integrated fluid properties calculator based on the “REFPROP-Database” – developed by the National Institute of Standards and Technology [11].

The “GESTIS Substance Database” [10] combines the information of data sheets about the risks of most fluids and standard properties (e.g. melting point etc.).

3.1 THE PLANT DESIGN

The thermo-oil cycle is designed with a 55kW heating rod (HR) and a circulation pump (P2) for supplying the HT-ORC with heat by transfer in the evaporator/superheater (HE). A 7,5kW synchro-generator (G) driven by a HT-turbine (T) feeds the primary power system. Improving the cycle efficiency by the recuperation of the condensation heat just conforms with the technical standard in the ORC technology.

Power plant components are designed for system operations up to a maximum temperature of 200°C, which fits the maximum main steam temperature at the turbine inlet $T_{h2} = 180^\circ\text{C}$ and enables the design of favourable low priced components (e.g. brazed heat exchanger).

Condensing the fluid against the ambient condition favours the installation of an air cooled direct condenser, which omits the need of an additional cooling water cycle. Hence the condensing temperature is fixed at 35°C (T_{h4}).

Table 1 shows the assumed components efficiencies, which are required as input for a later cycle simulation and useful in the process of the selection procedure. With the currently available cycle conditions (also listed in Table 2) and with the assumed isentropic turbine efficiency given in Table 1 it is possible to calculate the fluid condition at the turbine outlet (equation 1).

But before starting detailed cycle calculations it is necessary to pre-select organic working fluids (see Table 3).

Table 1: Components efficiencies (η)

Component	Description	Value
Turbine	Isentropic efficiency	$\eta_{s,T}$ 0.75
Feed pump	Isentropic efficiency	$\eta_{s,P}$ 0.80
Generator	Electric efficiency	$\eta_{el,G}$ 0.90
Heat exchanger	Component efficiency	η_{HE} 0.95

Table 2: Preliminary cycle conditions

Condition		Temperature [°C]
Turbine inlet	T_{h2}	180,0
Condenser outlet	T_{h4}	35,0

$$\eta_{s,turbine} = \frac{|h_3 - h_2|}{|h_{3,s} - h_2|} \quad (1)$$

3.2 PRE-SELECTION

The mean steam temperature (T_{h2}) at the turbine inlet of 180°C enables the use of high and low temperature working fluids. Cyclopentane is indicated by Fischer et al. [3] as a proven high temperature working fluid and iso-Pentane investigated as low temperature working fluid [2]. Novec 649 is specified as an effective heat conducting working fluid with a high safety standard.

The comparison of the pre-selected fluids (Table 3) follows by involving EC and TC.

Table 3: Pre-selected working fluids

Name	Number	Molecular-formula	Substance class	Critical temperature	Critical pressure
				°C	bar
				T_c	p_c
Cyclopentane	1	C_5H_{10}	Cyclic alkanes	238,6	45,7
Iso-Pentane	2	C_5H_{12}	Branched alkanes	187,2	33,8
Novec 649	3	$C_6F_{12}O$	Branched ketones	168,7	18,7

3.3 ELIMINATION CRITERIA (EC)

For the elimination of potential working fluids each EC needs the specification of a fixed range of values (v_i) as described in [8]. The pre-selected working fluid can be eliminated directly via any EC by comparison of the fluid specific value with its specified range of values. It has to be rejected if it is

out of the defined range. An accurate explanation for the definition of the range of values is given as follows (Table 4):

Table 4: Definition of the Elimination criteria (EC) and range of value (v_i)

Elimination criterion	Reasoning for specified validity of value	Range of values (v_i)
C₁ Boiling point (T_b)	To prevent the vaporization of working fluids at general laboratory conditions (1,013bar) the boiling point temperature is restricted to temperatures below 35°C.	$35^\circ\text{C} \leq T_b$
C₂ Melting point (T_m)	Permanent plant operation and a frozen fluid inside the plant should be avoided by the melting point criterion. The plant installation inside a permanent heated building allows a melting point with an upper boundary of -1°C .	$T_m \leq -1^\circ\text{C}$
C₃ Kinematic viscosity (ν)	A very low viscosity leads to power losses and raises the pump wastage. A high viscosity has a negative effect on the pumpability of the fluid. Therefore, the viscosity can vary between a maximum and a minimum value, which is mostly given by the manufacturer of the fluid.	$0,3 \frac{\text{mm}^2}{\text{s}} \leq \nu \leq 120 \frac{\text{mm}^2}{\text{s}}$
C₄ Thermo-stability (T_{max})	Designing the plant for an operating temperature of about 200°C with additionally 20°C safety margin enables a maximum temperature of 220°C .	$220^\circ\text{C} \leq T_{\text{max}}$
C₅ Condensation pressure (p_{h3})	According to the current state of technology the ORC systems should run safely with a vacuum up to 0,2bar. Fluids with a condensing pressure lower than 0,2bar depending on condensing Temperature (T_{h4}) are neglected.	$0,2\text{bar} \leq p_{h4}$
C₆ Flammability (T_{fl})	The flammability of organic working fluids is a very important safety characteristic, which should contain a high safety-tolerance regarding the maximum of the heat source temperature – in this case 200°C . Therefore, only fluids with an ignition temperature of about 50°C above the temperature level of the heat source are recommended.	$250^\circ\text{C} \leq T_{fl}$
C₇ Toxicity (X_T)	Substances which are harmful to health or dangerous to life are classified as hazardous substances according to the Globally Harmonised System (GHS) [13]. They have to be rejected. The “GESTIS Substance Database” [10] provides the information about the risks of most fluids.	$X_T = 0$ (none)
C₈ Ozone depletion potential (ODP)	Due to national or international prohibitions the consideration of working fluids with an ODP above zero would be wasted time.	$\text{ODP} = 0$ (none)
C₉ Cost of the working fluid	It should be noted that other criteria can be a much larger cost drivers than the cost of the substance itself (e.g. properties influencing component size & complexity, see e.g. C ₁₃ -C ₁₅). Due to the small plant capacity, which minimizes the amount of the fluid, substance costs are not considered.	– not considered –

Table 5 contains the fluid specific values for the comparison with the defined range of value of the EC. If a fluid specific value does not match with the defined range, the fluid has to be rejected (fail / “0”). Otherwise fluids pass the elimination process and are marked with “1”.

Table 5: Comparison of the fluid specific values with the defined range for the EC

			Cyclopentane		Iso-Pentane		Novec 649		
Elimination criteria (C _i)		w _i	Range of value (v _i)	Value	e _i	Value	e _i	Value	e _i
1	Boiling point	-	35°C ≤ T _b	49	1	28	0	49	1
2	Melting point	-	T _m ≤ -1°C	-94	1	-160	1	-108	1
3	Kinematic viscosity	-	0,3 ≤ ν ≤ 120	5,32	1	0,34	1	1,74	1
4	Thermostability	-	220°C < T _{max}	276,9	1	226,9	1	226,9	1
5	Condensation pressure	-	0,2bar ≤ p _{h3}	0.5	1	1.1	1	0.5	1
6	Flammability	-	250°C ≤ T _{fl}	320	1	420	1	-	1
7	Toxicity	-	X _T = 0	-	1	-	1	-	1
8	Ozone depletion potential	-	ODP = 0	-	1	-	1	-	1
9	Cost of the working fluid	-	–	Not included		Not included		Not included	
Fail (0) / pass (1):				1		0		1	

3.4 TOLERANCE CRITERIA (TC)

Tolerance criteria (TC) are designated for the rating of the potential working fluids, which have passed the pre-selection and the elimination process. For the ranking process a weighting factor (w_i) needs to be defined for each TC. The weighting of a TC depends on its significance and should be considered with respect to the area of system application, scientific literature and manufactures acknowledgment. Table 6 contains the grading system for the TC weighting used as follows.

For the ranking of working fluids, ranges of values (v_i) have to be assigned to each TC with respect to the evaluation system shown in Table 7. The “top ranking” for the most suitable range is rated with four points and a just acceptable range is rated with one evaluation point. Outside the defined ranges fluids are evaluated with zero points.

Table 6: Grading system for the weighting factor (w_i)

Weighting-factor (w _i)	Grading
4	Essential
3	Important
2	Basic
1	Less Important

Table 7: Measurement for the suitability of the ranges (v_i)

Evaluation number (e _i)	Suitability
4	Top-ranking
3	Satisfyingly
2	Basic-ranking
1	Just acceptable
0	Out of range

After compiling the TC (see Table 8) and completing the preparation for the fluid ranking the specific values of the pre-selected working fluids have to be calculated and compared with the evaluated ranges (v_i). Hence the working fluids are assigned with an evaluation number (e_i) for each TC with respect to the specified ranges.

In the ranking process, each fluid obtains a rating number (s_x) that depends on the achieved evaluation number (e_i) and the respective weighting factor (w_i). Therefore, the rating number or severity (s_x) for each fluid is defined as follows (equation 2):

$$s_x = \sum_{i=1}^n w_i \cdot e_i \quad (2)$$

Table 8: Definition of the Tolerance criteria (TC) with weighting and range of values (v_i)

Tolerance criterion	Reasoning for specified range of values and weighting	e_i	Range of values (v_i)
C₁₀ Enthalpy-slope ($\Delta h_{3,a-2}$) $w_{10} = 2$	Working fluids with an enthalpy-slope of about $120 \frac{\text{kJ}}{\text{kg}}$ in the region of superheated steam (turbine outlet to turbine inlet) are top ranked due to their high transfer of work, which can be converted by the turbine. Due to the direct influence on the cycle power production (equation 3) the enthalpy-slope is weighted as a basic criterion. $P_{el} = \Delta h_{3,a-2} \cdot \dot{m}_{\text{Fluid}} \quad (3)$	4	$120 \frac{\text{kJ}}{\text{kg}} \leq \Delta h_{3-2}$
		3	$60 \frac{\text{kJ}}{\text{kg}} \leq \Delta h_{3-2} < 120 \frac{\text{kJ}}{\text{kg}}$
		2	$30 \frac{\text{kJ}}{\text{kg}} \leq \Delta h_{3-2} < 60 \frac{\text{kJ}}{\text{kg}}$
		1	$10 \frac{\text{kJ}}{\text{kg}} \leq \Delta h_{3-2} < 30 \frac{\text{kJ}}{\text{kg}}$
		0	$\Delta h_{3-2} < 10 \frac{\text{kJ}}{\text{kg}}$
C₁₁ Thermal conductivity (λ) $w_{11} = 1$	For the first integration of the thermal conductivity (λ) into the procedure the top range is defined according to the thermal conductivity of water in its liquid phase (1,013bar, 20°C). For the comparison the fluid specific conductivity is calculated at the same condition. The thermal conductivity describes the ability of intermolecular heat transfer. Therefore, a high thermal conductivity is coupled to a favourable sizing of the heat exchangers. Due to the first consideration as tolerance criterion it is weighted as “less important”.	4	$0,6 \frac{\text{W}}{\text{m}\cdot\text{K}} \leq \lambda$
		3	$0,3 \frac{\text{W}}{\text{m}\cdot\text{K}} \leq \lambda < 0,6 \frac{\text{W}}{\text{m}\cdot\text{K}}$
		2	$0,1 \frac{\text{W}}{\text{m}\cdot\text{K}} \leq \lambda < 0,3 \frac{\text{W}}{\text{m}\cdot\text{K}}$
		1	$0,001 \frac{\text{W}}{\text{m}\cdot\text{K}} \leq \lambda < 0,1 \frac{\text{W}}{\text{m}\cdot\text{K}}$
		0	$\lambda < 0,001 \frac{\text{W}}{\text{m}\cdot\text{K}}$
C₁₂ Isobaric heat capacity (c_p) $w_{12} = 1$	The benchmark for the isobaric heat capacity (c_p) is liquid water at 20°C and 1,013bar. For the comparison the liquid isobaric heat capacity (c_p) of the working fluid is required at the same condition. This criterion is weighted as “less important” because its implementation and significance in the process has to be evaluated in more detail.	4	$4,19 \frac{\text{kJ}}{\text{kg}\cdot\text{K}} \leq c_p$
		3	$3,00 \frac{\text{kJ}}{\text{kg}\cdot\text{K}} \leq c_p < 4,19 \frac{\text{kJ}}{\text{kg}\cdot\text{K}}$
		2	$1,50 \frac{\text{kJ}}{\text{kg}\cdot\text{K}} \leq c_p < 3,00 \frac{\text{kJ}}{\text{kg}\cdot\text{K}}$
		1	$0,50 \frac{\text{kJ}}{\text{kg}\cdot\text{K}} \leq c_p < 1,50 \frac{\text{kJ}}{\text{kg}\cdot\text{K}}$
		0	$c_p < 0,50 \frac{\text{kJ}}{\text{kg}\cdot\text{K}}$
C_{13.1} Enthalpy of vaporization (E_v) $w_{13.1} = 1$	With respect to cycle power, The enthalpy of vaporization – at main steam pressure – is coupled with the working fluid mass flow (C_{14}) and the supplied heat. For the considered application, an enthalpy of vaporization range at approximately $275 \frac{\text{kJ}}{\text{kg}}$ allows system operation with a suitable working fluid mass flow ($0,2 \frac{\text{kg}}{\text{s}}$) by given heat supply (55kW) until reaching the saturated steam area. Due to the negative as well as positive effects of high enthalpy ranges during vaporization – discussed in more detail by Roedder et al. [8] – the weighting equates “less important”.	4	$250 \frac{\text{kJ}}{\text{kg}} \leq E_v \leq 300 \frac{\text{kJ}}{\text{kg}}$
		3	$E_v < 250 \frac{\text{kJ}}{\text{kg}}$ $300 \frac{\text{kJ}}{\text{kg}} < E_v$
		2	$E_v < 150 \frac{\text{kJ}}{\text{kg}}$ $400 \frac{\text{kJ}}{\text{kg}} < E_v$
		1	$E_v < 50 \frac{\text{kJ}}{\text{kg}}$ $500 \frac{\text{kJ}}{\text{kg}} < E_v$
		0	-
C_{13.2} Enthalpy of condensation (E_c) $w_{13.2} = 2$	During condensation the entropy inside the system decreases, hence heat energy has to be extracted. For an efficient single stage cycle the condensing heat should be as small as possible because it is not of further use for the system. Due to its influence on the cycle efficiency the enthalpy of condensation is weighted as a “basic” criterion.	4	$E_c \leq 50 \frac{\text{kJ}}{\text{kg}}$
		3	$50 \frac{\text{kJ}}{\text{kg}} < E_c \leq 100 \frac{\text{kJ}}{\text{kg}}$
		2	$100 \frac{\text{kJ}}{\text{kg}} < E_c \leq 400 \frac{\text{kJ}}{\text{kg}}$
		1	$400 \frac{\text{kJ}}{\text{kg}} < E_c \leq 1000 \frac{\text{kJ}}{\text{kg}}$
		0	$1000 \frac{\text{kJ}}{\text{kg}} < E_c$

C₁₄ Working fluid mass flow (\dot{m}_{Fluid})	<p>For the power production, the working fluid mass flow should be as high as possible (see equation 3) but with increasing mass flow the volume flow increases too (equation 4).</p> $\dot{V}_{\text{Fluid}} = \frac{\dot{m}_{\text{Fluid}}}{\rho} \quad (4)$ <p>Therefore, the working fluid mass flow needs an upper and a lower boundary. Its best available range for the present plant size is settled between $0,20 \frac{\text{kg}}{\text{s}} \leq \dot{m}_{\text{Fluid}} \leq 0,25 \frac{\text{kg}}{\text{s}}$. It should be possible to reach saturated steam condition by heating the fluid from 35°C (T_{h4}) up to 180°C (\dot{Q}_{to}) without involving the recuperation heat. The direct calculation of a mass flow requires the definition of the fluid condition at the turbine inlet (h_2) and after the feed pump ($h_{1,a}$) – without recuperator.</p> <p>Due to its direct influence on the cycle power production and also on the volume flow it is weighted relatively high.</p>	4	$0,20 \frac{\text{kg}}{\text{s}} \leq \dot{m}_{\text{Fluid}} \leq 0,25 \frac{\text{kg}}{\text{s}}$	
		3	$\dot{m}_{\text{Fluid}} > 0,15 \frac{\text{kg}}{\text{s}}$	$0,25 \frac{\text{kg}}{\text{s}} < \dot{m}_{\text{Fluid}}$
		2	$\dot{m}_{\text{Fluid}} > 0,10 \frac{\text{kg}}{\text{s}}$	$0,35 \frac{\text{kg}}{\text{s}} < \dot{m}_{\text{Fluid}}$
		1	$\dot{m}_{\text{Fluid}} > 0,05 \frac{\text{kg}}{\text{s}}$	$0,50 \frac{\text{kg}}{\text{s}} < \dot{m}_{\text{Fluid}}$
		0	$\dot{m}_{\text{Fluid}} < 0,05 \frac{\text{kg}}{\text{s}}$	$1,00 \frac{\text{kg}}{\text{s}} < \dot{m}_{\text{Fluid}}$
w₁₄ = 3				
C₁₅ Density at the turbine outlet (ρ_3)	<p>Due to the decreasing volume flow (\dot{V}) with increasing density (ρ) the plant size and cost remain small. Therefore, working fluids with a high density at the turbine outlet (ρ_3) are favoured due to their positive effect on the volume flow rate.</p> <p>Moreover a high fluid density can compensate the negative effect of a high working fluid mass flow on the volume flow.</p>	4	$4,0 \frac{\text{kg}}{\text{m}^3} \leq \rho_3$	
		3	$2,0 \frac{\text{kg}}{\text{m}^3} \leq \rho_3 < 4,0 \frac{\text{kg}}{\text{m}^3}$	
		2	$1,0 \frac{\text{kg}}{\text{m}^3} \leq \rho_3 < 2,0 \frac{\text{kg}}{\text{m}^3}$	
		1	$0,1 \frac{\text{kg}}{\text{m}^3} \leq \rho_3 < 1,0 \frac{\text{kg}}{\text{m}^3}$	
		0	$\rho_3 < 0,1 \frac{\text{kg}}{\text{m}^3}$	
w₁₅ = 3				
C₁₆ Main steam pressure (p_{h2})	<p>The main steam pressure depends on the turbine inlet temperature of the working fluid. It is a cycle variable which has direct influence on the cycle conduct (supercritical, subcritical, wet or superheated). As a reasonable simplification the main steam pressure is defined as equal to the evaporating pressure at the turbine inlet temperature (Table 2). Fluids with a pressure higher than 50bar are neglected.</p>	4	$p_{h2} \leq 15\text{bar}$	
		3	$15\text{bar} < p_{h2} \leq 20\text{bar}$	
		2	$20\text{bar} < p_{h2} \leq 30\text{bar}$	
		1	$30\text{bar} < p_{h2} \leq 50\text{bar}$	
		0	$50\text{bar} < p_{h2}$	
w₁₆ = 2				
C₁₇ Heat transfer coefficient (α)	<p>The heat transfer coefficient depends on the flow rate, the viscosity, the thermal conductivity, the geometric conditions of the cycle and the surface conditions. Hence the heat transfer coefficient can only be assumed for heat transferring components (e.g. evaporators, condensers or heat exchangers in general). The integration into the fluid selection process needs a more accurate analysis.</p>		– not considered –	
w₁₇ = 1				
C₁₈ Global warming potential (GWP)	<p>The global warming potential (GWP) of a fluid describes the negative effect after its release to the environment in contrast to carbon dioxide which has a GWP of “1”. That means a substance with a GWP of “2” is assumed to affect global warming two times stronger than carbon dioxide. The GWP can be obtained from the “GESTIS Substance Database” [10].</p>	4	GWP = 0 (none)	
		3	$0 < \text{GWP} \leq 100$	
		2	$100 < \text{GWP} \leq 500$	
		1	$500 < \text{GWP} \leq 1000$	
		0	$1000 < \text{GWP}$	
w₁₈ = 4				
C₁₉ Water pollution class (WGK)	<ul style="list-style-type: none"> • WGK1: light harmful • WGK2: harmful • WGK3: strong harmful 	4	no WGK	
		3	WGK1	
		2	WGK2	
		0	WGK3	
w₁₉ = 4				

C₂₀ Gross thermal efficiency (η_g)	The gross thermal efficiency (η_g) can be evaluated with the help of the p,h-diagram. It is a quick method to consider the ratio of the external heat input to the isentropic expansion work at which the pump work and the irreversibilities in the turbine are neglected. For a detailed analysis the net thermal efficiency must be considered in a full performance analysis.	4	$14\% \leq \eta_g$
		3	$11\% \leq \eta_g < 14\%$
		2	$7\% \leq \eta_g < 11\%$
		1	$5\% \leq \eta_g < 7\%$
		w₂₀ = 4	0
C₂₁ Molecular weight (M)	Working fluids with high molecular weight (M) have a larger amount of mass per volume (equation 3), which has to be transported by the pump. Hence compressing heavy working fluids requires a larger energy input of the feed pump and leads to a negative effect on the net electric efficiency by an increased internal energy demand of the system. $m = M * n = [\text{kg}] \quad (5)$	4	$MW \leq 100 \frac{\text{g}}{\text{mol}}$
		3	$100 \frac{\text{g}}{\text{mol}} < MW \leq 250 \frac{\text{g}}{\text{mol}}$
		2	$250 \frac{\text{g}}{\text{mol}} < MW \leq 400 \frac{\text{g}}{\text{mol}}$
		1	$400 \frac{\text{g}}{\text{mol}} < MW \leq 550 \frac{\text{g}}{\text{mol}}$
		w₂₁ = 2	0
C₂₂ Molecular complexity (MC)	A measurement for the complexity of a molecule can be the number of atomic bonds inside a molecule. For a user-friendly method of application the classification into cyclic, branched and single molecules is sufficient. Therefore, simple fluids with only one link should be classified as single molecules with strong interaction and not easily severable. Splitting branched molecules demand lesser energy due to their weakly cohesion and large contact surface. The cohesion inside a cyclic molecule-system is stronger than inside branched systems.	4	single structure
		3	cyclic structure
		2	branched structure
		1	–
		w₂₂ = 1	0

The fluid specific values for the comparison with the defined range of values (Table 8) are listed in Table 9, which also includes the calculation of the severity (s_x). The overall severity results in a maximum of 120 evaluation points in total. Iso-Pentane – although excluded during the elimination process – is also discussed in the ranking process.

Table 9: Comparison of the fluid specific values with the defined ranges for the TC (incl. ranking)

Tolerance criteria (C _i)		Unit	w _i	Cyclopentane		Iso-Pentane		Novec 649	
				Value	e _i	Value	e _i	Value	e _i
10	Enthalpy slope	$\frac{[\text{kJ}]}{[\text{kg}]}$	2	107,2	3	106,7	3	32,1	2
11	Thermal conductivity	$\frac{[\text{W}]}{[\text{m}\cdot\text{K}]}$	1	0,13	2	0,11	2	0,06	1
12	Isobaric heat capacity	$\frac{[\text{kJ}]}{[\text{kg}\cdot\text{K}]}$	1	1,79	2	2,25	2	1,10	1
13.1	Enthalpy of vaporization	$\frac{[\text{kJ}]}{[\text{kg}]}$	1	332,5	3	223,6	3	21,56	1
13.2	Enthalpy of condensation	$\frac{[\text{kJ}]}{[\text{kg}]}$	2	403,1	1	341,43	2	93,4	3
14	Working fluid mass flow	$\frac{[\text{kg}]}{[\text{s}]}$	3	0,093	1	0,095	1	0,313	3
15	Density (h_3)	$\frac{[\text{kg}]}{[\text{m}^3]}$	3	1,10	2	2,42	3	4,73	4
16	Main steam pressure	[bar]	2	5,8	4	14,6	4	17,6	3
17	Heat transfer coefficient	$\frac{[\text{W}]}{[\text{m}^2\cdot\text{K}]}$	-	-	-	-	-	-	-
18	Global warming potential	[-]	4	-	4	3	3	1	3
19	Water pollution class	[-]	4	1	3	2	2	1	3
20	Gross thermal efficiency	[%]	4	12,84	3	13,08	3	13,01	3
21	Molecular weight	$\frac{[\text{g}]}{[\text{mol}]}$	2	70	4	72	4	316	2
22	Molecular complexity	[-]	1	cyclic	3	branched	2	branched	2
Severity (s_x) =				83		79		82	

3.5 FINAL FLUID CHOICE

Based on the working fluid ranking, Cyclopentane obtains the best severity ($s=83$) with only one evaluation point ahead of Novec 649 with $s=82$. Iso-Pentane ($s=79$) was already rejected during the elimination process because it evaporates at too low temperature level while ambient pressure. The close match of the ranking justifies the need of a detailed cycle simulation and the comparison of the net electric efficiency for the two remaining fluid.

The simulation with “EBSILON®Professional” [12] suggests the selection of Cyclopentane due to the higher net electric efficiency (12,7%) in contrast to Novec 649 (12,1%).

4. RESULTS

For the elimination of working fluids the cost of the working fluid itself (C_9) is excluded from the process due to the addition of much higher cost driver (C_{14} & C_{15}) into the ranking process.

The consideration of additional eight tolerance criteria (C_{11} ; C_{12} ; $C_{13.1}$; $C_{13.2}$; C_{14} ; C_{17} ; C_{21} ; C_{22}) – compared to the earlier work of Roedder et al. [8] – was reviewed with respect to working effort and their utilization in the selection procedure.

In the presented work the thermal conductivity (C_{11}) was calculated with a simulation tool [12] that allows a simple integration into the selection procedure with only a slight demand of time.

The liquid isobaric heat capacity (C_{12}) – at ambient condition – is usually given by freeware substance-databases like “GESTIS” [10] or diverse other once or can also be calculated with any available calculation software and hence should be integrated into the rating process.

While using the p,h-diagram to consider the ratio of the external heat input to the isentropic expansion work – gross thermal efficiency (C_{20}) – the enthalpy of vaporization ($C_{13.1}$) and condensation ($C_{13.2}$) can also be achieved with nearly non additional work input.

For the integration of the heat transfer coefficient (C_{17}) an extensive calculation has to be performed. Hence it is the only TC, which is not considered in this work.

Due to heavy differences in the molecular weight (C_{21}) of working fluids and the increasing demand of energy consumed by the feed pump and hence its negative effect on the net electric efficiency the molecular weight should be included into the selection procedure.

The molecular complexity (C_{22}) is distinct in three categories with differences in their intermolecular cohesion, which is also confirmed by the thermostability of a working fluid (C_4) in the elimination process. Because it is not necessary to discuss criteria with the same meaning the molecular complexity can be omitted in favour of the thermostability. For the integration of the molecular complexity into the selection procedure the range of values needs a more complex classification.

5. CONCLUSIONS

In general, the integration of a standardized selection procedure into the early design phase of an Organic Rankine Cycle power plant is an assisting method, which pays off when several working fluids are to be considered.

The fluid selection is based on 21 criteria in total by exclusion of the working fluid cost (C_9) from the elimination process and the heat transfer coefficient (C_{17}) from the ranking process. It is shown that the ranking of the working fluid with the suggested tolerance criteria (C_{17} excluded) – leads to a representative result (see chapter 3.4), which is confirmed by a subsequent cycle simulation and the calculation of the net thermal efficiency.

In this work the integration of all reasonable criteria into the method was emphasized. Further investigations will be directed at a generalization of how to choose suitable weighting factors. It will also be necessary to show that the suggested method leads to customized results and shorter development times compared to a design process without application of an organized selection process ORC.

NOMENCLATURE

C	Criterion	[–]	\dot{Q}	Heat flow	$\left[\frac{\text{kJ}}{\text{s}}\right]$
e	Evaluation number	[–]	s	Rating number (severity)	[–]
EC	Elimination criterion	[–]	T	Temperature	[°C]
GHS	Globally Harmonised System	[–]	TC	Tolerance criterion	[–]
GWP	Global warming potential	[–]	v	Range of values	[–]
h	Specific enthalpy	$\left[\frac{\text{kJ}}{\text{kg}}\right]$	\dot{V}	Volume flow	$\left[\frac{\text{m}^3}{\text{s}}\right]$
HT	High temperature cycle	[–]	w	Weighting factor	[–]
LT	Low temperature cycle	[–]	X	Toxicity	[–]
\dot{m}	Mass flow	$\left[\frac{\text{kg}}{\text{s}}\right]$			
M	Molecular weight	[–]	α	Heat transfer coefficient	$\left[\frac{\text{W}}{\text{m}^2 \cdot \text{K}}\right]$
MC	Molecular complexity	[–]	η	Efficiency	[–]
ODP	Ozone depletion potential	[–]	λ	Thermal conductivity	$\left[\frac{\text{W}}{\text{m} \cdot \text{K}}\right]$
p	Pressure	[bar]	ν	Kinematic viscosity	$\left[\frac{\text{mm}^2}{\text{s}}\right]$
P	Power	[kW]	ρ	Density	$\left[\frac{\text{kg}}{\text{m}^3}\right]$

REFERENCES

- [1] Bao J., and Zhao L., 2013, A review of working fluid and expander selections for organic Rankine cycle, *Renewable and Sustainable Energy Reviews*(24), pp. 325–342.
- [2] Fischer J., Saleh B., Koglbauer G., Wendland M., 2007, Working fluids for low-temperature organic Rankine cycles, *Energy*(32), pp. 1210–1221.
- [3] Fischer J., Anh Lai N., Wendland M., Working fluids for high-temperature organic Rankine cycles, *Energy*, 2011(36), pp. 199–211.
- [4] Mohanraj M., Jayaraj S., and Muraleedharan C., 2009, Environmental friendly alternatives to halogenated refrigerants – A review, *International Journal of Greenhouse Gas Control*(3), pp. 108–119.
- [5] Papadopoulos A. I., Stijepovic M., and Linke P., 2010, On the systematic design and selection of optimal working fluids for Organic Rankine Cycles, *Applied Thermal Engineering*(30), pp. 760–769.
- [6] Quoilin S., Van Den Broek, Martijn, Declaye S., Dewallef P., and Lemort V., 2013, Techno-economic survey of Organic Rankine Cycle (ORC) systems, *Renewable and Sustainable Energy* (22), pp. 168–186.
- [7] Tchanche B.F., Papadakis G., Lambrinos G., Frangoudakis A., 2009, Fluid selection for a low-temperature solar organic Rankine cycle, *Applied Thermal Engineering* (29), pp. 2468-2476.
- [8] Rödder M., Neef M., Laux C., Priebe K.-P., 2015, Systematic fluid selection for organic Rankine cycles (ORC) and performance analysis for a combined high and low temperature cycle, *ASME-Paper GT2015-42432*, release in Proceedings of ASME Turbine Technical Conference and Exposition (TurboExpo), 15.-19. June 2015, Montreal, Canada
- [9] Breiung A., and Knosala R., 1997, Bewerten technischer Systeme: Theoretische und methodische Grundlagen bewertungstechnischer Entscheidungshilfen, Springer, Berlin
- [10] IFA Institut für Arbeitsschutz der Deutschen Gesetzlichen Unfallversicherung (German Social Accident Insurance), 2014, “GESTIS Information system on hazardous substances,” www.dguv.de/ifa/gestis-database,
- [11] Lemmon E. W., Huber M. L., McLinden M.O., 2013, “NIST Standard Reference Database 23, Fluid Thermodynamic and Transport Properties REFPROP, User's Guide,” National Institute of Standards and Technology (NIST)
- [12] Steag Energy Services, 2014, “EBSILON®Professional Program Documentation,”
- [13] United Nations Organization, 2013, “Globally Harmonized System of Classification, Labelling and Packaging of Chemicals,” GHS Rev.5, http://www.unece.org/trans/danger/publi/ghs/ghs_welcome_e.html.

EXPERIMENTAL STUDY OF AN ORC (ORGANIC RANKINE CYCLE) WITH THERMAL OIL FOR WASTE HEAT RECOVERY OF A DIESEL ENGINE.

Gequn Shu, Mingru Zhao*, Hua Tian, Guangdai Huang, Yongzhan Huo

* State key laboratory of engines, Tianjin University,
92 Weijin Road, Nankai District, Tianjin 300072,
China

zhaomr@tju.edu.cn, Tel:+86-138-2018-1525

ABSTRACT

Waste heat from exhaust gas of diesel engine could be recovered to increase engine's efficiency and decrease exhaust pollution. In this research, an Organic Rankine Cycle (ORC) test bench with thermal oil as heat transfer medium was set up to recovery the waste heat from a 240kW heavy-duty diesel engine. R123 was chosen for working fluid and expansion valve was employed temporarily to investigate the properties of waste heat. Experiments have been conducted to measure the available heat of exhaust gas in the different loads and speeds of engine. The results show the amount and the quality of waste heat that can be potentially recovered by this test bench during different conditions of engine, of which the maximum exergy and the potential power ability are 18.53kW, and 9.67kW separately. The maximum efficiency of exergy and potential power ability are 26.80% and 14.32% separately. Also, with thermal oil cycle integrated, the transient performance of the ORC test bench was investigated.

1. INTRODUCTION

With oil crisis and environmental pollution getting serious, the energy saving and emission reduction technology has become the main research direction in the ICE (internal combustion engine) area. The study (Dieter *et al.*, 2012) on diesel engine found that approximately 60% of the energy released by fuel is dissipated to the environment in the form of waste heat, which shows a great potential for diesel engine towards higher efficiency if the waste heat can be recovered. The Rankine cycle system is an efficient way to recover those heat (in comparison with other technologies such as thermo-electricity and absorption cycle air-conditioning). The idea of associating a Rankine cycle to an ICE has existed for a long time and the first technical developments showed up under the 70's energy crisis. For instance, Mack Trucks (1976) designed and built a prototype of ORC system operating on the exhaust gas of a 288 HP truck engine. A 450 km on-road test demonstrated the technical feasibility of the system and its potential market: an improvement of 12.5% of the fuel consumption was achieved. Systems developed today differ from those of the 70's because of the advances in the development of heat exchangers and expansion devices, plus the broader choice of working fluids. However, at the present time, Rankine cycle systems are under development, but no commercial solution on vehicle seems to be available yet.

Rankine Cycle has got a lot of attention for its high recovery efficiency and low impact on the backpressure of engine. However, considering the large variation of engine's working condition, SRC (steam rankine cycle) are unsuitable under low-and-medium duty for its needs of high temperature for superheating, where the organic working fluids show its advantages. Katsanos *et al.* (2012) conducted a theoretical study to investigate the potential improvement of the overall efficiency of a heavy-duty truck diesel engine equipped with a Rankine bottoming cycle for recovering heat from the exhaust gas. Two different working mediums, water and the refrigerant R245ca, are considered. The results under all operating conditions show that the brake specific fuel consumption improvement ranges from 10.2% (at 25% engine load) to 8.5% (at 100% engine load) for R245ca and 6.1% (at 25% engine load) to 7.5% (at 100% engine load) for water.

The ORC technology in cogenerative systems has by now reached a level of full maturity in biomass applications. In Europe, there are over 120 plants in operation with sizes between 0.2 and 2.5 MW electric. In these facilities, hot thermal oil is usually used as heat transfer medium, demonstrating a number of advantages, including low pressure in boiler, large inertia and simple adaptability to load changes, automatic and safe control and operation. Moreover, the transferred temperature for the hot side of ORC is lower, which ensures a very long working life of organic fluid. The utilization of a thermal oil boiler also allows operation without requiring the presence of licensed operators as for steam systems in many European countries. Several companies like Turboden, Pratt&Whitney have already made great achievements at biomass plants, of which the flue gas from boiler has the temperature as high as 1000°C. And the net electric efficiency can be above 18%. Although not as high as that of flue gas from biomass boiler, the temperature of exhaust gas from diesel engine can reach over 500°C, which is beyond the decomposition temperature of most regular organic fluids. So the thermal oil cycle were introduced by some researchers to deal with the high temperature of exhaust gas under heavy duty. Yu *et al.* (2013) did a theoretical study of an ORC system with thermal oil cycle for waste heat recovery of a 243kW diesel engine. R245fa was chosen as working fluid. The system shows that the maximum potential output power and recovery efficiency are as high as 14.5 kW and 9.2% separately. Jacek Kalina *et al.* (2011) compared the ORC containing thermal oil with the single and dual loop ORC when studying the WHR for gas engine theoretically. The results show that the recovery ability of ORC containing thermal oil is between the single and dual loop ORC. What's more, thermal oil cycle can avoid the use of gas-gas heat exchanger which is difficult to manufacture.

During this experiment, the highest temperature of thermal oil under each operating condition is in the range from 90 to 220 °C, which makes R123 the suitable working fluid. Although with micro toxicity and GWP of 120, the R123 shows the best performance when recovering low-and-mid temperature waste heat. Tzu-Chen (2001) investigated the working fluids Benzene (C₆H₆), Toluene (C₇H₈), p-xylene (C₈H₁₀), R113 and R123. He reported that R123 had a better performance in recovering a low-and-mid temperature waste heat. Wang *et al.* (2010) studied the relationship between the system performance, the pressure ratio and the mass flow rates of several organic working fluids. The results show that R123 owns the maximal thermal efficiency and net output at the same mass flow rate or heat input among the several working fluids. Also, R123 was selected as the working fluid because of its non-flammable properties, low boiling temperature, chemical stability and low cost. Moreover, it has many characteristics such as high cycle efficiency, high thermal conductivity and moderate working temperature and pressure. Zhou *et al.* (2013) set up an ORC bench using R123 to recover waste heat from low-temperature flue gas. The maximum recovery efficiency reaches 22%. Li *et al.* (2013) constructed a low-temperature regenerative ORC using R123. Finally the system obtained 6kW output power and 7.98% recovery efficiency. So it's necessary to investigate the maximum potential of the WHR system with R123 in the first time. Considering R123's drawbacks, R245fa will be the next choice for its lower toxicity and less damage to environment still high efficiency close to R123.

In this case, the experimental study of ORC containing thermal oil seems an interesting topic for WHR of diesel engine on vehicle. Despite of the extra weight and complexity, the thermal oil does help to the frequently changing operating conditions of engine on road. This paper focuses on the characteristics of waste heat from diesel engine and the potential recovery ability of ORC using R123 in all conditions. The whole working condition is conducted also to find out the limit of the test bench and to lay the groundwork for on-road test. What's more, the impacts of thermal oil cycle on the transient performance of the ORC test bench were investigated.

2. EXPERIMENTAL SETUP

In this research, the heat source is the exhaust gas from an 8.4L 6-cylinder heavy-duty diesel engine, of which rated power is 240kW. This kind of engine was turbo-charged and widely used on the line-

haul heavy trucks which are very likely to apply WHR techniques. The engine bench was equipped with a whole set of controlling and measurement device, which can keep the engine working steady under any specific condition with all the performance data recorded at the same time.

As shown in the Figure 1, the thermal oil cycle was added as the heat transfer medium, which can serve as a buffer to decrease the impact from the fluctuation of exhaust gas. Besides, since the highest temperature of exhaust gas can be close to 500°C, the thermal oil cycle effectively bring down the working temperature of R123 for its decomposition temperature is only 327°C, however, at the cost of lower quality of heat source, lower efficiency, higher irreversibility and longer response time.

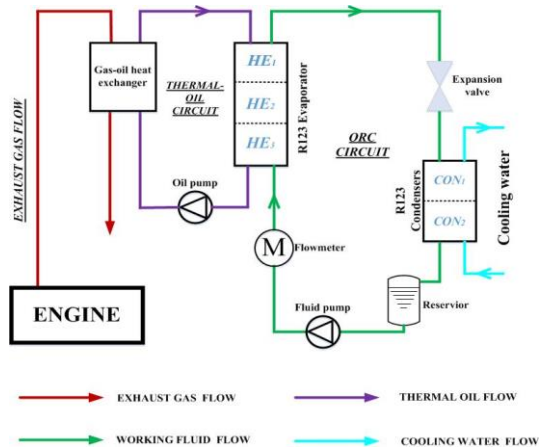


Figure 1: Structure of the ORC system

Dibenzyl-toluene (DBT) is chosen as thermal oil for its boiling point as high as 390°C, as well as its non-corrosiveness to metal which makes heat exchangers easy to manufacture. Also, DBT can resist oxidation well.

Table 1: Important parameters of heat exchangers

Name	Type	Heat transfer area
R123 evaporator	plate heat exchanger	4.61 m ²
R123 condenser	plate heat exchanger	5.18 m ²

Considering back pressure of engine, a shell-and-tube heat exchanger is chosen for thermal oil to absorb heat from exhaust gas. All the other heat exchangers in the thermal oil cycle and ORC system are plate heat exchangers as shown in Table 1. The oil pump is a 0.75kW centrifugal pump. A vortex shedding flowmeter (VSF) is installed to measure the volume rate of oil which is proved to be inaccurate because of its unexpected sensitiveness to the vibration of engine. Besides, the thermal oil can expand by as much as 25% under working condition which also makes it difficult to obtain its mass flow rate for the lack of its accurate density map. Those account for the absence of an energy balance analysis of thermal oil cycle. Then a 40L oil storage tank is installed above the whole system preparing to contain the expanded oil. When thermal oil get cold and shrink, they will flow back to system from tank by gravity.

The ORC system was set up with the thermal oil cycle as a whole test bench as shown in Figure 2. The chosen pump for ORC system is an 4kW plunger-driven diaphragm pump, for the membrane placed between the fluid chamber and the plunger zone ensures a perfect sealing of the circuit toward environment and allows reaching pressure as high as 3MPa, in spite of the low viscosity feature of the pumped liquid and the absence of any lubricant properties. Also, the mass flow rate can be controlled by adjusting the stroke length of plunger. A Coriolis flow meter was set before the pump inlet to measure the mass flow rate, while a damper was set after the pump to smooth the flow.



Figure 2: ORC system

An expansion valve was employed to temporarily take the place of the expander which are under manufacture. By controlling the expansion valve, the evaporating pressure can be adjusted. Since the mass flow rate of R123 is also influenced, the expansion valve was kept widely open during experiment to make sure the mass flow rate can be controlled by ORC pump more accurately and be large enough to absorb more heat from thermal oil.

A refrigerating unit using R22 as refrigerant was set up to produce cooling water whose temperature and flow rate can be adjusted conveniently. Therefore the condensing temperature and pressure of ORC system can be maintained in a certain range.

All the hot parts of the facility have been thermal insulated, also the test bench has been equipped with the necessary auxiliaries such as measurement devices, particular thermocouples and pressure sensors.

3. ANALYSIS OF EXPERIMENT AND RESULTS

In order to comprehensively analyze the characteristics of the waste heat form the exhaust gas, the experiments were conducted as the engine speed varied in the range of 1200 rpm to 2200 rpm with a 200rpm interval, and the engine load varied in the range of 20% to 100% with a 20% interval. The results are drawn as contour map to show the tendencies.

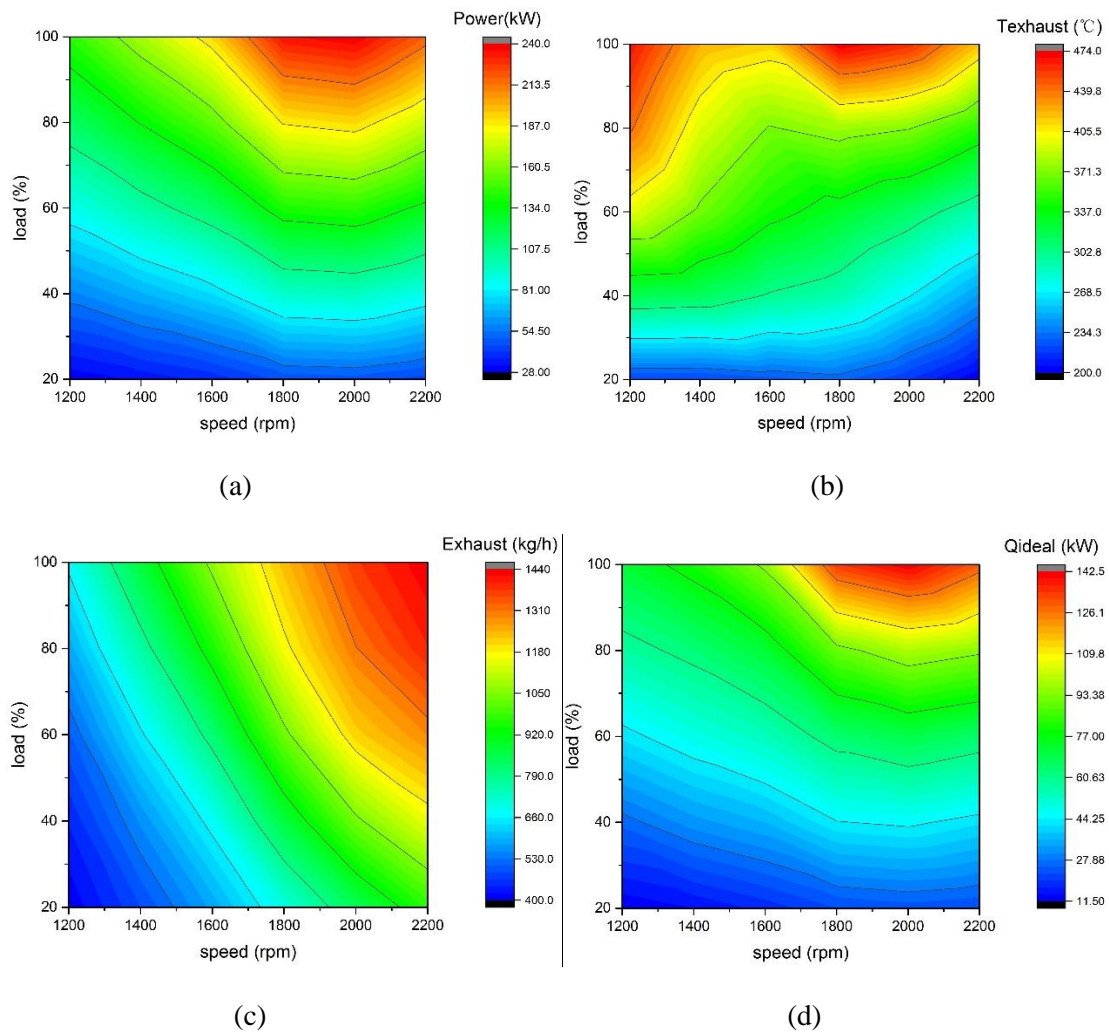


Figure 3: (a) Power output map; (b) Temperature map of exhaust gas; (c) Exhaust mass flow rate; (d) Q_{ideal} ;

According to the measured test data, the Power output map is shown in the Figure 3(a). At the rated condition as 2000rpm and 100%load, the effective power output of the diesel engine is 240 kW. To better observe the quality of the waste heat from exhaust gas, the temperature map of exhaust gas is shown in the Figure 3(b). When the engine speed goes up from 1200rpm to 1600 rpm, the temperature of exhaust gas decreases for the shorter combustion time of each cycle. When the speed goes above 1600rpm, the temperature slightly increases then decrease for the mutual effect of more air and shorter combustion time. The highest temperature appears as 474 °C at the working condition of 1800rpm and 100% load, instead of the rated condition whose power output is the largest. The exhaust mass flow rate as shown in the Figure 3(c) also helps to study the distribution of the waste heat. In the absence of EGR, the exhaust mass flow rate equals the sum of intake mass flow rate and fuel consumption rate under the ideal condition that fuel leakage is nonexistent. From the figure, the exhaust mass flow rate increases along with the engine speed for more intake air and tops as 1437.32 kg/h at the working condition of 2200rpm and 100% load. The figures above show that the temperature and mass flow rate of exhaust gas doesn't share the similar trend and further investigation is necessary.

Exhaust energy absorbed by thermal oil during experiments is calculated using an approximation method. $C_xH_yO_z$ can denote the average molecular composition for common diesel fuel because the petroleum-derived diesel fuel is a very complicated mixture of alkane, alkene and arene, with minimal

amount of sulphur and nitrogen which can be neglected. In this composition, x, y, and z respectively represent the moles of the C, H, O. Their mole ration is shown as the Equation (1) below:

$$x:y:z = 0.87:0.126:0.004 \quad (1)$$

The air is presumed as the mixture of nitrogen and oxygen with the mole ration of 3.098:1. Hypothetically, the combustion products only consist of carbon-dioxide, water, nitrogen, and oxygen for the usually oxygen-enriched combustion of diesel engine, of which nitrogen comes from air and oxygen is residual from combustion. Based on the atomicity balance principle, the mass fraction of combustion products is obtained by the Equation (2) below:

$$C_xH_yO_z + \left(x + \frac{y}{4} - \frac{z}{2}\right)(O_2 + 3.098N_2) = xCO_2 + \frac{y}{2}H_2O + 3.098\left(x + \frac{y}{4} - \frac{z}{2}\right)N_2 \quad (2)$$

According to the measured temperature and pressure, the exhaust energy in exhaust gas absorbed by thermal oil can be calculated by the Equations (3, 4) below:

$$h_{exh}(T, P) = \omega_{CO_2}h_{CO_2}(T, P) + \omega_{H_2O}h_{H_2O}(T, P) + \omega_{O_2}h_{O_2}(T, P) + \omega_{N_2}h_{N_2}(T, P) \quad (3)$$

$$Q_{exh} = m_{exh}(h_{exh}(T_{exhin}, P_{exhin}) - h_{exh}(T_{exhout}, P_{exhout})) \quad (4)$$

In practice, the temperature of exhaust is suggested above 120°C, for the possible corrosion to exhaust pipes and heat exchangers by the acid formed in the exhaust gas if the temperature decreases below 120°C. Assuming the temperatures of the exhaust gas after the heat exchanger under every working condition are all 120°C, the exhaust energy in exhaust gas that has been fully absorbed can be calculated by equations (3, 4) above. It is denoted as Q_{ideal} and shown in the Figure 3(d). Surprisingly the variation trend of Q_{ideal} is highly similar to that of power output in Figure 3(a). The maximum exhaust energy is obtained at rated condition as 142.4 kW, because the temperature and mass flow rate are all on a high level at this condition.

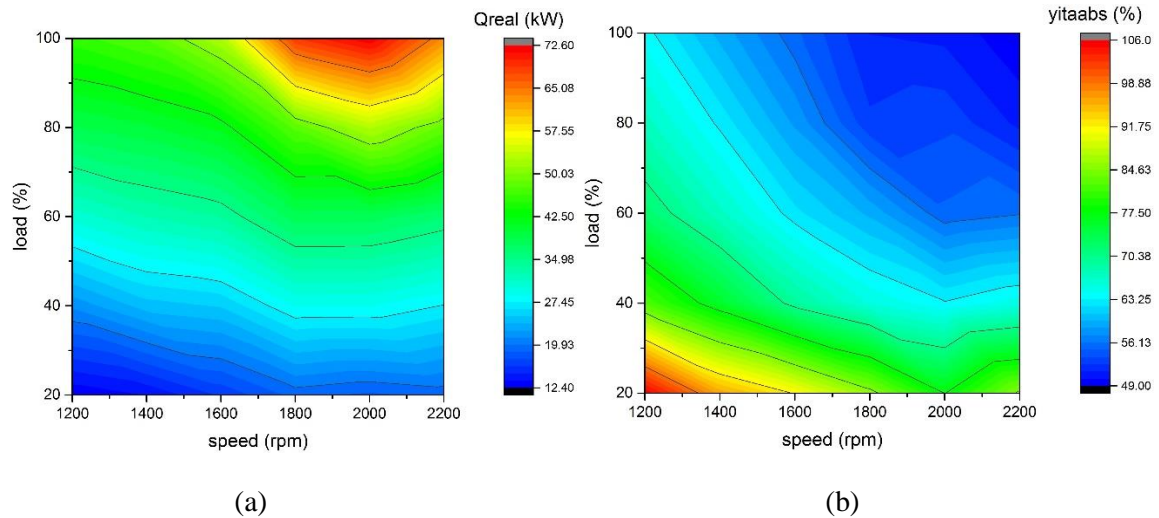


Figure 4: (a) Q_{real} ; (b) η_{abs} ;

But during this research, the exhaust energy cannot be fully recovered under all working condition. Based on the experiment data and equations above, the exhaust energy that is practically transferred to thermal oil can be calculated as shown in the Figure 4(a) and be denoted as Q_{real} . The similar trend

with Q_{ideal} shows that the amount and the quality of the waste heat in exhaust gas are all considerable under the high speed and heavy duty conditions, which from the figures are believed to be the suitable conditions to recover exhaust energy. The heat absorption efficiency as η_{abs} is defined as Equation (5) below. The Figure 4(b) shows that the higher speed and heavier load the condition is, the lower absorption efficiency it has. Values greater than 100% mean the temperature of exhaust gas after heat exchanger is below 120 °C, which also mean the available heat have been absorbed completely. With the maximum value as 106% and the minimal as 49.18%, the η_{abs} of most working conditions are below 70%, which means the capacity of heat exchanger are not efficient enough. The suitable working conditions for this heat exchanger are to be found under further study.

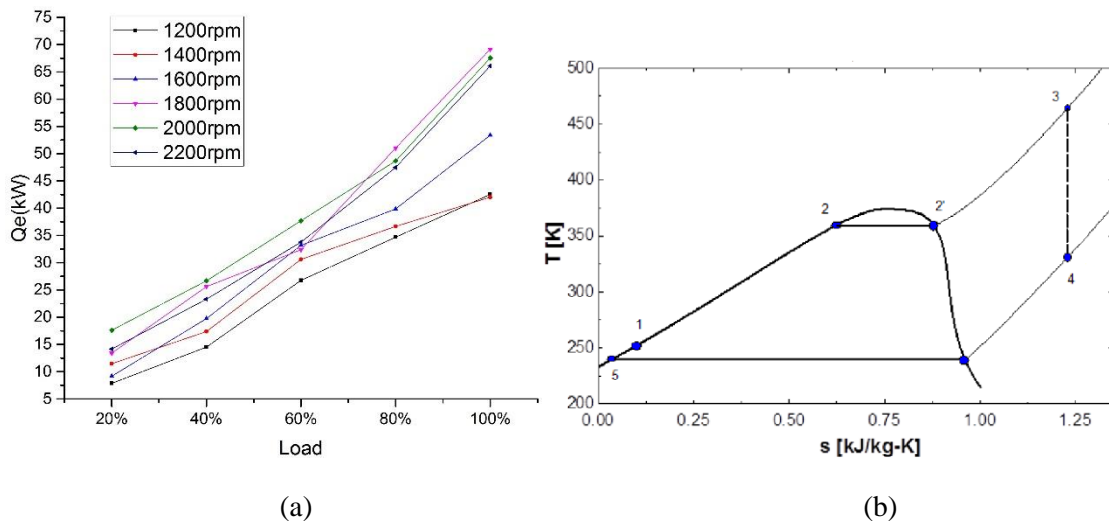
$$\eta_{abs} = \frac{Q_{real}}{Q_{ideal}} \cdot 100\% \quad (5)$$

However with the thermal oil onboard and the massive amount of it, two major consequences happened. First, the response of the whole ORC system becomes slow. Since there are more than one parameter needed to be adjusted such as mass flow rate of R123 and cooling water of which the temperature needs adjustment too, the steady state of the ORC system are difficult to maintain for recording. It usually takes more than half hour to be adjusted and stabilized. Second, the massive amount of the thermal oil leads to the massive amount of heat it carries as the heat transfer medium. Under the condition that the engine speed and load vary, especially from the heavy duty to the light duty, the situation may happens that the heat transferred from exhaust gas to thermal oil is less than that from thermal oil to R123, which leads to a misconception of Energy Non-Conservation. To reduce the impacts form above as much as possible, the rules below are followed during the experiments:

- 1, if the parameters vary within the range of less than 1% in 5 minutes, it can be seen as the quasi-stable state and ready for recording.
- 2, the adjustment of the parameters needs to be as minimal as possible to avoid the over-swing.

The waste heat absorbed by R123 as Q_e is calculated by the Equation (6) below and shown in the Figure 5(a). Affected by the thermal oil cycle, the maximum waste heat is absorbed as 69.14 kW at the condition of 1800rpm and 100% load instead of rated condition.

$$Q_e = m_{R123}(h_{R123}(T_{R123in}, P_{R123in}) - h_{R123}(T_{R123out}, P_{R123out})) \quad (6)$$



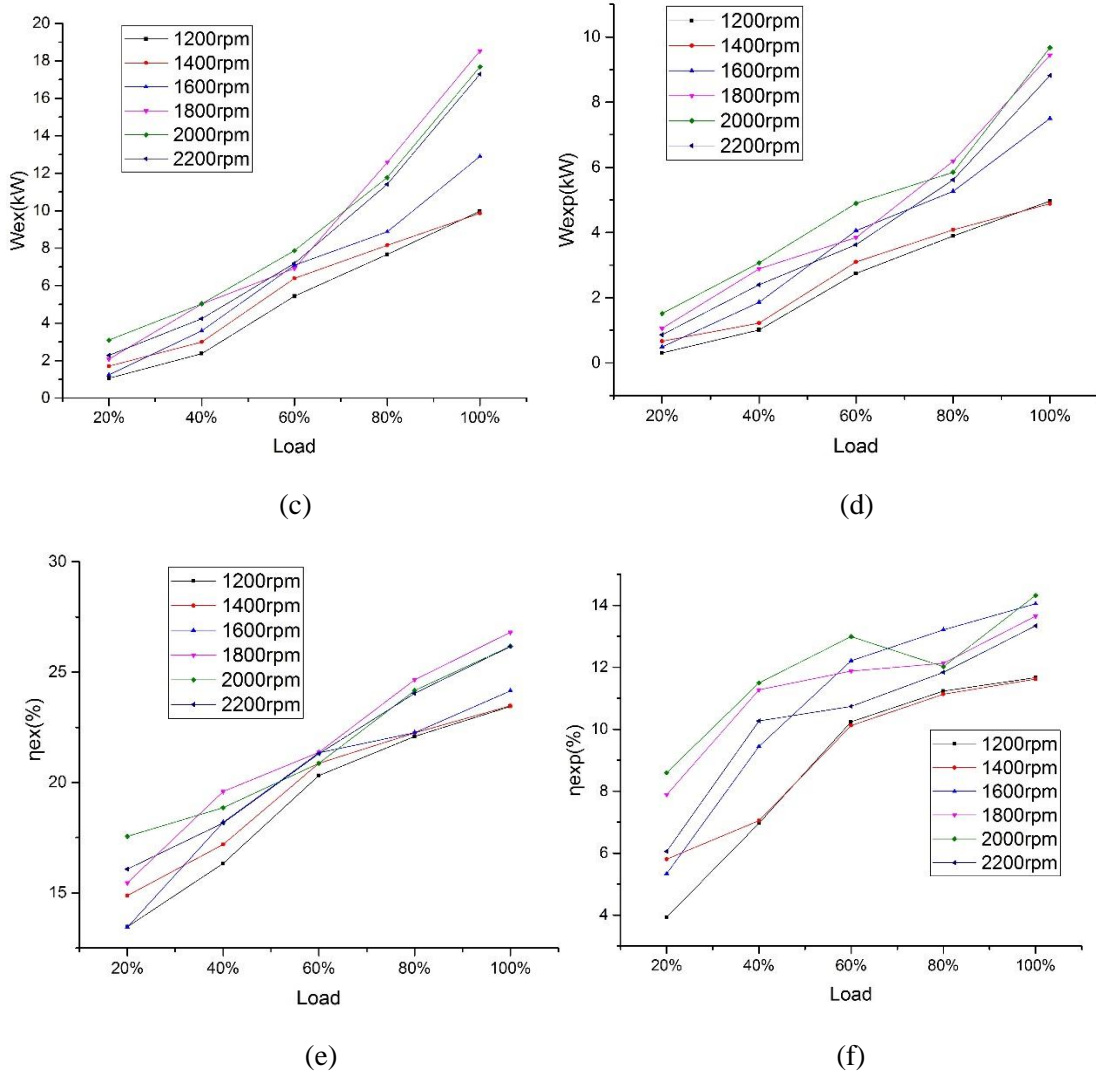


Figure 5: (a) Q_e ; (b) T-s map of R123; (c) W_{ex} ; (d) W_{exp} ; (e) η_{ex} ; (f) η_{exp} ;

Although the expander is unavailable yet, the potential power ability of R123 after evaporator can still be studied with an expansion valve. The Figure 5(b) is the T-s map of R123, point 1 to point 3 is the evaporation process with point 3 as the exit state after evaporation, of which the temperature and pressure are measured. Assuming the expansion process as isentropic, point 4 is the exit state, of which the temperature and pressure are measured. Subscript 0 are for the environmental state. The exergy and potential power ability by expander can be denoted as W_{ex} , W_{exp} separately and calculated by the Equation (7-10) below:

$$e_{ex} = (h_3 - h_0) - T_0(s_3 - s_0) \quad (7)$$

$$e_{exp} = (h_3 - h_4) \quad (8)$$

$$W_{ex} = m_{R123} \cdot e_{ex} \quad (9)$$

$$W_{exp} = m_{R123} \cdot e_{exp} \quad (10)$$

Figure 5(c) shows that the trend of W_{ex} is highly similar with that of Q_e for the obvious reason that the more heat R123 absorbed, the more work it can potentially make. The maximum exergy as 18.53kW is obtained at 1800rpm, 100% load condition. Its corresponding exergy efficiency as η_{ex} in Figure 5 (e) is 26.80%, with the definition of the exergy efficiency as the Equation (11) below:

$$\eta_{ex} = \frac{W_{ex}}{Q_e} \cdot 100\% \quad (11)$$

$$\eta_{exp} = \frac{W_{exp}}{Q_e} \cdot 100\% \quad (12)$$

The trend of W_{exp} in Figure (d) is not like that of Q_e for the condensing pressure at point 4, which determines h_4 , affects W_{exp} too. The maximum potential power ability by expander as 9.67kW is obtained at rated condition. Its corresponding potential power efficiency as η_{exp} in Figure 5 (f) is 14.32%, with the definition of the potential power efficiency as the Equation (12) above. The sudden fall at 2000rpm, 80% load condition results from the failure of maintaining the condensing temperature which leads to an unpleasantly high condensing pressure influencing W_{exp} as mentioned.

Despite of the negative impacts of the thermal oil, the inertia it brings to the ORC system can be helpful against the variation of engine condition. To investigate its positive impacts, the transient performance of ORC system when engine shuts down is studied. The light duty condition of 1200rpm and 20% load is chosen instead of the heavy duty because there could be serious damage to engine when it shuts down in a high temperature level. The Figure 6 shows the performance of ORC system when the engine shut down at 100th second and the data was recorded every 20 seconds. δT indicates the superheat degree of R123 after evaporator, which means vapor state when it's above zero. During the time from 100th second to 680th second, δT goes down obviously from 15.03 °C to 4.028 °C while Q_e only decreases from 7.452 kW to 7.108 kW and W_{ex} from 0.8818 kW to 0.8022 kW, which means the thermal oil has been transferring heat to R123 even though the engine has shut down. At around 700th second, δT eventually goes down below zero which means R123 is gas-liquid mixed state which has little ability to absorb heat and output power. Figure shows that after 700th seconds, Q_e goes down sharply to 1.423 kW and W_{ex} to 0.1034 kW which means the WHR system can keep outputting effective power for nearly 10 minutes after engine shuts down from a light duty condition. δT is proven to be a reliable indicator for safety that a positive superheat not only protects the expander blade from erosion, but also ensures the effective heat absorption and power output.

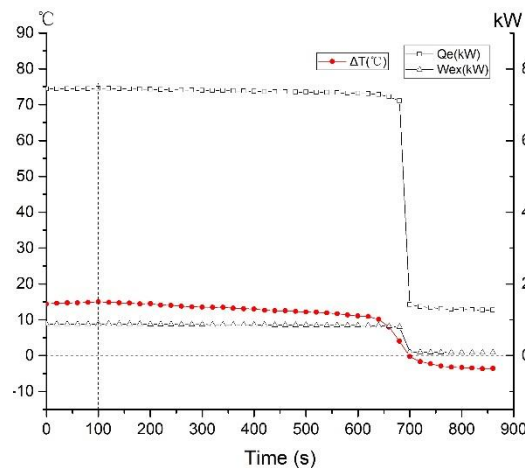


Figure 6: Transient performance of ORC system when engine shuts down

4. CONCLUSIONS

This paper elaborates the preliminary investigation of an Organic Rankine Cycle (ORC) test bench with thermal oil as heat transfer medium to recover the waste heat from a 243kW heavy-duty diesel engine. The conclusions are below:

- 1, The exhaust mass flow rate goes up along with engine speed, however the temperature doesn't share the same trend.
- 2, Although the temperature and the mass flow rate of exhaust gas at rated condition are not the highest, the exhaust energy at this condition are the largest, for the temperature and the mass flow rate are all above a high level.
- 3, The trends of Q_e and W_{ex} are highly similar, which mean the high speed and heavy duty conditions are the suitable conditions to recover exhaust energy. The maximum values of Q_e , W_{ex} and W_{exp} are 69.14 kW, 18.53kW, and 9.67kW separately. The maximum efficiency of exergy and potential power ability are 26.80% and 14.32% separately.
- 4, Despite of the difficulties the thermal oil adds to ORC system in experiment, the inertia it brings can be helpful against the variation of engine condition. And the superheat δT proves to be a reliable safety indicator.

NOMENCLATURE

h	specific enthalpy
ω	mass fraction
m_{exh}	mass flow rate of exhaust gas
m_{R123}	mass flow rate of R123
e	specific exergy

REFERENCES

- Fubin, Y., Xiaorui, D., Hongguang, Z., Zhen, W., Kai, Yang., Jian, Z., Enhua, W., Hao, L., Guangyao, Z., 2014, Performance analysis of waste heat recovery with a dual loop organic Rankine cycle (ORC) system for diesel engine under various operating conditions, *Energy Conversion and Management*, 80 (2014) 243–255.
- Guopeng, Y., Gequn, S., Hua, T., Haiqiao, W., Lina, L., 2012, Simulation and thermodynamic analysis of a bottoming Organic Rankine Cycle (ORC) of diesel engine (DE), *Energy*, 51 (2013) 281-290.
- Jacek, K., 2011, Integrated biomass gasification combined cycle distributed generation plant with reciprocating gas engine and ORC, *Applied Thermal Engineering*, 31 (2011) 2829-2840.
- Katsanos, C. O., Hountalas, D. T., Pariotis, E. G., 2012, Thermodynamic analysis of a Rankine cycle applied on a diesel truck engine using steam and organic medium, *Energy Conversion and Management*, 60 (2012) 68–76.
- Maoqing, L., Jiangfeng, W., Weifeng, H., Lin, G., Bo, W., Shaolin, M., Yiping, D., 2013, Construction and preliminary test of a low-temperature regenerative Organic Rankine Cycle (ORC) using R123, *Renewable Energy*, 57 (2013) 216-222.
- Naijun, Z., Xiaoyuan, W., Zhuo, C., Zhiqi, W., 2013, Experimental study on Organic Rankine Cycle for waste heat recovery from low-temperature flue gas, *Energy*, 55 (2013) 216-225.
- Sipeng, Z., Kangyao, D., Shuan, Q., 2013, Energy and exergy analyses of a bottoming Rankine cycle for engine exhaust heat recovery. *Energy*, 58 (2013) 448-457.
- Tzu-Chen H. Waste heat recovery of organic Rankine cycle using dry fluids. *Energy Conversion and Management* 2001,42.
- Wang, E, H., Zhang, H, G., Zhao, Y., Fan, B, Y., Wua, Y, T., Mu, Q, H., 2012, Performance analysis of a novel system combining a dual loop organic Rankine cycle (ORC) with a gasoline engine, *Energy*, 43 (2012) 385-395.
- Wang ZQ, Zhou NJ, Luo L, Zhang JQ, Tong DH. Comparison of thermodynamic performance for waste heat power generation system with different lowtemperature working fluids. *Journal of Central South University (Science and Technology)* 2010, 41(6):2424_9.
- Dieter, S., Thomas, L., Jürgen, G., Nadja, E., Michael, H., Ilona, K., 2012, Waste Heat Recovery for Commercial Vehicles with a Rankine Process, *Aachen Colloquium Automobile and Engine Technology* 2012.

AERODYNAMIC DESIGN OF RADIAL INFLOW TURBINE FOR MEDIUM SCALE ORGANIC RANKINE CYCLE SYSTEM

Lei Chen, Boaz Habib, Nick Inskip

Industry Development Division,
Heavy Engineering Research Association,
New Zealand.

lei.chen@hera.org.nz, boaz.habib@hera.org.nz, ninskip@hera.org.nz

ABSTRACT

The Organic Rankine Cycle (ORC) has been considered to be the most feasible technology among the existing approaches to convert low grade heat source (such as geothermal energy) and industrial waste heat into electricity. For a medium scale ORC system with a general power range of 50kW to 500kW, radial inflow turbines, with low mass flow rate and high pressure ratio, are applied more often than other types of turbines, because they are more efficient, adaptable, stable and cost-effective. When developing such a turbine, aerodynamic design is a step of vital importance. This paper presents a complete aerodynamic design process of a 100kW radial inflow turbine, including preliminary design, three dimensional modelling of blades and volute, and three dimensional numerical simulation. The preliminary design is carried out by using ANSYS RTD which can efficiently generate an optimal solution whilst fixing the mass flow rate, the pressure ratio and the blade speed ratio. Then, based on the preliminary design results, the cascade shape modelling of stator and rotor is conducted through in-house code and ANSYS BladeGen respectively. Following that, the three dimensional modelling of stator and rotor is conducted by stacking the cascades along a specified line. The volute is defined by a series of radial circular sections on the periphery of the turbine and the radii of the sections are obtained through the free vortex theory. ANSYS DesignModeler is used to perform three dimensional modelling of the volute. Finally, three dimensional numerical simulation of the radial inflow turbine is carried out by employing ANSYS TurboGrid, ICEM and CFX, where the R245fa is used as the working fluid. Detailed analyses of the flow field across the turbine stage and the volute are presented and the performance assessment of the turbine in terms of efficiency, blade speed ratio and mass flow rate is illustrated.

ADAPTING WASTE HEAT RECOVERY TECHNOLOGIES FOR LOW CARBON OFF-HIGHWAY VEHICLES

Apostolos Pesiridis^{1*}, Fuhaid Alshammari¹, Benjamin Franchetti²

¹ Brunel University London ² Entropea Labs, London, E8 1AB, UK

Corresponding author: apostolos.pesiridis@brunel.ac.uk

ABSTRACT

Waste Heat Recovery (WHR) technologies aim at recovering part of the otherwise wasted heat in the exhaust gases of a combustion engine and convert it to useful power, resulting in lower fuel consumption and pollutant emissions. Brunel University London, Entropea Labs and Mahle Powertrain have jointly optimised Waste heat Recovery technologies based on the Rankine cycle for other applications in the past. Experience gained in the design and manufacturing of the components for Organic Rankine Cycle (ORC) WHR systems for large displacement diesel engines is applied to increase the Off-Highway Vehicle (OHV) diesel engine fuel economy by 10% or higher. The project is funded by Innovate UK for a two-year period ending in May 2017. The proposed technology is modular, non-invasive and reversible, enabling it to be scaled across the range of new engine production irrespective of manufacturer while also being retrofittable to the large number of OHV engines already in service. Moreover, the technology and expertise has the potential to be further exploited by adapting it and scaling it to other transport and stationary power generation applications. The specific objectives of the project are: (1) ORC Model Development for ORC WHR applications, (2) Engine Simulation Development, (3) ORC WHR Component Development, (4) ORC WHR system performance demonstration and validation On-Engine, and (5) Validate retrofit capability in preparation for On-Vehicle demonstration. The potential impact from the realization of the project makes the technology highly competitive. The OHVs account for approximately 15% of all UK surface transportation emissions [1], achieving a retrofittable and scalable ORC-WHR technology, with 10% fuel efficiency increase, can account to a potential £1 billion (€1.4 billion) in fuel savings for fleet operators in the UK alone. In addition, the reduction in emissions will enable OEMs to meet the requirements outlined in pollution reduction legislation.

REFERENCES

- [1] ARCADIS, RPA, “Study in view of the revision of directives 97/68/EC on non-road mobile machinery (NRMM)”, December 2010.

ABOVE GROUND GEOTHERMAL AND ALLIED TECHNOLOGIES – PAVING THE RESEARCH ROADMAP

Boaz Habib¹, Nick Inskip¹, Lei Chen¹, Michail Karpenko¹, Mohammed Farid², Brent Young²

¹Heavy Engineering Research Association, New Zealand

²School of Engineering, University of Auckland

ABSTRACT

The Above Ground Geothermal and Allied Technologies (AGGAT) Research and Development (R&D) Programme is a collaborative initiative borne out of a Clean Energy development focus in the Heavy Engineering Industry of New Zealand. The programme is a positive testament to government, industry and academia as well as international experts working collaboratively to achieve a common objective of providing an R&D platform for growth in the clean energy technologies. The predominant focus of this programme is on the Organic Rankine Cycle using the research expertise of academic institutions and manufacturing capability of Heavy Engineering companies in NZ. Research is carried out in the areas of Technology Concepts, Turbines, Heat Exchangers, Control Systems, Materials and Fluids. The programme has been in operation for nearly three years now and has made progress towards establishment of pilot scale testing facilities on waste heat and geothermal based heat resource sites. Research progress update is provided along with opportunities identified for future collaboration especially with international partners.

CONNECTION OF A DISTRICT HEATING SYSTEM AND AN ORC GEOTHERMAL PLANT

P. Valdimarsson

Atlas Copco Energas GmbH
Gas and Process Division
Vegmúli 2, IS-108 Reykjavík, Iceland
e-mail: pall.valdimarsson@de.atlascopco.com
Web page: www.atlascopco-gap.com

ABSTRACT

Cogeneration of electricity and heat for district heating is feasible in colder climates, where a city having market for district heating is close to the plant.

Geothermal power plants usually produce base load. Heat load for district heating is dependent on the ambient temperature, and has a high peak to average heat load ratio. The production of district heating will reduce the electrical output of the geothermal plant, thus incurring lost revenue. This loss is the more, the higher the district heating load is. The characteristics of district heating consumption influence these losses as well, and certain measures to influence the consumer behaviour are necessary.

The minimization of this loss of electrical generation of the geothermal plant is crucial for the economics of the cogeneration.

This paper presents the cogeneration couplings suggested by Atlas Copco. Good temperature profiles for district heating supply and return are presented, and the relation between these temperature profiles and revenue loss is presented. Suggestions regarding tariff system and how the district heating consumer should be motivated are as well presented.

A NEW DESIGN OF AN ORC PLANT FOR HIGH ENTHALPY GEOTHERMAL RESOURCES

P. Valdimarsson*, **M. Sauerborn[†]**

Atlas Copco Energas GmbH
Gas and Process Division

*Vegmúli 2, IS-108 Reykjavík, Iceland

e-mail: pall.valdimarsson@de.atlascopco.com

[†]Schlehenweg 15, D-50999 Cologne, Germany

e-mail: markus.sauerborn@de.atlascopco.com

Web page: www.atlascopco-gap.com

ABSTRACT

The fluid in a high enthalpy geothermal field is saturated liquid with dissolved minerals and gases. The wells produce a mixture of mineralized brine, non-condensable gas and steam. The well fluid cannot be cooled below the silica saturation in the plant. The non-condensable gas has to be separated from the fluid at some stage and disposed of. This will all influence the power plant design.

The heat of the geothermal fluid is transferred to a working fluid in heat exchangers in an ORC plant. All heat transfer over a finite temperature difference will cause exergy loss, which will be less, the smaller the temperature difference is. But the cost of the heat exchanger will be higher the smaller this difference is, so an optimization has to be made.

The temperature profiles both for the geothermal fluid and the ORC working fluid are determined from the thermodynamic properties of the fluids. The selection of the working fluid has thus to be made with the thermodynamic properties of the complex geothermal mixture in mind.

Atlas Copco is proposing a novel way of fitting an ORC power plant to geothermal fluid from high enthalpy resources. This plant is described, and temperature-heat duty and Carnot efficiency-heat duty diagrams are used to describe how the ORC plant is optimized for each geothermal fluid mixture and enthalpy.

NOWASTE: WASTE HEAT RE-USE FOR GREENER TRUCK

L. Guillaume*, **V. Lemort***, **A. Perosino†**, **F. Bettoja†**, **T. Reiche‡**, **T. Wagner***

* Université de Liège, B49 Institut de Thermodynamique, Quartier Polytech 1, Allée de la Découverte 17, 4000 Liège, Belgium

e-mail: ludovic.guillaume@ulg.ac.be, vincent.lemort@ulg.ac.be

Web page: <http://www.labothap.ulg.ac.be>

† Centro Ricerche Fiat S.C.p.A., Strada Torino 50, Orbassano 10043, Italy

Web page: <http://www.crf.it>

e-mail: andrea.perosino@crf.it, federica.bettoja@crf.it

‡ Volvo Group Trucks Technology, Advanced Technology and Research

TER E70 2 10, 1 av Henri Germain 69800 St Priest, France

email: thomas.reiche@volvo.com

* AVL LIST GMBH

A-4400 Steyr, Im Stadtgut B2, Austria

Web page: <http://www.avl.com>

email: Thomas.Wagner@avl.com

ABSTRACT

Automotive world is rapidly changing driven by the CO₂ emission regulations worldwide asking for a significant fuel consumption reduction. The internal combustion engine will be the principal powertrain concept for the upcoming decades, especially when it comes to road transportation. Even if the efficiency of the ICE's has increased within the last years, around 30-50% of the fuel indicated energy is still lost via waste heat and could be partly recovered via secondary cycles as the Rankine cycle, Brayton cycle or Stirling cycle. However, preliminary studies have shown that for a heavy duty Diesel application the Rankine cycle offers the highest potential when it comes to efficient waste heat recovery.

The adoption of such technology in the automotive domain requires specific R&D activities to develop the components and identify the most appropriate system architectures and level of integration in order to achieve sustainable costs and the required level of reliability.

In this context, the EU has funded in the frame of the 7th framework program the project NOWASTE: a collaborative project between several companies and institutions: Centro Ricerche Fiat S.C.p.A., Volvo Technology AB, Dellorto SPA, Université de Liège, AVL List GMBH, Faurecia systems d'échappement SAS. This project has the goal to develop a waste heat recovery system based on Organic Rankine Cycle (ORC) for a Heavy Duty Truck application with the aim to realize fuel economy savings. The target applications have been chosen among the Iveco and Volvo fleets.

The partners have designed and realized two Rankine cycle systems suitable to be installed on board of a truck with the aim to convert the waste heat of the exhaust gases into useful energy to be used in mechanical or electrical form. The performances of these systems have been evaluated on engine test benches and are currently under evaluation also the system's on board performances.

MODELLING, EXPERIMENTATION AND SIMULATION OF A REVERSIBLE HP/ORC UNIT TO GET A POSITIVE ENERGY BUILDING

O. Dumont*, C. Carmo[†], S. Quoilin* and V. Lemort*

*Thermodynamics Laboratory, University of Liege,
Allée de la découverte, 17, 4000 Liege
Belgium
e-mail: olivier.dumont@ulg.ac.be

[†]Department of energy technology, Aalborg university
Fredrik Bajers Vej 5, 9100 Aalborg
Denmark
e-mail: cca@et.aau.dk

ABSTRACT

This paper presents an innovative building comprising a heat pump connected to a solar roof and a geothermal heat exchanger. This heat pump is able to invert its cycle and operate as an ORC (Fig. 1). The solar roof is producing large amount of heat throughout the year. This allows covering the building annual heating needs and, furthermore, electricity is produced thanks to the surplus of heat produced by the roof in the HP/ORC reversible unit. This paper is focusing on three main points: sizing, experimentation and simulation of the reversible unit. First, an optimal sizing of the components and fluid R134a shows promising performance with a net electrical energy produced over one year reaching 4030 kWh. Following that, a prototype has been build and has proven the feasibility of the technology. Finally, a dynamic simulation code including the building, the ground heat exchanger, the thermal energy storage, the solar roof and the reversible HP/ORC unit is developed and allows to perform a sensivity analysis. Annual results show that this technology allows to get a Positive Energy Building.

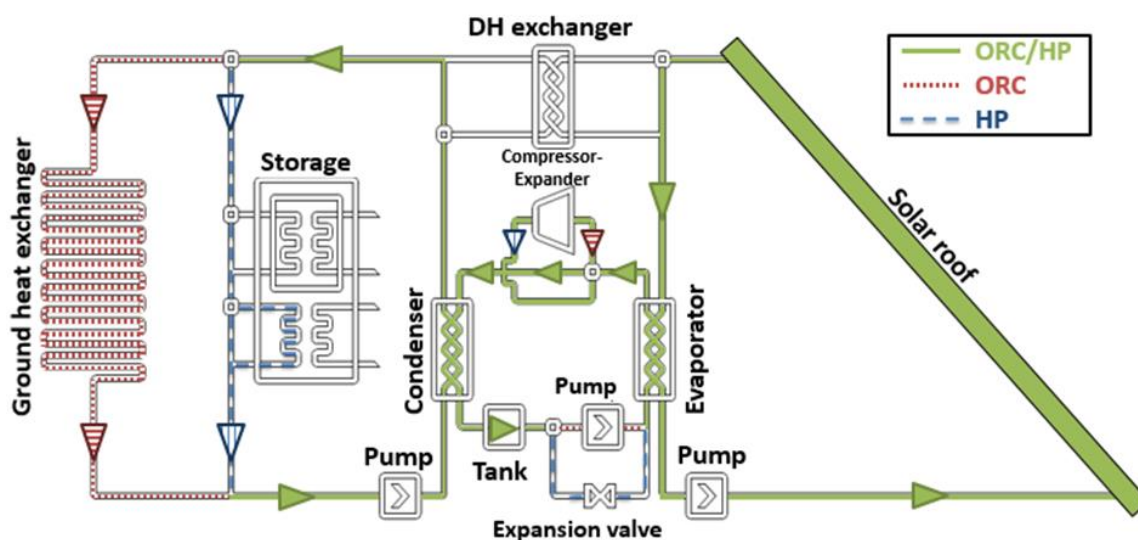


Figure 1: Hydraulic scheme of the HP/ORC reversible unit

EXPERIMENTAL VALIDATION OF A DOMESTIC STRATIFIED HOT WATER TANK MODEL IN MODELICA FOR ANNUAL PERFORMANCE ASSESSMENT

C.Carmo^{*,†,*}, O. Dumont[‡] and Mads P. Nielsen[†]

^{*,†} Aalborg University,
Dep. Energy Technology
Denmark

^{*}Insero Energy,
Denmark

[‡] Thermodynamics lab., Univ. Liège,
Belgium

e-mail: cca@et.aau.dk

ABSTRACT

The use of stratified hot water tanks in solar energy systems - including ORC systems- as well as heat pump systems is paramount for a better performance of these systems. However, the availability of effective and reliable models to predict the annual performance of stratified hot water tanks coupled with energy system solutions is limited. In this poster, a discretized model of a stratified tank developed in Modelica is presented. The physical phenomena to be considered are the thermal transfers by conduction and convection – stratification, heat loss to ambient, charging and discharging with direct inlet and outlet and immersed heat exchangers. Results of experimental and numerical investigations in a residential hot water tank with two immersed heat exchangers, one inlet and one outlet are presented and the performance of the model is assessed.

THERMO-ECONOMIC EVALUATION OF ORCS FOR VARIOUS WORKING FLUIDS

Pardeep Garg^{1*}, Matthew S. Orosz², Pramod Kumar¹⁺, Pradip Dutta^{1#}

¹Indian Institute of Science Bangalore
C V Raman Ave, Bengaluru, Karnataka, India

*E-mail: pardeep_1127@yahoo.com

+E-mail: pramod_k24@yahoo.com

#E-mail: pradip@mecheng.iisc.ernet.in

²Massachusetts Institute of Technology
Cambridge, MA, USA
E-mail: mso@mit.edu

ABSTRACT

A general thermoeconomic optimization of sub 500kW_e ORCs is developed using a 7-dimensional design space, with minimum investment cost per unit of nameplate electricity production as an objective function. Parameters used include working fluid, heat source temperature, pinch in condenser, boiler (HEX) and regenerator, expander inlet pressure and air cooled condenser area. Optimized power block configurations are presented for the application of ORCs with geothermal or waste heat sources and solar heat input for power scales of 5, 50 and 500 kW_e to facilitate rapid selection of design parameters across a range of thermal regimes. While R152a yields the lowest cost ORCs in the case of the former, isopentane is found to be more cost effective in the latter case for heat source temperatures between 125 and 275 °C.

1. INTRODUCTION

Increasing electricity demand necessitates the utilization of diverse energy resources, including the exergy potential of low temperature (< 300 °C) heat streams such as geothermal, waste heat from industrial processes or low concentration factor (< 100) solar collector systems. At sub steam-Rankine temperatures, the organic Rankine cycle (ORC) is a scalable thermodynamic solution for converting thermal resources (Velez et al., 2012) that can be configured to meet variable project demands. These resources are widely distributed in space, and consequently investment decisions for such inherently distributed generation projects require costly site and application-specific engineering and economic analysis. The design of ORC equipment optimized for unique resources and applications also involves a number of trade-offs and adds cost to projects.

Various working fluids have been proposed in the literature with optimized selections based on thermodynamic performance (Hung et al. 2010, Maizza and Maizza 2001, Wei et al., 2007 and Wang et al., 2011). However, when the strategic objective is minimized investment cost for a specific level of power output, the corresponding configuration and design operating conditions need not occur at the point of maximum efficiency (Quoilin et al. 2011). Work by Tempesti and Fiaschi (2013) and Lecompte et al. (2013) supports the above observation and underscores the need for a detailed thermo-economic evaluation of various ORC design parameters for comparison on an equivalent basis and generalizable across a wide range of ORC applications. This work presents such a study wherein the key design parameters influencing the specific cost of power from an air-cooled ORC are identified and used to formulate a 7-dimensional space to search for the minimum costs for applications with a) geothermal or waste heat sources and b) solar ORCs. Corresponding maps of operating parameters are generated to facilitate ORC engineers in the design of economic systems within constraints such as available heat source temperatures, maximum expander inlet pressures imposed, etc. Further, the effect of power scaling on these specific costs is evaluated for ORC capacities between 5 and 500kW_e.

2. Cycle details

The physical system considered in this paper consists of an ORC energized by a heat transfer fluid (HTF) that could be heated in two ways, forming Case A and B as follows:

Case A: The HTF gains enthalpy from geothermal or industrial waste heat or similarly relatively inexpensive sources (Figure 1). Here, the minimization of costs for a specific power output (i.e. \$/kW) are driven by the ORC capital expenditure at its performance envelope.

Case B: An ORC is coupled to a thermo-solar collector field via a thermal storage system (Figure 2) that maintains steady output in the ORC throughout the day. Here, the thermal source is a parabolic trough collector with significant cost. The optimization strategy in this case would be to configure the ORC to minimize the total system cost for a specific power output.

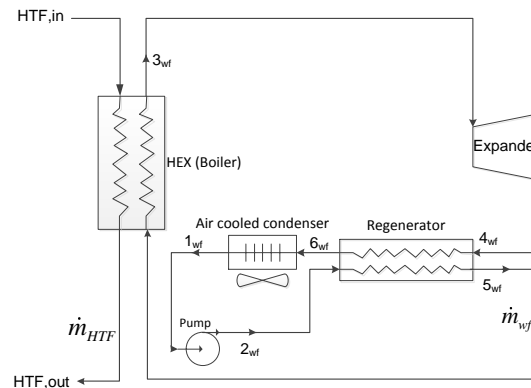


Figure 1. Schematic of an ORC which can be connected to a geothermal or waste heat recovery source.

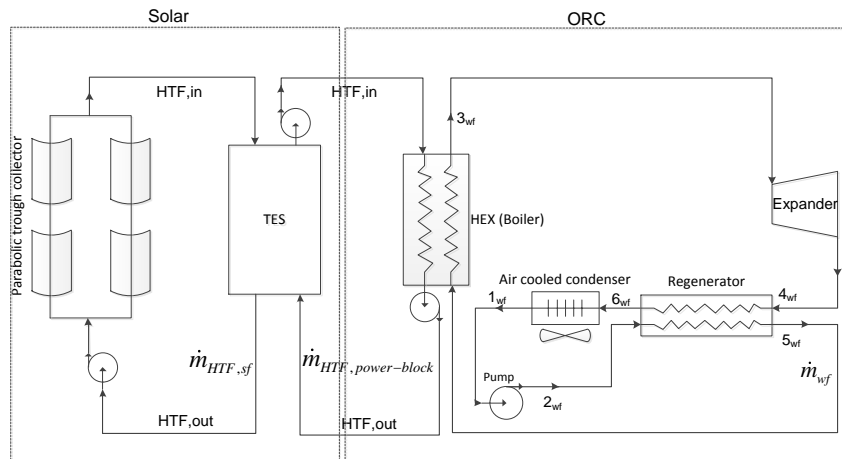


Figure 2. Schematic of an ORC connected to a solar source.

ORC component details:

The major components in a typical ORC include expander, heat exchangers (boiler, regenerator), air-cooled condenser (ACC), pumps, and VFD drives. For sub MWe ORC, positive displacement expanders are appropriate at the smaller scales where turbo-expanders suffer from high rotational speeds and lower isentropic efficiencies (Fiaschi *et al.*, 2012).

For the working fluid pump, a plunger type positive displacement device suitable for sub-MWe ORCs is coupled to a variable frequency drive to achieve the designed mass flow rates. The regenerator and boiler are modeled as plate heat exchangers which are limited to 60 bar and hence the high side cycle pressure ($p_{3, wf}$) is restricted to 60 bar. These heat exchangers are modeled for a pressure drop of 1.5 % of their pressures at the inlets on both cold and hot side along the length of heat exchanger using heat transfer and pressure drop correlations from literature sources (Martin, 1996 for single phase heat transfer, Würfel *et al.*, 2004 for two phase heat transfer and Piro *et al.*, 2004 for heat transfer in

supercritical regime) for sub- as well as trans-critical cycles. A 1-D numerical approach is employed to model these exchangers, accounting for the variation in the thermo-physical properties of the working fluid during heat transfer. The temperature profile of the HTF in the boiler is determined by a procedure based on minimization of entropy generation in the boiler (Garg et al., 2013). The expander chosen is scroll (connected to an electric generator) for which the overall isentropic efficiency is assumed to be 65% from thermal to electrical (Lemort et al., 2009). The cost function for scroll expanders is generated using a database of existing scroll compressors for HVAC applications. In the case of volume ratio > 2.89 , two or more scrolls are used in series. The condenser is air cooled and designed in such a way that the overall system cost is optimized taking into account its fan power. Commercially available condenser unit sizes are used in the analysis with the smallest and the largest surficial area ranging from 0.5 m^2 to 9.2 m^2 . In case of higher power levels requiring larger surficial areas ($>9.2 \text{ m}^2$), parallel units of condenser are considered. Modeling details of the condenser can be found in the Masters thesis of Monifa Fela Wright (2000). Major instruments considered in the power block include temperature and pressure sensors, flow meter, current transducers, data acquisition system, data processing and control systems. Details of the cost functions used in the analysis can be found in appendix A. Costs pertaining to the pipes and other accessories are not considered in this paper.

Solar-ORC details:

In the solar heat source case, the ORC described above remains identical with additional system components added including thermal energy storage (TES) system and a solar collector field. The storage type selected is pebble bed (efficiency assumed to be 95%) which can be economical for ORC systems (Hasnain SM, 1998). Modeling details of such a TES system can be found in Kshirsagar et al., 2015. Parabolic trough collector efficiency is modeled as a function of operating HTF temperatures (Kutscher et al., 2012). Solar calculations are performed for Vernal Equinox at the Tropic of Cancer (roughly the mean of extreme Indian latitudes) using the ASHRAE clear sky model. The clearness factor is selected to achieve an annual average DNI of $5.3 \text{ kWh/m}^2\text{-day}$. Annual average ambient temperature on such a location is $30 \text{ }^\circ\text{C}$. The thermal energy storage capacity and solar field are sized to ensure steady output of the plant at an ORC capacity factor of 0.5 throughout the year.

3. Methodology

Detailed component level models are developed and integrated in Matlab to simulate the systems described in cases A and B. For the given power capacity, investment cost of these systems is highly dependent on the operating conditions in their power blocks. Optimization proceeds by varying these operating conditions within the 7-dimensional space formed by working fluid type, HTF inlet temperature (heat source temperature), pinch in condenser, regenerator and HEX (boiler), expander inlet pressure and condenser area. The objective function is to minimize the specific cost of the system (C_{sp}) taking into account parasitic losses of working fluid and HTF pumping and fan power in condenser.

$$C_{sp} = \frac{\text{Total investment cost}}{\text{ORC output} - \text{parasitic losses}} \quad (1)$$

The algorithm to optimize the above power block is given in Figure 3. The parametric sweep was performed for 3 different power scales, 5, 50 and 500 kWe. Above 500 kWe, the expected technical setup changes (e.g., positive displacement expanders could be replaced by turbines and plunger pumps by centrifugal, etc.), hence this study is confined to small scale ORCs $\sim 500 \text{ kW}_e$ or below.

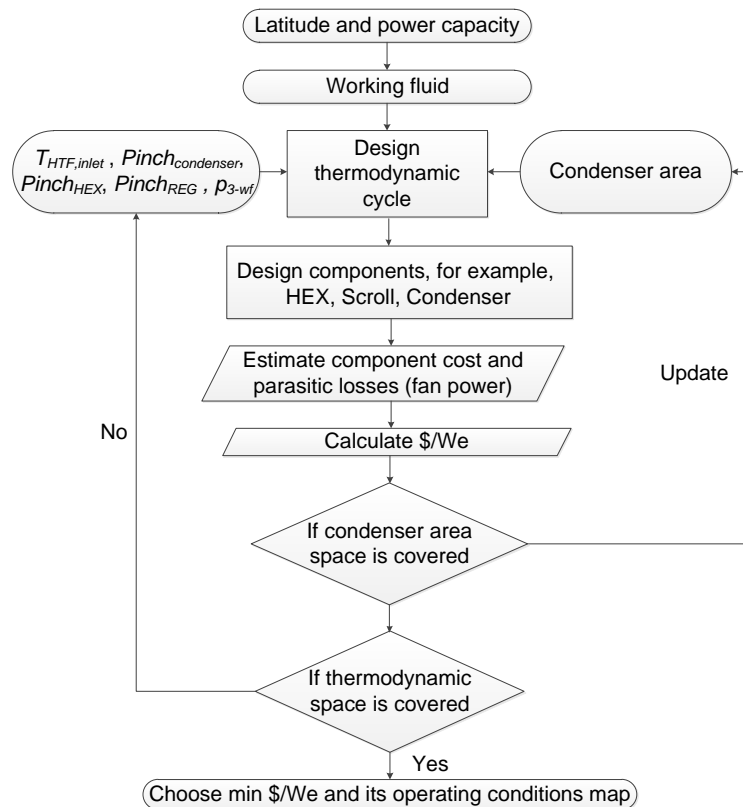


Figure 3. Algorithm to optimize the ORC system on thermo-economic basis

4. RESULTS AND DISCUSSIONS

Optimum C_{sp} values are calculated for 16 zero-ODP and positive condenser pressure (saturation pressure corresponding to 45 °C) working fluids for HTF supply temperatures between 125 and 275 °C in steps of 25 °C for the power capacities of 5, 50 and 500 kWe. To facilitate visualization of the data, only the 8 highest performing fluids are presented here (including isopentane and R245fa, two widely used fluids in ORCs). For some fluids, equations of state in the REFPROP property data base were extrapolated beyond their specified limits to enable a one to one comparison for the given HTF temperature, however, operating temperatures considered are well below the fluid thermal stability temperatures as suggested by Morgan and Munday (1935), Angelino and Invernizzi (2003), Hidaka et al. (2004), Moon et al. (2004) and Ito et al. (2014).

4.1 ORCs connected to geothermal or waste heat sources (Case A)

For a 5 kWe ORC, the optimum C_{sp} values are presented in Figure 4 against HTF_{in} temperature for different working fluids. At any temperature, C_{sp} is found to be a strong function of working fluid type, with a larger variance at lower temperatures; isopentane yields the highest C_{sp} whereas R152a and R161 compete at the low end. The trend for C_{sp} among different fluids is consistent at different temperatures. Certain fluids exhibit a sudden increase in cost with increase in HTF_{in} temperature due to transitioning from a sub to trans-critical cycle or due to excess heat duties of boiler and condenser in cases where a regenerator is not employed. While there is a significant potential for reducing C_{sp} with temperature in the case of isopentane, the same is not true in the case of R152a or R161 where the reduction in cost is just 10 % with increase in HTF temperature from 125 to 275 °C. Further, Figure 4 illustrates that an increase in efficiency is not always economically advantageous.

The corresponding map of optimum operating conditions is given in Figure 5 wherein the volumetric expansion ratio (v_4/v_3), expander inlet pressure ($p_{3,wf}$), pinch in condenser and HEX, condenser area and regenerator fractional cost are plotted. It is noteworthy that the lowest C_{sp} values are observed at the lowest volumetric expansion ratios in the expander at higher inlet pressures. Volume ratios as high as 20 are observed, requiring a multi stage expansion process or non-conventional scroll

expanders (Orosz et al., 2013). Also, higher pinch temperatures can be tolerated at higher $T_{HTF,in}$ temperatures. Optimized condensers converge on the smallest size possible in the domain of standard available air-cooled condensers considered. Further, improvement in efficiency via incorporating a regenerator is not economically justified for 5 kWe scale ORCs and hence optimized ORCs do not incorporate the regenerators. The rationale behind the exclusion of a regenerator at 5 kWe is justified by comparing the best cases with and without regenerator for minimum C_{sp} as shown in Figure 6. Also, Decreasing volumetric flow rate at the expander exhaust is found to be a key parameter for lower C_{sp} in cases of high condenser pressure fluids - with the exception of R134a which should have yielded a cost equivalent to that of R152a. In this case the penalty for lack of regenerator is relatively higher than for R152 and R161, where expansion significantly reduces the potential for heat recovery in the regenerator. The above analysis is extended to power scales of 50 and 500 kWe and is represented in Figures 7 to 11. Unexpectedly, the lowest C_{sp} values exhibit a jump at HTF temperature of 175 °C. At this temperature, power blocks without regenerator demand higher heat duties in HEX and condenser and hence optimum power blocks begin to employ a regenerator, resulting in higher C_{sp} .

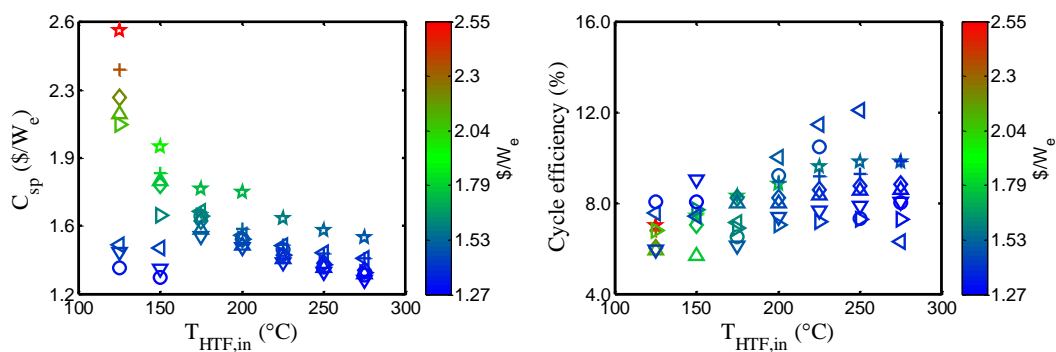


Figure 4. C_{sp} and cycle efficiency for various working fluids against $T_{HTF,in}$ temperatures for a 5 kWe ORC. Legend: ☆ ipentane, Δ butane, ▷ isobutane, + R245ca, ◇ R245fa, ◁ R134a, ○ R161, ▽ R152a.

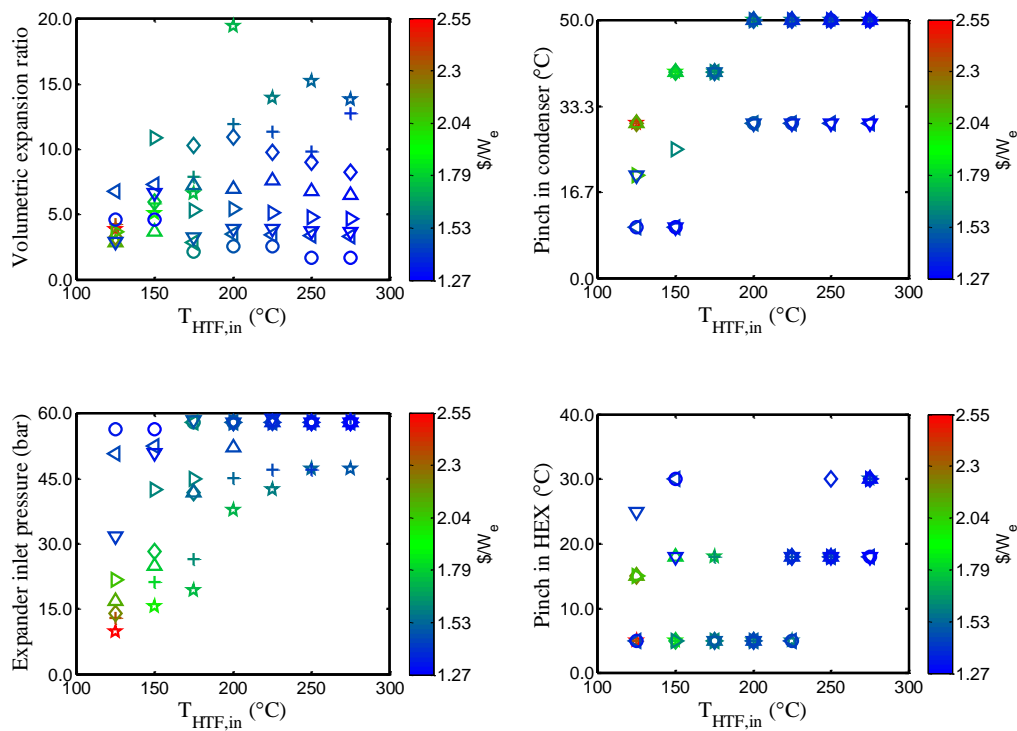


Figure 5. Corresponding map of optimum operating parameters for various working fluids against $T_{HTF,in}$ temperatures for a 5 kWe ORC. Legend: ☆ ipentane, Δ butane, ▷ isobutane, + R245ca, ◇ R245fa, ◁ R134a, ○ R161, ▽ R152a.

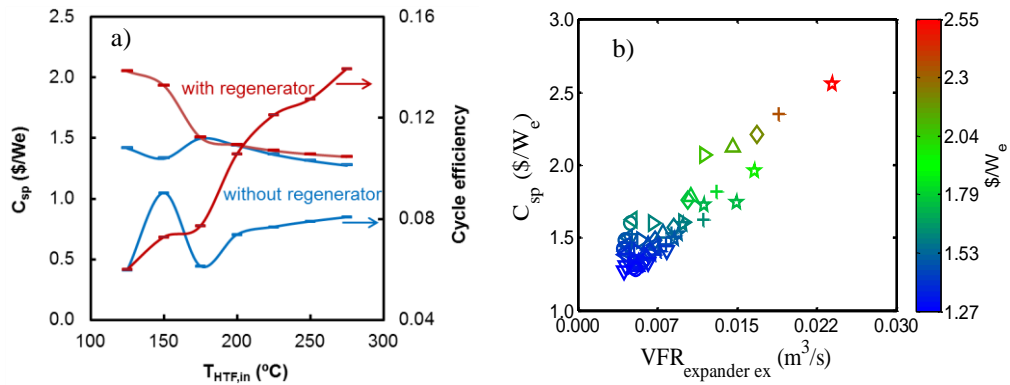


Figure 6. a) Comparison of the best cases with and without regenerator for minimum C_{sp} for a 5 kWe R152ORC. b) C_{sp} against the volumetric flow rate at the expander exhaust. Legend: ☆ isopentane, Δ butane, ▷ isobutane, + R245ca, ◇ R245fa, ◁ R134a, ○ R161, ▽ R152a.

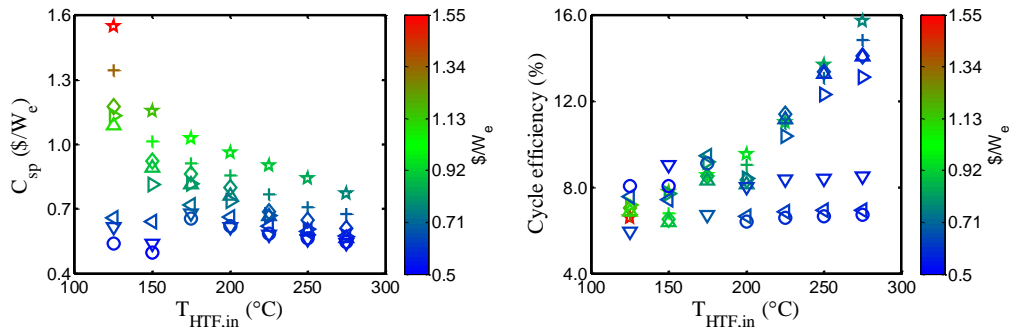
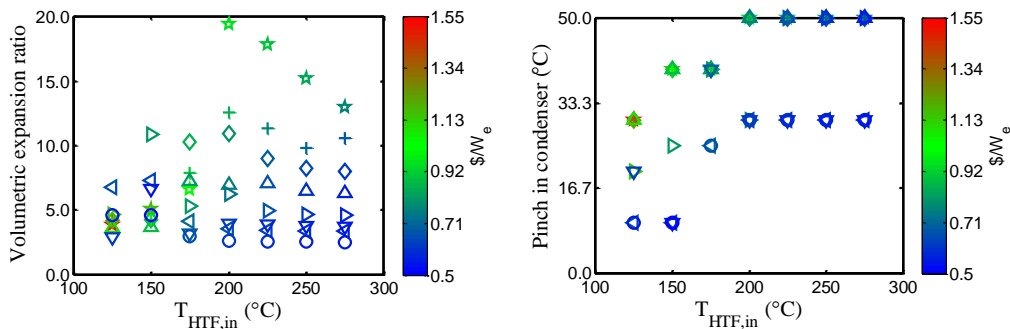


Figure 7. C_{sp} and cycle efficiency for various working fluids against $T_{HTF,in}$ temperatures for a 50 kWe ORC. Legend: ☆ ipentane, Δ butane, ▷ isobutane, + R245ca, ◇ R245fa, ◁ R134a, ○ R161, ▽ R152a.



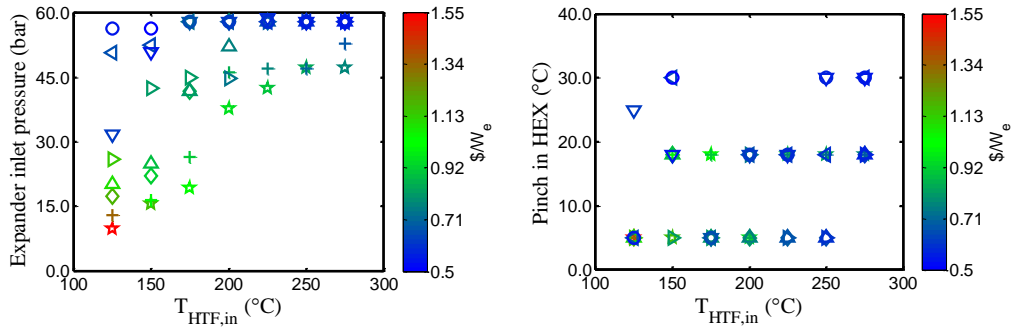


Figure 8. Corresponding map of optimum operating parameters for various working fluids against $T_{HTF,in}$ temperatures for a 50 kW_e ORC. Legend: ☆ ipentane, Δ butane, ▷ isobutane, + R245ca, ◇ R245fa, ◁ R134a, ○ R161, ▽ R152a.

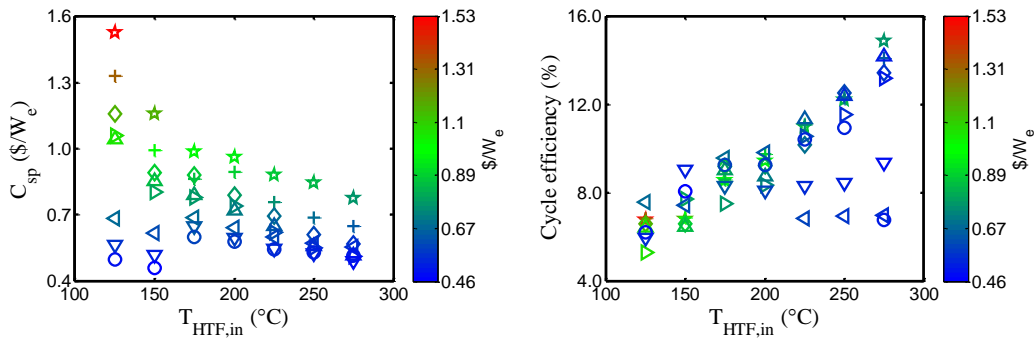


Figure 9. C_{sp} and cycle efficiency for various working fluids against $T_{HTF,in}$ temperatures for a 500 kW_e ORC. Legend: ☆ ipentane, Δ butane, ▷ isobutane, + R245ca, ◇ R245fa, ◁ R134a, ○ R161, ▽ R152a.

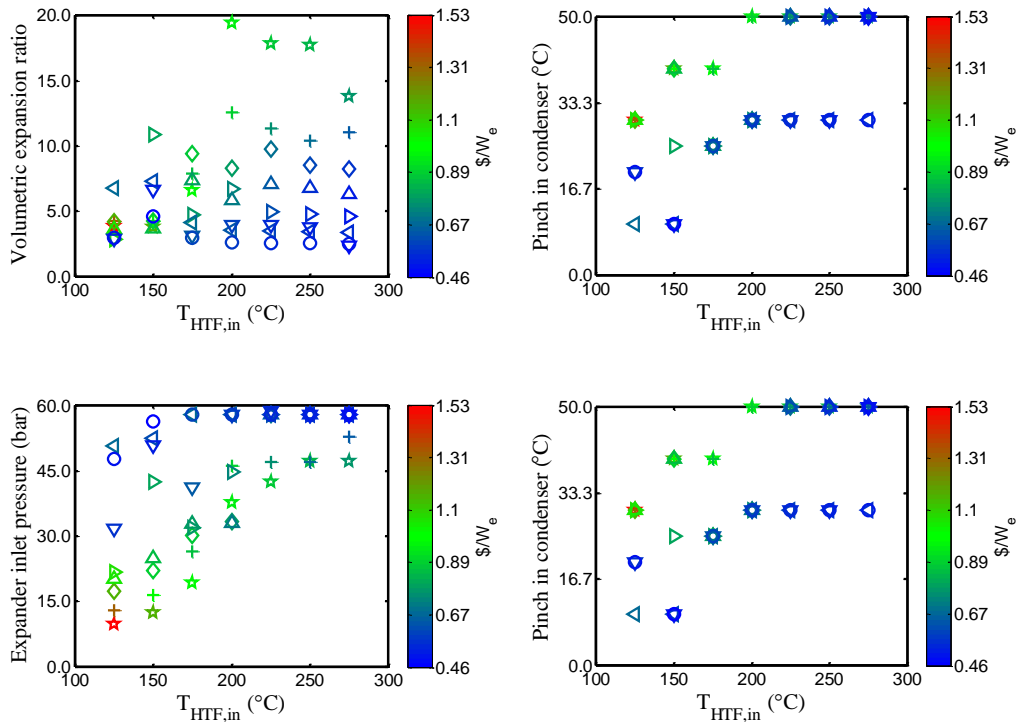


Figure 10. Corresponding map of optimum operating parameters for various working fluids against $T_{HTF,in}$ temperatures for a 500 kWe ORC. Legend: ☆ ipentane, Δ butane, ▷ isobutane, + R245ca, ◇ R245fa, ◁ R134a, ○ R161, ▽ R152a.

A cost break-down of the lowest C_{sp} ORC configurations is presented in Figure 11 for the power scales of 5, 50 and 500 kWe. At 5 kWe, instrumentation, DAQ system and controls represents a proportionally high fraction of total system costs, followed by ACC, scroll expander, pumps and HEX. The trend is reversed as the power scale goes up. While the absolute cost of instrumentation remains almost constant, the cost of volumetric machinery (pumps and scroll expander) scales linearly.

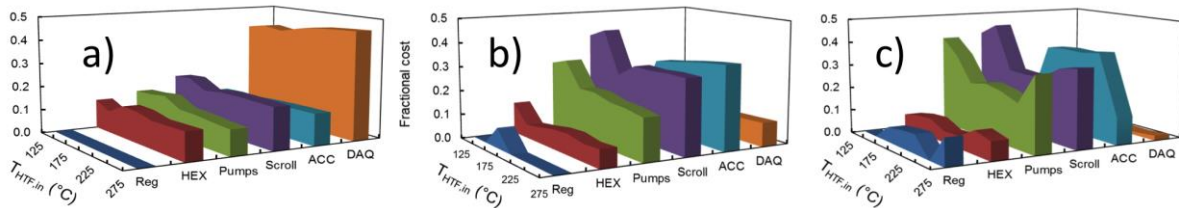


Figure 11. Cost break up for ORCs with lowest specific costs at various HTF operating temperatures. a) 5 kWe, b) 50 kWe and c) 500 kWe. Pump costs are inclusive of working fluid, HTF pumps and their VFD drives.

4.2 ORCs connected to solar heat source (Case B)

The initial investment cost for a solar-ORC per unit power produced is presented in Figure 12 for the different working fluids against $T_{HTF,in}$ temperature. At lower HTF operating temperatures, these costs are an order of magnitude higher than in ORCs with “free” thermal sources (Case A), but decrease by a factor of 4 across the range of $T_{HTF,in}$ temperatures, indicating the advantage of moving to higher operating temperatures. The trend among the working fluids is reversed with isopentane offering the lowest C_{sp} values and R161 or R152a the highest. Further, at higher HTF temperatures, there exist two distinct clusters of working fluids, at higher and lower costs levels. This trend can be mapped on the efficiency plot in Figure 12, emphasizing the fact that lower C_{sp} values are the direct result of higher cycle efficiencies, which in turn minimize the solar field area required and its associated cost. The corresponding map of optimum operating parameters is given in Figure 13. In solar-ORCs, this parameter space adjusts itself to maximize the cycle efficiency and hence pinch temperatures in condenser, regenerator and HEX tend to be minimized and ORCs tend to be regenerative. Similar exercises have been repeated for different power scales and are presented in Figures 14-17.

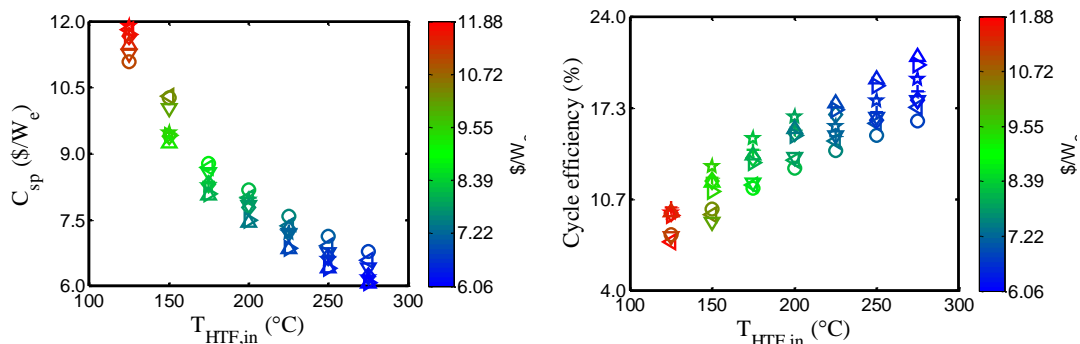


Figure 12. C_{sp} and cycle efficiency for various working fluids against $T_{HTF,in}$ temperatures for a 5 kWe solar-ORC. Legend: ☆ ipentane, Δ butane, ▷ isobutane, + R245ca, ◇ R245fa, ◁ R134a, ○ R161, ▽ R152a.

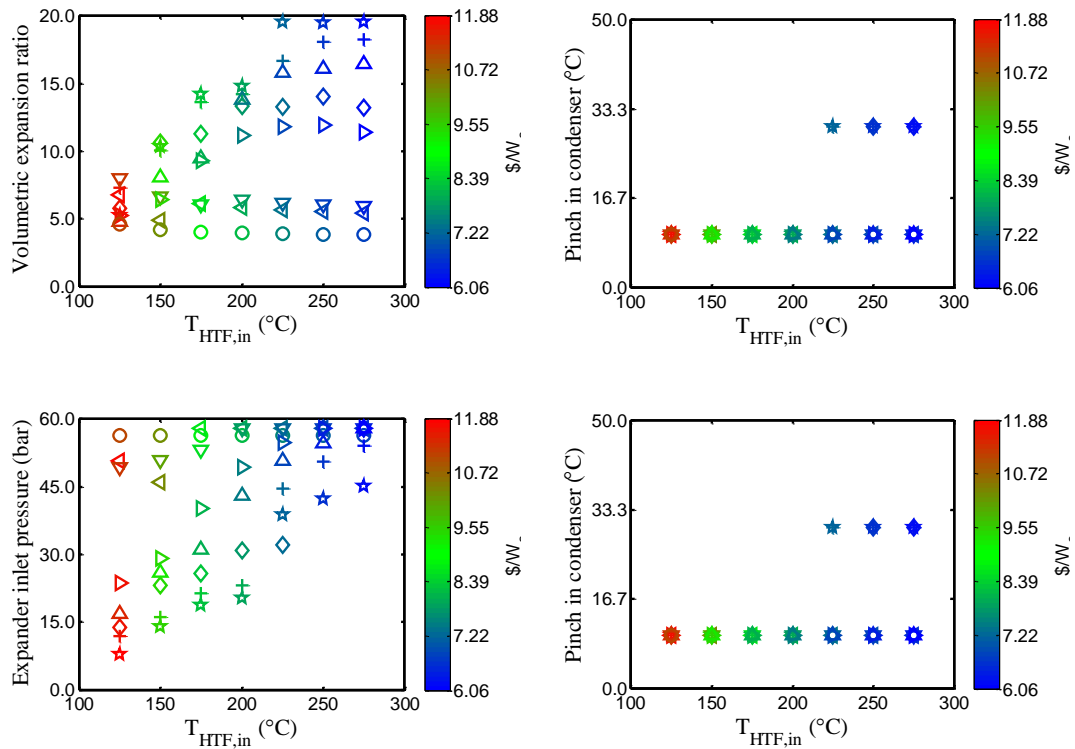


Figure 13. Corresponding map of optimum operating parameters for various working fluids against $T_{HTF,in}$ temperatures for a 5 kW solar-ORC. Legend: ☆ ipentane, Δ butane, ▷ isobutane, + R245ca, ◇ R245fa, ◁ R134a, ○ R161, ▽ R152a.

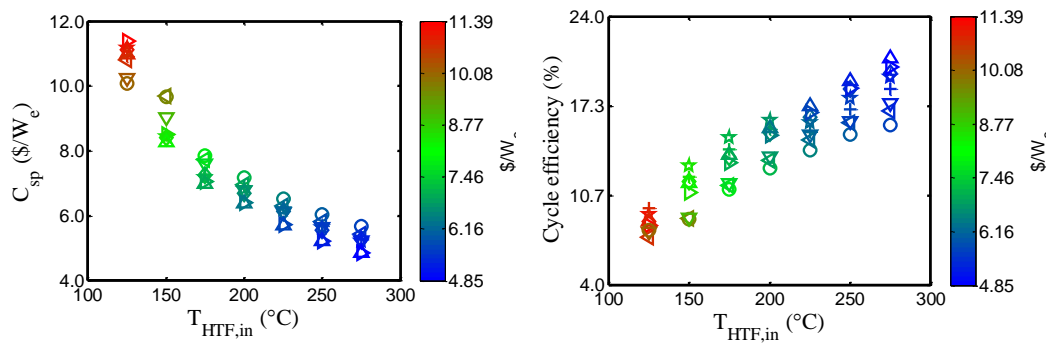
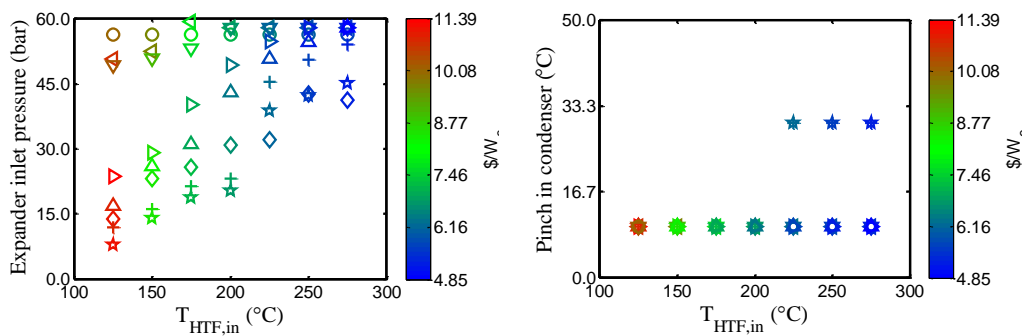


Figure 14. C_{sp} and cycle efficiency for various working fluids against $T_{HTF,in}$ temperatures for a 50 kW solar-ORC. Legend: ☆ ipentane, Δ butane, ▷ isobutane, + R245ca, ◇ R245fa, ◁ R134a, ○ R161, ▽ R152a.



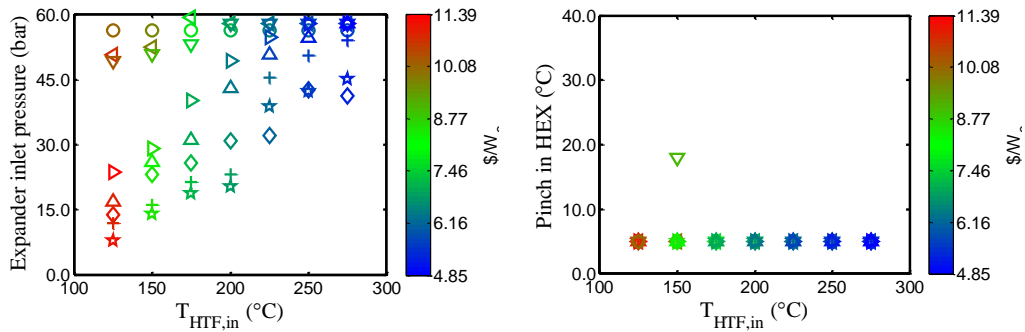


Figure 15. Corresponding map of optimum operating parameters for various working fluids against HTF,in temperatures for a 50 kW solar-ORC. Legend: ☆ ipentane, Δ butane, ▷ isobutane, + R245ca, ◇ R245fa, ◁ R134a, ○ R161, ▽ R152a.

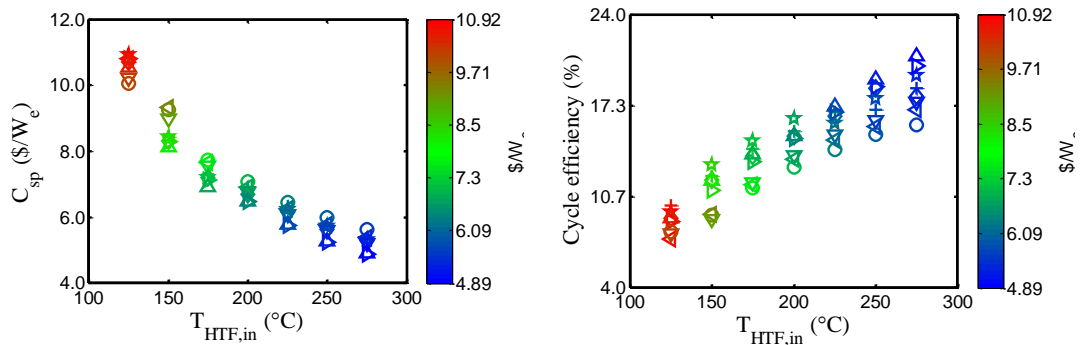


Figure 16. C_{sp} and cycle efficiency for various working fluids against HTF,in temperatures for a 500 kW solar-ORC. Legend: ☆ ipentane, Δ butane, ▷ isobutane, + R245ca, ◇ R245fa, ◁ R134a, ○ R161, ▽ R152a.

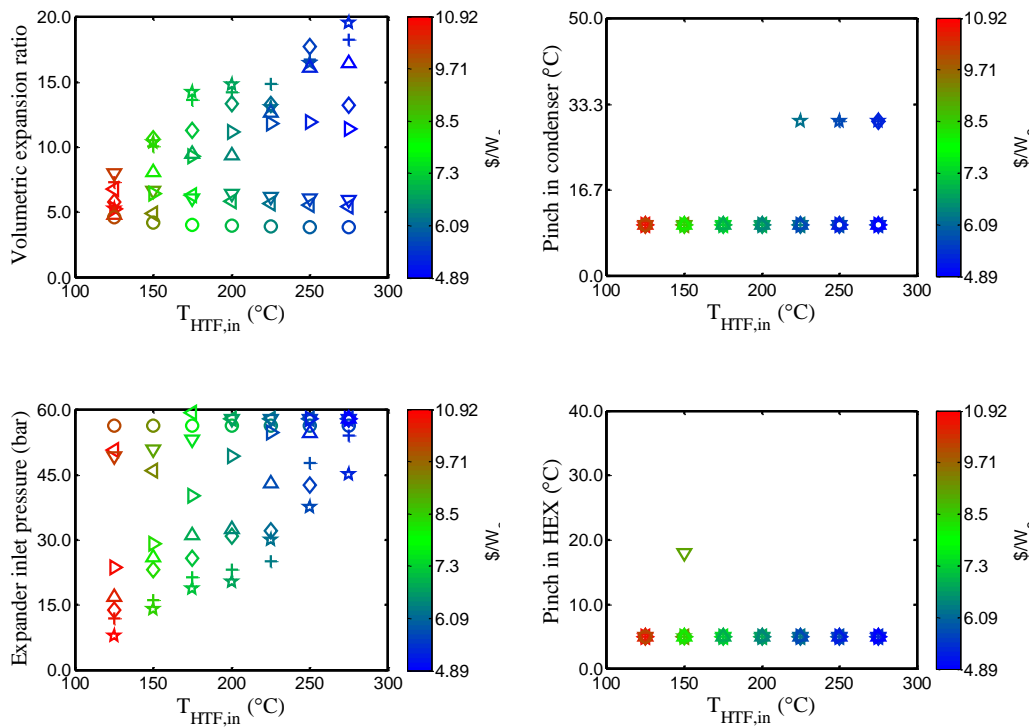


Figure 17. Corresponding map of optimum operating parameters for various working fluids against HTF,in temperatures for a 500 kWe solar-ORC. Legend: ☆ ipentane, △ butane, ▷ isobutane, + R245ca, ◇ R245fa, ◁ R134a, ○ R161, ▽ R152a.

Cost break-down for solar-ORCs is plotted in Figure 18 which indicates the solar field cost to be highest followed by power block and then storage system. Potential for further decrease in specific cost lies in the realization of higher temperature ORCs.

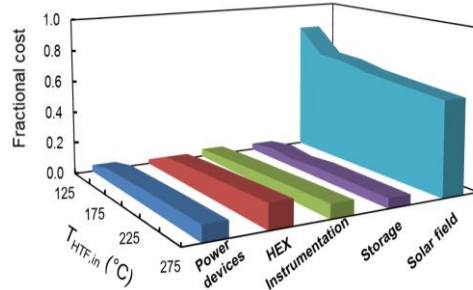


Figure 18. Cost break up of solar-ORCs with lowest specific costs at various HTF operating temperatures. 5 kWe is shown and 50 kWe and 500 kWe are omitted due to their close visual similarity. While power devices include pumps and expander, heat exchangers include regenerator, HEX and condenser.

Conclusions

The variable space formed by HTF supply temperature, pinch in condenser, regenerator and boiler, expander inlet pressure, condenser area and working fluid affects the ORC investment cost in a significant way. A tool developed to analyze the design space is applied for two major applications of ORCs, namely geothermal/waste heat and solar. The conclusions drawn from these two studies are well distinguished and summarized as follows:

ORC coupled to geothermal/waste heat source

- i. At any given temperature, R152a and R161 are found to yield the lowest cost. This cost pattern is attributed to their higher condenser pressures which imply lower volumetric flow rates at the expander exit (state of maximum volumetric flow rate) resulting in compact fluid machinery.
- ii. Some smaller ORCs may optimize their specific costs without incorporating a regenerator
- iii. Instrumentation costs are proportionally higher for smaller ORCs
- iv. Increase in HTF supply temperature does not yield a significant decrease in the lowest specific cost indicating diminishing returns with increased operating temperature.

ORC coupled to solar heat source

- i. Isopentane emerges as the best working fluid in solar ORCs at low HTF temperatures. However, at elevated temperatures, isopentane, R245fa and R245ca costs converge.
- ii. The regenerator cost is justified even at lower temperatures and lower power scales owing to higher cycle efficiencies and lower solar field costs.
- iii. The lowest cost of power generation at 5, 50 and 500 kWe are observed to be 5.9, 4.72 and 4.71 \$/We, respectively indicating asymptotic behavior of cost beyond 50 kWe.
- iv. Storage cost associated with a TES system designed for damping the solar insolation fluctuations on the power block side are found to be ~ 75 % of the power block. However, solar field cost remains a major contributing factor towards the total solar-ORC cost motivating to search for high temperature and hence more efficient ORCs requiring lower solar field area.

This work can contribute towards best practices that improve cost effectiveness of distributed ORCs. Future work involves the evaluation of the levelized cost of energy and appropriate business strategies for target ORC applications.

REFERENCES

- Angelino, G., Invernizzi, C. M., 2003, Experimental investigation on the thermal stability of some new zero ODP refrigerants, *Int. J. of Refrigeration*, 26, 1, 51-58
- Fiaschi, D., Manfrida, G., Maraschiello, F., 2012, Thermo-fluid dynamics preliminary design of turbo-expanders for ORC cycles, *Applied Energy*, 97, 601-608.

- Garg, P., Kumar, P., Srinivasan, K., Dutta, P., 2013, Evaluation of isopentane, R-245fa and their mixtures as working fluids for organic Rankine cycles, *Applied Thermal Engineering*, 51, 292-300
- Hasnain, SM. Review on sustainable thermal energy storage technologies. Part1. Heat storage materials and techniques, *Energy Convers Manage*, J1998, 39, 11, 1127-38
- Hidaka, Y., Oki, T., Kawano, H., 2004, Thermal Decomposition of Propane in Shock Waves, *Int J. of Chemical Kinetics*, 21, 8, 1
- Hung, T.C., Wang, S.K., Kuo, C.H., Pei, B.S., Tsai, K.F., 2010, A study of organic working fluids on system efficiency of an ORC using low-grade energy sources, *Energy*, 35, 3, 1403-1411
- Ito, M., Dang, C., Hihara, E., 2014, Thermal Decomposition of Lower-GWP Refrigerants, 15th *Int. Refrigeration & Air conditioning Conference*, 2591,1-10
- Kshirsagar, A., Garg, P., Kumar, P., Orosz, M.S., 2015, Identification of ORC parameters for optimization of thermal storage medium cost in solar ORC, accepted in ASME ORC 2015.
- Kutscher, C., Burkholder, F., Stynes, K., 2012, Generation of a Parabolic Trough Collector Efficiency Curve from Separate Measurements of Outdoor Optical Efficiency and Indoor Receiver Heat Loss, *J. of Solar Energy Engineering*, 134 / 011012-1, 1-6
- Lecompte, S., Huisseune, H., Broek, M.V.D., Schampheleire, S.D., Paepe, M.D., 2013, Part load based thermo-economic optimization of the Organic Rankine Cycle (ORC) applied to a combined heat and power (CHP) system, *Applied Energy*, 111, 871-881
- Lemort, V., Qoulin, S., Cuevas, C., Lebrun, J., 2009, Testing and modelling a scroll expander integrated into an Organic Rankine Cycle, *Applied Thermal Engineering*, 29, 14-15, 3094-3102
- Maizza, V., Maizza, A., 2001, Unconventional working fluids in organic Rankine-cycles for waste energy recovery systems, *Applied Thermal Engineering*, 21, 3, 381-390
- Martin, H., 1996, A theoretical approach to predict the performance of chevron-type plate heat exchangers, *Chemical Engineering and Processing: Process Intensification* 35 (4), 301-310
- Moon, D.J., Chung, M.J., Kwon, Y.S., Ahn, B.S., 2004, Thermally decomposing difluorochloromethane to tetrafluoroethylene; dimerization in fluidized bed reactor, *US6710215B2*
- Morgan, J.J., Munday, J.C., 1935, Thermal Decomposition of n-Pentane, *Industrial and Engineering Chemistry*, 27, 9, 1081-1086
- Orosz, M.S., Mueller, A.V., Dechesne, B.J., Hemond H.F., 2013, Geometric Design of Scroll Expanders Optimized for Small Organic Rankine Cycles, *J. Eng. Gas Turbines Power*, 135(4), 042303
- Qoulin, S., Declaye, S., Tchanche, B.F., Lemort, V., Thermo-economic optimization of waste heat recovery Organic Rankine Cycles, 2011, *Applied Thermal Engineering*, 31, 14-15, 2885-2893
- Tempesti, D., Fiaschi, D., 2013, Thermo-economic assessment of a micro CHP system fuelled by geothermal and solar energy, *Energy*, 58, 45-51
- Velez, F., Segovia, J.J., Martin, M.C., Antolin, G., Chejne, F., Quijano, A., 2012, A technical, economical and market review of organic Rankine cycles for the conversion of low-grade heat for power generation, *Renewable and Sustainable Energy Reviews*, 16, 6, 4175-4189
- Wang, E.H., Zhang, H.G., Fan, B.Y., Ouyang, M.G., Zhao, Y., Mu, Q.H., 2011, Study of working fluid selection of organic Rankine cycle (ORC) for engine waste heat recovery, *Energy*, 36, 5, 3406-3418
- Wei, D., Lu, X., Lu, Z., Gu, J., 2007, Performance analysis and optimization of organic Rankine cycle (ORC) for waste heat recovery, *Energy Conversion and Management*, 48, 4, 1113-1119
- Wright, M.F., 2000, Plate-fin-and-tube condenser performance and design for refrigerant R-410a air-conditioner, *Submitted as Master's Thesis at Georgia Institute of Technology*.
- Würfel, R., Ostrowski, N., 2004, Experimental investigations of heat transfer and pressure drop during the condensation process within plate heat exchangers of the herringbone-type, *International Journal of Thermal Sciences*, 43, 59-68
- Pioro, I.L., Khartabil, H.F., Duffey, R.B., 2004, Heat transfer to supercritical fluids flowing in channels—empirical correlations (survey), *Nuclear Engineering and Design*, 230, 69-91

ACKNOWLEDGEMENT

This research is based upon work supported by the Solar Energy Research Institute for India and the U.S. (SERIUS) funded jointly by the U.S. Department of Energy subcontract DE AC36-08G028308 (Office of Science, Office of Basic Energy Sciences, and Energy Efficiency and Renewable Energy, Solar Energy Technology Program, with support from the Office of International Affairs) and the Government of India subcontract IUSSTF/JCERDC-SERIUS/2012 dated 22nd Nov. 2012.

APPENDIX A

Cost functions for various components in US Dollars are as follows:

$$cost_{PHE} = 492.76 + 609.6A_{heat-transfer} \quad (A.1)$$

$$cost_{ACC} = NPU(1000A_{fan} + 173.3) \quad (A.2)$$

$$cost_{scroll} = (266.2 + 170976VFR_{outlet}) \left(0.6858 + 0.2732 \ln \left(\frac{VFR_{outlet}}{VFR_{inlet}} \right) \right) \quad (A.3)$$

$$cost_{tank} = 130V + 1140 \quad (A.4)$$

$$cost_{pump} = 19.7VFR_{inlet} \quad (A.5)$$

$$cost_{VFD} = 93.6\dot{W} + 110.1 \quad (A.6)$$

$$cost_{alternator} = 56.5\dot{W} + 8.9 \quad (A.7)$$

$$cost_{solar-field-per-sq.meter} = 245 \quad (A.8)$$

Cost per kg of the working fluids and HTFs considered is as follows:

$$cost_{ipentane} = 2.85 \quad (A.9)$$

$$cost_{R152a} = 3.51 \quad (A.10)$$

$$cost_{R134a} = 5.85 \quad (A.11)$$

$$cost_{isobutan} = 4.68 \quad (A.12)$$

$$cost_{R245ca} = 13.6 \quad (A.13)$$

$$cost_{butane} = 3.4 \quad (A.14)$$

$$cost_{R245fa} = 12.4 \quad (A.15)$$

$$cost_{R161} = 12.36 \quad (A.16)$$

$$cost_{EG,per,kg} = 1.6 \quad (A.17)$$

$$cost_{Therminol-VP1,per,kg} = 5.8 \quad (A.18)$$

Cost of instrumentation is as follows:

$$cost_{pressure-sensor} = 200 \quad (A.19)$$

$$cost_{temperature-gauge} = 50 \quad (A.20)$$

$$cost_{current-transducer} = 100 \quad (A.21)$$

$$cost_{relay} = 65 \quad (A.22)$$

$$cost_{data-aquisition} = 300 \quad (A.23)$$

$$cost_{processor} = 250 \quad (A.24)$$

$$cost_{user-interface} = 65 \quad (A.25)$$

$$cost_{network-cabel} = 300 \quad (A.26)$$

Number of instrument components considered as follows:

THERMOECONOMIC ANALYSIS OF ORGANIC RANKINE CYCLE USING ZEOTROPIC MIXTURES

Muhammad Imran^{†‡}, Muhammad Usman^{†‡}, Dong-Hyun Lee[‡] and Byung-Sik Park^{*†‡}

[‡]Korea Institute of Energy Research,
152 Gajeong-ro, Yuseong-gu, Daejeon, (305-343), South Korea
Email: bspark@kier.re.kr

[†]Korea University of Science and Technology
217 Gajeong-ro Yuseong-gu, Daejeon, (305-350), South Korea
Email: imran@ust.ac.kr

* Corresponding Author: Byung-Sik Park

ABSTRACT

The selection of the working fluid is an important part of design and optimization of ORC system as it affects the systems efficiency, design of ORC components, stability, safety and environmental impact. Present study aims to investigate the performance of ORC system using pure working fluids and zeotropic mixtures for low temperature geothermal heat source on the basis of thermodynamic and economic parameters of ORC system. Evaporator, expander, condenser and feed pump models are developed in MATLAB. The control volume approach is adopted for evaporator and condenser model with appropriate database of heat transfer and pressure drop correlations. For comparison, pure working fluids are taken as the base case. The ORC system with pure working fluid and zeotropic mixture under same heat and sink source conditions are optimized using multi objective genetic algorithm for maximum exergy efficiency and minimum specific investment cost. The exergy efficiency of ORC system with zeotropic mixture is improved by 14.33% compared to pure working fluid. The exergy destruction in evaporator and condenser is reduced by 24~30%. The fraction of more volatile component in zeotropic mixture affected the thermal and economic performance of ORC system, for current study the mass fraction of 40% of R245fa corresponds to optimum exergy efficiency and specific investment cost. For same condensing pressure and expander power, area of evaporator for pure working fluids and zeotropic mixture is also calculated. The required heat transfer area for zeotropic mixture is approximately 13% less than required for pure working fluid.

1. INTRODUCTION

Organic Rankine Cycle (ORC) system effectively recovers low grade and waste heat and reduces the energy cost and environmental impact (Imran et al. 2015). Working fluid selection is considered as an important part of the design and optimization of an ORC system since the properties of the working fluid affect efficiency of system, design and size of the system components, system stability and safety, and environmental impact. During last few years, extensive research had been conducted for selection methodologies (Bao & Zhao 2013) and operating characteristics of pure working fluids for various ORC applications (Chen et al. 2010).

Liu et al. (Liu et al. 2004) found that various working fluids at specific evaporation and condensation temperatures exhibited very similar thermal efficiencies although the thermal efficiencies were found to increase slightly with the critical temperature of the working fluids. They also used two improved parameters, total heat recovery efficiency and heat availability, to evaluate the performance of an ORC system, in lieu of traditional thermal efficiency indicators. Tchanche et al. (Tchanche et al. 2009) recommended R134A as the best working fluid for low temperature solar ORC systems among the 20

working fluids investigated. Lakew and Bolland (Lakew & Bolland 2010) pointed out that the selection of working fluid depends on the nature of the heat source, temperature level and the objective function. Saleh et al. (Saleh et al. 2007) screened out the best working fluid among 31 preselected working fluids using Backone equation of state. Hung et al. (Hung et al. 1997) shed light on that different slopes and shapes of saturation vapor curves were the most crucial characteristics of working fluids for ORCs, and that isentropic fluids were the most suitable for recovering low temperature waste heat. In later research, Hung et al. (Hung et al. 2010) found dry fluids could lead to a superheated state of vapor at the exit of the expander, reducing the network area in the TS diagram, as well as increasing the cooling load of the condenser.

The second law analysis of ORC systems indicate about 70~80% of exergy destruction occurs in evaporator and condenser (Saidur et al. 2012). The non-isothermal evaporation and condensation of zeotropic working fluids makes them ideal choice for better temperature profile match between heat source, sink and working fluid and thus reducing the exergy destruction and improving the efficiency of the ORC system. Zeotropic working fluids has gained much interest in last few years (Lecompte et al. 2014). Li et al. (2014) investigated the effect of mixture composition for various working fluids and concluded that there exist an optimum value of mixture composition corresponding to highest net power output. Heberle et al. (2012) performed the second law analysis of low temperature geothermal ORC system using zeotropic mixtures. The second law efficiency was improved by 4.3%. Dong et al. (2014) investigated the effect of mixture concentration, temperature glide, pressure ratio, and condensation pressure on first and second law efficiency. Most of the recent studies (Jung et al. 2015; Li et al. 2014; Liu et al. 2014; Zhao & Bao 2014) deal with parametric performance and exergy analysis of ORC system considering the simple modeling approach for evaporator and condenser.

Since zeotropic mixtures are considered superior to pure working fluids due to their non-isothermal evaporation and condensation. Therefore, design approach of evaporator and condenser as well as appropriate heat transfer and pressure drop correlations play key role in the accurate estimation of the potential of zeotropic mixture. Present study aims to investigate the potential of zeotropic mixtures for ORC application on the basis of cycle thermodynamic performance and economic assessment considering the detailed condenser and evaporator model.

2. SYSTEM DESCRIPTION

ORC system consist of evaporator, expander, condenser and a feed pump. The schematic of ORC system and TS diagram of the pure and zeotropic working fluid are show in Fig. 1.

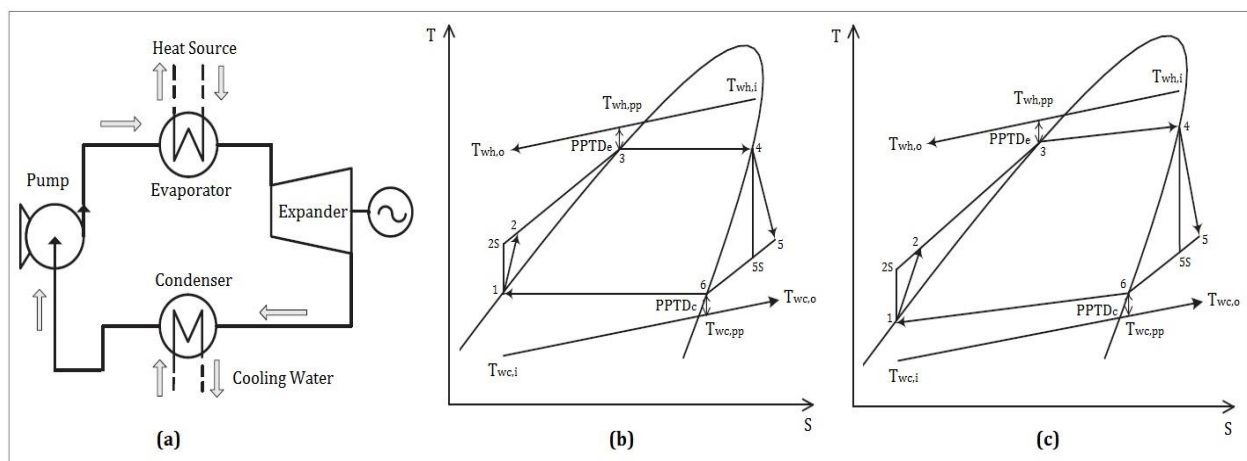


Figure 1: (a) Schematic of ORC (b) TS of pure working fluid (c) TS of zeotropic mixture

Two pure working fluids and their mixture has been considered in this study, detail of the working fluid and their characteristics are shown below in Table 1.

Table 1: Working fluid properties

Working Fluid		Physical Data				Environmental Data	
Name	Type	M (kg/kmol)	P _c (MPa)	T _c (C)	T _b (C)	ODP	GWP
Isopentane	Dry	72.15	3.380	187.2	27.8	0.00	20
R245fa	Dry	134.05	3.640	154.1	14.9	0.00	1030

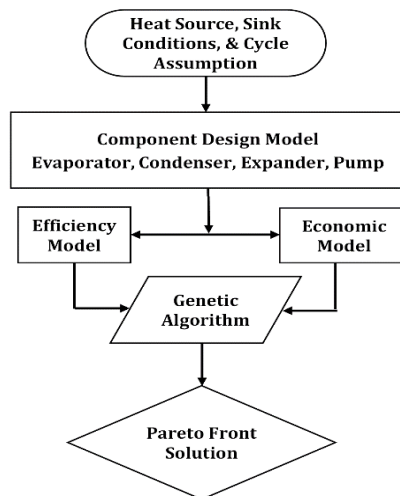
For ORC design & simulation, the heat source and sink conditions are presented in Table 2.

Table 2: Design conditions of orc system for modeling and simulation

Parameter	Value	Parameter	Value
Geothermal Water, Inlet Temperature	150 C	Cooling Water, Inlet Temperature	15 C
Geothermal Water, Inlet Pressure	5 bar	Pinch point Temperature, Evaporator	10 C
Geothermal Water, Mass Flow Rate	5 kg/s	Pinch point Temperature, Condenser	7 C
Isentropic Efficiency of Turbine	75%	Isentropic Efficiency of Pump	60%

3. THERMODYNAMIC MODELING

For complete ORC system modeling, an independent model of each component, evaporator, condenser, expander and working fluid pump are developed in MATLAB. Their inputs and outputs are connected to develop the single ORC model, consisting of two parts, exergy efficiency model and specific investment cost model. The ORC model is further optimized using multi objective genetic algorithm in MATLAB optimization environment. The results of each configuration of ORC system are compared at the optimum point. The detail layout of the complete model is presented in Figure 2.

**Figure 2:** Detailed Layout of the optimization approach

3.1 COMPONENT MODELING

3.1.1 Evaporator Model

The evaporator is divided into three parts, subcool, two phase and superheat section. The total area of the evaporator is given by

$$A = n \times A_p = n \times [L_p \times W_p] = n \times [(L_{sp} + L_{tp} + L_{sp}) \times W_p] \quad 1$$

The total number of thermal plates are known, the plate length for each section is calculated by log mean temperature approach, the calculation process is iterative and generalized layout of the design is presented in Fig. 3.

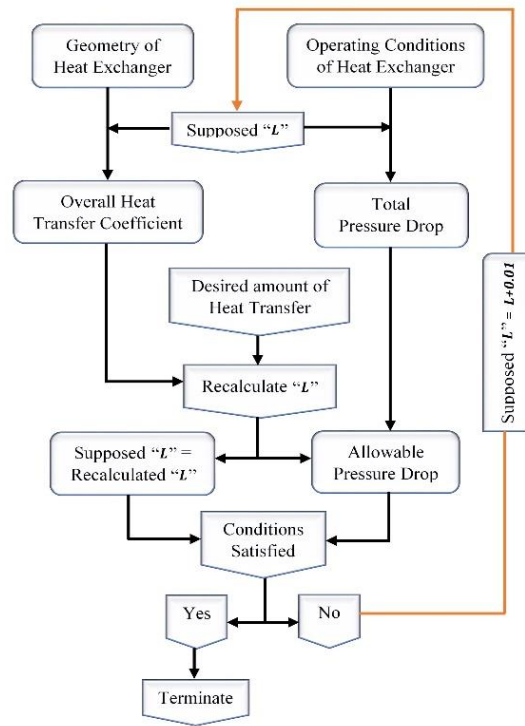


Figure 3: The design layout of plate heat exchanger

Initially, length of the plate is assumed and required plate length is recalculated based on the required amount of heat transfer, log mean temperature difference and overall heat transfer coefficient. The iterative process continues until the assumed length is equal to recalculated length.

Single Phase

The single phase Nusselt No. correlation for water in plate heat exchange is given by (Chisholm, D.; Wanniarachchi 1990)

$$Nu_w = 0.724 \left(\frac{6\beta}{\pi} \right)^{0.646} Re^{0.583} Pr^{0.33} \tag{2}$$

The single phase heat transfer coefficient for pure working fluids in plate heat exchanger (Hsieh & Lin 2002)

$$\alpha_{r,sp} = 0.2092 \left(\frac{k_f}{D_h} \right) Re^{0.78} Pr^{0.33} \left(\frac{\mu_m}{\mu_{wall}} \right)^{0.14} \tag{3}$$

For the zeotropic mixture, single phase heat transfer coefficient is estimated by Gnielinski correlation.

$$\alpha_{r,sp} = \frac{(f/8)(Re-1000)Pr}{1+12.7(f/8)^{0.5}(Pr^{2/3})} \quad \text{where as } f = [1.82 \log Re - 1.64]^{-2} \tag{4}$$

The plate length for single phase section is given by

$$L_{sp} = \frac{Q_{sp}}{U_{sp} \times LMTD_{sp} \times W_p \times n} \tag{5}$$

Two Phase

Since along the flow length of heat exchanger the vapor quality, temperature and concentration changes, therefore, control volume approach was adopted for evaporator modeling. The two phase section of evaporator is discretized and divided into N parts. The thermodynamic properties in each part are assumed constant and the variation in temperature difference is linear. The discretized temperature profile of two phase section of evaporator is shown in Fig. 4.

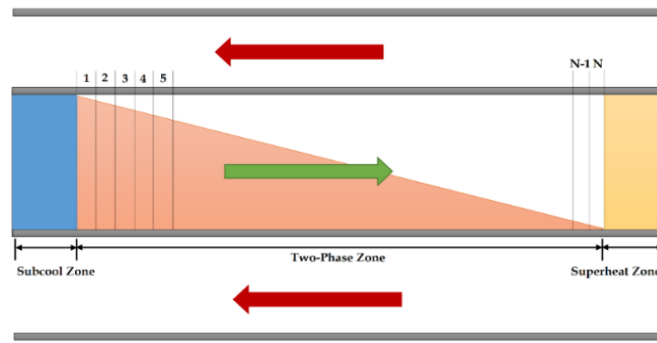


Figure 4: Control volume of two phase section of evaporator

The convective heat transfer coefficient for R245fa in plate heat exchanger (D. H. Han et al. 2003)

$$Nu = G_{e1} Re_{eq}^{G_{e2}} Bo_{eq}^{0.3} Pr^{0.4} \quad 6$$

where as

$$G_{e1} = 2.81 \left(\frac{P_{co}}{D_h} \right)^{-0.041} \left(\frac{\pi}{2} - \beta \right)^{-2.83}; G_{e2} = 2.81 \left(\frac{P_{co}}{D_h} \right)^{-0.082} \left(\frac{\pi}{2} - \beta \right)^{0.61} \quad 7$$

The equivalent Reynolds number and boiling number is given by

$$Re_{eq} = \frac{G_{eq} D_h}{\mu_f}; Bo_{eq,i} = \frac{q''}{G_{eq} \times i_{fg}}; G_{eq} = G \left[1 - x + x \left(\frac{\rho_f}{\rho_g} \right)^{0.5} \right] \quad 8$$

While two phase frictional factor is given by (D. H. Han et al. 2003)

$$f = G_{e3} Re_{eq}^{G_{e4}} \quad 9$$

where as

$$G_{e3} = 64710 \left(\frac{P_{co}}{D_h} \right)^{-5.27} \left(\frac{\pi}{2} - \beta \right)^{-3.03}; G_{e4} = -1.314 \left(\frac{P_{co}}{D_h} \right)^{-0.62} \left(\frac{\pi}{2} - \beta \right)^{-0.47} \quad 10$$

For the zeotropic mixture, two phase heat transfer coefficient is estimated by Jung's Correlation (Jung et al. 1989).

$$\alpha_{tp} = \frac{S}{c_{UN}} h_{UN} + C_{me} F h_l, S = \begin{cases} 4048 X_{tt}^{1.22} Bo^{1.13}, & \text{if } X_{tt} < 1 \\ 1 - 0.1 X_{tt}^{-0.28} Bo^{-0.33}, & \text{if } 1 < X_{tt} < 5 \end{cases}, C_{UN} = |1 + (b_2 + b_3)(1 + b_4)|(1 + b_5)$$

$$b_2 = (1 - X) \ln \left(\frac{1.01 - X}{1.01 - Y} \right) + X \ln \left(\frac{X}{Y} \right) + |Y - X|^{1.5}, b_3 = \begin{cases} 0, & \text{if } X \geq 0.01 \\ (Y/X)^{0.1} - 1, & \text{if } X < 0.01 \end{cases}, \quad 11$$

$$b_4 = 152(p/p_c)^{3.9}, b_5 = 0.92|Y - X|^{0.001}(p/p_c)^{0.66}, X/Y = 1, \text{ if } X = Y = 0$$

$$h_{UN} = \frac{1}{c_{UN}} \frac{h_1 h_2}{h_1 X_1 + h_2 X_2}, h_i = 207 \frac{k_i}{d} \left(\frac{q d_i}{k_i T_{sat}} \right)^{0.745} \left(\frac{\rho_c}{\rho_l} \right) Pr_l^{0.533}, d_e = 0.0146 \times 35 [2\sigma / (g(\rho_l - \rho_c))]^{0.5}$$

$$C_{me} = 1 - 0.35|Y - X|^{1.56}, F = 2.37 [0.29 + \frac{1}{X_{tt}}]^{0.85}, h_l = 0.023 \frac{k_l}{d} Re_l^{0.8} Pr^{0.4}$$

The plate length for two phase section is given by

$$L_{tp} = \frac{\sum_{i=1}^N Q_{(tp,i)}}{U_{(tp,i)} \times LMTD_{(tp,i)} \times W_p \times n} \quad 12$$

3.1.2 Condenser Model

The condenser model is similar to the evaporator model except the heat transfer correlation during condensation. For water side the heat same transfer correlations were used while for two phase condensation of pure working fluids is given by (D. Han et al. 2003).

$$Nu = G_{e5} Re_{eq}^{G_{e6}} Bo_{eq}^{0.3} Pr^{0.4} \quad 13$$

Where as

$$G_{e5} = 11.22 \left(\frac{P_{co}}{D_h} \right)^{-0.041} \left(\frac{\pi}{2} - \beta \right)^{-4.5}; G_{e6} = 0.35 \left(\frac{P_{co}}{D_h} \right)^{0.23} \left(\frac{\pi}{2} - \beta \right)^{1.48} \quad 14$$

For the zeotropic mixture, two phase condensation heat transfer coefficient is estimated by (Del Col et al. 2005).

$$\alpha_{tp} = \frac{\alpha_{f,m}\theta + (2\pi - \theta)\alpha_{c,m}}{2\pi}, \theta = \begin{cases} 0_{strat}, & \text{if } G < G_{strat} \\ 0_{strat} \left(\frac{G_{wavy} - G}{G_{wavy} - G_{strat}} \right)^{0.5}, & \text{if } G_{strat} < G < G_{wavy}, \alpha_{c,m} = \left(R_c + \frac{1}{\alpha_c} \right)^{-1} \\ 0, & \text{else} \end{cases}$$

$$\alpha_c = 0.003 \text{Re}_L^{0.74} \text{Pr}_L^{0.5} \frac{\lambda_L}{\delta} f_i, f_i = \begin{cases} 1 + \left(\frac{u_G}{u_L} \right)^{0.5} \left[\frac{(\rho_L - \rho_G)g\delta^2}{\sigma} \right]^{0.25}, & G > G_{strat} \\ 1 + \left(\frac{u_G}{u_L} \right)^{0.5} \left[\frac{(\rho_L - \rho_G)g\delta^2}{\sigma} \right]^{0.25} \frac{G}{G_{strat}}, & G < G_{strat} \end{cases} \quad 15$$

$$R_c = x C_{pG} \frac{\Delta T_{gl}}{\Delta h_m} \frac{1}{\alpha_G^0}, \alpha_G^0 = \alpha_G f_i, \alpha_G = \frac{\lambda_G}{d} 0.023 \text{Re}_G^{0.8} \text{Pr}_G^{0.33}$$

$$\alpha_{f,m} = F_m \left(R_f + \frac{1}{\alpha_f} \right)^{-1}, \alpha_f = 0.728 \left[\frac{\rho_L (\rho_L - \rho_G) g h_{LV} \lambda_L^3}{\mu_L d (T_{sat} - T_w)} \right]^{0.25}, R_f = x C_{pG} \frac{\Delta T_{gl}}{\Delta h_m} \frac{1}{\alpha_G}$$

$$F_m = \exp \left[-0.25 (1 - x) \left(\frac{G_{wavy}}{G} \right)^{0.5} \frac{\Delta T_{gl}}{T_{sat} - T_w} \right]$$

3.2 Energy & Exergy Analysis

Network and thermal efficiency of the ORC system is given by

$$W_{net} = \dot{m} [(h_4 - h_5) - (h_2 - h_1)] \quad ; \quad \eta_{thermal} = \frac{W_{net}}{Q_{evp}} \times 100 \quad 16$$

The physical exergy at i_{th} point of j_{th} component of ORC system is given by

$$\epsilon_{i,j} = \epsilon_{phy} = \dot{m} [(h - h_o) - T_o (s - s_o)] \quad 17$$

The exergy loss and exergy efficiency of the ORC component is shown in Table 3

Table 3: Exergy loss and exergy efficiency of orc components

Component	Available Exergy	Used Exergy	Exergy Loss	Exergy Efficiency
Pump	W_p	$\epsilon_2 - \epsilon_1$	$\epsilon_t = W_p - (\epsilon_2 - \epsilon_1)$	$\frac{\epsilon_2 - \epsilon_1}{W_p}$
Evaporator	$\epsilon_{wh,i} - \epsilon_{wh,o}$	$\epsilon_4 - \epsilon_2$	$\epsilon_e = (\epsilon_{wh,i} - \epsilon_{wh,o}) - (\epsilon_4 - \epsilon_2)$	$\frac{(\epsilon_4 - \epsilon_2)}{(\epsilon_{wh,i} - \epsilon_{wh,o})}$
Turbine	W_t	$\epsilon_4 - \epsilon_5$	$\epsilon_p = W_t - (\epsilon_4 - \epsilon_5)$	$\frac{\epsilon_4 - \epsilon_5}{W_t}$
Condenser	$\epsilon_5 - \epsilon_1$	$\epsilon_{wc,i} - \epsilon_{wc,o}$	$\epsilon_c = (\epsilon_5 - \epsilon_1) - (\epsilon_{wc,i} - \epsilon_{wc,o})$	$\frac{(\epsilon_{wc,i} - \epsilon_{wc,o})}{(\epsilon_5 - \epsilon_1)}$

The exergy efficiency of the system is given by

$$\eta_{exergy} = \frac{\sum \epsilon_{used}}{\sum \epsilon_{available}} = \frac{W_n}{\epsilon_e + \epsilon_p} \quad 18$$

4. ECONOMIC MODELING

Bare module cost method is one of the reasonable cost estimation approach for power plant equipment (Turton 2009) and has been used for cost estimation of ORC system as well (Imran et al. 2014; Wang et al. 2013). Generalized cost correlation of individual components ORC is given by

$$\text{Cost (\$)} = \frac{\text{CEPCI}_{2014}}{\text{CEPCI}_{1996}} \times F_S \times \hat{C}_b \times \{B_1 + (B_2 \times F_M \times F_P)\} \quad 19$$

Basic cost, \hat{C}_b , of the components is given by

$$\log \hat{C}_b = \{K_1 + K_2(\log Z) + K_3(\log Z)^2\} \quad 20$$

The pressure factor for heat exchanger is given by

$$\log F_p = \{C_1 + C_2(\log P) + C_3(\log P)^2\} \quad 21$$

Total cost, C_T is the sum of cost of evaporator, condenser, expander and working fluid pump. The specific investment cost (SIC) of ORC system is given by

$$\text{SIC} (\$/kW) = \frac{[C_T + OMC]}{[W_{net}]} \quad 22$$

Whereas OMC is operation and maintenance cost and is taken as 30% of total cost (Quoilin et al. 2011).

5. OPTIMIZATION APPROACH

The individual model of ORC components are connected in MATLAB with thermal and economic model. For pure and zeotropic working fluids, the ORC system was optimized for minimum specific investment and maximum exergy efficiency under logical bound of evaporation temperature, mass fraction of more volatile component and pinch point temperature in evaporator. The optimization was performed using multi objective genetic algorithm. The results of optimization of ORC system with pure and zeotropic working fluid are compared.

6. RESULTS AND DISCUSSION

There is trade off between exergy efficiency and specific investment cost so single value of decision variables cannot satisfy both objective functions simultaneously. Therefore, optimization results are presented in the Pareto Front form as shown in Table 4 and Fig. 5.

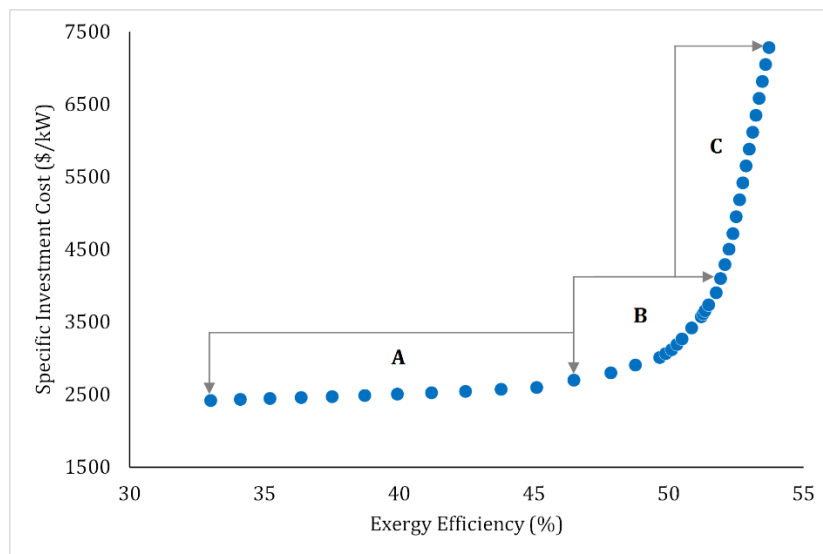


Figure 5: Pareto Front Solution of ORC system for zeotropic mixture

After the optimum operating point B, there is sharp increase in specific investment cost with slight increase in exergy efficiency. The optimization results in Table 3 shows that the exergy efficiency of ORC system with zeotropic mixture is 13.7% higher than ORC system with R245fa and 26.6% higher than R601a. From point A to point B the exergy efficiency has improved significantly with slight increase in specific investment cost, from point B to point C there is slight increase in exergy efficiency while there is sharp increase in specific investment cost. Point A present the low SIC and low efficiency, point C represent high SIC and high exergy efficiency, whereas point B shows the optimum range of exergy efficiency and SIC.

Table 4: Pareto Front Solution of ORC system with pure and zeotropic working fluids

Working Fluid	Optimized Parameters			Objective Functions		Cycle Performance	
	Mass Fraction	Evaporation Pressure	Pinch Pint Evaporator	Specific Investment Cost	Exergy Efficiency	Thermal Efficiency	Temperature Glide
	%	bar	C	\$/kW	%	%	C
R245fa	100	10.45	8.50	3692	44.73	8.79	0.00
R601a	100	6.15	9.20	3857	40.15	9.89	0.00
R245fa+R601a	40+60	8.45	8.25	3416	50.85	10.06	6.16

Based on the Pareto Front solution, under considered conditions an empirical correlation has been developed for specific investment cost.

$$SIC (\$/kW) = 0.078\eta^4 - 9.78\eta^3 + 403.13\eta^2 - 5403.38\eta \tag{23}$$

Empirical correlation is valid within given range of operating condition, and exergy efficiency

$$33\% \leq \eta_{ex} \leq 54\% \tag{24}$$

The exergy destruction for each working fluid is calculated at their optimum evaporation temperature and mass fraction. The exergy destruction and irreversibilities in ORC are shown in Fig. 6. The maximum exergy destruction occurs in evaporator and condenser, accounts more than 70% of total system exergy loss.

ORC system with zeotropic mixture has 21% less exergy destruction in evaporator and 28% less exergy destruction in condenser compare to ORC system with pure working fluid R601a and R245fa respectively.

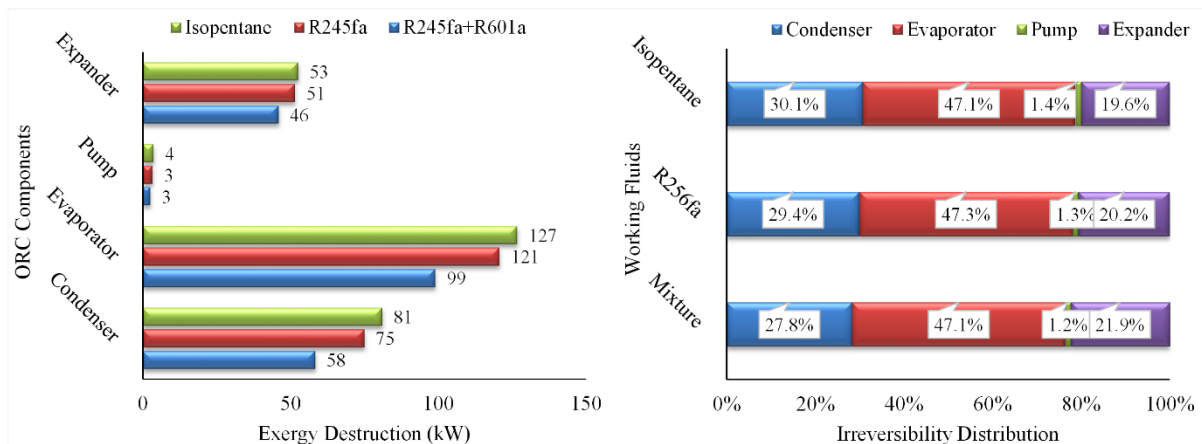


Figure 6: Exergy destruction of ORC components and irreversibilities distribution of ORC system

The effect of the evaporation temperature and mass fraction of more volatile component on exergy efficiency and specific investment has been estimated, as shown in Fig. 7.

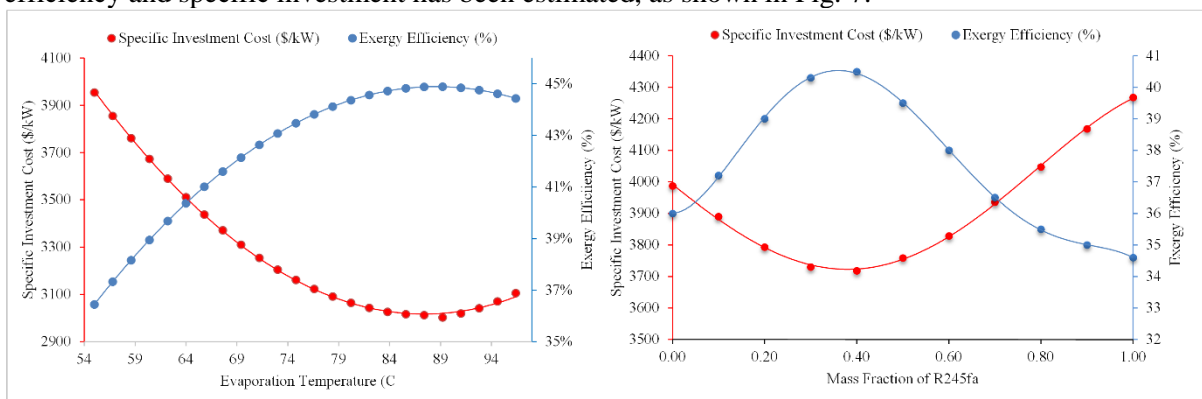


Figure 7: Effect of evaporation temperature and mass fraction of R245fa on exergy efficiency and SIC

With increase in evaporation temperature, the net power increase initially and after optimum evaporation temperature it start to decrease. As a result the SIC decrease with increase in evaporation temperature and after optimum evaporation temperature again start increasing. Since exergy efficiency is affected by both the net power output and total exergy destruction. Therefore exergy efficiency increases due to increase in net power and decrease in exergy destruction. However at elevated evaporation temperature the increase in exergy efficiency is not so sharp due to decrease in net power. There is an optimum value of mass fraction of more volatile component where the temperature glide is maximum and so the exergy efficiency and net power. At 40% mass fraction of R245fa the temperature glide was maximum, 6.16C, therefore, the exergy loss in evaporator and condenser was minimum. Similar trend was observed for net power of ORC system, the maximum power is observed at 40% mass fraction of R245fa. The net power decreased before and after the optimum value, 40%, of R245fa mass fraction. Therefore, the specific investment cost ORC system is minimum at optimum mass fraction of more volatile component R245fa.

Since the major advantage of zeotropic mixture is achieved in evaporator and condenser, therefor, for economic point of view, the evaporator and condenser area is estimated for each pure working fluid and zeotropic mixture. Under constant condensing temperature, degree of subcooling and turbine power, total heat transfer area of evaporator and condenser is estimated. Results of the comparison is shown in Table 5.

Table 5: Heat transfer area of evaporator & condenser

Component	Heat Transfer Area (m ²)		
	R245fa	R601a	R245fa-R601a
Evaporator	128	138	121
Condenser	141	144	126

7. CONCLUSIONS

Simulation study has been performed for the potential of zeotropic mixture application in ORC system and the results are compared with ORC using pure working fluids. Following conclusions can be drawn from the study. Due to non-isothermal evaporation and condensation, the exergy loss in evaporator and condenser is reduced considerably. The ORC system with zeotropic mixture has better exergy efficiency, 14.33% higher than ORC using pure working fluids. The overall exergy destruction has been reduced by 21% using the zeotropic mixture as working fluid. The composition of the mixture has an important effect on the ORC system performance, which is always associated with the temperature glide during the phase change of the mixture. Consequently, an optimal mixture concentration exists which maximizes the second law efficiency. For current study the optimum mass fraction of R245a is 40%. For constant condensing temperature, heat source amount and turbine power, required heat transfer area of evaporator and condenser using zeotropic mixture is relatively small compare to pure working fluids. The heat transfer area of evaporator and condenser has been reduced by 13% and 12% respectively. Although a number of studies have been conducted on zeotropic mixture but only limited experimental data is available about two phase heat transfer of zeotropic working fluids. Moreover the effect of composition shift has not been widely explored which is caused by the differential hold up in evaporator and condenser. Further experimentation of two phase heat transfer and data base of mixture properties is essential for accurate modeling of ORC system with zeotropic mixtures.

NOMENCLATURE

A	area, m ²	U	overall heat transfer coefficient, W.m ⁻² .K ⁻¹
B_o	boiling number	n	no. of thermal plates
CEPCI	chemical engineering plant cost index	Nu	Nusselt number
C_p	Specific Heat Capacity, J/kg.K	P	pressure, Pa
D_h	hydraulic diameter, m	Pr	Prandtl number
f	friction factor	q'	average heat flux, W.m ⁻²

G	mass velocity, $\text{kg}\cdot\text{m}^{-1}\cdot\text{s}^{-1}$	Q	heat transfer rate, kW
G_{start}	stratified flow transition mass velocity	Re	Reynolds number
G_{wavy}	wavy flow transition mass velocity	SIC	Specific investment cost, \$/kW
h	Specific Enthalpy, kJ/kg	T	temperature, °C
i_{fg}	enthalpy of vaporization, $\text{J}\cdot\text{kg}^{-1}$	x	liquid phase mass fraction
k	thermal conductivity, $\text{W}\cdot\text{m}^{-1}\cdot\text{K}^{-1}$	X_{tt}	Martinelli parameter
$LMTD$	Log mean temperature difference, °C	y	vapor phase mass fraction
\dot{m}	mass flow rate, $\text{kg}\cdot\text{s}^{-1}$		

Subscripts

eq	equivalent
f	liquid phase
g	vapor phase
p	plate
w	water
r	refrigerant side
sp	single phase
tp	two phase
f	liquid phase
g	vapor phase
w	water side

Greek Letters

β	chevron angle, degree
ϵ	Physical exergy, kJ
ρ	density, $\text{kg}\cdot\text{m}^{-3}$
μ	viscosity, $\text{kg}\cdot\text{s}^{-1}\cdot\text{m}^{-1}$
η	Efficiency
α	Heat transfer coefficient, $\text{W}/\text{m}^2\cdot\text{K}$
θ	Falling film angle

REFERENCES

- Bao, J. & Zhao, L., 2013. A review of working fluid and expander selections for organic Rankine cycle. *Renewable and Sustainable Energy Reviews*, 24, pp.325–342.
- Chen, H., Goswami, D.Y. & Stefanakos, E.K., 2010. A review of thermodynamic cycles and working fluids for the conversion of low-grade heat. *Renewable and Sustainable Energy Reviews*, 14(9), pp.3059–3067.
- Chisholm, D.; Wanniarachchi, A.S., 1990. 9. In *AICHE SPRING NATIONAL MEETING*. ORLANDO, FL.
- Del Col, D., Cavallini, a. & Thome, J.R., 2005. Condensation of Zeotropic Mixtures in Horizontal Tubes: New Simplified Heat Transfer Model Based on Flow Regimes. *Journal of Heat Transfer*, 127(3), p.221.
- Dong, B. et al., 2014. Analysis of zeotropic mixtures used in high-temperature Organic Rankine cycle. *Energy Conversion and Management*, 84, pp.253–260.
- Han, D., Lee, K. & Kim, Y., 2003. The characteristics of condensation in brazed plate heat exchangers with different chevron angles. *JOURNAL-KOREAN PHYSICAL SOCIETY*, 43(1), pp.66–73.
- Han, D.H., Lee, K.J. & Kim, Y.H., 2003. Experiments on the characteristics of evaporation of R410A in brazed plate heat exchangers with different geometric configurations. *Applied Thermal Engineering*, 23(10), pp.1209–1225.
- Heberle, F., Preißinger, M. & Brüggemann, D., 2012. Zeotropic mixtures as working fluids in Organic Rankine Cycles for low-enthalpy geothermal resources. *Renewable Energy*, 37(1), pp.364–370.
- Hsieh, Y.Y. & Lin, T.F., 2002. Saturated flow boiling heat transfer and pressure drop of refrigerant R-410A in a vertical plate heat exchanger. *International Journal of Heat and Mass Transfer*, 45(5), pp.1033–1044.

- Hung, T.C. et al., 2010. A study of organic working fluids on system efficiency of an ORC using low-grade energy sources. *Energy*, 35(3), pp.1403–1411.
- Hung, T.C., Shai, T.Y. & Wang, S.K., 1997. A review of organic rankine cycles (ORCs) for the recovery of low-grade waste heat. *Energy*, 22(7), pp.661–667.
- Imran, M. et al., 2015. Economic assessment of greenhouse gas reduction through low-grade waste heat recovery using organic Rankine cycle (ORC). *Journal of Mechanical Science and Technology*, 29(2), pp.835–843.
- Imran, M. et al., 2014. Thermo-economic optimization of Regenerative Organic Rankine Cycle for waste heat recovery applications. *Energy Conversion and Management*, 87, pp.107–118.
- Jung, D.S. et al., 1989. Horizontal flow boiling heat transfer experiments with a mixture of R22 / R114. *International Journal of Heat and Mass Transfer*, 32(1), pp.131–145.
- Jung, H.C., Taylor, L. & Krumdieck, S., 2015. An experimental and modelling study of a 1 kW organic Rankine cycle unit with mixture working fluid. *Energy*.
- Lakew, A.A. & Bolland, O., 2010. Working fluids for low-temperature heat source. *Applied Thermal Engineering*, 30(10), pp.1262–1268.
- Lecompte, S. et al., 2014. Exergy analysis of zeotropic mixtures as working fluids in Organic Rankine Cycles. *Energy Conversion and Management*, 85, pp.727–739.
- Li, Y.-R. et al., 2014. Potential of organic Rankine cycle using zeotropic mixtures as working fluids for waste heat recovery. *Energy*, 77, pp.509–519.
- Liu, B.T., Chien, K.H. & Wang, C.C., 2004. Effect of working fluids on organic Rankine cycle for waste heat recovery. *Energy*, 29(8), pp.1207–1217.
- Liu, Q., Duan, Y. & Yang, Z., 2014. Effect of condensation temperature glide on the performance of organic Rankine cycles with zeotropic mixture working fluids. *Applied Energy*, 115, pp.394–404.
- Quoilin, S. et al., 2011. Thermo-economic optimization of waste heat recovery Organic Rankine Cycles. *Applied Thermal Engineering*, 31(14-15), pp.2885–2893.
- Saidur, R. et al., 2012. Exergy analysis of solar energy applications. *Renewable and Sustainable Energy Reviews*, 16(1), pp.350–356.
- Saleh, B. et al., 2007. Working fluids for low-temperature organic Rankine cycles. *Energy*, 32(7), pp.1210–1221.
- Tchanche, B.F. et al., 2009. Fluid selection for a low-temperature solar organic Rankine cycle. *Applied Thermal Engineering*, 29(11-12), pp.2468–2476.
- Turton, R., 2009. *Analysis, Synthesis, and Design of Chemical Processes*, Prentice Hall. Available at: <http://books.google.com/books?id=YEJHAQAIAAJ>.
- Wang, J. et al., 2013. Multi-objective optimization of an organic Rankine cycle (ORC) for low grade waste heat recovery using evolutionary algorithm. *Energy Conversion and Management*, 71, pp.146–158.
- Zhao, L. & Bao, J., 2014. Thermodynamic analysis of organic Rankine cycle using zeotropic mixtures. *Applied Energy*, 130, pp.748–756.

ACKNOWLEDGEMENTS

The authors gratefully acknowledge the financial support provided by the Korea Institute of Energy Research and Korea University of Science and Technology (B4-5524).

INFLUENCE OF HEAT DEMAND ON TECHNO-ECONOMIC PERFORMANCE OF A BIOMASS/NATURAL GAS MICRO GAS TURBINE AND BOTTOMING ORC FOR COGENERATION

Sergio M. Camporeale^{1*}, Antonio M. Pantaleo²

¹Politecnico of Bari, Department of Mechanics, Mathematics and Management,
via Orabona 4, 70125 Bari, Italy
E-mail: sergio.camporeale@poliba.it

²University of Bari, DISAAT Department,
Via Amendola 165/A 70125 Bari, Italy
E-mail: Antonio.pantaleo@uniba.it

* Corresponding Author

ABSTRACT

This paper presents a thermo-economic analysis of small scale Combined Cycle power plant composed by a Micro Gas Turbine (MGT) and a bottoming Organic Rankine Cycle (ORC) for cogenerative application. For the topping cycle three different configurations are examined: 1) a simple recuperative micro gas turbine fuelled by natural gas, 2) an externally fired gas turbine (EFGT) with direct combustion of biomass, and 3) a dual fuel EFGT cycle, fuelled both by biomass and natural gas.

For the bottoming cycle, a saturated recuperative Rankine cycle is examined under two different condensation temperatures, in order to vary the ratio of heat to power generated. The research assesses the global energy efficiency and profitability of the different schemes, as a function of the thermal energy demand intensity, represented by the annual equivalent heat demand hours.

Keywords: CHP, microturbine, EFGT, ORC, biomass, dual fuel

1. INTRODUCTION

Small scale CHP (Combined Heat and Power) generation can contribute to a number of energy and social policy aims, such as the reduction of greenhouse gas (GHG) emissions and fossil fuel depletion, reduction of energy costs, increased decentralization of energy supply and improved energy security.

The use of biomass as an integrative energy source in natural gas fired plants has been widely addressed in literature [EC, 2009a,b; Franco and Giannini, 2005]. In small size range (50 kWe- 1 MWe), one interesting option is the use of dual fuel biomass/natural Micro Gas Turbines (MGT), in particular by means of Externally Fired Gas Turbines (EFGT) [Camporeale *et al.*, 2013]. A bottoming ORC could be coupled to the MGT in order to increase the electric efficiency of the system. The ORC are much more suited than conventional steam plants for small and micro generation from a few dozen to some hundreds kWe, because of the low enthalpy drop that allows a turbine expansion through few stages. There is a large literature on ORC cycles and in particular on the fluid selection for waste heat recovery applications (Chen *et al.*, 2010; Invernizzi *et al.*, 2011; David *et al.*, 2011). In the present work, different firing schemes are examined for the MGT: only biomass (B), only natural gas (NG) and dual fuel (B and NG) are considered as energy input and compared, as proposed in Pantaleo *et al.*, 2014 and Camporeale *et al.* 2014. The investment profitability is appreciated on the basis of thermo-economic methodologies [Pantaleo *et al.*, 2013, Al-Sulaiman *et al.*, 2013, Galanti *et al.*, 2013, Ferreira *et al.*, 2012, Pantaleo *et al.* 2014], with specific costs assessment proposed in [Pantaleo *et al.* 2013] and in light of the Italian policy measures for renewable energy and high efficiency CHP [Ministry Decrees, 2011, 2012].

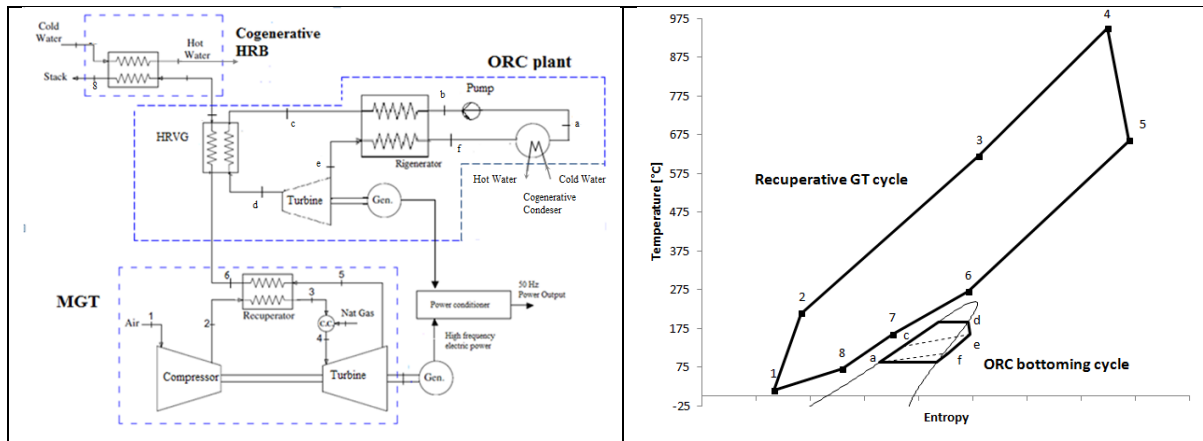


Figure 1 - MGT-ORC combined cycle for CHP generation, and related T-s diagram.

2. TECHNOLOGY OVERVIEW

2.1 Micro gas turbines fuelled by natural gas

Among distributed generation technologies, micro gas turbines (MGT) are expected to have steady growth in future energy systems, mainly for CHP applications. MGTs are typically single-shaft engines (Fig. 1), where compressor, turbine and electric generator have a common shaft rotating at high speed (typically between 60,000 and 90,000 rpm [Rosa do Nascimento *et al.*, 2013]). The high-frequency current from the generator is converted to grid frequency by an inverter, which enables variable-speed operation [Hamilton, 2003]. The turbine inlet temperatures (TIT) are typically in the range 800–1,000 °C, since no blade cooling systems are adopted, while the pressure ratio is low (3.5-5). A surface regenerative heat exchanger (recuperator) is used to increase the electric efficiency that can reach values of 30%. The turbine outlet temperature TOT is about 500-650°C, hence the material costs for the recuperator can be kept at a reasonable level. The total energy efficiency of a CHP-MGT is in the range 70–80%, and is influenced by the temperature of heat demand.

2.2 Externally fired micro gas turbines fuelled by biomass

Since several years, the use of biomass in MGT is considered a profitable option [Oberberger, 1998] for renewable energy production, however one of the key technical issues is the fuel quality. The EFGT cycle presents the advantages of gas turbines (low operational costs, high lifetime and reliability, relatively high energy efficiency even at small size) and the capability of using low quality biofuel. In the conventional scheme of an EFGT, the biomass is fed to an external furnace together with hot air coming from the turbine exhaust, and the turbine is fed by hot compressed air, heated in a high temperature heat exchanger (HTHE) to the required TIT by the hot gas of the biomass combustion. In this work, the following scheme has been selected: external combustion of biomass in a furnace, and heating of the MGT cycle working fluid (air) by means of a surface heat exchanger.

2.3 Natural gas/biomass dual fuelling

The external combustion of biomass combined with direct combustion of natural gas (often referred as “dual-fuel” or “cofiring”) is a promising, cost-effective and reliable small scale generation system, that offers plant flexibility, high conversion efficiency and possibility to use commercially available components. In conventional EFGT cycle the turbine inlet temperature is limited by material of the HTHE to 850–900 °C [Riccio *et al.* 2009; Yan and Eidensten, 2000; Ferreira and Pilidis, 2001; Knoef, 1998; Soltani *et al.*, 2013; Evans and Zaradic, 1996; Savola *et al.*, 2005; Cocco *et al.*, 2006; Riccio *et al.*, 2000, Camporeale *et al.*, 2014]. For this reason, a dual fuel configuration (biomass-natural gas) is investigated. With the internal combustion the TIT can reach a maximum TIT of about 950° compatible with the metal of the turbine blades, and consequently a higher efficiency and power output of the conversion process, with respect to only biomass input.

Table 1. Technical parameters for the topping MGT (AE Turbec T100, 2015)

Case study	Unit	100% NG	50-50% NG-B	100% B
Net electric power output (ISO)	kW	100.1	89.6	77.5
Turbine Inlet Temperature	°C	950	950	900
Energy input	kW	332.9	373.4	404.0
Net electric-efficiency. ISO	%	30.1	24.0	19.2
Gas temperature at turbine exit	°C	652.7	656.4	609.0
Exhaust gas temper. (recuperator exit.)	°C	270	272	262
Air mass flow rate	kg/s	0.7833	0.7833	0.7833

2.4 MGT+ORC combined cycles

The use of combined cycle schemes can increase the electric efficiency on respect to either two plants that compose the combined cycle. In this work, we consider a combined cycle composed by a MGT as topping cycle and an ORC as bottoming cycle, which converts part of the heat from the exhaust gas in useful work (Fig.1). In this scheme, the exhaust gas exiting the gas turbine is conveyed to a heat recovery heat exchanger that heats the organic fluid from liquid to saturated vapor or superheated vapor, depending on the chosen ORC cycle. It is composed by an economizer, an evaporator and, if present, a superheater. In analogy to gas-steam combined cycles, it is called Heat Recovery Vapor Generator (HRVG). In the HRVG, the organic fluid is brought to the thermodynamic condition requested for the admission in the turbine, while, on the other side, the gas exiting the HRVG has still a temperature suitable for cogeneration. Such heat is recovered in a cogenerative HRB where the gas can be cooled to a temperature that depends on the fluid temperature requested by the industrial or residential users. In the adopted configuration, a minimum gas temperature of 80°C is adopted. This limit can be applied either to MGT fuelling natural gas or EFGT fuelling biomass. In fact, in the adopted configuration of the biomass furnace, the products of biomass combustion do not contaminate the gas that flows across the turbine.

The bottoming cycle is an ORC in a recuperative configuration (Fig. 1). We considered the use of “dry fluids” that are characterized by a dry expansion in the turbine, avoiding drop generation that can damage turbine blades [Chen *et al.*, 2010]. In particular, the cycle contains a pump (a-b) that supplies the fluid to the recuperator (b-c). The recuperator pre-heats the working fluid using the thermal energy from the turbine outlet. The evaporator produces the evaporation of the organic fluid up to the requested condition, by recovering the heat from the topping cycle (c-d). Thus, the vapor flows in the turbine (d-e) connected to a high-speed electric generator. At the exit of the turbine, the organic fluid goes to the hot side of the recuperator (e-f) where it is cooled to a temperature a little higher than the condensation temperature. Finally, the condenser closes the ORC cycle (f-a). Two options are investigated for the condensation temperature:

- Option ORC1: low condenser temperature (40°C), Figure 2.(a); in this case the electric efficiency of the bottoming cycle is higher, but heat rejected by the ORC cannot be used for cogeneration;
- Option ORC2: high condenser temperature (100°C), Figure 2(b); in this case, the ORC output is lower, but the heat rejected at the condenser is useful for residential heating.

In both options, useful heat can be also recovered from the gas at the exit of the HRVG.

For the ORC cycle, considering that the exhaust gas temperature at the gas turbine outlet (recuperator exit) is 270°C, siloxanes and toluene are examined as suitable working fluids. The choices of thermodynamic parameters of the ORC cycle are related to the temperature of the heat to be recovered. In particular, turbine inlet temperature and evaporation pressure are the most influential properties. In relation to the choice of the evaporation pressure, p_{ev} , and of the maximum ORC cycle temperature, it is possible to examine saturated, superheated and supercritical cycles. A detailed discussion of the optimization of the cycle parameters can be found in [He *et al.* 2009; Kusterer *et al.* 2010]. Here some results can be summarized. The higher is the evaporation pressure in supercritical and subcritical cycles, the higher is the cycle efficiency. However, when the critical temperature is close to the heat source temperature, lower heat recovery efficiency is found. Furthermore, these cycles are characterized by high inlet / outlet turbine volumetric ratio. Therefore, the advantages of ORC cycles with very high-pressure levels are limited. For the above reasons, a simple recuperative ORC cycle is examined with a hexa-methyl-disiloxane “dry fluid”.

Table 2. Technical parameters for the bottoming ORC cycles (topping cycle MGT fuelling NG)

Description	Unit	ORC 1	ORC 2
Evaporation pressure	bar	8	8
Turbine inlet temperature	°C	192	192
Condenser temperature	°C	40	90
Available Thermal Flow from exhaust gas, \dot{Q}_{av}	kW	199.7	199.7
HRVG Heat flow, \dot{Q}_{rec}	kW	105.0	95.2
Heat recovery ratio, χ	%	52.6	47.8
Electric power output, $P_{e,ORC}$	kW	20.0	11.4
Cycle Efficiency, η_L	%	19.9	11.9
Overall efficiency as recuperative cycle, η_{rec}	%	10.0	5.7
Heat rejected from condenser	kW	83.44	79.4

3. PERFORMANCE ANALYSIS

The biomass/natural gas energy input ratio has been varied and the following schemes of the topping cycle have been examined: 100% of natural gas (NG), dual fuel scheme with 50% of energy input from biomass and 50% from natural gas (DF) and, finally, 100% of energy input from biomass (B). Thermodynamic simulations have been carried out by means of Gate-Cycle® software for the MGT and Cycle-Tempo® for the ORC section. Gate Cycle is a commercial software for thermal power plants including gas turbines, steam and combined cycles plants [<https://gettotalplant.com/GateCycle>, 2015]. The Cycle Tempo software is used for thermodynamic cycles and in particular organic and other non conventional fluids [<http://www.asimptote.nl/software/cycle-tempo/>, 2015]. Both the codes have been tested and validated by the authors. In the following, the methodologies for: (i) energy balances and efficiency analysis, (ii) primary energy savings and profitability of investment are reported.

3.1 First Law analysis and Definitions

All calculations are performed for ISO standard conditions (15 °C, 1.013 bar and 60% relative humidity). Based on the cycle thermodynamic analysis, the following equations are used to evaluate the net electric power output (P_e), the total thermal power input ($\dot{E}_{in,tot}$), electric efficiency (η_e), thermal power supplied to hot water for cogeneration (\dot{Q}_{th}), thermal efficiency (η_{th}), total (“first law”) efficiency for CHP generation (η_{CHP}).

The overall electric efficiency of the combined cycle $\eta_{e,cc}$ is reported in (1), where $P_{e,cc}$ is the electric power output of the combined cycle as reported in (2).

$$\eta_{e,cc} = \frac{P_{e,cc}}{\dot{E}_{in,tot}} \quad (1) \quad P_{e,cc} = P_{e,GT} + P_{e,ORC} \quad (2)$$

The energy input is due to the combustion of NG and biomass according to (3).

$$\dot{E}_{in,tot} = \dot{E}_{in,NG} + \dot{E}_{in,biom} = \dot{m}_{NG}LHV_{NG} + \dot{m}_{biom}LHV_{biom} \quad (3)$$

The energy performance of the bottoming cycle is evaluated from (i) the “internal thermal efficiency” of the bottoming cycle η_L of eqn (4), being $P_{e,ORC}$ the power output of the bottoming cycle and \dot{Q}_L the heat input to the bottoming cycle (heat recovered in the HRVG), and (ii) the “heat recovery ratio” or “HRVG efficiency χ , defined as the ratio between heat recovered \dot{Q}_L and heat rejected from the topping cycle \dot{Q}_{HR} .

$$\eta_L = \frac{P_{e,ORC}}{\dot{Q}_L} \quad (4) \quad \chi = \frac{\dot{Q}_L}{\dot{Q}_{HR}} \quad (5)$$

The heat rejected is here the sensible heat of the gas exiting the gas turbine, which is the theoretically available if the gas were cooled to the ambient temperature. Due to this reason, \dot{Q}_{HR} is also called “heat available” and indicated as \dot{Q}_{av} . The heat exchanged \dot{Q}_L in the HRVG, is evaluated in Eq.(6) from gas the temperature drop ($T_6 - T_7$), the mass flow rate \dot{m}_g exhausted by the gas turbine and the average specific heat $c_{p,g}$ of the exhaust gas. The available heat is given by Eq. (7).

$$\dot{Q}_L = \dot{m}_g c_{p,g}(T_6 - T_7) \quad (6) \quad \dot{Q}_{av} = \dot{m}_g c_{p,g}(T_6 - T_{amb}) \quad (7)$$

The overall efficiency of the bottoming cycle η_{rec} is defined as the ratio between $P_{e,ORC}$ and the heat rejected from the topping cycle \dot{Q}_{av} . From the above definitions,

$$\eta_{rec} = \frac{P_{e,ORC}}{\dot{Q}_{av}} = \chi \cdot \eta_L. \quad (8)$$

The maximum power output for the combined cycle is obtained when the product of η_L and χ is maximum. The exhaust gas exiting the evaporator has still enthalpy level suitable for cogeneration. The heat that can be recovered in the cogenerative HRB can be evaluated from the temperature drop ($T_7 - T_8$) of the exhaust gas. In this work, we assume a minimum temperature of 50°C for the return water from residential users. Therefore, assuming $\Delta T_{min} = 20^\circ\text{C}$, the minimum exhaust gas temperature $T_8 = 70^\circ\text{C}$ and the heat rate recovered can be evaluated from

$$\dot{Q}'_{th} = \dot{m}_g c_{p,g}(T_7 - T_8). \quad (9)$$

Useful heat for residential users can be recovered also from the condenser of the ORC plant, if the condensation temperature is sufficiently high. Assuming $\Delta T_{min} = 20^\circ\text{C}$, a condensation temperature of 90°C can be adopted. In this case, the heat flux rejected from the ORC plant is fully available for cogeneration,

$$\dot{Q}''_{th} = \dot{m}_v (h_f - h_a), \quad (10)$$

where \dot{m}_v is mass flow rate of organic fluid and $(h_f - h_a)$ is the enthalpy drop of the organic fluid across the condenser. The total thermal heat recovered for cogeneration is the sum of the heat recovered from exhaust gas and recovered from the heat rejected from the condenser

$$\dot{Q}_{th} = \dot{Q}'_{th} + \dot{Q}''_{th} \quad (11)$$

In the other case of condensation temperature lower than the temperature requested for cogeneration, the heat flux rejected by the ORC condenser is wasted to the environment. In this last case $\dot{Q}''_{th} = 0$. The instantaneous values of thermal efficiency, η_{th} , and first law (total heat and power) efficiency, η_{CHP} , of the plant, can be evaluated as

$$\eta_{th} = \frac{\dot{Q}_{th}}{\dot{E}_{in,tot}} \quad (12) \quad \eta_{CHP} = \eta_{e,CC} + \eta_{th} = \frac{P_{e,CC} + \dot{Q}_{th}}{\dot{E}_{in,tot}} \quad (13)$$

The energy performance of the plant has to be evaluated over the annual production of electric and useful thermal energy output, considering the annual fuel energy consumption. In this work, energy and economic evaluation are carried out under the hypothesis of baseload operation

$$E_{e,CC} = \int_0^{t_{an.}} P_{e,CC} dt, \quad E_{th} = \int_0^{t_{an.}} \dot{Q}_{th} dt, \quad E_{in,tot} = \int_0^{t_{an.}} \dot{E}_{in,tot} dt. \quad (14)$$

The annual averaged first law (total heat and power) efficiency is then

$$\bar{\eta}_{CHP} = \frac{E_{e,CC} + E_{th}}{E_{in,tot}}. \quad (15)$$

3.2 IFGT and EFGT gas turbine models

The natural gas fired IFGT simulation (case 1) is based on the MGT Turbec T100 having a maximum power output of 100 kWe when fuelling natural gas (AE-T100 data sheet, 2015). A recuperator is used to raise the net electric-efficiency from 16% of the simple cycle gas turbine to 30% of the recuperative Joule-Brayton cycle. The design hypotheses for these sections of the plant are described in [Pantaleo *et al.*, 2013]. The main performance data are in Table 1. In the case of dual combustion of biomass and natural gas, an EFGT scheme is adopted. The biomass feeds the external furnace while combustion air

is pre-heated in a dedicated heat exchanger, which recovers heat from exhaust combustion gas. Details of the EFGT scheme can be found in Pantaleo *et al.* (2013) and Camporeale *et al.* (2014). It should be noted that the combustion air is conveyed in the furnace by a fan independently from the gas flowing in the turbine. In this case, no dirty gas flows at the exhaust of the turbine, hence facilitating cogeneration and increasing the flexibility of input fuel, which could be particularly important in case of seasonal biomass availability. The results of the energy analysis reported in Table 3 (case A) show that option of 100% biomass fired EFGT is affected by a de-rated electric power on respect to option of 100% NG fired IFGT. The main causes are related to: (i) lower TIT (reduced to 900°C from the original 950°C of the turbine fuelled by NG,) and (ii) power absorbed by the fan of the furnace and the other auxiliaries.

Table 3. Energy performance of the different examined case studies.
Fuel type: NG: natural gas; DF: dual fuel natural gas/biomass; B: biomass

Description	Unit	MGT cogeneration			MGT + ORC 1 no cogeneration			MGT+ORC 1 cogeneration			MGT- ORC 2 cogeneration		
		NG	DF	B	NG	DF	B	NG	DF	B	NG	DF	B
Electric power output	kW	101.9	93.7	85.0	121.77	113.8	105.0	119.0	111.3	102.4	110.4	102.5	93.7
Thermal input	kW	332.2	348.6	366.4	332.2	348.6	366.4	332.2	348.6	366.4	332.2	348.6	366.4
Cogenerated Heat flux	kW	165.0	163.2	160.8				57.2	56.5	55.6	148.6	143.2	137.9
Electric efficiency	%	30.7	27.0	23.2	36.6	32.8	28.6	35.8	31.9	28.0	33.2	29.4	25.6
Thermal efficiency	%	49.7	46.8	43.9				17.2	16.2	15.2	44.7	41.1	37.6
CHP efficiency	%	80.3	73.7	67.1				53.0	48.1	43.1	77.9	70.5	63.2

3.3 Performance of ORC bottoming cycle

The topping cycle supplies exhausted gas (case NG, case DF) or air (case B) to the bottoming cycle at 270°C (262 °C in the case B, that is, 100% biomass), hence the suitable working fluid can be chosen among siloxanes. In particular, hexamethyldisiloxane –MM- with a critical temperature of 245.6°C has been chosen. From a previous analysis, where saturated, superheated and supercritical cycles were compared, the saturated cycles are considered the best choice. The evaporation pressure of 8 bar is selected in order to have a good electric power output with acceptable turbine volume ratio. The isentropic and mechanical efficiencies of the pump are set to 0.75 and 0.86, respectively, while turbine isentropic and mechanical ones are set to 0.8 and 0.96. A pressure drop of 2 kPa is assumed in all the heat exchangers.

Let us consider first the ORC cycle (indicated by “ORC-1”) with a condensation temperature of 40°C. The following discussion is referred to calculations carried out considering a MGT fuelling NG as topping cycle. From Table 2, it appears that about 53% of the available heat is recovered in the HRVG. The efficiency η_L of the bottoming cycle is about 20% that is relatively high if one considers that the maximum cycle temperature is 192°C. The overall efficiency η_{rec} of the bottoming cycle in such configuration is about 10 %. In this case, heat rejected from condenser is not useful for cogeneration but heat can be recovered from exhaust gas exiting the HRSG.

Then, let us consider the ORC cycle (indicated by “ORC-2”) with a condensation temperature of 90°C. From Table 2, it appears that about 48% of the available heat is recovered in the HRVG (5% less than ORC-1), while the efficiency η_L of the bottoming cycle is 11% that is about the half of the previous case due to the higher condensation temperature. The overall efficiency η_{rec} of the bottoming cycle in such configuration becomes about 6 %. In this case, heat flux rejected from condenser, about 80 kW, is useful for cogeneration as well as heat from exhaust gas of the HRVG.

About identical results are obtained with a dual-fuel MGT, since the temperature of the gas exiting the topping cycle is about the same (272°C) while some difference are obtained with MGT fuelling only biomass due to the lower temperature at the recuperator exit (262°C). A complete description of the combined cycle MGT+ORC under the different configurations is given in Table 3, where the performance of the gas turbine alone is also reported. The performance is examined for the MGT under cogeneration configuration while the combined cycle is examined under either only electric power production or cogeneration.

It appears that the combined cycle allows for a significant increase of the power output in all the cases with condensation temperature $T_c = 40^\circ\text{C}$, with an increase of the overall electric efficiency of about 5-6 %. However, there is a relevant reduction of the thermal efficiency η_{th} that drops from much more than 40% of the MGT alone to about 16% for the combined cycle: this is due to the utilization of the exhaust gas heat for the bottoming cycle. In the cases of combined cycle with ORC condensation temperature $T_c = 90^\circ\text{C}$, the electric efficiency is 3% higher than the simple MGT, but there is a low decrease of thermal efficiency with respect to the MGT, thanks to the utilization of the heat flux rejected from condenser. These results will be examined in the next section in order to identify the relative profitability and attractiveness of the different plant configurations.

4. Thermo economic methodology

The aim of the methodology is to provide a preliminary assessment of the global energy efficiency and profitability of the selected plant configurations as a function of the heat demand for cogeneration. For this purpose, the scenario of a baseload plant operation is assumed, with all electricity fed into the grid and cogenerated heat delivered to the load (50-70°C). The intensity of heat demand is taken into account by means of the equivalent hours of thermal energy consumption per year h_r , neglecting transients and part load efficiency. Further CHP operating strategies, including part load operation, can be found in previous works [Pantaleo *et al.* 2013, Camporeale *et al.*, 2014, 2015]. The plant is operated at rated power for the maximum number of hours compatible with maintenance (7,500 hr/year). The revenues from electricity are in the form of fixed guaranteed remuneration (for the natural gas-based fraction) and feed-in tariff [Ministry Decree, 2012] (for the biomass-based fraction), including white certificates for the quota of natural gas based high efficiency cogenerated energy [Ministry Decree, 2011]. In the case of only biomass fuel, this operating strategy is the most profitable one, since the feed-in price for biomass electricity is higher than the cost of electricity supply. The reason is that, according to Italian RES subsidy mechanism [Ministry Decree, 2012], only renewable electricity fed into the grid is eligible for feed-in tariff, while on-site electricity is not subsidized. However, in case of natural gas based electric generation, matching on site electric demand before feeding the excess to the grid could be more profitable, as resulting from [Pantaleo *et al.*, 2014a]. The calculation of incentives available for high efficiency cogeneration (HEC) is based on the assessment of the primary energy saving PES of the CHP plant, according to the procedures described in [Pantaleo *et al.*, 2013a, 2014b].

4.1 Financial appraisal

The financial appraisal of the investment is carried out assuming the following hypotheses: (i) 20 years of operating life; no 're-powering' throughout the 20 years; zero decommissioning costs; (ii) maintenance costs, fuel supply costs, electricity and heat selling prices held constant (in real 2015 values); (iii) duration of feed-in tariff for biomass electricity of 20 years and duration of HEC incentive for gas cogeneration of 10 years (as stated by the 'white certificates' mechanism, which also includes a multiplicative coefficient of 1.4 [Ministry Decree, 2011]); (iv) capital assets depreciated using a straight line depreciation over 20 years; (v) cost of capital (net of inflation) equal to 8%, corporation tax neglected, capital costs and income do not benefit from any support.

4.2 Costs and revenues assessment

The turnkey capital cost, including storage and civil work costs of the biomass section, is assumed from [Pantaleo *et al.*, 2013]. The cost of gas turbine recuperator is calculated assuming the maximum metal temperature of 1,000 °C and the use of Ni-Cr 40-20 alloy. The costs of ORC turbines vary in a wide

range depending on the technology. In this work, after personal interviews to ORC turbine manufacturers, a cost of 100 and 60 kEur is assumed for the 20 and 12 kW bottoming ORC turbine.

Table 4. Fuel consumption of the MGT plant with different configurations, CAPEX and OPEX of the investment, assuming baseload operation mode. NG: natural gas fuel; DF: dual fuel 50% natural gas and 50% biomass (referred to energy input); B: biomass

Fuel	Configuration	Fuel consumption		CAPEX (kEur)	OPEX (kEur/y)
		NG (Nm ³ /y)	Biom (t/y)		
NG	MGT+CHP	225,575	0	188	99.4
	MGT+ORC 1 without CHP ($T_c=40^\circ\text{C}$)			278	101.2
	MGT+ORC 1 + CHP ($T_c=40^\circ\text{C}$)			288	100.9
	MGT+ORC 2 + CHP ($T_c=90^\circ\text{C}$)			240	100.2
DF	MGT+CHP	118,352	312	289	83.2
	MGT+ORC 1 without CHP ($T_c=40^\circ\text{C}$)			379	85.3
	MGT+ORC 1 + CHP ($T_c=40^\circ\text{C}$)			389	85.1
	MGT+ORC 2 + CHP ($T_c=90^\circ\text{C}$)			349	84.2
B	MGT+CHP	0	657	470	65.0
	MGT+ORC 1 without CHP ($T_c=40^\circ\text{C}$)			560	67.4
	MGT+ORC 1 + CHP ($T_c=40^\circ\text{C}$)			570	67.1
	MGT+ORC 2 + CHP ($T_c=90^\circ\text{C}$)			530	66.1

Table 5. Electricity and heat selling prices; the feed-in tariff for biomass electricity includes remuneration for electricity fed into the grid and the subsidy; the white certificate is issued for primary energy saved through natural gas fuelled high efficiency CHP

Parameter	Eur/MWh
Natural gas electricity price PE_{NG}	150
Bio-electricity feed-in price PE_b	287
White certificate price	8.14
Thermal energy price PT_t	40

The fuel cost is assumed of 80 Eur/t and 40 cEur/Nm³ respectively for biomass and NG. These figures are obtained from market prices for wood chips in the Italian market and data from Italian Energy Authority for natural gas price for use in CHP plants (in this case, low tax rates apply in comparison to heating use) [Pantaleo *et al.*, 2013]. The O&M costs depend on the technology generation, the type of service and the capacity factor. In this work, the estimated O&M costs are 12 Eur/MWh for natural gas based electricity and 16 Eur/MWh for biomass based electricity, on the basis of global service contracts proposed by manufacturers of these small scale CHP plants to final customers. Biomass ash discharge costs are 70 Eur/t. In the case of biomass electricity generation, a plant self-consumption of 5% of generated electricity is assumed, which takes in account the energy consumption for biomass handling and furnace operation. The reference thermal and electrical efficiencies, to calculate the primary energy savings, are respectively 90% and 45.15% [Ministry Decree, 2011]. Table 4 summarizes the fuel consumption of the MGT with different fuels and the CAPEX and OPEX of the investments. The heat and electricity selling prices and the incentives for biomass electricity and HEC are reported in Table 5. The natural gas electricity price and the thermal energy price are estimated assuming the scenario of on site generation to match the heat and power demand of a block of residential buildings in the Italian energy market. In particular, the avoided electricity and thermal energy costs for residential end users are considered, assuming statistical data of electricity and natural gas costs from Italian Authority of Energy (AEEG, 2015) without taxes. In the case of thermal energy, the selling price is defined assuming

a reference scenario of natural gas based heating system (average thermal energy cost of 80 Eur/MWh) and a discount of 50% to incentivize customer to connect to the heating network of the CHP plant.

5. RESULTS AND DISCUSSION

5.1 Energy performance assessment

The first law cogenerative efficiency, $\bar{\eta}_{CHP}$, vs the equivalent hours of thermal load is reported in Figure 3. The plant configurations under investigation are: only MGT with cogeneration (MGT-cog), MGT+bottoming ORC and low T_C without cogeneration (MGT+ORC1), MGT + bottoming ORC with cogeneration and low T_C (MGT+ORC1-cog) and MGT + bottoming ORC with cogeneration and high T_C (MGT+ORC2-cog). These configurations are examined considering different input fuel mixes (natural gas, dual fuel and biomass). The following main conclusions can be drawn:

1. Input fuel: the use of natural gas presents the best energy performances, because of the higher conversion efficiency of the thermodynamic cycle on respect to the case of biomass;
2. Thermodynamic cycle: the use of bottoming ORC and low condensation temperature does not increase the global efficiency of the system (in particular at high heat demand levels) since, despite the higher electric efficiency of cases MGT+ORC1 with and without cogeneration, the cogenerated heat is lower (case MGT+ORC1-cog) or equal to zero (MGT+ORC1) on respect to case MGT-cog or MGT+ORC2-cog. At high energy demand levels (equivalent heat demand hours respectively above 4,000 – 3,500 and 3,000 for natural gas, dual fuel or biomass feed configurations) the use of only MGT presents higher global energy efficiency than the bottoming ORC2. However, the operating strategy to switch off the bottoming ORC during high heat demand periods, so increasing the cogenerated heat, could improve the energy performance (Pantaleo et al, 2015).

6.2 Profitability assessment

The internal rate of return (IRR) and net present value (NPV) of the investments are reported in Fig 4 and 5. The following considerations can be drawn:

1. Fuel mix: the dual fuel option presents the highest IRR, as a result of the trade-off between energy efficiency decrease and investment cost/electricity revenues increase when increasing biomass use; on the contrary, the option of only biomass input fuel presents the highest NPV, as a result of the highest investment cost of this technology, balanced by the highest revenues from electricity sales (mainly because of the high feed-in tariff available for biomass electricity);
2. System configuration: the bottoming ORC reduces the IRR of the investment in the case of natural gas fuel on respect to only MTG, even at high heat demand levels (where the bottoming ORC2 presents on the contrary the highest energy performance); this is not valid for the NPV and in the case of biomass fuel, where, at high energy demand levels, the case MGT+ORC2-cog presents higher NPV than case MGT-cog. On the contrary, at low heat demand levels and with dual fuel or only biomass options, the bottoming ORC cycle presents higher IRR than the only MGT option; this is due to the different electricity price for natural gas and biomass; in particular, and the higher ORC investment cost and reduced income from heat sale (less o no cogenerated heat) does not balance the increased revenues from electricity sale when using natural gas fuel.

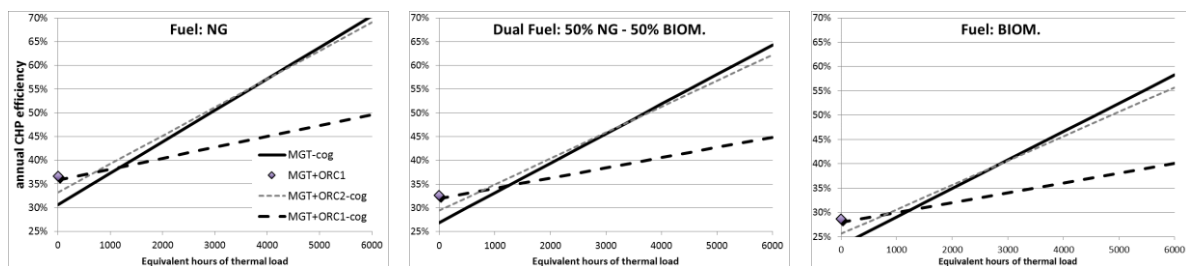


Figure 3. Annual CHP efficiency ($\bar{\eta}_{CHP}$) as a function of thermal energy demand.

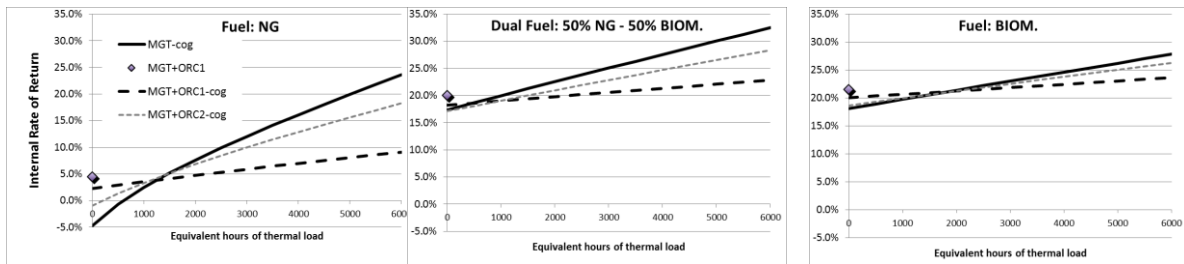


Figure 4. Internal Rate of Return (%) of the investments as a function of thermal energy demand equivalent hours for the case studies only natural gas (left), dual fuel (middle) and only biomass (right)

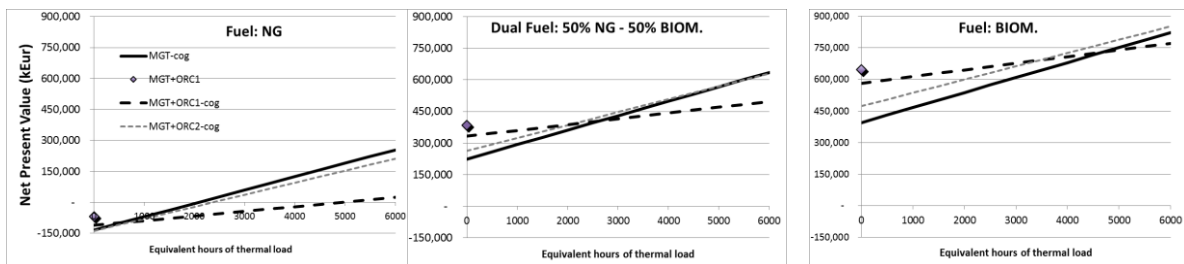


Figure 5. NPV (kEur) of the investments as a function of thermal energy demand equivalent hours for the case studies only natural gas (left), dual fuel (middle) and only biomass (right)

7. CONCLUSIONS

In this paper, the results of a thermo-economic assessment of micro gas turbine (100 kWe) with bottoming ORC fed by natural gas and biomass is presented. The systems configurations of MGT with cogeneration, MGT+bottoming ORC without cogeneration, and MGT with bottoming ORC and cogeneration at different condensing temperature are modelled, considering the three input fuel options of only natural gas, dual fuelling of natural gas and biomass, and only biomass. The results are used to inform a techno-economic methodology to estimate economic indices and energy performances in different scenarios. The influence of fuel characteristics on: (i) technical parameters, (ii) conversion efficiencies, (iii) capex and opex, (iv) profitability of investments are investigated.

The following main conclusions can be drawn:

(i) the global conversion efficiency ranged respectively between 30-70% and 23-60% for the natural gas and biomass fired case studies and the MGT with cogeneration, as a function of the thermal energy demand operating hours, with lower performances in case of biomass energy input. The combined cycle of the MGT with a bottoming ORC and low condensing temperature (case ORC 1) increases electric conversion efficiency to 36-28% and reduces the thermal efficiency to 17-15% respectively for the natural gas and biomass fired case studies. In the case of high condensing temperature (ORC 2), the electric and thermal conversion efficiencies are respectively of 33-25% and 45-38% for the natural gas and biomass fired cycles.

(ii) the ORC bottoming cycle increases the NPV when using biomass fuel, while the optimal IRR is obtained with dual fuel configurations; CHP investment profitability, and the incremental profitability of bottoming ORC on respect to MGT cycle, are highly influenced by thermal energy demand.

The scenario of 100% NG has the highest conversion efficiency and primary energy saving; however, the 100% biomass option has the highest NPV. This is due subsidies available by feed-in tariffs for electricity produced from biomass.

In conclusion, the profitability of adding a bottoming ORC is dependent on the trade-off between increased upfront costs, reduced heat available for cogeneration, and increased electricity generation. According to the simulation results, the bottoming ORC with low condensing temperature (ORC1) is profitable when using biomass fuel and with low heat demand levels, while the bottoming ORC with high condensing temperature (ORC2), despite presenting lower electric conversion efficiency, is more profitable than the only MGT cycle, at high energy demand levels. Further researches will be focused on algorithms to optimize the CHP operation with the option to switch on and off the bottoming ORC on the basis of the energy demand and other techno-economic parameters.

REFERENCES

- AEEG (Italian Authority of Electricity and Gas), statistical data, 2015
http://www.autorita.energia.it/it/dati/elenco_dati.htm, (accessed may 2015)
- AE-T100 Micro Turbine, Natural Gas, DATA SHEET, available from (accessed on Jan 4th, 2015)
http://www.ansaldoenergia.com/easyUp/file/ae-t100_micro_turbine_natural_gas_sheet_englis.pdf
- Al-Sulaiman FA, Dincer I, Hamdullahpur F. Thermoeconomic optimization of three trigeneration systems using organic Rankine cycles: Part I – Formulations. *Energy Conversion and Management*, 2013;69:199–208.
- C. He, C. Liu, H. Gao, H. Xie, Y. Li, S. Wu, J. Xu. “The optimal evaporation temperature and working fluids for subcritical organic Rankine cycle”. ELSEVIER, 2012.
- C. M. Invernizzi, P Iora, and R. Sandrini. “Biomass combined cycles based on externally fired gas turbines and organic Rankine expanders”. *Journal of Power and Energy*. DOI: 10.1177/0957650911415188
- Camporeale S, Ciliberti P, Torresi M, Fortunato B, Pantaleo A (2015), Externally fired micro gas turbine and ORC bottoming cycle: optimal biomass/natural gas CHP configuration for residential energy demand, Proceedings of ASME Turbo Expo 2015, Montreal, Canada, June 15-19 2015
- Camporeale S., Turi F., Torresi M., Fortunato B., Pantaleo A, Pellerano A. (2014) Part load performances and operating strategies of a natural gas-biomass dual fuelled microturbine for CHP operation, Proc. of ASME Turbo Expo 2014: Düsseldorf, Germany, June 16-20, 2014 GT2014- 27109, and ASME Journal of Engineering for Gas Turbines and Power
- Cheap, I.R., Fee, W., 1986, Conference Attendance of a Shoestring Budget, *Int. J. Cost-Effective Research*, vol. 7, no. 4: p. 78-93.
- Cocco D, Deiana P, Cau G. Performance evaluation of small size externally fired gas turbine (EFGT) power plants integrated with direct biomass dryers. *Energy* 2006;31(10-11):1459–1471.
- Decision 406/2009/EC of the European Parliament and of the Council of 23 April 2009
 Directive 2009/28/EC of the European Parliament and of the Council of 23 April 2009
- Duminil, M., 1995, Principes de la production du froid, Chapter 2, In: Côme, D., Ulrich. R., *La chaîne du froid – Le froid au service de l'homme*, Hermann, Paris: p. 33-144.
- Evans RL, Zaradic AM. Optimization of a wood-waste-fuelled indirectly fired gas turbine cogeneration plant. *Bioresource Technology* 1996;57: 117–26.
- Ferreira ACM, Nunes ML, Teixeira SFCF, Leão CP, Silva ÂM, Teixeira JCF, Martins LSB. An economic perspective on the optimisation of a small-scale cogeneration system for the Portuguese scenario. *Energy*, 2012;45(1):436–444.
- Ferreira SB, Pilidis P. Comparison of externally fired and internal combustion gas turbines using biomass fuel. *ASME J. Energy Resour. Technol.* 123 (2001) 291–296.
- Forbes-Pearson, S., 1996, Uses of Hydrocarbon Refrigerants, *Proc. Aarhus Meet.*, IIF/IIR: p. 439-446. Janna, S.W., 1986, *Engineering Heat Transfer*, PWS Publishers, Boston, 769 p.
- Fortunato B, Camporeale S.M., Torresi M., A Gas-Steam Combined Cycle Powered by Syngas Derived from Biomass, *Procedia Computer Science*, (2013) Volume 19, 736-745
- Franco A, Giannini N. Perspectives for the use of biomass as fuel in combined cycle power plants. *International Journal of Thermal Sciences*, 2005; 44(2):163–177.
- G. David, F. Michel, L. Sanchez. “Waste heat recovery projects using Organic Rankine Cycle technology – Examples of biogas engines and steel mills applications.” Geneve 2011- World Engineer’s Convention
- Galanti L, Massardo AF. Thermoeconomic Analysis of Micro Gas Turbine Design in the Range 25-500 kWe. Proceedings of ASME Turbo Expo 2010 (pp. GT 2010–22351; pp1–11).
- H. Chen, D.Yogi Goswami, E.K. Stefanakos. “A review of thermodynamic cycles and working fluids for the conversion of low-grade heat”. ELSEVIER, 2010
- Hamilton SL. The Handbook of Microturbine Generators. Tulsa: PennWell Corporation; 2003.
<http://www.asimptote.nl/software/cycle-tempo/>(accessed Jan. 3rd, 2015)
<http://www.autorita.energia.it/it/dati/condec.htm> accessed oct 2013
<https://gettotalplant.com/GateCycle/docs/GateCycle/index.html> (accessed Jan. 3rd, 2015)
- K. Kusterer, R. Braun, D. Bohn. “Organic Rankine cycle working fluid selection and performance analysis for combined application with a 2 MW class industrial gas turbine”. Proceedings of ASME Turbo Expo 2014: - GT2014 June 16 – 20, 2014, Düsseldorf, Germany
- Kautz M, Hansen U. The externally-fired gas-turbine (EFGT-Cycle) for decentralized use of biomass. *Applied Energy*. 2007;84(7-8):795–805.
- Knoef H. The indirectly fired gas turbine for rural electricity production from biomass, Project Brochure and Reports; 1998. Contract FAIR-CT95–0291.
- M. A. Rosa do Nascimento, L. de Oliveira Rodrigues, E. Cruz dos Santos, E. E. Batista Gomes, F. L. Goulart Dias, E. I. Gutiérrez Velásques, R. A. Miranda Carrillo. “ Micro Gas Turbine Engine: a Review”. *Progress in Gas Turbine Performance*, edited by Ernesto Benini, Published: June 19, 2013, DOI: 10.5772/54444
- Ministry Decree 5-09-2011 on incentives for High Efficiency Cogeneration in Italy (in italian)
 Ministry Decree 6-07-2012 on supporting mechanism for renewable electricity in Italy (in italian)

- Obernberger I. Decentralized biomass combustion: state of the art and future development. *Biomass and Bioenergy* 1998;14(1):33–57.
- P. Arvay, M. R. Muller, V. Ramdeen, *Economic Implementation of the Organic Rankine Cycle in Industry*, ACEEE Summer Study on Energy Efficiency in Industry, 2011, Editor: ACEEE, 529 14th Street, N.W., Suite 600, Washington, D.C. 20045, ISBN 0-918249-61-0
- Pantaleo A, Camporeale S, Shah N. Thermo-economic assessment of externally fired micro gas turbine fired by natural gas and biomass: applications in Italy, *Energy Conversion and Management*, (2013a);75:202-213
- Pantaleo A, Shah N, Keirstead J, Bioenergy and other renewables in urban energy systems (2013b) in *Urban Energy Systems – an integrated approach*, by J Keirstead and N Shah, Routledge, NY
- Pantaleo A, Candelise C, Bauen A, Shah N, ESCO business models for biomass heating and CHP: case studies in Italy, *Renewable and Sustainable Energy Reviews* (2014a) 30, 237-253
- Pantaleo A., Camporeale S., Shah N., Natural gas – biomass dual fuelled microturbines: comparison of operating strategies in the Italian residential sector *Applied thermal engineering*, (2014b)
- Pantaleo A, Ciliberti P, Camporeale S, Shah N (2015) Thermo-economic assessment of small scale biomass CHP: steam turbines vs ORC in different energy demand segments, *Proceedings of 7th International Conference on Applied Energy – ICAE, Abu Dhabi, March 28-31 2015*
- R. Tidball, J. Bluestein, N. Rodriguez, and S. Knoke (2010) Cost and Performance Assumptions for Modeling Electricity Generation Technologies, Report NREL/SR-6A20-48595, November 2010, available from <http://www.nrel.gov/docs/fy11osti/48595.pdf> (accessed Jan 4th, 2015)
- Riccio G, Chiaramonti D. Design and simulation of a small polygeneration plant cofiring biomass and natural gas in a dual combustion micro gas turbine *Biomass and Bioenergy* 2009; 33(11).
- Riccio G, Martelli F, Maltagliati S. Study of an external fired gas turbine power plant fed by solid fuel. In: *Proceeding of ASME turbo expo 2000*. ASME editor. Paper 0015-GT-2000
- Savola T, Tveit T-M, Laukkanen T. Biofuel indirectly fired microturbine state of the art. TKK, Laboratory of Energy Engineering and Environmental Protection, Espoo, http://eny.hut.fi/research/process_integration/bioifgt_Jan.pdf ; 2005.
- Soltani S, Mahmoudi SMS, Yari M, Rosen MA. Thermodynamic analyses of an externally fired gas turbine combined cycle integrated with a biomass gasification plant. *Energy Conversion and Management*, 2013; 70:107–115.
- Yan J, Eidensten L. Status and perspective of externally fired gas turbines, *J. Propulsion and Power* 2000; 16(4).

ACKNOWLEDGEMENT

The present work has been carried out within the program “SMART ENERGY BOXES - Systems research and development of electrical and thermal energy efficient generation, management and storage, integrated and interconnected in a Virtual Power Plant”, National Operative Program (PON), Italian Ministry of Education, University and Research, *MIUR prot.n.713/Ric., 29 October 2010*.

NOMENCLATURE

\dot{E}	energy flux	(kW)		
h	enthalpy	(kJ/kg)		
\dot{m}	mass flow	(kg/s)		
p	pressure	(bar) or (kPa)		
P	electric power	(kW)		
\dot{Q}	heat flux	(kW)		
T	temperature	(K) or (°C)		
W	work	(kJ/kg)		
η	efficiency			
χ	heat recovery factor			
subscripts			acronyms	
av	available		CHP	Combined Heat and Power generation
$biom$	biomass		HRB	Heat Recovery Boiler
cc	combined cycle		MGT	Micro Gas Turbine
g	exhaust gas		ORC	Organic Rankine Cycle
e	electric		LHV	Lower Heating Value
in	input		EFGT	Externally Fired Gas Turbine
gen	Electric generator		IFGT	Internally Fired Gas Turbine
L	Low (bottoming cycle)		MM	hexa-methyl-disiloxane
th	thermal		Fuel supply : NG = natural gas ; DF = dual fuel (50% natural gas and 50% biomass input energy) ; B= biomass	
rec	Recuperative cycle			

SIZING AND PARAMETRIC OPTIMIZATION OF A WASTE HEAT TO POWER PLANT BASED ON TRANSCRITICAL ORGANIC RANKINE CYCLE

Van Long Le^{1*}, Michel Feidt², Abdelhamid Kheiri², Vincent Lemort¹

¹University of Liège
Chemin des chevreuils 7, 4000 Liège, Belgium
E-mail: vanlong.le@ulg.ac.be

²University of Lorraine
2 Avenue de la Forêt de Haye, 54518 Vandœuvre-lès-Nancy, France

* Corresponding Author

ABSTRACT

In recent years, the transcritical (also called supercritical) organic Rankine cycle (Trans-ORC) has more and more aroused the attention for power generation from low-temperature heat source thanks to the better thermal matching between the heating and the cooling fluids of the high pressure heat transfer process. The absence of isothermal evaporation in transcritical ORC enables the heat source to be cooled down to a lower temperature despite an identical pinch point as in a comparable subcritical cycle. This leads to a greater utilization of the heat source. In other words, the transcritical cycle could produce more power with higher exergy efficiency compared to the subcritical one.

This paper aims at sizing a transcritical ORC to recover energy from a cooling circuit of turbine exhaust gas and optimizing the operating conditions of the cycle from a thermoeconomic point of view. Indeed, several potential organic fluids, which satisfy the screening criteria (e.g. safety, environment, thermophysical properties and availability), will be used as working fluid to evaluate the performance and the specific investment capital (SIC) of the plant. The operating conditions (i.e. turbine inlet temperature and pressure, condensing temperature and heat sink outlet temperature) of the plant will also be optimized to find out the most suitable working fluid for the studied cycle.

1. INTRODUCTION

Capturing and converting industrial waste heat into electricity is currently of a great concern. This not only improves energy efficiency of the industrial processes, but also reduces the thermal pollution caused by direct release of this heat into the environment. Over recent years, the transcritical ORC has aroused more and more attention for power generation from low-temperature heat source thanks to its advantages such as higher performance and less irreversibility. In a base Trans-ORC, the working fluid is first compressed above its critical pressure from sub-cooled liquid state (in the present work, the working fluid is assumed exiting the condenser in saturated liquid state). The working fluid is then heated, without isothermal phase change, by an external heat source (e.g. pressurized hot water) in high-pressure heat exchanger. In next step, the working medium releases its energy to drive the turbine blades during expansion process. The working fluid exits the turbine at superheated state, and is cooled down and then condensed by ambient air (dry cooling) or cooling water (wet cooling) before being pumped again to high pressure.

This work aims at sizing and then optimizing a small scale Trans-ORC to recover energy from a cooling circuit of turbine exhaust gas of a CHP (Combined Heat and Power) plant from landfill gas. According to the power range, the ORC systems could be categorized into (Vanslambrouck et al., 2011): micro-systems (0.5 – 10 kW_{el}), small systems (10 – 100 kW_{el}), medium systems (100 – 300 kW_{el}) and large systems (300 – 3000 kW_{el} or more). The process flow diagram and heat source and sink parameters for studied Trans-ORC are presented in Figure 1.

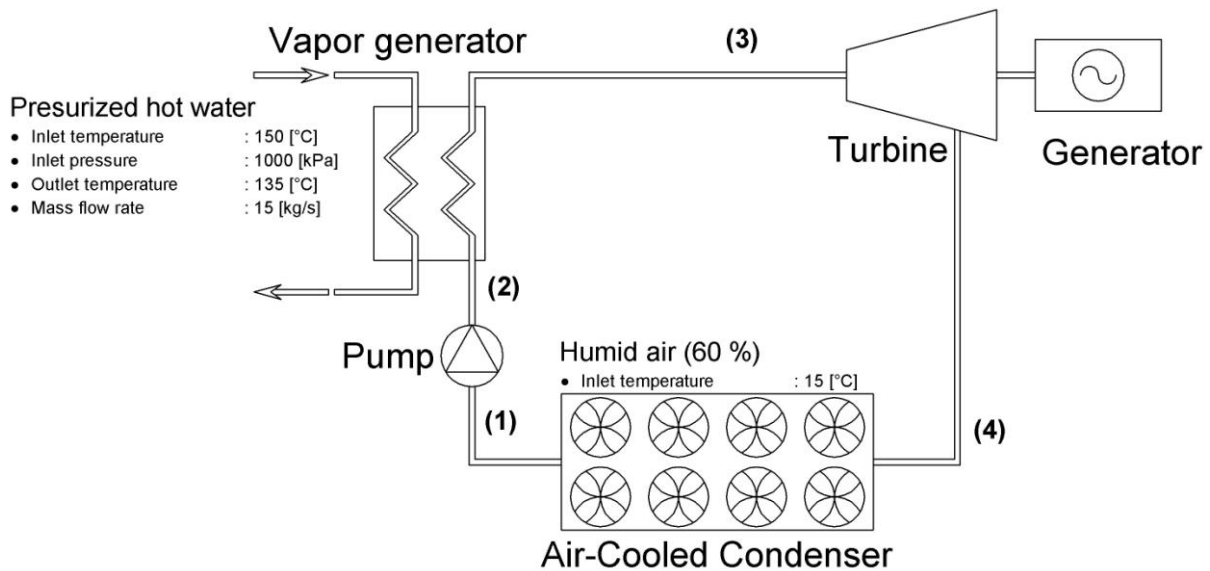


Figure 1: Process flow diagram

2. WORKING FLUID PROPERTIES

In practice, R134a and CO₂ are often used as working fluid for Trans-ORC. Although CO₂ has many desirable characteristics such as high thermal and chemical stability, low environmental impact, low cost and abundance in nature, the 80-160 bars operating pressure of the CO₂ transcritical cycle raises safety concerns. Therefore this medium is not taken into account in this study. Indeed, many factors could influence the selection of working fluid for any particular application including the ORC one. Many criteria have been proposed to find the best balance between working fluid properties, system architecture and application environment (cf. Figure 1).

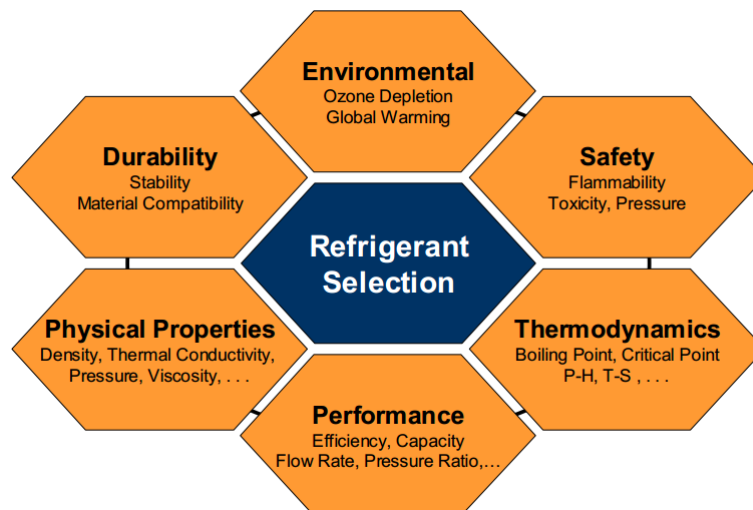


Figure 2: Factors influencing working fluid selection (Horn, 2011)

Some potential pure fluids, whose properties are available in the REFPROP database, are investigated as working medium. Those fluids satisfy selection criteria, i.e. GWP less than or equal to R134a GWP, critical temperature less than 115°C, maximum applicable temperature greater than 150°C, zero ODP, non-toxic and acceptable critical pressure. The thermophysical properties of the selected working fluids are computed by REFPROP (Lemmon et al., 2013) using Coolprop-EES interface (Bell et al., 2014). Some practical data of those working fluids are presented in Table 1.

Table 1: Working fluid data

Working fluid	R134a	R152a	R32	Propane (R290)	R1234ze(E)
Molecular weight	102.03 g/mol	66.05 g/mol	52.02 g/mol	42.08 g/mol	114.04 g/mol
T_c	101.1 °C	113.3 °C	78.1 °C	96.7 °C	109.4 °C
P_c	4059 kPa	4517 kPa	5782 kPa	4251 kPa	3635 kPa
T_b	-26.1 °C	-24.1 °C	-51.7 °C	-42.1 °C	-19.3 °C
ρ_c	511.9 kg/m ³	368.0 kg/m ³	424.0 kg/m ³	220.5 kg/m ³	489.2 kg/m ³
GWP	1370	133	716	< 20	6
Toxicity/Flammability**	A1	A2	A2L	A3	A2L
Materials	Good	Good	Good	Good	Good
Price (estimated)	6.85 \$/kg	3 \$/kg	3 \$/kg	1 \$/kg	37 \$/kg
Thermal conductivity*	0.01394 W.m ⁻¹ .K ⁻¹	0.01421 W.m ⁻¹ .K ⁻¹	0.01429 W.m ⁻¹ .K ⁻¹	0.01832 W.m ⁻¹ .K ⁻¹	0.008786 W.m ⁻¹ .K ⁻¹
Density*	4.258 kg/m ³	2.759 kg/m ³	2.153 kg/m ³	1.832 kg/m ³	4.774 kg/m ³
* Computed at temperature (25°C) and pressure (1 bar)					
**ASHRAE classification : A: lower toxicity; B: higher toxicity; 1: no flame propagation; 2: lower flammability; 3: higher flammability; 2L: lower flammability with a maximum burning velocity of < 10 cm/s					

3. EQUIPMENT SIZING AND CAPITAL COST ESTIMATION

3.1. Equipment purchase cost estimation

This work uses cost correlations as presented in (Seider et al., 2010) for estimating free-on-board purchase cost of equipment. The base cost of major equipment is estimated using the following

$$C_p^0 = e^{\{A_0 + A_1[\ln(S) + A_2[\ln(S)]^2 + \dots]\}} \quad (1)$$

Where

C_p^0 is base cost of equipment, US\$

A_0, A_1, A_2 are the estimation model constants

S is size factor or capacity of equipment

In addition to size, other factors, such as material of construction and operating pressure, are also taken into consideration for estimating equipment purchased cost. Therefore, the cost equations are often in the following form

$$C_p = F_M F_p C_p^0 \quad (2)$$

Where

C_p is the purchase cost of equipment, US\$

F_M is the material factor

F_p is the pressure factor

The values of constants for base cost estimation, i.e. A_0, A_1, A_2, \dots in equation (1), the material and pressure factors for estimating the purchase cost of centrifugal pump, shell and tube heat exchanger and fans are found in (Seider et al., 2010). To account for the inflation, Chemical Engineering Plant Cost Index (CEPCI), published in each monthly issue of the magazine Chemical Engineering, is used. As the cost correlations in (Seider et al., 2010) were developed using a CEPCI of 500, current purchase cost of equipment should be determined by

$$C_p = C_p^{500} \frac{\text{CEPCI}}{500} \quad (3)$$

Where

C_p^{500} is equipment purchase cost determined with CEPCI of 500

CEPCI is the present Chemical Engineering Plant Cost Index (CEPCI = 567.3 for the year 2013)

3.2. Plant capital investment

Besides purchase costs of equipment, many other costs must be accounted for plant capital investment. In this work, the total capital investment is determined to be the sum of components costs as shown in Table 2

$$C_{TCI} = \sum C_P + C_{wf} + C_{sp} + C_{sf} + C_{CCF} \quad (4)$$

Table 2: Components of total capital investment

Component	Description
Total equipment purchase cost (excluding installation costs)	$\sum C_P$
Cost for working fluid	C_{wf}
Total cost for spares, C_{spares}	Assumed to be zero
Total cost for computer, software and associated items, C_{comp}	Neglected
Cost of site preparation, C_{sp}	5% of $\sum C_P$
Cost of service facilities, C_{sf}	5% of $\sum C_P$
Cost of contingencies and contractor's fee, C_{CCF}	18 % of $(\sum C_P + C_{sp} + C_{sf})$
Cost of land, C_{land}	Assumed to be zero
Cost of royalties, $C_{royalties}$	Assumed to be zero
Cost of plant startup, $C_{startup}$	Assumed to be zero

3.3. Equipment sizing

For estimating the purchase cost of equipment, the size or capacity of the latter must be determined. Therefore, basic equations for equipment sizing and purchase cost estimation of some other ORC components (excluding the equipment covered in previous section, i.e. shell and tube heat exchanger, centrifugal pump and fan) are presented below.

Working fluid feed pump

A Centrifugal pump, of the radial type and with an isentropic efficiency of 70%, is used to raise the pressure of Trans-ORC working fluid. The shaft power of pump is computed as

$$\dot{W}_p = \dot{m}_{wf} (h_2 - h_1) \quad (5)$$

The pump motor power consumption is calculated from the pump shaft power in assuming a motor efficiency (η_{motor}) to be 95%

$$\dot{W}_m = \dot{W}_p / \eta_{motor} \quad (6)$$

Vapor generator

A general shell and tube heat exchanger with one shell pass and two tube passes is used for transferring heat from pressurized hot water to ORC working fluid. The heat rate transferred in the vapor generator is calculated as

$$\dot{Q}_h = \dot{m}_{wf} (h_3 - h_2) \quad (7)$$

The heat transfer coefficient and pressure drop of fluid flowing in heat exchanger shell side (i.e. hot water) are calculated using Kern method (Kern, 1950), while the supercritical heat transfer is computed by Jackson correlation (Jackson, 2002) with the Nusselt number determined as follows

$$Nu = 0.0183 \times Re^{0.82} \times Pr^{0.5} \times (\rho_w / \rho)^{0.3} \times (\bar{C}_p / C_p)^n \quad (8)$$

Indeed, Jackson correlation was obtained by modifying the correlation of Krasnoshchekov et al. which is valid within the following range (Krasnoshchekov et al., 1967):

$$8 \cdot 10^4 < Re < 5 \cdot 10^5, 0.85 < Pr < 65, 0.90 < \rho_w / \rho < 1.0, 0.02 < \bar{C}_p / C_p < 4.0, 0.9 < T_w / T_{pc} < 2.5$$

The index n in equation (8) depends on the values of wall tube temperature, T_w , and temperature of supercritical fluid in relation to its pseudo-critical temperature, T_{pc} , as mentioned in (Jackson, 2002). Jackson (2002) and previously, Jackson and Hall (1979) assessed the accuracy of many correlations. They found the correlation of Krasnoshchekov et al. (1967) and its modified version of Jackson (2002) to be the most accurate ones. Ninety seven percent of the experimental data were correlated with the accuracy of $\pm 25\%$ (Pioro and Duffey, 2007). The pressure drop of the supercritical fluid

inside the tubes is calculated as presented in (Le, 2014). Neglecting the fouling resistance, the overall heat transfer coefficient, U , of the shell and tube heat exchanger is computed as

$$\frac{1}{U} = \frac{1}{\alpha_o} + \frac{D_o}{D_i \alpha_i} + \frac{D_o \ln(D_o / D_i)}{2k_w} \quad (9)$$

Condenser

The heat rejection step of Trans-ORC is not realized by a shell and tube heat exchanger like for the heat addition but an air-cooled condenser (ACC). In an ACC, the hot process fluid flows through a bank of tubes, and ambient air is blown across the finned tubes by fans. The heat transferred from ORC working fluid to ambient air via condenser is determined as follows

$$\dot{Q}_c = \dot{m}_{wf} (h_4 - h_1) \quad (10)$$

The air-cooled condenser is considered with horizontal finned tube bundle. The air side heat transfer and pressure drop of ACC are calculated by the correlations of Ganguli (Ganguli et al., 1985). For tube side, Gnielinski correlation (Gnielinski, 1976) is used to calculate the heat transfer of single phase fluid, while Shah correlation (Shah, 2009) is used for the condensation in plain tube. According to the empirical correlation of Shah, there are two heat transfer regimes during the condensation in plain tube. The equations of two-phase heat transfer coefficient, α_{TP} , for each regime are presented below

In regime I (turbulent regime)

$$\alpha_{TP} = \alpha_l \quad (11)$$

In regime II (mixed regime)

$$\alpha_{TP} = \alpha_l + \alpha_{Nu} \quad (12)$$

Where

$$\alpha_l = \alpha_{LS} \left(1 + 3.8 / Z^{0.95}\right) \left[\mu_l / (14\mu_v)\right]^{(0.0058+0.557p_r)} \quad (13)$$

$$\alpha_{Nu} = 1.32 \text{Re}_{LS}^{(-1/3)} \left[\frac{\rho_l (\rho_l - \rho_v) g (k_l)^3}{(\mu_l)^2} \right]^{1/3} \quad (14)$$

The boundary between the regimes I and II is given by the following relation. Regime I occurs when

$$J_v \geq 0.98(Z + 0.263)^{-0.62} \quad (15)$$

Where J_v is the dimensionless vapor velocity defined as (Shah, 2009):

$$J_v = \frac{xG}{\left[gD\rho_v (\rho_l - \rho_v) \right]^{0.5}} \quad (16)$$

The Shah's correlating parameter Z is calculated as (Shah, 2009):

$$Z = (1/x - 1)^{0.8} p_r^{0.4} \quad (17)$$

The two-phase pressure drop of the fluid flowing inside the horizontal tube is the sum of two contributions (the momentum and the frictional pressure drop) and computed as described in (Le et al., 2014). The purchase cost of air-cooled condenser is estimated from its heat transfer surface area as in the following equation:

$$C_{P,ACC} = 6466 (A_{ACC})^{0.4} \text{CEPCI} / 500 \quad (18)$$

Fan motor

The fan motor power consumption is estimated by the equation (19) from pressure drop and mass flow rate of the air through the ACC. The fan efficiency, η_{fan} , and motor efficiency, η_{motor} , in equation (19) are assumed to be equal to 70% and 95%, respectively.

$$\dot{W}_{fan} = \frac{\Delta P_{air} \dot{m}_{air}}{\rho_{air} \eta_{fan} \eta_{motor}} \quad (19)$$

Turbine

In the present work, the isentropic efficiency of turbine is assumed to be 85%. The shaft Power output of the turbine, where heat losses are neglected, is determined as

$$\dot{W}_t = \dot{m}_{wf} (h_3 - h_4) \quad (20)$$

The purchase cost of turbine is determined as a function of its shaft power output (Seider et al., 2010):

$$C_{P,t} = 672.2 (\dot{W}_t)^{0.81} \text{ CEPCI} / 500 \quad (21)$$

Electrical generator

The electrical power output of generator is determined from the turbine power output with a generator efficiency of 95%

$$\dot{W}_{gen} = \dot{W}_t / \eta_{gen} \quad (22)$$

The purchase cost of electrical generator is calculated by the equation as presented in (Pierobon et al., 2013)

$$C_{P,gen} = 60 (\dot{W}_{gen})^{0.95}$$

Working fluid

In addition to the cost of equipment, the cost of working fluid must also be accounted for. In this work, the amount of working fluid is estimated as the liquid amount to fill the total volume of heat exchangers through which the working medium passes (Herrmann Rodrigues et al., 2010). The prices of tested working fluids were assumed from market surveys as shown in Table 1.

Global system

The net power output of Trans-ORC is considered as the difference between the power output of generator and the power consumption of the pump and fan motors

$$\dot{W}_{net} = \dot{W}_{gen} - \dot{W}_{motor} - \dot{W}_{fan} \quad (23)$$

The thermal efficiency of Trans-ORC is calculated as the ratio between system net power output to the heat transfer rate within vapor generator

$$\eta_{ORC} = \dot{W}_{net} / \dot{Q}_h \quad (24)$$

4. OPTIMIZATION

The optimization is performed by genetic method implemented in EES software (Klein, 2013). The parameters for the optimization are presented in Figure 1. The objective function is the specific investment capital (SIC) calculated hereunder:

$$\text{SIC} = C_{TCI} / \dot{W}_{net} \quad (25)$$

Many variables are taken into consideration for the optimization. In addition to the variable of operating conditions of the Trans-ORC, i.e. turbine inlet temperature (TIT); reduced pressure which is the ratio of turbine inlet pressure (TIP) to the critical pressure (P_c) of working fluid; condensing temperature and heat sink outlet temperature, the other variables concerning the shell and tube heat exchanger and the air-cooled condenser are also taken into consideration (cf. Table 3).

Table 3: Variables for SIC minimization

Variables	Lower	Upper
TIT	-	140 °C
$p_r = \text{TIP}/P_c$	1.01	3
T_{cond}	25 °C	50 °C
T_{cso}	18 °C	30 °C
ACC tube pass	1	4
Fluid velocity inside condenser and vapor generator tubes	0.15 m/s	3 m/s
Baffle spacing ratio = baffle spacing/shell diameter	0.2	1.0

During the optimization, the pinch (minimum temperature difference between heating and cooling curve) of heat transfer processes must be greater than 1°C, maximum pressure drop of fluids through heat exchangers (vapor generator and condenser) must be lower than 0.5 bar and vapor quality, x , of fluid exiting the turbine, calculated by the equation (26), must be greater than or equal to unity.

$$x = (h - h_{sat,l}) / (h_{sat,v} - h_{sat,l}) \quad (26)$$

5. RESULTS - DISCUSSION

According to the optimization results (Table 4), the lowest SIC (2641 \$/kW_{el}) is found with the system using R152a, while the highest one (3155 \$/kW_{el}) is observed with R32. Indeed, the R152a-based Trans-ORC system presents many advantages, i.e. moderate investment capital, highest net power output and thermal efficiency, moderate operating pressure and low working fluid GWP. One thing can limit the use of R152a is the fact that this fluid is mildly flammable.

Table 4: Results of SIC optimizations

Working fluid	R134a	R152a	R32	Propane (R290)	R1234ze(E)
\dot{W}_{net}	88.7 kW _{el}	102.9 kW _{el}	93.1 kW _{el}	89.3 kW _{el}	95.6 kW _{el}
η_{ORC}	9.2 %	10.7 %	9.7 %	9.3 %	9.9 %
TIT	140.0 °C	139.6 °C	140 °C	140 °C	140 °C
TIP	5420 kPa	5014 kPa	9253 kPa	6087 kPa	4206 kPa
p_r	1.335	1.11	1.6	1.432	1.157
T_{cond}	48.1 °C	44.4 °C	40.5 °C	43.8 °C	43.5 °C
T_{cso}	29.8 °C	29.9 °C	28.9 °C	29.5 °C	29.9 °C
SIC	2937 \$/kW _{el}	2641 \$/kW _{el}	3155 \$/kW _{el}	3075 \$/kW _{el}	3059 \$/kW _{el}
Avoided CO ₂ emissions*	231.5 t/year	268.5 t/year	243.0 t/year	258.9 t/year	249.5 t/year

* Annual operating hours is assumed to be 7884 h/year at full load with specific CO₂ emissions for electricity generation of 331g/kW_{el} (Clément, 2014)

In the case of a traditional working fluid for Trans-ORC system, i.e. R134a, although the net power output and thermal efficiency are the lowest for the optimum SIC, the SIC of R134a-based system together with two other systems using propane and R1234ze are competitive. Furthermore, as shown in T-s diagrams (Figure 3) of these working fluids, they exit the turbine at highly superheated state which presents a potential to install an internal heat exchanger as recuperator for improving the cycle performance. While the higher GWP of R134a and higher flammability of propane could limit the use of these working fluids, the high cost and mildly flammability of R1234ze are the challenges for its replacement to R134a as Trans-ORC working fluid.

At the present, the commercialized ORC modules are often subcritical ones. According to the data presented in (Vanslambrouck et al., 2011), the average prices of these turbine based ORC modules, excluding the installation cost, range from 1337 \$/kW_{el} (converted from 1000 €/kW_{el} with a 2011 yearly average exchange rate of 0.748 €/US\$) for a 2 MW-unit, to 2674 \$/kW_{el} (2000 €/kW_{el}) for a 500 kW-unit and up to 4011 \$/kW_{el} (3000 €/kW_{el}) for a 150 kW-unit. For waste heat recovery applications, the installation costs can go from 50% to 100% of the ORC module's cost. Comparing to these data, the studied Trans-ORC systems present a real potential for waste heat recovery application at small scale. Considering the working fluid properties presented in Table 1 and the SIC values, the greater are the critical and normal boiling temperatures, the smaller is the SIC. In the case of R1234ze, the SIC is higher than that for R134a-based Trans-ORC due to the high cost of working fluid.

The amount of annual avoided CO₂ emission for the electricity generation by recovering waste heat using a Trans-ORC is presented in Table 4 for each working fluid. This amount is calculated in assuming 7884 operating hours per years at full load of power plant.

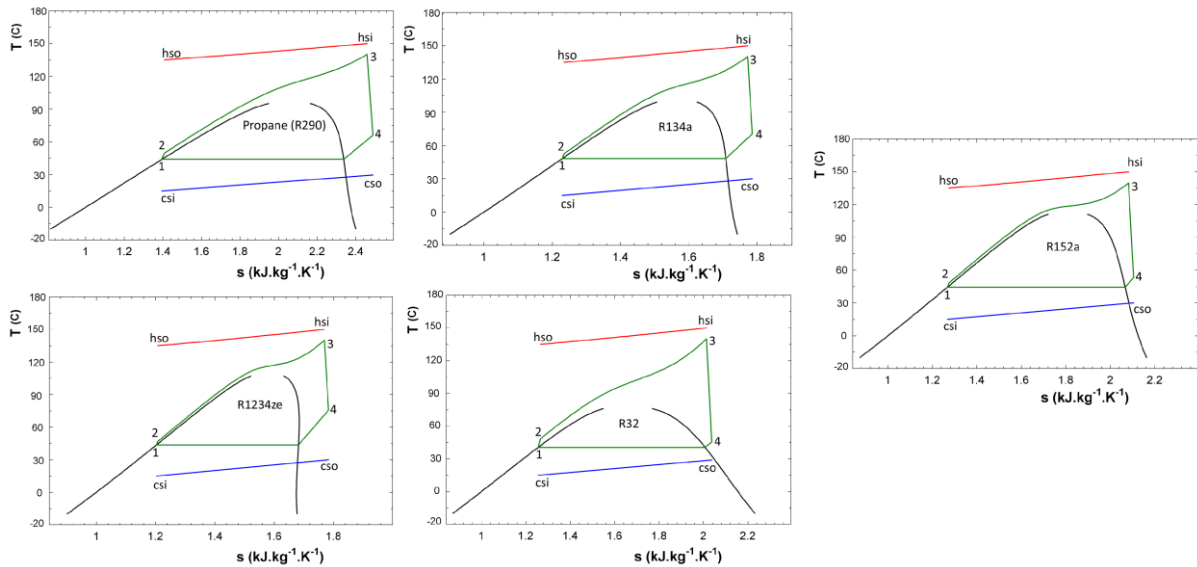


Figure 3: T-s diagram (green) of working fluids and temperature profile of heat source (red) and heat sink (blue) at minimum SIC

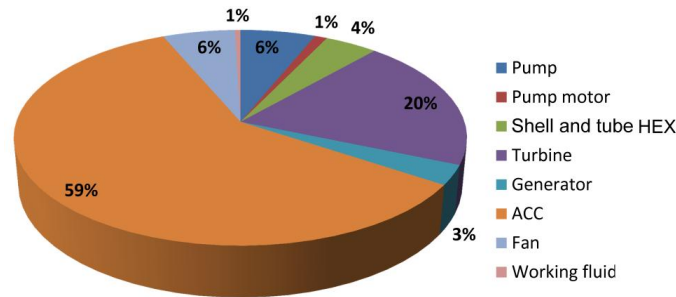


Figure 4: Repartition of purchase equipment cost of Trans-ORC (for the case of R152a)

Concerning the repartition of purchase equipment costs, the turbine and the air-cooled condenser are the most expensive components of Trans-ORC power plant (as shown in Figure 4) due to the low heat transfer coefficient and so the large required heat transfer surface area (e.g. $\sim 11.4 \text{ m}^2/\text{kWel}$ for the case of R152a). While the investment for the air-cooled condenser is more than half of total equipment purchase cost, this value for turbine is 20%. In the present work, the air-cooled condenser is considered with horizontal tubes. Indeed, other technologies such as A-frame and V-frame air-cooled condenser could also be considered to increase heat transfer coefficient. The other costs included in the total capital investment are presented in Table 5.

Table 5: Capital cost components (for the case of R152a)

Component	Value
Total cost for equipments (excluding installation costs)	208361 \$
Cost for working fluid, C_{wf}	948 \$
Cost of site preparation, C_{sp}	10465 \$
Cost of service facilities, C_{sf}	10465 \$
Cost of contingencies and contractor's fee, C_{CCF}	41443 \$
Total capital investment	271682 \$

6. CONCLUSIONS – PERSPECTIVES

This work presents the result of Specific Investment Capital (SIC) minimization for a Trans-ORC system that converts heat from cooling circuit of a turbine exhaust gas. Some potential working fluids

have been considered for the optimization of the system. According to the optimization results, the most interesting fluid is R152a with the highest net power output (102.9 kWel) and lowest SIC (2641 \$/kWel). However, the other fluids, i.e. R1234ze, R134a, or propane, present also the possibility to improve the performance and so the specific investment capital. The worst Trans-ORC in term of specific investment is found when R32 is used as working fluid. Indeed, this fluid operates at very high pressure (92.5 bars) to obtain a moderate net power output. For each tested working fluid, the optimum operating conditions are brought out by the mean of the SIC minimization. Regarding the repartition of purchase equipment costs, the most expensive component of Trans-ORC system is the air-cooled condenser followed by the turbine. Indeed, the condenser purchase cost contributes to more than half of the total equipment purchase cost, while the investment for the turbine excluding the electrical generator cost is of 20% of the total equipment cost.

NOMENCLATURE

D	Diameter	(m)
C	Cost	(US\$)
\bar{C}_p	$\bar{C}_p = (h_w - h) / (T_w - T)$	(kJ.kg ⁻¹ .K ⁻¹)
C_p	Specific heat	(kJ.kg ⁻¹ .K ⁻¹)
g	Acceleration constant	(m/s ²)
G	Mass flux	(kg.s ⁻¹ .m ⁻²)
h	Specific enthalpy	(kJ/kg)
\dot{m}	Mass flow rate	(kg/m ³)
k	Thermal conductivity	(kW.m ⁻¹ .K ⁻¹)
Nu	Nusselt number	(-)
P	Pressure	(kPa)
Pr	Prandtl number	(-)
p_r	Reduced pressure	(-)
\dot{Q}	Heat transfer rate	(kW)
Re	Reynolds number	(-)
SIC	Specific Investment Capital	(US\$/kW)
T	Temperature	(°C)
TIP	Turbine inlet pressure	(kPa)
TIT	Turbine inlet temperature	(°C)
U	Overall heat transfer coefficient	(kW.m ⁻² .K ⁻¹)
\dot{W}	Power	(kW)

Greek letters

α	Heat transfer coefficient	W.m ⁻² .K ⁻¹
η	Efficiency	(%)
μ	Dynamic viscosity	(kg.m ⁻¹ .s ⁻¹)
ρ	Density	kg/m ³

Subscript

1, 2, 3, 4	working fluid state points	l/v	liquid/vapeur
b	normal boiling point	m	motor
c	critical	p	pump
csi/cso	heat sink inlet/ outlet	sat	saturation
ex	external fluid	t	turbine
gen	generator	TP	two phases
h	hydraulic or hot	wf	ORC working fluid
hsi/hso	heat source inlet/outlet	w	wall

REFERENCES

- Bell, I. H., J. Wronski, S. Quoilin and V. Lemort (2014). *Pure and Pseudo-pure Fluid Thermophysical Property Evaluation and the Open-Source Thermophysical Property Library CoolProp*. Industrial & Engineering Chemistry Research 53(6): 2498-2508.
- Clément, L. (2014). Final report LIFE08 ENV/B/000040 CLIM-WASTENER. Bierges, Belgium, VERDESIS SA.
- Ganguli, A., S. S. Tung and J. Taborek (1985). *Parametric study of air-cooled heat exchanger finned tube geometry*. AIChE Symposium Series.
- Gnielinski, V. (1976). *New equations for heat and mass transfer in turbulent pipe and channel flow*. International Chemical Engineering 16: 359-368.
- Herrmann Rodrigues, L., E. Nie, A. Raza and B. Wright (2010). Low grade heat recovery. Senior Design Reports (CBE), University of Pennsylvania.
- Horn, B. V. (2011). A primer on HFOs Hydrofluoro-olefins Low-GWP refrigerants. 2011 ASHRAE Winter Conference. Las Vegas, NV.
- Jackson, J. D. (2002). Consideration of the heat transfer properties of supercritical pressure water in connection with the cooling of advanced nuclear reactors. 13th Pacific Basin Nuclear Conference. Shenzhen City, China.
- Kern, D. Q. (1950). *Process Heat Transfer*, McGraw-Hill
- Klein, S. A. (2013). EES: Engineering Equation Solver. Madison, F-Chart Software.
- Krasnoshchekov, E. A., V. S. Protopopov, F. VAn and I. V. Kuraeva (1967). *Experimental investigation of heat transfer for carbon dioxide in the supercritical region*. 2nd All-Soviet Union Conference on Heat and Mass Transfer, Minsk, Belarus.
- Le, V. L. (2014). *Feasibility study of subcritical and supercritical organic Rankine cycles (ORCs) for waste heat recovery*. Doctor of Philosophy Dissertation, University of Lorraine.
- Le, V. L., A. Kheiri, M. Feidt and S. Pelloux-Prayer (2014). *Thermodynamic and economic optimizations of a waste heat to power plant driven by a subcritical ORC (Organic Rankine Cycle) using pure or zeotropic working fluid*. Energy 78(0): 622-638.
- Lemmon, E. W., M. L. Huber and M. O. McLinden (2013). NIST Standard Reference Database 23: Reference Fluid Thermodynamic and Transport Properties-REFPROP. Gaithersburg, National Institute of Standards and Technology.
- Pierobon, L., T.-V. Nguyen, U. Larsen, F. Haglind and B. Elmegaard (2013). *Multi-objective optimization of organic Rankine cycles for waste heat recovery: Application in an offshore platform*. Energy 58(0): 538-549.
- Pirola, I. L. and R. B. Duffey (2007). *Heat Transfer & Hydraulic Resistance at Supercritical Pressures in Power Engineering Applications*. Three Park Avenue New York, NY 10016-5990, ASME
- Seider, W. D., J. D. Seader, D. R. Lewin and S. Widagdo (2010). *Product and process design principles: synthesis, analysis, and evaluation*, John Wiley.766
- Shah, M. M. (2009). *An Improved and Extended General Correlation for Heat Transfer During Condensation in Plain Tubes*. HVAC&R Research 15(5): 889-913.
- Vanslambrouck, B., I. Vankeirsbilck, S. Gusev and M. De Paepe (2011). *Turn waste heat into electricity by using an Organic Rankine Cycle*. 2nd European conference on Polygeneration Tarragona, Spain.

ACKNOWLEDGEMENT

The authors thank the French National Research Agency (ANR-10-EESI-001) who has funded the work reported in this paper.

PRELIMINARY INVESTIGATION INTO THE CURRENT AND FUTURE GROWTH AND AFFORDABILITY OF ORC ELECTRICITY GENERATION SYSTEMS

Michael Southon^{1*}, Susan Krumdieck¹

¹University of Canterbury, Department of Mechanical Engineering,
Christchurch, Canterbury, New Zealand
michael.southon@pg.canterbury.ac.nz

susan.krumdieck@canterbury.ac.nz

* Corresponding Author

ABSTRACT

The Organic Rankine Cycle (ORC) provides a way to produce power from heat resources that are at too low of a temperature to be competitively converted using steam-Rankine cycles. While ORC systems using geothermal, biomass, waste-heat, and solar resources currently provide less than 0.1% of worldwide electricity generation, their market growth has been historically steady, with new resource opportunities helping to marginally increase the installed capacity growth rate in recent years. This paper explores the current growth of ORC electricity generation systems, the theoretical limit of their future growth, and to what extent a policy-based market change will push ORCs towards meeting this potential.

The results from a survey of ORC manufacturers are presented, looking into the prevalence of existing ORC systems and the heat resources which they use. Estimates for the potential for future growth are made based on existing literature, and this is compared with current development. The historic trend for the growth of ORC generation capacity is presented, and it is proposed that if the low current annual growth rate continues, then ORCs are unlikely to become a globally significant energy conversion technology at current electricity demand levels.

The final part of this paper looks at the competitive advantage that ORCs get from GHG pricing, a non-technological factor that affects the growth rate of installed capacity. It is concluded that a truly significant penetration of ORC generation into the global energy mix would require a step change in the amount of resources that can be affordably developed; either through the introduction of new ways to cheaply access and convert resources, or through a massive shift in expenditure on energy systems, which may be unfeasible in future economic scenarios.

1. INTRODUCTION

From the 1970s until the mid 2000s, ORCs were primarily developed in order to generate electricity from geothermal resources in larger systems called ‘binary’ plants. Over the past decade, ORC systems have also started to be applied commercially to biomass and industrial waste heat resources, generally in regions with high electricity prices and subsidies directed at moving away from reliance on fossil fuels. During this time, the number of commercial suppliers of ORC systems has grown, improving the technology and increasing market competition. More recently, solar energy has also been collected and used in commercial ORC installations, as a supplement an existing heat source (Turboden, 2015).

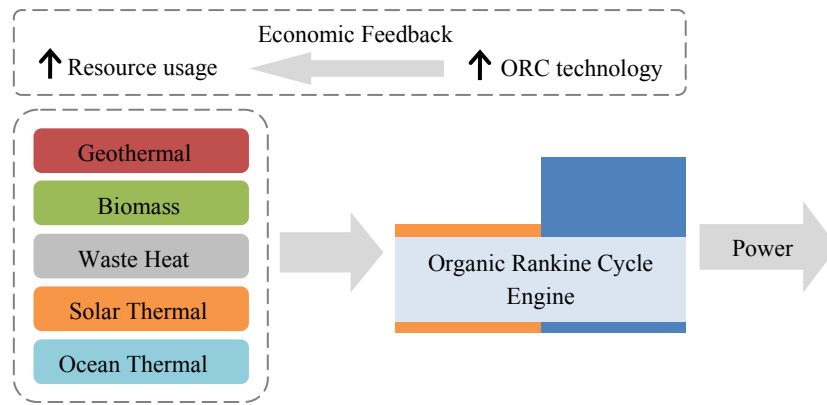


Figure 1: Common ORC resources, and the feedback of an improvement in ORC technology.

The applications for the power generated by ORC systems vary widely, with the majority of systems being used to provide electricity generation. There is however interest in using ORC systems other applications, such as direct shaft work in industrial plants (Quoilin *et al.*, 2013) and (Tchanche *et al.*, 2011), thereby marginally improving the overall efficiency and removing the need for a generator, which can be a significant cost at smaller scales.

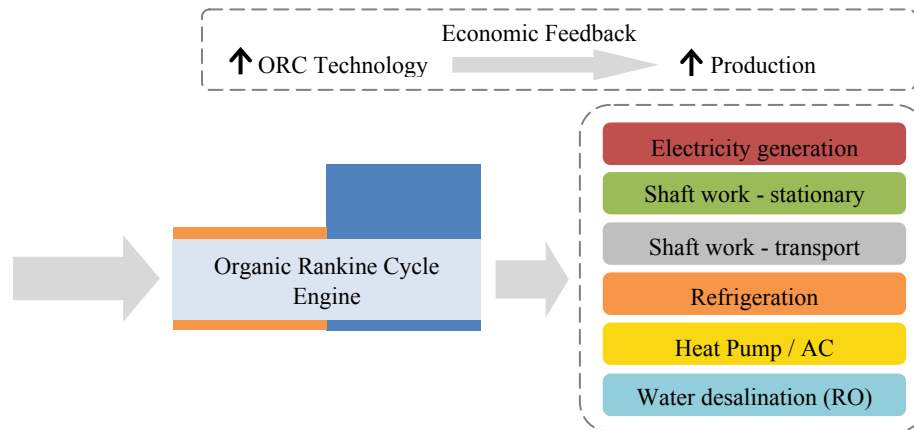


Figure 2: Proposed ORC applications, and the flow-on effect of an improvement in ORC technology.

The use of ORC systems specifically for electricity generation is studied in this paper. A survey of ORC manufacturers was undertaken to estimate the generation capacity currently operating from each ORC resource group. This capacity is compared to estimations in literature for the theoretical global potential of electricity from the heat resources used by ORCs. Lastly, as a factor which influences the growth of ORC technology that may soon undergo global changes, the effect that GHG pricing has on the competitiveness of ORC systems is investigated. These studies are intended to help inform preliminary predictions as to where ORC growth might lead to in future, and conclusions are drawn along those lines.

2. SURVEY OF ORC CAPACITY GROWTH

2.1 ORC Manufacturer Survey

A survey of ORC manufacturers was taken to determine how much generation comes from each resource, and for how long the development of the market for ORC systems has been underway. The size, installation date, and resource used for ORC systems from seventeen leading ORC manufacturers were surveyed. The survey data was gathered from manufacturer's websites and case studies. Only installations still currently in operation were included. The survey is not likely to be

exhaustive, especially pertaining to smaller manufacturers of waste-heat recovery (WHR) and biomass units. Systems that utilise heat from biogas burners were classed under WHR.

Table 1: Total installed capacity of ORC systems from 17 major manufacturers, as at the end of 2014. Data from (Exergy, 2015; ORMAT, 2015; Turboden, 2015) and others.

Manufacturer	2014 Capacity (MW)			Total
	Geothermal	Biomass	WHR	
ORMAT	1421.9	0	136.0	1558.0
Turboden	19.2	250.6	41.2	311.0
Exergy	122.5	2.4	3.3	128.3
TAS	22.0	0	134.0	134.0
Maxxtec/Adoratec	0	16.5	6.8	23.4
ENEX	105.3	0	0	105.3
Tri-O-Gen	0	0.3	2.6	2.9
Other manufacturers*	4.8	4.7	8.3	17.9
TOTAL	1705.9	275.6	332.8	2160.3

*Other manufacturers include GMK, EXERGY, Opcon, Cryostar, BEP-Europe, Bosch KWK, MANNVIT, ENERTIME, ElectraTherm and UTC.

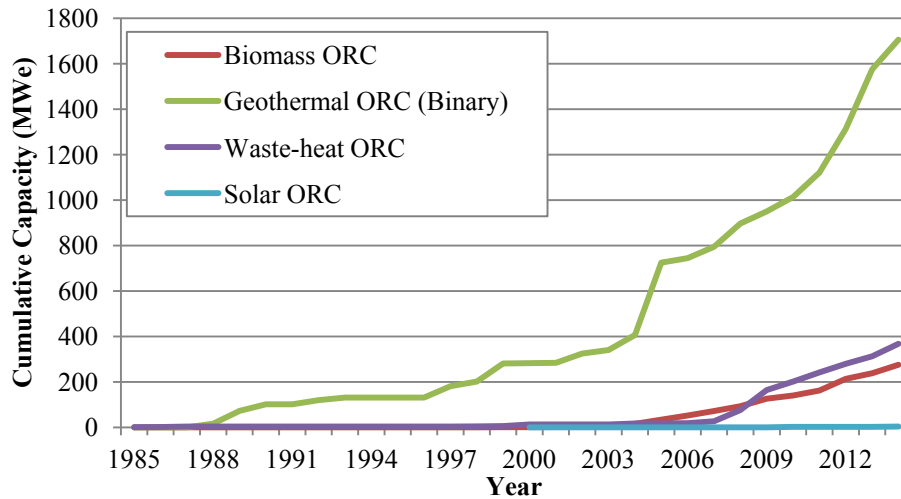


Figure 3: Growth of worldwide electricity generation capacity of ORC systems by resource type.

Figure 3 shows that geothermal ORC (binary) plants account for the majority of installed ORC capacity, with a significant amount of generation having been installed from the late 80’s onwards. In 2014, binary ORC systems accounted for about 20% of total geothermal generation (IEA, 2014). Biomass and WHR-ORCs have emerged more recently, with global capacity starting to grow from the mid 2000’s. The shape of the capacity growth curves indicate that ORC systems have undergone faster growth over the decade since 2005, which could perhaps be attributed to technology developments and the increasing price of other means of electricity production (IMF, 2015).

Table 2: Percentage generation capacity and average unit size from survey.

Heat Resource	Percentage of Total ORC Capacity	Max Unit Size (MW)	Min Unit Size (MW)	Average unit size (MW)
Geothermal	71.4	95	0.2	13.3
Biomass	13.1	8.0	0.07	1.1
WHR	15.3	5.3	0.0006	0.8*
Concentrating Solar**	0.2	2.0	0.1	0.9

*Excluding numerous very small (0.5 – 15 kW) gas pipeline compressor waste heat systems

** 2MW of concentrating solar generation is from an industrial waste heat/solar hybrid plant.

The survey results show that geothermal ORC systems are on average an order of magnitude larger than ORCs operating from other resources. Biomass, WHR and concentrating solar systems are of a similar average size, but the smallest commercial biomass and solar plants are currently much larger than the smallest WHR systems. This might be due to the additional equipment required to supply and transform biomass and solar resources (such as a boiler system), whose costs do not scale well to smaller sizes. Development is currently underway to commercialise smaller, domestic-scale biomass and solar powered cogeneration (heat and power) systems (Jradi and Riffat, 2014; Qiu *et al.*, 2012; Quoilin *et al.*, 2015).

2.2 Global capacity limit of ORC production

An important factor into whether the current ORC growth rates shown in Figure 3 can be expected to continue is the size of the available remaining resources, and at what price these resources can be utilised. Investigations relevant to the maximum practical potential, or capacity ceiling, of the development of energy resources using ORC systems are explored, and compared with current worldwide demand. These investigations are also presented in greater depth in (Southon, 2015).

2.2.1 Geothermal: In a study by (Ungemach, 2010), geothermal resources have been estimated to be able to provide a widely ranging potential of 70 GW to 2000 GW electrical capacity, depending on weather Enhanced Geothermal Systems (EGS) can be economically employed. A study by GNS science New Zealand also estimates that geothermal production could potentially reach to around 2000 GW using EGS systems (Chris J. Bromley & Ragnarsson, 2010). If about half of these systems were to use ORC energy conversion technology, an increase from around 20% currently, then a theoretical production capacity of 35 – 1000 GW, or 1.0 – 29 EJ per year assuming a 92% capacity factor, would be able to be provided using geothermal-ORC (binary) systems.

2.2.2 Biomass: It is apparent that a large expansion of biomass-ORC electricity production would be possible if ‘biomass – dedicated electricity’ systems were to become cost-effective; i.e. installations where biomass was produced for the sole purpose of electricity production. Estimates for the maximum potential of electricity generation through this means vary across a large range. In a review study by (Heinimo & Junginger, 2009), estimates for the additional thermal resource potential from managed biomass by 2050 were found to lie between 40 – 1100 EJ per year, with the higher side estimates assuming maximum land use change and technological advancements, particularly in agriculture. The IEA indicates that the annual energy production from biomass is currently around 46.6 EJ/yr (IEA, 2014). If all current and theoretical potential biomass resources were to be combusted in an ORC cycle with a net thermal efficiency of 20%, this would result in a potential production of 17.3 – 229.3 EJ of electricity annually, or an equivalent capacity of 610 – 8070 GW at a 90% capacity factor.

2.2.3 Waste-heat recovery (WHR): The potential for low-grade waste heat recovery using ORCs is small when compared with Biomass or Geothermal, as the resource is limited to industrial heat sources existing at the time. A survey of the low and high grade industrial waste heat recovery potential for the UK (McKenna & Norman, 2010) estimated that 36 – 71 PJ of heat was available to be recovered annually, although the authors indicated that this estimate is probably lower than the real value. If the high-side estimate for recoverable heat were to be converted by ORC systems with an average net thermal efficiency of 18%, 13 PJ of electricity could be produced annually. This figure is around 1% of the UK’s annual electricity generation of 1374 PJ in 2010 (OECD/IEA, 2015). If it is assumed that the worldwide proportion of recoverable waste heat to electricity generation is the same as for the UK, and that the global quantity of industrial waste heat remains unchanged into the future, then WHR using ORCs could mitigate an estimated maximum of 837 PJ annually, or 1% of current world electricity demand.

2.2.4 Solar: There have been many studies into the theoretical potential of solar electricity generation, with variations of up to nearly two orders of magnitude, depending on the assumptions used. For instance, a study using worldwide geographic data and stringent land-exclusion criteria estimated solar to have a massive 830 EJ per year electricity potential, many times greater than current

worldwide electricity demand (Trieb *et al.*, 2009). Other studies estimate a much smaller potential, such as 16.5 – 43.5 EJ (assuming a 30% capacity factor) in a study by (Castro *et al.*, 2015).

While it is likely that the majority of CSP growth will be met using steam-Rankine conversion technology, it is possible that the cost of high-temperature collectors may cause ORC systems to become more dominant going forward (Zarza, 2013). Rooftop thermal solar-ORC systems are also currently being investigated, due to their potential ability to work as a domestic heat pump in reverse operation (Quoilin *et al.*, 2015). From initial studies, these systems appear to provide a roof area-to-electricity conversion density of about $\frac{1}{4}$ that of an equivalent solar-PV system, as the energy collected is also used for heating purposes. In general, the theoretical potential energy yield of solar-ORC systems appear to be similar to that of biomass resources, but the lower capacity factor of solar generation results in a greater capacity requirement in order to reach this potential. If it is assumed that half of solar collection going forward were to use ORC energy conversion technology (up from near-zero currently), the range of estimates found would require a generation capacity of 870 – 44000 GW at a 30% capacity factor.

2.2.5 Summary of theoretical capacity potentials: Overall, the results of the studies investigated indicate that under a scenario of large-scale EGS development and significant land use change for biomass and solar collection, a significant penetration of ORC technology into the global energy mix is theoretically possible.

Table 3: Current and potential ORC electricity production, and total electricity production using all conversion technologies, from resources utilised by ORCs. Sources (EPIA, 2014; IEA, 2014; IRENA, 2013). Estimates of theoretical ORC capacity based on various studies as summarised in parts 2.2.1 – 2.2.4 of this paper. Further analysis of these studies is available in (Southon, 2015).

Resource	Current ORC Electricity Production (PJ/yr)	Current Electricity Production - all technologies (PJ/yr)	Theoretical potential maximum ORC electricity production estimate (PJ/yr)
Geothermal	50	240	1,000 – 29,000
Biomass	9.1	1,270	17,000 – 230,000
WHR	11.5	11.5*	840
Solar CSP	0.035	36	17,000 – 830,000
Rooftop Solar	0.0	615	
Total	71	2,170	36,000 – 1,090,000
Current worldwide electricity demand			81,600

*WHR figure is estimated as for low-temperature and discontinuous high-temperature resources only

The results in Table 3 indicate that there is significant remaining potential for the development of the heat resources used by ORC systems, which are currently developed to between 0.2% - 6.0% of their estimated potential capacity. ORC technology currently is a minority choice of energy conversion technology for geothermal, biomass and solar CSP resources, as the majority of development thus far has used steam-Rankine cycles.

Given the lower values for maximum potential capacity, a complete ‘replacement’ of current electricity generation resources would not be possible through the utilisation of ORC systems and their resources alone. Despite this, these estimates imply that under a scenario of significant land-use change for biomass and solar electricity production, much larger amounts of electricity production might be possible. Geothermal (EGS) and solar resources are estimated to have the largest potential to provide significant generation capacity, with ranges between 21% - 282% and 21% - 1017% of current global capacity respectively.

2.3 ORC capacity at current growth rates

The growth rate of ORCs systems may be impacted by several factors such as policy changes, changes to the price of other means of generation, changes to the demand for electricity, and the maturation of ORC technology leading to lower costs and increased resource access. If these and other factors were to remain unchanged, it could be argued that using past growth trends can be

expected to reasonably predict future ORC growth. This may be especially true for the more developed geothermal ORCs, but also to a smaller extent for less mature waste heat and biomass ORC technologies.

Several curve types were fitted to the capacity growth curves in Figure 3. For each curve type, the curve was truncated by earliest year in order to achieve a maximum coefficient of determination (R^2 -value), with a minimum period of five years. The R^2 -values of the trend lines for each resource are indicated in Table 4.

Table 4: Curve type, fit as determined by the coefficient of determination, and the truncation year necessary in order to achieve the maximum R^2 -value for each curve type, for the ORC capacity growth curves shown in Figure 3. The models that best fit each resource type are indicated in bold.

Resource	Curve Fit	R^2	Truncation year
Geothermal	Linear	0.986	2010
	Exponential	0.982	1989
	Power	0.947	2003
	Quadratic	0.990	2005
Biomass	Linear	0.979	2010
	Exponential	0.989	2009
	Power	0.998	2003
	Quadratic	0.997	1998
WHR	Linear	0.997	2009
	Exponential	0.947	1975
	Power	0.983	2008
	Quadratic	0.997	2009

Of the trend lines investigated, the best fits in terms of R^2 -value and amount of data covered are an exponential curve fit for geothermal generation from 1989 – 2015, and an exponential fit for WHR capacity from 1975 – 2015. This is because all the ORC resources were found to initially undergo relatively slow capacity growth for each resource, with a higher growth rate having occurred over the last decade, as can be seen in Figure 3. Factors that may have caused this increase in growth are; technology developments enabling access to a wider pool of resources, maturation of ORC technology leading to more technology providers and increased price competition, increasing worldwide electricity prices, increased worldwide electricity demand growth rates and the introduction of subsidies directed towards increasing renewable electricity generation. The omission of ORC systems that are now decommissioned may also have influenced the recorded growth trends.

It could be argued that if further significant changes to these growth factors were not to occur, a further increase in ORC capacity growth rates may not be expected, leading to a more linear trend line going forward. Figure 4 shows a linear curve fit to the to the capacity growth rate of ORC systems seen in recent years, as found from the survey.

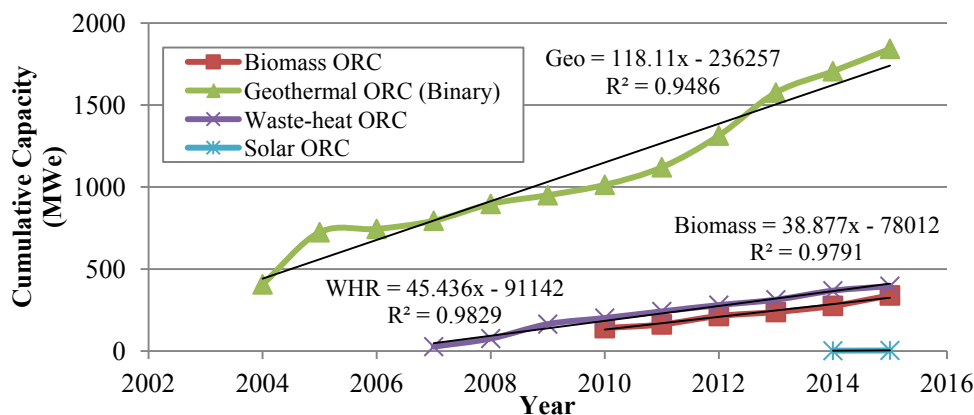


Figure 4: Resource-specific linear capacity growth trends for ORC systems.

The effect of a linear growth trend going forward on the global energy mix is shown in Table 5. Extrapolating the current growth rates using a linear trend line indicates that it will take nearly 150 years before annual electricity generation from ORCs will provide 1% as much electricity as current generation technologies. The years in which ORC systems can be expected to saturate their production potential are also indicated. Table 5 shows that in the year 2657 waste heat (WHR) will be the first resource to become fully saturated, if the resource potential were to remain at its current size.

Table 5: Years in which ORC systems will reach estimated theoretical potential resource limits, and 1% of current worldwide electricity production, if capacity continues to be added at current rates (linear extrapolation). Estimates of resource capacity potential adapted from various studies, as detailed in part 2.2 of this paper.

Resource	Theoretical future potential (PJ/yr)	Assumed average capacity factor	Year when potential capacity is achieved	Year of 1% current worldwide demand
Geothermal	1,000 – 29,000	0.92	2,292 – 69,000	2,238
Biomass	17,000 – 230,000	0.90	17,403 – 210,312	2,746
WHR	840	0.90	2657	2,638
Solar	17,000 – 830,000	0.30	1,058,311 +	52,715
Total ORC	36,000 – 1,090,000	0.88		2,160

3. ORC AFFORDABILITY UNDER GHG PRICING

As mentioned in part 2.3, ORC systems may become cheaper and more competitive through a variety of means, which will impact the rate at which new capacity is installed. As a policy intervention that may undergo changes in the near future with a potentially global influence (Mansell, 2015), greenhouse gas (GHG) pricing is highly relevant to ORC electricity production. GHG pricing mechanisms improve the competitiveness of ORC electricity over fossil-based generation, as a sufficiently large GHG price will incentivise the installation of new renewable generation in favour of established fossil-based systems.

3.1 GHG emissions from ORC energy systems

Selected lifetime-averaged gCO₂e/kWh figures for electricity generation from resources used by ORCs are presented in Table 6, as investigated for the IPCC fifth assessment report in (Schlömer *et al.*, 2014). A separate figure for ‘biomass after re-growth’ from (Weisser, 2007) is included, as the figure for the fifth assessment report assumes that the biomass fuel is dedicated energy crops or crop residues, and so is not applicable to current biomass ORC installations that often use forest wood. The ‘biomass – dedicated electricity’ values may become more applicable in the future however if large scale biomass-to-electricity conversion was pursued, as mentioned in part 2.2.2. Binary ORC plants are likely to sit at the lower end of the range of emission intensities given for geothermal, as these generally have higher reinjection rates compared to flash or steam technologies (Glassley, 2014).

Table 6: Estimated lifetime gCO₂e/kWh of ORC resources (Schlömer *et al.*, 2014) and (Weisser, 2007). The WHR-ORC figure has been estimated. The ‘%’ column indicates the relative median emissions intensity for each technology when compared to pulverized coal. The ‘cost’ column indicates the resulting lifetime-averaged cost in cents/ kWh of an imposed carbon price of \$25/tonne CO₂e.

Commercially Available Technologies	Min	Median	Max	%	¢/kWh
ORC resources					
Geothermal	6	38	79	4.6	0.10
Biomass – dedicated electricity	130	230	420	28	0.58
Biomass after re-growth	35	70	99	8.5	0.18
Concentrated Solar Power	8.8	27	63	3.3	0.07
WHR-ORC (estimated)		20		2.3	0.05
Fossil-fuel plants					
Coal - pulverised burner	740	820	910	100	2.05
Gas - CCGT	410	490	650	60	1.23

As it is not available in literature, a gCO₂e/kWh is estimated for WHR-ORCs. WHR-ORCs have no ongoing fuel costs, and so all of the CO₂ emissions from a WHR plant are embodied in the capital, operation and maintenance costs. As WHR plants generally cost somewhere in between onshore wind power and concentrating solar (Southon, 2015), and as the types of materials required for these systems are somewhat comparable (J.L. Sullivan *et al.*, 2010), the lifetime CO₂e/kWh is estimated to be in the range between these two plant types (1.3%-3.3% of pulverized coal). This estimate is not expected to apply for WHR-ORCs in situations where the process providing the waste heat has to be changed in order to accommodate the heat extraction, such as requiring additional heat or increasing fan power.

3.2 ORC competitiveness with coal electricity under GHG pricing

The cost of producing electricity can be represented using the Levelised Cost of Electricity (LCOE) shown in equation (1).

$$LCOE = \frac{\sum_{t=1}^n \frac{I_t + M_t + F_t}{(1+i)^t}}{\sum_{t=1}^n \frac{E_t}{(1+i)^t}} \quad (1)$$

Pulverised, scrubbed coal is a major source of electricity worldwide, with a historical LCOE of around \$0.06 / kWh (NREL, 2014). A simple economic model is used to explore the effect of GHG price on the competitiveness of ORC systems compared to standard pulverised coal electricity. The LCOE of theoretical geothermal (binary), WHR, biomass without heat sales, and CSP electricity were modelled using the following assumptions:

- Capacity factors of 92% for geothermal, 90% for biomass dedicated electricity and WHR, and 30% for CSP.
- Annual O&M costs of 5%.
- System lifetime of 20 years.
- Discount rate of 6%.
- Fuel cost for biomass dedicated electricity of \$0.015/kWh.

The lifetime-averaged cost/kWh of a nominal carbon price is then added to this LCOE to give the final electricity cost (LCOE'). The maximum ORC system investment price that still results in a LCOE' less than coal at 6¢/kWh can then be found for each carbon price, shown in Figure 5.

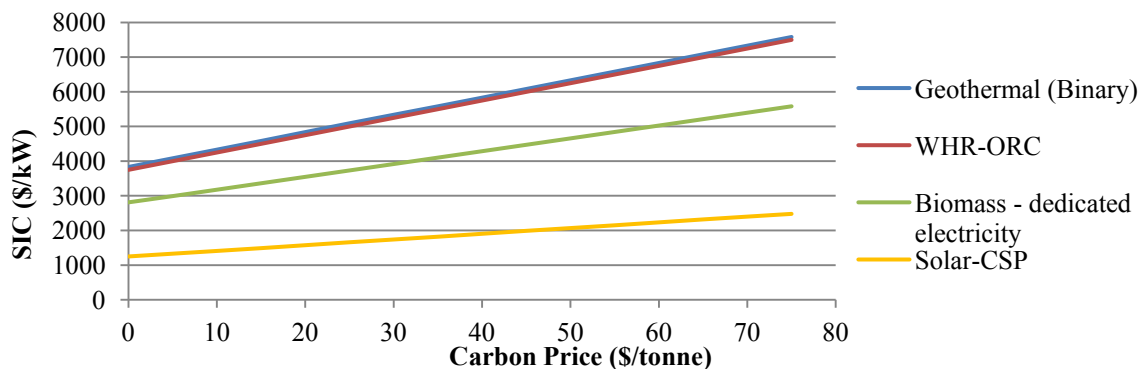


Figure 5: Maximum competitive cost/kW (SIC) for ORC systems in order to have a lower LCOE' than pulverised coal with a base price of 6¢/kWh under various GHG prices.

Figure 5 shows that a carbon price affects the maximum competitive cost of all the ORC system types investigated in a similar way, as they all produce far fewer GHG emissions than coal. At a GHG price of around \$38/tonne CO₂e, an ORC system can remain competitive at an SIC 1.5 times greater than if no carbon price was imposed. If it is assumed that all other technologies remained equal, the worldwide implementation of a policy such as this would increase the ORC capacity growth rate, reducing the time for ORCs to become a significant electricity production technology globally.

CONCLUSION

While ORC systems offer a low-CO₂ electricity solution when compared to energy-dense fossil fuel generation, their current capacity growth rate (from all energy resources) is far from sufficient for ORCs to soon become even a partial (1%) replacement for traditional electricity generation capacity, except in a few local regions and off-grid systems. In order for ORC generation to make a meaningful impact on GHG emissions in the 21st century (assuming no decrease in worldwide electricity demand), the means to affordably access and deliver as-yet-unharnessed energy resources will have to be developed and rapidly deployed.

This study found that ORCs are currently very far from being limited by the theoretical capacity of their heat resources at a global level, and so it is highly likely that there is also substantial room for growth of ORC capacity within many local electricity markets. Of the heat resources investigated, Enhanced Geothermal Systems (EGS) appear to offer the most promise for large-scale new development without having to implement significant land-use change, although many barriers still remain before EGS can fill this role. A carbon price was identified as one mechanism which could make ORCs more competitive; it was found that a GHG price of \$38/tonne would enable ORC systems to be competitive with pulverised coal at specific investment costs (SICs) 1.5 times greater than if no carbon price was implemented.

NOMENCLATURE

IEA	International Energy Agency	
EGS	Enhanced Geothermal Systems	
CSP	Concentrated solar power	
GHG	Greenhouse gas	
CO ₂ e	Carbon dioxide equivalent	
SIC	Specific Investment Cost	
LCOE / LEC	Levelised Cost of Electricity	
LCOE'	Levelised Cost of Electricity including additional carbon price	
I	Total investment outlay	(\$)
M	Operations, maintenance and repair expenditure	(\$)
F	Fuel expenditure	(\$)
E	Energy production	(kWh)
i	Chosen discount rate	(%)
n	System lifetime	(years)
Subscript		
t	Reference year	

REFERENCES

- Carlos de Castro, Margarita Mediavilla, Luis Javier Miguel, Fernando Frechoso. (2015). Global solar electric power potential: technical and ecological limits (Draft). *Energy Policy (Submitted)*.
- Chris J. Bromley, Mike Mongillo, Gerardo Hiriart, Barry Goldstein, Ruggero Bertani, Ernst Huenges, Arni, & Ragnarsson, Jeff Tester, Hirofumi Muraoka, Vladimir Zui. (2010). *Contribution of Geothermal Energy to Climate Change Mitigation: the IPCC Renewable Energy Report*. Paper presented at the World Geothermal Congress, 2010, Bali, Indonesia.
- EPIA. (2014). Global market outlook for photovoltaics. In G. M. Tom Rowe, Sinead Orlandi, Manoël Rekingier (Ed.): European Photovoltaic Industry Association.
- Exergy. (2015). References.
- Franz Trieb, Christoph Schillings, Marlene O'Sullivan, Thomas Pregger, Carsten Hoyer-Klick. (2009). *Global potential of concentrating solar power*. Paper presented at the SolarPaces, Berlin.

- Glassley, William E. (2014). Use of Geothermal Resources: Environmental Considerations Geothermal Energy (pp. 325-350): CRC Press.
- Heinimo, J., & Junginger, M. (2009). Production and trading of biomass for energy – An overview of the global status. *Biomass and Bioenergy*, 33(9), 1310-1320.
- IEA. (2014). Key World Energy Statistics: International Energy Agency.
- IMF. (2015). IMF Primary Commodity Prices. Retrieved from: www.imf.org/external/np/res/commod/index.aspx
- IRENA. (2013). Concentrating Solar Power: Technology Brief.
- Jradi, M., & Riffat, S. (2014). Modelling and testing of a hybrid solar-biomass ORC-based micro-CHP system. *International Journal of Energy Research*, 38(8), pp. 1039-1052.
- Mansell, Anthony. (2015). What role for carbon markets in the 2015 climate agreement? *BioRes*, 9(1). <http://www.ictsd.org/bridges-news/biores/news/what-role-for-carbon-markets-in-the-2015-climate-agreement>
- McKenna, R. C., & Norman, J. B. (2010). Spatial modelling of industrial heat loads and recovery potentials in the UK. *Energy Policy*, 38(10), 5878-5891. doi: <http://dx.doi.org/10.1016/j.enpol.2010.05.042>
- NREL. (2014). *Open EI Transparent Cost Database*. Retrieved from <http://en.openei.org/apps/TCDB/>
- OECD/IEA. (2015). *Statistics Report*. Retrieved from: <http://www.iea.org/statistics/>
- ORMAT. (2015). Global Projects. from <http://www.ormat.com/global-project>
- Qiu, Guoquan, Shao, Yingjuan, Li, Jinxing, Liu, Hao, & Riffat, Saffa B. (2012). Experimental investigation of a biomass-fired ORC-based micro-CHP for domestic applications. *Fuel*, 96(0), 374-382. doi: <http://dx.doi.org/10.1016/j.fuel.2012.01.028>
- Quoilin, S., Dumont, O., Lemort, V. (2015). Design, modeling and performance optimization of a reversible Heat Pump /Organic Rankine Cycle. *ASME Journal of Engineering for Gas Turbines and Power*, In Press.
- Quoilin, Sylvain, Broek, Martijn Van Den, Declaye, Sébastien, Dewallef, Pierre, & Lemort, Vincent. (2013). Techno-economic survey of Organic Rankine Cycle (ORC) systems. *Renewable and Sustainable Energy Reviews*, 22(0), 168-186. doi: <http://dx.doi.org/10.1016/j.rser.2013.01.028>
- Schlömer S., T. Bruckner, L. Fulton, E. Hertwich, A. McKinnon, D. Perczyk, J. Roy, R. Schaeffer, R. Sims, P. Smith, and R. Wisser. (2014). Annex III: Technology-specific cost and performance parameters *Climate Change 2014: Mitigation of Climate Change. Contribution of Working Group III to the Fifth Assessment Report of the Intergovernmental Panel on Climate Change*. Cambridge, UK and New York, USA: Cambridge University.
- Southon, M. (2015). *Performance and cost evaluation to inform the design of Organic Rankine Cycles in New Zealand*. (ME thesis), University of Canterbury <http://hdl.handle.net/10092/10591>
- Sullivan J.L., Clark C.E., Han J., and Wang M. (2010). Life-Cycle Analysis Results of Geothermal Systems in Comparison to Other Power Systems (Energy Systems Division,): UChicago, Argonne National Laboratory.
- Tchanche, Bertrand F., Lambrinos, Gr, Frangoudakis, A., & Papadakis, G. (2011). Low-grade heat conversion into power using organic Rankine cycles – A review of various applications. *Renewable and Sustainable Energy Reviews*, 15(8), 3963-3979.
- Turboden. (2015). References. from <http://www.turboden.eu/en/references/references.php>
- Ungemach, Pierre; Antics, Miklos. (2010, 11 June 2010). *Assessment of EGS potential*. Paper presented at the Technology Platform: Geothermal Electricity 3rd Meeting, Pisa, Italy.
- Weisser, Daniel. (2007). A guide to life-cycle greenhouse gas (GHG) emissions from electric supply technologies. *Energy*, 32(9), 1543-1559. doi: <http://dx.doi.org/10.1016/j.energy.2007.01.008>
- Zarza, Dr Eduardo. (2013). Increasing the efficiency of small scale CSP applications. from <http://social.csptoday.com/technology/increasing-efficiency-small-scale-csp-applications>

ACKNOWLEDGEMENTS

The project was supported by Heavy Engineering Research Association (HERA) as part of the Above Ground Geothermal and Allied Technology (AGGAT) program with funding from NZ Ministry for Business, Innovation and Employment contract: HERX1201. The corresponding author would like to thank the University of Liège for hosting them during the completion of this paper.

STUDY ON THE INFLUENCE OF EVAPORATOR OF ORC SYSTEM ON ENGINE PERFORMANCE

Chen Bei^{1,2*}, Hongguang Zhang^{1,2}

¹Beijing University of Technology, College of Environmental and Energy Engineering,
Beijing, China
E-mail: bc887410@126.com

²Collaborative Innovation Center of Electric Vehicles in Beijing,
Beijing, China
E-mail: bc887410@126.com

* Corresponding Author

ABSTRACT

In this paper, a simulation model of a fin-and-tube evaporator for the organic Rankine cycle (ORC) system is established by Fluent software. Then, the flow and heat transfer characteristics of the exhaust at the evaporator shell side are obtained, and then the performance of fin-and-tube evaporator of the ORC system is analyzed based on the aforementioned simulation results. Subsequently, the influence of evaporator of the ORC system on engine performance is studied. A simulation model of the engine is developed by using GT-Power under various operating conditions, the variation of engine power, torque and brake specific fuel consumption (BSFC) are obtained. Results show that, owing to the pressure drop caused by the evaporator of the ORC system, the diesel engine power and torque decreases slightly, while the BSFC increases slightly with the increase of exhaust back pressure. With the increase of engine speed, the power loss, the torque loss and the BSFC increment increase gradually, where the biggest change is less than 1%.

1. INTRODUCTION

With the development of economy, the car ownership is increasing rapidly; it will cause a lot of energy consumption and serious environmental pollution. Of the engine's fuel combustion energy, only about one third is converted into mechanical energy and the remaining is dissipated in the form of waste heat through the exhaust and the coolant system (Heywood JB, 1988).

Organic Rankine cycle (ORC) is an effective method for waste heat recovery and has been widely applied in many domains. Yari *et al.* (2011) investigated recovery waste heat from a gas turbine-modular helium reactor using different arrangements of organic Rankine cycles (ORCs) which included simple organic Rankine cycle, ORC with internal heat exchanger and regenerative organic Rankine cycle. The results showed that simple organic Rankine cycle is the best from the view of both thermodynamics and economics, the efficiency of this cycle was about 10% higher than that of without ORC system. Baik *et al.* (2012) proposed that the heat-transfer performance of the exchanger has a significant impact on the output power of the ORC. M. Hatami *et al.* (2014) recycled exhaust gas energy of gasoline engine and diesel engine by two different evaporators separately. The evaporators were simulated under three different kinds of turbulence model by Fluent software. Then, the variations of outlet temperature of exhaust and working fluid depended on the engine torque are obtained. The results showed that, simulation results which select the SST k- ω and RNG k- ϵ model are closer to experimental results. Borrajo-Pelaez R, *et al.* (2010) studied the performance of a plain fin-and-tube heat exchanger, and 3D numerical simulation method were used with higher heat transfer accuracy. Perrotin and Clodic (2004) presented the results of 2D and 3D CFD models of compact

louvered heat exchangers for the determination of heat transfer and pressure drop characteristics and local information analysis. 2D and 3D steady simulations were performed and compared to experimental results and correlations of the literature. J.F. Zhang *et al.* (2009) simulated the flow and heat transfer process of the spiral baffle plate heat exchanger shell side by Fluent software, and analyzed the mechanism of heat transfer use the field synergy principle. The results had a certain theoretical guiding significance for design the spiral baffle plate heat exchanger. Zhang *et al.* (2008) analyzed experimental and numerical heat transfer characteristics of a helically baffled heat exchanger combined with one three-dimensional finned tube. The results indicated that numerical investigations agree well with the measurements. Ozden *et al.* (2010) investigated the shell side design of a shell-and-tube heat exchanger by numerically modeling a small heat exchanger. The flow and temperature fields inside the shell were resolved using a commercial CFD package. The results showed that CFD simulations can pin point the source and the location of the weakness. Using CFD, together with supporting experiments, may speed up the shell-and-tube heat exchanger design process. Aytunc Erek *et al.* (2005) studied the influence of the geometric structure of the fin on heat transfer and resistance characteristics of heat exchanger based on the numerical simulation method use CFD software. The results showed that, the fin spacing has a considerable effect on the pressure drop. Therefore, taking as the heat transfer component of the ORC system, evaporator has an impact on ORC system, but also influences engine performance.

The main target of this research is to analyze the flow and heat transfer characteristics of the engine exhaust at the evaporator shell side and the influences of evaporator used in ORC system on engine performance under various operating conditions.

2. SIMULATION MODEL OF EVAPORATOR

2.1 Physical Model of Evaporator

In this paper, the flow and heat transfer characteristics of the exhaust at the evaporator shell side are obtained using Fluent software. The half section physical model of the fin-and-tube evaporator is shown in Fig.1. It consists of the front-end part, the main body, and the rear-end part. The main body is the heat convection place of the exhaust gas and the organic working fluid. The high temperature exhaust gas of diesel is at the evaporator shell side, the low temperature organic working fluid is in the tube side. The specific geometric parameters of fin-and-tube evaporator are shown in Table 1.

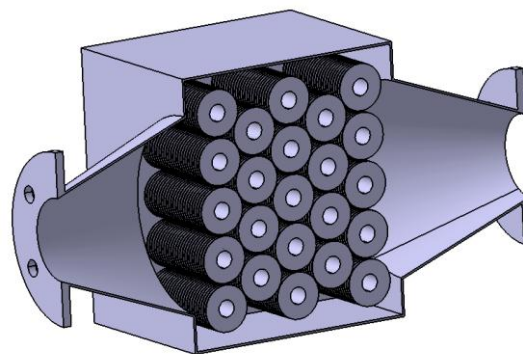


Figure 1: Physical model for the fin-and-tube evaporator

Table 1: Geometric dimensions of the fin-and-tube evaporator

Item	Parameter	Unit
Number of tube rows	5	-
Number of tubes in a row	4 or 5	-
Total number of tubes	23	-
Fin thickness	1	mm
Fin height	27	mm

Tube outside diameter	27	mm
Tube inner diameter	20	mm
Tube pitch	47×56	mm
Tube row alignment	Staggered	-

In order to ensure the accuracy of the flow and heat transfer calculation and simplify the numerical calculation, we used a quarter of the evaporator's physical model for calculations and make the following assumptions: (1) The thermal physical properties of the exhaust gas are set as constants based on the average exhaust temperature. (2) The temperatures of fins, round tubes and shells are set to average value. (3) The flow of exhaust gas at the evaporator shell side is turbulent, and the heat-transfer process is steady. (4) Ignore the free convection and gravity of the exhaust gas.

2.2 Boundary Conditions

In this paper, the fin-and-tube evaporator is used for recovery the exhaust heat of a diesel engine. We study the flow and heat transfer characteristics of the exhaust at the evaporator shell side at one steady operation point, where the engine speed is 2600 r/min and the engine torque is 180.7 N m. According to the engine test data, mass flow rate of the intake air is 0.06464 kg/s, the fuel injection rate is 0.00324 kg/s and the exhaust temperature at the inlet of the evaporator is 628 K. Thus, the mass flow rate of the exhaust, which is the summation of the intake air and the injected fuel, is 0.06788 kg/s. The exhaust pressure at the outlet is set to the ambient pressure. The boundary conditions are summarized in Table 2. In this study, the thermodynamic properties of the exhaust gas are set as constants based on the average exhaust temperature.

Table 2: The boundary conditions

Item	Parameter	Unit
Mass flow rate of exhaust gas	0.06788	kg/s
Temperature at evaporator inlet	628	K
Pressure at evaporator outlet	1.01×10^5	Pa
Temperature of fins and tubes	450	K
temperature of shells	555	K

2.3 Grid Generation and Numerical Method

The geometry model of evaporator is established using CATIA software. We used a quarter of the evaporator's physical model for calculations based on the principle of symmetry. We built 3D grid system using the commercial tool ICEM 14.5 and discretized it with unstructured elements of tetra/mixed type. The grid of evaporator model is shown in Fig.2.

A careful check for the grid-independence of the numerical solutions has been made to ensure the accuracy and validity of the numerical results. In order to verify the independence of grid system, three different grid systems were obtained. The first grid system has 3,314,020 cells, the second grid system has 4,426,733 cells, and the last one has 5,901,946 cells. Through the simulation calculation, the exhaust temperatures at the outlet of the evaporator for three different grid systems were obtained. The relative errors of the average exhaust temperature at the outlet are 0.42% and 0.21%, respectively. Thus, the solution precision of the last grid system is satisfactory.

The numerical calculations are used for Fluent14.5. A finite volume method is employed to discrete the governing equations. The SIMPLE algorithm is selected in these numerical calculations. The convergence criteria are the residual errors is less than 10^{-3} for the velocity and the momentum equations and the residual errors is less than 10^{-6} for the residual error for the energy equation.

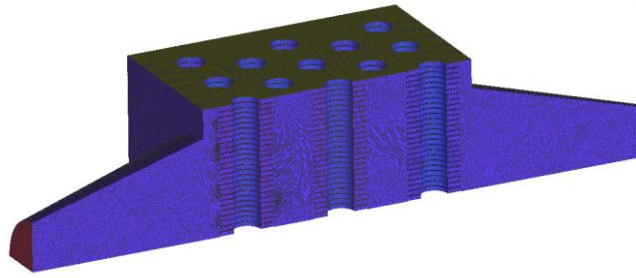
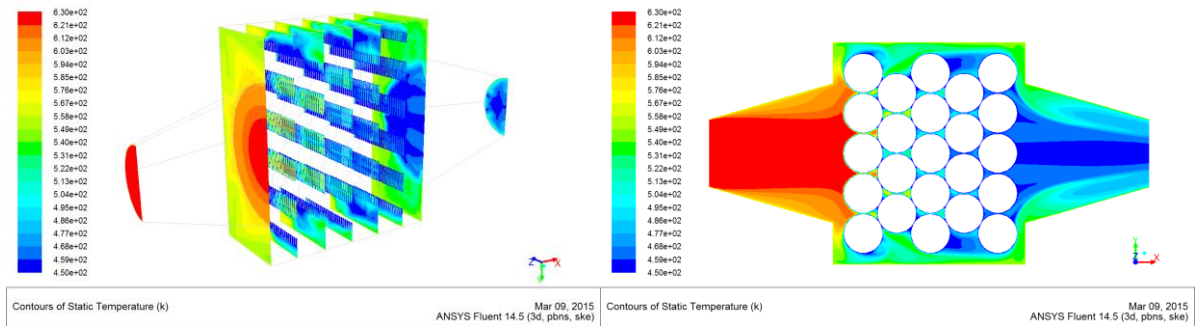


Figure 2: Grid of evaporator model

2.4 Results and Discussion of Evaporator Simulation



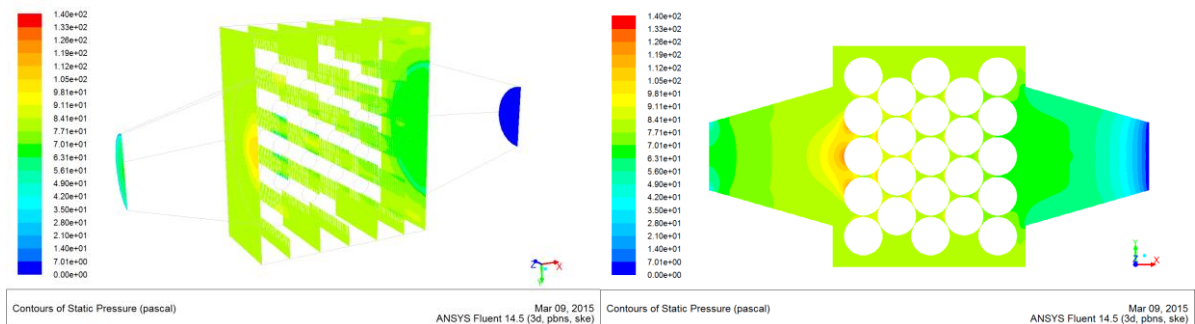
(a) Transversal surface section

(b) Center symmetry section

Figure 3: Temperature distribution of exhaust in the evaporator

In order to analyze the flow and heat transfer characteristics of the exhaust at the evaporator shell side, we chose 9 planes in different positions vertical to the x-axis. The specific locations are shown in Fig.3 (a). The center symmetry plane vertical to the z-axis is shown in Fig.3 (b). To reduce the workload, we used a quarter of the evaporator's physical model for calculations. Afterwards, we symmetrize the results along the symmetric plane. We use 5 planes in the middle along the direction of the exhaust flow to represent the planes through the centerlines of the tube bundles in each row.

The details of the temperature distribution in the evaporator are shown in Fig.3. The exhaust temperature of the area of front-end part approximately equals the inlet exhaust temperature of 628 K. The exhaust temperatures of the two corners far from the central area are relatively lower at approximately 520 K. In addition, the flow areas of the high-temperature exhaust gas are nearly round and expand gradually along the flow direction. The exhaust temperatures of the round areas decrease gradually, which means the high-temperature exhaust gas in the flow space between the first and second rows diffuses quickly. The temperature of the exhaust gas near the fin is low, so the heat exchange efficiency is better.



(a) Transversal surface section

(b) Center symmetry section

Figure 4: Pressure distribution of exhaust in the evaporator

The details of the pressure distribution in the evaporator are shown in Fig.4. The maximum pressure of the evaporator exists on central area of the first row of the bundles near the front-end part. The high-temperature exhaust in the tapered divergent pipe is blocked by the tube bundles of the first row, rapidly reducing the exhaust mass flow rate, leading to a rapid increase of the exhaust pressure. The maximum pressure of the evaporator is 141.34 Pa and is significantly lower than the maximum limit of 30 kPa. The pressure drop of exhaust gas between import and export of evaporator is about 53 Pa. It is the back pressure of exhaust under this work point of diesel engine.

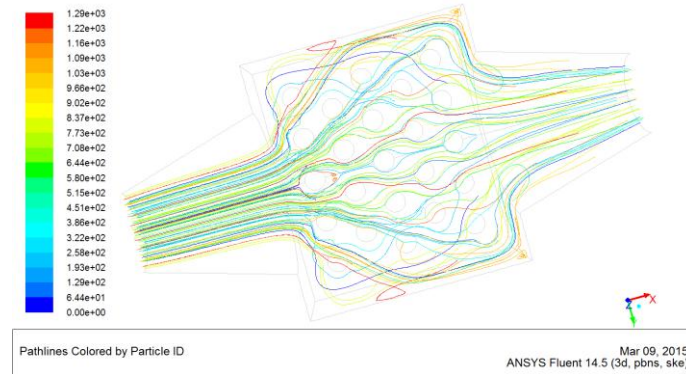


Figure 5: Streamlines of the exhaust gas in the evaporator

Streamlines of the exhaust gas in the evaporator are shown in Fig.5. The exhaust flow is well distributed, which means the convective heat transfer is fully developed in the center of the evaporator. In the two corners far from the center of the evaporator and near the front-end part, there little exhaust flow exists, resulting in a very poor convective heat transfer. However, the heat conduction process dominates in these regions and results in very low temperatures at the corners. Because the shape of the front-end part connecting with the main body is round, the exhaust flux entering into the main body is restricted in the domains close to the centers. The exhaust temperature of the central zones is quite low because of the cooling effects of the tube walls and the fins. Therefore, to ensure the exhaust flux is equally distributed in the spaces between the neighboring fin layers, the design of the shapes connecting the main body with the front-end and rear-end parts are very important.

According to the results of numerical simulation, the average exhaust temperature at the outlet of the evaporator is 473 K. The exhaust temperature is 491 K, according to the results of experiment. The error of the exhaust temperature at the outlet is 3.67 % which is in the reasonable scope. It verified the accuracy of the simulation mode. So the evaporator simulation model can be analyzed and researched. The reasons for error: only one point is measured for temperature sensor, but the result of numerical simulation is the average value in the face.

3. SIMULATION OF THE DIESEL ENGINE

3.1 Simulation Model of the Diesel Engine

In this paper BJ493ZLQ3 is selected as the research object. BJ493ZLQ3 is a diesel engine with inline four cylinders, four-stroke, forced water cooling, turbocharged intercooled, electronic control high pressure common rail. Technology parameters of the BJ493ZLQ3 diesel engine are showed in Table 3. A simulation model of the engine is developed based on GT-Power, the model includes: (1) The intake and exhaust system model. (2) Injector model. (3) Cylinder model. (4) Crankcase model. (5) Turbocharged system model. (6) The set of the system boundary conditions (temperature and pressure).

Table 3: Technology parameters of the BJ493ZLQ3 diesel engine

Item	Parameter	Unit
Cylinder diameter	93	mm
Stroke	102	mm
Compression ratio	17.4	-
Displacement	2.771	L
Rated power	85	kW
Rated speed	3600	r/min
Maximum torque	280	N m
Speed at max. torque	2300	r/min

In this paper, the simulation model of BJ493ZLQ3 diesel engine is built, which is shown in Fig.6.

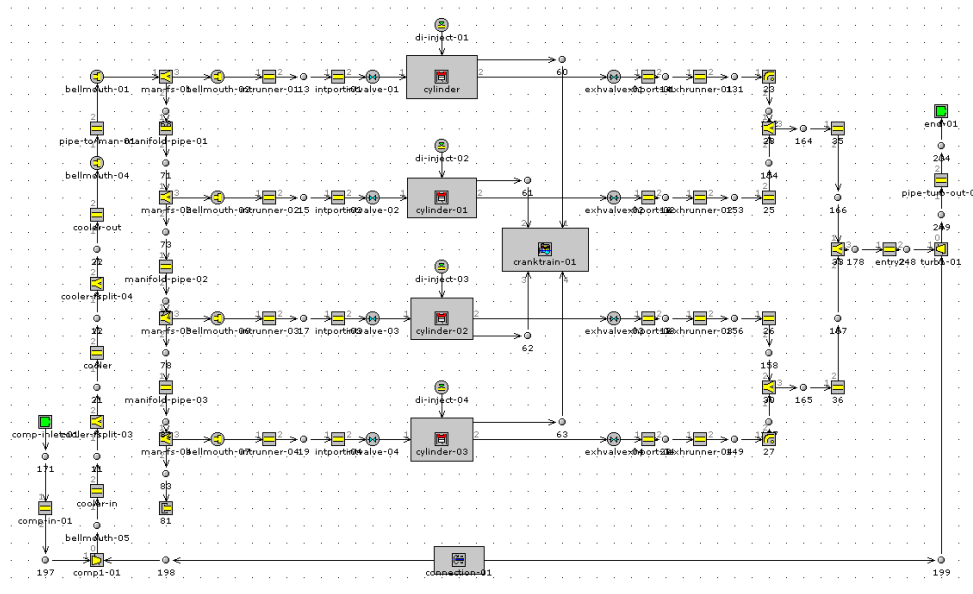


Figure 6: BJ493ZLQ3 diesel engine simulation model

3.2 Validation of Diesel engine Simulation Model

In order to ensure the simulation model can describe the actual operation of diesel engine and predict the performance of diesel engine effectively. The simulation results for various operating points are verified by using the experiment results of BJ493ZLQ3 diesel engine.

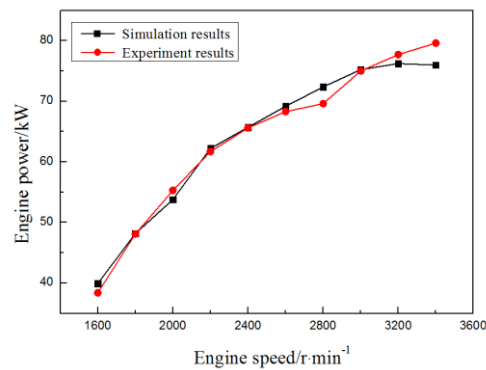


Figure 7: Simulation and experiment results of power at full load

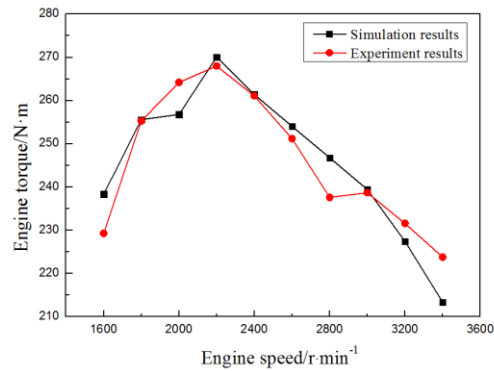


Figure 8: Simulation and experiment results of torque at full load

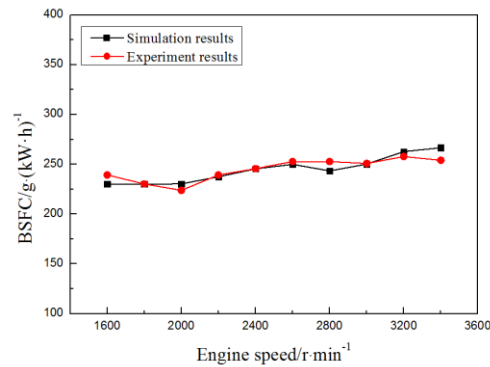


Figure 9: Simulation and experiment results of BSFC at full load

The simulation and experiment results of power, torque and brake specific fuel consumption (BSFC) of BJ493ZLQ3 diesel engine at full load are shown in Figures 7, 8 and 9. Simulation results have the similar variation trend with experiment results. At the speed of 3400 r/min, the relative error between simulation and experiment values of the power, torque and BSFC are all the biggest, which is 4.97%, 4.65% and 4.97% respectively.

According to the above-mentioned analysis, the maximum relative error between the simulation and experiment values is less than 5%. So, the engine simulation model can be employed with a high precision.

4. INFLUENCE OF EVAPORATOR ON THE ENGINE CHARACTERISTICS

In this study, the influence of evaporator of the ORC system on engine performance is studied under 6 operating conditions. The exhaust back pressure increment of engine exhaust is obtained according to the pressure drop between import and export of evaporator which is acquired from the simulation result. Then, a simulation model of the engine is developed by using GT-Power. The variation of engine power, torque and BSFC is discussed after equipping with evaporator of the ORC system under various operating conditions.

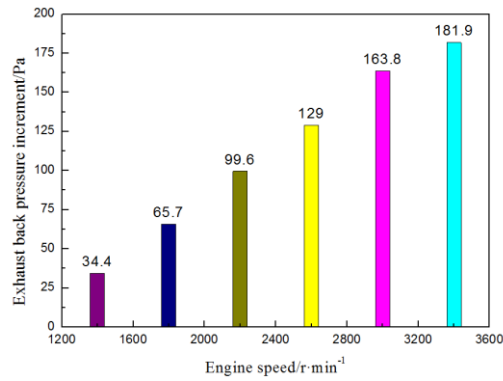


Figure 10: The exhaust back pressure increment of diesel engine under various operating conditions

The exhaust back pressure increment after equipping with evaporator of the ORC system under various operating conditions is shown in Fig.10. With the increase of engine speed, the engine exhaust back pressure increment increases gradually. The main reason is that, with the increase of engine speed, engine intake air mass flow rate increases gradually, which results in the increase of the exhaust mass flow rate, and then the pressure drop of engine exhaust increases at the evaporator shell side.

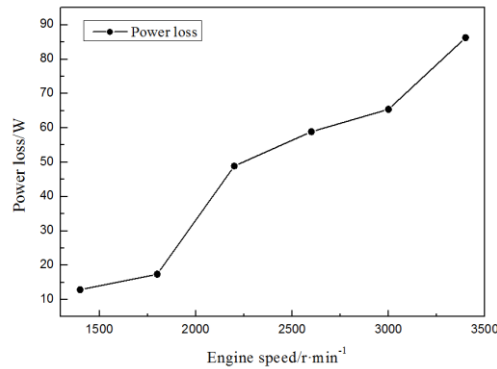


Figure 11: Power loss of diesel engine under various operating conditions

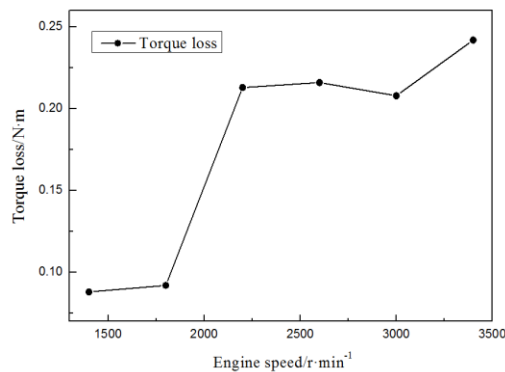


Figure 12: Torque loss of diesel engine under various operating conditions

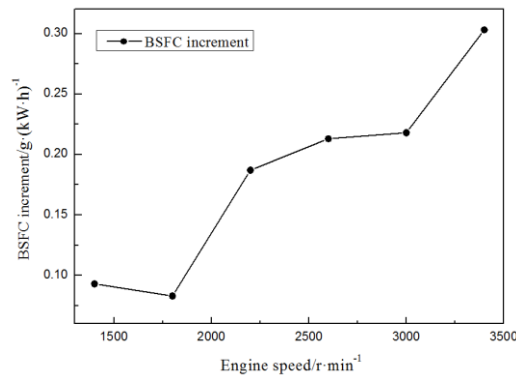


Figure 13: BSFC increment of diesel engine under various operating conditions

The power loss, the torque loss and the BSFC increment of diesel engine after equipping with evaporator of the ORC system under various operating conditions is shown in Fig.11-Fig.13. Equipped with the evaporator of the ORC system, the diesel engine power and torque decreases within a small range, while the BSFC increases within a small range with the increase of exhaust back pressure. With the increase of engine speed, the power loss, the torque loss and the BSFC increment of engine increase gradually. The main reason is that, diesel engine exhaust generated flow resistance in the shell side of evaporator after equipping with evaporator of the ORC system. Subsequently, exhaust back pressure of engine increased. With the increase of exhaust back pressure, residual gas pressure in cylinder of the diesel engine raised. This will not only increase the residual gas coefficient, furthermore, reduces the charging coefficient, but also increase the pumping loss. Finally, the engine power and torque decreased while the BSFC increased.

5. CONCLUSIONS

In this study, a simulation model of a fin-and-tube evaporator of an ORC system is established by Fluent software. Then, the flow and heat transfer characteristics of the exhaust at the evaporator shell side are obtained. Subsequently, the influence of evaporator of the ORC system on engine performance is studied.

- The exhaust gas temperatures decrease gradually along the flow direction at the evaporator shell side. The exhaust gas in the flow space between the first and second rows diffuses quickly. To ensure the exhaust flow is equally distributed in the spaces between the neighboring fin layers, the design of the shapes connecting the main body with the front-end and rear-end parts are very important.
- The maximum exhaust pressure occurs in the connection area between the front-end part and the main body because of the sudden reduction of the flow area. With the increase of engine speed, the engine exhaust back pressure increment increases gradually after equipping with evaporator of the ORC system.
- The diesel engine power and torque decreases within a small range, while the BSFC increases within a small range with the increase of exhaust back pressure after equipping with evaporator of the ORC system. With the increase of engine speed, the power loss, the torque loss and the BSFC increment of engine increase gradually.

REFERENCES

- Heywood JB., 1988, Internal Combustion Engine Fundamentals, *McGraw-Hill*, New York, p.673-674.
- Yari M., Mahmoudi S.M.S., 2011, A thermodynamic study of waste heat recovery from GT-MHR using organic Rankine cycles, *Heat Mass Transfer*, vol. 47: p.181-196.
- Baik Y, Kim M, Chang K, Lee Y, Yoon H., 2012, Power enhancement potential of a mixture transcritical cycle for a low-temperature geothermal power generation, *Energy*, vol. 47: p.70-76.
- Hatami M., Ganji D.D., Gorji-Bandpy M., 2014, Numerical study of finned type heat exchangers for ICEs exhaust waste heat recovery, *Case Studies in Thermal Engineering*, vol. 4: p.53-64.

- Borrajo-Pelaez R., Ortega-Casanova J., Cejudo-Lopez J.M., 2010, A three-dimensional numerical study and comparison between the air side model and the airwater side model of a plain fin-and-tube heat exchanger, *Applied Thermal Engineering*, vol. 30: p.1608–1615.
- Perrotin T, Clodic D., 2004, Thermal-hydraulic CFD study in louvered fin-and-flat-tube heat exchangers, *International Journal of Refrigeration*, vol. 27, no. 4: p.422–432
- Zhang J.F., He Y.L., Tao W.Q., 2009, 3D numerical simulation on shell-and-tube heat exchangers with middle-overlapped helical baffles and continuous baffles - Numerical model and results of whole heat exchanger with middle-overlapped helical baffles, *International Journal of Heat and Mass Transfer*, vol.52: p.5371–5389.
- Zhang Z.G., Ma D.B, Fang X.M., 2008, Experimental and numerical heat transfer in a helically baffled heat exchanger combined with one three-dimensional finned tube, *Chemical Engineering and Processing*, no. 47: p.1738–1743.
- Ozden E., Tari I., 2010, Shell side CFD analysis of a small shell-and-tube heat exchanger, *Energy Conversion and Management*, vol. 51, no. 5: p.1004–1014.
- Aytunc E., Bails O., Levent B., 2005, Effect of geometrical parameters on heat transfer and pressure drop characteristics of plate fin and tube heat exchangers, *Applied Thermal Engineering*, vol. 25, no. 14-15: p.2421-2431.

ACKNOWLEDGEMENT

This work was sponsored by the National Natural Science Foundation of China (Grant No. 51376011), the Beijing Natural Science Foundation Program (Grant No. 3152005), and the Scientific Research Key Program of Beijing Municipal Commission of Education (Grant No. KZ201410005003).

WASTE HEAT UTILIZATION OF MAIN PROPULSION ENGINE JACKET WATER IN MARINE APPLICATION

Errol L. Yuksek^{1*}, Parsa Mirmobin²

Calnetix Technologies, LLC
Cerritos, CA, USA

¹eyukse@calnetix.com

²pmirmobin@calnetix.com

KEYWORDS: waste heat recovery; organic Rankine cycle; R245fa; heat to electricity; heat engine; jacket water heat utilization; marine diesel propulsion engine; diesel generator fuel reduction; marine vessel emissions; sustainable maritime transportation

ABSTRACT

As world trade grows, fuel prices increase, and International Maritime Organization (IMO) emissions requirements tighten, there is more demand for the marine industry to employ innovative means of reducing the fuel consumption and emissions of shipping vessels.

The main propulsion engines of large shipping vessels produce great quantities of jacket water heat at temperatures below 95 °C, but this valuable heat energy is transferred to cooling systems and rejected to the world's oceans as waste. At the same time, the electrical needs of these vessels are sustained by burning diesel fuel to run generators. To utilize the jacket water waste heat Calnetix Technologies, in partnership with Mitsubishi Heavy Industries (MHI), has developed the Hydrocurrent™ 125EJW (Engine Jacket Water) Organic Rankine Cycle (ORC) to convert low-grade heat energy into grid-quality electric power.

Large vessels such as tankers, bulk carriers, and container vessels with an engine output of approximately 30 MW can output as much as 300 m³/hr of 80 to 95 °C jacket water from their main propulsion engines. When integrated into the jacket water and sea water systems of such vessels, the ORC unit can produce up to 125 kW of gross grid-quality electric power. To produce 125 kW of power, a diesel generator would consume as much as 250 metric tons of diesel fuel per year in addition to its generated emissions and maintenance requirements.

Calnetix Technologies has leveraged its core technologies to develop a new high efficiency ORC system that is compact and modular in design. In addition, the ORC unit has been certified by marine classification societies Nippon Kaiji Kyokai (NK) and Lloyd's Register (LR) for installation on any vessel without modification. The following is a description and validation of the commercially available, class society certified system that has been realized.

1. INTRODUCTION

A typical general cargo ship requires approximately 1 MW of electrical power whereas a modern Liquid Natural Gas (LNG) carrier may require power in excess of 12 MW. Ship electrical power is typically provided by a combination of main engine driven generators and auxiliary engine driven generators. International maritime regulations (International Convention for the Safety of Life at Sea (SOLAS), 1974) require at least two generators as part of the ship's main electrical system. Additionally, at least one generator needs to be independent of the speed and rotation of the main propellers and decoupled from the associated shaft.

The number of auxiliary engines and utilization of them versus the main engine is a subject of trade studies at vessel design and thereafter managed by Marine Fuel Management (MFM). The MFM has

the primary goal of reducing fuel usage. This is achieved by various means including route planning and throttle management. As well as reducing fuel consumption, considerations need to be given to other aspects of fuel usage at sea in order to comply with ever stiffening international marine pollution regulations like MARPOL 73/78 (Rizzuto and Soares, 2012).

By augmenting existing electrical power generating capability of ships, a more flexible and ultimately better optimized fuel management case can be constructed whereby the primary goal of fuel consumption as well as electrical power availability and pollution reduction goals can be attained. Additional power generation capability can always be achieved by adding more generators via main or auxiliary engine generators. However, this adds significant operating cost as well as adding to existing engine pollution. A better solution is to utilize the waste heat generated by the engines to power a heat recovery cycle. Already, heat from engine exhaust is used on many ships for steam generation (Ichiki et al., 2011). To date, low-grade heat such as engine coolant (jacket water) has been difficult to utilize. A review of literature existing on the subject of applying ORC technology to utilize the low-grade waste heat of marine diesel engines yields analytical research, but none affirming any real life application (Yu et al., 2013) (Yang and Yeh, 2015) (Song et al., 2015) (Soffiato et al., 2015) (Jin et al., 2012). The following describes a unique and commercially viable solution which aims to remove this barrier and tap into the low-grade jacket water heat to generate additional electrical power without incurring any additional fuel usage or added emissions. The subject being beyond investigation of a proposed system, the ORC system described has been fully tested and certified for use on any vessel.

2. HYDROCURRENT™ 125EJW ORC

As shown in Figure 1, the heat source, in the form of jacket water, is supplied from the engine at temperatures between 80 and 95 °C. This heat is transferred to the ORC's organic working fluid (R245fa) via a heat exchanger. Since the heat exchanger is used to elevate the temperature of the working fluid as well as turn the fluid into vapor, it is often referred to as the evaporator. A similar heat exchanger is used to condense the working fluid after expansion; this is referred to as the condenser. The coolant to turn the expanded fluid into liquid is supplied via readily available sea water.

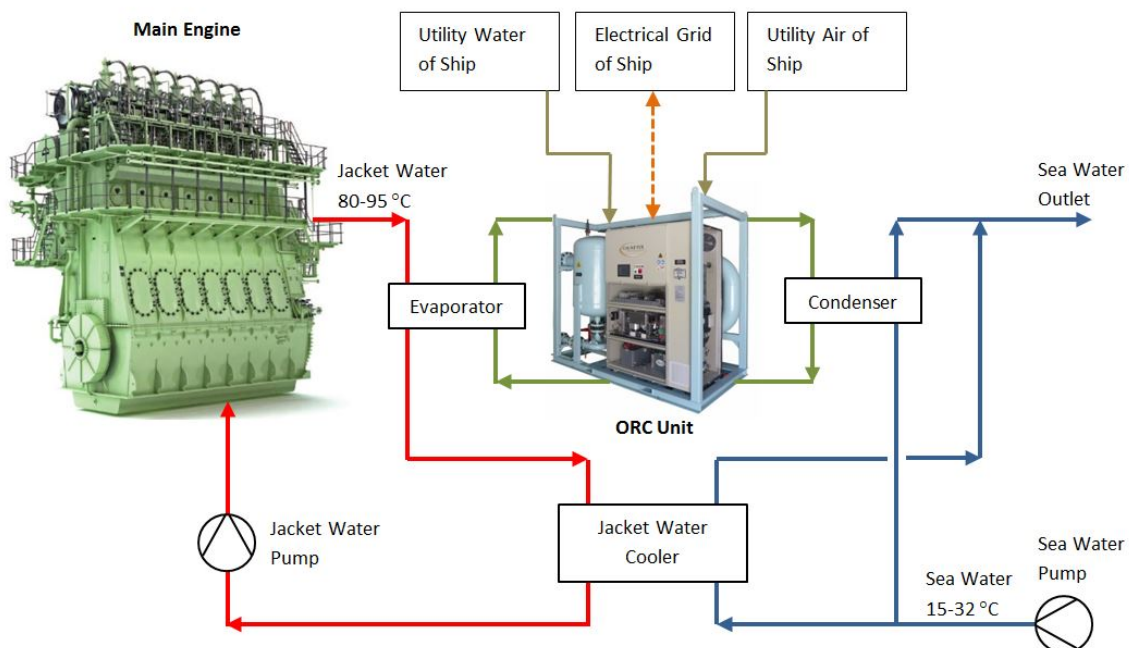


Figure 1: ORC system flow and ship interfaces. The engine pictured is a graphical rendering of a MAN G-type engine obtained from DIESELFACTS issue 1/2013 p. 5.

After the working fluid has been pressurized and evaporated it enters the Carefree Integrated Power Module™ (IPM). The high speed (16,500 rpm) turbine expander and permanent magnet generator are integrated into a single shaft within the IPM and this rotating assembly is supported by an active magnetic bearing system. The high speed generator converts the pneumatic power, developed from the working fluid, into electrical power. Electrical power from the generator requires conversion to meet the power quality and specification requirements of the ship. The conversion takes place in an active converter within the ORC unit. The electrical output power automatically synchronizes with the ship's grid voltage and frequency and maintains this synchronization irrespective of ship grid fluctuation or heat source changes.

Since the electrical power output of the ORC system is dependent on engine jacket water heat availability, the system is available whenever the main engine is in operation. By changing the power set point at the ORC unit, the power output can be modulated to meet the changing electrical load needs. This unique approach not only furnishes additional electrical power that can be readily modulated but it does so without increasing the ship's fuel consumption or pollution.

2.1 ORC Development

The ORC system as a whole utilizes the ship's main engine jacket water and sea water to facilitate evaporation and condensation of the organic working fluid in order to produce grid-quality electric power. At the design condition (125 kW gross power output), the ORC requires 208.6 m³/hr of 85 °C engine jacket water along with 341 m³/hr of 27 °C sea water. Figure 2 depicts the process flow diagram at the design condition.

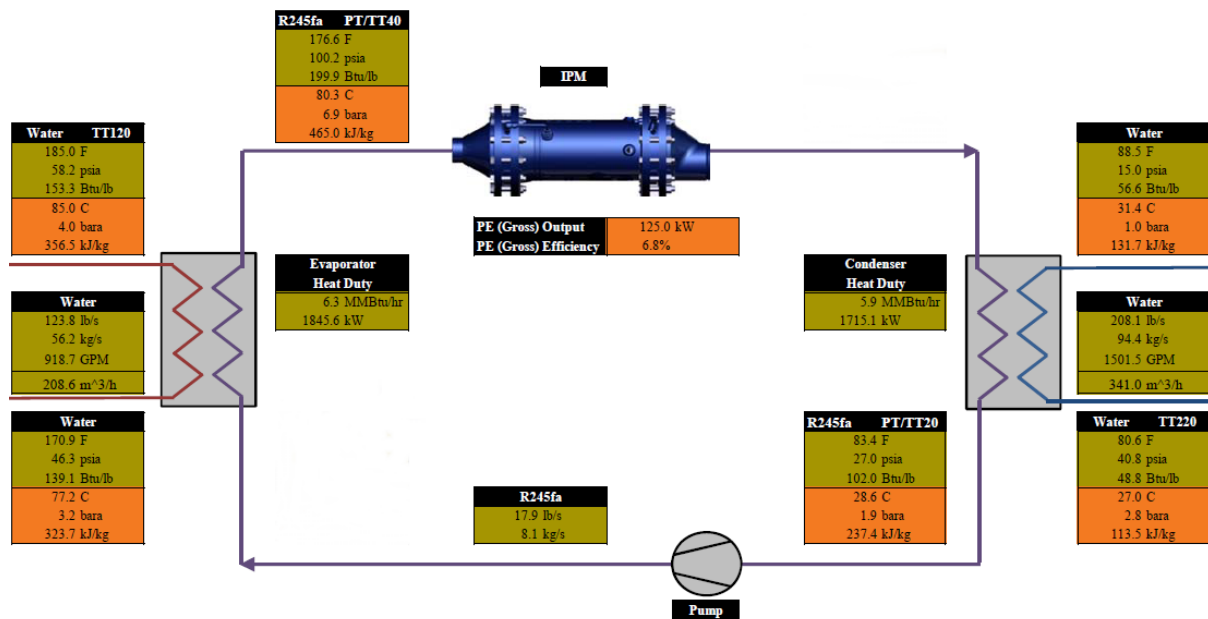


Figure 2: ORC process flow diagram at the design condition

The cycle begins with liquid working fluid stored in a receiver tank at temperature only a few degrees above that of sea water. The liquid is pumped to a higher pressure and circulated to an evaporator to absorb heat from the engine jacket water. The pressurized vapor is then expanded through the IPM's turbine which produces electrical power with its integrated generator. The working fluid is then cooled to a liquid state by the condenser utilizing cooling available from the ship's sea water system. The liquid is finally returned to the receiver tank to repeat the cycle.

Some key design features sought in the development of the ORC unit were: 1) Compact design for ease of integration into a new or existing ship engine, 2) Robust and reliable system requiring minimal maintenance, 3) Passive auxiliary system that does not interfere with normal ship functions. Design

efforts focusing on the most significant components of the ORC unit were important to the outcome of the development. Details of the function and analysis of the following ORC components will be discussed: 1) IPM - turbine and power generator, 2) Electrical Cabinet - power electronics, controls, and distribution, 3) Working Fluid Pump. Selection of the rotor-bearing system, working fluid pump and other components is based on extensive field evaluations on other Calnetix ORC systems.

2.2 Carefree Integrated Power Module™

The core of the ORC unit, the IPM provides the means to convert pneumatic power into electrical power. The IPM is a combination of a radial turbine and a Permanent Magnet (PM) generator. A cross-section along with overall dimensions and general materials of construction are shown in Figure 3. The alloy steel turbine and samarium-cobalt magnets of the generator are integrated into a single rotor shaft and supported by active magnetic bearings. This fundamental design feature brings numerous advantages over typical turbo-generators: 1) The PM generator provides higher efficiency and smaller size over other types of generators, 2) Magnetic bearings enable frictionless operation eliminating energy loss, wear and maintenance associated with otherwise lubricated bearings, 3) The integrated turbine and PM rotor eliminates a coupling and penetration between a turbine casing and generator eliminating associated mechanical shaft losses and working fluid leakage potential, 4) The integrated generator immersed in the working fluid flow eliminates a need for an external generator cooling system which reduces system cost and maintenance significantly.

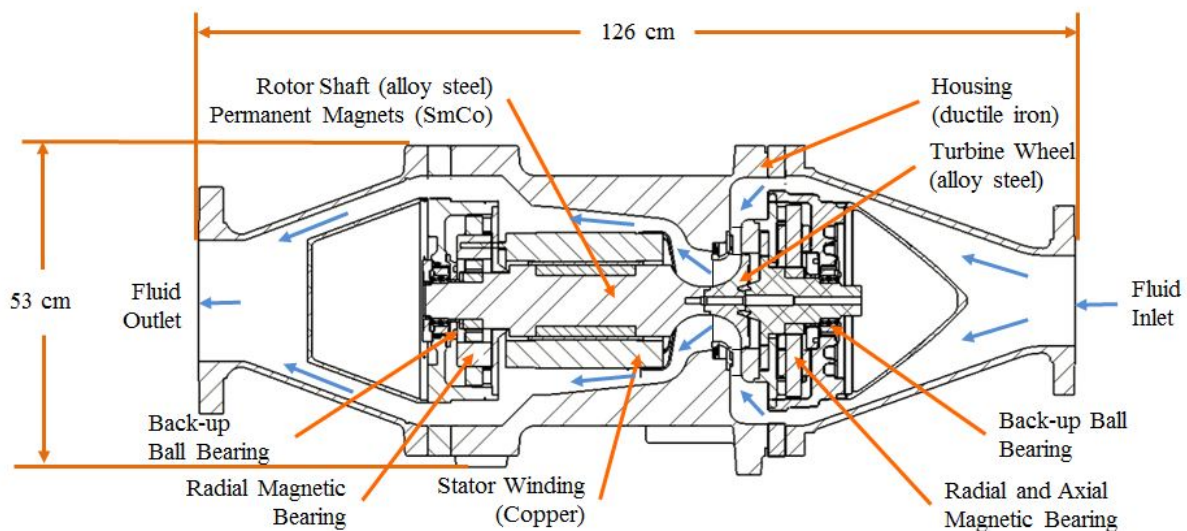


Figure 3: IPM cross-section

Design of the turbine is developed through an iterative process. Initially a mean-line analysis is carried out where size and speeds of the turbine are determined using efficiency speed maps. Thereafter, the performance of the turbine is characterized over a wide range of operating conditions. Additionally, the downstream aerodynamic losses are calculated and the entire IPM assembly is updated using a process simulation tool (Mirmobin and Sellers, 2015). Once an optimal operating point has been determined, detailed 3-D aerodynamic analysis is carried out. Any changes to the design are made at this time after which final designs of the turbine, wheel and diffusers are completed.

The turbine consists of a stationary nozzle and a shrouded radial wheel integrated with the rotor shaft. At nominal inlet conditions (6.9 bara and 80.3 °C), the turbine operates at an optimal speed of about 16,500 rpm at a rated terminal power of 137 kW. At the nominal pressure ratio of 3.0, the isentropic turbine efficiency (total to total) is about 90% and the specific speed is 0.82. To accommodate jacket water source temperature variation, the ORC control system maintains the level of superheat at the inlet to the IPM by modulating the working fluid pump speed and heat source valve position.

Therefore, there is little to no effect on vapor quality and subsequent turbine efficiency as the jacket water temperature varies.

The rotor is supported by five active magnetic bearings; one grouping is a combination radial-axial set like that of McMullen et al. (2000). The magnetic bearing design provides sufficient load capacity and load margin to ensure stable and robust operation under a variety of load sets. Sources of loading include the shaft weight, shaft unbalance, static offset (due to manufacturing variation), aerodynamic thrust, and external vibration. Selection of magnetic bearings was based on extensive use and field data from other Calnetix systems. Although conventional bearings could be used in this case, additional design considerations would need to be taken into account to ensure the bearings remain lubricated (cooled) whilst the coolant does not migrate into the working fluid and contaminate the system.

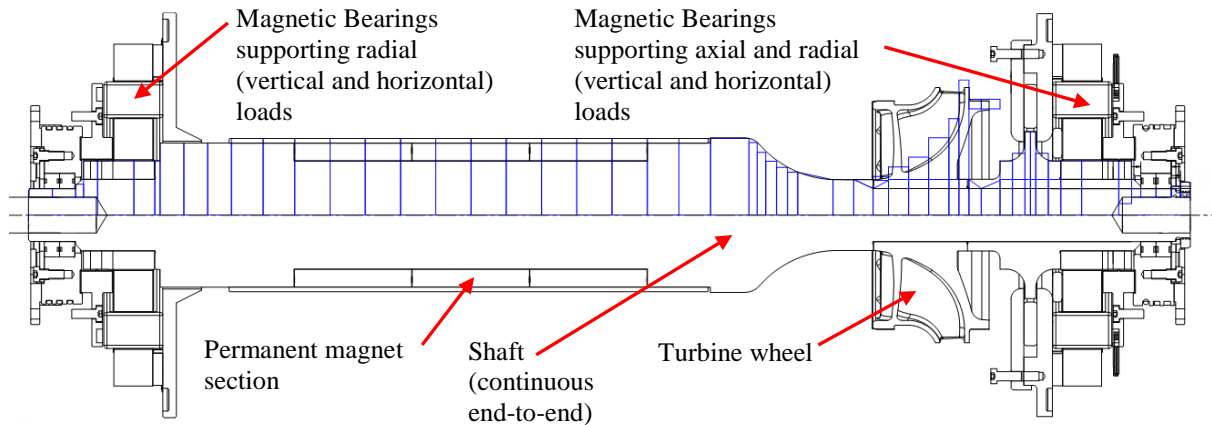


Figure 4: Rotordynamic model of IPM rotor

A rotordynamic model, shown in Figure 4, was constructed for dynamic modeling to identify natural frequencies and aid in magnetic bearing design and controls development. The rotordynamic model accounts for all mass and stiffness of the structure and couplings in between. Natural frequency of the rotor assembly is validated using a free-free resonance test. Free-free natural frequencies are determined by measuring excitation response of accelerometers affixed to rotor nodes of interest.

The magnetic bearing forces are calculated using a finite element analysis of the magnetic paths around the actuator. Permanent magnets provide a bias flux for the magnetic bearings which simplifies control with linear control response to control current commands, and when the rotor position is offset from the center can reduce the current required to maintain rotor levitation during operation; the low current consumption translates into a total IPM magnetic bearing power consumption of only about 200 W. Once the magnetic bearing design has been developed, the response of the magnetic bearing system (sensor, actuator and compensator) is modeled. The bearing design is validated with testing whereby forces exerted by the bearing system are measured for given displacements of the rotor.

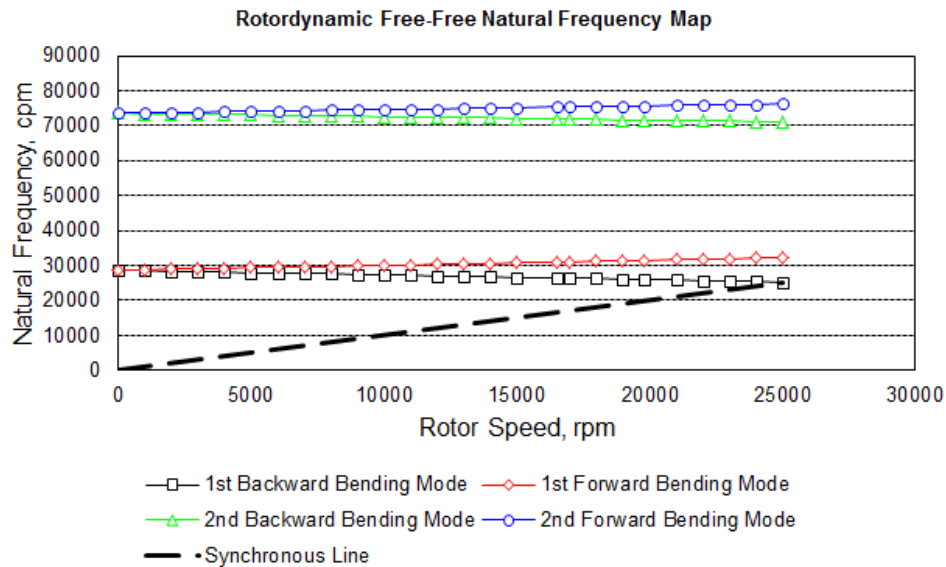


Figure 5: Free-free natural frequency map of IPM rotor

To ensure stable operation it is important to identify the natural frequencies of the rotor within the range of operating speeds, including overspeed. The overspeed limit required by marine classification societies NK and LR is 120% of the rated speed, in this case 19,800 rpm. Figure 5 depicts the free-free rotordynamic frequency map. In good practice a 15% design margin is sought between the first bending mode and the overspeed. Findings are that the first bending mode is excited at about 25,000 rpm which is well over 15% of overspeed.

2.3 Electrical Cabinet

The ORC unit is fitted with a multi-functional electrical cabinet with three primary sections: 1) Power Electronics, 2) Programmable Logic and Magnetic Bearing Controls, 3) Power Distribution.

The Power Electronics (PE) is a fully digitized motor controller with an active rectifier front end. The variable high-frequency power from the IPM generator is converted to regulated power that is synchronized to the ship's grid. Using Insulated Gate Bipolar Transistors (IGBT), the power of the IPM generator is converted from AC to DC. DC power is then converted back to AC at the grid voltage and frequency. The digital controls of the PE control the speed of the IPM as well as monitor the temperatures of the IGBTs and inductors. Speed and temperature limits are programmed within the firmware. Requiring minimal cooling water (less than 30 L/min), the PE delivers up to 125 kW of grid quality power at 440 VAC / 60 Hz or 380 VAC / 50 Hz with a conversion efficiency greater than 93% and a power factor 0.99 or greater. Total harmonic distortion (THD) of output power to the grid is no greater than 5% at 125 kW.

The Programmable Logic Controller (PLC) allows the ORC unit to operate autonomously. It monitors the temperatures and pressures necessary for proper operation as well as controls the automated engine jacket water and sea water source valves. Using temperature monitoring and the source valves the PLC ensures ship functions are unaffected when the ORC unit is offline. During operation, it actively prevents the ORC unit from cooling the engine jacket water below 75 °C or heating the sea water above 32 °C in order to safeguard the operation of the ship's fresh water maker.

The Magnetic Bearing Controller (MBC) provides 5-axis control of the IPM's active magnetic bearings. The MBC continuously monitors the rotor orbits and currents. Under adverse conditions such as high levels of unbalance or vibration the MBC sends a message to the PLC and the ORC system is shutdown in a controlled and safe manner.

The Power Distribution Unit (PDU) is the point of interface to the ship's electrical power supply. This section contains the necessary circuit breakers, contactors, filters and fuses to distribute the generated

power to the ship's grid. The PDU also provides grid power to the magnetic bearings, working fluid pump and other auxiliary loads within the ORC unit.

2.4 Working Fluid Pump

The working fluid pump is of centrifugal multistage design and is mounted horizontally to aid in achieving compactness of the skid. A special feature of the pump is its low suction head which accommodates particularly cold condensing conditions encountered in colder oceans. The pump's motor is 3-phase, 2-pole and is rated for 7.5 kW. Driven by a variable frequency drive, the pump is capable of varying the working fluid flow and pressure to compensate for varying heat source conditions and desired power generation settings.

2.5 Reliability and Maintainability

The ORC unit comprises a number of Commercial Off-The-Shelf components (COTS), particularly in the electrical cabinet and power converter. The reliability of such components is governed by industry standards.

Since the IPM's generator uses the expanded working fluid as coolant and the magnetic bearing system does not require any additional cooling, the entire IPM assembly is hermetically sealed. There are no rotating seals that require periodic maintenance. A hermetically sealed module together with non-wearing bearings provides an inherently reliable, long lasting power module.

3. ORC TESTING

Testing and validation of the ORC unit is primarily done in two phases - factory testing and sea trials. The following discussion addresses factory testing, sea trials are a subset of such tests conducted at sea for further validation of the design in actual operating environment.

Several aspects of the ORC system are tested as individual components before the system assembly is completed. Further testing is done at the system level to ensure conformance to system level requirements. The IPM is comprised of the high speed turbine expander together with the high speed PM generator. The rotating assembly is supported on an active magnetic bearing system. Due to the complexity of this module and significance in determining the overall ORC system performance, a number of component level tests are conducted and validated against requirements.

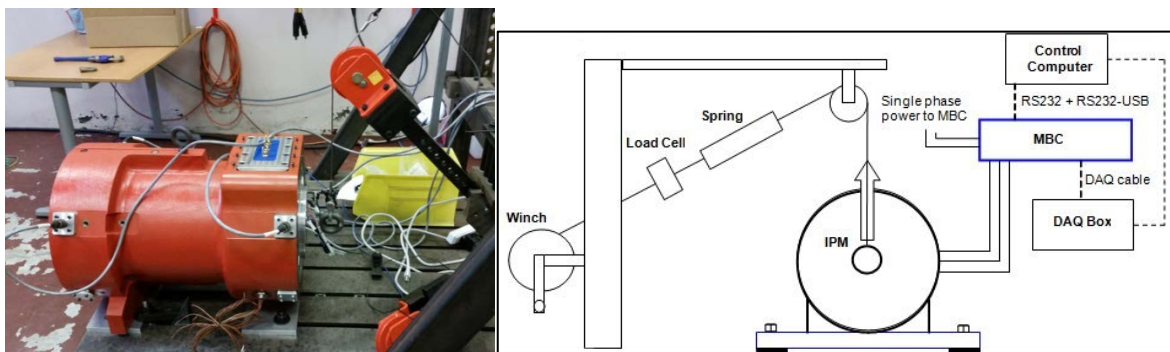


Figure 6: IPM under magnetic bearing load testing (left); IPM magnetic bearing load test setup (right)

Load capacity of the IPM magnetic bearings is validated using a load cell and MBC setup shown by Figure 6. The IPM magnetic bearing system is then tested by levitating and spinning the rotor independent of the overall ORC system. Using the MBC, the performance of the bearing system can be monitored and recorded for evaluation.

The PE is also tested independent of the ORC system whereby the active rectifier and inverter are tested to maximum load capacity and temperatures at the heat sink are monitored and recorded. Once these subassemblies have been tested and validated, the ORC system assembly takes place.

Thereafter, the system is tested at the Calnetix ORC Test Facility, shown in Figure 7, with representative heat source and condensing conditions. To validate turbine performance, the ORC system is operated at conditions which replicate engine jacket water using a closed loop of high pressure hot water.

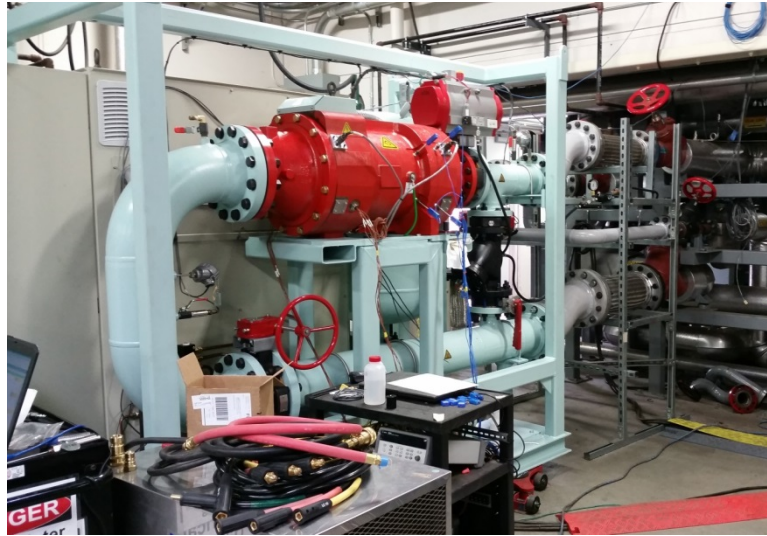


Figure 7: ORC under test at the Calnetix ORC Test Facility

In testing, the ORC unit is operated at several PE power output levels (between 50 and 125 kW). The IPM is fitted with pressure and temperature transducers both before and after the turbine. In addition, condensing conditions are varied to change the turbine pressure ratio so as to generate a full map of turbine performance and efficiency data for validation against design analysis.

The Gross Efficiency and Net Efficiency of the ORC are defined by equations (1) and (2). Equation (3) defines the Net Power Output of the ORC where the Parasitic Load includes the power of the working fluid pump, IPM magnetic bearings, and all other electrical loads within the ORC unit.

$$\text{Gross Efficiency} = \frac{\text{PE Power Output}}{\text{Rate of Heat Input}} \quad (1)$$

$$\text{Net Efficiency} = \frac{\text{Net Power Output}}{\text{Rate of Heat Input}} \quad (2)$$

$$\text{Net Power Output} = \text{PE Power Output} - \text{Parasitic Load} \quad (3)$$

The ORC and IPM turbine efficiencies are compared against design by measuring the rate of heat input from the hot water source, working fluid flowrate, IPM inlet and outlet conditions, PE and Net power outputs. The total to total isentropic efficiency was calculated using the measured generator power output, IPM inlet pressure and temperature, and the wheel outlet pressure. Viscous rotor losses and generator efficiency were not measured, so design correlations for these quantities were used in the calculation of the isentropic efficiency. In the full power test, the cooling water temperature was maintained at 27 °C and the ORC unit was operated to the maximum PE power output of 125 kW with an IPM speed of 16,500 rpm. Test measurements reported in Table 1 are average conditions measured while at steady state operation. The relative measurement uncertainty is the combined uncertainty of both the standard deviation of the measurement set and the inherent uncertainty of the calibrated instrumentation and fluid property calculations.

Table 1: Test vs. Design at PE Power Output of 125 kW

Description	Design Prediction	Test Measurement	Relative Measurement Uncertainty
Working Fluid Flowrate	8.1 kg/s	8.5 kg/s	0.50 %
IPM Inlet Temperature	80.3 °C	79.1 °C	0.95 %
IPM Inlet Pressure	6.9 bara	6.7 bara	0.28 %
PE Power Output	125.0 kW	125.3 kW	1.03 %
Net Power Output	119.1 kW	119.8 kW	1.03 %
Rate of Heat Input from Hot Water Source	1845.6 kW	1942.9 kW	2.21 %
Gross Efficiency	6.8 %	6.5 %	2.43 %
Net Efficiency	6.5 %	6.2 %	2.43 %
IPM Turbine Isentropic Efficiency (total to total)	90 %	89 %	2.43 %

4. CONCLUSIONS

In this paper the need to develop a heat recovery system utilizing low grade heat from ship engine jacket water has been outlined. Such a need arises to address the ever increasing electrical power demands of modern ships whilst reducing overall pollution emanating from power generating sources.

To achieve this goal, development of a novel low-grade heat source ORC system has been described. The ORC system not only achieves the primary goal of electric power generation without additional fuel consumption, it also adds to overall electrical power availability and adds a dimension to overall electrical system flexibility.

Performance test results have been provided and analyses of key performance metrics have been discussed. Much of the discussion in this paper has been focused at marine application of such architecture. It should be noted, with the abundance of low-grade heat sources, such as low-temperature geothermal, the same architecture, using the same ORC system, can be employed in many other low-grade heat recovery applications.

REFERENCES

- Yu, G., Shu, G., Tian, H., et al., 2013, Simulation and Thermodynamic Analysis of a Bottoming Organic Rankine Cycle (ORC) of Diesel Engine (DE), *Energy*, vol. 51, p. 281-290.
- Yang, M., Yeh, R., 2015, Thermo-economic Optimization of an Organic Rankine Cycle System for Large Marine Diesel Waste Heat Recovery, *Energy*, vol. 82, p. 256-268.
- Song, J., Song Y., Gu, C., 2015, Thermodynamic Analysis and Performance Optimization of an Organic Rankine Cycle (ORC) Water Heat Recovery System for Marine Diesel Engines, *Energy*, vol. 82, p. 976-985.
- Soffiato, M., Frangopoulos, C. A., Manente, G., et al., 2015, Design Optimization of ORC Systems for Waste Heat Recovery onboard an LNG Carrier, *Energy Conversion and Management*, vol. 92, p. 523-534.
- Rizzuto, E., Soares, C., 2012, Sustainable Maritime Transportation and Exploitation of Sea Resources, Taylor & Francis Group, London, p. 663-671.
- Mirmobin, P., Sellers, C., 2015, Advanced Thermodynamic Model of Organic Rankine Cycle, *ASME ORC 2015*, Brussels, Belgium.

- McMullen, P., Huynh, C., Hayes, R., 2000, Combination Radial-Axial Magnetic Bearing, *Proceedings of the Seventh International Symposium on Magnetic Bearings*, Zurich, Switzerland.
- Jin, J., Lee, H., Park, G., et al., 2012, Thermodynamic Analysis of the Organic Rankine Cycle as a Waste Heat Recovery System of Marine Diesel Engine, *Transactions of the Korean Society of Mechanical Engineers B*, vol. 36, no. 7: p. 711-719.
- Ichiki, Y., Keiichi, S., Kanaboshi, T., et al., 2011, Development of Super Waste-Heat Recovery System for Marine Diesel Engines, *Mitsubishi Heavy Industries Technical Review*, vol. 48, no. 1: p. 17-21.
- Hawkins, L., Zhu, L., Blumber, E., et al., 2012, Heat-To-Electricity with High-Speed Magnetic Bearing/Generator System, *GRC 2012 Annual Meeting*, Reno, NV.
- Hawkins, L., Zhu, L., Blumber, E., 2011, Development of a 125 kW AMB Expander/Generator for Waste Heat Recovery, *Journal of Engineering for Gas Turbines and Power*, vol. 133, no. 7.

TRANSIENT DUTY CYCLE ANALYSIS FOR MOBILE ORGANIC RANKINE CYCLE APPLICATIONS

Miles C Robertson[†], Aaron W Costall*, Peter J Newton and Ricardo F Martinez-Botas

*Corresponding Author, [†]Presenting Author

Department of Mechanical Engineering,
Imperial College London
City & Guilds Building
South Kensington Campus
London SW7 2AZ, UK
email: a.costall@imperial.ac.uk

ABSTRACT

Internal combustion engines have high exhaust energy at the tail pipe, and mobile organic Rankine cycle (ORC) systems have been proposed to harness this waste heat, thereby providing a significant opportunity for vehicle CO₂ emissions reduction. This paper discusses the impact of transient duty cycles on mobile ORC system performance. A thermodynamic model of an ORC system is presented, which includes a detailed heat exchanger model based on the Effectiveness-NTU method, and which has the ability to account for the thermal capacitance of the ORC system – which is of particular importance during vehicle start-up. Thermodynamic system simulations from start-up were performed based on four transient engine test cycles applied to a simulated 11.7L heavy-duty diesel engine: the Constant-Speed, Variable-Load (CSVL) cycle, the European Transient Cycle (ETC), the Non-Road Transient Cycle (NRTC), and the World Harmonized Transient Cycle (WHTC). For a fixed heat exchanger size, working fluid and ORC mass flow rate, it was found that the relatively high-load CSVL cycle (acting as a surrogate for an off-road machine) produced a peak average power of 9.0 kW from start-up, while the WHTC (representative of on-highway driving conditions) only delivered 3.2 kW. Results also indicate a very narrow band (5.5–6.2%) of peak exhaust energy recovery across all duty cycles, implying a close to linear scaling of ORC system power output with duty cycle intensity and engine size. The choice of vehicle/application is thus constrained by the ability to design an acceptable low-power ORC expander, suggesting that vehicles running the most heavily-loaded duty cycles stand to gain the most benefit from mobile ORC systems.

1. INTRODUCTION

Worldwide concern for lowering transport-related CO₂ emissions is driving internal combustion (IC) engine manufacturers to investigate new powertrain technologies. For example, the first fuel economy standards for US heavy-duty vehicles were announced in 2011 for years 2014–2018, with the largest trucks set a 20% target reduction by the end of that period (EPA, 2011). Unlike passenger car engines, heavy-duty diesel engines in commercial vehicle and off-road sectors are not well-suited for full electrification. Reduction of CO₂ emissions from these applications will continue to require improvements in conventional IC engine powertrains (Auto Council, 2011). Waste heat rejected to the exhaust is a significant portion of the fuel energy (Howey *et al.*, 2010), depending on the particular engine operating point, and waste heat recovery (WHR) technologies offer system efficiency enhancements in the near term (Greszler, 2012). Once the available high pressure and temperature energy is extracted (by turbocharging and, if present, turbocompounding), part of the remaining lower grade exhaust energy may be recovered via a bottoming cycle, such as the organic Rankine cycle.

ORC plants have been used for stationary power generation since the 1960s (Uusitalo *et al.*, 2011), taking advantage of biomass, geothermal, solar and numerous other heat energy sources. The benefits

of ORC applied to WHR in IC engines have been considered at various times since the late 1970s (Leising *et al.*, 1978; Aly, 1988; Endo *et al.*, 2007; Katsanos *et al.*, 2012) and more recently in the form of a Rankine (i.e., steam) cycle for a BMW turbocharged gasoline passenger car engine (Horst *et al.*, 2014). The heat rejected to the coolant and the exhaust system are the two common sources (some systems also utilize the EGR loop), and are typically categorized as low- and medium-grade, respectively (Sprouse and Depcik, 2013). This technology has been shown to deliver up to 13% improvement to fuel economy (DiNanno *et al.*, 1983). A recent large industrial research effort has sought to develop an ORC system for on-highway trucks under the US DOE SuperTruck program. This ORC WHR system contributed to the achievement of a brake thermal efficiency greater than 50% (Koeberlein, 2013). Nevertheless, duty cycles for on-highway trucks, city buses, various other commercial vehicles, and the vast number of off-highway machine applications are very diverse. In this work a thermodynamic system simulation is developed and applied transiently using reference duty cycle inputs from a selection of test cycles for heavy-duty engine applications. The purpose of this paper is to compare the influence of different duty cycles on mobile ORC system performance.

2. METHODOLOGY

2.1. System Level Overview

A basic schematic of the simulated ORC system is shown in Figure 1.

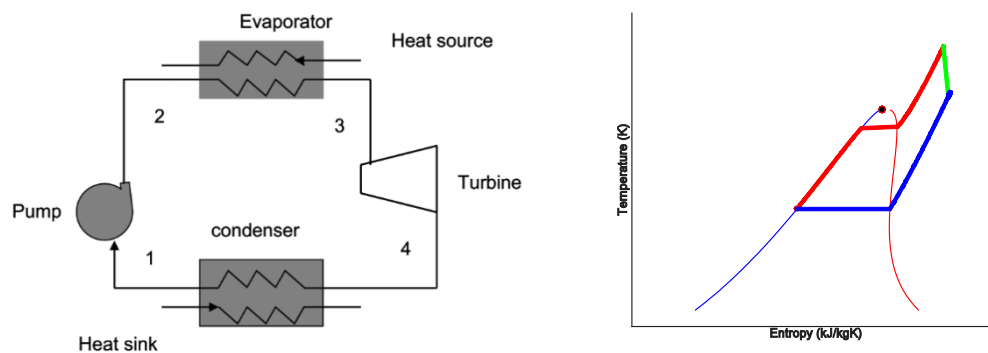


Figure 1: Basic block schematic of the ORC system (left) and corresponding T-S diagram (right)

The core layout consists of the fundamental Rankine cycle components – pump, evaporator, expander and condenser. A recuperator has been omitted from the design, due to the cost, weight and packaging penalties which make it unattractive for a mobile application. Although a recuperator increases cycle efficiency, this is of secondary importance to the ORC output power (Quoilin *et al.*, 2010).

2.2. Heat Exchanger Modeling

The focus of the current work is the accurate characterization of the transient heat flow between the vehicle exhaust flow and the ORC working fluid. A methodology was therefore developed which allowed modeling of the thermal capacitance of both fluid streams, along with the intermediate heat exchanger elements. The heat exchanger was modeled as a once-through/single pass design, consisting of an inner exhaust pipe enclosed by a concentric annular section containing the ORC working fluid. This design allows preheating, boiling and superheating of the working fluid within a single pipe. This avoids the requirement to hold excess fluid within a boiler drum, and the addition of unnecessary weight, which is to be discouraged in mobile applications (Quoilin *et al.*, 2013).

Considering practical aspects of ORC design, the Effectiveness-NTU method was chosen to allow compatibility with real-world evaporator design, along with the majority of heat transfer literature (e.g., Incropera *et al.*, 2006). By assuming quasi-steady behavior, a prediction of steady-state thermodynamic values can be generated, given the conditions at the current time step. An exponential relationship could therefore be defined, linking the temperature at the current time step, $T(t)$ to its infinite, steady-state solution, T_{inf} . This is shown in Equation (1), where the time constant $\tau(t)$ is an

unknown, defined from the thermodynamic conditions within the heat exchanger (Lachi *et al.*, 1997). An exponential projection of the temperature profile between the current time step and steady-state could therefore be drawn, before being truncated at the subsequent time step to provide an estimate of the transient temperature profile up to this point.

$$\frac{T(t)-T_{\text{inf}}}{T_0-T_{\text{inf}}} = e^{-t/\tau(t)} \quad (1)$$

Definition of the fluid time constant, τ , requires knowledge of the heat exchanger thermal capacitance. This is defined as the sum of the individual heat capacities of the exhaust gas, the ORC working fluid, and the heat exchanger pipe and casing metal (C_{exh} , C_{orc} , C_{pipe} , and C_{casing} , resp.), as in Equation (2) (Lachi *et al.*, 1997). Metal capacitances are constant, but fluid capacitances are time-varying, with temperature effects manifested in changes to specific heat capacity and density (altering the fluid mass contained in the heat exchanger, local fluid velocity and heat transfer correlations).

$$C(t) = C_{\text{exh}}(t) + C_{\text{orc}}(t) + C_{\text{pipe}} + C_{\text{casing}} \quad (2)$$

Fluid in the evaporator will be composed of different proportions of sub-cooled, boiling and superheated states, which are variable along the heat exchanger length. For example, a sub-cooled outlet state means wholly sub-cooled flow along the entire length of the heat exchanger; a boiling outlet implies portions of sub-cooled and boiling flow; while a superheated outlet requires all three phases within the heat exchanger. To accurately simulate the multi-phase phenomena within the heat exchanger, the three processes (sub-cooled, boiling and super-heated) were modeled separately, each with its own set of heat transfer coefficients and effectiveness relationships. The contribution from each process was determined iteratively from the ORC outlet enthalpy, with convergence achieved following successive calculations of a reference temperature (taken as the mean of the inlet and outlet values) to within a tolerance of 0.1°C. Single-phase flow was modeled using the Gnielinski forced heat transfer correlation (Incropera *et al.*, 2006) in Equation (5), where f is the wall friction factor. Two-phase ORC flow was modeled using the Gungor-Winterton boiling correlation (Gungor and Winterton, 1986) shown in Equation (6), where h_{TP} , h_l , and h_{pool} are respectively the heat transfer coefficients for two-phase, liquid and pool boiling, E is the enhancement factor, and S the suppression factor. Both models were validated against existing data prior to insertion in the model (Kakaç, 1991).

$$Nu_D = \frac{(f/8)(Re_D-1000)Pr}{1+12.7(f/8)^{1/2}(Pr^{2/3}-1)} \quad (5)$$

$$h_{\text{TP}} = Eh_l + Sh_{\text{pool}} \quad (6)$$

2.3. Cycle Specification and Heat Exchanger Sizing

The primary aspects of the ORC cycle simulation are listed in Table 1. A pressure ratio of 15 was chosen as a realistic value for a radial turbine expander. The low pressure level (160 kPa) assumes condensing to an ambient temperature of 300 K, maintaining a positive gauge pressure to avoid air ingress into the condenser (Badr *et al.*, 1985). Combined with the pressure ratio, this fixes the high pressure level at 2400 kPa. The heat exchanger volume is a key parameter, directly influencing working fluid velocity and its subsequent impact upon heat transfer and thermal capacitance correlations. Furthermore, it will be a significant contributor to overall mobile ORC system volume, which will be limited by packaging constraints. To investigate the effect of heat exchanger sizing on cycle transient characteristics, three sets of heat exchanger dimensions were used (Table 2). Designs **HE1** and **HE2** investigate differences caused by changing the volume of ORC fluid contained within the heat exchanger. **HE3** increases the volume of metal components and its thermal capacitance.

2.4. ORC Expander Modeling and Work Output

The selection of a radial turbine as the ORC expander was assumed in this work, and in order to include the effect of turbine size on overall cycle performance, an efficiency map based approach was used. The values of turbine efficiency in the map are dependent upon variations in density ratio and

size parameter, assuming operation at the optimum specific speed (Macchi and Perdichizzi, 1981). This method is useful since it does not assume constant turbine efficiency, but is much less complex than incorporating a full meanline model (e.g., Costall *et al.*, 2015).

Table 1: Summary of key cycle parameters

Parameter	Value
Working fluid	R245fa
Maximum temperature (°C)	300
High cycle pressure (kPa)	2400
Low cycle pressure (kPa)	160
Turbine pressure ratio (-)	15
Ambient (start-up) temperature (°C)	15

Table 2: Heat exchanger sizing combinations

	Exhaust Outer Dia. (mm)	Tube Thickness (mm)	ORC Outer Dia. (mm)	Casing Thickness (mm)	Description
HE1	70	6	96	6	Large ORC volume
HE2	70	6	86	6	Small ORC volume
HE3	70	12	92	12	Increased metal volume

2.5. Operating Logic Structure

In order to model the effects of vehicle start-up, several different modes of operation must be defined. These are shown schematically in Figure 2, and described here:

- (a) **Warm-up** occurs exclusively at the start of each simulation. The ORC fluid is assumed to begin at the ambient temperature (modeled as -10°C) – if this is below the condenser set-point temperature then the fluid is circulated round the evaporator and condenser at the minimum cycle pressure, until the condenser outlet set-point has been established.
- (b) **Sub-cooled** conditions at the heat exchanger outlet mean that no work can be extracted from the turbine. The most efficient path to boiling is therefore to circulate fluid around the heat exchanger to begin generating vapor. At this point the evaporator pressure is raised to its ‘high’ value (2400 kPa), assuming perfect pump pressure regulation.
- (c) **Boiling** conditions at heat exchanger outlet result in a mixture of vapor and steam – these are divided in the separator. Fluid is recirculated to raise evaporator inlet enthalpy, whilst vapor passes through the turbine and condenser, facilitating approximation of part-load operation.
- (d) **Super-heated** conditions at the heat exchanger outlet allow the entire ORC flow to be passed through the turbine and condenser – the other paths are closed off.

Optimal control of these modes is not attempted in the current work, though it is a major challenge for ORC applications, and examples of optimization tools are available (e.g., Peralez *et al.*, 2014).

2.6. Duty Cycle Data

A separate cycle simulation of an 11.7L Scania DC12 Euro 3 diesel engine validated against dynamometer test data (Hedbom, 2007) was used to generate maps of exhaust mass flow rate and temperature, at 89 full- and part-load operating points, between engine speeds of 600 and 2350 rpm. The transient thermodynamic ORC model interpolated this dataset at every instance in the four duty cycles listed in Table 3, obtaining the time-varying evaporator heat input powers shown in Figure 3.

3. RESULTS

3.1. Initial Transient Model Results

The time-varying exhaust conditions (generated in GT-POWER from duty cycle speed/load data) were used as an input to the transient thermodynamic ORC model, to generate cycle performance

predictions. Figure 4 shows how the proportion of sub-cooled, boiling and super-heated flow at the heat exchanger exit varies across a single WHTC duty cycle. Due to the once-through/single pass design, even when the heat exchanger outlet is super-heated, sub-cooled and boiling effects often dominate the entire heat exchanger length. In periods of high exhaust heat input, extended periods of super-heat are achieved, producing full (> 10 kW) turbine power. As heat input falls and superheat is lost, mass flow rate to the turbine is reduced, cutting output power (as a function of dryness fraction).

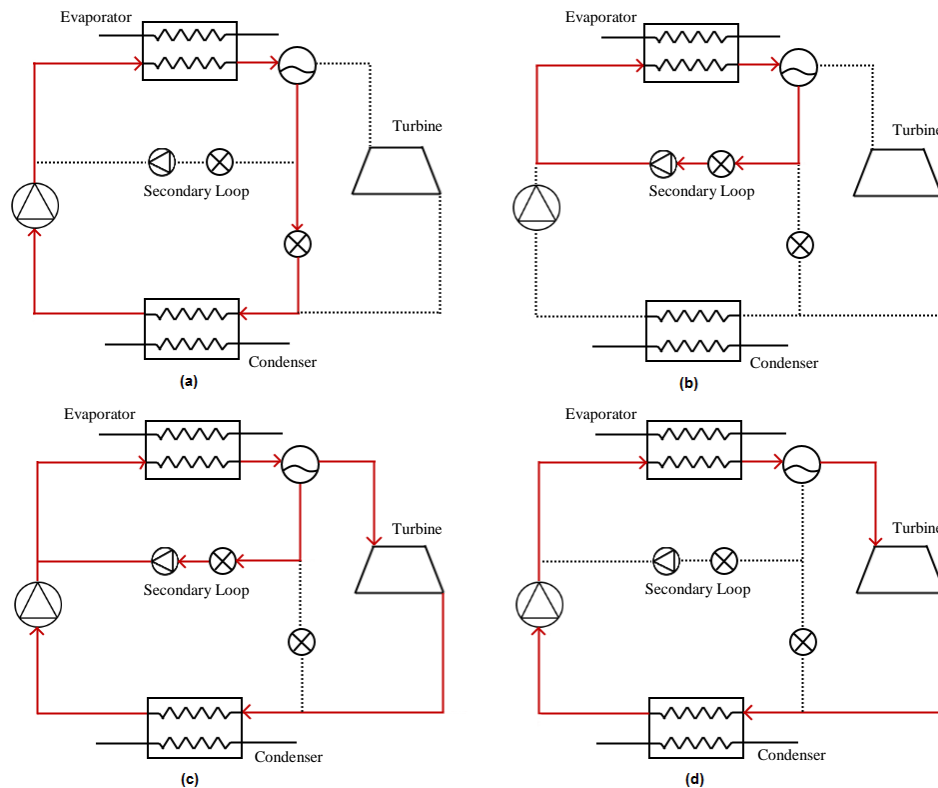


Figure 2: Flow paths are indicated in red for (a) warm-up, (b) sub-cooled, (c) boiling, and (d) super-heated

Table 3: Summary of duty cycles (DieselNet, 2015) used for transient thermodynamic ORC simulations

Duty Cycle	Originator	Length (s)	Focus
Constant-Speed, Variable-Load (CSVL)	US EPA	1200	Constant-speed engines; included here as a surrogate for off-road applications such as hydraulic excavators.
European Transient Cycle (ETC)	EU	1800	On-road; transient test cycle for truck and bus engines, used in part for heavy-duty engine emission certification.
Non-road Transient Cycle (NRTC)	US EPA/EU	1238	Off-road; transient engine dynamometer cycle for mobile off-road engines, for engine emission certification in the USA, EU and elsewhere.
World Harmonized Transient Cycle (WHTC)	UN ECE	1800	On-road; transient engine dynamometer cycle for heavy-duty engines, for engine emission certification worldwide.

Due to recirculation of saturated liquid back to the heat exchanger inlet, there is a deviation from expected behavior at high mass flow rates. In non-recirculating cycles, a sharp drop-off in average power is expected, as the exhaust flow no longer provides sufficient enthalpy to vaporize an increasing mass of fluid – a point will therefore be reached where zero power will be produced. In a recirculating cycle, it can be seen that as mass flow rate is increased, an increased proportion of saturated liquid will be produced, but this is recirculated to increase the heat exchanger inlet enthalpy. So, at large mass flow rates, no additional work will be extracted from the cycle, but rather than decreasing to zero, a minimum net power will be reached. This phenomenon is seen in Figure 5.

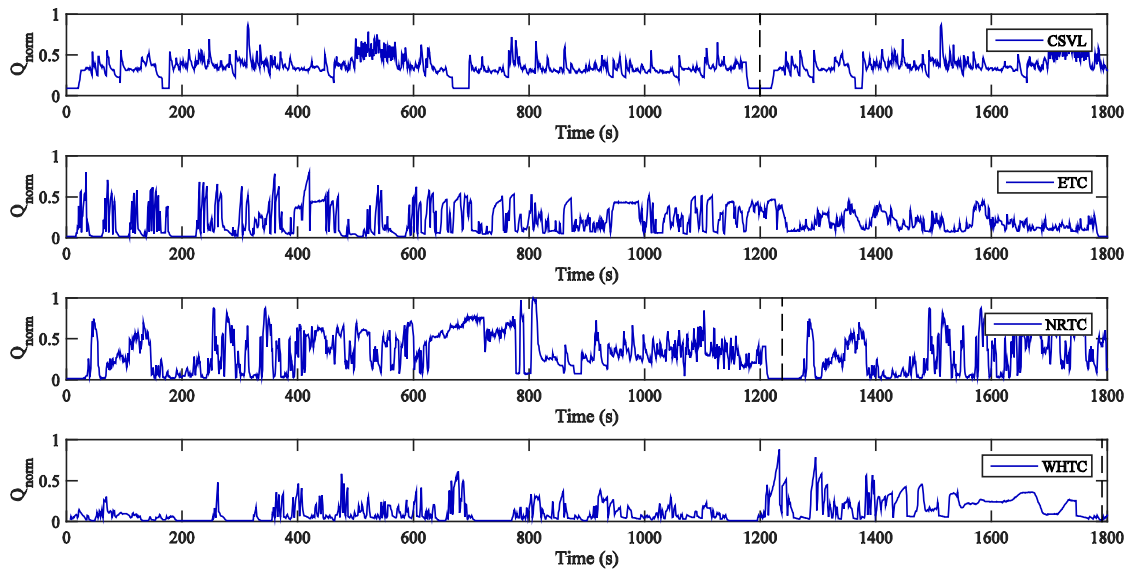


Figure 3: Time histories of normalized heat power, Q_{norm} , input into the ORC simulation for each duty cycle under examination (a broken vertical line denotes cycle repetition)

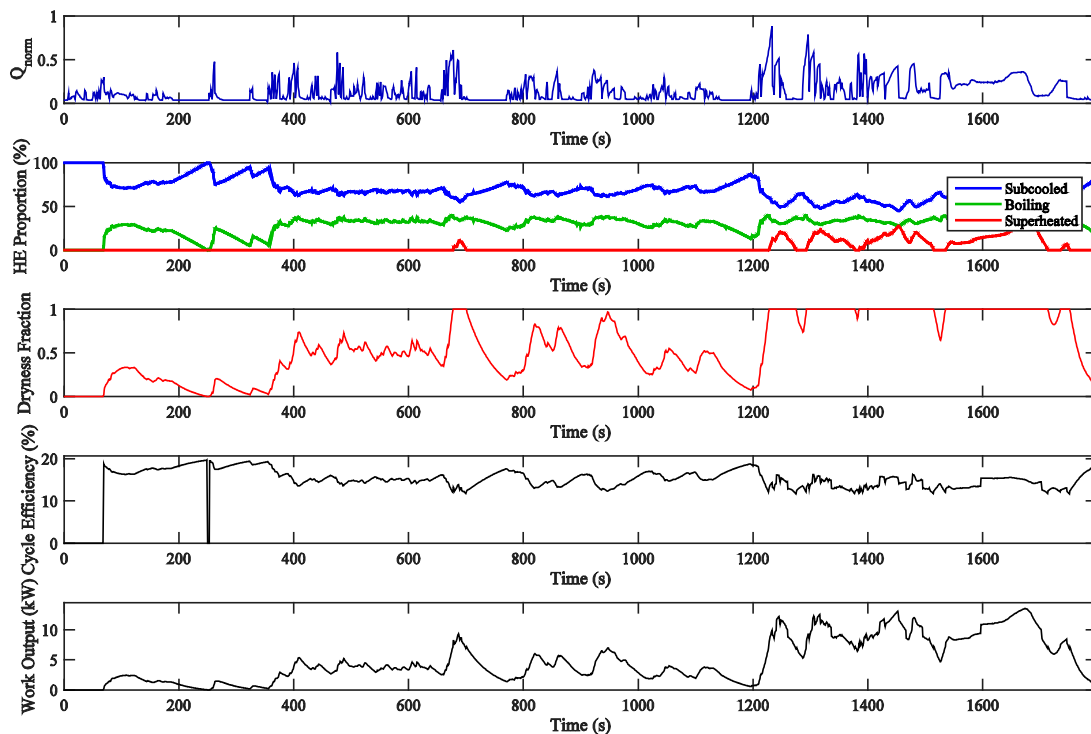


Figure 4: Key properties across a sample duty cycle (WHTC, 0.25 kg/s ORC mass flow rate). From top to bottom: normalized heat power (Q_{norm}); proportion of sub-cooled, boiling and superheated states (“HE Proportion”); dryness fraction; cycle efficiency; and work output

To illustrate the range of thermodynamic states encountered at the heat exchanger exit during a simulated duty cycle, Figure 6 presents two duty cycles (WHTC and CSVL) laid out on the T-S plane, superimposed on the R245fa saturation curve. The color map for each describes the relative proportion of time spent at each position on the 2400 kPa isobar. We may observe that the degree of variation across both duty cycles is very large – whilst in both cases the most time is spent under the saturation curve, there are extended periods of significant deviation from the optimal condition (on the saturated vapor line providing 100% mass flow to the turbine with no excess heat input). Secondly it

can be seen that the effectiveness of a heat exchanger sizing is highly dependent upon the nature of the heat source – whilst one cycle provides significant periods of super-heat (CSVL), another can fail to input sufficient power to fully vaporize the ORC working fluid.

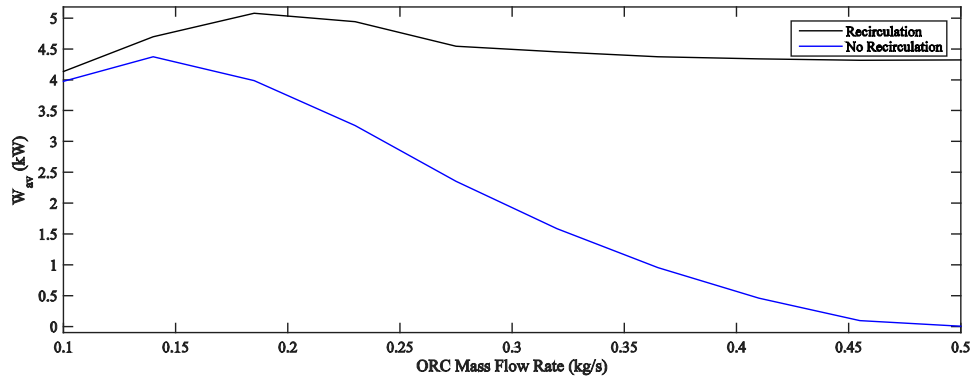


Figure 5: Sat. liquid recirculation raises average power output by increasing heat exchanger inlet enthalpy

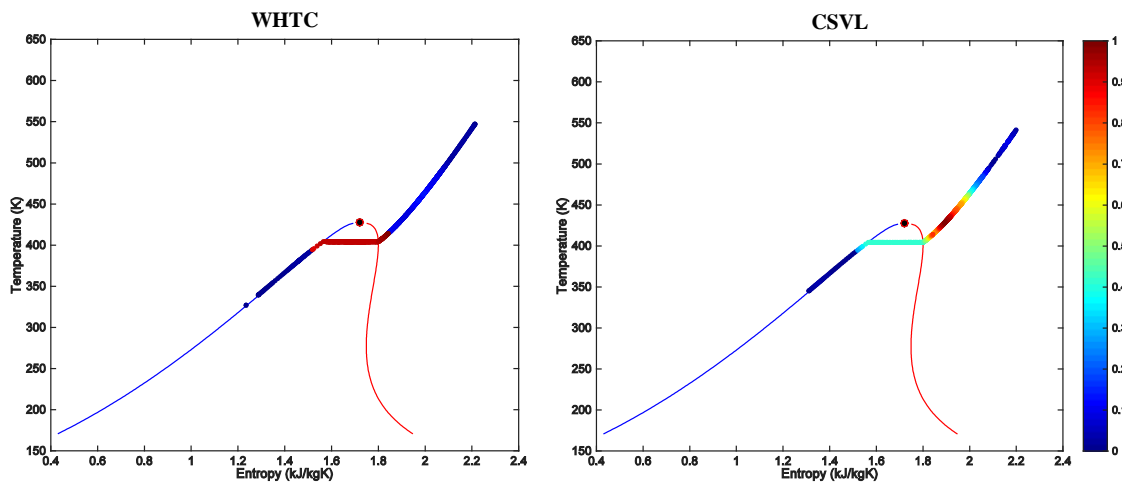


Figure 6: Range occupied in T-S plane for WHTC and CSVL duty cycles, with identical heat exchanger sizing and ORC mass flow rate set-points. Color map indicates fraction of time spent at each state

3.2. ORC Mass Flow Rate Variation

The primary figure of merit to maximize is the time-averaged power output across the entire duty cycle, which gives a pathway to quantifying potential fuel savings. ORC mass flow rate was set at the heat exchanger and in periods of saturated liquid recirculation from the heat exchanger outlet, the condenser mass flow was adjusted to meet this set-point. Ten simulations were conducted across each curve, as presented in Figure 7. Solutions that exceeded the R245fa maximum temperature of 300°C (where it would be stable for 100 hours (Angelino and Invernizzi, 2003)) were discarded, shown by the grey regions in Figures 7 and 8. Figure 7 shows a large difference between the average power output in each duty cycle. The CSVL cycle generates the highest output (9 kW), confirming the strong dependency between available exhaust energy and ORC system output. Sensitivity to heat exchanger size was quite modest, with less than 10% difference between designs. This is due to low exhaust-side convective heat transfer coefficients limiting the rate of heat transfer, irrespective of ORC pipe sizing.

3.3. Normalized ORC Power Recovery

To analyze the relative benefits of different duty cycles, each plot was normalized against the mean engine power, derived from temperature and mass flow rate traces. This gives a prediction of Exhaust Power Recovery (EPR), the time-averaged cycle efficiency over an entire transient duty cycle (Figure 8). It compares the power extracted to the theoretical maximum power available in the exhaust flow.

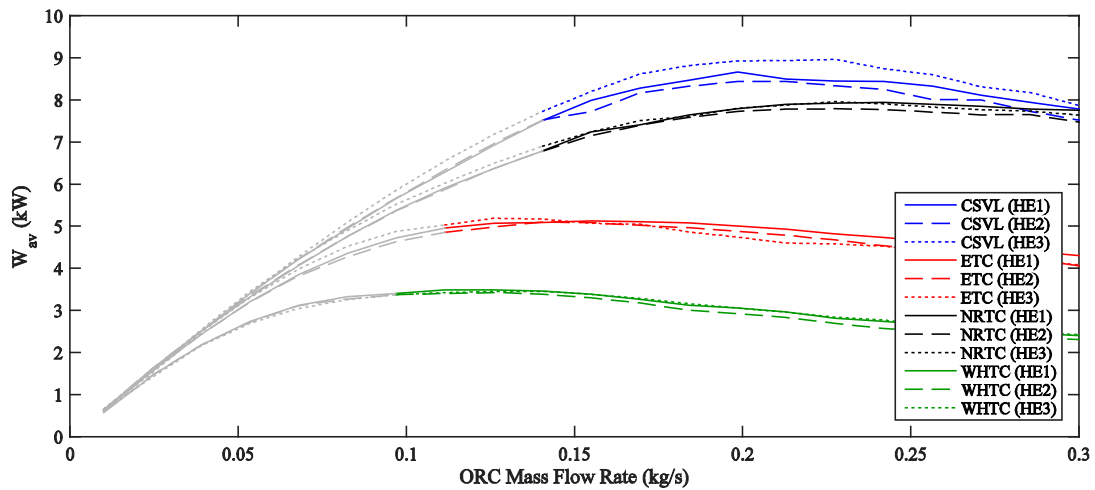


Figure 7: Cycle-averaged power output across each simulated duty cycle. Grey regions represent scenarios exceeding the maximum working fluid temperature.

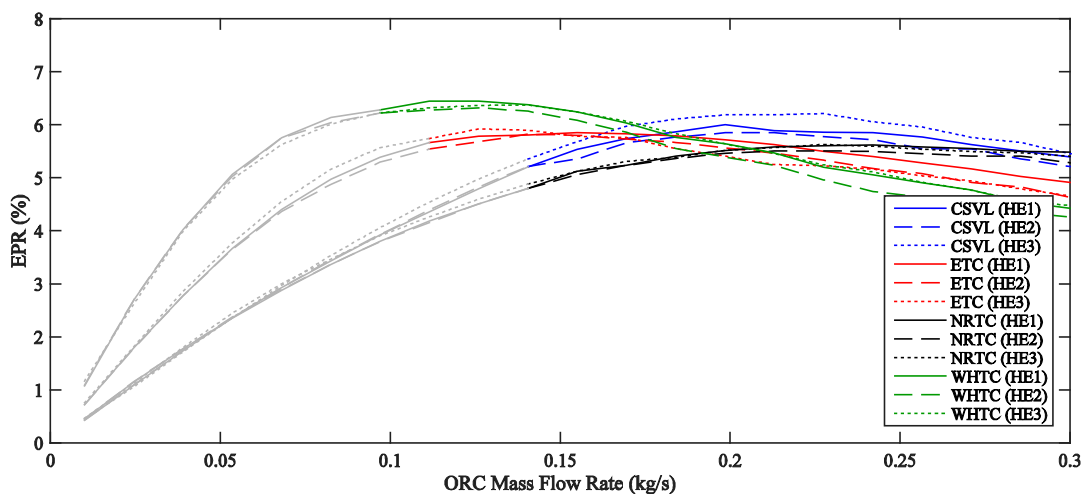


Figure 8: Exhaust Power Recovery (EPR) percentage for each duty cycle. Grey regions represent scenarios exceeding the maximum working fluid temperature.

Figure 8 shows that the peak values of Exhaust Power Recovery are at about the same level across all four duty cycles, with the highest (6.5%) being achieved by the low-power WHTC cycle. This is due to recirculation within the ORC system – this provides a pathway for fluid to be recirculated back to the heat exchanger inlet, allowing duty cycles which operate primarily at part-load to achieve increased efficiency. This is compounded by part-load operation increasing the proportion of boiling flow within the evaporator and therefore allowing increased heat exchanger effectiveness. While there is strong correlation between the available exhaust power and the level of ORC system output, it is also a relatively flat trend. Being taken from the point of exhaust entry to the ORC evaporator, this guarantees that as a given engine moves towards heavier duty cycles (and increased exhaust power ratings), ORC power output scales accordingly. A similar relationship may be valid across engine size, making mobile ORC systems promising for large heavy-duty diesel engines. With a key limitation on these applications being the ability to design turbomachinery to deliver acceptable isentropic efficiency at low power ratings, this scaling suggests that larger diesel engines stand to be the most promising candidates for initial mobile ORC system development.

4. CONCLUSIONS

This paper has detailed the development of a transient heat exchanger model based upon the NTU-effectiveness method, incorporating multiple operating states and correlations to accurately model

mobile ORC operation and start-up effects. A selection of reference transient duty cycles were taken as inputs to an engine simulation, providing mass flow and temperature boundary conditions to the ORC model, allowing insight into the transient cycle characteristics. For a fixed heat exchanger size, working fluid and ORC mass flow rate, different duty cycles were seen to produce a large variation in thermodynamic conditions at the evaporator outlet, along with the average power generated across a single duty cycle. Variation was such that a high-load CSVL cycle produced peak average power of 9.0 kW from start-up, whilst an on-highway WHTC only delivered 3.2 kW. Results were normalized against the theoretical exhaust power for each cycle, revealing a very narrow band (5.5-6.2%) of peak exhaust energy recovery across all duty cycles, suggesting a close to linear scaling of ORC system output with duty cycle output and engine sizing. The choice of vehicle/application is therefore primarily constrained by the ability to design acceptable low-power turbomachinery. A prediction is therefore made that vehicles running heavy duty cycles with high residual exhaust power have the potential to benefit the most from mobile ORC systems.

NOMENCLATURE

C	heat capacity	(kW K ⁻¹)
E	enhancement factor	(–)
f	friction factor	(–)
HE	heat exchanger	
h	heat transfer coefficient	(W m ⁻² K ⁻¹)
Nu	Nusselt number	(–)
ORC	organic Rankine cycle	
Pr	Prandtl number	(–)
Q	power (heat)	(kW)
Re	Reynolds number	(–)
S	suppression factor	(–)
T	temperature	(K)
t	time	(s)
W	power (work)	(kW)

Greek letters

τ	time constant	(s)
--------	---------------	-----

Subscripts

0	current value
av	time-averaged value
casing	referring to the heat exchanger metal casing
D	referred to diameter
exh	exhaust gas
inf	steady-state value
l	liquid
norm	normalized value
orc	ORC working fluid
pipe	referring to the heat exchanger metal piping
pool	pool boiling
TP	two-phase

REFERENCES

- Aly, A.E., 1988, Diesel engine waste-heat power cycle, *Applied Energy*, Vol. 29, p. 179-189.
 Angelino, G., Invernizzi, C., 2003, Experimental investigation on the thermal stability of some new zero ODP refrigerants, *Int. J. Refrigeration*, Vol. 26, p. 51-58.
 Auto Council, 2011, Commercial Vehicle & Off-Highway Low Carbon Technology Roadmap.

- Badr, O., Probert, S.D., O'Callaghan, P.W., 1985, Selecting a working fluid for a Rankine-cycle engine, *Applied Energy*, Vol. 21, p. 1-42.
- Costall, A.W., Gonzalez Hernandez, A., Newton, P.J., Martinez-Botas, R.F., 2015, Design methodology for radial turbo expanders in mobile organic Rankine cycle applications, *Applied Energy*, Article in Press, <http://dx.doi.org/10.1016/j.apenergy.2015.02.072>.
- DiNanno, L.R., DiBella, F.A., Koplrow, M.D., 1983, *An RC-1 organic Rankine bottoming cycle for an adiabatic diesel engine*, NASA, DOE/NASA/0302-1.
- DieselNet, 2015, Emission Test Cycles. Worldwide Engine and Vehicle Test Cycles, URL: <https://www.dieselnet.com/standards/cycles>, Accessed: 2015-03-20.
- Endo, T., Kawajiri, S., Kojima, Y., Takahashi, K., Baba, T., Ibaraki, S., Takahashi, T., Shinohara, M., 2007, Study on Maximizing Exergy in Automotive Engines, in: *Proceedings of the SAE 2007 World Congress and Exhibition*, SAE Technical Paper 2007-01-0257.
- EPA, 2011, Greenhouse Gas Emissions Standards and Fuel Efficiency Standards for Medium- and Heavy-Duty Engines and Vehicles, *Federal Register*, Vol. 76, No. 179, p. 57106-57513.
- Greszler, A., 2012, View from the Bridge – Commercial Vehicle Perspective, in: *Proceedings of the 18th Directions in Engine-Efficiency and Emissions Research (DEER) Conference*.
- Gungor, K.E., Winterton, R.H.S., 1986, A general correlation for flow boiling in tubes and annuli, *Int. J. Heat Mass Transfer*, Vol. 29, No. 3, p. 351-358.
- Hedbom, A., 2007, *SCANIA DC12 01 Euro 3 Engine. Emission Measurements for VTI and COST 346*, Report N52A-2005, Swedish National Road and Transport Research Institute (VTI).
- Horst, T.A., Tegethoff, W., Eilts, P., Koehler, J., 2014, Prediction of dynamic Rankine Cycle waste heat recovery performance and fuel saving potential in passenger car applications considering interactions with vehicles' energy management, *Energy Conversion and Management*, Vol. 78, p. 438-451.
- Howey, D., North R., Martinez-Botas, R., 2010, *Road transport technology and climate change mitigation*, Grantham Institute for Climate Change Briefing paper No 2.
- Incropera, F.P., DeWitt, D.P., Bergman, L., Lavine, A.S., 2006, *Fundamentals of Heat and Mass Transfer*, John Wiley & Sons, 6th Edition.
- Kakaç, S., 1991, *Boilers, Evaporators and Condensers*, John Wiley & Sons, 1st Edition.
- Katsanos, C.O., Hountalas, D.T., Pariotis, E.G., 2012, Thermodynamic analysis of a Rankine cycle applied on a diesel truck engine using steam and organic medium, *Energy Conversion and Management*, Vol. 60, p. 68-76.
- Koerberlein, D., 2013, *Technology and System Level Demonstration of Highly Efficient and Clean, Diesel Powered Class 8 Trucks*, DOE Hydrogen and Fuel Cells Program, and Vehicle Technologies Program Annual Merit Review and Peer Evaluation.
- Lachi, M., el Wakil, N., Padet, J., 1997, The time constant of double pipe and one pass shell-and-tube heat exchangers in the case of varying fluid flow rates, *Int. J. Heat Mass Transfer*, Vol. 40, No. 9, p. 2067-2079.
- Leising, C., Purohit, G., DeGrey, S., and Finegold, J., 1978, Waste Heat Recovery in Truck Engines, SAE Technical Paper 780686.
- Macchi, E., Perdichizzi, A., 1981, Efficiency Prediction for Axial-Flow Turbines Operating with Nonconventional Fluids, *ASME Journal of Engineering for Power*, Vol. 103, p. 718-724.
- Peralez, J., Tona, P., Sciarretta, A., Dufour, P., Nadri, M., 2014, Optimal Control of a Vehicular Organic Rankine Cycle via Dynamic Programming with Adaptive Discretization Grid, in: *Proceedings of the IFAC 19th World Congress*, p. 5671-5678.
- Quoilin, S., Declaye, S., Lemort, V., 2010, Expansion Machine and Fluid Selection for the Organic Rankine Cycle, *7th Int. Conf. on Heat Transfer, Fluid Mechanics and Thermodynamics*, p. 1-7.
- Quoilin, S., Van Den Broek, M., Declaye, S., Dewallef, P., Lemort, V., 2013, Techno-economic survey of Organic Rankine Cycle (ORC) systems. *Renewable and Sustainable Energy Reviews*, Vol. 22, p. 168-186.
- Sprouse, C. III and Depcik, C., 2013, Review of organic Rankine cycles for internal combustion engine exhaust waste heat recovery, *Applied Thermal Eng.*, Vol. 51, Nos. 1-2, p. 711-722.
- Uusitalo, A., Larjola, J., and Turunen-Saaresti, T., 2011, Background and summary of commercial ORC, in: *Proceedings of ORC 2011: First International Seminar on ORC Power Systems*.

A DUAL LOOP ORGANIC RANKINE CYCLE UTILIZING BOIL-OFF GAS IN LNG TANKS AND EXHAUST OF MARINE ENGINE

Taehong Sung¹, Sang Youl Yoon^{2*}, Kyung Chun Kim^{3*}

^{1,3}School of Mechanical Engineering, Pusan National University
Busan, Korea

¹taehongsung@pusan.ac.kr

³kckim@pusan.ac.kr

²Rolls-Royce and Pusan National University Technology Centre, Pusan National University
Busan, Korea

²yoonsy@pusan.ac.kr

* Corresponding Author

ABSTRACT

In this study, a dual loop ORC system for LNG carrier is analysed. First ORC system recovers heat from engine exhaust and releases heat to sea water. Second ORC recovers heat from exhaust sequentially and releases heat to boil-off gas. Due to very low-temperature of boil-off gas (around -160 °C), condensation temperature could be very low. Possible eight different refrigerants are screened and R218 refrigerant is revealed most suitable for the proposed cycle. Thermodynamic analysis shows maximum output is occurred at optimum evaporating temperature.

1. INTRODUCTION

In recent years, international natural gas market is gradually increased. Among fossil fuel, natural gas emits relatively a small amount of pollutants during the combustion (20% lower CO₂, 85-90% lower NO_x, hardly SO_x) compared to petroleum and coal. Natural gas is intensively reserved in specific areas and the producing areas are far from demand area like petroleum. Due to the significant investment cost for pipeline, liquefied form of natural gas is preferred for distances of above 2,000 km to be supplied by using transportations such as LNG carrier (Dobrota *et al.*, 2013).

During LNG supply process, boil-off gas (BoG) including evaporated volatile components (methane and nitrogen) is significantly generated. About 4-6% of the total LNG freight is converted in the form of BoG during typical 20-day voyage, and the generated BoG raises the pressure of the storage tank. In order to prevent potential risks, BoG needs to be removed from the tank properly. BoG is usually burned, re-liquefied, or re-used as fuel on board. Prior to the last-generation diesel engine, BoG was used as fuel for steam propulsion engine with the very low cycle efficiency. Since adopting diesel engine, BoG is re-liquefied with using Claud cycle (Moon *et al.*, 2007) for on board application. Very recently, BoG is re-considered to be used as a fuel in marine engine because (1) natural gas price is relatively competitive, (2) countries and harbors start to restrict the amount of diesel fuel consumption, and (3) dual fuel engine (DF engine) is introduced in market (e.g. Wärtsilä DF engine series) which has fuel flexibility. DF engine is preferentially adopted in LNG carrier where fuel natural gas could be easily obtained. In use of BoG as fuel, BoG of -160 °C is preheated to 0 ~ 25 °C using fuel preheater, and thus the useful cold energy is discarded during fuel preheating. The cold energy could be used for additional power generation as heat sink. In land application, available power generation cycles to be coupled with the LNG vaporization process in a Spanish LNG terminal (Querol *et al.*, 2011).

In marine application, the exhaust heat is used for operating turbo charger and steam service. Since released exhaust gas temperature is ranged about from 180 to 250 °C, the potential of useful thermal energy is still abundant for additional power generation. Hence, waste heat recovery of internal

combustion engine has been widely studied (Bombarda and Invernizzi, 2010, Vaja and Gambarotta, 2010, Wang *et al.*, 2011, Choi and Kim, 2013) with adopting ORC system. In this study, dual loop ORC system is proposed for utilizing both BoG cold energy and exhaust heat. Engine exhaust is sequentially utilized and each ORC systems use sea water and BoG as heat sink. High-temperature ORC (HT-ORC) loop is designed for use of R245fa refrigerant as working fluid, and low-temperature ORC (LT-ORC) loop is simulated with various working fluids.

2. DUAL LOOP ORC SYSTEM

2.1 System Description

Cycle design and simulation were conducted for Wärtsilä DF50 engine at 100% load. The key operating condition for cycle simulation is shown in Table 1. Marine engine exhaust gas is used for turbo charger and steam generation. In this study, a DF engine, a turbocharger and a steam generator are considered as single engine unit, and the exhaust gas temperature from the engine unit is assumed as 230 °C. Although BoG generation rate and temperature depends on the controlled tank pressure, those are assumed as 0.7 kg/s (engine fuel consumption rate) and -160 °C under the BoG pressure of 1 bar. The BoG is assumed as pure methane, because 99% of BoG is composed of methane. Figure 1 shows the schematic of proposed dual loop ORC system. HT-ORC operates using engine exhaust gas of 230 °C as heat source and sea water as heat sink. For LT-ORC operation, BoG and engine exhaust gas passed through HT-ORC are used as heat sink and heat source, respectively. The exhaust gas with the temperature of 75 °C is introduced into the evaporator of LT-ORC sequentially. Then, the rest of the thermal energy in the exhaust gas is used for raising the BoG temperature up to 25 °C because the appropriate temperature of the supply fuel is required for the operation of DF engine. The heat exchanger (HX1) in LT-ORC loop is acting as the BoG preheater and the condenser which is utilizing cold energy of BoG. Second heat exchanger (HX2) is an additional preheater which uses the rest of the heat in the exhaust gas passed through LT-ORC evaporator.

Table 1: Engine operating conditions

Engine output	17.1 MW
Air flow rate at 100% engine load	27.5 kg/s
Exhaust gas flow rate at 100% load	28.2 kg/s
Temperature after engine unit at 100% load	230 °C
BoG flow rate at 100% engine load	0.7 kg/s
BoG temperature	-160 °C
BoG pressure	1 bar

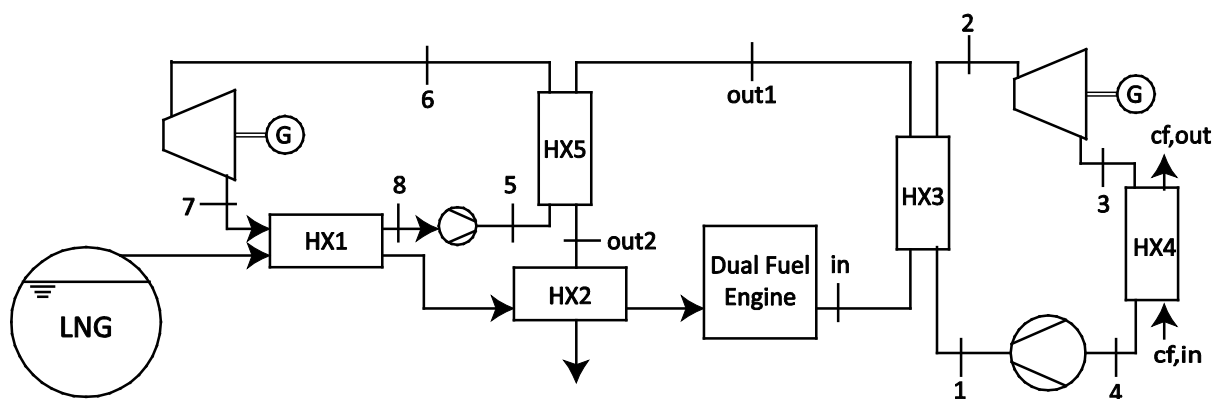


Figure 1: Dual loop ORC system for LNG carrier

2.2 System modeling

2.2.1. Turbine

\dot{m}_{ORC} is working fluid mass flow rate and h is the enthalpy. The power output \dot{W}_t and isentropic turbine efficiency η_t are

$$\dot{W}_{turb1} = \dot{m}_{o1}(h_3 - h_4) \quad (1)$$

$$\dot{W}_{turb2} = \dot{m}_{o2}(h_7 - h_8) \quad (2)$$

$$\eta_{turb1} = (h_3 - h_4)/(h_3 - h_{4s}) \quad (3)$$

$$\eta_{turb2} = (h_7 - h_8)/(h_7 - h_{8s}) \quad (4)$$

2.2.2. Condenser

The condenser heat duty \dot{Q}_c are

$$\dot{Q}_{cd1} = \dot{m}_{o1}(h_4 - h_1) = \dot{m}_{cf}(h_{cf,in} - h_{cf,out}) \quad (5)$$

$$\dot{Q}_{cd2} = \dot{m}_{o2}(h_8 - h_7) = \dot{m}_{BoG}(h_{BoG,in} - h_{BoG,out}) \quad (6)$$

2.2.3. Pump

The consumed power \dot{W}_p and isentropic efficiency η_p are

$$\dot{W}_{pp1} = \dot{m}_{ORC1}(h_2 - h_1) \quad (7)$$

$$\dot{W}_{pp2} = \dot{m}_{ORC2}(h_6 - h_5) \quad (8)$$

$$\eta_{pp1} = (h_{2s} - h_1)/(h_2 - h_1) \quad (9)$$

$$\eta_{pp2} = (h_{6s} - h_5)/(h_6 - h_5) \quad (10)$$

2.2.4. Evaporator

The heat duty of evaporator \dot{Q}_e are

$$\dot{Q}_{ev1} = \dot{m}_{o1}(h_3 - h_2) = \dot{m}_{in}c_{p,in}(T_{in} - T_{out1}) \quad (11)$$

$$\dot{Q}_{ev2} = \dot{m}_{o2}(h_7 - h_6) = \dot{m}_{in}c_{p,in}(T_{out1} - T_{out2}) \quad (12)$$

$c_{p,in}$ is heat source specific heat.

2.3 System efficiency modeling

Thermal efficiency can be defined as

$$\eta_{cyc1} = (\dot{W}_{t1} - \dot{W}_{p1})/\dot{Q}_{e1} \quad (13)$$

$$\eta_{cyc2} = (\dot{W}_{t2} - \dot{W}_{p2})/\dot{Q}_{e2} \quad (14)$$

3. RESULTS AND DISCUSSION

3.1 Cycle analysis

Figure 2 shows T-s diagram for the proposed dual loop ORC system. R245fa refrigerant is adopted as working fluid for HT-ORC which gives moderate performance characteristics and has proper material safety. HT-ORC specifications are shown in Table 2. Cycle maximum pressure is set to 20 bar due to high pressure gas regulation. HT-ORC produces 651.8 kW power output with 14.6 % thermal efficiency.

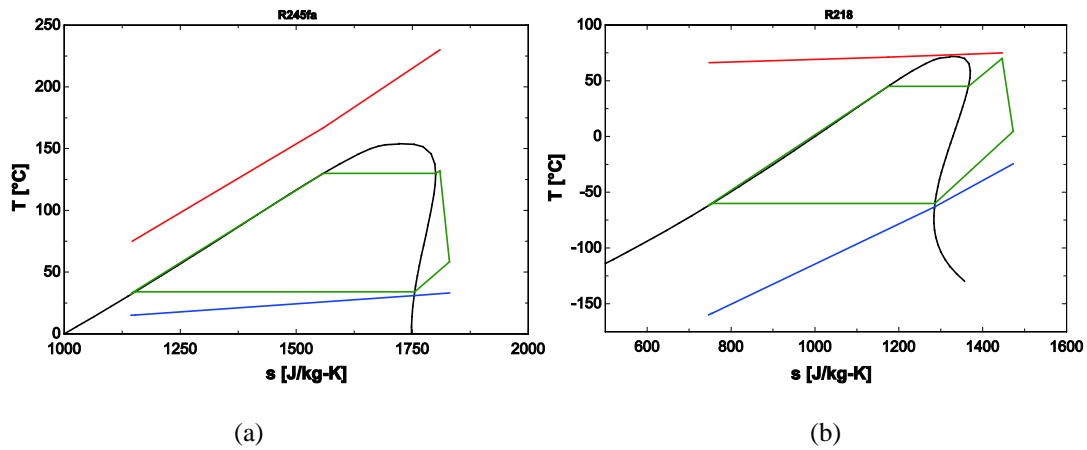


Figure 2: T-s diagram of (a) HT-ORC and (b) LT-ORC

Table 2: HT-ORC specifications

Refrigerant	R245fa
Evaporating temperature	130 °C
Condensing temperature	34 °C
Pressure ratio	11.5
Mass flow rate	18.1 kg/s
Power output	651.8 kW
Turbine efficiency	0.85
Pump efficiency	0.70
Cycle efficiency	0.146
Cooling source	Sea water
Cooling source temperature	15 °C
Cooling source mass flow rate	50.7 kg/s

3.2 Fluid selection for LT-ORC

Table 3 shows the physical properties, safety data and environmental data of eight screened refrigerants. All screened fluids has no ozone depleting potential, whereas three fluids (R143a, R125 and R218) shows relatively high global warming potential. Table 4 shows simulation condition for LT-ORC loop. The thermodynamic simulation results for LT-ORC system are shown in Table 5. Evaporating and condensing conditions, mass flow rate, volume flow rate, quality at turbine exit, power output, thermal efficiency and pressure ratio are shown in Table 5. LT-ORC with R218 refrigerant produces power output of 49.8 kW and recovers heat of 277 kW used in fuel preheating. Following factors are considered for suitable refrigerant selection for LT-ORC:

- (1) The system power output shall be as large as possible.
- (2) Dry expansion is preferred.
- (3) The system volumetric flow rate shall be as small as possible.
- (4) The system mass flow rate shall be as small as possible.
- (5) Pressure ratio be within acceptable range.

From Table 5, R218 has the highest power output, whereas, ammonia and R152a have the highest cycle efficiency. Ammonia also has the smallest mass flow rate and R41 has the smallest volume flow rate and pressure ratio. Ammonia, R152a and R134a shows wet expansion and higher pressure ratio compared to other refrigerants. It is obvious that there is no suitable refrigerant satisfying every design considerations at the same time.

LT-ORC loop with R41 produces much less power output. LT-ORC with ammonia, R152a and R134a has high power output, however pressure ratio is very high and wet expansion is required. LT-ORC with propane, R14a and R125 produce lower power output, however volume flow rate and pressure ratio are low. R218 is the most suitable for LT-ORC due to the highest power output and dry expansion characteristics with not bad pressure ratio and volumetric flow rate.

Table 3: Physical, safety and environmental data for the working fluids.

	T_{bp} (°C)	T_{fr} (°C)	T_c (°C)	P_c (bar)	$T_{sat@20bar}$ (°C)	Safety data	ODP	GWP
Propane	-42.11	-187.62	96.74	42.51	57.26	A3	0	~ 20
R143a	-47.24	-111.81	72.707	37.61	43.75	A3	0	3800
R125	-48.09	-100.63	66.023	36.18	39.82	A1	0	2800
R41	-78.31	-143.33	44.13	58.97	-0.79	-	0	97
Ammonia	-33.33	-77.65	132.25	113.33	49.35	B2	0	<1
R152a	-24.02	-118.59	113.26	45.17	72.65	A2	0	140
R134a	-26.07	-103.3	101.06	40.59	67.48	A1	0	<1
R218	-36.79	-147.7	71.87	26.4	59.31	A1	0	8600

Table 4: LT-ORC simulation conditions

Turbine Efficiency	0.85
Pump Efficiency	0.7
Turbine inlet temperature	70 °C
Condensation temperature	-60 °C
Ambient temperature	25 °C

Table 5: Thermodynamic results for the LT-ORC system

	T_{cd} (°C)	P_{cd} (bar)	T_{ev} (°C)	P_{ev} (bar)	M (kg/s)	V (m ³ /s)	x	W_{net} (kW)	η_{cyc}	r_p
Propane	-60	0.43	57.26	20.0	0.322	0.305	1.00	46.0	0.239	46.9
R143a	-60	0.53	43.75	20.0	0.606	0.255	1.00	44.0	0.223	37.7
R125	-60	0.54	39.82	20.0	0.836	0.262	1.00	44.8	0.214	36.8
R41	-60	2.52	-0.7909	20.1	0.310	0.064	1.00	32.3	0.177	7.96
Ammonia	-60	0.22	49.35	20.0	0.118	0.467	0.84	47.9	0.250	91.3
R152a	-60	0.15	65	16.9	0.430	0.701	0.92	48.1	0.250	112.4
R134a	-60	0.16	65	18.9	0.609	0.646	0.98	45.9	0.241	118.7
R218	-60	0.31	59.31	19.8	1.253	0.473	1.00	49.8	0.207	64.1

3.3 Thermodynamic analysis for LT-ORC system

In this chapter, thermodynamic analysis of LT-ORC for different evaporation temperature and condensation temperature is presented. Propane, R143a, R125 and R218 refrigerants are used as working fluids.

Figure 3 and Figure 4 show the change in the power output and cycle efficiency according to change of evaporation temperature. Turbine outlet pressure and turbine inlet pressure are fixed during the simulation. In all refrigerants, maximum power output is occurred which indicate optimum operating condition exist. On the other hand, maximum thermal efficiency is occurred only for R125. Thermal efficiency of the other refrigerants are linearly increased as evaporating temperature is increased. In all cases, the point of maximum thermal efficiency and maximum power output is not matched.

Figure 5 and Figure 6 show the power output and cycle efficiency of the variation of the condensation temperature at the optimum evaporation temperature. Increase in condensation temperature results in linear decrease in power output and thermal efficiency.

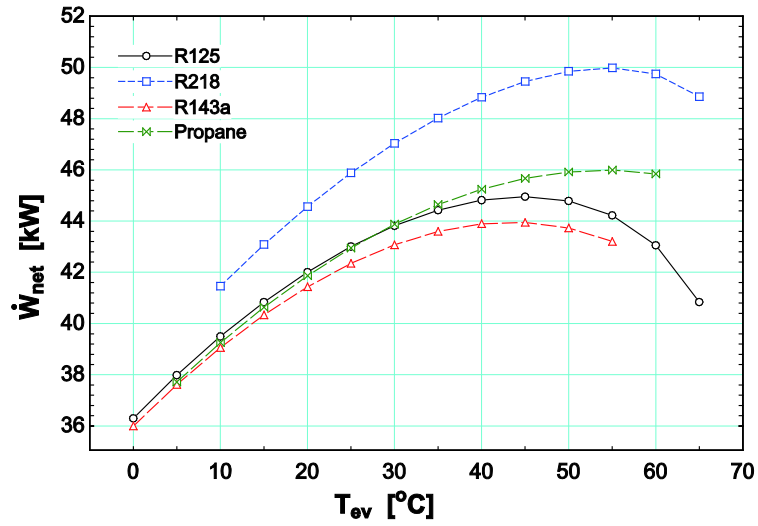


Figure 3: Power output of LT-ORC corresponding to evaporation temperature

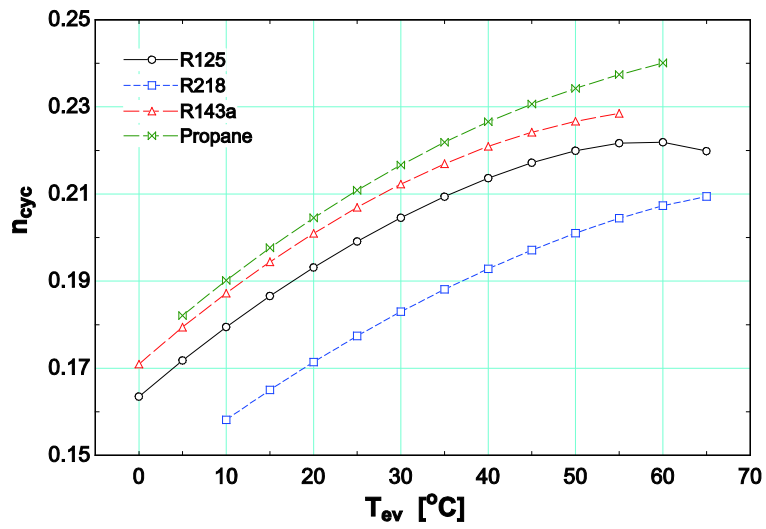


Figure 4: Cycle efficiency of LT-ORC corresponding to evaporation temperature

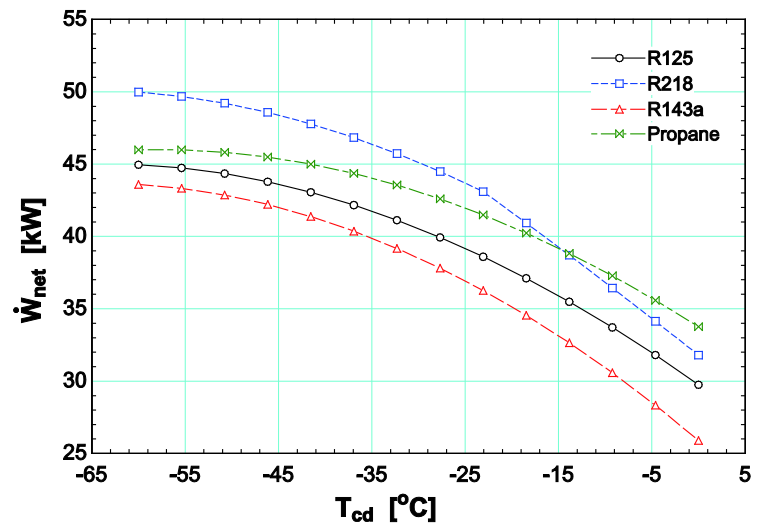


Figure 5: Power output of LT-ORC corresponding to condensing temperature

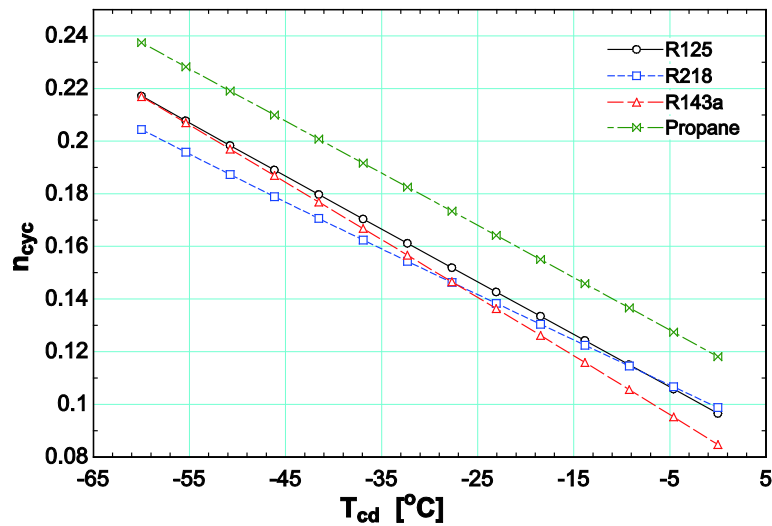


Figure 6: Cycle efficiency of LT-ORC corresponding to condensing temperature

4. CONCLUSIONS

A novel dual loop ORC system for waste heat recovery of LNG carrier has been described and analyzed. The proposed ORC system is intended to use the waste heat in engine exhaust gas and the cold energy in BoG. In order to investigate suitable working fluid and optimum operating condition for LT-ORC system, eight refrigerants including R218, R143, R125, propane were simulated with varying evaporation and condensation temperature. By using R218 refrigerant in LT-ORC loop, the highest power output of 49.8 kW was achieved from the waste heat in the exhaust gas passed through the HT-ORC loop. Also, the amount of additional waste heat recovery of 277 kW is expected during fuel preheating process.

NOMENCLATURE

BOG	boil-off Gas	(-)
c_p	specific heat	(kJ/K)
GWP	global warming potential	(-)
η	efficiency	(-)
M	mass flow rate	(kg/s)
ODP	ozone depleting potential	(-)
P	pressure	(bar)
Q	heat	(kW)
r_p	pressure ratio	(-)
T	temperature	(°C)
V	volumetric flow rate	(m ³ /s)
W	work	(kW)
x	quality	(-)

Subscript

1	HT-ORC
2	LT-ORC
c	critical
cf	cooling fluid
cyc	cycle
cd	condenser
ev	evaporator
fr	freezing

in	inlet
o	organic Rankine cycle
out	outlet
pp	pump
s	isentropic
sat	saturation
turb	turbine

REFERENCES

- Bombarda, P., Invernizzi, C. M., Pietra, C., 2010, Heat recovery from Diesel engines: A thermodynamic comparison between Kalina and ORC cycles, *Appl. Therm. Eng.*, vol. 30, no. 2: p. 212-219.
- Choi, B. C., Kim, Y. M., 2013, Thermodynamic analysis of a dual loop heat recovery system with trilateral cycle applied to exhaust gases of internal combustion engine for propulsion of the 6800 TEU container ship, *Energy*, vol. 58: p. 404-416.
- Dobrota, Đ., Lalić, B., Komar, I., 2013, Problem of boil-off in LNG supply chain. *Trans. Maritime Science*, vol. 2, no. 02: p. 91-100.
- International Energy Agency, 2013, *World Energy Outlook*
- Moon J, Lee YP, Jin Y, Hong E, Chang H., 2007, Cryogenic refrigeration cycle for re-liquefaction of LNG boil-off gas, *In. International Cryocooler Conference, Cryostar The Cryostar Magazine*, p. 629-635.
- Querol, E., Gonzalez-Regueral, B., García-Torrent, J., Ramos, A., 2011, Available power generation cycles to be coupled with the liquid natural gas (lng) vaporization process in a Spanish LNG terminal, *Applied Energy*, vol. 88: p. 2382-2390.
- Vaja, I., Gambarotta, A., 2010, Internal combustion engine (ICE) bottoming with organic Rankine cycles (ORCs), *Energy*, vol. 35, no. 2: p. 1084-1093.
- Wang, E. H., Zhang, H. G., Fan, B. Y., Ouyang, M. G., Zhao, Y., Mu, Q. H., 2011, Study of working fluid selection of organic Rankine cycle (ORC) for engine waste heat recovery. *Energy*, vol. 36, no. 5: p. 3406-3418.

ACKNOWLEDGEMENT

This research was partially supported by the Basic Science Research Program of the National Research Foundation of Korea (NRF) funded by the Ministry of Education (NRF-2013R1A1A2012173); partially by the Energy Efficiency and Resources of the Korea Institute of Energy Technology Evaluation and Planning (KETEP) and granted financial resource from the Ministry of Trade, Industry & Energy, Republic of Korea (No. 20112010100030); and partially by the National Research Foundation of Korea(NRF) in a grant funded by the Korea government (MSIP) through GCRC-SOP (No. 2011-0030013).

WATER-BASED RANKINE-CYCLE WASTE HEAT RECOVERY SYSTEMS FOR ENGINES: CHALLENGES AND OPPORTUNITIES

Gunnar Latz^{1*}, Olof Erlandsson², Thomas Skåre², Arnaud Contet²,
Sven Andersson¹ and Karin Munch¹

¹Chalmers University of Technology, Department of Applied Mechanics,
Gothenburg, Sweden
e-mail: latz@chalmers.se, sven.b.andersson@chalmers.se, karin.munch@chalmers.se

²TitanX Engine Cooling,
Sölvesborg, Sweden
e-mail: olof.erlandsson@titanx.com, thomas.skare@titanx.com, arnaud.contet@titanx.com

ABSTRACT

Much of the fuel energy in an internal combustion engine is lost as heat, mainly through hot exhaust gas. The high energy losses, and high temperatures of the exhaust gas, provide favorable conditions for applying a waste-heat recovery system. Among the available options, systems based on the Rankine cycle show the highest potential in terms of reducing fuel consumption.

Water or water-based mixtures have several advantages over organic fluids as working fluids for such applications of the Rankine cycle, in terms of cost, thermal stability, safety and complexity of the system. They also have several disadvantages, including possible freezing for pure water, high boiling temperature and high heat of vaporization. Hence, higher temperatures and amounts of waste heat are needed for reliable operation of the system. However, few experimental investigations have addressed the practical challenges associated with water and their effects on the performance and operation of a system in a driving cycle.

This paper presents results of experiments with a full-scale system for recovering waste heat from the exhaust gas recirculation (EGR) of a 12.8 L heavy-duty Diesel engine on a test bench. The working fluid used in the experiments was deionized water and a 2-cylinder piston expander served as an expansion device. The engine was kept in standard configuration, except for minor modifications required to implement the heat-recovery system. The prototype EGR boiler was designed to fit in the space initially designated for the production EGR cooler.

The assembly was operated in the operating points of the European Stationary Cycle (ESC). The results show that the trade-off between boiling pressure, sufficient superheating of the water and cooling of the EGR caused by the pinch-point in the boiler poses a major challenge when using water as a fluid. Low flow rates at low load points were challenging for boiler stability. During operation, the blow-by of working fluid into the lubrication system of the expander and vice versa was also problematic. Special steam-engine oil with high viscosity and good water separation capability was used to weaken this effect. The Rankine cycle-based test system attained a thermal efficiency of 10% with EGR as the only heat source. Results, major constraints and possible means to improve the system when using water as a working fluid are presented here. Simulation models developed for the EGR boiler and the piston expander supported this effort.

1. INTRODUCTION

Most of the fuel energy in an internal combustion engine is lost as heat. These losses can be reduced by using waste-heat recovery (WHR) systems, which have been widely discussed and investigated by various research groups in the last decade, as extensively reviewed by Sprouse and Depcik (2013) and Wang *et al.* (2011). Systems based on the Rankine cycle have been identified as the most appropriate for vehicle applications, in terms of efficiency, maturity and cost. Such systems could potentially

increase the powertrain efficiency of long-haul trucks (for which operating conditions are considered particularly suitable) by up to 30%, according to Wang *et al.* (2011). The most commonly discussed heat sources of the combustion engine are (in increasing order of temperature and hence quality of the utilizable heat) the engine coolant, charge air cooler, tailpipe exhaust gas and exhaust gas recirculation (EGR) system. Horst *et al.* (2014) noted that both charge air cooler and EGR are particularly attractive for heat recovery applications, since the recovered energy is removed from the load on the vehicle cooling system, while utilizing tailpipe exhaust gas adds additional heat to it.

Besides the choice of the heat source, the two main components that affect the conceptual design and performance are the working fluid used in the cycle and the expansion device, which is used to expand the generated vapor and produce the output work of the cycle. Optimal choices of the components are interdependent and depend on both the boundary conditions and requirements of the heat-recovery system (Seher *et al.*, 2012; Latz *et al.*, 2013). There are two main categories, based on the selected working fluid: organic Rankine cycle (ORC) if organic fluids are used and the traditional steam Rankine cycle if water is used.

Panesar *et al.* (2013) compared organic working fluids for a Euro 6 heavy-duty Diesel engine concept with high EGR rate, and concluded that acetone, R30 and R1130 provided better performance (under the chosen boundary conditions) than water, which was included in the tests for comparison. The drawback of water was the large amount of heat required to evaporate and superheat it, which reduced overall conversion efficiency. However, the cited authors noted that water also had substantial advantages, including its high thermal conductivity and absence of any health, environmental and safety issues. These advantages were also highlighted by Stobart and Weerasinghe (2006), who decided that water would be the most practical fluid to use in vehicle applications if the freezing issue could be overcome. Furthermore, Rayegan and Tao (2009) summarized the literature and concluded that no available organic fluid has all the desirable characteristics for an ORC application. Accordingly, Struzyna *et al.* (2014) found that various organics, including ethanol, acetals, siloxanes and ethers, lack long-term thermal stability at 275°C (the most stable were alkanes, cycloalkanes, aromatics and fluorinated hydrocarbons).

Two general conclusions that can be drawn from previous studies are that as heat-source temperatures rise beyond ca. 300°C (Ringler *et al.*, 2009) or 370°C (Sprouse and Depcik, 2013) the most efficient option switches from ORC to the steam Rankine cycle, and that neither option is clearly superior for applications at typical heavy-duty exhaust temperatures. However, at most operating points, temperatures in the high-pressure EGR system are higher than the 300-370°C threshold, and thus more suitable for steam systems, both theoretically and in terms of thermal stability of the fluid. Thus, several research groups have considered the performance of a heat-recovery system using EGR as a heat source and pure water or water-based mixtures as a working fluid (Howell *et al.*, 2011; Edwards *et al.*, 2012; Seher *et al.*, 2012). However, these studies have paid little attention to the operational challenges raised by using water as a fluid in a full-scale test system, such as the major limitations when using water as a fluid, interactions between the EGR and heat-recovery system, and key aspects of the expander design. Hence, the focal concerns of the study presented here were the operational challenges and bottlenecks related to the components of such systems, rather than the system performance *per se*.

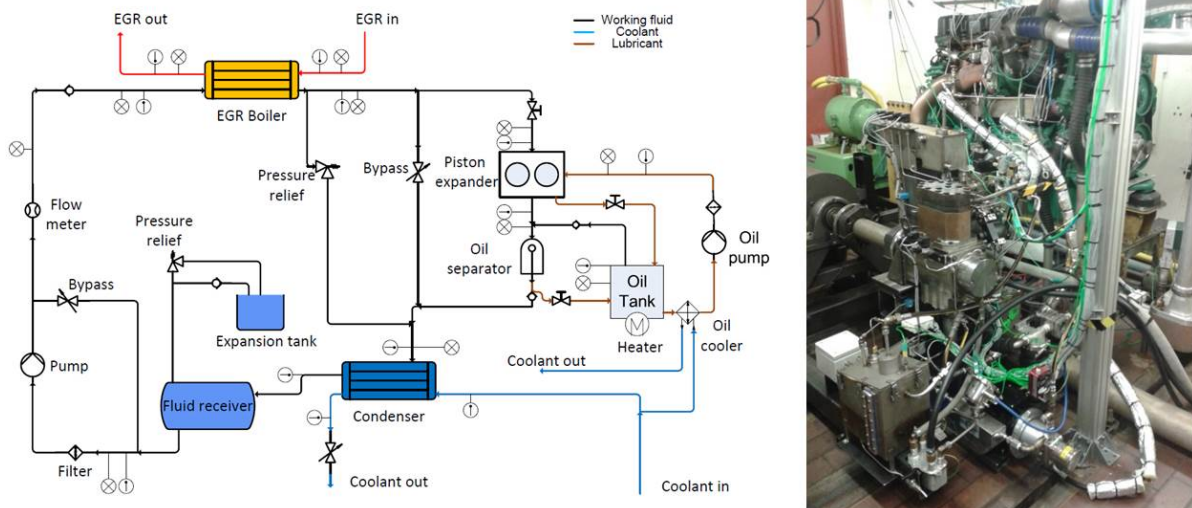
2. METHODOLOGY

This section briefly describes the experimental setup, the tests performed and simulations undertaken to support the experiments.

2.1 Experimental setup and components

The WHR system examined in this study utilized heat from the high-pressure EGR route of a heavy-duty Diesel engine. **Figure 1** displays the system layout and details of the measurement equipment

used to obtain the presented results. The water used as working fluid in the system was deionized, to avoid scale forming in the boiler. An observation glass was installed between the boiler and expander in order to check whether the working fluid was fully superheated or still in a two-phase state. The system was developed as a flexible tool for research purposes, neglecting packaging issues related to vehicle design, except that the EGR boiler replaced the production EGR cooler with only minor modifications to the bracketing on the engine.



Variable	Sensor principle	Range	Accuracy
Flow-rate (working fluid)	Coriolis	0 – 2.72 kg/h	0.2% of reading
Flow-rate (EGR)	Venturi with Δp -sensor	0-350 mbar	2% of reading (Δp)
Flow-rate (coolant)	Turbine flowmeter	0.8 – 80 liter/minute	2% of reading
Temperature	Thermocouple (K-type)	-40°C – 1100°C	< 2.4°C @ max. 600°C
Pressure	Piezoresistive	0 – 10 bar and 0 – 60 bar	0.25% of range

Figure 1: Experimental system layout and specification of the measurement equipment

The expansion device used in the heat-recovery system was a 2-cylinder, uni-flow (Stumpf, 1912) piston expander, in which live steam enters at the top of the cylinder and leaves after expansion through exhaust ports in the cylinder wall near the bottom dead center position of the piston (**Figure 2**). The inlet valve of the piston expander is actuated from inside the cylinder by a push-rod, driven by an eccentric cam sitting on top of the con-rod. The steam gets highly re-compressed after the piston closes the exhaust port on its way to top dead center. This reduces losses at the steam inlet, but sufficiently high live steam pressure and sufficiently low exhaust steam pressure are needed for the expander to produce any power. Tests with the presented expander showed that its operation required the live steam pressure to be at least 17 bar if the steam outlet pressure was 1 bar. Initially, it was designed for running on ethanol in a system utilizing more than only EGR heat, thus it was not expected to be optimal for the setup applied here (where 30 bar was the maximum specified pressure for the EGR boiler). However, the effect of this design drawback was one of the phenomena examined in the study.

A counter-flow plate heat-exchanger was constructed using plate-and-bar technology to operate as an EGR-boiler (evaporator), **Figure 2**. The height and length were set by the space available when it replaced the engine’s original EGR cooler, but the width was allowed to increase. Vertical plates were used to investigate the effects of gravity and phase separation.

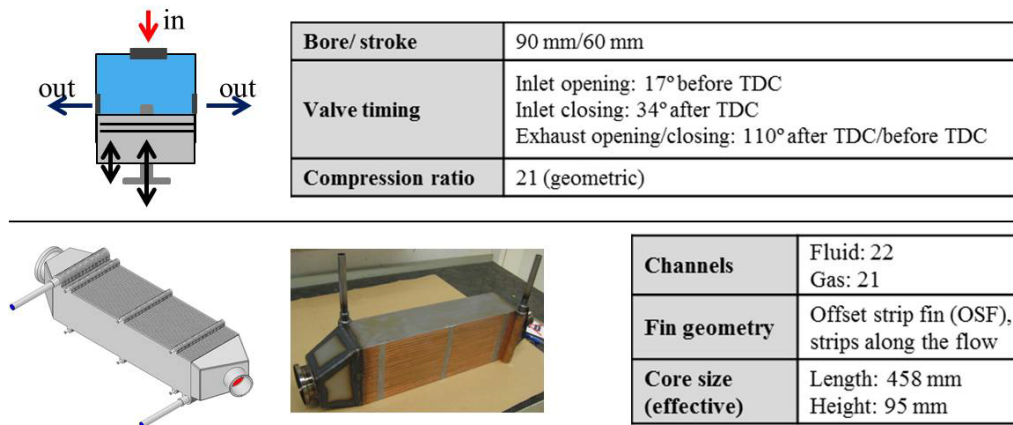


Figure 2: Schematic diagram and geometry of the uni-flow expander (upper image and table) and the EGR boiler (lower image and table)

Since this heat exchanger was considered to be a functional prototype for limited testing, no special measures were taken to minimize corrosion. The plates and turbulators were made of stainless steel and it was copper-brazed (vacuum), which was deemed acceptable for purposes of this study.

2.2 Experiments

To evaluate the potential for recovering heat from the EGR, the experimental system was operated with the expander bypassed to avoid oil contamination from its lubrication system. This would otherwise have affected the performance and reproducibility of the boiler tests. In these experiments the expander-bypass valve controlled the boiling pressure. However, tests with the expander engaged were also performed to validate the potential power output with the current expander design and the severity of the oil contamination issue.

2.3 Piston expander and EGR boiler simulations

A detailed model of the piston expander was implemented in the commercial 1-D flow simulation package GT-Suite. The model was then utilized to investigate optimal parameters for the expander and its performance limits when using water as a fluid in the heat-recovery system.

The boiler was sized using a TitanX in-house design tool based on a 0D lumped-element model (LEM) in Matlab[®]. The modeled heat exchanger was discretized into 20 elements along the flows (**Figure 3**) and all the channels were assumed to be under the same conditions. Partial boiling was allowed in elements, and where this occurred the overall heat transfer was iteratively weighted from boiling and single phase enthalpy parts to match the boiling start/end heat transfer energies. Cross-flow at entry and exits on the fluid side turbulator were ignored in the simulations. Factors and assumptions used are listed in **Table 1**.

Table 1: Factors and assumptions used for the boiler model

Modelling issue	Correlations/assumptions	Reference(s)
OSF heat transfer and pressure drop	Manglik/Bergles (single phase), Mandrusik/Carey (vaporization), Cooper (nucleate boiling for plain surface component)	Webb and Kim (2005)
Fluid properties	NIST Refprop data for water	Lemmon <i>et al.</i> (2013), Wagner and Pruss (2002)
Pressure drops	Single pressure drop factors (factors on dynamic pressure, evaluated at local conditions) <ul style="list-style-type: none"> • 1.4 at boiler connections (at restriction flow area) • 1.0 at inlet/outlet to channels (on turbulator flow area) 	-

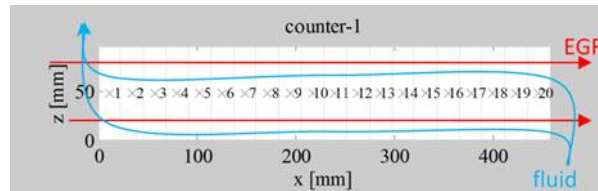


Figure 3: Discretization of the boiler in the lumped-element model.

In addition to the LEM, a working CFD model was developed at TitanX, with overall goals to investigate qualitatively and characterize local flow phenomena in fluid channels (and to a lesser extent) predict overall heat-exchanger performance. This CFD model, established in ANSYS Fluent, describes a single fluid and a single gas channel, as two separate CFD domains. The local projected heat transfer between the two domains is modeled from the LEM simulation described above and implemented as a continuous user-defined function (UDF). Variations in heat transfer strongly depend on the phase on the fluid side, thus the model uses fluid enthalpy as a parameter for the projected heat transfer coefficient (**Figure 4**). It should be noted that the model is only valid for one particular pressure, to characterize the specified heat transfer configuration, so it only provides qualitative results. The CFD model uses porous media for describing the offset strip fin (OSF) resistance, with differences in resistance along and across the fins (in a separate detailed module). It extends the analytic abilities provided by the LEM, by allowing exploration of effects on the system of fluid separation, inertia, gravity and variations of flows in the channels.

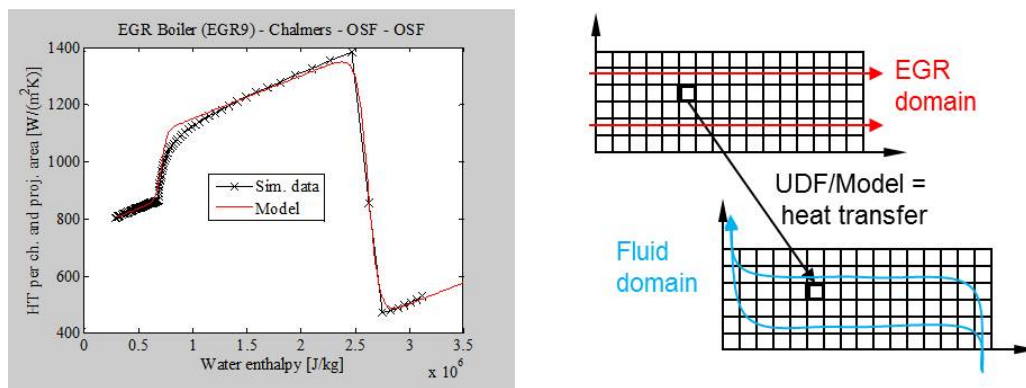


Figure 4: UDF (“Model”) describing projected heat transfer per channel and projected plate area. The principle of the UDF is illustrated by the figure to the right, showing CFD representations of an EGR- and a fluid channel.

3. RESULTS

This section presents findings from experiments with the system described above and complementary simulations of the piston expander and EGR boiler.

3.1 Experiments with the bypassed system at ESC points

The performance of the heat recovery system, in terms of heat transfer from the EGR, and EGR cooling capability, is displayed in **Figure 5**. Superheating clearly occurred at all covered ESC points and considered boiling pressures. The 25% load cases are excluded since it was not possible to achieve stable superheating at these points due to low EGR temperatures and flow. The engine could not be operated at full load with the applied setup either, due to limitations of the dynamometer. A problem associated with water, compared to organic fluids, is its limited capability to cool the EGR, mainly due to the high boiling temperatures and heat of evaporation, as previously reported in the theoretical study by Panesar *et al.* (2013). Hence, during the experiments reported here the EGR temperatures at the higher load points and boiling pressures were around 200°C, more than double the

temperatures (in degrees Celsius) maintained with the production EGR cooler, requiring corrective actions to the setup.

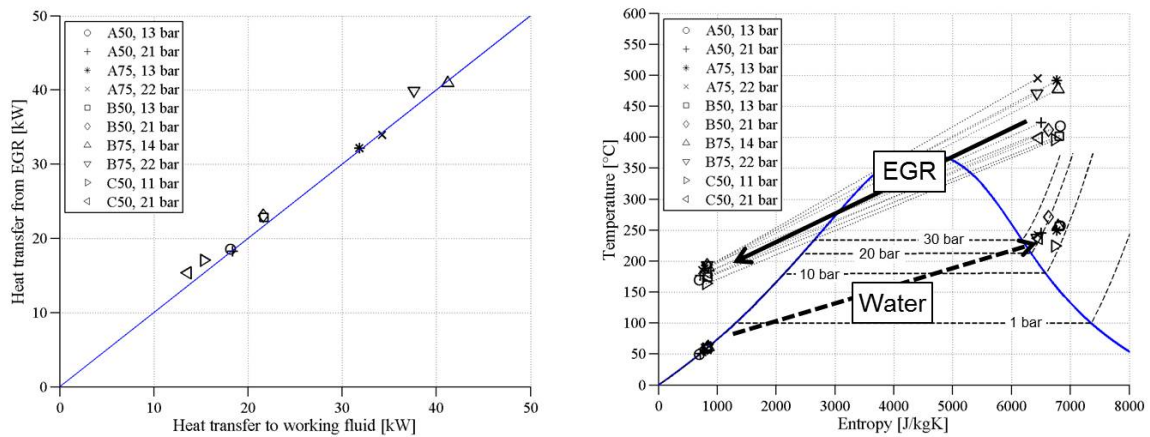


Figure 5: Heat transfer in the EGR boiler (left) and T-s diagram comparing fluid and EGR temperatures (right) at various ESC operating points and boiling pressures without an EGR after-cooler

To overcome the EGR temperature problem, an EGR after-cooler was designed that was intended to provide sufficient cooling and have minimal impact on the design of the EGR system (avoiding flow restrictions and any need for additional piping and brackets). The designed after-cooler replaced a horizontal section of the EGR route just before the EGR mixes with the charge air, and consists of a jacketed stainless steel pipe of identical diameter to the EGR pipe, supplemented with a helical copper coil inside. The jacket is cooled in parallel-flow configuration to the EGR, with the outlet water streaming through the copper coil in counter-flow direction to the EGR. This provides stable EGR temperatures below 80°C at all considered operating points. The after-cooler mounted in the EGR route as well as the distribution of EGR heat between the boiler and after-cooler is shown in **Figure 6**. Up to a third of the EGR heat goes to the after-cooler. The impact of the boiling pressure on this fraction is rather weak and less systematic than expected. However, at operating points with lower EGR temperatures (e.g. B50 and C50), high boiling pressures cause a reduction of heat utilization in the boiler due to the pinch-point limitation.

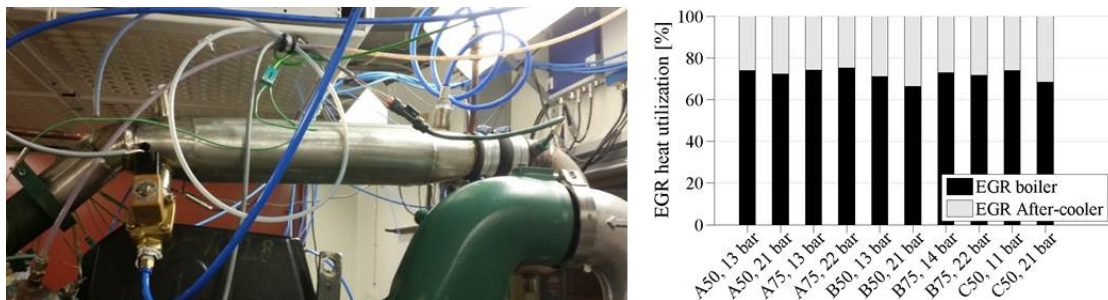


Figure 6: EGR after-cooler in the EGR route (left), distribution of EGR heat when cooled to 80°C (right)

3.2 Experiments with expander engaged

Following the tests with the bypassed system, the operation and performance of the current expander design was evaluated. Engine oil with SAE classification 15W40 was used for these initial tests. The oil circuit of the expander is constructed as a dry sump system, in which the external oil tank was electrically heated to 120°C to evaporate water from the lubrication system quickly and return the steam to the system downstream of the expander, as illustrated in **Figure 1**.

Figure 7 shows the steam boundary conditions and performance of the expander during a test in which the load was increased from B50 (with saturated vapor) to B65 (with superheated vapor) to

assess responses of the heat recovery system's efficiency and expander power output to the associated increases in inputs. The steam pressure increased due to the heat input. The expander speed was 600 rpm during the test (further increases of speed had no positive effect on power output). To assess the thermal efficiency of the Rankine cycle, the power output is related to the heat transferred in the boiler, while the expander's efficiency is assessed in terms of the isentropic enthalpy drop of the fluid over the expander. A general conclusion from this test is that the thermal efficiency achieved (between 5 and 10 %) is rather poor compared to the highest values reported in similar studies, as summarized for instance by Sprouse and Depcik (2013). This is because the expander used for the tests does not perform well, in the current configuration, under the given boundary conditions. Increasing the inlet steam pressure from 20 to 30 bar helps to double both the expander and thermal efficiency, indicating that the optimum inlet pressure for the expander lies beyond these values. One way to address this issue would be to increase the inlet pressure for the expander beyond 30 bar, but this was regarded as inadvisable in such early stages of testing the EGR boiler prototype. Lowering the condensation-side pressure below atmospheric level was not attempted, due to the risk of problematic air infiltration into the system. The remaining option was to modify the expander design by extending the steam admission phase or lowering the geometrical compression-ratio. These concepts, which can be used for adapting a uni-flow expander to given limitations in inlet pressures, are discussed in section 3.3.

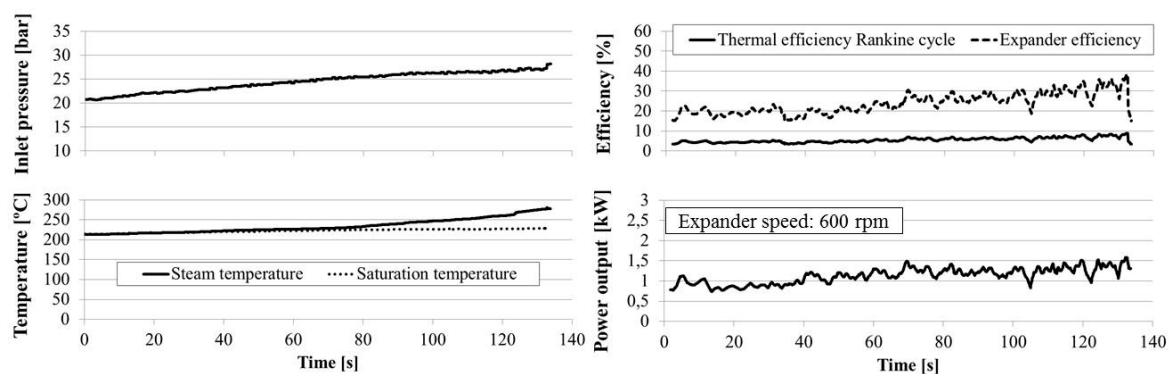


Figure 7: Boundary conditions (left) and performance (right) during an increase in load from B50 to “B65”

During expander operation, perceptible contamination of the working fluid with oil and vice versa was observed due to blow-by, resulting in unacceptable reductions in the oil's viscosity and hence the expander oil pressure for lubrication of the expander bearings. The water separation capability of the oil was poor and evaporation of the working fluid from the oil in the tank too inefficient to address these problems. Consequently, the oil was replaced with special steam engine oil, with a kinematic viscosity of 290 mm²/s at 40°C (DIN 51562-1), which has better properties in the presence of water.

3.3 Expander simulations

Effects of varying several parameters were investigated using the GT-Suite piston expander model. A particular objective was to assess potential strategies to improve the performance of a uni-flow expander when admission pressure is limited. One possibility is to decrease the expander compression ratio, and hence re-compression pressure (thereby shifting down the pressure required for efficient expander operation). Another alternative is to extend the admission phase by closing the inlet valve later in the expansion stroke, thus allowing more steam to enter the cylinder. The results indicate that at constant pressure boundary conditions both strategies provide similar increases in power output, but also similar increases in steam consumption.

The modeled dependence of the expander power output, and associated steam consumption, on the steam inlet pressure, compression ratio and expander speed are mapped in **Figure 8**. For comparison, the steam flow rates the boiler can supply at stable superheating levels are also listed. Projecting the 20-30 bar inlet pressure (at 600 rpm) for the experimental operating point characterized in **Figure 7**

on these maps, it can be seen that the power output between 1 and 2 kW can be confirmed by the expander model for the baseline compression ratio of 21. From the speed variation in the expander maps, it can be seen that increasing the expander speed beyond 600 rpm gives no improvement in power output at this compression ratio since the low inlet pressure is the power-limiting factor. The steam flow rate measured during the expander test described in section 3.2 could not exceed 6 g/s for this reason, which also caused the superheating temperature to increase over time (Figure 7). The model predicts a steam flow rate of 5 g/s for the same operating point. This deviation between the experimental and simulation results may be due to blow-by losses, which are not included in the simulation results.

It can also be seen that by reducing the compression ratio from 21 in the current design to 13, the expander could be operated at lower steam inlet pressure, achieving up to 3 kW in power output with 30 bar inlet pressure at a B50 operating point. In practice, this could be achieved by mounting a distance plate between the cylinder housing and crankcase of the expander, thus increasing the dead cylinder volume at piston top dead center. A consequence would be a 40% increase in steam consumption at this operating point, but the measured steam delivery rates of the boiler indicate that this could be covered. At the same configuration with a compression ratio of 13, an expander power output of 5 kW at 1200 rpm could be achieved for the B75 operating point. These results underline the sensitivity of the uni-flow piston expander’s performance to the system pressures.

From the measured steam delivery rates of the boiler it can be seen that the flow rate of steam has very weak dependency on the two boiling pressure levels. While the pinch point limitation in the boiler lowers the utilizable EGR temperature difference at high boiling pressures, the heat of vaporization for water is up to 20% lower under these conditions (explaining why the flow rates can be maintained overall).

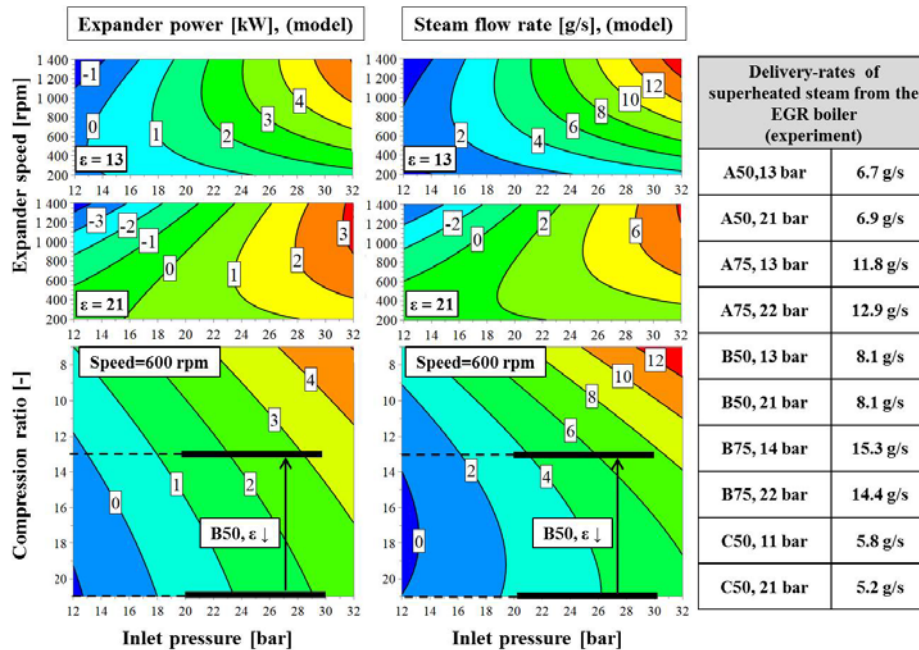


Figure 8: Modeled expander power and steam flow rate as functions of expander speed, compression ratio ϵ and inlet pressure (left). List of measured steam-delivery rates of the EGR boiler prototype (right).

3.4 EGR boiler simulations

Comparison of the LEM simulation and experimental data (Figure 9) reveals that the simulation overpredicts superheat in most cases. There may be many reasons for this, e.g. two-phase phenomena (model limitations in handling gravity or fluid separation, for instance), inaccuracies of coefficients

and correlations (related to fluids and geometry), other model limitations (e.g. channel-to-channel variations), fouling (which is ignored in the presented model), and heat losses to the surroundings.

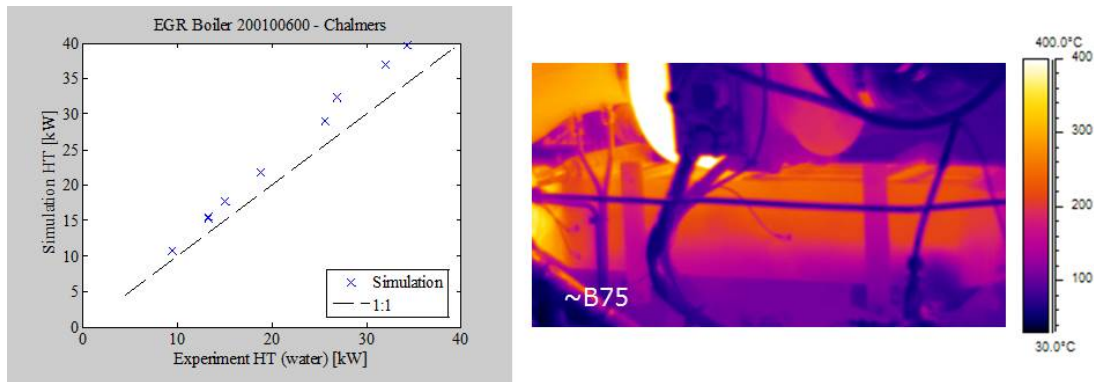


Figure 9: Comparison of simulation and experimental data (left). Engine load varies between A25 and B75, hence flows and pressures of both EGR and water also vary. Infrared image of the boiler side-plate (right). Fluid enters at the bottom right corner and exits at the top left corner. EGR flows from left to right.

Two-phase phenomena and characteristics in the EGR boiler were also explored in CFD simulations. Details are beyond the scope of this article, but the simulations revealed clear internal circulation on the fluid side: most of the liquid fluid immediately turns and flows along the bottom of the heat-exchanger. It gradually evaporates along the way and expands into the center region. However some of the vapor turns and flows in the reverse direction, creating a large steam “bubble” over the channel section that reduces both the effective heat transfer area and temperature difference, thereby reducing the overall heat-exchanger efficiency. This is likely the main reason for the difference between the LEM predictions and experimental data. It should be noted here that the engine, and hence boiler, are mounted in the same fashion in the test rig as in the truck, with a 4° angle to the horizontal plane, which further drives the liquid forward in the bottom of the vertical channels. Infrared images of the side-plate (**Figure 9**) support the CFD predictions, indicating that temperatures are significantly lower at the bottom of the heat-exchanger. The outer channel on the boiler is a fluid channel but the thick side-plate smears much of the gradients due to axial conduction in the wall. The images still clearly show that the liquid phase is not distributed over the height.

4. CONCLUSIONS

The goal of this study was to identify and characterize design component-level challenges associated with using a Rankine cycle-based system to recover waste heat from the EGR of a heavy-duty Diesel engine. The approach was to closely couple experiments using a full-scale demonstrator test bench system with simulations of processes in the EGR boiler and piston expander to highlight parameters and features that strongly influence the system’s overall performance. Water was used as the working fluid as it has promising potential in terms of both efficiency and convenience for applications at the considered heat-source temperatures.

The EGR boiler was designed as a plate-heat exchanger with vertical plates to investigate gravity effects in the boiler. CFD simulations and infrared images taken during the experiments showed the presence of internal flow circulation in the boiler. A steam “bubble” was formed, staying in the upper part of the boiler and reducing the area of effective heat transfer to the working fluid. The cooled EGR temperatures after the boiler were high (particularly at the A75 and B75 load points: up to 200°C , which is more than twice the temperature in degrees Celsius than the engine’s standard EGR cooler provides). Thus, an EGR after-cooler that further cooled the EGR to 80°C was built and mounted in the EGR route.

The maximal thermal efficiency of the system was just 10%, but the piston expander was not designed for use in the applied boundary conditions. A major bottleneck was the high re-compression of

exhaust steam due to the uni-flow operational mode. A 1D simulation model for the expander indicated that either reducing the compression ratio or extending the steam admission phase could double the expander's power output at current steam-delivery rates from the EGR boiler.

NOMENCLATURE

CFD	Computational fluid dynamics
EGR	Exhaust gas recirculation
ESC	European Stationary Cycle
ε	Compression ratio
HT	Heat transfer
LEM	Lumped element model
OSF	Offset strip fin
ORC	Organic Rankine cycle
TDC	Top dead center
UDF	User-defined function

REFERENCES

- Edwards, S., Eitel, J., Pantow, E., Geskes, P., Lutz, R., 2012, Waste Heat Recovery: The Next Challenge for Commercial Vehicle Thermomanagement, *SAE Int. J. Commer. Veh.*, vol. 5, no. 1, p. 395-406.
- Horst, T., Tegethoff, W., Eilts, P., Koehler, J., 2014, Prediction of dynamic Rankine Cycle waste heat recovery performance and fuel saving potential in passenger car applications considering interactions with vehicles' energy management, *Energy and Conversion Management*, vol. 78, p. 438-451.
- Howell, T., Gibble, J., Tun, C., 2011, Development of an ORC system to improve HD truck fuel efficiency, *Deer Conference 2011*, Detroit, Michigan, USA.
- Latz, G., Andersson, S., Munch, K., 2013, Selecting an Expansion Machine for Vehicle Waste-Heat Recovery Systems Based on the Rankine Cycle, *SAE Technical Paper* no. 2013-01-0552.
- Lemmon, E.W., Huber, M.L., McLinden, M.O., 2013, *NIST Standard Reference Database 23: Reference Fluid Thermodynamic and Transport Properties-REFPROP*, Version 9.1, National Institute of Standards and Technology, Gaithersburg.
- Panesar, A., Morgan, R., Miché, N., Heikal, M., 2013, Working fluid selection for a subcritical bottoming cycle applied to a high exhaust gas recirculation engine, *Energy*, vol. 60, p. 388-400.
- Rayegan, R., Tao, Y.X., 2009, A critical review on single component working fluids for organic Rankine cycles, *ASME Early Career Technical Journal*, vol. 8, no. 2, p. 1-8.
- Ringler, J., Seifert, M., Guyotot, V., Hübner, W., 2009, Rankine Cycle for Waste Heat Recovery of IC Engines, *SAE Technical Paper* no. 2009-01-0174,
- Seher, D., Lengenfelder, T., Gerhardt, J., 2012, Waste Heat Recovery for Commercial Vehicles with a Rankine Process, *21st Aachen Colloquium Automobile and Engine Technology*.
- Sprouse, C., Depcik, C., 2013, Review of organic Rankine cycles for internal combustion engine exhaust waste heat recovery, *Applied Thermal Engineering*, vol. 51, p. 711-722.
- Stobart, R., Weerasinghe, R., 2006, Heat Recovery and Bottoming Cycles for SI and CI Engines – A Perspective, *SAE Technical Paper* no. 2006-01-0662.
- Stumpf, J., 1912, *The una-flow steam engine*, R. Oldenbourg, Munich, 1912.
- Struzyna, R., Eifler, W., Menne, A., 2014, Suitability of selected working fluids for use in Waste-Heat-Recovery units, *IAV 4th Thermoelectrics Conference*, Berlin.
- Wagner, W., Pruss, A., 2002, The IAPWS Formulation 1995 for the Thermodynamic Properties of Ordinary Water Substance for General and Scientific Use, *J. Phys. Chem. Ref. Data*, vol. 31, no. 2, p. 387-535.
- Wang, T., Zhang, Y., Peng, Z., Shu, G., 2011, A review of researches on thermal exhaust heat recovery with Rankine cycle, *Renewable and Sustainable Energy Reviews*, vol. 15, p. 2862-2871.
- Webb, R.L., Kim, N.-H., 2005, *Principles of Enhanced Heat transfer*, 2nd edition, CRC Press, London.

ACKNOWLEDGEMENT

This study was conducted as a part of a waste-heat recovery project supported by the Swedish Energy Agency. The authors gratefully acknowledge the Agency's financial support.

EFFICIENT EVALUATION OF THERMOPHYSICAL PROPERTIES OF WORKING FLUIDS FOR ORGANIC RANKINE CYCLES

Matteo Pini, Salvatore Vitale, Giulio Gori
Antonio Rubino, Antonio Ghidoni

Delft University of Technology

ABSTRACT

The overall topic of this tutorial session is a description of the models that underpin the state-of-the-art thermophysical property libraries, and how these properties can be retrieved in a computationally efficient manner. The emphasis will be placed on the use of the REFPROP property library developed at the National Institute of Standards and Technology (NIST), though other libraries will also be described in some detail.

The first topic of the tutorial session will be a theoretical description of how the models (equations of state, mixture models, transport property formulations, etc.) are constructed. The emphasis of this section will be to describe the theory in a way that is relevant to end-users, such that they can understand the implications of these model formulations on their own code that they write.

Secondly, we will describe the use of the NIST REFPROP library to calculate the parameters of interest, including thermodynamic properties, derivatives of thermophysical properties, mixture phase envelopes, etc. An emphasis will be placed on the different means that can be used to maximize computational efficiency. Furthermore, the various options available for interfacing with REFPROP will be described, including the use of the CoolProp thermophysical property library.

Finally, we will present work that has been recently carried out to use the bicubic tabular interpolation methods of CoolProp to achieve computational speeds for fixed-composition mixtures from REFPROP that are on the order of the computational speed of mixtures that are treated as pseudo-pure fluids. This should be of particular interest to researchers that are carrying out dynamic simulation studies with zeotropic mixtures, as has been proposed in the literature for Organic Rankine Cycles.

PROTOTYPE OF THE DOMESTIC CHP ORC SYSTEM: CONSTRUCTION AND EXPERIMENTAL RESEARCH

Grzegorz Zywica*, Jan Kicinski, Tomasz Z. Kaczmarczyk,
Eugeniusz Ilnatowicz, Tomasz Turzynski, Sebastian Bykuc

Institute of Fluid-Flow Machinery, Polish Academy of Sciences
Gen. J. Fiszer 14 str., 80-231 Gdansk, Poland
e-mail: zywica@imp.gda.pl

* Corresponding Author

ABSTRACT

This paper presents the prototype of micro CHP ORC power plant, elaborated at the Institute of Fluid-Flow Machinery PAFI, Gdansk. The design and investigation of the micro CHP ORC (Organic Rankine Cycle) system are discussed. The source of heat is a newly-developed boiler, adapted to burn biomass. Electricity was generated thanks to a specially designed vapour microturbine. The gas bearings which are supplied by a working medium allow the turbogenerator to have a space-saving, hermetical structure. In the article the selected results of experimental studies are discussed. Thermal and flow characteristics were presented, allowing the evaluation of operating efficiency of boiler, heat exchangers, pumps, valves and other subassemblies. In addition, the test results concerning turbogenerator were attached, including its power output for various cycle parameters. The results obtained showed that the developed prototype operates in accordance with design solutions and the boiler's thermal output of 25 kW makes it possible to generate above 2 kW of electric power. The results also confirmed that this system may be used to develop a commercial version for this type of device.

1. INTRODUCTION

The micro CHP power plant with ORC is nowadays one of the fastest growing technologies, when it comes to combined generation of heat and power on a small scale. The popularity of this technology is based on a very broad scope of applications (Kicinski, 2013), since it can produce electricity irrespective of the type of heat source used. Depending on local energy resources, the ORC system can cooperate with different types of boilers, geothermic, waste heat and even as a kind of superstructure in bigger energy systems. Numerous research centers worldwide are being involved in the development of such high quality components or entire energy systems. The majority of scientific publications present the studies conducted on research installations under laboratory conditions. In the power range reaching several kW, commercially available solutions have hardly existed up to now.

The ongoing work is mainly intended to develop this ORC technology to the commercial level. An implementation of the technology is related with the need to overcome technical and economical barriers. The major technical problem is the construction of the expander. It is possible to apply solutions of various type in this power range, including screw expanders, scroll expanders, vane expanders or turbine expanders (steam micro-turbines). A systematic literature review on different types of expanders, mainly units up to 10 kWel, which are currently under development by industrial and research centers was presented in the article Qiu et al. (2011). None of the expanders reached series production status. According to Qiu et al. (2011), screw and blade expanders have the greatest number of advantages in the power range up to 10 kWel. The subject matter of the study on different types of expanders is the improvement in efficiency. The works are in progress in this scope either through experimental studies (Wang et al., 2011, Declaye et al., 2013, Hsu et al., 2014) or numerical

calculations (Clemante et al., 2012, Fiaschi et al., 2012, Klonowicz et al., 2014, Cordiner and Mulone, 2014). Research on expanders is also underway at the IMP PAN, in Gdansk. The last investigation showed, that the turbine expanders are the most attractive solutions in a domestic environment (Kaczmarczyk et al., 2013, Kicinski and Zywnica, 2014). They do not require an oil lubrication or dynamic seals and are very quiet, compared with other expanders. Higher rotational speed entails a reduction in the overall size of a turbine, so microturbines possess compact dimensions and low weight. The only rotating element is the rotor with a turbine and a generator, which does not wear out during use if bearing system had been properly designed (Kozanecki et al., 2014, Kicinski and Zywnica, 2012). They also allow for the achievement of satisfactory level of flow efficiency reaching 80% (Kosowski and Stepień, 2012).

Only very few small ORC systems, among the ones found in the literature, are based on steam micro-turbines. The main reason for this is the lack of ready-made commercially available solutions and the difficulties concerning the design and precise workmanship of micro-turbine elements. The example of such an installation was discussed in publication of Borsukiewicz-Gozdur (2013), but its slow-speed turbine generator (with the nominal power of 9 kW_{el}) was not intended for individual houses and was designed to make use of geothermal sources. The micro CHP biomass-fuelled systems review which may be used, among others, in a domestic environment was presented by Dong et al. (2009). The article also discusses the disadvantages and advantages of different technologies, it also emphasizes a great deal of potential for growth as far as cogeneration on a small scale is concerned. Experimental studies of biomass-fired ORC system are also described in the publications of Qiu et al. (2012) and Liu et al. (2010). Barberi et al. (2012) showed various CHP technologies adapted to domestic environment, taking into account different possible thermal energy sources such as combustion engines, Stirling engines, gas micro-turbines, ORC and thermophotovoltaic systems. Examples of systems for combined heat and electricity generation, which are still at the research stage, were also presented in other articles, e.g. (Pei et al., 2011, Minea, 2014). The article (Pei et al., 2011) shows in detail the research on the system with a steam micro-turbine integrated with outer gear and electricity generator. Literature concerning small ORC systems also pays much attention to modelling of such systems (Liu et al., 2011, Bouvenot et al., 2014).

The prototype of the CHP domestic energy system with ORC, which was developed at The Institute of Fluid-Flow Machinery (IMP PAN) in Gdansk, will be presented in the further part of the article. The fuel for the energy system is a biomass in the form of pellets. The electricity is produced using a high-speed oil-free steam micro-turbine. The energy system dimensions allow for its installation in houses. It is the first CHP energy system of that type in the country (and probably in this part of Europe). The prototype start-up took place in April 2014. Since then different types of experimental studies have been carried out aiming at the identification of characteristics of built device and its optimization.

2. THERMODYNAMIC CYCLE AND SYSTEM'S COMPONENTS

The prototype of the CHP domestic energy system with ORC was created within the framework of the research project co-financed by the European Union. The main objective of the project was to develop energy technologies enabling better use of renewable energy sources. This is why the ORC system which produces the electricity was integrated with biomass-fired boiler. Fuels of this type are easily accessible source of renewable energy and its quantity only slightly depends on weather conditions. Besides, biomass is one of the most popular fuels used for heating of family houses, especially in rural areas.

In the framework of prior design assumptions, demand for heating and for electricity was estimated in an average single-family house. On this basis, it was assumed that maximum capacities of the CHP system should be at level: approx. 25 kW of thermal power and approx. 2.5 kW of electric power. Under these assumptions it was possible to use the expanders of different types. On account of the highest potential for further development as well as operational aspects it was decided to apply the oil-free steam micro-turbine. Machines of this type, in the case of small ORC systems, have several advantages, the most important being high efficiency, no wear parts, hermetic housing and low noise (Kaczmarczyk et al., 2013, Kicinski and Zywnica, 2014, Kozanecki et al., 2014). Small dimensions

enable to develop compact structure for the entire device which is essential for the use of ORC system in a domestic environment.

After analyses and comparisons, mixture of substances under a trade name HFE-7100 was selected as the working medium (Mikielewicz et al., 2013a). This medium is a modern solvent, and is odourless and non-flammable. Its boiling point at atmospheric pressure is only 61°C. The thermodynamic cycle of the CHP system for the HFE-7100 was designed taking into account several criteria, such as: high efficiency of designed steam micro-turbine, purchase price of other components, net maximum electrical capacity, and availability of control and measurement apparatus in the market. The simplified diagram of the energy system is presented in Fig. 1. A characteristic feature of the cycle was the use of regenerative heat exchanger, which guarantees fairly higher efficiency of the cycle for the selected working medium. Temperature - entropy graph (T-s) for the chosen thermodynamic cycle is showed in Fig. 1. Theoretical energy generation efficiency, according to this cycle, was around 13 % at theoretical net electrical capacity of 2.7 kW. These results conformed (with a certain “safety margin”) with the original design intent.

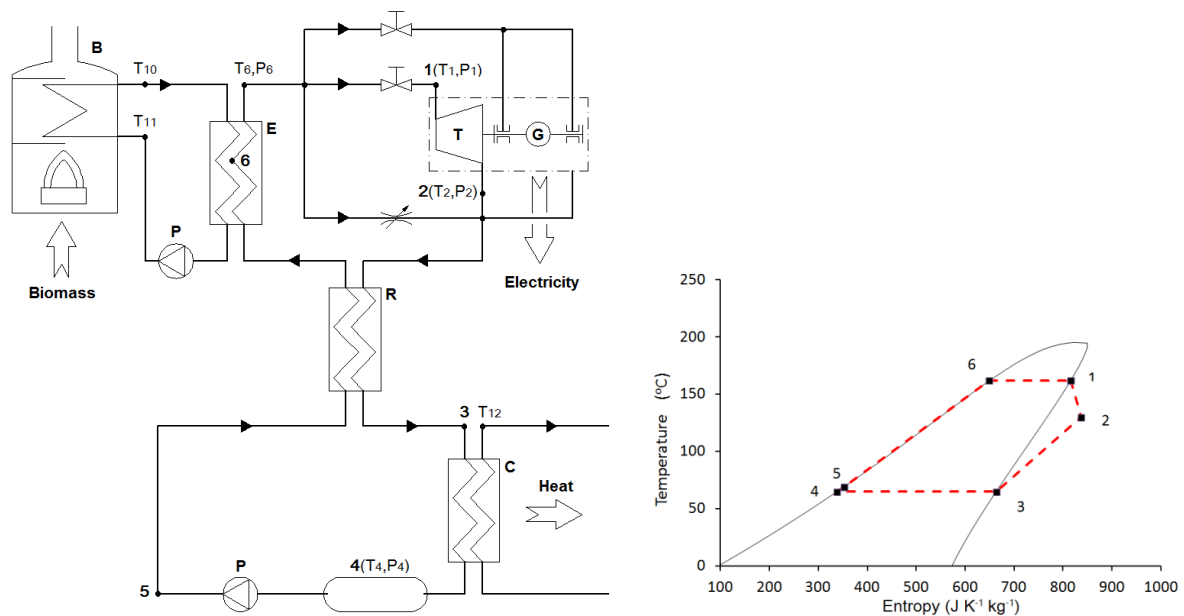


Figure 1: Diagram of the CHP ORC system with a biomass-fired boiler (B – boiler, P – pump, T – turbine, G – generator, E – evaporator, R – regenerator, C – condenser) and theoretical temperature-entropy graph for the ORC system with HFE-7100

On the basis of the characteristics of energy system cycle the selection criteria for all components were elaborated. Then the components were subject to theoretical analyses, design works and laboratory testing. The research was carried out in the laboratory specifically prepared for these tasks. Finally, the best constructional solutions have been selected to guarantee reliable operation and high efficiency of the entire machine. Specification of the basic parameters of the main components in the energy system is shown in Table 1.

Table 1: Basic parameters of the main components in the CHP ORC energy system.

Components	Basic properties
Boiler (biomass-fired)	Heat power (continuous) ~ 28 kW
Steam microturbine	Rated power – 2.7 kW (at 24 krpm)
Evaporator	Heat load – 25 kW
Regenerator	Heat load – 22.5 kW
Condenser	Heat load – 6.6 kW
Circulating pump	Nominal pressure difference – 10 bar Nominal capacity – 7.6 lpm

The listed components have successfully undergone experimental tests with the working medium in conditions close to target conditions. It has resulted in several innovative, alternative solutions of boilers (Kardas et al., 2014), circulating pumps (Kaniecki et al., 2013), heat exchangers (Mikielewicz et al., 2013b) and steam micro-turbines (Kicinski and Zywicka, 2013, Kozanecki et al., 2014, Stepien, 2013) while working on the components at the IMP PAN. When selecting components, a high level of durability and reliability as well as relatively low price were the important criteria, in addition to capacity demand and efficiency. The applied steam micro-turbine has gas bearings lubricated with steam of low-boiling medium, which allowed the use of hermetic casing. A high-speed generator with rare earth magnets was placed inside the casing, between the bearings. It is a four-stage radial turbine (two centripetal stages and two centrifugal stages). The applied micro-turbine should reach a flow efficiency up to 75% according to the design calculations. The visual appearance of the turbo-generator mounted on the frame of the micro power plant was presented in Fig. 2.



Figure 2: Photo of turbo-generator mounted on the frame of the micro power plant

3. DESIGNING AND BUILDING OF THE PROTOTYPE

The construction solution of the energy system was developed in the form of 3-dimensional, parametric CAD model, on the basis of the design assumptions and selected components. Then, after the preparation of the 2-dimensional technical documentation, the building of energy system at the laboratory of the IMP PAN commenced. The energy system installation together with the supporting structure and an automatic control and energy condition system was named “CHP module”. This module, during normal operation, allows generating electricity after being connected to any source of heat energy, in this case the multi-fuel boiler with thermal oil circulation. The CHP module cooperating with a boiler form a complete CHP ORC energy system, which allows to convert the chemical energy of fuel into thermal energy and electric power.

The main principles that have guided the process of design are listed below:

- logical grouping of prototype components around the biggest component – regenerative heat exchanger,
- arrangement of energy system components towards each other in such a way as to minimize length of the pipelines and to reduce the area occupied by them,
- realization of the following rule: hot vapour at the top, cold liquid at the bottom (micro-turbine - on the highest level, circulating pump - on the lowest level),
- the use of pipelines with diameters not less than nominal diameters of connecting components,
- the use of modular tank for the working medium, enabling the adjustment of the volume of the liquid in front of the pump,
- minimizing the number of angled connections and highly varying diameters of pipelines (trying to reduce pressure losses and drops),
- the use of flexible elements between joined components (compensation of thermal elongations, reducing the transmission of vibrations),
- replacing temporary fastenings by welded joints (improving the leaktightness of the installation) so long as maintaining the dismantling possibilities for any component,

- the use of standard joints and materials that are commonly sold on the market (the ease of rebuilding and repair),
- arrangement of components that support good air circulation, cooling the pump motors and automatics elements (air cooling from bottom to top),
- planning of so-called “transparency side”, on that side the control box was mounted and all screens, being a part of adjustment and measuring equipment which are visible there,
- the use of additional connections enabling easy serviceability of the system (e.g. filling, emptying, deaeration of the system).

When designing the energy system all publicly known principles of designing machinery were also used, maintaining relevant industry standards. The result of design works is presented in Fig. 3 in the form of 3D model.

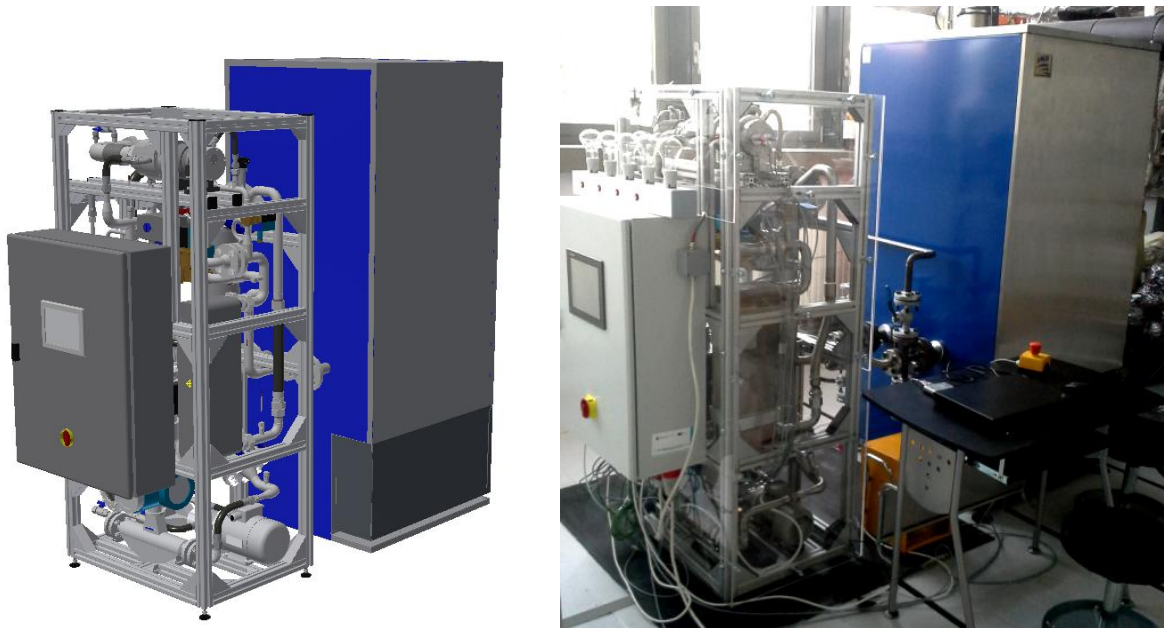


Figure 3: Three-dimensional CAD model and the prototype of the CHP ORC system

The control-measuring system based on universal PLC controller was created, in order to allow monitoring of the functioning of all components and conditioning of the electric energy. In addition, the energy system was fitted with a touch panel mounted on the control cabinet, displaying the most important operational parameters. The automatic control system allows for adjustment of operational parameters of the energy system components and also executive elements of the automatics, such as flow control valves. On the other hand, it also functions as a measurement & control system enabling achieving, visualizing and archiving of measured signals. The photo of the energy system with measurement & control system is showed in Fig. 3.

4. THE RESULTS OF EXPERIMENTAL INVESTIGATION

Experimental investigation of micro CHP ORC plant was made under laboratory conditions. The energy system was equipped with electric energy receivers: electric heater with 5 kW of power capacity, 10 bulbs of 1kW total power capacity. The take-up of heat energy from the condenser took place through the system filled with an aqueous solution of glycol fitted with outdoor dry air coolers. Combustion gases from the boiler were discharged through a stainless steel stack. During start-up tests the boiler was fired with biomass in the form of pellets, which was delivered to the furnace using an automatic feeding screw.

The aim of start-up tests was primarily to verify the correct functioning of all main components cooperating with each other in the ORC system and also checking whether the protective equipment and automatic control system are operating well (Kicinski et al., 2014). The start-up tests began before completing thermal insulation of the installation and some components (such as heat exchangers). It greatly facilitated searching for possible leakage points and allowed faster removal of leaks. It was connected with high heat losses that prevented the energy system from obtaining nominal operating parameters. Therefore, the effort was not aimed at achieving pre-determined micro-turbo-generator parameters during the first start-up attempts, but they were carried out only to check whether the steam micro-turbine functions properly. Preliminary tests lasted several hours in total. Selected measurement results were presented in the figures below.

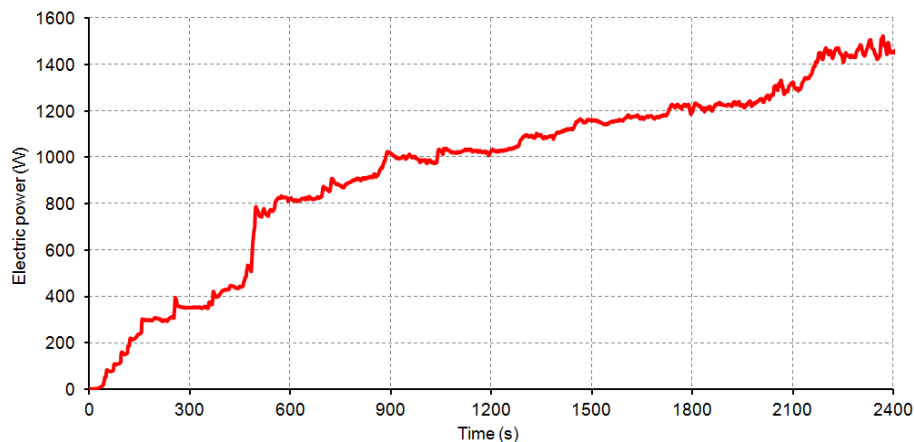


Figure 4: Electric power of the turbo-generator during preliminary tests of the CHP ORC energy system.

The amount of electricity generated during the 40 minutes start-up period is presented in Fig. 4. By adaptive control of the circuits the stable operation and a gradual increase in power output were obtained. The maximum electrical power was above 1500 W at the output of the electric energy conditioning system. The micro-turbine's shaft was operating with rotational speed around 18 000 rpm and around 6 000 rpm was still needed to reach nominal speed.

The temperatures of all the mediums that are present in the installations of the energy system measured during 2400 seconds are shown in Figures 5 and 6. The values of the temperature of low-boiling medium at different points of the ORC system are presented in Figure 5a. The temperatures after the evaporator and before the micro-turbine remained at similar levels and this was an indication of low heat losses. On the characteristics below, the gradual increase in temperature of the low-boiling medium before the pump may be also observed. That temperature was above 50 °C towards the end of the period concerned. The difference in temperature between the inlet and outlet of the micro-turbine was in the range of 10 to 22 °C. The temperature of HFE-7100 was measured in the tank at the pump inlet. The high degree of supercooling was achieved through the use of advanced cooling system with the fan and water spraying. In the figure 5b there is also a graph representing the absolute pressure of HFE-7100 at selected points in the ORC system. At the beginning of the test a vacuum procedure was done, to remove air from the ORC system. The highest pressure value reaching 11 bar took place directly at the outlet of the evaporator (P6). The pressure before the micro-turbine (P1) continued to increase together with gradual opening of the control valve. It was only marginally less than the pressure after the evaporator when the valve was fully open. The difference was approximately 0.3 bar. The vapour of the low-boiling medium after the micro-turbine, sharply declined its pressure to approx. 3 bar. The biggest pressure drop occurred at the end of measurement session, it was about 7.5 bar.

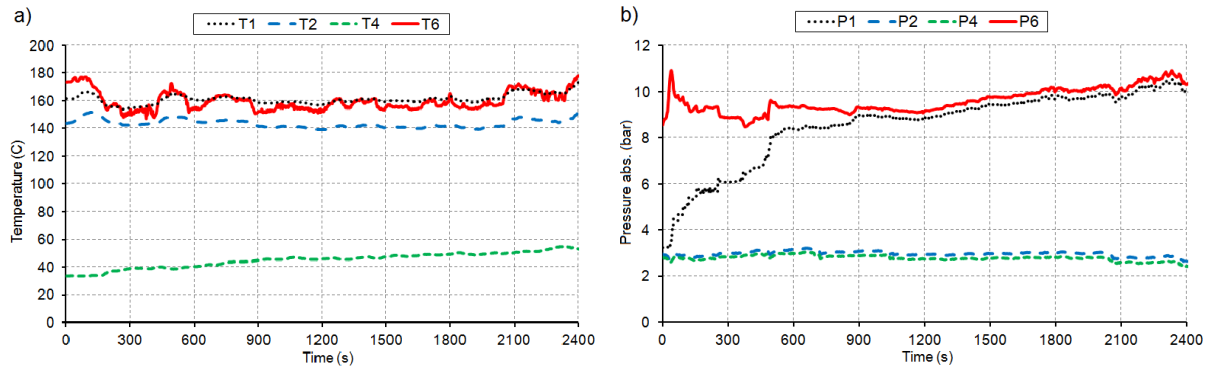


Figure 5: The temperature (a) and absolute pressure (b) of the HFE-7100 during tests performed on the ORC system (T1 – temperature at the inlet of the micro-turbine, T2 – temperature at the outlet of the micro-turbine, T4 – temperature of the medium in the tank at the inlet of the pump, T6 – temperature at the outlet of the evaporator, P1 – pressure at the inlet of the micro-turbine, P2 – pressure at the outlet of the micro-turbine, P4 – pressure in the tank at the inlet of the pump, P6 – pressure at the outlet of the evaporator).

Figure 6a presents the graph of thermal oil temperature in the inlet and outlet of the boiler. The maximum temperature at the evaporator inlet slightly exceeded 200 °C only for a short time and at its outlet amounted to around 150 °C. These parameters were stable over the period considered. A decrease of oil temperature has continued on the level of 50 °C during the tests. Figure 6b presents also the graph which shows the temperature of aqueous solution of glycol used to receive the heat in the condenser. The measurement was performed after the solution had flowed through condenser, therefore, after receiving heat energy from the working medium. At the end of measurements the temperature of the solution of glycol reached up to 70 °C and rose steadily, which was mainly the result of limited capabilities of heat consumption. This problem increased at high air temperature outside the building.

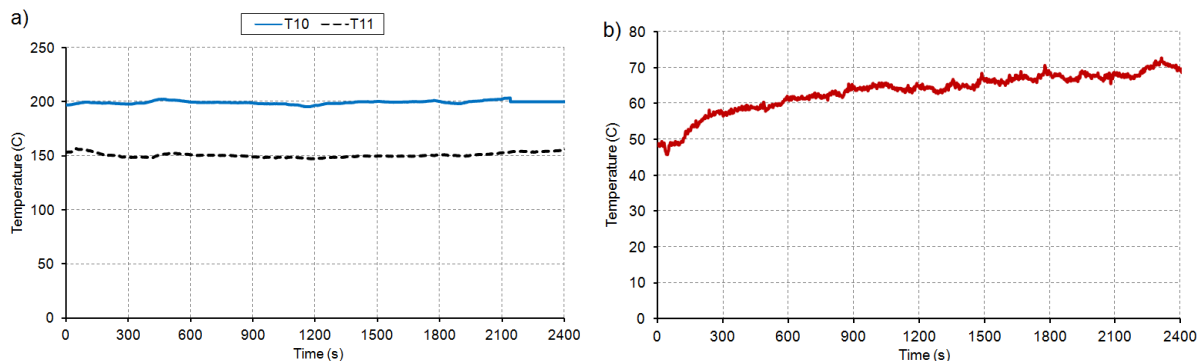


Figure 6: Temperature of the thermal oil (a) and aqueous solution of glycol (b) after the condenser (T12) during tests performed on the ORC system (T10 – temperature at the outlet of the boiler, T11 – temperature at the inlet of the boiler).

An important aspect to the tests performed on the ORC system is the flow rate of working medium. The measured value of flow rate for the low-boiling medium HFE-7100 was up to a maximum of 140 g/s. It constitutes 83 % of the nominal value of flow rate, which is 169 g/s. In terms of flow parameters, their optimal values for the micro-turbine have not been achieved during the tests. Both the level of pressure difference and flow rate was found to be below the design values. The flow rate of the thermal oil used as a heat-carrying agent between the boiler and the evaporator amounted to roughly 20 lpm. This value was close to the nominal value.

5. CONCLUSIONS

The article presents the prototype of the CHP ORC energy system. The preliminary research results were obtained from the tests during which the proper operation of all components in working medium heating and cooling processes was tested, and also from the tests in the operating mode in which the

micro-turbine generates electricity. The results confirmed the proper functioning of all components, automatic control system and the system receiving the electricity generated. The electrical power generated by the energy system was around 1.5 kW, because the installation was not yet fully prepared to achieve the nominal power. The turbine operation takes place with lowered pressure and flow rate of the working medium which impedes the performance of the system. The incomplete thermal insulation resulted in pretty high heat losses. In view of the obtained results and the past experiences, it can be said that when the installation is in optimum condition the built ORC energy system will make it possible to generate around 2.5 kW of electric power.

The target group of the developed micro power plant are the inhabitants of single-family houses, who, up to now, have been using biomass or other fuels to heat buildings. The works on the commercial version of the energy system are being planned in the near future. They will be carried out in cooperation with an industrial partner that have appropriate back-up facilities providing technology and marketing support and which already has its own distribution network in the market. It seems that, with the right policy of the country related to the use of renewable energy, the proposed domestic CHP ORC energy system can become a very attractive source of clean energy.

REFERENCES

- Barbieri, E.S., Spina, P.R., Venturini, M., 2012, Analysis of innovative micro-CHP systems to meet household energy demands, *Applied Energy*, 97: p. 723-733.
- Borsukiewicz-Gozdur, A., 2013, Experimental investigation of R227ea applied as working fluid in the ORC power plant with hermetic turbogenerator, *Applied Thermal Engineering*, 56: p. 126-133.
- Bouvenot, J.-B., Latour, B., Siroux, M., Flament, B., Stabat, P., Marchio, D., 2014, Dynamic model based on experimental investigations of a wood pellet steam engine micro CHP for building energy simulation, *Applied Thermal Engineering*, 73: p. 1041-1054.
- Clemente, S., Micheli, D., Reini, M., Taccani, R., 2012, Energy efficiency analysis of Organic Rankine Cycles with scroll expanders for cogenerative applications, *Applied Energy*, 97: p. 792-801.
- Cordiner, S., Mulone, V., 2014, Experimental-numerical analysis of a biomass fueled microgeneration power-plant based on microturbine, *Applied Thermal Engineering*, 71: p. 905-912.
- Declaye, S., Quoilin, S., Guillaume, L., Lemort, V., 2013, Experimental study on an open-drive scroll expander integrated into an ORC (Organic Rankine Cycle) system with R245fa as working fluid, *Energy*, 55: p. 173-183.
- Dong, L., Liu, H., Riffat, S., 2009, Development of small-scale and micro-scale biomass-fuelled CHP systems – A literature review, *Applied Thermal Engineering*, 29: p. 2119-2126.
- Fiaschi, D., Manfreda, G., Maraschiello, F., 2012, Thermo-fluid dynamics preliminary design of turbo-expanders for ORC cycles, *Applied Energy*, 97: p. 601–608.
- Hsu, S.-W., Chiang, H.-W. D., Yen, Ch.-W., 2014, Experimental Investigation of the Performance of a Hermetic Screw-Expander Organic Rankine Cycle, *Energies*, 7: p. 6172-6185.
- Kaczmarczyk, T., Ilnatowicz, E., Bykuc, S., Zywica, G., Kozanecki, Z., 2013, Experimental investigation of the ORC system in a cogenerative domestic power plant with a microturbine and an expansion valve, *ASME ORC 2013, 2nd International Seminar on ORC Power System*, Rotterdam, The Netherlands.
- Kaniecki, M., Henke A., Krzemianowski Z., 2013, Pump units for the micro CHP ORC system with low boiling agent, IFFM Publisher, Gdansk.
- Kardas D., Turzynski, T., Wardach-Swiecicka, I., Ronewicz, K., 2014, *Combustion and heat transfer in oil biomass boiler*. IFFM Publisher, Gdansk.
- Kicinski, J., 2013, Do we have chance for small-scale energy generation? The examples of technologies and devices for distributed energy systems in micro & small scale in Poland, *Bulletin of the Polish Academy of Sciences: Technical Sciences*, 61 (4): p. 749-756.
- Kicinski, J., Zywica, G., 2012, The numerical analysis of the steam microturbine rotor supported on foil bearings, *Advances in Vibration Engineering*, 11(2): p. 113-120.
- Kicinski, J., Zywica, G., 2014, *Steam microturbines in distributed cogeneration*, Springer.

- Kicinski, J., Zywicka, G., Kozanecki, Z., Ihnatowicz, E., Kaczmarczyk, T., Turzynski, T., Bykuc, S., Niewiadomski, J., Kardaś, D., 2014, *Preliminary studies of the micro CHP ORC prototype. Determination of the initial characteristics*, Internal Report of IFFM PAS, no 196/2014, Gdansk.
- Klonowicz, P., Borsukiewicz-Gozdur, A., Hanausek, P., Kryllowicz, W., Bruggemann, D., 2014, Design and performance measurements of an organic vapour turbine, *Applied Thermal Engineering*, 63: p. 297-303.
- Kosowski, K., Stepień, R., Włodarski, W., Piwowarski, M., Hirt, L., 2012, Partial admission stages of high efficiency for a microturbine, *Proc. VETOMC III International Conference*, Gdansk, p. 115-125.
- Kozanecki, Z., Kozanecka, D., Klonowicz, P., Lagodzinski, J., Gizelska, M., Tkacz, E., Miazga, K., Kaczmarek, A., 2014, *Oil-free micro-power turbomachinery*, IFFM Publisher, Gdansk.
- Kozanecki, Z., Tkacz, E., Lagodzinski, J., Miazga, K., 2014, Theoretical and experimental investigation of oil-free bearings and their application in diagnostics of high-speed turbomachinery, *Key Engineering Materials*, 588: p. 302-309.
- Liu, H., Qiu, G., Shao, Y., Daminabo, F., Riffat, S.B., 2010, Preliminary experimental investigations of a biomass-fired micro-scale CHP with organic Rankine cycle, *International Journal of Low-Carbon Technologies*, 5: p. 81-87.
- Liu, H., Shao, Y., Li, J., 2011, A biomass-fired micro-scale CHP system with organic Rankine cycle (ORC) Thermodynamic modelling studies, *Biomass and Bioenergy*, 35: p. 3985-3994.
- Mikielewicz, D., Mikielewicz, J., Ihnatowicz, E., Muszynski, T., Wajs, J., Rybinski W., 2013b, *Selected aspects of the design and testing of heat exchangers for domestic micro CHP ORC cycle*, IFFM Publisher, Gdansk.
- Mikielewicz, J., Mikielewicz, D., Ihnatowicz, E., Kaczmarczyk, T., Wajs, J., Matysko, R., Bykuc, S., Rybinski, W., 2013a, *Thermodynamic cycles of the domestic micro CHP ORC power plant*, IFFM Publisher, Gdansk.
- Minea, V., 2014, Power generation with ORC machines using low-grade waste heat or renewable energy, *Applied Thermal Engineering*, 69: p. 143-154.
- Pei, G., Li, J., Li, Y., Wang, D., Ji, J., 2011, Construction and dynamic test of a small-scale organic Rankine cycle, *Energy*, 36: p. 3215-3223.
- Qiu, G., Liu, H., Riffat, S., 2011, Expanders for micro-CHP systems with organic Rankine cycle, *Applied Thermal Engineering*, 31: p. 3301-3307
- Qiu, G., Shao, Y., Li, J., Liu, H., Riffat, S.B., 2012, Experimental investigation of a biomass-fired ORC-based micro-CHP for domestic applications, *Fuel*, 96: p. 374-382.
- Wang, W., Wu, Y., Maa, C., Liu, L., Yu, J., 2011, Preliminary experimental study of single screw expander prototype, *Applied Thermal Engineering*, 31: p. 3684-3688.
- Stepień, R., 2013, *Selected aspects of the design of multistage axial microturbines*, IFFM Publisher, Gdansk.

ACKNOWLEDGEMENT

The research work presented in this article was supported by the scientific project POIG.01.01.02-00-016/08 “Model agroenergy complexes as an example of distributed cogeneration based on local renewable energy sources”.

SMALL SCALE SOLID BIOMASS FUELLED ORC PLANTS FOR COMBINED HEAT AND POWER

Stefano Ganassin, Jos P. van Buijtenen*

Tri-O-Gen B.V.,
PO Box 25, 7470 AA Goor, The Netherlands
E-mail: Jos.vanbuijtenen@triogen.nl

* Corresponding Author

ABSTRACT

A high efficiency Organic Rankine Cycle (ORC) power unit of 170 kWe has been developed in The Netherlands. The ORC system is based on a thermally stable hydro-carbon as a working fluid, hence suitable for direct use of intermediate temperature heat sources. The unit is capable of transforming heat flows at temperatures between 350 and 530 °C into electricity. Typical applications involve the exhaust gasses of gas- or diesel engines and small gas turbines. Further applications include solid biomass combustion, incinerators, industrial residual heat and industrial flares.

This paper describes the application of biomass fuelled cogeneration (CHP) units, as in operation and on order now.

Wood or biomass is gaining interest as energy source for small district heating networks, while it is already widely used when available as a by-product, e.g. in sawmills. During combustion, temperatures reached are way above the level needed for the heating purpose. Hence, there is a considerable amount of exergy available, which can be used to generate electricity.

By applying an Organic Rankine Cycle (ORC) system, flue gasses from the wood combustor deliver their high temperature heat to be converted into electricity, leaving lower temperature heat to be supplied to the district heating grid, or to be used for local heating and drying.

This can be materialized in various ratios between power and heat, thus following the varying heat demand while maintaining total system efficiency.

An innovative system was developed, where the ORC is directly connected to the flue gas flow, without the need of an intermediate system. The system set-up, flue gas cleaning and evaporator cleaning methods are described in this paper, together with operational experience gained so far in several units.

1. INTRODUCTION

In recent years, the urge for utilizing all forms of available energy has increased significantly. One of these sources is heat, as can be generated by the combustion of wood and other residuals. The best way to utilize this energy is to convert it into electricity using a so-called Organic Rankine Cycle (ORC), while low temperature heat remains available for heating and drying purposes.

The development started in the early nineties at the Lappeenranta University of Technology in Finland, and was industrialized and commercialized by a Dutch company since 2002. Deployment took place since 2006, resulting in 30 units build so far, and 6 units on order or being commissioned. Most units so far utilize the residual heat from Internal Combustion Engines (ICE) exhausts, but already five units employ the heat generated by the combustion of biomass. This paper will highlight the ORC system as well as the specific technology used for the application of high temperature dust loaded flue gas as a heat source.

2. DESIGN OF THE ORC

Figure 1 shows the cycle scheme and the process of the Organic Rankine Cycle in the T-s diagram. Liquid working fluid is pumped from the storage vessel to the main pump, which is mounted on the same shaft as the turbine and the high-speed generator. The working fluid is compressed to its maximum working pressure and then enters the recuperator and subsequently the evaporator. Residual or waste heat is led through the evaporator, where the working fluid is heated up to the boiling point, evaporated and superheated. Then expansion takes place in the turbine, which drives the high speed generator and the main pump. After expansion, the sensible heat in the fluid is re-used in the recuperator, to preheat the liquid before it enters the evaporator. Below the recuperator the condenser is situated, where the vapor is condensed using a liquid coolant, before it flows back into the storage vessel.

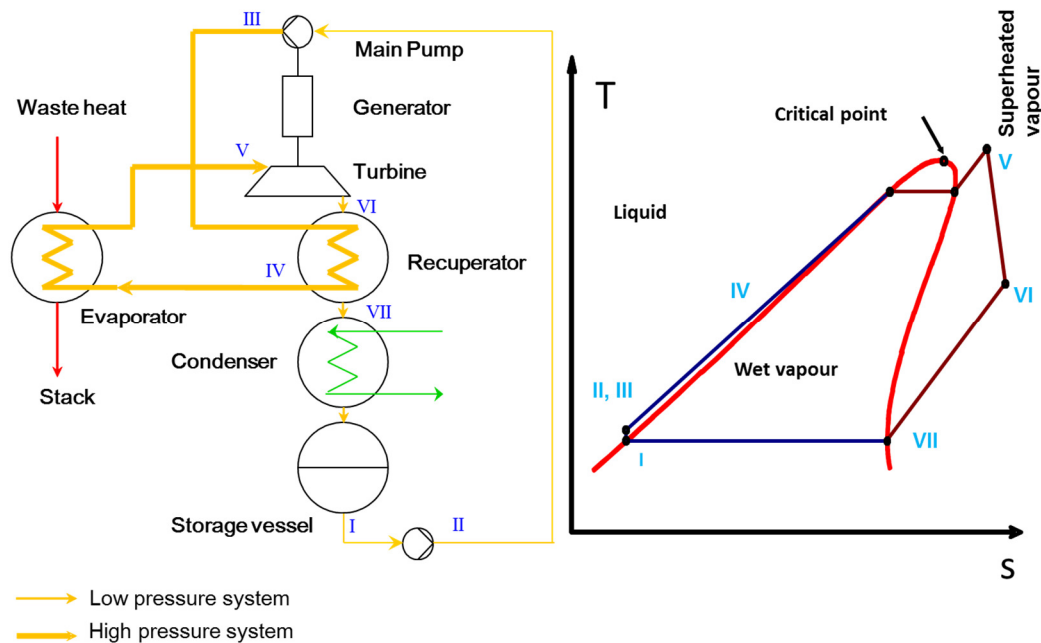


Figure 1: Cycle scheme and T-s diagram

This cycle uses toluene as working fluid. This allows a high value (320 °C) of the turbine inlet temperature thanks to its thermal stability. Moreover, the working fluid is used for lubrication and cooling of the turbo-generator which also embodies the main feed pump (van Buijtenen et al, 2003). This combination of turbine, generator and pump is running at high speed (25.000 rpm) without the need for a gearbox. This allows for a completely hermetic design, without the necessity of shaft seals. The turbine is a single stage radial inflow machine, driving an a-synchronous solid rotor induction type generator and the main radial pump. Speed is optimized for high turbine and pump efficiency. The recuperator and the condenser are plate and shell type heat exchangers.

The evaporator is of simple smooth pipe design, constructed out of horizontal U-shaped piping fixed at one side for free expansion. The small diameter pipes are made of stainless steel, and there is adequate access for cleaning. Allowable material temperature is well above the heat source temperature, so the evaporator is sufficiently safeguarded against no-flow conditions. The standard design can be sized to the specific conditions of the applications, as heat source temperature and flow.

Flue gasses are guided in a vertical direction from top to bottom through the evaporator. The lowest temperature is reached at the lowest point, where provisions are made to collect possible condensate during start and stop. The working fluid passes the series of pipes in a vertical direction from bottom to top, in once-through mode. There is no need for a drum, and the outflow conditions are controlled such that no liquid can be present while entering the turbine.

3. BIOMASS COMBUSTION AND ORC

3.1 Biomass combustion

There are several techniques to combust different kinds of biomass. Techniques are divided into grate firing and fluidized bed. To abate NO_x emission, there can be a certain amount of flue gas recirculation, affecting the resulting flue gas temperature, which typically ranges from 900 to 1100 °C. The term solid biomass refers to a large variety of organic substances, which ranges from clean, new wood from the wood production industry like sawmills, to demolition wood, and residues from wood harvesting and other agricultural processes like rice harvesting, sugar cane, olive plants et cetera.

These latter materials generally have no other application, and are considered as waste to get rid of through combustion. The resulting CO_2 emission would have been created anyway, but is using short cyclic carbon which is absorbed again in new crops. With this CO_2 neutral process useable electrical and thermal energy is produced in CHP mode replacing fossil energy. Although the burner has to be adapted to the kind of biomass, the ORC will remain similar in all cases, as the flue gas has to be cooled to 530 °C anyway. In order to reach the nominal power output, the amount of biomass to be burned might have to be adapted depending on calorific value and moist content.

3.2 Application to ORC

The heat energy generated from the combustion of biomass is generally used for heating and drying purposes. The required temperatures (50 to 100 °C) for heating and drying are well below the temperature generated by the biomass combustion. This means that a considerable amount of the available exergy (the measure for recoverable work from a flow of heat at a certain temperature) can be converted into electricity, generally considered as the higher valued form of useable energy, leaving the majority of the heat available for heating and drying. The available temperature trajectory is roughly from 1000 °C (flue gas) to the temperature needed for heating: typically 100 °C and below. However, due to the character of the flue gas that carries the energy (pressure and dust loading), this flue gas cannot directly be used for the generation of power as in a gas turbine. Another process has to take care of this, either in an open air cycle (indirectly fired gas turbine) or in a closed cycle using water (steam turbine) or using an appropriate organic fluid (Organic Rankine Cycle).

While normally ORC technology is considered to be suitable for low temperature heat sources, here the temperature is high, but the scale of the plant calls for something else than steam. One must realize, that even in large steam plants, live steam temperature will not exceed 540 - 600 °C, so the source temperature is reduced anyway. Moreover, this temperature will demand for a very high steam pressure and subsequently very low steam volume flow, not favorable for small plants. Organic fluids however, have a critical pressure at a much lower pressure than steam, so evaporation can still take place close to this critical point, hence reducing the heat exchange area for evaporation. Moreover, due to the positive slope of the right hand side boundary of the co-existence area, only a limited amount of superheating is necessary for completely dry expansion down to condenser pressure. Apart from these thermodynamic considerations, there are a number of arguments for applying ORC technology for small plants:

- During expansion, organic fluids will show a high volume flow at low enthalpy drop. This leads to the possibility of designing single stage turbines. Using water/steam, at a pressure over 60 bar (necessary to get sufficient thermodynamic cycle efficiency) one should at least use 3 to 4 stages. This would require axial turbine stages and eliminates the possibility to use radial turbine designs, which are known for being very suitable for small sizes (compare e.g. turbo-chargers for reciprocating engines).
- For small power plant (<500 kWe) steam cycles are often operated at even lower pressures (<20bar) and screw expanders are used instead of turbines. This solution however only achieves low efficiencies.
- Most organic fluids have good lubrication properties, so it can be used to lubricate bearings, eliminating the need for separating a conventional lubricant from the working fluid.

- Most organic fluids show a very low electric conductivity (practically 0), so electrical components might be subjected to it. This means that the generator can be cooled by operating in an environment of working fluid vapour.
- The use of organic fluids necessitates designing the system completely hermetic. As this can be done successfully based on the above elements, this leads to the advantage that units can be operated un-manned and/or remotely controlled and supervised automatically.
- In several countries, steam plants are required to be supervised by a qualified operator, adding to the operational costs of the plant.

Another characteristic of the biomass under consideration is its local availability, next to the local demand for heating and drying. This calls for relatively small plants, where gas turbine and steam cycle technology can perform only at rather low efficiencies. The logical choice then will be the Organic Rankine Cycle. Several solid biomass fueled ORC power plants in the range between 1 and 5 MWe have been installed in the last 10 years. These plants demand a heat input between 5 and 25 MWth, meaning that the feedstock must be collected in a large radius and transported to the power plant. The same counts for the heat distribution network, which must be extensive in order to allow complete absorption of the available heat. To avoid the heat losses of an extensive heat network and to avoid the cost and CO₂ production of feedstock transportation, the general tendency is to reduce the size of plants even further, to the range of 100 to 300 kWe. Moreover, the general tendency to more decentralized power generation is facilitated by the development of smart grid technology.

3.3 Direct Evaporation with flue gas from biomass combustion

Several ORC power plants are operated since several years powered by a solid biomass burner. When using flue gas from the combustion of biomass in an ORC evaporator, one has to take care of two facts, one being the high temperature of 900 to 1100 °C, and the other being the dust loading of such gases. As many working fluids of ORC systems are selected for the use of low temperature heat, chemical stability is not one of the criteria. So if such systems are to be used for high temperature flue gas, an intermediate circuit is used to transfer the heat to the ORC, using either thermal oil or pressurized water. Such an intermediate system requires extra equipment, leading to a loss in useable energy and requiring power for pumping.

The advantage of this ORC however, is that it is designed for higher temperatures: it uses a working fluid characterized by high temperature stability and requires a heat source temperature between 350 °C and 530 °C for continuous operation.

This ORC is therefore coupled with a hot gas generator biomass combustor (meaning a biomass combustor which is not equipped with an integrated heat exchanger). This direct evaporation requires of course special emphasis on safety. A safety system has been developed and deployed incorporating control of the burner in any abnormal situation that might jeopardize safe operation.

During normal operation the temperature of the gases coming from the combustion chamber is limited to 530 °C. This can be achieved in different ways:

1. mixing the hot flue gases with ambient air
2. mixing the flue gases with recirculated flue gas from the evaporator exit. This gas has a higher temperature and enthalpy than fresh air. Using recirculated flue gas instead of ambient air makes it possible to reduce the biomass consumption by 10 to 15%.
3. installing a heat exchanger (e.g. to produce hot water) before the ORC evaporator to extract heat and reduce temperature. This solution will require a bigger biomass combustor and it is only suitable when there is use for the extra heat.

3.4 Evaporator fouling and cleaning

Apart from the temperature, the high dust loading of the flue gases generated from biomass combustion must also be addressed.

Dust content of the flue gasses leaving the biomass burner may range from 1.000 to 10.000 mg/Nm³. By cooling the flue gas before cleaning, the temperature will drop below the so-called ash melting point, hence safeguarding downstream equipment from eutectic depositions.

After cooling the flue gas will be cleaned from dust down to a level of 200 mg/Nm³, using (multi) cyclones or other standard equipment depending on the burner technology and biomass characteristics,

before entering the evaporator. This cleaning is done at a temperature of 530 °C. Figure 2 shows the plant set-up as described.

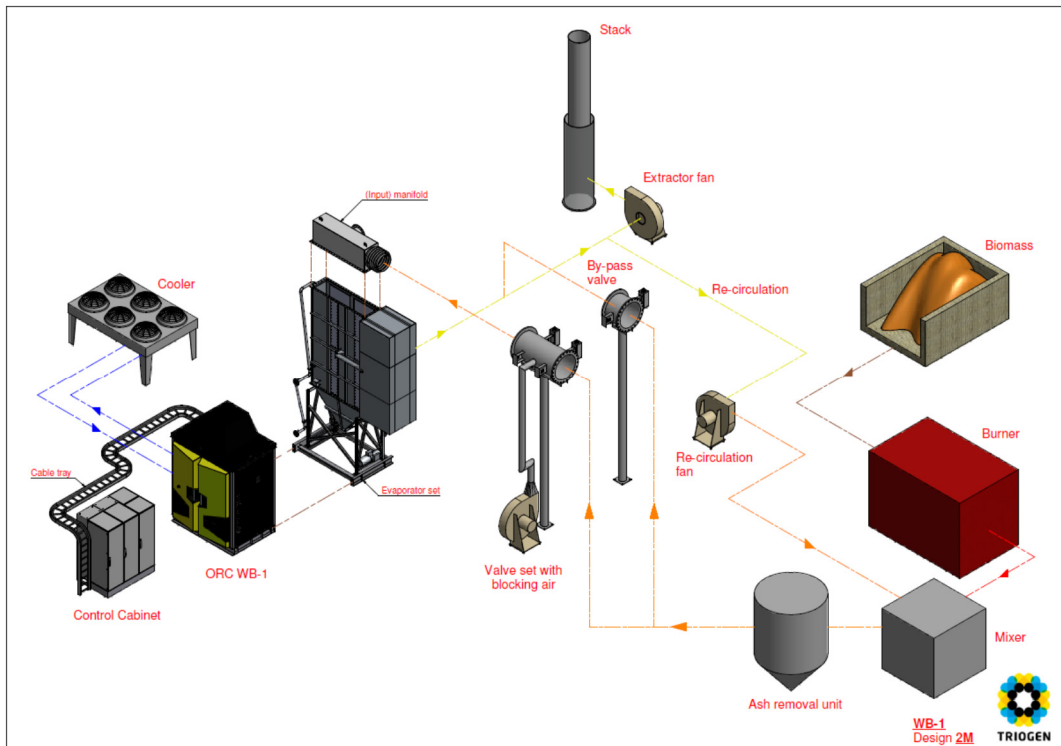


Figure 2: Schematic of a Biomass fired ORC plant.



Figure 3: Example of a biomass fired ORC plant

The value for dust content of the flue gas entering the evaporator is set as an attainable figure of 200 mg/Nm³ by this method. However, dust will still deposit on the pipes of the evaporator, and cleaning will be necessary. Fouling causes a reduced heat transfer to the pipes and rises the pressure drop of the flue gas on its flow path through the evaporator. Automatic on-line cleaning is applied at intervals set to certain values of these phenomena on the basis of first occurrences. As the dust will be dry as described above, several cleaning methods are being considered and tested.

Experience shows that the method to be applied depends on the type of biomass used, giving certain ash characteristics.

- Acoustic cleaning using a pneumatic horn proved to be effective in most cases, however care has to be taken for the noise emission.
- Mechanical brushes were abandoned because of the associated mechanical problems in the drives that had to move the brushes.
- Vibrational cleaning by exciting the pipes by so called shakers proved to be successful in some cases.
- Pneumatic cleaning, allowing a “shot” of air at high pressure to the pipes at distinct locations, looks promising at this moment, and is being tested.
- Shot cleaning using steel balls added to the flue gas flow and recovered from the bottom ash is under consideration.

In order to minimize the effect of fouling and facilitate cleaning, the evaporator as developed for clean flue gasses is adapted. Firstly, some extra heat transfer area is installed in order to maintain performance under mild fouling conditions. Secondly, the pitch at which the pipes are arranged can be varied, in order to tune the flue gas velocity to the flue gas density for keeping this more constant along the flow path. If particles with an abrasive character are expected, pipe wall thickness can be increased to ensure service life. External access to the heating surfaces is enabled through hatches in the evaporator covers, so manual cleaning can be done at regular intervals. Experience with actual operating plants is summarized in Table 1.

Table 1: Biomass combustion plants using ORC for electricity production

Plant	Fuel / Burner type	Operational since	Evaporator cleaning method	Heat use
A	Woodchips / Moving Grid	2012	Acoustic horn; once in 15 minutes. Manual cleaning every 2-3 months	Heat supply to offices (floor heating) and industrial equipment (55°C)
B	Woodchips / Fluidized Bed	2013	Acoustic horn	Heat supply to chicken stables and offices (floor heating 55°C)
C	Woodchips / Fluidized Bed	2014	Pneumatic cleaning	Heat supply to small swimming pool, houses and offices (55°C)
D	Residual wood from sawmill process / Moving grid	2013	Acoustic horn. Successful, constant good performance, manual cleaning as preventive maintenance every 6 months	Heat from coolant used in wood dryer (80°C)
E	Woodchips / Moving grid	Under commissioning	Pneumatic	
F	Rice hull / Fluidized Bed	Under commissioning	Shot cleaning	Heat from coolant to be used in the rice treatment process (80°C)

Pending local regulations, the system can be equipped with filters downstream of the evaporator, where values below 20 mg/nm³ are achievable. Temperature after the evaporator will be around 200 °C, hence well above the dew point. Conclusion here is that this ORC can utilize flue gas from biomass combustion in the ideal temperature range between ash melting point and dew point.

4. SYSTEM PERFORMANCE

The combination of an ORC with biomass combustion plants offers the opportunity to generate both electricity and heat from this renewable source. Like in typical combined heat and power plants (CHP), the high temperature available from the combustion process is used for power, while the essential residual heat is used for heating purposes. Biomass combustion plants have been built in many cases for heating only, and to get rid of organic remains of agricultural processes as well as in the wood industry.

Heat applications so far are the heating of local facilities like stables, swimming pools and offices, small district heating grids, pre-heating of water for industrial equipment for leather processing and rice treatment processes, the drying of production wood and of the remains of digestion processes.

Biomass/ORC plant can deliver heat from two sources: cooling water as used to cool the ORC condenser, as well as through further cooling of the flue gas to an acceptable level, as it leaves the ORC evaporator at approximately 200 °C.

An important parameter is the temperature at which the heat has to be used. For maximal power production, the ORC condenser should operate at the lowest possible temperature, which is 55 °C in this case. Cooling water is then available at 55 °C and has to be cooled to 35 °C. This temperature range can already be applied if the heating system is laid out for this low temperature (like a low temperature floor heating system, swimming pool or drying system). However, if there is a heat demand at higher temperature, the ORC condenser can deliver that at only a minor penalty on the electrical power. Maximum achievable temperature is 80 °C. In that case the ORC will be laid out such that the condenser temperature might vary depending on the heat demand temperature, so that always the optimum ration between heat and power can be reached. The achievable power as function of the heat supply temperature from the condenser is shown in Figure 3. If temperature demand is even higher, some heat from the remaining exhaust gases at 200 °C might be used (not considered in Table 2).

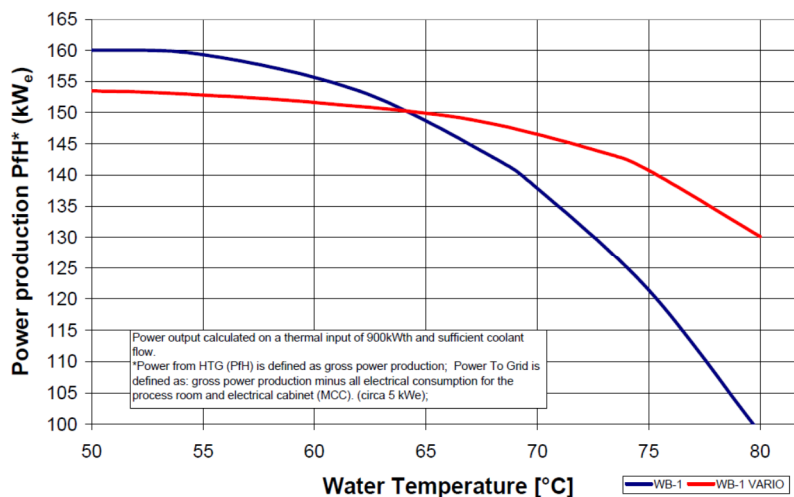


Figure 3: ORC electrical power as function of condenser cooling water temperature.

Of course, apart from delivery temperature, the amount of required heat can vary over time. Lower heat load might be accommodated by part load operation of the ORC by reducing heat input or by rejection of the excess heat. Some examples of typical performance specifications are given in table 2 below.

Table 2: Biomass combustion plants using ORC for electricity production (indicative values)

		CHP mode	POWER optimized
Burner power	kWth	~ 1100	~ 1100
ORC heat input	kWth	~ 900	~ 900
Stack losses (if unused)	kWth	~ 200	~ 200
Power output ORC	kWe	130	170
Heat rejected in coolant	kWth	~ 650	~ 650
Coolant outlet temperature	°C	80	55
General losses (mechanical and electrical)	kWth	~ 100	~ 100
ORC electrical Efficiency	%	~14,5	~18,9
CHP electrical efficiency	%	~11,8	~15,5
CHP system efficiency	%	~70,9	~74,6

5. CONCLUSIONS AND OUTLOOK

Because of the urge for renewable power and optimal use of all sources of energy, the application of combined heat and power should be realized in as much as possible instances. Thanks to the availability of ORC technology, this is now possible in cases where biomass is being used for heating and drying purposes. A different, counter intuitive, view on CHP is needed. The market asks for a system that first and foremost produces the demanded amount of heat energy, the electricity production should follow. This makes the electricity the byproduct and not the heat, as customary when a power station delivers also heat.

Local availability of solid biomass combined with local heat demand urges for tuning plant size to their volumes, avoiding large distances for biomass transportation and extensive heat networks. Moreover, the general tendency to more decentralized power generation is facilitated by the development of smart grid technology.

The whole system should be flexible for the ratio between heat and power. Varying heat demand, for example from seasonal effects or the needed temperature for drying (pending e.g. moisture content), can in this case be accommodated while ensuring maximum system efficiency through the VARIO® concept.

Evaporator cleaning is still a challenge, as the character of the dust deposit may vary largely with the kind of biomass and combustion technology used. So far, different cleaning methods have been applied successfully, on the basis of experience gained. A more sophisticated engineering approach should be developed.

References

J.P. van Buijtenen et al: DESIGN AND VALIDATION OF A NEW HIGH EXPANSION RATIO RADIAL TURBINE FOR ORC APPLICATION, *5th European Conference on Turbo-machinery, Praha, March 2003*

J.P. van Buijtenen: THE TRI-O-GEN ORGANIC RANKINE CYCLE: DEVELOPMENT AND PERSPECTIVES, *Power Engineer, Journal of the IDGTE, March 2009, Volume 13 Issue 1.*

J. Heinimo, J.P. van Buijtenen, J. Larjola, J. Backman: SMALL ELECTRICITY PRODUCTION WITH HIGH SPEED ORC TECHNOLOGY. *International Nordic Bioenergy 2003 conference, Jyvaskyla, 2/5 September 2003*

S. van Loo, J. Koppejan: THE HANDBOOK OF BIOMASS COMBUSTION & CO-FIRING. *Published by Earthscan Ltd, Dunstan House, 14a St Cross Street, London EC1N 8XA, UK. ISBN: 978-84407-249-1. (2008)*

ACKNOWLEDGEMENT

The authors wish to thank the management of Triogen B.V. for their permission to publish this paper.

START-UP RESEARCH ON THE LABORATORY MICRO CHP ORC TEST STAND

Sebastian Bykuć^{1*}, Łukasz Breńkacz², Grzegorz Żywica³

¹The Szewalski Institute of Fluid-Flow Machinery, Distributed Energy Department,
Gdańsk, Poland
sebastian.bykuc@imp.gda.pl

²The Szewalski Institute of Fluid-Flow Machinery,
Department of Turbine Dynamics and Diagnostics, Gdańsk, Poland
lukasz.brenkacz@imp.gda.pl

³The Szewalski Institute of Fluid-Flow Machinery,
Department of Turbine Dynamics and Diagnostics, Gdańsk, Poland
grzegorz.zywica@imp.gda.pl

* Corresponding Author

ABSTRACT

The paper presents the construction and the first results of analyzes performed on the newly built micro CHP ORC power plant test stand. The research covers initial start-up tests. This test stand has been built at the Institute of Fluid-Flow Machinery, Polish Academy of Sciences in Gdansk, Poland. It is a universal test stand where it is possible to examine among others micro turbines of various designs operating on a low boiling agent. The test stand is simulating Micro CHP based on ORC technology cogeneration unit producing electricity and heat as hot water up to 55°C (design conditions) applicable for low temperature heating (floor or wall heating systems). The supersonic turbine with a capacity of up to 3 [kW] was installed on the test stand. The HFE 7100 is a working medium in this system. This article briefly describes the construction of laboratory test stand, it is composed of turbine, pump, heat exchangers, regenerative heat exchanger and a set of sensors. The paper presents the results of experimental studies, for example graphs showing variations in temperature and in pressure at various measurement points on the test stand. The article also includes graphs of power generated by ORC turbine as a function of available pressure difference.

1. INTRODUCTION

There is a significant increase in the use of working fluids other than water in power plants and CHP systems, especially if the source temperature is lower than in traditional steam power plants. Different aspects of ORC systems including various heat sources (solar energy, geothermal fluids, waste heat), critical plant components (heat exchangers, expanders), thermodynamic cycle optimization and proper fluid selection were discussed in the literature (Angelino *et al.*, 1984). Different fluids for ORC systems are analyzed, some of them are pure fluids, mainly refrigerants (Maizza and Maizza, 2001, Borsukiewicz-Gozdur and Nowak, 2007) and some are mixtures of fluids (Angelino and Colonna, 1998, Bao and Zhao, 2013).

One can also observe the increasing number of papers dedicated to different aspects of turbines for ORC systems. Micro CHP systems requires small components. Literature indicates that the use of high-speed turbogenerator makes the ORC small, simple, hermetic and reduces significantly the maintenance expenses (Larjola , 1995). Different work summarized the findings of the marked research for the expanders, including turbines, and discussed the selection and choices of the expanders for the ORC-based micro-CHP systems (Qiu *et al.*, 2011). Numerical simulation of a radial

turbine designed to work in a system based on a toluene cycle was presented by Harinck *et al.* (2011). According to the numerical model the turbine efficiency for the design point is equal to about 70%. Small ORC high-speed turbogenerators with siloxans as working fluids were also investigated (Uusitalo *et al.* 2011). There are also some works dedicated to complete ORC CHP systems and its various types. Qiu *et al.* (2012) presented data from experiments with ORC for micro CHP and biomass boiler and HFE7000 working fluid in vane expander. Some construction, dynamic tests and experimental characterization of micro-scale ORC are reported by others (Pei *et al.*, 2011, Peris *et al.*, 2015). The performance potential of cycle modifications to the basic ORC was illustrated by Lecompte *et al.* (2015). Authors analyzed and discussed various types of cycles (transcritical, trilateral, cascade cycles and other) and identified potential future development, knowledge gaps and indicated the lack of experimental data in the subject.

The idea of combined production of heat and electricity on a small scale using ORC systems based on biomass is analyzed in the Institute for quite some time. Main works were focused on selection of a proper working fluid (Mikielewicz *et al.*, 2007), optimal working parameters (Mikielewicz *et al.*, 2006, Mikielewicz and Bykuć, 2006) and overall thermo dynamical cycle (Mikielewicz *et al.*, 2013). Some experimental works on first version of a test stand were carried out with ORC system and turbine measurements (Kaczmarczyk *et al.*, 2013). The dynamic aspects of microturbines were also analyzed (Kiciński and Żywica, 2014). The latest works relate to energy storage techniques for ORC CHP system (Bogucka-Bykuć *et al.*, 2014).

This paper presents the results of initial measurements carried out at the newly built testing rig for investigation of analysis of ORC systems performance. The goal of the experiments was neither the optimization of the system performance, nor the achievement of highest efficiencies. It was the dynamics of the phenomena occurring in the system, with the special interest and consideration of the start-up phase of the high-speed rotating turbine which was investigated. The characteristics of installation of the operation variant of the ORC with regenerative heat exchanger were determined. The entire system operating with a low-boiling agent HFE 7100 with various service conditions was tested.

2. THE LABORATORY TEST STAND CHARACTERISTICS

The test stand is built as an integrated mobile ORC system equipped with set of sensors and automatic control system (Breńkacz *et al.*, 2012). All components are placed on a supporting structure. Biomass fuel is used as a source of heat. The construction of test rig is allows for easy reconfiguration to connect different micro turbines, pumps, heat exchangers, valves, etc.

The 3D model was created in Autodesk Inventor Program. The view of this model as well as view of actual test rig are shown below on Fig. 1. In the described configuration a single-stage supersonic microturbine, developed (Kozanecki *et al.*, 2012a and 2012b) and tested (Bykuć *et al.*, 2014, Kiciński *et al.*, 2012) in IMP PAN was installed.

The laboratory test stand works like normal CHP system. Working medium (HFE 7100) is pumped through the circulation pump and regenerative heat exchanger to the evaporator, where evaporation and heating at specific and controlled parameters take place. In the next step it goes to a microturbine where its energy is converted into rotational motion of the rotor coupled to electric generator. The working medium expand in the turbine and then it is directed to regenerative heat exchanger, where it gives off some heat to preheat the liquid medium that is directed to an evaporator. Then the medium goes to the condenser where it changes phase. Water is used as a source of cooling. The working medium from the condenser flows into the tank, and next to the circulation pump, thereby closing the cycle. The laboratory test stand is equipped with sensors for measurements of temperature, mass flow rate, pressure, rotational speed and an appropriate set of safety sensors for correct work of the high-speed turbine.

Bearings in turbine use a vapor of the same working medium - HFE 7100 (HFE-7100 – Essential characteristics, 2006). The entire installation is a hermetically sealed structure.

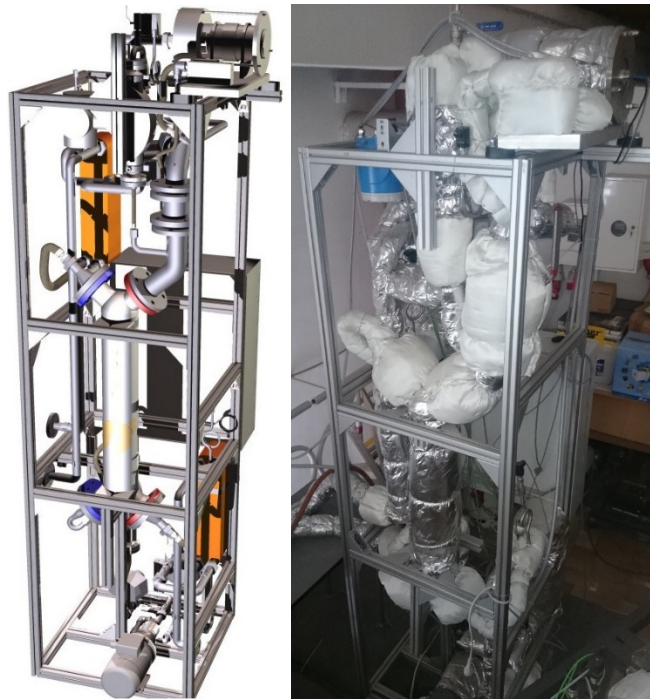


Figure 1: 3D model and view of laboratory test stand

The basic elements of the supersonic microturbine are single-stage radial impeller, electric generator with rare-earth magnets and a set of aerostatic bearings. All components are sealed in the body with a water jacket that cools the generator.

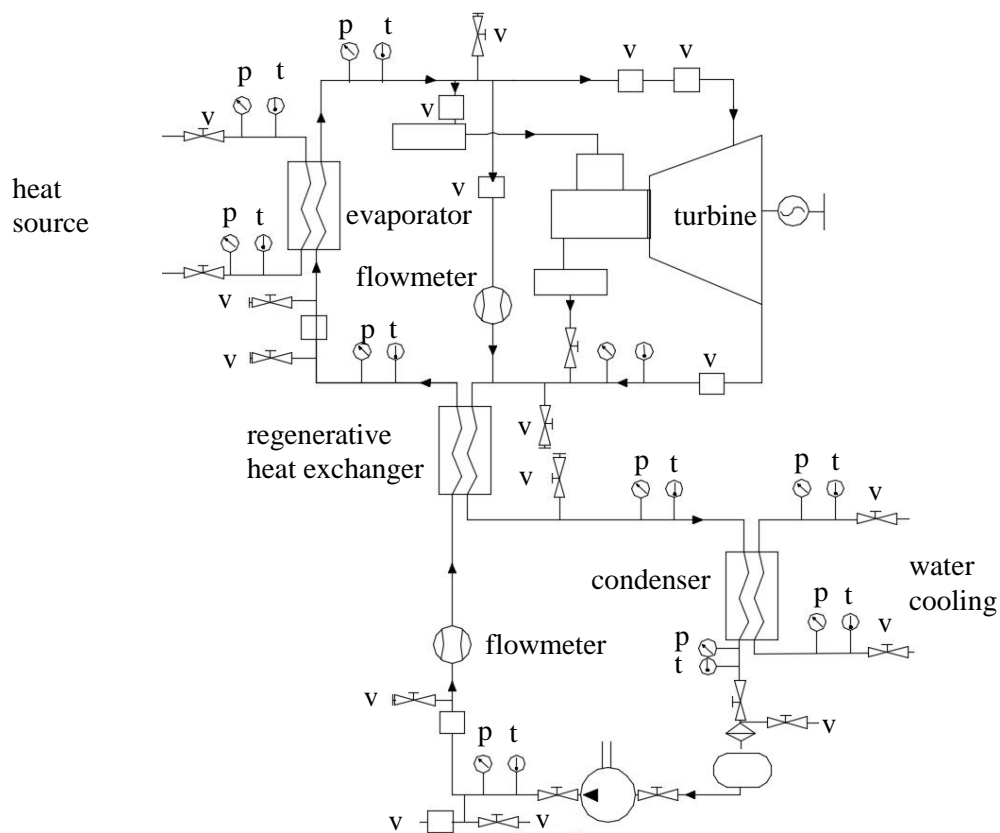


Figure 2: Schematic view of research test stand. v- valve, p – pressure measurement, t – temperature measurement

3. RESEARCH RESULTS

The testing rig is controlled from the level of one control panel. Fig. 3 presents a screenshot of control panel used to steer the testing rig. The most important points of regulation (i.e. EZZ1, EZZ2, EZZ3, EZO1, EZO2 valves) as well as pressure, temperature and flow measurement points in the installation are marked. EZZ1 and EZZ2 valves regulating flow via bypass installation as well as via turbine play the most important role in terms of the regulation of the whole installation. Appropriate settings of those valves enable achievement of a proper pressure value before turbine, proper running of a process of heating up of gas bearings and turbine as well as enable nominal speed to be reached by the turbine.

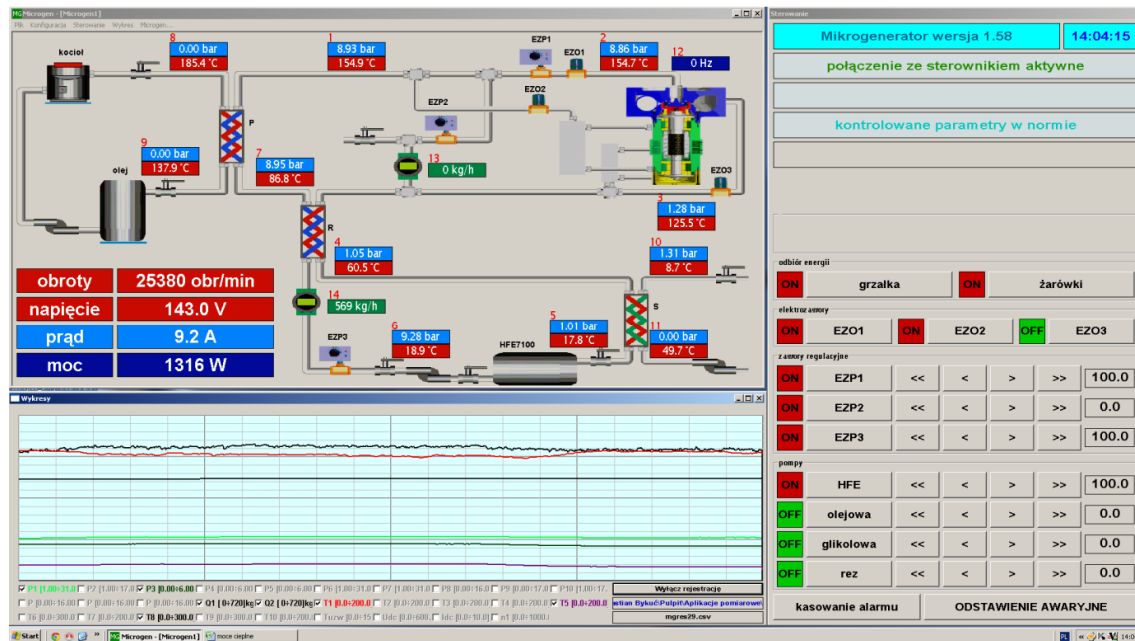


Figure 3: Control panel of the test stand

EZO1 and EZO2 valves are quick-closing valves and cut off inflow of working fluid into the turbine and bearings. Due to the application of slide bearings in the turbogenerator, working on the vapor of the working fluid, it is very important to prevent condensation of working agent in bearings and to maintain the proper flow during work performed with high speed. Therefore, the following is of great importance: a precise control of the temperature of the working agent at the inlet, assurance that work is performed in the area of superheated vapor and maintenance of the adequate pressure difference before and after turbine. An automatic system, set from the operator's level, cutting off inflow of fresh steam into the turbine - if any of the critical conditions are exceeded - is installed in the tested installation for safety reasons.

Graphs below exhibit the results of one of the series of measurements and start when turbine and its bearings are already fed (EZO2 valve is opened), turbine is heated up and rotates with speed of ca. 2000 rpm (EZZ1 valve is partially opened). The process of acceleration of the turbine is divided into three stages depicted in the below figures. First stage (Phase I) refers to interval of 0÷30 sec., second one (Phase II) refers to 30÷240 sec. and the last selected stage (Phase III) refers to 240÷970 sec. Those stages reflect settings of regulation valves EZZ1 and EZZ2.

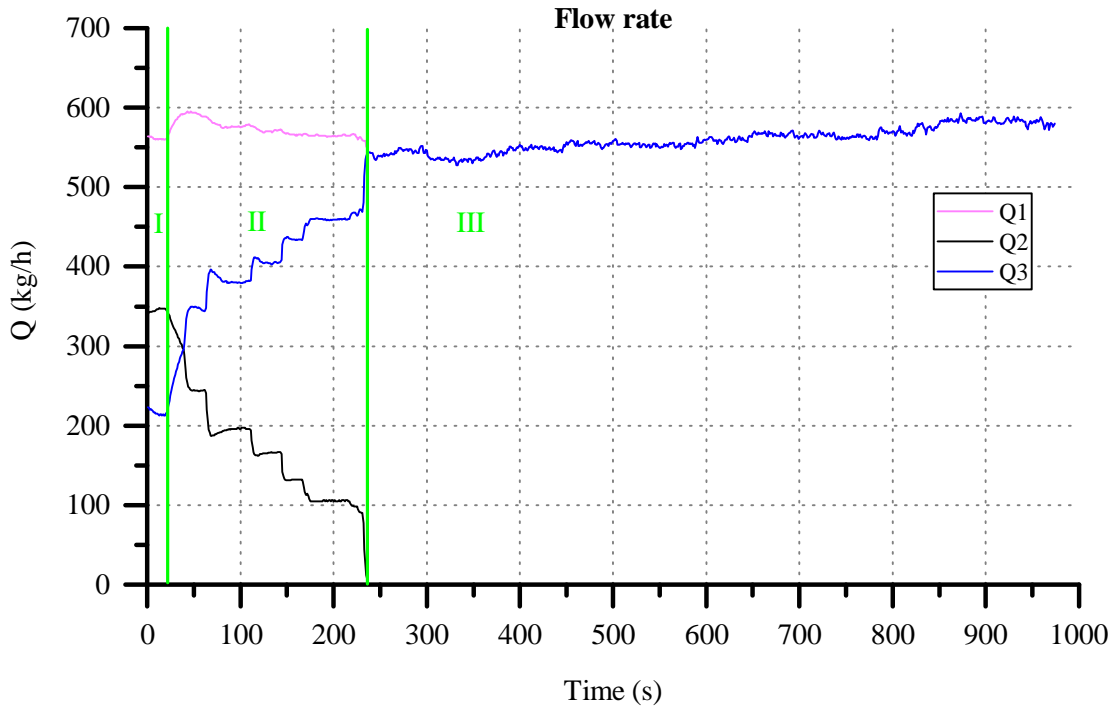


Figure 4: Mass flow rates (Q1- total flow rate, Q2-by-pass flow rate, Q3-turbine flow rate)

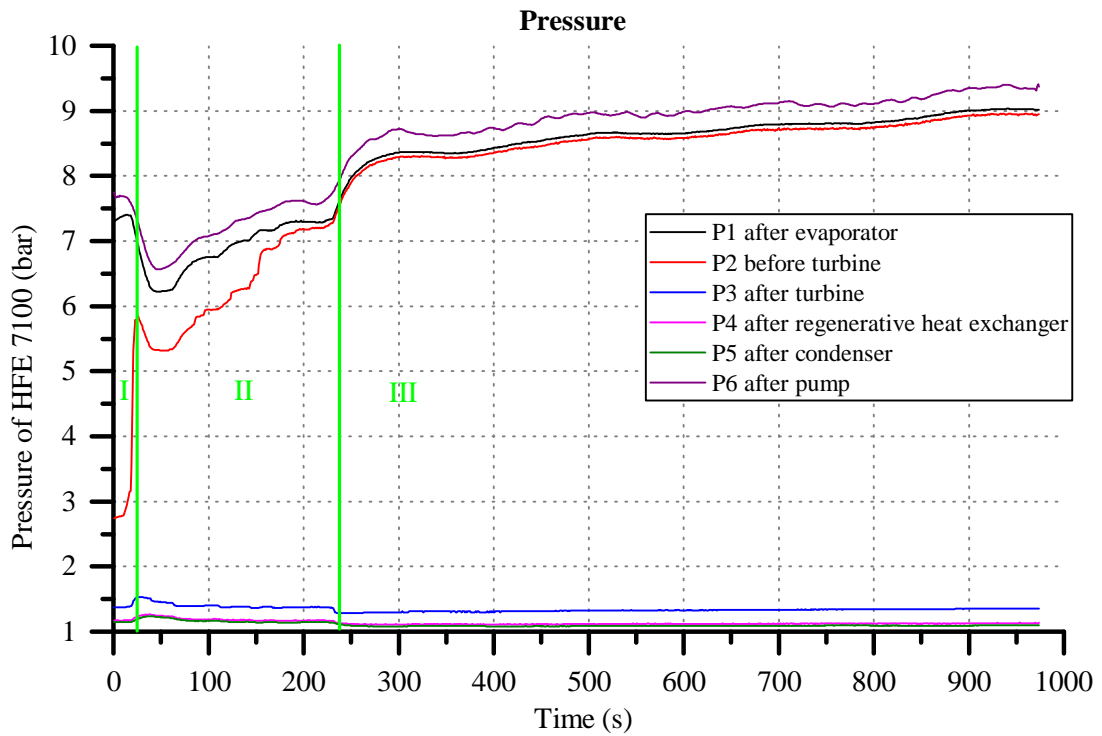


Figure 5: Pressure curves in the time domain obtained during startup

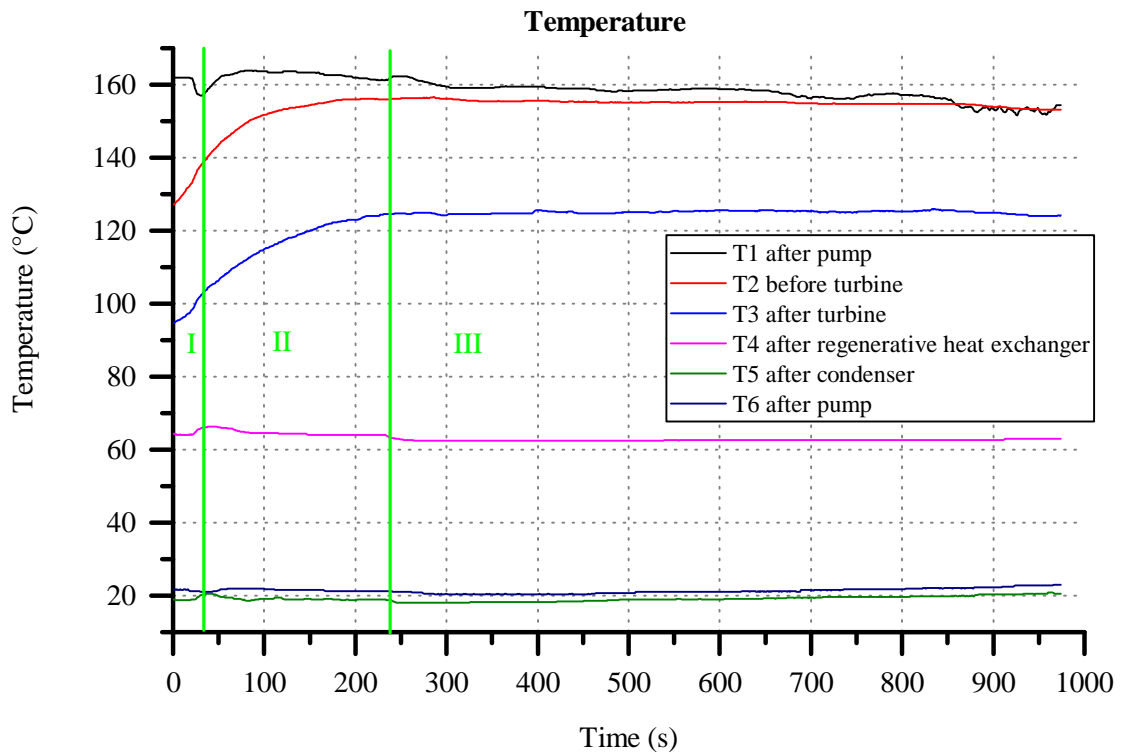


Figure 6: Temperature curves in the time domain obtained during startup

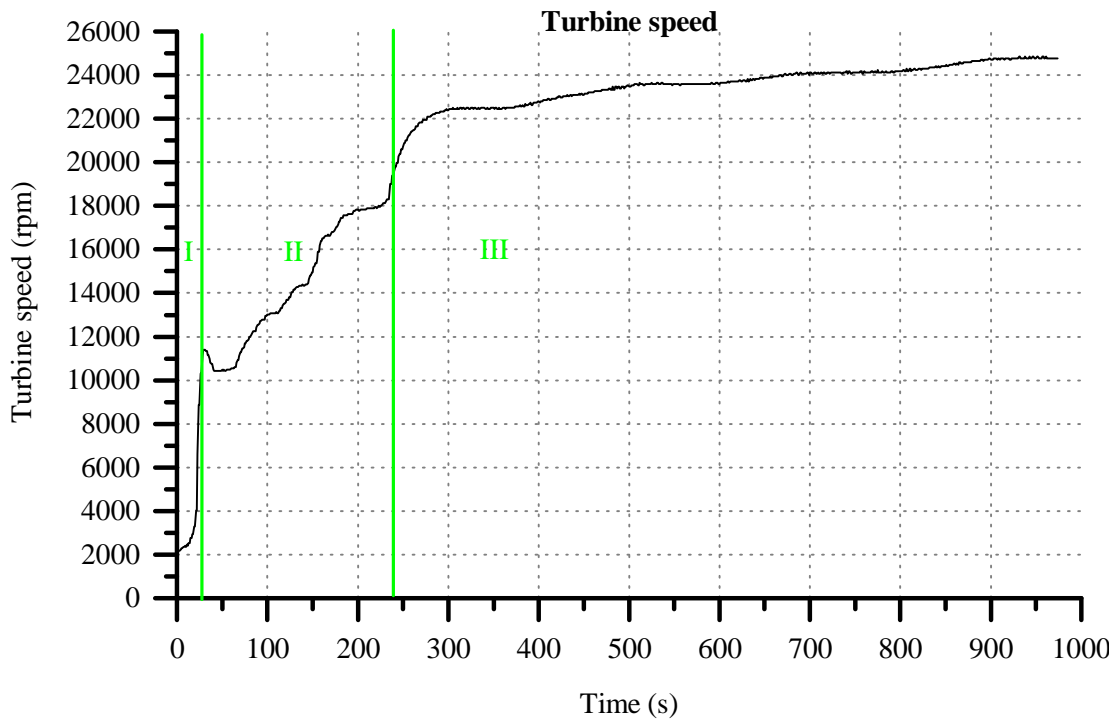


Figure 7: Rotational speed of turbogenerator in the time domain obtained during startup

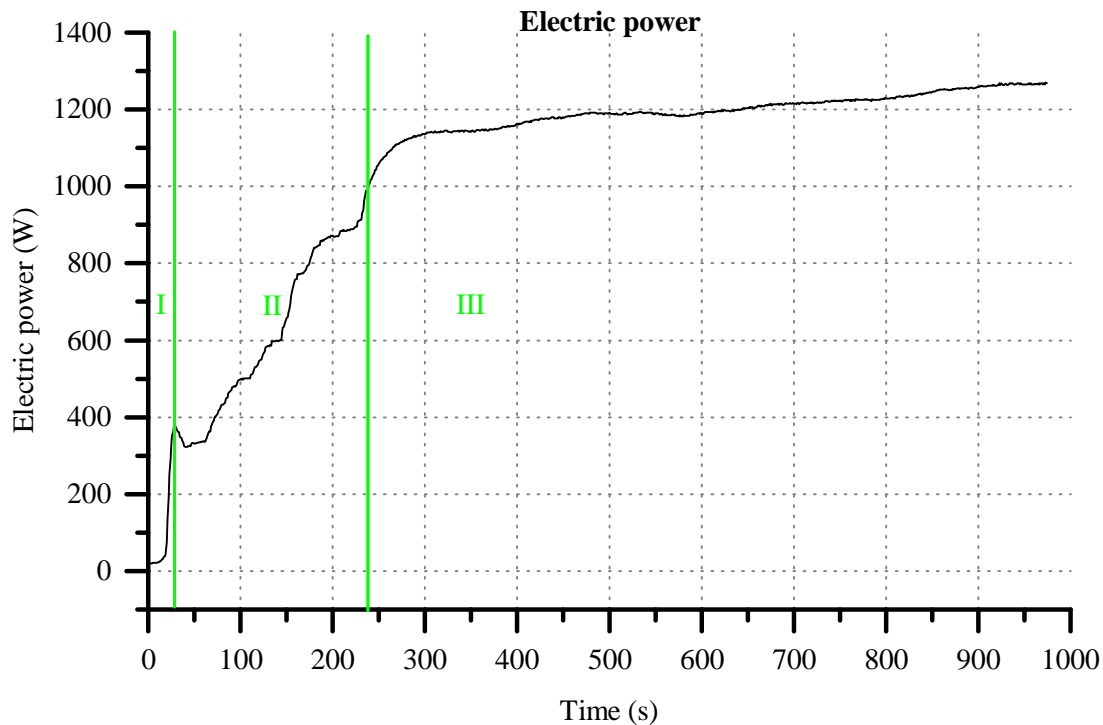


Figure 8: Power generated in the time domain obtained during startup

Fig. 4 presents the plots of the working fluid flows: total flow, bypass flow as well as calculated turbine flow. Placing the flow meters as presented it is possible to calculate the flow through the turbine without generation of additional pressure drops, decreasing the efficiency of the system. The unstable total flow of the working fluid stems from the settings of the inverter, the heating conditions, the cooling conditions as well as from the need of maintenance of the proper level of the working fluid in the tank.

As can be seen in case of Phase I, only 30 % of the total flow reaches turbine (EZP1 valve is only partially opened) and the remaining part flows via bypass. During this Phase, pressures are held at more or less constant level (Fig. 5). The pressure drop (ca. 0,5 bar) can be observed along the distance between pump and outflow from the evaporator. Due to throttling of the steam flow via EZP1 valve, pressure before turbine is ca. 4,5 bar smaller when compared to pressure in the outflow from evaporator.

The pressure drop (ca. 2,5 bar) on the regenerator after the turbine can be also observed. During this phase, the expansion in the turbine drops from ca. 2,7 bar and reaches 1,5 bar which makes it possible for the turbine to achieve speed of ca. 2000 rpm (Fig. 7) and generation of the trace amount of energy at the level of 20W (Fig. 8). During the Phase I, a small increase of temperature before and after turbine can be observed, which may be a sign of a turbine system not being enough heated up (Fig. 6). During Phase II, the settings of the EZP1 and EZP2 valves were changed with the aim of gradual increase of vapor flow through the turbine, and simultaneous decrease of the flow via bypass. During this measurement series, Phase II lasted ca. 200 sec. and took place within few steps. This Phase is ended up with a total closure of the EZP2 valve at the bypass and opening of the EZP1 valve. The gradual opening of the EZP1 valve and throttling of the EZP2 valve lead to the step increase of the flow via turbine flow system, whereas total mass flow was held almost constant (Fig. 4). At the beginning of Phase II, a rapid pressure drop of the steam (Fig. 5) in the system can be observed, due to the increase of the flow through the turbine. Simultaneously, the rotation speed of the turbine increases in steps from 2000 rpm up to ca. 11000 rpm during a few seconds (Fig. 7) and electric power generated increases to the level of ca. 380 W.

Next, the pressure starts to increase gradually up to the initial level at the end of the Phase II. Simultaneously a step increase of the rotation speed of the turbine is observed up to the level of

18000 rpm and generated power – up to ca. 1100W. The finalization of the Phase II due to the total closure of the bypass valve leads to the step increase of the flow through the turbine and this time also the increase of the pressure at the inflow to the turbine, and another increase of the rotation speed of the turbine as well as generated power.

Temperatures during this Phase are stable, however temperatures at the inflow and outflow from turbine are increasing in a uniform manner during the whole period, until they stabilize at the end of Phase II (Fig. 6). It is of major importance, from the safety point of view with respect to the performance of the high-rotation speed turbogenerator, to maintain the proper temperature and superheat of steam at the inflow to the bearings.

Phase III is initiated by the total cut off of the bypass and directing the total vapor flow through the turbine (Fig. 4). Since this moment, the increase of the pressure, the rotation speed and power of the turbogenerator result from the step increase of the rotation speed of the pump as well as slight increase of the temperature of the heat source.

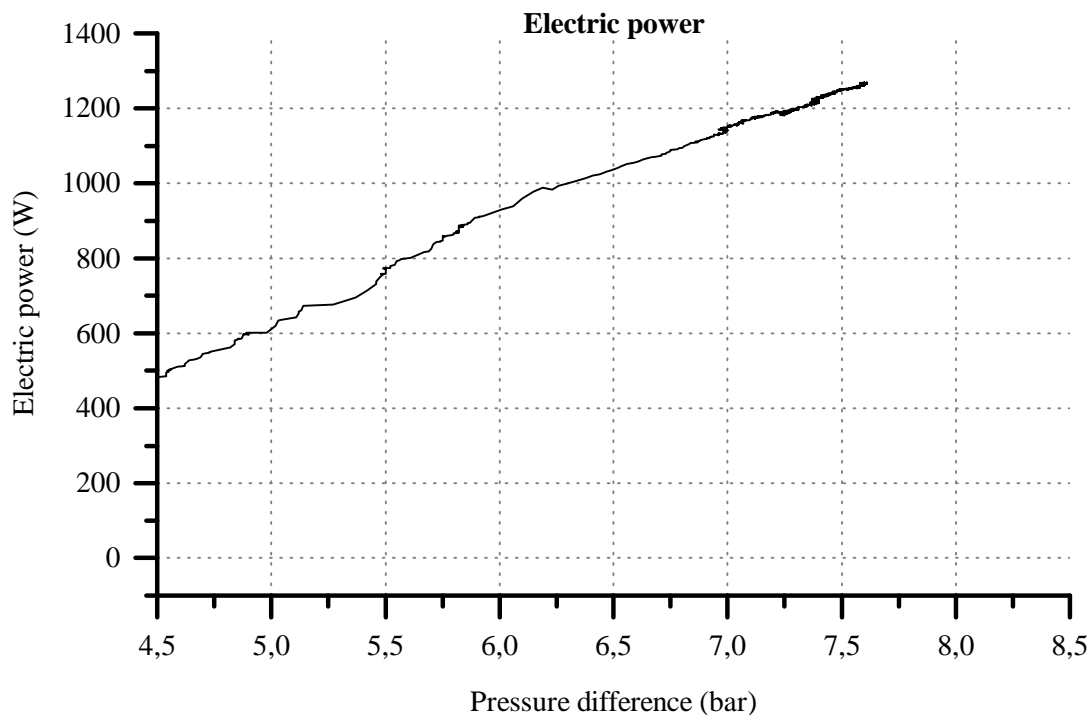


Figure 9: Power generated vs. available pressure difference between inlet and outlet of a turbine

During the work the linear increase of the power of the turbogenerator as a function of the increasing pressure difference was observed, as was expected (Fig. 9). The most important issue is the maintenance of the properly low level of the pressure in the condenser, i.e. assurance of the proper temperature of the cooling fluid, which may be a challenge.

4. SUMMARY AND CONCLUSION

The results of initial measurements carried out at the newly built testing rig for investigation of ORC systems performance were presented and analyzed. The goal of the experiments was the dynamics of the phenomena occurring in the system, with the special interest and consideration of the start-up phase of the high-speed rotating turbine. Curves of selected measures were obtained and it appeared that during the startup of turbine three characteristic phases may be shown. At the end of the measurement series under consideration the results shown below were obtained. The power of 1316 W was obtained on the terminals of the generator at the rotation speed of the turbine equal to 25380 rpm, pressure at the inflow to the turbine of 8,86 bar and temperature of ca. 155 °C. The expansion in the turbine occurred down to 1,28 bar and the flow of the working fluid was at the level of 569 kg/h. Optimization of the system performance was not the goal of executed works and values achieved are just exemplary. The results obtained will be used for formulating algorithms of automatic startup and working procedures of the laboratory test stand described.

REFERENCES

- Angelino, G., Colonna, Di Paliano, P., 1998, Multicomponent working fluids for organic Rankine cycles (ORCs), *Energy*,23(6):449–63.
- Angelino, G., Gaia M., Macchi E., 1984, A review of Italian activity in the field of organic Rankine cycles. *VDI Berichte – Proceedings of the International VDI Seminar*, vol. 539VDI Verlag, Düsseldorf, p. 465–482.
- Bao, J., Zhao, L.,2013, A review of working fluid and expander selections for organic Rankine cycle. *Renew Sustain Energy*, Rev;24:325–42.
- Bogucka-Bykuć, K., Włosiński, W., Bykuć, S., 2014, Towards development of prototype high-temperature latent heat storage unit as an element of a RES-based energy system (part 1). *Bulletin of the Polish Academy of Sciences Technical Sciences*, 62(3);489-494.
- Borsukiewicz-Gozdur, A., Nowak, W., 2007, Comparative analysis of natural and synthetic refrigerants in application to low temperature Clausius–Rankine cycle, *Energy*;32(4):344–52.
- Breńkacz, Ł., Bykuć, S., Niewiadomski, J., 2012, The project of the laboratory micro CHP ORC test stand with a high-speed supersonic turbine. The 2D and 3D drawings. Summary of additional materials required for install and connect of the turbogenerator (in Polish: Projekt stanowiska badawczego mikrośiłowni z turbiną naddźwiękową wysokoobrotową. Rysunki 2D, 3D. Zestawienie materiałów dodatkowych wymaganych do przyłączenia i montażu turbogenerators), *IMP PAN research report*, arch. no 844/2012, Gdańsk, Poland.
- Bykuć, S., Niewiadomski, S., Kaczmarczyk, T. Z., Żywica G., 2014, Start-up research of the supersonic microturbine with a target working medium on the laboratory micro CHP ORC test stand (in Polish: Badania rozruchowe mikro turbiny naddźwiękowej z docelowym czynnikiem roboczym na stanowisku badawczym mikrośiłowni ORC), *IMP PAN research report*, arch. no 121/2014, Gdańsk, Poland.
- Harinck J., Pasquale D., Pecnik R., Colonna P., 2011, Three-dimensional RANS simulation of a high-speed organic Rankine cycle turbine, in: *First International Seminar on ORC Power Systems ORC 2011*, Delft.
- HFE-7100 – Karta charakterystyki, 3M Poland Sp. z o.o.
- Kaczmarczyk, T., Ihnatowicz, E., Bykuc, S., Żywica, G., Kozanecki, Z., 2013, Experimental investigation of the ORC system in a cogenerative domestic power plant with a microturbine and an expansion valve, *ASME ORC 2013, 2nd International Seminar on ORC Power System*, Rotterdam, The Netherlands.
- Kiciński, J., Żywica, G., 2014, Steam microturbines in distributed cogeneration, *Springer monograph*.
- Kiciński, J., Żywica, G., Banaszek, S., 2012, Experimental research of the dynamic parameters and assessment of the dynamic state of the prototype super-sonic microturbine operating with a target working medium (in Polish: Badania eksperymentalne właściwości dynamicznych oraz ocena

- stanu dynamicznego prototypowej mikroturbiny naddźwiękowej podczas pracy z docelowym czynnikiem roboczym), *IMP PAN research report, arch. no 985/2012*, Gdańsk, Poland.
- Kozanecki, Z., Klonowicz, P., Więckowski, S., Łagodziński, J., Miazga, K., 2012, The concept, calculations and technical design of the alternative radial turbines for the third prototype of the turbogenerator operating with the small CHP ORC power plant (in Polish: Koncepcja, obliczenia i projekt techniczny alternatywnych turbin promieniowych III prototypu turbogeneratorsa funkcjonującego z modelową siłownią ORC), *IMP PAN research report, arch. no 22/2012*, Gdańsk, Poland.
- Kozanecki, Z., Marczyk, A., Więckowski, S., Łagodziński, J., Borkowski, 2012, Design and construction of the aerostatic bearing's component for the third prototype of the turbogenerator with the supersonic turbine. Tests of the machine equipped with aerostatic bearings and generation of electric power using air as a working fluid. (in Polish: Projekt i wykonanie podzespołu aerostaticznych łożysk gazowych III – go prototypu turbogeneratorsa z turbiną naddźwiękową oraz testy maszyny z łożyskami aerostaticznymi i generacją energii elektrycznej przy zastosowaniu powietrza jako czynnika roboczego), *IMP PAN research report, arch. no 632/2012*, Gdańsk, Poland.
- Larjola, J., 1995, Electricity from industrial waste heat using high-speed organic Rankine cycle (ORC), *Int J Prod Econ*, 1995;41(3):227–35.
- Lecompte, S., Huisseune, H., Van den Broek, M., Vanslambrouck, B., De Paepe, M., 2015, Review of organic Rankine cycle (ORC) architectures for waste heat recovery, *Renewable and Sustainable Energy Reviews*, 47 (2015) 448–461.
- Maizza, V., Maizza, A., 2001, Unconventional working fluids in organic Rankine-cycles for waste energy recovery systems, *Applied Thermal Engineering*;21(3):381–90
- Mikielewicz, J., Bykuć, S., 2006, The concept of the micro CHP power plant operating in the organic Rankine cycle (in Polish: Koncepcja mikrośiłowni kogeneracyjnej pracującej w obiegu Rankine'a, *Archiwum Energetyki*, tom XXXVI, Gdańsk, Poland.
- Mikielewicz, J., Bykuć, S., Mikielewicz, D., 2006, Application of renewable energy sources to drive Organic Rankine Cycle micro CHP, *Proc. of Heat Transfer and Renewable Sources of Energy*, p. 329-336, Międzyzdroje, Poland.
- Mikielewicz, J., Mikielewicz, D., Bykuć, S., 2007, Analysis of selected fluids for use in micro-chp for domestic applications, *Inter. Conf. University of Applied Sciences Bremen*, 08-09 Nov, Bremen.
- Mikielewicz, J., Mikielewicz, D., Ihnatowicz, E., Kaczmarczyk, T., Wajs, J., Matysko, R., Bykuc, S., Rybinski, W., 2013, Thermodynamic cycles of the domestic micro CHP ORC power plant, *IFFM Publisher*, Gdansk, Poland.
- Pei G, Li J, Li YZ, Wang DY, Ji J., 2011, Construction and dynamic test of a small-scale organic rankine cycle, *Energy*, (2011);36:3215–23.
- Peris, B. , Navarro-Esbrí, J. , Moles, F. , Martí, J. P., Mota-Babiloni A., 2015, Experimental characterization of an Organic Rankine Cycle (ORC) for micro-scale CHP applications, *Applied Thermal Engineering*, 79 (2015) 1-8.
- Qiu G., Liu H., Riffat, S., Expanders for micro-CHP systems with organic Rankine cycle, 2011, *Appl. Therm. Eng.*, 31.
- Qiu G., Shao Y., Li J., Liu H., Riffat, S., 2012, Experimental investigation of a biomass- fired ORC-based micro-CHP for domestic applications, *Fuel* 96, 374-382.
- Uusitalo, A., Honkatukia, J., Turunen-Saaresti, T., Larjola, J., Colonna, P., 2011 Suitability of siloxanes for a mini ORC turbogenerator based on high-speed technology, in: *First International Seminar on ORC Power Systems*, Delft.

ACKNOWLEDGMENTS

The research work presented in this article was supported by the scientific project POIG.01.01.02-00-016/08 “Model agroenergy complexes as an example of distributed cogeneration based on local renewable energy sources”.

FROM TECHNOLOGY DEVELOPMENT TO (PRE-SERIES) PRODUCT – THE EPACK HYBRID

Daniela Gewalt*, Katharina Rostek*, Andreas Schuster*, Richard Aumann*

*Orcan Energy GmbH,
Rupert-Mayer-Str. 44, D-81379 München
Germany
e-mail: daniela.gewald@orcan-energy.com
Web page: <http://www.orcan-energy.com>

ABSTRACT

Worldwide there is a potential resource of 4.300 GW_{th} of waste heat e.g. from engine power plants or industrial processes available that is nowadays left to dissipate naturally and equals the loss of 100 million litres of Diesel per hour, which show calculations based on data of DOE and Diesel & Gas Turbine World Wide.

The Organic Rankine Cycle (ORC) technology utilizes waste heat e.g. from biogas power, geothermal power and CHP plants or industrial processes and converts it CO₂-free into electrical energy. ORC plants and modules are commercially available and economically profitable only in large and medium scale applications with electric power outputs of 50 kW_{el} and larger. However, particularly large numbers of similar small scale waste heat sources, for example gas/diesel engine product families in CHP applications offer a huge potential for the implementation of standardized ORC modules. Especially in those applications part of the engine waste heat is often directly used e.g. in small heating networks or for fermentation and drying processes in biogas plants. This usually excludes the operation of an ORC module even if there is still a significant amount of waste heat that can be utilized only seasonally or is dissipated.

Considering such frequently found plant configurations the Orcan Energy GmbH has developed a flexible small scale “CHP-ready” ORC module – the ePack Hybrid – that can provide both, heat and power from the waste heat source by variable operation of an electricity-generation-only- and a CHP-mode. By the integration of a working fluid-to-water- and a fluid-to-air-condenser, the ePack Hybrid can provide hot water up to 80 °C if required or dissipate the condenser heat in the environment. According to the operational conditions (CHP share, required feed temperature, ambient air, etc.) the ePack Hybrid has a flexible net electric power output of 12 kW to 22 kW.

In order to take into account also further important market requirements as there are inter alia needs for excellent cost efficiency, high reliability, low maintenance effort and easy plug & play installation, the ePack design is based on standard off-the-shelf components and on innovative and patented system engineering. These technology features make the ePack Hybrid solution not only economically highly efficient but also outstandingly reliable.

With excellent results from extensive system tests and broad field experience with our ORC modules the ePack Hybrid is ready for commercialization and available as pre-series product.

The paper will explain the unique concept of the ePack Hybrid, and data from reference installations and operational experience of the installed ePack fleet will be presented.

1. THE EPACK HYBRID CONCEPT

The ePack Hybrid concept is based on technology experience gained during more than eight years of ORC development, and on specific requirements for small-scale ORC modules that are given by the market.

1.1 Market requirements

The focus market for the ePack Hybrid is the utilization of small-scale waste heat sources of internal combustion engines (ICE) in biogas plants, and of industry and heating processes. In these applications it is in many cases crucial to not just utilize the available waste heat for power production but to provide plant operators or process owners with the flexibility to still use part of the waste heat for heating purposes or as process heat, e.g. for fermenter heating, seasonal district heating or for drying processes (see Figure 1). The required temperature level for these heating purposes is between 50 °C (fermenter heating, drying processes) and 80 °C (district heating on cold winter days) while ICEs usually deliver hot water with a temperature level of 90 °C. In addition, the heat demand exists only seasonally and/or covers only a small part of the total available waste heat. Both, the seasonal character of heat demand and the requirement for temperature levels below typical ICE hot water temperature leaves a high potential for using ICE waste heat for power generation.

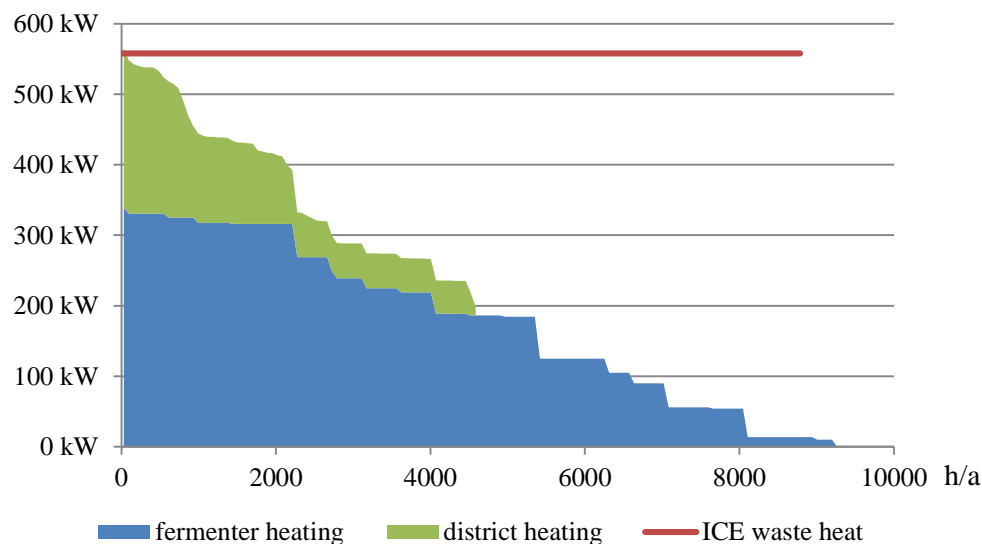


Figure 1: Typical annual heat demand for fermenter and district heating in a biogas plant

Besides this, further technical, operational and economical requirements are given for an ORC module. Amongst others, the most important ones are:

- Availability: firstly, the customer requires an ORC availability of more than 90 % and secondly it is mandatory for each ORC module not to influence the availability of the ICE it is coupled to. Thus, the ORC has to be operated and installed in such a way that it does not prevent the ICE from running in case of a shut down.
- Cost efficiency: an ORC module has to fulfil the typical requirements for return on invest (ROI) that are about three to four years in biogas applications but a maximum of two years in industrial applications. This includes all costs for the ORC module from investment to installation costs (CAPEX) and costs for service and maintenance over the ORC lifetime (OPEX).

- Plug & play installation: to ensure a fast and cost efficient installation, the ORC module has to be designed with a minimized number of simple interfaces. With a closed refrigerant cycle only interfaces for hot and cold water have to be connected to the existing ePack system. The electrical connection has to fulfil the requirements given by the transmission system operators for electricity. The engine shut down that is necessary for the ORC installation has to be as short as possible.

1.2 Product development – from market requirements to product

The development of the ePack Hybrid concept at Orcan Energy is based on long-term experience with the development of small scale, plug&play ORC products. The most important development principle thereby is to use off-the-shelf industrial standard components as basis for the ORC modules. This requires intensive tests for component qualification regarding application limits and reliability in order to fully rely on the given component's lifetime also in the ORC application.

The market driven product development at Orcan follows a stage gated product evolution process (PEP) which allows for a targeted and efficient development based on clear specifications and requirements. The stage-gate model not only improves the speed and performance of development but also reduces the risk of failure. It is based on testing prototypes at different levels of product maturity and immediately implementing the testing results in the following development steps. The PEP process also offers the possibility to quickly bring in modifications to the product in case the market requirements slightly change during the product development phase.

By such methodology, when launching the first ePack Hybrid Orcan Energy already had more than two years of field experience with in total more than 25 ePacks running more than 100.000 operating hours at a high availability level of nearly 95%, and generating more than 1 GWh_{el} of CO₂-free electricity.

1.3 Technology and operation concept of the ePack Hybrid

The ePack Hybrid converts waste heat in CO₂-free electric power and can provide heat at the same time in a CHP operational mode. If there is no heat demand, the heat can be dissipated into ambient air by the ePack Hybrid working in an electricity-generation-only mode. To enable both operational modes, two condensers – a water- and an air-cooled condenser – are incorporated in the ePack Hybrid. The water-cooled condenser is a usual plate heat exchanger, while the air-cooled condenser is constructed from micro-channel coils. The microchannel coils are directly integrated into the ePack casing, and the air volume flow which is needed for cooling of the coils is provided by two fans on top of the ePack.



Figure 2: The ePack Hybrid

According to the current heat demand the low pressure vapour flow after the expansion machine (screw expansion machine) is either directed into the water- (if heat is needed) or into the air-cooled condenser or it is split up between both condensers, if only part of the heat is needed. Instead of using valves or other mechanical devices to ensure the correct operation mode, thermodynamic effects are used and the amounts of heat in both condensers are controlled by the rotational speed of the fans. In all cases two important operation parameters have to be maintained:

- Suitable distribution of fluid in both condensers in order to ensure 100 % CHP operation, 100 % electricity-generation-only operation and all operating situations in between,
- Prevention from cavitation by sufficient sub-cooling of the working fluid in both condensers.

In order to control the ePack Hybrid condensation part only by thermodynamic effects, both condensers are connected in such a way that the pressure difference between them is equalized. The required filling level in both condensers for a sufficient sub-cooling of the fluid is ensured by a specifically calculated difference in height between the water and the air-cooled condenser. The gravitational pressure difference of the fluid due to the different heights of the two condensers then ensures the sufficient filling of the condensers. During operation the working fluid always flows into the “colder” condenser with the lower pressure level, which is at the same time always the condenser where the working fluid has to be. Thus the ePack Hybrid operation is in an intelligent way self-regulating.

- Electricity-generation-only and CHP-only mode: in this mode the heat cannot be used in the heating network and has to be dissipated into ambient air. Therefore the working fluid has to be condensed in the air-cooled condenser. This condenser is always the one with lower pressure level, because in this operation mode it's cooled by the air volume flow from the fans. The water-cooled condenser is not operating and has the temperature of the working fluid vapour after the expansion machine and thus a higher condensation

pressure than the air-cooled condenser. In CHP-only mode the fans are not operating and vice versa the air-cooled condenser has the temperature of the working fluid after the expansion machine and therefore the higher condensation pressure. Thus all the working fluid is automatically directed into the water-cooled condenser.

- Operation modes with partial heat demand: these operation modes can be covered flexibly by operating the fans with a distinct rotational speed, such that both condensers have the same condensation pressure. The control parameter is the temperature of the return flow from the heating system. If this temperature is increasing, the heat demand of the heating system is lower; if it is decreasing the heat demand is higher. By increasing the rotational speed of the fans, more heat is dissipated into ambient air and less heat is fed into the heating system by the water-cooled condenser and vice versa.

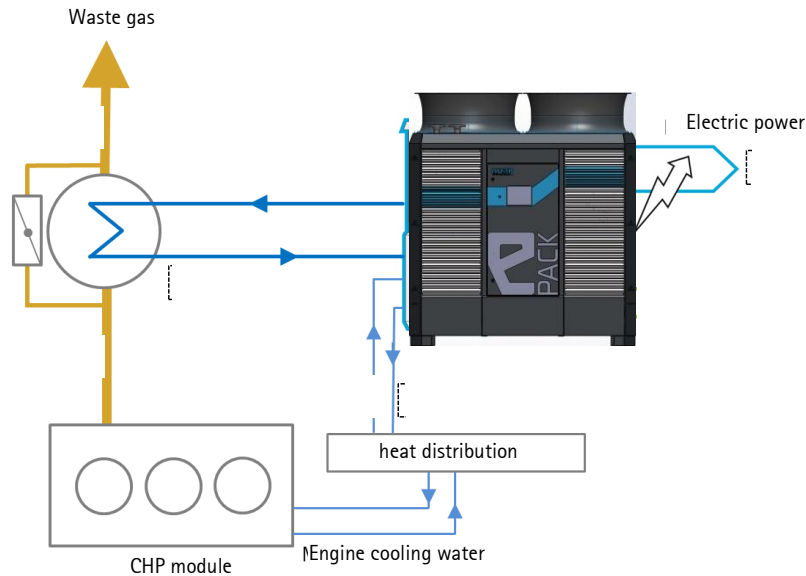


Figure 3: Integration of the ePack Hybrid into a ICE-CHP power plant with heating system

Figure 3 shows the integration of the ePack Hybrid in an ICE-CHP power plant with a heating system.

Based on performance measurements of several ePacks in operation and on well-known component parameters, the ePack Hybrid concept was firstly simulated and then completely designed, engineered and realized and tested in-house at the factory acceptance test bench. The simulation results are shown in Figure 4. They were calculated at a constant ambient temperature of 15 °C using the simulation software EES (Engineering Equation solver) with component models using the semi-hermetic modelling approach of the expansion machine as proposed by Quoilin and Lemort.

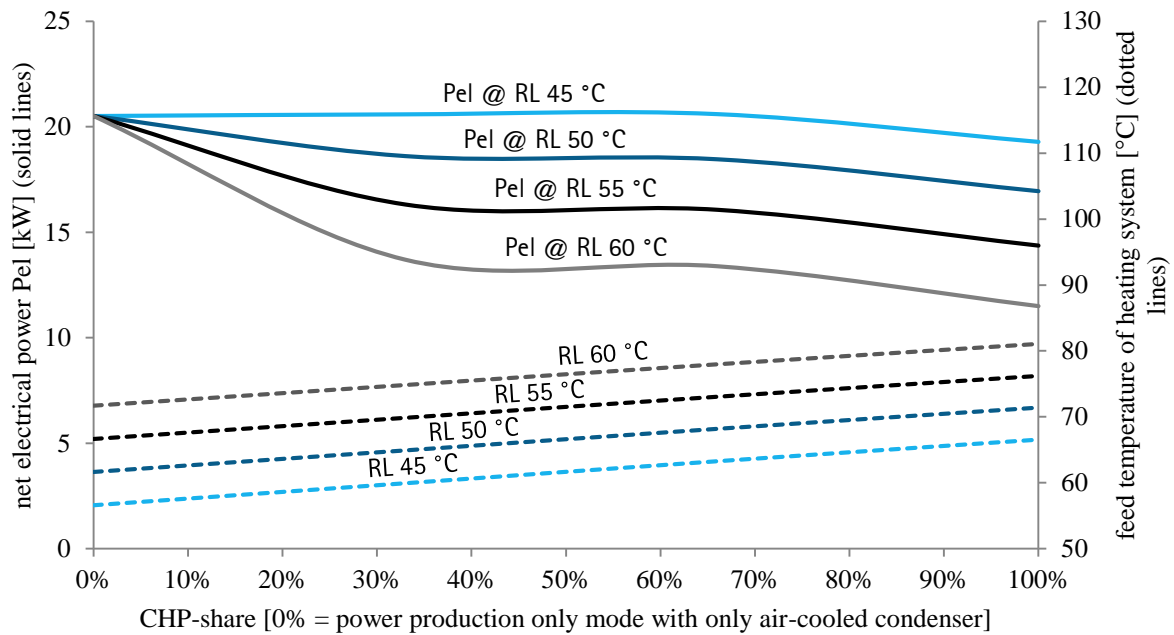


Figure 4: Simulation results for the ePack Hybrid in different operation modes

The net power output of the ePack Hybrid is mainly determined by three parameters: the CHP share, the return temperature of the heating system and the rotational speed of the fans. The maximum net power output can be gained in electricity-production-only mode with a CHP share of 0 %. In this mode lowest condensation pressures can be reached and therefore the enthalpy difference over the expansion machine is at its maximum. With increasing CHP share the net power output decreases due to increasing condensation pressures. Higher return temperatures from the heating system reinforce this effect. Between a CHP share of 40 % to 70 % the net power output has a plateau because the decreasing power output (due to higher condensation pressure levels) is partly compensated by lower power demand of the fans (due to lower rotational speed). Depending on the return temperature of the heating system, the ePack Hybrid can deliver feed temperatures of up to 80 °C, which is absolutely sufficient for most modern heating purposes.

By adjusting the feed temperature to the lowest level required for a specific application, the customer is able to maximise the power output of the ePack Hybrid.

2. OPERATIONAL EXPERIENCE

Orcan Energy has gained operational experience with small scale ORC modules since 2012. Up to now more than 20 ePack modules are installed in Germany in different applications, mainly in biogas power plants or as add-on to industry processes.

2.1 First operational experience with the ePack Hybrid at the factory acceptance test bench (FAT)

In order to check functionality, performance and quality of the ePack modules before installation and commissioning at a customer's site Orcan Energy has installed a test bench (factory acceptance test – FAT) where the ePacks are operated with hot water up to around 20 % of maximum load. This test bench was also used to verify the concept of the ePack Hybrid in real operation. Two different operation modes – electricity-generation-only, CHP-only and

especially the switching process between these two modes – were tested in the FAT. Some exemplary results are given in Figure 5.

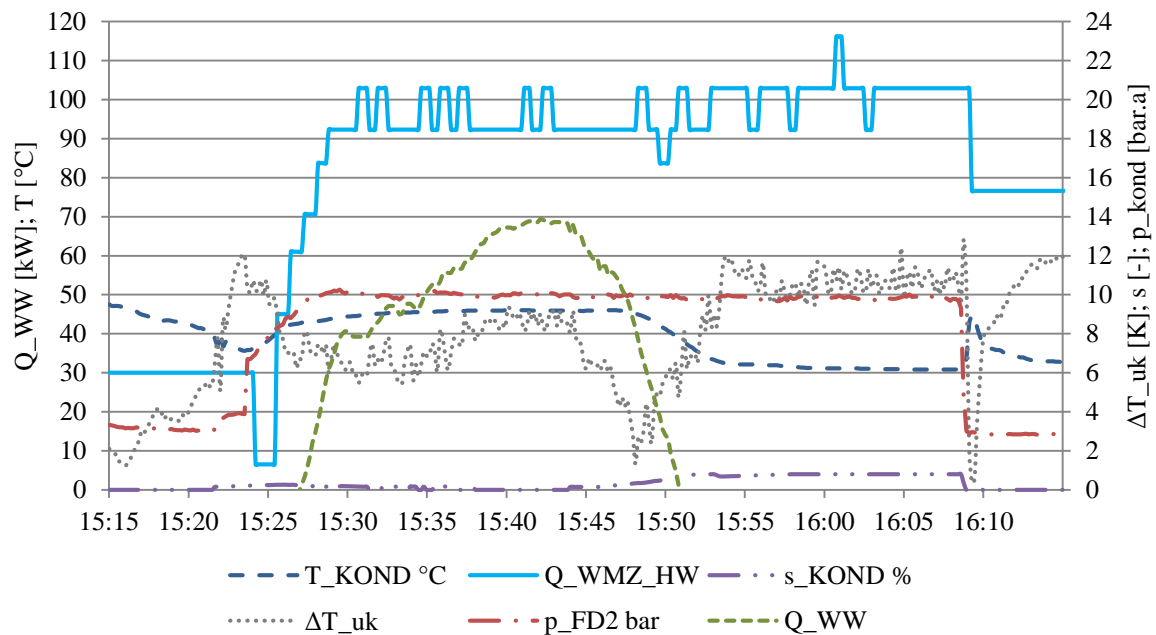


Figure 5: First test results of the ePack Hybrid operation in the FAT (electricity-generation-only mode, CHP-only mode and switching process)

Figure 5 shows that the ePack Hybrid steadily operates in both modes. The ePack Hybrid is starting in the CHP-mode with a heat input (Q_{WMZ_HW}) of around 100 kW. The fans are not running ($s_{KOND} = 0\%$) and the condensation heat is transferred to the heating system (Q_{WW}). At 15:45 the ventilators are starting and the condensing heat is transferred to the ambient by the integrated air cooled condenser. Therefore the heat transfer to the heating system (Q_{WW}) decreases to zero. The condensation temperature (T_{KOND}) is higher in the CHP-only mode. An indicator for the degree of operational stability is the subcooling (ΔT_{uk}) of the working fluid in the condensers. In an optimal operation mode the amount of subcooling should be the same in CHP-only and electricity-generation-only mode. The given test results reflect that the subcooling is around 8 K in CHP-only mode and 10 K in electricity-generation-only mode. During the switching process the subcooling slightly decreases but does not influence the cycle stability since it stays above zero and no cavitation problems of the feed pump are occurring.

Simulations and these tests in the FAT have shown that the ePack Hybrid is not only a sound concept but also working in a stable and reliable way even under changing conditions.

2.2 Field experience

The first ePack Hybrid is currently being installed at a customer's site in Germany. However, operational experience of the already installed fleet of Orcan ePacks with totally more than 100.000 operating hours already provides sufficient operational data with same or similar system components to answer the main questions regarding the ePack Hybrid's dynamic and part load operation at different ambient conditions. Especially the operation experience of three ePack sites can be transferred to the ePack Hybrid: two ePacks in biogas applications with an integrated condenser, which are basically the same ePack modules as the ePack Hybrid just without the water-cooled condenser, and one ePack which is integrated in an industrial heating system.

2.2.1 Dynamic and part load operation under different ambient conditions

Reliable operation of the ePack modules is crucial since the ePack has no influence on its heat source (the ICE) and has to follow the heat supply. It is also very important that the ePack is able to deliver electrical energy under different ambient conditions – at cold winter days as well as at hot summer days. The ePack is designed for a net electrical power output of 20 kW at an ambient temperature of 10 °C. Figure 6 shows an example of an ePack operating in the field under different conditions. If the heat source is stable, the ePack operates smoothly generating a stable net electrical output, if the heat source is fluctuating, the power output is fluctuating as well: the ePack operates reliably in a dynamic mode. At ambient temperatures below 10 °C the ePack delivers up to 22 kW of electrical power; at ambient temperatures up to 28 °C the ePack still generates around 15 kW with the air cooled condenser. The average net electrical power output over one year is 20 kW at an ePack-availability of 95 %.

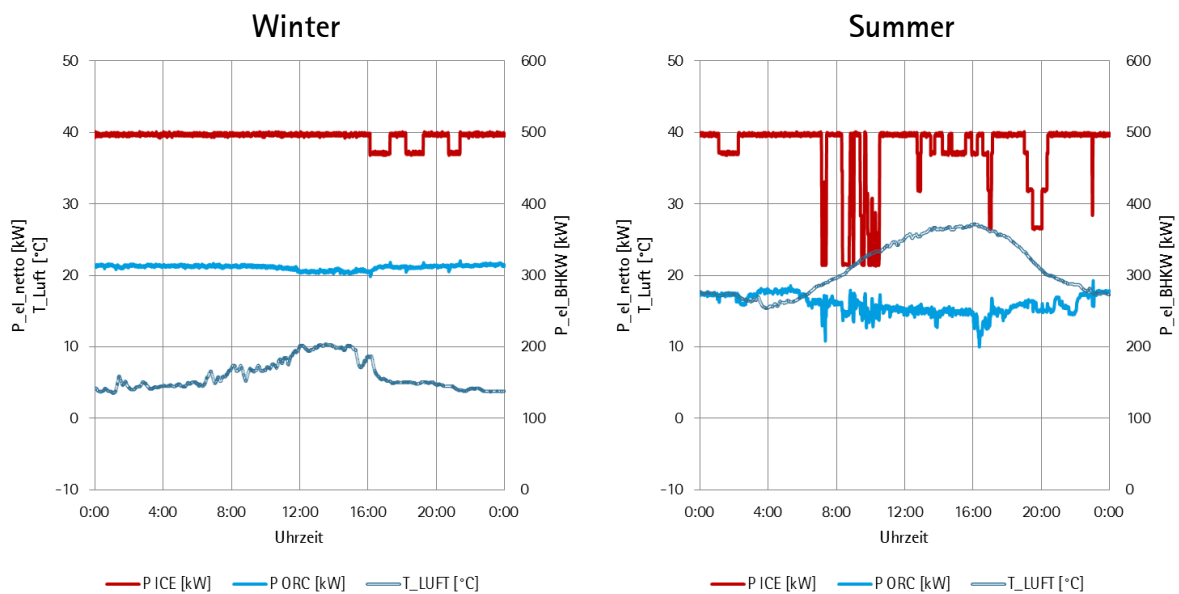


Figure 6: ePack operation in field under dynamic, part load and different ambient conditions

2.2.2 ePack operation as CHP module in an industrial heating system

When operating integrated into a heating system, the ePack performance is highly influenced by the return flow temperature of the heating system, which is the cooling temperature of the water-cooled condenser and therefore also determines the condensation temperature and pressure. In such configuration the ePack has to cope with highly fluctuating temperatures, and react to fast temperature changes, and has to deliver a maximum of electrical energy at the same time.

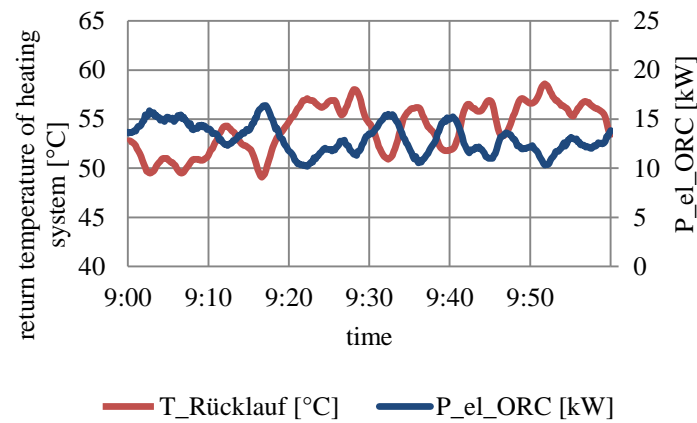


Figure 7: ePack operation as CHP module in an industrial heating system

Figure 7 shows data of an ePack operating as part of an industrial heating system. The ePack can respond very quickly to temperature changes of the heating system while still delivering a significant amount of net electrical energy of around 15 kW even at return flow temperatures ($T_{\text{Rücklauf}}$) of 50 °C to 55 °C.

3. CONCLUSIONS

The ePack Hybrid is a unique product which perfectly fits the waste heat market need of generating electricity and heat for downstream processes or district heating applications at the same time. Further significant customer requirements as in the first place high cost efficiency, but also quick and simple installation, compactness, and high reliability and availability are also fully met.

First tests of the ePack Hybrid have proven the functionality of the concept. The ePack Hybrid is reliably operating in the three different operation modes as there are: power-generation-only mode, CHP-only mode and the operational modes in between with a flexible share of CHP heat. The extensive operational experience with similar ORC modules that were sold in Germany by Orcan Energy since 2012 clearly demonstrates the reliable operation as power-generation units with an air-cooled condenser and as CHP unit with a water-cooled condenser even in highly dynamic or part load mode and at different ambient conditions. Therefore, it can be expected that also the ePack Hybrid – as it is based on same or similar components and system engineering – will operate in the same very stable and reliable way at customer sites.

REFERENCES

- Department of Energy (ed.), 2008, *Waste Heat Recovery: Technology and Opportunities in U.S. Industry*
- Department of Energy (ed.), 2004, *Energy Use, Loss and Opportunities Analysis U.S. Manufacturing and Mining*
- Diesel & Gas Turbine World Wide, 2009, *Power Generation Order Survey*
- Quoilin, S., Lemort, V. und Lebrun, J.: *Experimental study and modeling of an Organic Rankine Cycle using scroll expander*, Applied Energy, 2010, **87**(4), 1260-1268

Lemort, V., Quoilin, S., Cuevas, C. und Lebrun, J.: *Testing and modeling a scroll expander integrated into an Organic Rankine Cycle*, Applied Thermal Engineering, 2009, **29**(14-15), 3094-3102

F-Chart-Software, 2014, *EES – Engineering Equation Solver*, 2014.

INTEGRATED CHP CONCEPTS FOR ORC AND THEIR BENEFITS COMPARED TO CONVENTIONAL CONCEPTS

Christoph Wieland*, Dominik Meinel† and Hartmut Spliethoff‡

*,†,‡Technische Universität München, Lehrstuhl für Energiesysteme
Boltzmannstr, 15, 85748 Garching, Germany

‡Bavarian Center for Applied Energy Research,
Walther-Meißner-Str. 6, 15, 85748 Garching
Germany

*e-mail: wieland@tum.de
Web page: www.es.mw.tum.de

ABSTRACT

The present study investigates the flexibility and suitability of different Combined Heat and Power concepts. An integrated concept for heat decoupling with a two-stage ORC concept and turbine bleeding is introduced and compared with other state-of-the-art concepts. The flexibility of the integrated system is determined for different isentropic fluids and siloxanes. Under general circumstances siloxanes are not suitable for turbine bleeding, due to their dry expansion behavior. However, this picture changes in this CHP context. A comparison is made for different temperature levels of heat transfer fluid. Based on OMTS as the working fluid other CHP concepts are compared with this integrated concept. Its benefits are determined by calculating the produced electricity per year. Therefore, the integration of the CHP concept into a virtual district heating network based on annual load duration curves is investigated and the annual electricity revenues are calculated. Based on these electricity revenues per year higher manufacturing costs due to a higher system complexity are compared.

1. INTRODUCTION

The Organic Rankine Cycle (ORC) is an established technique for waste heat recovery, as well as for the utilization of biomass, geothermal energy and solar thermal energy (Schuster *et al.*, 2009). Several reviews on technological aspects and applications can be found in literature (Schuster *et al.*, 2009, Quoilin *et al.*, 2013 and Tchanche *et al.*, 2011). Its application is economically limited to the small to medium size range ($<1\text{kW}_e$ up to $>1\text{MW}_e$), but it enables the utilization of low temperature heat sources and its conversion to electricity.

The combined production of heat and power (CHP) is highly favorable for an operator from the economic point of view, since he is able to increase full load operational hours per year and has two different energetic products to sell. It is important to note, that the utilization of heat requires either a district heating network or an industrial process, where the heat can be used with minimal losses. In specific cases, the separate generation of electricity and heat can be more efficient from the primary energy point of view (Karl, 2009). In case of renewable energy sources and waste heat, where no additional CO₂ emissions are associated, CHP is always the better choice.

While medium scale CHP processes ($>1\text{MW}_e$) are already realized in existing plants by manufacturers (Bini and Manchiana, 1996, Knapik and Kittl, 2007), small scale CHP systems ($<10\text{kW}_e$) for residential applications have been addressed in scientific literature (Schuster *et al.*, 2009, Mago *et al.*, 2010).

It is the aim of this work to focus on flexible CHP systems, which are suitable for fluctuating heat sources and capable of achieving a significant coverage of the mid load heat demand. The latter minimizes the utilization of fossil fuel fired peak load boilers. The work is based on state of the art CHP concepts and innovative ORC cycle layouts. It is the objective of this paper to present an integrated CHP concept with a high flexibility and efficiency, which is derived from conventional power plants. This concept is based on a two-stage ORC with turbine bleeding, which has already

been discussed thoroughly in Meinel *et al.* (2014). It will be shown, that under these circumstances turbine bleeding can also be favorable for dry fluids, such as siloxanes.

2. COMBINED HEAT AND POWER (CHP)

2.1 CHP Concepts

Several configurations for CHP with an Organic Rankine Cycle can be found in literature (Karl, 2014, Mago *et al.*, 2010, Quoilin *et al.*, 2013). These concepts are shown in figure 1 and can be specified as follows:

- Serial concept: Heat extraction to district heating from the heat source and after ORC.
- Parallel concept: Heat from the heat source either to ORC or to district heating system.
- Serial/parallel concept: Heat extraction to district heating after ORC and, in order to increase the temperature, parallel to the ORC.
- Condensation concept (fixed σ): The district heat is supplied by the heat sink of the ORC in the condenser.
- Condensation concept (flexible σ): The district heat is supplied by the heat sink of the ORC in the condenser. Since a cooling tower is added in parallel to the district heating system, the heat extraction is decoupled from the power generation in the ORC
- Serial/condensation concept: These concepts are analogue to concepts d) and e), but they make use of excess heat from the waste heat source and increase the overall heat utilization.

The applicability and suitability of the above described concepts are strongly dependent on the temperature level of the (waste) heat source t_{WHS} and the temperature level of the district heating system t_{DHS} . In case of similar temperature levels for waste heat source and district heating system, with the waste heat source temperature being slightly higher ($t_{WHS} \geq t_{DHS}$) the parallel (a) or the

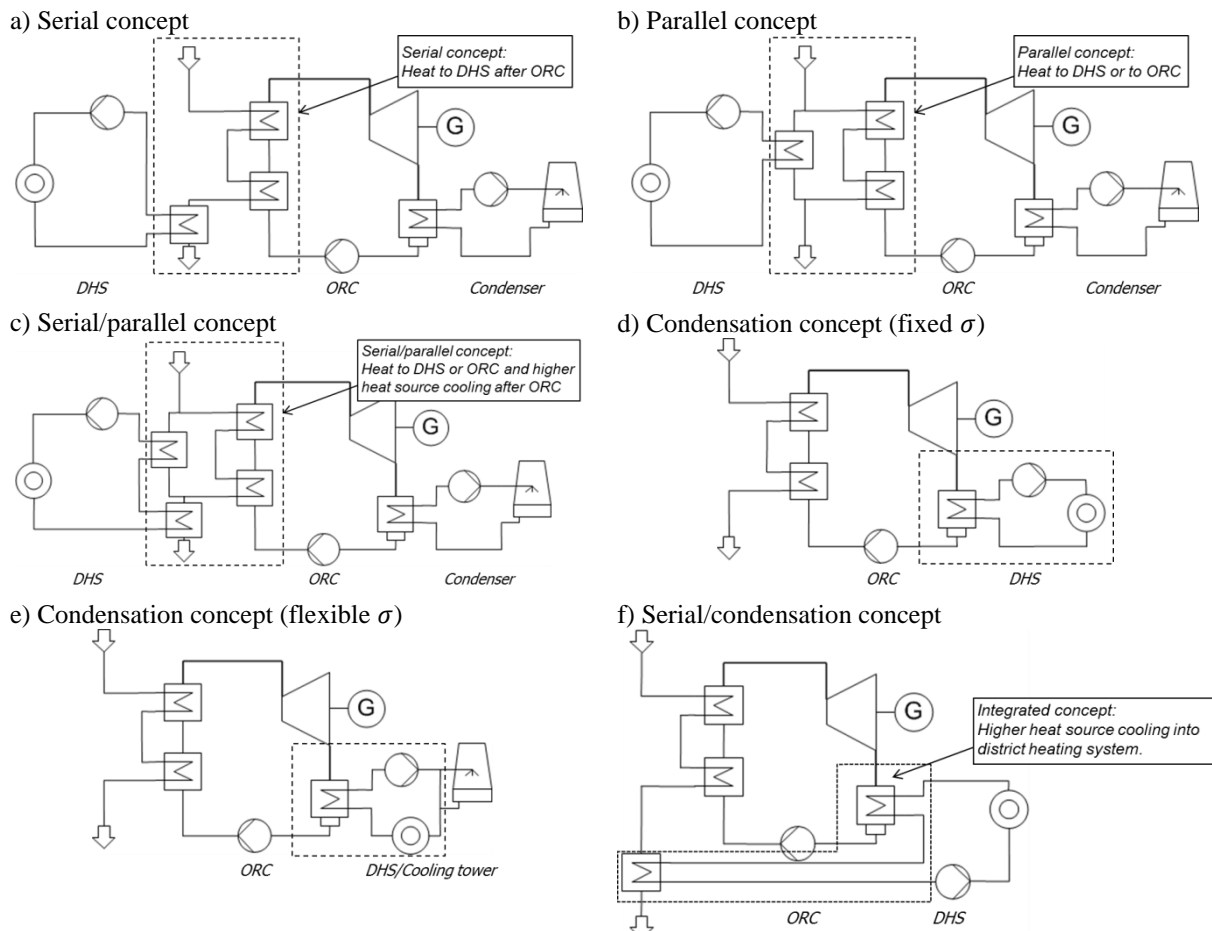


Figure 1: Qualitative schematics of common CHP concepts based on ORC systems.

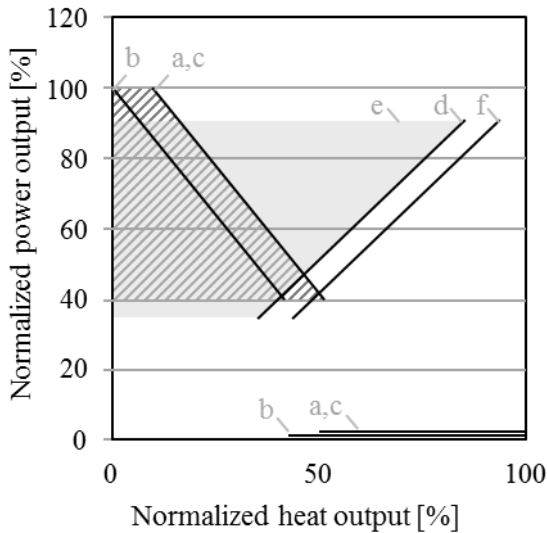


Figure 2: Qualitative $\dot{Q}_{DHS} - P_e$ -diagram for different CHP-concepts

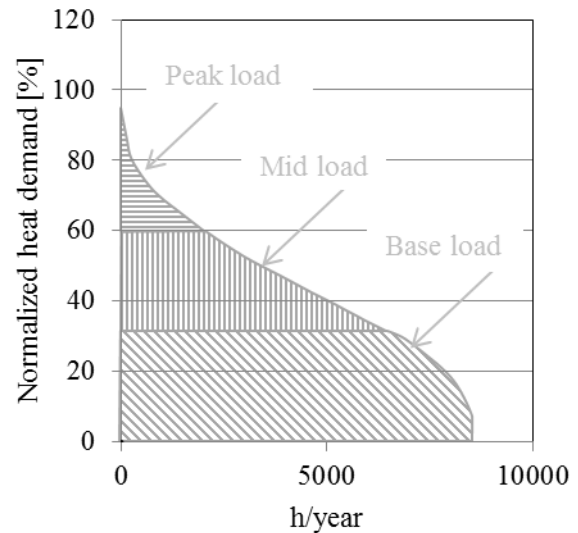


Figure 3: Annual load duration curve for an industrial consumer with different load zones

serial/parallel (b) concepts are favorable. Possible applications for these concepts cover geothermal, solar thermal and low temperature industrial waste heat in conjunction with district heating systems. Besides that, high temperature (waste) heat sources such as biomass in conjunction with high temperature process heat are suitable for these designs as well. Contrary to that, if the temperature level of the (waste) heat source is significantly higher than the temperature of the district heating system $t_{WHS} \gg t_{DHS}$ the serial concept (a) or one of the condensation concepts (d-f) are of better choice.

By comparing these concepts with each other, it has to be noted additional, that the concepts (a-c) can be used for any kind of heat sources, while the concepts (d-f) are chosen for applications where the heat source can be controlled and is on a high temperature level, e.g. biomass applications. Main reason for this is the flexibility of the concepts and the heat source utilization of these concepts, which is generally high. Therefore, the flexibility will be described more thoroughly in the next section.

2.2 Flexibility of CHP Concepts

The flexibility can be described in terms of the CHP coefficient σ , which is defined as the ratio between generated electrical power P_e and the heat flow to the district heating network \dot{Q}_{DHS} .

$$\sigma = \frac{P_e}{\dot{Q}_{DHS}} \quad (1)$$

While concepts (d) and (f) from figure 1 have a fixed CHP coefficient, the other concepts are characterized with a certain flexibility in this parameter. A qualitative characterization of the flexibility in a $\dot{Q}_{DHS} - P_e$ -diagram is shown in figure 2. The concept (e) is highlighted with the grey area. It shows a more flexible heat provision than the concepts (d) and (f). This flexibility is associated with a lower overall utilization efficiency of the heat source – one of the main advantages of this concept. The concepts (a-c) are all flexible concerning the CHP coefficient, which is denoted by the hatched area. The diagonal curves of (a-c) denote the full load operation for the concepts with the highest heat source utilization. The horizontal lines of (a-c) at the bottom of the diagram show the heat only mode, which is able to provide maximal heat to the district heating system. Note, that the above considerations neglect heat losses and assume a minimal part load for the ORC of $P_{min} = 0.4P_{max}$. Note also, that operation in the hatched area is associated with heat losses.

Based on this characterization, the concepts can be allocated to cover specific heat loads. For this purpose an annual load duration curve is exemplarily shown in figure 3. In this figure base load, mid load and peak load are shown qualitatively. While base load is supposed to lead to high full load operation hours (>7000 h/year), peak load has fairly small operational hours (< 2000 h/year). The more flexible a CHP system is, the more suitable it is for a high coverage of the heat demand (a-c, e). In all cases peak load is covered by a fossil fuel fired peak load boiler.

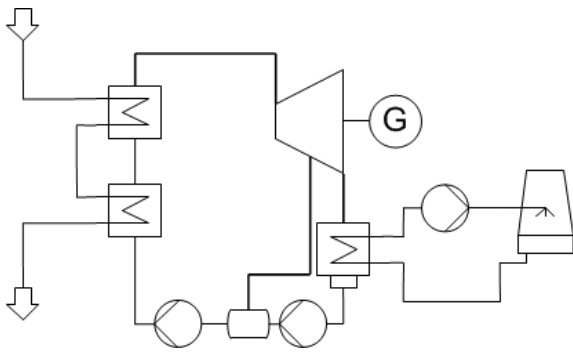


Figure 4: Two-stage ORC concept with turbine bleeding for regenerative pre-heating

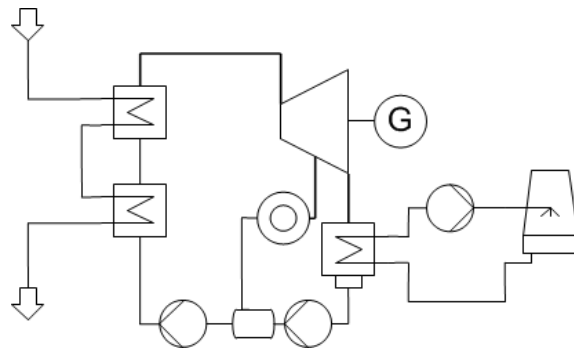


Figure 5: Integrated CHP concept with regenerative pre-heating

2.3 Operational strategies of CHP systems

In Vatopoulos *et al.* (2012) four major operation modes for CHP plants are distinguished: (1) Matching the electrical base load, additional power is purchased from the grid and heat is covered either by CHP or additional boilers; (2) Matching the thermal base load by meeting the base load in conjunction with a peak load boiler; (3) Matching the electrical load. For heat decoupling an additional boiler is used; (4) Matching thermal loads. Operation modes (3) and (4) can be considered as the classical electricity-driven and heat-driven operation.

A least cost strategy has been investigated by Hawkes and Leach (2007), which is not necessarily in line with the above mentioned ones. Hawkes and Leach (2007) investigated that least cost operational strategies can be a mix of the above mentioned operational strategies. It is apparent, that this operation mode is depending on the season and the overall coverage of the heat demand. Nevertheless, the heat-led operation leads always to minimal CO₂-emissions and to smallest primary energy consumption. In order to obtain a high coverage of the heat demand, flexible CHP systems are desired.

3. CONCEPT AND SIMULATION

3.1 Integrated CHP concept

In the literature a two-stage ORC with turbine bleeding has been investigated (Meinel *et al.*, 2014) This concept is shown schematically in figure 4, where the vapor from the turbine is extracted at an intermediate pressure level and used to saturate the working fluid in the liquid state in a direct contact heat exchanger. This measure increases the thermal efficiency of the ORC. It has been shown, that this concept is especially suitable for wet and isentropic organic fluids and that the performance increase is significantly better compared to a recuperator concept operated with the same fluid. The condensation temperature of the extracted fluid was in the range of 80 °C for R245fa. These findings suggested the investigation of heat extraction to a district heating system, which is integrated into the vapor extraction from the turbine. This concept is shown in figure 5.

It has to be noted, that this concept is associated with a higher system complexity due to the necessity of a multistage turbine and additional components (e.g. heat exchanger and pump). This results in higher investment costs. A further drawback of the system is the temperature level of the district heating system, which needs to be smaller than the evaporation temperature.

Table 1: Global specifications in the simulations

Parameter	Value	Parameter	Value
Mechanical efficiency	0.98	Supply temperature in heating network	80 °C
Generator efficiency	0.95	Return temperature in heating network	50 °C
Pump isentropic efficiency	0.90	Condensation temperature	30 °C
Turbine isentropic efficiency	0.80	Cooling water inlet temperature	20 °C
Pinch point specification	10 K	Temperature heat transfer media	240 °C/340 °C
Heat source scale	5 MW _t	Heat source temperature	490 °C

3.2 Simulation and boundary conditions

Simulations are carried out in Aspen V7.3, which is a well-known simulation tool for process engineering and offers a lot of component libraries, modules as well as fluid data bases.

The Peng Robinson equation of state is used to calculate fluid properties for these simulations. An overview of the applied boundary conditions, parameters and constraints is given in Table 1. The pressure level of the turbine bleeding was adjusted in order to meet the boundary conditions from the district heating and a given pinch point of 10 K. Furthermore, a pinch point of 10 K has been applied to all other heat exchangers. The temperatures for the district heating are in line with literature values found e.g. in Paar (2013) and Duminil *et al.* (2003). The heat source is assumed to originate from an internal combustion engine at a temperature level of $t_{WHS} = 490$ °C and ambient pressure (Karellas and Schuster, 2008). For simplification the gas composition is assumed to be equal to air. The energy content of the (waste) heat source is scaled to $\dot{Q}_{WHS} = 5$ MW_t and a thermal oil loop transfers this heat to the ORC. In the present study thermal oil temperatures of 240 °C (Karellas and Schuster, 2008) and 340 °C (Drescher and Brüggemann, 2007) are used, which are typical for waste heat recovery and biomass, respectively.

The working fluids in this study focus on isentropic fluids, but also include siloxanes, which are state-of-the-art for biomass applications. The next paragraphs explain the working fluid selection.

Among others, fluorinated alkanes such as 1,1,1,3,3-pentafluoropropane (R245fa) and the related 1,1,2,2,3-pentafluoropropane (R245ca) are considered, which are so called HFC. In particular R245fa is an often applied and investigated fluid and is used in experimental test rigs and operating plants nowadays.

In order to circumvent environmental-related issues, like high global warming potential, new molecules with lower impact on the climate are available. Thus, representatives of so-called fourth generation fluids (HFO) are included in the analysis, which are promising replacements for currently applied fluids. Namely cis-1,3,3,3-tetrafluoropropene (R1234zeZ) and trans-1-chloro-3,3,3-trifluoro-1-propene (R1233zd) are considered.

Cyclobutane, cyclopentene, furan and 2,5-dihydrofuran are selected from the group of cyclic molecules due to suitable critical parameters in the range of the chosen heat source temperatures.

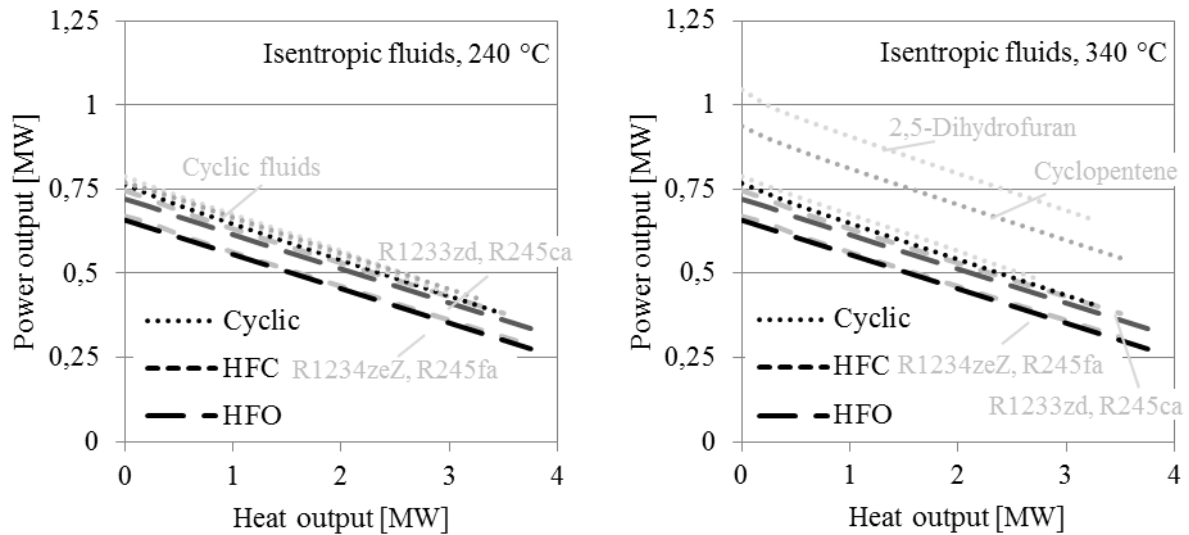
Commercially available systems for high temperature biomass and industrial waste heat applications are mainly operated by siloxanes. Siloxanes feature high critical temperatures in conjunction with good safety and environment-related properties. Thus in the present study several siloxanes are considered in the analyses as references. Depending on the heat source temperature hexamethyldisiloxane (MM), octamethylcyclotetrasiloxane (OMTS) and octamethyltrisiloxane (MDM) are simulated.

To conclude, representatives of hydrofluorocarbons (HFC), hydrofluoroolefins (HFO), cyclic compounds (Cyclic) and siloxanes (Siloxane) are investigated. Table 2 lists the considered working fluids and corresponding critical parameters as well as fluid type and characteristic.

Table 2: Investigated working fluids in the simulations including fluid type and critical parameters

Working fluid	Fluid type	t_{crit}	P_{crit}
cis-1,3,3,3-Tetrafluoropropene (R1234zeZ)	isentropic	150.08	35.30
1,1,1,3,3-Pentafluoropropane (R245fa)	isentropic	154.29	36.50
trans-1-Chloro-3,3,3-trifluoro-1-propene (R1233zd)	isentropic	165.56	35.70
Cyclobutane	isentropic	187.05	49.88

1,1,2,2,3-Pentafluoropropane (R245ca)	isentropic/dry	174.58	39.30
Furan	isentropic/dry	217.26	55.13
Cyclopentene	isentropic/dry	234.11	48.05
2,5-Dihydrofuran	isentropic/dry	269.10	55.13
Hexamethyldisiloxan (MM)	dry	245.68	19.13
Octamethyltrisiloxan (MDM)	dry	290.94	14.15
Octamethylcyclotetrasiloxan (OMTS)	dry	313.49	13.38



4. RESULTS

Since Meinel *et al.*, 2014 has shown that the efficiency of the two-stage concept with turbine bleeding performs best with isentropic working fluids, the first section focuses on these isentropic working fluids and the integrated CHP concept as shown in figure 5. For siloxanes the recuperation of the sensible heat becomes more and more favorable, due to the dry expansion behavior and the sensible heat content after the turbine outlet. Therefore a second section deals with siloxanes and a comparison of three different concepts. A final section presents a method to estimate annual electricity generation based on annual load duration curves.

4.1 Comparison of isentropic working fluids

In figure 6 results of the CHP simulations with the integrated concept for isentropic and wet working fluids are shown. Two different temperature levels of the thermal oil are investigated, which represent waste heat from internal combustion engines (240 °C) and biomass application (340 °C). For the 240 °C case all the fluids perform similar and only minor changes can be observed. Among the fluids Furan performs best generating up to 787.6 kW_e. The next ranked fluids in terms of electric power output are cyclopentene (-2.2 %) and 2,5-dihydrofuran (-2.3 %) with slightly less power output compared to furan. Note that at a condensation temperature of 30 °C cyclopentene, furan and 2,5-dihydrofuran expand into vacuum (Table 3), which causes higher investment costs for turbine and condenser. Noteworthy alternatives are cyclobutane (-3.0%) and R1233zd (-8.5%). Where especially R1233zd represents a good trade-off between environmental-related (low global warming potential, no ozone depletion potential), thermodynamic (relativ high power output) and economic aspects (no vacuum expansion).

Figure 6: Performance of isentropic fluids at different thermal oil temperatures

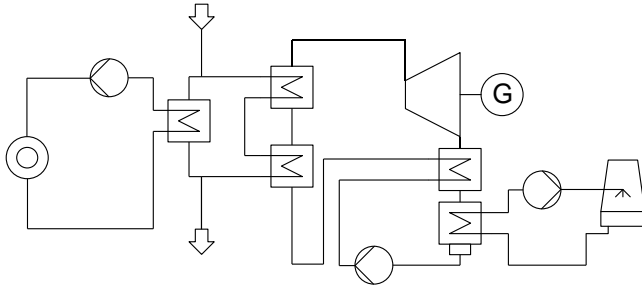


Figure 7: Parallel concept with recuperator concept for dry fluids (siloxanes)

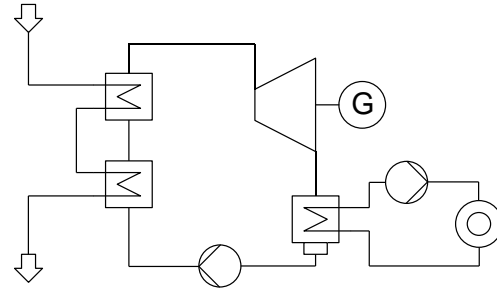


Figure 8: Parallel concept with recuperator concept for dry fluids (siloxanes)

For a thermal oil temperature of 340 °C only 2,5-dihydrofuran and cyclopentene as working fluids offer higher power outputs compared to the 240 °C-case. This increased power output is based on the fact, that the pinch point location changes from pre-heater outlet (240 °C) to the pre-heater inlet (350 °C) and no pinch point limitation occurs anymore. For the other fluids no significant increase in the power output is observed. With 2,5-dihydrofuran as the working fluid 1045.79 kW_e are generated followed by cyclopentene with 937 kW_e (-10.5%) and furan (-24.7%). Similar to the simulations at 240 °C cyclobutane (-26.6%) and R1233zd (-31.1%) are alternatives but seem more suitable for lower temperatures.

4.2 Comparison of siloxanes

Since siloxanes are suitable for high temperatures and mainly used for biomass applications, the comparison of these working fluids focuses only on the high temperature case of the thermal oil (340 °C). In order to evaluate siloxanes three different concepts are compared in terms of a $P_e - \dot{Q}_{DHS}$ -diagram:

1. Parallel concept with a recuperator to increase the thermodynamic efficiency (Figure 7). This concept is state-of-the-art for biomass fired power plants and process heat.
2. Condensation concept without a recuperator (Figure 8). This concept is state-of-the-art for biomass fired power plants and residential heating purposes.
3. Integrated CHP concept as shown in figure 5. This concept is beyond state-of-the-art for CHP applications.

Figure 9 shows the results for the three concepts and OMTS as working fluid. It can be seen, that the integrated concept offers a significantly higher power output compared to the parallel concept, if the capacity to the district heating system exceeds 1.25 MW_t. The condenser concept shows a lower electricity output for all operational conditions and becomes equal to the integrated concept with maximal heat decoupling. Note, that the CHP coefficients of the parallel concept and the integrated concept are variable, as was already described in section 2.2. The shaded triangle in figure 9 denotes operational points, where the proposed integrated CHP concept is more beneficial compared to the other designs.

For the other investigated siloxanes, MM and MDM the results are almost identical, which means, that a similar power and district heat output can be achieved. A comparison of the different siloxanes is shown in figure 10.

The recuperator cycle in general needs additional investments for the recuperator, which is an expensive component due to its size. The heat transfer from superheated vapor demands large surfaces. On the other hand side, the integrated concepts need additional components, as it was mentioned earlier, which causes additional costs as well. It is not the scope of this work to quantify

Table 3: Condensation pressures at a temperature of 30 °C

Working Fluid	p _{cond} @ 30 °C [bar]	Working Fluid	p _{cond} @ 30 °C [bar]
R245fa	1.77	Cyclobutane	1.83
R245ca	1.21	Cyclopentene	0.61
R1234zeZ	2.10	Furan	1.00
R1233zd	1.55	2,5-Dihydrofuran	0.29
MM	0.07	OMTS	0.03

these costs for the investigated concepts due to high uncertainties of available cost functions. In order to estimate benefits the power sales for the different concepts and different district heating systems will be compared. The procedure as well as the results will be described in the next section.

4.3 Estimation of economic benefits

For the economic calculation procedure an annual load duration curve is needed. If no measurement data are available, models are available in literature to approximate such curves. One of these models is the Sochinsky model, which determines the time dependent heat demand $\dot{Q}(\tau)$ in dependence of specific parameters:

$$\dot{Q}(\tau) = \dot{Q}_{max} \left(1 - (1 - m_0) \cdot \tau^{\frac{m-m_0}{1-m}} \right) \quad (2)$$

In the above equation \dot{Q}_{max} is the maximum heat demand of the district heating system and τ the hour of the year. The load factor m can be expressed as the ratio of full load operational hours per year z and the hours per year z_a :

$$m = \frac{z}{z_a} \sim \frac{z}{8760} \quad (3)$$

The uniformity factor m_0 is depending on the minimal \dot{Q}_{min} and maximal heat demand \dot{Q}_{max} in the district heating system and is determined through the following equation:

$$m_0 = \frac{\dot{Q}_{min}}{\dot{Q}_{max}} \quad (4)$$

The resulting normalized annual load duration curve is shown in figure 11 with $z = 2500$ and $\dot{Q}_{min} = 0.1\dot{Q}_{max}$. The grey curve represents data from a real district heating network in southern Germany. It can be seen, that both load profiles differ significantly. Note that real annual load duration curves differ in general, because they strongly depend on the type and number of consumers and are unique for each district heating system. In order to take these variations into account, both curves will be used in further investigations.

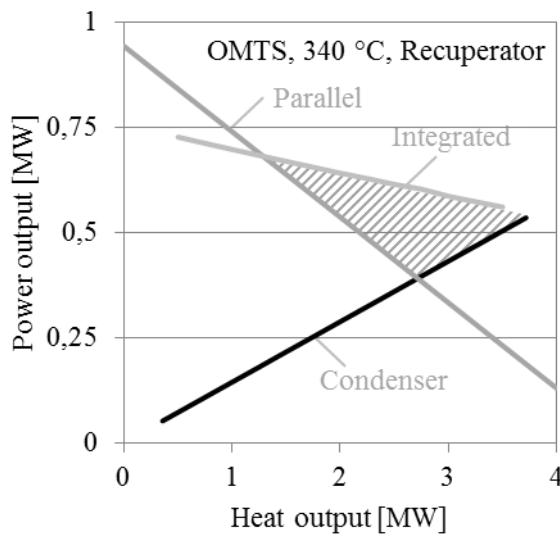


Figure 9: Comparison of CHP concepts with OMTS as a working fluid

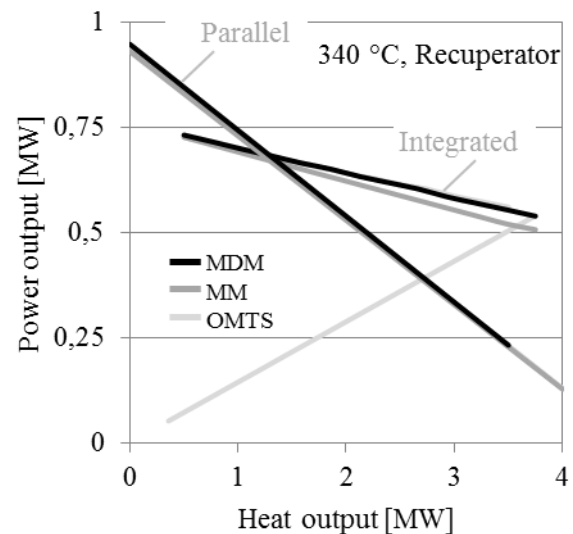


Figure 10: Comparison of different siloxanes as a working fluid

The integration of a CHP system into the district heating network is described by a cover ratio X_{CHP} which denotes the share of the maximal heat demand in the district heating system \dot{Q}_{max} which can be covered by the CHP system at full load operation $\dot{Q}_{CHP,max}$:

$$X_{CHP} = \frac{\dot{Q}_{CHP,max}}{\dot{Q}_{max}} \quad (5)$$

This cover ratio is varied for the different CHP concepts and the cumulated power is evaluated. Note that the part load behavior of the cycle is also taken into account ($P_{min} = 0.4 \cdot P_{max}$). Figure 12 shows the cumulated electricity over the cover ratio for the different concepts as well as the different annual load duration curves. For high cover ratios the parallel concept approaches the integrated concept, while the integrated concept is similar to the condenser concept for low cover ratios. In between the electricity generation of the integrated concept is significantly higher than for the other two concepts. These findings are valid for the Sochinsky model (solid line) as well as the real data of a district heating system (dashed line). Therefore, it can be concluded that the integrated concept is suitable for the whole range of cover ratios, while the condenser concept and the parallel concept are limited in their application.

According to Dötsch *et al.* 1998 cover ratios of $0.1 \leq X_{CHP} \leq 0.4$ are common for real CHP plants and offer best profitability due to high full load operation hours. Taking $X_{CHP} = 0.3$ and the annual load duration curve of Sochinsky, the integrated concept is able to generate almost 5200 MWh/a, while the condenser concept (3500 MWh/a) and the parallel concepts (1340 MWh/a) produce significantly less electricity.

Revenues can be calculated by taking electricity prices into account, which range around $c_e \approx 40$ €/MWh at the European stock exchange and $c_e = 105.50$ €/MWh for biomass applications of the considered CHP capacity according to the renewable energy act (EEG, 2014). These prices lead to annual revenues of $R_e(EEG) = 208\,000$ €/a and $R_e(EEG) = 548\,600$ €/a for the integrated concept and the Sochinsky-like district heating system.

5. CONCLUSIONS

In this study an integrated CHP concept is presented, which is based on a two-stage turbine bleeding ORC. The demand of the heating network is covered by decoupling heat from the steam extraction prior to the direct-contact heat exchanger. This integrated concept features a high level of flexibility due to the simultaneous adaption of the intermediate pressure in conjunction with a higher system performance due to regenerative pre-heating in the direct-contact heat exchanger.

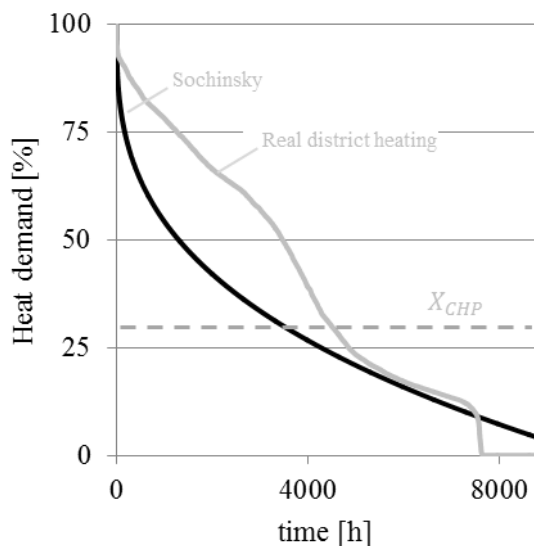


Figure 11: Annual load duration curve according to the Sochinsky model and real district heating data for southern Germany

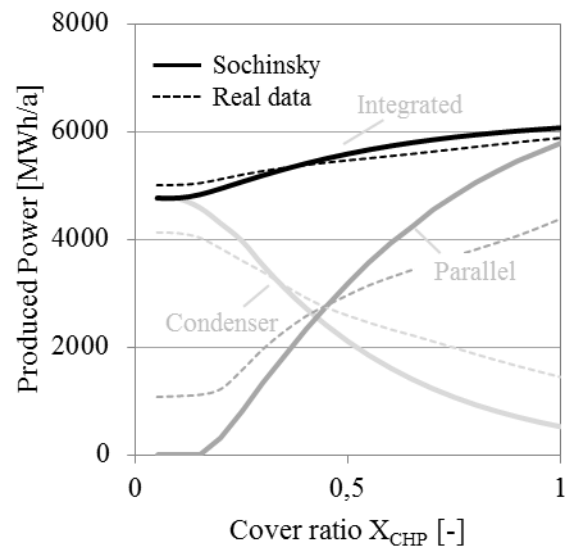


Figure 12: Annual cumulated power production for CHP integration in a district heating system in dependence of various cover ratios

First, the potential of the proposed system is characterized in terms of isentropic fluids. The investigated isentropic fluids are HFC, HFO and cyclic compounds. For waste heat applications R1233zd shows a good tradeoff between environment, thermodynamics and economics, although cyclic compounds have higher electricity output. For higher temperatures, similar to biomass applications, the cyclic compounds increase significantly in power output due to the absence of a pinch point limitation. Thus, this advantage might justify their application up to certain extent.

A comparison between different cycles for biomass applications with siloxanes as working fluids is presented, showing that the integrated concept has significant higher power output compared to other concepts.

The evaluation of the cumulated annual electricity production in dependence of the cover ratio within a district heating network shows, that the concept is flexible and applicable for the entire range of cover ratios.

In dependence of electricity prices the revenues per year are significantly higher and can justify also higher investments due to the higher system complexity of the presented integrated concept.

NOMENCLATURE

Parameter			Greek symbols		
c	prize	[€/MWh]	σ	CHP coefficient	[-]
p	Pressure	[bar]	η	efficiency	[-]
P	Power	[MW]	τ	time	h
\dot{Q}	Heat	[MW]	Abbreviations		
R	Revenue	[€/a]	CHP	Combined heat and power	
t	Temperature	[°C]	HFC	Hydrofluorocarbons	
X	variable/ratio	[-]	HFO	Hydrofluoroolefines	
z	time	[h/a]	Subscripts		
$cond$	condensation		max	maximum	
$crit$	critical		min	minimum	
DHS	District heating system		t	thermal	
e	electricity		WHS	Waste heat source	

REFERENCES

Bini, R.; Manciana, E., 1996, Organic Rankine Cycle Turbogenerators for combined heat and power production from Biomass, *3rd Munich Discussion Meeting "Energy Conversion from Biomass Fuels - Current Trends and Future Systems"*, ZAE Bayern, München

Drescher, U., Brüggemann, D., 2007, Fluid selection for the Organic Rankine Cycle (ORC) in biomass power and heat plants, *Applied thermal engineering*, vol. 27: p. 223-228.

Duminil, E., Tereci, A., Kesten, D., 2009, Economical aspect and environmental impact of renewable trigeneration in urban areas: Scharnhäuser Park case study, *International Conference on Renewable Energy Technologies and Polygeneration*, Poznan, Poland.

Dötsch, C., Taschenberger, J., Schönberg, I., 1998, Leitfaden Nahwärme. *Fraunhofer Umsicht Band 6*, Fraunhofer IRB Verlag, Oberhausen.

EEG, 2014, Gesetz für den Ausbau erneuerbarer Energien, *Deutscher Bundestag*, 21.7.2014

Hawkes, A, Leach, M., 2007, Cost-effective operating strategy for residential micro-combined heat and power, *Energy*, vol. 32, no. 5: p. 711-723

- Karellas, S., Schuster, A., 2008, Supercritical fluid parameter in organic rankine cycle applications, *Int. J. of Thermodyn.*, vol. 11, no. 3: p. 101-108.
- Karl, J., 2004, *Dezentrale Energiesysteme*, Oldenbourg, (ISBN 3-486-27505-4)
- Knapek, E., Kittl, G., 2007, Unterhaching power plant and overall system, *Proceedings European Geothermal Congress 2007*
- Mago, P.; Hueffed, A.; Chamra, L., 2010, Analysis and optimization of the use of CHP–ORC systems for small commercial buildings, *Energy and Buildings*, vol. 42, no. 9: p. 1491-1498
- Meinel, D., Wieland, C., Spliethoff, H., 2014, Effect and comparison of different working fluids on a two-stage organic rankine cycle (ORC) concept, *Applied Thermal Engineering*, vol. 63, no. 1: p. 246-253
- Paar, A., 2013, Transformationsstrategien von fossiler zentraler Fernwärmeversorgung zu Netzen mit höheren Anteilen erneuerbarer Energien, *Institut für Energie-und Umweltforschung Heidelberg GmbH*, Data sheet.
- Preißinger, M., Heberle, F., Brüggemann, D., 2012, Exergetic analysis of biomass fired double-stage Organic Rankine Cycle (ORC), *Proceedings of ECOS 2012*, Perugia, Italy.
- Quoilin, S., van den Broek, M., Declaye, S., Dewallef, P., Lemort, V., 2013, Techno-economic survey of Organic Rankine Cycle (ORC) systems, *Renewable and Sustainable Energy Reviews*, vol. 22: p. 168-186
- Schuster, A., Karellas, S., Kakaras, E., Spliethoff, H., 2009, Energetic and economic investigation of Organic Rankine Cycle applications, *Applied thermal engineering.*, vol. 29, no. 8-9: p. 1809-1817.
- Tchanche, Bertrand F.; Lambrinos, Gr; Frangoudakis, A.; Papadakis, G., 2011, Low-grade heat conversion into power using organic Rankine cycles – A review of various applications, *Renewable and Sustainable Energy Reviews*, vol. 15: p. 3963-3979
- Vatopoulos, K., Andrews, D., Carlsson, J., Papaioannou, I., Zubi, G., 2012, Study on the state of play of energy efficiency of heat and electricity production technologies, *Reference Report, Joint Research Centre of the European Commission*, (ISBN 978-92-79-25606-6).
- Wirths, A., 2008, Einfluss der Netzzrücklauftemperaturen auf die Effizienz von Fernwärmesystemen, *13th Dresdner Fernwärmekolloquium*.

A PERFORMANCE PREDICTION TOOL FOR ORC APPLICATIONS BASED ON MODELICA

Adrian Rettig^{1*}, Ulf Christian Müller¹

¹ Lucerne University of Applied Sciences and Arts
Technikumstrasse 21, CH-6048 Horw, Switzerland
E-mail: adrian.rettig@hslu.ch

* Corresponding Author

ABSTRACT

Converting waste heat to electricity using organic ranking cycle (ORC) technology is an effective method to improve energy efficiency and reduce costs. However, the waste heat source is often characterized by relatively large fluctuations in load, making it a demanding task to design and operate an ORC in an efficient and economically sound manner. A reliable performance prediction in an early project phase helps to create an economically successful operation and build the business case on a firm foundation. In this paper a prototype of such a prediction tool based on existing Modelica libraries is presented. A main emphasis lays on the control strategy that allows to reproduce part load behavior including autonomous shutdown and restart events. The suggested control strategy consists of two coupled layers, a state machine and a main controller operating different actuators. The state machine enables to switch between different control schemes, which is important for example for the transition of a running state to a shutdown procedure. The compiled ORC model simulates the electrical energy generated over a time period of 30 h with a deviation less than two percent compared to measurements of the real application. The model was applied to a test run with generic boundary conditions for a time period of 30 days and showed its capabilities to autonomously and reliably shut down and restart to normal operations.

1. INTRODUCTION

Large load fluctuations are an inherent nature of many waste heat sources making the application of an ORC system a demanding task. Compounding this challenge are the relatively tight profit margins of ORC projects in general, even with the support of governmental subsidies along with the tendency to use only a rough estimation in predicting performance. These factors increase the uncertainty when trying to create an economically successful operation. To build the business case on a firm foundation, performance prediction that takes into consideration all relevant operation aspects is inevitable. Therefore, a reliable performance prediction tool for the use in an early project phase is highly desired.

Dynamic simulation is an instrument to cope with varying operation parameters of many waste heat applications. Several authors have used dynamic modeling techniques to simulate the behavior of thermal power plants mainly in conjunction with designing and testing control strategies as well as for risk and safety assessment. Snidow and Malan (1988) used the Modular Modeling System (Smith et al., 1983) to simulate the behavior of an existing fossil power plant. Open-loop step test and closed ramp test were performed for validation purposes. Colonna and van Putten (2007) implemented a modular, hierarchical and causal modeling paradigm in the MATLAB/Simulink toolbox SimECS and applied it to a small biomass-fired Rankine Cycle. Several exemplary simulations starting from on-design and off-design stable operation were performed to validate the model (van Putten and Colonna, 2007). Fiorani (2009) also developed a Simulink library and showed the transients for a fuel step in a internal combustion engine and its interaction with various ORC and control configurations. In the last decade Modelica gained considerable attention in the modeling of dynamic and multidisciplinary systems. Casella and Leva (2006) developed the open Modelica library ThermoPower, which is used to model rather complex

thermal power plants. Casella and Pretolani (2006) investigated a typical combined-cycle power plant with the aim to speed up the startup time without compromising the life-time of critical components. Casella et al. (2013) also simulated the behavior of a commercially available ORC module using an open- and closed-loop approach. More recently Quoilin et al. (2014b) published the open Modelica library ThermoCycle as a framework for smaller energy systems such as heat pumps and ORC systems. Great emphasis was placed on implementing robust and computational efficient models (Quoilin et al., 2014a) using amongst others the very efficient fluid property calculation library CoolProp (Bell et al., 2014).

Waste heat applications using ORC often show significant operating hours in the part load regime with many automatic shutdown and startup cycles due to external limiting conditions such as high ambient temperatures or low heat source power. These factors should be taken into account to improve the prediction of the economic efficiency. Simulating startup and shutdown processes is a demanding task as stated by Casella and Pretolani (2006). In this reference it is noted that the direct initialisation of the plant model in the shutoff state is difficult to solve numerically due to the presence of low or zero flow rates and to the need of good starting values. As a work around the simulations in their study were initialized at the design point and then brought to idle from where the actual (warm) startup process was initiated. For a concentrated solar driven ORC plant, Ireland et al. (2014) used an alternative approach to avoid the numerical issues associated with the discontinuities in the working fluid density derivative present during rapid phase changes, e.g. while shutting down the plant. The Modelica models are based on the ThermoCycle library and consist of two submodels – an operating and an idling model, which are simulated concurrently. If shutdown conditions are met, only the idle model is brought down while the operating model keeps running at a virtual level avoiding phase changing issues in the evaporator. This approach allows the simulation of longer periods with recurring startups and shutdowns though the transient details of these processes are neglected. Erhart et al. (2013) simulated the shutdown and startup of a biomass fired ORC plant using the ThermoPower library. The simulation results match the measurements very well. No further details with respect to numerical issues are given. Felgner et al. (2011) directly coupled physical models with economical models using Modelica. The profitability of an ORC system on a typical farm biogas plant were assessed over a period of 25 years assuming boundary conditions and a shutdown of the ORC plant every second year for maintenance. Also a generic industrial waste heat application using ORC was investigated over a period of one week. This simulation included a strong variation of waste heat supply but no shutdowns. No further details on startup and shutdown procedures were given.

To study the performance of an autonomous operated ORC module including automated startup and shutdown procedures a performance prediction tool using Modelica is implemented. It is based on the ThermoCycle library (Quoilin et al., 2014b) in combination with the CoolProp software (Bell et al., 2014) necessary for calculating fluid properties and the StateGraph2 library (Otter et al., 2009) used for the higher-level control strategy. The setup and approach are described in more details in the following section.

2. SETUP AND APPROACH

A generic ORC system has been modeled inspired by an existing ORC plant of a small bio gas combined heat and power application in Klingnau (Switzerland). Figure 1 depicts the simplified layout of this plant. The heat from exhaust gases is transferred to a pressurized water circuit that is heated up to 130-150 °C before it enters the ORC module. The heat rejected by the module is discharged to a cold water circuit connected to an air cooler. The applied ORC module has a gross electrical power output of 30 kW at full load of the biogas engine, which has a rated power output of 625 kW_{el}. The ORC module contains a scroll type expander that is driven by the working fluid R245fa.

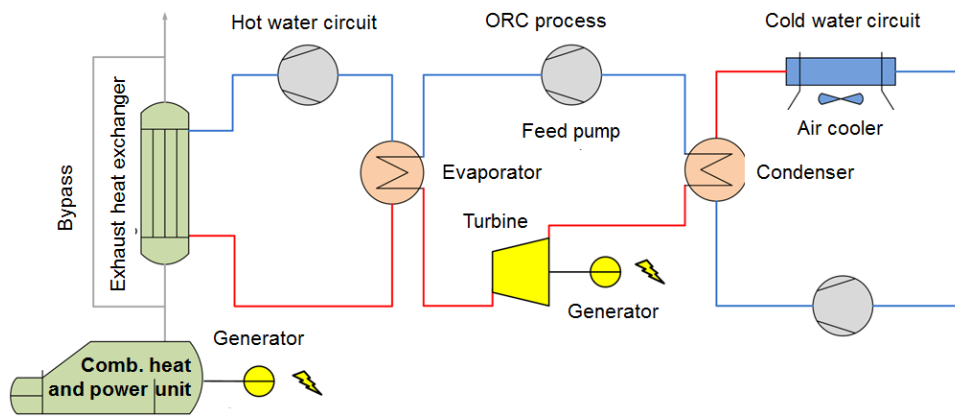


Figure 1: ORC plant of combined heat and power application. Source: Axpo Neue Energien AG

2.1 Modelica Model of the ORC Module

As only little data of the real ORC plant is currently available the topology, dimensioning as well as the control strategy are based on assumptions. To keep the model simple for testing the applicability of the derived control strategy as well as for testing the capability of performance prediction only the ORC module was taken into account within the scope of this study. Figure 2 shows parts of the overall Modelica model and the setup of the ORC module. It is a rather classical configuration. Most applied

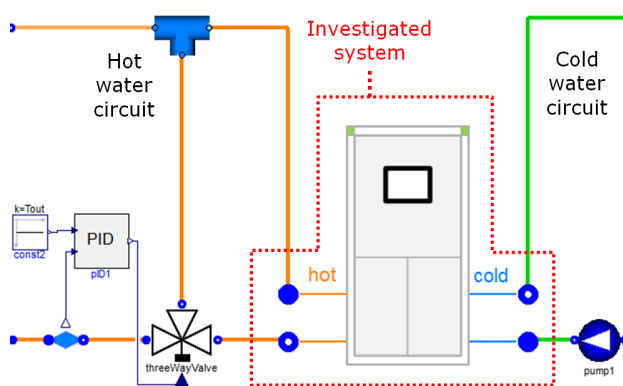


Figure 2: To keep the system simple for testing, the investigated model comprises the ORC module only.

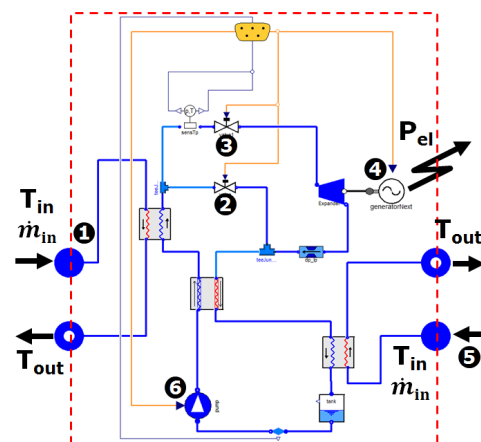


Figure 3: Assumed configuration of the ORC module. The numbered process data and actuators are altered by the controller.

models are standard or slightly modified components of the ThermoCycle library. The library comprises distributed and moving boundary heat exchanger models. Since during startup and shutdown the fluid may not be present as liquid, two-phase mixture and vapor concurrently, the distributed models seem to be more suitable as stated by Wei et al. (2008). During operation the expander bypass is closed and the expander inlet valve fully open. Both valve positions as well as the expander/generator speed may be altered by the controller during shutdown or startup phases. The expander model is extended by an additional simple leakage model. This maintains a small mass flow when the expander comes to rest, which leads to an increase of the numerical stability. The expander efficiency is correlated to the pressure ratio and the inlet pressure, see Section 2.3. The multi-stage radial pump is an own implementation inspired by Wetter (2013). It is based on the dimensionless flow and head coefficient. To enhance stability during initialization the pump characteristic is modified such that the head coefficient becomes a strictly monotonic function of the flow coefficient, see Figure 5.

2.2 Control Strategy

The real ORC plant shuts down and restarts autonomously depending on certain criteria. After reviewing the available process data, the relative power output of the internal combustion engine and the ambient temperature are assumed to trigger the shutdown and restart procedures. Additionally, the exceedance of the limits must persist for a certain time interval to prevent too frequent start/stop sequences. The model must be able to mimic these behaviors by a suitable control strategy. The suggested control strategy consists of two coupled layers, a state machine that keeps track of the current conditions and an actual controller comprising the subcontrollers of the different actuators, see Figure 4. The state machine is

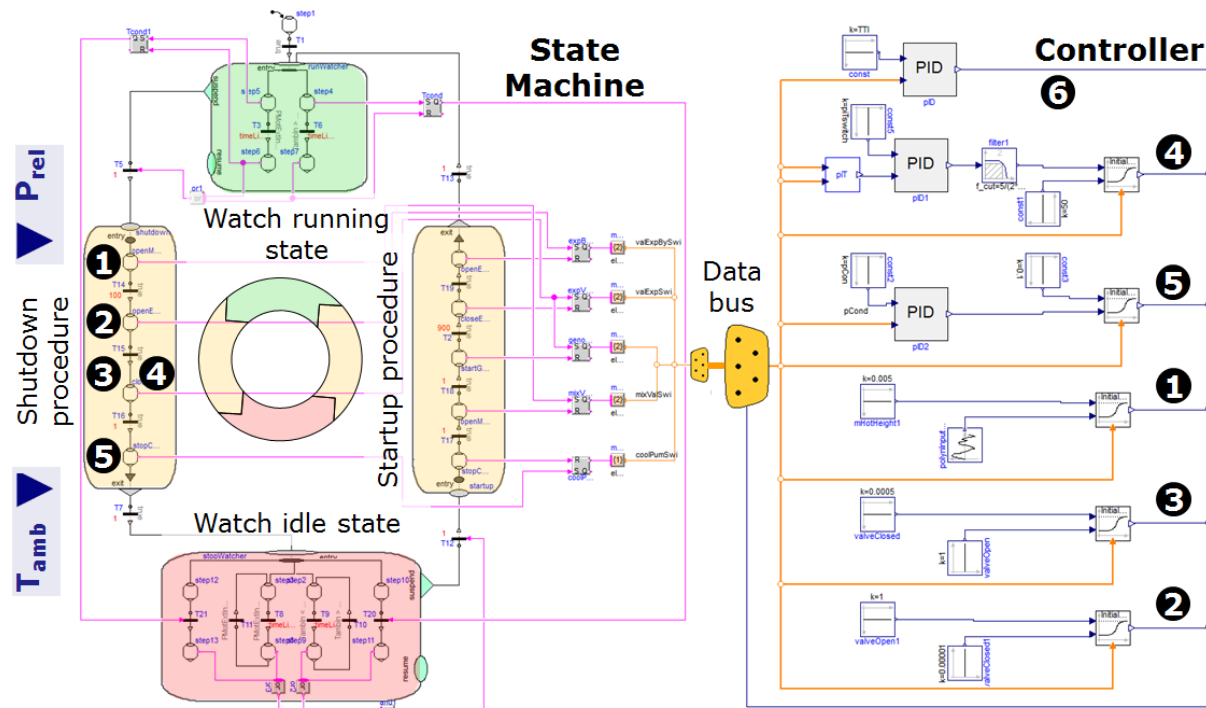


Figure 4: The control strategy consists of a state machine coupled with a controller. The numbers in the state machine and controller section correspond to the process data and actuators depicted in Figure 3.

implemented using the Modelica library StateGraph2 (Otter et al., 2009). The state machine is divided into four subparts, a running and idle state watcher as well as a shutdown and restart procedure. Due to numerical reasons the module is initially in the running mode as proposed by Casella and Pretolani (2006). As soon as the power or ambient temperature criteria is infringed for the time interval defined the running state is suspended and the shutdown procedure is initiated. The shutdown procedure consists of a sequence of steps to be performed. Each step triggers a switch that in turn alters the behavior of the controller (the numbers corresponds to the black numbers in Figure 2 and 4):

1. The hot water input to the module is decreased by fully opening a mixture valve, see Figure 2 left. Since this process is not modeled yet the mass flow into the module is prescribed as a mass flow source (open-loop control). By extending the model with a mixture valve, a corresponding closed-loop controller can easily be dropped in at the position of the current mass flow source.
2. With some time lag the expander bypass valve opens.
3. Simultaneously the expander inlet valve closes.
4. Concurrently also the generator stops. During the transition a closed-loop controller is applied to stabilize the simulation. By shutting down the generator too late the expander may create a very low (even negative) pressure at the expander inlet causing the fluid property calculation to crash. A sudden stop of the generator creates strong gradients, which in turn impact also the stability.

5. Finally, the cold water mass flow is shut down by switching from a closed-loop to an open-loop control and setting a near zero mass flow.
6. The feed pump control scheme is not changed. The feed pump controls the expander inlet temperature. As the heat input ceases the pump speed goes down trying to maintain the prescribed expander inlet temperature. It virtually shuts down itself. However, a small pump speed is maintained due to numerical reasons.

After processing all the shutdown steps the idle watch state becomes active. The ORC module remains in this state as long as the engine power and ambient temperature startup criteria are not fulfilled. As soon as the criteria are met the state proceeds to the startup procedure, where the reverse steps are performed. Finally, the running state is reached and maintained as long as no shutdown criteria arises.

The switch between different control schemes and signals is executed by a smooth transition function triggered by the state machine via a data bus. This increases the numerical stability significantly.

2.3 Model Calibration

Since no internal process data were available the heat exchanger areas were pragmatically calibrated based on few thermodynamic data received from the plant operator. These were the inlet and outlet temperature of the ORC module both for the hot and cold water circuit as well as the hot water inlet mass flow. The cold water mass flow rate is adjusted to keep the condenser pressure within limits, see Figure 3.

For the fine calibration a modified controller adjusted the expander efficiency to match the measured power output for different operating points. The calculated efficiencies are correlated to the expander pressure ratio and inlet pressure using a variant of the Pacejka formula as proposed by Declaye et al. (2013). Due to the small number of data points the adjusting of the fitting parameter is done manually. Figure 6 shows the calculated and reconstructed efficiencies. Most of the reconstructed efficiencies deviate by less than $\pm 5\%$ from the input values, see Figure 7. The derived correlation is finally implemented as a characteristic in the expander model.

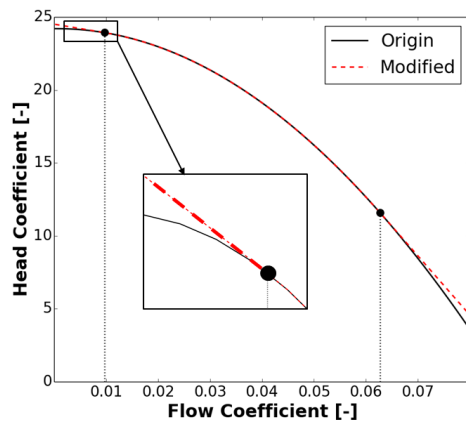


Figure 5: Dimensionless pump characteristic as a strictly monotonic function

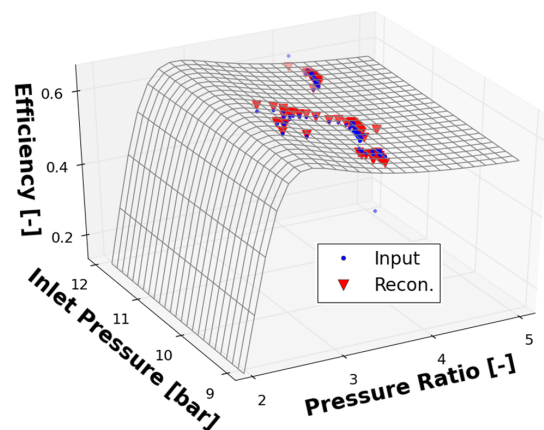


Figure 6: Deduced expander characteristic

3. RESULTS

To validate the model and the control concept a period of 30 hours is simulated and compared to measurements. There are two shutdown events within this period, one triggered by a low engine power output and the other by a too high ambient temperature. To avoid highly inefficient events during the simulation the input data are prepared as smooth piecewise polynomials as proposed by Quoilin et al. (2013). Figure 9 shows exemplarily the normalized measured and smoothed water inlet temperatures of

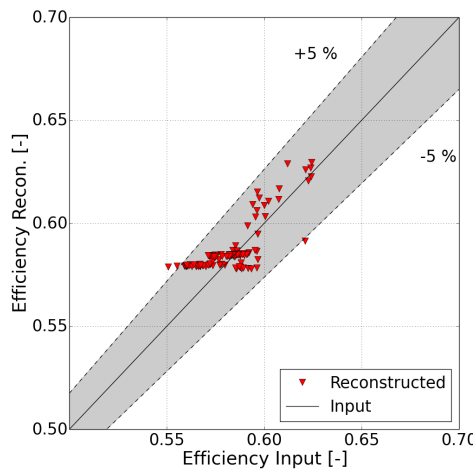


Figure 7: Reconstructed efficiencies using Pacejka formula

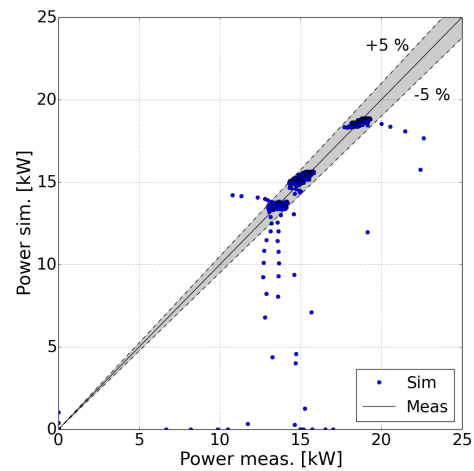


Figure 8: Simulated versus measured power for different points in time

the hot and cold side of the module. Additionally, a comparison between measurement and simulation is given for the outlet temperature on the hot side as well as the power output of the module. In operation the simulated outlet temperatures match the measurement well. During the shutdown period the outlet temperature cools down too fast. Raising the thermal inertia by increasing the thermal capacity of the heat exchanger and/or the fluid quantity did not improve the situation. As mentioned before a small mass flow rate is maintained within the module due to numerical reasons. Further investigations revealed that the temporal profile of the temperature during the shutdown period is very sensitive to this remaining mass flow rate. However, as this temperature discrepancy has a negligible effect on the performance prediction the deviation is acceptable. The simulated power output is well reproduced – of course also due to calibration, which is based on the measured power output. The deviation between the measured and simulated power is shown in more detail for different points in time in Figure 8. Most of the data points lie within a $\pm 5\%$ deviation range. The larger deviations originate from the transitions at shutdown and restart where the measurements show some peak values. These peak values are not covered due to the smoothed boundary conditions, see Figure 9. The simulated electrical energy generated over the period of 30 h is slightly lower than the energy derived from measurements. However, the deviation is less than two percent.

To further test the applicability of the model, generic boundary conditions are produced for a time period of 30 days. The input data consist of ambient temperature and engine power production. A mean ambient temperature of $19\text{ }^{\circ}\text{C}$ is assumed which corresponds to the long-term average value at Klingnau in July. A diurnal temperature variation of $16\text{ }^{\circ}\text{C}$ as well as some lower frequency variations to mimic changing meteorological conditions is superimposed sinusoidally to this average temperature. The engine is assumed to operate at a rather low power output with small sinusoidal variations in the vicinity of the 45% load. However, the data are chosen in a way that several shutdowns and restarts are triggered either by the ambient temperature and/or engine power criteria. Figure 10 shows the process data that triggers the shutdown and restart as well as the simulated electrical power of the ORC module. Within the first three days the module is shutdown three times due to high ambient temperatures. At day six the engine power output goes slightly below the shutdown limit. However, the lower limit is not infringed long enough to trigger the shutdown. Between day 13 and 16 as well as between day 21 and 22 frequent shutdowns are produced due to the minimum power and/or ambient temperature criteria.

4. DISCUSSION

The question may arise why there are automatic shutdown/restart sequences at all. Besides emergency stops and shutdowns for maintenance reasons there are performance issues. When the heat input to the

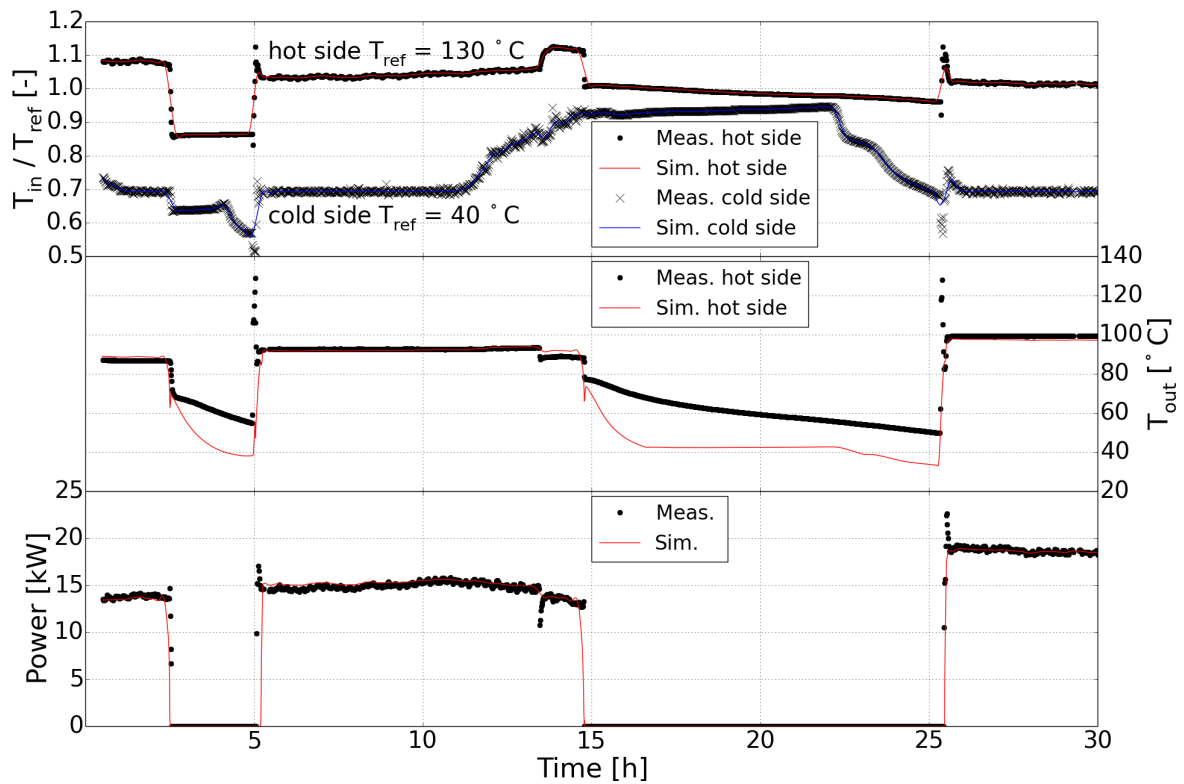


Figure 9: Top: Normalized water temperatures at the evaporator and condenser inlet. Middle: Measured and simulated water temperatures at the evaporator outlet. Bottom: Measured and simulated gross electrical power of the ORC module.

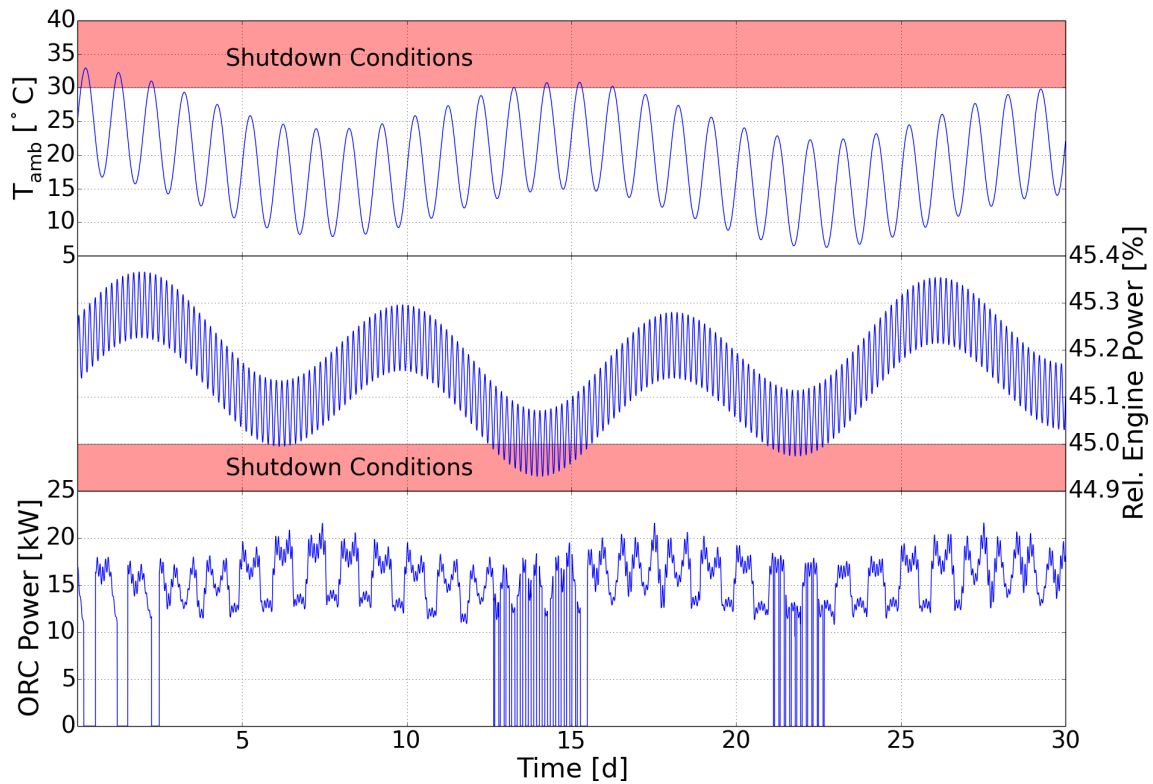


Figure 10: Top: Generically produced ambient temperatures. Middle: Generically produced relative engine power. Bottom: Simulated gross electrical power of the ORC module.

ORC system is low compared to the design point the total efficiency will significantly drop. When the electrical power consumption of the pumps and cooler fans exceed the generated electricity a shutdown may be more beneficial. Wearing concerns may be an other reason, e.g. due to insufficient lubrication of critical parts caused by unfavorable mass flows and pressure ratio at lower part load. Of course, in reality a proper dimensioning of the ORC plant will avoid excessive shutdown/restart cycles. However, operational caused fluctuations of the waste heat supply and/or altered process data due to modifications or a redesign of the main process are very common. Anticipation of such situations during the planning phase of an ORC plant are therefore highly recommended. A corresponding simulation tool helps to assess an expected operation behavior and power output of a future ORC plant by investigating different alternatives. Prior to building the plant the selected system can be tested on a virtual test bed revealing, for example, that a high portion of the operation hours lie within the part load regime with bad efficiency and possibly with many shutdown cycles. This would indicate a suboptimal sizing of the plant and corrective actions can be conducted in the planning rather than the commissioning phase.

The models developed within the scope of this work are a starting point for such a virtual test bed. So far, the investigated system comprises the ORC module only. The models need some further improvements and enhancements before applying them to a real world project. First of all, the ORC module should be expanded to an overall system model including at least peripherals such as exhaust heat exchangers, hot and cold intermediate circuits and air coolers. This allows to assess the overall performance taking into account auxiliary power consumption and the opportunity to derive and test alternative shutdown criteria, e.g. based on the overall performance. The implemented control system is fairly simple and probably not complete. Though the model is not crash-proofed, the simulations work fairly stable. However, more sophisticated control strategy may even improve stability and hopefully improve performance.

For the generic test run presented above the module shut down 30 times. It took about 33 minutes to perform the simulation task with Dymola 2015 FD01 having parallel execution capabilities on multiple cores. The simulations were conducted on a virtual machine assigned four Intel Core i7 processors. The calculation time is acceptable taking into account the many shutdowns, which significantly increase the CPU time. An analogous case was calculated where the ambient temperature and engine power was slightly shifted to avoid any shutdown. The CPU time reduced to about five minutes. The calculation time of an overall system simulation will definitely increase. This will be assessed in a future task.

Overall models may also be used for monitoring purposes. Simulations can be performed online with boundary conditions derived from measurements. Comparing the simulated power output with the measured power may show deviations. Corrective tasks such as cleaning heat exchangers or readjusting control parameters can then be initiated.

5. CONCLUSIONS

The Modelica library ThermoCycle together with the fluid property calculation package CoolProp provide robust and computationally efficient physically based models to simulate ORC systems. These were used to build up a simulation model of the Klingnau ORC plant. This simulation model reproduced the measured electrical power output within a ± 5 % deviation compared to the measured power. The simulated and measured electrical energy generated over the period considered deviated by less than two percent. A simple control strategy allowing for automatic shutdown and restart events was implemented and successfully tested with generic boundary conditions. The control strategy consists of two layers, a state machine and an actual controller comprising several subcontrollers. The state machine keeps track of the current conditions and switches between different control schemes, e.g. for the transition of a running state to a shutdown procedure. Using the Modelica library StateGraph2 proved to be a convenient way to model a corresponding state machine. In particular its graphical representation of the state flow is a valuable feature to test and track online the behavior of the controller and its interaction with the plant.

Finally, enhancing the model to an overall system will make it a viable tool to predict plant behavior and

performance in the planning phase. This ensures a suitable sizing and choice of optimal components. It will also be possible to use the models for optimizing and testing different control strategies as well as for monitoring and assessing the performance of existent plants. In the future, use of such simulation models will reduce the uncertainty when trying to create an economically successful operation and help build the business case on a firm foundation.

REFERENCES

- Bell, I. H., Wronski, J., Quoilin, S., and Lemort, V. (2014). Pure and pseudo-pure fluid thermophysical property evaluation and the open-source thermophysical property library coolprop. *Industrial & Engineering Chemistry Research*, 53(6):2498–2508.
- Casella, F. and Leva, A. (2006). Modelling of thermo-hydraulic power generation processes using Modelica. *Mathematical and Computer Modelling of Dynamical Systems*, 12(1):19–33.
- Casella, F., Mathijssen, T., Colonna, P., and van Buijtenen, J. (2013). Dynamic Modeling of Organic Rankine Cycle Power Systems. *Journal of Engineering for Gas Turbines and Power*, 135(4):042310.
- Casella, F. and Pretolani, F. (2006). Fast Start-up of a Combined-Cycle Power Plant: A Simulation Study with Modelica. In *Proceedings of the 5th International Modelica Conference, Vienna, Austria*, pages 3–10.
- Colonna, P. and van Putten, H. (2007). Dynamic modeling of steam power cycles. *Applied Thermal Engineering*, 27(2-3):467–480.
- Declaye, S., Quoilin, S., Guillaume, L., and Lemort, V. (2013). Experimental study on an open-drive scroll expander integrated into an {ORC} (organic rankine cycle) system with {R245fa} as working fluid. *Energy*, 55(0):173 – 183.
- Erhart, T., v.d. Broek, M., and Eicker, U. (2013). Dynamic Models for a heat-led Organic Rankine Cycle. Presented at the 2nd International Seminar on ORC Power Systems, ASME ORC 2013, Rotterdam, Netherlands.
- Felgner, F., Exel, L., and Frey, G. (2011). Component-oriented ORC plant modeling for efficient system design and profitability prediction. In *Clean Electrical Power (ICCEP), 2011 International Conference on*, pages 196–203.
- Fiorani, P. (2009). *Definition of an object oriented library for the dynamic simulation of advanced energy systems: Methodologies, tools and application to combined ice-orc power plants*. PhD thesis, University of Parma.
- Ireland, M. K., Orosz, M. S., Brisson, J. G., Desideri, A., and Quoilin, S. (2014). Dynamic Modeling and Control System Definition for a Micro-CSP Plant Coupled With Thermal Storage Unit. In *ASME Turbo Expo 2014: Turbine Technical Conference and Exposition*.
- Otter, M., Malmheden, M., Elmqvist, H., Mattsson, S. E., and Johnsson, C. (2009). A New Formalism for Modeling of Reactive and Hybrid Systems. In *Proceedings of the 7th International Modelica Conference, Como, Italy*, pages 364–377.
- Quoilin, S., Bell, I., Desideri, A., Dewallef, P., and Lemort, V. (2014a). Methods to Increase the Robustness of Finite-Volume Flow Models in Thermodynamic Systems. *Energies*, 7(3):1621–1640.
- Quoilin, S., Desideri, A., Bell, I., Wronski, J., and Lemort, V. (2013). Robust and Computationally Efficient Dynamic Simulation of ORC Systems: The ThermoCycle Modelica Library. Presented at the 2nd International Seminar on ORC Power Systems, ASME ORC 2013, Rotterdam, Netherlands.

- Quoilin, S., Desideri, A., Wronski, J., Bell, I., and Lemort, V. (2014b). ThermoCycle: A Modelica library for the simulation of thermodynamic systems. In *Proceedings of the the 10th International Modelica Conference, Lund, Sweden*, pages 683–692.
- Smith, L. P., Dixon, R. R., and Shor, S. W. W. (1983). MODULAR MODELING SYSTEM (MMS): A code for the Dynamic Simulation of Fossil and Nuclear Power Plants. Volume 1: Theory Manual.
- Snidow, N. and Malan, G. (1988). Development and Validation of a Dynamic Model of the Huntington Beach Unit 1 Fossil Power Plant using the Modular Modeling System. *Proceedings of the 1988 Conference on Power Plant Simulators and Modeling*.
- van Putten, H. and Colonna, P. (2007). Dynamic modeling of steam power cycles: Part II – Simulation of a small simple Rankine cycle system. *Applied Thermal Engineering*, 27(14-15):2566–2582.
- Wei, D., Lu, X., Lu, Z., and Gu, J. (2008). Dynamic modeling and simulation of an Organic Rankine Cycle (ORC) system for waste heat recovery. *Applied Thermal Engineering*, 28(10):1216–1224.
- Wetter, M. (2013). Fan and Pump Model That has unique Solution for any Pressure Boundary Condition and Control Signal. In *Proceedings of BS2013: 13th Conference of International Building Performance Simulation Association, Chambéry, France*, pages 3505–3512.

COMPARISON OF MOVING BOUNDARY AND FINITE-VOLUME HEAT EXCHANGER MODELS IN THE MODELICA LANGUAGE

Adriano Desideri^{1*}, Bertrand Dechesne¹, Jorrit Wronski², Martijn van den Broek³, Gusev Sergei³
Sylvain Quoilin¹, Vincent Lemort¹

¹ University of Liège, Thermodynamics laboratory,
Campus du Sart Tilman, Liège, Belgium
adesideri@ulg.ac.be

² Technical University of Denmark, Department of Mechanical Engineering,
Kongens Lyngby, Denmark

³ University of Gent, Department of Flow heat and combustion Mechanics,
Gent, Belgium

* Corresponding Author

ABSTRACT

When modelling low capacity energy systems such as a small (5–150 kW_{el}) organic Rankine cycle unit, the governing dynamics are mainly concentrated in the heat exchangers. As a consequence, accuracy and simulation speed of the higher level system model mainly depend on the heat exchanger model formulation. In particular, the modelling of thermodynamic systems characterized by evaporation or condensation, requires heat exchanger models capable of handling phase transitions. To this aim, the finite volume (FV) and the moving boundary (MB) approaches are the most widely used. The two models are developed and included in the open-source ThermoCycle Modelica library. In this contribution a comparison between the two approaches is performed. Their performance is tested in terms of model integrity and accuracy during transient conditions. Furthermore the models are used to simulate the evaporator of an ORC system and their responses are validated against experimental data collected on an 11 kW_{el} ORC power unit.

1. INTRODUCTION

The crucial role of dynamic modelling tools in tackling the challenges arising from the unsteady operation of complex physical systems has been generally accepted by the scientific community for the simulation of energy systems (Colonna and van Putten, 2007). Dynamic modelling is considered a reliable tool in energy system design, from evaluating and optimizing the system response time to the development and test of different control strategies. In recent years, the open-access language Modelica (Mattsson and Elmqvist, 1997) has been gaining momentum to be used for dynamic modelling of a wide range of dynamic systems. It allows describing continuous and discrete components in a physical way by writing self-consistent sets of casual and acasual equations, that are then transformed by the tool into an optimized set of hybrid differential-algebraic equations. Various libraries are available to model thermodynamic and thermal-hydraulic systems (Casella and Leva, 2005) with a focus on steam and gas cycles (e.g. ThermoSysPro, PowerPlants, ThermalPower, Thermo Power etc.) or refrigeration systems (e.g. TIL, AirConditioning etc.). Some of these libraries are open-access and only few of them are able to handle non-conventional working fluids thermo-physical properties. The authors recently presented ThermoCycle, a Modelica library targeting the modelling of low-capacity systems (Quoilin et al., 2014b). The library aims at providing a robust and efficient fully open-source suite of models for thermoflow systems, ranging from the computation of thermo-physical substance, through the coupling with the open-source CoolProp software (Bell et al., 2014), to the simulation of complex systems

together with their control strategies. When modelling low capacity systems, the governing dynamic is usually mainly concentrated in the heat exchanger (HE). In the particular case of heat exchangers involving two-phase flows, two commonly adopted HE modelling approaches are the finite volume (FV) and the moving boundary (MB) (Bendapudi et al., 2005). Both methods are based on the conservation laws of physics, where the governing dynamics are expressed in form of the conservation laws of energy, mass and momentum over a defined control volume. In a moving boundary model the fluid flow in the HE is divided in as many control volumes as the states (e.g. liquid, two-phase, vapour) in the fluid flow (in this work: from one to three). The control volumes size varies in time during transients, following the saturated liquid and the saturated vapour boundaries. The finite volume approach consists in discretizing the HE volume in a number of equal and constant control volumes. The conservation laws are then applied in each of the control volumes. The MB and FV methods have been applied starting from the late 70's for thermal system modelling (Dhar and Soedel, 1979) (MacArthur and Grald, 1987). The MB approach result in faster but sometimes less robust models (Bendapudi et al., 2005). Comprehensive literatures reviews by Bendapudi (2002), or Bonilla et al. (2015) show that moving boundary models have been proposed in several studies, but remain less common than FV models. A recent work from Bonilla et al. (2015) reports a clear review of the major MB heat exchanger models capable of handling two-phase flow, and presents a moving boundary library developed in the Modelica language for the modelling of direct steam generation parabolic through solar collectors.

This contribution presents a comparison between the MB and FV approaches to model heat exchanger components in a small capacity organic Rankine cycle (ORC) system. To that aim, the two types of heat exchanger model are developed in the Modelica language and are included into the open-source ThermoCycle library. The models are developed following an object oriented approach while minimizing the Modelica inheritance feature as to enhance model readability. In section 2 the modelling approach, the structure and the main characteristic of these models are presented. A comparison between the two approaches is analysed in section 3 in terms of model integrity by checking the mass and energy balance over a defined simulation time, and of model accuracy by comparing the outlet temperature and mass flow rate, considering as a reference a 100-control volumes (CVs) FV model proposed in Quoilin et al. (2014a). The capability of both models to be integrated in a higher level system model is assessed by using both approaches to simulate the evaporator of an organic Rankine cycle (ORC) unit model. In section 4 the ORC model is validated using transient experimental data from an 11 kW_{el} ORC test-rig equipped with a single screw expander. The results are finally summarized in section 5 and some concluding remarks are formulated.

2. HEAT EXCHANGER MODELLING

In this section the finite volume and the moving boundary models developed in the framework of the open-source ThermoCycle Modelica library are presented. The common assumptions considered for both the finite volume and the moving boundary approaches are reported in subsection 2.1. The structure and the governing equations for the MB and the FV models are described in subsection 2.2 and 2.3 respectively.

2.1 Assumptions

The heat exchanger models presented in this work are conceived to be integrated into a system model as one of the various components constituting the thermo-hydraulic system. The following assumptions are considered:

- The fluid flow through a control volume of the heat exchanger is described with a mathematical formulation of the conservation laws of physics: dynamic energy and mass balance, static momentum balance.
- The heat exchanger is considered as a 1-dimensional tube (z-direction) through which the working fluid flows.

- Kinetic energy, gravitational forces and viscous stresses are neglected.
- No work is done on or generated by the control volume.
- The velocity of the fluid is uniform over the cross sectional area (homogeneous two-phase flow).
- Pressure drop through the heat exchanger are neglected (constant pressure).
- The rate of thermal energy addition due to heat conduction is neglected in the fluid.
- The rate of thermal energy exchanged with the ambience by convection is considered.
- Thermal energy accumulation is considered for the metal wall of the tube.
- Thermal energy conduction in the metal wall is neglected in the circumferential and axial (z) direction.

2.2 Finite volume model

The finite volume heat exchanger model is object oriented, its structure being shown in Figure 1a. It is based on the connection of different subcomponents from the ThermoCycle library. Two fluid components simulating the flow of the fluid in the two sides of the heat exchanger and one wall component representing thermal energy accumulation in the metal wall. The conservation law of physics, describing the behaviour of the fluid through the heat exchanger, are derived by integrating the general 1-dimensional form of mass, energy and momentum balance over a constant volume. Considering the above mentioned assumptions, their final formulation for each CV is reported in Equations 1 to 3.

$$\frac{dM}{dt} = \dot{m}_{su} - \dot{m}_{ex} \quad \text{with} \quad \frac{dM}{dt} = V \cdot \left(\frac{\partial \rho}{\partial h} \cdot \frac{dh}{dt} + \frac{\partial \rho}{\partial p} \cdot \frac{dp}{dt} \right) \quad (1)$$

$$V\rho \frac{dh}{dt} = \dot{m}_{su} \cdot (h_{su} - h) - \dot{m}_{ex} \cdot (h_{ex} - h) + V \frac{dp}{dt} + A_1 \cdot \dot{q} \quad (2)$$

$$p_{su} = p_{ex} \quad (3)$$

where $\frac{\partial \rho}{\partial h}$ and $\frac{\partial \rho}{\partial p}$ in Equation 1 are considered to be thermodynamic properties of the fluid and are directly computed by the CoolProp library. The "su" (supply) and "ex" (exhaust) subscripts denote the nodes variable of each cell, A_1 is the lateral surface through which the heat flux \dot{q} is exchanged with the metal wall and V is the constant volume of each cell. Enthalpy and pressure at the center of the control volume are considered as the state variables. Thermal energy accumulation in the metal wall is expressed as:

$$M_w/N \cdot c_w \cdot \frac{dT_w}{dt} = A_{ext} \cdot \dot{q}_{ext} + A_{int} \cdot \dot{q}_{int} \quad (4)$$

where M_w is the total mass of the metal wall, N is the number of cells and c_w is the metal wall specific heat capacity. The secondary fluid is modelled as an incompressible fluid whose density and specific heat capacity are assumed constant within the heat exchanger length. The heat transfer through secondary fluid - wall and wall - working fluid is modelled with Newton's law of cooling. Both central and upwind discretization schemes are supported by the model.

2.3 Moving boundary model

The moving boundary model is developed following the object-oriented principles of abstraction, encapsulation and (limited) inheritance: two basic models are derived representing the fluid flow through a variable control volume in single and two phase state. The connection of these two basic models allows building dry, flooded or general evaporator and condenser models. The enthalpy of the fluid is assumed linear in each region of the tube (sub-cooled, two-phase, super-heated) and is computed as shown in Equation 5.

$$\bar{h} = \frac{1}{2} \cdot (h_a + h_b) \quad (5)$$

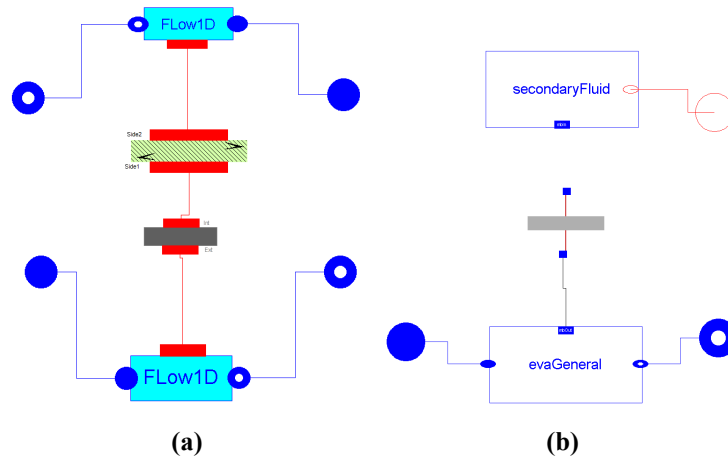


Figure 1: Representation of the finite volume (a) and the moving boundary (b) heat exchanger from the Dymola GUI.

where a and b subscripts denote the left and right boundaries of the region. Given a moving boundary control volume the mass and energy balance are defined by integrating the general conservation laws of physics over the length of the zone, as shown in Equations 6 and 7

$$A \cdot \int_{l_a}^{l_b} \frac{\partial \rho}{\partial t} dz + \int_{l_a}^{l_b} \frac{\partial \dot{m}}{\partial z} dz = 0 \quad (6)$$

$$A \cdot \int_{l_a}^{l_b} \frac{\partial (\rho \cdot h)}{\partial t} dz - A \cdot l \cdot \frac{dp}{dt} + \int_{l_a}^{l_b} \frac{\partial (h \cdot \dot{m})}{\partial z} dz = dl \cdot Y \cdot \dot{q} \quad (7)$$

where A is the cross sectional area, l_a and l_b are the lengths of the left and right boundaries of the region and Y is the channel perimeter. Assuming a constant pressure, the momentum balance is represented by Equation 3. As far as the one-phase region is concerned, the mass balance is derived solving Equation 6 by applying Leibniz rule to the first term and using the mean-value theorem such that the rate of mass flow change results in:

$$\frac{d}{dt} \int_{l_a}^{l_b} \rho dt = \frac{d}{dt} (\bar{\rho} \cdot l) \quad (8)$$

the mass balance for a one-phase region is equal to:

$$A \cdot \left[\bar{\rho} \cdot \frac{dl}{dt} + l \cdot \frac{d\bar{\rho}}{dt} - \rho_a \cdot \frac{dl_a}{dt} + \rho_b \cdot \frac{dl_b}{dt} \right] = \dot{m}_a - \dot{m}_b \quad (9)$$

where $\bar{\rho}$ is the average density of the region computed as a function of the pressure and of the average specific enthalpy, $\bar{\rho} \approx f(\bar{h}, p)$, l is the length of the region and $\frac{d\bar{\rho}}{dt}$ is calculated as:

$$\frac{d\bar{\rho}}{dt} = \frac{\partial \bar{\rho}}{\partial p} \cdot \frac{dp}{dt} + \frac{\partial \bar{\rho}}{\partial \bar{h}} \cdot \frac{d\bar{h}}{dt} = \frac{\partial \bar{\rho}}{\partial p} \cdot \frac{dp}{dt} + \frac{1}{2} \cdot \frac{\partial \bar{\rho}}{\partial \bar{h}} \cdot \left(\frac{dh_a}{dt} + \frac{dh_b}{dt} \right) \quad (10)$$

where $\frac{dh_{b/a}}{dt}$ are defined based on Equations 11 to 14 reported in Table 1. The energy balance is derived from equation Equation 7. Applying Leibniz rule to the first term and using the mean-value theorem allows to define the rate of energy change as:

$$\frac{d}{dt} \int_{l_a}^{l_b} (\rho \cdot h) dz = \frac{d}{dt} (\bar{\rho h} \cdot l) \approx \frac{d}{dt} (\bar{\rho} \cdot \bar{h} \cdot l) \quad (15)$$

with $\bar{\rho h} \approx \bar{\rho} \cdot \bar{h}$. The energy balance for the one-phase region results in:

$$A \cdot \left[\bar{\rho h} \frac{dl}{dt} + \bar{h} l \frac{d\bar{\rho}}{dt} + \bar{\rho} l \frac{d\bar{h}}{dt} + (\rho_a h_a) \cdot \frac{dl_a}{dt} - (\rho_b h_b) \cdot \frac{dl_b}{dt} \right] - A \cdot l_a \cdot \frac{dp}{dt} = \dot{m}_a \cdot h_a - \dot{m}_b \cdot h_b + \dot{Q} \quad (16)$$

Table 1: Specific boundary enthalpy derivative depending on the heat transfer and control volume.

	Evaporator	Condenser
Sub-cooled	$\frac{dh_b}{dt} = \frac{\partial h_l}{\partial p} \frac{dp}{dt}$ (11)	$\frac{dh_a}{dt} = \frac{\partial h_l}{\partial p} \frac{dp}{dt}$ (12)
Super-heated	$\frac{dh_a}{dt} = \frac{\partial h_v}{\partial p} \frac{dp}{dt}$ (13)	$\frac{dh_b}{dt} = \frac{\partial h_v}{\partial p} \frac{dp}{dt}$ (14)

In the two-phase region, the assumption of homogeneous two-phase flow condition allows to express the mean density as a function of the average void fraction $\bar{\gamma}$ as:

$$\bar{\rho} = (1 - \bar{\gamma}) \rho_l + \bar{\gamma} \rho_v \quad (17)$$

where the average void fraction is calculated integrating the local void fraction γ over the length of the region. $\bar{\gamma}$ is an indicator of the fraction of the total volume of the region occupied by fluid in vapour phase (Jensen, 2003). Substituting Equation 17 into Equation 8 and solving Equation 6 results in the mass balance for the two phase region:

$$A \left[((1 - \bar{\gamma}) \rho_l + \bar{\gamma} \rho_v) \frac{dl}{dt} + l \left((\rho_v - \rho_l) \frac{d\bar{\gamma}}{dt} + \bar{\gamma} \frac{d\rho_v}{dp} \frac{dp}{dt} + (1 - \bar{\gamma}) \frac{d\rho_l}{dt} \right) - \rho_a \frac{dl_a}{dt} + \rho_b \frac{dl_b}{dt} \right] = \dot{m}_a - \dot{m}_b \quad (18)$$

The energy balance for the two phase region is obtained from Equation 7 using Equations 17 and 15:

$$\begin{aligned} A \left[((1 - \bar{\gamma}) \rho_l h_l + \bar{\gamma} \rho_v h_v) \frac{dl}{dt} + l \left((\rho_v h_v - \rho_l h_l) \frac{d\bar{\gamma}}{dt} + \bar{\gamma} h_v \frac{\partial \rho_v}{\partial p} \frac{dp}{dt} + \bar{\gamma} \rho_v \frac{\partial h_v}{dp} \frac{dp}{dt} \right. \right. \\ \left. \left. + (1 - \bar{\gamma}) h_l \frac{\partial \rho_l}{dp} \frac{dp}{dt} + (1 - \bar{\gamma}) \rho_l \frac{\partial h_l}{\partial p} \frac{dp}{dt} \right) + (\rho_a h_a) \frac{dl_a}{dt} - (\rho_b h_b) \frac{dl_b}{dt} \right] - A \cdot l \cdot \frac{dp}{dt} \\ = \dot{m}_a h_a - \dot{m}_b h_b + \dot{Q} \end{aligned} \quad (19)$$

The option of imposing a constant average void fraction, i.e. $\frac{d\bar{\gamma}}{dt} = 0$, is supported by the model. The MB with constant void fraction is abbreviated as MBConstVF. The effect of such an assumption is analysed in section 4. The thermal energy balance in the metal wall for each control volume is expressed as:

$$\rho_w c_w A_w \frac{\partial T_w}{\partial t} = dl \cdot Y \cdot \dot{q}_{wf} + dl \cdot Y \cdot \dot{q}_{sf} \quad (20)$$

Applying Leibniz rule and solving the integral results in:

$$\rho_w c_w A_w \left[\frac{d}{dt} \int_{l_a}^{l_b} \partial T_w dz + T_w(l_b) \frac{dl_b}{dt} - T_w \left(l_a \frac{dl_a}{dt} \right) \right] = \dot{Q}_{wf} + \dot{Q}_{sf} \quad (21)$$

In order to simplify the resolution of the model, no energy, mass and momentum accumulation is considered in the secondary fluid. A linear temperature distribution is assumed and the thermal energy transfer with the metal wall is solved either with the semi-isothermal ε -NTU method or with Newton's law of cooling.

3. MODEL INTEGRITY

In this section a comparison between the FV and MB approach is performed with the aim of testing the model accuracy and integrity. The accuracy is defined as the agreement of the model-predicted output values with a reference system. The integrity is defined as the capacity of the model of respecting the

conservation of energy and mass. The FV and MB evaporator models are subjected to inlet enthalpy and pressure variations, whose value is limited to avoid any back-flow or any phase change at the working fluid outlet. The boundary conditions for pressure and enthalpy are defined in Equations 22 and 23.

$$p = 8.04 + 0.2 \cdot \sin(0.1 \cdot 2\pi \cdot t) \text{ [bar]} \quad (22)$$

$$h_{\text{su}} = 0.11 \cdot 10^5 + 0.2 \cdot 10^5 \cdot \sin(0.2 \cdot 2\pi \cdot t) \text{ [J/kg]} \quad (23)$$

The FV heat exchanger model is discretized using the upwind method and simulations are performed considering 10, 20, 40 and 100 CVs. The medium selected for these simulations is Solkatherm (SES36). The simulation is initialized in steady-state and lasts 625 seconds. The numerical solver is the DASSL and the relative tolerance is set to 10^{-4} . The integrity of the models is investigated by calculating the energy and mass balances over the whole simulation time for each model unit. The energy balance over each heat exchanger model is computed as:

$$\varepsilon_{\text{ener}} = \frac{(E_{\text{ext}} + E_{\text{su}} - E_{\text{ex}} - \Delta U)_{\text{wf}} + (E_{\text{ext}} + E_{\text{su}} - E_{\text{ex}} - \Delta U)_{\text{sf}} + (E_{\text{inlet}} - E_{\text{outlet}} - \Delta U)_{\text{wall}}}{E_{\text{ext,sf}}} \quad (24)$$

where E_{ext} is the overall thermal energy exchanged due to heat convection through the lateral surface, $E_{\text{ex/su}}$ is the total energy into/out of the system due to leaving/entering mass flow rate and ΔU is the total net increase of energy. They are calculated in Equation 25.

$$E_{\text{ext}} = \int_0^t \dot{Q} dt, \quad E_{\text{ex/su}} = \int_0^t \dot{m}_{\text{ex/su}} \cdot h_{\text{ex/su}} dt, \quad \Delta U = \int_0^t (U_{\text{final}} - U_{\text{init}}) dt \quad (25)$$

The conservation of mass is checked on the working fluid side as:

$$\varepsilon_{\text{mass}} = \sum_{i=1}^n \frac{M_{\text{ex}} - M_{\text{su}} - \Delta M}{M_{\text{su}}} \quad (26)$$

where $M_{\text{ex/su}}$ is the overall mass leaving/entering the system and ΔM is the net change in mass. Their values are computed using Equation 27.

$$M_{\text{ex/su}} = \int_0^t \dot{m}_{\text{ex,su}} dt \quad \Delta M = \int_0^t (V\rho_{\text{final}} - V\rho_{\text{init}}) dt \quad (27)$$

The accuracy of the models is investigated by comparing the model output enthalpy and mass flow rate with respect to a reference system, using as mathematical indicator the mean percentage relative error, $\bar{\varepsilon}$, defined in Equation 28. In this case the finite volume model with 100 CVs is taken as a reference.

$$\varepsilon(j) = 100 \cdot \frac{|X_s(j) - X_{\text{ref}}(j)|}{X_{\text{ref}}(j)} \quad \varepsilon = \sum_{j=1}^n |\varepsilon(j)| \quad \bar{\varepsilon} = \frac{\varepsilon}{n} \quad j \in [1, n]. \quad (28)$$

where $X_s(j)$ and $X_{\text{ref}}(j)$ are the j th sampled simulation and reference value of the selected variable and n is the number of sampling. Table 2 reports the benchmarking indicators for the integrity and accuracy simulations for the MB and FV models. The error on conservation of mass and energy balance is kept low by all the considered models. As expected the computational time increases exponentially with the increase of the number of CVs in the FV model. The MB approach results three order of magnitude faster than the finite volume with 100 CVs, allowing to maintain a good accuracy with respect to the 100 CVs FV model in terms of outlet mass flow and outlet enthalpy as the mean PRE value show. In Figure 2, the temperature profile for heat transfer calculation for the MB and FV model is depicted.

4. VALIDATION

In this section, the integration of the FV and MB heat exchanger models into a larger system model is validated against transient experimental data recorded on a 11 kW_{el} ORC unit. In subsection 4.1, the ORC test rig used to collect the experimental data is presented. subsection 4.2, reports a brief description of the different dynamic model components used to represent the whole ORC system. In subsection 4.3 the validation results are analysed.

Table 2: Benchmarking indicators for the integrity and accuracy test for the moving boundary and the finite volume models.

Model	MBConstVF	MB	FV 10 CVs	FV 20 CVs	FV 40 CVs	FV 100 CVs
$\varepsilon_{\text{mass}}$ [%]	$2.33 \cdot 10^{-13}$	$1.08 \cdot 10^{-12}$	$1.72 \cdot 10^{-13}$	$6.33 \cdot 10^{-13}$	$3.06 \cdot 10^{-14}$	$1.01 \cdot 10^{-12}$
$\varepsilon_{\text{ener}}$ [%]	$6.67 \cdot 10^{-12}$	$9.51 \cdot 10^{-12}$	$5.28 \cdot 10^{-12}$	$2.89 \cdot 10^{-12}$	$4.64 \cdot 10^{-12}$	$1.04 \cdot 10^{-12}$
$\bar{\varepsilon} h_{\text{ex}}$ [%]	0.55	0.69	3.16	1.06	0.31	0.0
$\bar{\varepsilon} \dot{m}_{\text{ex}}$ [%]	3.88	1.40	5.52	1.85	0.53	0.0
Time [s]	0.65	0.73	2.89	13.7	34.8	147

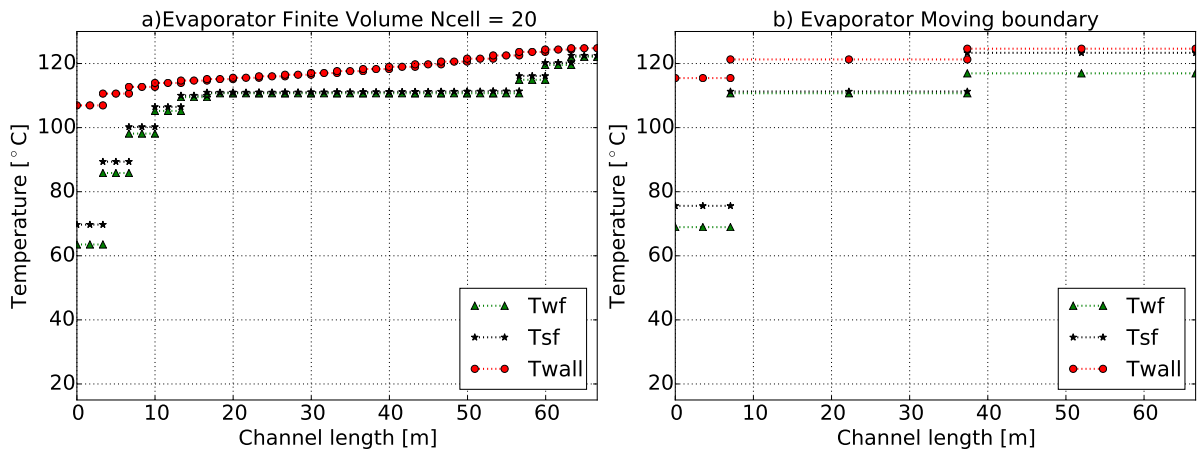


Figure 2: Temperature profile for heat transfer calculation in the finite volume and the moving boundary model. Each segment corresponds to one control volume.

4.1 ORC test rig facility

The ORC set-up used to acquire the experimental data for dynamic model validation is depicted in Figure 3a. The system is equipped with a single screw expander with a nominal shaft power of 11 kW. The same brazed plate heat exchanger type is used for the evaporator, recuperator and condenser. SES36 is the selected working fluid. Sensors are placed at the inlet and at the outlet of each ORC unit component. For further information on the test-rig, the range and the precision of the measurement devices the interested reader can refer to (Desideri et al., 2015).

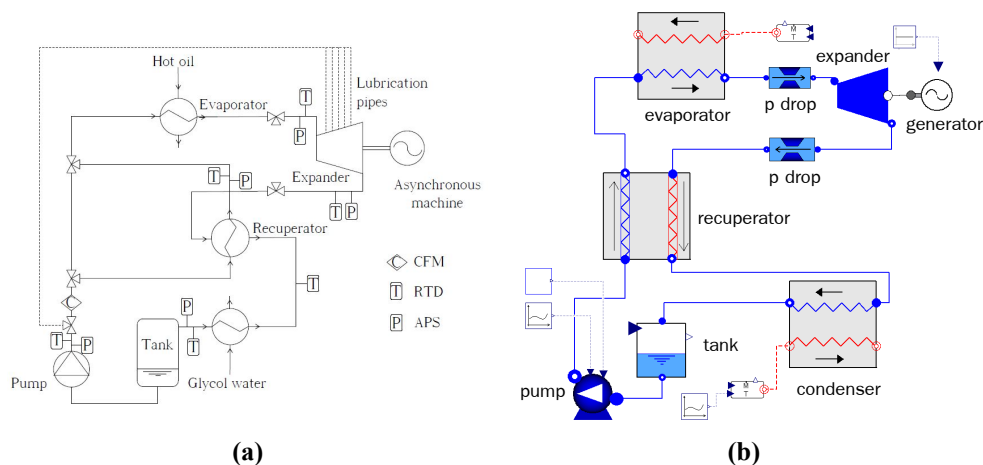


Figure 3: Process flow diagram of the ORC with sensors position (a). ORC system model from the Modelica-Dymola GUI.

4.2 ORC system modelica model

When modelling a low-capacity power unit, since the time constants characterizing the expansion and compression processes are small compared to those of the heat exchangers, semi-empirical (or lumped parameter) steady-state models can be used to simulate the expander and the pump components. The expansion machine is modelled by its effectiveness, expressed with a formulation proposed by Declaye et al. (2013), and the filling factor. The pump model is based on two empirical correlations, one for the effectiveness as a function of the pressure ratio and the pump speed, and one for the delivered mass flow rate as a function of the pump speed. The empirical coefficients for the different performance curves have been derived based on the acquired measurements of the test unit. A more detailed description of this process together with the values of the coefficients is reported in Desideri et al. (2014). The tank at the condenser outlet is modelled assuming thermodynamic equilibrium at all times and accounting for mass and energy accumulation. A lumped approach is applied for pressure drop modelling. Two pressure drop components are placed at the lowest vapour density part of both the low and high pressure lines accounting for laminar and turbulent phenomena. Finally the recuperator and the condenser components are modelled with the finite volume model. The evaporator is modelled using both the finite volume and the moving boundary to investigate the difference between the two approaches at a system level. The ORC model layout is shown in Figure 3b from the Modelica-Dymola graphical user interface.

4.3 Model validation

The transient response of the ORC unit is investigated by applying a downward step of 5 Hz to the pump rotational speed starting from a steady-state condition. The effectiveness of the finite volume and the moving boundary model is checked by replicating the pump step change experiment on the developed Modelica ORC model, using as an evaporator the finite volume and the moving boundary model. The

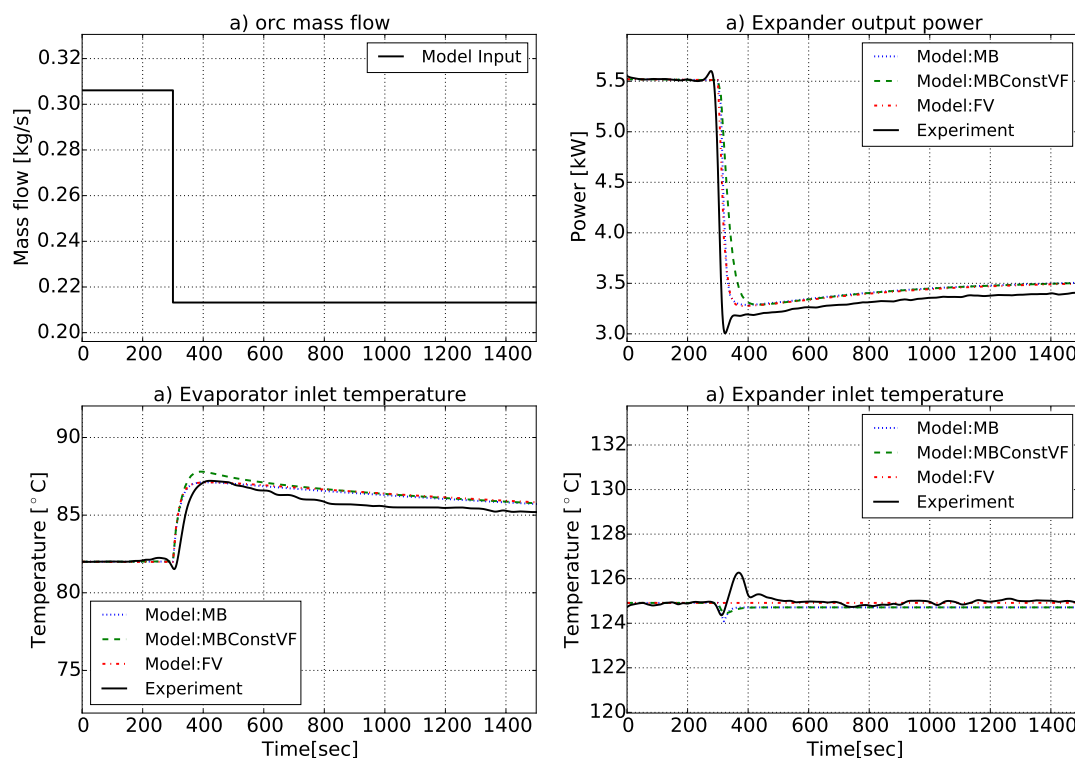


Figure 4: Downward-Upward 5 Hz step change to the pump rotational speed.

results are shown in Figure 4. The step down happens at $t=300$ seconds. Both models are able to well replicate the dynamics characterizing the system. It is interesting to note that when the void fraction is kept constant in the MB model, MBConstFV, the response of the model is slower compared to that of the real unit. This is explained by the fact that when the mass flow decreases the void fraction increases as

the portion of area occupied by the gas increases. As a consequence the thermal capacity decreases and this results in faster transients. Keeping the void fraction constant neglect such a phenomena resulting in a too slow response. It also results in a poor prediction of the outlet flow rate variations during transients.

5. CONCLUSIONS

In this work a comparison between the finite volume and moving boundary approach to model an evaporator is proposed. An integrity and stability test for each approach has been performed taking as benchmarking indicator the simulation speed, the conservation of mass and energy and the mean percentage relative error, $\bar{\epsilon}$, for outlet enthalpy and mass flow rate with respect to a 100 CVs finite volume. The FV and MB models are used in the Modelica model of an ORC system to simulate the evaporator component. The transient response of the model is compared against experimental results. The main outcomes of this study are summarized hereunder:

- The integrity test results allow to conclude that both the MB and FV approaches are well suited for modelling dynamic heat exchanger being characterized by a low error on the total conservation of energy and mass. Further, the MB is 3 orders of magnitude faster compared to a finite volume with a 100 CVs.
- The comparison against experimental transients demonstrates that the assumptions of constant void fraction in the MB approach overestimate the dynamics (i.e. leads to slower response times) making it unsuitable for modelling small capacity heat exchanger.

The proposed MB and FV models together with the test cases are open source and are available in the latest version of the ThermoCycle library. An experimental campaign focusing on the investigation of the specific dynamics characterizing the evaporator and condenser components is planned. The recorded data will be used to perform a more detailed validation of the FV and MB approach for modelling small capacity heat exchangers.

NOMENCLATURE

FV	Finite volume	T	Temperature	(°C)
MB	Moving boundary	t	Time	(sec)
CV	Control volume	l	Control volume length	(m)
n	samples time	ρ	Density	(kg.m ⁻³)
		\dot{m}	Mass flow rate	(kg.s ⁻¹)
Subscript		h	Specific enthalpy	(kJ.kg ⁻¹)
ex	Exit	E	Energy	(kJ)
su	Supply	U	Internal energy	(kJ)
ext	External	\dot{Q}	Thermal power	(kW)
v	Saturated vapor state	\dot{q}	heat flux	(kW.m ⁻¹)
l	Saturated liquid state	Y	Channel perimeter	(m)
		\dot{m}	Mass flow	(kg.s ⁻¹)
Symbols		γ	Void fraction	
p	Pressure	(bar)	ϵ	Relative error

REFERENCES

I.H. Bell, J. Wronski, S. Quoilin, and V. Lemort. Pure- and pseudo-pure fluid thermophysical property evaluation and the open-source thermophysical property library CoolProp. *Industrial & Engineering Chemistry Research*, 53:2498–2508, 2014.

- S. Bendapudi. A literature review of dynamic models of vapor compression equipment. Technical report, Herrick Laboratories, Purdue University, 2002.
- S. Bendapudi, J. Braun, E. Groll, and A. Eckhard. Dynamic model of a centrifugal chiller system—model development, numerical study and validation. *ASHRAE*, 2005.
- Javier Bonilla, Sebastian Dormido, and Francois E. Cellier. Switching moving boundary models for two-phase flow evaporators and condensers. *Communications in Nonlinear Science and Numerical Simulation*, 20(3):743–768, 2015. ISSN 1007-5704.
- F. Casella and A. Leva. Object-oriented modelling & simulation of power plants with modelica. In *Proceedings of the 44th IEEE Conference on Decision and Control, and the European Control Conference*, 2005.
- P. Colonna and H. van Putten. Dynamic modeling of steam power cycles.: Part I—modeling paradigm and validation. *Applied Thermal Engineering*, 27(2–3):467–480, 2007. ISSN 1359-4311.
- Sebastien Declaye, Sylvain Quoilin, Ludovic Guillaume, and Vincent Lemort. Experimental study on an open-drive scroll expander integrated into an ORC (organic Rankine cycle) system with R245fa as working fluid. *Energy*, 55(0):173–183, 2013. ISSN 0360-5442.
- A. Desideri, M. v. d. Broek, S. Gusev, V. Lemort, and S. Quoilin. Experimental campaign and modeling of a low-capacity waste heat recovery system based on a single screw expander. In *22nd International compressor engineering conference at Purdue*, 2014.
- A. Desideri, S. Gusev, M. v.d. Broek, V. Lemort, and S. Quoilin. Experimental comparison of organic fluids for low temperature ORC systems for waste heat recovery applications. *Energy Submitted for publications*, xx:xx, 2015.
- M. Dhar and W. Soedel. Transient analysis of a vapor compression refrigeration system. In *In proceedings of the XV International Congress of Refrigeration*, Venice, 1979.
- Jakob Munch Jensen. *Dynamic Modeling of Thermo-Fluid Systems*. PhD thesis, Technical University of Denmark, 2003.
- J.W. MacArtur and E.W. Grald. Prediction of cyclic heat pump performance with a fully distributed model and a comparison with experimental data. *ASHRAE Transactions*, 93(2):1159–1178, 1987.
- S.E. Mattsson and H. Elmqvist. Modelica - an international effort to design the next generation modeling language. In *Proceedings of the 7th IFAC Symposium on Computer Aided Control Systems Design*, 1997.
- S. Quoilin, I. H. Bell, A. Desideri, P. Dewallef, and V. Lemort. Methods to Increase the Robustness of Finite-Volume Flow Models in Thermodynamic Systems. *Energies*, 7:1621–1640, 2014a.
- S. Quoilin, A. Desideri, J. Wronski, I. H. Bell, and V. Lemort. ThermoCycle: A Modelica library for the simulation of thermodynamic systems. In *Proceedings of the 10th International Modelica Conference*, 2014b.

ACKNOWLEDGEMENT

The results presented in this paper have been obtained within the frame of the IWT SBO-110006 project The Next Generation Organic Rankine Cycles (www.orcnext.be), funded by the Institute for the Promotion and Innovation by Science and Technology in Flanders. This financial support is gratefully acknowledged.

ORCSIM: A GENERALIZED ORGANIC RANKINE CYCLE SIMULATION TOOL

Davide Ziviani^{1*}, Brandon J. Woodland², Emeline Georges³, Eckhard A. Groll, James E. Braun², W. Travis Horton², Michel De Paepe¹, Martijn van den Broek¹

¹ Gent University, Department of Flow, Heat and Combustion Mechanics,
Gent, Belgium

davide.ziviani@ugent.be, michel.depaepe@ugent.be, martijn.vandenbroek@ugent.be

² Purdue University, School of Mechanical Engineering, Ray W. Herrick Laboratories,
West Lafayette, Indiana, U.S.A.

bwoodlan@purdue.edu, groll@purdue.edu, jbraun@purdue.edu, wthorton@purdue.edu

³ University of Liege, Aerospace and mechanical Engineering Department, Energy Systems,
Liege, Belgium

emeline.georges@ulg.ac.be

* Corresponding Author

ABSTRACT

An increasing interest in organic Rankine cycle (ORC) technology has led to numerous simulation and optimization studies. In the open-literature different modeling approaches can be found, but general software tools available to the academic/industrial community are limited. A generalized ORC simulation tool, named ORCSim, is proposed in this paper. The framework is developed using object-oriented programming that easily allows improvements and future extensions. Currently two cycle configurations are implemented, i.e. a basic ORC and an ORC with liquid-flooded expansion. The software architecture, the thermo-physical property wrappers, the component library and the solution algorithm are discussed with particular emphasis on the ORC with liquid-flooded expansion. A thorough validation both at component and cycle levels is proposed by considering the aforementioned cycle architectures.

1. INTRODUCTION

An Organic Rankine cycle (ORC) is considered one of the most suitable systems to recover waste heat as well as to exploit renewable heat sources such as solar and geothermal. Although the technology is known, the optimization of such a system remains a key focus of ongoing research. Fluid selection, characterization of the cycle components and overall cycle analyses are a few of the common areas that researchers continue to explore (Quoilin et al., 2010; Woodland et al., 2014). In this context, a general ORC simulation framework, called ORCSim, is proposed to analyze such systems both at component and cycle levels. The cycle simulation is composed of a library of detailed models of each of the system components. While the general layout of the simulation tool and a brief introduction to the models of the components are outlined in Ziviani et al. (2015b), the present work focuses on a demonstration of the versatility of the tool. It can be applied to systems operating with different components, different working fluids and different hot/cold sources. Two ORC system architectures are considered in order to carry out a thorough validation, i.e. a standard ORC running with R245fa and an ORC with liquid-flooded expansion and internal regeneration, with R134a as the working fluid. In particular, the plate heat exchanger and expander models are described in detail because they present the highest level of complexity among the cycle components. An individual validation of these component models is also presented. The cycle simulation algorithm is explained along with the thermo-physical property routines. Finally, cycle simulations are carried out to validate the tool against experimental data.

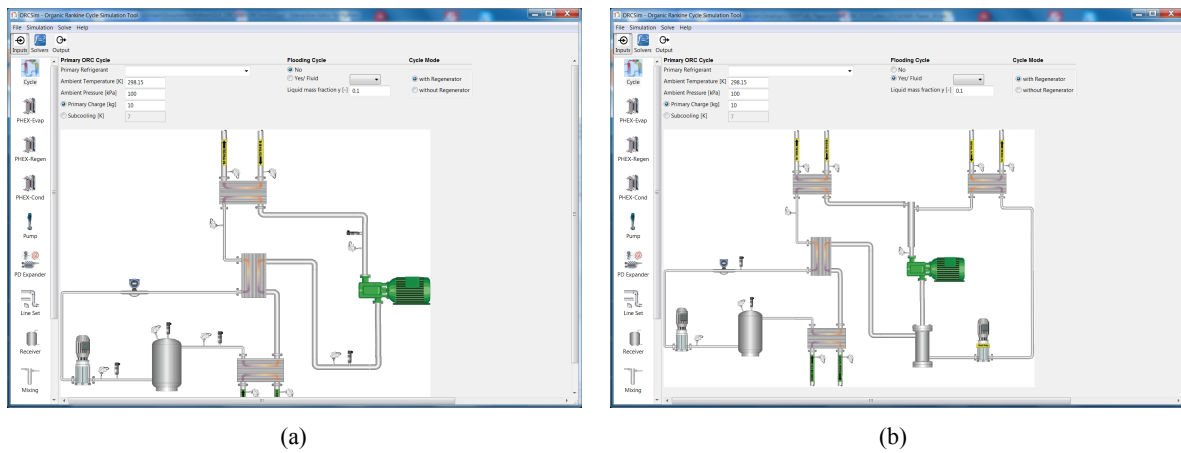


Figure 1: (a) ORC;(b) ORCLFE.

2. ORCSIM ARCHITECTURE

ORCSim is a Python-based simulation tool which takes full advantage of the object-oriented programming environment. Its architecture and solution scheme were originally derived from the open source software for air conditioners and heat pumps, ACHP¹. The first adaptation into an ORC simulation tool can be found in Georges (2012). The modularity of the code results in a flexible tool which allows the user to select not only the cycle configuration but also the desired type of model for each component. The graphical user interface (GUI) is shown in Fig. 1. Two cycle architectures are currently available and both are limited to subcritical applications: (i) standard organic Rankine cycle with/without internal regeneration, Fig. 1(a); (ii) organic Rankine cycle with liquid-flooded expansion and internal regeneration (Woodland et al., 2013), Fig. 1(b). The details of the GUI are described in Ziviani et al. (2015b).

2.1 Thermo-physical properties

In order to cover several ORC applications, the working fluid library has to be extensive, including both pure or pseudo-pure fluids as well as mixtures. Furthermore, many applications require thermal oils or other liquid heat transfer fluids to serve as the ORC heat source. The open-source thermo-physical property library CoolProp (Bell et al., 2014) has been used as the main source to retrieve properties for the wide range of refrigerants and incompressible fluids that may be used in ORC applications. This library implements the most accurate equations of state available in the literature, as well as highly efficient tabular interpolation methods to speed up property calculations. CoolProp can also be used as an interface layer around REFPROP (Lemmon et al., 2013). In this way, it is possible to make use of most of the features implemented in REFPROP as well as in CoolProp. A separate routine has been developed to compute the properties of the flooding mediums, typically lubricant oils, and of homogeneous mixtures of refrigerant and flooding mediums.

2.2 Pre-conditioning and cycle solver

The individual components of the ORC system are connected together in a cycle model. The solution of a simulation is initialized with a pre-conditioner, which calculates the first set of guesses of the evaporating and condensing temperatures and other required parameters. The pre-conditioner is basically equivalent to the main cycle to be solved with simplified models for the plate heat exchangers and expander. After the pre-conditioning loop is completed, the main solver drives three residuals to zero using a multi-variable Newton-Raphson algorithm. Two of these residuals are an overall energy balance and a conservation of mass flow rate between the pump and expander. Pressure drops through the system lines and heat exchangers are neglected so a momentum balance residual is not needed. The general form of

¹The ACHP website is at <http://achp.sourceforge.net>.

the overall energy balance, which also includes the flooding loop, is given by:

$$\dot{W}_{pp,r} + \dot{Q}_{ev,r} + \dot{W}_{pp,oil} + \dot{Q}_{ev,oil} - \dot{W}_{exp} - \dot{Q}_{cd,r} = 0 \quad (1)$$

The third residual is the total mass of refrigerant in the system. The user can select whether this residual is minimized directly, by specifying the total system charge, or indirectly, by specifying the condenser exit subcooling. The validations proposed in this paper are limited to the cases in which subcooling is imposed. Additional details regarding the solution scheme can be found in Ziviani et al. (2015b).

3. PLATE HEAT EXCHANGER MODEL

Only plate heat exchangers (PHEX) are considered in the current version because they are a common choice for waste heat recovery. The model is based on a moving-boundary approach and a validation is proposed for both evaporating and condensing streams.

3.1 Moving Boundary approach

An efficient moving-boundary algorithm is implemented to simulate the steady-state behavior of the heat exchangers. The model is based on the algorithm proposed by Bell et al. (2015). This model can accommodate evaporator and condenser duty, as well as cascade duty heat exchangers, in which phase-change occurs in both fluid streams. The model is robust and guarantees that the temperature profiles are physically-possible. The PHEX is modeled as a counterflow heat exchanger with two streams, i.e. hot and cold, separated by a wall. By imposing the inlet states of both streams and the geometric parameters, the algorithm determines the maximum possible heat transfer rate corresponding to 100% effectiveness. Then, the heat transfer rate is decreased due to internal pinch points, allowing for the possibility of phase change in both streams. The actual heat transfer rate is obtained iteratively by using a numerical solver with proper physical boundaries, i.e. the heat exchanger is divided into a number of zones corresponding to a phase, i.e. liquid, vapor or two-phase. The residual function to be driven to zero is given by,

$$r(\dot{Q}) = 1 - \sum_j w_j = 1 - \sum_j \frac{A_{req,j}}{A_h} \quad (2)$$

where w_j represents the j -fraction of the total heat exchanger length predicted from each zone. The correct solution is achieved once the sum of the length fractions of all the zones is equal to unity. The current model is suitable for sub-critical conditions only and the internal pressure drops are neglected. An extension has been added in the code with respect to Bell et al. (2015), to allow incompressible fluids, i.e. thermal oils, to be used as a heat source. In the solution process, if an incompressible fluid is selected, the algorithm excludes vapor and two-phase zones from the possible combinations by forcing the subcooled phase to be used. Thus, numerical artifacts have been added to eliminate the dependency on vapor quality.

4. EXPANDER MODEL

Different types of expander models have been included within the simulation frame: (i) an empirical model based on the Pacejka equation (for dry expansion only); (ii) a semi-empirical model based on the physics of the expander. Both models have been described and validated by the authors (Georges, 2012; Ziviani et al., 2015a) for a scroll and single-screw expanders under dry running conditions. In the following, the semi-empirical model is extended in order to allow for the liquid-flooded expansion process. The extension of the semi-empirical model to allow for liquid flooding, as well as the experimental data for a liquid-flooded scroll expander, were originally presented in (Georges, 2012). By considering the oil as an incompressible fluid and by assuming mechanical and thermal equilibrium between the refrigerant and the oil, the model is adapted by introducing a liquid fraction, i.e. ratio of the oil mass flow rate to the refrigerant mass flow rate, that accounts for different flooding ratios, $y_{oil} = \dot{m}_{oil}/\dot{m}_r$.

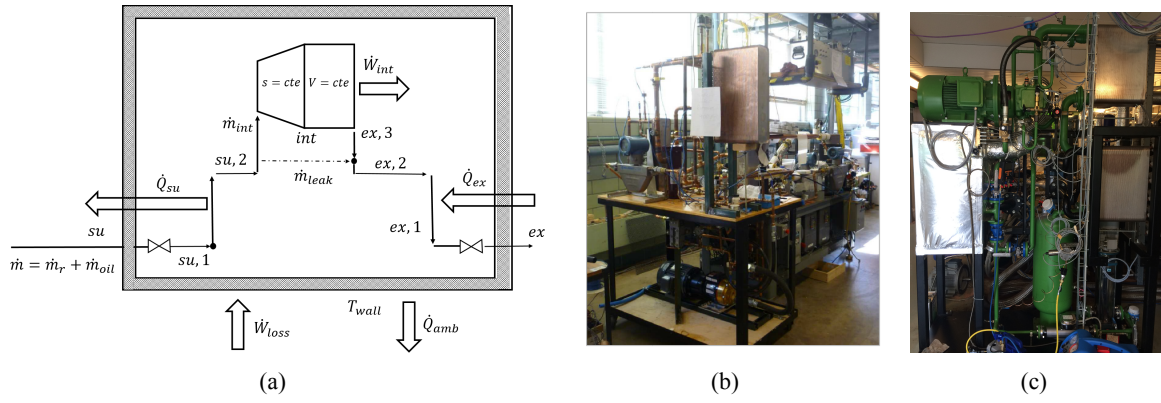


Figure 2: (a) Schematic of the semi-empirical model; (b) ORCLFE at Ray W. Herrick Laboratories, Purdue University; (c) ORC at UGent, Campus Kortrijk.

An effective built-in volume ratio, $r_{v,int}^*$, is defined due to the presence of oil in the expansion chamber:

$$r_{v,int}^* = \frac{r_{v,int} - a}{1 - a}, \quad (3)$$

where $a = \dot{V}_{oil,su} / \dot{V}_{dis,exp}$ is the fraction of the expander displacement volume that is occupied by oil. By considering the schematic proposed in Fig. 2(a), the expansion process is split into two steps, i.e. isentropic and constant volume, linked by a common internal state point. In particular, the isentropic step is computed by keeping the specific entropy of the mixture constant:

$$s_{m,int} = s_{m,su2} = s_{r,int} + x_{oil} s_{oil,int} = s_{r,int} + \left(\frac{\dot{m}_{oil}}{\dot{m}_r - \dot{m}_{leak}} \right) s_{oil,int} \quad (4)$$

where a new mass ratio, x_{oil} , has to be introduced to account for the internal leakage i.e. $\dot{m}_{r,int} = \dot{m}_r - \dot{m}_{leak}$ and the presence of oil. The internal isentropic work and the work at constant volume are expressed by:

$$\begin{aligned} w_{int,s} &= h_{r,su2} - h_{r,int} + x_{oil} (h_{oil,su2} - h_{oil,int}) \\ w_{int,V} &= (p_{r,int} - p_{r,ex2}) (v_{r,int} + x_{oil} v_{oil,su2}) \end{aligned} \quad (5)$$

The overall definition of the isentropic effectiveness is then given by:

$$\epsilon_{exp,s} = \frac{\dot{m}_{r,int} (w_{int,s} + w_{int,V}) - \dot{W}_{loss}}{\dot{m}_r [h_{r,su} - h_{r,ex,s} + y_{oil} (h_{oil,su} - h_{oil,ex,s})]}, \quad (6)$$

where the mechanical losses \dot{W}_{loss} are computed in the model as described in Ziviani et al. (2015a).

5. ORCSIM VALIDATION

The validation of the simulation tool has been carried out by considering two different ORC systems, shown in Fig. 2. The first one, Fig. 2(b), is an ORC with liquid-flooded expansion and internal regeneration (ORCLFE), where the high pressure and temperature refrigerant is homogeneously mixed before entering the expander with a lubricant oil at the same thermodynamic conditions in order to force the expansion toward a quasi-isothermal transformation. The working fluid is R134a and the lubricant oil is a 150 SUS polyol ester (POE) oil. The system includes four PHEXs (evaporator, oil heater, condenser and regenerator), two diaphragm pumps, a mixing section, an oil separator and a scroll expander (Woodland et al., 2013; Georges, 2012). Steam at around 105 °C and municipal water at around 15 °C are used as the hot and cold source, respectively. From the experimental results and data processing, 7 steady-state points have been obtained for different flooding ratios ($y_{oil} = 0 \sim 1$) with the rotational speed of the expander fixed at 2500 rpm, as reported in (Georges, 2012). The second system, Fig. 2(c),

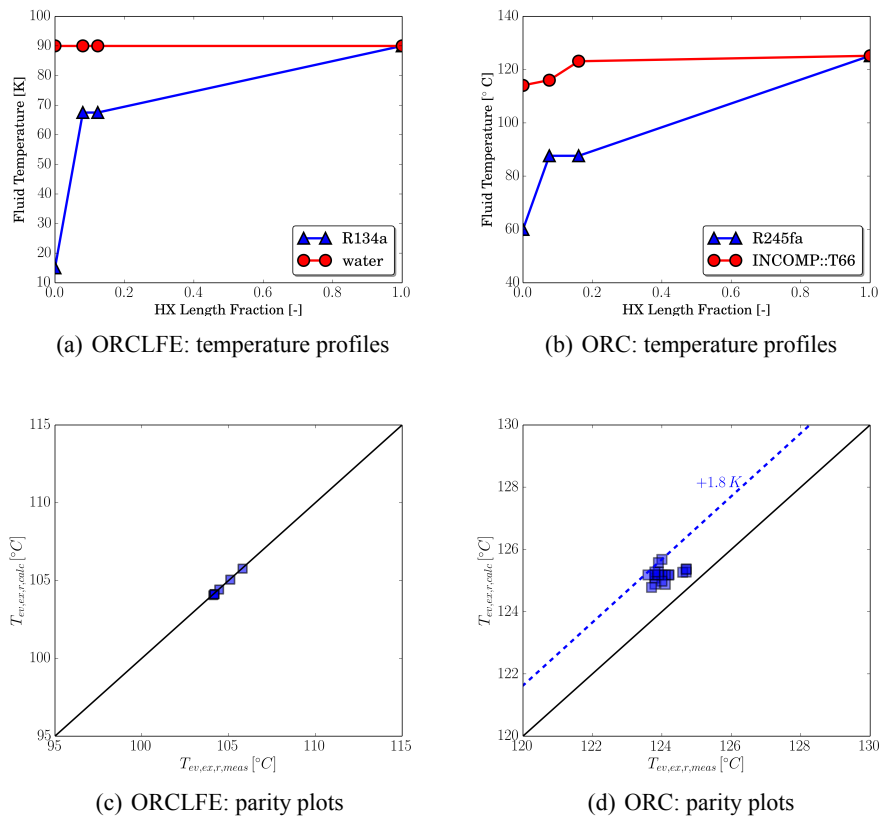


Figure 3: Validation of the PHEX model in the case of the evaporators.

is a standard ORC with regenerator derived from an industrial version. The system is composed of three identical PHEXs, a multi-stage turbopump, a liquid receiver and an 11 kW single-screw expander. The working fluid is R245fa. A thermal oil, therminol 66 (or simply T66), is used as the heat source. It is heated by means of a 250 kWe electric heater. Typical supply temperatures of the T66 are around 125 °C. The cooling medium is a mixture of water and ethylene glycol (around 30% by volume), which is cooled by a rooftop air-cooler unit. A total of 60 steady-state points have been identified at different expander rotational speeds (Ziviani et al., 2015a). Only the nominal speed of 3000 rpm is considered for the following validation, i.e. 21 steady-state points. The first part of the validation addresses the PHEX and expander components for each of the ORC systems. The second part is related to the overall cycle model and the estimation of the cycle efficiency.

5.1 Validation of PHEX model as evaporator

The validation of the moving-boundary model applied to the evaporators is carried out by imposing the mass flow rate and the inlet temperature and pressure of the heat source fluid and the refrigerant. The model is used to determine the heat transfer rate and the outlet temperatures. The first result that is possible to obtain is the temperature profile across the heat exchanger length for both streams. Fig. 3(a) shows the temperature profile in the case of the ORCLFE, where the hot stream is saturated steam and the working fluid is R134a. Similarly, Fig. 3(b) represents the temperature profile in the case of the standard ORC with T66 as the heat source fluid and R245fa as the working fluid. Note that the internal location of phase-change points is predicted by the model. In a design-stage analysis, this information would allow one to optimize the geometry of the evaporators. The parity plots of the calculated outlet temperature of the refrigerant, $T_{ev,ex,r,calc}$, with respect to the experimental data, $T_{ev,ex,r,meas}$, are shown in Fig. 3(c) and Fig. 3(d). In particular, Fig. 3(c) represents the outlet temperature for the evaporator installed in the ORCLFE. The relative error between calculated and measured values is negligible. This is due to the high heat capacity of the steam relative to the working fluid. It results in the limiting case

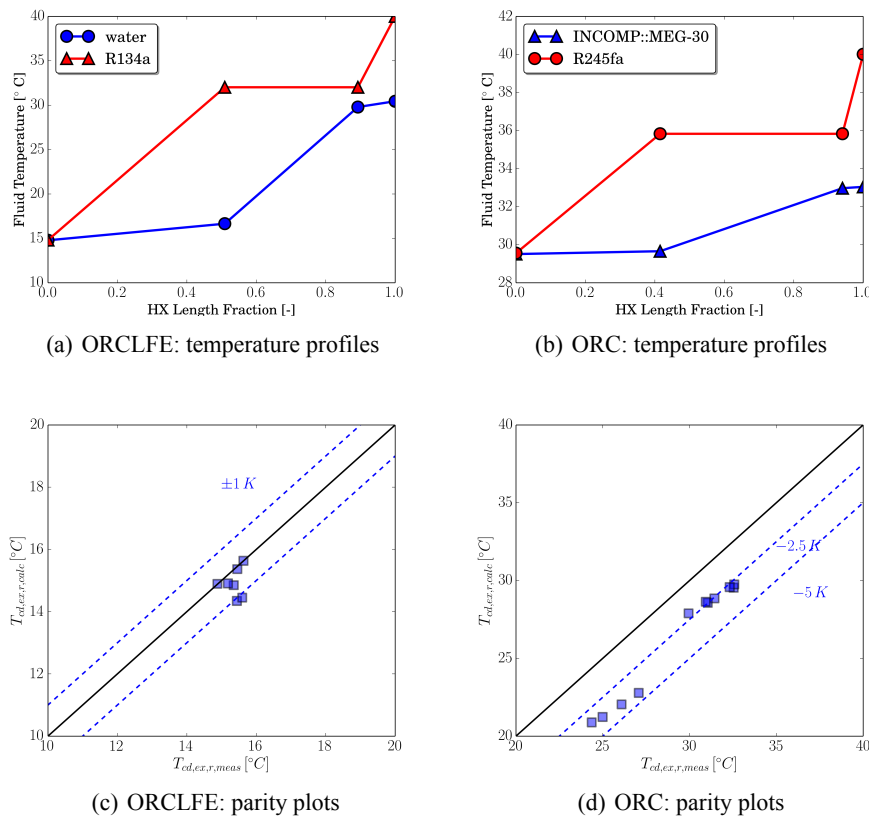


Figure 4: Validation of the PHEX model in the case of the condensers.

that the working fluid exit temperature is equal to the steam inlet temperature. In the case of the standard ORC with R245fa and T66 (Fig. 3(b)), the maximum heat transfer case is also apparent. However, the outlet temperature of the refrigerant is actually over-predicted by up to 1.8 K. A comparison between the thermo-physical property routines CoolProp and REFPROP has also been done in terms of computational time. By considering a single run of the PHEX model in the case of R134a and steam steady-state points, the same calculation has been performed using CoolProp, REFPROP called through CoolProp and native REFPROP. The PHEX simulation with CoolProp resulted to be 1.44 times faster than native REFPROP and up to 9.63 times faster than using CoolProp as an interface layer to REFPROP.

5.2 Validation of the PHEX model as condenser

In the same manner as for the evaporators, the PHEX model has been applied to the condensers by imposing the mass flow rate of both streams and the inlet conditions. For each of the ORC systems, two examples of the temperature profiles across the PHEX length and the parity plots of the outlet temperature of the refrigerant calculated and measured, $T_{cd,ex,r,calc}$ and $T_{cd,ex,r,meas}$, are shown in Fig. 4(c). It should be noted that the ORCLFE uses water as the cooling medium, while the standard ORC has an aqueous mixture of ethylene glycol. The outlet temperatures have been predicted within 1 K and 2.5 K, respectively. Only four points in the case of R245fa/ethylene glycol aq. have been predicted within 5 K. This represents an error in the predicted heat transfer rate of 11 %. The same results have been obtained with native REFPROP. In the current PHEX model, general heat transfer correlations are implemented in order to guarantee a general validity. An improvement could be made by integrating refrigerant-specific heat transfer correlations.

5.3 Validation of the expander model

The semi-empirical model proposed for the expanders aims to be general enough to cover different types of positive displacement machines and different operating conditions by adjusting a set of parameters.

As mentioned before, two different expanders have been considered in this study, i.e. a scroll expander with liquid-flooded expansion and a single screw expander. The model has been calibrated with the experimental points of each machine by means of a genetic algorithm. The procedure is explained in Ziviani et al. (2015a). It should be noted that the limited number of steady-state points obtained for the scroll expander under different flooding ratios does not allow for a validation of the model over a wide range of operating conditions. Nevertheless, it is possible to verify whether the model is able to capture the influence of the flooding medium. Regarding the single screw expander, a more comprehensive investigation and analysis of such a machine can be found in Ziviani et al. (2015a). The comparison between experimental data and calculated results is carried out by providing the expander rotational speed, inlet pressure and temperature, the expander discharge pressure and the ratio of the oil to the refrigerant mass flow rate. In the case of the single screw expander, the last parameter is set to zero. The result of the validation is a set of parity plots for the predicted refrigerant mass flow rate, the power output, the discharge temperature and the adiabatic efficiency. The validation of the scroll expander is shown in Fig. 5. Fig. 6 shows the four parity plots for the single screw expander. By comparing the results of both expanders, it is possible to notice that the model presents a better agreement in the case of the single screw expander, mainly because the complexity of two-phase, two-component flow within the working chamber is not involved. Despite this added complexity with the liquid-flooded scroll expander, the model is able to predict its performance with reasonable accuracy. Note that, while the mass flow rate is overestimated in all of the cases within 10% (Fig. 5(a)), the discharge temperature agrees within 1 K (Fig. 5(c)). The power output presents a larger deviation compared to the previous parameters, as shown in Fig. 5(b). The predictions have been improved by using a compressible two-phase flow model to calculate the pressure drop at the inlet port of the expander, as proposed by Morris (1991). The remarked difference between the measured and the predicted power is related to the presence of the oil and the consequent mechanical losses. The viscous effect of the oil increases with the flooding ratio. A proper viscosity model to take into account these losses should be introduced. The uncertainties of mass flow rate and power output within the model accumulate and directly affect the predictions of the adiabatic efficiency, as shown in Fig. 5(d).

5.4 Overall cycle validation

ORCSim is used to validate the cycle models of the ORCLFE and the standard ORC. The general definition of the cycle thermal efficiency for the ORC with liquid-flooded expansion is given by,

$$\eta_{ORCLFE} = \frac{\dot{W}_{exp} - \dot{W}_{pp,r} - \dot{W}_{pp,oil}}{\dot{Q}_{ev} + \dot{Q}_{oil}} \quad (7)$$

The definition is readily adapted for the standard ORC by dropping the terms related to the oil loop. The cycle simulations have been performed by using the condenser exit subcooling as a convergence criteria (in addition to the cycle mass flow and energy balances). Two examples of temperature-entropy plots of the cycle are shown in Fig.7 for both the ORCLFE and the standard ORC. For most of the points of the ORCLFE, the error on the prediction of the cycle efficiency is less than 25%. Higher accuracy has been obtained in the case of the standard ORC for several points. The parity plots are shown in Fig. 8.

6. CONCLUSIONS

In this paper, a general ORC simulation framework is presented. The architecture of the software has been described and its capabilities have been proven by considering two cycle architectures: an organic Rankine cycle with liquid-flooded expansion (ORCLFE) and internal regeneration using R134a with a scroll expander and a traditional ORC system using R245fa as working fluid with a single screw expander. The main results achieved are summarized below.

- A moving boundary model has been used to model PHEX. The model is general and it is able to capture the performance of an evaporator, a condenser or a regenerator. Thus, a wide range of

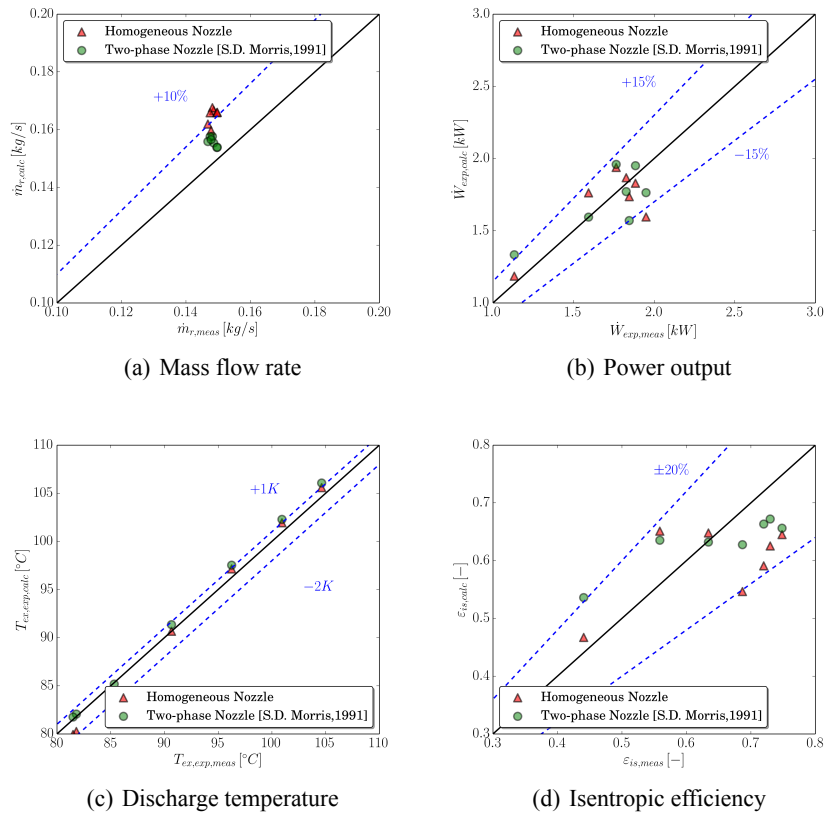


Figure 5: Scroll expander parity plots.

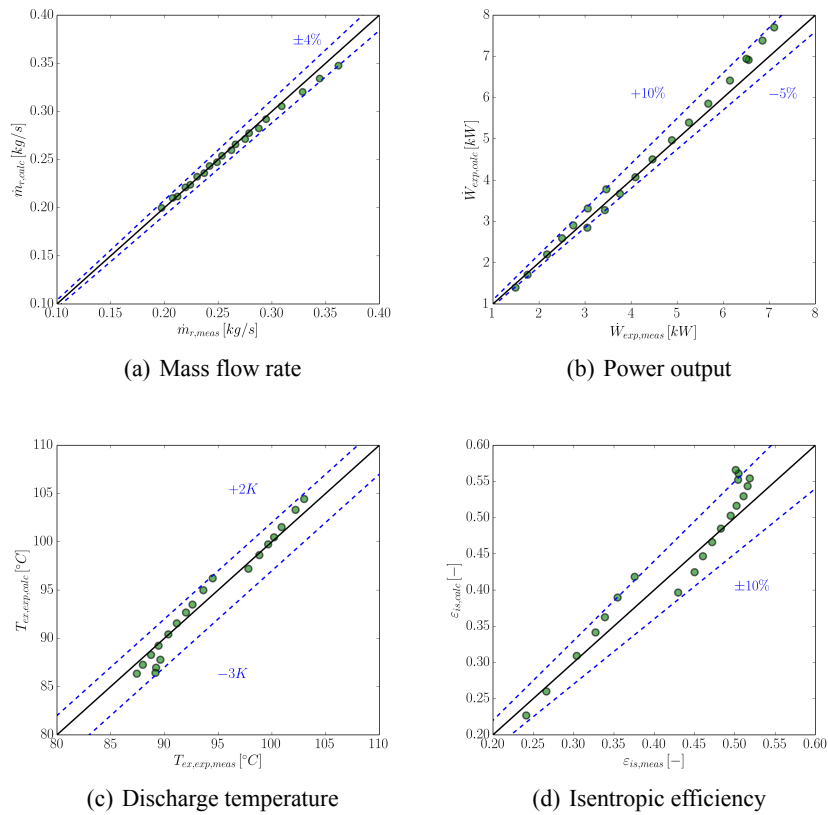


Figure 6: Single screw expander parity plots.

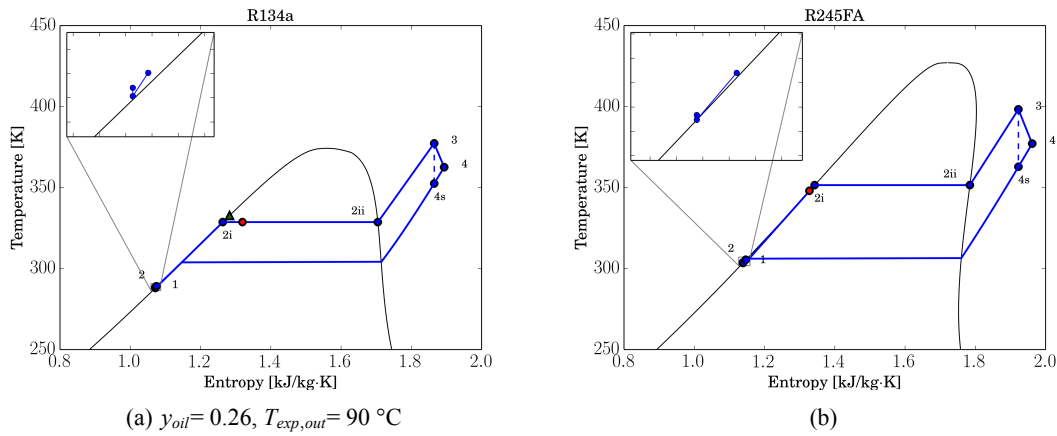


Figure 7: T-s diagram: (a) ORCLFE;(b) standard ORC.

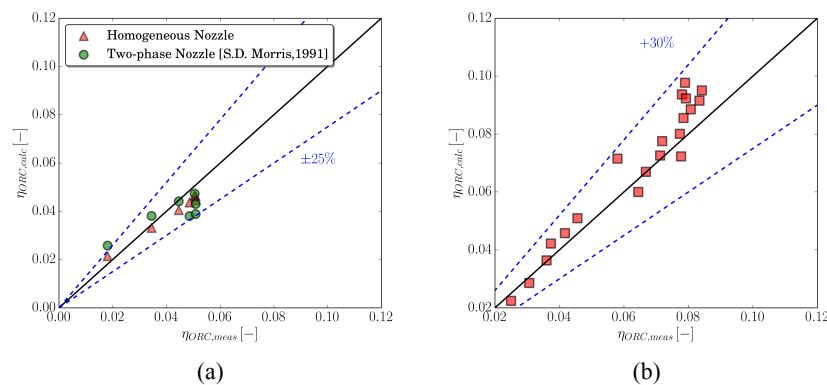


Figure 8: (a) ORCLFE cycle efficiency;(b) ORC cycle efficiency.

fluids, i.e. refrigerants, incompressible liquids, mixtures, etc., have been included. The model has been validated as an evaporator and a condenser for both ORC systems.

- A general semi-empirical model of an expander has been implemented to take into account the presence of different oil fractions. The model has been calibrated for two different expanders, i.e. scroll and single screw, showing good agreement with the experimental results. The agreement is not as good for the liquid-flooded scroll expander. Additional data and more model sophistication could yield improved results. The validation has been shown with a set of parity plots for mass flow rate, power output, discharge temperature and adiabatic efficiency.
- The validation of the overall cycle performance in terms of thermodynamic efficiency has also been carried out. The maximum relative error of 25.7% was obtained in the case of the ORCLFE. This is attributed to the fact that both fluids enter the evaporator in the two-phase state, making heat input measurement highly uncertain. Also, several uncertainties can be associated with the presence of oil in the expander model. For the ORC, the maximum relative error on efficiency prediction was 28.9% mainly because of the over estimation of the expander power output.

REFERENCES

- Bell, I. H., Quoilin, S., Georges, E., Braun, J. E., Groll, E. A., Horton, W. T., and Lemort, V. (2015). A generalized moving-boundary algorithm to predict the heat transfer rate of counterflow heat exchangers for any phase configuration. *Applied Thermal Engineering*, 79:192--201.
- Bell, I. H., Wronski, J., Quoilin, S., and V. L. (2014). Pseudo-pure fluid thermophysical property evalu-

- ation and the open-source thermophysical property library coolprop. *Ind. Eng. Chem. Res.*, 53:2498-2508.
- Georges, E. (2012). Investigation of a flooded expansion organic rankine cycle system. Master's thesis, University of Liege.
- Lemmon, E. W., Huber, M. L., and McLinden, M. O. (2013). Nist standard reference database 23: Reference fluid thermodynamic and transport prop-erties-refprop, version 9.1. National Institute of Standards and Technology, Standard Reference Data Program, Gaithersburg.
- Morris, S. D. (1991). Compressible gas-liquid flow through pipeline restrictions. *Chem. Eng. Process.*, 30:39--44.
- Quoilin, S., Lemort, V., and Lebrun, J. (2010). Experimental study and modeling of an organic rankine cycle using scroll expander. *Applied Energy*, 87:1260--1268.
- Woodland, B. J., Braun, J. E., Groll, E. A., and Horton, W. T. (2014). Methods of increasing net work output of organic rankine cycles for low-grade waste heat recovery. In *15th Int.Refrigeration and Air Conditioning Conf. at Purdue*, number 2190.
- Woodland, B. J., Krishna, A., Groll, E. A., Braun, J. E., Horton, W. T., and Garimella, S. V. (2013). Thermodynamic comparison of organic rankine cycles employing liquid-flooded expansion or a solution circuit. *Applied Thermal Engineering*, 61:859--65.
- Ziviani, D., Desideri, A., Lemort, V., De Paepe, M., and van den Broek, M. (2015a). Low-order models of a single-screw expander for organic rankine cycle applications. In *9th Int. Conf. on Compressors and their Systems, City University of London, London*, number 38.
- Ziviani, D., Woodland, B. J., Georges, E., Groll, E. A., Braun, J. E., Horton, W. T., De Paepe, M., and van den Broek, M. (2015b). Development of a general organic rankine cycle simulation tool: Orcsim. In *Proceedings of ECOS 2015: the 28th Int. Conf. on Efficiency, Cost, Optimization, Simulation and Environmental Impact of Energy Systems.*, number 50492.

NOMENCLATURE

A	area	(m ²)	\dot{W}	power	(W)	ev	evaporator	
h	specific enthalpy	(J/kg)	x	mass ratio	(-)	h	hot side	
\dot{m}	mass flow rate	(kg/s)	y	mass ratio	(-)	int	internal	
p	pressure	(Pa)	ϵ	adiabatic efficiency	(-)	m	mixture	
\dot{Q}	heat rate	(W)	η	cycle efficiency	(-)	pp	pump	
r_v	volume ratio	(-)	Subscript				oil	flooding fluid (oil)
s	specific entropy	(J/kg-K)	cd	condenser		r	refrigerant	
T	temperature	(K)	dis	displacement		req	required	
v	specific volume	(m ³ /kg)	ex	exhaust		s	isentropic	
\dot{V}	volume flow rate	(m ³ /s)	exp	expander		su	supply	
w	specific work	(J/kg)						

ACKNOWLEDGEMENT

The authors would like to acknowledge Ian H. Bell from NIST for his advice on numerous occasions regarding CoolProp and the Python programming language.

ANALYSIS AND COMPARISON OF DIFFERENT MODELING APPROACHES FOR THE SIMULATION OF A MICRO-SCALE ORGANIC RANKINE CYCLE POWER PLANT

Rémi Dickes*, Olivier Dumont, Arnaud Legros, Sylvain Quoilin, Vincent Lemort

Energy System Research Unit
Aerospace and Mechanical Engineering Department
Faculty of Applied Sciences
University of Liège
Belgium

* Corresponding Author (rdickes@ulg.ac.be)

ABSTRACT

When simulating a system based on the organic Rankine cycle (ORC), different modeling methods can be used to predict its performance. Each method is characterized by advantages, limitations and a level of complexity. This contribution aims to assess the impact of the modeling approach on the performance prediction of ORC systems. To this end, a 2.8 kWe ORC unit is investigated as case study. In this paper, the components of the test bench are modeled using different approaches of increasing complexity and each model is calibrated using experimental data from the test rig. The goodness of fit as well as the benefits and limitations of each modeling methods are analyzed and discussed.

1. INTRODUCTION

Because of the depletion of fossil fuels and global warming issues, the world of energy is undergoing many changes toward increased sustainability. Among the different technologies in development, power plant based on the organic Rankine cycle (ORC) are playing a key role in low-grade temperature applications such as waste heat recovery (Quoilin et al., 2011), geothermal power (DiPippo, 2004) or solar thermal energy (Georges et al., 2013). An organic Rankine cycle is a thermal power system used for the conversion of heat into mechanical work by means of the thermodynamic Rankine cycle. Its working principle and its components are similar to a conventional steam power plant but it uses an organic refrigerant as working fluid instead of water.

As for many other technologies, modeling and simulation of ORC systems is crucial for design, sizing or control purposes. From single polynomial correlations predicting the global power plant efficiency to detailed deterministic simulations of each component, several modeling approaches of different complexity levels can be used to predict the performance of an ORC. Each method has its advantages and limitations, and the most appropriate approach for one application is not necessarily the same for another. The objective of this work is to assess the impact of the modeling complexity on the performance prediction of ORC systems. To this end, a 2.8 kWe ORC unit is investigated as case study (Dickes et al., 2014). The test bench uses R245fa as working fluid and consists of a scroll expander, an air-cooled condenser, a gear pump, a recuperator and an oil-heated evaporator. In this paper, each component of the power plant is simulated with three different modeling methods and each model is calibrated using experimental data from the test rig. The goodness of fit as well as the benefits and limitations of the different modeling approaches are discussed. The following sections focus respectively on the pump, the evaporator, the condenser and the expander.

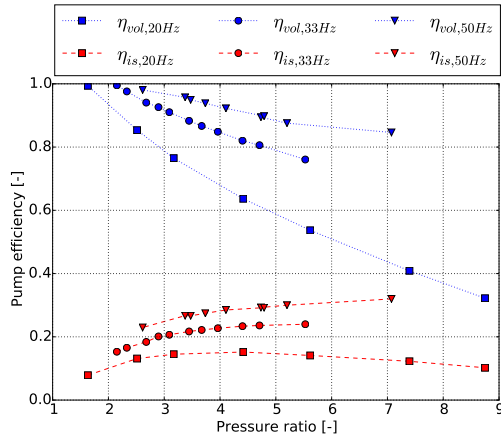


Figure 1: Experimental efficiencies of the gear pump in function of the shaft speed and pressure ratio

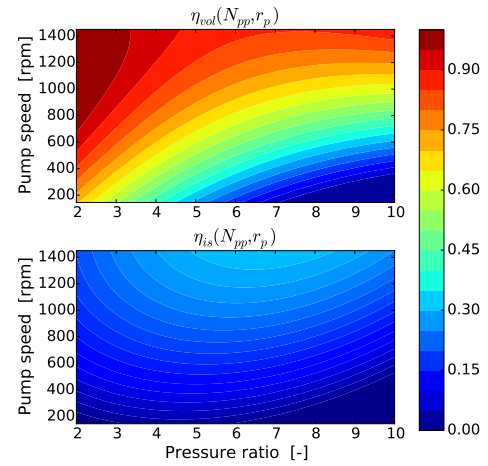


Figure 2: Second-order polynomial correlations modeling the pump isentropic and volumetric efficiencies

2. PUMP

The device used to pressurize the working fluid in the ORC test bench is a gear pump (model: Viking *SG-80550-M0V*). As shown in Figure 1, experimental measurements on the test rig demonstrate a significant influence of the pressure ratio and of the shaft speed on the pump performance (i.e. its isentropic efficiency $\eta_{is,pp}$ and its volumetric efficiency $\eta_{vol,pp}$). In order to predict the mechanical power consumption and the mass flow rate delivered by the pump, three different modeling approaches are investigated.

2.1 Constant-efficiency model (method PP_A)

A simple method to simulate a pump is to neglect the effect of the operating conditions on the machine performance. Such assumption allows to model the pump with constant volumetric and isentropic efficiencies i.e.

$$\eta_{is,pp} = \frac{\dot{m}_{pp}(h_{ex,is,pp} - h_{su,pp})}{\dot{W}_{mec,pp}} = \bar{\eta}_{is,pp} \quad \eta_{vol,pp} = \frac{\dot{V}_{su,pp}}{N_{pp}V_{dis,pp}} = \bar{\eta}_{vol,pp} \quad (1)$$

where \dot{m}_{pp} and $\dot{V}_{su,pp}$ are respectively the fluid mass and volumetric flow rates, $\dot{W}_{mec,pp}$ is the pump mechanical power, N_{pp} is the pump rotation speed and $V_{dis,pp}$ is the machine displacement volume. Based on experimental measurements or manufacturer data, the calibration of the two parameters $\bar{\eta}_{vol,pp}$ and $\bar{\eta}_{is,pp}$ is straightforward and can be performed with a single operating point. If data for several operating conditions are available, an average value of each efficiency is generally selected.

2.2 Physically-based model (method PP_B)

Alternatively, the pump can be simulated using a semi-empirical model (also referred to as lumped parameter model) which implements physically-based equations. In this work, the effective mass flow delivered by the pump \dot{m}_{pp} is calculated as an ideal mass flow rate $\dot{m}_{ideal,pp}$ to which an internal recirculation flow rate $\dot{m}_{lk,pp}$ is deduced. The mass flow rate characterizing the internal leakages is modeled by means of an incompressible flow through an equivalent orifice as suggested by Declaye (2015):

$$\dot{m}_{pp} = \underbrace{(\rho_{su,pp}N_{pp}V_{s,pp})}_{\dot{m}_{ideal,pp}} - \underbrace{(A_{lk}\sqrt{2\rho_{su}(P_{pp,ex} - P_{pp,su})})}_{\dot{m}_{lk,pp}} \quad (2)$$

where $P_{pp,ex}$ and $P_{pp,su}$ are respectively the pressures at the inlet and the exhaust of the pump, $\rho_{su,pp}$ is the inlet density of the fluid and A_{leak} is the surface area of the equivalent orifice. The mechanical consumption of the pump is calculated by adding mechanical losses $\dot{W}_{loss,pp}$ to the isentropic power $\dot{W}_{is,pp}$. These mechanical losses are calculated by means of constant losses \dot{W}_0 added to a term proportional to the isentropic power i.e.

$$\dot{W}_{mec,pp} = \underbrace{(\dot{W}_0 + K_0 \dot{V}_{su,pp}(P_{pp,ex} - P_{pp,su}))}_{\dot{W}_{loss,pp}} + \underbrace{(\dot{V}_{su,pp}(P_{pp,ex} - P_{pp,su}))}_{\dot{W}_{is,pp}} \quad (3)$$

Based on the identification of three parameters, namely A_{leak} , K_0 and \dot{W}_0 , the model can extrapolate the machine behavior while accounting for the influence of the operating conditions on the pump performance. The calibration of the parameters is performed by minimizing the deviation between the reference data and the simulation results. A minimum of two different operating points is required to identify the three parameters but the higher the number of data, the better the calibration.

2.3 Polynomial model (method PP_C)

Finally, a second-order polynomial correlation can be tuned to predict the pump efficiency as depicted in Figure 2. Such empirical model fits correctly the experimental data and provides good predictions of interpolated behaviors. However, extrapolations of the performance outside of the calibration range is unadvised. Indeed, the polynomial expressions could provide unrealistic values of $\eta_{is,pp}$ and $\eta_{vol,pp}$. The number of data points should also be high to avoid effects such as overfitting or the Runge's phenomenon. In this work, a second-order polynomial equation in function of the pressure ratio and the pump speed has been identified to best fit the experimental efficiencies of the pump:

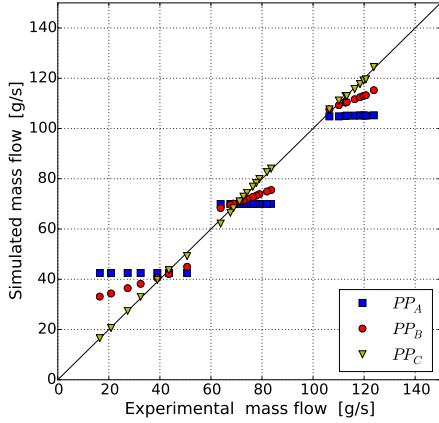
$$\eta_{is,pp} = \sum_{i=0}^2 \sum_{j=0}^2 a_{ij} r_p^i N_{pp}^j \quad \eta_{vol,pp} = \sum_{k=0}^2 \sum_{l=0}^2 b_{kl} r_p^k N_{pp}^l \quad (4)$$

2.4 Comparison of the results

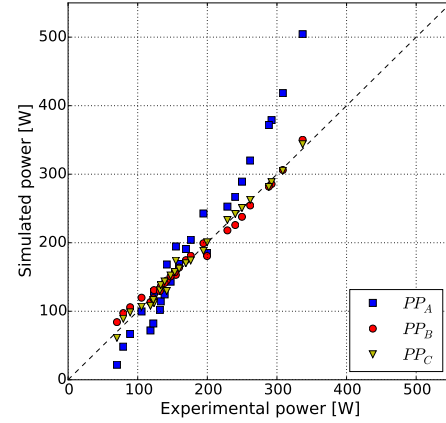
The three models PP_A, PP_B and PP_C are calibrated using an experimental database of 27 operating points. Detailed values of the parameters are given in the Appendix and the coefficients of determination R^2 resulting of the calibration are summarized in Table 1. The deviation between simulation results and experimental data is also illustrated in Figure 3. The basic constant-efficiency model (method PP_A) leads to the largest fitting residues and a maximum relative error of 160% and 69% is committed for the mass flow rate and for the mechanical power respectively. The second-order polynomial correlations demonstrate the best fit but they are characterized by severe modeling restrictions as discussed in section 2.3. The semi-empirical model PP_B which implements physically-based equations appears to be the best compromise between model complexity (only 3 parameters to be identified), goodness of fit and performance extrapolation. Although the mechanical power consumption is correctly reproduced, an alternative formulation of the recirculation losses should be investigated to improve the prediction of the pump mass flow rate.

3. EVAPORATOR AND CONDENSER

The evaporator and the condenser installed in the ORC test bench are respectively a counterflow brazed heat exchanger (model: Alfa Laval CB76-100E) and an air-cooled fin coil heat exchanger (model: Alfa Laval Solar Junior-121). Although the condenser presents a multipass crossflow arrangement, the number of passes for each tube in the air flow is considered high enough ($N_{pass} = 4$) to simulate the heat transfer as a counterflow configuration (Shah and Sekulic, 2003). For both the evaporator and the condenser, a single component performs the heat transfer resulting in the co-existence of three refrigerant phases inside the heat exchangers. In the case of the evaporator (resp. the condenser), the total surface area is divided in three zones (see Figure 4), namely the preheating (resp. the subcooling) zone, the vaporization (resp. the condensation) zone and the superheating (resp. the de-superheating) zone. In this



(a) Predicted mass flow rate vs. experimental data



(b) Predicted power vs. experimental data

Figure 3: Goodness of fit of the pump models PP_A, PP_B and PP_C

work, three different modeling methods are investigated to predict the performance of the evaporator and the condenser.

3.1 Constant-pinch model (method HEX_A)

A simple method to model a three-zone heat exchanger is to impose a constant pinch between the temperature profiles of the cold and the hot fluid. As depicted in Figure 5, the pinch θ can be located differently along the temperature profiles in function of the operating conditions and the type of heat exchanger (condenser or evaporator). In a general statement, one can formulate the constant-pinch paradigm as follows:

$$\min(\Delta T_c; \Delta T_l; \Delta T_v; \Delta T_h) = \bar{\theta} \quad \text{with} \quad \begin{cases} \Delta T_c = |T_{h,f,c} - T_{w,f,c}| \\ \Delta T_l = |T_{h,f,l} - T_{w,f,l}| \\ \Delta T_v = |T_{h,f,v} - T_{w,f,v}| \\ \Delta T_h = |T_{h,f,h} - T_{w,f,h}| \end{cases} \quad (5)$$

where the temperatures of the heat transfer fluid $T_{h,f,i}$ and the working fluid $T_{w,f,i}$ are referred as depicted in Figure 5. The calibration of the unique parameter $\bar{\theta}$ is straightforward and it can be performed using experimental results of a single point. If data in several operating conditions are available, a mean value of the pinch is chosen. The model is easily implemented but the assumption of a constant pinch over a wide range of conditions can lead to significant errors in the performance evaluation of an heat exchanger.

3.2 Three-zone model with constant heat transfer coefficients (method HEX_B)

Another approach to simulate the evaporator and the condenser is to decompose the modeling into the different zones of the heat exchanger. Each zone is characterized by a global heat transfer coefficient U_i and a heat transfer surface area A_i . The global heat transfer coefficient is evaluated by considering only two convective heat transfer resistances in series whereas the surface area is computed using the logarithm mean temperature difference method. In the case of the evaporator, both fluids have the same heat transfer surface area and A_i is evaluated in each zone as follows:

$$U_i = \left(\frac{1}{\alpha_{w,f,i}} + \frac{1}{\alpha_{h,f,i}} \right)^{-1} \quad A_i = \frac{\dot{Q}_i}{U_i \Delta T_{log,i}} \quad (6)$$

where $\alpha_{w,f,i}$ and $\alpha_{h,f,i}$ are the convective heat transfer coefficients of the two fluids, \dot{Q}_i is the heat power transferred in each zone and $\Delta T_{log,i}$ is the related logarithm mean temperature difference. In the case of

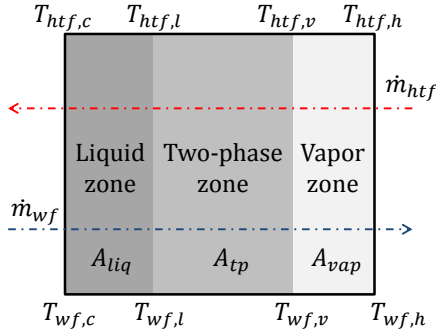


Figure 4: Three-zone moving-boundary model of an evaporator

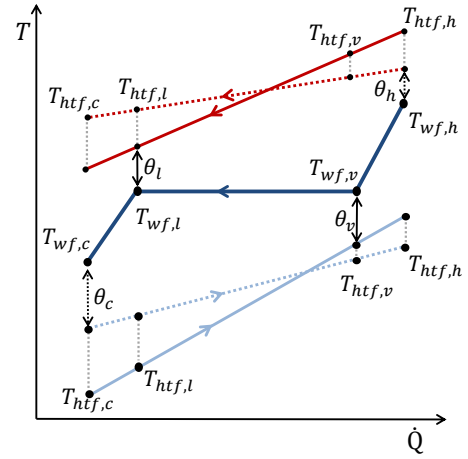


Figure 5: Pinch locations in a three-zone heat exchanger

the air-cooled condenser, the heat transfer surface area is not the same for the two fluids since it is a fin coil heat exchanger. For each zone, the surface area on the refrigerant side $A_{wf,i}$ is evaluated i.e.

$$U_i^* = \left(\frac{1}{\alpha_{wf,i}} + \frac{1}{\eta_{s,i}(A_{htf}/A_{wf})\alpha_{htf,i}} \right)^{-1} \quad A_{wf,i} = \frac{\dot{Q}_i}{U_i^* \Delta T_{log,i}} \quad (7)$$

where $\eta_{s,i}$ is the overall air-side surface efficiency and A_{htf}/A_{wf} is the ratio between the heat transfer surface areas of the two fluids. The efficiency $\eta_{s,i}$ is defined by Incropera and Witt (1996) as

$$\eta_{s,i} = 1 - \frac{A_{fin}}{A_{htf}} (1 - \eta_{fin,i}) \quad (8)$$

where A_{fin} is the fins area, A_{htf} is the total air-side heat transfer area and $\eta_{fin,i}$ is the fin efficiency. The calculation of the fin efficiency is performed using the Schmidt method. For the sack of conciseness, the set of equations leading to $\eta_{fin,i}$ is not provided in this paper. For any further information, refer to Stewart (2003) which provides a complete description of the modeling method. The temperature profiles inside the heat exchanger correspond to the situation in which the total surface area simulated by model is equal to the geometrical surface area of the component A_{hex} , i.e.

$$A_{hex} = A_{liq} + A_{tp} + A_{vap} \quad (9)$$

In this second modeling method, the convective heat transfer coefficients are assumed constant whatever the operating conditions. For the refrigerant, different values are assigned for each zone whereas a single coefficient characterizes the secondary fluid. Therefore, the semi-empirical model relies on four parameters: $\alpha_{wf,liq}$, $\alpha_{wf,tp}$, $\alpha_{wf,vap}$ and α_{htf} . The calibration of these parameters is not difficult if the reference database includes operating conditions with a unique zone on the refrigerant side (i.e. operating conditions with only a liquid phase, a vapor phase or two-phase in the refrigerant flow). In such conditions, the surface area of the zone is known ($A_{liq|tp|vap} = A_{hex}$) and the heat transfer coefficients can be identified easily. However, if the database used for the calibration consists of experimental points with multi-zone operating conditions, the calibration process becomes more challenging since the surface area dedicated to each zone is unknown. To identify the heat transfer coefficients, an optimization process must be performed over the complete database to minimize an error function. In this work, the temperature profiles are provided as inputs and the coefficients are optimized in order to minimize the global error committed on the surface area i.e.

$$\min \sum_{j=1}^M \frac{1}{M} \left| \frac{A_{hex} - A_{liq,j} - A_{tp,j} - A_{vap,j}}{A_{hex}} \right| \quad (10)$$

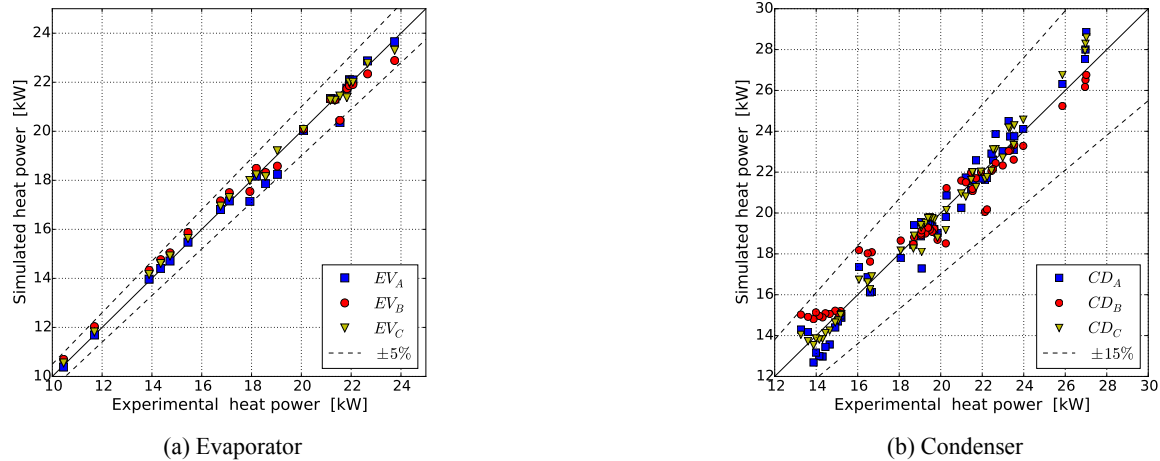


Figure 6: Predicted vs. experimental heat power transferred in the heat exchangers

3.3 Three-zone model with variable heat transfer coefficients (method HEX_C)

The third modeling approach investigated in this work is based on the same model paradigm of method HEX_B . However, instead of keeping the convective heat transfer coefficients constant in all operating conditions, it is proposed to account for the effect of the mass flow rate on the heat transfer by means of the following relations (Quoilin et al., 2008)

$$\alpha_{wf,i} = \alpha_{wf,n,i} \left(\frac{\dot{m}_{wf}}{\dot{m}_{wf,n}} \right)^{0.8} \quad \alpha_{hkf} = \alpha_{hkf,n} \left(\frac{\dot{m}_{hkf}}{\dot{m}_{hkf,n}} \right)^{0.8} \quad (11)$$

where $\alpha_{wf,n,i}$ and $\alpha_{hkf,n}$ are parameters illustrating the heat transfer coefficients of the fluids in case of nominal mass flow rates ($\dot{m}_{wf,n}$ and $\dot{m}_{hkf,n}$). Like for the second modeling approach, each zone on the refrigerant side is characterized by different coefficients whereas a single nominal heat transfer coefficient $\alpha_{hkf,n}$ is assigned for the secondary fluid. Four parameters must be identified and the calibration procedure has the same characteristics as discussed in section 3.2.

3.4 Comparison of the results

The three modeling methods are applied for both the condenser and the evaporator. The models are calibrated using experimental data from the test bench and the deviations between simulation results and experimental data are illustrated in Figure 6. Detailed values of the parameters are available in the Appendix and the coefficient of determination R^2 are summarized in Table 1. The constant-pinch model (method HEX_A) is the simplest method to implement and to calibrate. Since the operating points used for the calibration are with a relatively constant pinch, this modeling method demonstrates the second best fit to experimental data even though a single parameter is required. However, the ability of such modeling approach is limited for performance extrapolations over a wide range of operating conditions as explained in section 3.1. The three-zone moving-boundary model with constant heat transfer coefficients (method HEX_B) presents opposite characteristics. Its calibration is more complex and requires the use of an optimization process. Although it shows the lowest goodness of fit, the consideration of each zone in the heat exchanger makes it more reliable for performance extrapolation in different operating conditions. Finally, by accounting for the impact of the mass flow rate on the heat transfer, the method HEX_C demonstrates the best fit and the best ability for performance extrapolation. However, its calibration is as complex as for method HEX_B since it also requires an optimization process.

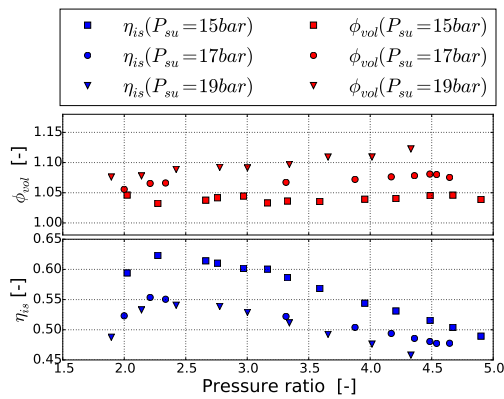


Figure 7: Isentropic efficiency and filling factor of the expander

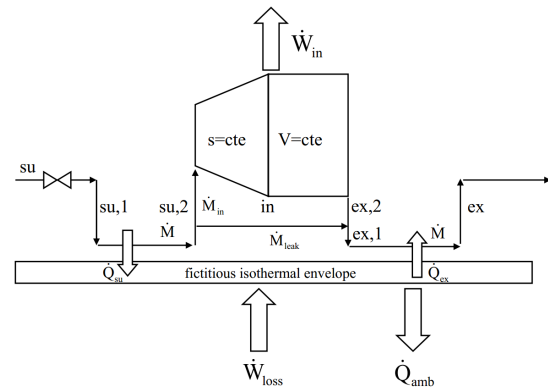


Figure 8: Semi-empirical model of the scroll expander (Lemort, 2008)

4. EXPANDER

The expansion process is performed by a scroll compressor modified to run in reverse as an expander (model: Copeland ZR34 K3E-ZD). It is directly connected to the grid and its shaft speed remains constant in any situation. As depicted in Figure 7, experimental measurements demonstrate an influence of the pressure ratio and the fluid supply conditions on the machine performance (i.e. the isentropic efficiency $\eta_{is,exp}$ and the filling factor $\phi_{vol,exp}$ (Quoilin, 2011)). In this contribution, three modeling methods are investigated to extrapolate the expander behavior in different operating conditions.

4.1 Constant-efficiency model (method EXP_A)

Similarly to the pump, the simplest method to simulate an expander is to assume a constant performance whatever the operating conditions. In such case, the isentropic efficiency $\bar{\eta}_{is,exp}$ and the filling factor $\bar{\phi}_{vol,exp}$ of the machine are identified and set constant as explained in section 2.1. However, the temperature range in an expander is higher than in a pump resulting in unnegligible heat losses if the expander is not thermally insulated. In order to account for the effect of these losses on the exhaust conditions, a third parameter AU_{loss} can be added to the model i.e.:

$$\dot{m}_{exp} (h_{su,exp} - h_{ex,exp}) = \dot{W}_{mec,exp} + AU_{loss} (\bar{T}_{exp} - T_{amb}) \quad (12)$$

4.2 Physically-based model (method EXP_B)

The second approach chosen for simulating the expander performance is the physically-based model proposed by Lemort (2008). The conceptual scheme of the model is shown in Figure 8 and a complete description of the governing equations can be found in Lemort et al. (2009). Besides of under- and over-expansion losses due to the fixed built-in volumetric ratio of the machine, the model accounts for internal leakages, mechanical losses, pressure drops at the inlet and heat losses. Unlike deterministic modeling methods which require the exact knowledge of the machine geometry (Dickes, 2013), the semi-empirical model can extrapolate the expander performance in a wide range of operating conditions by the identification of eight parameters. The calibration of the parameters is not direct and must be performed through an optimization process minimizing the global error committed on the model outputs (Lemort et al., 2009).

4.3 Polynomial correlations (method EXP_C)

A third modeling approach is to evaluate the expander performance by means of a second-order polynomial correlation. As discussed in section 2.3, these models are suitable to interpolate the machine behavior within the calibration range but extrapolations of the performance outside of this confidence domain is unadvised. In this work, a second-order polynomial equation in function of the supply density

Table 1: Goodness of fit for the different models
 (* : if heat losses are modeled in the expander)

Pump model	$R^2[\dot{m}_{pp}]$	$R^2[\dot{W}_{pp,mec}]$	$R^2[\dot{W}_{pp,elec}]$
PP _A	0.788	0.805	0.802
PP _B	0.951	0.981	0.982
PP _C	0.999	0.991	0.991
Evaporator model	$R^2[\dot{Q}_{ev}]$	$R^2[T_{wf,ex}]$	$R^2[T_{hf,ex}]$
EV _A	0.9995	0.9314	0.9043
EV _B	0.9994	0.7942	0.999
EV _C	0.9998	0.9479	0.9995
Condenser model	$R^2[\dot{Q}_{cd}]$	$R^2[T_{wf,ex}]$	$R^2[T_{hf,ex}]$
CD _A	0.968	0.748	0.987
CD _B	0.932	0.118	0.985
CD _C	0.981	0.86	0.996
Expander model	$R^2[\dot{m}_{exp}]$	$R^2[\dot{W}_{exp,mec}]$	$R^2[T_{wf,ex}]$
EXP _A	0.9826	0.9621	0.3695/0.9309*
EXP _B	0.9768	0.9848	0.8626
EXP _C	0.996	0.9906	0.3783/0.9151*

(ρ_{su}) and the logarithm of pressure ratio ($\ln(r_p)$) is used to characterize the isentropic efficiency and filling factor of the expander i.e.

$$\eta_{is,exp} = \sum_{i=0}^2 \sum_{j=0}^2 a_{ij} (\ln(r_p))^i \rho_{su}^j \quad \phi_{vol,exp} = \sum_{k=0}^2 \sum_{l=0}^2 b_{kl} (\ln(r_p))^k \rho_{su}^l \quad (13)$$

Similarly to method EXP_A, heat losses can be taken into account by using equation (12).

4.4 Comparison of the results

The three modeling methods EXP_A, EXP_B and EXP_C are calibrated using an experimental database of 53 operating points. The coefficients of determination R^2 from the calibration are summarized in Table 1 and detailed values of the parameters are provided in the Appendix. The constant-efficiency model permits a good fit of the experimental results if heat losses are taken into account, but significant errors are committed on the exhaust temperature otherwise. Since a constant efficiency is assigned to the machine performance while experimental measurements demonstrate an influence of the operating conditions, significant errors can be committed while extrapolating the machine performance out of the calibration range. In contrast to method EXP_A, the polynomial model accounts for the influence of the operating conditions on the expander performance and fits the best the experimental data. However, such correlation presents severe modeling restrictions as discussed in section 4.3 and it is more sensitive to the dataset used for the calibration. The semi-empirical model EXP_B overcomes these issues. By implementing physically-based equations, extrapolation of the expander performance can be performed out of the confidence range and the model calibration is less sensitive to the experimental points used as reference. However, the identification of the eight parameters is not as straightforward as for the two other methods since it requires a non-linear optimization process as explained in section 4.3.

5. CONCLUSION AND FUTURE WORK

The performance evaluation of an ORC system can be carried out using different modeling methods. In order to assess the impact, the advantages and the limitations of different approaches, a 2.8 kWe ORC unit is investigated as reference case. Each component of the micro-scale power plant is simulated by

Table 2: Characteristics of the different models
 (* : if heat losses are modeled in the expander)

	PP _A	PP _B	PP _C	HEX _A	HEX _B	HEX _C	EXP _A	EXP _B	EXP _C
Nbr. of parameters	2	3	8	1	4	4	2/3*	8	8/9*
Goodness of fit	-	+	+	≈	-	+	-/≈*	+	-/+*
Simplicity of calibration	+	≈	≈	+	-	-	+	-	+
Performance extrapolation	≈	+	-	-	≈	+	-/≈*	+	-
	+ : good			≈ : neutral			- : bad		

means of three modeling methods characterized by different levels of complexity. All the models are calibrated with experimental data from the test rig and a comparison is performed in terms of goodness of fit and calibration complexity. A deeper investigation about extrapolation capability will be performed by means of a cross validation process and by comparing the models prediction with other experimental datasets. The main observations of the current analysis are summarized in Table 2. In this paper, the components are considered alone. Future works will apply a similar analysis to the model of the whole system by interconnecting the models of each subcomponent. The global behavior of the test rig will be evaluated over a wide range of operating conditions and deviations between the different modeling approaches will be analyzed.

NOMENCLATURE

Symbols

A	surface area (m^2)
a, b	polynomial coefficients (-)
ΔT	temperature difference (K)
h	specific enthalpy (J/kg)
\dot{m}	mass flow (kg/s)
N	shaft speed (rpm)
P	pressure (Pa)
\dot{Q}	heat power (W)
r_p	pressure ratio (-)
T	temperature (K)
U	global heat coefficient ($W/m^2.K$)
V	volume (m^3)
\dot{V}	volumetric flow (m^3/s)
\dot{W}	Power (W)
α	convective heat coefficient ($W/m^2.K$)
η	efficiency (-)
φ	filling factor (-)
ρ	density (kg/m^3)
θ	pinch (K)

Subscripts

amb	ambiance
c	cold
cd	condenser
dis	displacement
ex	exhaust
exp	expander
ev	evaporator
h	hot
hex	heat exchanger
htf	heat transfer fluid
is	isentropic
l, liq	liquid
lk	leakage
log	logarithm
mec	mecanical
n	nominal
pp	pump
su	supply
tp	two-phase
v, vap	vapor
vol	volumetric
wf	working fluid

APPENDIX

The appendices include detailed values of the parameters for each model presented in this paper and additional Figures illustrating the deviations between simulation results and experimental data. The appendix is available in electronic form only at the following url: <http://hdl.handle.net/2268/180069>

REFERENCES

- Declaye, S. (2015). *Improving the performance of micro-ORC systems*. PhD thesis, University of Liège.
- Dickes, R. (2013). Design and fabrication of a variable wall thickness two-stage scroll expander to be integrated in a micro-solar power plant. Master's thesis, University of Liège.
- Dickes, R., Dumont, O., Declaye, S., Quoilin, S., Bell, I., and Lemort, V. (2014). Experimental investigation of an orc system for a micro-solar power plant. In *Proceedings of the 22nd International Compressor Engineering Conference at Purdue*.
- DiPippo, R. (2004). Second law assessment of binary plants generating power from low-temperature geothermal fluids. *Geothermics*, 33:565--586.
- Georges, E., Declaye, S., Dumont, O., Quoilin, S., and Lemort, V. (2013). Design of a small-scale orc engine used in a solar power plant. *International Journal of Low-Carbon Technologies*.
- Incropera, F. and Witt, D. D. (1996). *Fundamentals of Heat and Mass Transfer*. John Wiley and Sons, Inc.
- Lemort, V. (2008). *Contribution to the characterization of scroll machines in compressor and expander modes*. PhD thesis, University of Liège.
- Lemort, V., Quoilin, S., Cuevas, C., and Lebrun, J. (2009). Testing and modeling a scroll expander integrated into an organic rankine cycle. *Applied Thermal Engineering*, 29:3094--3102.
- Quoilin, S. (2011). *Sustainable energy conversion through the use of organic Rankine cycles for waste heat recovery and solar applications*. PhD thesis, University of Liège.
- Quoilin, S., Aumann, R., Grill, A., Schuster, A., Lemort, V., and Spliethoff, H. (2011). Dynamic modeling and optimal control strategy of waste heat recovery. *Applied Energy*, 88:2183--2190.
- Quoilin, S., Orosz, M. S., and Lemort, V. (2008). Modeling and experimental investigation of an organic rankine cycle using scroll expander for small scale solar applications. In *Proceedings of the 1st Eurosun Conference*.
- Shah, R. and Sekulic, D. (2003). *Fundamentals of Heat Exchanger Design*. John Wiley and Sons, Inc.
- Stewart, S. W. (2003). *Enhanced finned-tube condenser design and optimization*. PhD thesis, Georgia Institute of Technology.

DESIGN OF ORGANIC RANKINE CYCLE POWER SYSTEMS ACCOUNTING FOR EXPANDER PERFORMANCE

Angelo La Seta^{1*}, Jesper Graa Andreasen², Leonardo Pierobon², Giacomo Persico³, Fredrik Haglind²

¹ Technical University of Denmark, Department of Mechanical Engineering,
2800 Kongens Lyngby, Denmark, and
Politecnico di Milano, Dipartimento di Energia,
20156 Milano, Italy
anlse@mek.dtu.dk
angelo.laseta@mail.polimi.it

² Technical University of Denmark, Department of Mechanical Engineering,
2800 Kongens Lyngby, Denmark
jgan@mek.dtu.dk, lpier@mek.dtu.dk, frh@mek.dtu.dk

³ Politecnico di Milano, Dipartimento di Energia,
20156 Milano, Italy
giacomo.persico@polimi.it

* Corresponding Author

ABSTRACT

Organic Rankine cycle power systems have recently emerged as promising solutions for waste heat recovery in low- and medium-size power plants. Their performance and economic feasibility strongly depend on the expander. Its design process and efficiency estimation are particularly challenging due to the peculiar physical properties of the working fluid and the gasdynamic phenomena occurring in the machine. Unlike steam Rankine and Brayton engines, organic Rankine cycle expanders have to deal with small enthalpy drops and large expansion ratios. These features yield turbine designs with few highly-loaded stages in supersonic flow regimes. This paper proposes a design method where the conventional cycle analysis is combined with calculations of the maximum expander performance using a validated mean-line design tool. The high computational cost of the turbine optimization is tackled building a model which gives the optimal preliminary design of the turbine as a function of the cycle conditions. This allows to estimate the optimal expander performance for each operating condition of interest. The test case is the preliminary design of an organic Rankine cycle turbogenerator to increase the overall energy efficiency of an offshore platform. The analysis of the results obtained using a constant turbine efficiency and the method proposed in this paper indicates a maximum reduction of the expander performance of 10% – points for pressure ratios between 10 and 35. This work also demonstrates that this approach can support the plant designer on deciding the optimal size of the organic Rankine cycle unit when multiple exhaust gas streams are available.

1. INTRODUCTION

Environmental concerns stress the need for reducing greenhouse gas emissions and pollutants in the industrial, civil and transport sector. Organic Rankine cycle (ORC) power systems are an efficient and cost-competitive solution for heat-to-power conversion. These plants are nowadays regarded as a reliable technology for biomass and geothermal applications by virtue of the large operational experience. Current research efforts aim at enlarging their utilization range by progressing to the design of mini-ORC systems (3-20 kW) for challenging low heat source temperatures (90-150 °C) [6]. Concurrently,

ORC units are viable alternatives to steam Rankine cycle plants at high temperatures (300-500 °C), in niche sectors where the advantages of the ORC technology can be entirely exploited [5, 16].

In these applications, the turbine is arguably the most critical component owing to the small volumetric flow rates and the high expansion ratios [19]. The turbine performance tightly relates to the architecture of the thermodynamic cycle. Its design is of paramount importance for the technical and economic optimization of the power module. Numerous studies on the maximization of the cycle performance are available in the literature, see, e.g., [2, 17, 24, 26]. Few works address the feasibility of the turbine design, typically considered a posteriori or by setting bounds on the cycle parameters. As an example, Kang [14] selected the evaporation pressure of a 200 kW ORC unit with R245fa as working fluid considering a maximum expansion ratio of 4.11. Invernizzi et al. [13] employed the volumetric expansion ratio and the size parameter to identify a suitable working fluid for a bottoming mini-ORC unit. Astolfi et al. [3] performed a techno-economic optimization of a geothermal ORC power system. The cited authors estimated the number of turbine stages using information on the maximum volume flow ratio and the largest enthalpy drop.

The objective of this paper is to quantify how the variation of the expander efficiency influences the optimization of the thermodynamic cycle. A steady-state model of the thermodynamic cycle is coupled to a simulation tool capable of delivering the preliminary design of a single-stage turbine. This integration is performed optimizing the expander geometry for different boundary conditions of the cycle. A surrogate model of the turbine is then built to provide the maximum isentropic efficiency for each boundary condition. This approach gives a more realistic picture of the energy conversion efficiency of the system, when changing the key thermodynamic parameters of the cycle. The results are compared with those obtained assuming a constant isentropic turbine efficiency. This analysis demonstrates the impact of a proper modeling of the turbine for this class of power systems. The case study is the preliminary design of an ORC unit used to increase the overall energy efficiency of an offshore platform.

Section 2 presents the case study of this work. Section 3 describes the mean-line simulation tool for the design and optimization of the turbine. The results are then reported and discussed in Section 4. Concluding remarks are given in Section 5.

2. CASE STUDY

The case study is the power system installed on the Draugen oil and gas offshore platform, located 150 km from Kristiansund, in the Norwegian Sea. Three Siemens SGT-500 gas turbines are installed on the platform. The electrical power demand on board is 19 MW. Two turbines are kept in operation at all times, each covering 50 % of the load. The third is kept on stand-by, allowing for maintenance work. Despite the low energy conversion efficiency, this strategy ensures the necessary reserve power for peak loads and the safe operation of the engines.

The Siemens SGT-500 gas turbine is fed with natural gas and generates an electric power output of 16.5 MW. The mass flow rate and the temperature of the exhaust gases discharged by the engine are equal to $91.5 \text{ kg} \cdot \text{s}^{-1}$ and 625 K [24], respectively. The twin-spool engine employs two coaxial shafts coupling the low pressure compressor (LPC) with the low pressure turbine (LPT) and the high pressure compressor (HPC) with the high pressure turbine (HPT). The power turbine (PT) transfers mechanical power through a dedicated shaft to the electric generator (GEN). Recuperating the exhaust thermal power of the engines with an ORC unit may enhance their energy conversion efficiency. Figure 1 shows the layout of the power system, where one ORC unit is considered as bottoming unit for one gas turbine. The relatively low temperature of the exhaust gases enables to transfer the thermal energy directly to the once-through boiler (OTB), without the need for an intermediate oil loop. The working fluid first expands in the ORC turbine (TUR), and it is then cooled in the recuperator. In this way, the temperature of the organic compound at the OTB inlet may be increased by recovering energy from the superheated vapor exiting the turbine. The ORC fluid is then condensed and compressed to the highest pressure

level through the recuperator, thus closing the cycle. The selected organic compound is cyclopentane. According to the analysis performed by Pierobon et al. [24], this choice leads to the simultaneous optimization of net present value, plant efficiency and volume of the investigated ORC-unit. Moreover, this organic compound is already adopted for operating ORC systems in this range of temperature, see Del Turco et al. [10].

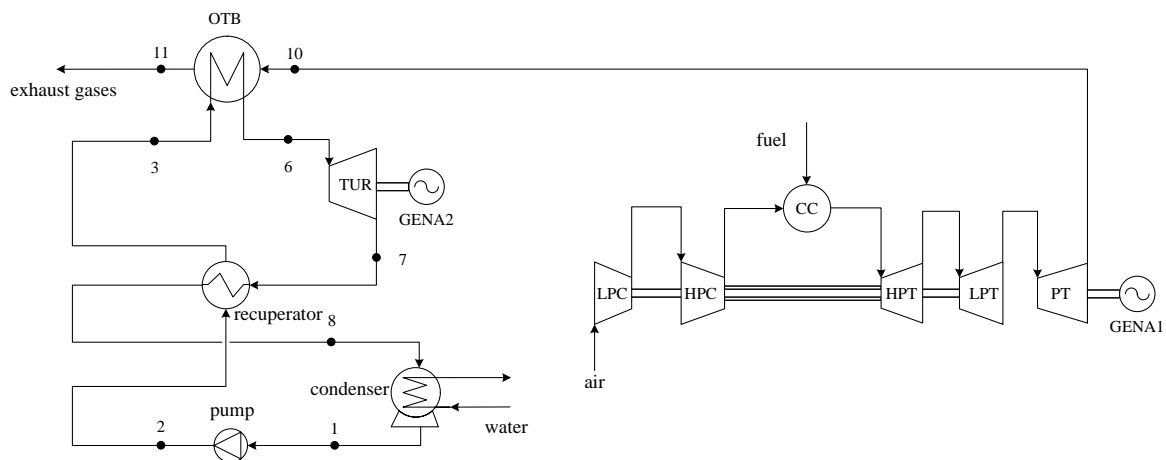


Figure 1: Simplified layout of the power system on the Draugen offshore oil and gas platform; the exhaust gases of one engine feed the organic Rankine cycle module. The two remaining gas turbines are not shown.

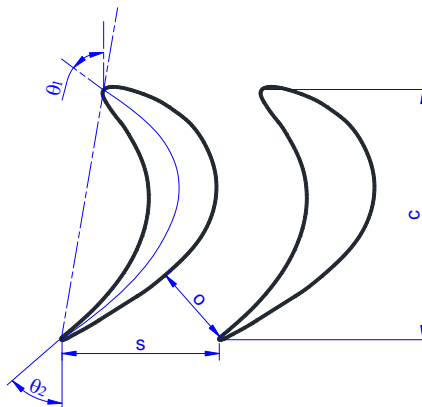


Figure 2: Main geometric blade parameters with relative nomenclature.

3. METHODS

3.1 The axial turbine simulation tool - TURAX

The large volume ratios and small enthalpy drops, commonly met in ORC turbines, entail higher volume flow ratios per stage compared to gas and steam turbines. The main problem is thus to distribute the load between stator and rotor in the most effective way. As discussed by Macchi [19], it is necessary to find a compromise between a pure impulse stage and a conventional configuration with a degree of reaction set to 0.5. The first one implies high Mach number of the relative velocity at the rotor inlet. Conversely, the latter demands large rotor blade height variations between inlet and outlet. A careful study is, therefore, necessary to find the optimal solution.

For the purpose of this work, a novel in-house code for turbine preliminary design, called TURAX, was written in the Matlab language. The simulation tool is the present result of ongoing development

at the Department of Mechanical Engineering, Technical University of Denmark, which began with a Master's Thesis work in 2013 [11]. For a given set of design parameters and boundary conditions, i.e., mass flow rate, inlet temperature, rotational speed and total pressure ratio, the simulation tool produces a preliminary design of a single- or multi-stage machine (see Figure 2 for the blade nomenclature) and an estimation of the total-to-total efficiency. Similarly to other preliminary design codes available in the literature, such as zTurbo [25], TURAX is based on one-dimensional approximation supported by proper correlations for the estimation of the losses and flow angles. The tool is combined with an external evolutionary algorithm to determine the optimal preliminary design.

The architecture of the code consists of three main parts:

1. Evaluation of the total inlet and total isentropic outlet thermodynamic states and of the total isentropic enthalpy drop. All these values remain constant during the design process.
2. Calculation of the set of first guess values for fluid angles, velocities and thermodynamic properties.
3. Iterative loop. Based on the first guess values, an iterative cycle runs until convergence is reached. The following steps are included in the iteration:
 - (a) Calculation of the nozzle blade opening with the Deich formula [9]. If the flow is supersonic, this step allows to account for converging-diverging shapes of nozzle blades.
 - (b) Evaluation of the blade and fluid angles. The blade angles θ_2 and θ_3 are obtained using the input parameters $(o/s)_n$ and $(o/s)_r$. The quantity o/s is the outlet section-to-nozzle pitch ratio. The subscripts "n" and "r" refer to the nozzle and the rotor. For a subsonic case, the fluid angles are calculated with the equation proposed by Ainley and Mathieson [1]. The Vavra correlation is used for supersonic cases [29].
 - (c) Updating of the fluid velocities with the calculated fluid angles and estimation of the thermodynamic properties and Mach numbers.
 - (d) Calculation of the turbine geometry, e.g., flare angles, blade height, by means of the continuity equation.
 - (e) Estimation of the turbine losses using the correlation proposed by Craig and Cox [7].
 - (f) Calculation of the total-to-total turbine efficiency. Check the difference with respect to the previous iteration and return to step 3a until the relative deviation is smaller than 10^{-4} .

The code is integrated with the optimization toolbox available in the Matlab language [28] to obtain the turbine layout which maximizes the total-to-total isentropic efficiency. The controlled elitist genetic algorithm, implemented as reported in Goldberg [12], is selected to find the optimal designs. Compared to gradient-based methods, a genetic algorithm is less prone to end its search in local minima of the problem and usually allows to converge towards global optima. This typically comes at the cost of an increased computational effort, due to the large number of the objective function evaluations [8]. Computational fluid dynamics tools tackle this issue by resorting to self-learning metamodels of the response surface [23]. However, in the present case the computational burden of a single evaluation is comparatively small, and it does not justify the use of metamodels. The genetic algorithm parameters are specified as follows: population size 900, generation size 200, crossover fraction 0.8, and migration fraction 0.2. These numerical values are selected to ensure the repeatability of the solution when different simulations are performed.

The vector of optimizing variables at hand reads

$$\bar{X} = [\psi, o_n, o_r, c_n, c_r, (o/s)_n, (o/s)_r, N], \quad (1)$$

where ψ is the stage work coefficient, and N is the rotational speed of the machine, if considered among the optimization variable. The geometric variables o and c are the blade throat opening and the axial

chord. Note that the possible choice of seeking for a turbine geometry optimized for a certain rotational speed implies the insertion of a gearbox. The initialization of the optimizer requires to set the upper and lower bounds limiting the optimization variables. The Reynolds number for the blade opening, the ratio of the rotor height at the inlet to the nozzle height at the outlet as well as the Mach number for the converging/diverging nozzles are input parameters equal to 10^5 , 1.1 and 1.4, respectively. The axial velocity component is assumed constant throughout the stage. Additional constraints on the geometry and thermodynamic variables are necessary to provide acceptable solutions from physical and technological perspectives. These conditions, established by Macchi and Perdichizzi [20], are accordingly implemented as non-linear constraints. Table 1 lists the upper and lower bounds imposed on the dependent and independent variables.

The simulation tool is fully integrated with the freely-available high-accuracy property library for the estimation of the thermophysical properties of fluids developed by Bell et al. [4]. The fluid database uses Helmholtz-free-energy-based equations of state, provided in a temperature-density-explicit form, as source of thermodynamic data for many relevant working fluids [27]. The described fluid library offers two distinct interpolation methods: a) Tabular Taylor Series Expansion (TTSE) as outlined by Miyagawa and Hill [21] and Watanabe and Dooley [30], and b) bicubic interpolation reported in the work of Keys [15]. Bell et al. [4] provides a detailed description of these methods and of the benefits in terms of computational cost. The TTSE method is selected for the turbine optimization and the cycle calculations reported in this work.

Table 1: Lower and upper bounds for the variables involved in the optimization of the turbine geometry. Additional constraints are also reported.

Variable	Lower bound	Upper bound
Stage work coefficient ψ [-]	2	6
Blade throat opening o [mm]	2	100
Axial chord c [mm]	10	100
Outlet section-to-nozzle pitch o/s [-]	0.225	0.7
Rotational speed (if optimized) [rpm]	2000	12000
Additional constraints		
Relative Mach number at the rotor inlet [-]	0	0.8
Relative Mach number at the rotor outlet [-]	0	1.4
Number of blades (both for nozzle and rotor) [-]	10	100
Flare angles [$^{\circ}$]	-25	25
Blade height to mean diameter ratio [-]	0.001	0.25
Axial chord to mean diameter ratio [-]	0	0.2

3.2 Model assessment

The software was verified using a similar code developed at the Politecnico di Milano [18]. Similarly to TURAX, this software can produce the optimal design of multiple stage axial-flow turbines. The code employs the same methods to estimate the fluid angles and the cascade losses. The test case for the comparison is the preliminary design of a single-stage axial machine for gas turbine applications. The expander rotates at 10000 rpm with a mass flow rate of $10 \text{ kg} \cdot \text{s}^{-1}$, a total turbine inlet temperature of 1123 K and an expansion ratio of 2. The comparison gives a relative error in isentropic efficiency lower than 0.2%. Lower deviations are observed for most of the relevant geometric and flow variables. The relative error in the absolute fluid angle at rotor outlet is 0.5%. This fluid angle is the highly sensible to the variations of the thermodynamic parameters. Given the relative errors reported above, the simulation tool is deemed reliable for preliminary design calculations.

3.3 Thermodynamic cycle calculation

The computation of the thermodynamic states is accomplished by applying the energy and mass balance equation to each plant constituent. This procedure yields the computation of the thermodynamic states at the inlet and outlet of each system component. Figure 3 illustrates the $T - s$ diagram for an ORC module with a turbine inlet pressure of 3 MPa, see Section 4. The nodes where the working fluid is in saturated conditions, i.e., 4, 5 and 9 in Figure 3, are not reported in the plant layout (Figure 1). The evaporation and condensation start inside the once-through boiler and the shell-and-tube condenser, respectively. A constant pressure specific heat capacity of $1100 \text{ J} \cdot \text{kg}^{-1} \cdot \text{K}^{-1}$ is used for the energy balance calculations involving the exhaust gases. Note that this work considers only subcritical cycle configurations.

The condensing pressure is equal to 0.1 MPa to prevent air leakages into the engine. The pinch-point temperature differences of the once-through boiler and internal recuperator are fixed to 10 and 15 K, respectively. The pump isentropic efficiency and the electrical efficiency of the generator are equal to 0.8 and 0.98 [24]. Additional assumptions are the following: no pressure loss in piping or heat transfer equipment, adiabatic system, steady-state condition and homogeneous flow in terms of thermodynamic properties. Note that the turbine inlet temperature is kept at 513.15 K to ensure the chemical stability of the working fluid. The reader is referred to Pasetti et al. [22] for an in-depth analysis of the cyclopentane decomposition at high temperatures. A gearbox efficiency of 0.96 is used when the rotational speed is included in the turbine optimization.

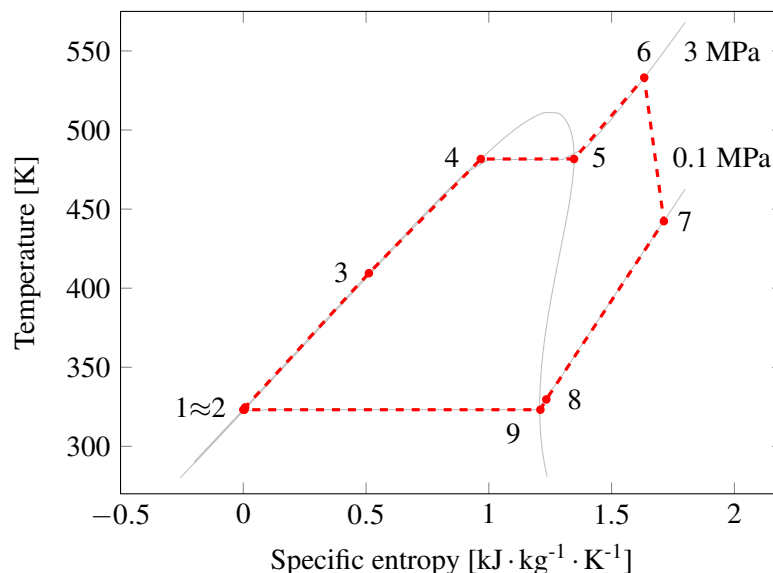


Figure 3: Saturation curve of cyclopentane in a $T - s$ diagram, showing the thermodynamic cycle state points of the organic Rankine cycle system.

4. RESULTS AND DISCUSSION

Figures 4 and 5 show the results for the turbine optimization at constant rotational speed (3000 rpm) and for the case where the rotational speed is optimized. The plots relate the total-to-total efficiency to the mass flow rate of the working fluid and the pressure ratio $\pi_e = p_{06}/p_{07}$. Each point in the figures represents a different optimal geometry obtained with a dedicated optimization. The efficiency curves initially increase, and, subsequently, flatten out. The results are in line with the trends reported by Macchi and Perdichizzi [20] for complex and monoatomic gases. As regarding the expander geometry, higher mass flow rates entail larger turbine sizes for the same pressure ratio. This results in wider blade channels and reduced relative influence of primary and secondary losses. Figure 6 shows an example of optimal geometry with relative velocity triangles. Removing the constraint on the rotational speed is extremely beneficial for the expander design. Figure 7 reports the optimal values obtained for this

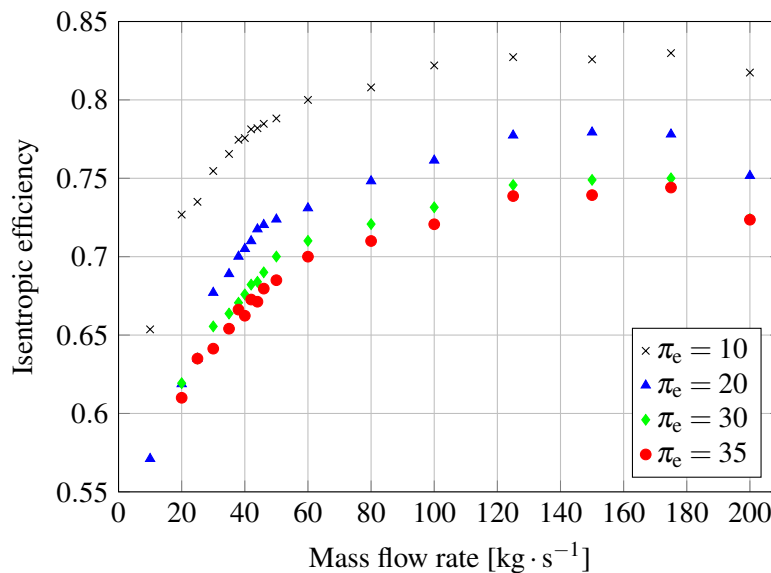


Figure 4: Surrogate turbine model at fixed rotational speed. Total-to-total isentropic efficiency versus mass flow rate at different turbine pressure ratios.

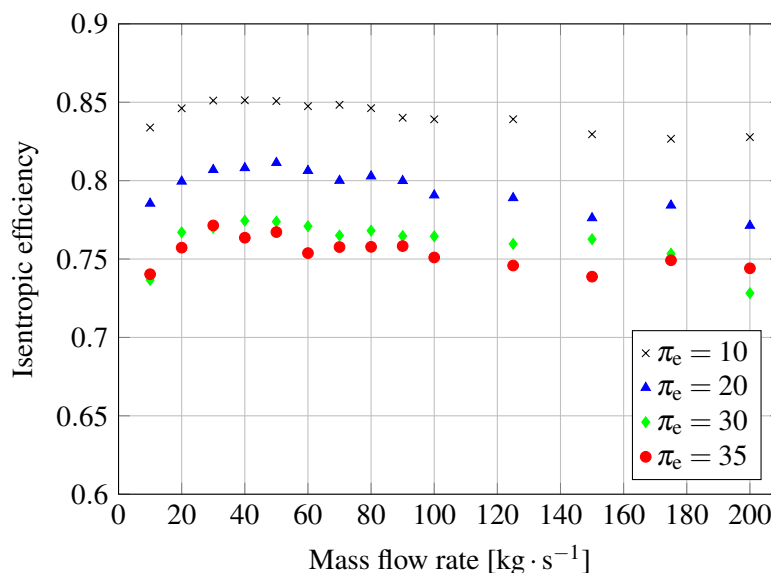


Figure 5: Surrogate turbine model at the optimal rotational speeds. Total-to-total isentropic efficiency versus mass flow rate at different turbine pressure ratios.

optimization variable. The highest gain in the turbine efficiency occurs at mass flow rates lower than $80 \text{ kg} \cdot \text{s}^{-1}$. In this region, increasing the rotational speed allows for higher blade heights. Conversely, operating at constant rotational speed leads to an increment of the cascade losses for decreasing mass flow rates.

Figure 4 reports a maximum in efficiency around $120 \text{ kg} \cdot \text{s}^{-1}$, while lower values are obtained for higher mass flow rates. This is caused by the increment of the profile losses in the nozzle. The rotor flare angle reaches the upper bound at around $120 \text{ kg} \cdot \text{s}^{-1}$. At higher mass flow rates, the expansion across the stator and the axial velocity components increase. This results in higher losses and lower efficiency.

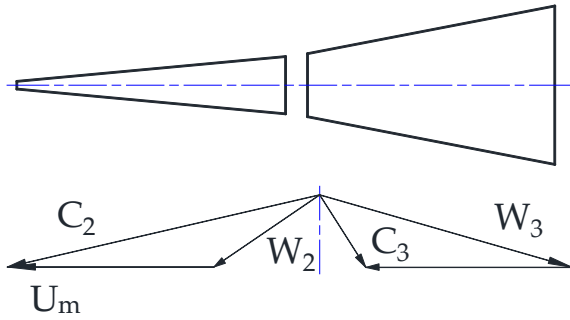


Figure 6: The turbine section channel and relative velocity triangles at $\pi_e = 20$ and $38 \text{ kg} \cdot \text{s}^{-1}$. The degree of reaction is 0.35.

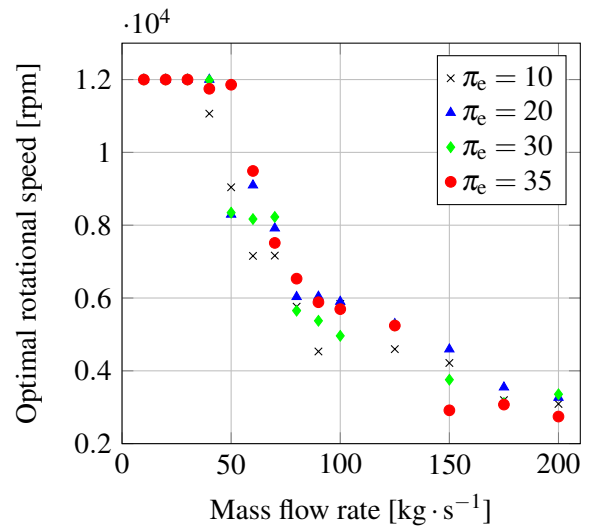


Figure 7: Optimal rotational speed versus mass flow rate at different turbine pressure ratios for the second surrogate model.

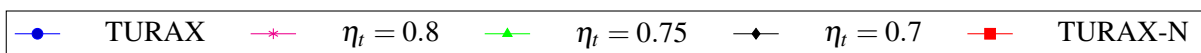
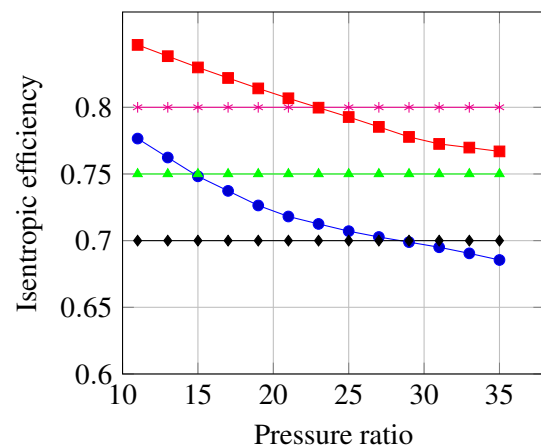
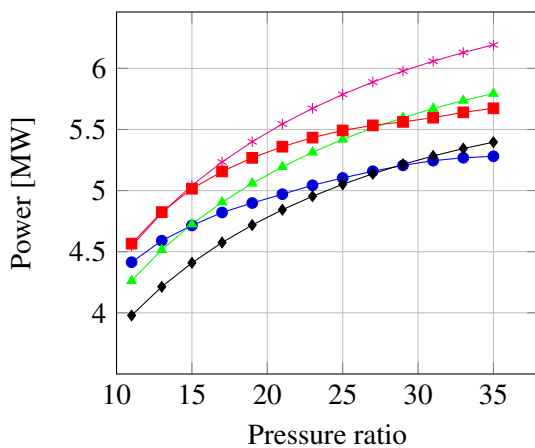


Figure 8: Single exhaust gas configuration. 8(a) Net power output versus pressure ratio and 8(b) Total-to-total turbine isentropic efficiency versus pressure ratio.

Figure 8a compares the ORC net power output at constant isentropic efficiency with that calculated using the turbine surrogate models. Given the assumptions reported in the previous section, the ratio π_e is the only variable affecting the power output. The circulating mass flow rate varies between 45 and $50 \text{ kg} \cdot \text{s}^{-1}$ for the reported range of π_e . The constant isentropic efficiency curves differ significantly compared to the trends observed with the surrogate models. This is owed to the progressive decrement of the expander performance at increasing pressure ratios, see Figure 8b. The computed isentropic efficiency decreases from 0.78 to 0.68 for the case with fixed rotational speed. The curve intersects the horizontal lines of constant efficiency. The intersections correspond to the values of pressure ratio for which the total-to-total efficiency coincides with the constant value. Accounting for the variability of the expander performance yields a maximum difference in power output of 900 kW, compared to the results obtained assuming a fixed turbine efficiency of 80%. This corresponds to a relative power decrement of 15%.

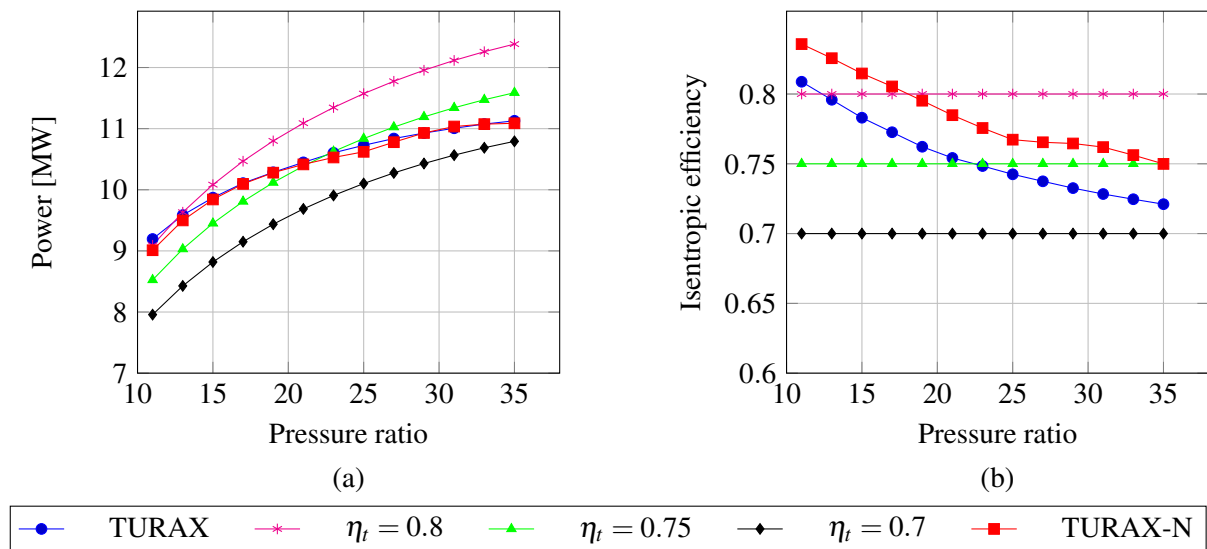


Figure 9: Multiple exhaust gas configuration. 9(a) Net power output versus pressure ratio and 9(b) Total-to-total turbine isentropic efficiency versus pressure ratio.

Figure 8b demonstrates that the optimization of the rotational speed increases averagely the expander efficiency of 8 %-points. The power curve is labeled as TURAX-N in Figures 8a and 8b. The improvement in power output is around 400 kW, corresponding to a relative increment of 7.4 %. This gain relates to the fact that the ORC unit operates in the range of mass flow rates where the expander efficiency is maximized. The highest power output occurs at the maximum available pressure ratio with just one stage, i.e., 35. Here the volumetric flow ratio reaches 43.5, a value close to the upper limit suggested by Macchi [19]. Further increments in the power output could be achieved by increasing the number of stages or adopting supercritical configurations. However, a larger number of stages implies higher investment costs. Moreover, the power curve in Figure 8b, obtained using the surrogate model, shows a progressively flattening trend for high values of pressure ratio. It is expected that the small power increments do not justify the technological (and economic) effort to operate at higher pressures. A complete techno-economic optimization should be carried out, in order to draw quantitative conclusions. However, such analysis is beyond the scopes of the current paper.

Figure 4 shows that the total-to-total isentropic efficiency of the turbine peaks at $120 \text{ kg} \cdot \text{s}^{-1}$. This value is around three times the mass flow rate of the ORC unit fed by the exhaust gases of one gas turbine. Given that on the Draugen platform two engines operate at the same time, the opportunity of harvesting the heat from both energy sources with one ORC unit arises. This investigation assumes perfect mixing of the two exhaust gases. The engines are also equally sharing the load. As reported in Figure 9a, the trend of power versus pressure ratio is similar to that presented in the previous test. However, the power output obtained with the surrogate model is proportionally larger, being the values of turbine efficiency around 10 % higher. The integration of the ORC unit with one engine produces a net power of 5.3 MW. Conversely, the use of the exhaust heat of two gas turbines gives a total output of 11.1 MW. Therefore, the latter plant configuration offers a relative power increment of 5 %, compared to the implementation of two separate ORC turbogenerators. As shown in Figure 9b, the use of one ORC unit for two engines reduces the benefit of optimizing the rotational speed of the turbine. The increment in efficiency is smaller compared to the case of two separate ORC power systems. Moreover, Figure 9a shows that the mechanical losses of the gearbox partially overshadow the gain in turbine efficiency.

5. CONCLUSIONS

This paper documents the development of a simulation tool for the preliminary design of axial turbines. The model is integrated with a freely-available high-accuracy property library. This integration gives the possibility to minimize the computational time using advanced interpolation methods. The simulation tool is combined with the thermodynamic model of the ORC process in the form of a surrogate model giving the optimal turbine geometry at different boundary conditions. The method is applied to design an ORC power system for offshore applications.

The results obtained computing the expander performance using the surrogate model are compared with those assuming constant turbine isentropic efficiency. The power curves present different trends with a maximum relative discrepancy of 15 % in power output. The curve flattens at high turbine expansion ratios, if the expander design is taken into account. This trend arises doubts as to the benefit of increasing the design-point pressure ratio. The optimization of the rotational speed of the turbine improves the expander performance of 8 %-points, with a correspondent relative increment in power of 7.4 %. The power outputs of a single ORC turbogenerator recuperating the exhaust heat from two gas turbines are compared to the ones of one unit for each engine. The superior performance of larger scale expanders enables to achieve a 5 % improvement of power output using a single ORC power system. This latter configuration makes the implementation of a gearbox less attractive. The increased mechanical losses partially overshadow of the higher turbine isentropic efficiency.

NOMENCLATURE

C	absolute fluid velocity [$\text{m} \cdot \text{s}^{-1}$]
N	rotational speed [rpm]
U	peripheral velocity [$\text{m} \cdot \text{s}^{-1}$]
W	relative fluid velocity [$\text{m} \cdot \text{s}^{-1}$]
\bar{X}	array of the optimizing variables
c	axial chord [m]
o	blade throat opening [m]
p	pressure [Pa]
s	blade pitch [m]

Abbreviations and acronyms

CC	combustion chamber
GEN	electric generator
HPC	high pressure compressor
HPT	high pressure turbine
LPC	low pressure compressor

LPT	low pressure turbine
ORC	organic Rankine cycle
OTB	once-through boiler
PT	power turbine
TUR	organic Rankine cycle expander

Greek letters

$\eta_{is,t}$	turbine isentropic efficiency
π_e	pressure ratio
ψ	stage loading coefficient
θ	blade angle [$^\circ$]

Subscripts

2	rotor inlet
3	rotor outlet
m	referred to average diameter
n	nozzle
r	rotor

REFERENCES

- [1] Ainley, D. and Mathieson, G. (1951). An examination of the flow and pressure losses in blade rows of axial-flow turbines. Technical report, Ministry of Supply - Aeronautical Research Council.

- [2] Andreasen, J. G., Larsen, U., Knudsen, T., Pierobon, L., and Haglind, F. (2014). Selection and optimization of pure and mixed working fluids for low grade heat utilization using organic Rankine cycles. *Energy*, 73:204–213.
- [3] Astolfi, M., Romano, M. C., Bombarda, P., and Macchi, E. (2014). Binary ORC (Organic Rankine Cycles) power plants for the exploitation of medium low temperature geothermal sources - Part B: Techno-economic optimization. *Energy*, 66:435–446.
- [4] Bell, I. H., Wronski, J., Quoilin, S., and Lemort, V. (2014). Pure and pseudo-pure fluid thermophysical property evaluation and the open-source thermophysical property library CoolProp. *Industrial & Engineering Chemistry Research*, 53(6):2498–2508.
- [5] Casati, E., Galli, A., and Colonna, P. (2013). Thermal energy storage for solar-powered organic Rankine cycle engines. *Solar energy*, 96:205–219.
- [6] Colonna, P. (2012). Developments from the early days, current status and an outlook on relevant research topics and new applications. In *Proceedings of International Symposium on Advanced Waste Heat Valorisation Technologies*, Kortrijk, Belgium.
- [7] Craig, H. and Cox, H. (1970). Performance estimation of axial flow turbines. *Proceedings of the Institution of Mechanical Engineers*, 185(1):407–424.
- [8] Deb, K. (2001). *Multi-objective optimization using evolutionary algorithms*. John Wiley & Sons, Inc., West Sussex, Great Britain.
- [9] Deich, M., Filippov, G., and Lazarev, L. (1965). *Atlas of Axial Turbine Blade Cascades*. C.E. Trans. 4563-4564. CEGB Information Services.
- [10] Del Turco, P., Asti, A., Del Greco, A., Bacci, A., Landi, G., and Seghi, G. (2011). The ORegen waste heat recovery cycle: Reducing the CO₂ footprint by means of overall cycle efficiency improvement. In *ASME Turbo Expo 2011*, pages 547–556, Vancouver, Canada.
- [11] Gabrielli, P. (2014). Design and optimization of turbo-expanders for organic rankine cycles. Master's thesis, Technical University of Denmark.
- [12] Goldberg, D. E. (1989). *Genetic Algorithms in Search, Optimization and Machine Learning*. Addison-Wesley Longman Publishing Co., Inc., Boston, MA, USA, 1st edition.
- [13] Invernizzi, C., Iora, P., and Silva, P. (2007). Bottoming micro-Rankine cycles for micro-gas turbines. *Applied Thermal Engineering*, 27(1):100–110.
- [14] Kang, S. H. (2012). Design and experimental study of ORC (organic Rankine cycle) and radial turbine using R245fa working fluid. *Energy*, 41(1):514–524.
- [15] Keys, R. G. (1981). Cubic convolution interpolation for digital image processing. *IEEE Proceedings. Nanobiotechnology Transactions On Acoustics, Speech, And Signal Processing*, 29(6):1153–1160.
- [16] Lang, W., Colonna, P., and Almbauer, R. (2013). Assessment of waste heat recovery from a heavy-duty truck engine by means of an ORC turbogenerator. *Journal of Engineering for Gas Turbines and Power*, 135(4):1–10.
- [17] Larsen, U., Pierobon, L., Haglind, F., and Gabrielli, C. (2013). Design and optimisation of organic Rankine cycles for waste heat recovery in marine applications using the principles of natural selection. *Energy*, 55(0):803 – 812.

- [18] Lozza, G., Macchi, E., and Perdichizzi, A. (1982). On the influence of the number of stages on the efficiency of axial-flow turbines. In *American Society of Mechanical Engineers, International Gas Turbine Conference and Exhibit, 27th*, London, England.
- [19] Macchi, E. (1977). Design criteria for turbines operating with fluids having a low speed of sound. *Von Karman Institute for Fluid Dynamics*, 2:1–64.
- [20] Macchi, E. and Perdichizzi, A. (1981). Efficiency prediction for axial-flow turbines operating with nonconventional fluids. *Journal of Engineering for Gas Turbine and Power*, 103(4):718–724.
- [21] Miyagawa, K. and Hill, P. G. (2001). Rapid and accurate calculation of water and steam properties using the tabular Taylor series expansion method. *Journal of Engineering for Gas Turbines and Power*, 123(3):707–712.
- [22] Pasetti, M., Invernizzi, C. M., and Iora, P. (2014). Thermal stability of working fluids for organic Rankine cycles: An improved survey method and experimental results for cyclopentane, isopentane and n-butane. *Applied Thermal Engineering*, 73(1):762 – 772.
- [23] Pasquale, D., Persico, G., and Rebay, S. (2013). Optimization of turbomachinery flow surfaces applying a CFD-based throughflow method. *Journal of Turbomachinery*, 136(3):1–11.
- [24] Pierobon, L., Nguyen, T.-V., Larsen, U., Haglind, F., and Elmegaard, B. (2013). Multi-objective optimization of organic Rankine cycles for waste heat recovery: Application in an offshore platform. *Energy*, 58(0):538–549.
- [25] Pini, M., Persico, G., Casati, E., and Dossena, V. (2013). Preliminary design of a centrifugal turbine for organic Rankine cycles applications. *Journal of Engineering for Gas Turbine and Power*, 135(4):1–9.
- [26] Quoilin, S., Orosz, M., Hemond, H., and Lemort, V. (2011). Performance and design optimization of a low-cost solar organic Rankine cycle for remote power generation. *Solar Energy*, 85(5):955–966.
- [27] Span, R., Wagner, W., Lemmon, E. W., and Jacobsen, R. T. (2001). Multiparameter equations of state—recent trends and future challenges. *Fluid Phase Equilibria*, 183:1–20.
- [28] The MathWorks, Inc. (2014). *Optimization ToolboxTM User's Guide*. The MathWorks, Inc., Natick, Massachusetts.
- [29] Vavra, M. H. (1969). Axial flow turbines. *Von Karman Institute for Fluid Dynamics*, 15.
- [30] Watanabe, K. and Dooley, R. B. (2003). Guideline on the Tabular Taylor Series Expansion (TTSE) Method for Calculation of Thermodynamic Properties of Water and Steam Applied to IAPWS-95 as an Example. Technical report, The International Association for the Properties of Water and Steam, Vejle, Denmark.

PAST AND CURRENT RESEARCH TRENDS IN ORC POWER SYSTEMS

Sylvain Quoilin

University of Liège
Faculty of Applied Sciences
Energy Systems Research Unit
Campus of Sart-Tilman, B49 (P33)
Chemin des Chevreuils, 7
B-4000 LIEGE (BELGIUM)
squoilin@ulg.ac.be

ABSTRACT

The past years have seen an almost-exponentially increasing number of published papers in the ORC research field. This profusion of publications sometimes makes it difficult to get a global picture of the main challenges and ongoing research.

Recent literature has also been characterized by a certain lack of originality, the same methods and approaches being repeated multiple times with few new relevant insights. It is therefore of primary importance to highlight the state-of-the-art and foster new and original research, potentially resulting in new technological improvements.

This keynote provides an overview of the state of the art and of the main research trends in ORC power systems. It does not aim at covering all research fields, but highlights and describes a few relevant topics originating from the previous ORC conferences and from the scientific literature. The main methods, mathematical tools and results are described in such a way to provide useful information for the replication of such studies. Recommendations are finally formulated, together with an open discussion regarding possible relevant future contributions in ORC research

TOWARDS THE OPTIMAL OPERATION OF AN ORGANIC RANKINE CYCLE UNIT BY MEANS OF MODEL PREDICTIVE CONTROL

Andres Hernandez^{1,2*}, Adriano Desideri², Clara Ionescu¹, Sylvain Quoilin²,
Vincent Lemort², Robin De Keyser¹

¹ Ghent University, Department of Electrical energy, Systems and Automation, Ghent, Belgium
andres.hernandez@ugent.be, claramihaela.ionescu@ugent.be, robain.dekeyser@ugent.be

² University of Liège, Aerospace and Mechanical engineering department, Liège, Belgium
adesideri@ulg.ac.be, squoilin@ulg.ac.be, vincent.lemort@ulg.ac.be

* Corresponding Author

ABSTRACT

In this paper the optimal operation of an Organic Rankine Cycle (ORC) unit is investigated both in terms of energy production and safety conditions. Simulations on a validated dynamic model of a real regenerative ORC unit, are used to illustrate the existence of an optimal evaporating temperature which maximizes energy production for some given heat source conditions. This idea is further extended using a perturbation based Extremum Seeking (ES) algorithm to find online the optimal evaporating temperature. Regarding safety conditions we propose the use of the Extended Prediction Self-Adaptive Control (EPSAC) approach to constrained Model Predictive Control (MPC). Since it uses input/output models for prediction, it avoids the need of state estimators, making of it a suitable tool for industrial applications. The performance of the proposed control strategy is compared to PID-like schemes. Results show that EPSAC-MPC is a more effective control strategy as it allows a safer and more efficient operation of the ORC unit, as it can handle constraints in a natural way, operating close to the boundary conditions where power generation is maximized.

1. INTRODUCTION

In recent years several studies have underlined the potential of low-grade heat recovery to reduce the amount of worldwide industrial energy consumption (IEA, 2010). The highly fluctuating nature of the heat source makes waste heat recovery (WHR) applications a challenging task. Organic Rankine Cycle (ORC) systems represent the most promising technology for WHR, where the main objectives to optimally operate the system are twofold: 1) keep the cycle in a safe condition and 2) maximize the net output power.

Safe operation of the ORC unit is important as it allows a longer life expectancy in all components. In this regard, an accurate regulation of the superheating represents an important task for the controller. The regulator has to guarantee a minimum value of superheating in order to maximize the efficiency, and to avoid the formation of liquid droplets at expander inlet that can damage the expansion machine (Wei et al., 2007). On the other hand, in order to maximize the output power, the evaporating temperature represents the most relevant controlled variable (Quoilin et al., 2011; Hernandez et al., 2015).

In this contribution we propose a two-layer control structure to guarantee the optimal operation of an ORC unit for waste heat recovery applications: an Extremum Seeking (ES) algorithm to find on-line the optimal evaporating temperature, which is later given as reference to a constrained Model Predictive Controller (MPC).

Extremum Seeking is a well developed research area which addresses the problem of objective value optimization when the objective function, its gradient and optimum value are unknown (Ariyur and

Krstic, 2003). In this study we make use of a perturbation based ES to find the evaporating temperature that maximizes the output power for the case of heat source variations. The performance of the ES algorithm is compared to the correlation obtained directly from the dynamic nonlinear model.

A possible drawback for ES algorithms appears for the case when the extremum causes other variables to violate safety limits. One option to tackle this situation is to design a complex ES algorithm which accounts for constraints as proposed in (De Hann and Guay, 2005). Here, instead we propose to use a simple ES algorithm and let a local controller to deal with constraints, e.g., taking actions for the cases when superheating is below a threshold value. The Extended Prediction Self-Adaptive Control (EPSAC) approach to constrained Model Predictive Control is proposed as local control strategy. Since it uses input/output models for prediction and not state-space models as in other MPC algorithms (Maciejowski, 2002), it avoids the need of state estimators, making of it a suitable tool for industrial applications. The performance of the proposed EPSAC-MPC strategy is compared to the one achieved using PI-like strategies.

The paper is structured as follows: a description of the ORC process is presented in section 2, followed by a brief description of the adaptive Extremum Seeking algorithm in section 3. Next in section 4 the EPSAC-MPC algorithm is formulated, followed by the discussion of the simulation results in section 5. Finally a conclusion section summaries the main outcome of this contribution.

2. PROCESS DESCRIPTION

This section describes the architecture and main characteristics of the ORC system used for evaluating the performance of the developed control strategies.

2.1 The Organic Rankine Cycle System

In order to assess the performance of the different developed control strategies, a dynamic model of the ORC system presented in Fig. 1 has been developed in the Modelica language using existent components from the ThermoCycle library (Quoilin et al., 2014). The developed model is then exported into Simulink/Matlab environment by means of the Functional Mock-Up Interface (FMI) open standard.

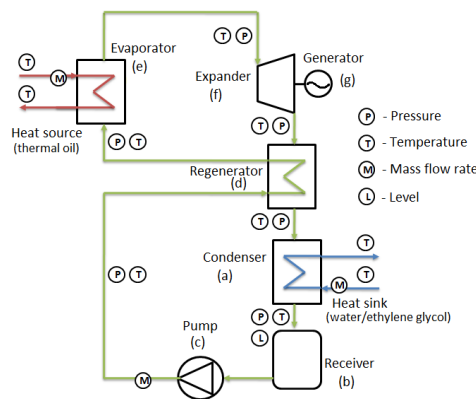


Figure 1: Schematic layout of the pilot plant available at Ghent University, campus Kortrijk (Belgium)

The system based on a regenerative cycle and solkatherm (SES36) as working fluid, shows a nominal power of 11 *kWe*. The expander is originally a single screw compressor adapted to run in expander mode. It drives an asynchronous generator connected to the electric grid through a four-quadrant inverter, which allows varying the generator rotational speed (N_{exp}). During the simulations performed in this paper, the generator rotational speed is kept constant at 3000 *rpm* to emulate an installation directly connected to the grid. The circulating pump (N_{pp}) is a vertical variable speed 14-stage centrifugal pump with a maximum pressure of 14 bar and 2.2 *kWe* nominal power.

Starting from the bottom of the scheme it is possible to recognize the liquid receiver (b) installed at the outlet of the condenser (a) where the fluid is collected in saturated liquid condition. From the receiver outlet, the fluid is pumped (c) through the regenerator (d) cold side, and the evaporator (e), where it is heated up to superheated vapor, reaching its maximum temperature at the evaporator outlet. The fluid, after being expanded in the volumetric machine (f), enters the regenerator hot side, and then it flows into the condenser (a) to close the cycle.

2.2 Conditions for optimal operation of an ORC unit

In order to optimally operate an ORC unit, two main conditions need to be satisfied: **1)** keep the cycle in a safe condition during operation and **2)** maximize the net output power. Safe operation of the ORC unit is important as it allows a longer life expectancy in all components. In this concern, an accurate regulation of superheating (ΔT_{sh}), is the main priority since a minimum value of superheating has to be guaranteed in order to avoid a wet expansion (i.e., formation of liquid droplets at the expander inlet that can damage the expansion machine). The superheating is defined as:

$$\Delta T_{sh} = T_{exp,su} - T_{sat,ev} \quad (1)$$

where $T_{exp,su}$ is the temperature measured at the inlet of the expander and $T_{sat,ev}$ the evaporating temperature, corresponding to the temperature at which the fluid undergoes the phase transition from saturated liquid to saturated vapor at the fixed evaporating pressure $p_{sat,ev}$.

$$T_{sat,ev} = f(p_{sat,ev}) \quad (2)$$

where f corresponds to a function that correlates the pressure for the refrigerant.

In order to maximize the output power the evaporating temperature represents the most relevant control variable (Quoilin et al., 2011), which needs to be adapted depending on the heat source conditions (Hernandez et al., 2015). The main terms to assess the performance of the ORC system are the net output power and the cycle efficiency, which are defined as:

$$\dot{W}_{el,net} = \dot{W}_{exp} - \dot{W}_{pump} \quad (3)$$

$$\eta_{cycle} = \frac{\dot{W}_{el,net}}{\dot{Q}_{in,ORC}} \quad (4)$$

where \dot{W}_{exp} is the expander electrical power, \dot{W}_{pump} is the pump electrical power and $\dot{Q}_{in,ORC}$ is the thermal power supplied to the ORC system in the evaporator.

2.3 Optimal evaporating temperature

The developed Modelica dynamic model has been used to gain insight on the system's dynamics, in particular on the relationship between superheating (ΔT_{sh}), evaporating temperature ($T_{sat,ev}$), pump speed (N_{pp}) and expander electrical power (\dot{W}_{exp}). The simulation consists on decreasing the pump speed N_{pp} from maximum to minimum in small steps. The same experiment is performed for different heat source conditions, temperature and mass flow, in the ranges $T_{hf} = \{90, 100, 110, 125\}^\circ C$ and $\dot{m}_{hf} = \{0.5, 0.8, 1.0, 1.5\} kg/s$, while temperature and mass flow in the heat sink T_{cf} and \dot{m}_{cf} were kept constant at $15^\circ C$ and $4 kg/s$, respectively. The results for the case of $\dot{m}_{hf} = 1.0 kg/s$ are depicted in Fig. 2, where the expander electrical power \dot{W}_{exp} is represented as a function of $T_{sat,ev}$ and ΔT_{sh} . Fig. 2a shows how, for each heat source condition, the expander output power initially grows for increasing evaporating temperature until it reaches a maximum. This is a consequence of the working fluid mass flow that is circulated in the system, see the pump rotational speed value. As the pump speed increases further, two-phase condition appears at the evaporator outlet and a lower output power is registered. Fig. 2b shows the relation between expander output power and superheating level for the same heat source conditions as in Fig. 2a. The power increases as the level of superheating decreases. Notice also that for values of superheating lower than $10^\circ C$ there is not much gain in the output power. Using the current data it is then possible to derive a correlation for the optimal evaporating temperature as a function of the heat source conditions:

$$T_{sat,opt} = -290.915 + 183.33 * \log_{10}(T_{hf}) + 10.636 * \dot{m}_{hf} \quad (5)$$

Equation (5) is valid in the range of $0.5 \leq \dot{m}_{hf} \leq 1.5 kg/s$ and $90 \leq T_{hf} \leq 125^\circ C$ given a constant saturation temperature in the condenser of $p_{sat,cd} = 1.4 bar$.

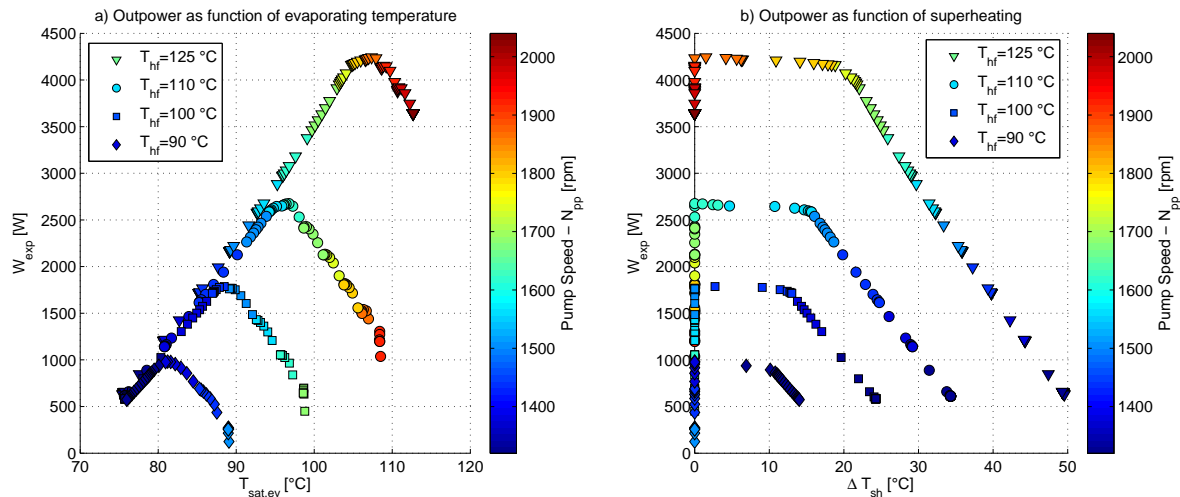


Figure 2: Understanding the operation of an ORC unit. Relationship between output power and a) evaporating temperature and b) superheating for four different heat source conditions $T_{hf} = \{90, 100, 110, 125\} \text{ } ^\circ\text{C}$ with $\dot{m}_{hf} = 1.0 \text{ kg/s}$.

3. ADAPTIVE OPTIMIZATION

As presented in section 2.3, in order to maximize the output power it is necessary to find the optimal evaporating temperature for some given heat source conditions. If a dynamic model of the system is known, one can then build a correlation which satisfies also safety conditions. However, there are two drawbacks in this approach: first, a validated dynamic model is not always available and second, there will be modeling errors and consequently a biased correlation.

In this contribution we follow a different approach, by using an Extremum Seeking (ES) algorithm to find the optimal evaporating temperature, which maximizes the output power without the need of a model. Extremum Seeking is a well developed field that addresses the problem of objective value optimization when the objective function, its gradient and optimum value are unknown (Ariyur and Krstic, 2003). These techniques are categorized into five main groups: sliding mode ES, neural network ES, approximation based ES, perturbation based ES and adaptive ES. From those the perturbation based ES framework is the most popular method in literature (Ariyur and Krstic, 2003). Since it has proved to be more robust to noise and dynamic effects in the system, thus producing smoother references which decrease the risk of instability (Zhang and Ordenez, 2012).

The control structure here proposed is depicted in Fig. 3. A *perturbation based ES algorithm* is in charge of finding the extremum $T_{sat,opt}$ that arises from the reference-to-output nonlinear map (i.e., $T_{sat,ev}$ to \dot{W}_{exp}), while a local feedback controller will keep the system stable at that equilibrium optimal point.

The ES algorithm works as follows: it sends a sine wave to the system as position reference together with an adaptation input:

$$T_{sat,opt} = \gamma \sin(\omega t) + \hat{T}_{sat,opt} \quad (6)$$

with some amplitude γ and modulation frequency ω . The adaptation signal $\hat{T}_{sat,opt}$ shifts the sine wave towards the gradient direction, thus (6) is the modulation phase of the algorithm. The response of the system to this signal is measured in the objective value (\dot{W}_{exp}). This output is filtered by a high-pass filter to eliminate the DC component and demodulated by the same sine signal to extract the gradient direction.

$$\zeta = W_{exp} \left(\frac{\omega_l}{s + \omega_l} \right) \left(\frac{s}{s + \omega_h} \right) (\gamma \sin(\omega t)) \quad (7)$$

This information is used to calculate the shift in the sine signal towards the gradient. Next the adaptation

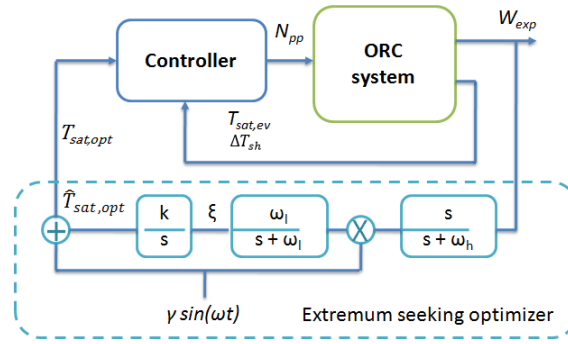


Figure 3: Perturbation based extremum seeking algorithm applied to the ORC system.

law is computed:

$$\hat{T}_{sat,opt} = \xi \frac{k}{s} \quad (8)$$

where k is a positive constant that specifies the adaptation speed. Since only the DC component of the demodulated signal is needed for gradient calculation, a low pass filter is often used. The amplitude and frequency of the sine wave signal and the cutoff frequencies of the filters are important design parameters. A detailed study of how the design of the perturbation signal affects the performance of the ES algorithm is presented in (Krstic, 2000).

4. MODEL PREDICTIVE CONTROL

A brief introduction to EPSAC algorithm is presented in this section. For a detailed description the reader is referred to (De Keyser, 2003; Hernandez et al., 2015).

4.1 Computing the Predictions

Using EPSAC algorithm, the measured process output can be represented as:

$$y(t) = x(t) + n(t) \quad (9)$$

where $x(t)$ is the model output which represents the effect of the control input $u(t)$ and $n(t)$ represents the effect of the disturbances and modeling errors, all at discrete-time index t . Model output $x(t)$ can be described by the generic system dynamic model:

$$x(t) = f[x(t-1), x(t-2), \dots, u(t-1), u(t-2), \dots] \quad (10)$$

Notice that $x(t)$ represents here the model output, not the state vector. Also important is the fact that f can be either a *linear* or a *nonlinear* function.

Furthermore, the disturbance $n(t)$ can be modeled as colored noise through a filter with the transfer function:

$$n(t) = \frac{C(q^{-1})}{D(q^{-1})} e(t) \quad (11)$$

with $e(t)$ uncorrelated (white) noise with zero-mean and C, D monic polynomials in the backward shift operator q^{-1} . The disturbance model must be designed to achieve robustness of the control loop against unmeasured disturbances and modeling errors (Maciejowski, 2002).

A fundamental step in the EPSAC methodology consists of the prediction. Using the generic process model (9), the predicted values of the output are:

$$y(t+k|t) = x(t+k|t) + n(t+k|t) \quad (12)$$

$x(t+k|t)$ and $n(t+k|t)$ can be predicted by recursion of the process model (10) and by using filtering techniques on the noise model (11), respectively (De Keyser, 2003).

4.2 Computing the optimal control action

A key element in linear MPC is the use of base (or free) and optimizing (or forced) response concepts (Camacho and Bordons, 2004). In EPSAC, the future response can be expressed as:

$$y(t+k|t) = y_{base}(t+k|t) + y_{optimize}(t+k|t) \quad (13)$$

The two contributing factors have the following origin:

- $y_{base}(t+k|t)$ is the effect of the past inputs, the apriori defined future base control sequence $u_{base}(t+k|t)$ and the predicted disturbance $n(t+k|t)$.
- $y_{optimize}(t+k|t)$ is the effect of the additions $\delta u(t+k|t)$ that are optimized and added to $u_{base}(t+k|t)$, according to $\delta u(t+k|t) = u(t+k|t) - u_{base}(t+k|t)$. The effect of these additions is the discrete time convolution of $\Delta U = \{\delta u(t|t), \dots, \delta u(t+N_u-1|t)\}$ with the impulse response coefficients of the system (G matrix), where N_u is the chosen control horizon.

The control ΔU is the solution to the following constrained optimization problem:

$$\Delta U = \arg \min_{\Delta U \in \mathbb{R}^{N_u}} \sum_{k=N_1}^{N_2} [r(t+k|t) - y(t+k|t)]^2 \quad (14)$$

subject to $A \cdot \Delta U \leq B$

where N_1 and N_2 are the minimum and maximum prediction horizons, N_u is the control horizon, $r(t+k|t)$ is a future setpoint or reference sequence. The various process input and output constraints can all be expressed in terms of ΔU , resulting in matrices A , B . Since (14) is quadratic with linear constraints in decision variables ΔU , then the minimization problem can be solved by a quadratic programming (QP) algorithm (Maciejowski, 2002; Camacho and Bordons, 2004).

5. SIMULATION RESULTS

The developed ES algorithm is tested in simulation using the proposed EPSAC-MPC strategy and two PI-like strategies. The heat source and heat sink profiles of the ORC system are depicted in Fig. 4. The main variation in the heat source is due to an increase in the temperature (T_{hf}) from 110°C to 120°C . Other heat source and heat sink variables are rather constant with some small variations around the operating point.

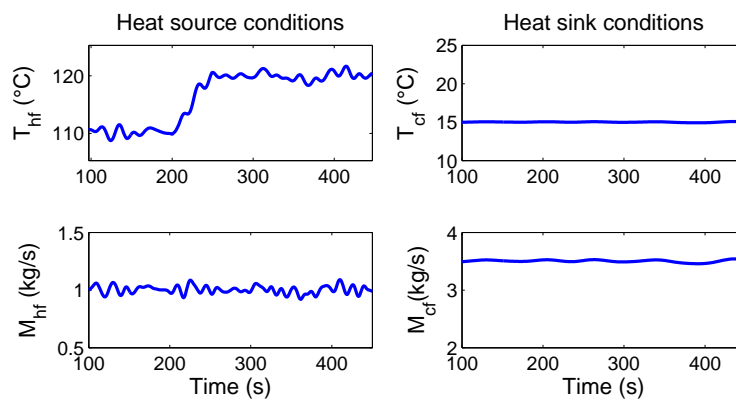


Figure 4: Temperature and mass flow rate of the defined heat source and heat sink.

5.1 Low-order model for prediction

MPC requires of a low-order model suitable for prediction. Following a similar approach as the one performed in (Hernandez et al., 2015), the model has been identified from the manipulated variable: pump

speed (N_{pp}) to the evaporating temperature ($T_{sat,ev}$) and superheating (ΔT_{sh}). Notice that the temperature T_{hf} in the heat source also influences $T_{sat,ev}$ and ΔT_{sh} , thus becoming a measured disturbance. As result we are interested on identifying a system consisting of 2 inputs (one manipulated and one measured disturbance) and 2 outputs.

A linear parametric identification is thus performed in the system using the prediction error minimization method from the data collected using a multisine excitation signal (Ljung, 2007). The identified model presented in (15) is in the form of discrete-time transfer functions for a sampling time $T_s = 1$ s .

$$\Delta T_{sh}(q) = \frac{-0.063q^{-1} + 0.059q^{-2}}{1 - 2.44q^{-1} + 1.955q^{-2} - 0.51q^{-3}} N_{pp}(q) + \frac{0.47q^{-1}}{1 - 0.51q^{-1}} T_{hf}(q) \quad (15a)$$

$$T_{sat,ev}(q) = \frac{0.066q^{-1} - 0.063q^{-2}}{1 - 2.42q^{-1} + 1.91q^{-2} - 0.49q^{-3}} N_{pp}(q) + \frac{0.0017q^{-11} - 0.0017q^{-12}}{1 - 3.6q^{-1} + 4.88q^{-2} - 2.95q^{-3} + 0.67q^{-4}} T_{hf}(q) \quad (15b)$$

5.2 Performance of ES with constrained EPSAC-MPC strategy

The MPC control objective consists in tracking the optimal setpoint generated by the optimizer (Fig. 3), while keeping the superheating above a desired threshold value to guarantee a safe operation. The control strategy must satisfy these conditions using only one degree of freedom (i.e. pump speed N_{pp}), while satisfying actuator constraints ($N_{pp,min} = 1320$ rpm; $N_{pp,max} = 2100$ rpm; $\Delta N_{pp} = 100$ rpm) and constraints at the process output ($\Delta T_{sh,min} = 10$ °C).

The EPSAC-MPC controller is tuned for horizons $N_1 = 1$, $N_2 = 15$ and $N_u = 1$. While the ES optimizer is tuned for $k = 1/38$, $\omega_l = 0.02$ rad/s, $\omega_h = 0.1$ rad/s, $\gamma = 0.05$ and $\omega = 0.06$ rad/s. Its performance is depicted in Fig. 5.

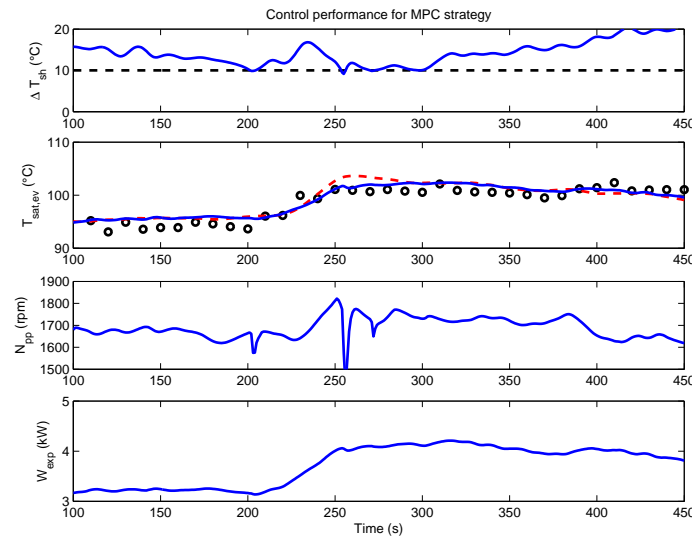


Figure 5: Control performance of MPC. Dashed-red line represents the ES optimizer while black-circles represents the optimizer obtained from the dynamic model.

Two important elements must be analyzed from results in Fig. 5. First, two optimal evaporating temperatures are present, one computed using the ES algorithm (dashed red line) and the other (black circles) computed from correlation (5). The ES algorithm is able to adapt properly to the heat source variation, maximizing the output power. Second, it is important to notice that in the time range between 250 and 300 seconds, the controller is not following the setpoint but it rather brings the evaporating temperature closer to the reference computed using correlation (5). This is due to the active constraint in superheating, which causes the controller to take actions in the pump to bring the system in a safer regime (i.e., $\Delta T_{sh} > 10$ °C). Remember that equation (5) was computed to ‘guarantee’ superheating will remain above 10 °C.

5.3 Performance of ES with PI-like strategies

The EPSAC-MPC strategy is replaced by two PI-like controllers, in order to compare the performance. The first strategy consists on a PI controller used to track the reference given by the ES optimizer. The second strategy consists in using a PI controller to track the optimal evaporating temperature unless superheating goes below the threshold value of 10°C , in which case a second PI controller for superheating with reference at ($\Delta T_{sh,ref} = 10^{\circ}\text{C}$) is activated, thus bringing the system back into a safer regime.

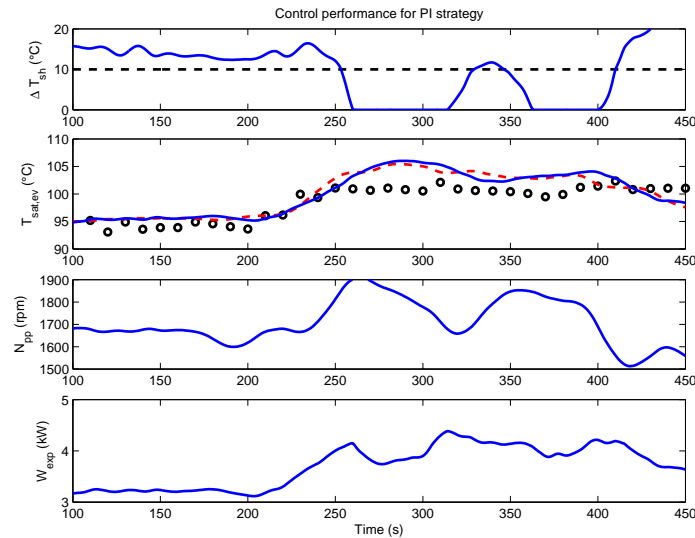


Figure 6: Control performance for a PI strategy. Dashed-red line represents the ES optimizer while black-circles represents the optimizer obtained from the dynamic model.

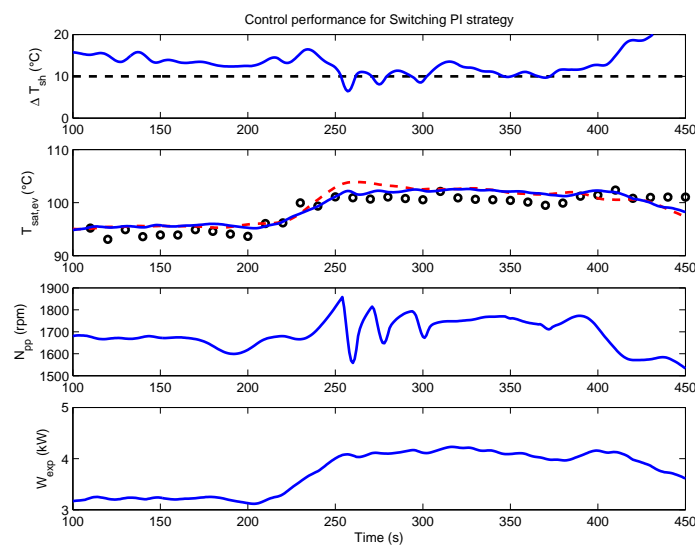


Figure 7: Control performance for a switching PI strategy. Dashed-red line represents the ES optimizer while black-circles represents the optimizer obtained from the dynamic model.

The result for the single PI strategy is depicted in Fig. 6. The ES optimizer (dashed red line) adapts the reference to the local PI controller, finding the point which maximizes the output power. As known from section 2.3 and Fig. 2 this maximum corresponds to zero superheating values. Since this strategy does not supervise superheating, once the controller tracks this reference the system reaches zero superheating, decreasing the generated power W_{exp} as observed at time 250 to 300 seconds and 350 to 400 seconds.

Next it is evaluated the performance of the switching PI strategy as depicted in Fig. 7. In this case the controller tracks the reference generated by the ES optimizer (dashed red line); but once it detects superheating values below 10°C , the PI controller for superheating becomes active. Thus avoiding that the organic fluid is in two-phase (i.e., gas and liquid phase) which would decrease the performance of the system as observed for the single PI strategy. Although the switching mechanism avoids superheating going to zero, it still reaches values near 5°C and requires of more aggressive control actions which increases power consumption in the pump compared to the EPSAC-MPC. Nevertheless, its simplicity is still remarkable.

5.4 Discussion of the obtained results

Although safety is highly important for Rankine cycles, it is also interesting to look into the net energy produced. Using results from Fig. 5 and Fig. 7, the net output power is calculated using (3). These values of net output power are further integrated over time to obtain the energy produced for each of the control strategies.

Taking the switching PI as a reference (100%), the EPSAC-MPC strategy allows increasing the *net energy production* by 21%. This is due to a better handling of the constraints, thus operating the system closer to the constraint for superheating while requiring a lower control effort (i.e., less power consumption in the pump) as observed in the results during the time from 250 to 300 seconds.

In an industrial context the single PI strategy solely is not safe to be applied, therefore its output power is not computed.

6. CONCLUSIONS

In this contribution a two layer control structure to achieve constrained optimal operation of an organic Rankine cycle unit for waste heat recovery applications is proposed. First, an optimizer based on a perturbation based extremum seeking algorithm is designed and implemented, to find the near-to-optimal evaporating temperature which maximizes energy production. Second, a constrained model predictive controller is implemented to track the optimal evaporating temperature given by the optimizer, while keeping the safety limit for superheating. Finally, the performance of the resulting loop is compared to PI control strategies. It is shown that a single PI cannot guarantee safety conditions, therefore a switching PI is proposed, resulting in a safer operation compared to a single PI but less effective compared to model predictive control since it violates safety limit for superheating and produces a lower net output power.

Future work will include the development of a multivariable control strategy by making use of the expander speed, as an additional manipulated variable.

NOMENCLATURE

ORC	Organic Rankine Cycle	
WHR	Waste Heat Recovery	
MPC	Model Predictive Control	
EPSAC	Extended Prediction Self-Adaptive Control	
PI	Proportional-Integral Control	
ES	Extremum Seeking	
\dot{m}	Mass flow rate	(kg/s)
\dot{W}	Power	(W)
N	Rotational speed	(rpm)
p	Pressure	(Pa)
T	Temperature	($^{\circ}\text{C}$)

Subscript		Greek letter	
el	Electric	η	Efficiency
ev	Evaporator	γ	Amplitude perturbation in ES algorithm
exp	Expander	α	Time constant reference trajectory in MPC
pp	Pump		

REFERENCES

- Ariyur, K. and Krstic, M. (2003). *Real-Time optimization by Extremum-Seeking Control*. John Wiley & sons.
- Camacho, E. F. and Bordons, C. (2004). *Model Predictive Control*, volume 405 pages. Springer-Verlag, London,, 2nd edition.
- De Hann, D. and Guay, M. (2005). Extremum-seeking control of state-constrained nonlinear systems. *Automatica*, 41:pp. 1567–1574.
- De Keyser, R. (2003). *Model based Predictive Control for Linear Systems*, chapter invited in UNESCO Encyclopaedia of Life Support Systems (EoLSS). Article contribution 6.43.16.1, Eolss Publishers Co Ltd, Oxford, 35p.
- Hernandez, A., Desideri, A., Ionescu, C., Quoilin, S., Lemort, V., and De Keyser., R. (2015). Experimental study of predictive control strategies for optimal operation of organic rankine cycle systems. In *Proceedings of the European Control Conference (ECC15)*, Linz, Austria.
- IEA (2010). Industrial excess heat recovery technologies & applications. Technical report, Technical report, Industrial Energy-related Technologies and Systems (IETS).
- Krstic, M. (2000). Performance improvement and limitations in extremum seeking control. *systems and control letters*, vol. 39:pp. 313–326.
- Ljung, L. (2007). *System identification: theory for the user*. Prentice-Hall.
- Maciejowski, J. (2002). *Predictive Control: With Constraints*. Pearson Education. Prentice Hall.
- Quoilin, S., Aumann, R., Grill, A., Schuster, A., and Lemort., V. (2011). Dynamic modeling and optimal control strategy for waste heat recovery organic rankine cycles. *Applied Energy*, Vol. 88:2183–2190.
- Quoilin, S., Desideri, A., Wronski, J., Bell, I., and Lemort., V. (2014). Thermocycle: A modelica library for the simulation of thermodynamic systems. In *Proceedings of the 10th International Modelica Conference*, Lund, Sweden.
- Wei, D., Lu, X., Lu, Z., and Gu., J. (2007). Performance analysis and optimization of organic rankine cycle (orc) for waste heat recovery. *J. Energy Conversion and Management*, Vol. 48:1113–1119.
- Zhang, C. and Ordonez, R. (2012). *Extremum-Seeking Control and Applications. A Numerical Optimization-Based Approach*. Advances in Industrial Control. Springer-Verlag.

ACKNOWLEDGEMENT

The results presented in this paper have been obtained within the frame of the IWT SBO-110006 project The Next Generation Organic Rankine Cycles (www.orcnext.be), funded by the Institute for the Promotion and Innovation by Science and Technology in Flanders. This financial support is gratefully acknowledged.

OPTIMAL CONTROL OF WASTE HEAT RECOVERY SYSTEMS APPLYING NONLINEAR MODEL PREDICTIVE CONTROL (NMPC)

Philipp Petr^{1*}, Christian Schröder¹, Jürgen Köhler¹, Manuel Gräber²

¹ TU Braunschweig, Institut für Thermodynamik
Hans-Sommer-Str. 5, 38106 Braunschweig, Germany
p.petr@tu-braunschweig.de
christian.schroeder@tu-braunschweig.de
juergen.koehler@tu-braunschweig.de

² TLK-Thermo GmbH
Hans-Sommer-Str. 5, 38106 Braunschweig, Germany
m.graeber@tlk-thermo.de

* Corresponding Author

ABSTRACT

This article describes an attempt for a real-time optimization of the net power output of an add-on Organic Rankine Cycle (ORC) system of a vehicle applying Nonlinear Model Predictive Control (NMPC). Therefore, a Modelica model library for satisfactorily accurate, fast vehicle and ORC models was developed. By means of the developed tool chain involving the optimizer MUSCOD II by the IWR Heidelberg, virtual simulation experiments of a waste heat recovery system for a long-distance bus could be realized. Results show an increase of the net power output of 7 % in part load engine operation in the European Transient Cycle compared to a conventional controller with optimum operation points optimized at steady-state conditions.

1. MOTIVATION FOR THE HOLISTIC OPTIMIZATION OF THE OPERATION OF A WASTE HEAT RECOVERY SYSTEM IN VEHICLES

In internal combustion engines, only a small part of fuel's chemical energy is transformed into mechanical energy. The residual is mainly wasted as thermal energy via the cooling system or as exhaust gas into the environment. Especially the exhaust gas still has a high exergetic potential, which can be converted into mechanical energy by means of an Organic Rankine Cycle (ORC). The recovered energy reduces the amount of mechanical energy provided by the combustion engine and therefore reduces the total fuel consumption. Virtual test drives of vehicles with waste heat recovery systems (WHRS) based on ORC promises a high fuel saving potential [1], [2], [3] and [4].

1.1 Interactions of the WHRS with Energy Systems in a Motor Vehicle

The integration and operation of an ORC in such a complex energy system represented by a motor vehicle affects many other subsystems (see Fig. 1). Interaction between these systems have to be considered in the design stage as well as in the development of operation strategies.

The combustion engine is affected by higher exhaust backpressure caused by pressure losses in the evaporator resulting in a slightly lower engine efficiency. Moreover, mechanical energy provided by the ORC reduces the load demand of the engine. This leads to a shift in the engine efficiency and the exhaust temperature, which has repercussions on the ORC itself. Furthermore, the condensing heat of the ORC significantly increases the load of cooling system. Under certain conditions, additional fans have to ensure target coolant temperatures. Admittedly, the power consumption of the additional fans exceed the additional power provided by the ORC, which results in a shutdown of the waste heat

recovery system. Not least, the additional weight of the ORC increases substantially the work load of the combustion engine.

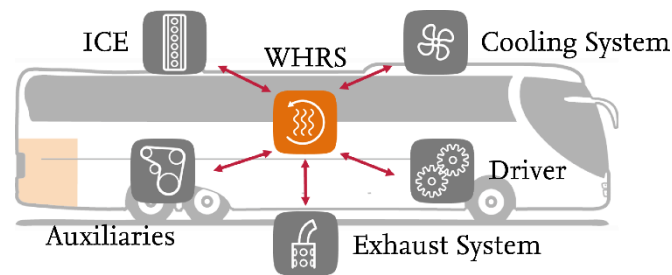


Figure 1: Interactions of the WHRS with other systems in mobile applications could influence the objective function (minimization of fuel consumption) substantially (i.e. power demand of additional fans).

In order to maximize the benefit of WHRS, interactions of different subsystems and their time constants should be integrated in the operation strategy in order to minimize shut down times of the WHRS and to maximize the recovered amount of exhaust exergy.

1.2 Variable Operation Points of the ORC Enables Waste Heat Recovery at Part Load Conditions

Focusing on the operation of the WHRS, car manufacturers currently consider a control approach with only one static operation point [1], [5], which is optimized for a representative driving cycle. Depending on actual exhaust enthalpy flow rate, the chosen operation point mostly differs from the current optimum operation point. Figure 2 shows a T-h diagram of an optimized operation point and one operation point which was designed for higher exhaust gas temperatures. It can be seen that the exhaust exergy used is significantly lower in the design operating point, which cannot compensate higher thermodynamic efficiencies. Thus, the second law efficiency for the adapted optimum operation point is 20 percentage points higher than for the fixed operation point. In the worst case, the WHRS is been shut due to low working fluid mass flow rates in part load conditions despite an still existing exhaust exergy potential.

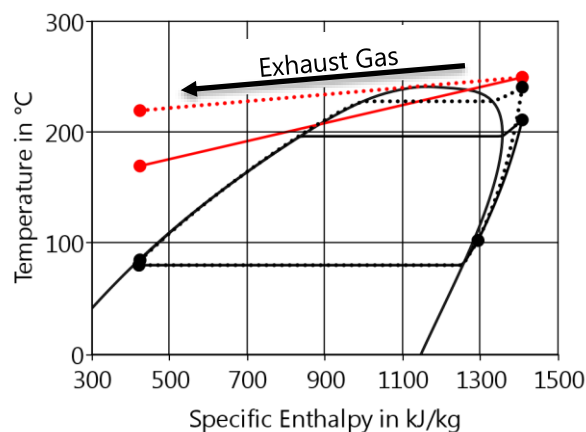


Figure 2: T-h-Diagram of two ORCs at different operation points with corresponding exhaust temperature course in the heat exchanger for an exhaust inlet temperature of 250 °C. Operation point optimized for higher loads (.....) shows poor usage of exhaust exergy compared to currently optimal operation point (—)

Enabling variable ORC operation points increases the benefit of the WHRS also in part load conditions, but requires the consideration of the dynamic behavior of the system (step response or time constants on excitation of the system). Optimized operation points calculated under steady state conditions differ from actual optimum control variables the more, the larger the time constants of the WHRS and the more dynamic the changes in the exhaust gas enthalpy flow rate are.

1.3 NMPC as One Promising Method to Minimize the Fuel Consumption for Real Drives

In order to maximize the benefit of a WHRS, the control strategy has to utilize variable operation points with respect to the system's dynamic behavior, future states of the ORC and dependencies of interacting systems. Conventional control strategies such as heuristic controls cannot fulfill these criteria. Nonlinear model predictive control (NMPC) is one method to meet this challenge. Based on a simplified nonlinear mathematical model of the system, an optimizer computes the ideal course of controlled variables for a certain prediction horizon. NMPC uses relevant information about the actual state of the vehicle and the predicted variables for real-time control. Relevant predicted data for the optimization are for example:

- Route including gradients and traffic
- Style of driving
- Comfort demand of passengers
- Ambient conditions (solar radiation, winds, temperature)

Due to fluid properties, the vehicle with its subsystems, especially the WHRS, is characterized by a high grade of nonlinearity. Hence, linear optimization approaches, as they are discussed in [6] and [7] for following given set points, are not applicable for set point optimization in large operation intervals. Therefore, efforts regarding fast and accurate nonlinear simulation models have to be done.

This article describes a first attempt of the development of an NMPC for a WHRS for a long distance bus. Therefore, a transient full vehicle simulation model of a long distance bus with a WHRS was set up. The WHRS model is based on a conventional ORC using Ethanol as working fluid and a Scroll expansion machine, which enables expansion in the two-phase region. The basis for the simulation study is the exhaust gas enthalpy flow rate of the part load section of the European Transient Cycle (ETC). As a first step, the chosen optimum criterion was set to the maximization of the ORC power output. To compare NMPC with heuristic control methods, optimum power points in steady state condition were calculated for each exhaust gas inlet state, which are adjusted by conventional Single-Input-Single-Output (SISO) controllers.

2. MODEL DESCRIPTION AND STEADY-STATE OPTIMIZED OPERATION POINTS FOR BENCHMARKING A CONVENTIONAL CONTROL STRATEGY

Basis for the development of the advanced control strategy is a conventional Organic Rankine Cycle, which is described in Fig. 3. The working fluid (Ethanol) leaves the feed pump in pressurized liquid state (1-2) and then enters in the evaporator, where it is heated and vaporized (2-3). In the expander (3-4), potential energy of the working fluid is converted into mechanical energy, which is used in the vehicle to drive auxiliaries. After the expansion, the working fluid is liquefied in the condenser. With re-entering the feed pump, the cycle starts again.

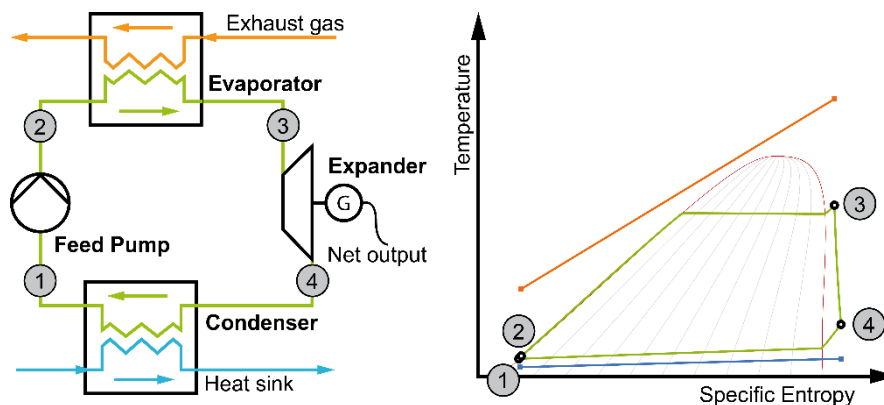


Figure 3: Investigated process configuration and T-s-Diagram. The working fluid is evaporated directly in the evaporator without using a secondary loop system

2.1 Transient Simulation Model in Modelica

For the evaluation of investigated control strategies, a transient simulation model of the ORC was set up in the programming language Modelica by means of the self-developed model libraries TIL and TILMedia. The evaporator is a physical model of a fin-and-tube heat exchanger, which is designed to a steady-state pinch point temperature of 10 K at the highest occurring exhaust gas enthalpy flow rate. The expansion machine model is efficiency based and represents a volumetric expander (scroll), which enables expansion in two-phase region. The condenser is connected to the vehicle cooling system, which supplies constant coolant temperature of 90 °C.

2.2 Optimum Operation Points in Steady State Conditions

In order to evaluate NMPC, a conventional control strategy based on steady-state optimized operation points was set up. Two degrees of freedom govern the net power output: expander inlet pressure and expander inlet enthalpy. The optimum operation point correlates not necessarily with the maximum cycle efficiency, but with the second law efficiency. A gradient-based optimization algorithm applied on a steady-state model of the ORC finds the optimum operation point for each boundary condition. Although the heat transfer coefficients depend on the mass flow rate of the exhaust gas and the working fluid as well as on the states in the heat exchanger, a constant pinch point temperature of 10 K in the evaporator was assumed. The expander inlet pressure was limited to 5 MPa.

Figure 4 shows the net power output of described ORC as a function of the expander inlet state. For low exhaust gas enthalpy flow rates (Fig. 4, left), optimum expander inlet state is located in the two-phase region, whereas it is in superheated region for high enthalpy streams (Fig. 4, right).

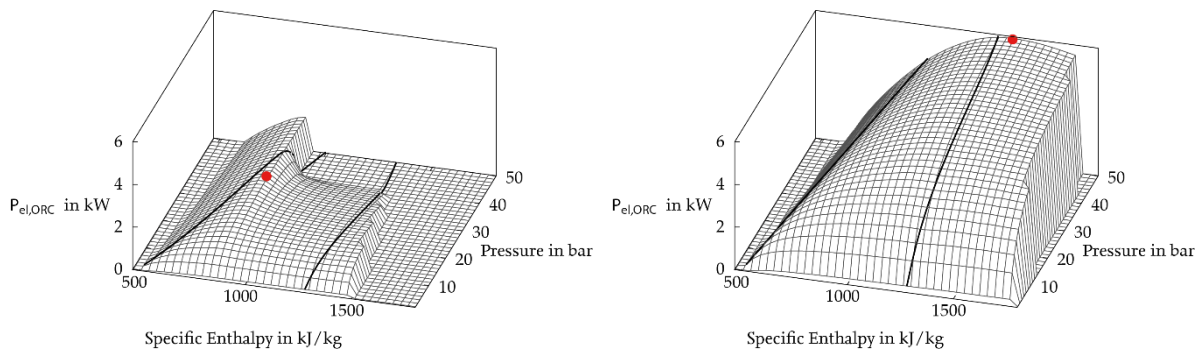


Figure 4: Net power output of ORC dependent on expander inlet pressure and enthalpy for low (left) and high (right) exhaust gas enthalpy flow rates. Projected fluid dew and bubble lines indicate the properties of mapped states. Working fluid: Ethanol, expander type: scroll, maximum pressure: 5 MPa

3. INTRODUCTION TO NMPC

This section introduces the theory of NMPC. The following NMPC scheme is derived based on the formulation and numerical solution approach of an Optimal Control Problem (OCP). Additionally, the key parameters influencing both solution quality and speed are discussed.

3.1 Optimal Control Problem (OCP)

The concept of this method is to calculate a specific control variable trajectory, which influences the dynamic behaviour of a plant in a way that it maximizes a given objective function. As a first step, the objective functions is the maximization of the net power output of the ORC over the considered horizon:

$$\max_{n_{pump}, n_{Expander}} P_{el,ORC} = P_{el,Generator} - P_{el,Pump} \quad 4.1$$

The optimal control trajectory is determined based on a mathematical model of the plant, which would be a system of semi-explicit differential algebraic equations of index 1. To achieve an optimal control trajectory, an objective function is needed as a benchmark of the system's performance. Therefore,

Lagrange-type terms can be used to maximize or minimize it over the entire time horizon or a Mayer-type term limits the target value to a set endpoint. In addition, a combination of the two known as a Bolza type objective function can be utilized. This leads to the general formulation of an OCP subject to several constraints. Besides the already described DAE system, we find path-constraints, e.g. a maximum temperature limit, which must not be exceeded at all times and point-constraints, defining boundaries only at definite instants. At last, the trajectories of the state variables have to be a solution to the initial value problem (IVP) with the given start values. Thus, the optimal control function must satisfy these constraints in order to be a valid solution of the OCP.

3.2 Nonlinear Model Predictive Scheme

In order to control a plant in a closed loop rather than an open loop setting, the OCP has to be solved repeatedly with up-to-date measurements of the system's states as initialization (Fig. 5). As proposed in [8], the real-time iteration approach is used, that performs only one Sequential Quadratic Programming (SQP) iteration per NMPC sample. Starting with a preparation phase, all functions and derivatives are evaluated, that do not depend on the current state x_0 . As soon as the new measurement of x_0 is available, the feedback phase starts with the computation of the control function $u(t)$, which is limited to a single Quadratic Programming (QP) due to the computation during preparation. Eventually, $u(t)$ can be given to the plant in the transition phase. Afterwards the new time sample starts according to the three phases.

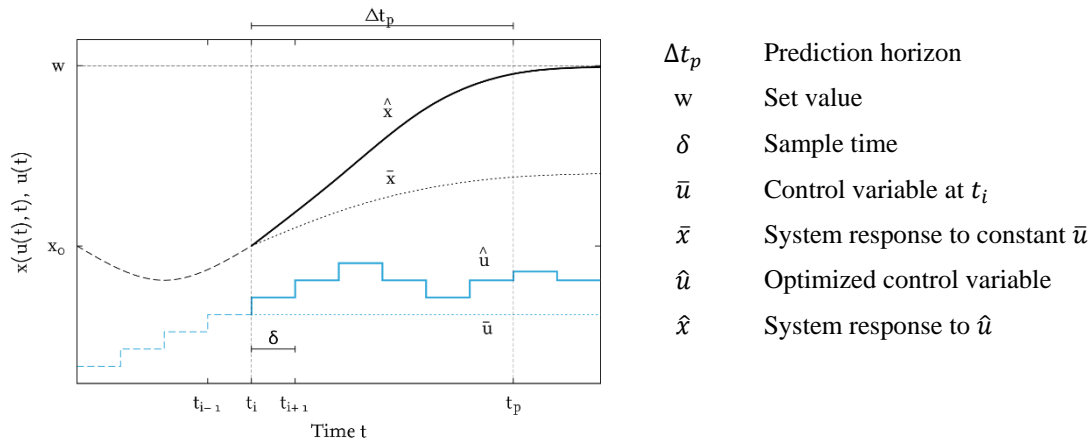


Figure 5: Nonlinear Model Predictive Control is a repeated solving of OCPs. At t_{i+1} , solving OCP restarts for the prediction horizon with current measured or estimated input values

3.3 Key Parameters in NMPC

The optimality of the solution as well as the computation time can be influenced not only by the complexity of the model, which is used for NMPC. A great impact also derives from the number of shooting knots N , hence the discretization of the NLP, and the prediction horizon Δt_p . Higher values lead to significantly increased numerical effort, but also to a better solution. A key parameter for online NMPC is the sample rate at which measurement data is provided and new control values are passed on to the plant. The optimization problem has to be solved fast enough to satisfy the required sample interval. Otherwise, the control values of the previous synchronization are used, which are usually not minimizing the objective function of the progressed system state. Table 1 shows the key parameters for the performed study:

Table 1: Key parameters for the performed study

Prediction horizon	4 s
Shooting knots	4
Sample rate	3,3 Hz

In this study, a higher prediction horizon shows only a slight increase in the ORC power output, but also in missing the real-time criterion (Intel Core™ i7-4770K CPU, 3,50GHz, 32GB RAM, Windows 8 - 64 bit)

3.4 Approach for a Prototype Setup

In this section, the software framework for a convenient setup of simulated and real-world NMPC loops is presented. The basic principle is to use different specialized software for each task and to couple it to a co-simulation master. Using Functional Mockup Interface (FMI) ensures integrity of the underlying plant model that is used in several places, and avoids error-prone and time-consuming model transformations.

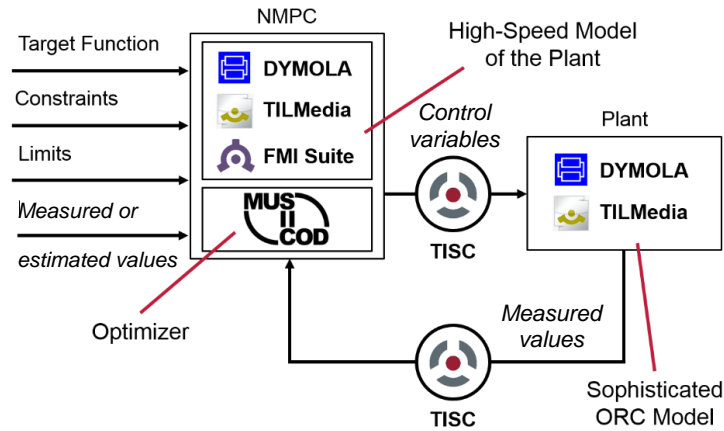


Figure 6: Used software framework for prototype NMPC attempt

The software framework for the NMPC prototype environment is described in Figure 6. For data exchange, the co-simulation platform TISC [9] is used to set-up a NMPC prototyping environment. TISC acts as master and manages data exchange between different clients. There already exist interfaces between TISC and a variety of simulation, visualization and measurement tools, e.g. Dymola, LabView, and Simulink. The user has to define types and names of variables to be sent and received for each client. Data routing between clients is automatically managed by matching variable types and names. The TISC type of time is Double, whereas all other variables are of TISC type Double Array. This definition enables the exchange of components of an NMPC loop. Hence, the virtual plant modeled in Modelica can be replaced easily by a real plant interfaced with LabView [8]. As optimizer, MUSCOD II of IWR at Heidelberg University, Germany as described in [10], [11] and [12], is proven to be appropriate.

4. NONLINEAR HIGH-SPEED MODEL FOR ONLINE OPTIMIZATION

The NMPC requires a nonlinear high-speed model, which maps real systems or, like presented in this study, a sophisticated model of the ORC accurately and which fulfils the demand of real-time optimization. Every component has been developed against certain requirements that need to be fulfilled in order to guarantee an efficient usage in the optimization process. The first key aspect is based on the solving process of the NLP. Like described in section 3, the SQP method is used in this case, which obligates that both the objective function and the constraints, thus all variables of the NMPC plant-model, are at least twice continuously differentiable with respect to the input $u(t)$ [10]. Any discontinuity in the state trajectories leads to a less efficient optimization and hence should be avoided. One key component for optimization of the transient operation of the ORC is the evaporator. Therefore, big effort is being made to map the physical characteristics of the real evaporator. For calculating the heat transfer, the NTU approach is used. To ensure continuous differentiability, the term

$$\dot{Q} = kA' \Delta T_o \left(\frac{1 - e^{-\theta L}}{\theta} \right) \quad 4.2$$

$$\text{with } \theta = kA' \left(\frac{1}{\dot{m}_1 c_{p1}} - \frac{1}{\dot{m}_2 c_{p2}} \right) \quad 4.3$$

is transformed with the help of the hyperbolic sine function. The term is now defined for equal heat capacity flow rates [13]:

$$\dot{Q} = kA'\Delta T_o e^{-\frac{\theta L}{2}} * \operatorname{sinhc}\left(\frac{\theta L}{2}\right) \quad 4.4$$

To take account of the different heat transfer coefficients of the working fluid in the different states, the heat exchanger is divided into three NTU sections (subcooled, two-phase and superheated). The mass balance in the three volume elements is calculated by

$$\dot{m}_{in} - \dot{m}_{out} = \left[\left(\frac{\partial \rho}{\partial p} \right)_h \frac{dp}{dt} + \left(\frac{\partial \rho}{\partial h} \right)_p \frac{dh}{dt} \right] V, \quad 4.5$$

whereas the energy balance is given by

$$m \frac{dh}{dt} = \dot{m}_{in}(h_{in} - h) - \dot{m}_{out}(h_{out} - h) + \dot{Q} + \frac{dp}{dt} V \quad 4.6$$

The thermal capacity of the heat exchanger wall is modeled by one differential state, which determines the transferred heat to the working fluid. Figure 7 shows a scheme of the model approach for the evaporator.

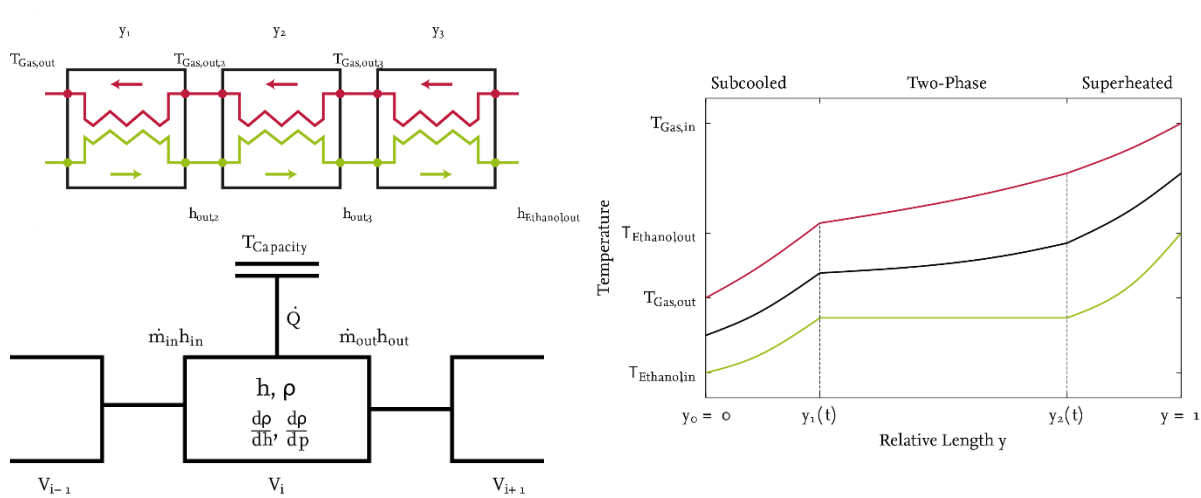


Figure 7: Evaporator Model. Consists of one cell for each working fluid phase. A modified NTU approach is used to calculate heat transfer coefficients. Transient conduct is modeled by finite volume elements

The total high-speed model is illustrated in Figure 8 (left). Efficiencies of the pump and the expander are mapped; component inertias are represented by first order elements.

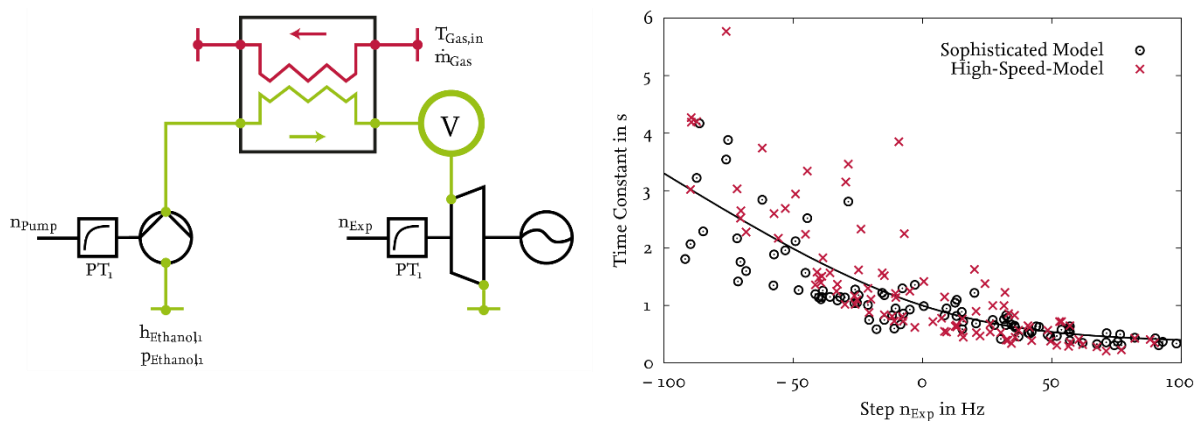


Figure 8: Scheme of high-speed model (left). Deviations in time constants on random pressure steps between high-speed and sophisticated model are acceptable (right)

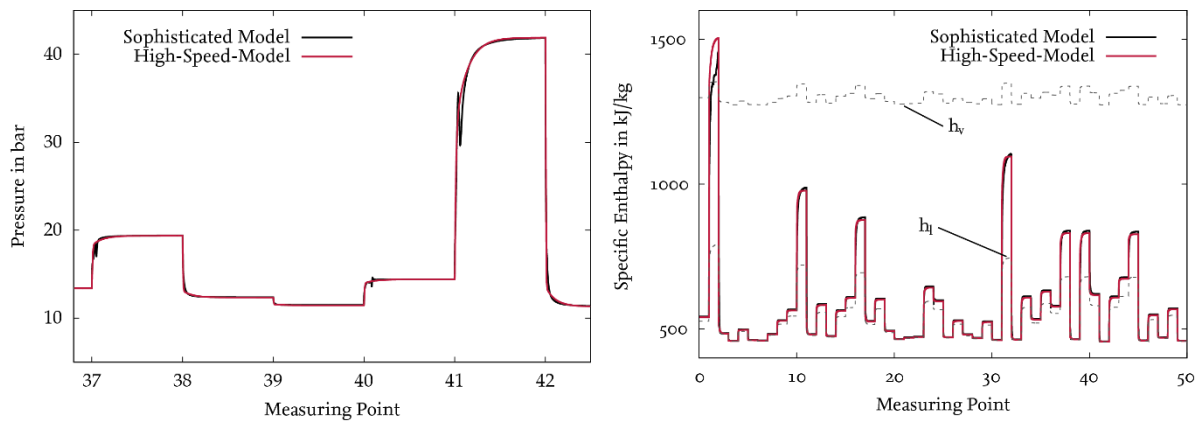


Figure 9: Step response on expander speed steps (left) and pump speed steps (right) of sophisticated and high-speed model

To evaluate the accuracy of the high-speed model, simulations with random steps on both models were carried out. Figure 9 shows only minor deviations in the step response for the sophisticated model and the high-speed model. Deviations in time constants are in accordance to low simulation times in acceptable intervals (Fig 8 right). The median error of the high-speed model for steady state target values are 5% for the expander inlet enthalpy and 1% for expander inlet pressure.

5. BENCHMARK OF NMPC AND CONVENTIONAL CONTROL IN THE URBAN PART OF THE EUROPEAN TRANSIENT CYCLE

In order to benchmark NMPC and the conventional control approach based on steady state optimized operation points in part load conditions, simulation experiments within the urban section of the European Transient Cycle (Fig. 10) were carried out for each control strategy.

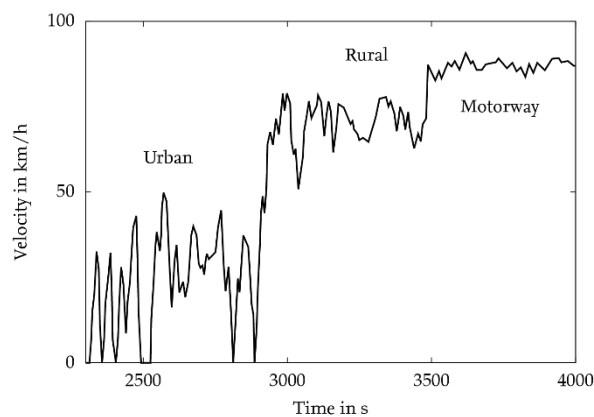


Figure 10: Velocity profile of the European Transient Cycle (ETC)

Figure 11 shows the course of expander inlet pressure and enthalpy over the cycle. It can be seen, that the conventional control cannot satisfactorily adjust the set values, which are calculated through steady state optimization. This is caused by the time constants of the ORC, which are not considered in steady state simulations. NMPC however tends to lower expander inlet pressures and higher expander inlet enthalpies.

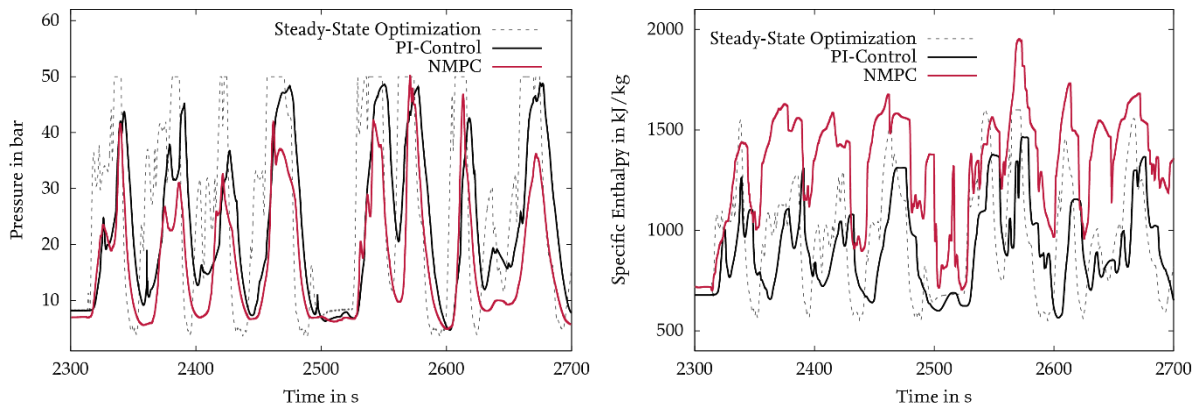


Figure 11: Course of expander inlet pressures (left) and inlet enthalpies (right). NMPC tends to higher inlet enthalpies and lower inlet pressures. Steady state operation points are not adjusted satisfactorily by PI-control

These different courses could be explained with focusing on the pump work, which affects the net output of the ORC. Because of the higher pressure steps of the PI-control, the pump work is significantly higher than of the NMPC (see Fig. 12, left) and the pump work of the steady state model.

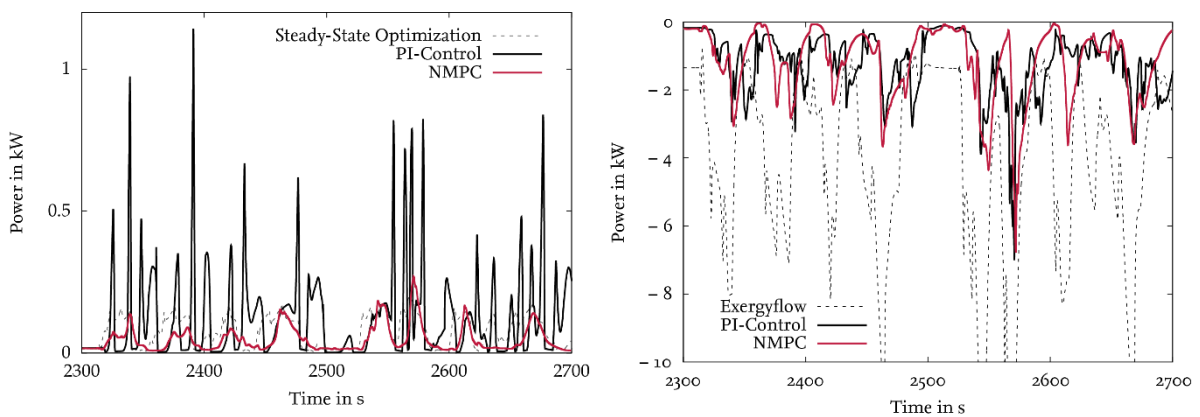


Figure 12 Pump work (left) and expander power output (right) of the ORC for both PI-Control and NMPC. NMPC show a 7 % higher average net power output

Thus, the expander power output of NMPC is not significantly higher (see Fig. 12, right), but cleared with actual pump work, NMPC provides a 7 % higher average net power output in part load operation of the internal combustion engine than the conventional control strategy based on operation points optimized in steady state conditions. Assuming that the ORC is shut down in part load operation for a conventional strategy with an operation point designed to high load operation, NMPC with variable operation points could increase the power output of the ORC by 15 %.

6. CONCLUSIONS

Optimal control approaches could increase the total system efficiency by considering interaction of several subsystems, future states and inertias of the thermal systems. NMPC is one promising method. At the TU Braunschweig and TLK-Thermo, a software tool chain was developed in order to facilitate NMPC for thermal systems. In this article, a NMPC approach for a WHRS of a long distance bus was developed. Particular challenge was the development of a high-speed model of the evaporator, which maps heat transfer coefficients and inertias accurately accomplishing the requirements of real-time optimization. In a simulation study, maximization of the WHRS net output in the part load section of the European Transient Cycle was considered. Results show an increase of the net power output of 7 % compared to a conventional controller with operation points optimized at steady-state conditions.

NOMENCLATURE

ETC	European Transient Cycle	FMI	Functional Mockup Interface
ICE	Internal Combustion Engine	IVP	Initial Value Problem
NLP	Nonlinear Programming	NTU	Number of Transfer Units
NMPC	Nonlinear Model Predictive Control	QP	Quadratic Programming
OCP	Optimal Control Problem	SQP	Sequential Quadratic Programming
WHRS	Waste Heat Recovery System		

REFERENCES

- [1] Horst, T. A., Tegethoff, W., Eilts, P., Koehler, J., 2014, Prediction of dynamic Rankine Cycle waste heat recovery performance and fuel saving potential in passenger car applications considering interactions with vehicles' energy management, *Energy Conversion Management*, vol. 78, pp. 438–451.
- [2] Espinosa, N., Tilman, L., Lemort, V., Quoilin, S., Lombard, B., Rankine cycle waste heat recovery on commercial trucks: approach, constraints and modelling. In: Proceedings of the international conference and exhibition on diesel engines, Rouen, France; 2010.
- [3] Sprouse, C., Depcik, C., 2013, Review of organic Rankine cycles for internal combustion engine exhaust waste heat recovery, *Appl. Therm. Eng.*, vol. 51, no. 1–2, pp. 711–722.
- [4] Boretti, A. A., 2012, Transient operation of internal combustion engines with Rankine waste heat recovery systems, *Appl. Therm. Eng.*, vol. 48, pp. 18–23.
- [5] Hartmann, A., 2014, Energie- und Wärmemanagement mit thermischer Rekuperation für Personenkraftwagen, Dissertation, TU Braunschweig.
- [6] Feru, E., Willems, F., De Jager, B., Steinbuch, M., 2014, Modeling and Control of a Parallel Waste Heat Recovery System for Euro-VI Heavy-Duty Diesel Engines,” *Energies*, vol. 7, no. 10, pp. 6571–6592.
- [7] Luong, D., 2013, Modeling, Estimation, and Control of Waste Heat Recovery Systems, Dissertation, University of California.
- [8] Gräber, M., Kirches, C., Scharff, D., Tegethoff, W., 2012, Using Functional Mock-up Units for Nonlinear Model Predictive Control, *9th International Modelica Conference*, p. 781-790.
- [9] Kossel, R., Löffler, M., Strupp, N. C., Tegethoff, W., 2011, Distributed energy system simulation of a vehicle, *Vehicle Thermal Management Systems Conference*, Institution of Mechanical Engineers, SAE International.
- [10] Bock, H. G., Plitt, K. J., 1984, A Multiple Shooting algorithm for direct solution of optimal control problems, *Proceedings 9th IFAC World Congress Budapest*, pages 243–247. Pergamon Press.
- [11] Diehl, M., 2001, Real-Time Optimization for Large Scale Nonlinear Processes, PhD thesis.
- [12] Leineweber, D. B., Bauer, I., Bock, H. G., Schlöder, J. P., 2003, An Efficient Multiple Shooting Based Reduced SQP Strategy for Large-Scale Dynamic Process Optimization (Parts I and II). *Computers and Chemical Engineering*, 27:157–174.
- [13] Tegethoff, W., Schulze, C., Graeber, M., Huhn, M.; Stulgies, N., Kaiser, C., Loeffler, M., 2011 TEMO Thermische Echtzeitfähige Modelle, Final Project Report.

WASTE HEAT RECOVERY RANKINE CYCLE BASED SYSTEM MODELING FOR HEAVY DUTY TRUCKS FUEL SAVING ASSESSMENT

V. Grelet^{1,2,3}, V. Lemort^{2*}, M. Nadri³, P. Dufour³, T. Reiche¹

¹ Volvo Trucks GTT ATR
1 av Henri Germain, 69800 Saint Priest
vincent.grelet@volvo.com, thomas.reiche@volvo.com

² Thermodynamics Laboratory – University of Liège,
Campus du Sart Tilman, B49, 4000 Liège, Belgium
vincent.lemort@ulg.ac.be

³ Université de Lyon, F-69622, Lyon, France, Université Lyon 1, Villeurbanne, France CNRS,UMR
5007, LAGEP,
dufour@lagep.univ-lyon1.fr, nadri@lagep.univ-lyon1.fr

* Corresponding Author

ABSTRACT

This paper presents a method to model heat exchangers used in waste heat recovery Rankine based systems in heavy duty trucks. The method is developed to predict both transfer and working fluid physical properties such as temperature and density after the heat exchange process. Due to the flexibility of such a model, it can be used for a numerous quantity of fluids including water-alcohol mixture. A validation of the developed model is shown and compared to steady state and dynamic test results. The model shows good performance as well in terms of accuracy, which is in the range of 5K error as in computational time which is faster than real time and makes it suitable for concept optimization, control and fuel economy evaluation.

1. INTRODUCTION

Driven by future emissions legislations and increase in fuel prices, engine gas heat recovering has recently attracted a lot of interest. In the past few years, a high number of studies have shown the interest of energy recovery Rankine based systems for heavy duty (HD) trucks engine compounding [Espinosa (2011), Sprouse III and Depcik (2013)]. Recent studies have brought a significant potential for such a system in a long haul truck which can lead to a decrease in fuel consumption of about 5% and reduces engine emissions. But many challenges have to be faced before the vehicle integration. The correct choice of fluids and system architecture is approached in [Mago et al. (2007), Latz et al. (2012)] and shows that system simulation is a critical part of the development work. Moreover, several papers focused on the control strategy which is important in order to optimize the energy recovery process and maximize the power production as to ensure a safe operation of the system when talking from a system point of view. The high number of interactions, both with the engine and the vehicle, constrains the system and challenge the control design. The system dynamic is mainly controlled by the heat exchangers behavior (i.e. evaporators and condenser) and dynamic models of these components are of two kind: moving boundary (MB) [Zhang and Zhang (2006), Bendapudi et al. (2008)] and finite volume (FV) [Feru et al. (2013), Vaja (2009)]. Usually more complex in terms of computational capacity needed due to the high number of system states, the FV approach has the advantage to be more powerful and robust concerning the prediction. Both approaches have been widely used in large power recovery system and control system design [Horst et al. (2013), Peralez et al. (2013)] and results in a simplification of the heat recovery

boiler/condenser geometry in a great extent (i.e. by representing the boiler by a straight pipe in pipe counterflow heat exchanger). The use of water-alcohol mixture can bring some advantages in the power recuperation and overcome both disadvantages of these fluids: high freezing temperature of water and flammability of alcohol [Latz et al. (2012)]. In those blends, Water Ethanol is promising and compliant with vehicle integration where both pure fluids are not. In the following a FV model of evaporators recovering heat from EGR and Exhaust in a serial arrangement (EGR as preheater and exhaust as superheater) using a mixture of 80% ethanol and 20% water by mass is presented and compared to steady state and dynamic tests. The paper is organized as follows. Section 2 presents the principle and the layout of the studied system. Section 3 presents the model itself and the resulting PDE system as well as the ODE discretized model. Section 4 compares modeling and experimental results when conclusions are drawn in section 5.

2. PRINCIPLE OF OPERATION AND STUDIED SYSTEM

2.1 Rankine process

The Rankine cycle is a widely used power generation cycle when it comes to turn heat into mechanical or electrical power. First, the working fluid is pumped from a tank at the condensing pressure to the evaporator at the evaporating pressure. Then the pressurized working fluid is pre-heated, vaporized and superheated in one or several heat exchangers. These heat exchangers are linked to the heat source. The superheated vapour expands from evaporating pressure to condensing pressure in an expansion device converting the pressure drop into mechanical work. Finally, the expanded vapour condenses through a condenser releasing heat into the cold sink (e.g. ambient air) and returns to the working fluid reservoir. In this process the changes of states in both the pump and the expander are irreversible and increase the fluid entropy to a certain extent. The process can be characterized as well by the Net Output Power (NOP) which corresponds to the generated power minus the pump consumption as well, as the cycle efficiency which is the ratio of the net output power by the heat flow rate recovered during the evaporation.

2.2 Studied system

The waste heat recovery system (WHRS) is compounded on a turbocharged 6 cylinder 13L 320kW HD engine using exhaust gas recirculation (EGR) and selective catalist reduction (SCR) to reduce the NOx emissions. The studied Rankine cycle is recovering heat from both EGR and exhaust, but unlike [Teng (2010)], heat exchangers (HEX) are arranged in a serial configuration in order to ensure low temperature of the EGR gases at the intake manifold inlet. This layout is also advantageous concerning the number of valves and actuators needed and simplify the control since there is a single controlled mass flow rate. The chosen working fluid is composed of water (20% wt) and ethanol (80% wt). The mass flow rate through the two boilers is controlled by the pump speed. The expansion machine is a turbine which has a higher power density than volumetric expanders [Kunte and Seume (2013)]. The working fluid is then condensed through an indirect condenser fed by coolant. Moreover the cycle is equipped with two bypass valves: one located in the exhaust stream to control the amount of energy introduced in the system and a second in front of the expander to prevent liquid to enter in the turbine and avoid blade erosion caused by liquid droplets into a high speed rotor. The experimental setup is fitted with pressure, temperature and mass flow sensors on the working fluid and gases flow. Pressures and temperatures are measured before and after each component in order to characterize their performance. Mass flow sensors are installed downstream the pump for the working fluid (based on the coriolis effect) and upstream their respective boiler for EGR and exhaust gases (based on the venturi effect). The sensors uncertainties given by the manufacturers are in the range of +/- 3K for the working fluid thermocouple, +/- 1.5% for the gases thermocouple, +/- 3% for the piezoresistive pressure sensors and 0.5% for the mass flow rates. Furthermore sensors performance can be influenced by other parameters such as the temperature field distribution among the pipe area for temperature sensors and the flow pulsation for the working fluid mass flow sensor. The complete experimental setup is presented in Figure 1. Recorded data during the test campaign are hereafter used to calibrate and validate the models of the EGR and exhaust gas boiler.

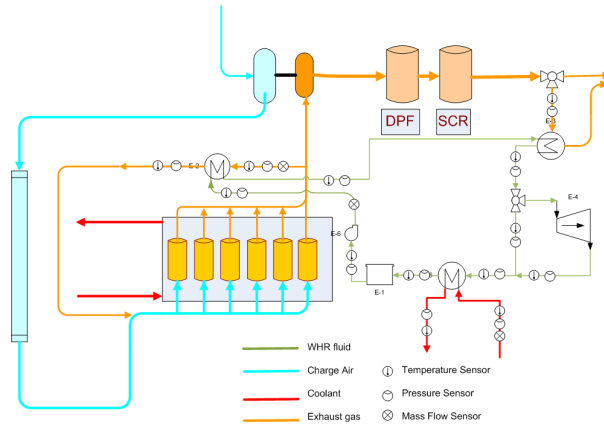


Figure 1: Experimental Setup

3. HEAT EXCHANGER MODEL

The models are developed to dynamically predict temperature and enthalpy of primary and secondary fluid (also called in the following working and transfer fluid) at the outlet of each boiler. This is critical when coming to control design to ensure a safe operation of the system and a proper operation of the EGR function. Safe means that the fluid is fully vaporized when entering the turbine in order to not destroy it. For the EGR, the aim is to have a gas temperature exiting the boiler at least equal to the one when using a classical cooler to not to disturb the emissions control strategy and the combustion process.

3.1 Modeling assumptions

Several assumptions have been made in order to simplify the dynamic problem. These ones are generally accepted when it comes to dynamic modeling of heat exchangers with phase change [Vaja (2009)].

- The transfer fluid is always considered in single phase i.e. no condensation in the EGR/exhaust gases is taken into account.
- The conductive heat fluxes are neglected since the predominant phenomenon is the convection.
- Pressure drop in each fluid (transfer and working fluids) is not considered.
- Both boilers are represented by a straight pipe in pipe counterflow heat exchanger, similarly to Vaja (2009), divided into n lumped sub-volumes in the longitudinal direction.
- Fluid properties are evaluated at the outlet of each sub-volume.
- Pressure dynamics is neglected since its time scale is very small considered to relevant HEX ones.

3.2 Governing equations

The model presented in this paper is based on mass (1) and energy conservation (2) equations.

$$A_{cross} \frac{\partial \rho_j}{\partial t} + \frac{\partial \dot{m}_j}{\partial z} = 0, \quad (1)$$

$$A_{cross} \frac{\partial \rho_j h_j}{\partial t} + \frac{\partial \dot{m}_j h_j}{\partial z} + \sum_{i=int}^{ext} \dot{q}_{jk} = 0, \quad (2)$$

$$\text{where: } \dot{q}_{jk} = \alpha_j P E_{exch_{jk}} (T_{wall_k} - T_j) \quad \text{with : } k = int, ext \text{ and } j = f, g, amb.$$

On the working fluid side, both conservation principles are applied whereas on the transfer fluid side the variation in density due to temperature and pressure change is neglected: therefore the continuity equation is not implemented in this region. These conservation principles at each node can be applied:

- Fluid Side (inner pipe): As pressure dynamics is neglected, the derivative term in density becomes:

$$\frac{\partial \rho_f}{\partial t} = \frac{\partial \rho_f}{\partial h_f} \frac{\partial h_f}{\partial t}. \quad (3)$$

By implementing equation (3) in (1) it takes the following form:

$$A_{cross} \frac{\partial \rho_f}{\partial h_f} \frac{\partial h_f}{\partial t} + \frac{\partial \dot{m}_f}{\partial z} = 0. \quad (4)$$

The energy conservation principle is then described by:

$$A_{cross_f} \frac{\partial \rho_f h_f}{\partial t} + \frac{\partial \dot{m}_f h_f}{\partial z} + \dot{q}_{f_{int}} = 0. \quad (5)$$

- Gas side (outer pipe): The density change due to temperature decrease in the heat exchangers is rather small (below a ratio of 2), therefore the continuity equation (1) is neglected and only the energy conservation principle (2) is applied where enthalpy is taking the following form:

$$h_g = c_{p_g}(T_g)T_g. \quad (6)$$

The energy conservation principle showed in equation (2) is then expressed under the following form:

$$\frac{\partial \dot{m}_g c_{p_g}(T_g)T_g}{\partial z} + \frac{\partial \dot{m}_g c_{p_g}(T_g)T_g}{\partial t} + \dot{q}_{g_{int}} + \dot{q}_{g_{ext}} = 0. \quad (7)$$

- Internal pipe wall: An energy balance is expressed at the wall between the two fluids and is written as follows:

$$\dot{q}_{f_{int}} + \dot{q}_{g_{int}} = \frac{\partial \dot{m}_{w_{int}} c_{p_{w_{int}}} T_{w_{int}}}{\partial t}. \quad (8)$$

- External pipe wall: Similarly to the internal wall the balance of the entering and leaving heat fluxes is done on the external wall:

$$\dot{q}_{g_{ext}} + \dot{q}_{a_{ext}} = \frac{\partial \dot{m}_{w_{ext}} c_{p_{w_{ext}}} T_{w_{ext}}}{\partial t}. \quad (9)$$

In addition to those equations, boundary and initial conditions are needed at $z = 0$ and $z = L$. Time dependent boundary conditions are used:

$$\begin{aligned} \dot{m}_f(t, 0) &= \dot{m}_{f_0}(t) & | & & \dot{m}_g(t, L) &= \dot{m}_{f_L}(t) \\ h_f(t, 0) &= h_{f_0}(t) & | & & T_g(t, L) &= T_{g_L}(t) \end{aligned} \quad (10)$$

The initial conditions for each state is given by:

$$\begin{aligned} \dot{m}_f(0, z) &= \dot{m}_{f_{init}}(z) & | & & T_g(0, z) &= T_{g_{init}}(z) & | & & T_{w_{int}}(0, z) &= T_{w_{int_{init}}}(z) \\ h_f(0, z) &= h_{f_{init}}(z) & | & & & & | & & T_{w_{ext}}(0, z) &= T_{w_{ext_{init}}}(z) \end{aligned} \quad (11)$$

3.3 Heat transfer

To model the convection from the transfer fluid to the pipe walls and from the internal pipe to the working fluid, a heat transfer coefficient (α) is needed. The convection from a boundary to a moving fluid is usually represented by the dimensionless Nusselt number (Nu), which is the ratio of convective to conductive heat transfer and is equal to:

$$Nu = \frac{\alpha l}{\lambda}, \quad (12)$$

where l represents a characteristic length and is, here, the hydraulic diameter. Numerous correlations to approach this number (α) can be found in the literature [Thome (2010)] and are usually derived from

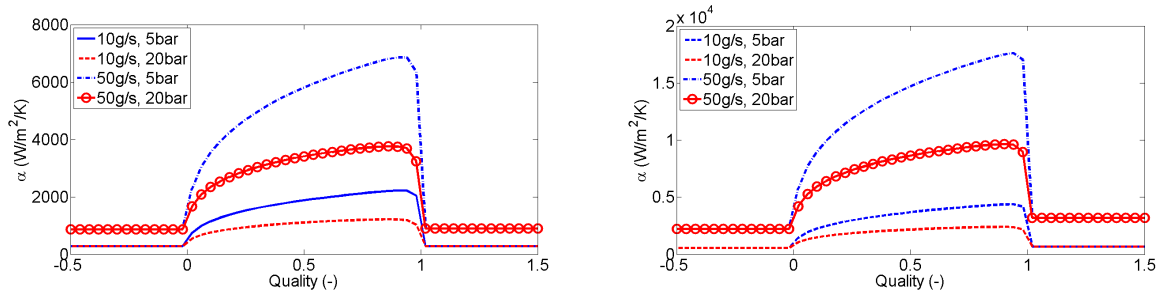


Figure 2: Heat transfer coefficient profiles EgrB (left) and ExhB (right)

experiments. Those correlations depend on the flow regime, the number of phases and the geometry studied. In single phase the following correlation is implemented:

$$Nu = CRe^n Pr^m, \quad (13)$$

where C is a constant, Re and Pr are dimensionless number (respectively Reynolds and Prandtl number). By integrating those numbers expressions in equation (13), it becomes:

$$Nu = C \left(\frac{4\dot{m}}{\pi d_h \mu} \right)^n \left(\frac{c_p \mu}{\lambda} \right)^m. \quad (14)$$

In the single phase region, the heat conductivity (λ), the viscosity (μ) and the specific heat (c_p) are assumed constant and the following expressions for the heat transfer coefficient is then derived:

$$\alpha_{f_{liq}} = \alpha_{f_{liq,ref}} \dot{m}_{f_{liq}}^n \quad | \quad \alpha_{f_{vap}} = \alpha_{f_{vap,ref}} \dot{m}_{f_{vap}}^n \quad | \quad \alpha_g = \alpha_{g,ref} \dot{m}_{g_{gas}}^n \quad (15)$$

where the constant α_{ref} and the exponent n have to be identified in liquid and vapor region for the working fluid and in single phase for the gas. In two phase, a correlation similar to [Horst et al. (2013)] is used to enhance the single phase heat transfer coefficient. This correlation corresponds to a tube arrangement and is practical since it creates continuity between single and two phase heat transfer coefficient and does not need transport properties such as viscosity or heat conductivity.

$$\alpha_{f_{2\phi}} = \alpha_{f_{liq}} \left\{ (1-x)^{0.01} \left[(1-x) + 1.2x^{0.4} \left(\frac{\rho_{liq}}{\rho_{vap}} \right)^{0.37} \right]^{-2.2} + x^{0.01} \left[\frac{\alpha_{liq}}{\alpha_{vap}} \left(1 + 8(1-x)^{0.7} \left(\frac{\rho_{liq}}{\rho_{vap}} \right)^{0.67} \right) \right]^{-2} \right\}^{-0.5}, \quad (16)$$

where x is the fluid quality defined as the quantity of vapor presents in the two phase flow:

$$x = \begin{cases} 0 & \text{if } h_f \leq h_{sat_{liq}} \\ \frac{h_f - h_{sat_{liq}}}{h_{sat_{vap}} - h_{sat_{liq}}} & \text{if } h_{sat_{liq}} \geq h_f \geq h_{sat_{vap}} \\ 1 & \text{if } h_f \geq h_{sat_{vap}} \end{cases} \quad (17)$$

Figure 2 show the working fluid heat transfer coefficient (α) for the EGR (left) and exhaust (right) boilers. For convenience, the quality (x) is not bounded between the interval $[0, 1]$ as shown in equation 17.

3.4 Working fluid properties

The working fluid properties are approximated using mathematical descriptions. This allows being independent from thermochemical database such as [Eric. W. Lemmon (2013)] and creates continuity in derivative terms during the single / two phase transition. The fluid properties will only be functions of pressure and enthalpy.

- Temperature model:

$$T_f = \begin{cases} a_{T_{liq}} h_f^2 + b_{T_{liq}} h_f + c_{T_{liq}} & \text{if } h_f \leq h_{sat_{liq}} \\ T_{sat_{liq}} + x (T_{sat_{vap}} - T_{sat_{liq}}) & \text{if } h_{sat_{liq}} \geq h_f \leq h_{sat_{vap}} \\ a_{T_{vap}} h_f^2 + b_{T_{vap}} h_f + c_{T_{vap}} & \text{if } h_f \geq h_{sat_{vap}} \end{cases} \quad (18)$$

where a , b , and c , are first order polynomial expressions function of pressure. The saturation temperature (T_{sat}) is approximated with the Wagner equation with adapted coefficient for liquid and vapor saturation [Kleiber et al. (2010)] and allows to make the transition between each phase.

- Density model:

$$\rho_f = \begin{cases} a_{\rho_{liq}} h_f^2 + b_{\rho_{liq}} h_f + c_{\rho_{liq}} & \text{if } h_f \leq h_{sat_{liq}} \\ \frac{1}{a_{\rho_{2\phi}} h_f + b_{\rho_{2\phi}}} & \text{if } h_{sat_{liq}} \geq h_f \leq h_{sat_{vap}} \\ a_{\rho_{vap}} h_f^2 + b_{\rho_{vap}} h_f + c_{\rho_{vap}} & \text{if } h_f \geq h_{sat_{vap}} \end{cases} \quad (19)$$

In single phase (*liq* and *vap*) the coefficient a , b , and c , are evaluated thanks to third order polynomial function of pressure similar to:

$$a_{\rho_{2\phi}} = \frac{1}{a_{\rho_{2\phi 1}} P_f + a_{\rho_{2\phi 0}}} \quad | \quad b_{\rho_{2\phi}} = \frac{1}{b_{\rho_{2\phi 1}} P_f + b_{\rho_{2\phi 0}}} \quad (20)$$

All coefficients mentioned before are evaluated thanks to fitting routines written in Matlab. Figure 3 show comparison between calculated temperature and density thanks to equation (18) and (19) and properties coming from [Eric. W. Lemmon (2013)] for pressure going from 1 to 80 bar.

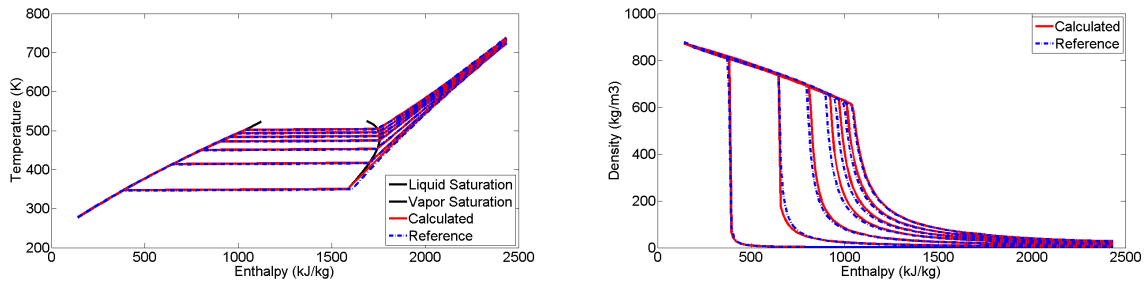


Figure 3: Temperature (left) and density (right) model validation

3.5 Discretization

To be implemented in the simulation environment, the continuous model mentioned by equations (4), (5), (7), (8), (9) are discretized with respect to space, based on finite differences method: The heat exchanger is divided into n longitudinal cells where a backward Euler scheme is applied for the space derivative terms. The dynamic response of the i th cell can be described by:

$$\begin{aligned} u &= [\dot{m}_{f_0} \quad P_{f_0} \quad h_{f_0} \quad \dot{m}_{g_L} \quad T_{g_L}] & Z &= \begin{bmatrix} 0 & 0 & 0 & 0 & 0 \\ 0 & 1 & 0 & 0 & 0 \\ 0 & 0 & 1 & 0 & 0 \\ 0 & 0 & 0 & 1 & 0 \\ 0 & 0 & 0 & 0 & 1 \end{bmatrix} \\ x_i &= [\dot{m}_{f_i} \quad h_{f_i} \quad T_{w_{int_i}} \quad T_{g_i} \quad T_{w_{ext_i}}] & Z\dot{x}_i &= f_i(x_i, u) \end{aligned} \quad (21)$$

$$f_i(x, u) = \begin{bmatrix} \frac{\dot{m}_{f_{i-1}} \frac{h_{f_{i-1}}}{\rho_{f_{i-1}}} \frac{\partial \rho_{f_{i-1}}}{\partial h_{f_{i-1}}} + \frac{1}{\rho_{f_{i-1}}} \frac{\partial \rho_{f_{i-1}}}{\partial h_{f_{i-1}}} \alpha_{f_i} A_{exch_{intf}} (T_{f_i} - T_{w_{int_i}})}{1 - \frac{h_{f_i}}{\rho_{f_i}} \frac{\partial \rho_{f_i}}{\partial h_{f_i}}} - \dot{m}_{f_i} \\ \frac{(\dot{m}_{f_{i-1}} h_{f_{i-1}} - \dot{m}_{f_i} h_{f_i}) - \alpha_{f_i} A_{exch_{intf}} (T_{f_i} - T_{w_{int_i}})}{\rho_{f_i} V_f} \\ \frac{\alpha_{f_i} A_{exch_{intf}} (T_{f_i} - T_{w_{int_i}}) + \alpha_{g_i} A_{exch_{intg}} (T_{g_i} - T_{w_{int_i}})}{\rho_{w_{int}} V_{w_{int}}} \\ \frac{\dot{m}_g c_{p_g} (T_{g_i}) (T_{g_{i-1}} - T_{g_i}) - \alpha_g [A_{exch_{intg}} (T_{g_i}^* - T_{w_{int_i}}) - A_{exch_{extg}} (T_{g_i} - T_{w_{ext_i}})]}{\rho_{g_i} V_g c_{p_g} (T_{g_i})} \\ \frac{\alpha_{amb} A_{exch_{ext_{amb}}} (T_{amb} - T_{w_{ext_i}}) + \alpha_{g_i} A_{exch_{extg}} (T_{g_i} - T_{w_{ext_i}})}{\rho_{w_{ext}} V_{w_{ext}}} \end{bmatrix}. \quad (22)$$

where the ambient temperature T_{amb} is assumed constant around the entire HEX.

4. HEX MODEL VALIDATION

4.1 Parameters identification

In the model presented above there are two kinds of parameters to identify. First: geometric parameters such as heat exchange area or cross section are usually given by the manufacturer or can directly be measured on the heat exchanger. Secondly: there are non-measurable parameters such as exponent in heat transfer correlation for each fluid. The identification process results into minimizing the error for each boiler on the working and transfer fluid outlet enthalpy or temperature using a feasible set of non-measurable parameters.

4.2 Steady state validation

First, the model is validated using steady state experimental results. To be representative of the engine map, 24 operating points corresponding to a speed/torque couple are used to compare experimental data to simulation results.

EGR evaporator: The comparison is done only for the EGR outlet temperature since in all measurements the working fluid is in two phase state. During the phase change, the temperature is more or less constant (a small temperature increase is observed for mixture) and comparison is not relevant on this criterion (major source of error coming from the pressure which is considered constant in both boilers). Figure 4 presents the temperature difference observed on both fluids: transfer (EGR) and working fluid (water ethanol mixture). The maximum deviation observed on the EGR temperature is 7.6 K and the average error is around 2.6K.

Exhaust evaporator: Figure 4 presents the temperature difference observed between the model and the experiments. Here both temperatures are relevant for comparison since the fluid is fully vaporized at the outlet. On the water ethanol side the maximum error is 9.2K and the mean deviation is around 4K. On the gas side the maximum error observed is 15.5K and the average difference is about 4.7K. Largest differences are observed on the exhaust which is not so important since accuracy on the working fluid is more significant for control purpose. The model predicts well the heat exchangers performance in steady state over the engine map. Main differences come from the non-dependency of the gas specific heat on air-fuel ratio (i.e. gases composition) and the uniform distribution of heat since the heat exchangers are simply represented by a single pipe. In reality, they are made of several channels and the working fluid is not necessarily homogeneously distributed between all the channels (this is also true for the gas). Last but not least, the heat losses are here represented by a single coefficient but in reality they are influenced by several parameters (external temperature and conditions). Moreover, one big issue was to have repetitiveness in the experiment. Indeed, the working fluid enters in the exhaust boiler in two phase state and it is assumed that the fluid distribution between each passage which was not homogeneous

creates those issues. In top of that, the different control loop actions (engine, Rankine and test cell) could have an influence on the experiments repetitiveness.

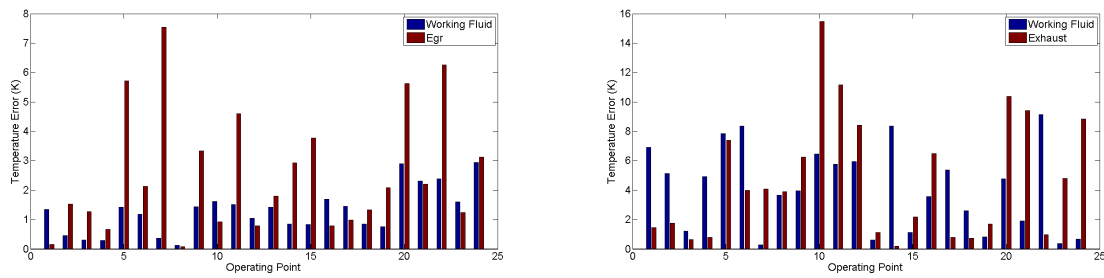


Figure 4: Temperature estimation error for the EGR (left) and Exhaust Boiler (right)

Steady state validation summary: Table 1 summarizes the model prediction error in steady state (relative error is the ratio of the absolute error and the maximum temperature difference across the heat exchanger).

	$T_{f_{out}EgrB}$		$T_{f_{out}ExhB}$		$T_{egr_{out}EgrB}$		$T_{exh_{out}ExhB}$	
	max	mean	max	mean	max	mean	max	mean
Absolute (K)	2.95	1.30	9.15	4.16	7.54	2.54	15.47	4.71
Relative (%)	0.57	0.29	8.84	3.28	2.34	0.61	8.61	3.40

Table 1: Evaporators steady state validation

4.3 Dynamic validation

The model is then compared to dynamic experiments where either working fluid mass flow or EGR and exhaust conditions can vary. Figure 5 presents the experimental inputs used in the model. Figure 6 shows

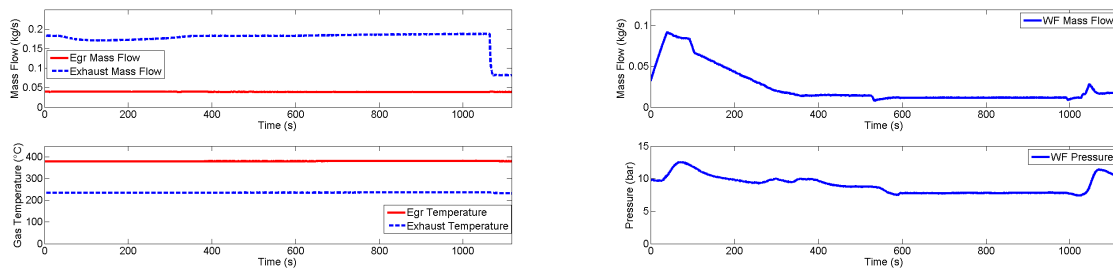


Figure 5: Experimental inputs: gas (left) and WF side (right)

the model predicted temperature versus the measured ones for respectively gas and working fluid sides. A large error can be observed a time 0 due to the initial conditions. It was difficult to have access to certain values in the experimental setup to correctly set initial conditions in the model (e.g. internal and external wall temperatures). Nevertheless, the dynamic behavior of the complete system is relatively well represented with a maximum deviation of 26 K on the working fluid predicted temperature and 20 K on the gas side. The EGR boiler behavior is better represented due to the more simple geometry. Indeed this component has only one core and the simple representation chosen is pretty correct whereas the exhaust boiler is composed of two cores but as the split between each core was not known it has been decided to represent it as a single core heat exchanger.

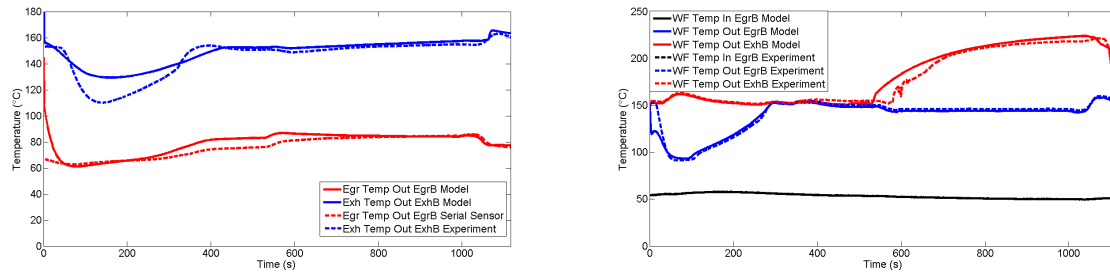


Figure 6: Experimental and modeled temperatures

Dynamic validation summary: Table 2 presents a summary of the predicted errors in dynamic, for several changes in the input disturbances. Even in dynamic, the model shows good overall performance with mean deviations below 2.5% while the computational complexity is low.

	$T_{f_{out}EgrB}$		$T_{f_{out}ExhB}$		$T_{egr_{out}EgrB}$		$T_{exh_{out}ExhB}$	
	max	mean	max	mean	max	mean	max	mean
Absolute (K)	4.5	1.5	25.9	2.3	7.9	2.8	20	4.2
Relative (%)	1.38	0.46	14.37	1.28	2.43	0.86	11.1	2.33

Table 2: Evaporators dynamic validation

5. CONCLUSION

A dynamic model of a serial boiler arrangement Rankine cycle using water ethanol mixture and recovering heat from EGR and Exhaust is presented and compared to experimental results. The model presents the advantage to be low in terms of computational needs and is suitable for control software integration. A more complete transient validation is needed to fully validate the model but first results show pretty good accuracy both in steady state and dynamic with an average error lower than 2.5% (relatively to the maximum temperature difference across the heat exchanger). Future work will focus on high level control strategy and optimization of the power recovery process on a complete vehicle environment. Low level control strategy is discussed in the companion paper [Grelet et al. (2015)].

REFERENCES

- Bendapudi, S., Braun, J. E., and Groll, E. A. (2008). A comparison of moving-boundary and finite-volume formulations for transients in centrifugal chillers. *International Journal of Refrigeration*, 31(8):1437 – 1452.
- Eric. W. Lemmon, M. L. H. (2013). Refprop nist standard reference database 23 (version 9.0), thermophysical properties division, national institute of standards and technology, boulder, co.
- Espinosa, N. (2011). *Contribution to the Study of Waste Heat Recovery Systems on Commercial Truck Diesel Engines*. PhD thesis, University of Liege.
- Feru, E., Kupper, F., Rojer, C., Seykens, X., Scappin, F., Willems, F., Smits, J., Jager, B. D., and Steinbuch, M. (2013). Experimental validation of a dynamic waste heat recovery system model for control purposes. In *SAE Technical Paper*. SAE International.
- Grelet, V., Dufour, P., Nadri, M., Lemort, V., and Reiche, T. (2015). Model based control for waste heat recovery rankine cycle system in heavy duty trucks. In *3rd International Seminar on ORC Power Systems (ORC15), 2015 (Accepted)*.
- Horst, T. A., Rottengruber, H.-S., Seifert, M., and Ringler, J. (2013). Dynamic heat exchanger model for performance prediction and control system design of automotive waste heat recovery systems. *Applied Energy*, 105(0):293 – 303.

- Kleiber, M., Wagner, W., Preisegger, E., Pfenning, A., and Neubronner, M. (2010). *VDI Heat Atlas Second Edition, Part D Thermophysical properties*. VDI Buch. Springer.
- Kunte, H. and Seume, J. (2013). Partial admission impulse turbine for automotive orc application. In *SAE Technical Paper*. SAE International.
- Latz, G., Andersson, S., and Munch, K. (2012). Comparison of working fluids in both subcritical and supercritical rankine cycles for waste-heat recovery systems in heavy-duty vehicles. In *SAE Technical Paper*. SAE International.
- Mago, P. J., Chamra, L. M., and Somayaji, C. (2007). Performance analysis of different working fluids for use in organic rankine cycles. *Proceedings of the Institution of Mechanical Engineers, Part A: Journal of Power and Energy*, 221(3):255–263.
- Peralez, J., Tona, P., Lepreux, O., Sciarretta, A., Voise, L., Dufour, P., and Nadri, M. (2013). Improving the control performance of an organic rankine cycle system for waste heat recovery from a heavy-duty diesel engine using a model-based approach. In *52nd Annual IEEE Conference on Decision and Control (CDC)*, pages 6830–6836.
- Sprouse III, C. and Depcik, C. (2013). Review of organic rankine cycles for internal combustion engine exhaust waste heat recovery. *Applied Thermal Engineering*, 51(1–2):711 – 722.
- Teng, H. (2010). Waste heat recovery concept to reduce fuel consumption and heat rejection from a diesel engine. *SAE International Journal of Commercial Vehicle.*, 3:60–68.
- Thome, J. R. (2010). *Wolverine Tube Inc Engineering Data Book III*. Heat Transfer Databook. Wolverine Tube Inc.
- Vaja, I. (2009). *Definition of an object oriented library for the dynamic simulation of advanced energy systems: Methodologies, Tools and Applications to Combined ICE-ORC Power Plants*. PhD thesis, University of Parma.
- Zhang, W.-J. and Zhang, C.-L. (2006). A generalized moving-boundary model for transient simulation of dry-expansion evaporators under larger disturbances. *International Journal of Refrigeration*, 29(7):1119 – 1127.

NOMENCLATURE

Acronyms

<i>EGR</i>	Exhaust gas recirculation
<i>HD</i>	Heavy duty
<i>HEX</i>	Heat exchanger
<i>NOP</i>	Net output power
<i>WHRS</i>	Waste heat recovery system

Greek letters

α	Heat transfer coefficient ($W/m^2/K$)
η	Efficiency (–)
λ	Heat conductivity ($W/m/K$)
ρ	Density (kg/m^3)

Latin letters

\dot{m}	Mass flow (kg/s)
\dot{Q}	Heat flow rate (W)
\dot{q}	Linear heat flow rate (W/m)
A	Area (m^2)
c_p	Specific heat ($J/kg/K$)
h	Enthalpy (J/kg)
Nu	Nusselt number (–)
P	Pressure (Pa)
PE	Perimeter (m)
Pr	Prandtl number (–)
Re	Reynolds number (–)

T	Temperature (K)
t	Time (s)
V	Volume (m^3)
z	Spatial direction (m)

Subscripts

<i>amb</i>	Ambient
<i>conv</i>	Convection
<i>cross</i>	Cross section
<i>egr</i>	EGR gas
<i>EgrB</i>	EGR boiler
<i>exh</i>	Exhaust gas
<i>ExhB</i>	Exhaust boiler
<i>ext</i>	External wall
<i>f</i>	Working fluid
<i>g</i>	Gas
<i>in</i>	Inlet port
<i>int</i>	Internal wall
<i>liq</i>	Liquid
<i>out</i>	Outlet port
<i>sat</i>	Saturation
<i>vap</i>	Vapor
<i>w</i>	Heat exchanger wall

MODEL BASED CONTROL FOR WASTE HEAT RECOVERY HEAT EXCHANGERS RANKINE CYCLE SYSTEM IN HEAVY DUTY TRUCKS

V. Grelet^{1,2,3}, P. Dufour^{2*}, M. Nadri², V. Lemort³, T. Reiche¹

¹ Volvo Trucks GTT ATR

1 av Henri Germain, 69800 Saint Priest

vincent.grelet@volvo.com, thomas.reiche@volvo.com

² Université de Lyon, F-69622, Lyon, France, Université Lyon 1, Villeurbanne, France CNRS, UMR 5007, LAGEP,

dufour@lagep.univ-lyon1.fr, nadri@lagep.univ-lyon1.fr

³ Thermodynamics Laboratory – University of Liège,

Campus du Sart Tilman, B49, 4000 Liège, Belgium

vincent.lemort@ulg.ac.be

* Corresponding Author

ABSTRACT

Driven by future emissions legislations and increase in fuel prices engine, gas heat recovering has recently attracted a lot of interest. In the past few years, a high number of studies have shown the interest of energy recovery Rankine based systems for heavy duty trucks engine compounding. Recent studies have brought a significant potential for such a system in a Heavy Duty (HD) vehicle, which can lead to a decrease in fuel consumption of about 5% [Wang et al. (2011)] and reduce engine emissions. But many challenges still need to be faced before the vehicle integration. This paper presents a control strategy development for waste heat recovery Rankine based systems in heavy duty trucks. Due to the highly transient operating conditions, improving the control strategy of those systems is an important step to their integration into a vehicle. It is shown here that moving to more advanced control strategies than classical PIDs lead to some gains in terms of performance. Due to the limited availability and high operational cost of test bench, the validation of such a controller is done on a representative and previously validated model.

1. INTRODUCTION

Idea of recovering heat and turning it into another form of energy is not new. By having a look in the long history of engine development, it has been introduced first through turbocharger technology and in for the commercial vehicle by the turbo-compound. Those two devices, helped the manufacturers to go through more and more stringent standards in pollutant emissions and to decrease the fuel consumption. However with nowadays engines, where those systems are present, it is hard to allocate more than 45% of fuel consumption to vehicle propulsion with classical solution. In the last decades, waste heat recovery systems (WHRS) based on Rankine cycle have attracted a lot of interest [Doyle and Kramer (1979) Oomori (1993) Wang et al. (2011)] and have shown a fuel economy potential between 5 and 10%, depending on the system complexity and the application. Contrary to stationary powerplants that use the same thermodynamic principle for electricity generation, a mobile application has very dynamic operating conditions which result into long and frequent transient behavior of the heat sources available on a vehicle. For such real driving conditions, control strategies must then be used to play a major role in the system efficiency. This topic is more and more addressed [Peralez et al. (2013), Luong and Tsao (2014)] since it is the final step for a good integration of the system into a vehicle. The control system should maximize the system performance and ensure a safe operation of the latter. Maximization of the performance is usually done by strategy optimization when safe operation means tight control of the manipulated variable(s). Here, we focus only on the second criteria since optimal strategy could only be done by taking into account all subsystems of the vehicle and not the WHRS as a standalone system. As the system dynamic is mainly controlled by the heat exchangers (HEX) behavior (i.e. evaporators and condenser) [Stobart et al. (2007), Quoilin et al. (2011)] it seems really important to focus on dynamic

performance of these components. Dynamic models of HEX are of two kinds: moving boundary (MB) and finite volume (FV). Both approaches have been widely used in control system design [Peralez et al. (2013), Pettit et al. (1998)] and result in a simplification of the heat recovery boiler/condenser geometry in a great extent (e.g. by representing the boiler by a straight pipe in pipe counterflow heat exchanger). The control issue tackled here deals with one key variable: the working fluid (WF) temperature before the expansion machine which should be accurately controlled by reducing the standard deviation around its set point. This paper is organized as follows, in the second section the Rankine process and the studied system are presented. Then, in the third section, developed control strategies are explained. Section four comparing the different controller implemented, on a validated simulation model [Grelet et al. (2015)]. Finally, conclusions are drawn and perspectives are opened.

2. RANKINE CYCLE PRINCIPLE AND STUDIED SYSTEM

2.1 Rankine process

The Rankine principle is shown in its temperature-entropy form in figure 1. It can be divided into four basic transformations:

- A liquid compression where the WF reaches the evaporation pressure ($1 \rightarrow 2$) by means of the pump power consumption (\dot{W}_{in}).
- An evaporation where the WF is heated up ($2 \rightarrow 3a$), vaporized ($3a \rightarrow 3b$) and superheated ($3b \rightarrow 3c$) by recovering heat from the heat source (\dot{Q}_{in}).
- An expansion where the fluid goes from the evaporation to the condensing pressure ($3c \rightarrow 4$). The pressure drop is converted by the expander into mechanical power on its shaft (\dot{W}_{out}).
- A condensation where the WF goes back to the liquid phase ($4 \rightarrow 1$) by giving heat to the heat sink (\dot{Q}_{out}).

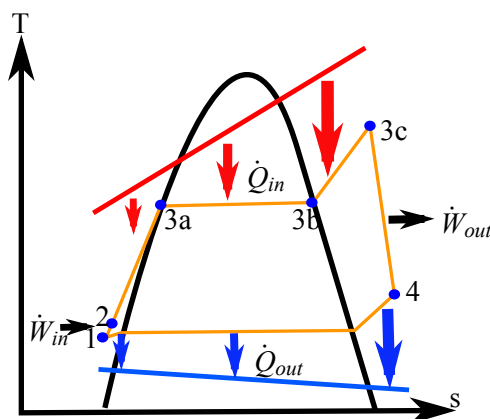


Figure 1: Temperature-Entropy diagram of the Rankine cycle

2.2 Studied system

For this application, the heat sources are the exhaust gas recirculation (EGR) and exhaust gases. The two evaporators linked to those sources are arranged in series, i.e. the WF passes first through the EGR boiler and then through the exhaust boiler. An electrical WF pump allows to control the mass flow rate in the system to achieve the control objective. The expansion machine is a kinetic turbine mechanically coupled to the engine and a liquid-cooled condenser is used to condense the WF. The WF is a water ethanol mixture showing better performance and which reduces the drawbacks of each pure fluid: freezing point of water and flammability for ethanol [Latz et al. (2012)].

3. CONTROLLER DEVELOPMENT

3.1 Control objective

As mentioned in section 1, the key parameter to control is the WF temperature before the expansion machine. This is even more critical for this system since it uses a high speed expansion machine which is very sensitive to wet steam. Indeed, during the expansion process the droplets formation could cause erosion of the blades and damage the turbine. In order to avoid this, it seems important to have a tight control of the inlet temperature to avoid wet steam from entering into the turbine. This is usually done by turning the temperature criterion into a superheating set point (superheat corresponds to the temperature difference between present value and vapor saturation temperature) which, when positive, guarantees fully vaporized fluid entering into the expander. As the focus is on the high pressurized branch of the circuit, only the evaporators are modeled.

3.2 Nonlinear heat exchanger model

The modeling methodology and model validation is presented in this paper companion [Grelet et al. (2015)]. Based on finite difference scheme, The governing equations and the boundary conditions are discretized in space domain. The obtained model takes the following form (see the nomenclature at the end for the abbreviation meaning):

$$Z \dot{x}_i = f_i(x_i, u), \quad (1)$$

$$\text{where: } u = [\dot{m}_{f,0} \quad P_{f,0} \quad h_{f,0} \quad \dot{m}_{g,L} \quad T_{g,L}], \quad (2)$$

$$Z = \begin{bmatrix} 0 & 0 & 0 & 0 & 0 \\ 0 & 1 & 0 & 0 & 0 \\ 0 & 0 & 1 & 0 & 0 \\ 0 & 0 & 0 & 1 & 0 \\ 0 & 0 & 0 & 0 & 1 \end{bmatrix}, \quad (3)$$

$$x_i = [\dot{m}_{f,i} \quad h_{f,i} \quad T_{w,int,i} \quad T_{g,i} \quad T_{w,ext,i}], \quad (4)$$

$$f_i(x_i, u) = \begin{bmatrix} \frac{\dot{m}_{f,i-1} \frac{h_{f,i-1}}{\rho_{f,i-1}} \frac{\partial \rho_{f,i-1}}{\partial h_{f,i-1}} + \frac{1}{\rho_{f,i-1}} \frac{\partial \rho_{f,i-1}}{\partial h_{f,i-1}} \alpha_{f,i} A_{exch,int,f}(T_{f,i} - T_{w,int,i})}{1 - \frac{h_{f,i}}{\rho_{f,i}} \frac{\partial \rho_{f,i}}{\partial h_{f,i}}} - \dot{m}_{f,i} \\ (\dot{m}_{f,i-1} h_{f,i-1} - \dot{m}_{f,i} h_{f,i}) - \alpha_{f,i} A_{exch,int,f}(T_{f,i} - T_{w,int,i}) \\ \frac{\rho_{f,i} V_f}{\alpha_{f,i} A_{exch,int,f}(T_{f,i} - T_{w,int,i}) + \alpha_g A_{exch,int,g}(T_{g,i} - T_{w,int,i})} \\ \frac{\dot{m}_g c_{pg}(T_{g,i})(T_{g,i-1} - T_{g,i}) - \alpha_g [A_{exch,int,g}(T_{g,i} - T_{w,int,i}) - A_{exch,ext,g}(T_{g,i} - T_{w,ext,i})]}{\frac{\rho_{g,i} V_g c_{pg}(T_{g,i})}{\alpha_{amb} A_{exch,ext,amb}(T_{amb} - T_{w,ext,i}) + \alpha_g A_{exch,ext,g}(T_{g,i} - T_{w,ext,i})}} \\ \frac{\rho_{w,int} V_{w,int}}{\rho_{w,ext} V_{w,ext}} \end{bmatrix}. \quad (5)$$

where the ambient temperature (T_{amb}) is assumed constant around the entire HEX.

3.3 The piecewise linear approach

Developing a first principle based model is often hard (most of the parameters presented in the model (1-5) are impossible to get from experimental results) and requires a lot of effort. Using a piecewise linear model approach could be a good trade-off between controller performance and development effort. If we consider the previous model to be a single input single output (SISO) plant of the form:

$$\dot{x} = f(x, u), \quad (6)$$

$$y = g(x, u), \quad (7)$$

where u is the WF mass flow entering into the EGR boiler and y is the WF temperature exiting the exhaust boiler. The dynamic relation between the variation of u and y (also called manipulated variable (MV) and controlled variable (CV)) around an operating point can be described by a first order plus time delay

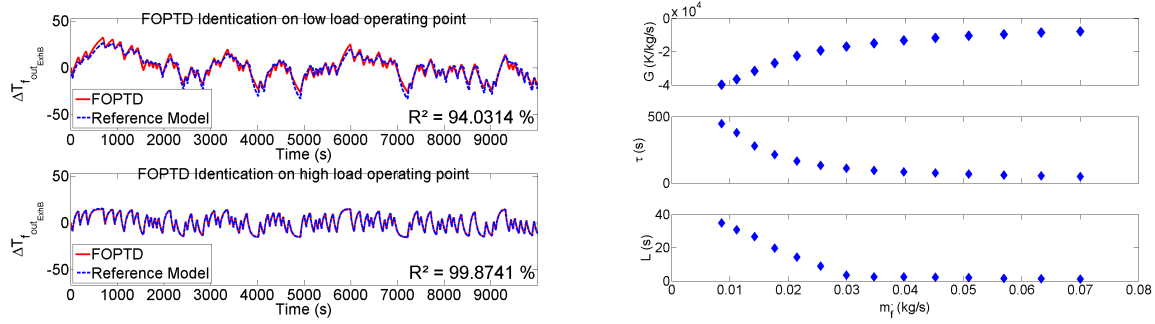


Figure 2: FOPTD model validation (left) and parameters identified (right)

(FOPTD) transfer function:

$$\frac{\Delta T_{f,L_{ExhB}}(s)}{\Delta \dot{m}_{f,0_{EgrB}}(s)} = \frac{G}{1 + \tau s} e^{-Ds}, \quad (8)$$

where the relation between the state ($h_{f,i}$) of equation (4) and the working fluid temperature (T_f) can be written:

$$T_f = (a_1 P_f + a_0) h_f^2 + (b_1 P_f + b_0) h_f + (c_1 P_f + c_0), \quad (9)$$

with a , b , and c fitted from thermodynamic database. Figure 2 shows a comparison of two different identified FOPTD model on a low and high engine load operating point and to the reference model presented in 3.2. As it can be seen on this figure the agreement is really good (94% for the low engine load point) and validates the choice of this model structure (8). The main drawback of doing this it is that FOPTD parameters varying a lot depending on the operating point where they are identified. Figure 2 shows gain, time constant and lag for the 14 identified FOPTD, hence demonstrating the nonlinearity of the system. By identifying FOPTD parameters around different relevant operating points and combining them by means of a weighting scheme a global linear model can be created. This global model is the sum of each weighted output of the N identified local models. The weighting method used in this paper is based on the validity of one model among N , obtained by comparing the local model outputs to the plant measurements. The current (at time k) modeling error between the process measure and the i th model output is:

$$\varepsilon_{i,k} = y_{P,k} - y_{i,k}. \quad (10)$$

3.3.1 Bayesian estimator: State of the art adaptive estimation technique is the Bayesian estimator [Banerjee et al. (1997), Aufderheide and Bequette (2003)]. The recursive Bayesian weighting scheme is the conditional probability of the i th model present in the N model bank to be true given the model population in the bank and its past history of probabilities. It assigns a weight between 0 and 1 (perfect fit of the i th model) to each model output in order to bound the global model output in the local models extreme values. The probability is calculated as follows:

$$p_{i,k} = \frac{\exp(-\frac{1}{2} \varepsilon_{i,k} K \varepsilon_{i,k}^T p_{i,k-1})}{\sum_{m=1}^N (\exp(-\frac{1}{2} \varepsilon_{m,k} K \varepsilon_{m,k}^T p_{m,k-1}))}, \quad (11)$$

where K is a convergence matrix used to accelerate the convergence to a single model and δ is an artificial small probability introduced to keep alive each model of the bank in the recursive scheme. The weight of each i^{th} model is then calculated according to:

$$W_{i,k} = \begin{cases} \frac{p_{i,k}}{\sum_{m=1}^N p_{m,k}} & \text{for } p_{i,k} > \delta \\ 0 & \text{for } p_{i,k} < \delta \end{cases} \quad (12)$$

The two tuning parameters of this scheme are the matrix K and the scalar δ and are tuned to achieved desired performance. If convergence to a single model is searched both are set relatively high whereas when more blending are wanted they are detuned and set at a low value. The global model output \tilde{y} is calculated by summing the weighted local models outputs at the current time k :

$$\tilde{y}_k = \sum_{i=1}^N W_{i,k} y_{i,k} \quad (13)$$

3.3.2 New proposed estimator: In order to reduce the tuning effort and to stay as simple as possible, a new method is here proposed to compute the local models weights. All values denoted by a superscript, $\tilde{}$, refer to normalized values.

$$\tilde{\varepsilon}_{i,k} = \frac{\varepsilon_{i,k}^2}{\sum_{m=1}^N \varepsilon_{m,k}^2}, \quad (14)$$

$$X_{i,k} = \prod_{j \neq i, j=1}^{j=N} \tilde{\varepsilon}_{i,k} (1 - \tilde{\varepsilon}_{j,k}), \quad (15)$$

$$\tilde{X}_{i,k} = \frac{X_{i,k}}{\sum_{m=1}^N X_{m,k}}. \quad (16)$$

The value \tilde{X}_i computed thanks to equation (16) is then filtered through a first order transfer function with unit static gain to obtain the current weight of each local model $W_{i,k}$:

$$W_{i,k} = \frac{1}{1 + T_S} \tilde{X}_{i,k}, \quad (17)$$

where T plays the same role as the convergence matrix K of equation (11), except that is a scalar instead of a matrix. The global model output is then calculated in the same way than with the Bayesian method.

$$\tilde{y}_k = \sum_{i=1}^N W_{i,k} y_{i,k}. \quad (18)$$

3.4 Gain scheduled PID

From the 14 identified FOPTD models, PID gains are offline computed and tabulated. These gains are then linearly interpolated function of the working fluid mass flow entering in the heat exchangers. In the rest of the study, parallel PID form are used with the addition of an anti wind-up to increase the overall performance of the controller. Gains are calculated using [Skogestad (2003)] where the tuning parameter is optimally set.

3.5 Nonlinear model inversion based controller

The model presented in the companion paper [Grelet et al. (2015)] and denoted by equation (1) can be reduced and inverted to be used as feed-forward term in the controller shown in figure 3. Principle and details of inversion is well explained in Peralez et al. (2013). The idea is to remove fastest dynamics in order to obtain an explicit expression of the desired MV u , in this case the WF mass flow (\dot{m}_{f_0}), function of the slowest states which are, here, the internal and external wall temperatures. Using the update of the input disturbances measure ($P_{f_0}, h_{f_0}, \dot{m}_{g_L}, T_{g_L}$), the system of equations defining the response of the i^{th} cell of the reduced model is then:

$$\begin{cases} 0 &= \dot{m}_f (h_{f_{i-1}} - h_{f_i}) + \dot{Q}_{f_{int_i}} \\ \frac{\partial T_{w_{int_i}}}{\partial t} &= \dot{Q}_{f_{int_i}} + \dot{Q}_{g_{int_i}} \\ 0 &= \dot{m}_g c_{p_g} (T_{g_{i-1}} - T_{g_i}) + \dot{Q}_{g_{int_i}} + \dot{Q}_{g_{ext_i}} \\ \frac{\partial T_{w_{ext_i}}}{\partial t} &= \dot{Q}_{g_{ext_i}} + \dot{Q}_{amb_{ext_i}}. \end{cases} \quad (19)$$

The expression of the feedforward term MV \dot{m}_f is then straightforward and equal to:

$$\dot{m}_f = \frac{\sum_{i=1}^N \dot{Q}_{f_{int_i}}}{h_{f_0} - h_{f_L}}. \quad (20)$$

The feedback part of the controller shown in figure 3 is composed of a gain scheduled PID and presented in section 3.4.

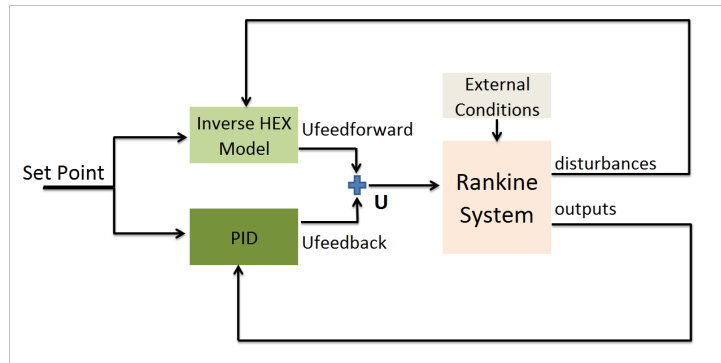


Figure 3: Model based controller structure

4. CONTROLLER PERFORMANCE

Each controller presented in section 3 is implemented under Matlab/Simulink and tested on the validated model presented in the companion paper [Grelet et al. (2015)]. A representative long haul truck driving cycle is used as simulation input (figure 4). Pump and turbine models are added to represent the high pressure part of the system.

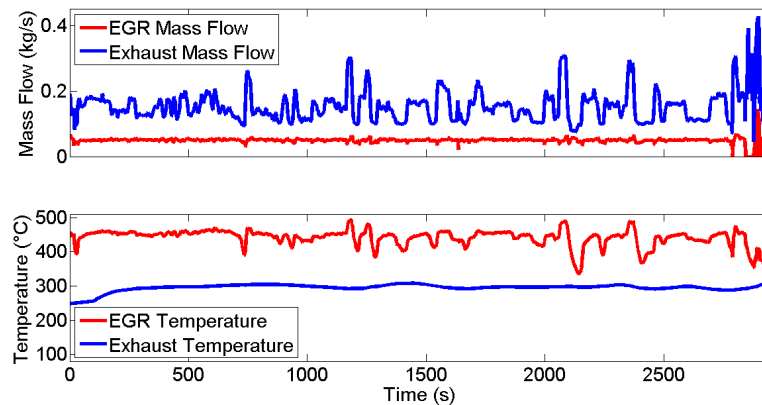


Figure 4: Driving cycle

4.1 Simulated system

The system is composed of an infinite sink at constant temperature, a first evaporator linked to the EGR gases, a second boiler recovering heat from the exhaust gases and a turbine expander. The simulated WF is composed of 20% water and 80% ethanol.

4.1.1 Pump model: The WF pump is simply represented by a fixed displacement and an isentropic efficiency. The volumetric efficiency will be a function of the outlet pressure. This law is identified

thanks to experimental data.

$$\dot{m}_f = \rho_{f,in} \frac{N_{pump}}{60} C_{c_{pump}} \eta_{vol,pump} \quad (21)$$

4.1.2 Turbine model: The turbine nozzle is represented by the following equation:

$$\dot{m}_f = k_{eq} \sqrt{\rho_{f,in} P_{f,in} \left(1 - \frac{P_{f,in}}{P_{f,out}} \right)^{-2}} \quad (22)$$

And the isentropic efficiency is calculated according to the following relation:

$$\eta_{is,turb} = \eta_{is,turb_{max}} \left(\frac{2c_{us}}{c_{us_{max}}} - \frac{c_{us}}{c_{us_{max}}} \right)^2, \quad (23)$$

where

$$c_{us} = \frac{u}{c_s} = \frac{\omega_{turb} R_{turb}}{2\sqrt{h_{in,turb} - h_{in,turb_{is}}}} \quad (24)$$

Model parameters (k_{eq} , $\eta_{is,turb_{max}}$, $c_{us_{max}}$ and R_{turb}) are fitted using data from supplier.

4.1.3 Actuator and sensors: Pump actuator, temperature and pressure sensors are represented by first order model, fitted with data from manufacturer data.

4.2 Tracking performance

Controllers are compared on their ability to follow a superheat set point (SP) calculated at each time step. A set point variation is done at $t = 1500s$ to better assess the controllers performance. Figure 5 shows the superheat tracking for the different controllers implemented.

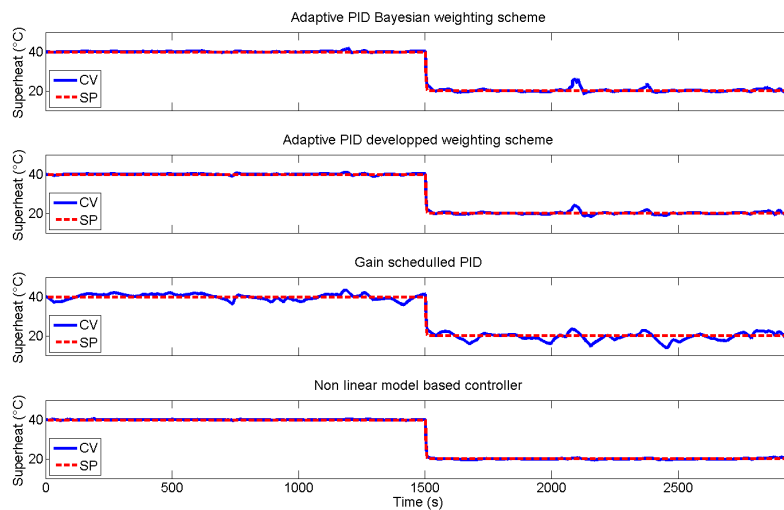


Figure 5: Superheat tracking

Gain scheduled PID can clearly be identified as the worst controller whereas the model based controller offers the best tracking performance. But it has to be recalled that the inverted model based control requires the perfect knowledge of all model parameter values (which is questionable), whereas the other models may be derived from various experimental process step responses. Concerning the adaptive PID, the performance is improved compared to the gain scheduling, where gains are identified off line, but it can be seen that the developed weighting scheme gives slightly better results especially when

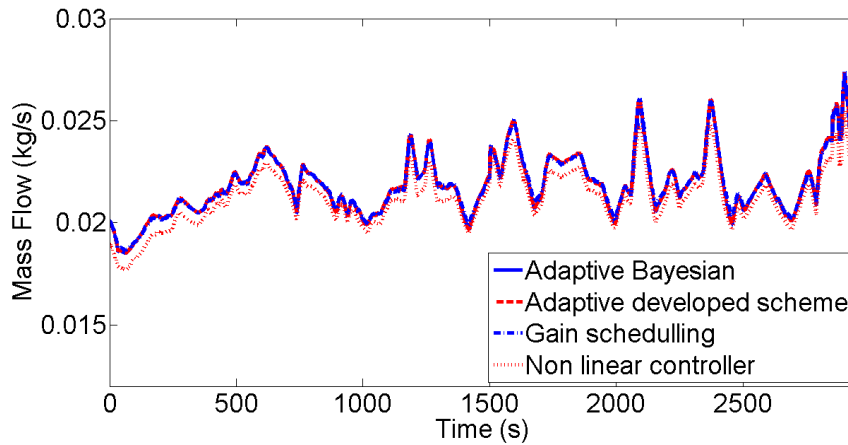


Figure 6: Manipulated variable

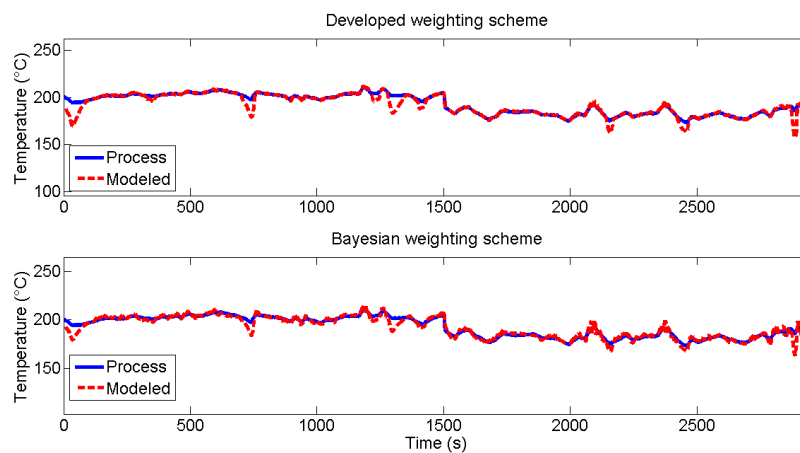


Figure 7: Global models outputs

large disturbances appear (at $t=2200s$ and $t=2400s$). This is highlighted when looking at the integrated absolute error (*IAE*) which is a classical performance index when comparing controllers performance. It is calculated using the following relation:

$$IAE = \int_0^{t_{sim\ final}} |CV(t) - SP(t)| dt. \quad (25)$$

Table 1 shows the *IAE* for the four controllers. As previously said, the inverted model based controller gives the best performance, followed by the adaptive strategy with the developed weighting scheme then the Bayesian weighting scheme and the gain scheduled strategy. Moreover, there are less tuning parameters (2) in the new proposed algorithm than in the Bayesian one. The new developed strategy gives better results compared to the Bayesian weighting scheme since the transition in PID parameters is smoother. The control inputs shown on figure 6 are similar but slightly different. Figure 7 shows the outputs of the global models weighted by the two methods showed in section 3.3. The Bayesian weighting scheme gives better results but creates chattering effect due to the fast changes in weights. This could be canceled by detuning the values of the convergence matrix K but not without affecting the controller performance. The developed weighting scheme includes by nature a low pass filter which avoid this effect.

Controller	IAE
Adaptive PID with Bayesian scheme	1044.17
Adaptive PID with new proposed scheme	958.09
Gain scheduled PID	4192.07
Non linear model based controller	417.54

Table 1: Integrated absolute error for the four implemented controllers

5. CONCLUSION

This study presented a new control strategy development of a waste heat recovery Rankine based system used in a long haul truck. Three different controllers are implemented and compared on a validated simulation model. Moreover, a weighting scheme for piece-wise linear approach was developed and compared to a state of the art weighting scheme. The global model outputs are similar but the developed scheme gives better results when the multi-model method is used to compute online optimal PID gains. This adaptive strategy improved significantly the performance of the PID compared to an offline gain scheduled strategy. The first principle nonlinear model based controller gave even better results but was costly in terms of development and parameter calibration, whereas the adaptive strategy requires minimum knowledge of the system and could be developed quite easily. However, the robustness of each controller still need to be investigated on an experimental setup.

REFERENCES

- Aufderheide, B. and Bequette, B. (2003). Extension of dynamic matrix control to multiple models. *Computers and Chemical Engineering*, 27(8–9):1079 – 1096.
- Banerjee, A., Arkun, Y., Ogunnaiké, B., and Pearson, R. (1997). Estimation of nonlinear systems using linear multiple models. *AIChE Journal*, 43(5):1204–1226.
- Doyle, E. DiNanno, L. and Kramer, S. (1979). Installation of a diesel-organic rankine compound engine in a class 8 truck for a single-vehicle test. In *SAE Technical Paper*, number 790646. SAE International.
- Grelet, V., Lemort, V., Reiche, T., Nadri, M., and Dufour, P. (2015). Waste heat recovery rankine cycle based system modeling for heavy duty trucks fuel saving assessment. In *3rd International Seminar on ORC Power Systems (ORC15), 2015 (Accepted)*.
- Latz, G., Andersson, S., and Munch, K. (2012). Comparison of working fluids in both subcritical and supercritical rankine cycles for waste-heat recovery systems in heavy-duty vehicles. In *SAE Technical Paper*. SAE International.
- Luong, D. and Tsao, T.-C. (2014). Linear quadratic integral control of an organic rankine cycle for waste heat recovery in heavy-duty diesel powertrain. In *American Control Conference (ACC), 2014*, pages 3147–3152.
- Oomori, H. Ogino, S. (1993). Waste heat recovery of passenger car using a combination of rankine bottoming cycle and evaporative cooling system. In *SAE Technical Paper*, number 930880. SAE International.
- Peralez, J., Tona, P., Lepreux, O., Sciarretta, A., Voise, L., Dufour, P., and Nadri, M. (2013). Improving the control performance of an organic rankine cycle system for waste heat recovery from a heavy-duty diesel engine using a model-based approach. In *52nd Annual IEEE Conference on Decision and Control (CDC)*, pages 6830–6836.

- Pettit, N., Willatzen, M., and Ploug-Sørensen, L. (1998). A general dynamic simulation model for evaporators and condensers in refrigeration. part ii: simulation and control of an evaporator: Modèle général dynamique pour évaporateurs et condenseurs frigorifiques. partie ii: Simulation et régulation d'un évaporateur. *International Journal of Refrigeration*, 21(5):404 – 414.
- Quoilin, S., Aumann, R., Grill, A., Schuster, A., Lemort, V., and Spliethoff, H. (2011). Dynamic modeling and optimal control strategy of waste heat recovery organic rankine cycles. *Applied Energy*, 88(6):2183 – 2190.
- Skogestad, S. (2003). Simple analytic rules for model reduction and PID controller tuning. *Journal of Process Control*, 13(4):291 – 309.
- Stobart, R., Hounsham, S., and Weerasinghe, R. (2007). The controllability of vapour based thermal recovery systems in vehicles. In *SAE Technical Paper*. SAE International.
- Wang, T., Zhang, Y., Peng, Z., and Shu, G. (2011). A review of researches on thermal exhaust heat recovery with rankine cycle. *Renewable and Sustainable Energy Reviews*, 15(6):2862 – 2871.

NOMENCLATURE

Acronyms

<i>CV</i>	Controlled variable
<i>EGR</i>	Exhaust gas recirculation
<i>FOPTD</i>	First order plus time delay
<i>HD</i>	Heavy duty
<i>HEX</i>	Heat exchanger
<i>IAE</i>	Integrated absolute error
<i>MV</i>	Manipulated variable
<i>SISO</i>	Simple input simple output
<i>SP</i>	Set point
<i>WHRS</i>	Waste heat recovery system

Greek letters

α	Heat transfer coefficient ($W/m^2/K$)
ε	Error (-)
η	Efficiency (-)
τ	Time constant (s)

Latin letters

\dot{m}	Mass flow (kg/s)
\dot{Q}	Heat flow rate (W)
A	Area (m^2)
C_c	Cubic capacity (m^3)
c_p	Specific heat ($J/kg/K$)
D	FOPTD lag (s)
G	FOPTD gain ($K/kg/s$)
h	Enthalpy (J/kg)
K	Bayesian recursive scheme convergence matrix (-)
k_{eq}	Turbine throat equivalent section (m^2)

N	Rotational speed (rpm)
P	Pressure (Pa)
p	Bayesian recursive scheme probability (-)
R	Turbine wheel radius (m)
T	Temperature (K)
t	Time (s)
V	Volume (m^3)
W	Weight (-)
X	Developed scheme raw weight (-)

Subscripts

<i>amb</i>	Ambient
<i>conv</i>	Convection
<i>cross</i>	Cross section
<i>EgrB</i>	EGR boiler
<i>ExhB</i>	Exhaust boiler
<i>exp</i>	Expander
<i>ext</i>	External wall
<i>f</i>	Working fluid
<i>g</i>	Gas
<i>in</i>	Inlet port
<i>int</i>	Internal wall
<i>k</i>	Current time step
<i>liq</i>	Liquid
<i>out</i>	Outlet port
<i>P</i>	Process
<i>sat</i>	Saturation
<i>vap</i>	Vapor
<i>w</i>	Heat exchanger wall

A NOVEL HYBRID SOLAR POWER GENERATION SYSTEM USING A-SI PHOTOVOLTAIC/THERMAL COLLECTORS AND ORGANIC RANKINE CYCLE

Jing Li, Pengcheng Li, Gang Pei*, Jie Ji, Jahan Zeb Alvi, Lijun Xia

Department of Thermal Science and Energy Engineering, University of Science and Technology of China,

Hefei, Anhui, China

E-mail: peigang@ustc.edu.cn; lijing83@ustc.edu.cn

ABSTRACT

A novel hybrid solar power generation system (HSPGS) is proposed. It mainly consists of photovoltaic/thermal (PV/T) collectors based on amorphous silicon (a-Si) cells, organic Rankine cycle (ORC), and inner-type heat storage unit. The PV/T collectors produce electricity directly via the cells, and the waste heat is carried away to the ORC for thermal power generation. Owing to the unique effect of thermal annealing, a-Si cells together with the ORC benefit from high temperature operation. Steady power generation is guaranteed by the heat storage unit. Compared with the conventional PV and solar ORC systems, the HSPGS can avoid or greatly reduce the usage of expensive battery, and has a much higher power efficiency. This work presents a close view of the HSPGS. Mathematic models are built and the system performance in the temperature range from 80°C to 150°C is estimated. Efficiency of about 12.5% can be achieved with a hot side temperature of 100°C.

1. INTRODUCTION

Solar ORC from tens of kWe to a few hundred kWe has great potential to meet the residential demand on heat and power. It has advantages over the highly concentrated solar thermal power technology in regard to the easier energy collection and storage, and the ability to supply energy near the point of usage. However, one critical problem of solar ORC is the low power efficiency. With a hot side temperature of 150 °C, the power efficiency is expected to be lower than 7%.

Photovoltaic (PV), is a simpler and more efficient way to generate electricity from solar irradiation. Heat can be also supplied to the consumers via the PV/T technology. Both power efficiency and cost-effectiveness of PV cells have been improved significantly in the past 10 years. One of the challenges associated with solar PV system is the energy storage. Currently lots of the PV systems are connected to the electric grid. Solar cells will generate electricity steadily throughout the day as long as the sun is shining. But when the sky is partly cloudy, solar power output from an entire region can fluctuate unpredictably. To mitigate the impact of this phenomenon, energy storage is a vital component of a more resilient, reliable and efficient electric grid. Energy storage will help lower consumer costs by saving low-cost power for peak times and making renewable energy available when it's needed the most. Aside from the grid-tied system, the off-grid PV system is preferable in remote areas for the sake of a silent, emission-free energy source, avoidance of the high cost of extending a utility line, and independence of homemade energy production. A backup energy source is essential for the stand-alone PV system. Unfortunately, the deployment of battery storage will dramatically increase the system cost. With a 5h lithium battery storage, the total system cost will be 30500RMB (about 5000 US\$)/kW, which is 4 times of that without storage (Li *et al.*, 2015).

Solar ORC technology is frequently compared with the PV technology to clarify its advantages. Nevertheless, cooperation of the two technologies can be more beneficial. A hybrid solar power generation system (HSPGS) based PV/T and ORC technologies is described in a patent (Li *et al.*, 2009). The cells absorb solar energy, part of which is converted into electricity directly and the rest is converted into heat. The heat is further utilized to drive the ORC and generate electricity. The HSPGS has the advantages over the conventional PV system regarding the replacement of expensive battery storage by heat storage, and is much more efficient than the solo solar ORC. Research on the HSPGS has also been reported (Li *et al.*, 2010, Kosmadakis *et al.*, 2011).

The selection of PV material is crucial for the HSPGS. Crystalline silicon (c-Si) cell has a high temperature coefficient of power at maximum power point (PMPP), which is about -0.41 to -0.50%/°C at standard test conditions (STC). The coefficient is negative with larger magnitude at higher temperature (King *et al.*, 1997). Given an efficiency of 18% at 25°C, the absolute decrement in the efficiency can be more than 10% when the operating temperature increases to 150°C. Gallium arsenide (GaAs) cell has a relatively low temperature coefficient of PMPP of about -0.20%/°C, but its efficiency at 25°C is generally higher than 25%, which may drop to 18% at 150°C. In the case of the c-Si and GaAs solar cells, the efficiency superiority of the HSPGS is not significant due to the great efficiency loss of the cells at high temperature. Though amorphous silicon (a-Si) cell is less efficient than c-Si and GaAs cells at normal operating temperature, it seems more suitable for the HSPGS application.

2. CHARACTERISTICS OF A-SI CELL

a-Si is the non-crystalline allotropic form of silicon. a-Si cell is the most well developed thin film cell. In China a total capacity more than 2.0 GW of a-Si cell can be produced annually (Hanergy, 2015). It can be deposited at low temperature onto a variety of substrates such as glass, plastic and metal, and thus produces savings on silicon material cost. One compelling characteristic of a-Si cell is the degradation in the power output when exposed to the sunlight, which is known as the Staebler–Wronski Effect (SWE). It is easy to achieve an initial a-Si cell efficiency of 10%, but it will drop to 7% or lower at stabilized state. The SWE has limited the development of a-Si cell despite of its relatively low cost, and makes it less competitive with c-Si cell. Notably, the common use of a-Si cell is subject to the ambient temperature. At higher operating temperature (>50°C), a-Si cell will benefit from the thermal annealing (Fanni *et al.*, 2009). The defects induced by light will decrease and even disappear, leading to an improved power generation.

A number of experiment results have indicated that a-Si cells perform better at higher operating temperature. For example, Del Cueto *et al.* (1999) investigated the temperature-induced changes in the performance of a-Si modules from different manufacturers in controlled light-soaking. Exposure of the modules was executed at low temperature (22±8°C) for about 1000 h, which was subsequently followed up with exposure at warm temperature (51±8°C) for about 500 h. The degradation at low temperature was recovered upon the subsequent warm soaking, resulting in an efficiency increment between 10% and 17%. Further investigation showed the operating temperature during light-soaking was the most important factor for determining stabilized cell performance, while the light intensity seemed to be the least important one (Roedern *et al.*, 2000). According to the four-year experiment conducted later on, higher minimum operating temperature led to higher performance levels of a-Si cell (Ruther *et al.*, 2005). Nikolaeva - Dimitrova *et al.* (2010) compared the seasonal variations on energy yield of a-Si, hybrid, and c-Si PV modules. The average efficiency of thin film modules in the hot month was greater than that in the cold month. Makrides *et al.* (2012) analyzed the effect of temperature on different grid-connected PV technologies over the period June 2006-June 2010. An increase in power for all the a-Si technologies was obvious during the warm summer season. These oscillations were due to both spectral effect and SWE. With the same spectral distribution, the efficiency of a-Si cell at mid-August was 8% higher than that at mid-February (Virtuani *et al.*, 2014). The dynamic degradation of a-Si cell at 25, 50 and 90°C was monitored (Pathak *et al.*, 2012a, Pathak *et al.*, 2012b, Rozario *et al.*, 2014). Higher operating temperature resulted in faster degradation and higher efficiency at degraded steady state (DSS). Some of the results are presented in Figure 1.

As demonstrated in the above works, the temperature coefficient of PMPP of a-Si cell at DSS is positive, which is contrary to that at STC. A value of about -0.21%/°C is common at STC. However, duration of the test is typically short. The cell is unable to experience a full annealing or degradation as the operation temperature changes. Evidences have shown the temperature coefficient of PMPP of a-Si cell for a short time scale of several hours is negative, while it is positive for a longer time scale of seasons (Ishii *et al.*, 2011). In fact, a-Si modules continue to show further change in maximum power even after they stabilize according to the international qualification standard IEC 61646. To perform sufficient preconditioning of thin-film modules prior to precision calibration, a new more complete standard procedure is needed (Kenny *et al.*, 2014).

The unique effect of thermal annealing makes a-Si cell especially suitable for PV/T application, where

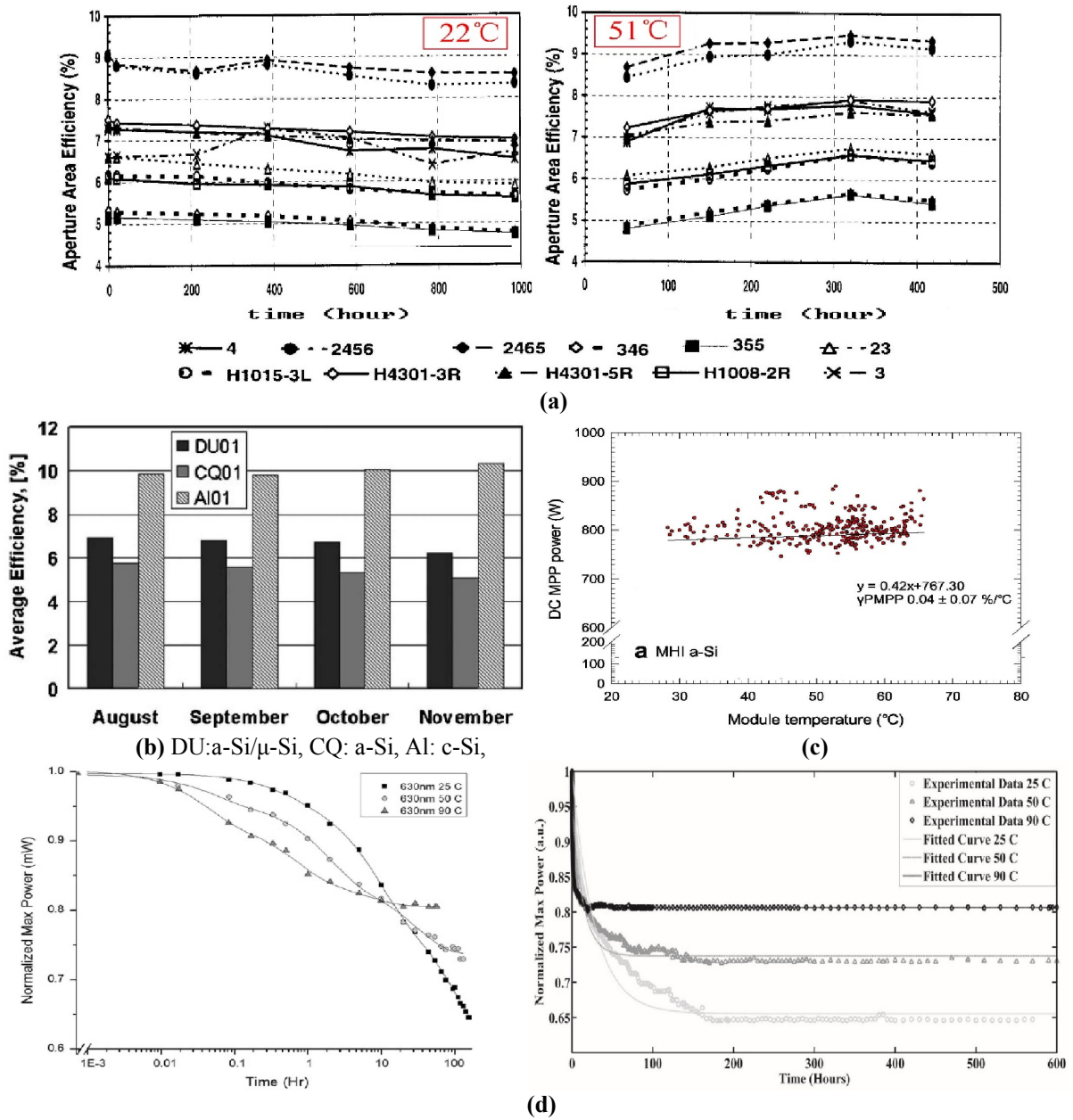


Figure 1: Variations of a-Si cell efficiency and power with time and operating temperature (a) by Del Cueto et al.,(b) by Nikolaeva -Dimitrova et al.,(c) by Makrides et al., (d) by Pathak et al.

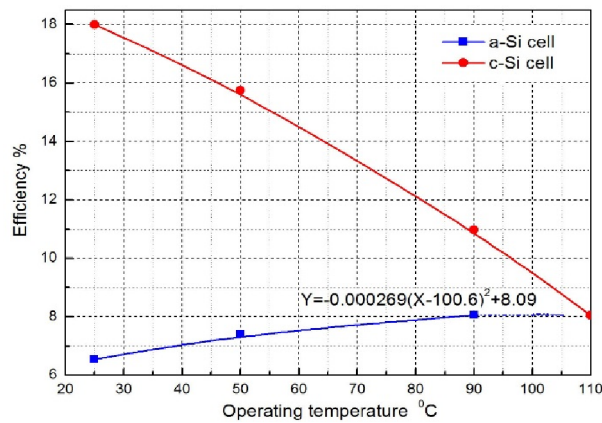


Figure 2: Variations of a-Si and c-Si cell efficiencies with the operation temperature

the operation temperature is higher than the ambient temperature. Research on the a-Si PV/T system is accumulating (Nualboonrueng *et al.*, 2012, Rahou *et al.*, 2014, Gaur *et al.*, 2014, Rozario *et al.*, 2014, Aste *et al.*, 2015). A comparison between a-Si and c-Si cell efficiencies at DSS under different operation temperature is shown in Figure 2 by using the results in Figure 1(d). At higher temperature, a-Si cell is competitive with c-Si cell in view of the efficiency, and the former is cheaper.

3. SYSTEM DESCRIPTION

The proposed HSPGS is shown in Figure 3. The system is composed of PV/T collectors, pumps, fluid storage tank with phase change material (PCM), expander, generator and condenser. It has the following innovative features:

- (1) a-Si cells characterized by positive temperature coefficient of PMPP at DSS are employed.
- (2) The working fluid is vaporized directly in the PV/T collectors.
- (3) An inner-type heat storage unit is embedded in the ORC to guarantee the stability of power generation.
- (4) The system is the first of its kind.

There are many types of collectors suitable for the medium-high temperature PV/T application, such as compound parabolic concentrators (CPC), evacuated tube heat pipe collectors, and evacuated flat plate collectors (FPC), as schematized in Figure 4. CPC collectors with small concentration ratio are able to accept a large proportion of the diffuse radiation incident on their apertures and concentrate it without the need of tracking the sun. CPCs would substantially performance better than FPCs at temperature above 80 °C while requiring only several adjustments for year-round operation. The evacuated tube heat pipe collectors use liquid–vapor phase change materials to transfer heat at high efficiency. These collectors feature a heat pipe (an excellent thermal conductor) placed inside a vacuum-sealed tube. The pipe is made of copper and attached to a black or blue fin that fills the tube. Both the pipe and fin absorb solar radiation. The fluid inside the pipe undergoes an evaporating–condensing cycle. The commercial collectors of this type are able to offer an efficiency of about 60% on the conditions of operating temperature of 100 °C, environment temperature of 20 °C, and radiation of 800Wm⁻². For the evacuated FPC collectors, they can offer work at over 50% efficiency at temperatures of 200°C due to the high-vacuum inside. In contrast to concentrating systems, they collector can utilize diffuse irradiation and without any tracking device (TVP Solar, 2015). The thin film of a-Si cell enables easier connection with the plate and better thermal conductivity in the PV/T. A sample of a-Si cell deposited on stainless steel is shown in Figure 5.

In the practical operation the system can have three modes:

I) The system needs to generate electricity and solar radiation is available. In this mode, valves 1, 2 and 3 are open. Pump 1 is running. The organic fluid is heated and vaporized through the collectors under high pressure. The vapor flows into the expander, exporting power in the process due to the pressure drop. The outlet vapor is cooled down in the condenser. The liquid is pressurized by pump 1

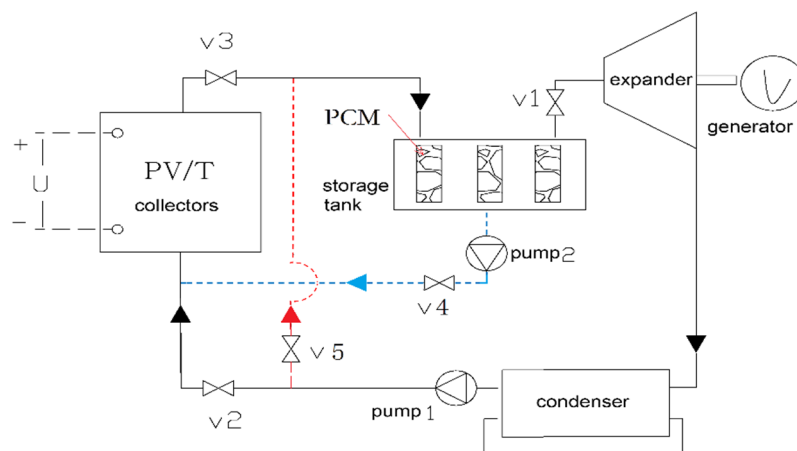


Figure 3: The scheme of the proposed HSPGS

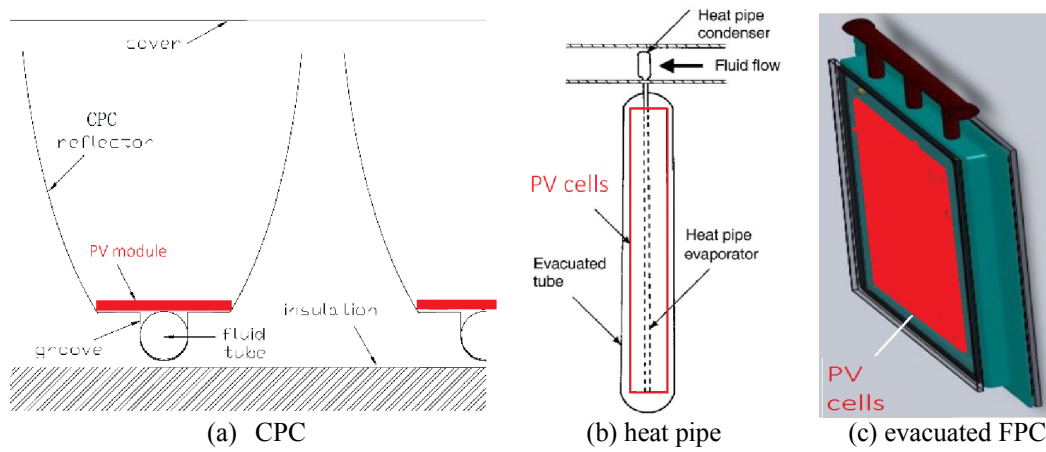


Figure 4: Collectors suitable for medium-high temperature PV/T application

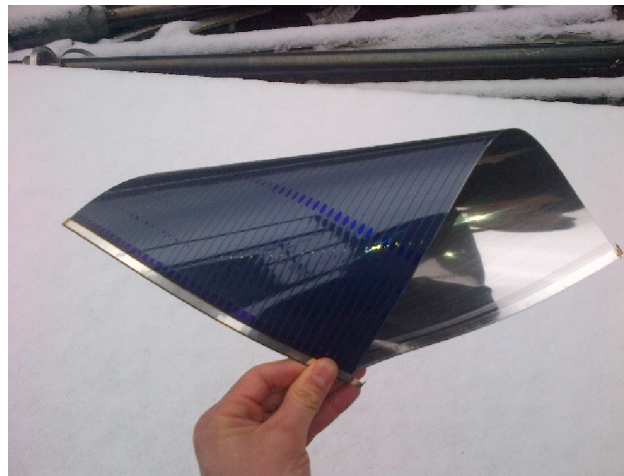


Figure 5: A sample of a-Si cell deposited on stainless steel

and is sent back to the collectors. By using a dry fluid super-heater is avoided. In case the irradiation is too strong, valve 4 can be open and pump 2 can run to prevent the working fluid from being superheated in the collectors. Aside from vapor, liquid/vapor mixture and liquid are allowed at the outlet of collectors. The liquid can drop in the fluid storage tank and won't harm the expander. Owing to this inner-type heat storage unit, the system can work smoothly without any complicated control strategy.

II) The system does not need to generate electricity but irradiation is well. Valves 3 and 4 are open. Pump 2 is running. In this mode, solar heat is transferred to the PCM by the organic fluid. Heat storage is in process.

III) The system needs to generate electricity but irradiation is very weak or unavailable. Valves 1 and 5 are open and pump 1 is running. Heat is released from the PCM and converted into power by the ORC. Mode I presents the simultaneous processes of heat collection and power generation, while Mode II or Mode III is the independent process of heat collection or power conversion.

4. THERMODYNAMIC MODELLING

The thermal efficiency of a solar collector is generally expressed by

$$\eta_c(T) = \eta_{c,0} - \frac{A}{G}(T - T_a) - \frac{B}{G}(T - T_a)^2 \quad (1)$$

The power output of PV cell is calculated by

$$W_{PV} = G \cdot S \cdot \eta_{PV}(T) \cdot x \quad (2)$$

The heat collection efficiency of a PV/T collector can be deduced as

$$\eta_{PVT}(T) = \eta_c(T) - \eta_{PV}(T) \cdot x \quad (3)$$

If a second order of approximation of $\eta_{PV}(T)$ is assumed, then $\eta_{PV}(T) \cdot x$ can be expressed by

$$\eta_{PV}(T) \cdot x = \eta_{PV,0} + aT + bT^2 \quad (4)$$

and

$$\eta_{PVT}(T) = \eta'_{c,0} - \frac{A'}{G}(T - T_a) - \frac{B'}{G}(T - T_a)^2 \quad (5)$$

$\eta'_{c,0}$, A' , and B' are the modified coefficients of the collector.

$$\eta'_{c,0} = \eta_{c,0} - \eta_{PV,0} - aT_a - bT_a^2 \quad (6)$$

$$A' = A + (a + 2bT_a)G \quad (7)$$

$$B' = B + bG \quad (8)$$

In a solar ORC system tens or hundreds of square meters of collectors are usually required, the temperature difference between neighboring collectors is supposed to be small. The fluid in the collector is mostly at liquid-phase or binary phase. For the binary phase region, the temperature is constant and it is easy to calculate the collector efficiency. For the liquid phase region, in order to reach an outlet temperature T_o of the fluid with an inlet temperature T_i , the required collector area is obtained by

$$S_l = \int_{T_i}^{T_o} \frac{mC_p(T)}{\eta_{PVT}(T)G} dT \quad (9)$$

The heat capacity of a liquid can be expressed by a first order approximation

$$C_p(T) = C_{p,0} + \alpha(T - T_0) \quad (10)$$

With $c_1 = A'/G$, $c_2 = B'/G$, the collector area according to Equations (5), (9) and (10) is calculated by

$$S_l = \frac{m}{c_2 G (\theta_2 - \theta_1)} \left[(C_{p,a} + \alpha\theta_1) \ln \frac{(T_o - T_a - \theta_1)}{T_i - T_a - \theta_1} + (C_{p,a} + \alpha\theta_2) \ln \frac{\theta_2 - T_i + T_a}{\theta_2 - T_o + T_a} \right] \quad (11)$$

θ_1 and θ_2 are the arithmetical solutions of Equation (12) ($\theta_1 < 0$, $\theta_2 > 0$).

$$\eta'_{c,o} - c_1\theta - c_2\theta^2 = 0 \quad (12)$$

$$C_{p,a} = C_{p,0} + \alpha(T_a - T_0) \quad (13)$$

The thermal efficiency of the collectors with fluid in the liquid phase is calculated by

$$\eta_{PVT,l} = \frac{m(h_{l,o} - h_{l,i})}{GS_l} \quad (14)$$

The thermal efficiency of the collectors with fluid in the binary-phase, and the overall PV/T collector efficiency are calculated by Equations (15) and (16), respectively,

$$\eta_{PVT,b} = \frac{m(h_{b,o} - h_{b,i})}{GS_b} \quad (15)$$

$$\eta_{PVT} = \frac{m(h_{b,o} - h_{l,i})}{G(S_l + S_b)} \quad (16)$$

The power generated by the cells in the liquid region of working fluid is calculated by

$$\begin{aligned} W_{PV,l} &= \int_0^{S_l} G \cdot \eta_{PV}(T) \cdot x dS \\ &= G \int_{T_i}^{T_o} \eta_{PV}(T) \cdot x \cdot \frac{mC_p(T)}{\eta_{PVT}(T)G} dT \\ &= M [N(T - T_a - \theta_1)^3 + L_1(T - T_a - \theta_1)^2 + K_1(T - T_a) + P_1 \ln(T - T_a - \theta_1)] \Big|_{T_i}^{T_o} \\ &\quad - M [N(T - T_a - \theta_2)^3 + L_2(T - T_a - \theta_2)^2 + K_2(T - T_a) + P_2 \ln(\theta_2 + T_a - T)] \Big|_{T_i}^{T_o} \end{aligned} \quad (17)$$

where

$$M = \frac{m}{c_2(\theta_2 - \theta_1)} \quad (18)$$

$$N = \frac{b\alpha}{3} \quad (19)$$

$$L_1 = 0.5[(2b\theta_1 + 2bT_a + a)\alpha + b(C_{p,a} + \alpha\theta_1)] \quad (20)$$

$$L_2 = 0.5[(2b\theta_2 + 2bT_a + a)\alpha + b(C_{p,a} + \alpha\theta_2)] \quad (21)$$

$$K_1 = \alpha[b(\theta_1 + T_a)^2 + a(\theta_1 + T_a) + \eta_{PV,0}] + (2b\theta_1 + 2bT_a + a)(C_{p,a} + \alpha\theta_1) \quad (23)$$

$$K_2 = \alpha[b(\theta_2 + T_a)^2 + a(\theta_2 + T_a) + \eta_{PV,0}] + (2b\theta_2 + 2bT_a + a)(C_{p,a} + \alpha\theta_2) \quad (24)$$

$$P_1 = [b(\theta_1 + T_a)^2 + a(\theta_1 + T_a) + \eta_{PV,0}](C_{p,a} + \alpha\theta_1) \quad (25)$$

$$P_2 = [b(\theta_2 + T_a)^2 + a(\theta_2 + T_a) + \eta_{PV,0}](C_{p,a} + \alpha\theta_2) \quad (26)$$

The power generated by the cells in the binary region of working fluid is calculated by

$$W_{PV,b} = G \cdot S_b \cdot \eta_{PV}(T_b) \cdot x \quad (27)$$

The PV efficiencies of the liquid-inside, mixture-inside and entire PV/T collectors are calculated by

$$\eta_{PV,l} = \frac{W_{PV,l}}{GS_l} \quad (28)$$

$$\eta_{PV,b} = \frac{W_{PV,b}}{GS_b} \quad (29)$$

$$\eta_{PV} = \frac{W_{PV,l} + W_{PV,b}}{G(S_l + S_b)} \quad (30)$$

The ORC efficiency is defined by the ratio of the net power output to the heat supplied,

$$\eta_{ORC} = \frac{W_t \cdot \varepsilon_g - W_p}{m(h_{b,o} - h_{l,i})} \quad (31)$$

The total efficiency of the HSPGS is

$$\eta_{HSPGS} = \eta_{PV} + \eta_{ORC} \cdot \eta_{PVT} \quad (32)$$

5. RESULTS AND DISCUSSION

To estimate the HSPGS performance, the evacuated FPC collector is exemplified. According to the test results by the international standards (EN 12975 and EN 12976), this kind of collector can have $\eta_{c,0}$ of 0.82, A of $0.399 \text{ W m}^{-2}\text{K}^{-1}$ and B of $0.0067 \text{ W m}^{-2}\text{K}^{-2}$ (Test Report, 2012). In this work, modest values are chosen, and $\eta_{c,0}$, A and B are 0.75, A of $0.80 \text{ W m}^{-2}\text{K}^{-1}$ and $0.0067 \text{ W m}^{-2}\text{K}^{-2}$ respectively. The heat loss coefficients related to radiation are then closer to those of commercial evacuated-type collectors. For the cell coefficients in Equation (4), some experiment results are typified as displayed in Figure 2. The PV efficiency above $90 \text{ }^\circ\text{C}$ is calculated by extending the curve. Evaporation and condensation processes are assumed to be isobaric while expansion and pressurization processes are adiabatic. The parameters in the simulation are summarized in Table 1.

Table 1: Parameters in the simulation

Parameter	Value	Parameter	Value
Ambient temperature	20 °C	$\eta_{PV} @ 25 \text{ }^\circ\text{C}$	6.55%
Condensation temperature	30 °C	x	1.0
Expander efficiency	0.75	$\eta_{c,0}$	0.75
Generator efficiency	0.80	A	$0.80 \text{ W m}^{-2}\text{K}^{-1}$
Pump efficiency	0.65	B	$0.0067 \text{ W m}^{-2}\text{K}^{-2}$
Radiation	800 W/m^2	Working fluid	R245fa

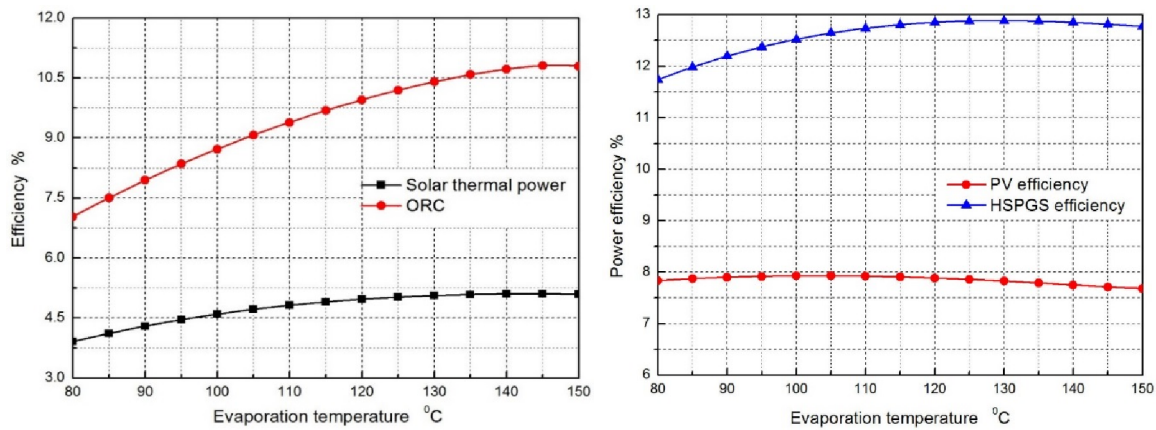


Figure 6: Efficiency variations with the ORC evaporation temperature (a) efficiencies of the ORC and solar thermal power generation, (b) efficiencies of PV cells and HSPGS

The variations of the ORC efficiency and solar thermal power efficiency ($\eta_{\text{ORC}} \cdot \eta_{\text{PVT}}$) with the evaporation temperature are shown in Figure 6(a). The ORC efficiency increases with the increment in the evaporation temperature until about 147 °C, at which the slope of the temperature- entropy (T - s) curve of R245fa saturation vapor changes from positive to negative. Due to the tradeoff between the ORC efficiency and solar energy collection efficiency, the solar thermal power generation efficiency first climbs up and then falls down with increment of the evaporation temperature. Its maximum value is 5.1% with an evaporation temperature of 142 °C.

The variations of the overall PV cells and HSPGS efficiencies with the evaporation temperature are shown in Figure 6(b). There are two effects on the PV efficiency regarding the increment in the temperature. One is the drop of the cell's open-circuit voltage (V_{oc}), and the other is the regenerative effect promoting the cell annealing. The temperature coefficient of V_{oc} for a-Si cell is about -0.39%/°C, which is generally independent on the exposure to sunlight (Ishii *et al.*, 2014). The thermal annealing mainly improves the fill factor (FF). With the two competitive effects, the PV efficiency no longer decreases in a monotone way as the evaporation temperature increases. The maximum overall PV efficiency is about 7.93% at the evaporation temperature of 104 °C. Both the efficiency and temperature at the peak point differ from those in Figure 2, which is attributed by the non-uniform temperature distribution in the PV array. The curve for the HSPGS efficiency is also like a parabola facing downward. The maximum HSPGS efficiency is 12.88% at the evaporation temperature of 130 °C.

6. CONCLUSION

In contrast to c-Si and GaAs cells, a-Si cell benefits from the thermal annealing at high temperature. The a-Si PV/T collector is an excellent match to the ORC. The efficiency of the hybrid system is much higher than that of the side by side solar ORC system (about 5.1% at 142 °C) and PV system (about 6.55% at room temperature). Because the collectors are shared by the PV and ORC systems, the cost of the HSPGS is expected to be lower than the total cost of the side by side systems.

At present the long-term experimental study of a-Si cells at high temperature is lacked, and it is difficult to estimate the lifetime of high temperature a-Si cells. However, it is worth mentioning some points as follows: (1) Solar cells available on the market generally have a permitted operating temperature up to 85 °C. The cell itself shall be able to operate at high temperature for years. The issue that really suffers from high temperature is the encapsulation. (2) The commercial cells are supposed to operate at normal temperature, so the encapsulation is not designed for high temperature applications. (3) High temperature PV/T systems have great potential to meet the consumers' multiple demands on cooling, spacing heating, drying and power. Research and development on this technology is being strengthened.

ACKNOWLEDGEMENT

This study was sponsored by the National Science Foundation of China (51476159, 51378483, 51206154, 51178442), Fundamental Research Funds for the Central Universities of China.

NOMENCLATURE

A	first coefficient of heat loss	$(\text{Wm}^{-2}\text{°C}^{-1})$
a	coefficient	(°C^{-1})
B	second coefficient of heat loss	$(\text{Wm}^{-2}\text{°C}^{-2})$
b	coefficient	(°C^{-2})
C	capacity	$(\text{Jkg}^{-1}\text{°C}^{-1})$
c, M, N, L, K, P	interim variables	
G	radiation	(Wm^{-2})
h	enthalpy	(J/kg)
m	mass flow rate	(kg/s)
S	area	(m^2)
T	temperature	(°C)
W	power	(W)
x	cover ratio	
θ	arithmetical solution	
α	coefficient	$(\text{Jkg}^{-1}\text{°C}^{-2})$
ε	efficiency	
η	efficiency	

Subscript

0,1,2	reference point
a	ambient
b	binary phase
c	collector
g	generator
HSPGS	hybrid solar power generation system
i	inlet
l	liquid phase
ORC	organic Rankine cycle
o	outlet
PV	PV cell
PVT	PV/T collector
p	pressure/pump

REFERENCES

- Aste, N., Leonforte, F., Del Pero, C., 2015, Design, modeling and performance monitoring of a photovoltaic–thermal (PVT) water collector. *Sol Energy*, vol. 112: p. 85–99.
- Del Cueto, J., von Roedern, B., 1999, Temperature-induced changes in the performance of amorphous silicon multi-junction modules in controlled light-soaking. *Prog. Photovolt: Res. Appl.*, vol. 7, no. 2: p. 101-112.
- Fanni, L., Pola, I., Burà, E., Friesen, T., Chianese, D., 2009, Investigation of annealing and degradation effects on a-Si PV modules in real operating conditions. *24th European Photovoltaic Solar Energy Conference*: p. 21-25.
- Gaur, A., Tiwari, G., 2014, Performance of a-Si thin film PV modules with and without water flow: An experimental validation. *Appl Energy*, vol. 128: p.184–191.
- Hanergy, thin-film solar power generation. www.hanergy.com/en/industry/industry_310.html 2015.05.10

- Ishii, T., Otani, K., Takashima, T., Ikeda, K., 2014, Change in I–V characteristics of thin-film photovoltaic (PV) modules induced by light soaking and thermal annealing effects. *Prog. Photovolt: Res. Appl.*, vol. 22, no. 9: p. 949–957.
- Ishii, T., Otani, K., Takashima, T., Kawai, S., 2011, Estimation of the maximum power temperature coefficients of PV modules at different time scales. *Sol Energy Mat Sol C*, vol. 95, no. 1: p.386–389.
- Kenny, R., Chatzipanagi, A., Sample, T., 2014, Preconditioning of thin-film PV module technologies for calibration. *Prog. Photovolt: Res. Appl.*, vol. 22, no. 2: p.166 – 172.
- King, D., Kratochvil, J., Boyson, W., 1997, Temperature coefficients for PV modules and arrays: measurement methods, difficulties, and results. *Photovoltaic Specialists Conference*, IEEE: p. 1183-1186.
- Kosmadakis, G., Manolakos, D., Papadakis, G., 2011, Simulation and economic analysis of a CPV/thermal system coupled with an organic Rankine cycle for increased power generation. *Sol Energy*, vol. 85, no. 5: p. 308–324.
- Li, J., 2015, Structural optimization of the ORC-based solar thermal power system, Chapter 2, *Structural optimization and experimental investigation of the organic Rankine cycle for solar thermal power generation*, Springer, Heidelberg: p. 41.
- Li, J., Pei, G., Ji, J., 2009, A hybrid solar ORC and PV system. Chinese Patent, CN200910144276.6.
- Li, J., Pei, G., Li, Y., Ji, J., 2010, Novel design and simulation of a hybrid solar electricity system with organic Rankine cycle and PV cells, *Int. J. Low-Carbon Tech.*, vol. 4, no. 5: p. 223-230.
- Makrides, G., Zinsser, B., Phinikarides, A., Schubert, M., Georghiou, G., 2012, Temperature and thermal annealing effects on different photovoltaic technologies. *Renew Energy*, vol. 43: p. 407-417.
- Nikolaeva - Dimitrova, M., Kenny, R., Dunlop, E., Pravettoni, M., 2010, Seasonal variations on energy yield of a-Si, hybrid, and crystalline Si PV modules. *Prog. Photovolt: Res. Appl.*, vol. 18, no. 5: p. 311–320.
- Nualboonrueng, T., Tuenpusa, P., Ueda, Y., Akisawa, A., 2012, Field experiments of PV-thermal collectors for residential application in Bangkok. *Energies*, vol. 5, no. 4: p.1229-1244.
- Pathak, M., Girotra, K., Harrison, S., Pearce, J., 2012, The effect of hybrid photovoltaic thermal device operating conditions on intrinsic layer thickness optimization of hydrogenated amorphous silicon solar cells. *Sol Energy*, vol. 86, no. 9: p. 2673–2677.
- Pathak, M., Pearce, J., Harrison, S., 2012, Effects on amorphous silicon photovoltaic performance from high-temperature annealing pulses in photovoltaic thermal hybrid devices. *Sol Energy Mat Sol C*, vol. 100: p. 199–203.
- Rahou, M., Othman, M., Mat, S., Ibrahim, A., 2014, Performance study of a photovoltaic thermal system with an oscillatory flow design. *J Sol Energy Engineering*, vol. 136, no. 1: p.011012.
- Roedern, B., del Cueto, J., 2000, Model for Staebler-Wronski degradation deduced from long-term, controlled light-soaking experiments. *MRS Proceedings*, Cambridge Univ Press: p. A10. 4.
- Rozario, J., Vora, A., Debnath, S., Pathak, M., Pearce, J., 2014, The effects of dispatch strategy on electrical performance of amorphous silicon-based solar photovoltaic-thermal systems. *Renew Energy*, vol. 68: p. 459-465.
- Ruther, R., Tamizh-Mani, G., del Cueto, J., Adelstein, J., Dacoregio, MM., von Roedern, B., 2005, Performance test of amorphous silicon modules in different climates - year three: higher minimum operating temperatures lead to higher performance levels. *Photovoltaic Specialists Conference*, IEEE: p.1635 – 1638.
- Virtuani, A., Fanni, L., 2014, Seasonal power fluctuations of amorphous silicon thin-film solar modules: distinguishing between different contributions. *Prog. Photovolt: Res. Appl.*, vol. 22, no. 2: p. 208–217.
- TVP Solar: www.tvpsolar.com/index.php?context=news-home&liv2=news&id_news=27, 2015.02.16.
- Institut für Thermodynamik und Wärmetechnik (ITW). 2012, Test report n.11COL1028.

OPTIMISATION OF A DOMESTIC-SCALE SOLAR-ORC HEATING AND POWER SYSTEM FOR MAXIMUM POWER OUTPUT IN THE UK

James Freeman, Klaus Hellgardt and Christos N. Markides*

Clean Energy Processes (CEP) Laboratory, Department of Chemical Engineering, Imperial College London
South Kensington Campus, London SW7 2AZ, UK
e-mail: c.markides@imperial.ac.uk

* Corresponding Author

ABSTRACT

A model is presented of a domestic-scale solar combined heating and power (S-CHP) system, featuring an Organic Rankine Cycle (ORC) engine and a 15-m² solar-thermal collector array. The system is configured for operation in the UK, incorporating high-efficiency non-concentrating solar collectors and an ORC working fluid buffer vessel to maintain continuous electrical power output during periods of intermittent solar irradiance. The solar collector array configuration and choice of ORC working fluid are examined, and the system electrical performance is optimised over an annual period of operation by simulating with London UK climate data. By incorporating a two-stage solar collector/evaporator configuration, a maximum net annual electrical work output of 1070 kWh yr⁻¹ (continuous power of 122 W) and a solar-to-electrical efficiency of 6.3% is reported with HFC-245ca as the ORC working fluid and an optimal evaporation temperature of 126 °C. This is equivalent to ~32% of the electricity demand of a typical (average) UK home, and represents an improvement of more than 50% over a recent effort by the same authors based on an earlier S-CHP system configuration and HFC-245fa.

1. INTRODUCTION

Solar energy has the potential to meet a significant proportion of household demands for heating and electricity in the UK, despite its comparatively low annual yield of incident solar radiation (~1000 kWh m⁻² yr⁻¹ for southern UK compared to ~1800 kWh m⁻² yr⁻¹ for parts of southern Europe). Distributed domestic solar-power provision is conventionally a choice of either electricity generation via photovoltaic (PV) devices, or water heating via solar-thermal collectors. The feasibility of installing these as side-by-side systems for provision of both heating and power is limited by cost and space availability. At present, the only available technologies that can provide both heating and power from the same area of solar collector array are hybrid PV-thermal (PVT) systems, which are expensive and have a limited ability to meet time-varying demand ratios for heating and power.

Organic Rankine cycle (ORC) systems are a promising alternative to PV-based technologies for electrical power generation from solar energy. The potential for solar-ORC systems to operate at lower temperatures and on smaller scales than solar-power systems based on steam-Rankine cycle technology opens up the possibility of developing the technology for geographical regions with a low solar resource and for distributed-level applications. Nonetheless, a significant amount of experimental and modelling research on these systems (Canada *et al.*, 2004; Manolakos *et al.*, 2009; Wang *et al.*, 2009; Jing *et al.*, 2010; Quoilin *et al.*, 2011) have focused on application to regions with abundant solar resource and collector array areas beyond the size of what could be easily accommodated on the roof of a domestic property. The aim of this paper is to assess the electricity generating potential of an ORC-based solar combined heating and power (S-CHP) system when operating at lower solar irradiance levels and smaller scales, namely, at a northern European location (specifically, London, UK) and a domestic roof-sized installation.

In an earlier work (Freeman *et al.* 2015a), the authors presented a system model of a domestic-scale S-CHP system and simulated its performance in the UK climate. The system model featured a solar

collector array, a basic four-component (*non-regenerative*) ORC engine and a hot-water cylinder. Both the ORC engine and the hot-water cylinder received a thermal energy input from the solar collector array to meet a variable demand for heating and power. The ORC working fluid was the hydrofluorocarbon (HFC) refrigerant R245fa, also investigated for use in low-temperature solar-ORC systems by Wang *et al.*, (2009) and Quoilin *et al.*, (2011); and chosen for its low flammability and global warming potential, and also its low saturation temperature at atmospheric pressure. The system's fixed flow-rates and fixed operating temperatures and pressures were selected for maximum work production on an "annual-average" day and then simulated over an annual period.

It was found that the total electrical work output was 700 kWh yr^{-1} (80 W average), and that the whole system capital cost was between £4400-5500. However, the system was only crudely optimised and several potential areas for performance enhancement were identified. In this paper, a wider range of working fluids will be considered in order to find the optimum fluid to maximise annual work output from the system in the UK setting. The performance of a given working fluid is dependent upon the evaporation temperature of the Rankine cycle, which is itself dependent upon the choice of solar-thermal collector design and the solar irradiance characteristics of the chosen location. Consideration will also be given to system configurations that enable efficient operation of the solar collector array and continuous power output under intermittent solar irradiance conditions.

2. MODELLING METHODOLOGY

2.1 System description

A schematic diagram of the investigated system is shown in Figure 1a. Pump 1 is used to pressurise the working fluid from a saturated liquid at State 1 to its evaporation pressure at State 2a. The fluid is then preheated to State 2b in the regenerator heat-exchanger, before mixing with the saturated liquid stream from the buffer vessel circulated by Pump 2. The combined fluid-stream at State 2c enters the evaporator where it is heated by the solar-collector fluid circulated by Pump 3. Fluid leaving the evaporator at State 3a then proceeds to the buffer vessel. The buffer vessel is assumed to be held at a constant temperature equal to the evaporation temperature of the ORC, such that working fluid may be stored in a two-phase state within. A similar concept was proposed earlier, in the work by Jing *et al.* (2010), where it was suggested that the buffer vessel temperature could be maintained by conduits filled with phase change material (PCM). Saturated liquid from the buffer vessel is recycled to the evaporator by Pump 2, meanwhile saturated vapour from the buffer vessel (State 3b) proceeds on to the expander where it is expanded to the condensation pressure, producing shaft work. Low pressure vapour is exhausted from the expander (State 4a) and cooled (de-superheated) in the regenerator (State 4b) before being returned to the initial saturated liquid condition (State 1) in the condenser.

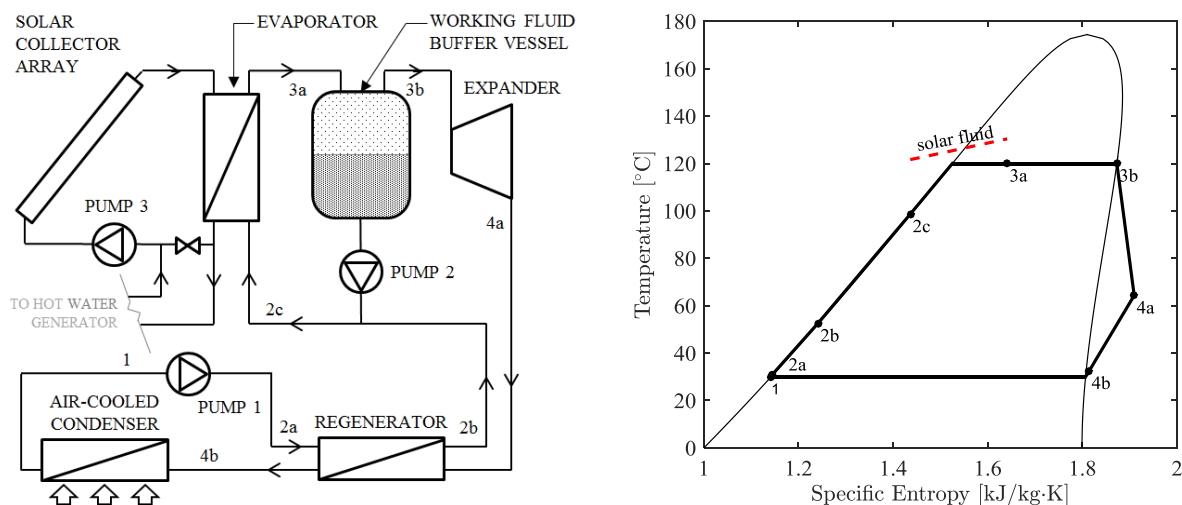


Figure 1: (a) Schematic diagram of the S-CHP system with a single-stage solar collector array; and (b) Temperature-entropy (T - s) diagram of the ORC with R245ca as the example working fluid.

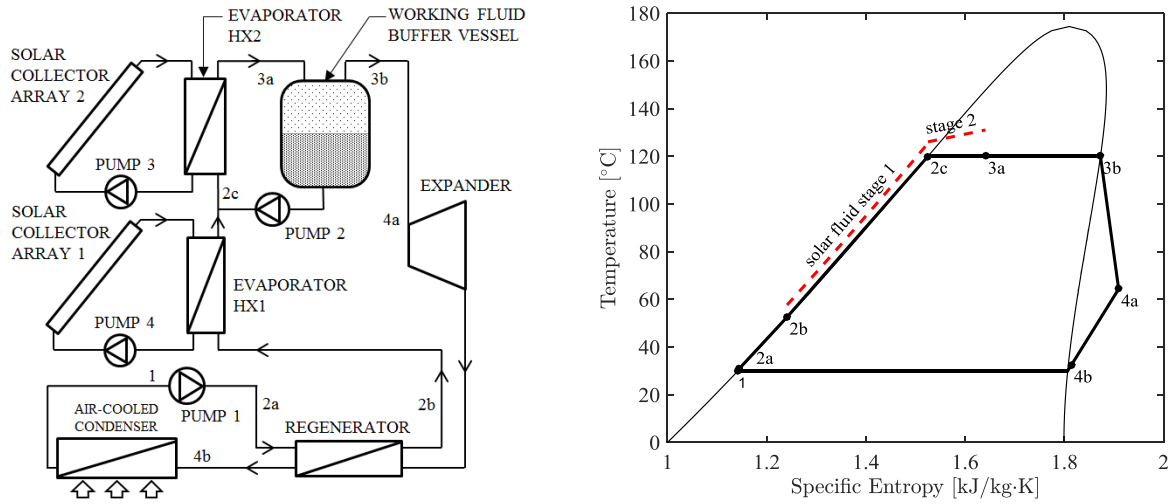


Figure 2: (a) Schematic diagram of the S-CHP system with two-stage solar collector array; and (b) Temperature-entropy (T - s) diagram of the ORC with R245ca as the example working fluid.

The benefits of the system design described are as follows: (1) the buffer vessel suppresses the variations in the expander inlet vapour quality due to the intermittency of the solar heat-source, so that periods of stable operation can be maintained for longer than for a system with no thermal/fluid store; (2) the design enables system operation with fixed flow-rates so that the pumps, expander and heat exchangers can operate at their design (best-efficiency) conditions; (3) the design enables a stable fluid temperature to be achieved at the evaporator outlet, which simplifies the task of identifying the optimal working fluid and evaporation temperature/pressure over the annual period in the chosen climate.

A variant of the aforementioned system will also be examined that incorporates a two-stage solar collector array, based on the configuration proposed by Jing *et al.* (2010). In the modified configuration shown in Figure 2, the ORC working fluid heat addition process is split into a separate sensible and latent stage, each served by a separate heat exchanger and dedicated section of the solar collector array (although the total collector array area remains the same as for the single-stage configuration). The sensible pre-heating stage occurs prior to mixing with the recirculated flow from the buffer vessel, and thus the two streams are closer together in temperature before mixing which is exergetically preferable. Furthermore, the lower average temperature of the solar collector circulating fluid in the first stage allows for a closer match in temperature between the fluid streams (illustrated by the red lines in Figure 2b), and a higher overall solar collector array efficiency. This configuration requires the inclusion of an additional pump and heat exchanger, the cost impact of which are discussed briefly in Section 3.3.

2.2 Solar collector array

The model of solar collector chosen for this study is the TVP SOLAR *HT-Power*, a high efficiency evacuated flat-plate collector highlighted for its potential in ORC applications in the study by Calise *et al.* (2015). The properties of the solar collector are listed in Table 1. In the aforementioned study, the diathermic oil DOWTHERM™ A (DOW, 1997) is chosen as an appropriate circulating fluid for this solar collector due to its temperature application range, and therefore the same fluid will be used for the simulations in the present work. The solar collector is modelled using the manufacturer's efficiency curve equation, where collector efficiency is expressed as a function of solar irradiance I_{sol} , ambient air temperature T_a , and mean solar collector temperature \bar{T}_{sc} :

$$\eta_{sc} = K_{\theta}\eta_0 - a_1 \cdot \frac{\bar{T}_{sc}-T_a}{I_{sol}} - a_2 \cdot \frac{(\bar{T}_{sc}-T_a)^2}{I_{sol}}. \quad (1)$$

For the calculation of the overall solar collector array efficiency, a modified expression is required that takes into account the non-linear decrease in collector efficiency with fluid temperature. Thus Jing *et al.*, (2010) derive the following expression for the collector array efficiency by integrating the

local collector efficiency over the total length of the array, provided that the inlet and outlet solar fluid temperatures ($T_{sf,in}$, $T_{sf,out}$) are known:

$$\eta_{sc,array} = \frac{(a_2/I_{sol})(\varphi_2 - \varphi_1)[c_{p,0}(T_{sf,out} - T_{sf,in}) + 0.5\alpha(T_{sf,out} - T_{sc,in})(T_{sf,out} + T_{sf,in} - 2T_{sf,0})]}{[c_{p,0} + \alpha(T_a - T_{sf,0} + \varphi_1)] \ln\left(\frac{T_{sf,out} - T_a - \varphi_1}{T_{sf,in} - T_a - \varphi_1}\right) + [c_{p,0} + \alpha(T_a - T_0 + \varphi_2)] \ln\left(\frac{\varphi_2 - T_{sf,in} + T_a}{\varphi_1 - T_{sf,out} + T_a}\right)}, \quad (2)$$

where $c_{p,0}$, α and T_0 are parameters that describe a linear variation of specific heat capacity with temperature for the solar heat-transfer fluid such that $c_{p,sc} = c_{p,0} + \alpha(T_a - T_{sf,0})$, and parameters φ_1 and φ_2 are the solution values (negative and positive, respectively) of the quadratic function $\eta_0 - a_1\varphi/I_{sol} - a_2\varphi^2/I_{sol} = 0$. By assuming that the quantity of solar radiation absorbed by the collector array is equal to the enthalpy rise of the heat-transfer fluid:

$$\dot{Q}_{sf} = \eta_{sc} A_{sc} I_{sol} = (\dot{m}c_p)_{sf} (T_{sc,out} - T_{sc,in}). \quad (3)$$

Finally, in order to calculate the pumping power required to circulate the solar fluid, pressure drops in the solar collector array are estimated using data provided by the manufacturer (see Table 1).

Table 1: System model parameters

Solar collector parameters ⁽ⁱ⁾		ORC parameters	
η_0	0.82	η_{pump}, η_{exp}	0.65, 0.75
a_1, a_2	0.399, 0.0067	η_{gen}	0.90
$K_{\theta(\theta=50^\circ)}$	0.91	ε_r	0.95
$\Delta P_{sc}^{(ii)}$ (kPa)	0.7	$T_{cond}^{(iii)}$ (°C)	30

(i) Information taken from HT-Power product datasheet (TVP SOLAR, 1997) and Calise *et al.* (2015); (ii) at $\dot{V}_{ref} = 51 \text{ L/m}^2/\text{hr}$; (iii) if $T_{sat}(P_{atm}) > 30 \text{ }^\circ\text{C}$, then $T_{cond} = T_{sat}(P_{atm})$

2.3 Heat exchanger model

A finite element method is used to model the heat transfer process in the evaporator. The evaporator is modelled as a counterflow concentric-tube heat exchanger, with the ORC working fluid flowing inside the tube and the solar heat-transfer fluid flowing in the annulus. The heat exchanger length is divided into N finite elements, and the enthalpy and temperatures of the ORC working fluid and solar collector heat-transfer fluid for the $(n+1)^{\text{th}}$ element are calculated from:

$$h_{wf,n+1} = h_{wf,n} + \frac{U\pi D_i N_{tubes} (T_{sf,n} - T_{wf,n})}{\dot{m}_{wf}} \Delta L, \quad (9)$$

$$T_{sf,n+1} = T_{sf,n} + \frac{U\pi D_i N_{tubes} (T_{sf,n} - T_{wf,n})}{(\dot{m}c_p)_{sf}} \Delta L, \quad (10)$$

where the total heat transfer coefficient between the fluid streams is $U = 1/(h_{c,i}^{-1} + h_{c,o}^{-1})$. Note that due to the counterflow arrangement of the heat exchanger, element $n = 1$ of the heat exchanger represents the working fluid inlet and the solar fluid outlet. The evaporator heat exchangers are approximately sized so that the ‘‘pinch-point’’ temperature difference between the fluid streams is $\Delta T_{pinch} \approx 5 \text{ K}$. The heat exchangers are sized with a suitable number of parallel tubes to achieve $Re \approx 3000$ in the solar fluid stream. Local heat transfer coefficients in the single-phase and two-phase heat exchanger stages are calculated following the methods in Incropera *et al.* (2006) and Wang and Touber (1991). With both fluid flow rates and the working fluid evaporator inlet temperature supplied as input parameters, the working fluid outlet and solar fluid inlet and outlet temperatures are solved so that $(\dot{m}\Delta h)_{wf} = -(\dot{m}\Delta h)_{sf}$. Finally, the pressure drops in the evaporator heat exchangers are calculated using the Reynolds number/friction factor correlations in Incropera *et al.*, (2006).

2.3 ORC engine model

The power required by the ORC pump and power output of the ORC expander are calculated using

their respective isentropic efficiencies (see Table 1):

$$\dot{W}_{\text{pump},1} = \dot{m}_{\text{pump}1}(h_{2a} - h_1)/\eta_{\text{pump}} , \quad (4)$$

$$\dot{W}_{\text{exp}} = \eta_{\text{exp}}\dot{m}_{\text{pump}1}(h_{3b} - h_{4a,s}) , \quad (5)$$

where h_1 is the specific enthalpy of the working fluid as a saturated liquid at the condensation pressure, h_{3b} is the specific enthalpy of the working fluid as a saturated vapour at the evaporation pressure and η_{exp} is chosen to be broadly representative of a generalised small-scale positive-displacement expander (Freeman *et al.* 2015). The change in enthalpy of the working fluid in the regenerator heat exchanger is calculated using an effectiveness parameter ε_r :

$$h_{2b} = h_{2a} + \varepsilon_r(h_{4a} - h_{4b'}) , \quad (6)$$

where $h_{4b'}$ is the specific enthalpy of the working fluid at the condensation pressure and at the temperature $T_{4b'} = T_{2a}$. The net electrical power output from the ORC system is:

$$\dot{W}_{\text{net}} = \eta_{\text{gen}}\dot{W}_{\text{exp}} - \dot{W}_{\text{pump},1} - \dot{W}_{\text{pump},2} - \dot{W}_{\text{pumps},3\&4} , \quad (7)$$

2.4 Fluid flow rates

The mass flow-rate of ORC working fluid circulated by pumps 1 and 2 is maintained at a fixed ratio of 1:2 such that $\dot{m}_{\text{pump}2} = 2 \cdot \dot{m}_{\text{pump}1}$. The solar heat transfer-fluid flow-rate circulated by Pump 3 is set for a temperature glide of $\Delta T_{\text{sf}} = 5$ K between the solar fluid inlet and the pinch point corresponding to the working fluid bubble point, for a design condition in which the vapour quality at the evaporator outlet $x_{3a} = 0.33$. Thus:

$$\dot{m}_{\text{pump}3} = (\dot{m}_{\text{pump}1} + \dot{m}_{\text{pump}2})(h_{3a} - h_{\text{bubble}})/c_{p,\text{sf}}\Delta T_{\text{sf}} , \quad (8)$$

For the two-stage collector configuration, the mass flow-rate circulated by Pump 4 is sized by a similar method as above to achieve an approximately parallel temperature glide between two fluid streams in the first stage heat exchanger, as shown in Figure 2b.

2.5 Working fluid buffer vessel

As mentioned earlier in Section 2.1, the presence of the buffer vessel at the evaporator outlet ensures that the working fluid always enters the expander as a saturated vapour at the chosen cycle evaporation temperature. Heat transfer in the buffer vessel is not treated in detail in this work. Following the approach of Jing *et al.* (2010), the buffer vessel is assumed to be perfectly insulated, zero-dimensional and of sufficient size to provide the required buffering for stable performance of the system over the entire annual period. Thus for each time-step of the annual simulation, the change in internal energy of the total fluid mass in the buffer vessel is:

$$\Delta U_{\text{bv}} = [(\dot{m}_{\text{pump}1} + \dot{m}_{\text{pump}2})h_{3a} - \dot{m}_{\text{pump}1}h_{3b} - \dot{m}_{\text{pump}2}h_{\text{bubble}}]\Delta t . \quad (11)$$

2.6 Annual simulations

For the annual assessment, the system performance is evaluated using London, UK annual climate data comprised of hourly solar irradiance and air temperature values (ASHRAE, 2001). An optimal tilt angle is chosen for the solar collector array in order to maximise the annual solar irradiation received (the optimal tilt angle calculated using the climate data set is found to be 40.5° for a due south orientation). The ORC system is operational during all hours in which the climatic conditions (solar irradiance and ambient air temperature) are sufficient such that $\eta_{\text{sc}} > 0$. During these hours, the ORC expander operates under constant flow-rate and power output conditions. If $h_{3a} > h_{x=0.33}$, then heat (enthalpy) is stored in the buffer vessel while if $h_{3a} < h_{x=0.33}$ then heat (enthalpy) is released from the buffer vessel. The area of the solar collector array is fixed at $A_{\text{sc}} = 15 \text{ m}^2$ (Freeman *et al.*,

2015a) and the fixed value for the mass flow-rate of Pump 1 is solved so that the net annual enthalpy gain by the buffer vessel is zero ($\sum_{hr=1}^{8760} \Delta H_{bv} = 0$). This procedure is repeated for each working fluid over the range of evaporation temperatures. The overall efficiency of the system operating over the annual period is evaluated as follows:

$$\eta_{\text{overall}} = \sum_{hr=1}^{8760} \dot{W}_{\text{net}} / \sum_{hr=1}^{8760} I_{\text{sol}} A_{\text{sc}} \cdot \quad (12)$$

The exergy efficiency of the system can be evaluated as the net annual work output from the ORC engine divided by maximum convertible work (or exergy) output from the solar collector array operating at its optimum temperature and flow-rate at each time-instant:

$$\eta_{\text{exergy}} = \sum_{hr=1}^{8760} \dot{W}_{\text{net}} / \sum_{hr=1}^{8760} \dot{X}_{\text{sc,out,max}} \cdot \quad (13)$$

Following the approach in Freeman *et al.* (2015b), the flow-rate of exergy in the fluid stream leaving the collector is calculated as the integral of the power produced by an infinite number of infinitesimal Carnot engines operating between the hot stream and the cold reservoir (in this case the ambient air), resulting in the following equation:

$$\dot{X}_{\text{sc,out}} = \eta_{\text{sc}} A_{\text{sc}} I_{\text{sol}} \left[\left(1 - (T_{\text{sc,out}}/T_a - 1) \right)^{-1} \ln(T_{\text{sc,out}}/T_a) \right] \cdot \quad (14)$$

3. RESULTS AND DISCUSSION

3.1 Comparison of working fluids under steady-state conditions for single-stage system

In order to understand how the optimum choice of working fluid and evaporation temperature/pressure varies with solar irradiance, the single-stage system is simulated under steady-state conditions. A range of hydrocarbon (HC), hydrofluorocarbon (HFC), hydrochlorfluorocarbon (HCFC) and chlorofluorocarbon (CFC) refrigerants are chosen that have been investigated in previous works on low temperature and solar ORC systems (Chen *et al.* 2010; Rayegan and Tao, 2011; Bao and Zhao 2013). Figure 3 shows the simulated power output from the system at a low irradiance level (150 W m^{-2}) and a high irradiance level (800 W m^{-2}), for the different working fluids considered herein and over a range of evaporation temperatures. For each irradiance level and working fluid the evaporation temperature is varied in finite increments and the system flow-rates are solved for a steady-state operation (corresponding to a vapour quality at State 3a of $x_{\text{wf}} = 0.33$, such that $\Delta H_{\text{bv}} = 0$). The resulting power output curves can then be used to identify the evaporation temperature that delivers maximum power output under steady-state irradiance conditions for each working fluid.

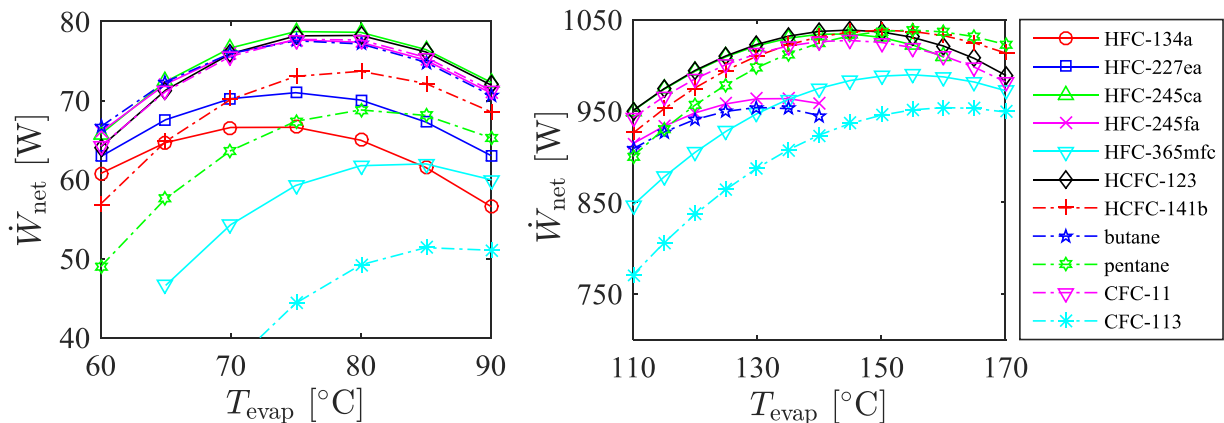


Figure 3: ORC net power output as a function of the evaporation temperature for conditions: (a) $I_{\text{sol}} = 150 \text{ W m}^{-2}$ and $T_a = 20 \text{ }^\circ\text{C}$; and (b) $I_{\text{sol}} = 800 \text{ W m}^{-2}$ and $T_a = 20 \text{ }^\circ\text{C}$.

It can be observed in Figure 3 that the highest net power outputs for both the low and high irradiance conditions are obtained with the fluids R245ca, R123 and R11. Furthermore, these fluids are found to perform well across a broad range of evaporation temperatures. The maximum net power output at the low irradiance level is 79 W (for working fluid R245ca), and is achieved at an ORC evaporation temperature of 78 °C. The maximum net power output at the high irradiance level is 1039 W (for working fluid R123) and is achieved at an ORC evaporation temperature of 144 °C. The corresponding solar collector array outlet temperatures in the low and high irradiance cases are 88 °C and 155 °C respectively. In both cases this is lower than the collector outlet temperatures corresponding to maximum exergy (calculated in Eq. 16), which are found to be 101 °C and 210 °C respectively. It can also be noted that the critical temperatures for most of the working fluids investigated (with the exception of R113 and R141b) are below 200 °C, and that this may restrict the attainable exergy efficiency of the system under higher irradiance conditions.

3.3 Comparison with two-stage system

For the following analysis, R245ca is chosen as the ORC working fluid of interest due to its favourable performance in the previous analysis and lower ozone depletion potential than R11 and R123. However, it should also be noted that at present R245ca is not widely available for purchase in bulk quantities in the UK. The steady-state simulations are repeated for the two-stage collector array configuration and the results compared with those for the single-stage configuration. For each steady-state condition, the system flow-rates and the relative areas of the first and second-stage collector arrays are solved so that the ORC working fluid leaves the first heating stage as a saturated liquid and the second heating stage as a two-phase fluid at the target vapour quality of $x_{w,f} = 0.33$ (illustrated by the T - s diagram in Figure 2b). The results are compared to the single-stage configuration in Figure 4. For the two-stage configuration the system is found to operate with a higher overall collector array efficiency, and the result is a 5% increase in maximum net power output in the low irradiance case and a 7% increase in maximum net power in the high irradiance case. It can also be observed that the peak power output for the two-stage configuration occurs at a higher evaporation temperature than for the single-stage configuration. This is most evident in the high irradiance case, for which the peak power output occurs at an evaporation temperature of 155 °C for the two-stage configuration compared to 144 °C for the single-stage configuration. For the two-stage system the ratio of the first-stage collector array area to total collector array area (also shown in Figure 4 on the right-hand y-axis) is found to increase with evaporation temperature. This can be easily understood by the increased ratio of sensible heating to latent heating of the Rankine cycle working fluid as evaporation temperature is increased. With the addition of the second stage heat exchanger, the overall heat transfer area increases by 42%. Taking this additional heat exchanger cost into account and also considering the need for the additional pump, the expected cost increase of the two-stage system relative to the single-stage system is in the region of €450-500. Thus the increase in system cost per additional Watt of nominal power output is approximately 6 €/W.

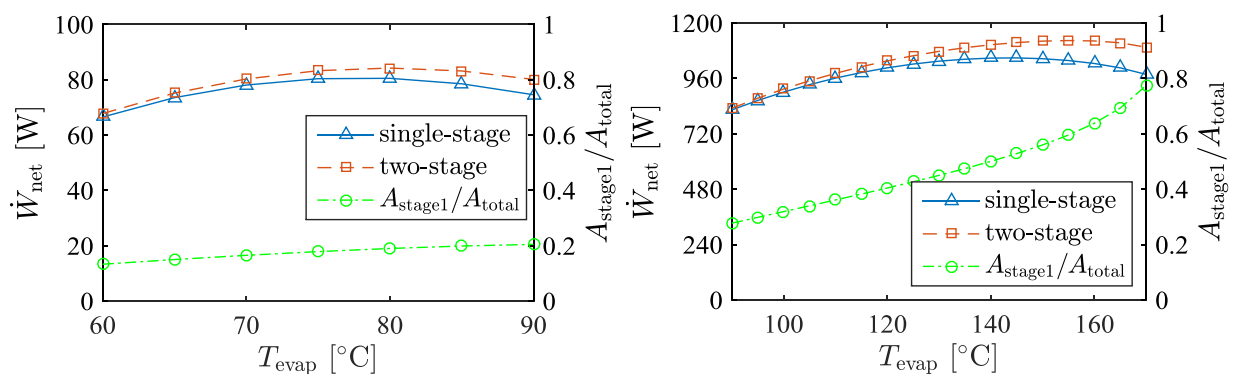


Figure 4: Comparison of the ORC net power output from single-stage and two-stage solar collector configurations (with the relative array areas of the two-stage configuration also shown), with R245ca as the working fluid and for conditions: (a) $I_{sol} = 150 \text{ W m}^{-2}$ and $T_a = 20 \text{ °C}$; and (b) $I_{sol} = 800 \text{ W m}^{-2}$ and $T_a = 20 \text{ °C}$.

Table 2: Results from the simulations of the annually optimised system with single-stage and two-stage collector configurations

Parameter	Unit	Single-stage collector configuration	Two-stage collector configuration
Optimal ORC working fluid	-	R245ca	R245ca
Optimal ORC evaporation temperature	°C	117	126
Solar collector array area (Stage 1 / Stage 2)	m ²	15 m ²	6.3 m ² / 8.7 m ²
Net annual work output	kWh yr ⁻¹	955	1070
Annually averaged net power output	W	109	122
Instantaneous/nominal net power output	W	403	481
Hours operational	hr yr ⁻¹	2372	2227
Mean solar collector array efficiency	-	44.0%	46.5%
ORC electrical efficiency	-	12.8%	13.6%
Annual overall efficiency	-	5.6%	6.3%
Annual exergy efficiency	-	52.2%	58.5%

3.2 Annual simulation of single-stage and two-stage system

The S-CHP system is simulated over an annual period with UK climate data for both the single-stage and two-stage solar collector array configurations and with R245ca as the working fluid. The ORC evaporation temperature and the relative sizes of the solar collector arrays (in the two-stage configuration) are optimised to deliver the highest net annual electrical work output from the system, and the results for the optimum settings are presented in Table 3. It is found that the system with the two-stage collector array configuration is able to deliver a 12% higher net annual work output than the single-stage system. The optimal ORC evaporation temperature is also found to be 9 °C higher for the two-stage system, resulting in a 19% increase in instantaneous power output from the ORC; however the higher temperatures in the system also result in a larger number of hours (under very low irradiance conditions) for which $\eta_{sc} \leq 0$, and therefore the total number of operational hours per year is reduced.

The maximum annual work output reported here is also found to be 53% higher than that in our earlier work (Freeman *et al.*, 2015a). The improvement can be specifically attributed to the various system modifications that have been made, as follows: (i) ~4% improvement due to the choice of working fluid; (ii) ~10% improvement due to the choice of solar collector module; (iii) ~8% improvement due to the addition of the regenerator heat exchanger; and (iv) ~12% improvement due to the two-stage collector array configuration. The remaining improvement (a further ~20%) in power output can be attributed to the manner in which the system was simulated and optimised, specifically; the use of monthly aggregated climate data in the prior work was found to result in a non-trivial reduction in calculated power output due to non-linearity in the relationship between solar irradiance and system power output, whereas in the present analysis, the peaks in solar irradiance are more effectively represented by the hourly resolution dataset.

4. FURTHER DISCUSSION AND CONCLUSIONS

A study of a domestic-scale solar combined heat and power (S-CHP) system has been undertaken in order to assess its electrical performance in a London UK setting. Challenges for the design and operation of the system and its components due to the intermittent nature of the UK solar resource were addressed by incorporating a working fluid buffer vessel, hypothetically sized to enable year-round operation. Thus, the system can be operated with fixed fluid flow-rates, limiting losses in component efficiencies due to part-load operation and enabling continuous power output for longer periods.

Of the range of working fluids investigated, R245ca was found to result in the highest net annual work output for the basic single-stage system design, which was 955 kWh yr⁻¹ (64 kWh yr⁻¹ per m² of solar collector) at a cycle evaporation temperature of 117 °C. This is equivalent to a continuous power output of 109 W when averaged over the whole year. A modified design incorporating a two-stage solar

collector array was found to offer a further 12% in annual work output (1070 kWh yr^{-1} , or 71 kWh yr^{-1} per m^2), due to the improvement in overall collector array efficiency. In the present design the two-stage collector array requires an additional pump and heat exchanger and therefore an associated increase in capital cost of the system; however future work will explore the possibility of directly heating the ORC working fluid in the solar collector, thus omitting the need for the secondary fluid circuit.

The results presented here suggest that the S-CHP system operating in a UK setting can be expected to provide in the region of 32% of the typical household demand for electricity (3300 kWh yr^{-1} according to OFGEM, 2011). While significant, this is still found to be less than half of the predicted electrical output for the same system when simulated in a southern European climate. The electrical performance can be compared to that of a mono-crystalline PV system which typically provides $110\text{--}120 \text{ kWh m}^{-2} \text{ yr}^{-1}$ in the UK climate (The Energy Saving Trust, 2011a), and thus for an equivalent array size (15 m^2) approximately 50% of household demand. The advantage of the S-CHP system design discussed here is the ability to also provide water heating and to store thermal energy during times of low electricity demand for better load profile matching, as well as a considerably lower capital expenditure (by at least one-third, and arguably up to one-half). However, overall system performance also depends on well-designed solar collectors, able to operate with high efficiency at high fluid temperatures while also making use of the large proportion of diffuse (scattered) radiation received in the UK. The new generation of evacuated flat-plate solar collector investigated here is a strong candidate technology for such an application.

Finally, it is emphasised that this paper has focused on the performance of the S-CHP system when optimised for maximum annual electrical power generation. In CHP operation, a proportion of the solar collector heat transfer fluid may be diverted to a domestic hot water cylinder (see the system schematic in Figure 1a), at the expense of a reduction in the thermal input to the ORC engine. Taking the water heating demand for a typical UK home to be around 2900 kWh yr^{-1} (The Energy Saving Trust, 2011a), the reduction in the annual electrical output from the S-CHP system in order to meet this heating demand can be expected to be in the region of 35–45%.

NOMENCLATURE

A	area	(m^2)
η_0, a_1, a_2	solar collector efficiency curve parameters	(–)
h	specific enthalpy	(J kg^{-1})
h_c	convective heat transfer coefficient	($\text{W m}^{-2} \text{ K}^{-1}$)
I_{sol}	solar irradiance	(W m^{-2})
K_{θ}	solar collector incident angle modifier	(–)
\dot{m}	mass flow-rate	(kg s^{-1})
P	pressure	(Pa)
s	specific entropy	(J kg K^{-1})
T	temperature	($^{\circ}\text{C}$)
t	time	(s)
U	overall heat transfer coefficient	($\text{W m}^{-2} \text{ K}^{-1}$)
x	vapour quality	(–)
ε	heat exchanger effectiveness	(–)
η	efficiency	(–)
W	work	(W)

Subscript

a	ambient air
bv	working fluid buffer vessel
bubble	bubble-point (saturated liquid condition)
exp	expander
gen	generator
i, o	inner, outer

in, outer	inlet, outlet
r	regenerator
s	isentropic process
sc, sf	solar collector, solar collector circulating fluid
wf	ORC working fluid
1,2,3...	cycle state points

REFERENCES

- ASHRAE, 2001, International Weather for Energy Calculations (IWEC Weather Files) Users' Manual and CD-ROM, Atlanta. Available from: apps1.eere.energy.gov/buildings/energyplus/cfm/weather_data.cfm [accessed 24/2/2015].
- Bao, J., Zhao, L., 2013, A review of working fluid and expander selections for organic Rankine cycle, *Renew. Sustain. Energy Rev.*, vol. 24: p. 325–342.
- Canada, S., Cohen, G., Cable, R., Brosseau, D., Price, H., 2004, Parabolic trough organic Rankine cycle solar power plant, *Solar Energy Technologies Program Review Meeting*, Denver, Colorado.
- Calise, F., D'Accadia, M.D., Vicidomini, M., Scarpellino, M., 2015, Design and simulation of a prototype of a small-scale solar CHP system based on evacuated flat-plate solar collectors and Organic Rankine Cycle, *Energy Convers. Manag.*, vol. 90: p. 347–363.
- Chen, H., Goswami, D.Y., Stefanakos, E.K., 2010, A review of thermodynamic cycles and working fluids for the conversion of low-grade heat, *Renew. Sustain. Energy Rev.*, vol. 14 no. 9: p. 3059–3067.
- Dow, 1997, Dowtherm A Heat Transfer Fluid product technical data. Available from: http://msdssearch.dow.com/PublishedLiteratureDOWCOM/dh_0030/0901b803800303cd.pdf?filepath=/heattrans/pdfs/noreg/176-01337.pdf&fromPage=GetDoc [accessed 24/2/2015]
- The Energy Saving Trust, 2011, A buyer's guide to solar electricity panels.
- The Energy Saving Trust, 2011, Here comes the sun: a field trial of solar water heating systems.
- Freeman, J., Hellgardt, K., Markides, C.N., 2015, An assessment of solar-powered organic Rankine cycle systems for combined heating and power in UK domestic applications, *Appl. Energy*, vol. 138: p. 605–620.
- Freeman, J., Hellgardt, K., Markides, C.N., 2015, An assessment of solar-thermal collector designs for small-scale combined heating and power applications in the United Kingdom, *Heat Transf. Eng.*, vol. 36, no. 14–15: p. 1333–1348.
- Incropera, F.P., DeWitt, D.P., Bergman, T.L., Lavine, A.S., 2006, *Fundamentals of Heat and Mass Transfer*, sixth ed., John Wiley & Sons, New Jersey.
- Jing, L., Gang, P., Jie J., 2010, Optimization of low temperature solar thermal electric generation with Organic Rankine Cycle in different areas, *Appl. Energy*, vol. 87: p. 3355–3365.
- Manolakos, D., Kosmadakis, G., Kyritsis, S., Papadakis, G., 2009, On site experimental evaluation of a low-temperature solar organic Rankine cycle system for RO desalination, *Sol. Energy*, vol. 83: 646–656.
- OFGEM (Office of Gas and Electricity Markets), 2011, Typical domestic energy consumption figures factsheet, Available from: <https://www.ofgem.gov.uk/ofgem-publications/76112/domestic-energy-consump-fig-fs.pdf> [accessed 24/2/2015].
- Quoilin, S., Orosz, M., Hemond, M., Lemort, V., 2011, Performance and design optimization of a low-cost solar organic Rankine cycle for remote power generation, *Sol. Energy* vol. 85: p. 955–966.
- Rayegan, R., Tao, Y. X., 2011, A procedure to select working fluids for Solar Organic Rankine Cycles (ORCs), *Renew. Energy*, vol. 36, no. 2: p. 659–670.
- TVP Solar, 2013, HT-Power Product datasheet. Available from: [http://www.tvpsolar.com/files/pagine/HT-Power%20Datasheet%20\(v4.2x\)\(ver3\).pdf](http://www.tvpsolar.com/files/pagine/HT-Power%20Datasheet%20(v4.2x)(ver3).pdf) [accessed 24/2/2015].
- Wang H. and Touber S., 1991, Distributed and non-steady-state modelling of an air cooler, *Int. J. Refrig.*, vol. 14, no. 2: p. 98–111.
- Wang, X.D., Zhao, L., Wang, J.L., Zhang, W.Z., Zhao, X.Z., Wu, W., 2009, Performance evaluation of a low-temperature solar Rankine cycle system utilizing R245fa, *Sol. Energy*, vol. 84: p. 353–364.

EFFECT OF TEMPERATURE DIFFERENCE ACROSS ORC BOILER ON THE THERMAL STORAGE MEDIUM COST IN A SOLAR ORC

Abhishek N. Kshirsagar¹, Pardeep Garg^{2†}, Pramod Kumar^{2#}, Matthew S. Orosz³

¹Pune Vidyarthi Griha's College of Engineering and Technology
Vidyanagari, Pune, Maharashtra, India
E-mail: kshirsagar_abhishek@yahoo.com

²Indian Institute of Science Bangalore
C V Raman Ave, Bengaluru, Karnataka, India
[†]E-mail: pardeep_1127@yahoo.com
[#]E-mail: pramod_k24@yahoo.com

³Massachusetts Institute of Technology
Cambridge, MA, USA
E-mail: mso@mit.edu

ABSTRACT

This paper identifies the key parameters to be optimized on a thermo-economic basis in a solar-ORC to minimize the storage cost associated with it. These parameters are ORC working fluid, its operating conditions and the heat transfer fluid used. A case study of a pebble bed thermal energy storage system is carried out using two working fluids in a 100 kWe ORC namely, R-245fa and R-134a for a wide range of expander inlet temperatures. Heat transfer fluids considered are ethylene glycol (for temperatures < 180 °C), Therminol VP-1 and Glycerol (for temperatures > 180 °C). Effect of these parameters is evaluated for the case scenario of suppressing the fluctuations in the ORC side arising due to solar insolation calculated using ASHRAE clear sky model. For a given energy storage, HTF temperature difference across the boiler and HTF mass required for storage and hence cost of PB-TES system are reported to be inversely co-related. Higher expander inlet temperatures in case of R134a ORC with Glycerol as an HTF are found to yield the lowest storage cost.

1. INTRODUCTION

Organic Rankine cycle (ORC) technology can be integrated with geothermal (Astolfi et al., 2014) or process heat available from industry (Wei et al. 2007) or renewable energy source such as a concentrated solar thermal system using parabolic trough collectors (Quoilin et al., 2011). In case when ORCs are directly coupled with solar, issues arising due to fluctuating nature of solar insolation are reported to adversely affect the ORC performance (Twomey et al., 2013). Thermal storage in this regard can help in suppressing the fluctuations and also provide an option for power generation during non-solar hours (Taljan et al. 2012). There exist a number of storage technologies which need to be optimized for the minimum cost depending on the application. In such a study, Herrmann and Kearney (2002) came up with a techno-economic analysis for the various existing storage technologies and emphasized on the need of reducing the cost of storage media. One possible way to reduce the cost of storage medium is to store partial amount of heat in the inexpensive rocks or pebbles as suggested by Meier et al., 1991. The technology is analyzed in a great detail by a number of researchers (Hasnain et al. 1998; Mawire et al., 2009; Singh et al, 2010 and Zanganeh et al., 2012) and simple modeling techniques are proposed. However, literature lacks the work on optimizing the cost of storage in conjunction with the ORC.

This paper analyzes the effect of ORC working fluid and its operating conditions on the cost associated with the pebble bed based thermal energy storage (PB-TES) tank designed to die out the

fluctuations arising due to varying solar insolation. In this regard, a procedure is developed to calculate the mass of HTF required in a PB-TES tank. HTF temperature difference across the boiler and the mass of HTF stored in a PB-TES tank (hence the cost of the storage system) are observed to be inversely co-related. This temperature difference in turn is found to be dependent on ORC working fluid and its operating conditions. The same is illustrated in a great detail for the two different working fluids in ORC namely, R245fa and R134a for different operating conditions in the power block.

2. SOLAR-ORC DETAILS

Physical layout of the solar-ORC considered in this paper consists of two closed loops, a) heat transfer fluid (HTF) and b) working fluid loop as shown in Fig. 1. In the HTF loop, cold HTF from a PB-TES is pumped to a parabolic trough collector where it gets heated up and is then sent for the storage in a PB-TES tank. Working fluid loop is a regenerative ORC where the expander exhaust heat is recovered to heat up the pump outlet fluid. The two loops interact via a heat exchanger termed as an HEX (boiler for the working fluid) in this paper where the HTF coming from a PB-TES tank is cooled and working fluid in turn is heated up to the expander inlet temperature.

2.1 ORC details

Low pressure and low temperature liquid at state 1_{wf} is pumped to higher pressures (state 2_{wf}). High pressure fluid at this state is preheated in a regenerator from state 2_{wf} to 5_{wf} by recovering heat from expander exhaust wherein the low pressure gas is cooled from state 4_{wf} to 6_{wf} . Remaining heat addition from state 5_{wf} to 3_{wf} occurs in a heater via a heat transfer fluid (HTF). Working fluid is then further expanded in a scroll device till state 4_{wf} . Regenerator outlet on low pressure side (state 6_{wf}) is then cooled in an air cooled condenser till state 1_{wf} to complete the cycle. Ideally, the pumping and expansion processes should be isentropic and heat transfer processes isobaric which in reality tend to deviate. Modeling details for such an ORC could be found in (Garg et al., 2013) and for the sake of completeness are repeated here.

- i. Power generation is 100 kW_e.
- ii. Minimum cycle temperature (T_l) is 45 °C.
- iii. Pump efficiency is 90 %.
- iv. Expander efficiency is 65 %.
- v. Pinch temperature in the regenerator and the HEX is set at 10 °C and the flow arrangement is counter flow type.

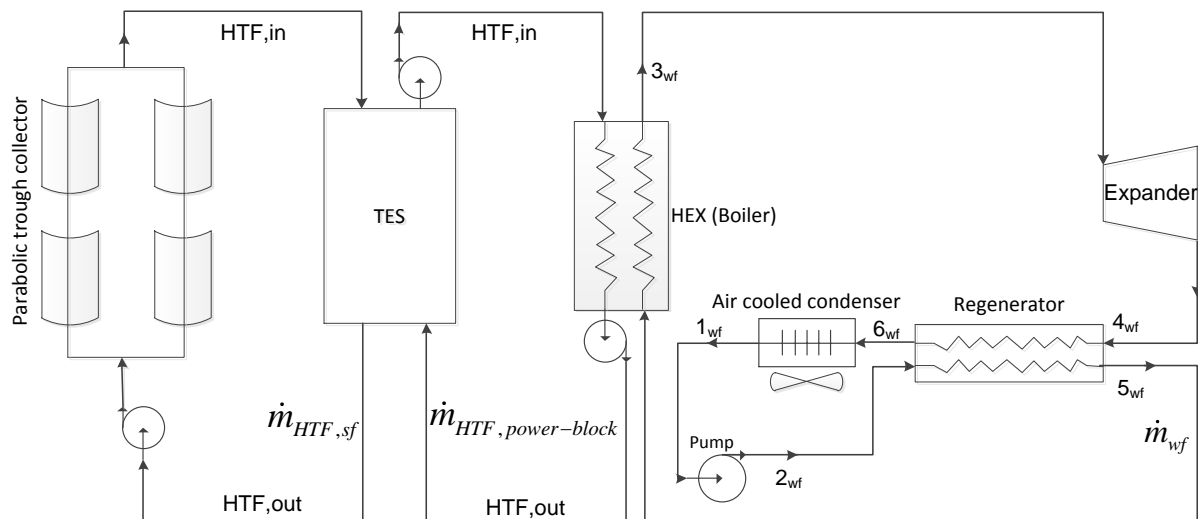


Figure 1: Schematic of an ORC

2.2 TES details

Heated HTF from solar field enters the PB-TES tank from the top where it loses heat to the pebbles and the cold HTF around. The same amount of cold HTF leaves the tank from the bottom side and is passed to the solar collectors to heat it up again. Control strategy followed in this loop is to regulate HTF mass flow rate to achieve steady HTF temperatures (also equal to HTF maximum temperature). In another loop, hot HTF from the PB-TES is passed on to the HEX (boiler for the working fluid) where it supplies the heat to the working fluid in the power block. Storage sizing is done in such a way that the fluctuations arising due to solar insolation are damped out, thus, ensuring the steady HTF operating conditions and ORC operation at its designed conditions throughout the day.

3. METHODOLOGY

To calculate the solar PB-TES costs associated with the ORC algorithm given in Fig. 2 is considered. Firstly, the ORC for the given operating expander inlet temperature is designed for the best efficiency. Solar insolation or DNI calculations are performed using ASHRAE clear sky model for which the details can be found in Appendix A. TES is modeled in such a way that temperature drop across the HTF in HEX and PB-TES are identical. In turn, these inlet and outlet temperatures of the PB-TES are governed by the operating conditions on working fluid side in power block discussed in detail in ahead.

3.1. Mass of storage media required

A bottom-up approach is followed to calculate the storage needs of a solar-ORC to damp the fluctuations in the operating conditions in the power block. Firstly, HTF operating conditions across the HEX i.e. HTF inlet and outlet temperature are calculated.

Calculation of HTF operating conditions in HEX

The procedure to calculate HTF operating conditions is based on pinch point analysis in the HEX. It is observed that pinch point in the HEX occurs at the liquid saturation line of the working fluid as shown in Fig. 4.

$$T_{HTF,pinch} = T_{2f,wf} + \Delta T_{pinch} \quad (1)$$

Further, to minimize the HEX irreversibility (Garg et al., 2013),

$$T_{HTF,in} = T_{3,wf} + \Delta T_{pinch} \quad (2)$$

Applying 1st law of thermodynamics to control volume across state 2_{wf} and 3_{wf}

$$\dot{m}_{HTF} c_{p,HTF} (T_{HTF,in} - T_{HTF,pinch}) = \dot{m}_{wf} (h_{3,wf} - h_{2f,wf}) \quad (3)$$

Having defined the thermodynamic properties on working fluid as well as HTF side, one can calculate the product of mass flow rate and specific heat of HTF

$$\dot{m}_{HTF} c_{p,HTF} = \frac{\dot{m}_{wf} (h_{3,wf} - h_{2f,wf})}{(T_{HTF,in} - T_{HTF,pinch})} \quad (4)$$

Once the above product is known, application of 1st law to the HEX can be applied to calculate the $T_{HTF,in}$

$$\dot{m}_{HTF} c_{p,HTF} (T_{HTF,in} - T_{HTF,out}) = \dot{Q}_{power-block} \quad (5)$$

Simplifying the above equation for $T_{HTF,out}$

$$T_{HTF,out} = T_{HTF,in} - \frac{\dot{Q}_{power-block}}{\dot{m}_{HTF} c_{p,HTF}} \quad (6)$$

where, heat required in the power block is

$$\dot{Q}_{power-block} = \frac{\dot{P}}{\eta_{ORC}} \quad (7)$$

For the transcritical cycle above mention procedure is modified to calculate $T_{HTF,out}$.

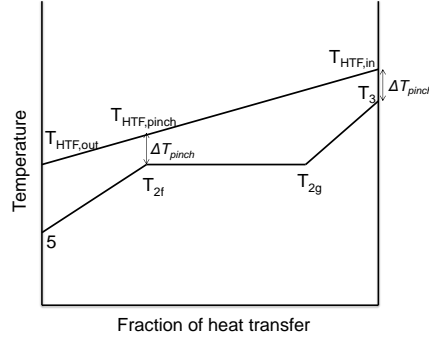


Figure 2. Temperature profiles of HTF and working fluid in a typical HEX.

PB-TES design

Let A_{solar} be the area of solar field required to generate power output (\dot{P}) for the full solar-day duration. Then, heat available from the collector whose efficiency is $\eta_{collector}$ is

$$\dot{Q}_{collector} = \eta_{collector} DNI_N A_{solar} \quad (8)$$

On a given day variation of $\dot{Q}_{collector}$ (derived using ASHRAE clear sky model with a cloud factor) with time is presented in Figure 3 along with $\dot{Q}_{power-block}$ which is steady in nature. Solar field area is designed in such a way that area under both the curves is identical. Mathematically,

$$area(ABCD) = area(AGHD) \quad (9)$$

or

$$\dot{Q}_{power-block} \Delta t_h = \int_{t_{1h}}^{t_{4h}} \dot{Q}_{collector} dt_h \quad (10)$$

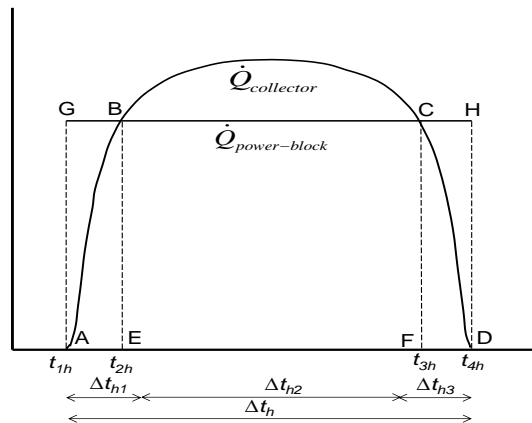


Figure 2: A standard DNI curve taken with constant output power

It can be noted that heat available from the collector exceeds that of required in the power block in the hours between t_{2h} to t_{3h} and can be stored in the PB-TES. The stored heat can then later be used in the hours between t_{1h} to t_{2h} and t_{3h} to t_{4h} when the heat available from the collector is not enough to run the power block. It can be appreciated that heat stored in the surplus hours should be equal to energy used

in the deficit hours for the steady operation of power block. Energy that needs to be stored in the PB- TES is thus given as

$$\Delta E_{PB-TES} = \text{area}(\text{arc}(BC)) - \text{area}(BCFE) \quad (11)$$

Or

$$\Delta E_{PB-TES} = \int_{t_2}^{t_3} \dot{Q}_{\text{collector}} dt_h - \dot{Q}_{\text{power-block}} \Delta t_{3h} \quad (12)$$

Further, this energy is stored in pebbles as well as HTF

$$\Delta E_{PB-TES} = \Delta E_{HTF} + \Delta E_{Pebble} \quad (13)$$

where,

$$\Delta E_{HTF} = M_{HTF} c_{pHTF} \Delta T_{HTF} \quad (14)$$

$$\Delta E_{Pebble} = M_{Pebble} c_{pPebble} \Delta T_{Pebble} \quad (15)$$

Further, condition of local thermal equilibrium is assumed to be valid in the PB-TES which makes the temperature of HTF and pebble equal. Break up of ΔE_{PB-TES} is given by Eq. 10 in the form of the porosity ($\varphi = V_{HTF}/V_{Total}$) in the tank.

$$\Delta E_{PB-TES} = (\varphi \rho_{HTF} c_{pHTF} + (1 - \varphi) \rho_{Pebble} c_{pPebble}) V_{Total} \Delta T_{HTF} \quad (16)$$

Knowing the value of ΔT_{HTF} and thermo-physical properties of the storage media, V_{Total} can be calculated. Eqs. (7), (10) and (4) are simplified to obtain M_{HTF}

$$M_{HTF} = \frac{\Delta E_{PB-TES}}{c_{pHTF} \Delta T_{HTF}} - M_{Pebble} \frac{c_{pPebble}}{c_{pHTF}} \quad (17)$$

Above equation establishes an inverse relationship between M_{HTF} and ΔT_{HTF} indicating the storage cost to be a strong function of working fluid in ORC and its operating conditions.

3.2. Storage Media properties

Pebble type considered here is fused silica with density of 2200 kg/m³ and specific heat of 740 J/kgK. Three different HTFs are considered, namely Ethylene Glycol, Therminol VP1 and Glycerol. For HTF operating temperatures lower than 180 °C, Ethylene Glycol is considered otherwise Therminol VP1 and Glycerol. Though, thermo-physical properties of HTFs are assumed to be the function of temperature as given in the Appendix B along with the cost functions, for the given operating conditions of HTF, thermo-physical properties are taken to be the average of those at inlet and outlet temperatures of HTF across HEX.

3.2.1 Assumptions:

- i. Pinch temperature in the HEX is 10 °C.
- ii. Porosity is taken as 0.45.
- iii. While the minimum cycle temperature is fixed at 45 °C, the maximum cycle temperature is considered to be variable.
- iv. In case when cycle efficiency becomes asymptote to the pressure ratio at a given expander inlet temperature, to avoid unnecessary high pressure ratio without having a substantial gain in efficiency, the optimum efficiency is chosen corresponding to a pressure ratio where

$$\left. \frac{\partial \eta}{\partial pr} \right|_{T_{3wf}} = 0.005 \quad (18)$$

4. RESULTS AND DISCUSSIONS

The storage model developed above is generic in nature and can be applied to any working fluid. However, the present paper considers R245fa and R134a to perform a detailed comparison in terms of

the storage cost. Storage cost for the rest of the working fluids is found to be somewhere between the cost of these two fluids and hence not presented. ORCs are designed in such a way that they operate at maximum efficiencies at the given expander inlet temperature. In this regard, the optimum pressure ratios in the cycle are plotted in Figure 3. It also shows the variation of optimum efficiency corresponding to pressure ratios with the expander inlet temperature for both the working fluids. In case of R245fa, optimum pressure ratio continues to increase with expander inlet temperature whereas in R134a the limit of 60 bar imposed on the high side pressure of the cycle is achieved and hence constant pressure ratios are observed for the temperatures beyond 200 °C. Also, the property data available in Refprop (Lemmon et al.) for R134a restricts its use in the ORC to 220 °C in comparison to 260 °C as observed in case of R245fa.

It can also be noticed that beyond ~ 140 °C, ORC efficiency increases almost linearly with expander temperature. Also, cycle efficiency is slightly lower (about 2-3 %) for R134a than R245fa under identical operating conditions which might result in higher storage needs as shown in Figure 4. Further, the storage requirements come down with expander inlet temperature because of higher cycle efficiencies.

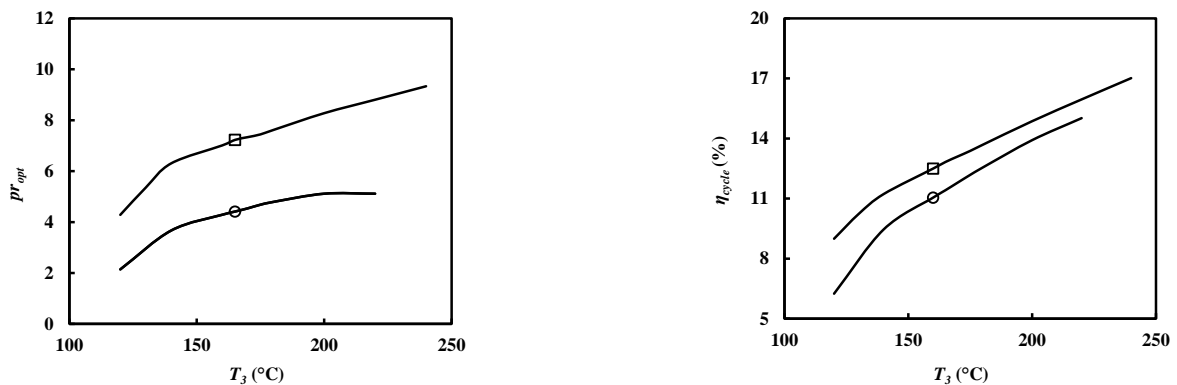


Figure 3: Variation of optimum pressure ratio and optimum efficiency in the ORCs with R245fa and R134a against the expander inlet temperature. Legend: \square R245fa, \circ R134a

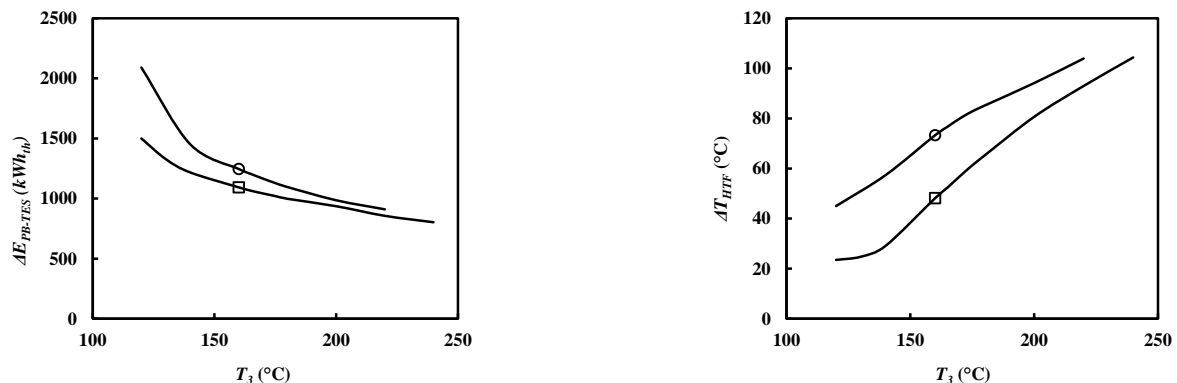


Figure 4: Thermal energy to be stored in PB-TES and HTF temperature difference across the HEX for ORCs with R245fa and R134a against the expander inlet temperature. Legend: \square R245fa, \circ R134a

Another important parameter which has a strong effect on storage namely temperature difference across HTF in the HEX (also across the PB-TES) is also plotted in Figure 4 for the corresponding operating conditions mentioned in the above figures. It is observed that ΔT_{HTF} increases with expander inlet temperature though the trend is found to be non-linear. The increase in ΔT_{HTF} with temperature can be explained on the basis of the fact that with increase in expander inlet temperature, optimum pressure ratio increases which lowers the amount of latent heat involved in the HEX. In an ideal counter flow HEX, where there is no change in the ratio of specific heats of the two fluids (HTF and working fluid) with respect to the heat transferred in it, the temperature profiles of the both fluids tend to remain parallel and the maximum temperature difference would be observed across HTF. This situation is generally realized in Brayton cycles (Garg et al., 2014) where irreversibility generation is

also found to be lower. Further, lower latent heat or no phase change involved in case of R134a in reference to R245fa makes ΔT_{HTF} higher for the former which could potentially reduce the storage cost.

Having known the ΔT_{HTF} and $\Delta EPB-TES$, the cost associated with the PB-TES can be calculated which is plotted in Figure 5. Notable observations are as follows:

- Storage cost as expected is a strong function of HTF type. Glycerol results in the lowest storage costs because of its lower cost per unit mass.
- For the given HTF, the storage cost keeps coming down with the expander inlet temperature because of higher cycle efficiency and higher ΔT_{HTF} .
- Lowest storage cost is observed for R245fa at the expander inlet temperature 250 °C with Glycerol as an HTF.

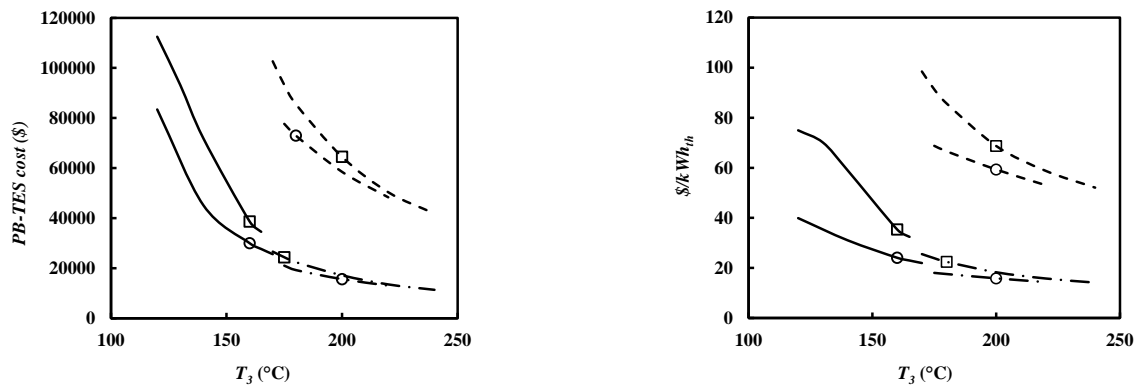


Figure 5: Variation of cost of PB-TES and cost of storage per unit of energy stored in the ORCs with R245fa and R134a against the expander inlet temperature. Legend: \square R245fa, \circ R134a, — Ethylene Glycol, — · — Glycerol, — — — Therminol VP1.

Further, the most sought after parameter in storage which is the storage cost per unit of thermal energy stored is also plotted in Figure 5. At any given expander inlet temperature, R134a shows the minimum cost per unit of energy stored in the PB-TES.

5. CONCLUSION

Paper analyzes the cost associated with the pebble bed based thermal energy storage system for the ORCs. A number of parameters are identified which can significantly affect the storage cost for example, HTF type, working fluid type and operating conditions in the ORC. A case study performed on the storage details for R134a and R245fa as working fluids in the ORC predicts the lower cost of storage for the formed in absolute terms as well as on the parameter of cost per unit of energy stored in. The lowest cost per unit of energy is found to be ~ 14 $\$/kWh_{th}$ which includes the cost of the HTF, pebbles and the tank. Further, this study can be extended to a number of working fluids in the ORC and various other HTFs possible with different operating temperature ranges to find the minimum storage cost.

REFERENCES

- Garg P., Kumar P., Srinivasan K., Dutta P., 2013, Evaluation of carbon dioxide blends with isopentane and propane as working fluids for organic Rankine cycles, *Applied Thermal Engineering*, Vol. 52, pp 439-448.
- Gregor Taljan, Gregor Verbi, Milos Pantos, Manfred Sakulin, Lothar Fickert, 2012, Optimal sizing of biomass-fired Organic Rankine Cycle CHP system with heat storage, *Renewable Energy*, vol. 41 p. 29-38
- Ulf Herrmann, David W. Kearney, 2002, Survey of Thermal Energy Storage for Parabolic Trough Power Plants, *Journal of Solar Energy Engineering*, Vol. 124/145-152
- G. Zanganeh, A. Pedretti, S. Zavattoni, M. Barbato, A. Steinfeld, 2012, Packed-bed thermal storage

- for concentrated solar power – Pilot-scale demonstration and industrial-scale design, *Solar Energy*, vol. 86 p. 3084–3098
- Mawire, M. McPherson, 2009, Experimental and simulated temperature distribution of an oil-pebble bed thermal energy storage system with a variable heat source, *Applied Thermal Engineering*, vol. 29 p. 1086–1095A.
- Hasnain SM. Review on sustainable thermal energy storage technologies. Part1. Heat storage materials and techniques, *Energy Convers Manage*, J1998;39(11):1127–38
- Quoilin, S., Orosz, M., Hemond, H., Lemort, V., 2011, Performance and design optimization of a low-cost solar organic Rankine cycle for remote power generation, *Solar Energy*, vol. 85, no. 5: p. 955-966.
- Orosz, M. S., 2012, ThermoSolar and photovoltaic hybridization for small scale Distributed Generation: Applications for Powering Rural Health, Doctoral dissertation, Massachusetts Institute of Technology.
- Orosz, M. S., Quoilin, S., Hemond, H., Sorce: A Design Tool For Solar Organic Rankine Cycle Systems In Distributed Generation Applications Curran, H. M., 1993, Mechanical systems and components, In: Lof, G. O. G., *Active Solar Systems*, MIT Press, Cambridge, MA: p. 693-94

Appendix A

The following model is used to calculate the DNI for a given location and at any time t for which a number of concerned terms are defined for the sake of completeness.

i. Hour angle, ω

$$\omega = (t - 12)15^\circ \quad (\text{A.1})$$

ii. Declination angle, δ

$$\delta = 23.45 \sin\left(\frac{360}{365}(284 + n)\right) \quad (\text{A.2})$$

iii. Solar altitude angle, β

$$\sin \beta = \cos l \cdot \cos \omega \cdot \cos \delta + \sin l \cdot \sin \delta \quad (\text{A.3})$$

iv. Solar azimuth angle, ϕ

$$\cos \phi = \frac{\sin \delta \cdot \cos l - \cos \delta \cdot \sin l \cdot \cos \omega}{\cos \beta} \quad (\text{A.4})$$

v. Wall solar azimuth, γ

$$\gamma = |\phi| \quad (\text{A.5})$$

vi. Angle of incidence, θ

$$\cos \theta = \cos \beta \cdot \cos \gamma \cdot \sin \alpha + \sin \beta \cdot \cos \alpha \quad (\text{A.6})$$

vii. Normal direct irradiation, G_{ND}

$$G_{ND} = \frac{A}{\exp\left(\frac{B}{\sin \beta}\right)} C_N \quad (\text{A.7})$$

Where C_N clearness number and constants A and B are referred from the data provided in the ASHRAE clear sky model handbook.

viii. Direct insolation available on the horizontal surface, DNI_H i.e. without axis tracking

$$DNI_H = G_{ND} \cdot \max(\cos \theta, 0) \quad (\text{A.8})$$

ix. Direct insolation available in the direction normal to sun, DNI_N i.e. with single axis tracking

$$DNI_N = \frac{DNI_H}{\cos \omega} \quad (\text{A.9})$$

Above equation is used to calculate the direct insolation available on the parabolic trough for a clearness coefficient of 0.6.

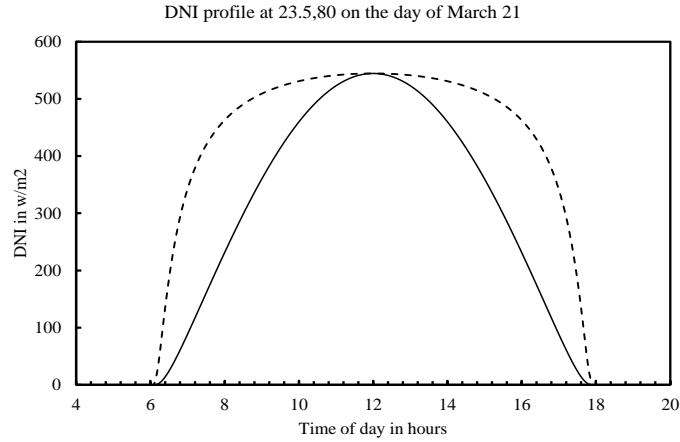


Figure A.1: The above figure shows the DNI profile Sinora, India (23.5, 80), on the day of vernal equinox.
 ————— Represents DNI without axis tracking and - - - - - represents DNI with single axis tracking.

Appendix B

Therminol VP-1

$$c_{p,HTF} = 1498 + 24.14 \times 10^{-4} T_{HTF,avg} + 59.9 \times 10^{-3} T_{HTF,avg}^2 - 29.879 \times 10^{-5} T_{HTF,avg}^3 + 44.172 \times 10^{-8} T_{HTF,avg}^4$$

$$\rho_{HTF} = 1083.25 - 90.797 \times 10^{-2} T_{HTF,avg} + 7.8116 \times 10^{-4} T_{HTF,avg}^2 - 2.36710^{-6} T_{HTF,avg}^3$$

$$cost_{HTF} = 2 \text{ \$/kg}$$

Ethylene Glycol

$$c_{p,HTF} = 2279.98862 + 4981.34 \times 10^{-3} T_{HTF,avg}$$

$$\rho_{HTF} = 1106.2 + 132.5 \times 10^{-3} T_{HTF,avg} - 8.7 \times 10^{-3} T_{HTF,avg}^2 - 0.02 \times 10^{-3} T_{HTF,avg}^3$$

$$cost_{HTF} = 6 \text{ \$/kg}$$

Glycerol

$$c_{p,HTF} = 2274.87 + 470.71 \times 10^{-3} T_{HTF,avg}$$

$$\rho_{HTF} = 1277 - 65.4 \times 10^{-2} T_{HTF,avg}$$

$$cost_{HTF} = 1.5 \text{ \$/kg}$$

$$cost_{tank} = 130V_{tank} + 1140$$

NOMENCLATURE

l	Latitude	(°)
ω	Hour angle	(°)
n	Day number	(-)
δ	Declination	(°)
β	Solar altitude angle	(°)
ϕ	Solar azimuth angle	(°)
γ	Surface solar azimuth angle	(°)
θ	Angle of incidence	(°)

α	Tilt angle	(°)
A	Apparent solar irradiation at air mass equal to zero	(W/m ²)
B	Atmospheric extinction coefficient	(-)
C_N	Clearness number	(-)
T	Temperature	(K)
M	Mass	(kg)
E	Energy	(J)
V	Volume	(m ³)
$A_{collector}$	Area of collector field	(m ²)
\dot{Q}	Power	(W)
\dot{P}	Output power	(W)
t	Time	(Hours)
c_p	Specific heat	(J/kgK)
η	Efficiency	(-)
ρ	Density	(kg/m ³)
\dot{m}	Mass flow rate	(kg/s)
φ	Porosity	(-)

Subscript

h	hour
HTF	heat transfer fluid
$Pebbles$	pebble
$PB-TES$	pebble bed thermal energy storage
$power-block$	power block
$collector$	collector
$Total$	total tank
wf	working fluid

Abbreviations

TES	thermal energy storage
HTF	heat transfer fluid
DNI	direct normal insolation
PB-TES	pebble-bed thermal energy storage
ORC	organic Rankine cycle
HEX	heat exchanger

ACKNOWLEDGEMENT

This research is based upon work supported by the Solar Energy Research Institute for India and the U.S. (SERIUS) funded jointly by the U.S. Department of Energy subcontract DE AC36-08G028308 (Office of Science, Office of Basic Energy Sciences, and Energy Efficiency and Renewable Energy, Solar Energy Technology Program, with support from the Office of International Affairs) and the Government of India subcontract IUSSTF/JCERDC-SERIIUS/2012 dated 22nd Nov. 2012.

ANALYSIS OF THERMAL ENERGY STORAGE SOLUTIONS FOR A 1 MW CSP-ORC POWER PLANT

David Sánchez^{1*}, Hicham Frej², Gonzalo S. Martínez³, José María Rodríguez³, El Ghali Bennouna²

¹University of Seville – ³AICIA, Thermal Power Group,
Seville, Spain
ds@us.es, gsm@us.es, jmrm@us.es

² Institut de Recherche en Energie Solaire et en Energies Nouvelles (IRESEN),
Rabat, Morocco
frej@iresen.org, bennouna@iresen.org

* Corresponding Author

ABSTRACT

Organic Rankine Cycle (ORC) power generation blocks have been principally used in the past couple of decades to recover medium grade heat from sources such as geothermal steam, biomass boilers and the exhaust of a realm of different industrial processes. In the past few years, a new philosophy of integrating thermal solar energy to an organic Rankine cycle has been assessed, the purpose of which is to develop a compact, water free and decentralized solution that offers the advantages of solar thermal power with low intermittency and the possibility to extend power generation to the night time at a relatively reasonable cost. To achieve these objectives, a proper storage system that is thermodynamically fit to the heat profile captured by the solar collector and to that of the power cycle must be identified.

This paper covers the selected criteria and the analysis done to identify the potential storage solutions adapted to a thermal solar – ORC system operating at temperature range between 170 C min and 300 °C max, while receiving energy in the form of sensible heat from the collector in order to eventually deliver it to a power organic Rankine cycle (ORC) that uses Cyclopentane as a working fluid. The system so developed will be integrated in the 1 MWe CSP-ORC facility based on Fresnel technology which is currently under construction at Iresen's facilities in Morocco.

The paper covers the optimisation process carried out to best match the characteristics of the thermal Energy storage system to the features of the ORC power block. Two alternative solutions are looked into: sensible heat storage and latent (phase-change) heat storage. A parallel analysis is presented from a multiple fold perspective (technical, economic...) showing that both technologies have particular advantages.

1. INTRODUCTION

The recognized need for electrical energy storage is not new, and many methods of storing energy have been devised over the years. Early last century, a U.S. patent application for a “*System of Storing Power*” was filed on June 7, 1907, by R.A. Fessenden and a patent (No. 1247520) was granted on November 20, 1917. In it, Fessenden stated: “*The invention herein described relates to the utilization of intermittent sources of power and more particularly to natural intermittent sources, such as solar radiation and wind power, and has for its object the efficient and practical storage of power so derived [...]. It has long been recognized that mankind must, in the near future, be faced by a shortage of power unless some means were devised for storing power derived from the intermittent sources of nature [...]. These sources are, however, intermittent and the problem of storing them in a practicable way, i.e., at*

a cost which should be less than that of direct generation from coal, has for many years engaged the attention of the most eminent engineers, among whom may be mentioned Edison, Lord Kelvin, Ayrton, Perry, and Brush”.

In spite of this acknowledgeable efforts, the problem of storing large amounts of accessible energy in a cost-effective and efficient manner has nevertheless remained one of the most difficult scientific and engineering problems known to date. Thus, as foreseen by Fassenden (1907), the advent of modern renewable energy sources greatly improved our ability to generate energy for several decades but not to store all of what we could produce. In the light of the fore cited arguments, the search for robust and cost-effective energy storage means has intensified in the last ten years.

The Research Institute for Solar Energy and New Energies (IRESEN) is currently developing a solar platform where research activities can be carried out in an environment with unmatched boundary conditions. Amongst different initiatives aiming to foster the development of solar power generation technologies, a 1 MWe Organic Rankine Cycle power system based on indirect vapor generation with linear Fresnel collectors is worth noting. This technology makes use of a heat transfer fluid (typically mineral or synthetic oils) which carries thermal energy from the solar field to a dedicated heat exchanger where organic superheated vapor is produced. This power generation facility is currently under construction and will expectedly come into operation in 2016. Performance specifications are given in Table 1.

Table 1: Performance specifications of the 1 MWe ORC power plant

Parameter	Units	Rated value
Rated Direct Normal Irradiation	W/m ²	850
Net Rated Power Output	kWe	900
Net Rated Efficiency of the ORC (Solar to electricity)	%	18
Collector type	-	Linear Fresnel
Number of solar field loops and total aperture area	- / m ²	7/11400
Efficiency of solar field all losses included	%	53
Solar field heat output	MWth	5000
Working fluid of power block	-	Cyclopentane
Reference dry bulb temperature (Dry cooling)	°C	30

The original design of the power plant does not incorporate thermal storage capabilities other than a buffer tank where a certain amount of hot heat transfer fluid is stored. Nevertheless, this system cannot be regarded as a true energy extending or shifting storage system as it only stores energy (sensible heat) for about twenty minutes and thus it is aimed at compensating for fast-passing clouds over the solar field only. Therefore, the buffer tank does not enable extended operation of the plant after sunset.

The aforecited characteristics of the power plant prevent it from delivering dispatchable electricity, hence eliminating one of the differential features of solar thermal electricity with respect to other renewable energy technologies like wind or photovoltaics. It is thus a primary target for IRESEN to develop thermal energy storage systems that could be integrated into these intermediate scale ORC power systems which are too large to consider electric batteries and too small to directly downscale the commercial technologies currently used in large CSP power plants (>50 MWe). The temperature difference between the steam cycle used in the latter and the ORC power block existing in the reference plant reinforces this statement.

With all the previous arguments in mind, this article approaches the design of a thermally-efficient and cost-effective thermal storage system to be integrated into the 1 MWe CSP-ORC power plant in Benguerir. The analysis starts off with the principles of energy storage and, then, a comparison amongst the different technologies available is presented before coming to conclusions with respect to the best candidate(s).

2. THERMODYNAMIC PRINCIPLES OF ENERGY STORAGE

To optimize the design and operation of the thermal energy storage (TES) system, this must be analyzed in terms of the First and the Second Laws of thermodynamics. The First Law yields the energy efficiency, which is the ratio from the energy delivered by the storage device during discharging to the energy supplied to it during the charging phase. This approach is interesting to detect two main inefficiencies:

- Heat losses to the surroundings. This is particularly important for systems that operate at very high temperature
- Residual energy not being delivered by the storage system. This is mainly due to temperature gradients between the energy source (typically a heat transfer fluid at high temperature) and the storage medium of the TES system.

This first law efficiency might nevertheless be misleading as it only accounts for the total amount of different forms of energy being transferred to and recovered from the TES system but it does not take into consideration how useful this energy is (energy quality); i.e. the potential to produce useful work in the power conversion system to which it is connected. Another complementary approach is thus needed, based on the second law. This provides a rational measure of the quality of this energy being transferred.

Figure 1 presents an elementary TES system whereby a heat transfer fluid, hereinafter called HTF, provides energy (E_{in}) to the tank during the charging process whilst the same or another fluid extracts a fraction (E_{out}) of the energy stored in the tank (E_{stored}).

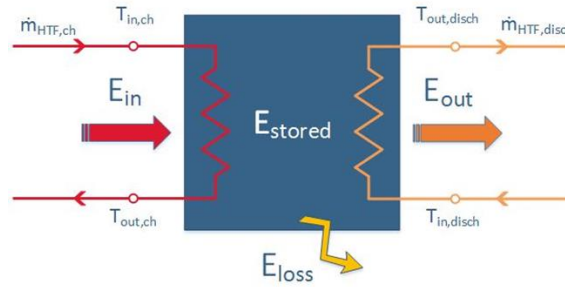


Figure 1: Scheme of an elementary TES system

The first law applied to the system in Figure 1 is equated as follows:

$$E_{in} = E_{out} + E_{loss} \quad (1)$$

Based on this balance, there are many different though valid definitions of the energy efficiency of TES systems. For example, Equations (1) and (2) provide valid definitions of energy storage efficiency:

$$\eta_{TES} = \frac{\text{Energy delivered by TES}}{\text{Energy supplied to TES}} \quad (2)$$

$$\eta_{TES} = \frac{\text{Energy delivered by TES} + \text{Energy remaining in TES after discharge}}{\text{Energy supplied to TES} + \text{Residual energy originally in TES}} \quad (3)$$

These equations have a similar foundation but they might yield different values under similar operating conditions. Therefore, many authors define different efficiencies for the charging and discharging phases:

$$\eta_{TES,charging} = E_{stored}/E_{in} \quad (4)$$

which describes the fraction of the total energy input (energy supplied plus pumping power) required to charge the storage tank that is effectively stored in it. A low value of $\eta_{TES,charging}$ indicates an ineffective heat transfer or a large amount of energy (sensible heat) carried by the hot fluid leaving the tank.

The discharging efficiency can be defined in a similar manner:

$$\eta_{TES,discharging} = E_{out}/E_{stored} \quad (5)$$

which describes the ratio of the energy delivered by the storage tank relative to the energy stored in it. The combination of charging and discharging efficiencies yield the overall efficiency of the TES system, which can be developed further with the introduction of Equation (1):

$$\eta_{TES,overall} = \eta_{TES,charge} \times \eta_{TES,discharge} = E_{in}/E_{out} = 1 - E_{loss}/E_{in} \quad (6)$$

On the other hand, as opposed to energy, exergy represents the maximum amount of work that can theoretically be performed by a system as this comes into equilibrium with its environment (once equilibrium is reached, the system no longer has the potential to perform work). If the process is ideal, then the work developed is highest; if on the contrary the process is irreversible, exergy is destroyed¹. It becomes therefore evident that exergy yields added value to reflect the thermodynamic and economic value of the storage system application. A second law analysis of the system is out of the scope of this work due to space limitations. It will thus be released in due time along with the techno-economic feasibility study.

3. ANALYSIS OF THERMAL ENERGY STORAGE OPTIONS

3.1 Layouts

Most thermal energy storage systems make use of a parallel configuration which means that the hot stream coming from the solar field is split: the main stream is used to drive the power block whilst the secondary flow is directed towards the thermal energy storage system, Figure 2 (top). The main advantage of such layout is the very high temperature achievable by the storage medium which, in turn, ensures that the efficiency of the power plant in discharge operation is closest to or even at the rated value.

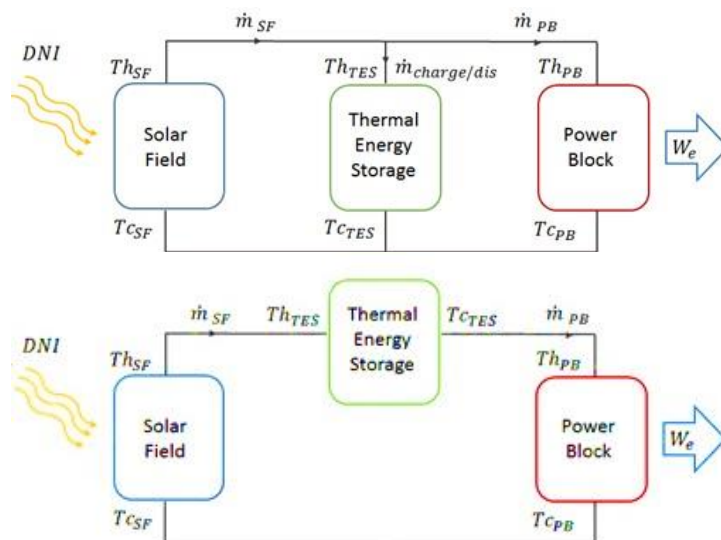


Figure 2: TES system integration layouts: parallel (top) and series (bottom).

¹ Note that, whilst energy is always conserved, exergy can be destroyed.

This layout is currently used by most commercial TES's and is particularly suitable for sensible heat storage, whether it be with of the single (thermocline) or multiple tank type. Ideally, a good design should yield equal or very similar return temperatures from TES ($T_{C_{TES}}$) and power block ($T_{C_{PB}}$) so that the temperature of the heat transfer fluid at the inlet to the solar field ($T_{C_{SF}}$) remains constant regardless of the type of operation (TES charge/discharge or power block only). Based on this rationale, the parallel layout is not advisable for latent heat storage inasmuch as the temperature drop of the heat source (hot heat transfer fluid) is much lower than in sensible heat solutions. For this reason, a series layout is preferred wherein the TES is placed upstream of the power block, Figure 2 (bottom). The main drawback of such layout is a reduction in live vapor temperature, though this is only effective when the TES system is being charged and, even in this situation, it can be attenuated by increasing the time needed to charge the system (i.e., reducing the HTF temperature drop and hence the heat transfer rate to the storage medium). Based on these standard configurations, four types of thermal energy storage systems are studied in this work:

- Sensible heat storage: thermal energy is stored by increasing the temperature of a storage medium. This can be either the heat transfer fluid used in the solar field (direct) or a different heat transfer medium (indirect). Also, for the latter case, two options are available:
 - Single tank configuration (thermocline). A storage tank with stratified temperatures.
 - Two tanks configuration. Hot storage medium with high energy content is stored in a hot tank from where it is pumped to a cold one when energy is demanded.
- Latent heat storage medium. In this case, the storage medium stores and releases energy by changing phase. Even though solid-liquid and liquid-gas storage is possible, the former is preferred for its higher energy density.

The main features of the four storage systems considered in this work are given below (note that a common specification to all of them is the capacity to operate the power plant at full load for one hour):

- Two tanks direct. The hot and cold tanks are located upstream and downstream of the vapor generator respectively. Their respective HTF levels are left free to vary between 15% and 98% so the ratio from useful HTF volume to vessel volume is 0.83 (Pacheco, 2002).
- Two tanks indirect. The storage medium is a HITEC binary molten salt with $C_{p,salt}=1.56$ kJ/kg and $\rho_{salt}=1900$ kg/m³. The sizing criterion of the hot and cold tanks remains the same.
- Single tank indirect (thermocline). The filler material is quartz rock and sand with a void fraction of 0.22 (Pacheco *et al.*, 2002). The properties of the filler are $C_{p,fill}=1.075$ kJ/kg and $\rho_{fill}=2600$ kg/m³. The tank is divided in 50 slices with similar height, where the energy balance equations are applied in each time step. The system is designed to keep the thermocline region during the charge/discharge cycles.
- Phase change storage. The properties of the storage medium are similar to those of sodium nitrite (NaNO₂) even if with a slightly higher melting temperature (280°C). This is done for generality and will have to be double checked and updated in future feasibility analyses. The properties of interest are $\lambda_{PCM}=212$ kJ/kg (latent heat) and $\rho_{PCM}=2260$ kg/m³. The ratio from PCM volume to vessel volume is 0.7375 (Laing *et al.*, 2010).

3.2 System model

The analysis presented in this document is based on elementary lumped volume models for the main components in the plant. The system is resolved in five minute steps (time discretization), meaning that the models are considered quasi stationary.

Turbine model

The Organic Rankine Cycle is of the recuperative type and operates with superheated live vapor. Given that cyclopentane is a dry fluid, the exhaust vapor from the turbine is also in the superheated region and hence its sensible heat is transferred to the subcooled liquid delivered by the pump. Such layout increases the thermal efficiency of the cycle though at the expense of a higher circulating mass flow rate through the solar field. This higher auxiliary power consumption is nevertheless compensated for

by a lower duty of the condenser which operates slightly above atmospheric pressure under any operating conditions (thus preventing oxygen infiltration). As a consequence of the recuperative layout, the vapor quality at condenser inlet is always lower than one.

The vapor turbine operates in sliding pressure mode and hence the next equation for live vapor conditions holds true

$$k_t = \dot{m}_{lv} / \sqrt{p_{lv} / v_{lv}} \quad (7)$$

where k_t is the flow function and remains constant for power settings higher than 25%. For lower loads, live vapor is throttled across the main stop valve to keep turbine inlet pressure constant.

TES system model

These models of the energy storage systems are based on elementary energy balances already described in section 2. First law applications result in Equation (8) for sensible heat systems and Equation (9) for phase change storage (these are the practical application of Equation (1)):

$$\dot{Q} = \dot{m}_{TES} C_{p, TES} (T_{h, TES} - T_{c, TES}) = \frac{dE_{TES}}{dt} = \frac{d}{dt} [M_{TES} C_{p, TES} (T_{h, TES} - T_{c, TES})] \quad (8)$$

$$\dot{Q} = \dot{m}_{TES} \lambda_{PCM} = \frac{dE_{TES}}{dt} = \frac{d}{dt} [M_{TES} \lambda_{PCM}] \quad (9)$$

Where T_h and T_c stand for hot and cold temperatures, M is the mass of storage medium and λ_{PCM} is the latent heat of the phase change material (storage medium). For direct systems, no additional heat transfer equations are needed as it is the heat transfer fluid flowing across the solar field which is stored in an insulated vessel. In this case, if no heat losses take place, the stored energy is available at the standard temperature level (i.e. live vapor temperature in discharge operation remains at the rated value). On the contrary, for indirect sensible heat systems, there is an inevitable reduction in the achievable live vapor temperature in discharge operation due to the terminal temperature difference of all heat exchangers. These heat transfer equipment are modelled with a simple $\varepsilon - NTU$ approach.

Solar field model

The model of the solar field is based on the common approach making use of *incidence angle modifiers* IAM for the transversal (θ_t) and longitudinal (θ_l) incidence angles, which are provided by the manufacturer to correct the reference optical efficiency of the solar field at noon ($\eta_{SF,0}$). These correction factors are applied to the incidence angle of the reference location (Benguerir, Morocco) to calculate the solar energy collected and they are then complemented by temperature dependent terms to account for heat losses (Haberle *et al.*, 2002)

$$\eta_{SF} = \eta_{SF,0} IAM(\theta_t) IAM(\theta_l) - a_1 \frac{(T_{SF,out} - T_{amb})}{DNI} - a_2 \frac{(T_{SF,out} - T_{amb})^2}{DNI} \quad (10)$$

where a_1 and a_2 are empirical coefficients. The net solar energy collected is then used to heat up the heat transfer fluid whose temperature at the outlet from the solar field ($T_{SF,out}$) is calculated by merely applying first law calculations.

3.3 Operating strategy

The operating strategy of the thermal energy storage system is not straightforward and it depends largely on the electric market where the power plant is operating. Thus, some operators opt for as fast as possible start-ups of the plant prior to TES lading. This maximizes the annual yield though it increases the risk that the TES system is not fully loaded at the end of the day when the environmental conditions are not good (for instance, hazy or cloudy sky and/or short winter days in the northern hemisphere). On the contrary, some operators decide to charge the TES system to full capacity before plant start-up. This ensures the extended operation but influences the annual yield negatively. This operation might make

sense though, if electricity prices in the morning are substantially lower than in the evening (Silva *et al.*, 2011).

The first strategy is adopted in this work whereby the plant starts up as soon as possible in the morning and, once it is operating at full capacity, the TES system is loaded. It must be noted though that, for plant start-up, the minimum DNI needed to produce positive net power and the minimum stable load are case-specific and hence they are very difficult to model with simple approaches. Thus, at this preliminary stage of the analysis, the following assumptions are made:

- Minimum DNI for plant start-up: 500 W/m². The minimum DNI depends on two factors:
 - Minimum stable load: the value of 500 W/m² is based on the experience of the authors.
 - Energy required to preheat the solar field and power block. The solar energy collected between sunrise and DNI=500 W/m² is used to preheat the system.
- Start-up time. Given the size of the plant, the expected start-up time will be fairly short and thus it is assumed that it falls within the time-step of the solver. It is here noted that this is still a conservative approach inasmuch as no electricity is produced until DNI=500 W/m².
- For DNI>500 W/m², the load increases up to the rated value. At this point, a fraction of the hot HTF coming from the solar field is diverted towards the TES system.
- Once the TES system is fully loaded, no more HTF is necessary and thus the surplus hot flow is used to increase the output of the plant to 110% the rated value (common industry practice).
- When DNI falls below 500 W/m², the storage system is discharged and used to keep the plant at full capacity for one additional hour.

These considerations apply to parallel configurations only. For integration in series (phase change), heat is supplied to the TES system when DNI reaches 500 W/m² (it is assumed that below this DNI the peak temperature achieved in the solar field is not high enough).

4. RESULTS

4.1 Daily performance

Figure 2 summarizes the most relevant features of the power plant incorporating a TES system of the direct type. The solar energy collected by the solar field and transferred to the heat transfer fluid (Q_{SF}) is directed towards the power block (Q_{PB}) to generate electricity once the minimum DNI is exceeded. The electric output (W_{ORC}) increases from this point up to full capacity and, then, thermal energy is progressively supplied to the thermal energy storage system (Q_{TES}). Once storage is completed, the plant output is increased to 110%.

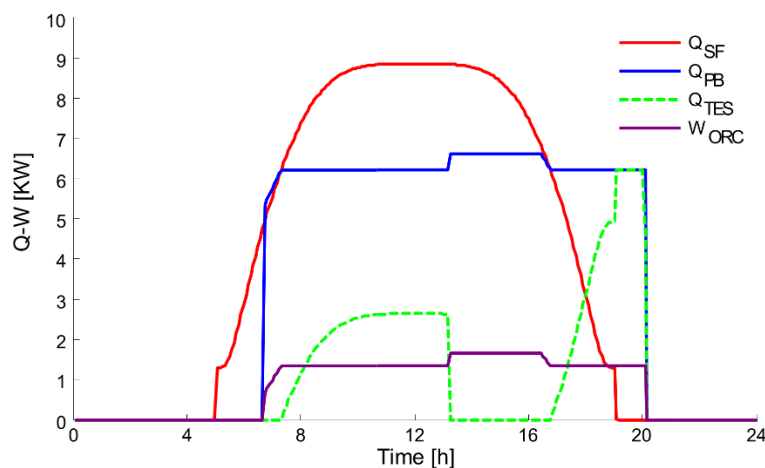


Figure 3: Performance of the direct sensible heat TES system.

In the evening, energy is dragged from storage to keep the plant operating at full capacity. It is worth noting in this regard that, rather than exhausting the storage system in order to further extend the

operation of the power block (at part load), the plant is shut-down when operation in rated conditions is no longer possible. This enables a faster start-up in the next morning as the storage system is not completely used up. The information displayed in Figure 3 is qualitatively applicable to all the systems based on sensible heat.

Figure 4 shows the performance of the latent heat system. Three salient differences are observed:

- Owing to the series integration (TES system upstream of the power block), electricity production and TES charging start at the same time. It is not possible to achieve full capacity prior to the charging phase. Note that even if this could be avoided by bypassing the TES system initially, it would lead to a more complicated operation of the vapor generator.
- It takes more time to charge the TES system completely. This is because the temperature drop of the HTF (energy carrier) across the TES system, i.e. the heat transfer rate, is much lower than in the other systems with parallel integration. There are two alternative solutions to compensate for this effect:
 - Increase the mass flow rate of hot HTF coming out from the solar field. This would increase pumping power at the solar field, therefore reducing net output.
 - Adopt a parallel integration. This would inevitably increase the HTF return temperature to the solar field, inasmuch as PCM storage systems take advantage of a very small temperature drop of the hot HTF. Pumping power would in turn be increased.
- Even if values will be provided later, it can be observed that more energy is dumped from the system than in the sensible heat arrangements (dumped energy is the fraction of available energy at the solar field that is not used by the power plant, neither for the power block nor for the storage system).

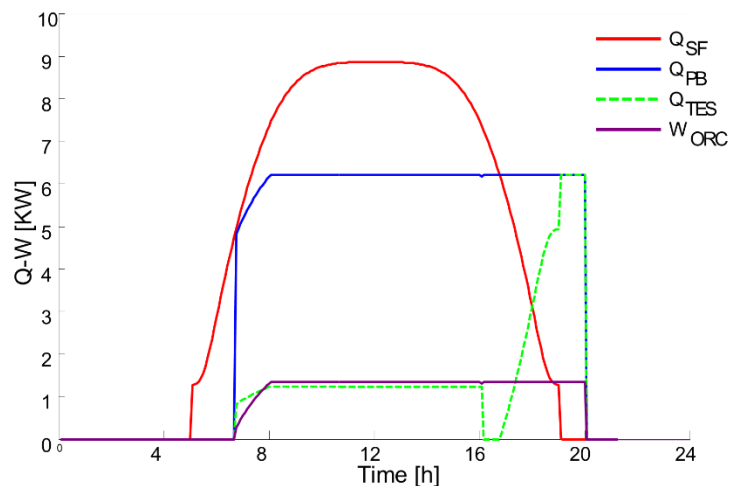


Figure 4: Performance of the indirect latent heat TES system.

4.2 Energy management

A comparison is provided in this section to show how energy is managed by the different TES systems, Figure 5. It is to note first that a common solar multiple of 1.5 is selected for all cases, which explains why the energy collected by the solar field (E_{SF}) and effectively transferred to the HTF leaving it (E_{EFF}) is constant in the cited figure. This effective energy is then split into two different streams. The majority of it drives the power block (E_{PB}), which produces electricity (W_{ORC}) whilst the smaller fraction charges the storage system (E_{Ch}). The surplus energy that cannot be used is dumped out of the system (E_{Dum}). This occurs when the storage system is already charged and the turbine operates at 110% load.

The most relevant observations in Figure 5 follow:

- All three sensible heat systems produce roughly the same electricity in a day, in spite of the slightly different heat addition to the power block. This is explained by the different power block efficiencies brought about by the operation in discharge conditions, Table 2. In other words, the live vapor conditions that are achievable during discharge are dissimilar.

- This can be confirmed by comparing, for these three systems, the amount of energy supplied to the power block (E_{PB}) and to the storage system (E_{Ch}). The indirect system exhibits lower values than the direct and thermocline solutions.
- Further to the previous point, it is also observed that dumped energy is highest for indirect systems. This makes sense in the light of the common solar field size and dissimilar energy demand by power block and storage.
- For the case of latent heat storage, the lower live vapor temperature brought about by the series integration has a visible negative influence on the efficiency of the power block. This influence is reflected in a lower electricity yield (W_{ORC}).
- The most remarkable difference between sensible and latent heat storage systems is the much higher dumped energy in the latter, due to the particular characteristics of the series integration and very low temperature drop of the HTF across it.

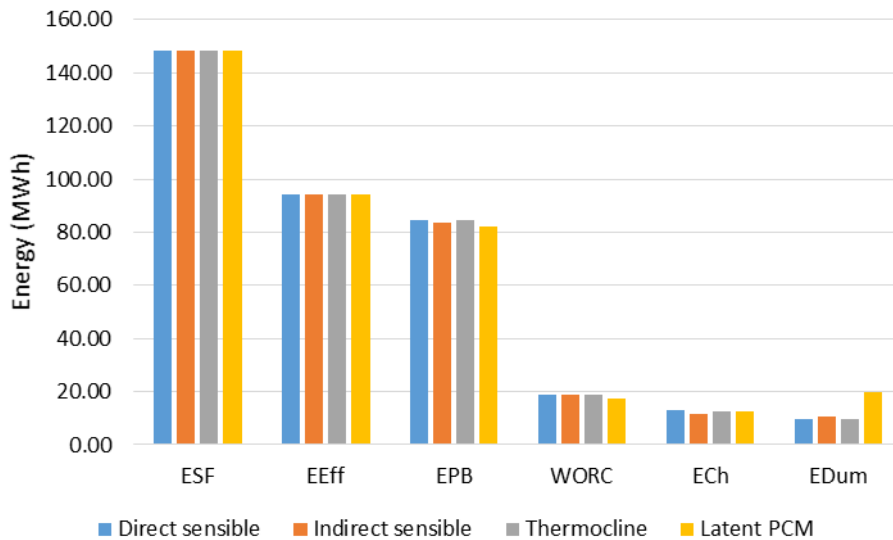


Figure 5: Energy management comparison.

Table 2: Daily average efficiency of power block

TES type	Direct sensible	Indirect sensible	Thermocline	Latent PCM
Average thermal efficiency of power block	22.25	22.29	22.13	21.23

4.3 Volume of storage medium

The thermal performance discussed so far provides a very useful insight into the benefits and drawbacks of each storage system. Nevertheless, when it comes to energy storage in the form of either sensible or latent heat, it is of capital importance to consider other techno-economic features. The first of these is the charging/discharging rate, which favors sensible heat storage, in particular of the direct type as already discussed previously. This can be ascertain by merely comparing the charging times in Figures 3 and 4.

On the other hand, the amount of storage medium is a critical factor affecting the economics of the TES system. Installation costs comprise two contributions: specific cost (€/ton) and total volume of the storage medium. Whilst the former is actually beyond the scope of this work (techno-economic analyses will be presented in future publications), the total volume of storage medium needed for each configuration is presented in Table 3. It is observed that in spite of the inherent simplicity and thermodynamic advantages, direct sensible heat storage is not interesting for it requires an extremely large volume of storage medium. This is because of the characteristics of the HTF and has a dramatic impact on the cost of the storage vessel.

On the other hand, PCM storage steps forth as a very interesting solution volume-wise. Nevertheless, the poorer thermodynamic performance and longer charging time are not compensated for by this advantage. Therefore, thermocline solutions are identified as the most interesting candidate with conventional two tank indirect storage solutions behind.

Table 3: Volume of storage medium

TES type	Direct sensible	Indirect sensible	Thermocline	Latent PCM
Volume of storage medium (m ³)	420	315	200	125

5. CONCLUSIONS

The main conclusions drawn from the work presented in this analysis are:

- Sensible heat storage systems enable faster charging processes and more agile operation.
- Latent heat systems exhibit poorer thermodynamic performance in comparison with sensible heat storage. This is most relevant when the energy dumped out of the system is compared.
- Direct sensible heat storage systems request a prohibitive amount of storage medium. It is thus not feasible in practice for the extended operating time required.
- Latent heat systems require the lowest amount of storage medium.
- Thermocline storage steps forward as the most leveraged solution, offering the best trade-off between thermodynamic performance and volume of storage medium

Future work include performing optimization analyses based on second law efficiencies and entropy analysis to identify where the main irreversibilities are located. Also, a more detailed analysis of operational aspects of the proposed solutions will result in a more clear picture of the reliability and agility of each TES system. This features are of paramount importance for the owners of these mid-scale facilities.

REFERENCES

- Fassenden, R., 1907, *System of storing power*, US Patent No. 1247520.
- Haberle, A., Zahler, C., Lerchenmüller, H., Mertins, M., Wittwer, C., Trieb, F., Dersch, J., 2002, The Solarmundo line focussing Fresnel collector. Optical and thermal performance and cost calculations, *SolarPACES International Symposium*, pp. 5-8.
- Pacheco, J., 2002, *Final Test and Evaluation Results from the Solar Two Project*, Sandia National Laboratories, Albuquerque, p. 55-63.
- Pacheco, J, Showalter, S, Kolb, W., 2002, Development of a Molten-Salt Thermal Storage System for Parabolic Trough Plants, *J. Solar. Eng.*, vol. 124.
- Silva, P., Astolfi, M., Binotti, M., Giostri, A., Manzolini, G., De Marzo, A, Merlo, L., 2011, Indirect molten salts storage management and size optimization for different solar multiple and sites in parabolic trough solar power plant, *SolarPACES International Symposium*.
- Laing, D., Bahl, C., Bauer, T., Lehmann, D., Steinmann, W., 2010, Thermal energy storage for direct steam generation, *Solar Energy*, vol. 85, p. 627-633.

ACKNOWLEDGEMENTS

The Research Institute for Solar Energy and New Energies in Morocco is gratefully acknowledged for funding this research work in the frame of the R&D program developed in the solar platform at Benguerir. Special thanks go to Mr. Badr Ikken for his continuous support of renewable energy development in the country.

THERMODYNAMIC ANALYSIS AND COMPARISON OF AN ORC-OFC COMBINED POWER GENERATION SYSTEM

Jianyong Wang, Jiangfeng Wang, Yiping Dai*

Institute of Turbomachinery
School of Energy and Power Engineering,
Xi'an Jiaotong University,
Xi'an 710049, Shaanxi, China
E-mail: ypdai@mail.xjtu.edu.cn

ABSTRACT

In this work, an ORC-OFC combined power generation system is proposed to improve the energy conversion efficiency for low grade heat sources. Mathematical models of the system are established to simulate the system under steady-state conditions. Effects of two key thermodynamic parameters including evaporation pressure and flash pressure on the system performance are examined. The analysis indicates that there exists an optimal evaporation pressure and an optimal flash pressure that yield the maximal net power output and system exergy recovery efficiency for the proposed system. Parameter optimizations by genetic algorithm are conducted for ORC, OFC and the proposed system under same heat source and restrictions, and the optimization results of the three systems are compared, showing that the ORC-OFC combined power generation system, with maximal exergy recovery efficiency reaching 16.70%, performs better than the ORC and the OFC.

1. INTRODUCTION

In recent years, with the overuse of fossil energy and the damage to environment, energy saving and emission reduction have been an important strategy for the development of most regions. More and more attentions have been paid to the utilization of the industrial waste heat and the renewable energy. This kind of energy belongs to low grade energy and the traditional steam power cycle is hard to convert this energy to electricity efficiently. Organic Rankine cycle (ORC), as one of the potential power generation cycles to recover the low grade energy efficiently, was proposed and has attracted much attention of researchers. Figure 1 shows the schematic diagram and the T - s diagram of the ORC. Generally ORC employs pure organic fluids as working fluids. Thus the working fluids evaporate at constant temperature during the heat addition process, whereas the heat source releases energy at decreasing temperature. The temperature mismatch between the heat source and the working fluid is one of the major sources of irreversibility for ORC. It's significant to maintain a good temperature match between the heat exchanger streams to decrease this type of irreversibility. Two methods are proposed to improve the temperature match. One is using zeotropic mixtures as working fluids. Based on different evaporation temperatures of two different fluids under the same pressure, the mixed working fluids evaporate at variable temperatures, performing a good temperature match with the heat source.

Some investigations have been done on the ORC with zeotropic mixtures as working fluids. Angelino and Colonna di paliano (1998) evaluated the merits of zeotropic mixtures as working fluids of ORC and conducted an analysis and an optimization for the zeotropic mixture ORC. Yang *et al.* (2013) studied effects of eight kinds of zeotropic mixtures on the performance of ORC for exhaust energy recovery of vehicle engine. Bao and Zhao (2013) made a summary of zeotropic mixture working fluids and corresponding cycle types for ORC. Chys *et al.* (2012) examined the effect of using mixtures as working fluids on the system performance of ORC, discussed a mixture selection method and suggested the optimal concentrations. They concluded that the use of suitable mixtures as working fluids had a positive effect on the ORC performance. Heberle *et al.* (2012) conducted

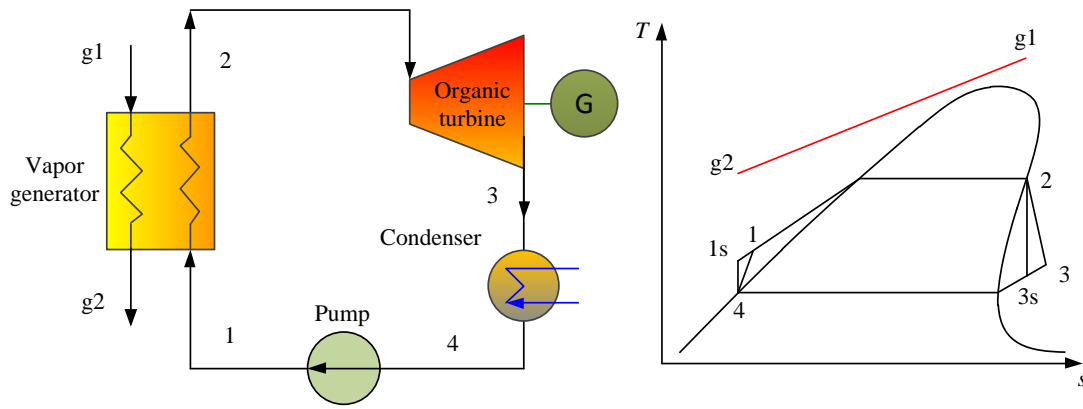


Figure 1: Schematic diagram and T - s diagram of organic Rankine cycle (ORC)

detailed simulations of ORC with two different groups of zeotropic mixture working fluids for low-enthalpy geothermal resources. The results showed that mixtures as working fluids lead to an efficiency increase. Some researchers made comparisons between pure-fluid ORC and mixed-fluid ORC. Garg *et al.* (2013) investigated the system performance of an ORC with isopentane, R245fa and their mixtures as working fluids for heat source temperature in the range of 385-425K. Aghahosseini and Dincer (2013) conducted a thermodynamic analysis and comparison of the low-grade heat source ORC with different pure and zeotropic mixture working fluids and the conclusions provided advice to selection of suitable working fluids for ORC. Andreasen *et al.* (2014) investigated the effect of mixed working fluids on the performance and the important design parameters of ORC by comparing using pure fluids and mixtures as working fluids. The results showed that mixed working fluid can increase the net power output of the cycle. But not every research proved the competitive advantages of using zeotropic mixture as working fluid. Li *et al.* (2011) evaluates the system performance of ORC with several pure fluids and one mixture as working fluids under different evaporation temperatures. The results showed the mixture-fluid ORC had lower efficiency than pure-fluid ORC. So whether using zeotropic mixtures as working fluid or not should depend on the specific cases.

The other method is making the working fluid heat transfer process at pressures above the critical pressure. The working fluid under supercritical state turns into some substance between liquid and vapor, which has no phase change during heat addition. Thus achieves a good temperature match with the heat source.

Several studies have been conducted on the supercritical or transcritical ORC. Gao *et al.* (2012) evaluated the system performance of a supercritical ORC using 18 different working fluids by several indicators and recommended two suitable working fluids according to some screening criteria. Karellas *et al.* (2012) investigated the influence of supercritical parameters of ORC on the heat

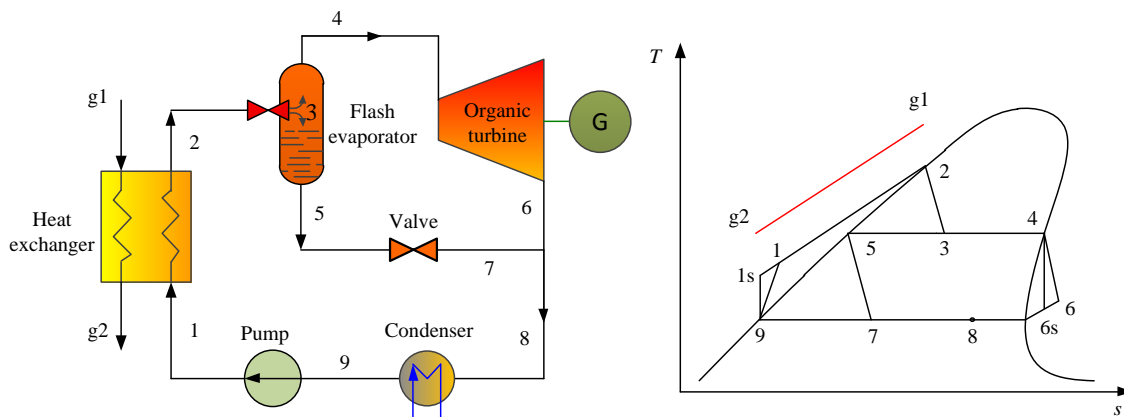


Figure 2: Schematic diagram and T - s diagram of organic flash cycle (OFC)

exchanger design. Some attention was paid to the comparisons between transcritical ORC and some other cycles, such as subcritical ORC, Kalina cycle and supercritical CO₂ cycle. Algieri and Morrone (2012) applied the transcritical ORC to the high-temperature biomass power generation case and made a comparison analysis with that using subcritical ORC. Shengjun *et al.* (2011) made a parameter optimization and a comparison of subcritical and supercritical ORC using different working fluids for low-temperature binary geothermal power system. Walraven *et al.* (2013) made a comparison among subcritical ORC, transcritical ORC and Kalina cycle under different pressure levels for low-temperature geothermal heat sources, and the results showed the transcritical ORC was one of the best. Schuster *et al.* (2010) conducted exergy analysis for sub- and supercritical ORC using different working fluids and the results indicated that supercritical parameters could improve the system efficiency of ORC. Baik *et al.* (2013) optimized a transcritical ORC using R125 and subcritical ORCs using several other pure fluids and compared the optimization results, which showed that the power output of the transcritical cycle was greater than that of subcritical ORCs under some conditions. They (Baik *et al.*, 2011) also demonstrated that the net power output of the R125 transcritical ORC produced more power than that of the CO₂ transcritical cycle by optimization and comparison. Chen *et al.* (2011) made a comparative study between a subcritical ORC using pure working fluids and a supercritical ORC using zeotropic mixture working fluids and the results showed the latter achieved higher thermal efficiencies than the former.

The two methods mentioned above all aim at forming a good temperature match in the heat exchangers, which may drive more working fluid for power generation. For the same purpose, Ho *et al.* (2012a) proposed an organic flash cycle (OFC) to potentially improve the energy conversion efficiency. The schematic diagram and the *T-s* diagram of the OFC are illustrated in Figure 2. As shown, the working fluid is just heated to saturated liquid under a high pressure in the heat exchanger, which avoids the constant-temperature evaporation and reduces the irreversibility. Then the working fluid is flashed to form two-phase fluids and separated to saturated vapor and saturated liquid in the flash evaporator. The saturated vapor is delivered into the organic turbine to produce power. Later Ho *et al.* (2012b) continued a further study that proposed several design enhancements to the basic OFC. Han and Kim (2014) also proposed an improvement that uses a two-phase expander instead of the throttle of the flash evaporator in the OFC, and carried out exergy analysis for their design.

This paper, based on ORC and OFC, proposes an ORC-OFC combined power generation system to recover the low-grade energy efficiently. The mathematical model of the system is established to simulate the system. Then the effects of several key thermodynamic parameters on the system performance are examined. Finally the system is parametrically optimized and compared with the ORC and the OFC under the same heat source and some same restrictions to verify the superiority of the proposed system.

2. SYSTEM DESCRIPTION

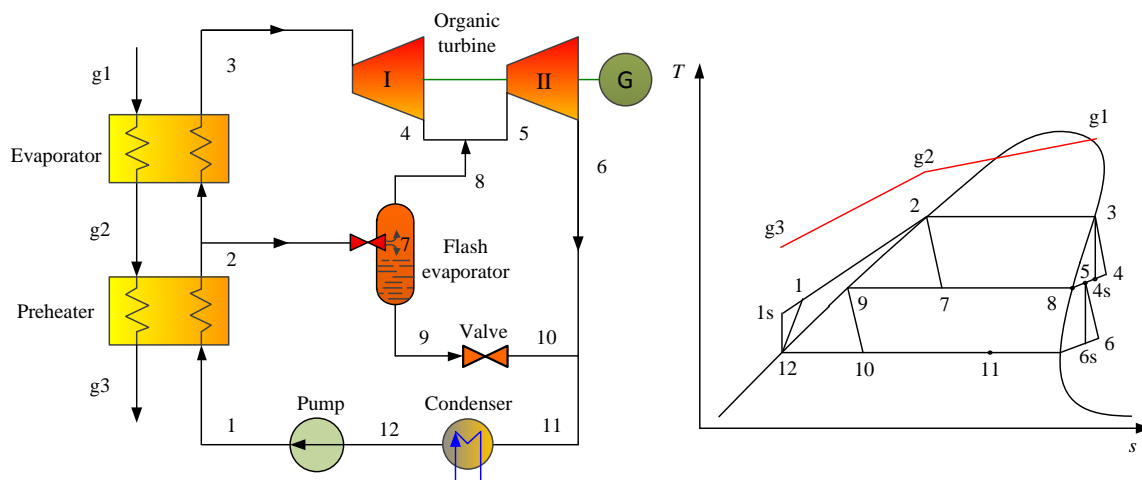


Figure 3: Schematic diagram and *T-s* diagram of ORC-OFC combined power generation system

Figure 3 illustrates the schematic diagram and the T - s diagram of the ORC-OFC combined power generation system. After being pumped to a high pressure state, the organic working fluid is fed into a preheater to absorb heat from the heat source to form saturated liquid. Then the saturated liquid working fluid at the outlet of the preheater is divided to two streams. One is delivered to a flash evaporator, and the other continues to be heated to saturated-vapor state by the heat source in an evaporator. The saturated organic vapor is expanded through the organic turbine I to generate power. The stream entering the flash evaporator is flashed to two-phase fluids firstly and then separated to saturated vapor and saturated liquid. The saturated vapor mixes with the exhaust working fluid from the turbine I and then is expanded through the organic turbine II. The saturated liquid from the flash evaporator mixes with the exhaust working fluid from the turbine II after being depressurized by a valve. Finally, the overall working fluid is condensed to saturated liquid in a condenser. The proposed system, combining ORC and OFC, could drop the exhaust temperature of the heat source and push more working fluid to generate power, thus improving the energy conversion efficiency for the heat source.

3. MATHEMATICAL MODELS AND PERFORMANCE CRITERIA

3.1 Mathematical Models

For system simulation, the mathematical models are established based on the law of mass, momentum and energy conservations. Some assumptions are made to simplify the theoretical models.

- (1) The system reaches a steady state.
- (2) The pressure drops in preheater, evaporator, flash evaporator, condenser and connection pipes are neglected.
- (3) There is no heat transfer between the equipment of the system and the environment.
- (4) The working fluids at outlets of the preheater and the evaporator are saturated liquid and saturated vapor, respectively.
- (5) The vapor stream and the liquid stream separated from the flash evaporator are saturated vapor and saturated liquid, respectively.
- (6) The streams at the condenser outlet are saturated liquid.
- (7) The turbine and the pump have a given isentropic efficiency, respectively.
- (8) The flow across the valve is isenthalpic.

Based on the above assumptions, the formulas of each component in the ORC-OFC combined power generation system are shown as follows.

Preheater:

$$m_{hs}(h_{g2} - h_{g3}) = m_{wf}(h_2 - h_1) \quad (1)$$

Evaporator:

$$m_{hs}(h_{g1} - h_{g2}) = m_3(h_3 - h_2) \quad (2)$$

Flash evaporator:

$$m_7 = m_8 + m_9 \quad (3)$$

$$m_7 h_7 = m_8 h_8 + m_9 h_9 \quad (4)$$

Turbine:

$$\eta_{tb} = \frac{h_3 - h_4}{h_3 - h_{4,s}} \quad (5)$$

$$W_{tb,I} = m_3(h_3 - h_4) \quad (6)$$

$$\eta_{tb} = \frac{h_5 - h_6}{h_5 - h_{6,s}} \quad (7)$$

$$W_{tb,II} = (m_3 + m_8)(h_5 - h_6) \quad (8)$$

Valve:

$$h_9 = h_{10} \quad (9)$$

Pump:

$$\eta_p = \frac{h_{1,s} - h_{12}}{h_1 - h_{12}} \quad (10)$$

$$W_p = m_{wf}(h_1 - h_{12}) \quad (11)$$

Fluids mixing:

$$(m_3 + m_8)h_5 = m_3h_4 + m_8h_8 \quad (12)$$

$$m_{wf}h_{11} = (m_3 + m_8)h_6 + m_9h_{10} \quad (13)$$

Net power output of the whole system:

$$W_{net} = W_{tb,I} + W_{tb,II} - W_p \quad (14)$$

3.2 Performance Criteria

In this paper, exergy recovery efficiency, based on the second law of thermodynamics, is employed to evaluate the system performance, being expressed as follows.

$$\eta_{exg} = \frac{W_{net}}{E_{in}} \quad (15)$$

where E_{in} is the exergy input to system, i.e. the initial exergy of the heat source.

When calculating the exergy value, it's assumed that only physical exergy of the steady flow is considered, whereas chemical exergy, macroscopic kinetic and potential energy are neglected. So the exergy input is expressed as

$$E_{in} = m_{hs}[(h_{g1} - h_0) - T_0(s_{g1} - s_0)] \quad (16)$$

4. PARAMETRIC ANALYSIS

The numerical simulation of the ORC-OFC combined power generation system is conducted by a program written in MATLAB and the thermodynamic properties of relevant fluids are calculated by REFPROP 9.01 (NIST, 2013). Before the simulation, some known conditions are assigned, as listed in Table 1. During the simulation, some restrictions should be imposed to ensure the simulation practically feasible. For example, the terminal temperature difference of the heat exchangers should be larger than 10°C to avoid an oversize heat exchange area; The quality of working fluid at the outlet of organic turbines should be larger than 0.9 to prevent the two-phase fluid corroding the turbine blades. Table 2 lists the thermodynamic parameters of each node of the system for one of the feasible simulation results, which is the base for the following parametric analysis. Table 3 shows the corresponding system performance.

Variations of some key system parameters have significant effects on the system performance. For example, the working fluid's evaporation pressure in the evaporator has direct effects on the mass flow rate of working fluid in the evaporator and the inlet pressure of the organic turbine I. The flash pressure in the flash evaporator influences the mass flow rate of the organic vapor generated in the flash evaporator, the back pressure of the organic turbine I and the inlet pressure of the organic

Table 1: Known simulation conditions

Term	Value	Unit
Working fluid	R245fa	/
Ambient temperature	20	°C
Ambient pressure	101.3	kPa
Heat source (hot air) temperature	150	°C
Heat source (hot air) pressure	150	kPa
Mass flow rate of heat source	10	kg s ⁻¹
Organic turbine isentropic efficiency	80	%
Pump isentropic efficiency	70	%
Pinch point temperature difference	10	°C

Table 2: Thermodynamic parameters of each node of the system

State	$t/^\circ\text{C}$	P/kPa	$h/\text{kJ kg}^{-1}$	$s/\text{kJ kg}^{-1}\text{K}^{-1}$	Quality	$m/\text{kg s}^{-1}$
1	34.14	1500.00	245.00	1.1515	0	5.11
2	107.85	1500.00	352.34	1.4635	0	5.11
3	107.85	1500.00	478.62	1.7950	1	2.61
4	86.88	800.00	469.66	1.8012	1	2.61
5	85.53	800.00	468.07	1.7968	1	3.30
6	52.11	200.00	447.27	1.8129	1	3.30
7	80.54	800.00	352.34	1.4697	0.2782	2.50
8	80.54	800.00	462.10	1.7800	1	0.70
9	80.54	800.00	310.04	1.3501	0	1.80
10	33.35	200.00	310.04	1.3669	0.3586	1.80
11	33.35	200.00	398.76	1.6564	0.8375	5.11
12	33.35	200.00	243.59	1.1501	0	5.11
g1	150.00	150.00	428.15	7.1280	/	10.00
g2	117.85	150.00	395.25	7.0471	/	10.00
g3	64.07	150.00	340.44	6.8963	/	10.00

turbine II. These effects will directly or indirectly impact the system performance. Therefore, the two thermodynamic parameters mentioned above (i.e. the evaporation pressure in the evaporator and the flash pressure in the flash evaporator) are selected to analyze their detailed effects on the system performance. The parametric analysis will be conducted based on the operating condition listed in Table 2 and when one thermodynamic parameter varies, the other parameters keep constant.

Figure 4 shows the effect of evaporation pressure on the net power output and the exergy recovery efficiency. As the evaporation pressure rises, the heat transferred from heat source to working fluid in the evaporator declines, resulting in a decrease in the mass flow rate of working fluid in the evaporator. However, the enthalpy drop across organic turbine I achieves an increase. Combined effected by the decreasing mass flow rate of the flow and the increasing enthalpy drop, the power output of organic turbine I presents a variation that increases firstly, reaches a top and then decreases. Due to the decreasing mass flow rate of working fluid through organic turbine II, the power output of organic turbine II drops. Additionally the power consumption of pump ascends with an increase of the evaporation pressure. Adding algebraic values of the above three items up, it's obtained that the net power output of system increases firstly and then decreases, which means that there is an optimal evaporation pressure yields the maximal net power output of system. The inlet parameters of the heat source keep unchanged, so the exergy input to system is constant. Therefore, the exergy recovery efficiency of system shows a similar variation with the net power output of system according to its definition.

Figure 5 shows the effect of flash pressure on the net power output and the exergy recovery efficiency. As the flash pressure increases, the back pressure of organic turbine I rises, leading to a decrease in the power output of organic turbine I. The increased pressure in the flash evaporator reduces the mass flow rate of the generated saturated vapor, so the mass flow rate of the working fluid entering organic turbine II declines. The enthalpy drop across organic turbine II increases with an increase of the flash pressure. Since the effect of the increased enthalpy drop overweighs the effect of the decreased mass flow rate of working fluid, the power output of organic turbine II increases. The power consumption of pump keeps constant. To sum up, the net power output of system shows a variation of increasing firstly and then decreasing. So does the exergy recovery efficiency of system.

Table 3: System performance

Term	Value	Unit
Power output of organic turbine I	23.35	kW
Power output of organic turbine II	68.68	kW
Power consumption of pump	7.20	kW
Net power output of system	84.83	kW
Exergy input	560.69	kW
Exergy recovery efficiency	15.13	%

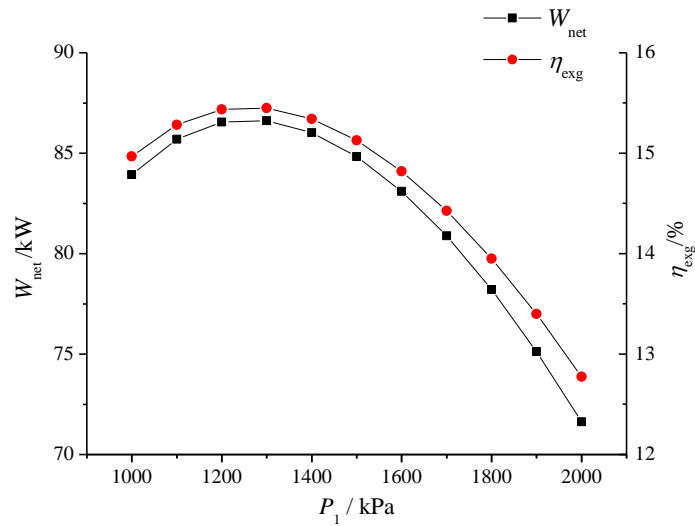


Figure 4: Effect of evaporation pressure on net power output and exergy recovery efficiency

5. OPTIMIZATION AND COMPARISON

Judging a power generation system being good or not, it should be compared with other types power generation systems. This paper would compare the proposed ORC-OFC combined power generation system with ORC and OFC power generation systems, respectively. Before comparison, the three systems would be optimized to their optimal performance state. The mathematical models of ORC and OFC, similar with parts of the mathematical model of ORC-OFC, will not present in this section. The system exergy recovery efficiency is selected as the objective function for the optimization. Different systems have different thermodynamic parameters needing optimization to obtain the maximal system exergy recovery efficiency. The ranges of optimization parameters of the three systems are listed in Table 4.

During the optimization, the three systems employ the same known simulation conditions listed in Table 1. Some restrictions, same with those mentioned in the parametric analysis section, are also set in the optimization process. The genetic algorithm (GA) (Dai *et al.*, 2009) is adopted as the optimization method to obtain the maximal system exergy recovery efficiency and find the corresponding optimal optimization parameters for the three systems. The operation parameters of GA are listed in Table 5.

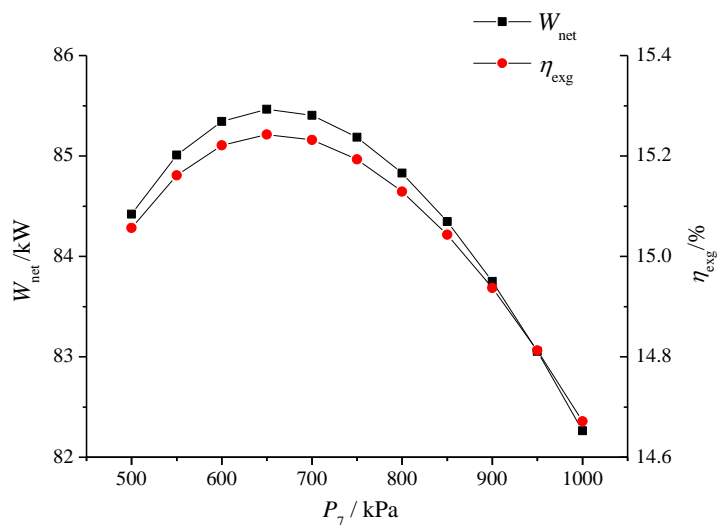


Figure 5: Effect of flash pressure on net power output and exergy recovery efficiency

Table 4: Ranges of optimization parameters for different systems

System	Thermodynamic parameters needing optimization	Range
ORC-OFC	Evaporation pressure/ kPa	[500,2800]
	Flash pressure/ kPa	[300,2500]
ORC	Evaporation pressure/ kPa	[500,2800]
OFC	Preheating pressure/ kPa	[500,2800]
	Flash pressure/ kPa	[300,2500]

Table 5: Operation parameters of GA

Term	Value
Population size	100
Crossover probability	0.8
Mutation probability	0.01
Stop generation	200

Table 6 shows the comparison results of the three power generation systems. It can be seen from the table that the ORC-OFC combined power generation system obtain the maximal exergy recovery efficiency, reaching 16.70%. Comparing the results of ORC and OFC, OFC pushes more working fluids to generate power and the enthalpy drop across turbine in OFC is also larger, so the power output of organic turbine in OFC is more than that in ORC. However, since the working fluids in OFC should be pumped to a much higher pressure before being heated to saturated liquid, OFC consumes much more power by pump than ORC. Therefore the net power output of OFC is less than that of ORC. Comparing with ORC and OFC, ORC-OFC combines the advantages of ORC and OFC that avoiding high power consumption of pump, pushing more working fluids for power generation and dropping the heat source exhaust temperature as low as possible, so ORC-OFC obtains the maximal net power output of the system. In conclusion, the ORC-OFC combined power generation system shows the best performance in the three systems.

6. CONCLUSIONS

Based on organic Rankine cycle (ORC) and organic flash cycle (OFC), an ORC-OFC combined power generation system is proposed to improve the energy conversion efficiency. By establishing the mathematical model to simulate the system under steady-state conditions, we analyzed the effects of two key thermodynamic parameters on the system performance, including evaporation pressure and flash pressure. Parametric optimizations with exergy recovery efficiency as the objective function are conducted for ORC, OFC and ORC-OFC respectively and the optimization results of the three

Table 6: Comparison results

Term	ORC-OFC	ORC	OFC
Evaporation/Preheating pressure / kPa	1289.5	1033.2	2800
Mass flow rate of fluid entering evaporator / kg s ⁻¹	3.00	3.50	/
Flash pressure / kPa	596.56	/	1132.0
Mass flow rate of fluid entering flash evaporator / kg s ⁻¹	4.05	/	6.61
Mass flow rate of saturated vapor generated in flash evaporator / kg s ⁻¹	1.20	/	3.63
Condensation pressure / kPa	200	200	200
Heat source exhaust temperature / °C	44.17	73.15	44.93
Power output of organic turbine / kW	I: 33.45	84.44	92.69
	II: 68.51		
Power consumption of pump / kW	8.33	3.16	18.60
Net power output of system / kW	93.63	81.28	74.09
Exergy input / kW	560.69	560.69	560.69
Exergy recovery efficiency / %	16.70	14.50	13.21

systems are compared. Some main conclusions drawn from the study are summarized as follows.

- (1) The ORC-OFC combined power generation system, having advantages of dropping heat source exhaust temperature and pushing more working fluids for power generation than ORC, meanwhile avoiding high power consumption of pump like that in OFC, shows great potential to improve the energy conversion efficiency for low grade heat sources.
- (2) There exists an optimal evaporation pressure and an optimal flash pressure that yield the maximal net power output and system exergy recovery efficiency for the ORC-OFC combined power generation system.
- (3) The optimization results show that the ORC-OFC combined power generation system, with maximal exergy recovery efficiency reaching 16.70%, performs better than the ORC and the OFC.

NOMENCLATURE

E	Exergy	kW
h	Enthalpy	kJ kg^{-1}
m	Mass flow rate	kg s^{-1}
P	Pressure	kPa
s	Entropy	$\text{kJ kg}^{-1}\text{K}^{-1}$
T	Temperature	$^{\circ}\text{C}$
W	Power output/consumption	kW

Greek symbol

η	Efficiency
--------	------------

Subscripts

hs	Heat source
p	Pump
s	Isentropic
tb	Turbine
wf	Working fluid

REFERENCES

- Aghahosseini, S., Dincer, I., 2013, Comparative performance analysis of low-temperature Organic Rankine Cycle (ORC) using pure and zeotropic working fluids, *Appl. Therm. Eng.*, vol. 54, no. 1: p. 35-42.
- Algieri, A., Morrone, P., 2012, Comparative energetic analysis of high-temperature subcritical and transcritical Organic Rankine Cycle (ORC). A biomass application in the Sibari district, *Appl. Therm. Eng.*, vol. 36: p. 236-244.
- Andreasen, J. G., Larsen, U., Knudsen, T., Pierobon, L., Haglind, F., 2014, Selection and optimization of pure and mixed working fluids for low grade heat utilization using organic Rankine cycles, *Energy*, vol. 73: p. 204-213.
- Angelino, G., Colonna di paliano, P., 1998, Multicomponent Working Fluids For Organic Rankine Cycles (ORCs), *Energy*, vol. 23, no. 6: p. 449-463.
- Baik, Y.-J., Kim, M., Chang, K.-C., Lee, Y.-S., Yoon, H.-K., 2013, A comparative study of power optimization in low-temperature geothermal heat source driven R125 transcritical cycle and HFC organic Rankine cycles, *Renew. Energ.*, vol. 54: p. 78-84.
- Baik, Y.-J., Kim, M., Chang, K. C., Kim, S. J., 2011, Power-based performance comparison between carbon dioxide and R125 transcritical cycles for a low-grade heat source, *Appl. Energ.*, vol. 88, no. 3: p. 892-898.
- Bao, J., Zhao, L., 2013, A review of working fluid and expander selections for organic Rankine cycle, *Renew. Sust. Energ. Rev.*, vol. 24: p. 325-342.

- Chen, H., Goswami, D. Y., Rahman, M. M., Stefanakos, E. K., 2011, A supercritical Rankine cycle using zeotropic mixture working fluids for the conversion of low-grade heat into power, *Energy*, vol. 36, no. 1: p. 549-555.
- Chys, M., van den Broek, M., Vanslambrouck, B., De Paepe, M., 2012, Potential of zeotropic mixtures as working fluids in organic Rankine cycles, *Energy*, vol. 44, no.1: p. 623-632.
- Dai, Y., Wang, J., Gao, L., 2009, Parametric optimization and comparative study of organic Rankine cycle (ORC) for low grade waste heat recovery, *Energ. Convers. Manage.*, vol. 50, no. 3: p. 576-582.
- Gao, H., Liu, C., He, C., Xu, X., Wu, S., Li, Y., 2012, Performance Analysis and Working Fluid Selection of a Supercritical Organic Rankine Cycle for Low Grade Waste Heat Recovery, *Energies*, vol. 5, no. 12: p. 3233-3247.
- Garg, P., Kumar, P., Srinivasan, K., Dutta, P., 2013, Evaluation of isopentane, R-245fa and their mixtures as working fluids for organic Rankine cycles, *Appl. Therm. Eng.*, vol. 51, no. 1-2: p. 292-300.
- Han, C. H., Kim, K. L., 2014, Exergetical analysis of organic flash cycle with two-phase expander for recovery of finite thermal reservoirs, *J. Therm. Sci.*, vol. 23, no. 6: p. 572-579.
- Heberle, F., Preißinger, M., Brüggemann, D., 2012, Zeotropic mixtures as working fluids in Organic Rankine Cycles for low-enthalpy geothermal resources, *Renew. Energ.*, vol. 37, no. 1: p. 364-370.
- Ho, T., Mao, S. S., Greif, R., 2012a, Comparison of the Organic Flash Cycle (OFC) to other advanced vapor cycles for intermediate and high temperature waste heat reclamation and solar thermal energy, *Energy*, vol. 42, no. 1: p. 213-223.
- Ho, T., Mao, S. S., Greif, R., 2012b, Increased power production through enhancements to the Organic Flash Cycle (OFC), *Energy*, vol. 45, no. 1: p. 686-695.
- Karellas, S., Schuster, A., Leontaritis, A.-D., 2012, Influence of supercritical ORC parameters on plate heat exchanger design, *Appl. Therm. Eng.*, vol. 33-34: p. 70-76.
- Li, W., Feng, X., Yu, L. J., Xu, J., 2011, Effects of evaporating temperature and internal heat exchanger on organic Rankine cycle, *Appl. Therm. Eng.*, vol. 31, no. 17-18: p. 4014-4023.
- NIST Standard Reference Database 23, 2013, NIST Thermodynamic and Transport Properties of Refrigerants and Refrigerant Mixtures REFPROP, Version 9.1.
- Schuster, A., Karellas, S., Aumann, R., 2010, Efficiency optimization potential in supercritical Organic Rankine Cycles, *Energy*, vol. 35, no. 2: p. 1033-1039.
- Shengjun, Z., Huaixin, W., Tao, G., 2011, Performance comparison and parametric optimization of subcritical Organic Rankine Cycle (ORC) and transcritical power cycle system for low-temperature geothermal power generation, *Appl. Energ.*, vol. 88, no. 8: p. 2740-2754.
- Walraven, D., Laenen, B., D'haeseleer, W., 2013, Comparison of thermodynamic cycles for power production from low-temperature geothermal heat sources, *Energ. Convers. Manage.*, vol. 66: p. 220-233.
- Yang, K., Zhang, H., Wang, Z., Zhang, J., Yang, F., Wang, E., Yao, B., 2013, Study of zeotropic mixtures of ORC (organic Rankine cycle) under engine various operating conditions, *Energy*, vol. 58: p. 494-510.

ACKNOWLEDGEMENT

The authors gratefully acknowledge the financial support by the National High-tech Research and Development Program (Grant No.2012AA053002).

PERFORMANCE POTENTIAL OF ORC ARCHITECTURES FOR WASTE HEAT RECOVERY TAKING INTO ACCOUNT DESIGN AND ENVIRONMENTAL CONSTRAINTS

S. Lecompte*, M. van den Broek, M. De Paepe

Department of Flow, Heat and Combustion Mechanics,
Ghent University, Sint-Pietersnieuwstraat 41, 9000 Gent, Belgium
Steven.lecompte@UGent.Be, Martijn.vandenBroek@UGent.Be, Michel.DePaepe@UGent.Be

* Corresponding Author

ABSTRACT

The subcritical ORC (SCORC), sometimes with addition of a recuperator, is the de facto state of the art technology in the current market. However architectural changes and operational modifications have the potential to improve the base system. The ORC architectures investigated in this work are: the transcritical ORC (TCORC), the triangular cycle (TLC) and the partial evaporation ORC (PEORC). Assessing the potential of these cycles is a challenging topic and is brought down to two steps. First, the expected thermodynamic improvement is quantified by optimizing the second law efficiency. Secondly, the influences of technical constraints concerning volumetric expanders are investigated. In the first step, simple regression models are formulated based on an extensive set of boundary conditions. In addition a subset of environmentally friendly working fluids is separately analysed. In the second step, two cases are investigated with the help of a multi-objective optimization technique. The results of this optimization are compared with the first step. As such the effect of each design decision is quantified and analysed, making the results of this work especially interesting for manufacturers of ORC systems.

1. INTRODUCTION

In view of increasing energy demand and environmental concerns it becomes essential to use our natural resources more efficiently. Between 1990 and 2008 the world energy use has already risen more than 40% [1]. Recovery of unused heat from industrial process is evidently an effective measure to make better use of our resources. Statistical studies show that low grade waste heat accounts for more than 50% of the total heat generated in the industry [2]. As such, many companies are interested to exploit new technologies to make valuable use of low grade waste heat.

Organic Rankine cycles (ORC) offer the possibility to generate electricity from the leftover waste heat, even with temperatures below 100°C [3]. Typical benefits associated with ORC are: autonomous operation, favorable operating pressures and low maintenance costs [4]. Waste heat applications roughly consist of up to 20% [5] of the ORC market, preceded by geothermal and biomass installations. Increasing the ORC performance would facilitate further market penetration.

At the moment, most commercially available ORCs have comparable design characteristics, i.e. they operate in the subcritical regime and with well accepted working fluids (WF). However, alternative cycle designs (with matching working fluids) have the potential for increased performance. Performance gains over the subcritical ORC (SCORC) are reported for, amongst others, multi-pressure cycles (MP) [6-9], triangular cycles (TLC) [10-12], cycles with zeotropic working fluids (ZM) [13-15] and transcritical cycles (TCORC) [10, 16-19]. Three cycle configurations, the SCORC, the partial evaporation cycle (PEORC) and the TCORC, are systematically analysed in this work. The

PEORC is a hybrid between the TLC and the SCORC. The working fluid in the PEORC enters the turbine in a state between saturated liquid and saturated vapour.

Assessing the potential of these cycles is a challenging topic and is brought down to two steps. This work provides the integration of these steps and extends two previous conference papers [20, 21] by investigating the effect of limiting the working fluids to an environmentally friendly set. In anticipation of new European F-gas regulations [22] the incentive is launched to restrict the use of fluids with a Global Warming Potential (GWP) value of > 150 . By 2015 this rule would apply to domestic freezers and refrigerators and by 2022 in extension to certain commercial installations. While the current rules apply for refrigerators and freezers an analogous restriction can be expected for power producing cycles.

In step one the second law efficiency is maximized. A large set of boundary conditions is considered to formulate simple regression models. These are used to compare alternative cycles in a first design iteration. To use the regression models the computational effort is low and no expert knowledge is required. In the second step, the effect of integrating volumetric expander design criteria is investigated. A multi-objective optimization is employed on two objectives: net power output and expander volume coefficient. A large computational cost is associated to this type of optimization but the cycle designer can now make the trade-off between expander sizing and cycle efficiency. In the current work, a specific case is analysed using this methodology and compared with the simple regression models from step one.

2. ALTERNATIVE ORC CYCLES

Three cycles architectures are investigated: the subcritical ORC (SCORC), the partial evaporation ORC (PEORC) and the transcritical ORC (TCORC). The cycle layout is identical for the three architectures and shown in Figure 1. The T-s diagram which introduces the nomenclature used is given in Figure 2.

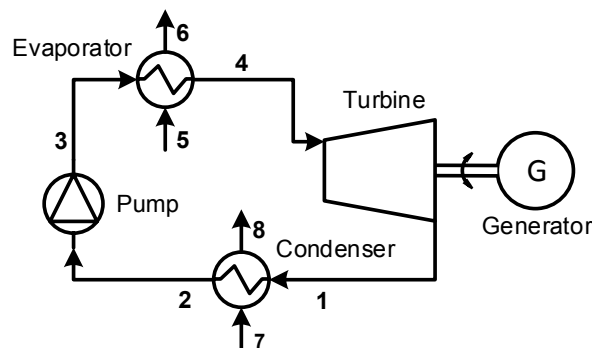


Figure 1: Basic ORC layout.

In a TCORC the evaporator is typically called a vapour generator because the two-phase state is omitted. In a TLC, only the pre-heating section remains and for the PEORC the working fluid evaporates to a state between saturated liquid and saturated vapour.

3. CASE DEFINITION

Two waste heat recovery cases are detailed in the second optimization step, see Table 1. Maximization of the ORC net power output (or second law efficiency) is key for these systems. Sometimes an artificial cooling limit is imposed to avoid condensation of flue gasses [23]. The condensed acids potentially give rise to corrosion and damage of the heat exchangers. In the investigated cases no upper cooling limit is imposed. The proposed cases and classification are based on data gathered in the ORCNext project [24].

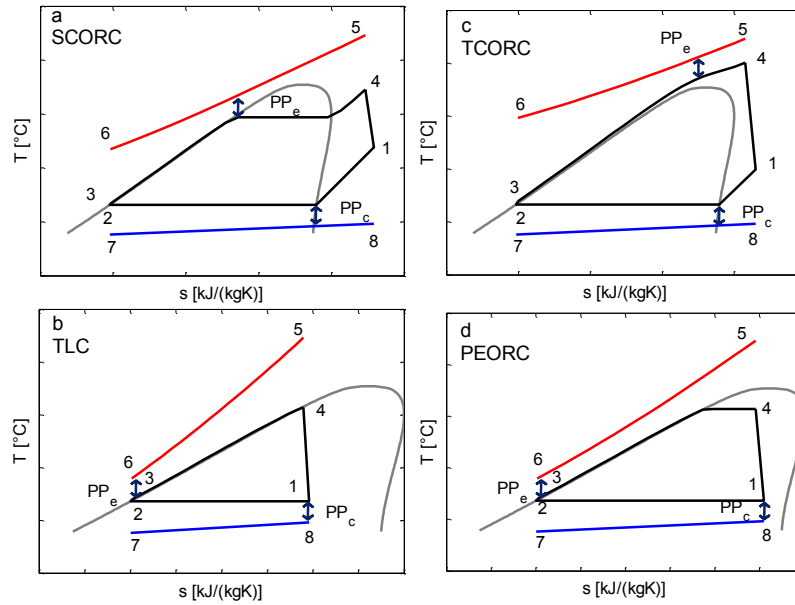


Figure 2: T-s diagrams for the SCORC, TCORC, TLC and PEORC.

Table 1: Definition of waste heat recovery cases.

Case	Case description	$T_{average}$ [°C]	Other applications
1	Flue gas from drying process	240	Exhaust gas internal combustion engines [4]
2	Flue gas from electric arc furnace	305	Cement industry [25] Exhaust gas turbine [4]

4. MODEL AND CYCLE ASSUMPTIONS

4.1 Cycle assumptions

The parameters characterizing the thermodynamic states of the ORC are shown in Table 2. The model assumes steady state operation of the system. Heat losses to the environment and pressure drops in the heat exchangers are considered negligible. No subcooling is considered. A discretization approach is implemented for modelling the heat exchangers. The evaporators are segmented into N parts to take into account changing fluid properties. Especially for the TCORC vapour generator this is essential. Details about the modelling approach are found in previous work by the authors [15, 32].

Table 2: Cycle assumptions.

Parameter	Description	Value
η_{pump}	Isentropic efficiency pump [%]	70
$\eta_{turbine}$	Isentropic efficiency turbine [%]	80
PP_e	Pinch point temperature difference in evaporator [°C]	5
PP_c	Pinch point temperature difference in condenser [°C]	5
T_5	Heat carrier inlet temperature [°C]	100-350
T_2	Cooling loop inlet temperature [°C]	15-30
ΔT_{cf}	Cooling loop temperature rise [°C]	10
i	Mass flow rate heat carrier [kg/s]	1

When changing N=20 to N=100 the calculated net power output of the TCORC changes less than

0.1%. To keep the calculation time acceptable $N=20$ segments is chosen. The condenser is divided into three zones: superheated, condensing and subcooling zone.

Thermophysical data are obtained from CoolProp 4.2.3 [26]. Only pure working fluids are considered, working fluid mixtures are out of scope. The working fluids under consideration all have a critical temperature above 60 °C to make sure two-phase condensation occurs. As such 67 working fluids remain. For the environmentally friendly set of working fluids the ozon depletion potential should be zero and the global warming potential must be lower than 150. This results in 48 remaining working fluids.

Furthermore, for the SCORC the maximum pressure is 0.9 times the critical pressure [15,17]. This is to avoid unstable operation in near-critical conditions. For the SCORC and TCORC the expansion process should end at a superheated state. For the multi-objective optimization (STEP 2) the cooling loop inlet temperature is fixed at 20 °C.

4.2 Performance evaluation criteria

The performance evaluation criteria will only be briefly explained here as these can be found in other works of the author [14, 20, 21]. The second law efficiency is defined as:

$$\eta_{II} = \frac{\dot{W}}{\dot{I}} \quad (1)$$

With \dot{I} the exergy flow:

$$\dot{I} = \dot{m} e \quad (2)$$

The specific exergy e for a steady state stream, assuming potential and kinetic contributions are negligible, is given as:

$$e = h - h_o - T_o(s - s_o) \quad (3)$$

For the dead state (T_o, p_o) the condenser cooling loop inlet temperature and pressure are chosen. Performance criteria for the expanders are formulated next. In this work volumetric machines are investigated and the volumetric coefficient is used as evaluation criteria:

$$VC = \frac{v_{exp,out}}{h_{in,exp} - h_{out,exp}} \quad (4)$$

The VC value is directly related to the size of the expander and permits to include general design ranges in the analysis. Realistic values of the VC in refrigeration and heat pump applications range between 0.25 and 0.6 m³/MJ [23]. In a theoretical study, Maraver et al. [23] report VC values between 0.26 and 936.50 m³/MJ for different waste heat carriers and working fluids.

5. OPTIMIZATION

When optimizing the ORC with the parameters given in Table 2 two degrees of freedom are left. Depending on the cycle types these are typically defined as:

- The superheating and evaporation pressure, for the SCORC.
- The vapour quality and evaporation pressure, for the PEORC.
- The turbine inlet temperature and supercritical pressure, for the TCORC.

In a previous paper [20] two dimensionless parameters, F_s and F_p , were introduced. Both have a range between 0 and 1. These parameters uniquely specify the operating state of the ORC. The benefit is that these two parameters fully cover the search space considering the three cycle architectures under investigation. Their definition is given below:

$$F_p = \frac{p_{wf,e} - p_{\min}}{p_{\max} - p_{\min}} \quad (5)$$

$$p_{\max} = 1.3p_{wf,crit} \text{ if } T_5 - PP_e > T_{wf,crit} \quad (6)$$

$$p_{\max} = p_{wf,sat}(T = T_5 - PP_e) \text{ if } T_5 - PP_e < T_{wf,crit} \quad (7)$$

$$p_{\min} = p_{wf,sat}(T = T_8 + PP_c) \quad (8)$$

$$F_s = \frac{s_4 - s_{\min}}{s_{\max} - s_{\min}} \quad (9)$$

$$s_{\min} = s_{wf,sat,liq}(p = p_{wf,e}) \text{ if } p_{wf,e} < p_{wf,crit} \quad (10)$$

$$s_{\min} = s_{wf,crit} \text{ if } p_{wf,e} > p_{wf,crit} \quad (11)$$

$$s_{\max} = s_{wf}(p = p_{wf,e}, T = T_5 - PP_e) \quad (12)$$

5.1 Maximization of η_{II} (STEP 1)

The boundary conditions for the optimization are a set $T_5 = [100, 120, 140, 160, 180, 200, 225, 250, 275, 300, 325, 350]$ °C, $T_7 = [15, 20, 25, 30]$ °C resulting in a total of 48 points. In each of these points a multistart algorithm [27] searches the global maximum of the second law efficiency ($\eta_{II,max}$). First, the multistart algorithm uniformly distributes 20 initial points in the search space (F_s, F_p) for the local solver to start. Next, a local solver based on a trust-region algorithm [20] starts at these trail points and the best solution is retained. Increasing the start points to 40 gave identical results.

5.2 Multi-objective optimization of VC and η_{II} (STEP 2)

Table 3: Settings of the genetic algorithm.

Parameter	Value
Generations	100
Population size	10000
Crossover rate	0.8
Migration rate	0.2
Mutation type	Gaussian (shrink = 1, scale = 1)
Pareto fraction	0.35

The multi-objective algorithm simultaneously maximizes η_{II} and minimizes VC. The VC is constrained to a range [0.1, 6.5]. The genetic algorithm implemented is based on the NSGA-II algorithm [28]. The settings of the genetic algorithm are provided in Table 3.

6. RESULTS AND TRENDS

6.1 Regression models (STEP 1)

The environmentally friendly working fluids resulting from the optimization are given in Table 6, Table 7 and Table 8 for respectively the SCORC, TCORC and PEORC. For the initial full set of working fluids we refer to a previous paper [20] by the authors. A simple regression model of the second law efficiency can be formulated in function of the T_5 and T_7 . The regression model takes the form:

$$\eta_{II,max} = a + \frac{b(cT_7 + 1)}{(dT_5 + 1)} \quad (13)$$

Goodness of fit statistics [29], the adjusted R^2 and sum square of errors (SSE) are provided in Table 4 and can be considered highly satisfactory. The regression coefficients are given in Table 5.

Table 4: Goodness of fit statistics.

Case	Adjusted R^2	SSE
All working fluids (all WF):		
SCORC	0.9917	0.0039
TCORC	0.9873	0.0055
PEORC	0.9976	0.00056
Environmentally friendly working fluids (env. WF):		
SCORC	0.9924	0.0041
TCORC	0.9944	0.0018
PEORC	0.9976	0.00056

Table 5: Regression coefficients.

Case	a		b		c		d	
	all WF	env. WF	all WF	env. WF	all WF	env. WF	all WF	env. WF
SCORC	0.7466	0.7548	1.357	1.735	3.043	2.488	-13.07	-14.6
PEORC	0.7408	0.7408	0.4796	0.4796	3.514	3.514	-8.184	-8.184
TCORC	0.7484	0.7228	0.9866	0.3061	3.083	2.846	-10.7	-4.624

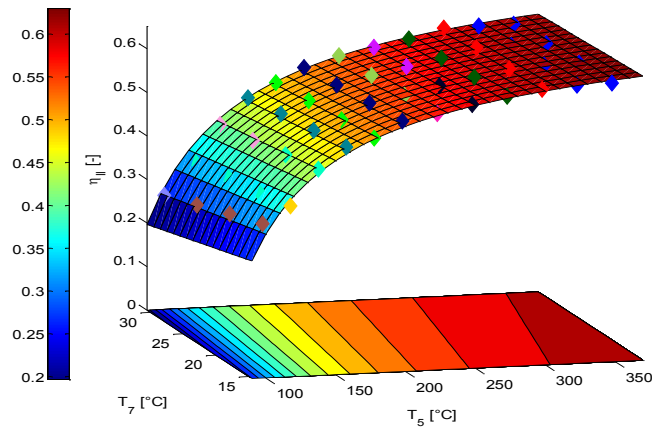


Figure 3: η_{II} optimization, full set of working fluids, surface fit for the SCORC.

For the full set of working fluids, the surface fit for the SCORC is given in Figure 3. The indicated points represent the results of the second law optimization, the colours correspond with the different working fluids. The performance benefit of the TCORC and PEORC over the SCORC are visualized in respectively Figure 4a and Figure 4b. It is clear that both the TCORC and PEORC result in increased second law efficiencies over the SCORC. An increase up to 13 % for the TCORC and 73% for the PEORC is observed at low temperatures (100 °C). However a strong dependency on the heat carrier temperatures should be noted. At high temperatures (350 °C) the relative increase in second law efficiency is reduced to around 2% and 5% for respectively the TCORC and PEORC.

When environmentally friendly working fluids are imposed, the PEORC working fluids do not change. However, as can be seen from Figure 5a (SCORC) and Figure 5b (TCORC), going to environmentally friendly working fluids results in an apparent performance decrease. Again, at low temperatures the performance decrease is the most noticeable (up to 12% for the SCORC and 6% for the TCORC). Furthermore no environmentally friendly working fluids are found for the TCORC under heat carrier inlet temperatures 100 °C and 120 °C. This indicates that there is still a gap for high performing environmentally friendly working fluids for transcritical operation.

6.2 Considering expander evaluation criteria (STEP 2)

Next we consider the effect of the expander performance criteria. As discussed in section 4.2 the VC ratio is directly related to the size of the equipment. Therefore, a multi-objective optimization is employed to simultaneously maximize η_{II} and minimize VC. Again, only the environmentally friendly set of working fluids is considered. The Pareto front for Case 1 and Case 2 are shown in Figure 6a and Figure 6b. Cyclopentane is already used in commercial ORC installations [30]. R1233ZDE is considered a low GWP alternative [31] for the well-known R245fa. Acetone is also considered a potential [32, 33] ORC working fluid.

It is clear that mainly the choice of the working fluid determines the VC. Only in second instance the operating conditions affect the relation η_{II} and VC. As expected, the optimal cycle type is always the PEORC. For Case 1 the VC varies between 0.342 ($\eta_{II} = 0.536$) and 5.957 ($\eta_{II} = 0.635$). For Case 2 the VC varies between 0.344 ($\eta_{II} = 0.536$) and 6.121 ($\eta_{II} = 0.611$).

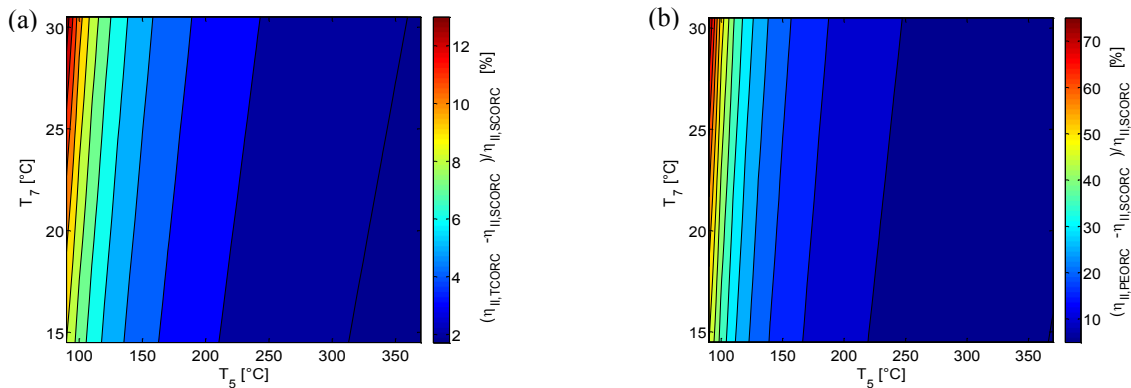


Figure 4: Relative difference η_{II} of (a) TCORC and (b) PEORC versus SCORC.

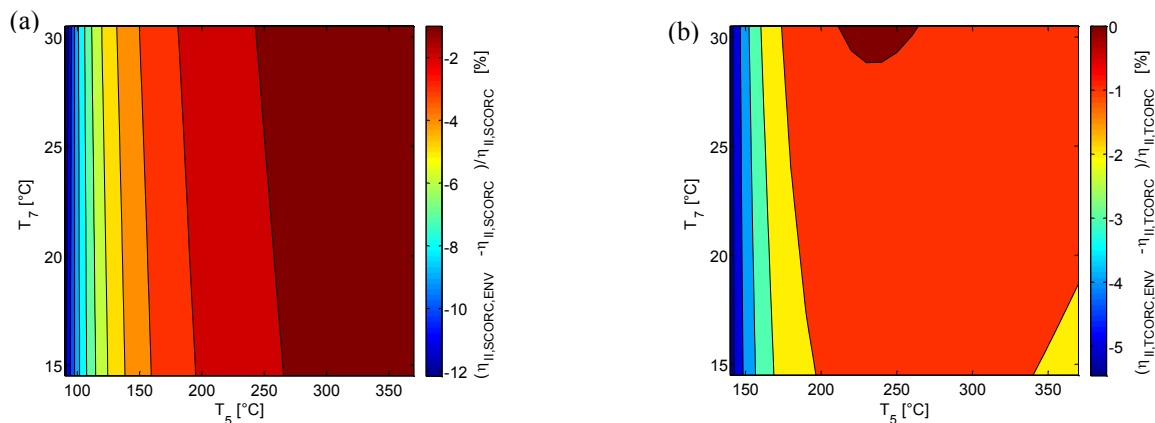


Figure 5: Relative difference η_{II} for full set versus environmentally friendly set of working fluids (a) SCORC (b) TCORC.

Table 6: SCORC environmentally friendly working fluids resulting from η_{II} maximization.

T_5/T_7 °C	15	20	25	30
100	R1234yf	R1234yf	R1234yf	R1234yf
120	R1234yf	R1234yf	R1234yf	R1234yf
140	R1234ZEE	R1234ZEE	R1234ZEE	R1234ZEE
160	R1234ZEE	R1234ZEE	R1234ZEE	Isobutane
180	Isobutane	Isobutane	Isobutane	Isobutane
200	Neopentane	Neopentane	Neopentane	Neopentane
225	R1233ZDE	R1233ZDE	R1233ZDE	R1233ZDE
250	n-pentane	n-pentane	n-pentane	n-pentane
275	Isohexane	n-Hexane	Isohexane	Cyclopentane
300	Cyclopentane	Cyclopentane	Cyclopentane	Cyclopentane
325	Acetone	Acetone	Acetone	Acetone
350	Acetone	Acetone	Acetone	Acetone

Table 7: TCORC environmentally friendly working fluids resulting from η_{II} maximization.

$T_s T_7$ °C	15	20	25	30
120	R1234yf	R1234yf	R1234yf	R1234yf
140	R1234yf	R1234yf	R1234yf	R1234yf
160	R1234ZEE	R1234ZEE	R1234ZEE	R1234ZEE
180	Neopentane	Neopentane	Neopentane	Neopentane
200	Neopentane	Neopentane	Neopentane	Neopentane
225	n-pentane	n-pentane	n-pentane	n-pentane
250	n-pentane	n-pentane	n-pentane	n-pentane
275	Cyclopentane	Cyclopentane	Cyclopentane	Cyclopentane
300	Cyclopentane	Cyclopentane	Cyclopentane	Cyclopentane
325	Acetone	Acetone	Acetone	Acetone
350	Acetone	Acetone	Acetone	Acetone

Table 8: PEORC environmentally friendly working fluids resulting from η_{II} maximization.

$T_s T_7$ °C	15	20	25	30
100	MD3M	MD3M	MD3M	MD3M
120	Water	MD3M	MD3M	MD3M
140	Water	Water	Water	D6
160	MD3M	D6	D6	D6
180	D4	MD2M	MD2M	MD2M
200	Water	Water	Water	D4
225	n-Dodecane	n-Dodecane	n-Dodecane	n-Dodecane
250	Water	Water	n-Dodecane	n-Dodecane
275	Water	Water	Water	Water
300	Water	Water	Water	Water
325	Water	o-xylene	o-xylene	o-xylene
350	Water	Water	Water	Water

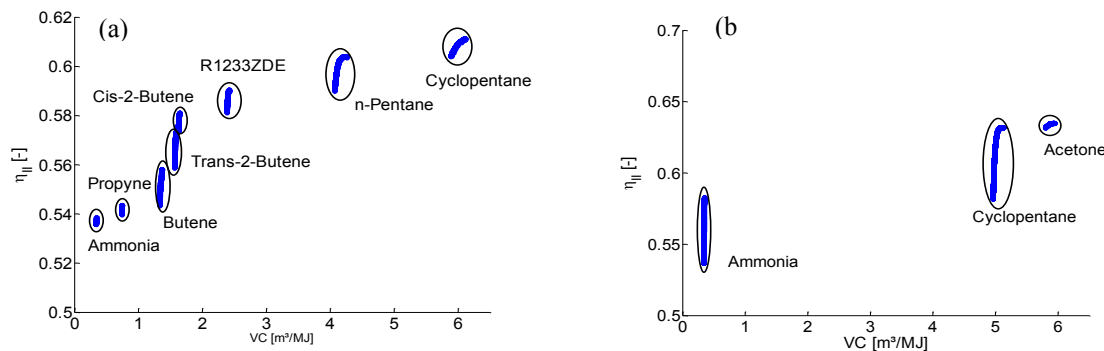


Figure 6: Pareto fronts of VC versus η_{II} for (a) Case 1 and (b) Case 2.

The results of applying the regression models from section 6.1 are given in Table 9. Considering the highest VC values, the reduction in second law efficiency is 5% for Case 1 and 4.9% for Case 2. As such, this optimization step is crucial for the ORC designer to make the final trade-off between cycle performance and expander size and complexity.

Table 9: Results of applying the regression models on the two cases ($T_7 = 20^\circ\text{C}$).

η_{II}	Regression model all WF			Regression model environmentally friendly WF		
	SCORC	TCORC	PEORC	SCORC	TCORC	PEORC
Case 1	0.588	0.605	0.643	0.581	0.602	0.643
Case 2	0.625	0.638	0.667	0.621	0.634	0.667

CONCLUSIONS

- Simple regression models are formulated. These have a low computational cost and are employed to make a first assessment between the SCORC, TCORC and PEORC:
 - Compared to the SCORC, the TCORC and PEORC have a relative increase in second law efficiency of 13% and 73% for a heat carrier temperature of 100°C

- For increasing heat carrier temperatures the performance benefit becomes lower: respectively 2% and 5% for the TCORC and PEORC with a heat carrier temperature of 350 °C.
- Considering environmentally friendly working fluids the second law efficiency is reduced with up to 12% for the SCORC and up to 6% for the TCORC. Again, for increasing heat carrier temperatures, the difference is lower.
- There is still a gap for high performing environmentally friendly working fluids for transcritical operation under low heat carrier temperatures.
- Pareto fronts of second law efficiency and volume coefficient are derived for two cases.
 - The choice of working fluid essentially determines the volume coefficient. The operating parameters have a secondary influence.
 - The second law efficiency is reduced in favour of a lower VC. For example, compared to the regression models, the second law efficiency reduces with 5% for Case 1 and 4.9% for Case 2 with the VC respectively 5.95 and 6.12.

NOMENCLATURE

η	efficiency	(–)
v	specific volume	(–)
e	specific exergy	(kJ/kg)
F	dimensionless ORC state parameter	(–)
\dot{m}	mass flow rate	(kg/s)
PP	pinch point temperature difference	(°C)
TCORC	transcritical ORC	(–)
TLC	triangular cycle	(–)
SCORC	subcritical ORC	(–)
PEORC	partial evaporation ORC	(–)
V	specific volume	(m ³ /kg)
VC	volume coefficient	(m ³ /MJ)
\dot{W}	power	(kW)
Subscript		
e	evaporator	
c	condenser	
crit	critical	
hf	heat carrier	
sat	saturated	
wf	working fluid	
0	dead state	

REFERENCES

- [1] International Energy Outlook 2011. U.S. Energy Information Administration 2011.
- [2] S. Quoilin, S. Declaye, B.F. Tchanche, V. Lemort. Thermo-economic optimization of waste heat recovery Organic Rankine Cycles. *Applied Thermal Engineering*. 31 (2011) 2885-93.
- [3] A. Schuster, S. Karellas, E. Kakaras, H. Spliethoff. Energetic and economic investigation of Organic Rankine Cycle applications. *Applied Thermal Engineering*. 29 (2009) 1809-17.
- [4] B.F. Tchanche, G. Lambrinos, A. Frangoudakis, G. Papadakis. Low-grade heat conversion into power using organic Rankine cycles – A review of various applications *Renewable and Sustainable Energy Reviews* 15 (2011) 3963 - 79.
- [5] S. Quoilin, M.V.D. Broek, S. Declaye, P. Dewallef, V. Lemort. Techno-economic survey of Organic Rankine Cycle (ORC) systems. *Renewable and Sustainable Energy Reviews*. 22 (2013) 168-86.
- [6] M. Kanoglu. Exergy analysis of a dual-level binary geothermal power plant *Geothermics* 31 (2002) 709 - 24.
- [7] M.Z. Stijepovic, A.I. Papadopoulos, P. Linke, A.S. Grujic, P. Seferlis. An exergy composite curves approach for the design of optimum multi-pressure organic Rankine cycle processes. *Energy*. 69 (2014) 285-98.
- [8] Z. Gnutek, A. Bryszewska-Mazurek. The thermodynamic analysis of multicycle ORC engine *Energy* 26 (2001) 1075 - 82.
- [9] A. Franco, M. Villani. Optimal design of binary cycle power plants for water-dominated, medium-temperature geothermal fields *Geothermics* 38 (2009) 379 - 91.

- [10] A. Schuster, S. Karellas, R. Aumann. Efficiency optimization potential in supercritical Organic Rankine Cycles Energy 35 (2010) 1033 - 9.
- [11] I.K. Smith. Development of the trilateral flash cycle system Part1: fundamental considerations. Proceedings of the Institution of Mechanical Engineers, Part A: Journal of Power and Energy. (1993).
- [12] J. Fischer. Comparison of trilateral cycles and organic Rankine cycles Energy 36 (2011) 6208 - 19.
- [13] F. Heberle, M. Preißinger, D. Brüggemann. Zeotropic mixtures as working fluids in Organic Rankine Cycles for low-enthalpy geothermal resources. Renewable Energy. 37 (2012) 364-70.
- [14] S. Lecompte, B. Ameel, D. Ziviani, M. van den Broek, M. De Paepe. Exergy analysis of zeotropic mixtures as working fluids in Organic Rankine Cycles. Energy Conversion and Management. 85 (2014) 727-39.
- [15] M. Chys, M. van den Broek, B. Vanslambrouck, M.D. Paepe. Potential of zeotropic mixtures as working fluids in organic Rankine cycles Energy 44 (2012) 623 - 32.
- [16] B. Saleh, G. Koglbauer, M. Wendland, J. Fischer. Working fluids for low-temperature organic Rankine cycles Energy 32 (2007) 1210 - 21.
- [17] Z. Shengjun, W. Huaixin, G. Tao. Performance comparison and parametric optimization of subcritical Organic Rankine Cycle (ORC) and transcritical power cycle system for low-temperature geothermal power generation Applied Energy 88 (2011) 2740 - 54.
- [18] Y.-J. Baik, M. Kim, K.C. Chang, S.J. Kim. Power-based performance comparison between carbon dioxide and R125 transcritical cycles for a low-grade heat source Applied Energy 88 (2011) 892 - 8.
- [19] S. Karellas, A. Schuster, A.-D. Leontaritis. Influence of supercritical ORC parameters on plate heat exchanger design. Applied Thermal Engineering. 33–34 (2012) 70-6.
- [20] S. Lecompte, H. Huisseune, M. van den Broek, M. De Paepe. Thermodynamic optimization of Organic Rankine Cycle architectures for waste heat recovery (under review). The 28th international conference on efficiency, cost, optimization, simulation and environmental impact on energy systems, Pau, France, 2015.
- [21] S. Lecompte, M. van den Broek, M. De Paepe. Techno-thermodynamic optimization of organic Rankine cycle architectures for waste heat recovery. 11th International Conference on Heat Transfer, Fluid Mechanics and Thermodynamics, Kruger National Park, South Africa, 2015.
- [22] The European Parliament. European Parliament legislative resolution of 12 March 2014 on the proposal for a regulation of the European Parliament and of the Council on fluorinated greenhouse gases. COM(2012)0643 – C7-0370/2012 – 2012/0305(COD)2014.
- [23] D. Maraver, J. Royo, V. Lemort, S. Quoilin. Systematic optimization of subcritical and transcritical organic Rankine cycles (ORCs) constrained by technical parameters in multiple applications. Applied Energy. 117 (2014) 11-29.
- [24] S. Lemmens, S. Lecompte, M. De Paepe. Workshop financial appraisal of ORC systems (ORCNext project: www.orcnext.be). 2014.
- [25] J. Wang, Y. Dai, L. Gao. Exergy analyses and parametric optimizations for different cogeneration power plants in cement industry. Applied Energy. 86 (2009) 941-8.
- [26] I.H. Bell, J. Wronski, S. Quoilin, V. Lemort. Pure and Pseudo-pure Fluid Thermophysical Property Evaluation and The Open-Source Thermophysical Property Library Coolprop. Industrial & Engineering Chemistry Research. 53 (2014) 2498-508.
- [27] Z. Ugray, L. Lasdon, J. Plummer, F. Glover, J. Kelly, M. Rafael. Scatter Search and Local NLP Solvers, A multistart Framework for Global Optimization. INFORMS Journal on Computing. 19 (2007) 238-340.
- [28] K. Deb. Multi-Objective Optimization Using Evolutionary Algorithms. Wiley2001.
- [29] R.L. Mason, R.F. Gunst, J.L. Hess. Statistical Design and Analysis of Experiments. John Wiley & Sons, Inc.2003.
- [30] P. Del Turco, A. Antinio, A.S. Del Greco, A. Bacci, G. Landi, G. Seghi. The ORegen™ Waste Heat Recovery Cycle: Reducing the CO2 Footprint by Means of Overall Cycle Efficiency Improvement. ASME 2011 Turbo Expo: Turbine Technical Conference and Exposition, Vancouver, British Columbia, Canada, 2011.
- [31] F. Molés, J. Navarro-Esbrí, B. Peris, A. Mota-Babiloni, Á. Barragán-Cervera, K. Kontomaris. Low GWP alternatives to HFC-245fa in Organic Rankine Cycles for low temperature heat recovery: HCFO-1233zd-E and HFO-1336mzz-Z. Applied Thermal Engineering. 71 (2014) 204-12.
- [32] R. Rayegan, Y.X. Tao. A procedure to select working fluids for Solar Organic Rankine Cycles (ORCs). Renewable Energy. 36 (2011) 659-70.
- [33] L. Pierobon, T.-V. Nguyen, U. Larsen, F. Haglind, B. Elmegaard. Multi-objective optimization of organic Rankine cycles for waste heat recovery: Application in an offshore platform. Energy. 58 (2013) 538-49.

ACKNOWLEDGEMENT

The results presented in this paper have been obtained within the frame of the IWT SBO-110006 project The Next Generation Organic Rankine Cycles (www.orcnext.be), funded by the Institute for the Promotion and Innovation by Science and Technology in Flanders. This financial support is gratefully acknowledged.

PERFORMANCE COMPARISON OF A NOVEL THERMOFLUIDIC ORGANIC-FLUID HEAT CONVERTER AND AN ORGANIC RANKINE CYCLE HEAT ENGINE

Christoph J.W. Kirmse, Aly I. Taleb, Oyeniyi A. Oyewunmi, Andrew J. Haslam,
and Christos N. Markides*

Clean Energy Processes (CEP) Laboratory, Department of Chemical Engineering,
Imperial College London, London SW7 2AZ, UK
E-mail: c.markides@imperial.ac.uk

* Corresponding Author

ABSTRACT

The Up-THERM engine is a novel two-phase heat engine with a single moving part—a vertical solid piston—that relies on the phase change of a suitable working fluid to produce a reciprocating displacement and sustained thermodynamic oscillations of pressure and flow rate that can be converted to useful work. A model of the Up-THERM engine is developed via lumped dynamic descriptions of the various engine sub-components and electrical analogies founded on previously developed thermoacoustic principles. These are extended here to include a description of phase change and non-linear descriptions of selected processes. The predicted first and second law efficiencies and the power output of a particular Up-THERM engine design aimed for operation in a specified CHP application with heat source and sink temperatures of 360 °C and 10 °C, are compared theoretically to those of equivalent sub-critical, non-regenerative organic Rankine cycle (ORC) engines. Five alkanes (from *n*-pentane to *n*-nonane) are being considered as possible working fluids for the aforementioned Up-THERM application, and these are also used for the accompanying ORC thermodynamic analyses. Owing to its mode of operation, lack of moving parts and dynamic seals, the Up-THERM engine promises a simpler and more cost-effective solution than an ORC engine, although the Up-THERM is expected to be less efficient than its ORC counterpart. These expectations are confirmed in the present work, with the Up-THERM engine showing lower efficiencies and power outputs than equivalent ORC engines, but which actually approach ORC performance at low temperatures. Therefore, it is suggested that the Up-THERM can be a competitive alternative in terms of cost per unit power in low-power/temperature applications, especially in remote, off-grid settings, such as in developing countries where minimising upfront costs is crucial.

1. INTRODUCTION

Primary energy efficiency, leading to a reduced consumption of fossil-fuel reserves and of related emissions to the environment, has been attracting increased attention in recent years. The present paper considers an innovative vapour-phase heat-engine concept termed ‘Up-THERM’. The Up-THERM engine was first proposed, designed and tested by company Encontech B.V. (<http://www.encontech.nl>) and is currently being further developed under the EU FP7 project Up-THERM (<http://labor1.wix.com/up-therm>) for combined heat and power (CHP) applications. The engine can be said to belong to a class of systems known as ‘thermofluidic oscillators’. Examples of single-phase thermofluidic oscillators include Sondhauss tubes (Sondhauss, 1850), thermoacoustic engines (Ceperley, 1979), Stirling (B. Kongtragool, 2003) and Fluidyne engines (Stammers, 1979). In particular, the Up-THERM engine is a *two-phase* thermofluidic oscillator akin to the ‘Non-Inertive-Feedback Thermofluidic Engine’ (NIFTE) (Markides and Smith, 2011; Solanki et al., 2012, 2013a,b), but also comprises a single solid piston (Glushenkov et al., 2012; Samoilov et al., 2013) much like gas-phase Stirling engines (rather than the liquid pistons employed in the NIFTE or Fluidyne engines). Similarly to the NIFTE, a constant temperature difference

applied between the hot and cold parts of the Up-THERM device results in the periodic evaporation and condensation of the working fluid in an unsteady thermodynamic cycle. This leads to unsteady oscillations of pressure, temperature, and volume within the engine, and the reciprocating vertical motion of the piston. By transforming the oscillatory movement of the fluid into unidirectional flow through check valves and hydraulic accumulators, power can be extracted by means of a hydraulic motor.

The Up-THERM engine can be thought of as an alternative to the more commercially mature organic Rankine cycle (ORC) engine: by relying on the phase-change of its working fluid, it is suitable for converting low-grade heat to useful mechanical power, and it is an external heat engine that can be used with a variety of heat sources. In particular, it promises *relatively* high efficiencies at low power outputs while being a more affordable solution compared to conventional systems. In this paper, we compare the efficiency and power output of an Up-THERM prime-mover design for a pre-specified CHP application to ORC equivalents, based on operation between the same heat source and sink temperatures, with the same heat input (indicative of scale and cost), and using the same (organic) working fluids.

2. UP-THERM ENGINE CONFIGURATION AND OPERATION

The Up-THERM engine concept is depicted in Figure 1a. The engine consists of a displacer cylinder, a connection tube and a load arrangement. The displacer cylinder comprises the hot and cold heat exchangers, the solid piston, a slide bearing, and a mechanical spring. The piston and cylinder wall together form a ‘piston-valve’ arrangement. Under operating conditions part of the space above the piston, at the very top of the displacer cylinder, is occupied by the working fluid in the vapour phase, which acts like a gas spring. The load arrangement consists of two check (non-return) valves, two hydraulic accumulators, and a hydraulic motor. The fluid flow directions are illustrated by black arrows.

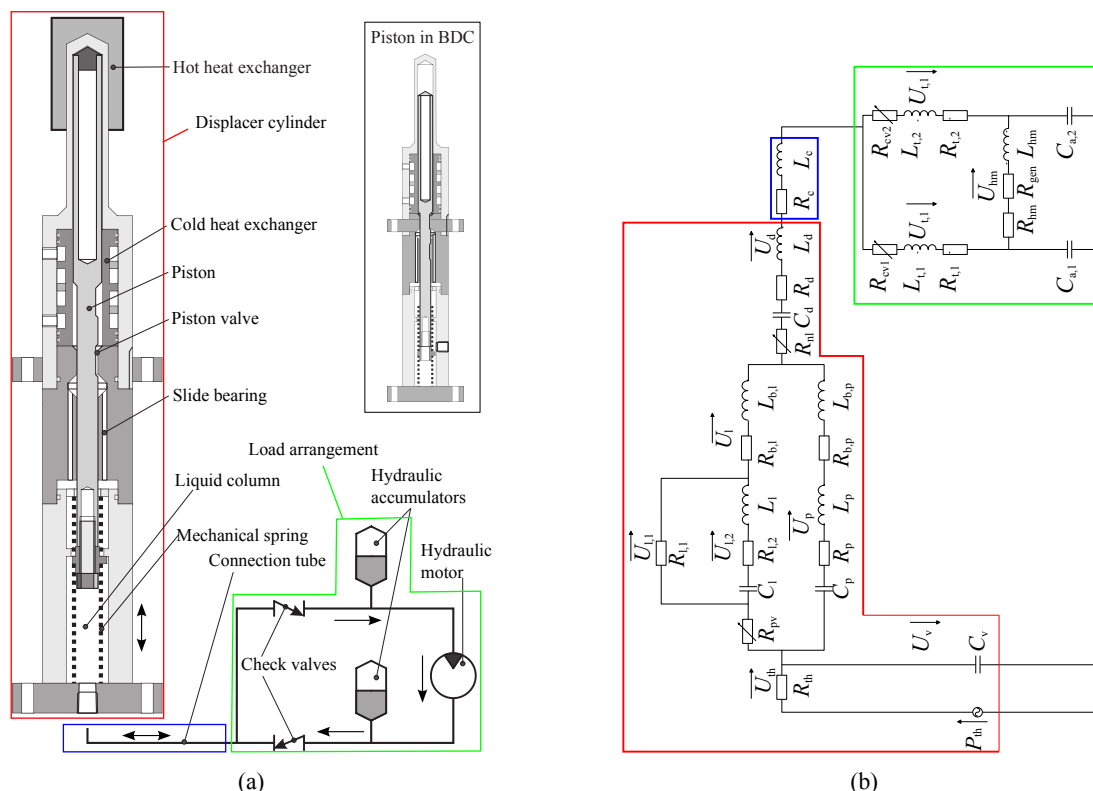


Figure 1: (a) Schematic of the Up-THERM engine with the piston at TDC and BDC (inset). (b) Circuit diagram of the Up-THERM; colours correspond to the engine components in (a).

Consider cyclic operation that starts with the piston at the top dead centre (TDC) position inside the displacer cylinder, as depicted in Figure 1a. The piston valve is open, the mechanical spring fully com-

pressed, and the vapour-liquid (VL) interface is in contact with the surface of the hot heat exchanger (HHX). Liquid working fluid evaporates and thus the pressure in the gas spring increases. This, together with the relaxation of the mechanical spring, leads to a downward movement of the solid piston and of the VL interface. Fluid flows from the compartment above the piston valve into the chamber below it, and into the adjoining connection tube. The piston valve eventually closes preventing continued fluid flow into the lower chamber. The pressure in the upper chamber continues rising, thus generating a pressure difference between both chambers. The pressure difference forces the piston to move downward and the valve re-opens. The pressures above and below the valve are thereby equalized and fluid flows through the valve. Due to the inertia of the piston and fluid, their downward movement continues. They overshoot their equilibrium position halfway between the HHX and cold heat exchanger (CHX).

The vapour, now in contact with the cold CHX surface, begins to condense, while the mechanical spring is compressed. When the piston reaches the bottom dead centre (BDC), the restoring forces of the mechanical spring and decreasing pressure in the gas spring reverse the direction of the piston and VL interface. The piston valve closes again, establishing a similar pressure difference as previously. After re-opening, fluid flows through the valve into the upper chamber while the pressure is equalized. The piston moves further upwards until it reaches the TDC, and the cycle repeats.

During the cycle, liquid oscillates (with zero mean flow) in the connection tube. The oscillating flow is transformed into a unidirectional flow by the two check-valves in the load arrangement, while the hydraulic accumulators act to dampen the amplitude of flow and pressure fluctuations. Thus, a steady unidirectional flow is provided to the hydraulic motor, where work can be extracted from the device.

3. MODEL DEVELOPMENT

3.1 Up-THERM engine

The approach taken for the modelling of the Up-THERM engine concept follows the earlier approaches by Ceperley (1979), Huang and Chuang (1996), and Backhaus and Swift (2000) as applied to thermoacoustic and thermofluidic devices, but also those taken for the modelling of the NIFTE, which is the most closely related device to the Up-THERM since it also exploits a phase-change of the working fluid between hot/cold heat exchangers. Inertial effects were neglected in the original effort of Smith (2004, 2005, 2006), however this early model was later extended to include these effects (Markides and Smith (2011); Solanki et al. (2012)), allowing for more realistic predictions of the operational and performance characteristics of the device. Markides et al. (2013) proceeded to introduce a non-linear temperature profile over the heat exchangers, resulting in further improvements in the predictions of the NIFTE's efficiency. The model was validated against experimental data, showing good agreement with the frequencies and efficiencies reported for an early-stage NIFTE prototype water pump (Solanki et al., 2013b; Markides et al., 2013). This approach (including the non-linear temperature profile) is deemed to be a suitable starting point for the modelling the Up-THERM engine. Full details of the modelling approach employed here for the Up-THERM can thus be found in these references.

Briefly, the engine is divided into sub-components. The dominant thermal or fluid-dynamic process taking place in each of these is modelled using first-order spatially lumped, ordinary differential equations (ODEs). For the following sub-components, we assume small fluctuations around an equilibrium point allowing us to linearize the ODEs: the piston; the slide bearing; the liquid column; the connection tube; the hydraulic accumulators; and the hydraulic motor. Electrical analogies are drawn such that the differential equations governing the dynamic processes are represented by passive electrical components (resistors, inductors, and capacitors). The models of each sub-component are interconnected to form an electrical circuit network that reflects the physical manifestation of the engine; see Figure 1b.

In more detail, force balances on the liquid volume in the connection tube and in the displacer cylinder are employed to derive the electrical analogies for these components. The Reynolds and Womersley numbers are assumed to be sufficiently low such that quasi-steady, fully developed flow can be assumed. In this case, linearized resistances can be used to represent viscous drag, linearized inductances represent

fluid inertia, and capacitances hydrostatic pressure differences (in the displacer cylinder only):

$$R = \frac{128\mu l_0}{\pi d^4}; \quad L = \frac{\rho l_0}{A}; \quad C = \frac{A}{\rho g}. \quad (1)$$

A force balance on the piston is combined with the Navier-Stokes equations for the surrounding leakage flow to derive the linearized electrical analogies for these two components. In the slide bearing, the fluid flows through two channels and hence is modelled as a liquid column. The piston slides through a third channel lubricated by a thin working-fluid film and experiences drag. Thus, the electrical components required to model the dynamics of the piston, leakage flow, and slide bearing are:

$$\begin{aligned} R_{1,1} &= \frac{128c_2 h_p \mu}{\pi c_1 c_3}; & R_{1,2} &= \frac{128c_2 h_p \mu}{\pi c_1 (c_1 - 2c_2 d_p^2)}; & C_1 &= \frac{\pi^2 c_1 (c_1 - c_2 d_p^2)}{64c_2^2 k_{ms}}; & L_1 &= \frac{64c_2^2 m_p}{\pi^2 c_1 (c_1 - 2c_2 d_p^2)}; \\ R_p &= \frac{64h_p \mu}{\pi d_p^2 c_1}; & C_p &= \frac{\pi^2 d_p^2 c_1}{32k_{ms} c_2}; & L_p &= \frac{32m_p c_2}{\pi^2 d_p^2 c_1}; & R_{b,p} &= \frac{16\mu h_b}{\pi^2 d_p^3 \delta}; & L_{b,p} &= \frac{4\rho_{ss} h_b}{\pi d_p^2}; \\ & & & & L_{b,1} &= \frac{4\rho h_b}{\pi d_b^2}; & R_{b,1} &= \frac{128\mu h_b}{\pi d_{b,1}^4}. \end{aligned} \quad (2)$$

In Eq. 2, three geometric constants are used: $c_1 = d_c^2 - d_p^2$, $c_2 = \ln(d_c/d_p)$, and $c_3 = c_2(d_c^2 + d_p^2) - c_1$.

The gas springs in the hydraulic accumulators are modelled using the linearized ideal gas law with:

$$C = \frac{V_0}{\gamma P_0}. \quad (3)$$

A torque balance is used to model the losses and inertia in the hydraulic motor. Ohm's law is used to calculate the power \dot{W}_{el} that can be extracted from the engine as a function of the flow rate U_{hm} through the hydraulic motor. The power is dissipated in the resistance R_{el} which is determined empirically.

$$R_{hm} = \frac{16\mu_{lub} d_s^3 h_s}{\pi \epsilon d_m^4 d_m^2}; \quad L_{hm} = \frac{8m_m}{\pi^2 d_m^4}; \quad \dot{W}_{el} = R_{gen} U_{hm}^2. \quad (4)$$

In addition to the linear descriptions of the aforementioned components, the gas spring above the piston, the piston valve, the two check valves, and the temperature profile over the heat exchangers are modelled non-linearly. The piston valve is described by a non-linear resistance:

$$R_{pv} = R_{min} + \frac{1}{2} R_{max} \left(-H \{P_{C,d} - \rho_{wfl} g h_{pv}\} + H \{P_{C,d} + \rho_{wfl} g h_{pv}\} \right), \quad (5)$$

using a Heaviside step function $H\{\cdot\}$, such that the valve opens and closes at the height h_{pv} .

The check valves and non-linear resistance R_{nl} in the displacer cylinder are also modelled using Heaviside step functions. The check valves are either open or closed depending on the flow direction U_d :

$$R_{cv} = R_{max,cv} H \{U_d\}, \quad (6)$$

while by introducing the non-linear resistance R_{nl} it is ensured that the vertical displacement amplitudes of the solid piston and liquid column are not larger than the height of the displacer cylinder itself:

$$R_{nl} = R_{max,3} \left(H \{P_{C,d} - \rho_{wfl} g h_3\} + H \{-P_{C,d} - \rho_{wfl} g h_3\} \right). \quad (7)$$

In the above equation h_3 is the maximum height of the liquid column. When reaching this height in the physical engine the piston/liquid column contacts a wall and cannot move further.

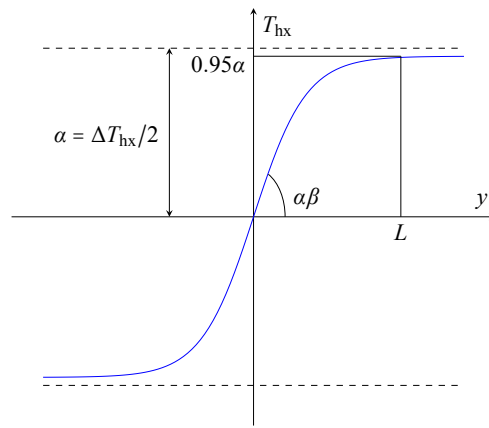


Figure 2: Non-linear temperature profile in the heat exchangers. At length L of the heat exchanger we assume that, by design, the temperature reaches 95% of its saturation value $\alpha = \Delta T_{hx}/2$.

The gas spring above the piston is modelled assuming an isentropic compression and expansion process ($PV^\gamma = \text{const.}$), where γ represents the heat-capacity ratio. Differentiating with respect to time, the temporal variations in the rate of change of pressure dP_v/dt of the gas spring can be expressed as:

$$\frac{dP_v}{dt} = \frac{\gamma (P_0 + P_v) U_v}{V_0 + V_v} = \frac{\gamma (P_0 + P_v) \left(\frac{P_{th} - P_v}{R_{th}} - U \right)}{V_0 + V_v}. \quad (8)$$

The interaction between the fluid at the vapour-liquid interface and the heat exchanger walls is the only nominally active thermal process in the device (corresponding to the thermal domain indicated by the subscript ‘th’ in Figure 1b), and is explained in more detail in Markides et al. (2013). As the vapour-liquid interface moves far away from (midway between) the equilibrium position between the CHX and HHX, it is assumed that the temperature on the heat exchanger wall T_{hx} is described by a non-linear static relationship that exhibits saturation at long distances from the equilibrium position:

$$T_{hx} = \alpha \tanh(\beta y), \quad (9)$$

where y is the distance of the vapour-liquid interface from the equilibrium position (see Figure 2) and $\alpha\beta$ is the gradient of the profile at equilibrium. Figure 2 illustrates the non-linear temperature profile.

The second law (exergy) efficiency is used here as a performance measure of the Up-THERM engine. It compares the work output of the cycle to the exergy input, and can be calculated from:

$$\eta_{ex} = \frac{\int R_{gen} U_{hm} dV_{hm}}{\int P_{th} dV_{th}}, \quad (10)$$

where $V_{hm} = \int U_{hm} dt$ is the volumetric displacement in the hydraulic motor and $V_{th} = \int U_{th} dt$ the ‘equivalent’ entropy flow (referred to the fluid domain, hence the volumetric conversion) due to thermal energy transfer to the working fluid over a cycle (Markides and Smith, 2011).

Finally, the first law (thermal) efficiency of the engine is calculated from:

$$\eta_{th} = \eta_C \eta_{ex}, \quad (11)$$

where η_C is the Carnot efficiency based on the average (external) heat-source and sink temperatures.

As stated earlier, we consider here the performance of a specific Up-THERM prime-mover design for a defined CHP application with a heat-source inlet temperature of 360 °C and a heat-sink inlet temperature of 10 °C, and with five alternative working fluids (*n*-pentane to *n*-nonane). This engine design and choice working-fluid properties fixes all system parameters, and allows the system of ODEs that describe the device’s operation to be solved from which the performance indicators of interest can be evaluated.

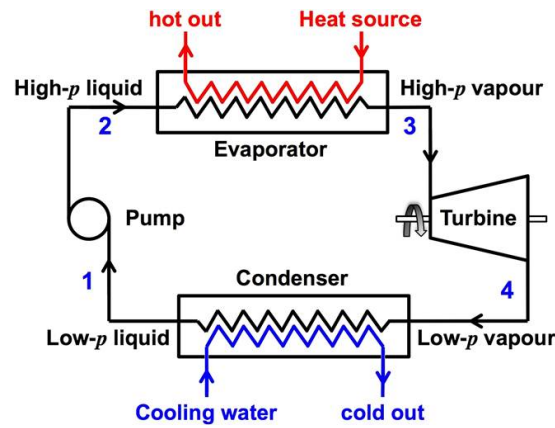


Figure 3: Simple schematic diagram of a non-regenerative ORC engine.

3.2 Organic Rankine cycle engine

A simple schematic of an ORC engine is presented in Figure 3. The working fluid is pumped from a saturated liquid at State 1 to State 2 before being pre-heated and vapourized in the evaporator with thermal energy taken from a hot fluid stream that acts as the heat source. For the purposes of maintaining our comparison, the working fluid remains in the sub-critical region throughout, and exits the evaporator as a saturated liquid; it is not superheated as there is little possibility to superheat in the Up-THERM engine. Moreover, superheating the working fluid during heat addition has been shown to be detrimental to ORC performance in some cases (Chen et al., 2010; Oyewunmi et al., 2014). The high-pressure vapour (State 3) generates power in an expander. The low-pressure vapour is then condensed to State 1, completing the cycle. The key processes of the cycle are described for completeness below.

The power required to pump the working fluid from State 1 to State 2 is:

$$\dot{W}_{\text{pump}} = \dot{m}_{\text{wfl}} (h_2 - h_1) = \dot{m}_{\text{wfl}} (h_{2s} - h_1) / \eta_{\text{is,pump}}, \quad (12)$$

with $\eta_{\text{is,pump}}$ being the isentropic efficiency of the pump, which is taken as 75%.

The heat extracted from the heat source is transferred to the working fluid assuming no heat losses and with a minimum pinch temperature difference of 10 °C in the evaporator. The heat addition process is assumed to be isobaric, thus the rate of heat input from the heat source is given by:

$$\dot{Q}_{\text{in}} = \dot{m}_{\text{wf}} (h_3 - h_2) = \dot{m}_{\text{hs}} c_{p,\text{hs}} (T_{\text{hs,in}} - T_{\text{hs,out}}). \quad (13)$$

The expander is assumed to have an isentropic efficiency $\eta_{\text{is,exp}}$ of 75%. Hence, the power generated on expanding the working fluid is:

$$\dot{W}_{\text{exp}} = \dot{m}_{\text{wf}} (h_3 - h_4) = \eta_{\text{is,exp}} \dot{m}_{\text{wf}} (h_3 - h_{4s}). \quad (14)$$

Most of the working fluids considered here are ‘dry’ and thus exit the expander in the superheated-vapour state. Therefore, heat is rejected as the working fluid is first de-superheated and then condensed to a saturated liquid isobarically. The rate of heat transferred to a cooling stream is given as:

$$\dot{Q}_{\text{out}} = \dot{m}_{\text{wf}} (h_4 - h_1) = \dot{m}_{\text{cs}} c_{p,\text{cs}} (T_{\text{cs,out}} - T_{\text{cs,in}}). \quad (15)$$

Finally, the thermal efficiency of the cycle is calculated from:

$$\eta_{\text{th}} = \frac{\dot{W}_{\text{net}}}{\dot{Q}_{\text{in}}} = \frac{\dot{W}_{\text{exp}} - \dot{W}_{\text{pump}}}{\dot{Q}_{\text{in}}}, \quad (16)$$

based on which an exergy efficiency η_{ex} can be determined via η_{C} as before.

The present study considers, from a purely theoretical thermodynamic perspective, the performance of equivalent ORCs to the proposed Up-THERM engines based on operation with the same working fluids, heat source/sink temperatures and heat inputs (indicative of scale/cost).

4. RESULTS AND DISCUSSION

Based on the above models, we proceed now to estimate the expected thermal and exergy efficiencies and power output from the Up-THERM heat engine, and to compare this with equivalent organic Rankine cycle (ORC) engine performance. For this purpose, we consider a heat-source stream inlet temperature of 360 °C and a heat-sink stream inlet temperature of 10 °C. The temperature drop/rise between the inlet and outlet in both heat exchangers is set to 30 °C; again this is done in order to match the external temperatures available to the ORC to those that are known to be available to the Up-THERM cycle. Since the flow rates and temperatures of the heat-source streams are similar in both systems, the heat inputs are therefore also similar, and any difference in power output reflects a different engine efficiency.

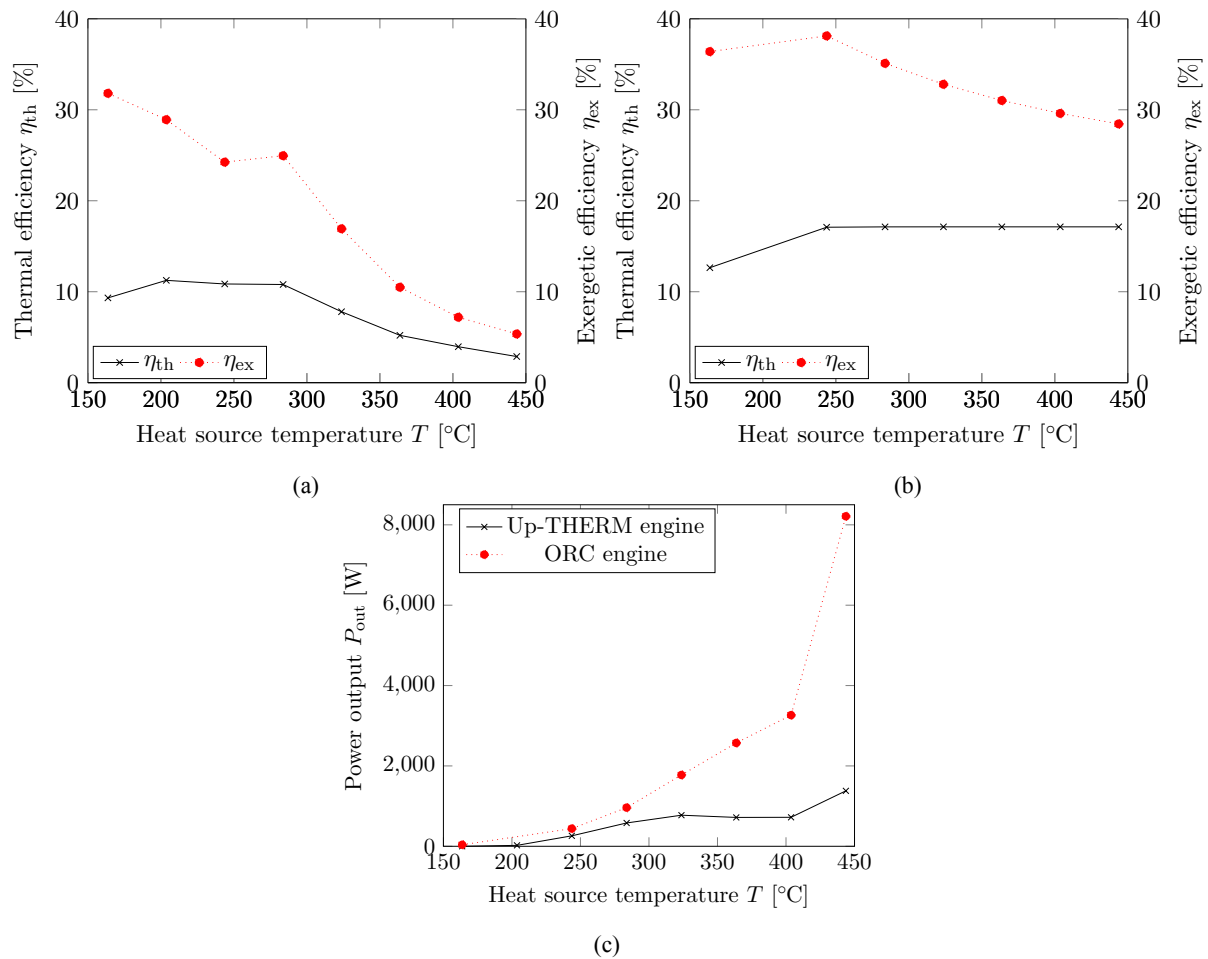


Figure 4: (a) Up-THERM efficiencies for different heat-source temperatures with n -hexane; (b) ORC efficiencies corresponding (a); and (c) Up-THERM and ORC net power-outputs.

Firstly we consider the two systems operating with the same working fluid (n -hexane) across a range of heat-source temperatures with the same heat sink; all other Up-THERM parameters (except those influenced by the change in equilibrium temperature and pressure) are kept constant. It is important to note from Figure 4(a), that as the heat-source temperature increases the efficiency of the Up-THERM engine first improves (at low temperatures) and then deteriorates again, even though the power output increases monotonically as demonstrated in Figure 4(c). (As the backpressure is increased the amplitudes of the pressure and volume oscillations throughout the system also increase, which leads to an increased flow rate through the hydraulic motor and hence to an increased power output.) At the lowest temperatures the predicted efficiency and power output of the Up-THERM approaches that of the ORC. This suggests that the Up-THERM may offer a competitive proposition when used with low-grade heat sources.

Table 1: Thermal and exergy efficiencies and power output as calculated by the Up-THERM and equivalent ORC engine models for five *n*-alkane working fluids.

Working Fluid	Up-THERM					ORC				
	η_{ex} [%]	η_{th} [%]	\dot{W}_{net} [W]	\dot{m}_{hs} [kg/s]	p_0 [bar]	η_{ex} [%]	η_{th} [%]	\dot{W}_{net} [W]	\dot{m}_{wf} [kg/s]	P_{23} [bar]
Pentane	5.37	2.97	1110	0.55	28.2	28.2	15.2	6090	0.073	30.4
Hexane	11.5	6.37	785	0.018	14.1	31.8	17.1	2250	0.020	27.1
Heptane	21.4	11.9	659	0.081	7.51	33.6	18.1	1080	0.080	24.4
Octane	19.1	10.6	195	0.027	4.13	34.3	18.5	366	0.0024	22.3
Nonane	18.7	10.3	47.2	0.0067	1.02	35.2	19.0	93	0.00055	19.2

Nevertheless, we are interested here in a particular CHP application for the Up-THERM where the heat-source temperature is relatively high (360 °C). Table 1 lists the main performance indicators of interest, namely the thermal and exergy efficiencies and power outputs, predicted by the Up-THERM and equivalent ORC engines models for a selection of working fluids. Additionally, the operating equilibrium/backpressure of the Up-THERM engine for each working fluid, the corresponding evaporation pressure for the ORC engine, and the (common) heat-source fluid-stream flow-rate and working-fluid flow-rate used in the ORC for maximum power are given. When the heavier alkanes are used in the Up-THERM this results generally in a higher efficiency, but a reduced power output due to the lower heat-input from the source. This is due to the lower gain and lower (pressure/flow) oscillation amplitudes that the heavier-hydrocarbon Up-THERM systems experience, given that the external temperature difference across which the device operates is fixed. Pentane is associated with the highest power output, in both the Up-THERM and ORC engines, at least for this application; however, the efficiencies of this working fluid are the lowest. For the Up-THERM, thermal efficiencies of up to 12% and exergy efficiencies of up to 21% (*n*-heptane), and power-outputs of up to 1.1 kW (*n*-pentane) are predicted.

It is clear that the ORC engine outperforms the Up-THERM engine in terms of power output and efficiency for all working fluids, and especially when the lighter hydrocarbons are used. This is a consequence of the relatively high temperature of the heat source in the presently investigated CHP prime-mover application (as identified previously in the discussion relating to Figure 4(c)). Both the power output and efficiencies of the ORC engine are about 2 – 5 times higher compared to that of the Up-THERM, depending on the working fluid. Nevertheless, this is a respectable performance from what is a non-optimized Up-THERM design, and also in light of the far lower capital and maintenance costs associated with this technology. Although not on-par in terms of our performance, the Up-THERM appears an interesting technology in terms of performance per unit cost.

5. CONCLUSIONS

In his work, a simple dynamic model of a novel two-phase thermofluidic oscillator featuring a single solid piston termed Up-THERM was developed. The sub-components of the engine are: the displacer cylinder with hot and cold heat exchangers and a solid piston; the connection tube, which links the displacer cylinder with a load arrangement; the load arrangement with hydraulic accumulators, check valves and a hydraulic motor, where power can be extracted from the cycle. The engine was described by a series of first-order spatially lumped ordinary differential equations (ODEs). For some components the ODEs were linearized. Components with a crucial impact on the performance of the engine were described non-linearly. The engine performance was examined with five alkanes as the working fluid. Specifically, the thermal and exergy efficiencies, as well as the power output of a particular Up-THERM engine design aimed for operation as a prime mover in a specified CHP application were evaluated for heat source and sink temperatures of 360 °C and 10 °C. The results were compared theoretically to those of equivalent sub-critical, non-regenerative organic Rankine cycle (ORC) engines. For this Up-THERM engine, thermal efficiencies of up to 12% and exergy efficiencies of up to 21% (*n*-heptane), and power-

outputs of up to 1.1 kW (*n*-pentane) were predicted. The power output and efficiencies of the ORC engine are about 2 – 5 times higher, depending on the working fluid. Thermofluidic oscillators, like the Up-THERM engine, are potentially cheaper to construct than currently available technologies such as ORCs. Since they have less moving parts they also offer the prospect of greater reliability and longevity. We have demonstrated that these advantages can be obtained while maintaining similar performance in terms of efficiency and power output. Accordingly, the Up-THERM engine represents an exciting new technology, particularly in the context of power generation in the developing world.

NOMENCLATURE

C	capacitance	$(\text{m}^4\text{s}^2/\text{kg})$
d	diameter	(m)
g	gravitational acceleration	(m/s^2)
h	height, enthalpy	$(\text{m}), (\text{J}/\text{kg})$
$H\{\cdot\}$	Heaviside step function	$(-)$
k	spring constant	(N/m)
L	inductance	(kg/m^4)
P	pressure fluctuations around equilibrium pressure	(Pa)
R	resistance	$(\text{kg}/\text{m}^4\text{s})$
U	flow rate	(m^3/s)
V	volume fluctuations around equilibrium volume	(m^3)
\dot{W}	power	(W)
α	half the temperature difference between HHX and CHX	$(-)$
γ	heat capacity ratio	$(-)$
δ	gap between piston and slide bearing	(m)
ε	gap between shaft and motor	(m)
μ	dynamic viscosity	(m^2/s)
ρ	density	(kg/m^3)

Subscript

0	equilibrium
a	hydraulic accumulator
b	slide bearing
c	connection tube
cv, pv	check valve, piston valve
d	displacer cylinder
el	electric
ex	exergy
gen	generator
hm	hydraulic motor
hx	heat exchanger
l	leakage flow
lub	lubricant
m	motor
min, max	minimum, maximum value
ms, vs	mechanical spring, vapour spring
nl	non-linear
p	piston
s	shaft
t	tube
th	thermal

wfl liquid working fluid

REFERENCES

- B. Kongtragool, S. W. (2003). A review of solar-powered Stirling engines and low temperature differential stirling engines. *Renewable and Sustainable Energy Reviews*, 7(2):131–154.
- Backhaus, S. and Swift, G. W. (2000). A thermoacoustic-Stirling heat engine: Detailed study. *Journal of the Acoustical Society of America*, 107(6):3148–3166.
- Ceperley, P. H. (1979). A pistonless Stirling engine-The traveling wave heat engine. *Journal of the Acoustical Society of America*, 66(5):1508–1513.
- Chen, H., Goswami, D. Y., and Stefanakos, E. K. (2010). A review of thermodynamic cycles and working fluids for the conversion of low-grade heat. *Renewable and Sustainable Energy Reviews*, 14(9):3059–3067.
- Glushenkov, M., Sprenkeler, M., Kronberg, A., and Kirillov, V. (2012). Single-piston alternative to Stirling engines. *Applied Energy*, 97(0):743–748.
- Huang, B. J. and Chuang, M. D. (1996). System design of orifice pulse-tube refrigerator using linear flow network analysis. *Cryogenics*, 36(11):889–902.
- Markides, C. N., Osuolale, A., Solanki, R., and Stan, G.-B. V. (2013). Nonlinear heat transfer processes in a two-phase thermofluidic oscillator. *Applied Energy*, 104(0):958–977.
- Markides, C. N. and Smith, T. C. B. (2011). A dynamic model for the efficiency optimization of an oscillatory low grade heat engine. *Energy*, 36(12):6967–6980.
- Oyewunmi, O. A., Taleb, A. I., Haslam, A. J., and Markides, C. N. (2014). An assessment of working-fluid mixtures using SAFT-VR mie for use in organic Rankine cycle systems for waste-heat recovery. *Computational Thermal Sciences*, 6(4):301–316. ID: 50af28c84073a421.
- Samoilov, A., Kirillov, V., Kuzin, N., Kronberg, A., Glushenkov, M., Taleb, A. I., and Markides, C. N. (2013). An external combustion heat engine with phase-change working fluid. In *Proceedings of the 13th UK Heat Transfer Conference, UKHTC2013*.
- Smith, T. C. (2004). Power dense thermofluidic oscillators for high load applications. In *Proceedings of the 2nd International Energy Conversion Engineering Conference, Providence (RI)*, pages 1–15.
- Smith, T. C. (2005). Asymmetric heat transfer in vapour cycle liquid-piston engines. In *Proceedings of the 12th International Stirling Engine Conference and Technology Exhibition*, pages 302–314.
- Smith, T. C. (2006). Thermally driven oscillations in dynamic applications. *PhD thesis, University of Cambridge, Cambridge, UK*.
- Solanki, R., Galindo, A., and Markides, C. N. (2012). Dynamic modelling of a two-phase thermofluidic oscillator for efficient low grade heat utilization: Effect of fluid inertia. *Applied Energy*, 89(1):156–163.
- Solanki, R., Galindo, A., and Markides, C. N. (2013a). The role of heat exchange on the behaviour of an oscillatory two-phase low-grade heat engine. *Applied Thermal Engineering*, 53(2):177–187.
- Solanki, R., Mathie, R., Galindo, A., and Markides, C. N. (2013b). Modelling of a two-phase thermofluidic oscillator for low-grade heat utilisation: Accounting for irreversible thermal losses. *Applied Energy*, 106(0):337–354.
- Sondhauss, C. (1850). Ueber die schallschwingungen der luft in erhitzten gläseröhren und in gedeckten pfeifen von ungleicher weite. *Annalen der Physik*, 155(1):1–34.
- Stammers, C. W. (1979). The operation of the Fluidyne heat engine at low differential temperatures. *Journal of Sound and Vibration*, 63(4):507–516.

ACKNOWLEDGEMENT

The research leading to these results has received funding from the 7th Framework Programme of the European Commission, grant agreement number 605826.

THERMODYNAMIC SIMULATION AND EXPERIMENTAL VALIDATION OF A CASCADED TWO-STAGE ORGANIC RANKINE CYCLE

Frithjof H. Dubberke*, Klaus-Peter Priebe*, Jadran Vrabec*, Maximilian Roedder[‡] and Matthias Neef[‡]

*University of Paderborn,
Warburger Str. 100, 33098 Paderborn, Germany
E-mail: f.dubberke@thet.upb.de
Web page: <http://thet.uni-paderborn.de>

[‡]University of Applied Sciences Düsseldorf,
Josef-Gockeln-Str. 9, 40474 Düsseldorf, Germany
Web page: <http://www.fh-duesseldorf.de>

ABSTRACT

Employing a zeotropic mixture as a working fluid in organic Rankine cycles (ORC) allows for an energetically favorable heat transfer to the evaporator due to its temperature glide. However, during heat discharge from the condenser, the temperature glide could become a disadvantage. Therefore, a cascaded combination of a two-staged ORC, where the high temperature (HT) cycle is operated with a zeotropic mixture and the low temperature (LT) cycle is operated with a pure fluid in supercritical mode, facilitates both favorable heat uptake from sensible heat sources as well as heat discharge to the environment [6].

As a test rig for according two-stage cycle innovations, an electrically heated cascaded organic Rankine cycle (CORC) was designed and commissioned at the University of Paderborn. To achieve a high efficiency in each cycle, the design strongly depends on the temperature level of the heat source. The integration of four electrical heating rods as a primary heat source into the HT cycle – each with 50 kW and one of them adjustable – the design enables for the specification of different temperature levels. The LT cycle is supplied with the discharged thermal energy of the HT cycle.

After successful commissioning of this two-stage CORC, experimental results are used to evaluate cycle and component performance to study the intended design. For this purpose, a detailed cycle simulation is performed with *EBSILON®Professional* [13], which can be fed with the operating parameters. The aim is to complement the flexible test rig with a suitable thermodynamic model that allows for the study of cycle variations, such as working fluid changes, hardware design improvements, etc.

First results on modeling and experimental validation are presented for a combination of two pure fluids that exemplify the heat integration between the HT and LT cycles. With a validated simulation tool based on energy and mass balances as well as suitable equations of state, the optimization of individual components of the CORC test rig, such as heat exchangers, pumps, condensers, turbines, as well as working fluids can be carried out rapidly and at low cost. The long-term goal of the present project is to put a two-stage CORC system into practical application.

1. INTRODUCTION

Many types of organic Rankine cycles (ORC) aiming at the recovery of exergy from waste heat have been described in the literature. Different cycle layouts and numerous components were studied for a wide variety of working fluids to obtain a better power cycle efficiency for the given heat source characteristics. Depending on the size and the economic situation of an individual project, cycle construction can be more sophisticated and complex to reach a higher power efficiency. The objective of the present experimental setup was to design and construct an ORC test rig that can help to identify

combinations of working fluids and operating conditions that exploit the maximum of the incoming energy from a waste heat source and thus achieve the maximum achievable utilization efficiency.

The cascaded ORC process (CORC) couples two organic Rankine cycles in a subsequent manner (cf. Fig. 1). It is intended to reach with this setup a higher exergetic performance than with conventional ORC by reducing dissipation losses [3].

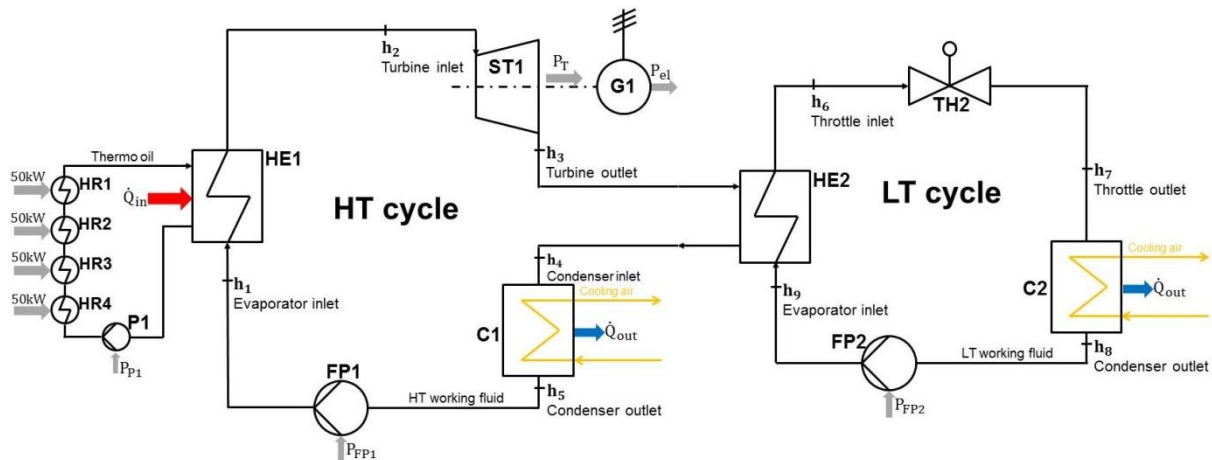


Figure 1: The two-stage ORC couples two organic Rankine cycles as a cascade (CORC).

To maximize the performance of the CORC process, zeotropic mixtures appear to be a reasonable choice as working fluids due to potentially low exergetic losses in the evaporator [9]. Having an almost constant temperature gradient ΔT as a driving force for the heat transfer from waste heat source to working fluid, because of the temperature glide of mixtures during evaporation, may significantly minimize exergetic losses there. Moreover, mixtures, depending on their components and composition, allow that their temperature glide is adjusted to the heat source characteristics. Although the heat sink for condensation is not isothermal [1], its difference in temperature is usually much smaller than the temperature glide of the zeotropic mixture. Therefore, the temperature glide during condensation towards a heat sink could be exergetically unfavorable and would neutralize a large part of the advantage during evaporation. Therefore, the second, i.e. low temperature (LT), stage of the present CORC utilizes the residual exergy from the condenser of the first, i.e. high temperature (HT), cycle. Transferring the process-flow sheet in Fig. 1 of the CORC into a temperature-entropy (T - S) diagram reveals the exergetic utilization of a given sensible waste heat source (cf. Fig. 2).

Fig. 2 shows a schematic example for a CORC where the HT cycle is operating with a zeotropic mixture working fluid in subcritical mode and the LT cycle is operating with a pure working fluid in supercritical mode [2, 7]. The goal is to minimize the area where the heat is brought into the cycle above ambient temperature, minimizing exergy losses [7]. In this work, the use of an internal heat exchanger (IHE) was not studied because it does not affect the exergetic utilization, but rather the thermal efficiency which is insignificant for rating the performance of a cycle.

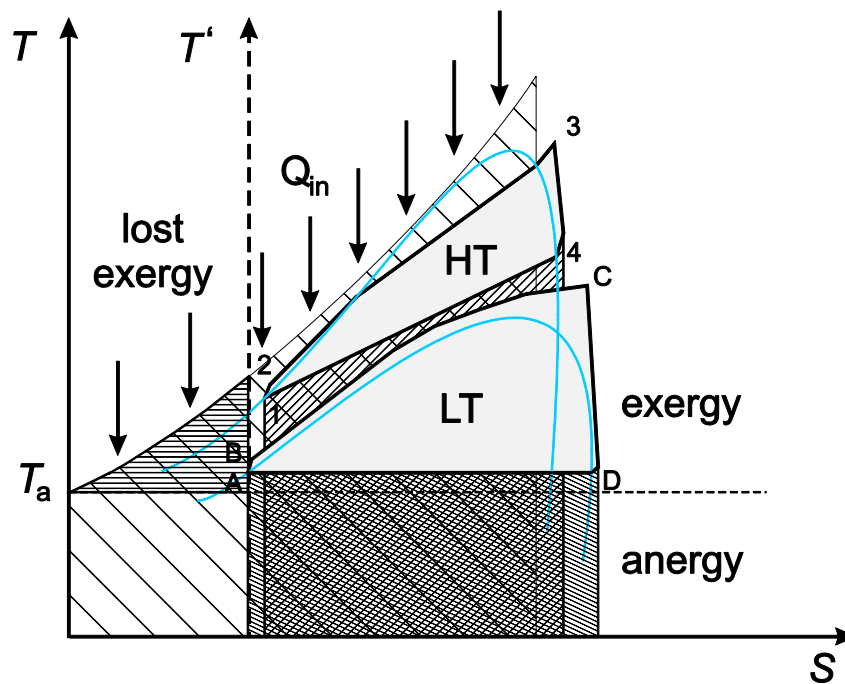


Figure 2: Exergetic analysis of the CORC process: The HT cycle cools the sensible waste heat source down to low temperatures; the LT cycle is linked to the HT cycle via a heat exchanger that acts as a condenser for the HT cycle and as an evaporator for the LT cycle.

2. CORC SETUP

For start-up and testing reasons of the CORC and its components, the HT cycle was filled with about 50 l of cyclopentane and the LT cycle with about 30 l of hexamethyldisiloxane (MM). Even though MM is not a classical low temperature working fluid and is therefore not very much suited for the LT cycle, it was chosen here for testing reasons in terms of its applicability for the installed pump and plate heat exchanger. In addition to its favorable safety in handling, MM might be suitable for trilateral ORC processes [4] and therefore its behavior in a throttle was of interest here.

Due to safety reasons for handling flammable or hazardous fluids, the CORC was placed outside of our laboratory building in a separate container. The CORC was designed in PN 100 for the HT cycle and PN 60 for the LT cycle according to AD 2000-Regelwerk B7. All flanges were sealed with meshed metal (chrome-nickel-molybdenum alloy, material no.: 1.4404) and strengthened graphite gaskets novaphit SSTCTA-L provided by Frenzelit [11], limiting the leakage rate to a tolerable amount.

The heating cycle (HC) was driven by a pump (Allweiler NTWH 25 200/01; cf. Fig. 3 (1)) which was capable of a mass flowrate of up to 450 g/s of therminol 66 [10] which was heated by four 50 kW electrical heating rods. The combined power could fully variably be adjusted from 0-200 kW up to a temperature of 350°C.

A progressive cavity pump (Netzsch Mohnopump: NM031SY12S; cf. Fig. 3 (4a,b)), based on a steel rotor, which is embedded into a chemically resistant synthetic stator with a helical geometry, worked up to a pressure of 4 MPa and was capable to feed a mass flowrate of up to 200 g/s. This model was used as a feed pump for both cycles.

The overall waste heat from the condensers was dissipated to the environment via an air-cooled heat exchanger outside of the container, which was connected by plate heat exchangers (GEA WTT PL 150; cf. Fig. 3 (5)) to the HT and the LT cycle. This separate cooling cycle worked on the basis of an ethylene-glycol/water mixture (1:1.25) and was fed by a pump (Grundfos TP 50-120/2) with a volume flowrate of 4.89 l/s.

The design of the CORC turbine (cf. Fig. 3 (6)) was based on an axially fed centrifugal pump that expanded the superheated vapor through its curved Laval nozzles that were embedded in a blade wheel (1.4305 / X8CrNiS) outwards to the radial expansion tube in the turbine casing (1.4006+QT / X12Cr13). Due to the impulse principle, the torque was mainly generated by the acceleration of the high velocity flow in the blades. The connection between turbine and generator, which was a six pole synchronous servomotor working at 50 Hz (type SK-190-1-30-560 T1), was done by a non-contacting magnetic coupling. For minimizing the gap losses in the turbine, the gap was designed as a labyrinth seal with 12 steps and a rotary shaft seal. Two angular ball bearings in o-arrangement and one deep groove ball bearing form the fixed bearing at the turbine side were used to minimize the slackness of the blade wheel. For cooling and lubrication of the rolling bearings, the casing was flooded with hydraulic oil (Mobil DTE 10 EXCEL 15) in a separate cooling cycle (BCC). The focus of this turbine lied on the application for testing different working fluids for a wide range of thermodynamic conditions and therefore its efficiency was initially subordinate.

The CORC control software framework is based on two systems: the graphical user interface (GUI), which was programmed in Agilent VEE, and a C program which provided functions for the GUI to access the programmable logic controller (PLC). The PLC worked for digital in- and output (DI/DO) and analog in- and output (AI/AO) which expect either a voltage from 0 to 10 V, a current from 4 to 20 mA or a resistance, such as in case of temperature (Pt1000) sensors. The AO connectors were used for setting the motor speed of the pumps by sending a signal from 0 to 10 V to the device. The DI could only detect an activated current (24 V) or deactivated current (0 V) and were used for receiving the error status from the devices. With the DO, variable frequency drives or non-controllable actors were turned on or off by sending a current to the device or their dedicated contactor. All these in- and output data were monitored and were accessible in the GUI. The alternative to a PLC is a hard-wired programmed logic controller (HPC), which was used for important security functions. A variable-frequency drive (VFD) frequency converter was applied in electro-mechanical systems to control pumps and generators.

The mass flowrate measurement worked with a differential pressure aperture according to DIN EN ISO 5167. To ensure that the maximum working temperature of the pressure sensors did not exceed 80°C, a flexible metal tube was used as an extension which was sealed with a copper gasket, respectively, PTFE to the piping system.

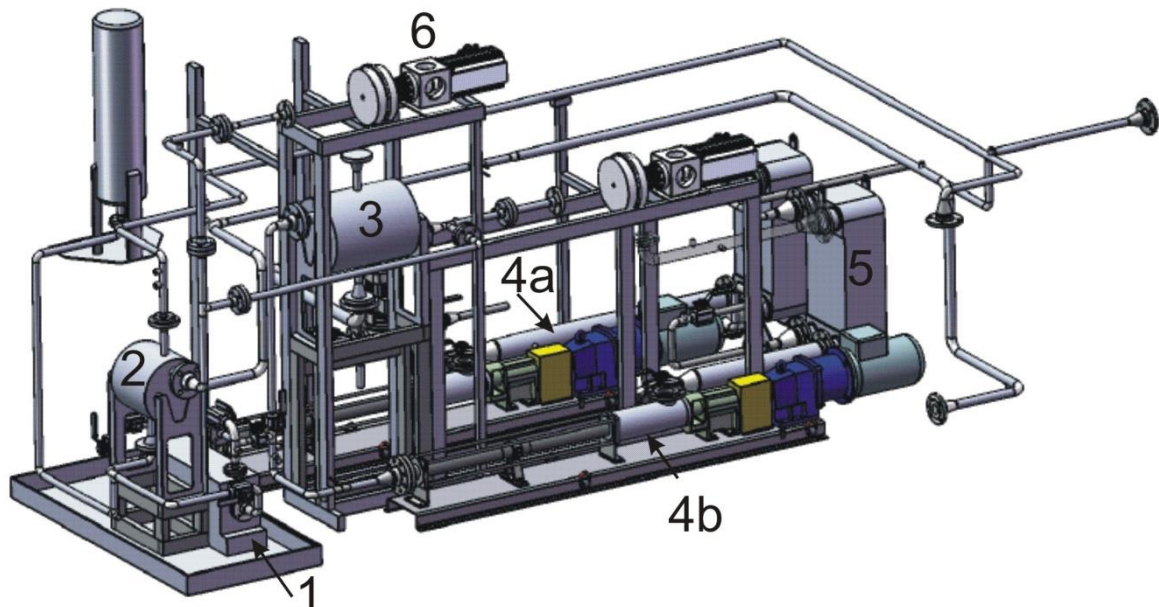


Figure 3: CORC design: 1: pump for heating cycle; 2: heat exchanger (HE1) of HT cycle; 3: heat exchanger (HE2) of LT cycle; 4a,b: feed pumps for HT and LT cycle; 5: condensers; 6: HT turbine and generator.

3. EXPERIMENTAL SETUP AND OPERATION

Before operating the CORC, a standardized safety procedure was carried out, such as checking sensors, valves and leakage in the piping and devices. First, the CORC cooling cycle with the air-cooled heat exchanger was started, before the heating cycle was fired up to a temperature of 180 °C with a thermo oil mass flowrate of about 400 g/s. After activating the cooling cycle (BCC) for the bearings of the turbine of the HT cycle, the turbine (ST1) was set to 3000 rpm. Subsequently, the mass flowrate of the HT cycle was increased by the feed pump FP1 until the inlet temperature of the heating cycle in heat exchanger HE1 stayed constant. This was done until the mass flowrate in the HT cycle and the temperature of the heating cycle was balanced at about 550 K and a mass flowrate of about 144 g/s with an overall transferred heat flow in HE1 of approximately 100 kW was reached.

After reaching a steady state in the HT cycle, the mass flowrate of the feed pump FP2 was set such that the maximum pressure of 0.8 MPa of the throttle TH2 in the LT cycle was reached. This was the case for a mass flowrate of 32 g/s of MM with a total heat flux of 10 kW in HE2.

4. MODEL DESIGN

The CORC structure was implemented in *EBSILON®Professional* [13], which is a simulation tool based on the thermodynamic equations of state and using the *REFPROP* database [12] for fluid properties. The first design calculation of the CORC builds the foundation for later off-design simulations and a system validation, which were not part of the present work. Therefore, the simulation model was generated with a strong association to the experimental setup. Component's efficiencies for the thermodynamic design were defined according to the manufacturer's instructions or in accordance with preceding experimental operations. The final flow diagram of the cycle is shown in Figure 4.

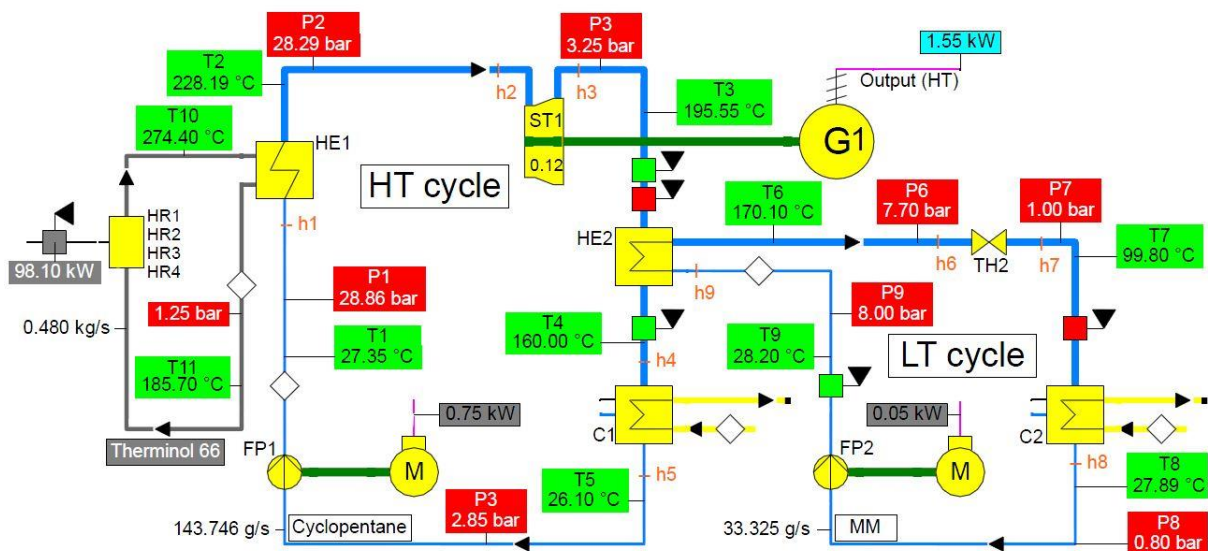


Figure 4: CORC design calculation with *EBSILON®Professional* for a steady state in case of an input heat flow of 98.1 kW.

MODEL COMPOSITION ON THE BASIS OF THE EXPERIMENTAL SETUP

The modelling started with the thermo oil cycle, which supplied 98.1 kW of electrically generated heat to the HT by HE1. For the thermo oil cycle calculation the thermodynamic properties of Therminol 66 [10] were manually implemented into the *EBSILON®Professional* thermoliquid-database. The thermo oil mass flow was calculated with the experimentally specified temperature

difference (T10-T11) and pressure. With the required input parameters of HE1 – working fluid mass flow, input temperature (T1) and main steam pressure (P1) – the thermodynamic start condition (h_1) for the HT calculation was defined. Pressure losses were taken into account by definition of a pressure drop inside a heat exchanger (e.g. 0.057 MPa – P1-P2). Here, the calculated turbine inlet condition (h_2) and the specification of the turbine outlet (h_3) enable for the calculation of the turbine characteristics. It was intended that the high temperature heat is transferred with a suitable high temperature difference (T3-T4), associated with the inlet temperature (T9) of the LT working fluid. However, the experimental system operation presented a high outlet temperature (T4) due to the low load in the LT. Condensing the HT working fluid against the ambient air leads to the condenser outlet condition (h_5).

With a given heat input into the LT and experimental definition of the HE2 inlet condition (h_9) the throttle inlet condition (h_6) was calculated with the given low temperature working fluid mass flow. The working fluid was throttled with a defined pressure drop known from the experiment before it passes through the condenser (C2), where it is also cooled down to ambient condition.

HIGH TEMPERATURE CYCLE

During a steady state operation, the high temperature working fluid was compressed up to 2.8 MPa, (state h_5 to h_1), before the driving heat flow from the electrical heater (98.1 kW) was transferred in the ECO/evaporator/superheater (HE1, state h_1 to h_2). This leads to heating of the working fluid mass flow (0.144 kg/s) from 27.4 °C up to its superheated steam state as shown in the T,s diagram in Figure 5. With the calculated turbine inlet temperature (228.2 °C) and given enthalpy slope, i.e. h_2 to h_3 , the isentropic turbine efficiency (0.12) was calculated with

$$\eta_{s,turbine} = \frac{|h_3 - h_2|}{|h_{3,s} - h_2|} \quad (1)$$

After expansion, the working fluid was still far in the superheated vapor state, due to the poor turbine efficiency, which enables the transfer of the excess heat into the LT cycle, i.e. h_3 to h_4 . Fig. 5 shows that the state h_4 is still superheated and that no condensation takes place in HE2 for the HT cycle. Therefore, the cyclopentane was condensed and supercooled only in the condenser (C1), i.e. h_4 to h_5 and a large part of the heat flow, which was assigned for the LT cycle, was dissipated to the environment.

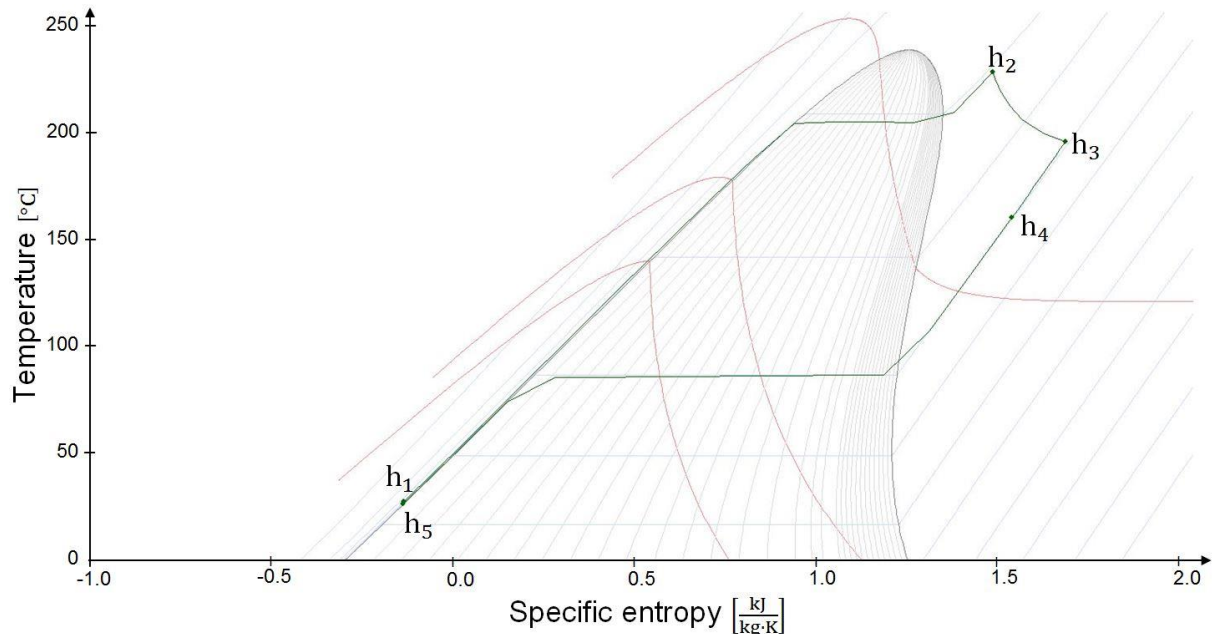


Figure 5: Temperature-entropy ($T-s$) diagram of the HT cycle.

LOW TEMPERATURE CYCLE

The working fluid MM of the LT cycle was compressed to 0.77 MPa before it is heated up to 170 °C in the HE2 to h_7 . Note that this state point was still in the liquid state, cf. Fig. 6. Subsequently, the fluid was throttled (TH1) through the two-phase region by a pressure drop of about 0.7 MPa, but did not pass the dew line (h_7 to h_8). As described above, the heat flow from the HT cycle to the LT cycle in HE2 was insufficient and rather poor so that most of the heat flow was condensed and supercooled from h_8 to h_9 in C2 to the ambient.

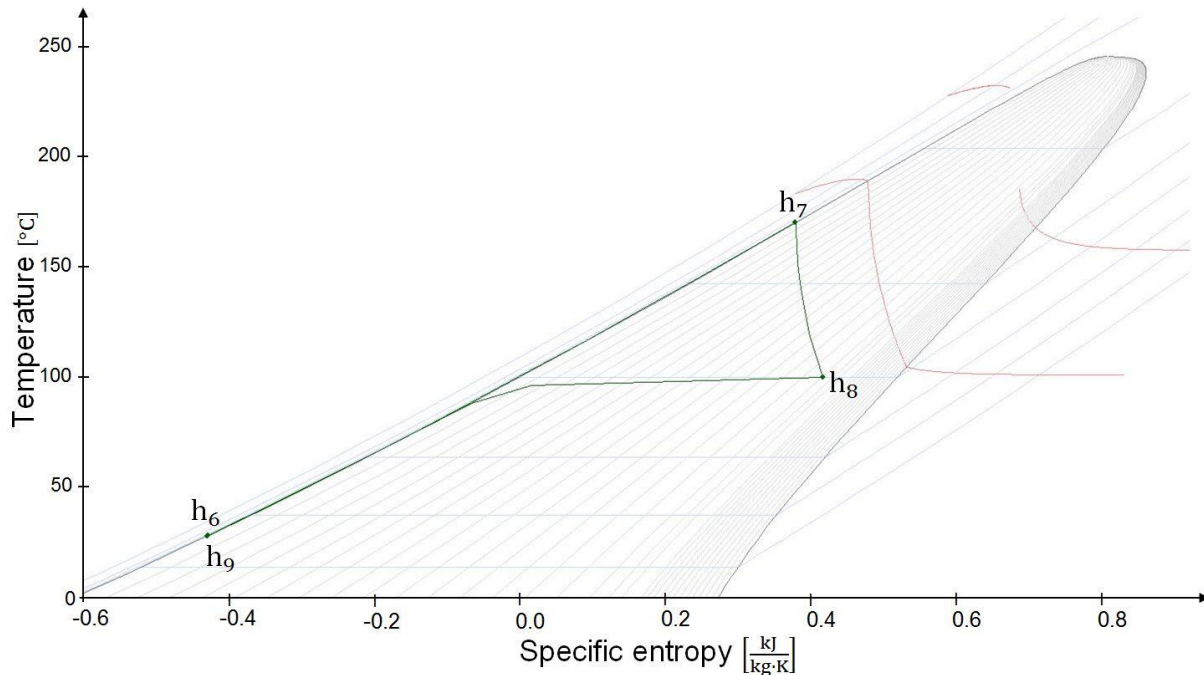


Figure 6: Temperature-entropy (T - s) diagram of the LT cycle.

5. EXPERIMENT VS. SIMULATION

In general, cycle simulations are performed using optimized operating parameters, with respect to a suitable electric cycle efficiency, to improve plant operation. Thus high cycle efficiencies are reached by adjusting the operating parameters gradually until the calculated ones are met. However, for the present vice versa approach, the simulation parameters were thoroughly deduced from the experimental data of the CORC power plant (cf. Table 1) in order to represent the design state of the current construction.

Table 1: Component efficiencies specified for the present CORC simulations.

Cycle	Abbrev.	Component	Efficiency	Isentropic
	ST1	Turbine		0.12
	G1	Generator	0.90	-
	FP1	Feed pump	0.85	0.80
	TH2	Throttle	-	-
	FP2	Feed pump	0.85	0.80

Hence, a suitable comparison between simulation and experiment, with a special focus on the temperature T_2 of the HE1 as an essential component, was performed by a separate comparison of the

cycle components (e.g. heat exchangers) in the following way: As listed in table 2 a steady state with a 98.1 kW heat flow brought into the HT was performed. For the simulation the temperatures HC in- and outlet (T10, T11) were implemented. T1 was calculated by the given isentropic efficiency of the feed pump FP1 and given pressure P1.

Table 2: Experimental data and simulation data – 98.1 kW

	Experimental data	Simulation data
Transferred heat	98.1 kW	98.1 kW
HC inlet (T10)	274.4 °C	274.4 °C
HC outlet (T11)	185.7 °C	185.7 °C
Mass flow HT	144 g/s	144 g/s
HE1 inlet (T1)	27.3 °C	27.4 °C
HE1 inlet (P1)	2.886 MPa	2.886 MPa
HE1 outlet (T2)	226.3 °C	228.2 °C
HE1 outlet (P2)	2.829 MPa	2.829 MPa
ST1 outlet (T3)	194.6 °C	195.6 °C
ST1 outlet (P3)	0.325 MPa	0.325 MPa
HE2 outlet (T4)	160.1 °C	160.0 °C
C1 outlet (T5)	22.0 °C	26.1 °C
C1 outlet (P5)	0.286 MPa	0.285 MPa
k*A (HE1)		1077 W/K

The simulation result for T2 (cf. Table 2) agrees well with the experimental result. Obviously, the implementation and description of the HE1 in the off design-simulation was well reproduced. The temperature T2 for the full load (Table 2) was determined backwards via the isentropic efficiency of ST1 and therefore the simulation agreed well.

6. CONCLUSIONS

This work presented the initial operation of the CORC setup at the University of Paderborn. The objective was to test the functions of all components and their interactions, with a special focus on the performance of the plate heat exchangers and the coupling of the heat flow between the HT and LT cycle. For the first design calculation a steady state CORC operation was performed and simulated with *EBSILON®Professional* at the University of Applied Sciences in Düsseldorf. It was shown that the simulation was able to accurately describe the operating conditions of the CORC, thus delivering a model which can be used for further off-design calculations and validation of experimental data.

Experimental and simulation results also show that the heat flow that is transferred from the HT cycle to the LT cycle via the heat exchanger HE2 is at present with 10 kW very small compared to the enthalpy offered by the HT cycle after expansion in the turbine. This might be due to the fact that the mass flowrate of the LT cycle was small and therefore HE2 was operated far away from its optimal operating conditions because of a low heat transfer coefficient at low flow velocity.

The next step of our project is to adjust HE2 and to extend the pressure range of the LT cycle to allow for higher flowrates. In addition, it is aimed at identifying a zeotropic mixture as a working fluid for the HT cycle and to adapt turbine TH1 to the according thermodynamic conditions. Before designing a turbine for the LT cycle, the heat flow should be optimized with an adequate supercritical working fluid which fits to the mixture of the HT cycle.

NOMENCLATURE

AI	Analog input	(–)
AO	Analog output	(–)
BCC	Cooling water cycle for bearings	(–)
C	Cycle or condenser	(–)
CORC	Cascaded two-stage organic Rankine cycle	(–)
DI	Digital input	(–)
DO	Digital output	(–)
FP	Feed pump	(–)
G	Generator	(–)
GUI	Graphical user interface	(–)
h_i	Specific enthalpy at cycle state i	(kJ/kg)
HE	Electrical heat exchanger	(–)
HC	Heating cycle	(–)
HT	High temperature cycle	(–)
LT	Low temperature cycle	(–)
M	Motor	(–)
MM	Hexamethyldisiloxane	(–)
ORC	Organic Rankine cycle	(–)
PLC	Programmable logic controller	(–)
Q	Heat flow	(kJ)
s	Specific entropy	(kJ/(kg K))
S	Entropy	(kJ/K)
T	Temperature	(°C)
ST1	Turbine	(–)
TH	Throttle	(–)
VFD	Variable-frequency driver	(–)

REFERENCES

- [1] Angelino G., Colonna P., 1998, Multicomponent Working Fluids For Organic Rankine Cycles (ORCs), *Energy*, vol. no. 23: p. 449-63
- [2] Chen H., Goswami D. Y., Rahman M. M., Stefanakos E. K., 2011, A supercritical Rankine cycle using zeotropic mixture working fluids for the conversion of low-grade heat into power, *Energy*, vol. no. 36: p. 549-555
- [3] DiPippo R., 2004, Second Law assessment of binary plants generating power from low-temperature geothermal fluids, *Geothermics*, vol. no. 33: p. 565-586
- [4] Lai N. A., Fischer J., 2012, Efficiencies of power flash cycles, *Energy*, vol. no. 44: p. 1-11
- [5] Lai N. A., Wendland M., Fischer J., 2010, Working fluids for high-temperature organic Rankine cycles, *Energy*, vol. no. 39: p. 199-211
- [6] Liu B., Rivière P., Coquelet C., Gicquel R., David F., 2012, Investigation of a two stage Rankine cycle for electric power plants, *Applied Energy*, vol. no. 100: p. 285–294.
- [7] Rant Z., 1956, Exergie, ein neues Wort für ‘Technische Arbeitsfähigkeit’, *Forsch. Ing. Wes.*, vol. no. 22: p. 36-37
- [8] Saleh B., Koglbauer G., Wendland M., Fischer J., 2007, Working fluids for low-temperature organic Rankine cycles, *Energy*, vol. no. 32: p. 1210-1221
- [9] Schuster A., Karellas S., Aumann R., 2010, Efficiency optimization potential in supercritical

Organic Rankine Cycles, Energy, vol. no. 35: p. 1033-1039

- [10] FRAGOL, Therminol Productinformation (FRAGOL SCHMIERSTOFF GMBH + CO. KG)
- [11] Frenzelit, novaphit SSTC Technical Datasheet (Frenzelit Werke GmbH)
- [12] Lemmon E. W., Huber M. L., McLinden M.O., 2013, "NIST Standard Reference Database 23, Fluid Thermodynamic and Transport Properties REFPROP, User's Guide," National Institute of Standards and Technology (NIST)
- [13] Steag Energy Services, 2014, "*EBSILON®Professional* Program Documentation"

ACKNOWLEDGEMENT

We gratefully acknowledge Deutsche Forschungsgemeinschaft (DFG) for funding the experimental setup of the CORC.

EXPERIMENTAL STUDY ON ADIABATIC TWO-PHASE EXPANSION IN A CYLINDER FOR TRILATERAL CYCLE

H. Kanno^{1,2*}, Y. Hasegawa², I. Hayase² and N. Shikazono²

¹ Railway Technical Research Institute, Drive systems, Vehicle control Technology Division,
2-8-38 Hikari-cho, Kokubunji-shi, Tokyo, Japan
E-mail: kanno.hiroshi.14@rtri.or.jp

² Institute of Industrial Science, The University of Tokyo,
4-6-1 Komaba, Meguro-ku, Tokyo, Japan
E-mail: shika@iis.u-tokyo.ac.jp

* Corresponding Author

ABSTRACT

In the present study, temperature and pressure measurements and visualization of two-phase adiabatic expansion for trilateral cycle are carried out. Experimental setup with piston and cylinder which mimics the reciprocating expander is constructed and boiling phenomenon is visualized. Working fluids are water and ethanol, and initial temperatures are 100 and 80 °C in this study. Output work is calculated from the $P - V$ diagram. In addition, filter-type sintered metal is fixed on the bottom of the cylinder to enhance boiling. The difference between measured and quasi-static pressures becomes larger and the adiabatic efficiency decreases as piston velocity is increased. With sintered metal filter on the bottom of the cylinder, the deterioration of adiabatic efficiency becomes moderate for both working fluids because of the initial captured bubbles in the sintered metal. The adiabatic efficiency for pore diameter of $d_{\text{pore}} = 20 \mu\text{m}$ and piston velocity 300 mm/s case is about 87 % for water, which is 1.05 times larger than that of the smooth surface condition. For ethanol, the adiabatic efficiency was about 92 % which is 1.18 times larger than that of the smooth surface condition. To investigate the feasibility of the two-phase expander, an experiment reproducing the intake and exhaust processes is conducted. The adiabatic efficiency increases with the increase of maximum piston velocity because of the reduction of heat loss. The sintered metal filter for boiling enhancement is also effective in an expander with intake and exhaust processes.

1. INTRODUCTION

In recent years, trilateral cycle attracts large attentions for waste heat recovery from moderate or low temperature heat sources (Smith et al., 1993, 1994, 1996, Fischer, 2011, Steffen et al., 2013). In the trilateral cycle, working fluid is pressurized and kept as a single liquid phase during the heating process. Heat is transferred from the heat source to the single phase working fluid, so the exergy loss can be drastically reduced because of favorable temperature profile matching between the heat source and the working fluid. In the expansion process, working fluid is flashed and becomes liquid-vapor two-phase. Thus, for the trilateral cycle system, the heat exchanger to reduce temperature difference and the two-phase expander are the key components.

For two-phase expansion or wet-vapor expansion, Lysholm turbine, scroll or reciprocating expanders have been investigated from the view point of erosion durability. Smith et al. (1993, 1994 and 1996) estimated the performance and cost of trilateral flash cycle using Lysholm twin screw turbine. They reported that the adiabatic efficiency of the expander can reach 70 %, and that the trilateral flash cycle can produce 1.8 times larger output power than a simple Rankine cycle for hot steam of 100 – 200 °C. Steffen et al. (2013) proposed a novel trilateral cycle using cyclone separator and reciprocating

expander, and simulated the influence of injection timing, material of cyclone, the size and frequency of reciprocating expander. They concluded that the effective thermal insulation of the cyclone wall is important, and found that large stroke volume and engine speed deteriorate isentropic efficiency of the expander due to the influence of injection timing. Bao et al. (2013) reviewed the advantages of several kinds of expanders from the view point of the working fluid, capacity and cost. They reported that reciprocating piston expander has the advantage of adaptability for variable working conditions and tolerance for two-phase expansion.

A two-phase expansion in adiabatic condition in constant volume chamber is called as flash evaporation. Yan et al. (2010) and Zhang et al. (2012) conducted an experimental study on static and circulatory flash evaporation, and investigated the steam-carrying effect. Saury et al. (2005) studied flash evaporation of water film and proposed a correlation between the dimensionless maximum mass flow rate, dimensionless initial temperature, depressurization rate, superheat and initial water height.

The above flash evaporation studies were carried out in a flash chamber, but did not focus on the output work which could be taken out from the system. Therefore, research on adiabatic two-phase expansion to generate output power or enhancing boiling in an expander is not fully investigated. As mentioned by Bao et al. (2013), reciprocating expander has several advantages for the two-phase expansion. However, experimental study for reciprocating two-phase expansion is still limited.

In this study, working fluid is expanded in a thermally insulated cylinder and boiling is visualized by the high speed micro scope to investigate the basic characteristics of adiabatic two-phase expansion in a reciprocating expander. The working fluid and the setup are warmed up before the expansion experiment to exclude the effect of heat loss. The pressure sensor and thermo-couple are embedded in the piston to measure vapor temperature. The output power is obtained from the measured $P - V$ diagram. The effect of piston velocity on adiabatic efficiency is evaluated. In addition, sintered metal filter is placed on the bottom of the cylinder to enhance boiling. To investigate the feasibility of the two-phase expander, continuous reciprocating expansion experiment is conducted. The adiabatic efficiency and heat loss are investigated and the effectiveness of the sintered metal is also evaluated.

2. TWO-PHASE EXPANSION EXPERIMENT

2.1 Experimental setup and procedure

Figure 1 shows the insulated cylinder for two-phase expansion experiment. In this study, water of 100 °C and ethanol of 80 °C are used as the working fluids. The cylinder is a double pipe made of polycarbonate. The piston with diameter of $D_p = 55$ mm is also made of polycarbonate. The bottom of the cylinder is made of thin stainless plate with thickness of 0.8 mm. The working fluid and the setup are heated up to the operating temperature by hot air in order to exclude the effect of heat loss. Then, the double tube and the back side of the cylinder bottom are vacuumed by a vacuum pump for thermal insulation before the expansion experiment. The temperatures of liquid and vapor phases are measured by the thermo-couples attached to the piston and the bottom of the cylinder. The pressure in the cylinder is measured by the pressure sensor embedded in the piston. Indicated work is obtained from a $P - V$ diagram.

Figure 2 shows the schematic of the experimental setup. Table 1 shows the physical properties of the stainless plate and the cylinder. Table 2 shows the experimental condition. The two-phase expansion experiments are carried out in the following procedure. First, the piston is initially set at $z_p = z_0$ by the linear actuator (EZC6D030M-K, Oriental Motor). Then, by operating the cross valves No.4, 5 and 6, the hot air from the heater (SD-2-2, Sakaguchi E.H VOC) is introduced to the insulation chamber (double-pipe cylinder) to warm up the setup. During this procedure, the flash chamber (test section) is connected to the vacuum pump (GLD-201B, Ulvac) by switching the cross valve 7 to purge the air in the test section. When the pressure in the test section becomes smaller than 0.001 MPa, the cross valves No. 7 and 8 are switched, and then the test section is connected to the syringe (1050-TLL, GL

Table 1: Physical properties of stainless plate and cylinder

	Stainless plate (SUS304)	Cylinder (polycarbonate)
ρ (kg/m ³)	9790	1200
C (kJ/kgK)	0.59	1.05

Table 2: Experimental condition

Parameter	Value
z_{liq} (mm)	6
z_0 (mm)	9
ε_{exp}	20
α_p (mm/s ²)	833
$v_{p,max}$ (mm/s)	1 – 300

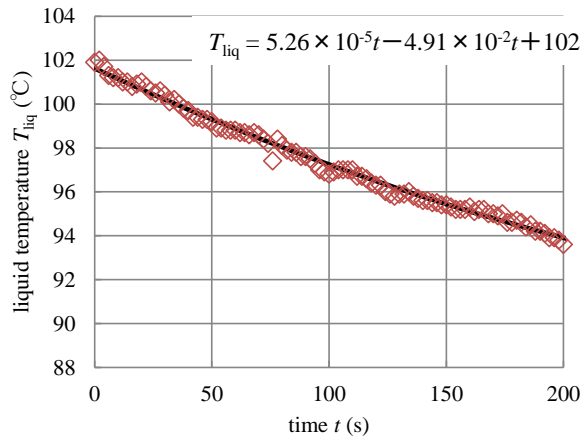


Figure 3: Liquid temperature change for water, 100 °C.

Table 3: Properties of sintered metal filter

Material	Pore diameter (μm)	Porosity (%)	Thickness (μm)
SUS304	5	80	0.37
	20	79	0.62
	75	87	0.87

$$\eta_{ad} = \frac{W_{exp}}{W'_{ise}} \quad (1)$$

$$W_{exp} = \int p_p dV_{cyl} \quad (2)$$

$$W'_{ise} = \int p'_{ise} dV_{cyl} \quad (3)$$

2.3 Experimental Results

Figure 4 and Figure 5 show the visualization results with smooth surface for water and ethanol, respectively. Boiling bubbles are observed from the edge of the bottom of the cylinder. The number and frequency of the boiling bubbles increase as the piston velocity is increased in both working fluids. Figure 6 shows the visualization for water with sintered metal filter of $d_{pore} = 20 \mu\text{m}$. The number of bubbles increased compared with the smooth surface case. The density of bubble departure sites also increased. Figure 7 shows the visualization for ethanol with sintered metal filter of $d_{pore} = 20 \mu\text{m}$. A lot of small bubbles are generated from the sintered metal filter, and the vapor-liquid interface is lifted by the bubbles. For both cases, boiling is enhanced by using sintered metal filter. In this experiment, the working fluid is heated from the bottom of the cylinder before the expansion process, and boiling bubbles are observed from the sintered metal during this heating process. It is considered that the small bubbles trapped by the sintered metal filter are the initial boiling sites. The small bubbles remained in the sintered metal filter before the expansion process are effective to enhance boiling in adiabatic expansion.

Figure 8 shows the $P - V$ diagram for water with piston speed of $v_{p,max} = 128 \text{ mm/s}$. The pressure decreases immediately and the pressure reduction becomes moderate afterwards. During the expansion process, the pressure becomes high with sintered metal filter compared with the smooth surface case. The pressure is generally higher for the sintered metal filter with larger pore diameters. Figure 9 shows the adiabatic efficiencies for water. Adiabatic efficiency decreases as the piston velocity is increased, while the efficiency becomes higher for larger pore diameters. In the case of $v_{p,max} = 300 \text{ mm/s}$ and $d_{pore} = 20 \mu\text{m}$, the adiabatic efficiency is about 87 % which is 1.05 times larger than that of the smooth surface case. In general, wettability of water is poor and the bubble diameter

observed in the visualization is larger than that of ethanol. Therefore, boiling is more enhanced when using large pore diameter filters.

Figure 10 shows the $P - V$ diagram for water with piston speed of $v_{p,max} = 128$ mm/s. The pressure reduction is restrained by the effect of boiling enhancement when using the sintered metal filter of $d_{pore} = 5$ and 20 mm. For $d_{pore} = 75$, boiling becomes unstable. In some cases, pressure is kept high, but in other cases, the pressure decreases immediately and recovers by following explosive boiling. Figure 11 shows the adiabatic efficiencies for ethanol. For $v_{p,max} = 300$ mm/s and $d_{pore} = 20$ μ m case, the adiabatic efficiency is about 92 % which is 1.18 times larger than that of the smooth surface case. When using the sintered metal filter of $d_{pore} = 75$, the adiabatic efficiency value varies due to the unstable boiling. For ethanol, wettability is better than water, and it is difficult to keep the initial nucleate bubble until the expansion process starts. From these results, it is considered that small pore diameter is preferable when using working fluids of good wettability.



Figure 4: Visualization for water with smooth surface. (a) $v_{p,max} = 8$ mm/s, (b) $v_{p,max} = 32$ mm/s and (c) $v_{p,max} = 128$ mm/s.



Figure 5: Visualization for ethanol with smooth surface. (a) $v_{p,max} = 8$ mm/s, (b) $v_{p,max} = 32$ mm/s and (c) $v_{p,max} = 128$ mm/s.

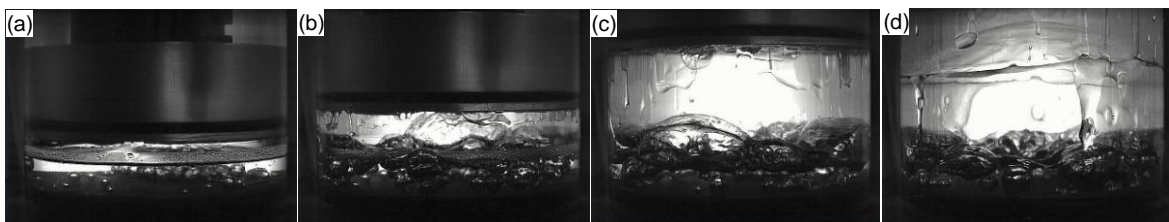


Figure 6: Visualization results for water with sintered metal filter of $d_{pore} = 20$ μ m and $v_{p,max} = 128$ mm/s. (a) $t = 0.05$, (b) $t = 0.1$, (c) $t = 0.2$, and (d) $t = 0.4$.

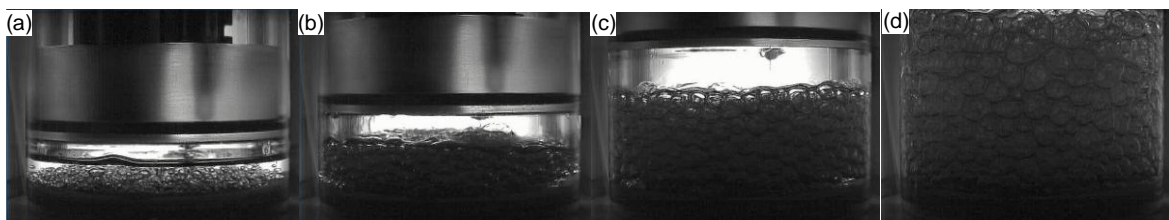


Figure 7: Visualization results for ethanol with sintered metal filter of $d_{pore} = 20$ μ m and $v_{p,max} = 128$ mm/s. (a) $t = 0.05$, (b) $t = 0.1$, (c) $t = 0.2$, and (d) $t = 0.4$.

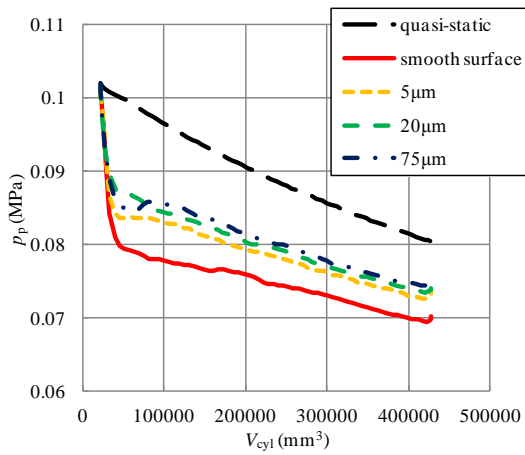


Figure 8: $P - V$ diagram for water and $v_{p,max} = 128$ mm/s.

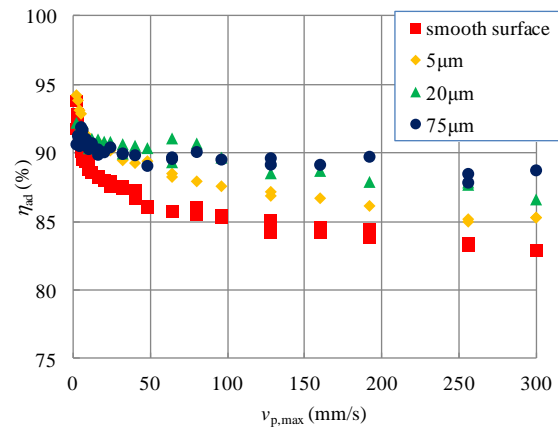


Figure 9: Adiabatic efficiencies for water.

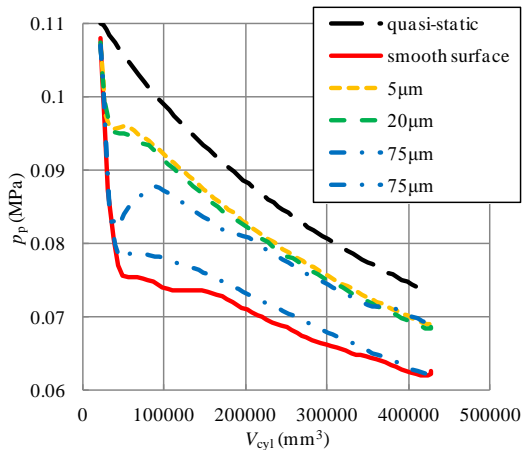


Figure 10: $P - V$ diagram for ethanol and $v_{p,max} = 128$ mm/s.

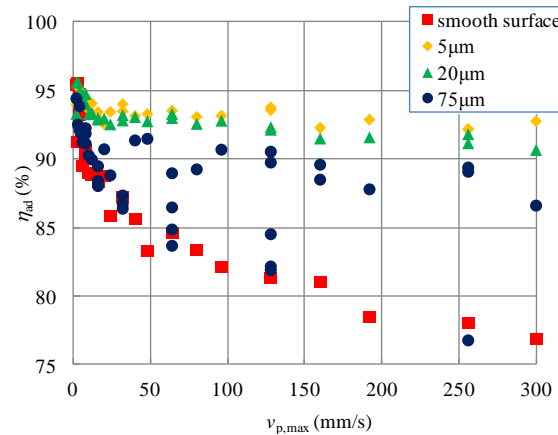


Figure 11: Adiabatic efficiencies for ethanol.

3. TWO-PHASE EXPANSION IN RECIPROCATING EXPERIMENTAL SETUP

3.1 Experimental setup and procedure

In the actual reciprocating expander, expansion process is divided into three processes, i.e. intake, expansion and exhaust. In the intake process, hot working fluid is introduced into the cold cylinder, so the heat loss deteriorates the adiabatic expansion, while the initial bubbles in the cylinder can enhance boiling.

Figure 12 shows the reciprocating experimental setup. The piston, cylinder and the mechanism of setup-warming and vacuum insulation are the same as the previous setup, while a mechanism to introduce hot working fluid into the cylinder is added. Water of 100 °C and ethanol of 80 °C are used as the working fluids. Working fluid in supply-tank No.1, pre-heater No.2, and heater No.4 is heated to the operating temperature T_0 . At the beginning of the expansion process, the heated working fluid is introduced by the plunger No. 3 pushed by the actuator No.11. The working fluid introduced into the cylinder No.5 is expanded by the piston moved by the actuator No.11. At the beginning of exhaust process, the exhaust valve is opened by DC solenoid and the working fluid in the cylinder is exhausted to the vacuum tank No.6. The back pressure in the vacuum tank is kept about 0.02 MPa.

In this experiment, the piston and the plunger for introducing the working fluid are accelerated and decelerated respectively. The cut-off timing which is the timing to stop introducing the working fluid is determined by the plunger displacement. Figure 13 shows the cut-off timing. The cut-off volume ratio $\varepsilon_{cut,vol}$ is defined by Eq. (4), and the expansion ratio ε_{exp} is defined by Eq. (5). Table 4 shows the experimental condition. The maximum piston velocity is changed by acceleration α_p . Note that the

acceleration is fixed as $\alpha_p = 96 \text{ mm/s}^2$ in the warming-up operation.

Warming-up operation including 10 cycles of intake, expansion and exhaust processes is conducted. After this warming-up operation, data during 5 cycles of intake, expansion and exhaust processes are collected. Figure 14 shows the example of warming-up operation and data acquisition operation. Liquid temperature T_{nozzle} measured in the inlet nozzle is gradually increased in the warming-up operation and kept at the operating temperature within the range of about $\pm 2 \text{ }^\circ\text{C}$ during the data acquisition operation. Output work is calculated by taking the average of 5 cycles of the $P - V$ diagram, and adiabatic efficiency is evaluated.

In this experiment, the initial temperature of the bottom plate before the expansion process is assumed to be the same as the saturated temperature of p_p before the expansion. Then, heat loss E_{loss} from the working fluid to the bottom plate is calculated. The isentropic efficiency which excludes the effect of the heat loss is defined as Eq. (6).

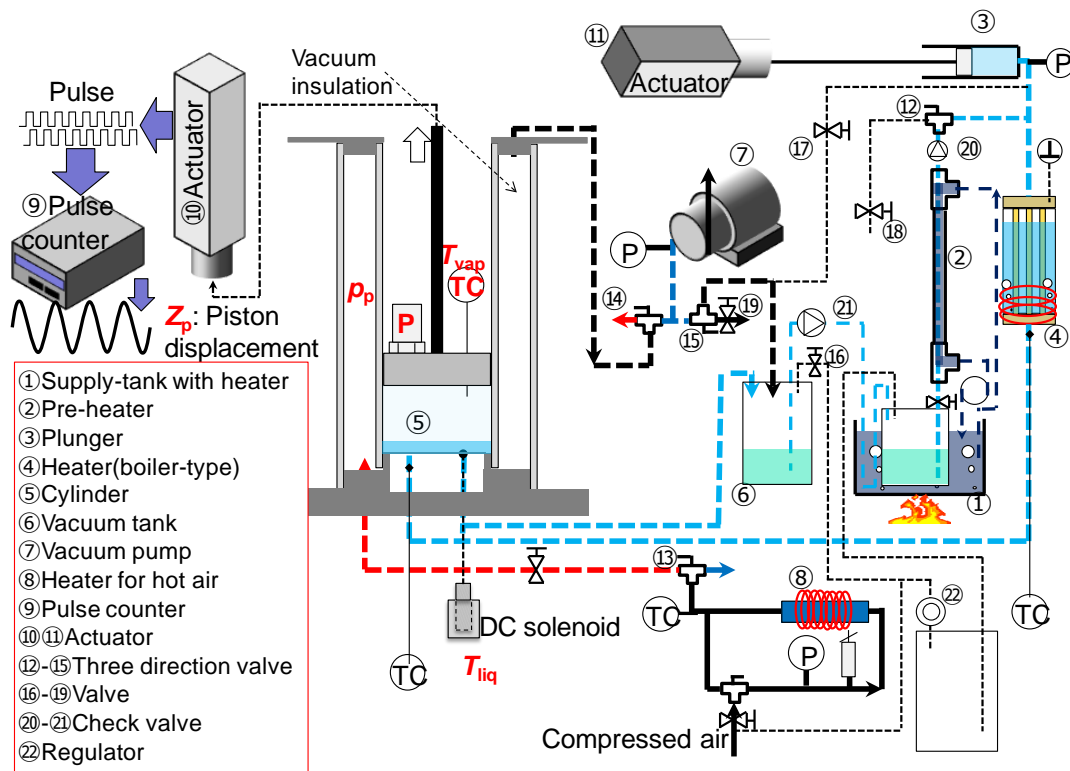


Figure 12: Schematic of the reciprocating experimental setup

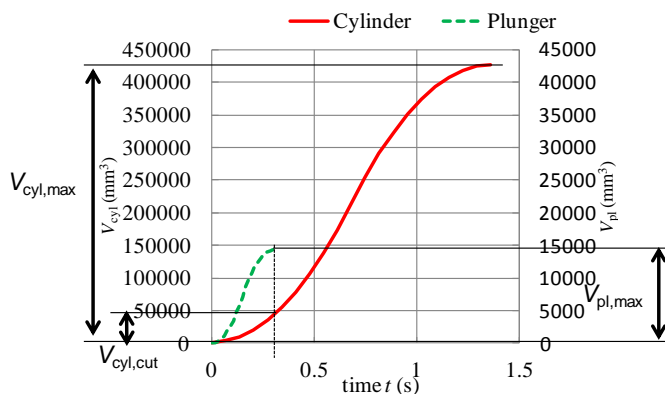


Figure 13: Cut-off point

Table 4: Experimental condition

Parameter	Value
z_{liq} (mm)	6
z_0 (mm)	0.5
z_{max} (mm)	180
α_p (mm/s^2)	10 - 769
$v_{p,\text{max}}$ (mm/s)	42.4 - 371.6
$\varepsilon_{\text{cut.vol}}$ (mm/s)	3
ε_{exp} (mm/s)	30

In warming-up operation, α_p is 96.2.

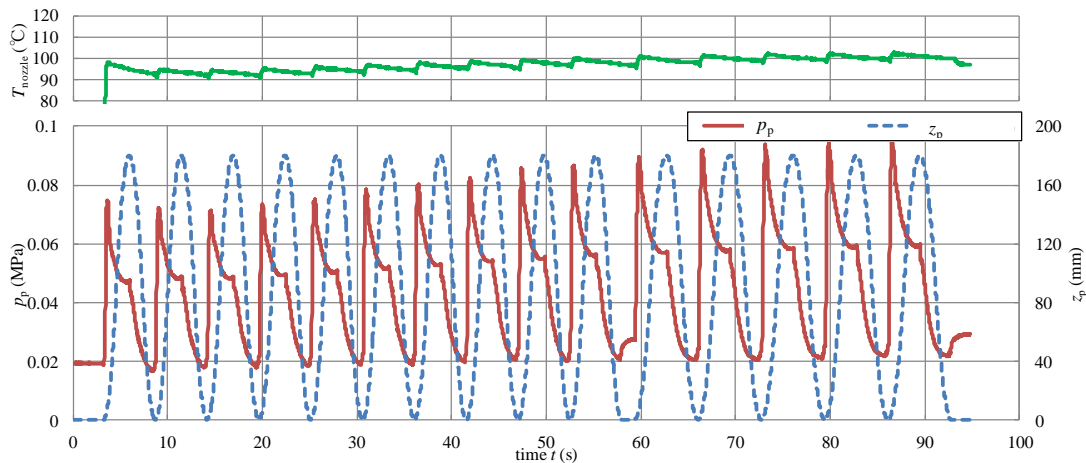


Figure 14: 10 cycles of warming-up operation and 5 data acquisition cycles for water at $\alpha_p = 47.8 \text{ mm/s}^2$.

$$\varepsilon_{\text{cut,vol}} = \frac{V_{\text{cyl,cut}}}{V_{\text{pl,max}}} \quad (4)$$

$$\varepsilon_{\text{exp}} = \frac{V_{\text{cyl,max}}}{V_{\text{pl,max}}} \quad (5)$$

$$\eta_{\text{ise}} = \frac{W_{\text{exp}}}{W_{\text{ise}} - E_{\text{loss}}} \quad (6)$$

3.2 Experimental results

Figure 15 shows the efficiencies with smooth surface and sintered metal filter of $d_{\text{pore}} = 20 \text{ }\mu\text{m}$ for water as a working fluid. The isentropic efficiency decreases or remains nearly constant with the increase of piston velocity, while the adiabatic efficiency increases because of the reduction of heat loss. It can be considered that the effect of heat loss becomes negligible when the piston velocity is high. When using the sintered metal filter, the adiabatic efficiency increases. However, the effect of the sintered metal filter becomes small as the piston velocity is increased.

Figure 16 shows the efficiencies for ethanol with smooth surface and sintered metal filter of $d_{\text{pore}} = 20 \text{ }\mu\text{m}$. The adiabatic efficiency of the sintered metal filter is about 5 % higher than that of the smooth surface case. From these results, the boiling enhancement is also important for the reciprocating expander with intake and exhaust processes, and the sintered metal filter should be also effective.

Ohman et al. (2013) reported that the adiabatic efficiency for vapor expansion in a Lyshol turbine is about 60 – 80 %, and it slightly decreases as the vapor quality measured at the inlet of the expander is reduced. Their study takes into account the electrical loss of generator and leakage loss to obtain adiabatic efficiency. In our reciprocating experiment, the maximum value of adiabatic efficiency is about 85 %, while the efficiency is defined by the indicated work. Therefore, if the mechanical and electrical losses are taken into account, the adiabatic efficiency should decrease a little from this value. From these results, the adiabatic efficiency of two-phase expansion can achieve nearly the same efficiency as the vapor expansion used for Rankine cycle. It is noted that the exergy efficiency of trilateral cycle is higher than that of Rankine cycle if the expander efficiencies are the same, which is shown by thermodynamic analysis in our previous study (Kanno et al., 2014).

For reciprocating expansion, several losses must be considered. For example, the injection loss due to the delay of the working fluid introduction, and non-equilibrium loss which is caused by the temperature difference between the liquid phase and vapor phase should be considered. To increase the adiabatic efficiency for high piston velocity conditions, reduction of non-equilibrium loss is important. Further investigation is required for understanding non-equilibrium loss.

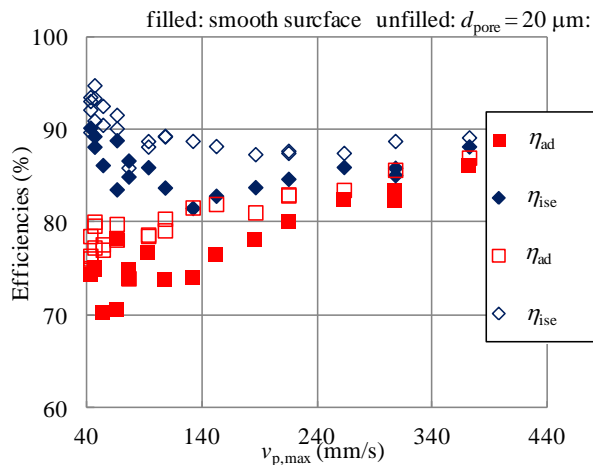


Figure 15: Efficiencies for water.

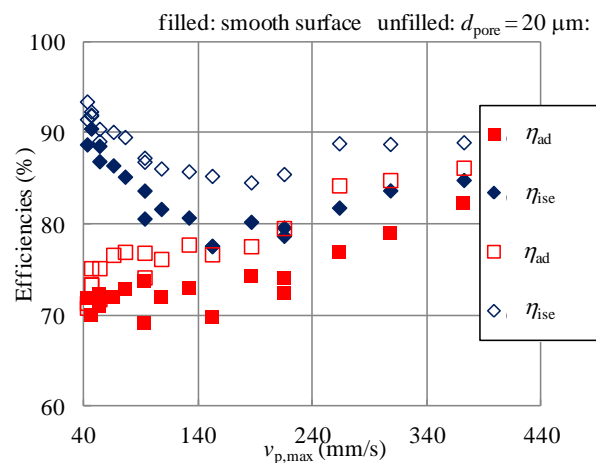


Figure 16: Efficiencies for ethanol.

4. CONCLUSIONS

An adiabatic two-phase expansion experiment in a cylinder with moving piston is conducted. From the experimental results, following conclusions are obtained.

When the heat loss is excluded, the adiabatic efficiency decreases with piston velocity. Sintered metal filter fixed on the bottom of the cylinder can enhance boiling. The adiabatic efficiency for pore diameter of $d_{\text{pore}} = 20 \mu\text{m}$ and piston velocity 300 mm/s is about 87 % for water, which is 1.05 times larger than that of smooth surface condition. The adiabatic efficiency is about 92 % for ethanol, which is 1.18 times larger than that of the smooth surface condition. In the actual reciprocating expander with intake, expansion and exhaust processes, the effect of heat loss to the setup cannot be neglected. However, the effect of heat loss decreases with the increase of the piston velocity. The sintered metal filter is also effective to enhance boiling for the reciprocating expanders with intake and exhaust processes. Reciprocating two-phase expander can achieve nearly the same adiabatic efficiency as the vapor expander. Thus, it is considered that trilateral cycle can achieve very high exergy efficiency as expected.

NOMENCLATURE

C	specific heat	(kJ/kgK)
D	diameter	(mm)
E	heat or energy	(J)
m	mass	(kg)
p	pressure	(MPa)
t	time	(s)
T	temperature	(°C)
v	velocity	(mm/s)
V	volume	(mm ³)
W	output work	(J)

Greek symbols

α	acceleration	(mm/s ²)
ε	volumetric ratio	(-)
η	efficiency	(%)
ρ	density	(kg/m ³)

Subscript

0	initial condition
---	-------------------

ad	adiabatic
cut	cut-off
cyl	cylinder
exp	expansion
ise	isentropic
liq	liquid
loss	loss
max	maximum
nozzle	nozzle
p	piston
pl	plunger
pore	pore
vap	vapor
vol	volumetric

REFERENCES

- Bao, J., Zhao, L., 2013, A review of working fluid and expander selections for organic Rankine cycle, *Renewable and Sustainable Energy Reviews*, vol. 24, pp. 325 – 342.
- Fischer, J., 2011, Comparison of trilateral cycles and organic Rankine cycles, *Energy* Vol. 36, pp. 6208 – 6219.
- Kanno, H., Shikazono, N., 2014, Thermodynamic Simulations of Rankine, Trilateral and Supercritical Cycles for Hot Water and Exhaust Gas Heat Recovery, *Mechanical Engineering Journal*, Vol. 1 , p. TEP0046.
- Lemmon, E.W., Huber, M.L., McLinden, M.O., 2010, NIST standard reference database 23: reference fluid thermodynamic and transport properties REFPROP version 9.0. Gaithersburg: *National Institute of Standards and Technology*, Standard Reference Data Program;
- Ohman, H., Lundqvist, P., 2013, Experimental investigation of a Lysholm Turbine operating with superheated, saturated and 2-phase inlet conditions, *Applied Thermal Engineering*, vol. 50, pp. 1211 – 1218.
- Oreijah, M., Date, A., Akbarzadaha, A., 2014, Comparison between Rankine Cycle and Trilateral Cycle in Binary System for Power Generation, *Applied Mechanics and Materials*, vol. 464, pp. 151-155.
- Saury, D., Harmand, S., Siroux, M., 2005, Flash evaporation from a water pool: Influence of the liquid height and of the depressurization rate, *International Journal of Thermal Sciences*, vol. 44, pp. 953–965.
- Smith, I.K., 1993, Development of the trilateral flash cycle system. 1. Fundamental considerations., *Journal of Power and Energy*, vol. 207, pp. 179-194.
- Smith, I.K., Dasilva, R.P.M., 1994, Development of the trilateral flash cycle system. 2. Increasing power output with working fluids mixtures, *Journal of Power and Energy*, vol. 208, pp. 135-144.
- Smith, I.K., Stosic, N., Aldis, C.A., 1996, Development of the trilateral flash cycle system. 3. The design of high-efficiency two-phase screw ex panders, *Journal of Power and Energy*, vol. 210, pp. 75-93.
- Steffen, M., Loffler, M., Schaber, K., 2013, Efficiency of a new Triangle Cycle with flash evaporation in a piston engine, *Energy*, Vol.57, pp. 295-307.
- Yan, J., Zhang, D., Chong, D., Wang, G., Li, L., 2010, Experimental study on static/circulatory flash evaporation, *International Journal of Heat and Mass Transfer*, vol. 53, pp. 5528–5535.
- Zhang, D., Chong, D., Yan, J., Zhang, Y., 2012, Study on steam-carrying effect in static flash evaporation, *International Journal of Heat and Mass Transfer*, vol. 55, pp. 4487–4497.

ACKNOWLEDGEMENT

This work has been partly supported by the Japan Science and Technology Agency (JST). The authors gratefully acknowledge for the financial support.

PERFORMANCE EVALUATION OF NGCC AND COAL-FIRED STEAM POWER PLANTS WITH INTEGRATED CCS AND ORC SYSTEMS

Vittorio Tola

Department of Mechanical, Chemical and Material Engineering, University of Cagliari,
Via Marengo 2, 09123 Cagliari, Sardegna, Italia
e-mail: vittorio.tola@dimcm.unica.it

ABSTRACT

A performance assessment of natural gas-fueled combined cycle (NGCC) power plants and pulverized coal-fired (PC) steam power plants, both equipped with a CO₂ removal system and integrated with an Organic Rankine Cycle (ORC), was performed. For large scale power plants (a fuel chemical power input of 1000 MW was assumed as reference for both NGCC and PC plants), post-combustion CO₂ removal systems based on chemical solvents are expected to reduce the net plant efficiency between 9-12 percentage points at 90% overall CO₂ capture. The recovery of low temperature heat, available from the solvent-based CO₂ removal systems and related process equipment, can be performed in order to increase the plant efficiency. In particular main low temperature heat sources available are: flue gas coolers upstream of the CO₂ capture unit (80-100 °C for NGCC and about 120 °C for PC), amine condenser of the CO₂ desorption column (100-110 °C) and amine reboiler water cooling (130-140°C). This paper evaluates low temperature heat recovery by means of an Organic Rankine Cycle (ORC) that can convert heat into electricity at very low temperatures. By producing additional electrical power by the ORC, the global performance of the above mentioned power plants can be improved. This study shows that the integration of CCS with the steam plant allows to recover a larger amount of waste heat in comparison to NGCC (more than 200 MW versus about 110 MW). As a consequence, integrating ORC technology with a post-combustion capture system leads to an increase of efficiency of about 1-1.5 percentage points for the NGCC plant and of about 2 percentage points for the steam plant, depending on the amount of low temperature heat available. Among several organic fluids available, N-Butane was assumed as organic operating fluid. Optimum cycle operating temperatures and pressures were identified in order to evaluate the most efficient approach for low temperature heat recovery.

1. INTRODUCTION

Carbon capture and storage (CCS) is expected to become an important strategy to reduce greenhouse gases emissions in the power sector. IEA studies estimate that CCS alone will account for 19% of the total CO₂ emissions reduction in 2050. Remaining 81% are due to energy system efficiency increase (38%), fuel switching (20%), renewable (17%) and nuclear (6%). Furthermore, coal-fired steam and natural gas-fired power plants are expected to contribute to about 65% and 30% respectively of the total installed power generation capacity equipped with CCS (IEA, 2010). Many studies, however, have shown that CO₂ capture from power plants, typically performed through post-combustion processes based on amines, is both very capital- and energy-intensive (Rubin *et al.*, 2007, Davison, 2007). In this context, thanks to its ability of convert heat into electricity at very low temperatures, Organic Rankine Cycle (ORC) can assume a fundamental role in recovering low temperature heat rejected from CO₂ capture plants and the auxiliaries required to enable them (Tola and Finkenrath, 2015). In fact ORC can produce additional electrical power improving global performance of the above mentioned power plants.

In post-combustion CO₂ removal process a large steam extraction from the power plant is required to supply the thermal energy necessary to solvent regeneration. This combination with additional

electrical energy for compressing and pumping the CO₂ up to a pressure suitable for transport and storage and for driving exhaust gas fans and solvent circulation pumps, causes substantial efficiency penalties to the power plant. As a result, near-term post-combustion CO₂ removal systems reduce the plant efficiency in the order of 8-12 percentage points at 90 % CO₂ capture (Tola and Pettinau, 2014, Mores *et al.*, 2013). Significant R&D projects are dedicated to the development of more efficient or less expensive capture and compression processes (Rubin *et al.*, 2012). For example, Finkenrath *et al.* (2007) and Jordal *et al.*, (2012) proposed exhaust gas recirculation (EGR) for natural gas combined cycles in order to increase the exhaust concentration of CO₂ and reduce costs associated with the capture unit. Little attention, however, has been given to recovering low temperature heat that is rejected from capture plants and the auxiliaries required to enable them.

This article will examine the performance impact of recovering low temperature heat with an Organic Rankine Cycle (ORC) that is integrated with a post-combustion CO₂ capture system of both pulverized coal-fired (PC) steam plant and natural gas combined cycle (NGCC). The analysis is based on fundamental thermodynamic analyses in order to evaluate the chance of heat recovery options based on ORC technology. The power section performance of both PC and NGCC were evaluated through simulation models based on the commercial software packages GateCycleTM. Models based on HYSYSTM software were used to evaluate performance of both ORC and CO₂ removal section.

2. PLANT CONFIGURATION

A simplified scheme of both PC and NGCC power plants is reported on Figures 1 and 2, respectively.

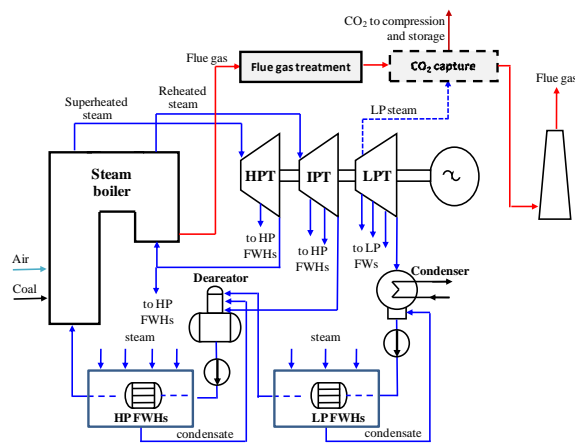


Figure 1: Simplified schemes of PC power plant

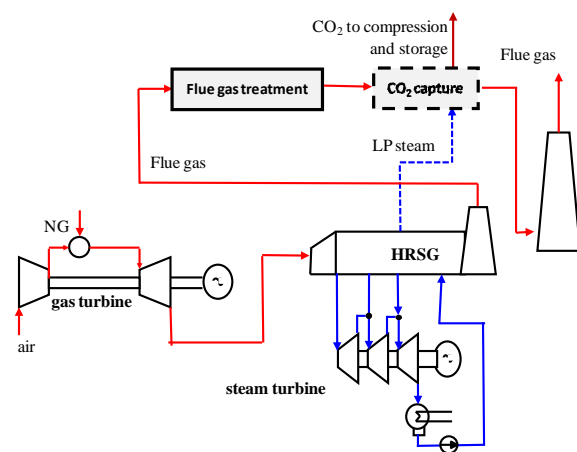


Figure 2: Simplified schemes of NGCC power plant

The steam power plant considered in this study is a generic medium-size (in the order of 400 MW of power output) pulverized coal-fired plant. The fuel chemical power input has been assumed equal to 1000 MW, corresponding to a mass flow of 39.4 kg/s of a coal with a lower heating value (LHV) of about 25.4 MJ/kg. The PC plant is based on a Rankine cycle with superheated and reheated steam and with eight regenerative steam extractions. A condenser pressure of 3.5 kPa has been assumed. The steam power plant has been considered equipped with a conventional tail-end flue gas treatment, which includes baghouse filters for particulate removal, a low temperature flue gas desulphurization system and a selective catalytic reduction denitrification system. Main cycle operating parameters are reported on table 1.

The natural gas combined cycle (NGCC) considered in this study is a generic medium-size (in the order of 600 MW) plant based on a typical gas turbine integrated with a heat recovery steam generator (HRSG) and a triple pressure steam cycle. For comparative purposes, a fuel chemical input equal to 1000.0 MW has been assumed also for the NGCC, corresponding to a natural gas mass flow of 20.0 kg/s (considering a natural gas LHV of 50 MJ/kg, as for methane). Table 2 shows main operating parameters of the NGCC.

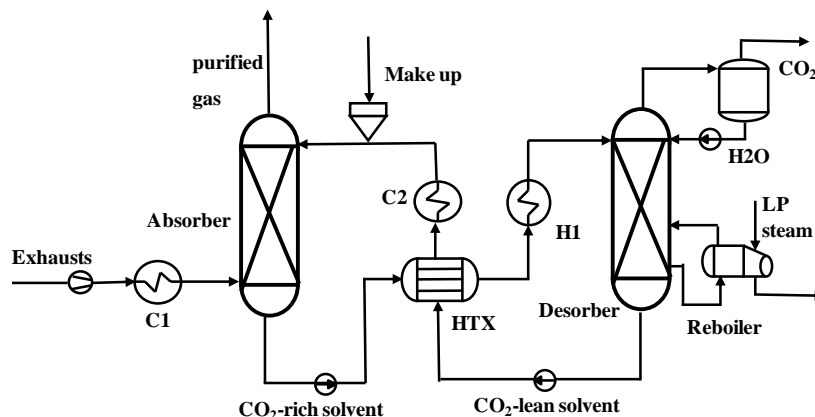
Table 1. Main operating parameters of the steam cycle

Fuel chemical power input	MW	1000.0
Coal mass flow	kg/s	39.4
Coal lower heating value (LHV)	MJ/kg	25.39
Air mass flow	kg/s	359.8
HP/IP/LP steam mass flow	kg/s	334.75/300.95/268.57
HP/IP/LP steam temperature	°C	537.9/540.0/322.6
HP/IP/LP steam pressure	MPa	25.0/3.4/0.7
Number of extraction		8
Extraction pressures	MPa	4.4/3.5/2.2/1.2/0.7/0.4/0.2/0.06
Deareator pressure	MPa	0.6
Condenser steam temperature and pressure	°C/kPa	26. 7/3.5
High/low pressure heat exchangers minimum ΔT	°C	-1.5/1.5

Table 2. Main operating parameters of the NGCC power plant

<i>Gas turbine</i>		
Fuel chemical power input	MW	1000.0
Natural gas mass flow	kg/s	20.0
Natural gas lower heating value	MJ/kg	50.0
Exhaust mass flow	kg/s	877.4
Exhaust temperature	°C	642.0
<i>Steam cycle</i>		
HP steam temperature/pressure	°C/MPa	565.0/16.3
IP steam temperature/pressure	°C/MPa	565.0/2.4
LP steam temperature/pressure	°C/MPa	311.0/0.45
Condenser pressure	kPa	3.5
Cooling water temperature	°C	17.0
Cooling water temperature rise	°C	6.7
Temperature difference in the condenser	°C	3.0

Both the steam and the NGCC power plants have been also studied in the more complex configuration considering a CO₂ capture and compression system, in the so-called PC-CCS and NGCC-CCS power plants. As mentioned, chemical absorption with amine-based solvents is currently considered the most suitable option for CO₂ removal from flue gases. In the present study, monoethanolamine (MEA) was chosen among the amines, despite its high energy requirements for the regeneration process, since it is one of the most proven and widespread technologies (Abu-Zhara *et al.*, 2007). Figure 3 shows a simplified scheme of the CO₂ removal section.

**Figure 3** Simplified scheme of the CO₂ removal section.

Exhaust gas is cooled to 30-50 °C and enters into the absorber, where the CO₂ is captured by the aqueous MEA solution. The CO₂-free gas is discharged from the top, while the CO₂-rich solvent is heated up to about 100 °C and sent to the regeneration column (Desorber). Inside the stripper a CO₂-water vapour mixture is released from the CO₂-rich solvent through the reboiler heat. In the upper section of the regeneration column a large fraction of steam condensates, whereas the CO₂-rich flow is sent to the compression section. The CO₂-lean solvent extracted from the bottom is cooled and recirculated back to the absorption column. Downstream the CO₂ removal section requirements for CO₂ transport and storage are matched through a conditioning and compression section. At first, the CO₂ compression process is carried out above the critical pressure (about 74 bar) in gaseous phase through intercooled compressors and then in liquid phase through a pump. In particular a pressure of 11 MPa and CO₂ purity above 99.5% are requested.

3. PLANT PERFORMANCE

3.1 PC and NGCC reference power plants

The reference PC power plant shows a net power output equal to 420.2 MW. The fuel chemical power input is 1000 MW plus a further thermal power of 13.3 MW, due to the flue gas treatment section. Globally the net efficiency of the plant is 41.47%. The flue gas treatment requires also an electrical power of 8.2 MW (about 2% of the overall PC power). The flue gas is characterized by a mass flow of 395.5 kg/s with a CO₂ molar fraction of 15.0%. The CO₂ emitted by the plant is equal to 87.6 kg/s corresponding to 735.9 g/kWh.

Better performance and lower CO₂ emissions are achieved with the NGCC power plant. At 15 °C ambient temperature, NGCC shows a net power output equal to 592.0 MW and a net efficiency of 59.2%. The flue gas is characterized by a mass flow of 877.4 kg/s with a CO₂ molar fraction of 4.1%. The CO₂ emitted by the plant is equal to 55.2 kg/s corresponding to 336 g/kWh.

3.2 Plants plus CO₂ removal systems

Lower performance is expected for both power plants when equipped with a CO₂ removal system. As a basis for the study, a post-combustion capture system based on a mixture of MEA (30 % by weight) and water and an absorber column temperature of 45°C have been assumed.

Figure 4 shows both the electrical power requirements of the CO₂ capture system (flue gas fan power and solvent compression power) and the specific thermal energy for the regeneration as a function of the CO₂ removal rate. Figure 5 shows CO₂ capture and emitted as a function of the CO₂ removal rate for both PC and NGCC power plants.

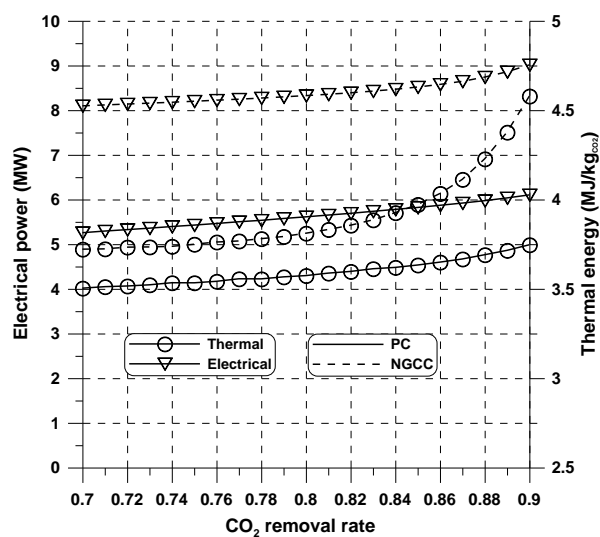


Figure 4 Electrical power requirements and specific thermal energy as a function of CO₂ removal rate

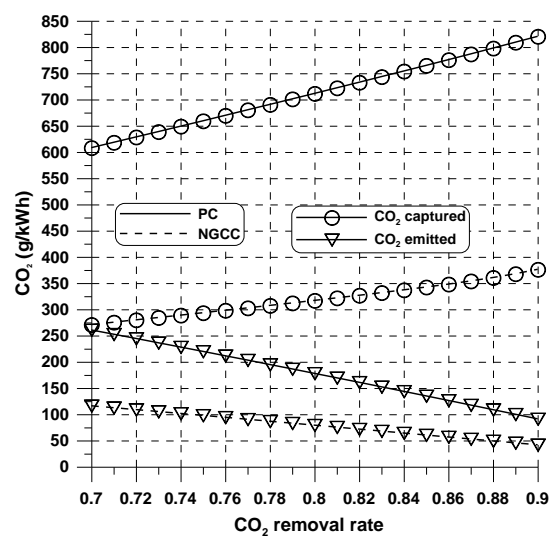


Figure 5 CO₂ captured and emitted as a function of CO₂ removal rate

NGCC is characterized by a larger flue gas mass flow to be treated in comparison to PC, with sensibly higher electrical power requirements. Besides, in PC plant, the higher CO₂ concentration in exhaust requires less solvent for CO₂ capture and consequently the specific thermal energy for solvent regeneration is lower. Figure 4 shows that electrical power requirements slightly increase with CO₂ removal rate, due to the larger power required by the solvent pump, in PC they range between 5.3 and 6.1 MW. Electrical consumptions of the NGCC are higher (about 3 more MW). For the PC power plant specific thermal energy required by the reboiler is about 3.5 MJ/kg assuming a CO₂ removal rate equal to 0.7 and increases up to 3.75 MJ/kg for a CO₂ removal rate equal to 0.9. Due to the lower CO₂ concentration in the flue gas, a higher specific thermal energy is required by the NGCC, up to 4.6 MJ/kg, assuming a CO₂ removal rate equal to 0.9. For the PC steam plant the amounts of CO₂ to be removed is larger, leading to higher values of both CO₂ captured and emitted in comparison to NGCC. As expected, Figure 5 shows that amounts of CO₂ captured and CO₂ emitted are increased and decreased respectively, increasing the CO₂ removal rate. At a CO₂ removal rate of 0.90, the amount of CO₂ captured is equal to 820.4 g/kWh (PC) and 376.3 g/kWh (NGCC). Both the plant show CO₂ emissions lower than 100 g/kWh, at a CO₂ removal rate of 0.90, in particular NGCC (41.8 g/kWh). Figures 6 shows the plant net power and the net plant efficiency reduction as a function of the CO₂ removal rate for both PC and NGCC. As expected, the introduction of the CO₂ removal system remarkably reduces net power of both plants. The power reduction is mainly due to steam extraction for amine regeneration, but also the CO₂ compression train and the electrical consumptions of the capture system, reported on figure 4, contribute. With reference to the NGCC plant, amine regeneration causes 77.2% of the total power reduction, whereas CO₂ compression and system requirements account for 15.1% and 7.7%, respectively. NGCC performance is more affected by CO₂ removal rate, due to the greater increase of the specific thermal energy required for solvent regeneration. Overall, NGCC net power decreases to 513.2 MW assuming a CO₂ removal of 70%, whereas it drops down to 475.4 MW for a CO₂ removal of 90%. PC net power reduction is more restrained, leading to a PC net power equal to 337.7 MW for a CO₂ removal rate of 0.9. As a consequence of power reduction, also net plant efficiency is largely reduced by the introduction of the CO₂ removal section. Figure 6 shows that in comparison to reference PC efficiency (41.5%) the net plant efficiency decreases of 15.6% and 19.6%, at 0.7 and 0.9 of CO₂ removal rate, respectively. Greater increases of the efficiency penalties with CO₂ removal rate are calculated for NGCC. In comparison to reference efficiency (59.2%), net plant efficiency decreases of 13.3% and 19.7%, at 0.7 and 0.9 of CO₂ removal rate, respectively. Globally, for a reference value of CO₂ removal rate equal to 0.9, net plant efficiency of PC and NGCC are equal to 33.3% and 47.5%, respectively.

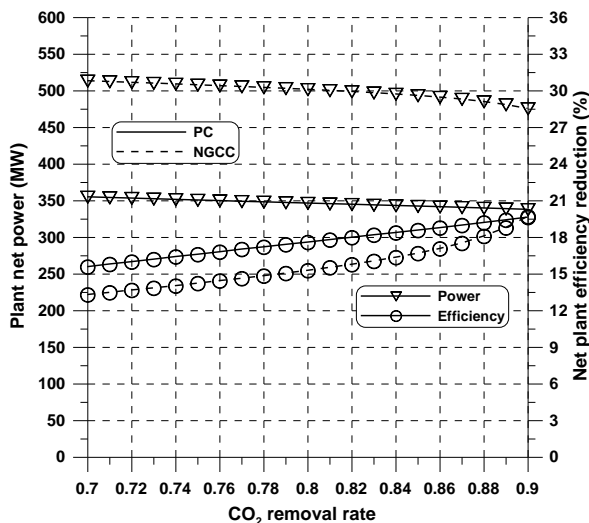


Figure 6 Plant net power and net plant efficiency reduction as a function of CO₂ removal rate

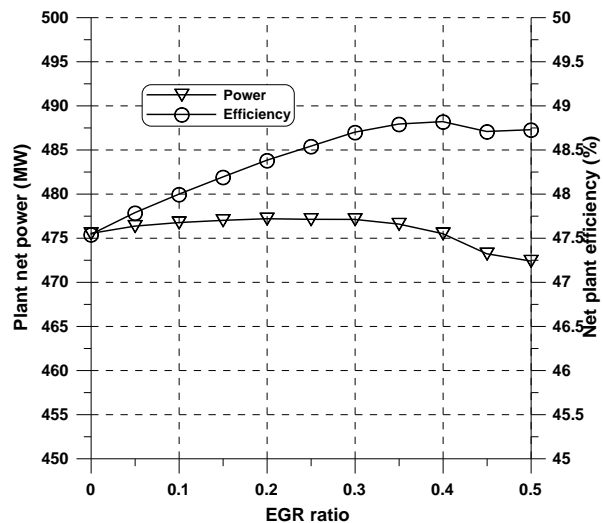


Figure 7 NGCC net power and net efficiency as a function of EGR ratio

3.3 Exhaust gas recirculation

Exhaust gas recirculation (EGR) has been developed mainly for oxy-fuel plants fed by coal, where exhaust gas is partially recycled back to the boiler with the aim of controlling flame temperature. EGR has also been proposed for post-combustion capture when using gaseous hydrocarbon fuels. In fact, key challenges of post-combustion capture are related to the high exhaust volumes and comparably low CO₂ concentration in the flue gas. For an NGCC with post-combustion capture, EGR increases the exhaust concentration of CO₂, improving the capture efficiency (lower energy requirements for the amine system) and substantially reducing capture equipment size and costs. Sipocz and Tobiesen (2012) reported that efficiency losses are reduced by approximately 1 percentage points and Rokke (2006) reported that capital expenditure for the capture unit is reduced by 20-30%.

Figure 7 shows both the net power plant and net plant efficiency of the NGCC as a function of the EGR ratio, defined as the ratio between the exhaust gas recirculated back to the compressor and the total exhaust gas mass flow. Results are reported for an exhaust gas cooling temperature equal to 30 °C. Figure 7 shows that an overall optimum in terms of net plant efficiency of about 48.8% could be expected at EGR ratios equal to 0.4. On the contrary, NGCC-CCS net power is just barely affected by EGR ratio. At an EGR ratio equal to 0.4, a net power of 475.5 MW has been calculated.

4. LOW TEMPERATURE HEAT SOURCES

Low temperature heat rejected from the solvent-based CO₂ removal system could be a potential energy source for enhancing plant performance of both PC and NGCC power plants. In fact so far little attention has been given to recovering the low temperature heat rejected from capture plants and the auxiliaries required to enable them. In particular this paper examines the effect of recovering this low temperature heat by a bottoming Organic Rankine Cycle (ORC) (Lecompte *et al.*, 2015).

Different sources of available low temperature heat from amine-based post-combustion CO₂ removal systems can be theoretically used for heat recovery in an ORC. In general the following major low-grade heat sources can be identified: (i) exhaust gas cooler, (ii) amine reboiler condensate cooling, (iii) stripper condenser, (iv) CO₂ compressor intercoolers and (v) lean solvent coolers.

In particular, cooling down exhaust gas leads to a discharge of a large amount of low temperature (80-120 °C, depending on technology) thermal energy. Furthermore, in the CO₂ capture section a large amount of waste heat is available from the stripper condenser (at 100-120 °C) and the amine reboiler condensate cooling (at 130-140 °C). In the stripper condenser a mixture of CO₂ and water vapor condensates making available both sensible and latent heat for heat recovery at a variable temperature. The saturated hot water (in the order of 4 bar) exiting from the reboiler unit is also available for feeding the ORC. Additional sensible heat could be recovered from CO₂ compressor intercoolers, at a temperature level dependent on the CO₂ compressor chain configuration. Since CO₂ compressors are generally characterized by low pressure ratios in order to reduce CO₂ compression work, temperature of the waste heat from compressor intercoolers would be insufficient for heat recovery in an ORC. Therefore heat recovery from the compressor intercoolers is not analyzed in this study. Furthermore, low temperature heat could be provided from cooling the lean-CO₂ solvent. Since this thermal energy is almost fully used to preheat the rich solvent, this potential heat source is not included in this study.

5. ORGANIC RANKINE CYCLE

5.1 ORC layout

Since waste heat sources at similar temperature are available in a post-combustion capture section, in this paper a parallel configuration of heat recovery has been selected. In fact, in series or cascaded layouts are potentially simpler in design, but their application typically would require a notable temperature difference between the waste heat sources used. In comparison, a parallel heat recovery layout comes with operational challenges related to controlling different and potentially fluctuating mass flow through each of the parallel heat exchangers in a single ORC loop. Nonetheless, a parallel heat recovery layout in principle allows for simultaneous heat recovery from different waste heat sources at very similar temperature.

5.2 ORC fluid

Depending on waste heat source temperature, different suitable organic working fluids can be selected. For this specific application, taking into account operating conditions, carbon dioxide and N-Butane are considered as potential ORC working fluids. In fact, both of them could be well matched with the available waste heat temperature levels by adjusting the cycle operating pressures. Table 3 shows CO₂ and N-Butane saturation pressure as a function of temperature.

Table 3. Saturation T and p for CO₂ and N-Butane

Temperature (°C)	Pressure (bar)	
	CO ₂	N-Butane
10	44.9	1.5
20	57.3	2.1
30	72.1	2.8
40	- *	3.8
50	-	4.9
60	-	6.4
70	-	8.1
80	-	10.1
90	-	12.5
100	-	15.3

* CO₂ critical point at 73.8 bar and 31 °C

CO₂ could be an interesting choice as organic working fluid, due to synergies in the fluid handling or safety infrastructure with the CO₂ capture system, lower costs and a better match with the exhaust gas cooling curve, due to the lack of vaporization in the operating range under consideration. However, CO₂ shows some disadvantages, in particular a higher pump work, due to the supercritical conditions, and higher equipment costs, due to the very high operating pressure required. For example, at 20 °C CO₂ condensates at 57.3 bar, whereas, N-Butane at a significantly lower pressure of 2.1 bar. Due to the lower operating pressure, N-Butane was selected as organic fluid for more detailed analysis.

5.3 Results

As previously mentioned, in this study the ORC system recovers waste heat simultaneously at slightly different temperature by using parallel waste heat exchanger arrangements. Due to the parallel flow configuration, all heat exchangers must operate at the same upper operating pressure of N-Butane. In addition, heat exchangers here considered do not include fluid superheating section and however N-Butane exits the evaporator at saturation conditions, with the highest operating temperature. As a consequence, the maximum operating pressure in the cycle is specified by saturation properties of N-Butane. Table 4 shows the main characteristics of the Organic Rankine Cycle.

Table 4. Main operating parameters of the Organic Rankine Cycle

Maximum cycle pressure (turbine inlet)	bar	6-12
Maximum cycle temperature (turbine inlet)	°C	58-88
Vapor fraction at the turbine inlet		1
Minimum cycle pressure (condenser)	bar	2.5
Minimum cycle temperature (condenser)	°C	25
Minimum ΔT at the heat exchanger	°C	5

A condenser pressure equal to 2.5 bar was fixed, corresponding to a condensation temperature of 25 °C. Since waste heat sources are available at different temperatures for both power plants, a sensitivity analysis has been carried out as a function of the maximum pressure of N-Butane in the Organic Rankine Cycle. A maximum ORC pressure in the range 6 and 12 bar was assumed, corresponding to a saturation temperature between 58 and 88 °C. A minimum temperature difference of 5 °C was assumed in the heat exchangers between the heat source and the organic working fluid. A higher pressure of organic fluid leads to a higher evaporation temperature, reducing the amount of heat that

can be recovered. On the other hand, a higher pressure inside the evaporator maximizes the turbine work, while additional required pump work to achieve the higher pressure is comparably low. For these reasons heat recovery can be optimized through a trade-off between key operating parameters. Figures 8 and 9 show the waste heat recovered as a function of the ORC maximum pressure for both PC (Figure 8) and NGCC (Figure 9) power plants. The figures report the total heat recovered and the heat recovered from each of the three different heat sources analyzed in this study. In particular, results of the NGCC are reported considering a reference scenario based on an EGR ratio equal to 0.4.

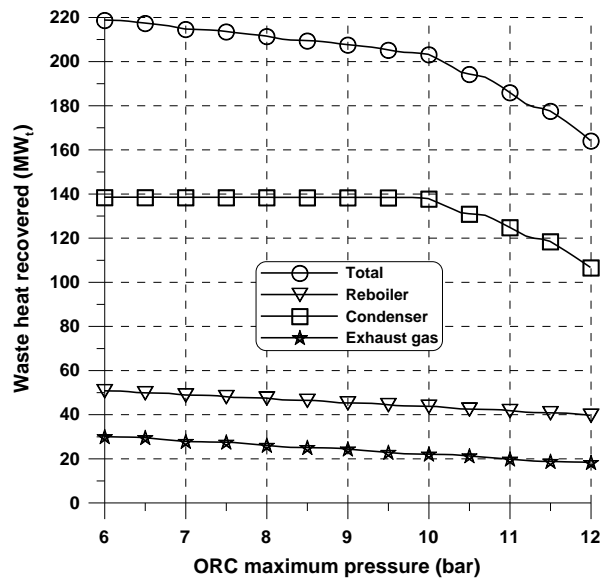


Figure 8 Waste heat recovered as a function of ORC maximum pressure

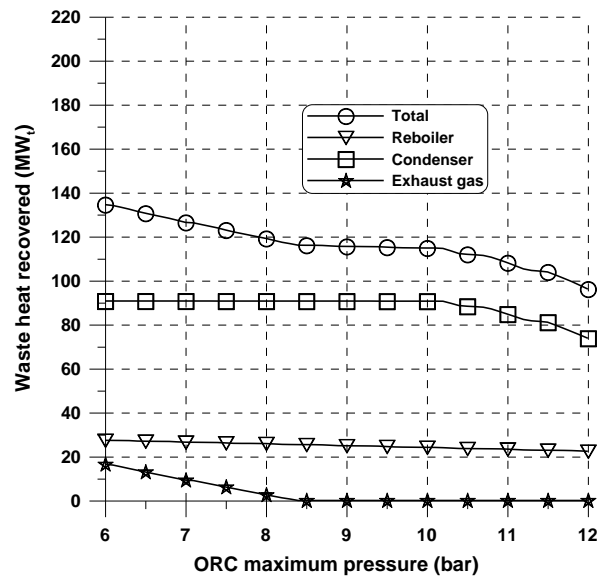


Figure 9 Waste heat recovered as a function of ORC maximum pressure.

Figures show that a larger amount of heat is recovered from the PC in comparison to NGCC. As mentioned above, an increase in the ORC maximum operating pressure reduces the overall waste heat recovery, and the single heat recovered, although not all the sources are impacted by a similar intensity. In both plants the largest amount of waste heat is recovered from the stripper condenser. An increase of the operating pressure results in a constant (about 138 MW and 91 MW for PC and NGCC, respectively) waste heat recovered from the stripper condenser until a maximum pressure of about 10 bar is reached. An even higher pressure reduces the possible waste heat recovery from the condenser, which has a water exit temperature slightly higher than 100 °C, since the pinch point minimum temperature difference is reached. Minimum amounts of waste heat equal to 106.5 MW (PC) and 73.8 MW (NGCC) are recovered for an operating pressure of 12 bar. On the contrary, the waste heat recovered from the amine reboiler condensate cooling is not affected significantly by the maximum cycle pressure, due to the comparably high temperature (up to 140 °C) of the saturated water that exits the amine reboiler. In particular, increasing the maximum operating pressure from 6 bar to 12 bar, waste heat recovery decreases from 50.6 to 39.5 MW (PC) and from 27.3 to 22.4 MW (NGCC). Lower amount of waste heat can be recovered from exhaust gas cooling. In the PC plant the heat recovered decreases from 29.7 to 18.0 MW, respectively at 6 and 12 bar. On the contrary, for NGCC, waste heat recovery from exhaust gas cooling is possible only at very low evaporation pressures of N-Butane. In particular the heat recovery would be 16.5 MW at 6 bar, while no waste heat recovery from exhaust gas cooling would be possible at maximum evaporation pressure higher than 8.3 bar. Figures 8 and 9 show also the total amount of waste heat that potentially could be recovered. Figure 8 shows that for the PC plant, the heat recovered would be 218.6 MW at 6 bar operating pressure. A relatively moderate reduction is obtained by increasing pressure up to 10 bar (203.0 MW), while at higher pressure a notable reduction of heat recovered can be noticed, mainly due to reduction in heat recovery from the stripper condenser. A minimum of 164.0 MW is recovered at a operating pressure of 12 bar. A similar trend is shown on Figure 9 for waste heat recovery from

NGCC. A maximum value of 134.5 MW can be recovered at 6 bar, whereas minimum heat recovery is equal to 96.1 at 12 bar. At 10 bar of operating pressure, waste heat recovered is equal to 114.8 MW. Figure 10 and 11 show the ORC net efficiency and the ORC net power as a function of ORC maximum pressure, for PC and NGCC plants respectively. In particular, figures show the total net power and the corresponding net power produced by ORC from each of the three heat sources.

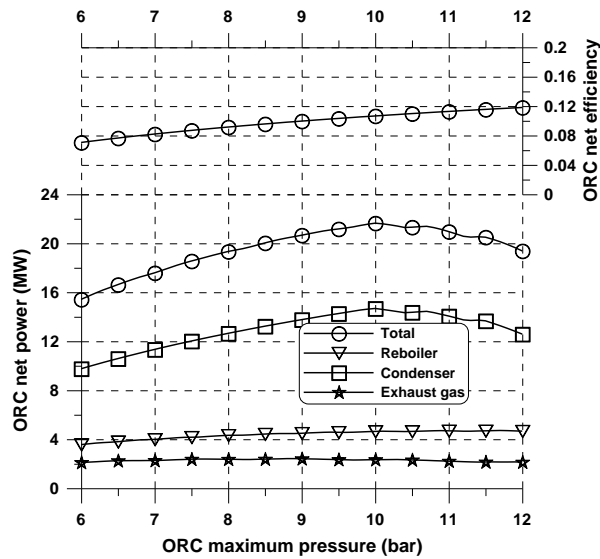


Figure 10 ORC net power and efficiency as a function of ORC maximum pressure

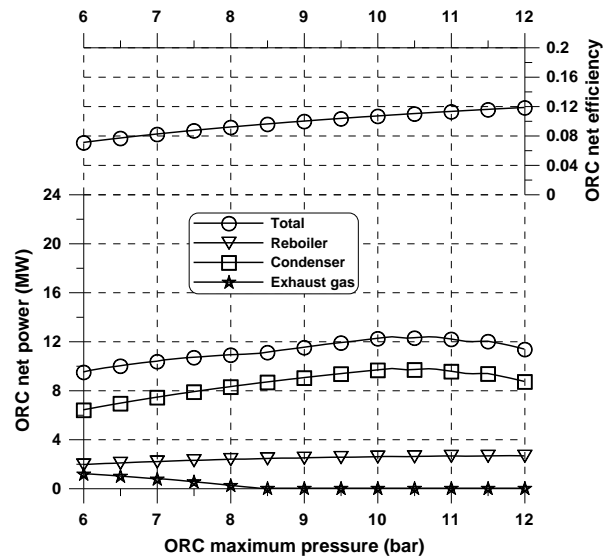


Figure 11 ORC net power and efficiency as a function of ORC maximum pressure.

Unlike waste heat recovered, ORC net efficiency increases with ORC maximum pressure. In particular, for the reference scenario based on a condenser pressure equal to 2.5 bar, cycle net efficiency increases from 7.1% (6 bar) to 11.8% (12 bar). As a consequence of opposite trend for waste heat recovered and net efficiency, the net power generated by the ORC system peaks at around 10.5 bar for PC and at 10 bar for NGCC. Since the largest amount of waste heat is recovered from the stripper condenser, not surprisingly the main contribution to the net Organic Rankine Cycle power stems from this heat source. The maximum net power that can be generated by the studied ORC system integrated with the PC-CCS is 21.6 MW (about 6.4% of the reference plant) at a total low-temperature heat input of 203.1 MW (ORC net efficiency of 10.7%). Due to the lower amount of heat recovered, ORC integrated with NGCC assures a lower additional power. In particular, a maximum additional power of 12.3 MW can be generated (about 2.6% of the NGCC-CCS plant with 40% EGR) at a total low-temperature heat input of 112.0 MW (ORC net efficiency of 11.0%). The overall impact of ORC integration on net power and efficiency is shown in Table 5, where plant performance is represented with or without CCS and ORC integration.

Table 5. Main plant performance

		PC	NGCC
Gross power of reference plant	MW	454.6	625.2
Net power of reference plant	MW	420.2	592.0
Net power of plant + CCS	MW	337.8	475.5
Net power of plant + CCS + ORC	MW	359.4	487.8
Net efficiency of reference plant	%	41.5	59.2
Net efficiency of plant + CCS	%	33.3	48.8
Net efficiency of plant + CCS + ORC	%	35.5	50.1

Table 5 shows that integrating CCS-power plants with an Organic Rankine Cycle assures a notably reduction of the influence of CO₂ capture penalization on plant power output. In general, considering that this study only evaluates the thermodynamic potential of heat recovery, the introduction of an

Organic Rankine Cycle would allow to increase the overall plant efficiency of 2.2 percentage points for the PC-CCS plant and of 1.3 percentage points for the NGCC-CCS plant. Globally the maximum net efficiency of the NGCC-CCS under investigation could thereby rise to 50.1%, whereas the maximum net efficiency of the PC-CCS increases up to 35.5%.

6. CONCLUSIONS

This paper analyses the option to recover low-grade heat from CO₂-capture processes for both pulverized coal steam plant and natural gas combined cycles by using Organic Rankine Cycle (ORC) technology. Potential waste-heat sources are identified and most appropriate ORC system layouts and working fluids are discussed. Under the assumption that N-Butane is used as an ORC working fluid, and low-grade heat sources are utilized in parallel in a single ORC loop, an overall power plant net efficiency improvement potential of 1.5-2.5 percentage points is estimated, depending on the power plant considered.

NOMENCLATURE

CCS	Carbon Capture and Storage
EGR	Exhaust Gas Recirculation
LHV	Lower Heating Value
MEA	Monoethanolamine
NGCC	Natural Gas Combined Cycle
ORC	Organic Rankine Cycle
PC	Pulverized Coal

REFERENCES

- IEA Report, 2010, Energy Technology Perspectives. Available: <http://www.iea.org> (Acc. February 23, 2015)
- Abu-Zahra M.R.M., Schneiders L.H.J., Niederer J.P.M., Feron P.H.M., Versteeg G., F., 2007. CO₂ capture from power plants. Part I. A parametric study of the technical performance based on monoethanolamine. *Int. Journal of Greenhouse Gas Control*, 1, 135-142.
- Davison J., 2007, Performance and costs of power plants with capture and storage of CO₂, *Energy*, 32, 7, 1163-1176.
- Finkenrath, M., Ursin, T.P., Hoffmann, S., Bartlett, M., Evulet, A., Bowman, M.J., Lynghjem, A., Jakobsen, J., 2007, Performance and cost analysis of novel gas turbine cycle with CO₂ capture. Paper GT 2007-27764, ASME Turbo Expo, Montreal, Canada.
- Jordal K., Ystad P.A.M., Anantharaman R., Chikukwa A., Bolland O., 2012. Design-point and part-load considerations for natural gas combined cycle plants with post combustion capture. *International Journal of Greenhouse Gas Control* 11, 271-282.
- Lecompte, S., Huisseune, H., VanDenBroek, M., Vanslambrouck, B., De Paepe, M., 2015. Review of organic Rankine cycle (ORC) architectures for waste heat recovery. *Renewable and Sustainable Energy Reviews*, 47, 448-461.
- Mores P.L., Godoy E., Mussati S.F., Scenna N.J., 2013. A NGCC power plant with a CO₂ post-combustion capture option. Optimal economics for different generation/capture goals. *Chemical Engineering Research and Design*, 92,7, 1329-1353.
- Røkke P.E., 2006. Environmental use of natural gas in a gas turbine. Doctoral thesis of Norwegian University of Science and Technology.
- Rubin, S., Chen, C., Rao, A.B., 2007. Cost and performance of fossil fuel power plants with CO₂ capture and storage, *Energy Policy*, 35, 4444-54.
- Rubin, E.S., Mantripragada, H., Marks, A., Versteeg, P., Kitchin, J., 2012. The outlook for improved carbon capture technology. *Progress in Energy and Combustion Science*, 38, 630-671.
- Sipöcz, N., Tobiesen, A., 2012. Natural gas combined cycle power plants with CO₂ capture – opportunities to reduce cost. *International Journal of Greenhouse Gas Control* 7, 98–106.
- Tola, V., Finkenrath, M., 2015. Performance evaluation of an Organic Rankine Cycle fed by waste heat recovered from CO₂ capture section. In course of publication on *International Journal of Thermodynamics*.
- Tola V., Pettinau A., 2014. Power generation plants with carbon capture and storage: A techno-economic comparison between coal combustion and gasification technologies. *Applied Energy*, 113, 1461-1474.

FLUID STABILITY IN LARGE SCALE ORCS USING SILOXANES - LONG-TERM EXPERIENCES AND FLUID RECYCLING

Erhart, T. ^{1*}, Gölz J., ², Eicker U. ¹ and van den Broek M. ³

¹ University of Applied Sciences, Schellingstrasse 24, 70174 Stuttgart, Germany
tobias.erhart@hft-stuttgart.de

² BIOP GmbH, Parkstrasse 37, 73630 Remshalden, Germany

³ Ghent University, 8500 Kortrijk, Belgium
*Corresponding Author

ABSTRACT

The results in this work show the influence of long-term operation on the decomposition of working fluids in eight different power plants (both heat-led and electricity-led) in a range of 900 kW_{el} to 2 MW_{el} . All case study plants are using Octamethyltrisiloxane (MDM) as a working fluid. The case study plants are between six to 12 years old. On one system detailed analyses, including the fluid distribution throughout the cycle, have been conducted. All fluid samples have been analysed via Head Space Gas Chromatography Mass Spectrometry (HS-GC-MS). Besides the siloxane composition, the influence of contaminants such as mineral oil based lubricants (and its components) has been examined. In most cases the original main working fluid has degraded to fractions of siloxanes with a lower boiling point (low-boilers) and fractions with a higher boiling point (high-boilers). As a consequence of the analyses, a new fluid management system has been designed and tested in one case study plant (case study number 8). The measures include fluid separation, cleansing and recycling. Pre-post comparisons of fluid samples have proved the effectiveness of the methods. The results show that the recovery of used working fluid offers an alternative to the purchase of fresh fluid, since operating costs can be significantly reduced. For large facilities the prices for new fluid range from € 15 per litre (in 2006) to € 22 per litre (in 2013), which is a large reinvestment, especially in the light of filling volumes of 4000 litres to 7000 litres per cycle. With the above mentioned method a price of € 8 per litre of recovered MDM can be achieved.

1. INTRODUCTION

Over the recent years a large number of ORCs (over 200) based on siloxanes as a working fluids have been taken into operation all across Europe. Siloxanes are advertised as uncomplicated and long lasting working fluids. Many siloxanes are classified as inflammable, and they are more stable than their carbon-organic equivalents. The bond energy of a siloxy group is significantly higher than the bond energy of a carbon chain (Zhou et al., 2006). There are only a few sources in literature describing the decomposition of siloxanes in high-temperature applications (250°C to 350°C) in detail, such as Grassie and Macfarlane (1978). Most studies are related to the use of poly-siloxanes as solids under oxygen and nitrogen atmospheres (Zhou et al., 2006). The Siloxy-bonds in siloxanes are very strong (809 kJ/mol), but compared to the methyl-silane group they are the weaker link. The methyl-silane decomposition takes place above 400 °C. In general, siloxanes have a tendency to polymerise or oligomerise above 300 °C. The equilibrium of the polymerisation and the product configuration depend on pressure and educt configuration. Formic acid may be produced during thermal decomposition. In thermal conversion siloxanes react to SiO₂, CO₂ and hydrocarbon residues (Dow Corning, 2013). Over longer periods of operation, cycle fluids degrade through decomposition or contamination. Strong oxidants, catalytic alloys or sulphur can trigger or accelerate the decomposition processes. Contaminants and decomposition products of cycle

fluids can lead to severe disturbances of the process. High-boilers, which are still liquid while the main working fluid is fully evaporated, can damage the turbine or heat exchangers by droplet impingement. Vaporous low-boilers can lead to cavitation in the feed-pump, galloping in the pre-heater, excessive super-heating in the evaporator and low heat transfer coefficients. The volume distribution across the cycle can significantly differ from the original design. As a consequence lower electric efficiencies and higher maintenance costs have to be expected.

2. METHODOLOGY

The authors have analysed the data of seven power plants across Europe. The focus was set on the following points:

- Operational mode: heat-led or electricity-led
- Total hours of operation and up-time per year
- Fluid quality: contaminations, degree of degradation, low-boilers, high-boilers
- Source temperature and degree of super-heating

Based on the above mentioned points a correlation between the cycle operation and the final working fluid composition was searched for. Besides the cause of the fluid decomposition and the contaminations, the removal of contaminations and the recycling of the working fluid was tested on one case study (number 8). Furthermore, the sequestration of fluid fractions across the cycle has been observed in this case study. The power plant for the recycling analysis is located in the city quarter Scharnhauser Park near Stuttgart. Since the year 2004 the power plant covers the demand of an area with an estimated population of 7000. The combined heat and power unit (CHP) is biomass driven and heat-led. A 7 MW_{th} furnace converts landscape preservation residues and wood chips into heat. The ORC is connected via a thermal oil cycle to the furnace. The system is controlled according to ambient temperature. The sink temperature levels are 60 °C/80 °C. The source temperature (thermal oil) of the OR-cycle is limited to 290 °C.

For all case studies fluid samples have been taken and analysed using the Head Space Gas Chromatography Mass Spectrometry (HS-GC-MS) method. In order to test the separation of contaminated working fluid mixtures distilling experiments have been conducted on various samples of case study number 8. For each distilling experiment the original working fluid sample (base fluid) and the products of the processes have been analysed.

3. RESULTS

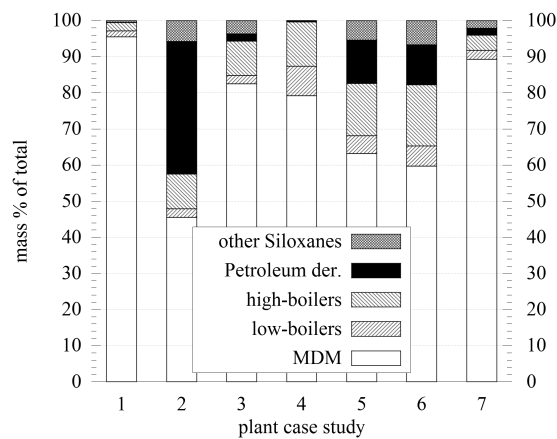
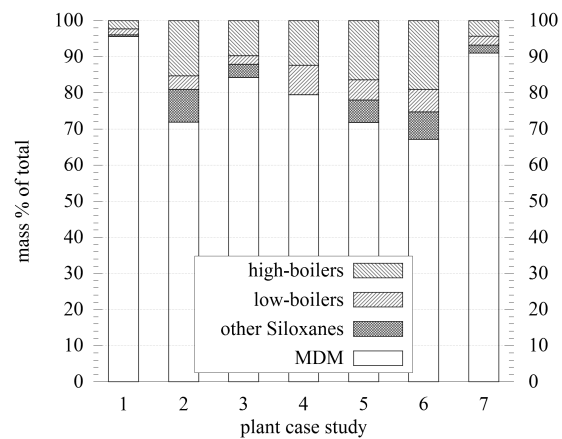
3.1 Analysis of working fluids from seven power plants

The following table shows an overview on the conditions under which the seven case study plants are working. For the sake of completeness the case study number 8 is listed as well. An operation time cannot be defined for case study 8, as major parts of the cycle have been replaced and the working fluid has been fully substituted.

Table 1: Boundary conditions for seven case study ORCs

case	$\vartheta_{source,max}$ [°C]	age [Y]	op.-time [h]	P_{max} [kVA]	operation mode, description
1	300	10.5	52500	1200	heat-led, district heating
2	300	12	90000	1280	electricity-led
3	313	5.5	45100	2000	heat-led, district heating
4	300	10.5	75600	1000	both, district heating
5	315	6	49200	1000	heat-led, district heating
6	310	7	57400	1000	both, district heating
7	308	7	38500	1000	heat-led, district heating
8	290	10	-	950	heat-led, district heating

In figures 1 and 2 the composition of the fluid samples from the seven different power plants are depicted. In figure 1 the lubricant fraction is included, in figure 2 only the siloxane fractions are depicted. The degree of degradation of the working fluid samples varies across a wide range (between 5% and 55%, respectively 5% to 34%).

**Figure 1: Composition of case study fluids including contamination****Figure 2: Composition of case study fluids, siloxane fractions only**

The following figure 3 depicts the total degradation of the original working fluid MDM for all case studies versus the operating time. As time is one of the main factors in chemical reactions a rough trend can be seen. However, the dispersion is very large.

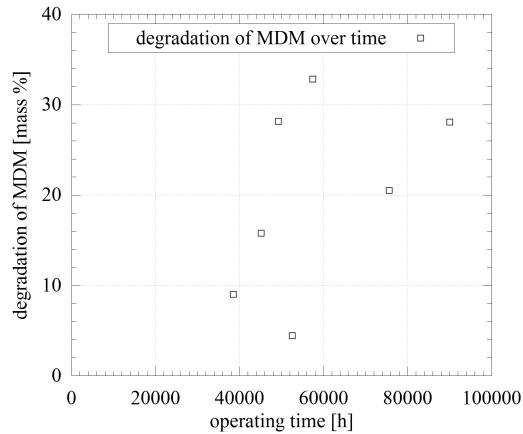


Figure 3: Degradation of working fluid vs. up-time

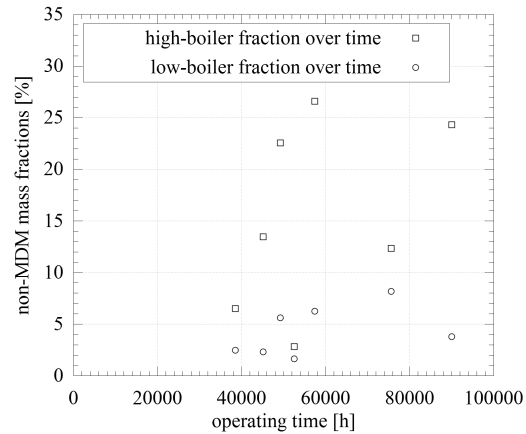


Figure 4: High- and low-boiler fraction in fluid samples vs. up-time

In figure 4 the development of the two categories of reaction products versus the operating time of the cycle is shown. The amount of high-boilers is significantly higher compared to the low-boilers. Besides the siloxane compounds in the working fluid, the samples were contaminated with varying fractions of petroleum derivatives. These contaminations usually come from a leakage located at the turbine shaft sealing. A certain leakage rate cannot be avoided, but some of the samples show massive contaminations (case 2, 5 and 6 in figure 1).

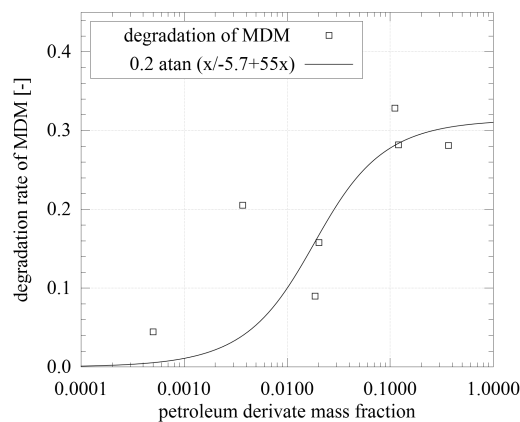


Figure 5: Degradation rate of MDM vs. petrol derivate fraction in cycle fluid

The data in figure 5 depict the degradation ratio of the original cycle fluid versus the measured fraction of lubricant residues on a logarithmic scale. The trend depicted in the diagram shows a correlation between the amount of hydrocarbon contaminants and the degradation of the original working fluid.

3.2 Fluid distribution within the cycle (case study 8)

In case of fluid degradation, the fluid composition throughout a cycle is not equal. Depending on the local thermodynamic state, the equilibrium of compounds shifts. This distribution of compounds across the cycle has been tested on power plant case study number eight. The following HS-GC-MS analyses in table 2 to table 5 show the results of various fluid samples taken from different points of the cycle. The first fluid sample (table 2) has been tapped from the pre-heater after a full stop of the cycle:

Table 2: HS-GC-MS analysis of cycle fluid (pre-heater after full-stop) (Erhart, 2015)

compound	abbr.	CAS	mass fraction
-	-	-	[%]
Octamethyltrisiloxane	L3 / MDM	107-51-7	79.2
Hexamethyldisiloxane	L2 / MM	107-46-0	7.55
Hexamethylcyclotrisiloxane	D3	107-52-8	0.592
Octamethylcyclotetrasiloxane	D4	556-67-2	4.93
Decamethyltetrasiloxane	L4 / MD2M	141-62-8	5.12
Decamethylcyclopentasiloxane	D5	541-02-6	0.535
Dodecanethylpentasiloxane	L5 / MD3M	141-63-9	1.7
Trimethylsilanol	MOH	1066-40-6	-

The second used fluid sample (table 3) has been taken from the reservoir of the vacuum pump (see figure 10). The large fraction of MM is very obvious. As the condensables in the condenser are fed back into the cycle and take part in the overall process, the low-boiling MM collects as vapour in the condenser shell. Consequently the vacuum pump takes the MM from there.

Table 3: HS-GC-MS analysis of cycle fluid (vacuum pump) (Erhart, 2015)

compound	abbr.	CAS	mass fraction
-	-	-	[%]
Octamethyltrisiloxane	L3 / MDM	107-51-7	50.9
Hexamethyldisiloxane	L2 / MM	107-46-0	45.5
Hexamethylcyclotrisiloxane	D3	107-52-8	0.898
Octamethylcyclotetrasiloxane	D4	556-67-2	1.4
Decamethyltetrasiloxane	L4 / MD2M	141-62-8	0.816
Decamethylcyclopentasiloxane	D5	541-02-6	0.099
Dodecanethylpentasiloxane	L5 / MD3M	141-63-9	0.238
Trimethylsilanol	MOH	1066-40-6	-
other poly-siloxanes	-	-	0.116

After a full stop of the cycle the sample presented in table 4 has been taken from the bottom of the recuperator (under liquid line). The analysis shows a large amount of high-boilers (MD2M and MD3M). After the turbine, the expanded vapour is transported through the recuperator. Meanwhile the saturation pressure of the high-boilers is reached. Furthermore, the flow of the vapour decelerates. Therefore, the high-boilers precipitate inside the recuperator shell. The high-boilers that are not evaporated before the turbine can damage the turbine blades.

Table 4: HS-GC-MS analysis of cycle fluid (recuperator reservoir) (Erhart, 2015)

compound	abbr.	CAS	mass fraction
-	-	-	[%]
Octamethyltrisiloxane	L3 / MDM	107-51-7	65.50
Hexamethyldisiloxane	L2 / MM	107-46-0	5.09
Hexamethylcyclotrisiloxane	D3	107-52-8	0.50
Octamethylcyclotetrasiloxane	D4	556-67-2	4.97
Decamethyltetrasiloxane	L4 / MD2M	141-62-8	11.00
Decamethylcyclopentasiloxane	D5	541-02-6	1.30
Dodecanethylpentasiloxane	L5 / MD3M	141-63-9	7.05
Trimethylsilanol	MOH	1066-40-6	-
other poly-siloxanes	-	-	4.56

The last sample (table 5) has been taken from the feed pump. It is the most representative for the fluid mixture involved in the overall thermodynamic process. Less than 80% of the original working fluid is left.

Table 5: HS-GC-MS analysis of cycle fluid (feed pump) (Erhart, 2015)

compound	abbr.	CAS	mass fraction
-	-	-	[%]
Octamethyltrisiloxane	L3 / MDM	107-51-7	78.3
Hexamethyldisiloxane	L2 / MM	107-46-0	3.6
Hexamethylcyclotrisiloxane	D3	107-52-8	0.543
Octamethylcyclotetrasiloxane	D4	556-67-2	4.04
Decamethyltetrasiloxane	L4 / MD2M	141-62-8	6.55
Decamethylcyclopentasiloxane	D5	541-02-6	0.92
Dodecanethylpentasiloxane	L5 / MD3M	141-63-9	3.96
Trimethylsilanol	MOH	1066-40-6	0.001
other poly-siloxanes	-	-	1.852

3.3 Distilling under laboratory conditions

In order to prove the feasibility of a working fluid separation, a laboratory test was conducted. The liquid educt samples was taken from the recuperator reservoir (liquid line).

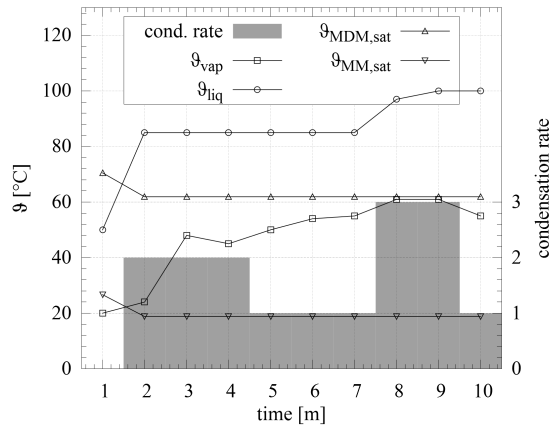


Figure 6: Distilling process of sample 1

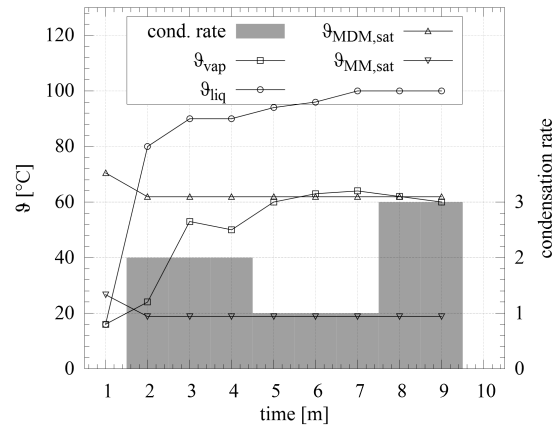


Figure 7: Distilling process of sample 2

Under a pressure of 40 mbar two fluid samples are evaporated and condensed, the results of the two experiments are shown in the figures 6 and 7. In the diagrams the saturation temperature of MDM and MM are given according to the measured pressure in the flask. The temperature of MM represents itself and all other low-boilers that evaporate below MDM. Furthermore, the temperatures of the boiling fluid mixture and the vapour are shown. The condensation rate is categorized (0-none, 1-low, 2-medium, 3-high) by observation. In experiment 1 the base fluid reservoir was first heated to a set-point of 85 °C and to 85 °C. In the second experiment the first temperature set-point was set to 90 °C. If the liquid temperature exceeds the saturation temperatures, evaporation occurs. If the measured vapour temperature is above or near to the saturation temperature condensation occurs. During the time steps 2,3 and 4 the condensation rate rises in both experiments; in that period the first distillates are taken. The first distillate usually contains the largest share of low-boilers. The second distillate, containing mainly MDM, is extracted during the time steps 8 and 9.

In the experiment number one, 54.2% of MDM could be recovered (figure 6) from the base fluid. In experiment number two 64.2% of the MDM could be recovered from the base fluid.

A detailed analysis of the distilling products of experiment number 2 (figure 7) showed: The first distillate contained 62.3% of MDM, 15.8% of MM, 19.92% of Petroleum derivatives and minor fractions of other siloxanes. The second distillate from the fluid sample contained 95.2% of MDM, and 2.4% of D4. The rest of the product was a mixture of various siloxanes (less than 1% each). The residue of the base fluid contained 25.5% MDM, 8.5% L4 and 18.4% L5. The lubricant was removed successfully from the original sample and no lubricant was in the product sample. Based on the experiences from the laboratory tests the condensation was tested in real scale.

3.4 Distilling and fluid treatment under field conditions

Unlike the laboratory set-up, under real conditions the base samples for fluid treatment can be of different origin. In this case study the main fluid source is the reservoir of the recuperator. As the distillation experiments in the last section show, this source contains a high fraction of high-boilers and lubricant. For the recovery of MDM and the elimination of lubricant fractions from the working fluid it is the perfect source. The distilling apparatus (1) built for the condensation of MDM from fluid mixtures with a high fraction of high-boilers, is depicted in figure 8. It is mounted on top of the multi-cyclone (2) and heated by the hot exhaust gases of the biomass furnace. A water cooled coil (3) is used for condensation.

Usually power plants of that type have a vacuum system removing inert gases and low-boilers. In the original layout of this power plant, the vacuum pump (claw type) extracts working fluid vapour, containing a high fraction of low-boilers and inert gas, from the condenser. The extracted fluid is usually released to the ambient. By doing so, the MDM in the extracted fluid is lost and the working fluid exhaust pollutes the environment. In order to avoid this, a reservoir has been added to the cycle. The

extracted mixture is collected in a vessel outside the turbine house ((1) in figure 9). In order to separate the low-boilers and inert gases from the mixture in the vessel, a second vacuum pump (membrane type) has been added. It can provide a lower pressure than the original pump ((2) in figure 9). The membrane pump and the external vessel are depicted on the very right margin of figure 10.

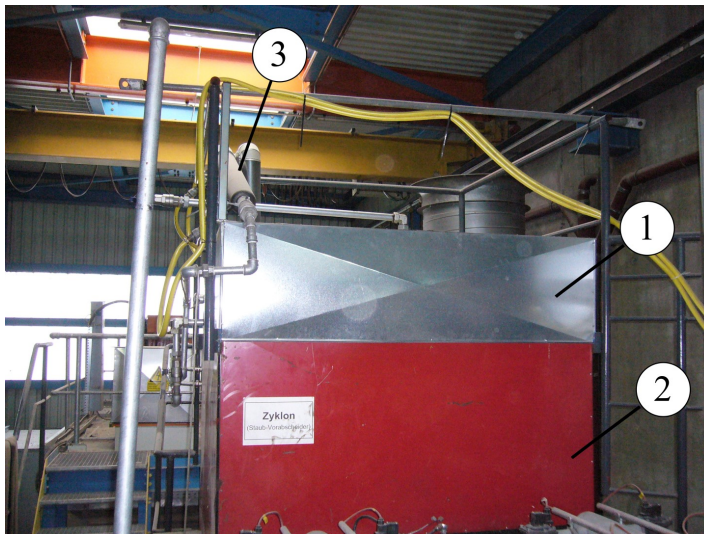


Figure 8: Distilling apparatus on top of multi-cyclone/ exhaust gas duct



Figure 9: New vacuum pump fluid reservoir and membrane pump

3.5 Cycle modifications

The modifications that were made in order to conduct the recycling procedures are depicted in figure 10. Besides the original vacuum pump, a membrane pump was installed (figure 10, right margin). Vapour from the condenser vessel is collected in a reservoir outside the turbine house where it partially condenses (figure 9). As the tests show (table 3), the fluid mixture from the vacuum pump contains a great share of MM. In order to remove the MM from the mixture, a pressure between 10 mbar and 43 mbar is necessary (ambient temperature in a range of 0 °C to 20 °C). This system is operated batch-wise, as soon as the capacity of the vessel is reached (200 litres) the membrane pump is started. After the end of the procedure, the remaining MDM is returned to the cycle.

The removal of working fluid with a high fraction of high-boilers is done via a drain in the recuperator vessel. With the original design of the cycle this was not possible. The liquid from this tap is evaporated in the distilling apparatus depicted in figure 8. Up to now there are no long-term operational experiences with this system. Although, with the modifications of the cycle, the costs for the recovery of one litre of MDM, with a purity of more than 95%, are estimated to € 8.

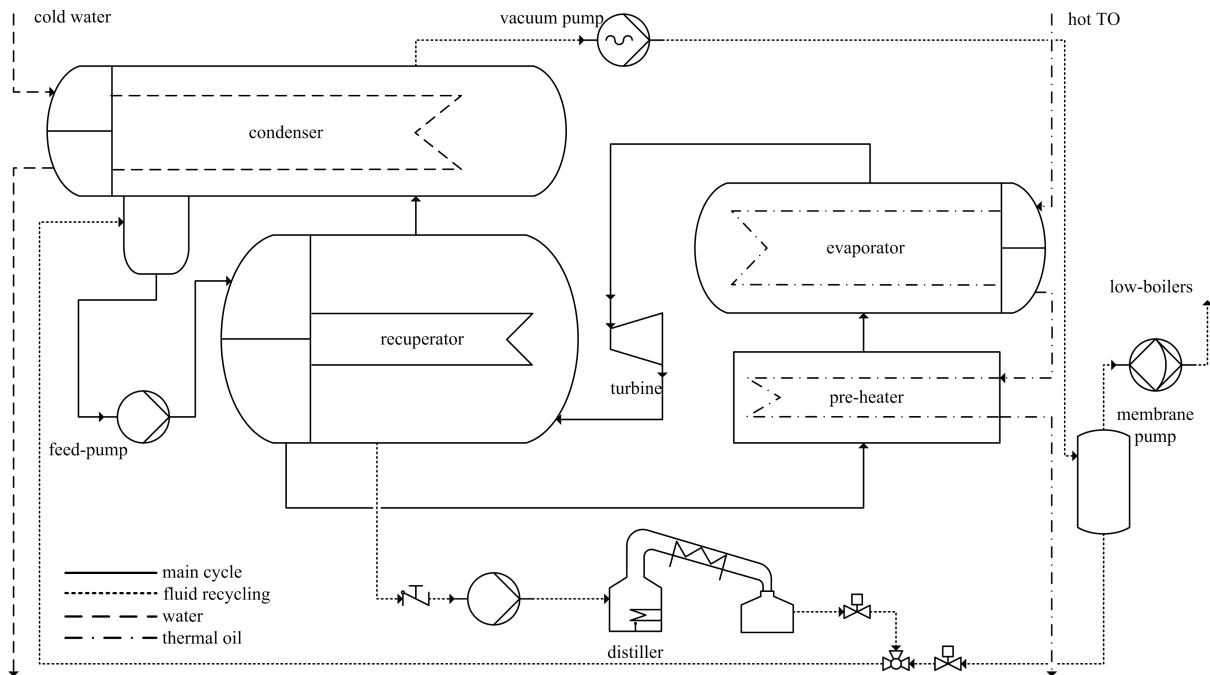


Figure 10: Cycle including all modifications Erhart (2015)

4. CONCLUSIONS

The following conclusions can be drawn from the observations in this paper:

- The degradation of MDM in ORCs is related with the amount of petroleum based lubricants. If this is related to the main component of the lubricant, to its additives or to the decomposition products of the lubricant is not clear.
- The decomposition process under the observed conditions, leads to a large amount of high-boilers in the working fluid.
- The fluid composition throughout the cycle differs significantly. A large fraction of high-boilers precipitate after the turbine. This offers the opportunity to remove these high-boilers from the system if the recuperator has a closed reservoir.
- Low-boilers can be removed from the cycle with the vacuum system by adding an additional membrane pump.
- The distilling of highly contaminated working fluid delivers 95% of pure MDM after the first treatment. Lubricants can be removed from the fluid reliably under laboratory conditions.
- The laboratory distilling tests have shown, that up to 64% of the MDM from the original fluid can be recovered.
- The economical effort of distilling contaminated fluid is far below the effort of a reinvestment in new working fluid. The costs for the distillation for one litre of pure working fluid are around € 8. Over the last years, the price for new working fluid ranged between € 15 and € 22.

Even though the number of analysed power plants is rather low, the data show the necessity for further investigation. The detailed chemical processes, especially the interaction of Hydrocarbons from the lubricant oil with MDM, could not be analysed in detail. A chemical analysis, under laboratory conditions, is necessary to determine the reaction kinetics of this complex process.

NOMENCLATURE

MM	Hexamethyldisiloxan	
MDM	Octamethyltrisiloxane	
D3	Hexamethylcyclotrisiloxane	
D4	Octamethylcyclotetrasiloxane	
MD2M/L4	Decamethyltetrasiloxane	
D5	Decamethylcyclopentasiloxane	
MD3M/L5	Dodecanethylpentasiloxane	
MOH	Trimethylsilanol	
CHP	Combined Heat and Power	
CAS	Chemical Abstract Service registry number	
HS-GC-MS	Head Space Gas Chromatography Mass Spectrometry	
TO	Thermal Oil, here Therminol66	
$\vartheta_{source,max}$	Temperature [°C]	-

Subscript

cond	condensing
max	maximum

REFERENCES

- Dow Corning, S. (2013). Safety datasheet - Dow Corning OS-20.
- Erhart, T. (2015). *Optimisation of heat-led CHPs based upon ORC technology*. PhD thesis, Strathclyde University of Glasgow.
- Grassie, N. and Macfarlane, I. (1978). The thermal degradation of Polysiloxanes, I. Poly(dimethylsiloxane). *European Polymer Journal*, 14(11):875 -- 884.
- Zhou, W., Yang, H., Guo, X., and Lu, J. (2006). Thermal degradation behaviors of some branched and linear Polysiloxanes. *Polymer Degradation and Stability*, 91(7):1471--1475.

ACKNOWLEDGEMENT

Many thanks to Eric Duminil, Xavier Jobard and Daniel Güerlich!

ORC DEPLOYMENT OPPORTUNITIES IN GAS PLANTS

John Harinck*^{1,2}, Ludovico Calderazzi³, Piero Colonna⁴ and Hugo Polderman⁵

¹Gensos B.V., Molengraaffsingel 12, 2629 JD, Delft, Netherlands (j.harinck@gensos.nl)

²Asimptote B.V., Martinus Nijhofflaan 2, 2624 ES, Delft, Netherlands

³Austex S.r.l., Via Brisa, 3, 20123, Milano, Italy

⁴Propulsion and Power, Delft University of Technology, Kluyverweg 1, 2629 HS, Delft, Netherlands

⁵Shell Global Solutions International B.V., Grasweg 31, 1031 HW, Amsterdam, Netherlands

ABSTRACT

Gas processing plants are characterized by large energy flows. Therefore it is key to maximize energy efficiency and to optimize utility balances. In the gas to liquid (GTL) complexes operated by Shell in Malaysia and Qatar, the highly exothermic Fischer Tropsch process is applied to convert gas into liquid hydrocarbon products. Most of the available thermal energy is used to cogenerate steam and to preheat feed streams, but still substantial additional cooling is required to reduce the temperature of intermediate streams for further processing. In the Qatar GTL plant this duty is in the order of 600 MW_{th}.

By means of a detailed investigation that included simulations and cost evaluation of both commercial ORC systems and dedicated advanced ORC concepts, it could be established that heat recovery by means of low-temperature ORC units is a feasible option. Prerequisite is that the ORC unit is directly coupled to the process, without an intermediate thermal fluid loop.

A parallel study focused on application of ORC systems in Liquefied Natural Gas plants. These plants waste large quantities of thermal energy in the form of high temperature exhaust gas from gas turbines used for power generation and gas compression. A similar evaluation of current ORC technology for the recovery of this high-temperature heat led to the conclusion that ORC systems can be more attractive than steam cycles for waste heat recovery from both mid-range gas turbine installations and a feasible option for larger systems in remote or arid locations where steam power plants are impractical. This still is a large scope of deployment, which is expected to increase given the potential for further developments in ORC technology, cost prices and market.

1. INTRODUCTION

Gas processing plants are characterized by large energy flows. In the gas to liquid (GTL) complexes operated by Shell in Malaysia and Qatar, the highly exothermic Fischer Tropsch process is applied to convert gas into liquid hydrocarbon products. Most of the available thermal energy is used to cogenerate steam and to preheat feed streams, but still substantial additional cooling is required. In the Qatar GTL plant, an amount of 600 MW_{th} has to be cooled away from temperatures between 130 and 185 °C. Another large currently wasted energy source is the hot exhaust from gas turbines in LNG plants, released at temperatures of 450-550 °C. Appropriate technology is sought to recover this energy and increase the energy efficiency of the plants, and Organic Rankine Cycle (ORC) power generation has been identified as a promising option.

Process simulations and cost evaluations have been performed to evaluate the power generation potential and economic feasibility of commercial as well as more innovative configurations for ORC units, when integrated in gas plants. The main results and conclusions of these studies are presented in Section 2 (GTL) and 3 (LNG) of this paper. Related studies and literature are, for instance, found in Stijepovic *et al.*, 2012, Jung *et al.*, 2014 and Chacartegui *et al.*, 2009.

2. LOW GRADE PROCESS WASTE HEAT RECOVERY

2.1 Specification of heat sources, sinks and assumptions

Figure 1 shows part of the heat recovery and cooling equipment in the syngas treating and separation train of a GTL plant of the size of Pearl. The specifications of the relevant streams are listed in Table 1.

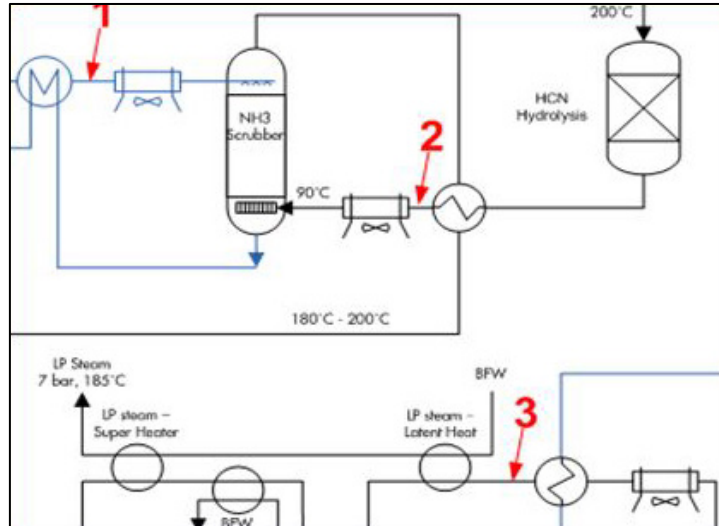


Figure 1: Process flow diagram representing the heat recovery and cooling equipment in the syngas treating and separation train of a GTL plant of the size of Pearl.

Table 1: Specification of process stream heat sources and ambient conditions.

Process stream		1	2	3
Medium		Water	Syngas mixture	Syngas mixture
Phase		Liquid, superheated	Gas, partially condensing	Gas, partially condensing
Pressure	bar	45	26.9	22
Pressure drop, assumed	bar	0.3	0.1	0.3
Temperature, inlet	°C	185	134	168
Temperature, outlet	°C	90 ^a	90 ^a	40 ^a
Heat available, based on specified outlet temperature	MW _{th}	30.6	208	269
Ambient temperature, dry bulb, daily maximum, seasonal/annual averages	°C	27 (winter), 43 (summer), 27 (annual mean)		
Ambient temperature, dry bulb, daily minimum, seasonal/annual averages	°C	10 (winter), 27 (summer), 27 (annual mean)		

^a Maximum allowed temperature limit for process stream outlet; lower return temperatures are preferred also for the downstream process operation.

Process stream 2 and 3 are syngas mixtures that partially condense in the stated temperature range, resulting in a curved temperature profile. This is an important characteristic for the determination of the optimal waste heat recovery (WHR) technology and configuration. The temperature profiles, i.e., the relation between the temperature and the thermal power during the cooling, are used to determine the match in temperatures between the process streams and the heat recovery system. The temperature profiles of process streams 2 and 3 are modeled using the PCPSAFT thermodynamic model (Gross and Sadowski, 2001) so as to take into account the effect of condensation and for stream 1 using RefProp (Lemmon *et al.*, 2010). These models, which are respectively implemented and accessed via FluidProp, an in-house program (Van der Stelt and Colonna, 2004), have been verified to represent the temperature profile of the source data to a sufficient accuracy for preliminary engineering evaluation.

The study is based on the following assumptions and considerations:

- A very important requirement is that, in order not to compromise plant operation, the process streams need to be cooled down to the maximum outlet temperatures indicated in Table 1.
- The process stream conditions do not vary significantly, so that the temperature and thermal energy flows, as specified in Table 1, are constant in time. Therefore, process stream part-load and transient operation were not considered in the waste heat recovery analysis.
- The seasonal and daily variation of the ambient temperature indicated in Table 1 is relatively large with respect to the average temperature, which is likely to have a large impact on the ORC power plant performance. This large variation also needs to be taken into account in the sizing of the air-cooled condenser of the ORC units. In this study, the performance evaluation and dimensioning of the air-cooled condensers of the envisaged ORC power plants are based on a design-point ambient temperature of 32 °C. At some locations, cooling water may be available in sufficient quantities for the ORC condensers, providing several advantages. For this case, cooling water conditions of 32 °C and 4.5 bar (supply flow) and 42 °C and 3 bar (return flow) are assumed.

2.2 Comparison of heat recovery configurations and full integration with process cooling

Various options exist for the integration of the waste heat recovery unit, using either Intermediate Heat Transfer Fluid (IHTF) loops and Direct Heat Exchange (DHE). IHTF loops offer control advantages, whereas DHE offers cost savings and higher efficiency (higher maximum cycle temperature). Process heat recovery configurations have been compared, and a preliminary evaluation led to the selection of the most interesting configuration with respect to feasibility, performance, cost and reliability for both greenfield and retrofit applications.

An important requirement is that the process streams need to be cooled down in order not to compromise the operation of the process plant. It is technically possible for ORC power plants to cool the process streams to the temperatures indicated in Table 1, except in very hot periods. Currently, a backup cooling system is still assumed to be installed. However, to minimize cost and plot space requirements, complete integration of the ORC power plants with the backup cooling system will be required. This is illustrated in Figure 2. This also depends on the degree of redundancy (parallel units) that is enforced.

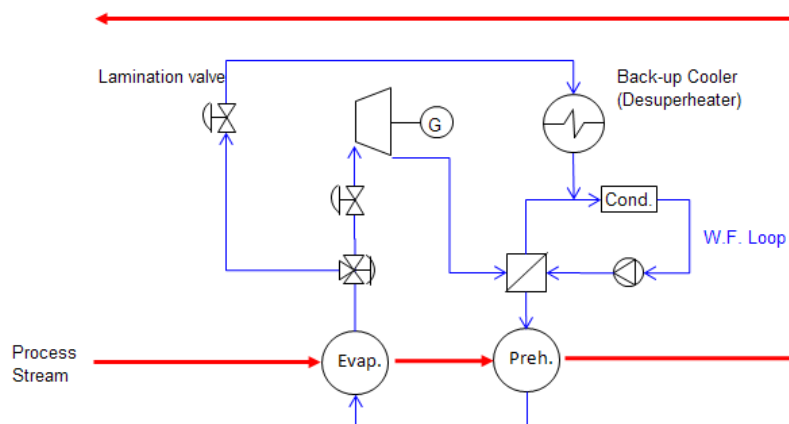


Figure 2: Example of integrated heat recovery: Direct Heat Exchange with back-up cooling on ORC low-pressure side.

The scheme of Figure 2 may be the preferred option in case DHE is applied. This implies that the process cooling becomes dependent on several ORC plant components, so availability of these components becomes a critical requirement for fail-safe process cooling. Careful heat exchanger dimensioning is required to avoid ending up with larger heat transfer surface and fan loads due to lower average rejection temperatures.

The scale up of ORC units beyond the current commercially available maximum unit power output may offer further advantages with respect to cost. The reduced parallelization associated with larger units, however, will affect the degree of redundancy and therefore availability.

2.3 Commercial ORC power plant solutions

This section presents the performance evaluation, based on thermodynamic cycle models, of the technical solutions proposed by various ORC vendors, for the recovery of waste heat from the processes specified in Table 1. These solutions are considered to be representative references for commercial and mature low-temperature ORC power plants of the required large capacity.

Thermodynamic cycle models were developed and validated based on the specifications of the technical proposals supplied by the ORC vendors for the three process heat sources. Conservative assumptions and values typically found for state-of-the-art ORC power plants were used for the isentropic efficiencies of the turbine and feed pump, pinch points and pressure drops of the components and degree of superheating. The models were developed in Cycle-Tempo, an in-house flow sheeting program for the steady-state simulation, design and verification of energy conversion systems (Van der Stelt *et al.*, 2002) marketed by Asimptote. All thermodynamic cycle simulations and coordination were done by Gensos, partner of Asimptote.

The steady-state operations of commercial ORC systems were simulated under various conditions, using these models. Given the assumed steady state environment of heat streams, the influence of ambient temperatures was investigated assuming a constant overall thermal conductance (UA-value) as calculated from the design-point condition (32 °C). The turbine and pump efficiency were assumed to remain constant at off-design conditions, which mainly refers to the varying condensation temperature.

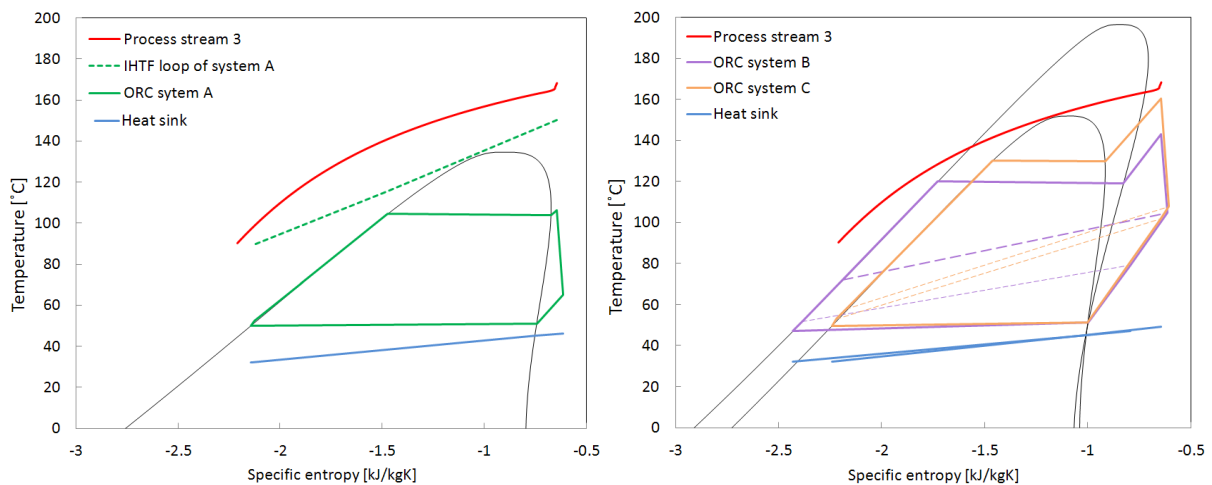


Figure 3: The thermodynamic cycles of three ORC systems using IHTF loop (left) and DHE (right) proposed by vendors, modeled with Cycle-Tempo at design-point conditions, shown in the temperature-entropy of the heat source. The entropy of the working fluids and heat sink medium is linearly scaled to that of the heat source. The dashed lines connect the heating and cooling temperature profiles that occur in the regenerator. Note the strongly curved temperature profile of the heat source due to partial condensation.

The results are summarized in Table 2. The ambient temperature variation reflects typical conditions for a location in the Middle East. As shown, the ambient temperature variation strongly determines net power output; at low ambient temperatures, the ORC power plants can deliver a significantly higher net power output.

Ambient temperature also affects the available cooling capacity. Process stream 1 and 2 can be cooled down to the required temperature of 90 °C using currently commercially available ORC power plants

for almost all ambient conditions. Process stream 3 should be cooled down to 40 °C, which is not feasible using commercial ORC power plants, due to dependence on the comparatively high and varying ambient temperature that is offset by pinch point temperature differences in the ORC system. An additional air-cooled process stream cooler is therefore required for this process stream. If water cooling were an option, then also this process stream can be cooled down to almost the required temperature.

Given the large thermal power available (Table 1) in comparison to the current maximum rating of commercial ORC power plants, an arrangement of two to three ORC units in parallel is required for process stream 2 and 3. The modularity offered by several units in parallel will be required anyway, to provide sufficient operational flexibility, redundancy/continuity and ease of maintenance.

Table 2: Performance predictions for current-technology ORC power plants recovering thermal energy from the process streams for a range of ambient temperatures (assuming air-cooled condensers) and water cooling. Results are also shown in case that sufficient cooling water were available to reject the heat through shell-and-tube condensers. Remaining auxiliary power consumptions other than fan and pump loads are necessarily excluded.

Process stream		1				
Ambient temperature	°C	10	27	32	43	Water cooling
Corresponds to		winter min.	annual mean	design	summer max.	-
Net electric power output	MW _e	4.86	3.71	3.34	2.78	4.25
Heat recovered	MW _{th}	34.3	31.4	30.6	29.2	35.4
Temperature, process outlet	°C	78	87	90	94	75
Water cooling duty	MW _{th}	-	-	-	-	30.8

Process stream		2					3				
Ambient temperature	°C	10	27	32	43	Water cooling	10	27	32	43	Water cooling
Corresponds to		winter min.	annual mean	design	summer max.	-	winter min.	annual mean	design	summer max.	-
Net electric power output	MW _e	27.1	17.6	15.1	10.8	21.1	37	27.9	25.0	20.3	31.7
Heat recovered	MW _{th}	246	212	201	195	224	253	234	201	218	265
Temperature, process outlet	°C	72	86	90	92	82	61	82	90	95	45
Water cooling duty	MW _{th}	-	-	-	-	201	-	-	-	-	231

2.4 Cost evaluation of ORCs for waste heat recovery in a GTL process

To assess the economic feasibility of ORC power recovery a P50¹ cost estimate has been developed for an ORC unit for syngas cooling in an actual GTL project. The project premises were taken from a study for a GTL plant with the size of Pearl in Qatar under development for realization in the US Gulf Coast area (Oil & Gas Journal, 2013).

Attention was restricted to the syngas cooler on process stream 3. The available heat is 269 MW_{th}, at a temperature of \cong 170 °C. Based on air cooling and the ambient temperature frequency distribution of Baton Rouge the yearly average recoverable electric power is estimated at 29.6 MW_e, see Figure 4. The pre-tax Net Present Value (NPV) of the electricity, at \$70 per MWh, including avoided CO₂ costs, would be of the order of 240 mlnUS\$. The project cost was estimated at 155 mlnUS\$. This figure is based on the detailed material take off cost calculation provided by the Asimptote

¹ A P50 cost estimate has a 50% probability of either underrunning or exceeding the final actual cost.

subcontractor Austex, complemented by Shell with further allowances, contingencies, premiums and costs, based on the Gulf Coast GTL premises. The resulting NPV would be 85 mlnUS\$, with a Value over Investment Ratio (VIR) of 0.55. In case water cooling can be applied, the value could be still somewhat higher, with an NPV of 100 mlnUS\$ and a VIR of 0.65. For a system with an ITHF loop the recoverable power is reduced to 19.3 MW_e, and the estimated cost increases to 181 mlnUS\$, resulting in a negative VIR.

For the evaluation the full cost of the secondary cooling was attributed to the ORC loop, i.e. no credit was taken for redundancy of the original air coolers. A substantial further economic optimization will be achieved by integrating the ORC condensers with the existing GTL air coolers.

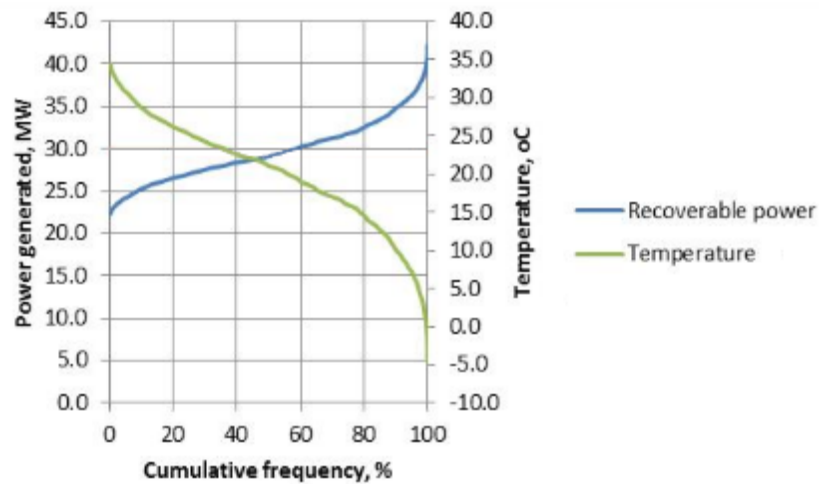


Figure 4: Temperature distribution and accompanying ORC power output. The yearly average recoverable electric power is estimated at 29.6 MW_e.

2.5 Dedicated and advanced ORC power plant configurations

In contrast to current commercial ORC power plants, future ORC systems dedicated to the considered process streams could be developed, given the very large drive that such a market could have. These future ORC systems may also include advanced cycle concepts such as novel working fluids, supercritical cycle pressures, and binary or ternary mixtures as working fluids. The potential performance gains of such dedicated and advanced cycle concepts has been investigated for the process streams in question (Table 1). The pinch point temperature differences and pressure drops used were as determined in the validation of the thermodynamic cycle models for the current state of the art.

The results indicate that optimal pure fluids and optimal cycle conditions would allow for performance gains in terms of net electric power output of approximately 20-35% and a 25-30 °C lower process outlet temperature, depending on the condensation behavior of the process stream. For process streams with limited or no condensation, working fluids with a critical temperature just below the process stream inlet temperature, leading to supercritical cycle conditions appear to provide the highest performance. For process streams with substantial (partial) condensation, working fluids with a critical temperature close to the process stream inlet temperature appear to yield the highest net power output and cooling capacity; in this case supercritical and subcritical evaporative cycle conditions result in equally good performance.

Zeotropic mixture fluids allow for potential performance gains, due to their non-isothermal isobaric condensation and evaporation. Preliminary cycle studies for the heat sources in Table 1 indicate potential gains of 30-35% in gross power output and 36-40 °C lower process outlet temperature (down to 20 °C above ambient conditions). This potential gain may however only be possible if, through careful expert heat exchanger design, a counter-current flow arrangement can be implemented and

working fluid fractionation risks can be minimized. Furthermore, zeotropic mixtures may require more costly heat exchanging equipment and higher fan loads.

3. HIGH GRADE GAS TURBINE EXHAUST HEAT RECOVERY

The feasibility and performance of ORC systems for gas turbine heat recovery in LNG sites was investigated and compared to that of conventional steam bottoming cycles. This part of the study aimed at identifying an application window for which current ORC systems can be more attractive than steam systems, as well as investigating performance gains that future, advanced ORC power plant configurations can potentially bring with continued technology developments and market sector penetration.

3.1 Specification of heat sources, sinks and assumptions

LNG facilities operated by Shell employ gas turbines (GTs) and conventional combined cycles (CCGTs) in various locations. This study focused more specifically on aeroderivative gas turbines (LM2500 and LM6000). A typical LNG site has 4-6 such turbines with a load percentage varying between 60-80%, with common operation at 80%.

To allow for generic conclusions for all LNG operations, a conceptual approach has been adopted. In this approach, the performance of ORC bottoming cycles is evaluated, using validated thermodynamic cycle models, for a range of exhaust temperatures between 400°C to 600°C, while the GT exhaust mass flow rate is set at 100 kg/s, for a range of ambient temperatures. The GT exhaust temperature ranges includes the GTs at both full load and part-load conditions. The reference GT exhaust mass flow rate of 100 kg/s is consistent with a medium-scale GT operating at full load (see, e.g., Del Turco *et al.*, 2011) and also allows for convenient scaling to different GT types and varying numbers of GT units. Like in the GTL case, the performance evaluation of the envisaged ORC power plants is based on a design-point ambient temperature of 32 °C. Using this approach, preliminary conclusions can be drawn for the various GT types, part-load operation, number of gas turbines in a set and the specific (ambient) location conditions relevant for LNG operations.

3.1 Commercial ORC power plant solutions

Thermodynamic cycle models of three ORC power plants, considered to be representative references for commercial and mature ORC power plant technology for GT waste heat recovery, and a conventional single-pressure, unfired, steam-based combined cycle power plant (CCGT) system were developed using the conservative assumptions stated in Section 2.3. The models were validated based on specifications of datasheets and technical proposals supplied by ORC vendors and literature (Gas Turbine World, 2012). The steady-state operation of the ORC systems and CCGT system were then simulated under the aforementioned condition ranges. For the off-design simulations, the sizes of all heat transfer equipment were fixed to the design value.

The results shown in Table 3 indicate that for this application CCGT systems currently still provide approximately 30%-45% more power output, on an equal specific capacity base, at gas exhaust temperatures of 450-550 °C (representative of the aeroderivative LM6000 PD) and nominal conditions. At higher temperatures, typical of heavy duty gas turbines, the gain in power output increases. If gas turbine load variations are frequent or large, the spread is smaller, since ORC systems are more flexible and tolerant to off-design conditions. DHE did not result in considerably higher power outputs as compared to the adoption of IHTF loops. IHTF loops were therefore assumed for subsequent simulations of commercial ORC solutions and DHE for advanced ORC power plant configurations.

The main reason for the lower output of ORC systems at high exhaust temperatures is the thermal stability limit of currently adopted working fluids (at most, approximately 350 to 400 °C, depending on the fluid), which imposes a limitation on the maximum turbine inlet temperature and thus power output. Water/steam does not have this limitation and CCGT systems can operate at much higher

turbine inlet temperatures and thus provide generally higher power outputs. The development of suitable organic fluids with higher thermal stability limits (and higher critical temperature while maintaining their low critical pressure) is therefore desirable. The ambient temperature appears to equally influence the power output for both ORC and CCGT systems.

Table 3: Main performance results based on thermodynamic cycle simulations for current state-of-the-art ORC systems compared to a (single-pressure) CCGT system, if coupled in a 1:1 mode to an LM6000 PD at 80% load (corresponding to an exhaust gas flow rate and temperature 94 kg/s and 503 °C, respectively) and air-cooled condenser with ambient temperature of 32 °C.

System	Gross power Output (MW _e)	Pump power (MW _e)	Fan Power (MW _e)	Net Power Output (MW _e)	Heat Recovered (MW _{th})
ORC system D	7.46	0.60	0.11	6.75	34.3
ORC system E (IHTF)	7.43	0.44	0.31	6.68	32.8
ORC system E (DHE)	7.61	0.36	0.35	6.90	33.5
CCGT	10.3	0.07	0.81	9.44	35.5

Application of ORC technology to GT WHR focuses on smaller installations, though a trend towards larger installations is noticeable. Figure 5 presents an indicative graphical representation of heat source temperatures and power outputs for which ORC and CCGT systems are considered viable. The feasibility limits shown for ORC and CCGT systems are based on current reference plants and therefore are merely an indicative representation of their current respective techno-economic viability. These limits may change due to progressing technological developments, reductions in cost prices, changes in the value of power or local regulations requirements. The thermal stability limit shown refers to the maximum temperature of currently adopted organic working fluids of ORC systems. The organic working fluids in ORC systems do not reach the heat source temperature, due to heat transfer surfaces (DHE) or the adoption of IHTF loops. Hence, heat sources with temperatures higher than the thermal stability limit can be recovered, although generally they will not lead to higher ORC system conversion efficiency and power output.

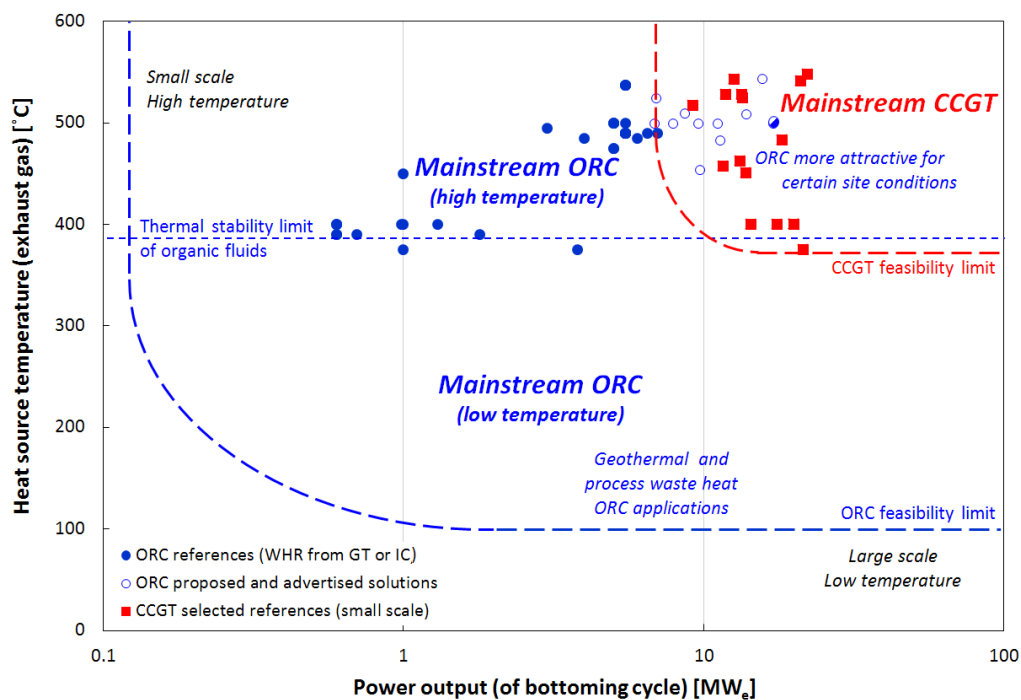


Figure 5: Heat source temperatures and power outputs for which ORC and CCGT systems are considered viable. This figure should only be used as an approximate indication; it was inspired by the figure from (Gaia,

2011) and constructed based on expert knowledge and experience, includes reference plants for ORC systems and CCGT systems and proposed solutions.

ORC systems can have a decisive advantage over CCGT systems in case of locations where water is not available, freezing conditions may be an issue, gas turbine load variations are frequent or large, or remote locations with limited operations support. ORC plants are fully automated and can sustain unattended operation (requiring no on-site supervision or qualified operator nor periodic manual checks or analyses of the working fluid), have zero water consumption, and automatically adapt to load variations without excessive penalties on turbine efficiency.

Given the potential for further performance improvement (up to 30%, see Section 3.2), standardization of manufacturing and economies of scale with increasing market adoption, cost price reductions are expected for ORC systems in the coming years, similarly to reductions that occurred for CCGT systems in previous decades. This would considerably enlarge the range of applications where ORC systems are more attractive than CCGT systems.

Although the state of the art in ORC systems does not provide the same power output as CCGT systems, it offers important operational and cost advantages with respect to simplicity and reliability of plant configuration, as well as safety aspects and requirement for skilled operators. These advantages lead to lower life cycle costs and, for small power output applications, may outweigh the (currently) higher specific investment costs as compared to CCGT systems.

3.2 Developments and advanced ORC power plant configurations

From the thermodynamic optimization point of view, opportunities exist to improve the performance of current ORC systems. These include (new) optimal working fluids with higher thermal stability and critical temperatures, the adoption of novel cycle configurations such as supercritical cycles (including CO₂ as fluid) and cascade ORC systems.

The results of a preliminary study, shown in Table 4, indicate that by employing more suitable fluids, optimized cycle conditions and more advanced ORC system concepts, the net output of ORC power plants could be increased up to 30% with respect to the current state of the art ORC systems at their (conservative) design cycle conditions. For the LNG application, this would make ORC systems comparable to CCGT with respect to performance. It should be noted that these results are demonstrational and do not necessarily represent the optimized solution for these concepts.

Table 4: Main performance results based on thermodynamic cycle simulations of (single-pressure) Rankine cycles for various high-temperature working fluids at optimized cycle parameters recovering heat, using Direct Heat Exchange, from an LM6000 gas turbine operating at 80% load (corresponding to an exhaust gas flow rate and temperature 94 kg/s and 503 °C, respectively, at a design ambient temperature of 32 °C).

Working Fluid	P _c (bar)	T _{max} (°C)	Gross Power Output (MW _e)	Pump Load (MW _e)	Fan Load (MW _e)	Net Power Output (MW _e)	Stack Temperature (°C)	Heat Recovered (MW _{th})	Gain ^a (%)
Cyclopentane	45.2	232	9.05	0.6	0.3	8.14	110	40.4	18%
Toluene	41.3	313	9.55	0.41	0.12	9.02	139	37.4	31%
Cyclohexane	40.8	274	9.58	0.49	0.16	8.93	136	37.8	29%
Pentane	33.7	190	7.74	0.6	0.62	6.53	110	40.4	-5%
MM	19.4	240	7.28	0.39	0.14	6.75	160	35.4	-2%
Steam	220	478	10.5	0.07	0.82	9.62	154	36.1	n/a

^a Gain is defined as the percentage increase in the net power output as compared to current state of the art ORC systems at their (conservative) design cycle conditions.

4. CONCLUSIONS

By means of a detailed investigation that included simulations of both commercial ORC systems and dedicated advanced ORC concepts, allowed to establish that the recovery of waste heat from gas to liquid (GTL) complexes operated by Shell by means of ORC systems is a feasible option. Prerequisite is that the ORC unit is directly coupled to the process, without an intermediate thermal fluid loop.

The similar evaluation of current ORC technology for the recovery of high-temperature heat from gas turbines exhausts in Liquefied Natural Gas (LNG) plants, led to the conclusion that ORC systems can be more attractive than steam power plants for waste heat recovery from both mid-range gas turbine installations and a feasible option for larger systems in remote or arid locations where steam cycles are impractical. This still is a large scope of deployment, which is expected to increase given the potential for further developments in ORC technology, cost prices and market.

REFERENCES

- Chacartegui R., Sanchez D., Munoz J.M., Sanchez T., Alternative ORC bottoming cycles FOR combined cycle power plants, 2009, *Applied Energy*, 86 (10), pp. 2162-2170.
- Gaia, M., 2011, 30 Years of Organic Rankine Cycle Development, *First International Seminar on ORC Power Systems*, September 22-23, 2011, Delft University of Technology, keynote.
- Gas Turbine World, 2012, *Gas Turbine World Handbook*, Pequot Publishing Inc. Fairfield, CT, United States.
- Gross, J. and Sadowski, G., Perturbed-Chain SAFT: An Equation of State Based on a Perturbation Theory for Chain Molecules, 2001, *Industrial & Engineering Chemistry Research*, 40 (4), pp. 1244-1260.
- Jung H.C., Krumdieck S., Vranjes T., Feasibility assessment of refinery waste heat-to-power conversion using an organic Rankine cycle, 2014, *Energy Conversion and Management*, 77, pp. 396-407.
- Lemmon, E.W., Huber, M.L., McLinden, M.O., 2010, *NIST Standard Reference Database 23: Reference Fluid Thermodynamic and Transport Properties-REFPROP*, Version 9.0, National Institute of Standards and Technology, Standard Reference Data Program, Gaithersburg, United States.
- OGJ Editors, Shell selects Louisiana site for \$12.5 billion, world-scale GTL facility, *Oil & Gas Journal Online*, September 24, 2013.
- Stelt, T.P. van der, and Colonna, P., 2004, Fluidprop: a program for the estimation of *thermophysical properties of fluids*. Energy Technology Section, Delft University of Technology, The Netherlands.
- Stelt, T.P. van der, Woudstra, N., Colonna, P., 2002, *Cycle-Tempo: a program for the thermodynamic analysis and optimization of systems for the production of electricity, heat and refrigeration*, Energy Technology Section, Delft University of Technology, The Netherlands.
- Stijepovic M.Z., Linke P., Papadopoulos A.I., Grujic A.S., On the role of working fluid properties in Organic Rankine Cycle performance, 2012, *Applied Thermal Engineering*, 36 (1), pp. 406-413.
- Turco, P. Del, Asti, A., Del Greco, A.S., Bacci, A., Landi, G., Seghi, G., 2011, The ORegen waste heat recovery cycle: Reducing the CO₂ footprint by means of overall cycle efficiency improvement, *Proc. ASME Turbo Expo*, GT2011, June 6-10, 2011, ASME, 1-10.

ACKNOWLEDGEMENT

The authors acknowledge Shell Global Solutions for allowing the publication of general results and conclusions of the two studies performed for Shell. The contacted ORC vendors, among them Turboden, Ormat and Exergy, are acknowledged for proposing technical solutions representative of the current state of the art.

ON HIGH LEVEL EVALUATION AND COMPARISON OF ORC POWER GENERATORS

Henrik Öhman^{1*}, Per Lundqvist²

¹KTH, Royal Institute of Technology,
Energy Technology, Stockholm, Sweden
henrik@hohman.se

²KTH, Royal Institute of technology,
Energy Technology, Stockholm, Sweden
per.lundqvist@energy.kth.se

* Corresponding Author

ABSTRACT

A review of the thermodynamic performance of ORCs from public, as well as non-public sources has revealed a correlation suitable to be used as a rule of thumb for high-level performance estimation of ORC power generators. Using the correlation, the limited amount of available test data can be generalised leading to a high level evaluation of the commercial benefits of any potential application for ORCs.

Power generators using ORC-technology exist in relatively low numbers. Furthermore, field installations seldom imply comparable boundary conditions. As ORCs generally operate at low temperature differences between source and sink it has been shown that their relative sensitivity to variations in temperatures i.e. the finiteness of source- and sink, is larger than the sensitivity of power generators operating with large temperature differences. Therefore the establishing of practical rule of thumb performance estimation, similar to the figure of merit, Coefficient of Performance, COP, as used in refrigeration and air conditioning industry, has previously not been successful.

In order to arrange field data in a manner suitable for comparison a refinement of suitable figures of merit was required. The suggested, refined terms are presented and explained as well as critically evaluated against the most common efficiency terms traditionally used.

The current lack of a performance rule of thumb leaves room for less serious vendors and laymen to make performance claims unrealistic to practical achievements. Scrutinizing such questionable statements requires detail process simulations and a multitude of technical assumptions. Hence argumentation becomes ineffective. If a suitable rule of thumb can be established argumentation against dubious claims would become significantly more forceful.

This paper suggests a new term to be used as rule of thumb and explains a method on how to use it.

1. INTRODUCTION

In the technical field of ORC power generators, as in most technical fields, the need for universally accepted figures of merit is substantial. Such terms are used daily by engineers and scientists to evaluate choices of many kinds. Design choices, development strategies, economic investments, career decisions are a few examples where figures of merit are used for rule of thumb decision. Only when resources are already allocated to feasibility studies, or similar, will someone spend the time to properly model the details of the conditions and thereby have the position to question any rule of thumb.

Technical fields lacking proper rules of thumb are susceptible to confusion, uncertainty and tend to attract the attention of enthusiasts with more or less respect for physical realities. It is not strange that

discussions then have a tendency to become more of debate than scientifically constructive argumentations. This is not only irritating but can also pose a significant entry barrier to the market. If potential investors need the expertise of gurus speaking incomprehensible language the likelihood of powerful market penetration is low. Furthermore enthusiasts claiming unrealistic future performances create excellent reasons to postpone any investment in current applications.

Establishing purely experience based figures of merit for specific technologies tend to require a large enough number of products in commercial use in combination with scientific endorsement of whatever entities used for comparison. Typically the environment of a technology can be limited to a few characteristic parameters, which then could be used for evaluation. Furthermore a clear reference of some representation of an ideal product/cycle has to be available. Compromises between scientific accuracy and practicality of communication are also required to gain acceptance. No figure of merit can be perfect, though over time the inapt terms will naturally disappear. However many still exist despite obvious logical imperfections. Two examples from industrial practice are volumetric screw compressors in the odd case measuring $>100\%$ volumetric efficiency and 2-phase compressors showing $>100\%$ isentropic efficiency. In the first case dynamic super-filling creates the illusion and in the second case the isentropic reference is badly chosen instead of an isothermal reference. The issue of choosing dubious definitions of figures of merit, as in the examples, cannot be entirely avoided and has to be addressed by educators and senior experts. However, the more implicit error of ill-defined methods is clearly a scientific matter. Communication about ORC technology performance is affected by both types of error.

Technologies for low temperature difference power generators, of which ORC is only one, are mature for market penetration, see example in Öhman (2012). Applications with available low grade heat are available in abundance as of many examples, Biscan and Filipan (2011). Need for heavy investments in new electric power generation is also well determined, see Breeze (2014). A number of industrial suppliers of ORC are offering products for different applications as seen in Öhman and Lundqvist (2013). In science a very high number of articles are published yearly on ORC technology, details of the plurality can be found in Öhman (2014). Environmental benefit of using low grade heat for power generation is furthermore evident to anyone educated in environmental concern. Yet, the number of commercially installed ORCs is not impressive. One way of improving implementation of ORCs in society would be to create universally accepted rules of thumb, guiding anyone involved in determining the quality of ORC-products.

2. FIGURES OF MERIT FOR ORC POWER GENERATORS

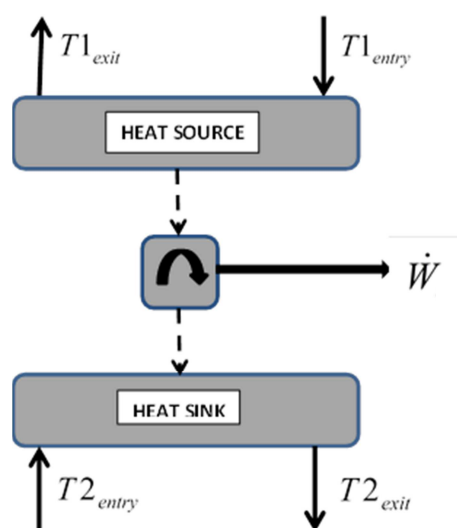


Figure 2. Schematic of a power cycle operating between a finite heat source and a finite heat sink.

Considering a schematic power cycle as of Figure 1, 1st law efficiency, here called thermal efficiency as of Equation (1), is a suitable figure of merit for some technologies, such as high temperature Internal Combustion Engines and Power plants. However, ORCs often operate with low temperature differences between source and sink and is therefore more sensitive to the nature of source and sink than high temperature systems.

$$\eta_{th} = \dot{W} / \dot{Q}_1 \quad (1)$$

where

$$\dot{Q}_1 = (T_{1entry} - T_{1exit}) / \alpha_1 \quad (2)$$

and if apparent heat capacity if the heat source is constant

$$\alpha_1 = 1 / (\dot{m} \cdot Cp) \quad (3)$$

Scientific papers of very shifting quality can be found claiming unrealistically high efficiencies of ORCs. A common simplification is to only consider the cycle itself. Temperatures of evaporator and condenser are used to calculate a reference Carnot efficiency, as of Equation (4). Any measure, or simulated, thermal efficiency of the ORC is then compared to the reference and the result is used as characterizing the system, as of Equation (5). Using this type of Carnot efficiency creates an illusion of being physically correct. First law efficiency, internal to the cycle, can sometimes be motivated when combined with some definition of “external” loss, such as Criterion P of Yan (1987) and Yan (1991). Also heat exchanger efficiency, as in Karellas and Schuster (2008) could be interpreted as an “external” loss. However when distinguishing between “internal” and “external” losses one cannot avoid making an assumption about the cycle, thereby biasing any comparison with a different cycle.

$$\eta_c = 1 - \frac{T_2}{T_1} \quad (4)$$

$$FM = \eta_{th} / \eta_c \quad (5)$$

A better, but still misleading, approach is to define a reference Carnot efficiency by using only the entry temperatures of the source and sink. This is a surprisingly common in literature. As no concern is taken to the temperature gradients in source and sink an infinitely small power cycle would appear more attractive than a larger one. Obviously this cannot serve as a universal figure of merit.

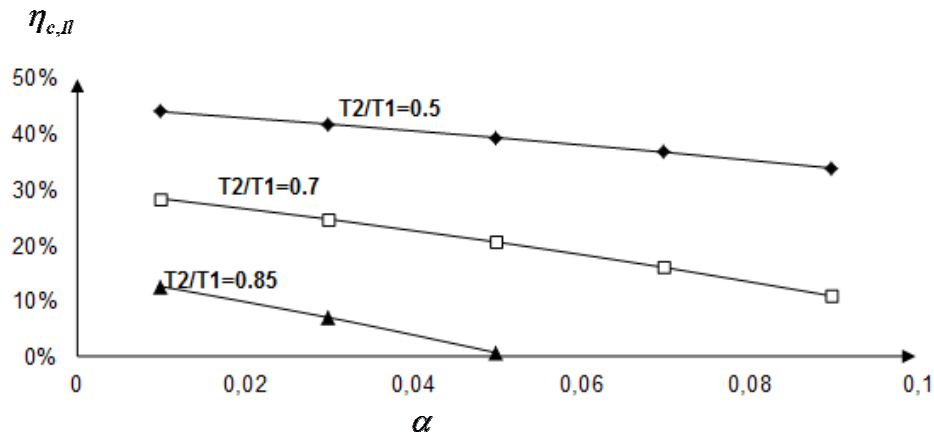


Figure 2. Integrated Local Carnot efficiency vs. inverse apparent heat capacity, α , with source and sink of equal finiteness, α_1 equals α_2 . Low temperature ratios show little sensitivity while high temperature ratios show high sensitivity to the finiteness. *From Öhman and Lundqvist (2013)*

Figure 2 shows relative sensitivity to source and sink finiteness as a function of source and sink entry temperature ratio. This is clear evidence of the poor suitability of thermal efficiency as figure of merit for ORCs.

Some authors prefer to use exergy analysis to solve the problem of comparing higher level performance of ORC. In some cases the exergetic efficiency, or 2nd law efficiency, is defined as in Equation (6). It is defined by comparing the work output to the exergy consumption from the source. Not only does Equation (6) leave out any characteristics of the heat sink, but it is also entirely dependent on a randomly chosen reference temperature.

$$\eta_{ex} = \dot{W} / [\dot{m}_1 \cdot (e_{1,entry} - e_{1,exit})] \quad (6)$$

Some authors use exergy efficiency, as defined in Equation (7), as reference for Equation (5). This approach is physically correct, according to standard textbooks such as Borgnakke and Sonntag (2009), but creates a dilemma explained later.

$$\eta_{ex} = \dot{W} / [\dot{m}_1 \cdot (e_{1,entry} - e_{1,exit}) + \dot{m}_2 \cdot (e_{2,entry} - e_{2,exit})] \quad (7)$$

In this case output work is related to the net exergy destruction. This approach serves excellently for further detailed studies on distribution of losses with a focus on cycle improvements. The dilemma created is that if we are to compare high level results between ORCs, operating at different conditions we need to refer to some reversible system, for which we need to define the net reference exergy conditions. Equation (7) only stipulates the exergy changes in the real system, not the exit exergy of the heat sink of the reference reversible system. Furthermore, if Equation (7) is applied to a reversible system it collapses to a simple 1st law relation where output work and heat sink exit temperature are unknown. I.e. an unsatisfactory iterative solutions method is required. Of the common methods used, this is the closest to be suitable as a figure of merit for ORCs. Unfortunately it cannot be used if the apparent heat capacity of any of the source or sink is a function of temperature. This is further discussed in section 4 of this paper.

An approach similar to Equation (5) is using the so-called Curzon-Ahlborn efficiency, as of Equation (8), as reference in Equation (5).

$$\eta_{CA} = \left(1 - \sqrt{T_2/T_1}\right) \tag{8}$$

η_{CA} was established by Curzon and Ahlborn (1975), though to a large extent preceded by Chambadal (1957) and Novikov (1958). The term is often used as a reference for plant efficiency as it assumes complete equalization of source and sink temperatures exiting the process. Though elegant, this reference will create a favor for very small systems compared to large ones due to 2nd law requirements. If source and sink are assumed similar the smallest power cycle will always operate at a higher average temperature difference. Curzon-Ahlborn efficiency is not suitable as reference for a figure of merit but it comes in very handy defining Utilization, defined in Equation (12), as will be seen later.

To emphasize the dilemma of high level performance comparison of ORCs Figure 3 and Figure 4 show calculated values of the above figures of merit as a function of Utilization for a combination of source and sink characteristics. Figure 3 shows thermal efficiency of a reversible power cycle. Figure 4 shows figures of merit for the same power cycle equipped with one irreversibility, a 10% transmission loss of work. Heat from the loss is assumed to leave the system immediately.

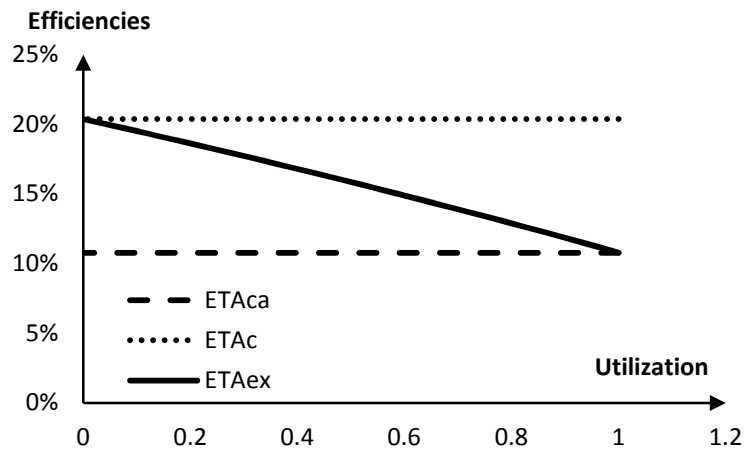


Figure 3. Thermal efficiencies of a reversible power cycle operating at entry temperatures 95/20degC and water flow of 100m3/h in source and sink. ($\eta_{CA}, \eta_C, \eta_{ex}$)

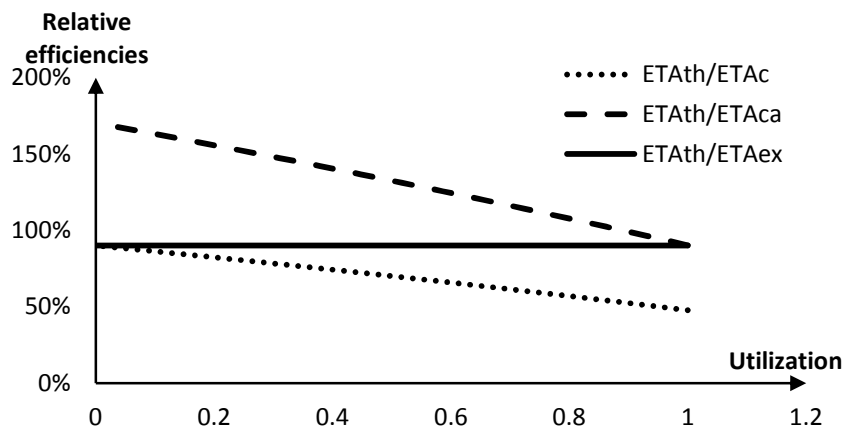


Figure 4. Figures of merit vs. Utilization for the power cycle in Figure 3 but with a 10% external loss of work.

Figures 3 and 4 explain that, of the described figures of merit, only exergy efficiency can be a reasonable reference considering that the thermodynamic *quality* of the power cycle solution is identical in all cases. It is a pity that there is such a difficulty in getting acceptance for the term exergy among practitioners. Entities based on iteration do not make it easier to get acceptance. On top of that variable apparent heat capacities would require each reference to be defined using arbitrary assumptions, being highly unsuitable in a reference for a figure of merit.

3. PROPOSED FIGURE OF MERIT, FRACTION OF CARNOT

From Chapter 2 we can conclude that a suitable figure of merit for ORC should yield results similar to using exergy efficiency as reference but also take variable apparent heat capacity of source and sink into account. Furthermore it should be possible to calculate it without iteration in order to ease the acceptance of the figure of merit among practitioners.

Luckily numerical methods provide a practical solution. Ibrahim and Klein (1996) describe a simple numerical approach, the so called Max Power Cycle. Numerically they defined the reversible work of a Max Power Cycle as Equation (9).

$$\dot{W} = \int_0^{\dot{Q}_1} \left(1 - \frac{T_{2l}}{T_{1l}}\right) \cdot d\dot{Q}_1 \quad (9)$$

Though not apparently solvable analytically this equation is easy to calculate numerically, without requiring iteration. Expressed as a summation we can write Equation (10), as of Öhman and Lundqvist (2012)

$$\eta_{c,II} = \frac{1}{n} \cdot \sum_{i=1}^n \left(1 - \frac{T_{2,i}}{T_{1,i}}\right) \quad (10)$$

where the summation is done in the dimension of heat transfer absorbed by the cycle from the heat source.

The chosen term, Integrated Local Carnot efficiency, represents the thermal efficiency of a reversible power cycle operating between a finite source and a finite sink. I.e. it creates an absolute reference for any figure of merit for power cycles. Note that this entity is physically identical to the exergy efficiency of Equation (7) if the apparent thermal capacities of the two streams are constant.

The proposed figure of merit, *Fraction of Carnot* then becomes defined as in Equation (11).

$$FoC = \eta_{th} / \eta_{c,II} \quad (11)$$

Fraction of Carnot describes how well the 1st and 2nd law potential of a particular combination of source and sink has been used, at a pre-defined rate of heat transferred from the source. If *FoC*, defined as of Equation (11), is plotted against Utilization we can draw conclusions from ORCs operating at very different conditions, as shown in Öhman and Lundqvist (2013). Utilization is defined according to Equation (12) and tells us how well the first law potential, of a combination of source and sink, has been used.

$$\psi_U = \dot{Q}_1 / \dot{Q}_{CA} \quad (12)$$

where \dot{Q}_{CA} is the rate of heat transfer from the heat source that would create fully equalized exit temperatures in source and sink using a reversible power cycle. This is calculated based on the Curzon-Ahlborn efficiency as of Equation (8).

$FoC(\psi_U)$ can be used as a universal figure of merit for low temperature difference power cycles, such as ORCs. As such it can be used to create general, high level comparison between different technical solutions. It will then work in a similar manner as Coefficient of Performance, COP, in refrigeration technology.

4. DISCUSSION ON PRACTICAL USE OF FRACTION OF CARNOT

As merely a proposed figure of merit little generalized investigations exist yet. However, Öhman and Lundqvist (2013) shows a correlation extracted from a wide range of applications and technologies, **Figure 5**. As shown in the reference too few data exists currently to make a comprehensive analysis of the statistical significance of the correlation. It should therefore be considered as preliminary.

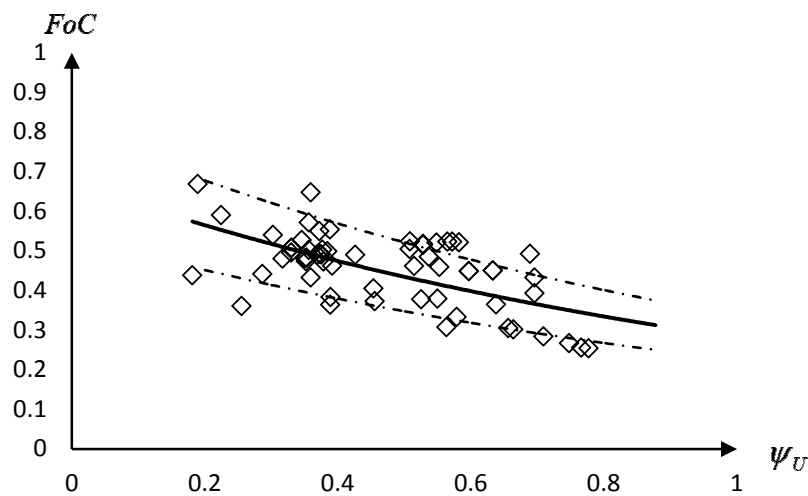


Figure 5. Correlation of Fraction of Carnot vs. Utilization as of Öhman and Lundqvist (2013). Data covering 0.2kW to 7.5MW electric power, heat sources from 73°C to 300°C, different working fluids and different thermodynamic cycles. Visual error bands of $\pm 20\%$ are indicated as dotted lines.

FoC , correlated with data from real systems, is well suited to make the currently very scattered performance data of few ORCs in different applications into a concentrated substitute for data from large number of, currently non-existing, operating real life units. Equation (13) expresses the correlation between Fraction of Carnot and Utilization.

$$FoC = 0,672 \cdot e^{-0,874 \cdot \psi_U} \quad (13)$$

As we receive more data from the field the correlation can be refined, however it is already more useful than any other candidate published.

In Öhman and Lundqvist (2014) a simplified method using the correlation for optimization, and sizing, of geothermal applications was shown. Not only was it possible to pre-estimate the expected power output but also the required heat transfer in evaporator and condenser could be pre-estimated. Thereby economic benefit, as well as a rough indicator of equipment size, could be established, allowing proper motivation for further detailed feasibility studies. That is an example on how a figure of merit, such as Fraction of Carnot, can be used. Note that this way an estimation of the optimal rates of heat transfer from the heat source, and to the heat sink, can be made. As a consequence rough

estimations on heat exchanger sizes are enabled by assuming basic process temperatures. Considering that heat exchangers are the major cost items in many ORCs an idea of expected product cost is possible to form. A pre-estimation of both investment and benefit can be made since the output power is also indicated by the correlation.

Hereby life is made easier for investors, legislators and practitioners in evaluating and promoting the best solutions. As a consequence market penetration of ORC may have a better chance to become significant. Inverting the argument, the lack of such a figure of merit is likely to harm the market penetration by allowing confusion and lack of confidence.

Of course once there are high numbers of ORC in the field, in each niche of temperature and heat capacity combinations of source and sink, a figure like *FoC* may become redundant. However, considering the vast number of possible combinations of source and sink characteristics that would require data from millions of ORC field units to become conclusive.

One could argue that Integrated Local Carnot efficiency should be named using exergy efficiency, based on the fact that Carnot efficiency can be derived from the 2nd law. Exergy efficiency could be numerically obtained in a similar manner as Equation (9) and Equation (10) as explained by Borgnakke and Sonntag (2009). This would however become confusing from two reasons; firstly a reversible system should logically always have an exergy efficiency of 1, secondly the risk of mixing up Equation (7) with Equations (9) and (10) would be apparent thereby making the consequential figure of merit ambiguous.

5. CONCLUSIONS

Lack of universally accepted figures of merit is a limiting factor for the implementation of ORC-technology in society in any significant magnitude.

Currently used figures of merit are not suitable due to lack of exact definitions of references and/or terminology alienating practitioners.

The term Fraction of Carnot offers a potential figure of merit useful for all low temperature difference power cycles.

Fraction of Carnot as a function of Utilization provides a general guide to which performance can be expected, from arbitrary ORC market products, as well as an estimation on physical size of the heat exchangers.

NOMENCLATURE

T	temperature	(K)
\dot{W}	rate of work	(kW)
\dot{Q}	rate of heat transfer	(kW)
α	inverse apparent heat capacity	(K/kW)
η_{th}	thermal (first law) efficiency	(-)
η_C	Carnot efficiency	(-)
η_{ex}	exergy (second law) efficiency	(-)
η_{CA}	Curzon-Ahborn efficiency	(-)
$\eta_{c,II}$	integrated local Carnot efficiency	(-)
n	integer	(-)
e	specific exergy	(kW/kg)
FoC	Fraction of Carnot (Figure of merit)	(-)
ψ_U	utilization	(-)
\dot{Q}_{CA}	heat transfer from source at $\psi_U = 1$	(kW)

FM	arbitrary figure of merit	(-)
\dot{m}	mass flow	(kg/s)
C_p	specific heat	(kJ/(kg,K))

Subscript

1	heat source
2	heat sink
entry	a flow entering the power cycle
exit	a flow leaving the power cycle
1	local

REFERENCES

- Biscan, D., Filipan, V., 2011, Potential of waste heat in Croatian industrial sector, 6th Dubrownik Conference on Sustainable Development of Energy Water and Environment Systems., SDEWES: FP 972.
- Breeze, P., 2014, An introduction to Electricity Generation, Chapter 1, *In: Power generation technologies, Second Edition*, Elsevier, Oxford, UK.: p. 9-13.
- Borgnakke, C., Sonntag, R. E., 2009, Availability, Chapter 10, *In: Fundamentals of Thermodynamics SI version*, John Wiley and Sons, Hoboken: p. 340-374.
- Chambadal, P., 1957, *Les centrales nucleaires*, Armand Coling, Paris, 458 p.
- Curzon, F., L., Ahlborn, B., 1975, Efficiency of a Carnot engine at maximum power output, *American Journal of Physics*, vol. 43, p. 22-24.
- Ibrahim, O., M., Klein, S., A., 1996, Absorption Power Cycles, *Energy*, vol. 21, no. 1: p. 21-27.
- Karrellas, S., Schuster, A., 2008, Supercritical Fluid Parameters in Organic Rankine Cycle Applications, *Int. J. of Thermodynamics*, vol. 11, no. 3: p. 101-108.
- Novikov, I., I., 1958, The efficiency of atomic power stations (A review), *Journal of Nuclear Energy II*, vol. 7, p. 125-128, (Translated).
- Öhman, H., 2012, Implementation and evaluation of a low temperature waste heat recovery power, *Energy*, vol. 48, p. 227-232.
- Öhman, H., 2014, *A survey of literature on low temperature power cycles in general and organic rankine cycles in particular*, KTH, Stockholm, doi:10.13140/RG.2.1.5000.1443, 23 p.
- Öhman, H., Lundqvist, P., 2012, Theory and method for analysis of low temperature driven power cycles, *Applied Thermal Engineering*, vol. 37, p. 44-50.
- Öhman, H., Lundqvist, P., 2013, Comparison and analysis of performance using Low Temperature Power Cycles, *Applied Thermal Engineering*, vol. 52, p. 160-169.
- Öhman, H., Lundqvist, P., 2014, Thermodynamic pre-determination of power generation potential in geothermal low-temperature applications, *Geothermal Energy*, vol. 2, no. 4: p. 1-10.
- Yan, J., 1987, The Thermodynamic Analysis of the Matching between Working Fluids and Variable-Temperature Heat Sources in a Cycle, (Chinese) Journal of Engineering Thermophysics, vol. 8, no. 4
- Yan, J., 1991, *On Thermodynamic Cycles with Non-Azeotropic Mixtures as Working Fluids*, (Thesis), ISBN 91-7170-059-5, Dept of Heat Technology. KTH, 26 p.

A MULTI SCALE METHODOLOGY FOR ORC INTEGRATION OPTIMIZATION IN AN INDUSTRIAL PROCESS

Cong-Toan Tran¹, Assaad Zoughaib^{2*}

MINES ParisTech, PSL Research University, CES - Centre for energy efficiency of systems,
Z.I. Les Glaizes – 5 rue Léon Blum 91120 Palaiseau, France

¹ cong-toan.tran@mines-paristech.fr

² assaad.zoughaib@mines-paristech.fr

* Corresponding Author

ABSTRACT

In industrial processes, a large amount of energy is usually lost as waste heat. This waste source reduces not only the energy efficiency of industrial processes but also contributes to greenhouse gases emissions and thermal pollution. In this context, The CERES-2 project (CERES denotes “Energy paths for energy recovery in industrial systems”), supported by the French National Research Agency, aims at developing a decision-making tool to identify the optimal solutions of industrial waste heat recovery. This platform leans on energy integration and multi-objectives optimization to identify and design the best waste heat recovery solutions, according to technical and economic criteria, for a given industrial process. The solutions gather direct heat recovery, heat pumping and electricity production technologies.

This paper presents how the developed multi scale methodology helps optimizing the integration and the architecture of an ORC in an industrial process.

On the process scale, CERES platform uses a MILP algorithm that uses Grand Composite Curve of the industrial process to specify the best integration location of the ORC in a systematic manner. The algorithm is based on exergy criteria and a simplified modeling of the ORC. This algorithm tests every possible couple of temperature level and chooses the best ones for the location of the heat recovery systems.

Once the ORC operating conditions defined, its detailed design and optimization is performed thanks to a model developed in Modelica language permitting to design the working fluid and the heat exchangers. The multi-objectives optimization of the cycle is performed by using self-adaptive version of Strength Pareto Evolutionary Algorithms 2 (SPEA2) implemented in CERES platform.

The methodology is successfully used in an industrial case where an ORC is integrated to the process.

1 INTRODUCTION

In France, the annual energy consumption in industry sector is about 456 TWh, of which 70 % is related to heating requirements. Although energy efficiency in France is one of the highest in the world, there are still significant sources of energy savings (Terrien 2008), especially via heat recovery (Center for Process Integration 2006). A number of studies show that it is theoretically possible to recover 10-25% of the energy consumption related to boiler fumes, ovens and driers (US Department of Energy 2000), that represents between 35 and 85 TWh per year for France (Dupont and Sapora 2009). The difficulties encountered by manufacturers to optimize their energy consumption can be divided into 3 groups:

- the variety of waste heat sources (nature, temperature ...);
- the variety of available production and recovery technologies;
- the different criteria to be considered for optimization: economic, energy, and environment.

Among the existing heat recovery methodologies, the method based on the pinch analysis, developed by Linnhoff (Linnhoff and Hindmarsh 1983), is considered as the most basic one. Other works have established the general rules for selection of appropriate utilities for a process (Bagajewicz and Barbaro 2003). The method has been successfully applied to a large number of process projects over the world. However, it requires a manual calculation procedure, so difficult to be used for a large system. In addition, there is no way to ensure that the found solution is the optimal one. These limitations require to develop alternative methodologies, such as mathematical programming approaches.

It should be noted that an adapted methodology has to be able to deal with a complex problem with many parameters and design variables (discrete or continuous) and result in technologically reliable solutions. The calculation time has to be also compatible with industrial requirements.

This paper presents a multi scale methodology allowing to integrate thermodynamic systems into an industrial process. This methodology is tested via a case study in which an integration of organic Rankine cycles (ORC) in an oil refinery process will be shown. In this case study, the results are obtained from CERES software, an open source tool developed by MINES ParisTech with supports of ANR and their 11 academia and industry partners (MINES ParisTech 2015).

2 METHODOLOGY

The methodology is composed of 3 sequential steps:

- The first step aims to identify waste sources and quantify heat recovery potential of the process. The pinch analysis is used in this step.
- Utilities are necessary to respond to the process energy requirements. So, the second step is to identify the most appropriate technologies (among the production and recovery technologies available, such as ORC system, heat pump, combined heat and power system) to be integrated in the process. The preliminary design of the identified systems is also investigated. An exergetic analysis is performed in this step.
- Finally, an optimal design of the selected system is performed thanks to optimization algorithms and mathematical solvers.

If the recovery potential analysis (first step) has been developed over decades, the identification of the most appropriate technologies (second step) and the optimal design (final step) are original since they combine the exergy analysis and the pinch method. In what follows, these two steps will be described.

2.1 Identification of the most appropriate technologies

The main challenge of an energy integration problem is to design a heat exchanger (HEN) network. There are a number of algorithms to design HEN. For minimizing the global cost (HEN and utilities), the algorithm picks up utilities in a set defined by the user. If too many utilities are available in the set, algorithm may crash down because of large number of combinatory possibilities. Moreover, potential relevant utilities that are not proposed will never be chosen. For this reason, it is necessary to carry out a preliminary phase aiming to select relevant utilities before the HEN design.

The algorithm developed in (Thibault, Zoughaib, and Pelloux-Prayer 2015) makes in one step automatic utility identification and pre-design. This algorithm is based on the Grand Composite Curve (GCC) utilization and a simplified exergy definition. Independently from their economical cost, utilities will be identified according to their energy efficiency, based on exergy criteria. The operating temperature levels of each selected utility are also specified.

To do so, the algorithm minimizes the exergy consumption / destruction of the process by selecting and sizing the appropriate utilities. It thus quantifies the available exergy flux (cooling at above ambient temperature) and the needs of exergy (heating above the temperature of the pinch point and cooling below the ambient temperature). In this analysis, a priori exergetic efficiency for the utilities is used, allowing to approach the performance of real energy conversion systems. The algorithm considers the following technologies: chiller, heat pump, ORC and CHP systems.

2.2 Design optimization

The previous step specifies the relevant utilities to recovery heat waste. This specification results in the temperature levels of hot and cold sources, and the powers of the utilities. In the next step, the utilities must be designed and optimized to achieve at least the exergy efficiency assumed previously. It is also necessary to check that the systems proposed are technically acceptable.

Among the variety of available production and recovery technologies, in this paper we focus on ORC system. In order to design an ORC system we first identify the appropriate refrigerant. According to (Ayachi et al. 2014), there is a strong correlation between the global exergy efficiency of the entire system (process and ORC) and the critical temperature of the refrigerant used in ORC system. As shown in Figure 1, an optimal critical temperature (for a heat source at 150°C) can be read from the hot source temperature and the pinch value (minimum temperature difference of heat exchanger). In particular, it appears a correlation for the optimal critical temperature of the refrigerant allowing to obtain a maximal exergy efficiency:

$$T_c \approx TIT_{\max} - 33 \text{ K} \quad (1)$$

where TIT_{\max} represents the highest turbine inlet temperature which can be reached for a given hot source temperature and a given pinch value of heat exchanger.

This correlation allows to identify the most appropriate refrigerant.

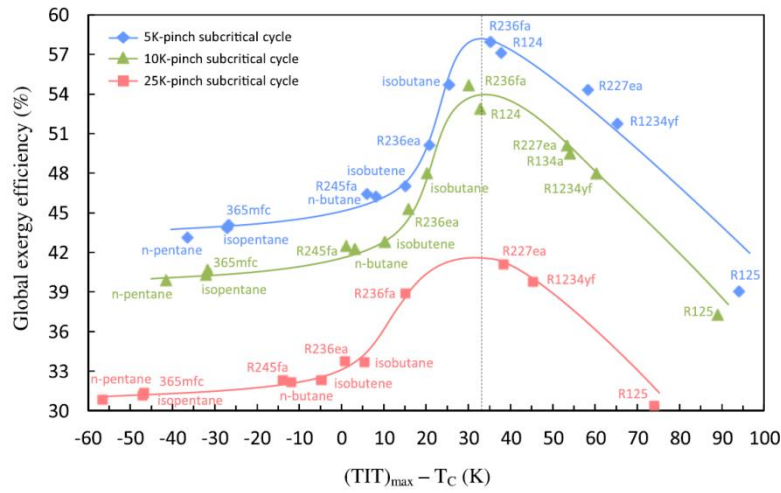


Figure 1: Refrigerant selection according to the temperature levels and the pinch of heat exchanger (Ayachi et al. 2014)

Once the refrigerant is identified, a multi-criteria optimization is performed for an ORC model (Figure 2). According to (Thieriot et al. 2011), optimization algorithms can be divided into two families: Gradient algorithms and Meta-heuristics algorithms. Meta-heuristic algorithms present a common characteristic: they combine rules and randomness to imitate natural phenomena. Within such methods, derivative computation is unnecessary. Most developed methods are evolutionary algorithms, genetic algorithms and simulated annealing. In this study we use Strength Pareto Evolutionary Algorithms 2 (SPEA2), one of the most common evolutionary algorithms.

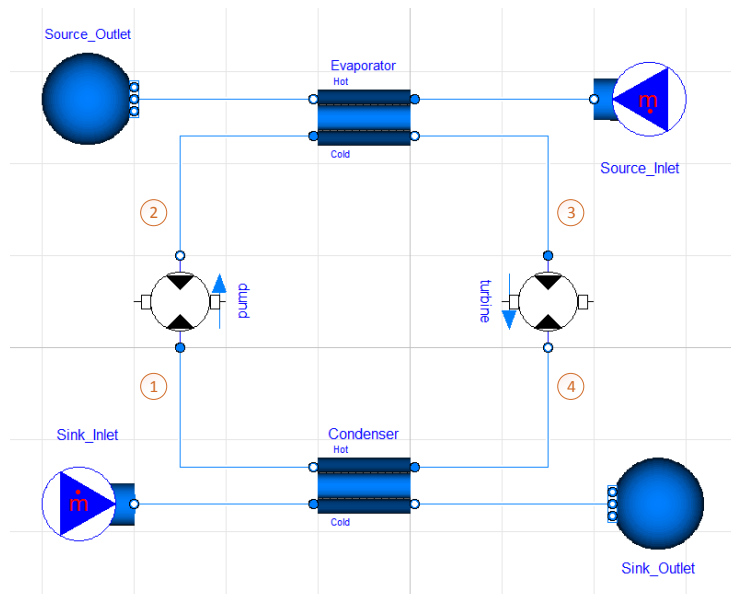


Figure 2. ORC model used in the optimization step

In what follows, we present the ORC model which will be used in the optimization step (Figure 2). The model is composed of 4 components defined via the following equations.

Pump:

$$\eta_{is,p} = \frac{h_{2,is} - h_1}{h_2 - h_1} \tag{2}$$

$$\dot{W}_p = \dot{m}_r (h_2 - h_1)$$

Turbine:

$$\eta_{is,t} = \frac{h_3 - h_4}{h_3 - h_{4,is}} \quad (3)$$

$$\dot{W}_t = \dot{m}_r (h_4 - h_1)$$

Evaporator and condenser:

$$\dot{Q}_h = \dot{m}_r (h_3 - h_2) \quad (4)$$

$$\dot{Q}_c = \dot{m}_r (h_4 - h_1)$$

Since no detailed heat exchanger design is done at this level, additional equations are used to take into account the pinch values set by the user.

Performances of the system:

$$\begin{aligned} \dot{E}x_h &= \dot{m}_h \left[(h_{h,in} - T_a s_{h,in}) - (h_{h,out} - T_a s_{h,out}) \right] \\ \dot{W}_{ORC} &= \dot{W}_t - \dot{W}_p \\ \eta_{En} &= \frac{\dot{W}_{ORC}}{\dot{Q}_h} \\ \eta_{Ex} &= \frac{\dot{W}_{ORC}}{\dot{E}x_h} \end{aligned} \quad (5)$$

3 CASE STUDY

We apply the presented methodology on a crude oil preheating process. The stream data (inlet and outlet temperatures, heating/cooling requirement) can be found in (Kemp 2006). For energy targeting an overall minimum temperature difference admissible $\Delta T_{\min} = 20$ K is considered. The grand composite curve (GCC) drawn from these streams is presented in red in Figure 3. Reading the GCC indicates that below the pinch temperature the process requires cooling needs of about 40 MW in a temperature range between 150 °C and 100 °C. We also observe a self-sufficient pocket of about 10 MW, situated between 100 °C and the ambient temperature.

The technology identification algorithm (the second step of the methodology presented) indicates how to use an ORC to fit the GCC, allowing to recover heat waste and produce maximum electricity. The algorithm is run by assuming a priori exergy efficiency of 50 % for the ORC unit. The following figures show the obtained results where the green line is the GCC of ORC units. The number of ORC units is limited to 1 (**Error! Reference source not found.**), then to 2 in cascade (Figure 4).

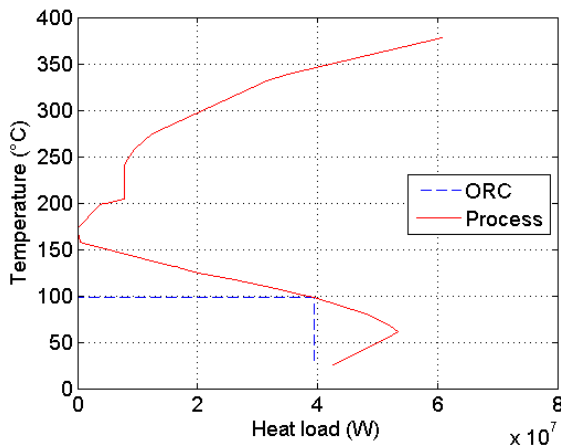


Figure 3: Integration of an ORC into the process

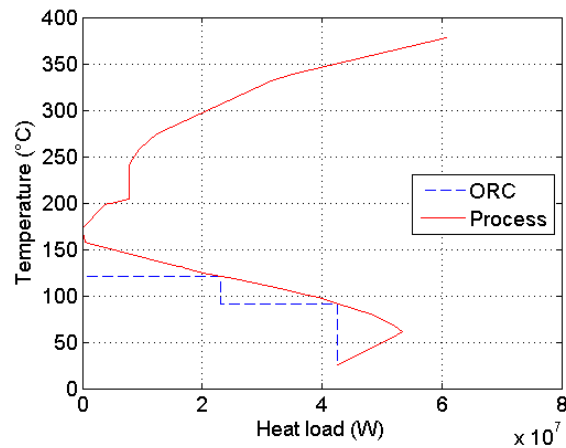


Figure 4: Integration of two ORC into the process

When the number of ORCs is limited to 1, the algorithm proposes to use an ORC at an average temperature of 100 °C. The ORC recovers a thermal power of 39 MW and produces 3.7 MW of electricity. When the use of 2 ORC is allowed, it is possible to cover all the available heat of the process. The two ORCs work at temperatures of 120 °C and 90 °C. In total they produce 4.3 MW of electricity. The small difference of the electric productions suggests using only one ORC, due to important investment costs of the ORC technology. For this reason, in what follows we focus to optimize a design of an ORC. As shown in (Error! Reference source not found.), the ORC have to work with a hot source whose temperature varies from 150 °C to 100 °C.

In this optimization study, the ORC model described in section 2.2 is used. In particular, the parameters of the model are shown in Table 1. These parameters are fixed.

<i>Parameter</i>	<i>Value</i>	<i>Unit</i>
Source	hot water	
Sink	cold water	
Ambient temperature	20	°C
Condensation temperature	25	°C
Pinch value of the evaporator	10	K
Pinch value of the condenser	3	K
Inlet hot source temperature	150	°C
Outlet target hot source temperature	100	°C
Isentropic efficiency of the pump and turbine	0,8	

Table 1: Parameters of the ORC model

First, according to Eq. (1), and after eliminating the candidates that does not fit safety and environmental requirements, we can determine that the optimal refrigerant is R1234yf. Then, we apply the SPEA2 algorithm to optimize the model. In particular, the evaporation pressure is varied, and the energy efficiency and exergy efficiency of the ORC are set as objective functions.

The multi-criteria optimization results are presented via a Pareto curve (Figure 5). Each point on the Pareto curve is a potential optimum. In this study, the ideal point is a hypothetical point at which two objective functions have their maximum values. However this point does not exist on the Pareto curve. So, the selection of the optimal point depends on the priority of the objectives and on the experience of the user. As an example, we can choose the closest point to the ideal point.

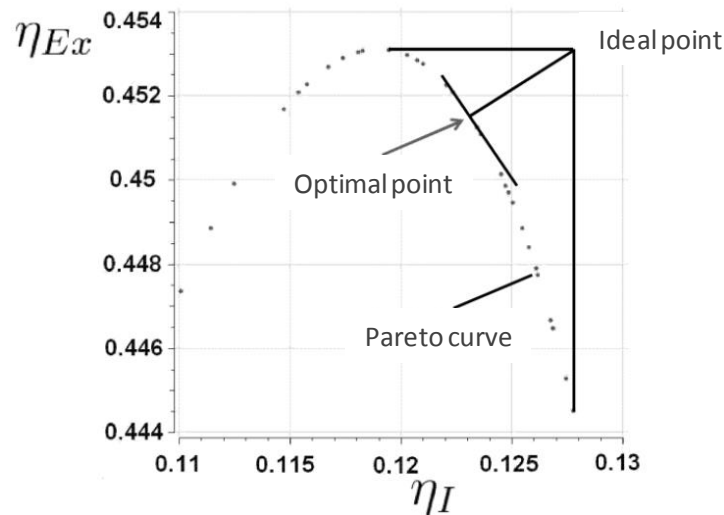


Figure 5: Optimization results (Pareto curve as functions of energy efficiency η_I and exergy efficiency η_{Ex})

It should be noted that the ORC model obtained by the optimization has an exergy efficiency of about 45 %, which is lower but close to the assumption of an exergy efficiency of 50 % used in the technology identification algorithm (the previous step).

It can therefore be concluded that the optimization results validate the technological relevance and the benefit on energy of an ORC integration solution for the crude oil preheating process. In further work, heat exchanger network design and utility selection based on economic criteria will assess the final profitability of such solution.

4 CONCLUSION

In conclusion, this paper has presented an approach for ORC integration in an industrial energy process. The method is based on energy and exergy analysis, aiming to offer the most appropriate solution to recover heat waste. The method is divided in different sequential steps such as process energy integration, selection, sizing and optimization of the utilities. It has been successfully used in an industrial case where an ORC is integrated to the process.

The method is a multi-scale approach going from a quick analysis of energy recovery potential to an identification of required utilities and, finally, to optimal design of the identified utilities. Therefore, the method provides a comprehensive analysis of energy integration problem.

5 NOMENCLATURE

Variable			Subscript	
η	efficiency		a	ambient
$\dot{E}x$	exergy	J	c	cold side
h	specific enthalpy	J/kg	en	energetic
\dot{m}	flow rate	kg/s	ex	exergetic
\dot{Q}	thermal power	W	h	hot side
s	specific entropy	J/(K.kg)	in	inlet
TIT	turbine inlet temperature	°C	is	isentropic
\dot{W}	electric power	W	out	outlet
			p	pump
			r	refrigerant
			t	turbine

6 REFERENCES

- Ayachi, Fadhel, Elias Boulawz Ksayer, Assaad Zoughaib, and Pierre Neveu. 2014. "ORC Optimization for Medium Grade Heat Recovery." *Energy* 68 (April): 47–56. doi:10.1016/j.energy.2014.01.066.
- Bagajewicz, Miguel J., and Andrés F. Barbaro. 2003. "On the Use of Heat Pumps in Total Site Heat Integration." *Computers & Chemical Engineering* 27 (11) (November): 1707–1719. doi:10.1016/S0098-1354(03)00149-2.
- Center for Process Integration. 2006. "UK Government Energy Demonstration Projects." Manchester.
- Dupont, M., and E. Saporá. 2009. "The Heat Recovery Potential in French Industry : Which Opportunities for Heat Pumps Systems ?" In *ECEEE*.
- Kemp, Ian C. 2006. *Pinch Analysis and Process Integration*. Pinch Analysis and Process Integration. Elsevier. doi:10.1016/B978-075068260-2.50009-2.
- Linnhoff, B., and E. Hindmarsh. 1983. "The Pinch Design Method for Heat Exchanger Networks." *Chemical Engineering Science* 38 (5) (January): 745–763. doi:10.1016/0009-2509(83)80185-7.
- MINES ParisTech. 2015. "Plateforme CERES - Outil D'intégration Énergétique et D'optimisation Des Systèmes, Procédés et Territoires." <http://www.ces.mines-paristech.fr/Logiciels/CERES/>.
- Terrien, Pascal. 2008. "ECLEER and Energy Efficiency in Industry." In *EDF Workshop Printemps de La Recherche*.
- Thibault, Fabien, Assaad Zoughaib, and Sandrine Pelloux-Prayer. 2015. "A MILP Algorithm for Utilities Pre-Design Based on the Pinch Analysis and an Exergy Criterion." *Computers & Chemical Engineering* 75 (April): 65–73. doi:10.1016/j.compchemeng.2014.12.010.
- Thieriot, Hubert, Maroun Nemer, Mohsen Torabzadeh-tari, Peter Fritzson, Rajiv Singh, and John John. 2011. "Towards Design Optimization with OpenModelica Emphasizing Parameter Optimization with Genetic Algorithms." In *8th International Modelica Conference*.
- US Department of Energy. 2000. "A Special Supplement to Energy Matters."

TUTORIAL

LOW-ORDER MODELS OF POSITIVE DISPLACEMENT EXPANDERS

Vincent Lemort

University of Liège
Belgium

ABSTRACT

The objective of this tutorial session is to be able to build and parameterize low order models of displacement expanders for use in Organic Rankine Cycle systems. The models that will be presented during the session will be provided to the participants in different formats: EES, Matlab and Modelica files.

The first part of the tutorial session will recall the main features of displacement expanders. The working operation of major families of displacement machines will be explained: screw, piston, scroll and vane expanders. Major performance indicators will be defined. The sensitivity of the expander performance with the operating conditions and design characteristics (volume ratio, etc.) will be discussed.

The second part of the session will deal with the lumped-parameter modeling (or “grey-box” modeling) of displacement expanders. Such models rely on a limited number of physically meaningful equations representing the major physical phenomena occurring inside the machine: heat transfers, leakages, friction, over and under expansion. We will discuss about the identification of models parameters based on measurements or information provided by manufacturers. Examples of use of such models will be given.

Finally, the last part of the session will introduce empirical (or “black-box”) models of displacement expanders. Such models consist of a set of empirical functions (such as polynomials) for the isentropic effectiveness and the filling factor. Their high numerical robustness and low-computational time make them suitable for dynamic simulation of ORC systems. Identification of such functions based on experimental data or on predictions by higher-order models will be discussed.

Participants are invited to bring their own laptop with updated versions of EES, Matlab or Dymola. However, this is not compulsory to follow the tutorial session.

Index

- Achaichia, Abdennacer, 569
Akasaka, Ryo, 782
Aki, Grönman, 328
Al-Dadah, Raya, 355
Aldi, Nicola, 392
Alimardani, Farzam, 876
Alshammari, Fuhaid, 959
Althaus, Wilhelm, 650
Alvi, Jahan Zeb, 1213
An, Qingsong, 201
An, Wei, 681
Andersson, Sven, 1060
Andreasen, Jesper Graa, 11, 1160
Antoniou, Nikolaos, 660
Astolfi, Marco, 289
Atakan, Burak, 570
Aumann, Richard, 1099
Auvity, Bruno, 121
Ayachi, Fadhel, 589
- Bülten, Björn, 650
Bardow, André, 32, 732
Bei, Chen, 1022
Bell, Ian, 365
Bellegem, Marnix Van, 412
Bellettre, Jérôme, 121
Benjamin Franchetti, Benjamin Franchetti, 959
Bennouna, El Ghali, 1243
Bettoja, Federica, 963
Blasiak, Przemyslaw, 742
Bohn, Dieter, 761
Brüggemann, Dieter, 2, 152
Braumakis, Konstantinos, 211
Braun, James, 1140
Braun, René, 761
Breńkacz, Lukasz, 1089
Broek, Martijn van den, 550, 1130, 1140, 1263, 1313
Bruno, Juan Carlos, 929
Bufi, Elio, 270
Buijtenen, Jos van, 670, 1080
Buratto, Carlo, 392
Burlaka, Maksym, 191
Bykuć, Sebastian, 1071, 1089
- Calderazzi, Ludovico, 1323
Camporeale, Sergio, 990
Cao, Yue, 600
Carmine, Margherita, 232
Carmo, Carolina, 964, 965
Casati, Emiliano, 244
Centemeri, Lorenzo, 462
Cheli, Renata, 232
Chen, Lei, 958
Chen, Lei Chen, 960
Chen, Liang, 610
Chen, Tao, 422
Chevalier, Philippe, 60
Chougule, Abhijeet, 532
- Cinnella, Paola, 270
Colasson, Stéphane, 580, 589
Collings, Peter, 818, 863
Colonna, Piero, 151, 244, 441, 472, 482, 1323
Contet, Arnaud, 1060
Coronas, Alberto, 929
Costall, Aaron, 1042
Cozzi, Fabio, 232
- D'haeseleer, William, 172
Da Lio, Luca, 828
Daenens, Dieter, 412
Dai, Xiaoye, 201
Dai, Yiping, 111, 600, 1253
DaSilva, Morgan, 121
David, Gilles, 1
Dechesne, Bertrand, 1130
Degroote, Joris, 513
Desideri, Adriano, 1130, 1173
Dickes, Rémi, 1150
Dimopoulos, George, 660
Dolz, Vicente, 311
Dossena, Vincenzo, 232
Dubberke, Frithjof H., 1283
Dufour, Pascal, 1193, 1203
Dumond, Olivier, 964
Dumont, Olivier, 1150
Dumot, Olivier, 965
Dutta, Pradip, 966
- Edel, Peter, 32
Eicke, Albrecht, 789
Eicker, Ursula, 1313
Eppinga, Quirijn, 670
Erhart, Tobias, 1313
Erlandsson, Olof, 1060
- Farid, Mohammed, 960
Feidt, Michel, 1002
Freeman, James, 1223
Frej, Hicham, 1243
Furuya, Osamu, 864
- G.M., Karthik, 382, 896
Gölz, Jürgen, 1313
Gaetani, Paolo, 232
Gaia, Mario, 131
Galindo, José, 311
Gallo, Mauro, 244
Ganassin, Stefano, 1080
Gao, Naiping, 681
Gao, Tieyu, 712
Garg, Pardeep, 382, 886, 896, 966, 1233
Gazet, Coline, 348
Georges, Emeline, 1140
Gewald, Daniela, 1099
Ghidoni, Antonio, 482, 1070
Gori, Giulio, 472
Gräber, Manuel, 1183

Grelet, Vincent, 1193, 1203
 Grob, Johannes, 650
 Groll, Eckhard, 1140
 Gross, Joachim, 32, 732
 Guardone, Alberto, 232, 244, 472
 Guenat, Elliott, 80
 Guillaume, Ludovic, 853, 963
 Gusev, Sergei, 550

Haberschill, Philippe, 580
 Habib, Boaz, 958, 960
 Haglind, Fredrik, 11, 1160
 Haller, Régine, 311, 771
 Harinck, John, 1323
 Hasegawa, Yusuke, 1293
 Haslam, Andrew, 1273
 Hasselmann, Karsten, 702
 Hayase, Isao, 1293
 He, Maogang, 630
 Head, Adam, 472
 Heberle, Florian, 152
 Hellgardt, Klaus, 1223
 Hemadri, Vinayak, 101
 Hernandez, Andres, 1173
 Horton, Travis, 1140
 Hu, Dongshuai, 600
 Huisseune, Henk, 412
 Hunstock, Björn, 650

Ihnatowicz, Eugeniusz, 338, 1071
 Imran, Muhammad, 620, 979
 Inskip, Nick, 958, 960
 Ionescu, Clara, 1173

Jari, Backman, 328
 Ji, Jie, 1213
 Joly, Clement, 191
 Josset, Christophe, 121
 Juha, Honkatukia, 328
 Juhasz, Jason, 41

Köhler, Jürgen, 1183
 Kærn, Martin Ryhl, 11
 Kaczmarczyk, Tomasz, 338, 1071
 Kakalis, Nikolaos Matthaïos, 660
 Kanno, Hiroshi, 1293
 Karellas, Sotirios, 211, 660
 Kaya, Alihan, 402, 412
 Keller, Claus-Peter, 41
 Keyser, Robin De, 1173
 Kheiri, Abdelhamid, 1002
 Kicinski, Jan, 1071
 Kim, Dokyun, 376
 Kim, Kyung Chun, 376, 1052
 Kirmse, Christoph, 1273
 Kolasinski, Piotr, 742, 751
 Kontomaris, Konstantinos, 41
 Kosmadakis, George, 222, 366, 412
 Kovacevic, Ahmed, 522
 Krumdieck, Susan, 255, 1012
 Kshirsagar, Abhishek, 886, 1233
 Kumar, Pramod, 382, 886, 896, 966, 1233

Kunte, Harald, 919
 Kusterer, Karsten, 761

La Seta, Angelo, 1160
 Laenen, Ben, 172
 Lampe, Matthias, 32, 732
 Landelle, Arnaud, 580
 Larsen, Ulrik, 11
 Latz, Gunnar, 1060
 Laux, Christoph, 938
 Lazova, Marija, 402, 412
 Lazzaretto, Andrea, 828
 Le, Van Long, 1002
 Lecompte, Steven, 1263
 Leduc, Pierre, 60
 Lee, Dong Hyun, 142, 280, 620, 979
 Lee, Si Woo, 142, 280
 Legros, Arnaud, 1150
 Lei, Biao, 540, 671, 817
 Lemmens, Sanne, 181
 Lemort, Vincent, 853, 963, 964, 1002, 1130, 1150,
 1173, 1193, 1203, 1350
 Leontaritis, Aris - Dimitrios, 660
 Leroux, Arthur, 60, 348
 Lever, Harold, 908
 Li, Gaosheng, 722
 Li, Guoqiang, 671, 907
 Li, Jing, 1213
 Li, Pengcheng, 1213
 Liu, Changwei, 712
 Liu, Jihua, 681
 Liu, Jin-Ming, 771
 Liu, Wei, 162
 Lundqvist, Per, 503, 1333

Müller, Ulf Christian, 1120
 Ma, Chongfang, 540, 610, 671, 817, 907
 Macchi, Ennio, 289
 Mahmoud, Saad, 355
 Manente, Giovanni, 828
 Manolakos, Dimitris, 222, 366, 412
 Markides, Christos, 22, 1223, 1273
 Martínez, Gonzalo S., 1243
 Martinez-Botas, Ricardo, 1042
 Mascuch, Jakub, 853
 Mathijssen, Tiemo, 244
 Meinel, Dominik, 162, 1109
 Melis, Julien, 311
 Mintsas, Andre-Charles, 60
 Mirmobin, Parsa, 432, 691, 1032
 Molés, Francisco, 807, 844
 Morini, Mirko, 392
 Moroz, Leonid, 191
 Mota-Babiloni, Adrián, 807, 844
 Mounier, Violette, 80, 937
 Mowill, Fredrik, 131
 Munch, Karin, 1060
 Muye, James, 929

Nadri, Madiha, 1193, 1203
 Navarro-Esbrí, Joaquín, 807, 844

Neef, Matthias, 938, 1283
 Nelson, Chris, 51
 Newton, Peter, 1042
 Nguyen, Denis, 589
 Nielsen, Mads, 965
 Ntavou, Erika, 366

 Obert, Benoît, 270
 Ohman, Henrik, 503, 1333
 Orosz, Matthew, 886, 966, 1233
 Oyewunmi, Oyeniya, 22, 1273

 Paepe, Michel De, 402, 412, 1140, 1263
 Paillette, Benoit, 348
 Pajot, Olivier, 80
 Pall, Valdimarsson, 961, 962
 Pallis, Platon, 660
 Pantaleo, Antonio, 990
 Papadakis, George, 222, 366
 Papantonis, Dimitris, 366
 Papastergiou, Aikaterini, 660
 Papes, Iva, 513
 Park, Byung Sik, 142, 979
 Park, Byung-Sik, 280, 620
 Park, Chun Dong, 142
 Passmann, Maximilian, 702
 Pauchet, Antonin, 348
 Paucker, Ralf, 650
 Pecnik, Rene, 441
 Pei, Gang, 1213
 Peng, Jie, 450
 Peris, Bernardo, 807, 844
 Perosino, Andrea, 963
 Persico, Giacomo, 493, 1160
 Pesiridis, Apostolos, 959
 Petr, Philipp, 1183
 Philominraj, Charles, 532
 Pierobon, Leonardo, 11, 1160
 Pietra, Claudio, 131
 Pinelli, Michele, 392
 Pini, Matteo, 472, 482, 1070
 Polderman, Hugo, 1323
 Preißinger, Markus, 2
 Priebe, Klaus-Peter, 1283

 Quoilin, Sylvain, 964, 1130, 1150, 1172, 1173

 Rödder, Maximilian, 1283
 Radulovic, Jovana, 797
 Rahbar, Kiyarash, 355
 Read, Matthew, 522
 Reiche, Thomas, 963, 1193, 1203
 Reinker, Felix, 702
 Rettig, Adrian, 1120
 Rinaldi, Enrico, 441
 Rivelin, Remi, 580
 Rizzi, Dario, 462
 Robertson, Miles, 1042
 Rodríguez, José María, 1243
 Rodriguez-Fernandez, Pablo, 493
 Roedder, Maximilian, 938
 Roskosch, Dennis, 570

 Rosset, Kévin, 80
 Rostamzadeh, Mohammadreza, 876
 Rostek, Katharina, 1099
 Roumpedakis, Tryfonas, 211
 Royo, Lucía, 311
 Rubino, Antonio, 1070
 Rudenko, Oleksii, 191

 Sánchez, David, 1243
 Saini, Ankit, 896
 Sakaue, Eiichi, 782, 864
 Sanvito, Massimiliano, 462
 Saravanan, Rajagopal, 929
 Sauerborn, Markus, 962
 Scharf, Roland, 640
 Schiffmann, Jürg, 80, 937
 Schilling, Johannes, 32, 732
 Schröder, Christian, 1183
 Schuller, Stéphane, 121
 Schuster, Andreas, 1099
 Sebelev, Aleksandr, 640
 Sellers, Chris, 432, 691
 Serafino, Aldo, 462
 Sergei, Gusev, 1130
 Serrano, David, 60
 Seume, Jörg, 919
 Shen, Li-li, 610
 Shi, Lin, 201
 Shikazono, Naoki, 1293
 Shu, Gequn, 948
 Simoni, Luke D., 41
 Skåre, Thomas, 1060
 Smague, Pascal, 60
 Smirnov, Maksim, 640
 Smith, Gregory, 569
 Smith, Ian, 522
 Smolen, Slawomir, 789
 Sonde, Ramakrishna, 532
 Song, Songsong, 559
 Southon, Michael, 1012
 Spadacini, Claudio, 462
 Spina, Pier Ruggero, 392
 Spinelli, Andrea, 232
 Spliethoff, Hartmut, 162, 1109
 Srinivasan, Vinod, 382, 896
 Stosic, Nikola, 522
 Strauch, Sabine, 650
 Subbarao, P.M.V, 101
 Suman, Alessio, 392
 Sung, Taehong, 1052

 Taklanti, Abdelmajid, 771
 Taleb, Aly, 1273
 Tanaka, Katsuyuki, 782
 Tartière, Thomas, 589
 Tauveron, Nicolas, 580, 589
 Thirumalai, N.C., 896
 Thomas, Raymond, 569
 Tian, Hua, 948
 Tian, Ran, 201
 Tola, Vittorio, 1303

Tona, Paolino, 60
 Tran, Cong-Toan, 1342
 Turunen-Saaresti, Teemu, 328
 Turzynski, Tomasz, 1071

Usman, Muhammad, 620, 979
 Uusitalo, Antti, 328

Vierendeels, Jan, 513
 Vitale, Salvatore, 472, 482, 1070
 Vodicka, Vaclav, 853
 Vourliotis, Panagiotis, 660
 Vrabec, Jadran, 1283

Wagner, Thomas, 963
 Walraven, Daniël, 172
 Wang, Hongjin, 70
 Wang, Jiangfeng, 111, 1253
 Wang, Jianyong, 1253
 Wang, Jingfu, 630
 Wang, Mingkun, 111
 Wang, Wei, 540, 610, 671, 817
 Wang, Xurong, 111, 600
 Weiß, Andreas, 301
 Weidtmann, Kristof, 761
 Wieland, Christoph, 162, 1109
 Wiesche, Stefan aus der, 702
 Wissink, Edo, 908
 Wong, Choon Seng, 255
 Woodland, Brandon, 1140
 Wronski, Jorrit, 1130
 Wu, Yuting, 540, 610, 671, 817, 907

Xie, Feibo, 681
 Xu, Jiamin, 712
 Xu, Xun, 712

Yang, Fubin, 90
 Yang, Yi, 111
 Yang, Young Min, 142, 280
 Yoon, Sang Youl, 376, 1052
 Young, Brent, 960
 Yu, Zhibin, 818, 863
 Yuksek, Errol, 1032
 Yun, Eunkoo, 376

Zabelin, Nikolay, 640
 Zhai, Huixing, 201
 Zhang, Congtian, 630
 Zhang, Hongguang, 70, 90, 559, 722, 1022
 Zhang, Lei, 422, 450
 Zhang, Xinxin, 630
 Zhang, Yangjun, 422, 450
 Zhang, Yeqi, 540, 671, 907
 Zhao, Mingru, 948
 Zheng, Ya, 111, 600
 Zhi, Ruiping, 671, 907
 Zhu, Jiangnan, 712
 Zhu, Tong, 681
 Zhuge, Weilin, 422, 450
 Ziviani, Davide, 550, 1140
 Zocca, Marta, 232

Zoughaib, Assaad, 1342
 Zywica, Grzegorz, 338, 1071, 1089